



# Sixth International Conference on Geosynthetics

**Conference Proceedings**

25–29 March 1998  
Atlanta, Georgia USA

**Soil Reinforcement Applications  
Geotechnical & Hydraulic Applications**

## **Cooperating Organizations**

Geoinstitute of ASCE (American Society of Civil Engineers)  
Canadian Geotechnical Society  
International Association of Geosynthetics Installers  
EDANA (European Association for the Nonwovens Industry)  
Geosynthetic Institute



**Organized under the auspices of the International  
Geosynthetics Society Sponsored by the  
Industrial Fabrics Association International  
and the North American Geosynthetics Society**

SPONSORED BY



SOLMAX



# Foreword

This Sixth International Conference on Geosynthetics, held in Atlanta in 1998, celebrated 21 years of international development of the geosynthetics discipline, much of it nurtured by the International Geosynthetics Society (IGS), under whose auspices the conference is held. For the past 15 years, the IGS, through the IGS Officers, the IGS Council, its committees, and the hard work of many individual members and their affiliated organizations, has fostered the development of this regular series of international conferences. The IGS also has been active in the development of chapters that provide local activities, including regional conferences and seminars, the publication of a directory and newsletter (IGS News), and associations with two first class international journals (*Geotextiles and Geomembranes* and *Geosynthetics International*), to name but a few of its many achievements.

The first of these international conferences (called the "International Conference on the Use of Fabrics in Geotechnics") was held in Paris, France in 1977. The subsequent conferences, held in Las Vegas, U.S.A. (1982), Vienna, Austria (1986), The Hague, The Netherlands (1990), and Singapore (1994), had a variety of titles, the most recent being the melodic but lengthy "International Conference on Geotextiles, Geomembranes and Related Products". Since the first conference, the geosynthetics discipline has matured. We have seen the adoption of terms like geotextiles and geomembranes (coined by J.P. Giroud in 1977), then geonets, geogrids, geocomposites, geosynthetic clay liners and geofoam, encompassed by the generic term "geosynthetics." The conference in Atlanta is the first to simply be called the International Conference on Geosynthetics signalling a maturity that fits with the passage of 21 years.

The maturing of the discipline also brings with it changes in the way these international conferences are run. There now are many regional and local conferences on geosynthetics; hence this conference has attempted to focus on papers that are likely to be of broader international interest rather than specific local interests. It is the first international conference on geosynthetics where all the final papers were peer-reviewed. This has involved a great deal of work for the Secretariat and the Session and Workshop Chairs, who coordinated the reviews of all the papers. Of the initial 428 papers for which abstracts were received, 185 were eventually accepted after peer review of the final papers. It was a challenge getting so many papers from so many parts of the world reviewed, corrected, and finally collected together in these proceedings. Many thanks to all those who contributed to this process; to the extent that the quality of papers has been improved by the review process, it is due to the diligence of the reviewers and the cooperation of the authors.

This is also the first conference in which there was no page limit on contributions. All papers had to be a minimum of four pages, but longer papers were accepted where the author and the reviewers agreed that a longer paper was appropriate. By providing this flexibility, we hope that the key details so often omitted from short conference papers have not been omitted here.

In another break with tradition, the first Giroud Lecture and the three Keynote Lectures all are contained in the proceedings available at the conference, and there will be no post-conference volume. The first volume of the proceedings includes the special lectures and the papers associated with the Environmental Applications theme. The second volume contains the papers relating to the two other primary conference themes: Soil Reinforcement Applications and Geotechnical and Hydraulic Applications.

In addition to the usual parallel sessions, we also have introduced a series of workshops, in which fewer papers are presented so as to allow more time for discussion of the topic by a smaller group of individuals keenly interested in the specific technical area. As usual, we have included some papers as posters where the author(s) can interact on a one-to-one basis with those interested in the topic. Finally, we will have three panel sessions dealing with "Users' Questions - Industry's Response" in the fields of Environmental Applications, Reinforcement Applications, and Hydraulic & Geotechnical Applications. The moderators of these sessions have been invited to write an article on their sessions to appear in the IGS News.

More than 100 people—including the Technical Committee members, the Sessions Chairs and Co-Chairs, the Workshop Chairs and Co-Chairs and numerous other individuals—reviewed papers and provided constructive advice to authors. Special thanks are due to the Conference Chair, Dr. R. M. Koerner, the Chairman of the International Advisory Board, Dr. J.P. Giroud, and the Intermediary to NAGS, Dr. B. Christopher, for their assistance to the Technical Committee. Special thanks are also due to Mr. S. Warner for the support of IFAI and to the IFAI staff, Ms. D. Fettig, Ms. J. McGovern and Ms. S. Kuehl, who were responsible for handling all the papers, correspondence and communications with reviewers and authors. Finally, thank you to the authors, for without your intellectual contributions, hard work and patience there would be no conference proceedings and no conference.

**R. Kerry Rowe**  
Chair, Technical Committee and Intermediary to the IGS  
Sixth International Conference on Geosynthetics

# Sixth International Conference on Geosynthetics

## **Chairman, Organizing Committee**

**Robert M. Koerner**

Geosynthetic Institute  
Drexel University  
USA

## **Chairman, Technical Committee and Intermediary to IGS**

**R. Kerry Rowe**

Dept. of Civil and Environmental Engineering  
University of Western Ontario  
CANADA

## **Chairman, International Advisory Board**

**Jean Pierre Giroud**

GeoSyntec Consultants  
USA

## **Intermediary to NAGS**

**Barry Christopher**

Consultant  
USA

## **Intermediary to IFAI**

**Stephen M. Warner**

Industrial Fabrics Association International  
USA

## **Secretary-General**

**Danette R. Fettig**

Industrial Fabrics Association International  
USA

## **Technical Review**

### **Committee Members**

**Hiroshi Miki**

Soil Mechanics Division  
Public Works Research Institute  
Ministry of Construction  
JAPAN

**Jochen Müller-Rochholz**

TBU/Fachhochschule  
Munster-Labor Fur Baustoffe  
GERMANY

**R. Kerry Rowe**

Dept. of Civil and Environmental Engineering  
University of Western Ontario  
CANADA

**Piero Sembenelli**

Consultant  
ITALY

**Barry Christopher**

Consultant  
USA

## **International Advisory Board**

**Chairman:**

**J.P. Giroud**

**Members:**

T. Akagi (Japan)  
R. Araujo (Panama)  
R.J. Bathurst (Canada)  
H. Brandl (Austria)  
D.A. Cazzuffi (Italy)  
S.H. Chew (Singapore)  
B.R. Christopher (USA)  
H.S. Chung (Korea)  
J.G. Collin (USA)  
S.P. Corbet (United Kingdom)  
R. Cossu (Italy)  
P. Delmas (France)  
G. den Hoedt (The Netherlands)  
V. Feodorov (Romania)  
R. Floss (Germany)  
M. Fukuoka (Japan)  
E. Gartung (Germany)  
F.W. Gassner (South Africa)  
J.P. Gourc (France)  
G. Heerten (Germany)  
R.D. Holtz (USA)  
R.A. Jewell (Belgium)  
C.J.F.P. Jones (United Kingdom)  
B.H. Kang (Korea)  
G.P. Karunaratne (Australia)  
J. Lafleur (Canada)  
C. Lawson (Malaysia)  
Z.Y. Liu (China)  
S. Martinetti (Italy)  
H. Miki (Japan)  
A.G. Mouw (The Netherlands)  
B. Myles (United Kingdom)  
H. Ochiai (Japan)  
J. Paul (United Kingdom)  
S.D. Ramaswamy (Singapore)  
S. Rammelan (Indonesia)  
P.E. Rimoldi (Italy)  
A.L. Rollin (Canada)  
R.K. Rowe (Canada)  
A. Sciuero (Italy)  
P. Sembenelli (Italy)  
P.E. Stevenson (USA)  
F. Tatsuoka (Japan)  
C.V.J. Varma (India)  
W. Voskamp (The Netherlands)  
Z.H. Wang (China)

# Table of Contents: Volume I

## **GIROUD LECTURE**

Analysis and Design of Veneer Cover Soils

R.M. Koerner and T.Y. Soong ..... 1

## **KEYNOTE LECTURES**

Geosynthetics and the Minimization of Contaminant Migration through Barrier Systems Beneath Solid Waste

R.K. Rowe ..... 27

Seismic Stability Against High Seismic Loads of Geosynthetic-Reinforced Soil Retaining Structures

F. Tatsuoka, J. Koseki, M. Tateyama, Y. Munaf & K. Horii ..... 103

Limit State Design of Geosynthetic Reinforced Soil Structures

A. McGown, K.Z. Andrawes, S. Pradhan & A.J. Khan ..... 143

## **ENVIRONMENTAL APPLICATIONS**

### **Landfill Design Issues**

Clogging Potential of Geosynthetic Leachate Collection Layers by Fine Particles From Sand Protective Layers

J.P. Giroud, M.F. Houlihan, R.C. Bachus & S. Qureshi ..... 185

Laboratory Investigation of the Effect of Coarse Stone Backfill on the Performance of Leachate Collection Pipe

R.W.I. Brachman, R.K. Rowe, I.D. Moore & A.R.M. Tognon ..... 191

HDPE Geopipes: Soil-Structure Interaction

H. Zanzinger & E. Gartung ..... 197

Effect of the Temperature on Tensile Behavior of Geomembranes

M. Tsuboi, S. Imaizumi & H. Miyaji ..... 201

Measuring the In-Situ Moisture Content of Geosynthetic Clay Liners (GCLs) Using Time Domain Reflectometry (TDR)

M.A. Eberle & K.P. von Maubeuge ..... 205

An Exposed Geomembrane Cover System for a Landfill

M.H. Gleason, M.F. Houlihan & J.P. Giroud ..... 211

Current Issues in Seismic Design of Geosynthetic Cover Systems

E. Kavazanjian, Jr. .... 219

Seismic Response of Landfills with Geosynthetic Liners

M.K. Yegian & H.U. Kadakal ..... 227



# Table of Contents: Volume I

## Leakage and Diffusion Through Liners

Evaluation of a Composite (Geomembrane/Clay) Liner for a Lagoon After 14 Years Use R.K. Rowe, Y.G. Hsuan, C.B. Lake, P. Sangam & S. Usher .....	233
Solubilities, Diffusion and Partition Coefficients of Organic Pollutants in HDPE Geomembranes: Experimental Results and Calculations W. Mueller, I. Jakob, R. Tatzky-Gerth & H. August .....	239
Water and Organic Solvents Transport Parameters in Geomembranes L. Durin, N. Touze & C. Duquennoi .....	249
Leakage Study Across an Offshore Waste Containment Bund S.A. Tan, S.H. Chew & G.P. Karunaratne .....	257
New Developments in Landfill Liner Leakage Evaluation J.P. Giroud, K.L. Soderman, M.V. Khire & K. Badu-Tweneboah .....	261
Evaluation of Liner System Performance Using Liquids Management Data J.F. Beech, K.W. Cargill & W.J. Huff .....	269
Comparison of Dye Testing and Electrical Leak Location Testing of a Solid Waste Liner System G.T. Darilek & L.V. Miller.....	273

## Liner Protection

Evaluation of the Effectiveness of HDPE Geomembrane Liner Protection K. Badu-Tweneboah, J.P. Giroud, D.S. Carlson & G.R. Schmertmann .....	279
Efficiency of Puncture Protection Layers H. Zanzinger & E. Gartung .....	285
A Rational Design for the Protection of Landfill Geomembrane Liners K.R. Reddy & R.E. Saichek .....	289
Effect of Geotextile on Dispersion of Tensile Stress Creating Within a Geomembrane Subjected to Deformation by Differential Settlement S. Imaizumi, T. Nomoto, M. Tsuboi & Y. Yokoyama .....	295

## Wrinkles (Waves) in Geomembranes

Laboratory Study of High Density Polyethylene Geomembrane Waves T.Y. Soong & R. M. Koerner .....	301
---	-----

# Table of Contents: Volume I

Installation Procedure and Welding of Geomembranes in the Construction of Composite Landfill Liner Systems- Focus on "Riegelbauweise" U.B.Averesch & R.T. Schicketanz .....	307
Bentonite Migration in Geosynthetic Clay Liners T.D. Stark .....	315
<b>Geomembrane Seams</b>	
Thermal Treatment of HDPE Geomembrane Sheets J. Mlynarek, M. Marcotte & P. Sarazin .....	323
The Influence of the Welding Parameters on HDPE Geomembranes A.L. Rollin, F. Montgrain, P. Lafleur & L. Maranda .....	331
Assessment of Seam Quality and Optimization of the Welding Process of HDPE Geomembranes G. Lüders .....	337
Automatic Ultrasonic Seam Tester for Bituminous Geomembranes - Development and Field Results B. Breul, J. Carroget & R. Herment .....	345
Evaluating the Stress Crack Resistance of HDPE Seams R.W.Thomas .....	349
<b>Geosynthetic Durability</b>	
Assessing the Long-Term Behavior of Geomembranes in Multi-factor Environments C. Maisonneuve, P. Pierson, C. Duquennoi & A. Morin .....	355
The Performance of Flexible Polypropylene Geomembranes in Covered and Exposed Environments A.I. Comer, Y.G. Hsuan & L. Konrath .....	359
A Fracture Mechanics Assessment for the Long-Term Durability of HDPE Geomembranes C.H. Popelar, C.J. Kuhlman & I.D. Peggs.....	365
Temperature Effect on the Stress Crack Resistance of High Density Polyethylene Geomembranes Y.G. Hsuan .....	371
Antioxidant Depletion During Thermal Oxidation of High Density Polyethylene Geomembranes Y.G. Hsuan & Z. Guan .....	375
Selecting a Geomembrane Material I.D. Peggs & R. Thiel .....	381

# Table of Contents: Volume I

Heat-Insulation Performance of Geomembrane Composite T.K. Tao, L. Yu & Y.N. Wu .....	389
Prediction of the UV Aging of Polypropylene Geotextiles-Landfills Case O. Artières, S. Gaumet & C. Bloquet .....	393
Geosynthetic Proficiency Testing G.R. Koerner .....	399
<b>Landfill Interfaces</b>	
Site Parameters Influencing Liner Strengths and the Impacts on Landfill Stability H.D. Sharma, D.E. Hullings & F. R. Greguras .....	405
Shear Strength and Deformation Considerations for Composite Landfill Liners in Hong Kong R.K. Frobel, M.A. Sadlier & J.W. Cowland .....	411
The Experimental Shear Strength Evaluation of Geomembrane - Clay Liner and Geomembrane-Geotextile Interfaces R. Floss & J. Fillibeck .....	417
Issues In Clay/Textured Geomembrane Interface Testing P.J. Sabatini, G.R. Schmertmann & R.H. Swan, Jr. ....	423
Geosynthetic Clay Liners at Field-Scale: Internal Shear Test Progress D.A. Carson, R. Bonaparte, D.E. Daniel & R.M. Koerner .....	427
The Influence of Geomembrane Surface Roughness on Geomembrane-Geotextile Interface Strength S.W. Lee, J.D. Frost & G.K. Righter .....	433
Variability of Interface Shear Strengths M. Snow, R. Mansour, R.H. Swan, Jr. & E. Kavazanjian, Jr. ....	439
Frictional Behavior of Landfill Liner Interfaces with Geonets A. De & T. F. Zimmie .....	443
Geosynthetic Interface Friction Testing in Germany - Effects of Test Setups W. Blümel & C. Stoewahse .....	447
The Influence of Equipment Style And Setup Dimensions on Sand/Geomembrane Direct Shear Test Measurements S.M. Bembem & D.A. Schulze .....	453
Evaluation of Soil Geosynthetics Interaction for Some Landfills in Algiers A. Bouazza .....	459



# Table of Contents: Volume I

## Reinforcement in Landfill Applications

Reinforcement Requirements at a Hazardous Waste Site A.T. Hendricker, K.H. Fredianelli, E. Kavazanjian Jr. & J.A. McKelvey III .....	465
Evaluation of a Geogrid Reinforced Slope Subjected to Differential Settlements J.G. Zornberg & E. Kavazanjian Jr. ....	469
High Strength Aramid Geogrids to Prevent Sliding on Steep Landfill Basal Slopes A. Plankel & D. Alexiew .....	475
Landfill Closure using Reinforced Soil Slopes K.W. Cargill & K.L. Olen .....	481
Geosynthetic Lining Systems Reinforcement by Geosynthetic Inclusion S. Lalarakotoson, P. Villard, & J.P. Gourc .....	487

# Table of Contents: Volume 2

## SOIL REINFORCEMENT APPLICATIONS

### Reinforced Soil Design Issues

Design Procedures for Reinforced Walls - A Historical Perspective R.R. Berg, T.M. Allen & J.R. Bell.....	491
---	-----

Aspects of Partial Factor Design of Reinforced Soil Walls T.S. Ingold .....	497
--	-----

A Comparison of Design Approaches for Reinforced Soil Structures in Europe J. Penman & R.A. Austin .....	501
---	-----

Recent Developments of the "Displacement Method" P. Lemonnier, P. Gotteland & A.H. Soubra .....	507
--	-----

Locally Loaded Geosynthetic Reinforced Soil Structure: Calculation Method E. Haza, P. Gotteland & J.P. Gourc .....	511
---	-----

Measuring Geotextile Strains with Strain Gauges S.R. Boyle & R.D. Holtz .....	517
--	-----

Soil Confinement Effect on Stress-Strain Properties of Geosynthetics Z. Yuan, R.H. Swan Jr., R.C. Bachus, V. Elias.....	523
--	-----

The Testing of Geosynthetic Reinforcements P.E. Stevenson, T.R. Skochdopole & A.D. Kelkar .....	529
--	-----

Geosynthetic Reinforcement: Are Geotextiles and Geogrids Interchangeable? C.J. Sprague .....	539
---	-----

Effect of End-Restraint in Geogrid-Soil Structures H. Ochiai, N. Yasufuku, T. Kawamura, T. Yamaji & T. Hirai .....	545
---	-----

Application of Dilatancy Models to Soils Reinforced by Geosynthetics H. Ohta, M. Hirata, A. Iizuka, T. Yamakami & K. Ohmori .....	551
--	-----

### Reinforced Soil Walls

Failure of Two Fabric Reinforced Segmental Block Walls in South Africa F.W. Gassner & G.M. James .....	559
---	-----

Preloaded-Prestressed Geogrid-Reinforced Soil Bridge Pier T. Uchimura, F. Tatsuoka, M. Tateyama & T. Koga .....	565
--	-----

# Table of Contents: Volume 2

Use of Fabric Reinforced Soil Walls for Integral Bridge End Treatment R.A. Reid, S.P. Soupir & V.R. Schaefer .....	573
Field Performance Test of a Geosynthetic-Reinforced Soil Wall with Rigid Facing Y.Tsukada, Y. Ochiai, H. Miyatake & N. Tajiri .....	577
Multi-Anchored Soil Retaining Walls with Geosynthetic Loop Anchors H. Brandl .....	581
Mechanically Stabilized Earth Wall Design: External Stability M.S. Meyers, R.A. Wetzels & R.R. Berg .....	587
Brick Faced Retaining Walls Reinforced with Geosynthetics - A Numerical Analysis M. I. M. Pinto, R.V.C. Pereira, M.L. Lopes & A. Mendonca .....	593
Large Deformations FEM Analysis of a Reinforced Earth Structure R. Arab, P.Villard & J.P.Gourc .....	597
Evaluation of Foundation Support for Geosynthetic Reinforced Soil Wall on Sloping Ground J. Otani, T. Hirai, H. Ochiai & S. Shinowaki .....	601
Parametric Study for Geosynthetic Reinforced Walls Under Sustained Earthquakes A. Carotti & P. Rimoldi .....	605
Influence of Reinforcement Stiffness, Length and Base Condition on Seismic Response of Geosynthetic Reinforced Retaining Walls R.J. Bathurst, K. Hatami .....	613
<b>Reinforced Slopes</b>	
The Verrand High Reinforced-Soil Structure G. Sembenelli & P. Sembenelli .....	619
Geogrid Reinforcement of Slopes for Earthquake Resistance at New U.S. Embassy in Caracas, Venezuela J.R. Lambrechts .....	625
The Construction of Steep Reinforced Slopes in Hilly Terrain C.R. Lawson & T.W. Yee .....	629
Case Study: Bluewater Retail & Leisure Destination-Major Reinforced Soil Slopes to Form Steep Sided New Lakes J.H. Dixon .....	637



# Table of Contents: Volume 2

Soil Bioengineering/Biotechnical Stabilization of a Slope Failure R.B. Sotir, J.T. Difini & A.F. McKown .....	643
Finite Element Analysis of Instrumented Geogrid Reinforced Slope A. Ghinelli & M. Sacchetti .....	649
<b>Durability and Long Term Behavior</b>	
The Assurance of Durability J.H. Greenwood .....	657
Long-Term Experience with Reinforced Embankments on Soft Subsoil: Mechanical Behavior and Durability K.H. Blume & D. Alexiew .....	663
Durability of Polyester and Polypropylene Geotextiles Buried in a Tropical Environment for 14 Years J.W. Cowland, K.C. Yeo & J.H. Greenwood .....	669
Study on Creep-Rupture of Polyester Tendons: Full Scale Tests P. Orsat, M. Khay & M. McCreath .....	675
Coated PET-Geogrids, Wovens and Yarns - Comparison of Longtime Performance Under Tension J. Müller-Rochholz, D. Alexiew, C. Recker & S.E. Lothspeich .....	679
The Effect of Oxygen Pressure, Temperature and Manufacturing Processes on Laboratory Degradation of Polypropylene Geosynthetics A. Salman, V. Elias & A. DiMillio .....	683
Conventional and Stepped Isothermal Methods for Characterizing Long Term Creep Strength of Polyester Geogrids J.S. Thornton, J.N. Paulson & D. Sandri .....	691
The Stepped Isothermal Method for Time-Temperature Superposition and its Application to Creep Data on Polyester Yarn J.S. Thornton, S.R. Allen, R.W. Thomas & D. Sandri .....	699
Modeling and Extrapolation of Creep Behavior of Geosynthetics T.Y. Soong & R.M. Koerner .....	707
Slow Strain Rate Modulus Assessment via Stress Relaxation Experiments T.Y. Soong & A.E. Lord, Jr. ....	711
Long Term Behavior Characterization of Soft Composites Under Biaxial Loading P. Mailler & M. Sotton .....	715

# Table of Contents: Volume 2

## GEOTECHNICAL & HYDRAULIC APPLICATIONS

### Construction with/on Marginal Soils

Design Guidance for Reinforced Soil Structures with Marginal Soil Backfills B.R. Christopher, J.G. Zornberg & J.K. Mitchell .....	797
Reinforcement of a Saudi Sabkha Soil Using Geotextiles S.A. Aiban, O.S.B. Al-Amoudi, I. Ahmed, H. Al-Abdul Wahhab .....	805
Long-Term Deformation of Reinforced Cohesive Soil Fills and Walls M. Fukuoka .....	811
Development of Woven Geotextiles for Reinforcing Cohesive Soil Filled Slopes - A New Approach S. Ariadurai, I.L. Whyte & P. Potluri .....	815
Large Scale Pullout Tests of Geotextile in Poorly Draining Soils S.H. Chew, S.A. Tan, K.H. Loke, P. Delmas & C.T. Ho .....	821
Soft Clay Embankment Reinforced by Geosynthetic Horizontal Drains M. Kamon, T. Akai, M. Fukuda & Y. Nanbu .....	825
Centrifuge Modeling of an Innovative MSES for Marginally Stable Slopes M.B. Mahmud & T.F. Zimmie .....	829
Hydraulic Effects of Using Dual-Function Geosynthetics in the Design of Multi-Layer Structures P. Gotteland .....	833
<b>Land Reclamation and Ground Improvement</b>	
The Mobilized Strength of Prefabricated Vertical Drains W. Voskamp, G. Troost & G.R. Koerner .....	839
Investigation of Some Factors Affecting Discharge Capacity of Prefabricated Vertical Drain N. Miura, J. Chai & K. Toyota .....	845
Design of a New Geocomposite Vertical Wick Drains for Ground Improvement J.N. Mandal & V.S. Kanagi .....	851
Critical Evaluation of Laboratory Drain Tests Simulating Field Conditions G.P. Karunaratne, S.A. Tan, S.H. Chew & S.L. Loh .....	855
Geotextiles for the El Dorado International Airport in Colombia A. Malagón .....	859

# Table of Contents: Volume 2

Testing and Analysis of Soft Foundation Treatment for Donggang Diking Project Q.Y. Luo .....	865
Electrokinetic Geosynthetics and Their Applications I.M. Nettleton, C.J.F.P. Jones, B.G. Clarke & R. Hamir .....	871
A Study of the Behavior of Geogrid Reinforced Stone Column J.S. Sharma .....	877
<b>Bearing Capacity</b>	
Geosynthetic Reinforced Unpaved Roads on Very Soft Soils: Construction and Maintenance Effects E.M. Palmeira .....	885
Numerical Analysis of a Pavement Base Reinforced with Geogrid M. Abramento .....	891
Improvement of Bearing Capacity of Soft Clay using Geogrids Y. Tanabashi, K. Yasuhara, K. Hirao, N. Kiyokawa & H. Itoh .....	895
The Bearing Capacity of a Reinforced Sand Layer Overlying a Soft Clay Subgrade M.J. Kenny .....	901
Supporting Capability of Geogrid Reinforced Soil Foundations N. Yasufuku, H. Ochiai & K. Kawamata .....	905
Theoretical Solutions for Stress and Strain Fields of a Geosynthetic-Reinforced Foundation Vertically Loaded by a Concentrated Force J. Han .....	911
Bearing Capacity of Strip Footing on Geogrid-Reinforced Slope C.S. Yoo & D.Y. Lee .....	915
A Study on the Coir Reinforcement for Strengthening Soft Soil Subgrades K. Rajagopal & S. Ramakrishna .....	919
Treatment of Container Stockyard Using Stress Distribution Ability of Geonet Z. Hong & H.R. Dao .....	923
<b>Roads and Pavements</b>	
A Geotextile-Wrapped Aggregate Highway Drain Evaluation G.P. Raymond, R.J. Bathurst & J. Hajek .....	929



# Table of Contents: Volume 2

Deformations and Damage of Nonwoven Geotextiles in Road Construction A. Watn, G. Eiksund & A. Knutson .....	933
Rut Prediction for Roadways with Geosynthetic Separators W.S. Tsai & R.D. Holtz .....	939
Quantifying the Separation Characteristic of Geosynthetics in Flexible Pavements I. Al-Qadi, B.J. Coree, T.L. Brandon, S.A. Bhutta & A.K. Appea .....	945
Geosynthetic-Reinforced Pavements: Overview and Preliminary Results S.W. Perkins, M. Ismeik, M.L. Fogelsong, Y. Wang & E.V. Cuelho .....	951
Cost Versus Reinforcing Effectiveness of Geotextiles in Pavement Works in Greece A.G. Kokkalis .....	959
A Study on Preventing and Repairing Road Frost Boiling by Applying Geotextile in Daqing Area J. Cao, Z. Huang, D. Zhao & J. Dai .....	963
Laboratory Study of the Dynamic Test System on Geogrid Reinforced Subgrade Soil D.T. Chang, W.J. Wang & Y. Wang .....	967
<b>Asphalt Pavements</b>	
Performance Prediction Model for Asphalt Overlays with Geotextile Interlayers on Cracked Pavements R.M. Rodrigues .....	973
Effectiveness of Synthetic Interlayers in Bituminous Pavements G. Dondi .....	977
Geotextile Within Asphalt Overlay on a Brazilian Road: A 13-year Case Study P.R. Aguiar & C.E.L. Paiva .....	985
Fracture Behavior of Geosynthetics in Asphalt Layers R. Lugmayr .....	989
Response Investigation and Design Guidelines for Asphalt Pavements with an EPS Geofoam Sub-base M. Duskov, L.J.M. Houben & A. Scarpas .....	993
<b>Filtration</b>	
Particles Washout Associated with the Retention of Broadly Graded Soils by Geotextiles J. Lafleur .....	1001
Geotextile Characteristic Opening Size: The Influence of Some Test Parameters M.C.P. Barroso & M.D.G. Lopes .....	1005

# Table of Contents: Volume 2

Permeability Requirements for Geotextile Filter Design R.J. Fannin, Y.C. Shi & Y.P. Vaid .....	1009
Geotextile Filter Design by Probabilistic Analysis D.C. Urashima & D. Vidal .....	1013
Filter Behavior of Hydraulically and Mechanically Damaged Geotextiles Y.H. Faure & Y. Kehila .....	1017
Large-Scale Performance Tests to Evaluate Filtration Processes T. Kossendey & G. Karam .....	1021
The Performance of a Geotextile Filter in Tropical Soil M.G. Gardoni & E.M. Palmeira .....	1027
Effect of Cavities Between Soil and Geotextile Filter on Permeability E. Güler & E. Baran .....	1033
Theoretical Basis for the Development of a Two-Layer Geotextile Filter J.P. Giroud, P. Delmas & O. Artières .....	1037
Aquatextiles: Use of Nonwoven Geotextiles for Filtration in a Municipal Water Treatment Plant E.A. Richards, J.D. Scott & D.W. Smith .....	1045
<b>Hydraulic Capacity of Geosynthetics</b>	
Turbulence and Dynamics in the Falling Head Test A. Bezuijen .....	1051
Factors Affecting Hydraulic Transmissivity of Geocomposite Drain Systems N. Rad, C. Gokmen & J.M. Stalcup .....	1055
Comparison of Transmissivity Tests DIN - ASTM - CEN J. Müller-Rochholz & Z. Bronstein .....	1059
The Optimization Analysis Between Processing Parameters and Physical Properties of Geocomposites Composed of Multi-Layered Nonwovens H.Y. Jeon & J.Y. Kim .....	1063
<b>Micro-Reinforcement &amp; Triaxial Testing</b>	
Static and Cyclic Behaviour of Sand Reinforced by Mesh Elements J.C. Morel & J.P. Gourc .....	1069

# Table of Contents: Volume 2

Stabilization of Earth Slopes with Fiber Reinforcement G.H. Gregory & D.S. Chill .....	1073
---	------

Effect of Geotextile Reinforcement on the Stress-Strain and Volumetric Behavior of Sand A.K. Ashmawy & P.L. Bourdeau .....	1079
---	------

Numerical Simulation of Dynamic Behavior of Soil With Reinforcement R.H. Chen & T.C. Chen .....	1083
--	------

## Railroads

Rail Transport Support Upgradation - Potential Evaluation of Innovative Geosynthetics V.K. Jain & A. Azeem .....	1089
---	------

The Use of Geotextiles for the Construction of the European High Speed Train Network F. De Meerleer & F. Donckers .....	1093
--	------

## Dams & Reservoirs

Geosynthetic System for the Facing of Bovilla Dam P. Sembenelli, G. Sembenelli & A.M. Scuro .....	1099
--	------

Long Term Performance of Exposed Geomembranes on Dams in Italian Alps D. Cazzuffi .....	1107
--	------

A Sail-Shaped Dam Made of High-Strength Composite Geomembrane K. Jiang & L. Yuan .....	1111
---	------

Use of a Synthetic Rubber Sheet for Surface Lining of Upper Pond at Seawater Pumped-Storage Power Plant H. Shimizu & Y. Ikeguchi .....	1115
---	------

A Scheme of Using Geosynthetics to Treat Cracks on a Reservoir Blanket Z.Y. Liu .....	1121
--	------

Installation Damage Field Tests on a Geomembrane and Waterproofing of the Selvet Dam H. Girard, D. Poulain, C. Mine & G. Potié .....	1125
---	------

## Rivers, Canals & Harbors

Bitumen Geomembranes in Irrigation - Case Histories from a Range of Climates B. Breul & R. Herment .....	1133
---	------

Construction Technology of Geotextile Mattresses for Bank Protection of Liaohe River, Liaoning Province, P.R. China D. Wang & X. Wang .....	1139
---	------

# Table of Contents: Volume 2

A New Structure for Protecting the Banks of Waterways J. Yan .....	1143
Alternative Design and Construction of an Under Seawater Road Tunnel using Geosynthetics in Greece A. Kollios .....	1147
Application and Testing of Geotextiles in Deep-Draft Quays F. Liang .....	1151
Jute Geotextiles U. Datta, P.K. Chatterjee, B. Chotopadhyay & A. Ghosh .....	1155
Abrasion Properties of Geotextiles Subject to Dynamic Loading W.S. Alexander .....	1161
Stability Criteria for Geosystems - An Overview K.W. Pilarczyk, M.K. Breteler & T. Stoutjesdijk .....	1165
Evaluation of Geosynthetic Fabric Containers to Contain Contaminated Dredged Sediment H. Moo-Young, T. Meyers & D. Townsend .....	1173
<b>Damage</b>	
Infrared Thermography of Damage in Geosynthetics M.P. Luong & M. Khay .....	1179
Influence of Reinforcement Damage on the Pull-out Resistance of Geogrids M.L. Lopes & T. Ayele .....	1183
Full-Scale Dynamic Tests on Geosynthetics as Waterproof Layer and Reinforcement of the Surface of Embankment J. Zhang & D.Y. Zou .....	1189
Performance Test to Simulate Geotextile Puncture under Dynamic Cyclic Loading G. Mannsbart, H. Breymann & M. Moser .....	1193

# Analysis and Design of Veneer Cover Soils

Robert M. Koerner

Professor and Director, Geosynthetic Research Institute, Drexel University, Philadelphia, Pennsylvania, USA

Te-Yang Soong

Research Engineer, Geosynthetic Research Institute, Drexel University, Philadelphia, Pennsylvania, USA

**ABSTRACT:** The sliding of cover soils on slopes underlain by geosynthetics is obviously an unacceptable situation and, if the number of occurrences becomes excessive, will eventually reflect poorly on the entire technology. Steeply sloped leachate collection layers and final covers of landfills are situations where incidents of such sliding have occurred. Paradoxically, the analytic formulation of the situation is quite straightforward. This paper presents an analysis of the common problem of a veneer of cover soil (0.3 to 1.0 m thick) on a geosynthetic material at a given slope angle and length so as to arrive at a FS-value. The paper then presents different scenarios that create lower FS-values than the gravitational stresses of the above situation, e.g., equipment loads, seepage forces and seismic loads. As a counterpoint, different scenarios that create higher FS-values also are presented, e.g., toe berms, tapered thickness cover soils and veneer reinforcement. In this latter category, a subdivision is made between intentional reinforcement (using geogrids or high strength geotextiles) and nonintentional reinforcement (cases where geosynthetics overlay a weak interface within a multilayered slope). Hypothetical numeric examples are used in each of the above situations to illustrate the various influences on the resulting FS-value. In many cases, design curves are also generated. Suggested minimum FS-values are presented for final closures of landfills, waste piles, leach pads, etc., which are the situations where veneer slides of this type are the most troublesome. Hopefully, the paper will serve as a vehicle to bring a greater awareness to such situations so as to avert slides from occurring in the future.

**KEYWORDS:** Analysis, Design, Limit Equilibrium Methods, Steep Slopes, Veneer Stability.

## 1 INTRODUCTION

There have been numerous cover soil stability problems in the past resulting in slides that range from being relatively small (which can be easily repaired), to very large (involving litigation and financial judgments against the parties involved). Furthermore, the number of occurrences appears to have increased over the past few years. Soong and Koerner (1996) report on eight cover soil failures resulting from seepage induced stresses alone. While such slides can occur in transportation and geotechnical applications, it is in the environmental applications area where they are most frequent. Specifically, the sliding of relatively thin cover soil layers (called "veneer") above both geosynthetic and natural soil liners, i.e., geomembranes (GM), geosynthetic clay liners (GCL) and compacted clay liners (CCL) are the particular materials of concern. These situations represent a major challenge due (in part) to the following reasons:

- (a) The underlying barrier materials generally represent a low interface shear strength boundary with respect to the soil placed above them.
- (b) The liner system is oriented precisely in the direction of potential sliding.
- (c) The potential shear planes are usually linear and are essentially uninterrupted along the slope.
- (d) Liquid (water or leachate) cannot continue to percolate downward through the cross section due to the presence of the barrier material.

When such slopes are relatively steep, long and uninterrupted in their length (which is the design goal for landfills, waste piles and surface impoundments so as to maximize containment space and minimize land area), the situation is exacerbated.

There are two specific applications in which cover soil stability has been difficult to achieve in light of this discussion.

- Leachate collection soil placed above a GM, GCL and/or CCL along the sides of a landfill before waste is placed and stability achieved accordingly.
- Final cover soil placed above a GM, GCL and/or CCL in the cap or closure of a landfill or waste pile after the waste has been placed to its permitted height.

For the leachate collection soil situation, the time frame is generally short (from months to a few years) and the implications of a slide may be minor in that repairs can oftentimes be done by on-site personnel. For the final cover soil situation, the time frame is invariably long (from decades to centuries) and the implications of a slide can be serious in that repairs often call for a forensic analysis, engineering redesign, separately engaged contractors and quite high remediation costs. These latter cases sometime involve litigation, insurance carriers, and invariably technical experts, thus becoming quite contentious.

Since both situations (leachate collection and final covers) present the same technical issues, the paper will address them simultaneously. It should be realized, however, that the final cover situation is of significantly greater concern.

In the sections to follow, geotechnical engineering considerations will be presented leading to the goal of establishing a suitable factor of safety (FS) against slope instability. A number of common situations will then be analyzed, all of which have the tendency to decrease stability. As a counterpoint, a number of design options will follow, all of which have the objective of increasing stability. A summary and conclusions section will compare the various situations which tend to either create slope instability or aid in slope stability. It is hoped that an

increased awareness in the analysis and design details offered herein, and elsewhere in the published literature which is referenced herein, leads to a significant decrease in the number of veneer cover soil slides that have occurred.

## 2 GEOTECHNICAL ENGINEERING CONSIDERATIONS

As just mentioned, the potential failure surface for veneer cover soils is usually linear with the cover soil sliding with respect to the lowest interface friction layer in the underlying cross section. The potential failure plane being linear allows for a straightforward stability calculation without the need for trial center locations and different radii as with soil stability problems analyzed by rotational failure surfaces. Furthermore, full static equilibrium can be achieved without solving simultaneous equations or making simplified design assumptions.

### 2.1 Limit Equilibrium Concepts

The free body diagram of an *infinitely* long slope with uniformly thick cohesionless cover soil on an incipient planar shear surface, like the upper surface of a geomembrane, is shown in Figure 1. The situation can be treated quite simply.

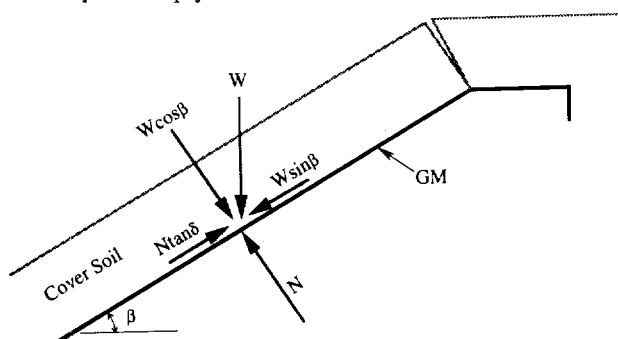


Figure 1. Limit equilibrium forces involved in an infinite slope analysis for a uniformly thick cohesionless cover soil.

By taking force summation parallel to the slope and comparing the resisting force to the driving or mobilizing force, a global factor of safety (FS) results;

$$FS = \frac{\sum \text{Resisting Forces}}{\sum \text{Driving Forces}} = \frac{N \tan \delta}{W \sin \beta} = \frac{W \cos \beta \tan \delta}{W \sin \beta}$$

hence:

$$FS = \frac{\tan \delta}{\tan \beta} \quad (1)$$

Here it is seen that the FS-value is the ratio of tangents of the interface friction angle of the cover soil against the

upper surface of the geomembrane ( $\delta$ ), and the slope angle of the soil beneath the geomembrane ( $\beta$ ). As simple as this analysis is, its teachings are very significant, for example:

- To obtain an accurate FS-value, an accurately determined laboratory  $\delta$ -value is absolutely critical. The accuracy of the final analysis is only as good as the accuracy of the laboratory obtained  $\delta$ -value.
  - For low  $\delta$ -values, the resulting soil slope angle will be proportionately low. For example, for a  $\delta$ -value of 20 deg., and a required FS-value of 1.5, the maximum slope angle is 14 deg. This is equivalent to a 4(H) on 1(V) slope which is relatively low. Furthermore, many geosynthetics have even lower  $\delta$ -values than 20 deg.
  - This simple formula has driven geosynthetic manufacturers to develop products with high  $\delta$ -values, e.g., textured geomembranes, thermally bonded drainage geocomposites, internally reinforced GCLs, etc.
- Unfortunately, the above analysis is too simplistic to use in most realistic situations. For example, the following situations cannot be accommodated:
- A finite length slope with the incorporation of a passive soil wedge at the toe of the slope
  - The consideration of equipment loads on the slope
  - Consideration of seepage forces within the cover soil
  - Consideration of seismic forces acting on the cover soil
  - The use of soil masses acting as toe berms
  - The use of tapered covered soil thicknesses
  - Reinforcement of the cover soil using geogrids or high strength geotextiles

These specific situations will be treated in subsequent sections. For each situation, the essence of the theory will be presented, followed by the necessary design equations. This will be followed, in each case, with a design graph and a numeric example. First, however, the important issue of interface shear testing will be discussed.

### 2.2 Interface Shear Testing

The interface shear strength of a cover soil with respect to the underlying material (often a geomembrane) is critical so as to properly analyze the stability of the cover soil. This value of interface shear strength is obtained by laboratory testing of the project specific materials at the site specific conditions. By project specific materials, we mean sampling of the candidate geosynthetics to be used at the site, as well as the cover soil at its targeted density and moisture conditions. By site specific conditions we mean normal stresses, strain rates, peak or residual shear strengths and temperature extremes (high and/or low). Note that it is completely inappropriate to use values of interface shear strengths from the literature for final design.

While the above list of items is formidable, at least the type of test is established. It is the direct shear test which has been utilized in geotechnical engineering testing for many years. The test has been adapted to evaluate geosynthetics in the USA as ASTM D5321 and in Germany as DIN 60500.

In conducting a direct shear test on a specific interface, one typically performs three replicate tests with the only



variable being different values of normal stress. The middle value is usually targeted to the site specific condition, with a lower and higher value of normal stress covering the range of possible values. These three tests result in a set of shear displacement versus shear stress curves, see Figure 2a. From each curve, a peak shear strength ( $\tau_p$ ) and a residual shear strength ( $\tau_r$ ) are obtained. As a next step, these shear strength values, together with their respective normal stress values, are plotted on Mohr-Coulomb stress space to obtain the shear strength parameters of friction and adhesion, see Figure 2b.

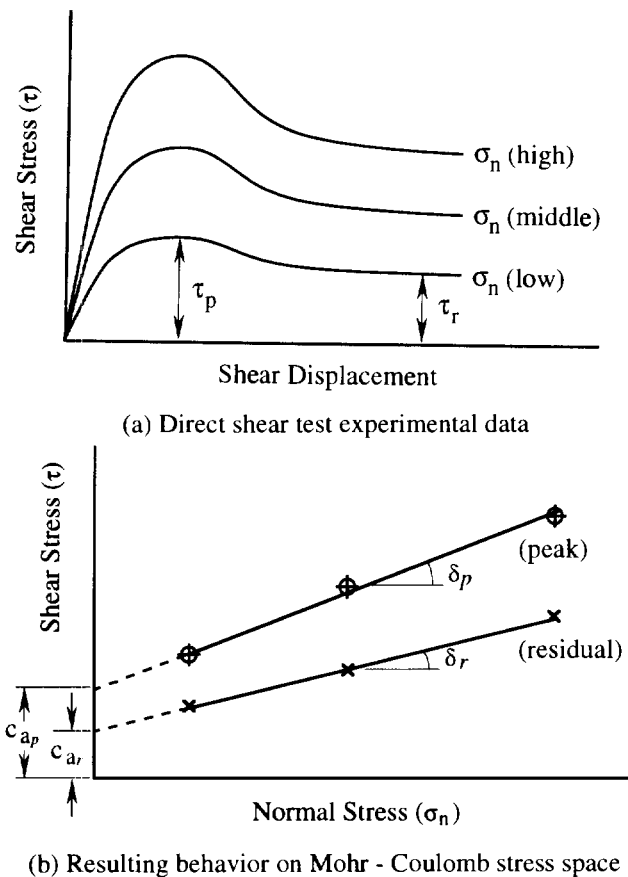


Figure 2. Direct shear test results and analysis procedure to obtain shear strength parameters.

The points are then connected (usually with a straight line), and the two fundamental shear strength parameters are obtained. These shear strength parameters are:

$\delta$  = the angle of shearing resistance, peak and/or residual, of the two opposing surfaces (often called the interface friction angle)

$c_a$  = the adhesion of the two opposing surfaces, peak and/or residual (synonymous with cohesion when testing fine grained soils against one another)

Each set of parameters constitute the equation of a straight line which is the Mohr-Coulomb failure criterion common to geotechnical engineering. The concept is readily adaptable to geosynthetic materials in the following form:

$$\tau_p = c_{ap} + \sigma_n \tan \delta_p \quad (2a)$$

$$\tau_r = c_{ar} + \sigma_n \tan \delta_r \quad (2b)$$

The upper limit of “ $\delta$ ” when soil is involved as one of the interfaces is “ $\phi$ ”, the angle of shearing resistance of the soil component. The upper limit of the “ $c_a$ ” value is “ $c$ ”, the cohesion of the soil component. In the slope stability analyses to follow, the “ $c_a$ ” term will be included for the sake of completeness, but then it will be neglected (as being a conservative assumption) in the design graphs and numeric examples. To utilize an adhesion value, there must be a clear physical justification for use of such values when geosynthetics are involved. Some unique situations such as textured geomembranes with physical interlocking of soils having cohesion, or the bentonite component of a GCL are valid reasons for including such a term.

Note that residual strengths are equal, or lower, than peak strengths. The amount of difference is very dependent on the material and no general guidelines can be given. Clearly, material specific and site specific direct shear tests must be performed to determine the appropriate values. Further, each direct shear test must be conducted to a relatively large displacement to determine the residual behavior, see Stark and Poepfel (1994). The decision as to the use of peak or residual strengths in the subsequent analysis is a very subjective one. It is both a materials specific and site specific issue which is left up to the designer and/or regulator. Even further, the use of peak values at the crest of a slope and residual values at the toe may be justified. As such, the analyses to follow will use an interface  $\delta$ -value with no subscript thereby concentrating on the computational procedures rather than this particular detail. However, the importance of an appropriate and accurate  $\delta$ -value should not be minimized.

Due to the physical structure of many geosynthetics, the size of the recommended shear box is quite large. It must be at least 300 mm by 300 mm unless it can be shown that data generated by a smaller device contains no scale or edge effects, i.e., that no bias exists with a smaller shear box. The implications of such a large shear box should not be taken lightly. Some issues which should receive particular attention are the following:

- Unless it can be justified otherwise, the interface will usually be tested in a saturated state. Thus complete and uniform saturation over the entire specimen area must be achieved. This is particularly necessary for CCLs and GCLs, Daniel, et al. (1993). Hydration takes relatively long in comparison to soils in conventional (smaller) testing shear boxes.
- Consolidation of soils (including CCLs and GCLs) in larger shear boxes is similarly affected.
- Uniformity of normal stress over the entire area must be maintained during consolidation and shearing so as to avoid stress concentrations from occurring.
- The application of relatively low normal stresses, e.g., 10, to 30 kPa simulating typical cover soil thicknesses, challenges the accuracy of some commercially available shear box setups and monitoring systems, particularly the accuracy of pressure gages.

- The issue of appropriate normal stress is greatly complicated if gas pressures are generated in the underlying waste. These gas pressures will counteract some (or all) of the gravitational stress of the cover soil. The resulting shear strength, and subsequent stability, can be significantly decreased. See Liu et al (1997) for insight into this possibility.
- Shear rates necessary to attain drained conditions (if this is the desired situation) are extremely slow, requiring long testing times.
- Deformations necessary to attain residual strengths require large relative movement of the two respective halves of the shear box. So as not to travel over the edges of the opposing shear box sections, devices should have the lower shear box significantly longer than 300 mm. However, with a lower shear box longer than the upper traveling section, new surface is constantly being added to the shearing plane. This influence is not clear in the material's response or in the subsequent behavior.
- The attainment of a true residual strength is difficult to achieve. ASTM D5321 states that one should "run the test until the applied shear force remains constant with increasing displacement". Many commercially available shear boxes have insufficient travel to reach this condition.
- The ring torsion shearing apparatus is an alternative device to determine true residual strength values, but is not without its own problems. Some outstanding issues are the small specimen size, nonuniform shear rates along the width of the specimen, anisotropic shearing with some geosynthetics and no standardized testing protocol. See Stark and Poepfel (1994) for information and data using this alternative test method.

### 2.3 Various Types of Loadings

There are a large variety of slope stability problems that may be encountered in analyzing and/or designing final covers of engineered landfills, abandoned dumps and remediation sites as well as leachate collection soils covering geomembranes beneath the waste. Perhaps the most common situation is a uniformly thick cover soil on a geomembrane placed over the soil subgrade at a given and constant slope angle. This "standard" problem will be analyzed in the next section. A variation of this problem will include equipment loads used during placement of cover soil on the geomembrane. This problem will be solved with equipment moving up the slope and then moving down the slope.

Unfortunately, cover soil slides have occurred and it is felt that the majority of the slides have been associated with seepage forces. Indeed, drainage above a geomembrane (or other barrier material) in the cover soil cross section must be accommodated to avoid the possibility of seepage forces. A section will be devoted to this class of slope stability problems.

Lastly, the possibility of seismic forces exists in earthquake prone locations. If an earthquake occurs in the vicinity of an engineered landfill, abandoned dump or remediation site, the seismic wave travels through the solid waste mass reaching the upper surface of the cover. It then

decouples from the cover soil materials, producing a horizontal force which must be appropriately analyzed. A section will be devoted to the seismic aspects of cover soil slope analysis as well.

All of the above actions are destabilizing forces tending to cause slope instability. Fortunately, there are a number of actions that can be taken to increase the stability of slopes.

Other than geometrically redesigning the slope with a flatter slope angle or shorter slope length, a designer can add soil mass at the toe of the slope thereby enhancing stability. Both toe berms and tapered soil covers are available options and will be analyzed accordingly. Alternatively, the designer can always use geogrids or high strength geotextiles within the cover soil acting as reinforcement materials. This technique is usually referred to as veneer reinforcement. Cases of both intentional and nonintentional veneer reinforcement will be presented.

Thus it is seen that a number of strategies influence slope stability. Each will be described in the sections to follow. First, the basic gravitational problem will be presented followed by those additional loading situations which tend to decrease slope stability. Second, various actions that can be taken by the designer to increase slope stability will be presented. The summary will contrast the FS-values obtained in the similarly crafted numeric examples.

## 3 SITUATIONS CAUSING DESTABILIZATION OF SLOPES

This section treats the standard veneer slope stability problem and then superimposes upon it a number of situations, all of which tend to destabilize slopes. Included are gravitational, construction equipment, seepage and seismic forces. Each will be illustrated by a design graph and a numeric example.

### 3.1 Cover Soil (Gravitational) Forces

Figure 3 illustrates the common situation of a *finite* length, uniformly thick cover soil placed over a liner material at a slope angle " $\beta$ ". It includes a passive wedge at the toe and has a tension crack of the crest. The analysis that follows is after Koerner and Hwu (1991), but comparable analyses are available from Giroud and Beech (1989), McKelvey and Deutsch (1991), Ling and Leshchinsky (1997) and others.

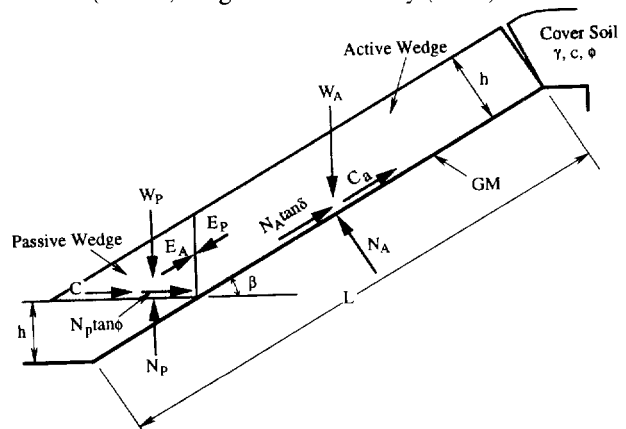


Figure 3. Limit equilibrium forces involved in a finite length slope analysis for a uniformly thick cover soil.

The symbols used in Figure 3 are defined below.

- $W_A$  = total weight of the active wedge  
 $W_P$  = total weight of the passive wedge  
 $N_A$  = effective force normal to the failure plane of the active wedge  
 $N_P$  = effective force normal to the failure plane of the passive wedge  
 $\gamma$  = unit weight of the cover soil  
 $h$  = thickness of the cover soil  
 $L$  = length of slope measured along the geomembrane  
 $\beta$  = soil slope angle beneath the geomembrane  
 $\phi$  = friction angle of the cover soil  
 $\delta$  = interface friction angle between cover soil and geomembrane  
 $C_a$  = adhesive force between cover soil of the active wedge and the geomembrane  
 $c_a$  = adhesion between cover soil of the active wedge and the geomembrane  
 $C$  = cohesive force along the failure plane of the passive wedge  
 $c$  = cohesion of the cover soil  
 $E_A$  = interwedge force acting on the active wedge from the passive wedge  
 $E_P$  = interwedge force acting on the passive wedge from the active wedge  
 $FS$  = factor of safety against cover soil sliding on the geomembrane

The expression for determining the factor of safety can be derived as follows:

Considering the active wedge,

$$W_A = \gamma h^2 \left( \frac{L}{h} - \frac{1}{\sin \beta} - \frac{\tan \beta}{2} \right) \quad (3)$$

$$N_A = W_A \cos \beta \quad (4)$$

$$C_a = c_a \left( L - \frac{h}{\sin \beta} \right) \quad (5)$$

By balancing the forces in the vertical direction, the following formulation results:

$$E_A \sin \beta = W_A - N_A \cos \beta - \frac{N_A \tan \delta + C_a}{FS} \sin \beta \quad (6)$$

Hence the interwedge force acting on the active wedge is:

$$E_A = \frac{(FS)(W_A - N_A \cos \beta) - (N_A \tan \delta + C_a) \sin \beta}{\sin \beta (FS)} \quad (7)$$

The passive wedge can be considered in a similar manner:

$$W_P = \frac{\gamma h^2}{\sin 2\beta} \quad (8)$$

$$N_P = W_P + E_P \sin \beta \quad (9)$$

$$C = \frac{(c)(h)}{\sin \beta} \quad (10)$$

By balancing the forces in the horizontal direction, the following formulation results:

$$E_P \cos \beta = \frac{C + N_P \tan \phi}{FS} \quad (11)$$

Hence the interwedge force acting on the passive wedge is:

$$E_P = \frac{C + W_P \tan \phi}{\cos \beta (FS) - \sin \beta \tan \phi} \quad (12)$$

By setting  $E_A = E_P$ , the resulting equation can be arranged in the form of the quadratic equation  $ax^2 + bx + c = 0$  which in our case, using FS-values, is:

$$a(FS)^2 + b(FS) + c = 0 \quad (13)$$

where

$$a = (W_A - N_A \cos \beta) \cos \beta$$

$$b = - \left[ (W_A - N_A \cos \beta) \sin \beta \tan \phi + (N_A \tan \delta + C_a) \sin \beta \cos \beta + \sin \beta (C + W_P \tan \phi) \right]$$

$$c = (N_A \tan \delta + C_a) \sin^2 \beta \tan \phi \quad (14)$$

The resulting FS-value is then obtained from the solution of the quadratic equation:

$$FS = \frac{-b + \sqrt{b^2 - 4ac}}{2a} \quad (15)$$

When the calculated FS-value falls below 1.0, sliding of the cover soil on the geomembrane is to be anticipated. Thus a value of greater than 1.0 must be targeted as being the minimum factor of safety. How much greater than 1.0 the FS-value should be, is a design and/or regulatory issue. The issue of minimum allowable FS-values under different conditions will be assessed at the end of the paper. In order to better illustrate the implications of Eqs. 13, 14 and 15, typical design curves for various FS-values as a function of slope angle and interface friction angle are given in Figure 4. Note that the curves are developed specifically for the variables stated in the legend of the figure. Example 1 illustrates the use of the curves in what will be the standard example to which other examples will be compared.

Example 1:

Given a 30 m long slope with a uniformly thick 300 mm cover soil at a unit weight of 18 kN/m<sup>3</sup>. The soil has a friction angle of 30 deg. and zero cohesion, i.e., it is a sand. The cover soil is placed directly on a geomembrane as shown in Figure 3. Direct shear testing has resulted in a interface friction angle between the cover soil and geomembrane of 22 deg. with zero adhesion. What is the FS-value at a slope angle of 3(H)-to-1(V), i.e., 18.4 deg?

Solution:

Substituting Eq. 14 into Eq. 15 and solving for the FS-value results in the following which is seen to be in agreement with the curves of Figure 4.

$$\left. \begin{aligned} a &= 14.7 \text{ kN / m} \\ b &= -21.3 \text{ kN / m} \\ c &= 3.5 \text{ kN / m} \end{aligned} \right\} \text{FS} = 1.25$$

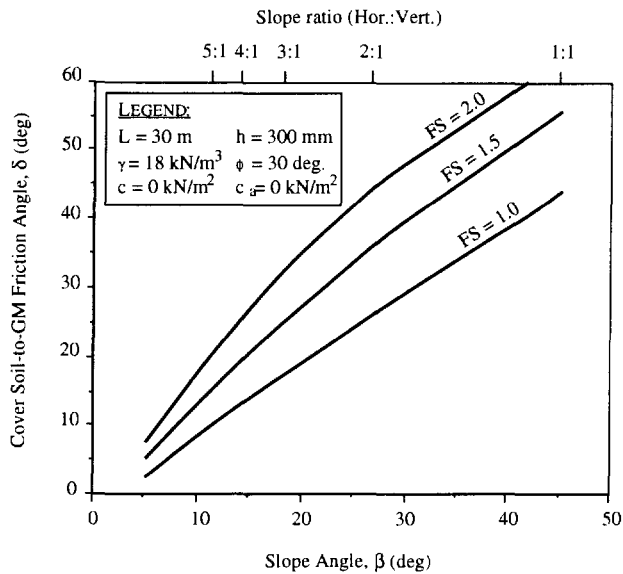


Figure 4. Design curves for stability of uniform thickness cohesionless cover soils on linear failure planes for various global factors-of-safety.

Comment:

In general, this is too low of a value for a final cover soil factor-of-safety and a redesign is necessary. While there are many possible options of changing the geometry of the situation, the example will be revisited later in this section using toe berms, tapered cover soil thickness and veneer reinforcement. Furthermore, this general problem will be used throughout the main body of this paper for comparison purposes to other cover soil slope stability situations.

### 3.2 Tracked Construction Equipment Forces

The placement of cover soil on a slope with a relatively low shear strength inclusion (like a geomembrane) should always be from the toe upward to the crest. Figure 5a shows the recommended method. In so doing, the gravitational forces of the cover soil and live load of the construction equipment are compacting previously placed soil and working with an ever present passive wedge and stable lower-portion beneath the active wedge. While it is necessary to specify low ground pressure equipment to place the soil, the reduction of the FS-value for this situation of equipment working up the slope will be seen to be relatively small.

For soil placement down the slope, however, a stability analysis cannot rely on toe buttressing and also a dynamic stress should be included in the calculation. These conditions decrease the FS-value and in some cases to a great extent. Figure 5b shows this procedure. Unless absolutely necessary, it is not recommended to place cover soil on a slope in this manner. If it is necessary, the design must consider the unsupported soil mass and the dynamic force of the specific type of construction equipment and its manner of operation.

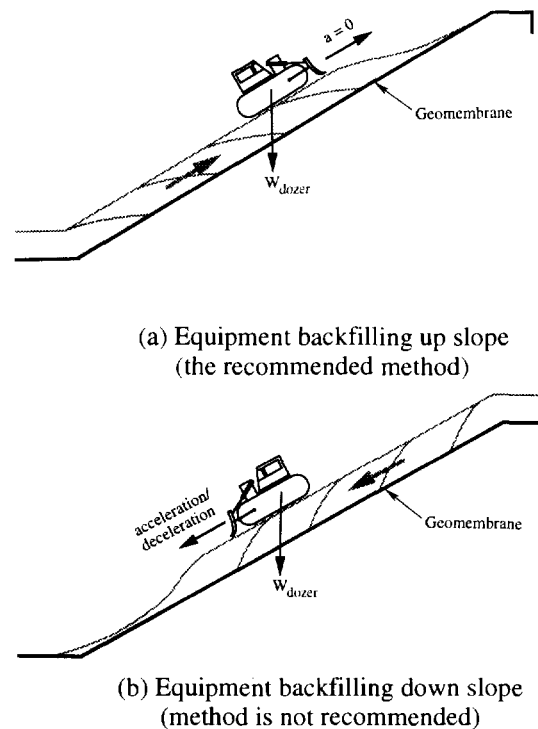


Figure 5. Construction equipment placing cover soil on slopes containing geosynthetics.

For the first case of a bulldozer pushing cover soil up from the toe of the slope to the crest, the analysis uses the free body diagram of Figure 6a. The analysis uses a specific piece of tracked construction equipment (like a bulldozer) characterized by its ground contact pressure and dissipates this force or stress through the cover soil thickness to the surface of the geomembrane. A Boussinesq analysis is used, see Poulos and Davis (1974). This results in an equipment force per unit width as follows:

$$W_e = qwI \quad (16)$$

where

$$\begin{aligned} W_e &= \text{equivalent equipment force per unit width at the} \\ &\quad \text{geomembrane interface} \\ q &= W_b / (2 \times w \times b) \end{aligned}$$

- $W_b$  = actual weight of equipment (e.g., a bulldozer)
- $w$  = length of equipment track
- $b$  = width of equipment track
- $I$  = influence factor at the geomembrane interface  
see Figure 7

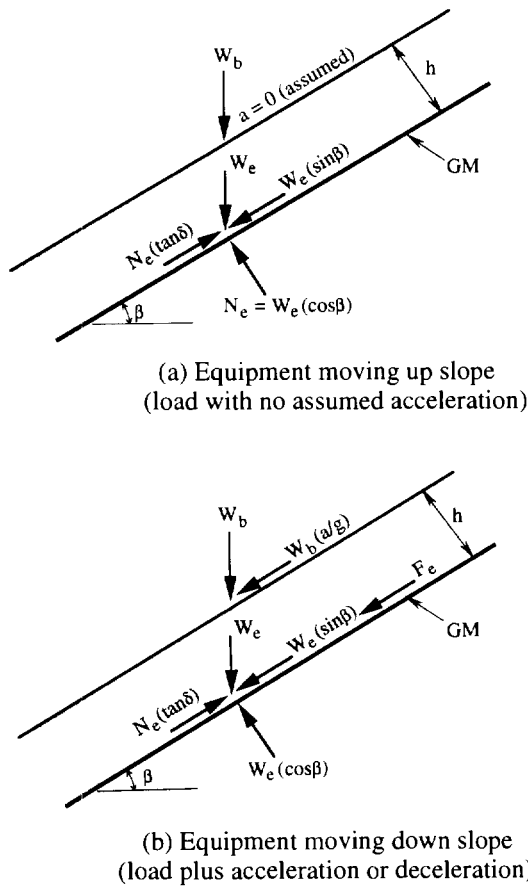


Figure 6. Additional (to gravitational forces) limit equilibrium forces due to construction equipment moving on cover soil (see Figure 3 for the gravitational soil force to which the above forces are added).

Upon determining the additional equipment force at the cover soil-to-geomembrane interface, the analysis proceeds as described in Section 3.1 for gravitational forces only. In essence, the equipment moving up the slope adds an additional term,  $W_e$ , to the  $W_A$ -force in Eq. 3. Note, however, that this involves the generation of a resisting force as well. Thus, the net effect of increasing the driving force as well as the resisting force is somewhat neutralized insofar as the resulting FS-value is concerned. It should also be noted that no acceleration/deceleration forces are included in this analysis which is somewhat optimistic. Using these concepts (the same equations used in Section 3.1 are used here), typical design curves for various FS-values as a function of equivalent ground contact equipment pressures and cover soil thicknesses are given in Figure 8. Note that the curves are developed specifically for the variables stated in the legend. Example 2a illustrates the use of the formulation.

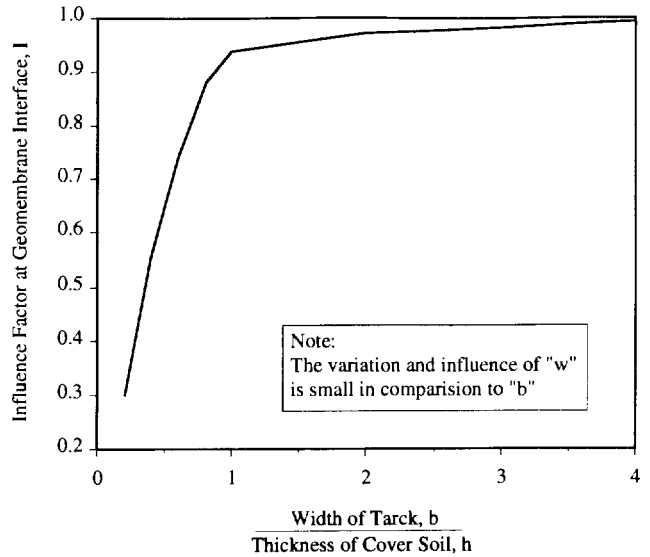
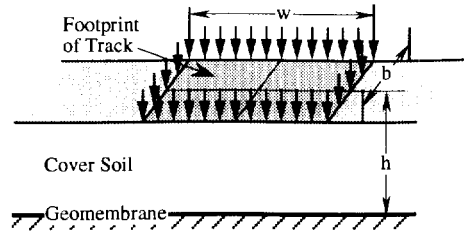


Figure 7. Values of influence factor, "I", for use in Eq. 16 to dissipate surface force of tracked equipment through the cover soil to the geomembrane interface, after Poulos and Davis (1974).

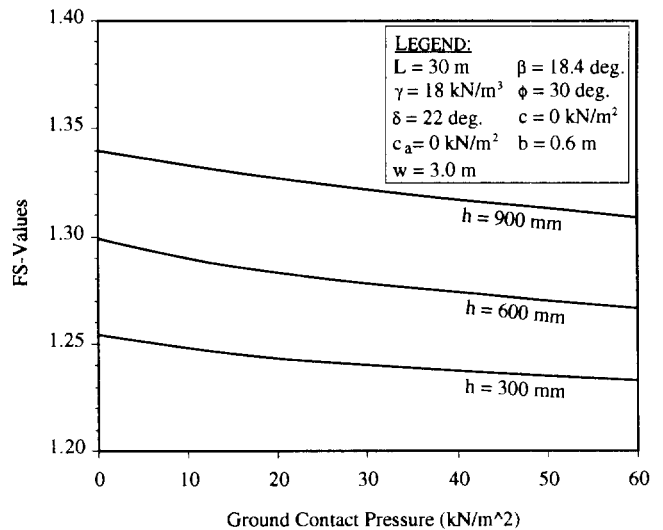


Figure 8. Design curves for stability of different thickness of cover soil for various values of tracked ground contact pressure construction equipment.

Example 2a:

Given 30 m long slope with uniform cover soil of 300 mm thickness at a unit weight of 18 kN/m<sup>3</sup>. The soil has a friction angle of 30 deg. and zero cohesion, i.e., it is a sand. It is placed on the slope using a bulldozer moving from the toe of the slope up to the crest. The bulldozer has a ground pressure of 30 kN/m<sup>2</sup> and tracks that are 3.0 m long and 0.6 m wide. The cover soil to geomembrane friction angle is 22 deg. with zero adhesion. What is the FS-value at a slope angle of 3(H)-to-1(V), i.e., 18.4 deg.

Solution:

This problem follows Example 1 exactly except for the addition of the bulldozer moving up the slope. Using the additional equipment load Eq. 16, substituted into Eqs. 14 and 15 results in the following.

$$\left. \begin{aligned} a &= 73.1 \text{ kN / m} \\ b &= -104.3 \text{ kN / m} \\ c &= 17.0 \text{ kN / m} \end{aligned} \right\} \text{FS} = 1.24$$

Comment:

While the resulting FS-value is low, the result is best assessed by comparing it to Example 1, i.e., the same problem except without the bulldozer. It is seen that the FS-value has only decreased from 1.25 to 1.24. Thus, in general, a low ground contact pressure bulldozer placing cover soil up the slope with negligible acceleration/deceleration forces does not significantly decrease the factor-of-safety.

For the second case of a bulldozer pushing cover soil down from the crest of the slope to the toe as shown in Figure 5b, the analysis uses the force diagram of Figure 6b. While the weight of the equipment is treated as just described, the lack of a passive wedge along with an additional force due to acceleration (or deceleration) of the equipment significantly changes the resulting FS-values. This analysis again uses a specific piece of construction equipment operated in a specific manner. It produces a force parallel to the slope equivalent to  $W_b (a/g)$ , where  $W_b$  = the weight of the bulldozer,  $a$  = acceleration of the bulldozer and  $g$  = acceleration due to gravity. Its magnitude is equipment operator dependent and related to both the equipment speed and time to reach such a speed, see Figure 9. A similar behavior will be seen for deceleration.

The acceleration of the bulldozer, coupled with an influence factor "I" from Figure 7, results in the dynamic force per unit width at the cover soil to geomembrane interface, "F<sub>e</sub>". The relationship is as follows:

$$F_e = W_e \left( \frac{a}{g} \right) \tag{17}$$

where

F<sub>e</sub> = dynamic force per unit width parallel to the slope at the geomembrane interface,

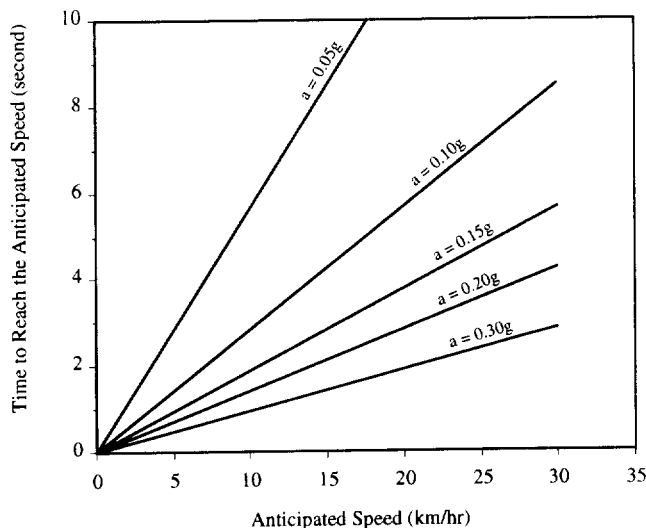


Figure 9. Graphic relationship of construction equipment speed and rise time to obtain equipment acceleration.

- W<sub>e</sub> = equivalent equipment (bulldozer) force per unit width at geomembrane interface, recall Eq. 16.
- β = soil slope angle beneath geomembrane
- a = acceleration of the bulldozer
- g = acceleration due to gravity

Using these concepts, the new force parallel to the cover soil surface is dissipated through the thickness of the cover soil to the interface of the geomembrane. Again, a Boussinesq analysis is used, see Poulos and Davis (1974). The expression for determining the FS-value can now be derived as follows:

Considering the active wedge, and balancing the forces in the direction parallel to the slope, the following formulation results:

$$E_A + \frac{(N_e + N_A) \tan \delta + C_a}{FS} = (W_A + W_e) \sin \beta + F_e \tag{18}$$

where

$$\begin{aligned} N_e &= \text{effective equipment force normal to the failure plane of the active wedge} \\ &= W_e \cos \beta \end{aligned} \tag{19}$$

Note that all the other symbols have been previously defined.

The interwedge force acting on the active wedge can down be expressed as:

$$E_A = \frac{(FS) [(W_A + W_e) \sin \beta + F_e]}{FS} - \frac{[(N_e + N_A) \tan \delta + C_a]}{FS} \tag{20}$$

The passive wedge can be treated in a similar manner. The following formulation of the interwedge force acting on the passive wedge results:

$$E_P = \frac{C + W_P \tan \phi}{\cos \beta (FS) - \sin \beta \tan \phi} \quad (21)$$

By setting  $E_A = E_P$ , the following equation can be arranged in the form of Eq. 13 in which the "a", "b" and "c" terms are as follows:

$$\begin{aligned} a &= [(W_A + W_e) \sin \beta + F_e] \cos \beta \\ b &= -\{[(N_e + N_A) \tan \delta + C_a] \cos \beta \\ &\quad + [(W_A + W_e) \sin \beta + F_e] \sin \beta \tan \phi \\ &\quad + (C + W_P \tan \phi)\} \\ c &= [(N_e + N_A) \tan \delta + C_a] \sin \beta \tan \phi \end{aligned} \quad (22)$$

Finally, the resulting FS-value can be obtained using Eq. 15. Using these concepts, typical design curves for various FS-values as a function of equipment ground contact pressure and equipment acceleration can be developed, see Figure 10. Note that the curves are developed specifically for the variables stated in the legend. Example 2b illustrates the use of the formulation.

#### Example 2b:

Given a 30 m long slope with uniform cover soil of 300 mm thickness at a unit weight of  $18 \text{ kN/m}^3$ . The soil has a friction angle of 30 deg. and zero cohesion, i.e., it is a sand. It is placed on the slope using a bulldozer moving from the crest of the slope down to the toe. The bulldozer has a ground contact pressure of  $30 \text{ kN/m}^2$  and tracks that are 3.0 m long and 0.6 m wide. The estimated equipment speed is 20 km/hr and the time to reach this speed is 3.0 sec. The cover soil to geomembrane friction angle is 22 deg. with zero adhesion. What is the FS-value at a slope angle of 3(H)-to-1(V), i.e., 18.4 deg.

#### Solution:

Using the design curves of Figure 10 along with Eqs. 22 substituted into Eq. 15 the solution can be obtained:

- From Figure 9 at 20 km/hr and 3.0 sec. the bulldozer's acceleration is 0.19g.
- From Eq. 22 substituted into Eq. 15 we obtain

$$\left. \begin{aligned} a &= 88.8 \text{ kN / m} \\ b &= -107.3 \text{ kN / m} \\ c &= 17.0 \text{ kN / m} \end{aligned} \right\} FS = 1.03$$

#### Comment:

This problem solution can now be compared to the previous two examples:

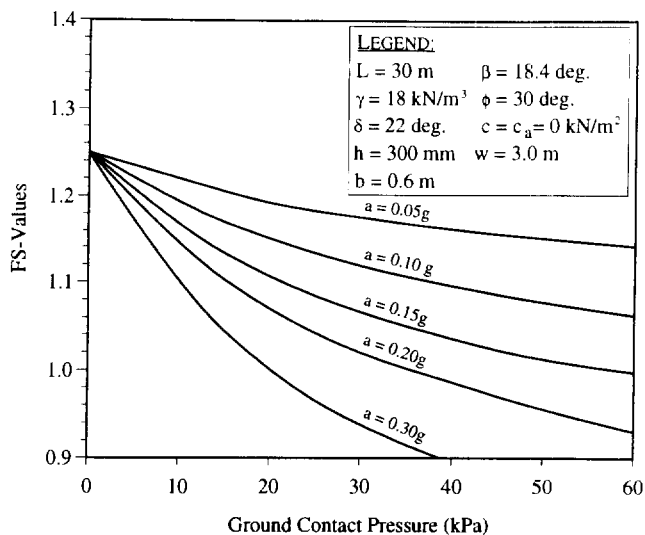


Figure 10. Design curves for stability of different construction equipment ground contact pressure for various equipment accelerations.

- |         |   |           |
|---------|---|-----------|
| Ex. 1:  | cover soil alone with no bulldozer loading  | FS = 1.25 |
| Ex. 2a: | cover soil plus bulldozer moving up slope   | FS = 1.24 |
| Ex. 2b: | cover soil plus bulldozer moving down slope | FS = 1.03 |

The inherent danger of a bulldozer moving down the slope is readily apparent. Note, that the same result comes about by the bulldozer decelerating instead of accelerating. The sharp breaking action of the bulldozer is arguable the more severe condition due to the extremely short times involved when stopping forward motion. Clearly, only in unavoidable situations should the cover soil placement equipment be allowed to work down the slope. If it is unavoidable, an analysis should be made of the specific stability situation and the construction specifications should reflect the exact conditions made in the design. The maximum allowable weight and ground contact pressure of the equipment should be stated along with suggested operator movement of the cover soil placement operations. Truck traffic on the slopes can also give as high, or even higher, stresses and should be avoided unless adequately designed. Additional detail is given in McKelvey (1994). The issue of access ramps is a unique subset of this example and one which deserves focused attention due to the high loads and decelerations that often occur.

### 3.3 Consideration of Seepage Forces

The previous sections presented the general problem of slope stability analysis of cover soils placed on slopes under different conditions. The tacit assumption throughout was that either permeable soil or a drainage layer was placed above the barrier layer with adequate flow capacity to efficiently remove permeating water safely way from the cross section. The amount of water to be removed is obviously a site specific situation. Note that in extremely



arid areas, or with very low permeability cover soils drainage may not be required although this is generally the exception.

Unfortunately, adequate drainage of final covers has sometimes not been available and seepage induced slope stability problems have occurred. The following situations have resulted in seepage induced slides:

- Drainage soils with hydraulic conductivity (permeability) too low for site specific conditions.
- Inadequate drainage capacity at the toe of long slopes where seepage quantities accumulate and are at their maximum.
- Fines from quarried drainage stone either clogging the drainage layer or accumulating at the toe of the slope thereby decreasing the as-constructed permeability over time.
- Fine, cohesionless, cover soil particles migrating through the filter (if one is present) either clogging the drainage layer, or accumulating at the toe of the slope thereby decreasing the as-constructed outlet permeability over time.
- Freezing of the drainage layer at the toe of the slope, while the soil covered top of the slope thaws, thereby mobilizing seepage forces against the ice wedge at the toe.

If seepage forces of the types described occur, a variation in slope stability design methodology is required. Such an analysis is the focus of this subsection. Note that additional discussion is given in Cancelli and Rimoldi (1989), Thiel and Stewart (1993) and Soong and Koerner (1996).

Consider a cover soil of uniform thickness placed directly above a geomembrane at a slope angle of “β” as shown in Figure 11. Different from previous examples, however, is that within the cover soil exists a saturated soil zone for part or all of the thickness. The saturated boundary is shown as two possibly different phreatic surface orientations. This is because seepage can be built-up in the cover soil in two different ways: a horizontal buildup from the toe upward or a parallel-to-slope buildup outward. These two hypotheses are defined and quantified as a horizontal submergence ratio (HSR) and a parallel submergence ratio (PSR). The dimensional definitions of both ratios are given in Figure 11.

When analyzing the stability of slopes using the limit equilibrium method, free body diagrams of the passive and active wedges are taken with the appropriate forces (now including pore water pressures) being applied. The formulation for the resulting factor-of-safety, for horizontal seepage buildup and then for parallel-to-slope seepage buildup, follows.

**The Case of the Horizontal Seepage Buildup.** Figure 12 shows the free body diagram of both the active and passive wedge assuming horizontal seepage. Horizontal seepage buildup can occur when toe blockage occurs due to inadequate outlet capacity, contamination or physical blocking of outlets, or freezing conditions at the outlets.

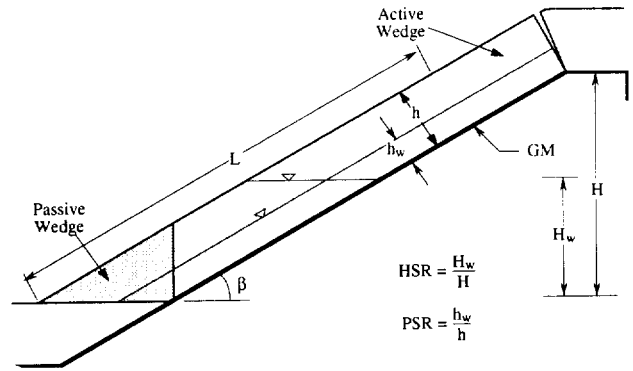


Figure 11. Cross section of a uniform thickness cover soil on a geomembrane illustrating different submergence assumptions and related definitions, Soong and Koerner (1996).

All symbols used in Figure 12 were previously defined except the following:

- $\gamma_{sat'd}$  = saturated unit weight of the cover soil
- $\gamma_t$  = total (moist) unit weight of the cover soil
- $\gamma_w$  = unit weight of water
- $H$  = vertical height of the slope measured from the toe
- $H_w$  = vertical height of the free water surface measured from the toe
- $U_h$  = resultant of the pore pressures acting on the interwedge surfaces
- $U_n$  = resultant of the pore pressures acting perpendicular to the slope
- $U_v$  = resultant of the vertical pore pressures acting on the passive wedge

The expression for finding the factor-of-safety can be derived as follows:

Considering the active wedge,

$$W_A = \left( \frac{\gamma_{sat'd}(h)(2H_w \cos \beta - h)}{\sin 2\beta} \right) + \left( \frac{\gamma_t(h)(H - H_w)}{\sin \beta} \right) \quad (23)$$

$$U_n = \frac{\gamma_w(h)(\cos \beta)(2H_w \cos \beta - h)}{\sin 2\beta} \quad (24)$$

$$U_h = \frac{\gamma_w h^2}{2} \quad (25)$$

$$N_A = W_A(\cos \beta) + U_h(\sin \beta) - U_n \quad (26)$$

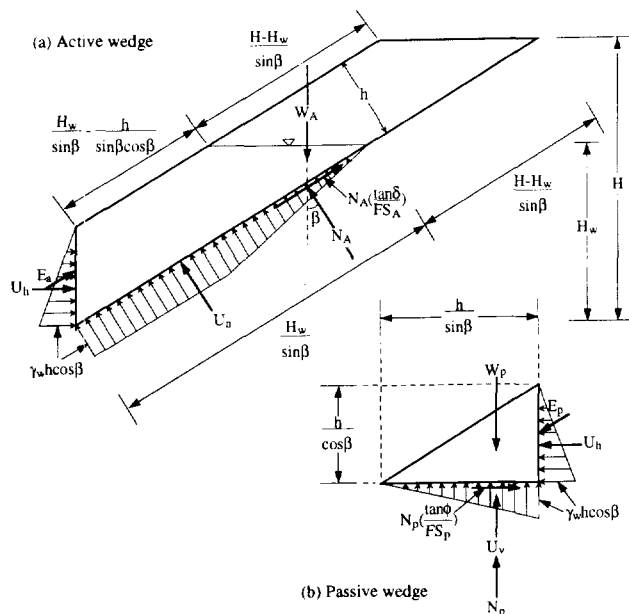


Figure 12. Limit equilibrium forces involved in a finite length slope of uniform cover soil with horizontal seepage buildup.

The interwedge force acting on the active wedge can then be expressed as:

$$E_A = W_A \sin \beta - U_h \cos \beta - \frac{N_A \tan \delta}{FS} \quad (27)$$

The passive wedge can be considered in a similar manner and the following expressions result:

$$W_P = \frac{\gamma_{sat} d h^2}{\sin 2\beta} \quad (28)$$

$$U_V = U_h \cot \beta \quad (29)$$

The interwedge force acting on the passive wedge can then be expressed as:

$$E_P = \frac{U_h (FS) - (W_P - U_V) \tan \phi}{\sin \beta \tan \phi - \cos \beta (FS)} \quad (30)$$

By setting  $E_A = E_P$ , the following equation can be arranged in the form of  $ax^2 + bx + c = 0$  which in this case is:

$$a(FS)^2 + b(FS) + c = 0 \quad (13)$$

where

$$\begin{aligned} a &= W_A \sin \beta \cos \beta - U_h \cos^2 \beta + U_h \\ b &= -W_A \sin^2 \beta \tan \phi + U_h \sin \beta \cos \beta \tan \phi \\ &\quad - N_A \cos \beta \tan \delta - (W_P - U_V) \tan \phi \\ c &= N_A \sin \beta \tan \delta \tan \phi \end{aligned} \quad (31)$$

As with previous solution, the resulting FS-value is obtained using Eq. 15.

**The Case of Parallel-to-Slope Seepage Buildup.** Figure 13 shows the free body diagrams of both the active and passive wedges with seepage buildup in the direction parallel to the slope. Parallel seepage buildup can occur when soils placed above a geomembrane are initially too low in their hydraulic conductivity, or become too low due to long-term clogging from overlying soils which do not have a filter. Identical symbols as defined in the previous cases are used here with an additional definition of  $h_w$  equal to the height of free water surface measured in the direction perpendicular to the slope.

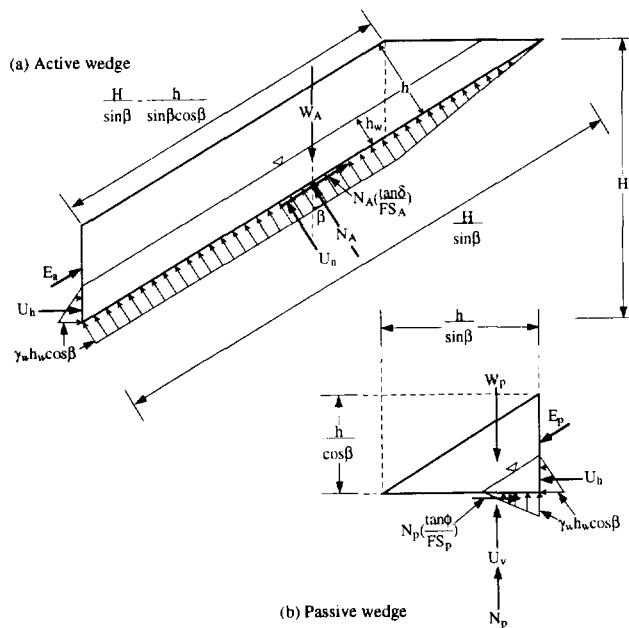


Figure 13. Limit equilibrium forces involved in a finite length slope of uniform cover soil with parallel-to-slope seepage buildup.

Note that the general expression of factor-of-safety shown in Eq. 15 is still valid. However, the a, b and c terms given in Eq. 31 have different definitions in this case owing to the new definitions of the following terms:

$$W_A = \frac{\gamma_t(h - h_w)(2H \cos \beta - (h + h_w))}{\sin 2\beta} + \frac{\gamma_{sat}d(h_w)(2H \cos \beta - h_w)}{\sin 2\beta} \quad (32)$$

$$U_n = \frac{\gamma_w h_w \cos \beta (2H \cos \beta - h_w)}{\sin 2\beta} \quad (33)$$

$$U_h = \frac{\gamma_w (h_w)^2}{2} \quad (34)$$

$$W_p = \frac{\gamma_t(h^2 - h_w^2) + \gamma_{sat}d(h_w^2)}{\sin 2\beta} \quad (35)$$

In order to illustrate the behavior of these equations, the design curves of Figure 14 have been developed. They show the decrease in FS-value with increasing submergence ratio for all values of interface friction. Furthermore, the differences in response curves for the parallel and horizontal submergence ratio assumptions are seen to be very small. Note that the curves are developed specifically for variables stated in the legend. Example 3 illustrates the use of the design curves.

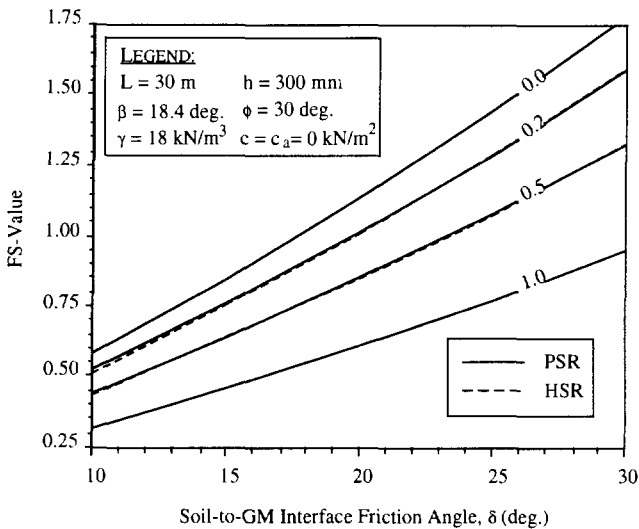


Figure 14. Design curves for stability of cohesionless, uniform thickness, cover soils for different submergence ratios.

**Example 3:**

Given a 30 m long slope with a uniform thickness cover soil of 300 mm at a dry unit weight of 18 kN/m<sup>3</sup>. The soil has a friction angle of 30 deg. and zero cohesion, i.e., it is a sand. The soil becomes saturated through 50% of its thickness, i.e., it is a parallel seepage problem with PSR = 0.5, and its saturated unit weight increases to 21 kN/m<sup>3</sup>. Direct shear testing has resulted in an interface friction angle of 22 deg. with zero adhesion. What is the factor-of-safety at a slope of 3(H)-to-1(V), i.e., 18.4 deg.

Solution:

Solving Eqs. 31 with the values of Eqs. 32 to 35 for the a, b and c terms and then substituting them into Eq. 15 results in the following.

$$\left. \begin{aligned} a &= 51.7 \text{ kN/m} \\ b &= -57.8 \text{ kN/m} \\ c &= 9.0 \text{ kN/m} \end{aligned} \right\} \text{FS} = 0.93$$

Comment:

The seriousness of seepage forces in a slope of this type are immediately obvious. Had the saturation been 100% of the drainage layer thickness, the FS-value would have been even lower. Furthermore, the result using a horizontal assumption of saturated cover soil with the same saturation ratio will give identically low FS-values. Clearly, the teaching of this example problem is that adequate long-term drainage above the barrier layer in cover soil slopes must be provided to avoid seepage forces from occurring.

### 3.4 Consideration of Seismic Forces

In areas of anticipated earthquake activity, the slope stability analysis of a final cover soil over an engineered landfill, abandoned dump or remediated site must consider seismic forces. In the United States, the Environmental Protection Agency (EPA) regulations require such an analysis for sites that have a probability of  $\geq 10\%$  of experiencing a 0.10 g peak horizontal acceleration within the past 250 years. For the continental USA this includes not only the western states, but major sections of the midwest and northeast states, as well. If practiced worldwide, such a criterion would have huge implications.

The seismic analysis of cover soils of the type under consideration in this paper is a two-part process:

- The calculation of a FS-value using a pseudo-static analysis via the addition of a horizontal force acting at the centroid of the cover soil cross section.
- If the FS-value in the above calculation is less than 1.0, a permanent deformation analysis is required. The calculated deformation is then assessed in light of the potential damage to the cover soil section and is either accepted, or the slope requires an appropriate redesign. The redesign is then analyzed until the situation becomes acceptable.

The first part of the analysis is a pseudo-static approach which follows the previous examples except for the addition of a horizontal force at the centroid of the cover soil in proportion to the anticipated seismic activity. It is first necessary to obtain an average seismic coefficient ( $C_s$ ). The bedrock acceleration can be estimated from a seismic zone map, e.g., Algermissen (1991), using the procedures embodied in Richardson, et al (1995). Such maps are available on a worldwide basis. The value of  $C_s$  is nondimensional and is a ratio of the bedrock acceleration to gravitational acceleration. This value of  $C_s$  is modified using available computer codes such as "SHAKE", see

Schnabel, et al. (1972), for propagation to the site and then to the landfill cover. The computational process within such programs is quite intricate. For detailed discussion see Seed and Idriss (1982) and Idriss (1990). The analysis is then typical to those previously presented.

Using Figure 15, the additional seismic force is seen to be  $C_S W_A$  acting horizontally on the active wedge. All additional symbols used in Figure 15 have been previously defined and the expression for finding the FS-value can be derived as follows:

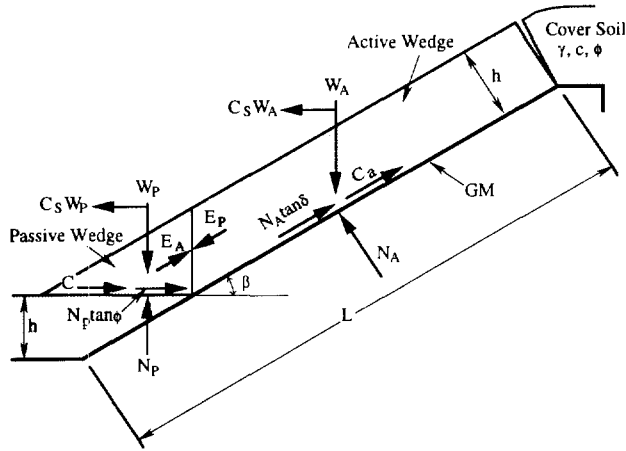


Figure 15. Limit equilibrium forces involved in pseudo-static analysis including use of an average seismic coefficient

Considering the active wedge, by balancing the forces in the horizontal direction, the following formulation results:

$$E_A \cos \beta + \frac{(N_A \tan \delta + C_a) \cos \beta}{FS} = C_S W_A + N_A \sin \beta \quad (36)$$

Hence the interwedge force acting on the active wedge results:

$$E_A = \frac{(FS)(C_S W_A + N_A \sin \beta)}{(FS) \cos \beta} - \frac{(N_A \tan \delta + C_a) \cos \beta}{(FS) \cos \beta} \quad (37)$$

The passive wedge can be considered in a similar manner and the following formulation results:

$$E_P \cos \beta + C_S W_P = \frac{C + N_P \tan \phi}{FS} \quad (38)$$

Hence the interwedge force acting on the passive wedge is:

$$E_P = \frac{C + W_P \tan \phi - C_S W_P (FS)}{(FS) \cos \beta - \sin \beta \tan \phi} \quad (39)$$

Again, by setting  $E_A = E_P$ , the following equation can be arranged in the form of  $ax^2 + bx + c = 0$  which in this case is:

$$a(FS)^2 + b(FS) + c = 0 \quad (13)$$

where

$$\begin{aligned} a &= (C_S W_A + N_A \sin \beta) \cos \beta + C_S W_P \cos \beta \\ b &= -[(C_S W_A + N_A \sin \beta) \sin \beta \tan \phi \\ &\quad + (N_A \tan \delta + C_a) \cos^2 \beta \\ &\quad + (C + W_P \tan \phi) \cos \beta] \\ c &= (N_A \tan \delta + C_a) \cos \beta \sin \beta \tan \phi \end{aligned} \quad (40)$$

The resulting FS-value is then obtained from the following equation:

$$FS = \frac{-b + \sqrt{b^2 - 4ac}}{2a} \quad (15)$$

Using these concepts, a design curve for the general problem under consideration as a function of seismic coefficient can be developed, see Figure 16. Note that the curve is developed specifically for the variables stated in the legend. Example 4a illustrates the use of the curve.

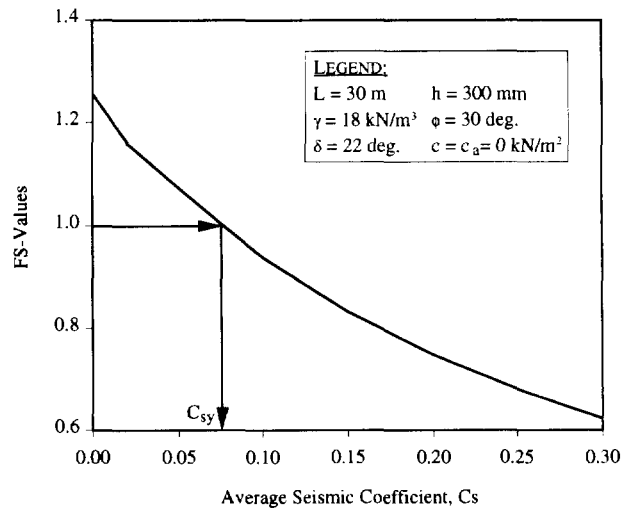


Figure 16. Design curve for a uniformly thick cover soil pseudo-static seismic analysis with varying average seismic coefficients.

**Example 4a:**

Given a 30 m long slope with uniform thickness cover soil of 300 mm at a unit weight of 18 kN/m<sup>3</sup>. The soil has a friction angle of 30 deg. and zero cohesion, i.e., it is a sand. The cover soil is on a geomembrane as shown in Figure 15. Direct shear testing has resulted in an interface friction angle of 22 deg. with zero adhesion. The slope angle is 3(H)-to-1(V), i.e., 18.4 deg. A design earthquake appropriately transferred to the site's cover soil results in an average seismic coefficient of 0.10. What is the FS-value?

**Solution:**

Solving Eqs. 40 for the values given in the example and substituting into Eq. 15 results in the following FS-value.

$$\left. \begin{aligned} a &= 59.6 \text{ kN / m} \\ b &= -66.9 \text{ kN / m} \\ c &= 10.4 \text{ kN / m} \end{aligned} \right\} \text{FS} = 0.94$$

Note that the value of FS = 0.94 agrees with the design curve of Figure 16 at a seismic coefficient of 0.10.

**Comment:**

Had the above FS-value been greater than 1.0, the analysis would be complete. The assumption being that cover soil stability can withstand the short-term excitation of an earthquake and still not slide. However, since the value in this example is less than 1.0, a second part of the analysis is required.

The second part of the analysis is directed toward calculating the estimated deformation of the lowest shear strength interface in the cross section under consideration. The deformation is then assessed in light of the potential damage that may be imposed on the system.

To begin the permanent deformation analysis, a yield acceleration, "C<sub>sy</sub>", is obtained from a pseudo-static analysis under an assumed FS = 1.0. Figure 16 illustrates this procedure for the assumptions stated in the legend. It results in a value of C<sub>sy</sub> = 0.075. Coupling this value with the time history response obtained for the actual site location and cross section, results in a comparison as shown in Figure 17a. If the earthquake time history response never exceeds the value of C<sub>sy</sub>, there is no anticipated permanent deformation. However, whenever any part of the time history curve exceeds the value of C<sub>sy</sub>, permanent deformation is expected. By double integration of the time history curve (which is acceleration), to velocity (Figure 17b) and then to displacement (Figure 17c), the anticipated value of deformation can be obtained. This value is considered to be permanent deformation and is then assessed based on the site-specific implications of damage to the final cover system. Empirical charts, e.g., Makdisi and Seed (1978) can also be used to estimate the permanent deformation. Example 4b continues the previous pseudo-static analysis into the deformation calculation.

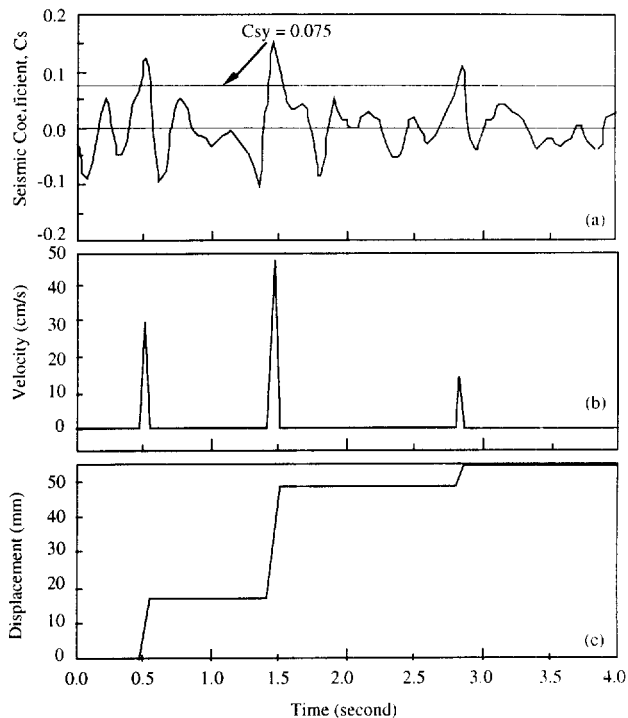


Figure 17. Hypothetical design curves to obtain permanent deformation utilizing (a) acceleration, (b) velocity and (c) displacement curves.

**Example 4b:**

Continue Example 4a and determine the anticipated permanent deformation of the weakest interface in the cover soil system. The site-specific seismic time-history diagram is given in Figure 17a.

**Solution:**

The interface of concern is the cover soil-to-geomembrane for this particular example. With a yield acceleration of 0.075 from Figure 16 and the site-specific (design) time history shown in Figures 17a, integration produces Figure 17b and then 17c. The three peaks exceeding the yield acceleration value of 0.075, produce a cumulative deformation of approximately 54 mm. This value is now viewed in light of the deformation capability of the cover soil above the particular interface used at the site. Note that current practice limits such deformation to either 100 or 300 mm depending on site-specific situations, see Richardson et al (1995).

**Comments:**

An assessment of the implications of deformation (in this example it is 54 mm) is very subjective. For example, this problem could easily have been framed to produce much higher permanent deformation. Such deformation can readily be envisioned in high seismic-prone areas. In addition to an assessment of cover soil stability, the concerns for appurtenances and ancillary piping must also be addressed.

#### 4 SITUATIONS CAUSING THE ENHANCED STABILIZATION OF SLOPES

This section represents a counterpoint to the previous section on slope destabilization situations, in that all situations presented here tend to increase the stability of the slopes. Thus they represent methods to increase the cover soil FS-value. Included are toe berms, tapered cover soils and veneer reinforcement (both intentional and nonintentional). Not included, but very practical in site-specific situations, is to simply decrease the slope angle and/or decrease the slope length. These solutions, however, do not incorporate new design techniques and are therefore not illustrated. They are, however, very viable alternatives for the design engineer.

##### 4.1 Toe (Buttress) Berm

A common method of stabilizing highway slopes and earth dams is to place a soil mass, i.e., a berm, at the toe of the slope. In so doing one provides a soil buttress, acting in a passive state thereby providing a stabilizing force. Figure 18 illustrates the two geometric cases necessary to provide the requisite equations. While the force equilibrium is performed as previously described, i.e., equilibrium along the slope with abutting interwedge forces aligned with the slope angle or horizontal, the equations are extremely long. Due to space limitations (and the resulting trends in FS-value improvement) they are not presented.

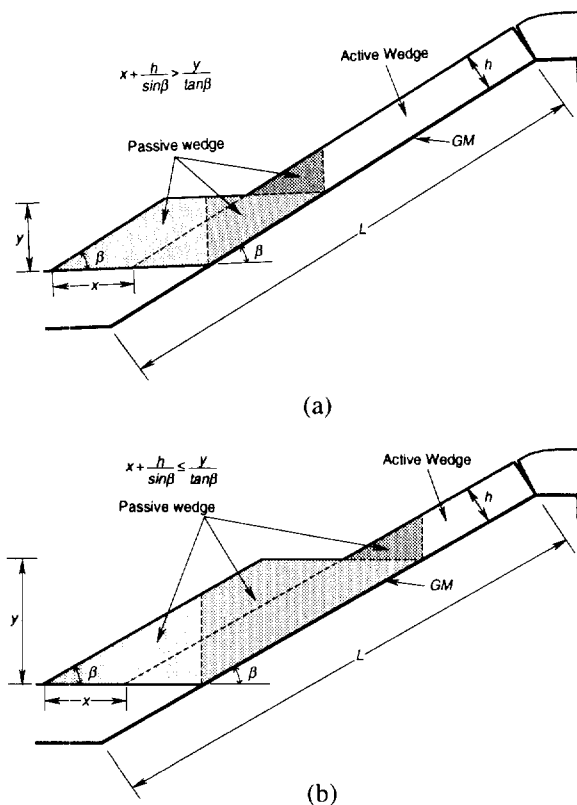


Figure 18. Dimensions of toe (buttress) berms acting as passive wedges to enhance stability.

##### Example 5:

Given a 30 m long slope with a uniform cover soil thickness of 300 mm and a unit weight of  $18 \text{ kN/m}^3$ . The soil has a friction angle of 30 deg. and zero cohesion, i.e., it is a sand. The cover soil is on a geomembrane as shown in Figure 18. Direct shear testing has resulted in a interface friction angle between the cover soil and geomembrane of 22 deg. and zero adhesion. The FS-value at a slope angle of 3(H)-to-1(V), i.e., 18.4 deg., was shown in Section 3.1 to be 1.25. What is the increase in FS-value using different sized toe berms with values of  $x = 1, 2$  and 3 m, and gradually increasing  $y$ -values?

##### Solution:

The FS-value response to this type of toe berm stabilization is given in two parts, see Figure 19. Using thickness values of  $x = 1, 2$  and 3 m, the lower berm section by itself is seen to have high FS-values initially, which decrease rapidly as the height of the toe berm increases. This is a predictable response for this passive wedge zone. Unfortunately, the upper layer of soil above the toe berm

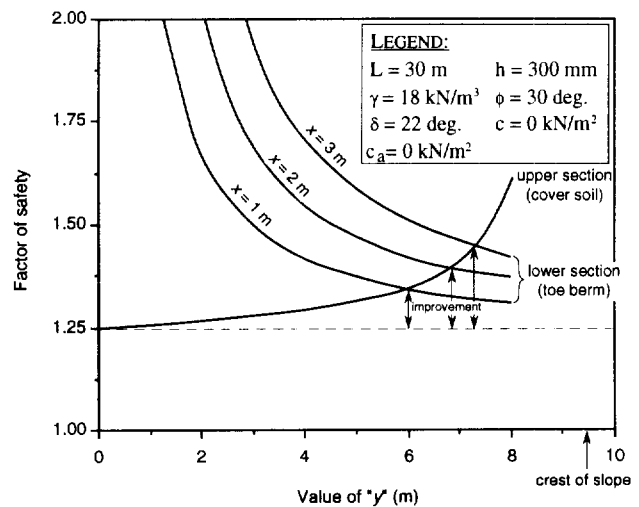


Figure 19. Design curves for FS-values using toe (buttress) berms of different dimensions.

(the active zone) is only nominally increasing in its FS-value. Note that at the crossover points of the upper and lower FS-values (which is the optimum solution for each set of conditions), the following occurs:

- For  $x = 1 \text{ m}$ ;  $y = 6.0 \text{ m}$  (63% of the slope height) and  $FS = 1.35$  (only an 8% improvement in stability)
- For  $x = 2 \text{ m}$ ;  $y = 6.8 \text{ m}$  (72% of the slope height) and  $FS = 1.37$  (only a 12% improvement in stability)
- For  $x = 3 \text{ m}$ ;  $y = 7.3 \text{ m}$  (77% of the slope height) and  $FS = 1.40$  (only a 16% improvement in stability)

##### Comment:

Readily seen is that construction of a toe berm is not a viable strategy to stabilize relatively thin layers of sloped cover soil of the type under investigation. Essentially what is happening is that the upper section of the cover soil (the

active wedge) above the berm is sliding off of the top of the toe berm. While the upper slope length is becoming shorter (as evidenced by the slight improvement in FS-values), it is only doing so with the addition of a tremendous amount of soil fill. Thus this toe berm concept is a poor strategy for the stabilization of forces oriented in the slope's direction. Conversely, it is an excellent strategy for embankments and dams where the necessary resisting force for the toe berm is horizontal thereby counteracting a horizontal thrust by the potentially unstable soil and/or water mass.

#### 4.2 Slopes with Tapered Thickness Cover Soil

An alternative method available to the designer to increase the FS-value of a given slope is to uniformly taper the cover soil thickness from thick at the toe, to thin at the crest, see Figure 20. The FS-value will increase in approximate proportion to the thickness of soil at the toe. The analysis for tapered cover soils includes the design assumptions of a tension crack at the top of the slope, the upper surface of the cover soil tapered at a constant angle " $\omega$ ", and the earth

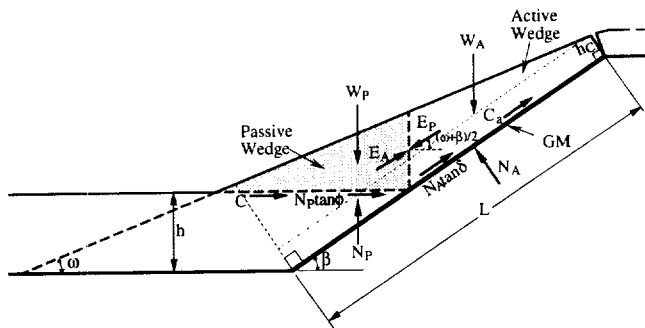


Figure 20. Limit equilibrium forces involved in a finite length slope analysis with tapered thickness cover soil from toe to crest.

pressure forces on the respective wedges oriented at the average of the surface and slope angles, i.e., the E-forces are at an angle of  $(\omega + \beta)/2$ . The procedure follows that of the uniform cover soil thickness analysis. Again, the resulting equation is not an explicit solution for the FS, and must be solved indirectly.

All symbols used in Figure 20 were previously defined (see Section 3.1) except the following:

- $h$  = thickness of cover soil at bottom of the landfill, measured perpendicular to the base liner
- $h_c$  = thickness of cover soil at crest of the slope, measured perpendicular to the slope
- $y$  = see Figure 20

$$= \left( L - \frac{h}{\sin \beta} - h_c \tan \beta \right) (\sin \beta - \cos \beta \tan \omega)$$

$\omega$  = finished slope angle of cover soil, note that  $\omega < \beta$

The expression for determining the FS-value can be derived as follows:

Considering the active wedge,

$$W_A = \gamma \left[ \left( L - \frac{h}{\sin \beta} - h_c \tan \beta \right) \left( \frac{y \cos \beta}{2} + h_c \right) + \frac{h_c^2 \tan \beta}{2} \right] \quad (41)$$

$$N_A = W_A \cos \beta \quad (42)$$

$$C_a = c_a \left( L - \frac{h}{\sin \beta} \right) \quad (43)$$

By balancing the forces in the vertical direction, the following formulations result:

$$E_A \sin \left( \frac{\omega + \beta}{2} \right) = W_A - N_A \cos \beta - \frac{N_A \tan \delta + C_a}{FS} (\sin \beta) \quad (44)$$

Hence the interwedge force acting on the active wedge is:

$$E_A = \frac{(FS)(W_A - N_A \cos \beta) - (N_A \tan \delta + C_a) \sin \beta}{\sin \left( \frac{\omega + \beta}{2} \right) (FS)} \quad (45)$$

The passive wedge can be considered in a similar manner:

$$W_P = \frac{\gamma}{2 \tan \omega} \left[ \left( L - \frac{h}{\sin \beta} - h_c \tan \beta \right) (\sin \beta - \cos \beta \tan \omega) + \frac{h_c}{\cos \beta} \right]^2 \quad (46)$$

$$N_P = W_P + E_P \sin \left( \frac{\omega + \beta}{2} \right) \quad (47)$$

$$C = \frac{\gamma}{\tan \omega} \left[ \left( L - \frac{h}{\sin \beta} - h_c \tan \beta \right) (\sin \beta - \cos \beta \tan \omega) + \frac{h_c}{\cos \beta} \right] \quad (48)$$

By balancing the forces in the horizontal direction, the following formulation results:

$$E_P \cos \left( \frac{\omega + \beta}{2} \right) = \frac{C + N_P \tan \phi}{FS} \quad (49)$$

Hence the interwedge force acting on the passive wedge is:

$$E_P = \frac{C + W_P \tan \phi}{\cos\left(\frac{\omega + \beta}{2}\right)(FS) - \sin\left(\frac{\omega + \beta}{2}\right) \tan \phi} \quad (50)$$

By setting  $E_A = E_P$ , the following equation can be arranged in the form of  $ax^2 + bx + c = 0$  which in our case is

$$a(FS)^2 + b(FS) + c = 0 \quad (13)$$

where

$$\begin{aligned} a &= (W_A - N_A \cos \beta) \cos\left(\frac{\omega + \beta}{2}\right) \\ b &= -\left[ (W_A - N_A \cos \beta) \sin\left(\frac{\omega + \beta}{2}\right) \tan \phi \right. \\ &\quad \left. + (N_A \tan \delta + C_a) \sin \beta \cos\left(\frac{\omega + \beta}{2}\right) \right. \\ &\quad \left. + \sin\left(\frac{\omega + \beta}{2}\right) (C + W_P \tan \phi) \right] \\ c &= (N_A \tan \delta + C_a) \sin \beta \sin\left(\frac{\omega + \beta}{2}\right) \tan \phi \end{aligned} \quad (51)$$

As usual, the resulting FS-value can then be obtained using Eq. 15. To illustrate the use of the above developed equations, the design curves of Figure 21 are offered. They show that the FS-value increases in proportion to greater cover soil thicknesses at the toe of the slope with respect to the thickness at the crest. This is evidenced by a shallower surface slope angle than that of the slope of the geomembrane and the soil beneath, i.e., the value of " $\omega$ " being less than " $\beta$ ". Note that the curves are developed specifically for the variables stated in the legend. Example 6 illustrates the use of the curves.

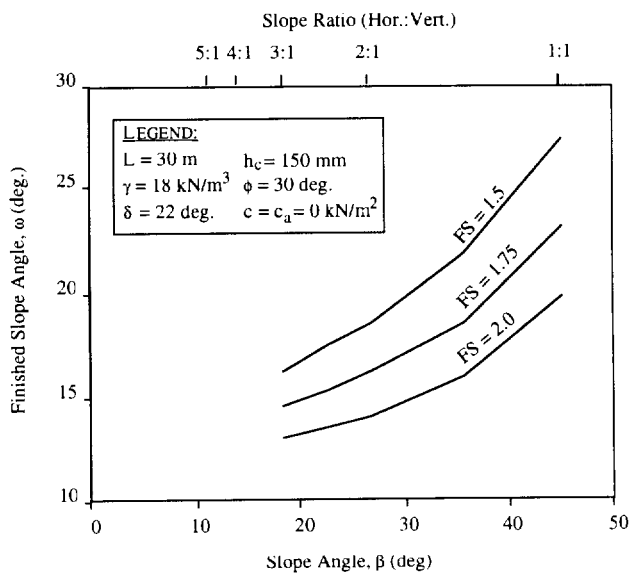


Figure 21. Design curves for FS-values of tapered cover soil thickness.

Example 6:

Given a 30 m long slope with a tapered thickness cover soil of 150 mm at the crest extending at an angle " $\omega$ " of 16 deg. to the intersection of the cover soil at the toe. The unit weight of the cover soil is 18 kN/m<sup>3</sup>. The soil has a friction angle of 30 deg. and zero cohesion, i.e., it is a sand. The interface friction angle with the underlying geomembrane is 22 deg. with zero adhesion. What is the FS-value at an underlying soil slope angle " $\beta$ " of 3(H)-to-1(V), i.e., 18.4 deg.?

Solution:

Using Eqs. 51, substituted into Eq. 15 yields the following:

$$\left. \begin{aligned} a &= 37.0 \text{ kN/m} \\ b &= -63.6 \text{ kN/m} \\ c &= 8.6 \text{ kN/m} \end{aligned} \right\} FS = 1.57$$

Comment:

The result of this problem (with tapered thickness cover soil) is FS = 1.57, versus Example 1 (with a uniform thickness cover soil) which was FS = 1.25. Thus the increase in FS-value is 24%. Note, however, that at  $\omega = 16$  deg. the thickness of the cover soil normal to the slope at the toe is approximately 1.4 m. Thus the increase in cover soil volume used over Example 1 is from 8.9 to 24.1 m<sup>3</sup>/m ( $\approx 170\%$ ) and the increase in necessary toe space distance is from 1.0 to 4.8 m ( $\approx 380\%$ ). The trade-offs between these issues should be considered when using the strategy of tapered cover soil thickness to increase the FS-value of a particular cover soil slope.

#### 4.3 Veneer Reinforcement - Intentional

A fundamentally different way of increasing a given slope's factor of safety is to reinforce it with a geosynthetic material. Such reinforcement can be either intentional or non-intentional. By *intentional*, we mean to include a geogrid or high strength geotextile within the cover soil to purposely reinforce the system against instability, see Figure 22. Depending on the type and amount of reinforcement, the majority, or even all, of the driving, or mobilizing, stresses can be supported resulting in major increase in FS-value. By *non-intentional*, we refer to multi-component liner systems where a low shear strength interface is located beneath an overlying geosynthetic(s). In this case, the overlying geosynthetic(s) is inadvertently acting as veneer reinforcement to the composite system. In some cases, the designer may not realize that such geosynthetic(s) are being stressed in an identical manner as a geogrid or high strength geotextile, but they are. The situation where a relatively low strength protection geotextile is placed over a smooth geomembrane and beneath the cover soil is a case in point. Intentional, or non-intentional, the stability analysis is identical. The difference is that the geogrids and/or high strength geotextiles give a major increase in the FS-value, while a protection geotextile (or other lower strength geosynthetics) only nominally increases the FS-value.



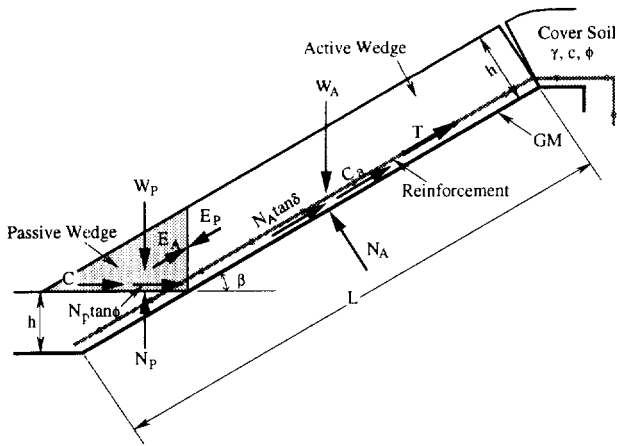


Figure 22. Limit equilibrium forces involved in a finite length slope analysis for a uniformly thick cover soil including the use of veneer reinforcement.

Seen in Figure 22 is that the analysis follows Section 3.1, but a force from the reinforcement “T”, acting parallel to the slope, provides additional stability. This force “T”, acts only within the active wedge. By taking free body force diagrams of the active and passive wedges, the following formulation for the factor of safety results. All symbols used in Figure 22 were previously defined (see Section 3.1) except the following:

$T = T_{allow}$ , the allowable (long-term) strength of the geosynthetic reinforcement inclusion

Consider the active wedge and by balancing the forces in the vertical direction, the following formulation results:

$$E_A \sin \beta = W_A - N_A \cos \beta - \left( \frac{N_A \tan \delta + C_a}{FS} + T \right) \sin \beta \quad (52)$$

Hence the interwedge force acting on the active wedge is:

$$E_A = \frac{(FS)(W_A - N_A \cos \beta - T \sin \beta)}{\sin \beta (FS)} - \frac{(N_A \tan \delta + C_a) \sin \beta}{\sin \beta (FS)} \quad (53)$$

Again, by setting  $E_A = E_P$  (see Eq. 12 for the expression of  $E_P$ ), the following equation can be arranged in the usual form in which the “a”, “b” and “c” terms are defined as follows:

$$\begin{aligned} a &= (W_A - N_A \cos \beta - T \sin \beta) \cos \beta \\ b &= - \left[ (W_A - N_A \cos \beta - T \sin \beta) \sin \beta \tan \phi \right. \\ &\quad \left. + (N_A \tan \delta + C_a) \sin \beta \cos \beta \right. \\ &\quad \left. + \sin \beta (C + W_P \tan \phi) \right] \\ c &= (N_A \tan \delta + C_a) \sin^2 \beta \tan \phi \end{aligned} \quad (54)$$

Again, the resulting FS-value can be obtained using Eq. 15.

As noted, the value of T in the design formulation is  $T_{allow}$  which is invariably less than the as-manufactured strength of the geosynthetic reinforcement material. Considering the as-manufactured strength as being  $T_{ult}$ , the value should be reduced by such factors as installation damage, creep and long-term degradation. Note that if seams are involved in the reinforcement, a reduction factor should be added accordingly. See Koerner, 1998 (among others), for recommended numeric values.

$$T_{allow} = T_{ult} \left( \frac{1}{RF_{ID} \times RF_{CR} \times RF_{CBD}} \right) \quad (55)$$

where

- $T_{allow}$  = allowable value of reinforcement strength
- $T_{ult}$  = ultimate (as-manufactured) value of reinforcement strength
- $RF_{ID}$  = reduction factor for installation damage
- $RF_{CR}$  = reduction factor for creep
- $RF_{CBD}$  = reduction factor for long term chemical/biological degradation

To illustrate the use of the above developed equations, the design curves of Figure 23 have been developed. The reinforcement strength can come from either geogrids or high strength geotextiles. If geogrids are used, the friction angle is the cover soil to the underlying geomembrane, under the assumption that the apertures are large enough to allow for cover soil strike-through. If geotextiles are used, this is not the case and the friction angle is the geotextile to the geomembrane. Also note that this value under discussion is the required reinforcement strength which is essentially  $T_{allow}$  in Eq. 55. The curves of Figure 23 clearly show the improvement of FS-values with increasing strength of the reinforcement. Note that the curves are developed specifically for the variables stated in the legend. Example 7 illustrates the use of the design curves.

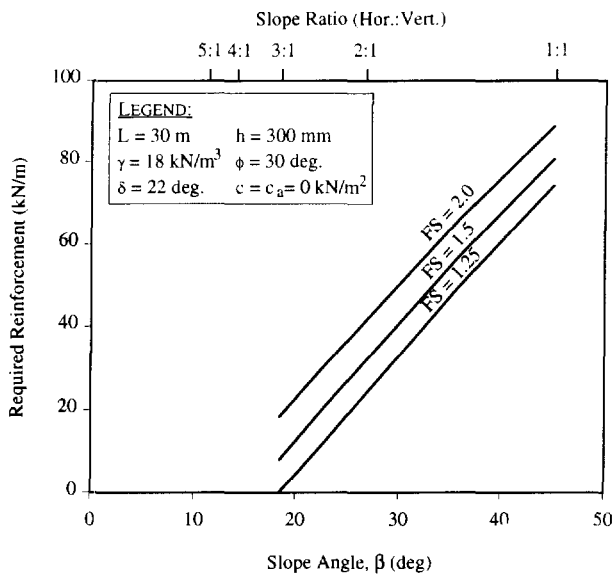


Figure 23. Design curves for FS-values for different slope angles and veneer reinforcement strengths for uniform thickness cohesionless cover soils.

**Example 7:**

Given a 30 m long slope with a uniform thickness cover soil of 300 mm and a unit weight of 18 kN/m<sup>3</sup>. The soil has a friction angle of 30 deg. and zero cohesion, i.e., it is a sand. The proposed reinforcement is a geogrid with an allowable wide width tensile strength of 10 kN/m. Thus reduction factors in Eq. 55 have already been included. The geogrid apertures are large enough that the cover soil will strike-through and provide an interface friction angle with the underlying geomembrane of 22 deg. with zero adhesion. What is the FS-value at a slope angle of 3(H)-to-1(V), i.e., 18.4 deg.?

Solution:

Solving Eqs. 54 and substituting into Eq. 15 produces the following:

$$\left. \begin{aligned} a &= 11.8 \text{ kN / m} \\ b &= -20.7 \text{ kN / m} \\ c &= 3.5 \text{ kN / m} \end{aligned} \right\} \text{FS} = 1.57$$

Comments:

Note that the use of  $T_{\text{allow}} = 10 \text{ kN/m}$  in the analysis will require a significantly higher  $T_{\text{ult}}$  value of the geogrid per Eq. 55. For example, if the summation of the reduction factors in Eq. 55 were 4.0, the ultimate (as-manufactured) strength of the geogrid would have to be 40 kN/m. Also, note that this same type of analysis could also be used for high strength geotextile reinforcement. The analysis follows along the same general lines as presented here.

**4.4 Veneer Reinforcement - Nonintentional**

It should be emphasized that the preceding analysis is focused on intentionally improving the FS-value by the inclusion of geosynthetic reinforcement. This is provided by geogrids or high strength geotextiles being placed above the upper surface of the low strength interface material. The reinforcement is usually placed directly above the geomembrane or other geosynthetic material.

Interestingly, some amount of veneer reinforcement is often nonintentionally provided by a geosynthetic(s) material placed over an interface with a lower shear strength. Several situations are possible in this regard.

- Geotextile protection layer placed over a geomembrane
- Geomembrane placed over an underlying geotextile protection layer
- Geotextile/geomembrane placed over a compacted clay liner or geosynthetic clay liner
- Multilayered geosynthetics placed over a compacted clay liner or a geosynthetic clay liner

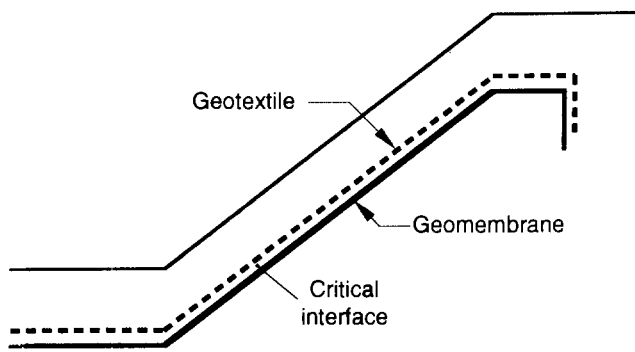
Each of these four situations are illustrated in Figure 24. They represent precisely the formulation of Section 4.3 which is based on Figure 22. On the condition that the geosynthetics above the weakest interface are held in their respective anchor trenches, the overlying geosynthetics provide veneer reinforcement, albeit of a nonintentional type. In the general case, such designs are not recommended although they can indeed provide increased resistance to slope instability of the weakest interface.

In performing calculations of the situations shown in Figure 24, the issue of strain compatibility must be considered. For the slopes shown in Figure 24 a and b, the issue is not important and the full wide width strength of the geotextile and geomembrane, respectively, can be used in the analysis. For the slopes shown in Figure 24 c and d, however, the complete stress vs. strain curves of each geosynthetic layer over the weak interface are necessary. The lowest value of failure strain of any one material dictates the strain at which the other geosynthetics will act. This will invariably be less than the full strength of the other geosynthetics. At this value of strain, however, the allowable strengths are additive and can be used in the analysis. Some detail on this issue is available in Corcoran and McKelvey (1995).

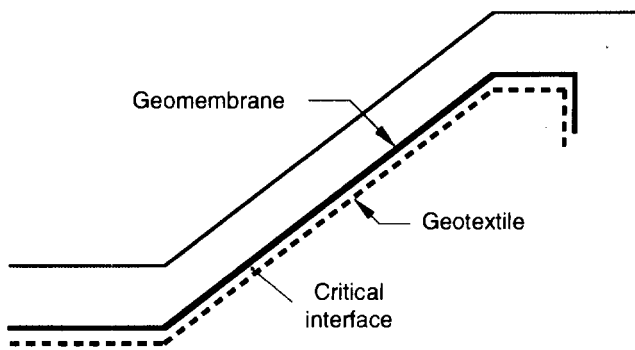
To illustrate the use of the above concepts, examples are given for the four situations shown in Figure 24.

**Example 8:**

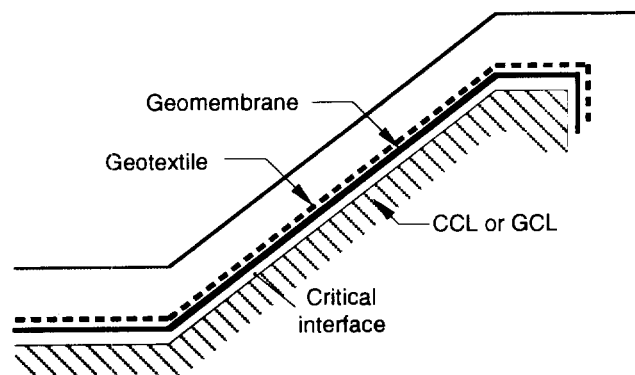
Given four 3(H)-to-1(V), i.e., 18.4 deg. slopes with cover soils as shown in Figures 24 a to d. In each case, the slope is 30 m long with 300 mm of uniformly thick cover soil at a unit weight of 18 kN/m<sup>3</sup>. The soil has a friction angle of 30 deg. and zero cohesion, i.e., it is a sand. The friction angle of the critical interface is 10 deg. What are the FS-values using the geosynthetic tensile strength data provided in the following table?



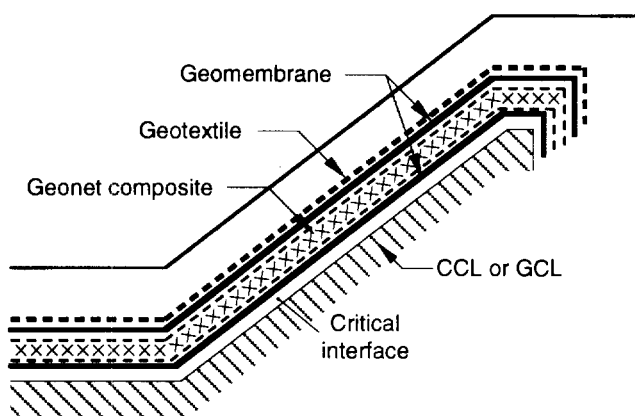
(a) Geotextile sliding on geomembrane



(b) Geomembrane sliding on geotextile



(c) Geotextile and geomembrane sliding on CCL or GCL



(d) Double liner system sliding on CCL or GCL

Values used for numeric examples of nonintentional veneer reinforcement.<sup>1</sup>

Slope type (figure)	GT strength <sup>2</sup> (kN/m)	GM strength <sup>3</sup> (kN/m)	GC strength <sup>4</sup> (kN/m)
24a	25	n/a	n/a
24b	n/a	15	n/a
24c	25	13	n/a
24d	25	13+13	36

Notes:

1. Strengths are product-specific and have been adjusted for strain compatibility.
2. Nonwoven needle punched geotextile of 540 g/m<sup>2</sup>
3. Very flexible polyethylene geomembrane 1.0 mm thick
4. Biaxial geonet with two 200 g/m<sup>2</sup> nonwoven needle punched geotextiles thermally bonded to each side

Solution:

Substituting Eqs. 54 into Eq. 15 results in the following data and respective FS-values.

Slope type (figure)	a (kN/m)	b (kN/m)	c (kN/m)	FS-value
24a	7.3	-9.7	1.5	1.15
24b	10.3	-10.3	1.5	0.82
24c	3.4	-9.0	1.5	2.45
24d	-11.0	-6.2	1.5	>10.0

Comments:

While the practice illustrated in these examples of using the overlying geosynthetics as nonintentional veneer reinforcement is not recommended, it is seen to be quite effective when a number of geosynthetics overlying the weak interface are present. On a cumulative basis, they can represent a substantial force as shown in Figure 24d. If one were to rely on such strength, however, it would be prudent to apply suitable reduction factors to each material, and to inform the parties involved of the design situation.

## 5 SUMMARY

This paper has focused on the mechanics of analyzing slopes as part of final cover systems on engineered landfills, abandoned dumps and remediated waste piles. It also applies to drainage soils placed on geomembrane lined slopes beneath the waste, at least until solid waste is placed against the slope. Numeric examples in all of the sections have resulted in global FS-values. Each section was presented from a designer's perspective in transitioning from the simplest to the most advanced. It should be clearly recognized that there are other approaches to the analyses illustrated in the various examples. References available in the literature by Giroud and Beech (1989), McKelvey and Deutsch (1991), Koerner and Hwu (1991), Giroud et al (1995a), Giroud et al (1995b), Liu et al (1997), and Ling and Leshchinsky (1997) are relevant in this

regard. All are based on the concept of limit equilibrium with different assumptions involving particular details, e.g.,

- Existence of a tension crack at the top of slope (filled or unfilled with water)
- Orientation of the failure plane beneath the passive wedge (horizontal or inclined)
- Specific details of construction equipment movement on the slopes in placing the cover soil, particularly the acceleration or deceleration, and the type of equipment itself (e.g., tracked versus wheel equipment)
- Specific details on seepage forces within the drainage layer, including the amount and its orientation
- Specific details on seismic forces, particularly the magnitude and the selection of interface strengths
- Specific details on the geometry of the toe berms or tapered cover soils
- Specific details on the strength and reduction factors used for intentional veneer reinforcement
- Specific details on the strain compatibility issues used with nonintentional veneer reinforcement.

When considering all of these site-specific details, it is readily seen that veneer cover soil analysis and design is a daunting, yet quite tractable, task. For example, one of the reviewers of this paper reanalyzed one of the examples presented herein and another reviewer reanalyzed all of the examples. Both used the analyses of Giroud et al (1995a) and (1995b). They found good agreement in all cases except the nonintentional veneer reinforcement with multiple geosynthetic layers, i.e., the last example presented. It is likely in this regard that different values of mobilized composite strength were being used.

Table 1 summarizes the FS-values of the similarly framed numeric examples presented herein so that insight can be gained from each of the conditions analyzed. Throughout the paper, however, the inherent danger of building a relatively steep slope on a potentially weak interface material, oriented in the exact direction of a potential slide, should have been apparent.

The standard example was purposely made to have a relatively low factor of safety, i.e.,  $FS = 1.25$ . This FS-value was seen to moderately decrease for construction equipment moving up the slope, but seriously decrease with equipment moving down the slope, i.e., 1.24 to 1.03. It should be noted, however, that the example problems were hypothetical, particularly the equipment examples in the selection of acceleration /deceleration factors. There are an innumerable number of choices to select from, and we have selected values to make the point of proper construction practice. Also, drastically decreasing the FS-value were the influences of seepage and seismicity. The former is felt to be most serious in light of a number of slides occurring after heavy precipitation. The latter is known to be a concern at one landfill in an area of active seismicity.

The sequence of design situations shifted to scenarios where the FS-values were increased over the standard example. Adding soil either in the form of a toe berm or tapered cover soil both increase the FS-value depending on the mass of soil involved. The tapered situation was seen to be more efficient and preferred over the toe berm. Both

Table 1. Summary of numeric examples given in this paper for different slope stability scenarios.

Exam- ple No.	Situation or condition	Control FS-value	Scenarios decreasing FS-values	Scenarios increasing FS-values
1	standard example*	1.25		
2a	equipment up-slope		1.24	
2b	equipment down-slope		1.03	
3	seepage forces		0.93	
4	seismic forces		0.94	
5	toe (buttress) berm			1.35-1.40
6	tapered cover soil			1.57
7	veneer reinforce- ment (intentional)			1.57
8	veneer reinforce- ment (non intentional)			varies

\* 30 m long slope at a slope angle of 18.4 deg. with sandy cover soil of 18.4 kN/m<sup>3</sup> dry unit weight with  $\phi = 30$  deg. and thickness 300 mm placed on an underlying geosynthetic with a friction angle  $\delta = 22$  deg.

designs, however, require physical space at the toe of the slope which is often not available. Thus the use of geosynthetic reinforcement was illustrated. By intentional veneer reinforcement it is meant that geogrids or high strength geotextiles are included to resist some, or all, of the driving forces that are involved. The numeric example illustrated an increase in FS-value from 1.25 to 1.57, but this is completely dependent on the type and amount of reinforcement. It was also shown that whenever the weakest interface is located beneath overlying geosynthetics they also act as veneer reinforcement albeit nonintentionally in most cases. The overlying geosynthetic layers must physical fail (or pull out of their respective anchor trenches, see Hullings, 1996) in order for the slope to mobilize the weakest interface strength layer and slide. While this is not a recommended design situation, it does have the effect of increasing the FS-value. The extent of increase varies from a flexible geomembrane to a nonwoven needle punched protection geotextile (both with relatively low strengths) to a multilayered geosynthetic system with 2 to 8 layers of geosynthetics (with very high cumulative strengths).

We conclude with a discussion on factor of safety (FS) values for cover soil situations. Note that we are referring to the global FS-value, not reduction factors which necessarily must be placed on geosynthetic reinforcement materials when they are present. In general, one can consider global FS-values to vary in accordance with the site specific issue of required service time (i.e., the anticipated lifetime) and the implication of a slope failure (i.e., the concern). Table 2 gives the general concept in qualitative terms.

Table 2. Qualitative rankings for global factor-of-safety values in performing stability analysis of final cover systems, after Bonaparte and Berg (1987).

Duration→ ↓Concern	Temporary	Permanent
Noncritical	Low	Moderate
Critical	Moderate	High

Using the above as a conceptual guide, the authors recommend the use of the minimum global factor-of-safety values listed in Table 3, as a function of the type of underlying waste for *static* conditions.

Table 3. Recommended global factor-of-safety values for static conditions in performing stability analyses of final cover systems.

Type of Waste→ ↓Ranking	Hazard- ous waste	Non- hazardous waste	Aban- doned dumps	Waste piles and leach pads
Low	1.4	1.3	1.4	1.2
Moderate	1.5	1.4	1.5	1.3
High	1.6	1.5	1.6	1.4

It is hoped that the above values give reasonable guidance in final cover slope stability decisions, but it should be emphasized that engineering judgment and (oftentimes) regulatory agreement is needed in many, if not all, situations.

## ACKNOWLEDGMENTS

The opportunity of writing and presenting this paper on behalf of IGS and its Nominating Committee as the 1998 Giroud Lecture is sincerely appreciated. Financial assistance in its preparation by the consortium of Geosynthetic Institute members is gratefully acknowledged.

## REFERENCES

Algermissen, S.T. (1991) "Seismic Risk Studies in the United States," *Proc. 4th World Conference on Earthquake Engineering*, Vol. 1, Santiago, Chile, pp. A1-14 to 27.

- Bonaparte, R. and Berg, R. (1987) "Long-Term Allowable Tension for Geosynthetic Reinforcement," *Proc. Geosynthetics '87*, IFAI, St. Paul, MN, USA, pp. 181-192.
- Cancelli, A and Rimoldi, P. (1989) "Design Criteria for Geosynthetic Drainage Systems in Waste Disposal," *Proc. of Sardinia '89*, 2nd Intl. Landfill Symposium, porto Conte, Sassari, Italy.
- Corcoran, G.T. and McKelvey, J.A. (1995) "Stability of Soil Layers on Compound Geosynthetic Slopes," *Proc. Waste Tech '95*, New Orleans, LA, USA: Environ Industry Assoc., pp. 301-304.
- Daniel, D.E., Shan, H.-Y. and Anderson, J.D. (1993) "Effects of Partial Wetting on the Performance of the Bentonite Component of a Geosynthetic Clay Liner," *Proc. Geosynthetics '93*, IFAI, St. Paul, MN, USA, pp. 1483-1496.
- Giroud, J.P. and Beech, J.F. (1989) Stability of Soil Layers on Geosynthetic Lining Systems," *Proc. Geosynthetics '89*, IFAI, St. Paul, MN, USA, pp. 35-46.
- Giroud, J.P., Williams, N.D., Pelte, T and Beech, J.F. (1995a) "Stability of Geosynthetic-Soil Layered Systems on Slopes," *Geosynthetic International*, Vol. 2, No. 6, pp. 1115-1148.
- Giroud, J.P., Bachus, R.C. and Bonaparte, R (1995b) "Influence of Water Flow on the Stability of Geosynthetic-Soil Layered Systems on Slopes," *Geosynthetic International*, Vol. 2, No. 6, pp. 1149-1180.
- Hullings, D.E. and Sansone, L.J. (1996) "Design Concerns and Performance of Geomembrane Anchor Trenches," *Proc. GRI-10 Conference on Field Performance of Geosynthetics*, GII, Philadelphia, PA, USA, pp. 245-259.
- Idriss, I.M. (1990) "Response of Soft Soil Sites During Earthquake," *Proc. Symposium to Honor Professor H. B. Seed*, Berkeley, CA, USA.
- Koerner, R.M. (1998) *Designing with Geosynthetics*, 4th Ed., Prentice Hill Book Co., Englewood Cliffs, NJ, USA, 761 pgs.
- Koerner, R.M. and Hwu, B.-L. (1991) "Stability and Tension Considerations Regarding Cover Soils on Geomembrane Lined Slopes," *Jour. of Geotextiles and Geomembranes*, Vol. 10, No. 4, pp. 335-355.
- Ling, H.I. and Leshchinsky, D. (1997) "Seismic Stability and Permanent Displacement of Landfill Cover Systems," *Jour. of Geotechnical and Geoenvironmental Engrg.*, ASCE, Vol. 123, No. 2, pp. 113-122.
- Liu, C.N., Gilbert, R.B., Thiel, R.S. and Wright, S.G. (1997) "What is an Appropriate Factor of Safety for Landfill Cover Slopes?" *Proc. Geosynthetics '97*, IFAI, St. Paul, MN, USA, pp. 481-496.
- Makdisi, F.I. and Seed, H.B. (1978) "Simplified Procedure for Estimating Dam and Embankment Earthquake-Induced Deformations," *J. of Geotechnical Engrg.*, ASCE Vol. 104, No. GT7, pp. 849-867
- Matasovic, N., Kavazanjian E. Jr. and Yan, L. (1997) "Newmark Deformation Analysis with Degrading Yield Acceleration," *Proc. Geosynthetics '97*, IFAI, St. Paul, MN, USA, pp. 989-1000.

- McKelvey, J.A. and Deutsch, W.L. (1991) "The Effect of Equipment Loading and Tapered Cover Soil Layers on Geosynthetic Lined Landfill Slopes," *Proceedings of the 14th Annual Madison Avenue Conference*, Madison, WI, USA, University of Wisconsin, pp. 395-411.
- McKelvey, J.A. (1994) "Consideration of Equipment Loadings in Geosynthetic Lined Slope Design," *Proc. 8th Intl. Conf. of the Intl. Asso. for Computer Methods and Advancements in Geomechanics*, Morgantown, WV: Balkema, pp. 1371-1377.
- Poulos, H.G. and Davis, E.H. (1974) *Elastic Solutions for Soil and Rock Mechanics*, J. Wiley & Sons, Inc., New York, NY, USA, 411 pgs.
- Richardson, G.N., Kavazanjian, E. Jr. and Matasovic, N. (1995) "RCRA Subtitle D (258) Seismic Design Guidance for Municipal Solid Waste landfill Facilities", EPA/600/R-95/051, U.S. Environmental Protection Agency, Cincinnati, Ohio, USA, 143 pgs.
- Schnabel, P.B., Lysmer, J. and Seed, H.B. (1972) "SHAKE: A Computer Program for Earthquake Response Analysis of Horizontally Layered sites," Report No EERC 72-12, Earthquake Engineering Research Center, University of California, Berkeley, CA, USA.
- Seed, H.B. and Idriss, I.M. (1982) "Ground Motions and Soil Liquefaction During Earthquakes," Monographs No. 5, Earthquake Engineering Research Center, University of California, Berkeley, CA, USA, 134 pgs.
- Soong, T.-Y. and Koerner, R.M. (1996) "Seepage Induced Slope Instability," *Jour. of Geotextiles and Geomembranes*, Vol. 14, No. 7/8, pp. 425-445.
- Stark, T.D. and Poeppl, A.R. (1994) "Landfill Liner Interface Strengths from Torsional Ring Stress Tests," *Jour. of Geotechnical Engineering*, ASCE, Vol. 120, No. 3, pp. 597-617.
- Thiel, R.S. and Stewart, M.G. (1993), "Geosynthetic Landfill Cover Design Methodology and Construction Experience in the Pacific Northwest," *Proc. Geosynthetics '93*, IFAI, St. Paul, MN, USA, pp. 1131-1144.





# Geosynthetics and the Minimization of Contaminant Migration through Barrier Systems Beneath Solid Waste

R. Kerry Rowe

Professor and Chair, Department of Civil and Environmental Engineering, University of Western Ontario, London, Ontario, Canada

**ABSTRACT:** Geosynthetics play a very important role in modern barrier systems designed to control contaminant migration from waste disposal sites. This paper discusses the effect of temperature, the importance of consideration of clogging of filters and drainage layers, the service life of compacted clay liners beneath geomembranes, the hydraulic conductivity and service life of geosynthetic clay liners (GCLs), diffusion through GCLs, the service life of geomembranes and composite liner systems in the design of these systems. It discusses why any evaluation of equivalence of liner systems should go beyond simple hydraulic equivalency and should consider issues such as diffusive transport and service life. Finally, it highlights the importance of considering conventional stability issues in addition to contaminant transport issues in the design and construction of landfill barrier systems.

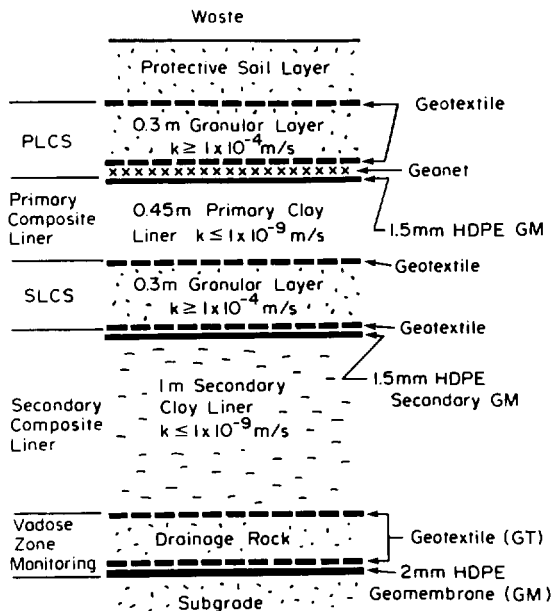
**KEYWORDS:** Liners, Geomembranes, GCLs, Leakage, Diffusion, Service life, Stability, Leachate collection

## 1 INTRODUCTION

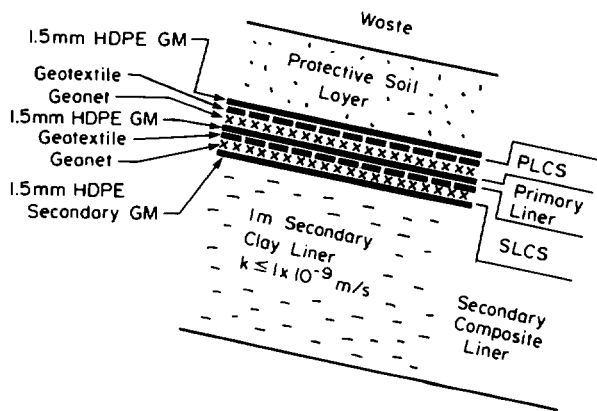
The protection of groundwater and surface water is now a major consideration in the design of waste disposal facilities in many countries. Typically, modern facilities will have a barrier system intended to limit contaminant migration into the surrounding environment to levels that will result in negligible impact. This system will generally include a primary leachate collection system intended to (a) control the leachate head acting on the underlying liner and (b) collect and remove leachate. The leachate collection system will typically incorporate a geotextile filter, a granular layer or geonet, and perforated collection pipes. The liner may range from a thick natural clay deposit to engineered liner systems involving one or more geomembrane (GM) and/or compacted clay liner (CCL) or geosynthetic clay liner (GCL). For example, Figure 1 shows a double composite liner system at the landfill base and a single geomembrane primary liner and composite secondary liner on the side slopes. Not all liner systems are this complicated. Many regulatory systems have both prescriptive designs (minimum) and also permit performance based design with appropriate justification (e.g. Germany 1993; USEPA 1994; MoEE 1996; and see Rowe 1997a for a discussion of the differences in these approaches). Figure 2 shows two simple composite liners involving a geomembrane (GM) over either a compacted clay liner (CCL) or a geosynthetic clay liner (GCL). It is assumed here that there is an attenuation layer (AL) between the base of the composite liner and an underlying aquifer. Since an aquifer is a geologic formation capable of yielding usable quantities of groundwater to wells or springs and since flow in the aquifer is principally in a horizontal direction, the aquifer that is present at some depth beneath many landfill sites often represents the

primary means by which contaminated groundwater can move off-site and impact on public health and safety. Thus a primary objective of the barrier system design is to minimize the escape of contaminants to groundwater and, in particular, to any underlying aquifer. Frequently, questions are raised concerning the equivalency of different systems such as those shown in Figure 2, or the need for double composite liners such as that shown in Figure 3. As discussed in Section 10, these questions should be addressed in terms of the objective of controlling the potential impact on groundwater quality to acceptable levels. However, this first requires consideration of the long term performance of the barrier system components, the different potential transport mechanisms such as advection (the movement of contaminants with flowing water/leachate) and diffusion (the movement of molecules or ions from regions of high concentration to regions of lower concentration), and the potential attenuation mechanisms such as biodegradation, sorption and dilution.

There are numerous factors requiring consideration in the design and construction of landfill barrier systems and there have been a number of excellent papers which provide an overview of many of these factors (e.g. Giroud & Cazzuffi 1989; Koerner 1990; Cazzuffi & Cancelli 1994; Gourc 1994; Bonaparte 1995; Gartung 1996; Daniel & Bowders 1996). The reader is referred to these papers for background on the different types of geosynthetics used in landfills, factors influencing their selection and factors to be considered in construction. This paper does not attempt to cover all of these issues but, rather, will focus in some greater detail on a number of important issues that have received limited attention in the literature and previous keynote lectures. In particular, attention will be focussed on (1) temperature in landfills; (2) the clogging of filters in leachate collection systems



(a) Base



(b) Side Slope

Figure 1. Schematic showing (a) base and (b) side slope of barrier system for Kettleman Hills Landfill (adapted from Bryne et al. 1992).

and their influence on collection system service life; (3) service life issues related to compacted clay liners, geosynthetic clay liners and geomembrane liners; (4) diffusion and attenuation of contaminants in liner systems; (5) leakage through composite liners; (6) equivalence of liner systems (in the context of items 3, 4 and 5 above); and (7) stability of barrier systems.

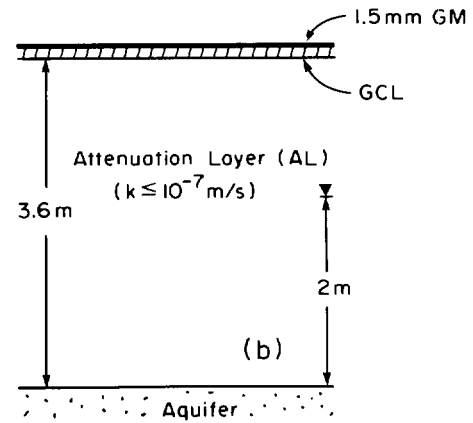
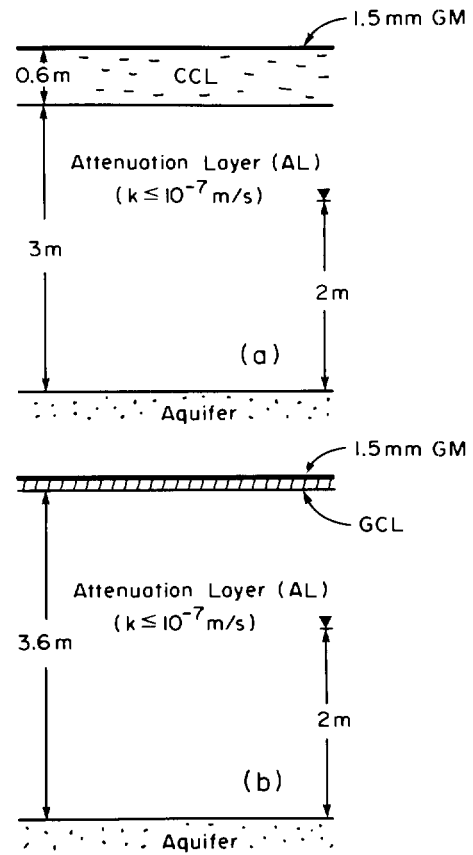


Figure 2. Schematic showing two single composite liner systems: (a) Geomembrane (GM) over 0.6 m compacted clay liner (CCL) over a 3 m thick attenuation layer (AL) over an aquifer; and (b) GM over a geosynthetic clay liner (GCL) over a 3.6 m thick attenuation layer.

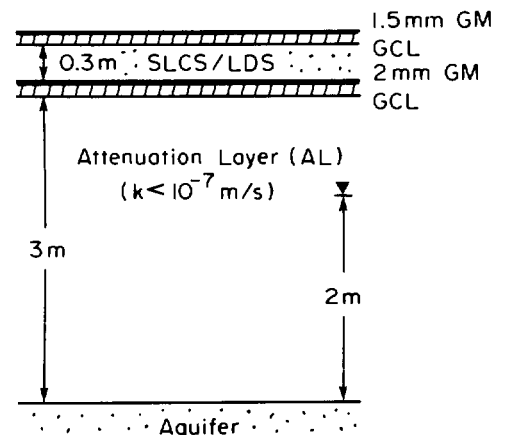


Figure 3. Double composite liner system.

## 2 LANDFILL TEMPERATURE

The temperature in a leachate collection system can have a significant effect on the rate of clogging of the leachate collection system (Rowe et al. 1997g). The temperature of the liner can have a significant effect on the service life of geopipes in the collection system and any geomembrane liner (see Section 7 and Koch et al. 1988; Koerner et al. 1992; Hsuan & Koerner 1995). Temperature also has implications with respect to potential fluid movement and moisture content decrease in a compacted clay liner (Collins 1993), especially below a geomembrane (see Section 4). Finally, it has implications with respect to the rate of contaminant diffusion through low permeability liners (i.e. geomembrane, compacted clay or geosynthetic clay liners) (see Section 10).

The literature contains a wide range of reported temperatures in landfills. High temperatures (50°C to 70°C) have been reported in a number of European landfills (Ramke 1989; Lechner & Lahner 1991). For example, Brune et al. (1991) reported (Figure 4) temperatures ranging from 24°C to 38°C in a leachate drain beneath 4-6 year old waste at the Altwarmbüchen Landfill. This landfill had been rapidly filled (10-20 m/a) and although it was in a methane forming phase after 4-6 years, the leachate was still acidic and very strong. In contrast, at the Venneberg Landfill the temperature in the drain only ranged from 14°C to 20°C. This landfill had been filled much slower (2 m/a) than the Altwarmbüchen Landfill and the leachate was only lightly loaded with both organic and inorganic contaminants. In both cases, the temperature was measured about 4 years after the landfill was completed over the drains.

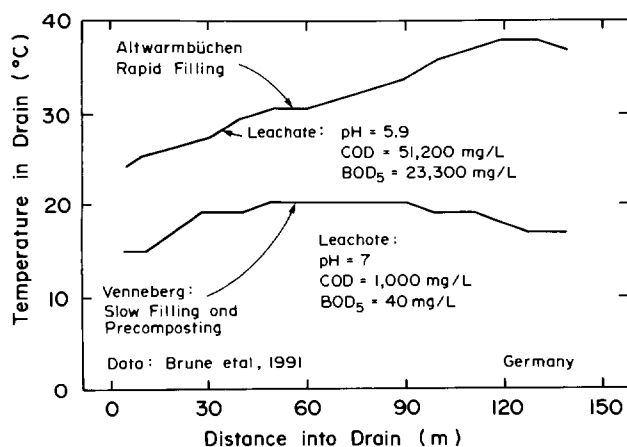


Figure 4. Temperature in drains at two German landfills approximately 4 years after last waste placed above the drains (modified from Brune et al. 1991).

High temperatures are often attributed to aerobic conditions, however, in both cases the generation of CO<sub>2</sub> and CH<sub>4</sub> provided evidence of anaerobic conditions. The primary differences between the two cases appear to have been (a) the rate of landfilling; (b) the thickness of waste; and (c) there had been pre-composting of the waste at the Venneberg Landfill. This illustrates that there is a relationship between the nature of the waste, landfilling practice and temperature.

There is also a relationship between location in the landfill and temperature. Figure 5 shows that the

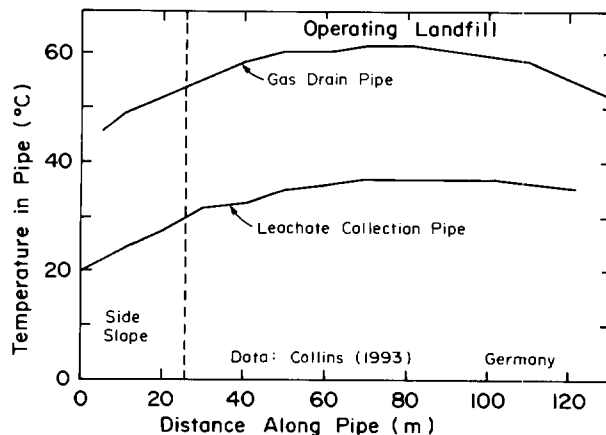


Figure 5. Temperature variation with distance in gas and leachate collection pipe at an operating landfill in Germany (modified from Collins 1993).

temperature increases with distance into the landfill and above the landfill base at an operating German landfill. Again, the temperatures at the level of the collection pipe are high (20-37°C). The temperature and the elevation of the gas collectors exceeded 60°C.

Figure 6 shows the variation in temperature with depth at two locations in an old German landfill (1936-1980). There is clear evidence of increasing temperature with depth from surface with the peak temperature being reached at a depth of about 30 m below the surface. The temperature then decreases towards the base of the landfill. The base temperature in 1990 (i.e. 10 years post-closure) ranged from 30° to 60°C in this landfill where the leachate level is reported to be 4-6 m above the base of the landfill.

The temperature profiles noted above are not restricted to Germany. Figure 7 shows a similar profile in a 30 m deep Japanese landfill. The landfill was filled very quickly (~10 m/a between 1976-1979). Trends similar to that noted above for the German landfill can be observed. The peak temperature, observed in 1985, was almost 70°C. The temperature generally decreased

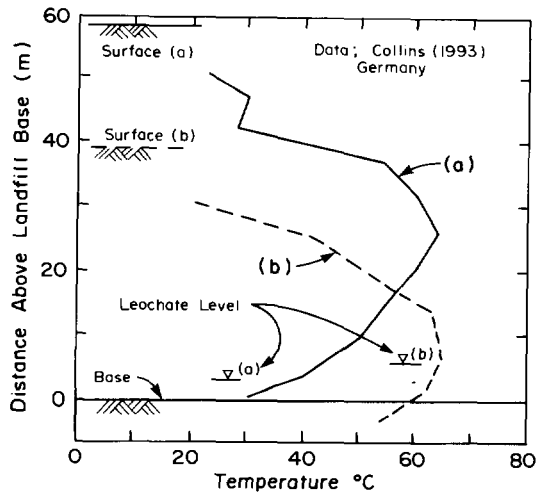


Figure 6. Temperature variation with depth at two locations in an old landfill (1936-1980) in Hannover, Germany (waste circa 1938 at bottom).

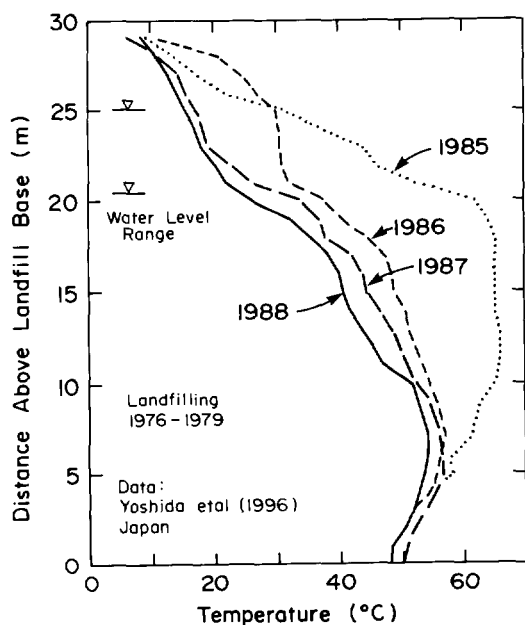


Figure 7. Temperature variation with depth in Tokyo Port Landfill (modified from Yoshida et al. 1996).

between 1985 and 1988. At the base of the landfill the temperature reached 50°C. The leachate mound is typically 20-25 m above the base of the landfill.

At the Brock West Landfill in Canada (Bleiker 1992), temperatures were found to increase from about 20°C near the surface to 60°C at a depth of about 20 m.

Conditions were anaerobic. Sludge had been disposed of at this landfill and the leachate mound was 22-25 m above the base.

However, not all researchers have encountered the high temperatures noted above. Koch et al. (1988) report temperatures above a landfill liner of between 20°C and 25°C. Haxo and Haxo (1989) report temperatures of 5°-20°C under anaerobic conditions.

Koerner et al. (1996a) have monitored the temperature above the liner at three different landfills in Pennsylvania, Florida and California, U.S.A. over periods of 6, 3 and 5 years respectively. Over the period monitored, the temperature on the liner has remained relatively constant within the following ranges: Pennsylvania 18-23°C; Florida 20-30°C; and California 10-30°C. The Pennsylvania landfill is in a humid area (mean annual precipitation of 1045 mm; mean annual temperature 12.6°C). There is an operational (0.6 m thick gravel) leachate collection system above the thermocouples on the liner and about 50 m of waste over the collection system. The Florida landfill is in a near tropical area (mean annual precipitation of 1920 mm; mean annual temperature 22.5°C). The landfill has a composite liner with a 0.7 m thick sand leachate collection system above the thermocouples on a 1.5 mm HDPE geomembrane. The California landfill has a mild, semi arid climate (mean annual precipitation of 450 mm; mean annual temperature 15.9°C). There is a geonet leachate collection layer and 0.3 m thick soil "operating layer" above the geomembrane being monitored. There is 3-11 m of waste over the thermocouple sensors (based on Figure 2, Yazdani et al. 1995). The Pennsylvania and California landfills have composite, low permeability final covers. The Florida landfill does not yet have a final cover. It would appear that these landfills are giving rise to temperatures at the base of the landfill much less than observed in the landfills previously discussed, although it remains to be seen whether this will continue.

It may be hypothesized that the limited amount of water in the waste combined with an operational leachate collection system, may be responsible for slowing biological activity which, in turn, is keeping the temperature low for at least the first five years. One can hypothesize several other possible reasons for the lower temperatures. Firstly, the waste in the U.S.A. may have a lower organic content than in other countries. While possible, it is unlikely that there is a significant difference in the nature of waste in large urban areas in the U.S.A. and Toronto, Canada where higher temperatures have been recorded at both the Brock West and Keele Valley Landfills. Secondly, thermocouples were directly on the geomembranes and measured temperatures over longer time periods than, say, spot measurement at other landfills. However, this is an unlikely explanation since at the Keele Valley Landfill discussed in the following

paragraph, similar but longer term monitoring above the clay liner has revealed a gradual increase in temperature with time as the water content of the waste increased. Finally, all three landfill liner systems were only 3-4 m above the water table that could provide a heat sink as groundwater movement removes heat from below the site. While possible, this also seems an unlikely explanation when one compares the conditions at these U.S. landfills with those at both the Brock West and Keele Valley Landfills in Toronto, Canada. For example, in the Keele Valley Landfill discussed in the following paragraph the water table was originally 2-3 m below the base of the pit (Reades et al. 1989) and hence 3-4 m below the top of the liner but the temperature in parts of the landfill has now risen to over 40°C as shown in Figure 8. The water table has now dropped to 4-6 m below the liner due to the reduced recharge after landfilling (Barone, personal communication) however, even so, it is likely that the groundwater at this landfill would be a greater heat sink than at the other sites due to the lower groundwater temperature in Toronto. Because of the likely similarity of the Keele Valley waste to U.S. waste, the longer term monitoring (13 years of data) and the similar proximity to groundwater, the Keele Valley Landfill provides an excellent contrast to the three U.S. landfills examined by Koerner et al. (1996a) since the major difference would appear to be the level of leachate mounding.

The Keele Valley Landfill (KVL) is located in an old sand and gravel pit in Maple, Ontario and is operated by the Municipality of Metropolitan Toronto. It became operational in 1983 and has recently been constructed to its maximum approved footprint of approximately 99 ha. It is still active and has an original estimated mass capacity of approximately 20 Mt. No sewage sludge has been disposed of at Keele Valley. The highest refuse contours are about 60 m above the liner and the proposed average thickness is about 30 m for the currently approved final contours. The average annual precipitation is 780 mm and the annual average temperature is 8.1°C. At the end of 1997 there was an intermediate 0.15 m thick sand cover over 60% of the site and a final cover (0.15 m of topsoil and 0.9 m of silty sand) over the remaining 40%. The leachate has mean annual COD of between 8,698 to 17,116 mg/L, mean annual BOD<sub>5</sub> of 3,641 to 12,367 mg/L and BOD<sub>5</sub>/COD ratio of 0.47-0.88 (Rowe 1995).

The KVL has an approximately 1.2 m thick compacted clayey till liner with a hydraulic conductivity of less than 10<sup>-10</sup> m/s (King et al. 1993). It has been constructed in four stages. In each stage, the liner is covered by about 0.3 m of sand intended to provide desiccation protection to the liner. In Stages 1 and 2, the primary leachate collection system consists of lateral french drains (50 mm, nominal diameter, stone) at spacings of about 65 m sloping towards the main collection pipes (spacing 200 m).

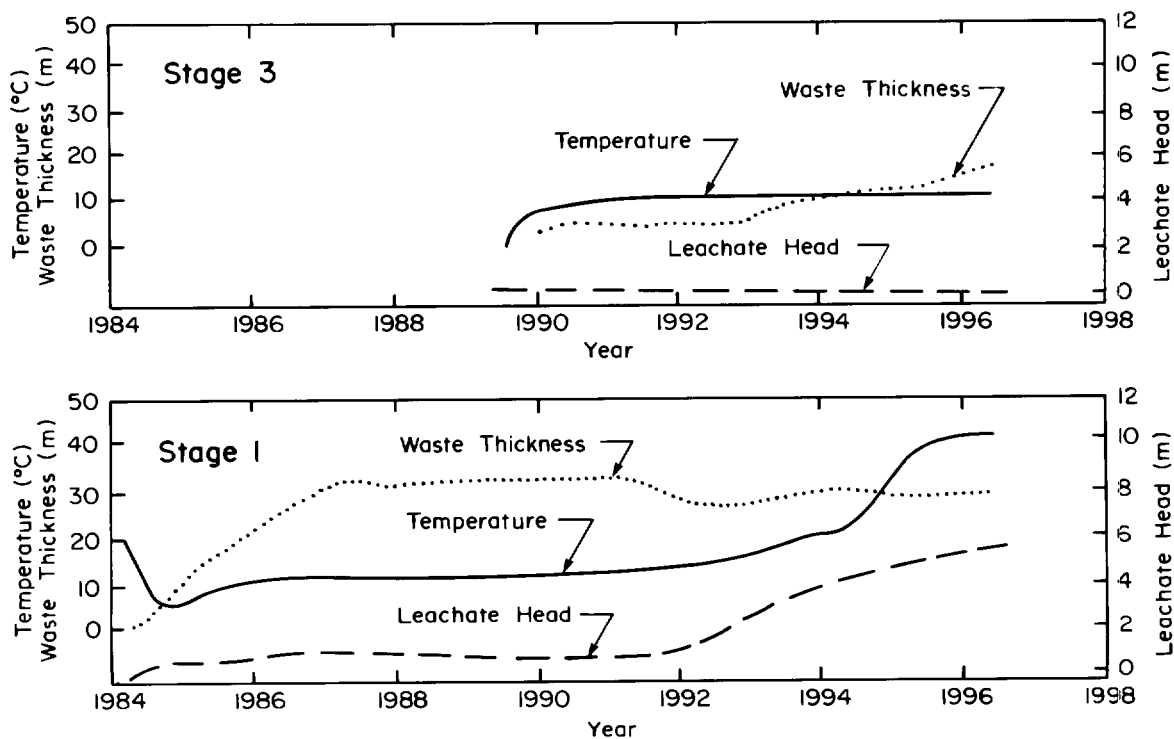


Figure 8. Variation in temperature, leachate head and waste thickness above base of landfill - Keele Valley Landfill, Canada (modified from Barone et al. 1997).

In Stages 3 and 4, there is a 0.3 m thick continuous stone drainage blanket of 50 mm clear dolomitic limestone over an approximately 0.3 m thick sand protection layer and clayey liner. A woven geotextile is placed between the stone and the sand. The waste is placed directly on the stone drainage layer.

At the Stage 3 monitor shown in Figure 8, the waste is up to 7 years old and over the 7 year period the leachate head has been at or below about 0.1 m and the temperature above the liner has been relatively constant at about 12°C (Barone et al. 1997) which is fairly consistent with the average leachate temperature (Fleming et al. 1997).

Examining the data for one Stage 1 monitor (Figure 8) it can be seen that for the first 8 years the head remained low and the temperature increased from a few degrees to about 12°C. However, since 1992 the leachate head has increased to 5.4 m and the temperature is now over 40°C. Based on five monitoring locations in Stage 1, the average temperature at the base of the landfill is 33.4°C and the average leachate head is 4-6 m. In contrast, based on thirteen monitors in Stage 3, the average temperature is 13.6°C and the average leachate head is less than 0.4 m. The relatively rapid increase in head in Stage 1 in the 1990s is attributed, at least in part, to attempts to rapidly stabilize the waste by injection of groundwater into the waste (now discontinued) and in part due to the nature of the collection system in this part of the site.

The data presented to this point would suggest that the temperature may vary depending on the rate of landfilling but that a significant factor affecting temperature is the water content of the waste and, in particular, the saturated thickness of the waste.

Apart from isolated saturated zones due to perching of leachate, the saturated thickness is related to the leachate head above the base. Figure 9 shows the data presented by Barone et al. (1997) plus some additional data. It shows a strong correlation between the temperature at the base of the landfill and the leachate head above the base.

As will be discussed in subsequent sections, potentially, the temperature at the liner can have a significant effect on diffusion through composite liner systems, the service life of the liner system, and the service life of plastic pipes in the leachate collection system. In turn, the temperature appears to be related to the water content of the waste and the level of leachate mounding. During the early life of the landfill, the temperature appears to be low if the water content of the waste is low. As the moisture content of the waste increases (e.g. due to moisture movement through the landfill cover or enhanced infiltration), the temperature appears to rise. However, as evidenced by the Keele Valley Landfill, the most significant factor appears to be the level of leachate mounding (the primary difference between Stages I and II, and III and IV). Thus the control of the leachate head may be important until the landfill is biologically stabilized. This highlights the importance of the design, construction and operation of the leachate collection system.

### 3 FILTERS IN LEACHATE COLLECTION SYSTEMS

Leachate collection systems may typically take the form of perimeter drains around the edge of the waste

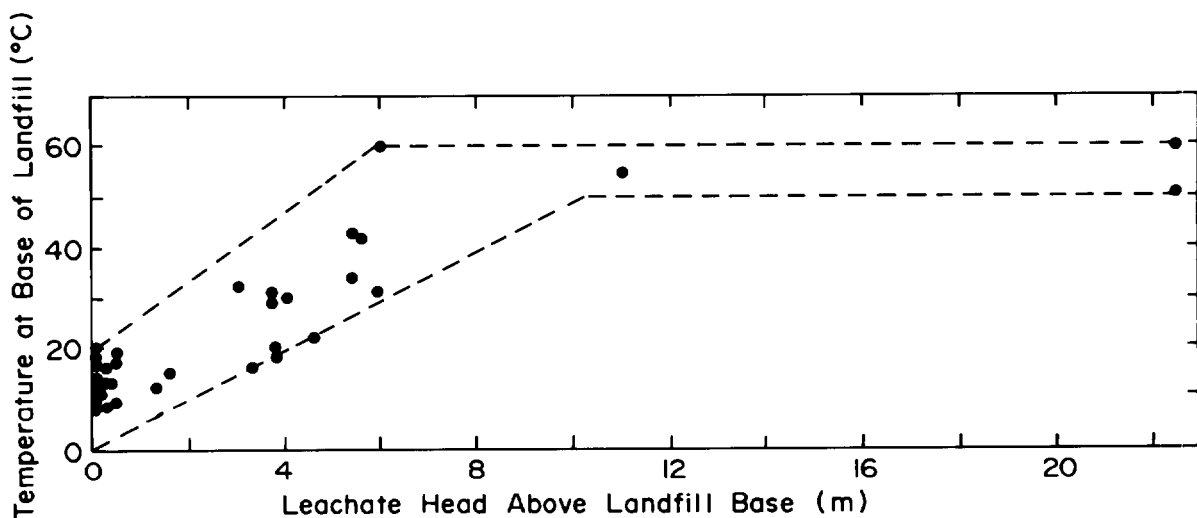


Figure 9. Variation in temperature at landfill base with leachate head for a number of landfills (modified from Barone et al. 1997).



and/or underdrain systems below the waste which may include either french drains (typically perforated pipes embedded in granular material; e.g. see Figure 10), at some spacing, granular drainage blankets with perforated pipes at some specified spacing (see Figure 11), and geosynthetic (geonet) drainage layers (e.g. see Figure 1b). Geotextiles are often used as filters between the waste and the drainage layer - especially when either coarse drainage material (e.g. gravel) or geonets are used to provide a drainage blanket (see Figures 1, 10 and 11). Key issues in the design of these systems is the need to provide adequate drainage, prevent structural failure (e.g. crushing, or other pipe failure) and to minimize clogging. Of these, the greatest challenge is minimizing clogging and prolonging the life of the leachate collection system.

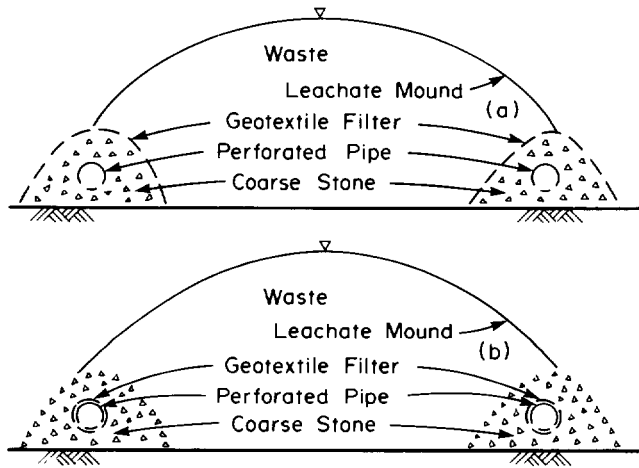


Figure 10. Schematic showing examples of poor leachate collection system designs (a) problematic; (b) even worse. Schematic also shows a leachate mound developed once there is excessive clogging of the geotextile filter and/or the drainage stone and/or the pipe. For details regarding calculation of mound height see Rowe et al. (1995b). Note: there would also be a mound to the left and to the right of the section shown and the mound would only be symmetric as a special case; generally, it would not be symmetric due to factors such as variability of clogging, hydraulic conductivity of waste etc. (modified from Rowe 1992).

### 3.1 Clogging of Leachate Collection Systems

Leachate typically flows down through the waste and into a granular layer (sand, gravel or crushed stone). It is usually intended that it will then flow through the void space between the solid particles in the granular media to plastic (usually High Density Polyethylene HDPE) collector pipes. These pipes are an essential component of the collection system and are perforated to allow leachate entry. The pipes typically conduct the leachate

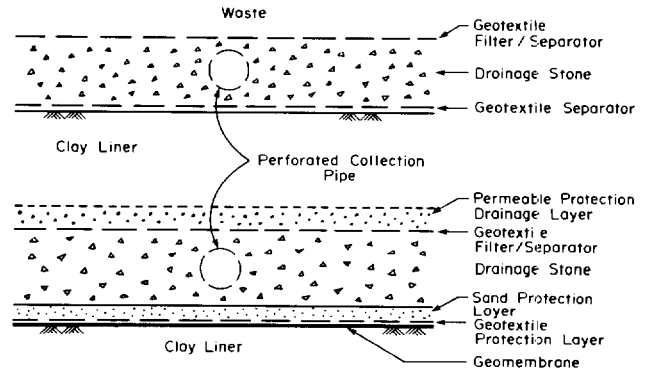


Figure 11. Schematic showing examples of blanket leachate collection system designs including a geotextile filter layer (modified from Rowe 1992).

to pumps that are used to remove the leachate from the landfill for treatment.

Leachate contains nutrients that will encourage bacterial growth within the waste, in geotextile filters, in granular drainage layers and around the perforations in the leachate collection pipes. Clogging of the leachate collection system involves the filling of the void space between solid particles as a result of a combination of biological, chemical and physical events. Particulate clogging can be a problem in some cases, but can be controlled by appropriate design (e.g. see Giroud 1996a). There is a growing body of evidence that a major component of the clogging is microbiologically related. For example, microbiological and chemical studies (Brune et al. 1991; Rowe et al. 1995c, 1997f,g and Rittmann et al. 1996) have shown that the clogging of drainage systems is the result of a mobilization process involving fermentative bacteria together with iron and manganese reducing bacteria, followed by precipitation processes involving primarily methanogenic- and sulfate-reducing bacteria. The clog typically has a soft (organic) and hard (predominantly  $\text{CaCO}_3$ ) component. The rate of clogging is related to the flow through the critical component of the system, the void size, the temperature in the collection system (generally higher temperature implies faster clogging) and the leachate chemistry (especially  $\text{BOD}_5$ , COD, TSS and Ca). The reduction in void space caused by biofilm growth and chemical precipitation (Brune et al. 1991; Vandevivere & Baveye 1992; Rowe et al. 1995c, 1997g; Fleming et al. 1997) results in a concurrent reduction in the hydraulic conductivity of these drainage systems and hence a reduction in their capacity to laterally transmit leachate. For example, Figure 12 shows the relationship between reduction in porosity (due to clogging) and the reduction in hydraulic conductivity of a granular medium with 6 mm diameter particles. This data was obtained by passing leachate

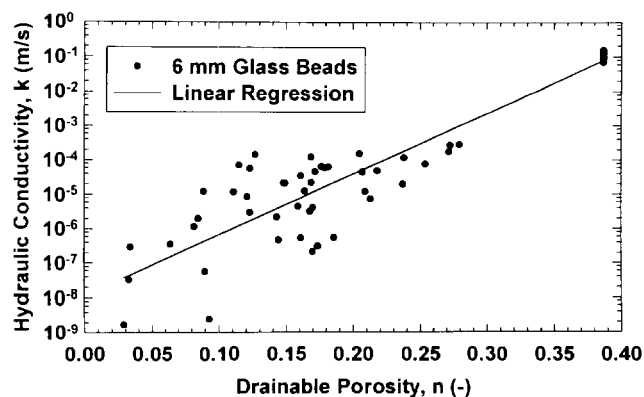


Figure 12. Variation in measured hydraulic conductivity of a granular medium (6 mm diameter particles) with decreasing drainable porosity due to biologically induced clogging resulting from permeation with landfill leachate.

through columns of glass beads. Different column tests were performed using actual Keele Valley Landfill leachate and synthetic leachate with a similar chemical composition (see Rowe et al. 1997f, g) and both gave a similar relationship between hydraulic conductivity and drainable porosity. The clog composition was typical of that encountered in the field by Brune et al. (1991) and Fleming et al. (1997) and more than 50% of the clog material (by dry weight) was calcium carbonate when the tests were terminated.

It must be recognized that "clogging" of a drainage layer is not synonymous with it becoming impermeable (Rowe et al. 1995b). On the contrary, a clogged sand blanket may still be substantially more permeable than, say, an underlying clay liner. "Clogging" of a drainage layer becomes significant when the hydraulic conductivity of the blanket drops to or below the hydraulic conductivity of the overlying waste. At this point, the reduction in hydraulic conductivity will result in the buildup of a leachate mound within the landfill that may subsequently result in increased temperature and decreased service life of any composite liner (see Sections 4 and 7) as well as potential impacts on surface water due to leachate seepage from the sideslopes of the landfill and increased contaminant migration through the barrier system and into the groundwater (see Section 10).

### 3.2 Field Examples of Clogging

Examples of clogging of leachate collection systems can be found in a number of existing landfills including Toronto's large Brock West Landfill where a 20 m high leachate mound built up during the first 11 years of operation (Dames & Moore 1992). Here, the primary leachate collection system consists of leachate collection

pipes at spacings ranging between 50 m (newer portions of the landfill) and 200 m (older portions of landfill). The collection system is reported to involve "french drains" with a perforated pipe in a pea gravel (5-10 mm diameter) pipe bedding. No geotextile was used. The landfill has accepted a significant quantity of sewage sludge in addition to MSW.

Another example of clogging of the drainage material around leachate collection pipes in the drain around a landfill has been reported by McBean et al. (1993), who noted that extensive clogging had resulted in excessive leachate mounding and leachate seeps. This design also involved french drains at wide spacing.

The Keele Valley Landfill provides two different examples of clogging. Firstly, there is a sand "protection" layer over the liner. Field exhumations (Reades et al. 1989) have shown that this sand blanket has become clogged and does not contribute to the hydraulic performance of the collection system, but rather, has become part of the "diffusion barrier" with the diffusion profile beginning at the interface between the more permeable waste (where lateral flow dominates) and the less permeable (clogged) sand blanket. Koerner and Koerner (1995b) reported similar clogging of a sand protection layer (Case 3, Table 1) where after 10 years the hydraulic conductivity dropped three orders of magnitude from  $4 \times 10^{-4}$  m/s to  $2 \times 10^{-7}$  m/s and leachate was flowing through the waste rather than the sand.

Exhumation of portions of the leachate collection system at the Keele Valley Landfill after four years (see Table 1 and Rowe et al. 1995c, 1997g; Fleming et al. 1997) indicated a three order of magnitude drop in the hydraulic conductivity of relatively uniform 50 mm stone near the leachate collection pipe (although the hydraulic conductivity was still sufficient to transmit leachate). Clogging was observed to be substantially less (Case 2, Table 1) in areas where a geotextile filter was used between the waste and the stone.

Koerner and Koerner (1994, 1995b) have described exhumations of three leachate collection systems (see Table 1, Cases 3, 4 and 5) and found excessive clogging of the geotextile in two cases where the geotextile was wrapped either around the perforated pipe or around the stone in a drainage trench. The reduction in hydraulic conductivity for these three cases and a fourth case (Case 6) involving geotextiles around well casing from a gas extraction system are summarized in Table 2.

### 3.3 Implications for Design

Research by Koerner et al. (1994) suggested that the hydraulic conductivity of geotextile decreased with increasing leachate flow rate. More generally, recent research by Rowe et al. (1998b) has indicated that clogging is directly related to the leachate mass loading

Table 1. Summary of observations from exhumation of collection systems in North America.

Waste Type <sup>1,2</sup> Age; Leachate	Collection System Design <sup>3</sup>	Key Observations
1.MSW & LI ~4 years COD=14,800 mg/L BOD <sub>5</sub> =10,000mg/L pH=6.3 Performance: ·Adequate at time of exhumation	·Blanket underdrain: Waste over 50 mm relatively uniform stone; 200 mm,SDR 11 HDPE pipe; 8 mm holes ·Pipe never cleaned ·No geotextile between waste and stone	·30-60% loss of void space in upper stone ·50-100% loss of void space near pipe ·Permeability of stone decreased from ~10 <sup>-1</sup> m/s to ~10 <sup>-4</sup> m/s ·All lower holes in pipe blocked; majority of upper holes blocked ·Large clog growth inside pipe
2.MSW & LI As for #1 above	·Blanket underdrain: waste over geotextile over 50 mm stone (rest as above) (GT: W;M <sub>A</sub> =180 g/m <sup>2</sup> , AOS=.475 mm, t <sub>GT</sub> =0.6 mm, ψ=0.04 s <sup>-1</sup> )	Substantially less clogging than observed in #1 above where there was no GT ·0-20% loss of void space in upper stone below geotextile
3.MSW & LI; LR ~10 years COD=31,000mg/L BOD <sub>5</sub> =27,000mg/L pH ~ 6.9 Performance: · No flow in LCS · High leachate mound	·Toe drain only ·Trench with 600 mm of crushed stone (6 to 30 mm) around geotextile wrapped 100 mm SDR 41 perforated PVC pipe (GT:HBNW; M <sub>A</sub> =150 g/m <sup>2</sup> , AOS=.15 mm; t <sub>GT</sub> =0.30 mm, ψ=1.1 s <sup>-1</sup> )	·Flow reduction noted after 1 year ·Pipe crushed (likely due to construction equipment) ·Substantial reduction in void space and cementing of stone. k reduced from 2.5×10 <sup>-1</sup> m/s to 1.2×10 <sup>-4</sup> m/s ·Sand (SW; AASHTO #10) layer above GM was clogged and leachate drained on top (not through this layer). k reduced from 4×10 <sup>-4</sup> m/s to 2×10 <sup>-7</sup> m/s ·Excessive clogging of GT (see Table 2)
4.MSW & LI; LR 6 years COD=10,000mg/L BOD <sub>5</sub> =7,500mg/L pH ~ 7.5 Performance: · Drain function- ing adequately	·Perimeter drain to control leachate seeps geotextile wrapped trench with 6-18 mm gravel and 100 mm SDR 30 HDPE perforated pipe (GT: W, M <sub>A</sub> =170 g/m <sup>2</sup> ; POA=7%, AOS=.25 mm; t <sub>GT</sub> =0.41 mm; ψ=0.9 s <sup>-1</sup> )	·Only small reduction in k of gravel from 5.3×10 <sup>-1</sup> m/s to 2.8×10 <sup>-1</sup> m/s ·Marginal clogging of GT (see Table 2)
5.ISS (included slurried fines 70% finer than 150 μm) 0.5 years COD=3,000 mg/L BOD <sub>5</sub> =1,000mg/L pH=9.9 Performance: · No flow in LCS	·Blanket underdrain: Waste over protection sand (0.075-4 mm) over geotextile (AOS=.19 mm) over pea gravel (1-20 mm) drainage layer; 100 mm diameter geotextile wrapped HDPE perforated pipe; 12 mm dia. holes (GT: NPNW, M <sub>A</sub> =330 g/m <sup>2</sup> , AOS = .19 mm; t <sub>GT</sub> =2.7 mm, ψ=1.8 s <sup>-1</sup> )	·High leachate mound ·Upper geotextile functioning (see Table 2, Case 5a) ·Pea gravel relatively clean ·Geotextile wrapping around perforated pipe excessively clogged (see Table 2, Case 5b) ·Once geotextile sock removed, leachate flowed freely ·Heavy geotextile sock clogging at location of perforations in pipe

<sup>1</sup>MSW≡Municipal Solid Waste; LI≡Light Industrial; ISS ≡ Industrial Solids and Sludge; LR ≡ Leachate Recirculation

<sup>2</sup>References: Cases 1 and 2 - Rowe et al. (1995c), Fleming et al. 1998; Cases 3, 4 and 5 - Koerner & Koerner (1995b)

<sup>3</sup>GT≡geotextile; W≡woven; HBNW≡heat bonded, nonwoven; NPNW≡needle punched, nonwoven; SDR≡Standard Dimension Ratio; see Section 14 for notation

Table 2. Summary of hydraulic conductivity ( $k_n$ ) and permittivity ( $\psi$ ) changes for geotextile exhumed from field application in landfills (based on Koerner et al. 1993 but as modified by G. Koerner, personal communication).

Case	Leachate		Geotextile	$M_A$ (g/m <sup>2</sup> )	AOS (mm)	$t_{GT}$ (mm)	Initial $k_n$ (m/s)	Final $k_n$ (m/s)	Initial $\psi$ (s <sup>-1</sup> )	Final $\psi$ (s <sup>-1</sup> )
	COD (mg/L)	TS (mg/L)								
3 <sup>1</sup>	31,000	28,000	HBNW	150	.15	.38	$4.2 \times 10^{-4}$	$3.1 \times 10^{-8}$	1.1	$8.2 \times 10^{-5}$
4 <sup>1</sup>	10,000	3,000	W	170	.25	.41	$3.7 \times 10^{-4}$	$1.4 \times 10^{-4}$	0.9	$3.3 \times 10^{-1}$
5a <sup>1</sup>	3,000	12,000	NPNW	220	.21	2.7	$4.9 \times 10^{-3}$	$8.5 \times 10^{-5}$	1.8	$3.1 \times 10^{-2}$
5b	3,000	12,000	NPNW	220	.21	2.7	$4.9 \times 10^{-3}$	$4.4 \times 10^{-8}$	1.8	$1.6 \times 10^{-5}$
6a <sup>2</sup>	24,000	9,000	NPNW	176	.21	2.2	$2.3 \times 10^{-3}$	$3.7 \times 10^{-5}$	1.1	$1.7 \times 10^{-2}$
6b	24,000	9,000	NPNW	176	.21	2.2	$2.3 \times 10^{-3}$	$1.6 \times 10^{-7}$	1.1	$7.3 \times 10^{-5}$
6c	24,000	9,000	NPNW	176	.21	2.2	$2.3 \times 10^{-3}$	$7.5 \times 10^{-7}$	1.1	$3.4 \times 10^{-4}$

<sup>1</sup>Refer to Table 1; <sup>2</sup>Geotextile around gas collection wells at depth of 3 m, 7.5 m and 15 m respectively

in terms of the mass of COD (Chemical Oxygen Demand) and calcium per unit area perpendicular to leachate flow. The leachate mass loading is a function of (a) the concentration of volatile fatty acids (represented in terms of COD) and metals (especially calcium) in the leachate; (b) the flow rate per unit area; and (c) elapsed time. Thus when leachate that is generated over a large area of the landfill is directed through a filter surrounding isolated drainage stone (french drains) (Figure 10a) or even worse, a filter wrapped around the pipe itself (Figure 10b), there is a confluence of flow across the filter and the confluence factor is approximately equal to the area of the landfill divided by the area of the filter material through which the leachate must flow. Since clogging depends on flow rate per unit area, this confluence of flow increases the mass loading per unit time and hence increases the rate of clogging of the geotextile and the drainage stone (it is assumed here that clogging of pipes is mitigated by regular cleaning). However, even more important is the effect that clogging has when it does occur. When the resistance to flow into the drainage pipe is increased, a leachate mound will develop in the waste between the drains (see Figure 10). This mound will maintain some flow to the pipe but will also increase flow out through the underlying liner. Based on this, Rowe (1992) cautioned against designs such as that shown in Figure 10. The field investigation discussed in the previous subsection confirms the soundness of this recommendation. Geotextile used to wrap drains or pipes showed a drop of hydraulic conductivity of between two and five orders of magnitude (to as low as  $4 \times 10^{-8}$  m/s: Case 5b, Table 2).

Rowe (1992) recommended the use of a suitably selected geotextile as a blanket filter above a blanket stone underdrain layer (Figure 11) and the findings of both Rowe et al. (1995c: Cases 1 and 2, Table 1) and Koerner and Koerner (1995b: Case 5a, Table 1) provide some evidence that a suitable blanket geotextile will

function adequately. These investigations demonstrated (Cases 2, 4 and 5) that the geotextile provided good protection to the stone, which experienced relatively little clogging compared to that observed when there was no geotextile filter between the waste and stone drainage medium (Cases 1 and 3). Geotextiles used as shown in Figure 11 will experience some clogging, however, even if a perched leachate mound developed above the geotextile, there would be no effect in terms of contaminant transport through the underlying liner. The level of leachate perching above the geotextile will depend on the leachate generated per unit area of the landfill and the hydraulic conductivity of the geotextile filter as discussed below.

In addition to these field examples, clogging of geotextiles in MSW leachate has been demonstrated by numerous laboratory studies (Cancelli & Cazzuffi 1987; Koerner & Koerner 1990, 1995b; Cazzuffi et al. 1991; Brune et al. 1991; Fourie et al. 1994 etc.). These studies show that the magnitude of the decrease in hydraulic conductivity  $k_n$  (and permittivity  $\psi$ ) will depend on the geotextile (e.g. openness of the pore structure), the flow rate, and the concentration of the leachate. Koerner and Koerner (1995b) provided data from a series of tests where mild leachate was passed through a number of different geotextiles yielding a decrease in hydraulic conductivity of between about two to five orders of magnitude at the highest flow rate examined. The worst hydraulic conductivity observed for nonwoven needle punched geotextile was similar to or higher than that observed in the field ( $6 \times 10^{-8}$  m/s in Table 3 vs  $4 \times 10^{-8}$  m/s in Table 2) under the most extreme conditions. Generally, the level of decrease was similar (four orders of magnitude) to that in the field under severe conditions. Koerner and Koerner (1995b) recommended that for mild leachate, a geotextile in contact with the waste should have the properties given in Table 4.

Giroud (1996a) has discussed the issue of geotextile

Table 3. Decrease in hydraulic conductivity of geotextiles permeated with leachate (average COD: 3000-4000 mg/L; BOD: 2000-2500 mg/L; TSS: 300-600 mg/L) at a rate of  $2 \times 10^{-5}$  m/s ( $620 \text{ m}^3/\text{a}/\text{m}^2$ ) (modified from Koerner et al. 1994).

Type of Filter	Unit Mass $M_A$ ( $\text{g}/\text{m}^2$ )	POA (%)	AOS (mm)	Thickness $t_{GT}$ (mm)	Initial $k_n$ (m/s)	Initial Permittivity $\psi$ ( $\text{s}^{-1}$ )	Equilibrium $k_n$ (m/s)	Flow to Equilibrium ( $\text{m}^3/\text{m}^2$ )
Uniform Sand					$4 \times 10^{-3}$		$2 \times 10^{-6}$	119
Well Graded Sand					$6 \times 10^{-4}$		$4 \times 10^{-7}$	170
W: Monofilament	200	32		0.7	$3.4 \times 10^{-3}$	4.8	$2.5 \times 10^{-6}$	51
W: Multifilament	270	14		0.8	$1.9 \times 10^{-3}$	2.4	$7 \times 10^{-6}$	51
W: Slit Film	200	7		0.4	$1.6 \times 10^{-4}$	0.4	$8 \times 10^{-8}$	43
W: Monofilament	250	10		0.6	$6.4 \times 10^{-4}$	1.0	$5 \times 10^{-8}$	76
Special NW/W	740		0.3	6.3	$1.5 \times 10^{-2}$	2.4	$3.5 \times 10^{-6}$	102
NPNW	130		0.21	1.1	$2.3 \times 10^{-3}$	2.1	$6 \times 10^{-8}$	76
NPNW	270		0.18	2.4	$3.6 \times 10^{-3}$	1.5	$1 \times 10^{-7}$	93
NPNW	540		0.15	4.7	$2.4 \times 10^{-3}$	0.5	$2 \times 10^{-7}$	85
HBNW	120		0.165	0.4	$2.4 \times 10^{-4}$	0.6	$4 \times 10^{-8}$	76
NPNW	220		0.12	2.0	$3.2 \times 10^{-3}$	1.6	$1.5 \times 10^{-7}$	68

Table 4. Koerner and Koerner's (1995b) recommended minimum values for geotextile filters for use with mild leachate ( $\text{TSS} \ \& \ \text{BOD}_5 \leq 2500 \text{ mg/L}$ ) and select waste over the geotextile (no hard or coarse material; for coarse or hard material over GT, the strength requirements may need to be increased).

Property	Woven Monofilament	Nonwoven Needle-punched
$M_A$ ( $\text{g}/\text{m}^2$ )	200	270
POA (%)	10	-
AOS (mm)	-	0.21
grab strength, N	1400	900
trapezoidal tear, N	350	350
puncture strength, N	350	350
burst strength, kPa	1300	1700

clogging as part of a broad review of filter design. He tentatively recommends that sand and nonwoven geotextile filters should not be used even if the waste has been stabilized to produce low strength leachate by pretreatment. Rather, he recommends the use of monofilament woven geotextiles with a minimum filtration opening size (AOS) of 0.5 mm and a minimum relative open area (POA) of 15%, with a preference for a POA greater than 30%. The rationale for these recommendations arises from the observations that (a) the specific surface area for monofilament woven geotextile is much smaller than for nonwoven geotextiles and this decreases the surface area for biofilm growth; (b) the woven filter allows more effective and rapid

movement of fine material (i.e. material not intended to be retained) and leachate through the filter; and (c) due to their compressibility, the filtration characteristics of a nonwoven geotextile vary with applied pressure and the critical filtration characteristics should be assessed under design pressures which could be up to 500 kPa. There is some evidence to suggest that geotextiles selected in accordance with Giroud's (1996a) recommendations are likely to experience less clogging and reduction in hydraulic conductivity with time (e.g. see Table 3) than geotextiles that simply meet the requirements of Koerner and Koerner (1995b and Table 4).

It is important to recognize that Giroud's (1996a) recommendations are based on the premise that we wish to minimize clogging of the filter. This may indeed be the case for some design situations (e.g. if one insists on using a design such as is shown in Figure 10a). However, the writer would argue that while excessive clogging is undesirable, the processes that cause clogging also provide leachate treatment and, in so doing, (a) decrease the potential for clogging at more critical zones (e.g. near collection pipes) and (b) reduce the level of leachate treatment required after removal of leachate from the landfill. Although the subject of ongoing research, it appears desirable to design the leachate collection system to maximize leachate treatment while maintaining its design function (see Fleming et al. 1997). Under these circumstances, and using a design such as the one shown in Figure 11, a sand or nonwoven geotextile filter may actually be desirable provided that the hydraulic conductivity did not drop to such a point as to cause perching of leachate that would have negative effects such as side seeps.

Based on published data, it appears unlikely that the

hydraulic conductivity of the geotextile selected in accordance with either Giroud's (1996a) or Koerner and Koerner's (1995) recommendations would be below  $4 \times 10^{-8}$  m/s (1.3 m/a) for normal conditions and more likely it would be of the order of  $1 \times 10^{-7}$  m/s or higher. If the geotextile was used in a blanket drain (e.g. see Figure 11), one can quickly establish that there would be negligible perched leachate on the geotextile for typical rates of leachate generation (less than  $3 \times 10^{-8}$  m/s or  $1 \text{ m}^3/\text{a}/\text{m}^2$ ). Thus, while recognizing that geotextiles will clog, based on the available data it appears that an appropriately selected geotextile used to protect gravel in a blanket drain will improve the performance and the service life of the drainage stone and not cause excessive perched leachate mounding.

The design and service life predictions for leachate collection pipes and drainage stone is beyond the scope of the present paper. The interested reader is referred to Rowe et al. (1994, 1997c,g) for more information. This is the subject of ongoing research.

#### 4 SERVICE LIFE OF COMPACTED CLAY LINERS BELOW GEOMEMBRANES

Composite liners consisting typically of a geomembrane over compacted clay have been widely adopted in "standard" landfill designs (e.g. Germany 1993; USEPA 1994, MoEE 1996). However, for the composite liner to perform adequately, it is essential that both the compacted clay and geomembrane meet the design specifications for the design life of each component.

The clay liner is intended to limit leakage through any holes in the geomembrane, act as a partial diffusion barrier and to provide attenuation of certain (e.g. organic) contaminants. To meet these requirements, it must maintain a hydraulic conductivity of less than or equal to the design value for the contaminating lifespan of the landfill (i.e. period of time during which the escape of contaminant due to a failure of the engineered system would have an adverse impact on the environment).

For a clayey liner, the service life is the period of time during which the bulk hydraulic conductivity of the liner may be expected to fall within the design range. Provided that a clayey liner has been properly designed and constructed and appropriate attention has been given to clay-leachate compatibility (see Rowe et al. 1995b), there is no reason to believe that it would not perform within the design range of hydraulic conductivity for thousands of years provided that it is not allowed to desiccate after placement. Desiccation can be related to a change in water content in the clay that could occur (a) after construction of the clay liner and before placing the geomembrane; (b) after placing the geomembrane and before covering with waste; and (c) after placement of

waste. These will be discussed below.

#### 4.1 Desiccation Before Placement of Waste

Desiccation can occur within hours after liner placement if the clay is not kept moist. The extent of desiccation cracking will depend on the mineralogy of the clay, the compaction water content and the degree and length of exposure to drying conditions. For example, in an experiment at the Keele Valley Landfill a compacted clay liner containing 20% clay size (clay minerals, mostly illite and chlorite) was found to crack to a depth of 120 mm (maximum width 12 mm) over a five week period (mostly in June) (Rowe et al. 1994). However, this form of desiccation is readily prevented by adopting appropriate construction procedures and, if it does occur, can be observed and rectified by removal and replacement of the cracked portion of the clay liner prior to placement of the geomembrane provided there is a good construction quality assurance program in place.

It has been shown that the temperature of a geomembrane exposed to the sun may rise to 80°C (Felon et al. 1992) and temperatures of 60°-70°C are not unusual. It has been shown (Pierson et al. 1993; Koerner & Koerner 1995a) that the temperature can be reduced by the use of a white coated geomembrane (see Table 5).

Table 5. Maximum temperature (°C) of exposed geomembrane in Philadelphia, U.S.A., Latitude 40° in different regions (after Koerner & Koerner 1995a).

Season of Year	Ambient Temperature	Black Geomembrane	White Geomembrane
Winter	5	13	2
Spring	22	46	38
Summer	30	70	57
Fall	18	35	28

However, Pelte et al. (1994) have also shown that while a white, glossy, reflecting coating adhering to the geomembrane surface effectively decreases the geomembrane temperature (relative to a black geomembrane) for given solar conditions, the placing of a thick white geotextile over the geomembrane only delays the heating of the underlying geomembrane and does not reduce the final temperature.

A high temperature at the geomembrane has the potential to cause (a) evaporation of water from the compacted clay liner into any air space between the clay and the geomembrane and (b) moisture movement from the region of higher temperature to the region of lower temperature. Mechanism (a) is significant in the context of heating and cooling cycles while mechanism (b) is most significant when there is a sustained temperature gradient

(Döll 1996). Both mechanisms cause a decrease in water content in the clay below the geomembrane which in turn can cause shrinkage and consequent desiccation. This is particularly likely to be a concern on side slopes where there can be condensation and movement of previously evaporated water downslope during the cooler portions of the cycle. Basnett and Bruner (1993) give an example where a compacted clay liner on a side slope was observed to desiccate through the full (0.3 m) depth with cracks of 12-25 mm width. This liner had been exposed to daily cycles of heating and cooling for a period of 3 years. Rowe et al. (1998a) also report severe desiccation cracking of a compacted clay liner below a geomembrane in a leachate lagoon. Here the geomembrane had been exposed to temperature cycles for 14 years. Cracking was restricted to the side slopes above the leachate level.

Corser et al. (1992) report results from a test liner/cover left exposed for six months (April-October; temperature of geomembrane reaching 43°C). The section where the geomembrane was in intimate contact with the clay (where a moisture content increase was observed) was found to have performed well. However, in areas where there was an air space between the geomembrane and clay (i.e. at wrinkles/waves) the clay had dried and cracked with cracks up to 6 mm wide extending to a depth of about 75 mm. In another section where there had been a 0.6 m thick soil cover over the geomembrane only very minor hairline cracks (many of which formed after the geomembrane was removed) were observed.

Bowders et al. (1997) performed laboratory simulations of heating cycles for two clays. In these tests there was the potential for some water loss as water vapour. It was found that steady state temperatures were established in the clay at depths of 0.2 and 0.3 m after about 7 days of heating. After 30 days, there was significant moisture drop in the highly plastic clay (PI ~42-48%) to a depth of about 0.17 m with a black geomembrane (average peak temperature ~ 64°C) but only minor moisture loss below the white geomembrane (average peak temperature ~ 59°C). After 60 days, the zone of significant desiccation had extended to 0.21 m and 0.07 m (black and white respectively) and cracks extended to depths of 0.3 m (full thickness) and 0.06 m for the black and white geomembranes respectively. Similar tests with a lower plasticity clay (PI ~ 28%) conducted for about 110 days showed less moisture loss in a given time period than the higher plasticity clay for both geomembranes and again the moisture loss and cracking were less for the white geomembrane, however some cracks extended to a depth of 0.3 m for both geomembranes. While these tests do not fully simulate field conditions, combined with the field observations noted earlier they serve as a warning that there can be significant desiccation of the upper 0.15 m of liner in 2 to 8 weeks and that while a white

geomembrane allows a little longer exposure before serious cracking (maybe 4 weeks), there is still a need to cover the geomembrane quickly.

Both the field cases and laboratory tests noted above illustrate that cracking of the clay liner does occur due to exposure to high temperature and that problems will be greatest on side slopes where there are wrinkles. The available evidence would suggest that provided the geomembrane is covered relatively quickly the depth of desiccation cracking is going to be limited to the upper portion of the clay liner. However, the presence of cracks in even the upper few centimeters could still be significant (especially on the base of the landfill) if these cracks were beneath a hole in the geomembrane since the cracked clay liner would more readily allow movement of leachate through the hole and along the crack. There is no evidence to suggest that the cracks will necessarily close up and even if they do there would still likely be an increase in hydraulic conductivity (due to the macrostructure that has been induced) relative to the original design value. The foregoing suggests that there is a need to cover the geomembrane with the protection layer and the leachate collection layer as soon as possible after placement of the geomembrane.

#### 4.2 Desiccation After Placement of the Waste

Holzlohner (1989, 1995) has suggested that the risk of desiccation of clay liners that have been covered and are no longer subject to solar heating depends on five prime factors: properties of the clay liner, properties of the underlying subgrade, overburden pressure, temperature gradient across the liner and the depth to groundwater. There is still much unknown about the potential for desiccation due to landfill induced thermal effects. As indicated in Section 2, high temperature can be achieved in landfills and this can be expected to create a thermal gradient to the groundwater that has the potential to move moisture away from the heat source (i.e. the landfill). When the clay is overlain by a geomembrane, there is no additional source of water from above and hence there is greater potential for desiccation of a clay liner as part of a composite liner due to thermal effects than for a clay liner used alone. Since there also appears to be a correlation between temperature (at the liner) and the leachate mound (see Figure 9), it would appear to be desirable to keep the leachate mound low and hence control the rate of biological degradation and consequent heat generation. This would minimize the potential for desiccation. This indicates the need to carefully monitor landfill temperature and performance when landfill operators cease leachate collection. If a significant increase in temperature was observed, consideration should be given to resuming leachate removal since a significant rise in temperature may (a)

increase the potential for desiccation cracking of the clay liner, (b) decrease the service life of the geomembrane liner (see Section 7) and (c) increase diffusion through the liner (see Section 10).

The risk of desiccation may be expected to be decreased in situations where there is a high overburden stress. Holzlöhner (1992) reported that cracking may be prevented if the soil suction  $S$  satisfies the expression

$$S \leq \kappa \sigma \quad (1)$$

where

$$\kappa = (K_r / (1 - K_r)) / \chi \quad (2)$$

and  $\sigma$  is the applied vertical pressure,  $K_r$  is the coefficient of earth pressure at rest and  $\chi$  ( $0 \leq \chi \leq 1$ ) controls the distribution of stress between pore water and pore air based on Bishop's (1959) extended effective stress principle. However, this approach has come under severe criticism by Heibrock (1997) who has developed an alternative approach based on the models of unsaturated soil behaviour proposed by Fredlund (1978) and an extension of shear strength concepts of Morris et al. (1992). Heibrock (1997) performed analyses to illustrate that the potential for cracking depends on the temperature rise at the top of the liner, the characteristics of the clayey liner, the unsaturated hydraulic conductivity of the subsoil below the liner and the depth to the water table below the liner. In one example, he predicts no cracking in 50 years with a temperature at the top of the liner of 25°C but predicts cracking to a depth of 1 m in 20 years with a temperature at the top of the liner of 40°C (all other things being constant). In a second example where the subsoil was changed from a silt loam to a loess with a much higher unsaturated hydraulic conductivity, there was no cracking predicted because the calculated downward vapour flux of water was much smaller than the suction induced upward liquid flux from the water table and hence no drying occurs and the water content approached the distribution of static isothermal equilibrium conditions. It should be cautioned that these predictions are soil specific and even so are based on many assumed and hard to determine parameters. However, the results do underline the need to carefully consider the potential for temperature induced cracking and the desirability of limiting the temperature at the top of the liner to the extent possible by the design and operation of the landfill.

Holzlöhner (1995) suggests that the potential water movement due to temperature gradient could be controlled by installing a geomembrane below the compacted clay (as well as above it). This can certainly be expected to reduce water loss from the compacted

clay liner but there may still be some movement of water and it may be anticipated that in this case there would be an increase in water content in the clay at the lower geomembrane and a decrease below the upper geomembrane. This may be expected to limit desiccation of the liner but care would be needed to assess the effect of the higher water content on the lower soil-geomembrane interface strength and design to avoid instability due to sliding at this interface (see Section 11).

Holzlöhner (1995) also claims that a drainage layer below the composite liner will increase the potential for desiccation. Although no evidence is presented to support this claim, one can anticipate that a drainage layer may have two potentially negative effects. Firstly, vapour would be transported from the soil to the drainage layer and then out of the drainage layer due to changes in atmospheric temperature and pressure. This would be expected to result in the removal of moisture from the adjacent soil and increase the chance of desiccation of the liner. Secondly, the drainage layer either alone or in combination with an underlying geomembrane may be expected to prevent any movement of water upward into the clay from the underlying groundwater table. Much more research is required to understand and improve designs for this situation. However, it would seem prudent to design systems such that the potential for moisture loss from the secondary drainage layer due to atmospheric pumping is minimized and to have a thick rather than thin compacted clay component to the composite primary liner. From the perspective of minimizing the effects of temperature on the hydraulic performance of the clay in these composite double liner systems, GCLs may provide a viable alternative to compacted clay as the clay component of a composite primary liner due to their capacity to (a) hold moisture and (b) rehydrate to gain much (but not all) of their initial hydraulic conductivity. However, there are a number of other factors that also need to be considered as discussed in Section 5.

## 5 HYDRAULIC CONDUCTIVITY AND SERVICE LIFE OF GCLs

There is growing interest in the use of geosynthetic clay liners (GCLs) as part of the base seal/bottom liner system in landfills. As part of a composite liner, a GCL may be expected to have a very long service life (hundreds/thousands of years) provided that:

(a) There is no significant loss of bentonite from the GCL during placement. This means that care will be required to avoid loss of bentonite into underlying drainage layers. An additional geotextile filter may be required to avoid bentonite loss for some GCLs (e.g. see Estornell & Daniel 1992). Care is also required to adopt



construction procedures that will maintain a uniform distribution of the bentonite in the GCL (the potential for bentonite movement may vary from one product to another and construction specifications should recognize this fact). This involves consideration of both loss of powdered or granular bentonite as well as scraping off of bentonite (e.g. due to physical or thermally induced movement).

(b) There is no significant lateral movement (thinning) of bentonite during and following hydration that would cause an uneven distribution of the bentonite in the GCL during the contaminating life of the facility. For example, wrinkles in a geomembrane may create a void or area of reduced stress into which bentonite in an underlying GCL could migrate (see Stark 1998). Likewise, care is needed on side slopes (especially steep side slopes) to avoid bentonite migration downslope both in the "dry" and hydrated state (as noted above, the potential for bentonite movement may vary from one product to another).

(c) The geosynthetic component of the GCL is not critical to the long term performance of the bentonite component of the GCL.

(d) Seams are installed to ensure intimate contact and the design and the construction procedures are such that the seams can not, and do not, open up during or following placement.

(e) The choice of GCL and the design are such that there is no significant long term loss of bentonite due to migration (internal erosion) through the GCL under the hydraulic gradients that may occur either during or after termination of the operation of the leachate collection system.

(f) The design hydraulic conductivity is selected based on tests that examine the equilibrium (i.e. long term) hydraulic conductivity of the GCL to the proposed leachate under conditions that simulate likely field conditions (i.e. similar hydrating conditions, applied stress, GCL and leachate characteristics).

Items (a), (b) and (c) can be addressed by appropriate design, specifications and construction procedures. If the geosynthetic component of the GCL is critical to the long term performance of the GCL then the service life of the GCL can not exceed the service life of the geosynthetic component. The service life of the geosynthetic component will depend on the polymer and additives used. Some polymers have the potential to degrade due to biological action. For example, Giroud (1996a) reports that there are fungi and bacteria that catalyze hydrolysis of polyester. In situations where the service life of the geosynthetic component is critical, it may be argued that HDPE should be used with additives (especially antioxidants) similar to that used in a geomembrane (see Section 7). However, if a long service life of the GCL is required, it would be better, where

practical, to adopt a design such that the geosynthetic component of the GCL is not critical to the long term performance of GCL. For example, one could avoid situations where the geotextile component is necessary to prevent movement of bentonite into underlying open void space in drainage stone. Likewise, one could avoid situations where one was relying on needle punching to provide long term shear resistance or where the geosynthetic component is required to prevent lateral migration of bentonite into areas of reduced stress (e.g. beneath a wrinkle).

The level of control of wrinkles (waves) in the geomembrane may need to be much higher when a GCL is used as part of the composite liner than when a CCL is used due to much thinner clay and the potential for clay movement within the GCL. If GCLs are going to be used in a base seal and are critical to system performance, it would seem prudent to develop and apply a technique for non-destructive checking of seam integrity following placement of the overlying layers to address item (d). It is noted the geotextile overlaps have been observed to move (open up) more than 0.5 m in some cases (Rowe et al. 1993) and hence it is certainly possible that movement could occur for GCLs (e.g. due to the construction practice adopted).

Items (e) and (f) can be addressed by appropriate hydraulic conductivity tests as will be discussed in the following subsection.

## 5.1 Hydraulic Conductivity of GCLs

A number of researchers (e.g. Schubert 1987; Shan & Daniel 1993; Daniel et al. 1993; Dobras & Elzea 1993; Ruhl & Daniel 1997; Petrov et al. 1997a,b; Petrov & Rowe 1997) have addressed the issue of GCL-leachate compatibility and the hydraulic conductivity and performance of GCLs in contact with various permeants under high gradient conditions that could occur in a base seal/bottom liner application. Table 6 describes the various GCLs that have been examined. Table 7 summarizes the published hydraulic conductivity values for a range of GCLs, leachate, applied stresses, and hydrating conditions. In the case of GCLs that include a geomembrane, the results presented in Table 7, and the following discussion, relate only to the bentonite component of the GCL.

The hydraulic conductivity of a GCL is highly dependent on the hydrating conditions and the applied effective stress during permeation. These factors combined with the method of manufacture, water content prior to hydration and mass of bentonite all significantly influence the GCL thickness and while there is some correlation between hydraulic conductivity,  $k$ , and thickness,  $H$  there is a great deal of scatter. Petrov et al. (1997b) showed that by plotting the bulk void ratio,  $e_B$ ,

Table 6. Nominal (published) characteristics of GCLs studied in hydraulic conductivity and/or diffusion tests summarized in Tables 7 and 11-13.

Generic Symbol	Product Name	Nominal <sup>(a)</sup> Mass/Area (kg/m <sup>2</sup> )	Bentonite <sup>(a)</sup> Mass/Area (kg/m <sup>2</sup> )	Upper <sup>(b)</sup> Geosynthetic	Lower <sup>(b)</sup> Geosynthetic	Method <sup>(c)</sup> of Construction
BF1	Bentofix NW	4.16	3.5	NW	NW	NP
BF2	Bentofix NS	5.39	4.9	W	NW	NP
BF3	Bentofix NW5000	5.55	4.9	NW	NW	NP
BF4	Bentofix BFG5000	5.50	4.7 <sup>(d)</sup>	W	NW:B	NP
BM	Bentomat SS	5.22	4.9	W	NW	NP
CL	Claymax 200R	5.05	4.9	W	W	G
GS	Gundseal*					
	Regular	Varies	5.0	-	GM	G
GSC	Gundseal*					
	"Contaminant Resistant"	Varies	5.0	-	GM	G

\*Hydraulic conductivity tests on bentonite removed from the GCL.

<sup>(a)</sup>ASTM D5261 <sup>(b)</sup>NW≡Nonwoven needlepunched; W≡Woven; GM≡HDPE Geomembrane; NW:B≡Bentonite impregnated <sup>(c)</sup>NP≡Needlepunched; G≡Glued <sup>(d)</sup>4.2 kg/m<sup>2</sup> between GTs, 0.5 kg/m<sup>2</sup> in NW:B.

rather than thickness, H, against hydraulic conductivity, k, one obtains a much better correlation and much less scatter of the data for a given permeant (e.g. see Figure 13). This is consistent with the conventional geotechnical engineering concept of a strong correlation between the void ratio and hydraulic conductivity.

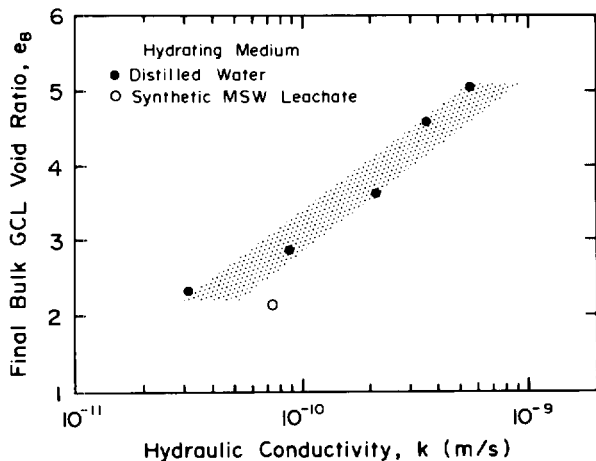


Figure 13. Final bulk GCL void ratio versus hydraulic conductivity for permeation of synthetic MSW leachate (modified from Petrov & Rowe 1997).

As shown in Table 7, the hydraulic conductivity to water of a number of commercially available GCLs ranges between about  $5 \times 10^{-11}$  m/s at "low" (3-4 kPa) confining stress to  $1 \times 10^{-11}$  m/s at "intermediate" (34-38 kPa) confining stress, and  $7 \times 10^{-12}$  m/s at "high" (109-117 kPa) confining stress. It is of interest to note that at a

confining stress of about 35 kPa the six products tested had a very similar hydraulic conductivity to water ( $7 \times 10^{-12}$  m/s to  $1 \times 10^{-11}$  m/s). Also, the test tended to be quite repeatable. For example, Petrov et al. (1997b) performed four tests with distilled water giving a mean value of  $1.28 \times 10^{-11}$  m/s with a range of  $1.4 \times 10^{-11}$  to  $1.2 \times 10^{-11}$  m/s. Four tests on the same product using tap water give a mean hydraulic conductivity of  $1.58 \times 10^{-11}$  m/s and a range of  $1.6 \times 10^{-11}$  to  $1.5 \times 10^{-11}$  m/s. The hydraulic conductivity values given for BF1 and water in Table 7 represent average values of between 4 and 7 tests. All other values given are individual values for a single test.

The confining stress at the time of hydration and the hydrating fluid can have a significant effect on the final hydraulic conductivity. A sample of BF1 that is hydrated at a low stress level (e.g. 3-4 kPa) and subsequently permeated with a 0.1 N NaCl solution ( $\text{Na}^+ \equiv 2300$  mg/L) at a low stress level has a hydraulic conductivity of  $1 \times 10^{-10}$  m/s whereas the same GCL (BF1) hydrated at 3-4 kPa but permeated at high stress (112 kPa) has a hydraulic conductivity of  $1.5 \times 10^{-11}$  m/s (almost one order of magnitude lower) and a sample hydrated with water and permeated at high stress (108 kPa) had a hydraulic conductivity of  $0.7 \times 10^{-11}$  m/s. This indicates the need to carefully consider the hydrating conditions and final stress level in any testing or selection of the hydraulic conductivity of the GCL to be used on a given project.

The permeating fluid can have a profound effect on the hydraulic conductivity of a GCL (see Table 7). Samples permeated with tap water and distilled water give very similar results but samples permeated with a real or synthetic landfill leachate may have a hydraulic conductivity an order of magnitude larger than that of

Table 7. GCL hydraulic conductivities under different testing conditions.

Generic Symbol	Hydrating Stress (kPa)	Final Confining Stress (kPa)	Hydrating Fluid	Permeating Fluid	Hydraulic Conductivity (m/s)	Reference
BF1	3-4	3-4	DW	DW	$5.2 \times 10^{-11}$	(a)
	35-37	35-37	DW	DW	$1.3 \times 10^{-11}$	(a)
	109-117	109-117	DW	DW	$7.5 \times 10^{-12}$	(a)
	34-35	34-35	TW	TW	$1.6 \times 10^{-11}$	(a)
	3-4	3-4	DW	0.01N	$5.3 \times 10^{-11}$	(b)
	3-4	14	DW	0.01N	$5.1 \times 10^{-11}$	(b)
	3-4	37	DW	0.01N	$3.8 \times 10^{-11}$	(b)
	3-4	69	DW	0.01N	$2.1 \times 10^{-11}$	(b)
	35	35	DW	0.01N NaCl	$1.5 \times 10^{-11}$	(b)
	107	107	DW	0.01N NaCl	$4.8 \times 10^{-12}$	(b)
	3-4	3-4	DW	0.1N NaCl	$1.0 \times 10^{-10}$	(b)
	3-4	12	DW	0.1N NaCl	$7.6 \times 10^{-11}$	(b)
	3-4	34	DW	0.1N NaCl	$5.3 \times 10^{-11}$	(b)
	3-4	73	DW	0.1N NaCl	$2.7 \times 10^{-11}$	(b)
	3-4	112	DW	0.1N NaCl	$1.5 \times 10^{-11}$	(b)
	36	36			$2.0 \times 10^{-11}$	(b)
	108	108			$7.3 \times 10^{-12}$	(b)
	4	4	0.1N	0.1N NaCl	$6.4 \times 10^{-11}$	(b)
	35	35			$2.1 \times 10^{-11}$	(b)
	113	113			$9.2 \times 10^{-12}$	(b)
	3-4	3-4	DW	0.6N NaCl	$6.3 \times 10^{-10}$	(b)
	3-4	12			$5.5 \times 10^{-10}$	(b)
	3-4	37			$2.2 \times 10^{-10}$	(b)
	3-4	74			$6.8 \times 10^{-11}$	(b)
	3-4	109			$2.7 \times 10^{-11}$	(b)
	35	35			$9.3 \times 10^{-11}$	(b)
	105	105			$2.1 \times 10^{-11}$	(b)
	3-4	3-4	0.6N	0.6N NaCl	$4 \times 10^{-9}$	(b)
	35	35			$7.6 \times 10^{-10}$	(b)
	111	111			$2.3 \times 10^{-10}$	(b)
	3-4	3-4	DW	2N NaCl	$2.6 \times 10^{-9}$	(b)
	3-4	12			$\sim 2 \times 10^{-9}$	(b)
	3-4	35			$\sim 2 \times 10^{-9}$	(b)
	3-4	75			$3.6 \times 10^{-10}$	(b)
	3-4	114			$1.6 \times 10^{-10}$	(b)
	33	33			$4.7 \times 10^{-10}$	(b)
	101	101			$6.2 \times 10^{-11}$	(b)
	3-4	3-4	2N	2N NaCl	$2.7 \times 10^{-8}$	(b)
	34	34			$1.2 \times 10^{-8}$	(b)
	107	107			$2.6 \times 10^{-9}$	(b)
3-4	3-4	DW	SL1	$5.5 \times 10^{-10}$	(b)	
3-4	15			$3.6 \times 10^{-10}$	(b)	
3-4	34			$2.1 \times 10^{-10}$	(b)	
3-4	72			$8.8 \times 10^{-11}$	(b)	
3-4	124			$3.1 \times 10^{-11}$	(b)	
31	31			$8.7 \times 10^{-11}$	(b)	
33	33	SL1	SL1	$7.3 \times 10^{-11}$	(b)	

Table 7 (contd.)

Generic Symbol	Hydrating Stress (kPa)	Final Confining Stress (kPa)	Hydrating Fluid	Permeating Fluid	Hydraulic Conductivity (m/s)	Reference
BF1	34	34	TW	E1	$7.3 \times 10^{-12}$	(a)
	33	33	TW	E2	$6.0 \times 10^{-12}$	(a)
	33	33	TW	E3	$4.1 \times 10^{-11}$	(a)
	32	32	TW	E4	$2.0 \times 10^{-9}$	(a)
BF2	35	35	TW	TW	$7.0 \times 10^{-12}$	(c)
	35	35	RL	RL	$< 1.0 \times 10^{-12}$	(c)
	35	35	SHWL	SHWL	$1 \times 10^{-11}$	(c)
	35	35	SL2	SL2	$2 \times 10^{-8}$	(c)
BM	35	35	TW	TW	$5 \times 10^{-12}$	(c)
	35	35	RL	RL	$2 \times 10^{-10}$	(c)
	35	55	SHWL	SHWL	$8 \times 10^{-10}$	(c)
	35	35	SL2	SL2	$1 \times 10^{-9}$	(c)
CL	35	35	TW	TW	$1 \times 10^{-11}$	(c)
	35	35	RL	RL	$7 \times 10^{-12}$	(c)
	35	35	SHWL	SHWL	$1 \times 10^{-10}$	(c)
	35	35	SL2	SL2	$3 \times 10^{-10}$	(c)
GS	35	35	TW	TW	$1 \times 10^{-11}$	(c)
	35	35	RL	RL	$3 \times 10^{-12}$	(c)
	35	35	SHWL	SHWL	$2 \times 10^{-11}$	(c)
	35	35	SL2	SL2	$4 \times 10^{-7}$	(c)
GSC	35	35	TW	SL2	$2 \times 10^{-11}$	(c)
	35	35	TW	TW	$1 \times 10^{-11}$	(c)
	35	35	RL	RL	$6 \times 10^{-12}$	(c)
	35	35	SHWL	SHWL	$3 \times 10^{-12}$	(c)
CL	35	35	SL2	SL2	$2 \times 10^{-7}$	(c)
	35	35	TW	SL2	$3 \times 10^{-12}$	(c)
	14	14	TW	TW	$2 \times 10^{-11}$	(d)
	14	14	TW	B	$4 \times 10^{-11}$	(d)
	5	14	TW	TW	$4 \times 10^{-11}$	(d)
	5	14	TW	E4	$2 \times 10^{-11}$	(d)
	5	35	TW	TW	$2 \times 10^{-11}$	(d)
	5	35	TW	SL3	$3 \times 10^{-11}$	(d)

References: (a) Petrov et al. (1997b); (b) Petrov & Rowe (1997); (c) Ruhl & Daniel (1997); (d) Rad et al. (1994)

Notes: DW=Distilled Water; TW=Tap Water;

SL1=Synthetic Leachate #1 Ref. (b); Acetic Acid=4000 mg/L; Propionic Acid=3000 mg/L; Butyric Acid=500 mg/L;  $\text{Na}^+$ =1615 mg/L;  $\text{K}^+$ =354 mg/L;  $\text{NH}_4^+$ =618 mg/L;  $\text{Ca}^{2+}$ =1224 mg/L;  $\text{Mg}^{2+}$ =473 mg/L;  $\text{Cl}^-$ =4414 mg/L;  $\text{HCO}_3^-$ =4876 mg/L;  $\text{NO}_3^-$ =40 mg/L;  $\text{SO}_4^{2-}$ =137 mg/L;  $\text{HPO}_4^{2-}$ =18 mg/L;  $\text{CO}_3^{2-}$ =156 mg/L; pH=6.2;  $E_b$ =-328 mV

SL2=Synthetic Leachate #2 Ref. (c); 0.15 M acetic acid (9000 mg/L), 0.15 M sodium acetate [ $\text{Na}^+$ =3450 mg/L],  $\text{Ca}^{2+}$ =1000 mg/L; 0.007 M salicylic acid [phenol=658 mg/L]

RL1=Real MSW Leachate Ref. (c);  $\text{Na}^+$ =368 mg/L;  $\text{Ca}^{2+}$ =112 mg/L;  $\text{Mg}^{2+}$ =100 mg/L;  $\text{Cl}^-$ =520 mg/L;  $\text{SO}_4^{2-}$ =4340 mg/L; pH=7; Acetone=116 mg/L; Benzene=9 mg/L; Phenol=2.5 mg/L; Toluene=11 mg/L; Ethylbenzene=41 mg/L; Xylene=130 mg/L; Chlorobenzene=87 mg/L; COD=687 mg/L;  $\text{BOD}_5$ =254 mg/L

RL2=Real Leachate: Ref. (d) Composition unknown

SHWL=Simulated Hazardous Waste Leachate Ref. (c); Acetone=4000 mg/L; Benzoic acid=2000 mg/L; Phenol=3000 mg/L; Chloromethane=1000 mg/L; Cadmium=100-200 mg/L

E1=Ethanol 25%, Water 75% (by mass) Ref. (a); E2=Ethanol 50%, Water 50% (by mass) Ref. (a); E3=Ethanol 75%, Water 25% (by mass) Ref. (a)

E4=Ethanol 100%, Water 0% (by mass) Ref. (a)

B=Benzene

water. Figure 14 shows an increase in the hydraulic conductivity of the BF1 GCL when permeated with synthetic leachate SL1 (see Table 7). At a low confining stress (3-4 kPa) the increase is by almost an order of magnitude. At an intermediate confining stress (30-35 kPa) the increase is by a factor of six.

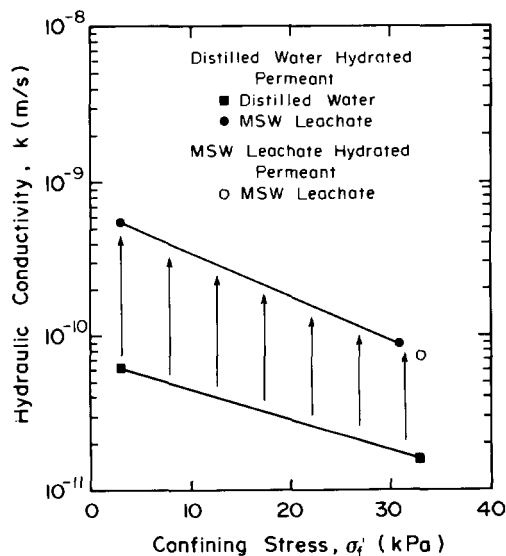


Figure 14. Hydraulic conductivity and hydraulic conductivity ratio versus static confining stress for permeation of synthetic MSW leachate (modified from Petrov & Rowe, 1997).

The increases in hydraulic conductivity evident in Figure 14 are not a problem if the barrier system has been designed based on the higher values that reflect interaction with leachate. However, it also should be recognized that the change in hydraulic conductivity will be highly dependent on the leachate. This is particularly evident when one compares the results given in Table 7 for the BF2 product at intermediate stress (30-35 kPa) for tap water ( $k \approx 7 \times 10^{-12}$  m/s), real leachate ( $k < 1 \times 10^{-12}$  m/s) and synthetic leachate SL2 ( $k \sim 2 \times 10^{-8}$  m/s) based on the tests of Ruhl and Daniel (1997). This clearly indicates the need to select the hydraulic conductivity giving due consideration to both the GCL and the leachate that it is likely to encounter. As indicated in Table 7, the hydraulic conductivity increases with the concentration of salts in the permeating solution. This needs to be considered when comparing the results for the two synthetic leachates and the "real leachate". The real leachate studied by Ruhl and Daniel (1997) (see Table 7) had a low concentration of cations ( $\text{Na}^+ \equiv 368$  mg/L;  $\text{Ca}^{2+} \equiv 112$  mg/L;  $\text{Mg}^{2+} \equiv 100$  mg/L) and actually gave a hydraulic conductivity lower than that with tap water. This may be due to the presence of bacteria that

can change the characteristics of the leachate during the test, typically causing an increase in pH and a consequent "dumping" or precipitation of some inorganic constituents (see Rowe et al. 1995b). This in turn can reduce the hydraulic conductivity due to (a) a reduction in pore space due to precipitation and bacterial clogging (see Rowe et al. 1995b) and (b) the formation of gas bubbles (typically methane or carbon dioxide) during anaerobic degradation of leachate. These gas bubbles can lodge in pore space and reduce the hydraulic conductivity unless special efforts are made to maintain the sample in a saturated state during the test. Both these mechanisms can occur in field applications, however it is not known to what extent this will occur and hence it is more conservative to use a chemically similar synthetic leachate. Since at typical laboratory temperatures it usually takes about 100 days for significant biological activity to be induced (see Rowe et al. 1997d, f), there is also the potential for changes in leachate characteristics and gas formation even using synthetic leachate in very long term tests.

Not all "synthetic" leachates are similar. The synthetic leachate used by Petrov and Rowe (1997) was modelled on Keele Valley Landfill leachate and has a very similar chemical composition to the real leachate. In contrast, the synthetic MSW leachate used by Ruhl and Daniel (1997) was not modelled on any specific leachate but was deliberately "designed" to have a high  $\text{Na}^+$  and  $\text{Ca}^{2+}$  content knowing that this would have a significant impact on Na-bentonite.

Considering the BF product, there is a clear trend in increasing hydraulic conductivity with increasing ionic strength of the leachate with Ruhl and Daniel's "real" leachate having the least effect ( $k < 1 \times 10^{-12}$  m/s), Petrov and Rowe's Keele Valley simulated leachate (SL1) having a modest effect ( $k \sim 7.3 \times 10^{-11}$  m/s) and Ruhl and Daniel's synthetic leachate (SL2) having the greatest effect ( $k \sim 2 \times 10^{-8}$  m/s) for samples hydrated and permeated with the same fluid at ~35 kPa. The value obtained by Ruhl and Daniel with synthetic leachate is very similar to that obtained by Petrov and Rowe with a 2N NaCl ( $\text{Na}^+ \equiv 46$  g/L) solution. Thus the high value obtained by Ruhl and Daniel is a little surprising compared to the other data in Table 7. Nevertheless, these results emphasize the need to perform tests on leachate with a composition similar to that expected in the actual landfill in order to obtain a realistic estimate of the GCL hydraulic conductivity in contact with leachate.

## 5.2 Hydration of GCLs

Since the hydration of GCLs with water prior to permeation with leachate generally results in a lower hydraulic conductivity, the level of hydration that can be

achieved prior to contact with leachate is an important question. Unfortunately, there is very little documented research on this topic. Daniel and Shan (1992) indicated that in contact with soil at the wilting point, bentonite can be expected to have a water content rise to about 50%. They performed a number of tests where the bentonite from a GCL (GS) was in contact with sand at different water contents. Table 8 summarizes the bentonite-water content after 40-45 days for bentonite placed in contact with (0.1-0.2 mm) sand at different water contents (at 14 kPa pressure). It can be seen that under these circumstances, the bentonite is very efficient in its uptake of water from the underlying soil. It may be expected that there would be less uptake of water if the GCL is placed on a dry geosynthetic drainage layer or on a drainage layer of stone at a typical (very low) water content, although test results would also be useful in these cases.

Table 8. Uptake of water by bentonite (interpreted from Daniel & Shan 1992).

Sand Initial Water Content (%)	Bentonite Water Content at 40-45 Days (%)
1	50
2	75
3	88
5	128
10	156
17	193

Bonaparte et al. (1996) performed hydration tests on three different GCL products in contact with a compacted clay (PL=22%, PI=19%,  $\omega_{opt}$ =20%) placed at three different water contents ( $\omega_{opt}$  -4%,  $\omega_{opt}$ ,  $\omega_{opt}$  +4%). Even for the driest soil ( $\omega \sim 16\%$ ) the GCL moisture content increased from initial values of 15-20% up to about 40% within 20 days. At the higher water content there was greater hydration. For compacted soil at  $\omega=24\%$ , after 75 days the GCL water content had increased to 70-90% depending on the product. Their test suggested that the uptake of moisture over a period of 25 days was not significantly affected by the applied pressure over the stress range of 5 to 390 kPa.

Daniel et al. (1993) examined the effect of partial hydration on the hydraulic conductivity of GCL:GS. They found that when the partially saturated GCL was permeated with concentrated hydrocarbons, the hydraulic conductivity was high (see Table 9) for a low initial water content (17% and 50%) but was close to that of water (except for TCE) at a water content of 100% and less than that due to water at higher water contents. Thus it was not necessary for the GCL to be fully saturated to have a low hydraulic conductivity.

Table 9. Summary of results of permeability tests on partially saturated bentonite (after Daniel et al. 1993)

Permeating Liquid	Hydraulic Conductivity (m/s)			
	17%	50%	100%	125%
Benzene	$3 \times 10^{-7}$	$2 \times 10^{-7}$	$5 \times 10^{-11}$	No Flow
Gasoline	$4 \times 10^{-7}$	$4 \times 10^{-7}$	$4 \times 10^{-11}$	No Flow
Methanol	$3 \times 10^{-7}$	$3 \times 10^{-7}$	$3 \times 10^{-11}$	No Flow
Tertbutylethylether	$2 \times 10^{-7}$	$3 \times 10^{-7}$	$< 1 \times 10^{-11}$	No Flow
Trichloroethylene	$4 \times 10^{-5}$	$4 \times 10^{-7}$	$3 \times 10^{-10}$	No Flow
Water	$1-2 \times 10^{-11}$	--	--	--

### 5.3 Effect of Holes in GCL

Shan and Daniel (1991) examined the effect of puncturing a CL type GCL by cutting out three holes in each 152 mm diameter specimen. The samples were allowed to hydrate under a confining stress of 14 kPa. The hydraulic conductivity to water was then measured as summarized in Table 10. Under these test conditions the bentonite swelled to completely fill the 12 and 25 mm diameter holes. However, two out of the three 75 mm holes were reported to have not sealed and left an opening of 12 mm diameter giving a hydraulic conductivity greater than  $2 \times 10^{-6}$  m/s (the upper limit measurable with the equipment used). These tests suggest that the GCL had the capacity to effectively self-heal small holes but not large holes or tears.

Table 10. Effect of punctures in a GCL:CL (after Shan & Daniel 1993)

Diameter of Punctures	Hydraulic Conductivity to Water (m/s)
No punctures	$2 \times 10^{-11}$
12 mm	$3 \times 10^{-11}$
25 mm	$5 \times 10^{-11}$
75 mm	$> 2 \times 10^{-6}$

## 6 DIFFUSION THROUGH GCLs

As will be discussed in more detail later, contaminants can migrate through a geomembrane by (a) diffusion through the geomembrane (see Section 8) and (b) advection through holes (see Section 9). The clay component of the composite liner serves two purposes: (a) it acts as a diffusion barrier and (b) it minimizes leakage through holes in the geomembrane. The growing interest in the use of GCLs as a replacement for

compacted clay liners raises the need to address the "equivalence" of the GCL and compacted clay liner with respect to both functions. This will be addressed in Section 10, however in order to make this assessment one must first have a knowledge of the diffusive and sorptive characteristics of GCLs as well as the hydraulic conductivity. Hydraulic conductivity was discussed in Section 5. In this section, the diffusion through GCLs will be addressed. Advection will be discussed in Sections 9 and 10.

Diffusion involves the movement of molecules or ions (in air, water or solid) as a result of their own random kinetic activity from areas of higher activity (concentration) to areas of lower activity (concentration). The movement of molecules or ions in porous media (including GCLs) is given by Fick's Law

$$f = -n_e D_e \frac{\partial c}{\partial z} \quad (3)$$

in which  $f$  is the mass flux [ $ML^{-2}T^{-1}$ ],  $n_e$  is the effective porosity [-],  $D_e$  is the effective diffusion coefficient [ $L^2T^{-1}$ ],  $c$  is the concentration in the GCL [ $ML^{-3}$ ] and  $z$  is the distance parallel to the direction of diffusion [L]. To date, little has been published concerning diffusion through GCLs. Rowe et al. (1997b) have developed an apparatus that can be used to measure the diffusion of various contaminants through a GCL. Details regarding the apparatus and test procedure are given in that paper and will not be repeated here. Briefly, the test involves placing a contaminant source on one side of a hydrated GCL and an uncontaminated receptor solution on the other side of the GCL (see insert to Figure 15). The change in concentration in both the source and receptor solution is then monitored with time as contaminant diffuses (with a hydraulic gradient of zero) from the source to the receptor solution.

Figure 15 shows the data obtained for a needle punched GCL BF2 (see Table 6 for nominal characteristics) for a sample confined to a hydrated thickness of 7.1 mm. By adjusting the effective diffusion coefficient and porosity, it is possible to obtain a theoretical fit to the source and receptor concentration using a computer program (Rowe & Booker 1983, 1997a). Based on this procedure, and using the total bentonite porosity,  $n=0.71$ , an effective diffusion coefficient,  $D_e$ , for chloride of  $1.5 \times 10^{-10} m^2/s$  was inferred giving a product  $nD_e = 1.05 \times 10^{-10} m^2/s$ . Due to the scatter of data inevitable in this type of test, there is some uncertainty and more than one combination of  $n$  and  $D_e$  could be used to fit the data shown in Figure 15. However, for the range of uncertainty, the value of  $nD_e$  only varies between 1.0 and 1.08  $m^2/s$ . It should also be noted that during a diffusion test there will be mechanisms other than molecular diffusion influencing

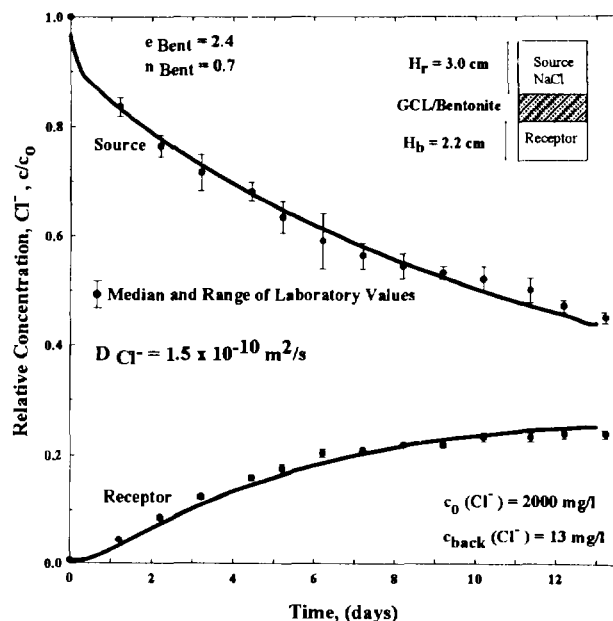


Figure 15. Variation in source and receptor concentration with time for a diffusion test on a needle-punched GCL BF2 (modified after Rowe et al. 1997b).

the movement of ions (see Rowe et al. 1995b) and  $D_e$  is really more a mass transfer coefficient than a true coefficient of molecular diffusion. A more detailed examination of anion exclusion and osmosis, and their potential effect on the effective porosity and diffusion coefficient is currently in progress and will be reported in a subsequent paper.

Similar tests have been performed for different products and different hydrated thicknesses of the GCL (see Table 11) and the diffusion coefficient and porosity is found to be a function of the void ratio which, in turn, is related to the confining stress and hydrating conditions. Similar tests to those reported in Table 11 can be performed for other contaminants (both inorganic and organic) and these tests are ongoing at the University of Western Ontario.

Diffusion can be an important consideration with respect to contaminant impact of well designed and operated landfill facilities. It can also impact on laboratory hydraulic conductivity tests. For example, Figure 16 shows the salinity ratio of various pore volumes of permeant in a hydraulic conductivity test on a GCL (BF1). As can be seen, the effluent is at 50% of the influent salinity after only 0.3 pore volumes. This early "breakthrough" could be misinterpreted as indicating a macro-structure and preferential flow paths however, in reality, it is diffusion of chloride ahead of the advective contaminant front and can be readily predicted using a diffusion coefficient of about  $4 \times 10^{-10} m^2/s$ .

The observation that there will be an "early" diffusive

Table 11. Chloride diffusion characteristics of some GCLs.

GCL	Applied Stress $\sigma_v'$ (kPa)	Hydrated Thickness $t_{GCL}$ (mm)	Effective Diffusion Coefficient $D_e$ ( $m^2/s$ )	Porosity $n$ (-)
BF3	20	11.1	$3 \times 10^{-10}$	0.80
	65	9.1	$2 \times 10^{-10}$	0.77
	100	7.1	$1.5 \times 10^{-10}$	0.71
	350	5.6	$0.4 \times 10^{-10}$	0.51
BF2	25	9.1	$2.5 \times 10^{-10}$	0.77
	140	7.1	$1.6 \times 10^{-10}$	0.68
	280	5.6	$0.7 \times 10^{-10}$	0.64
BF4	29	11.1	$2.9 \times 10^{-10}$	0.83
	100	7.1	$1.3 \times 10^{-10}$	0.74

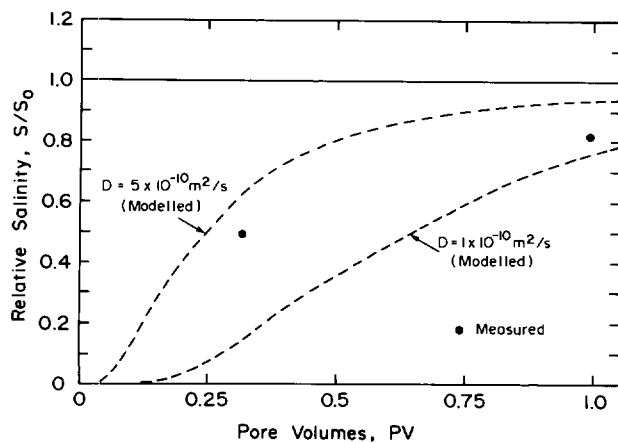


Figure 16. Effluent relative salinities versus pore volumes of salt solution; measured and modelled (after Rowe et al. 1997b).

movement of contaminant ahead of the advective front in hydraulic conductivity tests can be used to obtain an estimate of diffusion characteristics. For example, Lo (1992) used the program POLLUTE (Rowe & Booker 1983; 1997a) to fit the concentration profile in the effluent for tests performed using the GCL "CL" and obtained diffusion coefficients as summarized in Table 12. Separate batch tests were used to obtain the sorption coefficients given in Table 13. It was inferred that the diffusion coefficient for lead was greater than that for chloride while the diffusion coefficient for 1,2 dichlorobenzene was reported to be less than for

Table 12. Diffusion coefficient inferred by Lo (1992).

Liner Material	Effective Diffusion Coefficient $D_e$ ( $m^2/s$ )		
	Chloride	Lead	1,2 DCB
CL	$2.4 \times 10^{-10}$	$5.9 \times 10^{-10}$	$9.8 \times 10^{-11}$
Organo-Clay	$4.9 \times 10^{-10}$	$9.0 \times 10^{-10}$	$1.5 \times 10^{-10}$
HA-ALOH-Clay	$3.6 \times 10^{-10}$	$7.6 \times 10^{-10}$	$1.2 \times 10^{-10}$

chloride. Diffusion coefficients for the modified clays were up to 50% greater than for conventional bentonite. Compared to the modified clays, conventional bentonite gave the greatest sorption for lead (which was strongly retarded) but the sorption of the chlorobenzenes was very low. In contrast, the modified clays allowed substantial sorption of the chlorobenzenes. Finally, it should be noted that "sorption" of heavy metals is strongly pH dependent.

Table 13. Linear sorption coefficient  $K_d$  inferred by Lo (1992).

Liner Material	$K_d$ value (mL/g)			
	Lead (pH-7)	1,2 DCB	1,2,4 TCB	1,2,4,5 TECB
CL	6000	1.4	2.2	10
Organo-Clay	140	609	1320	4500
HA-ALOH-Clay	417	20	38	254

## 7 SERVICE LIFE OF GEOMEMBRANE LINERS

The exposure conditions of a geomembrane may be expected to be different depending on whether it is part of a composite primary or secondary liner. As a component of the primary liner, the geomembrane is subject to direct contact with leachate and temperatures higher than normal groundwater temperatures. As part of a secondary liner it is in contact with less leachate than the primary liner and this leachate will likely have experienced some attenuation due to cation exchange, precipitation and biodegradation as it migrates through the primary clay liner. The secondary geomembrane is also likely to be closer to natural groundwater temperature. However, depending on the design and operation of the secondary system, there is potential for exposure to atmospheric oxygen. Thus the service life of primary and secondary geomembrane liners may be expected to be different (Rowe et al. 1994).



## 7.1 Potential Failure Mechanisms

The two most important factors that affect the short-term performance of a geomembrane barrier are engineering design (including liner/leachate compatibility verification) and geomembrane manufacturing/installation CQC/CQA. Provided adequate engineering design is carried out and appropriate CQC/CQA procedures are followed during the manufacture and installation of the geomembrane, the geomembrane barrier component may be expected to perform satisfactorily in the short term. The design life (i.e. long-term performance) of the geomembrane is influenced primarily by the synergistic effects of chemical and physical stresses over an extended period of time. Primary considerations are the effect of temperature and the effect of tensile stresses over and above calculated design values (e.g. due to contact stresses that are related to the level of geomembrane protection, and stresses induced due to wrinkles/waves).

## 7.2 Geomembrane Protection

The provision of adequate protection to a geomembrane to strains induced by stones in a granular leachate collection layer is the subject of considerable debate. The debate largely hinges on the difference of design philosophy with respect to (a) providing sufficient protection to avoid holes in the geomembrane (i.e. puncture of the geomembrane); and (b) providing sufficient protection to control the strains due to indentation to a negligible (~ 0.25%) level (e.g. see Narejo 1995a,b; and discussion by Bishop 1996). Giroud et al. (1995) have developed a method of analysis for calculating geomembrane puncture resistance and Badu-Tweneboah et al. (1998) have developed an approach for evaluating the effectiveness of HDPE geomembrane liner protection. Reddy et al. (1996) evaluated the damage to a 1.5 mm HDPE geomembrane due to construction loads and concluded that "a geotextile as light as 270 g/m<sup>2</sup>...completely protects the geomembrane from construction loading". Wilson-Fahmy et al. (1996), Narejo et al. (1996) and Koerner et al. (1996b) provide an extensive examination of puncture protection of geomembranes. They showed that there is a linear increase in protection resistance with increasing thickness (mass per unit area) of the protection layer. However, the German approach (Brummermann et al. 1995; Saathoff & Sehrbrock 1995; Bishop 1996; Seeger & Müller 1996) goes beyond providing puncture protection and focuses on minimizing the contribution of indentation (and subsequent sensitivity to stress cracking) due to collection stones under long term loading condition to a very low strain level (~ 0.25%).

The differences between the U.S. and German approaches is partly a difference in philosophy.

However, there is also room to question the relatively arbitrary choice of 0.25% as a limiting strain (see Bishop 1996). Furthermore, the allowable strain can not be considered in isolation but, rather, must be considered in the context of the method of measurement used to assess whether this objective has been met for a given form of geomembrane protection. For example, Giroud (1996b) has quoted a case where the measured strain in a geomembrane that had been damaged, but not punctured, by stones was approximately 0.3% using a 5 mm scanning grid and an order of magnitude larger (3%) using a finer 0.5 mm scanning grid. Based on this, he argued that a limit of strain of say 0.5% with a scanning grid of 5 mm may really be equal to an allowable strain of 5%. By analogy, an allowable strain of 0.25% with a 5 mm scanning grid may really be an allowable strain of 2.5%. Notwithstanding these uncertainties, it would appear that the German approach is more likely to minimize tensile strains in the geomembrane than the U.S. approach; the need for the additional conservatism of the German approach remains an open question and may depend on the required service life of the geomembrane.

## 7.3 Wrinkles (Waves)

Wrinkles (also called waves in some papers) in a geomembrane are a source of considerable concern. It is well recognized that the high coefficient of thermal expansion and heating by the sun during construction play an important role in wrinkle formation. Conversely, these factors are important with respect to the development of potentially significant tensile stresses in the geomembrane if it is placed without wrinkles at a temperature significantly above its long-term ambient temperature. White geomembranes have been shown to lessen (but do not eliminate) the problem (Pelte et al. 1994; Koerner & Koerner 1995a). Giroud and Morel (1992) and Giroud (1995) showed that in addition to temperature, colour and the coefficient of thermal expansion, factors such as roughness and flexibility can also influence the size of wrinkles. Some have thought that wrinkles will "go away" due to applied pressure once the waste is placed, however findings by Stone (1984), Koerner et al. (1997) and Soong and Koerner (1998) cast doubt on that assumption and suggest that wrinkles may exist under even high pressure. In a series of laboratory tests conducted with normal stresses as high as 1100 kPa, they found that although there was a reduction in wrinkle height, the wrinkles remained. As a result of the wrinkle geometry and the applied stress, tensile strains of up to 3.2% were induced in the 1.5 mm thick HDPE geomembrane for an 80 mm high wrinkle at 23°C. In no case was intimate contact achieved in their tests even for the smallest wrinkle height studied (14 mm). Most

interestingly, it was found that even an increase in temperature up to 55°C (e.g. to simulate a high temperature in the landfill leachate) and an applied pressure of 700 kPa did not eliminate wrinkles and that the tensile strains for a 60 mm initial wrinkle increased from 3% at 23°C to 4.9% at 42°C and 55°C.

The presence of wrinkles (waves) in the geomembrane raises several concerns. Firstly, there is increased potential for contaminant migration through a hole in the geomembrane at or near the wrinkle (see Section 9). Secondly, there is increased potential for stress cracking due to the tensile strains that are induced by the wrinkle and these may be compounded by other tensile strains. This suggests the need for greater attention to reducing/avoiding wrinkles, possibly following the lines presently being advocated in Germany (Averesch & Schicketanz 1998). However, care is required to ensure that the elimination of wrinkles is not at the expense of inducing significant tensile strains in the geomembrane that could ultimately contribute to long term stress cracking, particularly at the toe of slopes. One may expect that in this situation, stress relaxation will play an important role but the long term stress in a geomembrane subject to tensile strain remains an open question and hence it would be prudent to minimize the tensile strains.

#### 7.4 Existing Long Term Performance Data

The relatively short history of geomembrane use in waste containment applications makes it rather difficult to predict a definitive service life for geomembranes. In Europe, polyethylene geomembranes were developed in the 1960s. Therefore, there is about 30 years of actual field experience with geomembranes used in canal and pond lining applications. Geomembranes have been extensively used as liners for landfills since the early 1980s. A study by Brady et al. (1994) examined the behaviour of HDPE in different environments over a period of 30 years. The results of tests on unaged and 30 year old specimens showed that there were no substantial changes in density, water adsorption value, and water extractable matter content. There was a small change in resistivity which was judged to be of no practical importance. There was no significant change in impact resistance after 15.5 years however a reduction of about 50% was observed over a 30 year period. The data from tensile tests showed that over the 30 year period the tensile strength remained essentially constant but there was a reduction in the strain at the peak (yield) strength and the HDPE became stiffer with time.

The oldest case histories which provide information on the field performance of geomembranes come from their use as canal/pond liners. Schmidt et al. (1984) carried out a series of physical index tests (yield, elongation,

break, and tear properties) on samples of polyethylene geomembranes from exposed and submerged geomembranes that had been in use for up to 16 years. The test results were compared with the original geomembrane material properties specified at the time of the geomembrane installation. The study concluded that there is typically a stiffening of the geomembrane with time, but that this is less significant for buried (unexposed) material. The major causes of failure to the liners was from physical/mechanical damage, rather than weathering/aging effects. The authors conclude that when polyethylene geomembranes are buried (i.e. protected), they showed only minor changes in physical performance over the observation period of 16 years.

Rollin et al. (1994) reported results obtained for samples of HDPE geomembrane that had been used in a contaminated soil containment facility for 7 years. Aging was found to increase the yield strength, decrease the tensile force required for rupture and lower the elongation at rupture. Aging was more severe for samples from the bottom of the cells than for samples from the slopes or cover.

In a study by Hsuan et al. (1991), HDPE geomembrane samples were taken from a 7 year old solid waste leachate lagoons. The samples were obtained from four different locations in the lagoons, ranging from areas continuously exposed to the atmosphere to those at the bottom of the impoundment, continuously covered by liquid. It was concluded that: (1) there was no substantial macroscopic change in the geomembrane sheets or seams after 7 years exposure at the site; (2) an evaluation of the stress crack resistance of the materials indicated that constant outdoor exposure had not caused substantial changes in the internal structure of the material; and (3) changes in the geomembrane were observed only on the molecular level and they did not affect the engineering/hydraulic containment properties of the geomembranes.

In contrast, Rowe et al. (1998a) conducted a similar study of a leachate lagoon liner after 14 years of operation. They observed very low standard oxidative induction (OIT) values for exposed geomembrane accompanied by a reduction in tensile break properties and stress crack resistance of the geomembrane. The results of the Melt Index test suggest that the degradation was induced by a chain scission reaction in the polymers. The geomembrane was severely cracked indicating that the material was highly susceptible to stress cracking. This was confirmed by SP-NCTL tests.

For geomembranes that were either covered by soil or leachate, the depletion of antioxidant was slower than for the exposed and partially exposed geomembranes. The amount of antioxidant present in these geomembranes seems to have been sufficient to protect the geomembrane from oxidation degradation over the 14 year

exposure period.

The results of the Rowe et al. (1998b) investigation substantiate the importance of the type and amount of antioxidant and stress crack resistance to the longevity of the geomembrane and suggest that these two properties should be evaluated and incorporated in the specification of a HDPE geomembrane to assure their quality.

## 7.5 Predictions of Service Life

While the most reliable method of determining the service life of geomembranes would be from exposure under the actual field conditions, this is not presently feasible due to the length of time that would be required to obtain useful results. Consequently, several "accelerated aging" tests have been developed which attempt to simulate long-term exposure of HDPE. However, in order to use these results one also needs an understanding of the mechanism of geomembrane aging and failure.

As discussed by Hsuan and Koerner (1995), there are two types of aging: physical and chemical. Physical aging involves a change in the crystallinity of the material but, by definition, there is no breaking of covalent bonds. Chemical aging involves degradation where there is breaking of covalent bonds and, eventually, a reduction in the engineering properties of the geomembrane. Conceptually, chemical aging can be considered to have three distinct stages: (a) depletion time of antioxidants; (b) induction time to the onset of polymer degradation; and (c) degradation of the polymer to decrease some property (or properties) to an arbitrary level (e.g., to 50% of the original value).

There are two key issues with respect to chemical breakdown: (a) the amount of antioxidant and its consumption and/or removal (e.g. by diffusion/leaching) from the geomembrane, and (b) the presence of an environment where oxidation can occur. Generally, conditions at the base of a landfill (i.e. above the primary liner) are anaerobic except for the first few years of operation. There is likely to be more persistent oxygen in the secondary leachate collection system (and hence above the secondary geomembrane) due to its separation from the biological processes ongoing in the landfill. Hsuan and Koerner note that the oxidation reaction of polyethylene can be increased in the presence of transition metals (e.g. Co, Mn, Cu, Pd and Fe). Since these are all potentially present in leachate, there is potential for the reduced presence of oxygen above the primary geomembrane liner to be at least partly offset by increased reactions due to the presence of the transition metals (amongst other things).

There is the potential for debate regarding the property(s) to be assessed with respect to the degree of polymer breakdown. In landfill base liner applications,

the real service life depends on the hydraulic and diffusive properties of the geomembrane. Provided that stress cracking does not occur, it is conceivable (and likely) that a geomembrane may lose strength and become brittle while still performing satisfactorily as a barrier. Therefore, the "hydraulic and diffusive service life" of a geomembrane may exceed the service life as determined by the degradation of physical properties such as tensile strength. This issue is the subject of current research by the writer and his coworkers at UWO. However, based on available information, it is also clear that it is desirable to minimize the physical degradation (by appropriate use of antioxidants) and to use geomembranes with adequate stress crack resistance since the most likely long term cause of loss of hydraulic resistance would be due to the formation of stress cracks in the geomembrane.

Koerner et al. (1993b) have recommended that geomembranes used as liners should not fail in 200 hours in a single point notched constant load test (SP-NCLT; ASTM D5397) at 30% of the yield stress. Studies at GRI have also led them to recommend minimum OIT values of 100 minutes for the standard test (D3895) or 400 minutes in the high pressure test (D5885). After oven aging at 85°C for 90 days (ASTM D5721), the geomembrane should retain 55% of the standard Std-OIT or 80% of the HP-OIT value. In the final assessment of service lives in this section, it is assumed that the geomembrane meets these criteria.

A number of investigators have addressed the issue of trying to assess the service life of geomembrane liners for landfills; these have ranged from "expert opinion" to quantification based on accelerated test data. A U.S. Environmental Protection Agency (USEPA) ad hoc committee considered the durability of polymeric landfill lining materials (i.e. HDPE) in landfills. Haxo and Haxo (1988) summarized the views of these U.S. experts who opined that (subject to numerous qualifications) the service life of geomembranes was likely to be in the order of hundreds of years. Tisinger and Giroud (1993) echo this opinion and state "that in properly designed and constructed facilities, HDPE geomembranes should be able to protect groundwater from leachate for hundreds of years".

Gray (1990) compared two methods of accelerated aging, which both use elevated temperature to simulate long-term HDPE exposure. The paper reviewed work carried out by the wire and cable industry which indicates the service life of HDPE insulation on cables (at a temperature of 40°C) is in the order of several hundred years.

Lord and Halse (1989) reviewed work carried out by the plastic pipe industry on the service life of HDPE pipes used in natural gas pipeline applications. These studies used elevated temperatures and stresses to

determine the ductile/brittle transition point of HDPE pipe, and predicted a service life of greater than 50 years for pipes under relatively high stresses (>7,000 kPa). For a geomembrane at the base of a landfill, the stresses will be much less and it is expected that accelerated aging tests at these lower stresses would indicate a longer service life (likely in the order of several hundred years).

Most of the work on natural gas pipeline service life has been carried out by Hoechst a.g., a German company. They have applied their pipe research expertise to the geomembrane area and conclude that the interaction with leachate is the largest concern in the service life of geomembranes. Although the stress fields in an HDPE pipe are different than those in a geomembrane liner, these studies indicate that the lifetime curves for pipes are applicable to geomembrane sheets with appropriate stress correction factors. Based on this work, Koch et al. (1988) conclude that: (1) The application of the Arrhenius extrapolation technique to predict the service life of HDPE has been confirmed over 30 years of testing. (2) Although various chemicals in landfill leachate have the potential to reduce the durability, since the concentration of organic compounds is low, the durability of HDPE in a domestic waste landfill can be assessed as similar to those in water containing a wetting agent. (3) Based on Arrhenius extrapolation, the time for mechanical/chemical alteration in an aqueous environment at 25°C is between 300 and 400 years assuming that leachate contains the same oxygen content as laboratory bath water. (4) Because of the anaerobic environment, with little or no oxygen, in a landfill environment, the actual time for chemical alteration should be longer than the times suggested by the laboratory data. (5) Considering all of these factors, the service life of these HDPE geomembranes could be expected to be considerably greater than 100 years.

None of the investigations and predictions noted above identified or directly considered the three stages of aging defined by Hsuan and Koerner (1995) although the accelerated aging test and hence the prediction would have incorporated all three components. However, it is useful to consider the three components in an attempt to improve estimates of service life. This can now be attempted based on the work of Hsuan and Koerner (1995) and Hsuan and Guan (1997) who have reported the results from two series of tests directed at assisting in the estimation of the depletion time of antioxidants in geomembranes. In both cases, samples of a single specific geomembrane were incubated at a series of temperatures (55, 65, 75 and 85°C). Samples were retrieved at various time intervals and evaluated by a number of tests for the physical, chemical and mechanical properties. The two test series were: (1) Series I: Nonstressed-Water Incubation: Hsuan and Koerner (1995) indicate that these tests were "designed to simulate

geomembranes that are exposed to liquids (water or leachate) on both sides and are essentially nonstressed". The HDPE samples were fully immersed in four water baths maintained at constant temperatures (as noted above). The data presented in the report for this series of tests spans a period of 30 months (2.5 years). Series III: Compressive Stress-Water/Air Incubation: These tests are said to be "intended to simulate geomembranes situated beneath solid waste landfills". The geomembrane is located between two (100 mm thick) layers of sand. The upper layer appears to be saturated and there is a 0.3 m water head acting on the geomembrane. The soil below the geomembrane is dry. The data presented in the report for this series of tests spans a period of 24 months (2 years). These tests were conducted with the geomembrane subjected to a vertical compressive stress of 260 kPa.

Two different Oxidative Induction Time (OIT) tests were performed and hence there is a (small) range to the interpretation of the results based on the two different methods. Based on the OIT values obtained at the four different temperatures, the results can be extrapolated back to the expected (lower) temperature of a primary geomembrane liner in a (North American) MSW landfill using the Arrhenius equation, assuming that the OIT depletion rate varies exponentially with the inverse of temperature (i.e. 1/T where temperature, T, is in °K). The values deduced by the writer, based on Hsuan and Koerner (1995) for Series I and Hsuan and Koerner (1997) for Series III, are given in Table 14. In their

Table 14. Calculated time for antioxidant depletion based on test data by Hsuan & Koerner (1995). (Original geomembrane had Std-OIT=80.5 min; HP-OIT=210 min; Density=948.8 kg/m<sup>3</sup>; Melt Index=0.23 g/10 min; Yield Stress=19.2 MPa)

Temp. (a) °C	Series I (b) Years	Series III (c) Years	Mean of I & III (d) Years	Mean of (c) & (d) Years
10	111	453	282	368
15	98	299	199	249
20	59	200*	130	165
25	44**	135	90	113
30	33	93	63	78
35	25	65	45	55
40	19	45	32	39
45	14	32	23	27
50	11	23	17	20
55	9	17	13	15
60	7	12	9.5	11

\* Value calculated by Hsuan & Koerner (1997)

\*\* Value calculated by Hsuan & Koerner (1995)

discussion of their experimental results, Hsuan and Koerner (1995) state that: "The shorter depletion time in Series I probably is due to the extraction rate of the antioxidant which is higher in Series I than in Series III conditions. The samples in Series I were exposed to moving water on all of their surfaces, whereas samples in Series III were exposed to stationary water on only one surface. It is known that moving water as in Series I tests actually causes leaching of antioxidants. Hence, the depletion time for incubation Series I probably is a very conservative value, since it is not common for both sides of the geomembrane to be exposed to moving liquids. In this regard, the results of the Series III tests seem to be more similar to HDPE geomembranes in service applications."

Considering the likely conditions in a landfill, the Series I depletion times given in Table 14 would appear to be too conservative since the geomembrane will not be subjected to moving water on both faces (as indicated by Hsuan and Koerner), however there is the potential for the movement of leachate adjacent to one face. This is likely to be less severe than the movement of oxygenated water but may be more severe than the stationary 0.3 m of water case examined in the Series III tests. The present writer averaged the depletion times between the Series I and III values based on the argument that this would correspond (approximately) to fluid movement on one face of the geomembrane and stationary condition on the other face. These depletion times are also given in Table 14. It could be argued that these interpolated depletion times represent a lower estimate of depletion time since the flushing fluid in the landfill environment is likely to be depleted in oxygen relative to the water used in the Series I tests. On this basis, the likely depletion time would lie between the mean value (column (d)) and the Series III value (column (c)) and the mean value is given for each temperature in the last column.

Based on the concept of aging outlined by Hsuan and Koerner and summarized earlier, the "service life" of a geomembrane would be the sum of the time to antioxidant depletion plus the induction time plus the time for degradation of the polymer. Hsuan and Koerner (1995) indicate an induction time of 12 years at 25°C. Hsuan and Koerner (1995) do not provide any information regarding degradation time in this report but indicate that this will be addressed in future reports (over the next decade).

Based on the Series III results, an induction time of 12 years and essentially ignoring the property degradation time, the service life of the geomembrane at 25°C would be about 150 years ( $135 + 12 = 147 \approx 150$  years). Based on the interpolated value of 113 and an induction time of 12 years, the service life would exceed 125 years. Recognizing that unstabilized 25 year old intact plastic has been found in landfills, it is not unreasonable to allow

at least 25 years for the degradation time, giving a service life of  $113 + 12 + 25 = 150$  years for a primary geomembrane at 25°C. If a secondary geomembrane is at a lower temperature, the service life would be expected to exceed 400 years at 10°C and 300 years at 15°C. Taking an intermediate value, the service life of a secondary geomembrane is estimated to exceed 350 years.

The service lives calculated above are reasonably consistent with earlier predictions or, to the extent that they differ, are more conservative at 25°C (or less). However, the rapid decrease in service life for temperatures above 25°C should be noted. As discussed in Section 2, landfill temperatures can increase rapidly to 40°C or more in a few years if leachate mounds to 6 m and this could reduce the service life of an underlying geomembrane to 40-75 years (with the range depending upon how the induction and degradation time decrease at 40°C). A temperature increase to 60°C (see Section 2) could reduce service lives to as little as one or two decades. In short, the service life of the geomembrane may be closely linked to the nature of the waste and the landfill operations and thus these should be carefully monitored.

## 8 DIFFUSION THROUGH GEOMEMBRANES

There are two primary mechanisms for contaminants to migrate through geomembranes: (a) "leakage" through holes and (b) diffusion through the intact geomembrane. Leaks are discussed in Section 9. In this section, attention will be focused on diffusive movement of both water and contaminants.

Geomembranes are not a conventional porous medium in which the pore size is large relative to both water and contaminant molecules. There is no "flow", in the conventional or Darcian sense, through an intact geomembrane. However, there can be movement of water and contaminant through the geomembrane due to molecular diffusion. The diffusive movement of a penetrant (contaminant or water) through a geomembrane where there are no defects such as pores, cracks or holes involves a cooperative rearrangement of the penetrant molecule and the surrounding polymer chain segments. The process requires a localization of energy to be available to allow a diffusive jump of the penetrant molecule in the polymer structure. The penetrant molecule and part of the polymer's molecular chain may share some common volume both before and after the jump. However, this jump will involve the breaking of some van der Waals forces or other interaction between the component molecules and polymer segments (Rogers 1985). Thus the diffusive motion depends on the energy available and the relative

mobilities of the penetrant molecules and polymer chains. This will depend on temperature and concentration, the size and shape of the penetrant, and the nature of the polymer.

### 8.1 Diffusive Transport

The diffusion of penetrant molecules through a geomembrane can be modelled by Fick's Law

$$f = -D_g \frac{\partial c_g}{\partial z} \quad (4)$$

in which  $f$  is the mass flux [ $ML^{-2}T^{-1}$ ],  $D_g$  is the diffusion coefficient in the geomembrane [ $L^2T^{-1}$ ],  $c_g$  is the concentration of the penetrant of interest in the geomembrane [ $ML^{-3}$ ] and  $z$  is the distance parallel to the direction of diffusion [ $L$ ]. Consideration of conservation mass then gives the governing differential equation for transient diffusion:

$$\frac{\partial c_g}{\partial t} = D_g \frac{\partial^2 c_g}{\partial z^2} \quad (5)$$

which must be solved for the appropriate boundary and initial conditions (see Rowe et al. 1995b for discussion of this related to landfills).

### 8.2 Sorption, Solubility and Henry's Law

When a geomembrane is in contact with a fluid (gas or liquid) for sufficient time to reach an equilibrium, there will be a relationship between the final equilibrium concentration in the geomembrane,  $c_g$  [ $ML^{-3}$ ], and the equilibrium concentration in the adjacent fluid  $c_f$  [ $ML^{-3}$ ]. This relationship may often be described by the Nernst distribution function (Rogers 1985) which may take a linear form (Henry's law):

$$c_g = S_{gf} c_f \quad (6)$$

where  $S_{gf}$  is variously called a solubility, partitioning or Henry's coefficient [-]. Alternatively, it may take a non-linear (e.g. Langmuir) form

$$c_g = \frac{S_a b c_f}{1 + b c_f} \quad (7)$$

where  $S_a$  and  $b$  are experimentally determined constants. The coefficients  $S_{gf}$ ,  $S_a$  and  $b$  may all vary with contaminant, phase of the fluid (gas or liquid) and temperature.

In the present context (see Rogers 1985; Naylor 1989),

the term "sorption" is a generalized term for the removal of the penetrant molecules from the fluid and its dispersal on or in the polymer. This may involve numerous processes including adsorption, absorption, incorporation in microvoids, etc. The distribution of penetrant may change with concentration, temperature and time and may change due to potential interaction with the polymer and swelling of the polymer matrix. Although much research has been conducted on sorption relating to plastics, there is limited recognition of its importance with respect to the design of landfills using geomembrane liners.

For the simplest case, where the permeant does not interact with the polymer (often, but not always, the case for HDPE geomembranes) or at low concentrations (Rogers 1985), Henry's law is obeyed and for this "Type I" sorption (Naylor 1989) the relationship between the concentration in the fluid and solid is given by Eq. 6 where, in principle,  $S_{gf}$  is a constant for the given molecule, fluid, geomembrane and temperature of interest (as will become evident later,  $S_{gf}$  will depend on the chemical composition of the fluid). Thus, substituting Eq. 6 into Eq. 4 gives the flux from a fluid on one side of a geomembrane to a similar fluid on the other side

$$f = -D_g \frac{\partial c_g}{\partial z} = -S_{gf} D_g \frac{\partial c_f}{\partial z} = -P_g \frac{\partial c_f}{\partial z} \quad (8)$$

where  $P_g$ , given by

$$P_g = S_{gf} D_g \quad (9)$$

is often referred to in the polymer literature as the permeability. This should not be confused with the old soil mechanics term "coefficient of permeability" (now called hydraulic conductivity) or the intrinsic permeability of a porous medium. It has nothing to do with Darcy's law or flow through the open voids within porous media.

Based on Eq. 9, the mass flux across a geomembrane of thickness  $t_{GM}$  is given by

$$f = S_{gf} D_g \frac{\Delta c_f}{t_{GM}} \quad (10)$$

or

$$f = P_g \frac{\Delta c_f}{t_{GM}} \quad (11)$$

where  $\Delta c_f$  is the difference in concentration in the fluid on either side of the geomembrane. It is possible to experimentally infer the value of  $P_g$  by performing a steady state experiment (see Figure 17) in which the

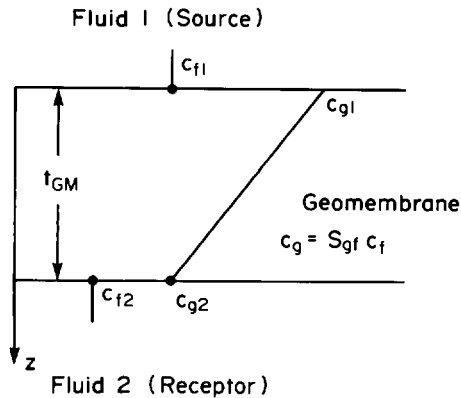


Figure 17. Diffusion across a geomembrane showing partitioning between the concentration in solution and the concentration dissolved in the geomembrane.

concentration is controlled at  $c_{f1}$ ,  $c_{f2}$  in the fluid on either side of the geomembrane and the flux,  $f$ , is measured. Thus

$$P_g = \frac{f t_{GM}}{\Delta c_f} \quad (12)$$

It follows from this that while a steady state test will allow the measurement of  $P_g$ , it does not allow the evaluation of either  $S_{gf}$  or  $D_g$  without additional tests. However transient contaminant transport is controlled by the diffusion coefficient,  $D_g$ , and not the permeability,  $P_g$ . This becomes evident when one substitutes Eq. 6 into Eq. 5 to give

$$S_{gf} \frac{\partial c_f}{\partial t} = S_{gf} D_g \frac{\partial^2 c_f}{\partial z^2} \quad (13)$$

and, on dividing by  $S_{gf}$ , this reduces to

$$\frac{\partial c_f}{\partial t} = D_g \frac{\partial^2 c_f}{\partial z^2} \quad (14)$$

which depends on  $D_g$  but not  $S_{gf}$  or  $P_g$ .

Thus it is important to distinguish between the Henry coefficient  $S_{gf}$  and the diffusion coefficient  $D_g$ . The Henry coefficient,  $S_{gf}$ , provides a measure of the discontinuity in concentration between the fluid and solid phase (as shown in Figure 17). The value of  $S_{gf}$  may be important with respect to mass balance calculations and is established from consideration of mass balance. In a two compartment diffusion test, such as the one shown in Figure 18, one can monitor the diffusion of the

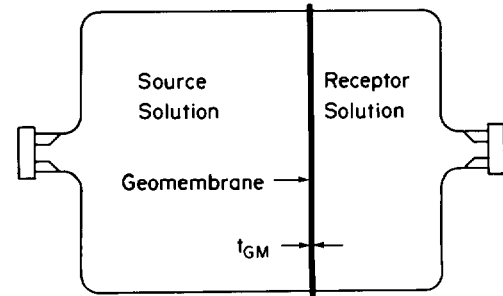


Figure 18. Two compartment diffusion cell used for measuring diffusion through a geomembrane.

contaminant of interest as it migrates from the source to the receptor with time. When an equilibrium is reached, the value of  $S_{gf}$  is given by

$$S_{gf} = \frac{c_{fo} V_s - c_{fF} (V_s + V_r) - \sum V_i c_i}{A t_{GM} c_{fF}} \quad (15)$$

- where
- $c_{fo}$  is the initial concentration of fluid in the source reservoir [ML<sup>-3</sup>]
  - $c_{fF}$  is the final equilibrium concentration in the source and reservoir [ML<sup>-3</sup>]
  - $V_s, V_r$  are the volumes of the source and the reservoir [L<sup>3</sup>]
  - $A$  is the area of geomembrane through which diffusion occurs [L<sup>2</sup>]
  - $t_{GM}$  is the thickness of the geomembrane [L]
  - $\sum V_i c_i$  is the mass removed by sampling events [M] ( $V_i$  and  $c_i$  being the volume and concentration removed at each sampling event).

The diffusion coefficient can then be calculated knowing the value of  $S_{gf}$  by fitting the variation of the source and effluent concentration with time using computer software that models the boundary conditions, phase change and transport through the geomembrane (e.g. Rowe & Booker 1997a). Table 15 summarizes a number of available techniques for obtaining  $D_g$  and  $S_{gf}$ .

It is important to note that there is a difference between phase change at the fluid/geomembrane boundary and sorption that occurs within the geomembrane itself as contaminant migrates through the geomembrane. Because plastic sheets are often very thin, the two have been confused in the literature. While this may be of little importance for very thin membranes, it is potentially important for thicker geomembranes. Sorption may occur, for example, when the contaminant absorbs to sorption sites in the geomembrane such as dispersed porous particles of high surface area (e.g. carbon black or silica gel). For this type of sorption, Eq. 5 is modified to

Table 15. Some techniques for measuring the partitioning and diffusion coefficients for geomembranes.

Technique	Method	Comments
Weight Gain	<p>Monitor increase in mass of geomembrane immersed in fluid of interest from initial value <math>m_o</math> until mass of geomembrane becomes constant at <math>m_\infty</math> (plot <math>(m_t - m_o)/(m_\infty - m_o)</math> vs <math>\sqrt{t}</math>)</p> $S_{gf} = \frac{\rho_{GM}(m_\infty - m_o)}{c_{fF}}$ $D_g = 0.049 t_{GM}^2 / t_{1/2}$	<p>Faster than alternative tests but each chemical must be examined separately. Prone to error due to mass loss when weighing (especially for VOCs).  <math>c_{fF}</math> = final equilibrium fluid concentration  <math>t_{1/2}</math> time to get; <math>(m_t - m_o)/(m_\infty - m_o) = 0.5</math></p>
Time Lag	<p>Monitor mass movement through geomembrane with time for test where <math>c_{t1} = \text{const}</math>, <math>c_{t2} = 0</math> (Figure 17), plot cumulative mass, F, through geomembrane against time and extrapolate steady state value to F=0 to obtain the time lag <math>\tau</math>. Thence</p> $D_g = t_{GM}^2 / (6\tau)$	
Pouch Method	<p>Geomembrane pouch filled with test permeant and immersed in liquid of known composition. Weight change of pouch is monitored as diffusion occurs.</p>	<p>Must avoid leaks in pouch; interpretation assumes diffusion through geomembrane is slow relative to that in fluid.</p>
Diffusion Test	<p>Diffusion from solution on one side of geomembrane to solution on other side. Change in source and receptor solution monitored with time. <math>S_g</math> calculated from Eq. 15 at equilibrium, <math>D_g</math> inferred from variation in source and receptor concentration with time.</p>	<p>May be used in conjunction with weight gain method to allow evaluation of parameters prior to equilibrium in the diffusion test.</p>

$$\frac{\partial c_g}{\partial t} = D_g \frac{\partial^2 c_g}{\partial z^2} - \frac{\partial S_g}{\partial t} \quad (16)$$

$\beta$  is an experimentally derived coefficient  $[M^{-1}L^3]$ .

where  $S_g$  may have a number of forms, including linear

$$S_g = K_g c_g \quad (17)$$

where  $S_g$  is the mass sorbed per unit volume  $[ML^{-3}]$   
 $K_g$  is the linear sorption coefficient  $[-]$  and  
 $c_g$  is the dissolved concentration  $[ML^{-3}]$   
 and Langmuir

$$S_g = \frac{\alpha \beta c_g}{1 + \beta c_g} \quad (18)$$

where  $\alpha$  is the limiting sorption mass per unit volume  $[ML^{-3}]$ , and

This sorption is distinct from the partitioning defined by Eq. 7. By combining Eq. 18 with linear partitioning between phases (Eq. 6), one can simulate the case where some of the molecules dissolved in the geomembrane are free to diffuse down the concentration gradient while other molecules are bound at a fixed number of adsorption sites or voids within the polymer.

### 8.3 Factors Affecting Diffusion Through a Geomembrane

The solubility and diffusion of a contaminant in a geomembrane will increase with increasing temperature. The diffusion coefficient tends to decrease with increasing penetrant size (molecular weight, molar volume or molecular diameter; see Berens & Hopfenberg 1982; Park & Nibras 1993). The shape of the molecule is also



important with linear, flexible and symmetrical molecules having higher mobility than rigid or non-symmetrical molecules (Salame 1960; Berens & Hopfenberg 1982; Saleem et al. 1989). For example, Saleem et al. (1989) showed that the diffusion coefficient for o-xylene is much lower than for p-xylene. This is attributed to the symmetrical nature of p-xylene (that has a dipole moment of 0) and the distorted shape of o-xylene with its two adjacent methyl groups (dipole moment = 0.62 debye). Berens and Hopfenberg (1982) showed that the diffusion coefficient for n-alkane and other elongated or flattened molecules are higher, by a factor of up to  $10^3$ , than the diffusion coefficients of spherical molecules of similar molecular weight.

The "permeability" ( $P_g = S_g D_g$ ) is highly dependent on the similarity of the penetrant and polymer. For example, strongly polar penetrant molecules have very low permeabilities through polyethylene (August & Tatzky 1984; Rowe et al. 1995a, 1996a) with the permeability being in the following order: alcohols < acids < nitroderivatives < aldehydes < ketones < esters < ethers < hydrocarbons (August & Tatzky 1984). Rowe et al. (1996a) noted that the diffusion of a number of different contaminants had the following order (lowest to highest): chloride < ethanoic acid < methyl ethyl ketone < 1,1 dichloroethane < dichloromethane < 1,2 dichloroethane. After 4 years there had been negligible diffusion of  $\text{Na}^+$  and  $\text{Cl}^-$  through the geomembrane and only minimal diffusion of ethanoic (acetic) acid. Similarly, August et al. (1992) found that there was negligible diffusion of heavy metal salts ( $\text{Zn}^{2+}$ ,  $\text{Ni}^{2+}$ ,  $\text{Mn}^{2+}$ ,  $\text{Cu}^{2+}$ ,  $\text{Cd}^{2+}$ ,  $\text{Pb}^{2+}$ ) from a concentrated (0.5 M) acid solution (pH=1-2) through HDPE over a 4 year test period.

For crystalline polymers, the crystalline areas act as "diffusion barriers" and diffusion appears to be primarily through the amorphous phase and hence one would expect that, as the crystallinity increases, the diffusion coefficients and solubility will decrease. For example, Park et al. (1995) reported that the permeability ( $P_g = S_g D_g$ ) of xylene in VLDPE was almost twice that through HDPE. Ashley (1985) has indicated that orientation can reduce permeability ( $P_g = S_g D_g$ ) of amorphous polymers by 10-15% and of crystalline polymers by over 50%.

#### 8.4 Diffusion of Water Through HDPE Geomembrane

Eloy-Giorni et al. (1996) performed a detailed study of water movement through intact geomembranes. Based on a series of experiments, they concluded that the concept of hydraulic conductivity (as defined by Darcy's Law) is not appropriate for describing water transport (and by inference the advective transport of contaminants) through hydrophobic geomembranes. In

particular, they demonstrated that a difference in pressure head across a geomembrane of up to 200 m had no significant effect on the movement of water molecules across a 1.7 mm thick HDPE geomembrane ( $\rho_g = 940 \text{ kg/m}^3$ ). Likewise, a head difference of up to 400 m had no significant effect on water movement across a 1 mm and 1.6 mm thick PVC geomembrane ( $\rho_g = 1260 \text{ kg/m}^3$ ). In these experiments, the driven flux of water (i.e. the flow of water across a geomembrane per unit area of geomembrane per unit time under conditions where there is a pressure head difference across the geomembrane) was less than or equal to the limit of accuracy of the apparatus ( $10^{-7} \text{ m}^3/\text{m}^2/\text{day} \leq 3 \times 10^{-5} \text{ m}^3/\text{m}^2/\text{a}$ ) and hence was negligibly small.

These findings, which were verified in several ways, are at variance with earlier results used by Giroud and Bonaparte (1989a) to establish permeation rates for geomembranes. Given the rigour of the recent experiments and the sophisticated techniques used, there is a reasonable likelihood that the 1996 results are more reliable than those used by Giroud and Bonaparte in 1989. If one accepts these results, then the only significant mechanism for water migration through the geomembrane is diffusion.

One may expect negligible water diffusion across a geomembrane in a composite MSW landfill liner for two reasons. Firstly, the permeability ( $P_g = S_g D_g$ ) of the geomembrane to water is extremely low. Based on the parameters given in Table 16 and Equation 10, one can

Table 16. Solubility and diffusion coefficient for water in three types of geomembrane (based on Eloy-Giorni et al. 1996).

	$S_g$ (-)	$D_g$ ( $\text{m}^2\text{s}^{-1}$ )	$\rho_g$ ( $\text{kgm}^{-3}$ )	$t_{GM}$ (mm)
HDPE	$8 \times 10^{-4}$	$2.9 \times 10^{-13}$	940	1.7
PVC	$7 \times 10^{-2}$	$4.4 \times 10^{-13}$	1260	1.0, 1.6
Bituminous	$9 \times 10^{-3}$	$8 \times 10^{-13}$	1150	5

show that the water flux,  $f$ , through a 1.5 mm thick HDPE geomembrane would be  $1.5 \times 10^{-13} \Delta c_f \text{ kg/m}^2/\text{s}$  (where  $\Delta c_f$  is in  $\text{kg/m}^3$  units) ( $1.3 \times 10^{-4} \Delta c_f \text{ L/ha/d}$ ) where  $\Delta c_f$  is the difference in the "concentration" of water on the two sides of the geomembrane. Thus, even with water on one side and zero relative humidity on the other side, the water flux would be very small. Secondly, apart from the low permeability of the geomembrane to water, one would expect there to be very little diffusive flux since the concentration gradient  $\Delta c_f$  is likely to be very small. For compacted clay liners, the soil water potential at the time of construction is typically -10 to -50 kPa and this corresponds to a relative humidity of about 99.5% (Daniel, personal communications). With water

(leachate) on one side of a geomembrane and compacted clay on the other side, the difference in relative humidity (and hence  $\Delta c_t$ ) is negligible. Thus, even with the presence of salts in the MSW leachate to influence the energy difference between the two sides of the geomembrane, the gradient in energy is so close to zero that, for all practical purposes, there will be no diffusion of water or water vapour across the geomembrane. This would appear to be the likely case for most of the service life of a geomembrane used as part of composite liner systems at the base of an MSW landfill. Thus, it would seem appropriate to revise the permeation rates suggested by Giroud and Bonaparte (1989a) to be, for all practical purposes, zero for HDPE geomembrane liners.

### 8.5 Diffusion of Contaminants Through HDPE Geomembranes

Although there is limited data on diffusion through geomembranes, there is enough to identify important issues and to provide a basis for the rational analysis and design of barrier systems that include a geomembrane.

Values of the Henry's coefficient  $S_{gf}$  and diffusion coefficient,  $D_g$ , based on the literature (including the work of the author and coworkers) are summarized in Table 17. These values provide a starting point, however the values should be used with caution since they are temperature and maybe concentration dependent. The values may also vary due to the chemical composition of the contaminant source, the polymer crystallinity, additives etc. and hence published values should only be used as an initial guide and do not replace experimentally determined values for the geomembrane of interest for projects where uncertainty regarding the diffusion coefficient or sorption could have a significant impact.

To illustrate the effect of leachate composition, consider the results for toluene and dichloromethane as summarized in Table 17. It can be seen that the value of  $S_{gf}$  reported for toluene ranges from 0.09 to 192 for pure and aqueous solution respectively and the values of diffusion coefficient range from  $4.4 \times 10^{-12}$  to  $0.18 \times 10^{-12}$ . It is also noted that the values of  $S_{gf}$  and  $D_g$  for aqueous solutions are reported to vary depending on the concentration. Based on the data by Park and Nibras (1993), average values of  $S_{gf}=96$  and  $D_g=0.47 \times 10^{-12}$  m<sup>2</sup>/s will be used in subsequent modelling of toluene in aqueous solution and values of  $S_{gf}=0.09$  and  $D_g=4.4 \times 10^{-12}$  m<sup>2</sup>/s will be used for pure toluene as summarized in Table 18. The variation in values for  $S_{gf}$  for the dichloromethane (DCM) is less than for toluene with  $S_{gf}$  ranging between 0.06 and 5.6 and the reported diffusion coefficients ranging between  $9 \times 10^{-12}$  and  $0.58 \times 10^{-12}$  m<sup>2</sup>/s for pure and aqueous solutions respectively. The values of  $S_{gf}$  and  $D_g$  to be subsequently used in modelling DCM diffusion through an HDPE geomembrane are given in

Table 18.

Fortunately, the variability between diffusion coefficients reported in the literature (see Table 17) is not as critical as it may appear. In essence, for a given contaminant, the geomembrane is either a good diffusion barrier (e.g. to water and hydrated ions such as Na<sup>+</sup>, Cl<sup>-</sup>, Zn<sup>2+</sup>, Ni<sup>2+</sup>, Mn<sup>2+</sup>, Cu<sup>2+</sup>, Cd<sup>2+</sup> and Pb<sup>2+</sup>) or it is not (e.g. organic compounds such as toluene, dichloromethane etc.) with many orders of magnitude difference in the permeability of the geomembrane ( $P_g=S_{gf} D_g$ ) for these two groups. Due to the very low permeation rates, it is very difficult to obtain the values of  $S_{gf}$  and  $D_g$  for hydrated ions however it is possible to obtain an estimate of the parameters. It may be anticipated that the solubility of hydrated ions will be less than unity. One option is to assume  $S_{gf}=1$  and deduce the value of  $D_g$  based on a two compartment diffusion test (see Figure 18). Since  $S_{gf}$  is likely smaller than unity, this approach may lead to some small mass balance error but in a field application it is likely not significant as demonstrated momentarily. The other option is to assume that  $S_{gf}$  is similar to that of water and deduce  $D_g$  from laboratory tests using  $S_{gf}=8 \times 10^{-4}$ . Figure 19 shows parameters deduced in both ways for a diffusion test conducted by Rowe et al. (1995a). Based on 2.5 years of data, they deduced an upper bound on the diffusion coefficient of chloride (assuming  $S_{gf}=1$ ) of  $6 \times 10^{-15}$  m<sup>2</sup>/s and indicated that the value would likely be reduced as more data became available. Figure 19 shows an additional two years of data and it can be seen that the concentration in the receptor remained low (the scatter of the data should be interpreted in the context of the very low concentrations - all lower than 0.2% of the source concentration). Assuming  $S_{gf}=1$ , it is now clear that the diffusion coefficient is less than  $3.2 \times 10^{-15}$  m<sup>2</sup>/s and likely less than  $2 \times 10^{-15}$  m<sup>2</sup>/s. Adopting the partitioning coefficient for water,  $S_{gf}=8 \times 10^{-4}$ , the diffusion coefficient is less than  $4 \times 10^{-13}$  m<sup>2</sup>/s and likely less than  $1 \times 10^{-13}$  m<sup>2</sup>/s. The theoretical fits using  $S_{gf}=8 \times 10^{-4}$  appear to better describe the observation than the fits for  $S_{gf}=1$ . These tests are ongoing and the diffusion coefficient will likely be reduced in the future as more data becomes available. However, there is already sufficient data to address practical issues as shown below.

Figure 20 shows the predicted migration of chloride through a composite liner system assuming no holes and no significant degradation of the geomembrane over the period being examined. It can be seen that the uncertainty regarding the precise parameters ( $S_{gf}=8 \times 10^{-4}$ ,  $D_g=1 \times 10^{-13}$  m<sup>2</sup>/s; versus  $S_{gf}=1$ ,  $D_g=2 \times 10^{-15}$  m<sup>2</sup>/s) is of little practical consequence and that the geomembrane (unlike the clay) is a very good diffusion barrier to Cl<sup>-</sup> (and likely other hydrated ions as already discussed). After 50 years the calculated peak impact is less than 3 mg/L and after 475 years it is less than 16 mg/L for the

Table 17. Partition and diffusion coefficients for various contaminants in PE geomembrane.

Chemical	Thickness <sup>+</sup>	Solution	$S_{gt}$	$D_g(\times 10^{12} \text{ m}^2/\text{s})$	Ref.
Acetic acid	2.0	4000 mg/L	-	$\leq 0.003$ <i>b</i>	[11]
	2.5	pure	0.0086 <i>ad</i>	0.52-0.58 <i>a</i>	[7]
	2.5	500-900 g/L	0.015 <i>ac</i>	0.11-0.29 <i>a</i>	[7]
Acetic acid ethyl ester	1.00	aqueous	0.021 <i>ad</i>	1.1 <i>b</i>	[7]
	2.00	aqueous	0.023 <i>ad</i>	-	[7]
Acetone	0.75	pure	0.012 <i>ad</i>	0.51 <i>a</i>	[8]
	1.00	aqueous saturated	0.20 <i>ac</i>	$< 0.0001$ <i>a</i>	[9]
	1.00	pure	0.009 <i>ad</i>	-	[7]
	2.00	pure	0.009 <i>ad</i>	-	[7]
	2.00	pure	-	0.26-1.0 <i>a</i>	[7]
	2.50	pure	0.0099-0.0112 <i>ad</i>	0.87-0.91 <i>a</i>	[7]
	2.50	10 % vol.	0.32 <i>ac</i>	0.66-0.84 <i>a</i>	[7]
	2.50	50 % vol.	-	0.88 <i>a</i>	[7]
	2.54	aqueous saturated	$> 0.013$ <i>ac</i>	-	[5]
	Benzene	0.15 <sup>**</sup>	pure	-	2.0 <i>a</i>
1.00		aqueous saturated	57.2 <i>ac</i>	0.037 <i>a</i>	[9]
1.50		pure	0.08 <i>ad</i>	2.2-3.3 <i>a</i>	[10]
0.75&2.54		pure	-	4.2 <i>a</i>	[2]
2.54		aqueous saturated	54.3 <i>ac</i>	-	[5]
Carbon Tetrachloride	0.15 <sup>**</sup>	pure	-	0.66 <i>a</i>	[15]
	1.00	pure	0.180 <i>ad</i>	2.4 <i>b</i>	[7]
	2.00	pure	0.200 <i>ad</i>	-	[7]
	2.00*	89.1 mg/L	-	57 <i>b</i>	[6]
	2.00	89.1 mg/L	-	48 <i>b</i>	[6]
Chlorobenzene	0.75	pure	0.083 <i>ad</i>	2.4 <i>a</i>	[8]
	1.00	pure	0.097 <i>ad</i>	3.6 <i>b</i>	[7]
	1.50	pure	0.110 <i>ad</i>	2.2-3.2 <i>a</i>	[10]
	2.00	pure	0.108 <i>ad</i>	-	[7]
Chloroform	0.15 <sup>**</sup>	pure	-	1.8 <i>a</i>	[15]
	1.00	pure	0.134 <i>ad</i>	5.9 <i>b</i>	[7]
	2.00	86.2 mg/L	-	17 <i>b</i>	[6]
	2.00*	86.2 mg/L	-	25 <i>b</i>	[6]
	2.00	pure	0.153 <i>ad</i>	-	[7]
Chloride	2.00	2000-4000 mg/L	-	0.002-0.005 <i>b</i>	[11]
	2.00	2000-4000 mg/L	0.0008 <i>be</i>	0.1-0.3 <i>b</i>	[16]
Cyclohexane	0.15 <sup>**</sup>	pure	-	0.61 <i>a</i>	[15]
	1.00	aqueous saturated	2378 <i>ac</i>	0.012 <i>a</i>	[9]
Dichloromethane	0.75	pure	0.06 <i>ad</i>	4.9 <i>a</i>	[8]
	0.75	13.1-234.4 mmol/L	1.8-2.9 <i>ac</i>	0.58-2.28 <i>a</i>	[8]
	0.75 & 2.5	pure	-	9.0 <i>a</i>	[2]
	0.76-2.54	100 mg/L	1.8-5.6 <i>bc</i>	-	[12]
	2.00	pure	-	2-10 <i>a</i>	[3]
	2.00	2-10 mg/L	-	1-3 <i>b</i>	[11]
	2.00	2-10 mg/L	2.3 <i>be</i>	0.95-1.2 <i>b</i>	[16]
1,1 Dichloroethane	0.75 & 2.54	pure	-	2.3 <i>a</i>	[2]
	2.00	2-10 mg/L	-	1-2.5 <i>b</i>	[11]

Chemical	Thickness <sup>+</sup> (mm)	Solution	S <sub>gf</sub>	D <sub>g</sub> (×10 <sup>12</sup> m <sup>2</sup> /s)	Ref.
1,2 Dichloroethane	0.75 -2.54	pure	-	2.3 <i>a</i>	[2]
	1.00	aqueous saturated	7.2 <i>ac</i>	6.8 <i>a</i>	[9]
	2.00	2-10 mg/L	-	3-6 <i>b</i>	[11]
Ethyl Acetate	0.75	pure	0.024 <i>ad</i>	0.79 <i>a</i>	[8]
EthylBenzene	0.75	pure	0.1 <i>ad</i>	2.8 <i>a</i>	[8]
Formaldehyde	1.00	37 % wt	0.004 <i>ad</i>	-	[7]
	2.00	37 % wt	0.003 <i>ad</i>	-	[7]
Heptane	2.50	pure	0.0646-0.0660 <i>ad</i>	1.52-1.74 <i>a</i>	[7]
<i>n</i> -Hexane	0.75	pure	0.006 <i>ad</i>	3.6 <i>a</i>	[8]
	2.50	pure	0.0646-0.0663 <i>ad</i>	2.08-2.47 <i>a</i>	[7]
Methyl ethyl ketone	2.00	2-10 mg/L	-	0.3-0.8 <i>b</i>	[11]
	2.50	pure	0.0179 <i>ad</i>	0.75 <i>a</i>	[7]
	2.50	pure	0.019 <i>ad</i>	0.86 <i>a</i>	[7]
	2.54	aqueous saturated	> 0.025 <i>ac</i>	-	[5]
<i>n</i> -Octane	0.75	pure	0.08 <i>ad</i>	1.9 <i>a</i>	[8]
Propanoic acid	2.50	pure	0.0212 <i>ad</i>	0.30 <i>a</i>	[7]
	2.50	pure	0.0209 <i>ad</i>	0.32 <i>a</i>	[7]
Tetrachloroethane	2.00	61.0 mg/L	-	78 <i>b</i>	[6]
	2.00*	61.0 mg/L	-	87 <i>b</i>	[6]
Tetrachloroethylene	1.00	pure	0.190 <i>ad</i>	3.8 <i>b</i>	[7]
	2.00	pure	0.217 <i>ad</i>	-	[7]
Toluene	0.15**	pure	-	1.8 <i>a</i>	[15]
	0.75	pure	0.09 <i>ad</i>	4.4 <i>a</i>	[8]
	0.75	0.28 - 5.0 mmol/L	63.5-151.0 <i>ac</i>	0.35-0.56 <i>a</i>	[8]
	0.76 - 2.54	100 mg/L	115-125 <i>bc</i>	-	[12]
	0.76 & 2.54	pure, 1.25 M	-	0.23 <i>a</i>	[2]
	1.00	0.05 % weight	-	0.23 <i>b</i>	[1]
	1.00	aqueous saturated	192 <i>ac</i>	0.51 <i>a</i>	[9]
	1.00	pure	0.080 <i>ad</i>	6.1 <i>b</i>	[7]
	1.00	aqueous	160 <i>ac</i>	0.2 <i>b</i>	[7]
	1.50	pure	0.09 <i>ad</i>	2.6-4.0 <i>a</i>	[10]
	2.00	pure	0.090 <i>ad</i>	-	[7]
	2.00	pure	-	0.18-4.0 <i>a</i>	[3]
	2.54	aqueous saturated	137 <i>ac</i>	-	[5]
1,1,1 Trichloroethane	2.54	aqueous saturated	78.2 <i>ac</i>	-	[5]
Trichloroethylene	0.75	pure	0.11 <i>ad</i>	12 <i>a</i>	[8]
	0.75	0.42-8.4 mmol/L	-	0.44-0.76 <i>a</i>	[8]
	0.76 - 2.54	100 mg/L	94-98 <i>bc</i>	-	[12]
	1.00	aqueous saturated	134.5 <i>ac</i>	0.52 <i>a</i>	[9]
	1.00	aqueous saturated	134.5 <i>ac</i>	0.50 <i>b</i>	[9]
	1.00	0.1 % weight	-	0.69 <i>b</i>	[1]
	1.00	pure	0.168 <i>ad</i>	10.8 <i>b</i>	[7]
	1.00	500 mg/L	-	0.6 <i>b</i>	[7]
	2.00	pure	0.190 <i>ad</i>	-	[7]
	2.00	61.0 mg/L	-	73 <i>b</i>	[6]
	2.00*	61.0 mg/L	-	85 <i>b</i>	[6]

Chemical	Thickness <sup>+</sup>	Solution	S <sub>gf</sub>	D <sub>g</sub> (×10 <sup>12</sup> m <sup>2</sup> /s)	Ref.
Trichloroethylene	2.50	pure	0.195-0.200 <i>ad</i>	7.70-8.40 <i>a</i>	[7]
	2.50	500 mg/L	189 <i>ac</i>	0.20-0.30 <i>a</i>	[7]
	2.54	aqueous saturated	131 <i>ac</i>	-	[5]
<i>m</i> -Xylene	0.15 <sup>**</sup>	pure	-	1.5 <i>a</i>	[15]
	0.75	pure	0.093 <i>ad</i>	3.7 <i>a</i>	[8]
	0.75	0.2-1.6 mmol/L	192.7-310.2 <i>ac</i>	0.31-0.36 <i>a</i>	[8]
	0.76-2.54	100 mg/L	365-370 <i>bc</i>	-	[12]
	2.54	aqueous saturated	366 <i>ac</i>	-	[5]
<i>o</i> -Xylene	0.15 <sup>**</sup>	pure	-	0.94 <i>a</i>	[15]
	2.54	aqueous	422 <i>ac</i>	-	[5]
<i>p</i> -Xylene	0.15 <sup>**</sup>	pure	-	1.6 <i>a</i>	[15]
	2.54	aqueous saturated	387 <i>ac</i>	-	[5]
<i>n</i> -Xylene	0.15 <sup>**</sup>	pure	-	1.8 <i>a</i>	[15]
Xylene	1.00	pure	0.083 <i>ad</i>	4.7 <i>b</i>	[7]
	1.00	aqueous	556 <i>ac</i>	0.2 <i>b</i>	[7]
	1.00	aqueous	-	1.8 <i>b</i>	[1]
	1.00	aqueous saturated	498.5 <i>a</i>	1.0 <i>ab</i>	[9]
	2.00	pure	0.095 <i>ad</i>	-	[7]
Water	1.70	-	≤ 0.0003 <i>ad</i>	≥ 0.4 <i>a</i>	[4]
	1.70	-	0.0008 <i>bd</i>	0.29 <i>b</i>	[4]
	2.00	-	-	0.4 - 9.0 <i>a</i>	[3]
	2.50	-	0.0008 - 0.001 <i>ad</i>	0.82 - 0.90 <i>a</i>	[7]
	-	-	-	1.6 -	[13]
	-	-	-	2.6 -	[14]

- [1] August & Tatzky (1984)  
[2] Britton et al. (1989)  
[3] Durin et al. (1998)  
[4] Eloy-Giorni et al. (1996)  
[5] Haxo & Lahey (1988)  
[6] Lubber (1992)  
[7] Muller et al. (1998)  
[8] Park & Nibras (1993)  
[9] Prasad et al. (1994)

- [10] Ramsey (1993)  
[11] Rowe et al. (1996)  
[12] Sakti & Park (1992)  
[13] Lord et al. (1988)  
[14] Hughes and Monteleone (1987)  
[15] Saleem (1989)  
[16] Present paper

- (a) Sorption/absorption/immersion  
(b) Permeation/diffusion  
(c) Solubility in GM/solubility in water  
(d) Mass of chemical/Mass of GM)  
(e) See text for methodology  
+ HDPE except where specified  
\* MLDPE  
\*\* LLDPE  
- Not reported/measured

Table 18. Values of  $D_g$  and  $S_{gf}$  used in modelling of contaminant migration across an HDPE geomembrane for Figures 20, 22-24.

Leachate	$D_g$ ( $m^2/s$ )	$S_{gf}$ (-)	Reference
Pure	$4.4 \times 10^{-12}$	0.09	(a)
Toluene			
Toluene*	$0.47 \times 10^{-12}$	96	(a)
DCM	$2.2 \times 10^{-12}$ **	1	(b)
(aqueous)	$1.0 \times 10^{-12}$	2.3	(c)
Chloride	$3.2 \times 10^{-15}$ **	1	(c)
	$2.0 \times 10^{-15}$ **	1	(c)
	$4 \times 10^{-13}$	0.0008	(c)
	$1 \times 10^{-13}$	0.0008	(c)

\*Aqueous Solution: Average values 5-90% of solubility.

\*\* $D_g$  calculated assuming  $S_{gf}=1$ .

(a) Park & Nibras (1993); (b) Rowe et al. (1995a); (c) this paper.

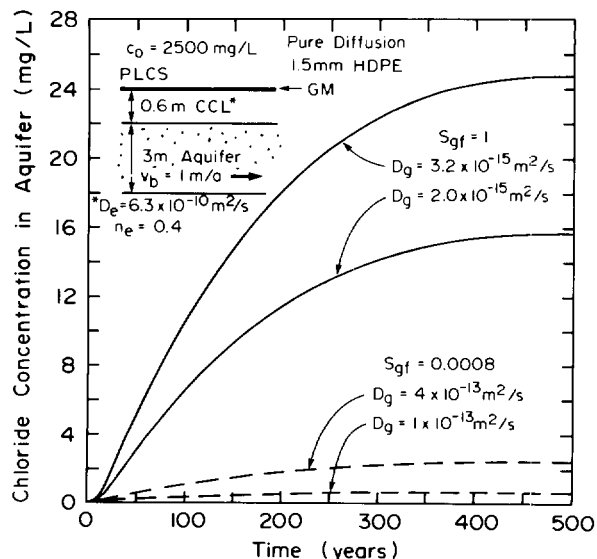


Figure 20. Calculated variation in chloride concentration in an aquifer due to diffusion through an HDPE geomembrane and 0.6 m CCL for different diffusion parameters  $D_g$ ,  $S_{gf}$ .

predictions using  $S_{gf}=1$  and its corresponding diffusion coefficient.

The tests conducted by Rowe et al. (1995a) were at concentrations of salt typical of landfill leachate. It should be noted that for solutes that dissociate completely to form ions, the mass transfer across a geomembrane may be proportional to concentration squared, and not just concentration as suggested by Ficks law, and hence the apparent "diffusion coefficient" may increase with increasing concentration (remembering the earlier caution that it may really be a mass transfer coefficient rather than a true diffusion coefficient that we use in our models). This is because in the geomembrane, the sodium and chloride (or other similar ion pairs) must diffuse as pseudo-molecules of sodium chloride rather than as ions and the concentration of ion pairs at the surface is proportional to the product of the sodium and chloride ions or the square of the concentration of sodium chloride in the adjacent aqueous solution as discussed by Cussler (1984).

For organic compounds in aqueous solution, the value of  $S_{gf}$  is strongly related to the solubility of the compound of interest in water. Generally, the lower the solubility in water, the greater the affinity for HDPE and the higher the value of  $S_{gf}$  when in aqueous solution. For DCM (see Table 18), the value of  $S_{gf}$  is of the order of unity and a range of values between 1 and 2.3 has only a small effect on the value of  $D_g$  that is deduced ( $0.95$  to  $2.2 \times 10^{-12} m^2/s$ ) (see Figure 21). To illustrate the fact that the precise choice of  $S_{gf}$  and  $D_g$  is not critical, calculations were performed for  $S_{gf} = 1$ ,  $D_g = 2.2 \times 10^{-12} m^2/s$  and  $S_{gf} = 2.3$ ,

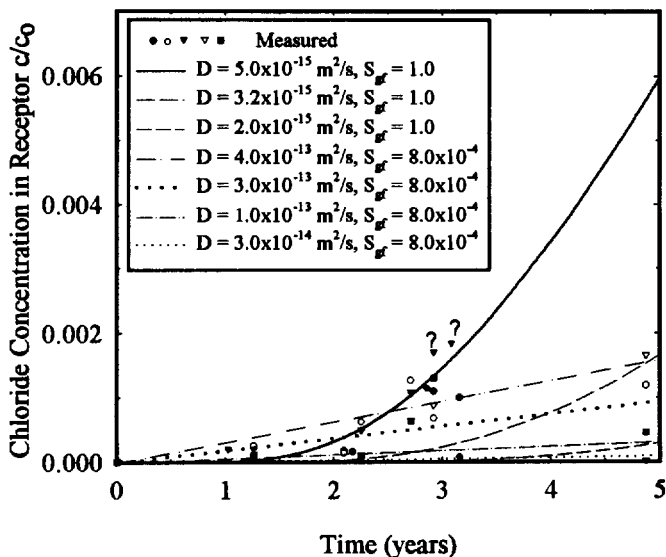


Figure 19. Variation in observed and calculated chloride concentrations in a two compartment diffusion test for a range of diffusion parameters  $D_g$ ,  $S_{gf}$ .

conditions examined and these two "likely upper" bound diffusion coefficients. Even for the most conservative interpretation of the current data, the peak increase in the aquifer (assuming no attenuation layer between the liner and aquifer) is less than 5 mg/L at 50 years and the peak is less than 25 mg/L at 475 years. As noted above, the combination of a low solubility ( $S_{gf}=8 \times 10^{-4}$ ) and the corresponding deduced diffusion coefficient gives a better fit to the experimental data shown in Figure 19 and gives much lower predicted impact (see Figure 20) than

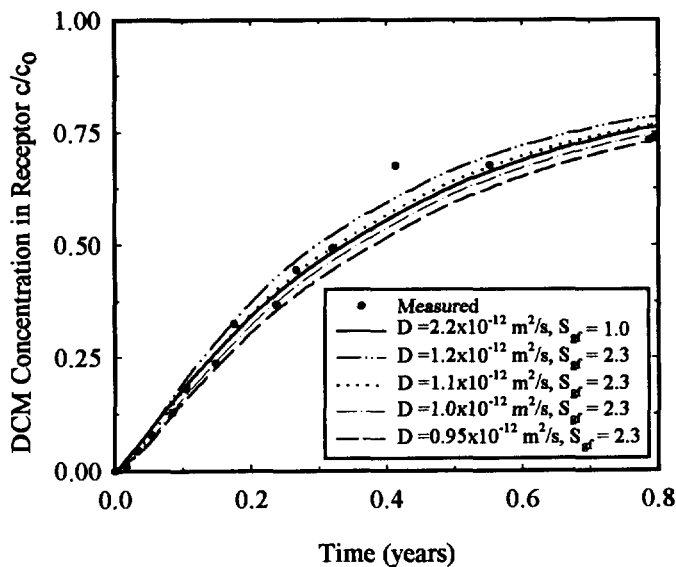


Figure 21. Variation in observed and calculated receptor dichloromethane (DCM) concentrations in a two compartment diffusion test for a range of diffusion parameters  $D_g$ ,  $S_{gf}$  (modified from Rowe et al. 1995a).

$D_g = 1 \times 10^{-12} \text{ m}^2/\text{s}$  (both combinations give a similar fit to the experimental data in Figure 21) as shown in Figure 22. The calculated increase in DCM concentration in an

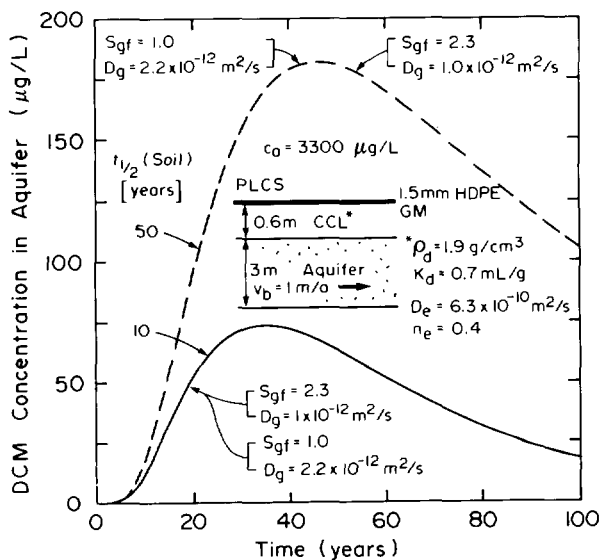


Figure 22. Calculated variation in DCM concentration in an aquifer due to diffusion through an HDPE geomembrane and 0.6 m CCL for different diffusion parameters  $D_g$ ,  $S_{gf}$  and half-lives in the clay.  $t_{1/2}$  (leachate) = 10 years.

aquifer below the composite liner is identical (to plotting accuracy) for the two cases. These calculations assume transport parameters in the clay as shown in the insert to Figure 22. Of particular note is the source concentration and half-life of DCM. The source concentration is based on data from the Keele Valley Landfill in Toronto (Rowe 1995). The half-life of 10 years is considered to be a reasonable value for MSW sites in Canada (see MoEE 1996; Rowe 1995). What is far less certain is the half-life of DCM in the underlying clay. Since the geomembrane acts as a selective barrier and effectively excludes volatile fatty acids that form the primary substrate for biodegradation in the landfill, one would anticipate slower degradation in the clay than in the leachate. This is the topic of current research at the University of Western Ontario. For the purposes of the current modelling, a half-life of 50 years was adopted. For this combination of parameters, and excluding the effects of consolidation, the concentration of DCM in the aquifer would be expected to reach 10-15  $\mu\text{g/L}$  after about 10 years and the Maximum Acceptable Concentration (MAC) of 50  $\mu\text{g/L}$  after 15 years. If the half-life was 10 years in the clay the peak impact at 35 years would be about 1.5 times the MAC for this combination of parameters. Clearly, some caution is required in the selection of half-lives. The impact on the aquifer can be reduced by the presence of either a thicker liner or an attenuation layer between the liner and the aquifer as will be illustrated in Section 10.

The published diffusion parameters for toluene (see Table 18) vary significantly depending on the test conditions, with low values of  $S_{gf}$  and high diffusion,  $D_g$  (e.g.  $S_{gf} = 0.09$ ,  $D = 4.4 \times 10^{-12} \text{ m}^2/\text{s}$ ,  $P_g = 0.4 \times 10^{-12} \text{ m}^2/\text{s}$ ) for pure solvent and high values of  $S_{gf}$  and low  $D_g$  (e.g. average values of:  $S_{gf} = 96$ ,  $D = 0.47 \times 10^{-12} \text{ m}^2/\text{s}$ ,  $P_g = 45 \times 10^{-12} \text{ m}^2/\text{s}$ ) for aqueous solutions. To examine this, Figure 23 shows the calculated variation in concentration with time in an aquifer for these two combinations of diffusion parameters ( $S_{gf}$ ,  $D_g$ ) and it can be seen that the parameters for aqueous contaminants give a much higher impact than those for pure solvent. However, the parameters for sorption ( $K_d$ ) and the half-life in the leachate and the soil are even more important. Results are given assuming no retardation ( $K_d=0$ ) and moderate sorption ( $K_d=3.9$ ) in Figure 23 for infinite half-life. Figure 24 shows similar results assuming a half-life in leachate of 10 years and soil of 50 years. Given that the drinking water objective for toluene is 24  $\mu\text{g/L}$ , it can be seen that the drinking water objective would be met only with moderate retardation and considering the toluene half-life as examined in Figure 24. The impacts for other cases would be reduced if there was an attenuation layer between the compacted clay liner and aquifer (as examined in Section 10). However, it is evident that the most critical liner parameters are the distribution

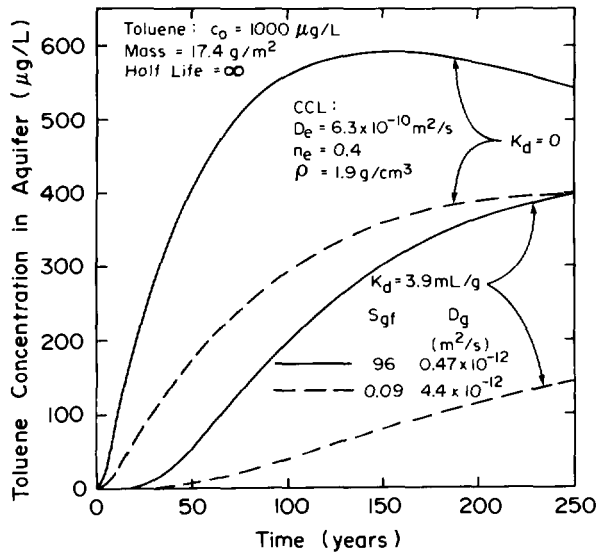


Figure 23. Calculated variation in toluene concentration in an aquifer due to diffusion through an HDPE geomembrane and 0.6 m CCL for published values of  $D_g$ ,  $S_{gf}$ . Assumed infinite half-life.

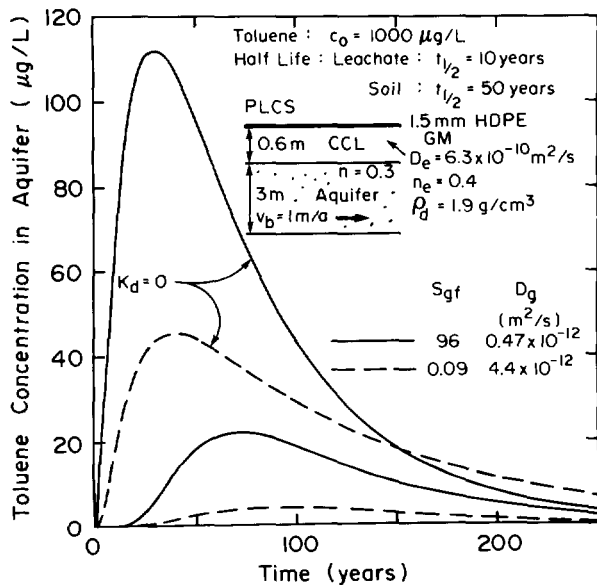


Figure 24. Calculated variation in toluene concentration in an aquifer due to diffusion through an HDPE geomembrane and 0.6 m CCL for published values of  $D_g$ ,  $S_{gf}$ . Assumed half-life of toluene: 10 years in leachate; 50 years in soil.

coefficient and the half-life in the clay. As discussed by Rowe et al. (1995b) and Rowe and Weaver (1997), care is required in the selection of  $K_d$  values based on published correlations.

Using computer codes like that used here (Rowe & Booker 1997) to get Figures 20, 22-24, one can establish the importance of diffusion as a transport mechanism through a geomembrane. For hydrated ions such as chloride examined in Figure 20, diffusion is not important for the diffusive service life of geomembrane (i.e. the length of time that it maintains this low diffusion coefficient) and the critical consideration will be leakage through holes. However, for certain organic contaminants (e.g. see Figures 22-24), the diffusive migration may be very significant for a well constructed liner (i.e. one with only a few holes), and should be considered if one is to ensure a safe design.

In the analysis, the migration of organic compounds through composite liners, key factors to be considered include (a) the retardation characteristics of the clayey component of the composite liner (see Rowe et al. 1995b) and (b) biodegradation of the organics as they migrate through the soil (see Rowe 1995; Rowe et al. 1996a, 1997d). Since the geomembrane provides a good barrier to volatile fatty acids and other nutrients in leachate, there is potential that the degradation rates for organic compounds below a geomembrane will be less than when a complete contaminant plume is migrating through soil due to the reduction in substrates.

## 9 LEAKAGE THROUGH COMPOSITE LINERS

### 9.1 Observed leakage Through Liners

Modern landfills typically have a primary leachate collection system (PLCS) intended to collect leachate and control the leachate head acting on the primary liner. A number of landfills have also been constructed with a second drainage layer below the primary liner (see Figures 1 and 3). This secondary drainage layer allows the collection of some or all of the water arising from consolidation of the clay liner as well as leachate that migrates through the primary liner. It also allows the control of the head acting on the secondary liner. The terminology used to describe this layer varies with it often being called either a secondary leachate collection system or a leak detection system. In this paper, the secondary drainage layer will be referred to as the secondary leachate collection system (SLCS).

Monitoring data from a secondary leachate collection system (SLCS) may provide insight regarding the effectiveness of composite primary liners. However, the interpretation of the data from SLCS requires careful consideration of sources of fluid other than leakage from the landfill (Gross et al. 1990). These include (a) water that infiltrated into the SLCS layer during construction; (b) water arising from compression and consolidation of the clay liner; and (c) groundwater water from outside of the landfill.



Bonaparte et al. (1996) examined data for 26 landfill cells containing GCLs as part of the composite primary liner. They identified three periods during which there may be very different flows to the SLCS: (a) the initial period of operation, (b) the active period of operation, and (c) post-closure period (after the final cover has been constructed). Table 19 summarizes the mean and standard deviations of the flows in the PLCS and SLCS. As might be expected, flow rates from the SLCS decrease as flow rates from the PLCS decrease. This is likely, at least in part, due to reduced head acting on the primary composite liner. The mean SLCS flow rates are small during both the active and post-closure period (0.7 and 0.2 lphd respectively). Peak flow rates are about an order of magnitude larger than the average values but are still quite small. If one eliminates construction water from the flows by examining systems with a geonet SLCS, it would appear that for a composite liner with a geomembrane and GCL, the hydraulic efficiency of the liner is in excess of 99.9% and the average flow rates potentially attributable to primary liner leakage are less than 11.2 and 24.3 lphd respectively. Data in the active period is limited but for the two cases reported the maximum mean and peak SLCS flow rates are 0.9 and 3.7 lphd respectively.

The SLCS flow rates reported by Bonaparte et al. (1996) are very low, however there is also potential for diffusive transport of organic compounds through a composite liner involving a geomembrane over a GCL with typical (unmodified) bentonite. Although data relating to potential diffusion through composite liners is limited, there is some evidence to suggest that this requires further evaluation. For example, Othman et al. (1996) report significant levels of 1,1 dichloroethane and dichloromethane (methylene chloride) in the SLCS for a landfill with a 1.5 mm thick HDPE geomembrane and 6 mm thick GCL composite liner and a 5 mm thick geonet SLCS. This same system had exhibited low SLCS flow rates (average value of 3.6 lphd from 14-21 months reducing to 0.7 lphd between 22-31 months) and inorganic chemistry that was not characteristic of leachate. This implies that any leakage through holes

in the geomembrane was very small. However, the concentration of DCM and 1,1 DCA are small but significant over a period of between 6 and 28 months after commencement of waste placement. This suggests possible diffusion through the GM/GCL system. Additional investigation would be required to confirm the hypothesis.

Table 20 summarizes data obtained in the "active operation" period for composite liners involving a geomembrane over compacted clay (CCL). The fluid collected in the SLCS is considerably greater than that obtained for the composite liners involving only a geomembrane and GCL. Othman et al. (1996) attributed much of the fluid collected in the SLCS of these systems to consolidation water from the overlying GCL. This hypothesis is supported by the leachate chemistry that is not similar to leachate. Generally, the volatile organic compound (VOC) concentrations in the SLCS were very low with only DCM being clearly evident at a low concentration and possible trace levels of other compounds for the landfill with a very thin CCL (450 mm thick). For this landfill, the SLCS flow rates were quite small (average value less than 15 lphd reducing to less than 3 lphd after about 3 years). Given (a) the thin liner and (b) the fact that consolidation of the liner increases the rate of contaminant transport and the mass flux across the clay liner (e.g. Smith 1997), there is the potential for organics that readily diffuse through the geomembrane and experience relatively little retardation in clay (such as DCM) to diffuse through the geomembrane and move through the clay in a couple of years.

Workman (1993) has also examined the chemistry of the fluid in the SLCS of a number of cells and detected several VOCs including chloroethane, ethylbenzene and trichloroethene at low concentrations. He hypothesizes that they migrated as gases from the primary to secondary system at the sideslopes. While this may be a reasonable hypothesis, the alternative hypothesis of migration through the primary liner by a combination of diffusion and consolidation induced advection warrants further consideration.

Table 19. Mean and standard deviations of flow in PLCS and SLCS for 6 landfill cells with a GCL as part of a composite primary liner (in lphd) (after Bonaparte et al. 1996).

	Average Flows					Peak Flows			
	Cells	PLCS		SLCS		PLCS		SLCS	
		Mean	sd	Mean	sd	Mean	sd	Mean	sd
Initial Period	25/26	5,350	3,968	36.6	68.5	14,964	11,342	141.8	259.9
Active Operation	18/19	276	165	0.7	1.1	752	590	7.7	13.7
Post-Closure	4	124	-	0.2		266	-	2.3	

Table 20. Average flow rates in PLCS and SLCS for landfills with composite liners involving GM and CCL (in lphd). (modified from Othman et al. 1996) [simple average of data after about 3 years].

Type	Primary Liner		SLCS		PLCS		SLCS		Period	
	GM	Clay	Material	Thick-ness (mm)	Average	Peak	Average	Peak		
Type	Thick-ness (mm)	Type	Thick-ness (mm)	Material	Thick-ness (mm)	(lphd)	(lphd)	(lphd)	(lphd)	(mo.)
CSPE	0.9	CCL	600	sand	450	1120	2076	113	260	41-93
HDPE	2.0	CCL	450	sand	300	4400	5790	59	152	35-54
HDPE	1.5	CCL	900	GN	5	1142	3985	167	275	42-66
HDPE	2.0	CCL	450	GN	5	53	170	1.5	10	34-58
HDPE	1.5	CCL	900	GN	5	1144	1371	60	102	30-37

Bonaparte and Gross (1993) examined the flow through composite primary liners underlain by a SLCS and based on their data it would appear that with Construction Quality Assurance (CQA), 19% of landfills had SLCS flow rates of 50 lphd or less (see Table 21) and 57% of landfills had SLCS flow rates of 200 lphd or less. For those landfills with no CQA, only 20% of landfills had SLCS flow rates of 200 lphd or less. This illustrates the benefits of CQA. The flows reported in Table 21 should be regarded as an upper bound to leakage since Bonaparte and Gross (1993) attribute most of these flows to consolidation water and hence it would not be due to leakage through the geomembrane. A better measure is given by the data in Table 20 where all of the average flows are less than 200 lphd and 60% are less than 100 lphd. In absolute terms, these flows are very small but, as will be discussed in subsequent sections, are generally much larger than would be expected due to leakage through a few holes in the geomembrane.

Table 21. Percentage of landfills with average measured flow rate in the SLCS in specified range for composite primary liners (modified from Bonaparte & Gross 1993).

Flow Rate (lphd)	With CQA	No CQA
<50	19%	-
50-200	38%	20%
200-500	27%	40%
500-1000	8%	40%
>1000	8%	
(Number of landfills)	37	5

## 9.2 Existing Solutions for Assessing Leakage

In the design of composite liner systems consideration needs to be given to the potential for water migration through the liner due to (a) diffusion (permeation) through the intact geomembrane (discussed in Section 8) and (b) flow through holes in the geomembrane. Giroud and Bonaparte (1989a,b) and Giroud et al. (1989) developed a set of equations that have been widely used for estimating the leakage through geomembrane liners underlain by compacted clay liners. These equations provide an approximate solution assuming that the gradient is near unity. This may be a reasonable assumption for low leachate mounds (e.g. design mounds of 0.03-0.3 m) and clay liners that are 0.6-0.9 m, but are not strictly valid for the levels of leachate mounding associated with termination of the operation or excessive clogging of a leachate collection system (e.g. 10-20 m) or even a modest leachate mound over a GCL. Recognizing this limitation, Giroud et al. (1992) extended the approximate solution to consider hydraulic gradients much greater than unity. They also provided a solution for large defects.

These Giroud and Bonaparte (1989a, b) and Giroud et al. (1989, 1992) solutions are all based on leakage experiments that were performed for geomembranes in contact with conventional compacted soil at low confining stress (Brown et al. 1987). They were not developed for the potentially better contact that could be achieved by having a geomembrane in contact with a GCL which itself is placed on a firm foundation layer. Wilson-Fahmy and Koerner (1995) recognized the limitation of the Giroud et al. (1989) solution for geomembranes over GCLs. Specifically, they noted that since the gradients were likely to be much larger than unity, the Giroud et al. (1989) approximations were no longer valid and it was necessary to solve the complete differential equation.

This they did using a numerical (finite difference) technique. They performed a parametric study to examine the leakage through holes of different radii (1, 3, 5 and 7 mm) for a range of transmissivities of the GM/GCL contact ( $10^{-8}$ ,  $10^{-9}$ ,  $10^{-10}$ ,  $10^{-11}$  and  $10^{-12}$  m<sup>2</sup>/s), hydraulic conductivities of the GCL ( $1 \times 10^{-10}$ ,  $1 \times 10^{-11}$ ,  $5 \times 10^{-11}$ , and  $1 \times 10^{-12}$  m/s) and GCL thicknesses (4, 7 and 10 mm).

Walton and Sagar (1990) and Walton et al. (1997) have suggested that for effective stresses corresponding to more than 0.5 m burial of the geomembrane there should be no gap between the geomembrane and the soil (wetted radius  $R=r_o$  in Figure 25) and hence for widely

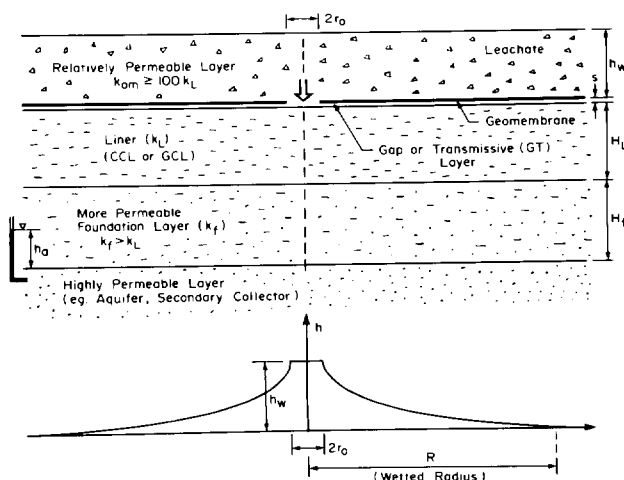


Figure 25. Schematic showing a hole of radius  $r_o$  in a geomembrane and the underlying strata together with the head distribution between the geomembrane and clay liner.

spaced small holes that are not infilled with soil, the leakage through any such hole would be given by Forchheimer's Equation (1930) for an ideal hole on a semi-infinite soil deposit

$$Q = 4r_o k_L h_w \quad (19)$$

where  $Q$  = leakage per hole (m<sup>3</sup>/s),  $r_o$  = radius of the hole (m),  $k_L$  = hydraulic conductivity of the liner below the geomembrane (m/s), and  $h_w$  = head loss across the geomembrane and the clay, taken here to be equal to the leachate head,  $h_w$ , above the geomembrane. As noted above, this equation represents idealized conductions of no lateral migration at the interface between the geomembrane and the underlying soil. They justify this assumption based on tests performed by Walton et al. (1997) involving fine sand above and below a

geomembrane with a hole. Except for the case where a low permeability soil is deposited as a slurry in contact with the geomembrane and it consolidates with time under a large compressive stress (e.g. see Garlanger et al. 1994; Giroud et al. 1994), Eq. 19 is likely to underestimate the leakage through holes in a geomembrane that is placed below a stone collection layer and protective geotextile and placed above a compacted clay liner or GCL. It also assumes that there are no wrinkles or waves in the geomembrane (after application of stress) near the location of the defect. Rowe and Booker (1998b) have extended this solution to consider a layer of finite depth. They suggest that the solution may be useful for assessing the leakage below a circular (or near circular) "wrinkle" (e.g. around a penetration in the geomembrane).

The scenario considered by Walton et al. (1997) corresponds, in principle, with the perfect contact case examined by Giroud and Bonaparte (1989b) who obtained an approximate expression for the "absolute minimum" leakage with perfect contact that was given by:

$$Q = \pi r_o^2 k_L (h_w + H_L) / H_L \quad (20)$$

where  $H_L$  is the liner thickness and all terms are as defined for Eq. 19 (it being assumed that the head at the base of the liner is zero:  $h_b = H_f$  in Figure 25 and  $k_f \gg k_L$ ). The flow calculated by Eq. 20 is plotted as (MIN) for two cases in Figure 26. They then obtained a second approximate solution for perfect contact:

$$Q = 2\pi r_o k_L (h_w + H_L) / (1 - r_o / H_L) \quad (21a)$$

that, for  $r_o / H_L \ll 1$ , reduced to

$$Q = 2\pi r_o k_L (h_w + H_L) \quad (21b)$$

Giroud and Bonaparte (ibid) argued that it was unreasonable for the flow to increase with increasing  $H_L$  and reduced Eq. 21b to

$$Q = 2\pi r_o k_L h_w \quad (22)$$

Equation 22 was used by Giroud and Bonaparte (1989b) to define flow for "perfect contact" (denoted (P.C.) in Figure 26). Equation 22 can be seen to be very similar to the exact solution for a deep layer (Eq. 19) but giving 57% greater flow. In 1994, Giroud et al. (1994) ceased to use Eq. 22 for perfect contact and adopted, instead, Forchheimer's Equation (Eq. 19).

Most recently Giroud (1997) and Giroud et al. (1997a-g) have published a series of papers addressing liquid migration through defects in a geomembrane (a) overlain by a permeable medium and underlain by a highly permeable medium (Giroud et al. 1997c); (b) underlain

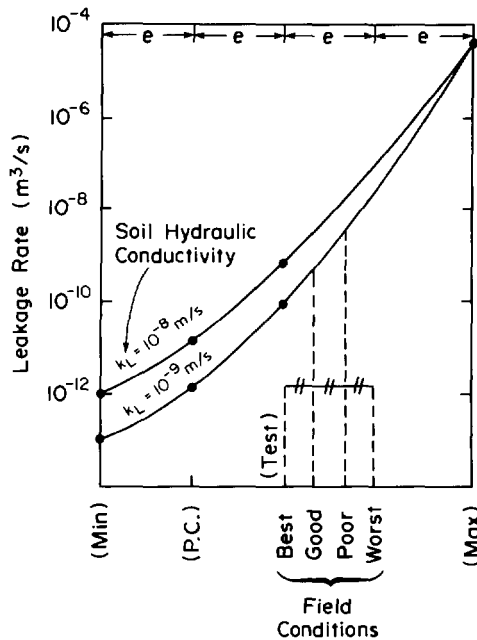


Figure 26. Leakage rate calculation from Giroud and Bonaparte (1989b) showing interpolation method used:  $h_w=0.03$  m;  $r_o=0.00564$  m.

by a saturated permeable medium (Giroud et al. 1997b); (c) underlain by a semi-permeable medium (Giroud et al. 1997g); and (d) underlain by a low permeability clay liner (Giroud 1997).

An excellent summary of these recent developments is given by Giroud et al. (1998). Of particular interest in the context of this present paper are the revised equations for leakage through composite liners due to circular or quasi-circular geomembrane defects given by Giroud (1997) which reduces to

$$Q=1.12C_{qo}[1+0.1(h_w/H_L)^{0.95}]r_o^{0.2}k_L^{0.74}h_w^{0.9} \quad (23a)$$

where  $C_{qo}$ =dimensionless coefficient that characterizes the quality of the contact between the geomembrane and the liner; and it is assumed that there is zero head at the bottom of the liner (i.e.  $h_a=H_f$  in Figure 25 and  $k_f \gg k_L$ ) and all other terms are as previously defined (or see Section 14: Notation). Equation 23 should only be used with the units specified (m for  $h_w$ ,  $H_L$ ,  $r_o$  and m/s for  $k_L$ ). As given above, Eq. 23 has a slightly different appearance than that given by Giroud (1997) due to the use of radius rather than diameter of the basic dimension of the defect. Two values of  $C_{qo}$  are given by Giroud (1997), based on Giroud et al. (1989),

$$C_{qo}=0.21 \text{ for good contact} \quad (23b)$$

$$C_{qo}=1.15 \text{ for poor contact} \quad (23c)$$

Good contact is defined (Giroud 1997) "as conditions where the geomembrane has been installed, with as few wrinkles as possible, on a low-permeability soil layer that has been adequately compacted and has a smooth surface." Poor contact is defined (ibid) as conditions where the geomembrane "has been installed with a certain number of wrinkles, and/or placed on a low-permeability soil that has not been well compacted and does not appear smooth."

Equation 23a represents the latest leakage equation from Giroud and supersedes equations in previous papers (e.g. Eq. 28 to be discussed subsequently). Giroud (1997) clearly identifies the limitations of Eq. 23 as (1) minimum and maximum radius of hole of 0.25 mm and 12.5 mm respectively; (2) liquid head,  $h_w$ , less than or equal to 3 m; (3) hydraulic conductivity of the liner,  $k_L$ , less than the value given by  $k_c$

$$k_L < k_c = (1.355r_o^{1.8} / [C_{qo}(1+0.1(h_w/H_L)^{0.95}h_w^{0.4})])^{1/0.74} \quad (24)$$

This latter condition is likely to be met provided conditions (1) and (2) above are met and  $k_L \leq 7 \times 10^{-9}$  m/s.

### 9.3 Comments on Contact Conditions

The leakage through a defect in a geomembrane overlying a low permeability layer necessarily depends on the contact between the geomembrane and the underlying soil as noted by Brown et al. (1987), Giroud and Bonaparte (1989b) and others. One can envisage three primary sources of imperfect contact as discussed below.

The first relates to protrusions that may exist causing a gap between the geomembrane and the underlying soil. Even for a well compacted soil, there may be protrusions related to particle size distribution (that in turn may be related to hydraulic conductivity) and these protrusions will create some gap in which water may flow. In the development of Eqs. 23, Giroud and Bonaparte (1989b) used Brown et al.'s (1987) test results as the basis of their "spacings",  $s$ , between the geomembrane and soil for "excellent field conditions" (see Table 22).

The second source of imperfection arises from undulations/ruts which result in the surface not appearing smooth. When compacting clay liners to obtain low hydraulic conductivity, it is usually desirable to compact at a water contents 2%-4% above the standard Proctor optimum value, however, this is often close to the plastic limit of the soil and it is difficult to obtain a smooth surface due to rutting that occurs from construction

Table 22. "Spacings",  $s$ , between geomembrane and soil for "excellent" or "best" field conditions as defined by Giroud and Bonaparte (1989b) based on Brown et al. (1987).

Soil Hydraulic Conductivity $k_s$ (m/s)	Geomembrane-Soil Spacing $s$ (mm)
$10^{-6}$	0.15
$10^{-7}$	0.08
$10^{-8}$	0.04
$10^{-9}$	0.02

equipment. This problem can be solved by compacting the upper layer of soil at a lower water content thereby allowing the preparation of a firm smooth surface and also reducing the potential of desiccation cracking. However, it should also be recognized that this layer will have a higher hydraulic conductivity than the rest of the liner and hence any ring infiltrometer tests on this layer may not be representative of the entire liner. However, the hydraulic conductivity of this layer is significant with respect to leakage through holes in the geomembrane. Thus a balance needs to be met between the desire to have the water content low enough to allow the preparation of a smooth surface but at the same time not so low as to increase the hydraulic conductivity of the layer above  $10^{-9}$  m/s under field stress conditions (with landfill loading applied).

The third source of imperfections affecting contact conditions is the presence of wrinkles (waves) in the geomembrane. The reader is referred back to Section 7.3 for a discussion of the need to eliminate wrinkles and the fact that wrinkles likely do not disappear when the waste is placed. The implications of this will be discussed further in Section 9.5.2.

When a geomembrane is placed over a geosynthetic clay liner (GCL), there is greater potential for obtaining good contact with a low permeability layer due to the fact that the GCL can be placed flat on a well compacted, smooth and firm foundation (e.g. see Giroud 1997). The factor controlling the leakage of an unwrinkled geomembrane over a GCL is the transmissivity of any geotextile between the geomembrane and bentonite (e.g. see Harpur et al. 1993). Where there are wrinkles in a geomembrane over a GCL, there is potential for the bentonite to "extrude" laterally and establish close contact between the geomembrane and clay provided there is sufficient applied compressive stress (e.g. see Giroud 1997) and the wrinkle is small. However, this also creates potential thinning of the GCL (see Stark 1998) which could impact on the GCL performance if there was significant bentonite movement. Also, for large wrinkles

there may be (a) significant thinning of the GCL adjacent to the wrinkle and (b) failure to fill the gap between the GCL and geomembrane. Thus, avoidance of wrinkles would appear to be important when a GCL is used to replace a compacted clay liner below a geomembrane.

A fundamental difference between the Forchheimer's Equation (1930) (Eq. 19) and Giroud (1997; Eqs. 23) is the potential for lateral fluid flow between the geomembrane and the underlying liner. This is related to the transmissivity between the geomembrane and liner. Walton et al. (1997) implicitly assume  $\theta=0$ .

As discussed by Brown et al. (1987) and Giroud and Bonaparte (1989b), if there is a gap that can be approximated by two smooth parallel plates then, based on Newton's viscosity theory, the transmissivity is given by

$$\theta = \frac{\rho g s^3}{12\eta} \quad (25)$$

where:  $\theta$  = hydraulic transmissivity of the empty space [ $m^2/s$ ];

$\rho$  = density of the liquid [ $kg/m^3$ ];

$g$  = acceleration due to gravity [ $m/s^2$ ];

$s$  = spacing between the geomembrane and the soil [ $m$ ]; and

$\eta$  = viscosity of the liquid [ $kg/m/s$ ].

The challenge is to relate the transmissivity  $\theta$  to the field contact conditions and hence derive leakage equations. In this context, and for the purposes of subsequent discussion, it is important to trace the genesis of the coefficients for "good" and "poor" contact as defined by Giroud (1997) and Giroud et al. (1998) to obtain Eq. 23. Giroud and Bonaparte (1989b) defined four reference conditions: "absolute minimum" leakage (Eq. 20), "perfect contact" (Eq. 22), "best contact" and "geomembrane alone". The "best" case was taken to correspond to "excellent field" conditions and based on the Brown et al. (1987) charts and using the value of spacing "s" given in Table 22 to calculate the transmissivity,  $\theta$ , using Eq. 25. This was then used in conjunction with charts published by Brown et al. (1987) to obtain empirical equations for the leakage rate and wetted radius under "best contact" conditions. For this case the flow was given in  $m^3/s$  for  $r_o$  and  $h_w$  in m units and  $k_L$  in m/s units by

$$Q = 0.785r_o^{0.2} k_L^{0.88} h_w \quad (26)$$

and plotted as "best" in Figure 26 for two cases.

The "maximum" geomembrane alone leakage conditions were taken to correspond to the maximum leakage rate ( $\theta \rightarrow \infty$ ) given by Bernoulli's equation (assuming zero hydraulic resistance below the geomembrane)

$$Q = \pi C_B r_o^2 \sqrt{2gh_w} \quad (27)$$

where  $g$ =acceleration due to gravity ( $m/s^2$ ),  $C_B$ =dimensionless coefficient related to the shape of the edges of the hole with  $C_B=0.6$  for sharp edges (Giroud & Bonaparte 1989a), and all other terms are as previously defined.

The values for the "absolute minimum" (MIN), "perfect contact" (PC), "best contact" (BEST) and "maximum" leakage (MAX) were plotted on a logarithmic scale (for a given soil hydraulic conductivity) as shown in Figure 26 with equal spacing between (MIN; Eq. 20), (PC; Eq. 22), (BEST; Eq. 26), (WORST: no data point) and (MAX; Eq. 27) points along the abscissa and a curve was fitted to these four data points (see Figure 26). The interval between "BEST" and the interpolated "WORST" point was then subdivided (arbitrarily in the absence of better alternatives: Giroud, personal communication) into three equal subintervals and "good" and "poor" contacts were taken as the flows corresponding to these intermediate points as shown in Figure 26.

Giroud et al. (1989) performed the interpolation described above for some 500 combinations of parameters and established the empirical equation:

$$Q = 0.785 C_{qo} r_o^{0.2} k_L^{0.74} h_w^{0.9} \quad (28)$$

where all terms are as defined for Eqs. 23 and  $C_{qo}$  is given by Eqs. 23b,c for "good" and "poor" contact. This equation was originally limited to low values of  $h_w$  and was subsequently extended (Giroud 1997; Giroud et al. 1998) to the most recent form given by Eq. 23.

Since the fundamental basis of a difference in flow (leakage) through the defect over the range between "perfect contact" ( $\theta=0$ ) and maximum flow ( $\theta=\infty$ ) is the difference in transmissivity of the "interface" zone between the geomembrane and the underlying soil (the clay liner in the context of this paper) it follows that it should be possible to relate these flows deduced for the cases of "good" and "poor" contact using Eq. 23 to values of  $\theta$ . It is also likely that leachate heads will exceed 3 m at some point during the service life of the geomembrane (see Sections 2 and 3) and hence it is useful to examine the implications of the empirical equation given by Eq. 23 for these conditions and the conditions associated with a GCL replacing a compacted clay liner. However, to do this one needs an analytical solution for leakage through the geomembrane liner. Such a solution is presented in the following section and this will be applied in Section 9.5 to address the issues raised above.

#### 9.4 General Analytical Solution for Leakage Through a Composite Liner

Consider a composite liner with a hole in the geomembrane as shown in Figure 25. The geomembrane rests on a low permeability layer of thickness  $H_L$  and hydraulic conductivity  $k_L$  (e.g. a compacted clay liner, CCL; or geosynthetic clay liner, GCL) which in turn rests on some more permeable (but not highly permeable) foundation layer (thickness  $H_f$  and hydraulic conductivity,  $k_f$ ) which rests on a highly permeable layer in which there is no significant matric suction. It is assumed that the geomembrane is not in perfect contact with the clay either due to small undulations creating a small gap of nominal thickness,  $s$ , or a geotextile (e.g. as part of a GCL) with transmissivity  $\theta$ .

Provided that the hydraulic conductivity of the liner is low relative to the other soil layers, the flow through the liner and foundation may be approximated as vertical and is given by

$$Q = k_s i_s A \quad (29a)$$

where  $Q$  = vertical flow [ $m^3/s$ ] through an area  $A$  [ $m^2$ ];  $k_s$  = harmonic mean hydraulic conductivity of the liner and foundation layer [ $m/s$ ];  $i_s$  is the mean gradient through the liner and foundation layer over the area  $A$  [-]; and

$$\frac{H_L + H_f}{k_s} = \frac{H_L}{k_L} + \frac{H_f}{k_f} \quad (29b)$$

$$i_s = \frac{H_f + H_L + h_w - h_a}{H_f + H_L} = 1 + \frac{h_w - h_a}{H_f + H_L} \quad (29c)$$

##### 9.4.1 Solution assuming hole is not on a wrinkle: circular hole

Following the rationale given by Giroud and Bonaparte (1989b) one can show that the head distribution beneath the geomembrane and acting on the low permeability liner is given by the solution to the equation

$$\frac{d^2 h}{dr^2} + \frac{1}{r} \frac{dh}{dr} - \alpha^2 h = \alpha^2 C \quad (30a)$$

$$\text{where: } \alpha^2 = \frac{k_s}{(H_L + H_f)\theta} \quad (30b)$$

$$C = H_L + H_f - h_a \quad (30c)$$

Equation 30 is to be solved subject to the boundary

conditions

$$h = h_w \quad \text{when} \quad r = r_o \quad (31a)$$

$$h = 0 \quad \text{when} \quad r = R \quad (31b)$$

and R is the wetted radius.

Extending the work of Jayawickrama et al. (1988), one can obtain the following analytical solution to Eqs. 30 and 31 and for the head h at position r:

$$h = (H_L + H_f + h_w - h_o)\Omega_o + (H_L + H_f - h_o)(\Omega_1 - 1) \quad (32a)$$

where

$$\Omega_o = \frac{K_o(\alpha r)I_o(\alpha R) - K_o(\alpha R)I_o(\alpha r)}{K_o(\alpha r_o)I_o(\alpha R) - K_o(\alpha R)I_o(\alpha r_o)} \quad (32b)$$

$$\Omega_1 = \frac{K_o(\alpha r)I_o(\alpha r_o) - K_o(\alpha r_o)I_o(\alpha r)}{K_o(\alpha R)I_o(\alpha r_o) - K_o(\alpha r_o)I_o(\alpha R)} \quad (32c)$$

and  $K_o$ ,  $I_o$  are modified Bessel functions of zero order that can be easily evaluated (Press et al. 1986). The solution given by Eq. 32 assumes that the wetted radius is known. In fact, R can be evaluated from the knowledge that at  $r=R$ ,

$$\frac{dh}{dr} = 0 \quad (33)$$

so the value of R can be obtained by finding the value that gives  $\frac{dh}{dr} = 0$  where, at  $r=R$ ,

$$\frac{dh}{dr} = (h_w + h_o - H_L - H_f)\Lambda_1 - (H_L + H_f - h_o)\Lambda_2 \quad (34a)$$

where

$$\Lambda_1 = \frac{-\alpha K_1(\alpha R)I_o(\alpha R) - \alpha K_o(\alpha R)I_1(\alpha R)}{K_o(\alpha r_o)I_o(\alpha R) - K_o(\alpha R)I_o(\alpha r_o)} \quad (34b)$$

$$\Lambda_2 = \frac{-\alpha K_1(\alpha R)I_o(\alpha r_o) - \alpha K_o(\alpha r_o)I_1(\alpha R)}{K_o(\alpha R)I_o(\alpha r_o) - K_o(\alpha r_o)I_o(\alpha R)} \quad (34c)$$

and  $K_1$ ,  $I_1$  are modified Bessel functions of order one. It is a simple matter to evaluate Eq. 34 to find the value of R for which Eq. 33 is satisfied.

The flow, Q, through the hole and low permeability

soil within the zone defined by the wetted radius is now given by the following closed form expression.

$$Q = \pi k_s [r_o^2 i_s + 2i_s \Delta_1 + 2i_s \Delta_2 - \frac{2h_w}{H_L + H_f} \Delta_2] \quad (35a)$$

where

$$\Delta_1 = -[R\lambda_1(r_o, R)K_1(\alpha R) + R\lambda_2(r_o, R)I_1(\alpha R)]/\alpha + r_o\lambda_1(r_o, R)K_1(\alpha r_o)/\alpha + r_o\lambda_2(r_o, R)I_1(\alpha r_o)/\alpha \quad (35b)$$

and

$$\Delta_2 = [-R\lambda_1(R, r_o)K_1(\alpha R) - R\lambda_2(R, r_o)I_1(\alpha R) + r_o\lambda_1(R, r_o)K_1(\alpha r_o) + r_o\lambda_2(R, r_o)I_1(\alpha r_o)]/\alpha \quad (35c)$$

$$\lambda_1(X, Y) = \frac{I_o(\alpha Y)}{K_o(\alpha X)I_o(\alpha Y) - K_o(\alpha Y)I_o(\alpha X)} \quad (35d)$$

$$\lambda_2(X, Y) = \frac{K_o(\alpha Y)}{K_o(\alpha X)I_o(\alpha Y) - K_o(\alpha Y)I_o(\alpha X)} \quad (35e)$$

and all other terms are as previously defined. Using Eq. 35, the leakage Q can be readily evaluated for any combination of layer properties, hole size or head. Eqs. 34 and 35 can be easily programmed using published code for Bessel functions (Press et al. 1986) and the results presented in this paper were obtained using the implementation by Rowe and Lake (1997).

#### 9.4.2 Solution assuming hole is on a wrinkle: circular hole

The previous subsection assumed that the defect occurred in an area away from a wrinkle. However, there is no reason that the defect could not be at the location of the wrinkle. In this case, the leakage will be substantially higher than given in the previous section. Here, we again assume a circular defect but in this case it occurs on a wrinkle of length L and width 2b (see Figure 27) where the height of the wrinkle is such that the transmissivity is much greater than between the geomembrane and the soil beyond. It is also assumed that  $L \gg b$  such that the effects of leakage at the ends of the wrinkle can be neglected. For this case, the head distribution beneath the geomembrane and acting on the low permeability liner is given by

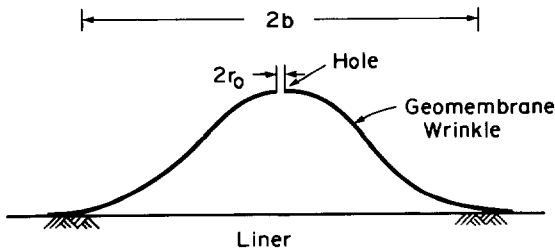


Figure 27. Schematic showing a wrinkle (wave) in a geomembrane with a hole in the wrinkle of radius  $r_o$ .

$$\frac{d^2h}{dx^2} - \alpha^2 h = \alpha^2 C \quad (36)$$

where  $\alpha$  and  $C$  are as defined in Eqs. 30b and c.

Equation 36 has the solution:

$$h = (h_w + C)e^{-\alpha(x-b)} - C \quad (37)$$

and the total flow is given by

$$Q = 2Lk_s \left[ b + \frac{1}{\alpha} (1 - e^{-\alpha(x-b)}) \right] \frac{H_L + H_f + h_w - h_a}{(H_L + H_f)} \quad (38)$$

where  $x$  is the wetted distance away from the centre of the wrinkle. If  $L \gg b$  then  $x$  must be established by one of three limits.

The first limit corresponds to the case where the flow is not limited by the hole and  $x$  tends to infinity. For this case, the flow is given by

$$Q = 2Lk_s \left[ b + \left( \frac{H_L + H_f}{k_s} \right)^{0.5} \right] \frac{H_L + H_f + h_w - h_a}{(H_L + H_f)} \quad (39)$$

The second limit recognizes that the flow may be controlled by (a) Bernoulli's equation if the permeability of the overlying layer is high enough or (b) by the capacity of the fluid to drain to the hole. The latter case corresponds to the case examined by Giroud et al. (1997c) where the limiting value of  $Q$  is obtained (iteratively) from

$$h_w = \left( \frac{r_o^2 q_o}{2k_{om}} + \frac{Q}{2k_{om}\pi} \left[ \ln \left( \frac{Q}{\pi r_o^2 q_o} \right) - 1 \right] + \frac{1}{4g^2} \left( \frac{Q}{1.88r_o^2} \right)^{4.5} \right)^{0.5} \quad (40)$$

where  $h_w$ ,  $k_{om}$ ,  $r_o$ ,  $q_o$  and  $g$  are all known,  $q_o$  is the liquid supply (e.g. permeation through the waste per unit area reaching the leachate collection system) in (m/s),  $k_{om}$  is the hydraulic conductivity of the permeable leachate collection layer over the geomembrane (m/s), and all

other terms are as previously defined. This expression reduces to the Bernoulli equation (Eq. 27) as  $k_{om}$  tends to infinity.

In discussing the third limit, we remember that for a circular hole the wetted radius ( $R$ ) is established by the condition  $dh/dr=0$  and corresponds to the point ( $r=R$ ) where the head  $h=0$  (Eq. 31b). For a plane problem  $dh/dx \rightarrow 0$  only as  $x$  tends to infinity, however  $h=0$  for a value of  $x$  which is quite finite and is given by

$$x = b - \ln \left( \frac{C}{C + h_w} \right) / \left( \frac{\theta(H_L + H_f)}{k_s} \right)^{0.5} \quad (41a)$$

$$C = H_L + H_f - h_a \quad (41b)$$

For the purposes of comparing leakage it makes some sense to compare the leakage in the zone where the head on the clay liner is greater than or equal to zero (taking the datum to be at the lower side of the geomembrane and noting that to satisfy the no flow condition a long way away from the hole, the head below the geomembrane tends to  $-C$  as  $x \rightarrow \infty$ ). Under these circumstances, the leakage can be calculated on a hand calculator by first calculating  $x$  from Eq. 41 and substituting this into Eq. 38. This will give a flow less than that given by Eq. 39. The leakage  $Q$  is therefore the minimum of the values calculated from Eqs. 41 and 38, and the value calculated from Eq. 40.

These calculations above assume that wrinkles with holes are spaced far enough apart such that they do not interact. This is valid provided that the distance between wrinkles is greater than  $2x$  (as calculated from Eq. 41). If wrinkles with holes are close enough that they could possibly interact then  $x$  should be taken as half the distance between the wrinkles with holes and the flow  $Q$  can be taken as the minimum of the value calculated from Eq. 38 (for the appropriate value of  $x$ ) and Eq. 40.

The foregoing equations are subject to the limitations that (1) the length of the wrinkle is much longer than its width, (2) the transmissivity of the space below the wrinkle is much higher than that between the geomembrane and the liner outside the wrinkle, (3) if there is more than one wrinkle with a hole, the wrinkles and holes are of similar size.

## 9.5 Calculated Leakage Rates for Composite Liners

### 9.5.1 Geomembrane in intimate contact with clay liner

Based on the equations presented in the previous subsections, it is possible to easily calculate the leakage through holes in a geomembrane for a range of conditions. Giroud's (1997) equations are very useful, however they do have a number of limitations that can be



readily overcome using Eqs. 34 and 35. Since the Giroud and Bonaparte (1989b) (now refined by Giroud 1997) equations have been widely used, it is of interest to infer the "transmissivity" that corresponds to "good" and "poor" contact for use in subsequent applications of Eqs. 34 and 35. Table 23 shows the leakage rate, Q, calculated from

Table 23. Backcalculated transmissivity and wetted radius corresponding to Giroud's (1997) latest equations:  $H_L=0.6$  m,  $H_f=0$ ,  $h_a=0$ ,  $k_L=10^{-9}$  m/s, small and large holes ( $r_o=0.001$  and  $0.00564$  m). Rounded to three significant digits.

Contact Hole	$h_w$ (m)	Q ( $m^3/s$ )	$\theta$ ( $m^2/s$ )	R (m)
Good small	0.003	$6.94 \times 10^{-11}$	$1.66 \times 10^{-8}$	0.149
	0.03	$5.54 \times 10^{-10}$	$1.63 \times 10^{-8}$	0.42
	0.3	$4.61 \times 10^{-9}$	$1.61 \times 10^{-8}$	1.2
	3	$5.08 \times 10^{-8}$	$2.06 \times 10^{-8}$	3.75
Poor small	0.003	$3.80 \times 10^{-10}$	$1.08 \times 10^{-7}$	0.348
	0.03	$3.04 \times 10^{-9}$	$1.03 \times 10^{-7}$	0.982
	0.3	$2.52 \times 10^{-8}$	$0.99 \times 10^{-7}$	2.81
	3	$2.78 \times 10^{-7}$	$1.26 \times 10^{-7}$	8.84
Good large	0.003	$9.82 \times 10^{-11}$	$1.53 \times 10^{-8}$	0.177
	0.03	$7.84 \times 10^{-10}$	$1.66 \times 10^{-8}$	0.499
	0.3	$6.51 \times 10^{-9}$	$1.73 \times 10^{-8}$	1.42
	3	$7.19 \times 10^{-8}$	$2.3 \times 10^{-8}$	4.39
Poor large	0.003	$5.38 \times 10^{-10}$	$1.08 \times 10^{-7}$	0.414
	0.03	$4.29 \times 10^{-9}$	$1.1 \times 10^{-7}$	1.17
	0.3	$3.57 \times 10^{-8}$	$1.11 \times 10^{-7}$	3.33
	3	$3.94 \times 10^{-7}$	$1.44 \times 10^{-7}$	10.4

Giroud's (1997) version of the leakage equation [Eq. 23] for a "small" and "large" hole and "good" and "poor" contact as defined by Giroud and Bonaparte (1989b). Table 23 also gives the transmissivity required in Eq. 35 to get the same flow as Eq. 23 for the contact, hole size and heads considered. Also shown are the corresponding wetted radii calculated from Eq. 34.

For given contact conditions and leachate heads,  $h_w$ , of 0.3 m or less, the transmissivities required to give the Giroud (1997) flows were very similar for both the "small" and "large" hole. This is as one would hope and expect since the hole size should not influence the contact conditions and transmissivity outside the hole. For "good" contact, the transmissivity was about  $1.6 \times 10^{-8}$  m<sup>2</sup>/s which

corresponds to an equivalent value of spacing, s, between the geomembrane and liner of about 0.027 mm. For "poor" contact the transmissivity was  $1.0 \times 10^{-7}$  m<sup>2</sup>/s corresponding to  $s=0.05$  mm. The backcalculated transmissivity for a 3 m leachate mound is about 25% higher than for heads of less than 0.3 m. While not particularly significant, this does indicate the error due to the approximation adopted by Giroud and Bonaparte (1989b) and Giroud (1997) and confirms their judgement in limiting the solution to cases for a head of 3 m or less.

The transmissivities deduced in Table 23 are for a 0.6 m thick compacted clay liner with  $k_L=10^{-9}$  m/s. Table 24

Table 24. Backcalculated (average) transmissivities and spacings corresponding to Giroud's (1997) equations for  $h_w=0.3$  m,  $H_L=0.6$  to 1.2 m; small and large hole ( $r_o=0.001$  &  $0.00564$  m). Rounded to two significant digits.

Liner $k_L$ (m/s)	Transmissivity, $\theta$		Spacing, s	
	Good Con-tact ( $m^2/s$ )	Poor Con-tact ( $m^2/s$ )	Good Con-tact (mm)	Poor Con-tact (mm)
$10^{-10}$	$3.2 \times 10^{-9}$	$2.0 \times 10^{-8}$	0.016	0.029
$10^{-9}$	$1.6 \times 10^{-8}$	$1.0 \times 10^{-7}$	0.027	0.050
$10^{-8}$	$8.6 \times 10^{-8}$	$5.5 \times 10^{-7}$	0.047	0.088

summarizes similar results for a head  $h_w=0.3$  m for a range of liner thicknesses and values of liner hydraulic conductivity. Based on the results presented in Table 25, it is possible to establish the following interpolation formulae for the transmissivity,  $\theta$  (in m<sup>2</sup>/s units), for a given liner hydraulic conductivity,  $k_L$  (in m/s units):

For good contact

$$\log_{10}\theta = 0.07 + 1.036(\log_{10}k_L) + 0.018(\log_{10}k_L)^2 \quad (42a)$$

For poor contact

$$\log_{10}\theta = 1.15 + 1.092(\log_{10}k_L) + 0.0207(\log_{10}k_L)^2 \quad (42b)$$

It is essential that the correct units be used in calculating a transmissivity from this equation.

Using a transmissivity,  $\theta=1.6 \times 10^{-8}$  m<sup>2</sup>/s, for "good" contact, Table 25 gives the calculated wetted radius, flows through a small and large circular hole and the leakage and Darcy velocity for 2.5 holes/ha for heads ranging from 0.003 to 30 m. For a head of 0.3 m, the leakage is quite small (~1 lphd) and even for a 30 m head (due to either a failed leachate collection system or termination of the operation of the collection system), the leakage is 100 lphd (or less). Table 25 also gives the calculated average Darcy flux beneath the wetted area ( $r \leq R$ ). For heads less than 5 m, this is relatively consistent at a value

Table 25. Calculated wetted radius, and leakage from circular holes for GM in good contact with a CCL for a range of head values based on Eqs. 34 and 35;  $H_L=0.6$  m,  $k_L=10^{-9}$  m/s, ( $\theta=1.6\times 10^{-8}$  m<sup>2</sup>/s). Rounded to two significant digits.

Small Hole ( $r_o=0.001$ m)						Large Hole ( $r_o=0.00564$ m)				
$h_w$ (m)	R (m)	Q (m <sup>3</sup> /s)	Leak- age* (lphd)	$v_a$ * (m/a)	$v_t$ ** (m/a)	R (m)	Q (m <sup>3</sup> /s)	Leak- age* (lphd)	$v_a$ * (m/a)	$v_t$ ** (m/a)
0.003	0.15	$6.7\times 10^{-11}$	0.01	$5.3\times 10^{-7}$	0.032	0.18	$1.0\times 10^{-10}$	0.02	$8.0\times 10^{-7}$	0.032
0.03	0.42	$5.5\times 10^{-10}$	0.1	$4.3\times 10^{-6}$	0.032	0.49	$7.6\times 10^{-10}$	0.2	$6.0\times 10^{-6}$	0.032
0.3	1.2	$4.6\times 10^{-9}$	1.0	$3.6\times 10^{-5}$	0.032	1.4	$6.1\times 10^{-9}$	1.3	$4.8\times 10^{-5}$	0.032
1.0	2.1	$1.4\times 10^{-8}$	3.1	$1.1\times 10^{-4}$	0.033	2.3	$1.8\times 10^{-8}$	4.0	$1.4\times 10^{-4}$	0.034
2.0	2.8	$2.7\times 10^{-8}$	5.9	$2.2\times 10^{-4}$	0.035	3.1	$3.5\times 10^{-8}$	7.6	$2.8\times 10^{-4}$	0.036
3.0	3.3	$4.0\times 10^{-8}$	8.7	$3.2\times 10^{-4}$	0.036	3.7	$5.1\times 10^{-8}$	11	$4.0\times 10^{-4}$	0.038
5.0	4.1	$6.6\times 10^{-8}$	14	$5.1\times 10^{-4}$	0.039	4.5	$8.4\times 10^{-8}$	18	$6.6\times 10^{-4}$	0.041
10.0	5.4	$1.3\times 10^{-7}$	28	$1.0\times 10^{-3}$	0.045	5.8	$1.6\times 10^{-7}$	35	$1.3\times 10^{-3}$	0.048
15.0	6.2	$1.9\times 10^{-7}$	41	$1.5\times 10^{-3}$	0.050	6.7	$2.4\times 10^{-7}$	52	$1.9\times 10^{-3}$	0.054
20.0	6.8	$2.5\times 10^{-7}$	54	$2.0\times 10^{-3}$	0.055	7.3	$3.2\times 10^{-7}$	69	$2.5\times 10^{-3}$	0.056
25.0	7.3	$3.1\times 10^{-7}$	68	$2.5\times 10^{-3}$	0.059	7.9	$4.0\times 10^{-7}$	86	$3.1\times 10^{-3}$	0.065
30.0	7.7	$3.8\times 10^{-7}$	81	$3.0\times 10^{-3}$	0.063	8.3	$4.8\times 10^{-7}$	100	$3.8\times 10^{-3}$	0.070

\* Assumes 2.5 holes/ha

\*\* Average Darcy velocity below wetted radius

between 0.03 and 0.04 m/a and for typical liner porosity implies an average linearized groundwater velocity of about 0.1 m/a. Neglecting the effects of consolidation, this alone implies that a conservative contaminant transported through a hole would migrate through a 0.6 m thick liner in 6 years and hence one can expect dilute leachate constituents to be detected in the leak detection system relatively quickly. One would expect that these constituents would have been diluted by (a) pore water from the clay liner that has been expelled due to consolidation; (b) any construction water in the secondary collection/leak detection system; (c) other water entering the system (if any). Also, the chemistry will not be a simple dilution of the leachate since (a) it will be combined with the pore chemistry of the clay water that will contribute inorganic constituents (such as Cl<sup>-</sup>, Na<sup>+</sup>, Ca<sup>++</sup>, Mg<sup>++</sup>, SO<sub>4</sub><sup>2-</sup>, etc.) in concentrations that will vary from clay to clay; and (b) inorganic and polar organics will leak through holes at one rate and volatile organic compounds (VOCs) will diffuse through the intact geomembrane at a second rate. Of these, the most telling sign of contaminant migration is likely to be the VOCs.

The use of a GCL in place of the CCL as the clay component of a composite liner can be expected to have some effect on leakage through holes in the geomembrane. Based on the tests performed by Harpur et al. (1993), it would appear that for the GCLs and conditions examined by them the transmissivity,  $\theta$ , between a geomembrane and GCL is in the range of  $6\times 10^{-12}$  m<sup>2</sup>/s to  $2\times 10^{-10}$  m<sup>2</sup>/s for GCLs with a woven or

nonwoven geotextile in direct contact with the geomembrane and  $3\times 10^{-12}$  m<sup>2</sup>/s for bentonite in direct contact with the geomembrane. Based on hydraulic conductivity tests with leachate (see Table 7), the hydraulic conductivity,  $k_L$ , of a GCL could lie within a wide range. For the purposes of the current comparison, three values of  $k_L$  ( $7\times 10^{-12}$  m/s,  $2\times 10^{-10}$  m/s and  $2\times 10^{-8}$  m/s) will be examined. To assess the potential for leakage through holes in a geomembrane underlain by a GCL, calculations were performed using Eqs. 34 and 35 for a range of values of  $k_L$  and  $\theta$  (using  $k_L=2\times 10^{-10}$  m/s;  $\theta=1\times 10^{-10}$  m<sup>2</sup>/s as base values) for a large hole ( $r_o=0.00564$  m,  $a=1$  cm<sup>2</sup>) and the results are presented in Table 26. It can be seen that even with significant clay leachate interaction ( $k_L=2\times 10^{-8}$  m/s) the leakage for 2.5 "large" holes/ha is very small at a design head of 0.3 m (less than 0.1 lphd) and even with a 30 m leachate mound the leakage is less than 5 lphd. It is of particular note that a variation in clay hydraulic conductivity from  $7\times 10^{-12}$  to  $2\times 10^{-8}$  m/s increased the flows by only about a factor of 5 at large heads (3 and 30 m). This is because at these high hydraulic conductivities the wetted radius is substantially reduced.

The implications from Tables 25 and 26 are that, for even large holes in good contact with either a CCL or GCL, the leakage would be very small for 2.5 holes per hectare; these flows are much lower than reported in Tables 19 and 20. Table 27 shows the effect of contact condition and the number of holes per hectare on leakage for large holes and (a) a CCL with good and poor contact and (b) a GCL with different combinations

Table 26. Wetted radius and leakage from circular holes for a GM in good contact with a GCL for a range of head, transmissivity and hydraulic conductivity values based on Eqs. 34 and 35;  $H_L=0.01$  m,  $H_T=0.6$  m,  $h_a=0$ ,  $k_t=10^{-6}$  m/s. Large hole ( $r_o=0.00564$  m). Rounded to two significant digits.

$k_L$ (m/s)	$\theta$ (m <sup>2</sup> /s)	$h_w$ (m)	R (m)	Q (m <sup>3</sup> /s)	Leakage* (lphd)	$v_a$ * (m/a)	$v_t$ (m/a)
$2 \times 10^{-10}$	$6 \times 10^{-12}$	0.03	0.01	$4.3 \times 10^{-12}$	0.0009	$3.4 \times 10^{-8}$	0.39
		0.3	0.02	$1.6 \times 10^{-11}$	0.003	$1.2 \times 10^{-7}$	0.43
		3	0.04	$9.8 \times 10^{-11}$	0.02	$7.7 \times 10^{-7}$	0.65
		30	0.07	$8.6 \times 10^{-10}$	0.2	$6.8 \times 10^{-6}$	1.8
$2 \times 10^{-10}$	$2 \times 10^{-10}$	0.03	0.03	$3.3 \times 10^{-11}$	0.007	$2.5 \times 10^{-7}$	0.38
		0.3	0.07	$1.9 \times 10^{-10}$	0.04	$1.5 \times 10^{-6}$	0.40
		3	0.17	$1.4 \times 10^{-9}$	0.3	$1.1 \times 10^{-5}$	0.52
		30	0.33	$1.3 \times 10^{-8}$	2.8	$1.0 \times 10^{-4}$	1.2
$2 \times 10^{-10}$	$1 \times 10^{-10}$	0.03	0.02	$2.0 \times 10^{-11}$	0.004	$1.6 \times 10^{-7}$	0.38
		0.3	0.05	$1.1 \times 10^{-10}$	0.02	$8.8 \times 10^{-7}$	0.40
		3	0.12	$8.0 \times 10^{-10}$	0.2	$6.3 \times 10^{-6}$	0.54
		30	0.24	$7.2 \times 10^{-9}$	1.6	$5.7 \times 10^{-5}$	1.26
$7 \times 10^{-12}$	$1 \times 10^{-10}$	0.03	0.08	$8.8 \times 10^{-12}$	0.02	$6.9 \times 10^{-8}$	0.01
		0.3	0.21	$6.1 \times 10^{-11}$	0.01	$4.8 \times 10^{-7}$	0.01
		3	0.53	$4.9 \times 10^{-10}$	0.1	$3.8 \times 10^{-6}$	0.02
		30	1.1	$4.5 \times 10^{-9}$	1.0	$3.5 \times 10^{-5}$	0.4
$2 \times 10^{-8}$	$1 \times 10^{-10}$	0.03	0.009	$1.3 \times 10^{-10}$	0.03	$1.1 \times 10^{-6}$	18
		0.3	0.01	$4.1 \times 10^{-10}$	0.09	$3.2 \times 10^{-6}$	20
		3	0.03	$2.4 \times 10^{-9}$	0.51	$1.9 \times 10^{-5}$	34
		30	0.05	$2.1 \times 10^{-8}$	4.5	$1.6 \times 10^{-4}$	100

\* Assumes 2.5 holes/ha.

of liner and transmissivity condition. As might be expected, the leakage increases linearly with the number of holes and almost linearly with leachate head for heads of 0.3 m or larger. Of particular interest are the leakages for a "design" head of 0.3 m. Under landfill operating conditions, one would expect the head in the primary leachate collection system to be less than 0.3 m and hence these values should represent an upper bound to the leakage that one would expect to detect in a SLCS under active and post-closure conditions for as long as the leachate collection system is operating to design specifications. Thus it is instructive to compare the numbers in Table 27 with those observed in field monitoring as reported in Tables 19 and 20. The easiest comparison is for systems involving a geomembrane over a GCL since there should not be any significant consolidation water in the flows recorded in the SLCS. From Table 19 it can be seen that under active conditions the mean flow is 7.7 lphd and even under "closed" condition it is 2.3 lphd. These substantially exceed that predicted in Table 27 even for a very large level of clay-leachate interaction and 40 holes per hectare. Indeed, one would need between 65 and 140 holes per hectare to explain the average post-closure

leakage. Since it is highly unlikely that there are this many large holes, an alternative explanation is required as discussed below. For geomembranes over compacted clay liners, the comparison is more difficult due to consolidation water contributing to the flow; however, even so, the flows are large enough to lead one to believe that more than leakage through "large" holes in good contact with the clay is required to explain the flows.

#### 9.5.2 Leakage through holes in a wrinkled geomembrane forming part of a composite liner

Wrinkles (waves) represent a particular concern due to the fact that available evidence suggests that (a) wrinkles remain after placement of waste and (b) local tensile strains are developed in the geomembrane at the wrinkle as discussed in Section 7.3. There is no reason to believe that holes will not occur at the location of wrinkles. On the contrary, given the local stress concentration, it is reasonable to hypothesize that holes would be more likely to occur at the location of a wrinkle. Thus it is of some interest to explore the implications of a hole coinciding with a wrinkle. As discussed in Section 9.4.2, one can develop a solution for a strip wrinkle. Table 28 presents

Table 27. Calculated leakage for different numbers of holes for a large hole ( $r_o=0.0054$  m). Based on Eqs. 34 and 35. Rounded to two significant digits.

	$h_w$ (m)	Leakage for number of holes per ha (lphd)				
		1	2.5	7.5	15	40
CCL	0.3	0.5	1.3	3.9	7.9	21
Good Contact <sup>1</sup>	3	4.4	11	33	67	180
	30	41	100	310	620	1600
CCL	0.3	2.8	7.0	21	42	110
Poor Contact <sup>2</sup>	3	24	60	180	360	970
	30	230	560	1700	-	-
GCL	0.3	0.02	0.04	0.12	0.25	0.66
Fair Condition <sup>3</sup>	3	0.1	0.3	0.92	1.8	4.9
	30	1.1	2.8	8.3	17	44
GCL	0.3	0.04	0.09	0.27	0.53	1.4
Poor Contact <sup>4</sup>	3	0.2	0.51	1.5	3.1	8.2
	30	1.8	4.5	14	27	72

1. Good Contact,  $\theta=1.6 \times 10^{-8}$  m<sup>2</sup>/s,  $k_L=1 \times 10^{-9}$  m/s,  $H_L=0.6$  m,  $H_f=0$
2. Poor Contact,  $\theta=1.0 \times 10^{-7}$  m<sup>2</sup>/s,  $k_L=1 \times 10^{-9}$  m/s,  $H_L=0.6$  m,  $H_f=0$
3. Fair Condition,  $\theta=2 \times 10^{-10}$  m<sup>2</sup>/s,  $k_L=2 \times 10^{-10}$  m/s,  $H_L=0.01$  m,  $H_f=0.59$  m
4. Poor Condition,  $\theta=1 \times 10^{-10}$  m<sup>2</sup>/s,  $k_L=2 \times 10^{-8}$  m/s,  $H_L=0.01$  m,  $H_f=0.59$  m

the results obtained for a strip wrinkle 3 m long and 0.2 m wide for both a compacted clay liner (CCL) and geosynthetic clay liner (GCL). Calculations were performed assuming a single small hole per wrinkle ( $r_o=0.001$  m), a percolation to the collection system of  $10^{-9}$  m/s and a hydraulic conductivity of the collection system of  $10^{-6}$  m/s unless otherwise noted. In no case did the hole (Eq. 40) limit the leakage and hence the same results would be obtained for  $r_o > 0.001$ . For comparison with Tables 25 and 26, the leakage and Darcy flux ( $v_a$ ) were calculated assuming 2.5 holes coinciding with wrinkles per hectare. (Since not all holes will coincide with wrinkles, this likely corresponds to more than 2.5 holes/ha.) Comparing the results in Table 28 with those in Tables 25 and 26, it can be seen that the coincidence of even a small hole with a wrinkle of the dimensions examined substantially increases

Table 28. Calculated leakage from a small hole ( $r_o=0.001$  m) in a wrinkle:  $L=3$  m,  $2b=0.2$  m,  $h_a=0$ ,  $q_o=1 \times 10^{-9}$  m/s.

Liner H $k_L$ $\theta$	$h_w$ (m)	Q (m <sup>3</sup> /s)	Leak- age* (lphd)
CCL	0.03	$3.0 \times 10^{-9}$	0.6
0.6 m	0.3	$2.4 \times 10^{-8}$	5.2
$1 \times 10^{-9}$ m/s	3	$2.4 \times 10^{-7}$	51
$1 \times 10^{-7}$ m <sup>2</sup> /s	30	$2.4 \times 10^{-6}$	510
CCL	0.03	$1.6 \times 10^{-9}$	0.3
0.6 m	0.3	$1.0 \times 10^{-8}$	2.2
$1 \times 10^{-9}$ m/s	3	$9.7 \times 10^{-8}$	21
$1.6 \times 10^{-8}$ m <sup>2</sup> /s	30	$9.6 \times 10^{-7}$	210
GCL	0.03	$7.8 \times 10^{-9}$	1.7
0.01m+	0.3	$1.3 \times 10^{-8}$	2.9
0.59m AL	3	$6.9 \times 10^{-8}$	15
$2 \times 10^{-10}$ m/s	30	$6.2 \times 10^{-7}$	130
$1 \times 10^{-10}$ m <sup>2</sup> /s			

\*Assumes 2.5 holes in wrinkles/ha

the leakage. The increase in leakage due to a wrinkle relative to that without a wrinkle is much greater for a GCL than for a CCL, however, for  $h_w \geq 3$  m the absolute magnitudes of the leakages are still smaller with the GCL than with the CCL for the cases considered.

Table 29 summarizes the calculated leakage (for 1 and 2.5 holes in wrinkles per hectare) for a range of wrinkle dimensions contact conditions and CCL and GCL properties. Also shown are the calculated leakage assuming that the area under the wrinkle is the same as for a strip of the dimensions shown but where the wrinkle is "circular" in shape.

For a "design" head of 0.3 m it can be seen that for a GCL with  $k_L \sim 2 \times 10^{-10}$  m/s, only a single hole in a wrinkle 5 m  $\times$  0.2 m is required to explain a leakage of about 2.3 lphd (see Tables 29 and 19) and that a hole in a 30 m  $\times$  0.2 m wrinkle will explain an average leakage of 7.7 lphd observed in field installations. For a greater level of clay-leachate interaction ( $k_L \sim 2 \times 10^{-8}$  m/s) the leakage is substantially higher.

Comparing observed results in Table 20 with calculated leakages in Table 29, it can be seen that one 5 m  $\times$  0.2 m wrinkle with a hole per hectare for a CCL and "good" contact or 3 m  $\times$  0.2 m and "poor" contact with a CCL would explain a leakage of 1.5 lphd, however seven 30 m  $\times$  0.2 m wrinkles with holes and "good" contact or three 30 m  $\times$  0.2 m wrinkles with holes and "poor" contact would be required to explain a leakage of about 60 lphd;

Table 29. Effect of wrinkle geometry on leakage: ( $2b=0.2$  m,  $q_o=10^{-9}$  m/s,  $k_{om}=10^{-2}$  m/s).

L (m)	$h_w$ (m)	Strip	Circle	Strip	Circle
		Leak- age (lphd)	Leak- age (lphd)	Leak- age (lphd)	Leak- age (lphd)
		CCL <sup>1</sup>		GCL <sup>2</sup>	
3	0.3	0.88	2.0	1.2	1.2
	30	84	120	64	48
5	0.3	1.5	2.4	2.1	2.0
	30	140	140	100	72
30	0.3	8.8	4.8	12	10
	30	840	250	640	360
		CCL <sup>3</sup>		GCL <sup>4</sup>	
3	0.3	2.1	8.2	45	44
	30	200	550	1700	1500
5	0.3	3.5	9.2	75	73
	30	340	600	2800	2500
30	0.3	21	15	390*	390*
	30	2000	880	4000*	4000*
		CCL <sup>5</sup>		GCL <sup>6</sup>	
3	0.3	2.2	5.1	3.1	3.1
	30	210	310	160	120
5	0.3	3.7	6.0	5.2	4.9
	30	350	360	260	180
30	0.3	22	12	31	26
	30	2100	620	1600	910

\* Flow controlled by Eq. 40 for a small hole

1. CCL,  $H_L=0.6$  m,  $k_L=10^{-9}$  m/s, "Good" Contact; 1 hole/ha
  2. GCL,  $H_L=0.01$  m,  $H_f=0.59$  m,  $k_L=2 \times 10^{-10}$  m/s,  $\theta=2 \times 10^{-10}$  m<sup>2</sup>/s; 1 hole/ha
  3. CCL,  $H_L=0.6$  m,  $k_L=10^{-9}$  m/s, "Poor" Contact; 1 hole/ha
  4. GCL,  $H_L=0.01$  m,  $H_f=0.59$  m,  $k_L=2 \times 10^{-8}$  m/s,  $\theta=2 \times 10^{-10}$  m<sup>2</sup>/s; 1 hole/ha
  5. CCL,  $H_L=0.6$  m,  $k_L=10^{-9}$  m/s, "Good" Contact; 2.5 holes/ha
  6. GCL,  $H_L=0.01$  m,  $H_f=0.59$  m,  $k_L=2 \times 10^{-10}$  m/s,  $\theta=2 \times 10^{-10}$  m<sup>2</sup>/s; 2.5 holes/ha
- Good Contact:  $\theta=1.6 \times 10^{-8}$  m<sup>2</sup>/s; Poor Contact:  $\theta=1 \times 10^{-7}$  m<sup>2</sup>/s

alternately, with poor contact a single wrinkle would need to be about 85 m  $\times$  0.2 m to explain an average flow of 60 lphd under a leachate head of 0.3.

For the results shown in Table 29, it was assumed that

$k_{om}=10^{-2}$  m/s and it was found that Eq. 40 controlled several cases involving a GCL with  $k_L=2 \times 10^{-8}$  m/s. The effect would be even greater for a lower hydraulic conductivity of the collection layer.

In summary, it appears that wrinkles associated with holes in the geomembrane can explain the observed leakage through composite liners (Table 19) involving a geomembrane over a GCL under both active and post-closure conditions and hence this hypothesis warrants further examination. Likewise, holes in a wrinkle will explain the low leakages observed through a geomembrane over a CCL but probably not the high values of flow rate observed in SLCSs (Table 20); this implies that other mechanisms such as consolidation of the CCL are required to explain the observed flow rates. Consolidation of the CCL may also give rise to earlier (diluted) contaminant arrival times in the SLCS than would otherwise be expected. The theory presented in Section 9.4.2 can be used to estimate the leakage for reasonable numbers of wrinkles. Comparing the results presented in Tables 27 and 29, it is clearly desirable to minimize wrinkles if leakage is to be minimized. It should be noted that the long term performance of geomembranes with wrinkles may be even worse than implied by these calculations due to the potential for the development of stress cracking and increased leakage through the geomembrane at the location of the wrinkle. This provides an incentive to minimize wrinkles.

## 10 CONTAMINANT IMPACT ASSESSMENT AND EQUIVALENCE OF LINER SYSTEMS

### 10.1 Impact Assessment

The assessment of the suitability of a liner system should, in principle, be related to the potential impact on water quality (especially groundwater) due to the proposed landfill and liner system. This assessment typically involves the solution of the advection-dispersion equation subject to appropriate boundary conditions (e.g. see Rowe et al. 1995b for a detailed discussion). Factors that influence the potential impact include (a) the landfill source concentration and its decay characteristics; (b) the advective flux (leakage) across the barrier system; (c) the thickness of any "attenuation" layer between the base of the low permeability liner(s) and the receptor aquifer (or distance to the water table if the liner is constructed in the unsaturated portion of the aquifer); (d) diffusion (especially for VOCs) across the barrier system; (e) sorption/retardation in the liner and underlying soil; (f) biodegradation; (g) dilution in the aquifer, (h) the service life of the engineered components of the landfill (e.g. covers/caps; leachate collection systems; liners); (i) the mode of operation of the landfill; and (j) consolidation of the liner and any underlying compressible soils.

Consolidation (item j) is usually not considered on the

grounds that it is transient and provides water for "dilution" of contaminants, however it should be noted that consolidation may be significant if one is calculating travel times and, in particular, first arrival times. As previously discussed, it may be hypothesized that the "premature" arrival of contaminant in leakage detection systems is, in part, attributable to failure to consider consolidation effects in assessing the expected travel times. More research is required into this aspect.

Items (a)-(i) can be readily modelled using existing contaminant transport theory and codes (e.g. Rowe and Booker 1997a). However, the factors considered in modelling impact tend to be regulatory driven and vary from one country to another and hence the assessment of what represents an "adequate" barrier system will vary from regulatory environment to regulatory environment. Thus one can not generalize about "equivalency" of liner systems since what is "equivalent" depends on what is being compared and how it is being compared.

It is possible to gain insight into how different barrier systems are likely to behave by modelling. In the following subsections, the potential impact of a landfill with two different composite liners (geomembrane over compacted clay; geomembrane over GCL) will be compared including consideration of diffusion, leakage through holes, contaminant biodegradation (for VOCs) and the finite service lives of the leachate collection system and geomembrane liner based on the factors discussed in previous sections of this paper. The comparisons will be limited by the use of assumed parameters that represent one hypothetical site. For any specific project, appropriate parameters should be established for that site. Then analyses such as those described in the following can be readily performed using the same techniques (Rowe & Booker, 1984, 1985, 1995, 1997a,b) to assess equivalency (and potential impact) for that site.

It is noted in passing that in some areas it is not practical to have an "unsaturated" zone below the base of the engineered barrier system and any assumption of the presence of an unsaturated zone must be specific to locations where that is practical. Secondly, when assessing dilution in an aquifer, it may not be reasonable to include the entire thickness of the aquifer in the dilution calculations for thick aquifers. Although beyond the scope of this paper, readers should be aware of the potential for plume localization in the upper few meters of an aquifer and this needs to be considered when assessing the thickness of the aquifer to be used in dilution calculations. In the following comparison, only the upper 3 m of the aquifer are considered to provide significant dilution.

As noted in Section 2, temperature may have an important effect on both hydraulic conductivity and diffusion coefficient. Table 30 gives the ratio of both the

Table 30. Effect of temperature on diffusion coefficient,  $D_T$ , hydraulic conductivity,  $k_T$ , in a liner at temperature  $T$  to values at 10°C.

Temperature, °C	$D_T/D_{10}$	$k_T/k_{10}$
10	1.0	1.0
20	1.4	1.3
25	1.6	1.5
35	2.0	1.8
50	2.7	2.4
65	3.5	2.9

diffusion coefficient and hydraulic conductivity at different temperatures to that at 10°C (see Collins 1993; Rowe et al. 1995b; Barone et al. 1997 for details of method of calculation). Domenico & Schwartz (1990) indicate that the groundwater temperature at a depth of 10-20 m is typically 1-2°C higher than local mean temperature and hence a temperature of 5-10°C would be typical groundwater temperature in the Northern U.S. and Southern Canada. From Table 30, it can be seen that diffusive and advective transport are 40% and 30% higher at 20°C than at 10°C and 100% and 80% higher at 35°C. If the liner temperature is to remain relatively constant, then constant diffusion and hydraulic conductivity parameters relevant to that temperature may be used. However, if the temperature of the liner changes with time (see Section 2) then some consideration may need to be given to the effect of the change in these parameters with temperature on the impact calculations. The approach proposed by Rowe and Booker (1997a) readily models change in  $D$  and the effect of a change in  $k$  with time as appropriate.

In the following examples, it will be assumed that the geomembrane and liner are at 20°C and that by the time the leachate mound begins to develop (30-50 years, or greater, post-closure) the temperature has stabilized. This is not necessarily the case since it is also assumed that the landfill has a low permeability final cover (cap) that is maintained ( $q_e=0.0003\text{m/a}\cong 8\text{ lphd}$ ) for this same period of time. Once the leachate collection system operation and cover maintenance are terminated, a leachate mound will develop and the temperature may increase since the organic waste may not have fully biodegraded in the low infiltration environment (see Section 2). This could be modelled using the Rowe and Booker (1997a) approach but is beyond the scope of the present paper. If the temperature were to increase, the impact would be greater for both systems examined in the following subsections.

## 10.2 Equivalency of Liner Systems

In North America, GCLs have been approved as

replacement for conventional compacted clay liners in at least 45 landfills and both Richardson (1997) and Giroud et al. (1997a) have discussed a number of aspects of equivalency between these systems. Giroud et al. (1997a) focus on the issue of leakage through GCLs and CCLs and steady state advective travel time (i.e. neglecting the effect of consolidation and diffusion on the first arrival time). Richardson (1997) discusses leakage and steady state travel time (also neglecting consolidation and diffusion effects) as well as chemical-absorption capacity and dilution potential. Rowe (1997b) has considered equivalency in terms of impact calculations that include consideration of leakage (in a similar manner to Giroud et al. 1997a and Richardson 1997) but has also examined the effects of diffusion, finite service life and biodegradation in the context of Ontario's draft landfill regulations (MoEE 1996). However, based on the material presented in this present paper, it is possible to go beyond these three recent evaluations. A detailed comparison would require a separate paper (in preparation) and the following is only intended to illustrate how a number of key factors may be incorporated.

Any comparison of equivalency of GCL and CCL as part of a liner system should consider: (a) the potential for clay/leachate interaction, (b) the interaction with the adjacent geomembrane, (c) the leachate head and corresponding gradient, and (d) diffusion and sorption. Inspection of Table 7 shows that the hydraulic conductivity of a GCL could potentially vary over many orders of magnitude, due to clay-leachate interaction, depending on the characteristics of the bentonite in the GCL and the leachate. However, as indicated in Table 27, even with a hydraulic conductivity as high as  $2 \times 10^{-8}$  m/s, a composite liner involving a GCL has the potential to give rise to substantially less leakage than a composite liner with a CCL having  $k_L \sim 10^{-9}$  m/s for a similar number of holes in the geomembrane. The explanation for this lies in the smaller potential for lateral migration between the geomembrane and GCL than for a geomembrane and CCL.

### 10.3 Comparison of Two Liner Systems: CCL versus GCL

For purposes of comparison of a conventional composite liner system and a composite system with a GCL replacing a 0.6 m CCL, the two liner systems shown in Figure 2 were examined using the parameters given in Table 31 and 32. For the cases involving a 0.6 m thick CCL, it was assumed that there was a 3 m thick attenuation layer (AL) between the CCL and the aquifer so that the combined thickness of the CCL and attenuation layer above the aquifer was 3.6 m (see Figure 2a). For cases involving a GCL two situations were examined. In the

Table 31. Parameters used in comparison of a GM over either a CCL or GCL composite liner system.

<b>Landfill Properties:</b>	
Length (m)	1000
Mass of waste/unit area, $M_w$ (t/m <sup>2</sup> )	25
Proportion of chloride in waste, $p$ (mg/kg)	1800
Proportion of DCM in waste, $p$ (mg/kg)	2.3
Proportion of benzene in waste, $p$ (mg/kg)	0.014
Initial concentration in leachate	
Chloride, $c_o$ (mg/L)	2500
DCM, $c_o$ ( $\mu$ g/L)	3300
Benzene, $c_o$ ( $\mu$ g/L)	20
Percolation through waste, $q_o$ (m/a)	
0-T1 years	0.0003
> T2 years	0.15
Half-life in landfill	
Chloride, $t_{1/2}$ (a)	$\infty$
DCM, $t_{1/2}$ (a)	10, $\infty$
Benzene, $t_{1/2}$ (a)	25, $\infty$
<b>Geomembrane Properties:</b>	
Thickness Primary, $t_{GM}$ (m)	0.0015
Thickness Secondary, $t_{GM}$ (m)	0.002
Diffusion coefficient Chloride, $D_g$ (m <sup>2</sup> /a)	$3 \times 10^{-6}$
[m <sup>2</sup> /s]	$[1 \times 10^{-13}]$
Diffusion coefficient DCM, $D_g$ (m <sup>2</sup> /a)	$3 \times 10^{-5}$
[m <sup>2</sup> /s]	$[1 \times 10^{-12}]$
Diffusion coefficient Benzene, $D_g$ (m <sup>2</sup> /a)	$2 \times 10^{-5}$
[m <sup>2</sup> /s]	$[6 \times 10^{-13}]$
Henry's coefficient Chloride, $S_{gf}$ (-)	$8 \times 10^{-4}$
Henry's coefficient DCM, $S_{gf}$ (-)	2.3
Henry's coefficient Benzene, $S_{gf}$ (-)	57
Number of holes/ha (-)	2.5
Hole radius, $c_o$ (m)	0.00564
Service life, SL (a)	
Primary	160
Secondary	360
<b>Attenuation Layer Properties:</b>	
Thickness, $H_f$ (m)	3 & 3.6
Hydraulic conductivity, $k_f$ (m/s)	$10^{-7}$
Distance to water table from bottom of attenuation layer, $h_a$ (m)	
	2
Diffusion coefficient, $D_e$ (m <sup>2</sup> /a)	0.03
Sorption, $\rho_d K_d$ (-)	0
Half-life in soil, $t_{1/2}$ (a)	
Chloride	$\infty$
DCM	10, 50, $\infty$
Benzene	25, 125, $\infty$
Porosity, $n_e$ (-)	0.3
<b>Aquifer Properties:</b>	
Thickness modelled, $h_b$ (m)	3
Porosity, $n_b$ (-)	0.3
Base Darcy flux (horizontal), $v_b$ (m/a)	1

Table 32. Clay liner properties used in comparison of composite liner systems.

	CCL	GCL
Thickness, $H_L$ (m)	0.6	0.007
Hydraulic Conductivity to Leachate, $k_L$ (m/s)	$1 \times 10^{-9}$	$2 \times 10^{-10}$
Diffusion Coefficient, $D_e$ ( $m^2/a$ )	0.02	0.005
Sorption, $\rho_d K_d$ (-)	0	0
Porosity, $n_e$ (-)	0.4	0.7
Geomembrane-Clay Transmissivity, $\theta$ ( $m^2/s$ )	$1.6 \times 10^{-8}$	$2 \times 10^{-10}$
Half-life in soil, $t_{1/2}$ (a)		
Chloride	$\infty$	$\infty$
DCM	10,50, $\infty$	10,50, $\infty$
Benzene	25,125, $\infty$	25,125, $\infty$

basic case (see Figure 2b), the attenuation layer below the GCL was assumed to be 3.6 m thick so that the thickness of soil above the aquifer was essentially the same as for the case with a CCL (see Figure 2a). As a sensitivity analysis, a second GCL case was also examined where the GCL was assumed to be resting on a 3 m thick attenuation layer; this corresponds to a simple replacement of the 0.6 m thick CCL in Figure 2a by a 0.007 m thick GCL. The potentiometric surface in the aquifer was assumed to be 2 m above the bottom of the attenuation layer in all cases.

The long term hydraulic conductivity of the CCL was taken to be  $10^{-9}$  m/s. For the GCL it was assumed that, due to clay-leachate interaction, the hydraulic conductivity increased to  $2 \times 10^{-10}$  m/s.

Three contaminants (chloride, DCM  $\equiv$  dichloromethane, and benzene) were examined. Due to uncertainty regarding organic carbon content of clay liners in a generic calculation, no sorption was considered. A range of half-lives for DCM and benzene was examined in the leachate, liner system and attenuation layer.

All time was measured relative to the mid time of landfill operation for a MSW landfill with an assumed 20 year operating period. Thus to know time relative to the start of landfilling one would add 10 years to the times given in the following discussion. Likewise, to know the time since landfill closure, one would subtract 10 years from the times given. It was assumed that a low permeability landfill cover (cap) will be maintained and the leachate collection system operated for a period  $T_1$  ( $T_1 = 40$  years and 110 years were examined; i.e. 30 and 100 years post-closure). During the period up to time  $T_1$ , the percolation through the waste was assumed to be  $3 \times 10^{-4}$   $m^3/m^2/a$  (8 lphd). The design leachate head during the period was assumed to be 0.3 m and the flows through the liner system for the period 0- $T_1$  are given in Table 33 for the two liner systems assuming 2.5 large (1  $cm^2$ ;  $r_o =$

Table 33. Leakage rates for systems considered.

Time Period (years)	Leachate Mound (m)	Leakage	
		(lphd)	(m/a)
<b>GM+GCL +3.6m AL</b>			
0-T1	0.3	0.04	$1.6 \times 10^{-6}$
T1-T2	6	0.59	$2.1 \times 10^{-5}$
T2-T3	12	1.1	$4.0 \times 10^{-5}$
T3-	~0	4100	0.15
<b>GM+0.6m CCL+3m AL</b>			
0-T1	0.3	1.4	$5.2 \times 10^{-5}$
T1-T2	6	22	$8.2 \times 10^{-4}$
T2-T3	12	43	$1.6 \times 10^{-3}$
T3-	2	4100	0.15
<b>GM+GCL alone</b>			
0-T1	0.3	0.03	$1.1 \times 10^{-6}$
T1-T2	6	0.58	$2.1 \times 10^{-5}$
T2-160	12	0.96	$3.5 \times 10^{-5}$
160-	~0	4100	0.15
<b>GM+GCL +3m AL</b>			
0-350	0.03	0.008	$2.8 \times 10^{-7}$

0.00564 m) holes per hectare. Under assumed design conditions, the leakage through both systems was small; but it was smallest for the system with the GCL.

After time  $T_1$ , the landfill cover was no longer maintained and the percolation was assumed to increase to  $0.15$   $m^3/m^2/a$  (4100 lphd).

Once the operation of the primary leachate collection system is terminated (at time  $T_1$ ), leachate will build up in the waste until an equilibrium is reached wherein the flow in through the landfill cover (cap) is balanced by the outflow through the liner system, leachate seeps from the sides of the landfill, and lateral migration above the intact liner system (if any). The magnitude of the leachate mound and the time needed to develop the mound depend on a number of factors including the porosity of the waste, the water content of the waste at the time of landfill cover (cap) failure, the thickness and hydraulic conductivity of the waste, and the landfill geometry. These factors will vary from site to site and a full discussion of modelling the development and equilibrium value of a leachate mound is beyond the scope of the present paper. For the purposes of illustration, it will be assumed that over a 20 year period following termination



of operation of the leachate collection system (at time  $T_1$ ), a leachate mound develops and at time  $T_2$  ( $T_2 = T_1 + 20$  years) an equilibrium is reached with a mound of 12 m. During the period from  $T_1$  to  $T_2$ , an average mound of 6 m was used to calculate the flow given in Table 33. More sophisticated modelling of this period is possible but not necessary for current purposes.

Between the time  $T_2$  (when the full leachate mound has developed) and a subsequent time  $T_3$  (when the geomembrane was assumed to fail), the leachate head remained at 12 m and the flows through the liner system were as given in Table 33. Both liners were very effective at controlling leakage even with a 12 m leachate mound but the system with the GCL allowed almost 40 times less leakage (43 lphd for CCL versus 1.1 lphd for the GCL) even allowing for some clay leachate interaction with the GCL.

At time  $T_3$  ( $T_3 = 160$  years; i.e. 150 years post-closure) the geomembrane was assumed to fail instantaneously. (One can easily model a gradual degradation however there is presently a paucity of data to justify modelling a gradual variation with time.) The clay component of the liner was assumed to remain intact but could not support a 12 m leachate mound. Thus the leachate mound reduced due to advective transport out of the landfill until an equilibrium was reached where there was sufficient mound to allow the full percolation of  $0.15 \text{ m}^3/\text{m}^2/\text{a}$  ( $4100 \text{ lphd}$  or  $4.7 \times 10^{-9} \text{ m/s}$ ) to migrate through the clay liner. It may be anticipated that when the geomembrane fails, whatever contaminant remains in the leachate will be readily transported down to the aquifer.

The leakage results given in Table 33 suggest that the GCL system is hydraulically as good as, if not better than, the system with a CCL. It should be noted that this comparison assumes that there is a low transmissivity geotextile ( $\theta \leq 2 \times 10^{-10} \text{ m}^2/\text{s}$ ) as part of the GCL in contact with the geomembrane; care is required in selection of the GCL since the uppermost geotextile on the GCL (the one in contact with the geomembrane) may vary considerably from one product to another. The leakage given in Table 33 also assumes that there are no holes in the wrinkles (or no wrinkles!); as illustrated in Section 9.5.2, a hole in a wrinkle can substantially increase leakage.

The initial peak concentration,  $c_o$ , of the various contaminants considered is given in Table 31. This represents the peak annual average value (see Rowe 1995; Rowe & Booker 1995 for a more detailed discussion of landfill leachate history). The finite mass of contaminant in the waste was modelled as described by Rowe et al. (1995b) using the proportion of contaminant mass in the waste and total mass of waste given in Table 31. Consideration of the finite mass of contaminant gives rise to a decrease in concentration in the leachate with time as contaminant mass is removed from the landfill by

leachate collection, by contaminant diffusion and advection through the liner system and, where appropriate, by other mechanisms such as biodegradation of organic compounds. As indicated by Rowe (1991, 1995), the decrease in concentration with time ( $c(t)$ ) can be approximately given by

$$c(t) = c_o \exp\left[-\left(\frac{c_o q_o}{p M_w} + \lambda\right)t\right] \quad (43)$$

where  $c_o$  is the initial (peak) (annual average) concentration in ( $\text{mg/L} \equiv \text{g/m}^3$ ),  $q_o$  is the percolation through the waste ( $\text{m/a}$ ),  $p$  is the proportion of contaminant (chloride here) in waste ( $\text{mg/kg}$ ),  $M_w$  is the mass of waste per unit area ( $\text{t/m}^2$ ),  $t$  is time (years: a),  $\lambda$  is the decay coefficient  $= \ln 2/t_{1/2}$  ( $\text{a}^{-1}$ ) where  $t_{1/2}$  is the contaminant half life (a). Thus the time required for the leachate concentration to reduce to a value of  $c(t)/c_o$  is given by

$$t = -\ln(c(t)/c_o) / \left[\frac{c_o q_o}{p M_w} + \lambda\right] \quad (44)$$

In the case of chloride, the concentration can only reduce due to mass being removed from the system ( $\lambda=0$ ). Since there is a low permeability final cover and a geomembrane primary liner, negligible mass is removed in the period  $0-T_1$  and the concentration in the landfill remains relatively constant. This can be appreciated by substituting the appropriate parameters into Eq. 43 ( $c_o=2500 \text{ mg/L}$ ,  $q_o=0.0003 \text{ m/a}$ ,  $p=1800 \text{ mg/kg}$ ,  $M_w=25 \text{ t/m}^2$  and  $\lambda=0$ ) and it will be found that the annual average concentration after 40 years has only dropped by about  $2 \text{ mg/L}$ . Once the final cover is no longer maintained and the leachate generation,  $q_o$ , increases to  $0.15 \text{ m}^3/\text{a}/\text{m}^2$ , ( $4100 \text{ lphd}$ ) more mass is removed from the landfill (by the collection of leachate at perimeter drains or, failing this, escape to surface water) and there is a much faster decrease in average leachate concentration with time than was the case with a low permeability cover. However, for these parameters it still takes another 280 years after the time  $T_1$  for the source concentration to decrease to 10% of the initial value (i.e. a total of about 320 years for  $T_1=40$  years). The model used to obtain the following results (Rowe & Booker 1997a) adopts a more sophisticated approach but yields a decrease in concentration with time similar to that which can be calculated from Eq. 43. For more details see Rowe et al. (1995b) and Rowe and Booker (1997a).

For contaminants that undergo biodegradation (e.g. DCM, benzene etc.) the time to reduce the concentration to acceptable levels may be much faster than for chloride but will depend on the assumed half-life,  $t_{1/2}$ . For example, for DCM the parameters given in Table 31 and

a DCM half-life in the landfill of 10 years, Eq. 44 can be used (remembering to use  $c_0$  in mg/L units) to predict that it will take about 30 years for the concentration in the leachate to reduce to 10% of the initial value ( $c(t)/c_0=0.1$ ). For a DCM half-life of 2 years (see Rowe 1995 and Rowe et al. 1997d), it would take only 6 years for the leachate concentration to decrease to 10% of the initial value by biodegradation. Thus from these simple hand calculations it can be seen that for a modest sized landfill (25 t/m<sup>2</sup>) and relatively high leachate generation (0.15 m<sup>3</sup>/a/m<sup>2</sup>) flushing out of contaminant (e.g. chloride) is very slow and that for organic contaminants a controlling parameter will be the half-life of that contaminant in the landfill and in the underlying soil as will be illustrated in the following examples.

For the period 0-T<sub>3</sub> (i.e. before the geomembrane fails), the dominant transport mechanism is diffusion although advection does make a measurable contribution for the case of a geomembrane and CCL. There will be a variation in concentration with distance below the geomembrane due to the diffusive resistance of the geomembrane, the clay and the attenuation layer. There is some dilution in the aquifer due to the horizontal flow however the effect of this is limited for the assumed horizontal Darcy velocity in the aquifer,  $v_b=1$  m/a, and the length of the landfill examined here. Thus the concentration calculated in the aquifer reflects the effect of several mechanisms including a decrease in landfill concentration due to flushing (i.e. due to  $q_0$ ) and biodegradation (where considered), the diffusive resistance of the liner system, and some dilution in the aquifer. Retardation of organic contaminants (e.g. due to sorption onto organic matter) is not considered in the following examples but can be readily modelled (as illustrated in Section 8) if the partitioning coefficient,  $K_d$ , is known for the particular contaminant and soil. More details regarding contaminant transport modelling and the controlling mechanism is given by Rowe et al. (1995b) and Rowe and Weaver (1997).

Analyses were first performed for dichloromethane (DCM), a chlorinated solvent often found in MSW leachate (Gibbons et al. 1992; Rowe 1995). In some regulatory environments, one can not include consideration of biodegradation in modelling impact. Assuming an initial source concentration of 3300 µg/L (Rowe 1995; MoEE 1996) and neglecting biodegradation, the calculated concentration in the aquifer (see Figure 28) would increase to about 14 µg/L at about year 40 (i.e. 30 years post-closure) which is well below the maximum acceptable concentration (MAC) in drinking water of 50 µg/L, however by year 110 (100 years post-closure) it would increase to about 250 and 230 µg/L for the CCL and GCL system respectively which exceeds the MAC. The peak impact at about year 180 would be around 1090 and 1070 µg/L for the CCL and GCL systems

respectively (see Figure 28). These values would be considered quite unacceptable in regulatory environments where no time limit exists on the period being examined. In order not to exceed the MAC, the initial concentration would need to be 150 µg/L or less under these conditions. However, these calculated impacts are very conservative (likely unrealistically so) since the calculation did not take account of any biodegradation. It is known that DCM degrades under anaerobic conditions in leachate and as it migrates through soil (Rowe 1995; Rowe et al. 1997). A DCM half-life in the leachate of 10 years can be assumed. Recognizing that the DCM half-life in soil below a geomembrane could be longer, a DCM half-life of 50 years was assumed in the clay and attenuation layer. The resulting contaminant impact curves are shown in Figure 28. In this case, the impact after 40 and 110 years is about 5-6 µg/L and 23-24 µg/L with the peak impact being about 24 µg/L (i.e. half the MAC: see Figure 29) for both systems shown in Figure 2. These calculations indicate that for DCM, the GCL and CCL systems shown in Figure 2 are equivalent with respect to contaminant impact. If the thickness of the attenuation layer below the GCL was reduced from 3.6 m to 3 m, the peak impact would increase to about 40 µg/L (see Figure 29) but this is still less than the MAC for the parameters considered.

Calculations were also performed for benzene assuming an initial source concentration of 20 µg/L. Again, the two systems shown in Figure 2 were equivalent. If one neglects biodegradation, they would both potentially exceed the MAC of 5 µg/L with a peak

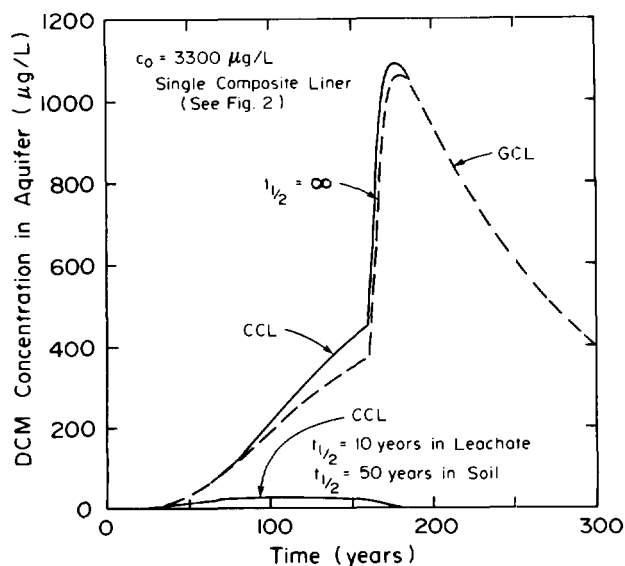


Figure 28. DCM impact curves in the aquifer below the composite liner systems shown in Figure 2 for different assumed half-lives ( $t_{1/2}$ ) of DCM.

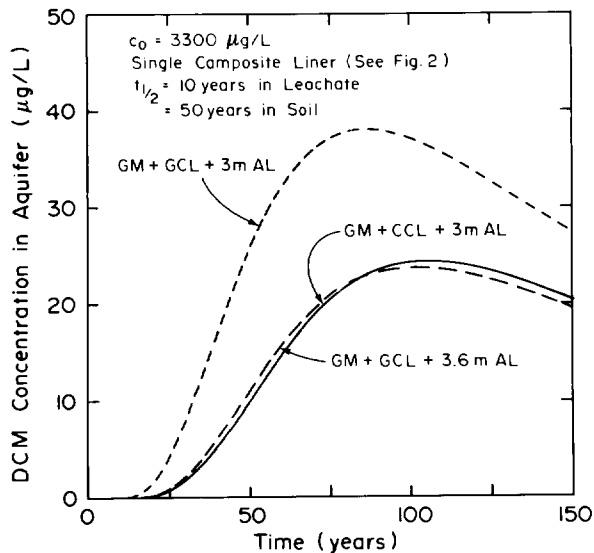


Figure 29. DCM impact curves in an aquifer below the two composite liner systems shown in Figure 2 for DCM half-lives  $t_{1/2}$  = 10 years in leachate, 50 years in soil.

impact of between 6 and 7 µg/L, however, if one considers half-lives of 25 years in the landfill and 125 years in the soil, the peak impact is less than 1 µg/L in both cases.

The migration of chloride was also examined since it is representative of conservative inorganic contaminants. As previously indicated, the diffusion coefficient for chloride is very low and for the low leakage rates that occur with only a few holes in the geomembrane the impact at the time of geomembrane failure (at  $T_3 = 160$  years) was less than 1 mg/L. However, since contaminants such as chloride do not degrade and the reduction in concentration can only occur due to dilution, there is considerable potential for impact when the primary geomembrane fails. Figure 30 shows the calculated variation in chloride concentration in the aquifer with time assuming the cover and collection system are maintained for (a) 40 years and (b) 110 years respectively, and assuming the service life of the geomembrane is 160 years. In both cases the impact greatly exceeds the typical drinking water objective for chloride of 250 mg/L. The greatest impact is for the case where the cover is maintained for 110 years and the lesser impact is for 40 years maintenance. At first this might seem counterintuitive, however it arises from the fact that cover failure implies increased infiltration into the landfill and even if the landfill underdrain system is not operated, leachate will mound and need to be collected at the perimeter drains (or else it will contaminate surface water). The leaching associated with

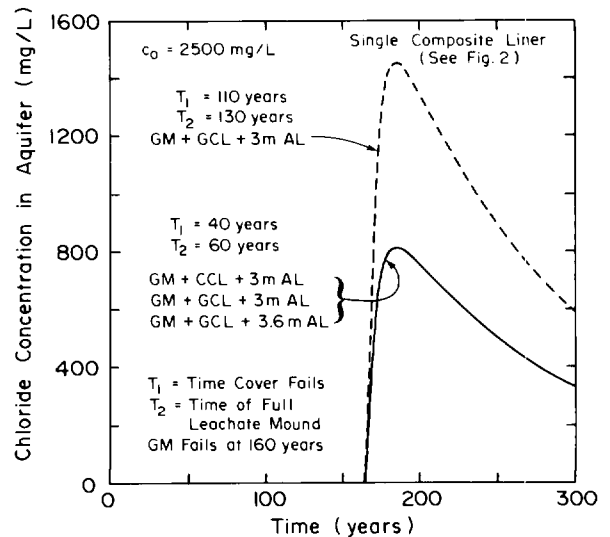


Figure 30. Chloride impact curve in an aquifer below the composite liner systems shown in Figure 2 showing the effect of maintaining the cover for periods  $T_1=40$  and 110 years. Geomembrane assumed to have service life to 160 years.

this will reduce the concentration of chloride in the landfill and hence when the geomembrane fails the impact on the aquifer is less. This highlights the desirability of early stabilization of the waste wherein the concentrations of contaminant in the waste (and hence leachate) are reduced to levels that would not cause an unacceptable environmental impact if the leachate was to escape to surface and groundwater without control (e.g. see Delaware 1995).

If one did intend to protect groundwater from contamination by chloride (and similar contaminants that can be leached by slightly acidic rainwater) without accelerating waste stabilization for a landfill of the size and characteristics considered here, it would be necessary to adopt a double lined system using either a CCL or GCL as part of the composite liner. Figure 3 shows one such system. The leachate conditions were the same as assumed previously for the primary collection system and the leakage volumes are as given in Table 33. Some readers may be surprised that the leakage through the primary composite liner shown in Figure 3 is less than through the composite liner shown in Figure 2b. As discussed by Rowe et al. (1995b), the leakage through a multi-layered soil system is controlled by the lowest hydraulic conductivity layer and the suction that may develop in an underlying unsaturated layer can actually increase leakage through a multilayered system relative to what would be obtained for the layer of less permeable soil alone. Thus, as noted by Giroud et al.

(1997a), an unsaturated mineral layer beneath a GCL does not improve the hydraulic performance relative to a GCL alone. On the contrary, the leakage through the system is increased if the soil below the GCL can sustain matric suctions. Typically, clayey and silty soils below a GCL can sustain significant matric suctions and it is generally not valid to adopt the assumption that the pressure head below the GCL in a multilayer system is zero. For calculating the leakage through the secondary composite liner, it was assumed that the head on the secondary liner would be kept to 0.03 m for the service life of the secondary geomembrane; this implies operation of the secondary leachate collection system for 350 years!

Figure 31 shows the calculated variation in

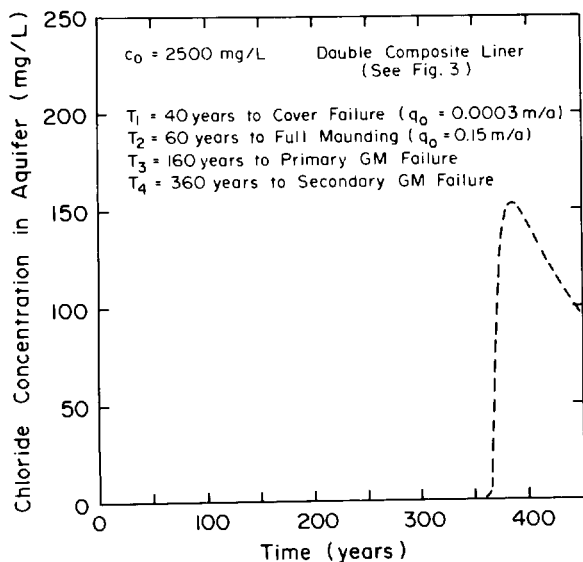


Figure 31. Chloride impact curve in an aquifer below the double composite liner system shown in Figure 3. Secondary geomembrane assumed to have a service life to 360 years.

concentration with time assuming that the secondary collection system is operated for the assumed service life of the geomembrane (i.e. until year 360; 350 years post-closure) and the peak impact is about 150 mg/L (i.e. well below the typical drinking water objective of 250 mg/L). This implies that if one was only required to meet the 250 mg/L objective, one could terminate operations earlier (essentially when the concentration in the leachate reached 250 mg/L); for the parameters adopted here (based on MoEE 1996) and a large landfill, this would be about 325 years. This implies that this landfill has a contaminating lifespan of at least 325 years. Once again, this highlights the desirability of early waste stabilization as an alternative to the long post-closure operating

period otherwise required to protect groundwater below large landfills. Clearly, the contaminating lifespan will change depending on assumed landfill conditions; generally, the larger the landfill (in terms of mass per unit area), the longer will be the contaminating lifespan and the required maintenance period unless there is accelerated stabilization.

#### 10.4 Summary

For landfills with a composite primary liner, the foregoing analyses and other analyses performed by the writer (Rowe et al. 1995b; Rowe 1997b) lead one to conclude that for well constructed liners (with relatively few holes in the geomembrane), contaminant transport of volatile organic compounds is governed by diffusive transport through the composite liner and any underlying soil. The impact of volatile organic compounds on water quality in any underlying groundwater will depend on: the peak source concentration ( $c_0$ ); the variation in source concentration with time; the diffusion coefficient and Henry's coefficient for the geomembrane; the diffusion coefficient and sorption characteristics of the clay component of the liner and the underlying attenuation layer; the biodegradation that occurs in the soil below the geomembrane; and dilution in the aquifer. The combined thickness of the clay component of the composite liner and the attenuation layer may be critical in terms of controlling impact on groundwater quality in any underlying aquifer for these contaminants.

Although data is limited and there is a need for more research, it appears that an HDPE geomembrane may provide a low permeability barrier to contaminants that are relatively soluble in water. For these contaminants, the diffusive transport across an intact geomembrane is low relative to that of the volatile organic compounds with low solubility and a low dipole moment (less than 1 debye). For the relatively soluble organic and inorganic contaminants, the number of holes and, in particular, the holes in contact with wrinkles may control the impact for the service life of the geomembrane. Once the primary geomembrane reaches its service life, many of the contaminants remaining in the leachate at this time will be readily transported across the clay component of the liner and the attenuation layer and impact may be largely controlled by dilution in the aquifer or by a secondary liner and collection system (if present). Thus for these contaminants the potential for concentration decrease with time in the landfill, the number of wrinkles and holes in the geomembrane, the service life of the primary geomembrane, the potential for dilution, and the presence of any secondary composite liner and operation of any secondary collection system will control the impact on groundwater beneath the site.

Finally, it is noted that it is possible that the

construction of a landfill may cause a change in groundwater quality even if there is no contaminant escape from the landfill! This may arise in situations where the construction of the landfill causes a reduction in recharge to an underlying aquifer (the "shadow effect") and/or a change in groundwater direction in the underlying aquifer as discussed by Rowe et al. (1995b). Likewise, construction of a landfill may cause a drop in groundwater levels below the landfill under some circumstances (Rowe et al. 1995b).

Using the modelling techniques adopted in Section 10.3, it is possible to assess equivalency of liner systems with respect to contaminant transport. For the specific cases considered in Section 10.3, it was shown that the composite liner with a GCL gave rise to less impact than a composite liner with a CCL even allowing for an increase in hydraulic conductivity of the GCL to  $2 \times 10^{-10}$  m/s due to clay-leachate interaction. However, it should be noted that in this comparison the total thickness of soil between the primary geomembrane and the receptor aquifer was held constant. In order to control the diffusion flux to a level similar to a CCL, it is necessary to couple the GCL with a soil layer that, while not having the hydraulic characteristics of a CCL, still provides diffusive (and potentially sorptive) resistance to contaminant migration.

It should be emphasized that when comparing liner systems, consideration should be given to factors such as:

- (a) The hydraulic resistance over the contaminating life-span of the landfill including the effects of leachate mounding and clay-leachate interaction for both compacted clays and GCLs. This will typically require clay-leachate compatibility tests (e.g. see Rowe et al. 1995b, Petrov & Rowe 1997). Consideration should also be given to the potential for internal erosion when there may be high gradients.
- (b) The contact conditions between the geomembrane and "clay". The geotextile component of the GCL may control transmissivity at the interface between the GCL and geomembrane and any assessment of leakage using the approach given in Section 9 should be based on experimental data for the proposed geomembrane and GCL under anticipated stress conditions.
- (c) The presence of wrinkles may be a problem with respect to the long term performance of composite liner systems in landfills. This may be particularly true for composite liners that incorporate a GCL due to the potential for clay movement in the GCL under applied pressure (see Section 7.3).
- (d) The level of construction CQA/CQC. The quality of a compacted clay liner is highly dependent on the construction control (e.g. compaction equipment, water content etc.). These CCL liners are also prone to desiccation cracking as discussed in Section 4.

GCLs are easier to place and their long term performance is less sensitive to desiccation effects however care is required to ensure that overlapped seams do not move and open up when overlying layers are placed.

- (e) The stability of the liner system and the potential for shear failure either at the interface between materials or within a layer itself both during construction and during placement of the waste (see Section 11).
- (f) The potential for diffusion, sorption and biodegradation. Since compacted clay liners are often not specified to have a minimum organic carbon content, sorption can not be relied on without independent tests. If sorption is required to control impact to a regulatory driven level, it is possible to specify a minimum organic carbon content and/or use modified clays in the GCL to achieve the desired level of sorption. For both compacted clay and GCL liner systems, some consideration should be given to the migration of metals, organic compounds and organo-metallic complexes that may be encountered in leachate.

From the discussion presented in this paper it is evident that there is potential for use of GCLs as part of composite liner systems in the base liners (base seals) of landfills provided that factors such as those itemized above are considered and addressed in the design and construction.

## 11 STABILITY OF BARRIER SYSTEMS

The preceding sections have focussed on the role of various geosynthetics with respect to reducing and controlling contaminant escape from a landfill. However, it is essential that in addition to contaminant transport considerations, adequate consideration be given to ensuring the stability of the barrier system (a) during liner construction, (b) during landfilling, and (c) after landfill completion. Failure in the barrier system prior to waste placement can occur if insufficient consideration is given to interface strength and/or the development of unanticipated seepage forces. Table 34 summarizes four cases where there were slides on slopes ranging from 4:1 (H:V) to 2.5:1. In three of the four cases, the failure arose due to low permeability of the drainage material. In one case, the as placed material had too low a hydraulic conductivity. In the other two cases, accumulation of fines gave rise to a build-up in seepage forces and subsequent failure. These cases illustrate the need to (a) select suitable materials, (b) have a design and construction plan that will minimize accumulation of fines, and (c) consider the potential climatic effect to impact on performance (e.g. heavy rainfall, freezing conditions). The design of landfill final cover (cap)

Table 34. Case histories involving slides of leachate collection layers before waste placement due to seepage forces (R.M. Koerner, personal communication).

No.	Upper Interface	Lower Interface	Slope Inclination (H:V)	Cover Soil Thickness (mm)	Approx. Slope Length (m)	Approx. Time After Construction (yr)	Cause of Seepage Force
1	NW-NP-GT	HDPE-GM	3:1	450	45	1-2	finer in stone
2	Stone	HDPE-GM	3:1	450	30	3-4	finer in stone
3	VFPE-GM	NW-NP-GT	2.5:1	300	20	0.2-0.5	low initial permeability
4	NW-NP-GT	PVC-GM	4:1	450	90 (3×30m)	1-2	ice wedge at toe of slope

Notes: GT = Geotextile      NW-NP = Nonwoven needle punched      HDPE = High density polyethylene  
 GM = Geomembrane      VFPE = Very flexible polyethylene      PVC = Polyvinyl chloride

systems is discussed in detail by Giroud and Beech (1989), Giroud et al. (1995a, b) and Koerner and Soong (1998) and the reader is referred to these papers for more details regarding the stability of covers and barrier systems on slopes.

Public aversion to the approval of new landfills has led to a general increase in the size of new landfills being constructed (since this maximizes the amount of waste that can be disposed of on a given footprint) and a tendency, when possible, to expand existing landfills laterally and/or vertically. In the construction of new landfills with complex barrier systems (e.g. see Figure 1), particular attention must be given to the potential for sliding within the barrier system before, during and after landfilling. This is illustrated with reference to the "Kettleman Hills" and "French" Landfills in the following subsections. When existing landfills are being expanded, it is common to include an engineered barrier system in the expanded portion of the landfill, even though the original landfill may not have incorporated any engineered barrier system. Particular care is required to integrate the new and old portions of the landfill and, in particular, to avoid stability problems when excavating at the toe of the existing landfill. This is illustrated with respect to the "Maine Landfill" and "Cincinnati Landfill" discussed subsequently.

#### 11.1 Kettleman Hills Slide as reported by Bryne et al. (1992)

The Kettleman Hills Landfill B-19 is a hazardous waste landfill with an engineered liner system as shown schematically in Figure 1. Construction of this phase had been completed and approximately 490,000 m<sup>3</sup> of waste and other material had been placed with the waste

reaching its maximum height (27 m) above the base when the failure occurred. The waste mass moved horizontally about 11 m and vertical slump of up to 4.3 m was observed along the sideslopes. Shortly after the failure, a study by Mitchell et al. (1990) and Seed et al. (1990) concluded that the failure was likely related due to failure in the liner system. Low shear strengths were identified for both the geomembrane/clay and geosynthetic/geosynthetic interfaces.

A second study was conducted during the removal of waste from the failed area and this study (Byrne et al. (1992) is reported to have established that failure involved: "slip along multiple interfaces within the landfill liner system. The predominant surface of sliding appeared to be the secondary clay/secondary geomembrane interface. In the upper portions of the northwest and southwest basal sideslopes" (see Figure 32), "the sliding surface corresponded to the primary geomembrane/secondary geotextile interface. In the toe regions of the northwest and southwest basal sideslopes, where the waste mass moved either directly or transversely away from those slopes, the failure mechanism was more complex and involved slip on multiple interfaces together with zones of distortion as a result of kinematic constraints to sliding on a continuous liner surface in these areas....The driving or destabilizing forces for the failure mechanism observed came from the waste located above the 2H:1V basal sideslopes located to the northwest and the southwest, and the resisting or stabilizing forces came from the waste located above both the essentially flat base of the landfill and the 3H:1V basal sideslope located to the northeast" (Figure 32). This complicated failure surface may have been caused by the stress dependent nature of the interfaces (Stark & Poeppel 1994).

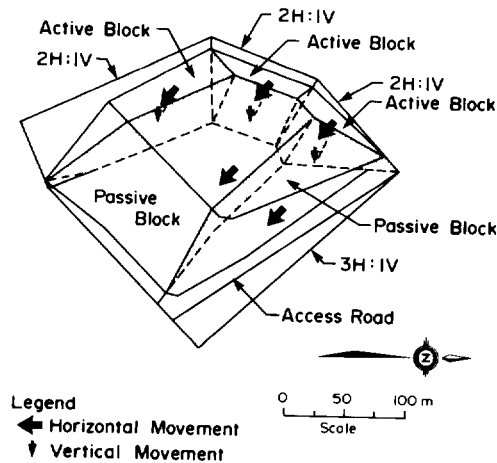


Figure 32. Displacement vectors for waste blocks during failure of the Kettleman Hills Landfill (modified from Byrne et al. 1992).

The failure appears to have been primarily the result of the low geomembrane/clay interface shear strength in the secondary liner system. The undrained behaviour of the interface about one year after construction is of particular note and was attributed to the fact that there was relatively little excess pore pressure dissipation near or within the geomembrane/clay interface due to the low hydraulic conductivity and coefficient of consolidation, and the length of the drainage path (since the geomembrane prevented drainage). The drainage path may, in part, explain why the secondary liner was more critical than the primary liner. Other interfaces also had low strength including the geomembrane/geonet interface ( $11^\circ$  peak;  $8^\circ$  residual) and geomembrane/geotextile ( $14^\circ$  peak;  $8^\circ$  residual).

This failure, and the subsequent investigations reported by Mitchell et al. (1990), Seed et al. (1990), Byrne et al. (1992) and Stark and Poepfel (1994) highlighted a number of important lessons to be considered in the design of barrier systems for landfills, including:

1. The interface behaviour between a geomembrane and compacted clay may be essentially undrained during landfilling and is quite sensitive to the as placed moisture content and dry unit weight of the clay. In this case, the undrained strength ranged from  $s_u = 26$ – $58$  kPa over the range of water content examined with a value of 45 kPa at the mean secondary liner water content.
2. The mean residual geomembrane/clay shear strength may be considerably lower than peak strength and is a function of the normal stress.
3. The geosynthetic/geosynthetic residual interface strength with conventional (smooth) HDPE geomembranes is quite low ( $8^\circ$  in this case).

4. There was a quite rapid decrease from peak to residual strength on all key interfaces as deformation occurs.
5. Peak strength may only be mobilized over a portion of the failure surface and at the onset of failure a significant portion of the interface may be at or near residual strength. Thus an evaluation of stability based solely on peak strengths is inappropriate. Stark and Poepfel (1994) have suggested that the use of peak strength may only be appropriate on flat or slightly inclined portions of the landfill.
6. Although 3D analyses may aid in interpreting stability of relatively complex geometric configurations (such as in this case), a conventional two-dimensional stability analysis along a representative cross-section provides an indication of potential problems (as in this case).
7. Appropriate laboratory strength tests appear to provide parameters that explain field behaviour provided they are performed for conditions representative of actual field conditions.
8. Particular care is required with compaction control of clay liners below geomembranes. A water content that is too low may lead to macrostructures and higher than specified hydraulic conductivity. A water content that is too high may give good hydraulic conductivity but low shear strength that could give rise to failure.
9. The effect of wetting of a clay liner (e.g. due to rainfall) after construction and before geomembrane placement needs to be considered in developing the design and construction plan.

## 11.2 French Slide as Reported by Ouvry et al. (1995)

A second example of the need to carefully design for barrier stability has been described by Ouvry et al. (1995). This municipal solid waste landfill had a barrier system consisting of at least 3 m of compacted clay ( $k < 1 \times 10^{-9}$  m/s) and 2 mm thick smooth HDPE geomembrane. At the base of the landfill a 190 g/m<sup>2</sup> spunbonded nonwoven geotextile was placed between the smooth geomembrane and the compacted clay (see Figure 33). The leachate collection system included a sand drainage blanket on the base, and sand and tyres (the tyres being to protect the geomembrane during compaction) on the 2:1 sideslope.

After compaction of the liner for Cell 1, the geomembrane was installed (December 1993) during a very wet period (234 mm of rain during the month of installation). Waste was then placed in the cell (see Figure 34) to an average thickness of 12–15 m (maximum 20 m) at the time of the waste slide.

The waste slide occurred in July 1994 and was reported to have occurred along the geomembrane/clay interface along the sideslopes and along the geotextile/clay interface at the base. The geomembrane was pulled out

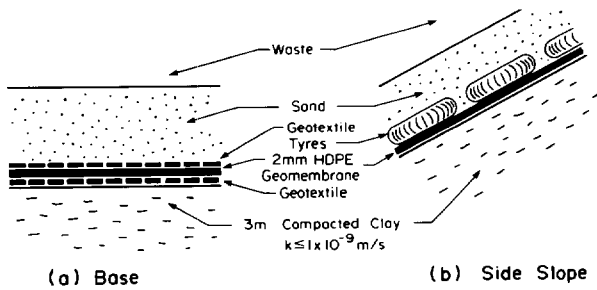


Figure 33. Schematic showing base and sideslope barrier systems for the French landfill (adapted from Ouvry et al. 1995).

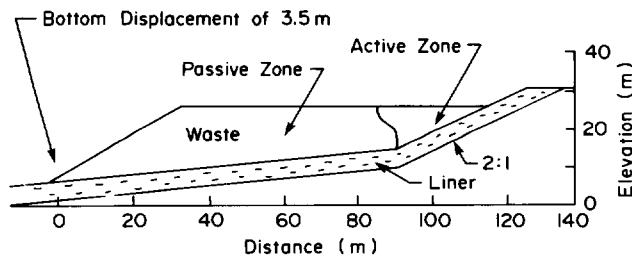


Figure 34. Schematic showing geometry of the base and waste at failure for the French slide (adapted from Ouvry et al. 1995).

of the anchor trench over a length of 60 m. The displacement at the top of the waste slide was 5-6.7 m. The moisture content of the clay from beneath the geomembrane was found to be 5-9% higher than it had been after compaction.

This case highlights a number of points made in the previous subsection, namely:

1. the importance of considering potential waste sliding when designing the landfill and developing its operations plan;
2. the critical nature of the geosynthetic/clay interface and the important role played by water content with respect to the shear strength developed at the interface;
3. the potential for a decrease in design interface strength due to events occurring during construction (heavy rainfall during placing of the geomembrane on the clay in this case).

### 11.3 Maine Slide as Reported by Reynolds (1991)

This landfill was initially developed as an unlined MSW

landfill on a soft marine clay with a soil profile consisting of a 3 m thick crust over 12 to 18 m of soft clay (vane strength 10-30 kPa). Stability calculations performed in 1986, assuming a waste density of 600 kg/m<sup>3</sup>, indicated that the maximum safe height of waste was 17 m. By 1989, the landfill had reached 22 m and it had been determined that the MSW density was about 1250 kg/m<sup>3</sup> (i.e. more than twice that assumed in the stability calculations). The increased density was attributed to the use of (a) more compactive effort, and (b) more daily and intermediate cover to control odour, birds and windblown waste.

As part of a 1989 landfill expansion, work started on constructing a liner system consisting of two layers of HDPE geomembrane over 0.6 m of recompacted clay over the marine clay in the expansion area (see Figure 35). The use of two layers of geomembrane is itself unusual and the rationale for this is not provided by Reynolds (1991). Trees were removed and 1-3 m of the stiff crust was removed to (a) remove some sand seams and (b) increase air space.

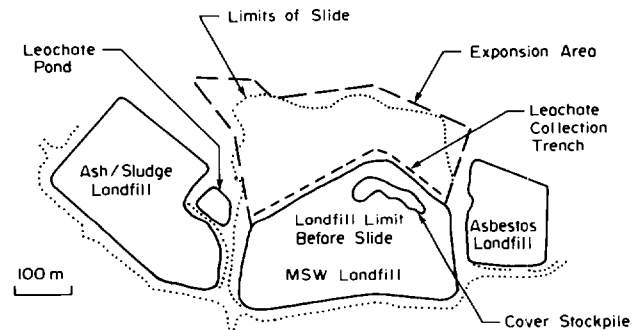


Figure 35. Schematic showing plan view of Maine slide (modified from Reynolds 1991).

Since the original landfill had no leachate collection system or engineered liner, a trench was excavated through the stiff clay at the western toe of the old landfill to allow interception of subsurface leachate flow from the landfill (see Figure 35). This combined with the stockpiling of cover soil over the westerly crest of the old landfill further reduced stability (see Figure 35) and following 10 days of rain (0.3 m) a landslide occurred involving some 500,000 m<sup>3</sup> of material (see Figure 35). The movement was reported to have lasted about 15 seconds. Figure 36 shows scale sketches for an east-west section both before and after the slide (Reynolds 1991). The slide was reported (Reynolds 1991) to have begun with a rotational failure under the original landfill slope (see Figure 36) and then retrogressed beneath the entire landfill, exiting at the eastern crest of the old landfill.



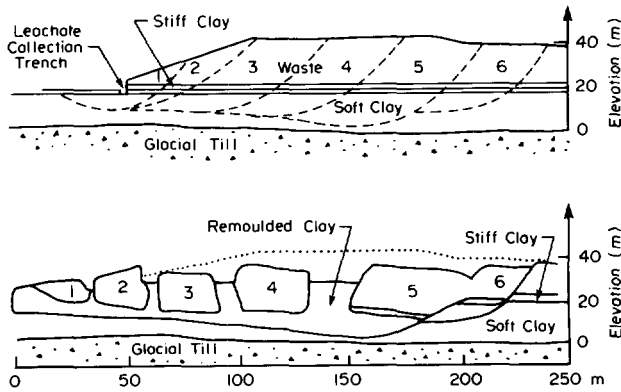


Figure 36. Schematic showing cross-section through the Maine slide (modified from Reynolds 1991).

During the slide the waste broke into large blocks which moved to the southwest, west and northwest on the remoulded soft clay which had lost up to 80% of its original strength (Figure 36). The block moved horizontally up to 50 m and at about 60 m from the original toe, the remoulded soft clay began to flow over the undisturbed surficial soil and extended up to 120 m from the original toe. Vertical walled crevasses up to 10 m deep were left between the blocks of waste when movement ceased (Figure 36). The post-failure investigation revealed that the average waste density (including daily and intermediate cover) was  $1520 \text{ kg/m}^3$  (range  $800\text{-}2000 \text{ kg/m}^3$  from  $10 \text{ m}^3$  test pits). The average shear strength parameters for the waste were  $c=24 \text{ kPa}$ ,  $\phi=27^\circ$  however large deformations were needed to mobilize this strength. The soft clay had a normalized strength ratio  $s_u/\sigma'_v=0.2$ .

This case illustrates a number of important points as follows:

1. as with most failures, there were a number of factors contributing to the failure;
2. the major cause of instability was the excavation of the stiff clay crust from the toe of the slope and excavation of the trench at the toe of the old landfill as part of the activity to construct an engineered barrier for the expansion portion of the site;
3. failure to recognize the actual waste densities contributed to the problem;
4. placement of a cover stockpile near the crest of the landfill decreased stability; and
5. heavy rains prior to the slide likely increased the density of the waste providing a trigger for the failure given the other conditions.

#### 11.4 Cincinnati Slide as Reported by Stark and Evans (1997)

This landfill experienced a significant waste slope failure in 1996. As reported by Stark and Evans (1997), the landfill covers about 93.6 ha and accepts an average of about 4,500 tonnes of waste per day. Initial development of the site began in 1945 and consisted of pushing waste over the edge of existing ravines where it came to rest on native soils consisting of a poorly sorted mixture of fine grained soil and angular rock fragments (colluvium). As a result of a 1994 approval for a 48 ha expansion and the requirements of US EPA Subtitle D (USEPA 1994), the operator was required to install a barrier system consisting of a leachate collection system, 1.5 mm HDPE geomembrane liner and a 1.5 m thick compacted liner in the expanded portion of the landfill.

The expansion involved creating a 40 m deep excavation at the toe of the existing landfill to allow installation of the barrier system. As the excavation was nearing completion after eighteen months, a major wasteslide occurred involving about  $1.3 \times 10^6 \text{ m}^3$  of waste. About 8 ha of waste slid into the 44 ha excavation and the toe of the slope moved about 250-300 m to the northern edge of the deep excavation.

At the time of the failure, the slope adjacent to the excavation was 2.6:1 (H:V) but some portions were steeper than 1.85:1 (H:V) and there was a 4.5-6 m nearly vertical excavation through the waste and colluvium at the toe. Stark and Evans report that the translational failure was thought to be due to mobilizing the post-peak shear strength ( $\phi \sim 10\text{-}12^\circ$ ,  $c' \sim 0$ ) in the colluvium, overbuilding of the waste above the approved elevation by about 12 m, excavating the toe that exposed the weak colluvium, and strain incompatibility between the waste and colluvium.

This case provides clear evidence that:

1. care is needed in the operational development of a landfill to avoid situations that could potentially cause overfilling and instability,
2. the interfaces between the waste and adjacent material (e.g. native or engineered liners) may be critical to the stability of waste slopes,
3. it is important to identify the geotechnical characteristics (including shear strength) of the native material on which the landfill is constructed and to calculate the stability of proposed slopes (it appears that the operational strength of the colluvium was the post-peak strength, not the peak strength), and
4. excavation of the toe of a slope can substantially increase the risks of a failure occurring.

## 11.5 Summary

Numerous landfills are safely constructed without stability problems. However, the four examples cited in this section illustrate the need for careful consideration to be given to the potential for sliding (a) during barrier construction, (b) during expansion of existing landfills and (c) during landfilling over the barrier system. Not illustrated here, but of importance nevertheless, is the potential for a failure at (or after) closure. The likelihood of failure occurring can be minimized by:

1. appropriate design and materials selection (including appropriate laboratory tests and stability analyses);
2. good CQC/CQA to ensure that the barrier system is installed as designed;
3. development plans for expanded landfills that limit toe excavation and overfilling and define allowable conditions for construction of the expansion area and a means of monitoring adherence to the development plans;
4. operations plans that include consideration of stability as the waste is placed and means of monitoring adherence to the operations plans;
5. contingency plans in the event of changed conditions occurring during construction (e.g. excessive rain, unexpected foundations conditions etc.); and
6. disposal alternatives so that waste can be diverted if expansion schedules are not met.

Provided that these issues are addressed, the numerous successful landfill construction projects not explicitly cited here illustrate that the well engineered barrier system can be safely constructed to provide a high level of environmental protection.

## 12 CONCLUSIONS

A number of key factors affecting the long term performance of landfill barrier systems (base seals) have been reviewed. It was shown that the temperature at the base of landfills is particularly sensitive to the type of waste, rate of landfilling and the saturated thickness of waste. In particular, leachate mounding on the base of the landfill (e.g. due to clogging of a leachate collection system or failure to remove leachate from the collection system) may result in a significant increase in temperature at the landfill liner. This in turn can increase both diffusive and advective contaminant transport through the liner system and can reduce the service life of both a geomembrane and underlying compacted clay liner.

Geotextile filters in landfill leachate collection systems do clog and may experience a drop in hydraulic conductivity of 2 to 5 orders of magnitude. The key issue is

whether or not they are excessively clogged. Currently, available evidence would suggest that when appropriately used in a drainage blanket, suitable geotextiles may increase the long term performance of the underlying granular drainage blanket without having any negative impact on the performance of the barrier system. However, geotextiles should be used with caution in areas of flow localization (e.g. around french drains, wrapping pipes etc.) in landfill leachate collection systems since excessive clogging can occur and this may cause leachate mounding and increased potential for the escape of contaminants.

Compacted clay liners potentially have a very long service life provided (a) adequate consideration is given to clay leachate compatibility in the selection of the clay and (b) there is no significant desiccation of the liner. Care needs to be given to minimizing/preventing desiccation both in the short term and the long term. Minimizing "short term" desiccation before waste placement can be achieved by appropriate design and construction. Minimizing "long term" desiccation after waste placement will require both appropriate design and landfill operations that limit the temperature at the base of the landfill. Particular care is required for thin (e.g. 0.6 m thick) compacted clay liners and for liners underlain by a secondary leachate collection/leak detection system.

The hydraulic conductivity of GCLs is sensitive to the permeant, the hydrating conditions and the applied stress. The hydraulic conductivity may increase several orders of magnitude for some permeating conditions. Thus the hydraulic conductivity needs to be assessed on a case by case basis (examining the proposed GCL permeated with leachate similar to that anticipated). However, a number of tests with real leachate and synthetic leachate whose chemical composition is based on real MSW landfill leachate have shown only modest increases in hydraulic conductivity (up to an order of magnitude). Calculations performed using the hydraulic conductivity of the GCL after interaction with MSW leachate suggest that a GCL may still be a very effective component of a composite liner system when combined with a well designed and constructed geomembrane liner.

Diffusion may be an important transport mechanism in well designed and operated landfills. Diffusion through geomembranes and GCLs has been discussed and parameters given. The rate of diffusive transport may be both concentration and temperature dependent. It is shown that some organic contaminants (e.g. volatile organic compounds, VOCs) can readily diffuse through HDPE geomembranes and that they may migrate through thin (~0.6 m) composite liners to detectable levels within less than a decade. The long term impact will depend on (a) the level of sorption that occurs in the clay liner and any attenuation layer above any potential

receptor aquifer; and (b) the level of biodegradation of organic contaminants that occurs in the waste and barrier system. Since the geomembrane is a selective barrier (providing considerable resistance to bacteria and primary substrates like volatile fatty acids but relatively little resistance to VOCs) the biodegradation in the soil below a geomembrane may be less than that observed in liners and aquifers where there is no geomembrane. More research is required to establish the magnitude of this effect.

Geomembranes provide an excellent diffusion barrier to inorganic contaminants and many organic contaminants. For these contaminants, the primary mode of contaminant transport is through holes in the geomembrane during the service life of the geomembrane. The leakage through composite liners has been examined. Field experience indicates that the leakage through composite liners is relatively small after waste placement and especially after the final cover has been constructed. However, the leakage is more than one would expect based on a few isolated holes in geomembranes assuming "good" construction. A new analytical solution for modelling leakage through holes in a geomembrane for a wide range of leachate heads and clay liner thicknesses has been presented both for isolated holes and holes in wrinkles (waves). It is shown that the presence of holes in wrinkles could explain the magnitude of the leakage observed in field applications with a leak detection system when allowance is also made for consolidation water arising from compacted clay liners.

The service life of GCLs and geomembranes is discussed. The service life of the geomembrane will be related to the type and amount of antioxidant used in the geomembrane, and the presence of stress concentration (e.g. at wrinkles, due to indentation by stones, etc.) and stress crack resistance. Based on existing data, the service life of a primary and secondary properly formulated HDPE geomembrane is projected to be of the order of 150 and 350 years (or greater) at temperatures of 25°C and 12°C respectively and assuming the conditions stated in Section 7, including (a) good design and construction practice; (b) the specified minimum oxidative induction time (OIT); (c) the specified minimum stress crack resistance; (d) negligible tensile stress concentrations in the geomembrane. It is noted that an increase in the temperature of the liner may substantially reduce the service life of the geomembrane.

Contaminant impact assessment is discussed in the context of the equivalence of liner systems. The use of GCLs as a replacement for a conventional compacted clay liner (CCL) has been discussed. By considering a specific example, it is shown that even allowing for an order of magnitude increase in hydraulic conductivity due to clay-leachate interaction, a GCL could replace a

conventional 0.6 m thick compacted clay liner and it still provides acceptably low impacts on an underlying aquifer. For the example examined, maintaining the same thickness of soil between the geomembrane and the aquifer (i.e. using a GCL and 0.6 m "foundation" layer to replace the 0.6 m CCL), the calculated impacts were less than for the CCL. If the CCL was replaced by a GCL alone, the calculated impacts were greater than for the CCL but with a 3 m attenuation layer between the GCL and aquifer were still acceptable during the service life of the geomembrane. These findings should not be generalized and each landfill should be considered on a case by case basis. The techniques used in Section 10 can be used to perform this assessment.

From the results presented in this paper it is evident that there is the potential for use of GCLs as part of composite liner systems in the base liners (base seals) of landfills provided that factors such as those itemized in the paper are considered and addressed in the design and construction. It should be emphasized that just as clay liners should be evaluated on a case by case basis, so should GCLs. Landfills vary in terms of mass loading and leachate characteristics and not all clays and GCLs have the same characteristics; even for a given GCL manufacturer there may be a range of products some of which are better suited than others for use in base liners.

It is shown that without stabilization of the waste there is the potential for significant impacts on groundwater due to recalcitrant contaminants once the primary geomembrane reaches its service life. These impacts can be minimized using a double composite liner. However, for large landfills the period of operation and maintenance of the leachate collection system may be of the order of hundreds of years.

Although the inclusion of various geosynthetics (e.g. geomembranes, geotextiles and geonets), clay liners, geosynthetic clay liners, and granular drainage layers may improve a landfill's performance by reducing contaminant escape, the implications of each layer and the potential interaction between layers (especially at interfaces) with respect to stability must be considered on a case by case basis. Potential failures may include sliding within the barrier system or general shear failures (landslide/waste slide) through the waste and underlying geological deposit (a) during liner construction, (b) during landfilling, or (c) after landfill completion. The need to carefully assess the stability of landfills is discussed and the lessons learned from four failures have been highlighted.

It is concluded that over the past decade very substantial advances have been made in understanding the behaviour of geosynthetics in barrier systems for landfills and that with appropriate design and construction, geosynthetics can be used to design a system that will provide excellent long term environmental protection.

This paper is dedicated to the memory of Professor John Booker - gentleman, scholar and friend. It was prepared with funding from the Natural Sciences and Engineering Research Council of Canada. The paper attempts to draw together both the author's research and the work of many other investigators. Explicit reference is made in the text to the sources of data (information relied upon). However, many individuals also provided suggestions, information and assistance in the preparation of the paper that can not be easily referenced. The author gratefully acknowledges Drs. J.P. Giroud and R.M. Koerner for their review of the entire manuscript and their constructive comments as well as to the following individuals who kindly offered their advice, information and, in some cases, their review of sections of the paper (in alphabetical order): Drs. F.S. Barone, R. Bonaparte, J.R. Booker, D.E. Daniel, E. Gartung, J.P. Giroud, J.P. Gourc, H. Haxo, Jr., G. Heibroek, Y.G. Hsuan, G.R. Koerner, R.M. Koerner, M. Othman, D. Smith, T. Stark and Messrs. R. Petrov, D. Stewart, K. von Maubeuge and the following graduate students who assisted in various aspects of the research reported herein: M. Armstrong (Section 3.2 and Figure 12), I.R. Fleming (Section 3.2), L. Hrapovic (Figures 19 and 21), C. Lake (Section 6, Table 11 and Figure 15), S. Millward (Table 30), P. Sangam (Sections 7.4 and 8, Table 17, Figures 19 and 21) and J. VanGulck (Figure 12).

## 14 NOTATION

AL	=	Attenuation Layer
AOS	=	apparent opening size (mm)
A	=	area perpendicular to flow and/or diffusion
a	=	area of hole in a geomembrane (cm <sup>2</sup> ; m <sup>2</sup> )
b	=	half width of a wrinkle (see Figure 27) (m)
C	=	H <sub>L</sub> + H <sub>f</sub> - h <sub>a</sub> (m)
CCL	=	Compacted Clay Liner
CSPE	=	Chlorosulphenated Polyethylene
c	=	contaminant concentration (mg/L, μg/L)
c(t)	=	contaminant concentration at time t (mg/L, μg/L)
c <sub>g</sub>	=	contaminant concentration in a geomembrane (mg/L; μg/L)
c <sub>f</sub>	=	contaminant concentration in solution (mg/L; μg/L)
c <sub>FE</sub>	=	final equilibrium concentration in fluid (mg/L; μg/L)
c <sub>IP</sub>	=	initial concentration in fluid (mg/L; μg/L)
c <sub>o</sub>	=	initial concentration (mg/L, μg/L)
D <sub>e</sub>	=	effective diffusion coefficient in soil (m <sup>2</sup> /s; m <sup>2</sup> /a)
D <sub>g</sub>	=	diffusion coefficient in a geomembrane (m <sup>2</sup> /s; m <sup>2</sup> /a)

D <sub>T</sub>	=	diffusion coefficient of temperature T (m <sup>2</sup> /s; m <sup>2</sup> /a)
D <sub>10</sub>	=	diffusion coefficient of temperature T=10°C (m <sup>2</sup> /s; m <sup>2</sup> /a)
e <sub>B</sub>	=	bulk GCL void ratio (-)
f	=	mass flux of contaminant (g/m <sup>2</sup> /a)
GCL	=	Geosynthetic Clay Liner
GM	=	Geomembrane
GN	=	Geonet
g	=	gravitational acceleration (m/s <sup>2</sup> )
HDPE	=	High Density Polyethylene
h	=	hydraulic head (m)
h <sub>a</sub>	=	potentiometric head in an aquifer (m)
h <sub>b</sub>	=	thickness of an aquifer (m)
h <sub>w</sub>	=	leachate head acting on top of a geomembrane (m)
H <sub>f</sub>	=	thickness of an attenuation (foundation) layer (m)
H <sub>L</sub>	=	thickness of a liner (CCL or GCL) (m)
i <sub>s</sub>	=	mean gradient across the liner and attenuation layer (see Eq. 29) (-)
K <sub>d</sub>	=	partitioning or distribution coefficient (mL/g)
K <sub>g</sub>	=	linear sorption coefficient for geomembrane (-)
K <sub>o</sub>	=	coefficient of earth pressure at rest (-)
k	=	hydraulic conductivity (m/s)
k <sub>f</sub>	=	hydraulic conductivity of a foundation/attenuation layer (m/s)
k <sub>L</sub>	=	hydraulic conductivity of clay liner (m/s)
k <sub>n</sub>	=	geotextile normal hydraulic conductivity (m/s)
k <sub>om</sub>	=	hydraulic conductivity of leachate collection layer (m/s)
k <sub>s</sub>	=	harmonic mean hydraulic conductivity of clay liner and attenuation layer (see Eq. 29) (m/s)
k <sub>T</sub>	=	hydraulic conductivity at temperature T (m/s)
k <sub>10</sub>	=	hydraulic conductivity at temperature T=10°C (m/s)
L	=	length of a wrinkle (m)
LCS	=	Leachate Collection System
LDS	=	Leak Detection System (also called a Secondary Leachate Collection System)
M <sub>A</sub>	=	mass per unit area (g/m <sup>2</sup> )
MSW	=	Municipal Solid Waste
M <sub>w</sub>	=	mass of waste per unit area (t/m <sup>2</sup> )
n	=	porosity (-)
n <sub>b</sub>	=	porosity in aquifer
n <sub>e</sub>	=	effective porosity (-)
P <sub>g</sub>	=	"permeability" of a polymer to a given contaminant (P <sub>g</sub> =S <sub>g</sub> D <sub>g</sub> ) (m <sup>2</sup> /s; m <sup>2</sup> /a)
PLCS	=	Primary Leachate Collection System
POA	=	percentage open area (-)
p	=	proportion of contaminant in waste (mg/kg)

Q	=	flow through a hole in a geomembrane (m <sup>3</sup> /s)
q <sub>o</sub>	=	permeation through landfill cover reaching the leachate collection system per unit area (m/s; m/a)
R	=	wetted radius (m)
r <sub>o</sub>	=	radius of a hole in a geomembrane (m)
S	=	soil suction (kPa)
S <sub>g</sub>	=	sorbed mass per unit volume of geomembrane (ms/L)
S <sub>gf</sub>	=	partitioning (solubility, Henry) coefficient (-)
SDR	=	Standard Dimension Ratio for pipes (-)
SLCS	=	Secondary Leachate Collection System (also called a Leak Detection System)
s	=	spacing between geomembrane and clay liner (m)
s <sub>u</sub>	=	undrained shear strength (kPa)
T <sub>1</sub>	=	time at which maintenance of landfill final cover (cap) and operation of the leachate collection system is terminated in example in Section 10.
T <sub>2</sub>	=	time at which equilibrium leachate mound is reached for an unmaintained landfill assuming no leachate collection from the underdrains but a fully functioning liner system in example in Section 10.
T <sub>3</sub>	=	time at which the geomembrane component of the primary composite liner is assumed to fail in the example in Section 10.
t	=	time (s,a)
t <sub>1/2</sub>	=	half-life (unless otherwise noted) (a)
t <sub>GM</sub>	=	thickness of a geomembrane (mm)
t <sub>GT</sub>	=	thickness of a geotextile (mm)
t <sub>GCL</sub>	=	thickness of GCL (mm)
VFA	=	Volatile Fatty Acids
VOC	=	Volatile Organic Compounds
v <sub>a</sub>	=	Darcy velocity (Darcy flux) through a layer (m/s; m/a)
v <sub>b</sub>	=	Darcy velocity (Darcy flux) in an aquifer (m/a)
v <sub>i</sub>	=	average Darcy velocity beneath the wetted radius around a hole in a geomembrane over a clay liner (m/a)
α	=	[k <sub>v</sub> /(H <sub>L</sub> +H <sub>i</sub> )/θ] <sup>0.5</sup> (-)
σ	=	applied vertical stress (kPa)
σ <sub>v</sub>	=	vertical effective stress (kPa)
ψ	=	geotextile permittivity (s <sup>-1</sup> )
ρ	=	density of a fluid (t/m <sup>3</sup> ; kg/m <sup>3</sup> ; g/cm <sup>3</sup> )
ρ <sub>d</sub>	=	dry density of soil (t/m <sup>3</sup> ; kg/m <sup>3</sup> ; g/cm <sup>3</sup> )
ρ <sub>GM</sub>	=	density of geomembrane (t/m <sup>3</sup> ; kg/m <sup>3</sup> ; g/cm <sup>3</sup> )
θ	=	transmissivity between geomembrane and clay liner (m <sup>2</sup> /s)
η	=	viscosity of a liquid (kg/m/s)
λ	=	decay constant = ln2/t <sub>1/2</sub> (a <sup>-1</sup> )

## REFERENCES

- Ashley, R.J. (1985) "Permeability and Plastics Packaging", In *Polymer Permeability*, Ed. J. Comyn, Chapter 7, pp. 269-308.
- August, H. and Tatzky, R. (1984) "Permeability of Commercially Available Polymeric Liners for Hazardous Landfill Leachate Organic Constituents", *Proceedings of International Conference on Geomembranes*, June 20-24, Denver, CO, Vol. I, Industrial Fabrics Association International, St. Paul, USA, pp. 163-168.
- August, H., Tatzky-Gerth, R., Preuschmann, R. and Jakob, I. (1992) "Permeationsverhalten von Kombinationsdichtungen bei Deponien und Altlasten Gegenueber Wassergefaehrdenden Stoffen", Report on the R&D Project 10203412 of the BMBF, published by BAM, Sub-Department IV.3, Landfill and Remedial Engineering, D-12200 Berlin, Germany.
- Averesch, U. and Schicketanz, R. (1998) "Installation Procedure and Welding of Geomembranes in the Construction of Composite Landfill Liner Systems: the Fixing Berm Construction Method", *Proceedings of 6th International Conference on Geosynthetics*, Atlanta, Industrial Fabrics Association International.
- Badu-Tweneboah, K., Giroud, J.P., Carlson, D.S. and Schmertmann, G.R. (1998) "Evaluation of the Effectiveness of HDPE Geomembrane Liner Protection", *Proceedings of 6th International Conference on Geosynthetics*, Atlanta, Industrial Fabrics Association International.
- Berens, A.R. and Hopfenberg, H.B. (1982) "Diffusion of Organic Vapors at Low Concentration on Glassy PVC, Polystyrene and PMMA", *Journal of Membrane Science*, 10, pp. 283-303.
- Barone, F.S., Costa, J.M.A. and Ciardullo, L. (1997) "Temperatures at the Base of a Municipal Solid Waste Landfill", *50th Canadian Geotechnical Conference*, Ottawa, October, Vol. 1, pp. 144-152.
- Basnett, C.R. and Bruner, R.J. (1993) "Clay Desiccation of a Single-Composite Liner System", *Proceedings of Geosynthetics 93*, Vancouver, Industrial Fabrics Association International, St. Paul, MN, pp. 1329-1340.
- Bishop, A.W. (1959) "The Principle of Effective Stress", *Teknisk Ukeblad*, 106(39), pp. 859-863.
- Bishop, D.J. (1996) "Discussion of 'A Comparison of Puncture Behavior of Smooth and Textured HDPE Geomembranes' and 'Three Levels of Geomembrane Puncture Protection' by Narejo, D.B.", *Geosynthetics International*, Vol. 3, No. 3, pp. 441-443.
- Bleiker, D.E. (1992) "Landfill Performance: Leachate Quality Prediction and Settlement Implications", M.A.Sc. Thesis, University of Waterloo.

- Bonaparte, R. (1995) "Long-Term Performance of Landfills", in *Geoenvironment 2000*, ASCE Geotechnical Special Publication 46, Ed. Y.B. Acar and D.E. Daniel, pp. 514-553.
- Bonaparte, R. and Gross, B.A. (1993) "LDCRS Flows From Double-Lined Landfills and Surface Impoundments", *Report to USEPA*, Contract 68-CO-0068, 65 p.
- Bonaparte, R., Othman, M.A., Rad, N.S., Swan, R.H. and Vander Linde, D.L. (1996) "Evaluation of Various Aspects of GCL Performance", Appendix F, *Report of 1995 Workshop on Geosynthetic Clay Liners*, D.E. Daniel & H.B. Scranton, EPA/600/R-96-149, pp. F1-F34.
- Bowders, J.J., Daniel, D.E., Wellington, J. and Houssidas, V. (1997) "Managing Desiccation Cracking in Compacted Clay Liners Beneath Geomembranes", *Proceedings of Geosynthetics '97*, Long Beach, Ed. L. Well and R. Thiel, Industrial Fabrics Association International, pp. 527-540.
- Brady, K.C., McMahon, W. and Lamming, G. (1994) "Thirty Year Ageing of Plastics", Transport Research Laboratory, Project Report 11, E472A/BG, ISSN 0968-4093.
- Britton, L.N., Ashman, R.B., Aminabhavi, T.M. and Cassidy, P.E. (1989) "Permeation and Diffusion of Environmental Pollutants Through Flexible Polymers", *Journal of Applied Polymer Science*, Vol. 38, No. 2, pp. 227-235.
- Brown, K.W., Thomas, J.C., Lytton, R.L., Jayawickrama, P. and Bahrt, S. (1987) "Quantification of Leakage Rates Through Holes in Landfill Liners", U.S. EPA Report CR810940, Cincinnati, 147 p.
- Brummermann, K., Blümel, W. and Stoewahse, C. (1995) "Protection Layers for Geomembranes: Effectiveness and Testing Procedures", *Proceedings of 5th International Conference on Geosynthetics*, Singapore, September 1994, pp. 1003-1006.
- Brune, M., Ramke, H.G., Collins, H. and Hanert, H.H. (1991) "Incrustation Processes in Drainage Systems of Sanitary Landfills", *Proceedings of 3rd International Landfill Symposium*, Sardinia, pp. 999-1035.
- Buss, S.E., Butler, A.P., Sollars, C.J. and Perry, R. (1995) "Migration of Organics Through HDPE Landfill Lining Material", *Proceedings of 5th International Landfill Symposium Sardinia 95*, Cagliari, Italy, pp. 377-385.
- Byrne, R.J., Kendall, J. and Brown, S. (1992) "Cause and Mechanism of Failure of Kettleman Hills Landfill", *Proceedings of ASCE Conference on Stability and Performance of Slopes and Embankments II*, pp. 1-23.
- Cancelli, A. and Cazzuffi, D. (1987) "Permittivity of Geotextiles in Presence of Water and Pollutant Fluids", *Proceedings of Geosynthetics '87*, New Orleans, pp. 471-481.
- Cancelli, A. and Cazzuffi, D. (1994) "Environmental Aspects of Geosynthetic Applications in Landfills and Dams", *Proceedings of 5th International Conference on Geosynthetics*, Singapore, Vol. 4, pp. 55-96.
- Cazzuffi, D., Cossu, R., Ferruti, L. and Lavagnolo, C. (1991) "Efficiency of Geotextiles and Geocomposites in Landfill Drainage Systems", *Proceedings of 3rd International Landfill Symposium*, Sardinia, pp. 759-780.
- Cohen, R.M. Rabold, R.R., Faust, C.R., Rumbaugh, J.O. and Bridge, J.R. (1987) "Investigation and Hydraulic Containment of Chemical Migration: Four Landfills in Niagara Falls", *Civil Engineering Practice*, Spring, pp. 33-58.
- Collins, H.J. (1993) "Impact of the Temperature Inside the Landfill on the Behaviour of Barrier Systems", *Proceedings of 4th International Landfill Symposium*, Sardinia '93, Vol. 1, pp. 417-432.
- Corser, P., Pellicer, J. and Cranston, M. (1992) "Observations on Long-Term Performance of Composite Clay Liners and Covers", *Geotechnical Fabrics Report*, Nov., pp. 6-16.
- Cullimore, D.R. (1993) *Practical Manual of Groundwater Microbiology*, Lewis Publishers Inc., Chelsea.
- Cussler, E. (1984) *Diffusion: Mass Transfer in Fluid Systems*, Cambridge University Press, Cambridge, 159 pp.
- Dames and Moore, Canada (1992) "Annual Monitoring Report, Brock West Landfill Site, 1991", Report submitted to Municipality of Metropolitan Toronto, Dept. of Works, December 1992.
- Daniel, D.E. and Bowders, Jr. J.J. (1996) "Waste Containment by Geosynthetics", *Proceedings of 2nd International Congress on Environmental Geotechnics*, Ed. M. Kamon, Balkema, Rotterdam, Vol. 2, pp. 49-66.
- Daniel, D.E. and Estornell, P.M. (1991) "Compilation of Information on Alternative Barriers for Liner and Cover Systems", *Rep. No. EPA600/2-91/002*, U.S. Environmental Protection Agency, Cincinnati, Ohio.
- Daniel, D.E. and Shan, H.Y. (1992) "Effects of Partial Wetting of Gundseal on Strength and Hydrocarbon Permeability", Report Submitted to Gundle Lining Systems Inc., 56 p.
- Daniel, D.E., Shan, H.Y. and Anderson, J.D. (1993) "Effects of Partial Wetting on the Performance of the Bentonite Component of a Geosynthetic Clay Liner", *Proceedings of Geosynthetics '93*, Industrial Fabrics Association International, St. Paul, Minn., 3, pp. 1483-1496.
- Delaware Solid Waste Authority (1995) "Landfill Bio-reactor Design and Operation", USEPA Report EPA/600/R-95/146, 230 pp.

- Dobras, T.N. and Elzea, J.M. (1993) "In-situ Soda Ash Treatment for Contaminated Geosynthetic Clay Liners", *Proceedings of Geosynthetics '93*, Industrial Fabrics Association International, St. Paul, MN, R.J. Bathurst, Ed., pp. 1145-1160.
- Döll, P. (1996) *Modelling of Moisture Movement Under the Influence of Temperature Gradients: Desiccation of Mineral Liners Below Landfills*, Ph.D. Thesis, Technical University of Berlin, 251p.
- Domenico, P.A. and Schwartz, F.W. (1990) *Physical and Chemical Hydrogeology*, John Wiley & Sons, New York, p318.
- Durin, L., Touze, N. and Duquennoi, C. (1998) "Water and Organic Solvent Transport Parameters in Geomembranes", *Proceedings of 6th International Conference on Geosynthetics*, Atlanta, Industrial Fabrics Association International.
- Eloy-Giorni, C., Pelte, T., Pierson, P. and Margarita, R. (1996) "Water Diffusion Through Geomembranes Under Hydraulic Pressure", *Geosynthetics International*, Vol. 3, No. 6, pp. 741-769.
- Estornell, P.M. and Daniel, D.E. (1992) "Hydraulic Conductivity of Three Geosynthetic Clay Liners", *ASCE Journal of Geotechnical Engineering*, 118(10), pp. 1592-1606.
- Felon, R., Wilson, P.E. and Janssens, J. (1992) "Résistance Mécanique des Membranes d'Étanchéité. Membranes Armées en Théorie et en Pratique", in *Vade Mecum Pour la Réalisation des Systèmes d'Étanchéité-Drainage Artificiels Pour les Sites d'Enfouissement Technique en Wallonie*. Journées d'Études ULg 92, edited by Monjoie, A., Rigo, J.M., Polo-Chiapolini, Cl. and Degeimbre, R., Liege University (Belgium).
- Fleming, I.R., Rowe, R.K. and Cullimore, D.R. (1997) "Field Observations of Clogging in a Landfill Leachate Collection System", Geotechnical Research Centre, University of Western Ontario, Research Report, GEOT-13-97, 42p.
- Forchheimer, P. (1930) *Hydraulik*, 3rd Edition, B.G. Teubner Ed., Leipzig und Berlin, Germany, 596p.
- Fourie, A.B., Kuchena, S.M. and Blight, G.E. (1994) "Effect of Biological Clogging on the Filtration Capacity of Geotextiles", *Proceedings of 5th International Conference on Geosynthetics*, Singapore, pp. 721-724.
- Fredlund, D.G. (1978) "The Shear Strength of Unsaturated Soils", *Canadian Geotechnical Journal*, No. 15, pp. 313-321.
- Garlanger, J.E., Fuleihan, N.F. and Riad, A.H. (1994) "Leakage Rates Through Geomembrane Liners Beneath Phosphogypsum Disposal Facilities", *Proceedings of 5th International Conference on Geosynthetics*, Singapore, September, pp. 923-928.
- Gartung, E. (1996) "Landfill Liners and Covers", in *Geosynthetics: Applications, Design and Construction*, Balkema, Rotterdam, Ed. M.B. de Groot, G. den Hoedt and R.J. Termaat, Vol. 1, pp. 55-70.
- Germany (1993) "The Third General Administrative Provision on Waste Avoidance and Waste Management Act", Technical Instructions on Recycling, Treatment and Other Management of Wastes from Human Settlements, Federal Gazette No. 99, 14 May 1993.
- Gibbons, R.D., Dolan, D., Keough, H., O'Leary, K. and O'Hara, R. (1992) "A Comparison of Chemical Constituents in Leachate From Industrial Hazardous Waste and Municipal Solid Waste Landfills", *Proceedings of 15th Annual Madison Waste Conference*, pp. 251-276.
- Giroud, J.P. (1995) "Wrinkle management for Polyethylene Geomembranes Requires Active Approach", *Geotechnical Fabrics Report*, Vol. 13, No. 3, pp. 14-17.
- Giroud, J.P. (1996a) "Granular Filters and Geotextile Filters", *Proceedings of Geofilters '96*, pp. 565-680.
- Giroud, J.P. (1996b) "Workshop on Testing of Geosynthetic Materials for Landfill Liners and Covers", *IGS News*, Vol. 12, No. 2, pp. 3-4.
- Giroud, J.P. (1997) "Equations for Calculating the Rate of Liquid Migration Through Composite Liners Due to Geomembrane Defects", *Geosynthetics International*, Vol. 4, Nos. 3-4, pp. 335-348.
- Giroud, J.P. and Beech, J.F. (1989) "Stability of Soil Layers on Geosynthetic Lining Systems", *Proceedings of Geosynthetics '89*, Vol. 1, pp. 35-46.
- Giroud, J.P. and Bonaparte, R. (1989a) "Leakage Through Liners Constructed with Geomembranes - Part I. Geomembrane Liners", *Geotextiles and Geomembranes*, Vol. 8, No. 1, pp. 27-67.
- Giroud, J.P. and Bonaparte, R. (1989b) "Leakage Through Liners Constructed with Geomembranes - Part II. Composite Liners", *Geotextiles and Geomembranes*, Vol. 8, No. 2, pp. 71-111.
- Giroud, J.P. and Cazzuffi, D.A. (1989) "Panelist Contribution - Uses of Geosynthetics for Environmental Control", *Proceedings of 12th International Conference on Soil Mechanics and Foundation Engineering*, Rio de Janeiro, August, pp. 3119-3125.
- Giroud, J.P. and Morel, N. (1992) "Analysis of Geomembrane Wrinkles", *Geotextiles and Geomembranes*, Vol. 11, No. 3, pp. 255-276 (Erratum: 1993, Vol. 12, No. 4, p. 378).
- Giroud, J.P., Bachus, R.C. and Bonaparte, R. (1995a) "Influence of Water Flow on the Stability of Geosynthetic-Soil Layered Systems on Slopes", *Geosynthetics International*, Vol. 2, No. 6, pp. 1149-1180.
- Giroud, J.P., Badu-Tweneboah, K. and Bonaparte, R. (1992) "Rate of Leakage Through a Composite Liner Due to Geomembrane Defects", *Geotextiles and Geomembranes*, Vol. 11, No. 1, pp. 1-12.

- Giroud, J.P., Badu-Tweneboah, K. and Soderman, K.L. (1994) "Evaluation of Landfill Liners", *Proceedings of 5th International Conference on Geosynthetics*, Vol. 3, Singapore, September, pp. 981-986.
- Giroud, J.P., Badu-Tweneboah, K. and Soderman, K.L. (1995b) "Theoretical Analysis of Geomembrane Puncture", *Geosynthetics International*, Vol. 2, No. 6, pp. 1019-1048.
- Giroud, J.P., Badu-Tweneboah, K. and Soderman, K.L. (1997a) "Comparison of Leachate Flow Through Compacted Clay and Geosynthetic Clay Liners in Landfill Liner Systems", *Geosynthetics International*, Vol. 4, Nos. 3-4, September, pp. 391-431.
- Giroud, J.P., Khatami, A. and Badu-Tweneboah, K. (1989) "Evaluation of the Rate Leakage Through Composite Liners", *Geotextiles and Geomembranes*, Vol. 8, No. 4, pp. 337-340.
- Giroud, J.P., Khire, M.V. and McKelvey, J.A. (1997b) "Rate of Leachate Migration Through a Defect in a Geomembrane Underlain by a Saturated Permeable Medium", *Geosynthetics International*, Vol. 4, Nos. 3-4, pp. 323-334.
- Giroud, J.P., Khire, M.V. and Soderman, K.L. (1997c) "Liquid Migration Through Defects in a Geomembrane Overlain and Underlain by Permeable Media", *Geosynthetics International*, Vol. 4, Nos. 3-4, pp. 293-321.
- Giroud, J.P., Rad, N.S. and McKelvey, J.A. (1997d) "Evaluation of the Surface Area of a GCL Hydrated by Leachate Migrating Through Geomembrane Defects", *Geosynthetics International*, Vol. 4, Nos. 3-4, pp. 433-462.
- Giroud, J.P., Soderman, K.L. and Badu-Tweneboah, K. (1997e) "Optimal Configuration of a Double Liner System Including a Geomembrane Liner and a Composite Liner", *Geosynthetics International*, Vol. 4, Nos. 3-4, pp. 373-389.
- Giroud, J.P., Gross, B.A., Bonaparte, R. and McKelvey, J.A. (1997f) "Leachate Flow in Leakage Collection Layers Due to Defects in Geomembrane Liners", *Geosynthetics International*, Vol. 4, Nos. 3-4, pp. 215-292.
- Giroud, J.P., Soderman, K.L., Khire, M.V. and Badu-Tweneboah, K. (1998) "New Developments in Landfill Liner Leakage Evaluation", *Proceedings of 6th International Conference on Geosynthetics*, Atlanta, Industrial Fabrics Association International.
- Giroud, J.P., Williams, N.D., Pelte, T. and Beech, J.F. (1995a) "Stability of Geosynthetic-Soil Layered Systems on Slopes", *Geosynthetics International*, Vol. 2, No. 6, pp. 1115-1148.
- Giroud, J.P., King, T.D., Sanglerat, T.R., Hadj-Hamou, T. and Khire, M.V. (1997g) "Rate of Liquid Migration Through Defects in a Geomembrane Placed on a Semi-Permeable Medium", *Geosynthetics International*, Vol. 4, Nos. 3-4, pp. 349-372.
- Gourc, J.P. (1994) "Geosynthetics and the Environment", The 1994 F. Brian Mercer Lecture, *Proceedings of 8th GRI Conference*, Industrial Fabrics Association International.
- Gray, R.L. (1990) "Accelerated Testing Methods for Evaluating Polyolefin Stability", *Geosynthetic Testing for Waste Containment Applications*, ASTM STP 1081, Robert M. Koerner, Ed., American Society for Testing and Materials, Philadelphia.
- Gross, B.A., Bonaparte, R. and Giroud, J.P. (1990) "Evaluation of Flow From Landfill Leakage Detection Layers", *Proceedings of 4th International Conference on Geosynthetics*, Vol. 2, The Hague, pp. 481-486.
- Gross, B.A., Bonaparte, R. and Othman, M.A. (1997) "Inferred Performance of Surface Hydraulic Barriers from Landfill Operational Data", *Proceedings of 1997 International Containment Technology Conference*, St. Petersburg, February.
- Harpur, W.A., Wilson-Fahmy, R.F. and Koerner, R.M. (1993) "Evaluation of the Contact between Geosynthetic Clay Liners and Geomembranes in Terms of Transmissivity", *Proceedings of GRI Seminar on Geosynthetic Liner Systems*, Ed. R.M. Koerner and R.F. Wilson-Fahmy, Philadelphia, PA, Industrial Fabrics Association International, pp. 143-154.
- Haxo, H.E., Jr. (1990) "Determining the Transport Through Geomembranes of Various Permeants in Different Applications", *Geosynthetic Testing for Waste Containment Applications*, Koerner, R.M. Ed., ASTM Special Publication 1081, Proceedings of Symposium, Las Vegas, NV, USA, January, pp. 75-94.
- Haxo, H.E., Jr. and Haxo, P.D. (1988) "Consensus Report of the Ad Hoc Meeting on the Service Life in Landfill Environments of Flexible Membrane Liners and Other Synthetic Polymeric Materials of Construction", Matrecon. Inc. Alameda, CA, U.S.A. Report to USEPA.
- Haxo, H.E., Jr. and Haxo, P.D. (1989) "Environmental Conditions Encountered by Geosynthetics in Waste Containment Applications", *Durability and Aging of Geosynthetics*, R.M. Koerner, editor, Elsevier Science Publishers Ltd.
- Haxo, H.E., Jr. and Lahey, T. (1988) "Transport of Dissolved Organics from Dilute Aqueous Solutions Through Flexible Membrane Liner", *Hazardous Waste & Hazardous Materials*, Vol. 5, pp. 275-294.
- Haxo, H.E., Jr. and Nelson, N.A. (1984) "Factors in the Durability of Polymeric Membrane Liners", *Proceedings of International Conference on Geomembranes*, Vol. II, Denver, Co., June 20-24.
- Haxo, H.E., Miedema, J.A. and Nelson, N.A. (1984) "Permeability of Polymeric Membrane Lining Material", *Proceedings of International Conference on Geomembranes*, Denver, USA, pp. 151-156.



- Heibroek, G. (1997) "Desiccation Cracking of Mineral Sealing Liners", *Proceedings of 6th International Landfill Symposium*, S. Margherita di Pula, Cagliari, Italy, October, Vol. 3, pp. 101-113.
- Holzlohner, U. (1989) "Moisture Behaviour of Soil Liners and Subsoil Beneath Landfills", *Proceedings of 2nd International Landfill Symposium*, Porto Conte. 1, pp. X1-X11.
- Holzlohner, U. (1992) "Austrocknung und Ribbildung in Mineralischen Schichten der Deponiebasisabdichtung. Wasser & Boden. No. 5, pp. 289-293.
- Holzlohner, U. (1995) "Moisture Balance, Risk of Desiccation in Earthen Liners", Chapter H of the "State of the Art Report: Landfill Liner Systems" Eds. U. Holzlohner, H. August, T. Meggyes, M. Brune, Penshaw Press, pp. H1-H22.
- Hsuan, Y.G. and Guan, Z. (1997) "Evaluation of the Oxidative Behaviour of Polyethylene Geomembranes Using Oxidative Induction Time Tests", *Oxidative Behavior of Materials by Thermal Analytical Techniques*, ASTM STP1326, A.T. Riga and G.H. Patterson, Eds. (in press).
- Hsuan, Y.G. and Koerner, R.M. (1995) "Long Term Durability of HDPE Geomembranes: Part I - Depletion of Antioxidants", GRI Report 16, 35p.
- Hsuan, Y.G. and Koerner, R.M. (1997) "Antioxidant Depletion Lifetime in High Density Polyethylene Geomembranes", *Journal of Geotechnical and Geoenvironmental Engineering*, ASCE (submitted).
- Hsuan, Y.G., Lord, A.E., Jr. and Koerner, R.M. (1991) "Effects of Outdoor Exposure on a High Density Polyethylene Geomembrane", *Proceedings of Geosynthetics '91*, Vol. 1, Atlanta, GA, Feb., pp. 287-302.
- Hughes, G.M. and Monteleone, M.J. (1987) "Geomembrane/Synthesized Leachate Compatibility Testing", in *Geotechnical and Geohydrological Aspects of Waste Management* (Eds. D.J.A. van Zyl, J.D. Nelson, S.R. Abt and T.A. Shepherd), Fort Collins, CO, Lewis Publishers Inc., Michigan, pp. 35-50.
- Jayawickrama, P., Brown, K.W., Thomas, J.C. and Lytton, R.L. (1988) "Leakage Rates Through Flaws in Membrane Liners", *ASCE Journal of Environmental Engineering*, Vol. 114, No. 6, pp. 1401-1419.
- King, K.S., Quigley, R.M., Fernandez, F., Reades, D.W. and Bacopoulos, A. (1993) "Hydraulic Conductivity and Diffusion Monitoring of the Keele Valley Landfill Liner, Maple, Ontario", *Canadian Geotechnical Journal*, 30(1), pp. 124-134.
- Koch, R., Gaube, E., Hessel, J., Gondro, C. and Heil, H. (1988) "Langzeitfestigkeit von Deponiedichtungsbahnen aus Polyethylene", *Mull und Abfall*, Vol. 8, pp. 348-361.
- Koerner, G.R. and Koerner, R.M. (1990) "Biological Activity and Potential Remediation Involving Geotextile Landfill Leachate Filters", *Geosynthetic Testing for Waste Containment Applications*, ASTM STP 1081, R.M. Koerner, Ed., American Society for Testing and Materials, Philadelphia, pp. 313-335.
- Koerner, G.R. and Koerner, R.M. (1994) "Design of Landfill Leachate-Collection Filters", *ASCE Journal of Geotechnical Engineering*, Vol. 120(10), pp. 1792-1803.
- Koerner, G.R. and Koerner, R.M. (1995a) "Temperature Behaviour of Field Deployed HDPE Geomembranes", *Proceedings of Geosynthetics '95*, Nashville, pp. 921-937.
- Koerner, G.R., Eith, A.W. and Tanese (1997) "Properties of Exhumed HDPE Field Waves and Selected Aspects of Waste Management", *Proceedings, 11th GRI Conference*, "Field Installation of Geosynthetics", pp. 152-161.
- Koerner, G.R., Koerner, R.M. and Martin, J.P. (1993a) "Field Performance of Leachate Collection Systems and Design Implications", *Proceedings of 31st Annual SWANA Conference*, San Jose, CA, pp. 365-380.
- Koerner, G.R., Koerner, R.M. and Martin, J.P. (1994) "Geotextile Filters Used for Leachate Collection System: Testing, Design and Field Behavior", *Journal of Geotechnical Engineering Division, ASCE*, Vol. 120, No. 10, October, pp. 1792-1803.
- Koerner, G.R., Yazdani, R. and Mackey, R.E. (1996a) "Long Term Temperature Monitoring of Landfill Geomembranes", *Proceedings SWANA's 1st Annual Landfill Symposium*, Publication GR-D 0401, pp. 61-73.
- Koerner, R.M. (1990) "Preservation of the Environment Via Geosynthetic Containment Systems", *Proceedings of 4th International Conference on Geosynthetics*, Vol. III, The Hague, pp. 975-988.
- Koerner, R.M. and Koerner, G.R. (1995b) "Leachate Clogging Assessment of Geotextile (and Soil) Landfill Filters", US EPA Report, CR-819371, March.
- Koerner, R.M. and Soong, T.Y. (1998) "Analysis and Design of Veneer Cover Soils", *Proceedings of 6th International Conference on Geosynthetics*, Atlanta, Industrial Fabric Association International.
- Koerner, R.M., Halse, Y.H. and Lord, A.E., Jr. (1990) "Long-term Durability and Aging of Geosynthetics", in *Waste Containment Systems: Construction, Regulation, and Performance*. ASCE Geotechnical Special Publication No. 26, *Proceedings of a Symposium in Conjunction with the ASCE National Convention*, San Francisco, California, Nov. 6-7.
- Koerner, R.M., Hsuan, Y. and Lord, Jr., A.E. (1993b) "Remaining Technical Barriers to Obtaining General Acceptance of Geosynthetics", *Geotextiles and Geomembranes*, Vol. 12, No. 1, pp. 1-53.

- Koerner, R.M., Hsuan, Y.G. and Lord, A.E. (1993c) "Stress Cracking Behaviour of HDPE Geomembranes and Its Prevention", GRI Report 9, 94 p.
- Koerner, R.M., Lord, A.E. and Hsuan, Y.K. (1992) "Arrhenius Modelling to Predict Geosynthetic Degradation", *Geotextiles & Geomembranes*, Vol. 11, pp. 151-183.
- Koerner, R.M., Wilson-Fahmy, R.F. and Narejo, D. (1996b) "Puncture Protection of Geomembranes Part III: Examples", *Geosynthetics International*, Vol. 3, No. 5, pp. 655-675.
- Lechner, P. and Lahner, T. (1991) "Materials for Leachate Collection Systems", *Proceedings of 3rd International Landfill Symposium*, S. Margherita di Pula, Cagliari, Italy, October 14-18.
- Lo, M.C. (1992) "Development and Evaluation of Clay Liner Material for Hazardous Waste Sites", Ph.D. Thesis, University of Texas, 283 pp.
- Lord, A.E., Jr. and Halse, Y.H. (1989) "Polymer Durability - the Materials Aspect", in *Durability and Aging of Geosynthetics*, R.M. Koerner, Editor, Elsevier Science Publishers Ltd.
- Lord, A.E., Koerner, R.M. and Swan, J.R. (1988) "Chemical Mass Transport Measurement to Determine Flexible Membrane Liner Lifetime", *Geotechnical Testing Journal*, ASTM, pp. 83-91.
- Luber, M. (1992) "Diffusion of Chlorinated Organic Compounds Through Synthetic Landfill Liners", Dept. of Earth Sciences, Waterloo Centre for Groundwater Research, University of Waterloo (complete report not available), 88p.
- Lundell, C.M. and Menoff, S.D. (1989) "The Use of Geosynthetics as Drainage Media at Solid Waste Landfills", *Proceedings of Geosynthetics '89*, San Diego, U.S.A., pp. 10-17.
- McBean, E.A., Mosher, F.R. and Rovers, F.A. (1993) "Reliability-Based Design for Leachate Collection Systems", *Proceedings of 4th International Landfill Symposium*, S. Margherita di Pula, Sardinia (T.H. Christensen, R. Cossu & R. Stegmann, Eds.), pp. 433-441.
- Mitchell, J.K., Seed, R.B. and Seed, H.B. (1990) "Kettleman Hills Waste Landfill Slope Failure. I: Liner System Properties", *Journal of Geotechnical Engineering*, ASCE, 116(4), pp. 647-668.
- MoEE (1996) Ontario Ministry of Environment and Energy proposed Regulatory Standards for New Landfilling Sites Accepting Non-Hazardous Waste.
- Morris, H., Graham, J. and Williams, D.J. (1992) "Cracking in Drying Soils", *Canadian Geotechnical Journal*, No. 29, pp. 263-277.
- Mueller, W., Jakob, R., Tatzky-Gerth and August, H. (1998) "Solubilities, Diffusion and Partitioning Coefficients of Organic Pollutants in HDPE Geomembranes: Experimental Results and Calculations", *Proceedings of 6th International Conference on Geosynthetics*, Atlanta, Industrial Fabrics Association International.
- Narejo, D.B. (1995a) "A Comparison of Puncture Behavior of Smooth and Textured HDPE Geomembranes", *Geosynthetics International*, Vol. 2, No. 4, pp. 699-705.
- Narejo, D.B. (1995b) "Three Levels of Geomembrane Puncture Protection", *Geosynthetics International*, Vol. 2, No. 4, pp. 765-769.
- Narejo, D.B. (1996) "Closure of Discussion of 'A Comparison of Puncture Behavior of Smooth and Textured HDPE Geomembranes' and 'Three Levels of Geomembrane Puncture Protection'", *Geosynthetics International*, Vol. 3, No. 3, pp. 443-444.
- Narejo, D., Koerner, R.M. and Wilson-Fahmy, R.F. (1996) "Puncture Protection of Geomembranes Part II: Experimental", *Geosynthetics International*, Vol. 3, No. 5, pp. 629-653.
- Naylor, T. de V. (1989) "Permeation Properties", *Comprehensive Polymer Science*, Eds. Booth, C and Price, C., Vol. 2, pp. 643-668.
- Othman, M.A., Bonaparte, R. and Gross, B.A. (1996) "Preliminary Results of Study of Composite Liner Field Performance", *Proceedings of 10th GRI Conference*, "Field Performance of Geosynthetics and Geosynthetic Related Systems", R.M. Koerner, G.R. Koerner & Y.G. Hsuan Eds., pp. 115-147.
- Ouvry, J.F., Gisbert, T. and Closset, L. (1995) "Back Analysis of a Slide in a Waste Storage Centre", *Recontres '95*, pp. 148-152.
- Park, J.K. and Bontoux, L. (1991) "Effects of Temperature, Repeated Exposure and Aging on Polybutylene Permeation by Organic Chemical", *Journal of Applied Polymer Science*, Vol. 42, pp. 2989-2995.
- Park, J.K. and Nibras, M. (1993) "Mass Flux of Organic Chemicals Through Polyethylene Geomembranes", *Water Environment Research*, Vol. 65, No. 3, pp. 227-237.
- Park, J.K., Sakti, J.P. and Hooper, J.A. (1995) "Effectiveness of Geomembranes as Barriers of Organic Compounds", *Proceedings of Geosynthetics 95*, IFAI, Vol. 3, February, pp. 879-892.
- Pelte, T., Pierson, P. and Gourc, J.P. (1994) "Thermal Analysis of Geomembranes Exposed to Solar Radiation", *Geosynthetics International*, Vol. 1, No. 1, pp. 21-44.

- Petrov, R.J. and Rowe, R.K. (1997) "Geosynthetic Clay Liner Compatibility by Hydraulic Conductivity Testing: Factors Impacting Performance", *Canadian Geotechnical Journal*, Vol. 34, No. 6.
- Petrov, R.J., Rowe, R.K. and Quigley, R.M. (1997a) "Comparison of Laboratory Measured GCL Hydraulic Conductivity Based on Three Permeameter Types", *Geotechnical Testing Journal*, ASTM, Vol. 20, No. 1, pp. 49-62.
- Petrov, R.J., Rowe, R.K. and Quigley, R.M. (1997b) "Selected Factors Influencing GCL Hydraulic Conductivity", *Journal of Geotechnical and Geoenvironmental Engineering*, ASCE, Vol. 123, No. 8, pp. 683-695.
- Pierson, P., Pelte, T. and Gourc, J.P. (1993) "Behaviour of Geomembranes Exposed to Solar Radiation", *Proceedings of 4th International Landfill Symposium*, Sardinia '95, Vol. 1, pp. 349-356.
- Prasad, T.V., Brown, K.W. and Thomas, J.C. (1994) "Diffusion Coefficients of Organics in High Density Polyethylene (HDPE)", *Waste Management and Research*, Vol. 12, pp. 61-71.
- Press, W.H., Flannery, B.P., Teukolsky, S.A. and Vetterling, H.T. (1986) "*Numerical Recipes*", Cambridge University Press, 818p.
- Rad, N.S., Jacobson, B.D. and Bachus, R.C. (1994) "Compatibility of Geosynthetic Clay Liners With Organic and Inorganic Permeants", *Proceedings of 5th International Conference on Geosynthetics*, Singapore, pp. 1165-1168.
- Ramke, H.G. (1989) *Leachate Collection Systems in Sanitary Landfilling: Processes, Technology and Environmental Impact*. Eds. Christensen, T.H., Cossy, R. and Stegmann, R. Academic Press, London, pp. 343-364.
- Ramsey, D.R. (1993) "Diffusivities of Organic Contaminants in High Density Polyethylene Geomembranes", *Proceedings of Geosynthetics 93*, Vancouver, Canada, pp. 645-657.
- Reades, D.W., King, K.S., Benda, E. et al. (1989) "The Results of On-Going Monitoring of the Performance of a Low Permeability Clay Liner, Keele Valley Landfill, Maple, Ontario", *Proceedings Focus Conference on Eastern Regional Ground Water Issues*, National Water Well Association, Kitchener, Ontario, pp. 79-91.
- Reddy, K.R., Bandi, S.R., Rohr, J.J., Finy, M. and Siebken, J. (1996) "Field Evaluation of Protective Covers for Landfill Geomembrane Liners Under Construction Loading", *Geosynthetics International*, Vol. 3, No. 6, pp. 679-700.
- Reynolds, R.T. (1991) "Geotechnical Field Techniques Used in Monitoring Slope Stability at a Landfill", *Proceedings of Field Measurements in Geotechnics*, G. Sorum, Ed., Rotterdam: Balkema, pp. 833-891.
- Richardson, G.N. (1997) "GCLs: Alternative Subtitle D Liner Systems", *Geotechnical Fabrics Report*, May, pp. 36-42.
- Rittmann, B.E., Fleming, I. and Rowe, R.K. (1996) "Leachate Chemistry: Its Implications for Clogging", North American Water and Environment Congress '96, Anaheim, CA, June, paper 4 (CD Rom) 6p, Session GW-1, Biological Processes in Groundwater Quality.
- Rohde, J.R. and Gribb, M.M. (1990) "Biological and Particulate Clogging and Geotextile/Soil Filter Systems", *ASTM STP1081*, pp. 299-312.
- Rogers, C.E. (1985) "Permeation of Gases and Vapors in Polymers", In *Polymer Permeability*, Ed. J. Comyn, Chapter 2, pp. 11-73.
- Rollin, A.L., Mlynarek, J., Lafleur, J. and Zanesco, A. (1994) "Performance Changes in Aged In-Situ HDPE Geomembrane", *Landfilling of Wastes: Barriers*, TH Christensen, R. Cossu and R. Stegmann Eds., E & FN Spon, pp. 431-443.
- Rollin, A.L., Vidovic, A., Denis, R. and Marcotte, M. (1990) "Microscopic Evaluation of High-Density Polyethylene Geomembrane Field-Welding Techniques", In *Geosynthetics: Microstructure and Performance*, ASTM STP 10760, Papers from the ASTM Symposium on Microstructure and the Performance of Geosynthetics, Orlando, Fla., Jan. 27, 1989.
- Rowe, R.K. (1991) "Contaminant Impact Assessment and the Contaminating Lifespan of Landfills", *Canadian Journal of Civil Engineering*, 18, pp. 244-253.
- Rowe, R.K. (1992) "Some Challenging Applications of Geotextiles in Filtration and Drainage", *Geotextiles in Filtration and Drainage*, Thomas Telford, London, pp. 1-12.
- Rowe, R.K. (1995) "Leachate Characterization for MSW Landfills", *Proceedings of 5th International Landfill Symposium*, Sardinia, Italy, Vol. 2, pp. 327-344.
- Rowe, R.K. (1997a) "The Design of Landfill Barrier Systems: Should There Be a Choice", *Ground Engineering*, August, pp. 36-39.
- Rowe, R.K. (1997b) "Contaminant Modelling - GCL Composite Liner Systems", Report to Terrafix Geosynthetics Inc., Geotechnical Research Centre, University of Western Ontario, London, Canada, May, 36 p.
- Rowe, R.K. and Booker, J.R. (1984) "The Analysis of Pollutant Migration in a Non-Homogeneous Soil", *Geotechnique*, Vol. 34, No. 4, pp. 601-612.
- Rowe, R.K. and Booker, J.R. (1985) "1-D Pollutant Migration in Soils of Finite Depth", *Journal of Geotechnical Engineering*, ASCE, Vol. 111, GT4, pp. 479-499.
- Rowe, R.K. and Booker, J.R. (1993) "POLLUTE v3 - 1D Pollutant Migration Through Non-Homogeneous Soil", Geotechnical Research Centre, Dept. of Civil Engineering, University of Western Ontario.

- Rowe, R.K. and Booker, J.R. (1995) "A Finite Layer Technique for Modelling Complex Landfill History", *Canadian Geotechnical Journal*, Vol. 32, No. 4, pp. 660-676.
- Rowe, R.K. and Booker, J.R. (1997a) "POLLUTE v.6.3 - 1D Pollutant Migration Through a Non-Homogeneous Soil", © 1983, 1990, 1994, 1997. Distributed by GAEA Environmental Engineering Ltd.
- Rowe, R.K. and Booker, J.R. (1997b) "Recent Advances in Modelling Contaminant Impact Due to Clogging", Keynote Paper, *9th International Conference of the Association for Computer Methods and Advances in Geomechanics*, Wuhan, China, November, No. 1, pp. 43-56.
- Rowe, R.K. and Booker, J.R. (1998a) "Modelling Impacts Due to Multiple Landfill Cells and Clogging of Leachate Collection Systems", *Canadian Geotechnical Journal* (In press).
- Rowe, R.K. and Booker, J.R. (1998b) "Theoretical Solutions for Calculating the Leakage Through Composite Liner Systems", Geotechnical Research Centre, Research Report, University of Western Ontario, London, Canada.
- Rowe, R.K. and Lake, C.B. (1997) "Program LEAK - A Program for Calculating Leakage Through Holes in a Geomembrane in Composite Liners", The University of Western Ontario, © 1997.
- Rowe, R.K. and Weaver, T.R. (1997) "Contaminant Transport in Groundwater", Keynote Paper, *Proceedings of First Australian-New Zealand Conference on Environmental Geotechnics*, Melbourne, November, pp. 97-114.
- Rowe, R.K., Barone, F.S. and Hrapovic, L. (1997a) "Laboratory and Field Studies of Salt Diffusion Through a Composite Liner", *Proceedings of 6th International Landfill Symposium*, S. Margherita di Pula, Cagliari, Italy, October, Vol. 3, pp. 241-250.
- Rowe, R.K., Caers, C.J. and Chan, C. (1993) "Evaluation of a Compacted Till Liner Test Pad Constructed Over a Granular Subliner Contingency Layer", *Canadian Geotechnical Journal*, Vol. 30, No. 4, pp. 667-689.
- Rowe, R.K., Hrapovic, L. and Armstrong, M.D. (1996a) "Diffusion of Organic Pollutants Through HDPE Geomembrane and Composite Liners and Its Influence on Groundwater Quality", *Proceedings 1st European Geosynthetics Conference*, Maastricht, October, pp. 737-742.
- Rowe, R.K., Hrapovic, L. and Kosaric, N. (1995a) "Diffusion of Chloride and Dichloromethane Through an HDPE Geomembrane", *Geosynthetics International*, 2(3), pp. 507-536.
- Rowe, R.K., Petrov, R.J. and Lake, C. (1997b) "Compatibility Testing and Diffusion Through GCLs", *Proceedings of 6th International Landfill Symposium*, S. Margherita di Pula, Cagliari, Italy, October, Vol. 3, pp. 301-310.
- Rowe, R.K., Quigley, R.M. and Booker, J.R. (1995b) *Clayey Barrier Systems for Waste Disposal Facilities*, E & FN Spon (Chapman & Hall), London, 390 pp.
- Rowe, R.K., Cooke, A.J., Rittmann, B.E. and Fleming, I.R. (1997c) "Some Considerations in Numerical Modelling of Leachate Collection System Clogging", Lead Lecture, *Proceedings of 6th International Symposium on Numerical Methods in Geomechanics*, Montreal, July, pp. 277-282.
- Rowe, R.K., Golder Associates, Fenco MacLaren and M.M. Dillon (1994) "Evaluation of Service Life of the Engineered Component of Landfills", Submitted to Interim Waste Authority (153 pages).
- Rowe, R.K., Hrapovic, L., Kosaric, N. and Cullimore, D.R. (1996b) "Biodegradation of Dichloromethane in Leachate", *North American Water and Environment Congress '96*, Anaheim, CA, June, Paper 356 (CD Rom) 6p, Session GW-9, Groundwater Contaminant Fate and Transport.
- Rowe, R.K., Hrapovic, L., Kosaric, N. and Cullimore, D.R. (1997d) "Anaerobic Degradation of Dichloromethane Diffusing Through Clay", *Journal of Geotechnical and Geoenvironmental Engineering, ASCE*, Vol. 123, No. 12, pp.1085-1095.
- Rowe, R.K., Lake, C., von Maubeuge, K. and Stewart, D. (1997e) "Implications of Diffusion of Chloride Through Geosynthetic Clay Liners", *Proceedings of Geoenvironment '97*, Melbourne, Australia, November, pp. 295-300.
- Rowe, R.K., Fleming, I., Cullimore, R., Kosaric, N. and Quigley, R.M. (1995c) "A Research Study of Clogging and Encrustation in Leachate Collection Systems in Municipal Solid Waste Landfills", Geotechnical Research Centre, University of Western Ontario, Report submitted to Interim Waste Authority Ltd., June, 128 p.
- Rowe, R.K., Hsuan, Y.G., Lake, C.B., Sangam, P. and Usher, S. (1998a) "Evaluation of a Composite (Geomembrane/Clay) Liner for a Lagoon After 14 Years of Use", *Proceedings of 6th International Conference on Geosynthetics*, Atlanta, Industrial Fabrics Association International.
- Rowe, R.K., Armstrong, M.D., Fleming, I.R., Rittmann, B.R. and Cullimore, R.D. (1998b) "Field and Laboratory Observations Relating to Clogging of Leachate Collection Systems", Geotechnical Research Centre, University of Western Ontario, Research Report.
- Rowe, R.K., Fleming, I.R., Armstrong, M.D., Millward, S.C., VanGulck, J. and Cullimore, R.D. (1997f) "Clogging of Leachate Collection Systems: Some Preliminary Experimental Findings", *Proceedings of 50th Canadian Geotechnical Conference*, Ottawa, October, Vol. 1, pp. 153-160.

- Rowe, R.K., Fleming, I.R., Armstrong, M.D., Cooke, A.J., Cullimore, R.D., Rittmann, B.E., Bennett, P. and Longstaffe, F.J. (1997g) "Recent Advances in Understanding the Clogging of Leachate Collection Systems", *Proceedings of 6th International Landfill Symposium*, S. Margherita di Pula, Cagliari, Italy, October, Vol. 3, pp. 383-392.
- Ruhl, J.L. and Daniel, D.E. (1997) "Geosynthetic Clay Liners Permeated with Chemical Solutions and Leachates", *Journal of Geotechnical and Geoenvironmental Engineering, ASCE*, 123(4), pp. 369-380.
- Saathoff, F. and Sehrbrock, U. (1995) "Indicators for Selection of Protection Layers for Geomembranes", *Proceedings of 5th International Conference on Geosynthetics*, Singapore, September 1994, pp. 1019-1022.
- Sakti, P.J., Park, K.J. and Hoopes, J.A. (1992) "Permeation of Organic Chemicals Through HDPE Geomembranes", *Water Forum 92*, ASCE, Baltimore, MD, pp. 201-206.
- Salame, M. (1961) "An Empirical Method for Predicting of Liquid Permeation in Polyethylene and Related Polymers", *SPE Transactions*, October 1961, pp. 153-163.
- Saleem, M., Asfour, A.A., De Kee, D. and Harrison, B. (1989) "Diffusion of Organic Penetrant Through Low Density Polyethylene (LDPE) Films: Effect of Size and Shape of the Penetrant Molecules", *Journal of Applied Polymer Science*, Vol. 137, pp. 617-625.
- Schmidt, R.K., Young, C. and Hewitt, J. (1984) "Long Term Field Performance of Geomembranes - Fifteen Years' Experience", *Proceedings of International Conference on Geomembranes*, Vol. II, Denver, Co., June 20-24, 1984.
- Schubert, W.R. (1987) "Bentonite Matting in Composite Lining Systems", *Geotechnical Practice for Waste Disposal '87*, R.D. Woods, ed., ASCE, New York, NY, pp. 784-796.
- Seed, R.B., Mitchell, J.K. and Seed, H.B. (1990) "Kettleman Hills Waste Landfill Slope Failure. II. Stability Analyses", *Journal of Geotechnical Engineering, ASCE*, 116(4), pp. 669-689.
- Seeger, S. and Müller, W. (1996) "Requirements and Testing of Protective Layer Systems for Geomembranes", *Geotextiles and Geomembranes*, 14, pp. 365-376.
- Shan, H.Y. and Daniel, D.E. (1991) "Results of Laboratory Tests on a Geotextile/Bentonite Liner Material", *Proceedings of Geosynthetics '91*, Industrial Fabrics Association International, St. Paul, MN, 2, 517-535.
- Smith, D.W. (1997) "One Dimensional Contaminant Transport Through a Deforming Porous Media: Theory and Solution for a Quasi-Steady-State Problem", Dept. of Civil, Surveying and Environmental Engineering, University of Newcastle Research Report 150.08.1997 (ISBN 0 7259 1004 6).
- Soong, T.Y. and Koerner, R.M. (1998) "Laboratory Study of High Density Polyethylene Geomembrane Waves", *Proceedings of 6th International Conference on Geosynthetics*, Atlanta, Industrial Fabrics Association International.
- Stark, T.D. (1998) "Bentonite Migration in Geosynthetic Clay Liners", *Proceedings of 6th International Conference on Geosynthetics*, Atlanta, Industrial Fabrics Association International.
- Stark, T.D. and Eid, H.T. (1994) "Drained Residual Strength of Cohesive Soils", *Journal of Geotechnical Engineering, ASCE*, Vol. 120, No. 5, pp. 856-871.
- Stark, T.D. and Evans, W.D. (1997) "Stability of Grandfathered Landfills", *ASCE Civil Engineering Magazine* (In press).
- Stark, T.D. and Poeppel, A.R. (1994) "Landfill Liner Interface Strengths From Torsional-Ring-Shear Tests", *Journal of Geotechnical Engineering, ASCE*, Vol. 120, No. 3, pp. 597-615.
- Stone, J.L. (1984) "Leakage Monitoring of the Geomembrane for Proton Decay Experiment", *Proceedings of International Conference on Geomembranes*, Denver, USA, Vol. 2, pp. 475-480.
- TA Siedlungsabfall (1993) Technische Anleitung zur Verwertung, Behandlung und Sonstigen Entsorgung von Siedlungsabfällen, Bundesanzeiger.
- Tisinger, L.G. and Giroud, J.P. (1993) "The Durability of HDPE Geomembranes", *Geotechnical Fabrics Report*, Sept., pp. 4-8.
- Underwriters Laboratory Standard UL 746 B (1987) "Polymeric Materials - Long Term Property Evaluation", Northbrook, IL.
- USEPA (1994) Office of the Federal Register, National Archives and Records Administration, Code of Federal Regulations, Vol. 40, "Protection of the Environment", Parts 190-259, Revised as of July 1, 1994.
- Vandevivere, P. and Baveye, P. (1992) "Effect of Bacterial Extracellular Polymers on the Saturated Hydraulic Conductivity of Sand Columns", *Applied and Environmental Microbiology*, 58, pp. 1690-1698.
- Walton, J.C. and Sagar, B. (1990) "Aspects of Fluid Flow Through Small Flaws in Membrane Liners", *Environmental Science and Technology*, 24, pp. 920-924.
- Walton, J.C., Rahman, M., Casey, D., Picornell, M. and Johnson, F. (1997) "Leakage Through Flows in Geomembrane Liners", *Journal of Geotechnical and Geoenvironmental Engineering, ASCE*, 123(6), pp. 534-539.
- Wilson-Fahmy, R.F. and Koerner, R.M. (1995) "Leakage Rates Through Holes in Geomembranes Overlying Geosynthetic Clay Liners", *Proceedings of Geosynthetics '95*, Industrial Fabrics Association International, pp. 655-668.

- Wilson-Fahmy, R.F., Narejo, D. and Koerner, R.M. (1996) "Puncture protection of Geomembranes Part I: Theory", *Geosynthetics International*, Vol. 3, No. 5, pp. 605-628.
- Workman, J.P. (1993) "Interpretation of Leakage Rates in Double-Lined Systems", *Proceedings of 7th GRI Conference*, pp. 91-108.
- Yazdani, R., Campbell, J.L. and Koerner, G.R. (1995) "Long Term In-Situ Measurement of a High Density Polyethylene Geomembrane in a Municipal Solid Waste Landfill", *Proceedings of Geosynthetics '95*, Vol. 3, pp. 893-905.
- Yoshida, H., Hozumi, H. and Tanaka, N. (1996) "Theoretical Study on Temperature Distribution in a Sanitary Landfill", *Proceedings of Second International Congress on Environmental Geotechnics*, Osaka, Vol. 1, pp. 323-328.

# Seismic Stability Against High Seismic Loads of Geosynthetic-Reinforced Soil Retaining Structures

F. Tatsuoka

Professor, Department of Civil Engineering, University of Tokyo, Tokyo, Japan

J. Koseki

Associate Professor, Institute of Industrial Science, University of Tokyo, Tokyo, Japan

M. Tateyama

Chief Research Engineer, Railway Technical Research Institute, Tokyo, Japan

Y. Munaf

Graduate Student, Department of Civil Engineering, University of Tokyo, Tokyo, Japan

K. Horii

Director, Engineering Department, Integrated Geotechnology Institute Limited, Tokyo, Japan

**ABSTRACT:** It is shown that there exists a big gap between the currently used design seismic coefficients  $(k_h)_{design}$  for retaining walls (RWs) and the ratio of the highest peak ground accelerations to the gravitational acceleration experienced during the 1995 Hyogo-ken-nambu Earthquake. It is argued that some factors for the above include; a) the use of conservative soil strength in the design; b) positive aspects of dynamic effects arising from ductility and flexibility of RW that are not considered in the pseudo-static approaches; and c) the use of a global safety factor larger than unity. It is suggested, at the same time, that the currently used  $(k_h)_{design}$  values should be increased appropriately to avoid such collapse of RWs as observed during the earthquake to a larger extent in the order of a) gravity type RWs, b) cantilever reinforced concrete RWs and c) geosynthetic-reinforced soil RWs having a full-height rigid facing. To evaluate dynamic earth pressure and failure zone size in unreinforced and reinforced backfill at high seismic loads more properly than the conventional pseudo-static methods, a modified pseudo-static approach is proposed, which takes into account the progressive process of the active failure in the backfill associated with shear banding and strain softening.

**KEYWORDS:** Seismic stability, Retaining walls, Pseudo-static analysis, Case histories, Model tests, Progressive failure

## 1. INTRODUCTION

It has been accepted that under static conditions, properly designed permanent geosynthetic-reinforced soil retaining walls (GRS-RWs) can be more cost-effective than, and can function equivalently to or even better than, conventional type retaining walls (RWs). Good performance of a number of GRS-RWs observed during a couple of recent very severe earthquakes in USA and Japan has shown that it is also the case under seismic conditions (e.g., Collin et al., 1992; White and Holtz, 1996; and Tatsuoka et al., 1996). Results obtained from recent theoretical and experimental works are consistent with the above (e.g., Bathurst and Alfalo, 1996). In this report, first some lessons from the seismic performance of representative types of RWs including GRS-RWs during the 1995 Hyogo-ken-nambu Earthquake will be summarized.

In the current aseismic design, RWs are designed to resist dynamic earth pressure, which is usually obtained by limit equilibrium-based pseudo-static stability analysis, mostly by the Mononobe-Okabe method (the original M-O method; Okabe, 1924; Mononobe and Matsuo, 1929). In such current aseismic design, conservative soil strength is

used (Table 1.1); for example, angles of internal friction, typically 35°, are assigned for cohesionless soils. These values are definitely lower than the actual peak friction angles  $\phi_{peak}$  for such densely compacted cohesionless backfill as realized in most permanent GRS-RWs. Rather, these values are similar to the residual frictional angles  $\phi_{res}$  for usual cohesionless soils. The use of such low design

Table 1.1 Typical soil strength values recommended for aseismic design of soil structures (Railway Technical Research Institute, 1997)

Type of backfill soil	Angle of internal friction, $\phi$
1) Well graded sand, gravel and muck from hard rock	40°
2) Ordinary sand and gravel	35°
3) Poorly graded sand	30°
4) Cohesive soil*	30°

\* For retaining walls not higher than 6 m and embankments not higher than 10m; cohesion is empirically replaced by shear resistance angle.

friction angles as above have been recommended for a reasonable conservatism, covering possible effects of progressive failure in the backfill and uncertainties of compaction level in each project (e.g., Bolton and Steedman, 1985; Jewell, 1991).

In the pseudo-static aseismic design methods that are employed in many countries including Japan, the design horizontal seismic coefficient  $(k_h)_{design}$  for RWs is usually as low as 0.1 - 0.2. On the other hand, after having experienced very serious damage to a great number of civil engineering structures during the 1995 Hyogo-ken-nambu Earthquake, a double-level aseismic design methodology has been proposed and accepted by Japanese civil engineers (JSCE, 1996). In this method, permanent civil engineering structures are first to be designed so as to maintain their serviceability against the specified lower level seismic load (Level 1). Level 1 seismic load is equivalent to the conventional seismic design load as described above, which is considered to be equivalent to the order of 200 - 300 gals in terms of the peak (horizontal) ground acceleration (PGA). At the same time, each structure should be designed against the higher Level 2 seismic load in such that although they are allowed to exhibit some plastic deformation, they should not collapse totally and can be remedied within a short period. Level 2 seismic load is considered to be equivalent to a PGA of the order of 600 - 800 gals. Following this recommendation, a number of Japanese aseismic design specifications and codes for reinforced concrete (RC) and steel civil engineering structures have been revised. Now, RWs cannot be an exception, and it is now required to develop a rational aseismic design method for RWs including GRS-RWs to survive such very high seismic load.

When a value of  $(k_h)_{design}$  equal to as high as 0.5 is employed, however, the seismic active earth pressure for cohesionless backfill obtained by the conventional pseudo-static approaches using the above-mentioned conservative friction angle becomes very high and the failure zone in the backfill becomes unrealistically very large and deep as shown later. Then, conventional type RWs as well as GRS-RWs are very difficult to be designed to have reasonable dimensions when they are to survive Level 2 seismic load. Yet,  $k_h = 0.5$  is still lower than  $PGA/g = 0.6 - 0.8$ , which was experienced by many collapsed and uncollapsed RWs during the 1995 Hyogo-ken-nambu Earthquake (n.b., the response maximum horizontal acceleration in the RWs should have been even higher). In the second part of the paper, reasons other than the use of conservative soil strength for inconsistencies between the conventional  $(k_h)_{design}$  values and the observed high  $PGA/g$  values will be discussed based on field and laboratory observations. The reasons will include positive net dynamic effects and the use of a global safety factor larger than unity.

In addition, the postulates used in the original M-O method will be examined based on field and laboratory observations and some theoretical considerations. Then, a modified pseudo-static approach to obtain reasonable design seismic active earth pressure and failure zone size for unreinforced and reinforced backfill subjected to very high seismic loads will be proposed.

Then, based on the information presented in this report, the values of  $(k_h)_{design}$  for Level 2 seismic load will be tentatively suggested as a function of analysis method, design soil strength and RW type.

## 2. SOME LESSONS FROM THE 1995 HYOGO-KEN-NAMBU EARTHQUAKE

The major lessons obtained from the performance of RWs including GRS-RWs during the 1995 Hyogo-ken-nambu Earthquake could be summarized as follows (Tatsuoka et al., 1996). Fig. 2.1 shows the locations of the RWs referred to below.

The damaged RWs could be categorized into the following three groups;

- a) slightly damaged; the RW deformed and/or displaced slightly, and its reuse was soon started after some remedy work;
- b) moderately damaged; the RW deformed and/or displaced noticeably, but did not totally collapse, and was demolished to be re-constructed, or was substantially repaired before reuse; and
- c) severely damaged; the RW totally collapsed to the ground, and was demolished to be re-constructed.

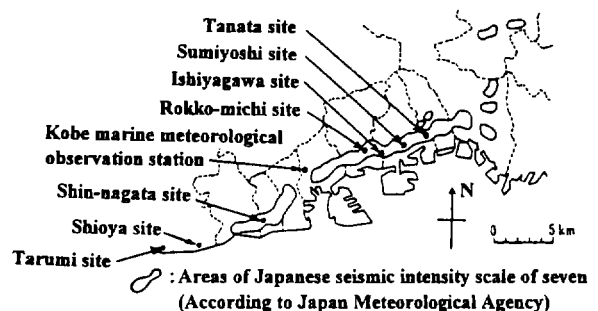


Fig. 2.1 Locations of typical soil retaining walls in Hyogo-ken-nambu referred to in the paper and Kobe Marine Meteorological Observation Station.

- 1) The GRS-RWs having a full-height rigid (FHR) facing at Tanata was slightly damaged; the wall deformed and displaced to some extent by sliding out at its base and overturning about its base (Fig. 2.2a), but it did not show a sign of ultimate failure, despite extremely high seismic loads at the site (the estimated PGA of about 800 gals or more) and use of reinforcement layers truncated to a same short length of  $L/H$  equal to 0.56. A recently constructed



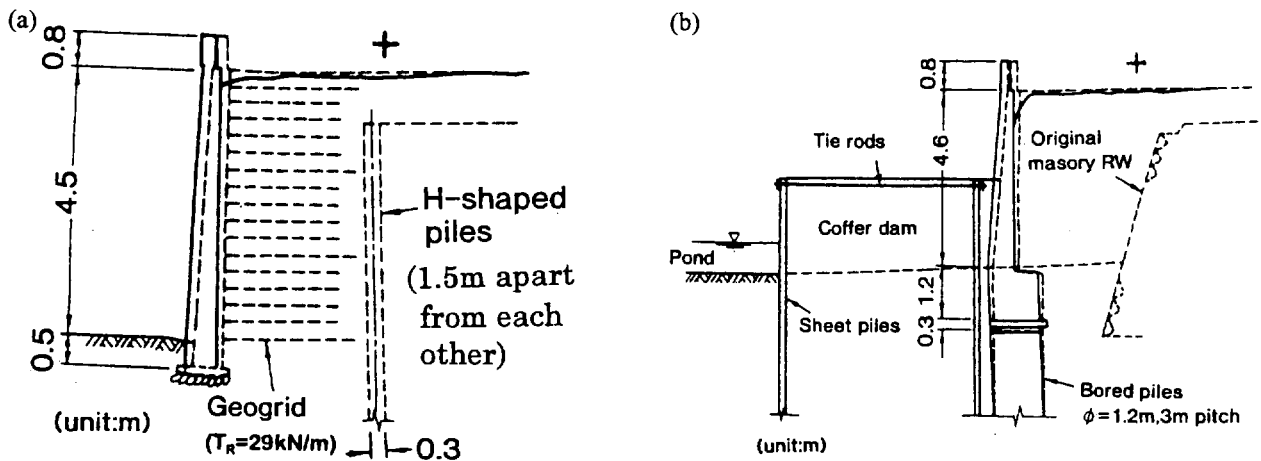


Fig. 2.2 Cross-sections before and after the earthquake of slightly damaged RWs at Tanata; a) a GRS-RW having a FHR facing (n.b., effects of the H-piles on the wall stability are considered to be very small); and b) a RC RW supported with a row of bored piles.

cantilever reinforced concrete (RC) RW supported with a row of bored piles (Fig. 2.2b), located adjacent to the Tanata GRS-RW, was also slightly damaged. Although the seismic load was less severe with an estimated PGA/g of the order of 0.5, similar GRS-RWs having a FHR facing located at Tarumi exhibited a limited amount of deformation and displacement (thus very slightly damaged). Cantilever RC RWs supported with a pile foundation constructed adjacent to these GRS-RWs

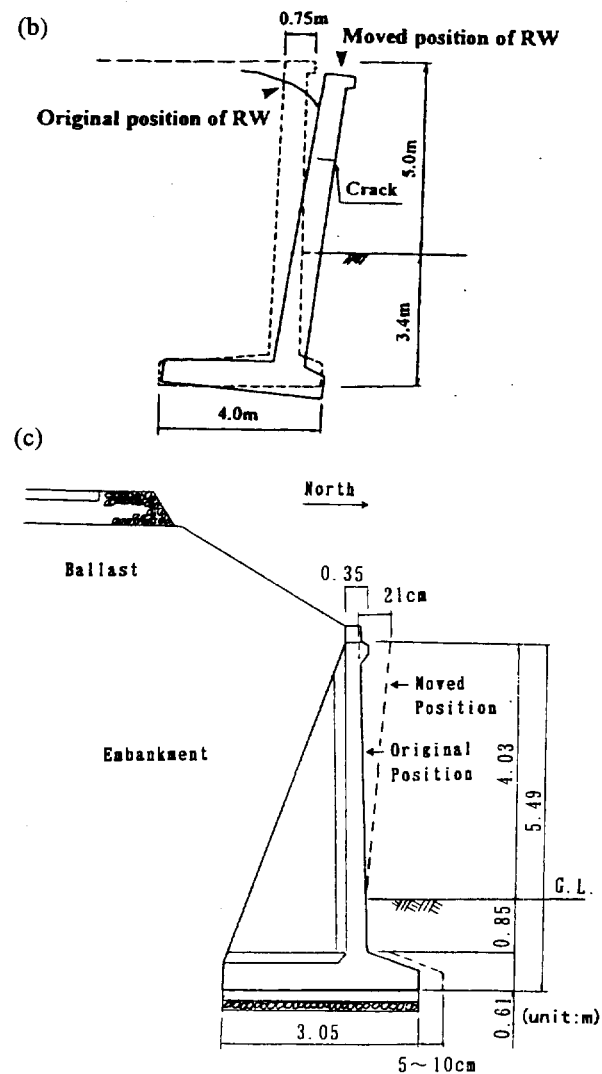
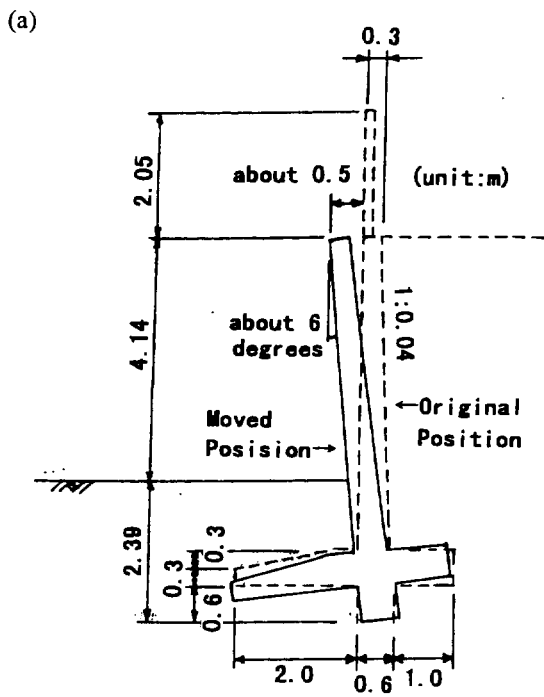


Fig. 2.3 Cross-sections before and after the earthquake of moderately damaged RWs; a) a RC retaining wall located at Rokko-michi; b) a cantilever RC RW at Ishiyagawa Station; and c) cantilever RC RW at Shioya Station

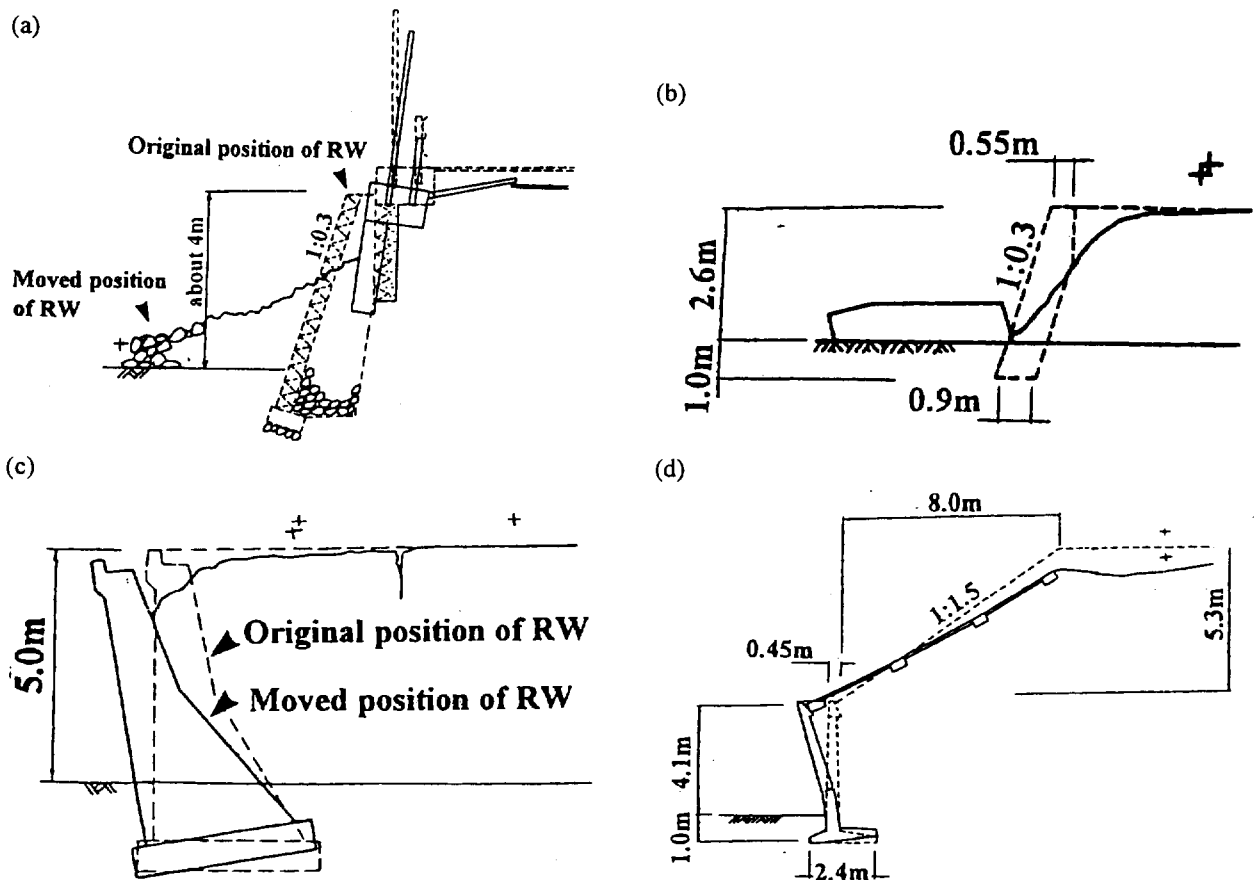


Fig. 2.4 Cross-sections before and after the earthquake of seriously damaged or totally collapsed RWs; a) a masonry RW between Setsu-motoyama and Sumiyoshi Stations; b) a leaning-type RW between Setsu-motoyama and Sumiyoshi Stations; c) a gravity-type RW at Ishiyagawa Station; and d) a poorly designed old cantilever RC RW at Shin-nagata Station

displaced similarly to the GRS-RWs. Subjected to the seismic loads similar to the Tanata GRS-RW, a reversed T-shaped cantilever RC RW at Rokko-michi (Fig. 2.3a) and those at Ishiyagawa (Fig. 2.3b) were moderately damaged. Although the seismic load was less severe, a cantilever RC RW at Shioya (Fig. 2.3c) was also moderately damaged. In comparison, a number of conventional gravity type RWs (masonry RWs and leaning type and gravity type unreinforced concrete RWs) and poorly designed old cantilever RC RWs such as that at Shin-Nagata which were located in the similarly very severely shaken areas were seriously damaged (Figs. 2.4a-d). In summary, the performance of the GRS-RWs with a FHR facing located in the severely shaken areas, particularly the one at Tanata, was satisfactory and equivalent to, or even better than, that of the recently constructed RC RWs. Reasons for these different performances should be understood.

2) The most dangerous failure mode of RW is over-turning about its bottom, because it is abrupt in a brittle and uncontrollable manner, which may result into very serious damage to structures and human beings located on the backfill and in front of the wall. A number of conventional

leaning and gravity type RWs collapsed in the overturning failure mode, triggered by large inertia force of RW and bearing capacity failure in the sub-soil below near the toe of RW, as typically seen in Figs. 2.4c and d. Sliding out of wall at the wall base is not preferable, but some amount should be admitted when subjected to very high seismic loads, because this failure mode is usually in a ductile manner, being not so abrupt as, and more stable than, the overturning failure mode. We need a relevant seismic design method for overturning at high seismic loads.

3) Fig. 2.5 shows the relationships between the safety factor and the  $k_h$  value for the Tanata GRS-RW and the RC RW at Rokko-michi obtained by the above-mentioned conventional pseudo-static design method using a design  $\phi$  value equal to  $35^\circ$  for the backfill. When based on this result, the Tanata GRS-RW should have failed by base sliding at  $k_h = 0.36$ . Despite its good seismic behaviour,  $k_h = 0.36$  is noticeably below the estimated values of PGA/g at the site (i.e., 0.8 or larger). We need an explanation for this large gap. There is a gap also for the cantilever RC RW at Rokko-michi. The gap is, however,

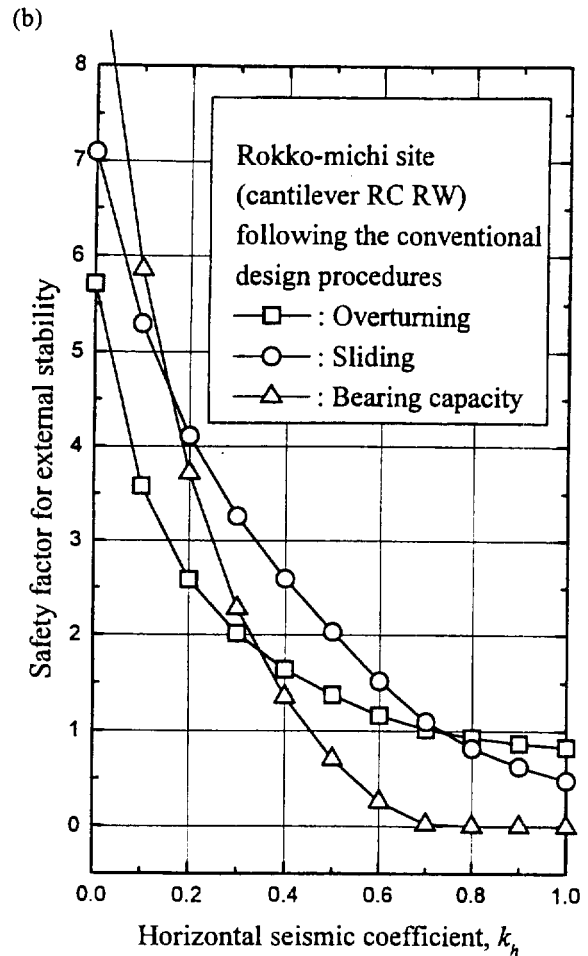
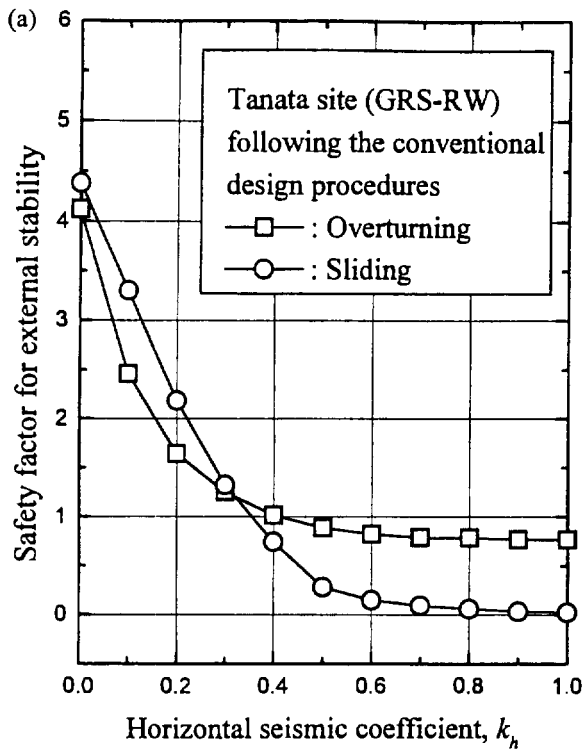


Fig. 2.5 Relationships between the safety factor and the  $k_h$  value for; a) the GRS-RW having a FHR facing at Tanata; and b) the cantilever RC RW at Rokko-michi, obtained using soil strength and simplification methods following the conventional design procedures (see Table 3.1 for calculation details).

smaller than that for the Tanata wall; the calculated critical  $k_h$  for bearing capacity failure in the sub-soil below the RW, leading to the overturning failure of RW, is higher (0.45), while the damage was severer.

4) The failure planes observed in the backfill of failed RWs, such as the gravity type unreinforced concrete RW at Ishiyagawa (Fig. 2.6a) and the leaning type unreinforced concrete RW along JR railway embankment between Setsu-motoyama and Sumiyoshi stations (Fig. 2.6b), were

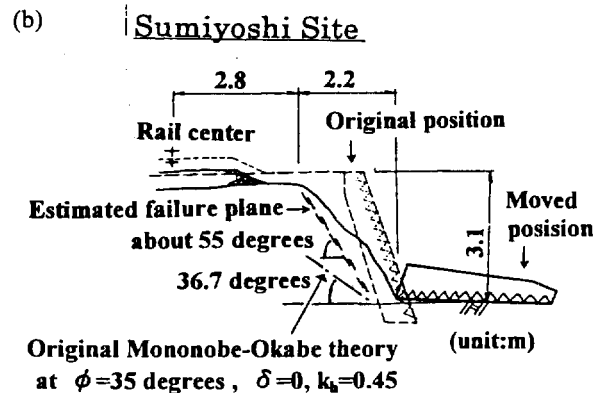
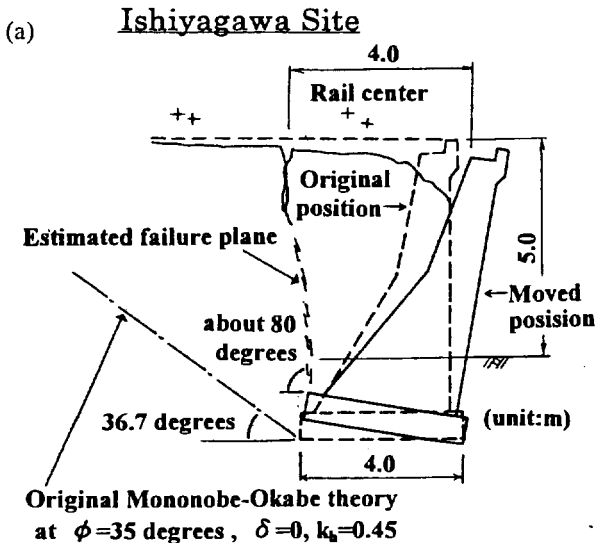


Fig. 2.6 Observed failure planes in the backfill; a) the gravity-type unreinforced concrete RW at Ishiyagawa Station; and b) the leaning-type RW along JR railway embankments between Setsu-motoyama and Sumiyoshi Stations.

much steeper than those predicted by the original M-O method using a conservative value  $\phi = 35^\circ$  and based on a tentative value of  $k_h$  equal to  $0.65 \cdot \text{PGA}/g = 0.65 \times 0.7 \approx 0.45$ . If the reinforcement layers should be extended well back the failure zone predicted for a high design  $k_h$  value by the original M-O method using a low design soil strength, we should use extremely long reinforcement layers.

5) Effects of facing type on the deformation of reinforced soil RW were observed; subjected to seismic loads which were less severe than that for the Tanata GRS-RW, discrete panel facings of several Terre Armee RWs exhibited relatively large deformation. Due to excessive wall deformation, the upper half of one major Terre Armee wall was rebuilt after the earthquake (Tatsuoka et al., 1996).

### 3. EXISTING PSEUDO-STATIC APPROACHES

In most of the aseismic design specifications, codes and guidelines used in Japan for relatively important RWs, seismic active earth pressure is evaluated by the original M-O method together with the assumption of hydrostatic distribution of dynamic earth pressures (static plus dynamic components). Alternatively, the trial wedge method, which is equivalent to the original M-O method for plane backslopes, is used for backfill having an irregular backslope. As mentioned earlier, conservative soil strength is used in these aseismic design procedures, as typically listed in Table 1.1. These design soil strength values are usually not a function of the degree of compaction, resulting in no differences in calculated stability between loosely and densely compacted backfills. Rather, the required degree of compaction is specified separately, not directly linked to static and seismic stability analyses. Note again that the use of conservative soil strength does not necessarily mean that the conventional aseismic design is conservative, because of the use of conservative  $(k_h)_{\text{design}}$  values.

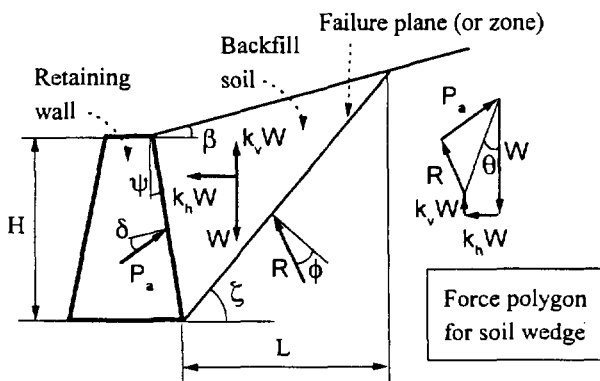


Fig. 3.1 Outline of the original Mononobe-Okabe method

In the original M-O method, the load equilibrium at the limit state (i.e., failure state) is examined for an assumed failure mechanism, and the maximum earth pressure is sought by trial and error changing the location and size of failure plane (Fig. 3.1). Fig. 3.2 shows the seismic active earth pressure coefficient  $(K_A)_{\text{seismic}}$ , plotted against  $k_h$ , for

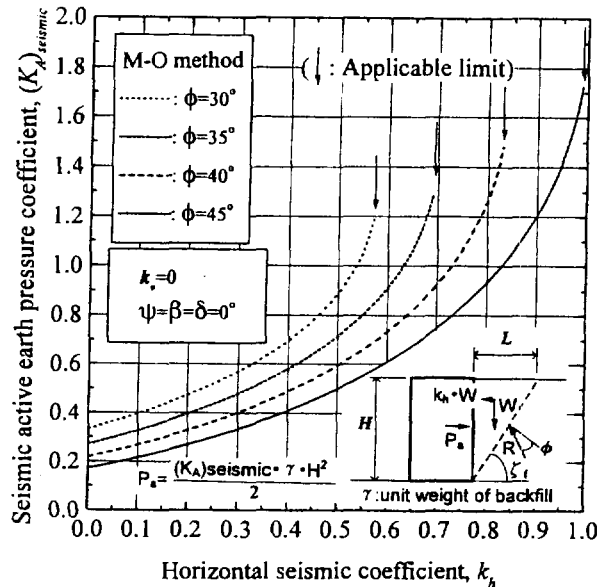


Fig. 3.2 Relationships between the seismic active earth pressure coefficient  $(K_A)_{\text{seismic}}$  and the horizontal seismic coefficient  $k_h$  obtained by the M-O method for  $\phi = 30, 35, 40, 45$  degrees for the simplest wall and backfill configuration.

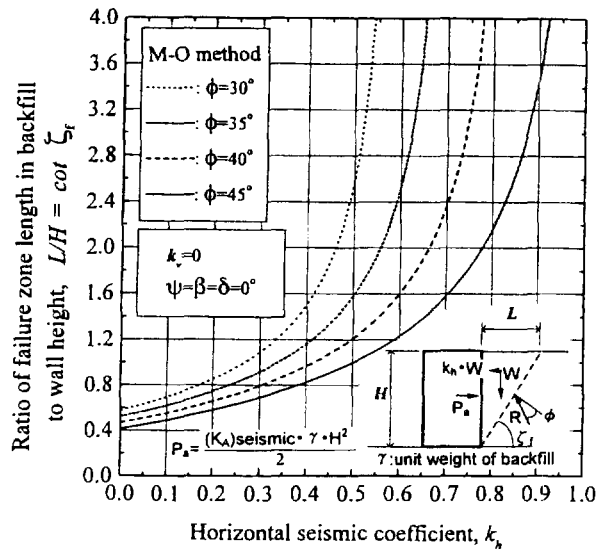


Fig. 3.3 Relationships between the size of failure zone in the backfill and the horizontal seismic coefficient  $k_h$  obtained by the M-O method for  $\phi = 30, 35, 40$  degrees, corresponding to Fig. 3.2.

the simplest wall and backfill configurations as shown in the figure, obtained by the original M-O method using  $\phi = 30^\circ, 35^\circ, 40^\circ$  and  $45^\circ$ , while Fig. 3.3 shows the size of the failure zone in the backfill. It may be seen that at a high  $k_h$  (about 0.5 or more), the use of conservative  $\phi$  values such as  $30^\circ$  results into very high  $(K_A)_{\text{seismic}}$  values with very deep and long failure planes.

The original M-O method is based on several postulates as summarized below:

- 1) The maximum earth pressure is obtained by changing the angle  $\zeta$  of the straight failure plane starting from the heel of the wall. Therefore, the angle  $\zeta_c$  for the critical failure plane is a function of  $k_h$  (and  $k_v$ ), and becomes smaller as the value of  $k_h$  increases.
- 2) The seismic coefficients  $k_h$  and  $k_v$  are usually applied uniformly in both vertical and lateral directions in the backfill (vertically or laterally non-uniform distributions of  $k_h$  (and  $k_v$ ) are used in some modified methods as discussed below).
- 3) The friction angle  $\phi$  is constant along the critical failure plane in homogeneous backfill. That is, the backfill soil is an isotropic and perfectly-plastic material, and the  $\phi$  value mobilized in the failure zone is independent of the previous wall movement which has occurred before the ultimate failure of RW. This is equivalent to not considering the progressive process of active failure associated with shear banding and strain softening in the backfill.
- 4) As a result of postulates 1, 2 and 3, the distribution of dynamic earth pressure is hydrostatic with the center of gravity at one third of the wall height ( $H/3$ ) when the backslope is level without surcharge.

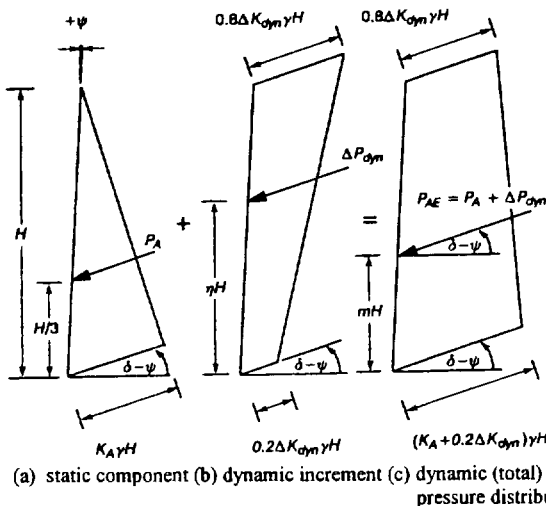


Fig. 3.4 Modified M-O method for GRS-RWs introducing a more realistic non-uniform vertical distribution of  $k_h$  (Bathurst and Cai, 1995); a) static component; b) dynamic increment; and c) dynamic (total) pressure distribution.

We should note, however, that these postulates are not relevant, as examined later in this paper in the light of the recent experimental results. For example, the postulate 3 is not relevant particularly for ductile RWs such as GRS-RWs, which can survive seismic loads largely exceeding the value at which the first active failure takes place in the backfill.

Several modifications have been proposed to alleviate some limitations of the original M-O method. The results of the previous model tests on conventional type RWs, including those by Ichihara and Matsuzawa (1973), revealed that the hydrostatic distribution assumption may be less conservative by itself. To apply to segmental GRS-RWs, Bathurst and Cai (1995) introduced a more realistic vertically non-uniform distribution of  $k_h$  (Fig. 3.4). In their method, however, a single straight failure plane starting from the heel of facing is assumed (as the original M-O method), irrespectively of the presence of reinforcement, and the reinforcement is considered to resist the seismic earth pressure obtained as above.

The two-wedge method (TW method; e.g., Jewell et al., 1984) has been used to design many GRS-RWs. This approach is particularly relevant for GRS-RWs having a FHR facing and short reinforcement (Horii et al., 1994; Fig. 3.5), since for such GRS-RWs, the failure zone consists of two wedges as observed in many model tests (Fig. 3.6a). Furthermore, the TW method can simulate single straight failure planes, thus covering the original M-O method. In the TW method, the pattern and location of failure plane is controlled by the presence of reinforcement.

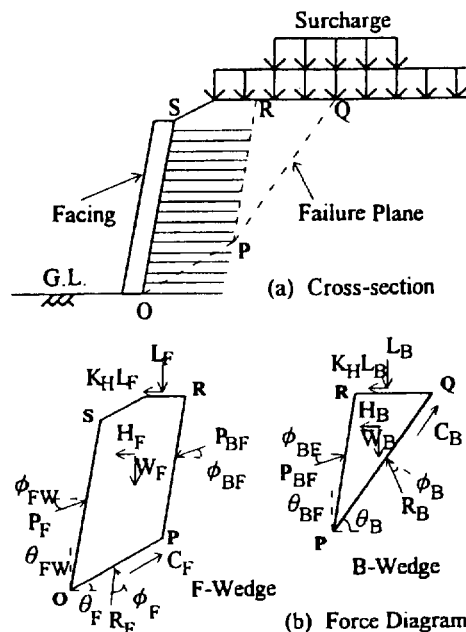


Fig. 3.5 The two-wedge method (Horii et al., 1994); a) cross-section; and b) force diagram.

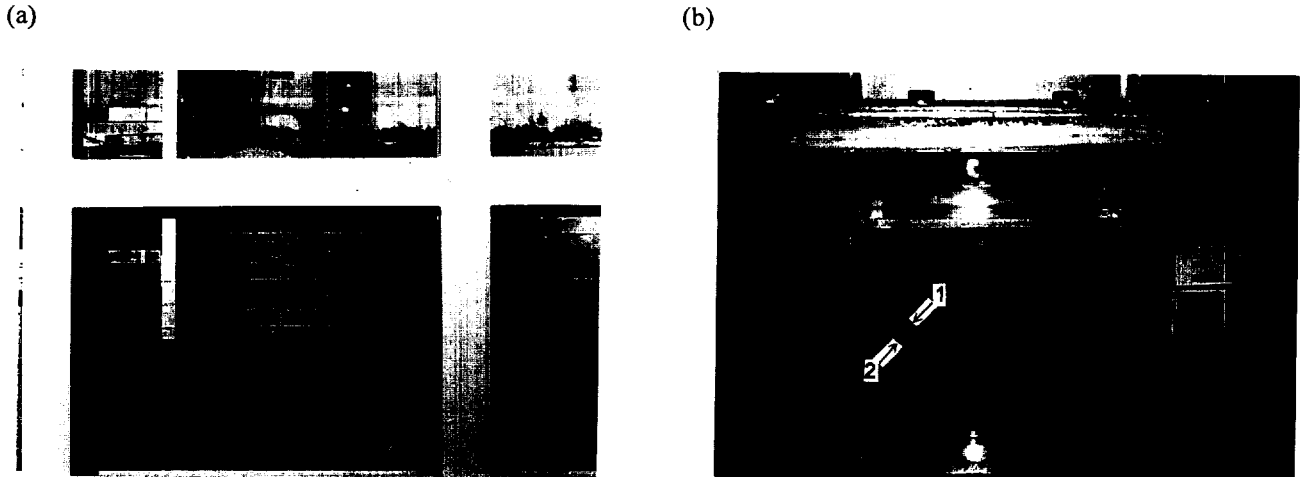


Fig. 3.6 a) Two-wedge failure mode observed in a model shaking test of GRS-RW having short reinforcements (see Fig. 4.6b and Fig. 4.7b for “Reinforced type 1”); and b) multiple failure planes observed in a model tilting test of GRS-RW having longer top reinforcement (see Fig. 4.6a and Fig. 4.7a for “Reinforced type 2”) (Koseki et al., 1997).

The design procedure proposed by Leshchinsky et al. (1995) for geosynthetic-reinforced slopes and segmental walls under static loads assumes a log-spiral failure plane in the backfill. Extending the above, Ling et al. (1997) considered seismic effects by introducing a uniformly-distributed horizontal seismic coefficient  $C_s$  for the whole backfill above and below the failure plane for the tieback failure analysis (Fig. 3.7). Log-spiral failure planes cover planar failure planes as assumed in the original M-O method by setting the pole of the log spiral at infinity, but may not sufficiently model such a two-wedge failure mechanism as shown in Fig. 3.6a.

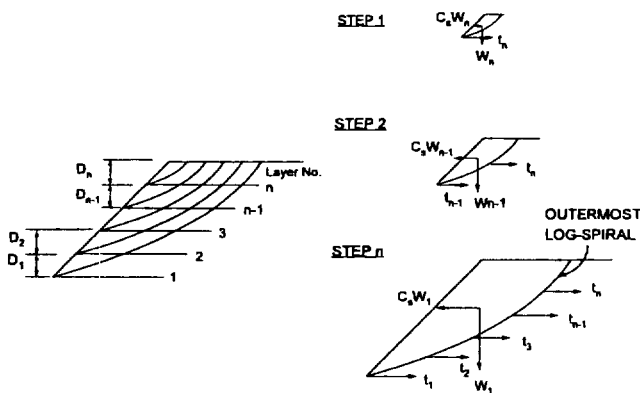
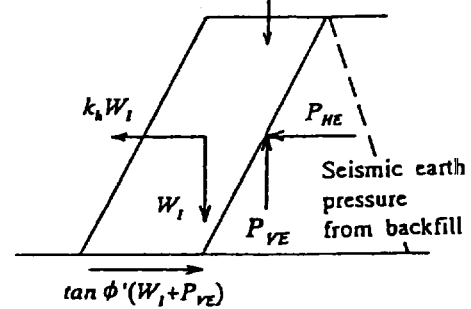


Fig. 3.7 Tie back failure analysis employing log-spiral failure plane and horizontal seismic inertia force (Ling et al., 1997).

Fukuda et al. (1994) analyzed the performance of a geogrid-reinforced slope of road embankment which survived the 1993 Koshiro-Oki Earthquake without any noticeable damage. In the aseismic design method proposed by Public Works Research Institute (1992) (Fig. 3.8a), the entire reinforced zone is regarded as a rigid body and seismic earth pressure acting from the unreinforced

backfill is evaluated by the trial wedge method or its equivalent (i.e., the original M-O method). They reported that when based on the external stability analysis described above, the safety factor of the wall against direct sliding along the wall base during the earthquake was 0.93, which is not consistent with the actual behavior. They considered that in the above method, no phase lag is introduced between the horizontal inertia force of the

(a) Reinforced zone as a pseudo-retaining wall



(b) Reinforced zone as a pseudo-retaining wall

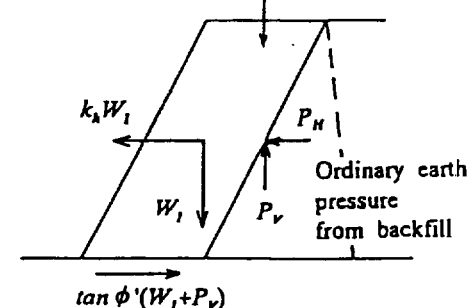


Fig. 3.8 Concept of horizontal inertia force and seismic earth pressure acting on the reinforced zone (Fukuda et al., 1994); a) when they are in the same phase; and b) when they have a phase-lag and increment of the earth pressure is zero at the maximum inertia force.

reinforced zone and the dynamic component of earth pressure acting on the back of the reinforced zone, as in many other design specifications. In order to explain this discrepancy, they assumed that the horizontal inertia force of the reinforced zone and the earth pressure acting on the back of the reinforced zone should have been out of phase. This assumption is consistent with observations in the small-scale model shaking table tests shown later. As an extreme case, they assumed that there was no dynamic component in the earth pressure when the inertia force was at its maximum, as schematically shown in Fig. 3.8b. The obtained safety factor was 1.23, which is more consistent with the actual behavior.

In the design guidelines of FHWA (1990), the value of  $(k_h)_{design}$  value assigned to the reinforced part of backfill is a half of that to be applied in evaluating the seismic thrust of the earth pressure acting from the unreinforced part of backfill by considering that these two forces are unlikely to peak simultaneously. For geosynthetic-reinforced segmental RWs, Bathurst and Cai (1995) proposed a factor of 0.6, instead of 0.5.

The major limitations inherent to the pseudo-static approaches as summarized above include the following:

- 1) Deformation and displacement of RW cannot be evaluated.
- 2) The effects of dynamic effects cannot be fully nor properly accounted for, as discussed by Tatsuoka et al. (1996). The major factors of the dynamic effects include;
  - a) dynamic ductility (the capability of deforming and/or

displacing without exhibiting ultimate failure against dynamic loads exceeding the yield strength of the structure); and b) dynamic flexibility (the property which causes phase lag in a RW reducing earth pressure on the RW in a positive way while it may increase the response acceleration in a negative way). In fact, among RWs having similar seismic safety factors evaluated by the pseudo-static approach, those having a higher dynamic ductility and larger positive effects of flexibility performed better during the Hyogo-ken-nambu Earthquake (Koseki et al., 1996). Fig. 3.9 shows the  $(k_h)_{critical}$  values at which the safety factor becomes unity for the several types of conventional type RWs (Figs. 2.2b, 2.3 and 2.4) and the Tanata GRS-RW (Fig. 2.2a) evaluated by the conventional pseudo-static approaches (i.e., the original M-O method and the conventional TW method) under the following two conditions;

- A) soil strength values and wall configurations are determined following the current design procedures; the  $\phi$  values are conservative, similar to the residual values, and passive pressure on part of the front face of underground part of RW is ignored (see Table 3.1); and
- B) peak soil strength values are used; for cohesionless soils, basically the peak friction angles estimated by relevant triaxial compression tests are used, which are larger than those described above, and the passive earth pressure on the front face of the underground part of RW is evaluated as it was at the time of the earthquake (see Table 3.2).

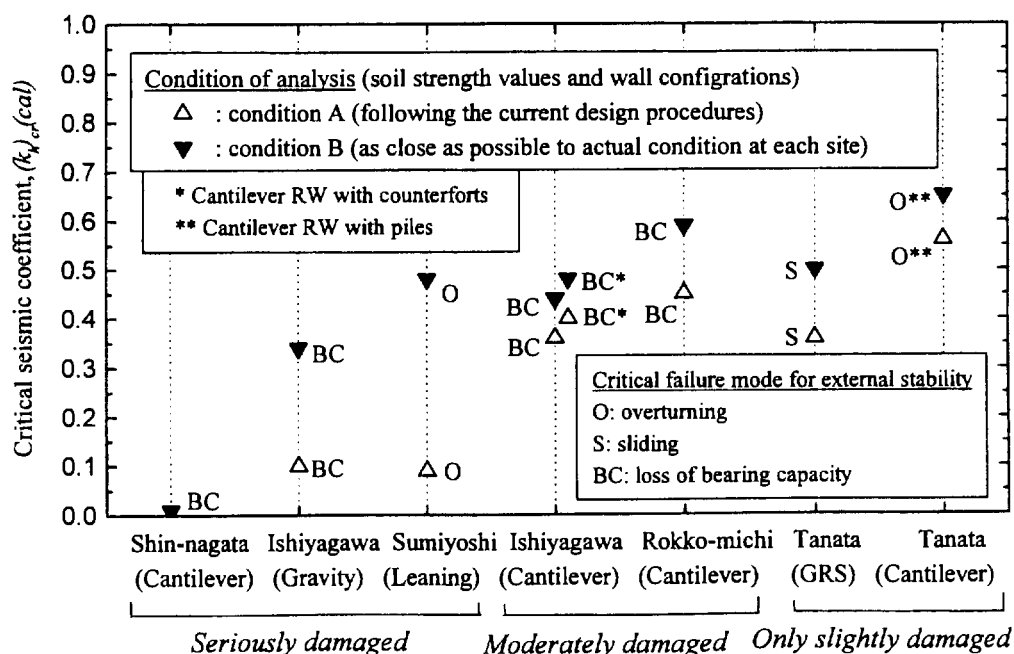
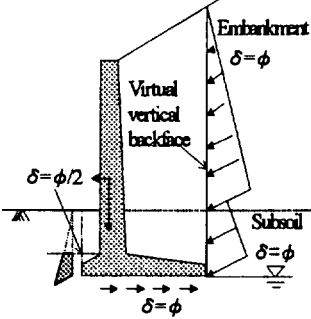
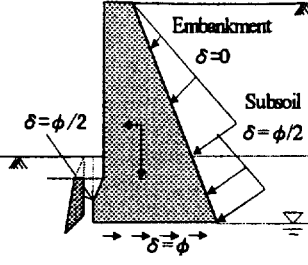
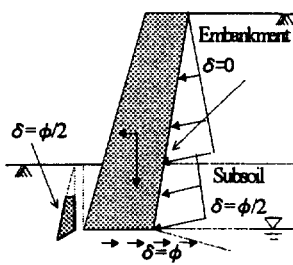
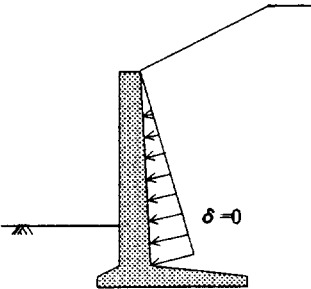
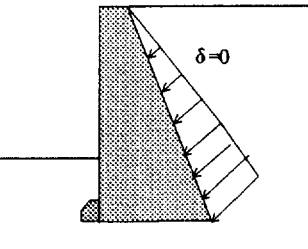
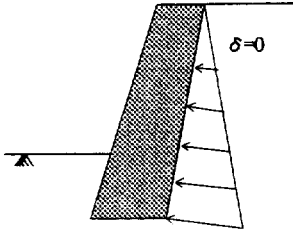


Fig. 3.9  $(k_h)_{crit}(cal)$  values for a safety factor equal to unity for ultimate failure of several conventional type RWs and the Tanata GRS-RW, evaluated by the current design methods (i.e., the original M-O method and the conventional two-wedge method) using two different soil strength values and wall configurations listed in Tables 3.1 and 3.2.

Table 3.1 Detailed calculation conditions used to obtain the  $(k_h)_{cr}(cal)$  values shown in Fig. 3.9 (using soil strength values and simplification methods following the current design procedures).

Site		Shin-nagata	Ishiyagawa	Sumiyoshi	
Type of RW		Cantilever RC	Gravity**	Leaning	
For external stability [condition A]	Soil property				
	Active earth pressure at the back face*	$\gamma$ (kN/m <sup>3</sup> )	17.7	19.6	19.6
		$C$ (kN/m <sup>2</sup> )	0.0	0.0	0.0
		$\phi$ (°)	30.0	35.0	35.0
$\delta$ (°)		30.0 (backfill), 30.0 (subsoil)	0.0 (backfill), 17.5 (subsoil)	0.0 (backfill), 17.5(subsoil)	
Passive earth pressure at the front face	$\gamma$ (kN/m <sup>3</sup> )	17.7	19.6	2.0	
	$C$ (kN/m <sup>2</sup> )	0.0	0.0	0.0	
	$\phi$ (°)	30.0	35.0	35.0	
	$\delta$ (°)	15.0	17.5	17.5	
Frictional resistance angle at bottom face	$\delta$ (°)	30.0	35.0	35.0	
Bearing capacity of subsoil	$\gamma$ (kN/m <sup>3</sup> )	15.7	17.7	19.6	
	$C$ (kN/m <sup>2</sup> )	49.1	0.0	0.0	
	$\phi$ (°)	0.0	35.8	41.8	

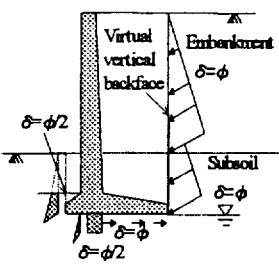
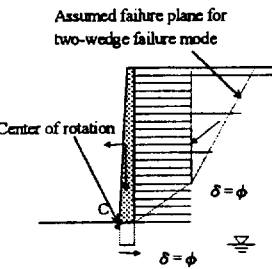
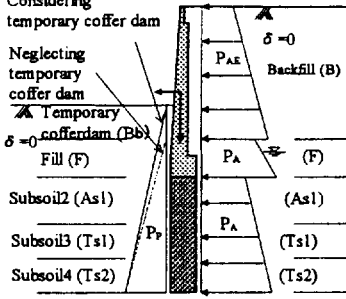
★ Surcharge was treated as equivalent backfill.

For internal stability [condition A]				
Concrete	$\gamma$ (kN/m <sup>3</sup> )	24.5	23.1 (24.5) **	23.1
	$\sigma_c$ (MN/m <sup>2</sup> )	11.8	7.7 (11.8) **	7.7
	$E_c$ (GN/m <sup>2</sup> )	29.9	28.3 (28.3) **	28.1
	Poisson's ratio	0.130	0.147 (0.147) **	0.177
Steel bar	$\sigma_s$ (MN/m <sup>2</sup> )	265	-(265) **	-
	$A_s$ (cm <sup>2</sup> /m)	19.355	-(77.6) **	-
	$E_s/E_c$	15	-(15) **	-

★★ For cantilever RC RW at Ishiyagawa, the same soil properties as shown for the gravity type RW at Ishiyagawa were employed except for the frictional angle at the virtual vertical backface for external stability, which was set equal to  $\phi$ . The properties of the concrete and the steel bar employed for the internal stability analysis of the cantilever RC RW at Ishiyagawa are indicated in the parentheses at the corresponding columns for the gravity type RW at Ishiyagawa.



Table 3.1 Detailed calculation conditions used to obtain the  $(k_h)_{cr}(cal)$  values shown in Fig. 3.9 (using soil strength values and simplification methods following the current design procedures). [continued]

Site		Rokko-michi	Tanata	Tanata						
Type of RW		Cantilever	Reinforced soil with FHR	Pile-supported cantilever RC						
For external stability [condition A]	Soil property									
		Note, $P_{AE}$ : seismic active earth pressure, $P_A$ : active earth pressure, $P_s$ : passive earth pressure								
		Active earth pressure at the back face*	$\gamma$ (kN/m <sup>3</sup> )	19.6	19.6	19.6				
			$C$ (kN/m <sup>2</sup> )	0.0	0.0	0.0				
			$\phi$ (°)	35.0	35.0	35.0				
	$\delta$ (°)	35.0 (backfill), 35.0 (subsoil)	35.0 (backfill), 35.0 (subsoil)	0.0						
Passive earth pressure at the front face	$\gamma$ (kN/m <sup>3</sup> )	19.6	2.0	19.6	19.6	17.4	18.9	19.7		
	$C$ (kN/m <sup>2</sup> )	0.0	0.0	0.0	0.0	0.0	0.0	0.0		
	$\phi$ (°)	35.0	35.0	35.0	35.0	27.0	37.0	44.0		
	$\delta$ (°)	17.5	35.0	0.0	0.0	0.0	0.0	0.0		
Frictional resistance angle at bottom face	$\delta$ (°)	33.0 (0.0 for the front face of shear key attached to the bottom of wall)		(Bb)	(F)	(As1)	(Ts1)	(Ts2)		
Bearing capacity of subsoil	$\gamma$ (kN/m <sup>3</sup> )	17.7	16.7	-	-	-	-	-		
	$C$ (kN/m <sup>2</sup> )	0.0	0.0	-	-	-	-	-		
	$\phi$ (°)	33.0	33.4	-	-	-	-	-		

★ Surcharge was treated as equivalent backfill.

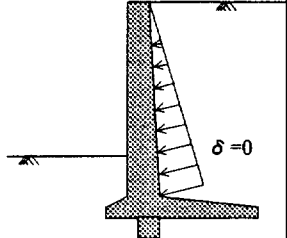
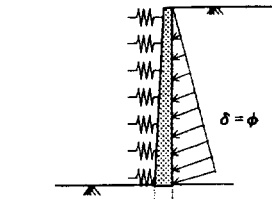
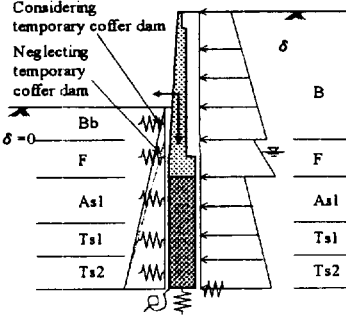
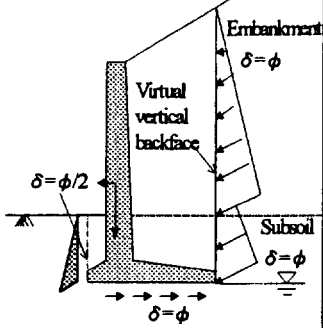
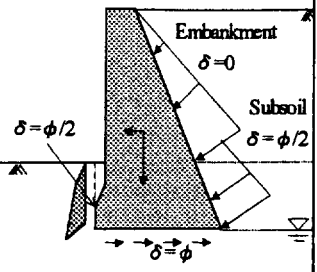
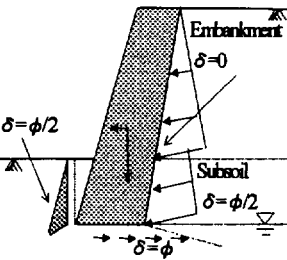
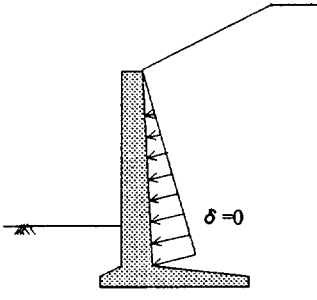
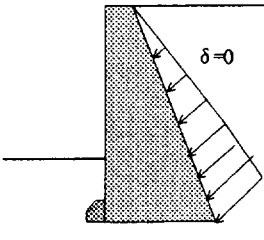
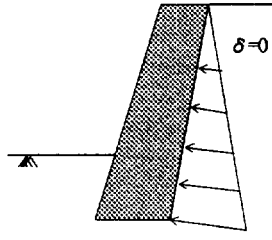
For internal stability [condition A]									
						RC wall		Pile	
		Concrete	$\gamma$ (kN/m <sup>3</sup> )	24.5	24.5	24.5	24.5		
			$\sigma_c$ (MN/m <sup>2</sup> )	11.8	20.6	11.8	20.6		
$E_c$ (GN/m <sup>2</sup> )	82.0		24.5	23.1	23.1				
Poisson's ratio									
Steel bar	$\sigma_s$ (MN/m <sup>2</sup> )	265	481	265	265				
	$A_s$ (cm <sup>2</sup> /m)	77.42	4.22	7.94	7.94				
	$E_s/E_c$	15	15	15	15				

Table 3.2 Detailed calculation conditions used to obtain the  $(k_h)_{cr(cal)}$  values shown in Fig. 3.9 (using soil strength values and wall configurations as close as possible to those at each site)

Site		Shin-nagata	Ishiyagawa	Sumiyoshi		
Type of RW		Cantilever RC	Gravity**	Leaning		
For external stability [condition B]	Soil property					
		Active earth pressure at the back face*	$\gamma$ (kN/m <sup>3</sup> )	16.1	17.5	18.1
		$C$ (kN/m <sup>2</sup> )	0.0	0.0	0.0	
		$\phi$ (°)	36.0	42.0	45.0	
Passive earth pressure at the front face	$\delta$ (°)	36.0 (backfill), 36.0 (subsoil)	0.0 (backfill), 21.0 (subsoil)	0.0 (backfill), 22.5 (subsoil)		
	$\gamma$ (kN/m <sup>3</sup> )	16.1	17.5	18.1		
	$C$ (kN/m <sup>2</sup> )	0.0	0.0	0.0		
	$\phi$ (°)	36.0	42.0	45.0		
Frictional resistance angle at bottom face	$\delta$ (°)	18.0	21.0	22.5		
	$\delta$ (°)	36.0	42.0	45.0		
Bearing capacity of subsoil	$\gamma$ (kN/m <sup>3</sup> )	17.3	18.9	19.7		
	$C$ (kN/m <sup>2</sup> )	49.1	0.0	0.0		
	$\phi$ (°)	0.0	35.8	41.8		

★ Surcharge was treated as equivalent backfill.

For internal stability [condition B]					
	Concrete	$\gamma$ (kN/m <sup>3</sup> )	23.2	22.7 (22.5) **	23.2
		$\sigma_c$ (MN/m <sup>2</sup> )	25.8	18.8 (30.5) **	18.6
		$E_c$ (GN/m <sup>2</sup> )	29.9	28.3 (28.3) **	28.1
		Poisson's ratio	0.130	0.147 (0.147) **	0.177
Steel bar	$\sigma_s$ (MN/m <sup>2</sup> )	481	-(481)	-	
	$A_s$ (cm <sup>2</sup> /m)	19.355	-(77.6)	-	
	$E_s/E_c$	15	-(15)	-	

★★ For cantilever RC RW at Ishiyagawa, the same soil properties as shown for the gravity type RW at Ishiyagawa were employed except for the frictional angle at the virtual vertical backface for external stability, which was set equal to  $\phi$ . The properties of the concrete and the steel bar employed for the internal stability analysis of the cantilever RC RW at Ishiyagawa are indicated in the parentheses at the corresponding columns for the gravity type RW at Ishiyagawa.

Table 3.2 Detailed calculation conditions used to obtain the  $(k_n)_{\alpha}(cal)$  values shown in Fig. 3.9 (using soil strength values and wall configurations as close as possible to those at each site) [continued]

Site		Rokko-michi	Tanata	Tanata						
Type of RW		Cantilever	Reinforced soil with FHR	Pile-supported cantilever RC						
For external stability [condition B]	Soil property									
		Active earth pressure at the back face*	$\gamma$ (kN/m <sup>3</sup> )	18.1	16.7	16.7				
		$C$ (kN/m <sup>2</sup> )	0.0	0.0	0.0					
		$\phi$ (°)	45.0	41.0	41.0					
Passive earth pressure at the front face	$\delta$ (°)	45.0(backfill), 45.0(subsoil)	41.0(backfill), 41.0(subsoil)	0.0						
	$\gamma$ (kN/m <sup>3</sup> )	18.1	16.7	17.7	16.7	17.4	18.9	19.7		
	$C$ (kN/m <sup>2</sup> )	0.0	0.0	0.0	0.0	0.0	0.0	0.0		
	$\phi$ (°)	45.0	41.0	30.0	32.0	27.0	37.0	44.0		
Frictional resistance angle at bottom face	$\delta$ (°)	22.5	41.0	0.0	0.0	0.0	0.0	0.0		
		33.0 (16.5 for the front face of shear key attached to the bottom of wall)	41.0	(Bb)	(F)	(As1)	(Ts1)	(Ts2)		
Bearing capacity of subsoil	$\gamma$ (kN/m <sup>3</sup> )	17.9	17.4	-	-	-	-	-		
	$C$ (kN/m <sup>2</sup> )	0.0	0.0	-	-	-	-	-		
	$\phi$ (°)	33.0	33.4	-	-	-	-	-		

★ Surcharge was treated as equivalent backfill.

For internal stability [condition B]					
				RC wall	Pile
Concrete	$\gamma$ (kN/m <sup>3</sup> )	24.5	24.5	24.5	24.5
	$\sigma_c$ (MN/m <sup>2</sup> )	11.8	20.6	11.8	20.6
	$E_c$ (GN/m <sup>2</sup> )	82.0	24.5	23.1	23.1
	Poisson's ratio				
Steel bar	$\sigma_s$ (MN/m <sup>2</sup> )	265	481	265	265
	$A_s$ (cm <sup>2</sup> /m)	77.42	4.22	7.94	7.94
	$E_s/E_c$	15	15	15	15

Table 3.3 List of the  $(k_h)_{cr}(cal)$  values obtained following the calculation conditions listed in Tables 3.1 and 3.2.

Site	Type of RW and condition of analysis	$(k_h)_{cr}(cal)$ for external stability			$(k_h)_{cr}(cal)$ for internal stability			Performance during the 1995 Hyogoken-nanbu earthquake	
		Overturning	Sliding	Bearing capacity	Compressive failure	Tensile failure	Shear failure		
Shin-nagata	Cantilever	A:	0.12	*	*	0.14	0.04	—	Severely damaged; very large tilting and sliding, cracking at middle height, large settlement of back slope embankment
		B:	0.24	0.16	0.01	0.40	0.23	—	
Ishiyagawa	Gravity	A:	0.25	0.64	0.10	1.97	0.47	—	Severely damaged; very large tilting, total or partial breakage at construction joints and total or very large overturning
		B:	0.63	0.78	0.34	5.20	1.14	—	
	Cantilever	A:	0.44	0.80	0.36	0.20	0.34	—	Moderately damaged; large tilting, cracking at middle height
		B:	0.89	1.23	0.44	0.80	0.78	—	
	Cantilever with counterforts	A:	0.56	0.63	0.40	0.51	0.19	—	Moderately damaged; large tilting
		B:	0.91	1.14	0.48	1.17	0.71	—	
Sumiyoshi	Leaning	A:	0.09	0.53	0.16	1.16	0.16	—	Severely damaged; complete overturning, partial breakage at ground surface level
		B:	0.48	1.06	0.49	2.23	0.77	—	
Rokko-michi	Cantilever	A:	0.72	0.73	0.45	0.52	0.68	—	Moderately damaged; large tilting
		B:	2.01	0.95	0.59	0.69	0.89	—	
Tanata	GRS	A:	0.41	0.36	—	1.29	1.22	—	Slightly damaged; slight tilting and sliding, partial minor cracking at middle height
		B:	0.60	0.50	—	1.74	1.69	—	
	Cantilever with piles**	A:	0.56	—	—	0.66 / 0.75	>1.0 / >1.0	0.99 / 0.82	Slightly damaged; slight tilting and sliding
		B:	0.65	—	—	0.77 / 0.80	>1.0 / >1.0	>1.0 / 0.92	
		A':	0.10	—	—	0.51 / 0.36	>1.0 / >1.0	0.82 / 0.24	
		B':	0.29	—	—	0.66 / 0.38	>1.0 / >1.0	0.96 / 0.32	

Condition A (upper line): using soil strength values and simplification methods following the current design procedures (refer to Table 3.1)

Condition B (lower line): using soil strength values and wall configurations as close as possible to those at each site (refer to Table 3.2)

\*At Shin-nagata site, safety factors against sliding and loss of bearing capacity even at  $k_h=0$  on condition A were smaller than 1.

\*\* For cantilever RW with piles at Tanata site, internal stability analyses were conducted on both the facing and the piles, and their results are listed in the table as " $(k_h)_{cr}(cal)$  for facing failure /  $(k_h)_{cr}(cal)$  for pile failure." Furthermore, another set of analyses was conducted by neglecting the presence of a temporary coffer dam in front of the RW, as denoted by conditions A' and B'.

Table 3.3 lists the summary of the results of the analysis with a global safety factor equal to unity. Here, the overturning failure of RW as a rigid body is assumed to occur about its toe. In actuality, overturning failure of RW may have resulted from bearing capacity failure in the subsoil below around the toe of RW, as observed with some RWs in the field (and in the laboratory as discussed later). It may be seen that when based on condition A, using conservative soil strength values, the calculated values  $(k_h)_{cr}(cal)$  of the two conventional gravity type (leaning and gravity types) RWs (Figs. 2.4b and 2.4c) are particularly low when compared with the others. However, for the purpose of evaluating different dynamic effects among these different RWs, the  $(k_h)_{cr}(cal)$  values obtained based on condition B, using more realistic soil strength values, are more informative. Then, it may be seen that except for the cantilever RC RW at Shin-nagata, these  $(k_h)_{cr}(cal)$  values are rather similar, despite their very different levels of damage. It is considered that positive net dynamic effects on the ultimate failure of RW may be one of the major reasons for their different seismic

behaviours. Note also that for many of the RWs (except for three cases), the  $(k_h)_{cr}(cal)$  based on condition A is much higher than 0.2, which is currently used for these types of RW. This difference is largely due to the use of a global safety factor, which is typically 1.5 for these types of RW.

When based on Table 3.3, the seismic stability of the pile-supported cantilever RC RW at Tanata (Fig. 2.2b) had increased largely by the presence of a temporary coffer dam in front of the RW, which was existing at the moment of the earthquake (cases A and B in Table 3.3); seemingly, the weight of the coffer dam have largely increased the overburden pressure in the sub-soil, thus have largely increased the passive earth pressure in the ground. Without these effects (cases A' and B'), the  $(k_h)_{cr}(cal)$  values of the RW becomes much lower, suggesting that the wall would have been damaged much more seriously than the GRS-RW at Tanata. On the other hand, the construction cost per wall length for the RC RW is about 2 - 3 times as high as that for the GRS-RW. These facts

indicate that the GRS-RW having a FHR facing could be much more cost-effective also from a viewpoint of seismic stability.

Note also that the value of  $(k_h)_{cr}(cal)$  for internal stability under condition B are similar to, or larger than, the estimated (PGA/g) values, except for an unusual case of the RC RW at Shin-nagata (see Table 3.3). Therefore, internal stability will not be discussed herein.

#### 4. ACTIVE FAILURE PROCESS IN THE BACKFILL

##### 4.1 Shear banding in PSC tests on sands and gravels

To examine the postulates with respect to soil properties used in the original M-O method, shear banding in granular materials will first be discussed. Densely compacted sand and gravel fails always associated with strain localization into a shear band (or shear bands) exhibiting strain softening. Therefore, the ultimate failure of the RW-backfill system is usually preceded by the active failure in the backfill associated with shear banding. Fig. 4.1 shows relationships between the shear stress level  $R_n$  and the shear deformation  $U_s$  of shear band for a variety of granular materials having a large range of particle size. These results were obtained from detailed observations of local deformation on the specimen's boundary  $\sigma_2$  surface in a series of plane strain compression (PSC) tests.  $R_n$  is defined as;

$$R_n = (R - R_{res}) / (R_{peak} - R_{res}) \quad (4.1)$$

where  $R$  is the principal stress ratio  $\sigma_1/\sigma_3$ , and  $R_{peak}$  and  $R_{res}$  are the peak and residual values of  $R$ .  $R_n$  is equal to 1.0 and 0.0 at the peak and residual states. The following important trends of behaviour have been found from Fig. 4.1 and related observations:

- In the post-peak strain softening regime, the stress level drops associated with yielding in a shear band and elastic rebound outside the shear band.
- The increment  $\Delta U_s$  by which the stress ratio drops from the peak value to the residual value is only about 5 - 10 times  $D_{50}$  for most of the granular materials (or less for Isomi gravel). This amount of shear deformation is very small when compared with the dimensions of usual full-scale RWs; for example, when the wall height  $H$  is 5 m and  $D_{50}$  is 0.2 mm,  $\Delta U_s = (10 - 20) \text{ times } D_{50}$  is only 0.4 - 0.8 % of  $H$ . This small figure suggests that the stress state in the shear band can become the residual state very rapidly after it develops associated with the active failure in the backfill.
- In PSC tests on sufficiently large specimens having height/width ratios larger than about 2.5 with well lubricated top and bottom ends, due to the weakening process inside the shear band, the first developed shear band further deforms without developing the second shear band(s). It would be also the case with the backfill of RW unless increasing seismic loads or backfill deformations or both change largely the principal stress directions in the backfill.

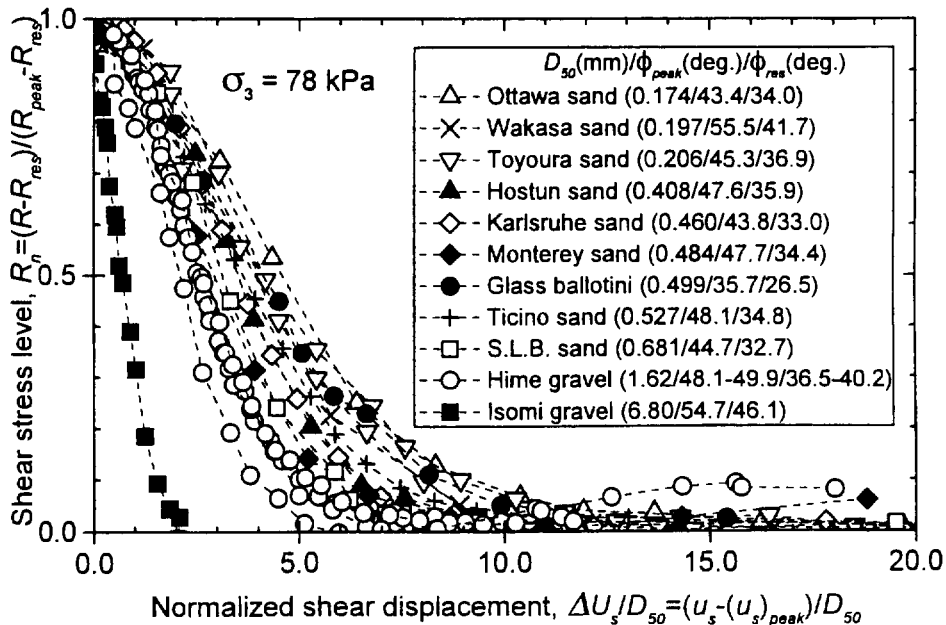


Fig. 4.1 Relationships between the shear stress level  $R_n$  and the shear deformation  $U_s$  of shear band from plane strain compression tests on a variety of granular materials with a large range of particle size (Yoshida et al., 1994; Yoshida and Tatsuoka, 1997).

These three features are relevant particularly for densely compacted backfill as that of reinforced soil RWs.

4.2 Active failure in PSE tests on sand

Yamada and Masuda (1997) performed a series of special plane strain tests in which specimens of Toyoura sand were rotated 90° after specimen preparation by air-pluviation so that the horizontal and vertical stresses  $\sigma_h$  and  $\sigma_v$  during the specimen preparation become, respectively, the axial

stress  $\sigma_a$  and the constant lateral stress  $\sigma_c$  during the plane strain tests (Fig. 4.2). The plane strain compression and extension tests were performed on specimens anisotropically consolidated at  $\sigma_a/\sigma_c (= \sigma_h/\sigma_v) = 0.375$ , which simulated, respectively, the passive and active failures from the  $K_0$  condition in the backfill behind a smooth vertical RW. In the active failure test (i.e., the plane strain extension test, PSE test; Figs.4.2c and d), the minimum earth pressure ( $\sigma_a$ )<sub>min</sub> with  $\phi_{peak}$  being mobilized (i.e., the active earth pressure ( $\sigma_h$ )<sub>a</sub>) was

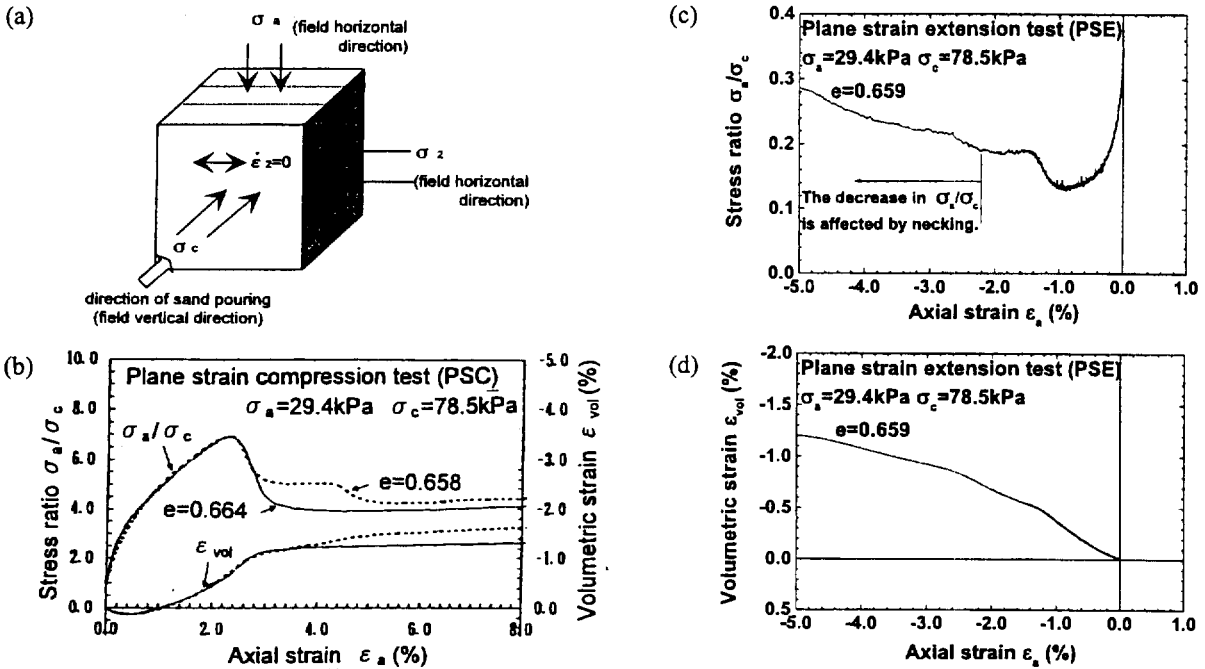


Fig. 4.2 a) Specimen configuration; and b) to d) relationships between the axial stress  $\sigma_a$  and the axial strain  $\epsilon_a$  from monotonic active and passive tests on saturated Toyoura sand at an axial strain rate of 0.125 %/min (Yamada et al., 1996).

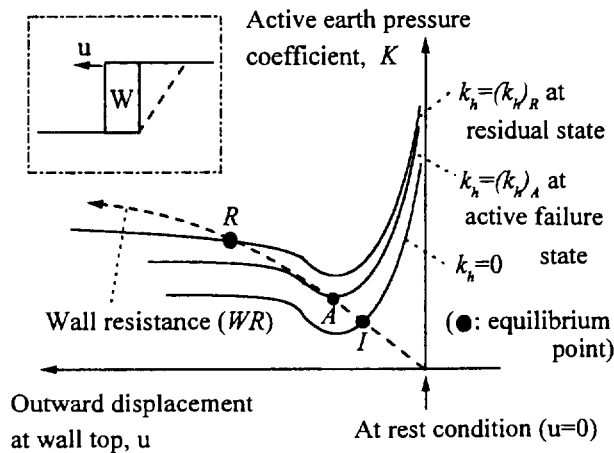


Fig. 4.3 Schematic diagram showing the active failure in the backfill and the ultimate failure of the RW.

attained at a very small axial strain of about -1.0 %. The minimum earth pressure state was followed by shear banding with the axial stress  $\sigma_a$  (i.e., the earth pressure  $\sigma_h$ ) increasing towards a larger value at the residual state and  $\phi_{mob}$  decreasing from  $\phi_{peak}$  to  $\phi_{res}$ . The basically same process occurred in the passive failure in the PSC test (Fig.4.2b).

It may also be inferred from Fig. 4.2c that for actual backfill soil, under static conditions or a certain seismic condition with a constant positive  $k_h$ , the pre-peak relationship between  $K$  ( $K_{static}$  or  $K_{seismic}$ ) and  $u$  is non-linear having a negative slope  $dK/du$ , while the post-peak relationship is also non-linear but having a positive slope (see Fig. 4.3). On the other hand, at a constant  $u$  (i.e., at a constant  $\phi_{mob}$ ), the relationship between  $K_{seismic}$  and  $k_h$  has a positive slope  $dK_{seismic}/dk_h$ . The existence of such opposite signs as shown above makes the seismic earth pressure properties very complicated and confusing.

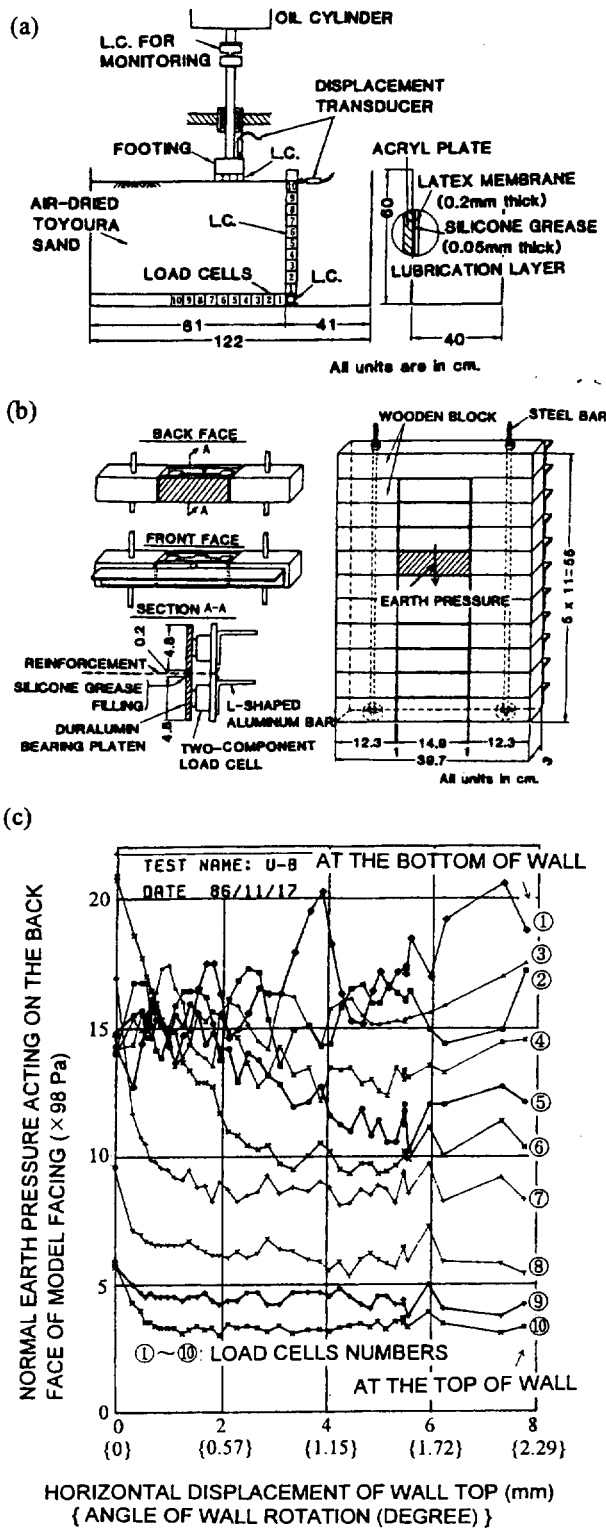


Fig. 4.4 a) Model configuration; b) details of model facing; and c) earth pressure acting on the back face of a 50 cm-high rough vertical retaining wall with backfill of air-dried Toyoura in a static model test controlling the rotation of the wall about its base (Tateyama, 1997).

### 4.3 Active failure in the backfill in model tests

**Static model test:** Tateyama (1997) measured by using ten load cells the earth pressure acting on the back face of a 50 cm-high model of rough vertical rigid RW with the backfill of air-dried Toyoura sand (Fig. 4.4). The model RW was rotated about its base at a controlled displacement rate. Similar to the above-mentioned PSE test, the minimum earth pressure was attained at a very small wall rotation (about 1.0°), which was equivalent to about -0.6 % lateral strain in the uniformly deforming active zone with  $\phi = 55^\circ$ . After this active failure state, at the lower part of the wall (i.e., load cell Nos. 1 to 6), the earth pressure increased associated with shear band development in the backfill. Measurements of strain field in the backfill showed that within the limit of wall rotation examined (about 2.2°), the first developed shear band further deformed without developing the second failure plane, likely due to essentially constant directions of the principal stresses in the backfill.

**Shaking table tests in a centrifuge:** Bolton and Steedman (1985) performed small-scale shaking tests of a 135 mm-high box RW model with the backfill of air-dried SLB sand ( $D_{50} = 0.225$  mm) in a centrifuge (Fig. 4.5a). The initial centrifuging to 80 g (g denotes the gravitational acceleration) and the first earthquake loading using roughly sinusoidal cycles having the maximum amplitude of 21 % of 80 g, which was equivalent to  $k_h = 0.21$ , caused a total rotation of 0.57° and a total base slip of 0.39 mm of the model RW. These wall displacements were seemingly enough to initiate the active failure in the backfill. The second earthquake loading having  $k_h = 0.33$  caused the ultimate failure of the RW with about a further 11 mm base slip and a visible failure plane developed in the backfill from the heel of the RW at an angle of  $(90^\circ - 25.5^\circ) = 64.5^\circ$  relative to the lateral direction. It is likely that the RW exhibited ductile behaviour, surviving higher seismic loads exceeding the value that caused the active failure in the backfill. The observed angle  $\zeta_r$  of the failure plane is slightly larger than the Coulomb failure angle equal to 58.4° at  $k_h = 0.21$  with  $\phi_{peak} = 50^\circ$  and the wall friction angle  $\delta = 2/3(\phi_{peak})$  obtained by;

$$\cot(\zeta_r) = -\tan(\phi + \delta) + \sec(\phi + \delta) \cdot \sqrt{\frac{\cos(\delta + \theta) \cdot \sin(\phi + \delta)}{\sin(\phi - \theta)}} \quad (4.2)$$

where  $\theta = \tan^{-1}(k_h)$ .

By using the ultimate failure seismic load  $k_h = 0.33$ , the failure plane angles predicted by the original M-O method using  $\phi_{peak} = 50^\circ$  and  $\phi_{res} = 34^\circ$  are, respectively, 52° and 36°, which are much smaller than the observed one. In a broad sense, this observation is consistent with the field behaviour (Fig. 2.6).

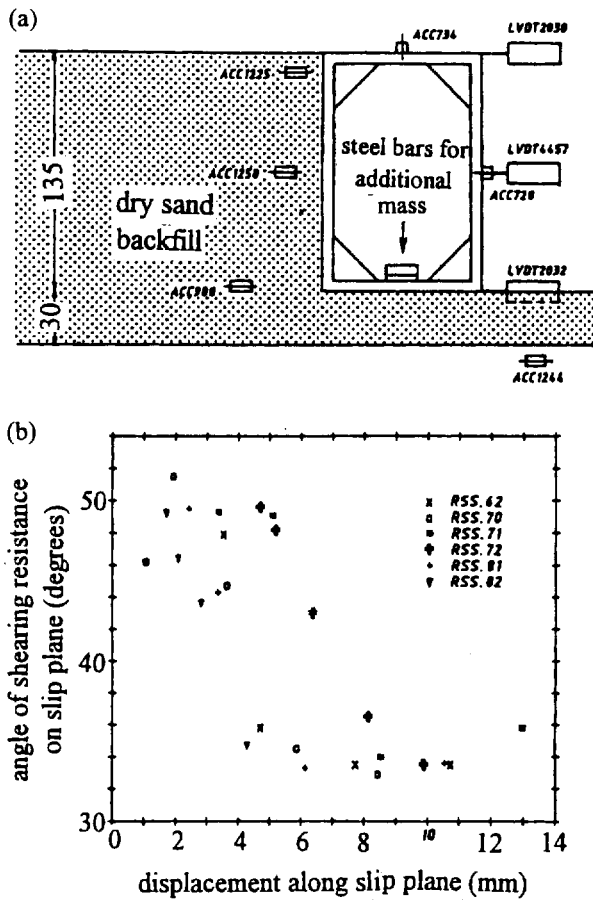
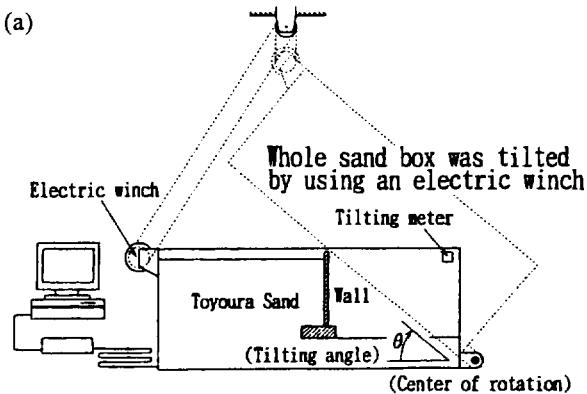


Fig. 4.5 Centrifugal shaking table tests on seismic stability of a box RW model with the backfill of air-dried SLB sand; a) test configuration (dimensions in mm); and b) relationships between the mobilized friction angle along the failure plane and the shear displacement across the shear band (Bolton and Steedman, 1985).

From the measured accelerations and displacements, the shear displacement increment across the shear band (or failure plane)  $\Delta U_s$  by which the stress changed from the peak value to the residual value was obtained to be about  $10 \cdot D_{50}$  (Fig. 4.5b), which is very consistent with the PSC



test results shown in Fig. 4.1. It was then concluded that “10 particle diameters is such a small relative slippage in a typical situation that it might alternatively be accepted that fully softened soil strengths  $\phi_{res}$  be invariably used on slip surfaces in sand irrespective of soil density.” This recommendation has actually been adopted in practice as discussed in INTRODUCTION. The present authors considers that this conclusion cannot be directly applied to the conventional pseudo-static approaches (e.g., the original M-O method and the conventional TW method), whereas this observation is essential for understanding and predicting better the behaviour of RWs at high seismic loads and for modifying properly the pseudo-static approaches, as discussed below.

“The seismic active failure in the backfill” and “the seismic ultimate failure of a RW” are different processes (Fig. 4.3). The seismic active failure could be defined as the mobilization of  $\phi_{peak}$  and associated start of shear banding under seismic loading conditions, while the seismic ultimate failure of a RW occurs when the seismic earth pressure exceeds the ultimate strength of the RW, usually occurring at a wall displacement larger than that at the active failure in the backfill. Therefore, it would be appropriate to assume that  $\phi_{res}$  is predominantly mobilized along the failure plane at the moment of the ultimate failure of RW, but not outside the failure plane (as suggested by Bolton and Steedman, 1985). This would be particularly relevant with ductile RWs, such as GRS-RWs, for which differences between the wall deformation at the seismic active failure in the backfill and that at the seismic ultimate failure of RW would be relatively large.

**Tilting and shaking table model tests:** Munaf et al. (1997) and Koseki et al. (1997) performed a series of small-scale static tilting tests, in which 50 cm-high models of several conventional types of RW and GRS-RWs having a FHR facing were brought to failure (Fig. 4.6a). The backfill was air-pluviated dense Toyoura sand, and each model RW was constructed on a 20 cm-thick sand layer. A model grid made of phosphor-bronze strips was

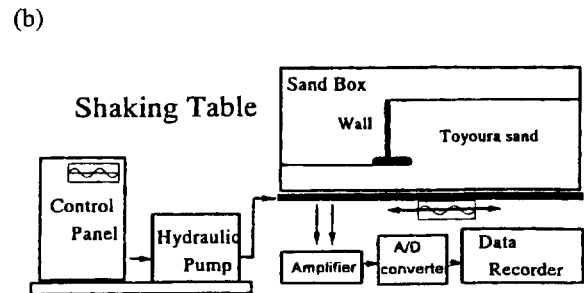


Fig. 4.6 a) Tilting tests and b) shaking table tests of cantilever-type RW model (Munaf et al., 1997).



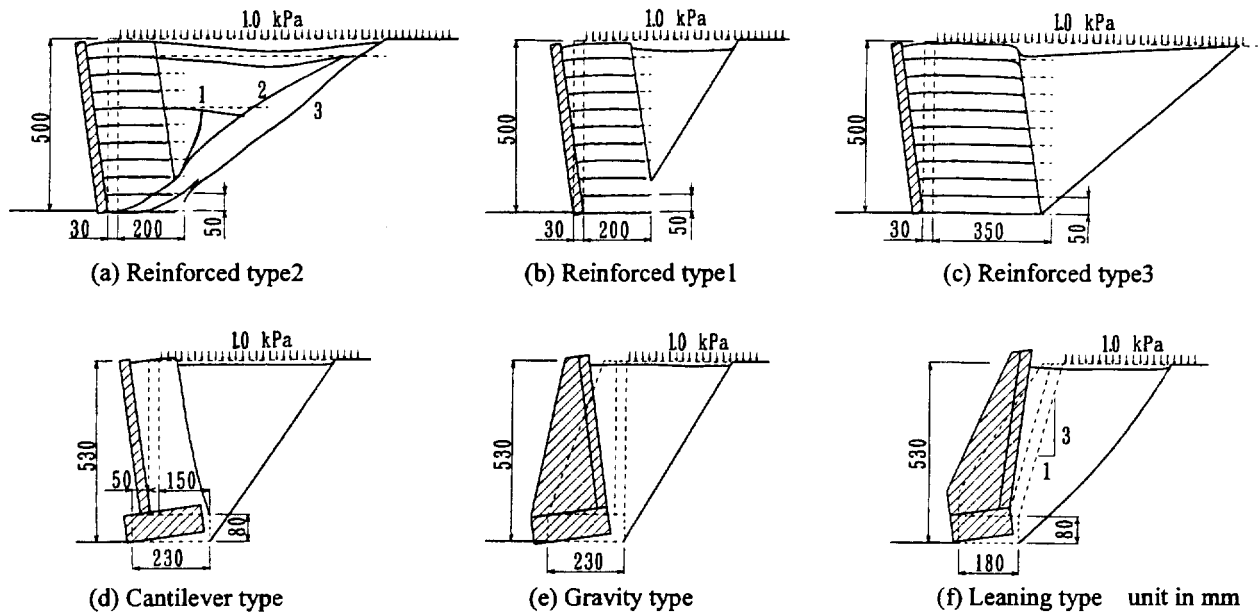


Fig. 4.7 Models of retaining walls showing their initial and displaced locations and observed failure planes; a) GRS-RW having a couple of extended top reinforcement layers, denoted as “Reinforced type 2” in Figs 4.8 and 6.2; b) GRS-RW having short reinforcement layers, denoted as “Reinforced type 1”; c) GRS-RW having moderately long reinforcement layers, denoted as “Reinforced type 3”; d) cantilever-type RW; e) gravity-type RW; and f) leaning-type RW (Koseki et al., 1997).

used to reinforce the backfill. A surcharge of 1.0 kPa, except for one test with 3.1 kPa, was applied on the backfill so as to increase the accuracy in the earth pressure measurements by increasing the pressure level in the backfill. Such static tilting model tests can simulate rather closely the stress conditions assumed in the original M-O method, except that the “vertical” stress (in the original vertical direction) decreases with tilting. In parallel, a series of shaking table tests were performed using the same RW models (Fig. 4.6b), in which the amplitude of sinusoidal waves at a frequency of 5 Hz used as input table acceleration was increased stepwise with an increment of 50 gals until the ultimate failure of RW was observed. The number of cycles at each step was about 50.

Fig. 4.7 shows the deformation of the models observed after failure in the shaking table tests. Commonly in the two series of model tests, only a single straight failure plane developed in the unreinforced backfill in back of the conventional type RWs, while a two-wedge mechanism was observed in the reinforced backfill (except for Reinforced type 2, in which multiple failure planes were observed as shown in Fig. 3.6b and 4.7a). This fact suggests that the pseudo-static approach for reinforced backfill should be different from that for unreinforced backfill such as the original M-O method. The seismic load  $k_h$  (i.e., the tilting angle or the amplitude of shaking

acceleration/g) could be increased further after the active failure plane started developing in the backfill, in particular with the reinforced soil models in the shaking table tests. However, in each test (except for Reinforced type 2), another deeper failure plane (or failure planes), which was (were) deeper than the first one, did not develop. Rather, as the  $k_h$  value increased, shear displacement was concentrated to the first developed failure plane.

Fig. 4.8 shows the relationship between the observed failure plane angle  $\zeta_f$  and the observed values of  $k_h$  at ultimate failure  $(k_h)_{cr}(obs)$ . For the GRS-RWs, the angle  $\zeta_f$  was defined for the failure plane of the back wedge developing in the unreinforced backfill behind the reinforced zone (except for Reinforced type 2). These  $\zeta_f$  values have been corrected for the initial wall configurations before deformations. Each value of  $(k_h)_{cr}(obs)$  was defined as the table horizontal acceleration/g or the tilting angle when a failure plane became clearly visible in the backfill and the wall displacement started increasing in an uncontrollable manner, when horizontal displacement at a wall top was about 5 % of the wall height. Note that single amplitude of the table horizontal acceleration at the active state was used to evaluate  $(k_h)_{cr}(obs)$ . Left-directed arrows next to some symbols mean that the respective failure plane started developing at a  $k_h$  below the  $(k_h)_{cr}(obs)$ . In Fig. 4.8, the theoretical relationships obtained by the original

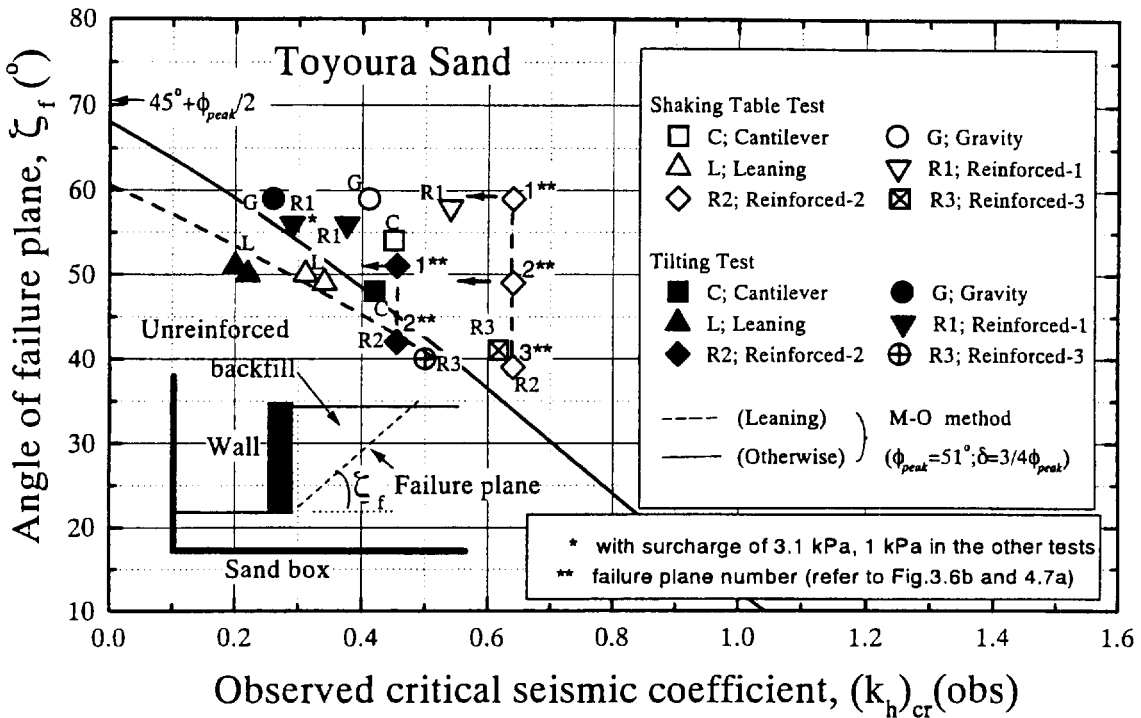


Fig. 4.8 Relationships between angle of failure plane and seismic coefficient at ultimate failure obtained from tilting and shaking table tests of model RWs (Koseki et al., 1997).

M-O method using  $\phi_{peak}$  of the backfill equal to  $51^\circ$  are shown. This  $\phi_{peak}$  value was determined based on results from PSC tests of the air-pluviated Toyoura sand used for the model tests prepared at the same density ( $e = 0.644$  to  $0.654$ ) as the model tests, performed at low confining pressure ( $= 9.8 \text{ kPa}$ ) with the  $\sigma_1$  direction being vertical. The frictional angle  $\delta$  at the interface between the wall back face and the backfill was assumed equal to  $3/4 \phi_{peak}$  ( $= 38^\circ$ ). The ratio of  $3/4$  is equal to the ratio of the angle of friction  $\phi_{SS} = \arctan(\tau/\sigma)_{max}$  on the horizontal failure plane from simple shear tests to the angle of friction  $\phi_{psc} = \arcsin\{(\sigma_1 - \sigma_3)/(\sigma_1 + \sigma_3)\}_{max}$  from PSC tests having the vertical  $\sigma_1$  direction, both obtained for air-pluviated Toyoura sand (Tatsuoka et al., 1991). The broken curve is for the leaning type RW having an inclined back face and the solid curve is for the other conventional type RWs having a vertical back face and the GRS-RWs (except for Reinforced type 2).

The following trends of behaviour can be observed from Fig. 4.8:

- a) In the tilting tests, the observed relationship between  $\zeta_f$  and  $(k_h)_{cr}(obs)$  is generally close to the respective theoretical relationship, irrespective of RW type. It was observed that the increase in  $k_h$  which could be made after the active failure plane started developing until the ultimate failure of RW was generally small,

in particular with the leaning type RW.

- b) For each type of RW, the failure plane angle  $\zeta_f$  is generally similar between the tilting and shaking table tests, while the  $(k_h)_{cr}(obs)$  value is larger in the shaking table test than in the tilting test. The difference depends on RW type, generally larger with the GRS-RWs than the three conventional types of RWs. Furthermore, it was observed that in the shaking table tests, the  $k_h$  value could be increased from the value where the active failure plane started developing without the ultimate failure of RW to a much larger extent than in the respective tilting test, in particular with the GRS-RWs. Therefore, in the shaking table tests on these GRS-RW models, there is no clear correlation between the failure plane angle  $\zeta_f$  and the  $(k_h)_{cr}(obs)$  value. This result indicates that in the shaking table tests, the failure plane angle  $\zeta_f$  is not totally controlled by  $(k_h)_{critical}$  and the difference in the  $\zeta_f$  value between the observation and the original M-O method should be explained by dynamic effects, as discussed later.

#### 4.4 Cyclic changes in earth pressure under dynamic loading conditions

**Dynamic earth pressure with an elastic backfill:** Only the simplest RW configuration illustrated in Fig. 4.9 will herein be discussed. The seismic earth pressure

coefficient  $K_{seismic}$  is defined as "the total earth pressure  $P''/(\gamma \cdot H^2/2)$ ". In general terms, the seismic earth pressure at a given moment is obtained from the equilibrium between the following two quantities;

- a) the earth pressure (in terms of coefficient  $K_{seismic}$ ) acting on the back face of RW, which is a function of wall displacement  $u$ , being affected by seismic loads; the lateral seismic coefficient  $k_h$  is assumed to be uniformly distributed in the backfill and its positive sign is defined for the inertia force acting towards the RW; and
- b) the resistance against the earth pressure (in terms of  $K_{seismic}$ ) of the RW supported by the subsoil, which is a function of  $u$ , being affected by the inertia force of the RW caused by the seismic coefficient  $(k_h)_w$ ;  $(k_h)_w$  may be different from  $k_h$  for the backfill.

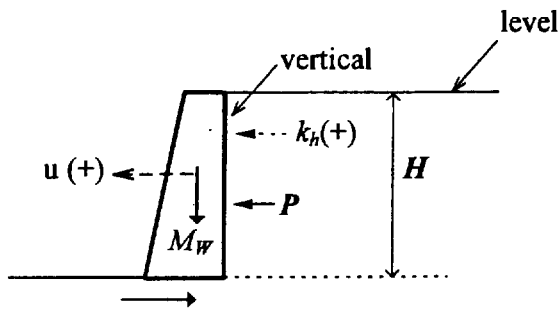


Fig. 4.9 Simple RW configuration.

Suppose that the backfill soil is a linear-elastic medium, and a rigid RW is supported linear-elastically with the subsoil (Fig. 4.10a). Suppose further that;

- a) the relationship between " $K_{seismic}$  as the load applied to the RW" and  $u$  is linear with a negative slope  $\alpha$  under static conditions or under a certain seismic condition with a constant  $k_h$ , and at a given  $u$ , the value of  $K_{seismic}$  increases proportionally with  $k_h$ ; and
- b) the relationship between " $K_{seismic}$  as the resistance of the wall" and  $u$  is also linear with a positive slope  $\beta$  under static conditions or under a certain seismic loading condition with a constant  $(k_h)_w$ , and at a given  $u$ , the value of  $K_{seismic}$  decreases proportionally with  $(k_h)_w$ .

Equilibrium state is obtained at the intersect of the two relationships for given values of  $k_h$  and  $(k_h)_w$ , such as point S under the static condition and point A at a seismic condition, Fig. 4.10a. With the values of  $k_h$  and  $(k_h)_w$  cyclically changing proportionally to each other and ignoring any phase difference between them, a linear relationship between  $K_{seismic}$  and  $u$  at equilibrium is then obtained, such as ASB in Fig. 4.10a. Similar relationships under different conditions are obtained as schematically shown in Fig. 4.10b. The slope  $\theta$  of the relationship is controlled by the values of  $\alpha$ ,  $\beta$  and the wall mass  $M_w$  among others. That is, the rate of increase in the seismic earth pressure with the increase in  $k_h$  and

$(k_h)_w$  (i.e., with the increase in  $u$ ) becomes larger, or the positive slope  $\theta$  becomes larger, as;

- a) the backfill becomes softer; i.e., the absolute value of negative  $\alpha$  decreases;
- b) the subsoil becomes stiffer and the RW becomes more rigid; i.e., the slope  $\beta$  increases; and
- c) the wall mass  $M_w$  decreases.

In this case, the active seismic earth pressure is the largest value during each cycle of dynamic loading. On the other hand, the rate of increase in the seismic earth pressure with the increase in  $k_h$  and  $(k_h)_w$  (i.e., with the increase in  $u$ ) becomes smaller, or the positive slope  $\theta$  becomes smaller, as;

- a) the backfill becomes more rigid ; i.e., the absolute of negative value of  $\alpha$  increases;
- b) the subsoil becomes softer and the RW becomes more flexible; i.e., the slope  $\beta$  decreases; and
- c) the wall mass  $M_w$  increases.

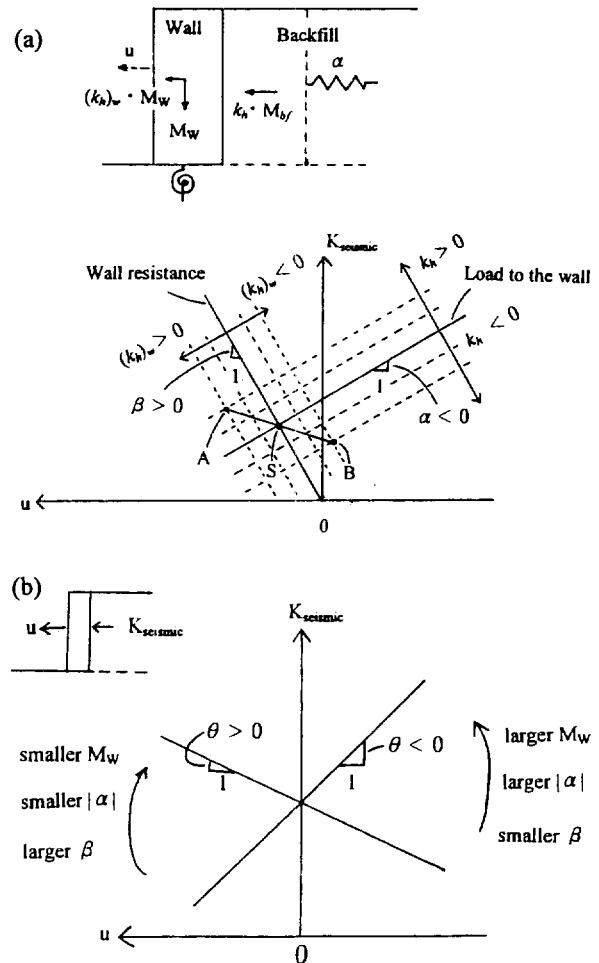


Fig. 4.10 Schematic figures showing the relationships between the dynamic earth pressure coefficient  $K_{seismic}$  and the wall displacement  $u$  with the elastic backfill and subsoil as a) the load and resistance; and b) that at the equilibrium.

In extreme cases, with the increase in  $k_h$  and  $(k_h)_w$  (i.e., with the increase in  $u$ ), the seismic earth pressure decreases, or the value of  $\theta$  becomes negative.

**Cyclic plane strain tests:** Actual backfill soil and subsoil are not linear elastic. Typical hysteretic relationships between “earth pressure  $\sigma_a = \sigma_h$ ” and “lateral strain  $\varepsilon_a = \varepsilon_h$ ” obtained from a cyclic plane strain test on isotropically consolidated Toyoura sand are presented in Fig. 4.11 (n.b., this behaviour is close to that of a  $K_0$  consolidated specimen under otherwise the same conditions, and see Fig. 4.2a for the specimen configuration). The results from two monotonic loading PSC and PSE tests are also plotted in Fig. 4.11 for comparison. The relationship after reversing the loading direction from a given stress state can be inferred from this result, which is essential information when interpreting the cyclically changing earth pressure acting in the backfill in shaking table tests.

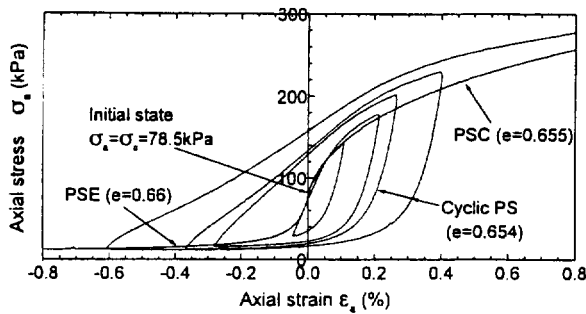


Fig. 4.11 Relationships between the axial stress  $\sigma_a$  and the axial strain  $\varepsilon_a$  from cyclic active and passive plane strain tests on Toyoura sand (Yamada et al., 1996).

**Dynamic earth pressure in backfill:**

Based on those shown in Fig. 4.10b and referring to the  $\sigma_h$  and  $\varepsilon_h$  relationships shown in Fig. 4.11, the relationship between  $K_{seismic}$  and  $u$  in one loading cycle when the RW reaction is still linear elastic can be inferred as below. When the wall mass  $M_w$  is relatively small and the wall resistance ( $\beta$ ) is relatively large, such a relationship as shown in Fig. 4.12a may result;

- a) With the increase in  $k_h$  from the static equilibrium state (point 1),  $K_{seismic}$  changes to a value at the seismic active earth pressure state (point 2). Under the pre-peak condition (i.e., before the active failure in the backfill), the rate of increase in  $K_{seismic}$  is decelerated by the effects of increasing  $\phi_{mob}$  with  $u$ , and  $K_{seismic}$  exhibits a relatively small change between points 1 and 2. Under the post-peak condition, on the other hand, the rate of increase in  $K_{seismic}$  is accelerated by the effects of decreasing  $\phi_{mob}$  with  $u$ , and  $K_{seismic}$  exhibits a larger increase. At the residual condition, where  $\phi_{mob}$  is independent of  $u$ ,  $K_{seismic}$  increases due solely to the increase in  $k_h$ .

- b) With the decrease in  $k_h$  from point 2,  $K_{seismic}$  changes to a value at the seismic passive earth pressure state (point 3), but the change may be small due to a decrease in the earth pressure caused by the decrease in  $k_h$ .
- c) With the increase in  $k_h$  from point 3,  $K_{seismic}$  first decreases as the earth pressure decreases at a high rate with the increase in  $u$  under the passive earth condition (see Fig. 4.11). Then,  $K_{seismic}$  exhibits a relatively small change due to an increase in the earth pressure caused by the increase in  $k_h$ .

On the other hand, when the wall mass  $M_w$  is relatively large and the wall resistance ( $\beta$ ) is relatively small, another relationship may be obtained (Fig. 4.12b);

- a) With the increase in  $k_h$  from point 1,  $K_{seismic}$  changes to a value at the seismic active earth pressure state (point 2), but the rate of increase is smaller than it is in the case illustrated in Fig. 4.12a.
- b) With the decrease in  $k_h$  from point 2,  $K_{seismic}$  first decreases or does not change largely due to dominant

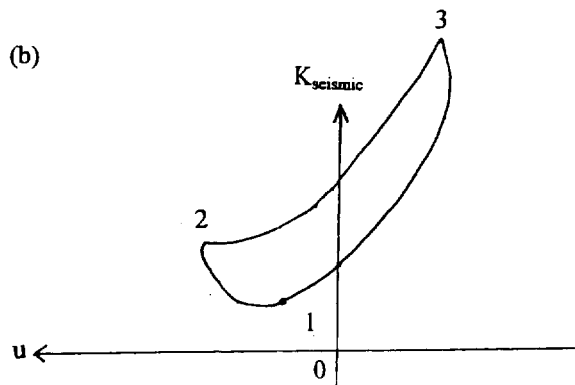
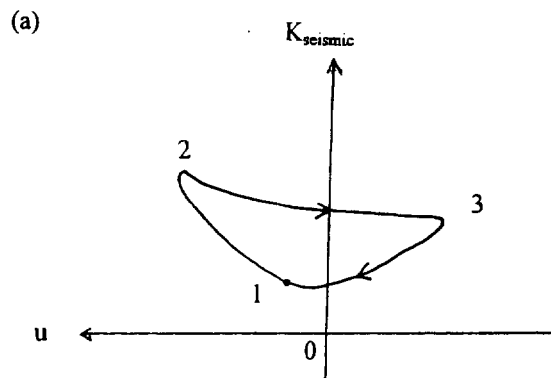


Fig. 4.12 Schematic diagrams showing the relationships between the dynamic earth pressure coefficient  $K_{seismic}$  and the wall displacement  $u$  at the dynamic equilibrium; a) when the wall mass  $M_w$  is relatively small and the subsoil resistance is relatively large; and b) when the wall mass  $M_w$  is relatively large and the subsoil resistance is relatively small.

effects of decreasing  $k_h$ , but soon increases at an increasing rate of increase to the seismic passive earth pressure value (point 3) as the effects of decreasing  $u$  on the increase in  $K_{seismic}$  under the passive earth condition becomes larger than those of decreasing  $k_h$  on the decrease in  $K_{seismic}$ .

- c) With the increase in  $k_h$  from point 3,  $K_{seismic}$  first decreases at a very large rate under the passive earth condition, accelerated by large outward inertia of the wall, and then increases at a smaller rate under the active earth condition.

The above consideration suggests that the peak active earth pressure is not necessarily the largest earth pressure in each cycle; even two peaks may appear in one cycle.

Matsuo et al. (1997) measured the earth pressures acting near the back face of the facing and the back face of the geogrid-reinforced Toyoura sand backfill in a shaking table test on a 140 cm-high GRS-RW model (EH3 and EH4 in

Fig. 4.13a). As seen from Fig. 4.13b, the earth pressure EH4 has two peaks in each cycle of shaking. The relationship between the earth pressure EH4 and the table acceleration in a representative cycle is shown in Fig. 4.13c; the numbers 1 to 3 attached to the relationship correspond to those shown in Fig. 4.13b. The largest earth pressure is attained at point 3 at the passive state where the facing is moving inwards and the wall never collapses. The second largest peak, much smaller than the largest one, is attained at point 2 at the active state with the facing moving outwards. The ultimate collapse of the wall may be caused by this type of active earth pressure. The pseudo-static stability analysis for RWs deals with this

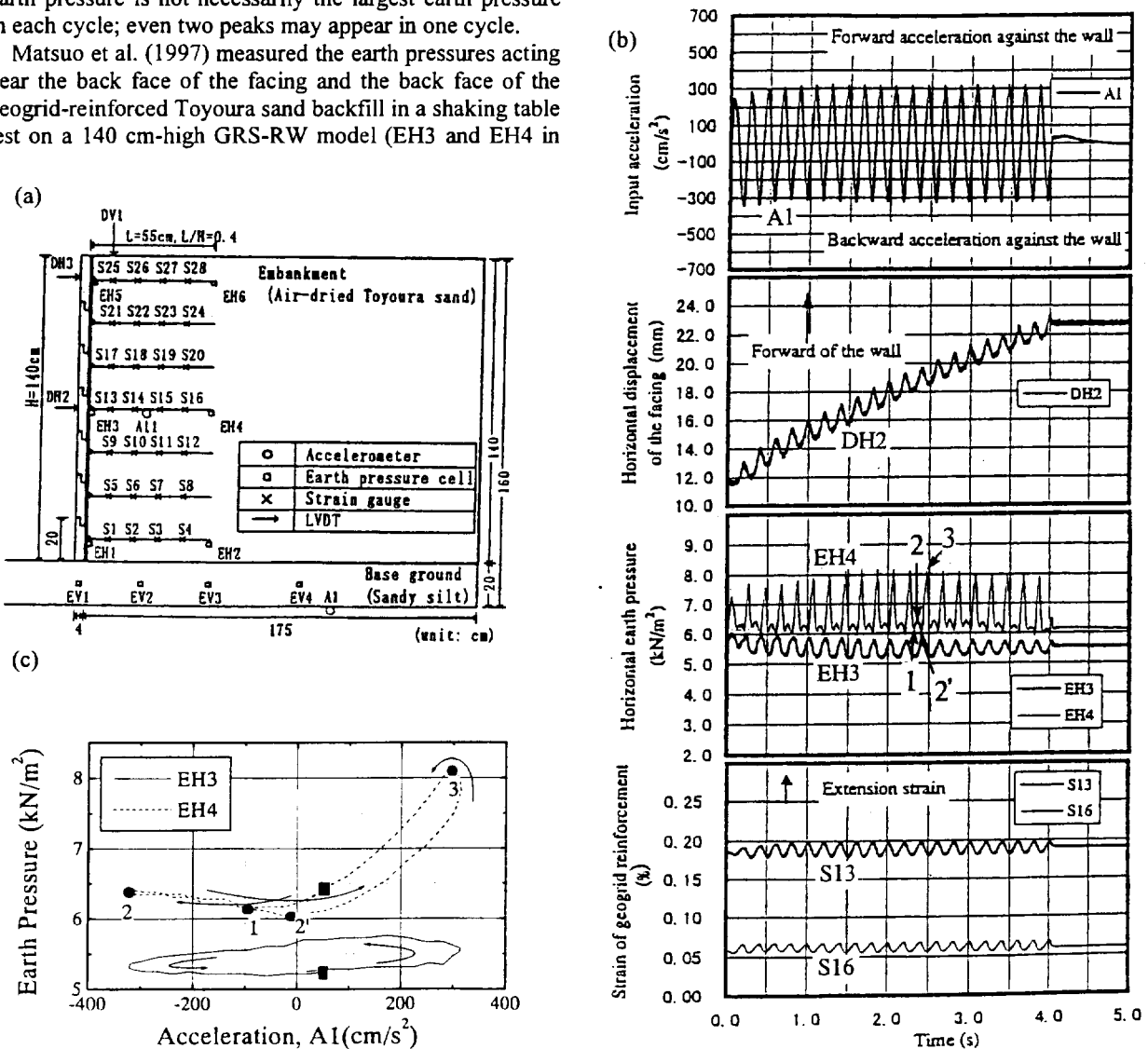


Fig. 4.13 Shaking table tests of GRS-RW model by Matsuo et al. (1997); a) test configuration for case 3; b) time histories at input acceleration of 320 gal; and c) representative hysteretic relationships between the earth pressure and the table acceleration. (A1: input acceleration; EH3 and EH4: earth pressures acting on the facing wall and the back of the reinforced soil; DH2: horizontal displacement; S13 and S16: tensile strain close to the free end and the connected end of the middle-height reinforcement.)

active earth pressure. This result shows that we should be very careful when interpreting earth pressure data from shaking table tests. In some previous cases, it seems that the largest earth pressure in one cycle was incorrectly considered as the dynamic active earth pressure.

The seismic earth pressure acting on the back face of the reinforced zone (EH4) is of the type illustrated in Fig. 4.12b for the case where the wall mass  $M_w$  is relatively large and the wall resistance is relatively low (low  $\beta$ ). These features result from the large mass and flexibility of the massive reinforced backfill zone in the model test.

On the other hand, the earth pressure EH3 shows a very small change in each cycle, having one peak at a moment when the state was changing from passive to active (see Fig. 4.13c). It seems that due to a smaller value of  $\beta$ , despite a smaller value of  $M_w$  of the facing, the behaviour of EH3 became somehow different from the type illustrated in Figs. 4.12a.

There is a noticeable time lag between the moments of peak earth pressure in EH3 and EH4. This phase lag in the reinforced zone helps in increasing the seismic stability of a reinforced soil RW (i.e., part of the dynamic effects). That is, the reinforced and unreinforced zones did not act as a rigid body, and therefore, as seen from Fig. 4.13b, the active earth pressure acting on the facing could be effectively resisted by tensile forces acting in the reinforcement layers. Fukuda et al. (1994) took advantage of this feature in the seismic stability analysis of a GRS-RW (see Fig. 3.8).

## 5. MODIFIED PSEUDO-STATIC APPROACH FOR HIGH SEISMIC LOADS

### 5.1 Seismic active failure process in unreinforced backfill

The progressive process of the seismic active failure in the backfill followed by the ultimate failure of RW discussed in Chapter 4 could be summarized as shown in Fig. 5.1;

1) Stage 1: The initial static equilibrium state I is attained, controlled by many factors such as those indicated in Fig. 4.10a and other construction details such as compaction procedure of backfill. We assume that the state I is attained before reaching the active failure state A in the backfill.

2) Stage 2: With an increase in  $k_h$  from zero to  $(k_h)_A$ , the backfill is subjected to the process of strain hardening, approaching the active failure state A in the backfill with the minimum earth pressure (i.e., the seismic active earth pressure). The angle  $\zeta_f$  of the failure plane that develops by the active failure is equal to " $45^\circ + \phi_{peak}/2 - \Delta\zeta$ ", where the fraction  $\Delta\zeta$  increases with the increase in  $(k_h)_A$ , while it is equal to zero when  $(k_h)_A = 0.0$ .

3) Stage 3: With a further increase in  $k_h$  from  $(k_h)_A$  to  $(k_h)_R$ , the backfill is subjected to strain softening associated with shear banding, approaching the residual earth pressure state R. As discussed before, only a very small wall displacement increment  $\Delta u$  is needed to reach the residual state. The  $\phi_{mob}$  values in the zones outside the shear band also decrease from  $\phi_{peak}$  to some values, but it is by elastic rebound. The possible maximum value of  $\phi_{mob}$  outside the shear band is still  $\phi_{peak}$ . So, unless the seismic active earth pressure arising from the second new failure plane having  $\phi_{peak}$  becomes larger than the earth pressure arising from the first failure plane with  $\phi_{residual}$ , the second failure plane does not develop and the earth pressure is controlled by the first failure plane (see Fig. 5.2).

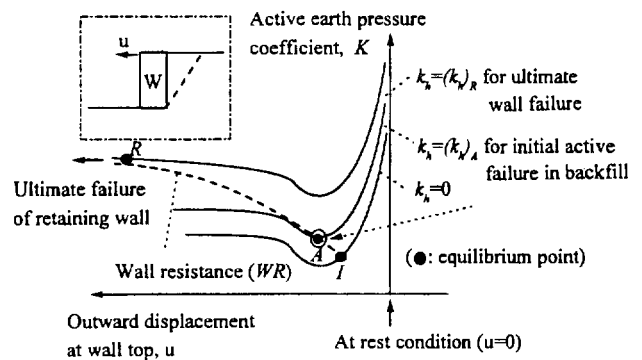


Fig. 5.1 Progressive process of mobilization of active earth pressure.

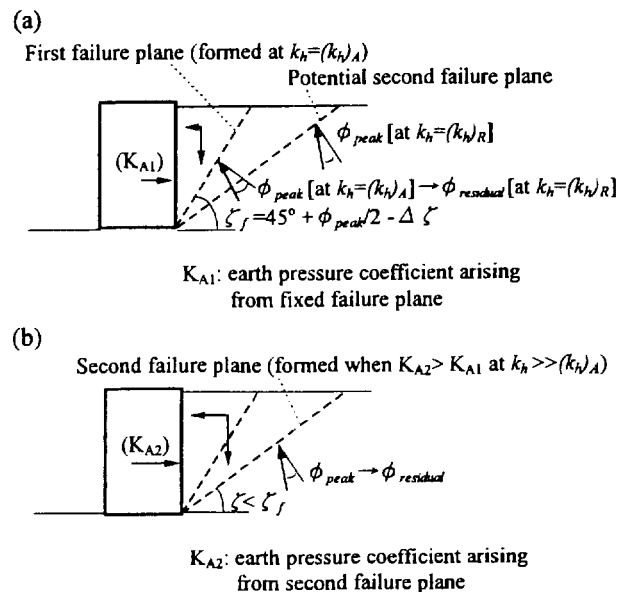


Fig. 5.2 Formation of failure planes considered in the modified method

### 5.2 Modified M-O method for unreinforced backfill (Koseki et al., 1997)

Usually, only a very small wall displacement  $u$  is needed for the active failure to take place in the backfill (about  $0.002 - 0.003 \cdot H$ ). Based on this fact, it is assumed in the modified method that except for the case of a rigid RW structure supported by perfectly rigid subsoil, the seismic active failure occurs in the backfill well before the seismic ultimate failure of the RW. In the conventional pseudo-static approaches including the original M-O method, the direction of failure plane is a function of  $k_h$  for which seismic earth pressure is to be obtained with  $\phi_{peak}$  mobilized along the failure plane. Unlike the above, it is assumed that the failure plane is fixed to the first-developed active failure plane, which is basically independent of  $k_h$ , and both  $\phi_{peak}$  and  $\phi_{residual}$  are used in the analysis. As a result, the fixed failure plane angle  $\zeta_f$  is generally smaller than the one predicted by the original M-O method, the difference decreasing with the increase in  $k_h = (k_h)_A$  at which the active failure plane first develops in the backfill.

Then, the very cumbersome procedure needed in the original M-O method to obtain the maximum earth pressure becomes unnecessary. In the modified method, the value of  $(K_A)_{seismic}$  is obtained by a very simple equation;

$$(K_A)_{seismic} = \left\{ \frac{\tan(\zeta_f - \phi_{residual}) + \tan \theta}{\cos(\zeta_f - \phi_{residual} - \delta)} \right\} \cdot \left\{ \frac{\tan \zeta_f}{\cos(\zeta_f - \phi_{residual} - \delta)} \right\} \quad (5.1)$$

where  $\zeta_f = 45^\circ + \phi_{peak}/2 - \Delta \zeta$ ;  
 $\delta$  = the wall friction angle; and  
 $\tan \theta = k_h$ .

Basically, the value of  $(k_h)_A$  should be determined by considering the deformability of RW system and other relevant factors, but it would not be simple. For practical purposes, the value of  $(k_h)_A$  and the corresponding failure plane angle  $\zeta_f$  may be obtained by the original M-O method using  $\phi_{peak}$ . Then, the value of  $\zeta_f$  decreases as the safety factor  $(F_s)_{static}$  for the static condition increases, since the first active failure occurs at a higher  $(k_h)_A$  as  $(F_s)_{static}$  increases.

Fig. 5.3 compares the relationships between  $(K_A)_{seismic}$  and  $k_h$  for a vertical frictionless RW with level backslope (without  $k_v$ ) obtained by the following three methods;

1. the original M-O method using  $\phi_{peak} = 50^\circ$ ;
2. the original M-O method using  $\phi_{residual} = 30^\circ$ ; and
3. the modified M-O method when  $(k_h)_A$  is equal to zero and 0.2.

In the modified M-O method, as long as using a fixed value of  $\zeta_f$  irrespective of  $k_h$ , the value of  $(K_A)_{seismic}$

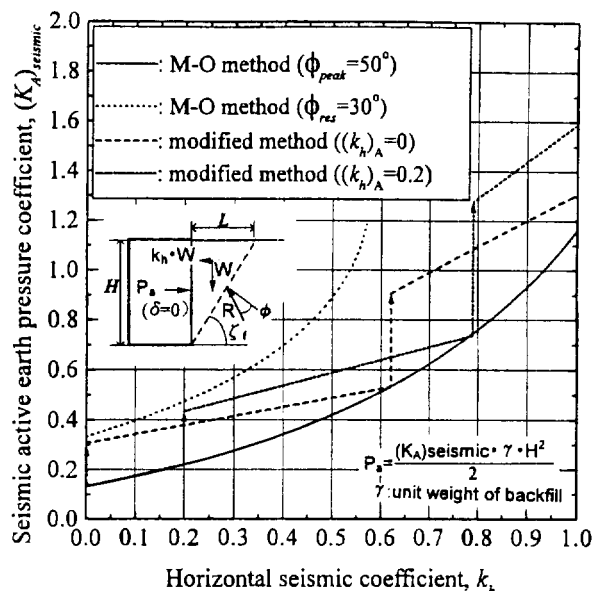


Fig. 5.3 Comparison of active earth pressure coefficient between the original and modified M-O methods for  $\phi_{peak} = 50^\circ$ ,  $\phi_{res} = 30^\circ$  and  $\delta = 0^\circ$  (Koseki et al., 1997a).

increases linearly with the increase in  $k_h$ . When the  $k_h$  value becomes a certain value  $k_h^*$ , the value of  $(K_A)_{seismic}$  obtained by the modified M-O method becomes the same with the value obtained the original M-O method using  $\phi_{peak}$ . Then, at the  $k_h^*$  value, the second deeper active failure plane is considered to develop as shown in Fig. 5.2b. The values of  $(K_A)_{seismic}$  at  $k_h$  values higher than  $k_h^*$  should be obtained for the second fixed active failure plane, which becomes larger than the respective value obtained for the first active failure plane. For this reason, each relationship between  $(K_A)_{seismic}$  and  $k_h$  consists of linear segments with discontinuities at the values of  $k_h^*$ . In actuality, the transition from the first active failure plane to the second one (and so on) would be somehow smooth.

The value of  $(K_A)_{seismic}$  at a given  $k_h$  obtained by the modified M-O method is always equal to, or larger than, the value obtained by the original M-O method using  $\phi_{peak}$ , while always smaller than the value obtained by the original M-O method using  $\phi_{res}$ . Therefore, the value of  $(K_A)_{seismic}$  by the modified M-O method does not become very large even at relatively high values of  $k_h$  where the values of  $(K_A)_{seismic}$  by the original M-O method using  $\phi_{res}$  become very large, or even infinite, or not possible to obtain.

Fig. 5.4 shows the relationships between the size of active failure zone, represented by  $L/H = \cot \zeta_f$ , and  $k_h$ , where  $L$  is the size of the failure zone on the crest of

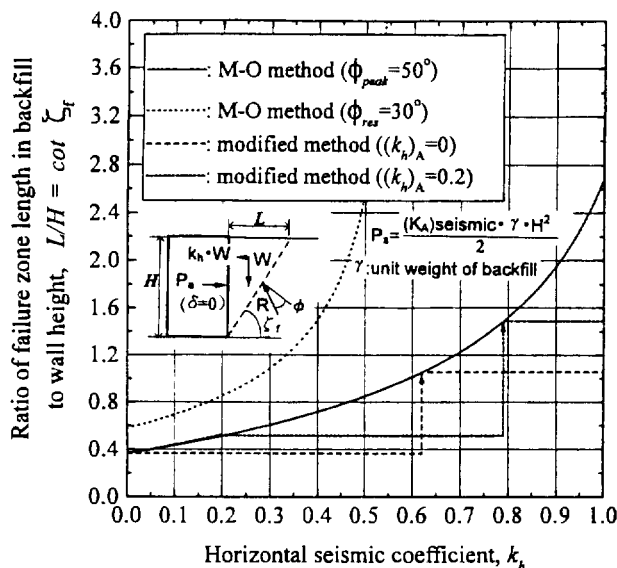


Fig. 5.4 Comparison of the ratio of failure zone length in backfill soil to wall height between the original and modified M-O methods for  $\phi_{peak} = 50^\circ$ ,  $\phi_{res} = 30^\circ$  and  $\delta = 0^\circ$  (Koseki et al., 1997a).

backfill, obtained by the above-mentioned three methods. The size of the active failure zone in the backfill by the modified M-O method is always equal to or smaller than those by the original M-O method using  $\phi_{peak}$  and always considerably smaller than those by the original M-O method using  $\phi_{res}$ . The failure zone size by the original M-O method becomes very deep and long at very high values of  $k_h$ , particularly when using  $\phi_{res}$ , and therefore, the relevant evaluation of the seismic stability of GRS-RWs having short reinforcement becomes very difficult. By the modified M-O method, on the other hand, realistic smaller and shallower failure planes, as observed in the Hyogo-ken-nambu Earthquake (see Fig. 2.6) and in the model tests (Fig. 4.7), are obtained.

As the modified M-O method uses both  $\phi_{peak}$  and  $\phi_{res}$ , it can take into account the effects of initial density of the backfill. On the other hand, in practice, their accurate evaluation would be not simple. In addition, in this method, the seismic active earth pressure is a function of  $(F_s)_{static}$ , which makes this method somewhat more complicated.

### 5.3 Modified two-wedge method for reinforced backfill

A modified two-wedge (TW) method is introduced below, in which the failure mechanism is represented by two wedges as in the conventional TW method to better simulate the seismic active failure in reinforced soil RWs,

particularly those of GRS-RWs having relatively short reinforcement. In the same way as the modified M-O method, the failure plane is basically not  $k_h$ -dependent; the first set of active failure planes with  $\phi_{peak}$  develops at  $(k_h)_A$ , and the seismic earth pressures at  $k_h$  higher than  $(k_h)_A$  are controlled by this first set of active failure plane with  $\phi_{res}$  until the seismic earth pressure controlled by the second set of failure plane with  $\phi_{peak}$  becomes larger.

The seismic active earth pressure coefficient  $(K_A)_{seismic}$  (for the earth pressure acting on the back face of FHR facing) was evaluated by the conventional TW method using either  $\phi_{peak} (= 45^\circ)$  or  $\phi_{res} (= 30^\circ)$  and the modified TW method using both  $\phi_{peak}$  and  $\phi_{res}$  for a typical configuration of GRS-RW (Fig. 5.5a), which was examined by Horii et al. (1994). The values of  $\phi$  used in the three analysis methods are shown in Fig. 5.5b. Fig. 5.5c compares  $(K_A)_{seismic}$  values when the safety factor for either overturning or sliding failure becomes the minimum. In this case, the first set of active failure plane is assumed to develop at  $(k_h)_A = 0.2$ . Note that this  $(k_h)_A$  value was selected rather arbitrarily. Similar to those shown in Fig. 5.3, the modified method yields reasonable earth pressure, which is between those obtained by the conventional TW method using  $\phi_{peak}$  and  $\phi_{res}$ . According to the modified TW method, even the use of short reinforcement layers can increase substantially the seismic stability of GRS-RW at high  $k_h$  values. This feature results from the intersection of many short reinforcement layers with the potential failure planes (Fig. 5.5a).

Fig. 5.5a compares the failure planes evaluated by the different methods when  $k_h = 0.5$ , in which those for unreinforced backfill obtained by the original M-O method using  $\phi_{peak}$  or  $\phi_{res}$  are also shown for comparison. It may be seen that those for the reinforced wall evaluated by the conventional TW method using  $\phi_{peak}$  and  $\phi_{res}$  are similar to the respective one obtained for unreinforced backfill by the original M-O method using  $\phi_{res}$ . On the other hand, the failure zone evaluated by the modified TW method is much smaller, being largely modified by the effects of reinforcement, despite that the reinforcement is generally short. Fig. 5.5d compares the size of the failure zone, where  $L'$  is the total length of the two wedges on the backfill crest. It may be seen that the failure zone evaluated by the modified TW method is considerably smaller, but more realistic, than those obtained by the conventional TW method.



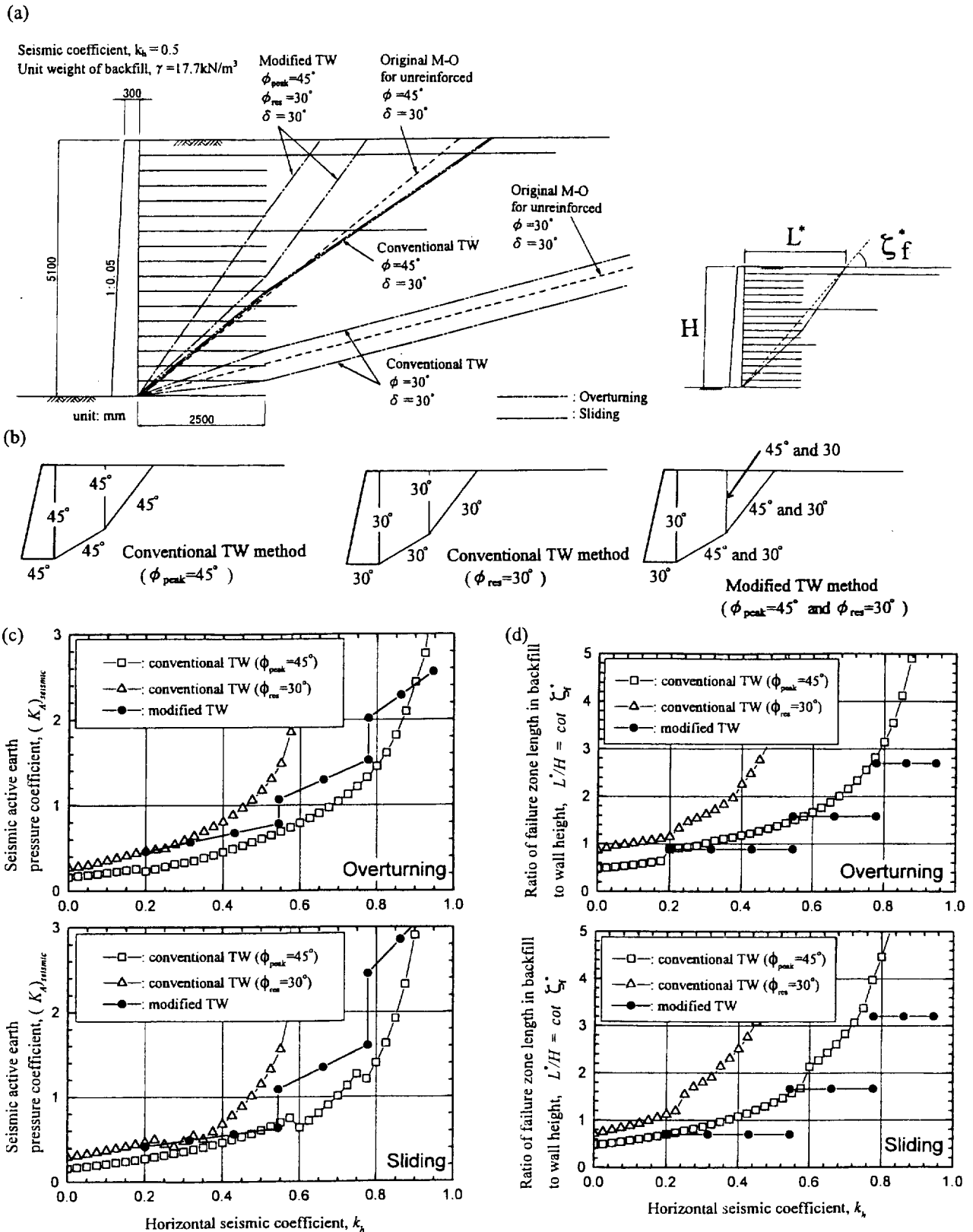


Fig. 5.5 Comparison between the conventional and modified TW methods for  $(k_h)_A = 0.2$ ; a) wall configurations with critical failure planes; b) values of  $\phi$  used in the analysis (the dimensions are not to scale); c) the coefficient  $(K_A)_{\text{seismic}}$  of active earth pressure acting on the facing; and d) ratio of failure zone length in backfill soil to wall height.

Table 5.1 Influencing factors included in different analysis and model testing methods.

		Failure plane for ultimate failure of RW				Dynamic force						
		Location		Shape		Amplification	Non-uniform seismic force	Phase lag in the backfill	Cyclic loading effects	Randomness of cyclic loads	Inclusion of vertical component	
		$k_h$ -dependent with a constant $\phi$	Fixed with $\phi_{res}$	Straight	Compound							
Analysis	M-O for unreinforced backfill	Original	Yes for any $k_h$	No	Yes	No	No	No	No	No	No	Possible
		Modified	Yes for the first failure	Yes	Yes	No	No	No	No	No	No	Possible
	Two-wedge for reinforced backfill	Conventional	Yes for any $k_h$	No	Yes	Yes	No	No	No	No	No	Possible
		Modified	Yes for the first failure	Yes	Yes	Yes	No	No	No	No	No	Possible
Model tests	Tilting tests		Perhaps yes for the first failure	Perhaps yes	Yes	Yes	No	No	No	No	No	No
	Shaking table tests	Uniform waves	Perhaps yes for the first failure	Perhaps yes	Yes	Yes	Yes	Yes	Yes	Yes	No	Possible
		Irregular waves	Perhaps yes for the first failure	Perhaps yes	Yes	Yes	Yes	Yes	Yes	Yes	Yes	Possible
	Actual seismic loads		Perhaps yes for the first failure	Perhaps yes	Yes	Yes	Yes	Yes	Yes	Yes	Yes	Yes

Note: "Yes" does not mean that the behaviour is exactly the same with that in each specific seismic event.

#### 5.4 Discussions on the modified pseudo-static approach

Among a number of the influencing factors for the seismic behaviour of GRS-RWs, Table 5.1 summarized the three major influencing factors; a) failure plane; b) soil strength; and c) dynamic force. It may be noted from Table 5.1 how better or poorly each analysis or model test method can simulate the actual seismic behaviour of GRS-RW. Shaking table tests using random loads could be better than those using uniform cyclic loads, and the latter could be better than pseudo-static analyses and tilting tests. It should be noted, however, that even 'yes' in this table does not necessarily mean that that particular analysis or model test method can simulate satisfactorily that factor involved in the actual behaviour of each specific GRS-RW subjected to specific seismic loads. The use in design of very sophisticated numerical analyses and model tests can be justified when nearly all the influencing factors are properly and sufficiently considered. In other words, simplified pseudo-static approaches could be still a useful engineering tool if they can reflect as better as possible the actual behaviour (such as the failure mode) and they use proper design soil strength values and seismic loads in a balanced way while taking into account the dynamic effects on the RW behaviour.

The modified TW method proposed above to evaluate seismic earth pressure in reinforced soil RWs cannot

simulate many dynamic aspects involved in the actual seismic behaviour of GRS-RWs. In particular, it is the case when it is assumed that  $k_h$  is uniformly distributed in the backfill without amplification and phase difference. Yet, the modified TW method can simulate the failure mode and earth pressure in the reinforced backfill subjected to high  $k_h$  values much better than the conventional TW method, particularly that using conservative soil strength. Similarly, the modified M-O method is more suitable for unreinforced backfill than the original M-O method.

At present, the field cases and the model tests which have been presented in this report have not been analyzed by the modified pseudo-static approach proposed above. This study is now being under way, and the results will be reported by the authors in the near future.

## 6. ULTIMATE FAILURE OF GRS-RWs

### 6.1 Ultimate failure observed in the field and model tests

Before considering a relevant aseismic design method for GRS-RWs to survive high seismic loads, observed ultimate failure of GRS-RWs will be reviewed.

Fig. 6.1 shows the relationships between the observed seismic coefficient  $(k_h)_{cr}(obs)$  and the calculated values

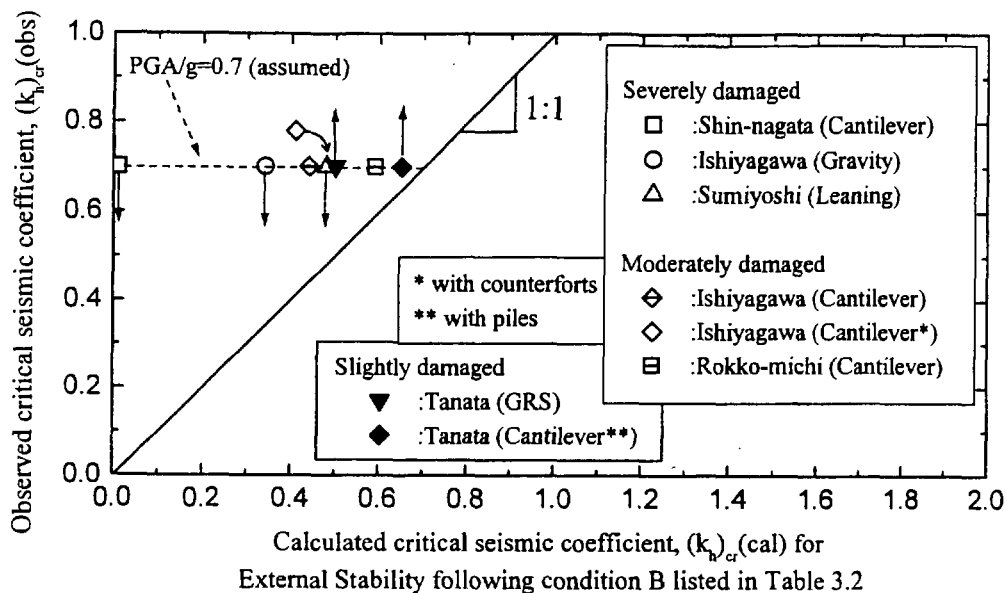


Fig. 6.1 Comparison of observed critical seismic coefficients  $(k_h)_{cr}(obs)$  to calculated values  $(k_h)_{cr}(cal)$  obtained following the conditions listed in Table 3.2 for RWs that experienced extra-ordinary high seismic loads during the 1995 Kobe Earthquake (Koseki et al., 1997).

$(k_h)_{cr}(cal)$  obtained by following the condition B shown in Table 3.2 (see also Table 3.3). Each  $(k_h)_{cr}(obs)$  value was plotted against a common PGA/g value, which was assumed to be equal to 0.7 and the same for these RWs. The upward arrows mean that the RWs were slightly damaged, thus the actual  $(k_h)_{cr}(obs)$  values for ultimate failure should be larger than the PGA/g value. The data points without arrows mean that the RWs were moderately damaged (albeit some deformation and displacement occurred), while the downward arrows mean that the RWs totally collapsed, implying that the actual  $(k_h)_{cr}(obs)$  values should be smaller than the PGA/g value. This result suggests that the ratios  $(k_h)_{cr}(obs)/(k_h)_{cr}(cal)$  is not the same among these RWs, which is likely to be larger in the order of; 1) the GRS-RW having a FHR facing at Tanata; 2) the cantilever RC RWs at Rokko-michi and Ishiyagawa; and 3) the gravity-type RWs at Ishiyagawa and the leaning-type RW at Sumiyoshi (particular the latter) (n.b., the cantilever RC RW at Tanata is not discussed herein, because this is not a usual case; the RW was supported by a temporary cofferdam in front of the wall at the time of the earthquake). This result suggests that the design value  $(k_h)_{design}$  should be different among different types of RW; under otherwise the same conditions, the value of  $(k_h)_{design}$  could be smaller for the GRS-RW.

As the amount of the field data is not sufficient, the data from the tilting and shaking table model tests, described in Figs. 4.6, 4.7 and 4.8, were analyzed. As the failure mode observed in all the tests was overturning, the results were first analyzed for this failure mode. Fig. 6.2a shows relationships between the critical seismic coefficients  $(k_h)_{cr}(cal)$  yielding a safety factor of unity against overturning obtained by the original M-O method and the

conventional TW method (Horie et al., 1994) and the observed seismic coefficients  $(k_h)_{cr}(obs)$ . For the pseudo-static analyses,  $\phi_{peak} = 51^\circ$  was used, obtained from PSC tests at  $\delta = 90^\circ$  at low confining pressures using the backfill of air-dried Toyoura sand. The wall friction angle  $\delta$  at the interface between the rough back face of the wall and the backfill was set  $3/4 \phi (= 38^\circ)$ . For the cantilever type RW, the angle of friction was set equal to  $\phi_{peak}$  along the vertical failure plane starting from the heel of the base part of the RW. For the GRS-RWs, the bearing capacity was evaluated for the facing base having a width of 3 cm, ignoring the surcharge effects of the backfill. The allowable vertical load at the facing base was set to the bearing capacity as obtained above, then the limit equilibrium for overturning was sought. As seen from Fig. 6.2a, for many of the data points, from the tilting tests,  $(k_h)_{cr}(obs)$  is much smaller than  $(k_h)_{cr}(cal)$ . This is likely due to;

- a) the effects of progressive active failure in the backfill were not considered by using  $\phi_{peak} = 51^\circ$ ; and
- b) the overturning failure could have been triggered by bearing capacity failure in the subsoil, which should have taken place before the safety factor for overturning failure obtained not considering the bearing capacity failure became unity. This infer is supported by the measured earth pressure on the base of the model.

Fig. 6.2b shows relationships between whichever the smaller value of  $(k_h)_{cr}(cal)$  yielding a safety factor of unity, against either overturning or bearing capacity failure, obtained by the original M-O method and the conventional TW method using  $\phi_{peak}$  and the observed seismic

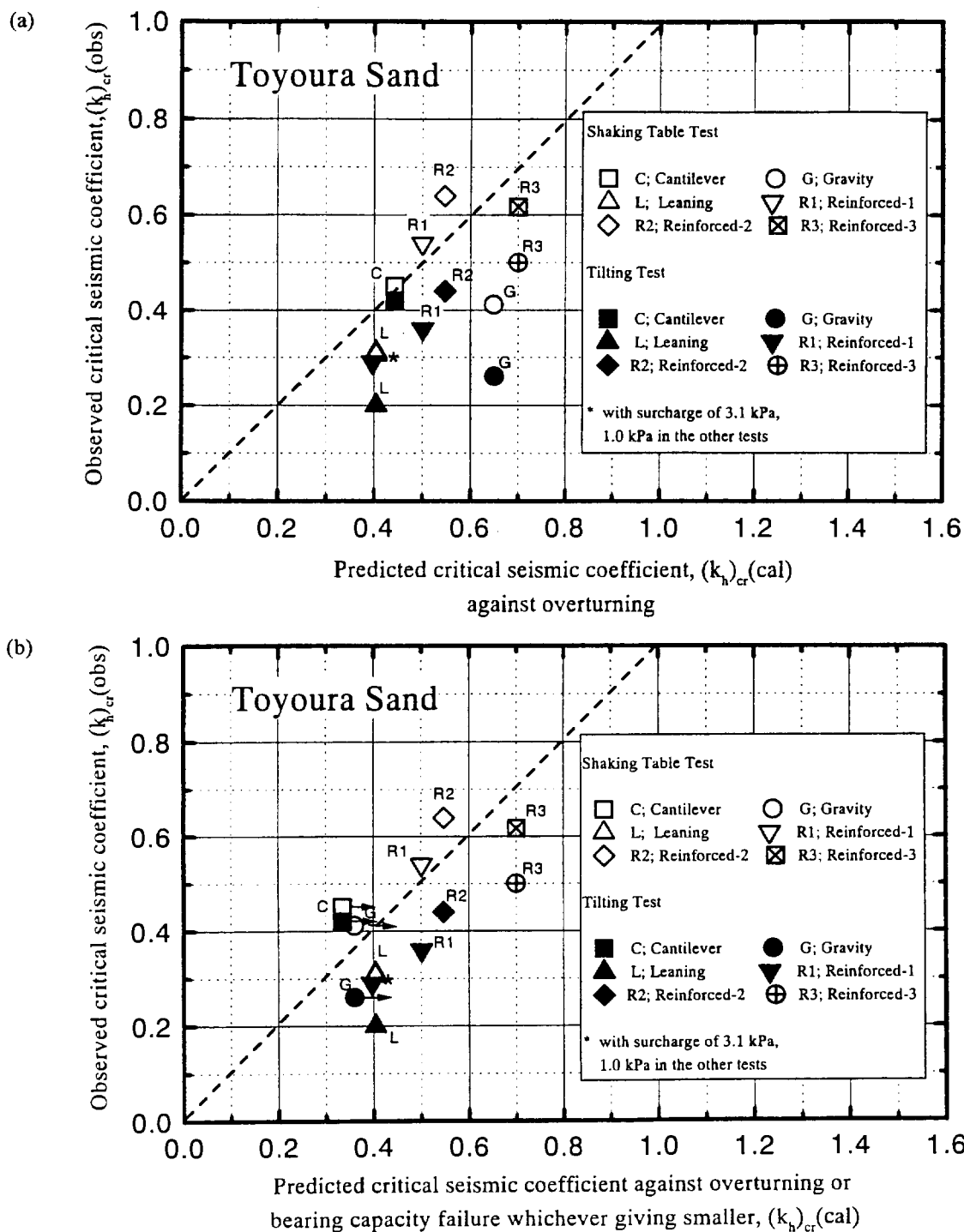


Fig. 6.2 Comparison of observed critical seismic coefficients  $(k_h)_{cr}(\text{obs})$  with predicted values  $(k_h)_{cr}(\text{cal})$  from tilting and shaking table tests of model RWs (Koseki et al., 1997).

coefficients  $(k_h)_{cr}(\text{obs})$ . For the GRS-RWs, the bearing capacity at the facing base has been taken into account for the data shown in Figs.6.2a and 6.2b. In so doing, the ultimate failure of RW due to the bearing capacity failure

has not been considered, since the wall can maintain its stability even when the load acting at the bottom of the facing reaches the bearing capacity of the subsoil, as demonstrated by a large-scale shaking test on a model of

GRS-RW (Murata et al., 1994). Lower  $(k_h)_{cr}(cal)$  values were obtained for bearing capacity failure with the cantilever and gravity-type RWs. The bearing capacity was evaluated assuming the subsoil thickness be sufficient to cause boundary-free subsoil failure despite that the actual thickness of the Toyoura sand layer was only 20 cm. Therefore, the safety factors against bearing capacity failure may have been somehow under-estimated. In Fig. 6.3b, this infer is indicated by arrows directing right shown next the data points for the cantilever and gravity-type RWs. The following trends may be seen from Fig. 6.2b:

1) The base width is the same, equal to 23 cm, among the gravity-type and cantilever RWs and the GRS-RW type 1 (see Fig. 4.7). The base width is 18 cm with the leaning-type RW, whereas the width between the top of the back face and the toe of the base is wider, equal to 33 cm. Despite the above, in the tilting tests, the GRS-RW type 1 and the cantilever RW have larger values of  $(k_h)_{cr}(obs)$  than the leaning-type and gravity-type RWs. In the shaking table tests, the GRS-RW type 1 is noticeably more stable than the others. This results are in a broad sense consistent with the full-scale field behaviour as shown in Fig. 6.1, suggesting a relatively high seismic stability of GRS-RWs having a FHR facing.

2) In the tilting tests, the ratio  $(k_h)_{cr}(obs)/(k_h)_{cr}(cal)$  is generally lower than unity (except for the cantilever RW). This result suggests that the conventional pseudo-static approaches using peak plane strain soil strength obtained when the  $\sigma_1$  direction is normal to the bedding plane direction over-estimate the stability of RW.

3) In the shaking table tests; the ratios  $(k_h)_{cr}(obs)/(k_h)_{cr}(cal)$  are generally larger than unity, except for the leaning type RW, and different among the different RWs. This fact corresponds to; a) the observation in Fig 4.8 that in the shaking table tests, at the same  $(k_h)_{cr}$ , the failure plane angles  $\zeta_f$  observed in the unreinforced backfill are generally larger than those predicted by the original M-O method using  $\phi_{peak}$ ; and b) that in the shaking table tests, the ultimate failure of RW took place at  $k_h$  noticeably larger than the value where the active failure started in the backfill, and the difference depended on the RW type. The difference can be considered to be due to the dynamic effects. It is to be noted that  $(k_h)_{cr}(cal)$  values that are smaller than those shown in Fig. 6.2a are obtained when evaluated by the modified pseudo-static methods proposed in this report, giving larger ratios  $(k_h)_{cr}(obs)/(k_h)_{cr}(cal)$ . In that case, larger dynamic effects are evaluated.

4) In the shaking table test results, the ratios  $(k_h)_{cr}(obs)/(k_h)_{cr}(cal)$  (shown in Fig. 6.2b) for the GRS-RW type 1 is similar to that for the cantilever RW, marginally larger than that for the gravity-type RW, and noticeably larger than that for the leaning-type RW. This trend is similar to that of the difference at a given  $(k_h)_{cr}(obs)$  value

between the measured value of  $\zeta_f$  and that predicted by the original M-O method using  $\phi_{peak}$  (shown in Fig. 4.8). The shaking table test results shown in Fig. 6.2 are, in a broad sense, consistent with the field full-scale behaviour of several representative types of RW which experienced extra-ordinary high seismic loads during the Hyogo-ken-nambu Earthquake (see Fig. 6.1). These results also suggest that the design values  $(k_h)_{design}$  to be used in the pseudo-static analysis should be different, being smaller in the order of i) GRS-RWs having a FHR facing, ii) RC RWs, and iii) leaning and gravity-type RWs.

5) In the shaking table tests, the value of  $(k_h)_{cr}(obs)$  is largest for the GRS-RW type 2 having a couple of long reinforcement layers at high levels in the backfill. As seen from Fig. 4.7a, in this model, multiple failure planes developed; the one numbered 1, which was steepest, developed first from the heel of the backfill zone reinforced with short reinforcement layers and stopped somewhere below the lowest longer reinforcement layers: then, the other two numbered 2 and 3 developed, which were inclined much more horizontally, and developed up to the crest of the backfill. On the other hand, the value of  $(k_h)_{cr}(obs)$  is marginally smaller for the GRS-RW type 3 having the moderately long same-length reinforcement layers than Reinforced type 2, while the total amount of reinforcement was similar. When reconstructing existing slopes to vertical GRS-RWs, the use of relatively short reinforcements is preferred, because the amount of slope excavation can be minimized. Based on the test result described above, using several long reinforcement layers at high levels as the model Reinforced type 2 can be recommended to effectively increase the seismic stability of GRS-RWs having a FHR facing, compared with the GRS-RW type 1.

6) In the shaking table tests, after the first active failure occurred in the backfill, the  $k_h$  value could increase to a higher level until the ultimate failure of RW took place, exhibiting larger positive net dynamic effects, in the order i), ii) and iii) listed in the term 4). It seems that the modified M-O method and the modified TW method are more relevant for aseismic design of RWs exhibiting larger positive net dynamic effects when subjected to high seismic loads.

## 6.2 Dynamic effects

Different ratios of "design  $k_h$ "/(PGA/g) have been proposed for different types of foundation structures and RWs, which include the following:

1) By comparing the seismic behaviour of port and harbor gravity-type caissons placed on underwater mounds with their  $k_h$  values calculated following the design specification, Noda et al. (1975) obtained the following relationship;

$$(k_h)_{critical} = \text{PGA/g} \quad (\text{PGA} \leq 200 \text{ gals}) \quad (6.1a)$$

$$(k_b)_{critical} = (1/3)(PGA/g)^{1/3} \quad (PGA \geq 200 \text{ gals}) \quad (6.1b)$$

When following this relationship,  $(k_b)_{critical} = 0.2, 0.246, 0.281, 0.309$  and  $0.333$  are obtained when  $PGA/g = 0.2, 0.4, 0.6, 0.8$  and  $1.0$ .

- 2) Seed and Whitman (1970) proposed a value of 0.85 for retaining walls and bridge abutments against significant wall displacements.
- 3) The design manual guidelines for Terre Armee RWs of FHWA (FHWA 1990) employs the following relationship to evaluate the maximum wall acceleration coefficient  $\alpha_m$  based on the maximum ground acceleration coefficient  $\alpha_0$ ;

$$\alpha_m = (1.45 - \alpha_0) \alpha_0 \quad (6.2)$$

Note that the horizontal inertia force of the reinforced backfill is reduced by half to consider the effects of phase lag as mentioned in 3. When following this relationship,  $(k_b)_{critical} = 0.25, 0.42, 0.51, 0.52$  and  $0.45$  are obtained when  $PGA/g = 0.2, 0.4, 0.6, 0.8$  and  $1.0$ .

These ratios  $(k_b)_{critical}/(PGA/g)$  are much lower than unity at high  $k_b$  values, which is seemingly due largely to the following three factors;

- a) underestimation of the soil strength used in evaluating the seismic stability of structure in terms of  $k_b$  to be compared with  $PGA/g$  (as in ordinary design procedures);
- b) simplifications in the design procedure leading to a safe side result such as that the passive pressure on the front face of the underground part of RW is ignored (but this could actually largely contribute to the seismic stability of actual RWs); and
- c) factors related to the so-called dynamic effects.

As seen from Figs. 4.8 and 6.2b, for the relatively

ductile RWs (i.e., the GRS-RWs), the value of  $(k_b)_{cr}(obs)$  is larger than the corresponding value in the tilting test. This feature is likely due to that the net dynamic effects were positive. The following factors are important for the so-called dynamic effects on the seismic behaviour of RWs;

- 1) dynamic ductility of RW, which is the capability of the RW to survive “accelerations/g” exceeding the pseudo-static ultimate strength  $(k_b)_{critical}$  by deforming without exhibiting seismic ultimate failure; this factor makes the structure more stable;
- 2) flexibility (or rigidity) of RW, resulting into the following three sub-factors;
  - a) phase difference in the lateral direction in the backfill, which usually increases with the RW flexibility, making also the RW more stable;
  - b) the coefficient  $\beta$  in Fig. Fig. 4.10a; for example, cantilever RC RWs, particularly those supported pile foundations, are rigid having a high value of  $\beta$ , resulting into higher seismic active pressure, while GRS-RWs are flexible having a low value of  $\beta$ , resulting into lower seismic active pressure; and
  - c) dynamic response of the structure, usually giving larger accelerations in the backfill than at the ground surface; this factor makes the RW less stable.

Related to the above factors 2a, 2b and 2c, in any shaking table test, the response acceleration, or dynamic amplification, is not uniform in both vertical and lateral directions, as typically seen from Fig. 6.3.

The difference in the  $(k_b)_{critical}$  value between shaking table and tilting tests using the same model should become

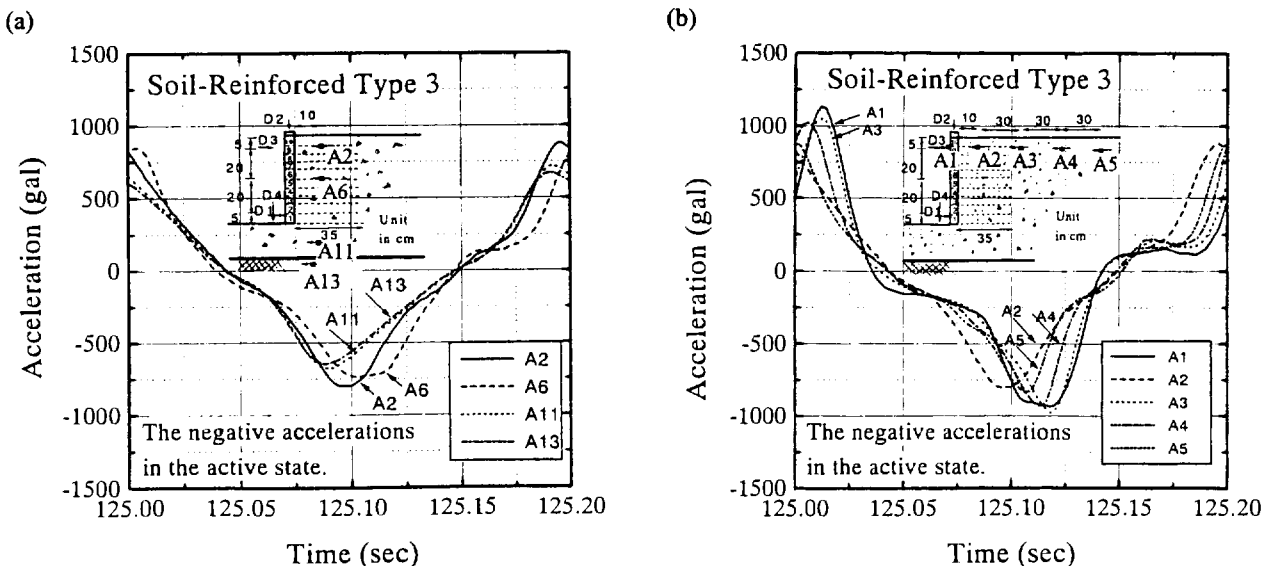


Fig. 6.3 Typical shaking table test of GRS-RW model (“Reinforced type 3”) performed by the authors; a) comparison of response horizontal accelerations in the vertical (A2, A6, A11 and A13); and b) lateral (A1 to A5) directions, at input acceleration of about 600 gal.

larger when the shaking table test uses random cyclic loads with the value of  $(k_h)_{critical}$  being defined as "the maximum table horizontal acceleration"/g at ultimate failure. For example, in the shaking table tests on the same type GRS-RW model having a discrete panel facing reported by Matsuo et al. (1997), the model wall failed by excessive outward deformation at a peak acceleration equal to 464 gals when the N-S component recorded at the Kobe Maritime Observatory during the 1995 Hyogo-ken-nambu Earthquake was used as the input random loads and at a single amplitude acceleration equal to 370 gals when twenty uniform sinusoidal waves were used as the input cyclic loads.

By using the cumulative damage theory, Murata et al. (1990) estimated the deformation of the GRS-RW having a FHR facing when subjected to a random cyclic loading based on the behaviour of the wall when subjected to uniform cyclic loadings at different acceleration levels. The procedure is similar to the one used for estimating the liquefaction strength of saturated sand when subjected to random seismic cyclic stresses based on the results obtained when subjected to uniform cyclic stresses (e.g., Tatsuoka et al., 1986). It was suggested by Murata et al. (1990) that for a given maximum input acceleration, the deformation of the model wall becomes much smaller when subjected to an irregular input motion than when subjected to a uniform motion, and the difference becomes larger as the number of cycles in the uniform motion increases, as the irregular motion becomes of more shock-type and as the RW becomes more dynamically ductile (i.e., factor 1 above).

### 6.3 Design $k_h$ values

The design value of  $k_h$ ,  $(k_h)_{design}$ , to be used in any pseudo-static analysis should reflect the fact that effects of the influencing factors, as listed in Table 6.1, are not perfectly, or are only poorly, reflected in the analysis. Therefore, the proper ratio of  $(k_h)_{design}$  to the PGA/g of the design seismic load should depend on, at least, the following six factors;

- 1) the analysis method (e.g., the original M-O method and the conventional TW method using either peak or residual soil strength, or the modified M-O method and modified TW method using both peak and residual soil strengths);
- 2) the ratio of the design soil strength to the true operating soil strength;
- 3) positive effects of simplification used in the design (e.g., no consideration of passive pressure on the front face of the underground part of facing);
- 4) the seismic ductility of RW, which depends on structure type (e.g., masonry, gravity, leaning, cantilever, or reinforced soil);- this factor is linked to the objective of aseismic design, which is different for Levels 1 and 2 seismic loads, as discussed before;

- 5) the seismic flexibility or rigidity of RW, which also depends on structure type and affects the dynamic response of RW; and
- 6) the global safety factor used in the aseismic design, which is usually 1.5 for RWs in Japan.

In the following, only design methods for Level 2 design seismic loads will be considered. Fig. 3.9 shows the values of  $(k_h)_{cr}(cal)$  giving the safety factor equal to unity for several RWs which experienced extra-high seismic loads during the 1995 Hyogo-ken-nambu Earthquake. These  $(k_h)_{cr}(cal)$  values were obtained by the conventional pseudo-static analyses (i.e., the original M-O method for the conventional type RWs and the conventional TW method for the GRS-RW) under the following two different conditions (see Table 3.3);

- A) the conventional design conditions using conservative soil strength (condition A; Table 3.1); and
- B) the conditions as close as the respective actual condition, while using peak soil strength (condition B; Table 3.2).

For all the data points, the estimated value of PGA/g is assumed to be 0.6 - 0.8 with an average of 0.7. As discussed before, to attain reasonable seismic stability, with a global safety factor equal to unity, the design value  $(k_h)_{design}$  should be larger than the value of  $(k_h)_{cr}(cal)$  for the collapsed types of RW, could be similar to the values of  $(k_h)_{cr}(cal)$  for the moderately damaged but uncollapsed types of RW, and could be smaller than the values of  $(k_h)_{cr}(cal)$  for the slightly damaged types of RW (note; for the cantilever RC RW at Tanata, this notion is valid only under the condition of the presence of the coffer dam in front of the wall, but it is not usual case and will not be discussed herein).

The following remarks are important:

- a) When based on the conventional pseudo-static analyses (i.e., the original M-O method for the conventional types of RW and the conventional TW method for GRS-RWs, both using conservative soil strength), the value of  $(k_h)_{cr}(cal)$  was 0.10 for bearing capacity failure leading to overturning failure with the gravity type unreinforced concrete RW at Ishiyagawa and 0.09 for overturning failure with the leaning type unreinforced concrete RW at Sumiyoshi, both of which totally collapsed. These results suggest that for masonry RWs and leaning and gravity types unreinforced concrete RWs, even when based on the conventional pseudo-static analyses using conservative soil strength, the use of  $k_h$  equal to 0.1 - 0.2 is unconservative for Level 2 design seismic load. Obviously, the design value  $(k_h)_{design}$  should be increased to a level much higher than 0.1 - 0.2, whereas it would be lower than, but a large fraction of, PGA/g of Level 2 seismic load (about 0.7- 0.8).
- b) When based on the conventional pseudo-static analyses using peak soil strength, the value of  $(k_h)_{cr}(cal)$  was 0.34

with the gravity type RW at Ishiyagawa and 0.48 for overturning failure with the leaning type RW at Sumiyoshi. Therefore, the use of  $(k_h)_{design} = 0.1 - 0.2$  in the conventional pseudo-static analyses using peak soil strength is more unconservative than the current design method using conservative soil strength and therefore never be acceptable.

c) It is to be noted again that these values of  $(k_h)_{cr}(cal)$  were back-calculated with an operating safety factor equal to unity. On the other hand, the allowable safety factor employed in the current aseismic design in Japan is typically 1.5. Part of the fraction 1.5 is considered to be assigned to uncertainties of load, and a lower allowance for uncertainties in the load is acceptable considering that the Level 2 seismic load is nearly the possible upper-bound design seismic load. Then, the suitable design value  $(k_h)_{design}$  can be set to be, say, 0.9 times the value of  $(k_h)_{cr}(cal)$  by which a given type of RW is moderately damaged but does not collapse with an operating safety factor equal to unity.

d) For the cantilever RC RWs, which were moderately damaged, when based on the conventional pseudo-static analyses using conservative soil strength, the values of  $(k_h)_{cr}(cal)$  was 0.36 and 0.40 for bearing capacity failure with the two cantilever RC RWs at Ishiyagawa and 0.45 for bearing capacity failure with the cantilever RC RW at Rokko-michi. This result suggests that the use of  $(k_h)_{design} = 0.1 - 0.2$  in the conventional pseudo-static analyses using conservative soil strength is also unconservative. However, the appropriate design value  $(k_h)_{design}$  should be smaller than that for masonry RWs and leaning type and gravity type unreinforced concrete RWs. A value between  $0.35 \times 0.9 \cong 0.3$  and  $0.45 \times 0.9 \cong 0.4$  would be appropriate. Perhaps, this value is appropriate also for modern RC RWs supported by a pile foundation.

e) For the cantilever RC RWs, when based on the  $(k_h)_{cr}(ob)$  values = 0.45 - 0.60 that were obtained by using peak soil strength, a value of  $(k_h)_{design}$  is around  $(0.45 - 0.60) \times 0.9 \cong 0.5$  would be appropriate.

f) For the Tanata GRS-RWs having a FHR facing, which was damaged only slightly, when based on the conventional pseudo-static analyses using conservative soil strength, the values of  $(k_h)_{cr}(cal)$  was 0.36 for base sliding. It seems that the use of  $(k_h)_{design}$  equal to 0.1 - 0.2 is unconservative, and a design value around  $0.35 \times 0.9 = 0.3$  or less would be appropriate. When based on peak soil strength, a value of  $(k_h)_{design}$  which is around  $0.5 \times 0.9 = 0.45$  would be appropriate.

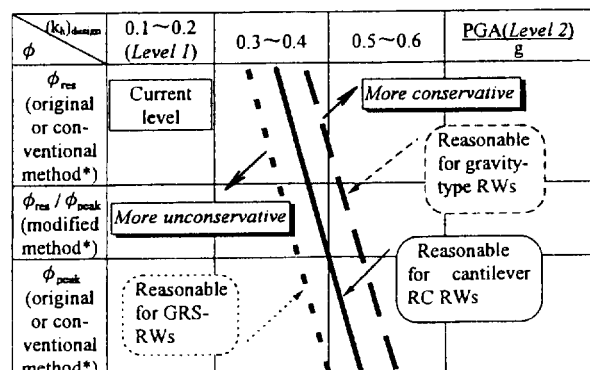
g) Summarizing the above, when based on the conventional pseudo-static analyses using conservative soil strength,  $(k_h)_{design}$  equal to 0.4, 0.35 and 0.3 would be appropriate for, respectively, a) masonry RWs and leaning

type and gravity type RWs, b) properly designed and constructed RC cantilever RWs and c) GRS-RWs having a FHR facing. This proposed classification is supported by the shaking table model test results shown in Figs. 4.8 and 6.2b.

h) If the conventional pseudo-static analyses using peak soil strength is employed, the design value  $(k_h)_{design}$  should be larger than those shown above;  $(k_h)_{design} = 0.55, 0.50$  and 0.45 would be appropriate for, respectively, a) masonry, leaning type and gravity type RWs, b) properly designed and constructed RC cantilever RW and c) GRS-RWs having a FHR facing.

i) When based on the modified pseudo-static approach proposed in this report, the  $(k_h)_{design}$  value would become higher than those used with the conventional pseudo-static analyses using conservative soil strength, becoming closer to the Level 2 PGA/g value (about 0.7). Considering that the failure mechanism can be better simulated, the use of the modified pseudo-static approach can be suggested for the aseismic design of GRS-RWs, particularly those having a FHR facing with relatively short reinforcement.

Based on the above and others, Fig. 6.4 was prepared. The design values  $(k_h)_{design}$  which are tentatively proposed for Level 2 seismic loads, are indicated by the three inclined lines, which are respectively for a) GRS-RWs having a FHR facing; b) cantilever RC RWs; and c) masonry, gravity and leaning types of RWs. Along each line, the value of  $(k_h)_{design}$  becomes smaller in the order of; a) the original M-O method and the conventional TW method using conservative soil strength; b) the modified M-O method and TW method using both peak and conservative soil strengths; and c) the original M-O method and the conventional TW method using peak soil strength.



\* The M-O method or the two-wedge method, depending on the soil structure type.

Fig. 6.4 Interrelations between seismic load (in terms of  $k_h$  or PGA/g), analysis method, structure type and seismic behaviour for Level 2 design load (tentative proposal).



6.4 Other important issues

**Effects of reinforcement length:** As discussed before, in the shaking table model tests described in Figs. 4.8 and 6.2, the GRS-RW having relatively long reinforcement (Reinforced type 3) was more stable than the GRS-RW having relatively short reinforcement (Reinforced type 1). In addition, the failure acceleration of the GRS-RW increased from 530 gals to 650 gals for over-turning failure by extending only a couple of top reinforcement layers (i.e., Reinforced type 2). Also in the shaking table tests on 100 cm-high grid-reinforced sand RW models performed by Murata, et al. (1990, 1992)(Fig. 6.5), under otherwise the same conditions, the GRS-RW model having longer reinforcement (case 2) was more stable than that having shorter reinforcement (case 1). This increase in the stability was attained by preventing the active failure plane starting from the heel of the reinforced zone to develop up to the backfill crest.

These results suggest that a shear band or failure plane is difficult to develop crossing reinforcement. Therefore, it is not relevant to always assume a single wedge to develop in reinforced backfill as in the unreinforced backfill. In particular, when based on the original M-O method using conservative soil strength assuming a single wedge, a very deep and largely inclined failure plane is predicted at a high  $k_b$  (see Fig. 5.5a); in that case, only one or two layers of short reinforcement can intersect with this failure plane, which may result into a design using long reinforcement layers from the bottom level. The modified TW method can properly evaluate the relatively high seismic stability

of the GRS-RW having short reinforcement at lower levels in the backfill.

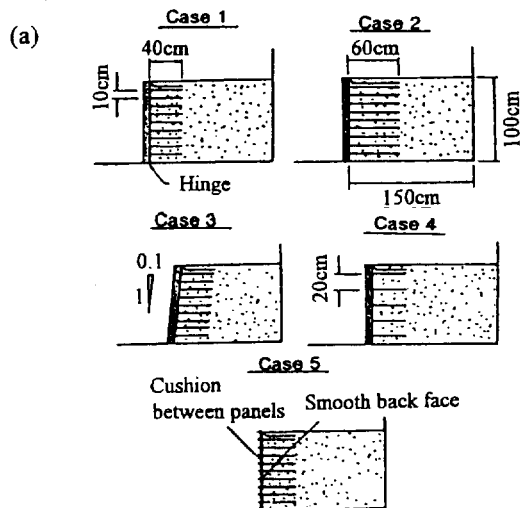
On the other hand, in the shaking table model tests on 100 cm-high models of vertical GRS-RWs having a discrete panel facing with reinforcement layers truncated to the same length performed by Matsuo et al. (1997) (see Fig. 4.13), the failure acceleration increased from 370 gals to 575 gals by increasing the length of reinforcement from  $L/H= 0.4$  to  $0.7$  under otherwise the same testing conditions. This test result is consistent with the shaking test results described above.

**Effects of facing rigidity:** The following trends of behaviour have been observed in the shaking table model tests of GRS-RWs with sand backfill (described so far in this report):

a) When the reinforcement was relatively short, such as  $L/H= 0.4$ , with a FHR facing, the predominant failure mode is overturning (Matsuo et al., 1997; Koseki et al., 1997).

b) In the tests on a 100 cm-high grid-reinforced sand model wall performed by Matsuo et al. (1997), under otherwise the same model configurations, when the facing was of discrete panels, the predominant failure mode was sliding with a failure plane passing inside the reinforced zone, resulting into a bulging deformation of the wall face.

c) In the tests by Matsuo et al. (1997), the effect of facing rigidity on the failure acceleration was small; the failure acceleration was 370 gals for a GRS-RW model having a discrete panel facing and 397 gals for a GRS-RW model having a FHR facing. It seems that this small difference



Case	Facing	NRL*	LR**	Slope of wall face	Note
1	One unit	10	40	Vertical	Standard
2	One unit	10	60	Vertical	Longer reinforcement
3	One unit	10	40	1:0.1(V:H)	Inclined facing
4	One unit	5	40	Vertical	Smaller NRL
5	Discrete	10	40	Vertical	Less rigid facing

\* NRL: Number of reinforcement layers.  
 \*\* LR: Length of reinforcement (in mm).

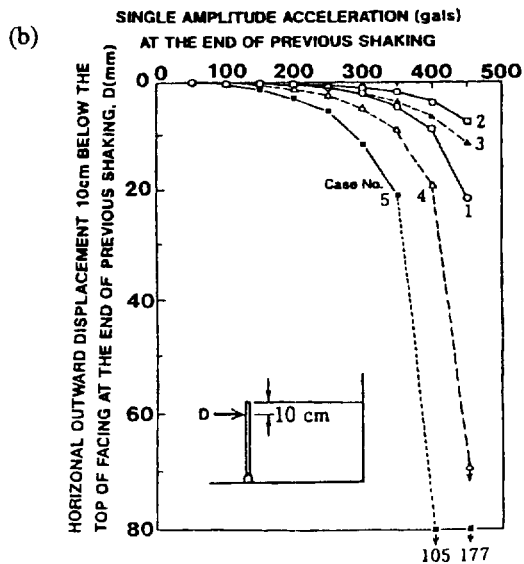


Fig. 6.5 Shaking table tests of GRS-RW models by Murata et al. (1992); a) test configuration; and b) relationships between table horizontal acceleration and outward displacement of wall.

resulted from that the stability of the GRS-RW having a FHR facing was relatively low. This was due likely to; a) relatively small pull-out resistance of the grid reinforcements resulting from; b) relatively short reinforcement length,  $L = 0.4H$ , with a relatively large vertical spacing  $S_v$  of reinforcement layers, 20 cm or  $S_v/H = 0.2$ ; and c) a low density of the backfill ( $D_r = 60\%$ ). On the other hand, in the shaking table tests presented in Fig.6.5, under otherwise the same conditions, the GRS-RW model having a FHR facing (case 1) was much more stable than that having a discrete panel facing (case 5), despite that the ratio of the reinforcement length to the wall height was  $L/H = 0.4$  as the tests by Matsuo et al. (1997). In these tests, the pull-out strength of grid was sufficiently large resulting from a small vertical grid spacing of 10 cm and a high density of the backfill ( $D_r = 94\%$ ). Similar positive effects of using a FHR facing has been observed in the model tests reported by Bathurst and Alfaro (1996), in which the pull-out resistance of geogrid was large enough. It is likely, therefore, that the effects of facing rigidity become more important as the pull-out strength of reinforcement becomes larger; a) by preventing the occurrence of sliding failure having a failure plane passing inside the reinforced zone and appearing at an intermediate height at the wall face; and b) by confining better the backfill adjacent to the facing.

**Effects of vertical acceleration (or  $k_v$ ):** Fig. 6.6 shows the plot of the combination of peak horizontal and vertical components of acceleration obtained from the time histories of acceleration recorded on the ground surface at Kobe Marine Meteorological Observation Station during the 1995 Hyogo-ken-nambu Earthquake. Table 6.2 shows the results of stability analysis of a typical GRS-RW having a FHR facing (see Fig. 2.2a) obtained by the conventional TW method using  $\phi = 41^\circ$  for the backfill. It may be seen that the safety factor for the worst combination with the largest ratio of the outward horizontal acceleration to the upward vertical acceleration along the envelop of the data points is lower by only 1 % than that obtained using only the peak horizontal acceleration. It can be concluded, therefore, that

differences in results between the pseudo-static analyses of reinforced soil structure having a cohesionless soil backfill with and without considering the effects of vertical seismic load components are usually very small. A similar conclusion has been obtained by Bathurst and Alfaro (1996). Therefore, when considering a high degree of uncertainty in other factors, it is not unreasonable not to use vertical component of seismic load in routine aseismic design of reinforced soil structures including GRS-RWs having a FHR facing.

**Evaluation of seismic ductility of RW:** This could be made in a very approximated way by the method introduced in Tatsuoka et al. (1996). In this method, the ductility is evaluated by the area between the curve showing the relationship between the safety factor  $F_t$  and the tilting angle of RW and the horizontal axis implying  $F_t = 0.0$ . However, the ductility could be better evaluated by estimating the deformation and displacement of RW by the method proposed by Newmark (1965) or its modifications, or the equivalent energy method described below, or the cumulative damage method.

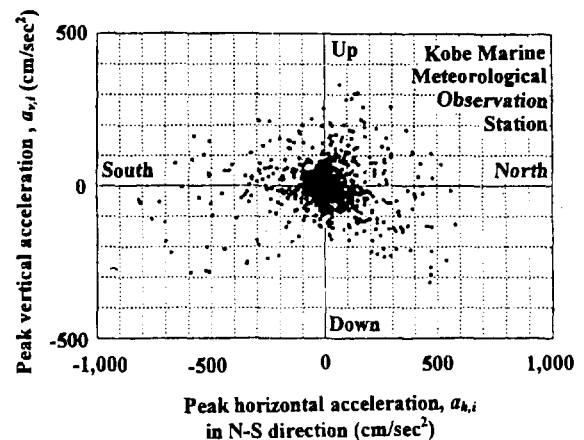


Fig. 6.6 Plot of the combination of horizontal and vertical components of acceleration obtained from the time histories of acceleration recorded on the ground surface at Kobe Marine Meteorological Observation Station during the 1995 Hyogo-ken-nambu Earthquake.

Table 6.2 Comparison of calculated critical seismic coefficients ( $k_h$ )<sub>cr</sub>(cal) following the conditions listed in Table 3.2 for GRS-RW at Tanata with or without considering the effects of vertical acceleration.

Calculated critical seismic coefficients ( $k_h$ ) <sub>cr</sub> (cal)	Neglecting effects of vertical acceleration	Considering north component as outward horizontal acceleration and corresponding vertical acceleration	Considering south component as outward horizontal acceleration and corresponding vertical acceleration
Overturning	0.597	0.591	0.626
Sliding	0.502	0.498	0.501

In the Newmark method, the displacement of a monolith during a seismic event is obtained as follows (Fig. 6.7):

1. The critical acceleration beyond which the monolith starts to slide is evaluated by a proper method such as pseudo-static analyses.
2. When the ground acceleration is in excess of the critical acceleration, the monolith is assumed to respond at a constant acceleration equal to the critical acceleration.
3. The residual displacement of the monolith relative to the ground is obtained by simply double-integrating difference between the accelerations of the monolith and the ground until the relative velocity of the monolith becomes zero upon the reversal of the ground acceleration direction.

Cai and Bathurst (1996a, b) and Ling et al. (1997) used this method to evaluate seismic residual lateral outward displacements of GRS-RW. On the other hand, only limited literature can be found on the method to evaluate the seismic overturning of retaining wall. Steedman and Zeng (1996) proposed a method to evaluate seismic rotation by rocking motion of large gravity walls placed on rigid foundations. Siddharthan et al. (1992) proposed a simple rigid plastic model for seismic tilting of rigid walls. Both methods consider both translation and tilting of the wall, and contact pressure on the bottom of the RW is evaluated by the method similar to the one used by the Japanese Railway Company (Haya et al., 1995 and RTRI, 1997). If the center of rotation of RW is assumed to be located near the toe of the wall, only a sliding mode of deformation is likely to occur, while when the center of rotation is located back the toe of the RW, a coupled (sliding and tilting) mode of displacement may result. It was also shown that the effects of the wall-soil friction angle  $\delta_1$  on the wall base be very large on the sliding displacement, while the effects of the wall-soil friction angle  $\delta_2$  on the wall back face be significant on the rotational displacement of the wall; a higher  $\delta_2$  results in a smaller rotational displacement.

The equivalent energy method (Fig. 6.8) has been proposed also by Newmark (1965) to estimate the seismic plastic deformation of a structure. Here,  $\tau_y$  and  $u_y$  are the yielding stress and displacement, and  $\tau_e$  and  $u_e$  are the elastic stress and displacement obtained without considering the effects of yielding. The total displacement  $u_m$ , which includes both the elastic and plastic components, is computed so that the elasto-plastic energy denoted by the total of the areas 1, 2 and 4 becomes equal to the elastic energy denoted by the total of the areas 1, 2 and 3. This method is popular in Seismic Structural Engineering to accommodate very high design seismic loads, such as Level 2, by allowing some plastic deformation of RC and steel structures. It is not certain whether this method is relevant also for soil structures, since they do not have an obvious yielding point. More

detailed discussion is beyond the scope of this short report.

**FEM analyses:** Even the failure of densely compacted unreinforced soil subjected to static loads is very difficult to be simulated by FEM, due mainly to the fact that proper simulation of strain localization into a shear band (or shear bands) and associated strain softening is an extremely complicated task (e.g., Tatsuoka et al., 1991). Complicated interaction between shear band deformation and reinforcement makes the failure analysis of reinforced soil more difficult (Kotake et al., 1997). Therefore, FEM analysis of the seismic failure of reinforced soil structure is still not a practical tool, and will not be discussed more.

**Rupture strength of reinforcement for seismic loads;** Recent laboratory deformation and strength tests on

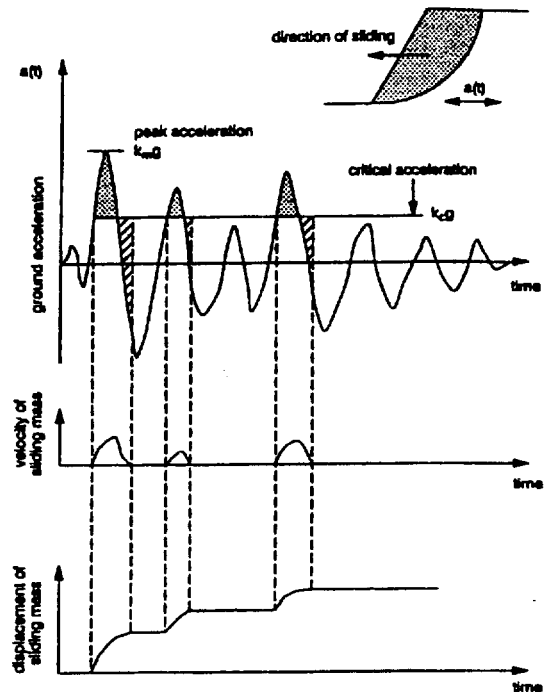


Fig. 6.7 Concept of Newmark's sliding block method (Cai and Bathurst, 1996a)

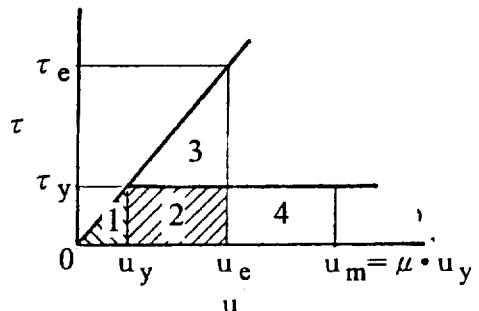


Fig. 6.8 Concept of equivalent energy method (Newmark, 1965)

geosynthetics showed that under the same strain rate, the strength after long-term creep is not smaller than that before creep (Bernardi and Paulson, 1997). This point is also discussed by Greenwood (1997). Therefore, no reduction factor is needed for the tensile strength of geosynthetic reinforcement to be used in seismic design compared with short-term design strength for static loads.

## 7. SUMMARY AND CONCLUSIONS

From the observations in the field, the model test results and the theoretical considerations summarized in this report, the following conclusions can be derived:

1. There exists a big gap between the design horizontal coefficients  $(k_h)_{design}$  used in the current pseudo-static aseismic design approaches for retaining walls (RWs) and the peak ground accelerations (PGA) divided by the gravitational acceleration ( $g$ ) experienced by a number of RWs during the 1995 Hyogo-ken-nambu Earthquake. This gap is due partly to; a) the use of conservative design soil strength; b) positive net dynamic effects that are not considered in the pseudo-static analyses; and c) the use of global safety factor larger than unity. At the same time, serious damage to a number of RWs during the earthquake shows that the current  $(k_h)_{design}$  values should be increased appropriately to avoid such damage.
2. In both the field behaviour and the laboratory model tests, for the same safety factor evaluated by the pseudo-static approach, the seismic stability of GRS-RW having a FHR facing was marginally higher than that of cantilever RC RWs not supported by a pile foundation, and noticeably higher than that of leaning and gravity-type RWs not supported by a pile foundation.
3. The observations in both the field and the laboratory revealed that large apparent inconsistencies exist in the size of failure zone between the conventional pseudo-static analyses and the actual observations.
4. In the laboratory static tilting model tests, irrespective of RW type, a failure plane or a set of failure planes developed in the backfill associated with the active failure in the backfill, followed by the ultimate failure or collapse of RW only at a slightly larger tilting angle. On the other hand, in the laboratory shaking table model tests, the ultimate failure or collapse of RW occurred at a later stage associated with relative large deformations and displacements of RW occurring after the first active failure plane developed in the backfill. The difference was due to positive net dynamic effects, which were different among the different types of RW. Yet, it is likely that the first developed active failure mechanism controlled the ultimate failure of the RW (except for the GRS-RW having several top or all long reinforcement layers). Therefore, similarly to the pseudo-static approaches, the static tilting tests are not appropriate to evaluate such seismic stability of RW as observed in the field and the shaking table tests.
5. The soil strength along the failure plane can drop very rapidly with very small shear deformation from the peak value to the residual value. It is very likely, therefore, that the peak strength along the failure plane has dropped to the residual value at the moment of the ultimate failure or collapse of RW.
6. Based on the above observations 1~5, a modified pseudo-static approach can be proposed to evaluate the dynamic active earth pressure acting on; a) the back face of RW with unreinforced backfill; and b) the back face of the full-height rigid facing of GRS-RW. The modified approach predicts smaller dynamic earth pressure and smaller failure zones in the backfill than those predicted by the conventional pseudo-static approaches using conservative soil strength, which is usually similar to the residual strength. According to the modified pseudo-static approach, the use of short reinforcement layers can increase largely the seismic stability of GRS-RW, particularly at high seismic loads. This estimation is consistent with the field and laboratory observations.
7. The design horizontal seismic coefficient  $(k_h)_{design}$  depends not only the PGA value of design seismic load, but also many other factors, among which; a) stability analysis method; b) design soil strength; c) simplification of wall configurations employed in the design; d) dynamic effects, among which the ductility and rigidity of RW and the frequency properties and randomness of seismic loads are important; and d) the global safety factor.
8. It is suggested that under otherwise the same conditions, the design value  $(k_h)_{design}$  for well-designed and constructed GRS-RW having a FHR facing could be marginally smaller than that for cantilever RWs and noticeably smaller than that for masonry RWs and leaning and gravity types RWs. When RWs are designed against Level 2 seismic loads by the conventional pseudo-static analysis using conservative soil strength, while using an allowable global safety factor equal to 1.5;
  - a) for masonry RWs and leaning and gravity types RWs; the use of  $(k_h)_{design} = 0.1 - 0.2$  is unconservative, and  $(k_h)_{design} = 0.40$  could be tentatively suggested;
  - b) for cantilever RC RWs; the use of  $(k_h)_{design} = 0.1 - 0.2$  is unconservative, and  $(k_h)_{design} = 0.35$  could be tentatively suggested; and
  - c) for GRS-RWs having a FHR facing; the use of  $(k_h)_{design} = 0.1 - 0.2$  may be unconservative, and  $(k_h)_{design} = 0.30$  could be tentatively suggested.
9. The use of several long reinforcement layers at high levels is effective to increase seismic stability of GRS-RWs.

## 8. ACKNOWLEDGMENTS

Funding for this study was provided by the Ministry of Education, Science, Sports and Culture, Japan. The authors wish to thank Messrs. S. Nishihara at Chuo Kaihatsu Co., K. Kojima at Railway Technical Research Institute, T. Tsutsumi at Public Works Research Institute, K. Hayano, T. Uchimura and T. Sato at University of Tokyo for their help in preparing the manuscript.

## REFERENCES

- Bathurst, R.J. and Cai, Z. (1995) "Pseudo-Static Seismic Analysis of Geosynthetic-Reinforced Segmental Retaining Walls", *Geosynthetics International*, Vol. 2, No. 5, pp. 787-830.
- Bathurst, R.J. and Alfaro, M.C. (1996) "Review of Seismic Design, Analysis and Performance of Geosynthetic Reinforced Walls, Slopes and Embankments", *Earth Reinforcement*, (Ochiai et al., eds.), Balkema (in print).
- Bernardi, M. and Paulson, J. (1997), "Is creep a degradation phenomenon?", *Mechanically Stabilized Backfill* (Wu, J.T.H. eds.), Balkema, pp. 289-294.
- Bolton, M.D. and Steedman, R.S. (1985) "Modeling the Seismic Resistance of Retaining Structures", *Proc. 11<sup>th</sup> ICSMFE*, Vol. 4, pp. 1845-1848.
- Cai, Z. and Bathurst, R.J. (1996a) "Deterministic Sliding Block Methods for Estimating Seismic Displacements of Earth Structures", *Soil Dynamics and Earthquake Engineering* 15, Elsevier, pp.255-268.
- Cai, Z. and Bathurst, R.J. (1996b) "Seismic-Induced Permanent Displacement of Geosynthetic-Reinforced Segmental Retaining Walls", *Canadian Geotechnical Journal*, Vol. 33, pp. 937-955.
- Collin, J.G., Chouery-Curtis, V.E. and Berg, R.R. (1992) "Field Observation of Reinforced Soil Structures under Seismic Loading", *Earth Reinforcement Practice* (Ochiai et al., eds), Balkema, Vol. 1, pp. 223-228.
- Federal Highway Administration (1990) "Reinforced Soil Structures Volume I. Design and Construction Guidelines", Publication No. FHWA-RD-89-043, p.100.
- Fukuda, N., Tajiri, N., Yamanouchi, T., Sakai, N. and Shintani, H. (1994) "Applicability of Seismic Design Methods to Geogrid Reinforced Embankment", *Proc. 5<sup>th</sup> International Conference on Geotextiles, Geomembranes and Related Products*, Singapore, pp. 533-536.
- Greco, V. R. (1997) "Stability of Retaining Walls against Overturning", *Journal of Geotechnical and Geoenvironmental Engineering*, Vol. 123, No. 8, pp. 778-780.
- Greenwood, J.H (1997) "Designing to Residual Strength of Geosynthetics Instead of Stress-Rupture", *Geosynthetics International*, Vol. 4, No. 1, pp. 1-10.
- Haya, H., Sawada, R. and Nishimura, A. (1995) "Loading and Vibration Tests for Spread Foundation", *Proc. of 10<sup>th</sup> Asian Regional Conference on SMFE*, Vol. 1, pp. 203-206.
- Horii, K., Kishida, H., Tateyama, M. and Tatsuoka, F. (1994) "Computerized Design Method for Geosynthetic-Reinforced Soil Retaining Walls for Railway Embankments", *Recent Case Histories of Permanent Geosynthetic-Reinforced Soil Retaining Walls* (Tatsuoka and Leshchinsky, eds.), Balkema, pp. 205-218.
- Ichihara, M. and Matsuzawa, H. (1973) "Earth Pressure during Earthquake," *Soils and Foundations*, Vol. 13, No. 4, pp. 75-86.
- Japan Society of Civil Engineers (1996) "Proposal on Earthquake Resistance for Civil Engineering Structures (Special Task Committee of Earthquake Resistance of Civil Engineering Structures)", *The 1995 Hyogoken-nanbu Earthquake - Investigation into Damage to Civil Engineering Structures-*, Committee of Earthquake Engineering, Japan Society of Civil Engineers, pp. 297-306.
- Jewell, R.A., Paine, N. and Woods, R.I. (1984) "Design Methods for Steep Reinforced Embankments", *Polymer Grid Reinforcement*, McGown et al. (eds.), Thomas Telford, pp. 70-81.
- Jewell, R.A. (1991) "Application of Revised Design Charts for Steep Reinforced Slope", *Geotextiles and Geomembranes*, Vol.10, pp.203-233.
- Koseki, J., Tateyama, M., Tatsuoka, F. and Horii, K. (1996) "Back Analyses of Soil Retaining Walls for Railway Embankments Damaged by the 1995 Hyogoken-Nanbu Earthquake", *The 1995 Hyogoken-nanbu Earthquake - Investigation into Damage to Civil Engineering Structures-*, Committee of Earthquake Engineering, Japan Society of Civil Engineers, pp. 101-114.
- Koseki, J., Munaf, Y., Tatsuoka, F., Tateyama, M., Kojima, K. and Sato, T. (1997) "Shaking Table and Tilting Tests of Geosynthetic-Reinforced Soil Retaining Wall and Conventional Type Retaining Wall Models", *Geosynthetics International* (submitted).
- Koseki, J., Tatsuoka, F., Munaf, Y., Tateyama, M., and Kojima, K. (1997a): "A modified procedure to evaluate active earth pressure at high seismic loads" *Soils and Foundations* (submitted).
- Kotake, N., Tanaka, T., Tatsuoka, F. and Yamauchi, H. (1997), "Numerical simulation of strain localization and failure in reinforced soil," *Proc. Int. Conf. on Deformation and Progressive Failure in Geomechanics*, IS Nagoya '97 (Asaoka, Adachi and Oka eds.), Pergamon Press, pp.247-252.
- Leshchinsky, D., Ling, H.I. and Hanks, G. (1995) "Unified Design Approach to Geosynthetic Reinforced Slopes and Segmental Walls", *Geosynthetics International*, Vol. 2, No. 5, pp. 845-881.
- Ling, H. I. and Leshchinsky, D. and Perry, E.B. (1997) "Seismic Design and Performance of Geosynthetic-Reinforced Soil Structures", *Geotechnique* (accepted)

- for publication).
- Matsuo, O., Tsutsumi, T. and Saito, Y. (1997) "Shaking Table Tests and Analysis of Geosynthetic-Reinforced Soil Retaining Walls", *Geosynthetics International* (submitted).
- Mononobe, N. and Matsuo, H. (1929) "On Determination of Earth Pressure during Earthquake", *Proc. World Engineering Congress*, Tokyo, Vol. 9, pp. 177-185.
- Munaf, Y., Koseki, J., Tateyama, M., Kojima, K. and Sato, T. (1997) "Model Tests on Seismic Performance of Retaining Walls", *Bulletin of Earthquake Resistant Structure Research Center*, No. 30, pp. 3-18.
- Murata, O., Tateyama, M., and Tatsuoka, F. (1990) "Shaking Table Tests on Sand Backfill Reinforced with Short Geogrid-Reinforcement with Various Types of Facings", *Proc. of 25<sup>th</sup> Japan National Conference on Soil Mechanics and Foundation Engineering*, pp. 2019-2022 (in Japanese).
- Murata, O., Tateyama, M., and Tatsuoka, F. (1992) "Loading Tests of Geosynthetic-Reinforced Soil Retaining Walls and Their Stability Analysis", *Earth Reinforcement Practice*, (Ochiai et al., eds.), Balkema, Vol. 1, pp. 385-390.
- Murata, O., Tateyama, M., and Tatsuoka, F. (1994) "Shaking Table Tests on a Large Geosynthetic-reinforced Soil Retaining Wall Model", *Recent Case Histories of Permanent Geosynthetic-reinforced Soil Retaining Walls*, (Tatsuoka and Leshchinsky eds.), Balkema, Vol. 1, pp. 259-264.
- Newmark, N.M. (1965) "Effects of Earthquakes on Dams and Embankments", *Geotechnique*, Vol. 15, No. 2, pp. 139-159.
- Noda, S., Uwabe, T. and Chiba, T. (1975) "Relation between Seismic Coefficient and Ground Acceleration for Gravity Quay Wall", *Report of Port and Harbour Research Institute*, Vol. 14, No. 4, pp. 67-111 (in Japanese).
- Okabe, S. (1924) "General Theory on Earth Pressure and Seismic Stability of Retaining Wall and Dam", *Journal of Japan Society of Civil Engineers*, Vol. 10, No. 6, pp. 1277-1323.
- Public Works Research Institute (1992) "Design and Construction Manual of Geotextile Reinforced Soil Structures", *Research Report of Public Works Research Institute*, No. 3117, 404 p. (in Japanese).
- Railway Technical Research Institute (1997): "Design Standard for Railway Foundations/Soil Retaining Structures", pp. 132-135 (in Japanese).
- Seed, H.B. and Whitman, R.V. (1970) "Design of Earth Retaining Structures for Dynamic Loads", *ASCE Specialty Conference on Lateral Stresses in the Ground and Design of Earth Retaining Structures*, pp. 103-147.
- Siddharthan, R., Ara, S., and Norris, G.M. (1992) "Simple Rigid Plastic Model for Seismic Tilting of Rigid Walls", *Journal of Structural Engineering*, Vol. 118, No. 2, pp. 469-487.
- Steedman, R.S. and Zeng, X. (1996) "Rotation of Large Gravity Walls on Rigid Foundations under Seismic Loading", *Analysis and Design of Retaining Structures against Earthquakes*, Geotechnical Special Publication No. 60, ASCE, pp.38-56.
- Tateyama, M. (1997) "Study on the Construction Methods for Reinforced Soil Retaining Walls using Facing Rigidity", Doctoral thesis, University of Tokyo, pp. 28-42 (in Japanese).
- Tatsuoka, F., Maeda, S., Ochi, K. and Fujii, S. (1986) "Prediction of undrained strength of sand subjected to irregular loading," *Soils and Foundations*, Vol.26, No.2, pp.73-90.
- Tatsuoka, F., Okahara, M., Tanaka, T., Tani, K., Morimoto, T. and Siddiquee, M. S. A. (1991) "Progressive Failure and Particle Size Effect in Bearing Capacity of a Footing on Sand", *Geotechnical Engineering Congress 1991*, Mclean, F., Campbell, D. and Harris, D., Editors, ASCE, Geotechnical Special Publication No.27, Vol. 2, pp.788-802.
- Tatsuoka, F., Koseki, J. and Tateyama, M. (1996) "Performance of Reinforced Soil Structures during the 1995 Hyogo-ken Nanbu Earthquake", *Earth Reinforcement*, (Ochiai et al., eds.), Balkema (in print).
- White, D.M. and Holtz, R.D. (1996) "Performance of Geosynthetic-Reinforced Slopes and Walls during the Northridge, California Earthquake of January 17, 1994", *Earth Reinforcement*, (Ochiai et al., eds.), Balkema (in print).
- Yamada, S., Masuda, T., Sato, T., Yamaguchi, I. and Tatsuoka, F. (1996) "Sand Behavior in Plane Strain Compression Test", *Proc. of 31<sup>st</sup> Japan National Conference on Geotechnical Engineering*, pp. 683-684 (in Japanese).
- Yoshida, T., Tatsuoka, F., Siddiquee, M. S. A., Kamegai, Y. and Park, C. S. (1994) "Shear Banding in Sands Observed in Plane Strain Compression", *Localisation and Bifurcation Theory for Soils and Rocks*, Chambon, Desrue and Vardoulakis (eds.), Balkema, pp. 165-179.
- Yoshida, T. and Tatsuoka, F. (1997) "Deformation Property of Shear Band in Sand Subjected to Plane Strain Compression and its Relation to Particle Characteristics", *Proc. of 14th ICSMFE*, Hamburg, Vol. 1, pp.237-240.

# Limit State Design of Geosynthetic Reinforced Soil Structures

A. McGown

Professor, Department of Civil Engineering, University of Strathclyde, Glasgow, U.K.

K.Z. Andrawes

Professor, Department of Civil Engineering, University of Strathclyde, Glasgow, U.K.

S. Pradhan

Former Research Student, Department of Civil Engineering, University of Strathclyde, Glasgow, U.K.

A.J. Khan

Research Student, Department of Civil Engineering, University of Strathclyde, Glasgow, U.K.

**ABSTRACT:** The governing principles of Limit Equilibrium Methods and the Limit State Approach for the design of reinforced soil structures are presented. The components, construction and behaviour of geosynthetic reinforced soil structures are described, including a discussion of their internal force equilibrium and strain compatibility. The Limit State Approach to design is strictly applied to geosynthetic reinforced walls, steep slopes and embankments with suggestions given for the selection of properties of materials, actions, geometrical data and behavioural mechanisms. The Partial Factors to be applied to these are indicated. Lastly, the development of a computer-aided Limit State Approach design method for geosynthetic reinforced soil structures is described and outcome designs are given.

**KEYWORDS:** Design, Partial Factors, Geosynthetic Reinforcement, Retaining Walls, Steep Slopes, Embankments.

## 1 INTRODUCTION

Geosynthetic reinforced soil structures were progressively introduced into modern civil engineering practice during the 1970's. The earliest applications were in road pavements, and embankment slopes, although there were some notable steep slopes and walls constructed, McGown and Ozelton (1973), Holtz and Massarsch (1976), Bell and Steward (1977) and Jarrett et al (1977). In most cases, a Limit Equilibrium Method was used to design these structures. In these designs, the soils were uniquely represented by their peak strengths and the geosynthetics by their short term strength, (the latter determined from constant rate of deformation tensile test data).

Little or no account was taken of the deformation characteristics of the soil, the geosynthetics or their interaction behaviours. Large global *Factors of Safety* were applied which were intended to ensure *explicitly* that collapse did not occur and to ensure *implicitly* that deformations under working conditions were not excessive. As implemented, many of these design methods were semi-empirical and they proved to be generally acceptable and economic compared to other technical solutions available at that date. As a result they allowed the rapid acceptance of geosynthetics.

At the same time as geosynthetics were being introduced, a fundamental change in the design of civil engineering structures was underway. This involved the introduction of deformations and strains as design criteria to be assessed and controlled in an *explicit* manner. These were incorporated into what is now known as the *Limit State Approach*, in which both collapse conditions, *Ultimate Limit States*, and operational conditions, *Serviceability Limit States*, are analysed. Another feature of this approach is the introduction of risk factors, *Partial Factors*, to replace the use of global Factors of Safety.

The Limit State Approach was rapidly adopted in structural engineering in the 1980's and it has been gaining acceptance in geotechnical engineering in the 1990's. A number of the latest codes of practice relating to geosynthetic reinforced structures in various countries now take account of Limit State principles (e.g. BS 8006, 1995), however in most cases, these include partial factors that ensure that the outcome designs are close to those based on the preceding semi-empirical Limit Equilibrium Methods.

This paper comprises four main parts together with an overall discussion. Part A describes the governing principles of the Limit Equilibrium Methods and the Limit State Approach. Part B describes the components and construction methods used to form reinforced soil

structures and identifies the factors influencing their internal force equilibrium and strains. In Part C the Limit State Approach to design is strictly applied to geosynthetic reinforced walls, steep slopes and embankments. The soil and material parameters, loads and Partial Factors to be used in Ultimate and Serviceability Limit State analyses are set out and discussed. Part D describes the development of a computer-aided Limit State Approach design for geosynthetic reinforced soil structures and examples of outcome designs are given.

## PART A - THE GOVERNING PRINCIPLES OF LIMIT EQUILIBRIUM METHODS AND THE LIMIT STATE APPROACH

### 2 LIMIT EQUILIBRIUM METHODS

Historically the main objective of employing Limit Equilibrium Methods to analyse soil structures, was to establish the load combinations that soil masses could support against ultimate failure/collapse with a suitable Factor of Safety. Such loadings were termed *Design Loads*. It was generally assumed that the soil structures would meet their serviceability requirements under *Working Loads*, which were equal to or less than the Design Loads. In some cases, quite separate volume change/settlement analyses were undertaken using Working Loads.

The Limit Equilibrium Methods dealt with the various conditions of ultimate failure of a soil mass, including problems such as earth pressures, bearing capacity, and slope stability. Solutions were often obtained by simple statics, assuming failure surfaces of various shapes, such as planar, circular, or log-spiral, and by using simple failure criteria. In addition, all the soil elements along the failure surface were assumed to have reached their peak strength.

One of the earliest contributions to the use of Limit Equilibrium Methods in soil mechanics was that of Coulomb in 1773. He proposed a simple failure criterion for soils and established the important geotechnical design concept of treating the soil mass as a continuum which he applied to the determination of the action of fills on retaining walls, Chen and Liu (1990) and Clayton et al (1993). Later, in 1857, Rankine similarly represented an infinite body of a granular fill as a continuum and developed his Limit Equilibrium Method for earth pressures. Only much later was it suggested that real soils do not behave as rigid plastic materials, that is they do not act in the simple continuum manner proposed by Coulomb and Rankine, Terzaghi (1936), Fig. 1(a). Terzaghi indicated that the peak strength of the soil was mobilised only after significant displacement of the soil mass and pointed out that most soils exhibit increase in strength with

strain, which is known as *Strain Hardening*. In dense sands, this is followed by plastic failure, which is associated with a drop in shear strength and is known as *Strain Softening*, Fig 1(b). Thus given that real soils are compressible and may be subject to Strain Softening, it may be suggested that there are situations where the peak strength of a soil cannot be mobilised over the entire shear surface at any one time. Roscoe (1970) confirmed this and showed from the results of triaxial tests that soils can reach the same shear strength by lateral expansion (*Active Case*) and by lateral compression (*Passive Case*), but at very different strain levels.

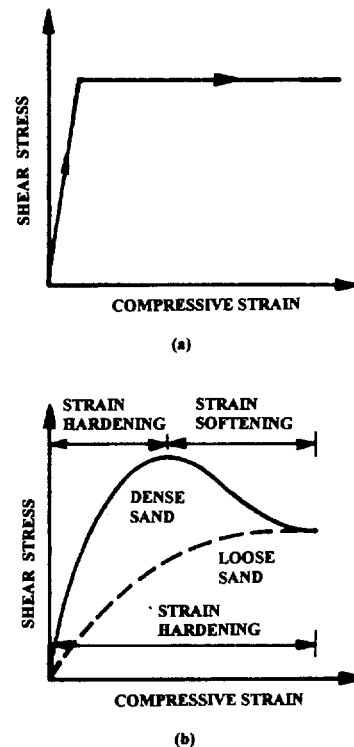


Fig. 1. Idealised and observed stress/strain behaviour of soil: (a) idealised and (b) observed (after Clayton, 1993)

As stated earlier, in some cases volume change/ settlement analyses were carried out to deal with the deformation of the soil at stress levels developed by the working loads, when no failure of the soil is usually involved. Solutions to this problem are obtained either by using the theory of elasticity or by a theory of consolidation, such as Terzaghi (1923) or Biot (1941). The elasticity approach is rational for problems involving short-term loads, however, it is obviously wrong to analyse all soil deformations using as a basis Hooke's law which is time-independent. In many cases the design must consider the influence of time on the deformations. Such behaviour may be modelled by



adopting the theory of viscoelasticity. However, in soil mechanics the complex multi-phase nature of the soils often requires a more complex approach.

### 3 THE LIMIT STATE APPROACH

#### 3.1 General Principles

The introduction to soil mechanics of design methods based on the Limit State Approach allows the following factors to be taken into consideration:

- (i) The nature and size of the soil structure, including any special requirements for the structure or its surroundings.
- (ii) The nature of the existing ground and groundwater conditions.
- (iii) The nature of the operational environment, including any seismicity.

To set the design requirements various *Geotechnical Categories* are introduced. In Eurocode 7 (1995), three categories are identified:

*Geotechnical Category 1* - Small or relatively simple soil structures, which may be designed using experience and qualitative geotechnical data and analysis.

*Geotechnical Category 2* - Conventional types of soil structures with no abnormal risks nor any exceptional ground or loading conditions, which may be designed using routine quantitative geotechnical data and analysis.

*Geotechnical Category 3* - Soil structures or parts of structures involving abnormal risks or difficult ground or loading conditions, which require to be designed using specialised non-routine quantitative geotechnical data and analysis.

For each geotechnical design problem, performance criteria during the period of construction and over the design life are set. Whenever a structure or a part of a structure operates at a level equal to any of the performance criteria, it is said to have reached a *Limit State*. Limit States are divided into two categories; *Ultimate Limit States (ULS)* and *Serviceability Limit State (SLS)*:

Ultimate Limit States are concerned with the safety, loss of static equilibrium or rupture of either a critical component or the entire structure. In brief, they set performance criteria such that no catastrophic damage can occur to a structure.

Serviceability Limit States are conditions, or performance criteria, beyond which the functional or aesthetic utility of a component or the entire structure are lost. The loss of serviceability may be due to deformation in the ground or deformation in the structure itself. For example, if a retaining wall supporting a bridge abutment deforms excessively, the serviceability of the bridge might be lost. Alternatively, due to a wall deformation there may be noticeable subsidence of a road subgrade which may cause discomfort to the users of that road or put the road out of service until proper maintenance is undertaken.

Two aspects of the Limit State Approach are of particular significance to geosynthetic reinforced soil structures. These are the considerations given to the *Strain Compatibility* of materials involved at the various Limit State conditions, and the assessment of the significance of internal and external environmental conditions on the durability of the materials used.

Designs based on the Limit State Approach require the identification of suitable *Calculation Models, Properties of Materials, Actions, Geometrical Data* and *Limiting Values of Deformations* etc.

The Calculation Models should consist of appropriate methods of analysis, based on valid *Behavioural Mechanisms*.

Design values of the Properties of Materials should be assessed directly for particular site conditions or derived from *Characteristic Values* based on field and laboratory test data.

Actions should include all loads, forces and displacements identified to be contributing to any specific Limit State condition. However, not all loads, forces or displacements will be treated as Actions in all Limit State analyses. Further the *Duration of Actions* needs to be considered, including changes in Actions resulting from changes in the Properties of Materials with time.

Geometrical Data should include all level, slope and other dimensional data important to the design and allowances made for variations in these.

Limiting Values should be chosen for each of the Limit States conditions.

The Limit State Approach does not use global Factors of Safety, instead Partial Factors are applied in the calculations where the uncertainties lie. The use of Partial Factors aims to distribute margins of safety to the places in the calculation where there are uncertainties. Also Partial Factors have the advantage that "margins of safety" can be

shared appropriately among the main parameters employed in the design. For example, a structure may be subjected to two actions, one adverse and the other beneficial, so that the nominal value of each cancels the other. Hence the resistance required for the structure will be very small or zero, on the basis of the nominal action. However, if in reality one of the actions is different from the expected value, the required resistance may be very high. This possible situation can be anticipated using Partial Factors, but could be missed in the global Factor of Safety approach.

Partial Factors relevant to soil structures have been suggested in Eurocode 7 (1995). Significantly, this suggests that different Partial Factors should be applied in the cases of favourable and unfavourable actions, Table 1. In the calculation of Serviceability Limit States, Eurocode 7 (1995) suggests the use of Partial Factors of unity.

### 3.2 Design Criteria

Design criteria are based on equating the effects of the destabilising actions and the stabilising actions. These are given in general terms by Eurocode 1 (1996) for both Ultimate and Serviceability Limit States as follows:

#### 3.2.1 Ultimate Limit States

For Ultimate Limit State analysis, static equilibrium and strength have to be verified so that the possible Ultimate Limit States are not exceeded.

##### (i) External Stability

When considering external Ultimate Limit States, the equilibrium or gross displacement of a structure are considered assuming the structure to be a rigid body. It must be verified that:

$$E_{d,dst} \leq E_{d,stab}$$

where,  $E_{d,dst}$  = Design value for the effect of the destabilising actions (direct, overturning or sliding), and

$E_{d,stab}$  = Design value for the effect of the stabilising actions (resisting).

##### (ii) Internal Stability

When considering internal Ultimate Limit States, rupture or excessive deformation of sections, members and connections, it must be verified that:

$$E_d \leq R_d$$

where,  $E_d$  = Design value of the effect of actions (internal forces, moments or vectors of several internal forces or moments), and

$R_d$  = Design value of the corresponding resistance (obtained from the design values of properties).

Table 1 Partial Safety Factors  
- Ultimate Limit States (Eurocode 7, 1995)

Case	Actions	Situations	
		Persistent -transient	Accidental
Permanent actions caused by structural and non-structural components, ground and groundwater			
- Loss of equilibrium: strength of structural materials or ground	unfavourable	1.10	1.00
	favourable	0.90	1.00
- Failure of structures or structural elements governed by the strength of materials	unfavourable	1.35	1.00
	favourable	1.00	1.00
- Failure of structures or structural elements governed by the strength of the ground	unfavourable	1.00 <sup>(1)</sup>	1.00 <sup>(1)</sup>
	favourable	1.00 <sup>(1)</sup>	1.00 <sup>(1)</sup>
Variable actions	unfavourable	1.50 <sup>(2)</sup>	1.00
Accidental actions	-	-	1.00

<sup>(1)</sup> In design calculations of lateral earth pressures, partial factors are used for the ground properties and for surface loads. Design earth pressures are not derived by multiplying characteristic earth pressures by partial factors.

<sup>(2)</sup> Unfavourable Variable Actions related to the failure of a structure or structural element governed by the strength of the ground should use a Partial Factor of 1.5/1.35 equal to 1.11.

### 3.2.2 Serviceability Limit States

It must be verified that no Serviceability Limit State is exceeded, using the following equation:

$$E_d \leq C_d$$

where,  $E_d$  = Design value of the effect of actions, (displacements, accelerations), and

$C_d$  = A nominal value or a function of certain design properties of materials related to the design effects of actions considered.

### 3.3 Material Properties for Ultimate Limit States

In geosynthetic reinforced soil structures the following four groups of material properties require to be identified for Ultimate Limit State analysis.

#### 3.3.1 Soils

In structural analysis, the ultimate tensile strength of low-carbon steels is usually ignored, and designs are based on the lower yield stress, Fig. 2(a). Thus it may be stated that structural engineers have decided not to utilise the strain-hardening which develops beyond the yield stress and in so doing they have decided to avoid the problems associated with progressive failure.

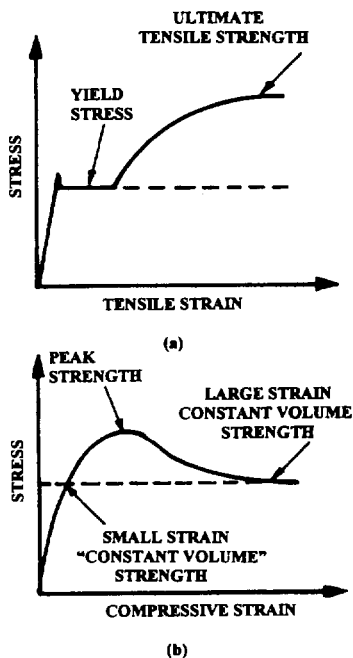


Fig. 2. Choice of steel and soil parameters for Ultimate Limit States (after Bolton, 1993)

In conventional geotechnical engineering practice the problems of progressive failure are avoided by geotechnical engineers neglecting the ultimate shear strength of soils in favour of the use of the peak shear strength of soils. However, peak shear strength is a transient value which is greatly dependent on the state of compaction of the soil and much less reliable than the ultimate shear strength. Additionally, the possibility of progressive failure is avoided, by the widespread use of large global Factors of Safety within analyses involving the peak shear strength of soils.

Ultimate Limit State analysis is concerned with collapse conditions, thus the ultimate large strain constant volume strength, Fig 2(b), (the large strain *Constant Volume Angle of Friction*,  $\phi'_{cv}$ ) should always be employed. Further given that at large strain, the constant volume shear strength is the lowest value achievable, at least in granular soils, then no Partial Factor is required for this parameter when it is used in designs.

Unfortunately, at the time of design the source of the soil to be used in the construction works may not be known and the quality of the compaction control may not be guaranteed. In such cases an appropriate design value for the angle of friction must be assumed based on the presumed nature of the soil and the compaction methodology most likely to be used. This assumed design value should be that for the large strain constant volume angle of friction of the soil presumed to be used. A small Partial Factor is appropriate in such cases.

#### 3.3.2 Geosynthetics

The choice of the design parameters for geosynthetic soil reinforcements to be used in Ultimate Limit State analysis has not yet been widely agreed. Some codes/design guides presently recommend the use of factored short term constant rate of deformation tensile test data, whilst others recommend the use of factored sustained load, (creep), test data. This matter will therefore be given detailed consideration in a later section.

#### 3.3.3 Soil Reinforcement Interaction

The choice of the design parameters for soil reinforcement interaction in Ultimate Limit State analysis has not yet been widely agreed. Some codes/design guides presently recommend the use of shear box test data and others pull-out test data. This matter will therefore be given detailed consideration in a later section.

### 3.3.4 Other Materials

For the Ultimate Limit State design of facings, in concrete, metal or other materials, connections and other components, relevant Limit State codes of practice may be followed, e.g. Eurocode 1 (1996).

### 3.4 Material Properties for Serviceability Limit States

As with Ultimate Limit State analysis, the following four groups of material properties require to be identified for Serviceability Limit State analysis.

#### 3.4.1 Soils

At working conditions, i.e., with actual working loads, the mobilised strains in and around soil structures can be relatively small. In such cases, the strains in the soil are likely to mobilise a friction angle between the at rest condition and peak strength, (i.e. between the *At Rest Angle of Friction*,  $(\phi'_o)$  and the *Peak Angle of Friction*,  $(\phi'_p)$ ). Hence, for Serviceability Limit States, no fixed value for the angle of friction can be suggested rather various values must be used, depending on the Serviceability Limit State being analysed.

#### 3.4.2 Geosynthetics

As for Ultimate Limit State analyses, there is no general agreement to date on the choice of the design parameters for Serviceability Limit State analyses. This matter will be dealt with in a later section.

#### 3.4.3 Soil Reinforcement Interaction

As for Ultimate Limit State analyses, there is no general agreement to date on the choice of the design parameters for Soil Reinforcement Interaction for Serviceability Limit State analyses. Thus this matter will be dealt with in a later section.

#### 3.4.4 Other Materials

For the Serviceability Limit State design of facings, in concrete, metal or other materials, connections and other components, relevant Limit State codes of practice may be followed, e.g. Eurocode 1 (1996).

### 3.5 Actions to be used in Designs

For any calculation the values of all the Actions must be known. Two categories of Actions have been defined in Eurocode 1 (1996):

*Direct Actions* - which are loads or forces applied to the soil structure, and

*Indirect Actions* - which are imposed or constrained deformations.

Within these two categories there are many *Types of Actions*, including *Permanent Actions*, (likely to act throughout a given design situation); *Variable Actions*, (likely to vary but with a mean value of significance); *Accidental Actions*, (likely to be of short duration and unexpected but of sufficient magnitude to cause severe consequences); *Fixed Actions*, (likely to be of known magnitude and direction with a fixed distribution over the structure); *Free Actions*, (likely to be of known magnitude and direction but a variable distribution over the structure); *Static Actions*, (likely to be stable and not cause significant acceleration of the structure or any of its components); *Dynamic Actions* (likely to cause acceleration of the structure or of its components), and *Quasi-static Actions*, (likely to be essentially static but have some dynamic effects).

Within design calculations it is necessary to identify *Representative Values* of the Actions known as *Characteristic Values*, in order to verify the Limit State conditions. These values should be established on a statistical basis to correspond to a prescribed probability of not being exceeded on the unfavourable side during the period taken into account in the design. Combinations of these are chosen to take account of the probability of simultaneous occurrence of the most unfavourable values of the independent Actions. This requires the identification of *Frequent* and *Quasi-permanent* values of Actions.

Frequent values are determined so that, (a) the total time during which the value of an Action is exceeded is only a small part of the chosen period of design life, or (b) the frequency of the exceedance of the values of Actions is limited.

Quasi-permanent Values are determined so that the total time during which the values of Actions are applied is a considerable part of the design life. Generally this means the Actions are applied for more than half of the design life.

Eurocode 1 (1996) generally requires that for Limit States with severe consequences, (generally Ultimate Limit States), design values shall represent the most unfavourable values which may occur in extreme circumstances and for Limit States with less severe consequences, (generally Serviceability Limit States), design value shall be the most unfavourable values which may occur in normal circumstances.

### 3.6 Partial Factors

Partial Factors need to be applied to the properties of materials, actions, geometrical data and behavioural models.

#### 3.6.1 Soils

The classical geotechnical Limit Equilibrium Methods were developed in the first half of this century following the pioneering work of Terzaghi (1925), but it was Krey (1926) who introduced the concept of global Factors of Safety with different values for slopes, retaining walls and foundations. Similar global Factors of Safety became customary for geotechnical design in Europe, North America and elsewhere during the first half of this century. The ranges for these global Factors of Safety are given in Table 2, Terzaghi and Peck, (1948). Taylor (1948) introduced separate Factors of Safety for the cohesive and frictional components of soil strength, ( $c$  and  $\tan \phi$ ) in the analysis of the stability of slopes. This approach was generalised by Brinch Hansen (1953 and 1956) when he proposed "Partial Factors" on different types of loads and the shear strength parameters of the soils used in the design of earth retaining structures and foundations. The principal numerical values of these "Partial Factors" related to soil structures are summarised in Table 3. The "Partial Factors" were chosen to give about the same estimates as conventional global Factors of Safety and have been used in the Danish Code since 1965, (Meyerhof, 1993).

The magnitudes of Partial Factors applied to the soil parameters in the modern Limit State Approach are governed by the reliability of the geotechnical information. The values of Partial Factors related to soils suggested in Eurocode 7 (1995) are given in Table 4.

#### 3.6.2 Geosynthetics

There is no general agreement to date on the choice of the Partial Factors for either Ultimate or Serviceability Limit State analyses involving geosynthetics. Thus this matter will be dealt with in a later section.

#### 3.6.3 Soil Reinforcement Interaction

There is no general agreement to date on the choice of the Partial Factors for either Ultimate or Serviceability Limit State analyses involving soil reinforcement interaction. Thus this matter will be dealt with in a later section.

Table 2. Values of Global Factors of Safety

Failure type	Item	Safety factor
Shear strength	Earthworks	1.3 to 1.5
	Earth retaining structures and excavations	1.5 to 2
Seepage	Uplift, heave	1.5 to 2
	Exit gradient, piping	2 to 3

Table 3. Values of Partial Factors in Various Codes

Item	Brinch Hansen		Denmark DS 415
	(1953)	(1956)	(1965)
Loads			
Dead loads, soil weight	1.0	1.0	1.0
Live loads	1.5	1.5	1.5
Environmental loads	1.5	1.5	1.5
Water pressure	1.0	1.0	1.0
Accidental loads	-	1.0	1.0
Shear strength			
Friction ( $\tan \phi$ )	1.25	1.2	1.2-1.25
Cohesion ( $c$ ) (slopes, earth pressures)	1.5	1.5	1.5

Table 4 Partial factors on ground properties for conventional design situations for ultimate limit states (Eurocode 7, (1995))

Ground Property	Partial Factor $\gamma_m$
$\tan \phi'$	1.25
$c'$	1.6
$c_u$	1.4

### 3.6.4 Other Materials

For the Partial Factors to be used in Ultimate or Serviceability Limit State designs of facings, in concrete, metal or other materials, connections and other components, relevant Limit State codes of practice may be followed, e.g. Eurocode 7 (1995).

### 3.6.5 Other Partial Factors

For any calculations the design values of the effects of Actions ( $E_d$ ) are determined from the design values of the Actions and Geometrical Data as well as the Properties of Materials. In some cases, the effects of the uncertainties in the Behavioural Model used in the calculations need to be considered explicitly and this may lead to the application of a *Coefficient of Behavioural Model Uncertainty* applied either to the Actions or to the internal forces and moments, whichever is the more conservative. For situations where deviations in the Geometrical Data will have a significant effect on the reliability of the structure, nominal geometrical design values may be modified to take account of the possibility of unfavourable deviations.

## PART B - REINFORCED SOIL STRUCTURES: THEIR COMPONENTS CONSTRUCTION AND BEHAVIOUR

### 4 TYPES OF REINFORCED SOIL STRUCTURES

The principal types of reinforced soil structures have been classified by Bonaparte et al (1985). They subdivided these structures into two broad categories, *Earth Structures* and *Load Supporting Structures*:

Earth Structures include walls, slopes, embankments, low permeability soil layers used in dams and waste containment facilities etc. Earth structures are not stable under their own weight and may or may not require to support significant external loads. The primary design criterion is the stability of the structure under its own weight and possibly external loads.

Load Supporting Structures include flexible pavements, unpaved roads, railroad track structures, and load supporting pads such as drilling pads, fabrication yards, and construction staging areas. These structures are usually stable under their own weight, and the primary design consideration is the ability of the structure to support the applied loads with limited deformations.

This paper is concerned only with the first category, the so-called Earth Structures, which may be sub-divided as follows:

### 4.1 Reinforced Soil Walls and Steep Slopes

Reinforced slopes and walls are typically constructed with alternating horizontal layers of compacted soil and reinforcement. With walls and very steep slopes, a facing is necessary to prevent localised surface erosion along the exposed side of the reinforced soil mass, which may lead to a progressive overall failure.

In these applications, the reinforcements strengthen the structure by adding tensile strength to the soil mass and by increasing soil strength as a result of increased soil confinement, Jewell (1980). This strengthening permits the construction of stable soil structures at angles steeper than the mobilised angle of friction of the soil. Examples of such soil structures include:

- (i) Vertical or near vertical soil walls with various types of facings such as full height panels, sectional panels and segmental concrete facings, "wrap around" facings and other facings such as timber, brick, or gabions, Fig. 3.
- (ii) Reinforced slopes used for embankment construction, natural slope stabilisation and excavations, Fig. 4.

The performance criteria for reinforced soil walls and steep slopes may be grouped into two categories. The first grouping is related to adequate stability against various internal and external collapse modes, McGown et al (1993a), Fig. 5. The second grouping is related to limits on deformations. These deformation limits are selected on the basis of architectural considerations regarding facing units, visual impact or on serviceability criteria imposed by supported structures, such as pavements and bridges.

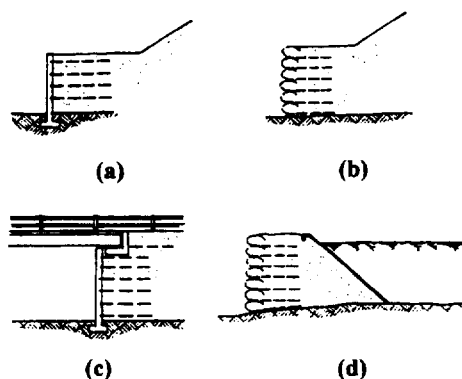


Fig. 3. Some examples of reinforced soil walls: (a) concrete faced retaining walls (b) "wrap-around" faced retaining wall (c) bridge abutment and (d) dam (after Bonaparte et al, 1985)

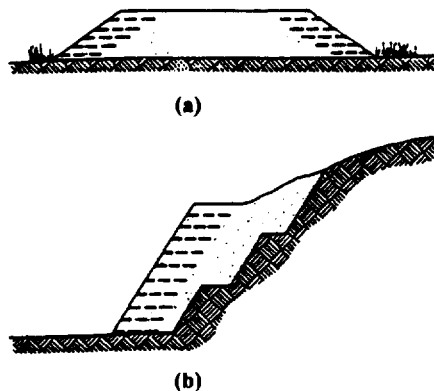


Fig. 4. Reinforced slopes: (a) embankment and (b) landslide repair (Bonaparte et al, 1985)

#### 4.2 Reinforced Embankments

Reinforced embankments on weak foundations are usually constructed by placing a layer of reinforcement, or a small number of soil and reinforcement layers, on the natural soil to produce a thin working pad on which the embankment is constructed in the conventional manner, Fig. 6.

There are at least two categories of weak foundations. If construction is to take place on a site underlain by a uniformly weak soil deposit such as soft clay, peat, or muskeg layers, the roles of the reinforcement are to increase the "margin of safety" against a slip-surface failure of the embankment and foundation soil, and to reduce lateral spreading and cracking of the embankment. If the foundation soil is locally weak, e.g. due to the presence of lenses of soft soil or sinkholes, the role of the reinforcement is to bridge the weak areas, (by the so called tension membrane effect), in order to reduce the risk of localised failure and to reduce differential settlements.

The two performance criteria usually considered for embankments are adequate external and occasionally internal stability, together with acceptable total and differential settlements, Fig. 5. Reinforcement placed at the embankment/foundation interface enhances stability and reduces embankment spreading. It should be noted that such reinforcements have little influence on the total time-dependent settlement of the embankment or the foundation soil, however, for non-uniform conditions, reinforcements at the embankment/foundation interface may reduce differential settlements, Bonaparte et al (1985).

## 5 COMPONENTS OF REINFORCED SOIL STRUCTURES

Reinforced soil structures consist of a number of components, including reinforced fill; retained fill; sub-soil; in-situ soil behind the reinforced fill; reinforcements; facing units and connections. The nature and important properties of these components are discussed in the following sections.

### 5.1 Reinforced Fill

The type of reinforced fill used in reinforced soil structures is dependent on the technical requirements of the structure and the basic economics associated with it. The main load transfer mechanism in reinforced soil structures is dependent on the shear forces developed at the soil-reinforcement interface. This major requirement of frictional forces has led to the use of cohesionless or slightly cohesive soil backfills with high friction angles, Yogarajah (1993). Most codes of practice and most design methods are based on the use of a suitable frictional backfill. For example, BS8006, (1995) requires a cohesionless fill with an effective angle of friction greater than  $25^\circ$  and with no more than 15% of the material less than  $63\mu\text{m}$  to be present. Generally, it has been suggested that granular materials should not contain more than 15% finer than 0.08mm, Lee (1978). Further, the reinforced fill is usually required to conform to certain electro-chemical and other conditions to reduce the corrosion/degradation of reinforcements.

From the point of view of operational performance the most important property of granular material is the relationship between the mobilised angle of friction and the tensile strains in the soil under plane strain conditions, Fig. 7. The plane strain apparatus should be used to determine this relationship but this is rarely the case. More usually the triaxial or shear box apparatuses are used to determine the peak angle of friction, ( $\phi'_p$ ), and constant volume angle of friction, ( $\phi'_{cv}$ ). However, various researchers have carried out experiments to find out the relationship between the mobilised angle of friction, ( $\phi'_m$ ), and the lateral tensile strain in the soil, ( $\epsilon_t$ ), Cornforth (1964), Barden et al (1969), Al-Hasani (1978) and Bolton (1986). According to their findings, the peak angle of friction, ( $\phi'_p$ ), of granular soils occurs at lateral tensile strains in the range 3 to 6% and the constant volume angle of friction, ( $\phi'_{cv}$ ), occurs at tensile strains in the range 6 to 12%, McGown et al (1993a), Fig. 7.

ULTIMATE LIMIT	SERVICEABILITY LIMIT	WITH FACING	NO FACING
1. Local stability at face of the fill	-		
2. -	Compressibility of the fill		
3. Integrity of facing	Displacement and deformation of facing		
4. Rupture of reinforcements and/or connections	Deformation of reinforcements and/or connections		
5. Reinforcement pull-out	Soil-reinforcement slippage		
6. Base sliding	-		
7. Bearing failure of sub-soil	Settlement of sub-soil		
8. Overturning	-		
9. Overall stability	-		

Fig. 5 Suggested Limit States for Walls, Steep Slopes and Embankments (McGown et al, 1993)



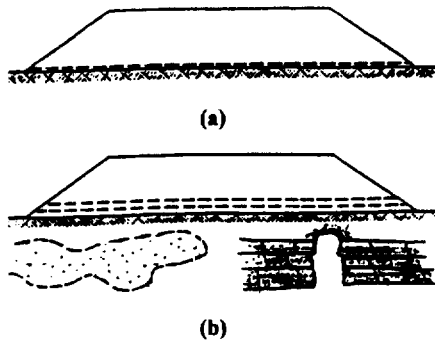


Fig. 6. Embankments on weak foundations: (a) embankment on uniform soft soil and (b) embankment on locally weak foundations (Bonaparte et al, 1985)

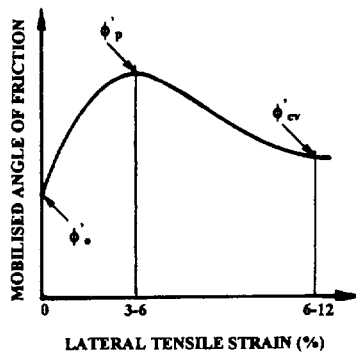


Fig. 7. Relationship between the mobilised angle of friction and tensile strain in cohesionless soil (after McGown et al, 1993)

In practice the maximum strain measured in reinforcing elements in walls is usually much less than 2%, Yogarajah (1993). At working conditions in walls, a mobilised angle of friction numerically equal to the value of the constant volume angle of friction, ( $\phi'_{cv}$ ), would appear to be the most appropriate value, Fig. 7.

A number of experiments and full-scale trials have been carried out to assess the use of cohesive backfills in reinforced soil structures, Murray and Boden (1979), Ingold (1981), Bonaparte et al (1989), Fourie and Fabian (1989) and Wu (1991). These show that cohesive soils may require a large amount of reinforcement with good adhesion and possibly good drainage qualities. Cohesive reinforced soil structures are presently being constructed in some countries on an increasing scale especially in Japan, Kasahara et al (1992), but these soils are not dealt with in this paper.

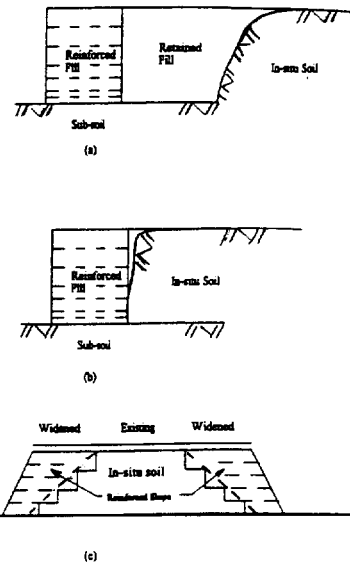


Fig. 8. Different sections of reinforced soil structures: (a) with retained fill (b) and (c) without reinforced fill (Pradhan, 1996)

## 5.2 Retained Fill

Fill behind the reinforced soil section may or may not be present depending on the site conditions, Fig. 8. Structures built to reinstate existing slopes or to widen an Existing road will not contain the retain fill, Fig. 8(b) and (c), instead they will have the in-situ soil behind the reinforced fill. Otherwise retained fills will be the same soil as that of the reinforced fill. The properties of the retained fill can govern the external stability of the reinforced soil structures. Hence, good quality retained fill should be used and its constant volume angle of friction ( $\phi'_{cv}$ ) needs to be appropriately determined.

## 5.3 Sub-Soil and In-Situ Soil Behind Reinforced Fill

The shear strength, (possibly, consolidated undrained, and drained parameters), and compressibility properties of the subsoil and the in-situ soils behind reinforced fills are important design parameters in reinforced soil structures.

Most of the design methods assume a competent foundation in the design of reinforced soil walls and steep slopes. In the case of embankments over a soft soil foundation, the properties of embankment materials themselves may not be critical rather the properties and changes in properties of the sub-soils with time may be the dominant influences. In-situ soil behind reinforced soil walls and steep slopes may have a significant effect on the length of the reinforcing elements required in the fill, hence the properties of these soils should be carefully determined, Pradhan (1996).

## 5.4 Reinforcing Elements

The type of materials used at the present time as reinforcing elements include steel, fibreglass and polymer synthetics in the forms of sheets, strips or grids. Some of the forms of polymer synthetic products, (so called *Geosynthetics*), are shown in Fig. 9. The choice of material and the form in which it is used (i.e., sheet, strip or grid) generally dictates the load transfer mechanism from the soil to the reinforcement. In the case of strips, sheets and grids with melded junctions, the load transfer mechanism at the soil/reinforcement interface is principally surface friction, while for grid with integral junctions, stress transfer is a combination of surface friction and bearing stresses developed at the junctions or protrusions, Fig. 10.

Two types of reinforcements have been identified by McGown et al (1978), *Relatively Inextensible* and *Relatively Extensible* reinforcements.

Relatively Inextensible reinforcements are defined as those which have rupture strains less than the maximum tensile strain in the soil without reinforcement, under the same operational conditions. The properties of this type of reinforcement are often independent of time and

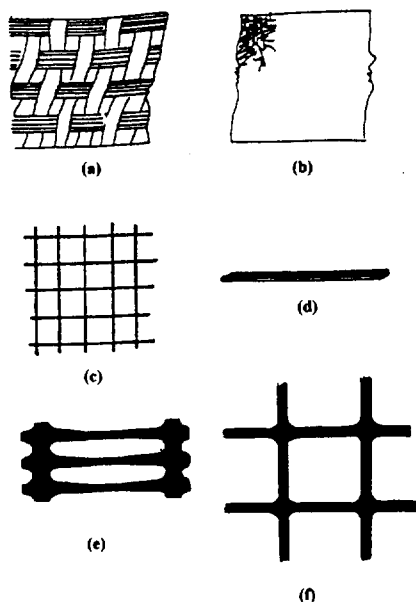


Fig. 9. Forms of geotextiles and related products: (a) wovens (b) non-wovens (c) nets and grids with melded junctions (d) straps (e) uniaxial grids with integral junctions and (f) biaxial grids with integral junctions

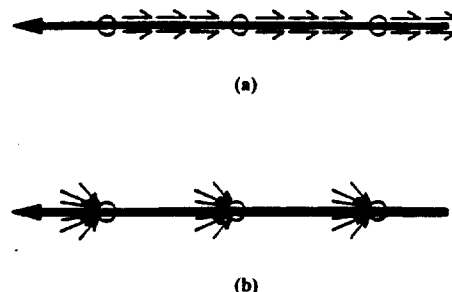


Fig. 10. Load transfer between soil and grid reinforcements (a) surface friction (b) bearing stress

temperature, in which case their stress-strain behaviour can be determined from short term, constant rate of deformation tensile tests.

Relatively Extensible reinforcements, which includes almost all geosynthetic strips, sheets or grids, are defined as those which have rupture strains larger than the maximum tensile strain in the soil without reinforcement, under the same operational stress conditions. The properties of this type of reinforcement are usually time and temperature dependent. For this reason, it has been suggested that long term, sustained load, (creep), tests at the appropriate temperature are required to determine their load-strain-time-temperature behaviour, Kabir (1984), McGown et al (1984a), Murray and McGown (1987), Andrawes et al (1986) and many others. Where the materials are highly compressible or change shape during straining, it has been further suggested that "in-soil" testing at appropriate confining stresses in the confining soil is required to determine representative load-strain-time-temperature behaviour, McGown et al (1982).

Embedding Relatively Inextensible reinforcements in soil, in the direction of the principal tensile strain, results in a net increase in the load carrying capacity of the soil and a reduction of soil boundary movements when compared to the soil alone under the same operational conditions. However, when rupture of the reinforcement occurs, the composite behaviour reverts back to the behaviour of the soil alone.

Embedding Relatively Extensible reinforcements in soil again results in a net increase in the load carrying capacity of the soil and a reduction of soil boundary movements when compared to the soil alone under the same operational conditions. The difference is that the extensibility of the reinforcements allows larger strains to occur without the reinforcements rupturing than for

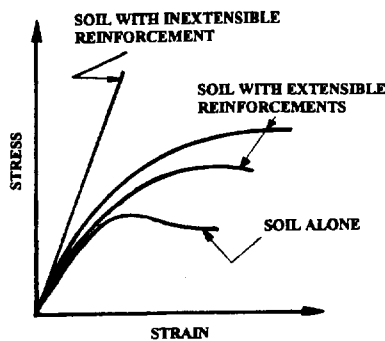


Fig. 11. Stress-strain behaviour of relatively extensible and inextensible reinforcements

Relatively Inextensible reinforcements. In these circumstances, the benefit of the mobilised tensile strength of the reinforcement exists even after the peak strength of the soil has been reached, Fig. 11, McGown et al (1978).

Relatively inextensible metallic reinforcement strips were the first type of reinforcing elements widely used in reinforced walls and steep slopes, Vidal (1969). These reinforcements have stiffnesses which do not allow the development of large enough soil boundary movements to mobilise Active earth pressures, McGown et al (1988 and 1992), Jones (1991), and Yogarajah et al (1993). Relatively Extensible reinforcements, such as geosynthetics, have stiffnesses which can allow the development of sufficiently large soil boundary movements to fully mobilise Active earth pressures. They are therefore potentially much more efficient than Relatively Inextensible reinforcements, in so far as they utilise the strength of the soil more effectively. However, they have to be carefully designed into structures in order to take account of possible long term creep (or stress relaxation) and degradation by UV exposure, thermal cycling and physical, chemical or biological attack. Nevertheless, because of the economic advantages they provide, they have become more and more widely accepted.

### 5.5 Facing Units

As stated earlier, reinforced soil walls and very steep reinforced slopes may require a facing to prevent localised surface erosion. Many types of facings can be used. Two of the most common are concrete panels, (incremental, full height and segmental) and "wrap around" facings. (the facing is provided by wrapping the reinforcement around the outside of the compacted soil layer), Fig. 3. Facings can be designed to be relatively rigid or flexible and lightweight, the latter when they are required to resist low pressures only, Jones (1993), Tatsuoka (1993). They generally represent a relatively

low cost per unit area of exposed surface, Jones et al (1987).

Unfaced slopes and embankments represent the condition of no restraint on the lateral soil boundary. Steep slopes and walls with facings represent various levels of lateral restraint conditions. The actual lateral soil boundary conditions depend upon four factors imposed by the nature of the facing employed, McGown et al (1993), Fig. 12:

- i) Axial compressibility
- ii) Lateral compressibility
- iii) Flexural rigidity, and
- iv) Frictional characteristics of the rear surface of the facing.

The effect of facing type on reinforced soil structures has been studied by various researchers, Fahim (1983), Ahmad (1989), Andrawes et al (1990), Loke (1991) and Saad (1993). Where a compressible boundary layer is present, the lateral earth pressure has been shown to greatly reduce during construction, Andrawes et al (1990), Yeo et al (1992) and Saad (1993).

### 5.6 Connections

Connections are important in walls and steep slopes which are faced. The connections between the reinforcement and the facings must be capable of transmitting the stress from the ends of reinforcement to the facing. The tensile load-deformation behaviour and flexural properties of the connections are important. Various forms of connections are possible such as, vertically sliding connections, loose fitting connections, rigid connections and connections tightened up during or after placement of the fill, McGown et al (1993).

Results from large scale model tests carried out on 2m high reinforced soil walls with different connection types have been reported by Andrawes and Yogarajah (1994). They showed that when the reinforcing elements were *Locked-on* to facing units, (with no horizontal or vertical movement allowed), the maximum tensile strain occurred close to the facing and thereafter was essentially linear away from the facing. In contrast, for loose fitting connections, the maximum tensile strain occurred away from the facing. For the latter case, larger shear resistance was mobilised in the soil and this resulted in reduced lateral earth pressures on the facing units.

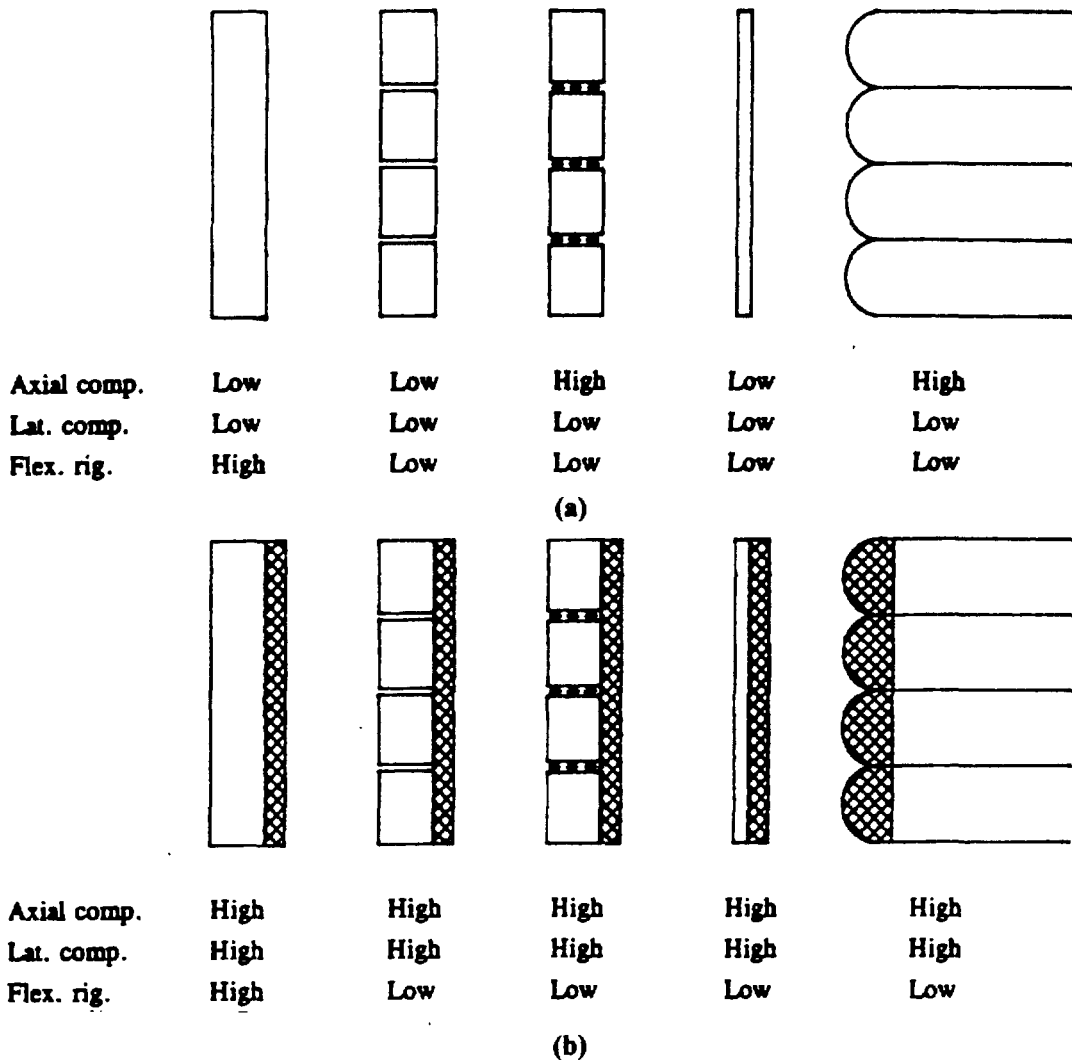


Fig 12. Factors relevant to the nature of the facings: (a) without and (b) with a compressible layer (McGown et al, 1993)

## 6 INTERNAL FORCE EQUILIBRIUM AND STRAIN COMPATIBILITY OF GEOSYNTHETIC REINFORCED SOIL STRUCTURES

The external force equilibrium and deformations of geosynthetic reinforced soil structures are treated in the same manner as for conventional soil structures. The main analytical difference for geosynthetic reinforced soil structures lies with the need to analyse the internal force equilibrium and strain conditions.

### 6.1 The Internal Role of Reinforcements

Soil deforms when it is loaded or allowed to deform under self-weight. In addition to any elastic distortion of

the soil particles themselves, shear deformation occurs as soil particle contacts realign. In so doing the soil mobilises shearing resistance. Deformations result in the development of a strain field in the soil, with both compressive and tensile strains developing as the soil shears, Fahim (1983).

When reinforcements which can develop bond, (either through frictional contact between the soil particles and planar surface areas or from soil bearing stresses on transverse surfaces), are placed in soil, any deformations in the soil will develop forces in the reinforcements. Whether or not tensile or compressive forces develop in the reinforcements, depends on whether they lie in the direction of tensile or compressive strains in the soil.

The mobilised reinforcement forces, ultimately limited by the available bond, act to alter the force equilibrium in the soil and so modify the strain field developed in the soil.

Studies have shown that reinforcements are most effective when aligned in the directions of principal strains in the soil, McGown et al (1978). If reinforcements are placed in or close to the direction of principal tensile strain in the soil, a tensile force develops which directly supports some of the applied loading and increases the normal stresses on potential rupture surfaces. This increased normal stress in turn develops greater frictional shearing resistance. This may be examined for the simple case of a singly reinforced wall, shown in Fig. 13. The self-weight loading of the soil causes a disturbing shear force, ( $P_s$ ), to act on the section of the shear surface shown in Fig. 13(a). The force polygon for an unreinforced wall is shown in Fig. 13 (b). This indicates that the earth pressure, ( $P_a$ ), on the wall would decrease with the increase of shearing resistance in the soil, ( $F$ ), (i.e. increase in the mobilised angle of friction,  $\phi_m$ ).

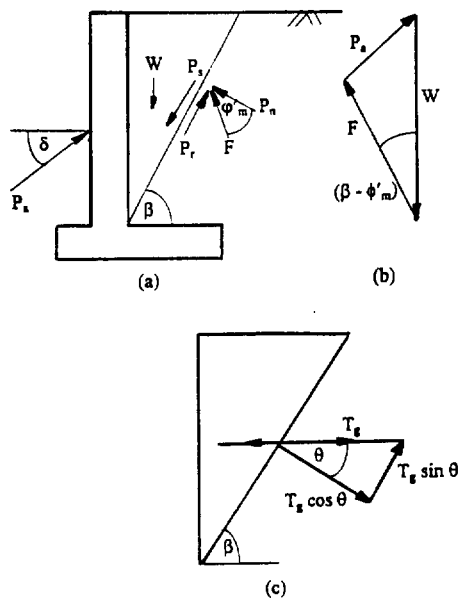


Fig. 13. Role of reinforcement: (a) forces on conventional retaining wall (b) force polygon and (c) components of reinforcement

Deformations in the soil will cause a tensile force to be mobilised in the reinforcement, ( $T_g$ ), and provide two additional components of resistance in the slope, Fig. 13 (c). The tangential component of the reinforcement force, ( $T_g \sin \theta$ ), directly resists the disturbing shear force in the soil, while the normal component of the force, ( $T_g \cos \theta$ ),

mobilises additional shearing resistance, ( $T_g \cos \theta \tan \phi'_m$ ). The net increase in shear resistance due to the reinforcement is then,  $\Delta P_r = T_g (\sin \theta + \cos \theta \tan \phi'_m)$ .

In practice, multiple layers of reinforcement are used and with a high *Concentration of Reinforcements*, theoretically no lateral earth pressure will be transferred to the wall. In fact, a high Concentration of Reinforcements in a granular soil would give the whole soil mass a “pseudo-cohesion” which would enable the granular soil mass to wholly or partly stand against its self weight and any imposed loads.

## 6.2 Internal Force Equilibrium

Equilibrium is considered in terms of *Required Forces* and *Available Forces*. The geometry of the structure (wall height etc.), loadings (external, self-weight, porewater pressures) and mobilised soil shearing resistance (friction) determine the Required Forces. The aim is to calculate both the magnitude and the distribution of the reinforcement forces needed to maintain equilibrium everywhere in the soil.

Possible reinforcement layouts (reinforcement type, spacing length) are then considered. A satisfactory reinforcement layout is one in which the Available Forces from the reinforcements exceed or equal the Required Forces everywhere in the soil. The calculation of the Available Forces involves consideration of the reinforcement material properties (strength and stiffness) and the available bond between the reinforcement and the soil. Clearly the Available Force in the reinforcement cannot exceed the strength of the material, and the magnitude of force selected governs the corresponding tensile strain in the reinforcement, Jewell (1988).

## 6.3 Internal Strain Compatibility

The link which determines whether a pair of Required and Available Force distributions are indeed balanced is the mobilised strains in the soil and the reinforcements. A common assumption made for geosynthetic reinforcements, due to their high level of bond, is that the tensile strains in the soil and the reinforcements are equal in the direction of the reinforcement. This concept is known as *Strain Compatibility*.

The Strain Compatibility of a reinforced soil structure is most conveniently represented in terms of the overall Required and Available Forces in the soil and the reinforcements respectively, plotted against the tensile strain in the soil and the tensile strain in the reinforcement, Jewell (1985).

The resulting *Strain Compatibility Curve* is most simply drawn for a propped wall construction. Initially both the

soil and the reinforcement have zero tensile strain, with the soil in the At Rest condition, i.e., the Required Forces for equilibrium taken by props are due to At Rest earth pressures, shown as point A in Fig. 14(c). Releasing the props disturbs the initial equilibrium, consequently tensile strains develop in the soil and in the reinforcement. This strain allows another equilibrium condition to be established, shown as the intersection of the Required and Available Forces, point B, in Fig. 14(c).

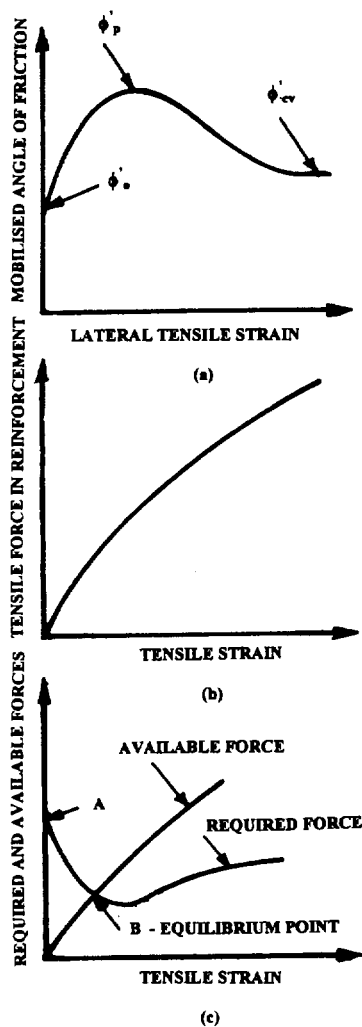


Fig. 14. The compatibility curve for determining the equilibrium of reinforced soil: (a) mobilised angle of friction - lateral tensile strain (b) tensile force in reinforcement - tensile strain and (c) strain compatibility curve (after Jewell, 1985)

An important feature of the Strain Compatibility Curve not always recognised, is that if creep strain occurs with time in the reinforcement, a decreasing load will require

to be carried by the reinforcement up to the strain required to mobilise the peak angle of friction of the soil. This suggests that if creep occurs in the reinforcement under working conditions, then a constant load is not applied to the reinforcements. Only if the change of load carried by the reinforcements under working conditions is not very significant, can this be overlooked.

It should be noted that Relatively Extensible reinforcements may have to strain quite considerably in order to mobilise significant forces and to contribute to the equilibrium of the structure. By definition, equilibrium calculations only examine stresses and forces and pay no attention to the strains in the soil mass as failure is approached. The generation of reinforcement forces depends on the reinforcement straining with the adjacent soil, thus when performing such calculations it is necessary to determine if the reinforcement forces can occur without exceeding tolerable deformations at the lateral soil boundary. An outcome of this is that a geosynthetic reinforced soil structure may have a reinforcement layout safe against Ultimate Limit States but it may excessively deform under self-weight and imposed loads.

Deformations developing in a reinforced soil structure depend on the *Concentration of Reinforcements*. This may be represented in terms of the stiffness of the structure. Thus if one reinforcement layout is found to deform unacceptably, the Concentration of Reinforcements, and so the stiffness of the system, can be increased in order to reduce the deformation of the lateral soil boundary. These additional reinforcements are not required from a force equilibrium point of view rather for deformation limitation. This concept is no different to that used by structural engineers to control excessive deflections in reinforced concrete beams.

All these concepts are included in the Limit State Approach, in which reinforcement layouts are determined both by Ultimate Limit State analysis, and by Serviceability Limit State Analysis.

## 7 CONSTRUCTION EFFECTS ON INTERNAL STRESSES AND STRAINS IN GEOSYNTHETIC REINFORCED SOIL STRUCTURES

### 7.1 Compaction and the Development of Interlock

Broms (1971), Aggour and Brown (1974) and Ingold (1979, 1980, 1981) investigated the effects of compaction on soil backfill behind rigid retaining walls. Based on empirical formulations, Broms (1971) and Ingold (1979, 1980, 1981) suggest that due to compaction stresses the assumption of At Rest lateral earth pressures at the back of rigid retaining walls, may be an underestimation of the horizontal stresses within the soil mass.

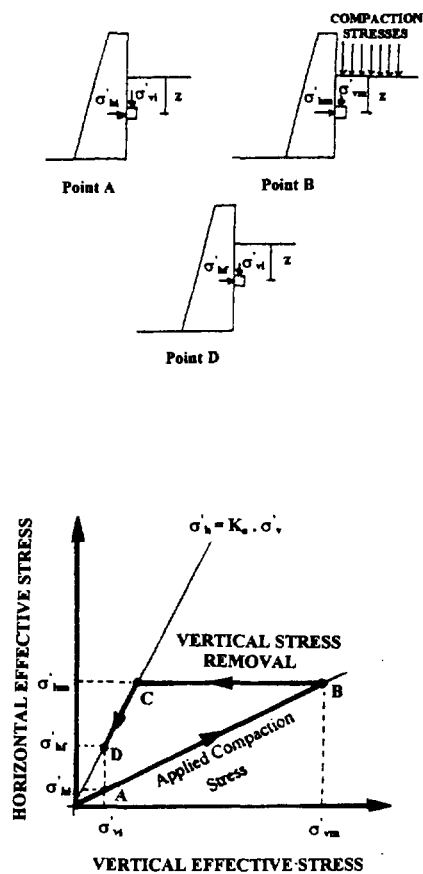


Fig. 15. Broms simplified compaction pressure theory (after Broms, 1971). where  $\sigma'_{hi}$  and  $\sigma'_{vi}$  are initial horizontal and vertical pressures before the application of compaction stress at  $K_0$  condition,  $\sigma'_{hm}$  and  $\sigma'_{vm}$  are increased horizontal and vertical pressure due to compaction stress at  $K_0$  condition and  $\sigma'_{hf}$  is "locked-in" horizontal pressure after removal of compaction stress.

These larger stresses were attributed to *Locked-in Stresses* within the soil mass. Broms (1971) suggested a simplified model of the development of these Locked in Stresses, Fig. 15. Ingold (1979), developed an analytical model, Fig. 16, to calculate the stresses generated due to compaction. He suggested that the horizontal earth pressures, ( $\sigma_{hcomp}$ ), caused by compaction can be calculated by:

$$\sigma_{hcomp} = \sqrt{(2p\gamma/\pi)}$$

where  $p$  is the weight per unit width of the compaction machine and  $\gamma$  is the unit weight of the soil backfill.

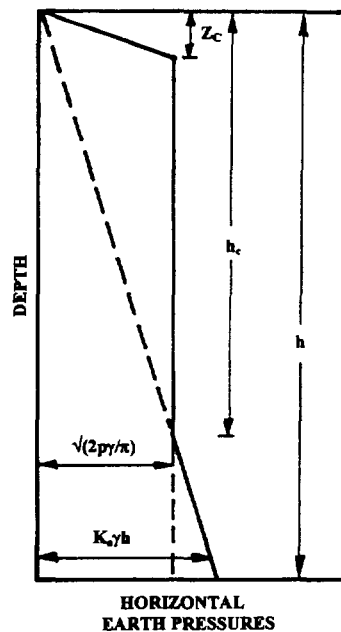


Fig. 16. Horizontal earth pressure due to compaction (Ingold, 1979) where  $z_c$  = critical depth below which there will be no reduction in the horizontal pressure.  $h_c$  = critical depth below which the active earth pressure exceeds the compaction induced pressure,  $p$  = weight per unit width of the compaction machine,  $\gamma$  = unit weight of soil,  $K_a$  = Rankine's coefficient of active earth

Broms (1971) and Ingold (1979) also compared roller and vibrator compaction machines of similar weights and suggested that the weight of a vibrator machine should be doubled to account for vibratory effects as these lead to increased locked-in stresses. Using this analogy and applying the above equation, the ratio of horizontal earth pressures from a vibrator and roller compaction machine of similar weights would be 1.4:1.

The effects of compaction on geosynthetic reinforced soil masses was carried out by Yogarajah (1993). McGown et al (1990 and 1994) suggested that when geogrids with integral junctions were used as reinforcements a mechanism developed which was additional to the interlock concept initially introduced by Mercer (1986). He identified the presence of *Static Interlock* mechanism based on the soil particles being locked into grids due to static loads. McGown et al (1990 and 1994) showed that an additional mechanism called *Dynamic Interlock*, was available and could be developed by repeated loading in soil masses containing geogrid reinforcements with integral junctions.

This Dynamic Interlock mechanism may be explained as follows:

- (i) During compaction of a soil backfill containing a geogrid with integral junctions, the compaction loads force soil particles into the apertures of the grids.
- (ii) When the compaction load is released, the grid attempts to return to its initial condition, but it is resisted from doing so by the particles within the apertures. This results in the development of *Locked-in Strains* within the geogrid, Fig. 17.
- (iii) The Locked-in Strains have a similar effect to a confining stress on the soil, therefore they increase the strength of the soil. This reduces the lateral earth pressures from the level that would be expected from the model given by Broms (1971) under At Rest conditions.

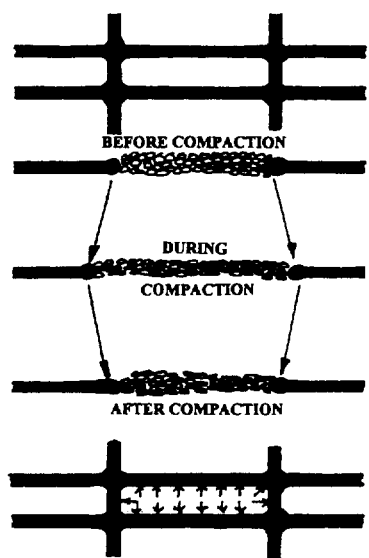


Fig. 17. Build-up of the dynamic interlock mechanism (Yogarajah, 1993)

The effectiveness of the Dynamic Interlock mechanism is dependent on the resilient nature of the polymeric material in the strands of the grid and the integrity of the junctions between the strands in the grid.

## 7.2 Horizontal Earth Pressures from Compaction against Rigid and Yielding Walls

Two limiting cases must be considered. Firstly, if the lateral boundary is not allowed to yield, the resulting pressures will be equal to or greater than those obtained under At Rest conditions. This case produces the upper

limit of the lateral pressure acting on the wall. Secondly, if the lateral boundary is allowed to yield sufficiently to mobilise large tensile resistance in the reinforcements and if the Required Forces and the Available Forces balance, theoretically there will be no horizontal pressure acting on the wall. This provides the lower limit case. However, even for this lower limit case the soil masses between the reinforcing layers may have a tendency to produce localised stresses near the facing. This develops because each soil layer between the reinforcement tends to act separately, causing the wall to be subjected to Active horizontal pressures over the depth of that layer.

Yogarajah (1993) carried out full scale tests on three full height panel walls. Walls 1 and 2 were compacted using a vibratory method, the props were released from bottom to top and top to bottom respectively. For Wall 3 a roller method of compaction was used for compaction and props were released from bottom to top in the same way as Wall 1. Figures 18, 19 and 20 show the horizontal earth pressure distributions on the facing of Walls 1, 2 and 3 respectively for two conditions; (i) full height fill before the reinforcements were attached and before prop removal, and (ii) full height fill after the reinforcements were attached then all the props removed.

Before prop removal, the horizontal earth pressures recorded at the rear of the facing panels, following vibratory compaction (Walls 1 and 2), were higher than the pressures recorded due to the roller compaction (Wall 3). The ratio of the pressures were approximately 1.8:1. Employing the Ingold (1979) mathematical model, a ratio of 1.96:1 is obtained for the two compaction machines used. The total force on the facing panels was carried by the props at this stage of construction. The horizontal earth pressures acting on the lower half of the full-height propped panel walls were less than the theoretical earth pressure At-Rest. This was caused by the Locked-in Strains developed within the geogrid reinforcement during compaction.

After attachment of the reinforcements to the facing panels and removal of the props, the walls started yielding outwards and tensile strains were developed in both the reinforcements and in the adjacent soils. According to the mechanism previously described the prop load was carried partly by the increasing stress in the reinforcements and partly by the adjacent soils. However, small pressures were recorded on the facings because of the tendency of the soil masses near the facing between the reinforcing layers to deform. These small pressures on the facings are evident in Fig. 18, 19 and 20, shown as horizontal pressures 7 days after prop removal.



Saad (1993) carried out tests on reinforced soil walls with compressible boundary. Figure 21 shows the distribution of horizontal earth pressure on the facing panels before prop removal and after 1 day and 6 months from prop removal. The results show that the horizontal pressure on the facing was much less than the Active earth pressure during construction. The reason may be attributed to the deformation of the compressible layer, and thereby that of the soil boundary. The induced deformation of the soil boundary due to the deformation of the compressible layer strains both the reinforcements and the adjacent soils and reduces the horizontal pressure on the facing panel. This is the same mechanism that operates for a rigid boundary after prop removal. The introduction of the compressible boundary thus allows the design of less

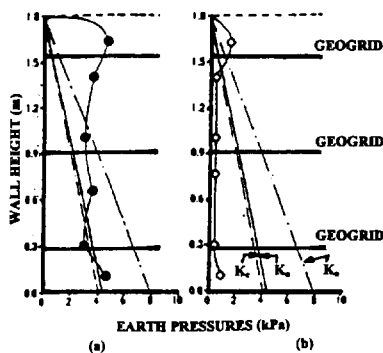


Fig. 18. Horizontal earth pressure distribution on 1.8m high Wall 1: (a) backfill height 1.8m and (b) 7 days after prop removal (after Yogarajah, 1993), where  $K_c$  = Coulomb's coefficient of active earth pressure,  $K_a$  = Rankine's coefficient of active earth pressure and  $K_o$  = Jaky's coefficient of earth pressure at rest.

robust props than for a wall with a rigid boundary. It may also be noted that most of the deformations occurred during construction hence the horizontal earth pressure on the facing remained almost unchanged after prop removal. This is highly significant, in that it shows that the compressible boundary helps not only in reducing the loads on the props during construction, but that it helps to reduce the post construction displacement of the wall.

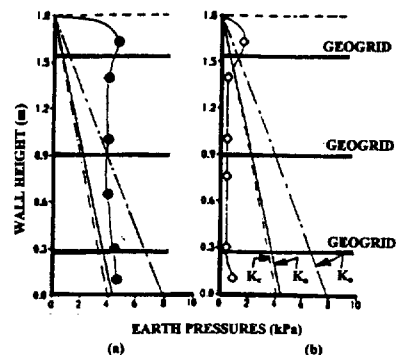


Fig. 19. Horizontal earth pressure distribution on 1.8m high Wall 2: (a) backfill height 1.8m and (b) 7 days after prop removal (after Yogarajah, 1993), where  $K_c$  = Coulomb's coefficient of active earth pressure,  $K_a$  = Rankine's coefficient of active earth pressure,  $K_o$  = Jaky's coefficient of earth pressure at rest.

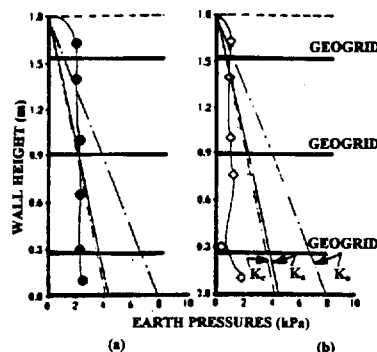


Fig. 20. Horizontal earth pressure distribution on 1.8m high Wall 3: (a) backfill height 1.8m and (b) 7 days after prop removal (after Yogarajah, 1993), where  $K_c$  = Coulomb's coefficient of active earth pressure and  $K_a$  = Rankine's coefficient of active earth pressure and

### 7.3 Strain Distributions Along Geosynthetic Reinforcements due to Compaction and Connecting Reinforcements to Facings

During construction of the three walls tested by Yogarajah (1993), the geosynthetic reinforcements were not attached to the facing panel. At the end of construction, strains in the range of 0.05 to 0.1% were recorded along the reinforcements layers in the three walls, Fig. 22. The strains can be attributed to the Dynamic Interlock due to placing and compaction of the reinforced backfill on the geogrids

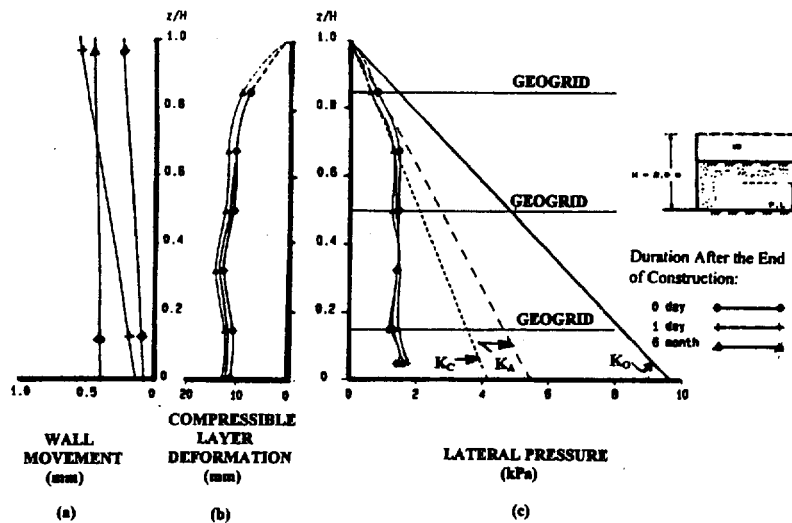


Fig. 21. Distribution of horizontal earth pressure: (a) wall movement, (b) deformation of geomattress, and (c) lateral earth pressure distribution after the end of construction on 2.0m high wall W6 (after Saad, 1993)

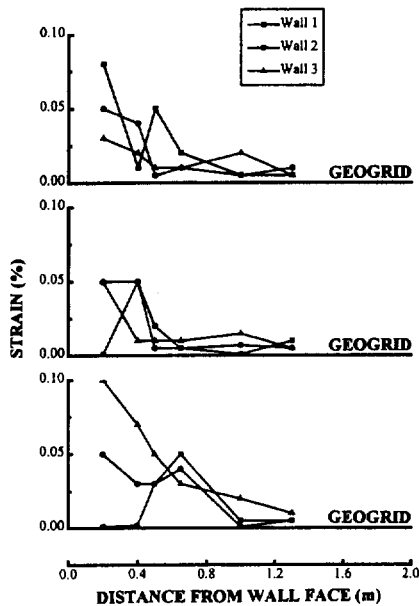


Fig. 22. Comparison of strain distribution along reinforcements at the end of construction on 1.8m high Walls (after Yogarajah 1993)

It was anticipated that the strains recorded along the reinforcement for the roller compaction method (Wall 3) would be higher than the vibrator compaction (Wall 1 and 2). In the roller compaction method, the rolling motion on the reinforced soil mass would have stretched the reinforcement. This additional stretching allowed larger amounts of soil particles to be embedded within the aperture of the geogrid used. Larger resistance to the contraction of the reinforcement would therefore have developed causing larger interlock forces and reduced horizontal earth pressures on the wall. The difference in behaviour, however, was not found to be significant.

After the 'hand tightening' of the reinforcements to the facing and removal of the props in Walls 1, 2 and 3, Yogarajah (1993) found that strains with similar distributions were recorded at all the reinforcement levels, Fig. 23. The strain distribution was not uniform, with small strains occurring at the front end of the reinforcements and increasing to a peak value along the reinforcement, before reducing to zero strains at the rear of the reinforcement. The positions of peak strains when joined together followed a straight line approximately  $0.18H$  away from the face of the wall. Obviously, if no slippage occurs between the reinforcement and the soil, the total displacement of the wall at the level of a particular reinforcement should be equal to the area of the strain diagram at the level of that reinforcement. This was confirmed by Yogarajah (1993).

A similar strain distribution was found by Saad (1993) for the geogrid reinforced walls with compressible boundary. Figure 24 shows the strain distribution along the reinforcements before prop removal with the

reinforcements unattached to the facing, with zero strain at the front end of the reinforcement and the locus of the peak tensions following a log-spiral line having its peak at a distance of  $0.3H$  from the facing at the top of the wall. The strain then drops back to zero at the rear end of the reinforcement.

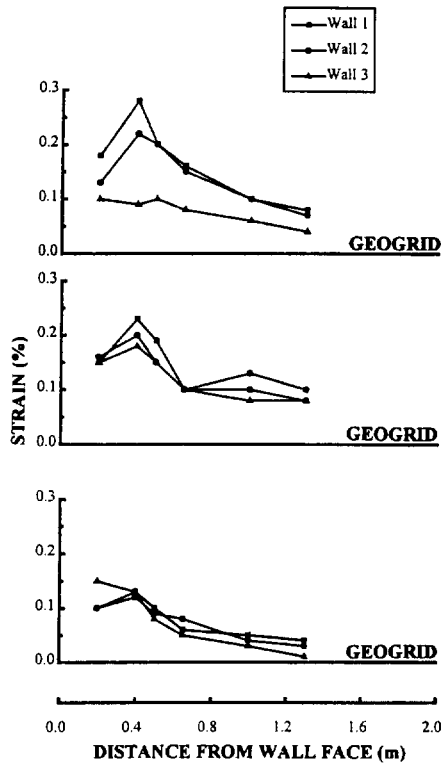


Fig. 23. Comparison of strain distribution along reinforcements 7 days after prop removal in 1.8m high Walls 1, 2 and 3 (after Yogarajah, 1993).

After the attachment of the reinforcements to the facings and removal of the props, the peak strain did not change significantly because almost all the movements of the compressible boundary had already occurred during construction. An appreciable change of strain, however, may be noted at the front end of the reinforcements, Fig. 25. This change of strain may be attributed to the 'hand tightening' of the reinforcements to the facings.

#### 7.4 Significance of Construction Effects on Design

The above sections are highly significant in terms of the approach to be taken to the design of geosynthetic reinforced soil structures. They emphasise the importance of the construction procedures in determining the internal stress-strain behaviour of geosynthetic

reinforced soil structures. Particularly important are the compaction procedures, imposed restrictions to lateral soil boundary movements and the nature and formation of connections between reinforcements and facings. Clearly construction procedures must be taken into account in design approaches and in particular in the Limit State Approach which involves assessment of the stress-strain behaviour of structures.

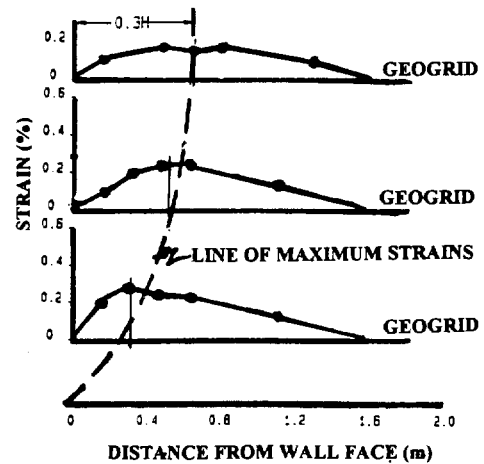


Fig. 24. Load/strain distributions along the geogrid reinforcements at the end of construction in 2.0m high wall W6 (after Saad, 1993)

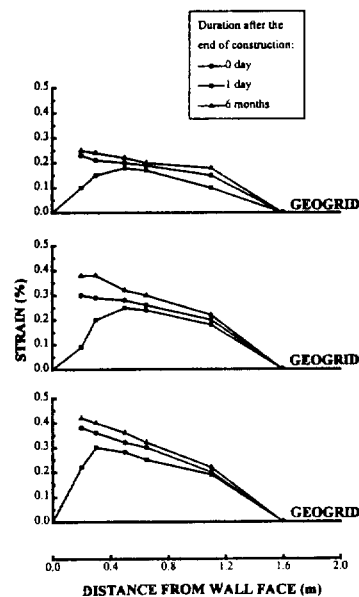


Fig. 25. Strain distributions along the geogrid reinforcements after the end of construction wall W6 (after Saad, 1993)

## PART C - THE LIMIT STATE APPROACH APPLIED TO GEOSYNTHETIC REINFORCED SOIL STRUCTURES

### 8 LIMIT STATE MECHANISMS APPLICABLE TO GEOSYNTHETIC REINFORCED SOIL STRUCTURES

The mechanisms related to the external stability and operational performance of geosynthetic reinforced soil structures is taken to be the same as for conventional soil structures. The main differences between conventional reinforced soil structures and geosynthetic reinforced soil structures are the mechanisms related to internal stability and operational performance.

#### 8.1 A Model for the Internal Ultimate Limit State Mechanism

The behaviour of geosynthetics is time, temperature and load dependent. The load-strain behaviour of geosynthetics may be determined either from constant rate of deformation tensile tests or long term sustained load (creep) tests, but the relationship between constant rate of deformation tensile test data and the long term load carrying capacity of geosynthetics has been shown to be highly product specific and test condition specific, Yeo (1985). In addition constant rate of deformation tensile test data do not provide the necessary stress-strain-time-temperature relationships needed for Limit State analyses. Thus constant rate of deformation tensile test data are not appropriate for use in the Limit State Approach. Long term, sustained load, (creep), test data should be used.

To simulate the long term, sustained load (creep) test conditions and to facilitate the direct application of the test data to the design of a prototype structure, a constant *Out of Balance Force* (OBF) must be applied to the reinforcements from the *End of Construction* (EOC) to the *End of Design Life* (EDL). Such a situation can be achieved only if the tensile strain in the soil is large enough to mobilise the large strain constant volume angle of friction, ( $\phi'_{cv}$ ), at the End of Construction. Thereafter, until the End of Design Life, the soil may strain further but the mobilised shear strength of the soil will remain constant, i.e. the constant volume angle of friction, ( $\phi'_{cv}$ ), will continue to be mobilised.

For the above condition, a *Model Limit State Mechanism* for geosynthetic reinforced soil structures can be identified. In this model it is assumed such that a constant load is applied to the reinforcements from the time of *Switch-on of Gravity* ( $t_{SOG}$ ) to the End of Design Life, ( $t_{EDL}$ ), Fig.26.

Now in practice all the loads are not applied instantaneously, although it is generally assumed that they are applied simultaneously at some point during the *Construction Period*, ( $t_{CP}$ ). An important point to realise is that the Construction Period may be much longer than the *Reinforcement Loading Period*, ( $t_{RL}$ ), depending on the construction procedures adopted. For example a wall may be fully propped until the fill is placed to full height, during which time the reinforcements will not be loaded. Only on removal of the props will the reinforcements be loaded. Thus great care must be taken when selecting the Reinforcement Loading Period, ( $t_{RL}$ ).

When the loads are "switched-on", at say two thirds the Reinforcement Loading Period, ( $2/3 t_{RL}$ ), they will develop a strain in the soil, ( $\epsilon_{SOG}$ ) sufficient to mobilise the large strain constant volume angle of friction of the soil, ( $\phi'_{cv}$ ). If such a situation is achieved, there will be no change in the Out of Balance Force from the time of Switch-on of Gravity to the End of the Design Life and the geosynthetic reinforcements will always carry the same load. Long term, sustained load, (creep), test data thus directly apply and the Model Limit State Mechanism applies.

#### 8.2 A Model for the Internal Serviceability Limit State Mechanism

As stated above, in practice all loads are not applied instantaneously. As for the Ultimate Limit State condition, it can be assumed that all the Serviceability Limit loads are applied at say two-thirds of Reinforcement Loading Period ( $2/3 t_{RL}$ ), although this depends on the construction procedures.

Normally, these loads mobilise an angle of friction in the soil, ( $\phi'_{mRL}$ ) less than the peak angle of friction ( $\phi'_p$ ), Fig. 27. With time, the soil and the reinforcement strain and at the End of Design Life, the mobilised angle of friction ( $\phi'_{mEDL}$ ) is likely to remain less than the peak angle of friction but higher than the mobilised angle of friction at the End of Construction Loading. As the mobilised shear strength of the soil increases with time, the force required to be carried by the reinforcements will gradually become less, which means that the applied force on the reinforcements will change with time. If the change is significant, then an iterative approach to the determination of the deformations in the soil and the reinforcements must be undertaken.

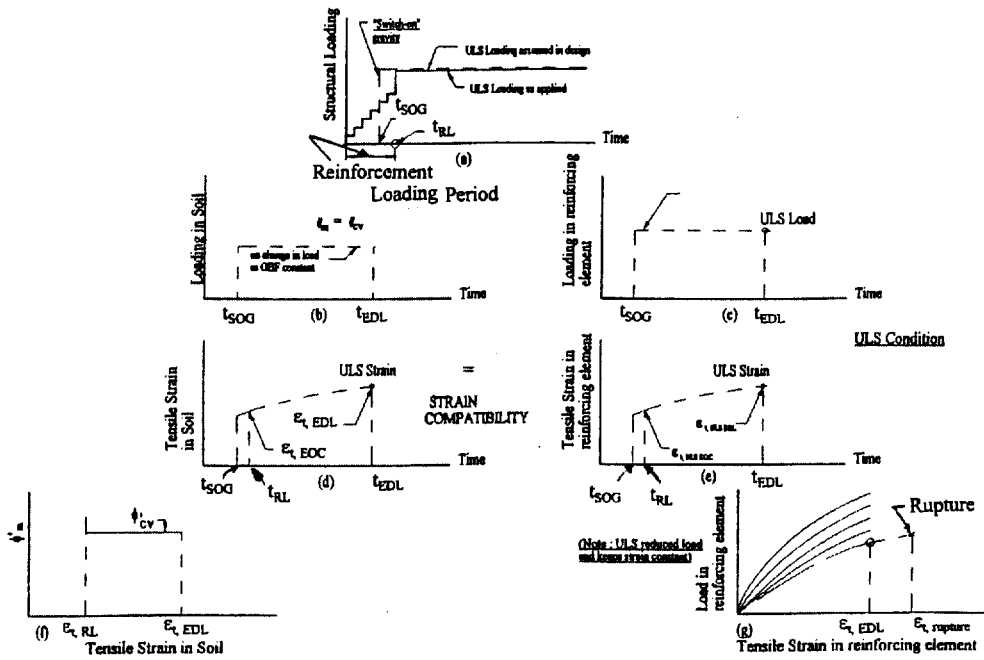


Fig. 26. Model ultimate limit state mechanism

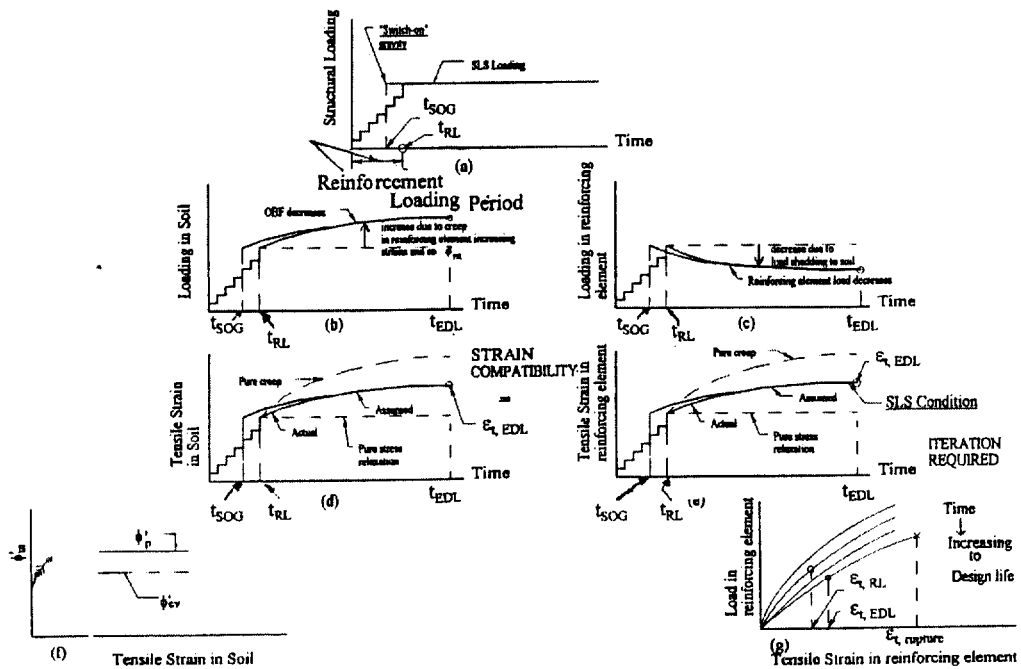


Fig. 27. Model serviceability limit state mechanism

## 9. MATERIAL PARAMETERS TO BE USED IN LIMIT STATE APPROACH DESIGNS OF GEOSYNTHETIC REINFORCED SOIL STRUCTURES

Geosynthetic reinforced soil structures act externally in the same manner as conventional soil structures, hence the choice of material design parameters is the same as for the Limit State analyses of conventional soil structures, which are covered by existing Limit State codes. The difference, once again, is related to internal behaviour.

### 9.1 Soil Properties

As stated previously, the collapse of geosynthetic reinforced soil structures will occur at relatively large deformations, hence the soil will have strained sufficiently to develop the large strain constant volume angle of friction, ( $\phi'_{cv}$ ). Therefore this value should be taken in all Ultimate Limit State analyses of geosynthetic reinforced soil structures.

To account for Serviceability Limit States, limiting strains have to be imposed. Depending on these limiting strains, an appropriate mobilised angle of friction requires to be selected. In general, it is likely that this value will be in the numerical range of at rest angle of friction ( $\phi'_o$ ) to peak angle of friction ( $\phi'_p$ ). Thus for Serviceability Limit State analyses values must be chosen from the relationship between mobilised angle of friction and strain ( $\phi'_m - \epsilon_t$ ) for the soil used, the choice of value will depend on the mobilised strain levels.

Bolton (1986), found that for many granular soils the constant volume angle of friction was in the numerical range of 32 to 37°. Further he suggested that the peak angle of friction is related to the constant volume angle of friction by the equation:

$$\phi'_p = \phi'_{cv} + 0.8 \psi$$

where  $\psi$  is the Angle of Dilatation.

Thus a reasonably close approximation of the shape of the ( $\phi'_m - \epsilon_t$ ) relationship for a dense granular soil may be postulated, as previously indicated in Fig.7 and a mathematical model may be used to represent this relationship, Pradhan (1996).

### 9.2 Geosynthetic Reinforcement Properties

Because of their tendency to creep or suffer stress relaxation, the properties of geosynthetic reinforcements should be determined from long term sustained load (creep) test data. As they are temperature dependent, the sustained load, at which a synthetic polymeric reinforcement element ruptures, must be determined for the operational temperature. The long term load to cause rupture at the End of the Design Life may be designated  $T_{g \text{ rupture EDL}}$ . The tensile strain at which this occurs is

termed the End of Design Life rupture tensile strain and is designated  $\epsilon_{t \text{ rupture EDL}}$ .

The Ultimate Limit State design strength of the reinforcing element at the end of design life, ( $T_{g \text{ ULS EDL}}$ ), may be derived in one of three ways, Fig. 28. Figure 28 (a) shows that the rupture load may be factored and the rupture strain kept constant, whereas Fig.28 (b) shows that the rupture load can be kept constant and the rupture strain factored. However, both the rupture load the rupture strain may be factored, as shown in Fig.28 (c). To date it would appear that the last case is being adopted and this is certainly the most conservative approach.

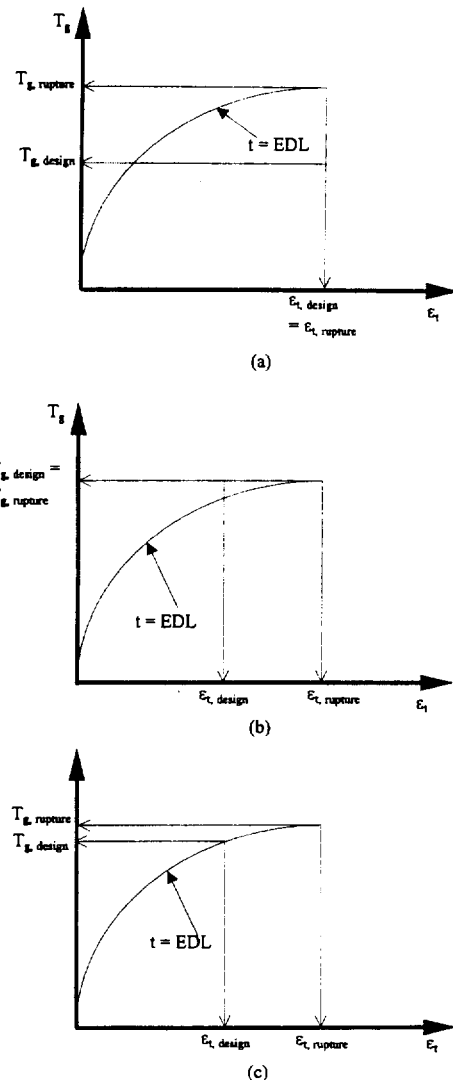


Fig. 28. Three ways of factoring the rupture strength/rupture strain of geosynthetics

For Serviceability Limit State analysis, the mobilised tensile strength of the reinforcement ( $T_{g \text{ MOB}}$ ) should be

derived from *Isochronous Stiffness* data using the mobilised tensile strain data. The isochronous stiffness data should be appropriate to the operational temperature and other factors which will influence the stiffness of the geosynthetic over the strain range appropriate to the Serviceability Limit State. Thus great care must be taken when choosing appropriate Isochronous Stiffness data.

### 9.3 Soil Reinforcement Interaction Properties

There are two limiting modes of soil reinforcement interaction, *Direct Sliding*; in which a block of soil slides over a layer of reinforcement, and *Pull-out*; in which a layer of reinforcement pulls out from the soil after it has mobilised the maximum available bond stresses.

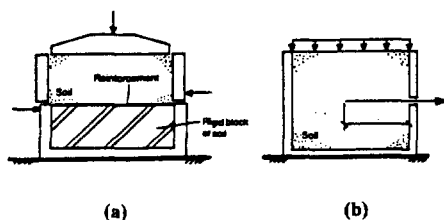


Fig. 29. Determination of friction coefficient between soil and reinforcement: (a) direct shear test; (b) pull-out test

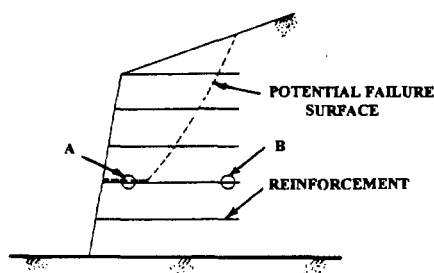


Fig. 30. Mechanisms of interaction in reinforced soil structures

The two tests commonly used to measure soil and reinforcement interaction are the *Direct Shear Test* and the *Pull-out Test*, Fig. 29. In typical reinforced soil structures, the mechanism represented by Direct Sliding is likely to occur in region A and Pull-out in region B in Fig. 30. Each of these tests has limitations in the modelling of the real problem, including differences in boundary conditions and in scaling.

The shortcomings of Direct Shear test are the small area of contact between the soil and reinforcement, the development of friction between the sides of the upper part of the box and the soil together with the development of friction at the edges of the top box due to the soil particles being wedged into the clearance space. However, the errors produced from the development of these frictions at the boundary and the interface usually have a negligible effect on the results as they would be of opposite sign, Butterfield and Andrawes (1972).

A considerable amount of research has been carried out on the Pull-out behaviour of soil reinforcements, including Schlosser and Vidal (1969), Bacot et al. (1978), Chang et al (1977), Schlosser and Elias (1978) and Schlosser and Guillox (1979). Such tests were originally considered to be a useful means of obtaining data for reinforced earth structures. However, their value for design purposes later became somewhat discredited when the measured interface friction coefficient was often found to be several times larger than that of the soil friction, Murray (1983). The interpretation of the Pull-out test results was realised to be complex when pronounced boundary condition effects were identified, Alimi et al (1977) and Schwab et al (1977). Later, Bacot et al. (1978) identified the influence of the length of reinforcement on the apparent coefficient of friction. More recently investigations have shown that test data are highly sensitive to boundary conditions, wall roughness, length of the reinforcement and the scale of the test, Palmeira and Milligan (1989). Because of the complex nature of the test, careful interpretation is required before it is used in the design of reinforced soil structures.

The Direct Shear test can be applied to the determination of the soil reinforcement interaction coefficient for sheet and strip reinforcements, the interaction mechanisms of these types of reinforcement being very similar, Jewell (1996). For geogrid reinforcements, however, the mode of interaction during Pull-out is quite different. Dyer (1985) and Milligan et al. (1990) showed that it is partly developed through the concentration of bearing stresses against the transverse members of the grid and partly developed by Direct Sliding. Thus the *Bond Coefficient* of grids can only be measured by Pull-out testing, Jewell (1996).

McGown et al (1984b) suggested the possibility of applying a Partial Factor to soil-reinforcement interaction coefficients. At present no Limit State code or design method specifies any such Partial Factor. However, it may be suggested that although only a small Partial Factor, equal to or slightly greater than unity, is required for cases where the Direct Shear test results would be applicable, where interaction coefficients are obtained using Pull-out test results a higher Partial factor will be required. Further, since the *Coefficient of Direct Sliding* and the *Coefficient of Bond* are both functions of soil angle of friction, care should be taken when applying such Partial Factors. If in the calculation of the coefficients, a factored soil angle of friction has been used, application of a further Partial Factor on the soil reinforcements interaction coefficients would give an extremely conservative value for use in design.

## 9.4 Other Material Properties

For other materials (concrete, steel connections etc.), a relevant Limit State code may be followed. Normally this exists for use in the design of reinforced concrete and steel structures and material properties can be appropriately selected.

## 10 ACTIONS TO BE USED IN LIMIT STATE APPROACH DESIGNS OF GEOSYNTHETIC REINFORCED SOIL STRUCTURES

To date no benefits related to the short duration of some Actions are taken. All self weight and externally applied Actions are considered to be long term, sustained Actions for the purposes of design. Some of the externally applied loads are not sustained over long periods, for example traffic loads. It has been considered that this assumption represents a conservative basis for estimating the long term rupture and operational strength of geosynthetics and is therefore an acceptable practice. However, it has yet to be determined just how conservative is this assumption. Further investigation of the behaviour of geosynthetics subject to combined sustained and transient loading will require to be undertaken before this can be determined.

## 11 PARTIAL FACTORS TO BE USED IN LIMIT STATE APPROACH DESIGNS OF GEOSYNTHETIC REINFORCED SOIL STRUCTURES

Partial Factors require to be applied to the Properties of Materials, Actions Geometrical Data and Behavioural Models. Existing Limit State codes deal with all these, but are not always in agreement, particularly relating to the Partial Factors to be applied to determine the design strength of geosynthetics and their interaction with soil either for Ultimate or Serviceability Limit State analyses. The Partial Factor for soil-reinforcement interaction has been discussed in Section 9.3, thus in the following section, the Partial Factor related to geosynthetics will be discussed.

### 11.1 Partial Factors for Geosynthetics

Four Partial Factors of major concern have been identified, Voskamp and Risseuw (1987), Jewell and Greenwood (1988), Greenwood and Jewell (1989) and Troost and Ploeg (1990). These are:

- Damage Factor*; to allow for the mechanical damage during construction.
- Environmental Factor*; to allow for the chemical environment and microbiological exposure in the ground.
- Material Factor*; to allow for the uncertainty inherent in the extrapolation of test data, and
- Overall Factor*; to allow for the properties of materials not meeting the manufacturers specification.

Partial Factors are applied to some value of the strength of the geosynthetic reinforcement. Thus the first stage must be to agree the *Reference Strength* to which Partial Factors need to be applied.

Bush (1988), Billing et al (1990), Watts and Brady (1990) and Koerner and Koerner (1990) have carried out tests to identify damage effects on geosynthetics on the basis of constant rate of deformation tensile tests. They defined the maximum load at rupture of the control materials under constant rate of deformation tensile testing as the Reference Strength. However, as stated previously, constant rate of deformation tensile test data depend on many factors such as rate of strain, temperature, etc., and in any case are not suitable for defining geosynthetic properties in Limit State Analysis.

Troost and Ploeg (1990), Viezee et al (1990) and Voskamp (1989) carried out long term sustained load (creep) tests to identify the damage effects on a range of geosynthetics. They defined the Reference Strength as the load to cause rupture of a control specimen at the End of Design Life, Fig. 31. Jewell (1996) has supported this definition but it should be noted that many geosynthetics show a wide range of scatter of their rupture strains at different load levels, Fig. 32. Hence the Reference Strength, defined on the basis of load at rupture for a specific design life time can be very difficult to identify, i.e. it can be difficult to select specific values of loads and strains at rupture for geosynthetics.

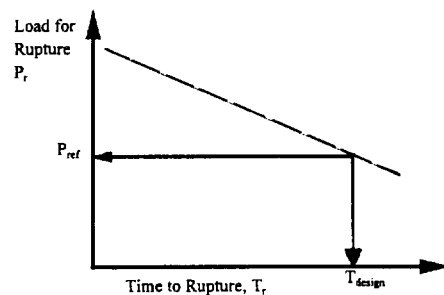


Fig. 31. Reference strength of geosynthetics (after Voskamp, 1990)

A number of manufacturers, for example Netlon (1997), define the Reference Strength as the load, obtained from the load-isochronous creep curves, corresponding to a Performance Limit Strain. Figure 33 shows a typical Sherby-Dorn plot for a geogrid and identifies the *Instability Strain Limit*. A lesser value is then adopted as the Performance Limit Strain for use in Limit Equilibrium Method designs, McGown et al (1984a). This is a very



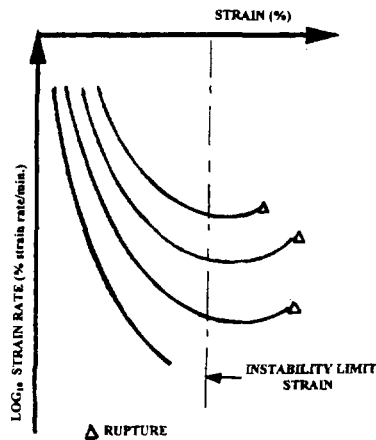


Fig. 32. Typical Sherby Dorn Plot

conservative approach. It is suggested that it would be more appropriate to suggest that the load to develop the Instability Strain, or a lesser defined Limiting Strain at the End of Design Life, should be used to define the Reference Strength for Limit State analyses. Partial Factors for use in Ultimate Limit State analyses should then be obtained by comparing the load carrying capacity of the geosynthetics corresponding to Instability Strain Limit, or to a lesser defined Limiting Strain at the End of Design Life, before and after damage and environmental attacks or due to manufacturing problems. For Serviceability Limit State analysis, the required Partial Factors can be suggested by comparing the load-isochronous curves (before and after damage) at strain levels appropriate to the Serviceability Limit conditions being analysed.

It should be noted that Partial Factors to be used with geosynthetics may be time dependant. Esteves (1996) carried out tests to identify damage effects on geosynthetics using long term sustained load (creep) tests. Figures 34 and 35 show the variation of the Partial Factor for a geogrid with time at large strain (10%) and at a relatively small strain (2%). It can be seen from these data that Partial Factors will vary with time and are therefore dependent on the Design Life of the reinforced soil structure.

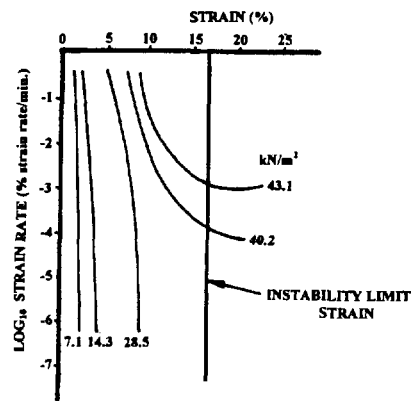


Fig. 33. Sherby Dorn plots for a geogrid at 20°C

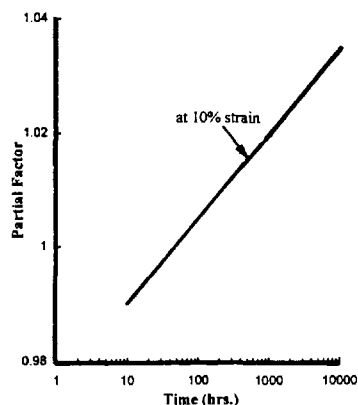


Fig. 34. Variation of damage Partial Factor for a geogrid with time at 10% strain (after Esteves, 1996)

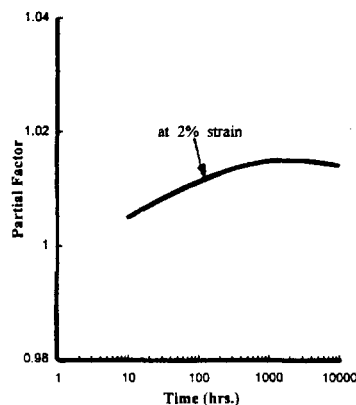


Fig. 35. Variation of damage Partial Factor with time for a geogrid at 2% strain (after Esteves, 1996).

## PART D - THE DEVELOPMENT OF AN INTEGRATED COMPUTER-AIDED LIMIT STATE APPROACH DESIGN METHOD FOR CATEGORY 2 GEOSYNTHETIC REINFORCED SOIL STRUCTURES

### 12 THE BASIS OF THE LIMIT STATE DESIGN PROGRAM

Recently a computer program has been developed for the design of Category 2 geosynthetic reinforced soil structures using the Model Limit State Mechanism outlined previously and assuming the principles of internal force equilibrium and strain compatibility, Pradhan (1996). The integrated program is capable of designing reinforced soil walls, steep slopes and embankments on soft soils, for both Ultimate Limit States and the Serviceability Limit States. Within the program two approaches are adopted:

- i) Design based on Ultimate Limit States with a check of Serviceability Limit States (ULS-SLS Approach).
- ii) Design based on Serviceability Limit States with a check of Ultimate Limit States (SLS-ULS Approach).

In the ULS-SLS Approach, the structure is first designed to satisfy the Ultimate Limit State external and internal criteria and then the Serviceability Limit States are checked for the given reinforcement layout. In the SLS-ULS approach, the structure is first designed to the Serviceability Limit State Criteria and then the external and internal Ultimate Limit States are checked.

For ULS analyses, the large strain constant volume angle of friction, ( $\phi'_{cv}$ ), of the soil is used and for the SLS analyses, the relationship between the mobilised angle of friction, ( $\phi'_m$ ), and lateral strain in the soil, ( $\epsilon_t$ ), is used. In all cases, a Partial Factor of unity is applied.

The design strength of the reinforcements for ULS analysis has been adopted using the method described in Fig. 28(c). As a basis, the load to develop the Instability Strain Limit at the End of Design Life has been chosen and Partial Factors adopted in the program, covering the damage, environmental, material and overall effects, as prescribed by the manufacturer of the products. For SLS analysis, appropriate Isochronous Stiffness data and mobilised strains have been used to obtain the mobilised tensile strength of the reinforcement.

A Partial Factor of unity has been adopted for the soil-reinforcement interaction for both ULS and SLS analysis.

All loads have been taken to be long term, sustained loads. The combinations of loads for ULS and SLS analysis have been chosen according to BS8006 (1995). Partial Factors applied to the Actions for ULS analysis have been chosen from Eurocode 1 (1996). For SLS analysis, a Partial Factor of unity has been applied to the Actions.

### 13 INPUTS FOR THE ULS - SLS DESIGN APPROACH

The Input parameters are chosen from a pre-selected range, e.g., loads, soils, reinforcements, temperature, facings and construction methods. Some of the properties are interrelated and values are assigned as default values, e.g., once the soil type is chosen, the default values and a suggested range of properties are displayed. The default value can be changed within the suggested range but if a value out of this range is chosen then a warning is given, suggesting that the value is "out of range". Some of the Inputs are restricted to default parameters which are dependent on other Inputs, e.g., for a sloped facing, a structure cannot have full height panels. Similarly segmental wall facings can only have either a vertical face or a specific inclination to the horizontal, which is dependent on the facing unit type.

#### 13.1 Inputs for Walls

##### 13.1.1 Load Types

The walls can be designed for one of the following loadings situations:

- i) No external loading
- ii) Surcharge load only
- iii) Bankseat load only
- iv) Surcharge and Bankseat load
- v) Sloped retained fill above the wall

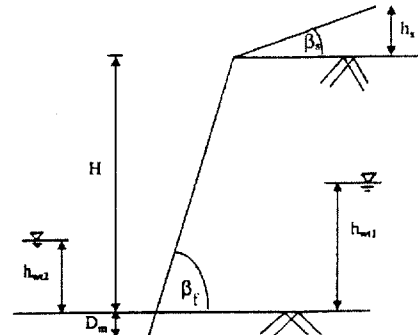


Fig. 36. Basic inputs for geometry of structure

##### 13.1.2 Basic Input

The basic inputs required for the analysis are:

- i) Design life of the structure (yrs)
- ii) Construction time (hrs)
- iii) Height of the structure above ground level, H (m)
- iv) Slope angle of the face of the structure,  $\beta_f$  ( $^\circ$ )
- v) Height of sloped retained fill,  $h_s$  (m)
- vi) Depth of embedment below ground level,  $D_m$  (m)

The parameters for defining the geometry of the structure are shown in Fig. 36.

### 13.1.3 Length of the Reinforcements

The option is given to define the minimum length of the reinforcements. The default value is 0.6 times the height of the structure. He user may define any other minimum length of the reinforcement.

### 13.1.4 Reinforced Fill, Retained Fill and Sloped Retained Fill Types

The following soil types are built into the program for the Reinforced, Retained and Sloped Retained fills:

- i) Well graded crushed rock.
- ii) Well graded sand and gravel.
- iii) Well graded sand.
- iv) Uniformly graded fine/medium sand.

### 13.1.5 Foundation Soil Types

The following soil types built in for the Foundation Soil are:

- i) Well graded crushed rock.
- ii) Well graded sand and gravel.
- iii) Well graded sand.
- iv) Uniformly graded fine/medium sand.
- v) Stiff clay.
- vi) Medium soft clay.
- vii) Soft clay.
- viii) Very soft clay.
- ix) Peat.
- x) Pulverised fuel ash.

### 13.1.6 Reinforcement Types

To date, the program is product specific.

### 13.1.7 Operational Temperature

The in-soil operational temperature in the structure has to be specified. The range of values included are between 5°C and 40°C, in increments of 5°C.

### 13.1.8 Facing Types

A range of Facing Types are available in the program and include:

- i) Full height panels.
- ii) Incremental panels.
- iii) External shutter wraparound.
- iv) Segmental facings.

In the program, if an out of range angle for the wall facing is chosen, information is given on alternative types of facings which are valid for the chosen facing angle .

### 13.1.9 Reinforcement Spacings

The maximum allowable spacing between the reinforcements may be restricted by the facing type and the minimum allowable spacing by the compaction layer thickness in the specification. In the program, the default values of maximum and minimum spacing are automatically chosen depending upon the type of facing.

### 13.1.10 Water Table

The water table can be entered as depth of water above or below the original ground level and it can be different within and outside the structure. A positive value represents the water table above the original ground level and a negative value represents the water table below the original ground level. A zero value represents the condition of no water table. The input data required for the depth of water are:

- i) Depth within the structure,  $h_{wt1}$  (m).
- ii) Depth outside the structure,  $h_{wt2}$  (m).

### 13.1.11 Construction Methods

The construction method is important in the case of the Serviceability Limit State as it dictates the mode of boundary deformation at the Serviceability Limit State condition.

The incremental construction method is applicable to all forms of facing except the full height panel wall construction. The full height panel has a series of separate construction methods, so that the range of methods is as follows:

- i) Incremental.
- ii) Full height panel: props released from Top to Toe.
- iii) Full height panel: props released from Toe to Top.
- iv) Full height panel: restrained at Toe during and after construction and props released at Top after construction.
- v) Full height panel: restrained at Top during and after construction and props released at Toe after construction.

To date compaction effects have not been included but this is now being introduced as it is known to be a very significant factor..

### 13.1.12 Mode of Boundary Deformation

The following ranges of modes of boundary deformation are given for the Serviceability Limit State condition:

- i) Rotation about Top.
- ii) Rotation about Toe.
- iii) Rotation about Top and Translation.
- iv) Rotation about Toe and Translation.
- v) Translation.
- vi) Others

The modes of boundary deformation are shown in Fig. 37.

### 13.1.13 Amount of Boundary Deformation

In the case of the modes of deformation (i) to (v), the slope of the boundary deformation at the Serviceability Limit State condition is defined in the form of deformations (mm) at the Top and the Toe of the facing. For the mode of deformation (vi), the shape of the deformations is entered by defining deformations (mm) at different depths. It may be noted that in the ULS-SLS approach the deformations given for the Top and Toe are only used to define the slope of the boundary, the output deformations of the boundary, (which can be different from these initial inputs), are calculated by an iteration process.

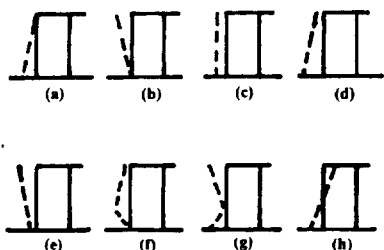


Fig. 37. Different modes of boundary deformation for retaining walls: (a) rotation about top, (b) rotation about toe, (c) translation, (d) rotation about top with translation, (e) rotation about toe with translation, (f), (g) and (h) others.

### 13.2 Inputs for Steep Slopes

The input parameters for Steep Slopes are no different from those of Walls except that the slope of the face of the structure has to be defined and full height panel facings cannot be chosen. The most common types of mode of deformation for Steep Slopes is Rotation about Top and Translation.

### 13.3 Inputs for Embankments

In the program, the embankments are assumed to have a slope angle less than or equal to the large strain constant volume angle of friction of the backfill material and they are resting on a weak Foundation Soil. Hence, a slope angle less than or equal to the large strain constant volume angle of friction of the backfill material has to be entered. The appropriate Foundation Soil type can be selected as one from (vi) to (x) mentioned previously in Section.

The program checks the external stabilities but does not need to check for internal stabilities. In the design, *Slope Change* or *No Slope Change* conditions can be chosen. If the *Slope Change* condition is chosen the slope of the embankment is changed until the most critical external stability is greater or equal to unity. If the *No Slope*

*Change* condition is chosen, the program does not change the slope of the embankment to be safe against all the external stabilities, however, it gives a warning that the Foundation Soil is not strong enough.

The program performs the Overall Stability Analysis for embankments using either a Total Stress Approach or an Effective Stress Approach. For the Total Stress Approach, the undrained shear strength, ( $C_u$ ), of the Foundation Soil at the surface has to be entered. The value of this undrained shear strength is programmed to change with time. It is also possible to vary the undrained shear strength linearly with depth, using the slope of the change in undrained strength versus depth relationship ( $m_c$ ).

For Effective Stress Analysis, Skempton's pore water pressure parameter 'A' at different times has to be entered.

No input for Serviceability Limit State Analysis is required to be entered for embankments having slope angle less than or equal to the large strain Constant Volume Angle of Friction of the embankment soil.

## 14 INPUTS FOR THE SLS-ULS DESIGN APPROACH

The input parameters in this approach are essentially the same as those for the ULS-SLS approach. The exceptions are that this approach is not appropriate for embankments and that the inputted lateral boundary deformations at the Top and Toe should represent the Serviceability Limit State values. These will determine the distribution of the reinforcements, which will then be checked for the Ultimate Limit State conditions.

## 15 OUTPUTS FROM THE ULS - SLS DESIGN APPROACH

The program checks the external and internal stabilities using the appropriate material properties and loadings and determines the deformations at force equilibrium at the End of Construction and at the End of Design Life.

### 15.1 Outputs for Walls and Steep Slopes

External Stability:

- Sliding Ratio
- Overturning Ratio
- Bearing Pressure
- Bearing Resistance

Internal Stability:

- Reinforcement Rupture Ratio
- Pull-out Ratio
- Sliding Ratio through reinforcements
- Sliding Ratio through reinforced fill layers.

Reinforcement Layout:

- Theoretical Layout
- Practical Layout

**Boundary Deformations:**

- At the End of Construction
- At the End of Design Life

**Force at Equilibrium:**

- Out of Balance Forces
- Available Forces

**15.2 Outputs for Embankments**

**External Stability:**

- Sliding Ratio
- Overturning Ratio
- Bearing Pressure
- Bearing Resistance
- Foundation Instability Ratio

**Reinforcement Layout for Slope Stability**

- Practical Layout

**Forces:**

- Required Forces and Available Forces
  - at the End of Construction (EOC)
  - after 1 year from EOC
  - after 5 years from EOC
  - after 10 years from EOC
  - after 120 years from EOC

**16 OUTPUTS FROM THE SLS-ULS DESIGN APPROACH**

The outputs from the SLS-ULS approach are similar to the outputs of the ULS-SLS approach with the difference that the calculated boundary deformations at the End of Construction and End of Design Life will be less than or equal to the Serviceability Limit State limiting values.

**17 SOME DESIGN EXAMPLES AND RESULTS**

**17.1 Walls**

A 5.0m high wall with flat top surface resting on a competent foundation has been designed . Well graded sand and gravel ( $\phi'_p = 40^\circ$  and  $\phi'_{cv} = 32^\circ$ ) was chosen as the Reinforced, Retained and Foundation Soils. Geogrids working at  $10^\circ\text{C}$  operational temperature were chosen. The mode of boundary deformation, the slope of boundary deformation and types of facings were varied to identify their effects on the amount of boundary deformation at the End of Design Life. Additionally, the design life of the structure was varied and its effect on the number of reinforcements and amount of boundary deformations at the End of Construction. The results of these analyses are shown in Figs. 38 to 42 and confirm the influence of the factors varied.

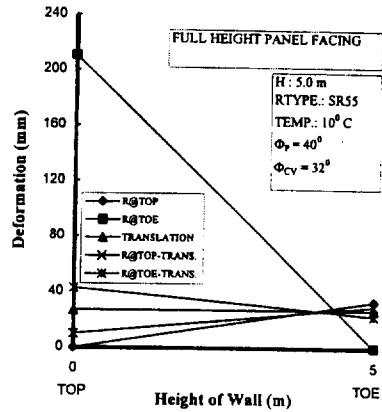


Fig. 38. Effect of mode of boundary deformation on the amount of boundary deformation at the end of design life.

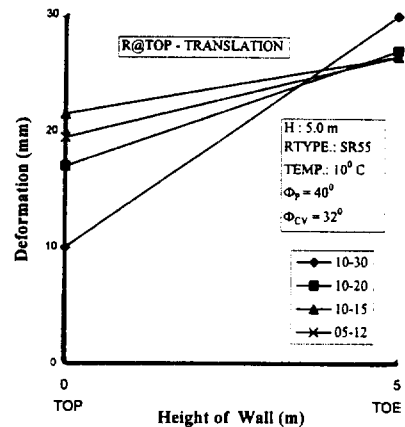


Fig. 39. Effect of the slope of the boundary deformation on the amount of boundary deformation at the end of design life.

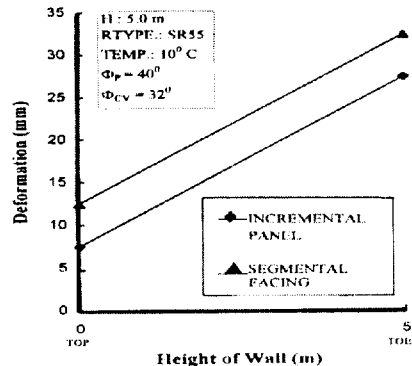


Fig. 40. Effect of facing type on the amount of boundary deformation at the end of design life.

## 17.2 Steep Slopes

A 5.0m high Steep Slope with a flat top surface resting on a competent foundation has been designed. Well graded sand and gravel ( $\phi'_p = 40^\circ$  and  $\phi'_{cv} = 32^\circ$ ) was chosen as the Reinforced, Retained and Foundation Soils. Geogrids working at  $10^\circ\text{C}$  operational temperature were chosen. The angle of the slope was varied to identify its effect on number of reinforcements and deformation at the End of Design Life. The results are shown in Fig. 43 and 44 and confirm the influence of the factors varied.

## 17.3 Embankments

A 5.0m high embankment with a flat top surface and a slope angle of  $30^\circ$  has been designed resting on a weak Foundation Soil. Medium soft clay was chosen as the Foundation Soil. Well graded sand and gravel ( $\phi'_p = 40^\circ$  and  $\phi'_{cv} = 32^\circ$ ) was chosen as the Reinforced and Retained Soils. Geogrids working at  $10^\circ\text{C}$  operational temperature was chosen and both the Slope Change and the No Slope Change conditions were adopted. The Total Stress Approach was used and the undrained shear strength at the surface and the rate of change of undrained shear strength with depth were varied to identify their effects on number of reinforcements for both the Slope Change and the No Slope Change conditions. The results are presented in Figs. 45, 46 and 47 and confirm the influence of the factors varied.

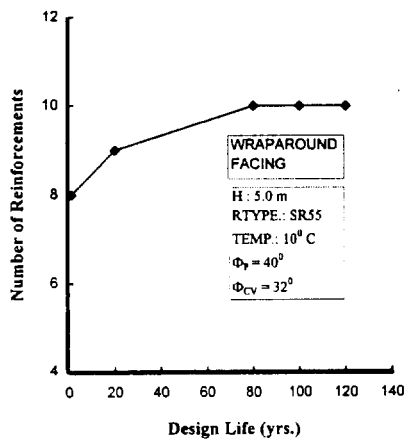


Fig. 41. Effect of design life on the number of reinforcements.

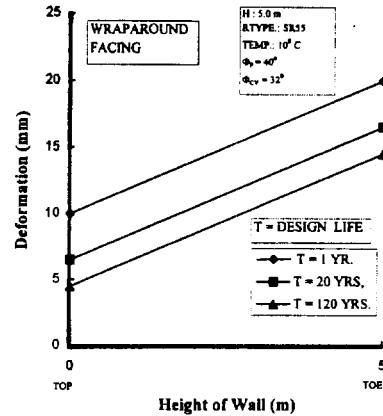


Fig. 42. Effect of design life on the amount of boundary deformation at the end of construction.

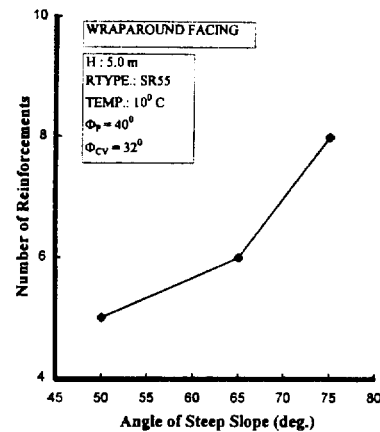


Fig. 43. Effect of angle of steep slope on the number of reinforcements.

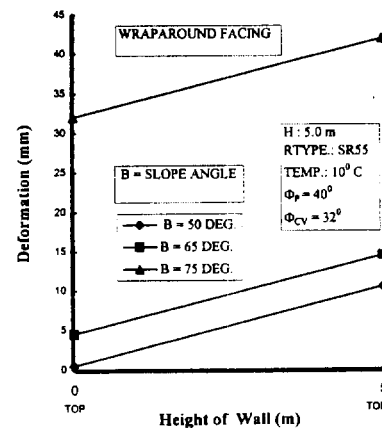


Fig. 44. Effect of slope of the structure on the amount of boundary deformation at the end of design life.

## 18 DISCUSSION AND CONCLUSIONS

The aim of this paper has been to demonstrate the methodology required in order to strictly apply the Limit State Approach to the design of geosynthetic reinforced soil structures. In the process of demonstrating the application of the Limit State Approach, the general principles of the Limit Equilibrium Methods, to date the most widely used design methods, were set out and the explicit and implicit assumptions involved have been highlighted.

From the detailed consideration of the Limit State Approach, it may be concluded that:

(i) The Limit State Approach allows consideration of the nature and size of soil structures, the nature of existing ground and groundwater conditions and the nature of the operational environment. It also allows the introduction of the concept of Geotechnical Categories to take account of the degree of complexity and/or importance of soil structures.

(ii) Two aspects of the Limit State Approach are of particular significance to geosynthetic reinforced soil structures, viz., the consideration given to the Strain Compatibility of the various materials within the soil structure and the assessment of the significance of internal and external environmental conditions on the durability of materials.

(iii) Designs based on the Limit State Approach required the identification of appropriate Calculation Models, Properties of Materials, Actions, Geometrical Data and Limiting Values. Design Values of the Properties of Materials are based on Characteristic Values determined on a statistical basis. The values to be used for collapse/failure and for serviceability conditions may well be very different.

(iv) Design criteria are based on equating the effects of the de-stabilising Actions and the stabilising Actions.

(v) Global Factors of Safety are not used in analyses, rather Partial Factors require to be applied to the Properties of Material, Actions, Geotechnical Data and Behavioural Models.

(vi) Particular attention requires to be given to the internal force equilibrium and strain behaviour of geosynthetic reinforced soil structures and to the effects of construction methods on these.

(vii) Detailed consideration requires to be given to the identification of model mechanisms applicable to the Ultimate and Serviceability Limit States.

The development of an integrated computer-aided Limit State Approach design for Category 2 geosynthetic reinforced walls, steep slopes and embankments has been

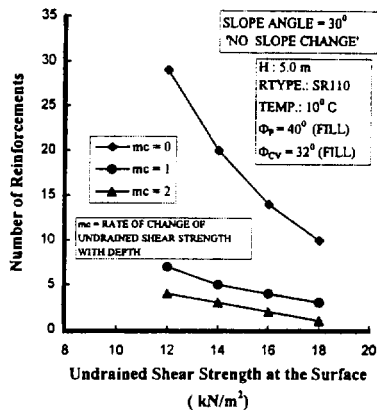


Fig. 45. Variation of number of reinforcements with undrained shear strength and with the rate of change of shear strength with depth for "no slope change" condition

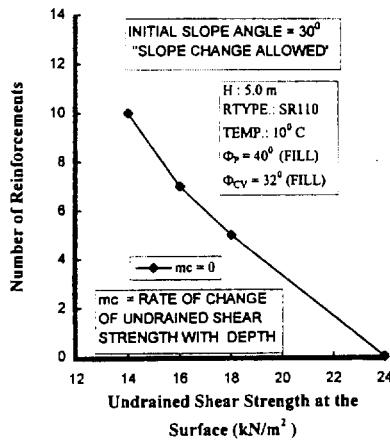


Fig. 46. Variation of number of reinforcements in an embankment slope with different undrained shear strengths for "slope change" condition.

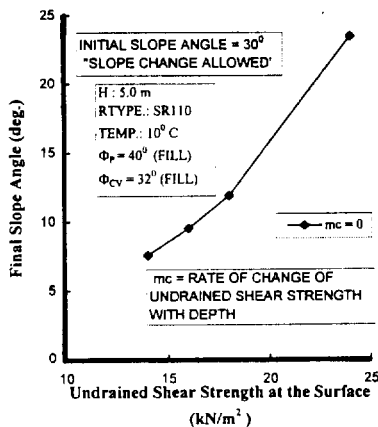


Fig. 47. Effect of undrained shear strength on the final slope angle for "slope change" condition.

presented. Details of the inputs required for the Ultimate and Servicability Limit State analyses have been given and the form of the outputs from the analyses set out. Some design examples have been included which indicate the significance of the various conditions and inputs included in the design program.

Overall, it has been shown that the Limit State Approach is ideally suited to the design of geosynthetic reinforced structures, taking into account many factors not included, nor possible to include, in Limit Equilibrium Methods of design. The computer-aided design package described showed that it is practically possible to apply the Limit State Approach to geosynthetic reinforced soil structures and to account for a wide range of the factors that influence their behaviour.

## REFERENCES

Aggour, M.S. and Brown, C.B. (1974) "The Prediction of Earth Pressure on Retaining Walls due to Compaction", *Geotechnique* 24, No.4, pp. 489-502.

Ahmad, F.(1989) "Model Studies of the Influence of Lateral Boundary Movements on Earth Pressures", *Ph.D. Thesis*, University of Strathclyde, Glasgow, pp. 90-141.

Al-Hassani, M.M. (1978) "Investigation of Stress-Strain Behaviour of Sand Tested in Plane Strain With and Without Sheet Inclusions", *Ph.D. Thesis*, University of Strathclyde, Glasgow, pp. 23-111.

Allen, T.M. and Bathurst, R.J. (1996) "Combined Allowable Strength Reduction Factor for Geosynthetic Creep and Installation Damage", *Geosynthetics International*, Vol.3, pp. 407-439.

Alimi, I., Bacot, J., Lareal, P., Long, N.T. and Schlosser, F. (1977) "Etude de l'adhérence sol armature", *Proc. 9th International Conference on Soil Mechanics and Foundation Engineering*, Tokyo, Vol.1, pp. 11-14.

Andrawes, K.Z., McGown, A. and Murray, R.T. (1986) "The Load-Strain-Time-Temperature Behaviour of Geotextiles and Geogrids", *Proc. 3rd International Conference on Geotextiles*, Vienna, Vol.3, pp. 707-712.

Andrawes, K.Z., Loke, K.H., Yeo, K.C., and Murray, R.T. (1990) "Application of Boundary Yielding Concept to Full Scale Reinforced Soil Walls", *Proc. International Reinforced Soil Conference*, University of Strathclyde, Glasgow, pp. 79-83.

Andrawes, K.Z. and Yogarajah, I. (1994) "Effects of Reinforcement Connections on the Behaviour of Reinforced Soil Retaining Walls", *8th International Conference of the Association for Computer Methods and Advances in Geomechanics*, May, pp. 1313-1318.

Bacot, J., Iltis, M., Lareal, P., Paumier, T. and Sangalerat, G. (1978) "Study of the Soil Reinforcement Friction Coefficient", *Proc. Symposium on Earth Reinforcement, ASCE Annual Convention*, Pittsburgh, Pennsylvania, pp. 157-185.

Barden, L., Ismail, H. and Tong, P. (1969) "Plane Strain Deformation of Granular Material at Low and High Pressures", *Geotechnique* 19, pp. 441-452.

Bell, J.R. and Steward, J.E. (1977) "Construction and Observations of Fabric Retained Soil Walls", *Proc. International Conference on the Use of Fabrics in Geotechnics*, Paris, pp. 123-128.

Billing, J.W., Greenwood, J.H. and Small, G.D. (1990) "Chemical and Mechanical Durability of Geotextiles", *4th International Conference on Geotextiles, Geomembranes and Related Products*, Hague, Netherlands, pp. 621 -626.

Biot, M.A. (1941) "General Theory of Three Dimensional Consolidation", *Journal of Applied Physics*, 12, pp. 155-164.

Bolton, M.D. (1986) "The Strength and Dilatancy of Sands", *Geotechnique* 36, pp. 65-78.

Bolton, M.D. (1993) "What are Partial Factors For?" *Danish Geotechnical Society*, ISLSD93, Vol.3/3, pp. 565-583.

Bonaparte, R., Holtz, R.D. and Giroud, J. P. (1985) "Soil Reinforcement Design Using Geotextiles and Geogrids", *Geotextile Testing and the Design Engineer*, Symposium Sponsored by ASTM Committee D-35 on Geotextiles, Geomembranes and Related Products, Los Angeles, pp. 69-116.

Bonaparte, R., Schmertmann, G.R., Chu, D. and Chouery-Curtis, V.E. (1989) "Reinforced Soil Buttress to Stabilise a High Natural Slope", *Proc. 12th International Conference on Soil Mechanics and Foundation Engineering*, Rio de Janeiro, pp. 1227-1230.

Brinch Hansen, J. (1953) "Earth Pressure Calculations", *The Danish Geotechnical Press*, Copenhagen.

Brinch Hansen, J. (1956) "Limit Design and Safety Factors in Soil Mechanics", *Bulletin No.1, Danish Geotechnical Institute*, Copenhagen, pp. 382-385.

Broms, B.B. (1971) "Lateral Earth Pressure Due to Compaction of Cohesionless Soils", *Proc. 6th International Conference of Soil Mechanics and Foundation Engineering*, Budapest, pp. 373-384.

BS8006 (1995) "Code of Practice for Strengthened/Reinforced Soils and Other Fills", British Standard Institution, pp. 1, 6-7, 43-44, 80-81, 98.



- Bush, D.I. (1988) "Evaluation of the Effects of Construction Activities on the Physical Properties of Polymeric Soil Reinforcing Elements", *International Geotechnical Symposium on Theory and Practice of Earth Reinforcement*, Fukuoka, Japan, 5-7 October, pp. 63-68.
- Butterfield, R. and Andrawes. K. (1972) "On the Angle of Friction Between Sand and Plane Surfaces", *Journ. of Terramechanics*, Vol. 8, No.4, pp. 15-23.
- Chang, J.C. and Forsyth, R.A. (1977) "Design and Field Behaviour of Reinforced Earth Wall", *Journ. Geotechnical Engineering Division, ASCE*, July, pp. 677-692.
- Chen, W.F. and Liu, X.L. (1990) "Limit Analysis in Soil Mechanics", *Developments in Geotechnical Engineering*, Vol.52, Elsevier Science Publishers B.V., pp. 1-4.
- Clayton, C.R.I., Milititsky, J. and Woods, R.I. (1993) "Earth Pressure and Earth-Retaining Structures", *2nd Edition*, Blackie Academic & Professional, pp. 21-25, 81-87.
- Cornforth, D.H. (1964) "Some Experiments on the Influence of Strain Conditions on the Strength of Sand", *Geotechnique* 14, pp. 143- 167.
- Dyer, M.R. (1985) "Observation of the Stress Distribution in Crushed Glass with Applications of Soil Reinforcement", *D. Phil. Thesis*, University of Oxford, UK.
- Esteves, S.A.C. (1996) "The Strength of Geosynthetics and Construction Effects", *M.Phil. Thesis*, University of Strathclyde, Glasgow, UK, pp. 108-109.
- Eurocode 1. Basis of Design and Actions on Structures. DD ENV 1991-1 1996. Basis of Design (together with United Kingdom Application Document), pp. 15-47.
- Eurocode 7. Geotechnical Design. DD ENV 1997-1 1995. General Rules (together with United Kingdom Application Document), pp. 5-7, 12-15, 72-86.
- Fahim, A.K. (1983) "Behaviour of Model Walls Retaining Reinforced and Unreinforced Backfills", *Ph.D. Thesis*, University of Strathclyde, Glasgow, UK, pp. 151-264.
- Fourie, A.B. and Fabian, K.J. (1989) "Geotextile Reinforced Clay Retaining Wall Models", *Proc. 12th International Conference of Soil Mechanics and Foundation Engineering*, Rio de Janeiro, pp. 1243-1247.
- Greenwood, J.H. and Jewell, R.A.(1989) "Strength and Safety: the Use of Mechanical Property Data", *Reinforced Embankments: Theory and Practice in the British Isles*, Thomas Telford, London, pp. 83-98.
- Holtz, R.D. and Massarsch, K.R. (1976) "Improvement of the Stability of an Embankment by Piling and Reinforced Earth", *6th European Conference on Soil Mechanics and Foundation Engineering*, Vienna, 1.2, pp. 473-478.
- Ingold, T.S. (1979) "The Effects of Compaction on Retaining Walls", *Geotechnique* 29, No.3, pp. 265-283.
- Ingold, T.S. (1980) "Reinforced Earth Theory and Design", *Journ. of Highway Engineering*, July, pp. 265-283.
- Ingold, T.S. (1981) "A Laboratory Simulation of Reinforced Clay Walls", *Geotechnique* 31, pp. 399-412.
- Jarrett, P.M., Lee, R.A. and Riddell, D.V.B (1977) "The Use of Fabrics in Road Pavements Constructed on Peat", *Proc. International Conference on the Use of Fabrics in Geotechnics*, Paris, pp. 19-22.
- Jewell, R.A. (1980) "Some Effects of Reinforcement on the Mechanical Behaviour of Soils", *Ph.D Thesis*, Cambridge University, UK, Art. 4.9-4.14, 5.1-5.27.
- Jewell, R.A. (1985) "Limit Equilibrium Analysis of Reinforced Soil Walls", *Proc. 11th International Conference of Soil Mechanics and Foundation Engineering*, San Francisco, Vol.3, Balkema, Holland, pp. 1705-1708.
- Jewell, R.A. (1988) "Compatibility, Serviceability and Design Factors for Reinforced Soil Walls", *International Geotechnical Symposium on Theory and Practice of Earth Reinforcement*, Fukuoka, Japan, 5-7 October, pp. 611-617.
- Jewell, R.A. and Greenwood, V.H. (1988) "Long Term Strength and Safety in Steep Soil Slopes Reinforced by Polymer Mat", *Geotextiles and Geomembranes*, Vol. 7, pp. 81-118.
- Jewell, R.A. (1996) "Soil Reinforcement With Geotextiles", *Special Publication 123*, Construction Industry Research and Information Association, London, UK, pp. 23-29.
- Jones, C.J.F.P., McGown, A. and Varney, D.J. (1987) "Construction Methods, Economics and Specifications", *The Application of Polymeric Reinforced Soil Retaining Structure edited by Jarrett, P.M. and McGown, A. (1988)*, NATO ASI Series, Series E, Applied Sciences, Vol. 147, pp. 573-611.
- Jones, C.J.F.P. (1991) "Construction Influences on the Performance of Reinforced Soil Structures", *Performance of Reinforced Soil Structures*, pp. 97-116.

- Jones, C.J.F.P., (1993) "Discussions: Slopes and Excavations", *Proc. of International Symposium on Earth Reinforcement Practice*, Fukuoka/ Kyushu/ Japan/ 11-13 Nov.1992, Ochiai, Hayashi & Otani (eds), Balkema, pp.972-975,
- Kabir, M.H. (1984) "In-isolation and In-soil Behaviour of Geotextiles", *Ph.D. Thesis*, University of Strathclyde, Glasgow, pp. 123-175.
- Kasahara, K., Kataoka, H., Yokota, Y., Arai, K., Machihara, H. and Nishikawa, S. (1992) "Development of New FTRP- Geogrid and its Application to Test Embankment", *Proc. International Symposium on Earth Reinforcement Practice*, Japan, pp. 357-362.
- Koerner, G.R. and Koerner, R.M. (1990) "The Installation Survivability of Geotextiles and Geogrids", *4th International Conference on Geotextiles, Geomembranes and Related Products*, Hague, Netherlands, pp. 597 -602.
- Krey, H. (1926) "Erddruck, Erdwiderstand und Tragfähigkeit des Baurgrundes", W. Ernst, Berlin (in German).
- Lee, K.L. (1978) "Mechanism, Analysis and Design of Reinforced Earth Walls", *ASCE Symposium on Earth Reinforcement*, Pittsburgh, Pennsylvania, pp. 62-76.
- Loke, K.H. (1991) "Effects of Lateral Boundary Yielding on Large Scale Unreinforced and Reinforced Soil Walls", *Ph.D. Thesis*, University of Strathclyde, Glasgow, pp. 73-154.
- McGown, A. and Ozelton, M.W. (1973) " Fabric Membrane in Flexible Pavement Construction Over Soils of Low Bearing Strength", *Civil Engg. and Public Works Review*, pp. 3-7.
- McGown, A., Andrawes, K.Z. and Al-Hasani, M.M. (1978) "Effect of Inclusion Properties on the Behaviour of Sands", *Geotechnique* 28, Vol. 3, pp. 327-346.
- McGown, A., Andrawes, K.Z and Kabir, M.H. (1982) "Load Extension Testing of Geotextiles Confined in Soil", *Proc. 2nd International Conference on Geotextiles*, Las Vegas, USA, pp. 793-798.
- McGown, A., Andrawes, K.Z., Yeo, K.C. and Dubois, D. (1984a) "The Load-Strain-Time Behaviour of Tensar Geogrid", *Proc. of the Conference on Polymer Grid Reinforcement*, London, pp. 11-17.
- McGown, A., Paine, N. and Dubois, D. (1984b) "Use of Geogrid Properties in Limit Equilibrium Analysis", *Proc. of the Conference on Polymer Grid Reinforcement*, London, pp. 31-36.
- McGown, A., Andrawes, K.Z. and Murray, R.T. (1988) "Control Yielding of Lateral Boundaries of Soil Retaining Structures", *Proc. Symposium Geosynthetics for Soil Improvement*, ASCE, Nashville, pp. 193-210.
- McGown, A., Yeo, K.C. and Yogarajah, I. (1990) "Identification of a Dynamic Interlock Mechanism", *Proc. of International Reinforced Soil Conference*, University of Strathclyde, Glasgow, UK, pp. 377-379.
- McGown, A., Loke, K.H., and Murray, R.T. (1992) "The Behaviour of Reinforced Soil Walls Constructed by Different Techniques", *Proc. ASCE Specialty Conference on Grouting, Soil Improvement and Geosynthetics*, Vol. 2, pp. 1237-1248.
- McGown, A., Andrawes, K.Z., Paul, J., Austin, R.A. (1993) "Limit State Design of Reinforced Soil Walls Slopes and Embankments", *Danish Geotechnical Society, ISLSD93*, Vol.1/3, pp. 275-284.
- McGown, A., Yogarajah, I., Andrawes, K.Z. and Saad, M.A. (1994) "Strain Behaviour of Polymeric Geogrids Subjected to Sustained and repeated Loading in Air and in Soil", *Geosynthetics International*, Vol.1, No.3, pp. 1-15.
- Mercer, F.B. (1986) "Critical Aspects of Industrial and Academic Collaboration", *The Royal Society Philips Lecture*, (Unpublished).
- Meyerhof, G.G. (1993) "Development of Geotechnical Limit State Design", *Danish Geotechnical Society, ISLSD93*, Vol.1/3, pp. 1-12.
- Milligan, G.W.E., Jewell, R.A., Housby, G.T. and Burd, H.J. (1990) "A New Approach to the Design of Unpaved Roads - Part 11", *Ground Engineering*, November, pp. 37-42.
- Murray, R.T. and Boden, J.B. (1979) "Reinforced Earth Wall Constructed with Cohesive Backfill", *International Conference on Soil Reinforcement: Reinforced Earth and Other Techniques*, Paris, Vol.1, pp. 569-577.
- Murray, R.T. (1983) "Studies of the Behaviour of Reinforced and Anchored Earth", *Ph.D. Thesis*, Heriott Watt University, Edinburgh, UK, pp. 88-99.
- Murray, R.T. and McGown, A. (1987) "Assessment of the Time Dependent Behaviour of Geotextiles for Reinforcement Soil Applications", *Durability of Geotextiles, RILEM Chapman and Hall*, pp. 52-73.
- Netlon (1997) *Tensar Geogrids in Civil Engineering: A Guide to the Products and Their Applications*, pp. 10-11.
- Palmeira, E.M. and Milligan, G.W.E. (1989) "Scale and other Factors Affecting the Results of Pullout Tests of Grids Buried in Sand", *Geotechnique* 39, pp. 511-524.
- Pradhan, S. (1996) "The Design of Synthetic Polymeric Reinforced Soil Structures: A Limit State Design

- Approach", *Ph.D. Thesis*, University of Strathclyde, Glasgow, UK, pp. 5-8, 67-69, 116-150.
- Roscoe, K.H. (1970) "The Influence of Strains in Soil Mechanics", *Geotechnique* 20, pp. 129-170.
- Saad, M.A. (1993) "Behaviour of Geogrid Reinforced Soil Wall Subjected to Controlled Lateral Deformation", *Ph.D. Thesis*, University of Strathclyde, Glasgow, UK, pp. 103-154.
- Schlosser, F. and Vidal, H. (1969) "la Terra Armee", *Bulletin de Liaison des Laboratoires*, Routiers Ponts et Chaussées, No. 41, pp. 101-144.
- Schlosser, F. and Elias, V. (1978) "Friction in Reinforced Earth", *Proc. Symp. on Earth Reinforcement, ASCE*, Annual Convention, Pittsburgh, Pennsylvania, pp. 735-763.
- Schlosser, F. and Guillox, A. (1979) "Etude du Frottement Sable Armature en Modele Reduit", *Proc. International Conference on Soil Reinforcement*, Paris, Vol. 1, pp. 151-156.
- Schwab, E.F., Pregel, D. and Broms, B.B. (1977) "Deformation Behaviour of Reinforced Sand at Model Tests Measured by the X-ray Technique", *Proc. International Conference on Use of Fabrics in Geotechnics*, Paris, Vol. 1, pp. 105-112.
- Tatsuoka, F. (1993) "Keynote Lecture: Roles of Facing Rigidity in Soil Reinforcing", *Proc. of International Symposium on Earth Reinforcement Practice, Fukuoka/Kyushu/Japan/11-13 Nov.1992*, Ochiai, Hayashi & Otani (eds), Balkema, pp. 831-870.
- Taylor, D.W. (1948) "Fundamentals of Soil Mechanics", *J. Wiley*, New York, pp. 414-417.
- Terzaghi, K. (1923) "Die Berechnung der Durchlassigkeitsziffer des Tones aus dem Verlug der Hydrodynamischen Spannungsercheinungen, Akademie der Wissenchaften in Wein, Sitzungsberichte, *Mathematisch Naturwissenschaftliche Klasse Part Ila*, 132(3/4): 125-138
- Terzaghi, K. (1925) "Erdbaumechanik", F. Deuticke, Vienna (in German).
- Terzaghi, K. (1936) "A Fundamental Fallacy in Earth Pressure Computations", *J. Boston Soc. Civil Engrs.* 23, pp. 71 - 88.
- Terzaghi, K. and Peck, R.P. (1948) "Soil Mechanics and Engineering Practice", *J. Wiley*, New York, pp. 232, 310, 395, 398-399, 403, 405, 411, 420, 429ff, 443ff, 455, 458, 465, 468, 490, 494, 497.
- Troost, G.H. and Ploeg, N.A. (1990) "Influence of Weaving Structure and Coating on the Degree of Mechanical Damage of Reinforcing Mats and Woven Geogrids Caused by Different Fills During Installation", *4th International Conference on Geotextiles, Geomembranes and Related Products*, Hague, Nederlands, Vol.3, pp. 609 -614.
- Vidal, H. (1969) "The Principle of Reinforced Earth", *Highway Research Record*, No.282, Washington, pp. 1-16.
- Viezee, D.J., Voskamp, W., den Hoedt, G., Troost, G.H. and Shmidt, H.M. (1990) "Designing Soil Reinforcement with Woven Geotextiles. The Effect of Mechanical Damage and Chemical Ageing on the Long Term Performance of Polyester Fibres and Fabrics", *4th International Conference on Geotextiles, Geomembranes and Related Products*, Hague, Nederlands, Vol.3, pp. 651 -656.
- Voskamp, W. and Risseeuw, P. (1987) "Method to Establish the Maximum Allowable Load Under Working Conditions of Polyester Reinforcing Fabrics", *Geotextiles and Geomembranes*, Vol. 6, pp. 173-184.
- Voskamp, W. (1989) "Determination of Allowable Design Strength of Polyester Reinforcing Mats", *Reinforced Embankments, Theory and Practice in the British Isles*, Thomas Telford, London, pp. 67-81
- Watts, G.R.A. and Brady, K.C. (1990) "Site Damage Trials on Geotextiles", *4th International Conference on Geotextiles, Geomembranes and Related Products*, Hague, Nederlands, Vol.3, pp. 603 -607.
- Wu, J.T.H. (1991) Editor, *Proc. of Int. Symposium on Geosynthetic Reinforced Soil Retaining Wall*, Denver, Colorado, pp. 3-77.
- Yeo, K.C. (1985) "The Behaviour of Polymeric Grids Used for Soil Reinforcement", *Ph.D. Thesis*, University of Strathclyde, Glasgow, UK, pp. 42-69.
- Yeo, K.C., Andrawes, K.Z. and Saad, M.A. (1992) "The Use of Compressible Boundary Layer in Reinforced Soil Structures", *Proc. of International Symposium on Earth Reinforcement Practice, Fukuoka/Kyushu/Japan/11-13 Nov.1992*, Ochiai, Hayashi & Otani (eds), Balkema, pp. 449-454.
- Yogarajah, I (1993) "Effects of Construction Procedures on the Behaviour of Geogrid Reinforced Soil Walls", *Ph.D. Thesis*, University of Strathclyde, Glasgow, UK, pp. 93-145.
- Yogarajah, I., McGown, A., Andrawes, K.Z. and Saad, M.A. (1993) "Identification of Appropriate Soil Parameters for Reinforced Soil Wall Design", *Danish Geotechnical Society, ISLSD93*, Vol.1/3, pp. 153-161



# Clogging Potential of Geosynthetic Leachate Collection Layers by Fine Particles From Sand Protective Layers

J.P. Giroud

Senior Principal, GeoSyntec Consultants, 621 N.W. 53rd Street, Suite 650, Boca Raton, Florida, 33487-8220, USA

M.F. Houlihan

Associate, GeoSyntec Consultants, 5950 Symphony Woods Road, Suite 510, Columbia, Maryland, 21044-3521, USA

R.C. Bachus

Principal, GeoSyntec Consultants, 1100 Lake Hearn Drive N.E., Suite 200, Atlanta, Georgia, 30342-1523, USA

S. Qureshi

Lafarge Gypsum, 11130 Sunrise Valley Drive, #100, Reston, Virginia, 20191, USA

**ABSTRACT:** Geosynthetic leachate collection layers used in landfills (e.g. geonet drainage layers overlain by geotextile filters) are often covered with a sand protective layer. If the sand contains fine particles and if the leachate infiltrating through the sand causes some of the fine particles to migrate, then the migrating fine particles may clog the geotextile filter or, if they pass through the filter, may clog the geosynthetic leachate collection layer. This paper presents an evaluation of the effect of migrating fine particles on the performance of the filter and the leachate collection layer. It is shown that a relatively small amount of migrating particles may clog geotextile filters and geonet leachate collection layers. It is unlikely that leachate flow will cause the migration of all of the fines contained in the sand protective layer; however, this paper indicates the importance of assessing the potential for fines migration and the consequences of this phenomenon.

**KEY WORDS:** Geosynthetic, Leachate collection layer, Geotextile, Filter, Clogging.

## 1 INTRODUCTION

### 1.1 Geosynthetics and the Need for Protection

Geosynthetic leachate collection layers used in landfills typically consist of a geonet. Geosynthetic leachate collection layers and the associated geosynthetics (i.e. the overlying geotextile filter and the underlying geomembrane liner) need to be protected from mechanical damage that may result from waste placement operations, and the geotextile filter needs to be protected from deterioration caused by sunlight. The required protection for these geosynthetics is typically provided by a soil protective layer (Figure 1). The degree of protection against

mechanical damage provided to the geosynthetics is a function of, among other factors, the thickness of the soil protective layer. The thickness of soil protective layers typically ranges from 0.3 to 1 m.

### 1.2 Sand Protective Layers Containing Fines

At many landfill sites, the material available for the soil protective layer is a sand containing fines. Fines are generally defined as particles smaller than a certain size (e.g. 75  $\mu\text{m}$  in the United States). Sometimes, a maximum fines content is specified, e.g. 5%. The maximum fines content specification is often treated by design engineers as a secondary consideration to which not much attention is paid, perhaps because no analytical approach has been available to rationally select the specified value. Furthermore, during construction, the specification may not be met, and/or conformance tests to check that the specification is met may not be performed. Based on the authors' experience, the specification regarding the fines content of a sand protective layer is not often well thought out, properly implemented, or seriously enforced.

As shown in this paper, the specification regarding the fines content of a sand protective layer is an important design consideration that must be carefully addressed because clogging of the leachate collection layer and/or its filter may result from the presence of fines in sand protective layers.

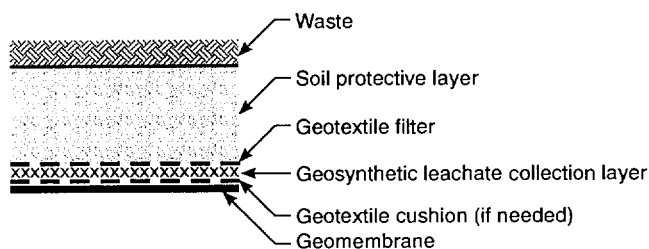


Figure 1. Soil protective layer overlying geosynthetics in a landfill liner system.

### 1.3 Potential Effects of Fines

If fines are “washed” by leachate flow (i.e. if fines migrate as leachate infiltrates through the sand protective layer), then the fines may accumulate on, or in, the geotextile filter, which impedes the flow of leachate toward the leachate collection layer; this problem is addressed in Section 4.2. If some of the migrating fines pass through the geotextile filter, they may accumulate in the leachate collection layer, thereby reducing its hydraulic conductivity and, consequently, its hydraulic transmissivity; this problem is addressed in Section 4.3.

Prior to evaluating the detrimental consequences of the migrating fines (Section 4), it is necessary to quantify the amount of fines contained in the soil protective layer (Section 2) and analyze the conditions that govern the mobility of these fines (Section 3).

## 2 DESCRIPTION OF SAND CONTAINING FINES

### 2.1 Particle Size Distribution of Sand Containing Fines

A typical particle size distribution curve of a sand containing fines is presented in Figure 2a. This curve can be broken down into three segments: AB, representing the fine fraction; BC, representing the coarse fraction; and CD, representing the very coarse fraction. Points B and C are the points of maximal curvature (i.e. minimal radius of curvature) of the particle size distribution curve. As indicated by Giroud (1996), the very coarse fraction, when it is a small portion of the total mass of soil particles (as is the case in Figure 2a where the very coarse fraction is less than 15% of the total mass), does not affect the mobility of the fine particles. Therefore, for the purpose of analyzing the effects of migrating soil particles, the particle size distribution curve can be truncated to eliminate the very coarse fraction (Figure 2b); this type of particle size distribution curve is used in the remainder of this paper.

The soil represented by the particle size distribution curve shown in Figure 2b comprises two distinct fractions: a fine fraction, characterized by the relatively flat curve AB, and a coarse fraction, characterized by the steep curve BC. The limit between the fine fraction and the coarse fraction, Point B in Figure 2, was selected, as indicated above, as the location of maximal curvature of the particle size distribution curve. In Figure 2, the abscissa of Point B is 0.12 mm (120 μm), and, in Figure 2b, the fine fraction proportion,  $f_M$ , is 6%. In this paper, the term “fine particles” is used to designate the particles of the fine fraction, i.e. the particles smaller than the abscissa of Point B, whereas the traditional term “fines” is used to designate particles smaller than 75 μm.

The particle size distribution curve shown in Figure 2 is that of a gap-graded soil if the AB portion of the curve

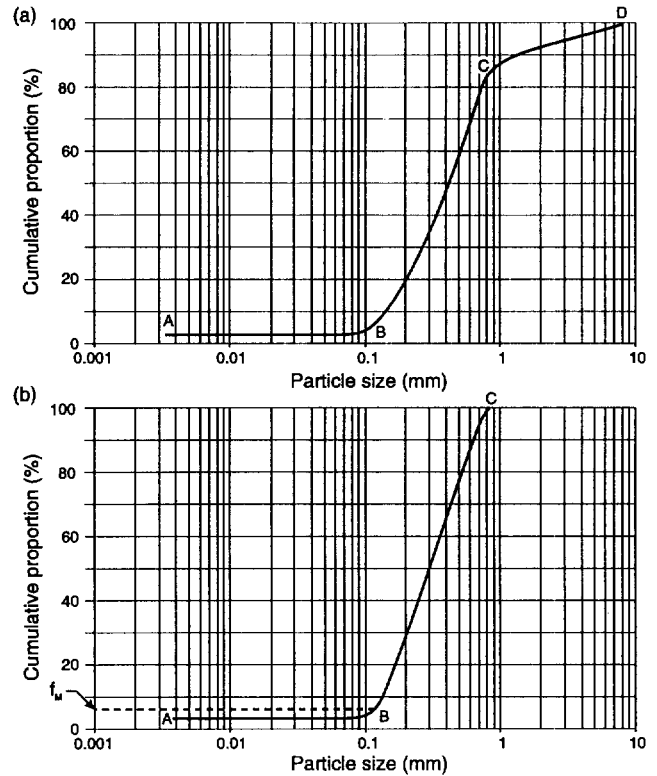


Figure 2. Typical particle size distribution curve of a sand containing fines: (a) fine fraction (AB), coarse fraction (BC) and very coarse fraction (CD), where B and C are points of maximal curvature; (b) particle size distribution curve after removal of the very coarse fraction.

includes, on the left of Point B, a plateau, which indicates a gap between the fine fraction and the coarse fraction. Filtration problems associated with gap-graded soils have been known for a long time (Giroud 1982). Herein, it is not assumed that the particle size distribution curve includes a plateau, but the problems discussed are similar to those of gap-graded soils.

As discussed in Section 3, the extent to which the fine fraction “fills” the pore space of the coarse fraction is an important factor governing the mobility of the fine particles. This is addressed in Section 2.2.

### 2.2 Critical Value of the Fine Fraction Proportion

The critical value of the fine fraction proportion,  $f_{M \text{ crit}}$ , is defined as the value of the fine fraction proportion,  $f_M$ , for which the fine fraction exactly fills the pore space of the coarse fraction. The value of  $f_{M \text{ crit}}$  (for which the derivation is not shown here) is:

$$f_{M \text{ crit}} = \frac{n_c (1 - n_r)}{1 - n_r n_c} \quad (1)$$

where:  $n_f$  = porosity of the fine fraction of the soil when the fine particles fill the pore space of the coarse fraction; and  $n_c$  = porosity of the coarse fraction, which can be expressed as follows:

$$n_c = n + f_M (1 - n) \quad (2)$$

where  $n$  is the porosity of the entire soil comprising the fine and the coarse fraction;  $n$  is obtained experimentally from simple volume measurements. Equation 2 makes it possible to eliminate the unknown parameter  $n_c$  from Equation 1. Combining Equations 1 and 2 gives:

$$f_{M\text{crit}} = \frac{(1 - n_f)[n + f_M (1 - n)]}{1 - n_f [n + f_M (1 - n)]} \quad (3)$$

The only unknown parameter in Equation 3 is the porosity of the fine fraction,  $n_f$ . Values of the order of 0.3 to 0.5 are typically assumed. Table 1 (which was established using Equation 1) shows that  $f_{M\text{crit}}$  does not depend much of the assumption made on  $n_f$  and is typically of the order of 20 to 40%. As a result, the fine fraction proportions of 5% or less used in typical specifications for sand protective layers are much smaller than  $f_{M\text{crit}}$ . In this paper, only cases where  $f_M$  is much smaller than  $f_{M\text{crit}}$  are considered, i.e., approximately:

$$f_M / f_{M\text{crit}} < 1/3 \quad (4)$$

where  $f_M / f_{M\text{crit}}$  is the degree of filling.

Table 1. Values of  $f_{M\text{crit}}$  (%).

Porosity of the fine fraction, $n_f$	Porosity of the coarse fraction $n_c$		
	0.3	0.4	0.5
0.3	23	32	41
0.4	20	29	38
0.5	18	25	33

### 2.3 Methodology for Evaluating the Degree of Filling

Based on the discussions presented in Sections 2.1 and 2.2, the methodology for evaluating the degree of filling of the pore space of the coarse fraction by the fine fraction of a soil composed of a coarse and a fine fraction can be summarized as follows:

- The proportion by mass of the fine fraction,  $f_M$ , is obtained from the truncated particle size distribution

curve of the soil;  $f_M$  is the ordinate of the point of maximal curvature that separates the portion of the curve representing the coarse fraction from the portion of the curve representing the fine fraction (Figure 2b).

- The porosity of the soil,  $n$ , is obtained experimentally.
- The porosity of the coarse fraction,  $n_c$ , is then calculated using Equation 2.
- An assumption is then made regarding the value of the porosity of the fine fraction,  $n_f$ . Typical values are assumed to range between 0.3 and 0.5.
- The value of  $f_{M\text{crit}}$  is then calculated using Equation 1 or 3, and  $f_M$  is compared to  $f_{M\text{crit}}$  to evaluate the degree of filling of the pore space of the coarse fraction by the fine fraction and to check if the condition expressed by Equation 4 is satisfied.

## 3 MOBILITY OF THE FINE PARTICLES

### 3.1 Mechanisms Governing the Mobility of Fine Particles

In a soil comprising two fractions (i.e. a coarse fraction and a fine fraction), the fine particles are located within the matrix formed by the coarse particles. All of the particles (coarse and fine) are subjected to drag forces from the downward flow of leachate. However, it is assumed herein that the matrix formed by the coarse particles is stable, implying that the drag forces do not dislodge the coarse particles. Therefore, only the mobility of the fine particles is considered. (Mobility is defined herein as the tendency of particles to migrate.) The drag forces tend to cause the fine particles to migrate through the matrix formed by the coarse particles. In other words, the drag forces tend to "wash" the fine particles through the matrix formed by the coarse particles. The mobility of the fine particles increases as the drag forces increase and the fine particles' resistance to the drag forces decreases.

The drag forces applied to the fine particles increase if the flow velocity increases. If the degree of filling of the pore space of the coarse fraction is small, i.e. if the condition expressed by Equation 4 is satisfied, the hydraulic conductivity of the soil is anticipated to be high and, consequently, the flow velocity is anticipated to be high. Therefore, in this case, the drag forces applied to the fine particles should be large, and the fine particles are likely to be mobile, thus the consideration in this paper of small degrees of filling.

A fine particle resists drag forces as a result of: (i) cohesive forces that attract the considered particle to other fine or coarse particles; (ii) physical interlocking of the fine particle within other fine particles; and (iii) entrapment of the fine particles within the matrix formed by the coarse particles. The first two mechanisms are discussed below, and the third one is discussed in Section 3.2.

Cohesive forces are difficult to quantify. Cohesive forces are conservatively neglected in the analyses

presented herein. As a result, the mobility of the fine particles predicted by the analysis presented herein is greater than the mobility that would be calculated if cohesion was taken into account.

Interlocking of the fine particles with other fine particles requires that fine particles be in contact with each other. Therefore, the portion, resulting from interlocking, of the resistance to drag forces increases as the amount of fine particles in the pore space of the coarse fraction increases. Only cases where the amount of fine particles is small are considered in this paper (see Equation 4 in Section 2.2). As a result, in the cases considered in this paper, the fine particles are not strongly interlocked.

If cohesion is negligible and interlocking is weak, as assumed in this paper, a significant number of fine particles are likely to migrate individually. In this case, the main factor that governs the ability of the fine particles to migrate is their size.

### 3.2 Influence of Particle Size on Particle Mobility

As indicated in Section 3.1, the mobility of the fine particles of a soil comprising a fine and a coarse fraction depends on their ability to pass between the coarse particles. In other words, the coarse fraction is acting as a filter with respect to the fine particles. Therefore, for the purpose of this analysis, the coarse fraction must be characterized by its filtration opening size. As shown by Kenney et al. (1985) and discussed by Giroud (1996), the filtration opening size of a granular material, such as the coarse fraction considered herein, is given approximately by the following equation:

$$O_F = D_{15}/5 \quad (5)$$

where:  $O_F$  = filtration opening size of the coarse fraction; and  $D_{15}$  = particle size of the coarse fraction such that 15% by weight of the particles of the coarse fraction are smaller than  $D_{15}$ . (Herein,  $D$  is used for the particles of the coarse fraction and  $d$  for the particles of the fine fraction.)

When fine particles migrate individually, they pass through the filter formed by the coarse fraction if they are smaller than the filtration opening size of the coarse fraction, i.e. if:

$$d \leq O_F \quad (6)$$

Combining Equations 5 and 6 gives the following condition for fine particles to migrate individually through the coarse fraction:

$$d \leq D_{15}/5 \quad (7)$$

However, if several particles smaller than  $O_F$  migrate at the same time toward the same area of the coarse fraction pore space, these particles may locally interlock and bridge the filter openings. If this mechanism takes place at many locations, it may gradually prevent many fine particles from migrating. For example, experience from grouting indicates that grout flows freely through a soil if the  $d_{85}$  of the grout particles meets the following requirement with respect to the  $D_{15}$  of the soil (Mitchell 1970):

$$d_{85} \leq D_{15}/25 \quad (8)$$

Grouting is an extreme case where many particles are likely to migrate at the same time into a given volume, whereas, in the case discussed in this paper (i.e. the case where the fine fraction proportion is small), only a small number of fine particles are likely to migrate at the same time. Nonetheless, Equation 8 provides a useful boundary for the case discussed in this paper, as shown below.

In conclusion all the particles that meet the condition expressed by Equation 8 should migrate through the coarse fraction: (i) if the amount of fine particles is small enough that particles are not interlocked (Equation 4); (ii) if leachate flow is able to overcome the cohesion between fine and coarse particles; and (iii) if the cohesion between fine particles is small enough that it will not prevent fine particles from migrating individually. (It is realized that restrictions of particle migration due to cohesion may be significant. For example, even gravel considered clean after thorough washing with water contains some fines.) Additionally, the particles that do not meet the condition expressed by Equation 7 cannot migrate through the coarse fraction, because they are entrapped due to their size. Therefore, the proportion by mass of the particles likely to migrate,  $f_{Mm}$ , is between a lower boundary,  $f_{Mm \min}$ , and an upper boundary,  $f_{Mm \max}$ :

$$f_{Mm \min} < f_{Mm} < f_{Mm \max} \quad (9)$$

Figure 3 shows how to obtain  $f_{Mm \max}$  from the value of  $d$  defined by Equation 7 and  $f_{Mm \min}$  from the value of  $d$  defined by Equation 8 (with  $d$  used instead of  $d_{85}$ ). Figure 3 shows that there is not a large difference between  $f_{Mm \min}$  and  $f_{Mm \max}$  if the particle size distribution curve of the fine fraction is relatively flat in the relevant region.

Often, the particle size distribution curve is known only for particles greater than, or equal to, 75  $\mu\text{m}$ . If the point of maximum curvature of the particle size distribution curve is close to 0.1 mm (100  $\mu\text{m}$ ), then only a small portion of the particle size distribution curve of the fine fraction is known and the method presented in Figure 3 can only be used if the particle size distribution curve is extrapolated. Alternatively, based on Figure 3, it may be assumed that  $f_{Mm}$  is approximately between  $f_M$  and  $f_M/2$  or  $f_M/3$ .



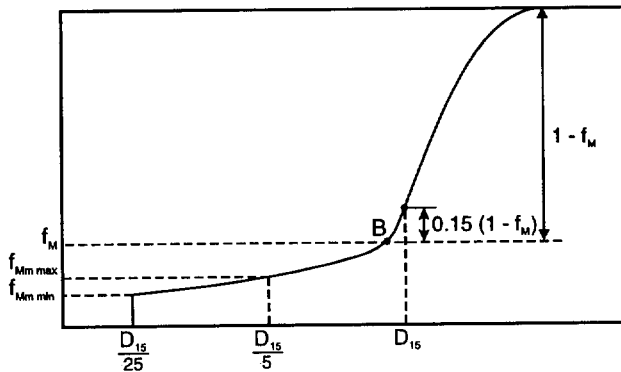


Figure 3. Determination of the amount of fine particles likely to migrate.

#### 4 EFFECTS OF MIGRATING FINE PARTICLES

##### 4.1 Overview

As indicated in Section 3.2, in a soil comprising two fractions, some fine particles can migrate through the coarse fraction. Depending on the opening size of the geotextile filter and other factors, these fine particles may pass through and/or accumulate in, or on, the geotextile filter. The effect of fine particles that accumulate on the geotextile filter is addressed in Section 4.2 and the effect of the fine particles that pass through the geotextile filter and may accumulate in the leachate collection layer is discussed in Section 4.3. A numerical example is presented in Section 4.4.

##### 4.2 Effect of Fine Particles on Filter

The fine particles that accumulate on, or in, the geotextile filter create a low-permeability layer that reduces the rate of leachate flow toward the leachate collection layer. The case where the particles accumulate on the filter is considered herein. Calculations (not presented here, but to be published elsewhere) show that the thickness of the low-permeability layer formed by fine particles accumulated on the geotextile filter is given by the following equation:

$$t_f'' = \frac{t}{n_c} \left( \frac{1-n_c}{1-n_f''} \right) \left( \frac{f_{MF}}{1-f_{MF}} \right) \quad (10)$$

where:  $t$  = thickness of the soil protective layer;  $n_f''$  = porosity of the fine fraction formed in the low-permeability layer by fine particles accumulated on the geotextile filter; and  $f_{MF}$  = proportion by mass of particles accumulated on the geotextile filter. Note that  $f_{MF} \leq f_M$ , the proportion by mass of the particles likely to migrate.

Table 2. Thickness of the low-permeability layer formed by fine particles accumulated on the geotextile filter in the case of a 0.6 m thick soil protective layer.

Proportion by mass of particles accumulated on the filter, $f_{MF}$ (%)	0.5	1	2	5
Thickness, $t_f''$ (mm)	14	28	57	147

Values of  $t_f''$  calculated using Equation 10 for  $t = 0.6$  m,  $n_c = 0.3$  and  $n_f'' = 0.5$  are presented in Table 2. It appears from Table 2 that the calculated thickness of the low-permeability layer formed by the fine particles accumulated on the filter may be significant, even when the proportion by mass of accumulated particles is relatively small (e.g.  $f_{MF} \leq 2\%$ ).

The effect of the low-permeability layer formed by fine particles accumulated on the geotextile filter on the flow of leachate toward the leachate collection layer can be evaluated by comparing the permittivity of this layer to that of the soil protective layer. According to Table 2, the thickness of the low-permeability layer formed by fine particles accumulated on the geotextile filter is of the order of 10 mm if the proportion by mass of the accumulated particles is of the order of 0.5%. If the hydraulic conductivity of this layer is  $1 \times 10^{-7}$  m/s, then the permittivity of this layer is  $1 \times 10^{-5}$  s<sup>-1</sup>. This value is approximately 20 times less than the permittivity of a 0.5 m thick sand protective layer with a hydraulic conductivity of  $1 \times 10^{-4}$  m/s (a hydraulic conductivity that corresponds to a sand containing approximately 1% fines). Clearly, a significant reduction of the leachate flow toward the leachate collection layer may be caused by the accumulation on the filter of as few as 0.5% of the particles (i.e. one tenth of the fines if the fines content is 5%).

##### 4.3 Effect of Fine Particles on Leachate Collection Layer

The fine particles that pass through the geotextile filter migrate into the leachate collection layer, where a significant fraction of the fine particles may tend to accumulate in areas where the leachate collection layer slope is gentle (e.g. 2%), as shown by sedimentation calculations. It is, therefore, important to evaluate if the leachate collection layer can accommodate these fine particles without becoming clogged. Calculations (not presented here, but to be published elsewhere) show that the thickness of leachate collection layer occupied by the accumulated fine particles is given by the following equation:

$$t_{fLCL} = \frac{t}{n_{LCL}} \left( \frac{1-n_c}{1-n_{fLCL}} \right) \left( \frac{f_{MLCL}}{1-f_{MLCL}} \right) \quad (11)$$

where  $n_{LCL}$  = porosity of the leachate collection layer;  $n_{fLCL}$  = porosity of the soil formed by the fine particles accumulated in the leachate collection layer; and  $f_{MLCL}$  = proportion by mass of particles accumulated in the leachate collection layer. Note that  $f_{MLCL} \leq f_M$ , the proportion by mass of the particles likely to migrate.

Values of  $t_{LCL}$  calculated using Equation 11 for  $t = 0.6$  m,  $n_c = 0.3$ ,  $n_{fLCL} = 0.5$ ,  $n_{LCL} = 0.3$  (granular leachate collection layer) and  $n_{LCL} = 0.8$  (geosynthetic leachate collection layer) are presented in Table 3. Table 3 shows that a typical 5 to 10 mm thick geosynthetic leachate collection layer is filled with fine particles, even if the amount of particles accumulated in the leachate collection layer is as low as 0.5 to 1% of the soil protective layer mass. In contrast, a 300 mm thick granular leachate collection layer is filled by fine particles only if the amount of particles accumulated in the leachate collection layer is approximately 10% of the soil protective layer mass.

Table 3. Thickness of leachate collection layer occupied by fine particles,  $t_{fLCL}$  (mm), in the case of a 0.6 m thick soil protective layer.

	Porosity of the leachate collection layer without fine particles, $n_{LCL}$	Proportion by mass of particles accumulated in the leachate collection layer, $f_{MLCL}$ (%)			
		0.5	1	2	10
Granular layer:	0.3	14	28	57	311
Geosynthetic layer:	0.8	6	11	21	117

#### 4.4 Numerical Example

Based on data presented in this paper, the following may be said about a 0.6 m thick sand protective layer containing 5% fines (a fines content generally considered acceptable): (i) the 5% fines content is small compared to the critical fine fraction proportion (which is of the order of 20 to 40%, according to Table 1) and, therefore, the condition expressed by Equation 4 is satisfied; consequently, the fines fill only a small portion of the pore space of the coarse fraction; as a result, the leachate flow velocity may be high and there is likely no interlocking between fine particles; thus, the fines are likely to be mobile unless they are retained on the coarse (i.e. sand) particles due to cohesion; (ii) more than one third or one half of these fines (i.e. approximately 2% by mass of the total soil) may pass through the coarse fraction (according to the comment at the end of Section 3.2), on the basis of their particle size with respect to the particle size of the coarse fraction; (iii) the 2% fines which are most mobile are the finest of the fines and many of them may be retained on the coarse

particles due to cohesion; however, if only one quarter of these fines, i.e. 0.5%, do migrate, the consequences may be significant; (iv) if the migrating fines accumulate on the geotextile filter, they can be expected to form a low-permeability layer at least 10 mm thick (according to Table 2), which may significantly reduce the rate of leachate flow toward the leachate collection layer; and (v) if, instead, the migrating fines pass through the filter, a portion of them may accumulate in the leachate collection layer, which would decrease the geonet hydraulic transmissivity (whereas the hydraulic performance of a typical 0.3 m thick granular leachate collection layer would not be significantly affected, according to Table 3).

## 5 CONCLUSION

The theoretical analysis presented in this paper shows that a small amount of fine particles, migrating under the action of leachate flow from a soil protective layer used in a landfill liner system, may clog the underlying geosynthetic leachate collection layer or its geotextile filter. The analysis presented herein does not take into account the cohesion that may retain fine particles on the coarse (i.e. sand) particles and, therefore, overestimates the amount of fine particles that may migrate. It is, therefore, recommended that, in specific cases where the above analysis indicates a risk of clogging, tests be conducted to determine the amount of fine particles that actually migrate in order to prepare adequate specifications.

## ACKNOWLEDGMENTS

The support of GeoSyntec Consultants is acknowledged. The authors are grateful to J. Lafleur and B.A. Gross for many valuable comments and to K. Holcomb and S.L. Berdy for assistance during the preparation of this paper.

## REFERENCES

- Giroud, J.P., 1982, "Filter Criteria for Geotextiles", Proceedings of the Second International Conference on Geotextiles, Vol.1, Las Vegas, August 1982, pp. 103-108.
- Giroud, J.P., 1996, "Granular Filters and Geotextile Filters", Proceedings of GeoFilters '96, Lafleur, J. and Rollin, A.L., Editors, Montréal, Canada, May 1996, pp. 565-680.
- Kenney, T.C., Chahal, R., Chiu, E., Ofogbu, G.I., Orange, G.N. and Ume, C.A., 1985, "Controlling Constriction Sizes of Granular Filters", Canadian Geotechnical Journal, Vol. 22, No. 1, pp. 32-43.
- Mitchell, J.K., 1970, "In-Place Treatment of Foundation Soils", Journal of the Soil Mechanics and Foundation Division, ASCE, Vol. 96, No. SM1, January 1970, pp. 73-110.

# Laboratory Investigation of the Effect of Coarse Stone Backfill on the Performance of Leachate Collection Pipe

R.W.I. Brachman

Graduate Student, Geotechnical Research Centre, The University of Western Ontario, London, Ontario, Canada

R.K. Rowe

Professor and Chair, Department of Civil and Environmental Engineering, The University of Western Ontario, London, Ontario, Canada

I.D. Moore

Professor, Geotechnical Research Centre, The University of Western Ontario, London, Ontario, Canada

A.R.M. Tognon

Graduate Student, Geotechnical Research Centre, The University of Western Ontario, London, Ontario, Canada

**ABSTRACT:** Laboratory test results conducted on a leachate collection pipe under simulated service conditions are presented for the particular case of a 320 mm outside diameter, 32 mm thick, HDPE drainage pipe surrounded by 50 mm crushed stone backfill. The testing facility and laboratory procedure are discussed. Pipe deformations were found to vary widely along the pipe axis. These measured variations are attributed to the discontinuous backfill support provided to the pipe by the coarse stone. Comparisons of deflections calculated from current design procedures indicates that the Modified Iowa equation over estimates pipe deflections. Equations based on the theory of elasticity applied to thick tubes provide good agreement with the measured deflections.

**KEY WORDS:** landfill, leachate collection system, laboratory tests, plastic pipe.

## 1 INTRODUCTION

Leachate collection systems are intended to control the hydraulic head acting on the barrier and therefore are an important component of modern waste disposal facilities. It is known that both geosynthetic and geologic materials of granular leachate collection systems (eg. geotextiles, pipes and stone, Figure 1) can experience clogging because of particulate, chemical and biological effects (see Rowe et al. 1995). Clogging reduces the effectiveness of leachate collection and may lead to an increase in hydraulic head acting on the landfill liner system.

Design measures intended to minimize the potential of clogging of the leachate collection system can lead to adverse service conditions for the pipe that are not experienced in typical buried pipe applications. For example, large particle size drainage stone is now commonly specified to minimize clogging (50 mm stone is desirable). The relatively large open void space and small surface area per unit volume provided by coarse stone help to minimize biologically induced clogging. However, there is a paucity of data that can be used to assess whether coarse stone has a detrimental effect on pipe performance. Because the stone particles are relatively large, coarse stone loads the pipe at discrete points around the outside surface rather than providing the more continuous support of other, traditional backfill materials (eg. sand, well graded gravel). The magnitude of the stress concentrations from coarse stone backfill, and their effect on the performance of the drainage pipes is presently unknown. Thicker polyethylene pipes are typically specified for use in landfill applications as a result of this uncertainty.

Previous testing conducted by various researchers has shown that plastic pipes can sustain large applied pressures. For example, Watkins (1987), Sargand (1993) and Zanzinger and Gartung (1995) have tested thick, small diameter plastic pipe for use in landfills. These tests did not involve the coarse drainage stone that is desirable to minimize clogging (gravel passing the 19 mm sieve, 25 mm crushed stone, and 8 to 16 mm stone, respectively, were tested). Also, the loading conditions imposed by Watkins differ from those expected to prevail under field conditions. Further, Brachman et al. (1996a) demonstrated that the boundary conditions of the test reported by Sargand were complex and had a significant effect on the pipe response.

Laboratory tests reported by Brachman (1997) conducted under axisymmetric loading conditions showed that coarse stone had an effect on the structural performance of 320 mm outside diameter (32 mm thick) polyethylene pipes, manifested by non-

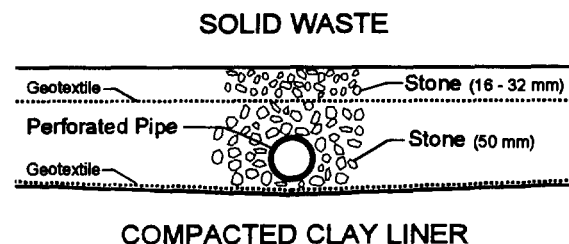


Figure 1. Section through a typical primary leachate collection system.

uniform pipe deformations and large variations in surface strain when backfilled with 50 mm (nominal size) crushed stone.

Laboratory testing of thick, high density polyethylene pipes is needed to assess the effect of coarse stone backfill on the structural performance of these pipes when buried below significant amounts of waste. The ability of design methods to calculate pipe deformations when used with coarse stone backfill must also be considered.

Test results for a 320 mm outside diameter, 32 mm thick, high density polyethylene pipe under simulated field conditions are presented. The nature of the loading applied to the pipe and the testing facility are briefly discussed. Pipe deflections measured at the crown, invert and springline, as well as vertical and horizontal diameter changes are presented to examine the response of the pipe to the applied load. Measured deflections are then compared to those obtained using current design procedures.

## 2 DESCRIPTION OF LABORATORY TESTS

Deep burial leads to large vertical and horizontal stresses in the drainage blanket containing the pipe. These conditions are closely simulated in the laboratory using the test facility described by Brachman et al. (1996b). A transverse section of the test cell is shown in Figure 2. The pipe specimen is centrally placed within a prism of soil that is 2 m wide  $\times$  2 m long  $\times$  1.6 m high. The soil is contained within a stiff steel structure. Lid and base units are connected with tie rods

capable of resisting large vertical pressures (1 MPa). The sidewalls consist of thick steel plates that are stiffened by four support frames. Vertical load is applied by a pressurized air bladder, providing a uniform vertical pressure across the top surface. Horizontal stresses develop in the soil by limiting the deflection of the sidewalls.

The sidewalls of the test cell were treated to reduce the boundary effects from friction. The interface consisted of a thick nonwoven geotextile (430 g/m<sup>2</sup>) and thin (0.1 mm) polyethylene sheet. This arrangement yielded a friction angle of 24°, determined from direct shear tests conducted over appropriate stress levels (25 to 150 kPa) and strain rate (0.41 mm/min). It is estimated that this level of friction reduces the vertical stresses reaching the pipe by roughly 15% and has only a small effect on the pipe diameter change (Brachman et. al 1996b).

Tests were conducted with 50 mm (nominal size) crushed dolomitic limestone as the backfill material. This material is a poorly-graded coarse gravel (GP) and consists of large angular particles with 70% finer than 50.8 mm sieve size and only 8% finer than 38.1 mm. The crushed stone was uncompacted and placed at an average density of 1520 kg/m<sup>3</sup>.

The tests were conducted on specimens of high density polyethylene (PE 3408) pipe with an average outside diameter of 320 mm and an average wall thickness of 32 mm (300 mm OD, DR11 nominal pipe size, where DR is the ratio of outside diameter OD to the minimum wall thickness). The 2 m long specimen contained three butt-fusion joints, located at the centre and 400 mm from each end.

Measurements of deformation were made at various locations

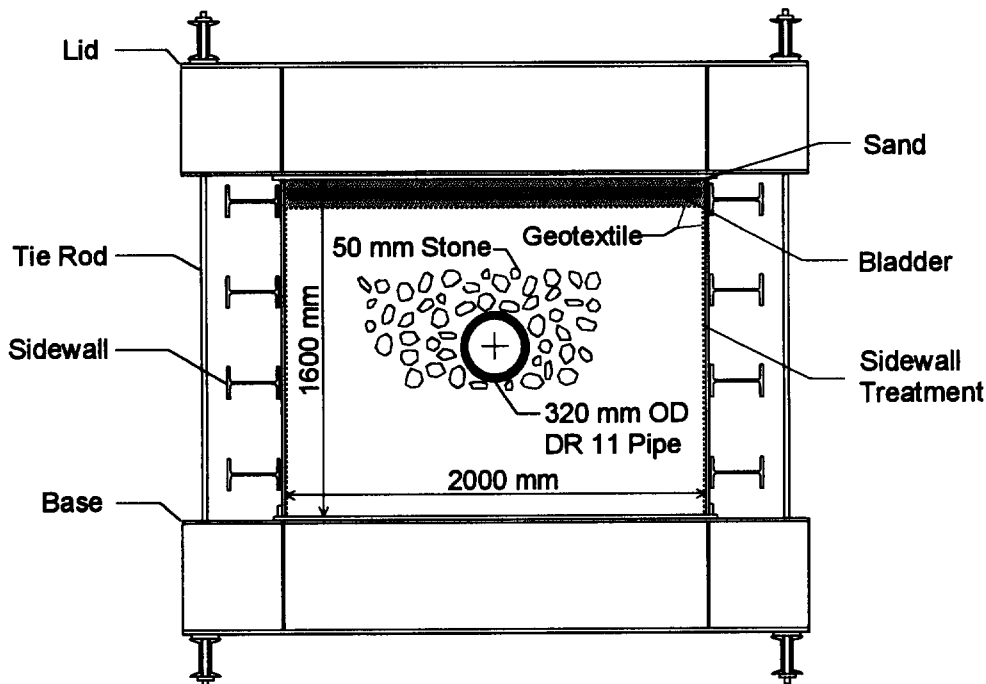


Figure 2. Transverse section through laboratory testing facility.

along the pipe using a laser analog sensor capable of translating and rotating to any position within the pipe. The tolerance associated to the deflection readings is estimated to be  $\pm 0.1$  mm.

Pressure in the bladder was rapidly increased by 50 kPa every 50 minutes and held constant until the next increment was applied. The maximum applied pressure was 250 kPa. Further testing has since been conducted using 1000 kPa pressure. Note that an overburden pressure of 250 kPa in the field corresponds to roughly 19 to 25 metres of waste, assuming that the unit weight of waste is between 13 to 10 kN/m<sup>3</sup>.

### 3 LABORATORY RESULTS

The pipe deformations measured in the laboratory are now presented. First, the measured deflections at the pipe crown, invert and springline are used to show the mode of pipe deformation. Second, the variation of diameter change along the pipe is considered to illustrate the effect of coarse stone backfill on the pipe response.

#### 3.1 Measured Pipe Deflections

Measured values of vertical deflections at the crown and invert ( $\delta_{cr}$  and  $\delta_m$ ) and horizontal deflections at the east and west springline ( $\delta_{sp E}$  and  $\delta_{sp W}$ ) of the pipe are plotted versus the applied bladder pressure in Figure 3. These values were measured near the centre of the pipe ( $z=880$  mm) and are typical of the results recorded for other locations along the pipe.

Downward vertical movements are shown as negative values while outward movements of the springline are taken to be positive.

The magnitude of the deflections increase linearly with an increase in bladder pressure apart from early data. The measured crown deflection was -9.3 mm at a pressure of 250 kPa, Figure 3. At this load level the mean of 17 crown deflection readings recorded at different locations along the pipe axis was -9.1 mm, with a standard deviation of 0.45 mm. The pipe did not remain level once load was applied, as the crown at one end of the pipe deflected 1.3 mm more than the other end. All intermediate measurements of crown deflection were between the values measured at the ends. No noticeable boundary effects from the sidewalls were observed. Also, the presence of the butt fusion joints caused no discernable effect on crown deflections.

The magnitude of the invert deflection measured at  $z=880$  mm was -5.7 mm at 250 kPa (Figure 3). At other locations along the pipe, the mean invert deflection was -6.2 mm with a standard deviation of 0.5 mm. Unlike the crown deflections, the maximum and minimum values were not measured at the ends of the pipe, but rather varied along the pipe with no apparent trend. This implies that the variation arises from the 50 mm coarse stone bedding upon which the pipe rests.

Lateral movements at the springline are also plotted in Figure 3. These values increase with pressure to 1.1 mm and 2.1 mm at the east and west springline, respectively. These values are small relative to the crown and invert deflections. The observation that west springline deflections are larger than those

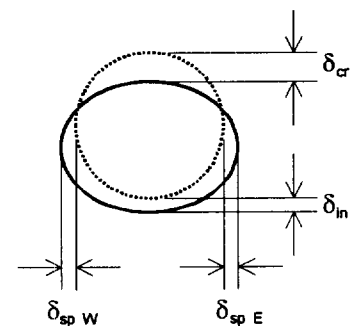
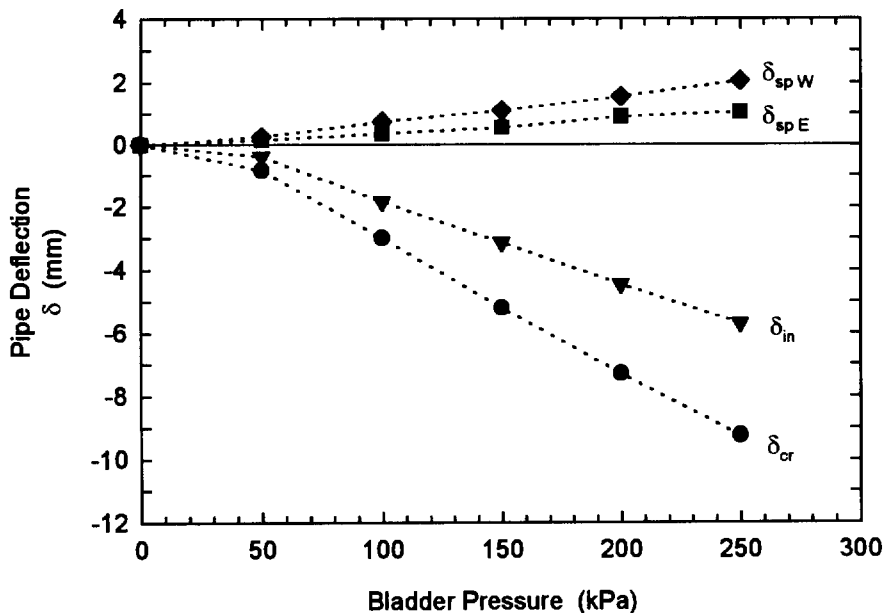


Figure 3. Measured pipe deflections at the crown, invert and springline.

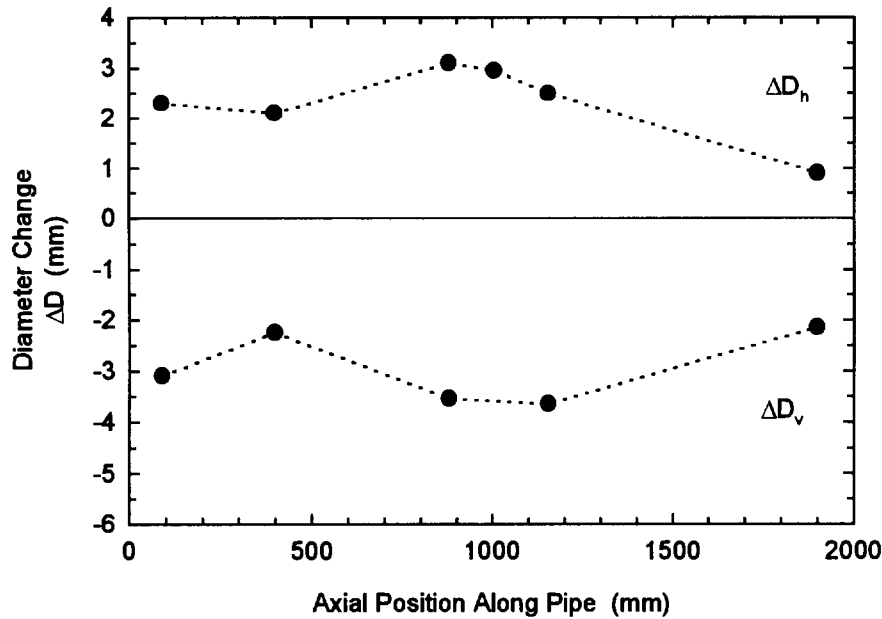


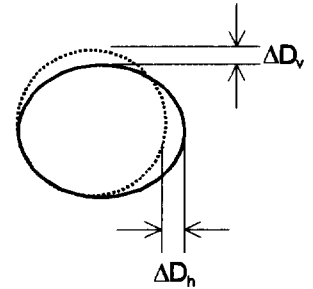
Figure 4. Variation of vertical ( $\Delta D_v$ ) and horizontal ( $\Delta D_h$ ) diameter change along the pipe axis at a bladder pressure of 250 kPa.

at the east springline was consistent along the length of the pipe. This suggests a lateral shift in the pipe. Lateral springline movements varied more than vertical movements of either the crown or invert. The mean deflection at the east springline was 0.7 mm (std. dev. 0.34), and 1.6 mm (std. dev. 0.46) at the west springline. The relatively large variations in springline deflection are probably a direct result of the discontinuous backfill support provided to the pipe by the coarse stone.

### 3.2 Measured Diameter Changes

The vertical ( $\Delta D_v$ ) and horizontal ( $\Delta D_h$ ) diameter changes are plotted in Figure 4 for various axial positions along the pipe at a bladder pressure of 250 kPa. Figure 4 shows a decrease in vertical diameter ( $\Delta D_v = \delta_{cr} - \delta_{in}$ ) and an increase in horizontal diameter ( $\Delta D_h = \delta_{p,e} + \delta_{p,w}$ ). There is a 70% difference in vertical diameter change varying from -2.2 mm near the end at  $z=1900$  mm, to -3.7 mm closer to the centre at 1156 mm. The mean vertical diameter change at this load level was -2.9 mm (std. dev. 0.71 mm). The magnitude of these values represent deflections of roughly 1% of the average pipe diameter at 250 kPa.

The small  $\Delta D_v$  value at  $z=1900$  mm results from a relatively small measured crown deflection and a relatively large invert deflection. This may have resulted from a boundary effect. However, similar vertical diameter changes were recorded at another location ( $z=398$  mm) implying that the variations in vertical diameter change are largely from the nature of the coarse stone backfill rather than a boundary effect.



The horizontal diameter change of the pipe also varies along the pipe axis. The mean  $\Delta D_h$  value is 2.2 mm (std. dev. 1.1 mm) with maximum value of 3.1 mm at  $z=880$  mm, and minimum value of 0.9 mm recorded at  $z=1900$  mm. Both east and west lateral springline deflections were small at  $z=1900$  mm, leading to the low value of  $\Delta D_h$ . This may possibly be a result of some boundary effect associated with the pipe in contact with the steel sidewall.

Overall, there is consistency between variations in vertical and horizontal diameter change with the maximum of the measured values occurring near the middle, and the minimum near the ends of the pipe.

This test shows that the coarse stone backfill does influence the deformation behaviour of the pipe. This is not surprising given the large particle size of the stone relative to the pipe. These measured variations do not, however, preclude the use of coarse 50 mm stone in direct contact with leachate collection pipes. Further study is required to ascertain the effect of the non-uniform deformations on the stresses within the pipe.

## 4 COMPARISON WITH DESIGN PROCEDURES

Limiting deflection is one structural performance criteria often considered when specifying leachate collection pipes. Various methods are available to estimate the pipe deflection for a proposed design. Calculations of deflections are now presented for the present pipe (320 mm OD, DR 11) backfilled with uncompacted, crushed stone, subject to an overburden pressure

of 250 kPa. These calculations are intended to provide a comparison of diameter changes between design values and those measured in the laboratory tests. Deflections are calculated using semi-empirical and theoretical based equations. For all cases, key parameters related to the stiffness of the soil are obtained from recommended values published in the literature. Calculations were performed with the AASHTO (1996) values for polyethylene pipe modulus of 758 MPa (short term) and 152 MPa (long term). The results are summarized in Table 1.

#### 4.1 Modified Iowa Equation

One commonly used method to estimate pipe deflections is the Modified Iowa equation (eg. see Howard 1977). This semi-empirical equation was originally developed to predict the horizontal diameter change of flexible metal pipes. Estimates of pipe deflection are a function of: soil support (characterised by the modulus of soil reaction,  $E'$ ), pipe stiffness, and empirical deflection lag ( $D$ ) and bedding constant ( $k$ ) parameters. Calculated deflections are largely dependent on the empirical parameter  $E'$ , which is a function of soil modulus, pipe size, type of material, and ratio of horizontal to vertical stresses (Gumbel 1983).

Diameter changes calculated using the Modified Iowa equation are presented in Table 1 for a range of  $E'$  values that Howard (1977) recommends for use with crushed rock material (7 MPa for uncompacted, to 20 MPa for compacted conditions). The diameter change calculated with the lower  $E'$  value (to represent material dumped in place) and the short term pipe modulus, is larger than the measured vertical diameter change by a factor of two. The Iowa equation assumes that the full prism load acts on the pipe. This neglects the redistribution of stresses (ie. arching) which may occur because of the difference in stiffness between the pipe and the backfill material.

Also, the Iowa equation is generally used under the assumption that vertical and horizontal diameter changes are of equal magnitude and opposite sign. For polyethylene pipes this is not necessarily the case, as the pipe experiences some circumferential shortening. As a result, the estimate of  $\Delta D_h$  using the Iowa equation ( $E_p=758$  MPa,  $E'=7$  MPa) is nearly three times the measured value.

Increasing  $E'$  from 7 MPa to 20 MPa (with  $E_p=758$  MPa) decreases the pipe deflection by 42%. Using the long term polyethylene modulus yields larger deflections, particularly for the case with the lower value of  $E'$ . Conceivably, a better estimate of  $E'$  for use in the Iowa equation could be made based on the measured deflections, or even from empirical relationships with the elastic soil modulus (Selig, 1990). However, care is required because of the empirical nature of the Iowa equation.

#### 4.2 Elastic Continuum Approach - Thin Tube Theory

Calculations of pipe deflection based on the theoretical solution of Höeg (1968) are also included in Table 1. This solution

considers the plane strain response of a thin, elastic, circular tube buried within an elastic, isotropic, homogeneous medium subject to biaxial stresses applied distant from the pipe. This approach explicitly considers the stiffness of the soil (Young's modulus  $E_s$  and Poisson's ratio  $\nu_s$ ) and the pipe ( $E_p$  and  $\nu_p$ ) as well as the loading conditions similar to those under deep burial in a landfill.

Estimates of elastic soil modulus can be made from the data of Selig (1990). For appropriate levels of confining stress,  $E_s$  varies between 20 to 40 MPa, for 85% and 95% of maximum dry density compaction levels (ASTM D698 test).

Calculations using the short term pipe modulus and  $E_s=20$  MPa are larger than the measured results by a factor of 1.55. The calculated vertical diameter changes are larger than the horizontal diameter changes by a factor ranging from 1.3 to 1.5 (for  $E_p=758$  MPa), depending on the soil modulus. This is consistent with the measured laboratory results, where  $\Delta D_v$  is 1.3 times larger than  $\Delta D_h$ . The elastic continuum approach estimates the mode of deformation similar to that measured in the laboratory tests.

The sensitivity of calculated values to changes in soil and pipe modulus are also shown in Table 1. Decreasing the modulus of the polyethylene to the AASHTO long term value of 152 MPa results in larger values of vertical diameter change, where as the horizontal diameter calculated may be smaller depending on the soil stiffness relative to that of the pipe.

Table 1. Comparison of measured and calculated diameter change at a vertical pressure of 250 kPa.

Method	Pipe Deformation (mm)			
	$E_p=758$ MPa <sup>1</sup>		$E_p=152$ MPa <sup>2</sup>	
	$\Delta D_v$	$\Delta D_h$	$\Delta D_v$	$\Delta D_h$
Measured				
Mean	-2.9	2.2		
Standard Deviation	0.7	1.1		
Modified Iowa <sup>3</sup>				
$E'=7$ MPa	-6.0	6.0	-12	12
$E'=20$ MPa	-3.5	3.5	-4.9	4.9
Elastic Continuum <sup>4</sup>				
Thin Tube Theory				
$E_s=20$ MPa	-4.5	3.4	-7.6	3.5
$E_s=40$ MPa	-2.9	1.9	-4.6	1.4
Elastic Continuum <sup>4</sup>				
Thick Tube Theory				
$E_s=20$ MPa	-2.8	2.1	-4.8	1.9
$E_s=40$ MPa	-1.8	1.1	-3.0	0.7

Notes: <sup>1</sup> Short term AASHTO modulus; <sup>2</sup> Long term AASHTO modulus; <sup>3</sup>  $E'$  from Howard (1977),  $D=1$ ,  $k=.083$ ; <sup>4</sup>  $E_s$  estimated from Selig (1990),  $\nu_s=0.2$ ,  $K=0.25$ ,  $\nu_p=0.4$ .

### 4.3 Elastic Continuum Approach - Thick Tube Theory

Thin ring theory, as assumed by Høeg, is typically satisfactory for pipes with  $DR > 50$ . However leachate collection pipes typically are much thicker than this limit. Thin tube theory assumes there is no radial variation of hoop stresses through the pipe wall and negligible radial stresses compared to the hoop stresses. The assumption of thin pipe response for use with thick leachate collection pipes is now assessed by presenting calculated deformations for thick elastic tubes using the method of Moore (1990).

The results from the thick tube analysis are also presented in Table 1, using the same values considered for the thin tube case. For soil modulus of 20 MPa and the short term AASHTO pipe modulus, the thin solution overestimates the pipe deflections by 40% when compared to values from thick theory. There is good agreement between calculations using thick theory and the measured values in the laboratory.

Increasing the soil modulus reduces pipe deflections. Decreasing the pipe modulus increases the vertical diameter change, while the horizontal diameter change decreases. These calculations show the importance of circumferential shortening when examining pipe deflection.

Although the calculation may be more tedious, the use of the thick elastic solution is recommended to estimate the deformation of leachate collection pipes. This method of analysis also allows calculation of stresses within the pipe. Additional study on the stiffness of coarse stone materials would be useful in characterising the response of these pipes.

## 5 SUMMARY

Measured deflections of a 320 mm outside diameter, 32 mm thick, high density polyethylene leachate collection pipe backfilled in 50 mm crushed stone have been presented. The average vertical and horizontal diameter changes were approximately -1% and 0.8%, respectively, of the mean diameter at an applied pressure of 250 kPa. Circumferential shortening of the pipe was observed as the decrease in vertical diameter was larger than the increase in horizontal diameter of the pipe. Variations in diameter change associated with discontinuities in support from the coarse stone backfill were noted.

Published values of modulus of soil reaction ( $E'$ ) for use in the Modified Iowa equation yielded large values of pipe diameter change. Analysis based on thick elastic tubes provided reasonable values of pipe deflection when compared with measured laboratory results.

Further testing and analysis is required to confirm these observations and to examine the effect of coarse stone on the stress distributions within the pipe.

## ACKNOWLEDGEMENTS

This research is part of a collaborative project investigating the clogging of leachate collection systems funded by the Natural Sciences and Engineering Research Council of Canada.

## REFERENCES

- AASHTO (1996) *Standard Specifications for Highway Bridges*, 16th Edition, American Association of State Highway and Transportation Officials, Washington, DC, USA.
- Brachman, R.W.I. (1997) "Hoop Compression Testing of HDPE leachate Collection Pipe", *Geosynthetics '97*, IFAI, Long Beach, CA, USA, pp. 337 - 350.
- Brachman, R.W.I., Moore, I.D., and Rowe, R.K. (1996a) "Interpretation of a Buried Pipe Test: Small Diameter Pipe in the Ohio University Facility", *Transportation Research Record*, 1541, pp. 64 - 70.
- Brachman, R.W.I., Moore, I.D., and Rowe, R.K. (1996b) "A New Laboratory Facility for Evaluating the Performance of Small Diameter Buried Pipes", *1996 Annual Conference of the Canadian Society for Civil Engineering*, CSCE, Edmonton, AB, Canada, pp. 72 - 83.
- Gumbel, J.E. (1983) *Analysis and Design of Buried Flexible Pipes*, Ph.D. Thesis, Department of Civil Engineering, The University of Surrey, United Kingdom.
- Høeg, K. (1968) "Pressure Distributions on Underground Structural Cylinders", *J. Soil Mech. Fdn. Eng.*, ASCE, Vol. 115(3), pp. 340 - 358.
- Howard, A.K. (1977) "Modulus of Soil Reaction Values for Buried Flexible Pipe", *J. Geotech. Eng. Div.*, ASCE, Vol. 103, GT 1, pp. 33 - 43.
- Moore, I.D. (1990) "Three Dimensional Response of Elastic Buried Tubes", *Int. J. Solids Structures*, Vol. 26, No. 4, pp. 391 - 400.
- Rowe, R. K., Quigley, R.M., and Booker, J.R. (1995) *Clayey Barrier Systems for Waste Disposal Facilities*, E & FN Spon (Chapman & Hall), London.
- Sargand, S.M. (1993) "Structural Performance of an HDPE Leachate Collection Pipe", *31st Annual International Solid Waste Exposition*, San Jose, CA, USA, pp. 381 - 402.
- Selig, E.T. (1990) "Soil Properties for Plastic Pipe Installations", *Buried Plastic Pipe Technology*, ASTM STP 1093, G.S. Buczala and M.J. Cassady (Eds.), ASCE, pp. 141 - 158.
- Watkins, R.K. (1987) *Structural Performance of Perforated and Slotted High-Density Polyethylene Pipes Under High Soil Cover*, Report Submitted to King County Solid Waste, Seattle, WA, USA, 13 pages.
- Zanzinger, H., and Gartung, E. (1995) "Large-scale Model Tests of Leachate Collection Pipes in Landfills Under Heavy Loads", *Advances in Underground Pipeline Engineering*, J.K. Jeyapalan and M. Jeyapalan (Eds.), ASCE, pp. 114 - 125.



# HDPE-Geopipes, Soil-Structure Interaction

H. Zanzinger

LGA, Geotechnical Institute, Nuremberg, Germany

E. Gartung

LGA, Geotechnical Institute, Nuremberg, Germany

**ABSTRACT:** Perforated geopipes are part of the leachate collection system at the base of solid waste landfills. Their structural performance depends on the embedment which is formed by a compacted clay layer, a geomembrane and a sand-bentonite cushion below and coarse gravel above the pipe. Two large scale model tests were carried out. A big geopipe-basal liner model was submitted to uniformly spread static loads up to 1200 kPa. The deformations of the 300 mm diameter pipes were measured by a mobile laser device and by strain gauges applied at the surfaces of the pipes. Earth pressure cells and extensometers recorded the deformation pattern and the load distribution within the soil layers surrounding the pipes. The evaluation of the data reveals a clear picture of the soil-structure interaction of the HDPE-geopipes at the base of high landfills. The test results facilitate the calibration of analytical and numerical methods of structural analysis.

**KEYWORDS:** Leachate Collection System, Landfills, Model Tests, Geopipes

## 1 INTRODUCTION

Leachate collection pipes at the base of solid waste landfills are submitted to high loads under as much as 50 to 70 m of waste material, or more. The pipes, typically 250 to 300 mm in diameter, consist of HDPE. They are embedded in coarse grained drainage gravel or crushed rock material and rest on the compacted clay liner (CCL) or on a special bedding of sand-bentonite above a geomembrane (GM). The structural performance of HDPE-geopipes (GPI) for leachate collection at the base of landfills is not well understood.

Zanzinger et al. (1992) reviewed the currently applied design methods and the influence of the range of typical soil parameters involved. The study comes to the conclusion that analytical models which are applied as a routine to the design of embedded flexible pipes under shallow soil cover do not describe the soil-structure interaction of heavily loaded flexible GPIs at the base of landfills with sufficient accuracy. Example calculations showed that numerical procedures based on the finite element technique facilitate the variation of material parameters and the mechanical behavior of ground conditions in a wide range. However, to properly apply them to design calculations, they ought to be calibrated by measured data obtained under field conditions. Since field measurements in the leachate collection system at the base of an operating landfill would require many years to obtain data under high cover of waste, and since the adverse conditions would strongly impede accurate measurements, large scale model tests were undertaken at the LGA Geotechnical Institute to determine the performance of drainage GPIs under heavy load.

## 2 TEST SETUP AND INSTRUMENTATION

The large scale of the model required very careful preparations. Designing the overall concept, selecting and acquiring the measuring instruments, developing the software for data recording and processing took much time.

A GPI of 315 mm nominal external diameter, with a wall thickness 28.7 mm, was selected for the large scale tests. The upper 2/3 of the GPI circumference were provided with slits, 7 mm wide and 132 mm long for the entry of leachate. The test setup accurately modeled field conditions at 1:1 scale with a CCL at the bottom, drainage gravel surrounding the GPI, and a layer of compressible material to simulate the mechanical properties of waste. The required dimensions of the physical model, width of the entire setup, thickness of the CCL and thickness of the waste-substitute were determined on the basis of finite element analyses to make sure that the measurements of the significant data would not be influenced by the boundaries. The dimensions are given in the cross section (Figure 1). The length of the model was 5.4 m. The model was confined by reinforced concrete elements which were braced against the walls of the test bin in one direction and tied together by steel rods in the other two orthogonal directions.

The load was applied by means of hydraulic flat jacks below the upper concrete beam. It was not easy to find a manufacturer for suitable rubber flat jacks which can reliably be pressurized to more than 1000 kPa. The first set of flat jacks failed during the suitability tests and the research project was delayed by one year. The lesson learned was, that sufficient time has to be allocated to manufacturing, testing and repair of the loading equipment.

The applied vertical load was measured and controlled by pressure gauges in the hydraulic system. In addition, the forces of the tie rods were monitored by force transducers.

In total 59 earth pressure cells were installed in the clay layer, in the drainage gravel and in the waste-substitute material for the determination of the magnitude and the

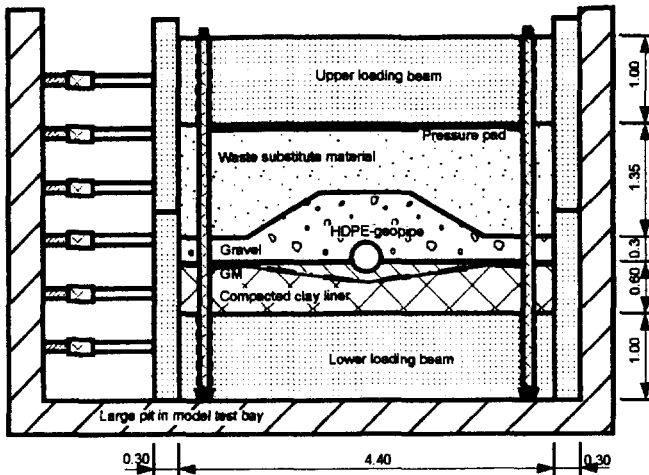


Figure 1. Cross section of the large scale model

distribution of vertical and horizontal stress components in the soil materials surrounding the GPI. The vertical deformation of the soil body was measured by 22 glass fiber rod extensometers, 16 extensometers were installed for the measurement of the horizontal deformation.

The GPI was equipped with 48 electrical resistance strain gauges at the external and 10 at the internal surface. The shape of the GPI was monitored by a mobile laser device, specially developed for this purpose. The laser traveled to 6 sections inside the GPI and took readings there of the distance between the center of the GPI and the wall by revolving around a horizontal axis. The interval of measurements was  $0.25^\circ$ , the precision of deformation measurements by laser technique was 0.1 mm. In order to evaluate the temperature influence on the measurements, thermocouples were installed near the upper and lower surfaces within the clay layer and attached to the GPI.

All measured data were recorded by computer. A special software was developed for data recording and processing. It was very important to have a certain redundancy in data acquisition. Since the great number of measuring instruments proved to be necessary, it was found useful to have different measuring systems for plausibility checks e.g. strain gauges and laser measurements of the GPI.

### 3 EXECUTION OF TESTS

The precast members of the concrete containment had to be placed by crane. The weight of single concrete members was up to 10 t, the entire weight of the confining concrete structure amounted to 235 t. The placement of approximately  $16 \text{ m}^3$  of clay and compaction by small vibratory roller in the laboratory was a challenge. 19.3 t of drainage gravel and about  $30 \text{ m}^3$  of waste substitute material consisting of a mixture of sand and saw dust, had to be handled. All soil materials used for the model test had undergone extensive standard soil mechanics suitability testing before selection.

The relevant soil properties were controlled throughout the installation process and during dismantling of the model. An important observation was that the CCL did not experience substantial changes in water content over the long duration of the model tests.

Plastic sheets and lubricants were placed at the interface between the concrete side walls and the model to reduce wall friction. The installation of all loading and measuring devices, transmission cables and water pressure hoses was carried out with great care. Their proper functioning was verified before the start of the loading test.

Two slightly differing test setups were examined. Figure 1 shows the cross section of the leachate collection GPI above a standard composite liner, consisting of a CCL and a 2.5 mm thick HDPE GM with smooth surfaces. This section was to be tested second. The first test was carried out on a model with the CCL only, so in test no. 1, the cross section looked like Figure 1, but without the GM and the sand-bentonite bedding between GM and GPI.

For test no. 1, the load was applied in 9 steps from 50 to 1200 kPa pressure in the flat jacks, for test no. 2 in 13 steps from 50 to 1300 kPa. The duration of the loading processes was governed by the response of the model to some extent, and by time required for maintenance and repair of some devices such as the mobile laser. The loading process of test no. 1 took 120 days, in case of test no. 2 it took 270 days in total.

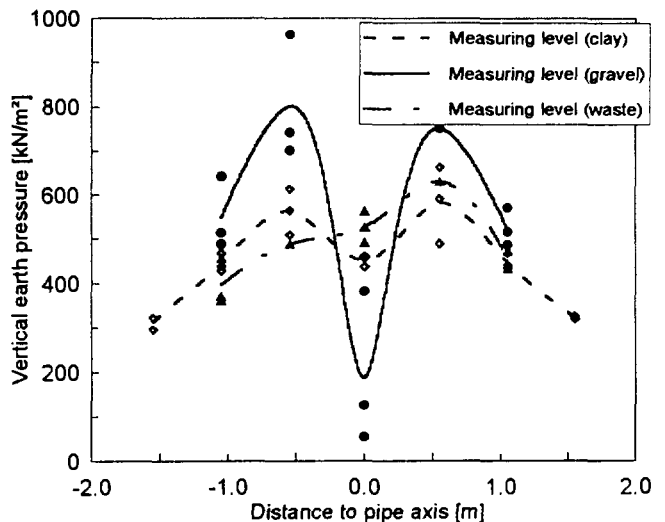


Figure 2. Vertical stress distribution, example for 700 kPa loading

### 4 RESULTS

#### 4.1 Behavior of the Soils

The stress measurements in the soil indicate that an interaction between the soil and the GPI takes place. The load applied at the surface of the model is carried by the soil

and the GPI. Stresses in the soil are redistributed in such a way, that a load carrying arch is formed in the gravel around the GPI. Figure 2 shows an example of the stress distribution in the soil measured in three horizontal planes. In the horizontal plane immediately above the GPI inside the gravel drainage layer, the vertical stresses besides the GPI are increasing and reach maximum values, above the crown they are decreasing and show a minimum. The vertical stresses in the CCL below the GPI qualitatively exhibit the same shape of the stress distribution curve, but less pronounced. The vertical stresses in the waste-substitute material appear to be unaffected by the stress concentration. Measurements of all loading steps reveal that the shape of the arch and the location of maximum stress concentrations in the drainage gravel are independent of the magnitude of the load. The vertical stresses are increasing linearly with increasing load.

The horizontal earth pressures in the midplane of the GPI are variable. They reach a maximum next to the GPI. Their minimum is located about three times the GPI diameter from the center of the GPI. The lateral deformations of the soil are almost zero at about 0.5 m from the center of the GPI. They occur near the maximum of vertical stresses.

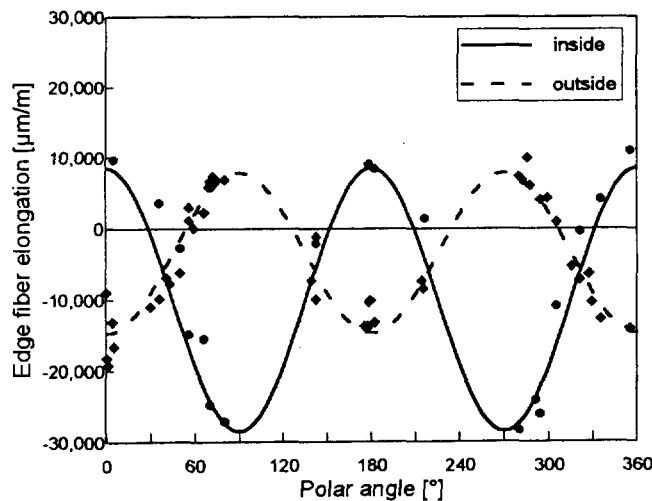


Figure 3. Strain in the GPI, example for 700 kPa loading

#### 4.2 Structural Behavior of the Geopipe

Precise measurements indicate that the GPIs are not exactly circular before they are loaded, but show a considerable deviation from the theoretical geometry of the cross section. Once the GPI is undergoing deformations under load, the mode of the deformation is kept, the magnitude of the deformations increases linearly with the applied load.

The strain and accordingly also the stress at the surface of the GPI is distributed in a sinusoidal pattern as shown for an example measurement on Figure 3. This applies to

the normal forces and to the bending moments as well. The normal forces and the bending moments can be deduced from the measured strains.

Maximum stresses occur at 0°, 90°, 180° (crown); 270°. In between there are locations of zero strains at 50°, 130°, 230° and 310°. These locations of zero strains are independent of the magnitude of loading. Once established, they remain geometrically stable during the entire loading sequence for all load steps.

In addition to the bending strains, the GPI experiences compressive strain due to the normal forces which reached the magnitude of 1% at elevated loads during the tests. This means that the deformed shape of the GPI is not exactly an ellipse. The lateral displacement  $\delta_v$  of the side walls is smaller than the vertical displacement (deflection)  $\delta_v$  of the crown. The relationship between these two displacements can be described by the simple formula  $\delta_v = -(1.2 \div 1.3)\delta_H$ . This result is interesting with respect to deformation measurements in the field. Since the GPIs at the base of an operating landfill will carry leachate and often also be covered by incrustations at the bottom, it is almost impossible to get correct measurements of the deformed shape of the leachate collection GPIs as expressed by a reduction of the vertical distance between crown and invert. It is much easier to measure the increase of the lateral distance between the side walls and deduce the vertical deformation from there.

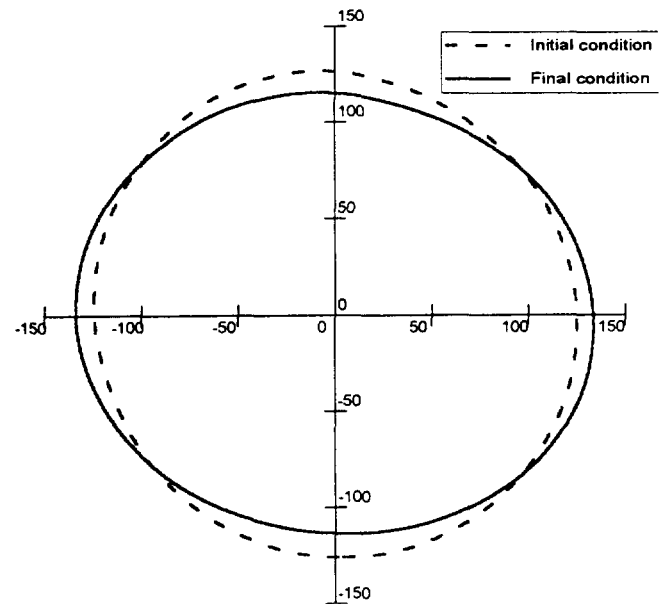


Figure 4. Example for the deformed shape of the GPI

The GPIs showed considerable deformations in the tests, an example is presented on Figure 4. The measured maximum values of clearance decrease amounted to 19% deflection under maximum vertical loads representative of about 65 m of waste material. There were no indications of an approach to structural failure under the applied loads.

At the interface between clay and gravel where the stiffness of the embedment conditions of the GPI change, finite element analyses indicate discontinuities in the distribution of stresses due to bending moments. The actual measurements taken at the large scale model however, do not reveal any irregularities in the shape of the stress distribution curve.

Under the test conditions, that is temperatures between 20° and 25 C and vertical loads up to about 800 kPa acting upon the drainage gravel surrounding the GPI for a maximum duration of the test of 270 days, no substantial creep was observed. Since essentially a linear structural response of the embedded GPI was observed, and no relevant creep effects occurred, it seems to be justified to use linearly elastic constitutive models for design analyses.

#### 4.3 Influence of the Geomembrane

The results of test no. 2, where the GPI was installed on a sand-bentonite bedding above the GM do not differ substantially from those of test no. 1, where the GPI rested directly on the CCL. A direct comparison of the stresses in the soils surrounding the GPI under equivalent vertical loads shows slightly smaller stress concentrations in the test with the GM and a comparison of the GPI deformations yields slightly larger deformations of the GPI under equivalent loads in the setup with the GM. These differences are marginal and do not call for special design rules for the GPIs above GMs although they indicate that the smooth surface of the GM has some affect on the structural performance of the GPI-soil system.

## 5 CONCLUSIONS

The large scale model tests show that at the base of landfills the structural performance of the GPIs is governed by the interaction with the surrounding soil. As the flexible GPI deforms, an arching effect develops inside the drainage gravel initiating vertical and horizontal stress redistributions. So the placement of the drainage blanket is important for the structural safety of the GPI. The shape and thickness (twice the pipe diameter above the GPI) of the drainage gravel according to German design practice is satisfactory. The waste material above the GPI embedment zone does not experience any stress redistribution due to the deformation of the GPI. So even if the waste has a certain strength and stiffness, it should not be taken into account in the design of the GPI.

There is no substantial difference in the performance between GPIs placed on CCL directly and GPIs placed on a sand-bentonite bedding above a smooth GM.

Under heavy loads GPIs experience considerable deformations and the deformation rather than the stability appears to be the controlling criterion. It is necessary to adjust analytical methods for the determination of GPI deformations according to the experience gained by the large

scale model tests, reported in this paper. Current design analyses may underestimate the magnitude of the expected deformations. When methods are applied which predict the deformations reliably, greater maximum deformations may be able to be tolerated than according to currently practiced specifications.

For the evaluation of the performance of GPI it is useful to determine the deformed shape of the GPI by the measurement of the lateral deformation. With the experience gained in the large scale model tests, it is possible to deduce the state of stress within the GPI from deformation measurements.

Not all problems concerning the behavior of embedded GPIs have been solved. To mention some open questions, the behavior of very thin walled GPIs or profiled GPIs cannot be judged on the basis of the present study on thick walled GPIs. Research on thin walled GPIs seems to be of primary interest with respect to economy. Another question that should be addressed is the influence of higher temperatures, and the performance of GPI junctions.

## ACKNOWLEDGMENTS

The research on the structural behavior of HDPE GPIs at the base of solid waste landfills was financially supported by the authorities of the State of Bavaria.

## REFERENCES

- Hoch, A., Zanzinger, H. and Gartung, E. (1990) "Design of Drainage Pipes below Landfills", *International Conference: Pipeline Design and Installation*, ASCE, New York, NY, USA, pp. 546-556.
- Moore, I.D. (1993) "HDPE Pipe for Burial under Landfill", *Sardinia 93: Fourth International Landfill Symposium*, Cagliari, Sardinia, Italy, pp. 1473-1482.
- Zanzinger, H., Gartung, E. and Hoch, A. (1992) "Grundsatzuntersuchung ueber die statische Berechnung von Rohrleitungen in Sickerwasserentsorgungssystemen bei Abfalldeponien", *Veroeffentlichungen des LGA-Grundbauinstituts*, Heft 61, 92 p.
- Zanzinger, H. and Gartung, E. (1995) "Large-scale Model Test of Leachate Pipes in Landfills under heavy Load", *Second International Conference: Advances in Underground Pipeline Engineering*, ASCE, New York, NY, USA, pp. 114-125.
- Zanzinger, H. (1996) "Großmaßstäblicher Modellversuch an Draenrohren in Deponien", unpublished research report, 324 p.

# Effect of The Temperature on Tensile Behavior of Geomembranes

Masayuki TSUBOI

Doctoral Student, Department of Civil Engineering ,Utsunomiya University, Utsunomiya City, Japan

Shigeyoshi IMAIZUMI

Department of Civil Engineering ,Utsunomiya University, Utsunomiya City, Japan

Hideki MIYAJI

R&P Technical Division of Toyo Tire & Rubber Co., Ltd., Inami-Town, Hyougo-Ken, Japan

**ABSTRACT:** Geomembranes have been used as a landfill liner to remove the leachate, which is generated from ash waste to prevent it infiltrating into the surrounding ground and groundwater. At the bottom of the landfill, the geomembrane is covered with protective soil but in many cases, the geomembrane on the slope is laid without protective soil or geotextile. Consequently, the geomembrane must be exposed for a long time. In this situation, there exists anchoring problems such as pull out of the anchorage when the temperature of a geomembrane decreases. This behavior is caused by thermal stress induced within a geomembrane. In this paper, tensile stress tests for four different geomembranes were conducted at temperatures ranging from  $-20$  to  $80^{\circ}\text{C}$ . Thermal stress tests were also conducted by decreasing the temperatures from  $80$  to  $-25^{\circ}\text{C}$ . The test results show that the relation between temperature and tensile strength are linear, and that the relation between temperature and Young's modulus is exponential. They also show that the results of co-energy evaluation which is the factor of safety of geomembrane for differential settlement.

**KEYWORDS:** Geomembrane, Thermal Stress, Young's Modulus ,Tensile Behavior

## 1. PROPERTIES OF THE GEOMEMBRANES TESTED

Four kinds of geomembrane with smooth surfaces and 1.5mm thickness were selected among geomembranes popularly used for a liner of a landfill in Japan. These are High Density Polypropylene (HDPE), Ethylene Propylene Diene Methylene Rubber (EPDM), Thermo Plastic Olefin (TPO) and Poly Vinyl Chloride(PVC).

## 2. TESTING METHOD

Two shapes of the specimen were tested. One was the #3 dumbbell shape with 100mm length and 5mm width at the neck indicated by the Japanese Industrial Standard. The other was an original square shape with 200mm length and 60mm width. The specimens were set in the jaws in the oven and tested after heating or cooling at a constant temperature for thirty minutes as shown in Figure 1. Elongation was estimated by measuring the distance between the two jaws.

The jaw separation speed was 50mm/min for dumbbell shaped specimens and 1mm/min for square shaped specimens. The slow(1mm/min) speed was selected ,because forces such as a downdrag force or a thermal stress increases slowly. In the case of the thermal stress test, the force was adjusted to zero at  $80^{\circ}\text{C}$  degree by moving the jaw separation slowly. Then, the temperature of the oven was decreased to  $-25^{\circ}\text{C}$  by decrements of  $10^{\circ}\text{C}$  in 30 minutes.

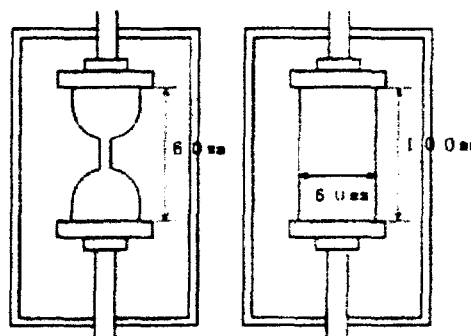


Figure 1. Setting of Specimens

## 3. TEST RESULTS AND DISCUSSIONS

### 3.1 Temperature effect on tensile strength

The tensile test were conducted by using dumbbell shaped specimens at a temperature of  $-25, 0, 20, 40, 60^{\circ}\text{C}$ . The test results was shown in Figure 2. Among the four kind of geomembrane, the values for HDPE indicated the yielding strength, while the others indicated peaking strength.

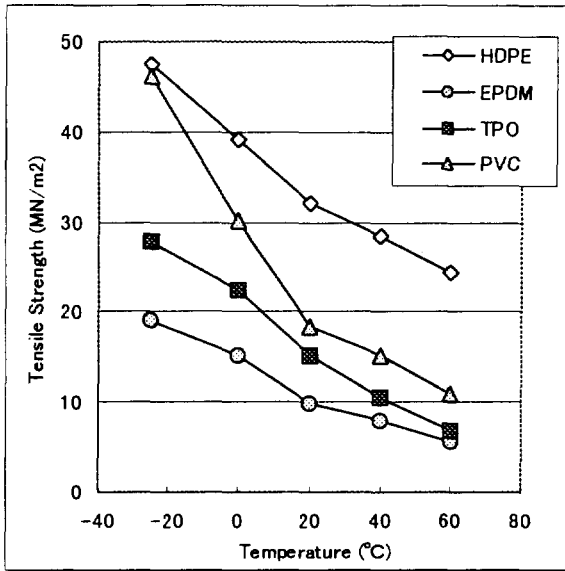


Figure 2. Temperature Effect on Tensile Strength

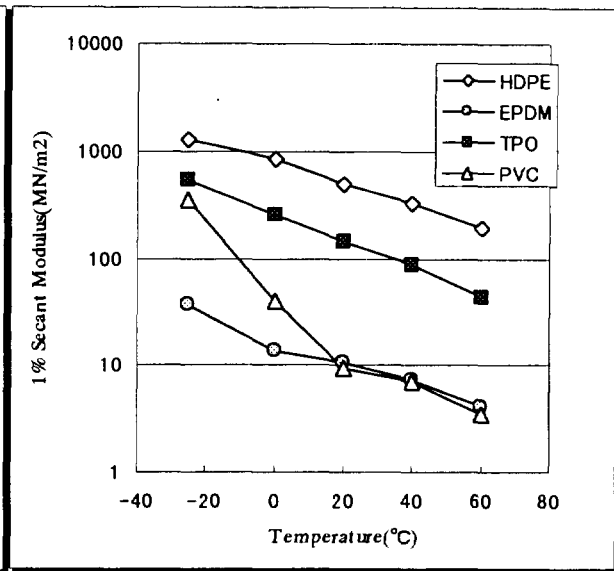


Figure 3. Temperature Effect on Young's Modulus

HDPE	$\sigma_t = -0.265t + 41.16$	MN/m <sup>2</sup>	(1)
EPDM	$\sigma_t = -0.167t + 14.70$	MN/m <sup>2</sup>	(2)
TPO	$\sigma_t = -0.255t + 21.36$	MN/m <sup>2</sup>	(3)
PVC	$\sigma_t = -0.421t + 32.14$	MN/m <sup>2</sup>	(4)

HDPE	$E = 794 \cdot 10^{-0.0102t}$	MN/m <sup>2</sup>	(5)
EPDM	$E = 17.6 \cdot 10^{-0.0102t}$	MN/m <sup>2</sup>	(6)
TPO	$E = 274 \cdot 10^{-0.0128t}$	MN/m <sup>2</sup>	(7)
PVC	$E = 43.1 \cdot 10^{-0.0340t}$	MN/m <sup>2</sup>	(8)

For all geomembranes tested, the tensile strength increases as the temperature decreases. The relationship between the temperature and the tensile strength is linear. The slope of the line, which indicates the ratio of tensile strength to temperature, is similar for all the lines, though PVC shows that the temperature affects tensile strength more severely than the other geomembrane types tested.

### 3.2 Temperature effect on Young's modulus

Young's modulus of geomembranes was investigated using square shaped specimens. The tests were conducted in the oven in which temperature was set at -25°C, 0°C, 20°C, 40°C, 60°C and the jaw was moving at the rate of 1mm/min. The secant modulus at 1% strain was calculated as the slope of the line connecting the origin to a point corresponding to 1% strain on the stress strain curves. The secant modulus at 1% for the geomembranes are shown in Figure 3.

There is large a difference in 1% secant modulus between the types of geomembrane. The modulus of HDPE at 20°C is the largest and is about fifty times that of PVC. The secant modulus of all geomembranes tested increases significantly with a decrease in temperature.

According to Figure 3, the relationship between the secant modulus and temperature is exponential, resulting in equations (5) to (8). Among the four geomembranes, the modulus of PVC is most sensitive to temperature. The other geomembrane types have similar slopes on a semilog plot, but the value of secant modulus are very different from each other.

### 3.3 Thermal Stress

Thermal stress was measured by square shaped specimens in the oven in which the temperature decreased slowly from 80°C to -25°C. The results are shown in Figure 4 and Figure 5.

The figures show that thermal stress occurred in all the membranes

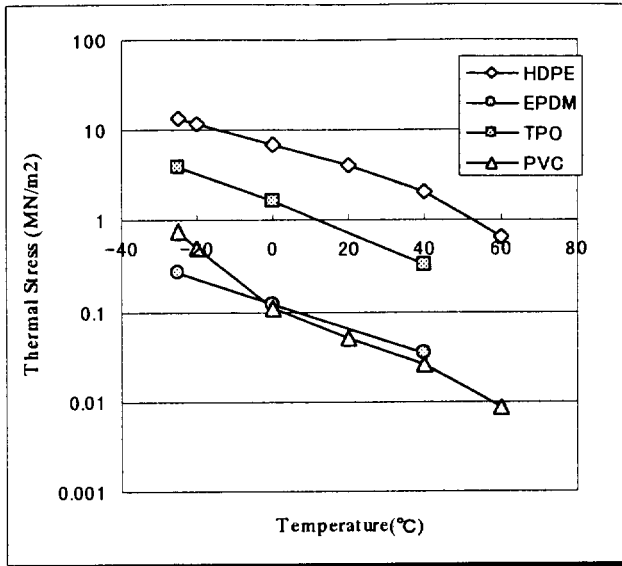


Figure 5. Thermal Stress

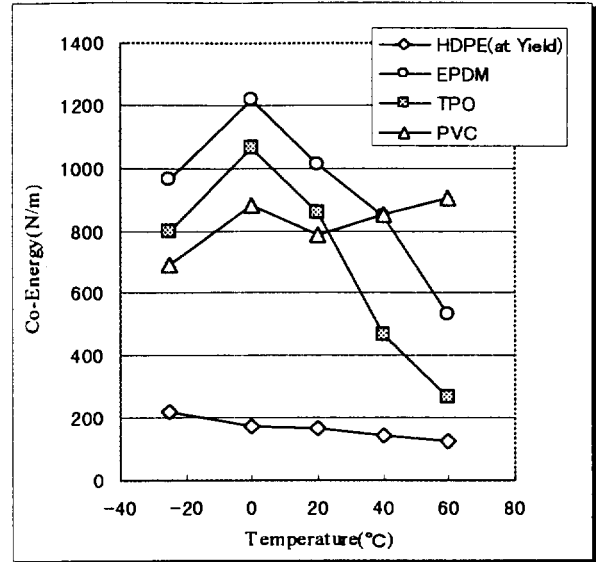


Figure 6. Co-Energy VS. Temperature

Table 1. Comparison of Thermal Stress (MN/m²) at 0°C

	Results	Calculated
HDPE	7.002	5.442
HPDM	0.119	0.099
TPO	1.628	1.347
PVC	0.109	0.102

$$\sigma_{ab} = \int \Delta \sigma dt = - \int_{tb}^{ta} \beta \cdot E_0 \cdot 10^{-\alpha t} dt \quad (9)$$

$$= -\beta \cdot E_0 \int_{0^{\infty}}^{tb} e^{-2.3025851\alpha t} dt = \frac{\beta \cdot E_0}{2.3025851\alpha} [e^{-2.3025851\alpha t}]_{0^{\infty}}^{tb} \quad (10)$$

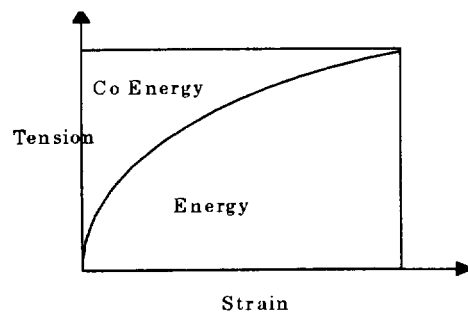
The thermal stress of HDPE was the largest. From Figure 5, the relation between the thermal stress and temperature is exponential

The authors presented the evaluation method by leading equation as (9) and (10).

The coefficient of thermal expansion  $\beta$  used for calculation is 0.00019 for HDPE, 0.00016 for EPDM, 0.00016 for TPO, and 0.00018 for PVC. The calculated thermal stress and test results at 0°C is shown in Table 1. The calculated thermal stress of EPDM and PVC from theoretical equation (10) was almost same as the test results, but that of HDPE and TPO, which indicated large values of thermal stress, were smaller than test results. The differences are assumed to depend on experimental errors at the setting specimens in jaws.

The tension of a membrane with 1.5mm thickness can be calculated from the thermal stress results. If the membrane is installed in the field during the day time when the surface temperature is 80°C, the tension that will occur at night time when the surface temperature is 0°C is 10.5kN/m for HDPE, 0.175kN/m for EPDM, 2.44 kN/m for TPO, and 0.164kN/m for PVC. The thermal stress of EPDM and PVC should be negligible, but that of HDPE and TPO would be significant.

### 3.4 Evaluation of Co-Energy



The concept of Co-Energy and the equation (11) was presented by Giroud .

$$s \cdot p \cdot \tan \phi = \int_0^T \epsilon \cdot dT \quad (11)$$

S; The total elongation of the geomembrane (equal to the settlement), P; Pressure, T; Tension,  $\epsilon$ ; Strain,  $\phi$ ; Friction angle. The integral of the equation (11) is equal to the area between the geomembrane tension-strain curve and tension axis up to the maximum tension value, which is shown co-energy area in the figure above. If P and  $\phi$  is the same, the maximum differential settlement S can be

evaluated by co-energy. So, the amount of the co-energy area from the test results can estimate the ability to withstand differential settlement. The results are shown in Figure 6.

The co-energy is different between the kinds of geomembrane. As the amount of HDPE was measured at yield point and that of the others were measured at break point, they should not be compared directly. The co-energy of EPDM, TPO and PVC is greater than HDPE. They present their peak at temperature of 0°C and decrease at lower and higher temperature than 0°C.

#### 4. CONCLUSION

- (1) Temperature effect on tensile strength: The tensile strength at break of EPDM, TPO, and tensile strength at yield of HDPE, increases linearly with decreasing temperature. PVC appears to be the most sensitive of the material tested.
- (2) Temperature effect on Young modulus: Young's modulus is different between the types of geomembrane tested and Young's modulus of HDPE is fifty times as large as PVC at 20°C. The modulus of all samples tested indicate an exponential increase with decreasing temperature.
- (3) Thermal stress: Thermal stress was measured in all cases. The thermal stress of HDPE and TPO is much larger than EPDM and PVC. The calculated thermal stress by theoretical equations was close to the test results for EPDM and PVC was significantly less than the test results for HDPE and TPO.
- (4) Temperature effect on co-energy: The value of co-energy shows changing according to the temperature of the testing and differences between the kinds of geomembranes. In case of HDPE, the value of the co-energy is the lowest and indicates a very small decreasing with increasing temperature. In case of EPDM, the value of the co-energy is the highest at the temperature from -25°C to 60°C and indicate the peak at 20°C. In case of TPO, the value is a little smaller than EPDM and indicates the almost same shape of the curves. In case of PVC, the incline of the curve indicate increasing the co-energy with temperature.

The thermal stress of EPDM and PVC would generally be negligible in the case of an exposed landfill liner. The thermal stress of HDPE and TPO may be significant. Since, thermal stress occurs only when the temperature changes, the temperature of the membrane under the thick protective soil may not be great concern because the temperature would be relatively stable. However, an exposed geomembrane on a steep side slope may result in large temperature changes. Thermal stress may be important for designing and installing exposed geomembranes on the steep side slope and the designer may need to account for these when designing anchorage for the geomembrane.

#### 5. REFERENCES

- J. P. Giroud: Quantification of Geosynthetic Behavior, Proceeding of the Fifth International Conference on Geotextiles, Geomembranes and Related Products, pp.3~27, 1994
- G. R. Koener · R.M. Koener: Temperature Behaviour of Field Deployed HDPE Geomembranes, Geosynthetics'95, pp.921—937, 1995
- R. Yazdani: Long Term In situ Strain Measurements of a High Density Polyethylene Geomembrane in a Municipal Solid Waste Landfill, Geosynthetics'95, pp. 893—905, 1995
- J. P. Giroud: Mechanical Design of Geomembrane Applications, Geosynthetics'93, pp.1455 ~ 1467, 1993
- Darryl E. Kilius: Cold Temperature Performance of Polypropylene Geomembranes and Seams, Geosynthetics Liner System, pp.197~207
- A.L.C. Comer: Effect of Freeze Thaw Cycling on Geomembrane Sheets and Their Seams, Geosynthetic'95, pp.853~866
- Hideki, Miyaji: Effect of Temperature on Tensile Behavior of Geomembrane, Proceeding of 11<sup>th</sup> Symposium I G S Japan, pp.110, 1996



# Measuring the In-situ Moisture Content of Geosynthetic Clay Liners (GCLs) Using Time Domain Reflectometry (TDR).

Matthew A. Eberle

*Geofabrics Australasia Pty Ltd, Australia.*

Kent P. von Maubeuge

*Naue Fasertechnik GmbH & Co. KG, Germany.*

**ABSTRACT:** A method that enables accurate in-situ measurement of moisture content in thin clay layers would advance performance monitoring of geosynthetic clay liners (GCLs) in many applications. The ability of a GCL to act as a gas or vapour barrier, or the friction/shear resistance of a GCL can be significantly affected by the degree of hydration of the bentonite within the geocomposite. Time domain reflectometry (TDR) emerged as a new technique to monitor soil-water content during the early 1980s. Advances in theoretical understanding and TDR equipment allows the technology to be used to continuously monitor in-situ moisture contents in a GCL at multiple locations, and remotely, if so desired. This paper will focus on the practical aspects of applying TDR technology to GCL testing and monitoring. These aspects include; obtaining relationships between gravimetric moisture content ( $w$ ) and apparent dielectric constant ( $K_a$ ), factors influencing the accuracy of measurements, and the effect of probe geometry and orientation on the GCL/soil influence zone. The results of some preliminary tests on a GCL under simulated prolonged evapotranspiration conditions are presented which indicate the potential of the technique.

**KEYWORDS:** Time domain reflectometry (TDR), Geosynthetic clay liners (GCL), Moisture content measurement, In-situ monitoring, Desiccation.

## 1. INTRODUCTION.

The moisture content or degree of hydration within a GCL will have an effect on many physical and chemical properties. Some of these properties include; the ability to act as a barrier to gases, vapours, and contaminants in landfill liners and secondary containment facilities, and the internal (mid-plane) shear strength and interface friction values (particularly in non-reinforced GCLs).

Removing GCL samples for oven drying is a direct and reliable method of measuring moisture content, however the technique is destructive, time consuming and highly impractical. There are a number of non-destructive options that can be employed to measure in-situ moisture content in a GCL that have evolved primarily out of the agriculture and forestry sectors.

## 2. ELECTRICAL RESISTANCE BLOCKS.

Electrical resistance blocks made from porous gypsum or fibreglass can be used as an indirect method of determining soil-water content. The technique relies on the equilibrium of soil-water potential in the block with that of the surrounding soil (White and Zegelin, 1995). Gypsum from the block dissolves in the pore water to provide electrolyte. Changes in electrical resistance in the embedded electrodes

within the block can be monitored with an AC or pulsed DC bridge. Fibreglass blocks rely on the electrolytes in the soil-water solution itself to provide conduction.

The electrical resistance in the blocks is sensitive to changes in electrolyte concentrations and electrical conductivity. Resistance blocks also tend to respond to soil matrix potential, not soil moisture, which leads to a hysteresis response between wetting and drying cycles (which subsequently require separate calibrations). The change in resistance of a block over the typical moisture content range in most granular soils is small, which limits the precision of the technique (Gardner, 1986). However, the fluctuation in gravimetric moisture content ( $w$ ) in a GCL can be very large in some cases, (up to 400%).

Gypsum blocks are not particularly suited to long-term monitoring of moisture content in soils as their pores become clogged with deposited material, and they gradually dissolve over time. This causes continual change in the relationship between electrical resistance and moisture content, leading to errors when using the original calibration (White and Zegelin, 1995).

In addition to the above mentioned disadvantages of resistance blocks, there are some practical difficulties embedding them within a GCL due to dimensional constraints. The advantages are that they are cheap and

many blocks can be multiplexed from a single hand-held meter (bridge) with relative ease. However, in order to use this technique with any precision, electrical conductivity and moisture content must be determined independently, and at regular intervals throughout the monitoring period.

### 3. TIME DOMAIN REFLECTOMETRY (TDR).

Time domain reflectometry (TDR) measurements relate measurements of apparent dielectric constant to volumetric water content. The application of TDR in soil water measurements was reported by Topp *et al* (1980). There are many potential advantages in using TDR in the measurement of gravimetric moisture content in GCLs over the electrical resistance (conductance) technique. These include:

- flexibility in probe (waveguide) geometry,
- insertion of probe into the GCL results in minimal damage to the GCL (non-destructive),
- a high level of accuracy,
- fewer calibration requirements,
- able to provide continuous soil water measurements through automation and multiplexing.

Some of the limitations of the TDR method include:

- relatively high equipment costs,
- possible limited applicability under highly saline conditions due to signal attenuation,
- soil-specific calibrations are required for soils having large amounts of bound water (eg. clays).

Signal attenuation can be a problem under saline conditions and in dense clays, but can be minimised by a combination of careful probe geometry selection and techniques involving coating the waveguides with some form of insulation. The inconvenience of having to perform soil-specific calibrations when dealing with some clays is minimised when applying the technology to GCLs as they contain relatively homogeneous bentonite clay.

#### 3.1 Theory.

The TDR technique involves sending a microwave pulse generated from the TDR cable tester/processor down a parallel transmission line of known length  $L$  embedded in the soil. The pulse propagates down the line and is reflected back from the end of the transmission line. It is possible to isolate the portion of the pulse representing the transit time,  $t(s)$ , in the buried waveguide/probe. The propagation velocity ( $v=2L/t$ ) is a function of the soil bulk dielectric constant,  $K_a$ , of the surrounding medium, which can be estimated from Eq.[1] (Topp *et al*, 1980),

$$K_a = (c/v^2) = (ct/2L)^2 \quad [1]$$

where  $c$  is the velocity of light in a vacuum ( $3 \times 10^8$  m/s). The bulk dielectric constant of the soil is governed by the dielectric of liquid water,  $K_{water} \rightarrow 80.36$  ( $20^\circ\text{C}$ ), as the dielectric of other constituents are much smaller, ( $K_{soil} \rightarrow 3$  to 5, and  $K_{air} \rightarrow 1$ ). Due to the large difference in dielectric constants, the electromagnetic pulse propagation time is very dependent on the water content of the soil (Figure 1) and relatively insensitive to soil composition and texture.

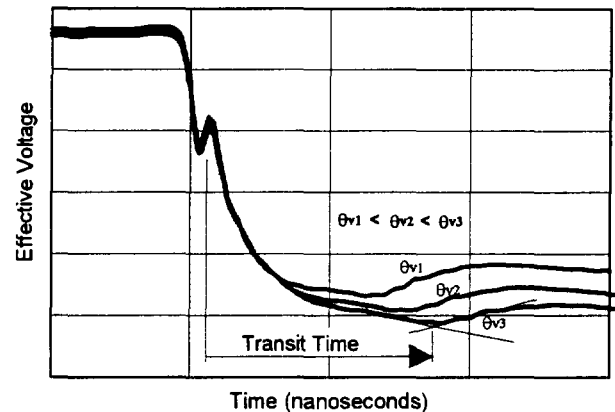


Figure 1: Sample traces measured in bentonite with various moisture contents (3-pronged waveguide)

#### 3.1.1 Establishing a $\theta_v(K_a)$ Relationship.

Several relationships between  $K_a$  and volumetric moisture content,  $\theta_v$ , have been established. The first approach developed by Topp *et al* (1980) utilises an empirically derived third order polynomial, fitted to observed relationships between  $K_a$  and  $\theta_v$ , for multiple soils.

$$\theta_v = -5.3 \times 10^{-2} + 2.92 \times 10^{-2} K_a - 5.5 \times 10^{-4} K_a^2 + 4.3 \times 10^{-6} K_a^3 \quad [2]$$

A second approach adopted by Dobson *et al* (1985) and Roth *et al* (1990) attempts to predict the bulk  $\theta_v(K_a)$  relationship based on the individual dielectric constants of the three soil components (soil particles, air and water). In this approach  $K_a$  is given by the mixing model,

$$K_a = [\theta_v K_{water}^\alpha + (1-\phi) K_{soil}^\alpha + (\phi-\theta_v) K_{air}^\alpha]^{1/\alpha} \quad [3]$$

with  $\phi$  the soil porosity, and  $\alpha$  a geometric factor relating to the spatial arrangement of the three phase mixture. Roth *et al* (1990) found a best fit  $\alpha=0.46$  for various soils (Zegelin *et al*, 1992).

The suitability of both of these approaches is limited when applied to GCLs due to a number of factors:

- the Topp calibration Eq.[2] was based upon test results on soils concentrated in the  $\theta_v < 0.5$  range, and subsequently fails to adequately describe the relationship for water contents exceeding 0.5 and fine textured, dense, heavy clay soils.
- predictions based on Eq.[3] require the bentonite porosity and dielectric constant (dry) to be known or estimated, which can potentially lead to additional errors in the methodology.

To avoid the problems associated with these two approaches, along with need to convert volumetric moisture contents to gravimetric moisture content ( $w$ ), it is a relatively simple task to construct a  $w(K_a)$  calibration for the particular TDR equipment and GCL being used. Because most TDR equipment can be integrated with software capable of reporting and logging  $K_a$  values for data reduction at a later stage, individual calibrations can be developed to replace default  $\theta_v(K_a)$  calibrations such as Eq.[2], which are not suitable for clays with high moisture contents.

### 3.1.2 Probe Geometry and Influence Zone.

Probably the most critical factor affecting the accuracy of the TDR technique when applied to measurements in GCLs lies in the selection of probe type and geometry. Zegelin *et al* (1992) describe a number of different coaxial insertion probes that have been used in soil water measurements. The electric field distribution of a 3-rod probe is shown in cross-section (qualitatively) in Figure 2. The sensitivity is highest within the soil in the immediate vicinity of the probe rods and falls off rapidly with distance from the conductors. Knight (1991) has shown that there is a strong weighting by the TDR measurement of water content close to the central rod of a three (or more) rod probe. A 3-rod probe is relatively easy to insert into a GCL and disturbance/damage to the insertion region can be minimised.

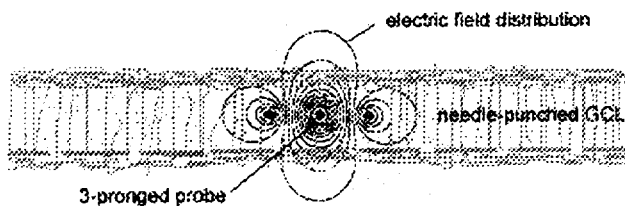


Figure 2: Approximate electric field distribution of 3-rod probe when inserted into a GCL.

There are limitations on the minimum length of TDR probes, and the ratio of probe rod-to-rod spacing to rod diameter. Clearly these limits are critical for measurements

in a thin layer of bentonite (only 6 to 10 mm thick). The lower limit on probe length is due to the accuracy of time-of-travel measurements of pulse propagation within the probe, which becomes questionable for probes less than 50 mm length (Zegelin *et al*, 1992).

### 3.1.3 Influence of Temperature ( $T$ ) on $K_a$ .

The dielectric constant of free water  $K_{water}$ , on which  $\theta_v(K_a)$  calibrations are based, is temperature dependent. In the field, ground surface temperatures can often exceed 50°C. In these situations, a temperature correction needs to be implemented (Eq.[4] → Handbook of Chemistry and Physics, 1974),

$$K_{water} = 78.54[1 - 4.579 \times 10^{-3}(T-25) + 1.19 \times 10^{-5}(T-25)^2 - 2.8 \times 10^{-8}(T-25)^3] \quad [4]$$

therefore, accurate measurement of moisture content will require simultaneous temperature monitoring when temperature fluctuations are expected.

## 4. TEST RESULTS FROM PRELIMINARY LABORATORY STUDY.

Prior to embarking on a large scale field trial using the TDR techniques discussed, the suitability for long-term in-situ monitoring of GCL moisture content was assessed in a laboratory trial, the results of which warrant further discussion.

### 4.1 Laboratory Test Method.

The laboratory study involved placing a GCL on a bedding layer of well graded sand (90% passing 4.75 mm sieve) in a large open box, with a 300 mm cover layer of the same sand over the GCL. A cross-section of the set-up is shown in Figure 3.

The sand had an initial gravimetric moisture content of around 8 to 10%, and the GCL was installed in a 'dry' state ( $w_{GCL} \approx 9\%$ ). A 1000 Watt halogen lamp was placed 250 mm above the sand in order to simulate a relatively hot and dry environment. A timer automatically cycled the lamp 'on' during non-working hours in the lab (15 hours per day) to limit exposure of the laboratory staff to glare resulting from the lamp during this cycle. A temperature sensor was placed centrally in the box at the surface level to monitor temperature during both cycles. The average temperature during the heating cycle was 43°C. The ambient temperature and humidity in the laboratory averages 23°C and 20% respectively.

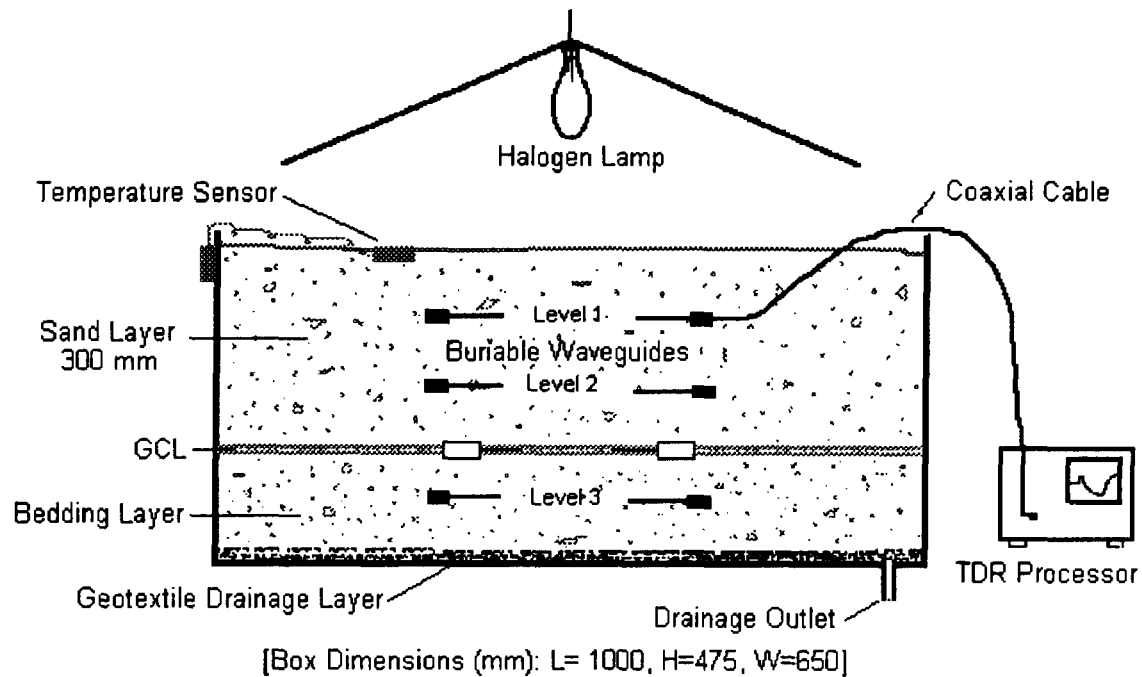


Figure 3: Schematic of test set-up and apparatus showing the position of the 2 mini-buriable waveguides (L=60 mm) within the GCL, and the 6 buriable waveguides (L=200 mm) in the surrounding soil.

#### 4.1.1 Probe Selection and Placement.

Probes (3-rod) were inserted in the GCL and surrounding material to monitor soil moisture. Two probes were inserted within the GCL, both had a rod length of 60 mm, a rod diameter of 1 mm, and the spacing between the two outside rods was 15 mm. TDR probes (3-rod) with a larger measurement volume were used in the sand material surrounding the GCL. These probes had a length of 200 mm, a rod diameter of 3 mm, and a spacing between outside rods of 40 mm. The probe locations are shown in Figure 3.

#### 4.2 Test Results.

The two moisture contents readings at each level in the soil profile were averaged and plotted against testing duration (Figure 4). The plot shows the moisture content within the GCL reached 100% in under 24 hours, and continued to gradually increase over the duration of testing to a maximum of 140% at around 1500 hrs. There is no evidence of significant drying within the GCL since this time. Probes at levels one and two indicate considerable drying in the cover soil as a result of the heating cycles. The water content in the bedding layer increased from 8% to 10.5%, possibly as a result of pore water movement towards the GCL due to condensation or suction.

#### 4.2.1 Discussion of Results.

The maximum moisture content that a GCL will reach is a function of confining stress. Previous experimental work by *Petrov et al* illustrates the relationship between confining stress and moisture content for a needle-punched GCL and a 'fibre-free' GCL (essentially the same needle-punched GCL with the needle-punched fibres cut). The presence of needle-punched fibres limits the swelling of the bentonite in the lower confining stress range, leading to lower fully-hydrated moisture contents, and subsequently lower hydraulic conductivity in comparison to a fibre-free sample (in the low confining stress range).

The relationship between confining stress and maximum hydrated moisture content was developed for the GCL used in testing (Figure 5). The peak moisture content reached in the GCL during the trial, as a result of wetting from the surrounding soil, is within approximately 20% of the expected maximum under confinement from the 300 mm cover soil.

The moisture content at which desiccation in the bentonite is expected to commence is typically between 70 and 90% (and is confining stress dependent). Although desiccation has not occurred to date in the trials, samples were deliberately dried in an oven to the point of significant cracking and TDR readings taken.

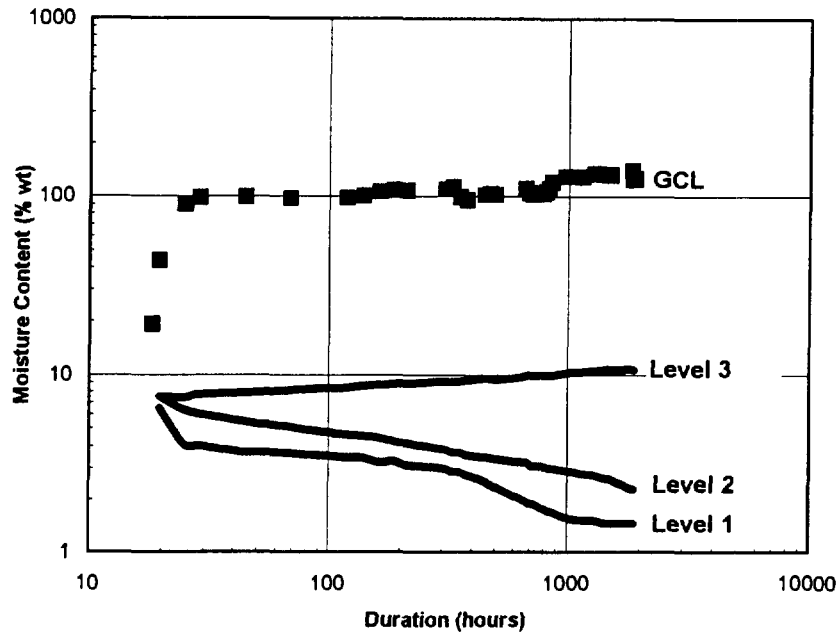


Figure 4: Moisture content within the GCL and throughout the soil profile versus duration of testing (approximately 2000 hrs to date).

The presence of air voids in the composite (due to cracking) was evident from the shape of the resulting TDR trace. Thus, careful monitoring of the waveform shape can potentially be used to indicate the onset of desiccation.

Additional tests were carried out in which 21°C air at 40 to 80% relative humidity was blown directly over the GCL. The GCL was confined with 9 kPa pressure over a drainage net, which allowed the air to pass directly over the GCL. The onset of desiccation occurred at 3000 hours, after which the moisture content within the GCL fell from 110% to 45% within two hours. The tests are ongoing and will be presented at a later date.

The ability of the GCL used in the trial to resist drying can, in part, be attributed to the hydrophilic nature of bentonite and to the moisture trapped beneath the GCL in the bedding layer, which appears to be continually hydrating/re-hydrating the GCL.

#### 4.2.2 Load Effects on the $w(K_d)$ Calibration.

In developing the  $w(K_d)$  calibration for the mini-buriable probes placed within the GCL, it became apparent that load effects were significant. To overcome the potential for error, the calibration was performed under the same

level of confinement as the GCL in the trial. The influence of confining stress or GCL bulk density on the calibration requires further investigation, but was beyond the scope of these preliminary trials.

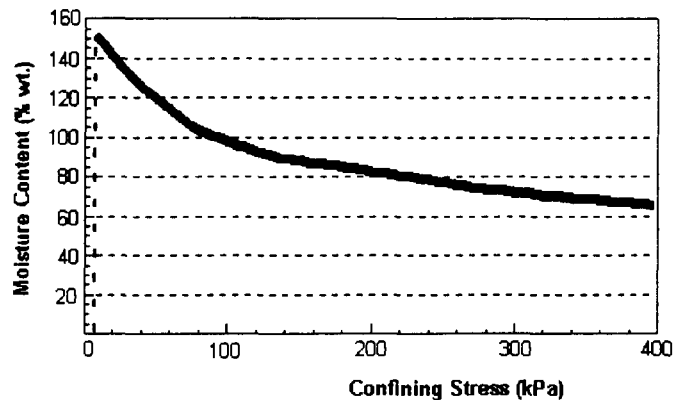


Figure 5: Fully hydrated moisture contents in the GCL under various confining stresses.

## 5. SUMMARY.

The trials performed illustrate the potential of TDR methods to monitor hydration levels within a GCL. In the

opinion of the authors, the level of accuracy is well within acceptable limits when appropriate calibrations and corrections for temperature are applied, and the probe type and geometry are carefully selected. Developments in telecommunications and data logging equipment make continuous remote monitoring of field sites feasible.

As for the test results, it has been shown that GCLs have the ability to hydrate from moisture in surrounding soils and remain hydrated for considerable periods without additional water being introduced.

In conclusion, a GCL may be a more appropriate mineral layer choice (as opposed to a compacted clay) in barrier applications where vapours and gases need to be contained, and the potential for desiccation in a compacted clay liner exists. A GCL will offer superior resistance to desiccation in the first instance, and if desiccation occurs, the bentonite has the ability to swell and heal cracks due to desiccation.

## 6. ACKNOWLEDGEMENTS.

The authors would like to thank Steve Zegelin of the CSIRO (Centre for Environmental Mechanics) in Canberra, Australia, and Steven Laird of Irricrop Technologies Pty Ltd, in Narrabri, Australia for their assistance in supplying and setting up equipment. The lab staff at the Geosynthetic Testing Service (GTS) in Albury, Australia, and at Naue Fasertechnik GmbH & Co. KG, Germany, need to be thanked as well.

## REFERENCES.

- Dobson, M.C., Hallikainen, F.T., and El-Rayes, M.T., "Microwave Dielectric Behaviour of Wet Soil. Part II Dielectric Mixing Models", *IEEE Trans. Geosci. Remote Sensing*, GE 23:35 (1985).
- Gardner, W.H., "Water Content", in *Methods of Soil Analysis. Part 1, Physical and Mineralogical Methods*, 2<sup>nd</sup> edition, A. Klute, Ed., Am. Soc. Agron. & Soil Sci. Soc. Am., Madison, WI, 1986, p493.
- Handbook of Chemistry and Physics*. 1974, 55<sup>th</sup> ed. CRC Press, Cleveland, OH.
- Knight, J.H., Discussion of "The Spatial Sensitivity of Time Domain Reflectometry Measurements" by J.M Baker and R.L Lascano, *Soil Sci.* 151:254-255, 1991.
- Petrov, R.J., Rowe, R.K., and Quigley, R.M., "Selected Factors Influencing GCL Hydraulic Conductivity", *Geotechnical Research Centre Report*, GEOT-3-96, Geotechnical Res. Centre, Uni. of Western Ontario, Canada, 1996.

- Roth, K., Schulin, R., Fluhler, H., and Attinger, W., "Calibration of Time Domain Reflectometry for Water Content Measurement Using a Composite Dielectric Approach", *Water Resour. Res.*, 26:2267 (1990).
- Topp, G.C., Davis, J.L., and Annan, A.P., "Electromagnetic Determination of Soil Water Content: Measurements in Coaxial Transmission Lines", *Water Resources Research*, Vol.16, No.3, Pages 574-582, June 1980.
- White, I., Zegelin, S.J., "Electric and Dielectric Methods for Monitoring Soil-Water Content", *Handbook of Vadose Zone Characterisation and Monitoring*, Lewis Publishers, 1995, pp 343-385.
- Zegelin, S.J., White, I., Russell, G.F., "A Critique of the Time Domain Reflectometry Technique for Determining Field Soil-Water Content" *Advances in Measurement of Soil Physical Properties: Bringing Theory into Practice*, Soil Science Society of America, Special Publication no. 30, 1992.

# An Exposed Geomembrane Cover System for a Landfill

M.H. Gleason

Project Engineer, GeoSyntec Consultants, Columbia, Maryland, USA

M.F. Houlihan

Associate, GeoSyntec Consultants, Columbia, Maryland, USA

J.P. Giroud

Senior Principal, GeoSyntec Consultants, Boca Raton, Florida, USA

**ABSTRACT:** Landfill closure represents a significant cost to owners and operators when the combined costs of cover system construction, maintenance of the cover system, and maintenance of the storm-water management system are considered. Owners and operators may reduce costs by constructing a cover system that consists of an exposed geomembrane (i.e., a cover system that does not include the typical drainage, vegetative support, and topsoil layers of the cover system), thereby eliminating the construction and maintenance costs associated with the portions of the cover system overlying the geomembrane. The advantages and disadvantages of the exposed geomembrane cover system, selection criteria for the exposed geomembrane, and key design considerations for the exposed geomembrane cover system are discussed in this paper. Two of the key design considerations, for which design approaches have only recently been developed, are then discussed in detail: (i) damage of the geomembrane by hail stones; and (ii) resistance of the exposed geomembrane to uplift forces caused by wind. Lastly, a case history for design is presented. By providing the necessary tools for selecting a geomembrane that is resistant to environmental factors, this paper can be used by landfill owners and designers as a basis to consider the exposed geomembrane closure approach for potentially appropriate sites.

**KEYWORDS:** Exposed geomembrane, Cover system, Landfills, Wind uplift, Hail impact.

## 1 INTRODUCTION

Solid and hazardous waste landfills are typically required to be closed with a cover system. The purposes of the cover system are to prevent direct contact of people and the environment with the waste, to prevent erosion of the waste materials, and to minimize infiltration of storm water (which causes leachate) into the landfill. From top to bottom, the components of a typical final cover system for a municipal solid waste landfill consist of: (i) a topsoil layer; (ii) a vegetative support soil layer; (iii) a drainage layer; (iv) a low-permeability layer (i.e., compacted clay or geomembrane); and (v) a soil final grading layer over the existing daily/intermediate cover layer and waste (Figure 1). Once constructed, such final cover systems require inspection and maintenance, such as mowing of vegetation and repair of eroded areas. In addition, construction of the typical final cover system represents a significant cost to owners and operators; this approach to closure may not be cost-effective, particularly in the cases where the design life of the cover system is relatively short (i.e., approximately 5 to 10 years), when future removal of the cover system may be required (e.g., for landfill reclamation), or when the landfill may be overfilled in the future. In these cases, it may be more cost-effective to construct an exposed geomembrane cover system. An example of the exposed geomembrane cover system is presented in Figure 2. As described in this paper, exposed geomembrane cover systems

represent a new direction in landfill cover system design that, depending on site-specific requirements, may represent a more cost-effective method of landfill closure.

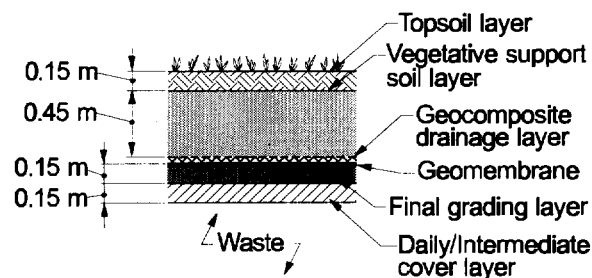


Figure 1. Typical Final Cover System

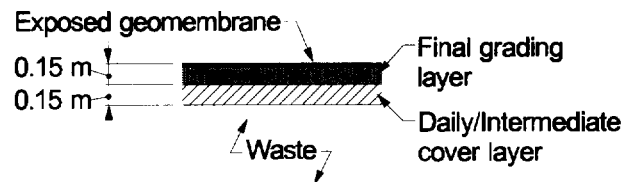


Figure 2. Exposed Geomembrane Cover System

In this paper, the applicability and design methods for an exposed geomembrane cover system are discussed; this discussion is focused on the design of an exposed geomembrane cover system for a 17-hectare landfill (Cell 1&2) at the Delaware Solid Waste Authority's (DSWA's)

disposal facility in Sussex County, Delaware. Based on experience from numerous designs of typical final cover systems and the design of this exposed geomembrane cover system, the advantages and disadvantages of exposed geomembrane cover systems are presented in Section 2. The design considerations required for selection of the exposed geomembrane component of the cover system are presented in Section 3. A summary of the design methods (e.g., geomembrane selection) and design features (e.g., geomembrane anchors) necessary to satisfy these considerations are then described in Section 4. The application of these design methods are described in the case history presented in Section 5. Finally, in the conclusion of the paper (Section 6), recommendations are provided regarding the applicability of exposed geomembrane cover systems to other sites.

## 2 ADVANTAGES AND DISADVANTAGES

### 2.1 Introduction

As indicated in Figure 2, the exposed geomembrane cover system represents a simpler design than the typical cover system (Figure 1), which results in several advantages. However, the functions performed by the materials overlying the geomembrane in the typical final cover system are not performed in the case of the exposed geomembrane cover system, which results in disadvantages. The advantages and disadvantages for the exposed geomembrane cover system are presented in the subsections 2.2 and 2.3 and should be reviewed prior to proceeding with any design.

### 2.2 Advantages

The typical advantages of an exposed geomembrane cover system are: (i) reduced construction cost; (ii) reduced soil maintenance requirements, (iii) increased landfill volume; (iv) easier access to landfilled materials for reclamation; (v) reduced post-construction waste settlement; (vi) reduced hydraulic head on the cover system barrier layer, and (vii) enhanced visual inspection. These advantages are described below.

*Reduced Construction Cost.* Elimination of the topsoil layer, vegetative support soil layer, and drainage layer components of the typical final cover system may reduce construction costs by as much as \$80,000 to \$120,000 per hectare, depending on site-specific conditions and the availability of construction materials at the site.

*Reduced Soil Maintenance Requirements.* The level of soil maintenance required for the exposed geomembrane cover system is expected to be much less than that required for a typical final cover system. Because the amount of soil on an exposed geomembrane cover system is limited, repairs to eroded areas would be minimized

and mowing of vegetation would be eliminated.

*Increased Landfill Volume.* Using an exposed geomembrane adds volume to the landfill if the final elevation of the geomembrane is set equal to the permitted final grades of the typical final cover system. For potential lateral landfill expansions, eliminating the soils overlying the geomembrane also results in added volume when the lateral landfill expansion is developed. In addition, because there is no potentially unstable material on top of the exposed geomembrane, it can be constructed on a slope that is steeper than a typical final cover system, thereby increasing landfill volume.

*Easier Access to Landfilled Materials for Reclamation.* Elimination of the cover soils allows the owner easier access to the waste in the event of future landfill reclamation without having to remove the existing cover soils.

*Reduced Post-Construction Waste Settlement.* Because an exposed geomembrane cover system is lighter than an a typical final cover system, post-construction settlement of the waste and settlement around landfill structures (i.e., landfill gas wells, drainage terraces, etc.) is reduced.

*Reduced Hydraulic Head on Cover System Barrier Layer.* Drainage off an exposed geomembrane cover system is not restricted by the hydraulic conductivity of cover drainage materials. Accordingly, the hydraulic head on the cover system barrier layer is reduced compared to a typical final cover system.

*Enhanced Visual Inspection.* Because the geomembrane is exposed, it may be easily inspected for damage; any identified damage may be inexpensively repaired.

### 2.3 Disadvantages

Several potential disadvantages of an exposed geomembrane cover system must be considered prior to initiating the design, including: (i) increased vulnerability to environmental damage; (ii) increased volume and velocity of storm-water runoff; (iii) susceptibility to uplift damage by landfill gas; (iv) limited vehicular access; (v) limited design life; (vi) limited regulatory approval; and (vii) aesthetic concerns. These potential disadvantages are described below.

*Increased Vulnerability to Environmental Damage.* Because the geomembrane is not protected by overlying cover soils, it is susceptible to damage from vandalism, animals, exposure to sunlight, low temperatures, and extreme weather (i.e., puncture from hail and damage from wind uplift). Potential damage to the exposed geomembrane from hail and wind is discussed in greater detail in Section 4 of this paper.

*Increased Volume and Velocity of Storm-Water Runoff.* Because there are no soils or vegetation over the exposed geomembrane, storm-water runoff is conveyed quickly



off of the cover system, resulting in increased peak flow quantities and increased runoff velocities. The increased peak flow quantity requires that storm-water drainage features (i.e., ditches and culverts) be designed for a greater flow capacity and that the on-site storm-water management ponds be designed for a significantly greater storage capacity than for a typical final cover system.

*Susceptibility to Uplift Damage by Landfill Gas.* Because there is no overlying cover soil to limit uplift of the geomembrane by landfill gas, a landfill gas collection and removal system must be designed to effectively collect landfill gas that is generated within the landfill.

*Limited Vehicular Access.* Vehicular access on the landfill is usually required to perform maintenance and associated repairs to damaged features on landfill cover systems. On a typical final cover system, light vehicles can usually drive on any soil-covered portion of the landfill cover system; for the exposed geomembrane cover system, vehicular access must be restricted to only the landfill cover access road.

*Limited Design Life.* Because the exposed geomembrane is not protected from environmental damage, it has an expected design life that is shorter than that of a geomembrane in a typical final cover system.

*Limited Regulatory Approval.* Because an exposed geomembrane cover system is not common, there may be concerns among regulators regarding its technical feasibility. Also because this cover system represents a departure from typical final cover systems, regulatory approval may be difficult, or may have strict limitations.

*Aesthetic Concerns.* A large landfill that is covered by an exposed geomembrane cover system may be perceived as less visually appealing than a landfill with a fully-vegetated typical final cover system.

### 3 DESIGN CRITERIA

To prevent impacts to the environment or excessive operation and maintenance costs, each of the disadvantages listed in Section 2.3 must be addressed and resolved during the cover system design. This paper is only focused on selection and design of the geomembrane component of the exposed geomembrane cover system. Design criteria that are directly related to selection of the geomembrane are presented in this section. The exposed geomembrane component of the cover system should be designed to meet the following criteria: (i) resist damage caused by exposure to sunlight; (ii) resist damage caused by low temperatures; (iii) resist damage caused by tensile strain due to downslope creep; (iv) resist puncture damage from hail stones; and (v) resist damage from wind. These criteria are discussed below.

*Resistance to Sunlight.* The geomembrane must not be adversely affected by long-term exposure to sunlight, which generates heat and contains ultra-violet radiation.

Therefore, geomembranes having plasticizers that could volatilize or geomembranes having components that could degrade during long-term exposure to ultra-violet radiation should not be used.

*Resistance to Low Temperatures.* The geomembrane polymer must not become brittle when subjected to low temperatures. The effect of low temperatures on the field performance of geomembranes is discussed in Giroud (1994) and Koerner and Koerner (1995).

*Resistance to Downslope Creep.* The combined action of gravity and thermal expansion/contraction of the geomembrane over long periods of time could lead to downslope creep of the geomembrane, thus creating additional stresses at the anchors. Desirable geomembrane properties are: (i) light color; (ii) low coefficient of thermal expansion; (iii) high interface friction with the underlying material; (iv) low bending modulus to minimize the formation of large wrinkles (Giroud and Morel, 1992); and (v) high tensile modulus and high activation stress to minimize creep. Only geomembranes that consist of a flexible polymer and are reinforced internally with a scrim can meet both the low bending modulus and high tensile modulus requirements.

*Resistance to Puncture from Hail Stones.* The exposed geomembrane would be susceptible to damage caused by extreme weather, including puncture from large-diameter hail stones. Geomembranes with a low resistance to puncture should not be used. Resistance to damage caused by hail stones is addressed in Section 4.2.

*Resistance to Wind Damage.* The geomembrane must have sufficient tensile strength and must be sufficiently anchored to the landfill slope to resist the tensile stresses caused by wind uplift. Use of unreinforced geomembranes, which have a relatively low tensile strength, would require closely spaced anchor trenches (i.e., 3-m to 5-m vertical intervals) or closely spaced surface anchors (such as sandbags, tires, or other ballast placed every 1 to 3 square meters on the landfill slope) to prevent wind damage. The surface anchors would be effective for short-term conditions; however, over a period of several years, they would likely move under the combined effects of wind, storm-water runoff, and thermal expansion/contraction of the geomembrane. In addition, the surface anchors would require regular maintenance, which could possibly offset the initial construction cost savings. A cost-effective design for providing protection against wind uplift damage involves selecting a geomembrane having a high tensile strength and constructing geomembrane anchors at widely spaced vertical intervals (i.e., 10 to 12 m). Resistance to damage caused by wind uplift is addressed in Section 4.3.

*Other Criteria.* There are other site-specific considerations that should be addressed, such as the potential for damage caused by vandalism or by animals (e.g., chewing or hooved animals). The owner or

operator should assess the risk and potential for this type of damage. A solution may be to construct a security fence to prevent unauthorized landfill access.

## 4 DESIGN METHODS

### 4.1 Introduction

In this section, design methods that can be used to address hail damage and wind uplift are presented. When using these methods, site-specific conditions must be considered, as described hereafter.

### 4.2 Hail Damage

To calculate the potential for damage to the exposed geomembrane by hail, a comparison must be made between the impact energy of a hail stone and the impact resistance of the exposed geomembrane. The impact energy of a hail stone is equivalent to its kinetic energy given by:

$$I_e = 0.5 M v_t^2 \quad (1)$$

where:  $I_e$  = impact energy of the hail stone (N-m);  $M$  = mass of the hail stone (kg); and  $v_t$  = terminal velocity of the hail stone (m/s). Therefore, the mass and terminal velocity of the hail stone must be calculated. The mass of the hail stone is a function of the hail stone density,  $\rho_h$  (kg/m<sup>3</sup>), and volume,  $V$  (m<sup>3</sup>):

$$M = \rho_h V \quad (2)$$

The volume is a function of the diameter,  $d$  (m):

$$V = \pi d^3/6 \quad (3)$$

hence,

$$M = \pi \rho_h d^3/6 \quad (4)$$

Now, the velocity of the hail stone is calculated. The driving force,  $F_g$  (N), on the hail stone is due to gravity:

$$F_g = M g \quad (5)$$

hence,

$$F_g = \pi \rho_h g d^3/6 \quad (6)$$

This force being constant, the hail stone tends to accelerate. However, this force is resisted by the drag force exerted by air,  $F_d$  (N), which is proportional to the square of velocity:

$$F_d = (1/2) \rho_a v^2 A c_d \quad (7)$$

where:  $\rho_a$  = density of air (1.225 kg/m<sup>3</sup>);  $c_d$  = dimensionless drag coefficient (range is typically 0.45 to 0.60);  $v$  = velocity of hail stone (m/s); and  $A$  = cross section of hail stone perpendicular to velocity (m<sup>2</sup>):

$$A = \pi d^2 / 4 \quad (8)$$

hence,

$$F_d = \pi \rho_a v^2 d^2 c_d / 8 \quad (9)$$

As the hail stone accelerates,  $F_d$  increases until it becomes equal to  $F_g$ :

$$F_d = F_g \quad (10)$$

At this point, the resulting force applied to the hail stone is zero and the velocity of the hail stone becomes constant (i.e.,  $v = v_t$ ). This constant velocity is calculated by combining equations 1, 2, and 3 (Straka, 1995):

$$v_t = [(4/3)(\rho_h / \rho_a)(gd / c_d)]^{0.5} \quad (11)$$

Finally, the impact energy of the hail stone is calculated by combining the derived Equations 1, 4 and 11;

$$I_e = (\pi \rho_h^2 g d^4) / (9 \rho_a c_d) \quad (12)$$

Equation 12 gives the impact energy for the case where hail falls in a direction perpendicular to the geomembrane. This is conservative because the impact energy is less if hail does not fall in a direction perpendicular to the geomembrane. One may be even more conservative by calculating the impact energy using Equation 1 with a value of  $v_t$  that is greater than that given by Equation 11 to account for an increase in the terminal velocity of the hail stone due to wind.

The factor of safety against puncture of the geomembrane by a hail stone must be greater than a specified value, e.g., 1.0. This factor of safety is calculated using the following equation:

$$\text{Factor of Safety} = I_r / I_e \quad (13)$$

where  $I_r$  is the impact resistance of the geomembrane measured in a test.

Because the hail stone impacts the geomembrane in the cross-plane direction, standard impact resistance tests that simulate in-plane impact are not appropriate. Rollin (1991, 1993) and Kilius (1993) present cross-plane geomembrane impact resistance data obtained from tests that used a large-scale dynamic testing apparatus. The apparatus is described as a "modified drop-weight

apparatus" in which the specimen is held taut while a mass is dropped from a fixed height. Using a different test method, Koerner et al. (1986) evaluated the cross-plane impact resistance of geomembranes with a floor-mounted pendulum device. For either of these test methods, the shape of the impact apparatus should be spherical in order to simulate the assumed shape of a hail stone. Impact resistance of the geomembrane is a function of the geomembrane material properties and the thickness of the geomembrane, and is reported in terms of energy.

### 4.3 Wind Damage

The resistance to wind uplift of the exposed geomembrane is a function of the tensile characteristics of the geomembrane, the landfill geometry, and the design wind velocity. The analyses for geomembrane wind uplift presented in this paper are based on the procedures developed by Giroud et al. (1995), extended by Zornberg and Giroud (1997). For a detailed design, these references should be reviewed. The analyses are organized into two criteria: (i) resistance of the exposed geomembrane to tensile failure caused by wind uplift; and (ii) resistance of the geomembrane anchor to the tensile forces caused by wind uplift on the geomembrane. The forces acting on the geomembrane that cause geomembrane uplift, geomembrane tension, and tensile forces at the geomembrane anchors are a function of the wind velocity and the exposed length of the geomembrane. The wind velocity may be selected based on the local building codes or other appropriate guidelines.

For the selected wind velocity, the wind uplift pressure (i.e., suction) on the geomembrane at or near sea level is given by the following equation (Giroud et al., 1995):

$$S = (0.05) \lambda v_w^2 \quad (14)$$

where:  $S$  = suction (Pa);  $\lambda$  = suction factor (dimensionless); and  $v_w$  = design wind speed (km/hr).

The recommended values for suction factor,  $\lambda$ , vary according to the location along the landfill slope, as indicated in Figure 3. The suction decreases slightly with increasing elevation above sea level (Giroud et al., 1995); this effect is conservatively ignored herein. Also, the suction given by Equation 14 can be slightly decreased to account for the weight of the geomembrane (Zornberg and Giroud, 1997); however, this effect is generally not significant and is also conservatively ignored herein. As a result, the effective suction,  $S_e$  (defined by Giroud et al., (1995) as the suction corrected for the site elevation and the geomembrane weight) is considered in this paper as equal to the suction expressed by Equation 14.

The effect of wind suction on the exposed

geomembrane is characterized by the term  $S_e L$ , where  $L$  is the length of exposed geomembrane.  $L$  is calculated using Equation 15 as follows:

$$L = h/\sin\beta \quad (15)$$

where:  $\beta$  = slope angle (degree); and  $h$  = vertical distance between geomembrane anchors (m).

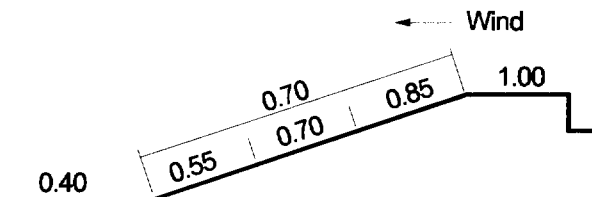


Figure 3. Recommended Values of the suction factor,  $\lambda$  (Giroud et al., 1995).

To evaluate the potential for tensile failure caused by wind uplift, the suction force acting over the length of geomembrane (i.e.,  $S_e L$ ) is compared to the ability of the geomembrane to resist this force. The properties of the geomembrane required for this analysis can be obtained from the stress-strain curve of the geomembrane, which may be established by performing American Society for Testing and Materials (ASTM) test method D 4885 (i.e., "Standard Test Method for Determining Performance Strength of Geomembranes by the Wide Strip Tensile Method"). The properties to be obtained from the stress-strain relationship are: (i) the allowable tensile strain,  $\epsilon_a$  (tensile strain at break for the reinforcing component of a reinforced geomembrane, or tensile strain at yield for unreinforced geomembranes); and (ii) the tensile stiffness,  $J$ , of the geomembrane.

The first part of the analysis involves calculation of the factor of safety for the geomembrane to resist rupture when subjected to the design wind event. Using the values obtained for  $S_e L$  and  $J$ , the normalized tensile stiffness for the geomembrane,  $J/S_e L$ , is calculated. Referring to Table 4 in the paper by Giroud et al. (1995) and using the calculated value of  $J/S_e L$ , the geomembrane strain,  $\epsilon_c$ , can be calculated. The factor of safety against geomembrane rupture (recommended to be a minimum of 1.5) is calculated by dividing the allowable geomembrane strain,  $\epsilon_a$ , by the strain calculated for the design wind speed,  $\epsilon_c$ :

$$FS_r = \epsilon_a / \epsilon_c \quad (16)$$

The second part of the analysis involves calculating the uplift force exerted on the geomembrane anchors. The required weight (hence the cross-sectional area) of the geomembrane anchor to resist the calculated uplift force can then be calculated. The geomembrane tension,  $T$ , is

calculated using Equation 17:

$$T = J \epsilon_c \quad (17)$$

where:  $T$  = tension in the exposed geomembrane (kN/m);  $J$  = geomembrane tensile stiffness (kN/m); and  $\epsilon_c$  = calculated strain (%). Using the strain calculated as indicated, the values for uplift distance,  $u$ , uplift angle,  $\theta$ , and normalized tension,  $T/S_e L$ , can be found from Table 2 of Giroud et al., (1995). These parameters are identified in Figure 4. The value of  $T$  calculated using Equation 17 may be confirmed by multiplying  $T/S_e L$  (obtained in Table 2 of Giroud et al., 1995) by  $S_e L$  to give  $T$ .

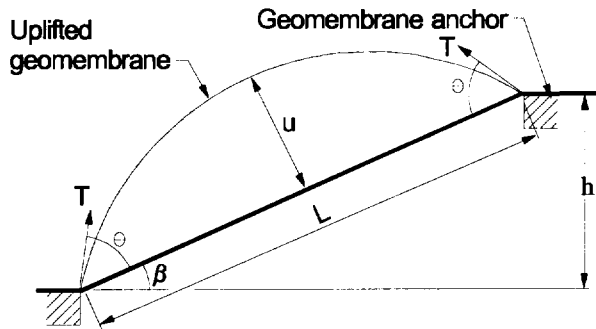


Figure 4. Exposed Geomembrane Uplift

A geomembrane anchor located on a slope between two portions of exposed geomembrane is subjected to the forces shown in Figure 5. The vertical component of these forces is a function of the uplift angle,  $\theta$  (identified in Table 2 of Giroud et al., (1995) and Figure 4 of this paper), the slope angle,  $\beta$ , and the tension,  $T$ , calculated in Equation 17. The weight of the geomembrane anchor required to resist the vertical components of the tensile forces acting on the geomembrane can be calculated using Equation 18.

$$W = T_d \sin(\theta_d - \beta) + T_u \sin(\theta_u + \beta) \quad (18)$$

where:  $W$  = weight per unit length of anchor trench (kN/m);  $T_d$ ,  $T_u$  = tension on geomembrane at the downslope and upslope side of the geomembrane anchor, respectively (kN/m);  $\theta_d$ ,  $\theta_u$  = uplift angle on the downslope and upslope side of the geomembrane anchor, respectively (degree); and  $\beta$  = slope angle (degree).

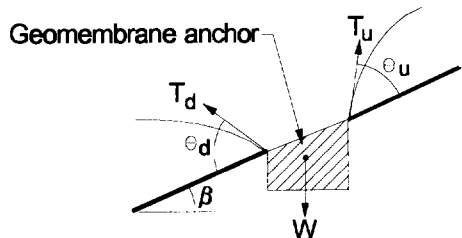


Figure 5. Tensions Acting on a Geomembrane Anchor

Assuming a continuous geomembrane anchor, the calculated anchor weight can be translated into a volume and a corresponding required area per unit width. For a geomembrane anchor consisting of soil, the required area per unit width is a function of the calculated vertical force,  $W$ , and the unit weight of the anchor soil,  $\gamma$ , and is calculated using Equation 19:

$$A_{\text{required}} = W / \gamma \quad (19)$$

The value for  $A_{\text{required}}$  is calculated assuming that the geomembrane is continuous through the cover system anchor. The calculation applies to uplift of the geomembrane anchor and does not apply to pullout of the geomembrane from the anchor. If the geomembrane is not continuous through the anchor or if the seam strength of the geomembrane is less than the geomembrane strength, then a geomembrane pullout calculation would be required. For this calculation, the soil/geomembrane interaction and/or the geomembrane seam strength would be required. These calculations are not provided in this paper.

## 5 CASE STUDY

### 5.1 Introduction

Use of the design equations and analyses presented in the previous sections is illustrated in the following case study, in which the impact of hail and wind uplift on an exposed geomembrane cover system is evaluated. The conditions presented in the case study are based on the design of an exposed geomembrane cover system for the DSWA's Cell 1&2 landfill. The geomembrane used for the design is a 0.9-mm thick green polypropylene geomembrane with a polyester scrim reinforcement. The following data are used for the analyses: (i) based on discussions with DSWA, a maximum hail stone diameter of 0.05 m was selected; and (ii) based on the local building code for structures in the area, the design wind velocity was 130 km/hr. The landfill has 4H:1V slopes (i.e., slope angle,  $\beta = 14^\circ$ ) and will have cover benches with corresponding drainage swales and geomembrane anchors spaced at 12 m vertical intervals (i.e.,  $h = 12$  m) (Figure 6).

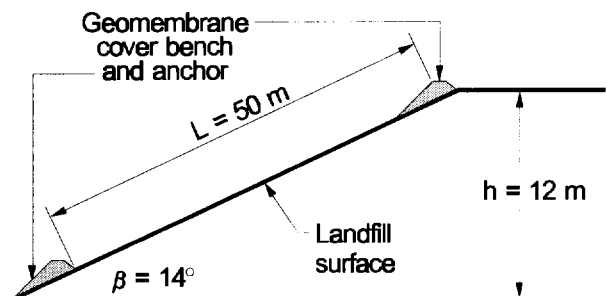


Figure 6. Case Study Landfill Slope Geometry

Using these data, the following analyses were performed: (i) calculation of the impact energy of the hail stone on the exposed geomembrane; and (ii) calculation of the total strain and tension in the geomembrane, and the minimum geomembrane anchor cross section required to resist the calculated uplift force. The analyses are described in the following two subsections.

## 5.2 Hail Impact

The impact energy,  $I_e$ , for a 0.05 m diameter hail stone assuming,  $g = 9.81 \text{ m/s}^2$ ,  $d = 0.05 \text{ m}$ ,  $\rho_h = 900 \text{ kg/m}^3$ ,  $\rho_a = 1.225 \text{ kg/m}^3$ , and  $c_d = 0.45$  is calculated using Equation 12 as follows:

$$I_e = [(\pi (900)^2 (9.81)(0.05)^4) / [(9)(1.225)(0.45)]] = 31.4 \text{ N}\cdot\text{m}$$

Therefore, to resist puncture by hail stones, the impact resistance,  $I_p$ , of the geomembrane must be greater than 31.4 N·m. The impact resistance is a function of the geomembrane polymer and thickness. The properties of the material underlying the geomembrane also affect the impact resistance (Koerner et al., 1986). The test results reported by Rollin (1991, 1993), Kilius (1993), and Koerner et al. (1986) were reviewed during the selection process of the geomembrane. As indicated from the published test results, the selected geomembrane has an impact resistance greater than the calculated impact energy, such that the factor of safety calculated from Equation 13 is greater than 1.0.

## 5.3 Wind Uplift

### 5.3.1 Introduction

Several geomembranes were considered for the design of the exposed geomembrane cover system. Calculations for the selected geomembrane are presented in this section. A reinforced geomembrane with a linear stress-strain curve characterized by a tensile stiffness,  $J=165 \text{ kN/m}$ , and a strain at break (i.e., of the reinforcement),  $\epsilon_b=27 \%$ , was selected for the design.

### 5.3.2 Analysis for Geomembrane Rupture

First, the factor of safety against tensile failure for the design wind speed is calculated. From Figure 3, the suction factor near the top of the slope is,  $\lambda=0.85$ . Ignoring the elevation factor and the mass of the geomembrane, the effective suction force,  $S_e$ , for a wind velocity,  $v_w$ , of 130 km/hr is calculated using Equation 14, as follows:

$$S_e = (0.05)(0.85)(130)^2 = 720 \text{ Pa}$$

Using Equation 15, the length of exposed geomembrane between the geomembrane anchors is:

$$L = 12 / \sin(14^\circ) = 50 \text{ m}$$

The suction force acting on this length is:

$$S_e L = (720)(50) = 36,000 \text{ N/m} = 36 \text{ kN/m}$$

And the normalized tensile stiffness is:

$$J/S_e L = (165 \text{ kN/m}) / (36 \text{ kN/m}) = 4.6$$

For  $J/S_e L = 4.6$ , Table 4 by Giroud et al. (1995) gives the calculated strain,  $\epsilon_c = 14.1\%$ . Using Equation 16, the factor of safety against geomembrane tensile failure is calculated, which is greater than the recommended minimum value of 1.5:

$$FS_r = (27\%) / (14.1\%) = 1.9$$

### 5.3.3 Geomembrane Anchor Analysis

Next, using the parameters obtained in the previous subsection, the tension caused by uplift and the required anchor area per unit width for the geomembrane is calculated. First, the uplift of the geomembrane is calculated. For the calculated strain,  $\epsilon_c = 14.1\%$  (obtained in subsection 5.3.2), Table 2 by Giroud et al. (1995) gives  $\theta = 50.3^\circ$  and  $u/L = 0.235$ . For an exposed geomembrane length,  $L = 50 \text{ m}$ , the total uplift,  $u$ , of the geomembrane is 11.75 m (Figure 4).

The wind generated tension,  $T$ , on the geomembrane is calculated from the normalized tension,  $T/S_e L$ . From Table 2 by Giroud et al., (1995),  $T/S_e L = 0.648$ ; multiplying this value by  $S_e L = 36 \text{ kN/m}$  gives  $T = 23.3 \text{ kN/m}$ . To confirm this value,  $T$  is also calculated using Equation 17:

$$T = J \epsilon_c = (165)(14.1\%) = 23.3 \text{ kN/m}$$

On either side of the geomembrane anchor it is assumed that the length of exposed geomembrane,  $L$ , and the suction factor,  $\lambda$ , for the slope are equivalent. Therefore,  $T_u = T_d$ , and  $\theta_u = \theta_d$  (Figure 5). For  $\theta_u = \theta_d = 50.3^\circ$ ,  $T_u = T_d = 23.3 \text{ kN/m}$ , and  $\beta = 14^\circ$ , the vertical force,  $W$ , required to resist uplift of the geomembrane anchor is calculated using Equation 18, as follows:

$$W = (23.3)\sin(50.3^\circ-14^\circ)+(23.3)\sin(50.3^\circ+14^\circ)=35 \text{ kN/m}$$

Assuming that the anchor consists of soil with a unit weight of  $18 \text{ kN/m}^3$ , the required cross-sectional area of the geomembrane anchor is calculated using Equation 19, as follows:

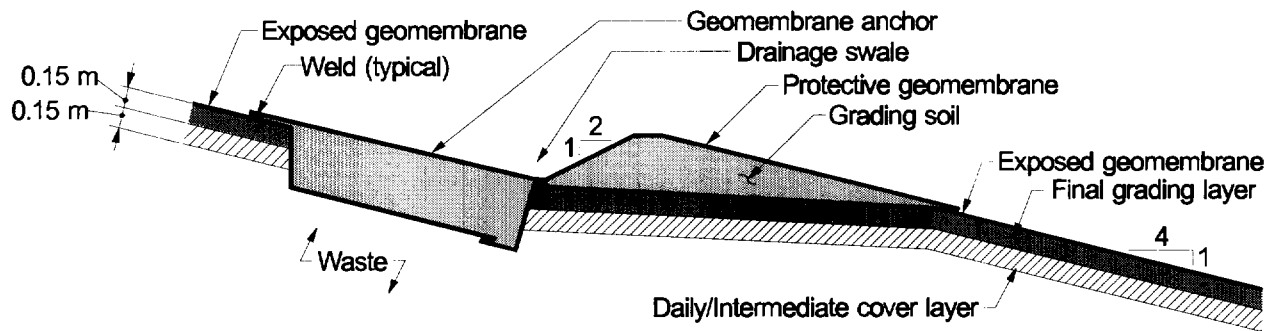


Figure 7. Exposed Geomembrane Anchor at Cover Benches

$$A_{\text{required}} = (35 \text{ kN/m}) / (18 \text{ kN/m}^3) = 1.95 \text{ m}^2$$

At the case study site, the geomembrane anchors on the cover system were designed to include a swale that conveys storm-water runoff from the landfill in a non-erosive manner. As indicated in Figure 7, the soils in the anchor trench and the soils that form the drainage swale are covered by a protective geomembrane that is welded to the exposed geomembrane in order to eliminate the potential for soil erosion at these locations.

## 6 CONCLUSION

An exposed geomembrane cover system may be appropriate at landfill sites when the design life of the cover system is relatively short or when overfilling or landfill reclamation are future possibilities. Sites that are considered for this application should also have adequate landfill gas collection systems and storm-water management controls. To design an exposed geomembrane cover system, a number of issues must be addressed. These issues are reviewed in this paper, and guidance is provided. Furthermore, design methods for two key issues, hail damage and wind uplift, are described and are illustrated using a case history. Considering the available design tools and the example provided by the case history, it is possible to safely design an exposed geomembrane cover system that can be constructed at a lower cost than a typical final cover system.

## ACKNOWLEDGMENTS

The authors acknowledge Messrs. N.C. Vasuki and R. Watson, and Ms. A. Germain for the opportunity to apply the design methods described in this paper to DSWA's Cell 1&2 landfill. The authors are grateful to Mr. J. O'Connor for his assistance in the preparation of the figures for this paper.

## REFERENCES

Giroud, J.P., and Morel, N., (1992) "Analysis of Geomembrane Wrinkles", *Geotextiles and*

- Geomembranes*, Vol. 11, No. 3, pp. 255-276. (Erratum: 1993, Vol. 12, No. 4, p. 378.)
- Giroud, J.P., (1994), "Determination of Geomembrane Shattering Cracks", *Geosynthetics International*, Industrial Fabrics Association International, Vol. 1, No. 2, pp. 149-180.
- Giroud, J.P., Pelte, T., and Bathurst, R.J., (1995) "Uplift of Geomembranes by Wind", *Geosynthetics International*, Special Issue on Design of Geomembrane Applications, Industrial Fabrics Association International, Vol. 2, No. 6, pp. 897-952.
- Kilius, D.E., (1993) "Cold Temperature Performance of Polypropylene Geomembranes and Seams", *Geosynthetic Liner System: Innovations, Concerns, and Designs*, Koerner, R.M., and Wilson-Fahmy, R.F., Editors, Proceedings of 1993 GRI Conference, Industrial Fabrics Association International, pp. 197-207.
- Koerner, G.R., and Koerner, R.M., (1995) "Temperature Behavior of Field Deployed HDPE Geomembranes", *Proceedings, Geosynthetics '95 Conference*, Nashville, Tennessee, USA, pp. 921-937.
- Koerner, R.M., Monteleone, M.J., Schmidt, J.R., and Roethe, A.T., (1986) "Puncture and Impact Resistance of Geosynthetics", *Proceedings, Third International Conference on Geotextiles and Geomembranes*, Vienna, Austria, pp. 677-682.
- Rollin, A.L., Lefebvre, M., Lafleur, J., and Marcotte, M., (1991) "Evaluation of Field Seam Quality by the Impact Test Procedure", *Proceedings, Geosynthetics '91 Conference*, Atlanta, Georgia, USA, pp. 223-237.
- Rollin, A.L., Lefebvre, M., Lafleur, J., and Mlynarek, J., (1993) "The use of Impact Test Procedure to Assess Seam's Brittleness", *Proceedings, Geosynthetics '93 Conference*, Vancouver, Canada, pp. 1559-1573.
- Straka, J., (1995) University of Oklahoma Meteorology Department, written communication with C. Furst of GeoSyntec.
- Zornberg, J.G., and Giroud, J.P., (1997) "Uplift of Geomembranes by Wind - Extension of Equations", *Geosynthetics International*, Industrial Fabrics Association International, Vol. 4, No. 2, pp. 187-207.

# Current Issues in Seismic Design of Geosynthetic Cover Systems

Edward Kavazanjian, Jr.

Principal, GeoSyntec Consultants, 2100 Main Street, Suite 150, Huntington Beach, California, USA

**ABSTRACT:** Current issues in the seismic design of geosynthetic cover systems for landfills include establishment of a rational seismic performance standard, determination of the allowable displacement, and evaluation of the seismic coefficient for use in pseudo-static analyses. Prevention of harmful discharge is a cost effective and environmentally protective alternative to current performance standards which require landfill covers to withstand the design earthquake without damage. Calculated seismic displacement is the most commonly used index of seismic performance. The allowable calculated displacement for a geosynthetic cover system depends upon the ability of the cover to sustain displacement without damage or discharge, the accuracy with which displacements can be calculated, and the feasibility of repair of damage to the cover. Rational selection of the seismic coefficient for a pseudo-static design analysis implicitly depends upon the allowable displacement. Evaluation of the seismic coefficient also depends on the potential for amplification and attenuation of ground motions.

**KEYWORDS:** Landfill, Cover, Geosynthetic, Seismic, Earthquake.

## 1 INTRODUCTION

Geosynthetic interfaces of low or reduced strength compared to soil or solid waste materials combined with the potential for amplification of free-field ground motions by the waste mass make seismic performance an important consideration in the design of geosynthetic cover systems. Even in areas of moderate seismicity, amplification of free-field ground motions and low interface strengths can combine to limit final cover side slope inclination and, hence, landfill capacity. Current issues in the seismic design of geosynthetic cover systems for landfills include the establishment of a rational seismic performance standard, determination of the allowable calculated permanent seismic displacement of cover system components, and determination of the appropriate seismic coefficient for pseudo-static design analyses.

In parts of the United States (e.g., California), current regulations require landfill cover systems to withstand the design earthquake "without damage." Experience with the seismic design of geosynthetic cover systems for landfills has shown that requiring the cover to unconditionally withstand the design earthquake without damage can be prohibitive. A rational, environmentally sound, and cost-effective alternative to this burdensome seismic performance standard is to require that the landfill cover system withstand the design earthquake without a discharge of contaminants that is harmful to human health or the environment.

The most commonly used index of the seismic performance of landfill cover systems is the calculated permanent seismic

displacement. However, little guidance exists as to what constitutes an allowable value of calculated permanent seismic displacement. Factors influencing the magnitude of allowable calculated permanent seismic displacement may include the seismic performance standard (e.g., without damage or without harmful discharge), the ability to detect and repair damage, design details of the cover system (e.g., the presence of penetrations through the geomembrane barrier layer), and the degree of confidence in the calculated displacement.

The seismic coefficient method is the most common analytical approach used in engineering practice for the seismic design of geosynthetic cover systems. In the seismic coefficient method, pseudo-static limit equilibrium analysis is used to design the cover system to achieve the required minimum factor of safety for a specified seismic coefficient. The seismic coefficient employed in pseudo-static limit equilibrium analysis is generally specified as a function of the free-field peak horizontal ground acceleration (PHGA) at the project site. Rational selection of the seismic coefficient depends upon allowable displacement considerations.

Due to the need to account for potential amplification of the free-field PHGA by the waste mass, seismic coefficient values established solely on the basis of the free-field PHGA generally incorporate significant conservatism. Reduction of the conservatism in seismic coefficient values associated with the potential for amplification requires relatively sophisticated project-specific seismic site response analysis. Project-specific response analyses may yield amplification factors lower than those based upon design charts. Project-specific response

analyses also facilitate averaging of spatially and temporally incoherent ground motions over the potential failure mass, another mitigating factor with respect to the relationship between peak ground acceleration and the seismic coefficient.

## 2 SEISMIC PERFORMANCE STANDARDS

In the United States (U.S.), federal regulations for design of municipal solid waste landfills require design of containment systems, including liners, covers, and facilities that control leachate and surface water, to “resist” the design earthquake. Interpretation of the term “resist” is left to the discretion of state regulatory agencies. Many state regulators strictly interpret “resist” to mean that the landfill containment system should unconditionally survive the design earthquake without damage. California explicitly requires solid waste landfill containment systems “withstand without damage” the design earthquake.

Experience with the seismic design of landfill cover systems shows that requiring a geosynthetic cover system to unconditionally withstand the design earthquake without damage is an extremely burdensome standard. Particularly when coupled with a relatively extreme design event (e.g., the prescriptive U.S. federal standard of a PHGA with a 90 percent probability of not being exceeded in 250 years), the “withstand without damage” seismic performance standard can severely limit cover slope inclinations and, hence, landfill capacity. Even in areas of relatively low seismicity (i.e., areas where the design PHGA equals 0.10 g to 0.20 g, where g is the acceleration of gravity), design of a geosynthetic cover system to unconditionally withstand the design earthquake without damage can be prohibitive due to the potential for amplification of ground motions and the low seismic resistance of many geosynthetic interfaces.

### 2.1 Damage threshold

Permanent seismic displacement is generally assumed to accumulate whenever the earthquake-induced horizontal acceleration averaged over the potential failure mass (termed the average acceleration) exceeds the seismic coefficient resulting in a factor of safety of 1.0 in a pseudo-static limit equilibrium analysis (termed the yield acceleration). Figure 1 presents yield acceleration values from infinite slope stability analyses (Matasovic, 1991) as a function of slope inclination and friction angle for a veneer failure surface with no cohesion. As many regulators consider permanent seismic displacement synonymous with damage, the yield acceleration values plotted in Figure 1 indicate that, even at slope inclinations as gentle as 4H:1V (4 horizontal to 1 vertical), many typical geosynthetic interfaces may possess insufficient strength to unconditionally resist even modest seismic loads (e.g., average accelerations greater than 0.1 g) without damage (i.e., with zero permanent seismic displacement).

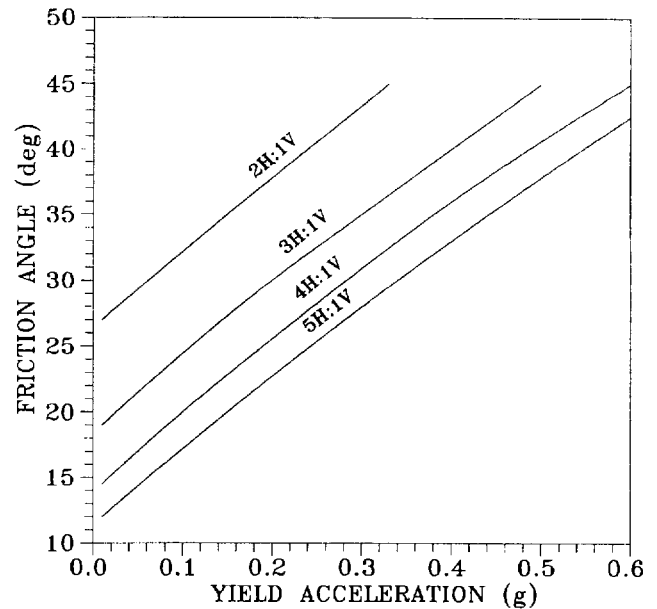


Figure 1 Yield Acceleration versus Friction Angle for an Infinite Slope with Zero Cohesion

#### 2.1.1 Mitigation measures for geosynthetic covers

The data in Figure 1 suggests that, for side slopes steeper than 4H:1V, use of a geomembrane with texturing on both sides may be required to satisfy the withstand without damage seismic performance standard for many geosynthetic cover systems. If a geosynthetic drainage element is employed on top of the geomembrane, it may be necessary to use a geocomposite with non-woven filter geotextiles heat-bonded on both sides of a drainage net in order to achieve unconditional stability. If a cohesion component of shear strength (i.e., interface adhesion) is relied upon to provide a yield acceleration sufficient to withstand the design earthquake without damage, it may be necessary to limit protective soil cover thickness, as the contribution of cohesion to the yield acceleration decreases with increasing cover soil thickness. In areas of moderate to high seismicity (i.e., areas where the design free-field PHGA is greater than 0.2 g), even these measures may not be sufficient for design of a cover that can unconditionally resist the design earthquake without damage.

### 2.2 Seismic performance of landfill cover systems

Observations of the performance of landfills in earthquakes indicate that solid waste landfill cover systems can sustain considerable damage without a discharge of contaminants harmful to human health or the environment. While there is no record of the performance of geosynthetic cover systems subject to strong shaking in earthquakes, observations of the performance of landfills with soil cover systems indicates that cracking and displacement of soil cover is the most common



mode of damage at landfills subjected to strong shaking in earthquakes (Anderson and Kavazanjian, 1995; Matasovic and Kavazanjian, 1996). In fact, cracking and displacement of cover soil has been noted in every post-earthquake damage survey of landfill facilities reported in the literature (Johnson, et al, 1991; Orr and Finch, 1990; Buranek and Prasad, 1991; Matasovic, et al, 1995). In some cases, cover soil displacement in excess of 0.5 m has been reported. Despite this prevalence of cover soil cracking and displacement and the occurrence of other modes of damage (e.g., disruption of the gas collection system), not one incident of a discharge of contaminants harmful to human health or the environment at a solid waste landfill facility has been attributed to earthquake ground motions. This satisfactory record of observed performance demonstrates clearly that design of landfill cover systems to unconditionally withstand the design earthquake without damage is not necessary, at least for short term protection of human health and the environment.

### 2.3 Alternative seismic performance standard

Design of landfill cover systems to withstand the design earthquake without a discharge of contaminants harmful to human health or the environment (i.e., design to “withstand without discharge”) provides a rational, cost-effective, and protective alternative to the “withstand without damage” seismic performance standard. Design to withstand without discharge requires consideration of seismically-induced discharge under both short-term and long-term conditions. Short-term discharge considerations may include mass movement of soil or waste and discharge of gas or leachate. For typical solid waste landfills, earthquake-induced damage to the cover will not result in harmful discharge in the short-term. However, earthquake-induced damage may result in harmful discharge in the long term if the integrity of the cover is not restored after the earthquake. Long-term discharge from a landfill due to seismically-induced damage to the cover system may result from both direct damage (e.g., an earthquake-induced tear in the geomembrane) and indirect damage (e.g., ultra-violet radiation-induced damage to the geomembrane resulting from loss of soil cover).

#### 2.3.1 Mitigation of potential for harmful discharge

To mitigate the potential for harmful discharge from the landfill, a post-earthquake response and recovery plan is an essential element of designing to withstand without discharge. The response and recovery plan should include guidelines for a comprehensive post-earthquake inspection to assess the earthquake-induced damage. The criteria for determining when a post-earthquake inspection is necessary is often based upon combinations of earthquake magnitude and site-to-source distance which induce the threshold value of free-field PHGA

with the potential for causing damage, considering amplification due to both foundation soils and the waste itself.

Identification of anticipated actions required for short-term repair and long-term restoration of the cover should also be included in a post-earthquake response and recovery plan. For many landfills, provisions in the post-closure Operation, Maintenance, and Monitoring Plan for cover damage that occurs under “normal” operating conditions may implicitly provide for response to and restoration of earthquake-induced cover system damage. However, explicit consideration should be given to response and recovery after a seismic event due to the potential for earthquake-induced damage to larger areas of the facility (compare to damage which occurs under “normal” operating conditions) and due to the potential impact of the earthquake on the availability of the required resources (e.g., materials, equipment, and/or skilled labor) for repair and restoration. Consideration should also be given to stockpiling special-order materials required for cover repair and to maintaining lists of approved suppliers and contractors (e.g., geomembrane installers) to facilitate cover repair.

## 3 ALLOWABLE DISPLACEMENTS

Calculated permanent seismic displacement is the most common measure used in practice for quantifying the seismic performance of a geosynthetic cover system. Due to the difficulty of designing a geosynthetic cover system that is unconditionally stable, seismic design criteria generally specify a value for the maximum, or “allowable,” calculated permanent seismic displacement for the cover system. However, little guidance exists as to the magnitude of the allowable calculated permanent seismic displacement for geosynthetic cover systems. There are some values for the allowable seismic displacement for geomembranes cited in the literature. These values tend to be based upon a 1992 survey of values used in engineering practice in the U.S. for seismic design of geosynthetic liner systems by Seed and Bonaparte (1992). However, the values cited by Seed and Bonaparte (1992) are often incorrectly referred to as “recommendations,” despite these authors specific caveat that they are merely reporting results of a survey of current practice.

The allowable value for the calculated permanent seismic displacement of a geosynthetic cover system logically depends upon the seismic performance standard (e.g., withstand without damage or withstand without harmful discharge), the level of confidence in the calculated displacement, and details of the cover system. If the seismic performance standard is to withstand without damage, the allowable calculated displacement will be small. For a cover system designed to the withstand without discharge standard, the allowable calculated displacement will be larger than for the withstand without damage standard. The accuracy of the displacement analysis is an essential consideration in establishing the allowable calculated displacement value.

### 3.1 Calculation of permanent seismic displacement

Permanent seismic displacement is generally calculated using Newmark's (1965) "sliding block on a plane" method of analysis. In a Newmark analysis, excursions of the time-history of the average acceleration of the potential failure mass above the yield acceleration of the mass are integrated to calculate the accumulated "permanent" seismic displacement. Theoretically, this calculated permanent displacement is a rigid body displacement that accumulates everywhere along the potential failure surface.

Conventional Newmark analyses generally employ a series of simplifying assumptions. The yield acceleration in a conventional analysis is usually calculated using residual shear strengths. Typically, only the horizontal component of the earthquake ground motion is considered in the analysis. Computation of the acceleration time-history of the failure mass is generally based upon a response analysis which ignores relative displacement along the failure surface (i.e., the seismic response analysis is "de-coupled" from the computation of permanent displacement.). These simplifying assumptions generally result in a conservative assessment of permanent seismic displacement. In fact, Anderson and Kavazanjian (1995) state that the permanent seismic displacement calculated in this conventional manner may be more appropriately considered an index of seismic performance rather than an engineering estimate of the anticipated displacement. These authors suggest that, in a conventional Newmark analysis, calculated displacement of 300 mm or less should be considered indicative of small displacement while calculated displacement of 1 m or more should be considered indicative of large displacement.

Seismic displacement analyses that are more advanced than the conventional Newmark analysis are available for seismic design of geosynthetic cover systems. These more advanced analyses include Newmark analyses which consider the degradation of shear strength from peak to residual conditions over the course of the earthquake and/or the coupling of earthquake ground motions and relative displacement. Finite element seismic deformation analyses with interface elements in which permanent seismic displacement is directly calculated are also available. However, these advanced analyses are not widely used in practice.

### 3.2 Current standards for cover system design

In current U.S. practice, the 150 to 300 mm of displacement cited by Seed and Bonaparte (1992) as the commonly employed allowable value for the calculated permanent seismic displacement of geosynthetic liner systems is sometimes also used as the allowable calculated seismic displacement for a geosynthetic cover system. However, an allowance is often made for the presumption that cover systems can reasonably be designed to sustain larger

displacements than liner systems because damage to cover systems is observable and repairable (Richardson, et al., 1994). Thus, the 150 to 300 mm allowable calculated displacement cited by Seed and Bonaparte (1992) for geosynthetic liner systems is often increased to values in the range of 500 mm to 1 m for the allowable calculated permanent seismic displacement of a geosynthetic cover system. Strictly speaking, because of the presumption that the cover can sustain some damage in the design event, these larger values may be applicable only if the withstand without discharge performance standard is employed. Allowable permanent seismic displacement values of 1 m are consistent with current practice for seismic design of slopes and embankments (Seed, 1979; ASCE 1983).

### 3.3 Recommended allowable displacement values

Based upon current standards of practice for the seismic stability of slopes and embankments, allowable values of calculated seismic displacement of 1 m, or more, should be acceptable for geosynthetic cover systems designed to withstand the design earthquake without discharge. When designing a cover system to withstand without discharge, provisions are needed to mitigate potential hazards associated with discharge of leachate and/or gas from disrupted conveyance systems (e.g., use of automatic shut-off valves, secondary containment, and/or articulated seismic joints) and facilitate post-earthquake repair of damage.

Multiple penetrations through geomembrane cover elements for gas and leachate collection or other purposes may limit allowable displacement to less than 1 m on an economic basis due to the cost of repair. However, if the anticipated displacement is above the geomembrane, there are no penetrations through the geomembrane on slopes, and benches provide sufficient capacity to retain cover soil that sloughs from the above, the allowable seismic displacement of a geosynthetic landfill cover system may be unlimited, provided the owner is prepared to repair and/or replace the protective soil cover and drainage layer (if any) on top of the geomembrane after a severe earthquake.

Based upon current standards of practice for seismic design of geosynthetic liner systems, 150 to 300 mm appears to be a reasonable range of values for the allowable calculated permanent seismic displacement of a geosynthetic cover system designed to withstand the design earthquake without damage. The upper end of the range (i.e., 300 mm) is more appropriate for simplified analyses which use upper bound displacement curves from generic Newmark displacement charts (e.g., Hynes and Franklin, 1984), residual shear strength, and/or simplified seismic response analyses. The lower end of the range (i.e., 150 mm) is more appropriate for more sophisticated analyses which strive to accurately calculate the permanent seismic displacement by using project-specific seismic response and formal Newmark displacement analyses.

Due to its simplicity, the seismic coefficient method remains the most common method of analysis used in practice for seismic design of geosynthetic cover systems. In the seismic coefficient method, the factor of safety for the cover system calculated in a pseudo-static limit equilibrium analysis using a specified seismic coefficient is compared to the minimum acceptable factor of safety to determine the adequacy of the design. The seismic coefficient equals the fraction of the weight of the potential failure mass that is applied as a horizontal force to the centroid of the mass in a pseudo-static limit equilibrium stability analysis. The seismic coefficient is typically specified as a fraction of the free-field PHGA of the design earthquake divided by the acceleration of gravity. Unless the criteria for seismic design is unconditional stability (zero seismic displacement), rational specification of the appropriate combination of seismic coefficient and pseudo-static factor of safety implicitly requires consideration of the allowable seismic displacement.

#### 4.1 Displacement basis for seismic coefficient values

Figure 2 presents a chart developed by Hynes and Franklin (1984) from the results of Newmark displacement analysis of 354 accelerograms from earthquakes of magnitude 5 to 8+. This figure presents mean, mean plus one standard deviation, and upper bound values for the calculated permanent seismic displacement from these records as a function of the ratio of yield acceleration to the peak acceleration of the time history used in the displacement analysis.

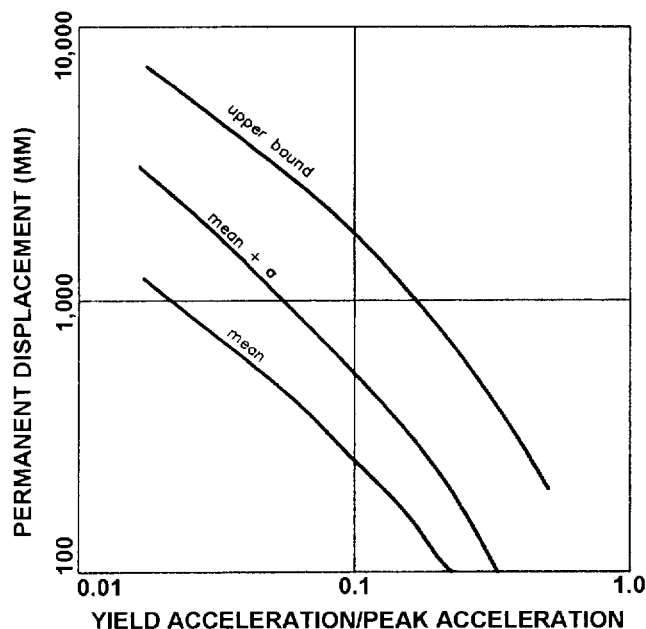


Figure 2 Calculated Permanent Seismic Displacement (after Hynes and Franklin, 1984)

Evaluation of the Hynes and Franklin data and experience with formal Newmark displacement analysis indicate that the mean curve in Figure 2 may be considered representative of the displacement potential of small magnitude earthquakes (magnitude less than or equal to 5.5) and of intermediate magnitude earthquakes (magnitude less than or equal to 6.5) at relatively short site-to-source distances (less than 10 km). On the same basis, the mean plus one standard deviation curve in Figure 2 may be considered representative of the displacement potential of intermediate magnitude events at site-to-source distances in excess of 10 km and larger magnitude events.

Evaluation of the data presented by Hynes and Franklin indicates that data points between the mean plus one standard deviation and upper bound lines in Figure 2 correspond either to very low intensity accelerograms from distant events or to synthetic accelerograms for very large magnitude (magnitude 8+) events and thus may not be representative of field conditions. Other important caveats on the applicability the Hynes and Franklin curves are that experience with seismic response and displacement analysis indicates that they may not be applicable to landfills on soft clay foundations, where amplification of long period motions by the foundation soils may significantly increase seismic displacement potential, and that the number of large magnitude events (magnitude greater than 7.4) in the data base is limited.

The Hynes and Franklin data indicates that when the ratio of yield acceleration to peak acceleration is greater than 0.4, calculated permanent seismic displacement will be small (less than 100 mm) for most situations encountered in practice. The data from Hynes and Franklin further indicates that calculated permanent seismic displacement will be less than 300 mm when the ratio of yield acceleration to peak acceleration is greater than 0.08 for small magnitude events and nearby intermediate magnitude events (i.e., for the mean curve in Figure 2) and 0.17 for more distant intermediate magnitude events and large magnitude events (i.e., for the mean plus one standard deviation curve). For a calculated permanent seismic displacement of less than 1 m, the Hynes and Franklin data indicates that the ratio of yield acceleration to the peak average acceleration should be greater than 0.03 for small magnitude events and nearby intermediate magnitude events and 0.06 for more distant intermediate magnitude events and large magnitude events.

Table 2 summarizes values of the ratio of yield acceleration to peak acceleration for various calculated permanent seismic displacement levels from Figure 2. Values from both the mean curve (i.e., for small magnitude events and nearby intermediate magnitude events) and the mean plus one standard deviation curve (i.e., for more distant intermediate magnitude events and large magnitude events) of Figure 2 are summarized in Table 2.

Table 2 Ratio of Yield Acceleration to Peak Acceleration as a Function of Calculated Permanent Seismic Displacement (based upon Hynes and Franklin, 1984)

Calculated Displacement	Mean	Mean + 1 Std. Dev.
100 mm	0.23	0.35
150 mm	0.17	0.27
300 mm	0.08	0.17
500 mm	0.05	0.11
1 m	0.03	0.06

#### 4.2 Amplification of free-field ground motions

The peak acceleration in Figure 2 and Table 2 represents the peak average acceleration of the potential failure mass, and not the free-field PHGA. Observations and analyses of the seismic response of solid waste landfills indicate that the free-field ground motions can be significantly amplified at the top of a landfill by the waste mass. This amplification can result in a landfill cover peak acceleration significantly larger than the free-field peak acceleration. Figure 3 presents amplification curves relating the free field PHGA to the peak acceleration at the top of an embankment or soft soil deposit developed by Singh and Sun (1995) for a 30-m-high landfill, by Idriss (1990) for soft soil sites, and by Harder (1991) for earth dams.

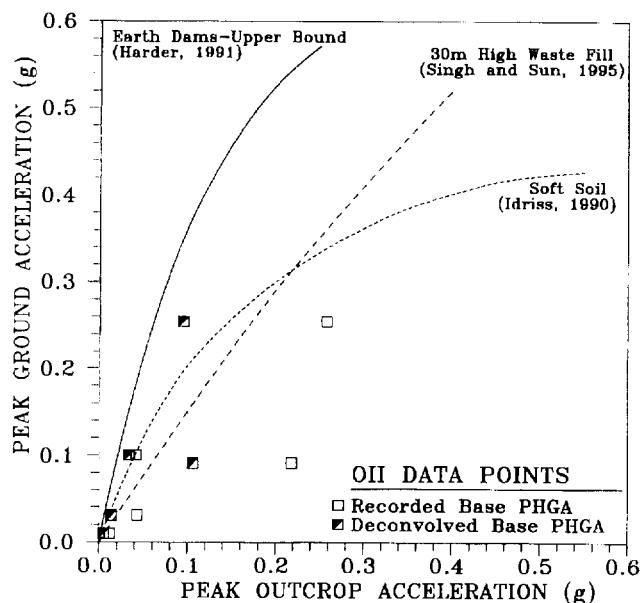


Figure 3 Amplification of Free-Field Ground Motions

Also plotted on Figure 3 are data points derived from the recorded motions at the OII landfill. Each OII data point is plotted twice, once using the peak acceleration recorded on

compacted fill at the base of the landfill as the “free-field” motion (Hushmand Associates, 1996) and once using the free-field PHGA evaluated by deconvolution in back analyses performed by GeoSyntec (1996). The results of the back analysis presented in Figure 3 indicate that amplification at the OII landfill was greater than reported by Kavazanjian and Matasovic (1995) based on the assumption that the motions recorded at the base of the landfill were free-field motions

The data plotted in Figure 3 indicate that the earthquake motions to which a landfill cover is subjected may be significantly greater than the free-field ground motions and that the Harder “upper bound” amplification curve for dams may also be appropriate as an upper bound for amplification by solid waste landfills. In order to account for the potential for amplification of the earthquake motions by the waste mass, the peak average acceleration of a potential cover system failure mass may be estimated from Figure 3 using the free-field PHGA and the Harder earth dam curve.

#### 4.3 Derivation of a displacement-based seismic coefficient

Table 2 and Figure 3 can be used to derive displacement-based seismic coefficient values for design of geosynthetic cover systems. The yield acceleration used to develop Table 2 represents the seismic coefficient for a factor of safety of 1.0. The peak acceleration used to develop Table 2 represents the peak average acceleration of the potential failure mass. Therefore, seismic coefficient values for specified levels of calculated permanent seismic displacement can be derived by multiplying the ratios presented in Table 2 by the peak average acceleration of the potential failure mass derived from the free-field PHGA using the Harder curve in Figure 3. For earthquakes of magnitude less than or equal to 6.5 within 10 km of the site and for any earthquake of magnitude less than or equal to 5.5, the ratios in the “Mean” column of Table 2 should be used. For earthquakes of magnitude greater than 6.5 and for earthquakes between magnitude 5.5 and 6.5 that are greater than 10 km from the site, the ratios in the “Mean + 1 Std. Dev.” column of Table 2 should be used.

Seismic coefficients derived from Table 2 should be used with a factor of safety of 1.0. Use of higher factors of safety (e.g., 1.1 or 1.15, as used with some methodologies) with a seismic coefficient derived from the Hynes and Franklin chart is not recommended, as their use would constitute unnecessary compounding of factors of safety. Furthermore, the ratios in Table 2 apply to the peak average horizontal acceleration of the failure mass and not to the free-field PHGA. The difference between these two peak acceleration values may be substantial. The relationship of the peak average horizontal acceleration of a potential failure mass to the free-field PHGA is influenced by two primary factors: amplification of the free-field ground motions by the waste mass (discussed in the previous section) and averaging of the earthquake ground motions over the potential failure mass.

#### 4.4 Attenuation by averaging of accelerations

A mitigating factor with respect to the seismic displacement potential of a geosynthetic cover system is the reduction in the peak average acceleration of a potential failure mass when compared to the peak acceleration of the mass. This reduction is due to the incoherence of the earthquake induced motions (i.e., to the spatial and temporal variability of the ground motions) of the potential failure mass. The phase difference (temporal incoherence) between motions at different points of the failure mass is particularly important in this respect. The ground motions at two points within the failure mass that are completely identical in all respects except for phase will cancel each other out entirely if they are 180 degrees out of phase. The larger the potential failure mass, the greater the reduction in the peak average acceleration compared to the peak acceleration, as incoherence increases with the size of the potential failure mass. Figure 4 illustrates the relationship between peak average acceleration and the size of the potential failure mass for a hypothetical landfill cover system.

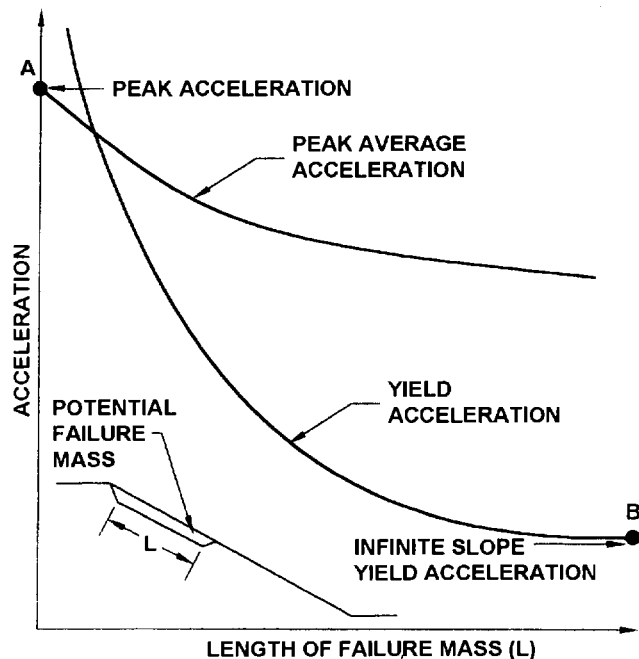


Figure 4 Yield Acceleration and Peak Average Acceleration Versus Size of Failure Mass

The seismic displacement potential of a geosynthetic cover systems is further mitigated by the inter-relationship between the size (length) of the potential failure mass and the yield acceleration. For veneer stability, shorter potential failure masses, which tend to have larger peak average accelerations than longer failure masses due to relatively small amounts of incoherence, serendipitously tend to have larger yield accelerations than the longer potential failure masses. The

yield acceleration tends to increase with decreasing size of veneer failure mass because as the potential failure mass decreases in size the contribution to the yield acceleration from the passive “buttressing” of the soil wedge at the bottom of the failure mass progressively increases the yield acceleration from the minimum value associated with infinite slope stability. The impact of the length of a potential veneer failure mass on yield acceleration is also illustrated in Figure 4.

The inter-relationship among yield acceleration, peak average acceleration, and the size of the potential failure mass illustrated in Figure 4 indicates that conventional seismic design analyses for geosynthetic cover systems which employ a seismic coefficient based upon the peak acceleration at the crest of a landfill (Point A in Figure 4) and a yield acceleration from an infinite slope veneer stability analysis (Point B in Figure 4) may be extremely conservative. Despite the conservatism associated with it, this conventional approach is commonly used in current practice due to its simplicity. Relatively sophisticated seismic response and limit equilibrium analyses are generally required to reduce the level of conservatism associated with such conventional analysis.

## 5 CONCLUSIONS

The low shear strength often associated with geosynthetic interfaces and the potential for amplification of earthquake ground motions by the waste mass combine to make seismic design an important consideration for geosynthetic cover systems for landfills, even in areas of low to moderate seismicity. Due to these factors, design of geosynthetic cover systems to be unconditionally stable when subjected to the design earthquake (i.e., so that the yield acceleration exceeds the peak average acceleration for all potential failure masses) is frequently burdensome and may be prohibitive.

Design of geosynthetic cover systems to withstand the design earthquake without a discharge of contaminants harmful to human health or the environment is a logical, cost effective, and environmentally protective alternative seismic performance standard to design for unconditional stability. A post-earthquake response and recovery plan is an essential element of designing a cover system to sustain damage in the design earthquake without a harmful discharge.

Due to the conservatism inherent to conventional Newmark seismic displacement analyses, wherein the calculated permanent seismic displacement is based upon seismic motions calculated in a de-coupled analyses and a yield acceleration calculated using residual shear strengths, geosynthetic cover systems may be assumed to be able to withstand the following calculated seismic displacements:

- at least 1 m for covers designed to withstand the design earthquake without a harmful discharge; and
- 150 to 300 mm for covers designed to withstand the design earthquake without damage.

With proper attention to detail, the ability of a geosynthetic cover system to sustain seismically-induced displacement of the overlying cover soil may be unlimited.

Generic Newmark seismic displacement analyses indicate that the seismic coefficient for use in pseudo-static limit equilibrium design analyses of geosynthetic cover systems may be a small fraction of the peak average acceleration of the potential failure mass. However, the potential for amplification of the free-field ground motions must be considered when evaluating the peak average acceleration of a potential failure mass. Observations and analyses of the seismic response of landfills indicate that the potential for amplification of earthquake motions at the top of solid waste landfills may be similar to that of earth dams.

The amplification potential of a landfill is mitigated by the reduction in the peak average acceleration of a potential failure mass due to the incoherence of earthquake ground motions and the increase in the yield acceleration of a failure mass of limited size compared to the yield acceleration calculated in an infinite slope veneer stability analysis. Detailed seismic response and limit equilibrium analyses are required to accurately account for these factors in landfill cover design.

## REFERENCES

- Anderson, D.G., and Kavazanjian, E., Jr. (1995), "Performance of Landfills Under Seismic Loading," Proceedings of the 3rd International Conference on Recent Advances in Geotechnical Earthquake Engineering and Soil Dynamics, St. Louis, Missouri, pp. 1557-1587.
- ASCE (1983), "Advisory Notes on Lifeline Earthquake Engineering," report prepared by the Technical Committees of the ASCE Technical Council on Lifeline Earthquake Engineering
- Buraneck, D. and Prasad, S. (1991), "Sanitary Landfill Performance During the Loma Prieta Earthquake," Proceedings of the 2nd International Conference on Recent Advances in Geotechnical Earthquake Engineering and Soil Dynamics, St. Louis, Missouri, pp. 1655-1660.
- GeoSyntec (1996), "Seismic Site Response Analyses, Seismicity, Settlement, and Slope Stability Work Plan Report No. SWP-6, Operating Industries, Inc. Landfill, Monterey Park, California," report submitted to Region IX, U.S. EPA, by GeoSyntec Consultants, Inc., Huntington Beach, California, for New Cure, Inc.
- Harder, Jr., L.S. (1991), "Performance of Earth Dams During the Loma Prieta Earthquake," Proceedings of the 2nd International Conference on Recent Advances in Geotechnical Earthquake Engineering and Soil Dynamics, St. Louis, Missouri, pp. 1613-1629.
- Hushmand Associates (1994), "Landfill Response to Seismic Events," report prepared for Region IX, U.S. EPA, by Hushmand Associates, Laguna Niguel, California.
- Hynes, M.E. and Franklin, A.G. (1984), "Rationalizing the Seismic Coefficient Method," Miscellaneous Paper GL-84-13, U.S. Army Engineer Waterways Experiment Station, Vicksburg, Mississippi.
- Idriss, I.M. (1990), "Response of Soft Soil Sites During Earthquakes," Proceedings of the Symposium to Honor Professor H.B. Seed, University of California, Berkeley.
- Johnson, M.E., Lundy, J., Lew, M. and Ray, M. E. (1991), "Investigation of Sanitary Landfill Slope Performance During Strong Ground Motion from the Loma Prieta Earthquake of October 17, 1989," Proceedings of the 2nd International Conference on Recent Advances in Geotechnical Earthquake Engineering and Soil Dynamics, St. Louis, Missouri, pp. 1701-1706.
- Kavazanjian, E., Jr. and Matasovic, N. (1995), "Seismic Analysis of Solid Waste Landfills," Proceedings of Geoenvironment 2000, ASCE Special Geotechnical Publication No. 46, pp. 1066-1080.
- Matasovic, N. (1991), "Selection of Method for Seismic Slope Stability Analysis," Proceedings of the 2nd International Conference on Recent Advances in Geotechnical Earthquake Engineering and Soil Dynamics, St. Louis, Missouri, pp. 1057-1062.
- Matasovic, N., Kavazanjian, E., Jr., Augello, A.J., Bray, J.D. and Seed, R.B. (1995), "Solid Waste Landfill Damage Caused by 17 January 1994 Northridge Earthquake," In: Woods, Mary C. and Seiple, Ray W., Editors, The Northridge, California, Earthquake of 17 January 1994: California Department of Conservation, Division of Mines and Geology Special Publication No. 116, pp. 221-229.
- Matasovic, N. and Kavazanjian, E., Jr. (1996), "Observations of the Performance of Solid Waste Landfills During Earthquakes," Proceedings of the 11th World Conference on Earthquake Engineering, Elsevier Science Ltd. Paper No. 341, 8 p. (on CD ROM)
- Newmark, N.M. (1965), "Effects of Earthquakes on Dams and Embankments," *Geotechnique*, Vol. 15, No. 2, pp. 139-160.
- Orr, W.R. and Finch, M.O. (1990), "Solid Waste Landfill Performance During Loma Prieta Earthquake," In: Landva, A. and Knowles, G.D., Editors, Geotechnics of Waste Fills: Theory and Practice, ASTM Special Technical Publication 1070, pp. 22-30.
- Richardson, G.N., Kavazanjian, E., Jr. and Matasovic, N. (1995), "RCRA Subtitle D (258) Seismic Design Guidance for Municipal Solid Waste Landfill Facilities," U.S. Environmental Protection Agency Report No. 600/R-95/051, 143 p.
- Seed, H.B. (1979), "Considerations in the Earthquake-Resistant Design of Earth and Rockfill Dams," *Geotechnique*, Vol. 29, No. 3, pp. 215-263.
- Seed, R.B., and Bonaparte, R. (1992), "Seismic Analysis and Design of Lined Waste Fills: Current Practice," Proceedings of the Conference on Stability and Performance of Slopes and Embankments - II, ASCE Special Geotechnical Publication No. 31, pp. 1521-1545.
- Singh, S. and Sun, J.I. (1995), "Seismic Evaluation of Municipal Solid Waste Landfills," Proceedings of Geoenvironment 2000, ASCE Special Geotechnical Publication No. 46, pp. 1081-1096.

# Seismic Response of Landfills with Geosynthetic Liners

M.K. Yegian

Professor and Chairman, Department of Civil and Environmental Engineering, Northeastern University, Boston, MA.

H.U. Kadakal

Research Assistant, Department of Civil and Environmental Engineering, Northeastern University, Boston, MA

**ABSTRACT:** Geosynthetic liners can have important effects on the seismic response of a landfill. Slip deformations occurring along a geosynthetic interface can limit the earthquake energy transmitted to the overlying waste or soil. A dynamic response analysis procedure is described in which a geosynthetic liner is replaced by an equivalent soil layer. The dynamic material properties of the equivalent soil layer were developed such that the response of the layer to earthquake excitation is similar to that of the geosynthetic liner it replaces. An example landfill cross section is analyzed using equivalent soil layers representing geosynthetic liners and the earthquake-induced accelerations within the landfill are calculated. The results obtained from the dynamic response analysis, that included the geosynthetic liners are compared with those that ignored the liners. It is demonstrated that smooth HDPE geomembrane/geotextile liners significantly reduce the landfill acceleration, beyond an input base acceleration of 0.2 g. Hence, a dynamic response analysis that assumes a complete shear transfer through the geosynthetic liners (not allowing slip) can significantly overestimate landfill accelerations. Such overestimation of landfill accelerations can lead to unrealistic values of landfill side slope displacements.

**KEYWORDS:** Friction layer, Geomembranes, Geotextiles, Landfills, Seismic design

## 1 INTRODUCTION

Earthquake ground motions when propagating through a landfill can induce permanent deformations of the waste fill, and slip displacements along geosynthetic liners used as impervious barriers. Such potential deformations, if excessive, can compromise the integrity of a landfill. To safeguard against this environmental hazard, in the U.S., federal regulations have been formulated that address the seismic vulnerability of new landfills.

The calculation of earthquake-induced permanent deformations of a landfill requires the investigation of the dynamic response of the landfill. In engineering practice, wave propagation analysis is performed to estimate the accelerations and shear stresses within the landfill that is experiencing a design level earthquake motion. In such an analysis, the presence of geosynthetic liners within the landfill cross section poses a significant challenge. Kavazanjian et al. (1991, 1995), Yegian et al. (1992), and Zimmi et al. (1994) have demonstrated that under dynamic excitations geosynthetic interfaces can transmit limited shear stresses. Stresses larger than this limiting level will induce slip displacements along the geosynthetic interface. In current engineering practice, to simplify the dynamic analysis of a landfill, the presence of geosynthetic liners is generally ignored. This practice effectively assumes that there is no slip induced along the liners during a seismic event. As will be illustrated in this paper, this assumption can lead to significant overestimation of the earthquake-induced shear stresses in a landfill, leading to unrealistic estimates of permanent deformations of the landfill.

This paper presents a brief description of a model that can be used to represent the dynamic response of

geosynthetic liners in wave propagation analysis of landfill cross sections. The paper includes an example analysis of a landfill. A discussion of the results is included to demonstrate the effect of the geosynthetic liners on the seismic response of the landfill.

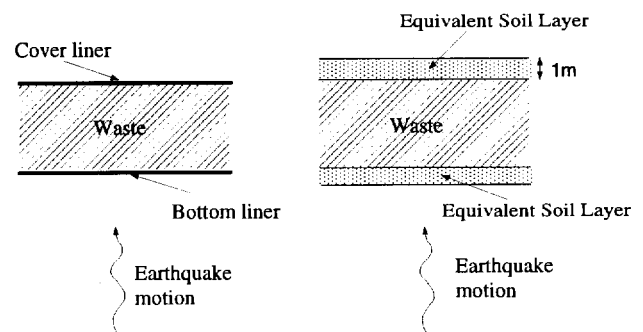


Figure 1. a) Waste fill with cover and bottom liners, b) Equivalent soil layers that replace the liners in dynamic response analysis.

## 2 MODELLING OF GEOSYNTHETIC LINERS

In engineering practice, the dynamic response of a landfill cross section is investigated, typically by considering a one-dimensional column of layered soil/waste fill profile. The earthquake-induced accelerations and shear stresses in each layer are computed using the equations that govern wave propagation through elastic media. The computer program SHAKE is commonly used for this purpose. In this SHAKE

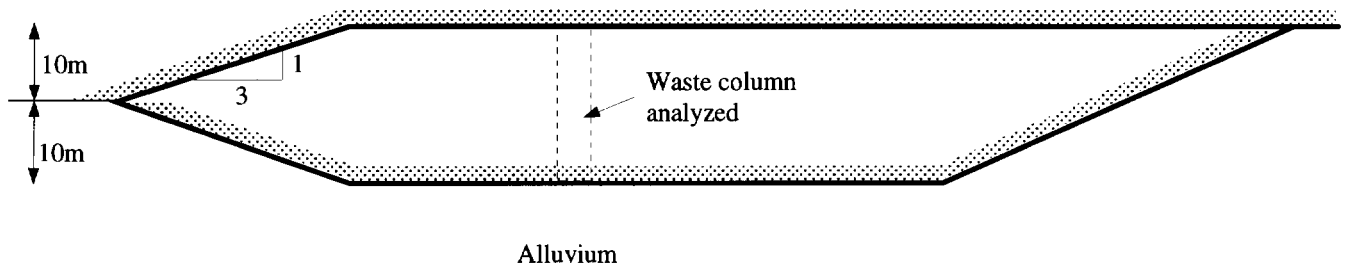


Figure 2. A simple landfill cross section analyzed to demonstrate the effect of geosynthetic liners on seismic response

analysis, the shear modulus and damping of each soil or waste fill layer are used together with the layer thickness and material unit weight. An earthquake motion is then specified, typically at the base of the landfill or at a nearby

outcropping of rock, and the accelerations and the shear stresses within the landfill profile are calculated.

To allow the performance of dynamic analysis of landfill cross sections that include geosynthetic liners, a model has been developed by (Yegian et al. 1996) that can represent the dynamic response of the liners in the analysis. Figure 1a shows a schematic diagram of a simple landfill profile consisting of a layer of waste fill, and cover and bottom geosynthetic liners. In Figure 1b, the same profile is shown except that the liners are replaced by equivalent soil layers that have identical dynamic response characteristics as the liner interfaces as measured in shaking table tests. The use of equivalent soil layers permits the dynamic response analysis of a landfill to be performed easily with the computer program SHAKE.

To illustrate the application of the procedure and to demonstrate the potential effects of geosynthetic liners on the dynamic response of landfills, the following example landfill is investigated using the equivalent soil layer model.

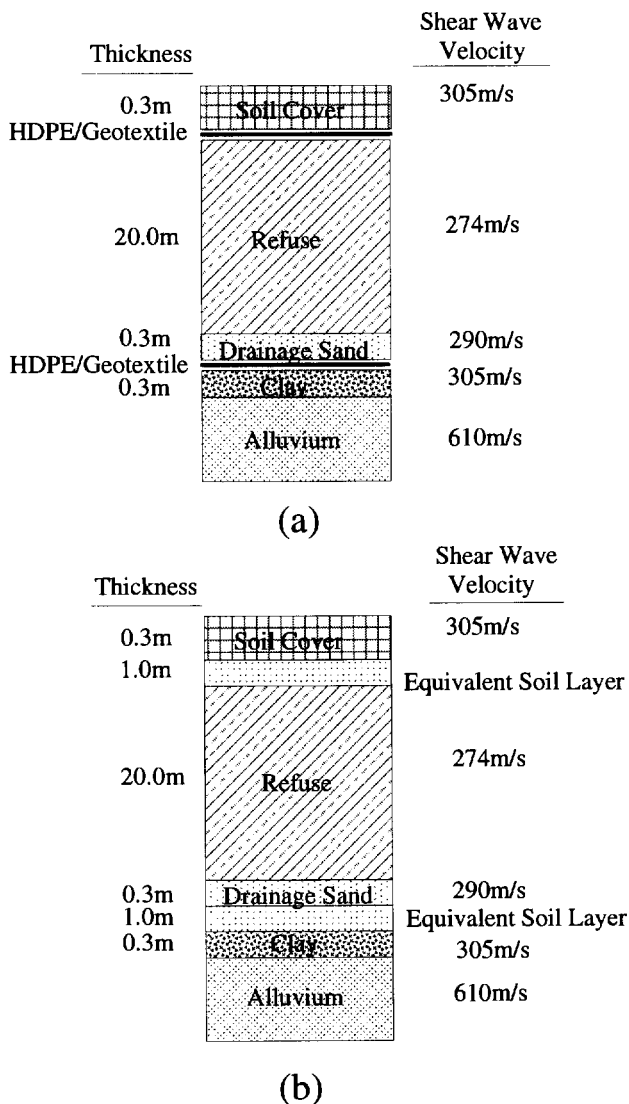


Figure 3. a) Soil/waste column analyzed, b) equivalent soil layers representing geosynthetic liners.

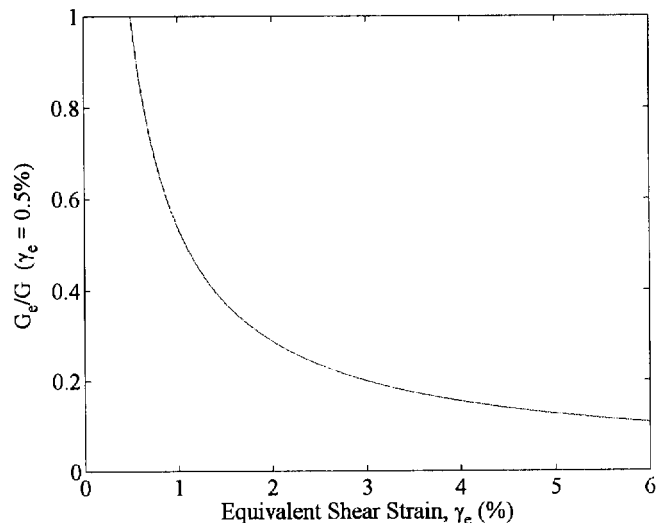


Figure 4. Shear modulus of equivalent soil layer normalized with respect to  $G_e$  at  $\gamma_e = 0.5\%$ .



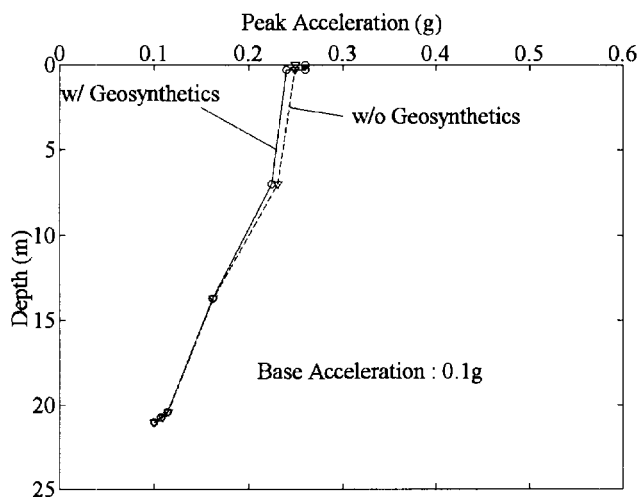


Figure 5. Peak accelerations with depth of landfill calculated with and without geosynthetic liners, and base acceleration of 0.1g.

### 3 EXAMPLE ANALYSIS OF A LANDFILL

Figure 2 shows a simple cross section of a landfill with cover and bottom geosynthetic liners. The dynamic response of this landfill profile was investigated by selecting a one-dimensional column as shown in Figure 2. The layer thickness and material properties of the landfill column are shown in Figure 3. In this landfill column, the geosynthetic liners (smooth HDPE geomembrane/geotextile) are replaced by equivalent soil layers. Figure 4 shows the equivalent shear modulus versus shear strain curve (of the selected interface) normalized by the shear modulus at an equivalent shear strain of 0.5%. The basis for selecting  $\gamma_e=0.5\%$  for normalizing is that this value corresponds to a slip amplitude of 0.5 cm below which an HDPE/geotextile interface observed to exhibit almost rigid behavior and its dynamic response is very difficult to record accurately based on shaking table tests. Thus, at displacement amplitudes smaller than 0.5 cm, for practical purposes an HDPE/geotextile interface can be assumed infinitely stiff. A hysteretic damping ratio of 0.43 was used for the equivalent soil layer. This damping, measured from the shaking table tests did not vary significantly for different slip amplitudes. In this example analysis the equivalent shear modulus at a shear strain of 0.5% were  $8622 \text{ kN/m}^2$  and  $210 \text{ kN/m}^2$  for the bottom and cover liners, respectively.

Using the equivalent shear moduli of the two liners and a damping ratio of 0.43, as determined from shaking table tests, the dynamic response of the landfill column was performed using the SHAKE program. The earthquake motion from the 1988 Spitak earthquake was normalized to 0.1 g and 0.4 g and used as input at the base of the landfill. Figure 5 shows the computed peak accelerations (with and

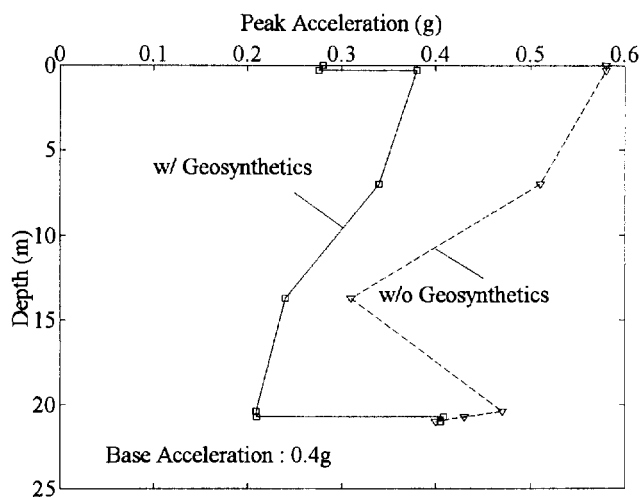


Figure 6. Peak accelerations with depth of landfill calculated with and without geosynthetic liners, and base acceleration of 0.4g.

without considering the geosynthetic liners) as a function of depth when the input earthquake motion had a peak acceleration of 0.1 g. The results show that the presence of the geosynthetic bottom and cover liners has no discernible effect on the acceleration within the landfill. This is not surprising because shaking table tests by Yegian and Harb (1995) show that slip deformations along smooth HDPE geomembrane/geotextile interfaces occur only at accelerations larger than about 0.2 g. Hence, if landfill accelerations are less than 0.2 g, ignoring the presence of smooth HDPE geomembrane/geotextile liners in the dynamic analysis of a landfill is reasonable.

Figure 6 shows peak accelerations, with and without geosynthetic liners, computed using an input motion scaled to 0.4 g. In this case, the bottom and cover geosynthetic liners have played an important role in modifying the earthquake motion propagating through the landfill. For example, the acceleration at the base of the waste fill is 0.47 g, if the geosynthetic liners are ignored in the analysis. Including the liner responses by using equivalent soil layers reduces the acceleration at the base of the waste fill by a factor of 2, to about 0.21 g. Similarly, if the liners are ignored the acceleration on top of the landfill is 0.58 g, and if the liners are included 0.28 g. Clearly, when the base acceleration is larger than 0.2 g, slip occurs along the geosynthetic liners thus limiting the accelerations transmitted through the liner interfaces. Ignoring this can unreasonably overestimate the landfill response.

Figure 7 summarizes the results of the dynamic analysis with and without considering the geosynthetic liners. The average acceleration of the waste fill is a parameter of importance in the calculation of the permanent deformations of the waste fill, and in the estimation of slip displacements along the side slope. In the example where

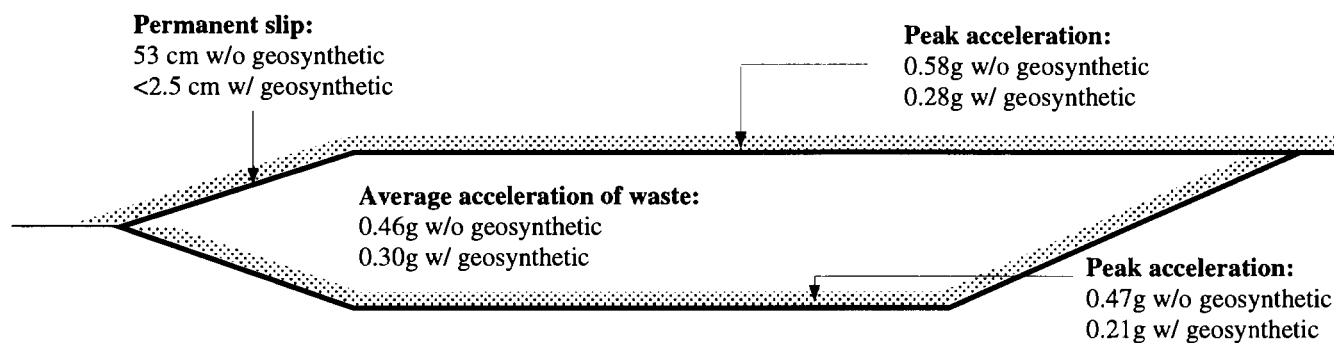


Figure 7. Results from seismic analysis of the example landfill showing the effect of geosynthetic liner on the landfill accelerations and side slope slip deformations.

the base acceleration was 0.4 g, the average acceleration of the waste fill is about 0.46 g, if the liners are ignored, and about 0.3 g if the liners are modeled in the dynamic response analysis of the landfill. These values of the average accelerations of the waste fill were used to calculate slip displacements along the side slope of the example landfill. The procedure of Yegian and Harb (1995) was used for the calculation of the side slope slip, assuming that the liner is a textured HDPE geomembrane/geotextile. The results again indicate that ignoring the dynamic response of the geosynthetic liners can lead to unrealistically large slip displacements (53 cm). Whereas, including the liner response the slip displacement on the slope is estimated to be less than one inch (< 2.5 cm).

#### 4 CONCLUSIONS

To perform realistic analysis of the seismic response of a landfill it is very important that geosynthetic liners are properly modeled. Beyond an acceleration of 0.2 g, slip displacements may occur along geosynthetic liner interfaces. This paper presents a model that can be used to represent the dynamic response of smooth HDPE geomembrane/geotextile liners in the seismic analysis of landfills.

Example analysis of a simple landfill profile is presented. The results demonstrate that smooth HDPE geomembrane/geotextile liners significantly reduce the accelerations and shear stresses transmitted through the landfill profile, especially when the base acceleration exceeds 0.2 g. Ignoring these effects can result in unrealistic estimates of seismic accelerations, shear stresses and permanent deformations in a landfill.

#### ACKNOWLEDGEMENTS

This research has been funded by a grant from the Earthquake Hazard Mitigation program of the National

Science Foundation. The authors express their appreciation to NSF and the program director Dr. Clifford Astill.

#### REFERENCES

- Kavazanjian, E.J., and Matasovic, N. (1995) "Seismic Analysis of Solid Waste Landfills", Geoenvironment 2000, Geotechnical Specialty Publication No.46, ASCE.
- Kavazanjian, E.J., Hushmand, B., and Martin, G.R. (1991) "Friction Base Isolation Using a Layered Soil-Synthetic Liner system", Proceedings of the 3<sup>rd</sup> U.S. Conference on Lifeline Earthquake Engineering, ASCE.
- Yegian, M.K., and Harb, J.N. (1996) "Dynamic Response of Geosynthetic Interfaces", PhD Dissertation Report No.CEE-96-01, Department of Civil and Environmental Engineering, Northeastern University, Boston, MA.
- Yegian, M.K., and Harb, J.N. (1995) "Slip Displacements of Geosynthetic Systems Under Dynamic Excitations", Earthquake Design and Performance of Solid Waste Landfills, Geotechnical Specialty Publication No.54, ASCE.
- Yegian, M.K., and Lahlaf, A.M. (1992) "Dynamic Interface Shear Properties of Geomembrane and Geotextiles", J. Geotech. Engrg., ASCE, 118(5), 760-779.
- Zimmie, T.F., De, A., and Mahmud, M.B. (1994) "Centrifuge Modeling to Study Dynamic Friction at Geosynthetic Interfaces", Proceedings of the Fifth International Conference on Geotextiles, Geomembranes and Related Products, Singapore.

# Evaluation of a Composite (Geomembrane/Clay) Liner for a Lagoon After 14 Years of Use

R.K. Rowe

Dept. of Civil and Environmental Engineering, University of Western Ontario, London, Ontario, Canada

Y.G. Hsuan

Geosynthetic Research Institute, Drexel University, Philadelphia, PA, USA

C.B. Lake and P. Sangam

Dept. of Civil and Environmental Engineering, University of Western Ontario, London, Ontario, Canada

S. Usher

Gartner Lee Ltd., Markham, Ontario, Canada

**ABSTRACT:** A 1.5 mm thick HDPE geomembrane was exhumed from a landfill leachate lagoon after 14 years of service. The differences in geomembrane properties that arise from five different exposure conditions are examined. The paper demonstrates the importance of antioxidant and stress crack resistance towards the longevity of the geomembrane. Severe cracking was observed in the geomembrane. Although most cracks were above the leachate level, the few below the level were sufficient to allow leachate to get between the geomembrane and clay liners. The diffusion profile through the clay implies that leachate has been in contact with the clay for most (if not all) of the 14 years of operation.

**KEYWORDS:** Liquid containment, Geomembrane, Clay liner, Aging, Diffusion

## 1 INTRODUCTION

Composite liners (geomembranes over clay) are now being widely used as the liner system for landfills and waste water lagoons. The understanding of factors associated with the design, selection of materials, construction quality, and long term protection of the composite liner has improved considerably over the past two decades. The importance of some of these factors can best be illustrated with reference to case records. The objective of this paper is to provide one such case record based on the exhumation of a 14 year old geomembrane from a leachate lagoon. This investigation examines: (a) the difference in geomembrane properties that can arise from different exposure conditions; (b) the influence of small cracks on the effectiveness of the geomembrane liner in the lagoon; and (c) the important role that the compacted clay can play as both an advection and diffusion barrier in the event of holes developing in the geomembrane.

## 2 FIELD INVESTIGATION AND GENERAL OBSERVATIONS

Due to expansion of the East Quarry Municipal Solid

Waste Landfill in the City of Niagara Falls, Ontario, Canada, one of two leachate lagoons was decommissioned in September 1996, after 14 years of service, to be replaced by another lagoon system at a different position in the landfill.

The lagoons were lined with a 1.5 mm (60 mil) thick HDPE geomembrane underlain by a more than 2 m thick compacted clay liner. There was no protection layer above the geomembrane which was directly exposed to the leachate and, above the leachate level, to the sun and atmosphere.

According to the operators of the landfill, the geomembrane component of the lagoon liners had a history of problems. During the lifespan of the lagoons, the two lagoons alternately had to be drained in order to clear out sludge from the lagoon and to patch defects that developed in the geomembrane liner.

When the lagoon was drained, the geomembrane at the bottom of the lagoon was like a "waterbed" with a significant amount of liquid trapped between the geomembrane and the clay. Even though the majority (93%) of cracks and holes were above the leachate level (see Figure 1), the remaining cracks/holes in the geomembrane along the side slopes appear to have been sufficient to allow leachate to get between the geomembrane and clay under conditions of zero effective

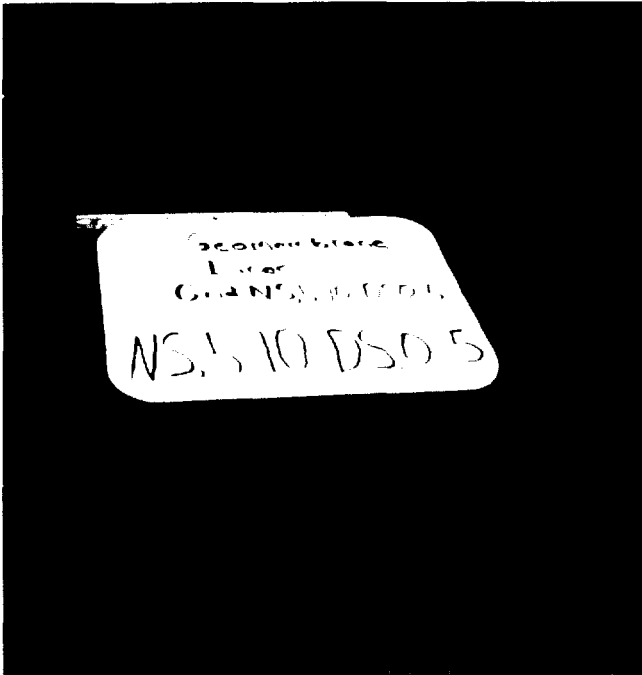


Figure 1. Photo of crack in geomembrane.



Figure 2. Photo of clay desiccation under geomembrane (above leachate level).

stress. There were no cracks or holes found in the geomembrane at the bottom of the lagoon at the time of decommissioning although 6 of the 54 patches were observed here. Many scratches were observed on the geomembrane from the bottom.

In total, 82 cracks, holes and patches were observed in the geomembrane over an area of 1352 m<sup>2</sup> (about 600 defects per hectare over the 14 year period of operation). Of these, 70% were above the leachate level and 30% were below the leachate level.

Samples were obtained from the anchor trench (NSNL: no sunlight exposure, no leachate exposure), above the leachate levels in the lagoon (SNL: sunlight but no leachate exposure), leachate level interface (MSL: sunlight and leachate exposure), and below the leachate level (NSL: no sunlight but leachate exposure). Selected samples were also taken from the bottom of the lagoon (NSLB: no sunlight, leachate/sludge exposure).

When the geomembrane was removed to expose the underlying clay liner, it was observed that clay liner sections above the leachate level were desiccated (see Figure 2). This phenomenon has been observed by others (Corser et al., 1992; Basnett & Brungard, 1992). The clay on the slopes below the leachate level and at the bottom was saturated and had an approximate 25-225 mm layer of black sludge present on the surface (the larger thicknesses generally occurred on the bottom of the liner).

### 3 GEOMEMBRANE TEST RESULTS

To assess the properties of the HDPE geomembrane, samples collected from locations in the five different exposure conditions were tested for their mechanical and physical and chemical properties. Unfortunately, due to the age of the lagoon, it was not possible to obtain the properties of the original geomembrane. Table 1 gives the values obtained on the 14 year old geomembrane removed from the lagoon. The carbon black content was within the typical range of 2-3% and will not be discussed further. Other properties are discussed in the following subsections.

#### 3.1 Density

HDPE geomembrane is a semi-crystalline polymer and its density is related to the degree of crystallinity. Any change in the density is regarded as a modification in the crystallinity. For example, any decrease in density implies a decrease of the crystalline content of the material. The density of the geomembrane under investigation was measured according to ASTM D792. Five specimens cut from samples from each exposure category were tested and the average values are presented in Table 1. The results are very similar for all locations and vary slightly between 0.965 and 0.967 g/cm<sup>3</sup>.

Table 1. Summary of average results for sheet samples

Location	$\rho_g$ (g/cm <sup>3</sup> )	CBC (%)	MI (g/10 min)	Std-OIT (min.)	SCR (hr.)	ITR (N)	Tensile Strength			
							Yield		Break	
							T (kN/m)	$\epsilon$ (%)	T (kN/m)	$\epsilon$ (%)
NSNL	0.965	2.58	0.36	3.5	3.5	284	37	11	33	646
SNL	0.967	2.64	0.5	1.8	2.6	271	37	11	25	379
MSL	0.967	2.67	-	3.3	-	284	37	10	26	479
NSL	0.966	2.73	0.41	6.3	3.1	284	37	11	32	703
NSLB	0.965	2.20	0.31	5.0	3.0	294	39	10	27	456

$\rho_g$  Geomembrane Density  
 CBC Carbon Black Content  
 MI Melt Index

ITR Initial Tear Resistance  
 $\epsilon$  strain  
 SCR Stress Cracking Resistance

These measured densities are for the geomembrane sheet and include the mass of the carbon black (which increases the overall density of the geomembrane). The density of the polymer can be back-calculated using the following equation given in ASTM D3350:

$$D_r = D_p - 0.0044C$$

where  $D_r$  is the density of resin,  $D_p$  is the density of the product and  $C$  is the weight percent of carbon black (obtained via ASTM D1603). Based on this, the calculated polymer density values were all very similar and the value of 0.954-0.955 g/cc falls within the high density range. The high density implies a high degree of crystallinity and a geomembrane that would be more susceptible to stress cracking than a less crystalline geomembrane. These days, HDPE geomembranes are made from medium density polyethylene with density less than 0.940 g/cc. Thus, properties of this geomembrane would not be the same as those of the current HDPE geomembrane.

### 3.2 Oxidative Induction Time Tests

The overall lifetime of a HDPE geomembrane is greatly dependent on the antioxidant package added to its formulation (Hsuan & Koerner, 1997). The initial step in the oxidation of HDPE geomembrane is the depletion of antioxidants. One laboratory accelerated aging study indicated that the antioxidants in the formulation must be essentially consumed before the mechanical property begins to degrade (Hsuan & Guan, 1997). Thus, by knowing the amount of antioxidant remaining in the geomembrane, the extent of the oxidation can be estimated. However, it should be emphasized that direct

comparison between different OIT values (expressed in minutes) is only applicable when the same type of antioxidant package is used, as in this case.

The amount of antioxidants in the 14 year old HDPE geomembrane was evaluated using two different oxidative induction time (OIT) tests: Standard (Std) OIT test and High Pressure (HP) OIT test. The Std-OIT test was performed according to ASTM D3895 at an isothermal temperature of 200°C and 35 kPa pressure, whereas the procedure for the HP-OIT test followed was ASTM D5885 at an isothermal temperature of 150°C and 3500 kPa. Tests were carried out on ten samples taken from the various locations. All ten samples were evaluated by the Std-OIT. Only six of the ten samples were evaluated by the HP-OIT test since the purpose of the HP-OIT test was merely to confirm the data of the Std-OIT tests. The consistency between HP-OIT and Std-OIT data suggests that the high isothermal temperature used in Std-OIT tests did not bias the result by destroying some of the antioxidants. Thus, the following discussion on the oxidation behaviour of this geomembrane will be based on the results of the Std-OIT tests. Modern geomembranes would be expected to have a Std-OIT value in excess of 100 minutes at the time of installation. However, the initial OIT values for this 14 year old membrane are unknown.

Table 1 shows the average results of the Std-OIT tests. The resulting values at ten different locations are all very short, signifying that there is only a limited amount of antioxidant remaining in this 14 year old geomembrane. As expected, geomembranes exposed to sunlight have the shortest OIT time of all. This is because the exposed geomembranes were subjected to both photo-oxidation and thermo-oxidation. In addition, the surface temperature of the exposed geomembrane was much

higher than the covered geomembrane; this further accelerated the thermo-oxidation. However, the OIT values from the north, south, east and west were similar. Thus the effect of the orientation with respect to the sun seems to be minor (the south and west slopes having slightly higher OIT values than the north and east slopes). Three of the six exposed samples had OIT values in the 1 minute range, suggesting that their antioxidant levels have almost reached zero. (A non-stabilized HDPE geomembrane has 0.5 minute of Std-OIT). Thus, oxidation degradation might already have started in the geomembrane at these locations, particularly on the surface.

For covered geomembranes, temperature is the crucial factor. Geomembranes which were fully covered by the leachate would experience the most consistent and lowest maximum temperature in the entire liner system since the leachate temperature would remain relatively constant through the year unlike the surface temperature which would be high in the summer. Thus, the relatively long OIT times measured for the leachate covered samples are reasonable. Approximately 5-6 minutes of Std-OIT were measured indicating that some antioxidant remained in these geomembranes. For the geomembrane that was located at the interface between the leachate and the sunlight, the OIT value of approximately 3 minutes falls between those of the fully exposed and the fully leachate covered geomembranes. Also, its value is very similar to the geomembrane that was located in the anchor trench. Due to the shallow depth of the anchor trench (approximately 0.75 m), the temperature of the geomembrane at this location would have reached the ambient temperature which could be 28°C in the summer season. Consequently, the oxidation of the anchor trench geomembrane proceeded faster than that covered by the leachate.

### 3.4 Melt Index Test (MI)

If oxidation degradation takes place in the polymer, the molecular weight of the polymer will be altered due to either a cross-linking or a chain scission reaction. The melt index (MI) test, ASTM D1238, is a qualitative method to assess molecular weight. A high MI value indicates a low molecular weight, and vice versa. Geomembrane samples were taken from the west slope at four different locations: anchor trench (NSNL), sunlight exposed region (SNL), below the leachate level (NSL) and at the bottom of the lagoon (NSLB). Tests were performed under the condition of 190°C and 2.16 Kg. Two replicates were tested for each sample. The MI results are shown in Table 1.

The MI value varies with the location of the geomembrane. The geomembrane that was completely covered by leachate has the lowest MI value, whereas

the fully exposed geomembrane shows the highest. The geomembrane at the anchor trench has a slightly lower value than that located at the leachate interface. Additionally, there is an inverse relationship between MI and OIT values; geomembrane with a high MI value has a low OIT value. The increase of the MI value suggests that the oxidation induced a chain scission in the polymer. This behaviour is different from that observed in some of the laboratory aging results obtained at oven aging temperatures in the range of 110-115°C at which a cross linking was observed (Thomas & Ancelet, 1993; Yim & Godin, 1993).

### 3.5 Tensile Properties

Tensile properties may be used to evaluate the macroscopic changes in a geomembrane. These properties were obtained in accordance with ASTM D638-90 (Type IV) with a strain constant rate of 50 mm/min. Tests were performed on 10 dumb-bell specimens cut from samples taken at different locations as previously described. The results presented in Table 1 show no significant difference in either the strength and strain values at yield. The yield strength varied from 37 to 39 kN/m and is higher than typical values (30 kN/m) while the yield strains were between 10 and 11% and were lower than typical values for new geomembrane (15%) today (all based on 25 mm gauge length).

Both the breaking strength and strain values are lower than expected for new material (50 kN/m). The highest values are observed for the anchor trench samples and samples from the slopes exposed to leachate. The lowest values are observed for samples exposed to sun and samples from leachate-sun interface (26 kN/m). However, a surprisingly low value of about 27 kN/m is observed for the bottom sample. This may be due to the highly scratched nature of the geomembrane on the bottom.

These results seem to agree with those reported by Rollin et al. (1994) who observed that, for a 7 year old HDPE, there was an increase of strength at yield and a decrease of both strength and strain at rupture. This behaviour of HDPE geomembrane suggests that the material has become brittle and hence is indicative of aging of the geomembrane.

### 3.6 Stress Cracking Resistance (SCR)

Stress cracking has been defined by ASTM D883 as an external or internal rupture in a plastic caused by tensile stress less than its short term mechanical strength. In this study, the SCR was assessed by the single point notched constant tensile load (SP-NCTL) test according to ASTM D5397-appendix instead of the bent strap

D1693 test. The notch was introduced from the exposed side of the geomembrane to minimize the surface effects such as scratches or surface degradation. Geomembrane samples were taken from the west side slope at four different locations and the results are given in Table 1. The overall failure time of this geomembrane is remarkably short; all specimens failed in less than 4 hours. The results suggest that the geomembrane is highly susceptible to stress cracking as reflected by the cracking behaviour observed in the field. Since there is no SP-NCTL test data on the original material, one can not conclude whether or not the short failure time was caused by the aging effect. Nevertheless, geomembranes at locations where they were covered or partially covered by soil or leachate show a very similar failure time. The geomembrane exposed to the sunlight shows a slightly lower failure time, suggesting that some degradation may have taken place in this portion of the geomembrane.

#### 4 DIFFUSION OF CONTAMINANTS INTO THE CLAY LINER

The geomembrane was underlain by a compacted clay liner in excess of 2 m thick. The liner was composed of 88-93% clay sized particles, a plastic limit of 23% and plasticity index of 18%. This low activity clay liner had a porosity of that typically ranged between 0.3 and 0.39 with an average value of about 0.33. The hydraulic conductivity below the leachate level was about  $2 \times 10^{-10}$  m/s (based on one laboratory test).

Figure 3 shows the observed chloride profiles with depth in the clay liner obtained by performing pore water squeezes and chemical analyses on samples from a borehole in the clay liner. The profile shows a generally consistent trend of chloride migration over a 14 year period. The depth of penetration of almost 2 m is consistent with expectations based on previous field cases (see Rowe et al., 1995) over a time period of the order of 14 years. The lower concentration at the surface (relative to 0.2 m depth) suggests that the average chloride concentration in the leachate over the year prior to exhumation was lower than the long term average concentration for the previous 13 years which gives rise to some back diffusion. This is consistent with the leachate chemistry data. The profile implies that the compacted clay liner performed well and the liner system protected the environment from contaminant escape over the 14 year operating life of the lagoon.

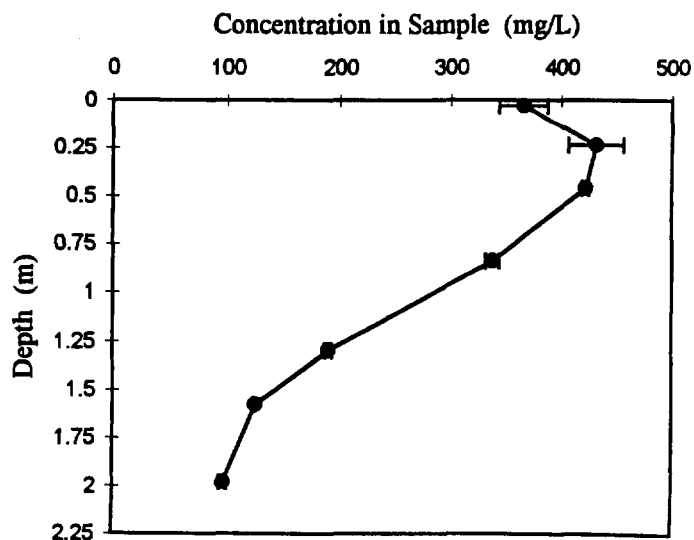


Figure 3. Variation in chloride concentration with depth in clay liner below the geomembrane after 14 years.

#### 5 SUMMARY AND CONCLUSIONS

Geomembrane samples were taken from five different locations of a 14 year old leachate lagoon. Their physical, chemical and mechanical properties were evaluated in order to assess the possibility of the degradation in the material during this service period. The overall amount of antioxidant present in the geomembrane was measured using the Std-OIT test. The OIT values at all five locations were relatively short, less than 7 minutes. Although the percent reduction in the 14 years service could not be estimated due to the unavailability of the original OIT value, the consumption rate at various locations of the lagoon was evaluated. As expected, the lowest OIT value was detected in the geomembrane that was constantly exposed to sunlight. A value as low as 1 minute was detected in some of the exposed geomembranes, implying only a small amount of antioxidant remaining in the geomembrane. Thus, some degrees of oxidation probably has already occurred in this part of the geomembrane, particularly on the exposed surface. The extent of the photo-oxidation has caused a reduction in tensile break properties and stress crack resistance of the geomembrane. The results of the Melt Index test suggest that the degradation was induced by a chain scission reaction in the polymers.

For geomembranes that were either covered by soil or leachate, their properties were largely the same. Their depletion of antioxidant was slower than the exposed and partially exposed geomembranes. The amount of antioxidant present in these geomembranes seems to be sufficient to protect the geomembrane from oxidation degradation as indicated by their relatively high tensile

break properties. Although tensile break properties of the bottom geomembrane showed a decrease, they might be due to surface scratches which appeared everywhere on this part of the geomembrane. The correlation between the OIT and tensile break properties of this 14 year old geomembrane illustrates the significant role of antioxidant in protecting the mechanical properties of the geomembrane.

The severe cracking observed on the geomembrane indicated that the material was highly susceptible to stress cracking, and this was confirmed by the results of SP-NCTL tests. The average failure time of unexposed geomembranes was 3 hours at 30% yield stress which is well below the current recommended value of 200 hours.

The results of this investigation substantiate the importance of the antioxidant and stress crack resistance towards the longevity of the geomembrane. Therefore, these two properties should be evaluated and incorporated in the specification of a HDPE geomembrane to assure their quality.

The presence of only a few small holes/cracks below the leachate level was, apparently, sufficient to allow leachate to get below the geomembrane and diffuse almost 2 m into the clay liner. However, notwithstanding the holes in the geomembrane, the liner system provided an excellent advective-diffusive barrier and provided the environmental protection required over the required service life of the lagoon liner system (14 years).

## ACKNOWLEDGEMENT

The authors very gratefully acknowledge the assistance of Niagara Waste Systems Limited in conducting the field sampling described in this paper. The testing and research was funded by the Natural Sciences and Engineering Research Council of Canada under a Grant to the senior author and by the Geosynthetic Research Institute at Drexel University. The authors also appreciate the assistance of Ms. C. Orsini in the preparation of Figure 3.

## REFERENCES

- Basnett, C. and Brungard, M. (1992). The clay desiccation of a landfill composite lining system. *Geotechnical Fabrics Report*, January/February, p. 38.
- Corser, P., Pellicer, J. and Cranston, M. (1992). Observations on the long term performance of composite clay liners and covers. *Geotechnical Fabrics Report*, November, pp. 6-16.
- Hsuan, Y.G. and Koerner, R.M. (1997). Antioxidant depletion lifetime in high density polyethylene geomembranes. *Journal of Geotechnical and Geoenvironmental Engineering, ASCE* (accepted for publication).
- Hsuan, Y.G. and Guan, Z. (1997). Evaluation of the oxidation behavior of polyethylene geomembranes using oxidative induction time tests. *Oxidative Behavior of Materials by Thermal Analytical Techniques*. ASTM STP1326, A.T. Riga and G.H. Patterson, Eds., American Society for Testing and Materials.
- Rollin, A.L., Mlyrek, J., LaFleur, J. and Zanesco, A. (1994). Performance changes in aged in-situ HDPE geomembrane. *Landfilling of Waste: Barriers*, T.H. Christensen, R. Cossu and R. Stegmann, Eds., pp. 431-443.
- Rowe, R.K., Quigley, R.M. and Booker, J.R. (1995). *Clayey Barrier Systems for Waste Disposal Facilities*. E & FN Spon (Chapman & Hall), London, 390 pp.
- Thomas, R.W. and Ancelet, C.R. (1993). The effect of temperature, pressure and oven aging on the high pressure oxidative induction time of different types of stabilizers. *Geosynthetics '93 Conference Proceedings*, Vancouver, British Columbia, Canada, Published by IFAI, St. Paul, MN, pp. 915-924.
- Yim, G. and Godin, M. (1993). Long-term heat aging stabilization study of polyethylene and its relationship with oxidative induction time (OIT). *Geosynthetics '93 Conference Proceedings*, Vancouver, British Columbia, Canada, Published by IFAI, St. Paul, MN, pp. 915-924.



# Solubilities, Diffusion and Partition Coefficients of Organic Pollutants in HDPE Geomembranes: Experimental Results and Calculations

W. Mueller, I. Jakob, R. Tatzky-Gerth and H. August  
Federal Institute for Materials Research and Testing, BAM, Berlin, Germany

**ABSTRACT:** Solubilities and diffusion coefficients of organic pollutants in HDPE geomembranes and the partition coefficients for acetone, acetic acid and trichloroethylene in the water-geomembrane system were measured in immersion tests. Solubilities and partition coefficients are the most relevant parameters in determining the permeation rate in geomembranes and in composite lining systems which include geomembranes. Theoretically these parameters can be obtained from calculations using group-contribution methods. Two methods (the UNIFAC procedure and the Retention-Index procedure) are described. The calculated results are compared with experimental values. It is shown that for various types of organic pollutant the calculated solubility and partition coefficient values agree with acceptable accuracy with the experimental results.

**KEYWORDS:** Diffusion, Permeability, Geomembranes, Composite Liner Systems, Performance evaluation

## 1 INTRODUCTION

The importance of the quantitative description of contaminant transport phenomena in liner systems appears to have increased considerably in recent years, in particular with respect to risk assessment for landfill construction and contaminated site containment, and equivalence or suitability considerations of different materials for liner systems.

Two contaminant and material dependent parameters are of fundamental importance in the description of the contaminant transport in a liner element. One is the partition coefficient, which represents the extent to which a contaminant from an aqueous solution can penetrate a liner material and be dissolved there, i.e. is distributed between the aqueous solution and the liner element or more generally is distributed between the liner material and an adjacent medium or another liner component. The other is the diffusion coefficient, which describes the degree of mobility of the dissolved contaminant within the liner material.

According to the second and third administrative provisions to the German waste avoidance and waste management act, concerning the technical standards for the treatment and disposal of waste (the so called TA Abfall and TA Siedlungsabfall), the composite liner comprising a geomembrane and a thick multilayered clay liner is the standard for municipal and hazardous solid waste landfills. Predominantly medium to high density polyethylenes (HDPE) are used for these purposes because these materials exhibit an extremely high chemical resistance and durability. The regulations in Germany require the certification of geomembranes for use in landfill liners and at present only this type of geomembrane is certified by the Federal Institute for Materials Research and Testing, BAM (BAM 1994).

In the following, the experimental results obtained from immersion tests for the determination of the partition and diffusion coefficients regarding the permeation of various contaminants, in particular from aqueous solutions, through HDPE geomembranes and composite liners, will be described. These experiments are the continuation of and supplement to

BAM's investigations in the field of contaminant transport in geomembranes already reported (August et al. 1984, 1992).

Special thermodynamically based calculation methods in engineering chemistry make it possible to calculate these parameters for a wide variety of undissociated contaminants in aqueous solution. Only this type of contaminant is of interest with respect to diffusion processes. Experiments lasting more than 10 years failed to yield any clues on solution or diffusion processes of hydrated cations and anions of dissociated molecules in aqueous solutions into geomembranes (Mueller et al. 1997b).

The experimental results for solubilities and partition coefficients will be compared with the calculated values. The comparison will indicate that these parameters can reliably be calculated for various kinds of contaminants. The calculation methods may therefore be used for the quantitative evaluation of contaminant transport through plastic liner and composite liner systems for landfills or the containment of contaminated sites.

## 2 THEORY

### 2.1 Partition Coefficient, Solubility and Diffusion Coefficient

If a geomembrane is submersed in an aqueous chemical solution, the molecules of the chemical may intrude into the plastic material. As the chemical concentration increases, increasing numbers of molecules will leave the geomembrane again. At a temperature  $T$  and pressure  $P$  a state of equilibrium between the amount of contaminant (mole fraction  $x_1$ ) of the chemical in the geomembrane and the amount of contaminant (mole fraction  $x_0$ ) in the aqueous solution, will be reached. The ratio of these two fractions is expressed by the partition coefficient:

$$\sigma' = x_1/x_0 \quad (1)$$

(The mole fraction of chemical dissolved in the plastic will be interpreted in the following as relating to one structural unit of

the polymer chain, e.g. CH<sub>2</sub> for polyethylene, and not the number of the polymer chains themselves).

In order to calculate  $\sigma'$  it is necessary to begin with the thermodynamic conditions of the state of equilibrium. The concentration partition at equilibrium is indicated by the chemical potential  $\mu(x, T, P)$  for the contaminant dissolved in water and that for it dissolved in plastic being equal. The dependency of the chemical potential of the dissolved contaminant on concentration is given by  $\mu(x, T, P) = \psi(T, P) + k_B T \log[\gamma(x, T, P)x]$ .  $k_B$  is the Boltzmann Constant,  $\psi$  is the chemical potential of the neat liquid chemical, being a function of T and P only.  $\gamma(x, T, P)$  is the activity coefficient which depends on the mole fraction, pressure and temperature. The function  $a = \gamma(x, T, P) \cdot x$  is called activity.

Thus in equilibrium the following holds:

$$\psi(T, P) + k_B T \log[\gamma_1(x_1)x_1] = \psi(T, P) + k_B T \log[\gamma_0(x_0)x_0] \quad (2)$$

from which it follows for the activities and concentrations of the solutions at equilibrium:

$$\gamma_1(x_1)x_1 = \gamma_0(x_0)x_0 \quad (3)$$

If the activities or the activity coefficients are known as a function of concentration, the two unknowns, partition coefficient  $\sigma'$  and mole fraction  $x_1$  in the geomembrane can be calculated from equations (1) and (3) for a particular  $x_0$  in the aqueous solution. At very low concentrations, the activity is proportional to concentration and, for a direct calculation of  $\sigma'$  using the proportionality constants  $\gamma_0$  and  $\gamma_1$ ,

$$\sigma' = \gamma_0 / \gamma_1 \quad (4)$$

can be assumed.

Usually, the concentration describing the contaminant content in a solution will be given by the volumetric concentration  $c$  (mass per volume) or by the mass fraction  $w$  (mass per mass). The corresponding partition coefficients are  $\sigma = c_1/c_0$  and  $\sigma'' = w_1/w_0$ . The relation of the partition coefficients is then given by:

$$\sigma' = x_1/x_0 \approx (V_p/V_L) \sigma \approx (M_p/M_L) \sigma'' \quad (5)$$

$V_L$  and  $V_p$  and  $M_L$  and  $M_p$  are respectively the mole volumes and mole masses of the water or the structural unit of the polymer.

If a geomembrane is immersed in the neat liquid chemical and the plastic is resistant to it some saturation concentration of the chemical dissolved by the plastic will be reached. The mass fraction (ratio of the mass of dissolved chemical to the mass of plastic) at saturation will be called the solubility  $s$ . An equation for the mole fraction  $x_p$  which corresponds to the solubility, can also be deduced directly from the equilibrium conditions (3). Since for the neat liquid chemical  $x_0 = 1$  and thus  $\gamma_0 = 1$ :

$$\gamma_1(x_p)x_p = 1 \quad (6)$$

must be true. Therefore, if the activity or the activity coefficient is known as a function of concentration, solubility can also be calculated according to (6).

Activities and activity coefficients and therefore the partition coefficients and solubilities can be calculated using the group-contribution methods. These methods consider the behaviour of chemicals in a solution to be determined additively by the properties of typical structural units of the dissolved molecules and by the interaction of these units with typical structural units of the solvent molecules. The structural units may be characterized by their properties volume, surface and interaction parameters with other units.

Two of these methods are used in the following. The partition coefficient can be determined directly by a method suggested by Piringier (1993), the so called Retention-Index method. The UNIFAC (Universal Functional Group Activity Coefficient) method is widely used and versatile but more complicated. An introduction is given by Reid et al. (1977). It is used to calculate the activities and activity coefficients of non-electrolytic liquid mixtures for various concentrations. Oishi and Prausnitz (1978) suggested an extension of this method which allows the activities of contaminants dissolved in amorphous polymers to be determined. Goydan, Reid and Tseng (1989) showed, that this method yields sufficiently exact results over a wide range of applications when compared with various similar methods for the determination of the solubility of organic contaminants in polymers.

Using group-contribution methods to analyze and parameterize a large amount of experimental results, Piringier (1993) derived the following empirical formula for the diffusion coefficient of contaminants in polymers at very low dilution:

$$D = \exp(A_p - 0,008 M_p - 10450 \frac{1}{T}) [m^2/s] \quad (7)$$

$M_p$  is the mole mass of the dissolved molecule, T is the absolute temperature measured in Kelvin and  $A_p$  is a materials parameter. For LDPE material the best fit to the data was obtained with  $A_p = 9$  and for high density PE materials with  $A_p = 5$  (Piringier 1993). For the medium density PE-copolymers used for the geomembranes we expect an intermediate value of  $A_p$  to give best results for the calculation of the diffusion coefficients.

The parameters  $\sigma$  and D can be determined experimentally using immersion tests. In an immersion test a sample of the geomembrane material of a particular geometry is immersed in the liquid chemical or its aqueous solution with the known, constant concentration  $c_0$ . The absorption of the chemical by the sample is measured from gradual mass increase  $\Delta G(t)$ . If the solubility of the chemical in the geomembrane material is limited, a saturation value  $\Delta G(\infty)$  for the increase in mass is reached during the test. For a diffusion process according to Fick's law with a constant diffusion coefficient D the increase in mass is proportional to  $(Dt)^2$  up to about 2/3 of the saturation

value. The proportionality factor depends on the geometry of the sample. For a plate with a large area compared to its thickness  $d$ :

$$\Delta G(t) = \Delta G(\infty) [4/(d \pi^{1/2})] (Dt)^{1/2} \quad (8)$$

The solubility  $s$  can be calculated for an immersion in the liquid chemical from the saturation value:

$$s = \Delta G(\infty) / G \quad (9)$$

The partition coefficient for immersion in the aqueous solution is determined from the concentration  $c(\infty) = \Delta G(\infty)/V$  of the chemical in the GM sample (density  $\rho_{GM}$ ), which is in equilibrium with the concentration of the chemical in the aqueous solution  $c_0$ :

$$\sigma = c(\infty) / c_0 = [(\Delta G(\infty) / G) \rho_{GM}] / c_0 \quad (10)$$

## 2.2 Permeability and Induction Time for Composite Liners

In the following we demonstrate the paramount importance of the partition coefficients for the contaminant transport in a liner. We show how these coefficients enter the formula for the steady state permeation rate and the induction time for the composite liner.

The concentration profile  $c(x)$  of the contaminant through the liner in the steady state can be split into different ranges:  $c_0$  is the initial concentration of the pollutant in the leachate,  $c_1(x)$  is the concentration profile in the geomembrane and  $c_2(x)$  that in the clay liner, we assume that the concentration beneath the liner should always be zero due to dilution by the groundwater. The concentration gradient which causes diffusion in the geomembrane, builds up by the adsorption and dissolution of contaminants on the surface of the geomembrane. The concentration conditions at the leachate/geomembrane interface ( $x=0$ ) as explained above are described by the partition coefficient  $\sigma_{0,1}$  thus:

$$c_1(0) = \sigma_{0,1} c_0 \quad (11)$$

In connection with the sealing layers geomembrane and mineral layer, a further parameter for the composite liner, i.e. partition coefficient  $\sigma_{2,1}$  for the interface between geomembrane and mineral layer ( $x = d_1$ ) is important:

$$c_1(d_1) = \sigma_{2,1} c_2(d_1) \quad (12)$$

In the simplest case  $\sigma_{0,1} = \sigma_{2,1}$ . Here it will be assumed that the partitioning of the contaminant between the geomembrane and leachate is similar to that between the geomembrane and the mineral layer pore water. Strictly speaking, however,  $\sigma_{2,1}$  depends on the properties of the interface between the two sealing components and  $c_1(d_1)$  and therefore it will differ from  $\sigma_{0,1}$ . In addition various chemicals in the leachate and in

contrast to the pure pore water effect the partition equilibrium.

For the diffusive transport of contaminants in the mineral layer pore water the effect of the pore structure on diffusion as well as the adsorbing effect of the "pore walls", i.e. the generally reversible adsorption of contaminants by chemical and physical bonding on the material of the mineral layer, should be considered in the diffusion equation. Pore structure will be described by a tortuosity factor  $\Gamma$ , by which the diffusion coefficient of the contaminant in water  $D_0$  is multiplied. Another partition coefficient  $k$  characterizes the contaminant partition between soil and soil water. Assuming once again linear equilibrium sorption, i.e. at any one time, for contaminant mass fraction  $c_3$  adsorbed by the soil particles and concentration  $c_2$  of the contaminants in the soil water,  $c_3 = k c_2$ , the following diffusion equations will be obtained:

$$R \frac{\partial c_2}{\partial t} = \Gamma D_0 \frac{\partial^2 c_2}{\partial x^2} \quad J_2 = -n \Gamma D_0 \frac{\partial c_2}{\partial x} \quad (13)$$

with the retardation coefficient  $R = 1 + \rho_d k/n$ , where  $\rho_d$  is the dry density of the mineral material and  $n$  its porosity.

In a mineral layer the permeation rate  $J_2$  and the induction time  $t_2$  are then given for an effective concentration  $c_0$  by:

$$J_2 = n \Gamma D_0 c_0 / d_2 \quad t_2 = R d_2^2 / 6 \Gamma D_0 \quad (14)$$

Under a steady contaminant supply the sorption in the mineral layer has no influence on the final permeation rate, it has however a substantial influence on the induction time. For a geomembrane the permeation rate  $J_1$  and induction time  $t_1$  of diffusive contaminant transport at a concentration  $c_0$  can be written as:

$$J_1 = \sigma_{0,1} D_1 c_0 / d_1 \quad t_1 = d_1^2 / 6 D_1 \quad (15)$$

Using permeability  $P$  as a material parameter, for the geomembrane and the mineral layer we define:

$$P_1 = \sigma_{0,1} D_1 \quad P_2 = n \Gamma D_0 \quad (16)$$

The permeability  $P$  and permeation rate  $J$  of the composite liner with a thickness  $d=d_1+d_2$  can now be easily calculated using the boundary conditions (11) and (12) from the conservation of contaminant fluxes in the steady state, i.e.  $J_1=J_2$ . This gives:

$$\frac{d}{P} = \frac{d_1}{P_1} + \frac{d_2}{(\sigma_{0,1}/\sigma_{2,1})P_2} \quad (17)$$

Finally the formula for the induction time of the whole system analogous to (17) should be given, which can also be easily calculated using a method suggested by J. C. Jaeger (Carslaw et al. 1959, Barrie et al. 1963). The induction time  $t$  of the composite liner is composed of the induction times  $t_1$  and  $t_2$  and

permeabilities  $P_1$  and  $P_2$  of its components as follows:

$$t = \frac{t_1 \left( \frac{d_1}{P_1} + \frac{3d_2}{(\sigma_{0,1}/\sigma_{2,1})P_2} \right) + t_2 \left( \frac{3d_1}{P_1} + \frac{d_2}{(\sigma_{0,1}/\sigma_{2,1})P_2} \right)}{\frac{d_1}{P_1} + \frac{d_2}{(\sigma_{0,1}/\sigma_{2,1})P_2}} \quad (18)$$

The permeation rate for the diffusion of a contaminant through the composite liner is determined according to (16) and (17) for given thicknesses ( $d_1 = 2.5$  mm and  $d_2 = 0.75$  m or 1.50 m for municipal waste landfills and hazardous waste landfills respectively) by diffusion coefficients  $D_1$  and  $D_0$ , partition coefficients  $\sigma_{0,1}$  and  $\sigma_{2,1}$  and soil parameters  $n$  and  $\Gamma$ . While parameters  $D_1$  and  $D_0$  and  $n$  and  $\Gamma$  vary by only approximately one order of magnitude for different contaminants and mineral materials, the partition coefficients  $\sigma$  of the various contaminants differ by many orders of magnitude. Thus the partition coefficient characterises the imperviousness of the composite liner for a variety of classes of contaminant. For example, the partition coefficient for cations and anions is practically zero since they cannot be dissolved out from the hydrated complex in the aqueous solution in the non-polar material polyethylene. As indicated previously, therefore, from the outset only undissociated organic and inorganic molecules have to be considered for diffusive contaminant transport.

Since the induction time depends on the square of the thickness, for a composite liner  $t_2 \gg t_1$ . Also the retardation capacity of the mineral layer may increase induction time considerably. The induction time  $t$  of the whole liner system is then determined according to (18) only by the thickness of the mineral layer and its sorption capacity. This does not apply for composite liners with particularly thin mineral layers such as GCLs.

This paper focuses on the determination of  $\sigma$  and  $D_1$ . A detailed discussion and evaluation of the other parameters mentioned above and therefore of contaminant transport in the composite liner is given elsewhere (Mueller et al. 1997b).

### 3 EXPERIMENT

The manufacturers and the resin specifications, thickness and crystallinity of the geomembranes used in the immersion tests and the identification number of the samples are listed in Table 1a. The corresponding parameters of the HDPE resins for certificated geomembranes are shown in Table 1b. The materials are high molecular weight, linear, medium density polyethylene with butene, hexene or octene co-polymer fractions. The first column of Tables 2a and 2b list the chemicals used as test liquids and as aqueous test liquid solutions for the immersion tests. Both non- or only weakly polar and polar organic test liquids were used.

Details of the experimental procedure and typical examples of mass gain versus time curves for samples immersed are given

elsewhere (Mueller et al. 1997a). The constant saturation value in the mass gain - time curve was used to calculate the mass fraction of the test liquid in the geomembrane, see (9). Tables 2a and 2b summarizes the results.

Table 1a. Properties (manufacturer, resin, thickness and crystallinity) of the test samples and sample numbers.

Sample number	Manufacturer	Product type	Thickness	Crystallinity <sup>2</sup>
48	AGRU GmbH	Hostalen GM 5040 T12	2.5 mm	(53.6 ± 0.5) %
139	GSE GmbH	Dowlex 2342 M	2.5 mm	(47.5 ± 0.5) %
a	Simona GmbH	unknown <sup>1</sup>	1.0 mm	(55.7 ± 0.5) %
b	SLT GmbH	Vestolen A 3512 R	2.0 mm	(51.3 ± 0.5) %

1) HDPE-resin of relatively high density (Dichte 0.954 g/cm<sup>3</sup>, MFI (190/5) 1.3 g/10min), no detailed data about the product available

2) with respect to a heat of melting of 293 J/g of fully crystallized HDPE

Table 1b. Characteristic data of the HDPE resins used for certificated geomembranes in landfill lining systems.

Product type	Density <sup>1</sup> [g/cm <sup>3</sup> ]	MFI <sup>1</sup> [g/10 min]	Ratio of MFI <sup>2</sup> [-]	carbon black <sup>1</sup> [wt.-%]
Hostalen GM 5040T12	0.946±0.002	0.85±0.15 (190/5)	19	2.15±0.15
Dowlex 2342 M	0.943±0.002	2.5±0.4 (190/5)	9	2.2±0.2
Fortiflex G36-24-149	0.947±0.003	23.0±3.0 (190/21.6)	18	2.35±0.25
Vestolen A 3512 R	0.942±0.003	1.6±0.2 (190/5)	9	2.1±0.3

1) Specification of the manufacturer according to the certification document, MFI: melt flow index according to DIN ISO 1133

2) Ratio of MFI (190/21.6) to MFI (190/5), measured at GM samples

The diffusion coefficient was determined according to (8) from the linear slope of the mass gain - square root of time curve valid for short times. The results are given in the second and third columns of Table 3a and 3b.

From the solubilities and diffusion coefficients determined from the immersion tests the expected permeation rates for the neat test liquids can be calculated according to (15). They are in good agreement with the directly measured rates obtained from permeation experiments. For trichloroethylene a rate of 50 g/m<sup>2</sup>d (Sample 48) and 56 g/m<sup>2</sup>d (Sample 139) was expected: measurement yielded 30 g/m<sup>2</sup>d and 61 g/m<sup>2</sup>d. For acetone a rate of 0.3 g/m<sup>2</sup>d (Sample 48 and Sample 139) was expected: measurement yielded 0.2 g/m<sup>2</sup>d on a 2.5 mm thick

geomembrane of Vestolen A 3512 R. For acetic acid a rate of 0.4 g/m<sup>2</sup>d was expected for sample a: measurement yielded a rate of 0.3 g/m<sup>2</sup>d.

Table 2a. Experimental results for the mass fraction of absorbed molecules in HDPE geomembrane from immersion test in neat polar liquids and their aqueous solutions.

Test liquid	Sample 48	Sample 139	Sample a	Sample b
Water	0.0008	0.0010	-	-
Methanol	-	-	0.001	0.001
Acetone	0.0099	0.0112	0.009	0.009
Aceton-water, 10 Vol.-%	0.0012	0.0013	-	-
Aceton-water, 50 Vol.-%	0.0050	0.0055	-	-
Methylethylketone	0.0179	0.0190	-	-
Acetic acid, conc.	0.0086	0.0086	-	-
Acetic acid, 0.50 kg/l	0.0036	0.0026	-	-
Acetic acid, 0.70 kg/l	0.0045	0.0036	-	-
Acetic acid, 0.90 kg/l	0.0062	0.0053	-	-
Propanoic acid, conc.	0.0212	0.0209	-	-
Acetic acid ethyl ester	-	-	0.021	0.023
Formaldehyde, 37 wt.-%	-	-	0.004	0.003

The values for the aqueous solutions were corrected for the absorbed water

The agreement between permeation and immersion experiments is also proved by the data in the last column of Table 3a. Permeation experiments had been performed on specimens taken from sample a - see August et al. (1984). Diffusion coefficients (last column of Table 3a) were then determined according to (15) from the permeation rates using the solubility from Table 2a and 2b. They are in good agreement with the values obtained from immersion experiments.

The diffusion coefficients given here cannot be considered to be the diffusion coefficients of a single molecule of a dissolved contaminant in the amorphous phase of the polymer. They are rather average quantities parametrising permeation and absorption processes based on Fick's Laws assuming a concentration independent diffusion coefficient. The diffusion processes however exhibit a pronounced dependence on the concentration. This is clear from the non-linear slope of the mass gain - time curve for liquids with very high solubility.

The Table 3b gives the diffusion coefficients in geomembranes determined from permeation and immersion tests on aqueous

solutions. The values decrease with decreasing concentration even for polar contaminants which are only slightly concentrated in the geomembrane. This effect is especially clear for non-polar test liquids which can be well dissolved in the geomembrane. The diffusion coefficients from tests on aqueous solutions are approximately one order of magnitude smaller than values obtained from tests using neat test liquids.

Table 2b. Experimental results for the mass fraction of absorbed molecules in HDPE geomembrane from immersion test in the neat nonpolar or only weak polar liquids and their aqueous solutions

Test liquid	Sample 48	Sample 139	Sample a	Sample b
Chloroform	-	-	0.134	0.153
Carbon tetrachloride	-	-	0.180	0.200
Trichloroethylene	0.195	0.200	0.168	0.190
Trichloroethylene-water, 0.5 g/l	0.046	0.060	-	-
Tetrachloroethylene	-	-	0.190	0.217
Chlorobenzene	-	-	0.097	0.108
Xylene (isomeric mixture)	-	-	0.083	0.095
Toluene	-	-	0.080	0.090
Pentane	0.0639	0.0631	-	-
Hexane	0.0663	0.0646	-	-
Heptane	0.0660	0.0646	-	-
Octane	0.0651	0.0634	-	-
Isooctane	-	-	0.047	0.051
Decahydro-naphthalene	0.1094	0.1074	-	-

The values for the aqueous solutions were corrected for the absorbed water

The chemicals are only dissolved in the amorphous regions of partially crystalline polymer. If a comparison is made with the calculated solubilities and partition coefficients for amorphous polyethylene, the mass gain for the dissolution of the chemical should only be related to the amorphous fraction of the sample. For this purpose the mass  $G_{\text{amorph}}$  of the amorphous phase in the geomembrane samples was determined from the degrees of crystallinity given in Table 1a. The partition coefficient  $\sigma$  was calculated from the saturation value of the mass gain for immersion in the dilute aqueous solution at concentration  $c_0$  according to (10) with  $G = G_{\text{amorph}}$  and the solubility for immersion in the liquid chemical according to (9) with  $G = G_{\text{amorph}}$ . The results for the solubilities and partition coefficients for the aqueous solutions corrected in this way are given in Tables 4 and 6.

concentrations to compare them with the measured values. For this purpose the value of activity  $a(x_0)$  was determined from the calculated activity curve for acetone in water, see Figure 1, for the specified concentration  $x_0$  of the aqueous solution. Figure 2 gives the activity curves for acetone in polyethylene. Since in equilibrium the activities are equal, the activity curve of acetone dissolved in the polymer yields the mass fraction  $w$  in the polyethylene at level of activity  $a(x_0)$ . For the aqueous solutions the calculated and measured values of the concentration in the polymer are in surprisingly good agreement. The calculations should therefore also yield reliable results for highly diluted aqueous solutions.

Table 5: Detailed comparison of calculated mass fractions with measured mass fractions in the systems aqueous acetone solution/polyethylene and aqueous acetic acid/polyethylene.

Test liquid	Mass fraction of the aqueous solution	Measured values of mass fraction of absorbed molecules with respect to the amorphous part of the HDPE-GM, Sample 48	Calculated mass fraction according to the method of Takeru Oishi and John. M. Prausnitz (UNIFAC)
Acetone, neat	1.0	0.022	0.021
Acetone-water	0.441	0.011	0.011
	0.081	0.003	0.004
Acetic acid	1.0	0.019	0.022
	0.855	0.014	0.014
	0.673	0.010	0.009
	0.486	0.008	0.006

Their activity coefficient was determined from the initial slope of the activity curve for  $x$  and  $w$  close to zero and the corresponding partition coefficient  $\sigma$  calculated according to (4) and (5). Table 6 shows a comparison of the experimental values measured and estimates with the results obtained by calculation. The estimated values are in square brackets. The estimated values were calculated as the ratio of solubility in the polymer (Table 2a and 2b) to solubility in water.

For aliphatic hydrocarbons the interaction parameters between the  $\text{CH}_2$  and the  $\text{H}_2\text{O}$  groups as given by Gmehling et. al. (1982, 1983), Tiegs et al. (1987) and Hansen et al. (1991) yield solubilities in water one or two orders of magnitude too high. Correspondingly partition coefficients estimated in this way would be much too small. For these cases it was necessary to fall back on the original interaction parameters given by Ried et al. 1977. The solubility in water is then in very close agreement with the measured values therefore the partition coefficients can be considered to be reliable.

Table 6. Partition coefficients for the system aqueous solution - polyethylene calculated with the UNIFAC method and the Retention-Index method compared with experimental and estimated results (values in brackets).

Test liquid	Partition coefficient, measured and estimated (square brackets)	Partition coefficient, calculated according to the UNIFAC-method	Partition coefficient, calculated according to the Retentions-Index method
Methanol-water	-	0.004	0.001
Acetone-water	0.032 <sup>a</sup>	0.016	0.106
Methylethylketone-water	[0.06]	0.173	0.403
Acetic acid, diluted	0.015 <sup>b</sup>	0.017	0.020
Propanoic acid, diluted	-	0.043	0.076
Acetic acid ethyl ester-water	[0.28]	0.42	0.930
Formaldehyde-water	0.015 <sup>c</sup>	-	0.009
Chloroform-water	[18]	19	22
Carbon tetrachloride-water	[238]	252	141
Trichloroethylene-water	189 <sup>d</sup>	-	114
Trichloroethylene-water	[135 <sup>f</sup> ]		
1,2-dichloroethane-water	[7 <sup>f</sup> ]	10	20
Tetrachlorethylen-water	[1357]	-	9972
Chlorobenzene-water	[209]	350	487
Benzene-water	[57 <sup>f</sup> ]	55	37
Xylene-water	[499 <sup>f</sup> ], [556]	1157	517
Toluene-water	[192 <sup>f</sup> ], [160]	254	206
Pentane-water	[1512]	3600	2800
Hexane-water	[5800]	22200	10700
Heptane-water	[24348]	131000	40600

<sup>a</sup>) 10 Vol.-% Acetone-water, <sup>b</sup>) 0.5 g/l acetic acid, <sup>c</sup>) 37 wt.-% formaldehyde, <sup>d</sup>) 0.5 g/l trichloroethylene-water

<sup>e</sup>) Data from Prasad et al. (1994) for the partition coefficient estimated from the ratio of measured solubilities

Using the UNIFAC method the temperature dependence of solubilities and partition coefficients can also be determined. This would however go beyond the scope of this paper.

Table 3a: Experimental results for the diffusion coefficient of test liquid molecules in HDPE geomembrane from immersion and permeation measurements with the neat test liquids.

Test liquid	Immersion test Sample 48 $D_1$ [ $10^{-12}$ m <sup>2</sup> /s]	Immersion test Sample 139 $D_1$ [ $10^{-12}$ m <sup>2</sup> /s]	Permeation test Sample a <sup>1</sup> $D_1$ [ $10^{-12}$ m <sup>2</sup> /s]
Water	0.82	0.90	-
Acetone	0.87	0.91	-
Methylethylketone	0.75	0.86	-
Acetic acid	0.58	0.52	-
Propanoic acid	0.30	0.32	-
Acetic acid ethyl ester	-	-	1.1
Chloroform	-	-	5.9
Carbon tetrachloride	-	-	2.4
Trichloroethylene	7.70	8.40	10.8
Tetrachloroethylene	-	-	3.8
Chlorobenzene	-	-	3.6
Xylene	-	-	4.7
Toluene	-	-	6.1
Pentane	2.44	2.90	-
Hexane	2.08	2.47	-
Heptane	1.52	1.74	-
Octane	1.08	1.31	-
Isooctane	-	-	0.44
Decahydro-naphthaline	0.35	0.36	-

§) Calculated from the permeation rate, see August et al. 1984, and from the solubilities of Table 2a and 2b according to (15)

#### 4 CALCULATIONS

The calculation methods applied are explained in great detail in the listed references, therefore they will not be extensively here. Activity  $a(x)$  of the aqueous solution of the test liquid with concentration (mole fraction)  $x$  was calculated using the UNIFAC method, see Reid et al. (1977) and the references given there. The activity  $a(w)$  of the test liquid dissolved in the polymer with a mass fraction  $w$  was calculated by the UNIFAC method as specifically extended for polymers by Oishi and Prausnitz (1978).

The amorphous regions of the polymer exhibit a large free volume. This has an effect on the molecules dissolved there which are spread throughout a greater free volume than in their

liquid phase. Therefore marked differences exist in the specific volumes of the liquid contaminant and that dissolved in the polymer which must be taken into account in the partition function of the solution and thus also in the activity. This is done in the extended UNIFAC method using an additional 'free volume' term, which depends on the density of the test liquid and of the polymer (Beret et al. 1975).

Table 3b. Experimental results for the diffusion coefficient of test liquid molecules in HDPE geomembrane from immersion and permeation measurements with aqueous solutions. The values put in brackets are quoted from (Prasad et al. 1994).

Test liquid	Immersion test, Sample 48 and data from the literature $D_1$ [ $10^{-12}$ m <sup>2</sup> /s]	Immersion test Sample 139 $D_1$ [ $10^{-12}$ m <sup>2</sup> /s]	Permeation test, Sample a <sup>1</sup> and data from the literature $D_1$ [ $10^{-12}$ m <sup>2</sup> /s]
Acetone-water 10 Vol-%	0.66	0.84	-
Acetone-water 50 Vol-%	0.88	0.87	-
Acetic acid, 0.50 kg/l	0.11	0.18	-
Acetic acid, 0.70 kg/l	0.15	0.22	-
Acetic acid, 0.90 kg/l	0.25	0.29	-
Trichloroethylene-water	0.20	0.30	0.6
Trichloroethylene-water	[0.52]	-	[0.50]
Benzene	[0.037]	-	-
Xylene	[0.10]	-	0.2 [0.10]
Toluene	[0.51]	-	0.2 [0.23]

§) Calculated from the permeation rate, see August et al. (1984), and from the calculated partition coefficients of Table 6 according to (15)

The amorphous polyethylene was modelled by the structural unit  $\text{CH}_2$  ( $M_p = 14.03$  g/mol) with the corresponding volume and surface and also interaction parameters. For the calculation the theoretical density of the amorphous part was not used but rather the actual density of the partially crystalline polymer (see Table 1a). Under this assumption the best agreement with the experimental data was achieved. The group parameters for a wide variety of structural units are given by Gmehling et al. (1982,1983),Tiegs et al. (1987) and Hansen et al. (1991). Figures 1 and 2 show examples of the calculated activity curves. The solubility was determined from these activity curves according to (6). The results are summarized in Table 4.

For those test liquids in Table 4 whose calculated values are shown in square brackets the calculated activity curve according to the extended UNIFAC method approaches unity only

asymptotically, see annotation to reference (Beret et al. 1975). Therefore a substantial error occurs in the estimate of solubility. In these cases the following method was chosen. Based on the assumption that the calculations are most reliable at low concentrations the tangent to the activity curve at low concentrations was determined. The mass fraction at which the ordinate of this tangent line equals 1 was then used to estimate solubility. The values are given in square brackets in Table 4. Obviously they are in very close agreement with the measured values.

Table 4. Solubilities (mass fraction) calculated with the extended UNIFAC-method by Oishi and Prausnitz for the test liquids in amorphous polyethylene compared with the experimental results. The calculated values put in brackets are extrapolated from the activity curve at low concentrations.

Test liquid	Measured values of mass fraction of absorbed molecules with respect to the amorphous part of the HDPE-GM		Calculated mass fraction according to the method of Oishi and Prausnitz
	Sample 48 *) Sample a	Sample 138 *) Sample b	
Water	0.002	0.002	
Methanol	0.002 <sup>a</sup>	0.002 <sup>b</sup>	0.004
Acetone	0.022	0.022	0.021
Methylethylketone	0.039	0.037	0.032
Acetic Acid	0.019	0.017	0.022
Propanoic acid	0.046	0.040	0.030
Acetic acid ethyl ester	0.048 <sup>a</sup>	0.047 <sup>b</sup>	0.065
Chloroform	0.305 <sup>a</sup>	0.312 <sup>b</sup>	0.325
Carbon tetrachlorid	0.409 <sup>a</sup>	0.408 <sup>b</sup>	[0.222]
Trichloroethylene	0.424	0.385	0.450
Tetrachloroethylene	0.432 <sup>a</sup>	0.443 <sup>b</sup>	0.442
Chlorobenzene	0.220 <sup>a</sup>	0.220 <sup>b</sup>	0.285
Xylene	0.189 <sup>a</sup>	0.194 <sup>b</sup>	[0.133]
Toluene	0.182 <sup>a</sup>	0.184 <sup>b</sup>	[0.439]
Pentane	0.139	0.121	[0.090]
Hexane	0.144	0.124	[0.105]
Heptane	0.144	0.124	[0.113]
Octane	0.142	0.122	[0.122]
Isooctane	0.107 <sup>a</sup>	0.104 <sup>b</sup>	[0.117]
Decahydro-naphthaline	0.238	0.207	[0.227]

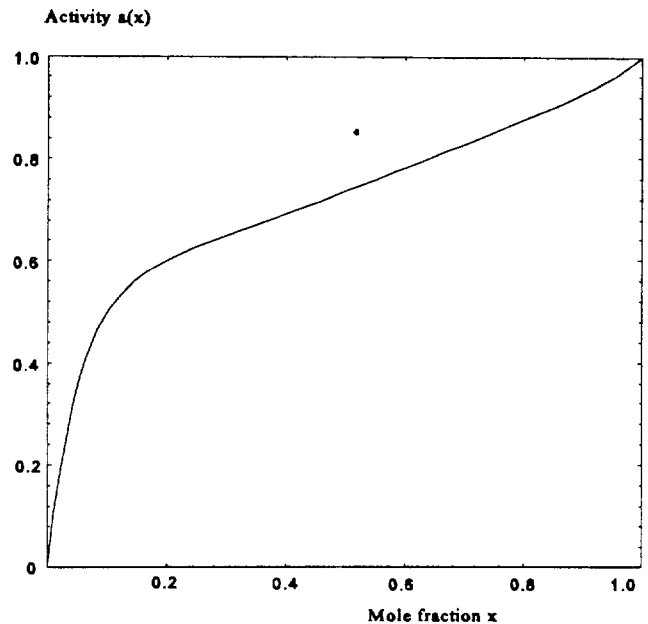


Figure 1. Illustrative example of activity versus mole fraction for aqueous acetone solutions. The curve was calculated with the UNIFAC-method.

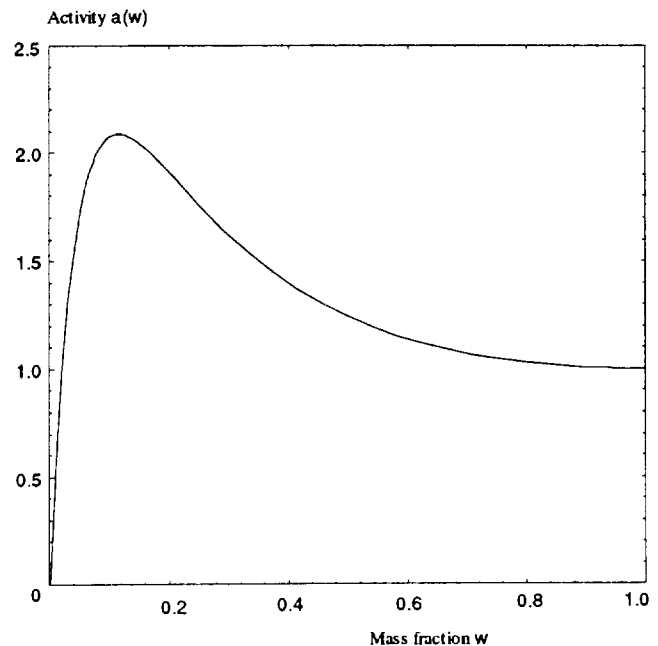


Figure 2. Illustrative example of activity versus mass fraction for acetone dissolved in amorphous polyethylene. The curve was calculated using the modified UNIFAC-method.

Table 5 shows the calculations for polyethylene/aqueous acetone solution and polyethylene/acetic acid at various



O. G. Piringer suggested a simple group contribution method for the direct calculation of the partition coefficient  $\sigma$ . A detailed explanation can be found in (Piringer et. al. 1993). The method is based on the comparison of the retention times in gas chromatography and is denoted as the Retention-Index-Method. The polyolefin is simulated here by the non-polar material Silikon OV 101. Increments for important structural units in the non-polar material Silikon OV 101 and in water are given by Piringer (1993). The calculation results are given in Table 6. The partition coefficients calculated according to the UNIFAC method are in every case in fairly good agreement with those calculated by the Retention-Index method.

The diffusion coefficients for compounds dissolved at low concentration in the geomembrane might be estimated according to (7) with an appropriate choice of the materials parameter  $A_p$ . With  $A_p = 7.5$  a fairly good agreement with the measured values in Table 3b is obtained.

## 5 DISCUSSION

The polyethylenes investigated here containing linear polymer chains with 5 to 15 ethyl-, butyl or hexyl side chains per 1000 C atoms, exhibit a complex morphology of finely-distributed crystalline and amorphous regions. A sample of black HDPE geomembrane with a typical mass of 6 g contains additionally approximately 150 mg of finely distributed carbon black particles and a few tens of grams of antioxidants. The parameters given here 'average out' influences and interactions acting in complex surroundings.

This is valid first of all for diffusion coefficients. The dissolved molecules interact with each other and change the surroundings and the conditions for migration in the polymer, which can be observed as swelling. Therefore the diffusion coefficient should depend on the concentration. It can be seen from both immersion tests and from permeation rates that the diffusion coefficient is considerably smaller at small concentrations from aqueous solutions than under a load with neat test liquids. Above all, the induction times are much shorter under a load with neat test liquids than with aqueous solutions. For a permeation process with a diffusion coefficient  $D$  increasing as a function of the concentration according to a simple rule, e.g.  $D(c) = D_0 e^{bc}$ , the induction time can be calculated (Frisch 1957 and annotation this reference) and a strong reduction in induction time is indeed obtained in comparison to that which would be obtained according to (15) at a low concentration and diffusion coefficient  $D_0$ .

The diffusion coefficients at high dilution depend on polarity and in particular on the size of the dissolved molecule. It might be estimated for various temperatures with formula (7). For the organic compounds the diffusion coefficient typically lay at a few times  $10^{-13}$  m<sup>2</sup>/s. The partition coefficients in Table 6 show a completely different behaviour. They vary by nearly 10 orders of magnitude. This proves the statement made at the beginning, that the partition coefficient is the fundamental determining factor for a wide variety of permeation rates for the different

pollutant classes.

These numbers enable a few simple estimates of diffusion in the composite liner. The diffusion coefficients in the mineral layer lay typically between a few times  $10^{-11}$  m<sup>2</sup>/s and  $10^{-10}$  m<sup>2</sup>/s. The porosity is a few times  $10^4$ . The permeability is then according to (16) typically around  $10^{-11}$  m<sup>2</sup>/s. The thickness of the mineral layer is greater by a factor of 400 than that of the geomembrane. Since the diffusion coefficients in the geomembrane are less than  $10^{-12}$  m<sup>2</sup>/s, in spite of its small thickness its diffusion resistance according to (16) and (17) exceeds that of the mineral layer if the partition coefficient is less than 0.025. This is the case for all easily water soluble test liquids. The geomembrane therefore not only completely prevents ionic diffusion it also contributes greatly to the diffusion resistance for all easily water soluble non-dissociated molecules. Hence the geomembrane is an indispensable element of an efficient engineering barrier not only as a barrier to convective transport but also as a diffusion barrier for easily water soluble substances.

The diffusion resistance of the geomembrane for non-polar or only weakly polar hydrocarbons is however low. The imperviousness is essentially determined by the mineral component. An additional increase in the diffusion resistance can however be achieved through the conditions at the interfaces. Assuming that the partition coefficient  $\sigma_{2,1}$  between the soil water and the geomembrane is greater than that  $\sigma_{0,1}$  between the leachate and the geomembrane, i.e.  $\sigma_{0,1}/\sigma_{2,1} < 1$ , this increases according to (17) the diffusion resistance of the whole system. Sufficiently convincing measurements for this are not yet available. There are however various arguments supporting this assumption.

In spite of the complex morphology and composition of the polyethylenes investigated, as mentioned at the beginning it can be seen that even a simple modelling of the amorphous regions with the CH<sub>2</sub> structural unit and taking into account the contribution of the free volume to the activity, assuming that contaminants can be dissolved in amorphous regions alone, the solubility can be predicted over a range of some orders of magnitude with an accuracy of up to a factor of 2. The calculated partition coefficients are in close agreement with those measured for HDPE geomembrane in aqueous solutions.

The UNIFAC-method has the advantage that it might be used to calculate partition coefficients at moderate temperature typically for landfills and for multicomponent solutions. In the waste body, due to chemico-biological and in exceptional cases due to hydration and oxidation processes, temperatures up to about 80° C can occur. In the basal liner beneath a state of the art drainage layer however, temperatures of more than 40° C have never actually been found. A temperature increase from 23° C to 40° C results in a tenfold increase in the permeability of the HDPE geomembrane.

The results of the Retention-Index method agree with those of the UNIFAC method. The calculation with the former method is much easier because only the influence of non-polar and aqueous surroundings on larger structural features like aromatics, aldehydes, alcohols, branches, Cl side groups, etc.

has to be taken into account. Even the accuracy achieved with this assumption is obviously sufficient for risk estimation or system comparison for the application of geomembranes in the field of ground water protection.

$$t_{ind} = \frac{6(4e^{\beta c_1} - 1 + e^{2\beta c_1}(2\beta c_1 - 3))}{4(e^{\beta c_1} - 1)^3} \frac{d^2}{6D_0}$$

## REFERENCES

- August, H., Tatzky, R., Pastuska, G. and Win, T. (1984) "Untersuchungen des Permeationsverhaltens von handelsueblichen Kunststoffdichtungsbahnen als Deponieabdichtungen gegenueber Sickerwasser, organischen Loesungsmitteln und deren waesserigen Loesungen", Report of the R&D-Project 10302208 of the BMBF, , published by BAM, Sub-Department IV.3, Landfill and Remedial Engineering, D-12200 Berlin, Germany.
- August, H., Tatzky-Gerth, R., Preuschmann, R. and Jakob, I. (1992) "Permeationsverhalten von Kombinationsdichtungen bei Deponien und Altlasten gegenueber wassergefaehrdenden Stoffen", Report on the R&D-Project 10203412 of the BMBF, published by BAM, Sub-Department IV.3, Landfill and Remedial Engineering, D-12200 Berlin, Germany.
- BAM (1994) "Guidelines for the Certification of Geomembranes as a Component of Composite Liners for Municipal and Hazardous Waste Landfills and for Lining Contaminated Land", published by BAM, Sub-Department IV.3, Landfill and Remedial Engineering, D-12200 Berlin, Germany.
- Barrie, J. A., Levine, J. D., Michaels, A. S. and Wong, P. (1963) "Diffusion and Solution of Gases in Composite Rubber Membranes", Trans. Faraday Soc., Vol. 59, p. 869.
- Beret, S. and Prausnitz, J. M. (1975) "Perturbed Hard-Chain Theory: An Equation of State for Fluids Containing Small or Large Molecules", AIChE Journal, Vol. 21, p. 1123-1132.
- The free volume term is determined by two parameters b and c ein. Parameter b is a proportionality constant of the order unity which enters the term for the reduced volume. With parameter c the rotational and vibrational external degree of freedom in addition to the translational degrees of freedom are taken into account. These are relevant for solvents with large molecules. Following the procedure of Oishi et al. (1978) and Goydan et al. (1989) we set b = 1.28 and c = 1.1. However especially for the large-chain hydrocarbons higher values of c might be more appropriate. Better agreement of the experimental value with calculated results are obtained for the solubility of the highmolecular hydrocarbons with greater values of c. However a detailed analyses of an optimized choice of the parameters for polyethylene is beyond the scope of this paper.
- Carlsaw, H. S. and Jaeger, C. J. (1959) *Conduction of Heat in Solids*, 2nd ed., Oxford University Press. Oxford, GB, p. 402.
- Frisch, H. L. (1957) "The Time Lag in Diffusion", J. Phys. Chem., Wash., Vol. 61, p.93.
- In this case the induction time is given by
- where  $c_1 = \sigma c_0$  is the equilibrium concentration in the surface of the geomembrane.
- Gmehling, J., Rasmussen, P. and Fredenslund, A. (1982) "Vapor-Liquid Equilibria by UNIFAC Group Contribution. Revision and Extension. 2", Ind. Eng. Chem. Process Des. Dev., Vol. 21, p. 118.
- Gmehling, J., Rasmussen, P. and Fredenslund, A. (1983) "Vapor-Liquid Equilibria by UNIFAC Group Contribution. Revision and Extension. 3", Ind. Eng. Chem. Process Des. Dev., Vol. 22, p. 676.
- Goydan, R., Reid, R. C. and Tseng, H.-S. (1989) "Estimation of the Solubilities of Organic Compounds in Polymers by Group-Contribution Methods", Ind. Eng. Chem. Res., Vol. 28, p. 45.
- Hansen, H. K., Gmehling, J., Schiller, M., Rasmussen, P. and Fredenslund, A. (1991) "Vapor-Liquid Equilibria by UNIFAC Group Contribution. Revision and Extension. 5", Ind. Eng. Chem. Res., Vol. 30, p. 2352.
- Mueller, W., Jakob, I., Tatzky-Gerth, R. and August, H. (1997a) "Stofftransport in Deponieabdichtungssystemen, Teil 1: Diffusions- und Verteilungskoeffizienten von Schadstoffen bei der Permeation in PEHD-Dichtungsbahnen", Bautechnik, Vol. 74, pp. 176-190.
- Mueller, W., Büttgenbach, B., Tatzky-Gerth, R. and August, H. (1997b) "Stofftransport in Deponieabdichtungssystemen, Teil 2: Permeation in der Kombinationsdichtung", Bautechnik, Vol. 74, pp. 331-344.
- Oishi, T. and Prausnitz, J. M. (1978) "Estimation of Solvent Activities in Polymer Solutions, Using a Group-Contribution Method", Ind. Eng. Chem. Process Des. Dev. , Vol. 17, p. 333.
- Prasad, T. V., Brown, K. W. and Thomas, J. C. (1994), "Diffusion coefficients of organics in high density polyethylene (HDPE)", Waste Management & Research, Vol. 12, p. 61.
- Piringer, O. G. (1993) *Verpackungen fuer Lebensmittel, Eignung, Wechselwirkungen, Sicherheit*, VCH Verlagsgesellschaft mbH, Weinheim, Germany.
- Reid, R. C., Prausnitz, J. M. and Sherwood, Th. K. (1977) *The Properties of Gases and Liquids*, 3rd ed., McGraw-Hill Book Company, New York, USA.
- Tiegs, D., Gmehling, J., Rasmussen, P. and Fredenslund, A. (1987) "Vapor-Liquid Equilibria by UNIFAC Group Contribution. Revision and Extension. 4", Ind. Eng. Chem. Res., Vol. 26, p. 159.

# Water And Organic Solvents Transport Parameters In Geomembranes.

L. Durin, N. Touze, C. Duquennoi

Cemagref, drainage and barrier engineering research division, B.P. 121, 92185 Antony cedex, FRANCE

**ABSTRACT:** To assess the efficacy of geomembranes against fluid transport, samples were tested in the presence of a concentration gradient and an hydraulic pressure gradient. Chemical diffusion tests were conducted by immersion of HDPE and EPR-PP in pure organic solvents such as acetone, dichloromethane and toluene. Water diffusion has been tested on various geomembranes such as HDPE, EPR-PP, PVC-P, EPDM, elastomeric bituminous and oxidized bituminous. Temperature influence on water diffusion rate was studied on PP, HDPE and PVC-P. Hydraulic permeation of water was studied on PVC-P, EPDM and a bituminous film with a permeation apparatus presented in this paper. Kinetic sorption curves are plotted from immersion tests. Diffusion coefficients and chemical permeation fluxes are calculated from experimental data. Immersion test is a valuable method for determining pure solvents diffusion coefficient if material swelling can be neglected. Application of Arrhenius Law to diffusion coefficient variation with temperature may be inaccurate. HDPE and EPR-PP seem to be more sensitive towards non polar solvents.

**KEYWORDS :** Geomembranes, Laboratory Tests, Permeability, Diffusion, Temperature Effects.

## 1 INTRODUCTION

Geomembranes are non porous materials which function is to act as a barrier against fluids such as water and pollutants. Various different methods have been used for estimating geomembrane behaviour towards fluid transport (August, 1984; Park, 1986). Transport phenomena in solids often refer to permeability, which is defined as the ability of a solid to be penetrated by a fluid. Distinction must be made between chemical and hydraulic permeability. Chemical permeability concerns the transport of molecules under a concentration gradient. Physical phenomena involved are the adsorption on surface, the diffusion through the geomembrane and the desorption. Hydraulic permeability is related to the transport of a under hydraulic pressure gradient.

Various studies aimed at determining mass flux from laboratory tests using pure (Haxo, 1990; Britton, 1989) or dilute organic solvents (Park, 1996). Authors often argue that when aqueous solutions are used, landfill conditions are better approached (Park, 1996). But few of them (Nguyen, 1996; Stessel, 1995) closely observed the influence of physical interaction between solvents and geomembranes on transport parameters evolution. Values obtained are rarely discussed considering their evolution along time. Nevertheless previous studies have shown that geomembrane ageing could also be controlled by transport phenomena (Durin et al. 1997, Duquennoi et al. 1995).

Because geomembranes are made of dense polymers, they are nonporous and laboratory experiments can last a long-time (at least 2 months). Two modes of transport (chemical and hydraulic permeation) through various geomembranes are compared in this paper by means of related parameters (diffusion coefficient, plasticizing coefficient, hydraulic and chemical permeation flow). It was aimed at determining if an increase of chemical gradient and of temperature could contribute to accelerate some processes without changes in phenomena. The last part of the paper describes a device used to evaluate water fluxes through geomembranes under hydraulic gradients (Eloy-

Giomi, 1993, Pelte, 1993, Touze, 1995). The method has become a standard in France to qualify the quality of geomembranes as far as hydraulic fluxes are concerned.

Three types of results are presented: (1) the effect of solvents type (organic and water) on diffusion coefficient value; (2) the effect of temperature on water diffusion; (3) the effect of water permeation under hydraulic pressure gradient.

## 2 DIFFUSION UNDER CONCENTRATION GRADIENT

### 2.1 Diffusion Coefficient Estimate

#### 2.1.1 Principle

Sorption tests through geomembranes can be described by an unidirectional Fickian diffusion in a medium bounded by two parallel planes (Crank, 1975). Solutions of second Fick's law (1) give the diffusion profile shape  $C(x, t)$  and permit the diffusion coefficient calculation from experimental profiles.

$$\frac{\partial C}{\partial t} = D \frac{\partial^2 C}{\partial x^2} \quad (1)$$

If the concentration of the diffusing solution adsorbed on the sample surface is called  $C_0$ , and the half-thickness of the sample is  $l$ , then boundary conditions for resolving (1) are (Crank 1975):

$$\begin{aligned} C &= C_0 & x &= -l, x = l \\ C &= C_1 & -l < x < l & \quad t = 0 \end{aligned}$$

For  $-l < x < l$  and  $t > 0$ , it gives (2):

$$\frac{C_x - C_1}{C_0 - C_1} = 1 - \frac{4}{\pi} \sum_{n=0}^{\infty} \frac{(-1)^n}{2n+1} \exp\left(-\frac{D(2n+1)^2 \pi^2 t}{4l^2}\right) \cos\left(\frac{(2n+1)\pi x}{2l}\right) \quad (2)$$

where  $D$  is the constant diffusion coefficient,  $t$  the time,  $n$  is a positive integer,  $C_x$  the concentration at the  $x$  distance from the surface.

If  $M_t$  is the quantity of diffusing matter in the membrane at time  $t$ , (2) leads to (3):

$$\frac{M_t}{M_\infty} = 1 - \frac{8}{\pi^2} \sum_{n=0}^{\infty} \frac{1}{(2n+1)^2} \exp\left[-D(2n+1)^2 \frac{\pi^2}{4l^2} t\right] \quad (3)$$

where  $M_\infty$  is the mass of diffusing matter absorbed when the sorption equilibrium is reached. Sorption ratio  $M_t / M_\infty$  is expressed as a function of time and the graph of sorption kinetic (Crank, 1975) is in general plotted with the reduced coordinates  $\left(\frac{M_t}{M_\infty}, \sqrt{\frac{Dt}{l^2}}\right)$ .

### 2.1.2 Sorption tests

Equation 2 is a trigonometric series which converges towards zero and infinity. When  $t$  tends to zero, it is assumed that the membrane surface reaches immediately equilibrium as soon as immersion begins ( $t = 0$ ). The diffusion coefficient  $D_0$  at the beginning of immersion can then be obtained from the half-sorption time  $t_{1/2}$  defined as

$\frac{M_{t_{1/2}}}{M_\infty} = \frac{1}{2}$ . If  $D_0$  is constant (Crank, 1975), equation 3 gives

$$D_0 \approx 0.0492 \times \frac{L^2}{t_{1/2}} \quad (4)$$

where  $L$  is the sample thickness.

When  $t$  tends towards infinity, it is considered that equilibrium is reached for a value of  $M_t / M_\infty$  equal to 90% of maximal sorption observed. Related time is called infinite time  $t_\infty$ . The diffusion coefficient  $D_\infty$  at equilibrium can be calculated from equation 3:

$$D_\infty = 0.212 \frac{l^2}{t_\infty} \quad (5)$$

Equations 4 and 5 give a good estimate of the diffusion coefficient if sorption is Fickian ( $D$  is a constant) and the geomembrane does not swell.

### 2.1.3 Evolution of diffusion coefficient with temperature.

Arrhenius law (6) says that an increase in temperature accelerates sorption rates:

$$D(T) = A \cdot \exp\left(-\frac{E}{RT}\right) \quad (6)$$

where  $A$  is a constant,  $E$  is the activation energy, independent from temperature  $T$ , and  $R$  the perfect-gas constant. The influence of a temperature variation on sorption was studied in order to determine if (6) could be used to estimate the diffusion coefficient at lower temperatures from results of tests conducted at high

temperature, assuming that the same value at the equilibrium could be reached faster in the latter case.

In the case of sorption tests conducted at three different absolute temperatures  $T_1 < T_2 < T_3$ , required times to reach the same value of sorption ratio are  $t_1 > t_2 > t_3$ . Then when (6) is verified one can obtain :

$$\ln\left(\frac{1}{t_2}\right) = \ln\left(\frac{1}{t_1}\right) + \frac{\frac{1}{T_2} - \frac{1}{T_1}}{\frac{1}{T_3} - \frac{1}{T_1}} \times \left(\ln\left(\frac{1}{t_3}\right) - \ln\left(\frac{1}{t_1}\right)\right) \quad (7)$$

## 2.2 Flow of Water and Solvents

If the diffusion coefficient  $D$  varies with the concentration, it can be described by Long's model (Favre, 1993):

$$D = D_0 \exp\left[\beta \left(\frac{M_t - M_{t=0}}{M_{t=0}}\right)\right] \quad (8)$$

where  $\beta$  is the plasticizing coefficient easily deduced from experimental diffusion coefficient value at equilibrium.

The chemical permeation flow,  $Q$ , under permanent regime is deduced from the conservation of mass. After integration along the sample half-thickness  $l$ , flow per unit volume,  $Q_v$ , is obtained from equation 9:

$$Q_v = \frac{-D_0}{\beta l \left[ \exp\left(\beta \left(\frac{M_t - M_0}{M_0}\right)_{x=l}\right) - \exp\left(\beta \left(\frac{M_t - M_0}{M_0}\right)_{x=0}\right) \right]} \quad (9)$$

Initial flow of chemical permeation per volume unit can be estimated for a membrane separating a medium with pure solvent at one face against void at the other face. Since the flow decreases during the experiment, because of the concentration gradient decreasing, initial flow is also the maximal during experiment.  $Q_v$  is easily converted in unit of mass,  $Q_m$  by:

$$Q_m = \rho Q_v \quad (10)$$

where  $\rho$  is the solvent density.

## 2.3 Experiments

### 2.3.1 Materials and methods

Table 1 presents the eight geomembranes tested. Crystallinity ratio for HDPE (High Density Polyethylene) was 80% and 20% for EPR-PP (Ethylene-propylene-rubber Polypropylene). Weighings were done with a balance (METTLER PE 360).

Table 1. Geomembranes tested with immersion tests.

	Bituminous	Bituminous	EDPM	HDPE	EPR-PP	EPR-PP	PVC
Thickness (mm)	4	3.9	1	2	1.5	1.2	1.5
Water (23, 40, 60°C)	×	×	×	×		×	×
Water (23°C)				×	×		
Acetone (23°C)				×	×		
Dichloromethane (23°C)				×	×		
Toluene (23°C)				×	×		

Selected solvents were nonpolar (toluene and dichloromethane), and polar (acetone and water). Five geomembrane samples were immersed in closed glass tanks containing 5 liters of pure solvent, under a temperature of 23°C. Sample dimensions at the beginning of experiment were 13 cm × 17 cm. Those dimensions were chosen in order to minimize edge effects. If L is the sample thickness and a is the radius of the circular aperture through which flow occurs, Crank (1975) states that edge effects on diffusion can be neglected if  $L/a \leq 0.2$ . Errors involved by such an approximation could lead to apparent differences between diffusion coefficient deduced from steady-state and time-lag measurements.

The tests of temperature influence on water sorption, were conducted with five 10 cm × 10 cm geomembrane samples immersed in glass tanks filled with one liter of distilled water. Experiments were conducted in incubators for immersions at 40°C and 60°C and in an air-conditioned room for 23°C tests.

In order to prevent any polymer degradation which would not be directly caused by solvent or water action, experiments were conducted in darkness, at a constant temperature and atmospheric pressure. At each selected time-lag, sample was removed, softly wiped with a special blotting paper and weighed. Kinetic curves ( $\frac{M_t - M_0}{M_0}; \sqrt{t}$ )

were plotted using the least square method assuming the experimental equation (deduced from equation 3):

$$\text{Abs.}\%(t) = \text{Abs.}\%(\infty) [1 - e^{-bt}] \quad (11)$$

with  $\text{Abs.}\%(t)$ , the percentage gain of matter absorbed at time t, b being a constant.

### 2.3.2 Results

#### 2.3.2.1 Immersion tests in solvents

Curve shapes show that the diffusion was Fickian. They present an asymptote when t tends towards infinity as showed in Figure 1, except for HDPE in water at 23°C for which equilibrium was not reached. The calculation method described above was followed and results are displayed in Table 2. Near the asymptote,  $M_t$  variations and errors on D decrease. There is always a difference between  $D_0$  and  $D_\infty$  as shown in Table 2. This can be attributed to the sample swelling which could increase edge effect. Every diffusion coefficient was under  $10^{-10} \text{ m}^2/\text{s}$  which was the maximum diffusion coefficient possible since pure solvents were used.

Stessel et al. (1995) have combined physical testing with chemical exposure. They showed that Hildebrand's solubility parameters could be a good indication of the permeability of a membrane to a liquid or vapour. They showed that HDPE Hildebrand's solubility was similar to the one of nonpolar solvents, helping melting process.

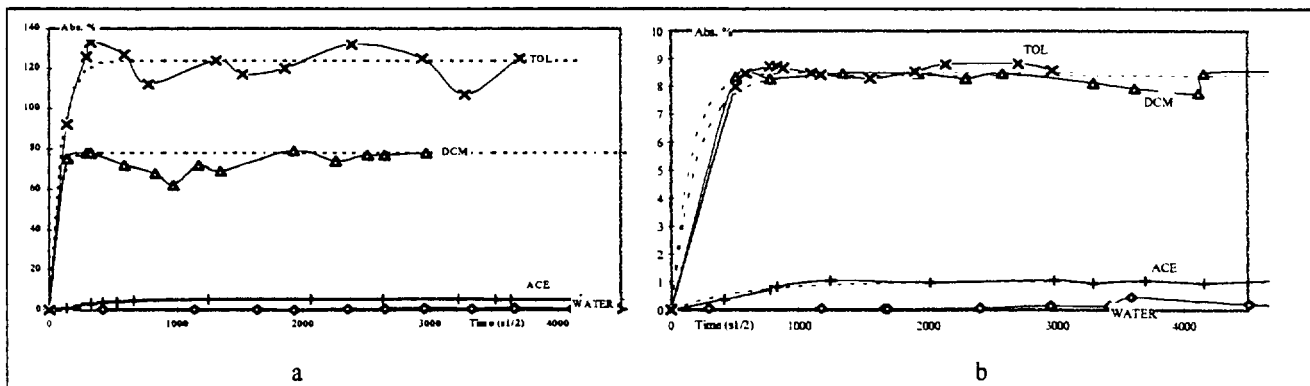


Figure 1. Kinetic sorption curves of PP (Fig. 1a) and HDPE (Fig. 1b) immersed in various solvents (TOL: toluene; DCM: dichloromethane; ACE: acetone), dotted line was calculated from (11).

Experiments showed in this paper seem to widen this hypothesis to PP since diffusion coefficients are higher in the case of immersion in non polar solvents (as dichloromethane and toluene).

Results also show that  $D_{\infty}$  is higher for PP than for HDPE. This can be attributed to the crystallinity which was lower for PP (20%) than for HDPE (80%). Results also show that  $D_{\infty}$  is smaller than  $D_0$  which is inconsistent with the hypothesis made on equation 2 ( $D$  is a constant along time).

Further research is conducted at present to verify the existence of a solvent-induced crystallization in polymer (Neogi, 1996) which could explain the difference between experimental and calculated curves particularly obvious in the case of PP immersed in dichloromethane (Figure 2.a). Values for water were not very accurate in the case of HDPE because equilibrium was not reached. The estimation of the absorbency for infinite time may be overestimated and this could explain the high diffusion coefficient for HDPE.

Table 2. Calculation of diffusion coefficient and chemical permeation flux from experimental data

	PP				HDPE			
	Water	Acetone	DCM	Toluene	Water	Acetone	DCM	Toluene
$D_0$ (m <sup>2</sup> /s)	$8 \cdot 10^{-15}$	$2 \cdot 10^{-12}$	$7.8 \cdot 10^{-11}$	$2.9 \cdot 10^{-11}$	$4.4 \cdot 10^{-13}$	$10^{-12}$	$10^{-11}$	$1.8 \cdot 10^{-11}$
$D_{\infty}$ (m <sup>2</sup> /s)	$1.5 \cdot 10^{-15}$	$4.5 \cdot 10^{-13}$	$1.6 \cdot 10^{-11}$	$6 \cdot 10^{-12}$	$9 \cdot 10^{-12}$	$2.6 \cdot 10^{-13}$	$2 \cdot 10^{-12}$	$4 \cdot 10^{-12}$
$Q_v$ (m <sup>3</sup> /m <sup>2</sup> /s)	$5.2 \cdot 10^{-12}$	$7 \cdot 10^{-11}$	$4 \cdot 10^{-8}$	$2.4 \cdot 10^{-8}$		$6 \cdot 10^{-12}$	$4.2 \cdot 10^{-10}$	$7.9 \cdot 10^{-10}$
$Q_m$ (g/m <sup>2</sup> /h)	0.0	0.2	193.4	75.6	0.0	2	2	2.5

Each flow was estimated by resolving equation 9. Integration was conducted on the half thickness, assuming the adsorption phase which precedes absorption was instantaneous and occurs on the first nanometers of the material. With a certain error we supposed that when sorption equilibrium was reached there was no concentration gradient between the surface and the inside of the polymer. Surface concentration at any time was then assumed to be equal to the concentration inside the sample at equilibrium. Results are presented in Table 2 with  $\frac{M_{\infty} - M_0}{M_0}(1) = 0$  and  $\frac{M_{\infty} - M_0}{M_0}(0) = \text{Abs.}(\infty)$ .

### 2.3.2.2 Immersion in water under various temperatures

Results obtained for the absorption of water at three different temperatures are presented on Figure 2. They have been obtained from another set of experiments. Diffusion coefficients and permeation fluxes could be determined at 23°C, for PP, HDPE and PVC-P, assuming that sorption equilibrium has been obtained. Curves shape seem to show that the diffusion was Fickian. For the other temperatures, sorption equilibrium has not been obtained, so that it was not possible to estimate diffusion coefficients. Results obtained are presented in Table 3. Diffusion coefficient values for HDPE, PP and PVC-P are somewhat strange for

water. PP has the lowest coefficient value; however a PP has a bigger amorphous phase than HDPE. Further research is necessary to determine if sorption equilibrium has really been reached, and to determine what is the role of the EPR contained in the PP geomembrane in the diffusion of water. For the bituminous and EDPM geomembranes, sorption curves exhibit an inflection point, indicating that the diffusion may not be Fickian. As the phenomenon responsible for this shape of curves has not yet been identified, diffusion coefficients could not be estimated.

An example of the diffusion coefficient variation with temperature is presented on Figure 3 for the PVC-P geomembrane. All results obtained have the same limitations, so that only one example is presented here. Figure 3 represents  $\ln(1/t)$  in function of  $1/T$ , for different percentages of absorption. Segments were based on the experimental points obtained at 23 and 60°C. The intermediate point, which was obtained at 40 °C, was presented with the uncertainty on its value. For most percentages of absorption, one can conclude that the three points are lined up. But the line slope varies in a significant manner with absorption, so that the assumption of a constant activation energy may not be accurate.

Table 3. Calculation of water diffusion coefficient and water permeation flux from experimental data (from Touze, 1995).

Geomembrane	$D_0$ (m <sup>2</sup> .s <sup>-1</sup> )	Plasticizing coefficient	Maximum percentage of sorbed water	$Q_v$ (m <sup>3</sup> .m <sup>2</sup> .s <sup>-1</sup> )	$Q_m$ (g.m <sup>-2</sup> .h <sup>-1</sup> )
HDPE	$1.38 \cdot 10^{-14}$	-1.68	$3.7 \cdot 10^{-2}$	$4.4 \cdot 10^{-12}$	$1.6 \cdot 10^{-5}$
PP	$6 \cdot 10^{-15}$	-0.44	0.59	$1.46 \cdot 10^{-11}$	$5.3 \cdot 10^{-5}$
PVC-P	$2.2 \cdot 10^{-14}$	-0.54	2.1	$8.21 \cdot 10^{-11}$	$2.9 \cdot 10^{-4}$

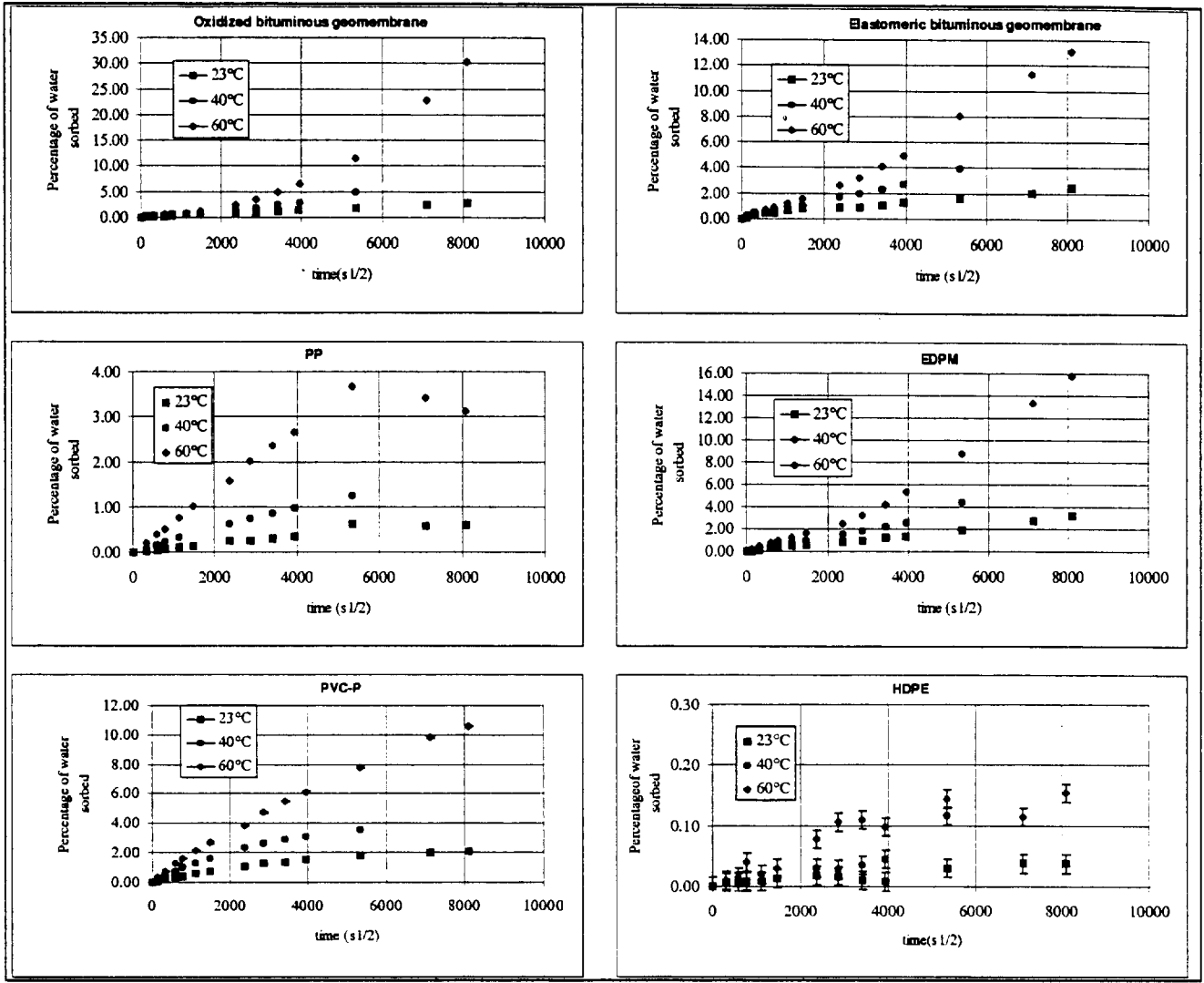


Figure 2. Kinetic sorption points for all the geomembranes tested in water, at 23, 40 and 60 °C.

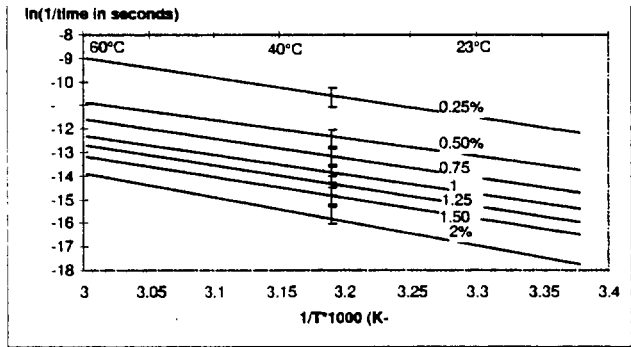


Figure 3. Arrhenius lines for different absorption coefficients of water in PVC-P

3 HYDRAULIC PERMEATION

3.1 Principle of measurement

Hydraulic permeation tests aim at estimating the flow of liquid going through an undamaged geomembrane under a

hydraulic pressure gradient. As hydraulic conductivity is not an intrinsic parameter of geomembranes (Eloy-Giorni, 1993), we will not present any interpretation of our results in terms of hydraulic conductivity, assuming Darcy's Law is not valid in geomembranes.

From an engineering point of view, water hydraulic permeation is far more representative than water vapour permeation. Koerner (1986) identified several problems inherent to water hydraulic permeation tests. When conducted with high hydraulic heads, tests resulted in leaks and failed specimens, whereas tests conducted with low hydraulic heads resulted in long test times and evaporation problems. The technical solution to this problem is presented in the following.

3.2 Materials and methods

3.2.1 Materials tested

Three different kinds of materials were tested: a 1.5mm thick plastified polyvinyl chloride geomembrane (PVC-P), a

1 mm thick ethyl-propylen-diene monomer geomembrane (EDPM) and a 0.4 mm thick bituminous film.

### 3.2.2 The permeation apparatus

Tests were conducted in a stainless steel cell, composed of two parts gripping the geomembrane (see Figure 4). At the downstream side of the geomembrane was a porous stainless steel disc, allowing liquid transfer, but preventing geomembrane deformation and failure since the upstream pressure was greater than the downstream one.

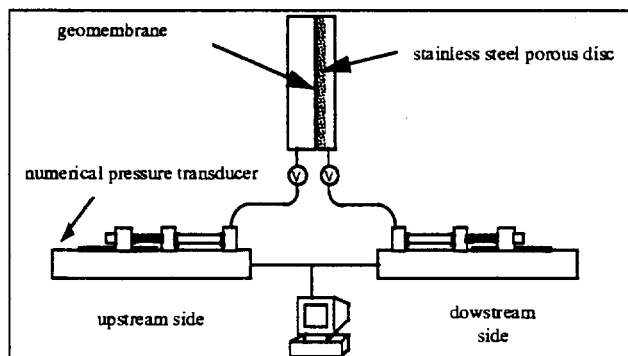


Figure 4. Apparatus of measurement of fluxes through geomembranes under hydraulic pressure gradients

Precise measurement and regulation of pressure was achieved by the use of two numerical pressure transducers (PT). Each of them was linked to one chamber (the upstream, or the downstream one) by rigid stainless steel tubes. PT allow to impose the desired pressure, and to measure the volume variations, on each side of the geomembrane.

As temperature variations can cause variations of the fluid volume and dilatation of the apparatus components, seven temperature captors have been put on the PT and on the cell. The eighth captor measures the laboratory temperature. These captors were necessary because the temperature could vary in spite of the control of room temperature. The variation of volume measured by the PT can be written as follows :

$$\Delta V_i = \Delta V_i(T) + \Delta V_i^P, \quad i \in \{\text{upstream, downstream}\} \quad (12)$$

With  $\Delta V_i(T)$  the variation of volume due to temperature variations and  $\Delta V_i^P$  the volume variation really due to permeation.  $\Delta V_i(T)$  were determined during calibration phases, described below :

$$\Delta V_i(T) = \sum_j \alpha_{ij} \Delta T_j, \quad i \in \{\text{upstream, downstream}\} \quad (13)$$

$$1 \leq j \leq 8$$

### 3.2.3 Test procedure

A disc of geomembrane, 20 cm in diameter, was put in the cell, after a month of immersion in the fluid used for the test. We assumed that this period of immersion was enough to saturate the geomembrane with the fluid and to limit concentration controlled transfers which could occur during the test. Then, the downstream and upstream side of the apparatus (cell plus pressure transducer) were filled with liquid. A calibration for the downstream and upstream sides was done before the measurement of liquid fluxes.

Downstream calibration was conducted with the two gates linking the PT to the cell being opened, the upstream PT pressure reaches 110 kPa, and the one of the downstream PT reaches 100 kPa. It is thought that this difference of pressure was enough to prevent any deformation of the geomembrane, and small enough to prevent any transfer through the geomembrane. Then the upstream gate was closed, and during a period varying from three to seven days, volume and temperature variations were recorded (see Figure 5). If any liquid leakage occurs, from the inside of the cell to the outside, it could be detected during this calibration.

In the absence of liquid leakage, volume variations can be linked to temperature variations by (13).

Upstream calibration was done after the downstream calibration. Pressures to be reached by the upstream and downstream PT were respectively 200 and 190 kPa. Once those pressures have been reached, the downstream gate was closed. This calibration allows to obtain correlation coefficients between temperature and upstream volume variations.

It is assumed that the relation between temperature variations and volume variations during the measurement phase will be the same as during the calibration phases.

The measurement was made after the calibration phases. The downstream PT pressure was sent to 100 kPa and the upstream PT pressure was maintained at 200 kPa. (see Figure 5).

Uncertainty on the flux value  $Q$  measured depends on uncertainties on volume variations  $d\Delta V$ , temperature variations  $d\Delta T_i$ , geomembrane surface  $dA$ , and on time measurements,  $dt$  :

$$\frac{dQ}{Q} = \frac{dA}{A} + \frac{dt}{t} + \frac{d(\Delta V^P)}{\Delta V^P} \quad (14)$$

with

$$d(\Delta V^P) = d(\Delta V) + d\sum_j (\alpha_j d\Delta T_j) \quad (15)$$



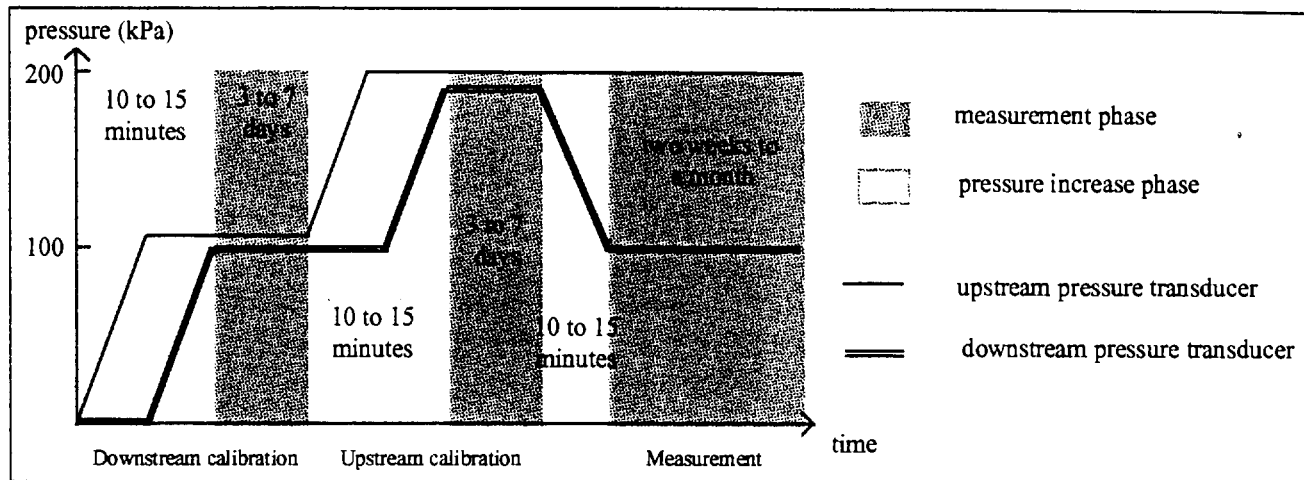


Figure 5. Variation of pressure of the two pressure transducers during the different phases of a measurement

### 3.2.4 Results

Table 4 summarizes results obtained in three different laboratories on the same PVC-P geomembrane. All the tests have been conducted in similar cells. The devices used for measurements were different. Eloy-Giorni, (1993) used a radioactive tracers method, and Pelte (1993) used graduated tubes.

All fluxes were the same order of magnitude. The flux given by Eloy-Giorni (1993) is bigger than the other ones as it is the total flux. The flux we obtained (Touze, 1995) is given by an interval, taking in account the uncertainties of the measurement.

Results obtained for the other two materials were presented in Table 5. One can notice that the permeation flux for the EDPM geomembrane was the same order of

magnitude as the one obtained for the PVC-P geomembrane. The flux obtained with the bituminous film was three orders of magnitude bigger, under a pressure gradient 10 times smaller. So the apparatus designed allows to make the difference between products that can be used for bottom landfill liners with little risks, and others. As previously mentioned, the method of measurement is now a standard in France and products exhibiting a water flow less than  $10^{-4} \text{ m}^3 \cdot \text{m}^{-2} \cdot \text{day}^{-1}$  under a pressure gradient of 100 kPa are considered as safe. It is ten times less than the flow of water through a 1 m liner of clay with a hydraulic conductivity of  $10^{-9} \text{ ms}^{-1}$  under the same conditions. One can observe that even if there is a great uncertainty on the measurement for low values of flow, one can ensure that PVC and EDPM geomembranes tested are safe, following the given criterion.

Table 4. Comparison of literature values of water fluxes in a PVC-P geomembrane

Pressure gradient (kPa)	Total flux ( $\text{m}^3 \cdot \text{m}^{-2} \cdot \text{day}^{-1}$ ) (Eloy-Giorni, 1993)	Volumetric flux ( $\text{m}^3 \cdot \text{m}^{-2} \cdot \text{day}^{-1}$ ) (Pelte, 1993)	Volumetric flux ( $\text{m}^3 \cdot \text{m}^{-2} \cdot \text{day}^{-1}$ ) (Touze, 1995)
100	$1.7 \cdot 10^{-6}$	$3 \cdot 10^{-7}$	$J < 9,3 \cdot 10^{-7}$

Table 5. Permeation fluxes obtained on different materials tested

Material	EDPM geomembrane	Bituminous film
Pressure gradient (kPa)	100	10
Volumetric flux ( $\text{m}^3 \cdot \text{m}^{-2} \cdot \text{day}^{-1}$ )	$< 5.9 \cdot 10^{-7}$	$4 \cdot 10^{-3}$

## 4 CONCLUSIONS

As far as transport of water and organic solvents in geomembranes is concerned, the elementary mechanisms involved in chemical permeation are molecular sorption and diffusion, whereas mechanisms involved in hydraulic permeation are still unidentified.

- Chemical permeation flux values for non polar solvents represent the upper bound for all diffusive flux. It has to be considered that these values are calculated as

an initial flux for the maximum concentration gradient possible (pure solvent on one face, void on the other face). Further research is necessary to verify if swelling can be neglected when calculating mass flux and if the diffusion coefficient decrease along time could be caused by crystallinity ratio increase.

- Arrhenius law cannot be used with confidence to estimate the evolution of the diffusion coefficient of water in the geomembranes tested. Another limitation is

that the validity of Arrhenius law is based on the assumption that the maximum absorption coefficient (at equilibrium) was the same whatever the temperature was. This does not seem to be valid.

- The permeation apparatus described here permits to compare different geomembranes behaviour towards water permeation under a hydraulic gradient. The method of measurement is now a standard and permits to make sure that geomembranes used in bottom liners are safe from an hydraulic point of view, if undamaged. It could present an interest in the study of soluble ions transport through geomembrane. It is thought, but still not verified, that the macroscopically measured hydraulic permeation rates in undamaged geomembranes do not represent porous-medium-like transport phenomena but should rather be related to microscopic mechanisms similar to sorption and diffusion. The apparatus presented could help in improving the knowledge of the phenomena involved by testing different pressure gradients.

## REFERENCES

- August, Hans and Tatsky, Renate (1984). Permeabilities of commercially available polymeric liners for hazardous landfill leachate organic constituents. *Proceedings of the International Conference on Geomembrane*, Denver (USA), IFAI, Vol.1, pp 163-168.
- Britton, L.N., Ashman, R.B., Aminabhavi, T.M. and Cassidy, P.E. (1989). Permeation and diffusion of environmental pollutants through flexible polymers. *J. Of Applied Polym. Sci.* Vol. 38, pp. 227-236.
- Crank, J. (1975). *The mathematics of diffusion*. Oxford Science Publications, UK, 414p.
- Duquennoi, C., (1995). Laboratory ageing of geomembranes in landfill leachates. *Fifth International Landfill Symposium*, Sardinia, Italy, pp 397-404.
- Durin, L., Duquennoi, C. (1997). The stability of HDPE and PP-based geomembranes in contact with organic solvents. *Sixth International Landfill symposium*, Sardinia, Italy, Vol.3, pp 217-228.
- Eloy-Giorni, C. (1993). Etude des transferts diffusifs dans les géomembranes : mécanismes et mesures à l'aide de traceurs radioactifs. Thèse de l'Université J. Fourier, Grenoble I-CEA, 174 p.(in French).
- Haxo, H.E. (1990). Determining the transport through geomembranes of various permeants in different applications. *Geosynthetic testing for waste containment applications*, ASTM special publication 1081, pp. 75-94.
- Koerner, R.M. (1986). *Designing with Geosynthetics*. Prentice Hall, 424 p.
- Neogi, P. (1996). Transport phenomena in polymer membranes. *Diffusion in Polymers (series 32: plastic engineering)*. pp 173-209.
- Nguyen, Q.T., Favre, E., Ping, Z.H. and Néel, J. (1996). Clustering of solvents in membranes and its influence on membrane transport properties. *J. Of Membrane Sci.* Vol. 113, pp. 137-150.
- Park, G.S. (1986). Transport principles-solution, diffusion and permeation in polymer membranes. *Synthetic membranes Sci.: Science, Engineering and applications*, Vol. 181, pp. 57-107.
- Park, J.K., Sakti, J.P. and Hoopes, J.A. (1996). Transport of organic compounds in thermoplastic geomembranes. I: Mathematical model. *J. Of Environ. Engin.* Vol. 122, pp. 800-813.
- Pelte, T., (1993). Etude théorique et expérimentale de la fonction étanchéité et du comportement thermique des géomembranes. Thèse Dr, Univ. J. Fourier, Grenoble 1, 253 p.(in French)
- Stessel, R.I., Hodge, J.S. (1995). Chemical resistance testing of geomembrane liners. *J. of Hazardous Materials*, Vol.42, pp. 265-287.
- Touze, N. (1995). Transferts d'eau dans les étanchéités synthétiques, minérales et composites. Mémoire fin étud. ENGEES, 133 p.(in French).

# LEAKAGE STUDY ACROSS AN OFFSHORE WASTE CONTAINMENT BUND

S.A. Tan

Senior Lecturer, Department of Civil Engineering, National University of Singapore

S.H. Chew

Lecturer, Department of Civil Engineering, National University of Singapore

G.P. Karunaratne

former Associate Professor, Department of Civil Engineering, National University of Singapore

**ABSTRACT:** This paper presents a study of potential leakage through an offshore waste containment bund from a FEM simulation of the steady state flow condition under the influence of the head difference between the waste pond and the open sea. It is assumed that under operating conditions, the waste pond may be kept at levels as high as 2m above mean sea level. For the study, the following liner systems are considered: (a) Dredge clay 2m thick ( $k=1 \times 10^{-8}$  m/s), (b) Geosynthetic clay liner 6 mm thick ( $k=1 \times 10^{-11}$  m/s), (c) Geomembrane liner 1 mm thick ( $k=1 \times 10^{-14}$  m/s) (d) Composite of Geosynthetic clay + 2m dredge clay (e) Composite of Geomembrane + 2m dredge clay. The results of the parametric study of the influence of bund hydraulic conductivity and the hydraulic head difference for the five alternatives are presented in the paper. Due to its very low comparative leakage potential, the system of geomembrane and 2m dredge clay layer cover on top of the geomembrane is used for the actual offshore waste containment bund design which is currently being constructed.

**KEYWORDS:** Containment, reservoir liners, modeling, performance evaluation

## 1 INTRODUCTION

Due to the scarcity of land for landfills, the Ministry of Environment of Singapore has embarked on the design and construction of an offshore waste disposal facility to cater for the end disposal of the incinerated residues of municipal and industrial wastes generated locally over the next 30 years. The facility involved the creation of a 30 ha offshore waste pond, by the bounding of the perimeter with 7 km of earth bunds in water depths varying from 10m at the shallow end to 20m at the deepest end from the offshore island of Pulau Semakau south of Singapore. For practical construction, the offshore bund will be created with stone revetments for shore protection, using geofabrics for separation and filtration between armour stones and hydraulic sand filling in the main body of the bund. However on the waste pond side of the bund, several geosynthetic liners were considered as possible protection layers to prevent leachate in the waste pond from contaminating the marine environment around the waste facility.

The southern coast of Singapore is in a low energy marine coastal environment due to the protection provided by the surrounding land masses. The fetch is generally short, and the directions of the maximum fetch rarely coincide with those of the strongest wind of about 8 m/s during the NE monsoon between December to March annually. Thus the average wave breaker height is less than 20 cm, and maximum wave height is less than 1 m, according to Chia et al, (1988). As there is no requirement for berthing facilities, the outer slope of the perimeter bund was designed using a conventional stone revetment structure of slope 1:3 with a 8 m berm for every 5 m rise in elevation from seabed levels, as shown in Fig. 1.

Detailed offshore site investigation was conducted at the proposed site for the offshore waste facility, and it was determined that the seabed soils consist mainly of 5m to 10m silty/clayey deposits on top of dense weathered sedimentary rocks of very low permeabilities, typical of the Jurong formation in the area. The silty/clayey deposits are from soft to firm consistency with very low permeabilities of less than  $10^{-10}$  m/s. Thus it is estimated that leakage through the seabed soils is a non-problem, as the offshore environment itself is a form of hydraulic barrier, with very low seepage gradient across the seabed soils underneath the waste facility, as shown by Lee et al, (1994).

## 2 LEAKAGE RATE EVALUATION

Giroud et al., (1994) have presented equations to evaluate the rate of leakage of liquids such as leachates through liners typically used in landfills including compacted clay liners (CCL), and several types of geosynthetic liners, geosynthetic clays liners (panels that consist of a layer of bentonite encapsulated between two geotextiles) and a composite where geomembrane is placed on low-permeability compacted clay or geosynthetic clay layer. The comparisons in Giroud's studies are only applicable to landfills where the head of leachate on top of the liner is small, i.e., typically less than 0.3m under one dimensional seepage condition. The relative effectiveness, and even ranking of the various liners compared in their study may be very different under the large liquid heads encountered in liquid impoundments (reservoirs), canals and dams.

For the two dimensional seepage analysis of an offshore containment bund, the finite element seepage program was

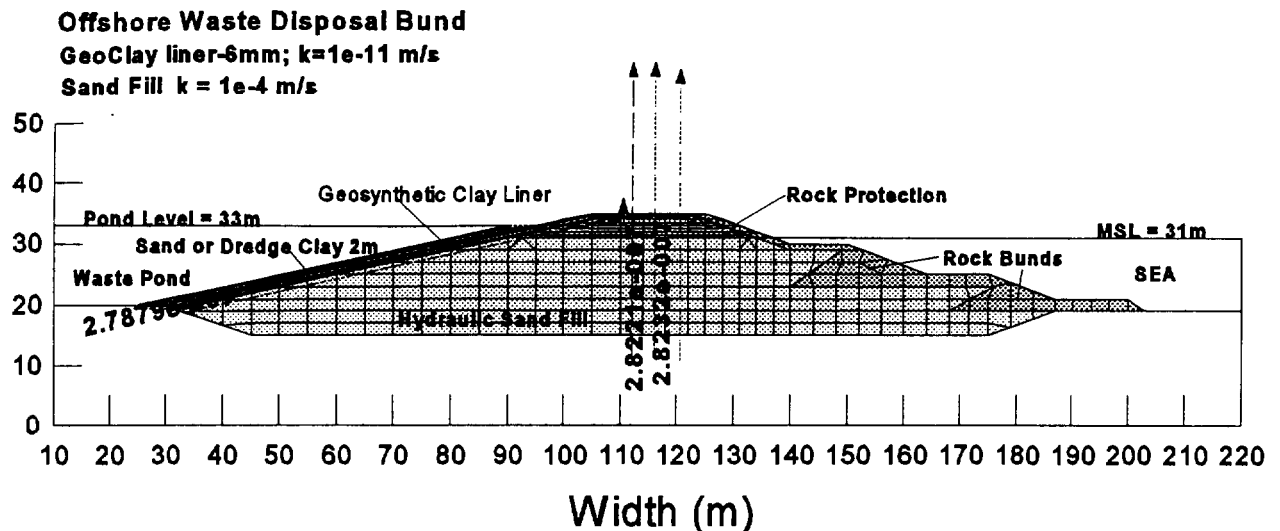


Fig.1 Typical Cross-Section of Offshore Containment Bund

used for the study. The software employed is SEEP/W by Geoslope, (1994), which is capable of modelling a 2D plane seepage analysis with saturated and unsaturated flows for both steady state and transient conditions. A typical cross-section of the offshore waste containment bund used is shown in Fig. 1. It consists of a rock bund revetment structure on the outer slopes of gradient 1:3, for shore protection purposes. The inner slopes are flatter with gradient of 1:5, and these slopes will be lined with approved liners. The liners under considerations are (i) 2m clay liner of dredged seabed clays placed directly on top of the hydraulic sand fill, (ii) geosynthetic clay liner covered by 2 m sand layer, (iii) geosynthetic clay liner covered by 2 m of dredged clays, (iv) geomembrane liner covered by 2 m sand layer, (v) geomembrane liner covered by 2 m of dredged clays. The analysis assumes that the dredged clay is 2 m thick with  $k=1 \times 10^{-8}$  m/s, as it cannot be compacted under water, the geosynthetic clay is 6 mm thick with  $k=1 \times 10^{-11}$  m/s, and the geomembrane is 1 mm thick with  $k=1 \times 10^{-14}$  m/s. All liner materials are assumed to be homogeneous and perfect, i.e no holes or cracks, zones of high permeability, or poor connection of panels and seams. The finite element mesh consists of 475, 8-noded quadrilateral isoparametric elements, with very thin elements to model the geosynthetic clay and geomembrane liners.

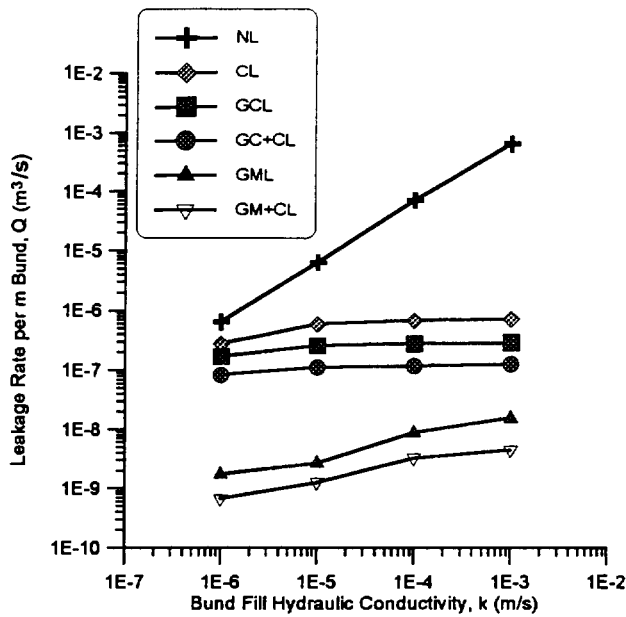
The hydraulic sand fill commonly used in Singapore reclamation projects are in the range of fine to coarse sands with very low silt contents. For bund construction, the silt contents are specified to be less than 5%, and for reclamation fill, the silt content must be less than 10%. Thus the range of possible sand permeabilities would be from as low as  $k=1 \times 10^{-6}$  m/s for fine sand with 10% fines, to as high as  $k=1 \times 10^{-3}$  m/s for coarse sand with less than 5% fines. The likely operative permeabilities for this project would be between  $k=1 \times 10^{-3}$  m/s to  $k=1 \times 10^{-4}$  m/s, with the latter as the most typical sand permeability to be encountered in the actual site.

The intended operating condition for the waste facility is to keep the pond levels at about mean sea level, which means theoretically, that there would be no net seepage from the waste pond to the sea, as there is no net head difference across the bund. For this comparative study, we assume steady-state condition, without consideration of the cyclical transient nature of the sea level due to the tides. With the sea kept at mean sea level, the seepage loss for the long term steady state condition of 2.0m, 1.5m, 1.0m, and 0.5m hydraulic head difference across the bund was considered in the study. The influence of tide on seepage loss across the bund using transient seepage analysis was reported by Tan et al, (1993).

### 3 COMPARISON OF LINERS

#### 3.1 Typical SEEP/W Results

Typical finite element steady state calculations involve iterations on the hydraulic conductivity functions which falls sharply as the sand desaturates into the negative pore water pressure zone of the unsaturated sand above the phreatic surface in the bund. For an all sand bund, convergence is rapid. For the sand bund with clay liner convergence may become difficult because of the sharp contrast in the hydraulic conductivities of the clay blanket and that of the sand bund. For all the finite element computations, a convergence tolerance of 0.001% difference on the norm of the nodal head vector between two successive iterations is applied. After convergence, the flux quantities across the bund is computed for four sections of the bund, one parallel to the inner slope and the remaining three vertical sections through the crest of the bund. All these flux values must be nearly the same when steady state seepage has been attained, as shown in a typical computation in Fig.1, where the leakage across a bund lined with a 6 mm thick Geosynthetic clay layer is calculated to be about  $2.8 \times 10^{-7}$  m<sup>3</sup>/s per m run of

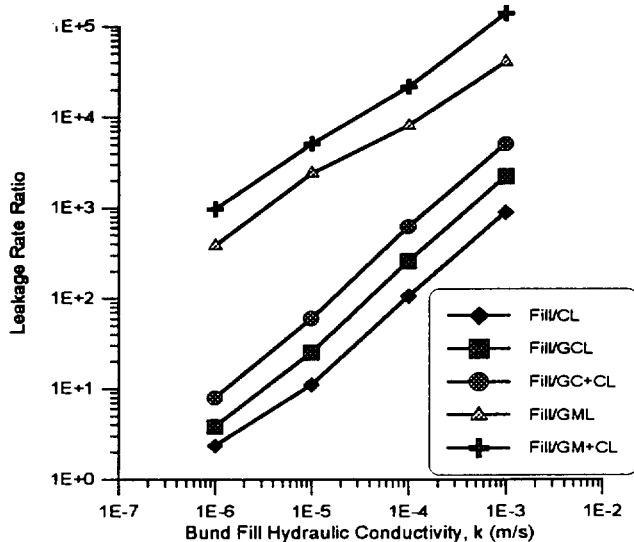


bund.

Figure 2. Leakage rate as function of bund permeability

### 3.2 Leakage Rate Comparisons

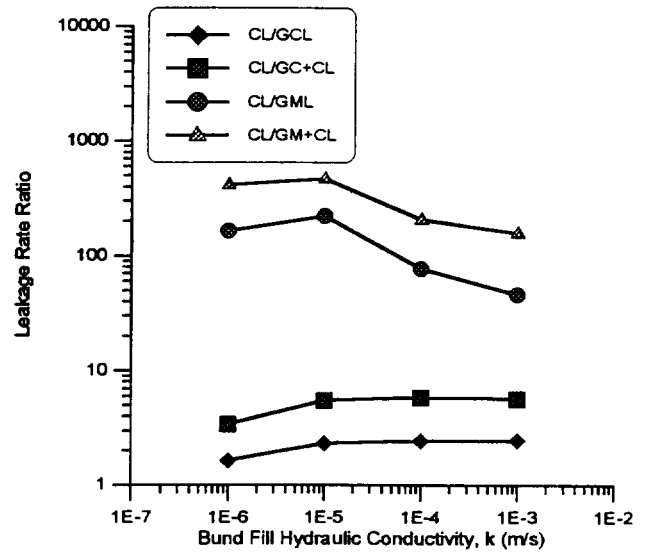
The leakage rate values per m run of bund for varying bund fill permeability is shown in Fig.2. The results showed that with the use of liners, the leakage rate can be reduced significantly, especially for bund fill with the higher permeability. For the sand bund without liner (NL), the leakage rate is a linear function of bund permeability as expected from Darcy's law,  $Q=kiA$ . However when the inside slope of the bund is lined with either a clay or geosynthetic liner, this linear behavior appear not to apply. The leakage rate performance



becomes less dependent on the bund permeability for the liner cases.

Figure 3. Leakage ratio as function of bund permeability

When the leakage rate for liners is compared to the case without liners (NL), the leakage rate ratio is some kind of linear function of bund permeability. It is obvious that the leakage reduction is greater for the higher bund permeability. At a bund permeability of  $10^{-4}$  m/s, a geomembrane liner would produce 10,000 times less leakage, whereas a geosynthetic clay or 2m clay liner would result in about a 100-200 times less leakage



than an unlined bund.

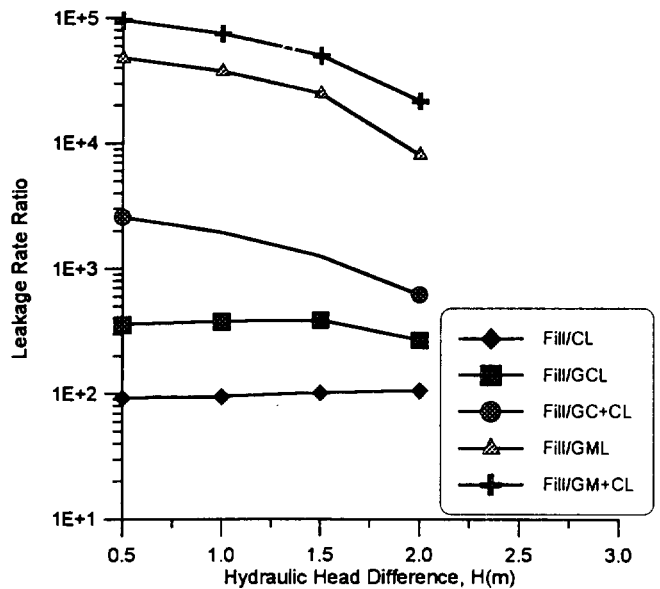
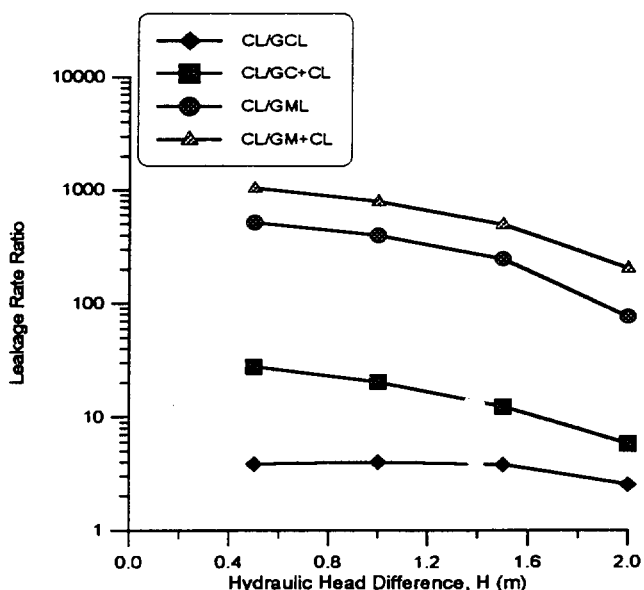


Figure 4. Comparison of Clay liner with other liners for different bund permeability

Figure 5. Leakage rate ratio as function of bund head difference

From Fig.4, it appears that a geosynthetic clay liner or geosynthetic clay with a 2m clay blanket is only about 1 to 7 times better than a 2m clay liner. A geomembrane liner would produce about 50-200 times less leakage than a clay liner, whereas a composite geomembrane with a 2m clay blanket is about 200-500 times more effective than a 2m clay liner. Thus a geosynthetic clay liner is comparable to a thick clay liner, whereas a non defective geomembrane liner is much better than a clay liner.

The leakage performance of an unlined compared to a lined bund for a bund permeability of  $10^{-4}$  m/s, and a bund head difference of 0.5 m to 2.0 m is compared in Fig.5. It appears that a 2m clay liner is 200 times more effective than the unlined bund for head difference from 0.5-2.0m. The geosynthetic clay liner is 300-400 times better than the unlined bund, whereas geosynthetic clay with the 2m clay liner is 600-2500 times better, with decreasing effectiveness at higher head difference. The geomembrane liner is 8000-50000 times more effective,



whereas the geomembrane with the 2m clay liner is 20000-100000 times more effective than an unlined bund, with decreasing effectiveness at higher head difference.

Figure 6. Comparison of Clay liner with other liners for various bund head difference

In comparing clay liner with the geosynthetic liner as in Fig.6, it is apparent that geosynthetic clay has comparable leakage rate to a 2m clay liner. A geosynthetic clay layer with a clay liner would be about 5-30 times better than the clay liner. A geomembrane liner is 80-500 times better, while a geomembrane with a 2m clay liner is about 200-1000 times better than a 2m clay liner, with the lower ratio at a higher head

difference.

#### 4 CONCLUSIONS

The paper has presented a comparative evaluation of different liners for an offshore waste containment bund for the assumed operating conditions of bund permeabilities from  $k=1 \times 10^{-6}$  m/s to  $k=1 \times 10^{-3}$  m/s, for bund head difference from 0.5m-2.0m. The study showed that geosynthetic liners are better than clay liners for the reduction of seepage across the bund. It appears that a 6mm geosynthetic clay liner would perform slightly better than a 2m dredged clay liner, whereas a 1mm geomembrane is far superior to a 2m dredged clay liner. The relative performance of geosynthetic liners to clay liners increases with higher bund permeabilities and lower bund head difference. The use of a geomembrane liner with a 2m dredged clay liner would produce a bund with extremely low leakage rate, and the composite liner system would provide a multiple barrier defence that would enhance the system performance taking into account that the thin geomembrane layer cannot be laid in a defect free condition, especially in an offshore underwater condition.

The geomembrane chosen for this particular project is a high performance geocomposite geomembrane consisting of a high strength polyester base fabric, coated with a highly resistant ethylene interpolymer alloy. This geomembrane is about 1 mm (40 mils) thick and has a unit weight of 1290 g/m<sup>2</sup>, making it self sinking in the offshore laying environment.

#### REFERENCES

- Chia, L.S., Khan, H., and Chou, L.M. (1988) "The Coastal Environmental Profile of Singapore", *ASEAN/US Coastal Resources Management Project*, Technical Publication 3.
- Giroud, J.P., Badu-Tweneboah, K., and Soderman, K.L. (1994) "Evaluation of Landfill Liners", *Fifth International Conference on Geotextiles and Geomembranes and Related Products*, Singapore, pp.981-986.
- Lee, S.L., Tan, S.A., Ng, K.Y., Yong, K.Y., and Karunaratne, G.P. (1994) "Seepage Study for Design of an Offshore Waste Containment Bund", *Developments in Geotechnical Engineering*, edited by Balasubramaniam et al, Bangkok, Thailand, pp.279-290.
- SEEP/W Manual, Version 3, (1994), Geoslope International, Calgary, Canada.
- Tan, S.A., Yong, K.Y., Ng, K.Y., and Lee, S., (1993). "Effect of Tidal Variation on Seepage Flow through an Offshore Waste Containment Bund", *Environmetet Geotechnique, De la decontamination a la protection du sous-sol, Ponts et Chaussées, Paris*, pp.277-284.

# New Developments in Landfill Liner Leakage Evaluation

J.P. Giroud

Senior Principal, GeoSyntec Consultants, 621 N.W. 53rd Street, Suite 650, Boca Raton, Florida, USA

K.L. Soderman

Project Engineer, GeoSyntec Consultants, 621 N.W. 53rd Street, Suite 650, Boca Raton, Florida, USA

M.V. Khire

Assistant Project Engineer, GeoSyntec Consultants, 621 N.W. 53rd Street, Suite 650, Boca Raton, Florida, USA

K. Badu-Tweneboah

Senior Project Engineer, GeoSyntec Consultants, 621 N.W. 53rd Street, Suite 650, Boca Raton, Florida, USA

**ABSTRACT:** This paper presents: (i) a new equation for calculating the rate of leakage through a composite liner due to geomembrane defects; (ii) a new equation that gives the rate of leakage through defects in a geomembrane placed on a semi-permeable medium; (iii) a new equation that gives the rate of leakage through a defect in a geomembrane liner taking into account the fact that the leachate collection material overlying the geomembrane hinders the flow of leachate toward the defect; and (iv) new equations for the design of leakage collection layers. Then, the paper presents a methodology based on these equations to select the optimal configuration of a double liner system.

**KEYWORDS:** Landfills, Liners, Geomembranes, Leachate, Leakage.

## 1 INTRODUCTION

The purpose of this paper is to provide information on new equations for the evaluation of the rate of leakage due to advective flow through defects in geomembranes included in liner systems and for the design of leakage collection layers. These equations were recently developed and published; references are made to the original publications for more details.

## 2 RATE OF LEAKAGE THROUGH COMPOSITE LINERS DUE TO GEOMEMBRANE DEFECTS

### 2.1 Presentation of the New Equation

In the context of this paper: (i) a composite liner consists of a synthetic component (a geomembrane) and a mineral component (a low-permeability soil or a GCL); and (ii) the mineral component is located beneath the geomembrane and is designated herein as "the low-permeability medium underlying the geomembrane". Semi-empirical equations are available to calculate the rate of leakage through a composite liner, due to geomembrane defects, when the leachate head on top of the liner is small compared to the thickness of the low-permeability medium underlying the geomembrane, whether the defect is small (Giroud et al. 1989) or large (Giroud et al. 1992). Equations are also available for the case where the leachate head on top of the liner is large compared to the thickness of the low-permeability medium underlying the geomembrane (Giroud et al. 1992, 1994); however, in such a case, graphs

are necessary to obtain the value of one of the terms of the equations, which is cumbersome. Giroud (1997) has shown that this term can be expressed analytically, which leads to entirely analytical expressions for the equations that give the rate of leakage through a composite liner, whether the leachate head on top of the liner is smaller or greater than the thickness of the low-permeability medium underlying the geomembrane. The equation in the case of a circular or quasi-circular defect is (Giroud 1997):

$$Q = C_{qo} \left[ 1 + 0.1(h/t_{UM})^{0.95} \right] a^{0.1} h^{0.9} k_{UM}^{0.74} \quad (1)$$

hence, for a circular defect:

$$Q = 0.976 C_{qo} \left[ 1 + 0.1(h/t_{UM})^{0.95} \right] d^{0.2} h^{0.9} k_{UM}^{0.74} \quad (2)$$

where:  $Q$  = leakage rate;  $a$  = defect area;  $d$  = defect diameter;  $h$  = leachate head on top of the liner;  $t_{UM}$  = thickness of the low-permeability medium underlying the geomembrane;  $k_{UM}$  = hydraulic conductivity of the low-permeability medium underlying the geomembrane; and  $C_{qo}$  = dimensionless coefficient that characterizes the quality of contact between the geomembrane and the underlying medium.

Equations 1 and 2 must be used with the following units:  $Q$  ( $m^3/s$ ),  $a$  ( $m^2$ ),  $d$  (m),  $h$  (m),  $t_{UM}$  (m), and  $k_{UM}$  (m/s). It should be noted that, when the leachate head on top of the liner is smaller than the thickness of the low-permeability medium underlying the geomembrane, the term in brackets in Equations 1 and 2 is approximately equal to 1. This term

is greater than 1 when the leachate head on top of the liner is greater than the thickness of the low-permeability medium underlying the geomembrane, which is often the case when this medium is a GCL.

Two typical values of  $C_{qo}$  are considered:  $C_{qogood}$ , the value of  $C_{qo}$  in the case of good contact; and  $C_{qopoor}$ , the value of  $C_{qo}$  in the case of poor contact. Definitions of good and poor contact are given by Giroud (1997). The following values were established by Giroud et al. (1989):

$$C_{qogood} = 0.21 \quad (3)$$

$$C_{qopoor} = 1.15 \quad (4)$$

Equations 1 and 2, and similar equations for rectangular defects and infinitely long defects given by Giroud (1997), supersede equations previously published by Giroud et al. (1992, 1994).

## 2.2 Limits of Validity of the Equations

The limits of validity of Equations 1 and 2 result from considerations such as: the experimental data supporting Equation 1, the restrictions to flow imposed by surface tension, and the range of applicability of Bernoulli's equation for free flow through an orifice. These limits can be summarized as follows (Giroud et al. 1997c):

- If the defect is circular, the defect diameter should be no less than 0.5 mm and not greater than 25 mm.
- The liquid head on top of the geomembrane should be equal to or less than 3 m.
- The hydraulic conductivity of the low-permeability medium underlying the geomembrane,  $k_{UM}$ , should be equal to or less than a certain value  $k_G$ . Giroud et al. (1997c) propose the following value for  $k_G$  in the case where the geomembrane defect is circular:

$$k_G = \left\{ 0.3891 d^{1.8} / \left[ C_{qo} \left( 1 + 0.1 (h/t_{UM})^{0.95} \right) h^{0.4} \right] \right\}^{1/0.74} \quad (5)$$

Values of  $k_G$  calculated using Equation 5 are given in Table 1.

Table 1. Maximum value,  $k_G$  (m/s), of the hydraulic conductivity of the medium underlying the geomembrane for Equations 1 and 2 to be valid in the case where  $C_{qo} = 0.21$  (good contact) and  $t_{UM} = 0.6$  m (from Giroud et al. 1997c).

Leachate head on top of the geomembrane, h (m)	Geomembrane defect diameter, d (mm)						
	0.5	1	2	3	5	10	11.284
0.01	$2.6 \times 10^{-7}$	$1.4 \times 10^{-6}$	$7.5 \times 10^{-6}$	$2.0 \times 10^{-5}$	$7.0 \times 10^{-5}$	$3.8 \times 10^{-4}$	$5.1 \times 10^{-4}$
0.03	$1.4 \times 10^{-7}$	$7.7 \times 10^{-7}$	$4.1 \times 10^{-6}$	$1.1 \times 10^{-5}$	$3.8 \times 10^{-5}$	$2.1 \times 10^{-4}$	$2.8 \times 10^{-4}$
0.1	$7.3 \times 10^{-8}$	$3.9 \times 10^{-7}$	$2.1 \times 10^{-6}$	$5.7 \times 10^{-6}$	$2.0 \times 10^{-5}$	$1.1 \times 10^{-4}$	$1.4 \times 10^{-4}$
0.3	$3.8 \times 10^{-8}$	$2.1 \times 10^{-7}$	$1.1 \times 10^{-6}$	$3.0 \times 10^{-6}$	$1.0 \times 10^{-5}$	$5.6 \times 10^{-5}$	$7.5 \times 10^{-5}$
1	$1.8 \times 10^{-8}$	$9.5 \times 10^{-8}$	$5.1 \times 10^{-7}$	$1.4 \times 10^{-6}$	$4.7 \times 10^{-6}$	$2.6 \times 10^{-5}$	$3.4 \times 10^{-5}$
3	$7.1 \times 10^{-9}$	$3.8 \times 10^{-8}$	$2.1 \times 10^{-7}$	$5.6 \times 10^{-7}$	$1.9 \times 10^{-6}$	$1.0 \times 10^{-5}$	$1.4 \times 10^{-5}$

## 3 RATE OF LEAKAGE THROUGH DEFECTS IN A GEOMEMBRANE ON A SEMI-PERMEABLE MEDIUM

### 3.1 Presentation of the New Equation

When a geomembrane is overlain and underlain by infinitely permeable media, the rate of leakage through a geomembrane defect is given by the classical Bernoulli's equation for free flow through an orifice:

$$Q = 0.6a \sqrt{2gh} = 0.15\pi d^2 \sqrt{2gh} = Q_B \quad (6)$$

As shown by Giroud et al. (1997c), Bernoulli's equation is valid if the hydraulic conductivity of the medium underlying the geomembrane is greater than:

$$k_B = 10^5 d^2 \quad \text{with } k_B \text{ (m/s) and } d \text{ (m)} \quad (7)$$

Values of  $k_B$  calculated using Equation 7 are given in Table 2. A comparison of Tables 1 and 2 reveals that  $k_G$  is always smaller than  $k_B$ . To evaluate the rate of leakage through defects in geomembranes underlain by a semi-permeable medium, i.e. when the hydraulic conductivity,  $k_{UM}$ , of the medium underlying the geomembrane is between  $k_G$  and  $k_B$ , Giroud et al. (1997c) have developed the interpolation method described below.

Interpolation between Equation 6 for flow through a defect in a geomembrane underlain by an infinitely permeable medium, and Equation 1 or 2 for flow through a defect in a geomembrane underlain by a low-permeability medium gives the following equation for the rate of leakage through defects in a geomembrane placed on a semi-permeable medium (Giroud et al. 1997c):

$$\log(Q_B/Q) = 0.74 \left[ \frac{\log(k_B/k_{UM})}{\log(k_B/k_G)} \right]^{\log(k_B/k_G)} \quad (8)$$

where  $Q_B$  is defined by Equation 6,  $k_B$  by Equation 7, and  $k_G$  by Equation 5.



Table 2. Hydraulic conductivity of the medium underlying the geomembrane below which Bernoulli's equation for free flow through an orifice is not theoretically valid,  $k_B$  (Equation 7), or not applicable for practical purposes,  $k_{UM\ min}$  (Equation 11) (from Giroud et al. 1997c).

Geomembrane defect diameter, d (mm)	0.5	1	2	3	5	10	11.284 (a = 1 cm <sup>2</sup> )
Theoretical, $k_B$ (m/s)	$2.5 \times 10^{-2}$	$1.0 \times 10^{-1}$	$4.0 \times 10^{-1}$	$9.0 \times 10^{-1}$	2.5	10	13
Practical, $k_{UM\ min}$ (m/s)	$2.5 \times 10^{-4}$	$1.0 \times 10^{-3}$	$4.0 \times 10^{-3}$	$9.0 \times 10^{-3}$	$2.5 \times 10^{-2}$	$1.0 \times 10^{-1}$	$1.3 \times 10^{-1}$

Combining Equations 5, 6, 7 and 8 gives:

$$\log Q = 0.3195 + 2 \log d + 0.5 \log h - 0.74 \left( \frac{5 + 2 \log d - \log k_{UM}}{n} \right)^n \quad (9)$$

where:

$$n = 5.5540 - 0.4324 \log d + 0.5405 \log h + 1.3514 \log C_{qo} + 1.3514 \log \left[ 1 + 0.1 \left( \frac{h}{t_{UM}} \right)^{0.95} \right] \quad (10)$$

The rate of leakage through a defect in a geomembrane underlain by a semi-permeable medium (whose hydraulic conductivity,  $k_{UM}$ , is greater than  $k_G$  and smaller than  $k_B$ ) can be calculated using Equation 9, which is equivalent to Equation 8. The genesis of the equation appears more clearly in Equation 8, whereas numerical calculations may be done more conveniently using Equation 9.

### 3.2 Example of Use of the Equation

Figure 1 shows a series of curves that represent the rate of leakage through a given geomembrane defect (diameter,  $d = 2$  mm) as a function of the hydraulic conductivity of the medium underlying the geomembrane for various leachate heads. Each curve in Figure 1 comprises three portions: the left-hand portion (straight line) represents Equation 2; the right-hand portion (plateau) represents Equation 6; and the central portion (curve) was interpolated using Equation 9. Both Equations 2 and 9 were used with  $C_{qo} = 0.21$  (Equation 3), i.e. assuming good contact between the geomembrane and the underlying medium. The limit value of the hydraulic conductivity between the left-hand portion and the central portion is  $k_G$  given by Equation 5 and Table 1; as shown in Table 1,  $k_G$  has a different value for each curve. The limit value of the hydraulic conductivity between the central portion and the right-hand portion is  $k_B$  given by Equation 7 and Table 2; as shown in Table 2,  $k_B$  has the same value for all curves related to the same value of  $d$ ; for example, for  $d = 2$  mm,  $k_B = 0.4$  m/s. Similar graphs for other values of  $d$  are given by Giroud et al. (1997c).

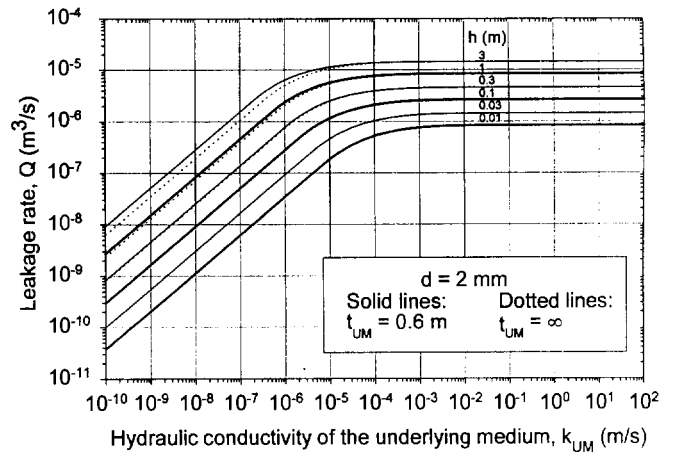


Figure 1. Rate of leakage through a 2 mm diameter defect in a geomembrane underlain by a medium, with a hydraulic conductivity  $k_{UM}$  and a thickness  $t_{UM}$ , overlain by a medium that is significantly more permeable than the underlying medium, for various values of the leachate head on top of the geomembrane,  $h$  (from Giroud et al. 1997c).

### 3.3 Limit of Applicability of Bernoulli's Equation

As indicated by Giroud et al. (1997c), Bernoulli's equation (Equation 6) provides a value of the leakage rate that is close to the value obtained using the interpolation method presented in Section 3.1, for values of the hydraulic conductivity of the medium underlying the geomembrane that are greater than  $k_{UM\ min}$  defined as  $k_B/100$ . Therefore, the practical limit of applicability of Bernoulli's equation is 100 times smaller than the theoretical limit of validity,  $k_B$ , hence, from Equation 7:

$$k_{UM\ min} = 10^3 d^2 \quad \text{with } k_{UM\ min} \text{ (m/s) and } d \text{ (m)} \quad (11)$$

Values of  $k_{UM\ min}$  calculated using Equation 11 are given in Table 2.

It is important to note that, for Bernoulli's equation to be applicable, the geomembrane must be not only underlain by a sufficiently permeable medium, but also overlain by a highly permeable medium. The required minimum hydraulic conductivity of the medium overlying the geomembrane is discussed in Section 4.

#### 4 RATE OF LEAKAGE THROUGH DEFECTS IN A GEOMEMBRANE OVERLAIN BY A PERMEABLE MEDIUM AND UNDERLAIN BY A HIGHLY PERMEABLE MEDIUM

##### 4.1 Presentation of the New Equation

As indicated in Section 3.1, when a geomembrane is overlain and underlain by infinitely permeable media, the rate of leakage through a geomembrane defect is given by the classical Bernoulli's equation for free flow through an orifice (Equation 6). Engineers designing landfills use Bernoulli's equation routinely without questioning its applicability. However, sometimes, absurd results are obtained, such as a calculated rate of leakage through a defect in a geomembrane liner greater than the total rate of liquid supply above the geomembrane.

The absurd results of the type indicated above are caused by an overestimation of the rate of leakage by Bernoulli's equation because this equation is based on the assumption that the hydraulic conductivity of the medium overlying the geomembrane is infinite. In reality, this hydraulic conductivity is not infinite; therefore, the flow of leachate toward the geomembrane defect is hindered and, as a result, the rate of leakage is less than in the ideal case of a geomembrane overlain by an infinitely permeable medium. Taking into account the fact that leachate does not flow freely toward the geomembrane defect, Giroud et al. (1997b) developed the following equation:

$$h = \left\{ \frac{a q_i}{2 k_{OM} \pi} + \frac{Q}{2 k_{OM} \pi} \left[ \ln \left( \frac{Q}{a q_i} \right) - 1 \right] + \frac{1}{4 g^2} \left( \frac{Q}{0.6 a} \right)^4 \right\}^{1/2} \quad (12)$$

where:  $q_i$  = rate of leachate supply on top of the medium overlying the geomembrane; and  $k_{OM}$  = hydraulic conductivity of the medium overlying the geomembrane.

It should be noted that, if  $k_{OM}$  is infinite, Equation 12 becomes identical to Equation 6, i.e. Bernoulli's equation for free flow through an orifice.

Equation 12 cannot be solved for  $Q$ . Therefore, iterations are necessary to determine  $Q$  when  $h$ ,  $a$ ,  $k_{OM}$  and  $q_i$  are known. Alternatively, graphical solutions can be used. An example is shown in Figure 2, and a series of similar graphical solutions is provided by Giroud et al. (1997b). Figure 2 shows that, in general, Bernoulli's equation overestimates the leakage rate. However, Figure 2 also shows that, for certain values of the leachate head on top of the geomembrane and the hydraulic conductivity of the medium overlying the geomembrane, Bernoulli's equation provides an excellent approximation of the leakage rate. This is further discussed in Section 4.2.

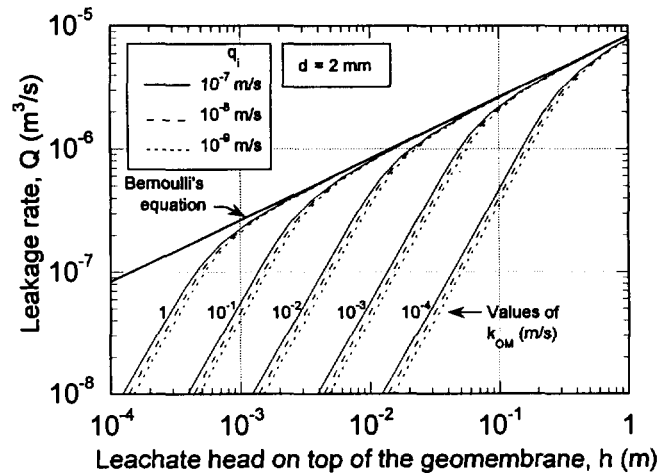


Figure 2. Graphical solution of Equation 12 for a geomembrane defect having a diameter of 2 mm.

##### 4.2 Limit of Applicability of Bernoulli's Equation

Comparing Equations 6 and 12, Giroud et al. (1997b) have shown that Bernoulli's equation gives the rate of leakage through a geomembrane defect with an error less than 5% if the hydraulic conductivity of the medium overlying the geomembrane,  $k_{OM}$ , is greater than:

$$k_{OM \text{ min } 5\%} = \frac{30 d^2}{h^{3/2}} \quad (13)$$

where the following units should be used:  $d$  (m),  $h$  (m) and  $k_{OM \text{ min}}$  (m/s).

It is interesting to note the consistency between two limits of applicability of Bernoulli's equation: the minimum value of the hydraulic conductivity of the medium *overlying* the geomembrane (given by Equation 13) and the minimum value of the hydraulic conductivity of the medium *underlying* the geomembrane (given by Equation 11). Equations 11 and 13 are consistent for  $h = 0.1$  m, which is remarkable because these two equations were established independently and are related to two different media.

##### 4.3 Relationship Between Liquid Supply and Leakage

For a given permeable medium (such as a leachate collection layer) overlying a geomembrane, the leachate head,  $h$ , and the leachate supply rate,  $q_i$ , are not independent. The leachate head depends on the leachate supply rate and varies as a function of the distance to the toe of the leachate collection layer slope. As shown by Giroud and Houlihan (1995), in a large number of cases, an excellent approximation of the average leachate head is given by the following equation:

$$h = \frac{q_i L}{2 k_{OM} \tan \beta} \quad (14)$$

where:  $\beta$  = slope angle of the permeable medium; and  $L$  = horizontal projection of the length of the permeable medium in the direction of the flow.

It is then possible to establish a direct relationship between the rate of leachate supply to the permeable medium,  $q_i$ , and the rate of leakage through the liner defect,  $Q$ . To that end, the leachate head,  $h$ , is eliminated by combining Equations 12 and 14, hence:

$$1 = (2/\pi) A [1 + C(\ln C - 1)] + B^2 (C/0.6)^4 \quad (15)$$

where  $A$ ,  $B$ , and  $C$  are dimensionless parameters defined as follows (Giroud et al. 1997b):

$$A = \frac{a k_{OM} \tan^2 \beta}{q_i L^2} \quad (16)$$

$$B = \frac{q_i k_{OM} \tan \beta}{gL} \quad (17)$$

$$C = \frac{Q}{a q_i} \quad (18)$$

Equation 15 provides a direct relationship between the rate of leachate supply,  $q_i$ , and the rate of leakage,  $Q$ . This direct relationship gives a definitive and quantitative answer to the following question often posed when practicing or teaching landfill liner design: is the rate of leakage through geomembrane defects greater if a geomembrane is overlain by a low-permeability leachate collection layer (which slows down the leachate flow toward the defects) or a high-permeability leachate collection layer (which reduces the leachate head over the geomembrane)? The answer to this question can be derived from Figure 3 which provides a graphical solution to Equation 15. Figure 3 shows that the rate of liquid migration through geomembrane defects decreases if  $A$  or  $B$  increases. From Equations 16 and 17, it appears that both  $A$  and  $B$  increase when  $L$  decreases and  $\beta$  and  $k_{OM}$  increase. The influence of  $L$  and  $\beta$  was already known through Equation 14: as  $L$  decreases or  $\beta$  increases, the leachate head decreases and, consequently, the leakage rate decreases. However, the influence of  $k_{OM}$  was not known because  $k_{OM}$  is a parameter in both Equations 12 and 14. Therefore, it is important to learn from the above discussion that, for a given situation defined by  $L$ ,  $\beta$  and  $q_i$ , the higher the hydraulic conductivity,  $k_{OM}$ , of the leachate collection layer, the lower the leakage rate. Therefore, the answer to the question posed above is that the rate of leakage through geomembrane defects is greater if a

geomembrane is overlain by a low-permeability leachate collection layer than by a high-permeability leachate collection layer. It should be noted that this conclusion is based on a demonstration that is limited, as is the scope of Section 4, to the case of geomembranes placed over a highly permeable medium. (However, the same conclusion would be reached if the geomembrane was placed on a low-permeability medium to form a composite liner because the rate of leachate migration through a composite liner is too small to have any significant impact on the leachate head on top of the liner. Therefore, in the case of a composite liner, it is obvious that the rate of leakage through geomembrane defects is greater if the leachate collection layer over the geomembrane has a low hydraulic conductivity than if it has a high hydraulic conductivity.)

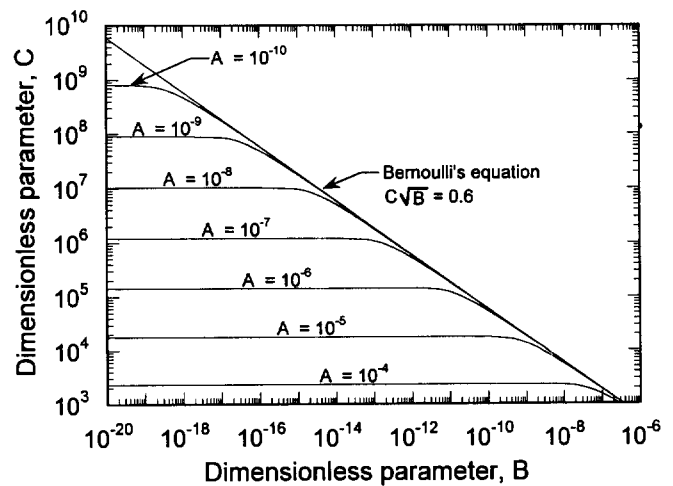


Figure 3. Graphical solution of Equation 15.

## 5 LEACHATE FLOW IN LEAKAGE COLLECTION LAYERS DUE TO DEFECTS IN GEOMEMBRANE LINERS

### 5.1 Presentation of the New Equation

Sections 2, 3 and 4 were devoted to the evaluation of the rate of leakage through geomembrane defects, considering several cases of hydraulic conductivities of the media overlying and underlying the geomembrane. Section 5 addresses the flow of leachate in the leakage collection layer located between the two liners in a double liner system. Since only leakage through defects in the primary liner is considered herein, and since the number of defects is generally limited, the leachate generally flows only in portions of the leakage collection layer called the wetted zones. If the defects in the primary liner are sufficiently far apart, the wetted zones related to the various defects do not overlap, and the boundary of the wetted zone related to one defect is approximately a parabola, as shown below.

The leachate flows downslope in the leachate collection layer overlying the primary liner (Figure 4a). A very small fraction of this leachate passes through the primary liner defect, D (Figure 4a). The leachate that has passed through the defect in the primary liner, first flows more or less vertically (DA in Figure 4a) through the leakage collection layer upper part, which is unsaturated. Then, when the leachate reaches (at Point A) the saturated portion of the leakage collection layer, it flows in all directions in the plane of the leakage collection layer (Figure 4a). It is therefore logical to assume that the leachate phreatic surface in the leakage collection layer is a cone with its apex at Point A located vertically beneath the defect in the primary liner (Figure 4a). Furthermore, for leachate to flow in all directions, the hydraulic gradient must be approximately the same in all directions. Since the hydraulic gradient is closely related to the slope of the phreatic surface, it may then be assumed that the slope of the cone generatrices is the same in all directions. The slope of the phreatic surface (i.e. the slope of the cone generatrix) in the downslope direction is approximately known: it is close to the slope angle,  $\beta$ , since the flow thickness is small compared to the length of the leakage collection layer. Therefore, it is assumed that the angle between a horizontal plane and all generatrices of the cone that form the leachate phreatic surface is  $\beta$  (Figure 4a), i.e. the cone axis is vertical.

From the foregoing discussion, it appears that the wetted zone (Figure 4b) is parabolic since the intersection of a cone and a plane parallel to a generatrix of the cone is a parabola. However, the actual wetted zone is only approximately parabolic because several simplifying assumptions were made, as indicated above.

Giroud et al. (1997a) showed that a consequence of the conical shape of the phreatic surface is the following relationship between the rate of leachate migration through the primary liner defect,  $Q$ , the hydraulic conductivity of the leachate collection layer,  $k$ , and the thickness of leachate in the leakage collection layer beneath the defect,  $t_0$  (Figure 4a):

$$Q = k t_0^2 \quad (19)$$

$t_0$  is the maximum thickness of leachate in the leakage collection layer (i.e. the distance between Point A and the secondary liner), hence the condition for the leachate collection layer to not be filled with leachate:

$$t_0 = \sqrt{\frac{Q}{k}} \leq t_{LCL} \quad (20)$$

Equations 19 and 20 are extremely simple and do not depend on the size of the defect in the primary liner or on the slope of the leakage collection layer.

## 5.2 Equation of the Boundary of the Wetted Zone

Giroud et al. (1997a) established the equation of the parabola that defines the wetted zone related to a single geomembrane defect. This equation is conveniently expressed as the width of the parabola at the horizontal distance  $x$  (Figure 4b) from the geomembrane defect:

$$W = \frac{2 t_0}{\sin \beta} \sqrt{1 + \frac{2 x \sin \beta}{t_0}} = 2 L \mu \sqrt{1 + 2(x/L)/\mu} \quad (21)$$

where  $L$  = horizontal projection of the length of the leakage collection layer in the direction of the slope; and  $\mu$  is a dimensionless parameter defined as follows:

$$\mu = \frac{t_0}{L \sin \beta} \quad (22)$$

## 5.3 Wetted Fraction

Typically, there are several defects in a primary liner. The frequency of defects,  $F$ , is defined as the ratio of the number of defects in the liner and the surface area of the liner. For example, if there are four defects per hectare,  $F = 4/10,000 = 4 \times 10^{-4} \text{ m}^{-2}$ . The total wetted zone generated by the defects consists of the individual parabolic wetted zones for the various defects. The wetted fraction is defined as the ratio of

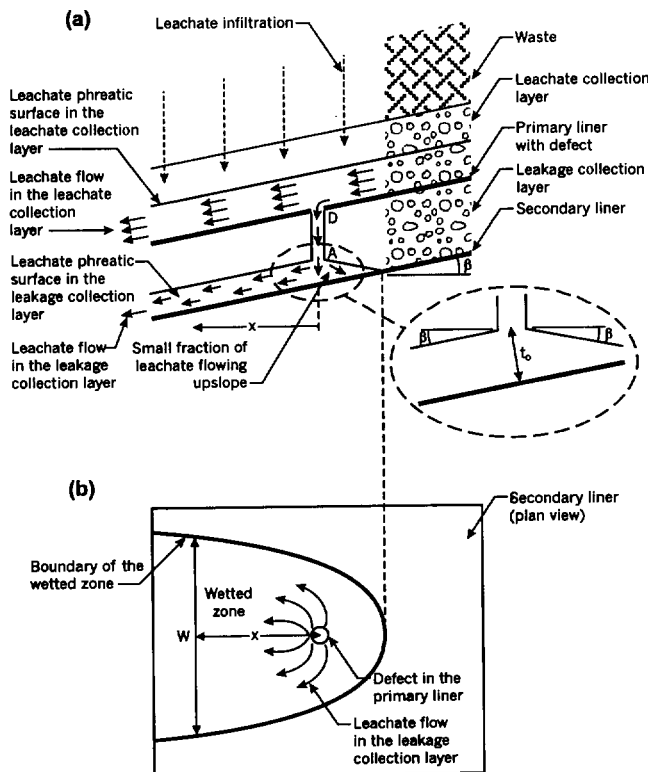


Figure 4. Leachate flow in the leachate collection layer, through a defect in the primary liner, and in the leakage collection layer: (a) cross section; (b) plan view.

the area of the total wetted zone and the surface area of the liner. The individual wetted zones may overlap; the smaller the defect frequency, the smaller the probability for the individual wetted zones to overlap. If the individual wetted zones do not overlap, which is the most frequent case since the defect frequency is generally small, two typical scenarios can be considered: (i) the worst scenario (Figure 5a) where all of the defects are located at the higher end of the primary liner slope, which results in the largest value for the wetted fraction; and (ii) the random scenario (Figure 5b) where the defects are located at random, which results in an average value for the wetted fraction. Using the equation of the parabola (Equation 21), Giroud et al. (1997a) calculated the wetted fraction,  $R_{w \text{ worst}}$  in the worst scenario, and  $R_{w \text{ rand}}$  in the random scenario:

$$R_{w \text{ worst}} = \lambda_{w \text{ worst}} F L^2 \quad (23)$$

where  $\lambda_{w \text{ worst}}$  is a dimensionless factor defined as follows:

$$\lambda_{w \text{ worst}} = \frac{2}{3} \mu^2 \left[ \left( 1 + \frac{2}{\mu} \right)^{3/2} - 1 \right] \quad (24)$$

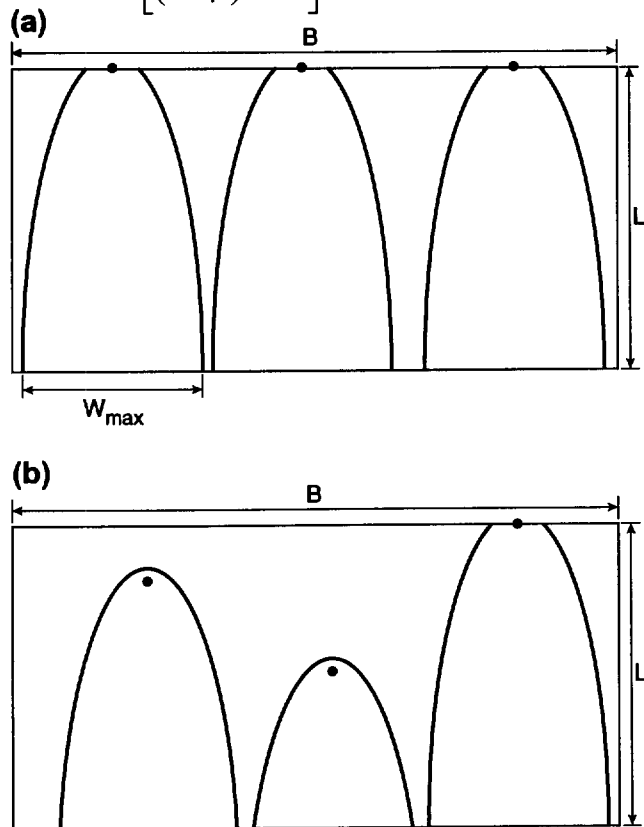


Figure 5. Leakage collection layer zones wetted by leachate migrating through several defects (•) in the primary liner, assuming no overlapping of wetted zones: (a) worst scenario where all of the defects are located at the high end of the primary liner slope; (b) random scenario where the defects are randomly distributed.

$$R_{w \text{ rand}} = \lambda_{w \text{ rand}} F L^2 \quad (25)$$

where  $\lambda_{w \text{ rand}}$  is a dimensionless factor defined as follows:

$$\lambda_{w \text{ rand}} = \frac{2}{15} \mu^3 \left[ \left( 1 + \frac{2}{\mu} \right)^{5/2} - 2 \right] \quad (\text{for } \mu \leq 2) \quad (26)$$

$$\lambda_{w \text{ rand}} = \frac{2}{15} \mu^3 \left[ \left( 1 + \frac{2}{\mu} \right)^{5/2} + \left( 1 - \frac{2}{\mu} \right)^{5/2} - 2 \right] \quad (\text{for } \mu \geq 2) \quad (27)$$

#### 5.4 Leachate Head on Top of the Secondary Liner

The leachate head on top of the secondary liner is zero outside the wetted zone. Inside the wetted zone, the leachate head varies from one point to another and an average value,  $h_{\text{avg}}$ , can be calculated. Based on the conical shape of the phreatic surface (Figure 4a) and using Equations 21 to 27, Giroud et al. (1997a) calculated the average leachate head on top of the secondary liner,  $h_{\text{avg worst}}$  in the worst scenario, and  $h_{\text{avg rand}}$  in the random scenario:

$$\frac{h_{\text{avg worst}}}{t_o \cos \beta} = \frac{3}{2 \mu \left[ \left( 1 + \frac{2}{\mu} \right)^{3/2} - 1 \right]} = \frac{\mu}{\lambda_{w \text{ worst}}} \quad (28)$$

$$\frac{h_{\text{avg rand}}}{t_o \cos \beta} = \frac{(5/3) + [15/(2\mu)] x_{\text{rand}} / L}{\mu \left[ \left( 1 + \frac{2}{\mu} \right)^{5/2} - 2 \right]} \quad (29)$$

It should be noted that  $h_{\text{avg rand}}$  is greater than  $h_{\text{avg worst}}$  because the wetted zone is smaller in the random scenario than in the worst scenario ( $R_{w \text{ rand}} < R_{w \text{ worst}}$ ). However, the total amount of leachate present at a given time in the leakage collection layer is greater in the worst case than in the random case.

As shown by Giroud et al. (1997a), if  $R_{w \text{ worst}}$  exceeds 2/3 or if  $R_{w \text{ rand}}$  exceeds 4/15, there is a high probability that the individual wetted zones will overlap. In this case, it would be extremely complex to determine the surface area of the wetted zone and, from a practical standpoint, it is preferable to use the approximate approach that consists of assuming that the entire surface area of the secondary liner is wetted (i.e.  $R_w = 1$ ). As shown by Giroud et al. (1997a), the values of the average leachate heads then become:

$$h_{\text{avg worst}} = \frac{F L Q}{k \tan \beta} \quad (30)$$

$$h_{\text{avg rand}} = \frac{F L Q}{2 k \tan \beta} \quad (31)$$

#### 5.4 Use of the Equations

To design a leakage collection layer, Equation 20 should be used. This extremely simple equation makes it possible to determine the required thickness of the leakage collection layer,  $t_{\text{LCL}}$ , as a function of the hydraulic conductivity of the leakage collection layer material,  $k$ , to accommodate a given leakage rate,  $Q$ .

To calculate the rate of leakage through the secondary liner (i.e. the rate of leakage into the ground), it is necessary to determine the head of leachate on top of the secondary liner. First, Equation 23 or 25 should be used to calculate the wetted fraction. If  $R_{w \text{ worst}}$  is less than 2/3 and  $R_{w \text{ rand}}$  is less than 4/15, Equations 28 and 29 can be used to calculate the leachate head in the worst and random case, respectively. If  $R_{w \text{ worst}}$  exceeds 2/3 or if  $R_{w \text{ rand}}$  exceeds 4/15, it should be assumed that the entire surface area of the secondary liner is wetted and Equations 30 and 31 must be used to calculate the average leachate head in the worst and the random case, respectively.

## 6 USE OF THE EQUATIONS TO SELECT THE OPTIMAL CONFIGURATION OF A DOUBLE LINER SYSTEM

The following methodology based on the equations presented in the preceding sections can be used to calculate the rate of leakage into the ground in the case of a double liner system: (i) calculate the rate of leakage through the primary liner; (ii) calculate the average head of leachate on top of the secondary liner; and (iii) calculate the rate of leakage through the secondary liner. Giroud et al. (1997d) used this methodology to compare two configurations of a double liner system: (i) in the first configuration, the primary liner is a geomembrane and the secondary liner is a geomembrane-GCL composite liner; and (ii) in the second configuration, the same two liners are in the inverse order, i.e. a geomembrane-GCL composite primary liner and a geomembrane secondary liner. They found that the rate of leakage into the ground is much less in the case of the second configuration, thereby showing that, from the viewpoint of minimizing advective flow of leachate, it is preferable to use the composite liner as the primary liner rather than as the secondary liner.

## 7 CONCLUSIONS

The new equations presented in this paper provide engineers designing landfills or evaluating landfill

performance with tools better than previously available. In particular:

- An entirely analytical method to calculate the rate of leakage through defects in the geomembrane component of a composite liner.
- An entirely analytical method to calculate the rate of leakage through defects in a geomembrane placed on a semi-permeable medium.
- An extension of Bernoulli's equation that eliminates the risk of absurd results such as those sometimes obtained with Bernoulli's equation, e.g. calculated leakage rate greater than the leachate supply rate.
- A set of equations that describe the flow of leachate in leakage collection layers and make it possible to design leakage collection layers and to calculate the leachate head on the secondary liner that is needed to calculate the rate of leakage through the secondary liner of a double liner system.

## REFERENCES

- Giroud, J.P. (1997) "Equations for Calculating the Rate of Liquid Migration Through Composite Liners Due to Geomembrane Defects", *Geosynthetics International*, Vol. 4, Nos. 3-4, pp. 335-348.
- Giroud, J.P. and Houlihan, M.F. (1995) "Design of Leachate Collection Layers", *Proceedings of the Fifth International Landfill Symposium*, Sardinia, Italy, October 1995, Vol. 2, pp. 613-640.
- Giroud, J.P., Khatami, A. and Badu-Tweneboah, K. (1989) "Evaluation of the Rate of Leakage through Composite Liners", *Geotextiles and Geomembranes*, Vol. 8, No. 4, pp. 337-340.
- Giroud, J.P., Badu-Tweneboah, K. and Bonaparte, R. (1992) "Rate of Leakage Through a Composite Liner due to Geomembrane Defects", *Geotextiles and Geomembranes*, Vol. 11, No. 1, pp. 1-28.
- Giroud, J.P., Badu-Tweneboah, K. and Soderman, K.L. (1994) "Evaluation of Landfill Liners", *Proceedings of the 5th International Conference on Geotextiles, Geomembranes and Related Products*, Singapore, Vol. 3, pp. 981-986.
- Giroud, J.P., Gross, B.A., Bonaparte, R. and McKelvey, J.A. (1997a) "Leachate Flow in Leakage Collection Layers Due to Defects in Geomembrane Liners", *Geosynthetics International*, Vol. 4, Nos. 3-4, pp. 215-242.
- Giroud, J.P., Khire, M.V. and Soderman, K.L. (1997b) "Liquid Migration Through Defects in a Geomembrane Overlain and Underlain by Permeable Media", *Geosynthetics International*, Vol. 4, Nos. 3-4, pp. 293-321.
- Giroud, J.P., King, T.D., Sanglerat, T.R., Hadj-Hamou, T. and Khire, M.V. (1997c) "Rate of Liquid Migration Through Defects in a Geomembrane Placed on a Semi-Permeable Medium", *Geosynthetics International*, Vol. 4, Nos. 3-4, pp. 349-372.
- Giroud, J.P., Soderman, K.L. and Badu-Tweneboah, K. (1997d) "Optimal Configuration of a Double Liner System Including a Geomembrane Liner and a Composite Liner", *Geosynthetics International*, Vol. 4, Nos. 3-4, pp. 373-389.

# EVALUATION OF LINER SYSTEM PERFORMANCE USING LIQUIDS MANAGEMENT DATA

J.F. Beech, Ph.D., P.E.

Principal, GeoSyntec Consultants, Atlanta, Georgia, USA

Kenneth W. Cargill, P.E.

Associate, GeoSyntec Consultants, Atlanta, Georgia, USA

William J. Huff, P.E.

Huff Engineering, P.C., North Babylon, New York, USA

**ABSTRACT:** The Town of Babylon (State of New York, USA) constructed a lined landfill using a double composite liner with a leakage detection system between the upper (primary) and lower liner. The primary liner was a composite on the base and a geomembrane on the slope. A requirement of the landfill construction and operation permit is that leakage through the primary liner be less than 180 liters per hectare day (lphd). Monitoring prior to operation revealed liquid was removed from the leakage detection system at rates above 180 lphd. A detailed analysis of the available data revealed that while some of the liquid was construction water, the liquid was also attributable to leakage through the primary liner. The source of leakage was considered to be a possible hole 3 mm in diameter approximately 800 mm up the side slope.

**KEYWORDS:** Geomembranes, Leakage, Landfills, Double-liner Systems, Case Study

## 1 INTRODUCTION

The Town of Babylon (State of New York, USA) constructed a municipal solid waste landfill using a double liner system designed in accordance with the governing regulatory requirements. The liner system on the base of the landfill is a double composite liner with a leachate collection system (LCS) above the upper composite (primary) liner and a leakage detection system (LDS) between the primary liner and the lower composite (secondary) liner. The liner system on the slope is similar to that on the base except the primary liner consists only of a geomembrane. A requirement of the landfill construction and operation permit is that leakage through the top liner be less than 180 liter per hectare per day (lphd). This leakage rate is referred to as the action leakage rate or ALR. The action leakage rate is a concept introduced by the U.S. Environmental Protection Agency (USEPA) and is used by the New York State Department of Environmental Conservation (NYSDEC) as the rate of leakage from the LDS that triggers interaction between the owner or operator and the agency to determine the appropriate response action for the leakage. The USEPA requires an ALR only for hazardous waste landfills, while the NYSDEC requires an ALR for municipal solid waste landfills as well as hazardous waste landfills. Another permit requirement is the monitoring of the LDS flow rates for a period of 30 days prior to operation to establish satisfactory performance of the top liner, in addition to monitoring during and after the active life of

the landfill. The results of monitoring prior to operation is the subject of this paper.

During the pre-operation monitoring period, liquid was removed from the LDS of the two cells comprising the landfill at rates on the order of 300 lphd and 650 lphd. An evaluation of a number of landfills revealed that landfills with a CQA program consistent with standard industry practice had top liner leakage rates less than 500 lphd, and typically less than 200 lphd [Bonaparte and Gross, 1990]. Therefore, the 180 lphd requirement of the permit is achievable, but leakage rates above 180 lphd sometimes occur. A detailed evaluation of the measured leakage rates was performed since the leakage rate defined by the permit was exceeded. In the remainder of the paper the liner system is described, the results of pre-operation monitoring are presented, the monitoring results are analyzed to identify the sources of liquid removed from the LDS, and conclusions are drawn.

## 2 DESCRIPTION OF LINING SYSTEM

The lining system for the landfill incorporates both geosynthetic and low-permeability soil components. The liner system configurations on the landfill base and slope are depicted in Figure 1. The liner system was designed to meet the governing regulatory requirements of the State of New York. The specific liner system components on the base of the landfill are, from top to bottom: (i) 0.6-m thick protective sand layer ( $k \geq 10^{-5}$  m/s); (ii) geotextile filter; (iii) geonet drainage layer; (iv) 1.5-mm thick smooth high-density polyethylene

(HDPE) geomembrane; (v) geosynthetic clay liner (GCL); (vi) 0.3-m thick compacted clay liner ( $k \leq 10^{-7}$  m/s); (vii) geotextile filter; (viii) geonet drainage layer; (ix) 1.5-mm thick smooth HDPE geomembrane; (x) 0.6-m thick compacted clay liner ( $k \leq 10^{-9}$  m/s).

The liner system components on the slopes are from top to bottom: (i) 0.6-m thick protective sand layer ( $k \geq 10^{-5}$  m/s); (ii) geocomposite drainage layer consisting of a nonwoven geotextile heat-bonded to each side of a geonet; (iii) 60-mil thick textured HDPE geomembrane; (iv) geocomposite LDS; (v) 1.5-mm thick textured HDPE geomembrane; (vi) 0.6-m thick compacted clay liner ( $k \leq 10^{-9}$  m/s). The textured HDPE geomembrane and geocomposite drainage layers used for the side slope liner system extend approximate 1.5 m onto the base of the landfill. The GCL forming part of the composite primary liner on the base is extended 1 m up the slope.

The landfill is divided into two, 1.3 ha and 1.4 ha, cells subsequently referred to as the eastern and western cells. The lining system is continuous between the cells; however, the LCS and LDS of each cell are hydraulically separated by a berm. The LCS and LDS of each cell are pitched to drain to a sump area. Liquids collected in the sump area are pumped from the landfill. Separate pumps are used to drain the LCS and LDS.

### 3. LDS MONITORING RESULTS

The quantity of liquid removed from the LDSs of the eastern and western cells as part of pre-operation monitoring was recorded by accumulating flowmeters. The measured LDS flow rate in both cells exceeded the ALR of 180 lphd during initial monitoring. However, the ALR applies only to liquid leaking through the primary liner into the LDS. Liquid leaking through the top liner is not the only possible source for liquid being removed from the LDS. When using leakage data to evaluate the performance of a primary liner it is important to take other sources of liquid into account [Bonaparte and Gross, 1990]. Other possible sources of liquid are discussed below.

**Construction water** is liquid that became trapped in the LDS during construction and continues to drain from the LDS after construction. The considered landfill lining system incorporates a geonet LDS. The voids in the geonet on the base of each cell could contain on the order of 38,000 liters of liquid if saturated. The rate of removal of construction water will depend primarily upon the grade at which the geonet is installed and its transmissivity. The rate of drainage of construction water from the LDS was estimated to range from 30 to 3,000 lphd.

**Consolidation water** is liquid squeezed from the clay component of the primary clay liner. Consolidation is the result of load being placed on the lining system. Consolidation of the clay liner can occur under the weight of the protective cover over the top liner. The rate

of consolidation water which can be produced due to this load was estimated to be on the order of 0 to 100 lphd.

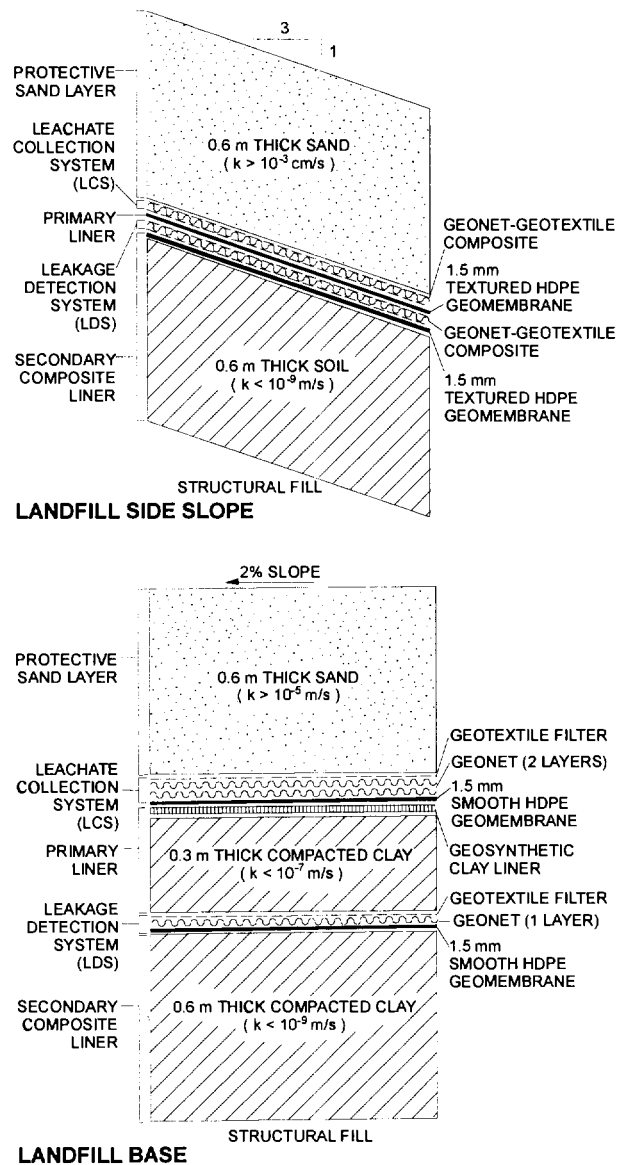


Figure 1. Liner System Configuration

**Infiltration** is liquid entering the LDS from outside the landfill or through the bottom liner. The rate will depend upon the source of infiltration (e.g., ground water surface water). The liner system is above the water table, and infiltration, if any, is expected to be negligible.

The daily liquid removal rate are plotted in Figure 2 for the eastern and western cells. The criteria used to evaluate liner system performance with respect to the 180 lphd ALR was the thirty-day average liquid removal rate. The first thirty-day average was calculated in June 1993. The western cell had a calculated 30-day average leakage rate of 240 lphd and the eastern cell had a leakage rate of 216 lphd on 24 June 1993. Since the thirty-day average



was above the 180 lphd threshold in both cells, it was concluded that either construction and consolidation water was not totally purged from the system, or there was a potential leak in the primary liner. On 10 July 1993 the pumps in the LCS sumps were turned off to allow precipitation to collect on the primary liner. This increase in hydraulic head on the primary liner created a small surcharge which accelerated the removal of any construction water, and would exaggerate conditions for leakage through the primary liner in the event a leak did exist.

The eastern cell did not perform as expected. As the hydraulic head increased on the primary liner, erratic liquid removal rates were measured. On 16 July, the daily rate of removal from the LDS reached 814 lphd (the 30-day average liquid removal rate was on the order of 260 lphd) and the hydraulic head was 610 mm (as measured in the eastern sump). From 17 July through 21 July the hydraulic head was increased to 740 mm, but the daily rate of liquid removal decreased to 198 lphd. This is what would be expected with the depletion of the construction and consolidation water. From 22 July through 18 August the hydraulic head increased to 1.01 m and the liquid removal rate started to increase. This increase was unexpected and could not be attributed to construction and consolidation waters.

The western cell performed as anticipated. As the hydraulic head increased on the primary liner, the rate of liquid removal from the LDS increased. On 17 July, the daily rate of removal from the LDS reached 308 lphd and the hydraulic head as measured in the western sump was 840 mm. From 18 July through 18 August the hydraulic head was increased to 1.27 m, but the daily rate of liquid removal gradually decreased to 49 lphd, as would be expected with the depletion of the construction and consolidation water. The western cell was determined to perform in accordance with the permit conditions and was not evaluated further.

#### 4. ANALYSIS OF DATA

As noted above, the liquid removal rate in the eastern cell increased significantly when the water level in the sump was raised above 740 mm. This increase in leakage rate was attributed to a hole in the top liner at least 740 mm vertical above the cell sump. At this elevation the hole was calculated to be above the GCL which extended a short distance (e.g., about 300 mm vertical) up the side slope. This observation was supported by the rapid response in the LDS to the height of liquid, which would be the case for leakage through a defect in a geomembrane overlying a free draining layer, as is the case on the slope. In order to estimate the size and location of the leak relative to the bottom of the cell, the data was analyzed using Bernoulli's equation for flow through an orifice [Giroud, 1984]:

$$Q = Ca\sqrt{2gh}$$

in which: Q = flow rate, C = dimension less coefficient related to the shape of the edge of the defect (assumed to be 0.6); a = area of orifice; g = gravity (9.81 m/s<sup>2</sup>); and h = height of liquid above the defect.

The conditions analyzed are shown in Figure 3. For two different water levels above the cell bottom, the rate of leakage is known; however, the height of liquid above the defect is unknown. Therefore, three unknowns exist: the height of liquid above the defect for each of the two different water levels, and the area of the defect. The available data and Bernoulli's equation were used to generate three equations with three unknowns. These equations are shown in Figure 3. Solving these equations yields an equivalent circular defect 3 mm in diameter located 785 mm vertical above the primary liner. The calculated height of the defect above the base is consistent with the elevation at which an increase in the leakage rate was observed.

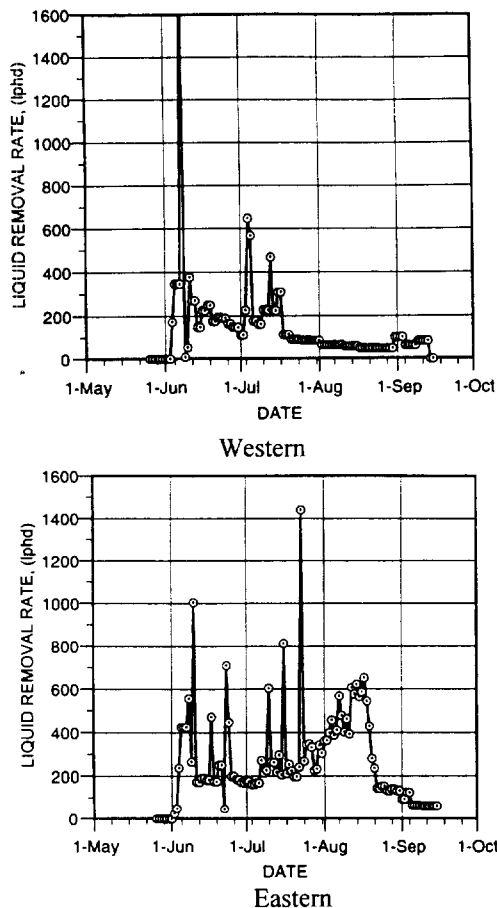
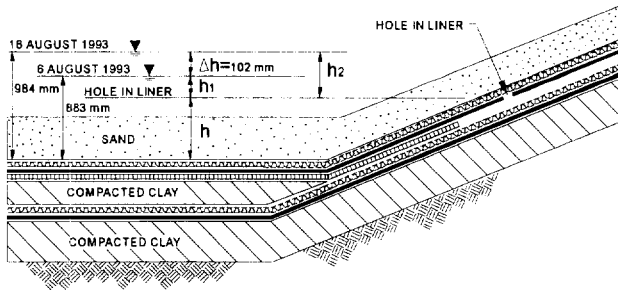


Figure 2. Daily Liquid Removal



### Known Relationships

$$Q_1 = 0.6a\sqrt{2gh_1} = 5.957 \times 10^{-6} \text{ m}^3 / \text{s}$$

$$Q_2 = 0.6a\sqrt{2gh_2} = 8.497 \times 10^{-6} \text{ m}^3 / \text{s}$$

$$h_2 = h_1 + 102 \text{ mm}$$

### Calculated Hole Area

$$\text{HOLE AREA} = 7.154 \times 10^{-6} \text{ m}^2$$

$$\text{HOLE DIAMETER} = 3 \text{ mm}$$

$$h_1 = 98 \text{ mm (3.8 in)}$$

$$h_2 = 200 \text{ mm (7.8 in)}$$

$$h = 883 - 98 = 785 \text{ mm}$$

Figure 3. Summary of Leakage Analysis

The calculated defect size is approximately the same as the typical size defect that may occur in geomembranes installed with good CQA practice [Giroud and Bonaparte, 1989]. In addition, the defect is located well above the primary geomembrane on the base of the landfill. The operating requirements of the cell requires the hydraulic head on the primary liner to be less than 300 mm. Given the location of the defect, the operational requirements to maintain the hydraulic head in the LCS less than 300 mm, and the potential to damage the liner during repair, the recommendation was made to place the cell into operation.

## 5 SUMMARY AND CONCLUSIONS

The initial rate of liquid removal from the LDS of a double-lined landfill exceeded the permitted rate of 180 lphd in both the eastern and western cells of the facility. An investigation into the potential sources revealed the

liquid in the western cell was due to construction and consolidation water. The leakage in the eastern cell was initially attributed to construction and consolidation water; however, later some of the liquid was attributed to leakage through the geomembrane liner on the side slope. The leak was attributed to a possible 3 mm diameter hole on the side slope. At this distance up the slope the hole would not impact normal operations. Therefore, the recommendation was made to place the landfill into service without repairing the geomembrane. The case history presented in this paper demonstrates that:

- liquid removed from the LDS shortly after construction is not necessarily an indicator of primary liner performance;
- careful monitoring and analysis of LDS liquid removal is needed to distinguish between leakage and other sources of liquid;
- liquid removal rate data can be used to estimate the locations and size of geomembrane primary liner defects; and
- leakage can occur in liners constructed with good CQA practice.

## ACKNOWLEDGMENTS

The support of GeoSyntec Consultants during the preparation of this paper is gratefully acknowledged. The efforts of Beth Gross in reviewing the paper are deeply appreciated. In addition, the authors wish to thank Ann Taylor for assistance in preparation of figures and Joyce Thomas for preparation of text.

## REFERENCES

- Bonaparte, R. and Gross, B.A. "Field Behavior of Double-Liner Systems," *Waste Containment Systems: Construction, Regulation, and Performance*, ASCE Geotechnical Publication No. 26, 1990, pp. 52 - 83.
- Giroud, J.P. "Impermeability: The Myth and a Rationale Approach," *Proceedings of the International Conference on Geomembranes*, Vol. 1, Denver, Colorado, USA, June 1984, pp. 157-162.
- Giroud, J.P. and Bonaparte, R., "Leakage Through Liners Constructed with Geomembranes - Part I. Geomembrane Liners," *Geotextiles and Geomembranes*, Vol. 8, No. 1, 1989, pp. 27-67.

# Comparison of Dye Testing and Electrical Leak Location Testing of a Solid Waste Liner System

G.T. Darilek

Principal Engineer, Leak Location Services, Inc., San Antonio, Texas, U.S.A.

L.V. Miller

Central Division Manager, Delaware Solid Waste Authority, Sandtown, Delaware, U.S.A.

**ABSTRACT:** Dye tracing and electrical leak location testing were independently conducted to detect and locate leaks in the primary geomembrane liner of two cells in a municipal landfill. Despite extensive quality control and quality assurance programs, water in the leak detection zone after construction indicated that the primary liner had a leak. Fluorescein dye tests were conducted by placing a fluorescent yellow/green dye in water impounded on the liner and then sampling the water drained from the leak detection zone for periods of at least 40 days. The samples of water were visually inspected and tested with a spectrophotometer. No dye was ever detected. An electrical leak location survey of the same areas located two leaks. One leak was a 90 x 76 mm (7.5 x 3 in.) hole that was near a leak detection drainage pipe. The other leak was a 25-mm (1-in.) diameter hole. The tests showed that dye testing was ineffective for detecting the presence of significant leaks in a liner system with sand above and below the leak. The electrical leak location method quickly and accurately located the leaks.

**KEY WORDS:** Leak detection, geomembranes, construction quality assurance, landfills, performance evaluation

## 1 INTRODUCTION

The lining system of a municipal solid waste landfill is the only barrier between the leachate generated and the local groundwater. The installation of the liner system is normally monitored with extensive quality control and quality assurance programs designed to insure that the specifications for materials and procedures for construction are met. Unfortunately, the completed lining system can be damaged during the installation of the leachate collection systems and the drainage/protection layers. Holes in the lining system can go undetected until long after landfilling in the area has started, making the location and repair of the holes almost impossible. Therefore, testing for leaks before waste is introduced can detect problems before they get worse.

The Delaware Solid Waste Authority (DSWA) initiated a post installation testing program that included dye tests and electrical leak location surveys for two cells of a disposal area with eight cells. The disposal area is comprised of two phases, each of which are divided into four drainage areas or cells. The tests on the two cells gave a good comparison of the two leak detection and location methods.

Figure 1 shows a cross section diagram of the typical cell construction. The diagram is not to scale. Each cell has dimensions of approximately 54 x 218 m (178 x 715 ft). The disposal area utilizes a double HDPE geomembrane liner system. The primary liner has a 600 mm (24 in.) protective drainage sand layer above the liner. The leak detection zone has a 300 mm (12 in.) layer of drainage sand between the liners. Leachate and leak detection pipe trenches formed in the primary liner and secondary liner respectively contain 150 mm (6 in.) perforated drainage pipes surrounded with ballast rock enveloped in a woven geotextile. The drainage pipes above the secondary and primary liners connect to common

headers which drain to separate internal sumps. All eight cells of the disposal area were dye tested. Only the last two cells were leak tested using the electrical leak location method.

## 2 DYE TESTS

The dye test included uniformly introducing a known concentration of fluorescent yellow/green fluorescein dye into the water impounded in each cell and then monitoring the water flowing into the leak detection sump for dye. Only one cell was tested at a time. The cells were filled with dyed water to a level just below the lowest berm. Because of the elevation of the lowest berm, only about half of each cell could be flooded. Therefore, the dye testing area in each cell was limited to approximately 50 x 125 m (160 x 410 ft). Samples of water were then collected from the secondary leak detection system and visually inspected under an ultraviolet lamp and analyzed using a spectrophotometer.

Cole-Parmer fluorescent yellow/green dye tracer was used to dye the primary water. The concentration of the dye in the water impounded on the primary liner was compared with the concentration of dye in the water collected in the secondary leak detection system using a Hach model DR/2000 spectrophotometer. The photometer was calibrated for absorbance of light at the 494 nanometer wavelength of the dye, and could detect the dye in concentrations of approximately 0.2 ppm. The minimum visible detectable concentration of the tracer using an ultraviolet lamp is one ppm. A higher initial dye concentration of 4 ppm was used to compensate for any moisture from construction in the leak detection system that would dilute the primary water and to compensate for biodegradation of the dye with time.

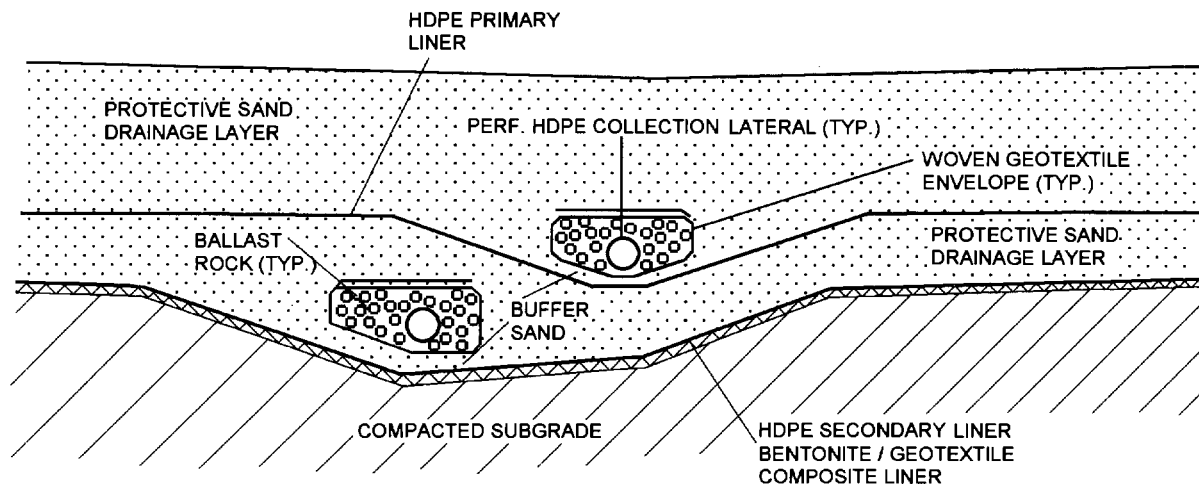


Figure 1. Typical Cross-Section View of Leachate and Leak Detection System

The maximum migration distance for the dye through the sand to a leak detection drainage pipe was approximately 14 m (46 ft). The minimum distance was approximately 1 m (3 ft). The estimated worst-case time necessary for the dye to migrate through the sand to the nearest part of the leak detection pipe was calculated using the equation from Giroud et al (1997):

$$t_{\text{travel}} = n x / (k \sin \beta \cos \beta); \quad (1)$$

where  $t_{\text{travel}}$  = leakage travel time;  
 $n$  = porosity of the sand;  
 $x$  = length of the leakage path;  
 $k$  = hydraulic conductivity; and  
 $\beta_L$  = slope of the leak detection layer.

The worst-case leakage travel time through the sand was calculated to be 38 days. The leakage travel time through the leak detection pipe was estimated to be a maximum of one day. Therefore, the dye tests were monitored for a minimum of 40 days. During the dye testing, two of the cells were tested in the summer where the increased temperature accelerated the biodegradation of the dye. Therefore, additional dye was added when the concentration of the dye decreased. Samples of the water in the leak detection sump were collected, analyzed, and stored twice a week.

### 3 RESULTS OF THE DYE TESTS

No dye was detected in any of the eight cells in the water collected from the leak detection zone using visual ultraviolet inspection and the spectrophotometer measurements. The absorbance of the water collected in the leak detection zone remained at a very low and constant level. The concentration of dye in the primary water decreased to the visible limit of 1 ppm in 16 to 28 days except for two cells that maintained a

visible concentration throughout the 40 days of monitoring. From previous tests, the dye in water that was not exposed to sunlight or high surface temperatures was much slower, requiring more than two months to degrade below the visible level.

### 4 ELECTRICAL LEAK LOCATION SURVEY

The electrical leak location method (Laine and Darilek, 1993) was used to search for leaks in two of the eight cells. The electrical leak location method is to apply a voltage across the liner and then detect the areas where electrical current flows through leaks in the insulating liner. Figure 2 shows a diagram of the principles of the method. Figure 3 shows an operator collecting the data. One electrode was placed in the sand on the primary liner. A second electrode was placed in the water at the end of a cleanout pipe in the leak detection zone. The electrodes were connected to a 300 VDC power supply. The geomembrane leak location survey was conducted by systematically making potential gradient measurements on the cover soil. Heavy vegetation on the sand layer along the survey lines was removed prior to the survey. Data was taken on survey lines spaced 760 mm (30 in.) apart. A measurement was taken every 760 mm with electrodes spaced 760 mm apart. The data was recorded using portable digital data loggers programmed so the operator could enter the survey parameters including file name, line number, starting position, position increment, and time interval between readings. The data collected with the digital data recorders was then downloaded to a laptop computer in the field and the data was plotted and analyzed for characteristic leak signals. The entire area of the two cells was surveyed using the electrical leak location method. The survey of 22,500 square m (5.5 acres) required eight man-days.

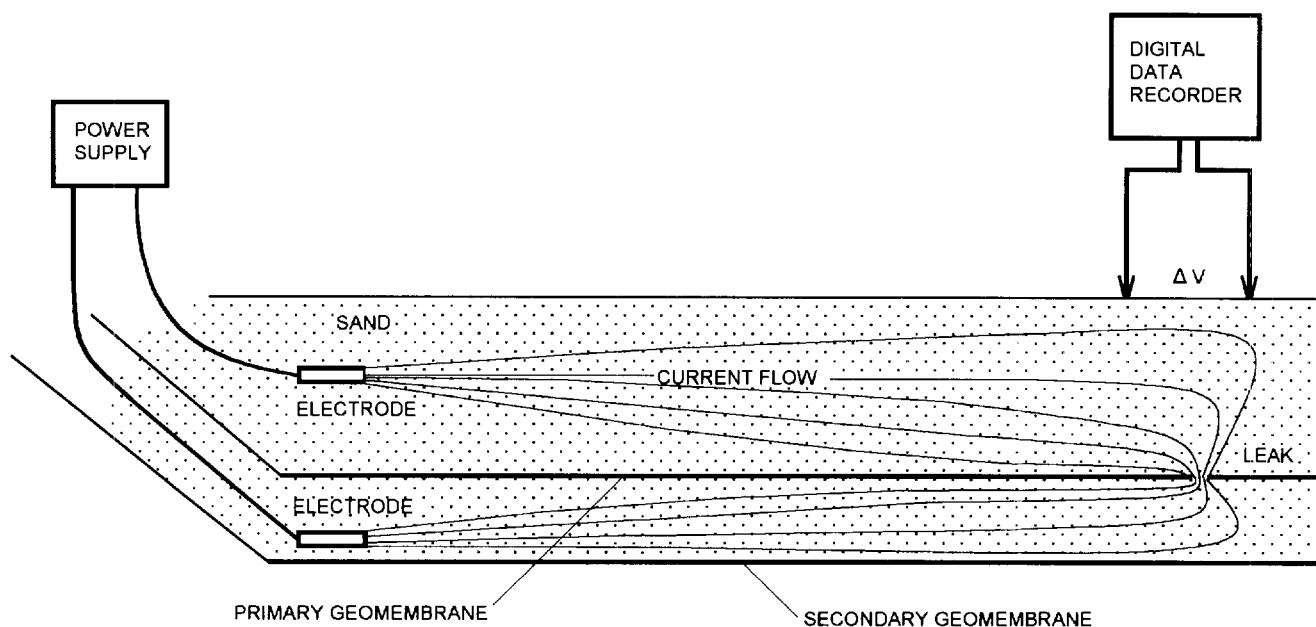


Figure 2. Principle of the Electrical Leak Location Method for Sand-Covered Geomembrane Liners

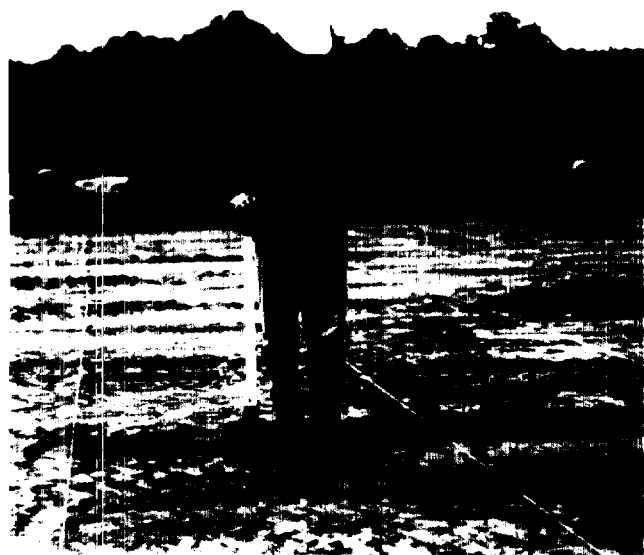


Figure 3. Geomembrane Electrical Leak Location Data Acquisition

## 5 RESULTS OF THE ELECTRICAL LEAK LOCATION SURVEY

Two leaks were found using the electrical leak location method. One leak was a 190 x 76 mm (7.5 x 3 in.) hole. It was excavated while the leak location survey crew was on the site. Figure 4 shows this leak in-situ with a 15 mm (6 in.) marker shown for scale. The second leak was a 25 mm (1 in.)

diameter hole. Figure 5 shows both leaks after they were cut from the parent material. A 300 mm (12 in.) scale is also shown in the photograph.

Considerable energy would be required to form leaks this large, so damage from machinery is suspected. The larger leak had scrape marks leading to the leak and the other edge of the leak had the torn piece of liner attached as a flap. The larger leak was found on the edge of a leachate collection trench, which was approximately 3 m (10 ft) from a leak detection drainage pipe under the primary liner. Visual observation of the excavated leak after a moderate rainfall showed approximately 75 mm (3 in.) of storm water flowing over the hole.

## 6 ANALYSIS

For the larger leak, the dye had to travel a distance of only 3 m (10 ft) through the sand on the primary liner, through the leak, through the sand in the leak detection zone, to the leak detection drainage pipe. The time required for this transit, again using equation (1), is approximately 8 days plus an additional day for the dye to flow down the leak detection drainage pipe. The absorbance of the primary water at the 8-day interval had decreased to 36 percent of the initial concentration, but was clearly visible. The absorbance of the water samples taken from the leak detection sump six, eight, and eleven days after the start of the test for that cell show no evidence of dye.

Since the completion of the construction of the disposal area, flow measurements were made of the water collected from each of the two phases. Each phase has four cells. The flow rate from Phase 2 has always been higher than Phase 1. This was originally believed to be due to the higher

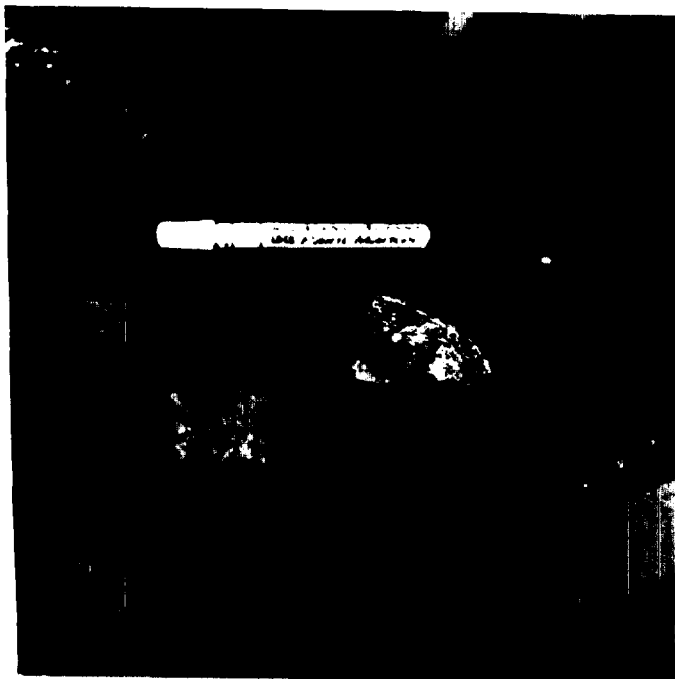


Figure 4. 90 x 76 mm (7.5 x 3 in.) Leak Found Using the Electrical Leak Location Method

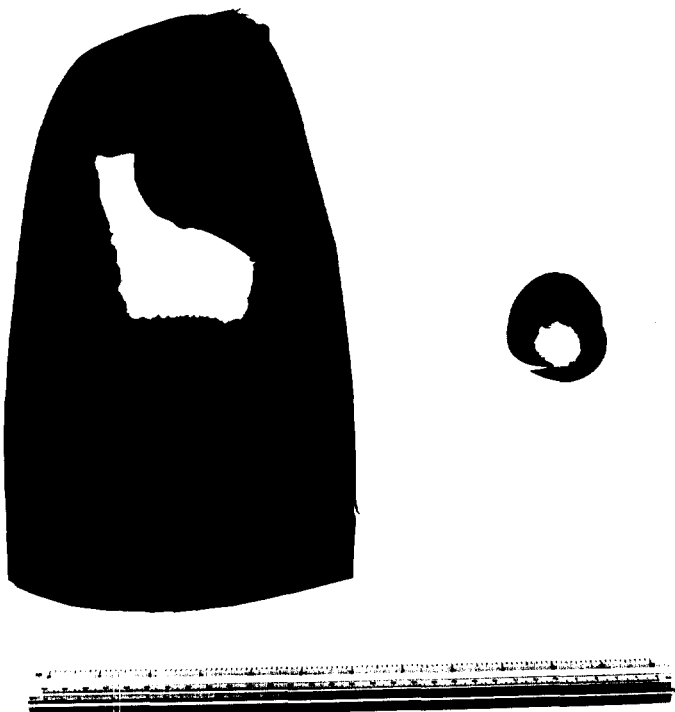


Figure 5. Samples of Geomembrane Liner Containing the Leaks Found Using the Electrical Leak Location Method

precipitation during the construction of Phase 2. Since landfilling has started in both phases the secondary flow rates have continued to decrease.

Prior to the repair of the holes, the flow rate was approximately 112 liters/10,000 sq m/day (lhd) (12 gallons/acre/day (gad)) for Phase 2 and 56 lhd (6 gad) for Phase 1. Since the repairs, the flow rate from Phase 2 has decreased to approximately 70 lhd (7.5 gad). The flow rate from Phase 1 has also continued to decrease to about 14 lhd (1.5 gad).

The secondary flow in Phase 2 dropped dramatically to approximately 70 lhd (7.5 gad) after patching the two holes. Because the flow before the leaks were repaired was approximately 112 lhd (12 gal/acre/day), the estimated leakage from the holes contributed 42 lhd (4.5 gad).

## 7 CONCLUSIONS

The tests showed that dye testing was ineffective for detecting the presence of significant leaks in a liner system with sand above and below the leak. Biodegradation of the dye significantly decreases the concentration of the dye during the long time required for water to flow to the leak detection sump. Considering that sand is a good filter for water, the failure of the dye test for the leak that was close to a leak detection drainage pipe may be because the sand adsorbed the dye from the water. Even if the dye tests would have indicated the presence of the leaks, the specific locations of the leaks would have been unknown.

The electrical leak location method not only detected the leaks, but also accurately located the leaks. The leaks were easily excavated for repair before waste was put in the disposal cell.

An electrical leak location survey for geomembrane liners is an effective method for detecting leaks present during the installation of the geomembrane liner or for detecting leaks caused by machinery while putting sand on the liner.

## ACKNOWLEDGMENTS

The authors thank N.C. Vasuki of Delaware Solid Waste Authority for his review of the original manuscript. The funding of the work reported was provided by the Delaware Solid Waste Authority.

## REFERENCES

- 1 Giroud, J.P., Gross, B.A., Bonaparte, R., and McKelvey, J.A., (1997) "Leachate Flow in Leakage Collection Layers Due to Defects in Geomembrane Liners", *Geosynthetics International*, Vol 4, Nos. 3-4.
- 2 Laine, D.L., and Darilek, G.T., (1993) "Locating Leaks in Geomembrane Liners Covered With a Protective Soil," *Geosynthetics '93*, IFAI, Vancouver, British Columbia, Canada, Vol. 3, pp. 1403-1412.

# Evaluation of the Effectiveness of HDPE Geomembrane Liner Protection

K. Badu-Tweneboah

Senior Project Engineer, GeoSyntec Consultants, 621 N.W. 53rd Street, Suite 650, Boca Raton, Florida, USA

J.P. Giroud

Senior Principal, GeoSyntec Consultants, 621 N.W. 53rd Street, Suite 650, Boca Raton, Florida, USA

D.S. Carlson

Senior Laboratory Technician, GeoSyntec Consultants, Materials Testing Laboratory, 621 N.W. 53rd Street, Suite 115, Boca Raton, Florida, USA

G.R. Schmertmann

Senior Project Engineer, GeoSyntec Consultants, 1100 Lake Hearn Drive, N.E., Suite 200, Atlanta, Georgia, USA

**ABSTRACT:** This paper presents an approach for evaluating the effectiveness of HDPE geomembrane liner protection. The approach is based on the use of multi-axial tension tests (ASTM D 5617) performed on geomembrane specimens after exposure to anticipated field conditions. A criterion based on the geomembrane mode of failure in the multi-axial tension test is used to determine if a certain type or level of mechanical damage is acceptable. An example from several studies conducted to evaluate the impact of a granular layer on a geomembrane is presented and discussed.

**KEY WORDS:** Geomembrane liner, Protection, Mechanical damage, Mode of failure, Multi-axial tension test.

## 1 INTRODUCTION

Geomembranes used in waste containment facilities are often overlain and/or underlain by granular drainage layers. Since coarse granular particles can potentially damage the geomembrane at points of contact, design measures are often taken to protect the geomembrane and limit damage to acceptable levels. Typical design measures include: requiring that certain characteristics of the granular material, such as maximum particle size, gradation, or angularity, are within specified limits; or including cushioning layers, such as geotextiles, between the geomembrane and the granular material. These design measures generally increase facility construction costs and there is therefore a need for designers to rationally evaluate their effectiveness.

The effectiveness of geomembrane protection measures is often evaluated through laboratory testing that is performed in two stages. The first stage is exposure, during which a geomembrane specimen is subjected to the anticipated field conditions of concern. The exposure conditions typically include anticipated stresses, temperatures, and loading durations. The second stage is evaluation, during which tests are performed to measure selected properties of the exposed geomembrane and the test results used to evaluate whether the degree of damage sustained by the geomembrane is acceptable. This paper provides information relevant to the evaluation stage of such testing. Specifically, the purpose of this paper is to discuss the use of multi-axial tension tests to evaluate

exposed high density polyethylene (HDPE) geomembranes and to present a criterion for assessing whether mechanical damage sustained by the geomembrane is within acceptable limits.

## 2 CRITERION FOR ACCEPTABLE DAMAGE

Consideration of acceptable levels of geomembrane damage is focused on the primary function of geomembranes used in waste containment facilities, i.e. to act as a hydraulic barrier. It is obvious that if punctures are observed in the geomembrane after the exposure stage of testing then the geomembrane will not function as an effective hydraulic barrier. In this case the level of damage is unacceptable and the evaluation stage of testing is not necessary. Other types of damage may decrease the ability of the geomembrane to resist rupture when subjected to the working loads and deformations that may develop throughout the life of the facility. The evaluation stage of testing is concerned with these other types of damage.

The ability of a geomembrane to resist rupture when subjected to loads and deformations results not from its strength, but from its ability to deform locally under concentrated loads and at locations where differential settlements occur. If the geomembrane has sufficient deformability, it can conform to the shape of adjacent material layers without the development of large internal stresses. This rationale leads to the following definition for acceptable levels of damage: for damage undergone by a geomembrane to be acceptable, the tensile strain

characteristics of the geomembrane must not be significantly affected.

The proposed criterion is based on the use of results from multi-axial tension tests performed in accordance with the American Society for Testing and Materials (ASTM) test standard D 5617. This test uses geomembrane specimens secured around the perimeter of a large diameter (greater than 450 mm) testing chamber. Pressure is applied to one side of the specimen to cause out-of-plane deformation. The pressure is increased until failure occurs due to rupture of the geomembrane. A virgin geomembrane with a uniform thickness must rupture at the top of the dome because this is the location where the stresses are highest. Since a large test specimen is used, the multi-axial tension test is more appropriate than many other small scale index tests. The mode of failure is an important characteristic with respect to the criterion proposed in this paper.

The important parameters that indicate the ability of a geomembrane to deform are the magnitude of tensile strain at yield and, to a lesser degree, the strain at break. However, the state-of-practice for predicting the stresses and strains in geomembranes used in waste containment facilities is not sufficiently detailed to justify a meaningful evaluation of the relative performance of geomembranes with slightly different stress-strain characteristics. Based on experience with multi-axial tension tests on mechanically damaged geomembranes, the authors have noted that the most significant indicator of damage for HDPE geomembranes may be when the geomembrane specimen ruptures at a location other than the top of the dome formed by the hydrostatically inflated geomembrane. If a geomembrane specimen ruptures at a location other than the top of the dome, this indicates that the specimen has been previously weakened at the location where the rupture occurs.

From the foregoing discussion, the following criterion has been developed: the mechanical damage undergone by a geomembrane is deemed unacceptable if the geomembrane specimen tested in a large diameter multi-axial tension test exhibits rupture at a location other than the center of the specimen and if this location is that of visible mechanical damage. The authors have used the approach and the criterion described above on several occasions and found that the proposed criterion always led to a clear and intuitively correct conclusion regarding what level of mechanical damage was acceptable.

In Section 3, an example from several studies conducted to evaluate the impact of a granular layer on a geomembrane is presented.

### 3 DESCRIPTION OF A TESTING PROGRAM

One of the studies conducted by the authors consisted of evaluating the need for a geotextile cushion between a

crushed rock layer and an HDPE geomembrane resting on a layer of compacted clay, thereby forming a composite liner to be used in an ore heap leach pad. The study included three steps:

- static compression loading to simulate the effects of the crushed rock layer on the geomembrane liner;
- visual examination of the geomembrane specimens after the compression tests to determine and record the locations of visible mechanical damage; and
- multi-axial tension tests to evaluate if the type or level of mechanical damage undergone by the geomembrane specimens was acceptable or not.

The materials used in the testing program consisted of a 1.5-mm thick HDPE geomembrane and four different proposed crushed rock materials designated A, B, C, and D. The particle-size distribution curves of the crushed rock materials are presented in Figure 1.

The static compression loading simulation was performed in a 450-mm diameter testing chamber. The size of the testing chamber was selected to be:

- more than five times the maximum particle size, which was 76 mm for material A, in order to eliminate the possible effects of arching which might have reduced the load applied to the geomembrane by transferring part of the load to the testing chamber; and
- less than the diameter (610 mm) of the pressure vessel used to perform the multi-axial tension test, in order to avoid the presence of locations where the geomembrane is damaged at or near the perimeter clamp, which could cause failures that are difficult to interpret.

One static compression loading was performed with each material A, B, C, and D. In each loading simulation, the geomembrane was underlain by a compacted clay layer to simulate the field conditions. The crushed rock material was then placed on the geomembrane and slightly tamped to produce a minimum of 100-mm thick uniform layer. A rigid steel platen was placed over the crushed rock material

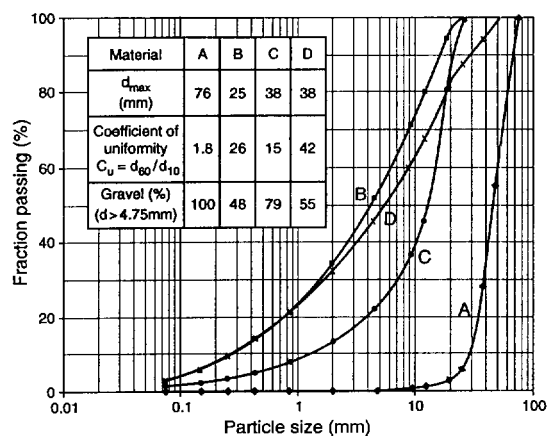


Figure 1. Particle-size distribution curves of crushed rock materials.



and a compressive stress of 860 kPa was applied to the top of the testing chamber to simulate the maximum anticipated field loading of 55 m height of ore, assuming an ore unit weight of 15.6 kN/m<sup>3</sup>.

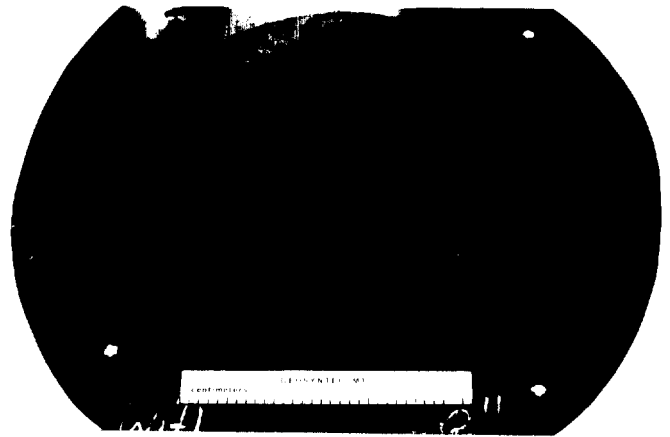
After 72 hours of sustained loading, the static compressive stress was removed and the geomembrane was carefully exhumed. The exhumed geomembrane was examined for any signs of damage and then subjected to a multi-axial tension test. The multi-axial tension tests were conducted on the geomembrane specimens generally within a few hours of exhumation. The multi-axial tension test was also conducted on a specimen of the virgin geomembrane in order to allow comparison between the failure modes and also obtain stress-strain data on the virgin geomembrane.

#### 4 SUMMARY AND DISCUSSION OF TEST RESULTS

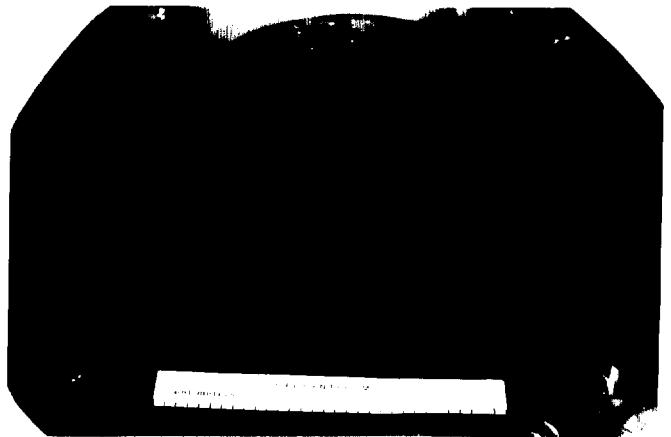
##### 4.1 Visual Examination After Compression Tests

Visual observations and the photographic documentation (Figure 2) of the exhumed geomembranes are summarized in Table 1 and can be described as follows:

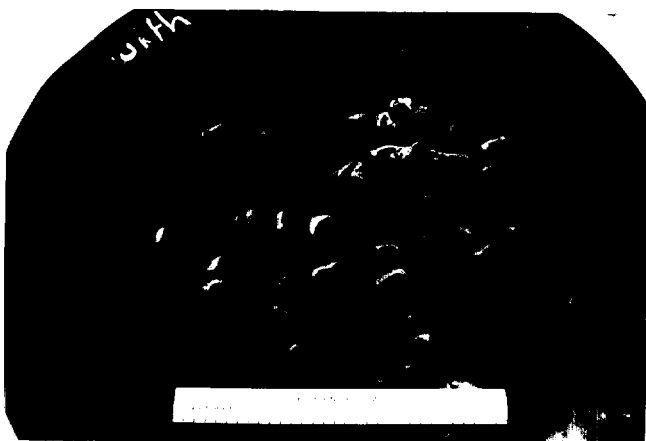
- The geomembrane that had been loaded with Material A showed significantly more damage than the other specimens. The imprints of the crushed rock material were visible at more than 50 locations on the upper surface of the geomembrane. Among these imprints, there were approximately 30 locations on the geomembrane surface which showed yield damage through the geomembrane thickness (i.e. where the imprints were also visible as protrusions on the lower surface of the geomembrane). However, no punctures were apparent at any of the contact points with Material A.
- The geomembrane specimen that had been loaded with Material B showed the least signs of damage. The



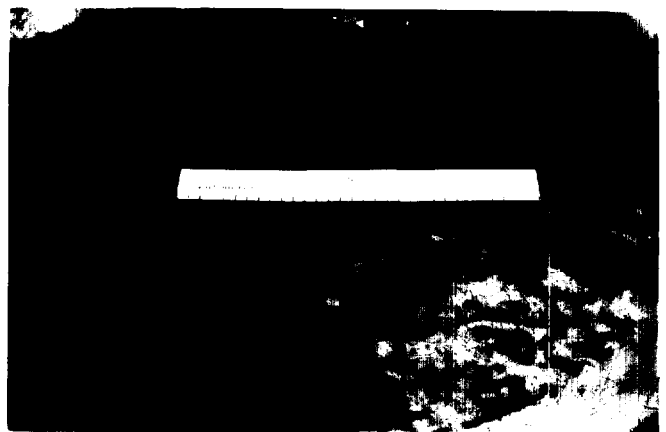
Material B



Material C



Material A



Material D

Figure 2. Photographic documentation of the imprints from Materials A, B, C and D.

Table 2. Summary of multi-axial tension test results (see Note 1)

Test feature	Geomembrane specimen				
	Virgin	A	B	C	D
Maximum tensile stress ("Peak") (MPa)	17.9	19.8	19.0	18.0	18.2
Tensile strain at maximum stress (%)	11.2	7.3	11.2	11.2	11.2
Maximum tensile strain (%)	23.0	11.2	14.5	21.4	27.4
Tensile stress at maximum strain ("Break") (MPa)	15.1	18.1	18.9	15.5	14.7
Mode of rupture (see Note 2)	DXL	LOC	DXS	DXL	DXL

Note 1: The stress and strain values presented in Table 2 are from actual test data. They are more accurate than the values that can be obtained from the curves in Figure 3 (especially the tensile strain at maximum stress, which is difficult to obtain with precision from the curves due to the shape of the curves).

Note 2: DXL = Geomembrane rupture at the center of the specimen diametrically in the cross-roll direction with a large yield zone; DXS = Geomembrane rupture at the center of the specimen diametrically in the cross-roll direction with a small yield zone; and LOC = Geomembrane rupture localized at a point where the geomembrane was in contact with one of the stones in the loading test.

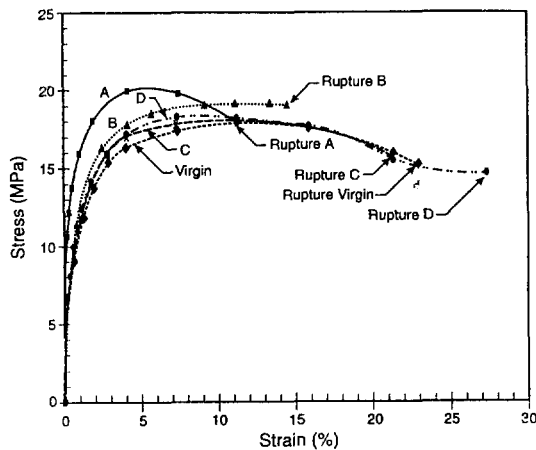


Figure 3: Multi-Axial Tension Test Stress-Strain Curves

- Material A significantly affected the geomembrane stress-strain curve (i.e. significantly lowering the tensile strain at peak) and significantly affected the mode of failure (i.e. geomembrane rupture at a point where the geomembrane had been damaged by a stone instead of being at specimen center).

It appears that the results of the multi-axial tension tests are consistent with the visual observations made on the geomembrane specimens following the compression loading simulation, which indicated the damage caused by Material A was far more severe than the damage caused by Materials B, C and D. Therefore, the results of the multi-axial tension tests are consistent with the criterion proposed in Section 2.

#### 4.3 Discussion of the Proposed Criterion

From the test results presented in Sections 4.1 and 4.2, it appears that the damage caused to the geomembrane by

Material A under the considered loading stress is unacceptable because it had two consequences that weakened the geomembrane and reduced its ability to resist mechanical actions during its service life: (i) it caused yield of the HDPE compound through the geomembrane thickness; and (ii) it caused a marked decrease in the yield strain of the geomembrane. In contrast, the damage caused by Materials B, C and D is acceptable.

Based on the above, an objective criterion for damage acceptability should be able to clearly distinguish between the geomembrane specimen that was loaded with Material A and the other geomembrane specimens. Several possibilities are considered:

- The maximum tensile stress (Table 2) does not provide any clear information.
- The tensile strain at maximum stress (Table 2) clearly distinguishes between the geomembrane specimen exposed to Material A and the other geomembrane specimens. Using the tensile strain at maximum stress as a criterion may therefore be appropriate. However, using the tensile strain at maximum stress as a criterion of geomembrane damage acceptability would have two drawbacks: (i) the peak of the stress-strain curves derived from multi-axial tension tests (Figure 3) is often not very marked and the determination of the strain at peak may be imprecise; and (ii) it would be difficult to develop a criterion that objectively distinguishes between an acceptable and an unacceptable strain reduction.
- The maximum tensile strain (Table 2) does not appear to provide results that are easy to interpret: damage to a geomembrane specimen results in an increase or a decrease of the maximum tensile strain.
- The tensile stress at maximum strain (Table 2) does not provide any clear indication.

imprints of the crushed rock material were visible at more than 100 locations on the upper surface of the geomembrane; however, none of these imprints resulted in yield damage through the geomembrane thickness as observed for the case of Material A.

- The geomembrane specimen that had been loaded with Material C showed moderate signs of damage by the overlying material. The imprints of the crushed rock material were visible at more than 50 locations on the surface of the geomembrane; however, none of these imprints resulted in yield damage through the geomembrane thickness as observed for the case of Material A. The imprints were slightly deeper and less uniform than those on the geomembrane specimen that had been loaded with Material B.
- The geomembrane specimen that had been loaded with Material D had a similar appearance as that loaded with Material B. The imprints of the crushed rock material were visible on more than 100 locations on the surface of the geomembrane; however, none of these imprints resulted in yield damage through the geomembrane thickness.

From the visual examination, it appears that Material A, caused significantly more damage than Materials B, C and D. From Figure 1, it appears that two characteristics that differentiate Material A from the three others and that may govern the ability of a granular material to cause a high degree of damage to a geomembrane are a large maximum particle size ( $d_{max}$ ) and a small value of the coefficient of uniformity,  $C_u$  (i.e. a very uniform particle size distribution curve). Indeed, these two parameters result in a smaller number of contacts between stones and geomembrane, hence higher contact forces for a given applied loading stress. This is confirmed by the number of imprints, which is less for Materials A and C than for Materials B and D (Table 1), and by the fact that Material A (large  $d_{max}$ , small  $C_u$ ) caused more damage than Material C (medium  $d_{max}$ , medium  $C_u$ ), which, in turn caused more damage than Materials B and D (medium  $d_{max}$ , very large  $C_u$ ). The angularity of the stones is another parameter that governs the ability of the stones to damage a geomembrane. However, no conclusion could be drawn from this testing program regarding this parameter since all four materials consisted of crushed stones of similar angularities.

## 4.2 Multi-axial Tension Tests

The results of the multi-axial tension tests, including the test performed on the virgin geomembrane specimen, are summarized in Table 2 and Figures 3 and 4. The interpretation of the results are as follows:

- The virgin geomembrane specimen and the geomembrane specimens that had been loaded with Materials C and D have similar stress-strain curves and the values of the maximum tensile strain, although different, are all between 20 and 30%. Also, they have the same mode of failure (Figure 4), i.e. rupture occurred at the center of the specimen, diametrically in the cross-roll direction, with a large yield zone.
- The geomembrane specimen that had been loaded with Material B has a stress-strain curve fairly similar to that of the virgin geomembrane, with approximately the same strain at peak (11.2%), but with a smaller strain at break. The failure mode (Figure 4) is rather similar to that of the virgin geomembrane, however, the yield zone is smaller in the case of the geomembrane specimen that had been loaded with Material B, which is consistent with the above comment about the strain at break.
- The geomembrane specimen that had been loaded with Material A has a strain at peak stress of approximately 7% whereas, in the four other cases, the strain at peak stress is approximately 11%. The mode of failure in the case of the geomembrane that had been loaded with Material A is distinctly different from the modes of failures with the four other geomembrane specimens (Figure 4). For Material A, the failure occurred at a point where the geomembrane had been damaged by a stone, in contrast with the four other specimens, where the failure occurred at the center of the specimen, i.e. independently from damage caused by the stones.

The above interpretations of the multi-axial tension tests may be summarized as follows:

- Materials C and D had essentially no effect on the geomembrane stress-strain curve and did not affect the mode of failure (i.e. geomembrane rupture at specimen center).
- Material B did not significantly affect the geomembrane stress-strain curve and did not affect the mode of failure (i.e. geomembrane rupture at specimen center).

Table 1. Summary of visual observations

Material	Holes	Imprints	Yield through	Yield size	Qualitative evaluation
A	None	>50	≈30	>2 mm×8 mm <5 mm×50 mm	Severe
B	None	>100	None	<1 mm×5 mm	Light
C	None	>50	None	<1 mm×5 mm	Light
D	None	>100	None	<3 mm diameter	Light

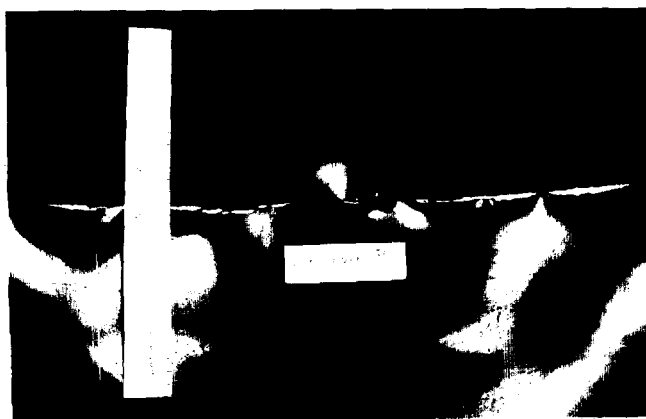
- The mode of rupture provides a clear distinction between the geomembrane specimen exposed to Material A and the other specimens, without the need for selection of a threshold property value separating acceptable from unacceptable damage.
- It may also be concluded that the damage, deemed unacceptable based on the mode-of-rupture criterion described above, also results in a decrease in tensile strain; however, the decrease in tensile strain does not provide an objective pass-or-fail criterion.

## 5 CONCLUSIONS

The paper has shown that a criterion based on the mode of rupture of a mechanically damaged geomembrane specimen subjected to a large-diameter multi-axial tension test provides a practical and defensible means to determine whether a certain type or level of mechanical damage is acceptable or not. The criterion is also consistent with the authors' observations from several mechanical damage studies.



Material A.



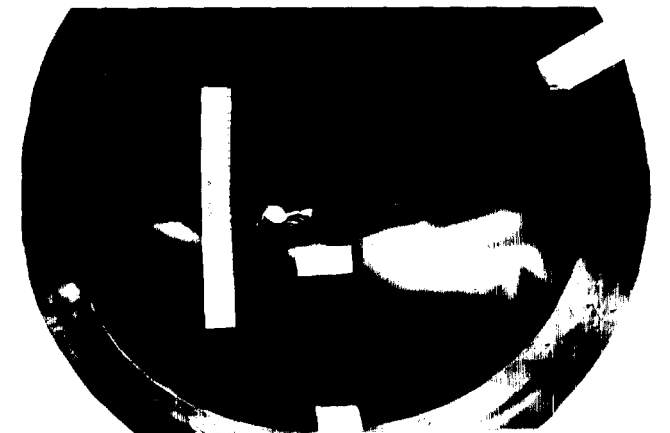
Material B.



Material C.



Material D.



Virgin Material.

Figure 4. Photographic documentation of geomembrane mode of failure during the multi-axial tension tests.

## ACKNOWLEDGMENTS

The authors are grateful to K. Holcomb, S.L. Berdy and R.P. Kari for assistance during the preparation of the paper.

H. Zanzinger

LGA, Geotechnical Institute, Nuremberg, Germany

E. Gartung

LGA, Geotechnical Institute, Nuremberg, Germany

**ABSTRACT:** Geomembrane liners at the base of solid waste landfills must be protected from stones and other sharp objects to properly act as liquid barriers. In Germany, where administrative instructions require very coarse grained drainage blankets above basal liners of solid waste landfills, special emphasis is placed on the selection of adequate protective layers. Their efficiency has to be demonstrated by tests according to the GDA-Recommendations of the German Geotechnical Society. The efficiency of six different geosynthetic protective layers was studied by large scale performance tests. The basal liner system, consisting of a compacted clay liner, a 2.5 mm thick HDPE-geomembrane, the protective layers and 0.3 m drainage stone of 16 to 32 mm were submitted to a uniformly distributed load increased step-wise up to 800 kPa. After more than two months loading, the geomembrane was exhumed and the deformations were examined by laser-measuring technique. The six protective layers lead to different results. All systems tested functioned successfully. A comparison of the performance observed by large scale testing and the assessment of the anticipated efficiency according to standard tests allows conclusions concerning the German protection efficiency test.

**KEYWORDS:** Geocomposites, Laboratory Tests, Landfills, Performance Evaluation, Puncture Resistance

## 1 INTRODUCTION

Basal liner systems of solid waste landfills consist of impermeable geomembranes (GM) and mineral sealing layers such as compacted clay liners (CCL) in combination. There may be a single GM like in the German standard composite liner (Gartung 1996) or there may be two GMs, e.g. the double liner system employed in many landfills in the USA (Koerner 1994). In any case, there have to be leachate collection and removal facilities immediately above the basal seal to prevent increasing hydraulic heads above the liner. The dewatering systems typically comprise a drainage layer of gravel or crushed stone of 16 to 32 mm diameter.

Below the overburden of the waste deposit the coarse grained drainage material exerts very high local stresses on to the GM which could cause puncturing. So protection layers are installed between the coarse drainage aggregates and the GMs to prevent failure of the polymeric seal. The requirements to be met by the protection layers have been established on the basis of engineering judgment, and they have been supported by theoretical models. For the protection of the primary GM liner in the USA, Wilson-Fahmy, Narejo and Koerner (1994) carried out extensive studies. In Germany, where only one HDPE-GM of at least 2.5 mm thickness is used as a component of the composite basal liner, theoretical arguments for the criteria required for adequate long-term performance of protection layers have been presented by Seeger and Mueller (1996). In either country laboratory tests are performed for the evaluation of the suitability of protection layers. These tests which differ in both countries are modeling the function of the protection layer under simplified boundary conditions.

The adequacy of such „index“-tests is not known, because there is no real long-term field experience with the performance of protectors. As a contribution to the discussion of GM protection issues, results are presented here of some large scale model tests which were carried out at the LGA Geotechnical Institute at Nuremberg in Germany.

## 2 STANDARD PROTECTION EFFICIENCY TESTS

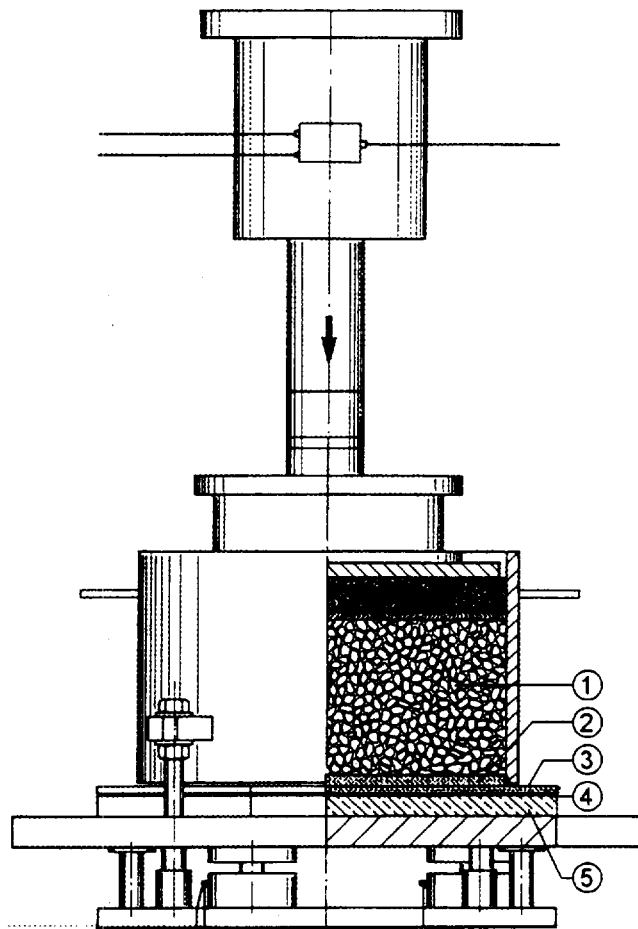
In the German standard test for the evaluation of the efficiency of protection layers, samples of the protector together with the GM of at least 300 mm, in our case 500 mm diameter, are submitted to loads in a device shown on Figure 1.

The coarse drainage aggregate above the protector consisted of natural river gravel 16 to 32 mm in the case reported here, and there was a 20 mm thick elastomer layer of 50 Shore hardness below the loaded test sample as specified in the GDA-Recommendations (1997). A vertical stress of 1,350 kPa at a temperature of 20°C was applied for 100 hours, and the resulting deformations at the lower surface of the GM were recorded by means of thin soft metal sheets. The deformed shape of the ductile metal sheets was transferred to plaster and after hardening, the micro-topography of the gypsum block was surveyed by laser to be evaluated with respect to the deduction of strains that occurred in the GM below the protecting geocomposite by data analysis. The results of the standard tests on the different products for protective layers reported here are presented on Table 2.

Table 1. Protection layer systems tested for this study

System No.	Type of geosynthetic	Polymer	Mass per unit area (g/m <sup>2</sup> )	Thickness at 2 kPa (mm)
1	geocomposite (geotextile/geomat/rubber)	PET/PA/rubber	6,646	12.2
2	geocomposite* (geotextile/geonet/geotextile)	HDPE and PP	2,025	12.9
3	geocontainer**(woven geotextiles linked with spacer threads)	HDPE and sand 0.1 to 1.0	≈70,000	≈50
4	geocontainer**(woven geotextiles linked with spacer threads)	HDPE and sand 0.1 to 1.0	≈56,000	≈40
5	geotextile*, nonwoven needlepunched	PP	4,274	26.8
6	geotextile, nonwoven needlepunched	PP	2,137	13.4
7 = 8	geocomposite** (geotextile/geomat/sand 0.1 to 1.0/woven+nonwoven geotextile)	PP/sand 0.1 to 1.0/HDPE	≈48,000	≈26

\* double layer    \*\* filled with sand on site



- ① Coarse gravel
- ② Protection layer
- ③ GM
- ④ Ductil metal sheet
- ⑤ Elastomer layer

Figure 1. German standard test device for puncture protection efficiency tests

### 3 GEOSYNTHETICS FOR PROTECTION

The cushioning effect of protectors for GMs can be achieved by mineral layers such as sand, by geosynthetic sheets or by combinations of these two types of materials. Out of the great number of different products available, 6 geosynthetic protection layers were selected for the study reported here. They are listed on Table 1.

The geocomposite product no. 1 consists of rubber tire chips enveloped by geotextiles. No. 2 is a geocomposite routinely installed in many civil and environmental applications for drainage purposes, it was tested as a double layer protector. The geocomposites no. 3 and no. 4 are essentially mattresses filled with sand at the construction site. They are tailored to the needs of the particular landfill site and prefabricated. Protectors no. 5 and no. 6 are very robust mechanically bonded nonwovens. They are applied as single or double layers at the base of landfills, depending on the amount of overburden; in the study reported here, the efficiency of single and double layers was tested. The protection geocomposite on test fields no. 7 and no. 8 contains sand. The sand is filled into prefabricated geosynthetic sheets at the construction site.

### 4 LARGE SCALE TESTS

At the LGA Geotechnical Institute large scale model tests were carried out, primarily for the determination of the soil-structure interaction of HDPE drainage geopipes and the surrounding soil (Zanzinger and Gartung 1998). The model was 5.4 m long, 4.4 m wide and 2.0 meters high. At the base it consisted of a composite liner, CCL of 0.6 m and HDPE GM of 2.5 mm thickness. The GM was protected against puncturing by a layer of geosynthetic protectors. The total area of 24 m<sup>2</sup> was subdivided into 8 test fields covered with 6 different products. In two cases two test fields were provided with identical protectors. The

Table 2. Comparison of results of different protection layer systems from laboratory and large scale tests

System No.	Protection efficiency test (according to GDA-recommendation E 3-9)		Large scale test	
	Average strain (%)	Peak strain $\epsilon$ (%)	Average strain (%)	Peak strain $\epsilon$ (%)
1	0.04	0.21	0.08	0.41
2	0.02	0.07	0.08	0.66
3	0.34	0.99	0.11	0.75
4	0.02*	0.19*	0.05	0.46
5	0.06	0.17	0.09	0.58
6	0.09	0.26	0.10	0.92
7	0.07	0.62	0.07	0.79
8 = 7	-	-	0.05	0.78

\* sample taken from a landfill construction site, tested at  $\sigma = 1,350$  kPa,  $\vartheta = 40^\circ$  C,  $t = 1,000$  h

drainage layer was composed of natural river gravel 16 to 32 mm, above which a mixture of sand-wood shavings was placed as a waste material substitute. The entire model was encapsulated with concrete slabs and tied together with high strength steel tension rods. So a uniformly distributed vertical stress representative of the over-burden of 60 m of solid waste could be applied via hydraulic flat jacks. Details of the loading procedure and the stress distribution within the model are given elsewhere (Zanzinger 1996).

For the quantitative determination of the performance of the protectors each test field was equipped with a 520 mm x 520 mm sheet of soft ductile metal at the lower surface of the GM in the zone of maximum vertical stresses below the foot of the structural arch which developed in the gravel adjacent to the geopipe. The recording procedure for the deformation measurement of the GM was the same as in the standard laboratory test. The metal sheet follows the deformation of the GM without any resistance, so also without developing any stress. After exhuming, the metal sheets depict the exact shape of the deformed GM. The micro-topography is then recorded by a plaster imprint which is surveyed with excellent precision by laser-measurements at 3 mm centers in two directions. As a result, a three dimensional image of the deformed GM is obtained. An example of the measured micro-topography is shown on the lower part of Figure 2.

Applying a detailed geometrical analysis to the deformation data, the distribution of strains in the GM is determined and plotted as shown on the upper part of Figure 2.

## 5 TEST RESULTS

Table 2 summarizes the most significant test results. It can be seen, that the average strains as well as the maximum strains determined in the standard laboratory test under a vertical stress of 1,350 kPa applied for 100 hours are somewhat smaller than the strains determined by the large scale test under a load representative of 60 m of waste

overburden applied for 6,500 hours (9 months). At test fields no. 7 and 8 where the protection is mainly achieved by about 20 mm of sand and the geotextiles are merely used as containers, hardly any differences between the two testing methods occurred.

Perhaps the most significant difference between the standard laboratory tests and the large scale test is their duration. The load was applied 65 times longer in the large

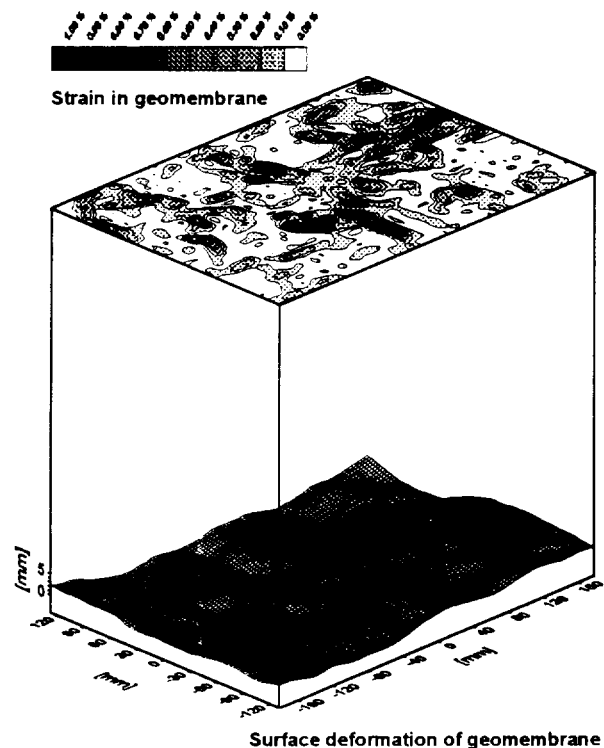


Figure 2. Image of the deformed GM and measured strain distribution

scale test than in the smaller lab tests. So it is conceivable that the larger deformations of the GM in the large scale test indicate the time dependent behavior of the polymeric geocomposites. But since there are also some other differences in the testing procedures, such as the stiffness of the base material: elastomer in one case, compacted clay in the other case and since the stress acting on the geomembrane in the large scale test is not exactly known, some other factors may also have contributed to the differences in the test results.

The performance of the sand filled geotextiles, test fields no. 3 and 4 and no. 7 and 8 is somewhat surprising. These systems which can certainly be considered suitable and durable because they employ mineral constituents, exhibit the largest values of maximum strains.

In case of the composite of test fields no. 3 and 4, the sand filled mattress with the greatest thickness and mass per unit area, the reason for the behavior can be assigned to the high degree of sand filling in the large scale test. The mattress transmits the vertical load along parallel lines. So the surface of the GM and below it the surface of the mineral sealing layer as well appear undulated. If the mattress is filled with less sand, this undulation can be minimized or avoided. This becomes evident, when the much smaller strains measured under conditions in the field (see Table 2, system no. 4: sample from a landfill side) are taken into account.

The protector no. 7 and 8 is thinner than the one of no. 3 / no. 4. The lower geotextile layer of the geocomposite is connected by welding points, and these welding points are stiffer than the surrounding elastic sections as matter of fact, the deformation of the GM is not caused by the drainage material above the protector but rather by the protector itself. So in the local region of the welding points there is an arching effect and the geomembrane is moving upwards.

These strains of the GM below sand filled protectors have to be regarded differently than those which are measured below pure geosynthetic protectors, because they are initiated by the structure of the protector. They are certainly tolerable at the recorded order of magnitude.

## 6 CONCLUSIONS

There is a difference in the maximum strains measured by standard protection efficiency tests and large scale field tests. If the large scale field tests are considered closer to actual field conditions, it turns out that the standard laboratory test underestimates the local maximum strains of the GM. So the lab test should be regarded as an index test rather than a performance test.

The local maximum strains of the geomembrane protected by geocomposites containing sand were greater than those of the tested geocomposites without mineral components. In all cases the maximum strains measured in the large scale test were less than 1 %. In our opinion all

geosynthetic protection layers tested in the study presented here, performed successfully and are suitable for use at the base of solid waste landfills.

## ACKNOWLEDGMENTS

The large scale tests for the study of the geopepe-soil interaction were financially supported by the Ministry of the Environment, the State of Bavaria. The support is gratefully acknowledged.

## REFERENCES

- BAM (1992) "Richtlinie fuer die Zulassung von Kunststoffdichtungsbahnen als Bestandteil einer Kombinationsdichtung fuer Siedlungs- und Sonderabfalldeponien sowie fuer Abdichtungen von Altlasten", Berlin, Germany, 47 p.
- Gartung, E. (1996) "Landfill Liners and Covers", *Geosynthetics: Applications, Design and Construction*, de Groot, den Hoedt and Termaat (eds.), A.A. Balkema, Rotterdam, The Netherlands, pp. 55-70.
- GDA-Empfehlungen (1997) *Geotechnik der Deponien und Altlasten*, 3. Auflage, Verlag Ernst & Sohn, Berlin, Germany.
- Koerner, R.M. (1994) *Designing with Geosynthetics*, 3rd ed., Prentice Hall, Englewood Cliffs, NY, USA, 704 p.
- Seeger, S. and Mueller, W. (1996) "Limits of Stress and Strain: Design Criteria for Protective Layers for Geomembranes in Landfill Liner Systems", *Geosynthetics: Applications, Design and Construction*, de Groot, den Hoedt and Termaat (eds.), A.A. Balkema, Rotterdam, The Netherlands, pp. 153-157.
- Wilson-Fahmy, R.F., Narejo, D.B. and Koerner, R.M. (1994) "A Design Methodology for the Puncture Protection of Geomembranes", GRI Report #13, Philadelphia, PA, USA, 93 p.
- Zanzinger, H. (1996) "Grossmassstaeblicher Modellversuch an Draenroehren in Deponien", unpublished research report, 324 p.
- Zanzinger, H. and Gartung, E. (1998). "HDPE-Geopipes, Soil-Structure Interaction", *6th International Conference on Geosynthetics*, Atlanta, GA, USA, 4 p.



# A Rational Design for the Protection of Landfill Geomembrane Liners

Krishna R. Reddy

Assistant Professor, Department of Civil & Materials Engineering, University of Illinois, Chicago, Illinois, USA

Richard E. Saichek

Graduate Research Assistant, Department of Civil & Materials Engineering, University of Illinois, Chicago, Illinois, USA

**ABSTRACT:** An adequate protective cover system is essential for preventing damage to the landfill geomembrane liner from impact, over-stressing, tearing, or puncturing during and after construction. The current method for ensuring protection of the geomembrane liner usually employs a soil layer that is 0.3 m thick, and in some cases uses a nonwoven geotextile between the soil and geomembrane for increased protection. The soil layer must possess a minimum hydraulic conductivity of  $1 \times 10^{-3}$  cm/s so that it also functions as a drainage layer. The optimal thickness and appropriate gradation of the soil to use in the protective cover and drainage layer have not been established. Furthermore, the optimal weight (or mass per unit area) of the geotextile has not been determined. In order to address these issues, field and laboratory tests were performed to determine the effects of soil gradation, presence of a geotextile, construction loading, and long-term waste loading on the geomembrane protection. The results of this testing demonstrated that a 0.3 m thick soil layer consisting of particles with  $D_{50}$  less than 30 mm and sphericity greater than 0.8 overlain on a  $270 \text{ g/m}^2$  nonwoven geotextile serves as an efficient protective cover system for a 1.5 mm thick HDPE geomembrane liner when it is constructed using construction equipment which exerts a ground pressure less than 30 kPa. This protective cover system was also found to be effective even under long-term waste loading up to a maximum pressure of 1400 kPa. However, a rational design approach taking into account site-specific conditions will provide the most optimal protective cover system for the geomembrane liners.

**KEYWORDS:** Geomembranes, Geotextiles, Landfills, Liner, Soils, Protective Cushioning, Installation Damage, Survivability

## 1 INTRODUCTION

An adequate protective cover system is essential for preventing damage to the landfill geomembrane liners from impact, over-stressing, tearing, or puncturing during and after construction. Currently, specific USEPA regulations on protective cover systems do not exist other than the stipulation that the leachate drainage layer which overlies directly above the geomembrane liner should be selected such that leachate head does not exceed 0.3 m. Some state landfill regulations additionally stipulate that the drainage layer material must possess a minimum hydraulic conductivity of  $1 \times 10^{-3}$  cm/s and a minimum thickness of 0.3 m. Many materials meet these requirements to be suitable for use in the drainage layer. These materials include soils, geosynthetics, recycled materials (e.g., shredded scrap tires), or a combination of these materials. Soils have been conventionally used; however, geosynthetics and recycled materials have also gained wide acceptance.

In addition to the efficient drainage of leachate, the designer must also assess the potential damage to the geomembrane liner during and after the construction of the drainage layer. Intuitively, there is a greater potential for geomembrane damage if a soil consisting of large size angular particles is used. Thus, the drainage layer material must be selected such that it serves a dual purpose, both as an efficient drainage medium and as an adequate geomembrane protective cover.

The common design practice is to use a soil layer to serve as a protective cover as well as a drainage layer. Optionally, a geotextile is placed above the geomembrane prior to the placement of the soil. The current approach to the selection of the soil type is mainly based on the minimum hydraulic conductivity requirement;

however, a wide range of soils can possess hydraulic conductivities equal to or greater than the required  $1 \times 10^{-3}$  cm/s. Therefore, an additional requirement which ensures maximum protection to the geomembrane liner is needed. In addition, the adequacy of using a 0.3 m thickness for the leachate drainage layer to serve as a protective cover is unknown. Furthermore, the necessity of using a geotextile above the geomembrane and, if necessary, the type of geotextile needed is unknown. Generally, protective cover systems are designed based on an empirical approach or the personal judgement of the designer. In order to develop a rational design approach, several researchers have performed both theoretical and experimental studies.

In this paper, an overview of previous studies performed on protective cover systems is provided first. Then, a summary of findings from a research study performed at the University of Illinois at Chicago (UIC) which involved both field and laboratory testing on protective cover systems is presented. Finally, a rational approach to the design of protective cover systems is outlined.

## 2 PREVIOUS STUDIES ON PROTECTIVE COVERS

Giroud (1992) evaluated the effects of placing a geotextile on the top, the bottom, or on both sides of the geomembrane on properties of the geomembrane. Puncture and impact tests were performed using a variety of 0.75 mm-thick geomembranes and 200, 400 and  $600 \text{ g/m}^2$  nonwoven needle punched geotextiles. These test results showed that using a geotextile either on top, bottom or on both sides increases the puncture and impact resistance over the geomembrane by itself. However, the combined effects of using a geotextile with soils over the

geomembrane were not investigated in this study.

Motan et al. (1993) performed laboratory testing using a pressure chamber in which a layer of angular gravel was formed by mounting particles with epoxy onto a plywood base, a geotextile was then placed, and finally a 1.5 mm thick smooth geomembrane was placed over the geotextile. Air pressure was applied in increments up to 815 kPa and then released. The geomembrane sample was removed and multi-axial tension tests were performed. This testing was repeated with geotextiles with four different weights of three different brands. Although beneficial effects of using a geotextile were observed, there was no consistent trend observed to conclude if one geotextile was better than the other. The testing conditions used in this study simulated protrusions from the subgrade. Only one particular soil was used and the soil particles were not allowed to move or reorient during the loading.

Koerner and his co-investigators reported a comprehensive investigation performed at Drexel University in order to determine the puncture protection of 1.5 mm thick HDPE geomembranes under different conditions and the results have been published in a three part comprehensive paper (Wilson-Fahmy et al., 1996; Narejo et al., 1996; Koerner et al., 1996). This investigation included a theoretical approach, an extensive laboratory experimental program, and a simplified design procedure. The theoretical approach is based on tensioned membrane theory and assumes axi-symmetric conditions on a geomembrane overlain on a single isolated protruding object rising above a firm subgrade. The effects of the height and top shape of the protrusion on the puncture resistance of geomembrane under the application of hydrostatic pressure were studied. The effects of the presence of geotextile between the geomembrane and the protrusion was also analyzed. Based on the comparison of pressures required for the initiation of yield conditions for a 1.5 mm thick HDPE geomembrane, it was concluded that an increase in the protrusion height, which is correlated to soil particle size, reduced the puncture resistance of the geomembrane. However, an increase in the radius of the protrusion shape, which reflects rounded or subrounded compared to angularly shaped particles, resulted in higher puncture resistance. In addition, it was determined that the effect of increasing the mass per unit area of the protection geotextile proved to significantly increase the puncture resistance of the geomembrane.

The above theoretical study was augmented with a laboratory testing program which involved: (1) hydrostatic pressure truncated cone puncture tests as per the standard test method ASTM D 5514, (2) similar tests except with cones substituted with isolated stones, (3) hydrostatic tests with geomembranes overlain on a bed of stones, and (4) geostatic tests which involved one truncated cone overlain by a geomembrane which in turn was overlain by a layer of sand and then was subjected to loading through the use of a rigid plate. The loading was gradually increased until failure of the geomembrane occurred. Some long-term tests were also conducted which involved loading to the fraction of its failure load and maintaining it for a long duration or until failure occurred. The different test variables considered in this testing program included different cone heights, different thicknesses of HDPE

geomembrane, and a 1.5 mm thick HDPE geomembrane with different protective geotextiles. The tests with isolated truncated cones or stones revealed that the geomembrane puncture resistance increases when: (1) the mass per unit area of the protective geotextile is greater, (2) protrusion heights are smaller, and (3) protrusion shapes are rounded as compared to angular. The arching and creep effects are also found to influence the geomembrane puncture resistance. All of these results are very useful in evaluating the geomembrane protection against isolated protrusions from the subgrade. In tests with a layer of packed stones, geomembrane failure could not be achieved; therefore, the signs of yield conditions were visually observed.

Using the puncture test data obtained using the isolated truncated cones and isolated stones, an empirical equation was suggested to calculate an allowable stress for a 1.5 mm thick HDPE geomembrane. This equation involves mass per unit area of the protective geotextile, protrusion height, and a series of modifying factors and partial factors of safety to account for the field conditions such as stone shape, packing density, soil arching, creep and chemical/biological degradation as well as a global factor of safety to account for uncertainties in the formulation.

The above study by Koerner and his co-investigators clearly documents the beneficial effects of using a geotextile to protect the geomembrane from damage due to isolated protrusions in the subgrade. The tests performed with a layer of stone closely simulated the protective cover and drainage layer over a geomembrane. However, the damage to the geomembrane in these tests was only assessed visually; therefore, quantification of the extent of physical changes that occurred for different stone types was subjective. The proposed design procedure is conservative because it is mainly based on the test results using isolated truncated cones or stones rather than test results using a bed of stone. Also, the values of different modification factors and partial factors of safety are required in using this procedure. In addition, the effects of construction loading are not addressed in this methodology.

Richardson (1996) investigated damage induced to a geomembrane when it is subjected to construction loading. A variety of geosynthetic cushions were evaluated to protect the geomembrane under two types of construction equipment loading conditions. A particular soil was employed with two different thicknesses 0.3 m and 0.6 m. It was found that even the lightest of geotextiles offered increased protection from scratches and dents. From laboratory wide width tensile testing, it was concluded that the recommended weight for a nonwoven geotextile, based on a factor of safety of three, was a 405 g/m<sup>2</sup> for a normal pressure of 345 kPa and linearly increased to approximately 1519 g/m<sup>2</sup> for a pressure of 2068 kPa. In this study, the yield strain and load correlated well with the visual damage to the geomembrane. However, other studies have found that physical changes to the geomembrane do not affect the yield strain and load, but the ultimate strain and load are affected (Reddy et al., 1996).

Among other countries, German regulations specify more stringent requirements on protective cover systems for the geomembrane liners (Brummermann et al., 1994). According to these regulations, if a strain as small as 0.25% is induced due to

local deformation of the geomembrane, the protective cover system is deemed unsuitable (Seeger and Muller, 1996). The yield stress of a 1.5 mm smooth geomembrane liner as determined by a wide strip tension test is approximately 18%. Even a third of this strain to reflect a factor of safety of 3 would be significantly higher than that of the German regulatory limit of 0.25%. Due to the strict regulations on the allowable strain in the geomembrane, the protective cover layer is constructed as a separate layer underneath the drainage layer. Three types of materials are commonly used for these protective cover layers: (1) nonwoven geotextiles with masses per unit area that are greater than 2000 g/m<sup>2</sup>, (2) sandfilled geotextiles or woven mattresses, and (3) nonwoven geotextiles with masses per unit area greater than 1200 g/m<sup>2</sup> that are covered with a coarse (0-8 mm) particle layer with a thickness of 15 cm or greater. Additionally, German systems use a geomembrane that has a 2.5 to 3 mm thickness and a drainage layer that employs a very coarse gravel that is graded from 16 to 32 mm (Seeger and Muller, 1996). Thus, it appears that the protective cover systems used in Germany are overly conservative.

### 3 RESEARCH ON PROTECTIVE COVERS AT UIC

Research conducted on protective covers for landfill geomembrane liners at UIC involved both field and laboratory testing to assess the performance of different protective cover conditions and to develop a rational design approach. An overview of the field and laboratory testing is provided in this section and the recommended rational design approach based on these test results is provided in the next section.

The procedures and results of field testing performed to evaluate different protective cover systems under construction loading have been described in detail by Reddy et al. (1996). This testing included seven test pads in order to determine the soil type, geotextile, and construction equipment that best protected the 1.5 mm thick smooth HDPE geomembrane liner. Two soils, a fine gravel and a medium gravel, were tested both with and without a 270 g/m<sup>2</sup> nonwoven geotextile. Two types of dozers, a light and a heavy dozer, were used for construction and reflected the typical field loading conditions. After the application of repetitive construction loading, geomembrane samples were exhumed, visually observed, and tested in the laboratory to assess the effects of physical changes on the properties of the tested geomembranes as compared to the virgin geomembrane. The laboratory tests performed on the exhumed geomembrane samples included wide strip tension, multi-axial tension, and water vapor transmission (WVT) tests. Typical results of multi-axial tension tests are presented in Figure 1.

These results showed that the physical changes in the geomembrane are reflected in the differences in the elongation at burst from multi-axial test and the ultimate strain and ultimate stress from wide strip tensile tests as compared to the values for the virgin geomembrane. The physical changes were significant for coarser soil and for heavy construction loading conditions. It was concluded from this study that a 270 g/m<sup>2</sup> nonwoven geotextile can significantly protect the geomembrane from

construction loading even when using construction equipment exerting a pressure of 46 kPa is used.

The field testing was complemented with a laboratory testing program in order to assess the protective cover systems under simulated long-term waste loading conditions. These tests were performed in a specially constructed simulation test setup. The details of the test setup and testing procedures have been given by Reddy and Saichek (1997). For these tests, an elastomer, which possessed compressibility similar to that measured for a typical compacted clay, was laid at the bottom of the test setup, and then a geomembrane was laid on the top of the elastomer. Different protective systems were installed over the geomembrane with different soils both with and without a geotextile. The soils used ranged from sand to gravel corresponding to D<sub>50</sub> values of 0.65 to 30 mm, respectively. The sphericity values ranged from 0.798 for the crushed gravel to 0.846 for the fine gravel. A rigid plate was placed on the cover system and incremental loading up to 1400 kPa was applied. The load was maintained constant for 48 hours and then gradually released. The geomembrane was then carefully exhumed and visually observed. Multi-axial tension, wide strip tension and WVT tests were performed similar to the field testing program in order to characterize the physical changes that the geomembrane had undergone due to loading. These test results also revealed that physical changes were reflected in the elongation at burst from multi-axial tests, and the ultimate stress and strain from wide strip tension tests. Overall, these long-term simulation testing results showed a similar trend in that a 270 g/m<sup>2</sup> geotextile adequately protected the geomembrane even when it was subjected to a high pressure of 1400 kPa. For long-term testing performed without a geotextile, the geomembrane elongation at burst and, generally, the stress and strain at break also decreased as the soil particle size increased. Figure 2 shows the changes in the elongation at burst observed as a function of mean particle size. The results for the tests incorporating a 270 g/m<sup>2</sup> geotextile are also shown in this figure. These results demonstrate that larger size particles cause more extensive physical changes as compared to smaller size particles, and the beneficial effects of incorporating a geotextile weighing 270 g/m<sup>2</sup> is clearly evident.

It should be noted that although valuable information has been obtained from this study, additional field and laboratory testing using distinctly different soils, types of geotextiles, and loading conditions is essential in order to create an extensive database which can then be utilized to develop design charts.

### 4 RATIONAL DESIGN APPROACH

In order to construct a protective cover system which will perform the functions of efficient drainage and adequate protection of the geomembrane, a rational design approach is outlined below:

Step 1: Obtain information on the subgrade and the liner components. Particularly, the type and thickness of the geomembrane must be known before the protective cover design can proceed.

Step 2: Select the type of material which will serve as both the protective cover and drainage layer. Potential materials can be

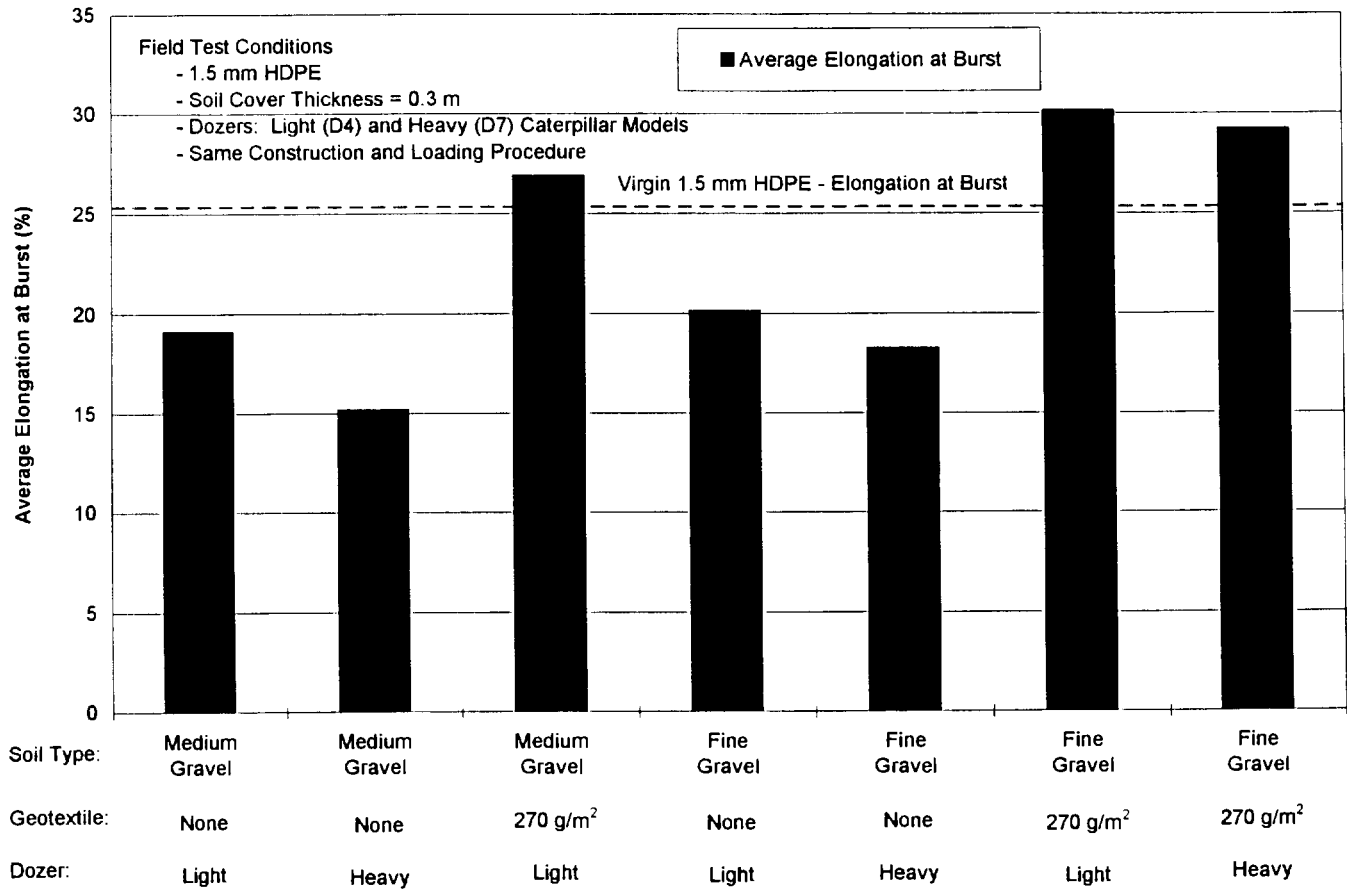


Figure 1. Evaluation of Field Performance of Protective Cover Systems Under Construction Loading

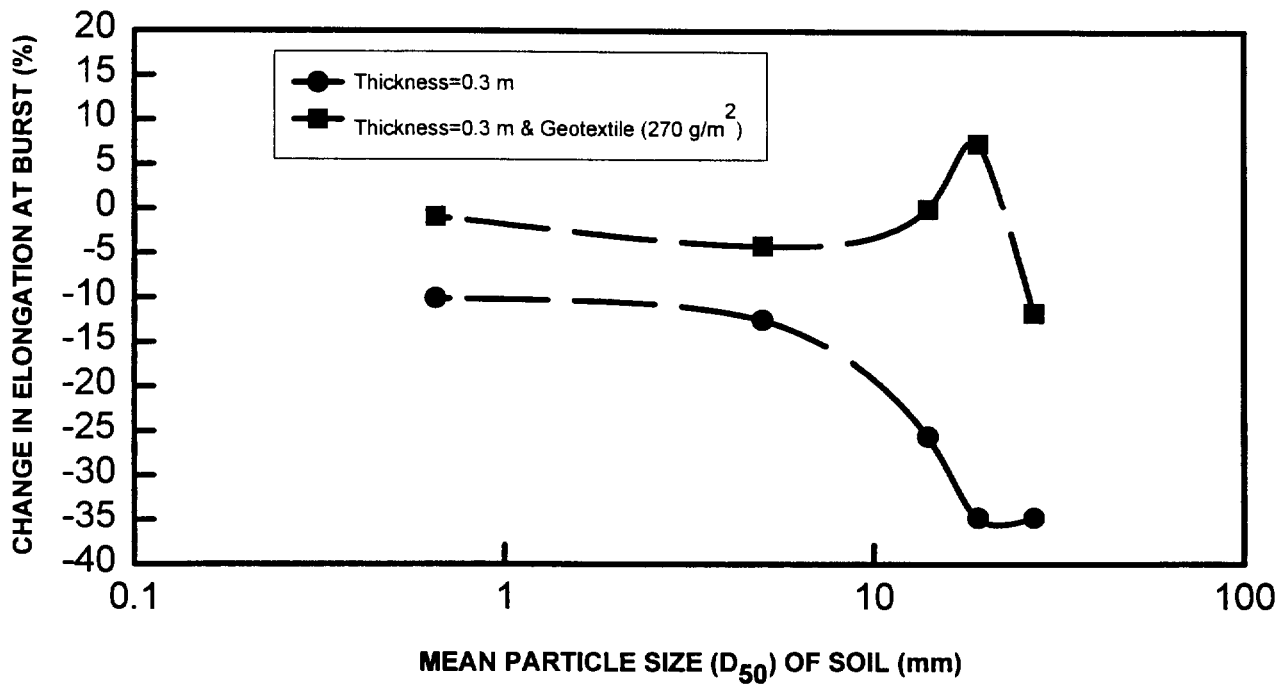


Figure 2. Evaluation of Protective Cover Systems Under Long-Term Waste Loading Conditions

either soils, geosynthetics, recycled materials, or a combination of these materials. For this paper, soils are considered as the suitable choice of materials. The different soil sources in the vicinity of the project site should be identified, and costs associated with procuring soils from these sources should also be obtained.

**Step 3:** Characterize the soils which have potential for use as protective and drainage materials as well as being cost-effective. The characterization must include particle shape, grain size distribution, density, hydraulic conductivity, durability, and shear strength. The soil must possess a minimum hydraulic conductivity of  $1 \times 10^{-3}$  cm/s and be compatible with the leachate characteristics of the expected waste material in order to be further considered.

**Step 4:** Determine the clogging potential of the soil. Standard filtration, retention, and clogging procedures can be followed as detailed by Koerner (1994). In addition to investigating physical clogging, biological activity should also be studied. Logically, soils containing relatively large voids and a high permeability are less likely to become clogged by finer particles or biological growth.

**Step 5:** Perform a protective performance evaluation of the potential soils under both construction and long-term loading conditions. This evaluation provides the necessary thickness of the soil and the necessity of using a geotextile. The UIC research results showed that a 0.3 m thick soil layer consisting particles with  $D_{50}$  in the range of 0.65 to 13 mm and sphericity greater than 0.8 placed over a  $270 \text{ g/m}^2$  nonwoven geotextile will provide adequate protection against low ground pressure (<30 kPa) construction equipment as well as long-term waste loading pressures up to 1400 kPa. These results may be used as an initial guidance for the selection of soil gradation; however, a site-specific testing program using the procedures developed at UIC (Reddy et al., 1996; Reddy and Saichek, 1997) is highly desirable.

**Step 6:** Evaluate the selected system for stability on the slopes to ensure that no sliding will take place within any material layer or along any interface.

**Step 7:** Stipulate QC and QA procedures in order to ensure that the materials, equipment, and construction procedures meet the specifications. The composition and placement of the first few lifts of waste should also be monitored to ensure that possibly damaging waste products, such as old concrete reinforcement bars, are not located directly on top of the protective cover soil.

## 5 SUMMARY

The current practice for geomembrane protection is to use a 0.3 m thick soil layer with or without an underlying geotextile. The protective soil layer also serves as the leachate drainage layer and must possess a hydraulic conductivity greater than  $1 \times 10^{-3}$  cm/s. Employing an excessively thick layer of protective cover soil is uneconomical, and using a layer that is too thin increases the susceptibility of the geomembrane to damage. The type of soil, particularly the shape and size of the particles, also influences the degree of protection offered to the geomembrane. In addition, the beneficial effects of the geotextile below the soil layer have not been well quantified.

Comprehensive field and laboratory testing undertaken at UIC was aimed at determining the adequacy of different cover systems during construction and under long-term waste loading conditions to protect a smooth 1.5 mm high density polyethylene (HDPE) geomembrane. The field investigation involved the testing of cover systems that were comprised of different soils with or without a geotextile and were subjected to various construction loads. The laboratory investigation involved the development of a simulation test apparatus and testing of various protective cover systems under incremental loads to simulate increasing waste heights. The laboratory simulated protective cover systems were comprised of a soil layer with varied soil type both with and without a geotextile. Damage to the geomembrane liner was quantified by performing water vapor transmission (WVT), multi-axial tension, and wide strip tension tests on the geomembrane samples exhumed after both field and laboratory simulation testing. These test results allowed the evaluation of the relative protective performance of different protective cover systems tested in this study.

The protective performance was found to depend on the soil type, incorporation of a geotextile, construction loading, and long-term waste loading. The geomembrane protection was found to be significantly dependent on the soil particle size. A 0.3 m thick layer of soil consisting of particles with  $D_{50}$  less than 30 mm and sphericity greater than 0.8 provided greater protection. Incorporation of a  $270 \text{ g/m}^2$  nonwoven geotextile significantly enhanced geomembrane protection. Additionally, the use of construction equipment with ground pressure less than 30 kPa caused less damage to the geomembrane. Protective cover systems meeting these criteria are found to perform satisfactorily under long-term waste loading up to 1400 kPa. Finally, a site-specific testing should be conducted, where possible, to determine the most efficient and economical protective cover system.

## ACKNOWLEDGMENTS

Financial support for this project was provided by Waste Management Inc. The National Seal Company made their laboratory facilities and personnel available for the geomembrane testing. The assistance of John Siebken of the National Seal Company is gratefully acknowledged. The authors are thankful to S. Motan, S. Bandi, M. Finy, and J. Rohr for providing valuable comments during the course of this research.

## REFERENCES

- Brummermann, K., Blumel, W., and Stoewahse, C. (1994) "Protection Layers for Geomembranes: Effectiveness and Testing Procedures", *Proc. of the Fifth International Conference on Geotextiles, Geomembranes and Related Products*, Singapore, Vol.3, pp.1003-1006.
- Giroud, J.P. (1992) "Geomembrane Protection", In: *A Design Primer: Geotextiles and Related Materials*, IFAI, St Paul, MN, pp.99-104.

- Motan, E.S., Reed, L.S., and Lundell, C.M. (1993)  
 "Geomembrane Protection by Nonwoven Geotextiles",  
*Geosynthetics '93*, IFAI, Vol.3, pp.887-901.
- Narejo, D., Wilson-Famy, R.F., and Koerner, R.M. (1996)  
 "Puncture Protection of Geomembranes Part II: Experimental",  
*Geosynthetics International*, Vol.3, No.5, pp.629-653.
- Koerner, R.M. (1994) *Designing with Geosynthetics*, Third Edition,  
 Prentice Hall, Englewood Cliffs, NJ.
- Koerner, R.M., Wilson-Famy, R.F., and Narejo, D.(1996)  
 "Puncture Protection of Geomembranes Part III: Examples",  
*Geosynthetics International*, Vol.3, No.5, pp.655-675.
- Reddy, K.R., Bandi, S., Rohr, J.J., Finy, M., and Siebken, J.  
 (1996) "Field Evaluation of Protective Covers for Landfill  
 Geomembrane Liners Under Construction Loading",  
*Geosynthetics International*, Vol.3, No.6, 1996, pp.679-700.
- Reddy, K.R., and Saichek, R.E. (1997) "Performance of Protective  
 Cover Systems for Landfill Geomembrane Liners Under Long-  
 term Waste Loading", *Geosynthetics International*, in review.
- Richardson, G.N. (1996) "Field Evaluation of Geosynthetic  
 Protection Cushions", *Geotechnical Fabrics Report*, IFAI, Vol.  
 14, No. 2, pp.20-25.
- Seeger, S., and Muller, W. (1996) "Requirements and Testing of  
 Protective Layer Systems for Geomembranes", *Geotextiles and  
 Geomembranes*, Vol.14, pp.365-376.
- Wilson-Famy, R.F., Narejo, D., and Koerner, R.M. (1996)  
 "Puncture Protection of Geomembranes Part I: Theory",  
*Geosynthetics International*, Vol.3, No.5, pp.605-628.

# Effect of Geotextile on Dispersion of Tensile Stress Creating within a Geomembrane Subjected to Deformation by Differential settlement

Shigeyoshi IMAIZUMI

Associate Professor, Department of Energy and Environmental Science, Utsunomiya University, Utsunomiya Japan

Tetsuya NOMOTO

Graduate Student, Department of Civil Engineering, Utsunomiya University, Utsunomiya Japan

Masayuki TSUBOI

Doctoral Student, Department of Civil Engineering, Utsunomiya University, Japan

Yukimitsu Yokoyama

Professor, Department of Civil Engineering, Utsunomiya University, Japan

**ABSTRACT;** Geomembranes such as HDPE and EPDM are used as a liner in waste landfill. When they experience deformation during service life time by differential settlement of subgrade soil or by the localized settlement around pieces of aggregate beneath the liner, tensile stress creates within the geomembrane. Non-woven geotextiles are also laid over and/or beneath it in order to protect against puncture from the gravel or sharp-edged material in waste. In this paper, first, a relation between amount of elongation  $S$ , creating maximum tensile stress  $\sigma_{max}$  and frictional coefficients  $\mu$  between geomembrane and the adjacent material is derived based on theory of elasticity. Next, model tests such that a geomembrane was laid on subgrade and the subgrade was forced to subside locally are presented. The tests' results showed that placing a geotextile between geomembrane and sand gave a meaningful effect on decreasing a tensile strain creating within geomembrane.

**KEY WORDS:** Geomembrane, Geotextile, Tensile Strain, Differential Settlement, Laboratory Test, Theory of Elasticity

## 1 INTRODUCTION

Geomembranes such as HDPE and EPDM are important component of a liner in waste landfill. When they experience deformation during service life time by differential settlement of subgrade soil or by the localized settlement around pieces of aggregate beneath the liner, tensile stress creates within the geomembrane. If the elongation is larger, creating maximum tensile stress may become larger and bring a rupture of the geomembrane. However the strain distribution and/or strain is, the authors think, is dependent on not only an elastic modulus and a thickness of geomembrane but also a frictional resistance between geomembrane and above/beneath materials. The frictional resistance is function of constrained stress (surcharge presser acting on it) and frictional coefficient between materials

Non-woven geotextiles are usually placed overand/or beneath the geomembrane for a purpose of protection from a puncture of it induced by the gravel or sharp-edged material in waste. Fortunately, a frictional coefficient between geotextile and geomembrane is usually much lower than that on intersurface between geomembrane and soil (Ingold; 1991). Therefor, placing a geotextile over and beneath is thought to have a function of decreasing the maximum strain even if gross elongation is same.

In this paper, the authors derive an elastic formula relating maximum stress (strain), surcharge pressure and frictional coefficient to a given elongation. Then they show the results of experiment where the modeled subgrade overlaid by geomembrane was forced to subside locally.

## 2 ELASTIC FORMULA

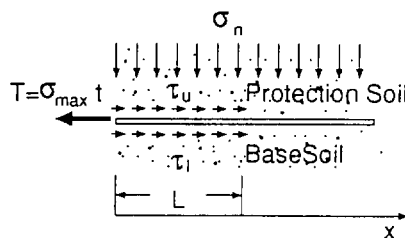


Fig. 1 Schematic drawing of geomembrane embedded in soil

Let us consider a situation that a geomembrane having a thickness of  $t$  and an elastic modulus of  $E$  is embedded in ground and one edge of the geomembrane is pulled by a force of  $T = \sigma_{max} \cdot t$  as shown in Fig. 1. The geomembrane should experience frictional resistance of  $\mu_U \cdot \sigma_n$  and  $\mu_L \cdot \sigma_n$  on top and bottom surfaces, respectively. Assuming that strain creates within an extent of  $L$  from the edge, the relation between tensile stress  $\sigma_x$ , strain  $\epsilon_x$  and infinitesimal deformation  $ds_x$  at point  $x \leq L$  is expressed as

$$\frac{ds_x}{dx} = \epsilon_x = \frac{\sigma_x}{E} \quad (1)$$

A equilibrium equation of force at point  $x$  is given by

$$\sigma_x \cdot t = \sigma_{max} \cdot t - \int_0^x (\mu_U + \mu_L) \cdot \sigma_n \cdot dx \quad (2)$$

Substituting Eq.(2) into Eq.(1) and then integrating  $ds_x$  over an extent of  $L$ , we can obtain an elastic formula (3) representing elongation  $S$  (Imaizumi et al., 1996).

$$S = \frac{(\sigma_{max} \cdot t)^2}{2 \cdot E \cdot (\mu_{tl} + \mu_L) \cdot \sigma_n} \quad (3)$$

The basic concept of this formula is thought to be just same as that of Co-energy presented by Giroud (1994).

Eq.(3) can be rewritten as Eqs.(4) and (5) for maximum stress  $\sigma_{max}$  and maximum strain  $\epsilon_{max}$ , respectively.

$$\sigma_{max} = \frac{\{2 \cdot S \cdot E \cdot (\mu_{tl} + \mu_L) \cdot \sigma_n\}^{0.5}}{t^{0.5}} \quad (4)$$

$$\epsilon_{max} = \frac{\{2 \cdot S \cdot (\mu_{tl} + \mu_L) \cdot \sigma_n\}^{0.5}}{(E \cdot t)^{0.5}} \quad (5)$$

From these equations, it is clearly pointed out that decreasing a frictional coefficient on intersurface between the geomembrane and the adjacent material can decrease the maximum tensile stress creating within it when same elongation of geomembrane is required..

### 3 EXPERIMENT

#### 3.1 Materials used

Dried Toyoura sand was used for both modeled base layer and protection layer over geomembrane liner. Two types of geomembrane, smooth surfaced HDPE and slightly textured EPDM, were used for a modeled liner. Two types of nonwoven geotextiles, continuous one with a thickness of 5 mm and stapled one with a thickness of 10 mm, were used for a protection layer beneath a liner. Mechanical properties of the geosynthetics are listed in Table 1. HDPE has a tensile strength about 3 times stronger and elastic modulus about 15 times larger than EPDM. Stapled nonwoven has the lowest strength among them.

Table 1. Mechanical properties of Geosynthetics

Type	Elastic Modulus (MN/m <sup>2</sup> )	Tensile Strength (MN/m <sup>2</sup> )	Yield strain (%)
HDPE	588.4	33.34	14
EPDM	39.2	9.81	640
C-N-GT	8.9	6.18	-
S-N-GT	0.13	0.33	-

C-N-GT; Continuous nonwoven geotextile  
S-N-GT; Stapled nonwoven geotextile

Table 2. Peak frictional coefficient between materials

	Toyoura		
	Sand	C-N-GT	S-N-GT
HDPE	0.36	0.16	0.16
EPDM	1.13	0.54	0.49

The amounts of frictional coefficients on intersurface between geomembrane and sand and geomembrane and geotextile were tested using direct shear test (Imaizumi et al. 1994) and are listed in Table 3. The value of frictional coefficient of HDPE geomembrane for geotextile is about 44 % lower than that for sand, and that of EPDM for geotextile is about 45 % lower than for sand.

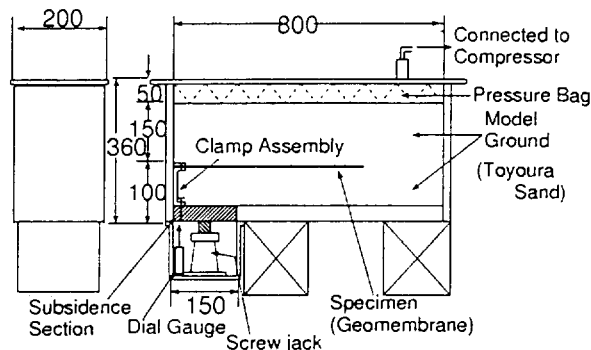


Fig. 2 Setting up of geomembrane in a container

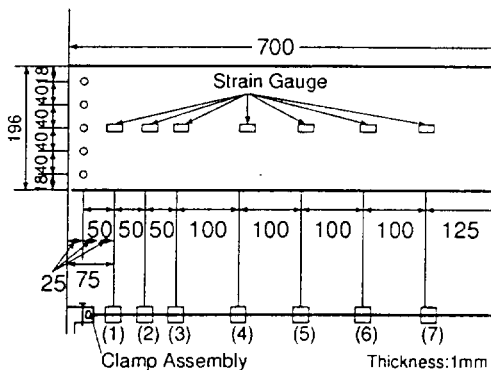


Fig. 3 Positions of strain gauges on geomembrane

#### 3.2 Testing Set-up and procedures

Modeled liner in landfill was constructed in container having a width of 200 mm, a length of 800 mm and a depth of 250 mm. A part of steel base with a length of 150 mm from its left end in the container can be forced to subside by electric screw jack (see Fig. 2).

First, Toyoura sand was rain-poured from a height of 750 mm to become a relative density of 95 %. The thickness of sand layer is 100 mm. Then a geomembrane with a width of 196 mm and a length of 750 mm was placed of which end was fixed to I-shaped steel mounted on subsiding base. In order to measure creating strain within a geomembrane, 16 strain gauges in total were pasted on top and bottom sides of geomembrane. Their pasting points are shown in Fig. 3.

After sand for a protection layer with a thickness of 150 mm was installed by a similar procedure employed for base layer, rubber-bag for air pressure was placed over the sand and steel cap was fixed to the container through bolts. In



some cases, nonwoven geotextile was placed beneath the geomembrane for protection.

The level of surcharge pressure was applied ranging from 98 to 196 kN/m<sup>2</sup> through air pressure rubber-bag. Then the subsiding part of steel base was forced to fall at moving rate of 1 mm/min. till it dropped by 40 mm. The strains creating in a geomembrane were measured through strain gauges at each 0.50 mm of base settlement and stored in diskette through data logger and personal computer.

#### 4 RESULTS AND CONSIDERATION

Axial strain was estimated as a mean value of measures of upper and bottom strains. Then gross elongation was calculated by integrating the estimated axial strains over entire length of geomembrane.

##### 4-1 Effect of type of geomembrane on strain distribution

Fig. 4 shows strain distributions of HDPE and EPDM without any protection layer of geotextile at gross elongation of 0.4 mm under a surcharge pressure of 98 kN/m<sup>2</sup>. In both cases, the amount of strain near the constrained left end is higher and decreases toward the other end, that is from point No.1 to point No.8, although point No.1 is not always highest. The point indicating the highest strain level is No.2 or No.3. This point is just over the edge of subsiding steel base. So, some additional pressure from arching behavior of soil may constrain the geomembrane and prevent inner geomembrane from stretching. Otherwise it is considered for some experimental error to be included.

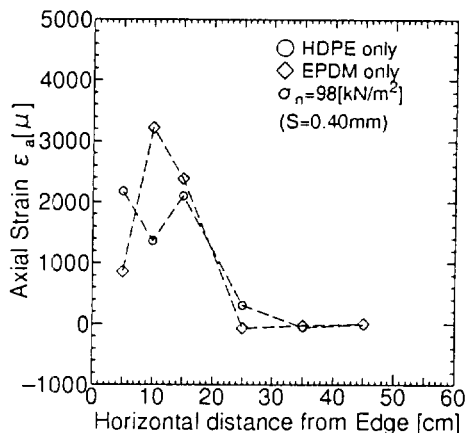


Fig. 4 Strain distribution of HDPE and EPDM without geotextiles

This result shows that the strain does not create uniformly along the geomembrane when the underlying base ground settles differently, while some designing for geomembrane liner assumes that the strain would distribute uniformly. The shape of distribution is almost similar as

one above mentioned in elastic consideration and presented by Giroud (1994).

In Fig. 4, HDPE has somewhat wider distribution and lower level of strain than EPDM. This difference seems to attribute to the difference of their rigidity and frictional property between sand. EPDM having lower rigidity about one-fifteenth of HDPE and larger coefficient about 3 times is apt to concentrate the strain.

##### 4-2 Effect of level of frictional coefficient or normal stress on strain distribution

Figs. 5 and 6 show comparison of strain distribution of geomembrane with continuous nonwoven geotextile to that without geotextile. When the geotextile was placed beneath the geomembrane, strains distribute over wider extent and its level situated just above subsiding base is lower. This trend is much distinct in case of EPDM. Therefore, placing a geotextile beneath a geomembrane is effective to decrease the maximum induced by differential settlement.

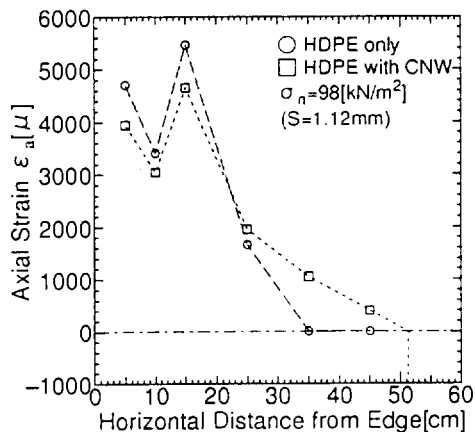


Fig. 5 Strain distribution of HDPE with and without continuous nonwoven geotextile

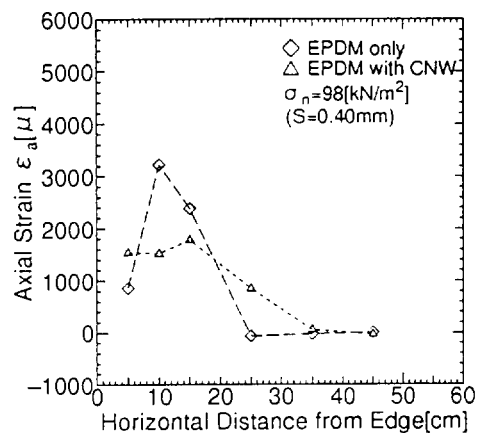


Fig. 6 Strain distribution of EPDM with and without continuous nonwoven geotextiles

Figs. 7 and 8 show the distributions of strain in case of changing a level of surcharge stress. In case of HDPE without geotextile, a trend that a shape of distribution becomes narrow with increasing of surcharge pressure is barely found. In case of EPDM with stapled nonwoven geotextile, the trend is practically recognized.

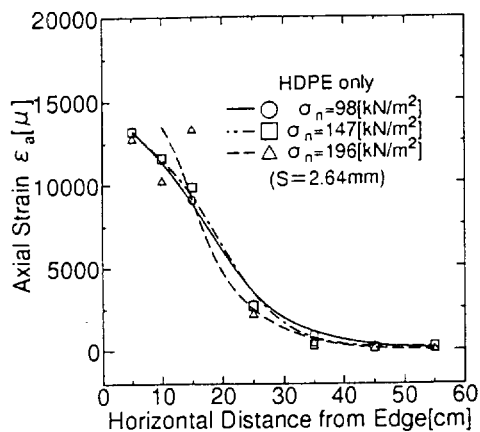


Fig. 7 Strain distribution of HDPE at surcharge pressure of 98, 147 and 196 kN/m<sup>2</sup>

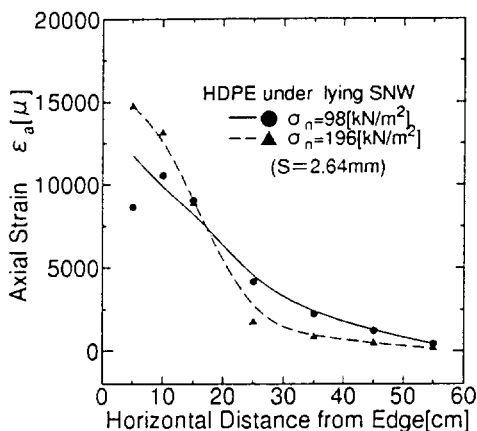


Fig. 8 Strain distribution of EPDM with stapled nonwoven geotextile at surcharge pressure of 98 and 196 kN/m<sup>2</sup>

## 5 CONCLUSIONS

- (1) Based on theory of elasticity, it is found that a amount of elongation of embedded geomembrane is functions of not only thickness and elastic modulus but also frictional coefficient and constrained stress.
- (2) EPDM having smaller rigidity and larger frictional coefficient have more localized strain distribution than HDPE.
- (3) Placing a geotextile beneath a geomembrane functions to decrease maximum induced stress practically.
- (4) Lager level of surcharge seems to make strain distribution localized.

In order to obtain more clear conclusion, the tests should be continued modifying a testing device and procedure.

## 6 ACKNOWLEDGMENT

The authors express their thanks Miss M.Abo for her helping the experiments in earnest. The financial support provided by Grant-in-Aid for Scientific Research (B) from The Ministry of Education, Science, Sports and Culture is also gratefully acknowledged

## REFERENCE

- Giroud, J.P. (1994) "Quantification of Geosynthetic Behavior", Fifth International Conference on Geotextiles, Geomembranes and Related Products, Special Lecture and Keynote Lectures, Singapore, pp.3-27
- Imaizumi, S., Nishigata, T. and Imura, K. (1994) "Effect of Variation in Sample Sizes on Soil-Polymer Interface Strength", Fifth International Conference on Geotextiles, Geomembranes and Related Products, Singapore, pp.423-426
- Imaizumi, S., Yokoyama, Y., Takahashi, S. and Tsuboi, M. (1996) "Elastic Formula for Pull-out Behavior of Embedded Geomembrane", Twelfth Southeast Asian Geotechnical Conference, Malaysia, pp.57-62
- Ingold, T.S. (1991) "Friction Testing", Geomembranes Identification and Performance Testing, Chapman and Hall, pp.176-203

# Laboratory Study of High Density Polyethylene Geomembrane Waves

Te-Yang Soong

Research Engineer, Geosynthetic Research Institute, Drexel University, Philadelphia, Pennsylvania, USA

Robert M. Koerner

Professor and Director, Geosynthetic Research Institute, Drexel University, Philadelphia, Pennsylvania, USA

**ABSTRACT:** The behavior of waves of the type seen in field deployed HDPE geomembranes was evaluated in laboratory tests. Four experimental variables were evaluated: normal stress, original wave height, geomembrane thickness and temperature. Twenty-five separate tests were conducted, each for 1,000 hours duration. Contact between the geomembrane and the subgrade soil was not achieved in any of the tests performed. The results suggest that if waves are to be avoided, the geomembrane must essentially be flat on the underlying subgrade before backfilling. Furthermore, tensile strains were monitored in each test with resulting values as high as 4.9%.

**KEYWORDS:** Geomembrane Waves, HDPE Waves, Laboratory Modeling, Geomembrane Installation.

## 1 INTRODUCTION

Geomembranes form the essential material component in many liner systems which require a liquid and/or vapor barrier. Such applications are landfill liners, landfill covers, liquid impoundment liners and other waste pile liners. The usual assumption in the placement of such liners (particularly for composite geomembrane/clay liners) is that they lay flat on the soil subgrade beneath them. Unfortunately, this is often not the case. Waves, or wrinkles, of different sizes often occur in the as-placed and seamed geomembranes, see Figure 1.



Figure 1. Photograph of waves in a field deployed and seamed geomembrane before backfilling or covering.

These waves have given the geomembrane community a certain amount of concern as to their behavior and/or fate after soil backfilling and/or covering by other geosynthetic materials. Figure 2 illustrates some possible deformation scenarios of geomembrane. The usual concerns expressed by many regulators, owners, engineers and installers are the following:

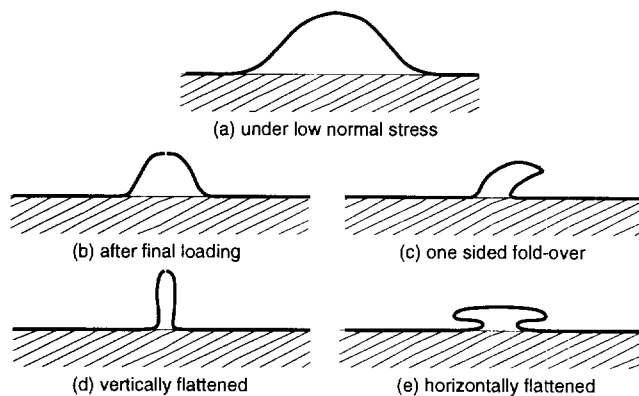


Figure 2. Deformation scenarios in geomembrane waves

- Intimate contact is not achieved. This allows for a potential leak through the geomembrane to spread over a relatively larger area as opposed to the area of the hole itself.
- Locations of large curvature suggest high stress concentrations. Such locations are susceptible with respect to stress cracking and/or a decrease in lifetime.
- The creation of "mini dams" which result in a less efficient removal of the liquid, as well as higher heads on the geomembrane.
- Cyclic heating and cooling might cause desiccation of underlying clayey subgrade soils.

The concern as to the ultimate fate of geomembrane waves should certainly receive attention insofar as a firm understanding of the problem. However, to date, all analyses and investigations into geomembrane waves have been semi-qualitative, e.g., see Giroud and Morel (1992) and Giroud (1995). A quantitative approach which evaluates the ultimate fate of geomembrane waves in a systematic and controllable manner is the focus of this study which is laboratory oriented. It is important to state that this study does not attempt to quantify the performance of geomembranes in the field stemming from the existence, or nonexistence, of such waves. What it does attempt to

quantify is the behavior of the waves as a function of the following four variables; normal stress, original wave height, thickness of geomembrane, and temperature.

Due to its common use in most environmentally related applications, high density polyethylene (HDPE) geomembranes were used throughout the study. In particular, one manufacturer's commercially available geomembrane was used. The only variation in material was the thickness of the specimens, which was one of the experimental variables. In all other cases, the thickness was maintained at 1.5 mm which is a commonly used value in many applications.

## 2 EXPERIMENTAL SETUP AND MONITORING

Four rigid boxes having dimensions of 300 mm long  $\times$  300 mm wide  $\times$  300 mm high were used to conduct the experiments. The front was fitted with a thick Plexiglas "window" to visually track and trace the profile of the wave's behavior. The waves were created by using geomembrane specimens longer than the inner length of the test box. After each specimen was placed in the box, sand backfilling was started from the end to the center of the box in a symmetrical manner. Consequently, the "slack" was "pushed" toward the center and, as a result, a reasonably symmetric wave was formed. The justification of using the relatively small test setups to simulate situations in the field are presented in an separate paper, see Soong and Koerner (1998). Along with steel reaction frames and a hydraulic pressurizing system, these boxes allow a application of normal pressure up to 1,500 kPa. This is equivalent to a solid waste landfill of approximately 125 m in height, i.e., a so-called "megafill". In addition, all four boxes can be simultaneously housed in a environmental room where constant environmental conditions can be maintained within ranges of 0 to 55°C temperature and 0 to 98% relative humidity. Photographs of a test box and the environmental room used in this study are shown in Figure 3. As seen in the figure, a data acquisition system was also available for strain gage measurements.

The experimental monitoring includes two parts: profile-tracing of the actual wave specimens and strain gage measurements. The latter part was used to quantify the tensile strains induced at different locations on the geomembrane wave specimens under various experimental conditions. The strain gages used in this study were electrical resistance (foil-type) strain gages having resistance of 120-ohms and gage length of 12.7 mm. With proper configuration, this particular type of gage measures strain within the range of  $\pm 5\%$  to an approximate accuracy of 0.25%. The installation procedure recommended by the gage manufacturer was followed. The surface cleaning and preparation was considered most critical in this regard.

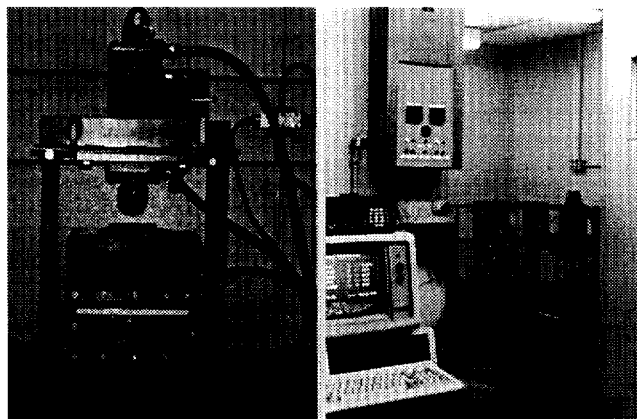


Figure 3. Photographs of one of the test boxes and the environmental room used in this study.

## 3 EXPERIMENTAL DESIGN

Four series of 1,000-hour experiments were designed and performed to evaluate the effect of the four experimental variables on the behavior of HDPE geomembrane waves. Table 1 presents the experimental design for normal stress, original height of wave, thickness of geomembrane, and temperature. As seen, the effects of different variables were evaluated by varying one particular parameter while holding the others constant. In all cases, smooth HDPE geomembranes were used and strain gages were attached to the wave specimens at different locations with constant readout over the duration of the tests.

Table 1. Experiments conducted in this study

Parameter Evaluated	Experimental conditions			
	Normal Stress (kPa)	Wave Height (mm)	Geomembrane Thickness (mm)	Testing Temp. (°C)
Normal Stress	180	60	1.5	23
	360			
	700			
	1100			
Original Wave Height	700	14	1.5	23
		20		
		40		
		60		
Geomembrane thickness	700	60	1.0	23
			1.5	
			2.0	
			2.5	
Testing Temp.	700	14	1.5	23
		20		42
		40		55
		60		

## 4 EXPERIMENTAL RESULTS

The results of the experiments will be given on an individual variable basis. The original and final (after 1,000 hours) shapes of the geomembrane waves along with the locations of strain gages will be presented in graphic form. Values of the maximum strain measured, along with wave heights and height-to-width ratios, corresponding to each of the tests will be given in table form.

### 4.1 Effect of Normal Stress

As listed in Table 1, a 1.5-mm thick HDPE geomembrane wave specimens with a 60-mm original wave height was subjected to four different normal stresses, namely; 180, 360, 700, and 1,100 kPa. The temperature was maintained at 23°C for all experiments over the entire duration of the experiments, i.e., 1,000 hours. The original (same for all specimens) and the final shapes of all test specimens, obtained via profile-tracing through the Plexiglas window, are shown in Figure 4.

Six strain gages, numbered from 1 to 6, were originally bonded at the locations shown on the uppermost curve in Figure 4 for all specimens. Gages 1 to 3 were on the upper surface near the center and gages 4 to 6 were bonded on the lower side of the geomembrane near the edges. This was necessary since the gages respond more accurately under tension than compression.

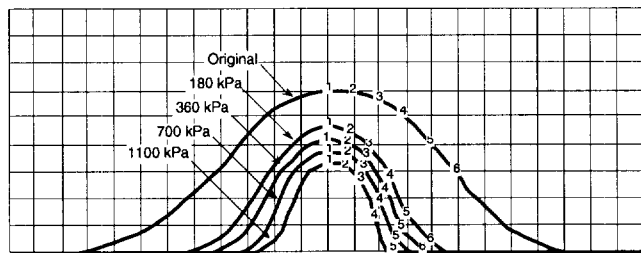


Figure 4. Original and final shapes of wave specimens under varying normal stress (gridlines have dimensions of 10 mm  $\times$  10 mm).

A typical strain gage measurement result of the test conducted under a normal stress of 700 kPa is shown in Figure 5 where the measured strain is plotted against time. It is seen that the upper portion of this particular wave specimen experienced considerable strain with a maximum tensile strain of 3.4% recorded near the crest of wave. Table 2 summarizes such information for this series of experiments.

As shown in Table 2 the final wave height decreases with increasing normal stress. However, the height-to-width ratio increases with increasing normal stress, even more significantly. It was seen that the effect on the height-to-width ratio is essentially doubled in comparison

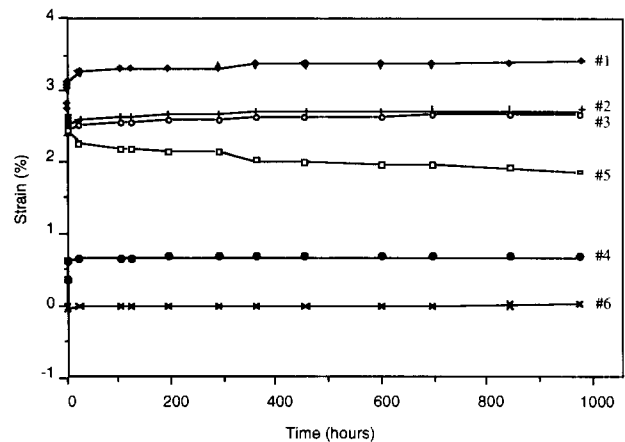


Figure 5. Strain measurement results of test conducted at 700 kPa

Table 2. Summarized results - Effect of normal stress

Normal Stress (kPa)	Final Wave Ht. (mm)	Final H/W <sup>1</sup> Ratio	Max. Strain (%)	Gage(s) of Max. Strain
0 (original)	60	0.47	+ 1.7 <sup>2</sup>	#1
180	47	0.47	+ 1.8	#1
360	42	0.51	+ 2.0	#1
700	38	0.58	+ 3.0	#1, 2 & 3
1100	34	0.62	+ 3.2	#2 & 5

1. Height-to-width ratio

2. "+" for tension, "-" for compression

with the effect on the final wave height. Since high height-to-width ratios generally indicate large curvatures and locations of high stress concentration, the overall effect of high normal stress is obviously unfavorable.

The maximum strain recorded in each experiment shows that tensile strain increases as normal stress increases. This is expected since the H/W values increase with greater curvature. Nevertheless, the geomembrane is tensioned significantly less than its yield point. (Note that the tensile yield strain for this geomembrane is in the range of 15 to 25% depending on the temperature.) Therefore, tensile yield is not challenged in any way.

### 4.2 Effect of Original Wave Height

The second series of 1,000-hour experiments was designed to evaluate the effect of the original wave height on the behavior of HDPE geomembrane waves. Five tests using 1.5 mm-thick wave specimens were conducted. The original wave heights were 14, 20, 40, 60, and 80 mm, respectively. All specimens were subjected to a constant normal stress of 700 kPa and maintained at a constant temperature of 23°C over the entire duration of the experiment. The original and final (after 1,000 hours) shapes of the test specimens are shown in Figure 6.

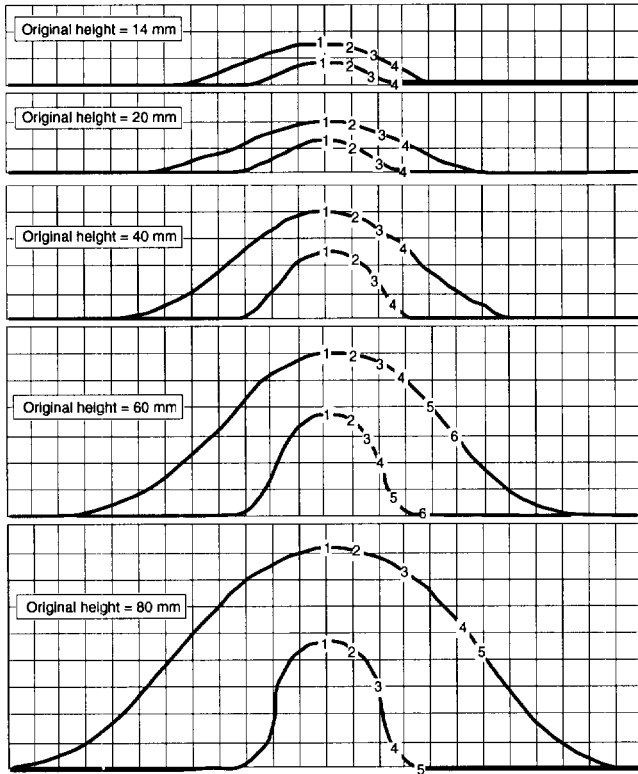


Figure 6. Original and final shapes of wave specimens with varying original height (gridlines have dimensions of 10 mm × 10 mm).

Table 3 was developed to summarize the test results. As seen, there was an approximate 40% reduction in height after 1,000 hours for all waves. As to the final H/W ratio, it increases with increasing original wave height. Note that for waves originally higher than 60 mm, the final H/W ratios exceeded a value of 0.5. There was no sign of achieving intimate contact between the specimen and the underlying subgrade after 1,000 hours, even for the wave with the smallest original height. With regard to the maximum strain recorded, an increasing trend is also seen with increasing original height.

Table 3. Summarized results - Effect of wave height

Original Wave Ht. (mm)	Original H/W <sup>1</sup> Ratio	Final Wave Ht. (mm)	Final H/W <sup>1</sup> Ratio	Max. Strain (%)	Gage(s) of Max. Strain
14	0.17	8	0.14	+ 0.2 <sup>2</sup>	#1
20	0.15	12	0.18	+ 1.2	#3
40	0.27	25	0.38	+ 2.4	#2 & 4
60	0.33	38	0.58	+ 3.0	#1, 2 & 3
80	0.33	47	0.65	+ 3.4	#2 & 4

1. Height-to-width ratio
2. "+" for tension, "-" for compression

#### 4.3 Effect of Geomembrane thickness

The third series of the experiments was designed to evaluate the effect of geomembrane thickness on the behavior of

HDPE geomembrane waves. Four tests using HDPE geomembrane wave specimens with thicknesses of 1.0, 1.5, 2.0, and 2.5 mm were conducted. The original heights of all specimens were approximately 60 mm. Owing to the various stiffness of the geomembranes having different thicknesses, a constant value of original H/W ratio could not be maintained, see Table 4. All specimens were subjected to a constant normal stress of 700 kPa and maintained at a constant temperature of 23°C over the entire duration of the experiments. The original and final (after 1,000 hours) shapes of the test specimens are shown in Figure 7.

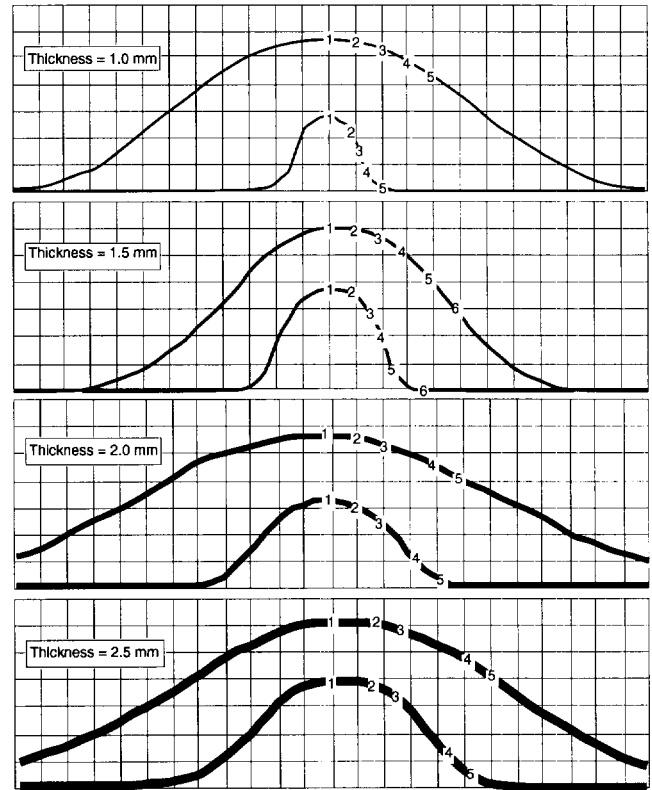


Figure 7. Original and final shapes of wave specimens with varying thickness (gridlines have dimensions of 10 mm × 10 mm).

The summarized results generated by this series of tests, including both the strain gage and the profile-tracing monitoring, are presented in Table 4.

Table 4. Summarized results - Effect of GM thickness

GM Thickness (mm)	Final Wave Ht. <sup>1</sup> (mm)	Original H/W <sup>2</sup> Ratio	Final H/W <sup>2</sup> Ratio	Max. Strain (%)	Gage(s) of Max. Strain
1.0	27	0.24	0.52	+ 2.5 <sup>3</sup>	#5
1.5	38	0.34	0.58	+ 3.0	#1, 2 & 3
2.0	33	0.18	0.34	+ 3.1	#1, 2, 4 & 5
2.5	38	0.21	0.32	+ 3.3	#2, 3, 4 & 5

1. Original wave height = 60 mm
2. Height-to-width ratio
3. "+" for tension, "-" for compression

As shown in Table 4, with the only exception being the 1.0 mm-thick geomembrane wave, the following observations were made. First, the thickness of geomembrane has very little effect on the final height of geomembrane waves. There was an approximate 40% reduction in height after 1,000 hours for all waves. In other words, the original height essentially determined the final height of the geomembrane waves. Second, the geomembrane thickness did show a significant effect on the final H/W ratio of the waves. That is to say, the final H/W ratio decreases with increasing geomembrane thickness. The latter observation can be interpreted in an alternative manner. That is, for waves with the same original height, thicker geomembranes resulted in smaller but wider voids beneath the wave. Third, the maximum strain recorded in each experiment shows that tensile strain increases as the thickness of geomembrane increases.

#### 4.4 Effect of Testing Temperature

The fourth series of experiments was performed to evaluate the effect of testing temperature on the behavior of HDPE geomembrane waves. Three sets of experiments, each consisting of 1.5-mm HDPE geomembrane waves with original heights of 14, 20, 40, and 60 mm, were conducted at temperatures of 23, 42 and 55°C.

The original shape of all waves were formed at 23°C with approximately 100 mm of sand backfill over them. Temperature was then increased, as necessary, to the desired value. This was meant to replicate field situations where the exposed geomembranes experience an increase in temperature after placement and seaming. The test boxes were then filled with sand, followed by a decrease in temperature back to 23°C, to simulate the decrease in sheet temperature of the field deployed geomembranes after the geotextile protection and drainage layers are placed. After approximately 24 hours, a constant normal stress of 700 kPa was applied. After another hour, temperature was increased from 23°C to the desired value and maintained for the rest of the experiment. The last step was intended to simulate a possible increase in the sheet temperature over the lifetime of landfills.

The original and final shapes of the test specimens, at three different temperatures, are shown in Figure 8. The summarized results generated from both parts of the monitoring is presented in Table 5. The values of maximum strain listed in the table correspond to the maximum final (after 1,000 hours) strain.

As seen in Table 5, temperature has only marginal effect on the final wave height and the final H/W ratio. For waves originally shorter than 40 mm, the maximum measured strain increases with increasing temperature. For waves originally higher than 40 mm, however, the maximum strain shows no clear trend with increasing temperature.

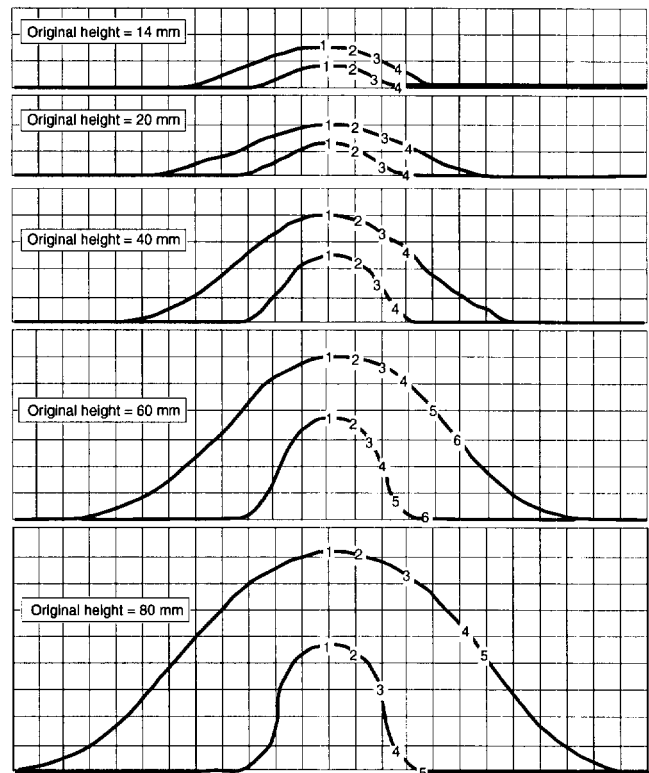


Figure 8. Original and final shapes of wave specimens having various original heights monitored at different temperatures (gridlines have dimensions of 10 mm × 10 mm).

Table 5. Summarized results - Effect of temperature

Original Ht. (mm)/ H/W <sup>1</sup> ratio	Temp. (°C)	Final Wave Ht. (mm)	Final H/W <sup>1</sup> Ratio	Max. Strain (%)	Gage(s) of Max. Strain
14 / 0.17	23	8	0.14	+ 0.2 <sup>2</sup>	#1
	42	10	0.19	+ 0.6	#4
	55	5	0.20	+ 1.3	#2
20 / 0.15	23	12	0.18	+ 1.2	#3
	42	14	0.21	+ 1.6	#4
	55	12	0.30	+ 2.1	#4
40 / 0.27	23	25	0.38	+ 2.4	#2 & 3
	42	25	0.42	+ 3.2	#3
	55	25	0.40	+ 2.1	#1
60 / 0.33	23	38	0.58	+ 3.0	#1, 2, 3 & 5
	42	30	0.52	+ 4.9	#1, 2, 3 & 5
	55	28	0.55	+ 4.9	#1, 2 & 5

1. Height-to-width ratio

2. "+" for tension, "-" for compression

## 5 SUMMARY OF TEST RESULTS

Summarizing remarks, subdivided according to the physical manifestation of the wave, are as follows:

### Regarding the wave heights:

- Wave heights decrease with increasing normal stress.
- An average of 40% reduction in wave heights was observed after 1,000 hours.
- Varying thicknesses of geomembranes had only a marginal effect on the final wave heights.
- Varying temperatures (after the wave was formed) had only a slight effect on the final wave heights.
- The final wave heights recorded from all experiments varied from 5 to 47 mm.
- Contact with the subgrade was not achieved after 1,000 hours, even for the smallest wave at the highest testing temperature.

### Regarding the height-to-width (H/W) ratio:

- The height-to-width ratio of the waves increased (approximately linearly) with increasing normal stress.
- The height-to-width ratio of the waves increased (approximately linearly) with increasing original wave heights.
- The height-to-width ratio of the waves decreased (approximately linearly) with increasing geomembrane thickness.
- Varying temperatures had only a marginal effect on the final height-to-width ratio of the waves.
- The final height-to-width ratios of the waves recorded from all experiments varied from 0.14 to 0.65.

### Regarding the tensile strain at the end of the experiments:

- The tensile strain at the maximum point of curvature of the waves increased (approximately linearly) with increasing normal stress.
- The tensile strain at the maximum point of curvature of the waves increased (approximately logarithmically) with increasing original wave height of the waves.
- The tensile strain at the maximum point of curvature of the waves increased (linearly) with increasing geomembrane thickness.
- The tensile strain at the maximum point of curvature of the waves increased with increasing testing temperatures for waves originally smaller than 40 mm.
- The tensile strain at the maximum point of curvature of the waves showed no clear trend with increasing testing temperatures for waves originally higher than 40 mm.
- The tensile strains recorded from all experiments were as high as 4.9%.

## 6 CONCLUSIONS

The above summarized observations have resulted in the following conclusions:

- Geomembrane waves, which are induced in the field during placement and subsequently maintained during seaming, distort greatly upon the application of even a nominal normal stress. The distortion accentuates the height-to-width ratio of the wave.
- Over the 1,000-hour experimental time of stress application for the main series of tests, the waves did significantly decrease (approximately 40%), however, they never disappeared.
- The maximum tensile stresses occur at locations of maximum tensile strain. These locations are on the anticipated side of the waves, i.e., tension along the upper surface of the wave near its crest and tension along the lower surfaces where the wave curvature changes to accommodate the horizontal subgrade beneath the wave. Note that compressive stresses occur on the opposite side of the geomembrane but they are of less concern than tensile stresses.
- The maximum tensile strain measured in this series of twenty-five 1,000-hour experiments was 4.9%. Note that yield of HDPE geomembranes is in the range of 15 to 25% strain (depending on the temperature), thus yielding of the geomembrane is not suggested.
- It is important to note that this study did not address the possible implications of the waves, their possible leakage scenarios, nor long-term performance of the geomembranes involved.

## 7 ACKNOWLEDGMENT

The funding for the preparation of this paper was provided by the U.S. EPA. Financial support via David A. Carson under contract CR-821448 is sincerely appreciated. Some additional funding was provided by the Geosynthetic Institute's consortium of member organizations.

## 8 REFERENCES

- Giroud, J.P. and Morel, N. (1992) "Analysis of Geomembrane Wrinkles", *J. of Geotextiles and Geomembranes*, Vol. 11, No. 3, pp. 255-276 (Erratum: 1993, Vol. 12, No. 4, p 378).
- Giroud, J.P. (1995) "Wrinkle Management for Polyethylene Geomembranes Requires Active Approach", *Geotechnical Fabrics Report*, Vol. 13, No. 3, pp. 14-17.
- Soong, T.-Y. and Koerner, R.M. (1998) "Behavior of Waves in HDPE Geomembranes", *J. Geotech. Engrg.* ASCE.



# Installation Procedure and Welding of Geomembranes in the Construction of Composite Landfill Liner Systems - Focus on "Riegelbauweise" -

Ulrich B. Aversch, Dipl.-Ing.

Institut für Baumaschinen und Baubetrieb, RWTH Aachen, Aachen, Germany

Rolf Th. Schicketanz, Dipl.-Ing.

Ingenieurbüro Schicketanz, Aachen, Germany

**ABSTRACT:** For an optimal composite sealing system one has to achieve, among others, that the geomembrane lies on the mineral layer in a so called "intimate contact". This requires a practically flat placement of the geomembranes over the whole area. The problems which you have to deal with when placing the geomembranes are to get the manufacturing conditioned imperfections under control as well as the waves in the geomembranes caused by sun or global radiation in order to achieve a flat surface before putting loads on the whole surface. This can be done by the "Riegelbauweise" ("Fixing Berm Construction Method" FBCM). Procedural and equipment parameters are presented.

**KEYWORDS:** Geomembrane Wrinkling, Installation, Intimate Contact, Riegelbauweise

## 1 INTRODUCTION

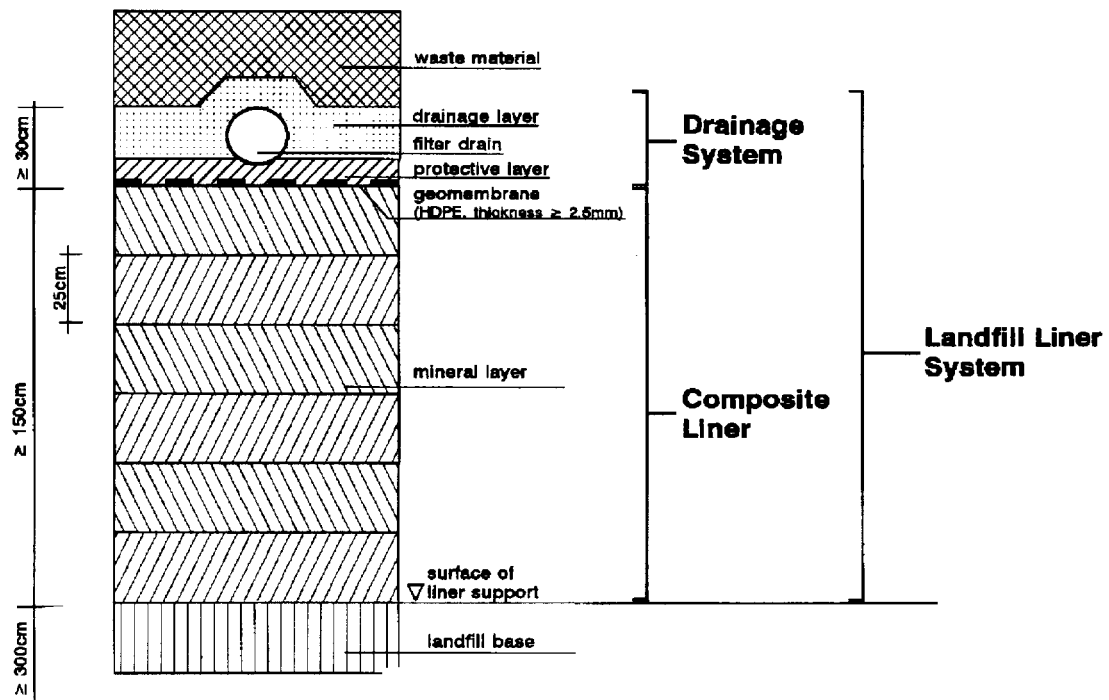
Landfills will continue to be indispensable in the foreseeable future. In order to avoid emissions the entire landfill area must be totally sealed and for this purpose cappings, side and base liners are used. The German guidelines "TA Abfall (1991)" and "TA Siedlungsabfall (1993)" advocate that landfill cappings and base liners consist of a combination of a mineral layer covered by a geomembrane (composite liner).

The composite liner consists of a minimum 75 cm mineral layer, as designed for a domestic waste landfill, or a minimum 150 cm mineral layer for a hazardous waste landfill, and a geomembrane (HDPE, thickness  $\geq 2.5$  mm).

This is supplemented by a drainage system consisting of a protective and a drainage layer. The protective layer might be composed of heavy-weight geotextiles ( $3.000 \text{ g/m}^2$ ) or of a combination of protective geotextile ( $1.200 \text{ g/m}^2$ ) overlaid with sand (0/8 mm) in a thickness of 15 cm. The drainage layer usually consists of graded permeable gravel (for example 16/32 mm). The composite liner and the drainage system together make up a landfill liner system, specially for base sealings (Figure 1).

The requirements on such a liner system, climatic considerations and the resulting scheduling commitments demand a meticulously drawn up structural and operational design for the implementation of the construction work and, in particular, for the utilisation of plant and machinery (Dornbusch et al. 1996).

Figure 1. Composite landfill liner system for hazardous waste (Germany).



## 2 PROCEDURAL AND EQUIPMENT PARAMETERS

The choice of effective plant and procedures is crucial for the technical and economic success of any building operation. This includes the scaling and performance-related coordination of the equipment line which must correspond to the particular requirements.

The various procedural steps in constructing a composite liner with a drainage system and the corresponding machinery are described in Aversch 1995 and are summarized in Figure 2 in the form of a process and an equipment line.

This paper focusses on the final procedural steps, beginning with the "Surface Treatment".

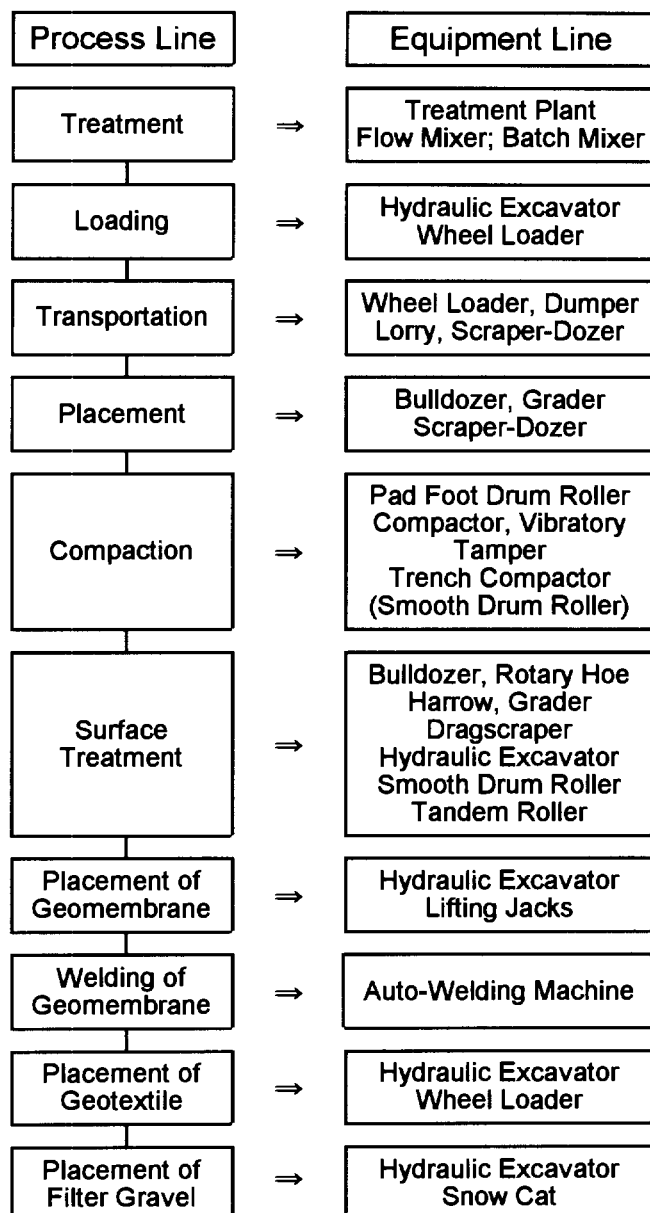


Figure 2. Process and equipment line.

## 3 SURFACE TREATMENT

The creation or rather the smoothing of the surface of a mineral layer poses the greatest difficulties for both personnel and machines. In order to obtain the intimate contact between the mineral layer and the geomembrane for the composite sealing effect, the clay surface must be plane, smooth and free of foreign matter, gravel or other objects. The surface of the mineral layer should not contain single grains of more than 10 mm diameter. Such grains must be fully embedded in the clay matrix. No mineral grains with sharp edges are allowed at the surface. According to the geomembrane approval directive set by BAM 1992 (Bundesanstalt für Materialforschung und -prüfung, Federal Institute for Materials Research and Testing), the surface of the compacted mineral layer must be absolutely clear of any abrupt changes in the surface structure. The BAM requirements allow for steps of at most 5 mm and level deviations of maximum 20 mm beneath a 4-m slat (screed) placed on top of the layer. Intolerable are deep dry-cracks, a wet or dusty-dry surface of the mineral layer during the installation of geomembrane, even when the required thickness of the mineral layer is achieved (Schicketanz 1992).

These requirements on the clay surface demand the utmost care in the implementation of the construction. This operational step can take up the same amount of time as the installation and compaction of an entire three-layer mineral liner (Aversch 1993).

Pad foot imprints cannot be levelled out by a smooth drum roller, even when using heavy models. Smoothing of the surface of a mineral layer according to the requirements demands a special procedural implementation. The following combination of techniques is favourable: the top layer must be superelevated (about the height of the pad feet), then compacted by foot drum roller. The additional millimeters will then be taken down by heavy levelling machines. For the smoothing process suitable machines are bulldozers without grousers (bogdozer model), graders or drag scrapers pulled by light tractors. The lighter the machine, the less damage will be done to the compacted clay layer, i.e. by track imprints.

Due to the possible development of shearing (which poses a threat to stability on embankments) and the subsequent breakdown in homogeneity, it is questionable to add further in-situ treatment of the earthen material by rotary hoe and harrow before the final surface treatment. However, this technique eliminates all disrupting imprints or surface roughness and a pre-smoothed surface of crumbly consistence is achieved.

A surface prepared in such a way has to be further treated by a combination of smooth rollers, consisting of heavy rollers (9-13 t) with smooth drum and ballon tyres, and light tandem rollers. Initially, one roller with smooth drum compacts the prepared surface; this can be carried out dynamically or statically. Further roughnesses, such as small hollows and wheel-prints of the rollers can only be removed using light compacting machines; any further passes using heavy rollers will create new defects. Suitable machines are tandem rollers with smooth drums and, possibly, dynamic vibration. The edges due to the shifting of the roller can be virtually avoided if the drums are displaced slightly with

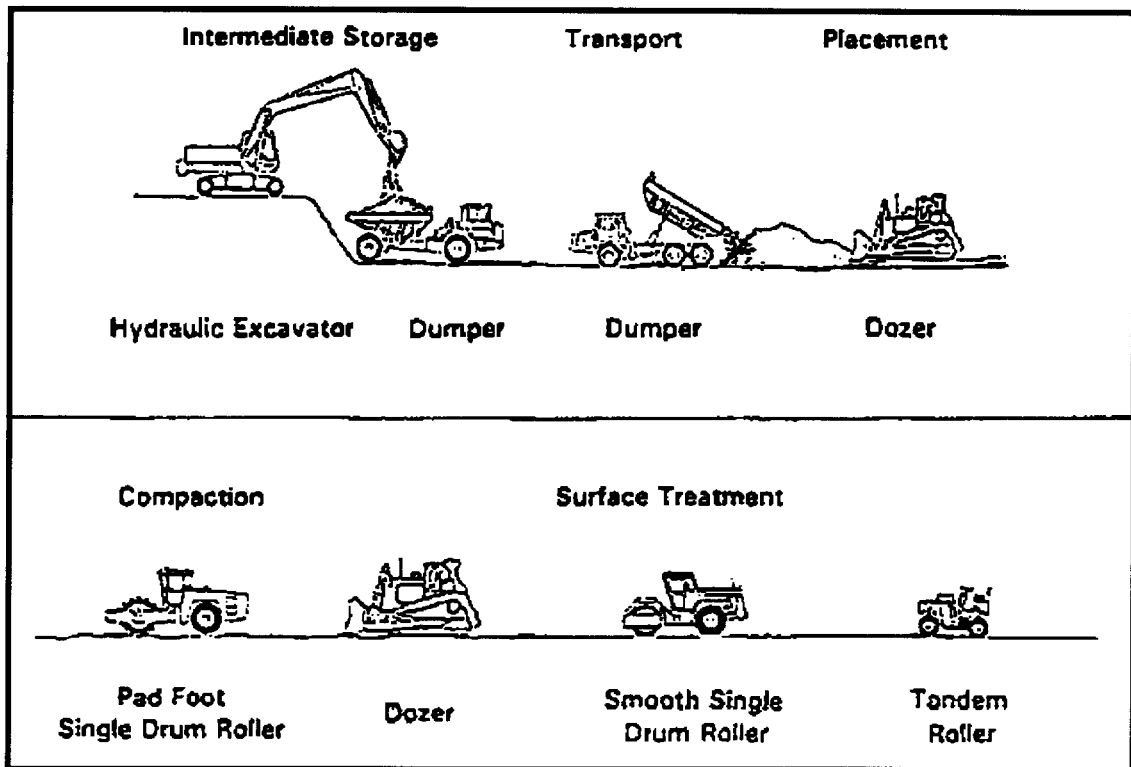


Figure 3. Equipment line for the construction of a mineral layer.

each transition (about 1/3 of the breadth of the drum). One possible process line for the implementation of the above procedural steps is shown in Figure 3.

#### 4 INSTALLATION OF GEOMEMBRANES

The installation of geomembranes poses another challenge to personnel, because they cannot drive over the clay surface with heavy machines and even inappropriate footwear might leave intolerable imprints. The heavy, rolled-up geomembrane can therefore only be brought in on and placed from on-site roads outside the construction section. Hydraulic excavators are most useful for this purpose. Spreader bars attached to the boom can pick up the geomembrane rolls from both sides of the steel cylinder core. The hydraulic excavator can access the geomembrane across the trench to the construction section from outside. The geomembrane can be unrolled either by lifting the rolls onto jacks at the construction section side and pulling down on the geomembrane manually, while maintaining a smooth underside or the entire roll with its core can be unrolled onto the construction section (with auxiliary support using ropes on embankments). Both installation techniques involve manual work.

Wheel loaders can generally be used for transporting the geomembranes on site, but because of their limited reach are less suitable than hydraulic excavators with long cantilevers or telescopic booms.

#### 5 WELDING OF GEOMEMBRANES

The geomembranes are welded at the edges with auto welding machines according to the DVS-Guideline 2225, Part 4 (1996). They become plasticised by an electrically heated and controlled heating wedge, and the edges are then pressed together by two pressure rollers and welded. The machine is entirely controlled by micro-processor. Furthermore, all the welding parameters and quality assurance data are memorized, such as welding speed, wedge temperature, welding pressure, ambient temperature, temperature of the membrane surface, date, time, machine number and installation contractor, company's logo and number of weld or site. The machines should have a serial interface so that a site's overall installation design can be monitored and depicted by PC with a graphics program (long-term documentation, database). In addition it is possible to monitor all the welds visually with the limiting values on screen simultaneously, and thus defects can be located immediately.

The need for simple landfill base geometries must be reiterated here as this will reduce the number of welds required.

#### 6 INTIMATE CONTACT WITH MINERAL LAYER ("RIEGELBAUWEISE")

The required flatness of the geomembranes has often been a matter of controversy (Figure 4). The geomembrane sealing

component has to be in full surface contact with the next sealing component - the mineral layer - so that the surcharges lead to an intimate contact. It is possible to observe many different on-site techniques being applied in order to achieve this result. Despite all the problems mentioned previously, it is possible to achieve an evenly placed geomembrane on a flat surface if the personnel and contract management are efficient and the installation is carried out conscientiously.



Figure 4. Example of a wavy geomembrane.

Intimate contact between the mineral layer and the geomembrane requires a flat placement of the geomembrane over the entire area. This can be achieved using the "Riegelbauweise" ("Fixing Berm Construction Method" FBCM) which has been developed and described by Schicketanz et al. 1991.

HDPE has a heat expansion coefficient of a factor of approx. 20 times higher than, for example, steel. This expansion can be used to attain complete flatness of the geomembrane in the cooler evening hours which could never be achieved by mechanical means.

The imperfections caused by the production and delivery of geomembranes as well as the waves in the geomembrane caused by sun or global radiation have to be under control in order to achieve a flat surface before the surface can be covered with the protective and drainage material.

According to the method of "Riegelbauweise" (FBCM) the geomembranes are placed following a layout-plan of placement in the morning on the prepared mineral liner surface. After about 1 hour (to adapt to the ambient temperature) the geomembranes are adjusted and stretched a little to eliminate the waves in the geomembrane condition on delivery and unrolling. Then the geomembranes are fixed with sandbags to prevent wind suction etc. After welding and testing of the seams and cleaning of the geomembrane surface, the geosynthetic protecting layer is spread.

Before it gets cooler in the evening, so called cross-"fixing-berms", consisting of protecting sand layer or drainage gravel, are placed on the geosynthetic protecting layer at the ends of the geomembranes and at special locations (e.g. hollows, grooves, toes) to fix the geomembranes and keep them in position. The fixing berms

should not exceed a distance of more than 30 to 50 m in order to avoid transverse contraction of the geomembranes. In the evening the lower temperature causes the geomembrane to become flat and subsequently the whole area can be spread with the protecting or drainage mineral layer either during the same night or in the early morning of the next day to prevent the built-up of condensed water underneath the geomembranes as well as the formation of new waves (figure 5).

The grading of the mineral protective layer to the designed level and the placement of the drainage layer is carried out some days later during normal day time, since a direct heat effect on the geomembranes is prevented by the complete coverage and thus also no new waves can form.

The installation of geomembranes in composite liners to cover the entire surface evenly is made possible by the utilisation of the physical characteristics of the geomembrane, and if the welders are experienced in their work, they can weld the geomembranes without creating any pockets in spite of the waves which invariably exist. This has been confirmed by on-site observations and is to be seen in figure 6 to 8.

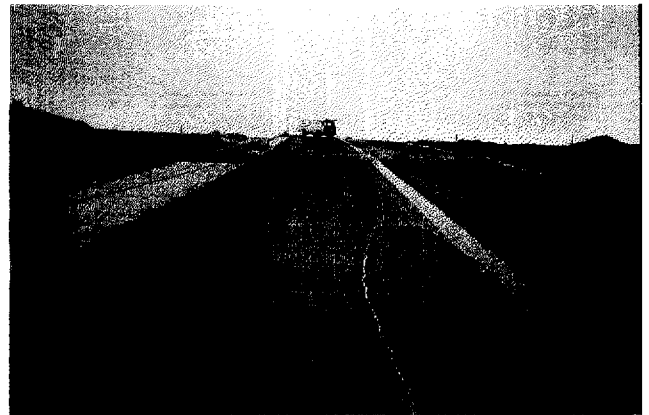


Figure 6. Example of a flat geomembrane on a landfill slope.

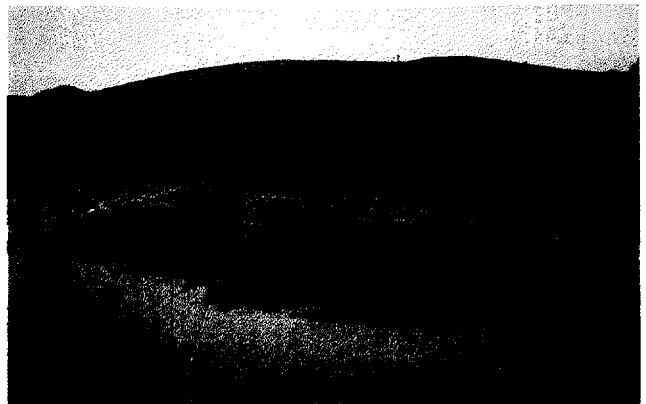


Figure 7. Example of a flat geomembrane on a landfill bottom.

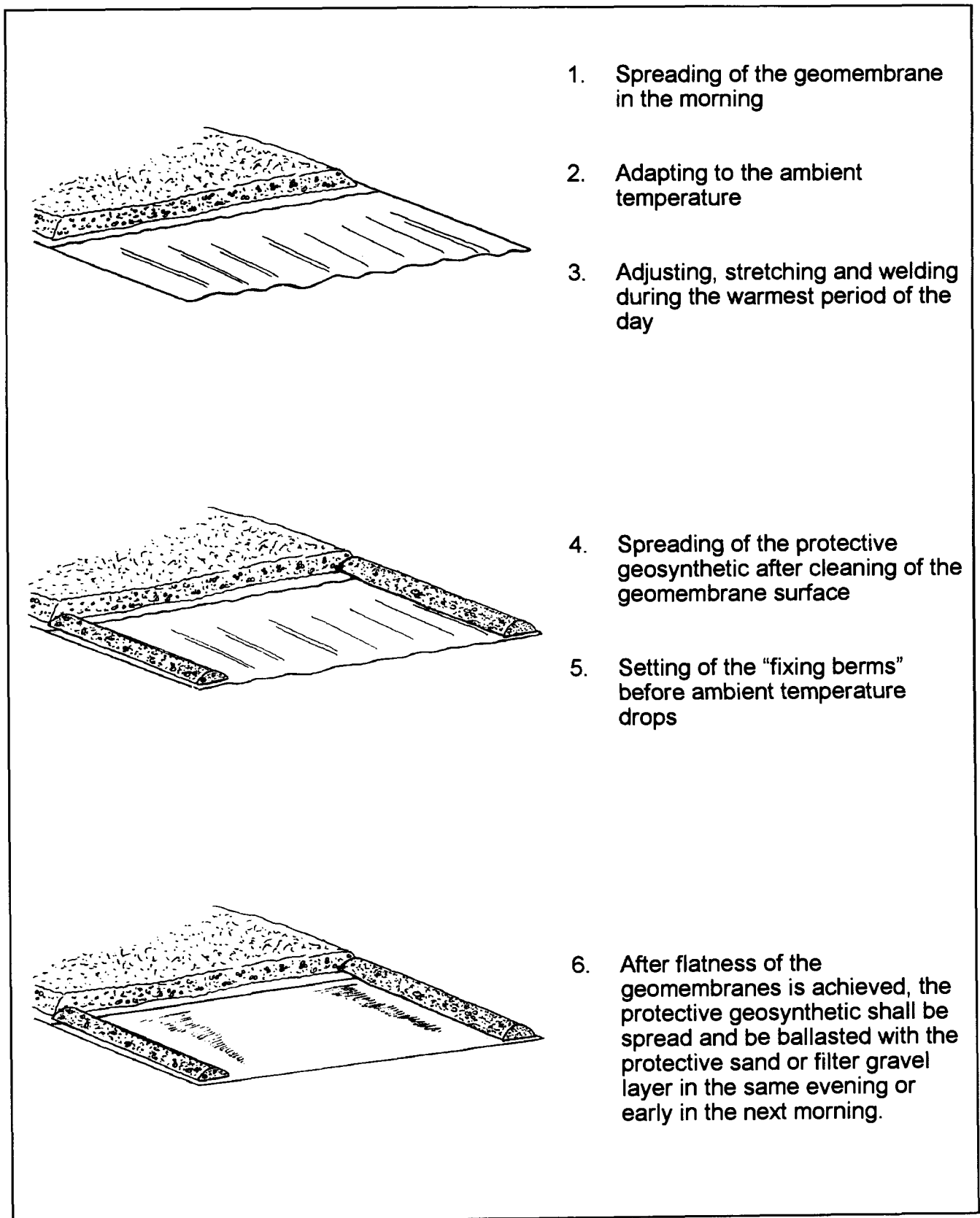


Figure 5. Flat placement of geomembrane by "Riegelbauweise".

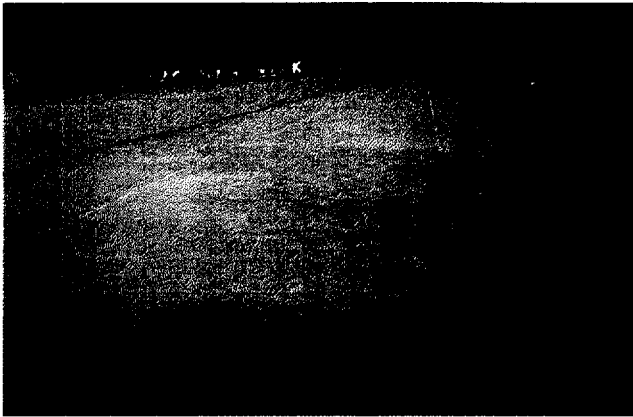


Figure 8. Example of a flat geomembrane on a landfill bottom.

## 7 STRESS LOAD ANALYSIS

The highest surface temperature measured in Germany on geomembranes of 2.5 mm thickness under direct sun exposure was not more than 60°C.

Since the fixing berms are placed later in the afternoon on the already cooling geomembranes, one can consider the temperature of the fixed geomembranes to be approx. 40°C. When covering the flat geomembrane with geosynthetics and protective sand layer or filter gravel, the temperature is usually not less than 15°C. With a temperature difference of  $\Delta T = 25 \text{ K}$  and a coefficient of linear thermal expansion of  $1.7 \times 10^{-4}/\text{K}$  the geomembrane will contain a strain of about 0.425%. At an accepted modulus of elasticity of about 600 MPa (MDPE) the induced stress is approximately 2.55 MPa, about 15% of the yield stress (about 17.5 MPa) of a common BAM-approved MDPE geomembrane (Seeger, S. and Mueller, W. 1996). This very low contraction stress level will additionally be reduced by stress relaxation while the geomembrane is in service. The service temperature of the geomembrane can - due to the increased leachate temperature - for the first 10 years be reckoned with up to about 35°C.

Therefore and on account of the MDPE resins used in Germany for geomembranes we see no danger of stress cracking or other kinds of failures when applying the "Riegelbauweise".

## 8 INSTALLATION OF PROTECTIVE LAYER AND DRAINAGE BLANKET

Analogous to the geomembrane, the protective geotextile can only be accessed to the placement area from the outside because it is not possible to allow heavy machinery to drive on the mineral layer or on the geomembrane. Correspondingly, there exists no actual installation equipment. Hydraulic excavators with articulated or telescopic booms are suitable.

This procedural step causes further implementation problems because geomembrane and geotextile cannot be accessed by heavy machinery. Bulldozers are therefore not

very suitable because of their high machine weight and shearing force which would impact on a geotextile or geomembrane; if a bulldozer is used it should be a bog-dozer model with plastic tracks.

The extensive installation of filter gravel by hydraulic excavator and excavator mats is out-dated because of its inefficiency. The use of hydraulic excavators with telescopic or articulated booms is feasible. They can reach the placement area from outside or from special construction roads on the placement area which are higher than 1.0 m, that is laterally, with the help of a long cantilever (range about 12 m). Because of its excellent levelling capacities the hydraulic excavator with a telescopic boom and power levelling shovel (cutting breadth 2.5 m) has proved useful on various sites.

A competitive alternative to hydraulic excavators are snowcats. The machines, originally designed for winter sports, have a low dead weight (2-6 t) and broad tracks (2 x 1.5 m), so that only low shearing forces and ground pressures (0.040 - 0.050 kg/cm<sup>2</sup>) are transmitted to the geotextile and geomembrane and no waviness in the geotextile or geomembrane will arise due to the installation of the protective layer. By way of comparison: a bulldozer exerts a ten times higher specific ground pressure than a snowcat.

Snowcats have proved effective on site. Even in slopes, especially if geogrids are installed, filter gravel can be pushed and placed easily and economically.

## 9 GEOSYNTHETIC CLAY LINERS (GCL)

At present the possible consequences of wrinkled geomembranes in combination with underlying GCLs are still under discussion. Some experts fear, that leakage paths may form or, moreover, hydrated bentonite might migrate into the hollows under the wrinkles.

Especially this fact reinforces the need of a flat installation of geomembranes to prevent wrinkles as much as possible to prevent any kind of flow path between the mineral sealing system and the geomembrane.

If wrinkles cannot be prevented during the installation phase it should be required to strengthen the internal shear strength of needle-punched GCLs to increase the internal shear strength and prevent the movement of bentonite laterally in the GCL. The use of non reinforced GCLs or partly reinforced GCLs (e.g. stitch bonded) would be critical for this application. Heerten et al. (1995) have demonstrated in their publication that there is a correlation between peel strength of the GCL and internal shear strength. Various testing programs have proven that GCLs can transmit a high shear strength in a needle-punched product without showing any creep behavior or pulling out of the fibers.

In any case, it is suggested - especially in base seals - to use GCLs with an appropriate peel resistance value and in addition have the geomembrane installed in such a way that wrinkles are avoided. Furtheron it is suggested that above items are construction quality controlled and should be already considered in the design phase and during the tender.

The choice of effective plant and procedures is crucial for a technically and economically successful construction project, along with the scaling of the equipment to correspond to requirements and the coordination of the equipment according to capacities.

Suggestions for a feasible equipment line for the construction of a composite liner incorporating a protective and a drainage system have been made above. The implementation of such a landfill liner system is highly demanding of personnel and machinery and requires the efficient implementation of construction procedures. In addition, various marginal conditions and risks as well as exacting schedule requirements increase the demands and thus exacerbate an already tense situation. The requirements which have to be met by a landfill liner system, weather factors and the resulting scheduling commitments, demand careful planning and sequential organisation of the construction work and particularly in the choice of machinery. Approved effectiveness of machinery, personnel and procedures are part of the performance-related requirements.

The landfill designer has to provide simple, even, non-curved geometries for the landfill base. Landfill designers should not seek to increase landfill volume by means of complex geometries, because in this way quality is reduced and the use of effective technology is prevented.

It is possible to construct a successful and economical composite liner with intimate contact of the layers by using the "Riegelbauweise" (FBCM), if it is carried out carefully and by well experienced personnel under effective management by the contractor.

## REFERENCES

- TA Abfall (1991) "2. Allgemeine Verwaltungsvorschrift zum Abfallgesetz" Bundesministerium für Umwelt, Naturschutz und Reaktorsicherheit, Bonn, Germany
- TA Siedlungsabfall (1993), "3. Allgemeine Verwaltungsvorschrift zum Abfallgesetz", Bundesministerium für Umwelt, Naturschutz und Reaktorsicherheit, Bonn, Germany
- BAM directive (1992) *Richtlinie für die Zulassung von Kunststoffdichtungsbahnen als Bestandteil einer Kombinationsdichtung für Siedlungs- und Abfalldeponien sowie für Abdichtungen von Altlasten*, Bundesanstalt für Materialforschung und -prüfung, Berlin, Germany
- Schicketanz, R. and Lotze, E (1991) "Erfahrungen mit der Fremdprüfung von Kombinationsabdichtungen", *Fortschritte der Deponietechnik 1991*, Seminar Haus der Technik, Essen, Germany
- Schicketanz, R. (1992) "Wirkungsweise der Kombinationsdichtung und Anforderungen an die mineralische Oberfläche", *Müll und Abfall*, 5/1992, pp. 287-295
- Schicketanz, R. and Lotze, E. (1992) "Prüfumfang bei der Qualitätssicherung von Kunststoffdichtungsbahnen", *Abdichtung von Deponien und Altlasten*, EF-Verlag GmbH, Berlin, Germany
- Averesch, U. (1993) "Bauverfahren bei der Herstellung von Kombinationsabdichtungen - Empfehlungen für einen optimalen Baubetrieb" *Fortschritte der Deponietechnik* Erich Schmidt Verlag, pp. 75-91
- Averesch, U. (1995) "Constructional Process Engineering and other problems specific to the construction of Composite Landfill Liner Systems" *SARDINIA 95 - Fifth International Landfill Symposium*, Christensen, T.H., Cossu, R., Stegmann, R. Vol 2, Siting, Lining, Drainage & Landfill Mechanics, pp. 115-130
- Dornbusch, J. and Averesch, U. and El Khafif, M. (1996) *Bauverfahrenstechnik und Qualitätsmanagement bei der Herstellung von Kombinationsabdichtungen für Deponien*, Shaker Verlag, Aachen, Germany
- DVS 2225, Teil 4 (1996) "Schweißen von Dichtungsbahnen aus Polyethylen (PE) für Abdichtungen von Deponien und Altlasten", DVS Verlag GmbH, Düsseldorf, Germany
- Seeger, S. and Mueller, W. (1996) "Limits of stress and strain: Design criteria for protective layers for geomembranes in landfill liner systems", *First European Geosynthetics Conference*, pp. 153-157, A.A. Balkema, Rotterdam, Netherlands
- Heerten, G., Saathoff, F., Scheu, C., von Maubeuge, K.P. (1995) "On the long-term shear behaviour of geosynthetic clay liners (GCLs) in capping sealing systems", *Proceedings of the international Symposium "Geosynthetic clay liners"*, pp. 141-150, Nürnberg, Germany





# BENTONITE MIGRATION IN GEOSYNTHETIC CLAY LINERS

Timothy D. Stark

Associate Professor, Department of Civil Engineering, University of Illinois at Urbana-Champaign, Urbana, Illinois, USA

**ABSTRACT:** Since the introduction of geosynthetic clay liners (GCLs) to waste containment facilities, one of the major concerns about their use has been the hydraulic equivalency to a compacted clay liner. Field observations and laboratory test results show that the thickness, or mass per unit area, of hydrated GCLs can decrease under normal stress, especially around zones of stress concentration, such as a sump or wrinkles in an overlying geomembrane. In a liner system, this decrease in GCL thickness can lead to an increase in fluid flux, regulatory non-compliance, and a decrease in leachate attenuation capacity and containment time. In a cover system, a reduced thickness of bentonite may lead to an increase in infiltration or gas migration through the GCL. Suggestions for protecting hydrated bentonite from stress concentrations are presented.

**KEYWORDS:** Geosynthetic Clay Liners, Flow Rates, Fluid Barrier, Permeability, Shear Strength

## 1 INTRODUCTION

In recent years, geosynthetic clay liners (GCLs) are increasingly being selected to replace compacted clay liners (CCLs) in composite liner and cover systems for waste containment facilities. Some of the advantages of GCLs over CCLs are: (1) lower and more predictable cost, (2) prefabricated/manufactured quality, (3) easier and faster construction, (4) reduced need for field hydraulic conductivity testing, (5) availability of engineering properties, (6) more resistance to the effects of wetting/drying and freeze/thaw cycles, (7) increased airspace resulting from smaller thickness, and (8) easier repair. Some of the disadvantages of GCLs versus CCLs include: (1) a potential for lower internal and interface shear strength, (2) a possible large post-peak shear strength loss in reinforced GCLs, (3) lower puncture resistance, (4) smaller leachate attenuation capacity, (5) shorter containment time, and (6) possibly higher long-term flux because of a reduction in hydrated bentonite thickness under the applied normal stress (Anderson and Allen 1995 and Anderson 1996). Koerner and Daniel (1995) concluded that GCLs can be considered hydraulically equivalent to CCLs if puncture and bentonite thinning do not occur.

## 2 BENTONITE MIGRATION IN GCLs

Field experiences, including the GCL slope stability research project in Cincinnati, Ohio (Koerner et al. 1996), show that bentonite will absorb moisture because of its high matric suction potential. An increase in water content is accompanied by an increase in compressibility regardless of the normal stress at which hydration occurs (Terzaghi et al. 1996).

Koerner and Narejo (1995) showed that if a circular piston is applied to a hydrated GCL, the bentonite will flow away from the load and the hydrated thickness of the GCL beneath the applied load will decrease. They concluded that

the soil covering a GCL must have a thickness ( $H$ ) greater than or equal to the diameter ( $D$ ) of the loaded area to adequately protect the GCL. Fox et al. (1996) presented results of similar GCL bearing capacity tests using three cover soils: a clean sand, a fine gravel, and a medium gravel. They recommended an  $H/D$  ratio between 1 and 2 to protect the GCL for this range of cover soils. The U.S. Army Corps of Engineers (United States 1995) requires a minimum cover soil thickness of 0.45 m, instead of an  $H/D$  ratio, before construction equipment can operate on top of a GCL.

The thickness of hydrated bentonite also may decrease under nonuniform normal stresses that may be imposed by the waste placed above the liner system. Stress concentrations in a liner system can cause hydrated bentonite to migrate to zones of lower stress. Stress concentrations are ubiquitous in a liner system, especially around a sump, under leachate collection pipes, at the edge of an anchor trench, at slope transitions, and around slope benches. Bentonite migration may be particularly important in sump areas because high hydraulic heads in a sump can increase leakage rates. In fact, Tedder (1997) recommended additional protection for sump areas. Stress concentrations can also be induced in a cover or liner system by a subgrade that contains stones or is uneven and/or contains ruts prior to GCL placement. Another possible mechanism for stress concentration development is local differential settlement caused by natural variations in foundation compressibility and shear strength, i.e., bearing capacity.

## 3 MIGRATION AT GEOMEMBRANE WRINKLES

The presence of wrinkles in an overlying geomembrane creates zones of nonuniform normal stress, which can cause hydrated bentonite to migrate into the airspace under the wrinkle. Figure 1 presents a typical pattern of wrinkles in a recently installed black, smooth high density polyethylene (HDPE) geomembrane. It can be seen that the liner has a

number of wrinkles, especially around the sump located in the foreground. (Note: sandbags in middle of photograph for scale.) The photograph was taken in the morning which probably reduced the number of wrinkles. In addition, there are a number of places around the sump and subsequent piping that lead to stress concentrations.

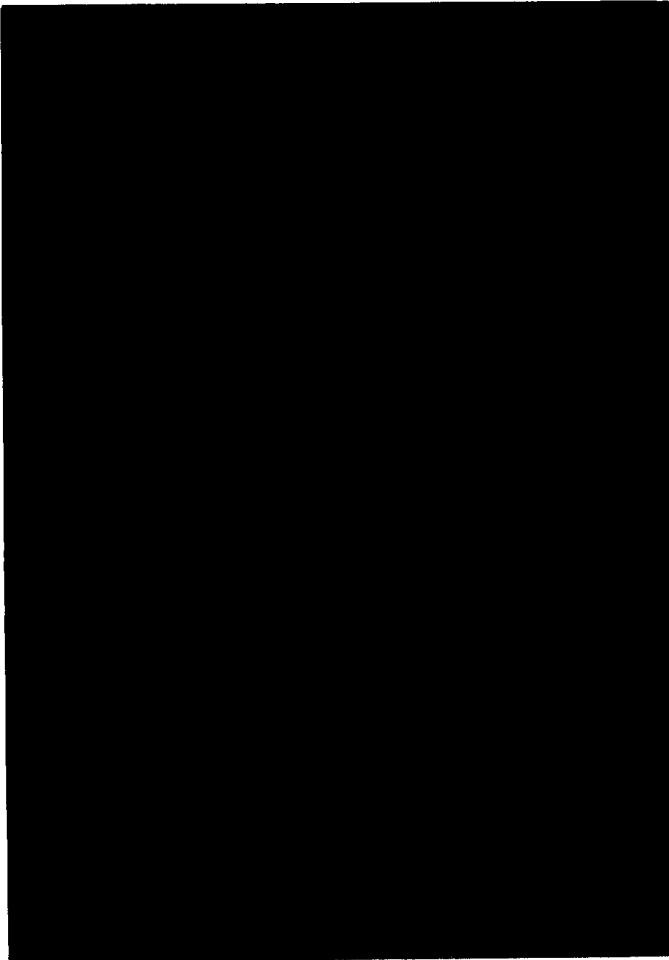


Figure 1. Typical pattern of wrinkles in a smooth HDPE geomembrane liner and around a sump.

Koerner (1996) and Soong and Koerner (1997) discussed the progress of a current research project investigating the fate of wrinkles in geomembranes. Current results indicate that the shape of a wrinkle or wave can change with time and normal stress, but the height does not appear to reduce substantially under a range of normal stresses. In addition, Eith and Koerner (1996) and Koerner et al. (1997) described a municipal solid waste landfill double liner system that was exhumed after eight years of service. The double liner system was constructed in 1988 and exhumed for a lateral expansion. After exhumation, a number of large wrinkles were found in the geomembrane. These observations show that wrinkles are not removed after installation, and can be long-term zones of nonuniform normal stress acting on an

underlying GCL. The lack of intimate contact due to wrinkles can result in hydrated bentonite migrating into the airspace under the wrinkle.

Anderson and Allen (1995) and Anderson (1996) showed that the thickness of a hydrated GCL can be reduced significantly in the vicinity of a geomembrane wrinkle. A normal stress of 958 kPa was applied to a hydrated GCL in the presence of a geomembrane wrinkle using a one-dimensional compression apparatus. These tests were conducted using a steel and plexiglass consolidometer measuring 0.3 m by 0.3 m. Two needle-punched GCLs were used in these compression tests. Both products consisted of woven upper geotextiles and nonwoven lower geotextiles. The non-woven geotextile of the GCL was placed on a horizontal layer of compacted sand while the woven geotextile was in contact with the geomembrane.

Both GCLs were hydrated under a normal stress of 9.6 kPa for 72 hours. The moisture content of the bentonite after hydration ranged from 100 to 150%. A 1.5 mm thick smooth HDPE geomembrane with a 50 mm wrinkle, as suggested by Giroud (1995), was placed on top of the GCL. Sand was then compacted along the sides and top of the wrinkle.

The normal stress was applied using a loading frame with a load cell at an average rate of 4.5 kN/min in one-dimensional compression. The normal force was increased for approximately 3.5 hours until a normal stress of 958 kPa was achieved. This normal stress was maintained for 3 hours and observations of the bentonite behavior were made. The shape or width of the wrinkle changed slightly but it did not disappear due to the normal stress of 958 kPa.

The hydrated bentonite migrated toward the void under the geomembrane wrinkle where the normal stress was at or near zero. The thickness of the GCLs under the wrinkle was 20 to 25 mm while the thickness farthest away from the wrinkle was less than 2.5 mm. The nominal manufactured thickness of the GCL was 7.0 mm. In addition, the upper woven geotextile separated from the GCL under the wrinkle and conformed to the shape of the wrinkle. This was caused by the additional pressure of the migrating bentonite breaking or pulling the needle-punched fibers out from the woven geotextile in the low confining stress area under the wrinkle. Along the edges of the GCL, where the bentonite was in compression, the needle-punched fibers remained intact.

In summary, the test results presented by Anderson and Allen (1995) indicate that migration of hydrated bentonite toward the area under a wrinkle in the 1.5 mm thick smooth HDPE geomembrane can occur. The migration of bentonite into the wrinkles of a geomembrane also has been observed at an operating landfill in Ohio (Evans 1997).

The migration of hydrated bentonite has implications for meeting regulatory requirements, including mass of bentonite per unit area and hydraulic performance. Thus, it

seems prudent to ensure a minimum long-term thickness or mass per unit area of hydrated bentonite to maintain hydraulic performance, leachate attenuation capacity, and leachate containment time in a GCL liner system. In a cover system, a minimum long-term thickness of hydrated bentonite should be maintained to reduce water infiltration and/or gas migration out of the landfill. The reduced thickness in a cover could be caused by vehicle traffic, slope transitions or benches, and geomembrane wrinkles.

#### 4 POSSIBLE SOLUTIONS

A number of possible solutions were considered to eliminate or reduce the potential migration of hydrated bentonite in a liner system. One possible solution is to use a CCL because of the low compressibility of the highly compacted soil. Another solution is to encapsulate the bentonite between two geomembranes to reduce the amount of hydration and the resulting increase in compressibility. This can be accomplished with planar geomembranes or geomembranes with protrusions. Multiple layers of GCL also can be installed at known points of stress concentration, e.g., sumps and changes in slope. The multiple layers of GCL initially provide a thicker layer of bentonite. Another possible solution involves reducing stress concentrations in the subgrade by smoothing changes in the geometry, reducing ruts, and removing rocks. The geomembrane also should be installed with a limited number of wrinkles. This can be accomplished by using geomembranes that are light-colored (white), exhibit a high friction coefficient (textured), and/or are flexible (Giroud 1995).

#### 5 MODIFICATION OF EXISTING GCLs

Another technique to ensure a minimum long-term thickness of hydrated bentonite is to modify existing GCLs to include an internal structure or stabilizer element. The stabilizer element would reduce the compression, and thus lateral squeezing, of hydrated bentonite in response to the stress concentrations in a liner or cover system. The internal structure would also protect the bentonite from concentrated stresses applied during handling, stockpiling, and construction, and may provide additional resistance to accidental puncture. Confining the bentonite in an internal structure will provide better assurance of the thickness or integrity of the bentonite. This protection is already provided in some bentonite waterproofing applications. It is anticipated that the bentonite would fill the entire depth of the internal structure. Therefore, the initial thickness of the GCL, or internal structure, would correspond to the desired bentonite thickness.

The modified GCL described herein utilizes a geonet as the internal structure or stabilizer element. This modified

GCL is fabricated by bonding one nonwoven geotextile to the geonet, filling the geonet with bentonite, and bonding the second geotextile. The internal structure facilitates bonding of the geotextiles and protects the bentonite, or other impermeable material, from the overlying normal stress. Heat bonding usually results in a strong bond between a geotextile and geonet, which has been observed for geosynthetic drainage composites. This bonding significantly reduces the potential for internal failure or shear through the bentonite. The internal structure also provides some puncture and tensile resistance to the GCL. If additional tensile resistance is required, the geonet could be replaced with a thick geogrid. Other variations of the modified GCL include the use of an internal configuration or structure that differs from a geonet or using a geomembrane that incorporates an internal structure (Stark 1997).

##### 5.1 Hydraulic Conductivity of Modified GCL

Stalcup and Rad (1994) conducted a falling head hydraulic conductivity test in accordance with ASTM D5084 (Standard 1993a) to evaluate the hydraulic conductivity of the modified GCL. The modified GCL described herein consisted of two 265 g/m<sup>2</sup> nonwoven geotextiles heat bonded to a geonet. The geonet was filled with 5 kg/m<sup>2</sup> of bentonite.

The modified GCL was consolidated at a confining stress of 35 kPa and then hydrated. The hydraulic conductivity value of  $4 \times 10^{-11}$  m/sec was measured using falling head hydraulic gradients ranging from 27 to 5. This value is in agreement with values (2 to  $5 \times 10^{-11}$  m/s) reported for existing fabric encased GCLs (Geotechnical Fabrics Report 1997).

##### 5.2 Shear Strength of Modified GCL

Swan (1994) conducted 0.3 m by 0.3 m direct shear tests in accordance with ASTM D5321 (Standard 1993b) to evaluate the shear strength of the modified GCL. The modified GCL was hydrated and sheared at the same normal stress. Two normal stresses, 100 and 290 kPa, were used in the tests. The modified GCL was allowed to hydrate for 24 hours under tap water immersion. The shear stress was applied at the rate of 1.0 mm/minute, as indicated in ASTM D5321. In both tests, failure occurred between the upper geotextile and a special direct shear gripping surface. The bond between the upper and lower geotextiles and the geonet did not fail or show any degradation. Table 1 presents the peak shear stress and secant friction angle for each test. These angles of internal friction correspond to a linear failure envelope that passes through the origin and the peak shear stress. The resulting friction angles are large, and comparable to the peak friction angle of a textured geomembrane/nonwoven geotextile (265 g/m<sup>2</sup>) interface

(Stark et al. 1996).

Table 1. Direct shear test results on modified GCL.

Normal stress (kPa)	Peak shear stress (kPa)	Peak secant friction angle (degrees)
100	115	49
200	174	31

Figure 2 presents the shear force-displacement relationships from the two 0.3 m by 0.3 m direct shear tests on the modified GCL. No post-peak strength loss was observed in the test at a normal stress of 100 kPa. In fact, the shear force-displacement relationship increases with increasing shear displacement due to necking or stretching of the geonet. The test at a normal stress of 290 kPa exhibited a reduction in shear force and friction angle of approximately 6 kN and 9 degrees, respectively. The post-peak strength loss is mainly attributed to the pulling out and/or tearing of the filaments from the nonwoven geotextile during shear (Stark et al. 1996). The geonet also necked or stretched during this test.

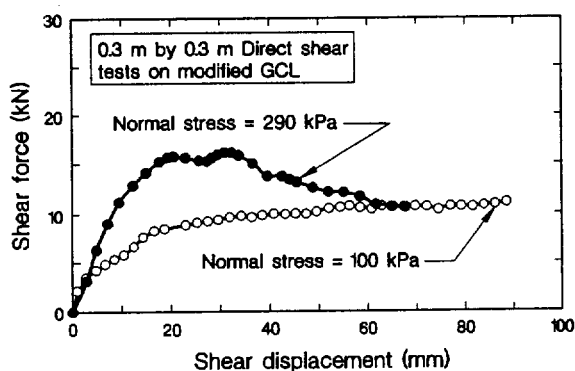


Figure 2. Shear strength of modified GCL after hydration (after Swan 1994).

### 5.3 Compressibility of Modified GCL

One-dimensional compression tests were conducted on the modified GCL in the 0.3 m by 0.3 m consolidometer used by Anderson and Allen (1995). The tests were conducted in the presence of a geomembrane wrinkle to demonstrate protection of the hydrated bentonite. The testing was performed both with and without bentonite in the geonet to distinguish between bentonite and geosynthetic compressibility.

For comparison purposes, the normal stress (958 kPa) and duration of the maximum normal stress (3 hours) used in the previously described tests by Anderson and Allen (1995) were used to test the modified GCL. However, to better simulate landfill loading rates, the normal stress was

applied at an average rate of about 2.5 kPa/min, instead of 4.5 kPa/min, until a normal stress of 958 kPa was achieved. As a result, approximately 6 hours of loading was required to obtain a normal stress of 958 kPa. However, this loading rate is still probably faster than actual landfilling.

Both modified GCL specimens were hydrated using the procedure described by Anderson and Allen (1995). The water content of the bentonite in the modified GCL after hydration was 172%. The specimen without bentonite was also hydrated, but moisture contents of the geosynthetics were not measured. After the normal stress was removed, the specimens with and without bentonite were measured to determine the variation of thickness across the specimen in the presence of a wrinkle.

#### 5.3.1 Modified GCL with bentonite

Table 2 presents the thicknesses of the GCL specimen with bentonite before and after loading to a normal stress of 958 kPa. The thickness of the GCL prior to hydration under a normal stress of 9.6 kPa for 72 hours was about 5.5 mm.

The thickness of the modified GCL increased slightly from approximately 5.5 mm to 5.8 and 5.9 mm along the right and left edges, respectively, during the hydration phase of the test. This is attributed to bentonite swelling into the nonwoven geotextile at a normal stress of 9.6 kPa. The thickness also increased slightly under the wrinkle at the center of the specimen. It is anticipated that this increase in thickness is also due to expansion of the bentonite during hydration.

Table 2. Thickness of modified GCL with bentonite.

Test Condition	Thickness at left edge (mm)	Thickness under wrinkle at center (mm)	Thickness at right edge (mm)
After hydration & prior to loading	5.9	5.7	5.8
After application of normal stress of 958 kPa	5.4	10.1	5.5
Change in thickness after loading	-0.5	+4.4	-0.3

Under a normal stress of 958 kPa, the GCL thickness at the outer edges decreased slightly to approximately the original thickness of 5.5 mm. This decrease is attributed to compression of the geotextile, compression of the geonet,

and possible squeezing of hydrated bentonite through the upper nonwoven geotextile toward the wrinkle or into the underlying bentonite. The bentonite probably initially migrated into the upper nonwoven geotextile during hydration under a normal stress of 9.6 kPa.

The interesting behavior occurred under the wrinkle near the center of the specimen where the thickness increased by 4.4 mm. Examination of the specimen after testing indicated that the increase in thickness was caused by bentonite swelling vertically into the nonwoven geotextile, the geotextile and geonet not being compressed under the wrinkle, and the geonet being slightly compressed along the edges and forcing hydrated bentonite toward the wrinkle area. It is also possible that hydrated bentonite in the nonwoven geotextile was squeezed or pushed from the left and right edges to the area under the wrinkle. It is important to note that the nonwoven geotextile remained bonded to the top of the geonet in the vicinity of the wrinkle instead of separating from the GCL as was observed in tests performed on a needle-punched GCL by Anderson and Allen (1995).

In summary, the modified GCL maintained a minimum thickness of 5.4 mm (near the initial thickness of 5.5 mm) after hydration and loading to a normal stress of 958 kPa in the presence of a geomembrane wrinkle.

### 5.3.2 Modified GCL without bentonite

Table 3 presents the thickness of the modified GCL specimen without bentonite before and after loading. The thickness of the GCL after hydration for 72 hours under a normal stress of 9.6 kPa was approximately 5.6 mm. As expected, the thickness of the modified GCL remained approximately constant during the hydration phase of the test because no bentonite was placed in the geonet. After loading to a normal stress of 958 kPa, the thickness at the left and right edges of the modified GCL showed little, if any, compression which is similar to the modified GCL with bentonite. The GCL thickness under the wrinkle remained essentially unchanged.

Comparison of Tables 2 and 3 shows that the modified GCL with and without bentonite exhibited similar thicknesses along the edges after loading to a normal stress of 958 kPa. The only discrepancy appears to be the area under the wrinkle where some hydrated bentonite swelled into the nonwoven geotextile and may have been pushed from the edges through the nonwoven geotextile to the wrinkle area.

In summary, the use of an internal structure in a GCL may provide some assurance of the minimum thickness or mass per unit area of the bentonite after installation. The long-term thickness can be prescribed by using an internal structure height that meets the desired thickness or mass per unit area. In addition, stress concentrations caused by handling, installation, uneven subgrades, rocks, sumps, piping, slope transitions, and geomembrane wrinkles will

not have to be reduced or modified because the bentonite is protected by the internal structure. The modified GCL also utilizes materials already approved and accepted for waste containment facilities.

Table 3. Thickness of modified GCL without bentonite.

Test Condition	Thickness at left edge (mm)	Thickness under wrinkle at center (mm)	Thickness at right edge (mm)
After hydration & prior to loading	5.6	5.5	5.7
After application of normal stress of 958 kPa	5.4	5.7	5.3
Change in thickness after loading	-0.2	+0.2	-0.4

## 6 CONCLUSIONS

Hydrated bentonite can migrate to areas of lower normal stress due to stress concentrations. Stress concentrations are ubiquitous in a liner system, especially around a sump and pipe locations, at the edge of an anchor trench, around slope transitions and slope benches, under geomembrane wrinkles, and above an uneven subgrade or rock. Possible solutions to eliminate or reduce the migration of hydrated bentonite include using a compacted clay liner, encapsulating the bentonite between two geomembranes to reduce the amount of hydration and the resulting increase in compressibility, installing multiple layers of GCL at known stress concentrations, eliminating stress concentrations in the subgrade by smoothing changes in geometry, reducing ruts and removing rocks, and/or installing geomembranes with a limited number of wrinkles. The number of wrinkles could be reduced using a geomembrane that is light-colored (white), exhibits a high coefficient of friction (textured), and/or is flexible (Giroud 1995). Another alternative is to modify existing GCLs to include an internal structure or stabilizer element as described herein. The stabilizer element appears to protect the bentonite from stress concentrations thereby reducing bentonite migration and provide additional puncture resistance.

## ACKNOWLEDGMENTS

Sam R. Allen of TRI/Environmental in Austin, Texas

supervised the 0.3 m by 0.3 m one-dimensional compression tests on the modified GCL. The author also acknowledges James D. Anderson of JANCO Engineering for his extensive review of this paper. The author invented the modified GCL. Patent rights have been assigned to Geosynthetics, Incorporated to which the author is a paid technical consultant.

## REFERENCES

- Anderson, J.D. (1996) "Are Geosynthetic Clay Liners (GCLs) Really Equivalent to Compacted Clay Liners", *Geotechnical News*, BiTech Publishing, Ltd., British Columbia, Canada, Vol. 14, No. 2, June, pp. 20-23.
- Anderson, J.D. and Allen, S.R. (1995) "What Are the Real Design Considerations When Using a Geosynthetic Clay Liner (GCL)", *Proceedings of the 9th Annual Municipal Solid Waste Management Conference*, Austin, TX.
- Eith, A.W. and Koerner, G.R. (1996) "Assessment of HDPE Geomembrane Performance in a Municipal Waste Landfill Double Liner System after Eight Years of Service", *Proceedings of 10th GRI Conf. on Field Performance of Geosynthetics and Geosynthetic Related Systems*, Drexel Univ., Philadelphia, PA, pp. 97-109.
- Evans, W.D. (1997). "Advisory on Structural Integrity Considerations for Incorporating Geosynthetic Clay Liners in Solid Waste Landfill Facility Designs," Div. of Solid and Infectious Waste Management, Ohio Environmental Protection Agency, August, 14 pp.
- Fox, P.J., DeBattista, D.J. and Chen, S.H. (1996) "Bearing Capacity of Geosynthetic Clay Liners for Cover Soils of Varying Particle Size", *Geosynthetics International*, Industrial Fabrics Assoc. International, St. Paul, MN, Vol. 3, No. 4, pp. 447-461.
- Geotechnical Fabrics Report (1997) "Specifier's Guide", Industrial Fabric Assoc. Intl., St. Paul, MN, pp. 144-145.
- Giroud, J.P. (1995) "Wrinkle Management for Polyethylene Geomembranes Requires Active Approach", *Geotechnical Fabric Report*, April, Vol. 13, No. 3, pp. 14-17.
- Koerner, G.R., Eith, A.W., and Tanese, M. (1997) "Properties of Exhumed HDPE Field Waves and Selected Aspects of Wave Management", *Proceedings of 11th GRI Conf. on Field Installation of Geosynthetics*, Drexel Univ., Philadelphia, PA, pp. 152-162.
- Koerner, R.M. (1996) *The GSI Newsletter/Report*, Geosynthetic Institute, Drexel University, Philadelphia, PA, Vol. 10, No. 2, June.
- Koerner, R.M., Daniel, D.E. and Bonaparte, R. (1996) "Current Status of the Cincinnati GCL Test Plots", *Proceedings of 10th GRI Conference on Field Performance of Geosynthetics and Geosynthetic Related Systems*, Drexel Univ., Philadelphia, PA, pp. 147-175.
- Koerner, R.M. and Daniel, D.E. (1995) "A Suggested Methodology for Assessing the Technical Equivalency of GCLs to CCLs", *Geosynthetic Clay Liners*, edited by Koerner, R.M., Gartung, E., and Zanzinger, H., A.A. Balkema, Rotterdam/Brookfield, pp. 73-98.
- Koerner, R.M. and Narejo, D. (1995) "Bearing Capacity of Hydrated Geosynthetic Clay Liners", *Journal of Geotechnical Engineering*, American Society of Civil Engineers, Vol. 121, No. 1, pp. 82-85.
- Soong, T.-Y. and Koerner, R.M. (1997) "Behavior of Waves in High Density Polyethylene Geomembranes: A Laboratory Study", *Proceedings of 11th GRI Conf. on Field Installation of Geosynthetics*, Drexel Univ., Philadelphia, PA, pp. 128-151.
- Stalcup, J.M. and Rad, N.S. (1994) "GCL Permeability Testing", Laboratory Testing Report prepared by GeoSyntec Consultants, Atlanta, GA, 6 pp.
- "Standard Test Method for Measurement of Hydraulic Conductivity of Saturated Porous Materials Using a Flexible Wall Permeameter - D5084", (1993a) American Society for Testing and Materials, Philadelphia, PA, Annual Book of Standards, Vol. 04.09, pp. 63-70.
- "Standard Test Method for Determining the Coefficient of Soil and Geosynthetic or Geosynthetic and Geosynthetic Friction by the Direct Shear Method - D5321", (1993b) American Soc. for Testing and Materials, Philadelphia, PA, Annual Book of Standards, Vol. 04.09, pp. 110-114.
- Stark, T.D. (1997) "Effect of Swell Pressure on GCL Cover Stability", *Proceedings of Symposium Testing and Acceptance Criteria for Geosynthetic Clay Liners*, Amer. Soc. for Testing and Materials, Special Technical Publication 1308, Larry W. Well, ed., pp. 30-44.
- Stark, T.D., Williamson, T.A. and Eid, H.T. (1996) "Effect of Textured HDPE Geomembrane/Geotextile Interface Shear Strengths", *J. of Geotechnical Engineering*, Amer. Soc. of Civil Engineers, Vol. 122, No. 3, pp. 197-203.
- Swan, R.H., Jr. (1994) "GCL Direct Shear Testing", Laboratory Testing Report prepared by GeoSyntec Consultants, Atlanta, GA, 8 pp.
- Tedder, R.B. (1997) "Evaluating the Performance of Florida Double-Lined Landfills", *Proceedings Geosynthetics '97 Conference*, Industrial Fabrics Association International, St. Paul, MN, Vol. 1, pp. 425-438.
- Terzaghi, K., Peck, R.B., and Mesri, G. (1996) *Soil Mechanics in Engineering Practice*, Third Edition, John Wiley & Sons, Inc., New York, NY, 549 pp.
- United States Army Corps of Engineers (1995) "Guide Specification for Military Construction: Geosynthetic Clay Liners - Section 02442", CEGS-02442, U.S. Army Corps of Engineers Waterways Experiment Station, Vicksburg, MS, August, 10 pp.

# Thermal Treatment of HDPE Geomembrane Sheets

Jacek Mlynarek, SAGEOS Geosynthetic Technology Center, Canada

Michel Marcotte, SOLMERS International Consultants, Canada

Pierre Sarazin, SAGEOS Geosynthetic Technology Center, Canada

**ABSTRACT:** To produce HDPE geomembrane sheets, heat is mixed with polymer pellets. The produced melt is then forced through an extruder and cooled down. Since thermoplastic material are known to have memory, heat treatment can access this memory and spell out some important information about the future behavior of the produced sheet, in particular if heat welded seams behavior is concerned. From the hypothesis that seam behavior will be controlled by parent material behavior under the same condition, different HDPE sheets were subjected to thermal treatment and their reaction measured. From more than 1500 tests, film blown extrusion sheets showed less reaction to thermal treatment. Moreover, the variability of their reaction through out the sheet itself is much less than the one of flat extruded sheets. DSC analysis confirmed these differences while tensile tests cannot see any significant differences. In that respect, thickness variation is an important parameter. It was found that thin geomembranes swell more significantly than the thicker ones. Finally, results reveals that thermal treatment procedure can be applied to identify type of extrusion process of any given HDPE geomembranes.

**KEYWORDS:** geomembrane, HDPE extrusion, thermal treatment

## 1 INTRODUCTION

In the past 15 years, worldwide landfill technology has rapidly adopted the use of high density polyethylene (HDPE) as a low permeability liners. This geomembrane material covers today most of the marketplace related to flexible membrane liners (FML). Since most of their use is concentrated in environmental protection facilities, their long term behavior is then of the utmost importance.

To create continuous liners over a large surface, HDPE geomembrane sheets are produced in continuously enlarged width and field welded through polymer fusion. As heat comes in the first stage of sheets production, heat is again supplied at the sheets' interface as welding procedure goes on. Heat supply is then one of the major component of any HDPE geomembrane sheet.

Today the geosynthetic society works intensively to understand basic properties of HDPE geomembranes as well as their long term behavior. It is understood that long term performance of liners could substantially be affected by inappropriate or excessive welding conditions such as too high roller pressure, overheating of the sheets and thermal shock within or in the vicinity of the fused area (Rollin et al, 1989). So

sheet's reaction to heat transfer and thickness variation as of some importance.

Struve (1993) has explained in details seven categories of parameters that affect wedge welding of geomembranes. All of them are related either to welding process, ambient weather, on-site conditions or technical ability of the operators to control wedge welder parameters. None of Struve's categories refer to behavior of the sheet itself (stress relaxation, molecules orientation). Koerner (1993) underlines a large number of operational variables, mentioning that « the type of the geomembrane, its thickness, its texture, the temperature of the sheet, and the orientation of the sheet probably all play a part in some respect ».

None of the reviewed authors had shown the influence of heat transfer to sheet itself except if this heat transfer exceed what the material can support. As a consequence, it seems that the only intrinsic property of the geomembrane sheet really taken into consideration for the selection of welding conditions (pressure and heat transfer) is geomembrane's thickness (Rollin & Fayoux, 1991, Struve, 1993). Maybe because only part of geomembrane thickness (20% to 30% according to Maranda, 1995) participates in welding process.

All engineers agree on the importance of welding temperature on the quality of a final seam. None however ask how geomembrane itself responds to this welding temperature e.g. what is its thermal reaction, understood as relaxation of stresses and/or of molecular orientation during heat application. This property took very little attention of geosynthetic scientists. Huneault (1992), Maranda (1995), Vermeersch et al. (1995) and Marcotte et al. (1995) have assumed that thermal behavior of geomembrane itself is an important factor in selection of geomembrane welding conditions. They carried out a thermal treatment test of samples taken from the seam area and from geomembrane sheet adjacent to the seams. The test was based on the dimensional stability tests. The results indicated that there are difference between thermal behavior of different seams samples.

In this paper the authors present results of a research on thermal treatment ( $T^2$ ) of HDPE geomembrane sheets. This research was undertaken in an effort to verify if geomembranes  $T^2$  behavior differ from one geomembrane to another and if it could play a role during welding and influencing,  $T^2$  behavior of seams.

Results of  $T^2$  testing of HDPE geomembranes are presented and discussed in this paper. The testing program was focused on geomembrane sheets only. At this step of research seams were excluded from the program.

## 2 THERMAL TREATMENT ( $T^2$ ) TEST

The test consists of immersion of the geomembrane samples into a hot (145°C) silicone bath placed in an oven under controlled temperature conditions and for a given time. Standard minimum time of immersion was 5 minutes while standard maximum time of immersion was 120 minutes. The initial size of samples was 6 cm x 1 cm, with the length (6 cm) taken in the machine direction, while width is in the transverse direction. Thickness of sample was also measured prior to immersion. At selected intervals of time of immersion samples were removed from the bath and then air cooled to room temperature. Their dimensions in machine direction (MD), transverse direction (TD) and sheet thickness (ST) were measured. The observed dimensional changes were analyzed and the deformation values were calculated using the following equation :

$$D_X (\%) = ((X_{\text{final}} - X_{\text{initial}})/X_{\text{initial}}) \times 100 \quad (1)$$

where :  $D_X$  = deformation of parameter X (MD, TD or ST)

Samples location on the width of geomembranes sheet is shown in Figure 1.

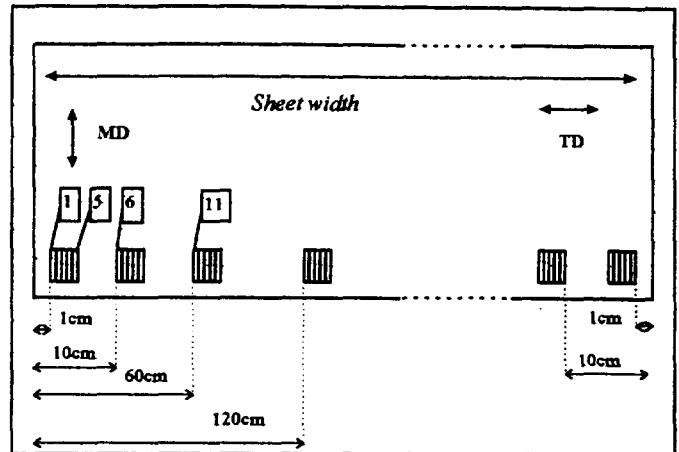


Figure 1. Location of samples on geomembrane sheets

In addition to thermal treatment testing some samples were analyzed by Differential Scanning Calorimetry thermal analysis procedure. Their tensile property was tested by ASTM D638-91.

Seven (7) commercially available HDPE geomembranes of 40, 60 and 80 mils of thickness have been selected for this testing program. Their properties specified by manufacturers are given in Table 1. Three (3) of them were produced by flat extrusion process and four (4) by blown film process. More than 1 500 samples have been tested during the program.

## 3 RESULTS

### 3.1 Thermal Treatment ( $T^2$ ) Test

Figure 2 shows a shape of samples of three geomembranes after 120 minutes of testing according to  $T^2$  procedure.

Figures 3 shows distribution of dimensional deformations of three parameters : machine direction, transverse direction and thickness. It can be noticed that thermal treatment ( $T^2$ ) behavior of blow film extruded geomembrane is much more uniform than the one manufactured by flat extrusion process. Also,



differences are observed between two flat extruded geomembranes.

Table 1. Properties of tested geomembranes as specified by manufacturers

ID*	Width (m)	Yield Strength (kN/m)	Break Strength (kN/m)	Elongation Yield/Break (kN/m)	Seams Shear (kN/m)	Seams Peel (kN/m)	Extrusion Process
-----	-----------	-----------------------	-----------------------	-------------------------------	--------------------	-------------------	-------------------

40 mils geomembranes

A	-	15.1	28	13/560	14.2	11.4	Blown
B	4.5	15.4	26.6	13/700	14	10.5	Flat
C	7.0	15.4	26.6	13/700	14	10	Blown
D	7.0	15	28	13/700	-	-	Flat

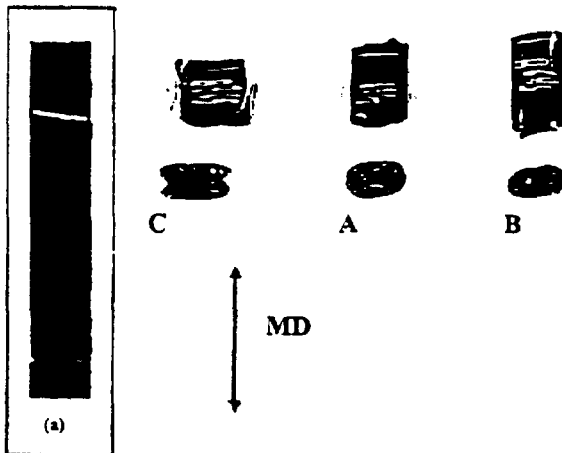
60 mils geomembranes

C	7.0	23.1	39.9	13/700	21	16	Blown
---	-----	------	------	--------	----	----	-------

80 mils geomembranes

A	7.0	30.3	56	13/600	28.4	22.8	Blown
B	4.5	30.8	53.2	13/700	28	21	Flat

\* ID : geomembranes manufacturer ID



Note : (a) shape of initial sample, before the thermal treatment

Figure 2. Samples of 40 mils geomembranes after 120 minutes of thermal treatment

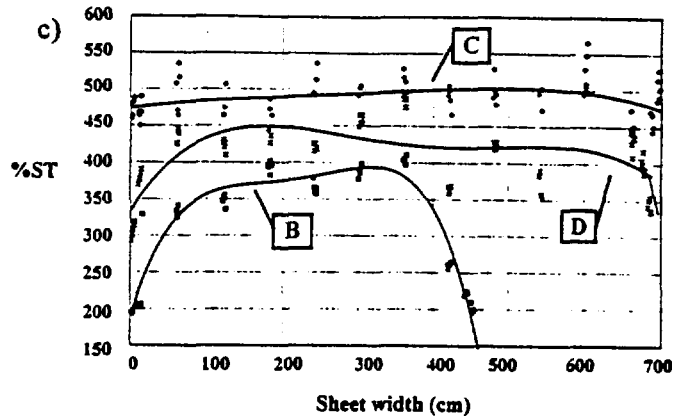
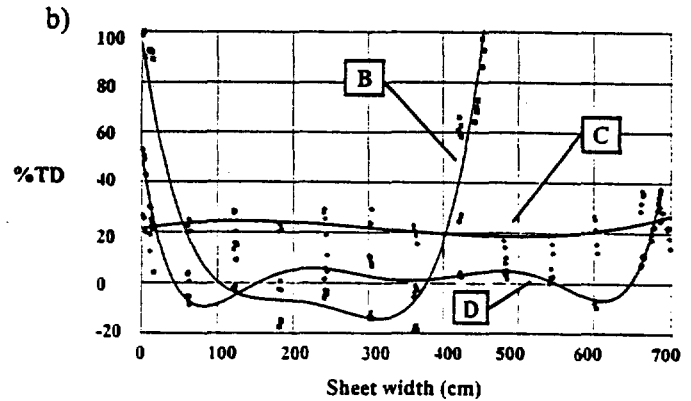
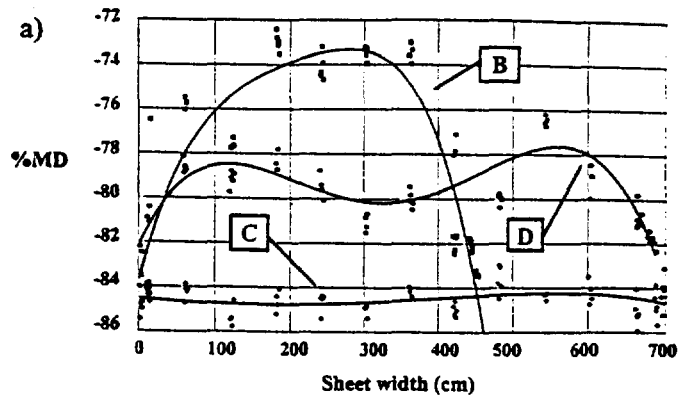


Figure 3. Thermal treatment results (dimensional deformation) in relation to sample position on the geomembrane sheet ; a) machine direction, b) transverse direction, c) thickness

Photos of samples after  $T^2$  in relation to sample location on the width of geomembrane sheet are presented in Figure 4. Figure 4a shows samples of flat extrusion process manufactured geomembrane while Figure 4b shows samples of blown film manufactured one. One column on these Figures represents samples taken at the same area of sampling. Three physical phenomena were observed during sampling. First, a

high shrinkage in machine direction was observed. It is clearly seen in Figure 2, where samples after T<sup>2</sup> are compare to original dimensions of the sample. Second, swelling process was observed in all samples. Finally, less pronounced changes were observed in transverse direction of each specimen as can be observed in Figure 2. Third, a variation of deformation in transverse direction was noted on the thickness of samples, as can be see in Figure 2, geomembrane C.

Figure 5 shows changes of dimensional deformation with time for machine direction dimension (Figure 5a) and for thickness (Figure 5b). These Figures also indicates the differences in TT behavior for different initial thickness of geomembranes. It can be noted that the dimensional deformation changes of the 80 mils geomembrane are less pronounced than the ones of the 40 mils geomembrane.

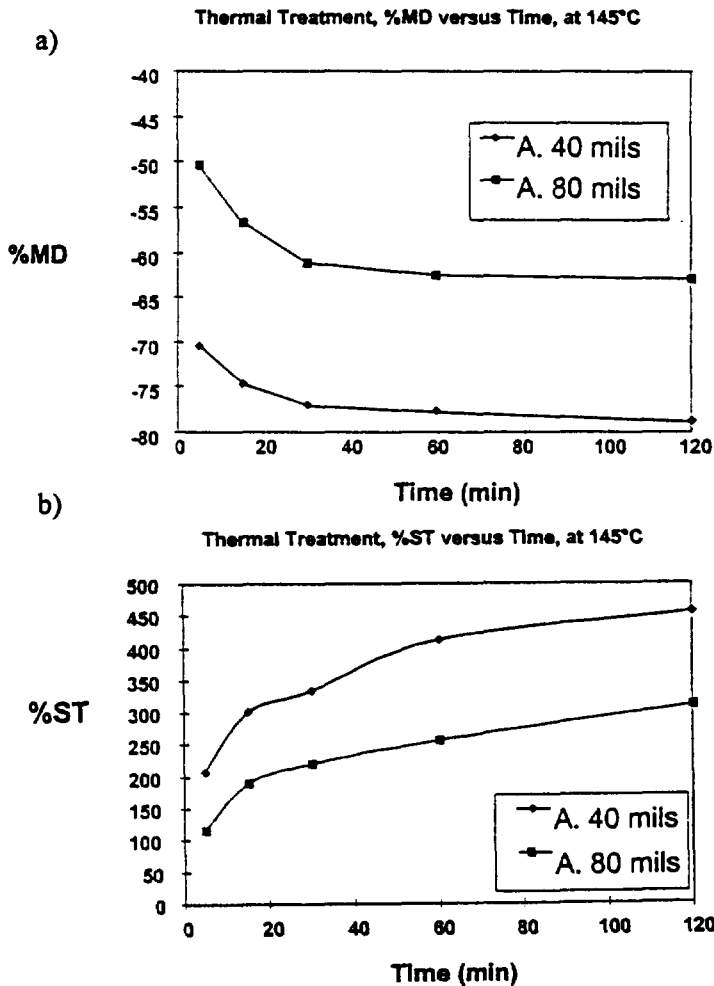
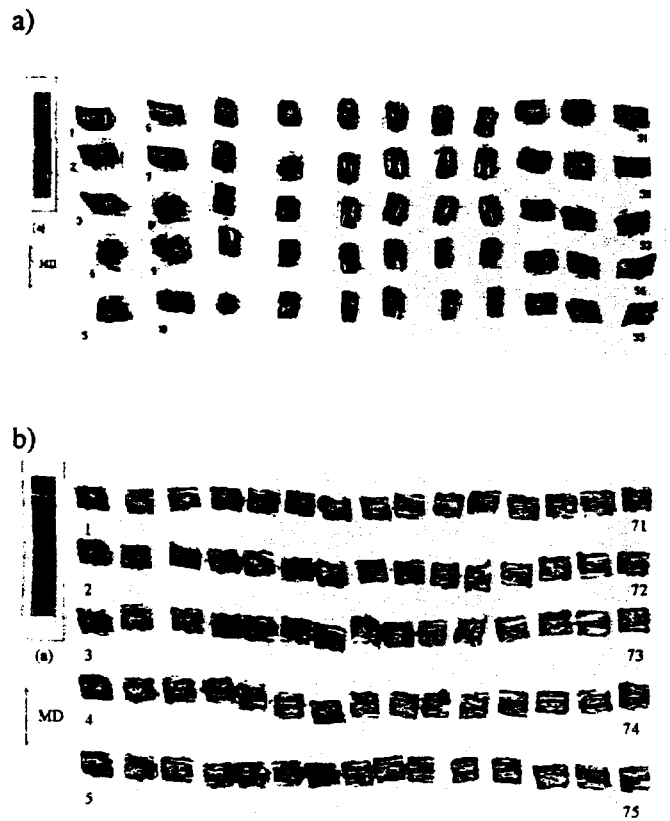


Figure 5. Dimensional deformation vs. time of immersion, a) machine direction b) thickness



Note: (a) shape of initial sample, before the thermal treatment

Figure 4. Photos of deformed samples after T<sub>2</sub> test in relation to their position geomembrane sheet  
a) flat extrusion geomembrane b) blown film geomembrane

Summary of measured deformation ratio at the edges and in the center of tested geomembranes of 40 mils thickness is presented in Table 2.

Table 2. Summary of deformation ratio of 40 mils initial thickness geomembranes

Geomembrane ID	Deformation ratio (%)					
	MD		TD		ST	
	Edge *	Center *	Edge *	Center *	Edge *	Center *
A (Blown Film)	-81	-80	10	-7	450	500
B (Flat extrusion)	-84	-73	100	-5	200	380
C (Blown Film)	-84	-84	25	25	490	500
D (Flat Extrusion)	-82	-80	50	0	350	425

\* Values read from deformation ratio curves at approximate of the edge and center of geomembrane sheets

### 3.2 Tensile test (ASTM D638-91)

Samples of two geomembranes, identified as B (flat extrusion) and C (blown film) were analyzed for their tensile behavior. The series of ASTM D638-91 tests were carried out on samples collected from the edge and from the center of geomembranes.

Tables 3 and 4 summarize tensile tests results for both geomembranes.

Table 3. Tensile test (ASTM D638-91) results of two geomembranes, C (blown film) and B (flat extrusion) - edge samples

Parameter	Geomembrane C				Geomembrane B			
	MD		TD		MD		TD	
	Values	Cv	Values	Cv	Values	Cv	Values	Cv
<b>Yield</b>								
- strength (N)	118	2.7	128	0.7	117	0.9	122	1.4
- elongation (%)	12.9	3.0	9.6	3.0	12.1	4.5	10.4	3.0
- displacement (mm)	3.2	3.0	2.4	3.0	3.0	4.5	2.6	3.0
<b>Break</b>								
- strength (N)	234	7.4	245	1.0	199	6.1	218	6.2
- elongation (%)	941.2	7.1	999.5	0.6	732.5	3.1	907.0	4.0
- displacement (mm)	235.3	7.1	249.9	0.6	183.1	3.1	226.8	4.0

Table 4. Tensile test (ASTM D638-91) results of two geomembranes, C (blown film) and B (flat extrusion) - center samples

Parameter	Geomembrane C				Geomembrane B			
	MD		TD		MD		TD	
	Values	Cv	Values	Cv	Values	Cv	Values	Cv
<b>Yield</b>								
- strength (N)	115	2.6	126	0.5	126	4.0	133	1.6
- elongation (%)	12.7	5.2	9.6	1.7	11.3	3.5	11.3	4.1
- displacement (mm)	3.2	5.2	2.4	1.7	2.8	3.5	2.8	4.1
<b>Break</b>								
- strength (N)	235	7.5	219	14.3	212	16.1	219	16.2
- elongation (%)	960.6	7.2	938.6	9.7	754.6	10.8	855.2	8.2
- displacement (mm)	240.2	7.2	234.7	9.7	186.7	10.8	213.8	8.2

### 3.3 Differential Scanning Calorimetry

DSC analysis was applied to measure the fusion temperature of two geomembranes. Samples for testing were taken from two locations on the geomembrane width, the edge and the center. Typical curves of DSC analysis for samples of flat extruded geomembrane B are shown in Figure 6 while values of fusion temperature are summarized in Table 5.

Table 5. Values of fusion temperature

Geomembranes ID	Peak Fusion Temperature ( °C)	
	Edge	Center
Geomembrane A (Blown Film Extrusion)	130.1	130.1
Geomembrane B (Flat Extrusion)	131.1	127.3

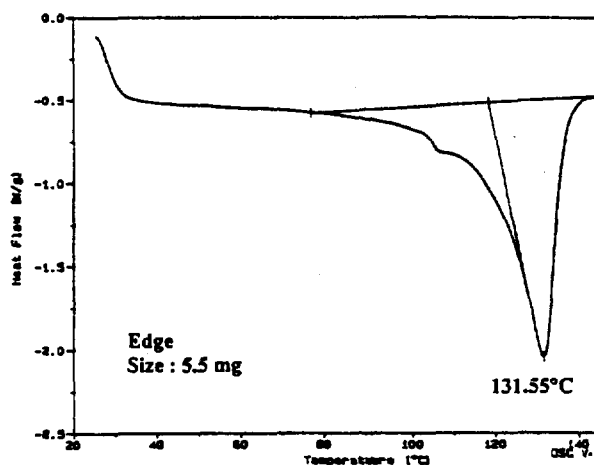
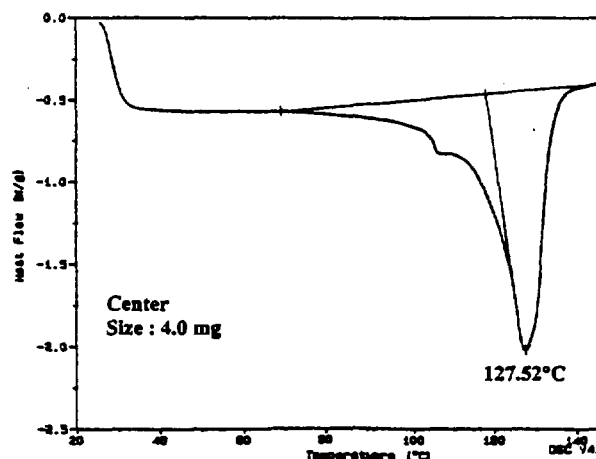


Figure 6. Examples of DSC curves for samples of geomembrane B

## 4 DISCUSSION

### 4.1 General

The specification of tested geomembranes, given by manufacturers, are very similar, as shown in Table 1. Also, simple statistical analysis of standard deviation of tensile results obtained during this program indicates that there is no significant difference between tensile property (ASTM D638) of HDPE geomembranes.

However,  $T^2$  indicates significant difference in thermal behavior of tested geomembranes. The visual observation indicates clearly that a shape of sample at the end of  $T^2$  depends on type of process as well as, in particular in case of flat extruded geomembrane, on position of samples on geomembrane sheets - Figure 4a. It can be also noted that the dimensional changes are very rapid at the beginning of thermal treatment and slows down with time, showing a tendency to equilibrium after about 60 minutes of treatment.

These differences in thermal treatment behavior of the geomembranes were never taken into consideration in selection of welding parameters.

### 4.2 Differences between geomembranes

$T^2$  deformation ratio distribution curves (Figure 3) indicate a significant difference in thermal behavior of blown film and flat extruded geomembranes.

Large differences in transverse direction and thickness deformation ratio can be noted for tested geomembranes (Table 2 and Figure 2). Machine direction deformation ratio varies very little, between -82% to -84%. The deformation ratio data indicates that the tested geomembranes react differently to temperature applications e.g. their thermal treatment behavior is different.

Simple statistical analysis of tensile test data presented in Tables 3 and 4 indicates that there is fair statistical discrepancy for the strength at yield in the transverse direction measurements between two geomembranes. There is no statistical difference between all other tensile testing parameters of both geomembranes.

### 4.3 Differences on the width of geomembranes

Blown film extruded geomembranes (manufacturers A and C) do not show large differences in deformation

ratio on the width of sheet, Figure 3 and Table 2 for all three, machine direction, transverse direction and thickness). On the other hand, flat extrusion geomembranes (manufacturers B and D) show different  $T^2$  behavior at the edge and in the center of the geomembrane sheet as shown in Figure 3.

The transverse direction (TD) and thickness deformations varied significantly as can be noticed in Table 2. Transverse direction deformation varies between 25% to 100% for the samples taken at the edge of geomembranes and between -5% to 25% for the samples from the center of the sheet. The negative value of the deformation of the sample in the center of the sheet could be an effect of the medium plane shrinkage. Thickness varies even more drastically, at the edge its deformation ratio for the same initial thickness of geomembranes varies between 200% to 500% while in the center sample between 375% to 500%.

Statistical analysis of tensile tests data indicates that there is no significant discrepancies between tensile behavior of geomembrane samples taken from the edge and from the center of tested geomembranes.

DSC analysis confirms the differences in thermal behavior of geomembranes noted during  $T^2$  tests (Table 5). Similarly to  $T^2$  results, a nonuniform behavior on the width of geomembrane sheet is observed for flat extruded geomembrane. As can be seen in Table 5, fusion temperature of the samples taken from the edge of the sheet is 131.1°C, while the center samples have fusion temperature 127.3°C. The DSC values of the blown film extruded geomembrane indicates uniform thermal behavior of the width of the geomembrane. A slight difference in fusion temperature of two geomembranes can also be noted in Table 5.

### 4.4 Thickness of geomembrane

The thinner geomembranes generate a higher deformation ratio than the thicker ones. Thus, it can be concluded that the relaxation of thermal stresses in these geomembranes are easier.

## 5 CONCLUSIONS

1. The typical specification of HDPE geomembranes, given by well known manufacturers, shows no important differences between HDPE geomembranes sheets. Tensile test results are very

similar for all the tested HDPE geomembranes from different manufacturers, indicating no significant differences between geomembranes.

2. The study reveals important difference in reaction to thermal treatment (thermal stresses relaxation) of different HDPE geomembranes. These differences, were never taken into consideration in selection of welding parameters.
3. Blown film extruded geomembranes indicates quite uniform reaction to both T<sup>2</sup> and DSC analysis. The deformation ratios and the fusion temperature values are very similar for the samples taken from different locations of the geomembranes.
4. On the other hand, flat extruded geomembranes show significant differences in thermal behavior of the samples taken at the edge and at the center of the geomembrane. These differences are confirmed by DSC tests.
5. T<sup>2</sup> confirms that the thickness is an important parameter in thermal behavior of geomembranes. It was found that the thin geomembranes swell under thermal treatment more significantly than the thicker ones.
6. Finally, results reveals that T<sup>2</sup> procedure can be applied to confirm the type of extrusion process of any given HDPE geomembranes.

## 6 RECOMMANDATIONS

More factual data is needed to understand thermal behavior of geomembranes to confirm authors observations.

Influence of thermal treatment (thermal stresses relaxation) on HDPE geomembranes seams is still little unknown. It is clear, however, that this behavior can have an influence on seaming process. It is thus recommended to relate the observed thermal treatment behavior of HDPE geomembranes to their seams quality.

## ACKNOWLEDGEMENTS

This research project was complete funded by SAGEOS Geosynthetic Technologies Center in collaboration with Ecole Universitaire d'Ingenieurs of Lille in France. The authors gratefully acknowledge material support from geomembrane manufacturers Agru America, Columbia Geosystems, GSE and National Seal. Special

acknowledgments are forwarded to Prof. J.Morcellet and Dr. D. Gueugnault of Ecole Universitaire d'Ingenieurs of Lille for their contribution in the research program reported in this paper.

## REFERENCES

- Hsuan Y.G., Yim G.K. and Koerner R.M. (1995), *Evaluation of Geomembranes Made from Different Blends of Polyethylene*, Proc. of Geosynthetics'95, Nashville, pp. 509-523
- Huneault (1992), *L'effet de l'opération de soudage sur les propriétés des géomembranes PEHD*, report for SOLMERS International, December 1992.
- Koerner R.M. (1993), *Overview - Data Acquisition and Control*, Proc. of the Workshop on Geomembrane Seaming, EPA/600/R-93/112, June 1993, pp.5 - 9
- Lu X., Zhou Z. and Brown N. (1994), *The Anisotropy of Slow Crack Growth in Polyethylene Pipes*, Polymer Engineering and Science, Vol. 34, No.2, January 1994, pp.
- Maranda L. (1995), *Comportement mécanique des soudures de géomembranes*, Master Thesis, Ecole Polytechnique of Montreal, June 1995.
- Marcotte M., Rollin A.L., Huneault M. and Lafleur J. (1995), *Effect of Welding Process on HDPE Seams Strength*, unpublished report, SOLMERS International, pages 12.
- Rollin A.L. and Fayoux D. (1991), *Geomembrane Seaming Techniques, in Geomembranes: Identification and Performance Testing*, Eds. A.L. Rollin and J.M. Rigo, Chapman and Hall, pp. 59-79.
- Rollin A.L., Vidovic A., Denis R. and Marcotte M. (1989), *Evaluation of HDPE Geomembranes Field Welding Techniques: Need to Improve Reliability of Quality Seams*, Geosynthetics'89, San Diego, pp. 443-455.
- Sarazin P. (1996), *Recherche pour la caractérisation des géomembranes PEHD*, SAGEOS/Ecole Universitaire d'Ingenieurs de Lille Report.
- Struve F. (1993), *Consistent Wedge Welders*, Proc. of 7th GRI Conference, Philadelphia, December 1993, pp. 9-23.
- Vermeersch O., Mlynarek J. and Morissette C. (1995), *Développement de la méthode de recuit pour l'analyse de la qualité des soudures*, SAGEOS Report, September 1995, pages 42.



# The Influence of the Welding Parameters for HDPE Geomembranes

A.L. Rollin and F. Montgrain, Solmers International, Longueuil, Canada

P. Lafleur and L. Maranda, École Polytechnique, Montréal, Canada

**ABSTRACT:** When in service, particularly in landfills, High Density Polyethylene (HDPE) may present fractures at the edge of seams upon the welding conditions used and their durability is questioned. Seams were performed in situ using a hot wedge welding machine and two commercial HDPE geomembranes 1,5mm (60 mils) thick. The evaluation of seams quality and its adjacent sheet has been performed by measuring properties using eight (8) different tests: seam shear and peel strengths; sheet crystallinity by the differential scanning calorimeter technique and by the gradient column method; residual stress in seam and membrane samples by dimensional changes in hot air and in silicone oil; seam brittleness level by the impact test developed at École Polytechnique and a high-sensitivity impact standard test. Temperature profile has been obtained simulating heat transfer involving a hot wedge machine using the method of finite differences. The simulation of the temperature profile indicated that the polymer sheet melts on about 20 to 30% of its thickness. Thermal gradients were found to be excessively high around the boundary of the melted zone, of the order of 50°C/mm of sheet width. It has been shown that the stress goes from compression in the weld to tension in the sheet indicating that the welding process does not induce stresses in the geomembrane but rather a stress gradient. Since it is known to be precursor of the stress-cracking phenomenon. Recommendations are made on the need to still improve welding machines and monitor welding. The measurement of the stress gradient build during seaming using the hot oil bath testing procedure should be investigated throughout to adapt it to HDPE geomembranes.

**KEYWORDS:** Geomembrane, Seams quality, Welding parameters, Heat transfer simulation

## 1 INTRODUCTION

### 1.1 The Concern

Often engineering structures fail because a geomembrane contains an unexpected flaw that is introduced, or gradually develops and becomes of a critical size that can cause rapid unexpected failure (Peggs 1994). Controlling welding process variables is then vital to achieving consistent wedge welds (Struve 1993). The various welding machines must monitor the desired variables to achieve consistent results over the widest possible range of field conditions and good well trained technicians must ensure that their machine performed well. It has been shown that seam quality is significantly influenced by speed, welding temperature, surface conditions and applied pressure (Peggs 1990, Rollin 1889a and b, Rollin 1991a, Rollin 1993, Rollin 1994, Struve 1993). These parameters may also significantly affect the long term behavior of the adjacent geomembrane. Thus, seam assessment criteria should include parameters for the adjacent geomembrane.

### 1.2 Seams

Sheets of two commercial HDPE geomembranes 1,5mm thick (shown in Table 1) were seamed in situ using a hot wedge welding machine (Maranda 1995) and the welding parameters were selected to span a wide range of acceptable conditions (Struve 1993): condition I being

identified normal and conditions II to IV being closer to non-acceptable limits. The welding procedure was performed under controlled conditions with the same machine such that the parameters influencing the seam quality are the welding speed, the welding temperature and the applied pressure as presented in Table 2.

Table 1. HDPE sheet properties

Sheet property/identification	GM A	GM B
Thickness (mm)	1,65	1,5
Tensile strength: yield point		
machine direction (MPa)	20,52	19,23
width direction (Mpa)	20,41	18,58

Table 2. Welding conditions

Welding conditions	Speed (m/min)	Temp. (°C)	Pressure
I	3	400	normal
II	2	400	normal
III	3	450	normal
IV	3	450	high

The influence of these welding parameters in the seam and in its adjacent sheet could be obtained by testing samples taken in the seams and in the sheet at distances from the center of the seam as shown schematically in Figure 1. It should be noted that samples collected at locations 1 and 2 are approximately 3,0mm thick.

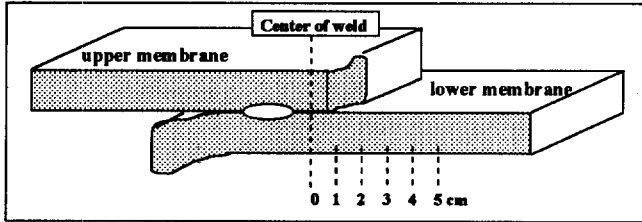


Figure 1. Schematic of a seam sample

## 2. EXPERIMENTAL

The evaluation of the seams and their adjacent membrane has been performed by measuring properties using eight (8) different methods. Firstly, a shear and a peel tests were performed on samples of produced seams to assess their acceptability as evaluated in the field by measuring their shear and peel strengths and identifying the location and the nature of the break. The ASTM D816 and D4437 modified test procedures were performed at a rate of 50mm/min. A total of 120 samples were tested and the results of the peel strength are presented in Table 3 and compared to Struve 1993 results. In all cases the Film Tear Bond criteria was respected.

Table 3. Seam peel resistance results

Peel resistance (N/mm)	GM A	GM B	Struve, 1993
minimum strength	21,6	17,7	19,3
maximum strength	26,6	21,6	24,4

It is generally accepted to identify the quality of an HDPE seam by calculating the critical ratio of the measured strength to the sheet strength at its yield point. As proposed (Peggs 1985) this factor should be greater than 90% for the shear resistance and 80% for the peel resistance. The calculated ratios for the shear test are all above the criteria and below for the peel test as presented in Table 4.

Table 4. Seam shear and pell resistance ratios

Seam shear resistance ratio (%)	GM A	GM B
I	99,7	102,9
II	103,4	101,3
III	101,1	101,8
IV	103,1	103,2
Seam peel resistance ratio (%)		
I	76,8	71,9
II	76,9	66,3
III	79,7	71,6
IV	74,1	65,6

The sheet crystallinity of the samples as a function of its location from the center of the welds has been calculated using a Scanning Differential Calorimeter (see Figure 2) and the density column method ASTM D1505 (see Figure 3). Forty (40) samples were tested at a rate of 10°C/min in

the SDC. The results indicate similar percentage of crystallinity in both membranes ranging from 75 to 79%.

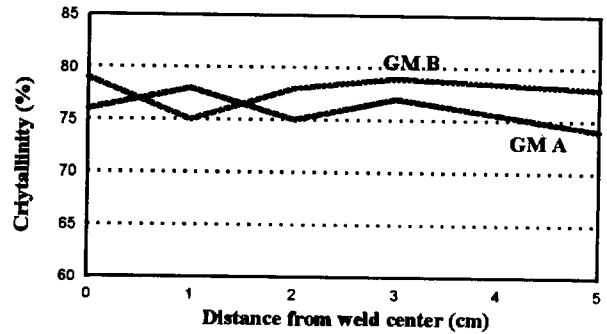


Figure 2. Sheet crystallinity by SDC

Two hundred (200) samples have been tested using the density column standard ASTM procedure. The results indicate a crystallinity ranging from 76,5 to 78,2% with a slight decrease in crystallinity at the seam edge located at 1cm from the weld center. It is interesting to note that this location corresponds to the melted polymer zone limit occurring during the welding process.

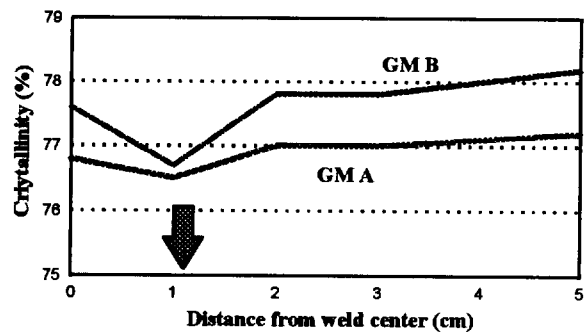


Figure 3. Sheet crystallinity by density column method.

Residual stresses in samples were identified using two dimensional stability tests: in hot air ASTM D1204 and in hot silicone bath. Samples of 10cm long and 1cm wide were placed in a oven at 130°C for an hour and samples of 6cm long in hot silicone oil at 140°C for 300s. The measured changes in the transverse direction (X axis) were in all cases the most drastic for both membranes (see Figure 4 for hot oil results) while the changes in the machine direction (Y axis) and the thickness (Z axis) were less pronounced (see Figures 5 and 6 for hot oil bath results). In Figure 4, the stresses go from compression in the weld to tension in the sheet indicating that probably the welding process did not induced stresses in the membrane but rather a stress gradient. This stress gradient is probably resulting from the relaxation of stresses within the sheet, stresses induced during the manufacturing process and not from the welding process. In any event this stress gradient is most probably responsible for seam brittleness.



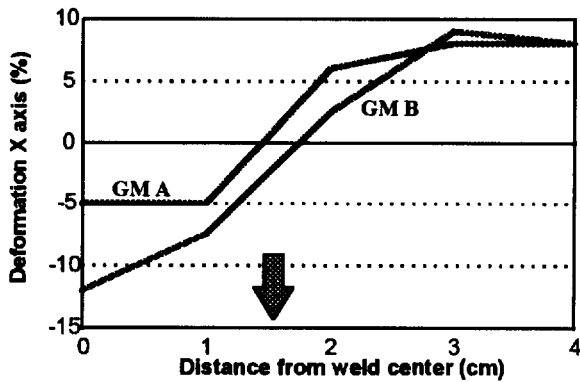


Figure 4. Transverse direction dimension variation

Obtained results indicated that the stress relaxation within the sheets were responsible for a decrease in the machine direction (sample width) of approximately 70% while the thickness increased by 2,5 times its value. The presence of the stress gradient in samples located at 1cm and 2cm from the weld center can be observed on Figures 5 and 6.

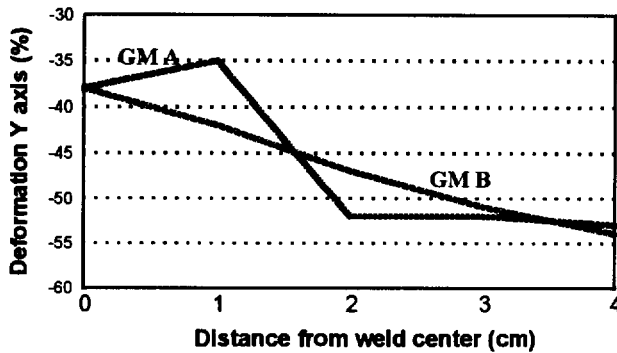


Figure 5. Machine direction dimension variation

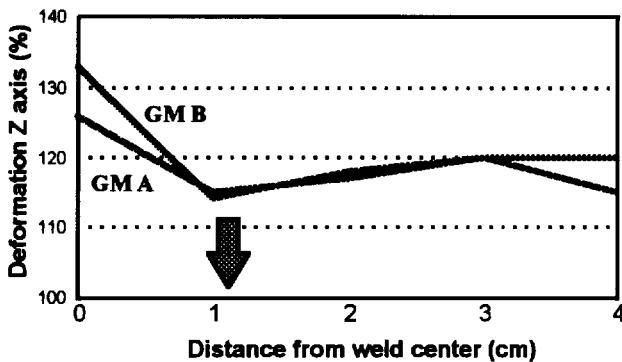


Figure 6. Thickness direction dimension variation

Seam brittleness can be detected using an impact test (Rollin 1991b). Samples were submitted to two impact test procedures: the Dynatup instrument and the impact test developed at Ecole Polytechnique (Rollin 1991b). The results are presented in Figures 7 and 8

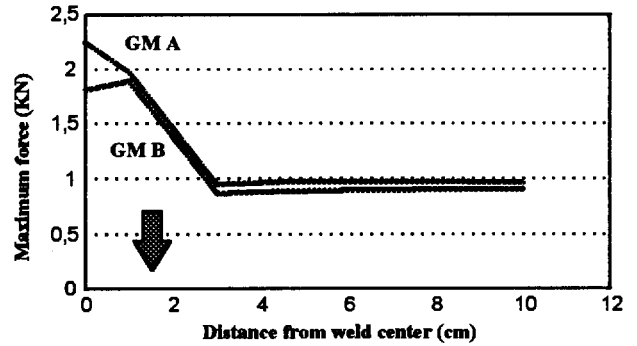


Figure 7. Dynatup apparatus impact test results

In the Dynatup device, an hemisphere rod of 12mm in diameter is dropped on a 76,2mm x 76,2mm sample with an impact energy ranging from 15 to 30J. The obtained results indicate that a greater impact energy has been necessary to rupture the samples within the weld than within the sheet itself. Visual observations of rupture samples indicated that the mechanism of rupture was ductile.

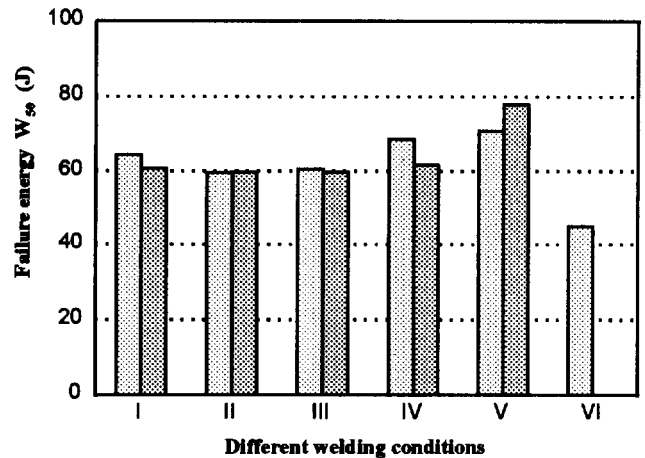


Figure 8. Ecole Polytechnique impact test results

Similarly the median impact energy necessary to rupture 1,5mm thick geomembranes GMA and GMB samples obtained with selected welding conditions (I to IV) are compared with already published data (Struve 1993, Rollin 1993). Overall, the results obtained over such a wide range of welding parameters are consistent. The higher values obtained of serie V are certainly related to improved machine design.

Thermal shock to HDPE sheet during welding can initiate stress cracking. In order to obtain the temperature gradients imposed on geomembrane during the welding process, temperature profile has been obtained simulating heat transfert involving a hot wedge machine and using the method of finite differences as shown schematically in Figure 9.

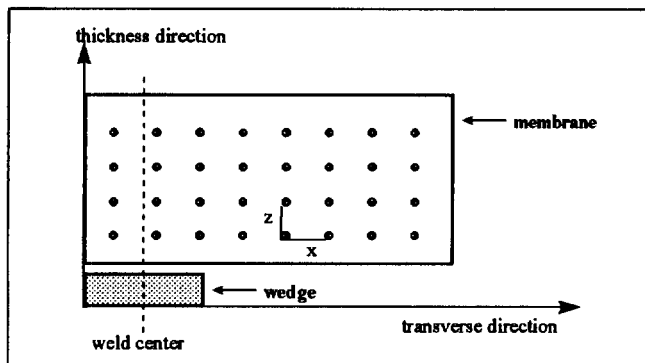


Figure 9. Heat transfer through the membrane

The temperature profile within the sheet at a specific time is function of the welding speed and the wedge temperature. Using the thermal conductivity equation in two dimensions for a transitional regime (1281 points), setting the heat transfer to both sheets identical and using a typical 75mm long and 37mm wide brass wedge, temperature profiles were obtained for a wide range of welding speed and temperature. The conductivity of the membrane was set at 0,48 W/m-°C (the HDPE conductivity is not affected by the black carbon content (Mesloh 1990)), of the wedge at 147 W/m-°C and at 0,0426 W/m-°C for air.

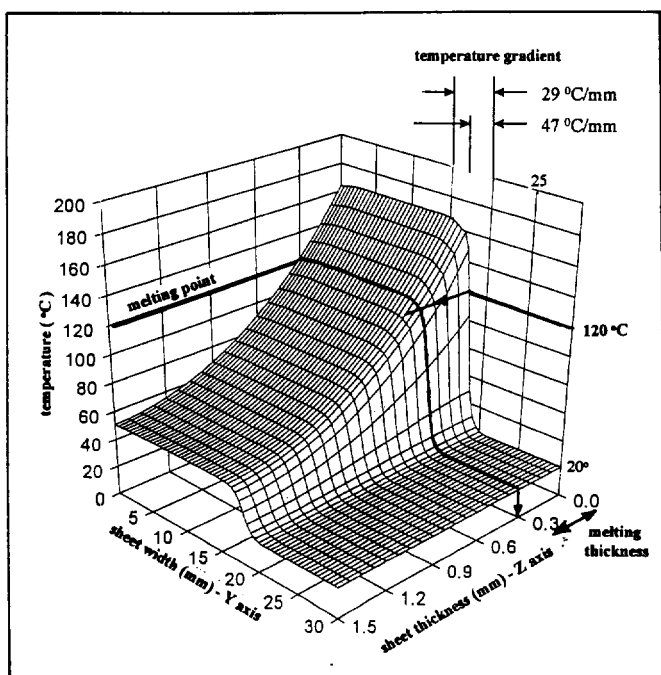


Figure 10. Simulated temperature profile

Temperature profiles such as the one presented in Figure 10 could be obtained for a wide range of welding speed and wedge temperature. From the temperature profile representing condition I, it can easily be found that the sheet melting thickness during the welding procedure ranges from 20 to 30% of its thickness and that the melted polymer limit correspond to edge of the wedge. The maximum temperature of 165 °C is located close to the

wedge and a large thermal gradient of the order of 50°C/mm of sheet width is located between 1,5 to 2,0cm from the center of the weld. The sheet surface temperature is approximately 55°C at a welding speed of 3m/min and raises to 75°C for a welding speed of 2m/min. The simulated temperature profiles indicated that excessive thermal gradients are generated at the boundary of the melted zone.

### 3. CONCLUSIONS

From the results obtained in this experimental study, the following conclusions can be drawn:

- the hot wedge welding process of HDPE geomembranes is responsible for stresses relaxation in manufactured sheets leading in the generation of large thermal gradients at the edge of the seams
- during the hot wedge welding process only a small fraction of the polymeric sheet is melted: 0,3mm in its thickness and 0,5mm at the edge of the weld
- the measurement of the dimensional variations of seams in hot oil bath or in an oven simulates best the welding process and is very sensitive to locate residual stresses in manufactured sheets
- the results obtained from most test procedures did not clearly differentiated between the welding conditions
- the simulated temperature profiles indicated that excessive thermal gradients are generated at the boundary of the melted zone and that a minimal fraction of the polymer is melted during the welding process

Recommendations are made on the need to still improve welding machines and to monitor welding parameters to lower the thermal gradient at the seam edge. The dimensional variations test standard should be investigated throughoutly since it can be performed easily. It would be interesting in the future to corrolate the impact energy measured by the impact test with the stress gradient generated with the hot oil bath testing procedure.

### ACKNOWLEDGEMENTS

The authors would like to thank Dr. J. Mlynarek and O. Veermersh from Sageos for their support during the testing phase of the project. The authors also acknowledge the efforts of Materiaux Techniques Cote personal for their involment in supplying products and welding the many geomembranes sheets. Finally a special thank is dedicated to Mr. Fred Struve whose comments materially improved the manuscript.

## REFERENCES

- Maranda, L. (1995) "Comportement mécanique des soudures de geomembranes", *Master thesis*, Chemical Engineering Departement, Ecole Polytechnique, June
- Mesloh, R.E. (1989) "Thermally Conductive Plastics", *Handbook of Applied Thermal Design*, McGraw-Hill, N.Y., part 6, chap. 5
- Peggs, I.D. and Little, D. (1985) "The Effectiveness of Peel and Shear Tests in Evaluating HDPE Geomembrane Seams", *Proc. Second Canadian Symp. On Geotextiles and Geomembranes*, Edmonton, pp 141-146
- Peggs, I.D. and Carlson D.S. (1990) "The Effects of Seaming on the Durability of Adjacent Polyethylene Geomembrane", *Proceedings of Geosynthetic Testing for Waste Containment*, Philadelphia, pp 132-142
- Peggs, I.D. and Rollin, A.L. (1994) "Seams in HDPE Geomembranes: The Quality Target", *Proceedings Fifth Int. Conf. On Geotextiles, Geomembranes and Related Products*, Singapore, pp 949-952
- Rollin, A.L., Vidovic, A., Denis, R. and Marcotte, M. (1989a) "Microscopic Evaluation of HDPE Geomembrane Field Welding Techniques", *Geosynthetics: Microstructure and Performance*, Ed. I.D. Peggs, ASTM Special Technical Publication 1076, Orlando, pp 34-47
- Rollin, A.L., Vidovic, A. and Denis, R. (1989b) "Evaluation of HDPE Geomembrane Field Welding Techniques: Need to Improve Reliability of Quality Seams", *Geosynthetics '89*, San Diego, pp 443-455
- Rollin, A.L. (1991a) "Microanalysis of Polyethylene Geomembrane Seams", *Geomembranes Identification and Performance Testing*, Ed. A.L. Rollin and J.M. Rigo, Chapman and Hall, Chapter 12, pp 24-267
- Rollin, A.L., Lefebvre, M., Lafleur, J. and Marcotte, M. (1991b) "Evaluation of Field Seams Quality by Impact Test Procedure", *Geosynthetics '91*, IFAI, Atlanta, pp 223-237
- Rollin, A.L., Marcotte, M., Lafleur, J. and Mlynarek, J. (1993) "The Use of Impact Test Procedure to Assess Seams brittleness", *Geosynthetics '93*, IFAI, Vol. 3, pp 1559-1573
- Rollin, A.L., Vidovic, A. Ciubutariu, V. (1994) "Assesment of HDPE Geomembrane Seams", *Landfilling of Wastes: Barriers*, Edited by Christensen, Cossu and Stegmann, Chapman & Hall, pp 377-391
- Struve, F. (1993) "Consistent Wedge Welders", *Proceedings 7<sup>th</sup> GRI Seminar*, December, Philadelphia, pp 9-23



# Assessment of Seam Quality and Optimization of the Welding Process of HDPE Geomembranes

G. Lüders

Bundesanstalt für Materialforschung und -prüfung, Berlin, Germany

**ABSTRACTS:** Using GM's made of two different commercial resins 50 double track fusion seam test samples were produced by systematic variation of some welding parameters. The results of short term and long term peel tests were correlated with the ratio of the thickness reduction of the seam  $s_f$  to the thickness of the molten surface layer  $L_o$ . The ratio  $s_f / L_o$  is an important process parameter, reflecting the interaction of welding parameters. Thus, all seams appear to be quite acceptable in the short term test, independent of the ratio  $s_f / L_o$ . However, the long term tests revealed peeling of the seams and the time to failure  $t_f$  strongly depends on  $s_f / L_o$ . We found a pronounced maximum in the failure time at  $s_f / L_o = 0.7$ , where the lifetime was improved by a factor of 5 to 10. It is therefore shown that the long term peel test is appropriate to evaluate the quality even of acceptable seams. An optimization of the welding process is possible. Time plots of peeling, micrographs of the fracture surface and annealing experiments indicate that the time to failure depends on the structural and thermal homogeneity of the seam at given welding conditions.

**KEYWORDS:** Geomembranes, weld seams, peel separation, failures, quality assurance

## 1 INTRODUCTION

In the construction of composite landfill liners, HDPE geomembrane sheets are placed and welded together one by one over the mineral layer to form a single large-area geomembrane liner. Appendix E of German TA Abfall (1991) and TA Siedlungsabfall (1993) states the suitability of the geomembrane and the welding technology must be verified under a process of certification. The relevant BAM Guidelines (BAM 1992), which are based in the main on the requirements of DVS 2225 (DVS 1991-1996), consider welding to be the only suitable seaming method. The Clarification section of the BAM Guidelines states that a suitable test method and further knowledge on the mechanical long-term performance of the weld seams and their dependencies on the welding parameters are still required to enable seam quality to be evaluated.

In the following paper the initial results of our investigations will be detailed with regard only to the welding parameters used in one and the same hot wedge welder of a construction-site-tested type. These are connected to earlier long-term peel tests in which peel of the weld area was observed but no relationship between failure time and welding parameters could be established (Bielefeld et al. 1991).

## 2 REMARKS ON WELD SEAM BEHAVIOUR UNDER DESTRUCTIVE LOADING

As is well known, short-term mechanical testing methods such as tensile shear tests per DVS 2203 (DVS 1985), are not able to differentiate appropriately the strength of overlap weld seams. It is not the weld area itself but the base material adjacent to the seam edge which always suffers brittle or yield failure; this is because the weld area is stiffened locally and the test periods are not long enough to activate any processing-related defects in the seam plane (Knausenberger et al. 1983). The process which enables the determination of seam quality in tensile tests on hole-notched hot wedge butt weld seams, i.e. a tensile load

perpendicular to and hole-notching in the weld plane, is not feasible for overlap weld seams in geomembranes. In long-term tensile tests, too geomembrane weld seams always fail in the base material near the seam edge. Establishing a relationship between failure time and seam geometry and welding parameters is difficult for a number of reasons (Bielefeld et al. 1991). Peel tests per DVS 2225 can basically only differentiate between 'good' (meeting the requirements) and 'poor' seams, however they can be used on construction sites and form part of QC/QA. In peel tests, too, the weld area remains undisturbed while the base material elongates at the seam edge. The maximum tensile force is measured, from which yield stress can be calculated. The weld area only peels if welding conditions are far below the requirements of the Guidelines, based on extensive practical experience. It is only this type of 'poor' seam which permits measurement of peel resistance.

What seam quality evaluation should (or must) be based on still remains to be determined (Müller and Lüders 1995):

- Seam edge break with an undisturbed weld area under practice-relevant (long-term) tensile loading, or
- failure of the weld area under long-term peel loading.

The general belief that peel forces do not occur in the field during landfill construction and operation and are therefore irrelevant in practice have lately been proved incorrect by the discovery of peeled seams in excavated geomembrane samples (Peggs et al. 1994). Analytical considerations on seam performance in short-term peel tests have revealed that the stress maximum in seam edge yield related to the yield stress in the base material, known as the Film Tearing Bond (FTB per NSF 1993), fails to provide any information on seam quality. Its evaluation must, therefore, be based on the failure, i.e. peel, of the weld area (Peggs 1996).

### 3 EXPERIMENTS

#### 3.1 Geomembranes

Two BAM certified geomembranes, based on ethylene-butene copolymer (GM1) and ethylene-octene-copolymer (GM2) both with a narrow molecular mass distribution were used in the tests (Table 1).

Table 1. Materials properties (in part, manufacturer's data)

GM		1	2
Density	[g/cm <sup>3</sup> ]	0.942	0.943
MFI 190/5 <sup>1</sup>	[g/10 min]	1.6	2.5
MFR 190/21.6 / 190/5		9	9
M <sub>w</sub> /M <sub>n</sub>		4.8	3.4
Carbon black	[% by mass]	2.1	2.2
Yield stress	[N/mm <sup>2</sup> ]	18	16.8
T <sub>c</sub> (DSC-peakmaximum)	[° C]	125	124
Thickness	[mm]	2.5	2.5

<sup>1</sup> Melt flow index at 190 °C under a 5 kg loading

#### 3.2 Weld Seam Sample Preparation

Welding was performed using a hot wedge welding machine of a construction-site-tested type known world-wide. Roller pressure and speed were transferred mechanically to the two part-seams by rollers above and below the geomembrane. Welding parameters were recorded using a data acquisition system with memory cards and evaluated using DOS software.

- Two 'open' thermo-elements in the hot wedge (HW) contact areas to measure the interface temperature of the geomembrane emerging at the HW tip during test welding (not quite correct!).
- The lower limit of the gap difference between the rollers on the left and right part-seams was 0,05 mm
- Width of the part seams 15 mm; total length of a weld seam: 9m; range of length applied 1m to 8.5m selected from the seam length range for which, according to the welding records, the roller pressure was constant and equal to the nominal value.
- Test specimens from the weld seam samples were sawned across the seam and finally planed down on each side to a width of 15 mm ± 0.05.

#### 3.3 Long-term Peel Test

The investigation was aimed at finding the relationship of failure time as a function of the welding parameters and not at determining the absolute values of failure time. Preliminary tests indicated that there was no significant difference in parameter dependency between the two part seams. Thus it was

possible to concentrate the investigation on one specific part-seam ( GM1 on part seam 1, GM2 on part seam 2 ). Weld seam failure time was determined on at least six test specimens, taken from different parts of the seam at at least 40cm intervals.

Testing was carried out in mechanical advantage test set-ups with horizontal load lever compensation in water at 80°C containing 2% by mass surfactant and time/elongation recorded. Following a 10 minute pre-loading period at 10% of the main load, the test load was applied automatically (test start). Breaking with no deformation over the long term is not representative of realistic conditions for seam peel so a test load high enough to obtain relatively short failure times could be chosen. A 4 N/mm linear load was chosen for GM1 and 6 N/mm for GM2, which prevented yield in the seam edge and ensured uniform seam failure due to a fast peel. The results obtained exhibited a normal distribution. The arithmetic mean of a minimum of 6 (maximum 18) measurement results was used as the failure time.

### 4 RESULTS TO THE RELATIONSHIP BETWEEN FAILURE TIME AND REDUCTION IN THICKNESS

Failure time was investigated in long-term peel tests on weld seams which differed in the combination of their welding parameters. Seam variants produced at

- hot wedge temperatures T<sub>HW</sub> 280; 350; 400 and 450°C
- roller pressures F 800; 1100 and 1400N
- welding speeds V 0.8; 1.5 and 2.5 m/min

were tested. In short-term peel tests per DVS 2225 all but one seam yielded at the seam edge and thus they comply with the requirements.

Seam strength measured as peel resistance always increases with decreasing thickness until the minimum melt flow is reached (Potente 1977). Beyond this (s<sub>t</sub> = 0.1 - 0.2mm) the seam peels no further and at this point yield stresses at the seam edge, which are of course independent of the reduction in thickness and without exception lay on a high plateau, can be measured. Because peel in the weld area and yield at the seam edge are two completely different failure types the results are not therefore suitable either for establishing a definition of a welding factor, or for including this in a closed relationship with the welding parameters (Michel 1995).

Seam strength measured as failure time reacts to every change in process conditions. The reduction in thickness behaves in parallel or inversely with failure time, i.e. the relationship is undefined similar to the that with failure time in tensile shear tests (Bielefeld 1991). For a meaningful relationship between seam quality, measured as failure time in peel tests, and process parameters to be formulated, the reduction in thickness alone is not suitable. A new reference quantity is therefore needed. With regard to butt welded seams, the so-called the ratio in thickness reduction is used (Michel 1988).

When applied to hot wedge welding, the reduction in thickness s<sub>t</sub> is, analytically speaking, the distance by which the gap between the two rollers is reduced until the selected roller pressure F reaches equilibrium with the flow resistance of the molten material of the two sheets (Figure 1). Flow resistance can be compared with normal stress σ<sub>22</sub> when molten material

Reduction of the thickness $s_t$ with roller pressure $F =$ flow resistance	
Flow resistance = (normal stress $\sigma_{22}$ ) = $f(V, L_o)$	
Reduction in thickness $s_t = f(F, V, T)$	Melt depth $L_o = f(T, V (t_H))$
rheological process conditions	thermal process conditions
$s_t / L_o$ Ratio in thickness reduction	

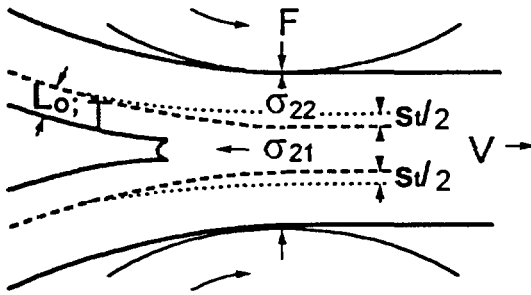


Figure 1. Scheme to explain terms in the ratio in thickness reduction

is exposed to a shear stress  $\sigma_{21}$  e.g. in a cone-plate-viscometer. It is perpendicular to the shear plane and equals force  $F$ , required to prevent the cone and the plate from drifting apart, i.e. to keep their distance constant. In equilibrium with roller pressure  $F$ , flow resistance is a function of speed  $V$  and melt depth  $L_o$ .

The melt depth depends on the HW temperature and the pre-heat period  $t_H$ , i.e. on speed, too. It can be therefore considered as the result of the thermal history of the geomembrane. The melt depth predetermines not only the melt depth in the geomembrane, however, but also, simultaneously, the most important initial geometric condition for the melt flow in the seaming phase.

The ratio of the reduction in thickness to melt depth - the ratio in thickness reduction  $s_t / L_o$  - is then approximately the ratio of the thickness of extruded to input melt under the above equilibrium conditions in the seaming phase, i.e. a measure for melt flow. Thus the ratio in thickness reduction ought to represent a parameter for the combination of all the process conditions to which seam properties could be related. Whether this is actually the case in a welding process, in which rheological and thermal conditions are determined by partly freely chosen and partly dynamically adjusted parameters, will be investigated following.

## 5. THE RATIO IN THICKNESS REDUCTION $s_t / L_o$ USED TO OPTIMISATION OF THE WELDING PROCESS

While microscopic measurements are not appropriate to measure the input molten layer Fourier's equation for non-steady heat conduction in the following derivation (Michel 1995) was applied to calculate melt depth  $L_o$ .

$$L_o = 1.905(1 - \theta_c) \sqrt{a_{eff} t_H} \quad (1)$$

where:

$$\theta_c = \frac{T_c - T_{GM}}{T_{HWP} - T_{GM}}$$

$T_c$  = crystalline melting point for HDPE (table 1);  $T_{GM}$  = geomembrane temperature;  $T_{HWP}$  = temperature at the hot wedge tip (HWP), depending on the selected speed and nominal value  $T_{HW}$  (used as interface temperature);  $\theta_c$  = temperature (dimensionless);  $t_H$  = pre-head period, calculated for a 7cm effective HW length;  $a_{eff}$  = effective thermal conductivity, according to (Potente 1977); 1.905 = correction factor.

Failure time values measured in long-term peel tests and the ratio  $f_o$  of the yield stress from short-term peel tests to the yield stress in the base material are plotted in Figure 2 as a function of the ratio in thickness reduction.

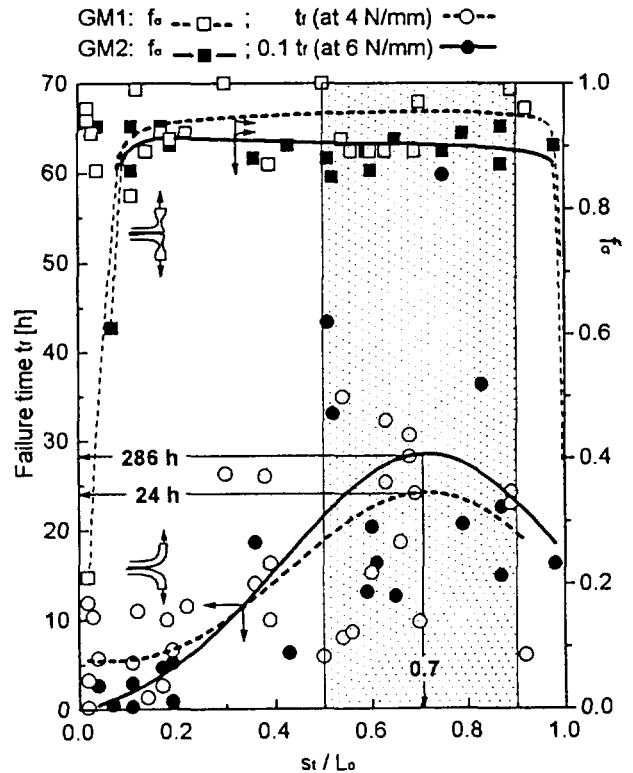


Figure 2. Failure time  $t_r$  in long-term peel test and yield stress ratio  $f_o$  in short-term peel test as a function of the ratio in thickness reduction  $s_t / L_o$

Over almost the whole range of  $s_1/L_0$  between 0 and 1 the yield stress ratio exhibits a high plateau at  $f_0 = 0.9$ , as is already well known (Michel 1995). However the failure time obtained as an average of all values reaches a maximum at  $s_1/L_0 = 0.7$  for both resins. Compared to the shortest failure time measured the life time was improved by a factor of 5 to 10. For butt weld seams a maximum was found at  $s_1/L_0 = 0.75$  (Michel 1988). This agreement is surprising considering the rather different seam geometries and processes involved in the two welding methods. Since the loci of maximum of the failure time coincide for weld seams of both materials (GM1 and GM2),  $s_1/L_0 = 0.7$  can be considered as an invariable optimization value for HDPE, i.e. in the range around this  $s_1/L_0$  value (e.g. 0.5-0.9 in Figure 2) the interaction of the selected welding parameters is optimum with regard to the production of the seams investigated. An analysis of the dependency of the failure time on each of the adjustable parameters (T, V, F) alone turned out not to be appropriate. For the welding practice it is on the other hand of importance to determine the optimum values for the adjustable parameters F and V in order to keep the  $s_1/L_0$ -value in the above optimum range. Thus the dependency of the failure times on V and F is shown in figure 3 and 4 by assigning the respective values for V and F to each of the data point of figure 2 (as in figure 2 each data point is given by its failure time and the corresponding  $s_1/L_0$ -value).

Figure 3 shows the areas characterized by the average seam melt depth  $L_0$  with failure times contained in them and placed according to the corresponding  $s_1/L_0$  values.

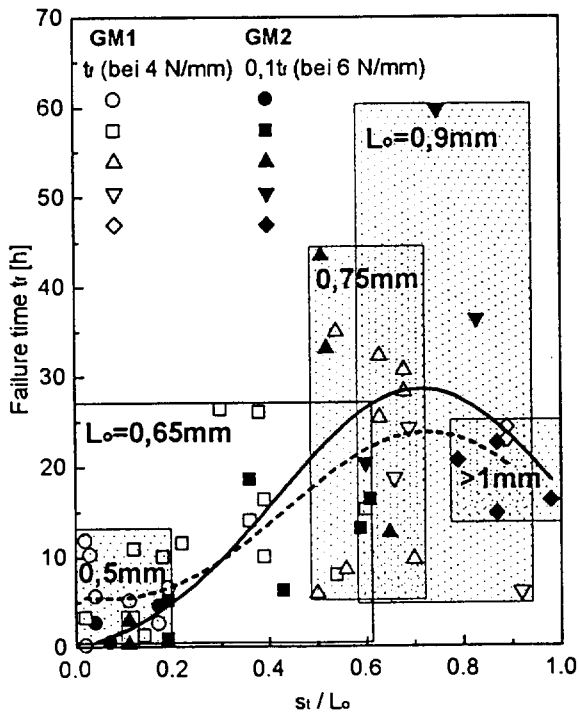
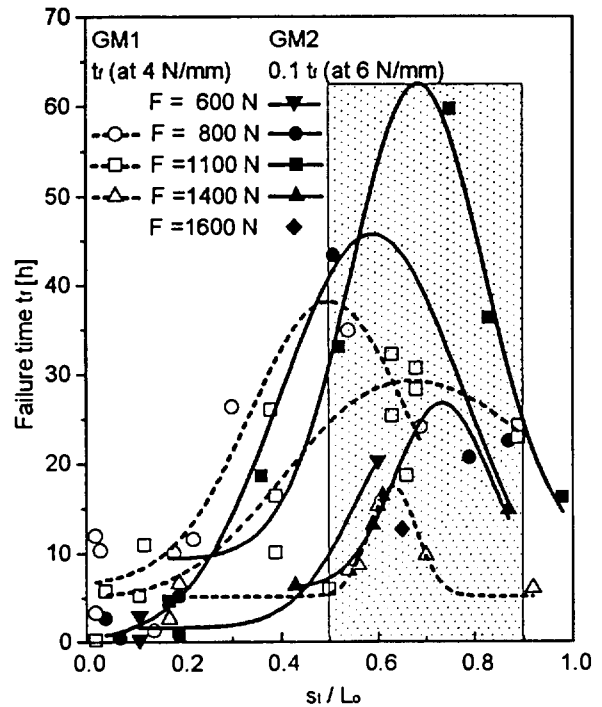


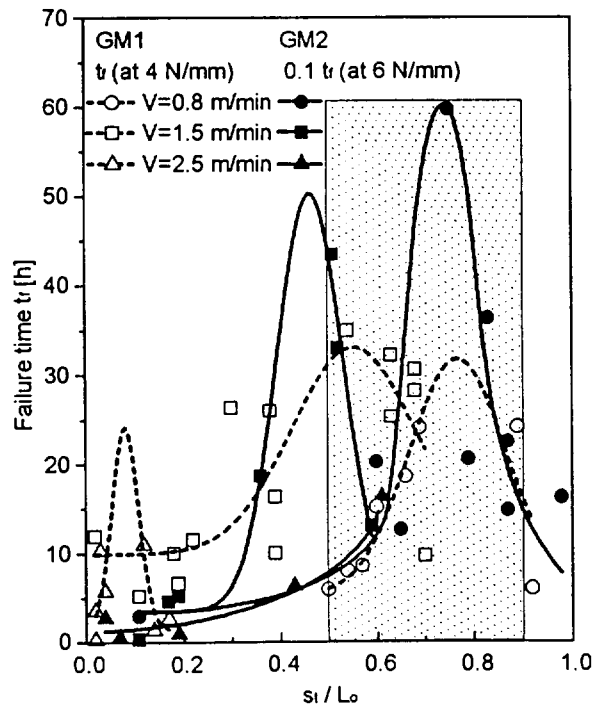
Figure 3. Failure time  $t_r$  as a function of the ratio in thickness reduction  $s_1/L_0$  with melt depth  $L_0$  as a parameter

It can be seen that seams with long failure time require melt depths between 0.75mm and 0.90mm, i.e. reaching the failure time maximum depends decisively on the pre-heat conditions - pre-heat period and temperature.

In Figure 4 it can be seen clearly that failure time attributed to roller pressures  $F=800$  and  $1100$  N and velocities  $V=1.5$  and  $0.8$  m/min exhibits high values in the marked  $s_1/L_0$  range between 0.5 and 0.9.



(a)



(b)

Figure 4. Failure time  $t_r$  as a function of the ratio in thickness reduction  $s_1/L_0$ : (a) with roller pressure F as a curve parameter, (b) with speed V as a curve parameter



To formulate the optimum parameter combination in Table 2 temperature must be taken directly as a welding parameter, because it does not represent an optimization variable.

Table 2. Optimum parameter combinations

GM	$s_f/L_o$	$L_o$ [mm]	F [N]	V [m / min]	$T_{HW}$ [°C]	$t_f$ increase [h]
1	0.55	0.75	800	1.5	400	24- 34
	0.78	0.90	1100	0.8	350	24- 32
2	0.50	0.75	800	1.5	400	286-430
	0.75	0.90	1100	0.8	350	286-597

The wider the  $s_f/L_o$  basis of the maxima attributed to the single parameters, the easier the optimization. They can be then made easily to coincide, thus the corresponding parameter combination can be determined by the same reduction in thickness ratio. The results in Table 2 indicate that low to medium roller pressure values and velocities result in the greatest failure times. This does not exclude however that other parameter combinations, in particular when they are graded more closely than in this work may provide even better results. Pre-requisite is however that the actual pre-heat conditions ensure adjusting the reduction in thickness ratio. This is no more the case at e.g. 2.5m/min (Figure 4b, GM1, open triangle). Here the pre-heat time is so short that the geomembrane cannot be molten deep enough (Figure 3,  $L_o = 0.5mm$ , open circle). An 'optimum' ratio in thickness reduction can then be achieved though with an extremely high roller pressure, but the failure time is only increased slightly (Figure 4a, 1400 N, GM1, open triangle †, 1600 N, GM2, rhombus). A calculative estimation suggests that the effective HW length must be a minimum of 11cm to achieve  $L_o = 0.75mm$  at 2.5m/min.

On the other hand Figure 3 indicates clearly (GM2, solid triangle †) that failure time also remains short at  $L_o = 0.75mm$  when roller pressure was too low (Figure 4a,  $F = 600 N$ , solid triangle †). In order to increase melt flow of  $s_f/L_o = 0.1$  with regard to failure time optimization, either  $L_o$  must be increased up to 0.9mm (solid triangle † in Figures 3 and 4a) or even better F must be increased up to 800 or 1100 N.

## 6 ADDITIONAL REMARKS ON THE RELATIONSHIP BETWEEN SEAM PROPERTIES AND FAILURE TIME

The causes of the quality-determining properties of a weld seam deviating from those of the base material are nearly always attributed to the consequences of a thermo-rheological restructuring process. The positional variable secondary crystallisation in the thermally effected zone (Kamenowa et al.) and the flow-induced crystallisation in the zone influenced by shear (Kojima 1979; Aciemo et al. 1978) leave a morphologically unhomogeneous seam area weakened by the complex effect of frozen-in stresses (Ehrenstein 1979). Failure was consistently predicted in the fibrillar shear structure in the

molten/solid transition zone for butt weld seams (Egen 1985) and also observed in peeled weld seams (Bielefeld 1991; Gehde 1992). The question of whether or not this failure criterion holds for weld seams of all parameter combinations was investigated.

In Figure 5 e.g. failure time of annealed weld seams (2h and 120°C) is compared with the failure time of non-annealed weld seams (GM1, Figure 4a). The annealing effect depends on the  $s_f/L_o$  position and is maximum at high roller pressures.

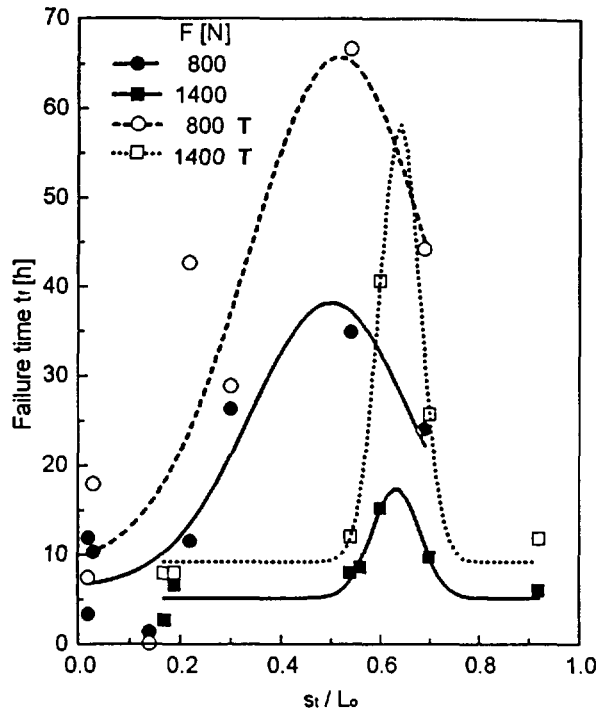
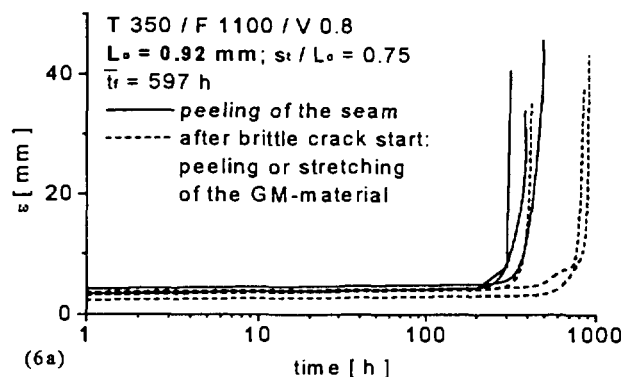


Figure 5. Failure time  $t_{tr}$  of annealed (T) and non-annealed weld seams of GM1 as a function of the ratio in thickness reduction  $s_f/L_o$  with roller pressure as a curve parameter 2h/120°C

The time plot of peeling measured as clamp distance against time is uniform for all seam samples with high failure time (Figure 6a). Scattering increases with decreasing failure time. The steep increase becomes unsteady and is often characterized by a step at the beginning (Figure 6b).



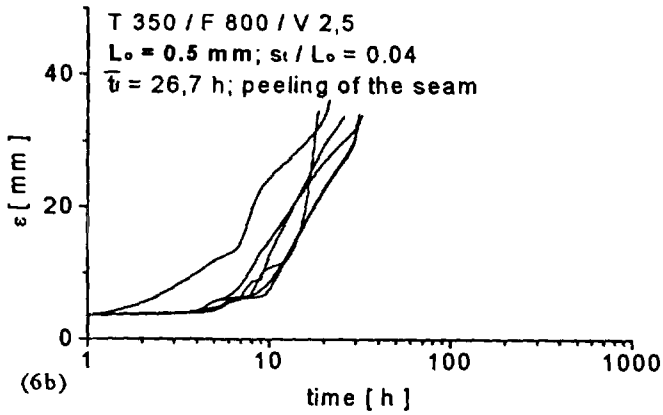


Figure 6. Distance between the clamps  $\epsilon$  in the peel test as a function of time: (a) GM2 seam samples of high failure time  $t_f$  and high melt depth  $L_o$ ; (b) GM2 seam samples of low  $t_f$  and small  $L_o$ .

Simple microscopic illustration of the fracture interfaces of peeled seams shows that there are inhomogeneities there which are characteristic of some parameter combinations (Figures 8a-d). The results illustrated here exemplarily provide indications for seam quality, which is explained in a summarised way using the scheme in Figure 7.

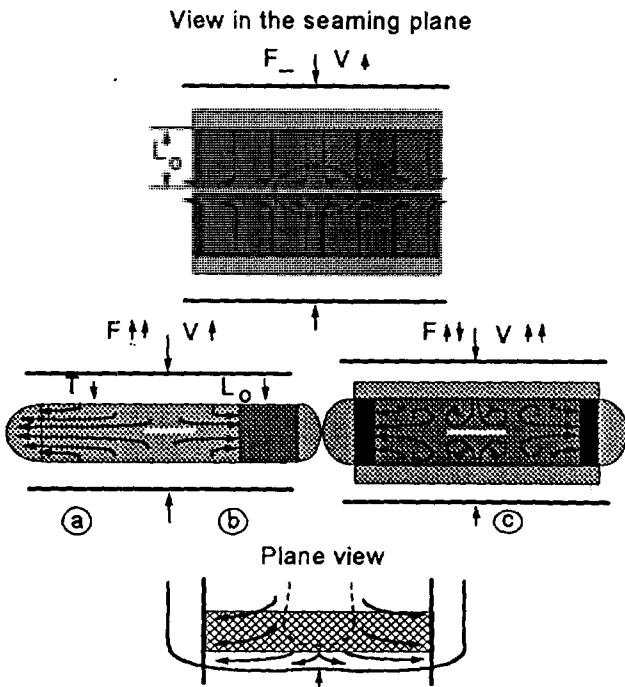
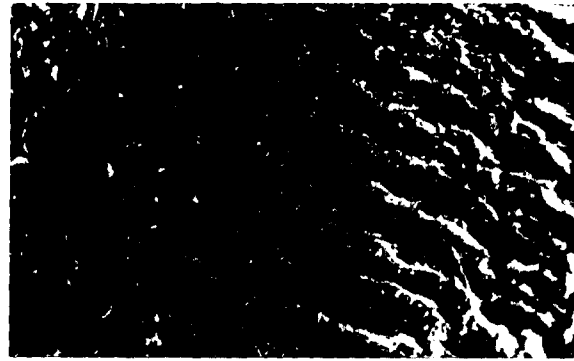


Figure 7. Melt flow in the weld area (schematic)

In the final phase of the welding process orientations left behind by melt flow in the loading plane freeze quickly. Considering the melt flow illustrated schematically by arrows it becomes clear that the more the (bright) transitional area is affected by the relative movement of the (dark) molten mass towards the seam edge, the more widespread the development of fibrillar shear structures. At high roller pressure and a low temperature orientation spreads as far as into the bead (a in Figure 7) which is then often split at the end of the peel process in the centre (Figure 8d).



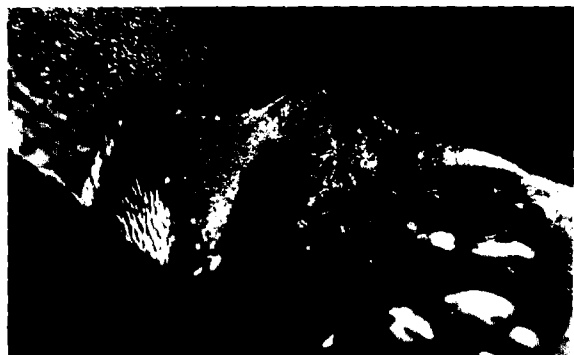
8a. Fracture surface of a GM1 seam sample [16x];  $s_r/L_o=0.69$   $t_f=24\text{h}$ ; detail: transition seam centre to side; welding direction ↓



8b Fracture surface of a GM1 seam sample [10x];  $s_r/L_o=0.04$   $t_f=6 \text{ h}$ ; V ↑↑; detail: seam centre vortexing and lacking in molten material; welding direction -



8c. Fracture surface of a GM1 seam sample [6.5x];  $s_r/L_o=0.17$   $t_f=3.5 \text{ h}$ ; F ↑↑; detail: seam centre containing no molten material; welding direction ↓



8d. Bead near test channel of a GM1 seam sample [6.5x];  $s_r/L_o=0.56$ ;  $t_f=8.6 \text{ h}$ ; T ↓↓; F ↑↑; detail: splitting and adhesion rupture due to extensive orientation; welding direction ↘

Because of the heat content transported to the seam edge by the molten material a relaxation back into the spherulitic structure and regaining of strength isotropy can be expected (b in Figure 7).

This is not only of special importance in seams with small melt depth  $L_0$ , where it may explain the step in plots of Figure 6a. It could also explain that seams with sufficient high heat content ( $L_0$ ;  $T$ ;  $V$ ) after brittle groove cracking in the root of the bead notch the peel front runs frequently into the geomembranes material or the material of the residual cross section exhibits yielding (Figure 6b), i.e. the behavior of the weld area in the peel test becomes similar to that of the geomembranes material due to the more extensive annealing after welding.

At high velocity, vortexing occur in the molten mass (c in Figure 8, Figure 7b), as has already been suggested as elastic turbulence for extreme flow conditions in butt weld seams [20]. In all three cases the molten mass may be displaced from the centre of the seam (Figure 7c). On peeling only adhesion ruptures can be then observed in the centre of the seam between two each other close adjacent interfaces.

The farther the ratio in thickness reduction from the position of the failure time maximum, the greater the extent of structural and thermal inhomogeneity. Correspondingly, seams with long failure times peel evenly and leave bright fracture interfaces, finely structured probably by crazing (Figure 7a). With decreasing failure time mixed failure increasingly prevails, consisting of extensive yielding of more or less flat, spliced ribbons and adhesion ruptures in plane areas which exhibit a large number of faults and a shortage of molten material due to vortexing and/or high orientation. In such cases seams fail both in and near the weld plane.

## 7 SUMMARY AND CONCLUSIONS

Hot wedge weld seams in long-term peel tests always fail due to peel in the weld area. Failure time and access to the open seam ensure an assessment of seam quality.

The absolute values of failure time depend closely on the geomembrane's material. They are between one and 40 hours at 80°C in water with 2% surfactant (GM1, 4N/mm), however they may reach in spite of high loads even several hundred hours (GM2, 6N/mm). The relationship between failure time and welding parameters can be illustrated convincingly by using the ratio of the experimentally obtained reduction in thickness  $s_r$  to the calculated melt depth  $L_0$  of the geomembrane, i.e. the ratio in thickness reduction  $s_r / L_0$  as a reference figure. The  $s_r / L_0$  locus of failure time maxima with the parameters melt depth, roller pressure and speed may serve to optimize welding conditions and process-relevant seam quality assessment. It can also be used to recognize the limitations of hot wedge welding, such as

- principal limitations: the pre-heat conditions cannot be freely chosen but must be adjusted to the welding speed and
- practical limitations for the actual material and the welding machine used.

For seam quality standard  $s_r / L_0 = 0.7$  can be used which has been experimentally established as an invariant optimization quantity for HDPE. Parameter combinations near this value, i.e. falling in the range 0.5 to 0.9, are supposed to provide only

seams of good quality. Whether or not this finding holds under construction site conditions, it will be investigated in the future.

Failure time and failure performance depend closely on the type and extent of melt flow. Peel performance and annealing in seams suggest the consequences of rheologic phenomena, such as frozen-in orientation and melt vortexing in the seam centre and the displacement of molten material from the seam centre. The farther the  $s_r / L_0$  value from the optimum range 0.5-0.9, the stronger these phenomena.

A structural and thermal inhomogeneity over the seam width indicates that in such cases the seam strength also differs widely. It is, as a rule, higher in the lateral segments of the weld area into which molten material flows, thus making heat available to reduce orientation by relaxation.

## REFERENCES

- Aciemo, D.; La Mantina, F. R.; Marucci, G. (1978) "Mechanisms of Polymer Crystallisation from Flowing Solutions", *Polymer Engin. Sci.* 18 (1978) p. 10
- BAM Guidelines for the Certification of Geomembranes as a Component of Composite Liners for Municipal and Hazardous Waste Landfills as well as for Lining Contaminated Land, Bundesanstalt für Materialforschung und -prüfung Berlin 7/92
- Bielefeldt, K.; Glück, L.; Klingenuß, H., "Assessment of Long-term Performance of Weld Seams of Geomembranes for Landfill Basal Liners and Cappings" *Research Report SKZ FV 187, Würzburg 1991, FKZ 14704668 BMFT*
- Egen, U. (1985) *DVS Research Reports on Welding Technology* Vol. 4, Deutscher Verlag für Schweißtechnik, Düsseldorf
- Ehrenstein, G.W. (1979) *Polymer Materials, Structure and Mechanical Performance*, Carl-Hanser-Verlag, München
- Gehde, M. (1992) "Welded Joints on Landfill Geomembranes - Tests and Failure Performance", *Die sichere Deponie, Würzburg, Proceedings 8. Fachtagung*, pp. 59-88
- Guidelines DVS 2225, "Seaming of Geomembranes Made of Polymer Materials for Earthworks and Hydraulic Engineering":  
 Part 1: Welding, Gluing, Vulcanisation (2/1991)  
 Part 2: Site Testing (8/92)  
 Part 3: Requirements on Welding Machines and Welding Apparatus (2/93)  
 Part 4: Welding of Polyethylene Geomembranes for Lining Landfills (2/96)
- Guidelines DVS 2203, "Testing of Joints in Thermoplastics", Part 2 (7/85)
- Kamenowa, L. A. et al., "Study of Relations Between the Welding Parameters, The Morphology and Mechanical Characteristics of Polypropylene Welded Joints", IiW Doc. XVI
- Knausenberger, R.; Menges, G.; Schmachtenberg, E. (1983), "A Fast Method of Determining the Long-term Performance of Weld Seams", *DVS-Berichte*, Vol. 84, Düsseldorf, Deutscher Verlag für Schweißtechnik 1983.
- Kojima, M. (1979) "Growth Front of Polypropylene Spherulites" *J. Polymer Science* 17 (1979)

- Müller, W.; Lüders, G.(1995): "Geomembranes".  
 In: Holzlöhner, U.; August, H.; Meggyes, T.; Brune, M.  
 (Eds.) *Landfill Liner Systems*. A State-of-the-Art Report.  
 Bundesanstalt für Materialforschung und -prüfung, Berlin.  
 Penshaw Press Sunderland, U. K.
- Michel, P.(1995) "Quality Assurance for Geomembrane  
 Welding", *Die sichere Deponie* Würzburg, Proceedings  
 11.Fachtagung, pp. 167-205
- Michel, P.(1988) *DVS Research Reports on Welding  
 Technology* Vol. 18, Deutscher Verlag für Schweißtechnik,  
 Düsseldorf
- National Sanitation Foundation (1993), International Standard  
 54, Flexible Membrane Liners, Ann Arbor MI, USA: NSF
- Peggs, I. D.(1996):"A Reassessment of HDPE Geomembrane  
 Seam Specifications" *Geosynthetics*, De Groot, Den Hoedt  
 & Termaat (Eds.), Balkema, Rotterdam
- Peggs, I. D.; Glos G. H.; Haxo, H. E. jr.(1994): "A  
 Geomembrane Liner Failure: Design, Installation and  
 Communication Lessons Learned. Proceedings of *Fifth  
 International Conference on Geotextiles, Geomembranes  
 and Related Products*, pp. 1077-1080, Singapore (IGS)
- Potente,H.(1977)"On the Theory of Hot Wedge Butt Welding",  
*Kunststoffe* 67 (1977) pp. 98-102
- TA Abfall (1991): " Second General Administrative Provision  
 to the Waste Avoidance and WasteManagement Act, Part 1:  
 Technical Instructions on the Storage, Chemical, Physical  
 and Biological Treatment, Incineration and Disposal of  
 Waste Requiring" Particular Supervision of 12.3.1991,  
 Gemeinsames Ministerialblatt, No. 8, 1991.
- TA Siedlungsabfall (1993): "Third General Administrative  
 Provision to the Waste Avoidance and Waste Management  
 Act: Technical Instructions on Recycling, Treatment and  
 Storage of Municipal Waste" of 14.5.1993, *Müll-Handbuch*,  
 E. Schmidt, Berlin, Vol. 1, 0675. pp. 1-52

# AUTOMATIC ULTRASOUND SEAM TESTER FOR BITUMINOUS GEOMEMBRANES - DEVELOPMENT AND FIELD RESULTS

B. Breul

Colas S.A., Direction Recherche et Développement, 92653 Boulogne Billancourt, France

J. Carroget

Colas S.A. Laboratoire Central de Recherche, 78114 Magny les Hameaux, France

R. Herment

Société des Pétroles Shell, Direction Bitumes, 92563 Rueil Malmaison, France

**ABSTRACT:** Bituminous geomembranes have been tested with hand-held ultrasonic equipment for twenty years. Colas has developed a mechanised seam tester for seam widths of up to 20cm, offering greater precision, reliability and speed. It consists of a 20cm-wide horizontal cylinder in which 24 ultrasound pick-ups bathe in a liquid medium. The rubber membrane conforms to irregular surfaces and is constantly wetted to provide intimate contact with the geomembrane. A VDU displays the data. Testing proceeds at a rate of 100 metres of seam per hour, compared with 50-80m per day with manual apparatus. The machine will work equally well on sloping linings. Readings are made every millimetre as the it progresses. Flaw detection resolution is 5mm<sup>2</sup> but the software only registers flaws larger than 1.5 cm<sup>2</sup>.

**KEYWORDS:** , Ultrasound, Seams, Testing, Geomembranes, Quality Control.

## 1 COLETANCHE® REINFORCED BITUMINOUS GEOMEMBRANE

Colétanche reinforced bituminous geomembrane is manufactured in 4m-wide rolls and consists basically of a needle-punched infinite polyester fibre geotextile impregnated with RI00/40 blown bitumen or a bitumen/elastomer mix. Thickness ranges from 3.3mm to 5.6mm. The geomembrane therefore meets French Standard NFP 84500, which requires that a geomembrane must be more than 1mm thick and more than 1.5m wide with a permeability coefficient expressed as the flow passing through it of less than 10<sup>-4</sup> m<sup>3</sup>/m<sup>2</sup> per day. The rolls are unwound on site with a 20cm overlap for the hot air seam.

The permeability coefficient of this geomembrane is very low over the whole width (the Darcy K coefficient is less than 10<sup>-13</sup> m/s) but when assessing overall in-place watertightness, one must consider any damage sustained by the geomembrane as it is laid, and seam quality. Since the bituminous geomembrane is thick and reinforced, it displays excellent resistance to puncturing by the granular covering material frequently applied as protection. It is also robust in terms of chance damage during the laying process, such as puncturing by a stone wedged in the sole of a workman's boot, a frequent source of damage to thinner membranes<sup>1</sup>. This means that it is very often sufficient simply to test seams to ensure that the whole waterproofing system meets the specification<sup>2</sup>.

Seam testing is also relevant to PVC, HDPE, EPDM and other types of geomembranes although not for geosynthetic clay liners which are not geomembranes under the NFP

84500 definition because they cannot be welded together. Geomembrane seam testing methods include the electric comb, double weld with central channel, and vacuum and ultrasound apparatus. The last-mentioned method yields what can be considered an X-ray image of the seam, immediately identifying flaws that need repairing.

## 2 MANUAL ULTRASOUND TESTING

Bituminous geomembrane seams have been tested for the last twenty years with hand-held ultrasound apparatus<sup>3</sup> working in the 1-3 MHz frequency band. Figure 1 illustrates the return echoes that are picked up and displayed on the oscilloscope when there is no discontinuity in the ultrasonic waves crossing the seam between the emitter and receiver. Figure 2 shows the echo pattern when the seam is flawed.

## 3 AUTOMATED ULTRASOUND TESTING

### 3.1. Test Machine

The CAC 94 automatic machine was designed in 1994 for automatic testing of seams widths up to 20cm. It weighs 200kg and has two steering wheels and two drive wheels. It tows a horizontal rubber cylinder, 21cm wide, filled with a conducting liquid, and contains 24 ultrasound pick-ups, set back 1cm from the cylinder wall so that they are unaffected as the rubber deforms when travelling over irregular surfaces. A spray bar meters a wetting agent ensuring

continuity between the ultrasound gear and the test seam. The positions of the flaws detected are marked on the membrane. The machine also carries a computer with liquid crystal screen.

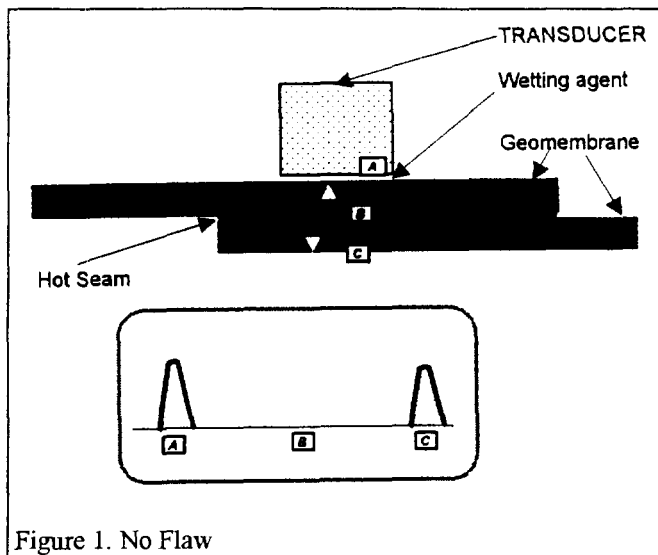


Figure 1. No Flaw

This machine progresses at a rate of 100m per hour, as compared with 50-80m per day with hand-held apparatus.

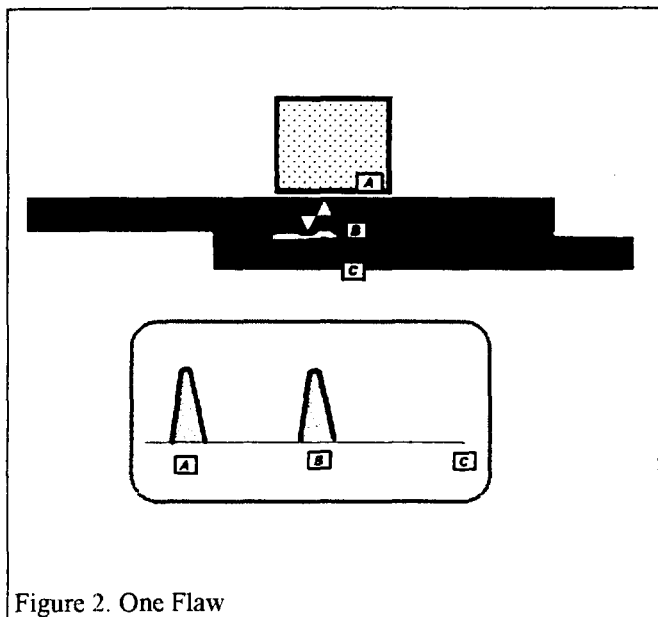


Figure 2. One Flaw

### 3.2 Procedure

Figures 3, 4 and 5 show the interfaces encountered by the ultrasound waves:

A: Transducer/conducting liquid interface

B: Wetting agent/top membrane interface

C: Top membrane/bottom membrane interface

D: Bottom membrane/underlying soil interface.

Figure 3 shows the echo received from a sound seam, while figure 4 is the echo from a flaw at interface C. Figure 5 shows the display when no wetting agent is used. Readings are made every millimetre as the machine moves along the seam. Each transducer sweeps a strip parallel to the direction of travel. Each strip is subdivided into virtual rectangles for ease of processing and recording. This produces a grid map, with each rectangle measuring 9mm x 5mm approx. Adjacent flaws must aggregate more than 1.5 cm<sup>2</sup> in size, otherwise they are ignored by the software.

## 4 VALIDATION PROCEDURE

The machine was validated by comparing the results from manual and automatic testing of a seam 1.5m long and 20cm wide into which 0.2mm-thick brass inserts of various shapes had been placed. The inserts produce the same signature as an air bubble of the same area. The inserts ranged in size from 50 cm<sup>2</sup> to 1.5 cm<sup>2</sup> and were scattered in random fashion in the seam.

It was found that the map produced by the automatic machine resembled a radiographic image whereas the manual procedure aggregated multiple adjacent flaws into a single flaw, and sometimes failed to detect flaws that were known to exist (Table 1, figure 6).

## 5 PRACTICAL APPLICATIONS

### 5.1 Preparation

Before use on site, transducer response is checked by using a standard plate of constant thickness and acoustic impedance. The machine is then calibrated on a single thickness of the geomembrane as delivered to site in order to check that transducer response always indicates a flawed seam.

### 5.2 Examples of Field Use

The machine has been used both on the flat and on sloping linings such as at the Strasbourg municipal solid waste incinerator bottom ash stabilising yard in 1996. At the 38m-high Ortolo rockfill dam in Corsica with bituminous geomembrane upstream facing sloping 1 vertical for 1.7 horizontal, the machine was winched up from the toe to the dam crest; seams were 70m long.

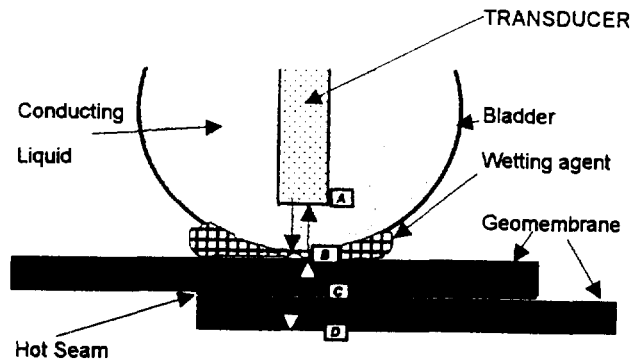


Figure 3 : NO FLAW

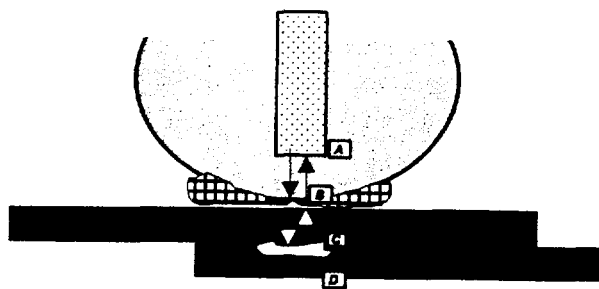
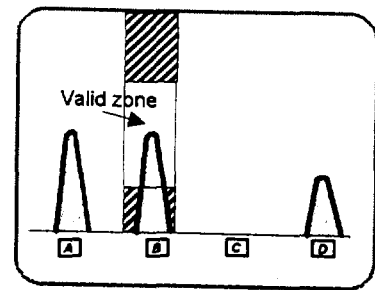


Figure 4 : ONE FLAW

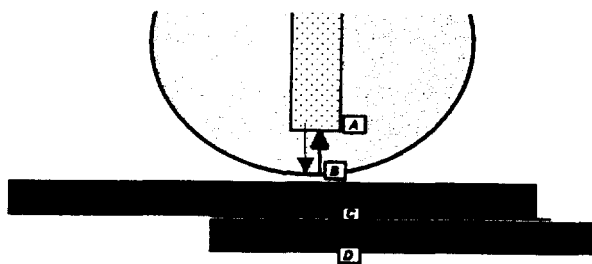
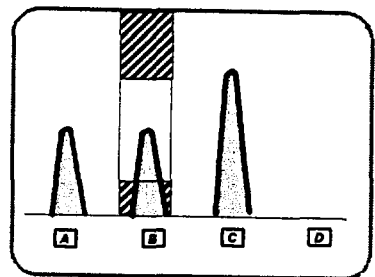
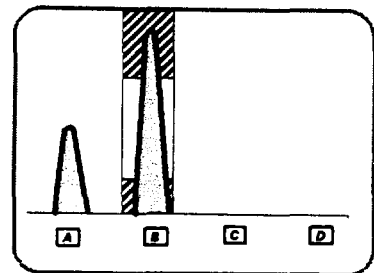


Figure 4 : NO WETTING AGENT



In all, field tests have revealed seam flaws needing repair amount to 1-2 ‰ of total seam footage.

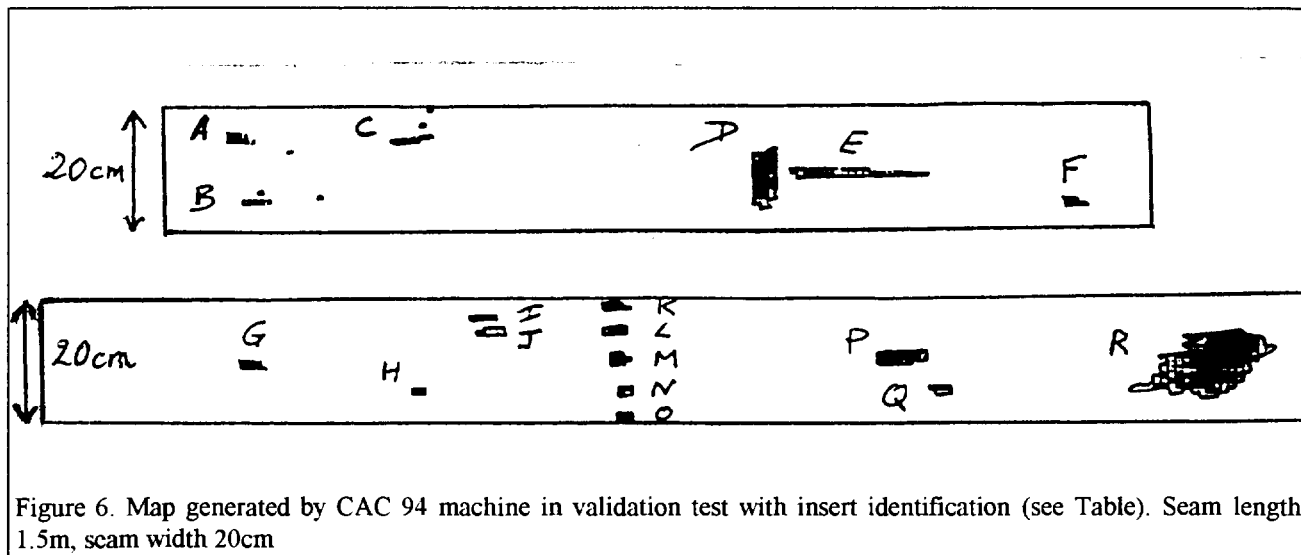
6

## CONCLUSIONS

Seam quality control using the CAC mechanised seam tester is now standard practice. The stated goals of precision, reliability and rapidity have been achieved. It would appear that this test has led to an improvement in seaming quality.

Table 1. Comparison of Manual and Mechanised Testing of Geomembrane Seam with Brass Inserts - Seam Width 20cm, Length 1.5m

Insert Area (cm <sup>2</sup> )	Area from Manual Test (cm <sup>2</sup> )		Mean (cm <sup>2</sup> )	Area from CAC 94 Automatic Machine						Mean (cm <sup>2</sup> )	Insert (see map)
1.5	1.5	1.5	1.5	2.6	2.6	3.0	2.6	1.7	2.6	2.5	A
1.5	1.5	1.5	1.5	2.6	2.6	3.0	1.3	3.0	1.3	2.3	B
2.0	3.0	7.5	5.3	2.2	1.7	1.7	1.7	3.0	2.6	2.2	C
10.0	5.0	13.0	9.0	11.0	13.0	12.0	12.0	13.0	13.0	12.3	D
10.0	4.0	12.5	8.3	8.7	13.0	8.2	7.8	8.2	9.1	9.2	E
1.5	1.5	2.3	1.9	1.7	2.6	2.6	2.2	2.2	2.2	2.3	F
1.5	2.0	0.0	1.0	0.0	0.0	0.0	0.0	0.0	0.0	0.0	G
1.5	1.5	1.5	1.5	2.6	2.6	1.7	2.2	1.7	2.6	2.2	H
1.5	1.5	1.0	1.3	1.3	2.2	1.7	2.2	1.3	2.2	1.8	I
2.0	0.0	0.0	0.0	1.7	2.6	2.6	1.7	1.7	3.0	2.2	J
1.5	0.0	2.0	1.0	0.0	0.0	0.0	0.0	1.7	1.7	0.6	K
2.0	1.5	1.5	1.5	1.7	2.6	3.9	2.6	1.7	1.7	2.4	L
2.0	1.5	1.5	1.5	2.2	1.7	3.5	1.3	1.7	2.6	2.2	M
2.0	2.0	3.0	2.5	1.7	1.7	2.2	2.2	1.7	1.7	1.9	N
2.0	0.0	0.0	0.0	1.7	2.6	3.5	2.2	2.2	3.0	2.5	O
6.0	8.8	10.5	9.6	6.1	5.6	8.2	5.2	8.7	5.6	6.6	P
1.5	3.8	0.0	1.9	2.2	2.2	2.2	1.3	2.2	1.3	1.9	Q
50.0	24.0	32.5	28.3	54.0	50.0	57.0	50.0	55.0	58.0	54.0	R



REFERENCES

- [1] J.P. Gosset, B. Breul, P. Garnier & V. Nosko (1993), Hazardous Waste Landfill with Double Liner and Electrical Damage Control. Recontres 93, CFGG Congress
- [2] G. Ossena, B. Breul & R. Herment (1994), Bituminous Geomembrane Cap to Radioactive Waste Landfill, Quality Program, 5th Int Conf on Geotextiles, Geomembranes and Related Products, Singapore
- [3] L'Ospedale Dam - Corsica's Reservoir will Store 3 Mm<sup>3</sup> for Dry Years, Construction Industry International, 1979



# Evaluating the Stress Crack Resistance of HDPE Seams

R.W. Thomas

Vice President and Technical Director, TRI/Environmental, Inc., Austin, Texas, USA

**ABSTRACT:** Forty three (43) field seams were collected over the construction seasons of 1995 and 1996 in the United States. The seams were made from sheet supplied by at least 4 different manufacturers, were both smooth and textured, and included fusion and extrusion welds. The seams also ranged in thickness from 1 to 2 mm and were made by at least 5 different types of welding machines. The stress crack resistance of these seams was determined by a constant load test at 80°C. Results showed that 30% of the seams failed in less than 100 hours and that extrusion seams were more susceptible to crack formation than fusion seams. The main failure modes for the seams were also determined. Fusion seams broke primarily through the top sheet at the root of the squeeze-out bead. Extrusion seams showed five different failure modes but the most prevalent one was a crack directly through the extruded bead. This mode of failure raises important questions about the stress crack resistance of the welding rod used to make extrusion seams.

**KEYWORDS:** HDPE, Geomembranes, Laboratory Tests, Stress Cracking, Seams

## 1 INTRODUCTION

The phenomenon of slow crack growth (stress cracking) in HDPE geomembranes has been studied for over ten years and is still not well understood. Certain resin characteristics like density, molecular weight, molecular weight distribution and co-monomer type and distribution are believed to affect stress crack resistance, but it is not known exactly how. Therefore, this is one property of HDPE that needs to be continually monitored for quality assurance and to minimize the potential for field fractures. The main way to evaluate a materials stress crack resistance is with ASTM D5397, "Evaluation of Stress Crack Resistance of Polyolefin Geomembranes Using Notched Constant Tensile Load Test". This test is one of the best tools available for evaluating the stress crack resistance of smooth geomembranes and its development has directly led to improved resins and a reduction in the numbers of stress cracks that have occurred in the field.

The test has several limitations, however. First, it has limited use as a QC/QA tool because it is a relatively long test. The most common performance requirement for an acceptable geomembrane is a failure time greater than 200 hours under a load of 30% of the yield strength when tested by the appendix to D5397. This is over eight days which is too long for a QC/QA test. One way to accelerate the test is by increasing the temperature (Hsuan 1995, Thomas 1997).

Secondly, this test cannot be performed on textured geomembranes or seams. Tests on textured sheet are important because the texturing processes create flaws in the surface of the sheet and it is important to know if these flaws can lead to stress cracks. Tests on seams are important because historically, nearly all of the stress cracks found in the field started at a seam.

A modification of ASTM D5397 was developed several years ago in Germany by workers at a Federal Institute called Bundesanstalt für Materialforschung and prüfung, or BAM (Müller 1992). This test was subsequently used in the USA to

study stress cracking of textured geomembranes (Thomas 1993), and different types of seams (Thomas 1993, 1994, 1995). The test has been called the BAM test, and is a constant load stress crack test that is run at a higher temperature (80°C vs. 50°C), uses a specimen with more surface area (10 cm<sup>2</sup> vs 0.5 cm<sup>2</sup>) and does not involve a notch.

The purpose of this study was to use the BAM test to study the stress crack resistance of selected HDPE seams installed in the USA during the construction seasons of 1995 and 1996.

## 2 EXPERIMENTAL PROCEDURES

### 2.1 Seam Samples

Forty three (43) seam samples were collected from sites all over the USA. It is believed that they are a fairly good representation of the types of seams being made. Specific information is not known about all of the seams, except for the site they were from. However, it is known that they included sheet made from at least 4 different manufacturers and the seams were made by at least 5 different brands of welders. Otherwise, the exact resin, sheet manufacturer, installer, and welding machine were not known. All of the seams studied passed destructive peel and shear tests.

Thirty eight (38) seams were made from 1.5 mm (0.06 in) sheet, two were made from 1.0 mm (0.04 in) sheet, and three were made from 2.0 mm (0.08 in) sheet.

The seams were divided into four main classes. They were smooth/fusion, textured/fusion, smooth/extrusion, and textured/extrusion. Seams joining smooth sheet to textured sheet were considered to be textured seams. The numbers of each type are given in Table 1. An attempt was made to keep a balanced sample set, but this was not possible. It was more difficult to obtain extrusion seams because they are tested less frequently than fusion seams.

Table 1. Types of field seams evaluated.

Seam Type	Number of Samples
Smooth/Fusion	15
Textured/Fusion	11
Smooth/Extrusion	7
Textured/Extrusion	10

## 2.2 The BAM Stress Crack Test

The test specimens were rectangular bars, cut with a die and of the dimensions 1.25 cm x 15.2 cm (0.5 in x 6.0 in). They were mounted in modular lever arm devices, each capable of holding 5 specimens. The stress crack solution was 5% Igepal CA-720 in DI water, the test temperature was  $80 \pm 1^\circ\text{C}$ , and the applied stress was 4.0 MPa (580 psi).

The test was run by first mounting five replicate specimens in shear into a test device. This means that the top sheet was placed in one clamp and the bottom sheet on the other end of the seam placed in the other clamp. Then, the device was mounted onto the side of a constant temperature bath containing the stress crack solution. After about five minutes, the loads were applied to the lever arms and the timers on the devices set to zero. Placing the load on the specimens within five minutes is believed to allow them to become loaded more gradually, since they had not yet reached the test temperature. As each specimen failed, it tripped a switch causing the timer to stop. If no specimens failed within a specified time, the experiment was terminated.

## 3 RESULTS AND DISCUSSION

### 3.1 Failure Times

In nearly all cases, the average reported is the result of five test specimens. In two cases, specimens slipped from the grips, so the remaining 3 or 4 failed specimens were averaged. The average failure times of the 43 seams ranged from 17 to over 500 hours. Since the main focus of this paper was on fast failure times it was decided after a few months to terminate the tests once they reached 300 hours. The variability in the average failure times was relatively constant among the different sample types. A summary of the results in terms of failure time ranges is shown in Table 2.

These results clearly show that extrusion seams are more susceptible to cracking than fusion seams. Most of the fusion seams lasted over 300 hours while only a few of the extrusion seams did. Also, most of the extrusion seams failed in less than 200 hours, with 41% failing in less than 100 hours. Overall, 13 of 43, or 30% of the seams tested failed in less than 100 hours. Eight of the 13 failed in 50 hours or less.

Table 2. Summary of average failure times (43 samples).

Failure Time(hrs)	Smooth Fusion	Textured Fusion	Smooth Extrusion	Textured Extrusion
<100	3 (20%)	3 (27%)	5 (71%)	2 (20%)
100-200	1 (7%)	2 (18%)	1 (14%)	4 (40%)
200-300	3 (20%)	0 (0%)	0 (0%)	2 (20%)
>300	8 (53%)	6 (55%)	1 (14%)	2 (20%)

Two important questions that need to be addressed are:

1. Why do some seams fail more quickly than others?, and
2. How good is good enough?

The first question is related to a number of factors which affect the stress crack resistance of the seams. First, the stress crack resistance of the base sheet is an important consideration. The generally accepted minimum value for a geomembrane is 200 hrs, when tested by the Appendix to ASTM D5397. Most of the resins on the US market today have average stress crack values from 500 to 1000 hours. There are also a couple of resins that can easily exceed 2000 hours in this test. It has been shown that seams made from great resins will be less susceptible to stress cracks than seams made from average resins (Thomas 1995).

A second factor which affects the stress crack resistance of the seams is the welding process itself. During seaming, events can occur which may affect stress crack resistance. It has already been shown that the geometry of the hot wedge and drive wheels is an important factor (Thomas 1995). Additionally, the wedge temperature, drive roller pressure, and welding speed are important variables. During extrusion seaming, the surface of the sheet is ground and preheated before the extrusion bead is put in place. Over-grinding can leave stress crack initiation sites in the joint, as can overheating. The quality of the welding rod is another variable. It may or may not be made from the same resin as the sheet. And, even if it is, its stress crack resistance can be compromised by high temperatures or long dwell times in the extrusion gun.

A belief held by the author is that, in general, one can hardly do anything to hurt an excellent resin, but average resins can produce seams that might be considered unacceptable. Again, it is important to decide what level of performance is desired. Obviously, a seam that lasts 200 hours in this test is better than one that lasts 100 hours, but how does one know that a 100 hour seam is not acceptable?

The answer to this question is important because even though seam samples can fail in an accelerated test does not mean the seams will fail in the field. On the other hand, it would seem prudent to expect some minimum performance to further reduce the potential for field failures. Fast failure times might also be indicative of correctable quality problems in the seams.

One way to consider how long a seam should last is by comparing seam results with results from ASTM D5397 performed at 80°C (Thomas 1997). Results from that study showed that the test is accelerated by at least 8 times when run at 80°C and a load of 20% of the yield stress. That means that 200 hours in the notched test at 50°C is about equal to 25 hours in the test at 80°C. Obviously, if a seam breaks as quickly as a notched sample, the seam would essentially be like a defect equivalent to a razor blade cut to a depth of 20% of the thickness of the sheet. So, one would expect a seam sample to last much longer than a sample with a notch in it. Therefore, a seam requirement of 100 hours in the BAM test would suggest that the seam was 4 times more resistant than the minimum required notched sheet stress crack resistance. The stress crack resistance of the seam is definitely a result of both the stress crack resistance of the sheet and the amount of stress placed into the seam during the seaming process (Thomas 1995). That means that the 100 hours minimum time could be reached by a good resin with a significant amount of internal stress in the seam, or a minimally acceptable sheet made into a seam with very little internal stress. Either way, 100 hours seems to be a reasonable and obtainable value.

### 3.2 Failure Modes

The modes of failures for all of the specimens that broke were examined independently from the failure times. The failure times are greatly influenced by the resin, but the locus of failure can provide valuable information about the “weak link” in the seam. The crack will start at some location under stress that contains a flaw.

There were three different failure modes associated with double track fusion seams. They were: 1) a crack in the top sheet at the base of the squeeze-out bead, 2) the same location in the bottom sheet, and 3) a crack forming in the sheet away from the weld. Only one sample cracked in the sheet. It was a textured sheet seam and the fact that it failed in the sheet suggested that the sheet itself was more susceptible to cracks than the seam. The crack appeared to start at a thin spot in the geomembrane. The distribution of the failures modes found in the fusion seams is shown in Table 3. It is clear from these results that most of the fusion seams tested failed in the top sheet. This was true for both smooth and textured seams.

Table 3. Fusion seam failure modes (42 specimens).

Failure Mode	Number (% of Total)
Top sheet at squeeze out	27 (64%)
Bottom sheet at squeeze out	10 (24%)
In the sheet	5 (12%)

The total number of specimens available for failure mode analysis was 42 even though there should have been 60 since 12 fusion samples with 5 replicates failed in less than 300 hours. However, three sets of seams tested early in the study were discarded and three individual specimens slipped from the grips.

There were five different failure modes observed for extrusion seams. They were: 1) failure through the extrusion bead, 2) failure through the top sheet under the extruded bead, 3) failure through the top sheet at the edge of the extruded bead, 4) failure through the bottom sheet under the bead, and 5) failure through the bottom sheet at the edge of the extruded bead.

The distribution of these failure modes through the samples tested is shown in Table 4.

Table 4. Extrusion seam failure modes (70 specimens).

Failure Mode	Number (% of Total)
Through the extrudate	43 (61%)
Top sheet under bead	4 (6%)
Top sheet at edge of bead	3 (4%)
Bottom sheet under bead	12 (17%)
Bottom sheet at edge of bead	8 (11%)

The most common and surprising failure mode was directly through the extruded bead. This occurred over 60% of the time and was more common in smooth seams than textured seams (80% vs. 48%). The most surprising fact about this failure mode was the length of some of the cracks. There were beads that were over 7.6 mm (0.3 in) tall. This failure mode suggests that the stress crack resistance of the welding rod itself needs to be considered. It is possible that either a different resin is being used to make the rod, or the rod is somehow damaged during the extrusion process.

Failures through the top sheet either under the bead or at the edge of the bead were relatively rare. There were only 7 specimens that failed this way and 6 of them were textured.

Failures in the bottom sheet either under the bead or at the edge of the bead were the second most common modes. Most of these were found in textured sheet (15 vs. 5). In fact, there were no failures in smooth sheet that occurred at the edge of the bead, they all failed at a location under the bead. Close examination of one of the samples that failed under the bead showed that the cracks grew from grinder marks that had not been remelted during the extrusion process.

The failures at the edge of the extrusion bead in textured sheet may have been a result of sheet thinning in that area. It is reasonable to assume that if the sheet thins, it would have a higher stress causing cracks to grow there more quickly.

Of the failures cataloged above, the ones that failed in less than 100 hours are examined again in Table 5. These results give an indication why the seams failed so quickly.

Table 5. Failure modes of 13 seams failing in <100 hours.

Seam Type	Failure Mode
Sm./Fusion (3)	100% - top sheet at squeeze out
Tex./Fusion (3)	66% - top sheet at squeeze out 33% - in the sheet
Sm./Extrusion (5)	100% - through the extrudate
Tex./Extrusion (2)	50% - bottom sheet under bead 50% - bottom sheet edge of bead

Close examination of these 13 seams shows that causes of early failures can be found in most cases. The smooth/fusion seams all failed by a crack in the top sheet at the base of the squeeze out bead. It was discovered that one failed because of a bad resin. The failure time of the sheet by the notched stress crack test was 65 hours, which is much less than the required 200 hours. The other two appeared to be overheated. One was a 1.0 mm (0.04 in) seam that had large ripples throughout the seam. The other was a 1.5 mm (0.06 in) seam that had been distorted to the point that the cross-section of the seam was shaped like a stretched out letter Z.

Two of the textured/fusion seams failed in the top sheet at the root of the squeeze out and the other failed in the sheet. The seams looked acceptable, but it was possible that there were thin spots at the edges. The seam that failed in the sheet was made from a textured sheet that appeared to have many thin spots. It also failed quickly ( $51 \pm 4$  hours), which indicates that the stress crack resistance of the textured sheet itself should be considered.

All of the smooth/extrusion seams failed through the extruded bead. This mode of failure proves that the stress crack resistance of the welding rod needs to be controlled. All of these seams would probably have surpassed 100 hours with a higher quality welding rod.

The textured/extrusion seams all failed in the bottom sheet, with half cracking at the edge of the bead and half cracking under the bead. It appeared as if sheet thinning was the cause of the failures at the edge and overheating caused cracks under the bead. The sample that cracked under the bead showed puckering underneath the bottom sheet.

This brief analysis suggested that the seams that failed in less than 100 hours all had some type of quality defect. This supports the selection of 100 hours as a minimum acceptable failure time. It is strongly believed that all of these times can be easily improved by learning more about the relationship between the seaming process and the stress crack resistance of the resulting seams.

#### 4 SUMMARY AND CONCLUSIONS

This paper presented results of stress crack tests performed on 43 field seams made in the USA during the construction seasons of 1995 and 1996. The failure times and the different failure modes were reported. The results obtained lead to the following conclusions.

1. Extrusion seams are more likely to fail by stress cracking than fusion seams. This is extremely important when one considers the appropriateness of cutting holes in fusion seams to test them and repairing the resulting hole with an extrusion seam.
2. The main failure mode for extrusion seams was a crack through the extruded bead. This means that the stress crack resistance of the welding rod is a new and important consideration.
3. Seams that failed in less than 100 hours likely had quality defects that can be corrected.
4. The BAM test has proven to be a very effective tool for evaluating the quality of seams. More work is required to discover why seams break quickly and how to make seams that survive longer in this test. Longer times in the BAM test will certainly improve the reliability of a geomembrane over its service lifetime.

#### REFERENCES

- Hsuan, Y.G. and Koerner, R.M. (1995) "The Single Point Notched Constant Tension Load Test: A Quality Control Test for Assessing Stress Crack Resistance", *Geosynthetics International*, Vol. 2, No. 5, pp. 831-843.
- Thomas, R.W. and Woods-DeSchepper, B. (1993) "Stress Crack Testing of Unnotched HDPE Geomembranes and Seams", *Proceedings of the 7th GRI Seminar*, Philadelphia, PA, pp. 116-125.
- Thomas, R.W. and Woods-DeSchepper, B. (1994) "The Environmental Stress Crack Behavior of Coextruded Geomembranes and Seams", *Fifth International Conference on Geotextiles, Geomembranes and Related Products*, Singapore, Vol. 3, pp. 945-948.
- Thomas, R.W., Kolbasuk, G.M. and Mlynarek, J. (1995) "Assessing the Quality of HDPE Double Track Fusion Seams", *Sardinia '95 Landfill Conference*, pp.415-428.
- Thomas, R.W. and Siebken, J. (1997) "Increasing the Temperature of the Notched Constant Tensile Load Environmental Stress Crack Resistance Test", *Geosynthetics '97*, Long Beach, CA, Vol. 1, pp. 191-200.
- Müller, W. (1992) personal communication.

# Assessing the Long-term Behavior of Geomembranes in Multi-factor Environments

C. Maisonneuve

PhD Student, LIRIGM, BP53X, 38041 Grenoble Cedex 09, France

P. Pierson

Professor, LIRIGM, BP53X, 38041 Grenoble Cedex 09, France

C. Duquennoi

Engineer, CEMAGREF, Parc de Tourvoie, BP 121, 92185 Antony Cedex, France

A. Morin

Engineer, INERIS, BP2, 60550 Verneuil en Halatte, France

**ABSTRACT:** The objective of this paper is to analyse the effects of aging on geomembrane durability and to design an accelerated test (few months duration). This test takes into account the different aging parameters without changing the aging mechanisms observed on site. Different analysis and mechanical tests are considered to characterize the geomembrane changes. Results show good agreement with observations on site.

**KEYWORDS:** Geomembrane, Mechanical properties, Stress cracking, Polymeric aging.

## 1 INTRODUCTION

Geomembranes have been used almost all over the world for about three decades. During these years the variability of applications of geomembranes has been constantly increasing. Nowadays, the environment in which geomembranes are used is very different from an application the another.

Among all the problems encountered by engineers and scientists in this context of technological diversity, the question of durability is one of the most important in terms of engineering and scientific complexity.

The problem of geomembrane durability has been addressed by researchers like Haxo (1989) and Koerner (1990). Their pioneering work, besides setting the bases for future research, enabled considerable enhancements in material developpement and engineering practice. But not all has been done! To the simple question "how long will this particular geomembrane perform in this particular case of application?", no simple answer can be found, and moreover, no widely accepted method can be found to answer it. Most of the time, and particularly when environmental issues are at stake, the answer is crucial.

The lack of a ready-made method to evaluate the durability of geomembranes is mainly due to the fact that in many cases, physical, chemical and biological stresses of the geomembrane and their effects on the material are not very well known. This, in turn, is due to the lack of measurements, either of the stresses themselves or of their separate aging effects on the geomembrane geomembranes.

An objective of the study presented herein is to set up

the bases of a method to accelerate the aging of by increasing the value of pertinent individual form of stresses. Our final goal is to predict the durability of geomembranes under given conditions.

The research program involved four french laboratories: CEMAGREF (Agricultural and Environmental Engineering Research Institute), INERIS (National Institute for Industrial Environment and Risks) and LIRIGM (Research Laboratory on Geology and Mechanics, Grenoble University), LRPC (Regional Research Laboratory of Civil Engineering of Lyon), under financial support from ADEME (National Agency for Environmental Protection and Energy Saving).

## 2 AGING OF GEOMEMBRANES: THEORETICAL FRAMEWORK.

### 2.1 Definitions

The following definitions and theoretical framework to aging studies are based on well-established methods in the field of polymer aging (Verdu, 1984). These methods have been validated and successfully applied in such domains as automobile, electronic equipment, pipes, etc...

Aging is defined as a slow and irreversible evolution of material properties under environmental stresses.

Durability should not be confused with aging. It is the ability of a material or a structure to withstand aging in such a way that its properties remain in the limits of acceptability for a given use.

The service life of a material or a structure is the time during which its properties remain in the limits of acceptability for a given use. In order to estimate the service life of a geomembrane, it is not only necessary to predict its aging but to define the limits of acceptability of its properties.

Natural aging is defined as aging under condition in use.

Artificial aging is defined as aging in a specific, controlled device, either in the laboratory or on site. The quality of artificial aging depends on its closeness to natural aging.

Artificially accelerated aging is defined as accelerated aging by the means of artificial conditions. Aging mechanisms are supposed to be similar to those occurring in field condition but in an accelerated way.

Aging environment is a set of external factors likely to influence aging of a material or a structure.

It has to be underlined that aging depends on numerous environmental parameters: some parameters can be isolated and others are interacting.

The typical example to illustrate this lack of data concerns the long-term behavior of geomembranes used in landfill barriers. The physico-chemical environment to which a geomembrane is exposed at a landfill bottom is generally reducing and light-free. These conditions are thought to be favorable to geomembrane durability, because polymers are usually affected by photo-oxidation aging processes which can reasonably be neglected here. On the other hand, the leachate in which the geomembrane is continuously immersed is a complex aqueous solution of low concentration chemicals which have a potentially long-term deteriorating effect on geomembranes, especially when combined with mechanical stress and temperature. This already complex situation is furthermore complicated by the extreme difficulty of *in situ* observations : solicitation measurements are very scarce and sample collection and analysis is impossible most of the time. It is therefore necessary to develop tests in which aging mechanisms are similar to those occurring in field conditions but in an accelerated way.

The effect of interacting chemical and mechanical stresses can be illustrated by the now famous example of stress cracking of High density polyethylene (HDPE) (Hsuan et al., 1993) further developed in part 3 of the present article.

### 3 ACCELERATED AGING: TESTS AND RESULTS

Results presented herein concern HDPE geomembrane 2 mm thick and flexible polypropylene (FPP) geomembranes. The main reason for this presentation is that full results and interpretations are available on the HDPE material and that FPP is quite new.

Chemical, thermal and mechanical aging conditions have been selected on the base of literature. Different geomembrane types have all been immersed in the same immersion medium at 23 and 60 °C, under constant uniaxial tensile strain (5% for HDPE and 10% for FPP). The synthetic immersion medium (SIM, presented in table 1) is an aqueous solution of selected active chemicals, considered as a collection of aging-triggering agents. The SIM is designed to age the geomembranes without modifying natural aging mechanisms, each solvent representing a chemical family, known to be interacting with geomembranes.

Table 1. Initial SIM composition

Compound	Concentration
Cyclohexanone	30 g/l
Phenol	3 g/l
Perchloroethylene	0.1 g/l
Xylene	0.1 g/l
Heptane	0.1 g/l
Surfactant	10 g/l
pH	2

Samples are regularly taken out from the tanks (every 2 months with a maximum immersion time of 8 months). Samples are then weighted (before and after drying at 60°C (or 30°C for samples immersed at 23°C) during 48 hours) and tested using analytical and mechanical methods.

#### 3.1. Results On HDPE Samples

Physico chemical analysis was presented in "Accelerated aging tests for geomembranes used in landfills" (Maisonneuve et al., 1997). As it is thought that aging first affects the surface of geomembrane, such analysis cannot detect changes at the surface of the material because the polymer is melting due to the high temperature during analysis. Surface analyses would be more appropriate. More thorough experiments are underway. Only Oxidative Induction Times (OIT) which gives the time for oxidation in isothermal conditions decreased (table 2). It shows a loss of antioxidants.

Duquenois et al. (1995) also noticed a small loss of ester-type antioxidant after 27 months, in leachate at 50°C.

Tensile tests and shear tests show a decrease in strength at yield (table 2) and an increase in strain at yield with aging on both seamed and non seamed samples.

To confirm this result, the relaxation modulus has been assessed by measuring the stress in a sample maintained at a fixed strain. The residual modulus is higher in stressed non-immersed samples at 23°C than in stressed samples

immersed in the SIM at 60°C for the same fixed strain (table 2).

It can be induced by the internal lubrication in the polymer due to the absorption of components.

Moreover, we also detect an increase in strain for samples immersed in water at 60°C, during the same time, but no change happens for samples in SIM, at 23°C. This change is an important result because Giroud (1984) has demonstrated that failures of HDPE geomembranes are governed by the yield strain on the order of 10%.

Castaldo (Eurogeo,1996) noticed similar mechanical variation for 3 different HDPE immersed in a synthetic medium at elevated temperature (50°C and 70°C).

A possible interpretation of these observations is that modification of mechanical properties at yield described above depends first of temperature.

Table 2. Variations between 8 months aged HDPE samples and reference HDPE samples for different tests and analyses

Tests	Variations* (%) in	
	water, 60°C	SIM, 60°C
tensile test		
strength at yield	1	-0.5
strain at yield	3.2	5.4
shear test		
strength at yield	3	-15.2
strain at yield	4	10.8
peel test	No significant results	
relaxation	modulus	air, 23°C
		SIM, 60°C
	non seamed sample	-70.7
	seamed sample	-79.5
mass	before drying	0.1
	after drying	0
thickness	No significant results	
density	No significant results	
permeation	Soon available results	
DSC	No significant results	
OIT	Time to oxydation	-56
TG	Soon available results	
MFI	No significant results	

\* Aged samples are immersed 8 months in pure water and in SIM, at 60°C; they are then tested after drying 48h at 60°C. The relaxation test compares stressed sample in air and in SIM during 8 months.

A very important phenomenon to be considered for semi-cristalline polymers in the visco-elastic state (like

HDPE) is stress cracking. To induce it, notched samples are immersed in different media (SIM, surfactant in solution or pure water) under constant stress. Two types of break can be developed:

- Ductile break obtained with a stress large enough to produce a fast yield point: Interlamellar chain tension produces intra-cristallite break.

- Brittle break obtained with a smaller stress: Break occurs in the amorphous zone (inter-cristallite break).

Our first results on HDPE immersed in SIM show the transition from brittle break to ductile break which occurs at about 40% of the stress at yield. When comparing results obtained with SIM and with water, the influence of the immersion medium is noticeable: No break was observed in water after 2000h, whereas break occurred after 10h for HDPE in SIM for the same stress level.

The immersion medium has a growing reactivity with high pH, a low viscosity and a low surface tension (Courard, 1996). We can compare our result to results found by Hsuan et al (1993) : they compare the effect of different incubation media. The medium composed by 10% IGEPAL Co630 in 90% tap water will be seen to be a very aggressive incubation liquid compared to other fluidslike 100% tap water or air (i.e. no liquid immersion).

To induce stress cracking in field, it must have a point at which a crack can initiate (simulated by notched sample in laboratory). Condition of a crack initiation point could be an imperfection scratch, carbon black agglomeration or other anomaly but will most likely be at the location of a seam (Carson,92).

These data clearly show solvent absorption by the geomembrane, increased both by temperature and the SIM.

### 3.2 Results On FPP Samples

This geomembrane is a rubber modified polypropylene and it is very difficult to characterize the molecular properties because the different components interact during physico chemical analysis: it is then impossible to separate them. In this particular case, physico chemical analysis do not appear to be good indicators of aging. More thorough experiments are underway.

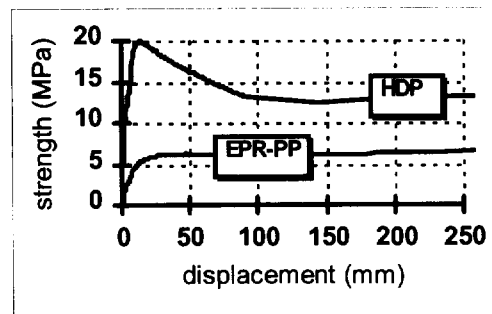


Figure 2. HDPE and FPP tensile test.

Like HDPE, we focused our research on mechanical tests. The yield point is not as distinct as in HDPE (figure 2) because of the Ethylene Propylene Rubber included in PP. However, in tensile tests, we observed a decrease of the pseudo- yield strength, as in HDPE.

Mass variation, measured after 2 months immersion tests are presented table 3.

Table 3. Mass variation on FPP

T = 23°C	T = 60°C
SIM	SIM
+ 5 % before drying	+ 5 % before drying
+ 2% after drying	- 0.5% after drying
Water	Water
+ 1% before drying	+ 2% before drying
0% after drying	0% after drying

Absorption is noticeable for samples immersed in SIM and water. In water immersion, the variation is reversible. In SIM, at 60°C, the mass is inferior to initial mass, the copolymer seem to be attacked by the solvents. In SIM, at 23°C, solvents are still present in the copolymer after drying, the heat to extract solvents during drying is probably not important enough.

#### 4 CONCLUSION

Physico chemical analysis did not evidence aging phenomena on HDPE and FPP, except for the loss of antioxidants.

We suppose that for both HDPE and FPP, modification of mechanical properties at yield first depends on temperature.

Stress cracking tests show the importance of the immersion medium to develop cracks. This phenomenon is very important because break is obtained under the same conditions on site and during our experiments.

Solvent absorption by immersed samples depends both on temperature and on immersion medium.

HDPE and FPP geomembranes have a good resistance to the applied stresses. Additional analyses are necessary to correlate mechanical stresses with a change in structure.

Similar modification are noticed on accelerated aging geomembrane and on 'natural' aging geomembrane: this accelerated aging process seems to be a good way to understand the long term behavior of geomembranes. Next step consists on determining accelerated aging factors by comparing the effects of accelerated aging to the effects of aging on site. Other materials and sollicitations should also be considered.

#### ACKNOWLEDGEMENTS

This study was partially financed by ADEME and could be achieved. The aging study on HDPE and on FPP was conducted at INERIS laboratory (which supported a PhD work with ADEME on this subject) and at IRIGM, university of Grenoble (France).

#### REFERENCES

- Castaldo S., Viviani G., Cazzuffi D., Fede L. (1992) "Chemical compatibility of geomembranes in presence of synthetic landfill leachate", *Geosynthetics: Applications, Design and Construction*, De Groot, Den Hoedt and Termaat (eds). Rotterdam.
- Courard V., Rigo J.M (1992) "Oxidative induction time: A quality assurance measurement to predict environmental stress-cracking", *Geosynthetics: Applications, Design and Construction*, De Groot, Den Hoedt and Termaat (eds). Rotterdam.
- Duquennoi C., Bernhard C., Gaumet S. (1995) "Laboratory aging of geomembranes in landfill leachates", *Proceedings of the 5th International Landfill Symposium*, Sardinia '95, Cagliari, pp.397-404.
- Giroud J.P. (1984) "Analysis of Stresses and Elongations in Geomembranes" *Proceeding of the International Conference on Geomembranes*, volume 2, Denver, CO, USA, June 1984, pp.487-486.
- Haxo H. E., Jr. (1989) "Compatibility of Flexible Membrane Liners and Municipal Solid Waste Leachates", *15th Annual Research Symposium on Remedial Action, Treatment and Disposal of Hazardous Waste*, Cincinnati, OH, USA.
- Hsuan Y.G., Koerner R.M. and Lord A.E. Jr (1993) *Stress Cracking Resistance of High Density Polyethylene Geomembranes*, ASCE, Journal of Geotechnical Engineering, Vol.119, No.11, pp. 1840-1857.
- Koerner R.M. (1990) *Long term durability and aging of geomembranes*, Waste Containment Systems; Construction, regulation and performance, Geotechnical special publication n°26, American Society of Civil Engineers, pp. 106-134.
- Maisonneuve C., Pierson P., Duquennoi C., Morin A. (1997) "Accelerated aging tests for geomembranes used in landfills", *Proceedings of the Fifth International Landfill Conference*, Sardinia '97, Cagliari.
- Rollin A. L., Mlynarek J., Lafleur J., Zanescu A. (1991) "The investigation of a seven year old HDPE geomembrane used in a landfill", *Proceedings of the Third International Landfill Conference*, Sardinia '91, Cagliari, vol. 1, 667-677.
- Verdu J. (1984), *Vieillessement des plastiques*, AFNOR Techniques.



# Performance of Flexible Polypropylene Geomembranes in Covered and Exposed Environments

Alice I. Comer  
U. S. Bureau of Reclamation, Denver, CO, USA

Yick G. Hsuan  
Geosynthetic Research Institute, Drexel University, Philadelphia, PA, USA

Linda Konrath  
Civil and Architectural Engineering, Drexel University, Philadelphia, PA, USA

**ABSTRACT:** The U. S. Department of Interior, Bureau of Reclamation (Reclamation) began investigating the long term properties of flexible polypropylene (fPP) geomembranes as early as 1989. This paper presents the performance of fPP geomembranes at two field test sites in which the geomembranes were either covered by soil or partially exposed to direct sunlight. The buried fPP continues to have good mechanical properties after 6 years. The particular stabilization package used in the exposed fPP was found to be inadequate to prevent ultraviolet (UV) degradation. The exposed section of the geomembrane showed cracking after 26 months. Furthermore, the UV degradation was substantiated in a laboratory acceleration test using a UV weatherometer. This indicates that UV weatherometer exposure and subsequent testing can be used for screening to evaluate the UV resistance of differently formulated fPP geomembranes.

**KEYWORDS:** flexible polypropylene, geomembrane, ultraviolet resistance,

## 1 INTRODUCTION

In 1989 Reclamation began a study on the laboratory evaluation of a new type of geomembrane that was being developed. This new geomembrane is a co-polymer of propylene and ethylene (Kilius and Shah, 1995). It is generically referred to as flexible polypropylene (fPP). The laboratory studies gave rise to two separate field installations. The fPP geomembrane involved in these two case histories was supplied by one manufacturer who also formulated the stabilization package.

The first field installation by Reclamation of a fPP geomembrane was in April, 1992. A 0.75 mm (30 mil) thick geomembrane was used as liner in a test section of a canal near Belle Fourche, South Dakota, United States. The geomembrane was placed directly on the soil subgrade and covered with 0.4 m (16 in) of soil. Thus the geomembrane was fully covered during the duration of the test program. Coupons were retrieved from the test section after 3, 4 and 6 years. The possible changes in physical and mechanical properties were evaluated.

The second field installation was in May 1994. A 1 mm (40 mil) thick fPP geomembrane was used as a liner in a salinity gradient solar pond near El Paso, Texas, United States. Details of the concept and principles of solar pond behavior have been described by Lichtwardt and Comer, 1996. The geomembrane in the upper portion of the pond was not covered and thus it was exposed directly to the ambient environment. The geomembrane in the lower portion of the pond was covered by a brine solution which varied in concentration, with fresh water on the surface and concentrated brine on the bottom. The geomembrane at the bottom of the pond reached temperatures as high as 90°C. In order to monitor the geomembrane properties during the

testing period, test strips were installed on the northern slope of the pond. The strips were retrieved at different time intervals so that the change in material properties could be evaluated. Additionally, laboratory acceleration tests were performed on this 1.0 mm thick geomembrane in order to evaluate the long-term behavior of fPP material. Two accelerated incubation protocols were carried out: water incubation at elevated temperatures and accelerated weathering incubation using an ultraviolet weatherometer.

This paper presents the results obtained from both field sites so that the performance of fPP geomembranes under two different service conditions can be compared and contrasted. In addition, data obtained from the laboratory and field coupons will be compared in order to assess the merit of the respective acceleration tests.

## 2 fPP GEOMEMBRANE USED AS A CANAL LINER

Belle Fourche Irrigation District Personnel prepared a previously determined leaking 150m (500 ft) long section of the Belle Fourche canal for placement of a geomembrane. This preparation included removing all protrusions (e.g., stress) in the subgrade which were larger than 20 mm (3/4 in.). A fPP geomembrane was selected for this test site to examine its long term performance in a canal lining application. The fPP was factory fabricated into panels so that the only seaming required was a transverse weld between ends of the adjacent panels. Panels were folded, rolled, and placed on pallets which were delivered to the job site.

The 0.75 mm (30 mil) unreinforced fPP was hand-placed in the canal as shown in Figure 1. The ends of the



Figure 1 - Hand-placed the fPP geomembrane in the canal.

adjacent panels were to be wedge welded. However, problems were encountered welding the fPP geomembrane in the sun using a welder which was originally designed to weld high density polyethylene (HDPE) geomembranes. Therefore, the panels were welded using a hot air gun aided by a hand-held roller. These seams were determined to be adequate since canal linings are not generally required to provide 100 percent seepage control.

Following placement of the geomembrane, coupons were attached to the geomembrane both above and below the water for monitoring purpose. The geomembrane was then covered by a protective layer comprised of 0.2 m (8 in) of soil topped by 0.2m of sand and gravel so as to provide for erosion resistance.

### 2.1 Test results of field coupons

Transport of water in this location is provided during the summer months only. Therefore, the test coupons were removed following 2, 3 and 5 irrigation cycles, i.e., 3, 4 and 6 years of duration. The results of mechanical property testing are reported in Table 1.

The mechanical properties of tensile, tear, and seam peel and shear have not changed significantly over the 6 years that the fPP has been buried. Whether the soil covered geomembrane is above the water line or beneath it does not seem to have an effect on the mechanical properties. The unreinforced fPP continues to have excellent elongation properties and adequate tensile and seam properties.

Water district personnel report that the fPP geomembrane has stopped the seepage problems that were present prior to the installation.

Table 1. Properties of Belle Fourche buried fPP geomembrane sheets and seams. (values are the average of 5 replicates)

Year	1994	1995	1997
<b>Geomembrane sheet</b>			
Tensile stress (kN/m)	14.8 (A) 14.7 (B)	15.1 (A) 15.4 (B)	14.2 (A) 14.8 (B)
Tensile elongation (%)	1173 (A) 1206 (B)	1253 (A) 1315 (B)	1233 (A) 1200 (B)
Graves tear (kN/m)	0.063 (A) 0.067 (B)	0.064 (A) 0.066 (B)	0.065 (A) 0.064 (B)
<b>Field Seams</b>			
Peel strength (kN)	0.055 (A) 0.085 (B)	0.077 (A) 0.066 (B)	0.11 (A) 0.065 (B)
Shear strength (kN)	0.14 (A) 0.13 (B)	0.18 (A) 0.17 (B)	0.15 (A) 0.18 (B)
<b>Factory Seams</b>			
Peel strength (kN)	0.16 (A) 0.16 (B)	0.15 (A) 0.15 (B)	0.16 (A) N/A (B)
Shear strength (kN)	0.22 (A) 0.21 (B)	0.22 (A) 0.21 (B)	0.22 (A) N/A (B)

Note: (A) = Above the waterline  
(B) = Below the waterline  
N/A = not available

### 3 fPP GEOMEMBRANE USED AS A SOLAR POND LINER

Five test sample strips were installed on the north slope of the solar pond noted in the introduction. However, the strips were placed 6 months after the pond being constructed. The length of the strips extends from the anchor trench to the bottom of the pond so that coupons from different zones of the pond can be taken for analysis. Parallel to the field study, coupons of the geomembrane were evaluated by two laboratory accelerated incubation methods: UV degradation and thermo-oxidation. Both field and laboratory coupons were tested for their tensile properties and melt flow rate (MFR). Table 2 gives the method used for each test and the parameters that were monitored. The results obtained from the field and laboratory coupons are presented in this section.

Table 2. Tests and test parameters used in the solar pond study.

Test	ASTM Method	Test Parameter
Tensile	D 638 Type IV	break stress/break strain
Melt Flow Rate	D 1238	value at 2.16 Kg/230°C

#### 3.1 Test results of retrieved field coupons

The field sample strips were retrieved after 6 and 12 months duration. Coupons were taken from six different zones along the length of the strip. The zone location and exposure condition of the coupons are described in Table 3.

Table 3. Description of the field coupons

Code	Zone	Exposure Conditions
1	Trench	ambient temperature/no UV
2	Exposed	ambient temperature/UV
3	Upper Liquid	water/ambient temperature/limited UV
4	Middle Liquid	brine solution at 30-50°C
5	Lower Liquid	brine solution at 50-70°C
6	Base Storage	brine solution at 70-93°C

Tensile tests were only performed in the machine direction of the geomembrane. For each coupon, five tensile replicates and three MFR replicates were tested. The average values were compared to their corresponding original value to obtain the percent retained value. Figure 2 shows the percent retained of each test at six different zones as described in Table 3. After 12 months, both tensile properties and MFR value of the geomembrane remained largely unchanged, although MFR values at the exposed zone are higher than the other zone locations.

However, after 26 months of service, before the 24 month old strip sample being retrieved, cracking was observed on the geomembrane in the exposed zone, i.e., Zone 2. This indicates that the geomembrane was undergoing UV degradation. Coupons were cut from the geomembrane in this particular zone for property evaluation. The change in properties is shown in Figure 3. The tensile break stress and break strain have dropped approximately 50% whereas the melt flow rate value increased 400%. On the other hand, the geomembrane that was covered either by soil or solution did not show any cracking, and their properties remained almost the same.

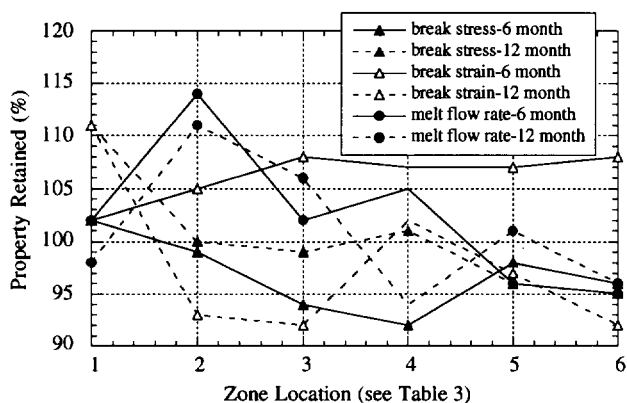


Figure 2. Properties retained of field coupons at different locations.

### 3.2 Test results of laboratory coupons

The long term durability of this particular fPP geomembrane was evaluated after exposure to two laboratory accelerated procedures: water incubation at elevated temperatures and ultraviolet exposure.

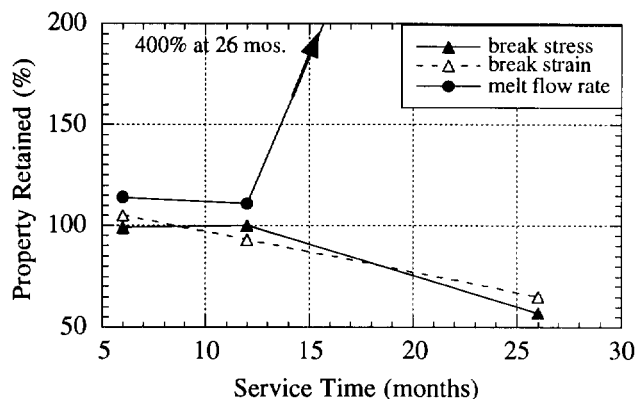


Figure 3 - Properties retained of field coupons in Zone 2.

#### 3.2.1 Water incubation study

The water incubation test was meant to simulate the effect of high temperature on the geomembrane in a liquid medium. Water was used instead of the brine solution due to the difficulty of maintaining the salt concentration. Coupons were incubated in separate water baths at temperatures of 55, 65, 75 and 85°C. The incubated coupons were removed from the baths on three month intervals. Tensile and MFR tests were performed on the retrieved coupons. Figure 4 shows the property retained values of the geomembrane coupons during the 12 months of incubation at 85°C. There is essentially no change in the properties, since the change is within the variation of the test method itself. Similar behavior was observed at the three lower incubation temperatures.

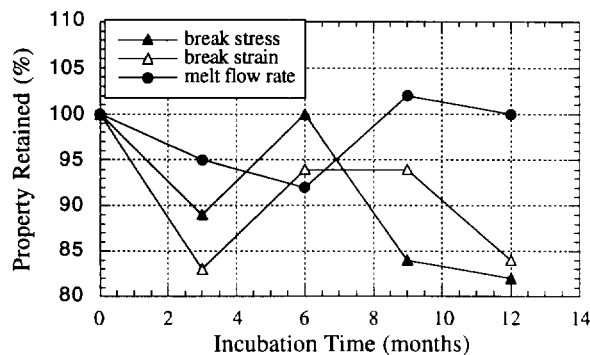


Figure 4. Changes in properties of geomembrane incubated in water bath at 85°C.

#### 3.2.2 UV exposure study

To simulate field conditions of the geomembrane located in the exposure zone (Zone 2 of Table 3), geomembrane coupons were incubated in a fluorescent UV weatherometer. The incubation procedure was according to ASTM D 5208. The condition of the incubation was set to be 5 hours of UV light at 60°C followed by a 3 hours

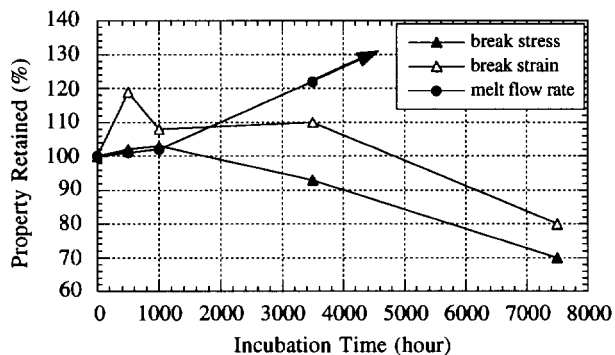


Figure 5. Changes in properties of UV exposed coupons

condensation at 50°C. Coupons were removed from the apparatus after 500, 1000, 3500 and 7500 hours of incubation time. Tensile and MFR tests were performed on the removed coupons. The test results are presented by plotting the property retained against the incubation time, as shown in Figure 5.

The tensile break stress and break strain do not show changes until 3500 hours after which their values decrease significantly. For the MFR value, it gradually increases after 1000 hours. It was impossible to measure the MFR value for the 7500 hour coupon due to its rapid flow. The increase in MFR value indicates that a chain scission reaction is taking place in the polymer. The UV degradation probably started between 3500 and 7500 hours. Furthermore, many regions in the 7500 hours coupons became so brittle that cracking resulted during cutting of the test specimens. Thus, the break stress and break strain at 7500 hr could be much lower than values that are shown in Figure 5.

### 3.3 Correlation between field and laboratory studies

In the water incubation study, test results are consistent between the laboratory coupons and field-retrieved coupons, even though the immersion solutions are not the same. After 12 months incubation, there was no substantial change in either tensile properties or MFR values at temperatures as high as 85°C.

For the UV acceleration study, cracking was noticed in coupons exposed for 7500 hr. Also cracking was observed in the field after 18 months. This suggests that the UV degradation of the geomembrane can be estimated using the fluorescent UV weatherometer. The correlation between the UV acceleration test and the field condition can be quantified based on the total UV radiation energy as described by Hsuan and Koerner, 1993. The calculation procedure is presented as follows:

- Step 1 - Determine the total UV radiation energy in the 295-385 nm range at the field site. Since the site is located at El Paso, Texas, this value is estimated using data published by South Florida Test Service for their Arizona site (South Florida, 1993). From May 1993 to June 1995, the total UV energy was measured to be 696 MJ/m<sup>2</sup>. This value is considered to be the approximate amount of energy that the field

exposed geomembrane was subjected to during its 26 months of service life.

- Step 2 - Calculate the total UV energy being generated by the weatherometer during 7500 hours of incubation. The weatherometer is equipped with UVA-340 lamps with peak emission at 343 nm. The UV energy from 295-400 nm is 39 W/m<sup>2</sup>. The actual UV light time in 7500 hours = 7500 \* 5/8 = 4687 hr. The total energy generated = 4687 hr \* 39 W/m<sup>2</sup> = 658 MJ/m<sup>2</sup>.
- Step 3 - Compare the results of the previous two steps where it is seen that the field (696 MJ/m<sup>2</sup>) is quite close to the laboratory (658 MJ/m<sup>2</sup>) which is encouraging insofar as laboratory simulation studies are concerned.

## 4 CONCLUSION

In the two case histories reported in this paper, buried and exposed fPP geomembrane were monitored for changes in the as-received properties. The buried fPP canal liner continues to retain essentially all of its mechanical properties after 6 years of service. The field performance indicates that the geomembrane has stopped the seepage problems that were present prior to the installation. For the exposed fPP geomembrane, cracking was observed after 26 months, indicating that this particular stabilization package is inadequate to protect the geomembrane under the site ambient environment. An accelerated laboratory test using a UV weatherometer showed good correlation to the field performance. Thus, it seems that the UV weatherometer could be used to evaluate different UV stabilization packages being used in the fPP geomembrane.

## ACKNOWLEDGMENTS

Laboratory testing by the Bureau of Reclamation was performed by John Schaffer of the Materials Engineering and Research Laboratory. Linda Konrath was supported by the NSF Research Experience for Undergraduates, Project number CMS-9312772.

## REFERENCES

- Hsuan, Y. and Koerner, R.M. (1993), "Can Outdoor Degradation be Predicted by Laboratory Acceleration Weathering?" Geotechnical Fabrics Report, November, No. 8, pp. 12-16.
- Kilius, D.E. and Shah, B.A. (1994), "Polypropylene Resins for Geomembranes", Proceedings of the 8th GR1 Conference on Geosynthetic Resins, Formulations and Manufacturing, Published by IFAI, pp. 31-38.
- Lichtwardt, M.A. and Comer, A.I. (1997), "Geosynthetics in a Salt-Gradient Solar Pond Environment," Geosynthetics' 97, IFAI, Vol. 1, pp. 551-560.
- South Florida Test Service News, (1993 to 1995), Monthly Solar Energy Data, Miami, Florida, USA.

Table 2 - Status and information on the commercial pipe samples

Code	Pipe Producer	Diameter (inch)	Profile	Resin Composition	Status
1	I	18	Type S - annular	100% virgin resin (VR-1)	R
2	I	18	Type S - annular	Blended resin - reprocessed resin (RR-1)/post consumer resin (PCR-1)	R
3	I	18	Type S - annular	Blended resin - (VR-1/RR-1/PCR-1)	R
4	II	24	Type S - annular	100% virgin resin (VR-2)	R
5	III	24	Type S - annular	Blended resin - two virgin resins (VR-3)/(VR-4)	R
6	III	24	Type S - annular	Blended resin - (VR-3/PCR-2)	R
7	IV	24	Type S - annular	100% virgin resin (VR-5)	P
8	V	24	Type S - annular	100% virgin resin (VR-6)	R
9	II	24	Type S - helical	100% virgin resin (VR-7)	R
10	I	24	Type S - annular	100% virgin resin (VR-8)	R
11	II	36	Type S - annular	100% virgin resin (VR-2)	R
12	V	36	Type S - annular	100% virgin resin (VR-9)	R
13	IV	36	Type S - annular	100% virgin resin (VR-10)	P
14	I	36	Type S - annular	100% virgin resin (VR-1)	R
15	I	48	Type S - annular	100% virgin resin (VR-1)	R
16	II	48	Type S - Honeycomb	100% virgin resin (VR-11)	R

Note: Type S - This type of pipe has a full circular cross-section, with an outer corrugated pipe wall and a smooth inner liner. Corrugation may be either annular or helical.

Virgin resin (VR) = material in the form of pellets, granules, powder, floc, or liquid that has not been subjected to use or processing other than that required for its initial manufacture.

Reprocessed resin (RR) = regrind or recycled-regrind material that has been processed for reuse by extruding and forming into pellet or by other appropriate treatment. (The reprocessed resins typically are not in-house materials, but are sold by other manufacturers that make different types of products).

Post consumer resin (PCR) = materials generated by a business or consumer that have served their intended end use, and that have been separated or diverted from solid waste from the purpose of collection, recycling and disposition.

R = received

P = promised to be delivered before the end of November.



# A Fracture Mechanics Assessment for the Long-Term Durability of HDPE Geomembranes

C.H. Popelar

Institute Engineer, Materials and Structures Division, Southwest Research Institute, San Antonio, Texas, USA

C.J. Kuhlman

Senior Research Engineer, Materials and Structures Division, Southwest Research Institute, San Antonio, Texas, USA

I.D. Peggs

President, I-CORP INTERNATIONAL, Ocean Ridge, Florida, USA

**ABSTRACT:** A fracture mechanics methodology for predicting the life expectancy of PE geomembrane liners under service conditions is presented. The approach builds upon the experience and success gained in developing a lifetime assessment capability for PE natural gas pipes. It combines slow crack growth testing with fracture mechanics analyses to predict the life expectancy of the liner. Correlations for the time for initiation of crack growth and the crack growth rate with the stress intensity factor are developed. It is demonstrated that the bidirectional shifting method and shift functions, developed for PE pipes, can also be used to quantify the influence of temperature on the failure process in PE geomembranes. The correlation for the crack growth rate can be integrated for the field loads to predict the liner's life expectancy. This approach can be used to establish the admissible initial defect size for a prescribed loading and service life, and as a basis for specifying inspection requirements, and quality control and assurance standards.

**KEYWORDS:** Geomembranes, Stress Cracking, Fractures, Temperature Effects, Failures

## 1 INTRODUCTION

Geomembranes are used to line evaporation, ash and other ponds of electrical power stations in the United States, Canada and Europe in addition to solid waste and hazardous waste landfills. Geomembranes are often used as the primary barrier to prevent intrusion of contaminants into the adjoining soil and ground water. Therefore, long-term durability is essential to the reliable performance of these barriers.

Premature failures of a number of uncovered liquid impoundment and solid waste lining systems in North America and Europe have occurred (Peggs et al. 1988). In many instances these failures could be traced to cracking originating at scratches and gouges produced during the installation of the geomembrane, near seams or at other stress risers. Frequently, the driving force for the failure of liners in uncovered ponds is due to thermal contraction stresses that may result from large changes in ambient temperature with the onset of the winter season if proper precautions are not exercised in the design and installation of the geomembrane.

While several different materials have been used in geomembranes, high density polyethylene (HDPE) is often the material of choice because of its better chemical resistance to degradation by harsh chemicals and aggressive leachates. Like other polymers, polyethylene is a viscoelastic material and, therefore, is susceptible to time-dependent failures at stresses significantly less than its yield strength. Stress rupture tests are frequently performed to evaluate the susceptibility of a geomembrane material to

time-dependent failure. A typical test is the notched constant tensile load (NCTL) test (ASTM 1993). In this test a dumbbell shaped face-notched specimen is subjected to a constant tensile load in the presence of a surfactant (e.g., Igepal) at an elevated temperature, and the time to failure as a function of the applied stress is measured. Examples of the application of this test method to HDPE geomembrane materials along with data can be found in Hsuan et al. (1993) and Lord et al. (1993). Failure at the higher stress levels is characterized by a ductile collapse of the remaining ligament or net section. By contrast, the failure at lower stresses exhibits little ductility at the macroscopic level and generally results from slow crack growth (SCG). The latter failures are often referred to as brittle because of their slit-like appearance even though there is evidence of ductility at the microscopic level.

To date, no quantitative relationship between the time to failure in an NCTL test and the actual service life of a geomembrane liner has been established. Until recently, a similar situation existed for the time-dependent failure of PE natural gas distribution pipes which exhibit the same type of service failures as geomembrane liners. Over the last decade a fracture mechanics methodology has evolved under support from the Gas Research Institute that permits making lifetime forecasts for medium and high density PE gas pipes and fusion joints for the system operating conditions (e.g., internal pressure and temperature) (Kanninen et al. 1990, Popelar, S.F. et al. 1991, Pfeil et al. 1993). In this methodology slow crack growth tests, performed on laboratory fracture specimens, are used to develop empirical relations for the time for initiation of

crack growth and the rate of crack growth as a function of a measure of the crack driving force and temperature. In these tests, temperature and stress are used to accelerate the failure process. The influence of temperature on the crack growth resistance and the life expectancy is quantified through bidirectional shifting (Popelar, S.F. et al. 1993, Pfeil et al. 1993). These data and the crack driving force for defects in the pipe or its joints are used to determine the life expectancy of the component for prescribed operating conditions.

Because of the many similarities between the time-dependent failure in PE geomembrane liners and gas pipes, it is reasonable to expect that the technology developed for predicting the life expectancy of medium and high density PE gas pipes and butt fusion joints can be extended to geomembrane applications. The objective of this paper is to demonstrate that the accelerated testing and fracture mechanics methodology developed for PE natural gas distribution systems can be extended to make realistic and useful forecasts for the durability of geomembranes at service conditions. A long-range goal is to identify manufacturing, seaming, construction, quality assurance, and maintenance procedures that will help ensure the failure-free, long-term service performance of geomembranes.

## 2 FRACTURE MECHANICS METHODOLOGY

### 2.1 Stress Intensity Factor

The stress and strain fields exhibit a  $r^{-1/2}$  singularity at the tip of a crack in a linear viscoelastic continuum (Kanninen and Popelar 1985). The strength of these fields is determined by the stress intensity factor  $K$  which depends linearly upon the applied load and is a function of the crack length and the geometry of the cracked body. Expressions for stress intensity factors of different flawed bodies can be found in fracture mechanics handbooks (e.g., Tada et al. 1985). Strain concentrations at the crack tip in a polymer usually result in the formation of a narrow rarefied (crazed) zone emanating from the tip. Crack growth proceeds by systematic formation and failure of the crazed zone. This zone is not explicitly included in the development of expressions for the crack tip fields. If the size of the crazed zone is small compared to the size of the region over which the singular fields dominate, then it can be argued that whatever happens within the crazed zone must be controlled by the singular crack tip fields. The local crack tip fields will be identical in two flawed bodies for the same loading mode (e.g., Mode I) if their stress intensity factors are equal. Therefore, the crack growth time history in one body can be expected to be the same as that in a second body of the same material, thickness and temperature if their stress intensity factors are equal. Hence, data gathered from one body (e.g., the test specimen) can be transferred to the second body

(e.g., the geomembrane liner) to predict the crack growth history in the latter under its loading.

In general, the stress intensity factor can be expressed as

$$K = \frac{P}{W} \sqrt{\pi a} Y(a/W) \quad (1)$$

where  $P$  is the applied load per unit width,  $a$  is the crack length,  $W$  is the thickness or dimension of the body in the direction of potential crack growth, and  $Y(a/W)$  is a dimensionless function that depends upon the geometry of the cracked body.

### 2.2 Life Prediction

Suppose that the crack growth rate  $da/dt$  and the time  $t_i$  for initiation of crack growth determined in laboratory SCG tests conducted at temperature  $T$  can be correlated with the stress intensity factor and can be expressed functionally as

$$\frac{da}{dt} = F(K; T) \quad (2)$$

and

$$t_i = G(K_o; T) \quad (3)$$

where  $K_o$  is the initial stress intensity factor corresponding to the initial crack length  $a_o$ . Laboratory tests are frequently conducted at temperatures greater than the anticipated service temperature in order to accelerate the crack growth process. Provided that the fracture mode remains brittle, stresses greater than those experienced in the field are often applied in laboratory tests to further accelerate the failure process. The stress intensity factor accounts for different stress levels.

Popelar, C.F. et al. (1990) and Popelar, C.H. et al. (1991), (1993) have demonstrated that material property data for medium and high density PE natural gas pipe materials gathered at temperature  $T$  can be translated to an arbitrary reference temperature  $T_r$  (e.g., the service temperature) through bidirectional shifting. Bidirectional shifting of SCG data requires that time  $t$  and the stress intensity factor  $K$  be replaced by the reduced time  $t/a_T$  and  $Kb_T$ , respectively. The horizontal  $a_T$  and vertical  $b_T$  shift functions are given, respectively, by

$$a_T = \exp[-0.109(T - T_r)] \quad (4)$$

and

$$b_T = \exp[0.0116(T - T_r)] \quad (5)$$



where  $T$  and  $T_R$  are expressed in degrees Celsius or Kelvin (Popelar, C.F. et al. 1990). The horizontal shifting is based upon the classical time-temperature superposition principle for the rate process phenomenon in thermorheologically simple materials. Because of its semicrystalline nature, PE is a thermorheologically complex material. Vertical shifting is required in addition to horizontal shifting to account for variations in its mechanical properties (e.g., slow crack growth resistance) resulting from changes in its crystallinity with temperature. Consequently, Equations (2) and (3) for the crack growth rate and time for initiation of crack growth at the arbitrary temperature  $T_R$  become

$$\frac{da}{dt} = a_T F(Kb_T; T) \quad (6)$$

and

$$t_i = G(K_o b_T; T) / a_T \quad (7)$$

Equation (6) can be viewed as the nonlinear equation of motion for the crack tip and Equation (7) provides the initial condition. The integration of Equation (6) subject to the initial condition of Equation (7) provides the failure time

$$t_f = t_i + \frac{1}{a_T} \int_{a_o}^{a_f} \frac{da}{F(Kb_T; T)} \quad (8)$$

at the reference temperature for isothermal loading wherein  $t_i$  is given by Equation (7) and  $a_f$  is the final flaw size that may be determined from a criterion for unstable crack growth. Equation (8) can be used to predict the life expectancy of a geomembrane for a prescribed loading and initial flaw size  $a_o$  or, conversely, to determine the permissible initial flaw size for a prescribed design life and loading history. The methodology provides a rigorous approach for establishing a quality assurance program which currently relies upon rules of thumb for which there may be no theoretical basis (e.g., scratches and gouges deeper than ten percent of the geomembrane thickness are not permitted).

The task of making estimates for the life expectancy of geomembranes reduces to one of establishing the correlations in Equations (2) and (3), demonstrating that they hold irrespective of the load and initial flaw size, and justifying the use of the shift functions of Equations (4) and (5). The process of establishing these correlations is described in the following sections.

### 3 SLOW CRACK GROWTH TESTS

The 2-mm thick material used in the tests is a HDPE material taken from a liner that served as an uncovered cap of a mixed waste landfill. It had an NCTL ductile/brittle

transition time of approximately 20 hours at 50°C in a 10 percent Igepal solution.

Blanks, 102-mm long by 12.7-mm wide, were cut from this material. A centrally located face notch was sliced into the specimen at a very slow rate with a scalpel blade to minimize damage. The notch depth was systematically varied from 28% to 57% of the liner thickness. The notches were oriented parallel to the extrusion direction.

Grips were attached to the specimens so that the test section was 75-mm long. Figure 1 is a schematic of the SCG test setup which is located in a precision oven for performing controlled elevated temperature tests. The specimen is dead loaded through the core of a liner variable differential transformer (LVDT) which is used to measure the load-point displacement of the specimen that is automatically recorded with an A/D board and a PC. Tests were performed for different combinations of load, initial notch depth and temperature.

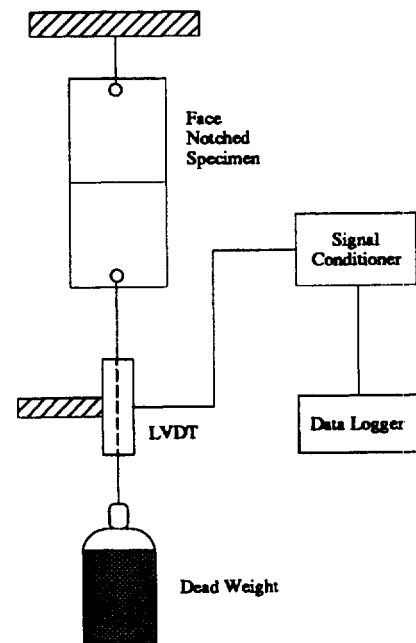


Figure 1. Schematic of slow crack growth test setup.

Figure 2 depicts a typical measured variation of the load-point displacement with time for a test conducted at 81°C. A careful examination of the record reveals an inflection point nearly 25 hours after loading. Empirical data show this point to be the time for initiation of crack growth. Prior to this time the displacement is due to viscoelastic creep of the specimen, and afterwards the displacement is due primarily to crack growth and secondarily to creep. Failure of the specimen occurred approximately 53 hours after loading. Depending upon the initial value of the stress intensity factor and test temperature, typical test durations may vary from a few days to several weeks or more.

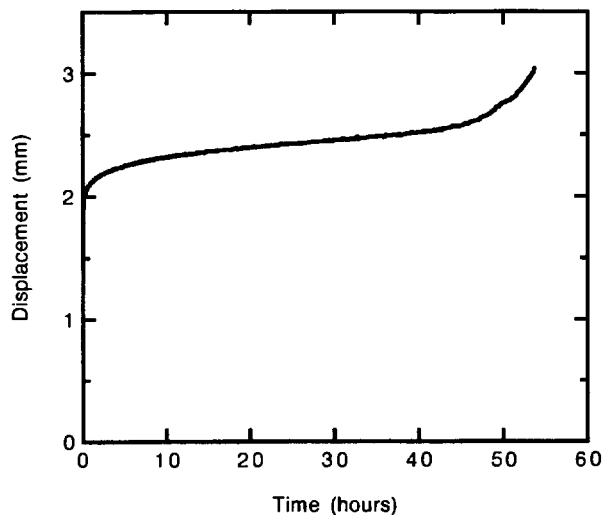


Figure 2. Typical measured load-point displacement history.

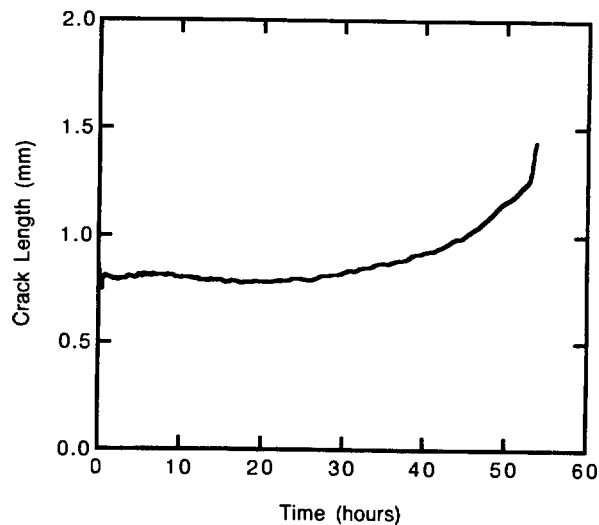


Figure 3. Crack length history deduced from measured load-point displacement record of Figure 2.

#### 4 SLOW CRACK GROWTH RESULTS

Prior to crack initiation, the SCG test can be viewed as a creep test from which the creep compliance of the material can be determined. This creep compliance is used in a quasi nonlinear viscoelastic fracture model (Popelar, S.F. et al. 1993) of the specimen to deduce the crack growth history from the measured load-point displacement record. Figure 3 shows the crack growth history deduced from the load-point displacement record in Figure 2. The validity of this approach was established by comparing the measured crack length at the end of the test with the deduced length. The local slope of the curve in Figure 3 provides the crack growth rate  $da/dt$ , and the crack length and load determine the corresponding stress intensity factor  $K$  per Equation (1).

Figure 4 shows the correlation of the stress intensity factor with the crack speed for tests conducted at 61°C and 81°C. The straight lines represent the best least square power law fit to the respective data. While there is some scatter in the data, the stress intensity factor appears to be an appropriate fracture mechanics parameter for characterizing SCG — considering that results are for a variety of loads and initial notch lengths. Figure 5 depicts the correlation of the time for initiation of crack growth  $t_i$  with the initial stress intensity factor  $K_0$  from tests at 61°C and 81°C. The accelerating influence of an elevated temperature on the crack growth rate and the initiation time is clear from these figures.

The bidirectional shifting method, using the shift functions established for PE gas pipe materials, can be used to develop master curves. Figures 6 and 7 depict, respectively, the resulting master curves at a reference temperature of 81°C for the crack growth rate and the time

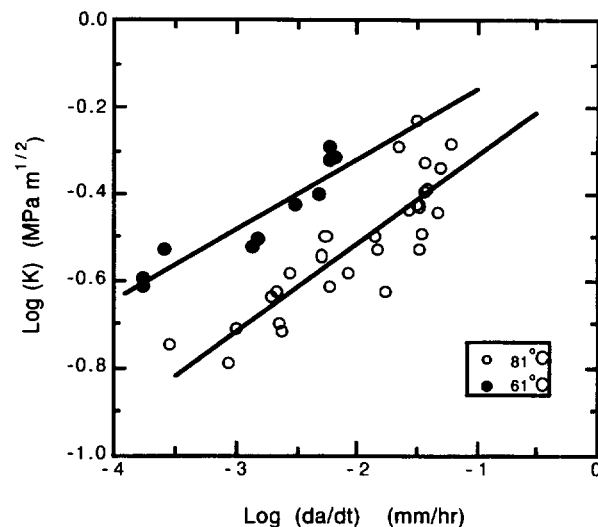


Figure 4. Correlation of the stress intensity factor and the crack growth rate at 61°C and 81°C.

for initiation of crack extension. These master curves exhibit good coherence with the shifted 61°C data interspersed with the 81°C data. Note that the reference temperature is completely arbitrary and has no influence upon the coherence of the master curve. The straight lines are best least square fits to the data and are given by

$$da/dt = F(K; 81^\circ\text{C}) = 6.8K^{5.3} \quad (9)$$

and

$$t_i = G(K_0; 81^\circ\text{C}) = 5.44 \times 10^{-4} K_0^{-6.9} \quad (10)$$

liner's installation temperature is 50°C. While the ambient temperature was assumed to remain constant in this example, seasonal changes can be included. In this case not only will the thermal stress and, hence, the crack driving force vary with time, but also the shift functions will vary with time. These time-dependencies must be taken into consideration when integrating the equation of motion for the crack tip, Equation (6).

The purpose of Figure 8 is simply to illustrate the fracture mechanics methodology and several simplifications were made in developing it. The influence of stresses other than thermal ones is neglected and will further reduce the life expectancy. The mean data for the initiation time and crack growth rate were used. A more detailed statistical analysis could be used to provide predictions for a prescribed confidence level which may additionally reduce the life expectancy by as much as a decade.

## 5 CONCLUSIONS

An investigation of SCG in a HDPE geomembrane material has been performed. A fracture mechanics methodology for predicting the life expectancy of geomembranes for service conditions has been developed and demonstrated for a surface crack that grows through the thickness of the liner. The methodology, which is based upon earlier developments for PE natural gas pipes, can be used to predict the life expectancy of a liner for prescribed service loads and size of an initial defect, or to determine the permissible initial defect size for prescribed service loading and life. SCG tests at different temperatures were conducted for specimens having various initial notch depths and loads. Correlations between the stress intensity factor and the time for initiation of crack extension, and the crack growth rate demonstrate that the stress intensity factor is an appropriate measure of the crack driving force in this HDPE material. Coherent master curves for the initiation time and crack growth rate were obtained using the bidirectional shifting method and shift functions developed for PE pipes. The accelerated testing approach, presented herein, permits developing critical SCG data for making long-term durability assessments (e.g., lifetime forecasts on the order of 100 years or more) relatively quickly. An example was presented that demonstrated how the methodology may be used to establish a rational basis for specifying inspection requirements and quality control and assurance standards. Finally, it is through a methodology of the type presented herein that the long-term performance of PE geomembranes can be quantified.

## ACKNOWLEDGMENTS

The authors are grateful to the Electric Power Research Institute for the support of this work under Contract Number WO1457-13 and to Project Manager, Dean Golden.

## REFERENCES

- ASTM (1993) "Standard Test Method for Evaluation of Stress Crack Resistance of Polyolefin Geomembranes Using Notched Constant Tensile Load Test," ASTM D 5397-93, American Society for Testing Materials, Philadelphia, pp. 356-359.
- Hsuan, Y.G., Koerner, R.M., and Lord A.E., Jr. (1993) "Notched Constant Tensile Load (NCTL) Test for High-Density Polyethylene Geomembranes," *Geotechnical Testing Journal*, Vol. 16, pp. 450-457.
- Kanninen, M.F., O'Donoghue, P.E., Popelar, C.H., and Kenner, V.H. (1990) "A Viscoelastic Fracture Mechanics Assessment of Slow Crack Growth in Polyethylene Gas Distribution Pipe Materials," *Engineering Fracture Mechanics*, Vol. 36, pp. 903-918.
- Kanninen, M.F. and Popelar, C.H. (1985) *Advanced Fracture Mechanics*, Oxford University Press, New York.
- Lord, A.E., Jr., Hsuan, Y.G., and Koerner, R.M. (1993) "Time-Temperature Superposition in Mechanical Durability Testing of Polyethylene Geomembranes," *Geotechnical Testing Journal*, Vol. 16, pp. 259-262.
- Peggs, I.D., and Carlson, D.S. (1988) "Stress Cracking of Polyethylene Geomembranes: Field Experience," *Durability and Aging of Geosynthetics*, (R.M. Koerner, Ed.), Elsevier Applied Science, London, pp. 195-271.
- Pfeil, M.C., Kenner, V.H., and Popelar, C.H. (1993) "A Fracture Mechanics Evaluation for the Life Expectancy of Polyethylene Butt Fusion Joints," *Engineering Fracture Mechanics*, Vol. 44, pp. 91-107.
- Popelar, C.F., Popelar, C.H., and Kenner, V.H. (1990) "Viscoelastic Material Characterization and Modeling for Polyethylene," *Polymer Engineering and Science*, Vol. 30, pp. 577-586.
- Popelar, C.H., Kenner, C.H., and Wooster, J.P. (1991) "An Accelerated Method for Establishing the Long Term Performance of Polyethylene Gas Pipe Materials," *Polymer Engineering and Science*, Vol. 31, pp. 1693-1700.
- Popelar, C.H. (1993) "A Comparison of the Rate Process Method and the Bidirectional Shifting Method," *Proceedings of the Thirteenth International Plastic Fuel Gas Pipe Symposium*, American Gas Association, November 1-4, pp. 151-161.
- Popelar, S.F., Popelar, C.H., and Kenner, V.H. (1991) "Creep Crack Growth in Joints of a Thermoplastic," *International Journal of Fracture*, Vol. 50, pp. 115-130.
- Popelar, S.F., Popelar, C.H., and Kenner, V.H. (1993) "Time-Dependent Fracture of Polyimide Film," *Journal of Electronic Packaging*, Vol. 115, pp. 264-269.
- Tada, H., Paris, P.C., and Irwin, G.R. (1985) *Stress Analysis of Cracks Handbook*, Second Edition, Paris Productions Inc., St. Louis.



# Temperature Effect on the Stress Crack Resistance of High Density Polyethylene Geomembranes

Y. G. Hsuan

GRI, Drexel University, Philadelphia, PA 19104

**ABSTRACT:** The current status of stress crack resistance testing of HDPE geomembranes is the single point notched constant tensile load (SP-NCTL) test per ASTM D 5397-appendix. Since more than 200 hours is required to arrive at an acceptance decision, the quest is to use higher temperature to reduce the testing time. The results of this study indicate that the testing temperature can be increased to 70°C to obtain the maximum acceleration on the failure time. Using this temperature, instead of the current standard temperature of 50°C, results in an additional acceleration factor of 4.7 over the factors inherent in the test method itself. Using 70°C it is possible that a quality control procedure can be crafted to give a "go/no go" result within 48 hours.

**KEYWORDS:** stress crack resistance, slow crack growth, polyethylene, geomembrane.

## 1 INTRODUCTION

Stress cracking as defined in ASTM D883 is "an external or internal crack in a plastic caused by a tensile stress less than its short-term mechanical strength". The stress cracking mechanism can be divided into two categories: rapid crack propagation and slow crack growth. Cracking that is caused by the rapid crack growth mechanism takes place extremely fast and generally extends to a large area by shattering in a dendritic pattern. This type of failure does not commonly occur in the high density polyethylene (HDPE) geomembrane unless subzero temperatures exist (Peggs 1990). Comparatively, cracking that is induced by the slow crack growth mechanism proceeds relatively slowly and is generally limited in its extent. The crack propagation rate varies with the material, magnitude of the tensile stress and temperature. Cracks caused by slow crack growth have been observed in HDPE geomembranes used as surface impoundment liners. (Hsuan, et. al., 1993; Peggs and Carlson, 1988). Such field observations indicate the importance of slow crack growth resistance of HDPE geomembranes with respect to their long term performance. An effective test method should be utilized to assess such property in the minimum amount of testing time.

In the United States, the ASTM D 5397 "Notched Constant Tensile Load (NCTL) Test" is the standard method to evaluate slow crack growth resistance, generally called the stress crack resistance (SCR), of HDPE geomembranes. The incubation conditions specified in the method include a constant temperature immersion at 50°C and a specific incubation solution which consists of 10% surfactant (Igepal® CO-630) mixed with 90% tap water. Both the temperature and incubation solution have an accelerating effect on the crack propagation rate, in particular the temperature (Lord et. al., 1993). However, in the HDPE polyethylene pressure gas pipe industry, 80°C is the commonly used incubation temperature to accelerate crack growth rates (Brown 1993). For HDPE geomembranes, Thomas and Siebken (1997) performed the NCTL test at

80°C using a different surfactant (CA-720). They have found a good correlation between test results at 50°C and 80°C incubation. However, there was no available data at the intermediate temperatures.

This paper presents the result of a series of NCTL tests performed at temperatures of 50, 60, 70 and 80°C in an incubation medium of 10% CA-720 and 90% water. Two different geomembranes were evaluated to verify the effect of temperature on crack growth rate in such a surfactant solution environment.

## 2 TEST MATERIALS

Two commercially available HDPE geomembranes were included in this study. They are designated as Samples A and B. The nominal thickness of both samples is 1.5 mm. The geomembranes were produced by different manufacturers and by different processes: blown sheet and flat sheet extrusion. The density, crystallinity and melt index values are given in Table 1.

Table 1. Material properties of Samples A and B.

Property	ASTM Method	Sample A	Sample B
Density (g/ml)	D 1505	0.9492	0.9490
Melt Index (g/10 min.)	D 1238	0.29	0.15
Heat of Fusion* (J/kg)	D 4037	123	124

\* Heat of Fusion is directly proportional to crystallinity of the polymer

## 3 TEMPERATURE EFFECT ON TENSILE YIELD BEHAVIOR

The tensile yield properties of the geomembranes was evaluated according to ASTM D 638 Type IV. These data are necessary since the NCTL test is performed at given percentages of the yield stress. Furthermore, the yield stress

varies with temperature and it must be evaluated accordingly. Tests were performed in an environmental chamber in order to achieve the designated temperatures which varied from 20 to 80°C.

Thomas and Siebken (1997) found that the yield stress decreased as the test temperature increased in a linear relationship. Similar behavior was also obtained for the two geomembranes used in this study. Figure 1 shows the effect of temperature on the yield stress of Samples A and B. The slope of the line, which may be related to the percent crystallinity of the polyethylene, is 0.23 MPa/°C.

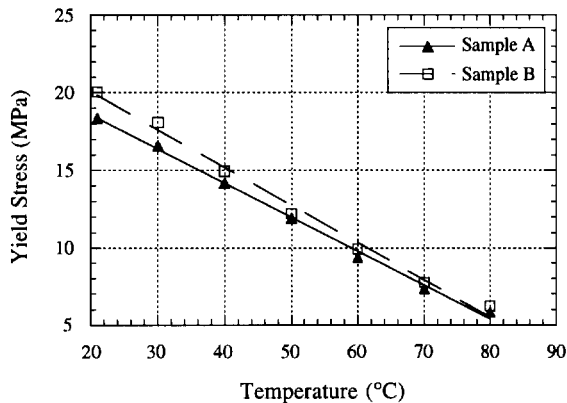


Figure 1. Tensile yield stress at different temperatures.

Besides lowering the yield strength, the increase in temperature actually influences the yielding behavior of the test specimens. Figure 2 shows the stress/strain curves of Sample A at different test temperatures. The yield region consists of two peaks, referred to as double yielding. This complex yielding behavior was observed in a variety of polyethylene copolymers by Lucas et. al. (1995). As temperature is increased, the first yield peak gradually diminishes whereas the second yield peak becomes more

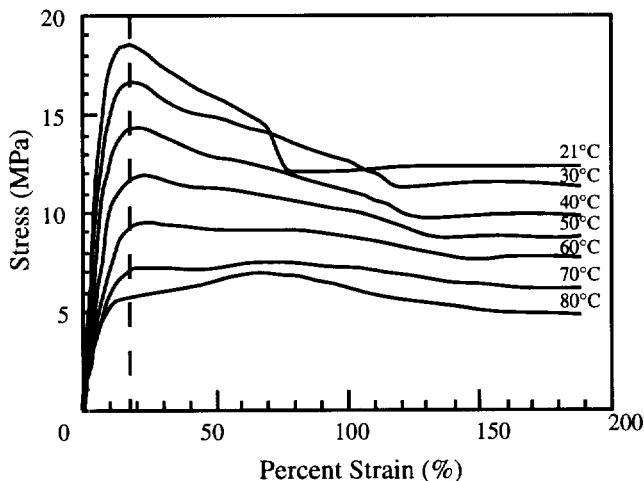


Figure 2. The yield behavior at different temperatures

pronounced. In both geomembrane samples, the second peak became the predominant yield peak at temperatures above 70°C. Lucas et. al. (1995) have proposed that the first peak corresponds to the yielding of original perfect crystallites in the material. The second peak is induced by the yielding of the newly formed crystallites. As the test temperature increases, the energy requirement for secondary recrystallization is reduced. A greater amount of less perfect crystallites can be melted and recrystallized. As a result, an enhanced second yield peak is obtained, particularly above 70°C.

In this study, the first yield peak was used to analyze the temperature effect on the yield stress, and it was also utilized to calculate the applied stress of NCTL tests.

#### 4 TEMPERATURE EFFECT ON STRESS CRACK RESISTANCE

The stress crack resistance (SCR) of Samples A and B were evaluated by the NCTL test. This section presents the test details and results of the NCTL tests.

##### 4.1 NCTL Test Procedures

The NCTL test was performed according to ASTM D5397 at temperatures of 50, 60, 70 and 80°C. The incubation solution used in the test consisted of 10% surfactant with 90% of water. Instead of a minimum of 10 applied stresses as required in the standard method, only the lower stresses that induce brittle failure were utilized. This included applied stresses ranging from 15 to 30% of the yield stress at room temperature. Three specimens were tested at each stress level. The failure time of each specimen was recorded to the nearest 0.1 hour. The average failure time was used in the data analysis.

Due to the high elevated testing temperatures used in the study, a different surfactant was used than the one specified in the standard method. As explained by Thomas and Siebken (1997), the surfactant CO-630, which is a type of ethoxylated alkylphenol compound, becomes immiscible with water in a temperature range of 52-56°C. Thus another type of ethoxylated alkylphenol, CA-720, was selected due to its high immiscible temperature range, that being 86-90°C. Furthermore, CA-720 is rather sensitive to NaCl. If it is mixed with 10% NaCl solution, the immiscible temperature range drops to 56-60°C. To minimize such effect, deionized water was used throughout the study.

##### 4.2 NCTL Test Results and Analysis

The NCTL test data are presented by plotting percent yield stress against average failure time on a log-log scale. Figures 3 and 4 present the brittle response curves for Samples A and B, respectively. The slopes of these curves are very similar, indicating that the same failure mechanism took place in all tests.

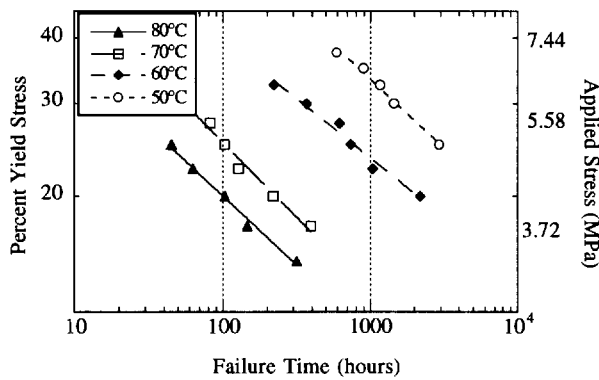


Figure 3. NCTL test response curves for Sample A.

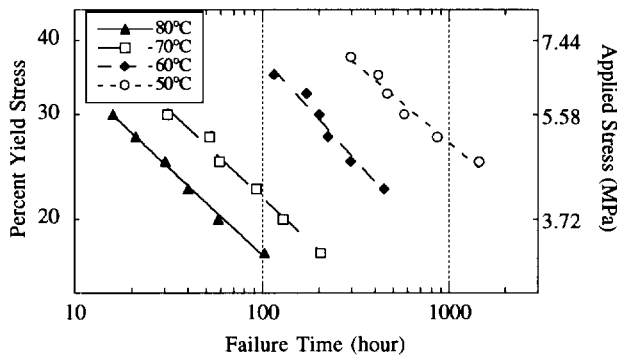


Figure 4. NCTL test response curves for Sample B.

In the above curves, the failure time decreased as the testing temperature increased, indicating that crack propagation was accelerated by the temperature. However, the acceleration seems to slow down between 70 and 80°C in comparison to the lower temperatures. The actual temperature effect on the failure time is unable to be evaluated by presenting the data using percent yield stress at room temperature, as shown in Figures 3 and 4. This is because the yield stress also decreased as temperature increased.

To determine the temperature dependence on the time to failure, the applied stress at each test temperature is normalized to the corresponding yield stress at that temperature. The normalized stress ( $\sigma/\sigma_y$ ) data is plotted against average failure time on a log-log scale as shown in Figures 5 and 6 for Samples A and B, respectively. The resulting curves are somewhat different to those appearing in Figures 3 and 4. The 70 and 80°C lines overlap one another. This implies that there is no temperature acceleration at elevated temperatures above 70°C. In other words, at a same percent yield stress, a similar failure time will be obtained at temperatures of 70 and 80°C and presumably (although not evaluated) still higher temperatures.

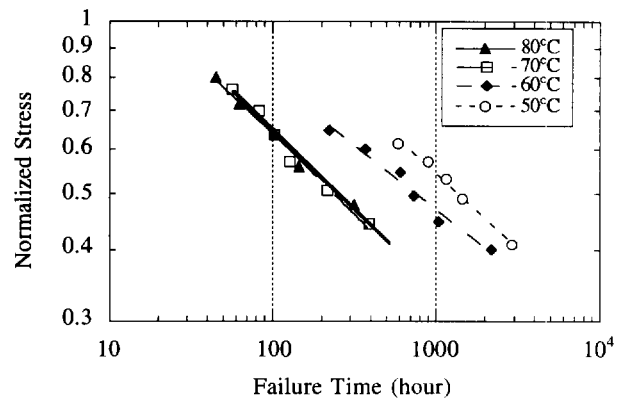


Figure 5. Normalized stress vs. failure time for Sample A.

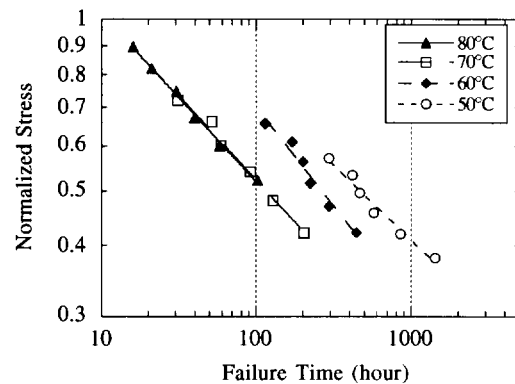


Figure 6. Normalized stress vs. failure time for Sample B.

Conversely, from 50 to 70°C, temperature clearly accelerates the crack growth rate. The relationship between temperature and failure time can be expressed by the Arrhenius equation, shown as Equation 1. Figure 7 presents an Arrhenius plot at four different normalized stresses for both Samples A and B. A linear relationship is obtained. The same behavior was also found for Sample B. The activation energy of the failure mechanism is found from the slope of the lines to be 73.5 kJ/mol.

$$t_f = A \exp(E/RT) \quad (1)$$

where:

- $t_f$  = failure time (minutes)
- A = constant
- E = activation energy (= 73.5 kJ/mol)
- R = gas constant (8.31 J/mol.K)
- T = temperature (K)

Similar tests were performed by Lu and Brown (1990) on a HDPE pipe resin in forced air ovens at temperatures from 24 to 80°C. A linear relationship between failure time and inverse temperature was obtained up to 70°C. Also the linearity ceased at 80°C for the low applied stresses. The failure time at 80°C was somewhat similar to that obtained

at 70°C. This may suggest that the unexpected SCR behavior found at 80°C test on geomembranes was not induced by this particular test environment but by the change in the material, such as secondary recrystallization. Tests performed in both water and air could verify whether the unexpected behavior observed at 80°C is due to internal or external factors. Such experiments are currently ongoing.

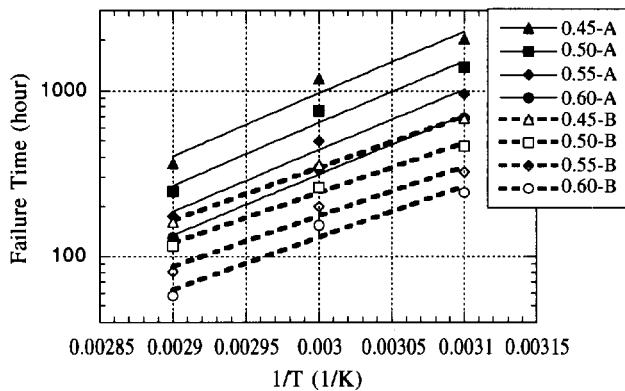


Figure 7. Failure time against inverse temperature at different normalized stresses for Samples A and B.

Regarding the temperature acceleration factor (AF), at the same normalized stress value of 0.5, the average AF of two tested samples between 50°C and 70°C is 4.7. Using the current SCR specification (GRI-GM 10, 1997), a minimum failure time of 200 hours at 30% yield stress of room temperature at test temperature of 50°C is required. After being normalized to the yield stress at corresponding test temperature, the 30% becomes 50% of the yield stress at 50°C. Thus at the same normalized stress, i.e., 50% yield stress at 70°C, the failure time will be 4.7 times faster, reducing the testing time to 43 hours. (Note that the 50% yield stress at 70°C is approximately equal to 20% of the yield stress at room temperature).

## 5 SUMMARY AND CONCLUSION

The effect of temperature on SCR of two HDPE geomembrane samples was evaluated at temperatures of 50, 60, 70 and 80°C using the brittle region of the NCTL test. Additionally, tensile tests were performed at these temperatures to obtain the corresponding yield stress (which decreased linearly as temperature increased).

For the NCTL test results, the failure time decreased as temperature increased. From 50 to 70°C, the failure time increased exponentially with the temperature. However, the acceleration seems to cease between 70 and 80°C.

The results of this study indicate that the maximum temperature that can provide acceleration in performing the NCTL test is 70°C. At the same normalized stress value,

the failure time at 70°C is 4.7 times faster than that at 50°C.

## ACKNOWLEDGMENT

The funding of this research was provided by the Geosynthetic Institute's Consortium of Member Organizations. The author also appreciates the assistance of Mr. Derrick Whitaker in performing the tensile tests. Mr. Whitaker is supported by NSF Research Experience for Undergraduates Program, Project number CMS-9312772.

## REFERENCES

- Brown, N. and Lu, X (1993) "Controlling the Quality of PE Gas Piping Systems by Controlling the Quality of the Resin" Proceedings of Thirteenth International Symposium for Plastic Fuel Gas Pipe, San Antonio, TX, Nov. Published by American Gas Association, pp. 327-338.
- Hsuan, Y.G. Koerner, R.M. and Lord, A.E. Jr. (1993) "Stress-Cracking Resistance of High Density Polyethylene Geomembranes" Journal of Geotechnical Engineering, ASCE, Vol. 119, No. 11, pp. 1840-1855.
- Lord, A.E. Jr. Hsuan, Y.G. and Koerner, R.M. (1993) "Time-Temperature Superposition in Mechanical Durability Testing of Polyethylene Geomembranes" Geotechnical Testing Journal, GTJODJ, Vol. 16, No. 2, pp. 259-262.
- Lu, X. and Brown, N. (1990) "The Ductile-Brittle Transition in a Polyethylene Copolymer" Journal of Materials Science, 25, pp. 29-34.
- Lucas, J.C. Failla, M.D. Smith, F.L. and Mandelkern, L. (1995) "The Double Yield in the Tensile Deformation of the Polyethylenes", Polymer Engineering and Science, Vol. 35, No. 13, pp. 1117-1123.
- Peggs, I.D. Carlson, D.S. and Peggs, S.J. (1990) "Understanding and Preventing "Shattering" Failures of Polyethylene Geomembranes", Proceedings of Fourth International Conference on Geotextiles, Geomembranes and Related Products, The Hague, pp. 549-554.
- Peggs, I.D. and Carlson, D.S. (1988) "Stress Cracking of Polyethylene Geomembranes: Field Experience" *Durability and Aging of Geosynthetics*, R.M. Koerner ed., Elsevier, pp. 195-271.
- GRI-GM 10 (1997) "Specification for the Stress Crack Resistance of HDPE Geomembrane Sheet", Geosynthetic Institute, Philadelphia, PA 19104.
- Thomas, R.W. and Siebken, J. (1997) "Increasing the Temperature of the Notched Constant Tensile Load Environmental Stress Crack Resistance Test" Geosynthetics'97 Conference Proceedings, IFAI, St. Paul, MN., pp. 191-200.



# Antioxidant Depletion During Thermal Oxidation of High Density Polyethylene Geomembranes

Y. G. Hsuan  
GRI, Drexel University, Philadelphia, PA 19104

Z. Guan  
GRI, Drexel University, Philadelphia, PA 19104

**ABSTRACT:** In this study, forced air oven aging was utilized as the acceleration procedure to simulate the thermo-oxidation process in five high density polyethylene (HDPE) geomembranes containing different antioxidant packages. The geomembrane coupons were incubated at four different temperatures; 115, 95, 75 and 65°C. After a predetermined period of time, incubated coupons were removed from the oven and subsequently evaluated for the consumption of antioxidants, along with possible changes of physical and mechanical properties. The consumption of antioxidants with time was monitored by both standard oxidative induction time (Std-OIT) and high pressure oxidative induction time (HP-OIT) tests. The results indicate that both OIT tests can effectively track the consumption of antioxidants that consist of hindered phenols and phosphites. However, for antioxidant packages that contain thiosynergists or hindered amines, the HP-OIT is the appropriate test. The study also demonstrates that the tensile break properties of the geomembrane remain unchanged until all the antioxidants are consumed. Based on the reduction rate of OIT, the depletion time of antioxidants at a 20°C site temperature was extrapolated using the Arrhenius equation. The average depletion time of hindered phenol and phosphite types of antioxidants is 80 years. The addition of thiosynergists and hindered amines further extended the depletion time in an amount which is still under investigation.

**KEYWORDS:** oxidative induction time, aging, polyethylene, geomembrane, oxidation.

## 1 INTRODUCTION

High density polyethylene (HDPE) geomembranes have been widely used as liquid barriers in landfill applications for both liners and covers. Since geomembranes in such applications are typically covered by soil or by other geosynthetics; neither sunlight nor elevated temperatures are of concern. However, oxidation remains as a key degradation mechanism regarding the long-term durability of the material. For protection against oxidation during the service period, antioxidants are added into the formulation of the geomembrane. As long as antioxidants are present in the material, the physical and mechanical properties of the geomembrane can be preserved (Hsuan and Koerner, 1997). Thus the long term performance of HDPE geomembranes is greatly dependent on the depletion time of the antioxidants.

There are many different types of antioxidants and each performs somewhat differently. Oven aging is the most commonly used laboratory incubation method to investigate the performance of antioxidants in polymers (Gray, 1990; Gugumus, 1996). Coupons are incubated in forced air ovens at elevated temperatures for a sufficient time so as to deplete the antioxidants and start the oxidative degradation process. At that time, the physical and mechanical properties of the material begin to degrade. The temperature of the ovens should be high enough to increase the reaction in order to obtain results within a reasonable time frame, but cannot be too high that the reaction mechanism and material's structure are altered. Temperatures as high as 110°C to 120°C have been utilized in evaluating HDPE geomembranes by researchers (Gray, 1990; Thomas and Ancelet, 1993; Yim and Godin, 1993).

In this study, five different commercially available HDPE geomembranes were incubated in four ovens at

temperatures of 115, 95, 75, and 65°C. The incubated coupons were periodically removed from the ovens and were then evaluated for their remaining antioxidants using two types of oxidative induction time (OIT) tests together with the physical and mechanical properties.

## 2 INCUBATION TEST PROCEDURES

The oven aging incubation procedure was performed according to ASTM D5271. Coupons with dimensions 100 mm wide and 180 mm long were taken from each geomembrane sample. The coupons were freely hanging in forced air ovens maintained at temperatures of 115, 95, 75, and 65°C.

Specimens were taken from the incubated coupons at a monthly intervals for antioxidant evaluation. They were taken at three month intervals for physical and mechanical tests.

## 3 EVALUATION TESTS

Properties of the incubated coupons were monitored by thermal analytical, physical and mechanical tests. Table 1 shows the tests that were included in this study.

Table 1. Test used to evaluate incubated geomembranes.

Test	ASTM Method	Property Evaluated
Std-OIT	D3895	Amount of antioxidant
HP-OIT	D5885	Amount of antioxidant
Melt Index	D1238	Molecular weight
Tensile	D638 - IV	Stress and strain

The depletion of antioxidants were monitored by two OIT tests. OIT is the time required for the geomembrane test specimen to be oxidized under a specific pressure and temperature. For the same antioxidant package (type and amount), the OIT is proportional to the quantity of the antioxidant (Howard, 1973). However, for different antioxidant packages, direct comparison between two single OIT values can be misleading and caution must be used.

Once the polymer starts to oxidize, there will be either a cross-linking reaction or a chain scission reaction taking place, resulting in a change in molecular weight. The melt index test is a qualitative method to assess molecular weight of polymers. A decrease in melt index value indicates an increase in the molecular weight (i.e., crosslinking) and vice versa. Melt index tests were performed only at the incubating temperatures of 115 and 95°C.

As the oxidation proceeds further, it will eventually induce changes in the engineering properties such as tensile properties. Five tensile parameters are included in the analysis: modulus, yield stress and yield strain, and break stress and break strain. It should be recognized that break strain has the greatest sensitivity towards molecular changes in the polymer. Again, only coupons at the two higher incubation temperatures were tested for tensile properties.

#### 4 TEST MATERIALS

Five commercially available HDPE geomembranes were included in the study. They are designated as Samples A to E. All samples have a nominal thickness of 1.5 mm. The five geomembranes were produced by four manufacturers. They included both blown sheet and flat sheet extrusion processes. The physical and chemical properties of the original unaged material were evaluated and the data is presented in Table 2.

Table 2. Average properties of original geomembrane

Sample	Anti-oxidant <sup>1</sup>	MI <sup>2</sup> (g/10 min)	Std-OIT <sup>3</sup> (min)	HP-OIT <sup>4</sup> (min)
A	a	0.23	122±7%	262±6%
B	a	0.15	129±1%	280±1%
C	a	0.29	156±5%	368±3%
D	b	0.15	1267%	1125±12%
E	c	0.46	144±9%	1499±9%

Note:

- a = hindered phenols & phosphites  
b = hindered phenols, phosphites & thiosynergists  
c = hindered phenols, phosphites & hindered amines
- MI = melt index
- Std-OIT = Standard OIT
- HP-OIT = High pressure OIT

Regarding the antioxidant package in each geomembrane, only the type (not the quantity) of each antioxidant component was known.

The original Std-OIT values were very similar in all five samples even though they contained different antioxidant packages. Contrary, a large difference in the HP-OIT values was observed. The thiosynergists and hindered amines led

to a much higher OIT value in Samples D and E. This is because these two antioxidants have a maximum effective temperature below 200°C (Fay and King, 1993). Subsequently, their performance cannot be properly evaluated by the Std-OIT test which uses an isothermal temperature of 200°C. On the other hand, at an isothermal temperature of 150°C in the HP-OIT test, the presence of these two types of antioxidants was able to be assessed. Thus, the HP-OIT is the proper test for antioxidant packages containing thiosynergists or hindered amines.

#### 5 TEST RESULTS AND DISCUSSION

Since the focus of this paper is on the depletion of the antioxidants, the OIT results will be emphasized.

##### 5.1 Results of Std-OIT and HP-OIT Tests

The test data indicate that the normalized Std-OIT decreased exponentially over time regardless the antioxidant package type, see Figures 1 and 2. The reduction behavior was very similar for Samples A, B and C. On the other hand, the OIT depletion rate of Samples D and E increased greatly at incubation temperatures 95°C and 115°C, particularly for Sample D.

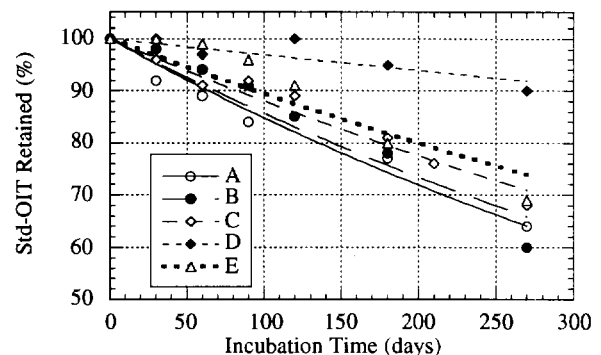


Figure 1. Change in percent retained of Std-OIT values at an incubation temperature of 65°C

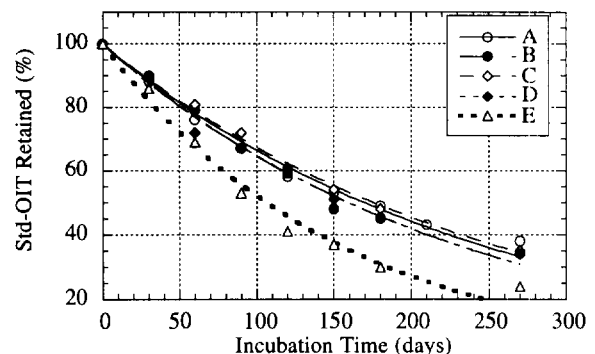


Figure 2. Changes in percent retained of Std-OIT values at an incubation temperature of 95°C

In comparison, the HP-OIT exhibited different responses depending on the antioxidant package, as shown in Figures 3 and 4. Samples A, B and C which contained the same antioxidant types behaved similarly; their OIT values decreased exponentially with incubation time at all incubation temperatures.

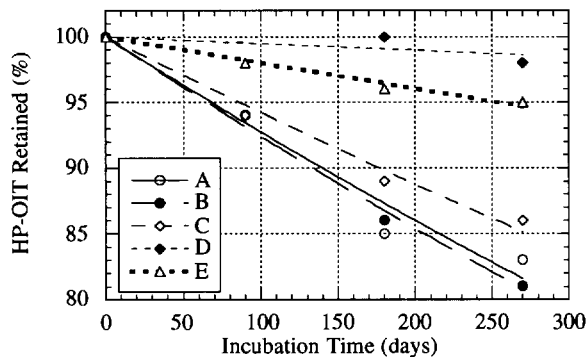


Figure 3. Changes in percent retained of HP-OIT values at an incubation temperature of 65°C.

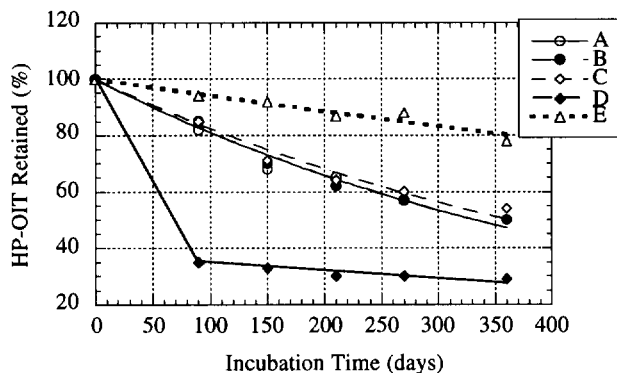


Figure 4. Changes in percent retained of HP-OIT values at an incubation temperature of 95°C.

Similar to the Std-OIT, Sample D which consists of thiosynergists also showed a rapid depletion in OIT values at 95°C and 115°C incubation temperatures. However, the OIT value maintained almost unchanged after the significantly drop in the first 90 days. The rapid reduction in OIT values at 95°C and 115°C suggest that substantial amount of thiosynergist was quickly consumed at these two elevated incubation temperatures. Since the depletion occurred within such short period, as indicated by the HP-OIT results, volatilization probably was the primary consumption mechanism rather than oxidation. There may be a high concentration of thiosynergists near the surface of the coupons. The depletion rate for the remaining additives seems to be relatively slow and is sufficient to protect the geomembrane from being oxidized.

For Sample E, which contained hindered amines, its OIT value decreased exponentially with time but at a much

slower rate than samples with only phosphite and hindered phenols.

## 5.2 Comparing Std-OIT, HP-OIT and Other Material Properties

In order to demonstrate the importance of the antioxidants toward the long term physical and mechanical properties of the geomembrane, changes in MI value and tensile properties are compared to the two OIT results at incubation temperatures of 115 and 95°C.

Since Samples A, B and C contain the same antioxidant types, their properties behaved in a similar manner throughout the incubation period. Sample A was selected to represent this group of three samples. Figures 5 and 6 depict the change of each property with incubation time at 95°C and 115°C, respectively.

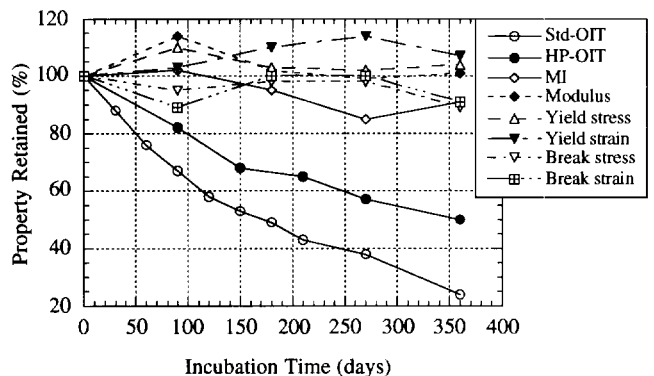


Figure 5. Changes in properties with incubation time at 95°C for Sample A.

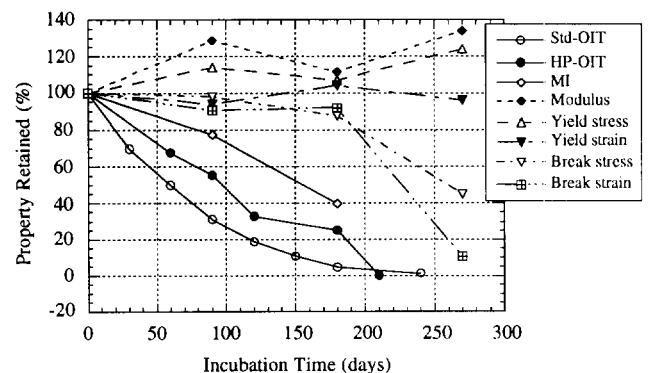


Figure 6. Changes in properties with incubation time at 115°C for Sample A.

Based on Figures 5 and 6, the behavior of this group of geomembranes can be summarized as follows:

- The depletion of antioxidants using both Std-OIT and HP-OIT measurements were very similar. Actually, a linear correlation was found between them. Thus either

one of the tests can be used to evaluate these types of antioxidant packages.

- Regarding the correlation between OIT and tensile properties, the data at 115°C indicates that tensile break properties remain essentially unchanged as long as antioxidants are still present. After 180 days, the tensile break properties dropped significantly when both OIT values approached zero.
- As for the MI value, it behaved differently at these two incubation temperatures. At 115°C, the MI value decreased steadily with time even though the OIT was still at a fairly high value. Such behavior was also observed by Thomas and Ancelet (1993) under similar test environment. However, at 95°C, the MI value remained largely unchanged while the Std-OIT value decreased to 20%. Hsuan and Koerner (1997) observed essentially no changes in MI value as the Std-OIT decreased to less than 10% at temperature of 85°C in a soil incubation condition. The decrease in MI value at 115°C probably was due to cross linking resulted from oxidation reactions. Since the onset of the melting peak begins at about 60°C and reaches the peak at 128°C, some amount of the crystalline phase are in the molten stage at 115°C. Such change in microstructure can substantially enhanced the oxidation degradation which most likely not occurs at the low service temperature. Thus the incubation temperature at 115°C seems to be too high to evaluate the durability of HDPE geomembranes.
- Regarding the MI value in evaluation of polymer degradation, it probably has a higher sensitive than the tensile test. However, it may be difficult to establish a correlation with the tensile behavior. Data from longer incubation times could verify this hypothesis.

For Samples D and E, their change of properties with time at 115°C are given in Figures 7 and 8, respectively. The Std-OIT and HP-OIT behaved very differently for both samples. In Sample D, the Std-OIT value gradually decreased to less than 5% in 270 days, whereas the HP-OIT value maintained at 20% after the initial rapid reduction. In spite of the low Std-OIT value, the tensile properties remained unchanged. Sample E is somewhat similar to Sample D in their Std-OIT results. After 270 days, the Std-OIT value reached 2% while the HP-OIT value was still at 60%. Clearly, the presence of hindered amines was being detected by the HP-OIT. At the same time, the tensile properties showed no significant changes. The test data further confirmed that the HP-OIT test reflects more the "true" state of the antioxidants present in these two geomembranes. The Std-OIT test measures mainly the depletion of the hindered phenol and phosphite antioxidants.

Regarding the MI value, again a reduction was only detected at 115°C in both samples. Sample D showed the least decrease in the MI value than all other four geomembranes.

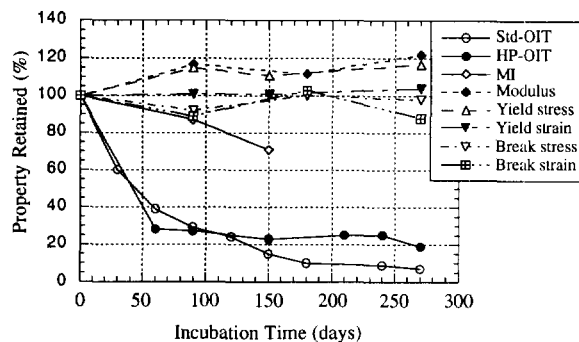


Figure 7. Changes in properties with incubation time at 115°C for Sample D

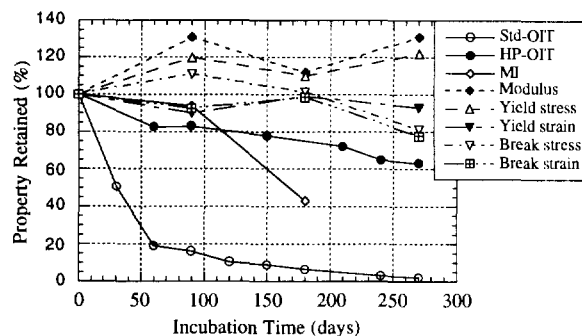


Figure 8. Changes in properties with incubation time at 115°C for Sample E.

## 6 ANTIOXIDANT DEPLETION TIME

The significance of antioxidants to the longevity of the geomembranes has been qualitatively illustrated. It is of value to use this data to quantify the depletion time of the antioxidants, since within this time period, the engineering properties of the geomembrane are unchanged. In this section, the methodology used to predict the depletion time of the antioxidants is based on OIT reduction rates obtained from three elevated incubation temperatures. Data obtained from the 115°C is not included due to the possible changes in the material's structure as stated earlier. Furthermore, Samples D and E were not analyzed. The evaporation of the antioxidants in Sample D, make the high temperature data not possible to be analyzed. For Sample E, the current reduction in the HP-OIT value at the lower incubation temperatures are too small to actually predict the depletion rates.

For Samples A, B and C, the depletion of OIT decreased exponentially with time. The generalized equation for OIT depletion curves as those shown in Figures 1 and 2 can be expressed by Equation (1). The depletion rate of the OIT at each incubation temperature can be determined by curve fitting.

$$\text{OIT} = P * \exp(- S*t) \quad (1)$$

where:

$$\text{OIT} = \text{OIT time (min.)}$$

- P = original OIT of the geomembrane (min.)  
 S = OIT depletion rate (min./day)  
 t = incubation time (days)

The next step is to extrapolate the OIT depletion rate to a lower (and site specific temperature), using the Arrhenius equation described in Equations (3) and (4).

$$S = A \cdot \exp(-E/RT) \quad (3)$$

$$\ln(S) = \ln(A) + (-E/R) \cdot (1/T) \quad (4)$$

- where: S = OIT depletion rate  
 E = Activation energy of the antioxidant depletion reaction under this test condition (kJ/mol)  
 R = gas constant (8.31 J/mol.K)  
 T = test temperature in absolute Kelvin (degrees K)  
 A = constant

A linear relationship is established between  $\ln(S)$  and inverse temperature. Figure 9 shows the Arrhenius plots for the Std-OIT testing of Samples A, B and C. Similar behavior is also obtained for the HP-OIT.

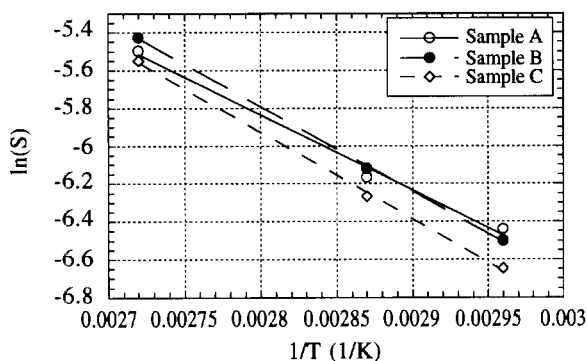


Figure 9. Arrhenius plot for Std-OIT test data.

The resulting activation energies of these samples are very similar regardless the type of OIT test, since similar reactions are being evaluated. The average activation energy value (slope of the lines in Figure 9) is 36 kJ/mol.

Based on the resulting Arrhenius equations, the OIT depletion rates at a typical site specific temperature can be extrapolated. To select a site specific temperature, Koerner, G.R., et. al. (1995) and Yazadini, et. al. (1995) found that the temperatures at the base of two municipal landfills in Pennsylvania and California vary between 19 and 22°C. Thus 20°C was used as the extrapolation temperature to calculate depletion rate using Equation 4. Using the obtained depletion rate, the required time to deplete all the antioxidants in the coupons at 20°C was calculated using Equation 1. However, before proceeding with the calculation, two boundary conditions must be established. They are the intrinsic OIT values that a pure unstabilized (i.e., no antioxidants) HDPE resin can possess in the two

respective OIT tests. Both Std-OIT and HP-OIT tests were performed on a pure HDPE resin. The Std-OIT was measured to be 0.5 minutes and HP-OIT to be 20 minutes. These two values are taken to be the OIT values when essentially all of the antioxidants in the incubated HDPE geomembranes are consumed (i.e., the OIT time in Equation 1). Table 3 shows the time required to consume all antioxidants from the three coupons at 20°C. In other words, these are the predicted antioxidant depletion times at temperature of 20°C under the simulated test conditions presented in this study.

Table 3. Required time to consume all the antioxidants

Sample	Antioxidant Depletion Time (year)	
	Std-OIT	HP-OIT
A	60	70
B	80	50
C	100	110

The predicted lifetimes from both Std-OIT and HP-OIT tests are reasonably close, although Sample B showed a unexpected low value using the HP-OIT test. The overall average lifetime of this antioxidant package under the test environment is 80 years. This is substantially shorter than the predicted value obtained from a separate incubation test that simulated a landfill liner condition. In that case, a 200 year depletion time was found (Hsuan and Koerner, 1997). This difference can be contributed by two factors. One is caused by the different oxygen concentrations between the two incubation environments. In the forced air oven, the concentration of oxygen is relatively high (21%) and is constantly being circulated. Comparatively, the oxygen is limited in a simulated landfill incubation test. Second is due to the evaporation of the antioxidants. The constant air circulation in the forced air oven can accelerate the antioxidant diffused out from the polymer as well as oxygen diffused into the polymer. Thus the forced air oven incubation procedure is a very severe test condition. It does not represent typical field situations, since at least one side of the geomembrane is always in contact with soil even for exposed applications.

Nevertheless, the air oven incubation is an ideal index test procedure for the evaluation of different antioxidant packages and for manufacturing quality control purposes. It can achieve the desired result within a relatively short time.

## 7. SUMMARY AND CONCLUSION

The consumption of antioxidants in five commercially HDPE geomembranes incubated in forced air ovens at elevated temperatures of 115, 95, 75 and 65°C was assessed. The results can be summarized as follows:

- The OIT test is ideally suited to track the depletion of antioxidants in the geomembrane. The OIT value decreased exponentially with incubation time in most of the tested geomembranes.

- For geomembrane Samples A, B and C that contain combination of hindered phenols and phosphites, the Std-OIT test can be used as well as the HP-OIT test. For geomembrane Samples D and E that contain either thiosynergists or hindered amine, the HP-OIT is the appropriate test.
- The 115°C incubation temperature is too high for aging evaluation. In addition, geomembranes that consist of thiosynergists, should not be incubated at temperatures 95°C and above due to the rapid evaporation of the thiosynergists.
- The antioxidants in the geomembrane must be completely consumed before the physical and mechanical properties begin to change.
- The antioxidant depletion time was predicted using the Arrhenius equation and found to be approximately 80 years for Samples A, B and C.
- For Samples D and E, which contained thiosynergists or hindered amines, the depletion time appears to be longer in comparison to Samples A, B and C. The depletion times of these two antioxidant packages are still under investigation.
- The time of 80 years for depletion of antioxidants is shorter than the results obtained from a separate study using a simulated landfill incubation setup. In that study, the predicted antioxidant depletion time is 200 years. The differences in these two values is caused by the amount of oxygen available. In this study, oxygen is constantly circulating in the forced air oven. While this incubation method is appropriate for research into different types of antioxidants or for manufacturing quality control, it does not represent in-situ condition.

Due to the significance of the antioxidant to the long-term durability of geomembranes, the performance of the antioxidants in the geomembrane should be properly evaluated by the user community (designers and/or owners). Since the Std-OIT and HP-OIT tests can effectively monitor the overall amount of antioxidants present in the geomembrane, the consumption rate of different antioxidant types can be compared and verified after the geomembrane is incubated in a properly designed procedure.

In a recently developed manufacturing quality control specification for HDPE geomembranes (GRI, 1997), the antioxidant packages are being evaluated. A minimum of 100 minutes of Std-OIT or 400 minutes of HP-OIT is recommended. Also the consumption rate of the antioxidant is limited to 55% for Std-OIT and 88% for HP-OIT, after the geomembrane is exposed in a forced air oven at a temperature of 85°C for 90 days.

#### ACKNOWLEDGMENT

This research is supported by the National Science Foundation, via its Geomechanical, Geotechnical and Geo-Environmental System (G3S) program under Grant No. CMS-9312772.

#### REFERENCES

- Fay, J.J. and King, R.E. (1993) "Antioxidants for Geosynthetic Resins and Applications", *Geosynthetic Resins, Formulations and Manufacturing*, Hsuan, Y.G. and Koerner, R.M., ed., GRI Conference Series, IFAI, St. Paul, MN, pp. 77-96.
- Gray, R.L. (1990) "Accelerated Testing Methods for Evaluating Polyolefins Stability", *Geosynthetic Testing for Waste Containment Applications*, ASTM STP1081, Robert M Koerner, editor, American Standard of Testing and Materials, pp. 77-96.
- GRI-GM 13 (1997) "Standard Specification for Test Properties, Testing Frequency and Recommended Warranty for High Density Polyethylene (HDPE) Smooth and Textured Geomembranes", Geosynthetic Institute, Philadelphia, PA 19104.
- Gugumus, F., (1996) "Thermooxidative Degradation of Polyolefins in the Solid State, Part I to Part IV", *Polymer Degradation and Stability*, Vol. 52, pp. 131-159.
- Howard, J.B. (1973) "Data for Control of Stability in Polyolefin Wire and Cable Compounds", *Polymer Engineering Science*, Vol. 13, No.6, pp. 429-434.
- Hsuan, Y.G. and Koerner, R.M. (1997) "Antioxidant Depletion Lifetime in High Density Polyethylene Geomembranes", Accepted by ASCE, *Journal of Geotechnical and Geoenvironmental*.
- Hsuan, Y.G. and Guan, Z. "Evaluation of the Oxidation Behavior of Polyethylene Geomembranes Using OIT Tests", *Oxidative Behavior of Materials by Thermal Analytical Techniques*, ASTM STP1326, A.T. Riga and G.H. Patterson, Eds., American Standard of Testing and Materials.
- Koerner, G.R. and Koerner, R.M. (1995) "Temperature Behavior of Field Deployed HDPE Geomembranes" Geosynthetics'95 Conference Proceeding, IFAI, St. Paul, MN, pp. 921-938.
- Thomas, R.W. and Ancelet, C.R. (1993) "The Effect of Temperature, Pressure and Oven Aging on the High Pressure OIT of Different Types of Stabilizers" Geosynthetics'93 Conference Proceeding, IFAI, St. Paul, MN, pp. 915-924.
- Yazadini, R. Campbell, J.L. and Koerner, R.G. (1995) "Long-Term In-Situ Strain Measurements of a HDPE Geomembrane in a Municipal Solid Waste Landfill", Geosynthetics'95 Conference Proceeding, IFAI, St. Paul, MN, pp. 893-906.
- Yim, G. and Godin, M. (1993) "Long-Term Heat Aging Stabilization Study of Polyethylene and Its Relationship with OIT", Geosynthetics'93 Conference Proceeding, IFAI, St. Paul, MN, pp. 921-938.

# Selecting A Geomembrane Material

Ian D. Peggs

I-CORP INTERNATIONAL, Inc.; Ocean Ridge, FL, USA

Rick Thiel

Thiel Engineering; Oregon House, CA, USA

**ABSTRACT:** As the number of available geomembrane materials Polyethelene (PE), Poly (vinyl chloride) (PVC), Polypropylene (PP), Chlorosulfonated Polyethylene (CSPE), Polyester (PET), Polyurethane (PUR), and their alloys) increases and their range of applications widens, it is becoming more important that the proper selection of material, and even resin within one material type, be made. This cannot be done on an emotional basis, nor can it be done without a thorough knowledge of geomembrane performance. A technically based protocol is presented for selecting a material for each specific geomembrane application. The important parameters for each geomembrane application are identified and rated on a scale of 1 to 5 in terms of their significance to the project. The candidate materials are then rated on a scale of 1 to 10 for each of the parameters. The two ratings are multiplied and then totaled for each material to provide a technically based overall rating of geomembrane materials for the specific project. Examples are provided for different types of facilities, which highlight the materials, operations and maintenance characteristics that influence the performance of geomembranes in different lining applications.

**KEYWORDS:** Geomembrane, liner, design-by-function

## 1 INTRODUCTION

The selection of a geomembrane material for landfill or liquid impoundment lining systems is often based on the prescriptions of federal, state or provincial regulations, or is based on the selection of the material that will most easily proceed through appropriate permitting processes. For the past several years high density polyethylene (HDPE) has enjoyed the position of geomembrane-of-choice and, in fact, "HDPE" has become almost synonymous with the word "geomembrane". However, in a few instances, such as for the containment of black liquor at pulp mills (Peggs et al, 1993), for the containment of nitric acid and due to inadequate specification of resin properties, this has led to liner failures. In such instances alternative materials or resins would have provided better service, but the knowledge or appropriate mechanisms for the selection of the better materials or resins were not in place or were ignored.

The conditions under which geomembranes are used in lining systems are wide and varied. Geomembranes are required to provide service as the only, primary, or secondary liner of basal lining systems. The single, or primary geomembrane may be exposed to ultraviolet radiation or may be covered

with soil, or it may be covered with a wide range of liquid chemicals. The primary geomembrane may be placed on an imported well-prepared soil layer, while a secondary geomembrane (never exposed to UV radiation except during installation) may be placed on a not-so-well-prepared (rough) natural subgrade. While the primary geomembrane may be constantly exposed to a chemical the secondary geomembrane will not, or should not. If the primary geomembrane is exposed to UV radiation, it may also be exposed to wide variations in temperature (if liquid levels are varied) while the secondary geomembrane is not exposed to such wide changes in temperature. Thus, the service conditions experienced by primary and secondary geomembranes in the same basal liner may be quite different. There are similar, and more, differences required for the performance of geomembranes in landfill caps and floating covers, when compared to basal liners. Geomembranes in caps are subjected to differential settlement, permanent shear stresses, temperature variations, and perhaps vegetation root penetration that basal liner are not. They must be able to tolerate deformation far more readily than basal liners. Then there are different requirements for geomembranes used as canal liners, dam facings, vertical cut-off walls, fuel

farm secondary containment, and portable storage for fuel and water.

There are many geomembrane materials available today - HDPE, Very Low Density Polyethylene (VLDPE), Linear Low Density Polyethylene (LLDPE), coextruded PEs, Poly (Vinyl chloride) (PVC), PVC alloys, Polypropylene (PP) (reinforced and unreinforced), Ethylene Propylene Diene Monomer (EPDM), Chlorosulfonated Polyethylene (CSPE), Bitumen (roll and spray products), Polysulfide (PS), Polyurethane (PUR) (roll and spray products), and Polyester (PET) - all with different performance characteristics. With this wide range it is inappropriate to assume that one material, even a regulatory prescribed one, will provide optimum, even adequate, performance. Even though many regulations and project specifications allow "proven equal" materials, the time and expense of proving equality are more than most facility owners are willing to incur. Thus, innovation and progress are stifled.

It is also necessary to understand that, just as there are many different geomembrane polymers, so there are many different HDPE resins with different performance characteristics. While all of these have very similar conventional strength, density, and deformation characteristics, their long term mechanical durabilities (stress rupture resistance) can vary by a factor of more than 1000. Thus, specifying "HDPE" alone is akin to requiring a bridge to be made simply out of "steel". One needs to be much more specific to obtain adequate or optimum performance from the installed facility.

Therefore, a technical approach based on polymer performance, geomechanics, constructibility, and other factors has been developed for the selection of the most appropriate geomembrane for each project specific application. Cost considerations then become a secondary, rather than the primary, reason for material selection. By using this approach the increasing number of geomembrane failures that are occurring might be reversed.

## 2 METHODOLOGY

The first step in the process is to identify all of the factors that are important for the successful performance of the geomembrane in the specific application in the specific project. As previously indicated, such factors will be different for primary and secondary liners, caps, and floating covers. Not

only should basic material mechanical, physical, and chemical performance be considered, so also must installation conditions (temperature, wind), time between installation and designed service conditions, operational requirements, and maintenance requirements. Will the landfill liner/cover be left exposed before waste is placed? Will select waste be placed as the first layer? Will the liquid level be constant, or high in winter and low in summer, or vice versa? Will the owners want to make their own repairs? A complete listing should be made of all of these requirements.

The second step is to identify the relative significance of each of these parameters (requirements) on a scale of 1 to 5, with 5 being "most significant" and 1 being "of little (but still some) significance". Thus, UV resistance for an exposed leachate lagoon liner will receive a 5 rating, while for a secondary basal liner it will receive a 1, unless for some reason, during installation, sections of it were to be left exposed for some time, when it might receive a 2. Clearly, these ratings are somewhat subjective and are based on the experience of the rater.

Some of the factors and their relative significances in solid waste and liquid impoundment facilities are listed in Tables 1 and 2 respectively. Note that that these should not be considered complete for any real facility since environmental conditions have not been defined. Also note the differences between primary and secondary geomembrane liner requirements.

When all the significant parameters for each of the geomembrane components have been identified and rated, a number of candidate geomembrane materials (three to five) should be identified. Clearly, experience and judgment are usually required to develop the initial 'short list' of candidate geomembranes. Cost should not be a factor at this stage of the selection process.

The performance of each of these candidate materials is then rated against each of the required parameters on a scale from 1 (poor) to 10 (excellent). A scale of 1 to 10 for only 3 or 5 materials allows emphasis to be given to extremely good or poor performance as required. The complete parameter/material rating system can be presented as shown in Table 3.

The significance and performance ratings (1 to 5 and 1 to 10) are multiplied to provide an adjusted rating for each parameter/material combination. All of the adjusted ratings for each material are then totaled to



**TABLE 1 Some Landfill Geomembrane Parameters and Their Significance**

PARAMETERS	SIGNIFICANCE		
	Primary	Secondary	Cap
Leachate Resistance	5	3	1*
UV Resistance	3	2	4
Oxidation Resistance	4	2	4
Flexibility For Subgrade Contact	5	4	5
Biaxial Stress/Strain	4	3	5
Puncture Strength	1	1	1
Puncture Strain	5	5	5
Interface Friction	4	3	5
Stress Cracking Resistance	5	5	5
Loss Of Additives	5	3	5
Seamability (Window)	5	5	3
Number Of Field Seams	3	2	2
Detail Seamability	4	3	3

\* Assuming no condensates

**TABLE 2 Pond Liner and Floating Cover Parameters and Their Significance**

PARAMETERS	SIGNIFICANCE	
	Liner	Cover
Liquid Resistance	5	4
UV Resistance	2	5
Oxidation Resistance	3	5
Subgrade Contract	5	1
Biaxial Stress/Strain	4	3
Puncture Strength	1	4
Puncture Strain	4	1
Interface Friction	4	1
Stress Cracking Resistance	5	2
Loss Of Additives	4	3
Seamability (Window)	3	3
Detail Seamability	4	3

TABLE 3 Rating Procedure

	MATERIAL 1			MATERIAL 2		MATERIAL 3	
	Sig.	Perf.	Adj.	Perf.	Adj.	Perf.	Adj.
PARAMETERS REQUIRED	A	B	A x B	C	A x C	D	A x D
<b>TOTAL</b>			<b>F</b>		<b>G</b>		<b>H</b>

KEY: Sig. - Significance Per. - Performance Adj. - Adjusted

A 1- 5 1 little importance, 5 very important  
 B, C, D 1-10 Performance of material for this parameter; 1 poor, 10 good  
 F, G, H Totals Rating of each material to meet service requirements, highest is best.

generate the final material rating. The highest value identifies the most technically appropriate material for that specific geomembrane application. Only now should factors such as cost be considered. And with this system, one generates a means of partially demonstrating "equivalency" of different materials.

As with any contrived rating system, experience and judgment are required in the final evaluation. There may be some technical parameters of overriding importance that are not adequately reflected in a subjective tabular rating. For example, achieving a minimum acceptable factor of safety for slope stability is often a fundamental design criteria that must be met with no compromise. In this case there is an absolute pass/fail criterion that candidate geomembranes must meet to qualify for further evaluation. Slope stability analyses on a specific project may reveal that only an aggressively textured geomembrane will be able to satisfy the requirements, and that textured polyethylene geomembranes are the only material available that is manufactured with such surfaces. But then the significance of that factor on the stress rupture resistance may have to be given more weight as well. Thus, the tabular matrix would then shift its emphasis from a range of fundamental polymer types, to a range of available polyethylene properties.

### 3 EXAMPLES

Four situations, all of which are contrived, and all of which are intentionally incomplete (so as not to become "prescriptions"), are described below.

**CASE 1 - THE PRIMARY AND SECONDARY GEOMEMBRANES OF AN MSW LANDFILL.** The secondary geomembrane will be placed on a coarse stony subgrade in a cold winter with the primary placed on a GCL in the following hot summer. The primary geomembrane will be covered immediately. Local regulators are aware of PP, and PVC, but are most comfortable with HDPE.

In this case the secondary geomembrane will have to tolerate subgrade scratching damage during installation and will have to tolerate puncture strains from the coarse subgrade. It will have to have some resistance to UV radiation since it may be exposed for up to 6 months. It will also have to have a low expansion coefficient so that excessive wrinkles are not formed at the high summer temperatures when it will be covered.

The evaluation presented in Table 4 indicates HDPE is most acceptable for the primary geomembrane, while PP is most suited for the secondary geomembrane.

While it is an accepted fact that a composite liner constructed from a geomembrane and mineral layer/GCL produce the optimum lining system, similar recognition has not effectively been given to the benefits of using two different materials in double geomembrane lining systems, where the negative aspects of the primary geomembrane are complemented by the positive aspects of the secondary. Thus the chemical resistance and strength of an HDPE geomembrane can be complemented by the strain tolerance, low expansion coefficient, flexibility, and stress cracking resistance of a more flexible geomembrane. The secondary geomembrane does not require the same chemical resistance since it is not constantly exposed to the contained liquid, but it will conform better to the subgrade because of its flexibility (providing a better composite action than will HDPE). In cold environments compensation wrinkles in a flexible secondary geomembrane will not present a problem when placing an HDPE primary geomembrane, also with compensation wrinkles, on top of it, as might happen if the primary HDPE geomembrane were placed on top of a wrinkled secondary HDPE geomembrane. There is much to be said for having primary and secondary geomembranes made from different materials. (Note that the decision to use different materials for primary and secondary liners may also need to take into account the need to weld the primary and secondary liners together in the anchor trench to prevent water from entering the leak detection system. This is a site-specific issue that could be incorporated into the rating procedure.)

**CASE 2 - THE EXPOSED PRIMARY GEOMEMBRANE IN A PULP MILL BLACK LIQUOR POND** that will be installed in the summer in a location where winter temperatures can reach -40°C. The pond will mostly be empty except for three-week plant maintenance periods. "Detergents" will not be skimmed off the liquor. The black liquor enters the pond site at a temperature of 82°C.

Although efforts are made to reduce the temperature of the black liquor by cascading or spraying it into the pond, the liquid is still relatively warm. But is this necessary if exposed black liners regularly experience temperatures of 80°C in the summer sun? Chemical resistance to the liquor is of extreme importance as is the concern of thermal contraction of the geomembrane at low winter temperatures. Compensation wrinkles may need to be built-in in the summer installation.

Table 5 indicates PP and CSPE appear to be technically the most suitable materials.

**CASE 3 - A CO-DISPOSAL (MSW/CDD) LANDFILL CLOSURE CAP** where temperatures vary somewhat but are never very high. Installation occurs in the summer. The waste is subject to differential settlement. There is an active landfill gas removal system incorporated in the lining system. The geomembrane is placed on a GCL on 3:1 slopes.

The cap will have to tolerate the strains of differential settlement, and the stresses induced by some temperature changes. Maximum temperatures are not so high that loss of plasticizers from PVC is of concern.

Table 6 indicates that PVC is technically the optimum geomembrane. However, slope stability analyses indicate that the interface friction between PVC and the underlying GCL is not adequate to meet the minimum required factor of safety of 1.5. In this case, consideration of a well-textured LLDPE is warranted if its interface shear strength is able to meet the requirements.

**CASE 4 - AN UNDERGROUND CONCRETE RESERVOIR** for storage of irrigation water for a golf course. There are many square concrete pillars supporting the roof. All corners between pillars and floor, and walls and floor, are right angles. There are cracks in the floor.

Table 7 indicates that a spray on polyurea liner is the optimum liner for this application.

Clearly these examples have been contrived to generate different solutions and should not be considered complete, either in the parameters of significance, nor in the selection of candidate geomembrane materials, but they do provide examples of the types of thought processes and evaluations that are required for the successful selection and functioning of a geomembrane. There is not one geomembrane material that will be suited for all applications.

Even though this methodology may lead the specifier to an appropriate geomembrane material, care still needs to be taken in the details of the final specification. For example, when specifying HDPE, the stress rupture performance characteristics (stress cracking resistance) should be matched with the criticality of the specific lining installation.

Finally, it should be noted that there are many benefits to be gained from using different, but

TABLE 4 MSW Landfill: Overview of Liner Selection Process

PARAMETER	SIG		HDPE				PP				PVC			
	P	S	P		S		P		S		P		S	
			rate	adj.	rate	adj.	rate	adj.	rate	adj.	rate	adj.	rate	adj.
Leachate Resistance	5	3	10	50	10	30	8	40	8	24	5	25	5	15
Welding window	2	5	7	14	7	35	10	20	10	50	5	10	5	25
Puncture strain	3	5	5	15	5	25	10	30	10	50	8	24	8	40
Stress cracking resistance	5	5	6	30	6	30	9	45	9	45	8	40	8	40
Expansion coefficient	3	5	5	15	5	25	10	30	10	50	6	18	6	30
Notch sensitivity	2	5	5	10	5	25	8	16	8	40	10	20	10	50
UV resistance	1	3	8	8	8	24	7	7	7	21	4	4	4	12
Regulatory acceptance	3	3	10	30	10	30	1	3	1	3	3	9	3	9
CQA-ability	3	3	10	30	10	30	1	3	1	3	7	21	7	21
				196		254		194		287		171		242

P = Primary

S = Secondary

Sig = Significance

TABLE 5 Black Liquor Pond

PARAMETER	SIG	HDPE		PP		CSPE	
		Perform.	adj.	Perform.	adj.	Perform.	adj.
Black liquor resistance	5	1	5	7	35	6	30
Stress cracking resistance	5	4	20	9	45	10	50
Thermal contraction	4	4	16	7	28	10	40
UV resistance	5	8	40	7	35	10	50
Number of field seams	4	3	12	3	12	6	24
Total seams	3	10	30	8	24	1	3
Repairability	3	6	18	6	18	3	9
Puncture strain	1	3	3	10	10	1	1
			144		207		207

TABLE 6 Landfill Closure Cap

PARAMETER	SIG	HDPE (textured)		PVC (embossed)		LLDPE (textured)	
		performance	adj.	performance	adj.	performance	adj.
Gas permeability	1	8	8	4	4	6	6
Biaxial strain tolerance	5	2	10	9	45	8	40
Intimate contact	5	2	10	9	45	7	35
Thermal expansion	4	3	12	5	20	2	8
Interface friction	5	8	40	4	20	8	40
Stress cracking resistance	5	4	20	9	45	8	40
Seamability	1	4	4	4	4	4	4
			100		183		173

TABLE 7 Concrete Reservoir

PARAMETER	SIG	HDPE		PP		SPRAY POLYUREA	
		performance	adj.	performance	adj.	performance	adj.
Intimate support	5	2	10	6	30	10	50
Stress cracking resistance	4	4	16	8	32	10	40
Biaxial strain	5	4	20	7	35	9	45
Biaxial strength	4	10	40	7	28	4	16
Number of seams	3	4	12	4	12	10	30
Chemical resistance	1	10	10	8	8	6	6
Thermal expansion	3	2	6	6	18	9	27
			114		163		214

complementary, materials for the primary and secondary geomembranes of double lining systems.

#### 4 CONCLUSIONS

A simple technically based procedure has been developed for the selection of the most appropriate geomembrane material for project specific applications. The procedure takes into account the operational and maintenance requirements of the facility as well as the mechanical, physical, and chemical performance characteristics of the material.

The procedure also provides information for a basic assessment of technical equivalency of different materials.

As with all engineering construction materials, experience, judgment, and a knowledge of the performance of such materials in such applications is essential in order to mobilize the optimum performance of the finished product.

#### REFERENCES

Peggs, I.D., Dewijn, T., and Lewis, D.R. (1993),  
"Geomembranes for the Containment of Pulp Mill  
Hot Black Liquors: Problems and Remediation",  
Proceedings of Geosynthetics '93, IFAI, St. Paul,  
MN. pp 1357-1372.

# Heat-Insulation Performance of Geomembrane Composite

T. K. Tao

Professor, Hydraulic Engineering Department, Nanjing Hydraulic Research Institute, Nanjing, P. R. China

L. Yu

Graduate Student, Nanjing Hydraulic Research Institute, Nanjing, P. R. China

Y. N. Wu

Engineer, Nanjing Hydraulic Research Institute, Nanjing, P. R. China

**ABSTRACT:** This paper presents the preliminary study on heat-insulating performance of the geomembrane composite. The authors find that generally the thermal diffusivity of the geomembrane composite is slightly smaller than that of the concrete and 10~30 times smaller than that of simple geomembrane, and will decrease with the increase of thickness of geotextile associated with geomembrane. In this paper, a typical dike is presented as a application case for checking the heat-insulating effect of geomembrane composite. It is expected that the geomembrane composite will be used in the place of the concrete as the heat-insulating layer in civil engineering.

**KEYWORDS:** Geomembrane composite, Thermal diffusivity, Laboratory test, Heat insulation

## 1 INTRODUCTION

Geomembrane composite is a material composed by the geomembrane and geotextile. Since it has multi-functions such as seepage prevention and drainage, geomembrane composite was successfully widely applied in civil engineering in China, such as, in the main cofferdam at Shuikou Hydroelectric Station (Tao, 1989), in Lijiaqing earth dam (Tao, 1990), in the Core of Zhushou Reservoir dam (Tao, 1993), in the Xiaolingtou Rock-fill dam (Tao, 1996) to replace the clay or concrete impervious barrier and sand cushion.

The geomembrane composite is usually associated with the geotextile (in general needle-punched geotextile). The geotextile associated with the geomembrane is of fiber structure, thus is non-homogeneous, porous and anisotropic. These characteristics make the geotextile to have good heat-insulation performance, so that the geomembrane composite has both geomembrane and geotextile properties as well as impervious and heat-insulation functions. Formerly, the people have not attached importance to this special property of the geotextile.

The aim of this paper is to investigate whether the geomembrane composite is able to be used as heat-insulation layer in civil engineering.

Analytic results indicate that the seepage-prevention and heat-insulation effect of the geomembrane composite is fairly significant. So, the geomembrane composite can be used as a new type of engineering material to replace the concrete impervious and heat-insulation liner in civil engineering. It is a new application field in civil engineering for the geomembrane composite.

## 2 HEAT CONDUCTION EQUATION AND THERMAL DIFFUSIVITY

### 2.1 Heat Conduction Equation

Based on the heat conduction theory and energy conservation law, differential equation of heat conduction in terms of rectangular coordinates for the non-homogeneous and anisotropic area with inner heat source is

$$\frac{\partial t}{\partial \tau} = \left( a_x \frac{\partial^2 t}{\partial x^2} + a_y \frac{\partial^2 t}{\partial y^2} + a_z \frac{\partial^2 t}{\partial z^2} \right) + \frac{A}{C_p \rho} \quad (1)$$

where  $t$ —temperature;  $\tau$ —time;  $a$ —thermal diffusivity;  $A$ —inner heat generated per unit volume;  $\rho$ —density;  $C_p$ —specific heat at constant pressure.

From Eq.(1) it can be seen that the main characteristic for heat conduction is thermal diffusivity,  $a$ , which is defined by

$$a = \frac{\lambda}{\rho C_p}$$

where  $\lambda$  denotes the thermal conductivity.

The parameter,  $a$ , denoted the area where inner heat propagates per unit time. Since  $\rho$  is the mass density, the specific heat  $C_p$  must have the dimension of heat per unit mass and per temperature difference. If the specific heat is based on unit weight, the specific weight  $\gamma$  must be used in place of  $\rho$ . Therefore the dimension of the thermal diffusivity,  $a$ , is  $m^2/h$ .

Thus, it follows the research on thermal diffusivity of geomembrane composite first in laboratory.

### 2.2 Thermal Diffusivity of Geomembrane Composite

Geomembrane composite is a kind of thin plate material, according to the transient thermal diffusivity theory of infinite plate (Chapman, 1974), a test apparatus which is suitable for transient thermal diffusivity of infinite plate is developed. The test apparatus consists of water tanker composed by a heating chamber and a measuring chamber, of a auto-temperature controlling

Table 1 Test results of thermal diffusivity

No.	Specifications	Thermal diffusivity (m <sup>2</sup> / h)
1	Single geomembrane PVC with a thickness of 0.5 mm	0.06211
2	0.5 mm PVC with 250 g / m <sup>2</sup> NPGT on both sides	0.00798
3	0.5 mm PVC GM with 300 g / m <sup>2</sup> NPGT on both sides	0.00502
4	0.5 mm PVC GM with 400 g / m <sup>2</sup> NPGT on both sides	0.00358
5	0.5 mm PVC GM with 450 g / m <sup>2</sup> NPGT on both sides	0.00269
6	0.5 mm PVC GM with 500 g / m <sup>2</sup> NPGT on both sides	0.00207
7	Single geomembrane PVC with a thickness of 0.7 mm	0.05946
8	0.7 mm PVC GM with 300 g / m <sup>2</sup> NPGT on both sides	0.00475
9	0.7 mm PVC GM with 500 g / m <sup>2</sup> NPGT on both sides	0.00201
10	Concrete with a thickness of 100 mm	0.002995

Note: GM— geomembrane composite; NPGT— needle-punched nonwoven geotextile.

system, and of a auto-detecting system. Geomanbrane composite No.2~ No.6, No.8 and No.9, and single geomembrane No.1, No.7 are used in the tests as shown in Table 1.

The thermal diffusivity of the concrete plate (No.10) obtained by use of the test apparatus above-mentioned is 0.002995 m<sup>2</sup> / h, it is similar to that (0.0032 m<sup>2</sup> / h) obtained by use of "Measuring Apparatus for thermal diffusivity of Concrete" in "The Hydraulic Concrete Test Codes" approved by the Ministry of Water Resources and Electric Power of China in June 1982. Therefore, the test apparatus developed for determining the thermal diffusivity of geomembrane composite is reliable.

From Table 1, it can be seen that

— The thermal diffusivity of geomembrane composite is similar to that of concrete and it is relatively small and generally belongs to 10<sup>-3</sup> m<sup>2</sup> / h;

— The thermal diffusivity of geomembrane composite decreases with increase of thickness (or mass per unit area) of the geotextile associated with the

geomembrane;

— For the single geomembrane, the thermal diffusivity is the largest, it decreases slightly with increase of thickness of the geomembrane.

### 3 HEAT-INSULATING PERFORMANCE OF GEOMANBRANE COMPOSITE

As a calculation example, the authors take a dike installed between the intake and outlet of a power station, the dike axis is parallel to the coast line, so a discharge channel on one side of the dike near the coast is formed and is protected from the action of waves, while the other side of the dike fronts to the open sea. The water level, owing to the draining of heat water, in the discharge channel will be slightly higher than that of the open sea. The calculation profile of the heat-insulation liner within the dike is shown in Figure 1.

The dike is situated on the alluvial-slope from the land. The composite lining is placed below the base of the whole discharge channel, and extended within the

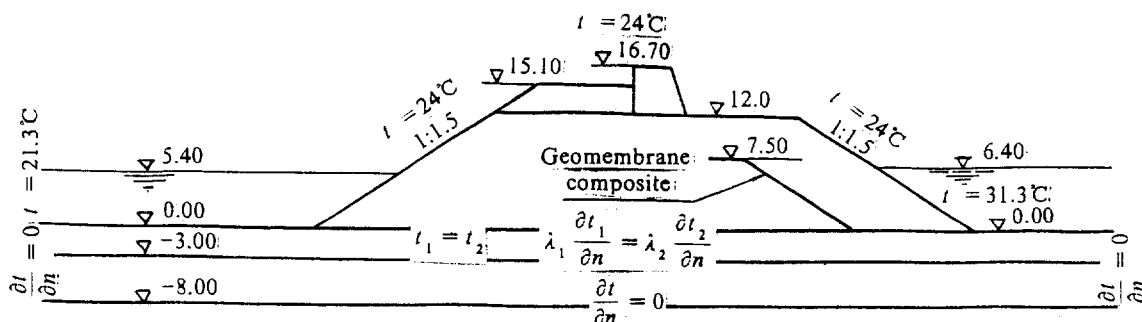


Figure 1. Computation section of dike and boundary conditions.



dike to the distance of 5 m perpendicular to the side-slope and the elevation of 7.5 m. Both sides of the impervious liner are filled with gravels 20~80 mm in granular diameter as a transition layer, the thickness being 1 m on both sides.

Eq. (1) is employed for calculating heat-insulating performance of the dike. For the inner thermal source of the discharge channel, it is prominent that heat transfer induced by joint seepage of the geomembrane composite will cause temperature rise of water, and the following can be written.

$$\frac{\partial \theta}{\partial \tau} = \frac{A}{\rho C_p} = QW \quad (2)$$

where,  $\theta$  denotes temperature rise of sea water;  $Q$ , thermal seepage discharge induced by the joints of the composite;  $W$ , temperature rise per unit volume of hot water in discharge channel.

Generally, there is a joint every 20 m of width for the geomembrane composite in engineering practice. Owing to the seepage discharge of heat water caused by the joint can maintain constant for a certain head difference, so the temperature rise due to heat transfer per unit volume caused by seepage discharge is also constant, for example, in the case calculation carried out by the authors, the constant value  $W = 10^\circ\text{C} / \text{m}^3$  have been obtained. Then the inner thermal source can be considered as a constant, thermal diffusivity of the geomembrane composite liner is assumed to be isotropic.

### 3.1 Boundary Conditions and Calculation Parameter

The region for heat-insulation calculation is 100 m long, and 110 m wide, from the foundation elevation of -8.0 m to the crest elevation of 12.0 m. There are 5 joints in the composite along the dike.

Temperature boundary: for the temperature of sea water, local annual average atmospheric temperature, i. e.  $21.3^\circ\text{C}$  is used; for water temperature in the discharge channel, because the temperature of water in discharge

channel is  $10^\circ\text{C}$  higher than that of the seaward side of the dike,  $31.3^\circ\text{C}$  is employed; for the temperature of the dike surface above the water surface of discharge channel,  $24^\circ\text{C}$  is used because there is a rise of the temperature of  $2.7^\circ\text{C}$  due to the solar radiation according to data of concrete gravity dam; the other boundaries are treated as adiabatic boundary ( $\partial T / \partial n = 0$ ) (see Figure 1).

The thermal diffusivities of various media for the heat-insulation calculation domain of the dike are shown in Table 2.

Table 2 Thermal diffusivities of various media

Materials	Thermal diffusivity ( $\text{m}^2 / \text{h}$ )
Cobble boulder	0.20
Medium coarse sand	0.01
Mild clay	0.002
Sea water	0.50
Composite No.6	0.00207
Concrete (No.10)	0.002995

### 3.2 Calculated Results and Their Analyses

The calculated results for heat-insulation calculation of the dike are shown in Figure 2 and indicate that

- (1) The heat-insulating effect of composite No.6 is fairly significant: a large quantity of heat conduction is insulated.
- (2) Owing to the temperature discontinuity between the water surface and the dike surface on the discharge channel side, there is a large temperature gradient at their interface.
- (3) The boundaries of the foundation and both sides of the dike in the heat-insulation calculation domain are treated as adiabatic boundaries, so the distribution of temperature rise contours is similar to the shape of the placement of the composite, and the temperature rise contours of other part present almost uniform perpendicular

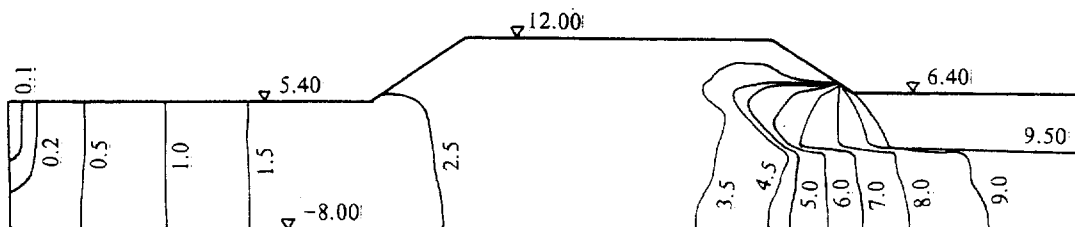


Figure 2. Contours of temperature rise distribution for geomembrane composite liner.

distribution.

(4) Calculations for the dike with concrete heat-insulating wall are carried out, as shown in Figure 3. one can find that the temperature rise contours are obviously concentrated on the position of placement of concrete. It can be seen that the heat-insulating effect of concrete is also satisfactory.

(5) Comparing Figures 2~3, it can be seen that the distributions of temperature rise contours on the seaward side of the dike are almost identical; the reason is that seaward boundary of the calculation domain is treated as an adiabatic boundary. Therefore, the determination of the boundary conditions is the key to the analysis of the temperature field. The exact determination of dike surface temperature and seawater temperature, and the exact determination of boundary locations and conditions of the sea domain and discharge channel are still complex problems to be resolved. In this paper, the authors have to simplify these problems to show the heat-insulation effect of the composite.

#### 4 CONCLUSIONS

This paper has presented the preliminary study on the heat-insulating properties of the geomembrane composite, it can be seen that the geomembrane composite has both the properties of geomembrane and geotextile. Therefore, the geomembrane composite has good impermeous and heat-insulating property. The following conclusions can be obtained.

(1) The thermal diffusivity of geomembrane composite is usually small and is similar to that of concrete. It decreases with increase of the thickness (or mass per unit area) of the geotextile associated with the geomembrane.

(2) The heat-insulating effect of the geomembrane composite is remarkable, and it can prevent most of the heat conduction accross the geomembrane composite. For the calculation, the exact determination of boundary conditions is the key to the analysing the temperature fields. But the exact determination of boundary conditions

of the sea domain and discharge channel are still complex to be resolved, so the authors have to make some simplifications.

(3) The thermal diffusivity and heat insulating effect of geomembrane composite is about the same of concrete, however, the geomembrane composite is a soft material and can be suitable to the dynamic condition of engineering (as earthquake). Moreover, the geomembrane composite have other advantages: low cost, easy construction and maintenance. So that it is expected that the geomembrane composite will be used in place of concrete as heat-insulating material.

#### REFERENCES

- Chapman, A. J., 1974. *Heat transfer*, New York, The Macmillan Company.
- Tao Tong-Kang, 1989. *A Geomembrane Composite Used to prevent Seepage in the Main Cofferdam at Shuikou Hydraulic Station*, Technical Report S 8931, Nanjing Hydraulic Research Institut. (in Chinese)
- Tao Tongkang, Tang R. and Chen M., 1990. Application of Geomembrane Composite in Impervious Lining System of Lijiaqing Dam, *Proc. of Fourth International Conference on Geotextile, Geomembranes and Related Products*, Balkema, Vol.2, The Hague, The Neetherland, pp. 463-466.
- Tao Tongkang, Li D.F., and Yan J., 1995. Calculation of Coupled Stress and Seepage for Dams with a Geomembrane Composite Liner, *Geosynthetics International*, Vol. 2 No.4, pp.707-721.
- Tao Tongkang, Yan J., Tao X. and Zhou H., 1996. Application of Geotextile Composite Liner for Infiltration Prevention in XiaoLingTou Rock-Fill Dam, *Geosynthetics International*, Vol. 3 No.1, pp.125-136.
- The Ministry of Water Resources and Electric Power, PRC of China, 1983, *Hydraulic Concrete Test Codes (SD 105-82)*, Beijing, Water Resources and Electric Power Press. (in Chinese)

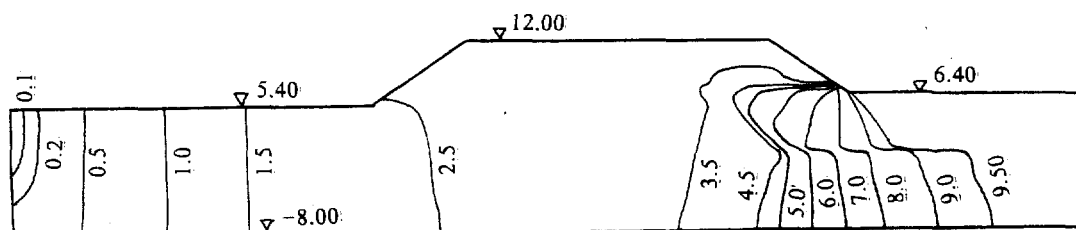


Figure 3. Contours of temperature rise distribution for concrete impervious wall.

# Prediction of the UV Ageing of Polypropylene Geotextiles - Landfills case

O. Artières

Dr.-Ing., Bidim Geosynthetics S.A., Bezons, France

S. Gaumet

Dr., CNEP (Centre National d'Evaluation de Photoprotection), Université Blaise Pascal, Clermont-Ferrand, France

C. Bloquet

Dr., France Déchets, Gargenville, France

**ABSTRACT:** Geotextiles may be exposed to long weathering periods when used as a filter in drainage systems or geomembrane protection layer in specific applications such as landfills. There is therefore an urgent need to develop specific products able to offer the required durability of their functional characteristics for several months or years. The paper presents a methodology to assess the UV durability of polymers. This mechanistic approach firstly analyses the chemical degradation process of the polymer when exposed to natural weathering. Then it describes the rules able to control artificial accelerated ageing by keeping all the parameters into a representative range. The experimental investigation on polypropylene geotextiles in landfills is proposed as an example of this methodology.

**KEYWORDS:** Ageing, Geotextiles, Landfills, Ultraviolet Effects, Weathering Resistance

## 1 INTRODUCTION

Geotextiles are made of polymers, the most common being polypropylene, polyethylene and polyester. These pure polymers are sensitive to UV radiations which cause catalytic photo-oxidation reactions. These reactions in turn lead to breaks in the molecular chains, causing the degradation of the products. Polymer chemists have been aware of this phenomenon for a considerable number of years (but, we will see, the chemical mechanisms have only been discovered recently). They have found anti-UV and anti-oxidant stabilisers able to halt these reactions. These molecules are mixed with the polymer before it is melted.

In most earthwork applications, geotextiles are unwrapped and quickly covered in soil. Geotextile manufacturers have therefore adjusted the quantity of stabiliser into the polymer so that the products are not damaged after a few weeks' exposure. In such conditions, and in absence of any other chemical or mechanical erosion, geotextile will last for decades, as demonstrated in the sites built since the mid-sixties. Geotextile samples taken from a 25 years old earthdam have shown for example no significant damage (Delmas et al. 1994).

The damage becoming apparent on some geotextiles used in waste containment sites within periods ranging from 3 months to 2 years (Gisbert et al. 1997) stems from the disparity between these historical applications on one side, and the new constraints of landfill operation on the other side. In these applications, geotextiles are often installed on slopes as filter above a drainage layer or as geomembrane protection. They may be exposed for several months or years to weathering before being covered, instead of several weeks in current earthwork applications.

When geotextiles are exposed to sunlight for the whole period during which the site is in operation, special protection must be designed. One solution should be to

cover the geotextiles by a thin layer of soil. Another possibility is to impregnate them with a protective resin. One example of this technique is the Maraval's overflow-dike in southern France (Kern, 1977). The geotextile reinforced wall of the dike is exposed to permanent weathering. No deterioration has been observed on the site since it was built in 1976. A third possibility is to adjust the UV stabiliser content to the period of exposure.

In response to this specific requirement, a research program has been set up by Bidim Geosynthetics, producer, and France Déchets, landfill operator, to assess the effective lifetime of geotextiles laid in landfill, with the technical support of C.N.E.P. institute, from Clermont-Ferrand University, specialised in photodegradation of polymers. The paper focuses specially on the methodology used to assess the ageing of polymer products. Its principles are quite new in the area of geosynthetics even if it is used for several years in other industrial sectors (pipes, cars, fine arts, etc...). Some important results are given in the case of polypropylene geotextiles, but most of the principles apply to other types of geosynthetics.

## 2 AGEING METHODOLOGY

The methodology used in this study to predict geotextiles lifetime combines two complementary analyses on:

- Polymer durability through a mechanistic approach, as proposed by Blaise Pascal university (Lemaire 1996);
- Product lifetime through a functional approach.

### 2.1 Polymer Durability

#### 2.1.1 The conventional method : the simulation approach

A large part of the research and development on polymer

durability is based on an empirical approach developed in the early 1950s, with the expansion of polymeric materials. Laboratory testing was set up to reproduce the phenomena causing the degradation of the polymeric systems on a shorter time scale. Those systems were handled as macroscopic units characterised by their physical properties. The polymeric substrate was treated as a "black box" to which all the possible environmental physicochemical stresses—light, heat, mechanical, O<sub>2</sub>, liquid and gaseous water, O<sub>3</sub>, pollutants—were applied.

The devices designed for laboratory ageing experiments tried to simulate qualitative and quantitative environmental stresses as exactly as possible. For example, the choice of xenon light sources in simulation units (Weather-O-Meter, Xenotest) instead of medium-pressure mercury was justified on the fact that the spectral distribution of the light emitted as a semicontinuum was close to that of daylight (except in the range 240-300 nm which needs to be strictly filtered out). However, the fundamental concepts of photochemistry, especially the existence of vibrational relaxation of excited states in the condensed phase, would allow the relevant use of medium-pressure arcs.

But the stress simulation approach has some negative aspects:

- The control of the temperature of the exposed surfaces, which is an important parameter of photoageing, is not seriously considered.
- Water sprinkling designed to simulate rain could be questioned as well, because many of the effects of water are not produced in this manner. The first effect of water on a solid surface is to provoke the mechanical abrasion of the external oxidized layers and to wash out low molecular weight compounds that have migrated to the surface of samples.
- The degradation criteria are mainly based on the variations of the physical or mechanical properties. This "black box" approach connecting macroscopic and microscopic changes could not be rationalised, because many different chemical evolutions could have the same physical consequences.
- It is difficult to identify the actual origin of an observed degradation if many physical and chemical stresses are applied simultaneously.
- As there is no control of the real chemical reactions occurring inside the polymer, the environmental stresses should be applied at their exact level with a time scale as close as possible to the real time scale in outdoor conditions and without accelerated conditions to ensure relevancy.

Therefore, any relationship obtained with the simulation approach between, on one hand, lifetimes in natural weathering conditions, and on the other hand, lifetimes in artificial ageing, is nothing more than an experimental correlation whose variations cannot be explained.

Despite these difficulties, the simulation approach has been developed steadily since 1950. Most standards are based on such experiments, and in many cases, results are

consistent with the long-term behaviour of the polymer. Still many predictions have caused significant accidents, especially when the degradation criteria were based on laboratory results. The simulation approach had both succeeded and failed without being able to explain it.

### 2.1.2 The mechanistic approach

With this approach, the polymer durability is predicted from its chemical evolution which is observed when relevant physico-chemical stresses are applied. When a polymeric material is submitted to moderate environmental stresses, the degradation of most physical properties is attributable to chemical ageing: the polymer should be treated as a "photochemical" reactor in the presence of light and as a "thermal" reactor without light. Therefore, it should be possible to pinpoint the exact nature of the chemical events responsible for the physical detriment.

The mechanistic approach requires therefore to control both the analysis methods assessing the polymer chemical evolution and the laboratory accelerated conditions.

### 2.1.3 Analysis of the chemical evolution of the polymer

The analysis and follow-up of the chemical evolution of a polymeric material submitted to light, heat, O<sub>2</sub>, H<sub>2</sub>O, and other potentially degrading elements occurring in artificial conditions—as well as in natural weathering or real use conditions—have two advantages. Firstly, they allow the correlation to be relevant, based on the comparison of ongoing chemistry. Secondly, because the extent of the chemical evolution can be related to the exposure duration in either average (weathering) or well-defined (artificial ageing) conditions, the lifetime in-laboratory conditions can be converted into lifetime in-use conditions.

This analysis is complex for the following reasons:

- The analysis should be carried out in the solid state;
- The degradation products should be considered at very small concentrations;
- Chemical evolution includes many mechanisms.

But usually, the most important route involves a photo-oxidation or a thermo-oxidation mechanism whose products are formed in concentrations high enough to be observed in vibrational spectrophotometry. It allows identification of the main intermediate oxidation products (i.e., hydroperoxides, ketonic groups, and alcoholic groups), the main conversion route of those intermediate products, and the major final products that accumulate in the matrix (e.g., acidic, ester and lactonic groups).

### 2.1.4 The recommended accelerated testing

Acceleration is at the moment the recommended technique due to the impossibility of extrapolating data collected in nonaccelerated conditions. But the usual techniques of homogeneous kinetics cannot be applied to handle the chemical transformation of a polymer matrix through

ageing due to the complexities of the reactions that take place and because of the heterogeneity of a semicrystalline matrix which is oxidized in only a very small part of its amorphous zones.

CNEP and Blaise Pascal University formulated a set of principles that provoke accelerated chemical evolutions in solid polymers and that obey the same mechanisms as the nonaccelerated evolutions :

- For each polymer system, the ageing process should be controlled via chemical analysis so that both ageing processes have the same intermediate products, the same conversion pathway for each intermediate, and the same final products or functional groups accumulating in the matrix.
- Acceleration should be stopped when chemical distortions such as enhanced cross-linking resulting from biradical recombinations are observed.
- Photoageing acceleration should take place as a result of high light intensity and high temperatures. It should not result from shorter wavelengths of light. Temperature increase should be limited so that the photothermal transformation will exceed any pure thermal conversion.
- Mechanical stress does not generally influence chemical reaction rates, but it does modify the correlation between the chemical evolution and the variations of physical properties.

Accelerated testing is only valid when one unique dynamic process controls the ageing in natural and artificial conditions. In many outdoor uses of polymeric systems, photo-oxidation is the main detrimental mechanism. Thus, the artificial conditions must accelerate photo-oxidation without introducing some irrelevant control attributable to an oxygen starvation effect or to a stabilizer migration. In the first case, oxygen diffusion is a competitive dynamic process that does not exist in environmental conditions. In the second case, stabilizers are expected to migrate on the time scale of natural weathering, an equivalent migration should be introduced into the artificial conditions. Dark periods throughout exposure are sometimes required for that reason.

When low temperature thermo-oxidation is the controlling detrimental mechanism in weathering conditions, it is difficult to accelerate ageing simply by increasing temperatures. In that case, acceleration should be limited and analytically controlled.

## 2.2 Geosynthetic lifetime

Many of the studies undertaken on geosynthetic lifetime after weathering refer to the loss of mechanical characteristics of the product, specially the tensile resistance. If this approach is relevant for products for which tensile strength is a functional characteristic for the long term, such as geotextile or geogrid for reinforcement, in most of the other geosynthetic functions, tensile strength is mainly required during installation stage. This

characteristic must therefore keep the required value only for a short term period corresponding to several weeks, except for specific applications as discussed before such as landfills, where the product is not immediately covered.

On the contrary, functional characteristics must exceed the designed service values during the whole service life of the work. The lifetime of geosynthetics should be evaluated through the variation of these functional characteristics. Table 1 gives the corresponding functional characteristics in case of the geotextiles for filtration and geomembrane protection studied in this program (CFG 1995).

## 3 EXPERIMENTAL STUDY

The ageing methodology previously discussed was applied in the case UV ageing of polypropylene geotextiles in landfills.

### 3.1 Geotextiles

2 types of geotextiles representative of the products used in landfills for the filtration and for geomembrane protection functions were exposed to outdoor weathering and artificial ageing. Their characteristics are given in Table 1.

### 3.2 Natural Weathering

#### 3.2.1 Outdoor sites

Four European sites at different latitudes were chosen for their specific climatic conditions (Table 2). Geotextiles were installed in June 96. A weathering period of 1 year is already available.

Table 1. Characteristics of the analysed geotextiles (1)

Function	Filtration	Protection
Functional characteristic	Opening size (3): 110 $\mu\text{m} \pm 10 \mu\text{m}$ Permittivity (4): 2.8 $\text{s}^{-1} \pm 0.4 \text{s}^{-1}$	Protection efficiency of a geomembrane: 1.0 $\text{kN} \pm 0.2 \text{kN}$ (2) Thickness (5): 4.0 $\text{mm} \pm 0.2 \text{mm}$
Characteristic for installation	Elongation (6): 75 % $\pm 10$ % Dyn. perforation: 22 $\text{mm} \pm 2 \text{mm}$ (7)	Tensile strength (6): 35 $\text{kN/m} \pm 3 \text{kN/m}$ Dynamic perforation: 10 $\text{mm} \pm 2 \text{mm}$ (7)
Identification	Polymer: Type:	Polypropylene Continuous filament needle-punched nonwoven
Mass (8):	180 $\text{g/m}^2$	500 $\text{g/m}^2$

Notes : (1) Average value and relative variation ranges including product and test variations for this study; (2) Protection efficiency for a HDPE 1.5 mm geomembrane : increase of puncture resistance due to the geotextile (NF P84507); (3) NF G38017; (4) NF G38016; (5) EN 964-1; (6) EN ISO 10319; (7) EN 918; (8) : EN 965

Table 2. Climatic conditions of the outdoor sites

Site	Villeparisis Aubière	Bellegarde Oria		
City	Paris	Clermont	Nîmes	Almeria
Country	France	France	France	Spain
Latitude	48°5N	45°5N	43°5N	36°5 N
Longitude	2°E	3°E	4°E	2°W
Altitude	80 m	330 m	60 m	200 m
Annual sun exposure	1600 h	1800 h	2700 h	3000 h
Annual global radiance	18 J/m <sup>2</sup>	50 J/m <sup>2</sup>	-	-
Min. Monthly	+3 °C	-1 °C	+5 °C	+12 °C
Aver. Temp.				
Max Monthly	+19 °C	+25 °C	+24 °C	+25 °C
Aver. Temp.				

### 3.2.2 Geotextile installation

The geotextiles were exposed in a Southwards direction and inclined on a 45° angle to meet extreme conditions. As described on figures 1, 2 and 3, the exposed area allows a sampling of strips at 4 ageing periods. The size of each strip is sufficient to carry out the tests listed in Table 1. Test specimen are localised in such a way that the effect of the product heterogeneity is low. The variations between the strips are mainly due to the action of weathering.

The geotextiles were fixed on a HDPE geomembrane to reproduce the current landfill situation, except in Clermont-Ferrand, where the smaller sized samples are exposed on a frame allowing air circulation on both sides.

### 3.3 Artificial ageing

In outdoor conditions, the most detrimental effect on polypropylene systems results from the photothermal oxidation due to the UV, heat and O<sub>2</sub> conjugated influences. Water has been shown not to be a major stress (see § 2.1.1). The lifetime prediction of PP systems is therefore based on the experimental results obtained in SEPAP 12.24, an unit in which the accelerated photoageing is attributable to the combined effect of light intensity and heat only. The acceleration factor is largely dependant on the nature of the polymer (Lemaire 1996).

This unit described by Tang et al. (1982) is built as a parallelepipedic chamber with medium-pressure mercury arcs lamps located at each of the 4 corners. They emit between 280 and 405 nm and a borosilicate double envelope filters out any low-intensity radiations with wave length < 290 nm. The emissions are delivered with a constant intensity and a spectral distribution over 4000 h. As long as the relative percentages of short and long wavelengths are considered, the medium-pressure mercury source emission is a closer approximation to daylight than xenon source emission.

24 samples fixed on a rotating support in the centre of the chamber receive a homogeneous distribution of

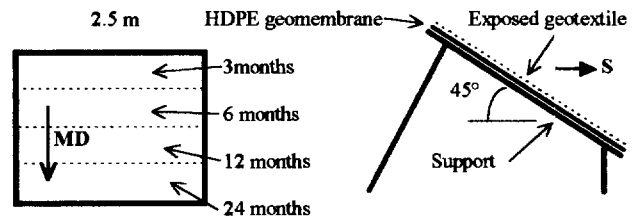


Figure 1. Panels for outdoor exposure (MD: Machine direction).

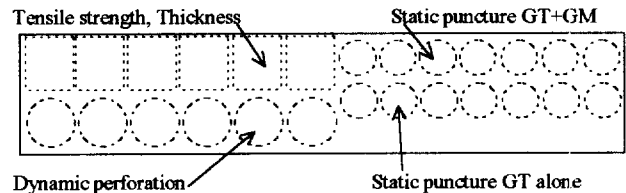


Figure 2. Positioning of the test specimen on a strip of geotextile for protection (2.5 m x 0.5 m).

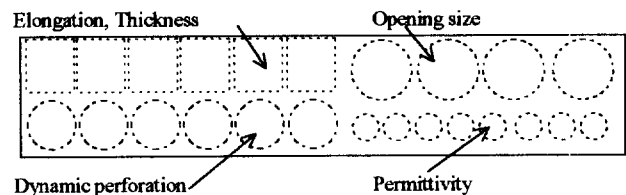


Figure 3. Positioning of the test specimen on a strip of geotextile for filtration (2.5 m x 0.5 m).

radiation. The temperature of the exposed surface of a reference film is controlled and maintained constant between 50 and 80°C (±1°C). The reference film is chosen to have the same surface properties (same colour and processing) as the other 23 samples. This unit was used in our study with a temperature of 60°C.

## 4 POLYPROPYLENE (PP) PHOTOOXIDATION

As discussed before, the control of the accelerating factors applied during artificial ageing is based on the knowledge of the type and rate of the chemical reactions occurring in the polymer during outdoor exposure.

### 4.1 Chemical mechanism

The mechanism of PP photothermal oxidation has been thoroughly examined for many years by most groups working in polymer. The most recent and the most complete version of the photooxidation mechanism is presented on Figure 4 (Delprat et al. 1995; Vaillant et al. 1994). The proposed mechanism is based on :

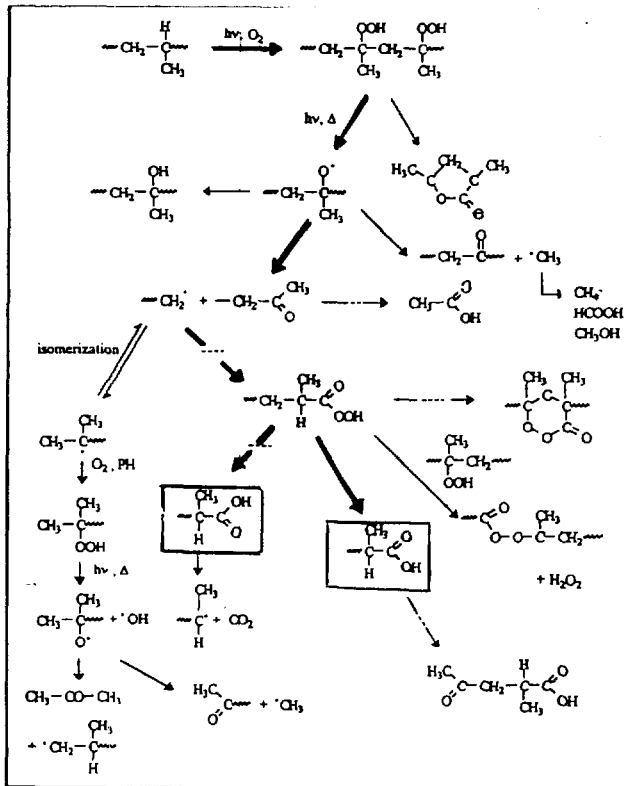


Figure 4. The main photooxidation route of PP

- the identification of the various photoproducts formed on the macromolecular chains, observed through FTIR spectrophotometric and microspectrophotometric measurements, with or without derivatization reactions;
- the identification of the various low molecular weight products through mass spectrometry.

The complete picture could be useful when the main oxidation route is well identified among all the possible conversions of intermediate products. That main route is represented on Figure 4. Among the final photoproducts which accumulate in the matrix, the chain end acidic groups  $\text{CH}_3\text{—C—COOH}$  were selected as "critical photoproducts", i.e. products of which the concentration was found to be correlated with the variations of functional characteristics.

From direct comparison of the formation rate of the critical photoproducts between the accelerated conditions of a SEPAP 12.24 unit and the first phase of in-use weathering conditions, the lifetime of unstabilized PP materials could be predicted.

The lifetime of stabilized PP is predicted from the comparison of the loss rate of stabilizers between artificial accelerated conditions and natural weathering.

#### 4.2 Identification of the Polymer Ageing

Using the correlation between the variations of physical

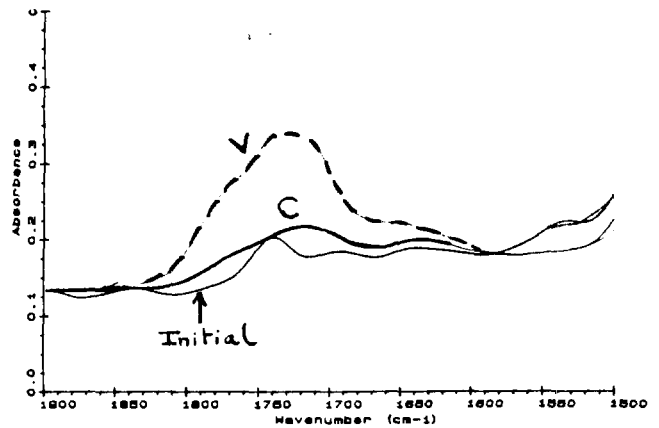


Figure 5. FTIR spectrum of 2 filtration geotextiles samples after 6 months weathering. V: Villeparisis on geomembrane - C: Clermont-Ferrand without support.

properties and the variation of the critical product concentrations under accelerated conditions, we can determine the lifetime of the polymeric material in the artificial condition. This result is converted into an estimate of the lifetime in weathering conditions using a predetermined acceleration factor based on the corresponding chemistry.

The loss rate of stabilizers and the chemical evolution of the polymer is analysed using FTIR (Fourier Transform Infra Red) spectroscopy in photoacoustic mode (PAS). This technique allows the analysis of the first 15  $\mu\text{m}$  near the surface of non translucent samples without specific preparation of the samples.

The FTIR spectral evolutions and the observed stoichiometry events at the molecular scale are the same with artificial ageing and outdoor weathering. This proves that SEPAP 12.24 units at 60°C reproduce well the outdoor PP ageing. For example, the growth of the main critical photoproduct (acid) is followed at 1720  $\text{cm}^{-1}$ . A typical FTIR spectrum is given on Figure 5.

## 5 BENEFITS OF THE METHODOLOGY

When the main target of the experimental study was the definition of the type and content of the UV stabiliser to be used in the geotextiles produced by one of the authors, 2 general results of great significance must be pointed out.

### 5.1 Influence of the Support

Even with lower climatic conditions (Table 2), the photooxidation rate in Villeparisis was found to be much higher than in Clermont. Spectrophotometric analysis of the Villeparisis samples shows that the UV stabilisers totally disappeared and that the concentration of the main critical photoproduct is about 3 times higher than in Clermont (Figure 5). The explanation corresponds to a

problem of air circulation around the sample : when samples are laid on a geomembrane, air doesn't circulate and the geotextile's temperature increases. The geomembranes acts also as a dark body which accumulates the sun energy and maintains the surrounding temperature at an high level over a longer period. Therefore, the stabiliser loss rate, the oxidation kinetic and the correlation between accelerated ageing and outdoor exposure cannot be the same. In this case, as discussed in § 2.1.4, the acceleration procedure has firstly to take into account this migration of stabilisers by keeping dark periods, and secondly to adjust the temperature of the ageing chamber at least to the level measured on the site by controlling the stoichiometry of the reactions

This result points out 3 main conclusions. Firstly, the conventional approach would not be able to explain these differences of behaviour. Secondly, the stabilisation level of a geotextile laid on a geomembrane must be much higher than for a geotextile laid on a soil with the same weathering conditions and during the same period. Thirdly, each specific application need specific outdoor exposure. It is false to extrapolate existing data to another situation.

## 5.2 Geotextile Durability

In many studies, geosynthetic ageing is related to the loss of tensile strength, even if this is not an essential characteristics. Our investigation has shown that significant loss of tensile strength doesn't necessarily means that the fonctionnal characteristics decrease with the same ratio. Table 3 gives the changes of the functional characteristics of a filtration and of a protection geotextile having the same level of stabilisation after one year's exposure in Villeparisis. Even with a 55 % reduction of its tensile strength, the fonctionnal behaviour of the filtration geotextile is still correct.

For the geomembrane protection geotextile, the reduction of the protection efficiency is also lower than the loss of tensile strength. It is know that even if the initial tensile modulus of the geotextile is of great importance to

Table 3. Geotextile characteristics and their variations (in brackets) after 12 months weathering in Villeparisis compared to the initial values. (1)

Function	Filtration	Protection
Functional characteristic	Opening size : 120 µm (0%) Permittivity : 3.7 s <sup>-1</sup> (+32%)	Protection efficiency of a geomembrane: 0.7 kN (-20%) Thickness : 4.2 mm (0%)
Tensile strength loss	-55 %	-25 %
(as comparison)		

Notes : (1) The geotextiles have both the same level of stabilisation and are laid on a geomembrane. If the measured value is found inside the variation range of the characteristic, it is assumed that there is no significant change.

protect the geomembrane against high strain, the geotextile thickness is also a major factor to decrease the local stress (Wilson-Fahmy et al., 1996).

## 6 CONCLUSION

The geotextile lifetime exposed to a long period of weathering should be assessed by combining : (i) the evaluation of the polymer durability based on a mechanistic approach to be sure that the same chemical reactions occur between natural weathering and artificial ageing; (ii) the changes of the functional characteristics of the products, instead of the tensile strength when it is not justified.

This methodology applied in the case of geotextiles used in landfills shows the efficiency of these tools to explain the high level of ageing when they are laid on a geomembrane.

Finally, the designer should use the fonctionnal approach to specify minimum values for each of their essential characteristics that the geosynthetics have to keep before being covered.

## REFERENCES

- CFG 1995 *Recommandations pour l'utilisation des géosynthétiques dans les centres de stockage de déchets*, Fascicule n°11, Comité Français des Géosynthétiques, c/o ITF, Bagneux, France, 50 p.
- Delmas Ph., Faure, Y.H., Farkouh, B., and Nancey A. (1994) "Long Term Behaviour of a Geotextile as a Filter in a 24-Year Old Earth Dam: Valcros", *Fifth International Conference on Geotextiles, Geomembranes and Related Products*, Singapore, pp. 1199-1202.
- Delprat, P., Duteurtre, X., and Gardette, J.L. (1995), *Polym. Degrad. Stab.*, Vol. 50, p. 1.
- Gisbert, Th., Bloquet, C. and Artières, O. (1997) "Geotextiles exposed to UV in landfills", *Rencontres '97*, Reims, France, CFG, Ph. Delmas & J.P. Gourc Editors, Tome 2, pp. 110-116.
- Kern F. (1977) "Réalisation d'un barrage en terre avec parement aval vertical au moyen de poches en textile", *1er Colloque International sur l'emploi des textiles en géotechnique*, Paris, France, ENPC, pp. 91-94
- Lemaire, J. (1996) "Predicting Polymer Durability", *Chemtech*, October, pp. 42-47.
- Tang, Ly, Sallet, D., Lemaire, J. (1982), *Macromol.*, Vol 16, p. 1437.
- Vaillant, D., Lacoste, J., and Dauphin, G. (1994), *Polym. Degrad. Stab.*, Vol. 45, p. 355.
- Wilson-Fahmy, R.F., Narejo, D., Koerner, R.M. (1996), *Puncture protection of geomembranes Part I: Theory, Geosynthetics International*, Vol 3, n°5, pp. 603-628



# Geosynthetic Proficiency Testing

G. R. Koerner

Geosynthetic Institute, Drexel University, Philadelphia, PA USA

**ABSTRACT:** A major tasks of the Geosynthetic Accreditation Institute's Laboratory Accreditation Program (GAI-LAP) is monitoring and evaluating laboratory test data measurement reliability. The program has developed data bases for assessing measurement reliability among geosynthetic testing laboratories. This paper describes the data base development and how it is utilized as a benchmarks from which proficiency test results are evaluated. It is felt that this type of an accreditation program is more challenging in assessing a laboratory's capability of performing specific tests than are programs that only check the existence of a quality system. While a quality system is indeed important to a laboratory performing tests, it is the actual test-by-test capability that is ultimately important to the end user of geosynthetic test results. It is this type of capability that is monitored and evaluated by the program.

**KEY WORDS:** Geosynthetic, laboratory testing, proficiency testing, precision, bias.

## 1 BACKGROUND

Test data reliability and quality are indeed worldwide concerns. A laboratory is not only expected to work efficiently but also expected to provide quality results in accordance with a well conceived quality system.

Upon observing questionable laboratory results in the recent past and realizing that many geotechnical and materials testing laboratories were starting fledgling geosynthetics test laboratories, the Geosynthetic Accreditation Institute (GAI) under the umbrella of the Geosynthetic Institute (GSI), began Geosynthetic Accreditation Institute's Laboratory Accreditation Program (GAI-LAP) in 1995. The program is intended to assure that a laboratory is capable of properly providing advertised tests.

Program representatives audit laboratories based on two international quality standards. The labs are directed to use ISO Guide 25 as their model for conducting business and encouraged to draft their quality manual, as per ISO 9003. Although the program suggests the use of these standards, it does not profess to be affiliated with ISO. Rather, the program is a hybrid one which tailors the above two standards to serve the immediate needs of the geosynthetic testing community. Also it should be made clear that this program does not "certify" laboratories, per se, nor the results that come from them. The intent of the accreditation program is to provide credentials to a laboratory showing that it has met requirements in regards to equipment and documentation for specific standard test methods.

Figure 1 shows a flow chart which highlights the accreditation process. As can be seen in the flow chart, there is considerable exchange of information and documentation prior to an actual audit. When successfully fulfilled, an on-site audit is conducted. At the audit, documentation, procedures and general laboratory protocol are first verified. When completed the auditor proceeds to supply the laboratory technician(s) samples of geosynthetics for which a data base exists. The technician prepares test specimens, tests

them in accordance with the appropriate standard and is required to have results fall within  $\pm 2$  standard deviation of a data base average. After progressing through the laboratories repertoire of tests an audit report is prepared summarizing all general and specific deficiencies. At the closing meeting these deficiencies are brought to the attention of management. Upon closing these deficiencies, the laboratory's accreditation is granted and a fee is paid.

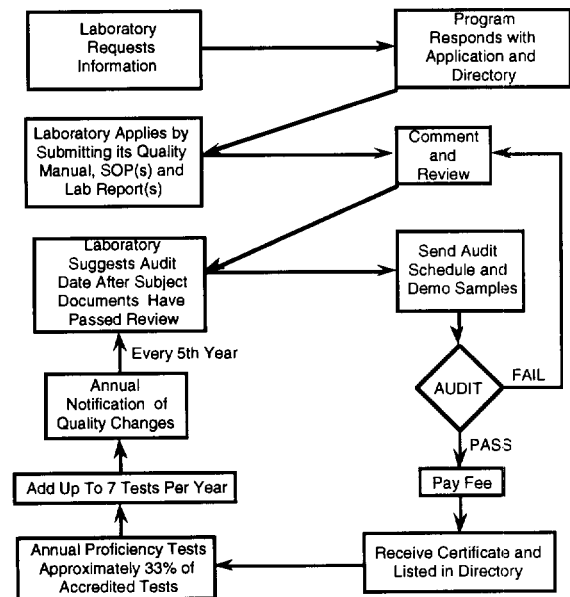


Figure 1. Program flow chart.

In subsequent years, the laboratory enters into a loop where off-site proficiency testing is required for approximately 20% of the laboratory's accredited tests. Every five years an on-site audit is conducted. In 1996 and 1997, proficiency testing was carried out among 19 laboratories. Using Geosynthetic Institute's laboratory as a reference, submitted results are compared with established data base averages.

At present, 80 data bases have been generated which involve 11 different rolls of "standard" geosynthetic materials. These materials are the following:

- HDPE smooth geomembrane
- HDPE textured geomembrane
- VFPE smooth geomembrane
- PVC geomembrane
- Scrim reinforced PP geomembrane
- Needle punched nonwoven geotextile
- Slit film woven geotextile
- GCL
- Geonet
- Stiff geogrid
- Flexible geogrid

One hundred test specimens are cut from samples of these rolls and are conditioned prior to testing. In order to obtain representative test specimens from the samples, no more than 10 specimens are cut from a particular roll width. In addition, no specimens are taken within 300 mm of the roll edge. All data base test specimens are evaluated on the same equipment, by the same technician. No more than 10 replicates of any given test are performed in a single day. The data base results are statistically analyzed by JMP® (1994). This computer program is a user friendly statistical software package. A histogram and control chart are generated for each data base. Values such as mean and standard deviation of each data set are determined.

Proficiency data bases are repeatability rather than reproducibility data bases. Repeatability testing is defined as "conducted in one laboratory by one technician on the same piece of equipment." Conversely, reproducibility testing is defined as "conducted at several laboratories by various technicians on different pieces of equipment." This has created some anxiety with participating laboratories because two standard deviations of a repeatability database is a smaller window of acceptability than that of a reproducibility data base. In addition, such a small window ( $\pm 2\sigma = 95\%$  confidence limit) is unprecedented in geotechnical testing industry to which geosynthetic testing is often compared. Many federal agencies such as AASHTO (1995) and ASTM (1993) use a 99% confidence limit ( $\pm 3\sigma$ ) as their grading requirement.

## 2 PROFICIENCY TEST RESULTS

Results of the 1996 and 1997 proficiency tests are presented in Tables 1 and 2 respectively. The tables are subdivided into two parts illustrating numeric results of the data bases and an analysis of the laboratory submittals with respect to them. Data bases are described by the average (Avg. 1), upper control limit (UCL) and lower control limit (LCL). In this regard, the UCL is defined as "plus two standard deviations of the data base average" where the LCL is defined as "minus two standard deviations of the data base average." In

contrast, laboratory submittals are illustrated by an average (Avg. 2), maximum (Max.) and minimum (Min.) of the results submitted that year. In addition, results are rated based on the following grading requirements which represents a 95% confidence limit of each data base in question.

5 = data within  $\pm 0.5$  standard deviation of average,  
4 = data within  $\pm 1.0$  standard deviation of average,  
3 = data within  $\pm 1.5$  standard deviation of average,  
2 = data within  $\pm 2.0$  standard deviation of average, and  
1 = data  $> 2.0$  standard deviation of data base average.

Finally, the above numeric ratings are averaged on an individual test basis, by way of a grade point average (GPA). This number can be thought of as a score for how well the submitted results match the data base in question. Five (5) indicates a good match where two (2) signifies a poor one. Note that a grade of one (1) is considered unacceptable and requires corrective action to be taken on the part of the submitting laboratory.

## 3 DISCUSSION

Depending on ones perspective the results presented in Tables 1 and 2 hold promise as well as disappointment. As can be seen in Table 1 the task of constructing a geosynthetic data base for a particular test and material is achievable. During the course of conducting this effort there have been many skeptics. Discussions about aging of the test material, damage during transit and vagueness of the test standards have been encountered. After 2 years of work, and 178 attempts at matching with 28 data bases, the merits of this exercise are apparent.

When the average GPA is calculated for both 1996 and 1997, a score of 3.5 is obtained. This quite respectable value highlights the success of this overall endeavor.

As far as test scores are concerned it is seen that three groupings can be considered.

Tests with statistical results between 5 and  $>4$ , e.g., Melt flow index (D 1238), Transmissivity (D 4716), Thickness (D 5199), Break Stress (D 638), Break Strain (D638), Density (D 1505), Mullen Burst (D 3786), Mass/Area (D 5261), Peak Friction Angle (D 5321), and 2% Secant Modulus (D 5323).

Tests with statistical results between  $<4$  and  $>3$ , e.g., Geomembrane Tear (D 1004), Permittivity (D 4491), 10% Modulus (D 882), Apparent Opening Size (AOS) (D4751), Puncture (D4833), Thickness (D5199), and Residual Friction Angle (D 5321).

Tests with statistical results between  $<3$  and  $>2$ , e.g., Specific Gravity (D 792), Grab Tensile (D 4632), Yield Stress (D 638), Yield Strain (D 638), Stiffness (D1388), Carbon Black Content (D 1603), Trap Tear ( D 4533), Wide Width Tensile (D4595).

Table 1. 1996 proficiency test results.

#	ASTM	Description	Units	Data Base			Lab Submittals			Rating					GPA <sup>g</sup>
				Avg. 1 <sup>a</sup>	UCL <sup>b</sup>	LCL <sup>c</sup>	Avg. 2 <sup>d</sup>	Max <sup>e</sup>	Min <sup>f</sup>	5	4	3	2	1	
1	D638	Yield Stress	kN/m	27.8	31.0	24.7	29.2	30.8	27.5	2	2	2	2	0	3.5
2	D792	Specific Gravity	—	0.951	0.956	0.946	0.955	0.956	0.954	0	1	1	3	0	2.6
3	D1004	Geomembrane Tear	N	231	240	223	231	240	227	1	2	0	2	0	2.6
4	D1238	Meltflow Index condition P	g/10 min.	1.2	1.4	1.0	1.2	1.35	1.2	3	0	1	0	0	4.5
5	D3786	Mullen Burst	MPa	5.3	5.9	4.8	5.6	5.8	5.2	3	6	1	0	0	3.6
6	D4491	Permittivity	sec <sup>-1</sup>	0.91	1.21	0.61	0.82	1.20	0.61	2	1	2	0	1	3.5
7	D4595	Wide Width Tensile	N/m	36.6	43.6	29.6	41.1	43.4	36.6	0	0	2	1	0	3.0
8	D4632	Grab Tensile	kN	1.6	1.8	1.4	1.6	1.7	1.5	0	0	2	1	0	2.3
9	D4716	Transmissivity	m <sup>2</sup> /sec	4.2	5.0	3.4	4.4	4.8	4.1	4	0	1	0	0	4.6
10	D5199	Thickness	mm	0.69	0.79	0.58	0.66	0.66	0.66	1	0	0	0	0	5.0
11	D5321	direct shear	degrees	16.4	19.3	13.5	17.3	19.0	15.5	1	0	0	1	0	3.5

Table 2. 1997 proficiency test results.

#	ASTM	Description	Units	Data Base			Lab Submittals			Rating					GPA <sup>g</sup>
				Avg. 1 <sup>a</sup>	UCL <sup>b</sup>	LCL <sup>c</sup>	Avg. 2 <sup>d</sup>	Max <sup>e</sup>	Min <sup>f</sup>	5	4	3	2	1	
1	D638	Yield Stress	kN/m	30.5	32.0	28.9	31.0	32.6	27.0	0	4	1	4	3	2.5
		Yield Strain	%	17.4	19.8	15.0	18.0	24.8	15.0	1	2	3	2	4	2.5
		Break Stress	kN/m	53.0	60.6	45.5	48.5	56.4	47.3	4	7	1	0	0	4.3
		Break Strain	%	697	855	539	782	1819	630	9	1	0	0	2	4.3
2	D882	10% Modulus	MPa	89.9	117.0	62.9	83.9	158.8	62.9	4	0	2	1	1	3.6
3	D1004	Geomembrane Tear	N	240	254	227	236	249	229	0	1	0	0	0	4.0
4	D1388	Stiffness	g/cm	5.8	10.3	1.2	16.7	63.0	0.5	0	1	0	0	2	2.0
5	D1505	Density	g/cm <sup>3</sup>	0.948	0.951	0.945	0.949	0.950	0.947	2	3	0	0	0	4.4
6	D1603	C.B. Content	%	2.34	2.41	2.27	2.37	2.72	2.13	1	4	0	3	2	2.9
7	D3786	Mullen Burst	MPa	5.3	5.8	4.8	5.4	5.4	5.4	1	0	0	0	0	5.0
8	D4491	Permittivity	sec <sup>-1</sup>	0.95	1.3	0.6	1.03	1.26	0.89	1	1	0	1	0	3.7
9	D4533	Trap Tear	N	774	930	619	690	935	561	2	2	1	3	3	2.7
10	D4595	Wide Width Geotextile	kN/m	36.6	43.6	29.6	42.2	42.2	42.2	0	0	0	1	0	2.0
11	D4751	AOS	mm	0.13	0.18	0.08	0.09	0.11	0.05	0	2	0	0	1	3.0
12	D4833	Puncture	N	814	988	641	752	975	467	3	2	2	1	2	3.3
13	D5199	Thickness	mm	0.64	0.69	0.58	0.63	0.66	0.60	0	2	1	0	0	3.7
14	D5261	Mass/Area	g/m <sup>2</sup>	251	265	244	255	265	251	5	0	0	1	0	4.5
15	D5321	Peak Friction Angle	degrees	24.5	27.0	22.0	24.9	26.3	24.0	3	0	1	0	0	4.5
16	D5321	Residual Friction Angle	degrees	15.0	18.0	12.0	14.7	17.0	12.0	1	1	1	1	0	3.5
17	D5323	2% Secant Modulus	MPa	335.4	412.7	258.1	345.1	412.6	280.4	3	0	1	1	0	4.0

<sup>a</sup>Avg. 1 = Average of data base<sup>b</sup>UCL = Upper control limit of data base<sup>c</sup>LCL = Lower control limit of data base<sup>d</sup>Avg. 2 = Average of laboratory submittals<sup>e</sup>MAX = Maximum laboratory submittal<sup>f</sup>MIN = Minimum laboratory submittal<sup>g</sup>GPA = Grade Point Average

The rating of one (1) for some of the tests performed by accredited labs gives rise to concern and deserves some discussion. It should be mentioned that not matching the data base is not always the fault of the submitting laboratory. If results are reproduced by the majority of laboratories but are rated as one (1), the database shall be brought into question. In addition, it should be noted that a 95% confidence level ( $\pm 2\sigma$ ) of a repeatability data base is a very small target and that there are several suspected reasons for low ratings. The most evident being existing confusion with respect to gray areas of some ASTM standards. Gray areas such as gripping, preloading, conditioning and strain rate still persist in standard which offer guidance instead of clearly defining test conditions. These gray areas are most notable with performance rather than index tests and are particularly evident for test methods not specific to geosynthetics.

From a review of Table 1 and 2, there does not appear to be a trend as far as category of test, i.e., physical, mechanical, hydraulic or chemical. It was surprising to find that physical and mechanical results were not easier to match than hydraulic or chemical tests. In addition, trends showing that force and pressure measurements were easier to match than deformation and strain measurement did not materialize.

It was surprising to note that the submitted performance test responses matched very well with their respective data bases. Namely, transmissivity (ASTM D4716) and direct shear (ASTM D5321) responses had a combined average GPA of 4.0. However, in all cases the cross sections examined were rather simple geosynthetic ones. For example, a geonet between two rigid platens for the transmissivity test and a geomembrane against a geonet for the direct shear test were used. The effect of adding soil to the respective cross section has yet to be evaluated.

It was interesting to note significant material variation on any given roll of geosynthetic. Such variation were more significant across the roll width and were particularly noticeable with needle punched nonwoven geotextiles. Such results corroborate current efforts in writing specifications around the minimum average roll value (MARV) for geotextiles as mentined by Koerner (1994).

Along with the positive correlations drawn from matching the lab submittals to the data base, there were several shortcomings. The first of which was the determination of stiffness via ASTM D1388. This relatively obscure test caused a great deal of difficulty for laboratories who have all passed an on-site audit. While determining the corrective actions for outliers, it was determined that unit conversion mistakes were the root cause of the two incorrect submittals. It appears that United States laboratories loose sensitivity for the order of magnitude of results when reporting results in metric units.

The second general test shortcoming was in regard to grip slippage or stress concentration imparted by testing grips. Ideally a grip should not initiate failure while it should allow a specimen to break within the gage length

as it prevents slippage. Grip problems were encountered with the tear test, ASTM D4533, and the puncture test, ASTM D4833. In cases where stress concentrations was encountered with the tear test, results were lower than anticipated. Such conservative results are a disservice to the material. Conversely, when slippage was encountered with the tear test, results were higher due to realignment of the specimen from a tearing mode to quasi tensile mode. In cases where slippage was encountered with the puncture test, results were lower due to a "yielding puncture" rather than a "crisp rupture" of the material. Due to these findings, it is felt that in general more attention should be placed on how geosynthetic specimens are gripped prior to testing.

A related area of concern is the preload or manner in which specimens are loaded into grips. This issue appears to have an effect on the failure strain and modulus results generated from data acquisition systems. Although not a major source of problems in either the 1996 or 1997 proficiency test results, it is envisioned that as the data base values become more refined, such subtleties shall become significant.

#### 4 SUMMARY AND CONCLUSIONS

It is felt that the work presented in this paper illustrates the merits of geosynthetic proficiency testing. The author believe that analyzing quantitative results (via proficiency testing) is a more viable means of assessing a laboratory's quality than merely discussing its attributes. By making proficiency testing the focus of an accreditation program, rather than a voluntary aside, one creates a better program. It has been shown that geosynthetics lend themselves well to proficiency testing and that results within the 95% confidence level are attainable using repeatability data bases.

#### ACKNOWLEDGMENTS

The author would like to take this opportunity to thank members of GSI for their insight and financial support in regard to this work. In addition, an acknowledgment of the geosynthetic testing laboratories who have participated in this program is expressed.

#### REFERENCES

- AASHTO proficiency testing, 1995, TX DOT, Austin TX, pp. 416.
- ASTM data base development, 1993, ASTM Philadelphia, PA, pp. 234.
- JMP® Statistics and Graphics Guide, 1994, SAS Institute Inc., Cary, NC, pp. 213.
- R. M. Koerner, 1994, Designing with Geosynthetics, Prentice Hall, Englewood Cliffs, NJ, pp. 22.

# Site Parameters Influencing Liner Strengths and the Impacts on Landfill Stability

H. D. Sharma

Associate, Geosyntec Consultants, Walnut Creek, California, USA

D. E. Hullings

Project Engineer, EMCON, San Jose, California, USA

F. R. Greguras

Supervising Engineer, EMCON, San Jose, California, USA

**ABSTRACT:** Liners below landfills may be constructed either over relatively permeable materials (sands and silty sands or a drainage layer) or over relatively low permeability formations (silts and clays). These conditions either allow full drainage and consolidation of the low-permeability liner component or allow only partial drainage and consolidation. These varying field conditions will have different impacts on mobilized liner interface strengths. The mobilized strengths influence factors such as construction sequencing, final height and slope of the landfill, and both static and seismic stability. This paper presents the results of interface strengths under various subgrade drainage conditions and presents their impacts on landfill stability and airspace by citing case histories.

**KEYWORDS:** Interface strength, Landfills, Liners, Stability.

## 1 INTRODUCTION

The importance of composite lining systems, which include both a geomembrane and low-permeability soil components, to reduce the potential for leakage has been recognized for years in the development of the modern sanitary landfill. The composite liner, however, has introduced variables that need to be considered in landfill design; among them the interface shear strength between the geomembrane and low-permeability soil. The importance of this parameter has been recognized for years, as evidenced in the literature references, with emphasis placed on laboratory shear strength testing, especially the direct-shear test described in American Society of Testing and Materials (ASTM) D 5321.

ASTM D 5321 is an important step in evaluating shear strengths, but leaves much to be determined by the design engineer "to simulate field conditions." While the authors acknowledge the importance of simulating field conditions, more information is required on how this is to be done. Two variables, drainage and consolidation, that ASTM D 5321 currently leaves unspecified, can impact tests. In an attempt to address these issues, we offer the following.

## 2 DRAINAGE AND CONSOLIDATION OF SOIL

### 2.1 Effects of Drainage and Consolidation on Shear Strengths of Low-Permeability Soil

The impacts of drainage and consolidation are described in any number of standard soil mechanics text books (Lambe and Whitman 1969; Terzaghi, Peck and Mesri 1996), but a short discussion is appropriate here as it directly affects the evaluation of interface strengths. Soils tested in the unconsolidated undrained (UU) condition usually represents short-term conditions. In laboratory testing, such as triaxial tests (ASTM D 2850), the soil is not permitted to drain either during the initial application of confining pressure nor during shearing. Pore pressures are not dissipated and shear strengths ( $S_u$ ) are constant (e.g., strengths do not increase with confining pressure) for saturated cohesive soils.

Triaxial testing (ASTM D 4767) that allows drainage during the initial application of confining pressure but does not permit drainage during shearing is referred to as consolidated undrained (CU). This represents soils that have consolidated under load, but are sheared quickly so that pore pressures generated during shearing are not dissipated.

Shear strengths under CU, for total stress conditions, are presented by the Mohr-Columb equation:

$$\tau = c + \sigma \tan \phi \quad (1)$$

where:  $\tau$  = shear stress;  $c$  = cohesion, which is the shear strength intercept when the normal stress is equal to zero;

$\sigma$  = total normal stress on the failure plane at failure; and,  
 $\phi$  = angle of internal friction.

Testing conducted at strain rates slow enough to allow drainage during shearing represent consolidated drained (CD) conditions. Consolidated drained conditions may also be estimated by measuring pore pressures during the CU triaxial test and accounting for them to determine effective stresses. These conditions typically reflect long-term conditions. Cohesion is usually low or negligible under drained conditions for normally consolidated or slightly over consolidated soils.

## 2.2 Effects of Drainage Conditions on Interface Shear Strengths

For typical design and testing purposes, the low-permeability soil is considered initially saturated. Compacted low-permeability soil liners are usually well compacted at moisture contents above optimum, which results in a soil placed near saturation. Initial moisture migration from compacted soil to the geomembrane/soil interface due to factors, such as, thermal gradient effects is enough to saturate the soil near the interface. Compression under load may also increase the degree of saturation. To model these field conditions, interface strength testing is conducted under submerged conditions and the top of the clay is sprayed with water prior to placement of geomembrane.

Two distinct models are generally considered for drainage conditions. Low-permeability soil constructed over a relatively permeable soil subgrade or a subdrain should consolidate quickly, less than one year, and consolidated shear strengths are considered (Figure 1a). Liners constructed over relatively low-permeability subgrades or a naturally occurring layer of low-permeability soil may not consolidate quickly (Figure 1b).

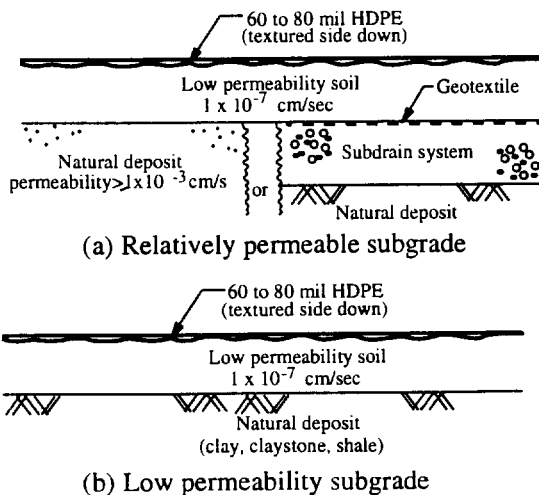


Figure 1. Field conditions representing relatively permeable and low permeability subgrades

In this case, unconsolidated strengths are typically considered, at least for short-term to intermediate conditions. It should be noted that textured HDPE geomembrane has been used and post-peak strengths have been considered in the analyses.

## 3 RELATIVELY PERMEABLE SUBGRADE

### 3.1 Consolidation

Low-permeability soil liners constructed over relatively permeable subgrades are likely to consolidate and increase in strength over time. Interface shear strengths between textured geomembrane and the soil should likewise increase in strength due to consolidation if the texturing is sufficient enough to push the failure plane into the upper surface of the soil as opposed to the geomembrane sliding above the surface. The time required to consolidate the soil near the interface is related to the soil characteristics, specifically the coefficient of consolidation, according to the following equation:

$$t = \frac{TH^2}{c_v} \quad (2)$$

where:  $t$  = the time for consolidation to occur,  $T$  = appropriate time factor for desired percent consolidation,  $H$  = length of the drainage path (thickness of the layer for single drainage), and  $c_v$  = coefficient of consolidation from consolidation test (ASTM D 2435).

For most practical purposes, 90 percent consolidation is probably sufficient to consider the soil consolidated and even 50 percent consolidation may be enough to result in measurable increases in strength. The above equation is applicable to relatively permeable subgrades such as a natural granular deposit, leachate detection, or subdrain layer beneath a primary clay liner. In such cases 90 percent consolidation is likely to occur within a year (e.g., assuming a 610 mm thick layer with  $c_v = 1 \times 10^{-4} \text{ cm}^2/\text{sec}$ ).

In cases where consolidation of the soil liner can be substantiated, testing should be conducted to reflect consolidated conditions. For the interface shear strength testing, we have applied the full overburden load test load for about 16 hours and allowed the sample to consolidate under this load prior to shearing. Generally, clay samples 25-mm-thick used in the interface shear strength test should consolidate (80 to 90 percent) within 12 hours. The test apparatus should allow for drainage beneath the soil sample. In such situations, shear rates of 1 mm per minute would most closely represent consolidated undrained conditions. This CU strength is appropriate for modeling

seismic conditions and is an appropriate value for long-term static conditions.

### 3.2 Soil Testing

One of the short comings of the direct-shear testing (ASTM D 5321) is that drainage conditions are not easily controlled. When simulating consolidated conditions, the impact of consolidation during shearing is probably not significant compared to initial consolidation prior to shearing. The dissipation of pore pressure during shearing, however, does have an impact of whether the test can be considered drained or undrained. While attempting a CU test, true undrained conditions can not be achieved since some dissipation of pore pressure is allowed during shearing. True CD conditions may be approached if shear rates are low enough to prevent pore pressures from accumulating. Shear rates slower than 0.1 mm per minute are usually required which results in shearing times in excess of one day.

In an attempt to overcome these short comings, the authors typically conduct shear strength testing on the soils alone using triaxial testing where drainage conditions can be controlled. Unconsolidated undrained triaxial shear testing for saturated samples is conducted to represent short-term strengths. This strength should represent worst-case conditions and be lower than the consolidated interface shear strengths under typical refuse loading (greater than 240 kPa). UU strengths may be used to analyze interim refuse slopes where consolidation of the soil liner may not yet be appreciable.

Consolidated undrained triaxial shear strengths should represent the upper limit of strength. This testing is important, however, in that it reflects the effects of consolidation on soils and is conducted under known drainage conditions. In addition to triaxial shear testing, consolidation tests may also be conducted to determine coefficients of consolidation under various load increments. This is important, along with fill sequencing, in determining how much consolidation may be achieved.

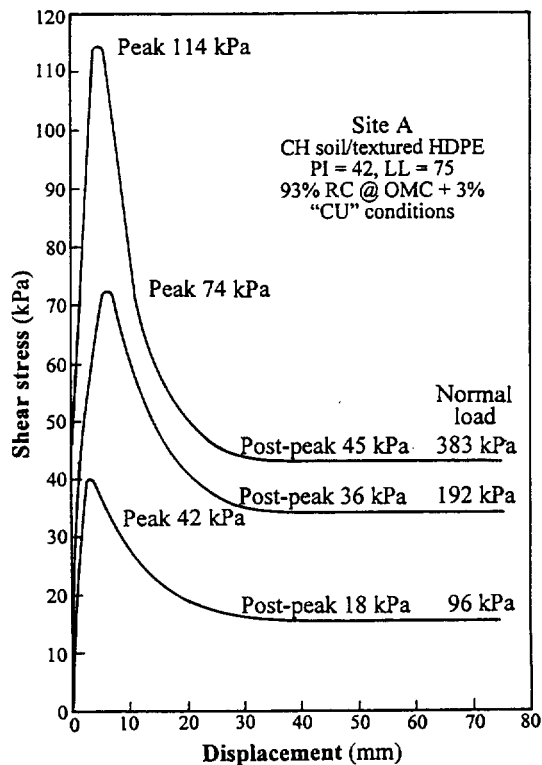
### 3.3 Case Histories

#### 3.3.1 Compacted clay/HDPE liner system

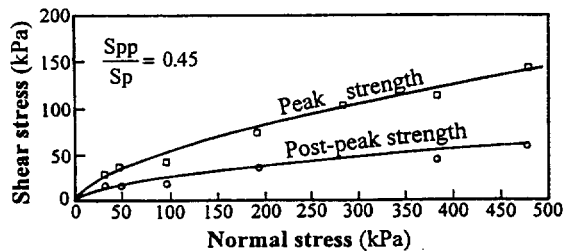
Consolidated shear strengths were used in the design of a municipal solid waste landfill along the California Central Coast (Site A). Low-permeable soils were available for soil liner construction from a nearby borrow source, while subgrade soils were generally sands that allowed for consolidation. Groundwater was more than one meter below the liner.

At 93 percent relative compaction (ASTM D 1557), the UU shear strength of the soil met the required 38 kPa short-term strength. The CU triaxial compression strength

(total stress) was a friction angle of 13.5 degrees with a cohesion of 53 kPa. The CU interface shear strength (post-peak) with textured HDPE geomembrane was represented in a two-part curve to model non-linear behavior; a friction angle of 10.5 degrees under loads less than 190 kPa and 4 degrees with a cohesion of 21 kPa at higher loads. The peak interface strength of 11 degrees with a cohesion of 39 kPa is roughly 80 percent of the CU clay strength. As shown in Figure 2, under high loads the interface strength falls between UU and CU triaxial soil strengths. Note the significant drop in post peak interface shear strengths from peak strengths that has been associated with plastic clays. (Sharma, et al. 1997). Consolidation tests resulted in a coefficient of consolidation around  $1 \times 10^{-3} \text{ cm}^2/\text{sec}$  which allows for significant consolidation of the clay within months. The landfill was designed using CU post-peak interface strengths. The stability of interim refuse slopes was also checked using the UU triaxial soil strength.



(a) Shear stress-displacement relationship



(b) Shear strength envelopes

Figure 2. Interface strength for consolidated conditions (Site A: permeable subgrade)

### 3.3.2 Admix soil/HDPE liner system

Another MSW site in the Southern California area (Site B), where the excavated subgrade materials are predominately coarse-grained sandstone, required either imported low-permeability clay or screening site material and admixing with 7 percent high-swelling sodium bentonite. To achieve static stability (factor of safety = 1.5) and seismic deformation (average 6 inches) requirements, an admixed low-permeability material was specified. A field test pad fill confirmed that the admixed material could meet the field permeability requirement of  $1 \times 10^{-7}$  cm/s.

A saturated, UU triaxial compression strength of 76.8 kPa and CU triaxial compression strength (total stress) of a friction angle of 19.5 degrees with a cohesion of 23.8 kPa were achieved on the selected admix soil design with specimens remolded at 92 percent of the maximum dry density (ASTM D 1557) at 5 percent above optimum moisture content.

Two series of saturated direct shear interface tests (ASTM D 5321) between the selected admix soil and the 1.5 mm thick textured high-density polyethylene (HDPE) geomembrane were performed (Figure 3). The first series of tests were performed under partially consolidated conditions where the soil was submerged for at least 16 hours under a 6 kPa overburden pressure, the load ramped to the selected normal overburden pressure, and then sheared at 1 mm per minute. The second series of tests were performed under similar consolidated conditions described for the first series testing, the load ramped to the selected normal load, and the soil was allowed to consolidate under the full load for 1 to 4 hours (80 to 90 percent consolidated) prior to shearing.

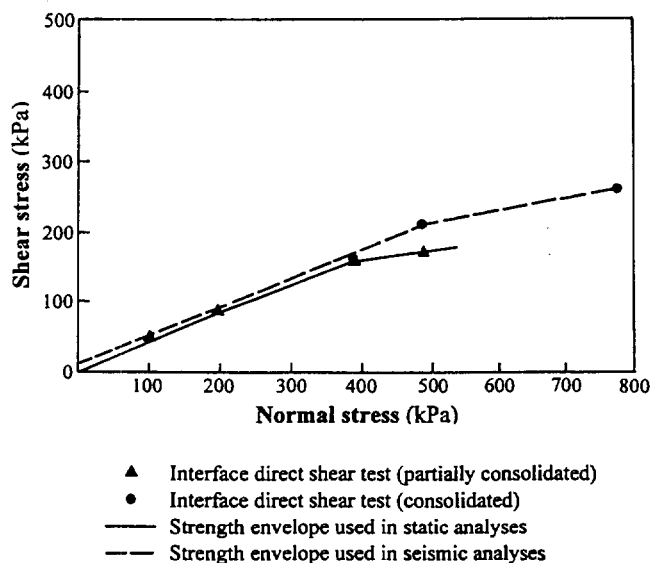


Figure 3. Interface strengths for relatively permeable subgrade, Site B

The static stability analyses for fill sequencing were performed using the saturated, interface shear strength envelope for partially consolidated soil conditions. The seismic stability analyses were performed using the saturated, interface shear strength envelope for the consolidated site conditions. The basis for using the higher strength envelope to assess seismic and long-term static conditions is due to the following:

- The coefficient of consolidation from a laboratory test performed on an admix specimen ranged from  $1 \times 10^{-3}$  to  $2 \times 10^{-3}$  cm<sup>2</sup>/s.
- A low-permeability admix material will be underlain by predominately coarse-grained materials which will provide a drainage path.
- The thickness of the low-permeability admix material is limited to 0.6 m, therefore, about 90 percent of field consolidation should occur within 30 days.
- The probability of the design earthquake occurring before completion of 90 percent of consolidation is very small.

## 4 LOW-PERMEABILITY SUBGRADE

### 4.1 Testing

Low-permeability subgrades are slow to drain and do not permit rapid consolidation of the soil liner. With a constant unsaturated vadose zone beneath the liner, consolidation of the soil liner is probably inevitable (on a long-term basis), but should not be counted on for near term conditions (during landfill operations).

Direct-shear interface strength testing in these cases should be conducted to simulate UU conditions as closely as possible. As noted earlier, however, consolidation and drainage during shearing (ASTM D 5321) do not allow testing under true UU conditions. To approximate this state, the soil sample is placed under a setting load (6 to 24 kPa) and submerged overnight. The full load is placed immediately before shear (immediately in this case means applying the load quickly in stages of about 50 kPa per minute). The amount of the setting load may have minimal impact at high overburdens, but should be considered carefully especially for testing under low overburdens (50 kPa or less).

Triaxial testing under saturated UU conditions should also be performed to develop soil strength data under controlled drainage conditions. Slope stability analyses should be performed for both direct-shear interface and triaxial strengths. Although interface strengths should be no greater than the internal soil strengths, consolidation during testing may have increased the interface strengths resulting in a higher interface strength than soil strength.



Testing under CU conditions is not required for this scenario since consolidation is not expected under this field condition.

## 4.2 Case Histories

### 4.2.1 Compacted high plasticity clay/HDPE over shale subgrade

A site in the San Francisco Bay Area is being developed as an MSW landfill over a foundation consisting largely of shale (Site C). Excavated weathered shale is recompacted as a 610 mm-thick soil layer over the shale. A dendritic patterned subdrain system is being installed to collect isolated subgrade seeps, but the spacing of the drainage trenches is thought to be too large to dissipate pore pressures in the soil layer in the near term.

Testing under UU conditions has resulted in an interface shear strength friction angle of 7.5 degrees under normal stresses less than 290 kPa with a slightly lower friction angle under higher stresses (Figure 4). The friction angle for lower stresses under CU conditions is about 10 degrees. The soil itself has an undrained shear strength of 34 kPa. These relatively low strengths have a significant impact on allowable refuse slopes and landfill capacity. The interface shear strengths have limited landfill refuse heights to 100 feet to maintain a minimum static factor of safety of 1.5 with a maximum allowable seismic displacement of 1 foot.

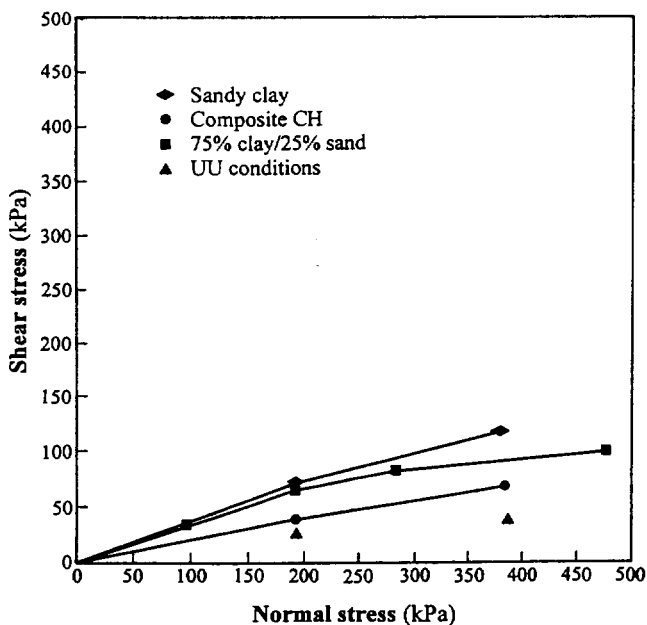


Figure 4. Interface strengths for low-permeability subgrades, Site C

To avoid staging over long periods and to potentially increase refuse slopes, we are currently evaluating enhancing the subdrain system and improving the clay strengths. Remembering that the relatively low post-peak strengths are associated with plastic clays, we have initiated testing a blended soil consisting of 75 percent clay (site shale) and 25 percent on-site silty sand. The blended soil has a lower plasticity index and a CU interface strength approximated with a friction angle of 16 degrees. Together with the enhanced subdrain, the higher strengths may permit a substantial vertical expansion. Testing under UU conditions is underway to determine if adequate strengths can be achieved without enhancing the subdrain system.

### 4.2.2 Compacted high plasticity clay/HDPE over claystone subgrade

A similar situation occurs in a Colorado landfill (Site D) where the landfill is constructed largely on claystone. Interface shear strength (between clay and HDPE) testing for the first composite-lined cell for this landfill resulted in an adhesion of 19 kPa and friction angle of 9° for CL type soil and adhesion of 9.5 kPa and friction angle of 5° for CH type soil (normal load range from 100 to 500 kPa) under undrained conditions (Figure 5). On-site clays with lower plasticities (CL soil with PI equal to about 20 to 22) have higher strengths, but were difficult to identify in the field, and selectively excavate in sufficient quantities to construct the low-permeability soil layer.

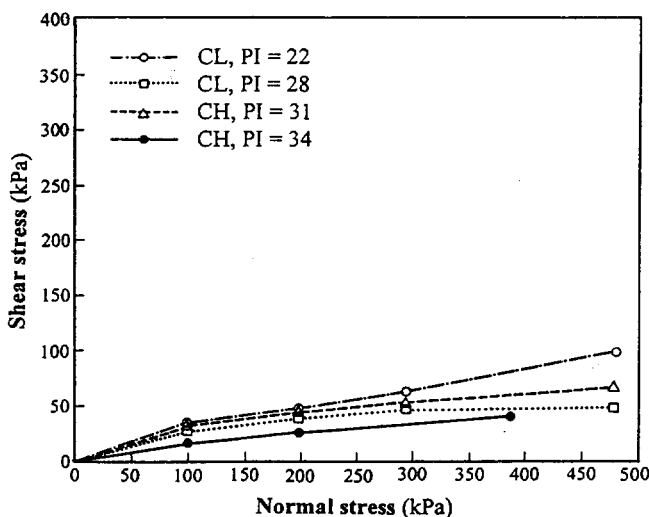


Figure 5. Interface shear strengths for low-permeability subgrade, Site D

The low interface shear strengths, barely sufficient for originally permitted refuse slopes, have impacted vertical expansion plans. Current permitted capacity is 19 million m<sup>3</sup> but expansion plans were to increase the capacity to 37 million m<sup>3</sup>. The initial thought was to provide a subdrain to allow the clay to consolidate, but initial interface testing under CU conditions at 290 kPa normal load showed minimal increase in strength over UU conditions (a shear strength of 56 kPa compared to 53 kPa). The current plan is to admix bentonite with on site-silty sands (similar to Site B) or blend the plastic clays with sand (similar to Site C) to achieve a shear strength with an internal friction of 16 degrees.

## 5 CONCLUSIONS AND RECOMMENDATIONS

Based on the results of laboratory tests, analyses, and case histories cited in this paper, the following conclusions and recommendations can be made:

- Subgrade drainage conditions should be considered in the soil and interface strength testing program and eventual landfill liner design.
- For relatively permeable subgrade conditions, CU triaxial and interface tests (with normal loads allowed to consolidate) should be performed. For low-permeability subgrade conditions, UU triaxial and interface tests (where shearing occurs immediately upon application of the full normal load) should be performed.
- The application of UU or CU interface shear conditions for fill sequencing analyses depends on project-specific soil characteristics, fill sequencing, and drainage conditions.
- Differences in UU and CU strengths vary ranging from negligible difference (Site D) to differences only at large normal loads (Site B) to about 20 percent increase in CU strength over UU strengths (Site C).
- For compacted soil liners consisting of highly plastic clays (CH), exhibiting low undrained interface strength, blending the clay with sandy material should increase interface shear strengths while maintaining low permeability. This approach can provide additional airspace for landfills with slope stability constraints.

## REFERENCES

- ASTM (1997) Annual Book of Standards, American Society for Testing and Materials, West Conshohocken, PA, USA, Volumes 04.08 and 04.09, Test Methods D 1557, D 2435, D 2850, D 4767, and D 5321.
- Lambe, T.W. and Whitman, R.V. (1969) Soil Mechanics, John Wiley and Sons, Inc., New York, NY, USA.
- Sharma, H.D., Hullings, D.E., and Greguras, F.R. (1997) "Interface Strength Tests and Application to Landfill Design," Geosynthetics '97, IFAI, Volume 2, Long Beach, CA, USA, pp. 913-926.
- Terzaghi, K., Peck, R.B., and Mesri, G. (1996) Soil Mechanics in Engineering Practice, Third Edition, John Wiley and Sons, Inc., New York, NY, USA.

# Shear Strength and Deformation Considerations for Composite Landfill Liners in Hong Kong

R.K. Frobels  
Principal, R.K. Frobels & Assoc., Lakewood, Colorado, USA

M.A. Sadler  
Principal, Geosynthetic Consultants Australia, Melbourne, Australia

J.W. Cowland  
Geotechnical Engineering Office, Hong Kong

**ABSTRACT:** Geosynthetic clay liners (GCLs) are often used as one layer of a composite landfill liner, with a geomembrane forming the other layer. GCLs offer significant advantages over compacted clay liners in terms of their ease of installation. Some recent experience with the testing and use of a variety of GCL products is presented particularly with respect to complex liner systems on steep slopes in Hong Kong, which require careful consideration to determine appropriate internal and interface shear strengths to be used in design.

**KEY WORDS:** Geosynthetic Clay Liners, Geomembranes, Protection, Interface and Internal Shear, Slopes.

## 1. INTRODUCTION

Geosynthetic clay liners (GCLs) have been rapidly adopted as an alternative for compacted clay liners in many landfills around the world, and they have been widely used in composite liners for landfills in Hong Kong.

Hong Kong has a mountainous terrain, with many steep sided valleys, or canyons, which have 25° to 40° natural side slopes rising from near sea-level to a height of a few hundred metres. Three new landfills are being constructed and operated in these valleys, and the liner systems are being placed on some very steep and high slopes. With building development at the toe of these landfills, stability is an important issue.

Multilayer lining systems using geomembranes and GCL's can have relatively low internal and interface shear strengths, so they have the potential to act as a slip planes, and often form the weakest link in stability considerations. The naturally low shear strength of the bentonite component of GCL's has required careful measurements of their strength, with due consideration to the use of these measurements in design.

## 2. TYPICAL COMPOSITE LINER

A typical Hong Kong landfill liner comprises a geomembrane overlying a geosynthetic clay liner. A groundwater drainage layer is usually placed below the liner, and a leachate drainage layer is placed above the liner.

Depending on various design and availability considerations, these drainage layers may comprise crushed granitic rocks (with a geotextile cushion to protect the liner) or geonets. A typical arrangement is shown in Figure 1.

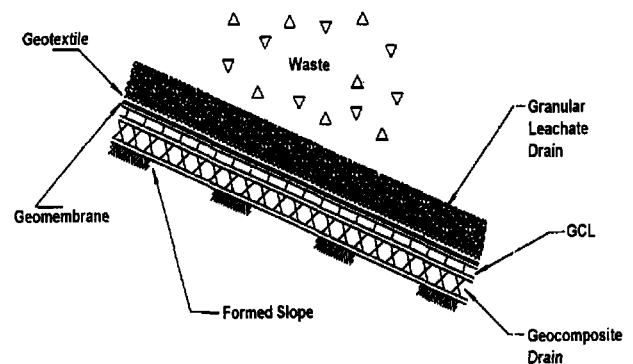


Figure 1. Typical Hong Kong Composite Lining System

The geomembrane is usually a 2mm thick sheet of high density polyethylene (HDPE), with either textured or smooth surfaces. The GCLs are usually needlepunched with woven or non-woven geotextiles on each side of the bentonite, which may be in powder or granular form. Whilst powdered bentonite can be more effective in terms of distribution and hydration performance, it can be more difficult to retain within the GCL during transportation and placement.

GCLs based on woven geotextiles offer the capacity for better tensile strength at less elongation, compared to non-woven geotextiles. However, the non-woven geotextiles are more effective at retaining the bentonite gel, although there may still be enough weeping to reduce the interface shear strength. The tendency for bentonite to weep through woven geotextiles allows these materials to have better self-sealing properties at the overlap joints. Products using non-wovens require additional bentonite at the seams, which some manufacturers introduce at the roll edge during manufacture.

Some GCLs have a woven geotextile on one side and a non-woven on the other side, and some have a composite geotextile with a woven material within the non-woven base.

### 3. DESIGN ISSUES TO BE CONSIDERED

#### 3.1 Maximum and Minimum Induced Stresses

The maximum depth of waste planned for Hong Kong's landfills is currently around 150 metres. With a possible unit weight of 1.4 tonnes/cubic metre (Cowland et al, 1993), this depth of waste could impose a stress of around 2000 kPa on the GCL. At the other extreme, the depth of soil overlying a GCL in a landfill cap may be less than one metre, giving rise to an induced stress as low as 10kPa. In addition, the stresses on a GCL on a side slope will vary from the top to the bottom of the slope. So the normal stresses to be considered in the GCL shear strength testing programme may need to range from 10 to 2000 kPa.

Although high ultimate loadings may be expected, it is still possible for a slip failure to occur at low normal loads during construction of the liner, caused by the downdrag of an overlying granular leachate drainage or protection layer.

#### 3.2 Degree of Hydration

The internal and interface shear strength of a GCL usually decreases as it becomes wet. Although the overlying geomembrane will help to keep it dry, with the typical lining system there is a groundwater drain immediately below the GCL. Experience has shown that with its high affinity for water, the bentonite component of a GCL will soon start to become hydrated even when only a small amount of moisture is present in the underlying drainage medium.

Some designers try to keep the GCL dry by encasing it between two geomembranes. However, the long term effectiveness of this measure, given the possibility of minor leaks or other damage or deterioration of the geomembrane, is unknown.

Examination of two liner systems, where it was known that heavy rainfall had penetrated through the geomembrane, and remedial action was required, has shown a surprising extent of lateral moisture travel along the GCL/geomembrane interface. It was observed that water easily travels through compressed wrinkles in the geomembrane to wet a large surface area of the underlying GCL.

#### 3.3 Relevant Shear Surface

The bentonite layer within a GCL can have a low shear strength, especially when hydrated, resulting in a low internal shear strength through the mid-plane of the GCL. In addition, the bentonite can be squeezed through the openings of the geotextiles, producing a low friction surface at the interface between the GCL and the adjacent material.

Exhumation after a construction failure has shown that slip surfaces can pass through the mid-plane of the GCL, and also along interfaces between the GCL and adjacent layers. Thus, the testing should be arranged to examine both these potential failure modes.

### 4. GCL SHEAR TESTING CONSIDERATIONS

Shear strength parameters of GCLs for both internal and interface shear are determined following the form of the standard American Society for Testing and Materials (ASTM) test method D 5321-92 for geosynthetics (ASTM, 1992). However, when this test method was first developed for geomembranes and geotextiles, GCLs were not considered and there is on-going work to further develop this ASTM test method for GCLs.

It is generally considered that the shear box should be at least 300 mm square, as smaller boxes will introduce excessive edge effects and give distorted results, particularly if granular materials are involved. Figure 2 illustrates schematically a large scale shear box. A constant normal compressive stress is applied to the apparatus and one section of the box moves in relation to the other. The shear force and corresponding displacement is recorded and shear stress is plotted against normal compressive stress.

Although ASTM D 5321-92 provides guidance for shear displacement rates, with emphasis on the need for slow rates to dissipate pore water pressures, a lot of testing has been carried out using a default shear displacement rate of 60 mm/hr.

The GCL is usually hydrated in the shear box, under the design normal load, for 24 hours just prior to shear. However, more information is needed on the impact of different hydration times and boundary materials.

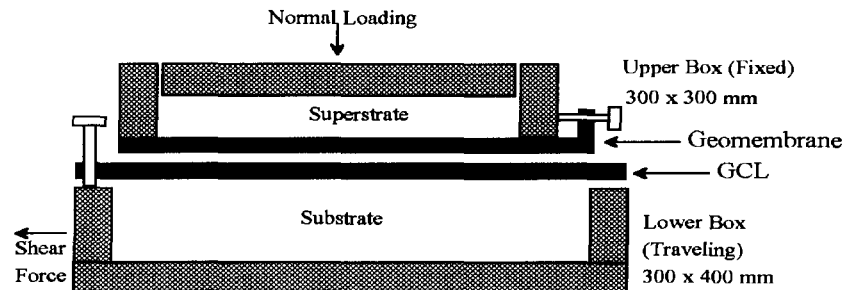


Figure 2. Typical Interface Shear Test Device

## 5. A SITE SPECIFIC TEST PROGRAMME

During a recent project, the deformation and shear strength of the interface between a smooth HDPE geomembrane and a needle-punched GCL, resting on coarse granular material, was examined. The main issues were the deformation imposed on the geomembrane by the interaction of the various granular surfaces and protective layers of geotextile, and the shearing capacity of the various interfaces in the liner system.

### 5.1 Deformation Testing

The deformation testing was carried out in a large scale geostatic test apparatus as shown in Figure 3, and as described by Frobel & Winneke (1993). Various combinations of geosynthetics and granular layers were under consideration for different stages in the design development.

The geostatic test is a relatively new performance test intended to provide a view of behaviour under field loading conditions. The layers of geosynthetic and granular materials are placed into a cylindrical vessel, where they are subjected to appropriate loadings, with submergence to achieve hydration as required.

Deformation is measured by the use of a highly deformable thin zinc plate which is placed under the geomembrane and which retains the deformed shape on disassembly. As yet, there is no standard test method for this new test.

Testing of protection layer materials for this project included both 1050 and 1200 gram/m<sup>2</sup> needlepunched non-woven geotextiles. The results indicated that the deformation performance of these very heavy products was influenced more by the tightness of the needed mat than by small variations in unit weight.

### 5.2 Degree of Hydration

Two series of hydration tests under load were carried out for this project. In the first, a number of GCL samples were hydrated for 24 hours under a constant confining stress of either 175, 350, 700 or 1000 kPa. The moisture content in the samples under 175 kPa confining stress was found to be in the range of 75 to 90% after 24 hours. Samples hydrated under larger stresses were found to have lower moisture contents, with values of 40 to 50% being measured after 24 hours under a load of 1000 kPa.

In the second series, specimens of a GCL were hydrated for different times under a stress of 10 kPa or a stress of 700 kPa. Initial hydration occurred more quickly under the lower stress, however, in neither case was hydration complete after 24 hours. These results are shown in Figure 4, and can be compared with Stark (1996) who found that a GCL under a load of 40 kPa was still hydrating after 250 hours.

It is strongly recommended that the degree of hydration (i.e. moisture content of the GCL) must be reported with the shear strength results.

### 5.3 Interface Direct Shear Testing

The interface direct shear testing for this project was carried out in a 300 x 400 mm direct shear box, using the various combinations of geosynthetics and granular layers that were under consideration in the design.

It was found that 10 - 20 mm angular drainage gravel under a GCL significantly deformed the interface between the GCL and an overlying geomembrane, which increased the interface friction angle by about 2 - 3°, but it had a detrimental effect on the integrity of the geotextile components of the GCL which allowed the bentonite gel to weep.

Non-woven geotextiles appeared to more successfully contain the bentonite gel than woven geotextiles.

## 6. SHEAR BOX TEST METHODOLOGY

Some of the many apparatus set up questions for GCL shear testing that are not answered by ASTM D 5321-92 include hydration method, loading period, displacement rates and fixing methods. The following discussion is based on direct experience.

### 6.1 Gripping Methodology

It is important that the gripping methodology for testing the internal shear strength of GCLs be carefully considered.

One system is to use sharp, one-way serrated steel surfaces that grip into the surface of the geotextile on either side of the GCL to uniformly force the shear plane into the hydrated bentonite/fiber structure. In addition, extensions of the GCL fabric are wrapped around the top and bottom plates to effect a positive tensile strain across the full width of the GCL fabric. Bolting of end sections is not recommended, due to tearing at bolt holes and disturbance of the specimen.

### 6.2 Hydration

After hydration under load, the normal stress applied should not be relieved before shearing. Thus, the sample should be hydrated in the shear box, unless a method can be found to maintain the normal stress during specimen transfer to the shear box. In view of the need to hydrate for some time, and the scarcity of large shear boxes, this issue requires further development.

### 6.3 Displacement Rate

Significant pore pressures are generated within the bentonite clay component of a GCL, and thus displacement rates reflecting consolidated-drained (CD) conditions should be considered.

The ASTM test method D 3080-90 (ASTM, 1990), gives a method for calculating the time to failure to achieve CD conditions. By using the time to failure from consolidation tests, and a required total displacement during shear (20 to 30 mm for reinforced GCLs), the displacement rate can be calculated. These displacement rates should be in the range of 1 to 10 mm/hr in order to reflect CD conditions.

For instance, it was found in one programme of GCL interface shear testing that the friction angles measured at a displacement rate of 2.4 mm/hr were 1 - 2° lower than at a displacement rate of 60 mm/hr. Faster displacement rates will result in indications of higher internal shear strength and should be avoided for design test purposes.

## 6.4 Area Corrections

In a square shear box, the contact or stressed area of a GCL decreases with increased displacement. Consequently, the compressive stress decreases, resulting in an increase in shear stress. So, it is important to apply an area correction, especially for larger displacements for GCL tests run under CD conditions. Alternatively, a shear box which has one half of the box longer than the other can be used to keep the shear area constant.

## 7. USE OF SHEAR STRENGTH DATA IN DESIGN

Having obtained strength data from careful testing, the designer needs to consider various aspects in the use of this data in design.

### 7.1 Peak or Residual Strength

With increasing strain, needlepunched GCLs typically exhibit shear strengths that rise to a peak and then fall to a residual value.

The difference between peak strength and residual can be relatively small for interfaces but can be quite large for internal shear. With needlepunched GCLs the peak shear strength is based on mechanical rather than friction bonds and is usually achieved after 20 - 30 mm of displacement, and thus the question of whether to use peak or residual strength is very significant.

Based on limited knowledge of landfill failures it would be unwise for the designer to rely on peak strength throughout the lining system. From a finite element back analysis of the Kettleman Hills Landfill failure, Byrne (1994) found that the onset of progressive failure mobilises residual strengths on the side slopes, although the peak strength may still be relied upon for a proportion of the base.

As noted by Koerner (1994), the analysis of side slope liner stability is complicated for a multi-layered liner and leachate collection system. The unit load of the waste gravitationally induces shear stress through the leachate collection system onto the liner and then onto the groundwater collection system. Depending on the frictional characteristics of the surfaces involved, it is possible that only a portion of the induced shear stress is transmitted to the layer below.

It is possible therefore, when a low friction slip surface is built into the upper part of the system, that some interfaces may not progress past their peak strength. However, extensive laboratory and field measurements, and a thorough finite element or finite difference analysis of the stresses and strains in the system would seem to be needed to determine whether individual interfaces should be designed using the measured peak or residual strengths.

## 7.2 Deformation of the Shear Surface

With a coarse granular leachate drainage layer above the lining system, and high normal loads, it is likely that the shear surface will become deformed. This deformation may result in an increase of the interface friction angle. However, in order to utilise this increased friction angle, the designer needs to be confident that the same deformation will occur in the laboratory and the field. The gravel used in laboratory tests needs to be truly representative of the gravel used in the landfill. Also, the normal loads in the laboratory tests should be varied to ensure the deformation would still exist with lower than expected normal loads in the field.

## 7.3 Landfill Loading Sequence

Load should be placed above the GCL as soon as possible after installation, in order that it does not get the chance to go into free swell and weaken, due to any moisture that may be available.

With a low strength lining material being placed on steep slopes, it would appear that there is a high chance of a slip occurring. However, Giroud and Beech (1989) have demonstrated that many of the stability problems associated with these materials can be avoided by utilising an incremental balanced method of placing the overlying load, using toe buttresses, and these methods have been used successfully in Hong Kong.

## 8. CONCLUSIONS

The GCLs currently being used in landfill liners and caps have the potential to act as slip planes, as the bentonite they contain has a low shear strength, especially when wet. For the designer, it is important to incorporate shear strengths obtained from relevant and independent testing into the design of the landfill. The designer needs to consider the complete range of loads that may be exerted on the GCL, the possible degree of hydration, and all possible shear surfaces. For drained shear strength parameters, it is important to maintain a low rate of strain during the test.

The determination of GCL shear strength needs to be both material specific and project specific. With the rapid development of GCLs incorporating different geotextiles and methods of bonding them together, it is not possible to rely on previous test results. The designer needs to know the shear strength characteristics of the individual product to be used in his landfill.

Obtaining reliable GCL interface and internal strength parameters is difficult and not recommended for laboratories with minimal GCL experience. Conformance test procedures must be described in detail and should

model the existing or design site conditions using the actual site soil materials and geosynthetics specified in the design.

It is not adequate to simply state the required GCL friction angle in the specifications for a project. Designers must specify in detail the test parameters required to generate design oriented values.

## ACKNOWLEDGEMENT

This paper is published with the permission of the Director of Civil Engineering of the Government of the Hong Kong Special Administrative Region.

## REFERENCES

- ASTM (1990). "Direct Shear Test of Soils under Consolidated Drained Conditions", ASTM 3080-90, Philadelphia, USA.
- ASTM (1992). "Determining the Coefficient of Soil and Geosynthetic or Geosynthetic Friction by the Direct Shear Method", ASTM D 5321-92, Philadelphia, USA.
- Byrne R.J. (1994). "Design Issues with Strain-Softening in Landfill Liners", Proceedings of Waste Tech '94, National Solid Wastes Management Association, South Carolina, USA, Section 4, pp. 1-26.
- Cowland J.W., Tang K.Y. & Gabay J. (1993). "Density and Strength Properties of Hong Kong Refuse", Fourth International Landfill Symposium, Sardinia, Italy, pp. 1433-1446.
- Frobel R.K. & Winneke C.J. (1993). "Large Scale Performance Test Methods for Geomembrane Systems used in Heap Leach Pad Applications", Randol Gold Mining Forum, Beaver Creek, Colorado, USA, 15p.
- Giroud J.P. & Beech J.F. (1989). "Stability of Soil Layers on Geosynthetic Lining Systems", Geosynthetics '89 Conference, San Diego, USA, pp. 35-46.
- Koerner R.M. (1994). "Designing with Geosynthetics", Prentice Hall, 783p.
- Stark T.D. (1996). "Effect of Swell Pressure on GCL Cover Stability", Testing and Acceptance Criteria for Geosynthetic Clay Liners, ASTM STP 1308, pp. 30-44.

# THE EXPERIMENTAL SHEAR STRENGTH EVALUATION OF GEOMEMBRANE - CLAY LINER AND GEOMEMBRANE - GEOTEXTILE INTERFACES

R. Floss

Professor, Institute for Foundation Engineering, Technical University of Munich, Germany

J. Fillibeck

Research Associate, Institute for Foundation Engineering, Technical University of Munich, Germany

**ABSTRACT:** When calculating the slope stability of geomembrane-lined slopes in waste disposal applications, the shear behavior between the lining components have to be evaluated. The paper discusses the shear strength of compacted clay liners (CCLs), CCL/geomembrane and geomembrane/geotextile interfaces. The dependence between matric suction of the CCL and shear strength is shown. Shear tests between compacted clay liners and geomembranes demonstrate the influence of several test conditions (e. g. duration of consolidation, shear speed, normal stress and water content of the CCL). In addition, 1000 hours creep tests between geomembranes and geotextiles were conducted to evaluate the long term shear strength behavior.

**KEYWORDS:** Shear strength, Testing, Friction, Geomembranes, Compacted Clay Liner

## 1 INTRODUCTION

According to the relevant regulations, composite sealing layers - consisting of a mineral seal (compacted clay liner, CCL) a geomembrane (GM) and a geotextile protection layer (GT) - are current state of the art in Germany. Prior to installation, it needs to be proven that shear forces are transferred into the subsoil from the top of the cross section downward. The starting point of such slope stability proofs are shear box tests which determine the maximum transmittable shear forces within the sealing system. As the test conditions under which such shear box tests have to run are not yet clearly defined, the Arbeitskreis Grundwasserschutz AK-GWS (Working Group 'Groundwater Protection') initiated a research project to investigate the influence of various test conditions on the shear strength of the sealing system. Triaxial tests with CCLs under saturated and partly saturated conditions were carried out to show the influence between matric suction and shear strength. Direct shear tests between CCLs and GMs demonstrate the influence of drainage conditions, texturing of the GM and matric suction in dependent on the normal stress. Further tests were carried out on the long term effects of the shear properties between GTs and the GMs. The results of the research project which were carried out at the Institute for Foundation Engineering at the Technical University of Munich are given below in an abridged format.

## 2 CHARACTERISTIC DATA OF THE MATERIAL

Tests with one smooth GM and three textured GMs were carried out. All four GMs were manufactured of HDPE having a thickness of 2.5 mm. Furthermore, two highly plastic clays (a clay called 11A and a kaolinite clay) and a mixed grained soil (mixture of a coarse grained soil and

the kaolinite clay) were used for the investigation. Table 1 illustrates the characteristics of these three clays.

Table 1. Characteristic magnitudes of the testing soils

	Clay 11A	Kaolinite clay	Mixed grained material
$w_L$ (%)	58,8	73,6	
$w_p$ (%)	21,9	29,8	
$\rho_{Pr}$ (t/m <sup>3</sup> )	1,63	1,43	1,95
$w_{Pr}$ (%)	20,2	27,1	11,0

The clay used for the investigation were placed near optimum moisture content and compacted with standard proctor-energy. As a protection layer a mechanically bonded PP-nonwoven was used in these tests. The nonwoven had a mass per unit area of  $m_A > 1200$  g/m<sup>2</sup> (DIN EN 965) at a thickness of  $d = 8$  mm (DIN EN 964 TI-2).

## 3 SHEAR STRENGTH OF PARTLY SATURATED COMPACTED CLAY LINERS

CCLs are generally installed partly saturated in the field. The degree of saturation decisively influences the shear strength of the CCL and also the interface CCL/GM, as shown below.

### 3.1 Theory

Because of capillary and adsorptive forces partly saturated soils tend to absorb water. A negative pore water pressure incurs (suction), which is dependent on the grain size and pore size distribution of the soil. The discrepancy between



pore water pressure  $u_w$  and the pore air pressure  $u_a$  within the sample is described as matric suction. Referring to Bishop (1955) the matric suction increases the intergranular pressure  $\sigma'$  (1). The parameter  $\chi$  depends on the degree of saturation  $S_r$  of the soil. For saturated soils it can be stated that  $\chi = 1$  and for "dry" soils  $\chi = 0$ . The effectiveness of the matric suction can be described as a pre-stressing of the soil.

$$\sigma' = \sigma - u_a + \chi(u_a - u_w) \quad (1)$$

According to Coulomb the shear strength  $\tau_f$  of saturated soils is expressed by the effective cohesion  $c'$  and the effective angle of the internal friction  $\phi'$ .

$$\tau_f = c' + \sigma' \tan \phi' \quad (2)$$

Fredlund et al. (1978) define the matrix friction angle  $\phi^b$  (3). They assume that the parameter  $\chi$  is constant when the soil is compacted to the same water content and density. This results in the shear strength of partly saturated soils (4).

$$\tan \phi^b = \chi \tan \phi' \quad (3)$$

$$\tau_f = c' + (\sigma' - u_a) \tan \phi' + (u_a - u_w) \tan \phi^b \quad (4)$$

The shear parameters  $c'$  and  $\phi'$  are independent of the matric suction and can be determined under saturated conditions.

### 3.2 Test Description and Test Results

Within the framework of the research project the shear parameter  $c'$ ,  $\phi'$  and  $\phi^b$  of the clay 11A were determined at saturated and partly saturated conditions (D-Tests) using the triaxial apparatus. The "saturated" tests were carried out according to DIN 18137-2 at a back pressure of  $u_w = 5$  bar. The "partly saturated" tests were carried out at a constant water content and a pore pressure of  $u_a = 4$  bar. The change of the matric suction in the "partly saturated" tests was measured with a tensiometer located on the top pressure plate. Table 2 shows the average results of 9 tests at  $w_a = 23\%$ .

Table 2. Results of the triaxial test with clay 11A

$w_a$ (%)	$c'$ (kN/m <sup>2</sup> )	$\phi'$ (°)	$\phi^b$ (°)	$R^2$ (-)	$\chi$ (-)
23	30.6	14.6	12.8	0.92	0.87

The high regression coefficient  $R^2$  shows that the shear strength of the partly saturated soil can be represented well by means of the equation of Fredlund et al. (1978).

Figure 1 shows the result on a stress diagramm. The increase of the shear strength as a result of capillary forces at lower normal stresses can clearly be recognized. At the same time it is noticed that while the mean stress increases, the matric suction decreases. When the values reach 800 kN/m<sup>2</sup>, the sample's stresses are so high that the formerly partly saturated samples have changed into saturated samples by way of consolidation.

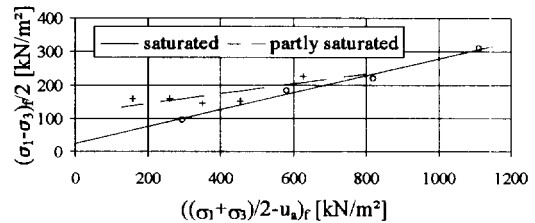


Figure 1. Partly saturated and saturated tests (Clay 11A,  $w_a = 23\%$ )

According to the test results, it can be summarized that even in high saturated conditions the increase of the shear strength of compacted clays is considerably high under low confining stresses because of the matric suction. This matric suction also influences decisively the shear behavior of the CCL / GM interface as shown in the next chapter.

## 4 SHEAR STRENGTH AT THE COMPACTED CLAY LINER / GEOMEMBRANE- INTERFACE

### 4.1 Test Description

The following describes the influence of different test parameters which influence the shear test results between the CCL and the GM. As this is the shear strength between two different material types the shear parameters are renamed. Adhesion  $a$  and interface friction angle  $\delta$  take the place of cohesion  $c$  and the angle of internal friction  $\phi$ . The corresponding critical condition between two materials according to Coulomb is as follows:

$$\tau_f = a + \sigma \tan \delta \quad (5)$$

Both a 30 cm x 30 cm (30x30-SG) and a 10 cm x 10 cm (10x10-SG) direct shear apparatus were used for this investigation. Within the framework of the research project the basic comparability of both shear apparatus' regarding the maximum shear stress could be proven (Fillibeck and Heyer, 1995). Since the matric suction cannot be measured at the interface, the evaluation of the test results is shown in a  $\sigma/\tau_f$ -diagramm whereas  $\sigma$  is the acting total normal stress differentiated from the confining stress. Figure 2 shows a schematical test setup of the direct shear apparatus 30x30-SG. It is important that the compaction of the soil sample is not carried out on top of the GM and that the soil

sample has a constant thickness so that the normal stress can be transferred evenly.

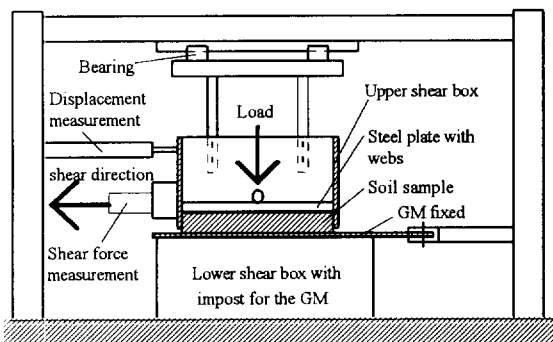


Figure 2. Schematic cross section of the 30x30-SG

The shear force was applied by means of a plate with webs (Figure 3) in order to achieve a fairly constant distribution of the shear stress across the interface.

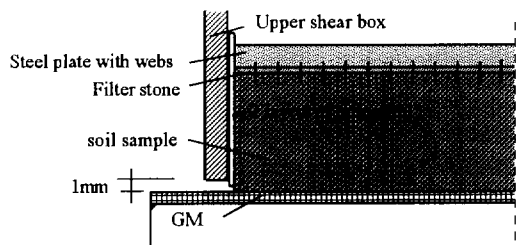


Figure 3. The direct shear apparatus 30x30-SG as a detail

As the top part of the shear box cannot be displaced in the vertical direction, the normal stress transfer must be possible without significant loss of stresses due to side wall friction between the soil sample and the upper shear box. Measurements show a reduction of the normal stress of up to 20% due to this effect. To avoid this, two layers of teflon foil were installed between the soil sample and the wall of the shear box (figure 3). In addition the smallest possible thickness of the clay layer was chosen.

In the case of the shear tests carried out in the direct shear apparatus 10x10-SG the geomembrane was also placed in the lower shear box and the compacted soil in the upper shear box.

#### 4.2 Drained Shear Tests with Partly Saturated CCLs

Figure 4 shows drained shear tests (shear speed after consolidation  $v = 0.3$  mm/h) between three GMs and the kaolinite clay ( $w_a = 30\%$ ). Comparatively the shear strength of the kaolinite clay alone is shown by a dotted line.

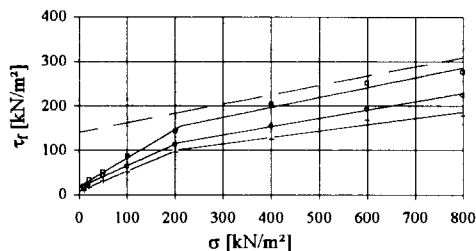


Figure 4. D-tests between kaolinite clay and 3 GMs

The  $\sigma/\tau$ -behavior can be shown with two straight lines which are valid for two different normal stress ranges (high and low). Shear parameters can thus be assigned to each normal stress range. Under very low normal stresses the high internal shear strength of the CCL cannot be transmitted to the GM, as there occurs no intimate contact between the GM and the CCL. The shear behavior corresponds to the shear behavior of a coarse grained soil with high friction angle and only little or no adhesion. The intimate contact improves with increasing normal stresses. The shear properties of the test soil under higher normal stresses develops progressively. In the high normal stress range the best possible intimate contact is achieved.

As expected, the shear behavior between the GM and the CCL is clearly influenced by the texturing of the GM. Under high normal stresses, some textured GM/CCL interfaces can almost reach the shear strength of the respective CCL alone.

#### 4.3 Comparison between UU-Tests and D-Tests

As known in soil mechanics, the difference in shear strength between UU-tests (unconsolidated, undrained tests) and D-tests (drained tests) of a fine grained soil because of existing pore water pressure is well known. The following considers whether pore water pressure or pore air pressure influences the shear strength of the interface between GM and partly saturated CCL.

UU-tests were carried out with a shearing speed of  $v = 10$  mm/h. Such tests were compared with results from D-tests performed with a shearing speed of  $v = 0.3$  mm/h (after the primary consolidation). It was assumed that possibly existing pore water and excess air could not decrease at fast shearing rates. Figure 5 shows representative results of tests carried out with a textured GM and clay 11 A ( $w_a = 23\%$ ).

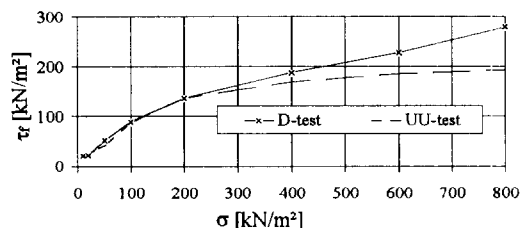


Figure 5. Comparison between UU and D-tests

In the lower normal stress range (at  $\sigma < 200 \text{ kN/m}^2$ ) decreasing pore water pressures and trapped pore air pressures do not develop within the shear plane between the CCL and the GM due to the high stiffness of the CCL. At this stage, intimate contact between the CCL and GM has not yet developed. Only if high normal stresses are achieved, pore water and trapped pore air pressures do develop within the clay directly after applying the load. These pore water and trapped pore air pressures also influence the shear strength within the interface. These can decrease during the D-Test whereas the shear strength increases compared to the UU-Test. In the case of an increase of the normal stress to  $\sigma > 800 \text{ kN/m}^2$  the additional normal stresses are only absorbed by means of trapped pore water pressures. Consequently, the shear strength which is achieved in the UU-Test does not further increase, as evidenced by the asymptotic nature of the  $\sigma/\tau$ -curve in figure 5.

The question needs to be asked at which normal stresses does differing results between drained and undrained tests occur. The answer certainly depends on the water content of the soil and on the compacting process used to prepare the soil specimen. In general when CCL's are compacted on the wet side of proctor-optimum it can be assumed, that the shear speed and duration of consolidation under low normal stresses only slightly influence the shear behavior. Note that this condition is typical for CCL's.

#### 4.4 Comparison between Tests with Partly Saturated and with Saturated CCLs

On several occasions it is assumed that the capillary and adsorptive forces, which are responsible for the high shear strength between CCLs and GMs, can at least partly get lost in excessive situations. This can be the case if - for example - perspiration occurs on the bottom side of the GM as a result of temperature differences or if rainwater is collected under the geomembrane during installation. In order to consider this condition, tests with saturated CCLs were carried out according to Bembem & Schulze (1995). For these tests the soil samples were installed into the shear box partly saturated and subsequently consolidated in a water bath so that the negative pore water pressure approached zero.

Figure 6 shows the results of tests which are carried out with partly saturated and saturated samples (D-Tests) between the smooth geomembrane and the clay 11A.

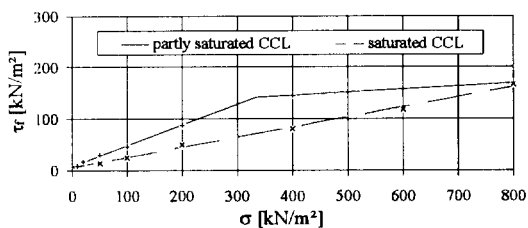


Figure 6. D-Tests with partly saturated and saturated CCLs

The shape of the  $\sigma/\tau$ -curve of the series of tests carried out with the saturated CCL proceeds fairly linearly in the whole range of the normal stress. Under low normal stresses, the water content of the soil sample increases during consolidation (up to 7%). Thus its strength decreases significantly. The result of this is - in contrast to the tests carried out with the partly saturated samples - that already under low normal stresses a good contact between the soil sample and the geomembrane is achieved. Under very low and under very high normal stresses the shear strength of the tests carried out with partly saturated samples and those carried out with saturated samples are comparable. Under very low normal stresses still no extensive contact is achieved between the partly saturated CCL and the GM. Under high normal stresses ( $\sigma \geq 800 \text{ kN/m}^2$ ) the partly saturated CCL is so excessively compressed that saturation appears after the consolidation.

In the middle range of the normal stress, the shear strength of the partly saturated tests is considerably higher than the shear strength of the saturated tests.

#### 4.5 Test Procedures for the Practical Application

Referring to the test results above, the following test procedures can be proposed:

For stability calculations under low normal stresses (e. g.  $\sigma \leq 50 \text{ kN/m}^2$ ) during construction, usually partly saturated tests have to be carried out. It is recommended to choose a water content for the shear test which is slightly higher than the installation moisture content. To prevent the increase of the water content of the CCL after installation, constructive measures have to be taken, by means of covering the CCL directly after its placement with a GM and a drainage layer and installation of drainage trenches to collect the rain water. Thus shear tests can be run at a high speed (e. g.  $v = 10 \text{ mm/h}$ ) with a reduced consolidation time.

For stability calculations under low normal stresses for the post-installation condition (e. g. landfill cap) partly saturated, drained shear tests can be used. However only if it is ensured that the water content of the CCL cannot increase. Field investigations have shown that this is normally the case for landfill caps. It is recommended to choose a water content slightly higher than the installation water content. Water saturated tests show a comparable worst case condition.

For stability calculations under high normal stresses (e. g. base sealing of landfills) drained tests should be carried out (shear speed  $v = 0.3 \text{ mm/h}$ ) because it is often the case that the normal stress does not increase in such a way that pore pressures occur. As long as the CCL can adsorb water due to capillarity from the ground water, saturated tests should be carried out.

Because of the nonlinear dependence between the normal stress and the shear stress, normal stresses have to be used for the shear tests which are close to the normal stress occurring on site. The shear parameters which are calculated

by linear regression from the test results are only valid for the range of the chosen normal stresses. If shear tests were carried out under higher normal stresses, an appropriate friction angle can be used which is calculated by linear regression through the origin of the coordinates.

## 5 SHEAR STRENGTH AT THE GEOMEMBRANE / GEOTEXTILE INTERFACE

Usually shear tests between geotextiles and geomembranes are determined by constant shear speed. However, in practice the interface is mostly developed at a constant shear stress which is better simulated by a stress controlled test. Because of the creep behavior of geosynthetics, it has been investigated in the research project, if the results of strain controlled tests compare to those of stress controlled tests and which displacements appear close to the peak value as a function of the time.

### 5.1 Comparison of Stress and Strain Controlled Shear Tests

Tests were carried out in the 10x10-SG and 30x30-SG shear boxes. In both cases the geotextile was placed in the upper shear box.

At stress controlled shear tests the failure in the interface is induced by increasing the shear stress step by step. In contrast to strain controlled tests, the shear rate is not constant. After increasing the shear stress the shear rate  $dx/dt$  is measured as a function of the time. The shear force is increased once the shear rate drops below 0.05 mm/min. In each case 4 shear tests were carried out at normal stresses of 50, 100 and 300 kN/m<sup>2</sup>.

For the strain controlled shear tests a shear rate of 10 mm/h was chosen. 10x10-SG tests were carried out at a normal stress of 10, 20, 50, 100, 200, 400 and 800 kN/m<sup>2</sup> and under a normal stress of 10, 20, 50, 100, 200 and 300 kN/m<sup>2</sup> in 30x30-SG. In Table 3 the friction angles of the shear tests between the geotextile and two different geomembranes are given.

Table 3. Stress and strain controlled shear tests

Shear test	10x10-SG	10x10-SG	30x30-SG
	stress contr.	strain contr.	strain contr.
	$\delta$ (°)		
KDB I	28.3	29.6	28.3
KDB II	15.7	16.5	15.9

It is obvious from these results that the stress controlled shear tests correspond very well to the strain controlled shear tests. Thus the strain controlled shear test which can be carried out easier can be regarded more suitable for the determination of the shear parameters. Also it can be noted

that there exists a good conformity between the 30-30-SG and the 10x10-SG results.

### 5.2 Creep Test

The stress controlled creep tests were carried out in the 10x10-SG. The shear stress was kept constant for about 1000 hours. During this time the shear speed was monitored. The creep shear stress was determined by the chosen stress intensity  $D$  which is defined as the ratio between the creep shear stress and the maximum shear stress gained from the strain controlled shear test. To analyse the creep tests the potential equation (6) was used to describe the shear speed  $dx/dt$  in dependence of the time  $t$ .

$$\frac{dx}{dt} = A_1 \times t^{-m} \quad (6)$$

In a double logarithmic scale the potential function is a straight line with the inclination  $-m$ . The smaller the constant  $m$  the more it creeps (higher creep potential). The constant  $A_1$  is the shear speed at the time  $t = 1$ . The shear displacement  $x$  can be calculated by integration of the potential equation (7).

$$x = \int \frac{dx}{dt} dt = \frac{A_1}{1-m} t^{(1-m)} + x_G \quad m \neq 1 \quad (7)$$

For  $t \rightarrow \infty$ , and  $m > 1$  the shear displacement  $x$  is close to the constant  $x_G$ . The  $t/x$ -curve approaches a horizontal asymptote which meets the displacement axis at  $x_G$ . For  $m < 1$  there is no horizontal asymptote ( $x \rightarrow \infty$ ). In Figure 7 the creep curve of a test with a textured GM under  $\sigma = 300$  kN/m<sup>2</sup> and a stress intensity  $D = 95\%$  is shown. Table 4 shows some test results for a textured GM.

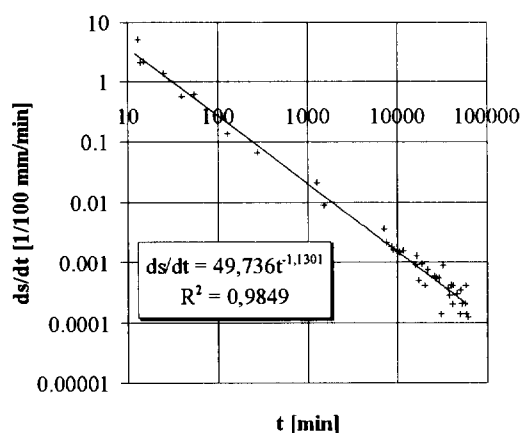


Figure 7. Creep test between the textured GM and the geotextile ( $D = 95\%$ ,  $\sigma = 300$  kN/m<sup>2</sup>)

Table 4. Results of creep tests

$\sigma$	D	creep function $x = A_1 / (1 - m) t^{(1-m)} + x_G$	$x_G$
[kN/m <sup>2</sup> ]	[%]	[1/100 mm]	[mm]
50	90	$-250,1 t^{-0,24} + 274,6$	2,7
	95	$-394,7 t^{-0,21} + 361,0$	3,6
300	90	$-193,0 t^{-0,12} + 185,9$	1,9
	95	$-382,3 t^{-0,13} + 280,3$	2,8

The constant  $m$  was in all the tests higher than 1 even with the stress intensity  $D = 95\%$ . This means that the shear speed decreased in such a way that the shear displacement approached  $x_G$  for  $t \rightarrow \infty$  (Table 4). The value  $x_G$  approximately corresponds to the shear displacement of the stress controlled shear test. Therefore no large creep displacements are expected which is very important for landfill applications.

After testing the creep behavior for 1000 hours the shear stress was increased until failure. The maximum shear stresses rose from 10% to 40% when comparing with the short term tests. This can be explained by the reduction of the stress peaks during the creep test (redistribution of the stress). If the shear stress is increased quickly, e. g. in the stress or strain controlled shear test, the interface between geotextile and GM is stressed irregularly and a progressive failure is the consequence. If the shear stress is kept constant prior to failure (e. g. in the creep test), the highly stressed areas of the interface can be reduced (relaxation). As a consequence, no progressive failures occur and the maximum shear stress after this relaxation is higher than the one in the stress controlled test. For practical applications it is important to know, that the shear parameters from stress or strain controlled short term tests are safe and reliable.

## 6 SUMMARY

This paper treats the shear strength of composite sealing layers consisting of a compacted clay liner (CCL), a geomembrane (GM) and a geotextile protection layer (GT). The influence of selected test conditions on shear test results is shown.

The comparison of triaxial shear tests with saturated and partly saturated CCLs show the dependence of capillary and adsorptive forces (matric suction) on the shear strength. It proved that under small normal stress the shear stress of partly saturated soils increases quite visibly due to matric suction. Matric suction diminishes with increasing normal stress and the shear stress response approaches that of the saturated soils.

The matric suction also influences the shear strength of the CCL / GM-interface. Shear tests showed a bilinear dependence between normal stress and shear stress.

Therefore the shear strength of this interface can be described quite well by 2 pairs of shear parameters for an upper and a lower range of normal stress. Under low normal stress, the influence of the shear speed and consolidation time upon the shear strength with partly saturated CCLs is negligible but increases with higher normal stress. Compared to tests with saturated CCLs the shear strength with partly saturated CCLs is - normal stress dependent - recognizable higher.

At the interface between the GT and the GM the long term shear behavior was investigated under constant shear stress. The results of the creep tests (duration 1000 h) showed that even under a high stress intensity the occurring deformations decreased quite quickly. The calculated displacements are almost equivalent to the measured displacements of shear tests under constant shear speed. After the creep tests the maximum shear forces increased compared to the maximal shear stress measured in tests under constant shear speeds. Therefore shear tests with constant shear speeds (e. g. 10 mm/h) are conservative and reliable.

The published test results of the investigated shear interfaces show that with suitable materials slope inclinations of 2.5 : 1 to 3 : 1 (H:V), safe designs utilizing composite lining systems can be achieved.

## ACKNOWLEDGMENTS

The research reported in this paper was sponsored by the working group Groundwater Protection e. V. in particular by the companies Naue Fasertechnik GmbH & Co. KG, Frank Deponietechnik GmbH, GSE Lining Technology GmbH and Ursuplast GmbH & Co. KG. The authors express their appreciation for the given support.

## REFERENCES

- Bemben, S. M., Schulze, D. A. (1995) "The Influence of Testing Procedures On Clay/Geomembrane Shear Strength Measurements", Geosynthetics Conference Nashville Tennessee, 1995
- Bishop, A. W. (1955) "The Use of the Slip Circle in the Stability Analysis of Slopes", Geotechnique 5, 1955
- Fillibeck, J., Heyer, D. (1995) "Bestimmung der Scherparameter zwischen mineralischer Abdichtung und Kunststoffdichtungsbahn", Süddeutsches Kunststoffzentrum, 11. Fachtagung "Die sichere Deponie", 1995
- Fillibeck, J., Heyer, D., Floss, R. (1997) "Das Scherverhalten von Dichtungssystemen mit Kunststoffdichtungsbahnen", Geotechnik, No 2, 1997
- Fredlund, D. G., Morgenstern, N. R., Widger, R. A. (1978) "The Shear Strength of Unsaturated Soils", Canadian Geotechnical Journal, No. 15, 1978

# Issues in Clay / Textured Geomembrane Interface Testing

Paul J. Sabatini, Gary R. Schmertmann, and Robert H. Swan Jr.  
GeoSyntec Consultants, Atlanta, Georgia, USA

**ABSTRACT:** This paper presents the results and interpretation of interface direct shear testing using varying shear displacement rates and normal stresses on compacted clay / textured geomembrane interfaces. The testing included eight clay soils from project sites throughout the United States and two HDPE textured geomembranes. Seventeen pairs of interface direct shear tests were performed where one test was run at a relatively rapid shear displacement rate (fast test) and another test was run at a slower rate (slow test). Shear displacement rates varied from 1 to 5 mm/min for the fast tests and from 0.01 to 0.1 mm/min for the slow tests. Testing normal stresses ranged from 10 to 960 kPa. The test results reveal that larger shear strengths are sometimes measured in the slow test and sometimes in the fast test.

**KEYWORDS:** shear strength, laboratory tests, soils, geomembranes, interface testing, direct shear testing

## 1 INTRODUCTION

Liner and cover systems for modern landfills often contain layers of soil and geosynthetic materials. The shear strength of the weakest interface within these systems, under both long-term and short-term loading conditions, is often required for slope stability analyses. These shear strengths are commonly evaluated using the results of laboratory interface direct shear tests.

The weakest interface within liner and cover systems is often that between a compacted clay soil layer and a geomembrane. In conducting direct shear tests on this interface, pore pressures in the clay are not commonly measured. Without knowledge of pore pressures near the interface, it is not known whether the measured interface shear strength is appropriate for short-term or long-term loading conditions. This issue has been discussed by previous investigators (e.g., Fishman and Pal, 1994).

Common practice in the United States is to perform laboratory interface direct shear testing in accordance with the American Society for Testing and Materials (ASTM) D 5321 test standard. The test standard includes a default shear displacement rate of 1 mm/min for testing soil/geosynthetic interfaces. This displacement rate is appropriate for evaluating short-term strengths of clay/geomembrane interfaces as it typically results in peak strengths being achieved after a shearing duration of 5 to 50 minutes. This displacement rate may be too rapid, however, to evaluate the long-term strength of clay/geomembrane interfaces, particularly when the compacted clay is at or near saturation. Many engineers may assume that shear strengths measured using the default shear displacement rate are conservative for both short-term and long-term conditions.

This paper presents the results of laboratory interface direct shear testing using varying shear displacement rates and normal stresses on clay / textured geomembrane interfaces from project sites throughout the United States. Seventeen pairs of comparative results were obtained by

performing a test using a relatively rapid shear displacement rate (fast test) and another using a relatively slow rate (slow test). Differences in measured shear strengths from the fast and slow tests are discussed. The test results were accumulated from project-specific testing performed by the authors' firm between 1993 and 1995. Although not part of a systematic testing program designed specifically to evaluate the effect of shear displacement rate, the results provide a set of data believed to be valuable to practicing engineers.

## 2 INTERFACE DIRECT SHEAR TESTS

### 2.1 Test Device and Procedures

The interface direct shear tests were conducted in accordance with ASTM D 5321 using a direct shear device that consists of an upper shear box and a lower shear box. The upper box measures 300 mm by 300 mm (plan) by 75 mm (high). The lower box measures 300 mm by 360 mm (plan) by 75 mm (high).

Each test specimen included a compacted clay / textured geomembrane interface. Although other soil and geosynthetic materials were included in some of the test specimens, the reported test results all involve shearing on the compacted clay / textured geomembrane interface. The steps used to set up each test are described below.

- A lower bedding layer was compacted into the lower shear box. The bedding layer consisted of either a concrete sand or a site-specific soil.
- The geomembrane was placed on top of the lower bedding layer and attached to the lower shear box. The direction of shear was the same as the machine direction of the geomembrane. For some tests, the geomembrane was wetted with a fine mist of water.
- The clay soil was compacted away from the geomembrane in the upper shear box to specified

moisture and compaction conditions to a thickness of 25 to 50 mm and then placed on the geomembrane.

- A normal stress was applied to the complete test specimen and the test specimen was then soaked (submerged in water) or consolidated (no submergence) for a period of time prior to shearing.

After the soaking or consolidation period was complete, the test specimen was sheared at a constant rate of deformation. Shearing was conducted until a peak shear strength was measured and then continued until a stable, large-displacement shear strength was achieved.

## 2.2 Soil Properties and Geomembrane Materials

Index properties, including percent passing the US Standard No. 200 sieve (%P200), Atterberg limits (LL, PI), and compaction results (optimum water content,  $w_{opt}$ , and maximum dry unit weight,  $\gamma_{D(max)}$ ), for the eight clayey soils used are provided in Table 1. The soils used are typical for compacted clay components of liner and cover systems and range from sandy and clayey silts to sandy clays and silty clays of medium to high plasticity.

Textured HDPE geomembranes from two different manufacturers were used in the testing. The geomembranes ranged in thickness from 1.5 to 2.0 mm.

Table 1. Properties of Clay Soils.

Clay Soil No.	%P200 (%)	LL	PI	$w_{opt}^{(1)}$ (%)	$\gamma_{D(max)}^{(1)}$ (kN/m <sup>3</sup> )
1	93	77	48	27.2 <sup>(2)</sup>	14.5 <sup>(2)</sup>
2	-	-	-	14	18.5
3	-	-	-	15	17.4
4	59-80	49	17	13	18.9
5	-	72	45	20.6	16.8
6	-	-	-	34.3 <sup>(2)</sup>	13.2 <sup>(2)</sup>
7	70	-	-	17.2 <sup>(2)</sup>	17.6 <sup>(2)</sup>
8	81	35	18	12.1	19.4

Notes: (1) Modified Proctor compaction test (ASTM D 1557) unless otherwise noted.

(2) Standard Proctor compaction test (ASTM D 698).

## 2.3 Test Conditions

The compaction conditions, soaking and consolidation times, normal stresses, and shear displacement rates for each test specimen are reported in Table 2. For the comparative test pairs, both tests were performed with the same soil and geomembrane materials, target clay compaction conditions, and test specimen configuration. Other features of the testing were as follows:

- Target clay compaction conditions for all the tests reflect typical values specified for landfill liner and cover system construction, with the target water content being above the optimum water content.

- Shear displacement rate for the slow test of each pair was ten to one hundred times slower than the fast test.
- Wetting, soaking, and consolidation conditions were not always the same for both tests in each comparative test pair. These conditions reflected anticipated project-specific field conditions and loadings.

## 3 INTERFACE DIRECT SHEAR TEST RESULTS

### 3.1 Overview

Test results including change in water content and peak and large-displacement shear strength are summarized in Table 2. The ratios of both peak and large-displacement shear strength measured during fast tests to those measured during slow tests vary from 0.7 to 1.4. These results are discussed subsequently.

### 3.2 Influence of Normal Stress Levels on Shear Strength

Previous investigators have indicated that differences in interface shear strength from fast and slow tests can be attributed, in part, to the existence of drained versus undrained conditions during shear (Bemben, 1993; Fishman and Pal, 1994; Takasumi et al., 1991). Fishman and Pal (1994) also suggested that these differences may be affected by pore pressure generation during undrained shear. If a saturated clay tends to dilate during shear, as for a heavily overconsolidated material, negative pore pressures may develop in fast tests. Conversely, if a saturated clay tends to compress during shear, as for a normally consolidated material, positive pore pressures may develop in fast tests. Pore pressure development will affect the shear strengths measured in fast tests. These characteristics may be relevant in evaluating shear strengths from fast and slow tests.

Compaction of a clay soil induces an apparent preconsolidation pressure,  $p_c'$ . For compacted clays tested at normal stresses lower than  $p_c'$ , the clay will be more likely to behave as an overconsolidated material and may develop negative pore pressures in fast tests. These negative pressures would result in larger shear strengths than in slow tests. For compacted clays tested at normal stresses higher than  $p_c'$ , the clay will be more likely to behave as a normally consolidated material and may develop positive pore pressures in fast tests. These positive pressures would result in smaller shear strengths than in slow tests. Although the value of  $p_c'$  was not evaluated for the compacted clays used in the testing, the influence of the testing normal stress was considered.

To evaluate the influence of testing normal stress, the ratios of peak shear strength measured during fast and slow tests were plotted as shown in Figures 1 and 2. Figure 1 shows the results for tests performed at relatively

low normal stresses (i.e.,  $\sigma_n < 40$  kPa), and Figure 2 shows the results for tests performed at higher normal stresses (i.e.,  $\sigma_n > 40$  kPa). For landfills, low normal stresses are generally present in cover systems and high normal stresses are generally present in liner systems.

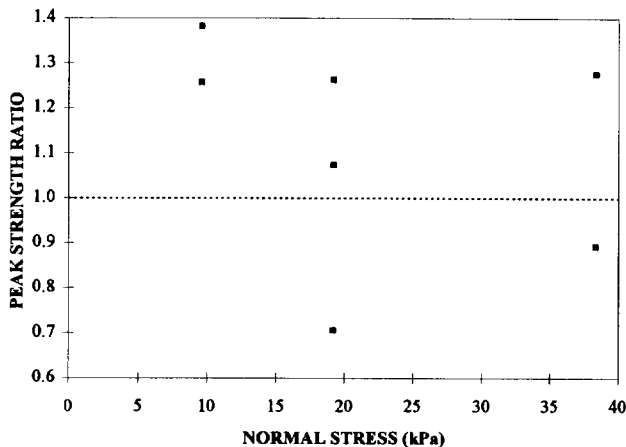


Figure 1. Peak Strength Ratios at Low Normal Stresses.

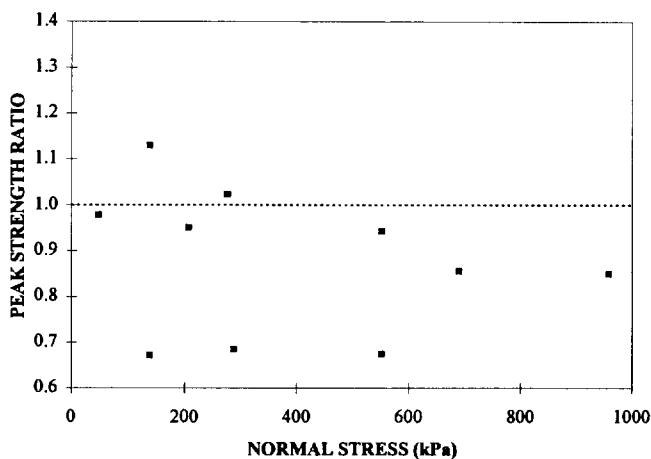


Figure 2. Peak Strength Ratios at High Normal Stresses.

Five of the seven comparative test results shown in Figure 1 indicate that, at low normal stresses, fast shear tests result in greater shear strengths than slow tests (i.e., peak strength ratio  $> 1$ ). Eight of the ten comparative test results shown in Figure 2 indicate that, at high normal stresses, fast shear tests result in lower shear strengths than slow tests (i.e., peak strength ratio  $< 1$ ). These results are generally consistent with the possible influence of normal stress previously described. Similar trends are apparent for the large displacement strength data.

### 3.3 Limitations

In addition to shear rate and normal stress, other testing factors may affect pore pressure conditions during shear and measured interface shear strength. Some of these

factors include initial saturation of the clay soil and changes in saturation during consolidation and shear. Saturation conditions during shearing could not be assessed as sufficient water content and volume change measurements are not available. The type and quality of geomembrane texturing was not considered, but it also effects measured strength. Although all tests were conducted by the same laboratory, unknown testing variability exists. Based on these uncertainties, the trends illustrated in Figures 1 and 2 are considered preliminary.

## 4 CONCLUSIONS

The results of 17 pairs of comparative direct shear tests on compacted clay/textured geomembrane interfaces were evaluated. Each comparative test pair included one test at a relatively fast shear rate and one test at a relatively slow shear rate, and used the same clay soil, textured geomembrane, compaction conditions, and test specimen configuration. Interpretation of the comparative test results is considered preliminary due to unknown testing variability, differences in clay moisture conditions, and the limited number of comparative tests.

The test results are generally consistent with the hypothesis that at low normal stresses the compacted clay/textured geomembrane interface may behave as an overconsolidated material, and at high normal stresses the interface may behave as a normally consolidated material. The results suggest that the interface strength measured in laboratory direct shear tests, using a shear rate such as 1 mm/min, may be unconservative for use in long-term stability analyses of cover systems and other soil/geosynthetic systems subjected to low normal stresses. The results imply that it is prudent to establish project-specific shear displacement rates, moisture conditions, and loading conditions when evaluating the shear strength of compacted clay/textured geomembrane interfaces.

## 5 REFERENCES

- Bemben, S.M. and Schulze, D.A. (1993) "The Influence of Selected Testing Procedures on Soil/Geomembrane Shear Strength Measurements", *Geosynthetics '93*, Vol. 2, Vancouver, Canada, pp. 619 -631.
- Fishman, K.L. and Pal, S. (1994) "Further Study of Geomembrane/Cohesive Soil Interface Shear Behavior", *Geotextiles and Geomembranes*, Vol. 13, pp. 571-590.
- Takasumi, D.L., Green, K.R., and Holtz, R.D. (1991) "Soil-Geosynthetics Interface Strength Characteristics: A Review of State-of-the-Art Testing Procedures", *Geosynthetics '91*, Vol. 1, Atlanta, USA, pp. 87 -100.



Table 2. Interface Direct Shear Test Conditions and Results.

Clay Soil No.	Test No.	$\gamma_{Di}$ (1) (kN/m <sup>3</sup> )	$w_i$ (2) (%)	R.C.(3), R.W.C(4) (%)	Soaking time (hr)	Cons. time (hr)	Normal stress, $\sigma_n$ (kPa)	Disp. rate (mm/min.)	$\Delta w$ (5) (%)	Peak shear stress, $\tau_p$ (kPa)	Large disp. shear stress, $\tau_{ld}$ (kPa)	$\tau_{fast}/\tau_{slow}$ (peak)	$\tau_{fast}/\tau_{slow}$ (large disp.)		
1	1F	13.8	32	95,+5	0	0	19	1.02	5.3	8.8	7.9	0.71	0.85		
	1S	13.7	32.4	95,+5	0	16	19	0.10	3.2	12.5	9.3				
2	2F	16.7	15.4	90,+1.5	24	0	10	5.08	9.2	9.0	8.7	1.38	1.35		
	2S	16.7	15.4	90,+1.5	24	0	10	0.08	7.1	6.5	6.4				
	3F	16.7	15.5	90,+1.5	24	0	19	5.08	6.9	13.2	12.8			1.26	1.30
	3S	16.7	15.5	90,+1.5	24	0	19	0.08	5.6	10.5	9.8				
	4F	16.7	15.4	90,+1.5	24	0	38	5.08	5.4	23.5	22.8			1.28	1.25
	4S	16.7	15.4	90,+1.5	24	0	38	0.08	5.6	18.4	18.2				
3	5F	15.8	16.3	90,+1.5	24	0	10	5.08	8.3	7.4	6.9	1.25	1.20		
	5S	15.6	16.6	90,+1.5	24	0	10	0.08	10.2	5.9	5.7				
	6F	15.6	16.9	90,+1.5	24	0	19	5.08	6.0	12.8	12.3			1.07	1.18
	6S	15.7	16.2	90,+1.5	24	0	19	0.08	10.0	11.9	10.4				
	7F	15.8	16.3	90,+1.5	24	0	38	5.08	5.6	18.7	17.4			0.89	0.92
	7S	15.6	16.6	90,+1.5	24	0	38	0.08	8.7	20.9	19.0				
	4	8F	17.8	16.5	95,+3	12	0	48	5.08	10.0	31			21	0.98
8S		17.9	15.8	95,+3	12	0	48	0.08	8.3	32	27				
9F		17.8	16.5	95,+3	12	0	287	5.08	10.0	74	70	0.68	0.65		
9S		17.9	15.4	95,+3	12	0	287	0.08	7.3	108	108				
10F		17.9	16.4	95,+3	12	0	958	5.08	10.0	256	239	0.83	0.78		
10S		18.0	15.6	95,+3	12	0	958	0.08	8.0	307	307				
5	11F	15.0	25.9	90,+5	0	0	138	1.02	-0.8	90	70	1.13	1.02		
	11S	15.1	25.7	90,+5	0	12-14	138	0.05	-1.2	79	68				
	12F	15.1	25.1	90,+5	0	0	276	1.02	-0.5	155	141			1.02	1.06
	12S	15.2	24.5	90,+5	0	12-14	276	0.05	-1.3	152	133				
	13F	15.2	24.6	90,+5	0	0	552	1.02	-1.6	249	239			0.95	0.92
	13S	15.0	26.1	90,+5	0	12-14	552	0.05	-0.8	263	259				
6	14F	12.5	38.5	95,+4	0	0	138	1.02	1.2	59	59	0.67	0.81		
	14S	12.4	38.5	95,+4	0	40(7)	138	0.01	-2.3	88(6)	73				
	15F	12.4	38.5	95,+4	0	0	690	1.02	0.5	235	235			0.86	0.90
	15S	12.5	38.5	95,+4	0	40	690	0.01	-2.4	274(6)	261				
7	16F	16.7	18.4	95,+2	0	0	552	5.08	0.7	177	163	0.68	0.65		
	16S	16.8	19.1	95,+2	24	0	552	0.05	0.8	261	252				
8	17F	17.4	16.4	90,+4	0	3	207	1.02	0.7	149	149	0.95	0.95		
	17S	17.4	16.5	90,+4	0	20	207	0.01	-0.1	157	157				

Notes: (1) Dry unit weight of compacted clay soil at placement.  
(2) Water content of compacted clay soil at placement.  
(3) R.C. = Target Relative Compaction =  $(\gamma_{Di} / \gamma_{D(max)}) * 100\%$   
(4) R.W.C = Target Relative Water Content =  $w_i - w_{opt}$

(5)  $\Delta w$  = water content measured in soil adjacent to interface at end of test -  $w_i$   
(6) Sliding was not observed at the clay/geomembrane interface at peak load, indicating that the clay/geomembrane shear strength is at least as strong as value reported.  
(7) Consolidation for test 14S consisted of 24 hr at 69 kPa followed by 16 hr at 138 kPa.

# Geosynthetic Clay Liners at Field-Scale: Internal Shear Test Progress

D. A. Carson

Environmental Engineer, US Environmental Protection Agency, Office of Research and Development, National Risk Management Research Laboratory, Cincinnati, Ohio, USA

R. Bonaparte

President, GeoSyntec Consultants, Atlanta, Georgia, USA

D. E. Daniel

Professor and Head of Civil Engineering, University of Illinois at Urbana-Champaign, Urbana, Illinois, USA

R. M. Koerner

Director, Geosynthetic Institute, Philadelphia, Pennsylvania, USA

**ABSTRACT:** Geosynthetic Clay Liners (GCLs) are increasingly popular as a barrier material in waste containment. While GCLs have many desirable engineering properties, long-term performance issues are not documented. This information is critical for designers and regulators to prudently implement GCLs in waste containment. With the cooperation and assistance of GCL manufacturers and consultants, US EPA initiated a field study to examine the performance of GCLs on slopes. The project purpose is to assess field performance and to verify design parameters associated with the application of GCLs in waste containment applications. The two slope angles, 2H:1V and 3H:1V, were selected to model GCL performance in a challenging situation. The experiment aims to reveal the internal shear properties of the GCLs by forcing the internal bentonitic clay to provide stability for the entire cross section. The experiment is designed to force the shear plane inside the clay of the GCL. The experimental design includes cross sections with varying GCL product and varying drainage materials.; These 13 field plots are monitored for displacement and moisture content. The slope experiment has been underway since the Spring of 1995, and this paper summarizes the experimental design, monitoring techniques, and interim results.

**KEYWORDS:** Geosynthetic clay liner (GCL), Landfill cover, Solid waste containment, Shear strength

## 1 INTRODUCTION

Geosynthetic Clay Liners (GCLs) are often considered in modern landfill cover design. GCLs have consistent and desirable hydraulic properties, and may be easier to reliably construct in cover applications than a compacted clay liner (CCL). GCLs provide a reasonable alternative to CCLs in composite waste containment cover applications. This research effort was initiated with the assistance of GCL manufacturers to gain greater understanding of the shear and slope stability characteristics of GCLs.

Technical documentation covers GCL development from their introduction as an engineering material through to their field performance (Daniel and Estornell, 1991, Daniel and Boardman, 1993, Daniel and Scranton, 1996, Koerner, Gartung and Zanzinger, editors, 1995). Technical comparisons between GCLs and CCLs when used in waste containment applications have been made between GCLs and CCLs and are detailed in Daniel and Boardman (1993). Like any engineering material, GCLs must be chosen for use based on site-specific characteristics, and specifiers must understand the impacts of changing engineering properties over time.

One property that remains unproven in the long-term is internal shear strength which relates directly to geotechnical slope stability. The curiosity about this property emerges from our understanding of the technical properties of

bentonitic clay, commonly used in GCLs. Bentonitic clay has undesirable engineering properties when hydrated, such as low shear properties under low overburden pressures. Relatively low overburden pressures are present in most landfill cover applications.

Modern landfill covers contain many natural and geosynthetic components, presenting the designer with multiple stability design issues. A multilayer system contains multiple interface friction conditions. Some materials, like GCLs, present an internal friction situation with potential to change with varying moisture conditions. Landfill covers containing geosynthetics and/or natural barrier materials will remain stable only if the interface and internal shear properties remains stable over time. Landfill covers are a common application for GCLs.

Some GCLs are specifically designed to serve in slope applications. These materials are made with particular attention paid to the stabilization of internal shear properties. This can be accomplished by joining the top and bottom textiles with one or a combination of techniques. The techniques utilized for the GCLs involved in this research include stitching, needle-punching, and heat burnishing. All intend to feed fibers through the GCL clay material and join the two textiles. This project focuses on only one property, the internal shear characteristics of GCLs. Other interfaces and shear properties were selected to be satisfactory for the

purposes of this experiment.

## 2 MATERIALS AND METHODS

Utilizing GCLs being manufactured at the time of project initiation, the project was constructed at full scale beginning in November, 1994. Thirteen (13) test plots were constructed and instrumented for physical displacement, and for soil and GCL clay moisture conditions, the primary indicators of slope stability and long-term performance.

Drainage materials were of two types, drainage sand, and a geosynthetic drainage composite consisting of a drainage net thermally bonded to nonwoven geotextiles on both surfaces.

Cover soils were consistent on the slopes at approximately 1 m thickness.

## 3 EXPERIMENTAL DESIGN

Slopes of 3H:1V (18.4 degrees) and 2H:1V (26.6 degrees) were selected to represent two conditions. The slopes were intended to represent typical landfill cover applications, and a more aggressive slope nearer the minimum factor of design safety (for this particular experiment), respectively. Each plot consists of two roll widths, to include a field constructed seam running vertically along the length of the slope. Slope lengths were to accommodate a 9.2 m vertical elevation change. This resulted in GCL panel lengths of 29 m for the 3H:1V slopes, and of 20 m for the 2H:1V slopes. Each plot is separated by a drainage area in approximately 3 m widths to accommodate monitoring, plot isolation and drainage.

### 3.1 GCLs Involved in Study

Five products from all four GCL manufacturers (at the time of project initiation) were included in the study. The GCLs included in this study are described in Table 1.

Table 1. GCLs involved in study.

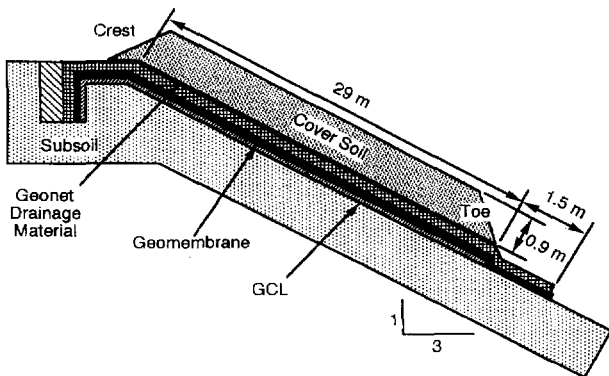


Figure 1. Cross section of 3H:1V test plot. (Scranton, 1996)

Product	Substrate GT as Field Placed	Superstrate GT as Field Placed	Top/bottom Joining Technique	Roll Width
				m
Bentofix NS	NP-NW	NP-NW	heat burnished	4.7
Bentofix NW	W-SF	NP-NW	heat burnished	4.7
Bentomat ST	NP-NW	W-SF	needle punched	4.6
Claymax SP500	W-SF	W-SF	stitched, 100 mm spacing	4.2
Gundseal	HDPE-T GM or none	none or HDPE-T GM	adhesive bonded	5.3

Key: GT = geotextile  
 NP-NW = needle punched nonwoven geotextile  
 W-SF = woven slit film geotextile  
 HDPE-T GM = high density polyethylene, textured both sides, (GM orientation varied per plot)

Table 2 describes the configuration of the test plots and the identifying letter. The cross section of a typical plot is presented in Figure 1 (for 3H:1V slopes).

Recall that all plots have geosynthetic erosion control products applied to rapidly establish vegetation, except plot M, which is an experimental control. Project plots are similar in construction except for these details:

- 1) Some cross sections contained composite barriers consisting of a GCL overlain by a geomembrane, and some had only a GCL used without a geomembrane, and
- 2) Some cross sections contained geosynthetic drainage composites, and others had GCL overlain by sand and a geotextile to form a drainage layer.

Table 2. Description of plot cross sections.

Plot	GCL	Cross Sections (described from top to bottom)
A	Gundseal	cover/GC/GM/GCL (bentonite up)/subgrade
B	Bentomat ST	cover/GC/GM/GCL/subgrade
C	Claymax SP500	cover/GC/GM/GCL/subgrade
D	Bentofix NS	cover/GC/GM/GCL (NW GT side up)/subgrade

E	Gundseal	cover/GC/GM/GCL (bentonite down)/subgrade
F	Gundseal	cover/GC/GM/GCL (bentonite up)/subgrade
I	Bentofix NW	cover/GC/GM/GCL/subgrade
J	Bentomat ST	cover/GT/granular drain/GCL/subgrade
K	Claymax SP500	cover/GT/granular drain/GCL/subgrade
L	Bentofix NW	cover/GT/granular drain/GCL/subgrade
M	None (Control)	cover/subgrade
N	Bentofix NS	cover/GC/GM/GCL (NW GT side up)/subgrade
P	Gundseal	cover/GC/GM/GCL (bentonite up)/subgrade

Key: GC = geotextile/geonet/geotextile drainage composite, thermally bonded  
 GM = geomembrane  
 GCL = geosynthetic clay liner  
 GT = geotextile  
 NW GT = nonwoven geotextile  
 † = replaced plots G and H, lost prior to testing  
 \* = units: degrees

### 3.2 Instrumentation

Two key parameters that would indicate the performance of the plots are moisture properties, to determine hydration of subgrade and GCL, and movement of the GCL panels down slope. To monitor this behavior, three instruments were utilized.

#### 3.2.1 Moisture Sensor in Soil Subgrade

Subgrade soil is monitored by the use of dielectric resistance moisture probes calibrated to the subgrade soils. Probes are positioned beneath each plot. To monitor subgrade moisture, gypsum blocks were employed were placed at evenly spaced intervals in a column at three positions along the slope length. Each probe has electrical leads that extend beyond the boundary of each panel to accommodate measurement. The location of the sensors is shown in Figure 2.

#### 3.2.2 Moisture Sensor in or near Bentonitic Clay

Sensors at the GCL/subbase interface are similar in function to the gypsum blocks used for soil subgrade, but consist of fiberglass wafers. These probes were inserted into the interface between GCL and soil subbase. On occasion, probes are inserted into the clay portion of a GCL blanket. Sensors are calibrated to function in site soils. The GCL bentonite probes were placed in a similar grid as the soil subgrade sensors, with electrical leads that also extended beyond the boundary of each panel.

#### 3.2.3 GCL Deformation - Translational Movement

Motion is monitored by a series of steel wires designed to detect motion in the textiles that form the top and bottom of each GCL individually. The sensors are comprised of braided stainless steel wire encased in plastic sleeve tubing to allow movement of the wire inside the sleeve. The wires were connected to the GCL in a 5 row by 2 column grid along the vertical centerline of each GCL panel. The wire displacement sensors are attached to both the top and bottom textile of each

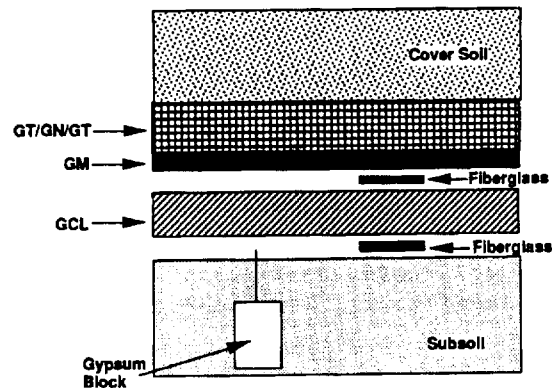
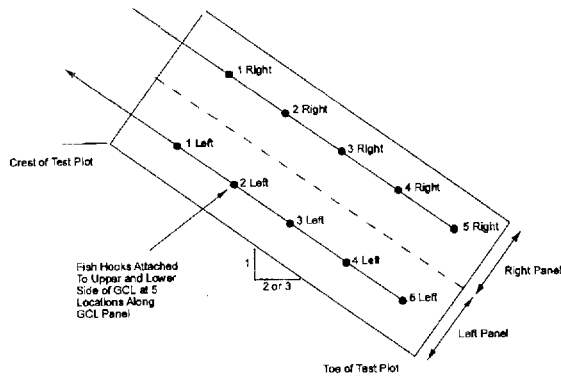
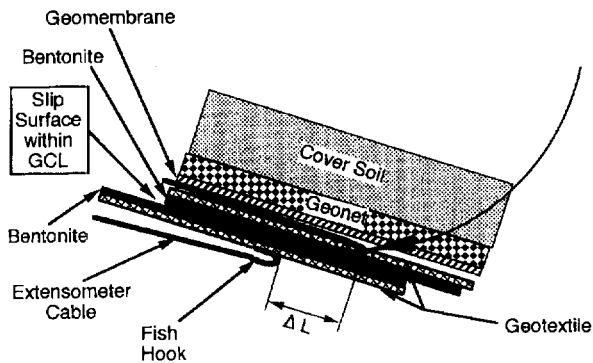


Figure 2. Location of Moisture Sensors, typical. (Scranton, 1996)

GCL panel. This monitoring configuration would allow the detection of translation movement and therefore, internal shear motion. The design was slightly modified for Gundseal, a GCL which is comprised of granulated bentonite adhered to a geomembrane overlain by an extremely lightweight geotextile web (or in most cases, no geotextile at all). Monitoring displacement data for Gundseal products is difficult in this experiment due to the inability to monitor both surfaces effectively. The steel wires are brought to the surface monitoring area at the crest of each slope (in two locations per plot, one for each panel) and the wires are exposed on tables with motion indicators attached.



**Figure 3.** Plan view of arrangement of displacement gauges.



**Figure 4.** Cross-section of displacement gauge location.

## 4 CONSTRUCTION SEQUENCE

Construction of each plot followed the following chronological sequence:

- Subgrade preparation (wet conditions prevailed)
- GCL deployment
- Geomembrane deployment and seaming (where required)
- Drainage layer installation (either geocomposite or GCL/sand/geotextile)
- Cover soil emplacement
- Removal of bottom buttress
- Installation of erosion control geosynthetics
- Hydro seeding of slope surface

### 4.1 EXPERIMENTAL COMMENCEMENT

Near the end of construction, the largest supportive force, the soil toe buttress (necessary for construction) was removed, and the overlying geosynthetics were then severed, marking the beginning of the experiment.

## 5 RESULTS AND DISCUSSION

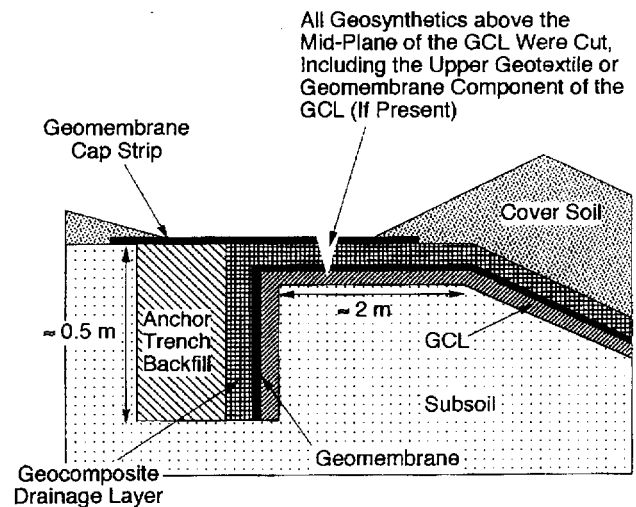


**Figure 5.** Severing of overlying geosynthetics.

Results are being collected as the project progresses. This paper provides a brief overview and discussion of data collected up to the point of writing. Below is a discussion of events that have occurred.

### 5.1 Field Performance - Short Term

Shortly after construction, two interface shear slides occurred. Two slopes (former plots G and H) were lost in translational slides at 20 and 50 days after construction, respectively. In each case, the underlying GCL (in these cases, a woven slit-film material interfaced with textured geomembrane), which remained intact. The two plots were later replaced with another plot P. These slides revealed no useful information regarding internal shear properties.

All other plots remained stable throughout the construction process, showing minimal motion.

### 5.2 Field Performance - Long-Term

Experiments formally began with the severing of overlying geosynthetics. This was done so that the geosynthetics could not contribute to slope stability in a tensile fashion. Textiles and/or geomembranes were carefully severed at each layer. For GCLs other than Gundseal, only the bottom geotextile remained intact. For Gundseal, only the geomembrane remained intact (for bentonite up applications). After severing, it is primarily the clay that resides within any individual GCL that resists movement on each plot.

#### 5.2.1 Interface Slides

Plot F experienced an interface slide between the underlying GCL and the overlying geomembrane at approximately 10 months into the experiment. As with the post-construction slides discussed earlier, the GCL remained on the slope, while overlying materials slid. Panel F was constructed such that the clay of the GCL was positioned between two geomembranes, and this arrangement should prevent massive hydration of bentonitic clay within this cross section. Yet wetting of the GCL progressed quickly, indicating a malfunction in slope construction or site management.

### 5.2.2 Subbase Failure

In May of 1997, approximately 700 days into the experiment, Plot I experienced a subbase failure in the soil beneath the plot. Subbase soils were found to contain a pocket of highly plastic clays, and over time, the slope became unstable and a soil slide occurred. The GCL was performing satisfactorily until this event occurred.

### 5.2.3 Investigative Disassembly

In June of 1997, approximately 730 days into the experiment, Plot K was experiencing significant tensile stretching (little evidence of any internal shear), on the order of 900 mm of stretching over a length of 16.5 m. This plot was disassembled in an attempt to learn from the plot before any slide occurred. Disassembly allowed access to the GCL, which was observed to be intact.

### 5.3 Data Summary

Data is summarized in Table 3. The table shows indications of deformation and hydration status at the time of writing. As can be seen from this data, some motion is detected on 2H:1V plots at the time of writing.

## 6 PROJECT STATUS

This effort will continue as long as possible. Monitoring continues on a monthly basis. Final technical project reports will be forthcoming from the authors and US EPA in 1997 and upon project conclusion.

Plot	Maximum Total Deformation (mm)	Maximum Differential Deformation (mm)	Hydration Status	
			GCL/ Subgrade	Subgrade
A	30	10	low	moderate
B	30	25	low	moderate
C	30	10	wet	wet
D	35	15	wet	wet
E	30	10	moderate	wet
F	Slid		wet	wet
I	Slid		wet	wet
J	900	30	moderate	wet
K	Disassembled	75	moderate	moderate
L	800	125	moderate	moderate
M			unknown	unknown
N	30	10	wet	wet
P			low	low

## ACKNOWLEDGMENTS

This project is funded by US EPA via cooperative agreement CR-821448 with David Carson as technical project officer. The grantees and key members associated with the project (in addition to the authors) are: George Koerner - Geosynthetic Research Institute at Drexel University, John Bowders, Jr., and Heather Scranton - The University of Texas at Austin, Majdi Othman - GeoSyntec Consultants Inc., Robert Landreth (retired), Mike Davis, Taras Bryndzia, Lynnann Hitchens, Donna Fisher, Jim Horton, and Scott Ebert - US EPA National Risk Management Research Laboratory, Remediation and Containment Branch. Further, this project is supported in kind by the GCL manufacturers who were represented at the time of project initiation by Robert Trauger - CETCO, John Fuller and Richard Carriker - Claymax (now CETCO), Richard Erickson, Fred Struve, Jim Anderson, Mark Cadwallader - Gundle Lining Systems (now GSE), Larry Lydick and Ted Dzierzbicki of National Seal Corporation, who also provided construction services and related geosynthetics. This project is also supported with in kind contributions from Waste Management Inc., Cincinnati, Ohio, managed by David Bower and formerly by John Stark. This project received geosynthetic materials for erosion control from many suppliers as a subset study. Many participants have moved to other positions after the time of project initiation. Their commitment and support of this project is greatly appreciated.

## REFERENCES

Table 3. Project data summary at approx. 750 days.

Daniel, D.E., and Boardman, B.T. (1993) *Report of Workshop on Geosynthetic Clay Liners*, EPA/600/R-93/171, US EPA Office of Research and Development, Cincinnati, Ohio.

Daniel, D.E. and Estornell, P.M. (1991) *Compilation of Information on Alternative Barriers for Liner and Cover Systems*, EPA/600/2-91/002, US EPA, Office of Research and Development, Risk Reduction Engineering Laboratory, Cincinnati, Ohio.

Daniel, D.E. and Scranton, H.B. (1996) *Proceedings of 1995 Workshop on Geosynthetic Clay Liners*, EPA/600/R-96/149, US EPA, Office of Research and Development, National Risk Management Research Laboratory, Cincinnati, Ohio.

Koerner, R.M. Gartung, E., and Zanzinger, H., editors. (1995) *Proceedings of an International Symposium on Geosynthetic Clay Liners*, A.A. Balkema Publishers, Rotterdam, Netherlands.

Scranton, H.B. (1996) *Field Performance of Sloping Test Plots Containing Geosynthetic Clay Liners*, thesis presented to the Graduate School of the University of Texas at Austin in partial fulfillment of the requirements for the degree of Master of Science in Engineering.

# The Influence of Geomembrane Surface Roughness on Geomembrane-Geotextile Interface Strength

Seok-Won Lee

Graduate Research Assistant, School of Civil and Environmental Engineering, The Georgia Institute of Technology, Atlanta, Georgia, USA

J. David Frost

Associate Professor, School of Civil and Environmental Engineering, The Georgia Institute of Technology, Atlanta, Georgia, USA

Gregory K. Righter

Geotechnical Engineer, Geo-Hydro Engineering Inc., Kennesaw, Georgia, USA

**ABSTRACT:** This paper summarizes the results of a study which uses the recently developed Optical Profile Microscopy technique (Dove and Frost, 1996) as the basis for investigating the role of geomembrane surface roughness on the shear strength of geomembrane/geotextile interfaces. The results show that interface friction can be quantitatively related to the surface roughness of the geomembrane. The peak and residual interface strengths increase dramatically through the use of textured geomembranes as opposed to smooth geomembranes. For the textured geomembranes, the peak interface strength is mainly mobilized through the micro-texture of the geomembrane, however, the residual interface strength is primarily attributed to macro-scale surface roughness which pulls out and breaks the filaments from the geotextile. The results of this study can be used to provide a quantitative framework that can lead to a significantly improved basis for the selection and design of geotextiles and geomembranes in direct contact.

**KEYWORDS:** Geomembranes, Geotextiles, Surface roughness, Interface strength

## 1 INTRODUCTION

Geomembranes are commonly designed to be in contact with soils or other geosynthetics. A textured geomembrane with roughened top and/or bottom surfaces is used to increase the shear resistance mobilized with soils or other geosynthetics as compared to the shear resistance mobilized along smooth geomembrane interfaces. The recently developed Optical Profile Microscopy (OPM) technique (Dove and Frost, 1996) can be used to provide a quantitative measure of surface roughness for geomembranes and enable the role of geomembrane surface roughness on the shear strength of geomembrane/geotextile interfaces to be investigated.

It has been observed that geomembrane surface topography affects not only the shear resistance but also the shear mechanisms operating at the interface. Stark et al. (1996) investigated the interface shear strength between geomembranes and geotextiles using a torsional ring shear device. They reported that the textured geomembranes yielded a substantial increase in interface shear strength over smooth geomembranes (Figure 1).

Based on a quantitative measure of surface roughness, the relationship between surface roughness and geomembrane/geotextile interface shear strength is evaluated in this paper. More importantly, the role of

geomembrane surface roughness on the shear mechanisms of geomembrane/geotextile interfaces is investigated.

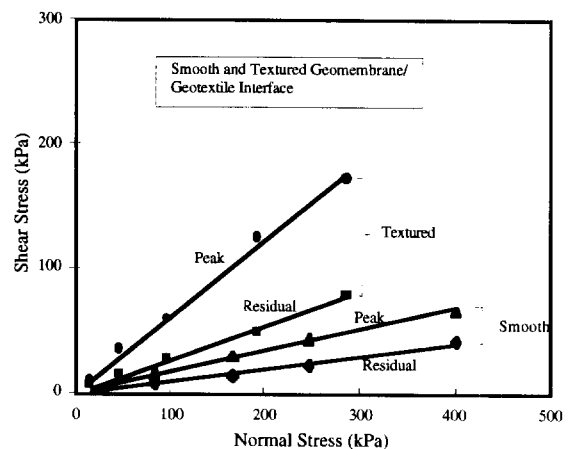


Figure 1. Comparison of failure envelopes for smooth and textured geomembrane/geotextile interfaces (after Stark et al. 1996).

## 2 EXPERIMENTAL STUDY

### 2.1 Surface Roughness Parameter



The surface roughness of geomembranes can be characterized by the recently developed Optical Profile Microscopy (OPM) technique (Dove and Frost, 1996). The OPM technique uses digital image analysis to quantify the profile roughness on three cross-sections of a geomembrane oriented at 120 degrees to each other.

Theoretically, the two-dimensional profile roughness parameter,  $R_L$ , is defined as the ratio of the actual length of the profile to the projected length of the profile. Similarly, the three-dimensional surface roughness parameter,  $R_S$ , is defined as the ratio of the actual area of the surface to the projected area of the surface. Values of  $R_S$  can vary from 1.0 for perfectly oriented surfaces to infinity, theoretically, although the resulting surface roughness parameter ranges, in practice, from about 1.05 for "smooth" geomembranes to greater than 1.70 for "heavily textured" geomembranes.

Since the measurement of real area of geomembrane surface is not an easy task, the surface roughness parameter,  $R_S$ , can be derived, in practice, from the stereology-based relationship (Gokhale and Drury, 1990). More details of this procedure is provided by Dove and Frost (1996).

## 2.2 Surface Roughness Characterization

Three coupons oriented at 120 degrees to each other and approximately 50mm in length are taken from the geomembrane samples. The three sections are placed vertically into a mold filled with a plaster of Paris mixture. After the mixture hardens, the polished surfaces are captured with a CCD camera and evaluated using an image analysis system (Dove and Frost, 1996).

## 2.3 Geosynthetics Used in the Interface Shear Tests

One smooth and three textured HDPE geomembranes which are considered to be representative of the range of textures and texture patterns presently available to designers were utilized in this study. In addition, four different geotextiles were used.

- Dura Seal HD and Friction Seal HD geomembranes manufactured by National Seal Co.
- GSE Friction Flex geomembrane manufactured by GSE Lining Technology, Inc.
- Poly-Flex textured HDPE geomembrane manufactured by Poly-Flex, Inc.
- Trevira Spunbond 110/550 geotextile : Continuous filament polyester nonwoven needle punched fabric manufactured by Hoechst-Celanese with a mass per unit area of 16 oz/yd<sup>2</sup>.
- Amoco #4506, #4510, and #4516 geotextiles : Staple filament polypropylene nonwoven needle punched

fabric manufactured by Amoco with a mass per unit area of 6, 10, and 16 oz/yd<sup>2</sup>, respectively.

## 2.4 Geomembrane Specimen Preparation

The geomembrane specimens were glued to the underside of a 1/4 inch thick 4 inch square aluminum plate using a spray epoxy. The geomembranes were oriented so that the machine direction of the roll was parallel to the shear direction of the plate. The adhesive was allowed to cure for 24 hours under a normal stress of approximately 10 kPa. The geomembrane was then trimmed flush with the rear and side edges of the aluminum plate, leaving excess geomembrane extending from the leading edge. The excess geomembrane was then wrapped completely around the leading edge of the plate, cemented, clamped and allowed to cure overnight. The geomembrane - aluminum plate combination was then bolted to the underside of a 4 inch square aluminum block (Figure 2). This configuration prohibits relative displacement between the geomembrane and the aluminum plate. It also provides a smooth leading edge, allowing the geomembrane to be sheared against the geotextile without peeling back and folding under.

## 2.5 Geotextile Specimen Preparation

The geotextile specimens, approximately 6 inches wide by 10 inches long, were glued to a flexible geomembrane backing using a spray epoxy. After curing overnight, the geotextile - geomembrane combination was placed on the testing platform of the direct shear apparatus, with the machine direction of the geotextile parallel to the shear direction (Figure 2). The geotextile was secured by fastening a 1 inch wide metal bracket along the rear and two side edges of the specimen. The geomembrane backing was used to give the underside of the geotextile added rigidity. The backing in combination with the metal brackets eliminated the relative displacement that would take

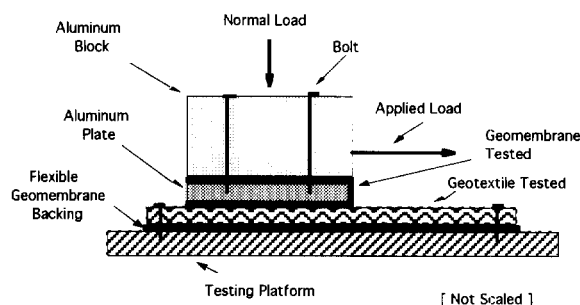


Figure 2. Schematic geomembrane/geotextile interface shear test configuration.

place if the geotextile was fastened directly to the metal testing platform of the direct shear apparatus.

## 2.6 Interface Shear Tests

A modified large displacement direct shear test apparatus was used to measure the shear strength of the geomembrane / geotextile interfaces. This device was used to permit large displacements and hence residual conditions to be achieved in the tests. The tests were conducted at normal stresses of 50, 100, and 150 kPa. The geomembrane was placed on top of the geotextile, after which the normal stress was applied via a metal cross arm and series of dead weights (Figure 2). The geomembrane-aluminum block was then fastened to the direct shear arm and sheared at a constant rate of 0.08 in/min. A load cell and LVDT mounted on the apparatus were used to measure the shear force and displacement, respectively. The test data was collected and displayed on a computer via a LabView data acquisition system.

## 3 RESULTS

### 3.1 Geomembrane Roughness Determinations

The average values of  $R_s$  determined for each geomembrane sample along with the standard deviation are shown in Table 1.  $R_s$  values measured in this study agreed well with those from the previous study reported by Dove et al. (1997).

### 3.2 Effect of Geomembrane Surface Roughness on Interface Shear Strength

Figure 3 shows typical plots of the shear stress - horizontal displacement relationship for geomembrane/ nonwoven geotextile interfaces. As expected, the tests performed using the more textured geomembranes result in a higher peak strength. It is also shown that as the surface roughness of the geomembrane increases, the displacements required to achieve peak and residual strength increase. One interesting aspect of the plot is the relative shape of the different curves. The stress-displacement curve corresponding to the smooth geomembrane results in an initial rise in strength which remains constant once the peak strength is mobilized. The stress - displacement curves for the more textured geomembranes, however, exhibit an initial rise and well defined peak, followed by a decrease to a residual state. This trend is consistent throughout the various textured geomembrane / nonwoven geotextile combinations tested. This is principally attributed to the fact that sliding of the geotextile is the

Table 1. Results of surface roughness determinations.

Geomembrane	Average $R_s$	Standard Deviation	Texture Descriptor*
NSC Dura Seal	1.09	-	Smooth
GSE Friction Flex	1.25	0.03	Slightly Textured
NSC Friction Seal	1.51	0.05	Moderately Textured
Poly-Flex Textured	1.68	0.12	Moderately /Heavily Textured

\* : Proposed by Dove and Frost (1996)

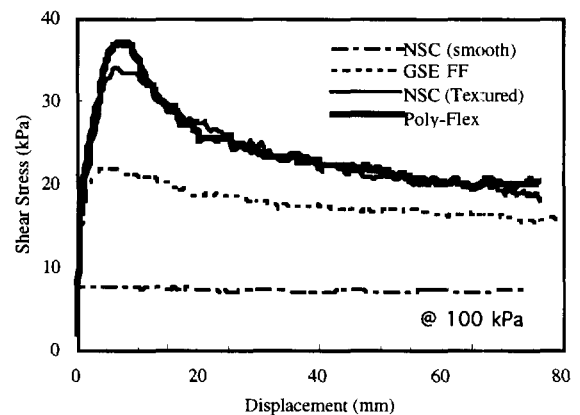


Figure 3. Typical stress-displacement curves : geomembranes/Amoco #4510 geotextile.

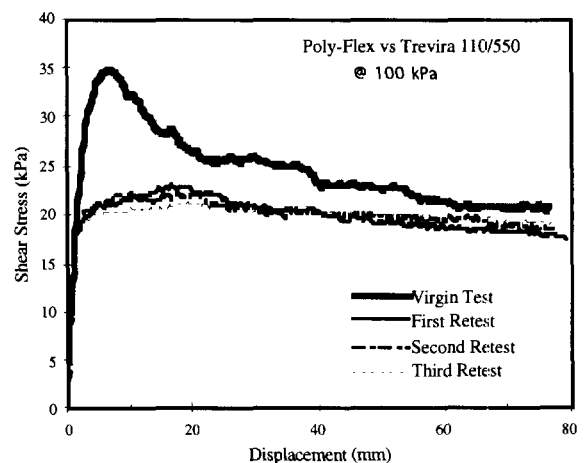


Figure 4. The impact of reusing geomembrane.

main mechanism for smooth geomembrane interfaces, however the pulling out and tearing of the filaments from the geotextile and the breaking of micro-textured asperities from the geomembrane are key mechanisms for textured geomembrane interfaces. This phenomenon is well defined by investigating the impact of reusing geomembranes.

Figure 4 illustrates the impact of reusing a geomembrane specimen on the shear stress - horizontal displacement relationship for Poly-Flex textured geomembrane / nonwoven geotextile interface. This plot shows the results of a series of four tests, the first of which involved using both a virgin geomembrane specimen and a virgin geotextile specimen. In the other three tests, the original geomembrane specimen was reused and sheared against a new geotextile specimen in each test. In addition to reducing the magnitude of the peak interface strength, reusing the geomembrane specimen also effects the shape of the shear stress - horizontal displacement curve. The test performed using virgin textured geomembrane specimens results in a stress - displacement curve exhibiting a sharp rise, peak and decrease in shear strength. The subsequent tests do not exhibit the same trend. Instead, the shear stress - horizontal displacement curve more closely resembles that of a smooth geomembrane, in which the shear strength rises to a peak value with little or no subsequent reduction in strength.

The data presented in this figure suggests micro-texture on virgin geomembrane specimens contributes significantly towards the peak strength of a textured geomembrane / nonwoven geotextile interface. More importantly, the micro-texture can be removed by a relatively small amount of displacement, resulting in a substantial loss of strength. For the textured geomembranes, the peak strength is induced by the tearing of micro-texture geomembrane asperities. After all the micro-texture is removed by the geotextile filaments, the strength reduces to a residual state where the pulling out and the tearing of the filaments in the geotextile occurs. Thus, the residual state is primarily controlled by the macro-scale surface roughness.

Figure 5(a) shows the peak interface friction angle as a function of the surface roughness,  $R_s$  at a normal stress of 100 kPa. All interface friction angles presented herein are secant values computed for an adhesion intercept of zero. It is observed that the peak interface friction angle increases rapidly with small changes in roughness up to a certain  $R_s$  value, above this roughness, the rate of increase of peak interface friction angle with the change in roughness decreases. As hypothesized, the peak strength is mainly mobilized by the geomembrane micro-texture and not the global roughness which includes both macro-scale roughness and micro-scale roughness. For the moderately and

heavily textured geomembrane, even though the  $R_s$  value which is much more affected by the macro-scale roughness, changes in a broad range, the micro-texture does not follow the trend of  $R_s$  values at the same rate. This make the rate of increase of peak interface friction

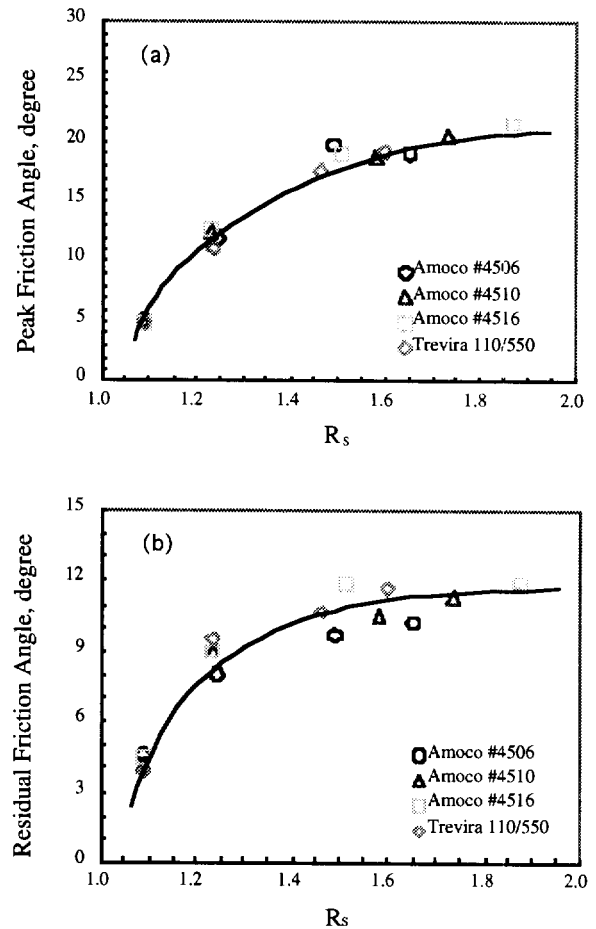


Figure 5. Peak and residual interface friction angles.

Table 2. Results of roughness decrease by reusing of geomembrane.

Geomem-brane	No. of Tests	Virgin $R_s$	Reused $R_s$	% Decrease
GSE	1	1.238	1.233	0.4
Slightly Textured	4	1.271	1.244	2.1
NSC	1	1.523	1.511	0.8
Moderately Textured	1	1.508	1.489	1.3
	2	1.729	1.392	19.5
	7	1.768	1.452	17.9
Poly-Flex	1	1.670	1.653	1.0
Moderately/Heavily Textured	2	1.729	1.633	5.6
	4	1.742	1.600	8.2
	7	1.587	1.492	6.0

angle decrease with the change in roughness,  $R_s$  for moderately and heavily textured geomembranes.

Figure 5(b) shows residual interface friction angle as a function of  $R_s$  for a normal stress of 100 kPa for different geotextiles. As with the peak interface friction angle, it is noted that the residual interface friction angle also increases rapidly with small changes in roughness up to a certain  $R_s$  value, after which, the rate of increase of residual interface friction angle with the change in roughness decreases. Even though the trend is the same as for the peak interface friction angle, the mechanism for the residual interface friction angle is somewhat different. The residual strength is primarily a function of macro-scale surface roughness, since almost all the micro-texture is removed at displacements near the peak stress. This means that beyond a certain value of surface roughness, the residual strength is mainly attributed to the pulling out and tearing of the filaments from the geotextile, and consequently the real strength is influenced by the more pronounced geomembrane asperities, and is a function of strength of the geotextile itself.

Table 2 shows the amount of decrease in surface roughness resulting from the reuse of textured geomembranes. The decrease in surface roughness increases dramatically when the same geomembrane is used multiple times. Single reuse of the geomembrane where the micro-texture influences the peak strength shows that the surface roughness,  $R_s$ , decreases by about 0.4%, 1.1%, and 1.0% for slightly, moderately, and moderate/heavily textured geomembranes, respectively. However, multiple reuse of a geomembrane induces large decreases in surface roughness, where, as described, the shear strength may come from the geotextile itself.

### 3.3 Effect of Geotextile on Interface Shear Strength

Figure 6 presents the effect of geotextile mass per unit area on textured geomembrane/geotextile interface strength at 100 kPa normal stress. The curve shows the results from the same textured geomembrane sheared against the same type of geotextile, with the only difference being the mass per unit area. The trend is for the geotextile with the higher mass per unit area to peak at both a higher stress and a higher degree of displacement at normal stresses less than 100 kPa. This can be explained by the difference in geotextile thickness. Geotextiles with more mass per unit area are thicker. As the geomembrane is sheared against the geotextile, the top of the geotextile is displaced while the bottom is fixed to the geomembrane backing. Displacement rearranges the geotextile fabric, stretching the fibers between the moving geomembrane and the stationary base. The fibers of the thicker fabric can

stretch over a longer distance, resulting in a higher horizontal displacement. The higher strength comes from the increase in fibers per unit area.

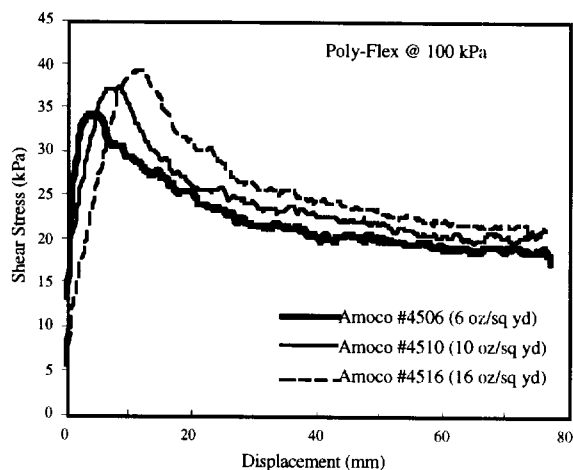


Figure 6. Effect of geotextile mass per unit area.

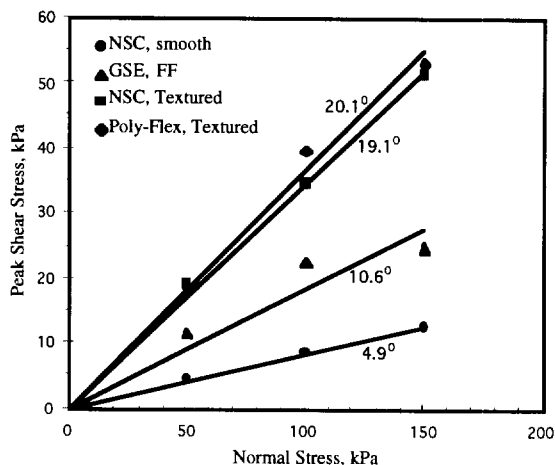


Figure 7. Peak failure envelope for geomembrane/geotextile interface.

### 3.4 Failure Envelope

Figures 7 and 8 present the peak and residual failure envelopes for the geomembrane/geotextile interfaces, respectively. It can be seen that the failure envelopes are approximately linear within the normal stress range tested, although the failure envelope clearly has some degree of curvature. It is also noted that the peak and residual interface strengths are increased dramatically by the use of textured geomembranes instead of smooth geomembranes. However, the post peak strength loss is

substantially greater with a textured geomembrane as shown in Figure 9 where the sensitivity is plotted as a function of roughness.

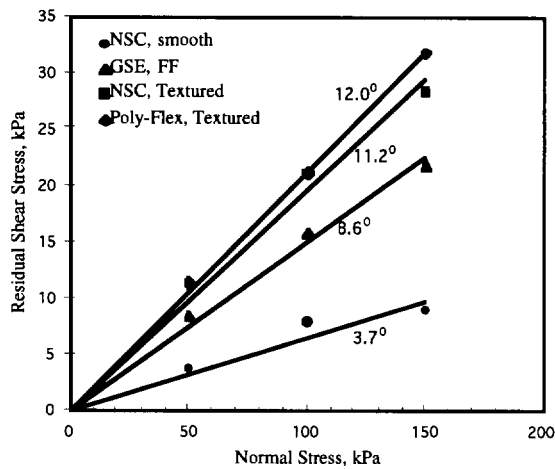


Figure 8. Residual failure envelope for geomembrane/geotextile interface.

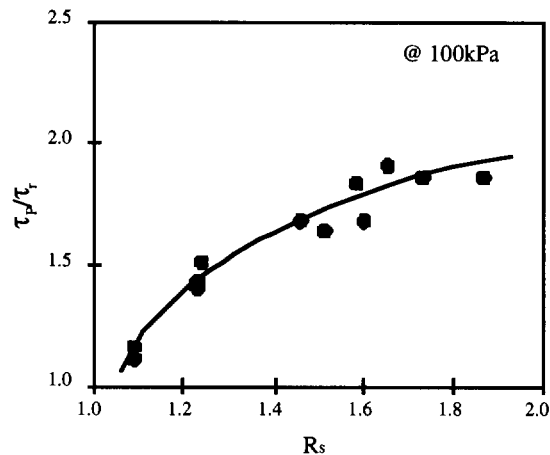


Figure 9. Interface strength sensitivity.

#### 4 CONCLUSIONS

This paper has quantitatively illustrated the influence of geomembrane surface roughness on geomembrane/geotextile interface strength. The results show that surface roughness has a first-order effect on the strength of geomembrane/geotextile interfaces. The following conclusions are based on the data and interpretation presented in this paper:

1. Textured geomembranes mobilize higher peak and residual shear strengths than smooth geomembranes.

2. The sliding of the geotextile is the main mechanism for the smooth geomembrane surfaces, however pulling out and tearing of the filaments from the geotextile and the tearing of micro-texture at asperities from geomembrane are key mechanisms for textured geomembrane surfaces.
3. For the textured geomembrane, the peak interface strength is mainly mobilized by the micro-texture of geomembrane asperities.
4. For the textured geomembrane, the residual interface strength is primarily attributed to the pulling out and tearing of the filaments from the geotextile, and consequently is attributed to the characteristics of the geotextile (e.g., filament entanglement, filament strength, filament length/diameter) and how it interacts with the geomembrane macrotopography.
5. The geotextiles with the higher mass per unit area induce the higher strength and the higher degree of horizontal displacement at peak stress at normal stresses less than 100 kPa.
6. The interface sensitivity can also be quantitatively related to the geomembrane roughness.

#### REFERENCES

- Dove, J.E. and Frost, J.D. (1996) "A Method for Measuring Geomembrane Surface Roughness", *Geosynthetics International*, Vol. 3, No. 3, pp. 369-392.
- Dove, J.E., Frost, J.D., Han, J. and Bachus, R.C. (1997) "The Influence of Geomembrane Surface Roughness on Interface Strength", *Geosynthetics '97*, San Diego, CA, USA, Vol. 2, pp. 863-876.
- Gokhale, A.M. and Drury, W.J. (1990) "A General Method for Estimation of Fracture Surface Roughness: Part 1. Theoretical Aspects", *Metallurgical Transactions A*, Vol. 21A, pp. 1193-1199.
- Stark, T.D., Williamson, T.A. and Eid, H.T. (1996) "HDPE Geomembrane/Geotextile Interface Shear Strength", *Journal of Geotechnical Engineering*, ASCE, Vol. 122, No. 3, pp. 197-203.

# Variability of Interface Shear Strengths

M. Snow

Manager of Engineering Services, Golder Associates, Inc., Irvine, California, United States

R. Mansour,

Design and Construction Section Head, Kern County Waste Management Department, Bakersfield, California, United States

R.H. Swan Jr.

Laboratory Manager, GeoSyntec Consultants, Atlanta, Georgia, United States

E. Kavazanjian Jr.

Principal, GeoSyntec Consultants, Huntington Beach, California, United States

**ABSTRACT:** The interface shear strength between various components of liner and cover systems is an important parameter in evaluating the stability of these systems. Typical stability analyses for liner and cover systems do not explicitly consider the potential variability of the interface shear strength. This paper presents the results of several interface shear conformance tests performed as part of the construction quality assurance program for two composite liner system projects. Interfaces tested include geonet/smooth geomembrane, hydrated geosynthetic clay liner/textured geomembrane, and compacted clay liner/textured geomembrane. The test data provides insight on the statistical distribution of interface shear test results. The data provided are expected to be useful in: (i) evaluating the reliability of interface shear strengths established during the design phase; (ii) performing probability-based stability analyses for liner and cover systems; and (iii) evaluating construction quality assurance interface shear conformance test results.

**Keywords:** Statistical, Shear, Strength, Stability, Construction, Interface

## 1 INTRODUCTION

Slope stability is an important design consideration for waste containment systems employing geosynthetic layers. These geosynthetic layers have the potential for creating interfaces with low shear strengths when combined with other geosynthetic layers or weak soil layers. The presence of these low shear strength interfaces has been an important factor in slope stability failures (Mitchell et al. 1990). As a result, the evaluation of these interface shear strengths has received significant attention. In the current state-of-the-practice, slope stability analyses are performed using interface shear strengths based on prior experience, published data, and/or limited site-specific testing. In addition, these slope stability analyses do not consider the variability of interface shear strengths. These variabilities can result from geosynthetic material manufacturing processes such as geomembrane texturing (Dove et al., 1997), from errors inherent in the testing procedure (Criley and Saint John, 1997), or from variations inherent within natural soil materials. The variability in geosynthetic material manufacturing can be manifested from roll to roll or within individual rolls. Understanding the variabilities of these interface shear strengths can provide useful insight into interpreting slope stability results and can form the basis for performing probabilistic slope stability analyses.

This paper presents the results of interface shear conformance testing performed as part of the construction quality assurance program for two composite liner system

projects in California. The interfaces tested include a geonet/smooth high-density polyethylene (HDPE) geomembrane, hydrated geosynthetic clay liner (GCL)/textured HDPE geomembrane, and compacted clay liner/textured HDPE geomembrane. The statistical distributions of the test results presented and are characterized. The statistical nature of the test results forms the basis for evaluating the confidence level for the specified minimum shear strength.

For both case histories presented, the cover material stability on the slopes was obtained by progressively placing the cover materials in a wedge configuration as the waste disposal operations proceeded up the slope.

## 2 GENERAL TESTING PROCEDURE

The interface shear testing presented herein was performed in general accordance with the American Society for Testing and Materials (ASTM) D 5321 standard test procedure. The shear box apparatus measured 300 mm by 300 mm. The tests were performed at a displacement rate of 1.02 mm/min. Post-peak shear strengths were measured at displacements varying from 43 to 58 mm. The ASTM D 5321 standard test procedure does provide some flexibility in the selection of test parameters which can significantly affect the interface shear strength test results (Sharma et al., 1997). As a result, the project specific details of the interface shear testing procedures are presented in the following section. All tests were

performed at the same laboratory using procedures standardized within the laboratory and consistent with ASTM D 5321.

### 3 PROJECT DESCRIPTIONS

#### 3.1 Shafter-Wasco Landfill Module 2

The Shafter-Wasco Landfill is located about 4.4 km west of the City of Shafter, California. The landfill is an "area-fill" operation with 3 horizontal:1vertical (3H:1V) side slopes about 6-m high. Module 2 was completed in June 1995 and included about 96,000 square meters of lined surface area. Construction of Module 2 included an alternative to the regulatory prescriptive composite liner system comprised of (top to bottom): (1) 340 g/m<sup>2</sup> nonwoven geotextile; (2) additional 205 g/m<sup>2</sup> nonwoven geotextile on the side slopes; (3) geonet; (4) 1.5-mm thick smooth on top textured on bottom HDPE geomembrane; (5) GCL; and (6) 0.45-m thick select subgrade layer with a maximum saturated hydraulic conductivity of  $1 \times 10^{-7}$  m/s. The GCL included a 270 g/m<sup>2</sup> needlepunched nonwoven geotextile and a 110 g/m<sup>2</sup> woven geotextile. The two geotextiles were needlepunched together with a layer of bentonite between them. The interface shear strength for the liner system was specified to have a minimum friction angle value of 7 degrees.

Twenty-five interface shear conformance test series were performed as part of the construction quality assurance program. In this paper, the results of 21 test series performed in two groups will be discussed. The two groups of tests complied with the intent of the specifications. Each test series consisted of three tests (i.e., total of 63 tests) performed at different confining pressures. The first group consisted of twelve (12) test series with the select subgrade, GCL, and HDPE geomembrane components prepared as a sandwich. The HDPE geomembrane was attached to the shear box while the GCL was not attached. For these tests, peak strength displacements occurred at the select subgrade/GCL interface (Group 1a) and post-peak strength displacements occurred at the GCL/textured HDPE geomembrane interface (Group 1b). The second group (Group 2) consisted of nine (9) test series with all the liner system components prepared as a sandwich. The geosynthetics for these tests were not attached to the shear box and were overlain by a second layer of compacted soil. For these test series peak and post-peak strength displacements occurred at the geonet/smooth HDPE geomembrane interface. For each of the Group 1 and 2 test series, geosynthetics were obtained from different rolls on-site and a single bulk sample of select subgrade soil was used for all tests.

For each test the select subgrade material was placed at about 4 percent wet of the optimum moisture content and compacted to 90 percent of the maximum dry density, obtained in accordance with the ASTM D 1557 standard test method. The GCL was hydrated for 24 hours under a confining pressure of 14.4 kPa. The materials were then sheared at normal stresses of 36, 72, and 144 kPa.

#### 3.2 Bena Landfill Network 4

The Bena Landfill is located 27 km east of Bakersfield, California. The landfill is operated as a canyon fill. Network 4 of the Phase 1 development has 3H:1V side slopes up to 25.3m high. Construction of Network 4 was completed in 1995 and included about 111,540 square meters of lined surface area. Network 4 included an alternative to the regulatory prescriptive composite liner system comprised of (top to bottom): (1) geocomposite drainage layer (i.e., geonet sandwiched between two nonwoven 205 g/m<sup>2</sup> geotextiles); (2) 2-mm thick textured on both sides HDPE geomembrane; and (3) 0.6-m thick compacted clay liner with a maximum saturated hydraulic conductivity of  $1 \times 10^{-8}$  m/s. The interface shear strength of the liner system was specified to have a minimum friction angle value of 11 degrees.

Eighteen interface shear conformance test series were performed as part of the construction quality assurance program. Each test series consisted of three tests (i.e., total of 54 tests) performed at different confining pressures. The tests were performed with the compacted clay, HDPE geomembrane, and geocomposite prepared as a sandwich. The geomembrane was not attached to the shear box while the geocomposite was. For 46 tests the peak (Group 3a) and post-peak (Group 3b) strength displacements occurred at the compacted clay liner/textured HDPE geomembrane interface. For the remaining eight (8) tests, peak and post-peak strength displacements occurred at the geocomposite/textured HDPE geomembrane interface. The test series were performed using samples of the geosynthetic materials obtained from different rolls on-site and a single bulk sample of the clay material.

For each test the clay was compacted to about 4 percent wet of the optimum moisture content and to 90 percent of the maximum dry density, obtained in accordance with ASTM D 1557. The clay was subsequently hydrated for 24 hours under a confining pressure of 14.4 kPa. The materials were sheared at normal stresses of 108, 216, and 432 kPa.

### 4 TEST RESULTS

In evaluating the variability of interface shear test results, an important consideration is what form of the test data

should be used. For interface shear testing this leads to a consideration of: (1) the form of the reported test results; (2) the form of the specified minimum value; and (3) the shape of the statistical distribution.

In accordance with ASTM D 5321, the following interface shear test results are typically reported: (1) shear stress plotted against shear displacement; and (2) shear stress plotted against normal stress. In addition, a best fit line is used to define an angle of friction (i.e., slope) and an apparent adhesion (i.e., y-intercept) on the shear stress versus normal stress plot for each series of three tests. The apparent adhesion value obtained from this best fit line can be an important factor in stability analyses where low confining loads are dominant (e.g., veneer stability). However, the reliability of the apparent adhesion value obtained from a best fit straight line is questionable when the true nonlinear nature of the shear stress versus normal stress plot (Sharma et al., 1997) is considered. At low normal stresses, the best fit line may overestimate the apparent adhesion value. Giroud et al. (1990) suggested the use of an apparent friction angle for veneer stability problems. This apparent friction value combines both friction and adhesion into one parameter and is represented by a best fit line passing through the zero value of the y-intercept. The use of an apparent friction angle or slope value, without a separate apparent adhesion value, to represent the interface shear strength is consistent with the current practice of specifying a minimum interface friction angle for material conformance.

To evaluate the apparent friction angle, or slope value, the interface shear strength values obtained for the Group 1a, 1b, 2, 3a and 3b tests were normalized with respect to normal stress. This normalization allows the normalized interface shear strength for each test result to be grouped with test results obtained at other normal stresses. In addition, a singular normalized interface shear strength value simplifies statistical characterizations and allows each test result to be verified for compliance with the specified minimum friction angle value. However, normalization does not explicitly account for the apparent adhesion value or the nonlinear nature of the shear stress versus normal stress plot. The apparent adhesion is implicitly represented in the statistical distribution of the normalized test data while the nonlinear behavior may influence the statistical variations in the data.

Histograms of the normalized test data for Groups 1a and 1b are presented on Figure 1. A histogram of the normalized test data for Group 2 is presented on Figure 2. It should be noted that the peak and post-peak values were identical for all Group 2 tests, which is typical of geonet/smooth geomembrane interfaces. A histogram of the normalized test data for Groups 3a and 3b are presented on Figure 3. Data where displacements occurred at the geocomposite/textured HDPE geomembrane were not included in Figure 3.

Assuming a normal distribution, the sample arithmetic mean and standard deviation for each group of test data are presented in Table 1. Assuming a normal distribution, Table 1 also presents a lower estimate of the true

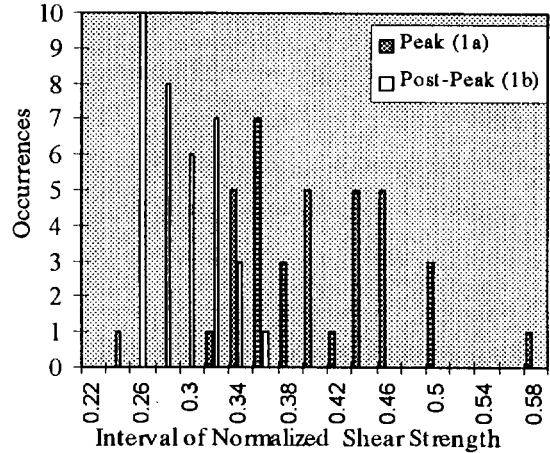


Figure 1. Histogram of Group 1 interface shear data.

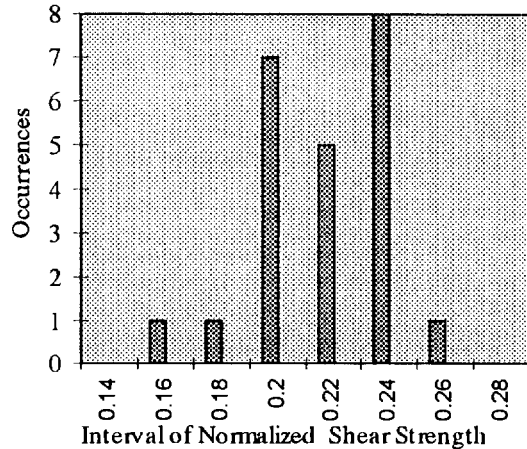


Figure 2. Histogram of Group 2 interface shear data.

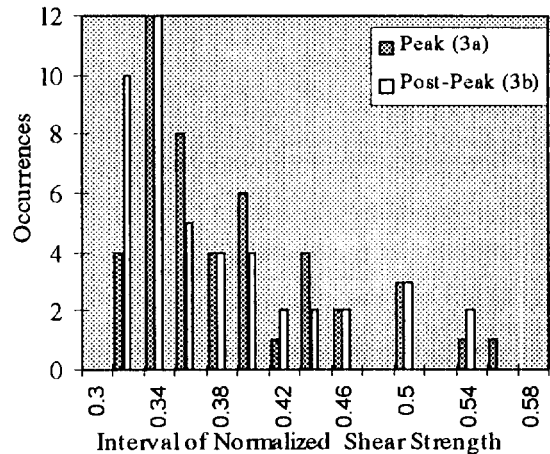


Figure 3. Histogram of Group 3 interface shear test data.



population mean corresponding to a 2.5 percent probability of the true mean being less than the lower estimate using the Student-t distribution. The standard deviations given in Table 1 for Groups 1a and 3,

Table 1. Summary of interface shear statistical parameters.

Statistical Parameters	Test Group				
	1a	1b	2	3a	3b
Sample Mean	0.400	0.287	0.215	0.381	0.370
Lower True Mean Estimate	0.380	0.276	0.206	0.363	0.352
Sample Standard Deviation	0.060	0.032	0.024	0.062	0.062

soil/geosynthetic interfaces, are significantly less than the standard deviations presented by Criley and Saint John (1997) also for soil/geosynthetic interfaces. It is not clear why the variations observed in this testing program are less than those observed by Criley and Saint John. However, variability between different laboratories may explain some of the differences observed.

Using the lower (i.e., 5 percent) estimate of the population mean and a 95 percent confidence interval, the test data also indicate that:

- the lower confidence limit for the Group 1a (i.e., GCL/select subgrade) results is 0.281;
- the lower confidence limit for the Group 1b (i.e., GCL/textured geomembrane) results is 0.224;
- the lower confidence limit for the Group 2 (i.e., geonet/textured geomembrane) results is 0.167;
- the lower confidence limit for the Group 3a (i.e., compacted clay/textured geomembrane) results is 0.261; and
- the lower confidence limit for the Group 3b (i.e., compacted clay/textured geomembrane) results is 0.25.

## 5 CONCLUSIONS

The variability of interface shear strength described herein can be considered significant by geotechnical standards. The variability occurred even with the use of a single laboratory, standardized test procedures, and a single soil sample (where applicable). It is believed that the observed variability in the test results can be primarily attributed to the geosynthetic materials. The variability of the geosynthetic materials typically results from roll to roll variations in characteristics. However, variations across rolls may also be a contributing factor.

Based on the data presented herein, the statistical significance of a non-conforming (i.e., a test result less than the minimum specified value) test result can be evaluated. This can be observed in the Group 3 test results

where 10 normalized residual interface shear strength results were less than the specified minimum value, yet 75 percent of the results were greater than the specified minimum value. This supported the acceptance of the non-conforming interface shear strength results for this project. In addition, the data presented herein can be used to perform probabilistic slope stability analyses where the statistical distribution of the interface shear test results can be used to optimize liner and cover designs.

The standard deviations presented herein can also be used to predict and/or optimize the required number of conformance samples on projects with similar interfaces based on a Student-t distribution analysis.

## REFERENCES

- ASTM D 5321 (1992), "Standard Test Method for Determining the Coefficient of Friction of Soil and Geosynthetic or Geosynthetic and Geosynthetic Friction by the Direct Shear Method", American Society for Testing and Materials, Philadelphia, Pennsylvania.
- ASTM D 1557, (1991) "Test Method for Laboratory Compaction Characteristics of Soil Using Modified Effort (56,000 ft-lbf/ft<sup>3</sup> (2,700 kn-m/m<sup>3</sup>))", American Society for Testing and Materials, Philadelphia, Pennsylvania.
- Criley, K.R. and Saint John, D., (1997) "Variability Analysis of Soil vs. Geosynthetic Interface Friction Characteristics by Multiple Direct Shear Testing", *Proceedings of Geosynthetics '97*, Long Beach, California, Industrial Fabrics Association International, Vol. 2, pp. 885-897.
- Giroud, J.P., Swan Jr., R.H., Richer, P.J., and Spooner, P.R., (1990) 'Geosynthetic landfill cap: laboratory and field tests, design and construction', *Proceedings 4<sup>th</sup> International Conference on Geotextiles, Geomembranes and Related Products*, The Hague, pp. 493-498.
- Dove, J.E., Frost, J.D., Han, J., and Bachus, R.C., (1997) "The Influence of Geomembrane Surface Roughness on Interface Strength", *Proceedings of Geosynthetics '97*, Long Beach, California, Industrial Fabrics Association International, Vol. 2, pp. 863-876.
- Mitchell, J.K., Seed, R.B., and Seed, H.B., (1990) "Stability Considerations in the Design and Construction of Lined Waste Depositories", *Geotechnics of Waste Fills - Theory and Practice*, American Society for Testing and Materials, ASTM STP 1070, pp. 207-224.
- Sharma, H.D., Hullings, D.E., and Greguras, F.R., (1997) "Interface Strength Tests and Application to Landfill Design", *Proceedings of Geosynthetics '97*, Long Beach, California, Industrial Fabrics Association International, Vol. 2, pp. 913-926.

# Frictional Behavior of Landfill Liner Interfaces with Geonets

Anirban De

Senior Staff Engineer, GeoSyntec Consultants, Walnut Creek, California, U.S.A.

(formerly Graduate Student, Department of Civil Engineering, Rensselaer Polytechnic Institute, Troy, New York, U.S.A.)

Thomas F. Zimmie

Professor, Department of Civil Engineering, Rensselaer Polytechnic Institute, Troy, New York, U.S.A.

**ABSTRACT:** In this paper the frictional characteristics of geotextile / geonet and geomembrane / geonet interfaces are discussed. The shear strength properties of such interfaces demonstrate some interesting characteristics. The possible effects of parameters such as specimen size, orientation of geonet, normal stress, number of cycles and shearing rate were investigated under monotonic (commonly known as static) and cyclic loading conditions. It has been observed that the interface friction angle is largely dependent on the direction and orientation of the strands forming the net, with respect to the direction of shearing motion.

**Keywords:** Landfill liner, Landfill cover, Geonets, Interface friction, Direct Shear tests

## 1. INTRODUCTION

The stability of multi-layer liner systems is of great concern in the design of modern landfills with relatively steep side slopes. The different components of such liners include interfaces that have been known to possess low friction properties. The interface shear strength at such interfaces, therefore, play a major role in the stability of landfill slopes.

Geonets are commonly used in landfill liner systems to function as drainage layers. They are usually placed in contact with other geosynthetic surfaces, such as geotextiles or geomembranes. In order to perform appropriate design procedures, it is important to understand the various factors that influence the frictional properties at such interfaces.

## 2. EXPERIMENTAL APPROACH

This paper presents results from a research project in which the interfacial friction properties of different common geosynthetics used as landfill liner components were

studied. In this study twelve different geosynthetic interfaces were studied. The details of the project are published in De (1996). In this paper the important features regarding the frictional behavior of geonet/geotextile and geonet/smooth geomembrane interfaces are presented.

The geonet used in the tests was a medium density polyethylene and had a thickness of 5.2 mm (205 mils). The geotextile used in the tests was a continuous filament, non-woven needle punched fabric made of polypropylene material with mass per unit area of  $270 \text{ g/m}^2$  (8 oz/yd<sup>2</sup>). The geomembrane (smooth) was a high density polyethylene having a thickness of 1.5 mm (60 mils).

### 2.1 Orientation of Geonet

The geonet was tested at different angles of orientation between the major direction of the strands forming the interface and the direction of sliding motion. It is believed that the amount of shearing resistance offered by a geonet during sliding is influenced by its orientation with respect to the direction of sliding. This is best explained with the help of the schematic shown in Figure 1.

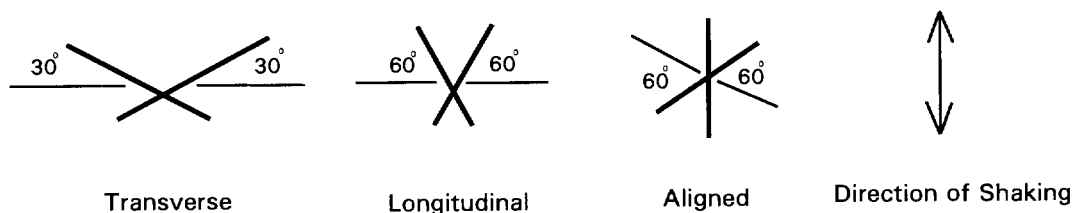


Figure 1. Orientation of geonet mesh

The orientation in which one of the strands is along the direction of the force is termed aligned. The case where the strands are at 60° with the direction of the force is termed transverse. When the strands are at 30° to the force direction, the orientation is termed longitudinal. The three orientations were treated as three different surfaces and tested accordingly.

The influence of orientation of geonet on its frictional properties has also been observed by other researchers, viz. Geotek (1987) and Mitchell et al. (1990).

The frictional behavior of these interfaces were studied under both monotonic and cyclic loading conditions.

## 2.2 Apparatus

The monotonic and cyclic tests reported here were performed using a direct shear device that tested specimens 900 cm<sup>2</sup> (144 in<sup>2</sup>) in area. The shear force was controlled by means of servo-hydraulic actuators. The normal force was produced by means of a pneumatic control system.

## 3. EXPERIMENTAL RESULTS

### 3.1 Monotonic Tests

The test results are classified as geonet / geotextile, and geonet / smooth geomembrane. The tests were performed in a direct shear apparatus using a stroke-controlled mode at a displacement rate of 1.27 mm/min. Four direct shear tests were conducted for each interface at different normal stress levels between 21 and 43 kPa (3 to 6 psi). Each piece of geonet specimen was used for two consecutive tests and the orientation and the side of the geonet was altered after one test, so that transverse and longitudinal tests were performed alternately. The geotextile specimens were reused in three to four consecutive tests. A fresh geomembrane specimen was used in every test. The details can be found in De (1996).

#### 3.1.1. Geonet/geotextile interfaces

The results from the monotonic direct shear tests on geotextile/geonet tests are presented in Figure 2. Plots of shear stress versus displacement for all three orientations, tested under the same normal stress, are presented for comparison.

The plots in Figure 2 exhibit significant differences in the behavior of the three orientations when subjected to shear stress. For the transverse orientation, the shear stress continues to increase after the peak. In the case of the longitudinal orientation, the stress continues to remain at about the level where the peak occurs. Finally, in the case where the strands are aligned in the direction of the force, there is a slight reduction in the shear stress.

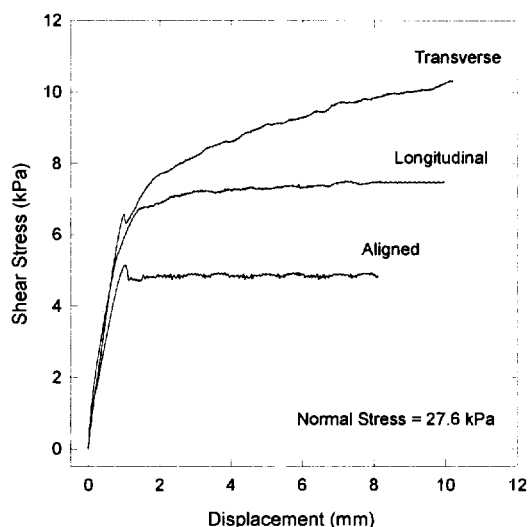


Figure 2. Shear stress versus displacement results from direct shear tests: geotextile over geonet (transverse, longitudinal and aligned)

The cause for this orientation dependent behavior of the geonet strands is not completely understood. It appears that an arrangement of the strands along or almost along the direction of the force leads to an elasto-plastic type behavior, whereas an arrangement where the strands face sideways to the direction of loading leads to a strain hardening effect.

The results of peak shear stress versus the normal stress for four tests on each geotextile/geonet interface are shown in Figure 3. It can be seen from the figure that the shear stress versus normal stress behavior in the case of the transverse and longitudinal orientations is not linear, and dependent on normal stress. In the case of the aligned orientation the relationship appears to be linear. The cause for this behavior is not known; however it may be caused by deformation of the geotextile under high stress. Unfortunately, these interfaces could not be tested at a wider range of normal stresses to confirm this theory, because of limitations in the testing apparatus.

Because of the stress dependent nature of the friction angles for the transverse and longitudinal orientations, it was deemed appropriate to report the static friction angle values as ranges, instead of single values, as was done for the other interfaces.

For the transverse orientation, the calculated peak friction angles ranged from 14.5° to 22°, with the smallest value associated with the highest normal stress (41.4 kPa) and the largest value associated with the lowest normal stress (20.7 kPa) used in these tests. In the case of the longitudinal orientation, the value of residual friction angle was between 14° (for 41.4 kPa normal stress) and 17° (corresponding to 20.7 kPa stress). The behavior of the aligned orientation appears to be more linear, and the peak friction angle is about 10.5°.

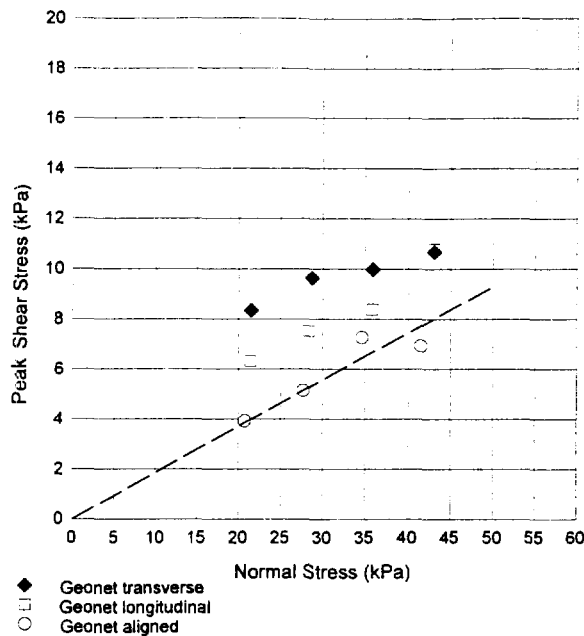


Figure 3. Peak shear stress versus normal stress from direct shear tests: geotextile over geonet (transverse, longitudinal and aligned)

From a practical standpoint, geonet orientation could play a significant role in liner interface behavior after sliding is initiated in the field. For the case of sliding along a geonet oriented transversely to the direction of movement, the amount of slip occurring after the shear strength of the interface is exceeded will be relatively small. However, where sliding occurs in a direction parallel to the direction of the strands, larger displacements can result following slippage, due to the relatively low value of residual shear strength.

### 3.1.2. Geonet/geomembrane interfaces

Experiments similar to the ones described in the last section were performed on geonet/smooth geomembrane interfaces. For a detailed account the reader is referred to De (1996).

Figure 4 shows the plots of shear stress at peak versus normal stress for interfaces between smooth geomembrane and geonet in three orientations. In this case the residual friction angle appears to be less dependent on the orientation of the geonet, than in the case of the interfaces involving geotextile. The minimum value of friction angle of  $8^\circ$  corresponds to the aligned orientation and the maximum value is about  $11^\circ$  for both the transverse and the longitudinal orientations.

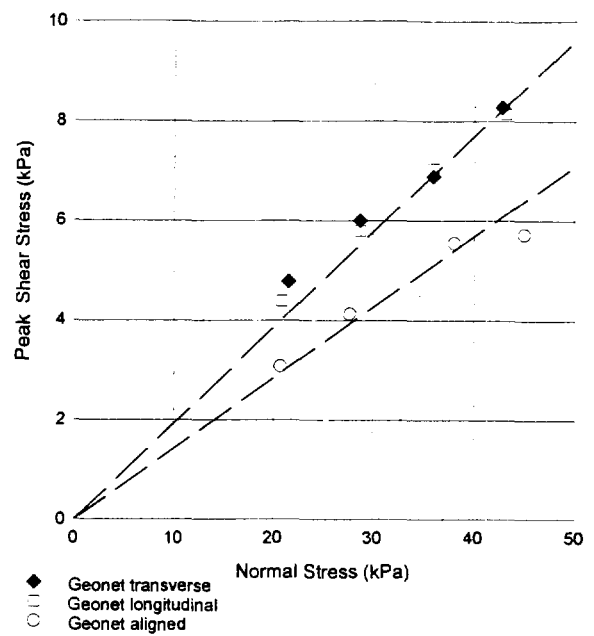


Figure 4. Peak shear stress versus normal stress from direct shear tests: smooth geomembrane over geonet (transverse, longitudinal and aligned)

## 3.2 Cyclic Tests

Sinusoidal displacement-controlled excitation was applied to the geosynthetic interfaces in the cyclic direct shear tests. The peak dynamic friction angle at the end of each cycle was calculated on the basis of the peak shear stress and the normal stress.

### 3.2.1. Geonet/geotextile interfaces

In the case of the geonet/geotextile interfaces, the dynamic friction angle was found to be dependent on normal stress and no variation was observed due to the number of cycles of loading.

### 3.2.2. Geonet/geomembrane interfaces

The dynamic shear stress behavior of geonet/ smooth geomembrane interfaces appeared to depend both on the normal stress and the number of cycles of loading. Figures 5, 6 and 7 show plots from tests performed on geonet/geomembrane (smooth) interfaces with the geonet oriented in the transverse, longitudinal and aligned orientations, respectively.

It can be seen from Figure 5 that the dynamic friction angle varies quite substantially with the number of cycles of loading. For the first cycle the dynamic friction angle is approximately  $11^\circ$ , for all normal stress levels. Then there is a very rapid increase in the value of dynamic

friction angle for about the next five to ten cycles. After that the increase is at a much slower pace, and the rate of increase is related to normal stress, with the lowest normal stress showing the most rapid increase.

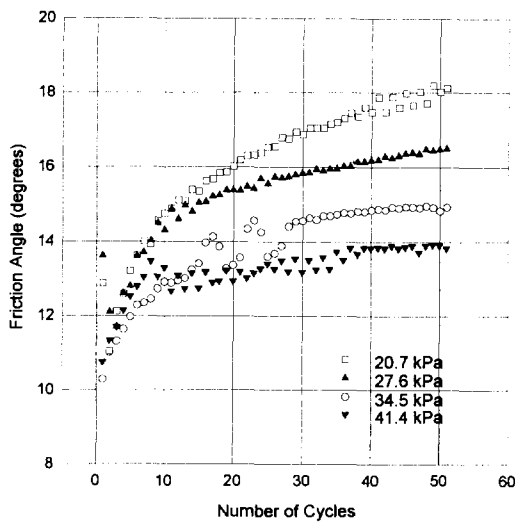


Figure 5. Variation of friction angle with number of cycles from tests using the direct shear device: Smooth geomembrane over geonet (transverse)

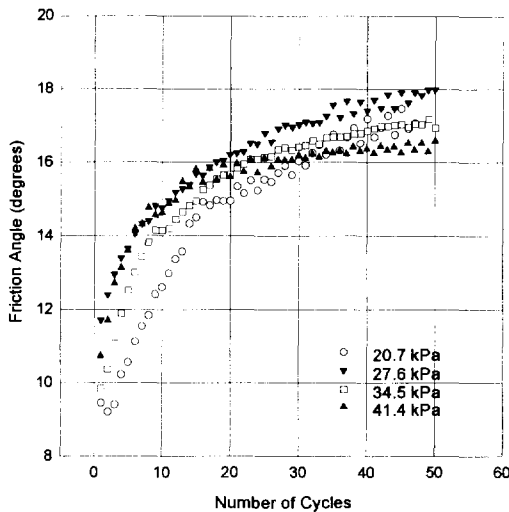


Figure 6. Variation of friction angle with number of cycles from tests using the direct shear device: Smooth geomembrane over geonet (longitudinal)

Plots of dynamic friction angle with number of cycles of loading for longitudinal and aligned orientations of the geonet are shown in Figures 6 and 7. The basic nature of the curves are similar to those in Figure 5. However, the dependence on normal stress is not as prominent in Figure 6, and absent in Figure 7.

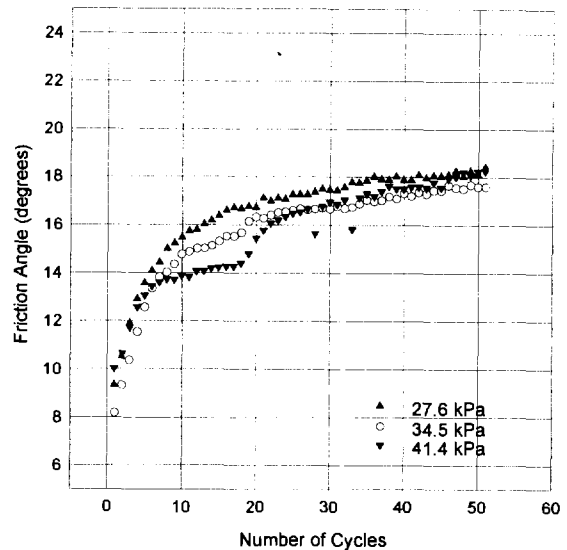


Figure 7. Variation of friction angle with number of cycles from tests using the direct shear device: Smooth geomembrane over geonet (aligned)

#### 4. CONCLUSIONS

From the experimental results it may be concluded that the following parameters have an influence on the monotonic and cyclic shear behavior of geonet interfaces:

- a) orientation of the geonet strands;
- b) normal stress (for transverse and longitudinal);
- c) number of cycles of shear loading.

The dynamic friction angle obtained at the end of the first cycle of a cyclic direct shear test is close to the value obtained from a monotonic shear test.

#### REFERENCES:

- De, A. (1996) *Study of Interfacial Friction of Landfill Geosynthetics : Static and Dynamic*, Ph. D. Thesis, Department of Civil Engineering, Rensselaer Polytechnic Institute, Troy, New York, USA.
- Geotek (1987) *Direct Shear Testing of Friction Liner Material*, Report for Gundle Lining Systems, Project 2166.
- Mitchell, J. K., Seed, R. B. and Seed, H. B. (1990) "Kettleman Hills Waste Landfill Slope Failure. I: Liner-System Properties," *Journal of Geotechnical Engineering*, ASCE, Vol. 116, No. 4, pp. 647-668.

# Geosynthetic Interface Friction Testing in Germany

## - Effect of Test Setups -

W. Blümel

Professor, Institute of Soil Mechanics and Foundation Engineering, University of Hannover, Germany

C. Stoewahse

Research Engineer, Institute of Soil Mechanics and Foundation Engineering, University of Hannover, Germany

**ABSTRACT:** An interlaboratory friction test program, initiated by the German Society of Geotechnical Engineering (DGGT), was organized and evaluated by the authors. As a main part of this program friction tests between a geotextile and a rough geomembrane as well as between a Standard Sand and a geotextile were performed by several German testing institutions. Some selected results of this interlaboratory test program are presented with special reference to effects induced by different test setups. Results of additional investigations performed by the authors with a modified testing device, where the vertical resultant force in the friction plane can be controlled during testing, help to explain the high scattering of data obtained by the interlaboratory tests. Mainly based on the results of the program a working group of DGGT has proposed preliminary recommendations for investigation of friction between different geosynthetics and between soils and geosynthetics. Some main proposals are presented in the conclusions as a basis for further discussion.

**KEYWORDS:** Interface Friction, Geotextiles, Laboratory Tests, Landfills, Direct Shear Testing

### 1 INTRODUCTION

Landfill sealing systems usually consist of different materials like compacted clay, granular soils, geomembranes and geotextiles. For stability calculations the parameters of friction between the components of the sealing systems have to be determined experimentally.

Friction tests for geosynthetic-geosynthetic or soil-geosynthetic interfaces are mainly performed in devices which are comparable with direct shear equipment commonly used in soil mechanics. Data obtained from such friction tests with geosynthetics performed by different institutions often do not correspond to each other. This leads to complex discussions and problems in defining friction parameters for design work. Different testing devices, setups, procedures etc. seem to be the cause for this situation.

The determination of reliable friction parameters for the components of liner systems is of central importance for stable and economical constructions. This includes the choice of partial safety factors in relation to the scattering of test data. Slope failures may occur, if friction available under in situ conditions is overestimated by friction tests performed with boundary conditions, that are not covering all critical stages during building and life of a landfill structure or any other geotechnical construction with inclined layers of geosynthetics and soils.

Caused by the problems explained above a working group of the German Society of Geotechnical Engineering (DGGT) has performed interlaboratory tests, which were organised by the authors at the Institute for Soil Mechanics and Foundation Engineering (IGBE) of the University of Hannover. These arrangements also included basic work for evaluating and summarising test results. The main aim

of the activities of the working group are preliminary recommendations for the investigation of friction between different geosynthetics and between soils and geosynthetics.

### 2 INTERLABORATORY TESTING PROGRAM

As a main part of the interlaboratory test program friction between the following materials was investigated:

- nonwoven PP-geotextile, 1200 g/m<sup>2</sup>, vs. rough textured geomembrane
- sand according to the European Standard EN 196-1 vs. nonwoven HDPE-geotextile, 300 g/m<sup>2</sup>.

The grading of the Standard Sand is given in Table 1.

Sieve Size mm	Cumulative Sieve Residue %
2.00	0
1.60	7 ± 5
1.00	33 ± 5
0.50	67 ± 5
0.16	87 ± 5
0.08	99 ± 1

Table 1. Grading of Standard Sand

The first test series was performed with only few instructions given by the organizers. The participants were allowed to choose several boundary conditions like the type

of test setup, fixation of geosynthetics etc. with their own engineering sense and experience. But it has to be pointed out that the participants received more instructions concerning the test conditions than normally given by construction companies, consultants, etc. for project tests.

The results of the first test series show significant variations in the characteristics of friction stress vs. displacement curves as well as in magnitudes of the peak friction stress values. Some results of the first test series are published by Blümel et al. (1996 a, b). Further details about the scattering of test data are given by Blümel et al. (1997).

Generally it can be stated that the scattering of data was unsatisfactorily high in all investigated cases. Therefore, it was decided to perform a second test series where all participants received more detailed instructions concerning the boundary conditions and testing procedure. The testing procedures recommended in this second test series were developed by the working group of DGGT after a discussion with the participants of the first interlaboratory test series.

About twenty institutions participated in each interlaboratory test series. All devices used for the tests had friction interfaces of at least 30 cm square. For all tests a constant rate of displacement of 10 mm/h was proposed. The vertical load was applied to the samples one hour before starting the displacement. Tests had to be performed with four different loads to meet the following values of average vertical stresses in the friction interface: 20/50/100/200 kN/m<sup>2</sup>. The tests were run without submerging the samples.

### 3 SELECTED RESULTS

#### 3.1 Friction Between a Geotextile and a Geomembrane

Test instructions defined two different test setups to conduct these friction tests.

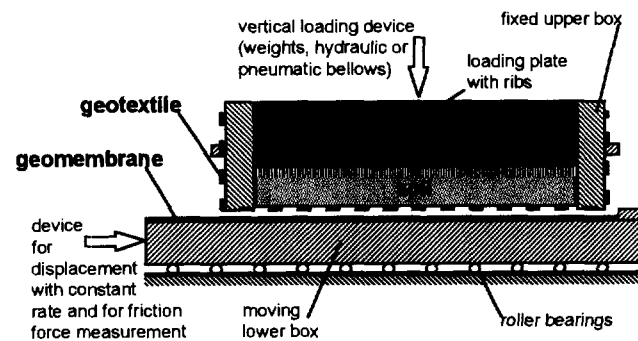


Figure 1. Test setup for geotextile-geomembrane interface friction

The first type of test setup for determination of geotextile-geomembrane interface friction is shown in Figure 1. The geotextile is clamped to the upper box of the shear device. The upper box is partly filled with Standard Sand. The geomembrane is fixed to a rigid support in the lower box.

This type of test setup also opens possibilities to investigate friction with those soils that will be placed above the geotextile in the liner system. It has to be taken into consideration that granular soils neighbouring the geosynthetics can affect the interface friction behaviour.

Typical friction stress vs. displacement curves for a vertical stress of 100 kN/m<sup>2</sup> obtained with the first type of test setup are shown in Figure 2. Nearly all data generated by the different institutions fits together quite well. This is true for the characteristics of the curves as well as for the peak friction stresses.

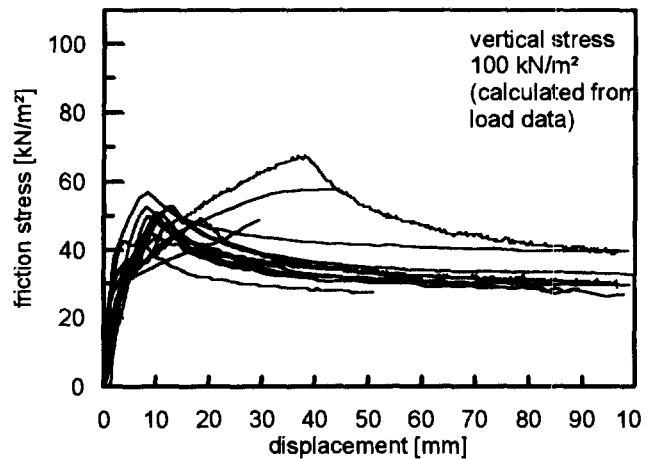


Figure 2. Friction stress vs. displacement measured with test setups according to Figure 1

A second test setup as shown in Figure 3 could also be used for investigating friction between two geosynthetics. The geotextile is fixed to a rigid block placed inside the upper box. The geomembrane is fixed to a rigid support in the lower box in the same way as described above.

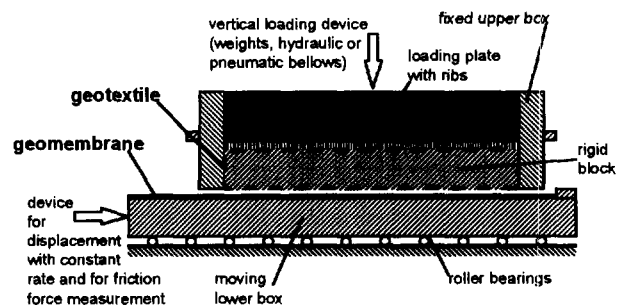


Figure 3. Modified test setup for geotextile-geomembrane interface friction

The coefficients of variation of peak and residual friction stresses are in the same magnitude for both test setups. For a small vertical stress of 20 kN/m<sup>2</sup> the coefficient of variation of the peak friction stress reaches about 30 % but decreases with increasing vertical stresses. For 200 kN/m<sup>2</sup> the coefficient of variation is about 13 %. Interlaboratory direct shear tests in soil mechanics led to coefficients of variation of the same magnitude.

The friction stress vs. displacement curves obtained with the two test setups displayed in Figure 2 and 4 show only little differences concerning the form of the curves which doesn't seem to be significant. Relative friction stress maxima before reaching the absolute peak values measured with the second type of test setup may be caused by tilting of the rigid block placed in the upper box.

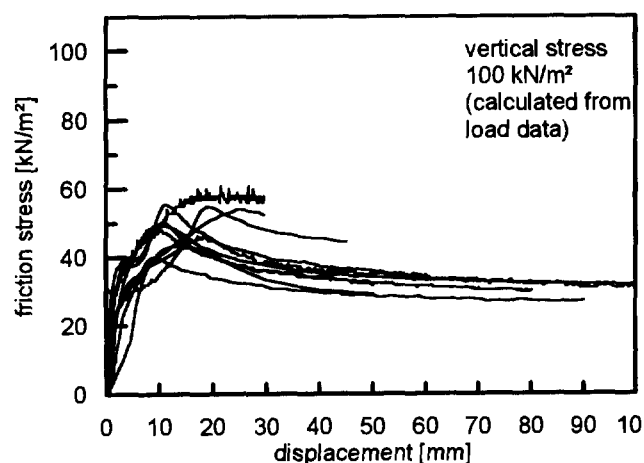


Figure 4. Friction stress vs. displacement measured with test setups according to Figure 3

### 3.2 Friction Between Standard Sand and a Geotextile

Friction stress vs. displacement curves obtained at a vertical stress of 100 kN/m<sup>2</sup> for the interface between Standard Sand and a geotextile, 300 g/m<sup>2</sup>, are shown in Figure 5. The geotextile is fixed uniformly to a rigid support in the lower box and additionally is clamped on one side. Standard Sand as defined in EN 196-1, was placed in a dry state in the upper box with a density of 1.8 g/cm<sup>3</sup>. Sketches of the setups used by the participating institutions are shown in Figure 6 and Figure 8.

As in the case discussed in chapter 3.1 the participants were supplied with detailed information concerning the boundary conditions of the tests. Nevertheless, the data generated by the institutions for friction between sand and geotextile scatter within a wide range. This is true for peak and residual friction stress values. The coefficients of variation calculated from the friction stresses at a displacement of 30 mm are between 40 % for a vertical stress of 20 kN/m<sup>2</sup> and 23 % for a vertical stress of 200 kN/m<sup>2</sup>. In addition, friction stress vs. displacement curves

differ in shape. Some curves do not show any significant peak friction value at all. Others were obviously faulty due to insufficient test setups and were omitted from the evaluation.

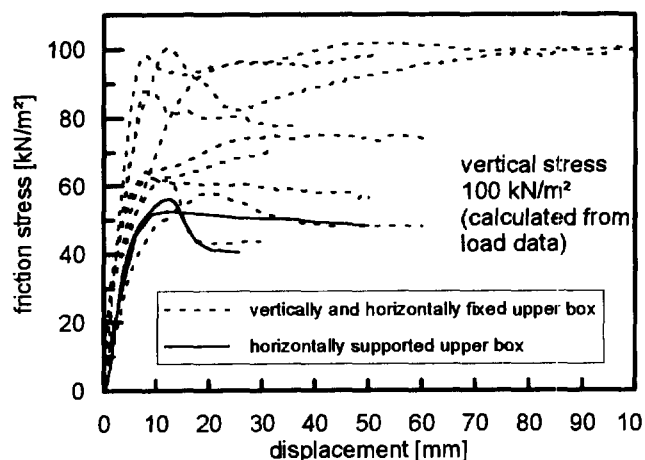


Figure 5. Friction stress vs. displacement for sand-geotextile interface obtained with two different setups according to Figure 6 and 8

Additional tests were performed by the authors in order to identify specific factors which may affect the friction in the sand-geotextile interface, e. g. the method of fixation of the geotextile to the support or the rate of displacement. It was found that the rate of displacement is not a significant factor. But the method of fixation of the geotextile to the rigid support is likely to have an effect. Insufficient fixation can lead to friction stress vs. displacement curves without any friction peak value. Other possible reasons for the scattering of data caused by the test setup like the height of the sand filled into the upper box or the use of smooth or ribbed loading plates could not be identified from the interlaboratory test data.

Devices of different manufacturers were used by the participants. Seven participants used an equal type of testing device but the scattering of data delivered by this subgroup was found to be in the same range as for the whole group.

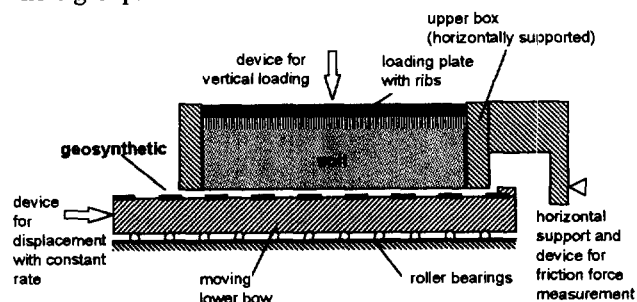


Figure 6. Test setup with horizontally supported upper box for soil-geosynthetic interface friction



In general, devices with a movable lower box were used for the tests, some with a completely fixed upper box (with vertical and horizontal support) and others with an only horizontally supported upper box. For the latter type of test setup we have to recognize that effects as explained in Figure 7 may occur during testing.

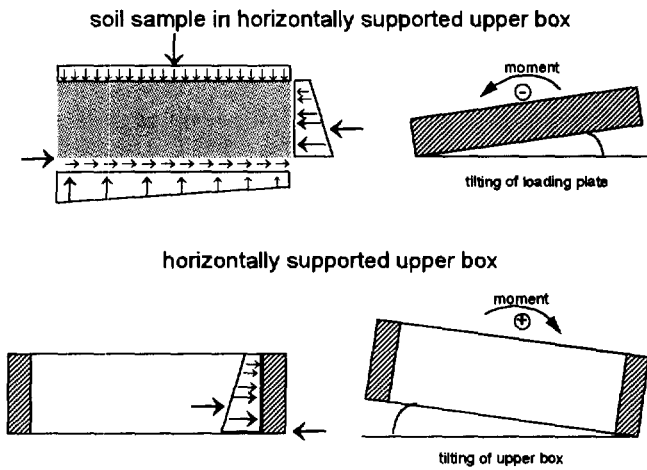


Figure 7. Interaction forces, stresses and deformations occurring in a test setup according to Figure 6 (Wernick 1979)

For the test setup with completely fixed upper box vertical friction stresses can occur at the inner walls of the upper box which will lead to a reduction of the average vertical stress in the friction interface (Figure 9).

These effects are well known in soil mechanical direct shear testing (Kast 1986; Jewell 1989). Especially for test devices of the type discussed in this paper with larger dimensions than commonly used for soil testing we have to take these effects into our considerations concerning the evaluation and interpretation of test data.

The type of test setup shown in Figure 6 has an upper box, which is only horizontally supported at one point. The type with a completely fixed upper box is displayed in Figure 8. The upper box is fixed vertically and horizontally and therefore no displacement or rotation of the box is possible, but the loading plate can rotate within a small range.

The friction stresses measured in tests with a fixed upper box are in most tests higher than those obtained from tests in the device with an only horizontally supported upper box. But we have to regard that the number of data obtained with the latter type of construction is very small. Furthermore, the results of the friction tests for the geotextile-geomembrane interface show nearly no differences for test setups with fixed and horizontally supported upper box.

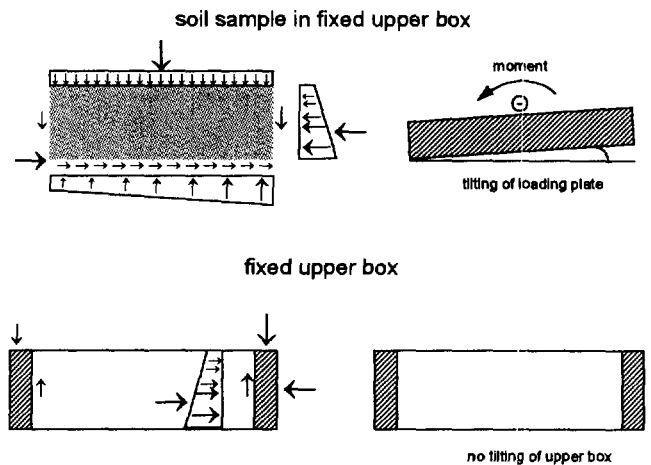


Figure 9. Interaction forces, stresses and deformations occurring in a test setup according to Figure 8

#### 4 ADDITIONAL INVESTIGATIONS

Depending on the test device the vertical load is applied to the top of the sample with weights, hydraulic jacks or hydraulic or pneumatic bellows. A stiff plate is often used for load distribution over the test area. The distribution and magnitude of the normal stress acting in the friction interface during testing is unknown.

The assumption that a constant vertical stress derived from the load applied to the top of the sample is acting in the friction interface is most probably valid for testing devices with a point supported upper box (Figure 6) before starting horizontal displacement. This assumption is questionable for devices with a fixed upper box as effects like friction between test material and internal walls of the upper box can occur.

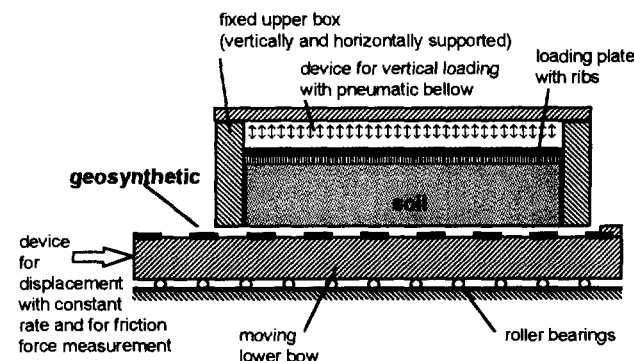


Figure 8. Test setup with completely fixed upper box for soil-geosynthetic interface friction

To investigate such effects, the testing equipment used by the authors was modified. To determine the average vertical stress acting in the friction interface during horizontal displacement the vertical forces at the corners of the fixed upper box were measured. A sketch of the device is shown in Figure 10. The equipment was manufactured by Wille-Geotechnik GmbH, Göttingen/Germany.

By summarizing the values of the vertical support forces the resulting vertical force acting in the friction interface can be obtained. The air pressure in the bellow is regulated during horizontal displacement of the lower box in order to keep the resulting vertical force and average vertical stress acting in the friction interface at a constant value. Information about the vertical stress distribution in the interface can also be obtained with this setup.

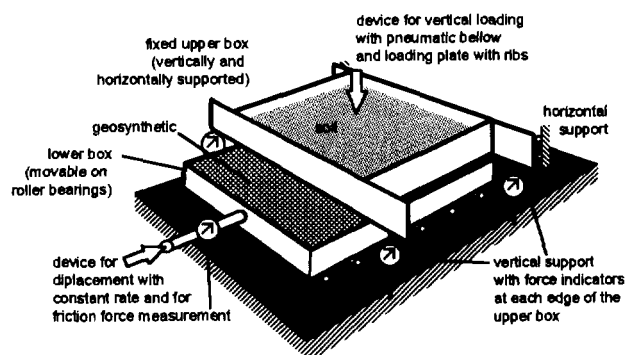


Figure 10. Modified test setup with measuring devices to keep a constant vertical stress in the friction interface

Friction tests for the interface between Standard Sand and a nonwoven geotextile of 300 g/m<sup>2</sup> and direct shear tests for Standard Sand were performed. One series of tests was carried out with a constant load applied to the top of the sample and the other with a constant vertical force in the friction interface. The tests were performed under conditions of repetition. The boundary conditions were the same than those chosen for the interlaboratory testing program described above. Several tests were done for both series to meet the following values of vertical stresses: 20/50/100 kN/m<sup>2</sup>.

Figure 11 shows the friction stress vs. displacement curves obtained from tests with a fixed upper box with the two different methods of controlling the vertical stress. The scattering of test data for the case with a constant pressure applied to the top the sample is smaller than in the interlaboratory test program. The coefficient of variation derived from the measured peak friction stresses in these tests under conditions of repetition is only about 5 %. The shape of the friction stress vs. displacement curves is similar, but certain variations in the curves are found for greater values of displacement after passing the peak friction value. All data obtained from the tests with a constant vertical force in the interface show very good conformity.

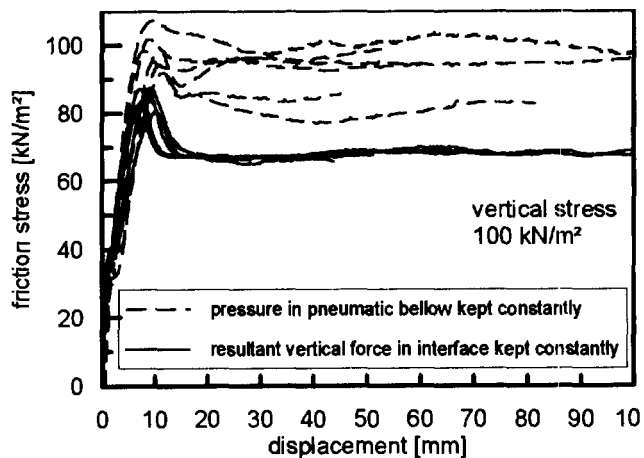


Figure 11. Friction stress vs. displacement for sand-geotextile interface with two different procedures of vertical stress control during testing

The peak friction stresses obtained from the tests with vertical stress controlled by measurement during horizontal displacement are significantly smaller than those found for tests with constant pressure on top of the sample. In the latter case the average normal stress in the shear plane increased to about 130 kN/m<sup>2</sup> at a normal stress of 100 kN/m<sup>2</sup> applied to the top of the sample. In the tests with a constant normal stress in the shear plane of 100 kN/m<sup>2</sup> the air pressure in the loading equipment decreased to about 75 kN/m<sup>2</sup>. These effects are most probably caused by interaction and compulsory forces between soil and box during shear. Shibuya et al. (1997) obtained comparable results in direct shear tests on sand with a fixed upper box device and constant load on top of the sample.

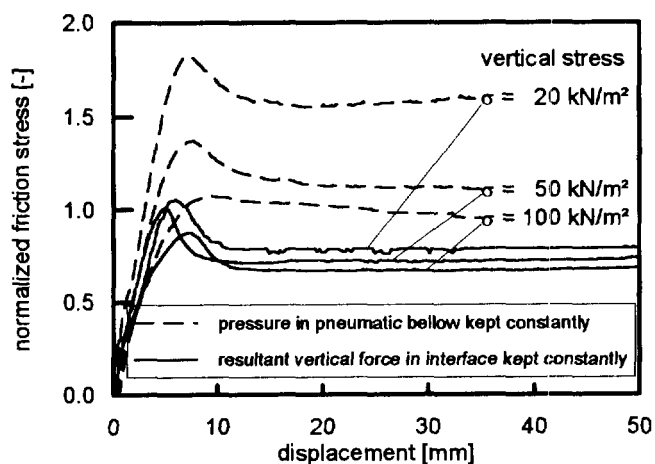


Figure 12. Normalized friction stress vs. displacement for sand-geotextile interface with two different procedures of vertical stress control during test

For further evaluation the friction stress data was divided by the vertical stress. In Figure 12 these

normalized friction stresses vs. the displacement are plotted. It can be seen from this plot that the deviations are decreasing with increasing vertical stress.

## 5 CONCLUSIONS

The determination of friction properties between different geosynthetics and between soil and geosynthetic in direct shear devices is complicated due to high scattering of data. Test equipment, boundary conditions, test procedures and the mechanical properties of soil affect the characteristics of the friction stress vs. displacement curves and the magnitude of the peak friction stresses. Therefore, the experimental investigations, test setups and boundary conditions should be in accordance with the expected situations at the site as well as possible.

The institutions which are performing the friction tests, have to be provided with detailed information about the type of construction and about the construction materials. The properties of the tested soils have to be considered.

The German preliminary recommendations on friction testing with geosynthetics prescribes standard test setups and boundary conditions of testing in order to minimize effects resulting from different setups and procedures. The method of load application and its effect have to be regarded and reported together with the results of the friction tests and other boundary conditions.

To cover data scattering observed under conditions of comparison it is recommended to carry out a sufficient number of tests by two different institutions for each project. Friction tests have to be performed with at least three different normal stresses. The vertical stress that is relevant for the project and the stability calculations, must be within this range. The test with this vertical stress must be carried out three times. The determination of test conditions, data evaluation and derivation of friction parameters for design calculations has to be done in close cooperation with the engineers responsible for design and stability calculations.

Based on further evaluations of friction tests with other geosynthetics and soils, which are not presented in this paper, it is recommended that adhesion derived from friction test results should be introduced into stability calculations only in special cases, e.g. for interfaces between cohesive soils and geomembranes. Considering all possible site conditions during building and during life of the structure the engineers responsible for the project must agree that adhesion will act continuously. Safety factors for the design value of the adhesion have to cover scattering of test data especially at low normal stresses.

## ACKNOWLEDGMENTS

The authors thank all colleagues and institutions for their contributions to the interlaboratory testing program.

## REFERENCES

- Blümel, W., Brummermann, K., Lottmann, A. & Stoewahse C. (1996a) "Reibung zwischen Erdstoffen und Geokunststoffen im direkten Scherversuch", *Braunschweiger Deponieseminar 1996*, Mitt. IGB TU-BS, H. 51.
- Blümel, W. & Brummermann, K. (1996b) "Interface Friction between Geosynthetics and Soils and between different Geosynthetics", *Geosynthetics: Applications, Design and Construction*, De Groot, Den Hoedt & Termaat (eds), Balkeema, Rotterdam, pp.209-216.
- Blümel, W., Saathoff, F. & Stoewahse, C. "On the stability of inclined sealing systems", *Proc. of the 6<sup>th</sup> International Landfill Symposium*, Sardinia 1997, paper submitted for publication
- Gartung, E. & Neff, H. K. (1997) "Empfehlungen des Arbeitskreises 'Geotechnik der Deponiebauwerke' der DGGT e. V., E 3-8: Untersuchung der Reibung zwischen verschiedenen Geokunststoffen sowie zwischen Geokunststoffen und Erdstoffen in Rahmenschergeräten", *Bautechnik* 74, H. 9
- Jewell, R. A. (1989), "Direct shear tests on sand", *Geotechnique*, Vol. 39, No. 2, pp. 309-322
- Kast, K. (1986) "Geführte direkte Scherversuche an bindigen Erdstoffen", *Bautechnik*, H. 8, pp. 271-277
- Shibuya, S., Mitachi, T. & Tamate, S. "Interpretation of direct shear box testing of sands as quasi-simple shear", *Geotechnique*, Vol. 47, No. 4, pp. 769-790
- Wernick, E. (1979) "A 'true direct shear apparatus' to measure soil parameters of shear bands", *Proc. Seventh European Conference on Soil Mechanics and Foundation Engineering*, Brighton, Vol. 2, pp. 175-182

# The Influence Of Equipment Style And Setup Dimensions On Sand/Geomembrane Direct Shear Test Measurements

S.M Bemben

Geotechnical Engineering Consultant, 147 Victoria Road, New Britain, Connecticut, USA.

D.A . Schulze

Senior Vice President, Laboratory Services, GZA Geoenvironmental, Inc., Newton Upper Falls, Massachusetts, USA.

**ABSTRACT:** The results of a testing program employing two sands and two geomembranes with a commercial direct shear device are presented. Two avenues of direct shear device modifications were utilized. The first avenue was to employ new upper shear boxes having 7.5 x 7.5 and 15 x 15 cm areas, as well as the original 30.5 x 30.5 cm area upper box, all upon longer length lower boxes so as to maintain a constant area of shear (termed new style). The second avenue was to employ each of the three sizes of upper boxes over identically sized lower boxes so as to create a constantly decreasing area of shear (termed old style). The paper compares the effects of size of shearing area, new and old style shearing boxes, size of the fixed gap between upper box and top of geomembrane, and thickness of sand layers on peak and residual stress ratios.

**KEYWORDS:** Friction, Geomembranes, Laboratory tests, Shear strength, Sand

## 1 INTRODUCTION

Every direct shear test requires selection of materials to be tested, test equipment, setup criteria, and rate of shearing movement. The purpose of this study is to determine the effects of size of shearing area, new and old style shearing boxes, size of the fixed gap between upper box and top of geomembrane and thickness of sand layers on peak and residual stress ratios for combinations of two sands and two geomembranes.

The most extensive guideline for sand/geomembrane testing is ASTM (1992). It will frequently be referenced.

## 2 EQUIPMENT, MATERIALS AND SETUP PROCEDURES

### 2.1 Direct Shear Device

The shear device employed was the same basic unit with improvement modifications previously described by Bemben and Schulze (1995). It is a commercial unit manufactured by Boart Longyear Company. Two new avenues of modifications were designed, fabricated and utilized by the writers. The first avenue was to employ upper shear boxes having 7.5 x 7.5 and 15 x 15 cm areas, as well as the original 30.5 x 30.5 cm area upper box, all upon longer length lower boxes (termed new style herein). The second avenue was to employ each of the three sizes of upper boxes over identically sized lower boxes topped by geomembranes having top surfaces flush with the top of the box (termed old style herein). The various shear box areas employed for both the new style and old style tests are presented in Table 1.

Table 1. Sand/geomembrane setup sizes.

Setup size	Top box sand area (cm x cm)	Geomembrane area (cm x cm)
SM1	30.5 x 30.5	35.5 x 43.2
SM2	30.5 x 30.5	30.5 x 30.5
SM3	15.2 x 15.2	30.5 x 38.1
SM4	15.2 x 15.2	15.2 x 15.2
SM5	7.6 x 7.6	30.5 x 38.1
SM6	7.6 x 7.6	7.6 x 7.6

As shearing movements occur, the upper box is fixed and the lower box displaces laterally. The rate of displacement was 0.1 cm/min. This is in accord with ASTM (1992) for dry and nearly dry sands. Shear force corrections for friction losses associated with movements of the traveling container were made in accord with ASTM (1992).

### 2.2 Geomembranes

Two geomembranes were employed. Geomembrane 1 was a textured high density polyethylene liner manufactured by GSE Lining Technology, Inc. and having their HDT designation. Geomembrane 2 was a smooth high density polyethylene liner manufactured by GSE Lining Technology, Inc. and having their HD Designation.

For new style tests the geomembranes were clamped to the leading edge of the lower traveling box. For old style tests the geomembranes were fastened to plywood support blocking by finishing nails. For textured membrane tests, the direction of travel during shearing was in the direction of roll production. Textured geomembranes were generally used for two tests and smooth geomembranes

were always used once. Textured geomembranes were from two rolls of different thicknesses and smooth were from one roll.

### 2.3 Sands

Two sands were employed. Sand 1 was a medium sand having subangular particles which is commercially available under the name Flint Sand. Sand 2 was fine to coarse sand having angular particles and was from a glacial deposit. Grain size distributions are presented in Table 2. The two sands are classified SP and SW-SM, respectively, by the Unified Sand Classification System.

### 2.4 Setup Criteria

#### 2.4.1 Fabrication of Sand Layers

For tests with Sand 1, the sand was compacted air dry to a unit weight of 17.66 kN per cubic meter. For tests with Sand 2, the sand was compacted to a dry unit weight of 17.59 kN per cubic meter with a water content of 3%. The sands were maintained with the same water contents during shearing as those during fabrication.

The total height of sand is called the sand layer thickness. When the sand layer thickness was 2.5 cm or less, the sand layer thickness was fabricated by one compacted lift; when the sand layer thickness was greater than 2.5 cm, it was fabricated by employing the minimum number of multiple compacted sand lifts of equal thickness not exceeding 2.5 cm. (For example, a 5.7 cm thickness is composed of three 1.9 cm lifts). Sand was compacted in lifts, first by direct hand tamping with a 2.5 kg weight having a 5 cm diameter and then by hand tamping with the same weight onto a steel plate. Six measurements with calipers were made to control the thickness of each compacted lift.

#### 2.4.2 Gap Setting and Load Transfer Plates

The gap is the space between the bottom of the top box and the top of the geomembrane. The gap is set and remains constant during sand fabrication and shearing movements.

Table 2. Grain size distributions.

Sieve number	Opening (mm)	Percent passing	
		Sand 1	Sand 2
4	4.76	100	100
10	2.00	100	91
20	0.840	100	77
40	0.420	28	48
60	0.250	2	31
100	0.149	0	18
200	0.074	0	11

Load transfer plates were provided at the top of the sand layer in accordance with ASTM (1992). The plates were unbonded pieces of Geomembrane 1 which were cut slightly less in area than the area of the box.

## 3 PRESENTATION OF DATA

Data pertaining to 48 direct shear tests are presented in Tables 3 through 5. Data are also presented by Figures 1 through 5. The definitions of peak and residual stress ratios are shown by Figure 5.

Table 3. Listing of Sand 1/Geomembrane 1 tests.

Test	Setup size	Thickness sand (cm)	Gap (cm)	Stress ratio		Figure
				peak	residual	
1.1	SM3	1.9	0.38	0.68	0.56	1
1.2	SM3	1.9	0.53	0.75	0.47	1
1.3	SM3	2.5	0.38	0.76	0.56	1
1.4	SM3	2.5	0.53	0.74	0.48	1
1.5	SM3	2.5	0.53	0.70	0.48	1,2
1.6	SM3	2.5	0.53	0.73	0.48	1
1.7	SM3	2.5	0.76	0.56	0.48	1
1.8	SM3	3.8	0.53	0.75	0.45	1
1.9	SM3	5.7	0.53	0.80	0.33	1
1.10	SM3	6.4	0.38	0.97	0.30!	1
1.11	SM3	3.8	0.38	0.71	0.46	1
1.12	SM3	2.5	0.53	0.70	0.49	2
1.13	SM3	2.5	0.53	0.67	0.48	2
1.14	SM4	3.8	0.44	0.76	*	3
1.15	SM5	1.9	0.38	0.72	0.45	1
1.16	SM6	1.9	0.53	0.56	*	3
1.17	SM1	2.5	0.25	0.71	0.56	1
1.18	SM1	2.5	0.43	0.76	0.47	1
1.19	SM1	2.5	0.61	0.77	0.47	1
1.20	SM1	3.8	0.25	0.80	0.52	1
1.21	SM1	3.8	0.61	0.77	0.45	1
1.22	SM1	3.8	0.76	0.76	0.46!	1
1.23	SM1	5.8	0.20	0.91	0.60!	1
1.24	SM1	5.8	0.76	0.70	0.26!	1
1.25	SM1	5.8	0.37	0.73	0.45	1,2
1.26	SM1	5.8	0.37	0.92	0.45	2
1.27	SM1	5.8	0.37	0.65	0.41	2
1.28	SM2	5.7	0.53	0.89	*	3
1.29	SM2	3.8	0.51	0.73	0.55	3

Notes: Tests 1.12 and 1.26 are at 24 kPa normal stress, tests 1.13 and 1.27 are at 96 kPa and all other tests are at 48 kPa; \*denotes vague residual value as shown by presented stress ratio-shear movement curves; ! denotes ratio decreasing at end of test.

## 4 DISCUSSION OF NEW STYLE SETUP DATA

Table 4. Listing of Sand 2 / Geomembrane 1 tests.

Test	Setup size	Thickness sand (cm)	Gap (cm)	Stress ratio		Figure
				peak	residual	
2.1	SM1	2.5	0.71	0.84	0.64	4
2.2	SM1	3.8	0.71	0.92	0.69!	4
2.3	SM1	1.8	0.71	0.75	0.71	4
2.4	SM1	1.8	0.81	0.77	0.72	4
2.5	SM1	3.8	0.96	0.80	0.63	4
2.6	SM2	2.5	0.69	0.84	*	3
2.7	SM3	1.8	0.71	0.73	0.63	4
2.8	SM3	2.5	0.38	0.87	0.71	4
2.9	SM3	2.5	0.71	0.79	0.62	4
2.10	SM3	2.5	0.53	0.78	0.61	4,5
2.11	SM3	3.8	0.71	0.95	0.63	4
2.12	SM3	3.8	0.38	0.85	0.72	4
2.13	SM4	2.5	0.61	0.78	*	3

Note: See notes following Table 5.

Table 5. Listing of Sand 2/Geomembrane 2 tests.

Test	Setup size	Thickness sand (cm)	Gap (cm)	Stress ratio		Figure
				peak	residual	
3.1	SM3	1.8	0.66	0.48	0.33	4
3.2	SM3	2.5	0.36	0.56	0.38	4
3.3	SM3	3.8	0.36	0.51	0.38	4
3.4	SM3	2.5	0.66	0.48	0.32	4,5
3.5	SM1	2.5	0.82	0.44	0.31	4
3.6	SM1	1.8	0.82	0.49	0.34	4

Notes: Tests 1.12 and 1.26 are at 24 kPa normal stress, tests 1.13 and 1.27 are at 96 kPa and all other tests are at 48 kPa; \*denotes vague residual value as shown by presented stress ratio-shear movement curves; ! denotes ratio decreasing at end of test.

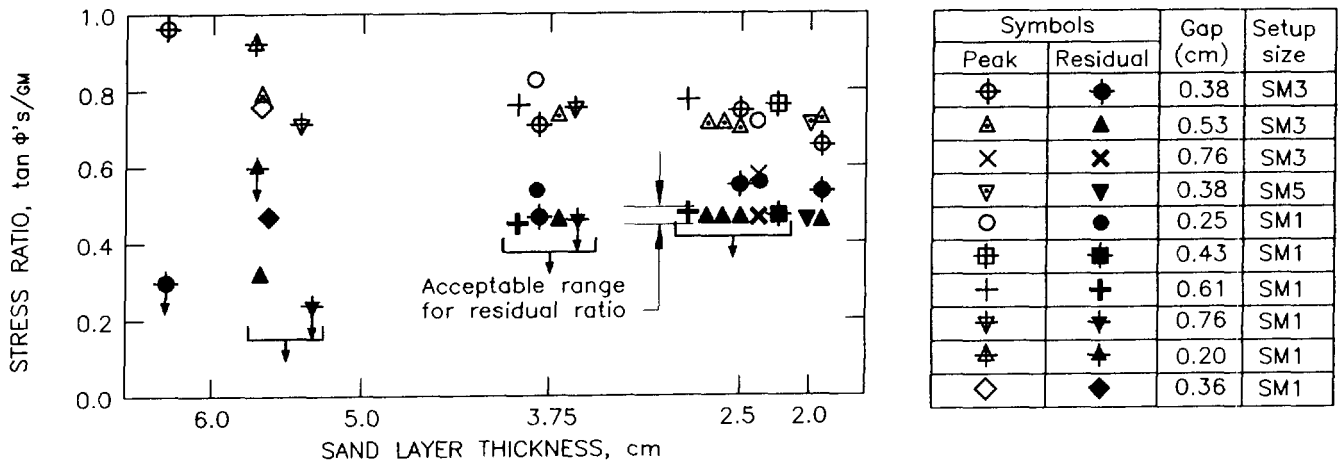


Figure 1. Effects of sand layer thickness and gap size on peak and residual stress ratios for Sand 1 / Geomembrane 1 using new style shear box.

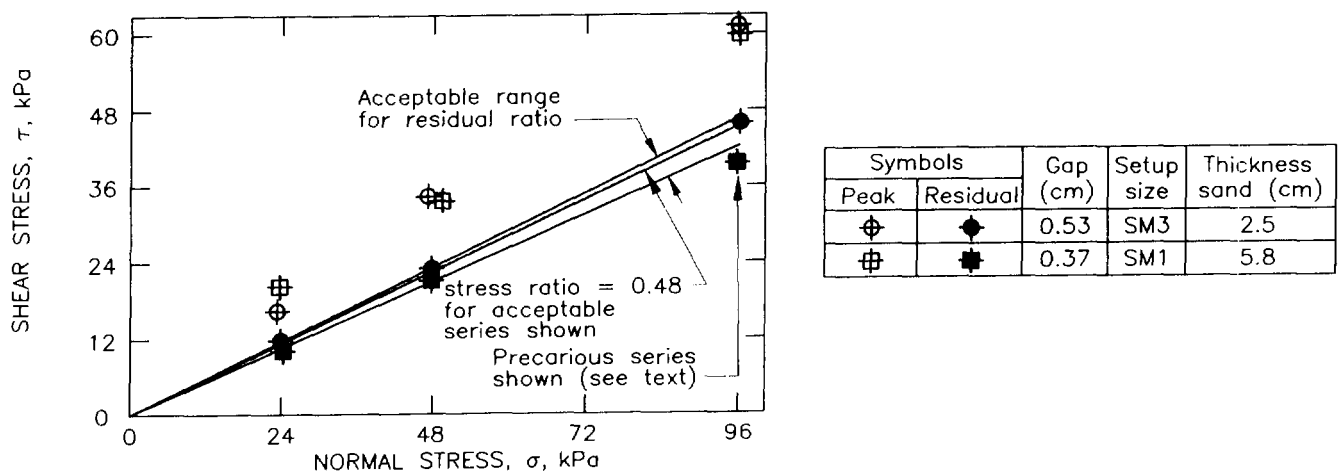
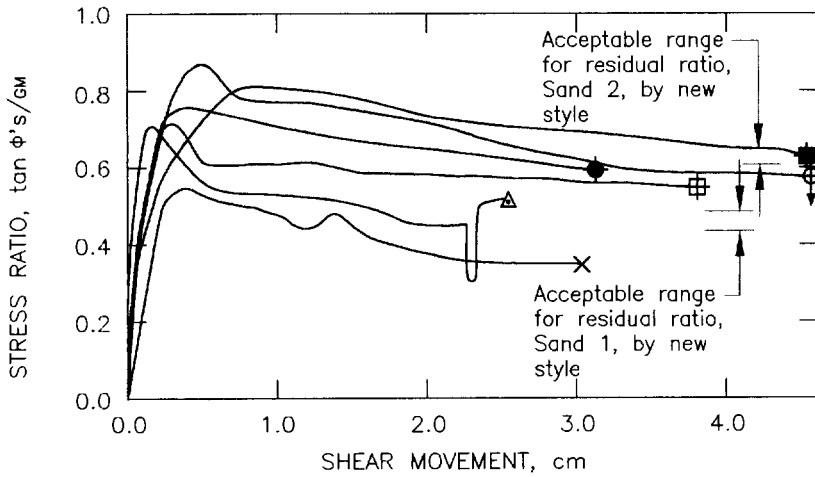
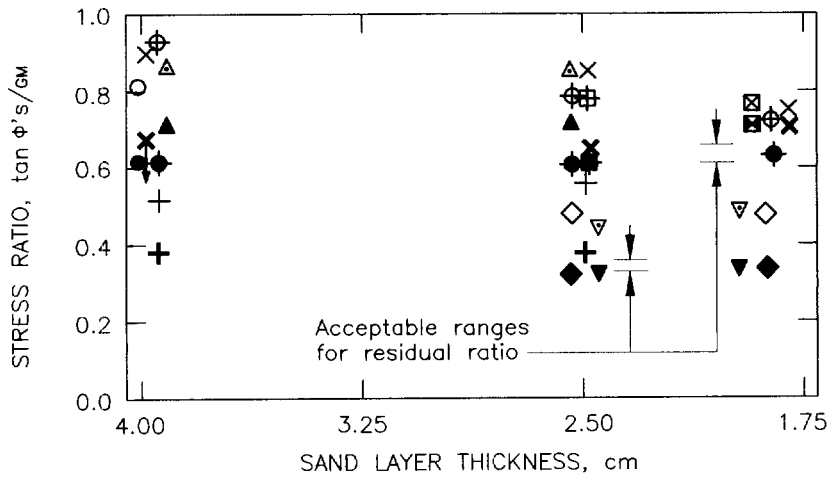


Figure 2. Effect of acceptable and unacceptable sand layer dimensions on shear stress envelopes for Sand 1/Geomembrane 1 tests.



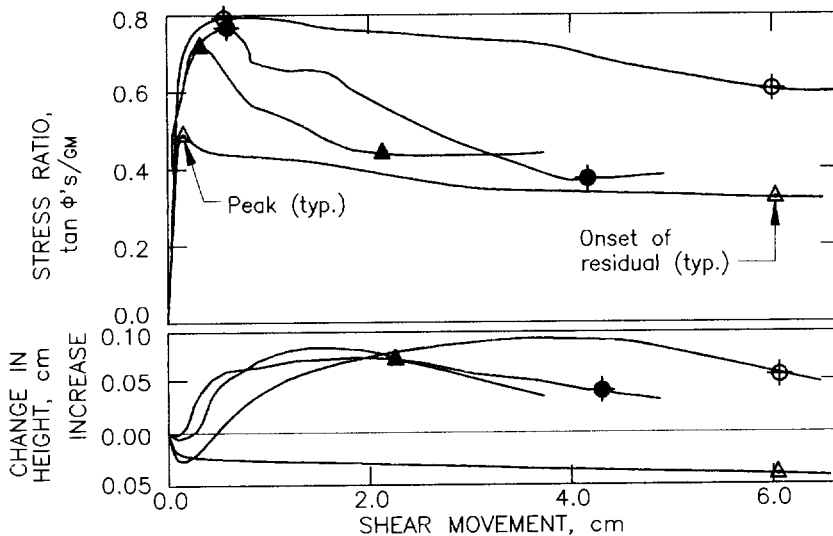
Symbol	Gap (cm)	Setup size	Thickness sand (cm)	Test	Sand
⊕	0.51	SM2	5.7	1.28	1
⊞	0.53	SM2	3.8	1.29	1
△	0.44	SM4	3.8	1.14	1
×	0.51	SM6	1.9	1.16	1
◆	0.61	SM4	2.5	2.13	2
⊞	0.69	SM2	2.5	2.6	2

Figure 3. Effect of sand layer dimensions on stress ratio – shear movement curves for Sand 1/ Geomembrane 1 and Sand 2/Geomembrane 2 using old style shear box.



Symbols		Gap (cm)	Setup size	Geomembrane
Peak	Residual			
⊕	◆	0.71	SM3	1
⊞	⊞	0.53	SM3	1
△	▲	0.38	SM3	1
×	×	0.71	SM1	1
○	●	0.96	SM1	1
⊞	⊞	0.81	SM1	1
◇	◆	0.66	SM3	2
+	+	0.36	SM3	2
▽	▼	0.82	SM1	2

Figure 4. Effects of sand layer thickness and gap size on peak and residual stress ratios for Sand 2/ Geomembrane 1 and Sand 2/Geomembrane 2 using new style shear box.



Symbol	Gap (cm)	Setup size	Test	Sand	Geomembrane
⊕	0.54	SM3	2.10	2	1
△	0.66	SM3	3.4	2	2
◆	0.53	SM3	1.9	1	1
▲	0.53	SM3	1.8	1	1

Figure 5. Comparison of stress ratio and change in height – shear movement curves for Sand 1/ Geomembrane 1, Sand 2, Sand 2/Geomembrane 1, and Sand 2/Geomembrane 2 tests.

## 4.1 Residual Stress Ratios

### 4.1.1 Effect of Sand Layer Dimensions

Residual stress ratios versus sand layer thickness are shown by Figures 1 and 4. Bands of data comprising the writers' appraisal of acceptable ranges for residual ratios are indicated for each combination of materials. (It will be shown that the development of acceptable residual stress ratio values requires the selection of proper sand layer thickness and gap size dimensions). For Sand 1/Geomembrane 1, the range is 0.45 to 0.49; for Sand 2/Geomembrane 1, the range is 0.61 to 0.69, and for Sand 2/Geomembrane 2, the range is 0.31 to 0.34.

The range of sand layer thickness values for which the bands of each combination of materials apply is seen to be from the smallest thickness up to at least 2.5 cm providing the acceptable range of gap values also exists.

Relatively thick layers are unacceptable for shear box testing. The residual stress ratios are typically too low when too thick layers are involved. This is largely due to vertically directed shear stresses arising between the inside walls of the upper shear box and the sand within as the sand tries to move upward and downward. Such movements are shown by Figures 5. As the sand dilates during early shear, the shear stresses arising at the walls of the upper box produce an increased downward force on the failure surface resulting in a too large peak shear stress. As shear movement continues and the sand contracts, the shear stresses at the wall surfaces are reversed. If the reversal is not completed when shearing movement is stopped, either a residual shear stress state will not be reached, or it will be incorrect. ASTM (1992) provides that the "stationary" upper box "should be adjustable" to compensate for deformations of the sand. No definition is given for "adjustable".

A different problem exists for the smallest sand layer thickness for the Sand 2/Geomembrane 1 case shown by Figure 4. The layer thickness to maximum particle size is (1.8cm/0.48cm) or 3.75. ASTM (1992) requires the ratio to be 6 or larger. It is surmised that this requirement allows sufficient ease for the larger particles to move about as shearing is ongoing. Thus, the measured residual stress ratios for the locked in grains of the too thin layer are higher than the acceptable range even though the gap is acceptable.

### 4.1.2 Effects of Gaps and Area Sizes

The size of the gap affects the measured residual stress ratio. If the gap is too small, the measured residual stress ratio will be too large or may be cyclic in nature. For Sand 1, Figure 1 shows that the gap must be greater than 0.38 cm; for Sand 2, Figure 4 shows that a gap of 0.53 cm is large enough; this is also about 0.3 cm larger than  $D_{85}$ . This conflicts with ASTM (1992) which allows the gap to

be as small as  $D_{85}$  of the sand. The sounds of grinding sand particles during shearing were emitted when the gaps were too small. All gaps larger than the minimum sizes were acceptable.

Figures 1 and 4 show that the setup size has no effect on the acceptable residual stress ratio providing the proper sand layer dimensions and gap sizes exist. The possibility of using a shear box of lesser area than the 30.5 x 30.5 cm standard size is provided by ASTM (1992).

## 4.2 Peak Stress Ratios

### 4.2.1 Effect of Sand Layer Dimensions

Peak stress ratios versus sand layer thickness are shown by Figures 1 and 4. Bands of data showing the ranges in the peak stress ratios at each value of sand layer thickness can be envisioned. They have much larger spread than the bands of acceptable range for residual stress ratios. The discussion will be limited to the range of acceptable sand layer thickness associated with acceptable residual stress ratio behavior, namely, up to 2.5 cm.

The bands of the sand/textured geomembrane combinations are sloping. The peak values increase with increasing sand layer thickness. This behavior is surmised to be due to the volume change behavior during shear previously described. With increasing sand layer thickness, the wall area providing downward stresses during early shear movements increases and, hence, the excess normal stress on the failure plane increases. Because the excess normal stress increases with increasing sand layer thickness, the peak shear stress does likewise.

Figure 4 shows the peak shear stress ratio does not increase with sand layer thickness for the sand/smooth geomembrane case. Figure 5 shows the sand layer thickness does not experience dilatancy during shear, hence the vertical wall shear stresses are very small. The failure mechanism is deduced to be sliding of the intact sand layer over the smooth geomembrane. The creation of the peak stress ratio is attributed to the angular sand particles biting into the geomembrane. The smooth geomembranes had readily visible scratches in the direction of travel.

### 4.2.2 Effects of Gaps and Areas

At any one sand layer thickness, the effect of gap size on measured peak stress ratios is usually about 0.1 in magnitude. Usually, the case is that the smallest gap employed presented the highest peak stress ratio and the largest gap presented the lowest.

Figures 1 and 4 show that the setup size has no effect on the band of peak shear stress ratios providing that proper sand layer dimensions and gap sizes are in effect.



### 4.3 A Precarious Failure Envelope Situation

Two failure envelopes developed from Sand 1/Geomembrane 1 tests are shown by Figure 2. The failure envelope using the SM3 setups involves Tests 1.5, 1.12 and 1.13. These test setups meet the previously presented sand layer dimensions, gap sizes and other setup criteria. As expected, the residual failure envelope is within the acceptable range. Figure 2 also shows for the SM3 setup tests, that residual stress ratios are independent of the normal stress and peak stress ratios are dependent on the normal stress.

The failure envelope using the SM1 setups involves Tests 1.25, 1.26, and 1.27. The sand layer thickness is greater than 2.5 cm; hence, poor test results are anticipated. The residual stress ratio for the 96 kPa normal stress is too low. Not shown are the results for six other tests at 24 kPa, 48 kPa and 96 kPa normal stress with gaps of 0.20 and 0.76 cm. The stress ratios for the set at 48 kPa are shown on Figure 1. These six tests concluded with the stress ratio decreasing without ever experiencing a true residual case. Only by a fortuitous chance setup combination of the too small 0.37 cm gap with the too thick sand layer dimensions involved did the SM1 setups produce the precarious envelope.

## 5 DISCUSSION OF OLD STYLE SETUP DATA

Stress ratio-shear movement curves for Sand 1/Geomembrane 1, and Sand 2/Geomembrane 2 are presented by Figures 1 and 3. The stress ratios have not been corrected for changes in the area of the failure plane. This is acceptable ASTM (1992).

With the exception of Test 1.16 (the small SM 6 setup), the peak stress ratios are in fairly good agreement with those for new style setups having the same sand layer thickness.

It is very difficult to ascertain the residual stress ratios. The stress ratio-shear movement curves usually have decreasing ratios from the peak to the end of the test. The writers feel old style setups are usually inferior to new style setups for ascertaining residual stress ratios. But, the junior writer's laboratory has produced some stress ratio-shear movement curves (with other sands) from which residual stress ratios were reasonably discerned.

## 6 CONCLUSIONS

The following conclusions derive from the described direct shear testing program using the cited equipment, normal stresses, materials and setup dimensions and procedures. Extensions to other situations should only be made with appropriate considerations.

1. New style setups are superior to old style setups for

testing of sand/geomembrane combinations.

2. For new style setups, the residual stress ratio for each sand/geomembrane combination is a unique value if proper sand layer thickness and gap size dimensions are used.
3. For new style setups, the peak stress ratio for each sand/geomembrane combination is not a unique value. The value depends on sand layer thickness, gap size, and normal stress level but not on size of area.
4. ASTM (1992) promulgates the use of too small gap sizes. This setup criterion results in too large peak and residual stress ratio measurements.
5. For each sand/geomembrane combination setup, the improper selection of layer thickness and gap size dimensions can lead to widely varying improper test data.
6. The minimum acceptable thickness of a sand layer is governed by the size of the largest sand particle. The maximum acceptable thickness is governed by the combination of the roughness of the inside walls of the upper box and the volume change during shear behavior of the sand.
7. The use of 15.2 x 15.2 cm top box sand areas on lieu of conventional 30.5 x 30.5 cm areas does not create any loss of test data accuracy.

## ACKNOWLEDGMENTS

The laboratory testing and publication costs were funded by GZA Geoenvironmental, Inc. as in-house research. The writers express their gratitude to Matt Trettel, the laboratory technician who performed all the tests. Gratitude is also extended to GSE Lining Technology, Inc. who provided funding to the senior writer for project expenses.

## REFERENCES

- ASTM (1992) Standard Test Method for Determining the Coefficient of Sand and Geosynthetic or Geosynthetic and Geosynthetic Friction by the Direct Shear Method, D5321-92, American Society for Testing and Materials, West Conshohocken, PA, USA, pp.332-336.
- Bemben, S.M. And Schulze, D. A. (1995) 'The Influence of Testing Procedures on Clay/Geomembrane Shear Strength Measurements', *Geosynthetics* '95, IFAI, Nashville, TN, USA, Vol.3, pp.1043-1056.

# Evaluation of Soil-Geosynthetics Interaction for Some Landfills in Algiers

A. Bouazza

Senior Lecturer, Department of Civil Engineering, Monash University, Melbourne, Victoria, Australia

**ABSTRACT:** The paper presents the results of a study concerning the potential use of geosynthetics in some MSW landfills in the Algiers (Algeria) area. The study focussed on the evaluation of interface shear strength between the different components of the proposed liner. Sand/woven geotextile, sand/non woven geotextile, sand/textured PVC geomembrane (locally made), and clay/PVC (smooth and textured) geomembrane systems have been investigated. It was found that efficiency on friction varied from 0.82 to 0.97 for sand/geotextiles and geomembranes systems and from 0.16 to 1.22 for the clay/geomembranes and geotextiles systems. Locally made textured geomembranes showed good promise in terms of efficiency and can contribute to a safe disposal of domestic waste. More importantly, the results showed that a minimum composite liner can be constructed taking into account the availability of some local materials. Thus avoiding the common practice of dumping the waste in a big open hole without a minimal protection.

**KEYWORDS:** Geotextiles, Geomembranes, Landfills, Liners, Interface friction

## 1 INTRODUCTION

The economic boom that most of the industrialised countries of the world have experienced in the past has brought both increased industrial and urban waste disposal problems. Industrial treatment sludges, along with an array of other industrial, hazardous and domestic waste, have been indiscriminately dumped into either disused rock quarries and sand pits, or in areas previously considered to be undesirable. Only minimal attention has been given to the control of leachate to prevent spread of contaminants in surface water and ground water. As a result, the total environmental and societal costs of landfilling have for a long time not realistically been considered. Programs for cleaning up many old sites, such as those identified by the Superfund program in the United States and in the contaminated land inventories in the European Community, have mainly started over the last decade.

Over the last decade considerable attention has been focused on environmental issues. Indeed, ground and groundwater protection and restoration of contaminated soils and waters are issues that have come under increased public scrutiny. It has become necessary to design and construct safe waste disposal facilities which employ the best of the available technologies. Nowadays, landfill waste containment systems often are comprised of several layers of geosynthetics and natural soils. Typically, the soil layers are predominantly fine grained and consists of large amounts of clay. Soils and geosynthetics are used in a liner system to serve as drainage and collection layers as well as hydraulic barriers. In most systems, the clay layer and a geomembrane are placed in direct contact to form a composite barrier and to increase the total effectiveness of the hydraulic barrier to contaminant migration out of the landfill. Multiple barrier and collection layers are often combined to provide redundancy to the design. However, in developing countries the above concept of

design is still in its infancy due mainly to the lack of guidelines, regulations, expertise, or funding. It is worth noting that funding when available is in competition with more basic needs such as those for housing, education or adequate nutrition.

The main problem which prompted the present study was linked to the state of the main refuse landfill situate at Oued-Smar 15 kms east of Algiers, Algeria (Figure 1).

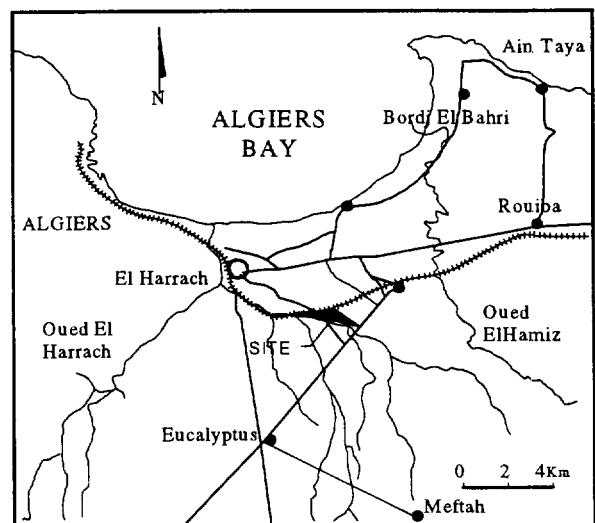


Figure. 1 Site location

This landfill receives approximately 580000 t/year of wastes of all sorts. The typical refuse in the Oued-Smar landfill consists of 72% food (including, fibres, shells, etc.), 9% papers, 8% plastics, 4% textiles, 1% glass, and 5 % of other materials (Bouazza, 1993). Twenty years after its opening, it shows the signs of a poorly designed landfill. Unpleasant and unhealthy odours are emerging from the site, repulsive aspects which play a negative role on the neatness and the protection of the site.

Furthermore, the poor level of leachate migration control added to the fact that it is inadequately lined resulted in soil and groundwater pollution. There was a strong need to replace the existing landfill by a new landfill with a composite liner.

The work presented in this paper was part of a study of lining systems for some potential landfills to be constructed around the Algiers area (Algeria). This study has been carried out in the prospect of possibly usage of, locally (Algerian) made PVC geomembranes, local soils and imported geotextiles in the new composite liner.

## 2 MATERIALS

The geosynthetics used in the present study consisted of woven geotextile (GTw), non-woven geotextile (GTnw), textured PVC (GM), and smooth PVC (GM). The PVC geomembranes were selected because of their availability locally. The clay used was from the El-Harrach area where the main Algiers landfill is sited. All samples were taken at a depth of about 4-5 m. The physical properties from laboratory tests, conducted according to AFNOR standards methods, are: unit weight =  $17.10 \text{ kN/m}^3$ , natural moisture content = 12%, optimum moisture content (omc) = 14.5%, liquid limit = 38%, plasticity index = 17%. The mineralogical analysis of the sample showed that the clay was of a kaolin type. The sand was a medium clean uniform sand. It had the following properties: maximum porosity  $n_{\text{max}} = 48\%$ , minimum porosity  $n_{\text{min}} = 28\%$ , specific gravity  $G_s = 2.65$ , uniformity coefficient  $C_u = 1.9$ , shape = subrounded

## 3 TESTING PROCEDURE

A 100 mm x 100 mm shear box was used to determine the interface shear strength of the soil/geosynthetics systems in a non saturated state (dry condition). Conventional shear box tests were initially conducted to ascertain the internal angle of friction of the clay and the sand. Further shear box tests were then conducted but with clay or sand in the upper half of the box only, with the geosynthetic element material in the lower half. The lower half of the box was occupied by a hardwood block and the geosynthetic material was glued firmly to the surface of the block. The geosynthetic was aligned so that shearing occurred in a direction parallel to the longitudinal axis, along shearing direction. The block was adjusted so that the surface of the geosynthetic was flush with the top edge of the bottom half of the box, in order to ensure shearing could only occur at the interface. The clay was compacted in the standard proctor mold and then specimens were trimmed and placed into the upper split box. Sand samples were prepared by pluviating sand directly into the upper box to achieve a relative density

( $I_p$ ) of 65%. A normal pressure varying from 100 to 400 kPa was applied. The shearing rate was 0.1 mm/min. Once, the samples have been prepared and the desired normal stress applied, the sample was left for about thirty minutes to come to equilibrium and then sheared to failure.

## 4 RESULTS AND DISCUSSION

The interface shearing resistance between geosynthetic and soil is generally expressed by two parameters:

- 1) angle of friction ( $\phi_{\text{GT} \text{ or } \text{GM}}$ ) due to the friction between the soil particles and the geosynthetic surface;
- 2) adhesion ( $C_i$ ) due to the interface force holding soil particles at the geosynthetic surface, obviously in a cohesionless soil  $C_i = 0$ .

The contact efficiency, or efficiency on friction, (E) is then defined as the ratio of the tangent of the friction angle ( $\phi_{\text{GT} \text{ or } \text{GM}}$ ) for the soil-geosynthetic interface, to the tangent of the friction angle ( $\phi$ ) for the soil alone.

The data reported in this paper were obtained for normal pressures ranging from 100 kPa to 400 kPa. The results obtained with sand are presented in Table 1 while the results obtained with clay are presented in Table 2.

It is obvious to see that the friction angle ( $\phi_{\text{GT} \text{ or } \text{GM}}$ ) between geosynthetics and soils are smaller than the internal angle of friction ( $\phi$ ) of soil alone, except for the GTnw/clay system. In the latter, the shear tests have generated an efficiency value well above 1.00, indicating a perfect contact. This is probably due to the good interlocking between the clay particles and the geotextile fibres. This is further enhanced by the roughness and the random orientation of the fibres in the nonwoven geotextile. A similar behaviour has been noticed when testing nonwoven geotextile/peat interface strength (Bouazza & Djafer-Khodja, 1994). The interface friction angle of non-woven geotextiles (GTnw) and woven geotextiles (GTw) in contact with sand is  $32^\circ$  and  $34^\circ$  respectively mobilising 89 % and 96 % of sand's friction angle. The interface friction angle of textured PVC (GM) in contact with sand is  $30^\circ$  and mobilised 82 % of the sand friction angle. The above results indicate that the interface friction angles of geotextiles and textured PVC (GM) with sand are close to those obtained for sand alone. The friction angle between clay and textured PVC (GM) is  $22^\circ$  which mobilised 73 % of the clay friction angle. Whereas the smooth PVC geomembrane was found to have an efficiency of approximately 17 %. The low interface friction angle value and efficiency attained in the present case with the smooth PVC (GM) represent a high risk potential of failure due to slippage (Bouazza, 1996).

Table1. Peak interface friction results for geosynthetics/sand system.

	Sand alone	GTw	GTnw	PVC GM
$\phi$ (°)	35	-	-	-
$\phi_{p,n/GT}$ (°)	-	34	32	-
$\phi_{p,n/GM}$ (°)	-	-	-	30
E	-	0.96	0.89	0.82

Table2. Peak interface friction results for geosynthetics/clay system.

	Clay alone	GTnw	smooth PVC	textured PVC
$\phi$ (°)	29	-	-	-
C (kPa)	35	-	-	-
$\phi_{p,n/GT}$ (°)	-	34	-	-
$C_s$ (kPa)	-	22	-	-
$\phi_{p,n/GM}$ (°)	-	-	5	22
$C_s$ (kPa)	-	-	9	14
E	-	1.22	0.16	0.73

Figure 2 shows typical direct shear data for the interface between the compacted clay and the different types of PVC (GM). The shear stress is plotted as a function of the horizontal displacement for a normal stress,  $\sigma_n = 200$  kPa. The measurements indicate that the roughness of the textured PVC (GM) contributes to the increase in the amount of the shear resistance at the clay/PVC (GM) interface. Apparently the rough surface of the textured PVC (GM) creates better interlocking with the clay material than the smooth surface of the second PVC (GM). One can also notice that the sample with a textured surface shows a peaking of shear strength at small displacements of less than 0.8 mm. Whereas the sample with smooth surface shows a flatter shear displacement curve. Another feature is also depicted in Figure.2. Indeed, one can also notice that the residual strength of the soil/smooth PVC (GM) system is almost identical to its peak value. Whereas in the soil/textured PVC (GM) system the drop from peak to residual strength value is more significant.

Composite liners, consisting of compacted clay and geosynthetic materials, are generally used in MSW landfills as they have proved to be an effective barrier against contamination of soils and groundwaters. However, the use of a composite liner requires that greater attention be paid to the stability of the landfill. The failure of a liner system can be catastrophic in terms of the harm it can do to the environment and the monetary cost to the community. The investigation of the sudden slope failure of the Kettleman Hills waste landfill in California, USA (Mitchell et al. 1990, Seed et al., 1990, Byrne et al., 1992) indicated clearly that failure occurred by sliding along one or more interfaces within the landfill liner system. The results of the geosynthetics interface shear test reported by Mitchell et al. (1990) in connection with the Kettleman Hills failure investigation as well as the results reported by Martin

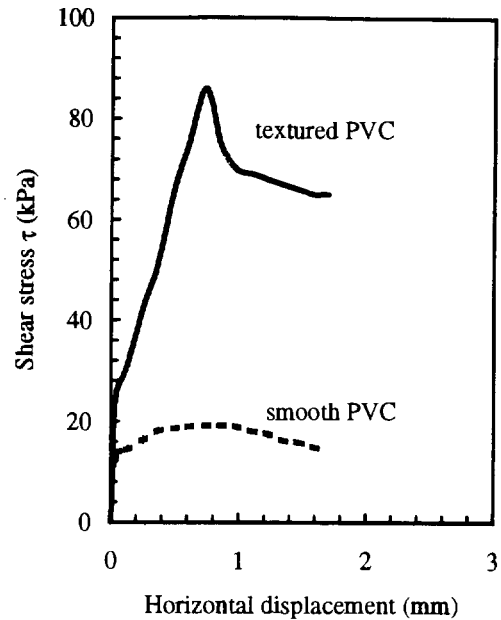


Figure 2: Shear displacement relationship for smooth and textured PVC (GM) at  $\sigma_n = 200$  kPa.

et al (1984), Williams and Houlihan (1986), Negussey et al. (1989), Pasqualini et al. (1993) and Stark et al. (1996) are particularly instructive examples of the values and variabilities of interface shear resistances. However, published values of interface friction cannot be used for design of a specific project, without at least careful review of test materials, test conditions and test methods. For design purposes, an interface friction should be determined on a site specific basis. The present results provide some data for the local engineers, obviously more work needs to be carried out to optimise any solution to the safe disposal of wastes.

Perhaps more importantly, Giroud et al. (1995) queried whether a developing country should adopt or adapt landfill regulations and designs from countries with stringent environmental regulations. Their answer was that waiting to construct a landfill with a state of the art system in a developing country is likely to result, over time, in more pollution of the environment than accepting lower standards and immediately constructing a landfill with a liner built using local materials. The present results show indeed that local materials such as PVC (GM) and clay or sand can achieve an acceptable performance and present a viable economic alternative. However, extreme precautions should be taken when using PVC geomembranes. Indeed, Masada et al. (1994) stressed the fact that PVC geomembranes show rapid aging upon prolonged exposure to leachate and also that clay/PVC interface shear strength is susceptible to undergo a large reduction when exposed to leachate.

In the present specific case, it appears that the use of textured locally made PVC (GM) can alleviate certain environmental issues and contribute to the "safe" disposal of domestic waste. Economically, this is also a viable alternative for local authorities since the cost of having a composite liner is reduced. However, one should stress that this is not the panacea to all waste disposal problems in Algeria. Proper regulation should be put forward. More testing encompassing all aspects linked to landfill design are needed in order to optimise the locally made material.

#### ACKNOWLEDGMENTS

This work has been carried out while the author was lecturing at the University of Sciences & Technology of Algiers, Algeria. The help provided by the ENTP (Algiers) and the LTPC (Algiers) is gratefully acknowledged.

#### REFERENCES

- Bouazza, A. (1993). "Compacted clayey soils as cover material for landfills", *Proceedings International Conference On Waste Disposal by Landfill*, Bolton, U.K, pp. 405-407. Rotterdam: Balkema.
- Bouazza, A. (1996). "Evaluation of soil PVC-geomembrane interface for landfill stability", *Proceedings 1st European Geosynthetics Conference, EUROGEO1*, Maastricht, The Netherlands, pp.189-192
- Bouazza, A. and Djafer-Khodja, S. (1994). "Friction characteristics between nonwoven fabric and peat", *Geotextiles and Geomembranes*, vol. 13, No 12, pp. 807-812.
- Byrne, R.J., Kendall, J. and Brown, S. (1992). "Cause and mechanism of failure, Kettleman hills landfill B-19, Unit 1A", *Stability and Performance of Slopes and Embankments*, ASCE. *Geotech. Special Publication No. 31*, vol. 2, pp. 1188-1520.
- Giroud, J.P., Bonaparte, R. and Sembenelli, P. (1995). "Selection of waste containment systems in developing countries", *Proceedings 5th International Landfill Symposium*, Cagliari, Italy, pp.149-157.
- Martin, J.P., Koerner, R.M. and Whitty, J.E. (1984). "Experimental friction evaluation of slippage between geomembranes, geotextiles, and soils", *Proceedings International Conference on Geomembranes*, pp. 191-196. St Paul, IFAI.
- Masada, T., Mitchell, G.F., Sargand, S.M. and Shashikumar, B. (1994). "Modified direct shear study of clay liner-geomembrane interfaces exposed to landfill leachate", *Geotextiles & Geomembranes*, vol. 13, pp. 165-179.
- Mitchell, J.K., Seed, R.B. and Seed, H.B. (1990). "Kettleman hills waste landfill slope failure I: liner-system properties", *Journal of Geotechnical Engineering, ASCE*, vol. 16, No 4, pp. 647-668.
- Negussey, D., Wijewickreme, W.K.D. and Vaid, Y.P. (1989). "Geomembrane interface friction", *Canadian Geotech. Journal*, vol.26, pp. 165-169.
- Orman, M.E. (1994). "Interface shear-strength properties of roughened HDPE", *Journal of Geotechnical Engineering., ASCE*, vol. 120, No 4, pp.758-761.
- Pasqualini, E. , Sani, D. and Rocatto, M. (1993). "Factors influencing geomembrane interface friction", *Proceedings International Conference On Waste Disposal by Landfill*, Bolton, U.K, pp. 349-356. Rotterdam:Balkema.
- Seed, R.B., Mitchell, J.K. and Seed, H.B. (1990). "Kettleman hills waste landfill slope failure II: Stability analysis", *Journal of Geotechnical Engineering., ASCE*, vol. 116, No 4, pp. 669-689.
- Stark, T.D., Williamson, T.A. and Eid, H.T. (1996). "HDPE geomembrane/geotextile interface shear strength", *Journal of Geotechnical Engineering., ASCE*, vol. 122, No 3, pp.197-203.
- Williams, N.D. and Houlihan, M. (1986). "Evaluation of friction coefficients between geomembranes, geotextiles and related products", *Proceedings. 3rd International Conference. on Geotextiles*, Vienna, Austria, pp. 891-896.

# Reinforcement Requirements at a Hazardous Waste Site

A.T. Hendricker  
Project Coordinator, McColl Site Group, 2655 Rosecrans Avenue, Fullerton, CA, USA

K.H. Fredianelli  
Project Manager, Parsons Engineering Science, Inc., 100 W. Walnut Street, Pasadena, CA, USA

E. Kavazanjian, Jr.  
Principal, GeoSyntec Consultants, 2100 Main Street, Suite 150, Huntington Beach, CA, USA

J.A. McKelvey, III  
Senior Project Engineer, GeoSyntec Consultants, 2100 Main Street, Suite 150, Huntington Beach, CA, USA

**ABSTRACT:** A case history on the use of geosynthetic reinforcement for remedial action of a Southern California hazardous waste site is presented. The site consists of twelve pits containing highly acidic organic compounds and oil-based drilling muds. The organic compounds in the pits originated from oil and petroleum sludges, which have high percentages of sulfuric acid. The selected remedy for the site was to provide long-term isolation of the waste using a geosynthetic cover system and a soil-bentonite vertical barrier. Selection of the cover system components required consideration of the chemical compatibility between the waste and the geosynthetics and the ability of the cover to withstand differential settlement of the underlying wastes. The paper discusses the chemical compatibility test program, design and construction of the reinforced cover system used for this project and lessons learned during construction.

**KEYWORDS:** Reinforcement, Differential Settlement, Geogrid, Geocell, Chemical Compatibility.

## 1 INTRODUCTION

This paper presents a case history of the design and construction of a reinforced geosynthetic cover system at a Southern California hazardous waste site. The paper presents: (i) background information of the site; (ii) design considerations for the remedial action; (iii) the chemical compatibility testing program used to evaluate the long-term durability of the components of the cover system; and (iv) issues which arose during construction.

## 2 BACKGROUND

Twelve pits containing petroleum sludges and oil-based drilling muds exist at the site. The sludges were generated by the production of high-octane aviation fuel and were placed in the pits between 1942 and 1946. Between 1952 and 1964, the site was used for disposal of oil-based drilling muds. These wastes and their reaction products and byproducts are found as liquid, gas and solid phases within the pits. At the time of deposition, essentially all of the waste materials were mobile. Over time, much of the waste has hardened. Since deposition, the wastes have been present at the site without an engineered containment system. During the post-deposition period, occasional tar seeps and malodorous gaseous emissions emanated from the pits.

The solid and semi-solid material present in the pits consist of a thin layer of surface soil having a thickness between 0.8 and 1.7m, soil mixed with waste, drilling muds and soft flowable tar varying in thickness between 0.3 and 2.6m, and solidified waste having a measured thickness

from 0.6 to 7.8m. These materials are neither present in equal proportions or are they distributed evenly within the pits.

The drilling muds are a thixotropic semi-solid sludge, which can behave as a very viscous fluid. The tar portion of the waste is a black, moist, viscous material with the potential for mobility. Flowable tarry waste had seeped through the overburden soil cover to the surface at approximately fifty locations within nine of the twelve pits. Figure 1 shows one of the waste seeps observed at the site. The tar emerged to the surface in a viscous state but solidified following exposure to the atmosphere into a glassy substance that exhibited a tendency to fracture. The solidified waste, the predominant content of the pits, is a hard, friable immobile material that is the end product of a series of chemical reactions that have occurred among the various materials within the pits.

Beneath the pits are native soils consisting of thin beds of intermixed sands, silts and clays. There is no engineered lining system beneath the pits. However, the solidified waste is anticipated to act in a manner similar to an asphalt liner. The regional groundwater table is located 43 to 73m beneath the pits. There are isolated, transient lenses of perched water around the site at elevations higher than the regional groundwater table. The source of the perched water is likely infiltration and leaking drainage culverts. The highest transient lens of perched water is 3m below the bottom of the deepest pit.

Key considerations of the selected source remedy for the site were to: (i) provide a cover system that includes a barrier layer and a gas collection and treatment system over the pits to minimize infiltration of water and release of



Figure 1- Flowable waste seep through existing soil cover.

hazardous or malodorous gas emissions; (ii) provide a subsurface vertical barrier around the pits to minimize outward lateral migration of mobile waste or waste by-products and inward lateral migration of subsurface liquid; and (iii) provide slope stability improvements for unstable slopes at the site. As the focus of this paper is on the reinforcement requirements of the cover system, discussion of the subsurface vertical barrier will not be presented.

### 3 DESIGN CONSIDERATIONS

In addition to encapsulating the waste, the design of the cover system also considered long term use of the facility. Several slopes at the site required reconfiguration to resist seismic events deemed probable in the area. By designing geogrid-reinforced walls at the toe of these slopes, the grades of the slopes could be flattened sufficiently to achieve acceptable performance during the design seismic event. Other improvements included extending an adjacent golf course over the more stable pits, creating three holes and a water hazard. The other portions of the site were to be landscaped to a park-like setting.

The design of the cover system was complicated by the inhomogeneity of the material in the pits. Slight to moderate subsidence was observed in various areas over the pits. Considering this observation, there was a concern that additional overburden from the landscaping could aggravate any differential settlement of the cover system. Furthermore, the drilling muds of variable thickness were considered likely to generate significant differential settlement. To minimize stresses on the barrier layer of the cover system (a geomembrane) due to differential settlement, it was concluded that reinforcement was needed beneath the cover system. Two types of reinforcement were used based on the varying overburden stresses proposed. Over the pits containing high percentages of drilling muds, the cover system stress on these materials was limited in the design to minimize long-term settlement.

In these areas, a cellular confinement system (geocell) was used because the stiffness of the three-dimensional geocell is greater than that of two dimensional sheet reinforcement (i.e., geogrid) and does not require initial deformation to support the design loads. Over the pits that did not contain drilling mud, the design allowed placement of 4.6m of fill for the golf course. In these areas, geogrid reinforcement was used.

Further complicating the design was the highly acidic nature of the waste, derived from sulfuric-based petroleum sludges. As many materials typically used for cover systems perform poorly in a highly acidic environment, material selection was based on a chemical compatibility testing program.

### 4 CHEMICAL COMPATIBILITY

Due to the nature of the wastes and the extent of reactions and transformations occurring in the pits, many constituents of the waste exist at varying concentrations in different phases. Of particular importance to the constituent interactions are the sulfur compounds found in the liquid phase of the waste. These sulfur compounds are the result of catalyst-based reactions involving various organics, acidic clays, and the sulfate anion. The origin of the sulfur within the pits is the petroleum sludges. Typical acid concentration for these sludges was 90 percent sulfuric acid when initially placed in the pits, but is believed to be less now since reactions with organics and infiltrating precipitation have been occurring over time. The pH of the waste averaged 3.5, and ranged from 1 to 8.1, depending on the composition of the waste at the sampling location.

Selection of the materials to be used in the chemical compatibility program was based on a literature search on chemical resistance of polymeric materials. Based on the very low pH of the waste, polyethylene materials were selected. However, the literature review indicated that the organic compounds in the waste could be soluble in polyethylene, leading to a decrease in strength and an increase in ductility. Furthermore, the polyethylene could oxidize in the presence of the waste, leading to possible environmental stress cracking. Accordingly, both chemical exposure and environmental stress cracking tests were conducted on the polyethylene materials proposed for use in the cover system.

Due to the unsaturated conditions in the waste, it was not possible to obtain enough liquid from within the pits to perform laboratory analysis. However, a waste-derived liquid was prepared from samples of the waste for use in the chemical compatibility program. This waste-derived liquid (WDL) had a pH of less than one. Samples of the polyethylene geomembrane and geocell proposed for use were placed in exposure tanks containing both the waste-derived liquid and flowable tar. Polyethylene geogrid samples were not tested as the proposed material had a

higher density than the geomembrane and geocell materials, and hence was considered to be more resistant. However, it was agreed that any strength reduction noticed in the geomembrane and geocell samples would be applied equally in the design of the geogrid.

Figure 2 shows the influence of both waste-derived liquid and tar exposure on the geomembrane.

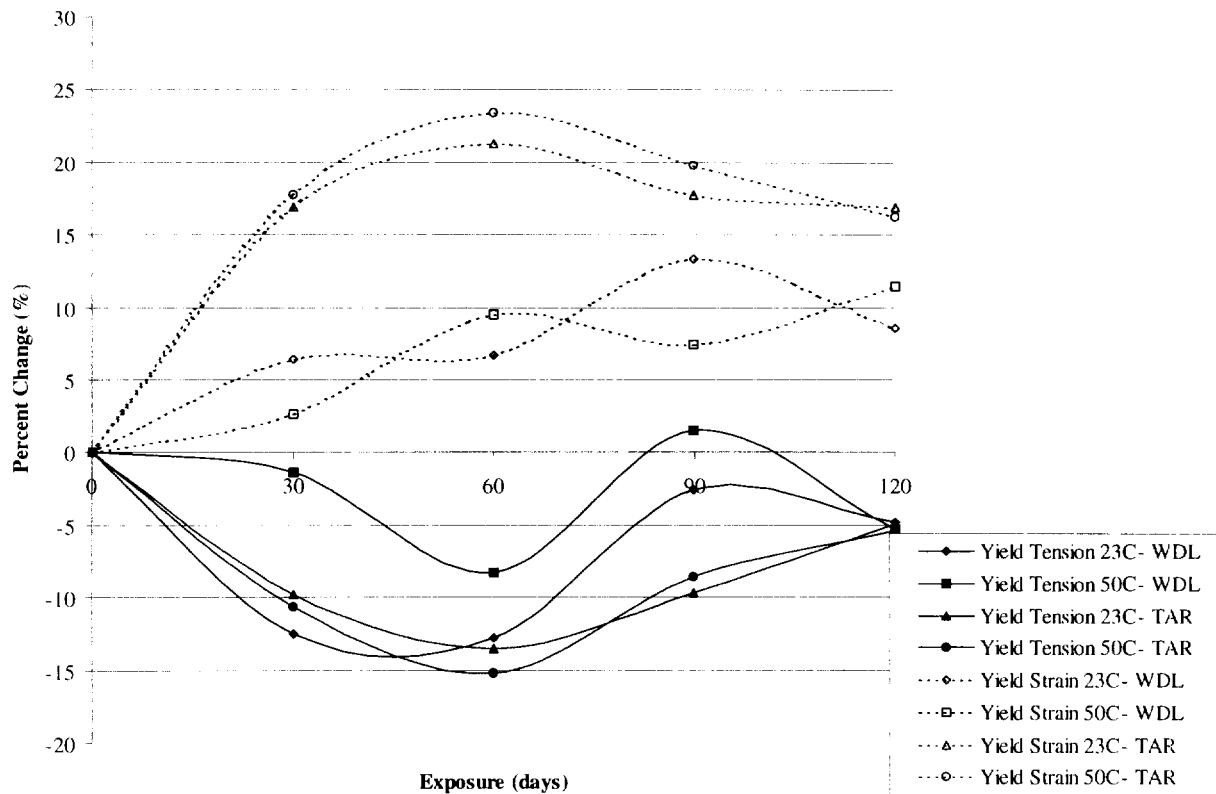


Figure 2. Chemical compatibility test results from geomembrane exposure tests in waste-derived liquid (WDL) and tar. While the data lacks a time dependent trend, softening of the polyethylene was observed upon initial contact with the waste.

The results of the exposure testing suggested that the polyethylene materials softened upon initial contact with both the tar and waste-derived liquid. Related properties such as puncture resistance and trapezoidal tear strength were similarly effected. Chemical concentration and elevated temperature appeared to influence the results of some of the exposure testing. However, the data lacked a time dependent trend, as shown in Figure 2 for the geomembrane testing.

To evaluate the effect of exposure on surface oxidation and related stress crack resistance, notched constant tensile load tests were performed. Samples of the geomembrane and geocell were retrieved from the waste exposure vessels after the samples were exposed to the waste-derived liquid for periods up to 120 days. The samples were then notched and placed in a surfactant bath. The samples were then loaded at a constant tension equal to 30 percent of the

materials yield strength. After 400 hours of exposure, the tests were terminated. No samples had tensile breaks prior to the 400 hour testing duration, suggesting that the stress crack resistance of the materials was still adequate following waste exposure.

Based on the results of the chemical compatibility program, reduction factors were included in the design of the reinforcement materials. Where waste exposure was considered to be possible, reduction factors of up to fifty percent were used in relevant design properties such as tensile strength and puncture resistance. In the reinforced earth structures, waste exposure was not anticipated, as these structures were placed above the barrier layer and/or outside the limits of the cover system. Accordingly, the chemical degradation reduction factors used in the design were typical values for conventional structures.



## 5 CONSTRUCTION

Extensive coordination was required during construction of the remedial action due to the complexity of the site and the schedule constraints of the project. In order to meet the project schedule, portions of the cover system had to be completed in phases, which caused some minor problems, as discussed below.

The geogrid reinforcement for the cover system over the more stable pits was constructed with two layers of uniaxial reinforcement placed orthogonal to one another. Connections at the end of each geogrid roll were provided by Bodkin joints. Adjacent geogrid panels did not have any permanent mechanical connections. This was found to be somewhat problematic, as additional care was required during placement of the overlying gas collection sand to minimize geogrid separation. After the connections were made, the geogrid was covered with sand and then pull taut using a backhoe to pull on the free end of the geogrid as shown in Figure 3.



Figure 3- Each geogrid panel was pulled taut by anchoring one end in soil and pulling on the free end with a backhoe.

A geocell reinforcement layer was constructed over the pits containing high percentages of drilling muds. While the construction of this reinforcement layer proceeded at a slower pace than the geogrid reinforcement, it did provide an immediate platform to support load. As the bearing capacity of the underlying drilling mud was quite low, the geocell provided load distribution, increasing the overall bearing capacity of the cover system.

A total of three reinforced earth structures were constructed at the site. One of the structures was necessary to provide a working pad for construction of the subsurface vertical barrier. This reinforced earth structure had to support the excavator with a gross operating weight of 1,100 kN that was used to dig the soil-bentonite cutoff wall. Another reinforced earth structure at the site had to span a portion of completed cutoff wall. Due to concerns that the

stress of the reinforced earth structure on the underlying soil-bentonite cutoff wall would lead to excessive deformation of the wall due to consolidation of the cutoff wall backfill, a flexible wall fascia was selected. As shown on Figure 4, the fascia consisted of galvanized wire baskets used to form a geogrid wrap-back. Each reinforced earth structure on the site used this type of facing. In one instance during construction, the wrap-back was not sufficiently tensioned, which led to deformation of the wall fascia during compaction of the wall backfill. Although the deformation was unsightly, the integrity of this wall was not compromised.



Figure 4- One of the reinforced earth structures completed during construction. Galvanized wire baskets were used to form the geogrid wrap-back earth structures.

## 6 SUMMARY

The chemical compatibility testing program performed during the design phase for this hazardous waste site remedial action provided several lessons. Although the literature can provide insight on many polymer degradation mechanisms, actual testing of the materials is required for competent design. The exposure testing performed to assess chemical compatibility allowed rational formulation of degradation reduction factors for use during the design, thereby limiting the use of conservative assumptions.

Construction observations also provided lessons. The techniques used to tighten the geogrid were successful in that the geogrid was not damaged during installation. Geocell was found to be an acceptable reinforcement over very soft materials. It became clear during construction of the reinforced earth structures that specifications need to clearly describe the tensioning of the wrap-back portion of the geogrid for acceptable construction of the wall fascia.

# Evaluation of a Geogrid-Reinforced Slope Subjected to Differential Settlements

Jorge G. Zornberg, Ph.D., P.E.  
GeoSyntec Consultants, Huntington Beach, California, U.S.A.

Edward Kavazanjian Jr., Ph.D., P.E., G.E.  
GeoSyntec Consultants, Huntington Beach, California, U.S.A.

**ABSTRACT:** A geogrid-reinforced toe buttress was constructed in 1987 under the direction of the Environmental Protection Agency (EPA) in order to enhance the stability of the southeastern slopes of the Operating Industries, Inc. (OII) Landfill Superfund site. The landfill is located approximately 16 km east of downtown Los Angeles, in an area of high seismicity. The front of the approximately 4.6 m high, 460 m long toe buttress was founded on concrete piers. However, as the back of the reinforced slope was founded on waste, the structure has been subjected to more than 0.6 m of differential settlements since its construction. Finite element analyses were performed to evaluate the long-term integrity of the geogrid reinforcements under the loads induced by 30 years of additional differential settlements followed by the design earthquake. The calculated maximum strains in the geogrid reinforcements after the long-term static and design seismic loadings are well below the allowable strain, indicating that the integrity of the toe buttress should be maintained even when subjected to large differential settlements and severe earthquake loads.

**KEYWORDS:** Finite Element Analysis, Landfills, Reinforcement, Seismic Loads, Settlement Analysis.

## 1 INTRODUCTION

A geogrid-reinforced toe buttress was constructed in 1987 under the direction of the Environmental Protection Agency (EPA) in order to enhance the stability of the southeastern slopes of the Operating Industries, Inc. (OII) Landfill Superfund site. The toe buttress is immediately adjacent to a residential development. The waste slopes behind the toe buttress are up to 37 m high, with intermediate slopes between benches up to 18 m high and as steep as 1.3H:1V. The approximately 460 m long, 4.6 m high toe buttress was founded on concrete piers at the front of the buttress and reinforced using HDPE geogrids. However, as the back of the reinforced buttress was founded on waste, the toe buttress has been subjected to significant differential settlements since its construction.

A thorough evaluation was undertaken to assess the long-term integrity of the reinforced toe buttress and, consequently, the stability of the southeastern landfill slopes behind the toe buttress. Analyses calibrated on the previous performance of the toe buttress were used to predict its future performance considering 30 years of additional settlement followed by the design (maximum credible) earthquake. The analyses of the toe buttress included three distinct components: (i) interpretation of monitoring data to evaluate the history of differential settlements in the toe buttress area and to project the future differential settlements to which the structure will be subjected over the next 30 years, (ii) analysis of the

global stability of the southeastern slopes of the landfill, assuming that the internal integrity of the toe buttress is maintained; and (iii) evaluation of the internal integrity of the geogrid-reinforced toe buttress, subjected to the predicted long-term differential settlements followed by the design earthquake, using nonlinear finite element analyses.

The scope of this paper is limited to some aspects of the element evaluation. Subsequent publications will present further aspects of the long-term and seismic evaluation of the geogrid-reinforced toe buttress. The finite element analyses presented herein were performed in three sequential phases: (i) toe buttress construction, modeled by sequentially activating soil and bar elements in the reinforced soil zone; (ii) development of differential settlements beneath the toe buttress, simulated by imposing incremental displacements at the base of the reinforced soil mass; and (iii) earthquake loading, modeled pseudo-statically by applying horizontal body forces, representing the maximum average acceleration estimated from a finite element site response analysis, to the reinforced soil mass.

## 2 BACKGROUND INFORMATION

Schematic profiles through the toe buttress and the waste slope along the southeastern perimeter of the OII Landfill are illustrated in Figure 1. Reinforced cast-in-place concrete piers were constructed along the roadway which

was located at the toe of the landfill, along the property line, in areas where the natural ground surface continued to slope downward beyond the property line (Figure 1a). Piers were not installed in areas where the ground surface was level beyond the toe of the waste slope (Figure 1b). A total of 201 piers, 0.9-m in diameter, were installed at 1.8-m center to center spacing along approximately 360 m of the 460 m long toe buttress.

An assessment of the available information on the geometry of the bottom of the waste beneath the toe buttress was undertaken to aid in the toe buttress global stability evaluation. The logs for the 201 concrete piers drilled along the toe buttress, along with historical aerial photos and limited data from borings through the waste, provided relevant information regarding the depth of the waste in the toe buttress area. This available information indicated that the bottom of the waste in the vicinity of the toe buttress area slopes down at an approximately 1H:1V inclination from the property line into the landfill.

Visual observations and survey data indicate that, since its construction in 1987, significant differential settlements have taken place over the width of the toe buttress along most of its alignment. The presence of the concrete piers under the front edge of the buttress and the increasing thickness of the waste towards the back of the buttress both contributed to the substantial differential settlements observed over the width of the toe buttress. Settlement profiles at eight stations along the toe buttress were measured in October 1992 and in April 1996. The results from the 1996 survey showed that, while the differential settlement rate at most of the stations along the toe buttress has decreased since 1992, significant differential movements were still occurring.

Because the settlement surveys were not tied to an external reference, it was assumed that the elevation of the toe buttress surface immediately above the drilled piers was fixed. The settlements monitored at the back of the toe buttress were projected forward in time to evaluate the potential for future settlements. Settlement was projected for each individual cross section as a straight line on a semi-logarithmic plot. The differential settlements projected 40 years beyond the end of construction (until year 2027) was less than 1.17 m for every cross section but one. For Cross Section 3 the projected differential settlement was 1.98 m. However, because of the inconsistency of the data for Cross Section 3, the projected differential settlement of 1.98 m for this section was considered to be an outlier. A differential settlement of 1.17 m was considered a conservative projection of the settlement at the back of the toe buttress over the next 30 years for the purpose of evaluation of the long-term integrity of the toe buttress. Nevertheless, in response to EPA comments, the performance of the toe buttress when subjected to a projected differential settlement of 1.98 m was also evaluated.

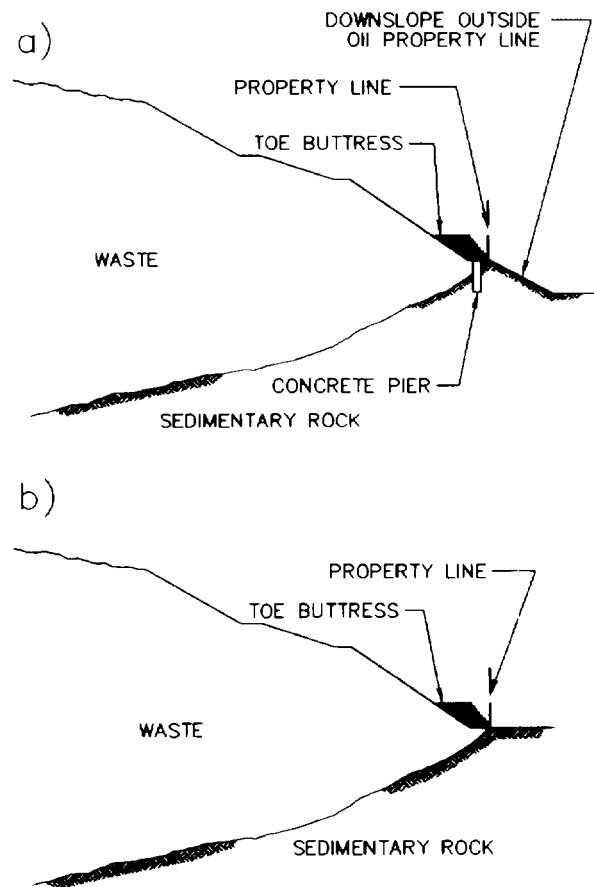


Figure 1: Typical profiles of the toe buttress at the OII Superfund Landfill.

### 3 MATERIAL PROPERTIES

The reinforcement elements used in the toe buttress were Tensar SR2 geogrids. Manufacturing of these reinforcement products had been discontinued by the time of this investigation. Consequently, the geogrid material properties needed for the analyses undertaken in this study were evaluated primarily on the basis of information available from the literature on this type of geogrid reinforcement. This literature information was supplemented with creep tests performed on archived geogrid samples provided by the geogrid manufacturer. A 10 percent limiting strain was established from the literature as a conservative estimate of the allowable geogrid strain for long-term static loading of this reinforcement (Bonaparte and Berg, 1987). A 20 percent limiting strain was established from the literature as the allowable geogrid strain for rapid earthquake loading (McGown et al., 1984). The laboratory testing program performed as part of this investigation included wide width tensile tests and creep tests followed by rapid loading to failure. The main objective of this testing program was to address concerns expressed by EPA that

sudden loading after an extended period of creep could reduce the allowable geogrid strain to a value less than that obtained from wide width testing. However, the test results verified that an allowable strain of 20 percent in the geogrid was applicable to the case of static creep followed by rapid seismic loading.

Construction records indicated that the toe buttress fill is a sandy gravel classified as GP using the Unified Soil Classification System. Specifications required a minimum relative compaction of 95 percent, based on modified Proctor compaction test, except within 0.61 m of the toe buttress face. The constitutive relationship used in the finite element analyses to model the backfill behavior is the hyperbolic model proposed by Duncan, et al. (1980). Hyperbolic model parameters for the backfill material were obtained from triaxial test results reported in the literature for a sandy gravel of similar grain size distribution and compaction characteristics (Zornberg and Mitchell, 1994). The parameters for the gravel constitutive model obtained from these triaxial test results are presented in Table 1.

As a component of the comprehensive investigation of the seismic performance of the OII landfill of which this investigation was part (GeoSyntec, 1996), a field sampling and laboratory testing program was undertaken to characterize the static and dynamic mechanical properties of the waste at the OII landfill. Direct shear test results were used to determine the shear strength properties of the waste material for the finite element analyses presented herein. Simple shear test results were used to define the hyperbolic stress-strain parameters required to characterize the behavior of the waste material in the finite element analyses. The hyperbolic parameters used in the finite element analyses to characterize the waste material are summarized in Table 1. Based upon data from the field investigation, a uniform unit weight of 15.7 kN/m<sup>3</sup> was used for the solid waste material in the analyses.

#### 4 FINITE ELEMENT EVALUATION OF THE TOE BUTTRESS

The integrity of the reinforced toe buttress subjected to the projected differential settlements followed by the design earthquake loading was evaluated via finite element analysis. The analysis was performed using the finite element code GeoFEAP developed at the University of California at Berkeley for analysis of geotechnical problems (Espinoza et al., 1995). Both material and geometric nonlinearity were considered in the analysis in order to account for the constitutive behavior of the materials and for the large displacements. The strains induced in the geogrid reinforcement were modeled using three sequential analyses: (i) construction

of the toe buttress, (ii) gradual increase of differential settlement, and (iii) earthquake loading.

The finite element mesh used in the analyses consisted of 1082 nodes, 1028 plane strain elements for representation of soil and waste, and 140 bar elements for simulation of the reinforcements. A relatively fine mesh discretization between reinforcement layers was found essential for the proper representation of the behavior of the soil layers.

Table 1. Hyperbolic soil parameters for the backfill and waste materials

Parameter	Parameter definition	Backfill	Waste
$K$	Young's modulus coefficient	913	212
$n$	Young's modulus exponent	0.6	0.61
$R_f$	Failure ratio	0.64	0.7
$c$ (kPa)	Cohesion	0.0	28.7
$\phi_0$ (°)	Friction angle at 1 atm.	46.1	31
$\Delta\phi$ (°)	Friction angle reduction parameters	5.3	0.0
$K_B$	Bulk modulus number	250	212
$m$	Bulk modulus exponent	0.8	0.61
$K_{ur}$	Unload-reload modulus coefficient	1485	428
$K_\theta$	At-rest lateral earth pressure coefficient	0.35	0.4

Construction of the toe buttress was modeled by sequentially activating soil and bar elements in the reinforced soil zone, as illustrated in Figure 2. Tensile strains were induced in the reinforcement during construction by the selfweight of the backfill material. The maximum reinforcement strain estimated in the construction analysis occurs in reinforcement level 7, located 2.7 m above the base of the 4.57 m high reinforced slope. The maximum strains that develop during construction in the geogrid reinforcements are very small, with a maximum strain of less than 0.4 percent. Figure 3 shows the strain distribution computed in reinforcement level 7 during the different stages of construction of the toe buttress. The different stages indicated in this figure correspond to the

placement of the soil layers during construction simulation.

The second phase in the finite element modeling of the toe buttress consisted of imposing differential settlement at the base of the reinforced soil mass, as illustrated in Figure 4. Strain and tension in the reinforcements were induced by progressively increasing the base settlements in a triangular pattern, with zero settlement at the front of the mesh and the maximum settlement at the back of the finite element mesh. A total of 2.0 m of differential settlement was imposed at the base of the finite element mesh to simulate the long-term differential settlement of 1.20 m projected for the surface of the toe buttress. The maximum geogrid strain computed after imposing this differential settlement occurs in reinforcement level 3, located 0.9 m above the base of the toe buttress. Figure 5 shows the strain distribution estimated in the reinforcement level 3 due to increasing differential settlements. The differential settlement was imposed considering ten intermediate stages.

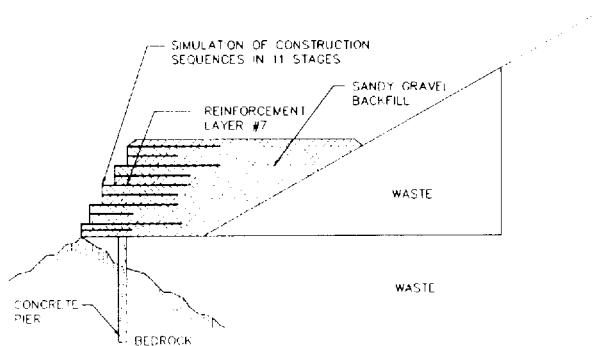


Figure 2: Finite element simulation of the construction sequence of the toe buttress.

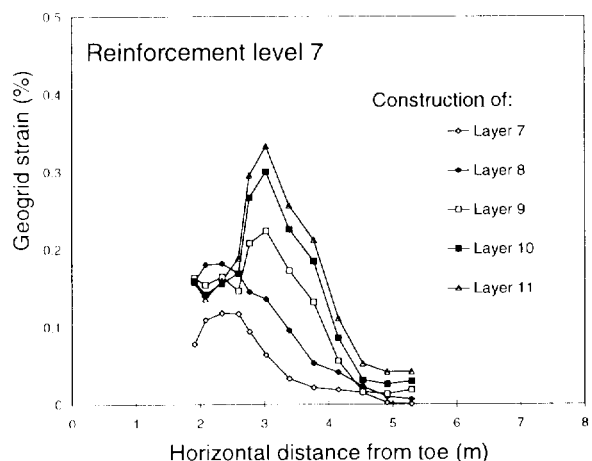


Figure 3. Estimated geogrid strains induced during construction.

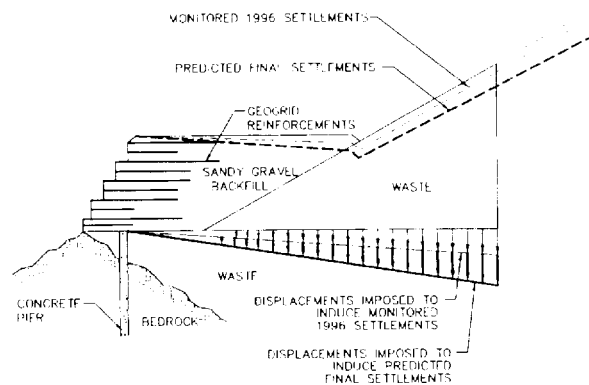


Figure 4: Finite element simulation of the differential settlements in the toe buttress.

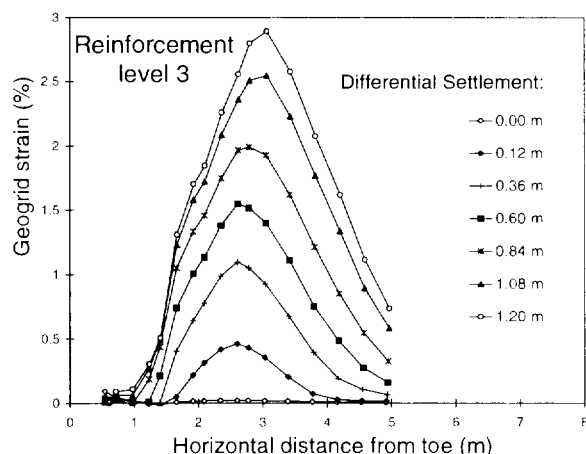


Figure 5. Estimated geogrid strains induced by increasing differential settlements.

The current (1996) average differential settlement at the back of the toe buttress is approximately 0.60 m. From the results shown in Figure 5, the maximum tensile strain in the geogrid reinforcements computed for the current condition is approximately 1.5 percent. Moreover, Figure 5 shows that the maximum tensile strain in the geogrid reinforcements computed for the long-term condition (i.e. after reaching 1.20 m of differential settlements on the surface of the toe buttress) is approximately 2.9 percent. Both the current and long-term geogrid strain levels predicted in the finite element analyses are well below the maximum static strain level of 10 percent established for the geogrid reinforcements. Extrapolation of the finite element results to larger strain levels indicates that it would require approximately 3.9 m of settlement between the crest of the toe buttress and the drainage ditch at the back of the structure to induce the

maximum allowable static strain of 10 percent in the geogrids. This exceeds by a factor of almost two the maximum long-term settlement of 1.98 m considered for Cross Section 3. As discussed previously, this magnitude of settlement was considered an outlier, but was addressed in response to EPA concerns.

To model the impact of seismic loading on the performance of the toe buttress, horizontal body forces corresponding to the maximum average acceleration estimated for the toe buttress area were applied to the active reinforced soil wedge, as shown in Figure 6. The design earthquake was a magnitude 6.9 earthquake on a blind thrust fault immediately below the site. A pseudo-static acceleration of 1.0 g, estimated in a finite element site response analysis as the maximum average acceleration of the toe buttress in the design earthquake, was used for the analyses presented herein. The earthquake-induced strains are most significant in the upper reinforcement layers of the toe buttress, in contrast to the results of the previous static phases of the analysis. Reinforcement level 9, located 3.66 m above the base of the 4.57 m high toe buttress, shows the maximum estimated tensile strain when the structure is subjected to the design pseudo-static seismic loading.

Figure 7 shows the strain distribution estimated in reinforcement layer 9 during application of the seismically-induced horizontal body forces. The strain distributions that correspond to the end of construction and to the long-term differential settlement are also shown in the figure (the 0.0 g cases). The final stage shown in the figure corresponds to the results obtained after applying the design earthquake loading (1.0 g). The magnitude of the maximum tensile strain in the reinforcement at this stage of the analysis is approximately 8.5 percent, considerably lower than the 20 percent allowable strain for combined static and dynamic loads. The 1.0 g pseudo-static seismic load induced a 6.7 percent strain increase in the reinforcement. Extrapolation of these results indicates that a seismic coefficient of more than 1.5 g would be required to induce an incremental strain of 10 percent in the geogrids (10 percent is the difference between the rapid and the creep limited allowable strains).

The numerical results obtained in the three phases of the finite element analyses show that the maximum geogrid strain estimated after each phase of the study does not occur at the same elevation. The maximum strain due to construction loading occurs at midheight of the reinforced toe buttress, while the maximum strain due to differential settlement occurs towards the base of the structure and the maximum strain due to earthquake loading occurs towards the top of the slope. The results of the finite element analysis presented herein show that the integrity of the toe buttress should be maintained even when the toe buttress is subjected to the projected long-term differential settlement followed by the design

earthquake loads. The predicted strain level in the geogrid reinforcement for the combined effect of these anticipated loadings is well below the allowable strains for combined long-term static and earthquake loading.

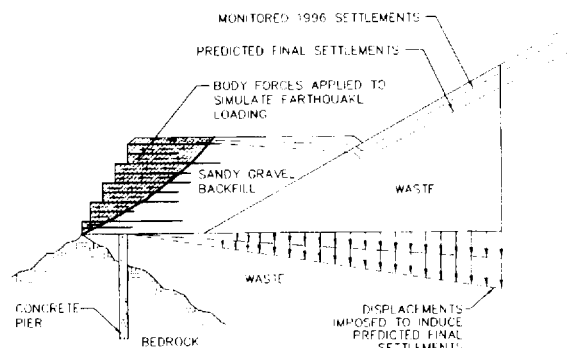


Figure 6: Finite element simulation of earthquake loading in the toe buttress.

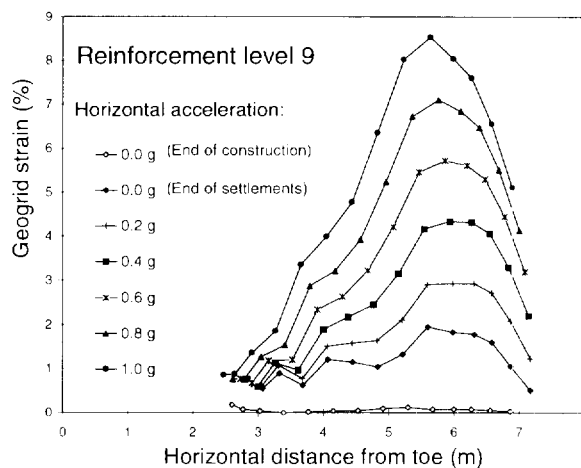


Figure 7. Estimated geogrid strains induced by seismic loads.

## 5 SUMMARY AND CONCLUSIONS

A geogrid-reinforced toe buttress was constructed in 1987 under the direction of the EPA in order to enhance the stability of the southeastern slopes of the OII Landfill Superfund site. The toe buttress is immediately adjacent to a residential development. The waste slopes behind the toe buttress are up to 37 m high with intermediate slopes between benches up to 18 m high and as steep as 1.3H:1V. The landfill is located 16 km east of downtown Los Angeles, in an area of high seismicity.

The approximately 4.6 m high, 460 m long toe buttress was built using sandy gravel as backfill material.

The front of the structure was founded on concrete piers. However, as the back of the toe buttress was founded on waste, the structure has been subjected to more than 0.6 m of differential settlements since the end of its construction. In response to concerns regarding the internal stability of the reinforced soil structure, finite element analyses were performed to evaluate the long-term integrity of the geogrid reinforcements under static and seismic loads. The analyses considered 40 years of settlement followed by the design earthquake. The finite element modeling evaluated the strains induced in the geogrid reinforcement considering both material and geometric nonlinearity. The analyses were performed in three sequential phases: (i) toe buttress construction, modeled by sequentially activating soil and bar elements in the reinforced soil zone; (ii) gradual increase in differential settlements, simulated by imposing incremental displacements at the base of the reinforced soil mass; and (iii) earthquake loading, modeled by applying horizontal body forces representing the maximum average acceleration estimated in a finite element site response analysis.

A total of 2.0 m of differential settlement was imposed on the base of the finite element mesh to simulate long-term differential settlement. The maximum strain in the geogrid reinforcements calculated after this long-term static loading is less than 3.0 percent, well below the allowable static strain of 10 percent. The calculated maximum geogrid strain induced by construction, long-term differential settlement, and earthquake loading is approximately 8.5 percent, well below the allowable strain of 20 percent established for rapid loading. The results of this study indicate that the integrity of the geogrid-reinforced toe buttress should be maintained even when subjected to large differential settlements and severe earthquake loads.

#### ACKNOWLEDGMENTS

This study was part of the seismic investigation undertaken at the OII Landfill. The support of New Cure Inc. (NCI), in particular of Mr. Kenneth Hewlett and Dr. Lester LaFountain, is gratefully acknowledged. The review and suggestions provided by Dr. David Espinoza of GeoSyntec and the contributions of the members of the Seismic Working Group organized by NCI and the EPA Technical Review Panel are also greatly appreciated.

#### REFERENCES

- Bonaparte, R. and Berg, R. R. (1987) "Long-Term allowable Tension for Geosynthetic Reinforcement", *Geosynthetic'87*, IFAI, New Orleans, Louisiana, USA, pp. 181-192.
- Duncan, J. M., Byrne, P., Wong, K. S., and Mabry, P. (1980) *Strength, Stress-Strain and Bulk Modulus Parameters for Finite Element Analyses of Stresses and Movements In Soil Masses*, Report UCB/GT/80-01, Department of Civil Engineering, University of California, Berkeley, California, USA.
- Espinoza, R. D., Taylor, R. L., Bray, J. D., Soga, K., Lok, T., Rathje, E. M., Zornberg, J. G., and Lazarte, C. A. (1995) *GeoFEAP: Geotechnical Finite Element Analysis Program. PART I - User's Guide*, Geotechnical Research Report No. UCB/GT/95-02, October 1995, Department of Civil and Environmental Engineering, University of California, Berkeley, California, USA.
- GeoSyntec Consultants (1996), "Summary Report of Findings, Report no. SWP-9, Operating Industries, Inc. Landfill, Monterey Park, California" Prepared for New Cure, Inc.
- McGown, A., Andrawes, K. Z., Yeo, K. C., and DuBois, D. D. (1984) "The Load-Strain-Time Behavior of Tensar Geogrids", *Polymer Grid Reinforcement in Civil Engineering*, The Institution of Civil Engineers, London, UK, pp. 11-17.
- Zornberg, J. G. and Mitchell, J. K. (1994) "Finite element prediction of the performance of an instrumented geotextile-reinforced wall". *Eight International Conference of the International Association for Computer Methods and Advances in Geomechanics (IACMAG '94)*, Vol. 2, Morgantown, WV, USA, pp. 1433-1438.

# High-Strength Aramid Geogrids to Prevent Sliding On Steep Landfill Basal Slopes

A. Plankel

Dipl.-Ing., Plankel, Pelzl & Partner, Lauterach, Austria

D. Alexiew

Dr.-Ing., HUESKER Synthetic GmbH & Co., Gescher, Germany

**ABSTRACT:** A landfill with steep basal slopes of 1V:2H is in the stage of filling. High-strength geogrids are required to ensure the sliding stability of the drainage gravel layers and parts of the waste. For some slopes aramid geogrids with 1200 kN/m and 550 kN/m ultimate tensile strength at less than 3 % ultimate strain have been selected. It is the first application of such geogrids as 'antisliding' reinforcement on landfill slopes. Formulation of the problem, general philosophy and considerations, and first measurement results are presented.

**KEYWORDS:** Geogrids, Landfills, Slope stabilization, Measurements, High-Strength

## 1 INTRODUCTION

For basal and capping systems of landfills multilayered structures consisting of soils and different geosynthetics are used. A world-wide overview of standardized solutions can be found, e.g. in Van Impe et al., 1996, the typical German solutions, which are similar to those in Austria, e.g. in Gartung, 1995, and alternative actual solutions e.g. in Alexiew et al., 1995, Alexiew and Sobolewski, 1997. All these 'sandwiched systems' have a common characteristic: they comprise some interfaces, in which the shear resistance could be lower than in the soils and geosynthetics themselves. The interface with the lowest resistance controls the sliding stability of multilayered slopes. If the shear resistance is not sufficient, the layers above this critical plane would slide downwards. In practice, a reliable solution is to lay an appropriate geogrid in the (soil)layers tending to slide on the critical plane. The geogrid has to be installed on the entire slope from the toe up to the crest, reinforcing throughout the layer, and anchored.

Recommendations are given e.g. in Alexiew, 1994, calculation procedures among many others in Koerner, 1994, Alexiew, 1994, and Alexiew and Sobolewski, 1997. The problem is shown in general in Figure 1, for a typical case.

## 2 GENERAL CONSIDERATIONS FOR REINFORCEMENT AGAINST SLIDING

### 2.1 Importance of Interaction ('Why a geogrid?')

A geogrid is recommended as reinforcement due to the high coefficient of interaction (bond coefficient) to the mineral layer to be reinforced and prevented from sliding.

The definition for geogrids (IGS, 1996) asks for mesh sizes larger than the constituents (bundles, strips, ribs etc.), which is the most important condition to ensure good interaction. Soil-grading related criteria are used also, e.g.  $B_{GG} \geq 3.5 \times d_{50}$  (Koerner, 1994, p. 338) or  $a \geq 1.67 \times d_{80}$  (DB AG-TL, 1997), where  $B_{GG}$  or  $a$  is the minimum mesh size

respectively;  $d_{50}$  and/or  $d_{80}$  is the grain size of soil for 50% and 80% passing, respectively. Contrarily to Koerner, 1994, p. 386 and Mannsbart, 1996, no geotextile or geocomposite without open aperture should be used because of the risk of insufficient bond, especially for saturated conditions accompanied by seepage pressure. For example, the use of woven geotextile as soil reinforcement in a multilayered system on a German landfill resulted in a general 'landslide' just around a month after installation. At the same time, geogrid reinforcements have been successfully used for both very long or very steep permanent slopes (Martin and Simac, 1995, Alexiew and Sobolewski, 1997).

### 2.2 Importance of Displacements and Strains

Simplified limit equilibrium analyses are mostly used for stability calculations, taking into consideration the driving and retaining forces along the entire slope, and resulting in one single scalar equation. The driving forces are generated by weight and seepage (and building machines in the construction stage), the retaining ones by friction, adhesion (which has to be assumed very carefully, if at all) and, if necessary for stability by the retaining force in the geogrid (Figure 1).

Despite some details, all calculation methods of this type usually have a common characteristic: all elements of the multilayered system are assumed to be absolutely stiff. Only force equilibrium is being analysed without taking into account displacements and strains.

Strictly speaking, such a concept is not fully correct (Long et al., 1994; Alexiew, 1994) Displacement compatibility (say limitation of sliding displacements in this case) is an important matter. Large displacements could result in reduction of interface shear resistance from 'peak' to 'residual' values, followed by loss of stability, or in tension stresses in the underlayered geomembrane, which is usually not allowed, etc.

Consequently, not only the strength, but the strain of a geogrid can control the design.



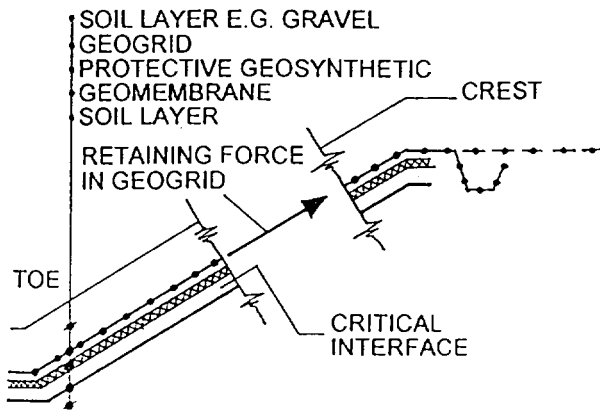


Figure 1. Geogrid reinforcement against sliding: typical case

From the theoretical point of view the ideal geogrid should mobilize the maximum tensile force at nearly zero strains, and should have zero additional long-term strain due to creep. Note, that the second condition (low creep) is more important (Alexiew, 1994), because the major part of short-term strains takes place usually during installation of the soil layer (Figure 1) by heavy equipment. During this process the layer tends to slide, and stresses the geogrid. In this way, until end of construction, the short-term strains are 'pre-consumed', tacitly compensated, and thus, of secondary importance. So, for a veneer slope, after completion only creep strain under the long-term constant load is of importance. Basal slopes are stepwise additionally loaded even after completion of drainage layer by the waste being filled, thus alternately short-term and creep strains can take place.

Geogrids, meeting perfectly all the 'ideal' conditions mentioned above, are not available yet. Nevertheless, a classification can be made in order of best-fitting the 'ideal geogrid':

- aramid (both short-term and long-term strains (creep) are extremely low);
- high-tenacity polyester (short-term strain is relatively low, long-term strain (creep) is very low);
- high-density polyethylene, drawn (short-term strain is low, long-term strain (creep) is relatively high).

### 2.3 Influence of Temperature

At the basal slopes of municipal waste disposals relatively high temperature can develop due to biological degradation of waste. Increasing temperature reduces the moduli and increases the creep tendency of geosynthetics, resulting in higher strains or creep rupture without increase of external load. Aramid and high-tenacity polyester are nearly insensitive to this phenomenon; for polyethylene and polypropylene the reduction of moduli and the increase of creep are noticeable.

## 2.4 Reliability of Design Calculations

As stated earlier, the most calculation procedures to determine the required force in the geogrid on a slope are based on simple equilibrium analyses. Advanced FEM-analyses are used by way of exception. Note, that the scatter of input parameters for design are of great importance for the results (e. g. required reinforcement force), and may have even a greater influence than the calculation method itself. In particular, a really exact stability calculation of a landfill basal slope seems very difficult because of feature of waste (scattering parameters, compaction, unsteady seepage etc.) Thus, assumptions and safety factors have to be set on the safer side (resulting in a stronger geogrid).

## 3. LANDFILL BÖSCHISTOBEL: STEEP MULTILAYERED BASAL SLOPES

### 3.1 Project Description

The landfill Böschistobel in the region Vorarlberg in Austria is located at the base of a steep mountain slope. This circumstance results in steep (1V:2H) and long (up to 160 m) slopes for nearly the half of the landfill area (Figure 2 and 3). The interface 'protective non-woven / HDPE liner' controls the sliding stability. The latter is insufficient not only due to slope steepness, but additionally due to horizontal base inclination required for drainage.

The slope multilayered system (Figure 4) is being constructed up from berm to berm depending on the filling of waste. More informations can be found in Fock and Plankel, 1996.

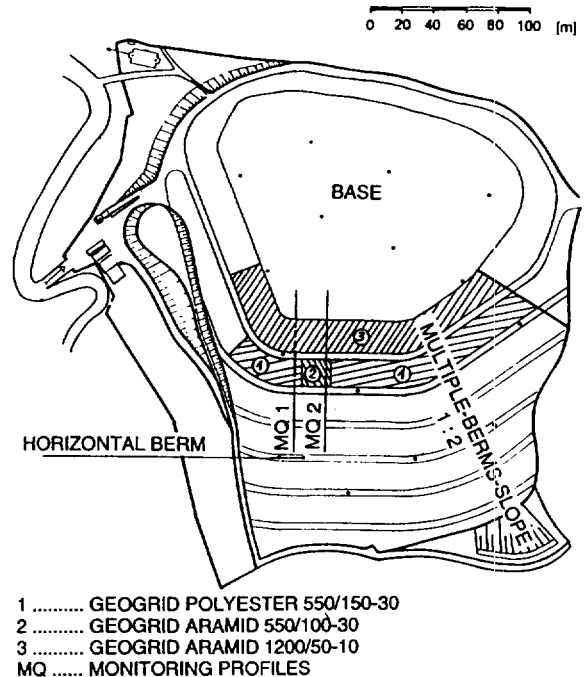


Figure 2. Situation of the Landfill

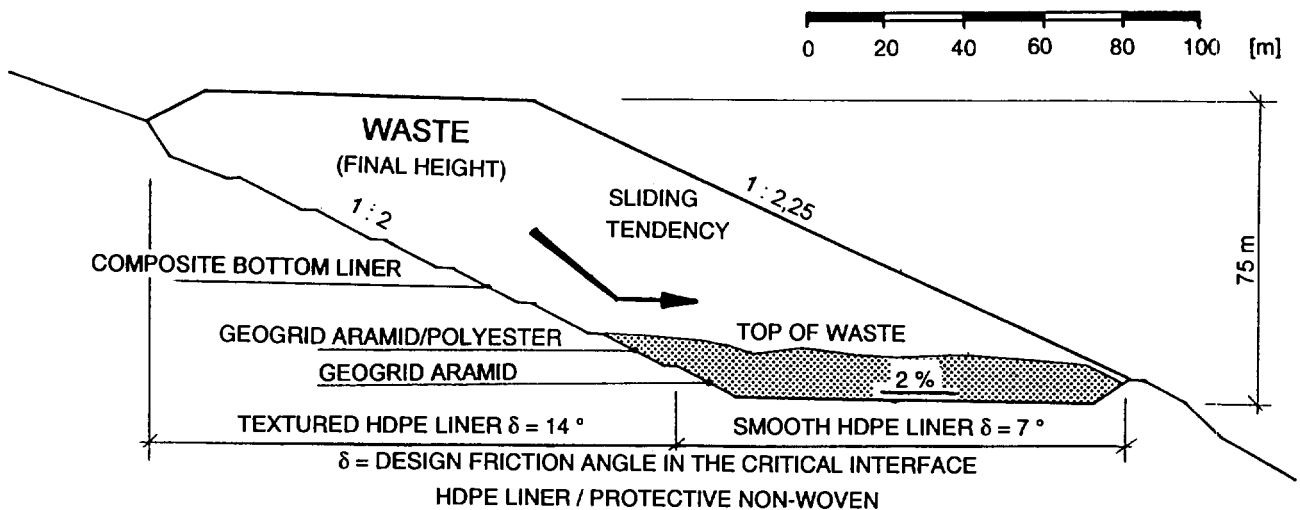


Figure 3. Multiple-Berms-Slope-Design, Cross Section

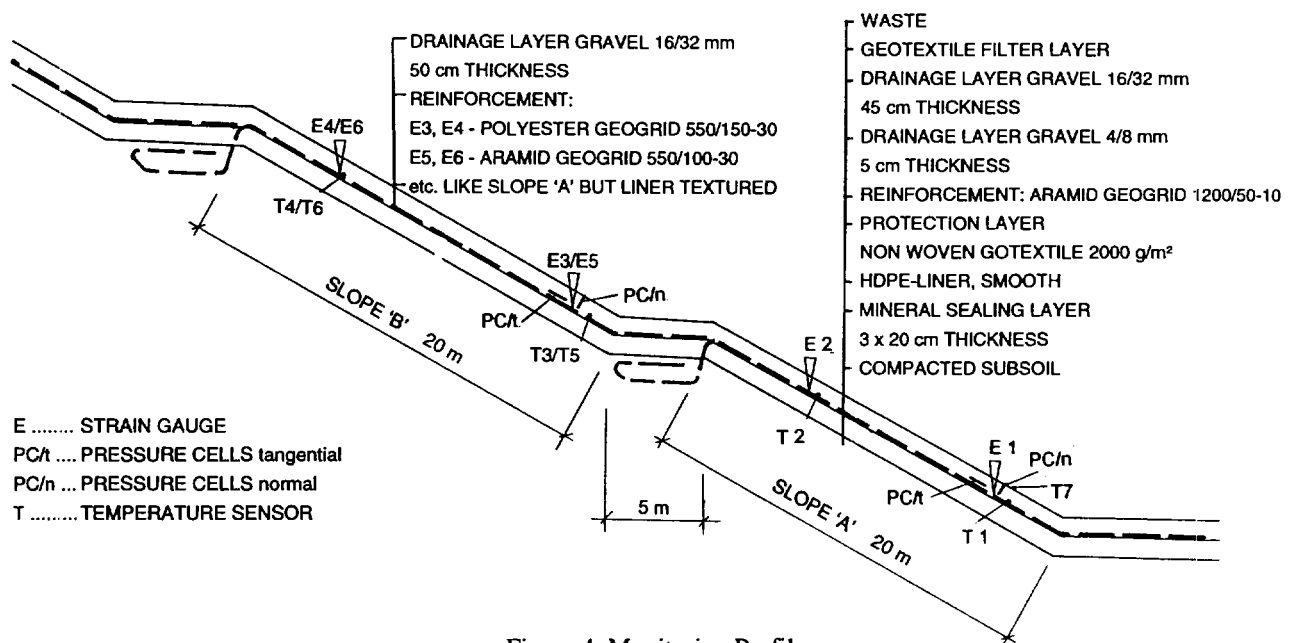


Figure 4. Monitoring Profile

Two groups of stability analyses have been performed. The first one comprises only the local sliding stability of the slope with the drainage gravel layer. The second one comprises the global stability of slope, base and waste fill for different stages. The analyses resulted for slope 'A' (Figure 4) in a geogrid with 1200 kN/m ultimate tensile strength (UTS), and for slope 'B' in a geogrid with 550 kN/m UTS.

### 3.2 Aramid Geogrids

For the entire slope 'A' (Figure 4 and position 3 in Figure 2) an aramid geogrid with 1200 kN/m UTS (Fortrac® 1200/50-10) was selected.

This geogrid had been primarily developed and applied to solve problems with overbridging sinkholes already in 1993 (Alexiew, 1997), being the first one in this class of strength. For slope 'B' an aramid geogrid with an UTS of 550 kN/m (Fortrac® 550/100-30) was chosen (position 2 in Figure 2), and a polyester geogrid with 550 kN/m UTS also on adjacent sections.

Both aramid geogrids are knitted (unfortunately, in Fock and Plankel, 1996, they are incidentally described as woven). Even the 1200-geogrid meets the criterion (IGS, 1996) for constituents to be thinner than the mesh size.

The exact stress-strain curves of the geogrids are shown in Figure 5.

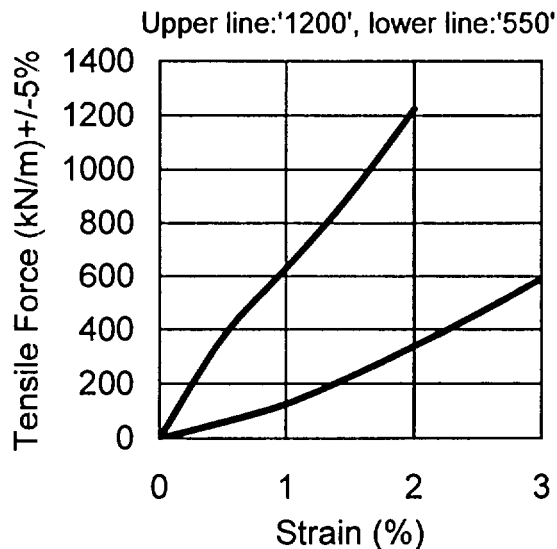


Figure 5. Stress strain curves for the aramid geogrids 550 and 1200

Due to their mechanical behavior (very high tensile stiffness and very low creep strain) the aramid geogrids are close to the 'ideal' as mentioned in Section 2.2. Although the stability analysis applied does not take into consideration displacements and elongation, limitation of deformations to a possible minimum has been an important aim of design in this case according to the considerations in Section 2.2.

### 3.3 Measurement Program

At the slopes of the landfill Böschtobel a measurement program is being performed. The focal point in this paper is the behavior of the sections with the aramid geogrids: for the aramid geogrid 1200 the lower part (slope A) of the measurement profile MQ 1 on Figure 2, and for the aramid geogrid 550 the upper part (slope B) of MQ 2 in Figure 2.

The aims are:

- to register the strains of both aramid geogrids;
- to monitor the pressures in the gravel layer normal and parallel to the slope plane;
- to register the temperature in the geogrid-reinforced gravel layer (upper and lower side).

The data should clarify the real behavior of the aramid geogrids (e.g. are they really minimizing deformations on the slopes under increased temperature also), the correctness of design assumptions and simplified dimensioning procedures. The strains of the geogrids are measured by strain gauges fixed directly on them, with a measurement basis of 1000 mm and 0.01 mm sensitivity, which is important for high-modular geogrids. The pressures in the gravel layer are monitored by pneumatic cells both normal and tangential to the slope. The measurements were started in January 1996 parallel to waste filling. The gauges are depicted in Figure 4.

Because the filling of waste progresses slower than expected, a final data set is not available yet. Nevertheless, the

data are presented so far because of the lack of any information on the behavior of extremely high-strength geogrids under the conditions described.

### 3.4 Test Results and Preliminary Analysis

The bulk density of the waste was determined by a comparison of volume and registered weight. The waste volume in different stages of the filling was determined by geodetical survey. The average bulk density amounts to  $\gamma = 10 \text{ kN/m}^3$  and  $\gamma = 11 \text{ kN/m}^3$  for lower and larger fill heights, respectively. Thus, for the 'vertical load' lines in Figures 7 and 8  $\gamma = 10 \text{ kN/m}^3$  is set. Note, that for design calculations  $\gamma = 12 \text{ kN/m}^3$  has been assumed.

Filling of waste and temperature on top (T 1) and bottom (T 7) of the drainage layer is shown in Figure 6. After a rapid raise of temperature within the first two months the temperature stayed almost constant during a period of 1.5 years. The temperature sensor on the geogrid (i.e. bottom of the drainage layer) shows values from 30 to 36 °C, the sensor on top of the drainage layer shows temperatures from 32 to 39 °C.

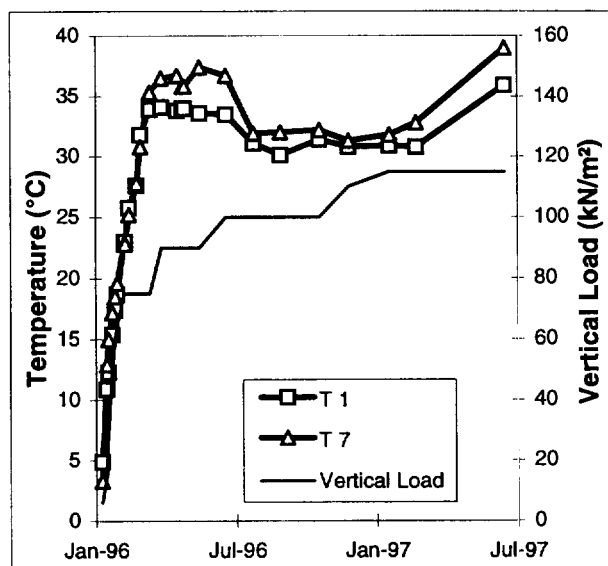


Figure 6. Development of temperature and vertical load

The strains reached a maximum of  $\epsilon = 0,61 \%$  in the aramid geogrid 1200/50-10 on slope 'A' at a vertical load of approximately  $120 \text{ kN/m}^2$  (Figure 7). Although in winter 1996/97 the load was increased by 15 - 20  $\text{kN/m}^2$  (i.e. 15 - 20 %) the strain in the geogrid did not increase significantly. Under 'vertical load' the vertical load just over the points E 1 and E 5 respectively is mentioned.

In the aramid geogrid 550/100-30 (slope 'B') the strains reached a maximum of  $\epsilon = 0,32 \%$  at a vertical load of  $50 \text{ kN/m}^2$  (Figure 8).

At the beginning of the filling of waste strains increased rapidly up to 0,2 %. From July to December 1996 strains increased up to  $\epsilon = 0,28 \%$  without increasing of load.

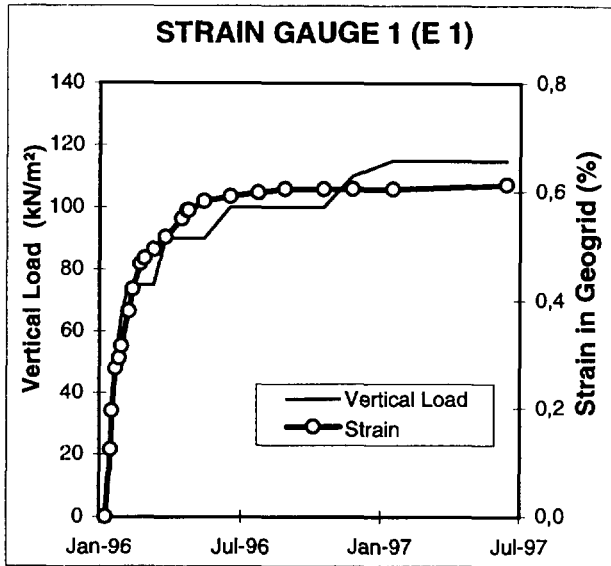


Figure 7. Development of vertical load above E 1 and strain in geogrid 1200/50-10

After December 1996 the load was increased by approximately 12 kN/m<sup>2</sup> (i.e. ~ 20%), the strains in the geogrid increased only by 10 - 15 %.

It is known, that the aramid geogrids used are practically insensitive to the registered temperatures of about 30 °C to 35 °C and to creep/relaxation also for the period treated. Therefore, the short-term stress-strain relations may be used to determine the tensile forces in this case exactly enough for engineering purposes.

Accordingly, the tensile force is around 400 kN/m for slope A and around 45 kN/m for slope B. The corresponding stress ratio SR (=mobilized force/UTS) amounts to SR<sub>A</sub> = 30 % (geogrid 1200) and SR<sub>B</sub> = 8 % (geogrid 550). Thus, the relation of stress ratios is SR<sub>A</sub>/SR<sub>B</sub> = 30 %/8 % = 3.75.

On the other hand, the ratio of mobilized force vs. vertical load (say waste height above measurement point)  $\zeta$  is for slope A  $\zeta_A = 400/115 = 3.48$  and for slope B  $\zeta_B = 45/50 = 0.90$ , respectively (dimensions are intentionally ignored). Thus, the relation  $\zeta_A/\zeta_B$  amounts to  $3.48/0.90 = 3.87$ , which is nearly equal to 3.75 (=SR<sub>A</sub>/SR<sub>B</sub>, see above). Consequently, the registered response of both aramid geogrids is analogous, and data sets harmonize well.

For slope A the stress ratio of about 30 % is in acceptable agreement with the simplified calculation methods, parameter assumptions and (relatively conservative) factors of safety applied in design (Sections 2.4 and 3.1).

For slope B the registered stress ratio of around 8 % is surprisingly low to date, and the value of  $\zeta_B$  also. Underestimation of shear interface resistance on the textured HDPE-liner here, or overestimation of the load by waste could be the reasons. It is quite possible that the waste redistributes the load downslope, or that the geogrid needs more time for full response corresponding to 'delayed' waste self-compaction. The development of load by waste, geogrid strain

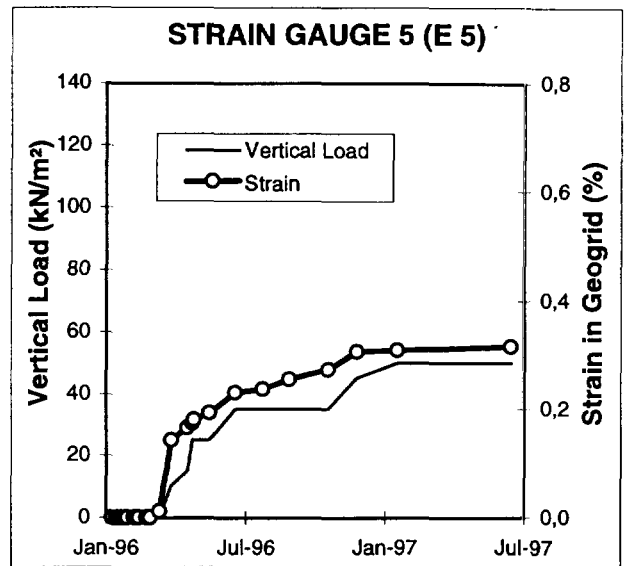


Figure 8. Development of vertical load above E 5 and strain in geogrid 550/100-30

and stresses in the gravel are shown in Figure 9 for the zone E 5 (Figure 4). The pressure cells indicate a 'delayed' increase of stresses without increase of waste height, in the same periods, which seems to be an indication of time-depending redistributions in the waste.

A vertical load (i.e. weight of waste) of 50 kN/m<sup>2</sup> should result in a pressure normal to the slope plane of  $\sigma_n = 50 \cos 26,5^\circ = 44,7$  kN/m<sup>2</sup> and pressure parallel to the slope plane of  $\sigma_t = 50 \sin 26,5^\circ = 24,4$  kN/m<sup>2</sup>. The measurements in June 1997 show values of  $\sigma_n = 55$  kN/m<sup>2</sup> and  $\sigma_t = 19$  kN/m<sup>2</sup>, indicating a good correspondence with theoretical values (with some delay).

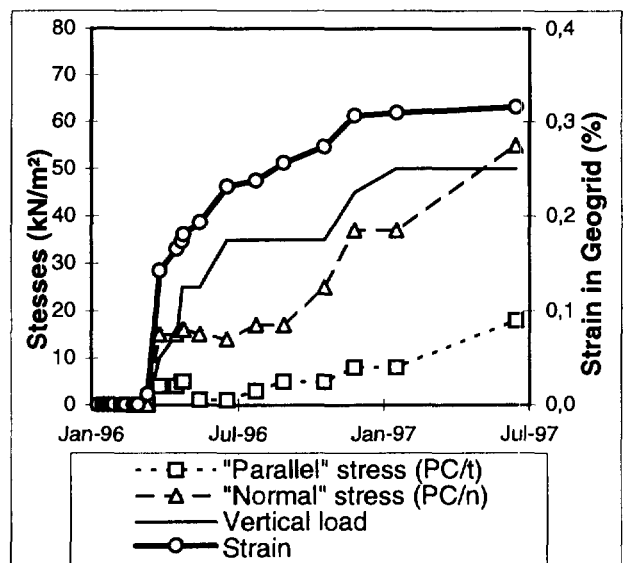


Figure 9. Development of strain, tangential pressure, normal pressure and vertical load above E 5

#### 4. CONCLUSION

Aramid geogrids with 1200 kN/m and 550 kN/m UTS and ultimate strain of 2 % to 3 % have been used for the first time on steep landfill basal slopes.

The aim is to ensure local (gravel layer) and global (waste fill) stability against sliding at low displacements. Pressures, strains and temperature are being measured.

The following conclusions can be made to date:

- the geogrids used really ensure sufficient stability at very low displacements at increased temperatures
- the good agreement of geogrid strains in the drainage gravel layer and progress of waste falling on it indicates a perfect bond of the geogrids
- the stress ratio of the 1200-geogrid on a slope with smooth HDPE-liner corresponds well to the design assumptions; the simplified design calculations (equilibrium of forces only, displacement compatibility ignored) seem to be acceptable, at least for the extremely high-modulus reinforcement used
- the stress ratio of the 550 geogrid on a slope with textured HDPE-liner is lower than expected; high interface shear resistance and/or downslope waste load redistribution could be the reasons
- the measured pressures in the drainage layer correspond well with the calculated ones by simple equilibrium analyses.
- the temperatures in the drainage layer are relatively low for a municipal landfill base (convection on the slope)

The measurements are going on. Further long-terms data will be reported later.

#### REFERENCES

- Alexiew, D., (1994) "Bemessung geotextiler Bewehrungselemente für Dichtungssysteme auf geneigten Flächen", 10. Fachtagung 'Die sichere Deponie', Süddeutsches Kunststoff-Zentrum, Germany, Conference Proceedings, SKZ 1994, pp. 197 - 212.
- Alexiew, D., et. al., (1995) "On the Slope Stability of Landfill Capping Seals Using GCL's", *International Symposium on Geosynthetic Clay Liners, Nürnberg, Germany*, Conference Proceedings, Balkema, Rotterdam, 1995, pp. 151 - 158.
- Alexiew, D., (1997) "Bridging a Sink-Hole by High-strength High-modulus Geogrids", *Geosynthetics '97, Long Beach, USA*, Conference Proceedings, Vol. 1, pp. 13 - 24.
- Alexiew, D., Sobolewski, J., (1997), "Effiziente Oberflächenabdichtung - zwei Praxisbeispiele für steile Deponieoberflächen", 1. Österreichische Geotechniktagung, Wien, 1997, Conference Proceedings, pp. 317 - 336.
- DB AG - TL 918 039, 1997, "Technische Lieferbedingungen 'Geokunststoffe'", Issue April 1997.
- Fock, G., Plankel, A., (1996), "Case Study on Geogrids to Prevent Sliding of Waste in a Landfill", *Geosynthetics: Applications, Design and Construction, De Groot, den Hoedt & Termaat (eds), 1996, Balkema, Rotterdam*, pp. 537 - 540.
- Gartung, E., 1995, "German Practice in Landfill", *IGS Landfill Containment Seminar, Glasgow 1995*.
- IGS, 1996, "Recommended Descriptions of Geosynthetic Functions, Geosynthetic Terminology, Mathematical and Graphical Symbols", p. 4.
- Van Impe, W.F., et. al., 1996, "Waste Disposal and Containment", *Second International Congress on Environmental Geotechnics, Osaka, Japan, 1996*.
- Koerner, R.M., 1994, *Designing with Geosynthetics, Third Edition, Prentice Hall, Englewood Cliffs, New Jersey 07632, 1994*.
- Long, J.H., et. al., 1994, "Geosynthetic Loads in Landfill Slopes: Displacement Compatibility", *Journal of Geotechnical Engineering, Vol. 120, No. 11, 1994*, pp. 2009 - 2025.
- Mannsbart, G., 1996, "Reinforcing Geotextiles for the Slope of a Waste Disposal Site", *Geosynthetics: Applications, Design and Construction, De Groot, den Hoedt & Termaat (eds), 1996, Balkema, Rotterdam*, pp. 541-544.
- Martin, J.S., Simac, M.R., 1995, "The Design and Construction of 168-Meter-Long Geogrid Reinforced Slopes at the Auburn, N.Y., Landfill Closure", *Geosynthetics '95, Nashville, USA, Conference Proceedings*, Vol. 2, pp. 771 - 784.

# Landfill Closure Using Reinforced Soil Slopes

Kenneth W. Cargill

Associate, GeoSyntec Consultants, Atlanta, Georgia, USA

Kara L. Olen

Formerly of GeoSyntec Consultants, Atlanta, Georgia, USA

**ABSTRACT:** Through the innovative use of reinforced soil slopes and a shingled geomembrane liner, a steep-sided hazardous waste landfill was capped in an economical manner. This paper presents a case history describing the technical solution to the difficult task of construction of a capping system over a steep waste mound which was up to 42 m above the surrounding ground surface and where only limited regrading was possible. Stability issues associated with the design of reinforced soil slope modules and the arrangement of modules to achieve global stability are discussed.

**KEYWORDS:** Caps and closures, Case study, Geogrids, Reinforcement, Steep slope.

## 1 INTRODUCTION

The Town of Babylon Landfill is located in Suffolk County, Long Island, New York. The site, an inactive hazardous waste landfill, covers approximately 19 ha and has waste deposits down to 21 m below and up to 42 m above the surrounding ground surface. The steepness of existing waste slopes, some of which were up to 1 horizontal to 2 vertical (1H:2V) and which averaged steeper than 2H:1V, prevented capping using a conventionally designed final cover system due to restrictions on waste regrading. Regrading of the landfill to achieve slopes on which a conventional cover system could be constructed was not possible due to limits on the final landfill height and lack of alternate landfilling locations for the excavated waste.

In consultation with the New York State Department of Environmental Conservation (NYSDEC), an innovative system of reinforced soil slopes was selected from alternatives presented in a focused feasibility study (GeoSyntec, 1992). The Record of Decision described these slopes as, *"...a multiple-tiered reinforced soil wall bench system. Each bench will be covered with a final cover system..., using a geomembrane as the hydraulic barrier, with additional geomembrane sections incorporated within the reinforced soil walls to create a shingled hydraulic barrier over the covered slopes."*

The final closure system design for the steeper slope sections incorporated a shingled geomembrane within

geogrid-reinforced soil slope modules. The project included a total length of approximately 4,300 m of these modules which were up to 6.1 m high. In the most critical section, the reinforced soil slope modules were stacked to a total height of about 36 m. The design minimized infiltration of precipitation and release of landfill gas even though the geomembrane was not continuous throughout the cap. A discussion of the final closure system in conventionally capped areas and how the total system functioned to minimize infiltration, control landfill gas release, and manage surface-water runoff is presented elsewhere (Cargill and Olen, 1997). The area of final closure at the Town of Babylon Landfill is shown in Figure 1 where reinforced soil slopes are highlighted.

## 2 REINFORCED SLOPE MODULE DESIGN

While stability is the most important factor in the design of the reinforced soil slopes, other factors also played a role in the final selection of a slope cross section profile at the Town of Babylon Landfill. Minimization of excavation was required due to the classification of the landfill as a Class 2 inactive hazardous waste site. Minimization of waste excavation required consideration of additional fill requirements, landfill boundaries, and cost. These requirements were optimized in the final design by establishing and using a variety of soil slope standard sections, or modules, which could be stacked as required to closely match the existing slopes.

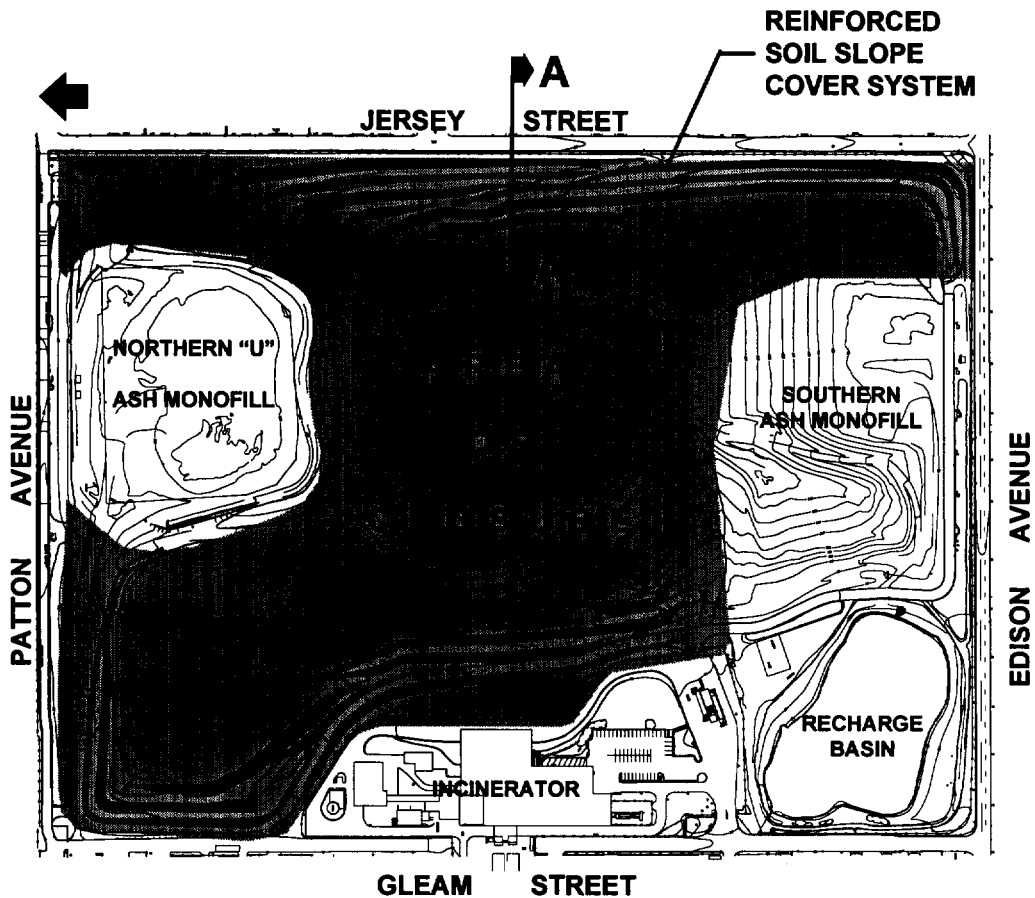


Figure 1. Town of Babylon Landfill area of closure and location of reinforced soil slopes.

These modules were first designed for individual stability and then assembled into stable configurations of multiple modules best fitting the existing landfill slope and also minimizing both required excavation and placement of additional fill behind the reinforced soil slopes. The face slope of the three basic modules used in the design are 1H:2V, 1H:1.5V, and 1H:1V. A standard maximum height of 6.1 m was chosen for the modules in order to comply with the state requirements (NYSDEC, 1988) that the vertical distance between drainage swales not exceed 6.1 m for slopes steeper than 3H:1V. A standard top bench width of 6.1 m was selected to provide space for a drainage swale between the slope shoulder and the toe of the next slope module. This width also provided space for equipment to maneuver

during slope construction and access for vehicles during post-closure maintenance.

The arrangement of the various slope modules was dependent on the geometry of existing landfill slopes on which they were built. Where possible, preference was given to building steeper modules at the lower elevations and less steep modules higher on the landfill in order to provide a more gradual tie-in to the flatter slopes at the top of the landfill. However, the specific geometry of the existing slopes often were better suited to a configuration of steeper slopes at the higher elevations. Thus, the final design contained both configurations.

The method of analysis used for design of reinforcement was a two-phase process. First, a preliminary reinforcement design based on the methodology presented in the Federal Highway

Administration (FHWA) Geotextile Engineering Workshop (1989) was performed. The FHWA method is based on design charts from which a horizontal tensile reinforcement force and length of reinforcement are calculated. Second, the preliminary design was analyzed in detail by the methodology incorporated in the computer slope stability program XSTABL (Sharma, 1992). The purpose of the detailed design was to minimize the module section, and thus minimize any required waste excavation, and to check the actual factor of safety based on selected reinforcement length and spacing. If the actual factor of safety did not meet the required minimum factor of safety, reinforcement spacing and lengths were adjusted and the second step repeated.

Material properties selected for the reinforced soil slope design were based on laboratory testing of locally available soils and typical geosynthetic reinforcement strengths. The laboratory testing of a bank-run, silty sand from a local pit indicated a minimum friction angle,  $\phi$ , of  $31^\circ$  and a cohesion intercept of  $184 \text{ kN/m}^2$ . For the slope design,  $\phi = 31^\circ$  and  $c = 0 \text{ kN/m}^2$  were used. The allowable geosynthetic tensile strength selected for design after reduction for creep and other typical factors of safety for construction and environmental factors was  $20.4 \text{ kN/m}$ . Based on a review of geosynthetic product literature, this value was considered reasonable and attainable. As a part of the contract specifications, the contractor was required to submit evidence that the geosynthetic reinforcement used met the minimum allowable strength. The contractor selected high-density polyethylene (HDPE) geogrids.

### 3 MODULE STABILITY

Each of the slope modules was initially designed for a minimum factor of safety of 1.25. This factor of safety was recommended in the focused feasibility study and approved by NYSDEC. It was considered adequate since the reinforced slopes were constructed on existing stable waste slopes and a detailed program of construction quality assurance was planned. The actual factor of safety was greater than the design value of 1.25 because of the actual number of geosynthetic reinforcement layers. The final factor of safety for each module was calculated based on the required tension forces indicated by the XSTABL analysis.

The preliminary maximum reinforcement spacing for each module was calculated using the FHWA method for a  $FS = 1.25$  and resulted in the following:

Module	Upper 2/3 of Slope	Lower 1/3 of Slope
1H:2V	1.36 m	0.82 m
1H:1.5V	1.84 m	1.10 m
1H:1V	2.83 m	1.70 m

In order to use the reinforcement efficiently, a secondary reinforcement was specified to wrap individual steps in the slope face and where primary reinforcement was not required. To maintain a uniform slope appearance and provide slope face stability and erosion resistance, a maximum secondary reinforcement spacing of 0.46 m was selected. The final spacing selected for primary reinforcement was:

Module	Upper 2/3 of Slope	Lower 1/3 of Slope
1H:2V	0.91 m	0.46 m
1H:1.5V	1.37 m	0.91 m
1H:1V	1.37 m	1.37 m

Using the above final primary reinforcement spacing and a reinforcement length of 3.96 m, the factors of safety for reinforcement and for block sliding of the slope modules was calculated by XSTABL. Results of the calculations are summarized below:

Module	Reinforcement Factor of Safety	Sliding Block Factor of Safety
1H:2V	2.6	2.5
1H:1.5V	2.0	1.8
1H:1V	2.0	1.3

### 4 MODULE CONSTRUCTION

Figure 2 shows the arrangement of the primary and secondary reinforcement in a slope module. The primary reinforcement consisted of a uniaxial HDPE geogrid and the secondary reinforcement was a biaxial HDPE geogrid. The shingled geomembrane hydraulic barrier, gas management components, and the drainage swale atop each module are also indicated in the figure.



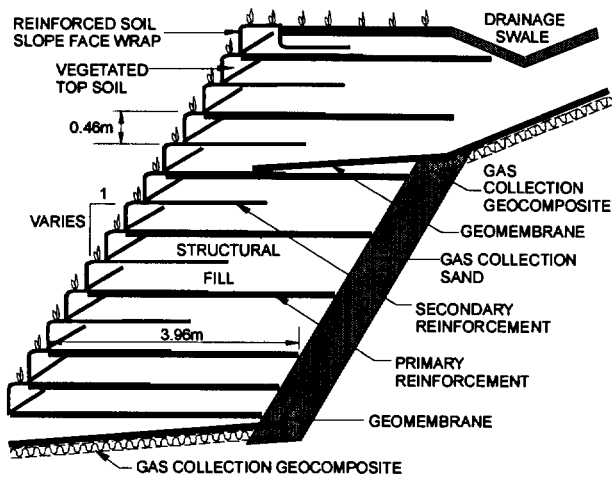


Figure 2. Slope module geometry and reinforcement arrangement.

The secondary reinforcement was installed at each slope face setback and was used to wrap the slope face for erosion protection as shown in Figure 3. Figure 3 also shows how the secondary reinforcement was used to wrap the slope face and support a wedge of topsoil within a seeded erosion control mat until vegetation could be established.

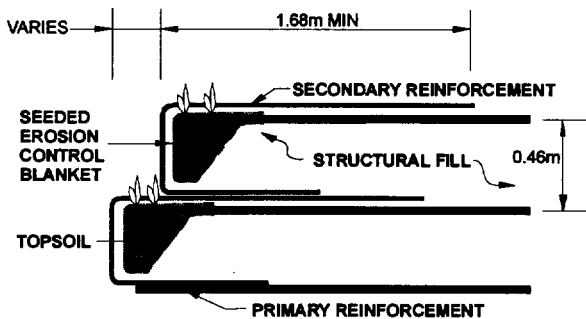


Figure 3. Typical reinforced soil slope face wrap.

Slope face support during construction was provided by a welded wire fabric which was allowed to remain in place after construction. Figure 4 shows the wire mesh formwork and initial vegetation on the slope face.



Figure 4. Reinforced soil slope faces with secondary reinforcement wrap and wire mesh formwork.

A reinforced soil slope module under construction is shown in Figure 5. This module is located on the eastern side of the landfill. The level of primary and secondary reinforcement shown in the photograph is approximately 10 m above the street level shown on the right in the photograph and illustrates the proximity of the landfill to the public road. The reinforcement is in the second module going up the slope.



Figure 5. Module construction on eastern landfill slope looking north.

The system of reinforced soil slope modules under construction on the western slope is shown in Figure 6. The photograph illustrates the proximity of the landfill to the incinerator facility shown on the left in the photograph and the existing slope steepness.

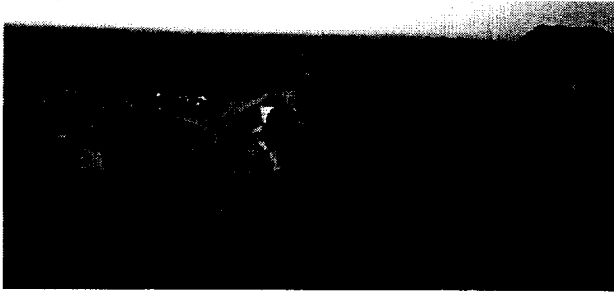


Figure 6. Module system construction on western landfill slope looking north.

## 5 GLOBAL STABILITY

The final arrangement of the reinforced soil slope modules in plan view for the Town of Babylon Landfill is shown in Figure 1. Once the system of reinforced soil slope modules was assembled in the most efficient manner for cut and fill minimization, the global stability of the overall slope was also calculated using XSTABL. For this calculation, a waste strength of  $\phi = 28^\circ$  and  $c = 5 \text{ kN/m}^2$  was used. This waste strength was selected based on published values (Landva and Clark, 1990, Singh and Murphy, 1990) and a back analysis of several existing

slopes at the Town of Babylon Landfill. A critical cross section of the assembled reinforced slope modules on the eastern side of the landfill as indicated by Section AA in Figure 1 is shown in Figure 7 along with the trace of the potential failure surface. The calculated factor of safety for this surface was 1.3.

A photograph of the completed reinforced soil slopes on the eastern side of the landfill looking west is shown in Figure 8. Three soil slope modules are shown stacked in the photograph. A photograph of the completed reinforced soil slopes on the western side of the landfill looking north is shown in Figure 9. This is approximately the same area shown in Figure 6 during construction. Also seen in the photograph is the layout of drainage swales and downchutes for storm water management of the landfill final closure system.

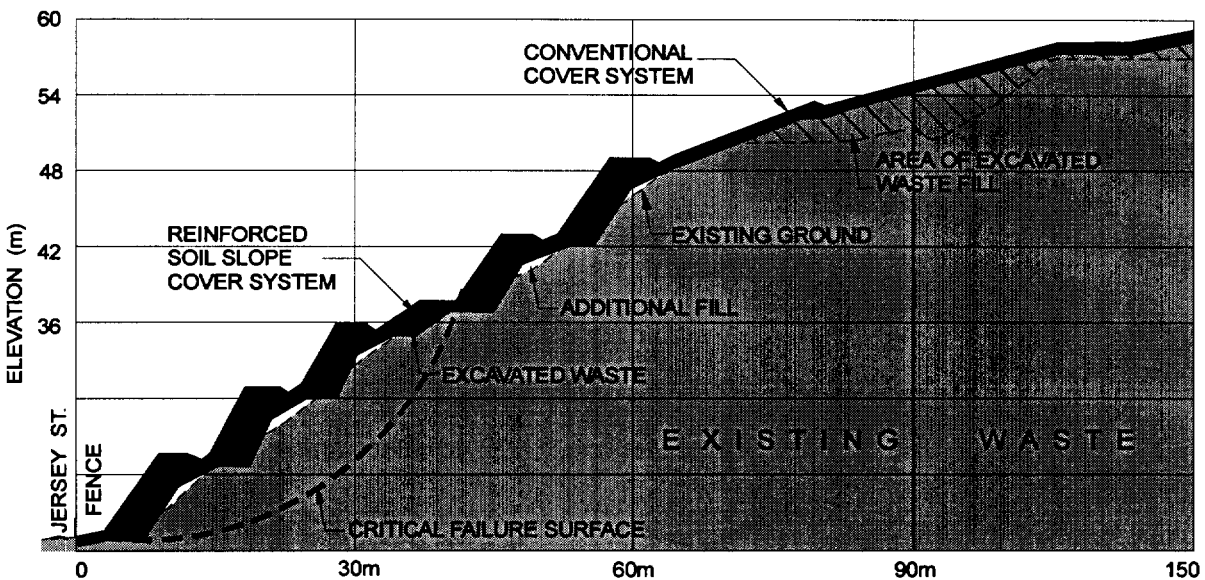


Figure 7. Critical cross-section through waste mound. (Section AA from Figure 1.)

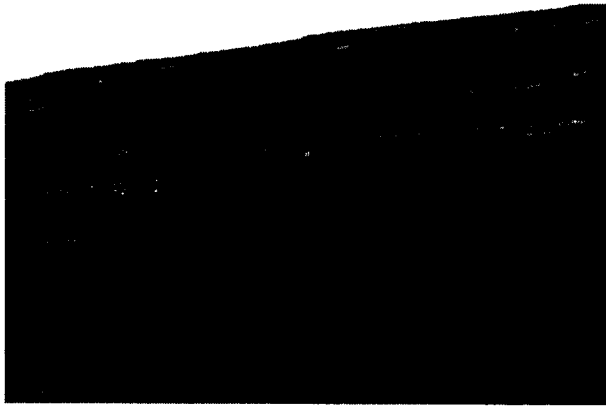


Figure 8. Completed reinforced soil slope on the eastern side of the landfill looking west.



Figure 9. Completed reinforced soil slopes on the western side of the landfill looking north.

## 6 CONCLUSIONS

This paper has presented a case study of how geosynthetic reinforced soil slopes were used as a component of a final closure system for a hazardous waste landfill. Through an arrangement of individually stable reinforced soil slope modules, excavation of waste was minimized and global slope stability was maintained. The reinforced soil slopes containing a shingled geomembrane functioned with conventionally capped waste areas to minimize landfill gas release and control surface water runoff. The design illustrates an innovative use of reinforced soil slopes which regulatory agencies and designers should consider for application at other sites with existing steep slopes and where excavation must be minimized.

## ACKNOWLEDGEMENTS

The support of GeoSyntec Consultants during the preparation of this paper is gratefully acknowledged. In addition, the authors wish to thank Ann Taylor for assistance in preparation of figures and Joyce Thomas for preparation of text.

## REFERENCES

- Cargill, K. W. and Olen, K. L. (1997) "An Innovative Final Closure System", 2nd Annual Landfill Symposium, Solid Waste Association of North America, Sacramento, California, USA, pp. 79-85.
- GeoSyntec Consultants, P.C. (1992) "Focused Feasibility Study for Closure of the Town of Babylon Landfill", prepared for Town of Babylon, Lindenhurst, NY, USA, 58 p.
- Landva, A.O. and Clark, J.I. (1990), "Geotechnics of Waste Fills", Geotechnics of Waste Fills - Theory and Practice, ASTM STP 1070, Arvid Landva, G. David Knowles, Editors, American Society for Testing and Materials, Philadelphia, PA, USA, pp. 86-103.
- New York State Department of Environmental Conservation (1988) "6 NYCRR Part 360, Solid Waste Management Facilities, Title 6 of the Official Compilation of Codes, Rules, and Regulations", New York State Department of Environmental Conservation, Division of Solid Waste, Albany, NY, USA.
- Sharma, S. (1992) "Slope Analysis with XSTABL", Interactive Software Design, Inc., Moscow, ID, USA, 144 p.
- Singh, S. and Murphy, B. J. (1990) "Evaluation of the Stability of Sanitary Landfills", Geotechnics of Waste Fills - Theory and Practice, ASTM STP 1070, Arvid Landva, G. David Knowles, Editors, American Society for Testing and Materials, Philadelphia, PA, USA, pp. 240-258.
- U.S. Department of Transportation Federal Highway Administration (1989) "Geotextile Engineering Workshop", Publication No. FHWA-HI-89-002, pp. 119-144.

# Geosynthetic Lining Systems Reinforcement by Geosynthetic Inclusion

S. Lalarakotoson

Lirigm, Joseph Fourier University, Grenoble, France

P. Villard

Lirigm, Joseph Fourier University, Grenoble, France

J.P. Gourc

Lirigm, Joseph Fourier University, Grenoble, France

**ABSTRACT:** Slope stability is an important concern in the design of waste containment facilities equipped with sophisticated lining and cover systems. An engineering solution consists of placing a high-strength geosynthetic reinforcement into the cover layer above the low friction angle interface. In order to simulate in situ conditions of geosynthetic lining systems (low confining stress, gravity load control), an experimental research was conducted on an inclined plane apparatus with a large size testing box (100 cm x 70 cm x 30 cm). A numerical simulation of the laboratory experiments with a 2D Finite Element model and a 1D Finite Difference model was also carried out in order to provide a fine interpretation of experimental data.

**KEYWORDS:** Geosynthetic Lining System, Inclined Plane, Geosynthetic reinforcement, Finite Element Method, Finite Difference Method.

## 1 INTRODUCTION

Recent landfills usually include composite systems - more or less complex - made of soil layers (vener, drainage) and geosynthetics (geomembrane, geonet, geotextile) in order to isolate waste from environment.

Low storage capacities or small available areas lead sometimes to the choice of high angles and lengths for the waste fill slopes. This results in a potential sliding failure due to an insufficient shear strength or in an excessive deformation of components which, with a short or long term evolution of geosynthetics and interfaces parameters, can be harmful to the protection function. To avoid stability problems, a solution consists in reinforcing the geosynthetic lining system with a geosynthetic such as a geotextile or a geogrid.

This paper deals with reinforcement by inclusion of a geosynthetic within the soil layer. This technique of reinforcement has been investigated by means of an inclined plane apparatus devised at the Lirigm, which reproduces the field working conditions : low confinement and gravity load control.

Concurrently, two numerical models have been developed in order to provide a fine interpretation of experimental data. Validity of interface characterization on inclined plane device and the fact of taking into consideration interface nonlinearity in the models are evaluated by comparison with experimental data.

## 2 THE LABORATORY MODEL

The diversity of geosynthetics and the versatility of their combinations may increase significantly the complexity of liner systems. Fortunately, it is possible to get an insight into the mechanism of reinforcement by means of a relatively simple scheme.

A schematic side view of the test apparatus is shown in Figure 1.

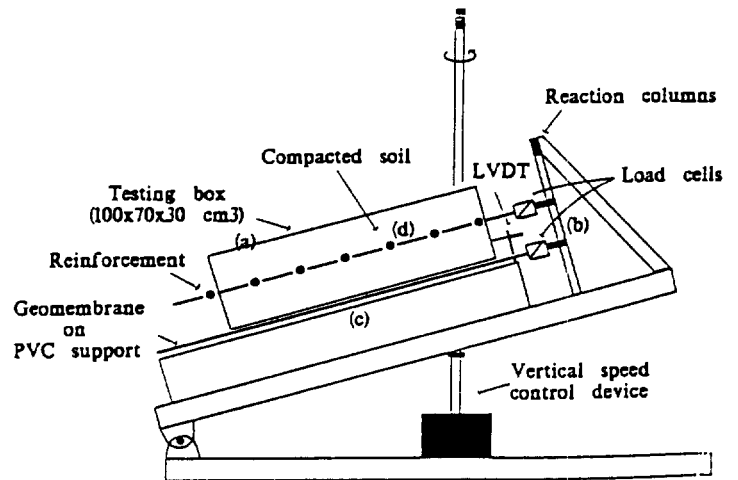


Figure 1. Schematic view of the inclined plane apparatus.

The reference case, ie unreinforced, includes a compacted soil layer filling an orthogonal rigid box (a), a geomembrane placed on a rigid horizontal PVC support and connected to an anchorage device (b). The PVC support is fixed on a tilting base plane (c). The box is supported on the base plane by means of metallic rollers on both sides.

In the present case, the reinforcement consists in placing a geosynthetic halfway up the thickness of the soil (d). The anchorage device allows a variation of the reinforcement vertical position.

The system is sollicitated by tilting progressively the plane at low constant vertical rate (0.5°/mn for an inclination of 30°) - which assures quasi-static conditions. The global state of the system can be described by the angle of plane inclination, the relative displacement of the box and the maximal axial force mobilized within the different geosynthetics. A continuous monitoring of these parameters is made through suitable data acquisition devices.

The main features of the laboratory model are the low confinement which has a great influence on the behaviour of the soil and interfaces, the control by gravity load, the maximal sollicitation of the reinforcement without toe buttress effect which has to be considered in field cases.

The inclined plane apparatus allows also a direct measure of the peak frictional resistance of geosynthetic interfaces under low confinement (2.5 and 5 kPa) and an indirect estimation of the residual friction by means of a compression load cell placed at the toe of the testing box.

### 3 TESTS RESULTS

All tests on reinforcement by geosynthetic inclusion were conducted with the standard sand EN 196-1, at a dense state ( $D_r \sim 80\%$ ). The water content is about 2%.

Three geosynthetics were used as reinforcements :

- a non-woven needle punched geotextile, in PP (Gt TGX),
- a biaxial woven geogrid, in PET (Gg TFM),
- an uniaxial stretched geogrid, in HDPE (Gg TFS).

With these materials, it was possible to investigate the influence of some important parameters as axial tensile stiffness, interaction with soil and bending rigidity (flexibility).

The main mechanical characteristics of the materials and interfaces are summarised in Table 1. Inclined plane apparatus was used for interface characterization (shear stiffness  $k_s$  and friction angles  $\Phi$ ). The two geogrids have comparable axial tensile stiffnesses ( $J$ ) but the Gg TFS is less flexible, due to its structure. Among the 3 geosynthetics, the Gt TGX is the more flexible and extensible material.

Table 1. Mechanical parameters of geosynthetics and interfaces.

Interface	$k_s$ (kN/m <sup>3</sup> )	$\Phi_{peak}$ (°)	$\Phi_{res}$ (°)
Geomembrane/PVC	$10^5$	20	16
Sand/Geomembrane	$10^5$	27	21
Sand/Gt TGX	$10^3$	45	32
Sand/Gg TFM	$10^3$	45	32
Sand/Gg TFS	$10^3$	17	-
<b>Geosynthetic</b>	<b>J (kN/m)</b>		
Geomembrane	125		
Gt TGX	15		
Gg TFM	650		
Gg TFS	650		
<b>Sand (50-150 kPa) <math>C_{peak}=2.5</math> kPa, <math>\Phi_{peak}=39^\circ</math>, <math>\Phi_{res}=32^\circ</math> (<math>\sigma=5</math> kPa : <math>\Phi_{peak} \sim 47^\circ</math> - value extrapolated)</b>			

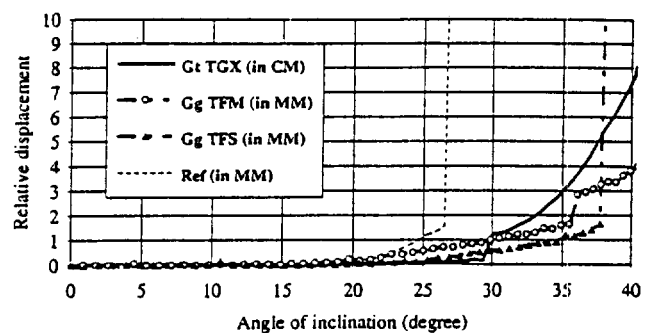


Figure 2. Relative displacement of the testing box for an increasing inclination.

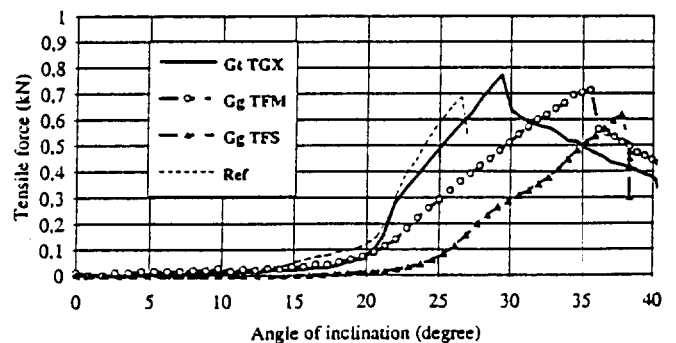


Figure 3. Evolution of the load within the geomembrane.

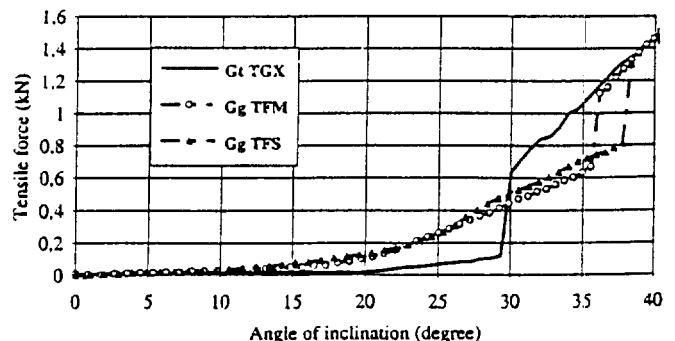


Figure 4. Evolution of the load within the reinforcement.

The test plane is progressively inclined until 40°, the end of the test. In these conditions, general sliding of the testing box was observed before a 40° inclination for the reference case (without reinforcement) and for the Gg TFS unlike the Gt TGX and Gg TFM cases (Figure 2).

The evolution of the relative displacement of the box and the loads developed within the geomembrane and the reinforcement are shown in figures 2-4. The laboratory model response shows an initial phase (low inclination value) with a very low axial force developed within the geosynthetics (Figure 3: geomembrane, Figure 4: reinforcement). The tensile solicitation of the geosynthetics begins for an inclination of about 20°, which corresponds to the Geomembrane/PVC interface peak frictional angle. The maximal tensile force developed within the geomembrane is obtained when the sliding between the sand and the geomembrane occurs (comparison between figures 2 and 3). After the initiation of the sliding process, a more effective solicitation of the geosynthetic reinforcement and a significant decrease of the geomembrane tensile force can be observed (figures 3 and 4).

- For an inclination less than 27° ( $\beta_c$ : limit of stability without reinforcement), it's worth noting that the tensile mobilization of the geomembrane is significantly mitigated by the existing reinforcement (Figure 3).

Efficiency depends mainly on the reinforcement axial stiffness, as shown clearly. The difference of behaviour between the Gg TFM and the Gg TFS demonstrates the influence of the material flexibility which tends to delay the axial tensile mobilization by an initial lack of reinforcement sheet flatness.

The Sand/Geomembrane sliding produces a threshold on the load carried by the reinforcement (Figure 4). This jump arises from the postpeak nonlinear behaviour of the Sand/Geomembrane interface, as observed with the inclined plane apparatus ( $\Phi_{peak} = 27^\circ - \Phi_{res} = 21^\circ$ ). Load transferred by friction to the geomembrane is partially reported towards the reinforcement. The same jump is also trapped on the evolution of the load carried by both geosynthetics because of the remanence of the viscoelastic geomembrane tensile force (Figure 5).

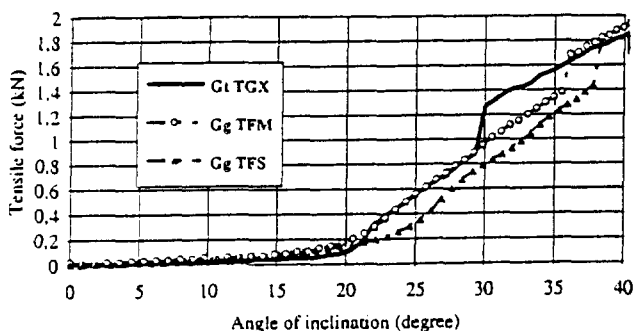


Figure 5. Evolution of the load carried by both geosynthetics.

- For an inclination more than  $\beta_c$ , a partial sliding may occur on the Sand/Geomembrane interface and the main purpose of the reinforcement is the stabilization of the soil layer. The Sand/Reinforcement friction becomes the main parameter as indirectly illustrated by the failure with the Gg TFS which has the lowest friction with the soil (Table 1).

## 4 NUMERICAL SIMULATIONS

Two numerical models of the reinforcement test were built as tools for the interpretation of the experimental data.

Given the smallness of strains observed within the soil and the low solicitation of the geosynthetics, a linear elastic behaviour was assumed for these materials.

To explain the evolution of the load within the components, nonlinear postpeak response of the interface (Dense Sand/Geosynthetic) was roughly idealized by an abrupt drop from peak to residual shear stress level.

### 4.1 The 2D - Finite Element model

The Finite Element mesh used is shown in Figure 6. The model combines continuum element for the soil, bar elements for geosynthetics and zero-thickness - type elements for the discretization of the interfaces.

An elastic perfectly plastic law describes the interface behaviour. The formulation adopted takes into account the postpeak response as indicated above. The improved linear interface element proposed by Kaliakin V.N. and Li J. (1995) is used for interface discretization. It allows, among other, to avoid stability problems with high shear stress gradient.

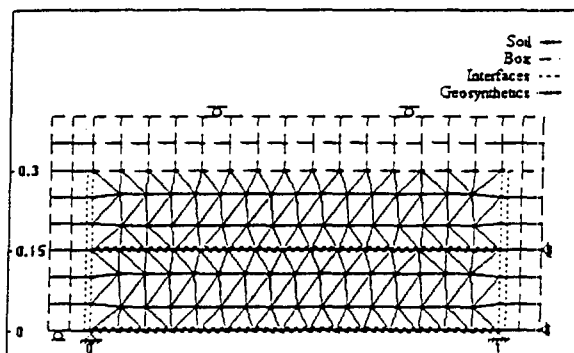


Figure 6. The Finite Element mesh used.

### 4.2 The 1D - Finite Difference model

The principle of reinforcement by inclusion consists in anchoring the soil layer by the reinforcement. The load transfer between the soil and the reinforcement depends on their relative displacement. If an homogeneous

displacement is assumed throughout the thickness of the soil, the reinforced system may be considered as layers connected with interface mechanisms (Figure 7). The Finite Differences method proposed by Gilbert R.B. et al (1993) can then be used for predicting axial load developed in the components.

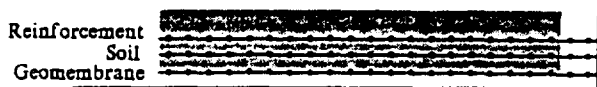


Figure 7. Finite Difference discretization.

This model accommodates easily the interface postpeak behaviour by means of a simple nonlinear Shear Stress/Relative Displacement relation. Interface nonlinearity is integrated by an nonlinear elastic approach which assures displacement compatibility. Unlike the Finite Element model, the load path is not taken into account here.

#### 4.3 Comparison with experimental results

The geosynthetic axial modulus ( $J$ ) (Table 1) used for numerical simulations was obtained from secant modulus of Load-Strain index curve, within the range of solicitation observed with experimentations. The Young's modulus of the soil was extrapolated from triaxial tests in order to take into account the influence of the confinement ( $E = 10^3 \text{ kN/m}^2$ ,  $\nu = 0.3$ ,  $\gamma = 18 \text{ kN/m}^3$ ). The interface normal stiffness ( $kn$ ) was assigned a very high value ( $10^7 \text{ kN/m}^3$ ) to prevent incompatibility in the normal direction.

Globally, the responses of the two models are in agreement with the experimental results. According to the experimental results, the Finite Differences model behaves surprisingly better than the Finite Element model after the partial sliding of the Sand/Geomembrane interface. The difference between the two models is more evident with the Gt TGX in which case the observed sliding is more important (figures 8-9). Such difference informs about the influence of the partial sliding that tends to erase the memory of shear stress mobilization along the interface.

#### 5 CONCLUSION

Tests carried out with inclined plane apparatus showed the effectiveness of reinforcement by geosynthetic inclusion due to a significant increase in the stability angle or a decrease - in a factor down to 3.5 - of the geomembrane tensile force.

Optimal reinforcement working requires a great stiffness of the reinforcement sheet and a sufficient interaction with the soil, basal mechanics being the anchoring of the soil layer by the reinforcement sheet.

The idealization of the nonlinear interface behaviour considered here seems to be sufficient. Nevertheless, it requires accurate characterization of the maximal and residual frictions, which is possible using inclined plane apparatus. For such systems, numerical simulations must take into account the occurrence of partial interface sliding.

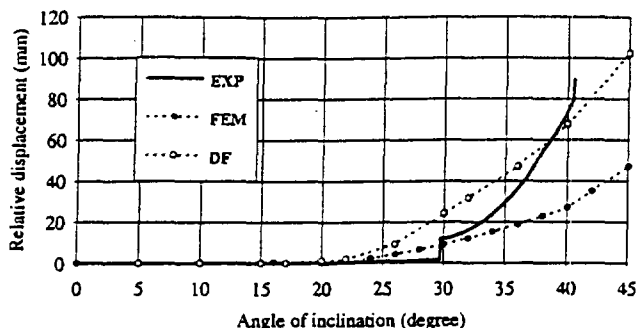


Figure 8. Comparison between the relative displacement measured and calculated (Gt TGX).

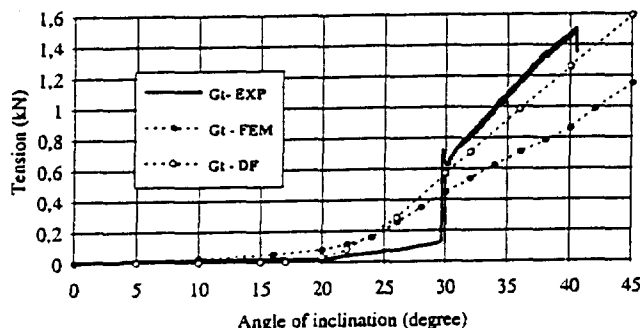


Figure 9. Comparison of the load measured and calculated within the reinforcement (Gt TGX).

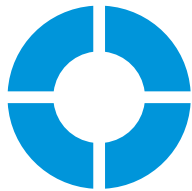
#### REFERENCES

- Gilbert R.B., Long J.H., Daly J.J. (1993). Structural integrity of composite geosynthetic lining and cover systems. *Geosynthetics '93, Vancouver - Canada*, pp. 1389-1401.
- Jewell R.A. (1993). Keynote lecture: Links between the testing, modelling and design of reinforced soil. *Earth Reinforcement Practice, Ochai, Hayashi & Otani (eds), Balkema - Rotterdam, 1993*, pp. 755-772.
- Kaliakin V.N., Li J. (1995). Insight into deficiencies associated with commonly used zero-thickness interface elements. *Computers and Geotechnics, vol.17, 1995*, pp. 225-252.

SPONSORED BY



SOLMAX



agru

The Plastics Experts.



# Design Procedures for Reinforced Soil Walls — A Historical Perspective

R.R. Berg

P.E., Consultant, Ryan R. Berg & Associates, Inc., St. Paul, Minnesota, USA

T.M. Allen

P.E., State Geotechnical Engineer, Washington Department of Transportation, Olympia, Washington, USA

J.R. Bell

Ph.D., P.E., Professor Emeritus, Oregon State University, Corvallis, Oregon, USA

**ABSTRACT:** The progression of analysis procedures, used in the United States, for internal design of geosynthetic reinforced soil retaining walls are summarized in this paper. Procedures are presented in chronological order over the past twenty-four years, to track changes in practice, from first use through current codes. Both the resistance and the load computations, and the combined effect of the two, are examined. It is concluded that large changes in design conservatism have not occurred since first use of geosynthetic reinforced soil walls; and that performance of existing structures is applicable to new design codes and guidelines. This documentation is directed towards researchers, practitioners, and regulators, and gives guidance for future research and development of codes for reinforced soil walls.

**KEYWORDS:** History, Reinforcement, Retaining walls, Safety factors, Reinforcement specifications & guidelines.

## 1 INTRODUCTION

Geosynthetic reinforced soil (GRS) retaining walls were first used in North America in 1974 for construction of geotextile reinforced walls supporting logging roads in northwestern United States. Use of GRS walls have grown steadily since this initial project. Significant increases in the use of GRS walls were realized with the introduction of geogrid soil reinforcement elements in 1982 and with the introduction of segmental retaining wall units in 1985. Today, GRS walls are routinely used on private land development projects and are becoming more commonplace in transportation works. It is anticipated that recent guidelines (Elias and Christopher 1997; FHWA 1997) and codes (AASHTO 1997) for highway works will spur use of GRS walls and that they will be routinely used throughout North American highways.

Growth in usage of GRS walls is partially attributable to the success of constructed works. Confidence in engineering of these walls today is based upon performance of GRS structures to date. To better understand this behavior, it is useful to the engineer to understand how design procedures have evolved over time. Were the successfully performing structures constructed to date designed with procedures more or less conservative than current guidelines and codes? This question is addressed within, specifically for the internal stability of GRS walls, by examining changes in the geosynthetic reinforcement design tensile strength and soil load determination procedures.

## 2 GEOSYNTHETIC TENSILE RESISTANCE

Internal stability analysis of a reinforced soil wall is performed to quantify required strength and vertical spacing of

the geosynthetic reinforcements. A safe, long-term allowable design strength (LTADS) of the geosynthetic reinforcement needs to be quantified for this analysis. Procedures for quantifying LTADS of geosynthetics have evolved over time, as summarized below. Note that connection strength limitations are not addressed, thereby, assuming that connection does not limit LTADS for purposes of comparisons within this paper. Common terminology is used within this paper to present the various procedures. In general, the basic form of the equation used to calculate the LTADS is:

$$LTADS = \frac{T_{ULT}}{RF \times FS} \quad (1)$$

where

$T_{ULT}$  = average value of ultimate wide width strength;

RF = product of reduction factors, or partial factors of safety, to account for creep, installation damage, chemical degradation and biological degradation; and

FS = overall factor of safety for other (e.g., material, geometric, loadings) uncertainties.

### 2.1 Forest Service Procedures

A 1977 U.S. Forest Service (USFS) manual (Steward et al. 1977) documents a design procedure for geotextile walls. The procedures in this manual were used for the design of a forest service wall constructed in 1974 (Bell et al. 1975), the first GRS wall built in North America. The LTADS is computed with Equation 2. The ultimate strength of the geotextile reinforcement (time frame is prior to introduction of geogrids) is measured with the Oregon State University (OSU) ring test. The OSU ring test ultimate tensile strength,

$T_{ult-OSU}$ , is approximately 80% of the wide width tensile strength (ASTM D4595 1986) for nonwoven needle-punched geotextiles. A FS of 1.5 to 1.75 is recommended, with the higher factor generally for use with heavy live loads (e.g., log haul trucks). Reduction factors, RFs, are not used for these temporary walls.

$$LTADS = \frac{T_{ult-OSU}}{FS} \quad (2)$$

## 2.2 Geogrid Procedure

An allowable strength procedure for geogrids was presented in a 1983 (Netlon) manual published in the United Kingdom. This procedure is presented in Equation 3. The creep limited strength,  $T_c$ , is the highest (tested) load level that precludes exceeding 10% strain or rupture, over the design life. An installation damage factor,  $RF_{ID}$ , is used to further reduce the creep-limited strength. This factor is quantified as the ratio of the ultimate strength of undamaged to damaged specimens. An overall factor of safety value of 1.35 is recommended.

$$LTADS = \frac{T_c}{RF_{ID} \times FS} \quad (3)$$

The approach in Equation 3 was modified for North American practice (Tensar 1986), for a particular product. The  $RF_{ID}$  was incorporated into the overall FS, as shown in Equation 4. An overall factor of safety value of 1.5 was recommended for use with Equation 4.

$$LTADS = \frac{T_c}{FS} \quad (4)$$

For the product addressed in the 1983 (Netlon) and 1986 (Tensar) manuals, the LTADS value calculated with Equation 3 is approximately equal to the value computed with Equation 4 for gravelly sand soils.

## 2.3 1987 Task Force 27 Procedure

The Task Force 27 (AASHTO 1990) procedure (implemented as early as 1987) for computing a LTADS uses a partial reduction factor approach (Bonaparte and Berg 1987). The LTADS is the lesser of the following two, limit state and serviceability state, equations.

$$LTADS \leq \frac{T_l}{RF_D \times RF_{ID} \times FS} \quad (5a)$$

$$LTADS \leq \frac{T_w}{RF_D \times RF_{ID}} \quad (5b)$$

Where

$T_l$  = highest tension level at which the creep strain-rate continues to decrease with log-time within the required design lifetime and which precludes brittle or ductile failure;

$T_w$  = tension level at which total strain is not expected to exceed 5% within the design lifetime; and

$RF_D$  = durability reduction factor, 1.10 minimum.

A minimum  $RF_{ID} = 1.25$  with Equation 5a is required if fill source is unknown at time of design. A 1.5 minimum FS is also required with Equation 5a. No minimum  $RF_{ID}$  is stated for Equation 5b.

## 2.4 1989 FHWA Report

The FHWA research report (Christopher et al. 1989) presented two procedures for quantifying LTADS of geosynthetics. The first procedure, stated as being complex and requiring extensive long-term strength testing, is the partial reduction factor approach presented by Bonaparte and Berg (1987). The second procedure, which can be used in absence of sufficient test data, is to calculate the LTADS with the following simplified equation:

$$LTADS = \frac{T_{ULT} \times CRF}{RF_{ID} \times RF_D \times FS} \leq T_s \quad (6)$$

where

$T_s$  = long-term tension capacity of the geosynthetic at a selected design strain (usually 5% or less); and

CRF = creep reduction factor (ratio of creep limit strength obtained from creep tests to ultimate strength).

$RF_D$  and  $RF_{ID}$  should be based upon product specific data, but not less than 1.1, each. A minimum FS value of 1.5 is recommended for permanent walls.

## 2.5 1991 AASHTO

The 1991 American Association of State Highway and Transportation Officials (AASHTO) Standard Specifications for Highway Bridges followed procedures for LTADS computation as presented in the Task Force 27 (AASHTO 1990) report (i.e., Equations 5a and 5b). However, a minimum  $RF_{ID}$  of 1.25 was stated.

## 2.6 1993 NCMA Procedure

Two optional methods for calculating LTADS are presented within the National Concrete Masonry Association (NCMA) design manual. Method A is a partial reduction factor

approach with a minimum  $RF_{ID}$  of 1.05, adapted from an FHWA publication (Berg 1993), as follows:

$$LTADS = \frac{T_{ULT-MARV}}{RF_{CR} \times RF_{ID} \times RF_{CD} \times RF_{BD} \times FS_{MU} \times FS_{to}} \quad (7a)$$

where

$T_{ULT-MARV}$  = minimum average roll value of ultimate tensile strength, which is typically 5 to 15% lower than  $T_{ULT}$ ;

$RF_{CR}$  = partial factor of creep deformation (ratio of  $T_{ULT}$  to creep limit strength), based upon not exceeding a 10% total strain;

$RF_{CD}$  = partial factor for chemical degradation;

$RF_{BD}$  = partial factor for biological degradation, with a minimum combined  $RF_{CD}$  and  $RF_{BD}$  of 1.1;

$RF_{MU}$  = partial factor for material uncertainty, 1.5 minimum; and

$FS_{to}$  = factor of safety against tensile overstress, 1.2 minimum.

Method B is similar to European practice and borrows heavily from the work of Jewell and Greenwood (1988). This method decouples the FS against overall uncertainties from the calculation of LTADS, and uses creep rupture to define CRF. The LTADS is calculated as:

$$LTADS = \frac{T_{ULT-MARV} \times CRF}{RF_{BD} \times RF_{CD} \times RF_{ID} \times RF_{CE} \times FS_{to}} \quad (7b)$$

where

$RF_{CE}$  = material factor for extrapolation of creep data, 1.3 to 1.5 typical for permanent walls.

## 2.7 1994 and 1996 AASHTO

The 1994 and 1996 AASHTO Standard Specifications for Highway Bridges followed equations (i.e., 5a and b) for LTADS computation as presented in the 1991 AASHTO manual. However, the overall factor of safety, FS, minimum was increased to 1.78. A minimum  $RF_{ID}$  and  $RF_D$  of 1.1 and 1.05, respectively, were stated in the commentary.

## 2.8 Current FHWA/AASHTO Guidelines

The current FHWA (Elias and Christopher 1997) and AASHTO (1997) guidelines present the following equations for quantifying LTADS.

$$LTADS = \frac{T_{ULT-MARV}}{RF \times FS} \quad (8)$$

Where

RF = product of applicable reduction factors (i.e.,  $RF = RF_{CR} \times RF_D \times RF_{ID}$ ), with a minimum value of 1.1 for both  $RF_D$  and  $RF_{ID}$ , and with  $RF_{CR}$  based upon creep rupture; and FS minimum of 1.5 is recommended.

An alternative procedure for LTADS is to use a default overall reduction value, RF, of 7, as shown in Equation 9. Application of this alternative is limited to conditions stated within the guidelines.

$$LTADS = \frac{T_{ULT-MARV}}{7 \times FS} \quad (9)$$

## 2.9 Current NCMA Guidelines

The current NCMA (1997) design manual uses the same equation (similar nomenclature) as the current FHWA/AASHTO (i.e., Eq. 8).

## 3 LOAD DETERMINATION

The lateral driving load to be resisted by the geosynthetic reinforcements is a function of the soil mass and surcharge loads, and, in some analyses, the overturning moment on the reinforced fill due to the retained backfill. The soil mass and surcharge loads are factored by a lateral earth pressure coefficient to compute reinforcement loadings. Design and analysis procedures over time have varied by the assumed lateral pressure coefficient and inclusion or not of the overturning moment effect. In general terminology, the tension in the  $i$ th layer of reinforcement, not including surcharge loads, is calculated as:

$$T_i = K \sigma_{vi} s_{vi} \quad (10)$$

where

$K$  = lateral pressure coefficient;

$\sigma_{vi}$  = vertical pressure at the depth of the  $i$ th layer; and

$s_{vi}$  = effective vertical spacing (i.e.,  $\frac{1}{2}$  distance to reinforcement above plus  $\frac{1}{2}$  distance to reinforcement below) of the  $i$ th layer of reinforcement. The procedures for determining the lateral load are summarized in Table 1 in terms of lateral pressure coefficient used and whether or not overturning (OT) effects are included in the computation of  $\sigma_{vi}$ .

The USFS manual (Steward et al. 1977) focused on the design of geotextile wrap-around walls for log-haul roads. These walls have a relatively short design life and are subject to large live loadings. The load is determined using the approach described by Bell et al. (1975). An at-rest lateral earth pressure coefficient (i.e.,  $1 - \sin \phi'$ ) is used. The normal pressure ( $\sigma_{vi}$ ) is the sum of the weight of the rein-

Table 1. Load computation procedures.

Procedure	K	$\sigma_{vi}$
1977 USFS	at-rest	w/o OT
Geogrid - 1983	active Rankine	w/ OT
- 1987	active Rankine	w/o OT
1987 Task Force 27	active Rankine	w/ OT
1989 FHWA	1.0 to 1.5 active Rankine	w/o OT
1991, 1994 & 1996 AASHTO	active Rankine	w/ OT
1993 & 1997 NCMA	active Coulomb	w/o OT
1997 FHWA /AASHTO	active Rankine	w/o OT

OT — Overturning force from retained backfill.

forced fill (i.e., product of unit weight of soil,  $\gamma$ , and height of fill above  $i$ th layer of reinforcement,  $h_i$ ), uniformly distributed surcharge loads ( $w_s$ ), and other surcharge loads.

The 1983 (Netlon) geogrid wall design manual recommended use of active lateral earth pressure coefficient,  $K_a$ , with either the tie-back wedge or the coherent gravity analysis procedure. The tie-back wedge method with overturning effect was used extensively for design of geogrid walls in North America starting in 1983 (e.g., Berg et al. 1984; Tensar 1986; Berg et al. 1987). A Rankine active lateral earth pressure coefficient (i.e.,  $\tan^2(45 - \phi/2)$ ) is used with this procedure. The vertical pressure, assuming a Meyerhof-type of pressure distribution of the overturning force generated by the retained backfill, is shown in Equation 11, for level backfill conditions. The subscripts  $w$  and  $b$  refer to the reinforced wall fill and the retained backfill, respectively, and  $l$  is the length of reinforcement.

$$\sigma_{vi} = \gamma_w h_i + w_s K_{ab} \left( \gamma_b h - i + 3 w_s \right) \left( \frac{h_i}{l} \right)^2 \quad (11)$$

The overturning of component of  $\sigma_{vi}$  was deleted from the load computation (Simac 1990; Tensar 1990), at least in private practice, subsequent to and based upon discussions at the 1987 NATO Workshop on geosynthetic reinforced soil walls (Jarrett and McGown 1988). The method for calculating LTADS did not change, therefore, Equation 4 is applicable with this revised load determination procedure.

In the 1987 Task Force 27 (AASHTO 1990) procedure, the tie-back wedge method of analysis is recommended for analysis of geosynthetic reinforced retaining walls. The tension in the reinforcement is calculated as a function of the vertical stress induced by gravity, uniform normal surcharges

and active thrust from the retained fill (i.e., Eq. 11), multiplied by the Rankine active earth pressure coefficient.

FHWA research in the late 1980's (Christopher et al. 1989) led to a recommended stiffness approach for quantifying the lateral pressure coefficient. With this approach, a Rankine lateral earth pressure coefficient equal to  $K_a$  was recommended for geotextile reinforcements. A varying coefficient of  $1.5 K_a$  at the top of wall to  $1.0 K_a$  at a distance of 6 m below top of wall, and lower, was proposed for geogrid reinforcements.

The 1991, 1994, and 1996 AASHTO Standard Specifications for Highway Bridges followed procedures for load computation as presented in the Task Force 27 (AASHTO 1990) report.

Rankine theory was used for quantifying the  $K_a$  coefficient until the NCMA design procedure for segmental retaining walls (Simac et al. 1993) was published. A Coulomb theory is recommended in this manual, which allows for direct incorporation of the beneficial effects of wall face batter and interface friction between the fill soil and wall face. The NCMA procedure (Simac et al. 1993; NCMA 1997) for calculating the internal stability lateral load (without surcharge loads) is:

$$P_a = \frac{1}{2} \gamma_w K_{aC} H_e^2 \cos(\delta_i - \psi) \quad (12)$$

where

$P_a$  = active earth force acting over the effective height of the wall, per unit width of wall;

$\gamma_w$  = moist unit weight of wall infill soil;

$K_{aC}$  = Coulomb active earth pressure coefficient;

$H_e$  = effective height for battered walls;

$\delta_i$  = wall to soil friction angle; and

$\psi$  = total wall inclination from vertical.

The second edition of the NCMA design manual (1997) does not change the procedure for determining the soil load for internal stability analysis. The NCMA design procedure is one of the two procedures currently in widespread use in North America. The other procedure in widespread use was developed for the design of highway walls, with select granular fill, and is referred to as the simplified coherent gravity method.

The new FHWA manual (Elias and Christopher 1997) and the recent update to AASHTO bridge manual (1997) incorporated features of the stiffness, tie-back wedge, and coherent gravity approaches for analysis of walls — resulting in the simplified coherent gravity method. With this procedure an active Rankine lateral earth pressure, over the entire wall height, is recommended for computation of geosynthetic (both geotextiles and geogrids) reinforcement loads. Overturning effects are not included in the vertical pressure.

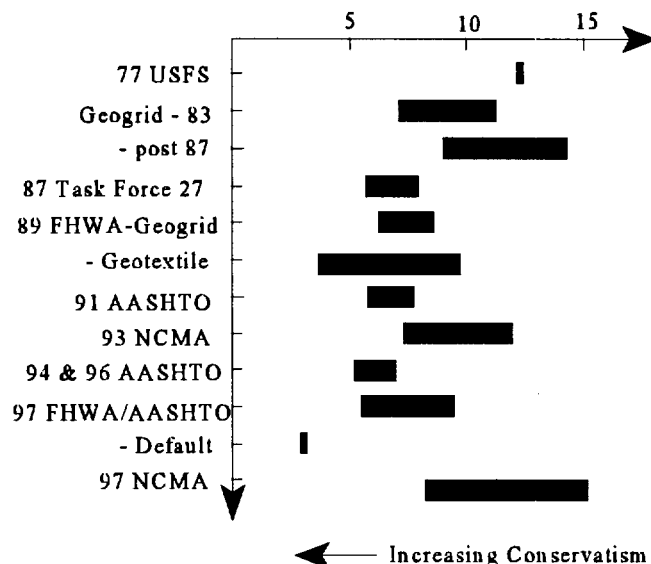
The changes in procedures to quantify the LTADS of geosynthetic reinforcement and the internal lateral load on GRS walls are quantified in Table 2. The values in Table 2 are based upon typical ranges of values for the partial factors used in practice, from the authors' experience. The resistance,  $R$ , is the LTADS in terms of percentage of ultimate wide width strength ( $\%T_{ULT}$ ). The load,  $L$ , is the total load on the wall, without surcharges, using the assumptions listed in Table 2, expressed as  $P/H^2$ , where  $P$  is the total force on the wall per unit length of wall. The  $R/L$  in Table 2 is a normalized ratio for comparing the various procedures, and not a design parameter. The lower the  $\%T_{ULT}$  used the more conservative the procedure. Also, with other factors remaining equal, the higher the assumed load the more conservative the method. Therefore, the lower the  $R/L$ , the more conservative the combination of resistance and load computations. The trend of  $R/L$  ratios over time and range of individual procedures are illustrated in Figure 1.

Table 2. Quantifying  $R/L$  ratios.

Procedure	Resistance ( $\%T_{ULT}$ )	Load ( $P/H^2$ )	$R/L$ Ratio
1977 USFS	~ 53	4.3	~ 12.3
Geogrid			
- '83	25 to 40	3.54	7.1 to 11.3
- post-87	25 to 40	2.77	9.0 to 14.4
1987 Task Force 27	20 to 28	3.54	5.7 to 8.0
'89 FHWA			
- Geogrid	20 to 27.5	3.2	6.3 to 8.6
- Geotextile	10 to 27.5	2.77	3.6 to 9.9
1991 AASHTO	20 to 27.5	3.54	5.8 to 7.8
1993 NCMA	16 to 28	2.3	7.0 to 11.7
1994 & 1996 AASHTO	18 to 24.3	3.54	5.1 to 6.9
'97 FHWA & AASHTO	14.6 to 26	2.77	5.3 to 9.4
- w/ Default	8.6	2.8	3.1
1997 NCMA	19 to 35	2.3	8.3 to 15.2

## Assumptions:

wall fill  $\phi = 34^\circ$   $\gamma = 19.6 \text{ kN/m}^3$   
retained backfill  $\phi = 30^\circ$   $\gamma = 18.8 \text{ kN/m}^3$   
 $H = 6 \text{ m}$  (1989 FHWA geogrid case)  $l/H = 0.7$   
batter =  $0^\circ$ ,  $\delta = \frac{3}{4}\phi$ , and  $FE = 1.3$  (NCMA cases)

Figure 1.  $R/L$  ratio trends and ranges.

## 5 CONCLUSIONS

The trend of change in the resistance to load relationship ( $R/L$  ratio) is illustrated in Figure 1. Observed trends are generalized and based upon assumptions previously stated. More precise results could be revealed by examining specific case histories over time. The following can be concluded from this plot.

1. Transportation specific procedures (i.e., FHWA, AASHTO) are more conservative than non-transportation specific procedures (i.e., geogrid, NCMA).
2. Transportation procedures have, generally, increased in conservatism throughout their development, primarily due to increases in resistance reduction factors. Calculated loads have decreased somewhat during this period.
3. The 1997 FHWA/AASHTO default value of 7 is more conservative than all of the procedures examined.
4. Large changes in conservatism with transportation procedures have not occurred since 1987.
5. Large changes in conservatism with non-transportation procedures have not occurred since first use in 1975.
6. Performance of existing structures is applicable to new design codes and guidelines.

## 6 REFERENCES

AASHTO (1997) *Interims to Standard Specifications for Highway Bridges*, Sixteenth Edition, 1996, American Association of State Highway and Transportation Officials, Washington, DC, USA.

- AASHTO (1996) *Standard Specifications for Highway Bridges, Sixteenth Edition*, American Association of State Highway and Transportation Officials, Washington, DC, USA.
- AASHTO (1994) *Standard Specifications for Highway Bridges, Fifteenth Edition*, 1992 with 1993 and 1994 Interims and Commentary, American Association of State Highway and Transportation Officials, Washington, DC, USA.
- AASHTO (1991) *Standard Specifications for Highway Bridges, Fourteenth Edition*, 1989 with 1990 and 1991 Interims and Commentary, American Association of State Highway and Transportation Officials, Washington, DC, USA.
- AASHTO-AGC-ARTBA (1990) *Task Force 27 Report: In Situ Soil Improvement Techniques*, American Association of State Highway and Transportation Officials, Washington, DC, USA, 324 p.
- ASTM (1997) D 4595 - 86 (Reapproved 1994) Standard Test Method for Tensile Properties of Geotextiles by the Wide-Width Strip Method, *Soil and Rock (II): D 4943 - latest, Geosynthetics*, Vol. 04.09, West Conshohocken, PA, pp. 961 - 971.
- Bonaparte, R., and Berg R.R. (1987) Long-Term Allowable Design Loads for Geosynthetic Soil Reinforcement, *Proceedings of the Geosynthetics '87*, IFAI, Vol. 1, New Orleans, LA, USA, pp. 181-192.
- Bell, J.R., Stille, A.N. and Vandre, B. (1975) Fabric Retaining Walls, *Proceedings of the 13<sup>th</sup> Annual Engineering Geology and Soils Engineering Symposium*, Moscow, ID, USA.
- Berg, R.R. (1993) *Guidelines for Design, Specification, & Contracting of Geosynthetic Mechanically Stabilized Earth Slopes on Firm Foundations*, U.S. Department of Transportation, Federal Highway Administration, Washington, DC, USA, FHWA-SA-93-025, 87 p.
- Berg R.R., La Rochelle, P., Bonaparte, R., and Tanguay, L. (1987) Gaspe' Peninsula Reinforced Soil Seawall - Case History, *Proceedings of Soil Improvement - A Ten Year Update*, J.P. Welsh, Ed., Geotechnical Special Publication No. 12, ASCE, pp. 309-328.
- Berg, R.R., Bonaparte, R., Chouery, V.C., and Anderson, R.P. (1986) "Design, Construction, and Performance of Two Geogrid Reinforced Soil Retaining Walls," *Proceedings of the IIIrd International Conference on Geotextiles*, Vienna, Austria, pp. 401-406.
- Christopher, B.R., Gill, S.A., Giroud, J.P., Juran, I., Schlosser, F., Mitchell, J.K. and Dunnicliff, J. (1989) *Reinforced Soil Structures: Volume I. Design and Construction Guidelines*, U.S. Department of Transportation, Federal Highway Administration, Washington, DC, USA, FHWA-RD-89-043, 287 p.
- Elias, V. and Christopher, B.R. (1997), *Mechanically Stabilized Earth Walls and Reinforced Soil Slopes, Design & Construction Guidelines*, FHWA-SA-96-071, U.S. Department of Transportation, Federal Highway Administration, Washington, DC, USA, 371p.
- FHWA (1997), *Degradation Reduction Factors for Geosynthetics, Federal Highway Administration Geotechnology Technical Note*, U.S. Department of Transportation, Federal Highway Administration, Washington, DC, USA, 5 p.
- Jarrett, P.M. and McGown, A., eds. (1988) *The Application of Polymeric Reinforcement in Soil Retaining Structures, Proceedings of the NATO Advanced Research Workshop on Application of Polymeric Reinforcement in Soil Retaining Structures*, Kingston, ON, Canada, June 1987, Kluwer Academic Publishers, Dordrecht, The Netherlands, 637 p.
- Jewell, R.A. and Greenwood, J.H. (1988), Long-Term Strength and Safety in Steep Slopes Reinforced by Polymer Materials, *Geotextiles and Geomembranes*, Vol. 7, pp. 81-118.
- NCMA (1997) *Design Manual for Segmental Retaining Walls*, 2<sup>nd</sup> Edition, J. Collin Ed., National Concrete Masonry Association, Herdon, VA, USA, 289 p.
- Netlon Limited (1983), *Guidelines for the Design & Construction of Reinforced Soil Retaining Walls Using Tensar Geogrids*, Blackburn, England, 39 p.
- Simac, M.R., Bathurst, R.J., Berg, R.R., and Lothspiech, S.E. (1993) *Design Manual for Segmental Retaining Walls*, 1<sup>st</sup> Edition, National Concrete Masonry Association, Herdon, VA, USA, 336 p.
- Simac, M.R. (1990) *Design Methodology for MIRAGRID™ Reinforced Soil Retaining Walls*, Mirafi Inc., Charlotte, NC, 110 p.
- Steward, J.E., Williamson, R. and Mohny, J. (1977), *Guidelines for Use of Fabrics in Construction and Maintenance of Low-Volume Roads*, USDA, Forest Service, Portland, OR, USA.
- Tensar (1986), *Guidelines for the Design of Tensar Geogrid Reinforced Soil Retaining Walls*, TTN:RW1, The Tensar Corporation, Morrow, GA, USA.
- Tensar (1990), *Guidelines for the Design of Tensar Geogrid Reinforced Soil Retaining Walls*, TTN:RW1.1, The Tensar Corporation, Morrow, GA, USA.

# Aspects of Partial Factor Design of Reinforced Soil Walls

T. S. Ingold

Consulting Engineer and Honorary Professor of Geotechnical Engineering, The University of Birmingham, UK

**ABSTRACT:** In assessing margins of safety, geotechnical engineers have traditionally worked in terms of lumped factors of safety, often defined as the ratio of restoring force to disturbing force, that are calculated using soil parameters which are judged to be representative. This approach is lucid in so far as it deals with raw, unfactored, values of soil properties. In contrast, partial factor design deals with design disturbing forces, which are raw values artificially enhanced by partial factors, and design restoring forces which are raw values artificially depressed by partial factors. How these partial factors are applied has a major affect on the end result with this also being heavily influenced by the use of characteristic values of soil parameters. Certain approaches to partial factor design are more lucid than others and this is illustrated by making comparisons between some of the approaches prescribed in BS 8006 : 1995, "Strengthened/reinforced soils and other fills", and the pre-standard Eurocode ENV-1997-1 : 1994, "Geotechnical design - Part 1 : General rules".

**KEYWORDS:** Reinforced soil, Retaining walls, Design, Safety factors, Specifications

## 1 INTRODUCTION

Traditionally, geotechnical engineers factor design values of soil properties by judgment with this judgment, perhaps aided by regression analyses, accounting for a multitude of variables such as test method, validity of test results and variability of results. The resulting value is a raw, unfactored, value which is used for design.

In assessing soil induced forces involved in, say, base sliding of a retaining wall, of given geometry, then, for a cohesionless soil of given unit weight  $\gamma$ , these forces will be a function of  $\phi'$ , the effective stress internal angle of shearing resistance of the soil. The function maybe  $K_a$ , if considering a raw lateral disturbing force,  $D$ , or  $\tan\phi'$  if considering a raw horizontal restoring force,  $R$ . The lumped factor of safety against sliding may then be defined, traditionally, as  $F=R/D$ . Provided  $F$  equals, or exceeds, some prescribed value, typically 1.5 to 2.0, then there is deemed to be an adequate, definitive, margin of safety against forward sliding. Although definitive,  $F$  is a combined margin of undefined error and/or ignorance. Nonetheless, prescribed values have stood the test of time.

In contrast, non-geotechnical engineers often have the luxury of designing with well controlled materials, and loads, whose parameters are well documented. In this case it is possible to generate a general distribution of, say, material strengths and applied loads. Statistical analyses may be applied to these distributions to determine theoretical values of partial load and partial material factors which are then applied to statistically determined values of load and strength. The end result is that, when the partial factors are applied it, is possible to define the probability of the design load exceeding the design strength. So, for example, such an approach may define a probability of failure of 1 in 10,000. Clearly, this approach is totally different to the lumped factor of safety approach.

There has long been a move in Europe towards partial factor design and so the code of practice, BS 8006 : 1995,

"Strengthened/reinforced soils and other fills" was written in a partial factor format. The essence of this is that a partial load factor,  $f_t$ , is used to enhance a raw disturbing force,  $D$ , whilst a partial material factor,  $f_m$ , is used to depress a raw restoring force,  $R$ . An adequate margin of safety, against attaining an ultimate limit state, is deemed to operate when the identity  $f_t D \leq (R/f_m)$  is satisfied. A similar approach is proposed in the European pre-standard Eurocode 7, or just EC-7, which is formally entitled Eurocode ENV-1997-1 : 1994, "Geotechnical design - Part 1 : General rules".

## 2 BS 8006 AND EUROCODE 7

BS 8006 prescribes a variety of different partial material factors,  $f_m > 1$ , with different numerical values, to be applied to material strengths, such as those for soil or soil reinforcement, to define a design strength. It is important to note that soil unit weight,  $\gamma$ , and  $\tan\phi'$  are allotted a partial material factor of unity. So, in other words, these two parameters are not factored. Load factors,  $f_t > 1$ , with different numerical values, are applied to loads to determine design loads and these factors differ in magnitude from one prescribed loading condition to another. In addition, there is a further group of partial material factors, such as  $f_s > 1$ , which applies to specific failure modes such as bearing capacity, forward sliding or reinforcement pull-out. Table 1 presents some selected examples of partial load factors.

Table 1. Selected partial load factors from BS 8006

Load factor, $f_t$ , applied to	Loading case		
	A	B	C
Mass of the reinforced soil body	1.5	1.0	1.0
Earth pressure behind structure	1.5	1.5	1.0

Table 2. Selected partial factors from BS 8006

Soil material factor, $f_m$ , applied to $\tan\phi'$	1.00
Factor, $f_s$ , on sliding across reinforcement	1.30
Factor, $f_{ms}$ , on ultimate bearing capacity	1.35

BS 8006 considers two limit states; the ultimate limit state of collapse and a predefined serviceability limit state appropriate to the structure under consideration. In assessing the latter, all partial factors are set to unity per Case C in Table 1. In assessing the ultimate limit state of collapse, the code is formulated in such a way that partial factors with a value greater than unity are only applied to raw pressures or forces. So, taking the example of base sliding, stability is deemed satisfied if  $f_t D \leq (R/f_m)$ .

Since BS 8006 partial factors operate on what are effectively raw forces, the identity  $f_t D \leq (R/f_m)$  may also be expressed as  $R/D \geq f_t f_m$ . This formulation is identical to the traditional lumped factor of safety format in which  $R/D$  must equal or exceed a prescribed minimum value of  $F$ . For forward base sliding the prescribed value of  $F$  traditionally falls between 1.5 and 2.0. Loading case A of Table 1, a worse case for base sliding, implies a value of  $f_t$  of 1.5 and, for a perfectly rough basal reinforcement, Table 2 implies a material factor,  $f_s = f_m$ , with a value of 1.3. The product of these two factors is 1.95 which is essentially the value of the conventional lumped factor of safety  $F$ .

Indeed, the values of partial factors in BS 8006 were formulated such that  $f_t f_m = F$ . This formulation, with due regard for any interaction between various factors, was extensively calibrated against well established and proven design methods, as well as observed performance of existing structures, to render numerical values of partial factors which, with regard for commercialism, are consistent with adequate margins of safety. Perhaps more importantly, partial factors are applied in a lucid manner which has a linear effect on design loads and strengths.

Table 3. Selected partial factors from EC-7

Case	Favourable load	Unfavourable load	$\tan\phi'$
A	0.95	1.00	1.10
B	1.00	1.35	1.00
C	1.00	1.00	1.25

Eurocode 7 has a similar format to BS 8006 but has three loading cases pertaining to the ultimate limit state, per Table 3, as opposed to two cases, cases A and B of Table 1, in BS 8006. Like BS 8006, EC-7 sets all partial factors to unity when considering a serviceability limit state. EC-7 does not prescribe material factors which can be applied to assess internal stability nor partial factors which apply to specific failure modes such as base sliding.

For loading cases A and C, EC-7 prescribes the use of a materials factor,  $f_m > 1$ , on  $\tan\phi'$ . This gives a design value of friction angle  $\phi_d = \tan^{-1}([\tan\phi'] / f_m)$ . If, for example, lateral soil thrusts were being calculated to BS 8006 then  $\phi'$  is not factored and the resulting coefficient of earth pressure used in design is  $K_a$ , the conventional coefficient of active earth pressure. If  $\phi_d$  is used as the design value then the resulting earth pressure coefficient might be denoted as  $K_d$ . It is reasonable to assume that the  $f_m$  value defined in EC-7 is a component used with the objective of achieving a uniform, target, overall margin of safety, but, if the effects of  $f_m$  are assessed it transpires that resulting margins of safety are not uniform.

Figure 1 shows a plot of  $K_d/K_a$  against  $f_m$  for a range of unfactored values of  $\phi'$ . For soil with  $f_m = 1$ , per BS 8006, and  $\phi' = 20^\circ$  then  $\phi' = \phi_d = 20^\circ$  and the value of  $K_d/K_a$  is unity since  $K_d = K_a$ , but if  $f_m = 1.25$ , per EC-7, the value of  $K_d/K_a$  increases by 15 % so implying a concealed load factor component of 1.15. For  $\phi' = 50^\circ$  then, as before  $K_d = K_a$  per BS 8006, but according to EC-7,  $K_d/K_a$  increases by 38 % so implying a concealed load factor component of 1.38. So, the EC-7 approach introduces a non-linearity in margins of safety which penalise better quality soils and fills. This non-linearity varies according to which aspect of stability is being considered. If calculating tensile forces applied to reinforcement then  $K_a$  and a sine function is involved. If considering base sliding then both a sine and tangent function are involved.

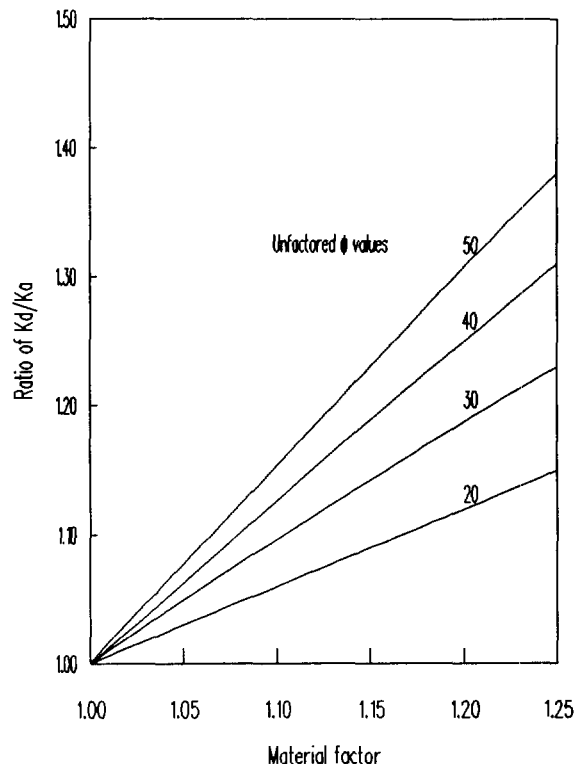


Figure 1. Nonlinear effect of partial material factor on design value of lateral earth pressure coefficient



### 3 BASE SLIDING

Eurocode 7 does not give partial factors for internal stability so the following sections illustrate various aspects of the BS 8006 and EC-7 approaches by considering base sliding and bearing capacity in terms of  $\phi'$  and the ratio,  $\lambda$ , of wall base width,  $L$ , to wall height,  $H$ .

Conventional, lumped factor of safety, design defines the factor of safety against base sliding as :

$$(\gamma LH \tan\phi') / (\frac{1}{2}K_a \gamma H^2) = F \quad (1)$$

If  $F$  is some limiting target value to be achieved and  $L/H$  is written as  $\lambda$ , then Equation 2 can be rearranged as :

$$(2 \lambda \tan\phi') / (FK_a) = 1 \quad (2)$$

The corresponding EC-7 formulation is :

$$(2 f_w \lambda \tan\phi_d) / (f_t K_d) = 1 \quad (3)$$

where  $\phi_d = \tan^{-1}([\tan\phi'] / f_m)$  and  $f_w$  is a load factor on favourable dead load which may be less than unity. The corresponding BS 8006 Case B formulation is :

$$(2 \lambda \tan\phi') / (f_s f_t K_a) = 1 \quad (4)$$

For given raw values of  $\phi'$  values of  $\lambda$  can be determined for a given partial factor set.

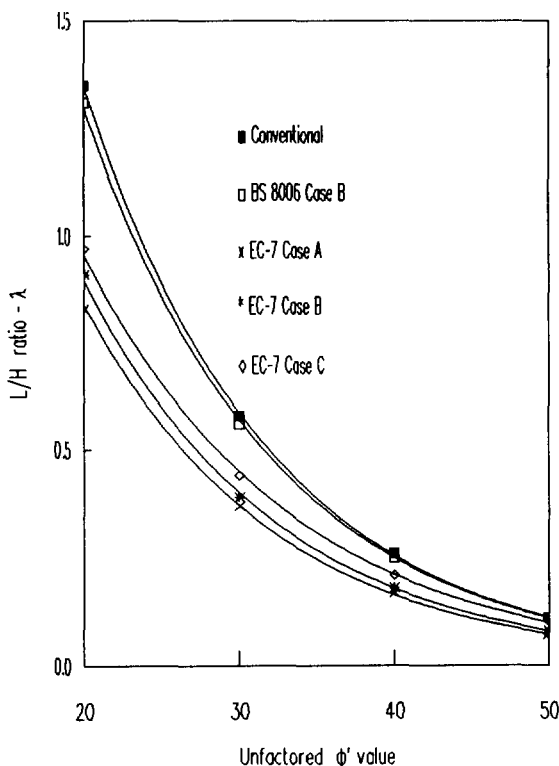


Figure 2. Base width to height ratio -  $\lambda$  against  $\phi'$  values

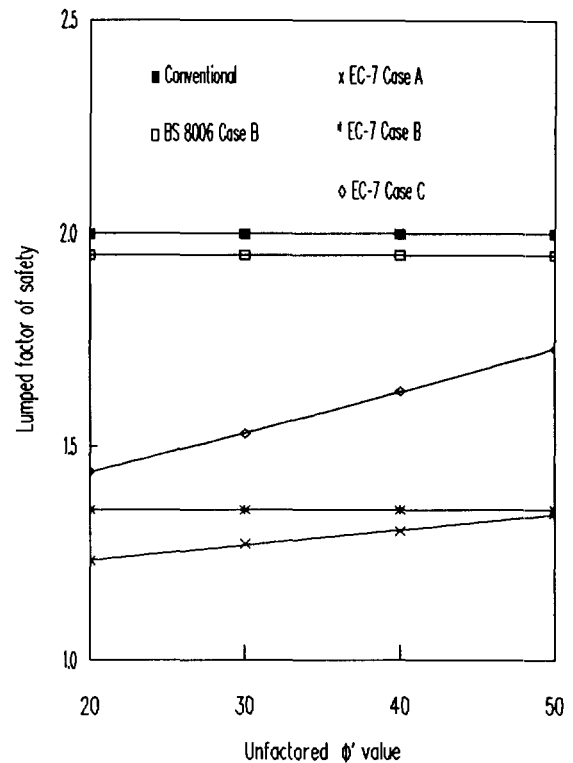


Figure 3. Conventional lumped factor of safety against  $\phi'$

For each partial factor set and a given value of  $\phi'$ , Figure 2 presents the value of  $\lambda$  required by a given partial factor set to achieve an adequate margin of safety as defined by that partial factor set. As expected, values of  $\lambda$  for the conventional lumped factor of safety approach and BS 8006 Case B almost coincide. The EC-7 partial factor sets are closely grouped and, for a given value of  $\phi'$ , these generally indicate a requirement for a lower value of  $\lambda$  than BS 8006. To investigate the reasons for this, the  $\lambda$  values derived from each partial factor set were reanalysed to determine what conventional lumped factor of safety they would produce.

The results of these reanalyses are presented graphically in Figure 3 which is a plot of equivalent lumped factor of safety against unfactored  $\phi'$ . As expected conventional analysis produces a constant factor of safety, of 2.00, which is independent of  $\phi'$ . The same applies to BS 8006 Case B, with a constant value of 1.95, and to EC-7 Case B where the constant value is 1.35. Case A produces a variable factor of safety as does Case C which is the worst case for base sliding. The non-linearity effect of applying a material factor, greater than unity, to  $\tan\phi'$  is well illustrated by Case C where the equivalent factor of safety increases from 1.44 for  $\phi' = 20^\circ$  to 1.73 for  $\phi' = 50^\circ$ . It can be seen that in general EC-7 results in lower margins of safety against base sliding than BS 8006 and, in particular, it penalises better quality fills and soils which have higher  $\phi'$  values.

## 4 BEARING CAPACITY

To investigate the effects of different partial factor sets on margins of safety against bearing capacity failure, analyses have been carried out on a simple wall, with a constant value of  $\lambda$  of 0.7, founded at ground surface. The common theme of all partial factor sets is that the design ratio,  $\rho$ , of available design bearing capacity to applied design pressure should be equal to or greater than unity. The results of these analyses are presented in Figure 4 as plots of  $\rho$  against  $\phi'$ . For all partial factor sets a  $\rho$  value of unity or greater is obtained for  $\phi'$  greater than 30 to 33°. In particular the worst threshold case from BS 8006, Case B, is obtained at  $\phi' = 32^\circ$  whilst from EC-7 the worst case is Case C which is obtained at  $\phi' = 33^\circ$ . This indicates that, for the wall geometry analysed, BS 8006 and EC-7 render almost identical margins of safety against bearing capacity failure.

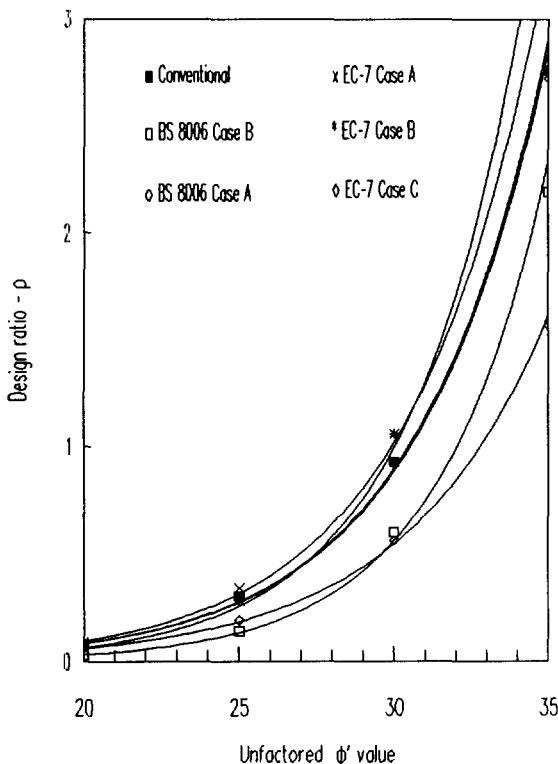


Figure 4. Variation of design ratio,  $\rho$ , with unfactored  $\phi'$

## 5 CHARACTERISTIC VALUES

The above analyses assume deterministic values of soil properties such as  $\phi'$  but BS 8006 and EC-7 imply the use of characteristic values. If statistical methods are used, the characteristic value should be derived such that the calculated probability of a worse value governing the occurrence of a limit state is not greater than 5%. Upper or lower values are used according to the problem.

Designing with characteristic values of  $\phi'$  for fills is not problematical since the designer can require a specified characteristic value. However, the effects of using characteristic values for insitu soils may be problematical.

Consider a wall imposing a pressure of 120 kN/m<sup>2</sup>. A designer might have 9 test results for the  $\phi'$  value of the foundation soil which are 32, 33, 34, 35, 36, 35, 37, 40 and 33°. The mean is 35° which leads to an ultimate bearing capacity of 670 kN/m<sup>2</sup> and lumped factor of safety of 5.6. The characteristic value is 31° which leads to a ultimate bearing capacity of 350 kN/m<sup>2</sup> and a lumped factor of safety of 2.9. If the designer had say only 3 results of 32, 35 and 38° the mean would still be 35° and the designer would calculate the same result as before. The characteristic value of this set is 30° for which the bearing capacity is 300 kN/m<sup>2</sup> with a notional factor of safety of 2.5. Hence, quality, quantity and distribution of test data may have as large an influence on margins of safety as the various partial factors which may be applied.

## 6 CONCLUSIONS

Traditionally geotechnical design employs lumped factors of safety and a key element in deriving these is the veracity of the soil parameters used. This is largely a matter of engineering judgment. In theory, if factors of safety are greater than unity, then there should be no failure. In fact failures do occur occasionally and these often call into question the judgment of the designer.

In Europe the move is away from lumped factor of safety design towards partial factor design. Since partial factors are applied to enhance raw loads, and to reduce raw strengths, the designer deals with design loads, and strengths, which are distorted from raw values. The aim of this distortion is to wean geotechnical design away from a deterministic approach to a probabilistic approach.

Some of the mathematical manipulations prescribed in partial factor design, such as factoring characteristic  $\phi'$  values, tend to produce distorted, nonlinear, design values. This tends to cloud the application of engineering judgment and it remains to be seen whether partial factor design introduces a real probability of failure which is lower or higher than that currently associated with traditional lumped factor of safety design.

## REFERENCES

- BSI (1995) *Code of practice for Strengthened/reinforced soils and other fills*, BS 8006 : 1994, British Standards Institution, London, UK.
- CEN (1994) *Geotechnical design - Part 1 : General rules*, Eurocode ENV-1997-1 : 1994 Comité Européen de Normalisation, Brussels, Belgium.

# A Comparison of Design Approaches for Geosynthetic Reinforced Soil Structures In Europe

J. Penman and R.A. Austin

Tensar Division, Netlon Limited, New Wellington Street, Blackburn, UK

**ABSTRACT:** The use of geosynthetic materials to reinforce soil structures has become widespread in recent years. Traditional methods for the design of these structures using polymeric reinforcement are based on a limit equilibrium approach which can lead to a conflict in the design of different parts of the same structure. In a bridge for example, the deck itself is likely to be designed using a limit state approach while the supporting reinforced soil abutment could be designed using a limit equilibrium method.

For reinforced soil walls, the most popular design methods currently used in Europe are based on the tie-back wedge approach. For reinforced soil embankments the most common methods use modified forms of Bishop or Janbu equations for circular and non-circular slip surfaces respectively, the method outlined in the UK Department of Transport technical note HA 68/94 or chart based design methods. All these wall and embankment design methods are based on limit equilibrium principles.

The publication of the UK code of Practice for strengthened/reinforced soils and other fills, BS 8006 introduced alternative methods for the design of reinforced soil structures using limit state principles. The paper describes the advantages and limitations of both limit equilibrium and limit state approaches and outlines the economic implications of using the various methods in different conditions.

**KEYWORDS:** Design, Limit equilibrium, Limit state, BS 8006, Walls, Embankments

## 1 INTRODUCTION

When reinforced soil techniques were originally developed, only three or four methods were routinely used for the design of structures. With the wider acceptance of this developing technology, many countries now have at least one approved method for the design of walls and embankments and each is slightly different to the ones used elsewhere.

Since the introduction of modern soil reinforcement techniques by Vidal in the 1960's and the pioneering work for the design of reinforced soil embankments undertaken by Jewell in the 1970's, we have moved on to other more refined and flexible methods of analysis. However, the original coherent gravity method, Vidal (1966) and revised embankment design charts, Jewell (1990) are still very much in use today.

Whilst it is appreciated that many other design methods and Standards exist, this paper focuses on the methods most commonly used at present for the design of geosynthetic reinforced soil structures in Europe.

## 2 LIMIT EQUILIBRIUM METHODS

### 2.1 General

The limit equilibrium approach for the design of reinforced soil structures is based on the application of global factors of safety. Thus for external stability calculations, minimum target values are set which must not be exceeded in the design, while for internal stability calculations, a factor of

safety is applied to the reinforcement creep limited strength to determine the safe design strength.

Full details of the limit equilibrium design methods discussed in this paper can be found in Netlon Limited (1997).

### 2.2 Reinforced Soil Walls

#### 2.2.1 Tie-back Wedge Method

This method was one of the earliest developed for reinforced soil walls and is still very much in use today. Most of the more recent limit equilibrium design methods for geosynthetic reinforced soil walls could be regarded as variations of this traditional approach.

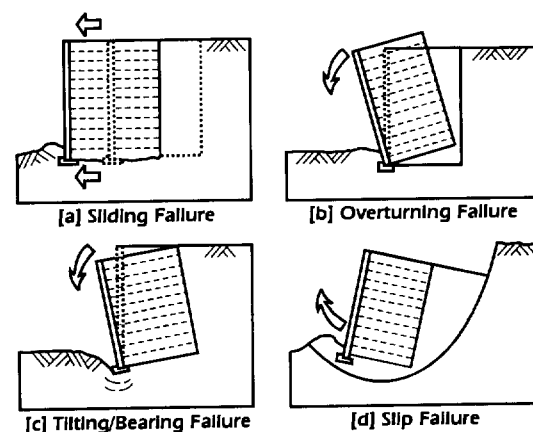


Figure 1. Main failure mechanisms for reinforced soil walls

The external stability of the structure is assessed based on the assumption that it behaves as a rigid body and the possible failure mechanisms are shown in Figure 1. Due to the large strains which develop in the soil, critical state soil parameters ( $\phi'_{cv}$ ,  $c'_{cv}$ ) are generally adopted in design.

Although overturning failure is usually included in external stability calculations, in the absence of any large horizontal loads (e.g. in bridge abutments), it is unlikely to be a problem. A target factor of safety of 2.0 is usually adopted for sliding while for bearing, the vertical pressure exerted by the reinforced soil block is normally calculated and compared with the allowable bearing pressure of the foundation soil. In the past, a trapezoidal pressure distribution was generally adopted for bearing capacity calculations, the vertical pressure being greater at the toe than at the back of the structure. This approach has now largely been replaced by a uniform Meyerhof pressure distribution which takes account of the eccentricity of the applied load at the back of the block in the calculation of the applied pressure.

In general, the base width of the reinforced soil block is chosen to satisfy external stability requirements with regard to sliding, overturning and bearing. A slope stability computer program is then used to check for potential slip failures at the back of the structure.

The internal stability of a reinforced soil wall is essentially concerned with the tension and pull-out failure mechanisms shown in Figure 2. For the purposes of the analysis, a uniform frictional fill is assumed and horizontal soil pressures are taken to be in the active condition throughout the structure; the at rest pressure which may develop during the construction phase will reduce to the active pressure when temporary supports are removed.

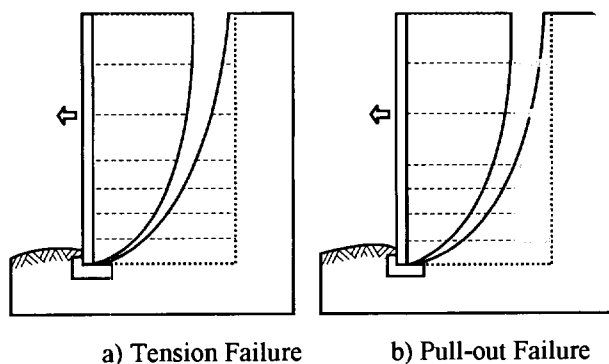


Figure 2. Tie-back wedge internal failure modes

In order to assess potential rupture, it is assumed that the reinforcement will carry tension as a result of the self-weight of the fill and the external loading. These tension components can be evaluated separately and combined to give the total tension to be carried by an individual layer of reinforcement. External vertical and horizontal line loads may also be included thus enabling forces from bridge abutments and parapets to be taken into account.

In order to investigate potential pull-out failure of the reinforcement, it is necessary to consider separately the possibility of inclined failure planes passing through the wall forming unstable wedges of soil bounded by the front face of the wall, the ground surface and the potential failure plane, Figure 3. For the purposes of the analysis, it is assumed that each wedge behaves as a rigid body and friction between the facing and the fill is ignored. A series of potential failure planes emanating at various heights behind the face of the wall are investigated and for each, a check is made to ensure that the total restoring force provided by all layers of reinforcement cut by the wedge exceeds the out of balance force, usually by a factor of two.

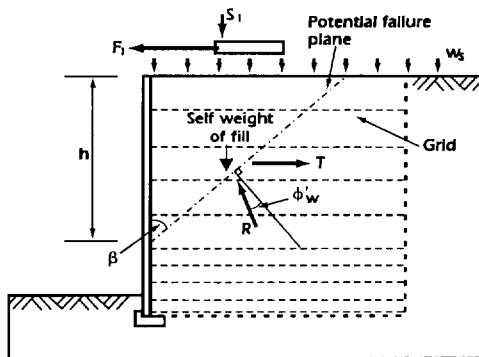


Figure 3. Tie-back wedge pull-out failure mechanism

## 2.2.2 The Deutsches Institut für Bautechnik Design Method

This design method, based on German DIN standards, has gained widespread acceptance in mainland Europe and is becoming increasingly popular in other parts of the world.

Although the method is based on the tie-back wedge approach, there are a number of important variations. For external stability calculations, these include a reduced target factor of safety of 1.5 for sliding and a specific method for the consideration of bearing failure which by modifying the Terzaghi bearing capacity equation, takes account of the inclination of the resultant force due to the active pressures at the back of the reinforced soil block. An additional check is included to ensure that the resultant force acts in the middle third of the base, this effectively replacing the overturning calculation in the traditional tie-back wedge method.

Internal stability calculations concentrate mainly on a consideration of reinforcement pull-out with the traditional single-part wedge being replaced by a two-part mechanism, the base of the upper wedge passing along the back of the reinforced soil block. An additional check is however required for structures with flexible faces; for each layer of reinforcement, it is necessary to ensure that the design strength (or the anchorage strength if a full-strength connection is not used) is not exceeded by the active pressure on the face.

Critical state soil parameters are used in the design and the reinforcement strengths adopted in the designs referred to in this paper are detailed along with the appropriate methodology in Deutsches Institut für Bautechnik Certificate No. Z-20.1-102 (1990).

### 2.3 Reinforced Soil Embankments

#### 2.3.1 Slip Circle Method

Until fairly recently, rigorous stability analyses of reinforced soil embankments generally took the form of a circular slip circle analysis using one of the methods of slices e.g. Bishop's method, Figure 4.

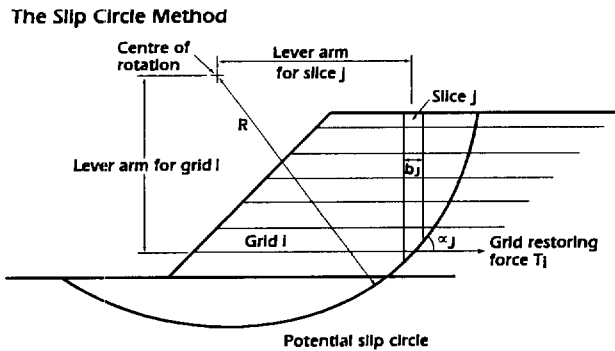


Figure 4. Bishop slip circle method

For each circle, the disturbing moment of the soil mass is compared with the restoring moment provided by the soil and the reinforcement and a factor of safety against failure calculated. If the minimum factor of safety is greater than the target value (usually around 1.3 for permanent structures), the design is deemed to be satisfactory in terms of stability.

Such an analysis is rapidly carried out using computer software developed by some individual manufacturers and the commercial software packages now available. It should be borne in mind however that the method of incorporating reinforcement into the design often varies between these software packages.

#### 2.3.2 The UK Department of Transport Design Method

The UK Department of Transport Advice Note HA 68/94 gives guidance on the design requirements for the use of reinforced soil and soil nailing techniques in embankments. A series of tables are provided in the document which are aimed at providing a simple method enabling engineers to produce independently replicable designs. However, in order to take full advantage of the economy in the design method outlined in HA 68/94, a computer program is necessary.

The HA 68/94 design method involves the consideration of two-part wedge failure mechanisms, Figure 5. Critical state soil parameters are used in the analysis but apart from

the normal factors applied to the strength of the reinforcement, no other factors of safety are present in the design. A general discussion of the principles involved in the HA 68/94 method and some of the potential difficulties with its application are discussed in Penman (1996 and 1996a).

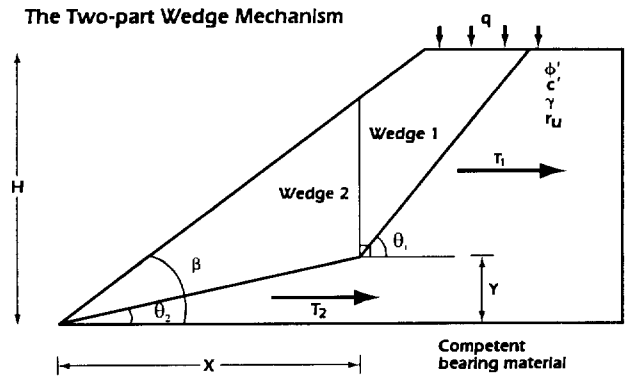


Figure 5. HA 68/94 two-part wedge failure mechanism

Although HA 68/94 is gaining widespread popularity, a number of implicit restrictions often require an alternative method to be used. These restrictions include the presence of a complicated embankment geometry, multiple fill types, the presence of horizontal loads and a less than fully competent foundation soil.

Comparisons using the modified design charts published by Jewell (referred to earlier) have not been included in the comparison exercise described below. However it is stated in Appendix A of HA 68/94 that the use of a  $\phi'_{12}/\phi'$  ratio of 0.5 for inter-wedge friction, yields similar reinforcement layouts to those achieved using the Jewell charts.

## 3 LIMIT STATE METHODS

### 3.1 General

The object of a limit state approach is to apply appropriate partial factors where they are required i.e. the greatest partial factors should be applied where there is the greatest uncertainty.

The publication of BS 8006 heralded a new approach to the design of reinforced soil structures. The Code of Practice adopts limit state principles for the design of walls and embankments whereby individual partial factors are applied to the various forces acting on the structure and the soil/reinforcement properties. It is questionable however whether BS 8006 has been successful in following the limit state objective of applying partial factors where they are required most; notwithstanding its endeavour to follow current practice, it is difficult to justify a partial factor of 1.5 for soil unit weight while a partial factor of unity is applied to the friction angle, there surely being greater uncertainty with the latter than the former.

It is stated in BS 8006 that provided a reinforced soil structure is unlikely to undergo excessive differential settlement, peak effective shear strength parameters can be used for design i.e.  $\phi'_p$ ,  $c'_p$ . It should be appreciated however that with the exception of some industrial fills (e.g. Pulverised Fuel Ash), an effective cohesion value of zero is normally adopted.

BS 8006 clearly distinguishes two parts to the design process, the ultimate and serviceability limit states. As such it is the only document discussed in this paper which refers directly to the key issue of boundary deformation. Unfortunately, BS 8006 is vague in terms of how serviceability should be addressed and much is therefore left to the individual designer.

## 4 COMPARISON OF DESIGN METHODS

### 4.1 General

A number of designs have been undertaken for each of the various methods described above; the analyses were carried out using Netlon Limited's Winslope and Winwall computer programs for the design of reinforced soil structures, Figures 6 and 7. Each design was based on the use of the Tensar® range of HDPE geogrids and where possible, soil parameters were chosen such that the geogrid quantities were not governed by the normal maximum practical spacing criteria.

As the limit equilibrium and limit state methods use constant volume and peak shear strength properties respectively, clearly any comparison between methods adopting these two approaches is sensitive to the relationship assumed between the constant volume and peak values for a particular soil. For the purpose of this exercise, a  $\tan\phi'_p / \tan\phi'_{cv}$  ratio of 1.3 has been used throughout. For each design case, the most cost effective method was given a cost rating of 1.00, the relative cost

of using the other methods being based on typical current prices of the products used in the design.

### 4.2 Wall Design Methods

The results of the cost comparison exercise for walls are shown in Table 1. The most striking feature that comes out of the comparison exercise is the inefficiency of the traditional tie-back wedge approach for all but the smallest of structures. The main reason for this is the longer grid lengths required to satisfy the target factor of safety of 2.0 for sliding, although the method of dealing with the internal stability requirements is also slightly less efficient for the tie-back wedge than the Bautechnik and BS 8006 methods.

The Bautechnik method, in general uses shorter grid lengths than the BS 8006 method but the grid quantities required to satisfy internal stability criteria are significantly less in the BS 8006 method. Overall, for the examples considered in this paper, it would appear that for structures up to 3m high, the traditional tie-back wedge approach may be the most cost effective while for medium sized structures (3m to 8m high), the approach outlined in BS 8006 provides the most cost effective layouts. It should be appreciated however that for different soil and loading conditions, the 'switch in efficiency' between design methods will be at different heights of structure. Similarly, the relationship between the constant volume and peak strength properties for a particular soil will have a considerable effect on the relative performance of the limit equilibrium and limit state methods.

In addition to comparisons being made based on height of structure, the way the design methods deal with inclined faces and water pressure was also investigated. For inclined faces (Cases 7 and 8) the benefits gained by reducing the active earth pressures were equally well reflected in all three methods but when water pressure is present (Cases 9 and 10), it would seem that the BS 8006 method deals with these in a slightly more cost effective manner.

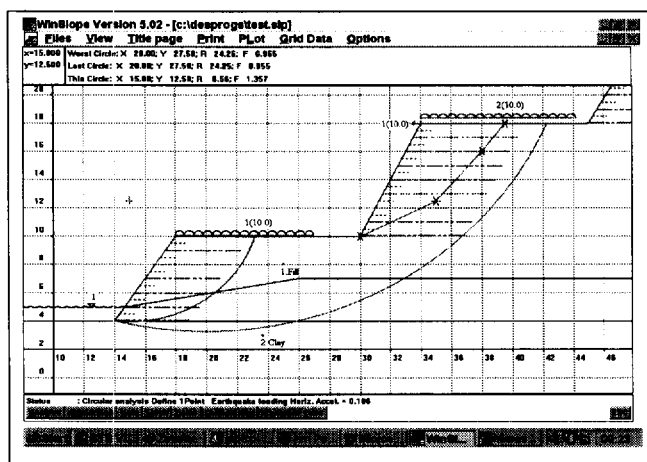


Figure 6. Winslope computer program

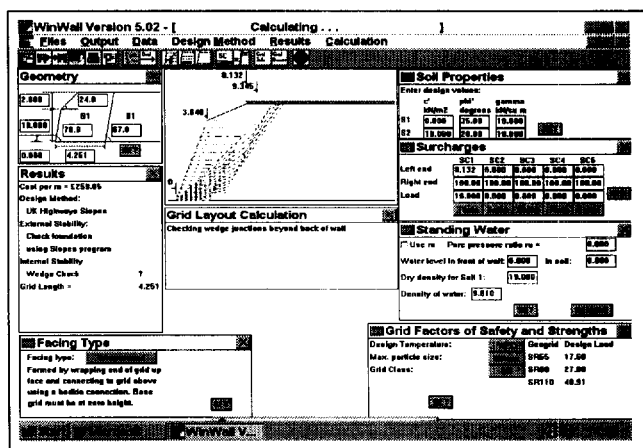


Figure 7. Winwall computer program

### 4.3 Embankment Design Methods

The results of the cost comparison exercise for embankments are shown in Table 2. It should be appreciated when examining the results that the actual reinforcement layout used to determine the cost ratio for a particular design method is based on both the minimum reinforcement requirement derived from the analysis and the maximum vertical spacing between reinforcement layers; for the latter this was 1.0m throughout. Although this undoubtedly has an effect on the overall costs used in the analysis, it is unlikely to affect the overall cost ranking of the design methods.

Possibly the most noticeable feature of the results for embankments is the significant economy attained by using a limit state approach rather than the traditional limit

equilibrium method for slip circle analyses. It would appear that the difference becomes greater for higher embankments and for shallower embankments constructed with comparatively weak fill (e.g. high plasticity clay).

The two types of HA 68/94 analysis carried out demonstrate the economy which can be attained by using a computerised approach to this method, with the inclusion of inter-wedge friction as opposed to the simplified method using the tables within HA 68/94. It should be appreciated however that in order to use a high value for inter-wedge friction (such as the value of 0.5 used in this exercise), it is necessary to check the stability of two-part wedges behind  $T_{max}$  (Love and Bond, 1996).

Table 1. Results of comparison exercise for walls

Case	Description	Bautechnik		Tie-back Wedge		BS 8006	
		Cost Ratio	Grid Length	Cost Ratio	Grid Length	Cost Ratio	Grid Length
1	3m high, 90° wall, $\phi'_{cv}=28^\circ$	1.08	2.00m	<b>1.00</b>	<b>2.60m</b>	1.10	3.00m
2	4m high, 90° wall, $\phi'_{cv}=28^\circ$	1.08	2.60m	1.13	3.40m	<b>1.00</b>	<b>3.00m</b>
3	5m high, 90° wall, $\phi'_{cv}=28^\circ$	1.06	3.00m	1.05	4.30m	<b>1.00</b>	<b>3.00m</b>
4	8m high, 90° wall, $\phi'_{cv}=28^\circ$	1.03	4.80m	1.22	6.80m	<b>1.00</b>	<b>5.60m</b>
5	12m high, 90° wall, $\phi'_{cv}=28^\circ$	<b>1.00</b>	<b>7.20m</b>	1.49	10.30m	1.14	8.40m
6	16m high, 90° wall, $\phi'_{cv}=28^\circ$	<b>1.00</b>	<b>9.60m</b>	1.64	16.60m	1.17	11.60m
7	4m high, 80° face, $\phi'_{cv}=28^\circ$	1.18	2.40m	1.34	3.80m	<b>1.00</b>	<b>3.00m</b>
8	8m high, 80° face, $\phi'_{cv}=28^\circ$	1.09	4.80m	1.41	7.60m	<b>1.00</b>	<b>5.60m</b>
9	As case 2 with water pressures	1.05	3.50m	1.45	5.60m	<b>1.00</b>	<b>4.00m</b>
10	As case 4 with water pressures	1.02	6.30m	1.67	10.30m	<b>1.00</b>	<b>5.90m</b>

Table 2. Results of comparison exercise for embankments

Case	Description	Bishop (Limit Eq.)		Bishop (Limit State)		HA 68/94 ( $\phi'_{12} = 0$ )		HA 68/94 ( $\phi'_{12} = 0.5$ )	
		Cost Ratio	Base Grid Length	Cost Ratio	Base Grid Length	Cost Ratio	Base Grid Length	Cost Ratio	Base Grid Length
1	4m high, 60° face, $\phi'_{cv} = 30^\circ$	1.23	2.80m	<b>1.00</b>	<b>2.00m</b>	1.33	2.00m	1.24	2.30m
2	8m high, 60° face, $\phi'_{cv} = 30^\circ$	1.37	5.30m	1.15	4.80m	1.08	5.25m	<b>1.00</b>	<b>4.75m</b>
3	12m high, 60° face, $\phi'_{cv} = 30^\circ$	1.66	8.00m	1.38	7.00m	1.12	8.00m	<b>1.00</b>	<b>8.00m</b>
4	4m high, 45° face, $\phi'_{cv} = 30^\circ$	1.34	3.40m	<b>1.00</b>	<b>2.40m</b>	1.43	3.40m	1.23	2.80m
5	8m high, 45° face, $\phi'_{cv} = 30^\circ$	1.50	6.00m	<b>1.00</b>	<b>4.60m</b>	1.47	6.75m	1.28	5.75m
6	12m high, 45° face, $\phi'_{cv} = 30^\circ$	1.66	8.00m	<b>1.00</b>	<b>7.00m</b>	1.29	10.0m	1.11	8.50m
7	4m high, 1 in 2 face, $\phi'_{cv} = 30^\circ$	1.72	4.80m	<b>1.00</b>	<b>3.80m</b>	1.87	7.30m	1.68	6.50m
8	8m high, 1 in 2 face, $\phi'_{cv} = 30^\circ$	1.56	10.50m	<b>1.00</b>	<b>7.00m</b>	2.03	14.5m	1.83	13.00m

n.b.  $\phi'_{12}$ =inter-wedge friction

Perhaps the most surprising feature of the results is the relative performances of the HA 68/94 and limit state slip circle methods. It would appear that despite the absence of a global factor of safety on soil strength for the HA method, with the exception of reasonably large embankments with steep faces (greater than or equal to 60°), there are considerable savings to be attained using the limit state slip circle approach.

## 5. CONCLUSIONS

The paper has reviewed the design methods most commonly used in Europe for the design of reinforced soil structures. It is clear that while there are many similarities between the methods used for the design of reinforced soil walls, several important differences exist which in some cases result in significant variation in the amount of reinforcement required to satisfy the various design criteria. Similar differences are observed in embankment design methods.

Overall it is not possible to indicate one particular design method for walls or embankments which consistently yields more cost effective reinforcement layouts. It would appear however that the limit state methods proposed in BS 8006 are economic in most cases.

There is the possibility that individual designers will select their own favourite methods for walls and embankments without being aware of the appropriateness of other approaches. However, when a particular method is chosen simply based on cost, it is important that the designer understands fully the design philosophy and reasons for the economy. In the case of HA 68/94 for example, the adoption of a high inter-wedge friction angle requires additional checks to be made to ensure a safe embankment design is achieved.

## ACKNOWLEDGEMENT

The writers would like to acknowledge the efforts of Mr. Paul McCombie in developing the design software used for the analyses referred to in this paper.

## REFERENCES

British Standards Institution. BS 8006: *Code of practice for strengthened reinforced soils and other fills*: 1995, BSI, London.

*Certificate No. Z-20.1-102*, Deutsches Institut für Bautechnik, Berlin, 1990.

Department of Transport, *HA 68/94 Design methods for the reinforcement of highway slopes by reinforced soil and soil nailing techniques*, HMSO, UK, 1994

Jewell, R, *Revised design charts for steep reinforced slopes*, Proc. Symp. Reinforced embankments - theory and practice, Cambridge, Thomas Telford, pp18-30, 1990.

Love, J and Bond A, *discussion on 'The computerised design of reinforced soil structures' by Penman, J and McCombie, P (1996)*, Ground Engineering, Emap Construct, London, January/February 1997, p36.

Netlon Limited, *The design of reinforced soil structures using Tensar geogrids*, 1997

Penman, J and McCombie P, *The computerised design of reinforced soil structures*, Ground Engineering, Emap Construct, London, November 1996, pp 36-37 and December 1996, p33.

Vidal, H, *La terre armée*, Annls L'Inst Tech de Batement et des Travaux Publics, Serie Matériaux 30, Puppement No. 223-4, July-August 1966.





displacement field along the failure surface defined by a vertical top displacement  $y_1$  (see Figure 1), (ii) the anchored membrane concept (see Figure 2), and (iii) the geosynthetic extensibility. The local equilibrium of each sheet is considered, coupled with the tension constitutive model of the reinforcement and of that in friction of the soil-geosynthetic interface (elasto-perfectly plastic behavior). Faced with the problem of the determination of the soil stiffness modulus, a simplified mechanism of the membrane behavior has been considered by the authors: (a) The reinforcement tension is constant all along the membrane zone  $B_1B_2$  (see Figure 2) and is equal to the ones at  $B_1$  and  $B_2$ ; (b) This tension is either assumed to act in the horizontal direction or in the direction of the tangent to the failure surface (maximum inclination); And (c) the modeling of the geosynthetic behavior is considered either with a small or large displacements assumption. Note that the corresponding software "Cartage" is widely used in France for practical design work.

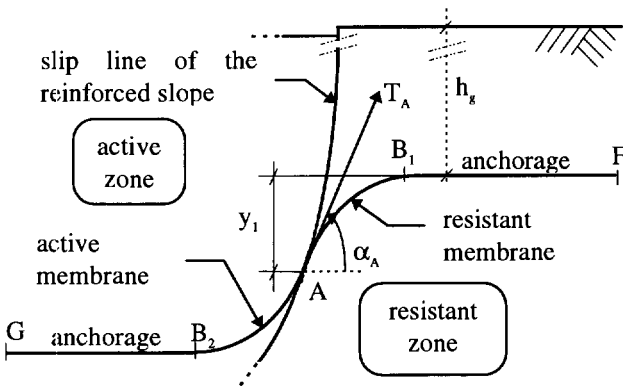


Figure 2: Anchored membrane concept.

## 2.2 Modified "Displacement Method"

This method considers a more rigorous mechanism (circular shape) of the membrane behavior. The determination of the reinforcement tension  $T_A$  (see Figure 2), which is also assumed to be constant all along the circular membrane zone, is based on the local equilibrium of this zone. Thus, the reinforcement tension and its inclination  $\alpha_A$  depend on the vertical top displacement  $y_1$  and the soil stiffness modulus. Note that the corresponding software "Membrane" is used essentially for research (Gotteland, 1991).

## 2.3 "Variational Displacement Method"

The problem has been split into two different parts:

- Global equilibrium of the sliding mass  
Applying the variational limit equilibrium method, elaborated by Baker and Garber (1977) in the case of unreinforced slopes, to the one of reinforced slopes, it

has been shown that (i) the trace of the critical failure surface is a log spiral (see Figure 1), and (ii) the only moment equilibrium equation of all forces acting on the sliding mass is enough for the determination of the safety factor  $FS$ , defined with respect to the shear strength parameters of the soil.

- Local equilibrium of the reinforcement sheets

In order to assess the reinforcement contribution to the stability, the variational calculus has been applied to the equilibrium of the membrane zone in the neighborhood of the failure surface, considering the principle of the "displacement method" (i.e.: the anchored membrane concept, see Figure 2). The variational approach allows the determination of the optimal shape (log spiral) as well as the optimal position of the sheet for which one obtains the extremal tension at the intersection with the failure surface. Thus, the tension is no longer assumed to be constant along the membrane zone. Furthermore, this method provides the tension distribution and the relative soil-geosynthetic displacements all along the sheets.

## 2.4 Comparison Of The Different Models

Table 1 shows the comparisons of some principles of the three above mentioned models, regarding (a) the global equilibrium of the sliding mass (columns 1 to 3) and (b) the local equilibrium of the reinforcements (columns 4 to 6). Note that the listed principles are those which differ from each other. It appears that the "Displacement Method" has gained in rigour in its two latter developments (i.e. less a priori assumptions). The improvement provided by the "Modified" model consists of a more rigorous determination of the reinforcement tensions. With the present model, it provides an improvement on the determination of both the safety factor (no a priori assumptions concerning the failure surface shape, nor the normal stress distribution along this surface), and the reinforcement tension (no a priori assumptions concerning the shape of the membrane zone, nor its critical position).

## 3 COMPARATIVE CASE STUDY

In order to show the developments of the "displacement method", the three above mentioned models have been applied to a 6m high wall reinforced with 11 geosynthetic layers. All other data required for the analysis are presented in Figure 3. For all three models, the safety factor  $FS$  of the soil in shear is set to 1.5. Note that all "Cartage" results correspond to the assumption of large displacements with a horizontal reinforcement tension (see §2.1).

Table 1. Comparison of some principles of the three models

Name	1. Limit equilibrium method	2. Failure surface shape	3. Search for critical failure surface	4. Critical position of the membrane zone (as rest)	5. Tension in B <sub>1</sub> B <sub>2</sub> (see Fig.2)	6. Inclination of tensions (null) or (maximum)
“Cartage”	“Perturbation”	any (circular more used)	manual	(as rest)	(constant)	(null) or (maximum)
“Membrane”	“Perturbation” Fellenius Bishop Jambu	(circular) (bilinear) (mixed)	manual	(fixed)	(constant)	(fixed)
Present model	Variational	Log-spiral*	automatic	result of minimisation process*	non constant*	result of minimisation process*

Notes: Terms in parentheses () refer to a priori assumptions, and the one followed by \* refers to analytical result.

### 3.1 Failure Surfaces

Concerning the two first models (i.e. “standard” and “modified”), and for each potential slip line (circular shape) considered, a critical vertical top displacement  $y_{ic}$  corresponding to  $FS=1.5$  is determined. The critical slip circle (represented in a dotted line in Figure 3), which is the same in both models, corresponds to the larger  $y_{ic}$  value considering six different potential slip circles (Gourc et al, 1989).

For the present model, the slip line shape is a log spiral and the critical position (represented in Figure 3) corresponds to the critical  $y_i$  value (called  $y_{ic}$ ) which provides a safety factor  $FS=1.5$  as its minimum value, considering 860 different log-spirals passing through the toe of the wall.

Note that these two lines are rather close to each other in the lower half part of the wall, then the log-spiral is placed further away from the facing than the circle. Nevertheless, regarding the difference in the determination of the critical position of the failure surface in each model, the scatter between these positions is small.

### 3.2 Critical Vertical Top Displacements

Concerning the critical vertical top displacements  $y_{ic}$ , the standard model gives 26mm, the modified one gives 50mm, and the present one gives 88mm (see Figure 3). Thus, it seems that there is a tendency in the development of the method for an increase of this key parameter.

### 3.3 Critical Tension Distributions

Figure 4 shows the distribution of the critical tensions and of their inclinations along the failure surfaces. It is interesting to note that the tension distribution of the present model is close to the one of “Cartage” in the

upper half part of the wall, and close to the one of “Membrane” in the lower half part. Plus, the present model gives the lowest maximal tension  $T_{max}$  (presented in Figure 4), which is reached in the lowest sheet in each model. Nevertheless, the scatter between these tension distributions is rather small.

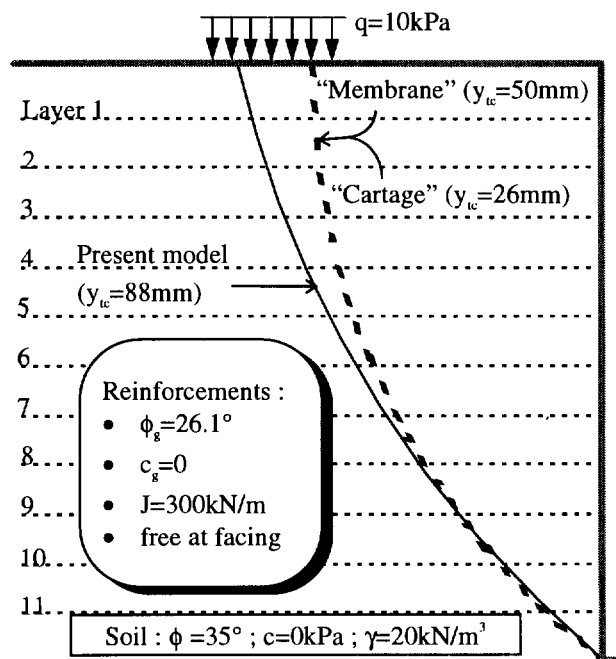


Figure 3. Case study - Critical positions of the theoretical failure surfaces

### 3.4 Critical Tension Inclination Distributions

Concerning the tension inclinations, the distributions as given by “Membrane” and the present model (null for “Cartage”) are very different from each other. “Membrane” distribution decreases continuously with the depth, while the one of the present model passes through a minimum value at the second layer (see

Figure 4), then from the 8<sup>th</sup> layer and deeper it reaches the maximal inclination distribution, which corresponds to tensions tangent to the failure surface (the log-spiral of Figure 3).

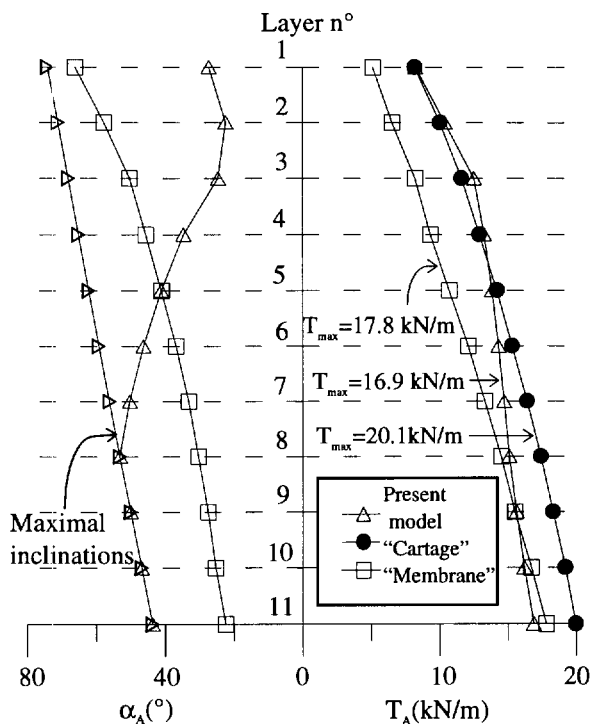


Figure 4. Comparative study (case study of Figure 3)

### 3.5 Discussion

The present comparison study shows that (i) the critical failure surfaces obtained with the three models are close to each other (see Figure 3), (ii) the reinforcement tension distributions along the failure surface are similar (see Figure 4), but (iii) the obtained critical vertical top displacements  $y_w$  has been increased significantly from one model to its following development (92% between the two first, and 76% between the two last). However, the latter parameter is difficult to correlate to actual measurements, and further research should be performed on the validation of these models on real structures build and tested to failure.

## 4 CONCLUSION

This paper presents the recent developments of the "displacement method". This method, which is the standard in France for the design of geosynthetically reinforced earth structures, has since been improved at least twice. The first improvement concerns the determination of the reinforcement tensions, the second one also concerns the determination of the safety factor of the structure. Indeed, the originality of the latter is

the application of the variational calculus on both the equilibrium of the sliding mass and the one of the membrane zone in the vicinity of the failure surface. This analysis allows a significant decrease in the number of a priori assumptions considered in the previous models. A comparative study on a 6m high wall has shown that the rigour tends to increase the obtained critical top displacement.

## REFERENCES

- Baker, R. and Garber, M. (1977) "Variational Approach to Slope Stability", *9th Int. Conf. on Soil Mechanics and Foundation Engineering*, Tokyo, Japan, Vol. 2, pp. 9-12.
- Fidler, P., Gotteland, Ph., Gourc, J. P. and Haidar, S. (1994) "Evolution of the 'Displacement Method' applied to soil reinforced structures", *Int. Conf. on Geotextiles, Geomembranes and related products*, Singapore, pp.225-228.
- Gotteland, Ph. (1991) *Renforcement des sols par géosynthétiques ; dimensionnement et validation* Ph.D thesis, Grenoble University, France, 384 p.
- Gourc, J. P., Ratel, A. and Delmas Ph. (1986) "Design of fabric retaining walls : the Displacements Method", *Third Int. Conf. on Geotextiles and geomembranes*, Vienna, Austria, session 3A/1, pp. 289-294.
- Gourc, J. P., Ratel, A. and Gotteland, Ph. (1988), "Design of reinforced soil retaining walls : Analysis and comparison of existing methods and proposal for a new approach". *The Application of Polymeric Reinforcement in Soil Retaining Structures*, Nato Asi Series, Applied Sciences, Vol. 147, pp.24-67.
- Gourc, J. P., Gotteland, Ph. and Delmas, Ph. (1989), "Parametric study of geosynthetic reinforced retaining walls using the displacement method". *Geosynthetics '89*, San Diego, USA, pp. 112-123.
- Lemonnier, P. (1995) *Application de la méthode variationnelle au problème de la stabilité des talus renforcés par des nappes géosynthétiques*, PhD thesis, I.N.S.A Lyon, France, 483 p.
- Lemonnier, P. and Soubra, A. H. (1997) *Recent development of the "displacement method" for the design of geosynthetically reinforced slopes - Comparative case study*, Rencontres'97, CFG, Reims, France, Vol. 2, pp. 28AF-31AF (10p.).
- Yoshioka, A., Delmas, Ph., Gourc, J. P. and Gotteland, Ph. (1990) "Validation of the 'displacement method' on an experimental reinforced wall at failure" *Int. Conf. on Geotextiles, Geomembranes and related products*, The Hague, Netherlands, Vol. 1, pp.61-66.

# Locally Loaded Geosynthetic Reinforced Soil Structure: Calculation Method

E. Haza

Ph.D., Lirigm, Grenoble University, France

P. Gotteland

Assistant Lecture, Lirigm, Grenoble University, France

J.P. Gourc

Professor, Lirigm, Grenoble University, France

**ABSTRACT:** This article presents a proposed method for the preliminary design of geosynthetically reinforced soil structures, adapted to the case of localised surface loads. The first section describes two modifications made to the basic calculation method: firstly, to consider the deformable nature of geosynthetics and, secondly, to consider a local equilibrium calculation of each reinforcement. In the second section, an attempt is made to validate the proposed initial modifications on the basis of results obtained using an experimental structure locally loaded up to its failure point. The local approach seems satisfactory.

**KEYWORDS:** Retaining wall, Reinforcement calculation method, concentrated top load, Prediction, Experimentation.

## 1. INTRODUCTION

Geosynthetically reinforced soil embankments with flexible facings are commonly used in France for retaining purposes; their ability to bear is also currently being studied at the Grenoble Lirigm laboratory. This article will concentrate on this function for case where the head of the structure is locally loaded.

Little is known about structures with flexible reinforcement sheets which are locally loaded at the head. Observation of the way in which instrumented embankments fail (Matichard and al., 1992, Lensiewska and al., 1992) shows that the reinforcing sheets in the upper part of the embankment are placed under high stress by the slab which perforates the embankment, and that the tensile force and slope of the reinforcing sheets in the shear zone are greatly reduced towards the base of the embankment. This behaviour is the reverse of that of a structure with no localised overload or which is evenly overloaded, where the sheets at the base are under greatest tensile forces.

On a reference experimental structure (Gourc and al., 1995) (Photo 1), an attempt will be made to validate a preliminary design method for these structures which is quick and easy to use: the modified double-block method (shortened to DB), based on the limit equilibrium calculation principle. This method is sufficiently widely used to study the stability of structures which are either not overloaded or evenly overloaded.



Photo 1. The GARDEN experimentation

## 2. THE DOUBLE-BLOCK METHOD (DB)

With the DB method, the active part of the embankment is divided into two rigid blocks placed side by side and assumed to be slipping. The slip line is bilinear, with kinematic convexity condition.

The points where the slip line intersects the facing (point A) and the upper surface of the embankment (point C), as well as the positions of the slope break point and the inter-block line (point B) are selected by the user (Figure 1).

The limit equilibrium of the double block is calculated by applying a resultant horizontal thrust  $P$ , redistributed throughout the reinforcing sheets  $j$  (tensile forces  $T_j$ ) (Figure 1). The slip line is assimilated to the line along

which the maximum tensile forces are accommodated in the reinforcing sheets. The equality  $\Sigma T^j = P$  is checked.

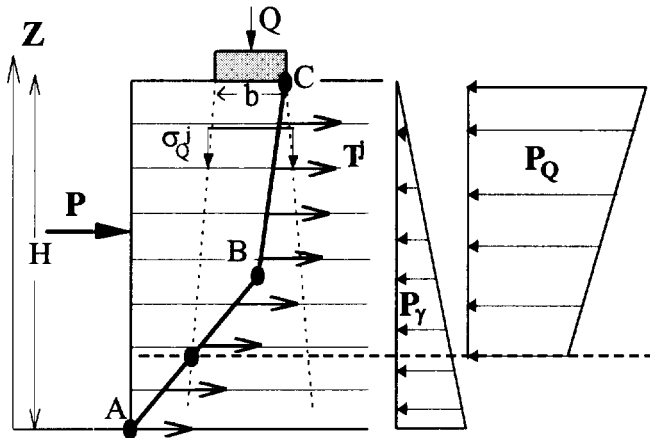


Figure 1. Double-Block method principle.

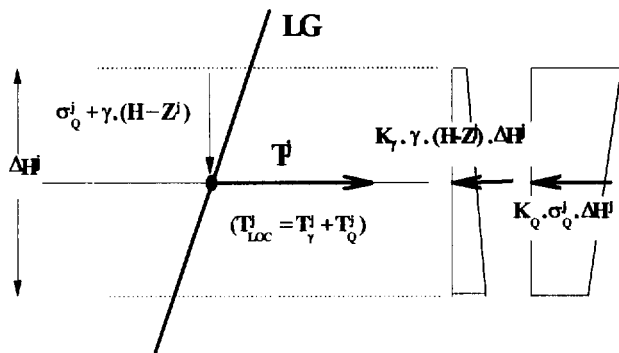


Figure 2. Local equilibrium of a reinforcing sheet j.

The distribution used for the resultant vertical stress of the localised overload Q is almost vertical inside the embankment (angle of distribution  $\phi_{soil}/4$ ). The vertical stress at the reinforcing sheet j which is applicable in the distribution zone will be called  $\sigma_Q^j$ .

The safety coefficient F is applied to the mechanical properties of the earthfill. The theoretical failure of an embankment is thus obtained when  $F=1$ .

Two approaches are proposed for the preliminary design, one known as *overall* and the other *local*.

### 2.1 Overall Approach (OA)

Overall equilibrium of the unstable area is considered to be ( $\Sigma T^j = P$ ).

In a first option (OA1), the tensile forces  $T_{OA1}^j$ , mobilized in the reinforcement sheets, are fixed; the value of F is deduced.

A second option (OA2) consists in fixing F and then deducing a uniform tensile force distribution throughout

the reinforcement ( $T_{OA2}^j = T_{OA2}$ , except on case of anchorage problem). The critical slip line is obtained for the maximum value of  $T_{OA2}$ .

### 2.2 Local Approach (LOC)

Another approach consists in studying the local equilibrium of the complex [soil+reinforcing sheet] at the level of each reinforcing sheet for a predefined slip line (Figures 1 and 2).

The action of the localised head load Q is separated from the action of the deadweight of the soil. This means that a different distribution can be considered for each of these actions along the slip line.

The double-block equilibrium thrust  $P_Q$  is calculated for the double-block only subjected to Q, for a density of the soil body in the double-block assumed to be zero. In accordance with the observations already made, the distribution made is one whereby the upper reinforcing sheets which are under greater tensile forces. The distribution of  $P_Q$  is trapezoidal. The proposed hypothesis consists in assuming that the reinforcing sheets are under tensile forces only if their intersection with the slip line is included in the top load area of influence (Figures 1 and 2).

A thrust coefficient  $K_Q$  is calculated on the basis of  $P_Q$  to determine local tensile forces  $T_Q^j$  :

$$K_Q = \frac{P_Q}{\sum_j \sigma_Q^j \cdot \Delta H} \quad (1) \quad \text{and} \quad \begin{cases} T_Q^j = K_Q \cdot \sigma_Q^j \cdot \Delta H^j \\ \Sigma T_Q^j = P_Q \end{cases} \quad (2)$$

For the action of weight of the soil, the conventional triangular distribution hypothesis is considered. The thrust  $P_\gamma$  is calculated, equilibrium resultant of the double-block under its own weight, on the basis of which the thrust coefficient  $K_\gamma$  and the local tensile forces  $T_\gamma^j$  are deduced.

$$\begin{cases} T_\gamma^j = K_\gamma \cdot \gamma \cdot (H - Z^j) \cdot \Delta H^j \\ \Sigma T_\gamma^j = P_\gamma \end{cases} \quad (3)$$

The tensile force in the reinforcing sheet j is then obtained by (Figure 2):  $T_{Loc}^j = T_Q^j + T_\gamma^j$ .

Given the cases examined, where the overload Q is high compared with the soil weight, the tensile forces  $T_Q^j$  will be generally high compared to the tensile forces  $T_\gamma^j$ , and thus predominant in the design of the structure.

### 3. COMPARISON WITH EXPERIMENTAL RESULTS

#### 3.1 Experimental structures

The GARDEN programme ("Geotextile": Application in Reinforcement: Experimentation and Normalisation) consisted in loading to failure point two embankments with cellular facings (Löffel type), at an 80° slope (Photo 1).

These embankments have a total height  $H = 4.35$  m, and are reinforced by geosynthetics having a tensile strength ( $T_p$ ) and different stiffness moduli, with local head loading (Gourc and al., 1995). The loading system is presented on the Figure 3.

An exhaustive assessment of the behaviour of these two structures has been made (Haza, 1997). They were hardly instrumented (Figure 4).

One of these embankments is shortly presented here : the embankment reinforced by a non-woven polyester geosynthetic (NW embankment, Figure 5). The other embankment is reinforced by a woven polyester geosynthetic (W embankment, figure 6).

The mechanical properties of the earthfill are  $\phi = 36^\circ$ ,  $C = 4$  kPa and  $\gamma = 19$  kN/m<sup>3</sup>.

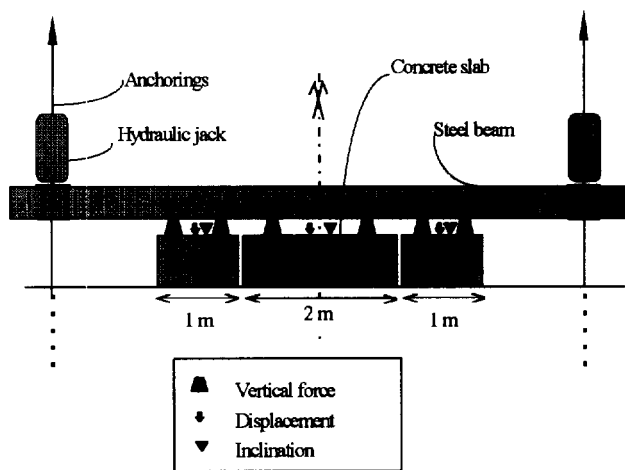


Figure 3. Loading system of both experimental embankments.

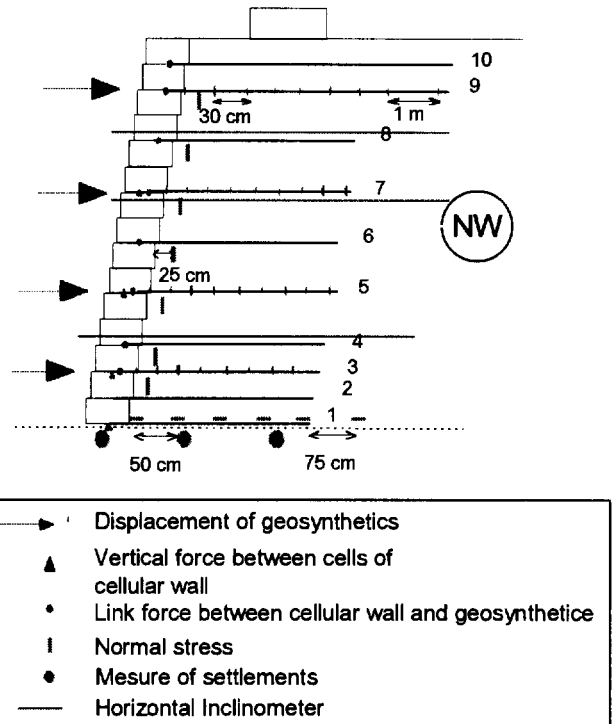


Figure 4. Instrumentation of the NW embankment.

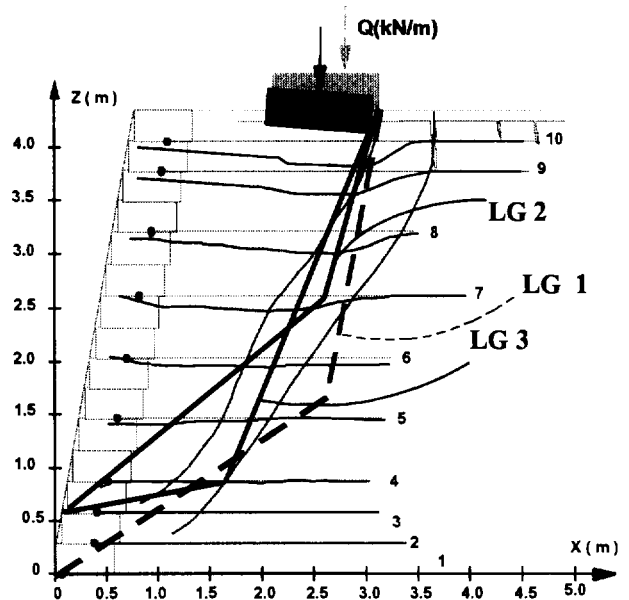


Figure 5. NW embankment profile - slip lines retained for the reverse calculations.

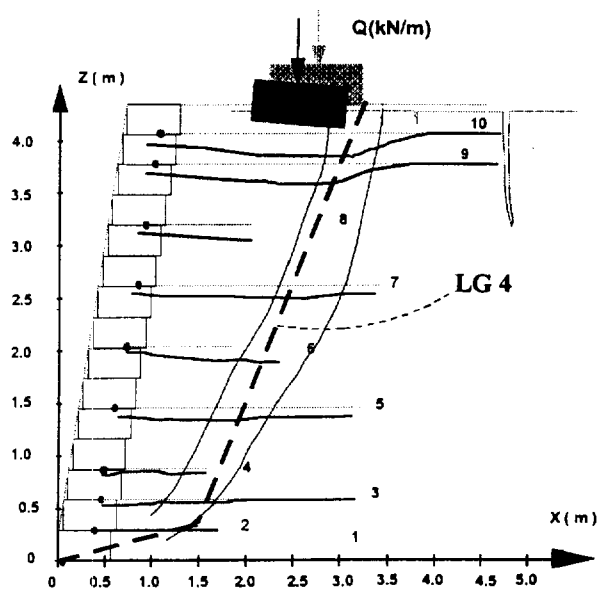


Figure 6. W embankment profil - slip line retained for the reverse calculations.

### 3.2 Preliminary design stage

#### 3.2.1 Definition of profiles: overall approach (OA)

The preliminary design of these experimental structures was carried out using the overall approach (OA2): the safety coefficient was fixed ( $F = 1$ , theoretical failure reached), as was the maximum load considered at the conceptual design stage  $Q = 330$  kN/m.

The critical slip line was obtained (LG 1 in the NW embankment, Figure 7). The selected tensile strength of the geosynthetic used was equal to  $T_{OA2}$  ( $T_f = T_{OA2} = 25$  kN/m in the NW embankment).

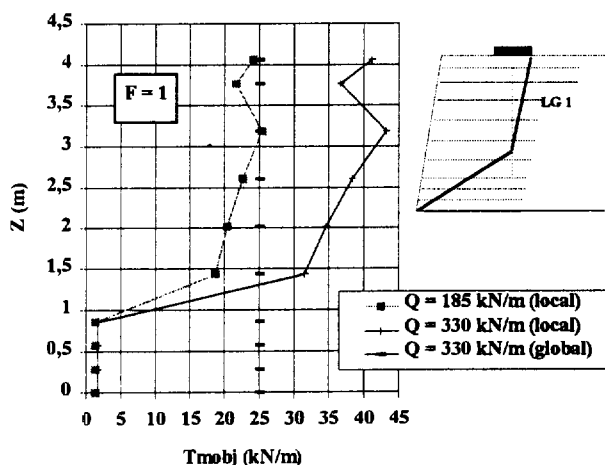


Figure 7. Preliminary design stage - tensile force distribution (NW embankment).

However, since the anchoring strength of the two upper sheets is low ( $< T_f$ ), these sheets were made longer. Thus, the NW embankment is reinforced by eight 3 m long sheets and two 4 m long upper sheets and the W embankment is reinforced by three 3 m long sheets and two 4 m long upper sheets (Figures 5 and 6).

#### 3.2.2 Forecast failure load: local approach (LOC)

For  $Q = 330$  kN/m,  $F = 1$  and slip line LG 1 defined above, the tensile force distribution  $T_{LOC}^j$  gives values much higher than  $T_f (= 25$  kN/m) in the upper two thirds of the NW embankment (Figure 7).

A new loading condition  $Q$  was then calculated compatible with a maximum tensile force value  $T_{LOC}^j$  closer to  $T_f$ . A value of  $Q_{LOC}^F = 185$  kN/m was obtained for a maximum value of  $T_{LOC}^j = 25$  kN/m (Figure 7). The same value of  $Q_{LOC}^F$  was obtained for the W embankment, for a maximum value of  $T_{LOC}^j = 44$  kN/m ( $= T_f$ ).

### 3.3 Feedback from experimentation

At the end of the test, the maximum load applied on the two embankments was  $Q_{EXP} = 230$  kN/m.

By measuring the displacement of reinforcing sheet points at failure, the range of maximum reinforcement sheet strain zones can be obtained (Figures 3 and 4). The distribution of experimental tensile forces  $T_{EXP}$  can then be estimated (Figure 8, in the NW embankment). Observations of the two embankments confirmed that the upper sheets work much harder than the others, and tend to bend considerably (Gotteland and al., 1997).

The critical slip line selected for the preliminary design in the NW embankment (LG 1) was not exactly within the range of maximum tensile force values. In the following discussion, two other slip lines included within this range, LG 2 and LG 3, were considered in the NW embankment for carrying out the reverse calculation using the DB method. The slip line LG 4, included within the range of maximum tensile force values, was considered in the W embankment for the reverse calculation (Figures 5 and 6).

#### 3.3.1 Reverse calculation: overall approach (OA)

The forecast failure load in the overall approach (§ 3.2.1) was 330 kN/m, a value much higher than the load observed under experimental conditions ( $Q_{EXP} = 230$  kN/m).

The overall approach (OA1), with  $Q_{EXP} = 230$  kN/m and  $T_{OA1}^j = T_{EXP}^j$  applied along the line LG 2 and the deeper line LG 3, gives safety coefficient values of  $F = 0.66$  and  $F = 0.995$  respectively (Figure 8). Therefore,



with the overall approach, the safety coefficient  $F$  depends closely on the slip line chosen, although the two lines considered are relatively close. A satisfactory result is obtained for line LG 3 ( $F \approx 1$ ).

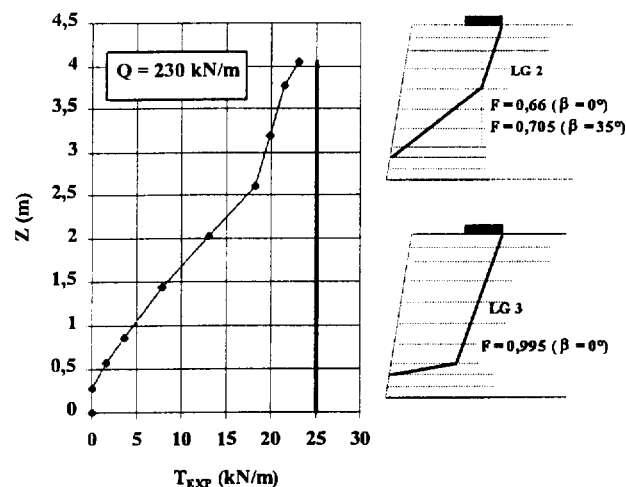


Figure 8. Experimental tensile force distribution in the NW embankment.

### 3.3.2 Overall approach: proposed development

In the shear zone, flexible reinforcing sheets become deformed. Therefore, the stress that builds up here does not remain horizontal.

A vertical component of the tensile forces along the shear line, taken into account in the active double-block equilibrium, was introduced into the calculation (Haza, 1997).

In the light of the observations, it is proposed to divide up the active zone of the embankment into two simplified zones :

- a "top" zone (above point B, Figure 1), where the tensile forces that build up in the reinforcements are all inclined at the same angle  $\beta$ ,
- a "bottom" zone (below point B, Figure 1), where the tensile forces remain horizontal.

As before, the option (OA1) is applied in the NW embankment with  $Q = Q_{EXP} = 230$  kN/m, by imposing  $T_{OA1}^j = T_{EXP}^j$  but inclining the "top" forces at  $\beta = 35^\circ$  (inclination of sheet n°10 measured when the structure was dismantled). To ensure that only the upper reinforcing sheets were inclined, line LG 2 is considered because point B is high up in the embankment.  $F = 0.705$  in place of 0.66 was obtained. By inclining these forces, a slight increase in the safety coefficient  $F$  was observed; it nevertheless remains less than 1.

### 3.3.3 Local Approach (LOC)

During the preliminary design, the foreseeable failure load obtained ( $F = 1$ ) is less than the failure load measured experimentally ( $Q_{LOC}^F (=185$  kN/m) <  $Q_{EXP} (=230$  kN/m)).

To compare the results of the local approach with the overall approach, the slip lines LG 2 and LG 3 are also used in the NW embankment (Figure 9), and the slip line LG 4 in the W embankment (Figure 10).

By applying  $F = 1$  and  $Q = Q_{EXP} = 230$  kN/m, the tensile forces distribution calculated along the slip line LG 2 is much higher than the distribution obtained experimentally, whereas along LG 3 it is closer. Thanks to the low position of point B on line LG 3, the deeper-lying reinforcement sheets in the embankment can also take part in the overload double-block equilibrium because they are directly involved in load distribution within the embankment (Figure 9). The thrust  $P_Q$  is thus distributed among a greater number of reinforcement sheets, thereby reducing the tensile forces  $T_{LOC}^j$ . Meanwhile, the tensile forces distribution calculated along the slip line LG 4 in the W embankment is not so close to the distribution obtained experimentally (Figure 10). The very large vertical space between the sheets at the middle level of the W embankment can be an explanation of this result.

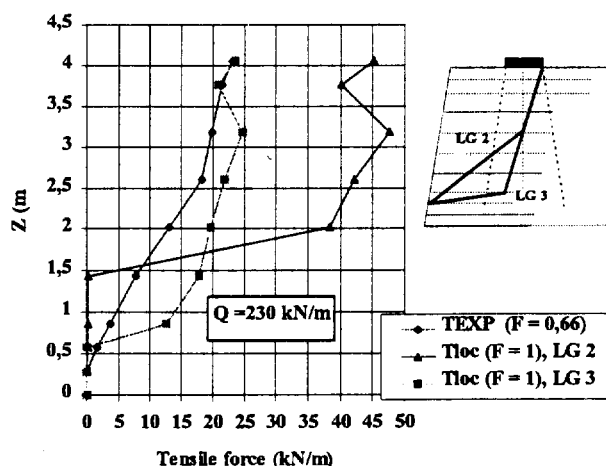


Figure 9. Reverse calculation by the local approach (NW embankment)

As the point B (Figure 1) is near the bottom of the embankment, its exact position has little bearing on the values of  $T_{LOC}^j$ ; the same is true for the position of point A, as the level of participation of the lower sheets remains very low.

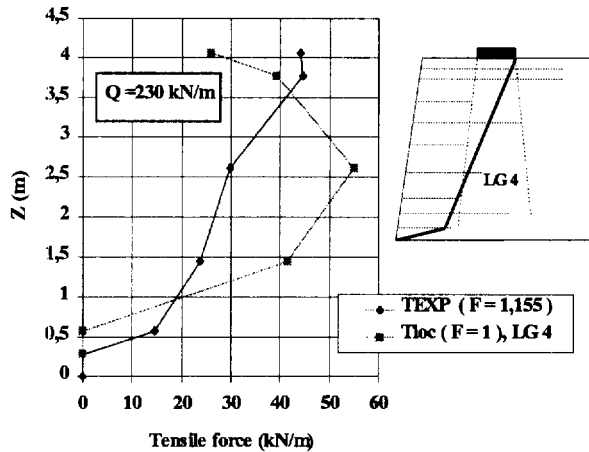


Figure 10. Reverse calculation by the local approach (W embankment).

This type of slip line, emerging at C, just upstream of the loading slab, with a high angular opening, would seem to match the local approach modelling system used here.

The same type of slip line could be used for the design of reinforced embankment whose geosynthetic is more or less stiff. Indeed, we observed, during the GARDEN experimentation, that the position of the experimental slip line is similar in both embankments (Figures 5 and 6). However, the stiffness moduli of the geosynthetics were different ( $J_{NW} = 95 \text{ kN/m}$ ,  $J_W = 340 \text{ kN/m}$ ).

#### 4. CONCLUSIONS

The operating and failure mechanisms of geosynthetically reinforced earth structures, with local head loading condition, are still relatively unknown. This paper proposes the outlines of a simple and fast calculation method for the preliminary design of such structures. Two modifications to the double-block method, the first to take into account the deformable nature of the reinforcing material (Overall Approach), and the other to take into

account a distribution of the tensile forces produced by Local Approach, are used to approximate the observed behaviour on experimental structures subjected to massive deformation.

The Local Approach proposed gives promising results and should become even more satisfactory with possible allowance being made for the angle of inclination of the tensile forces, i.e., consideration for the deformable nature of the reinforcing sheets.

We have suggested (Haza, 1997) a design method which needs now to be validated on several experimental results.

#### REFERENCES

- Gotteland P., Gourc J.P., Villard P. (1997) Geosynthetics reinforced structures as bridge abutments; Full scale experimentation and comparison with modelisations, *Proceedings of the Int.Symposium on Mechanically Stabilized Backfill*, Denver, U.S.A., 10 p., to be edited.
- Gourc J.P., Gotteland P., Haza E., Perrier H., Baraize E. (1995) Geotextile Reinforced Structures as Bridge Abutments : full scale experimentation, *Proceedings of the VI<sup>th</sup> International Conference on Geosynthetics*, Nashville, USA, pp 79-92.
- Haza E. (1997) Massif en terre renforcé par géosynthétiques, chargé localement en tête : expérimentation et méthode de calcul , Ph. D, *University of Grenoble*.
- Matichard Y., Thamm B., Sere A. (1992) Behaviour of a geotextile reinforced earthwork under surface loading, *Proceedings of seiken symposium NO.11*, Tokyo, Japan, pp 117 - 130.
- Yoshioka A., Delmas P., Gourc J.P., Gotteland P. (1990) Validation of the « displacement method » on an experimental reinforced wall at failure, *Proceedings of the IV<sup>th</sup> Int. Conf. on Geotextiles, Geomembranes and Related Products*, The Hague, Neatherland, pp 61 - 66.

# Measuring geotextile strains with strain gages

Stanley R. Boyle  
 Engineer, Shannon & Wilson, Inc., Seattle, Washington, USA

Robert D. Holtz  
 Professor, Department of Civil Engineering, University of Washington, Seattle, Washington USA

**ABSTRACT:** Laboratory research was undertaken to evaluate the effectiveness of electrical resistance strain gages to measure geotextile strains. At low strains, typical of those observed in geosynthetic reinforced soil slopes and walls, the strain gages were found to underrecord total strain and incremental strain in both in-isolation and in-soil load-elongation tests on both polypropylene and polyester woven geotextiles. The degree of underrecording decreased with increasing geotextile strain. Strain gages were effective for measuring the strain distribution in geotextiles and for monitoring geotextile creep.

**KEYWORDS:** Geotextiles, reinforcement, strain gages, strain measurements, testing

## 1 INTRODUCTION

To evaluate the effectiveness of electrical resistance strain gages for measuring strains in reinforcement geotextiles, a series of load-elongation tests were performed on woven polypropylene and polyester geotextiles to which strain gages had been attached. Specimens 100 mm long by 200 mm wide were tested in isolation and confined in soil. Three polypropylene woven slit film geotextiles (PP1, PP2, and PP3) and two polyester woven multi-filament geotextiles (PET1 and PET2) were included in the test program, Table 1.

Table 1: Geotextiles tested.

Material	Material and Description	Strength <sup>1</sup>
PP1	Polypropylene, woven, slit-film	26 (15) <sup>2</sup>
PP2	Polypropylene, woven, slit-film, 2 layer stitch-bonded	49 (15) <sup>2</sup>
PP3	Polypropylene, woven, slit-film, 3 layer stitch-bonded	77 (15) <sup>2</sup>
PET1	Polyester, woven, multi-filament	215 (10) <sup>3</sup>
PET2	Polyester, woven, multi-filament	175 (10) <sup>2</sup>

<sup>1</sup> Wide width strength, kN/m, and associated (elongation, %), ASTM D 4595.

<sup>2</sup> Manufacture supplied data from Industrial Fabrics Association International (1990, 1992).

<sup>3</sup> Average value from Allen et al. (1992).

In-isolation wide width tests were performed using an MTS testing machine which had been fitted with hydraulically operated clamps, in accordance with ASTM D 4595. The geotextiles were loaded to failure at rates of 10%/min and 1%/min. In an attempt to eliminate end effects, overall elongation of the geotextiles was measured using a "scissors" type displacement measurement device,

Figure 1. The scissors were attached to the geotextiles by pushing needles, mounted at the end of each arm, through the geotextile. The distance between the needles at the beginning of each test, approximately 60 - 75 mm for 100 mm gage length specimens, was used as the initial gage length for calculating overall strains in the woven geotextiles. No measurable reduction in strength resulted from insertion of the needles.

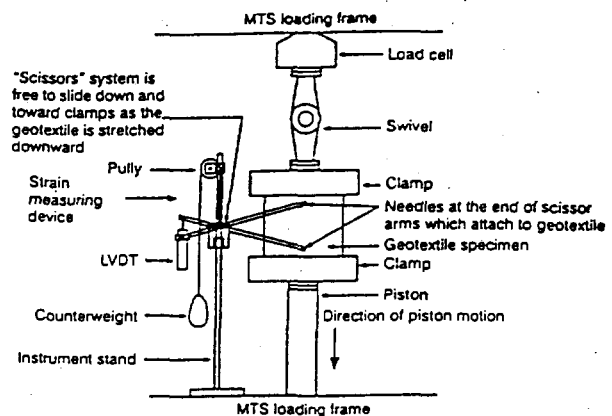


Figure 1: In-isolation test device.

In-soil tests were conducted using a plane strain unit cell device (UCD), Figure 2. During UCD tests, horizontal deformation of the soil is resisted by an applied lateral confining pressure and by tensile loads induced in the reinforcement. Elongation and tension in the geosynthetic specimen are measured, respectively, by LVDT's and load cells connected to the clamps which grip the reinforcement at both ends. Stiff end plates, to which the clamps are mechanically linked, ensure the reinforcement and soil

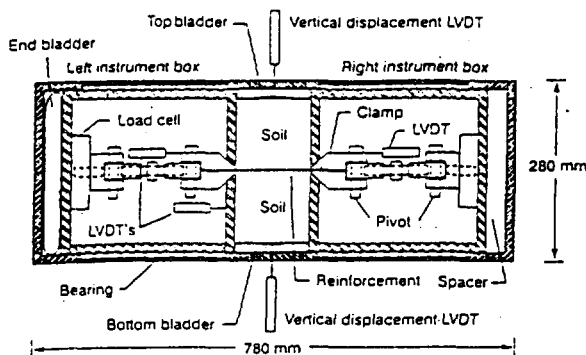


Figure 2: Unit Cell Device (UCD).

displace equally in the lateral direction during loading and that the faces of the specimen remain orthogonal. Because the UCD is a load control device, with load applied vertically to the soil specimen, neither the vertical nor horizontal (reinforcement) strain rates could be controlled, but they could be measured.

Dimensions and yield strain of the high-elongation strain gages used in the testing program are presented in Table 2. A single gage was attached at the center of each in-isolation specimen. Two or three gages were used in the in-soil tests; they were positioned along the length of the geotextile specimen to permit measurement of the strain distribution. After preparing the surface with a primer, the Tokyo Sokki Kenkyujo, Co., Ltd. Model YL-series gages were attached to the polypropylene woven geotextiles using a cyanoacrylate type CN adhesive. The BLH, Inc. SR-4 type, model PA-series gages were attached to the polyester geotextiles using an SR-4 adhesive, without priming the surface. To protect the strain gages during soil compaction and load application in the in-soil tests, the strain gages and their lead wires were coated with type MB-4 rubber cement and then covered with a small piece of 0.3 mm thick latex rubber.

Table 2: Strain gages tested.

Gage Type	Gage Length and Width (mm)	Backing Length and Width (mm)	Yield Strain (%)
YFLA-2	2 x 1.8	7.5 x 4	10 - 15
YL-10	10 x 3	20 x 7	10 - 20
YL-20	20 x 3	30 x 7	10 - 20
PA-3	19 x 11	51 x 13	10
PA-7	6.4 x 7.5	29 x 9.5	8

Additional details on the in-isolation test procedure and results; UCD design, operation, test procedure and results; geotextile sample preparation; and strain gage tests are presented in Boyle (1995a, b), Gallagher (1995), and Boyle et al. (1996).

## 2 RESULTS

### 2.1 In-isolation Test Results

The YL-20 strain gages, attached to the woven polypropylene slit-film geotextiles, PP1, PP2, and PP3, appeared to work adequately until they reached the gage yield strain or the backing started to debond from the geotextile, conditions that typically occurred between 6% and 12% strain. In all cases the YL-20 strain gages reported less strain than was recorded for the overall specimen.

To facilitate evaluation of strain gage performance we looked at the ratio of strain gage strain to total strain (SR), defined as:

$$SR = \epsilon_{sg}(t) / \epsilon_{total}(t) \quad (1)$$

where:

$\epsilon_{sg}(t)$  = strain gage strain at time t

$\epsilon_{total}(t)$  = total overall strain at time t

The SR for a given strain gage-reinforcement combination changed throughout each test and differed from one test to another, Figure 3. After the first 1% strain the SR typically increased to a maximum that occurred between 3% and 8% overall strain.

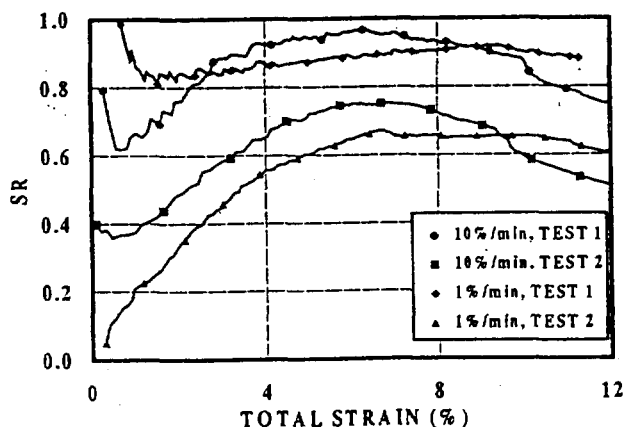


Figure 3: SR versus overall specimen strain for in-isolation test on PP2 with YL gages.

To reduce the influence of initial strain readings on the analysis, an incremental strain ratio, ISR, was defined:

$$ISR = \frac{\epsilon_{sg}(t_2) - \epsilon_{sg}(t_1)}{\epsilon_{total}(t_2) - \epsilon_{total}(t_1)} \quad (2)$$

For the YL gages, as shown in Figure 4, the ISR results fell in a slightly narrower band than was exhibited by the SR. The pattern of ISR versus total strain for the three polypropylene geotextiles were similar. The ISR generally increased to a maximum between 3% and 8% total strain, and then decreased at larger strains (Gallagher, 1995; Boyle, 1995a). The decrease in ISR, and SR, after about 8% strain likely results from debonding of the strain gage from the geotextile or may be due to yielding of the strain gage. At small strains, i.e. 0.5%, ISR values were typically in the range 0.1 to 0.5. The ISR values for the YL-20 gages tested in isolation increased to a maximum at strains greater than 3%. These maximums were typically between 0.8 and 1.2, although values as high as 1.3 were found. Thus, at higher strains, the incremental strain measured by the strain gages was relatively accurately measured. However, strains of this magnitude have not been commonly reported for instrumented wall case histories (Allen et al., 1992; McGown et al., 1993).

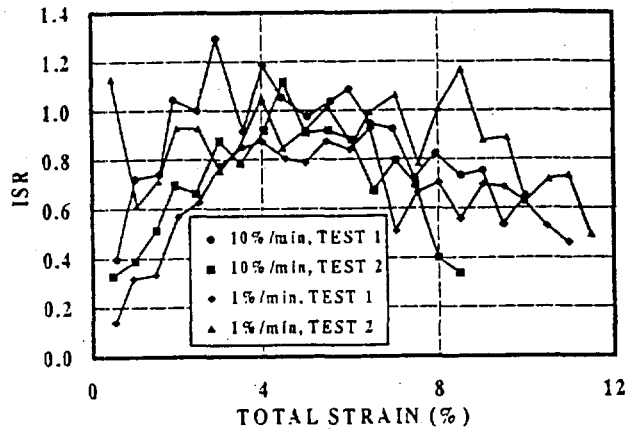


Figure 4: ISR versus overall specimen strain for in-isolation test on PP2 with YL gages

Tests with PA-3 gages attached to polyester reinforcement PET2 met with only limited success. Only two of the in-isolation tests conducted with these strain gages produced reasonable results (Gallagher, 1995). For these two tests, the initial ISR values of 0.78 and 0.91 were higher than the initial values for the YL-20 gages attached to the polypropylene geotextiles. The maximum ISR values were approximately 1.1. ISR values on this order indicate the strain gages were not underrecording incremental strain substantially. However, the non-incremental strain ratio, SR, did underrecord strains, and was sensitive to the initial "zero" strain gage reading selected. Because the PA-3 gages tended to debond from the polyester geotextile at strains between 1% and 3%, evaluation of strain gage performance at higher strains was not possible on the woven polyester geotextiles.

## 2.2 In-Soil Test Results

The pattern of strain recorded by the YL strain gages when attached to the polypropylene geotextiles, including creep strain, was similar to the pattern for overall lateral (geotextile) strain in the majority of the UCD strain gage tests conducted, Figure 5. This similarity, plus the smooth, continuous nature of the data, was interpreted as evidence that the strain gages were behaving properly. As in the isolation tests, the gages underrecorded total strain, Figures 5, 6, and 7. For YL gages attached to polypropylene reinforcements PP1, PP2, and PP3, the SR ranged from 0.3 to 1.0. As occurred in the in-isolation tests, during the initial stages of each test SR increased with increasing strain, Figure 6. Since total strain was limited (by the UCD device) to less than 6% in the in-soil tests, debonding or yield of the strain gages did not occur.

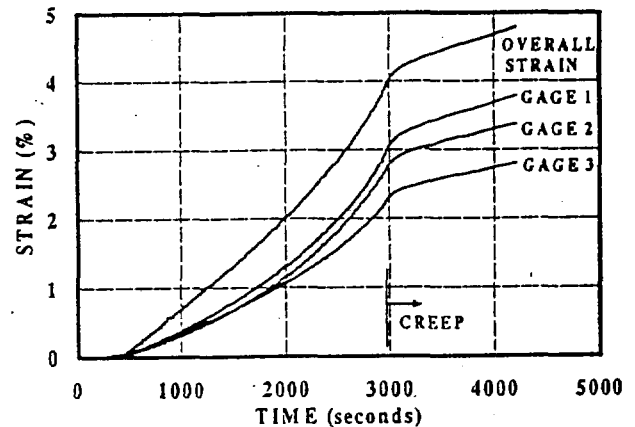


Figure 5: Overall specimen strain and strain gage measured strain for in-soil test, PP2 with YL-10 gages.

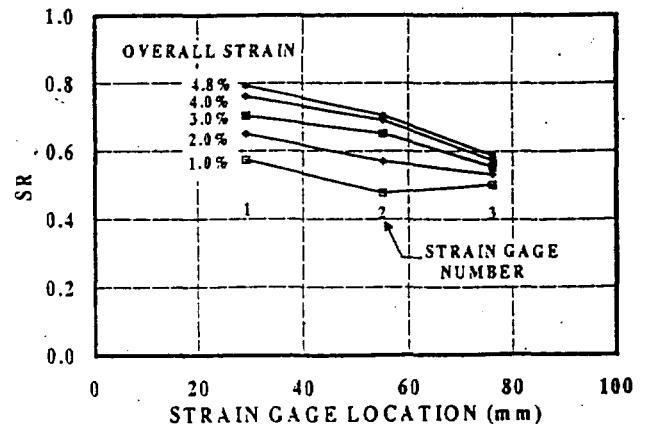


Figure 6: SR for gages at different locations along in-soil test specimen, PP2 with YL-10 gages.

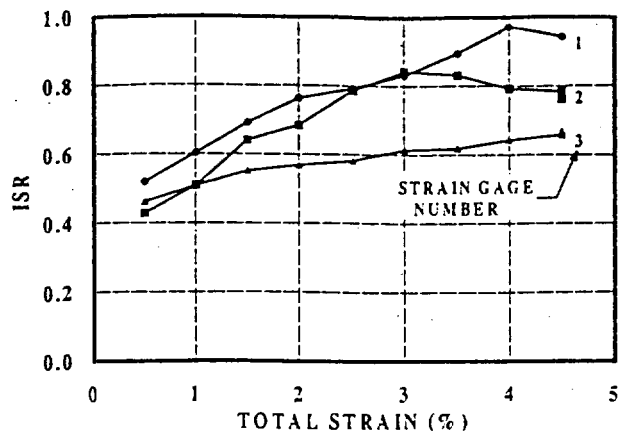


Figure 7: ISR for gages at different locations along in-soil test specimen, PP2 with YL-10 gages.

There was less fluctuation in the ISR values for the YL strain gages in in-soil tests than was recorded in the in-isolation tests, Figure 7. The smoothing of the response may be due to the reduction of specimen flexibility by confinement in soil. As with the in-isolation tests, the ISR for in-soil tests tended to increase with increasing overall specimen strain. Initial ISR values (e.g., at 0.5% strain) for the three different length YL gages were between 0.20 and 0.80. At higher strains ISR generally fell in the range 0.3 to 1.10, although maximums as high as 1.32 were observed, see Table 3. While SR or ISR values near 1.0 would indicate relatively accurate measurement of geotextile strains, the SR and ISR did not approach or exceed 1.0 until strains greater than 3% were attained. This is three times the strain reported in geosynthetic reinforced walls (Allen et al., 1992; McGown et al., 1993).

Table 3: Range of SR and ISR values.

Strain	YL-series gages		PA-series gages	
	In-Isolation	In-Soil	In-Isolation	In-Soil
<b>SR</b>				
0.5%	----	0.3 - 0.8	----	0.3 - 0.7
4% - 6%*	0.5 - 1.0	0.4 - 1.0	----	0.3 - 0.7
<b>ISR</b>				
0.5%	0.2 - 0.7	0.2 - 0.8	0.8 - 1.0	0.4 - 0.7
4% - 6%*	0.8 - 1.3	0.3 - 1.3	0.7 - 1.1	0.1 - 0.9

\* Range at 1% to 2% used for PA gages.

Only two in-soil tests were conducted with PA-7 gages, both mounted on Reinforcement PET1. In these tests the ISR at 0.5% strain fell between 0.4 and 0.7, but ranged as wide as 0.1 to 0.9 at higher strains. These values are lower than was observed in the in-isolation tests for PA-3 gages attached to PET2. As with the in-isolation tests, the PA

gage responses were somewhat erratic and strains to only a few percent were recorded.

### 2.3 Discussion

The SR and ISR values for the YL gages in the in-soil tests were more uniform and less erratic than for the in-isolation tests. While the in-soil and in-isolation ISR values were similar, there was slightly less variation in the in-soil ISR values at each strain level, Table 3. From these tests, neither in-soil or in-isolation resulted in more accurate measurement of geotextile strains. At strains less than 2% the initial ISR for in-isolation tests were somewhat, though not significantly, lower than for in-soil tests. At strains from 4% to 6% in-isolation ISR values were slightly higher than in-soil values. Initial ISR values were also slightly lower for in-soil tests with YL-2 gages (7.6 mm length) than for the longer YL-10 (20.5 mm) and YL-20 (30.5 mm) gages. The PA gages did not behave better in-soil than in-isolation, and we experienced difficulties with their adhesion to the geotextiles under both test conditions. The in-isolation ISR values were closer to 1.0 than were the in-soil ISR values. This difference may be related to the different strain gage lengths; the longer PA-3 gage may be better at recording overall strain than the shorter PA-7 gage.

An insufficient number of tests were performed to conclude that the strain gages attached to geotextiles behaved better in in-soil tests than in in-isolation tests, or vice-versa, or that longer gages perform better than shorter ones. There is, however, sufficient data to conclude that strain gages of the type tested can be expected to underrecord both total and incremental strain when attached to woven polypropylene slit-film or woven polyester multi-filament geotextiles, especially at low strains. A number of factors may contribute to this phenomenon:

- Overall strain includes global rearrangement of the fibers and tightening of the weave. Tightening of the weave with increasing strain may partially explain the increase in SR and ISR values, and their leveling off after the first few percent strain.
- Strain gages are intended for application to smooth, flat surfaces; these conditions are not met when the gages are attached to woven geotextiles where the gages pass over multiple weaves in both the machine and cross-machine directions. The height and length of these "bumps" may be expected to change throughout the test as the reinforcement is strained. This change in degree of flatness of the gage may modify the gage resistance, thus affecting the output.
- The strain gages were not attached to a single geosynthetic fiber oriented in the direction of straining. They were attached to three parallel slit film strips or three parallel filament bundles, and the gages crossed strips and filament bundles oriented perpendicular to the

direction of strain. The independent action of the parallel slit-films or filament bundles to which the gages were attached can be expected to influence gage performance.

- d) In the in-soil tests, it is possible, even likely, that the geotextile sheets were arched very slightly when tested. The presence of such an arch, while unconfirmed, would result from the soil not being perfectly flat when the UCD specimen was constructed or from deformation of the soil during loading. During straining this arch may be increased, removed, or reversed, depending upon specimen behavior. Any change in the reinforcement orientation would influence the gage reading. This effect may be compensated for by attaching complementary gages directly opposite each other on each side of the geotextile specimen.

With the exception of item (d), these complicating factors are inherent to the nature of woven geotextiles and must be recognized as contributors to uncertainty when interpreting strain gage data.

Because the gages attached to the geotextiles did not accurately record overall strains, to estimate the true strain in a geotextile from strain gage measurements, it is necessary to apply a correction factor, CF. Such a factor can be computed by taking the reciprocal of SR and ISR (i.e.,  $CF_{SR} = 1/SR$  and  $CF_{ISR} = 1/ISR$ ). Emphasizing typical test results, instead of the full range of variation presented in Table 3, we believe representative correction factors for the geotextile reinforcements and strain gages used in our program are as follows:

Table 4: Correction factors.

Strain (%)	YL - series gages		PA -series gages
	0.5	4 - 6	0.5
$CF_{SR}$	2.5-1.0	1.7-1.0	2.5-1.4
$CF_{ISR}$	5 - 1.7	2.0-0.9	2.5-0.9

The selection of representative correction factors is somewhat subjective, and is based upon our assessment of the quality of all of the tests conducted in the program, and involves some engineering judgment. Because of the spread in CF values, and the somewhat subjective nature in their selection, it is impractical to select a single correction factor to apply to a given strain gage reading. Instead, if correction factors are to be applied, we recommend a probable range be computed for the corrected strain gage measurement, and that this range be used in estimating overall geotextile strain from strain gage measurements. When using strain gage data to estimate true geotextile strains, our test program illustrates that the potential for error is greatest at low strains (less than 1%). This is unfortunate because for geosynthetic reinforced walls, for example, reported typical strain values are often of this magnitude (Allen et al., 1992; McGown et al., 1993).

In our program, the difference between the measured overall geotextile strain and that measured with strain gages is similar to that reported by Allen et al., (1992) for a 12.6 m high instrumented geotextile reinforced wall. The reinforcements and strain gages used in our program were the same or similar products and by the same manufacturers as those used by Allen et al. For measuring overall geotextile strain in the field, Allen et al., used mechanical extensometers. The extensometers tended to record greater strain than the electrical resistance strain gages in almost all cases.

Despite the apparent limitations and inaccuracies associated with using strain gages to measure overall and incremental strain of geotextiles, the test results provide evidence that strain gages can be effectively used to measure strain distribution and creep of geotextiles confined in soil, Figures 5, 6, and 7. The effectiveness of using strain gages to measure strain distribution and to record creep in geotextiles, as was found in our laboratory program (Boyle, 1995a), was also observed by Allen et al., (1992) in a full scale instrumented wall. Therefore, despite the inability to use strain gages to determine the true strain in geotextiles with confidence, strain gages appear to be useful instruments for determining the distribution of strain along woven geotextiles and for recording creep.

### 3 CONCLUSIONS

In this study, in the first few percent strain, i.e., at strains typically observed in geosynthetic reinforced walls, strain gages underrecorded by 20% to 80% both total and incremental strain. The degree of underrecording decreased at strains between 4% and 8% strain, and the incremental strain ratio was on the order of 1.0 in some cases. Because of the inaccuracies involved, we suggest that a range of probable geotextile strain values, not a single value, be reported when adjusting field strain gage data. This is an especially important consideration at small strains, e.g., less than 1%.

Despite our inability accurately measure the true geotextile strain using strain gages attached to woven geotextiles, we did find that strain gages could be effectively used to identify the distribution of strain along the geotextiles. Strain gages were also found to be effective for monitoring creep in geotextiles.

### ACKNOWLEDGMENTS

This research was funded by the Washington State Department of Transportation, and their financial support is greatly appreciated. We thank T.M. Allen for his many helpful discussions and M. Gallagher for his assistance in conducting the laboratory tests.

## REFERENCES

- Allen, T.M., Christopher, B.R., and Holtz, R.D. (1992), "Performance of a 12.6 m high geotextile wall in Seattle, Washington," *Geosynthetic-Reinforced Soil Retaining Walls*, Proceedings of the International Symposium on Geosynthetic-Reinforced Soil Retaining Walls, Denver, J.T.H. Wu ed., A.A. Balkema Publ., Rotterdam, pp. 81-100.
- Boyle, S.R. (1995a), *Deformation of Geosynthetic Reinforced Soil Retaining Walls*, Ph.D. Dissertation, University of Washington, 391 p.
- Boyle, S.R. (1995b), "Unit cell tests on reinforced cohesionless soils", *Proceedings of Geosynthetics '95*, Nashville, Vol. 3, pp. 1221-1234.
- Boyle, S.R., Gallagher, M. and Holtz, R.D. (1996), "Influence of strain rate, specimen length, and confinement on measured geotextile properties", *Geosynthetics International*, Vol. 3, No. 2, pp 205-225.
- Gallagher, M. (1995), *In-isolation wide width tests on geotextiles*, Master of Science Thesis, University of Washington.
- Industrial Fabrics Association International, 1989, "1990 Specifiers Guide", *Geotechnical Fabrics Report*, Vol. 7, No. 7, 120 p.
- Industrial Fabrics Association International, 1992, "1993 Specifiers Guide", *Geotechnical Fabrics Report*, Vol. 10, No. 7, 196 p.
- McGown, A., Yogarajah, I. and Yeo, K.C. (1993), "Choice of soil properties for limit state analysis of reinforced soil retaining structures", *Retaining Structures*, Proceedings of Conference on Retaining Structures, Cambridge, C.R.I. Clayton, ed., Thomas Telford Publishers, London, pp. 529-540.



# Soil Confinement Effect on Stress-Strain Properties of Geosynthetics

Z. Yuan, R. H. Swan, Jr., and R. C. Bachus  
GeoSyntec Consultants, Atlanta, Georgia, USA

V. Elias  
Earth Engineering & Sciences, Inc., Baltimore, Maryland, USA

**ABSTRACT:** A confined extension test device was designed and fabricated for measuring the response of geosynthetic materials confined in soil. A series of confined extension tests was performed on each of five selected geosynthetic materials using the confined extension test device. Each test series consisted of one unconfined extension test and two confined extension tests, each conducted at a different level of normal stress. The test data were presented in the form of stress versus strain curves. Using the test data, secant moduli at select strain levels were calculated. A comparison was made between unconfined and confined moduli for each geosynthetic material to quantify the soil confinement effect on stress-strain properties. A comparison was also made between the relative increase of moduli at the same strain level among the five geosynthetic materials to demonstrate the different responses of these geosynthetic materials under soil confinement.

**KEYWORDS:** confined extension test, soil confinement, geosynthetics, geogrids, geotextiles, stress, strain, modulus.

## 1 INTRODUCTION

In the design of geosynthetic-reinforced soil structures, the tensile strength and modulus of the reinforcing material are important design parameters. These two parameters are commonly obtained from the wide-width tensile test, described in the American Society for Testing and Materials (ASTM) Standard Test Method D 4595. This test is conducted under unconfined (i.e., in-air) conditions which do not fully simulate field conditions. Under field conditions, the geosynthetics are almost always confined within soil. Questions have been raised regarding the potential beneficial effects on the stress-strain properties of the geosynthetics due to soil confinement.

To address these questions, several researchers have studied the effect of soil confinement on stress-strain properties of various geosynthetic materials using different test devices. These devices include: (i) the in-soil test device developed by McGown et al. [1982] and modified by Wilson-Fahmy et al. [1993]; (ii) the zero-span test device by Christopher et al. [1986]; (iii) the pullout test device by Holtz [1977] and Juran et al. [1991]; (iv) the modified triaxial test device by Ling et al. [1991] and Wu [1991]; (v) the plane strain unit cell device (UCD) by Boyle [1995]; (vi) the automated plane strain reinforcement (APSR) cell by Whittle et al. [1993]; and (vii) the modified direct shear test machine by Leshchinsky et al. [1987]. Characteristics of these test devices were described in detail in the final report to the Federal Highway Administration (FHWA) by Yuan et al. [1997].

After an extensive literature review and several series of test trials using different in-soil confined extension test devices, it was found that an in-soil test apparatus based on the initial design by McGown et al. [1982] including the revisions by Wilson-Fahmy et al. [1993] could be modified to provide a nearly constant strain rate and a nearly constant tensile load over the confined test specimen length. Using this device, the confined response of a geosynthetic material measured using the in-soil test apparatus can be directly compared with the unconfined response (ASTM D 4595) of a geosynthetic material to assess the overall effect of soil

confinement. This led to the decision to design and fabricate a new device which is conceptually similar to the in-soil test apparatus for use in a comparative testing program. Using the modified device, herein referred to as the confined extension test device, the confined stress-strain response of geosynthetics at different confining stresses were compared with the unconfined response of the same geosynthetic to evaluate the effect of soil confinement.

## 2 TEST PROGRAM

### 2.1 Testing Materials

The materials used in the testing program included five geosynthetic and two soil materials. A brief description of each geosynthetic material and its ultimate wide-width tensile strength as tested in accordance with ASTM D4595 are summarized in Table 1. Beach sand and silty sand were

Table 1. Summary of geosynthetic properties.

Geosynthetic Materials	Description	Tensile Strength (kN/m)
Geosynthetic PP-10	Staple-filament needle-punched polypropylene nonwoven geotextile	19.7
Geosynthetic PP-11	Slit-film and multi-filament polypropylene woven geotextile	70.1
Geosynthetic PP-12	Mono-filament polypropylene woven geotextile	40.3
Geosynthetic PE-13	Extruded polyethylene geogrid	86.0
Geosynthetic PET-14	Polyester geogrid	85.5

used as the two soils in the testing program. For each of the two soil materials, a particle-size analysis was performed; results are shown in Figure 1. Based on the

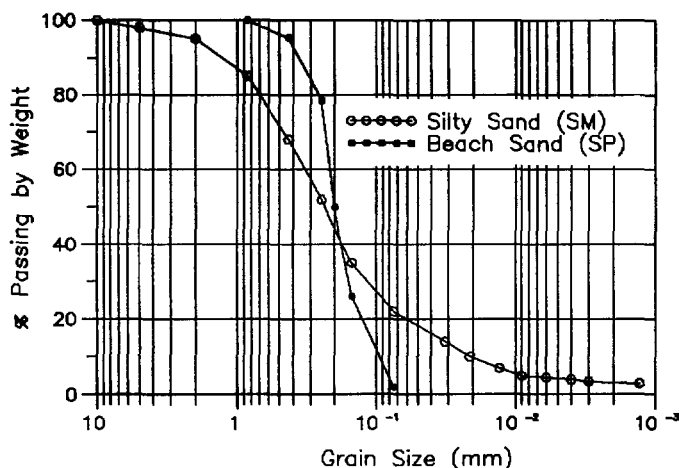


Figure 1. Particle-Size distribution curves for beach sand and silty sand.

results of particle-size analyses, the beach sand and silty sand were classified as SP (poorly-graded sand) and SM (silty sand), respectively, in accordance with the Unified Soil Classification System. A standard Proctor compaction test and direct shear tests were also performed on each of the two soils; results are summarized in Table 2. The

Table 2. Summary of compaction and direct shear test results.

Soil Material	Maximum dry unit weight and optimum moisture content (ASTM D 698)	Peak shear strength parameters <sup>(1)</sup> (ASTM D 3080)
Beach sand	16.1 kN/m <sup>3</sup> at 11.5%	30° and 0.5 kPa
Silty Sand	15.4 kN/m <sup>3</sup> at 21.5%	34° and 7.6 kPa

direct shear tests were conducted on remolded beach sand and silty sand specimens compacted to 95 percent of maximum dry unit weight at optimum moisture content. Tests were conducted at normal stresses ranging from 14 to 63 kPa and a displacement rate of 1 mm/min.

## 2.2 Test Equipment

A new confined extension test device was designed and fabricated. As mentioned previously, the confined extension test device is conceptually similar to the in-soil test apparatus developed by McGown et al. [1982] and modified by Wilson-Fahmy et al. [1993]. These earlier devices consisted of a stationary confining box while a moving box was developed by the authors. The detailed cross-section drawing of the confined extension test device

is shown in Figure 2. The device consisted of the following major components:

1. a rigid supporting table with overall plan dimensions of 1,070 mm in length by 710 mm in width;
2. a confinement box with internal dimensions of 430 mm by 305 mm in plan and 150 mm in depth;
3. a flexible pneumatic diaphragm loading device (air bladder system) at the top and bottom of the confinement box for applying normal stresses to the test specimen; and
4. a 150-mm diameter hydraulic cylinder for applying tensile loads to the geosynthetic specimen.

The hydraulic cylinder was mounted on the front of the supporting table. A constant rate of strain was achieved by manually adjusting the rate of air or hydraulic flow into the hydraulic cylinder. A constant load test or a confined creep test can be conducted by maintaining a constant pressure within the hydraulic cylinder.

The confined extension test device was calibrated through several series of preliminary and calibration tests prior to being used for the confined extension testing program. These tests were conducted to evaluate: (i) the friction between the confinement box and steel rollers; (ii) the uniformity of strain distribution along the geosynthetic specimen length; and (iii) the reproducibility of test results. The results of the calibration tests are detailed in the final report to FHWA and indicate that: (i) the friction between the confinement box and steel rollers did not vary with confining pressures and the maximum friction was approximately 40 N; (ii) the strain distribution along the geosynthetic specimen length was approximately uniform for a normal stress up to 138 kPa; and (iii) the confined extension test device produced similar results for three specimens of a given geosynthetic subject to the same test conditions.

## 2.3 Testing Procedure

A testing procedure was developed to conduct confined extension tests using the confined extension testing device. This testing procedure consisted of the following steps:

1. *Preparation of Test Specimen:* Soil was compacted into the lower half of the confinement box above the lower air bladder system to form the lower confining layer. A previously prepared geosynthetic specimen with each end of the specimen cast in a low-temperature curing epoxy resin was placed on top of the confining soil layer. The two clamp ends of the geosynthetic specimen were then connected to the corresponding clevis as shown in Figure 2. A pretension force was then applied to the geosynthetic specimen to eliminate slack within the geosynthetic specimen. Additional soil was compacted into the upper half of the confinement box to form the upper confining layer. The upper air bladder system was then installed on top of the upper confining layer.
2. *Apply Normal Stress:* A normal stress was applied to the test specimen by pressurizing the upper and lower air bladder loading systems simultaneously.
3. *Apply Tensile Loads:* After the application of normal stress, the geosynthetic specimen was loaded under a

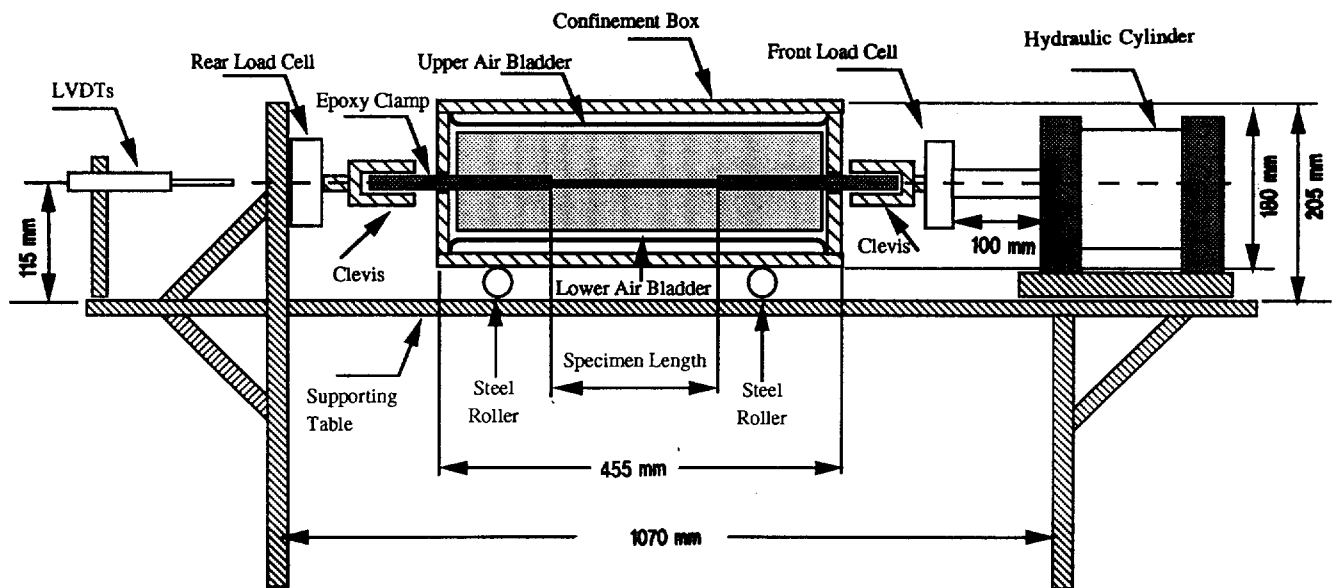


Figure 2. Details of confined extension test device.

constant rate of displacement as measured on the front specimen clamp.

Tensile loads were measured at the front and rear end of the geosynthetic specimen using two electronic load cells. Displacements at the front and rear ends of the geosynthetic specimens were measured using two linear variable differential transformers (LVDTs), each connected to a "tell-tail" wire which was attached to the geosynthetic specimen within the confinement box. Load and displacement data were recorded using a computer data acquisition system.

There were five major test variables involved in the testing procedure established for conducting confined extension tests. These variables were: (i) pretension force; (ii) strain rate; (iii) aspect ratio; (iv) thickness of the confining soil; and (v) boundary friction on the upper and lower surfaces of confining soil. The first three test variables were selected in accordance with ASTM D 4595 as follows:

1. **Pretension Force:** A total pretension force equal to 1.25 percent of the expected breaking force was applied to each geosynthetic specimen. However, the total pretension force was not less than 45 N or greater than 222 N in any case. The pretension force was applied to the geosynthetic specimen prior to placement of the upper confining soil layer.
2. **Strain Rate:** A constant rate of strain of 10 percent per minute was applied to the geosynthetic specimen in the confined extension test.
3. **Aspect Ratio:** An aspect ratio of 2:1 was used for geotextile specimens with a specimen width of 200 mm. For the geogrid, the test specimen was trimmed in such a way that it had a length containing at least two complete apertures in the direction of testing and a width containing at least five ribs in the cross-test direction.

The soil thickness and boundary conditions were selected

based on the results of two preliminary confined extension tests, as will be described below.

The effect of soil thickness on the confined response of geosynthetics was investigated through a series of confined extension tests on Geosynthetic PP-10 confined between two layers of beach sand with thicknesses ranging from 10 to 76 mm. The test results, as shown in Figure 3, indicate that there was little difference among the confined responses of Geosynthetic PP-10 when it was confined between 25- to 76-mm thick soil layers. However, the effect of soil confinement was reduced when the thickness of the soil layer was reduced to 10 mm due to the fact that cracks developed throughout the thickness of the soil layers, resulting in partial confinement of the geosynthetic specimen. To provide full confinement of the geosynthetic specimen, a soil thickness of 76 mm was then selected for all of the confined extension tests in this study.

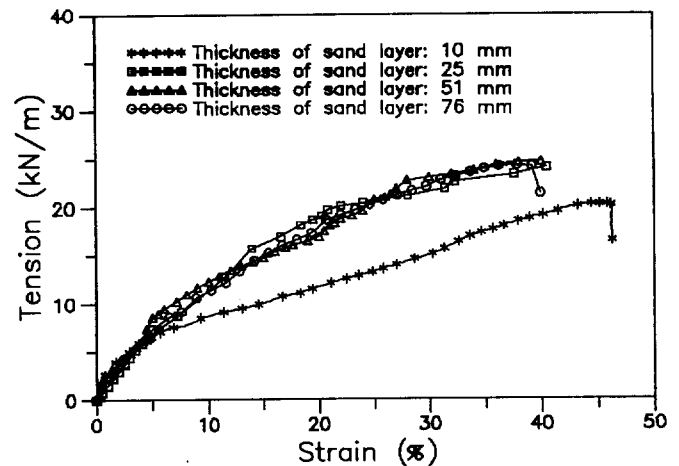


Figure 3. Responses of Geosynthetic PP-10 confined within various thicknesses of beach sand layers.

The effect of the boundary friction on the confined response of geosynthetics was investigated through a series of confined extension tests on Geosynthetic PP-10, each test conducted under one of the following two boundary conditions:

1. Condition 1: no lubrication between the air bladder and confining soil while the confinement box was allowed to move; and
2. Condition 2: lubrication between the air bladder and confining soil while the confinement box was fixed to the supporting table during testing.

The lubrication was achieved by placing two layers of lubricated latex membranes on the contact surface between the bladder and confining soil. In each test the geosynthetic specimen was confined between 10-mm thick beach sand layers in order to directly compare the effect of the boundary condition. The test results, as shown in Figure 4,

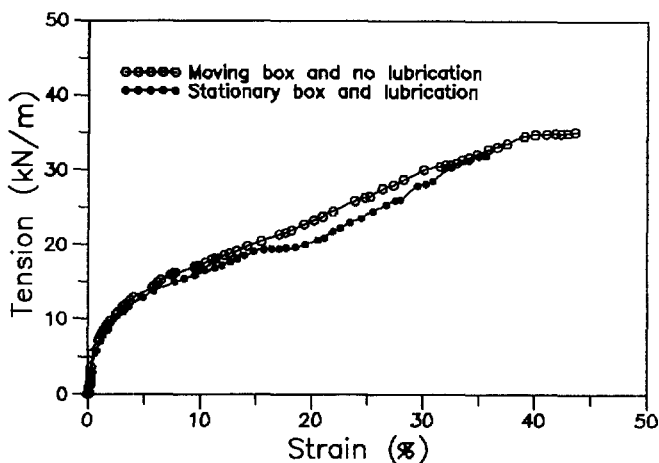


Figure 4. Confined responses of Geosynthetic PP-10 under lubricated and unlubricated boundary conditions.

indicate that the confined stress-strain curves of Geosynthetic PP-10 are very similar when tested in accordance with conditions 1 and 2. Because of the small difference between these results, condition 1 was selected for the boundary condition during the testing program.

### 3 TEST RESULTS

Ten test series were conducted in the testing program. Each test series consisted of one unconfined and two confined extension tests on one of the five selected geosynthetic materials. Each geosynthetic material was confined within beach sand (Test Series 1 through 5) or silty sand (Test Series 6 through 10) under two different normal stresses (69 and 138 kPa). For each test, tensile loads and displacements were measured at the front and rear end of the geosynthetic specimen by load cells and LVDTs, respectively, and recorded using the computer data acquisition system. The load and displacement data were subsequently used to develop the tensile force (i.e., load

divided by initial specimen width) versus strain (i.e., total displacement divided by initial specimen length) curves.

To quantify the improvement due to the soil confinement, secant moduli at 1, 5, and 10 percent strain levels and peak strength were calculated for each test and summarized in Table 3. For this paper, the secant modulus at 5 percent strain was selected to quantify the effect of soil confinement. The improvement of secant moduli at 5 percent strain was plotted versus confining pressure for each geosynthetic material confined in the beach sand and in the silty sand as shown in Figures 5 and 6, respectively.

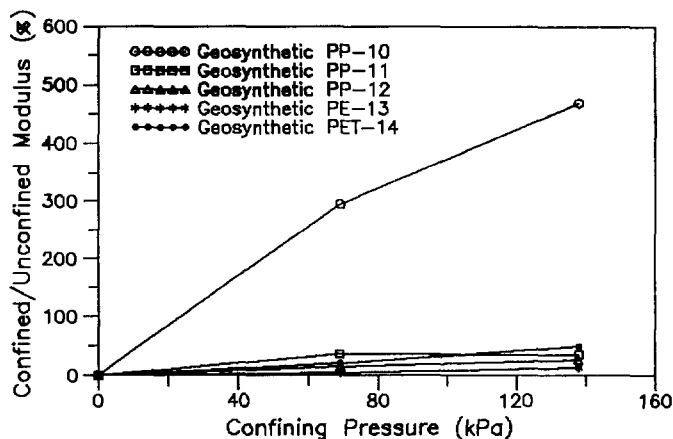


Figure 5. Confinement effect of beach sand on secant modulus at 5 percent strain.

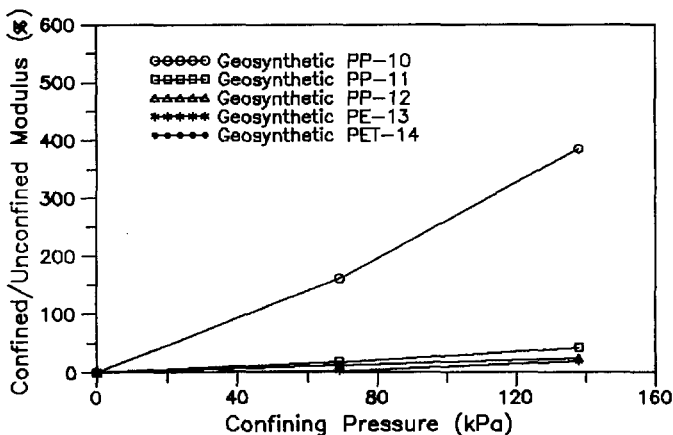


Figure 6. Confinement effect of silty sand on secant modulus at 5 percent strain.

In these plots "improvement" is defined as the ratio of the confined secant modulus to the unconfined secant modulus at a strain level of 5 percent. These figures clearly demonstrate that the Geosynthetic PP-10 is significantly affected by soil confinement and the other four geosynthetic materials are less affected by soil confinement. The comparison between Figures 5 and 6 indicates that the confinement effect of the beach sand is greater than that of the silty sand.

Table 3. Summary of confined extension test results.

Test Series Number	Geosynthetic Material <sup>(1)</sup>	Confining Material <sup>(2)</sup>	Confining Pressure (kPa)	Modulus at 1% Strain (kN/m)	Modulus at 5% Strain (kN/m)	Modulus at 10% Strain (kN/m)	Peak Strength (kN/m)
1	PP-10 in machine direction	in-air beach sand beach sand	0	81.9	59.0	62.7	19.8
			69	137.1	232.5	162.4	26.5
			138	341.9	335.8	246.8	37.1
2	PP-11 in cross machine direction	in-air beach sand beach sand	0	674.7	618.1	560.4	88.0
			69	828.5	840.7	706.8	95.7
			138	790.0	836.8	715.2	108.6
3	PP-12 in machine direction	in-air beach sand beach sand	0	559.6	417.1	326.5	49.7
			69	783.4	480.8	381.2	56.2
			138	957.9	527.0	424.7	61.8
4	PE-13 in machine direction	in-air beach sand beach sand	0	1135.9	832.7	680.5	85.6
			69	1221.7	868.6	693.4	85.9
			138	1290.4	948.5	675.4	86.7
5	PET-14 in machine direction	in-air beach sand beach sand	0	989.7	930.3	837.0	92.3
			69	907.5	1097.4	914.0	94.5
			138	962.1	1361.1	983.4	103.7
6	PP-10 in machine direction	in-air silty sand silty sand	0	81.9	59.0	62.7	19.8
			69	116.9	153.3	108.1	24.3
			138	277.8	286.0	233.8	31.5
7	PP-11 in cross machine direction	in-air silty sand silty sand	0	674.7	618.1	560.4	88.0
			69	934.3	731.4	620.6	98.6
			138	1089.6	879.9	769.4	104.4
8	PP-12 in machine direction	in-air silty sand silty sand	0	559.6	417.1	326.5	49.7
			69	644.3	467.4	364.5	52.8
			138	754.1	520.5	393.0	60.0
9	PE-13 in machine direction	in-air silty sand silty sand	0	1135.9	832.7	680.5	85.6
			69	1296.3	854.0	726.0	84.5
			138	1322.9	991.6	768.4	87.4
10	PET-14 in machine direction	in-air silty sand silty Sand	0	989.7	930.3	837.0	92.3
			69	1174.8	1046.3	875.7	97.7
			138	1397.9	1250.4	984.9	105.1

Notes: (1) For Geosynthetics PP-10, PP-11 and PP-12, each test specimen was 200 mm in width and 100 mm in gage length. For Geosynthetics PE-13 and PET-14, each test specimen had two full apertures in the machine direction and five ribs in the cross-machine direction.

(2) For each confined extension test, the geosynthetic specimen was confined between two 76-mm thick layers of beach sand or silty sand.

#### 4 CONCLUSIONS

A confined extension test apparatus was designed, fabricated, calibrated, and used in a comparative testing program. The advantages of the test apparatus fabricated for this study include: (i) ease of the test set-up; (ii) well-defined boundary conditions; and (iii) ease of test interpretation. Based on the results of the calibration tests, a nearly uniform distribution of tensile strain along the specimen length was achieved. Because of this relatively uniform distribution, the confined stress-strain response of the geosynthetic was readily obtained from the measured data and used for a direct comparison with the unconfined response of the geosynthetic to evaluate the effect of soil confinement. Further evaluations can be performed using this device to study the effects of full and partial confinement and creep behavior of geosynthetic materials.

Based on the results of the ten confined extension tests series, the following conclusions can be drawn:

1. Soil confinement significantly improves the moduli and strength of Geosynthetic PP-10. As the confining pressures increases, the moduli and strength of this material similarly increases. The 5 percent moduli of Geosynthetic PP-10 increased by approximately 200 to 400 percent when confined in the beach sand and 50 to 300 percent in the silty sand under confining pressures of 69 and 138 kPa.
2. Under the same confining pressure, the confined response (i.e., modulus and strength) of Geosynthetic PP-10 in beach sand is greater than that of Geosynthetic PP-10 in silty sand.
3. There is a noticeable effect of confinement with respect to the confined response for the two woven geotextiles and two geogrids (Geosynthetics PP-11, PP-12, PE-13, and PET-14) when confined in the beach sand and in the silty sand; the increase of the 5 percent moduli ranged from approximately 5 to 30 percent among Geosynthetics PP-11, PP-12, PE-13, and PET-14 at a normal stress of 138 kPa. These increases can be considered significant with respect to unconfined moduli of the same materials although considered less significant when compared with the increase of the 5 percent moduli for the nonwoven geotextile (Geosynthetic PP-10).
4. Improvement of the confined stress-strain properties for a given geosynthetic material may be primarily related to: (i) internal friction between fibers or yarns; (ii) alignment of curved fibers or yarns (i.e., tortuosity); and (iii) interlocking of soil within openings or apertures of geosynthetics.

#### ACKNOWLEDGEMENTS

The research presented in this paper was supported by the FHWA. The support of the FHWA is greatly appreciated. The authors would like to thank Drs. B. Christopher, R.M. Koerner, and R.D. Holtz for their comments on the original

report of this research program submitted to the FHWA on which this paper is based.

#### REFERENCES

- Boyle, S.R. (1995), "Unit Cell Test on Reinforced Cohesionless Soils", *Proceedings of Geosynthetics '95*, Nashville, Vol. 3, Feb, pp. 1221-1234.
- Christopher, B.R., Holtz, R.D., and Bell, W.D. (1986), "New Tests for Determining the In-Soil Stress-Strain Properties of Geotextiles", *Proceedings of 3<sup>rd</sup> International Conference on Geotextiles*, Vol. 3, Vienna, pp. 683-688
- Holtz, R.D. (1977), "Laboratory Studies of Reinforced Earth Using a Woven Polyester Fabric", *International Conference on the Use of Fabrics in Geotechnics*, Paris, Vol 2, pp. 149-154.
- Juran, I., Farrag, K.H., and Richmond, L. (1991), "Short and Long Term Performance of Polymeric Geogrids", *Proceedings of Geosynthetics '91*, Vol. 2, Atlanta, Feb, pp. 587-599.
- Leshchinsky, D. and Field, D.A. (1987), "In-Soil Load Elongation, Tensile Strength and Interface Friction of Nonwoven Geotextile", *Proceedings of Geosynthetics '87*, New Orleans, pp. 238-249.
- Ling, H.I., Wu, J.T.H., and Tatsuoka, F. (1991), "Effectiveness of In-Membrane Test in Simulating Strength and Deformation Characteristics of a Nonwoven Geotextile Under Operational Conditions", *Proceedings of Geosynthetics '91 Conference*, Atlanta, Feb, Vol. 2, pp.601-614.
- McGown, A., Andrawes, K.Z., and Kabir, M.H. (1982), "Load-Extension Testing of Geotextiles Confined In-Soils", *Proceedings of 2<sup>nd</sup> International Conference on Geotextiles*, Las Vegas, pp. 793-798.
- Whittle, A.J., Larson, D.G., Germaine, J.T., and Abramento, M. (1993), "A New Device for Evaluating Load-Transfer in Geosynthetic Reinforced Soils", *ASTM STP 1190*, pp. 1-15.
- Wilson-Fahmy, R.F., Koerner, R.M., and Fleck, J.A. (1993), "Unconfined and Confined Wide-Width Tension Testing of Geosynthetics", *ASTM STP 1190*, pp. 49-63.
- Wu, J.T.H. (1991), "Measuring Inherent Load-Extension Properties of Geotextiles for Design of Reinforced Structures", *Geotechnical Testing Journal*, Vol. 14, No. 2, Jan, pp. 157-165.
- Yuan, Z., Swan, R.H., Bachus, R.C., and Elias, V. (1997), "Development of Protocol Confined Extension/Creep Testing of Geosynthetics for Highway Applications", Submitted to the Federal Highway Administration, U.S. Department of Transportation.

# The Testing of Geosynthetic Reinforcements

Peter E. Stevenson

Project Manager, The Tensar Corporation, Atlanta, Georgia

Todd R. Skochdopole

Manager of Research and Development, The Tensar Corporation, Atlanta, Georgia

Ajit D. Kelkar, Professor, North Carolina A&T State University, Greensboro, NC

**ABSTRACT:** Concurrent with a product development program, a review of the testing of reinforcements was conducted. Review of more than 100 published articles revealed that: (1) Researchers have identified 14 issues of concern to the design engineer as well as the manufacturer of geosynthetic reinforcements. (2) The geosynthetic and geotechnical community have not fully exploited the technical resources (data base and knowledge) of the textile industry. (3) Data for reinforcement products is inconsistently reported, resulting in potential misinterpretation. (4) Little research has been conducted on the testing of high performance geosynthetic reinforcements. This paper will review the above and present a test methodology that: (1) addresses the issues of concern, (2) is based on detailed research and experimentation, (3) is easily verified, is repeatable and reproducible.

**KEYWORDS:** Mechanical properties, tensile strength, modulus, testing, woven fabrics, knit fabrics, specifications.

## 1 INTRODUCTION

Much research has been conducted on the type of wide width testing represented by ASTM D4595 and ISO 10319 in hopes of establishing a relationship between laboratory testing and the plane strain conditions a geosynthetic experiences in use. The references cited in this paper represent the key portion of the work that deals with some aspect of wide width testing of geosynthetics. 53 references in the literature explore wide width testing. Less than 10 address reinforcements and 5 of the 10 report serious concerns about current methodology and the results of its application to high strength materials (Haliburton 1978; Myles et al. 1986; Rowe et al. 1986; Leschinsky et al. 1990; Brand et al. 1991). In the period from 1977 (Finnigan 1977) through the present, 14 issues of concern have been identified with the testing of reinforcements with many of these concerns yet unresolved. The research reported here focuses specifically on the testing of textile products employing high tenacity industrial quality multifilament textile yarns from such polymers as polyester (PET), polyamide (nylon), and polyvinyl alcohol (PVA).

The specific concerns about testing of reinforcing products expressed in the literature are: (1) the effect of sample gauge (length) on reported values including tensile strength, extension and modulus, (2) the effect of test speed, i.e. strain rate on reported values: one specific issue is the difference between ASTM at 10% and ISO at 20% per minute, (3) the effect of fabric structure (weave) on reported values, (4) the effect of jaw or grip types on reported values, (5) the control of sample slippage in grips, (6) the amount of tolerable slippage in clamping devices, (7) the accuracy of various extension measurement systems,

(8) the effect of the extension measurement system on the reported values, (9) the effect of sample width on reported values, (10) the effect of preload on reported values, (11) the definition, measurement and reporting of modulus, (12) which modulus is important?, (13) what portion of the sample does a reported modulus represent?, (14) is there a demonstrated relationship between single end yarn test values and fabric test values?

The research reported in this paper is directed toward developing a repeatable and reproducible test method for textile reinforcements. This presentation focuses on 8 of the concerns. The issues addressed are sample length, sample gauge (area of extension measurement), method of extension measurement, fabric structure, test preloads and modulus. Reference is made but specific research is not reported for jaw types, slippage, sample width and yarn to fabric relationship. The investigation includes both conventional roller grip systems and pressure clamping systems. The pressure clamping system incorporates a technique used in other disciplines for very strong materials. This technique is the application of sacrificial tabs to the clamping area of the specimen, thus permitting very high jaw pressures without specimen damage. A second modification to test protocol involved the use of long samples, 0.508 m between grips. Long samples have two benefits, first the sample geometry is similar between roller and tab systems and longer samples reduce the effect of variation in test speed on results. It is important to note that, the techniques employed in this work are applicable to conventional textiles produced from multifilament yarns based on polymers whose glass transition point is at or above the testing temperature. It is the authors opinion that the techniques in the test method that produce meaningful

information for very strong textiles will not be necessary for other textile based geosynthetics such as nonwovens or separation membranes. A specific caution applies to robust fabrics produced from polypropylene yarns. While the variations in test results caused by variation in testing speed can be substantially neutralized for fibers, yarns and fabrics produced from nylon and polyester, the same cannot be said for polypropylene textiles unless tests are conducted at temperatures below  $-10^{\circ}\text{C}$ . Given an accurate description of applicability, technique, preparation, equipment, and clear and accurate reporting requirements, this methodology can be incorporated in the standard test methodologies already extant in the geosynthetics industry.

## 2 RESULTS OF THE INVESTIGATION

### 2.1 The Importance of Fabric Structure on the Testing of High Strength Reinforcements.

Several researchers have noted that the structure of a product has a profound impact on the performance of that product in a testing protocol. Research can be interpreted to describe the structure of the reinforcement (fabric) as the dominant condition of the testing protocol (Rowe and Ho 1986). This concept is confirmed by a text sponsored by the NGO (Balkema 1986), which conducts a detailed discussion of the effects of fabric and yarn crimp, sample width, and cross contraction under load in confined and unconfined tests with the conclusion that the structure of

the fabric and the size of the sample will dominate the protocol and dictate the hierarchy of the results. Figures 1 and 2 present comparative test results for two groups of fabrics. For both groups all conditions are uniform except sample structure. Figure 1 presents 6 fabrics produced to the same performance specification, (5 of these fabrics employ a common warp in different structures, the sixth was produced separately). Figure 2 presents an additional 5 fabrics, all from a common warp of a different polymer. The wide variation in the curves and the shape of the curves demonstrates the dramatic effect of fabric structure on the results from a tensile test. Fabric structure is manipulated by the designer/producer to achieve a performance level. Test conditions cannot "correct" the impact of structure on results because structure clearly has

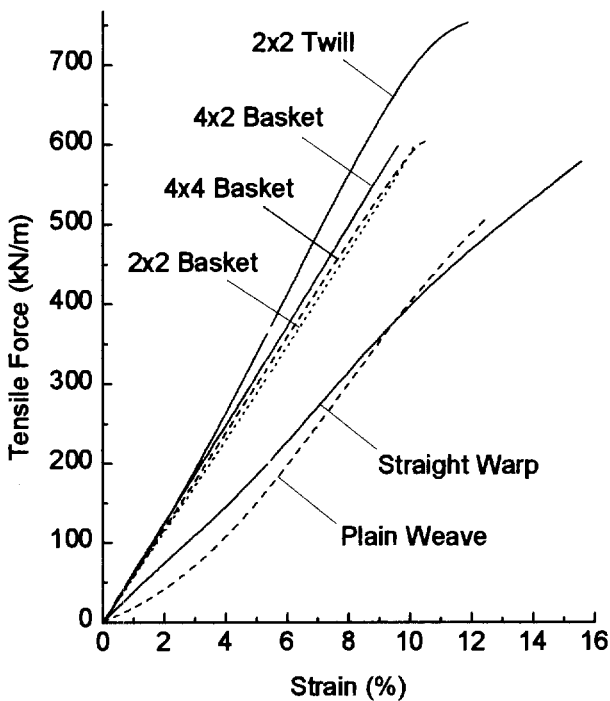


Figure 1. Performance Variation of Polyester Fabric Structure

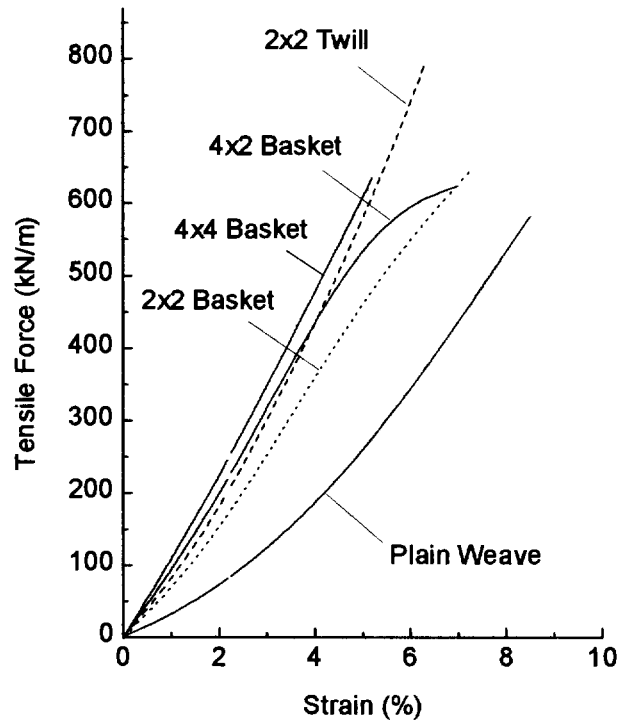


Figure 2. Performance Variation of PVA Fabric Structure an impact on performance.

### 2.2 The Effect of Preloads on Test Results

Three widely referenced test methods for the reporting of geosynthetic properties are ASTM D4595, ISO 10319:1993 and BS 6906. Subtle differences in test conditions and important differences in reporting exist between the methods. Both ISO and the British Standard cite a maximum preload of 1% of breaking strength while ASTM allows 1.25% not to exceed 0.73 kN/m. The ASTM method appears more conservative for very high strength materials: however, ISO and BSI recommend stress strain curves that



include any initial elongation established in the application of preload. ASTM allows the presentation of data without reporting the initial elongation and acknowledges in a note that ASTM does not have agreement on the point of origin (zero position). Myles (1986) clearly defined the logic and the method in which to record the test initiation, a "daylight" point and total offset to be used for calculation

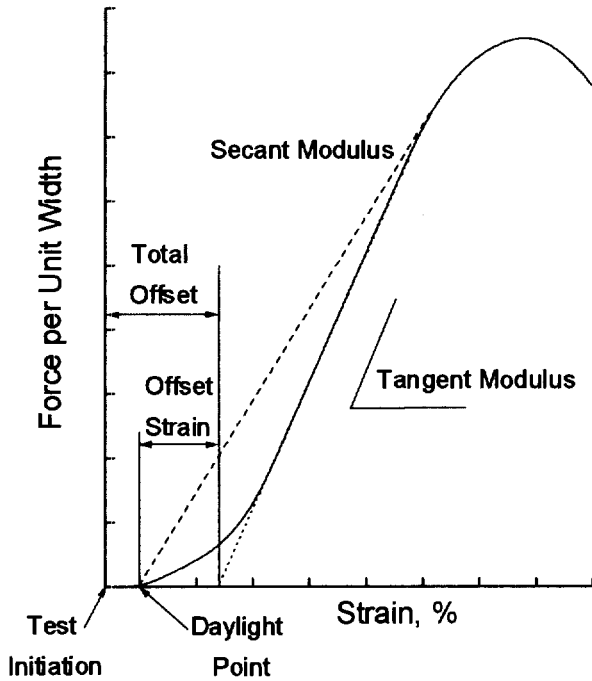


Figure 3. Stress-Strain Curve with Complete Test Results

of secant and tangent moduli as shown in Figure 3.

The test methods cited above are employed equally for a wide range of geosynthetics. The significance of tensile strength and modulus are not the same for all classes of geosynthetics. Unreported stress, strain and modulus data on a filter is not a concern to the designer. Any such unreported data on products used in critical structures is, or should be, a significant concern. One illustration of the importance of accurate reporting is the effect of preloads. Figure 4 presents the effect of preload variation on a set of identical samples tested on roller grips. The significance of geosynthetic performance at low strain is increasingly recognized as significant to the working range of successful construction projects (Craig 1997, Fakher et al. 1996). Current specifications are frequently governed by strength requirements at strains of 5%. Because testing preload has such profound effect on reported data at low strain values, it is essential that the design engineer have both a good understanding of test protocol and accurate data in order to employ reinforcements in such designs. Figure 4 demonstrates that application of a 222 N preload results in a 15 to 20% increase in reported load at 5% strain and that

successively higher preloads more than double T5 values. Ultimate strength is nearly independent of preload; however, there can be a modest decrease in ultimate strain as preload increases. Figure 5 demonstrates that preloads

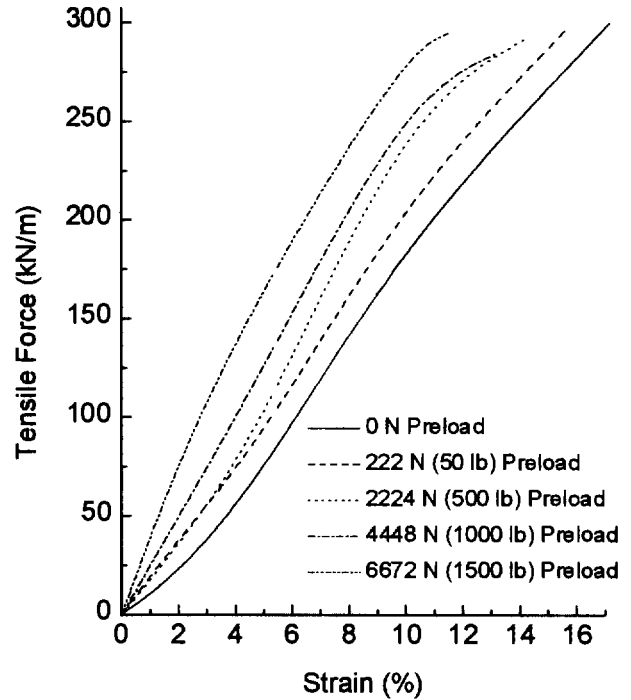


Figure 4. Effect of Preload on Identical Samples Using Roller Grips

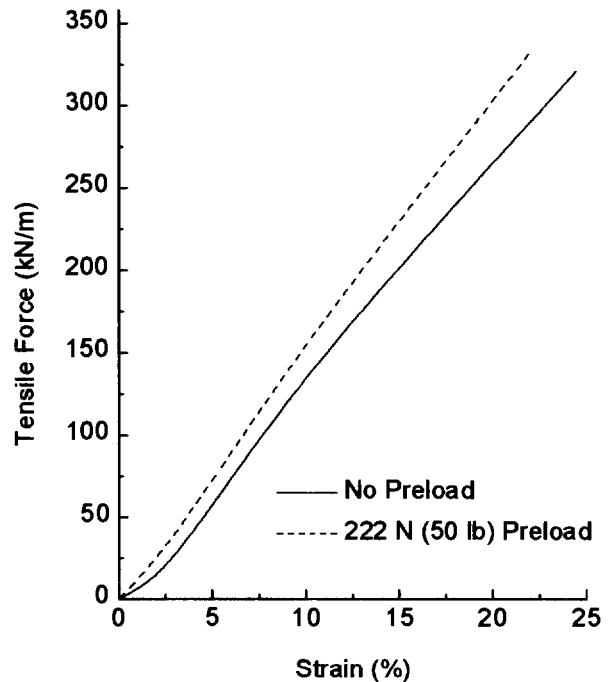


Figure 5. Effect of Preload on Identical Samples Using Tab Grips

produce the same data inflation in the tab system that was seen in figure 4 for roller testing. Figure 6 presents 2 widely different fabric structures produced to the same specification tested under no preload and under a high preload using roller grips. Clearly preloads inflate data regardless of fabric structure or gripping system. When employing roller grips, the use of preload in testing of very strong geosynthetic reinforcements is obviously necessary in order to remove slack and to seat samples in the testing device. The recording of preloads applied in testing of very strong geosynthetic reinforcements is important, and the full reporting of extension when applying preloads is essential to insure data is presented in complete form. The reporting of tests performed on high strength textiles should

are related to segments of the stress strain curve. The ISO and BSI definitions are compatible with ASTM in language; however, the ISO and BSI curves, with the reporting of extension from test initiation, clearly include data that ASTM excludes. The point is that the reporting of a value at 2% or 5% strain on a secant calculated from a body of data that omits part of the specimen extension data should be of little value to the designer of a critical structure.

During the execution of a test, data for the entire curve can be recorded. With the salient data available for analysis, information concerning any, and every, segment of the load elongation curve can be observed. Initial modulus should be defined as the linear portion of the test curve from the initiation point to the point where the curve

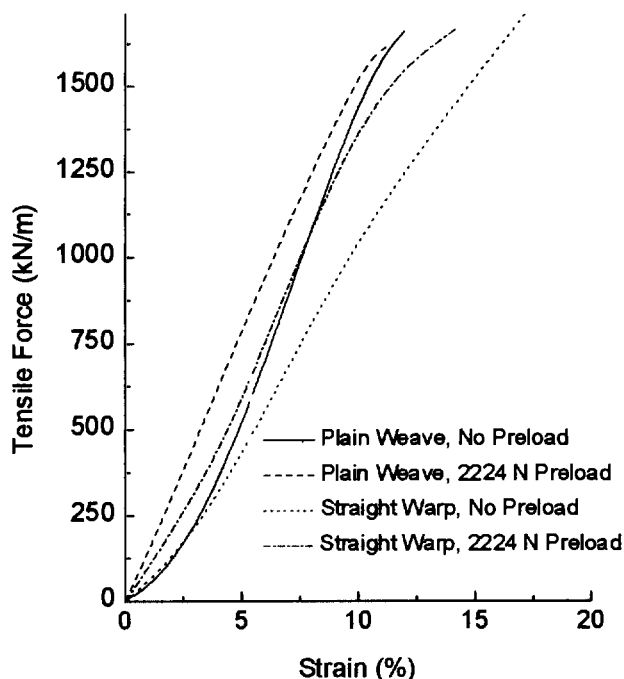


Figure 6. Effect of Preload Regardless of Structure, Using Roller Grips

include test initiation, daylight point and the total offset as mentioned by Myles (1986).

### 2.3 The Definition of and Reporting of Modulus

Due to poor agreement between sources, the definitions of modulus can be problematic for the authors of specifications and test reports on reinforcing geosynthetics. The problem is the selection of the portions of the curve to be included in the calculations. ASTM D4595 defines initial tensile modulus as “the ratio of change in tensile force per unit width to a change in strain (slope) of the initial portion of the force per unit width strain curve.” ASTM also defines offset modulus and secant modulus in similar terms with the clear intent that all of these concepts

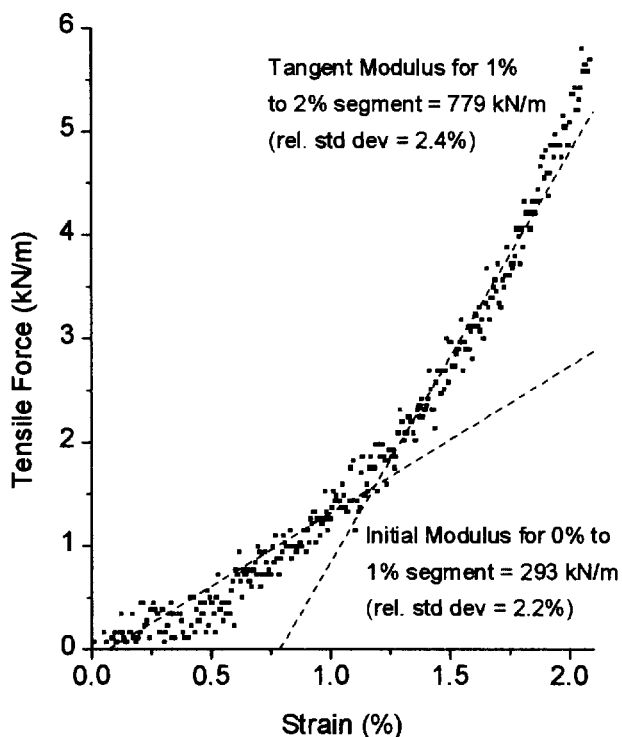


Figure 7. Measurement of Initial Modulus Data Using Tab System with No Applied Preload

shifts to non linearity. Figure 7 presents 2 best fit lines for 2 segments of a stress strain curve. Segment (a) represents 0 to 1%. Segment (b) represents 1 to 2%.

### 2.4 The Effect of Sample Gauge on Test Results

One of the principle concerns of the research community in its review of wide width testing on reinforcements was the effect of sample gauge. The authors conclude that the 100 mm sample gauge has proven to be inadequate for reinforcements. Finnigan (1977), Sisson (1977) and Van

Leeuwen (1977) all cited standard testing protocols for strong fabrics as the textile strip method in which sample length was typically 2 to 4 times the width. Recognition that the strip concept of sample configuration is most appropriate for strong tensile members is recognized repeatedly throughout the literature, ASTM D5035, a strip test, is representative of the standard method for testing strong textiles and employs long thin specimens. The NGO (Balkema 1986) provide discussion of the mechanisms of testing and effects of gauge, width and structure. The concept of long sample lengths is common to the textile industry reflecting the producers understanding that short sample lengths inflate strength and extension while deflating modulus. Pan et al. (1997) showed that a small variation in length of textile reinforcements had a large effect on results. Experiments were conducted using long samples, up to 0.508 m, in the sacrificial tab method in search of a neutral gauge for multifilament textile products using polyester, polyamide or other industrial fibers. Data indicates that a small variation in length of textile reinforcements has a large effect on results. The experiments indicate that for multifilament textile products using polyester, polyamide or other industrial fibers both the effects of sample length and of variations in test speed are greatly reduced by long specimens. Figure 8 presents the effect of strain rate on initial modulus as a function of specimen length. Initial modulus is defined as "the linear portion of the test curve from the test initiation point to the point where the curve shifts to nonlinearity". Figure 9 presents the effect of strain rate on segment (3%-ULT)

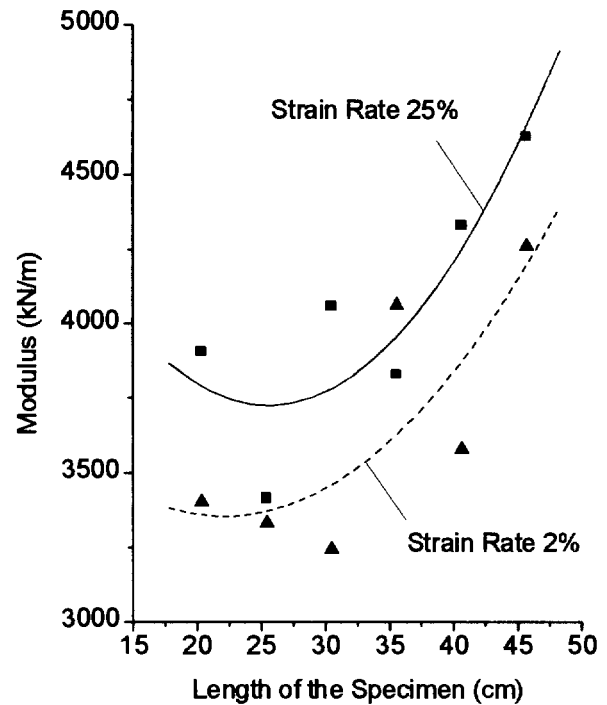


Figure 9. Effect of Strain Rate on Segment (3%-ULT) Modulus

modulus as a function of specimen length and Table 1 presents a comparison of standard deviation for initial and segment modulus.

Table 1. Comparison of Standard Deviation for Initial and Segment Modulus

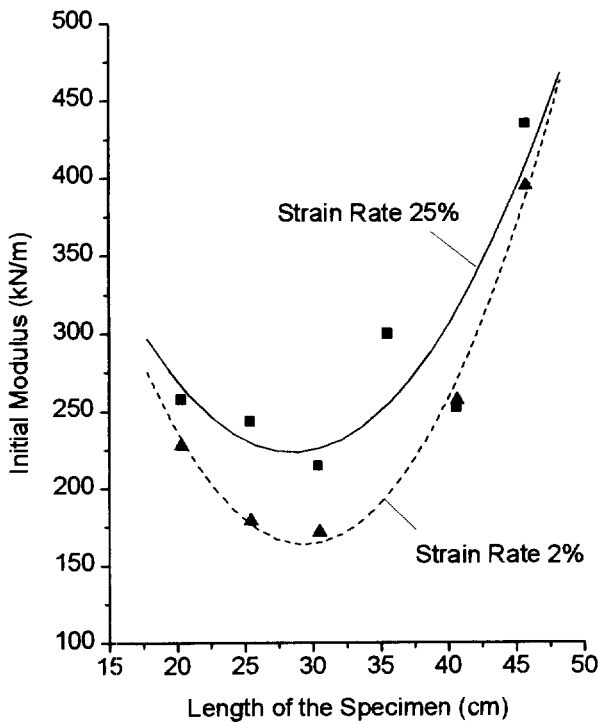


Figure 8. Effect of Strain Rate on Initial Modulus

Length of Specimen, cm	% Strain Rate per min	% Standard Deviation of Initial Modulus	% Standard Deviation of Segment Modulus
20.3	25	2.2	0.8
20.3	2	0.9	0.5
25.4	25	2.1	0.8
25.4	2	1.3	0.4
30.5	25	2.6	1.1
30.5	2	1.1	0.4
35.6	25	2.7	0.9
35.6	2	1.4	0.8
40.6	25	2.2	1.6
40.6	2	1.0	0.4
45.7	25	2.6	1.3
45.7	2	1.0	1.3

## 2.5. Strain Measurement

The measurement of strain in testing of geosynthetics is widely acknowledged to be difficult and it is particularly so for the high strength materials used in reinforcements. The ISO method dictates that the extensometer be capable of measuring the distance between two reference points on the specimen without any damage to the specimen or slippage in relation to the specimen and resulting in a measurement representing the true movement of the reference points. The four strain measurement techniques cited in the literature and the ISO test method are mechanical, optical, infrared or electrical devices. Mechanical devices include both crosshead movement (displacement of the clamps) and lvdt's (linear displacement measurement devices) or mechanical devices attached to the specimen. Optical devices include video and laser systems. All of which observe a small section of the specimen. The principle issues are specimen damage, rate of strain and confirmation of accuracy. The experiences reported by Brand and Pang (1991) and Leschinsky and Fowler (1990) define the difficulties experienced in accurate measurement of strain on very strong geosynthetic materials regardless of device type, and reflect the broad concern that accuracy needs to be verified by comparison of two or more measurement techniques. Figure 10 presents a comparison of curves from specimens in which extension was recorded simultaneously for both displacement and an optical device. The excellent agreement at low strain is most significant to the designer

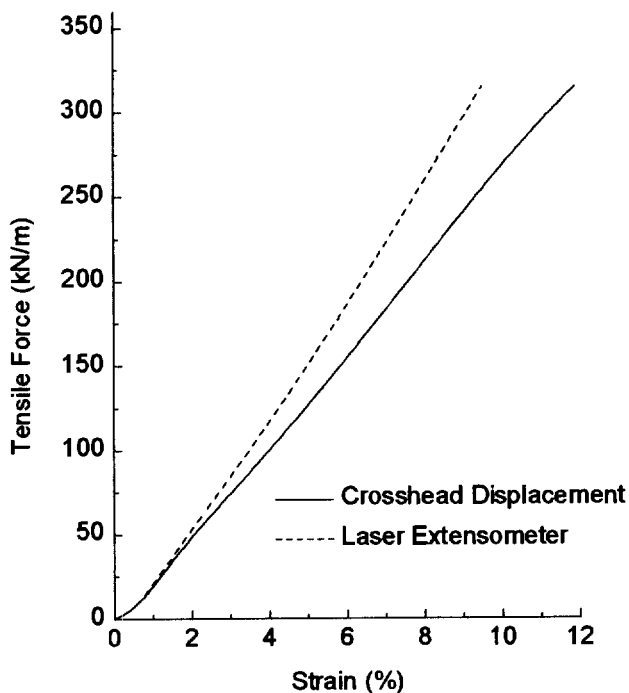


Figure 10. Effect of Extension Measurement Device Using Tab System

of reinforced structures.

Specimen damage or distortion that influence test results can be evidenced in two principal forms. Sample slippage in clamps resulting in partial or major deformation can influence test results necessitating that the specimen be discarded. More frequent is the seating slippage typical of roller devices and the slight distortion of samples in the clamp area in normal strip tests. In both instances, accurate measurement and recording of strain is essential to determine whether the slippage materially affects the results. Figure 11 compares the results of identical specimens with data recorded by lvdt and by crosshead.

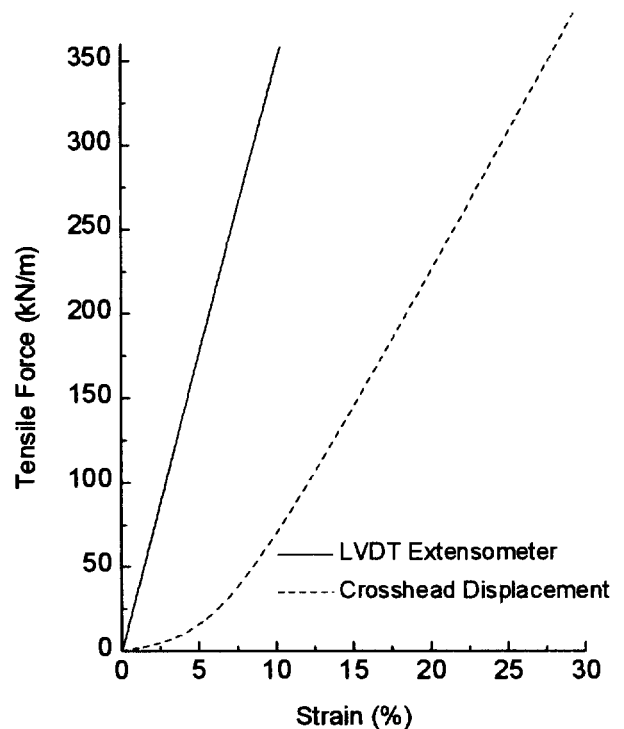


Figure 11. Effect of Extension Measurement Device Using Roller Grips

The crosshead data presentation shows initiation and the process of sample slippage during the test. The lvdt data is presented from preloaded initiation only and masks the slippage and elongation at initiation. It is interesting to note that the device has the effect of truncating the stress strain curve at ultimate while recording consistent data at low loads.

Figure 7 illustrates that for non slipping grips, crosshead displacement data from a correctly calibrated instrument will provide strain information for an entire sample geometry rather than a small nonrepresentative sector. Some practitioners have expressed concern about the accuracy of displacement measurement. The conventional testing machine does experience deformation in the

conduct of a tensile test. Error introduced by this deformation is corrected by subtracting machine displacement from the data. To demonstrate accuracy we tested a calibrated aluminum bar. The specified modulus of the specimen was 68.95 GPa. Strain gages recorded a modulus of 68.1 GPa. Crosshead displacement recorded modulus of 54.0 GPa. Displacement values corrected for machine deformation were 68.4 GPa, essentially zero error. Tests conducted on fabrics with loads at 31.1 kN and extension of 12 to 16% experienced machine deformation of less than 0.1%. Failure to correct for this deformation results in test error of less than 0.5% leading to the conclusion that displacement is an accurate measurement.

Finally, rate of strain is shown to be problematic in measurement as it is calculated as a percentage of sample gauge (a length measurement). For those geosynthetics that can be tested in a 100 mm length by 200 mm width geometry, the speed of the test is easily recorded by conventional means. High strength materials are typically tested in the much different longer than wide geometry, dictated by equipment load capacity and clamping devices. Brand and Pang (1990) report that strain rate for an entire sample tested by roller grips was typically 6% not the expected 10% prescribed by the method ASTM D4595. The NGO, Balkema (1986) explains that the phenomena occurs because of differences in strain characteristics in different portions of the specimen. Strain in the vicinity of the clamps is plane in nature while strain in the center of the sample tends to be linear. Goswami et al. (1996) present variation in strain for different sites on the specimen as the norm for textile type materials. The necessity to observe either the total area or a large portion of the specimen to accurately record strain rate necessitates the simultaneous employment of a combination of techniques such as displacement and optical devices and a mandatory comparison of the data. The definition of sample length, the strain measurement gauge used, the strain measurement system used and the observed test speed must be clearly reported.

## 2.6 Jaws, grips and other devices

Strong geosynthetics such as reinforcements experience great difficulty in sample gripping. Experienced researchers (Haliburton 1978; Myles 1986, 1987; Rowe et al. 1986; Richardson et al. 1987; Leschinsky and Fowler 1990; Brand and Pang 1991) cite grip failure as a key concern. The principal test methods, ASTM, ISO and BSI, recognize the issue of the difficulty of sample gripping and permit the utilization of roller or capstan grips. Roller grips typically require sample lengths of 1.829 m, width up to 0.203 m and typical spacing between rollers of 0.508 m. Because the sample geometry used in rollers is larger than most extension measurement tools, it seems obvious that displacement could be a critical measure of sample strains.

Unfortunately, the large amount of slippage that occurs in roller grips throughout the test negates the application of these techniques for low strain values in roller testing, although displacement can be quite accurate in recording ultimate strain. Equally problematic is the application of other devices. Typical optical devices observe a pencil line wide strip 0.203 m high, and mechanical/electronic devices also observe a very narrow, 0.101 m long section of a specimen with the result that when applied to roller tested specimens, these extension measurement systems represent the area observed and not the specimens performance.

Roller grips have several other awkward characteristics beside large sample geometry including the need to permit a sample to seat itself. The process of seating, also described as the application of preload, involves a certain extension of the sample. Accurate reporting requires that this extension be recorded as per Figure 3. Another issue of difficulty caused by large sample geometry of 1.829 m length, 0.508 m grip separation and sample widths up to 0.203 m is incompatibility with the general definition of wide width sample geometry: 100 mm gauge length by 200 mm width. In terms of strain measurement, this definition results in the apparent observation of, and reporting on, of a 0.101 m section of a 0.508 m or longer sample. Leschinsky and Fowler (1990) and Brand and Pang (1991) reported that different areas of a fabric were seen to extend at different rates and that any 100 mm by 200 mm section of a large sample would not be representative of the sample, or the product. The phenomenon that extension is not uniform over a large sample is documented elsewhere in textile literature (Goswami et al. 1996).

Sample widths vary according to the test device load capability, but in every case an equal number of yarn ends should be tested in each specimen of a sample or a testing program. In our work the separation from center of barrel to center of barrel was fixed at 0.508 m. Extension was measured by displacement or lvdt with the lvdt found to be acceptable for measurement of low strain values but strongly influenced by sample geometry at ultimate. Figure 9 compares identical specimens with extension recorded by displacement compared to lvdt. The lvdt could be observed to distort the specimen, break fiber and prematurely fail the specimen at very high strain.

The jaw used in the sacrificial tab system employed in our work is a hydraulic clamp with a wide pressure range. For very strong fabrics with tensile exceeding 700 kN/m, grip pressures exceeded 20.7 MPa insuring control of slippage in the grips. The typical specimen length exceeds 0.610 m permitting mounting of 0.0508 m sacrificial tabs on each end of the specimen and leaving a 0.508 m separation between clamps. As in roller testing, sample width is dictated by load cell capability but in every case an equal number of yarn ends is maintained between specimens.

## 2.7 Sample preparation

Care is taken in mounting samples in grips to avoid skew. Sacrificial tabs of light metal are adhesive bonded on both sides of specimens destined for pressure clamps, with tab separation of a minimum of 0.508 m. Adhesives are selected to have minimal influence on samples. For many light load fabrics, under 130 kN/m, protective tabs are unnecessary.

The sample preparation technique attempts to achieve yarn (and filament) alignment. The sacrificial tab permits very high pressures across the clamped face of the specimen which prevents the specimen from slipping out of the clamp. Simultaneously, the soft adhesive that binds the tab to the sample permits some relative slippage within the specimen permitting the maximum degree of uniform alignment and engagement of a high proportion of the filaments in the specimen. Slippage is observed in the two procedures at different times. Slippage is first observed on rollers in the early stages of the test, continues through much of the procedure and reduces to nil when approaching ultimate. Slippage is observed in pressure clamps at the end of the test. This small distortion develops late in the test and allows the continued loading of a majority of the filaments in the specimen.

## 3 CONCLUSIONS

The following conclusions are presented in the same order as the listing of the 14 concerns. 1. For textiles with uniaxial orientation of strength members (yarns), sample length influences test results. Shorter lengths inflate tensile values while deflating modulus. A practical solution to insure comparable results is to employ sample lengths in pressure grips that are comparable to roller grip separation distances. This permits the observation of similar geometry of the specimens. 2. Increased test speed inflates results; however, longer samples reduce the effect. Polyolefin materials are far more greatly affected by variation in speed. 3. Fabric structure dominates testing. Manipulation of other testing aspects: polymer, fiber form, test speed, sample geometry, grips, or protocols cannot reduce the impact of structure on fabric performance. 4. Test grips are part of a system and each system, roller or pressure can be employed to achieve accurate and repeatable results. 5. Slippage is also part of the system when testing strong materials and is in fact desirable in order to achieve consistent and meaningful results. 6. Tolerable slippage is observed and recorded by developing correlation between extension measurement systems. 7. Extension measurement is a critical element and a contentious issue in testing of high strength fabrics. Certain devices, lvdts, can be satisfactory for part of the test and may invalidate another portion of the test. There is a potential lack of confidence

in, or familiarity with, displacement and its influence of sample geometry and speed. Accurate displacement measurement can be performed simultaneously with other measurements and compatibility of two measurements insures good understanding of the test process and the recognition of flawed results. The test operator must take care to report the strain measurement gauge and the sample length, particularly when these measurements are different. 8. Extension measurement is defined by sample geometry, test speed, the physical area the device measures and the location of the device on the sample. Extension measurement techniques must be reported in detail to avoid undue masking of results. 9. Strong reinforcements are essentially uniaxial in orientation with each strength member (yarn) parallel to the next. In strip testing, whether 1.016, 0.203 or 0.0508 m in strip width, the entire sample is gripped and width does not play a significant role in the test except where the grip system is incapable of achieving uniform pressure. For reinforcements, sample width identifies the limits of the apparatus, not the reinforcement. In all cases testing must insure that an equal number of yarn ends are tested from sample to sample within a nominal specimen width. 10. Preload is a necessary element in testing of strong materials if roller systems are used. If not properly reported, preloads can mask test result information. 11-13. Modulus is the second contentious issue in testing of reinforcements. Clearly the meaningful moduli are related to certain segments of the data curve. In terms of reinforcements for critical structures it is not agreed whether the meaningful value is a secant of a very large segment or the actual value of a specific segment, for example: the modulus of the segment between 2% and 5% strain. 14. The relationship between single end yarn data and fabric performance is clearly evident; however, the relationship is not represented by a simple ratio. Some of the influences on the translation efficiency of a yarn strength to a fabric are: processing conditions, fabric structure, and testing systems. For a given product from a specific system, the relationship of yarn to fabric is a constant.

## REFERENCES

- A.A. Balkema Publishers*, Old Post Road, Brookfield, VT 05036-9704, USA Fax 1 802 276 3837 ISBN 90 6191 624 0
- Bais-Singh, Smita and Goswami, Bhuvanesh, C., 1996, "Deformation Behavior of Spun-Bonded Nonwovens: Measurement" Proceedings of INDA-TEC 96, *International Nonwovens Conference*, Hyatt Regency Crystal City, Crystal city, VA., pp. 29.1-29.19
- Brand, E.W. and Pang, P.L. R., 1991, "Durability of Geotextiles to Outdoor Exposure in Hong Kong",

- Journal of Geotechnical Engineering*, Vol. 117, No. 7, pp. 979-1000.
- Craig, B. "Report on the joint BGS/IGS meeting "Use of Geosynthetic Materials with Improved Reinforcement Capabilities", 4 December, 1996, University of Manchester, Ground Engineering, April, 1997.
- Fakher, A., Jones, C.F.J.P., & Zakaria, N-A.B., "The Influence of Dimensional Analysis on the Interpretation of Model Loading Tests on Reinforced Ground", *Earth Reinforcement: Proceedings of the International Symposium on Earth Reinforcement, Fukuoka, Kyushu, Japan 12-14 November 1996*, Edited by Hidetoshi Ochiai, Noriyuki Yasufuku, Kiyoshi Omine A.A. Balkema Publishers, Old Post Road, Brookfield, VT 05036-9704, USA Fax 1 802 276 3837 ISBN 90 5410 833 9
- Finnigan, J.A., 1977, "The Creep Behavior of High Tenacity Yarns and Fabrics Used in Civil Engineering Applications", *Proceedings of the International Conference on the Use of Fabrics in Geotechnics, L'Ecole Nationale Des Ponts et Chaussees*, Vol. 2, Paris, France, April, 1977, pp. 305-309.
- Geotextiles and Geomembranes, edited by R. Veldhuijzen Van Zanten, pp. 61-78
- Haliburton T.A., Anglin C.C. and Lawmaster, J.D. 1978, "Testing of Geotechnical Fabric for Use as Reinforcement", *Geotechnical Testing Journal*, Vol. 1, No. 4, pp. 203-212
- Jones, C.F.J.P., Fakher, A, Hamir, R. & Nettleton, I.M. "Geosynthetic Materials with Improved Reinforcement Capabilities", *Earth Reinforcement: Proceedings of the International Symposium on Earth Reinforcement, Fukuoka, Kyushu, Japan 12-14 November 1996*, Edited by Hidetoshi Ochiai, Noriyuki Yasufuku, Kiyoshi Omine A.A. Balkema Publishers, Old Post Road, Brookfield, VT 05036-9704, USA Fax 1 802 276 3837 ISBN 90 5410 833 9
- Leschinsky, D. and Fowler, J., 1990, "Laboratory Measurement of Load Elongation Relationship of High-Strength Geotextiles", *Geotextiles and Geomembranes*, Vol. 9, No. 2, pp. 145-164.
- Myles, B. and Carswell, I.G., 1986, "Tensile Testing of Geotextiles", *Proceedings of the Third International Conference on Geotextiles*, Vol. 3, Vienna, Austria, April 1986, pp. 713-718
- Pan, N, Chen, H.C., Thompson, J., Inglesby, M.K., Khatua, S., Zhang, X.S., and Zeroinian, S.H., 1996, "Fiber Initial Modulus as a Function of Fiber Length", *The Fiber Society, General Technical Conference*, Hotel Viking, Newport, Rhode Island, October 14-17,
- Rowe, R.K. and Ho, S.K., 1986, "Determination of geotextile Stress-Strain Characteristics Using a Wide Strip Test" *Proceedings of the Third International Conference on Geotextiles*, Vol. 3, Vienna, Austria, April 1986, pp. 885-890.
- Sissons, C.R., 1977, "Strength Testing of Fabrics for Use in Civil Engineering", *Proceedings of the International Conference on the Use of Fabrics in Geotechnics, L'Ecole Nationale Des Ponts et Chaussees*, Vol. 2, Paris, France, April, 1977, pp. 287-292
- Van Leeuwen, J.H., 1977, "New Methods of Determining the Stress-Strain Behaviour of Woven and Non Woven Fabrics in the Laboratory and in Practice", *Proceedings of the International Conference on the Use of Fabrics in Geotechnics, L'Ecole Nationale Des Ponts et Chaussees*, Vol. 2, Paris, France, April, 1977, pp. 299-304.





# GEOSYNTHETIC REINFORCEMENT: ARE GEOTEXTILES AND GEOGRIDS INTERCHANGEABLE?

C. Joel Sprague, P.E.  
Sprague & Sprague Consulting Engineers, Greenville, SC, USA

**ABSTRACT:** Geosynthetically reinforced soil structures have become acceptable, cost-effective alternatives to conventional geotechnical structures. Yet, it is interesting to note that many geosynthetically reinforced soil structures are specified in such a fashion that only geogrid but not geotextile reinforcement may be used, or vice versa. Why is this? This paper explores this question using tables and charts of relevant, performance-oriented properties and a survey of more than 50 State DOT and FHWA engineers questioned about their preferences related to the use of geotextiles and geogrids for reinforcement applications. In general, there appear to be no overriding technical or economical reasons to rely on proprietary, product-specific designs/specifications when using geosynthetic reinforced soil structures. Conversely, there are several arguments for the widespread use of generic design, specification, and procurement procedures.

**KEY WORDS:** geotextiles, geogrids, reinforcement, specifications

## 1 INTRODUCTION

Though the use of tensile inclusions in soil structures dates back several thousand years to the construction of religious structures in ancient Babylonia, it was only three decades ago that Henri Vidal, a French architect, pioneered modern earth reinforcement techniques. These techniques involved the incorporation of resisting elements into a soil mass to complement the soil's compressive strength and together to act in a composite fashion to improve the mechanical properties of the soil mass. Vidal patented his system, which used steel strips to provide the reinforcement, and named the system "Terre Armee" in France and "Reinforced Earth" in the United States. The first Reinforced Earth wall was constructed along California State Highway 39 in 1972.

Mitchell and Villet (1987) detailed and expanded on this historical perspective, noting that beginning in the early 1970's, experimentation using geotextiles as soil reinforcement was conducted in Europe and the United States. The U.S. Forest Service constructed full-scale wrapped-face walls in the Siskiyou and Olympic National Forests using geotextiles in 1974 and 1975 and developed construction and design guidelines based on this experience. Under FHWA sponsorship, highway departments in New York, Colorado, and Oregon constructed geotextile reinforced walls in the early 1980's. These geotextile reinforced walls were compared to walls constructed with steel inclusions and all were found to perform well.

This success attracted other candidate forms of plastic inclusions such as geogrids. Beginning in about 1984, Tensar geogrids were introduced specifically for soil reinforcement. These geogrids were manufactured of

polyethylene - a different polymer than used in the geotextiles. Polypropylene and polyester were the polymer of choice for geotextiles.

Since 1986, the use of reinforced soil systems, which are also called mechanically stabilized earth (MSE), in the United States has significantly increased. The primary types of MSE systems which have emerged include: mechanically stabilized earth walls (MSEW); reinforced soil slopes (RSS); reinforced embankments over soft foundations (RESF); and reinforced liners and caps. MSEW and RSS have become especially important in highway construction as their use reduces the required width of new right-of-way and facilitates construction within existing limited right-of-way. RESF are recognized as a cost-effective alternative to traditional techniques for constructing earthen embankments over low strength foundations. Additionally, critical environmental applications of geosynthetic reinforcement have emerged, including the reinforcement of landfill and lagoon liner and cap systems on steep slopes and over weak subgrades or underlying voids.

Free draining granular material is the preferred backfill material in reinforced soil structures. Therefore, the use of reinforced soil structures - primarily MSEW and RSS - has been somewhat limited in cases where high quality backfill material is not readily available. Mitchell and Zornberg (1994 & 1995) observed that the inherent low strength, moisture instability, possible volume changes, and creep potential, along with the corrosive potential of saturated soils, are common concerns associated with the use of fine-grained, cohesive backfills. They further noted that as successful experiences are documented and consistent design methodologies are developed for these poorly

draining backfills, even greater growth in the use of reinforced soil structures will be possible.

Clearly, there has been substantial acceptance of geosynthetic reinforced soil structures and much of the growth has been the result of aggressive marketing by companies providing candidate geosynthetic soil reinforcement materials. Therefore, much of the experience gained to-date is with those reinforcement materials which are marketed most aggressively and "packaged" with proprietary designs. Yet, this growth has been fraught with argument as competing proprietary systems claim superior performance or dependability. In response, independent researchers and Federal and State engineers have advanced the development of generic design techniques and material specifications such as AASHTO (1997) MSEW specifications and the FHWA's RSS guidelines by Berg (1993) and the DEMO 82 educational effort discussed by DiMaggio (1996). This new generation of generic design techniques and specifications recognizes the suitability of both geotextiles and geogrids for soil reinforcement.

This paper details the key issues associated with the use of geosynthetics as soil reinforcement and provides comparative data for common reinforcing geosynthetics. Additionally, required product documentation, relative costs, and a summary of geosynthetic reinforcement use by state Departments of Transportation (DOT) are presented.

## 2 REINFORCEMENT DESIGN INPUTS

### 2.1 Overview

Geosynthetic reinforcement systems incorporate geotextiles and/or geogrids as horizontal layers within a soil backfill to resist outward movement of the reinforced soil mass. The geosynthetic interacts with the soil by adding a tensile force and this tensile force is transferred to the soil mass through unique geosynthetic/soil interaction mechanisms. Both tensile force and soil interaction must be determined for each candidate geosynthetic.

### 2.2 Allowable Tensile Strength

The allowable tensile strength of a geosynthetic is input into reinforced soil analyses in order to determine the reinforced factor of safety. Allowable geosynthetic design strengths must be determined by testing and analysis methods that account for the long-term dimensional stability and durability of the full geosynthetic structure. Dimensional stability is characterized by the ability of the geosynthetic to sustain long-term load in-service without excessive creep strains. Durability factors include site damage, chemical degradation and biological degradation. These factors may theoretically cause deterioration of either the geosynthetic's tensile elements or the geosynthetic/soil stress transfer mechanism of the geosynthetic structure according to Berg

(1993). To account for dimensional stability and durability, allowable tensile strength,  $T_a$ , for the geosynthetic is determined using a partial factor of safety approach such as Equation 1 from Berg (1993).

$$T_a = T_{ult} / (FS_{CR} \times FS_{ID} \times FS_{CD} \times FS_{BD} \times FS_{JNT}) \quad (1)$$

$T_a$  = allowable geosynthetic tensile strength;

$T_{ult}$  = ultimate geosynthetic tensile strength;

$FS_{CR}$  = partial factor of creep deformation;

$FS_{ID}$  = partial factor of safety for installation damage;

$FS_{CD}$  = partial factor of safety for chemical degradation;

$FS_{BD}$  = partial factor of safety for biological degradation;

$FS_{JNT}$  = partial factor of safety for joints.

The allowable tensile strength,  $T_a$ , is often referred to as the long-term design strength, or LTDS. (Long-term allowable design load, or LTADL, is also used by some.) Many geosynthetic manufacturers can provide typical LTDS values for each of their candidate reinforcement materials. It is important to recognize that these "typical" LTDS values reflect factors of safety derived from laboratory and/or field testing which may or may not simulate the project conditions under consideration. Therefore, the designer must consider whether the partial factors of safety inherent in any "typical" LTDS value are applicable.

### 2.3 Partial Factors of Safety.

The partial factors of safety used to calculate the allowable tensile strength of the geosynthetic are intended to address the issues which provoke the greatest arguments between competing reinforcing systems. These factors of safety are either based on laboratory/field testing of the candidate material or are assigned based on "default" values derived from worst-case experience. An example of default values as recommended by Berg (1993) and typical testing-derived values is shown in Table 1.

Table 1. Typical Geosynthetic Reinforcement Default and Testing-Derived Values for Partial Factors-of-Safety

FS	Partial Factors of Safety					Composite
	ID	CR	CD	BD	J/S	
Default	3.0	5.0	2.0	1.3	2.0	78
Tested	1.2	2.0	1.1	1.0	1.01	2.64

KEY: FS=factor of safety; ID=installation damage; CR=creep; CD=chemical degradation; BD=biological degradation; J/S=joint/seam

The magnitude of default values virtually assures that a material supplier will do product-specific testing to derive the factors of safety to be used to calculate allowable tensile strength. If one were to use only default values, the

candidate geosynthetic would be able to claim an allowable tensile strength equal to only 1/78th of the ultimate tensile strength of the material. Certainly, this would likely make the candidate material uneconomical. Conversely, product-specific testing can be done to clearly define the unique limitations of a material without excessive conservatism. Guidance is commonly given in well written specifications such as Berg (1993) on how to determine factors of safety through laboratory/field testing. For example, one state DOT (WSDOT,1996) requires that ASTM D 5818 be the basis for  $FS_{ID}$  and that ASTM D 5262 along with a detailed data extrapolation technique be the basis for  $FS_{CR}$ . Additionally, this DOT gives a general approach to determining  $FS_{CD}$  and  $FS_{BD}$  based on the geosynthetic polymer.  $FS_{JNT}$  is not addressed, so presumably joints/seams are not permitted. It is important to note that the use of partial factors of safety does not identify any combined effects of the various forms of degradation. In the future, FS values derived from testing that examines the combined, and perhaps synergistic effects of two or more forms of degradation will be used. These types of testing are currently under development.

As shown in Table 1, using factors of safety derived from testing, the allowable tensile strength would typically be on the order of 38% of the ultimate (i.e. composite  $FS=2.64$ ), rather than the 1.2% of ultimate resulting from the use of default values. Composite factors of safety for calculating LTDS are commonly range from 2.0 to 4.0, depending primarily on the polymer.

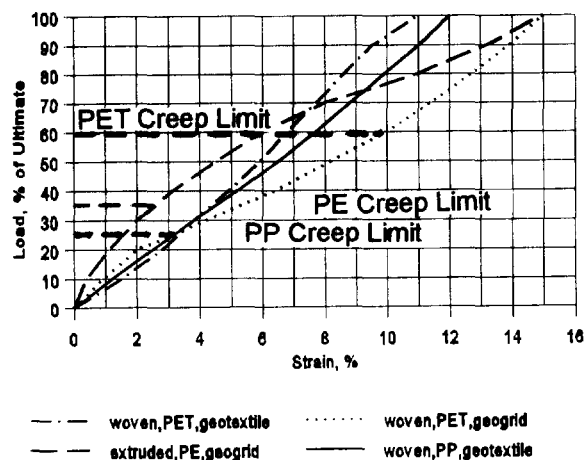


Figure 1. Geosynthetic Strength Characteristics

## 2.5 Creep.

As shown in Table I, creep potential is usually the greatest "factor" in LTDS calculations. Characteristic strength properties and associated creep limits of various geosynthetic types are presented in Figure 1. Creep potential limits the allowable tensile strength to no more than the creep limited load and strain. Therefore, as shown

in Figure 1, PET geosynthetics can safely mobilize higher strengths and strains than can PE or PP. This explains the generally lower composite factor of safety used to calculate LTDS for PET geosynthetics ( $FS = 1.8 - 2.0$ ) versus that used for PE or PP ( $FS = 3 - 4$ , or more).

## 3 GEOSYNTHETIC/SOIL INTERACTION

### 3.1 Overview

As noted earlier, along with tensile strength, a geosynthetic's interaction with the soil must be characterized as a part of the design process. Geogrids mobilize a different kind of interaction with the soil than the frictional behavior relied on by geotextiles. Instead of a continuous frictional surface, geogrids have large openings, or apertures, which allow the soil to be continuous through the inclusion. Geogrids transfer stress to the soil through passive soil resistance on transverse members of the grid and limited friction between the soil and horizontal surfaces of the geogrid. Geotextiles transfer stress to the soil through the friction created across its entire surface area.

Two types of soil/geosynthetic interaction must be quantified: pullout and direct shear. In both cases, the quantification of stress transfer must be accomplished through laboratory testing. As with Factors of Safety, specific guidance, especially on the range of normal loads to be used, is commonly given in well written specifications on how to determine pullout and direct shear coefficients through laboratory/field testing.

### 3.2 Pullout Resistance.

Pullout coefficients are used in stability analyses to compute mobilized tensile force at the front and tail of each reinforcement layer in MSEW and RSS systems. According to Berg (1993) design of MSEW and RSS for permanent applications requires evaluation of long-term pullout performance with respect to three basic criteria:

1. pullout capacity should be adequate to resist the design tensile force with an appropriate factor of safety; and
2. allowable displacement should be greater than the relative geosynthetic to soil displacement required to mobilize the design tensile force; and
3. the pullout load should be smaller than the critical creep load.

The long-term pullout interaction coefficient is quantified by laboratory testing such as is outlined by Berg (1993). For geotextiles, this simply requires a quick effective stress pullout test since only surface friction is involved. For geogrids, sufficient long-term junction strength must be considered in addition to or as a part of pullout testing, since soil bearing on transverse ribs may be an important component of grid pullout resistance. This may require

creep testing of the junctions or the entire soil/grid system or cutting transverse ribs to remove the junctions from the testing. Therefore, much more testing may be required in order to qualify a candidate geogrid for pullout resistance as compared to a geotextile. The  $C_i$  value from pullout testing is used to calculate the bond length behind a critical failure surface using Equation 2.

$$L = PO_{ult} \text{ or } PO_{0.75 \text{ in}} / (2 \times C_i \times \sigma \times \tan\phi) \quad (2)$$

Where:

$L$  = bond length beyond a failure plane;  $\sigma$  = normal load;  $\tan\phi$  = the tangent of the soil's friction angle;  $C_i$  = interaction coefficient (See Tables 2a and 2b);  $PO_{ult}$  = the highest load resisted by the embedded reinforcement; and  $PO_{0.75 \text{ in}}$  = the pullout capacity associated with a movement of less than 0.75 inches (19mm) of the leading edge of the reinforcement sample.

Table 2a: Typical Short-term Geosynthetic/Soil Interaction Coefficients for Pullout,  $C_i$

Interface with Soil	Normal Stress					
	500 psf		1000 psf		2000 psf	
	Clay	Sand	Clay	Sand	Clay	Sand
W,PP,GTX	0.60	0.90	0.65	0.90	0.70	0.90
W,PET,GTX	0.70	1.00	0.80	1.00	0.90	0.95
W,PET,GG	0.70	1.00	0.90	1.00	0.90	1.00
EX,PE,GG	>0.7	>0.9	>0.7	>0.9	>0.7	>0.9

KEY: W=woven; EX=extruded; PP=polypropylene; PET=polyester; GTX=geotextile; GG=geogrid. Based on Cowell & Sprague (1993); Collin & Berg (1993); unpublished reports

Table 2b: Typical Long-term Geosynthetic/Soil Interaction Coefficients for Pullout,  $C_i$

Interface with Soil	Normal Stress					
	500 psf		1000 psf		2000 psf	
	Clay	Sand	Clay	Sand	Clay	Sand
W,PP,GTX	0.60	0.90	0.65	0.90	0.70	0.90
W,PET,GTX	0.70	1.00	0.80	1.00	0.90	0.95
W,PET,GG	n/a	0.90	n/a	1.00	n/a	1.00
EX,PE,GG	>0.7	>0.9	>0.7	>0.9	>0.7	>0.9

KEY: W=woven; EX=extruded; PP=polypropylene; PET=polyester; GTX=geotextile; GG=geogrid; n/a=not available. Based on Cowell & Sprague (1993); Collin & Berg (1993); unpublished reports

Cowell and Sprague (1993) provided the following general conclusions based on extensive pullout testing:

1. Geogrids and geotextiles having similar strength properties also have similar ultimate pullout capacities and coefficients of interaction.
2. The pullout capacity at 0.75 inches of displacement for the geotextiles tested was significantly lower (50 to 67%) than that obtained for geogrids of similar strengths.

3. Junction strength of geogrids and the contribution to pullout resistance contributed from transverse ribs does not have a significant affect on pullout performance. (See long-term values in Table 2b)

One additional conclusion can be drawn concerning the sensitivity of a design to variation in  $C_i$ . If equation 2 is solved for length, given a required pullout, it can be shown that for  $C_i$  in the range of 0.7 to 0.9, a minimum length of 1 m controls for reinforcement layers below approximately 1 m of soil depth.

### 3.2.1 Pullout in the Design of RSS Structures.

The ultimate load is taken to be less than or equal to the LTDS and from this the bond length required is calculated. A factor of safety, typically on the order of 1.5, is applied to this length. In RSS applications, strains are typically controlled by using a 10% creep limit strain in the selection of the LTDS. RSS structures can tolerate more movement than MSEW, therefore  $PO_{0.75 \text{ in}}$  is not typically used for RSS.

### 3.2.2 Pullout in the Design of MSEW Structures.

For the design of MSEW structures, especially those with concrete facing panels, not only is the required bond length calculated as with RSS structures, but the limiting strain of the wall face can be critical. It is important to check if the LTDS can be mobilized within a limiting strain in order to assure that wall face movements remain within tolerable limits. Therefore, both the  $C_i$  and the  $PO_{0.75 \text{ in}}$  must be checked to see how they may affect the design.

### 3.3 Direct Shear.

Direct shear coefficients are used in checking the factor of safety against sliding of an overlying soil mass. This sliding is a consideration in all reinforced soil systems. Soil/geosynthetic direct shear resistance is determined by laboratory testing. As can be seen in Table 3, geotextiles and geogrids are both highly efficient in transferring interface shear stresses, especially with sand.

Table 3: Typical Geosynthetic/Soil Interaction Coefficients for Direct Shear,  $C_s$

Interface with Soil	Normal Stress					
	500 psf		750 psf		1000 psf	
	Clay	Sand	Clay	Sand	Clay	Sand
W,PP,GTX	0.60	0.85	0.60	0.90	0.60	0.90
W,PET,GTX	0.75	0.90	0.80	0.95	0.90	0.95
W,PET,GG	0.80	0.90	0.85	0.95	0.90	0.95
EX,PE,GG	>0.9	>0.9	>0.9	>0.9	>0.9	>0.9

KEY: W=woven; EX=extruded; PP=polypropylene; PET=polyester; GTX=geotextile; GG=geogrid. Based on Koutsourais, et al (1991); The Tensar Corp. (1986); unpublished reports

MSEW designs may also require quantification of the geosynthetic/facing connection strength using large-scale pullout testing for each unique geosynthetic/facing combination. Still, experts continue to debate the magnitude of the forces, if any, which are exerted at the face.

#### 4 DOCUMENTING GEOSYNTHETICS

Consideration and approval of candidate geosynthetics by owner/agency personnel requires that the geosynthetic supplier provide sufficient evidence of the proposed material's suitability and additional evidence of the manufacturer's/supplier's capabilities. The Federal Highway Administration (FHWA) requirements for documentation in all submittals are detailed by Berg (1993) as follows:

- \* History of material development.
- \* Current capability to supply material.
- \* Polymer and additive composition of geosynthetic.
- \* Practical applications of material.
- \* Representative list of users.
- \* Typical LTDS and interaction values.
- \* Typical unit costs.
- \* Laboratory test data, comprehensive literature review, and the interpretation and extrapolation used to determine the partial factor of safety should be presented for:
  - Creep performance: Range of loads for 10000 hours.
  - 75 year creep extrapolation.
  - Installation damage.
  - Ultimate strength.
  - Chemical resistance.
  - Biological degradation.
  - Joint (seam/connection) strength.
  - Long-term pullout coefficient.
  - Direct sliding coefficient.

#### 5 COST CONSIDERATIONS

An important factor in the increasing acceptance of a technology is increasing cost-effectiveness. Although there are many factors associated with the as-built cost of any geosynthetic reinforced soil structure, including project size, backfill type, and contractor familiarity to name a few, it is useful to examine the relative material costs associated with various candidate geosynthetic reinforcements. Commonly, geogrids are somewhat more costly per unit LTDS than are woven geotextiles but, geogrids may be more cost-effective for providing lower initial strain levels and higher soil interaction, if needed. Typical pricing of geogrids ranges from 0.0015 to 0.001 \$/m<sup>2</sup> per unit LTDS for low to high strengths, respectively. Woven geotextiles commonly range from .001 to .006 \$/m<sup>2</sup> per unit LTDS.

As note earlier, the FHWA has taken the lead in providing guidance in the implementation of generic design techniques and material specifications associated with geosynthetic reinforced soil systems. Still, individual owners/agencies are free to exercise their own judgements as to the appropriateness of following the FHWA lead. Tables 4a and 4b summarize a telephone survey of state Departments of Transportation (DOTs) conducted by the author in the fall of 1996. The survey solicited responses on the use of geosynthetic reinforced soil structures, reinforcement preferences, and reasons why preferential specifications may be used on any given project.

Table 4a. Survey of State DOTs - Use of Geosynthetic Reinforced Soil Systems

U.S. Region	Number of States Using Reinforced Soil System								
	MSEW			RSS			RESF		
	C	T	n/u	C	T	n/u	C	T	n/u
Northeast	1	4	2	3	3	1	1	0	6
Mid-Atl.	3	1	2	3	0	3	2	0	4
Southeast	2	4	2	4	2	2	4	2	2
Midwest	2	2	2	3	2	1	1	1	4
Southwest	2	2	1	2	2	0	1	2	2
Plains	4	0	0	1	2	0	0	0	0
West	5	1	0	3	2	1	1	1	4
Far West	5	1	1	3	1	3	4	1	2
Total States	24	15	10	22	14	13	14	7	28

KEY: MSEW=mechanically stabilized earth walls; RSS=reinforced soil slopes; RESF=reinforced embankments over soft foundations; C=commonly used; T=Trials use only; n/u=not used.  
NOTE: RI,NV,PR did not respond.

Table 4b. Survey of State DOTs - Geosynthetic Reinforcement Preferences

U.S. Region	Number of States						
	Preferred Reinforcement			Reason for Preference			
	Gen- Future	Gen- eric	Prop- erties	Exper- ience	Cns/ Vendor		
Northeast	0	5	2	3	0	2	6
Mid-Atl.	0	2	2	2	0	1	4
Southeast	3	6	2	3	0	3	4
Midwest	1	4	0	5	0	1	5
Southwest	1	5	0	1	2	2	4
Plains	0	4	0	2	2	3	4
West	0	4	1	3	1	3	4
Far West	2	3	3	2	3	2	2
States Responding	44	44	44	44	43	43	43

KEY: Gtx=geotextile; GG=geogrid; Gen.Future=plan generic use in future  
NOTE: RI,NV,PR did not respond. 5 states did not indicate a preference. 6 states did not state a reason for a preference.

Tables 4a and 4b reveal the following trends:

1. Most Departments of Transportation (DOTs) are commonly using at least one form of geosynthetic reinforced soil structure.
2. Geogrids have been the most often used geosynthetic reinforcement to-date, largely because of vendor/consultant influences and greater experience with these materials.
3. Many DOTs intend to use non-preferential, more generic design/specification approaches in the future.

A further indication of the acceptance of and support for geosynthetic reinforced soil structures is the recently initiated effort to develop manuals and software and teach associated courses on mechanically stabilized earth technology. Geosynthetic reinforcement and associated design/construction technologies will be presented. This effort is called Demonstration Project No. 82, or Demo 82 for short, and has as its explicit purpose according to DiMaggio (1996): "to optimize the acceptance and implementation of mechanically stabilized earth technology in routine design and construction practice."

## 7 CONCLUSIONS

Generally, geotextiles and geogrids are interchangeable in reinforcement applications. It appears that there are no overriding technical or economical reasons to rely on proprietary, product-specific designs/specifications when using geosynthetic reinforced soil structures. Conversely, the following observations support the use of generic design, specification, and procurement procedures:

1. Geotextiles and geogrids have been successfully used for over 2 decades in all types of reinforced soil structures.
2. Generally accepted design techniques have been developed which are equally compatible with geotextiles and geogrids.
3. Geotextiles and geogrids have been tested and found to provide suitable and comparable tensile and soil/geosynthetic interaction properties.
4. Geotextiles and geogrids can be quickly tested to confirm compliance with generic project-specific requirements.
5. A wide range of suitable, proven products is available representing the full range of strength/strain/interaction properties typically required in reinforced soil structures.
6. Many owners/agencies now commonly using geosynthetic reinforced soil structures are inclined to encourage more generic design, specification, and procurement of geosynthetic reinforcement in the future to assure fairness and cost-effectiveness.

The generic design, specification, and procurement of geosynthetic reinforced soil structures appears to evolve naturally as the designer/owner gains sufficient understanding of and experience with the associated technology.

## ACKNOWLEDGMENTS

The author would like to thank David Andrews of Synthetic Industries for his valuable review of the original report upon which this paper is largely based.

## REFERENCES

- AASHTO (1997), "Interim Specifications - Standard Specification for Highway Bridges Division I, Section 5 - Retaining Walls & Division III, Section 7 - Earth Retaining Systems", American Association of State Highway and Transportation Officials (AASHTO), Washington, DC.
- Berg, R.R. (1993), "Guidelines for Design, Specification, and Contracting of Geosynthetic Mechanically Stabilized Earth Slopes on Firm Foundations, FHWA-SA-93-025, FHWA, Washington, D.C.
- Collin, J.G., and Berg, R.R. (1993), "Comparison of Short-term and Long-term Pullout Testing of Geogrid Reinforcement", Geosynthetic Reinforcement Testing Procedures, ASTM, Philadelphia, PA, pp. 184-194
- Cowell, M.J. and Sprague, C.J. (1993), "Comparison of Pullout Performance of Geogrids and Geotextiles", Proc. of Geosynthetics '93, Vancouver, IFAI, pp. 579-592.
- DiMaggio, J.A. (1996), "Update on Demonstration Project No. 82", Geotechnical Fabrics Report, Oct./Nov., p. 43.
- Koutsourais, M.M., Sprague, C.J., and Pucetas, R.C. (1991), "Interfacial Friction Study of Cap and Liner Components for Landfill Design", Geotextiles and Geomembranes, Vol. 10, Nos. 5-6.
- Mitchell, J.K. and Villet, W.C.B. (1987), "Reinforcement of Earth Slopes and Embankments", NCHRP Report No. 290, Transportation Research Board, Washington, D.C., pp. 5-8, 126-129.
- Mitchell, J.K., and Zornberg, J.G. (1994), "Reinforced Soil Structures with Poorly Draining Backfills, Part I: Reinforcement Interactions and Functions", Geosynthetics International, Vol. 1, No. 2, pp. 103-147.
- Mitchell, J.K., and Zornberg, J.G. (1995), "Reinforced Soil Structures with Poorly Draining Backfills, Part II: Case Histories and Applications", Geosynthetics International, Vol. 2, No. 1, pp. 265-307.
- The Tensar Corporation (1986), "Guidelines for the Design of Tensar Geogrid Reinforced Soil Retaining Walls", TTN:RW1.
- WSDOT (1996), "Geosynthetic Reinforcement Product Submission and Approval Requirements", Washington State Department of Transportation, FOSSC Materials Laboratory, Tumwater, WA.

# Effect of End-Restraint in Geogrid-Soil Structures

H. Ochiai, N. Yasufuku, and T. Kawamura  
Department of Civil Engineering, Kyushu University, Fukuoka, Japan

T. Yamaji  
Ministry of Transport, Tokyo, Japan

T. Hirai  
Mitsui Petrochemical Industrial Products, Ltd., Tokyo, Japan

**ABSTRACT:** Reinforcing effects of geogrid-soil structures depend on the end-restraint condition of the geogrid. Two types of end-restraint, fixed-end and sliding-end, were experimentally investigated by using a prototype shear apparatus that has been developed for this purpose. Main conclusions are: 1) In order to obtain a significant effect of reinforcement, one end of each geogrid in the soil structure should be fixed on the facing of the soil structure in such a way that the geogrid and the soil in the moving soil mass do not move relative to each other, and 2) For the fixed-end type, there exists an additional confining effect which increases the normal stress on the potential sliding plane in addition to the effect due to the tensile force of geogrid.

**KEYWORDS:** Reinforcement, Geogrids, End-restraint

## 1 INTRODUCTION

Earth reinforcement techniques have become useful and economical solutions to many problems in geotechnical practice but there are some points concerning the reinforcing mechanism of soil-reinforcement system that

need to be clarified.

In geogrid reinforced soil structures, such as the one shown in Figure 1, the end-restraint condition of the geogrid may have considerable influence on the reinforcing effect. In this research, two types of end-restraint, fixed-end and sliding-end, have been investigated experimentally by using a small prototype shear apparatus which has been developed for this purpose. An expression has been proposed to evaluate the reinforcement effect quantitatively.

## 2 MODEL OF END-RESTRAINT

The two types of end-restraint investigated are shown in Figures 1a and 1b.

**Fixed-end:** Figure 1a shows the fixed-end type of restraint. One end of the geogrid is fixed on the facing and the geogrid and the soil in the moving soil mass do not move relative to each other.

**Sliding-end:** Figure 1b shows the sliding-end type of restraint. The geogrid is not fixed on the facing and the geogrid and the soil may move relative to one another.

## 3 TEST APPARATUS AND TEST PROCEDURE

### 3.1 Test apparatus

The apparatus has two bellofram-cylinders on the right and left sides to model the types of end-restraint. In the fixed-end type, the left side of the geogrid is fixed to the upper box and the tensile force of geogrid is provided by the right bellofram-cylinder. In the sliding-end type, the tensile force of geogrid is provided by both sides of the bellofram-cylinder.

A sketch of the test apparatus and the shear box are shown in Figure 2, details can be found in Ochiai et al (1996). The shear box is rectangular in shape and is of size 200 × 200 × 380mm. The shear box has two halves, the

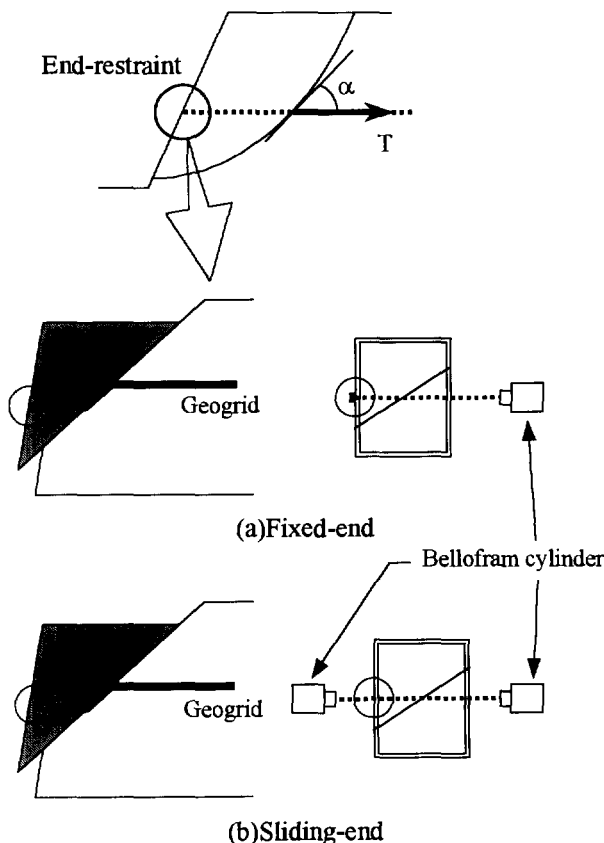


Figure 1. Model of end-restraint in in-situ and laboratory test conditions

upper box and the lower box, with a common sliding plane. The two halves of the shear box are connected and guided by frictionless linear motion bearings on the sliding plane. Three types of shear boxes with different sliding angles are prepared for this study. The shear force,  $S$ , along the sliding plane is provided by the vertical surcharge load. The normal component of the tensile force on the geogrid on the sliding plane is canceled out by the reaction on the linear motion bearings. Therefore, the normal component of reinforcement effect due to tensile force of geogrid,  $T \cdot \sin \alpha \cdot \tan \phi$ , cannot be mobilized in the tests.

### 3.2 Specimen

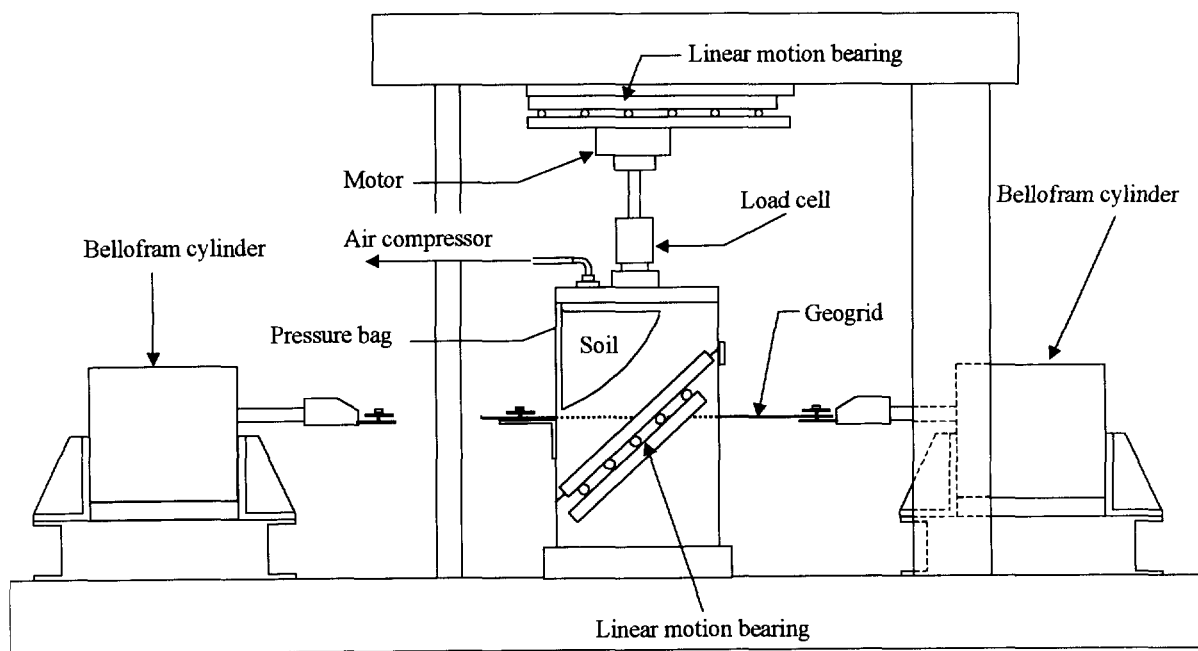
Dry Toyoura sand, which is a standard sand used for testing

in Japan, was used and four kinds of geogrids with varied shape properties were used as reinforcement materials. The physical and strength properties of sand are shown in Table 1 and Figure 3 respectively. The strength values of sand were obtained using the test apparatus shown in Figure 2 for the conditions of the relative density,  $D_r=90\%$ , and the sliding angle,  $\alpha=30^\circ, 40^\circ, 50^\circ$ .

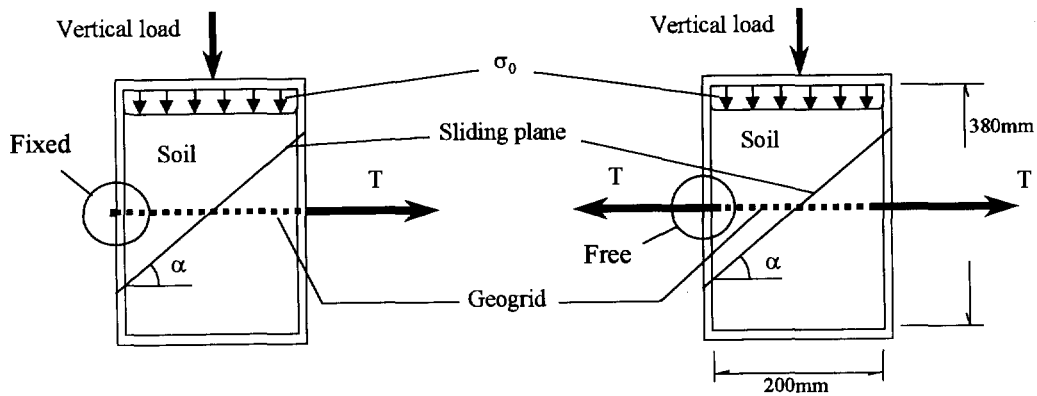
The geogrid measurements are defined in Figure 4 and the properties of geogrids are summarized in Table 2.

### 3.3 Test procedure

Sand is poured through multiple sieves in order to construct a homogeneous specimen. The relative density of the sand,  $D_r$ , is about 90%. After applying a constant tensile force to



(a) Test apparatus



(b) Shear box in fixed-end test

(c) Shear box in sliding-end test

Figure 2. Sketch of test apparatus and the shear box



the geogrid,  $T$ , and an overburden pressure,  $\sigma_0$ , the tests are carried out by vertically loading at a constant speed of 0.35mm/min which is the same as the speed used in the

Table 1. Physical properties of sand

Specific gravity of soil particle, $G_s$	2.64
Maximum void ratio, $e_{max}$	0.971
Minimum void ratio, $e_{min}$	0.601
Uniformity coefficient, $U_c$	1.7
Mean particle size, $D_{50}$ (mm)	0.18

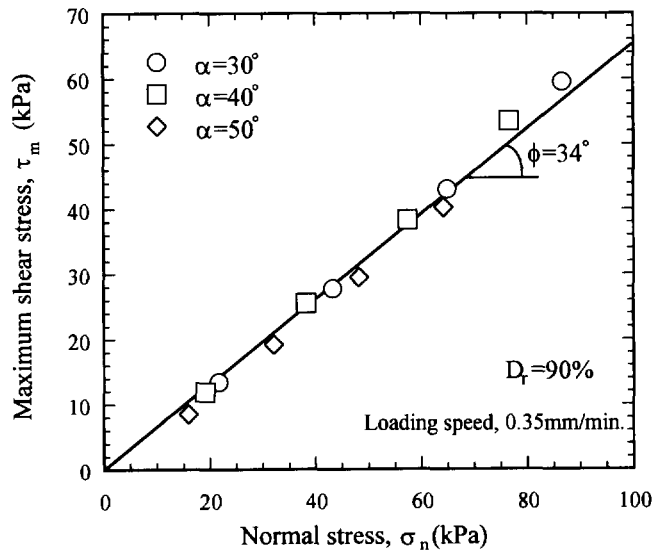


Figure 3. Strength properties of sand

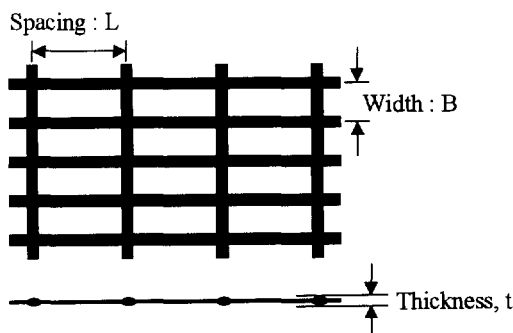


Figure 4. Geogrid measurements

Table 2. Properties of geogrids

	Tensile strength (kN/m)	Spacing L(cm)	Width B(cm)	Thickness t(cm)
Geogrid A	76.6	0.89	0.94	0.13
Geogrid B	37.2	5.42	2.79	0.10
Geogrid C	28.4	2.97	0.83	0.06
Geogrid D	76.6	1.78	0.94	0.13

tests on sand samples. The test conditions are summarized in Table 3.

Table 3. Test conditions

Type of end-restraint	Fixed-end, Sliding-end
Tensile force applied to geogrid, $T$ (kN)	0.373, 0.981, 1.961
Overburden pressure, $\sigma_0$ (kPa)	25, 50, 75, 100
Sliding angle, $\alpha$ (°)	30, 40, 50

## 4 TEST RESULTS AND DISCUSSION

### 4.1 Effect of end-restraint

Figure 5 shows the typical relationships between shear force on the sliding plane,  $S$ , and shear displacement,  $D$ , obtained from a series of tests. The same tendency is observed in the fixed-end and sliding-end types. The curves in Figure 5 are approximated by hyperbolas given by the equation

$$S = \frac{D}{a \cdot D + b} \quad (1)$$

$a$  and  $b$  are constants in which  $1/a$  is the asymptotic line of the curves and is approximated as the maximum value of shear force,  $S_m$ , on the sliding plane. The relationships between the ratio,  $S_{m(F)}/S_{m(S)}$ , and the normal stress on the sliding plane,  $\sigma_n$ , are shown in Figure 6 in which  $S_{m(F)}$  and  $S_{m(S)}$  are the maximum values of shear forces for the fixed-end and the sliding end tests respectively. The maximum value of shear force for the fixed-end test is larger than that of the sliding-end test. Higher reinforcing effects in fixed-

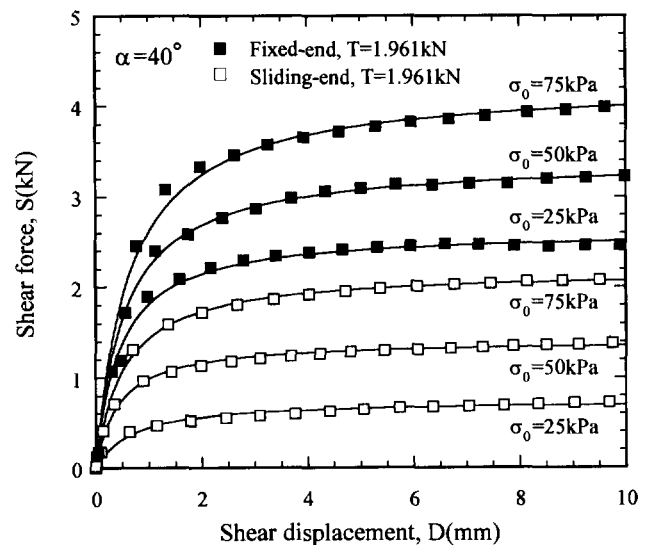


Figure 5. Relationships between shear force,  $S$ , and shear displacement,  $D$

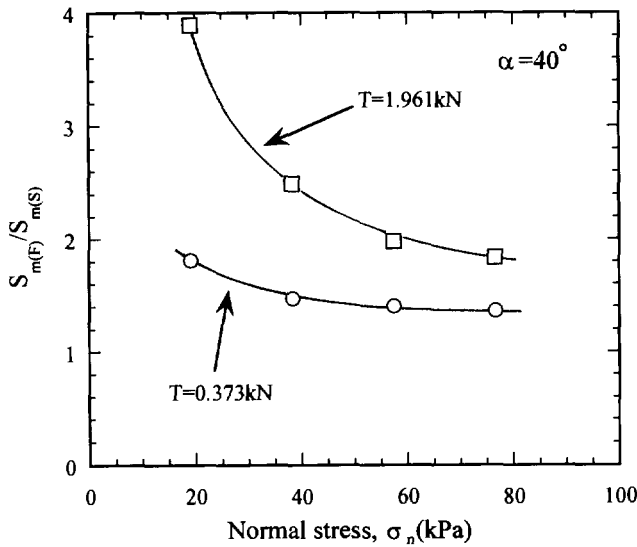


Figure 6. Relationships between  $S_{m(F)}/S_{m(S)}$  and normal stress,  $\sigma_n$

end tests were observed in both small normal stress values and large tensile force of geogrid. The reinforcing effects in sliding-end test is not mobilized, especially in small normal stresses,  $\sigma_n$ , because there is little friction between geogrid and soil.

The maximum values of shear stress measured in the tests are used to investigate the reinforcing effect in the two types of end-restraint conditions. The maximum value of shear stress on the sliding plane is calculated as

$$\tau_m = \frac{S_m}{A'} \quad (2)$$

where  $A'$  is the area of the sliding plane. Typical test results are shown in Figure 7. For sand samples, the relation between  $\tau_{m(N)}$  and  $\sigma_n$  is a straight line through the origin with an inclination of  $\tan\phi$  as shown in Figure 3;

$$\tau_{m(N)} = \sigma_n \cdot \tan\phi \quad (3)$$

in which  $\phi$  is the internal friction angle of sand.

For geogrid-reinforced sand, the relationship will, in general, be expressed as follows;

$$\tau_{m(R)} = \tau_1 + \{(1 + \beta) \tan\phi\} \sigma_n \quad (4)$$

where  $\tau_1$  is the intercept on the  $\tau_m$  axis and  $\beta \cdot \tan\phi$  is the increment in slope of the reinforced lines from the sand line. The values of  $\tau_1$  and  $\beta$  depend on the end-restraint conditions. The value of  $\tau_1$  in the sliding-end type is approximately equal to zero, whereas the value in the fixed-end type changes with the tensile force of geogrid,  $T$ , as shown in Figure 7. The values of  $\beta$  in the two end-restraint

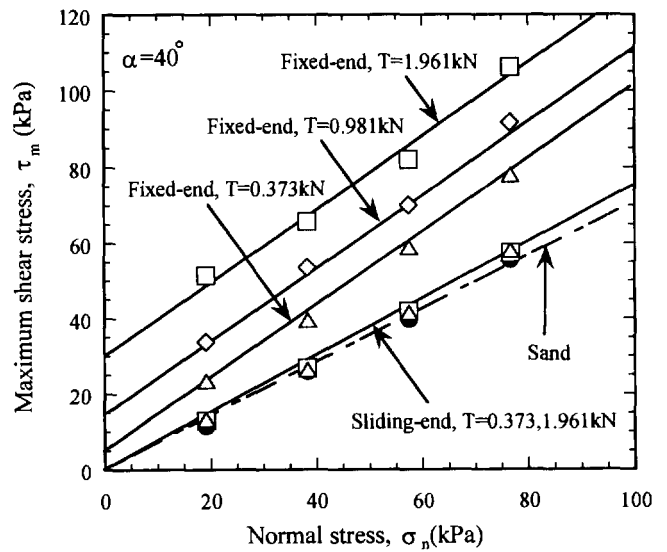


Figure 7. Relationships between maximum shear stress,  $\tau_{max}$ , and normal stress,  $\sigma_n$

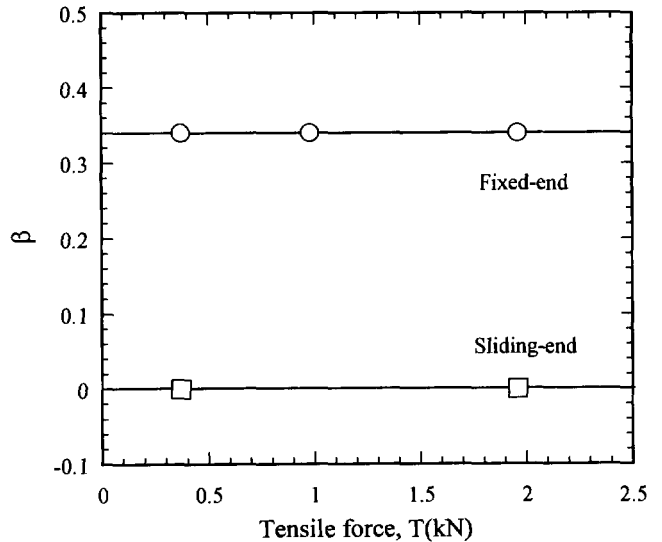


Figure 8. Relationships between  $\beta$  and tensile force,  $T$

conditions are summarized in Figure 8 where  $\beta$  is approximately equal to zero in the sliding-end type and has a constant value in the fixed-end type irrespective of the tensile force of geogrid,  $T$ , i.e.

$$\text{Fixed-end: } \tau_1 \neq 0, \beta \neq 0 \quad (5)$$

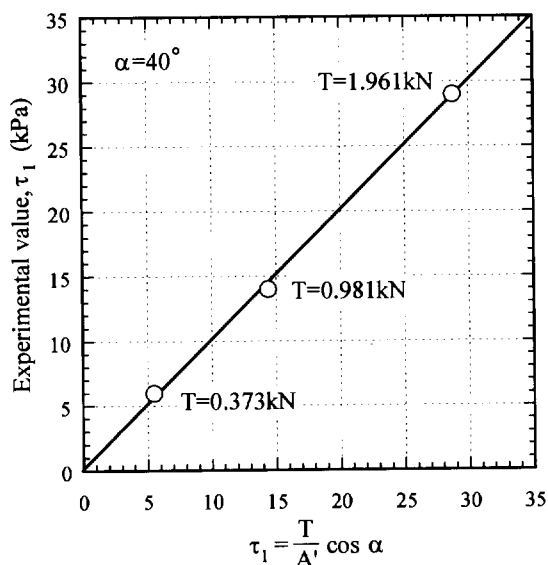
$$\text{Sliding-end: } \tau_1 \approx 0, \beta \approx 0 \quad (6)$$

In conclusion, a significant effect of reinforcement cannot be obtained in the sliding-end type. In order to obtain a significant effect of reinforcement, the geogrid should be fixed on the facing of the soil structure in such a way that the geogrid and the soil in the moving soil mass do not move relative to each other.

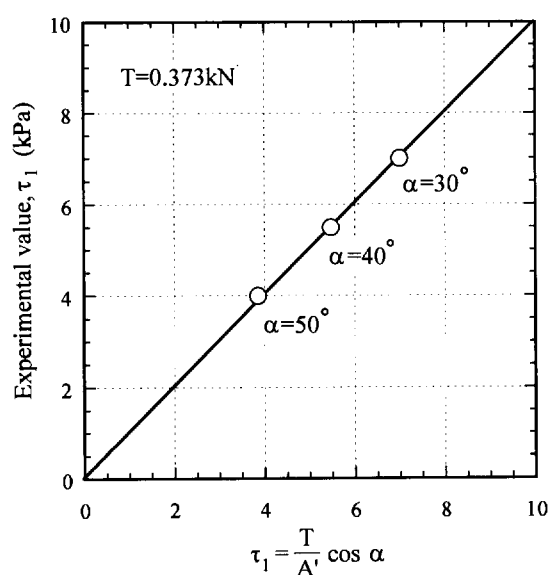
## 4.2 Evaluation of reinforcement effect in fixed-end type

### 4.2.1 Evaluation of $\tau_1$

The design of the apparatus is such that the normal component of tensile force on the sliding plane is not transmitted to the soil and therefore a component of reinforcement effect,  $T \cdot \sin \alpha \cdot \tan \phi$ , due to tensile force of geogrid,  $T$ , cannot be mobilized in the tests. Therefore, the observed reinforcement effect due to the tensile force,  $T$ , is a component along the sliding plane,  $\tau_1$ .



(a) Different tensile forces of geogrid,  $T$



(b) Different sliding angles,  $\alpha$

Figure 9. Comparison between experimental results and calculated values of  $\tau_1$

$$\tau_1 = \frac{T}{A'} \cos \alpha \quad (7)$$

The calculated values from Equation (7) and the experimental results in Figure 7 are almost the same as shown in Figures 9a and b. Therefore, Equation (7) well expresses the experimental results under different tensile forces,  $T$ , and sliding angles,  $\alpha$ .

### 4.2.2 Evaluation of the coefficient $\beta$

The  $\beta$  in Equation (4) can be considered to be a coefficient for the increment in normal stress on the sliding plane due to the placement of geogrid in soil. The coefficient  $\beta$  will therefore depend on the density of the soil and the shape of geogrid. A shape index,  $R$ , for evaluating the shape characteristics of the geogrid has been proposed by the authors (Ochiai et al, 1996) as follows;

$$R = \frac{2t(B+L) \frac{A}{B \cdot L}}{A} = 2t \left( \frac{1}{B} + \frac{1}{L} \right) \quad (8)$$

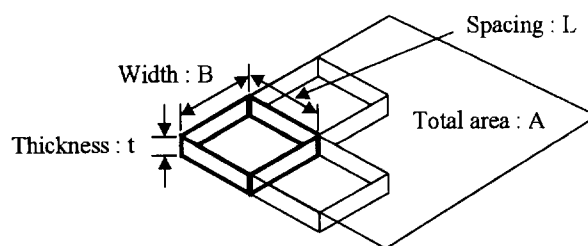


Figure 10. Description of measurements in the shape index

where notations in Equation (8) are shown in Figure 10. It is noted that the value of  $R$  represents the effects in which the soil is confined into the aperture of geogrid, and is pressed by the surface of geogrid. Four kinds of geogrids with different values of  $R$  were used in this study. A unique  $\beta$ - $R$  relationship can be observed by comparing the shape index  $R$  and the coefficient  $\beta$  as shown in Figure 11.

In fixed-end tests, where the geogrid and the soil in the moving soil mass do not move relative to each other, the geogrid restricts the deformation of soil and therefore an additional normal stress,  $\beta \cdot \sigma_n$ , is induced on the sliding plane as illustrated in Figure 12. This effect of soil reinforcement may be called the confining effect (Ochiai et al 1996).

Thus, the maximum value of shear stress,  $\tau_{m(F)}$ , measured in the fixed-end tests may be expressed as

$$\tau_{m(F)} = \frac{T}{A'} \cos \alpha + (1 + \beta) \sigma_n \tan \phi \quad (9)$$

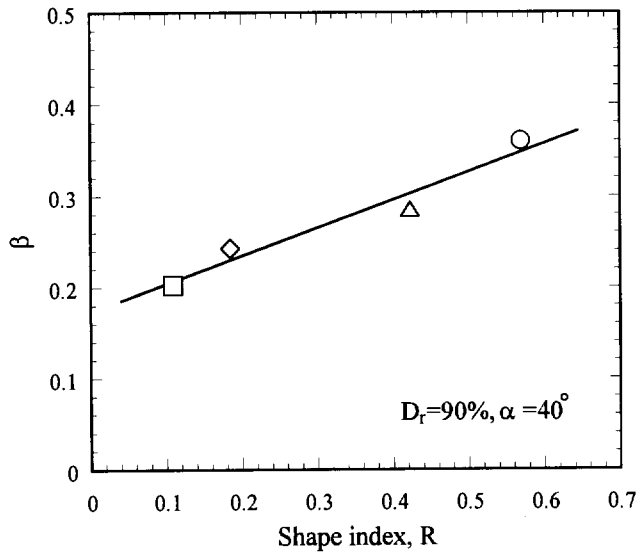


Figure 11. Relationship between  $\beta$  and shape index, R

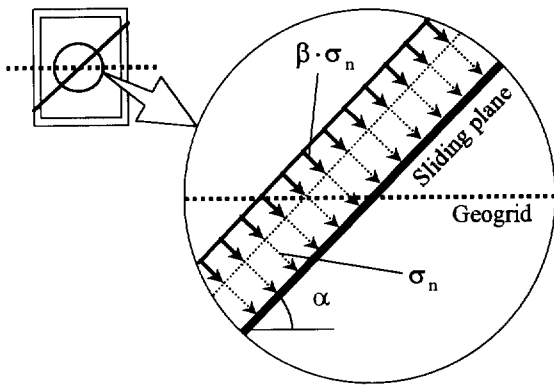


Figure 12. Condition of normal stress around the geogrid

## 5 REINFORCEMENT EFFECT IN GEOGRID-SOIL STRUCTURES

The test apparatus used in this study was designed such that the normal component on the sliding plane of tensile force of geogrid,  $T \cdot \sin \alpha$ , is directly transmitted to the lower box and not to the soil. Therefore, the normal component of reinforcement effect due to the tensile force of geogrid,  $T \cdot \sin \alpha \cdot \tan \phi$ , is not mobilized in the test. However, this component of reinforcement effect is considered to exist in in-situ conditions and is therefore added to the value obtained from the laboratory test. Thus the maximum values of shear stress in geogrid-soil structures may be expressed as follows;

$$\tau_{m(F)} = \frac{T}{A'} (\cos \alpha + \sin \alpha \cdot \tan \phi) + \{(1 + \beta) \sigma_n\} \tan \phi \quad (10)$$

where  $\beta \cdot \sigma_n$  is an additional normal stress on the sliding

plane induced by the restriction of soil deformation due to the placement of geogrid in soil.

## 6 CONCLUSIONS

A series of tests has been performed to clarify the effect of end-restraint in geogrid-soil structures. It has been concluded that:

1. In order to obtain a significant effect of reinforcement, one end of the geogrid should be fixed on the facing of the soil structure in such a way that the geogrid and the soil in the moving soil mass do not move relative to each other.
2. For the fixed-end type, there exists an additional confining effect which increases the normal stress on the potential sliding plane in addition to the effect due to the tensile force of geogrid. The maximum value of shear stress,  $\tau_{m(F)}$ , in the geogrid-soil structure may therefore be expressed as

$$\tau_{m(F)} = \frac{T}{A'} (\cos \alpha + \sin \alpha \cdot \tan \phi) + \{(1 + \beta) \sigma_n\} \tan \phi$$

## REFERENCE

- Ochiai, H., Yasufuku, N., Yamaji, T., Guang-Li Xu and Hirai, T. (1996) "Experimental evaluation of reinforcement in geogrid-soil structure", *Proc. of International Symposium on Earth reinforcement (IS Kyushu 96)*, Balkema publishers, Vol. 1. pp. 249-254

# Application of Dilatancy Models to Soils Reinforced by Geosynthetics

H. Ohta

Professor, Department of Civil Engineering, Kanazawa University, Kanazawa, Ishikawa, Japan

M. Hirata

Graduate Student, Department of Civil Engineering, Graduate School of Kanazawa University, Kanazawa, Ishikawa, Japan

A. Iizuka

Associate Professor, Department of Architecture and Civil Engineering, Kobe University, Kobe, Hyogo, Japan

T. Yamakami

Technical Officer, Department of Civil Engineering, Kanazawa University, Kanazawa, Ishikawa, Japan

Y. Yokota

Engineer, Maeda Kohsen Co. Ltd, Fukui, Japan

K. Ohmori

Instructor, Department of Civil Engineering, Kanazawa University, Kanazawa, Ishikawa, Japan

**ABSTRACT:** This paper aims at rationally explaining the mechanical behavior of the soil structure reinforced by geosynthetics. The attention is paid to confining effect by the geosynthetics under shearing in this paper. The confining effect is interpreted as the mechanical interaction such that the reinforcement material works so as to prevent dilative deformation of soils. Then, elasto-plastic constitutive models which can describe the dilative deformation of soils under shearing are introduced and applied to the finite element simulation of the mechanical behavior of soil structure reinforced by geosynthetics. A full-scale in-situ model test, which was carried out in Kanazawa, Japan, is chosen to analyze. After verification of applicability of employed methodology to the analysis of the model test, the computed results are compared with the monitored behaviors of the soil structure reinforced by geosynthetics in the model test.

**KEYWORDS:** Geosynthetic reinforcement, Dilatancy of compacted soils, Elasto-plastic model, Finite element simulation

## 1 INTRODUCTION

The behavior of the soil structure reinforced by geosynthetics is governed by the mechanical interaction of soils and geosynthetic materials. In the numerical simulation of the behavior of such soil structure, appropriate modeling of its mechanical interaction is required. The authors tried to explain the reinforcement mechanism by geosynthetics throughout a series of finite element numerical simulations for a full scale in-situ model test (Ohta et al, 1996), where soils were simply modeled as non-linear elastic materials by employing the hyperbolic constitutive relation. However, observed behaviors in the in-situ model test could not be well explained. Particularly, the development of strain localization, which was prominently observed in the test, could not be well expressed. This has led the authors to feel the importance of introducing the contraction/dilatation characteristics of soils under shearing into the numerical simulation. Then, this paper focuses on the dilatancy characteristics of soils and the reinforcement mechanism is tried to be interpreted as that the geosynthetics work so as to confine the dilation of soils under shearing. The elasto-plastic models for soils are introduced to describe the dilatancy characteristics of compacted soils of which the reinforced soil structure is composed. An idea to specify input parameters needed in the analysis for the compacted soils is proposed and a series of finite element simulations of full scale in-situ model test are carried out. Finally the results obtained are

compared with monitored behaviors in the test.

## 2 MODEL TO DESCRIBE DILATANCY OF COMPACTED SOILS

### 2.1 Sekiguchi and Ohta's Model

A model employed in this paper is the elasto-plastic constitutive model proposed by Sekiguchi and Ohta (1977). This model had been primarily developed for naturally consolidated-saturated clays and can be regarded as an extension of the original Cam Clay model. The shear behavior of heavily over-consolidated clays is represented by strain-softening material with dilation in this model. The positive volumetric strain (dilation) which the model yields varies with the over-consolidated ratio,  $OCR$ . Higher  $OCR$  produces greater dilation under shearing. When this model is applied to the compacted unsaturated soils that tend to dilate under shearing, some idea on how the compacted soils can be modeled as the heavily over-consolidated saturated clays is required. The section 4.2 is devoted to evaluate the material properties of compacted soils as the heavily over-consolidated clay.

When this model is incorporated into a finite element code, a problem arises, that is, the conventional judgement criterion by Hill (1958) cannot distinguish the subsequent loading (elasto-plastic response) in the strain softening region from the unloading (elastic response). Asaoka et al. (1994) introduce a new criterion which can judge the

subsequent loading in the strain-softening region. The new judgement criterion is employed here and is briefly summarized as follows.

When the plastic strain increment is given by the following associated flow rule as,

$$\dot{\epsilon}_{ij}^p = \Lambda \frac{\partial f}{\partial \sigma_{ij}}, \quad (1)$$

proportional constant  $\Lambda$  can be expressed in terms of plastic strain increment as,

$$\Lambda = \frac{L}{X}, \text{ and } L = \frac{\partial f}{\partial \sigma_{ij}} C_{ijkl}^e \dot{\epsilon}_{kl}^p, \\ X = \frac{\partial f}{\partial \sigma_{ij}} C_{ijkl}^e \frac{\partial f}{\partial \sigma_{kl}} + h, \text{ } h = \frac{\partial f}{\partial \sigma_{ij}} \delta_{ij}, \quad (2)$$

where  $\dot{\epsilon}_{ij}^p$  is the incremental plastic strain tensor,  $\sigma_{ij}$  is the stress tensor,  $C_{ijkl}^e$  is the elastic stiffness tensor,  $f$  is the yielding function. In the case of Sekiguchi and Ohta's model, the yielding function  $f$  is given as,

$$f = MD \ln \frac{p}{p_0} + D \eta^* - \epsilon_{ij}^p \delta_{ij} = 0, \quad (3)$$

where  $M$  is the critical state parameter,  $D$  is the dilatancy coefficient proposed by Shibata (1963),  $p$  and  $p_0$  are mean stresses at the current state and at the reference state, respectively,  $\eta^*$  is generalized deviatoric stress ratio defined by

$$\eta^* = \sqrt{\frac{3}{2} \left( \frac{s_{ij}}{p} - \frac{s_{i_0 j_0}}{p_0} \right) \left( \frac{s_{ij}}{p} - \frac{s_{i_0 j_0}}{p_0} \right)}, \text{ } s_{ij} \text{ is the deviatoric stress tensor } (= \sigma_{ij} - p \delta_{ij}).$$

Now, since the plastic coefficient  $X$  of Eq.(2) always stays positive, the loading or unloading can be judged by the sign of scalar function  $L$  of Eq.(2) as,

loading (elasto-plastic)	if $L > 0$	
neutral	if $L = 0$	(4)
unloading (elastic)	if $L < 0$	

This judgement criterion is incorporated into the finite element program, DACSAR (Iizuka and Ohta, 1987). 4-node quadrilateral constant strain element is employed in the finite element discretization. Fig.1 indicates the verification of F.E. program. Computed effective stress paths of triaxial undrained shear are compared with theoretical curves where  $q$  is the deviatoric stress by

$$q = \sqrt{\frac{3}{2} s_{ij} s_{ij}}.$$

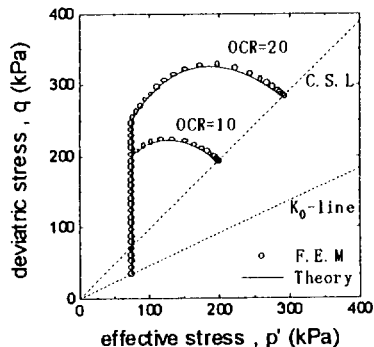


Figure 1 Stress paths of Sekiguchi and Ohta's model

## 2.2 Drucker and Prager's Model

Another model employed is the elasto-plastic constitutive model of which the yielding function is Drucker and Prager's type. This model always yields the dilation without strain-softening. The amount of dilation is determined by the input parameters,  $c$  and  $\phi$  regardless of how much the soils are over-consolidated. Drucker and Prager's yielding function is given as,

$$f = \alpha I_1 + \sqrt{J_2} - k = 0, \quad (5)$$

where  $I_1$  is the first invariant of stress tensor ( $I_1 = p$ ),  $\sqrt{J_2}$  is the second invariant of deviatoric stress tensor ( $\sqrt{3} \sqrt{J_2} = q$ ) and  $\alpha$  and  $k$  are constants relating with the cohesion  $c$  and the internal friction angle  $\phi$  as,

$$\alpha = \frac{\tan \phi}{\sqrt{9 + 12 \tan^2 \phi}} \text{ and } k = \frac{3c}{\sqrt{9 + 12 \tan^2 \phi}}. \quad (6)$$

The associated flow rule is employed and the model is incorporated into the finite element program, DACSAR. Fig.2 compares computed effective stress paths of triaxial undrained shear with theoretical ones. Good agreements are obtained.

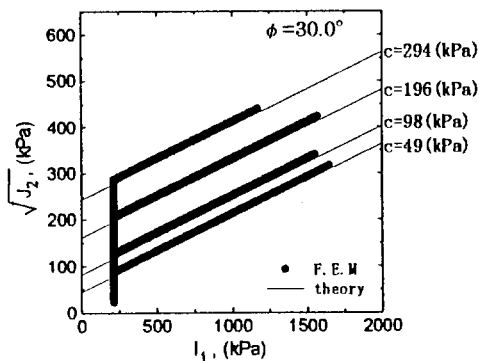


Figure 2 Stress paths of Drucker and Prager's model

## 3 SIMULATION OF FULL SCALE IN-SITU MODEL TEST

### 3.1 Full Scale In-situ Model Test

A full scale in-situ model test was conducted during the period from July, 20, to August, 8, '92 in Kanazawa, Japan, in order to investigate the reinforcement mechanism by geosynthetics (Nishimoto et al., 1992, Ohta et al., 1996). A beam shaped soil structure reinforced by geosynthetics was designed and the resistance capability of the structure against the bending moment was investigated. Fig.3 shows the side view of the test embankment that was 2.75 m high, 42.5 m long and 4.5 m wide, including supporting berm. In the construction of the test embankment, the soil was spread over up to 10 cm thickness and compacted sufficiently by the vibration roller. The degree of compaction was controlled by the dry unit weight

measured by RI (radioisotope) method. The geosynthetics (Adem#G-6, Maeda Kohsen Co.) were placed at every 50 cm. The experiment began by removing steel H piles, which were supporting the reinforced portion by geosynthetics, in the order by the number in Fig.4. The deformation of the reinforced soil structure was measured by photographic observation of the position changes of markers installed at every 25 cm interval on the side of the embankment. The measured maximum deformation at each step is summarized in Table 1. In the experiment, when the #10 steel H pile was removed at Step 9, the structure failed.

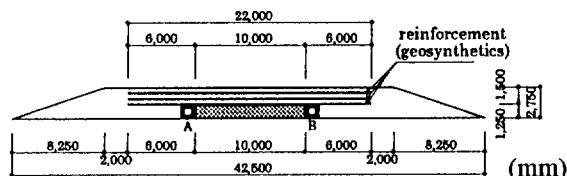


Figure 3 Side view of test embankment

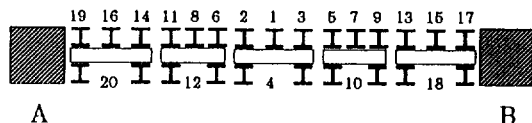


Figure 4 Position of supporting steel H piles  
Table 1 Step in experiment and results

step	No. of steel pile to be moved	maximum deformation (m)
1	No.1	0.000
2	No.1~No.2	0.150
3	No.1~No.3	0.319
4	No.1~No.5	0.438
5	No.1~No.6	0.590
6	No.1~No.7	0.770
7	No.1~No.8	0.880
8	No.1~No.9	>1.200
9	No.1~No.10	>1.200

### 3.1 Applicability of Constitutive Models

The soils were sampled from the test site and served to one-dimensional compression (oedometer) tests and constant volume shear box (CV-SBT) tests in the laboratory. The soil samples were consolidated in the shear box by the vertical pressure of 39.2, 78.4, 156.8 and 313 kPa and then were sheared under the constant volume. Fig.5 shows the effective stress paths obtained from CV-SBT tests for undisturbed compacted soil samples. Experimental effective stress paths in Fig.5 are quite similar to typical behaviors of over-consolidated clays. The authors believe that constitutive models which can explain dilation of a soil element are applicable to the compacted soils, when the effective stress paths in Fig.5 are compared with those in Figs.1 and 2.

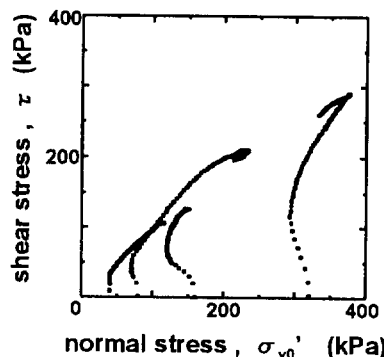


Figure 5 Effective stress paths of compacted soils

### 3.2 Evaluation of Material Parameters Needed in Analysis

The soils used in the full-scale test were sampled from the site and were prepared at the water content of 20, 23, 25, 27 and 30 %. These loose disturbed soils were served to CV-SBT tests. The soils were consolidated in the shear box by the vertical pressure of 39.2, 78.4, 156.8 and 313 kPa and then were sheared under the constant volume. The results obtained are shown in Fig.6, where the upper figure of Fig.6 presents the relationship between the dry unit weight  $\rho_d$  and the consolidation pressure  $\sigma'_v$  and the lower one shows the equivalent 'undrained' strength,  $s_u$ , obtained from CV-SBT for very loose disturbed samples. The increase rate of 'undrained' strength results in  $s_u/\sigma'_v = 0.234$ .

Next, the undisturbed compacted soil samples of which natural water contents varied from 20.6 to 23.4 % in-situ were served to the consolidation and shear tests in the same manner. The plots of test results for undisturbed samples are added to Fig.6 and then Fig.7 is obtained. The plots for undisturbed samples seem to form straight lines with in-situ water contents as shown in Fig.7. When these lines are extended to compression lines obtained from consolidation tests in the shear box for very loose disturbed samples, the equivalent pre-consolidation pressures  $\sigma'_{v0}$  can be estimated. Thus, the equivalent pre-consolidation pressures  $\sigma'_{v0}$  and the equivalent over-consolidation ratios can be specified for in-situ compacted soils as in Table 2.

The 'undrained' strengths ( $\blacktriangle$ ) obtained from shear tests for undisturbed compacted samples can be converted to its equivalent N.C. 'undrained' strengths by using the following equation,

$$\left(\frac{s_u}{\sigma'_{v0}}\right)_{NC} = OCR^{-\bar{\lambda}} \left(\frac{s_u}{\sigma'_v}\right)_{OC} \quad \text{and} \quad \bar{\lambda} = 1 - \frac{\bar{c}_s}{C_c} \quad (7)$$

where  $C_c$  and  $\bar{c}_s$  are gradients of compression lines in Fig.6 and the equivalent swelling line in  $e - \log \sigma'_v$  space of Fig.7. Thus converted strengths are plotted in the lower figure of Fig.7 as  $\blacksquare$  and agree with the broken line indicating  $s_u/\sigma'_v = 0.234$ .

Then, input parameters needed in Sekiguchi and Ohta's model can be specified as follows. The N.C. undrained

strength obtained from the constant volume shear box test has been theoretically derived from Sekiguchi and Ohta's model as (Ohta et al., 1985),

$$\left(\frac{s_u}{\sigma'_{v0}}\right)_{NC} = \frac{1+2K_0}{3\sqrt{3}} M \exp(-\Lambda), \quad (8)$$

where  $K_0$  is the coefficient of earth pressure at rest,  $M$  is the critical state parameter ( $=\frac{6\sin\phi'}{3-\sin\phi'}$ ,  $\phi'$ : effective internal friction angle) and  $\Lambda$  is the irreversible ratio (see, Iizuka and Ohta, 1987). Therefore, by employing the empirical relations:  $M = 1.75\Lambda$  (Karube, 1975),  $K_0 = 1 - \sin\phi'$  (Jaky, 1944), Eq.(8) can be expressed as the function of only  $\phi'$  shown in Fig.8. Now, since the increase rate of strength  $(s_u/\sigma'_{v0})_{NC}$  is given as 0.234 in Fig.6, the effective internal friction angle is specified as 27.5 degree for in-situ compacted soils. Other parameters needed in Sekiguchi and Ohta's model are also specified in the manner shown in Fig.9. Thus obtained input parameters are summarized in Table 3. In the numerical simulation, since the equivalent pre-consolidation pressures of in-situ compacted soils vary in wide range from 931 to 2058 kPa as in Table 2, two cases ( $\sigma'_{v0} = 980$  kPa: Case 1, 1960 kPa: Case 2) are considered.

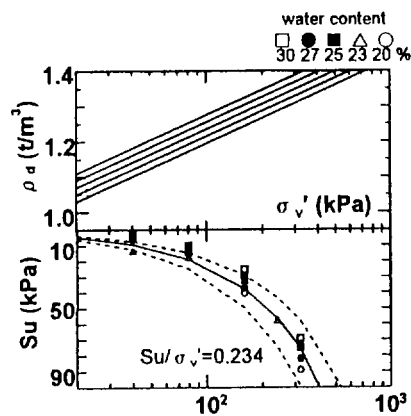


Figure 6 Experimental relation of  $\rho_d$ ,  $\sigma'_v$ , and  $s_u$

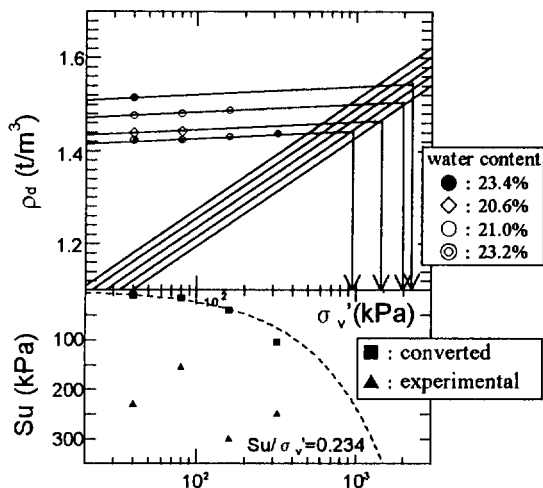


Figure 7 Evaluation of preconsolidation pressure

Table 2 Specified over-consolidation ratio

effective overburden pressure $\sigma'_{v0}$ (kPa)	water content w (%)	equivalent preconsolidation pressure $\sigma'_{v0}$ (kPa)	over consolidation ratio OCR
39.2	23.4	2058.0	52.50
78.4	20.6	1470.0	18.75
156.8	21.0	1960.0	12.50
313.6	23.2	931.0	2.97

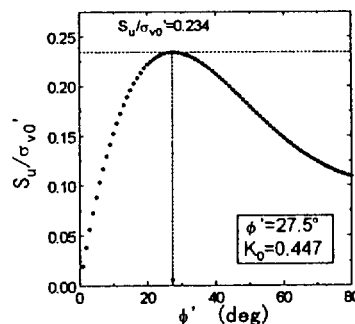


Figure 8 Evaluation of effective internal friction angle

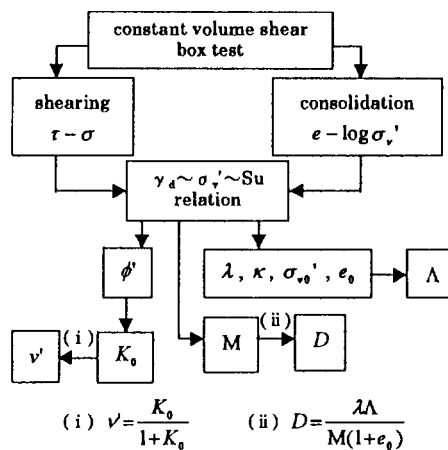


Figure 9 Specification procedure of parameters

Table 3 Parameters for Sekiguchi and Ohta's model

$\Lambda$	$K_0$	$M$	$\lambda$
0.85	0.54	1.09	1.92
$D$	$e_0$	$v$	
0.85	0.77	0.35	

Triaxial CU tests were also carried out for undisturbed soil samples. The results obtained are summarized in Table 4 and the input parameters ( $c'$  and  $\phi'$  in terms of effective stress) needed in Drucker and Prager's model can be specified. However, two test results shown in Table 4 happened to quite differ each other. Therefore, two cases in the numerical simulation are considered as shown in Table 4.



Table 4 Parameters for Drucker and Prager's model

	case3	case4
effective cohesion : $c'$	0.18	0.11
effective internal angle : $\phi'$	34.1	26.3
Lame's constant : $\lambda$ (kN/m <sup>2</sup> )	333.2	245.0
Lame's constant : $\mu$ (kN/m <sup>2</sup> )	166.6	122.5
unit weight of the soil : $\rho_t$ (t/m <sup>3</sup> )	1.707	

Fig.10 indicates the experimental result of uniaxial extension test for geosynthetics materials used in the field model test. The linearly elastic model is applied to represent the stress and strain relationship of the geosynthetics in Fig.10 and the bar element in the F.E. simulation is employed. The input parameters are summarized in Table 5.

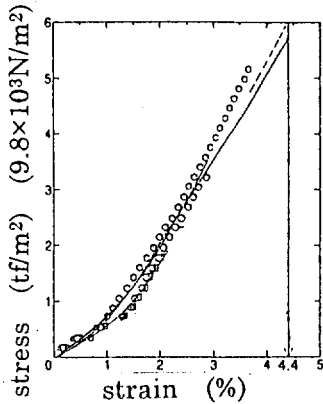


Figure 10 Stress and strain relation of geosynthetics  
Table 5 Parameters for geosynthetics

geosynthetics	
max. extension force : $N_f$ (kN/m)	58.8
sectional area : $A \times$	1337.7
Young's module : $E$ (kN)	

### 3.3 Comparison of Finite Element Simulations

The finite element mesh employed in the simulation of the full-scale in-situ model test is shown in Fig. 11. The 4-node constant strain finite element and the forward incremental calculation scheme are used. The supporting portion indicated by shaded part in Fig.7 is removed following the order in the experiment as shown in Table 1. Table 6 indicates the step number when the axial force of a

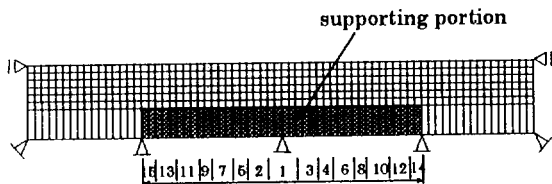
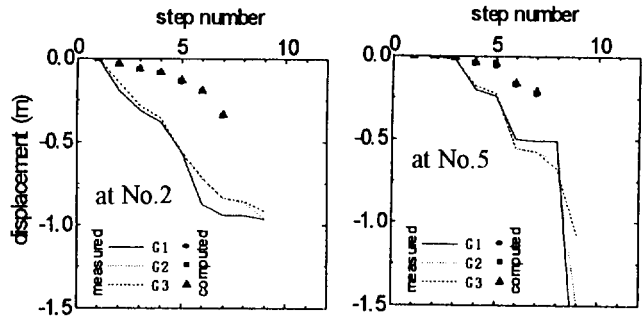


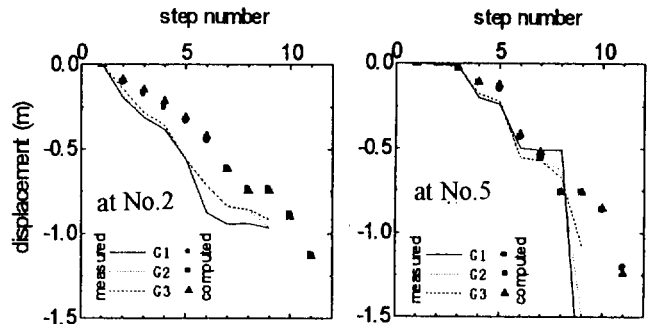
Figure 11 Finite element mesh in simulation

Table 6 Step number when the structure failed

Sekiguchi-Ohta's model	case1	step=7
	case2	step=8
Drucker-Prager's model	case3	step=12
	case4	step=11



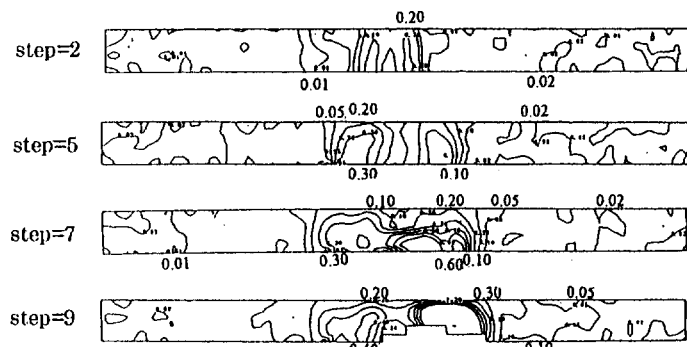
(a) In case of Sekiguchi and Ohta's model



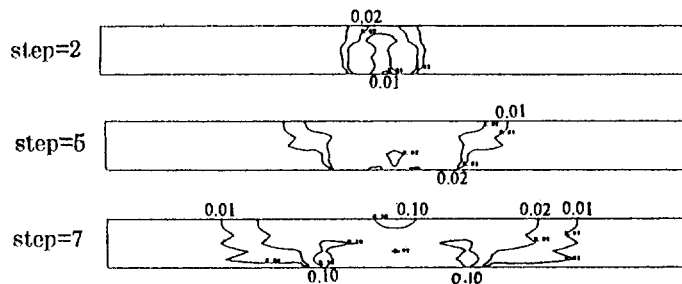
(b) In case of Drucker and Prager's model

Figure 12 Computed and monitored deformations

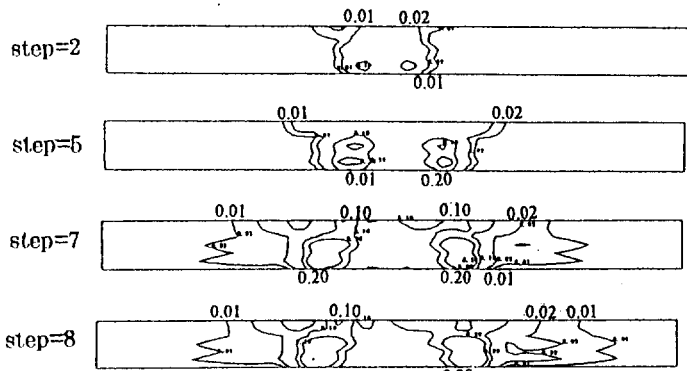
bar element exceeded its strength and the structure failed. In Figs.12, the computed predictions and the monitored behaviors are compared above positions of steel H piles of No.2 and No.5 (refer to Fig.4), in which the horizontal axis in the figure represents the step number shown in Table 1. The labels G1, G2 and G3 indicate the geosynthetics placed, that is, G1 is at the upper layer, G2 is at the middle layer and G3 is at the lower layer. As seen from figures, the monitored deformations are larger than our predictions. It would be because the geosynthetics hung down in experiment when the support was removed and then soils between geosynthetics were loosened. Figs.13 illustrates the contours of shear strain distribution. The results of Case 1 (Sekiguchi and Ohta's model) and Case 4 (Drucker and Prager's model) are chosen to be compared with the monitored result in Fig.13, because there was not much differences between results of Case 1 and Case 2 nor between results of Case 3 and Case 4. Fig.13(d) is added to be compared with the numerical result of the hyperbolic model which does not consider the dilation under shearing (Ohta et al., 1996). At earlier step such as at Step 2, the hyperbolic model does not explain the sharp distribution of strain localization which is observed as in Fig.13(a). The dilatancy models seem to qualitatively explain the monitored development of strain localization from earlier



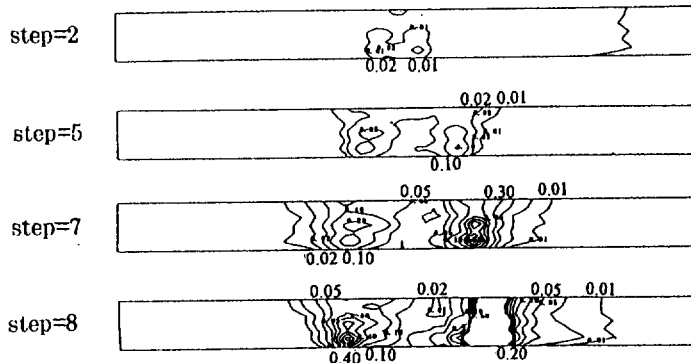
(a) Observed shear strain distribution



(b) In case of Sekiguchi and Ohta's model



(c) In case of Drucker and Prager's model



(d) In case of hyperbolic model

Figure 13 Comparison of shear strain distribution,  $\gamma$

step. In the case of Sekiguchi and Ohta's model, the shear strain localization concentrates in narrower zone, which is closer to monitored tendency, but distributes in wider region in the case of Drucker and Prager's model. However, the quantitative agreement with monitored distribution of shear strain has not been achieved. The authors guess that it is because the soils were considerably loosened resulting in being less stiff when the steel H piles were removed.

#### 4 CONCLUDING REMARKS

A beam shaped soil structure reinforced by geosynthetics was designed to investigate the resistance capability of the structure against the bending moment and was constructed as a full-scale model test. The monitored behavior of the full-scale model test and its numerical predictions are compared. In numerical simulation, dilatancy models are introduced in order to capture the development of strain localization in the beam shaped soil structure reinforced by geosynthetics. Specification procedure of input parameters needed in the models is presented. The compacted soils used in the full-scale model test are represented by the over-consolidated clays equivalent to them. It is found that dilatancy models qualitatively explain the monitored behaviors in the field model test. However, the above results were obtained for a rather unique test setup and more precise examination on general applicability of dilatancy models is required.

#### REFERENCES

- Asaoka, A., Nakano, M. and Noda, T. (1994) "Soil-water Coupled Behaviour of Saturated Clay near/at Critical State", *Soils and Foundations*, Vol.34, No.1, pp.91-105.
- Hill, R. (1958) "A general theory of uniqueness and stability in elastic-plastic solids", *J.Mech. Phys. Solids*, Vol.6, pp.236-249.
- Iizuka, A. and Ohta, H. (1987) "A Determination Procedure of Input Parameters in Elasto-viscoplastic Finite Element Analysis", *Soils and Foundations*, Vol.27, No.3, pp.71-87.
- Karube, D. (1975) "Unstandardized Triaxial Testing Procedures and Related Subjects for Inquiry", *Proc. 20th Symposium on Geotechnical Eng.*, pp.45-60 (in Japanese).
- Nishimoto, T., Tsutsui, H. and Morikage, A. (1992) "Joint Project of Full Scale Model Test for Reinforcement by Geosynthetics", *Research Institute Report, Magara Co.* (in Japanese).
- Ohta, H. and Hata, S. (1977) "Strength of Dynamically Compacted Soils", *Proc 9th ICSMFE, Tokyo*, Vol.1, pp.239-242.
- Ohta, H., Hiura, Y., and Kuniyasu, I. (1978) "Strength Mobilized in Compacted Earth Structures at Failure", *Proc. Symposium on Soil Reinforcing and Stabilizing Techniques in Eng. Practice*, Sydney, pp.385-401.
- Ohta, H., Nishihara, A. and Morita, Y. (1985) "Undrained Stability of  $K_0$ -consolidated Clays", *Proc. 11th ICSMFE*, Vol.2, pp.613-616.
- Ohta, H., Goren, S., Iizuka, A., Yamakami, T., Yamagishi, K. and Moroto, N. (1996) "Numerical Simulation of Beam-shaped Soil Structure Reinforced by Geosynthetics", *Proc. Int. Symp. on Earth Reinforcement, Fukuoka*, Vol.1, pp.255-260.
- Sekiguchi, H. and Ohta, H. (1977) "Induced Anisotropy and Time Dependency in Clays", *Proc. 9th ICSMFE, Specialty Session 9*, pp.229-237.
- Shibata, T. (1963) "On the Volume Changes of Normally Consolidated Clays", *Annals, Disaster Prevention Research Institute, Kyoto University*, No.6, pp.128-134, (in Japanese).



annual evaporation exceeds the annual precipitation. Hence, the design allowed for no phreatic surface in the backfill.

The shear resistance of the concrete blocks was included in determining the depth of reinforcement required and excluded in determining the reinforcement force required.

The design of the hockey-field wall was based on the same principles, as outlined above. The detail of this wall is shown in Figure 2.

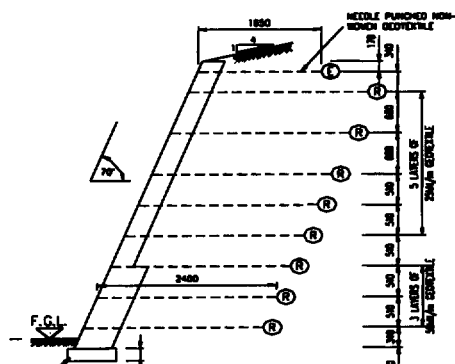


Figure 2: Specified detail of hockey field wall

FIGURE 2

The depth of the reinforcement geotextiles was specified as 2.4m (0.49 H), for the highest section of 4.9m high. The bottom part of the wall was reinforced using woven multi-filament polyester geotextiles with a maximum tensile strength of 50 kN/m. The upper part was reinforced with woven polyester geotextiles of a maximum tensile strength of 25 kN/m. The height of wall reduced along the length of the wall, and at a height of 2.6m, the wall reverted to a gravity structure. Hence this backfill was not reinforced, but 500mm deep blocks were used over the lower section of the wall.

The design was based on a 1:4 slope of the fill at the top of the wall.

### 3. FAILURE DESCRIPTION

#### 3.1 Athletics track wall

The facing blocks of the wall collapsed, as a result of the lower blocks being sheared by the horizontal deformation of the wall and reinforced backfill. At the top of the fill extensive large cracks formed, upto 75mm

wide. Heavy rainfall resulted in sheet flow runoff from the field flowing into some of the cracks.

Immediately after the collapse of the athletics track wall, seepage was noted over the lower 700mm of the backfill, in areas where stormwater had not flowed into the tension cracks of the soil.

The deformed soil mass kept moving vertically over the next few weeks, until a vertical displacement of around 0.7m existed at 2.4m to 2.8m from the back of the wall. This position coincided with the trench for the irrigation pipes of the sportsfield, and the edge of the athletics track subsoil drainage. Sections of the pipes had been repaired in the past, and the pipe junctions were pulled apart by the movement of the failed wall. The foundation of the concrete blocks had rotated by around 14°, and moved laterally. The deflected reinforced soil mass remained intact for numerous months, before being removed by excavation for remediation of the wall.

#### 3.2 Hockey field wall

The facing of the wall next to the field light mast collapsed over a 20m section, with a portion of the surcharge slope at the top of wall lying on top of the collapsed blocks. A 7m long section adjacent to this moved horizontally by over 150 mm, and opened up a 75mm wide tension crack near the top of the surcharge slope. The concrete blocks near the bottom of this wall section were also extensively cracked.

To the south of the light mast the wall supported a car park with a wall height of 3.74m and a wall slope of 70°. The area 2.5m behind the top of the wall settled by around 100mm, and a crack of 20mm wide existed at the back of the settled area. The wall had an outward bulge of between 130mm and 170mm near the mid-height. These measurements can not be exactly quantified, as no completion survey had been carried out on the wall, upon completion of construction.

### 4. AS-CONSTRUCTED DETAILS

#### 4.1 Athletics track wall

The detail of the as-constructed wall is shown in Figure 3. This detail applies over most of the wall length. The end sections of the wall of lower height had no geotextile in the backfill, but a larger and heavier concrete block was used.

The bottom layers of reinforcement geotextile were missing in the fill, as well as the top layer of reinforcement geotextile. The short layer of non-woven geotextile at the top of the wall was installed to minimise the risk of erosion gullies forming behind the blocks.

This wall had a short section where no geotextiles were installed in the backfill, but the rest of the wall backfill was reinforced with either three or four layers of a woven multi-filament polyester geotextile with a tensile strength of 25kN/m.

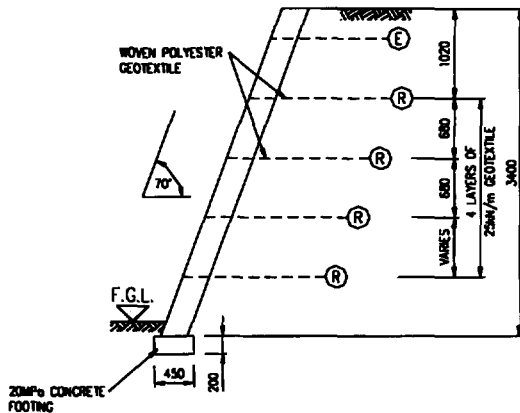


Figure 3: As-constructed athletics track wall

The backfill to the reinforced section as well as under the athletics track, consisted of a silty clay to clayey sand, with a Plasticity Index varying between 24 and 32, and a liquid limit above 43. The soil also classified as medium expansive on the van der Merwe chart for active soils. The tested shear strength of the soil is:

$$\phi' = 26,3^\circ$$

$$c' = 6 \text{ kPa}$$

#### 4.2 Hockey field wall

The detail of the as-constructed wall is shown in Figure 4 and Figure 5.

The wall in Figure 4 was specified to be constructed as per the athletics track wall detail, to a maximum height of 3.74m. The car park at the top of the wall started 2m from the back of the wall, at the highest section of the wall. The depth of the reinforcement geotextiles was specified as 1,8m deep, and they were installed to that depth. The spacing and type geotextiles were however not installed to specification, with sections of the wall having the erosion control geotextile replacing sections of the upper two layers of

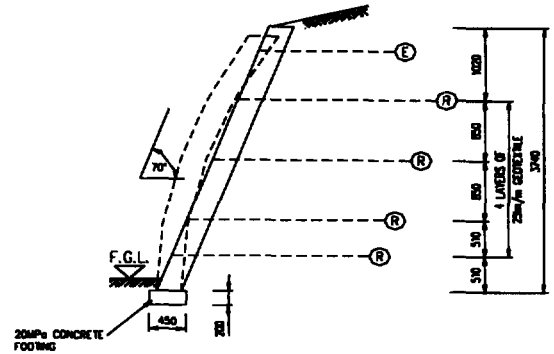


Figure 4: As-constructed hockey field wall, below carpark

reinforcement geotextiles. The tensile stiffness of the non-woven geotextile is between 20% to 30% of that of the woven reinforcement geotextile specified.

The wall in Figure 5 was built to a maximum height of 3.7m, compared to a design height of 4.9m. The toe of the wall and the breakpoint of the top of the slope above the wall were fixed, resulting in a steeper surcharge slope at the top of the wall. This slope varied between 17° and 25° to the horizontal, compared to the 14° design slope. The backfill to the wall, as well as the slope above the wall, consisted of a clayey sand to gravely silt.

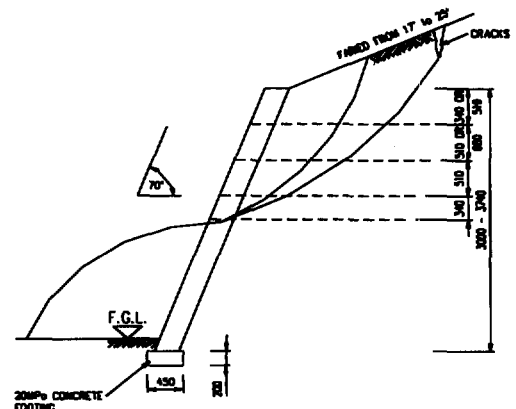


Figure 5: As-constructed hockey field wall, below sloped section

Laboratory analyses of soil samples from both walls confirmed that they were active soils, with a low shear strength, similar to the backfill of the athletics track wall. The reinforcement to the backfill varied considerably over the highest portion of the wall. A 20m section of the highest wall collapsed, while other sections deflected excessively. During reconstruction of the wall, a layer of alluvial soil was also exposed near the base of the reinforced fill where the wall had collapsed. The sections

where the wall had been designed and built as gravity walls, performed satisfactorily. The slope at the top of the wall was less than 14°.

## 5. BACK ANALYSIS:

The failures of the walls was back analysed, based on the following design deviation conditions:

- Reduced shear strength of poor backfill.
- Incorrect reinforcement geotextiles position.
- Geometry deviation.
- Seepage through backfill.

Each condition was analysed separately, and then in combinations, to determine the impact on the wall stability, resulting from the non-compliance's with the original design. The analysis was carried out using a dual wedge analysis program.

### 5.1 Reduced Shear Strength and Position of Geotextiles

Due to the variation of moisture content in South African soils between summer and winter, the 'cohesion' measured in laboratory tests on active soils (high PI), is seldom realised in the field over the long term. Hence the case of no cohesion was included in the analysis, as the walls had stood for nearly three years. For the back analysis, the full concrete block shear strength (including mechanical interlock) was included.

Wall I = Athletics track

Wall II = Hockey field

P/R = Ratio of provided to required

<b>Case – Poor Backfill:</b>	<b>P/R</b>
<b>Wall I</b>	
As-Constructed (3 layers)	0,86
As-Constructed (4 layers)	1,00
Geotextile spacing as specified	1,36

#### **Wall II – Collapse**

As specified slope at top, bottom geotextile missing	0,64
As specified slope at top, geotextiles as specified	2,5

#### **Wall II – Deflected**

As-Constructed (overall stability)	1,19
As specified geotextiles	1,87
As-constructed (force in geotextiles)	1,11

The analysis shows that the reduced shear strength of the soil plus the incorrect spacing of the geotextiles brings the wall close to ultimate limit state for wall I, and "beyond" ultimate limit state for the collapsed wall II. The deflected wall II results in service loads in the geotextiles with a margin of only 10% above what would be normally considered a maximum for the ultimate limit state for the geotextiles used. Geotextiles loaded to this level are expected to give rise to large deflections and excessive creep. This was clearly the case on site.

The reduced shear strength of the soil on its own is unlikely to result in a state of collapse. For a collapse to occur, one would expect the ratio of provided to required to be well below 1,0.

The "temporary situation," where a cohesion of 6kPa is effective, results in a reduction in the stresses of the geotextiles by a factor of 2.5. Also, the factor of safety for overall stability of Wall I is 1.9 and Wall II is 2.3. Hence, no stability or deflection problems would be expected. This was the case for a period of three years from construction.

### 5.2 Geometry Deviation

Wall II has a further complication, where the slope above the wall was constructed at a slope, which is very close to incipient failure, for a shallow sloughing failure. It can be shown that should such a failure be mobilised, that the upper 1.0m height of the wall, as built, would be at a point of incipient failure. Such a slide results in the top of the wall being pushed over, releasing the clamping effect of the blocks at the front of the geotextiles. Hence, the local stability at the top of the wall is at the limit of equilibrium, where the slope at the top of the wall approached the shear strength of the fill. ( $c' = 0\text{kPa}$ ).

The overall stability was also analysed, based on variation of the angle of the upper slope. The result of this analysis is shown below:

<b>Case – Poor Backfill:</b>	<b>P/R</b>
25° slope at top, as specified geotextiles	0,79
17° slope at top, as specified geotextiles	0,95
14° slope at top, as specified geotextiles	1,15

### 5.3 Seepage

The effect of a phreatic surface in the reinforced backfill to the wall was analysed. For this a simple  $r_u$

$$= \left( \frac{\sigma}{\gamma_w h_w} \right) \text{ factor was used on the lower failure surface}$$

of the dual wedge analysis. Using a value of  $r_u=0,1$ , the following results were obtained.

#### Case: Poor Backfill with Phreatic

Surface:	P/R
As-Built (3layers)	0,82
As-Built (4 layers)	0,91
Geotextiles – as specified	1,15
Geotextiles as specified, granular backfill	2,3

Again, it can be seen that a phreatic surface alone would probably not have been sufficient to collapse the wall.

From the above analyses, it can be concluded that in order for the wall to fail, at least two non-compliance's to the original design were required. On this basis the following scenarios were identified as having resulted in the collapses:

Wall I (Athletic track): Missing geotextiles at the base of the wall in conjunction with low shear strength soil.

Wall II (Hockey wall): Steep surcharge slope, in conjunction with low shear strength soils.

Incorrect spacing of geotextiles with the low shear strength soils lead to serviceability failure of the carpark wall.

## 6. REMEDIATION OF THE WALLS

### 6.1 Athletic Track Wall

The athletics track wall was rebuilt, using an imported granular fill. The fill was reinforced with five layers of a woven polyester geotextile with a tensile strength of 50kN/m, at a uniform depth of 2.5m into the fill. Due to space constraints, the excavation next to the athletics track had to be temporarily supported, using driven soil anchors. In the area where the soil remained very wet, subsoil drains were installed at the interface between the clayey soil and the imported granular fill. The owner of the sportsfield was also requested to carry out leakage

tests on the irrigation system to minimise the risk of saturation and erosion due to leaking water pipes.

### 6.2 Hockey Field Wall

The section of the hockey field wall that had been built too low, and had not deflected excessively, was reinforced with either one, two or three rows of 6m long soilnails, spaced at 1,6m horizontally. These soilnails consisted of 20mm diameter galvanised high tensile steel bars encased in grout.

The number of nails depended on the extra height of wall to be placed ontop of the existing wall, and the final height of the wall. The maximum wall raise was 1,8m ontop of an existing 3,1m high wall. The nails were designed to ensure overall stability of the wall, and the added wall height was reinforced with woven polyester geotextiles. These geotextiles were specified to have a tensile strength of 50kN/m, spaced at 680mm vertical centres and 2,5m deep. A silty sand was specified for the backfill.

The collapsed wall sections, and sections where the backfill and wall had deflected excessively (visibly), were rebuilt. The poor shear strength of the soil dictated that the depth of the geotextiles needed to be 77% of the final wall height. The granular fill used for the reinforced fill allowed the use of a cheaper woven polypropylene tape multi-filament geotextiles with a tensile strength of 35kN/m over the upper 3,5m of the wall, and a woven polyester geotextiles of 50kN/m for the lower section.

All the above work was completed by end of 1996, and has been performing satisfactorily to date.

## 7. CONCLUSIONS

From the above, the following conclusions can be drawn:

- Geotextile reinforced backfill walls are structures that are robust to variations from the design specifications.
- Collapse of such a structure is usually as a result of two or more substantial deviations from the design specifications.
- Geotextile reinforced retaining walls have a ductile and a brittle component. The brittle component is the facing, while the backfill acts as a ductile component of the structure.

## ACKNOWLEDGEMENTS

The authors wish to thank the owners of the retaining walls, as well as the wall contractors, for their permission to publish this case history.

## REFERENCES

1. HA68/94, 1994, Design Methods for the Reinforcement of Highway Slopes by Reinforced Soil and Soil Nailing Techniques. Design Manual for Roads and Bridges, Vol. 4, Section 1, Part 4, HMSO.
2. The Practice of Soil Reinforcement in Europe, 1995. Dr. T.S. Ingold (Editor), Symposium by IGS, 18 May 1995, Thomas Telford, London.
3. Nelson N.S.C., Wu J.T.H, 1993, Investigating Performance of Geosynthetic – Reinforced Soil Walls, Report No. CDOT-UCD-R-93-21, University of Colorado, Denver.
4. Greenwood J.H., 1990, The Creep of Geotextiles, 4<sup>th</sup> International Conference on Geotextiles, Geomembranes and Related Products, Den Hoedt (ed.), The 28 May to 1 June, 1990, The Haque, Netherlands.
5. Report No. 1555/1008/1/G, Wates, Meiring & Barnard (Pty) Ltd, March 1995, “Geofabric Pullout Tests”.
6. Day, R.W., Axten G.W. (1989), “Surficial stability of compacted clay slopes”, Journal of Geotechnical Engineering, ASCE, 115(4), p577-580.
7. Pradel D, Raad G (1993), Affect of Permeability on Surficial Stability of Homogenous Slopes, Journal of Geotechnical Engineering, ASCE, Vol. 119(2), p315-332.



# Preloaded-Prestressed Geogrid-reinforced Soil Bridge Pier

T.Uchimura

Research Associate, Department of Civil Engineering, University of Tokyo, Japan

F.Tatsuoka

Professor, Department of Civil Engineering, University of Tokyo, Japan

M.Tateyama

Senior Research Engineer, Japan Railway Technical Research Institute

T. Koga

Kyushu Railway Company (JR Kyushu)

**ABSTRACT:** The first prototype preloaded and prestressed geogrid reinforced soil bridge pier was constructed to support temporary railway girders. An abutment of geogrid-reinforced soil retaining wall, which was not preloaded nor prestressed, was also constructed. The behavior of the pier and the abutment during and after construction and in service was carefully observed. By preloading and prestressing, the gravel backfill of the pier became very stiff against static and dynamic load compared to the abutment. Cyclic triaxial loading tests on the backfill gravel were performed to understand the contribution of the preloading and prestressing to the high performance of the pier.

**KEYWORDS:** Preloading, Prestressing, Geogrid-reinforced soil, Bridge pier, Full-scale loading test, Cyclic triaxial test

## 1 INTRODUCTION

A new construction method, the preloaded and prestressed (PLPS) reinforced soil method, has been proposed; a reinforced backfill is made very stiff against vertical load by vertical preloading and prestressing (Tatsuoka et al. 1996a.)(Figure 1). A similar method taking advantage of preloading has been proposed by Adams (1997), but it does not take advantage of effects of prestressing. The mechanisms of the PLPS method, which will be mentioned later, were demonstrated by tests on a full-scale model embankment and creep-relaxation tests on large triaxial specimens of the backfill gravel (Uchimura et al. 1996).

In this paper, the construction and the behavior of the first prototype PLPS geogrid-reinforced soil bridge pier is

reported. This pier was constructed in the summer of 1996 to support temporary railway girders and has been opened to service since the summer of 1997. The comparison of the behavior between the PLPS pier and an ordinary geogrid-reinforced soil abutment, which was not preloaded nor prestressed, proved that preloading and prestressing can restrain three kinds of vertical compression of the backfill: creep compression under long-term static compressive load; the amplitude of compression by dynamic loading (i.e. transient cyclic loading); and residual compression by many times of cyclic loading.

Cyclic triaxial loading tests on the backfill gravel was performed to understand the effects of preloading and prestressing on the behavior of the pier under cyclic load in service. The results showed that when a very well compacted backfill is sufficiently preloaded and prestressed at an appropriate stress level, the settlement at the pier crest and the reduction in the tie rod tension caused by many times of cyclic loading can be very small.

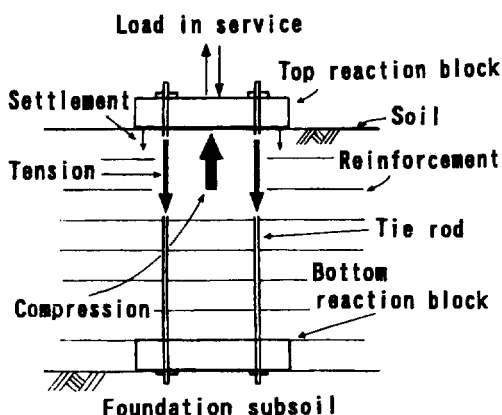


Figure 1. A schematic diagram of preloaded and prestressed reinforced soil (Tatsuoka et al. 1996a.).

## 2 OUTLINE OF PLPS METHOD

### 2.1 Construction Procedures

The typical construction procedures are as follows (Tatsuoka et al. 1996a):

1. The sub-soil is improved if necessary, usually by in-situ cement-mixing; a pile foundation is not used because of its high cost.
2. A rigid bottom reaction block, which is usually a reinforced concrete (RC) block, is constructed at the

bottom level of the backfill.

3. Four steel tie rods are installed vertically with their bottom ends anchored to the bottom reaction block.

4. The backfill is constructed, being reinforced with geogrid and involving the tie rods within it. Usually, well-graded gravel is used. Good compaction of the backfill is essential.

5. A top reaction block is constructed on the top of the completed backfill.

6. Hydraulic jacks are set at the top ends of the tie rods, supported by the top reaction block.

7. The backfill is preloaded by using the jacks. To develop as large as possible compression of the backfill during this stage, high preload kept constant for a long period or many times of cyclic loading may be applied.

8. The load is decreased from the preload level to a prescribed non-zero prestress level.

9. The top ends of the tie rods are fixed to the top reaction block (usually by using nuts), and the jacks are removed. After this, a vertical stress remaining in the backfill in equilibrium with the tie rod tension works as prestress.

## 2.2 Mechanisms

The mechanisms of this method could be summarized as follows (Tatsuoka et al. 1996a) :

1. The backfill needs to be reinforced to support much higher preload than an unreinforced backfill.

2. The preloading and subsequent unloading makes the backfill stiffer and nearly elastic against external loads applied on the top reaction block. The amount of unloading from the preload level should be larger than the maximum design load; otherwise, the compressive stress activated in the backfill during service may exceed the maximum stress during preloading, resulting in occurrence of larger plastic deformation of the backfill. On the other hand, the load should not be decreased to a very low level or zero to avoid swelling and associated softening of the backfill (Tatsuoka et al. 1996b).

3. The compressive prestress activated in the backfill under prestress condition leads to high stiffness, thus a high integrity, of the backfill.

4. The load working on the top of the backfill is always in equilibrium with the sum of the external load applied on the top reaction block and the tie rod tension. Therefore, when external compressive load is applied, the reduction in the tie rod tension associated with vertical compression of the backfill results in a reduction of load increment on the backfill. This mechanism decreases the backfill settlement.

5. Large part of the tensile strains in the reinforcements induced by preloading remains after the load is decreased to the prestress level. Therefore, the reinforcement can confine the backfill more efficiently.

6. If a well compacted backfill is preloaded by sufficiently large load for a long period, relatively large creep

deformation develops in the backfill, resulting in very small long-term rate of the relaxation of the tie rod tension under the prestressed condition..

7. The backfill may deform in the simple shear mode during a seismic event. When the backfill is very well compacted, large dilatation of the backfill may occur associated with seismic shear deformation. But such dilatation is restrained by the tie rods, resulting in a considerable increase in the tie rod tension and compressive stresses in the backfill. Therefore, a high seismic stability can be expected.

## 3 PROTOTYPE PLPS GEOGRID-REINFORCED SOIL BRIDGE PIER

### 3.1 Design and Construction

The first prototype PLPS geogrid-reinforced soil bridge pier was constructed to support two 16.5 m long steel bridge girders for a single railway track in Fukuoka City, Japan (pier P1 in Figure 2a). The bridge is planned to be used for about three years from August 1997. The cross-section of the pier is 6.4 m x 4.4 m, and the height of the backfill is 2.7 m. The design dead load by the girder weight and live load by train loads including impact load are 196 kN and 1,280 kN, respectively.

On the other hand, one of the abutments for the girder was constructed as an ordinary geogrid-reinforced soil retaining wall (GRS-RW) without preloading and prestressing (abutment A2 in Figure 2a).

First, a subsoil of an about 9 m-thick very soft clay deposit was improved by in-situ cement-mixing forming nine 9 m-long 0.8 m in diameter cement-mixed soil columns (Figure 2b). In addition, the whole cross-section of the pier was improved by cement-mixing for the 1 m-thick surface soil layer to form the bottom reaction block. The lower ends of four steel tie rods, which were originally produced for prestressed concrete, were anchored into the cement-mixed soil columns for a length of 4 m. The nominal yield tensile force of each tie rod is 1,034 kN.

The backfill was constructed with a help of gravel-filled bags stacked along the four sides of each gravel layer, while wrapping around the bags with the reinforcement. A well graded gravel of crushed sandstone ( $D_{max} = 30$  mm,  $D_{50} = 0.9$  mm,  $U_c = 16.5$ ,  $\phi = 60^\circ$ ) was used. A hand-operated 30 kg-vibration compactor and a hand-operated 60 kg-tamper were used to compact the backfill; larger machines could not be used because of small available working space. A geogrid reinforcement of polyvinyl alcohol coated with polyvinyl chloride (PVC) was used, whose nominal rupture strength is 73.5 kN/m and the nominal stiffness is 1,050 kN/m at strains less than 1 percent. The arrangement of the reinforcement was determined for a GRS-RW with one facing at the end under

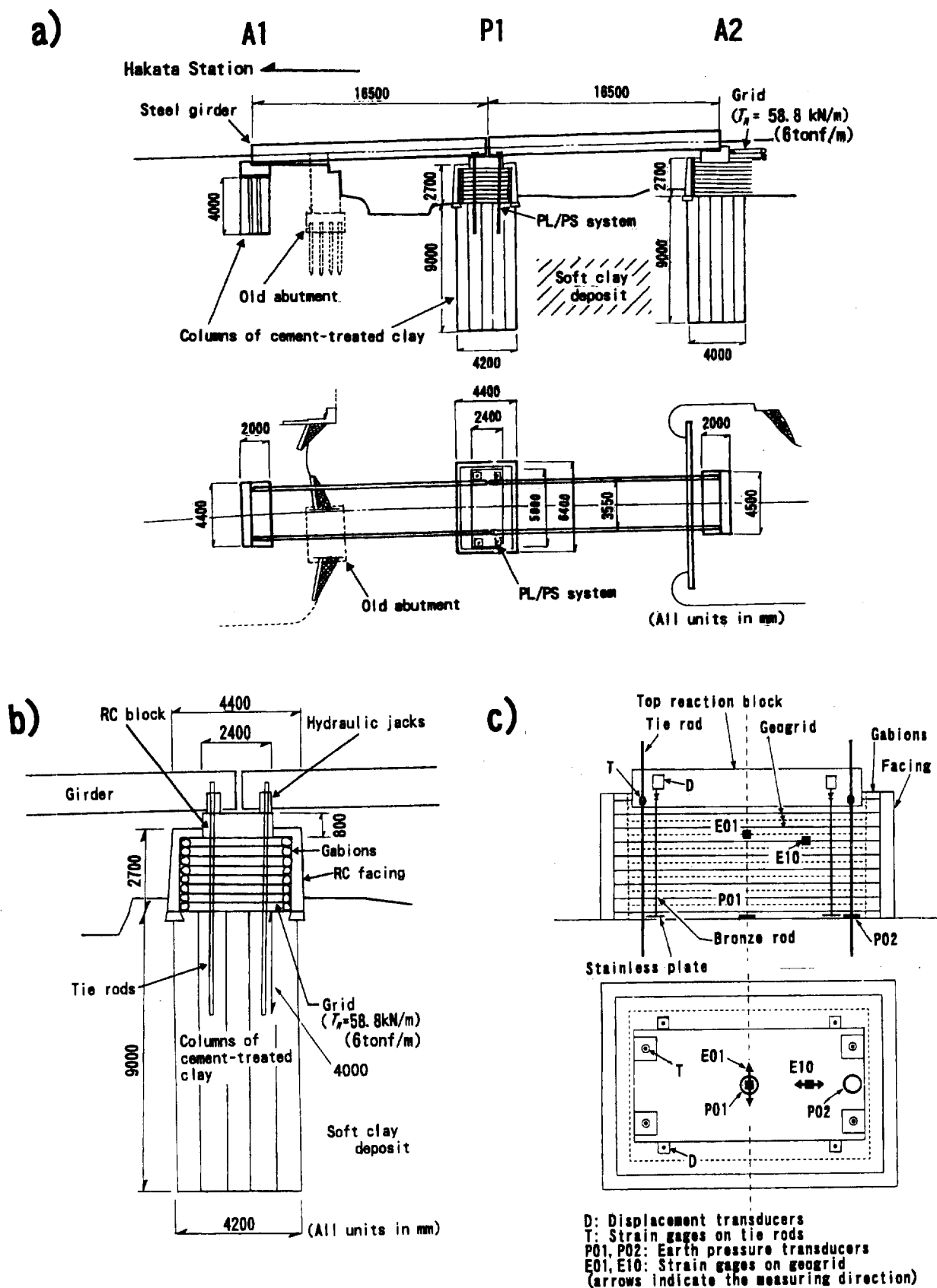


Figure 2. a) A bridge construction project involving the first prototype PLPS reinforced soil pier; b) detail of the pier; c) arrangement of the instrumentation described in this paper (Tatsuoka et al. 1996b).

plane strain condition with the same height as the actual pier, instead of the actual pier having a rectangular prismatic shape. As the result, the vertical spacing of the reinforcement was designed to be 30 cm. However, the pier has two pairs of wall faces in two orthogonal directions; therefore, each cross-section having one pair of wall faces were designed independently. By overlapping the two cross-sections, the actual average vertical spacing of the reinforcement became 15 cm.

The construction of the backfill took five days by a team of five workers. Preloading started ten days after casting the top reaction RC block (5 m-long, 2.4 m-wide and 0.8 m-thick). Then, full-height rigid facings were cast-in-place on the four wall faces. The total construction period was about 1.5 months. The construction cost for the pier was about a half of that for an equivalent conventional RC pier supported by a pile foundation.

The abutment A2 was constructed by the same method using the same materials as the pier, except that it has only one wall face retained by reinforcement with a vertical spacing of 30cm, and the both sides are exposed slopes (1.5:1.0 in H:V) without a facing.

### 3.2 Instrumentation

For the measurement of vertical compression, four stainless anchor plates for the pier and two plates for the abutment were embedded at the bottom of the backfill (Figure 2c). Brass rods placed inside PVC pipes were vertically installed through the backfill and connected to the anchor plates at the lower ends. The vertical displacement of the top of the rods relative to the top of the backfill have been measured with displacement transducers. The average compression of the pier and the abutment was calculated based on these measurements.

The tie rod tension has been measured with electric resistance strain gages attached to the tie rods. The earth pressure has been measured at the center (P01) and near the tie rods (P02) at the bottom level of the backfill with strain-gage-type pressure transducers of 20 cm in diameter. The tensile strains of the reinforcement have been measured by strain gages attached to the grid at 32 points. Strains in horizontal two directions, orthogonal each other, have been measured separately.

### 3.3 Preloading

For a period of ten week days, preload was applied by using four hydraulic jacks (Figure 3). The total net preloading period was 72 hours, however, because the preloading was allowed only during daytime due to a restraint at the site. During nighttime, the tie rods were fixed to the top reaction block with the backfill under prestressed condition.

In the first day, the vertical load was increased step by

step up to 1,960 kN (from the origin to Point 1 in Figure 4); each step consisted of a load increment of 196 kN applied within 2 minutes or less and a pause keeping the load constant for 30 or 60 minutes. In the fifth day, the load was decreased to 905 kN (Point 10), followed by reloading. In the sixth day, the load was increased to 2,350 kN (after Point 11). In the seventh day, the load was decreased to zero (Point 13), followed by reloading. In the tenth day, the load was decreased to about 1,100 kN (Point 16) and then the backfill was left under prestressed conditions for three days. Finally, the load was increased to 2,350 kN (Point 17), maintained for three hours, decreased again to 980 kN (Point 18), and since then, the backfill has been left under prestressed condition.

Figure 4 shows the relationship between the total tie rod tension,  $T$ , and the backfill compression. During the preloading stage, the tie rod tension was the same as the amount of the preload working on the crest of the backfill. A total settlement of 8 mm occurred through the whole preloading period. During unloading and reloading by 1,400 kN in the last day, the rebound and re-compression were nearly the same and equal to only 0.4 mm, indicating a very high stiffness and nearly elastic deformation of the backfill. According to Tatsuoka et al. (1996a), the Young's modulus  $E$  for vertical elastic strains of such gravels measured by triaxial tests can be expressed as  $E = E_0 \cdot (\sigma_v / p_0)^m$ , where  $m=0.57$  and  $E_0$  is the  $E$  value when the vertical stress  $\sigma_v$  is equal to  $p_0 = 98$  kPa. Based on this relationship, by fitting the theoretical elastic rebound and reload curves to those measured with the pier,  $E_0=400$  MPa is obtained. The theoretical curve for elastic settlement is also plotted to start from the origin in Figure 4; this curve indicates the elastic component of the compression. The plastic component of the compression is obtained as the difference between the elastic component and the integrated value of the instantaneous compression increments caused at each loading step. The difference between the total compression and the instantaneous (elastic plus plastic) component is the time-dependent (viscous) component. The viscous component is found to be more than a half of the total compression and its ratio to the total compression increases with the load level. Therefore it is important to remove potential creep deformation of the backfill by sufficient preloading.

It may also be seen from Figure 4 that the average stiffness of the backfill when reloaded from Point 10 is noticeably smaller than the value when reloaded from a higher load level (e.g., from Point 7). Moreover, the average stiffness when reloaded from the zero load (from Point 13) is smaller than the above. This behavior is likely due to the effects of swelling and softening of the backfill when the load is decreased largely or to zero. This result shows the importance of maintaining sufficiently high prestress in the backfill (Tatsuoka et al. 1996b).

Figure 5 shows the relationship between the total tie rod

tension and the earth pressure measured at the center (P01) and near the tie rods (P02) at the bottom of the backfill. The average pressure, equal to the applied load divided by the total cross-sectional area (5.8 m x 3.8 m) of the pier, is nearly the same as the measured earth pressure increments. Furthermore, the earth pressures at P1 and P2 are almost the same as each other, while showing a highly linear relationship with the tie rod tension. These results show

that the stress distribution was nearly uniform at the bottom of the backfill and that the bottom reaction block made by in-situ cement-mixing functioned as a nearly rigid mass.

### 3.5 Long-term Behavior under Static Load Condition

After the preloading stage, the full-height rigid concrete facings were cast-in-place, and then two steel girders, each

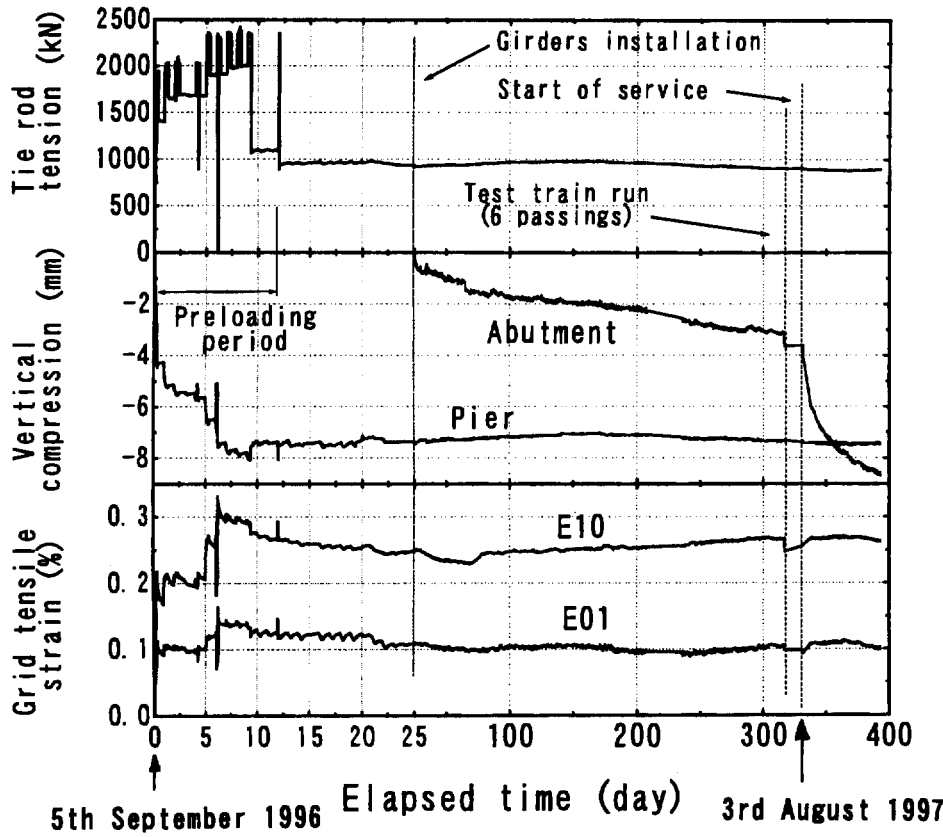


Figure 3. Long-term behavior during and after preloading and in service; tie rod tension; vertical compression of the pier and the abutment; tensile strain of the grid.

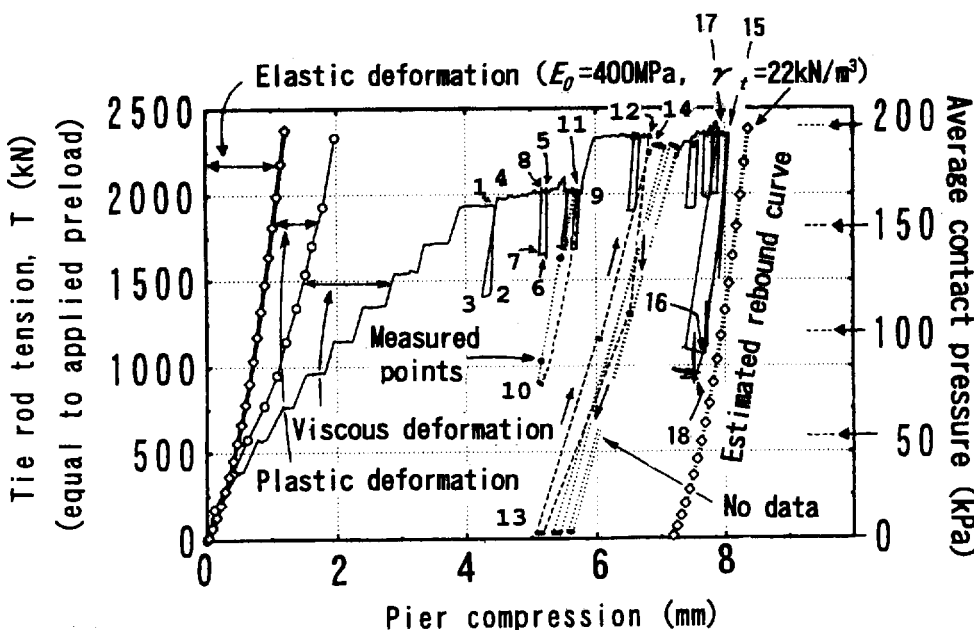


Figure 4. Relationship between the tie rod tension and the settlement of the pier (Tatsuoka et al. 1996b).

weighing 211 kN, were installed on the pier and the abutments. The instantaneous compression of the pier by a girder weight of 211 kN was only 0.04 mm, while that of the abutment by a girder weight of 105 kN was ten times larger, equal to 0.4 mm. Then, the behavior of the pier and the abutment was observed for ten months (Figure 3).

The tie rod tension and the compression of the pier P1 appear to have changed slightly for this long period, but this is likely to be annual change due to temperature effects. The tensile strain in the reinforcement kept almost constant without showing any creep extension.

On the other hand, the abutment A2 showed noticeable creep compression by the self weight and the girder weight. Although the measurement of the abutment compression started just before the girder installing, the total compression has reached 3.1 mm by the summer of 1997.

The difference shows the first advantage of preloading and prestressing that makes long-term creep deformation of the backfill under static load condition very small.

### 3.6 Short-term Behavior at Train Passing

On 19 July 1997, a diesel locomotive of 637 kN in weight passed 6 times over the bridge for inspection. The residual compression of the pier P1 was 0.02 mm, while that of the abutment A2 was 0.52 mm.

Since 3 August 1997, the bridge has been opened to

service. Figure 6 shows the behavior of the pier P1 and the abutment A2 at the first train passing in service; the train consisted of 2 coaches, each weighing 353 kN without passengers.

The amplitude of compression of the pier was 0.02 mm, which was equivalent to a vertical strain of 0.001 percent; this very small strain also suggests nearly elastic behavior of the pier. The tie rod tension responded to the pier compression. The change in tensile strain in the

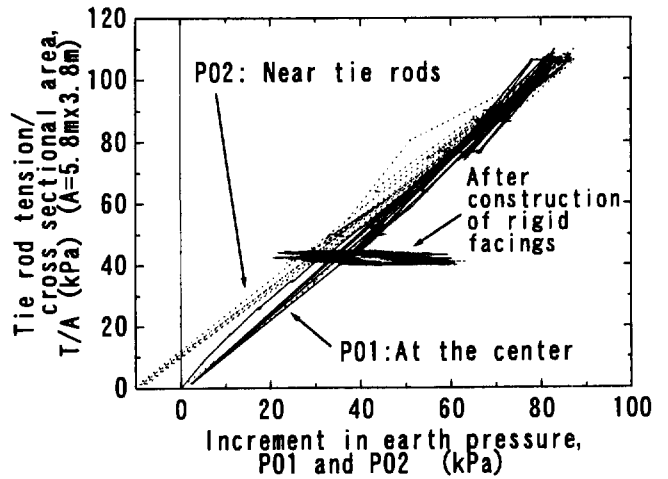


Figure 5. Relationships between the earth pressure P1 and P2 and the tie rod tension.

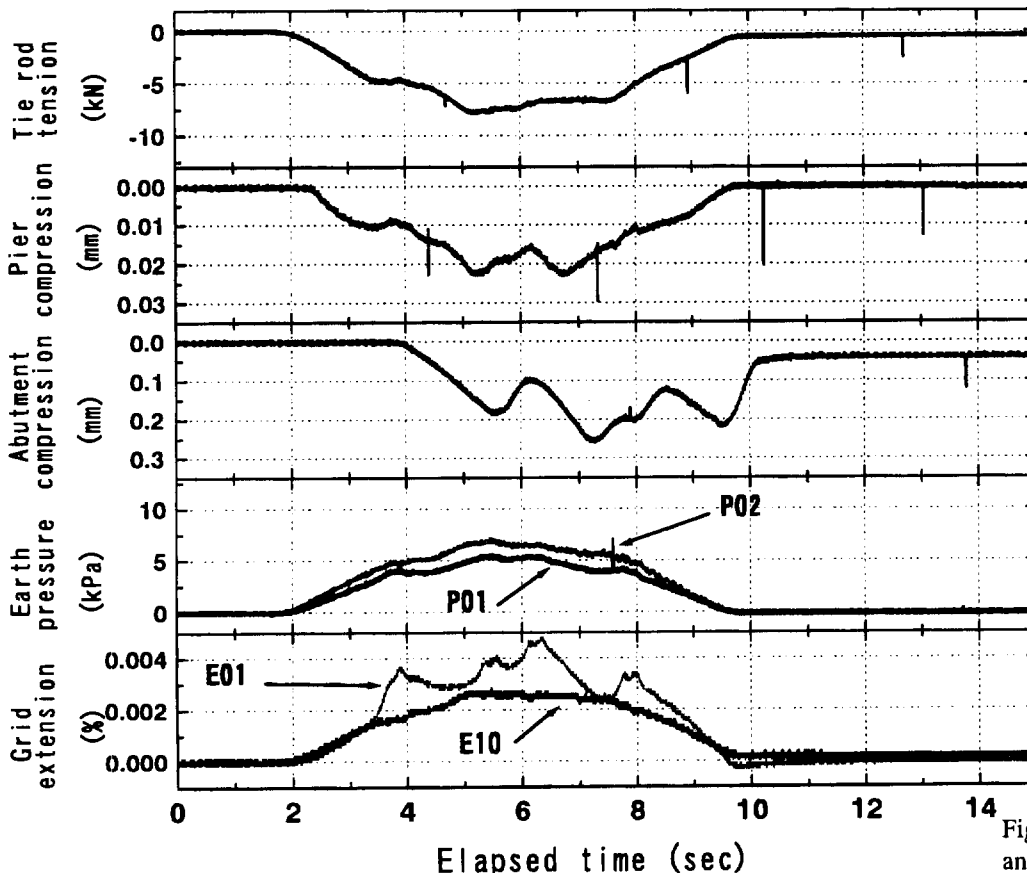


Figure 6. Behavior of the pier and abutment at train passing.

reinforcement was very small and elastic, which was due to very small compression of the pier. Apparently, the train road was not supported by the corresponding very small increase in the tensile force in the reinforcement alone, but the backfill having highly elastic properties with high stiffness actually supported the train load; these backfill properties could be achieved by sufficiently large preloading and prestressing, which was possible only with a help of reinforcement.

On the other hand, the amplitude of the compression of the abutment was 0.2 mm; this is not a harmful quantity, but 10 times larger than that of the pier.

The difference shows the second advantage of preloading and prestressing that makes the amplitude of compression by dynamic loading very small.

### 3.7 Long Term Behavior in Service

The behavior of pier and abutment in service has been observed for 2 months (Figure 3). On average, 125 trains, each consisting of two to four coaches, each weighing 30 to 40 tons without passengers, pass over the bridge every day.

The residual compression of the pier was 0.08 mm. Corresponding to that, the tie rod tension decreased by 17.3kN. The tensile strains in the reinforcement did not change largely; as a whole, they have been constant. On the other hand, the abutment showed a residual compression of 5.1 mm. It is still compressing rapidly, even though the compression rate is decreasing. Some maintenance will be necessary. This difference shows the third advantage of preloading and prestressing that makes the residual compression by many times of cyclic loading very small.

## 4 BEHAVIOR AGAINST CYCLIC LOAD

The comparison of the behavior between the pier and the abutment subjected to many times of train passing showed several advantages of preloading and prestressing, by which temporary and residual compression of the backfill against cyclic loading was very effectively restrained. In order to understand these effects of the PLPS method, cyclic triaxial compression tests were performed at a constant confining pressure ( $\sigma_h = 49$  kPa) on a large square prismatic unreinforced specimen (23 cm x 23 cm x 60 cm high) of the backfill gravel ( $\rho_d = 1.95$  g/cm<sup>3</sup> and  $w = 3.3$  percent) (Figure 7). Axial and lateral strains were measured by a set of LDTs, a device to measure small local strains on the surface of the specimen. An LDT consists of a phosphor bronze strip with strain gages attached at the center, supported at the both ends with two hinges glued to the specimen surface. Figure 8a shows the time history of the deviator stress  $q = \sigma_v - \sigma_h$ . The primary loading (PL) was conducted at a stress rate of  $dq/dt = 49$  kPa/min. C1 and C2 mean creep loading stages for 6 hours at a constant

$q = 98$  and  $196$  kPa, respectively. CYC1 to CYC5 mean cyclic loading stages of 500 cycles, in which  $q$  changed between 98 and 196 kPa for CYC4 and between 0 and 98 kPa for the others. PL simulated a short-time preloading without creep compression, while C2 simulated a long-time preloading with creep compression at the peak load.

Figures 8b and 9 show the test results. Even after some creep (C1), the vertical compressive strain  $\epsilon_v$  increased noticeably (by 0.013 percent) during the first cyclic loading stage CYC1. During CYC2 after PL, the increase in  $\epsilon_v$  by cyclic loading was nearly zero. On the other hand, during CYC3 after C2 and CYC5 after CYC4,  $\epsilon_v$  decreased during cyclic loading (by 0.006 percent and 0.007 percent respectively). During CYC4,  $\epsilon_v$  increased noticeably (by 0.023 percent) by cyclic loading, but the double amplitude stiffness  $\Delta q / \Delta \epsilon_v$  is about 2.5 times larger than those during CYC1 to CYC5 at the lower  $q$  level.

The test results suggest the following:

1. If the backfill is not preloaded, it may be compressed largely by cyclic loading (CYC1). This trend of behavior was actually observed with the abutment A2.
2. For the same amplitude of cyclic stress and number of loading cycles, the settlement of the backfill becomes very small after preloading; this trend becomes more obvious after the occurrence of the creep deformation or cyclic loading during the preloading stage. This trend of behavior was actually observed with the pier P1.
3. The higher prestress on the backfill causes higher stiffness of the backfill during cyclic loading. But if the stress level is near the maximum stress during preloading, residual compression becomes larger.
4. To make both of the amplitude and residual value of compression by cyclic loading very small, the backfill should be preloaded at sufficiently high stress level, and the prestress should be some non-zero level; otherwise it leads

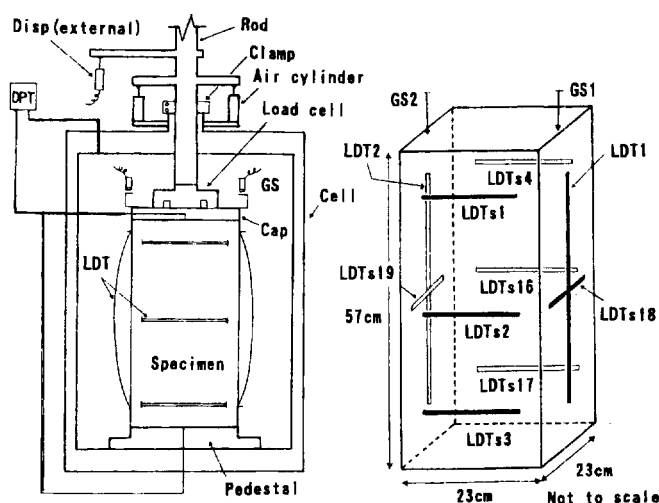


Figure 7. Schematic diagram of the large scale triaxial test (Uchimura et al. 1996).

to a large amplitude of compression during cyclic loading. On the other hand, the prestress should not be very high so that the maximum stress during cyclic loading does not approach the maximum stress during preloading. Some intermediate prestress level is appropriate.

## 5 CONCLUSIONS

The behavior of the first prototype PLPS geogrid-reinforced soil bridge pier was observed during and after construction and in service. Compared to a bridge abutment of geogrid-reinforced soil constructed without preloading and prestressing in the adjacent place at the same time, the pier showed very small transient and long-term deformation. The different performances demonstrated significant effects of the preloading and prestressing procedures in restraining creep compression under long-term static compressive load; the amplitude of compression by dynamic loading; and residual compression by many times of cyclic loading. The results of triaxial cyclic loading tests on a specimen of the backfill gravel also showed a high efficiency of preloading and prestressing, particularly preloading with creep compression or cyclic loading, to restrain temporary and residual compression of the backfill. Both field and laboratory observations showed that it is not preferable to unload the prestress to zero because it leads to a large amplitude of compression during cyclic loading. On the other hand, to make the residual compression very small, prestress should not be very high so that the maximum stress during cyclic loadings does not approach the maximum stress during preloading.

## ACKNOWLEDGMENTS

The authors deeply appreciate the help in this research of Messrs. Tsuru, H. and Maeda, T. of Kyushu Railway Company Dr. Koseki, J. and Mr. Sato, T. of Institute of Industrial Science, University of Tokyo, Mr. Maruyama, D. of University of Tokyo and Mr. Nakamura, H. of Nihon University, and Messrs. Sugimura, Y. and Ishihara, M., graduate school of the university of Tokyo.

## REFERENCES

Adams, M. (1997) "Performance of a prestained geosynthetic reinforced soil bridge pier", Int. Sym. On Mechanically Stabilized Backfill, Balkema, Feb.1997 (Wu eds.), Denver, CO, USA (to appear).  
 Tatsuoka, F., Uchimura, T. and Tateyama, M. (1996a) "Preloaded and prestressed reinforced soil", Soils and Foundations, JGS, Vol. 37, No. 3, pp.79-94  
 Tatsuoka, F., Tateyama, M, Uchimura, T. and Koseki, J. (1996b) "Geosynthetic-Reinforced Soil Retaining Walls as Important Permanent Structures, The 1996-1997 Mercer

Lecture", Geosynthetic International, IGS, Vol. 4, No. 2, pp.81-136

Uchimura, T., Tatsuoka, F., Sato, T., Tateyama, M. and Tamura, Y. (1996) "Performance of preloaded and prestressed geosynthetic-reinforced soil", Balkema, Int. Symp. on Earth Reinforcement, Fukuoka, Japan, (Ochiai et al., eds), Vol. 1, pp.537-542.

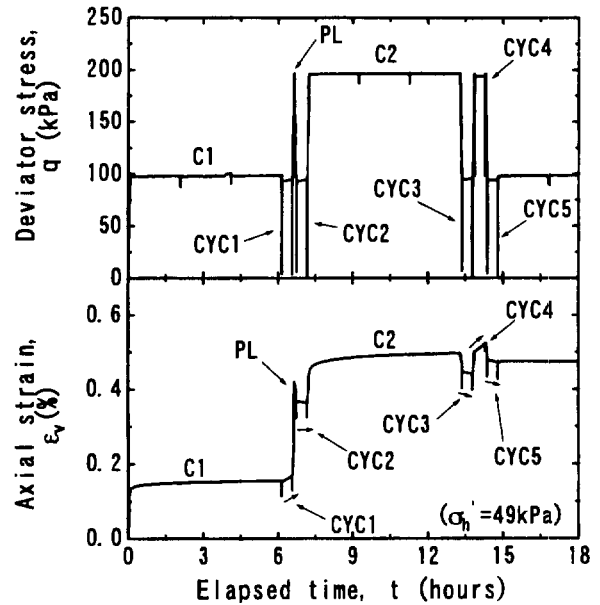


Figure 8. Time histories of a) deviator stress,  $q$  and b) axial strain,  $\epsilon_v$ . Only the first and the last loading cycles are shown for each cyclic loading.

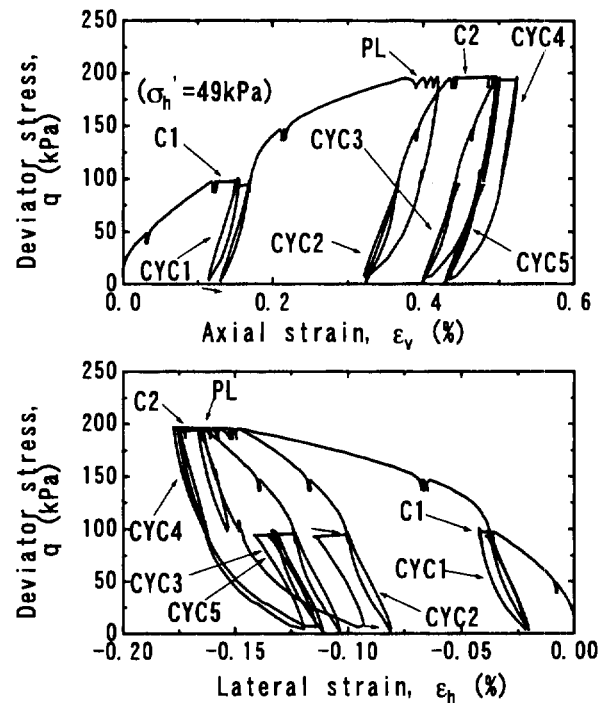


Figure 9. Results of a triaxial cyclic loading test. Relationships between a) deviator stress,  $q$  and axial strain  $\epsilon_v$ , b)  $q$  and lateral strain,  $\epsilon_h$ .



# Use of Fabric Reinforced Soil Walls for Integral Bridge End Treatment

R.A. Reid

Assistant Professor, Civil & Environmental Eng. Dept., South Dakota State Univ., Brookings, South Dakota, USA

S.P. Soupir

Graduate Research Assistant, Civil & Environmental Eng. Dept., South Dakota State Univ., Brookings, South Dakota, USA

V.R. Schaefer

Professor, Civil & Environmental Eng. Dept., South Dakota State University, Brookings, South Dakota, USA

**ABSTRACT:** The problem of void development under bridge approach slabs has been correlated to the use of integral abutment bridges (Schaefer and Koch, 1992). The observation of the occurrence of voids under approach slabs, even in cases where no traffic had yet occurred led to a hypothesis of thermally-induced movements of bridge beams/abutment walls as the mechanism causing the void development. As a result of identification of the mechanism of void development, changes to the approach system needed to be made to accommodate this mechanism. A method used by the Wyoming Department of Transportation, and subsequently by the South Dakota Department of Transportation, uses a fabric reinforced soil wall behind the abutment to build a vertical, self contained wall capable of holding a vertical shape and forming a void behind the abutment. This paper will detail the design concept used by the South Dakota Department of Transportation, present data obtained from instrumented bridges currently being monitored, and show how this system alleviated the integral bridge abutment approach problems.

**KEYWORDS:** Geotextile, Temperature Effects, Retaining Walls, Integral Abutment, Pavements

## 1 INTRODUCTION

The problem of void development under bridge approach slabs has been correlated to the use of integral abutment bridges (Schaefer and Koch, 1992). The observation of the occurrence of voids under approach slabs, even in cases where no traffic had yet occurred, led to a hypothesis of thermally-induced movements of bridge beams/abutment walls as the mechanism causing the void development. As a result of identification of the mechanism of void development, changes to the approach system needed to be made to accommodate this mechanism. For this project the approach system design consisted of a geotextile reinforced soil wall behind the abutment resulting in a vertical, self-contained wall capable of holding a vertical shape and forming an air gap between the abutment and retained backfill. This design was based on a system used by the Wyoming Department of Transportation (WYDOT). It was hypothesized that the gap behind the abutment would allow for the thermally-induced movement of the abutment without affecting the backfill. Three bridges were constructed in South Dakota using this design. The field portion of this study consisted of monitoring the variations in gap width between the abutment and geotextile wall and development of voids under the approach slab. This paper will review the design of the bridge systems and geotextile soil wall, data collection and measurement, preliminary analysis and conclusions.

## 2 PREVIOUS RESEARCH

Although numerous factors contribute to the differential movements between bridge abutments and the approach areas to the bridge, previous research has shown that void development under approach slabs to integral abutment bridges occurs due to the elongation and contraction of the bridge beams due to temperature variations. As the bridge beams expand and contract they alternately push into and pull away from the backfill behind the abutment wall, leading to the development of a void near the abutment wall under the approach slab. The observation of such voids in the field has been reported by Jorgenson (1983), Kramer and Sajer (1991), and Schaefer and Koch (1992). The size of the void varies markedly, with Schaefer and Koch (1992), who surveyed 140 bridges in South Dakota, reporting measured voids from 13 to 360 mm (1/2 to 14 in.) in depth and extending as much as 3 m (10 ft.) away from the abutment wall. The study concluded that the development of the voids under the approach slab to integral abutment structures was an inherent problem in the use of integral abutment systems. The void development was not considered to be isolated to one mechanism resulting from abutment movement, but rather to be the result of the cumulative effects of embankment bulging as the backfill deforms, approach slab uplift, backfill densification as particle breakage occurs, and backfill deformation as passive failure occurs in the backfill. The relative contribution of each of these mechanisms

has not been discerned to date. It was suggested that the largest increases in void size occurred when passive failure likely occurred and this mechanism was probably the most important one.

Edgar, et al. (1989) investigated the use of a reinforced soil wall as a means to prevent void development under the approach slab in highway embankments. This research determined that retaining the backfill with a geotextile wall, thereby creating a gap between the retained fill and bridge abutment, reduced the applied stresses to the soil to near zero. The reduction of the passive stress to near zero eliminates the passive failure mechanism in void development. Consequently, this system was adopted for use in the construction of three bridges in South Dakota based on the hypothesis that the presence of a gap between the abutment and retained fill would prevent or greatly reduce void development under the approach slabs.

### 3 BRIDGE BACKFILL DESIGN

The backfill design used by the WYDOT was adapted by the South Dakota Department of Transportation (SDDOT) for replacement of a single concrete bridge, 134 m (440 ft) in length, on Highway 73 across the White River near Kadoka, SD in the spring of 1996. This design was also used on two concrete bridges, 122 m (400 ft) in length, on Interstate 29 across the Big Sioux River south of Brookings, SD. The southbound bridge was constructed in the fall of 1996 and the northbound bridge in the summer of 1997. These three bridges are being monitored to measure seasonal variations in the gap spacing and for the development of voids under the approach slab. This design has been adopted for all new bridge construction in South Dakota.

Design of the backfill system followed current SDDOT bridge design and construction practices except for the presence of the woven geotextile wall. Prior to the implementation of this design methodology, backfill material consisted entirely of select granular material. This expensive backfill was used since it had been shown to reduce void development because of its greater passive resistance. This backfill contained material with less than five percent passing the #200 sieves and extended the depth of the abutment and back at typically a 1:2 slope. A design developed by the WYDOT incorporated the use of a gap between a reinforced soil wall and the abutment wall. During construction of the three bridges monitored in this project, a 15.4 cm (6 in) cardboard spacer was placed against the concrete abutment. The wrapped face geotextile wall was then constructed against the cardboard, which acted to maintain the gap and control the alignment of the wall face. The first three layers of the reinforced soil wall were 30.5 cm (1 ft) thick and the top layer thickness

varied with respect to grade specifications. A fabric overlap of 1.2 m (4 ft) was used on all layers of the wall. Upon completion of the wall, the cardboard spacer was saturated with water and removed. The backfill material was the same select backfill used in previous SDDOT designs. Based on the results of this project, the state may specify less expensive backfill materials in the future. The drainage pipe was installed in the bottom most layer of the geotextile wall. A general illustration of this backfill design is shown in figure 1.

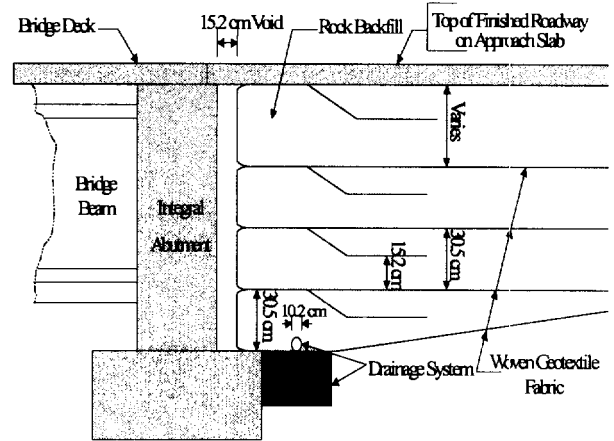


Figure 1. Typical geotextile reinforced soil wall behind the bridge abutment.

### 4 DATA COLLECTION

Over the course of this three-year project (1996-1999) physical measurements of the gap width, bridge length, and void development were obtained. More detailed instrumentation of these bridges was not feasible due to limited funding.

The gap width between the reinforced soil wall and the bridge abutment was monitored to determine if the abutment came in contact with the reinforced soil wall, thereby creating a passive pressure condition on the backfill. Also, if the abutment and wall do not come in contact, this data would be used to determine if a smaller gap width would be appropriate. To monitor gap width on the White River abutments, four vertical rows of four holes each were drilled through each abutment between the bridge beams. In each row, the approximately 5 cm (2 in) diameter hole locations were evenly spaced on the vertical profile of the wall. Initial measurements of the gap width at each hole location were recorded after the supporting cardboard had been removed. For the I-29 bridges, four vertical rows of three holes each were installed in each abutment

between the bridge beams.

A second series of holes were formed into the approach slab to monitor the formation of voids beneath the slab. These holes were installed with removable caps to cover the hole but allow access for measurement. Void measurement locations measuring 5 cm (2 in) in diameter are located at 0.46 m (1.5 ft), 0.76 m (2.5 ft), 1.68 m (5.5 ft), and 4.72 m (15.5 ft) back from the face of the abutment. These measurements can be made along the centerline, along the centers of the driving lanes, and at the edges of the approach slab.

Physical measurements were also taken to monitor the thermal expansion and contraction of the bridge deck. Nails driven into the bridge deck served as bench marks for measurements of bridge deck movement. Three benchmarks were installed at 0.6 m (2 ft) from the guardrails at the midpoint of the span of the bridge and on the north and south ends of the bridge. Additional benchmarks were placed on the centerline of the bridge at the midpoint and on both ends.

In addition, air temperatures were recorded each time field measurements were made.

## 5 DATA

The gap width of the White River Bridge has been monitored for a full one-year temperature cycle. Gap width measurements are being taken on two Interstate 29 bridges. The southbound lane has been monitored since completion in November of 1996 and at the time of writing is going through its first high temperature cycles. The northbound lane is near completion and initial gap width readings have been recorded. Figure 2 shows the approximate gap measurement hole locations in between the bridge beams. Due to the space limitations of this paper, only the results from the south abutment of the White River Bridge are shown, see figure 3.

Due to the distance from Brookings this bridge is located, readings on the gap width for the White River bridge were made about every three months, with readings scheduled to ensure readings were taken in the high temperature and low temperature periods in a one-year cycle.

Monitoring of the void development under the approach slab on the White River Bridge will start after the summer of 1997. The thermal expansion and contraction of the bridge system relative to the backfill system is currently being evaluated. No significant findings can be presented on these subjects until two full years of data have been recorded.

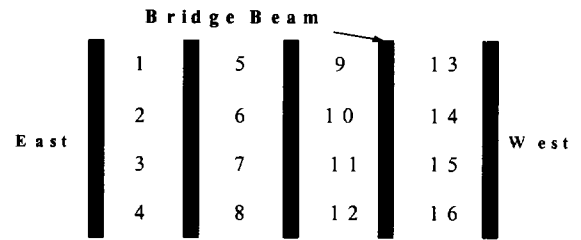


Figure 2. White River Bridge south abutment hole configuration.

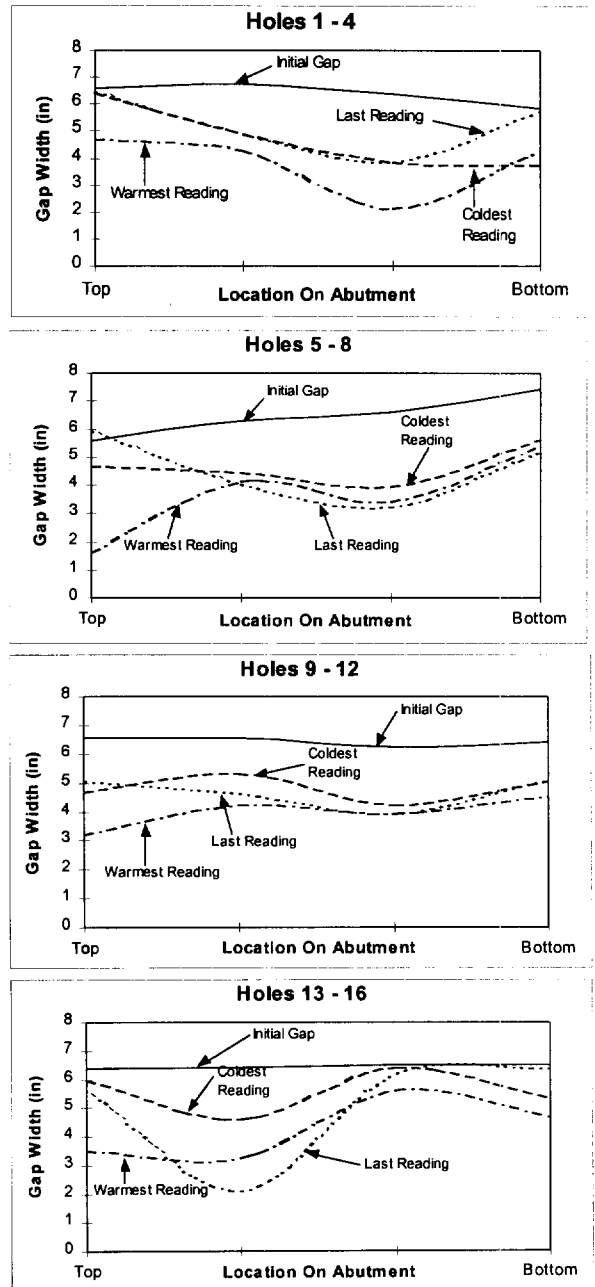


Figure 3. White River Bridge south abutment gap width for a one-year temperature cycle.

Gap width measurements taken from the White River Bridge and the one completed I-29 Bridge show changes in the gap width due to seasonal variations in temperature. The south abutment of the White River Bridge was constructed first. Based upon the limited number of readings taken thus far, the gap widths on this bridge are somewhat more scattered than the others. This has been attributed to the construction of the wall, which was visually observed and noted to be less than ideal. The south abutment was the first reinforced soil wall built by that particular construction company and was the first wall to be constructed by the State of South Dakota in a bridge end backfill application. Construction techniques were refined considerably following construction of the south abutment, which lead to a higher quality of construction for the north abutment. Due to improved construction practices, the north abutment displayed a larger initial gap measurement. Thus, it is essential to ensure all the layers of the wrapped faced reinforced soil wall are pulled very tight to reduce deformations after the cardboard is removed. The results show that experience in construction improved the performance of the north abutment backfill system.

The top of the abutment, which is integral to the bridge deck, undergoes the most movement. In most cases, the gap width for the upper two-thirds of the abutment changes more than the lower third. This suggests that a point of rotation exists in the foundation piling system below the bridge abutment. It can be observed in figure 3 that the minimum measured gap corresponds to the warmest temperatures, 100°F (38°C). Even measurements corresponding to the coldest temperature, 0°F (-18°C), are smaller than the initial gap, indicating a closure of the gap as the abutment cyclically moves. However, the data also shows that the initial gap has not fully closed in even the warmest temperatures, indicating the geotextile wall is functioning as intended. In all cases, the gap has remained open and prevented the abutment from pushing against the backfill and void development has not occurred.

## 7 CONCLUSIONS

At this early stage of the project conclusions as to the effectiveness of this design methodology in preventing void development will not be made. The data must be recorded over a longer time period to establish the repeatability of the data. Additional monitoring is necessary to distinguish how much of the gap closure is due to the initial movement of the wrapped face geotextile wall or is due to temperature induced abutment movement. The quality of construction of the backfill wall may also affect closure of the gap.

Therefore, quality control measures must be taken during construction. However, from one year's data it appears that the 15.2 cm (6 in) gap will provide sufficient space to allow for both movement of the abutment, movement of the soil wall related to inadequate construction, and movement due to creep of the geotextile soil wall.

## 8 ADDITIONAL WORK

Additional research, not discussed in this paper, is also being performed as part of this project. Alternative backfill materials and designs are being studied and tested in a SDDOT model bridge facility and will be the subject of future papers.

## 9 ACKNOWLEDGMENTS

This research was funded by the South Dakota Department of Transportation, project SD96-02. The support of the SDDOT is sincerely appreciated.

The contents of this report reflect the views of the authors who are responsible for the facts and accuracy of the data presented herein. The contents do not necessarily reflect the official views or policies of the South Dakota Department of Transportation, the State Transportation Commission, or the Federal Highway Administration. This report does not constitute a standard, specification, or regulation.

## 10 REFERENCES

- Edgar, T.V., Puckett, J.A., and D'Spain, R.B. (1989), "Effects of Geotextiles on Lateral Pressure and Deformation in Highway Embankments," Final Report to the Wyoming Highway Department, Department of Civil Engineering, University of Wyoming, Laramie, WY.
- Jorgenson, J.L. (1983), "Behavior of Abutment Piles in an Integral Abutment in Response to Bridge Movements," Transportation Research Record 903, Transportation Research Board, Washington, D.C., pp. 72-79.
- Kramer, S. L. and Sajer, B. (1991). "Bridge approach slab effectiveness." Final Report, Research Project GC 8286, Task 35, Washington State Transportation Center, University of Washington, Seattle, Washington, December.
- Schaefer, V.R. and Koch, J.C. (1992), "Void Development Under Bridge Approaches," Final Report No. SD90-03 to the South Dakota Department of Transportation, Department of Civil and Environmental Engineering, South Dakota State University, Brookings, SD.

# Field Performance Test of a Geosynthetic-Reinforced Soil Wall with Rigid Facing

Y. Tsukada, Y. Ochiai and H. Miyatake

Public Works Research Institute, Ministry of Construction, Tsukuba, Japan

N. Tajiri

Fukken Co., Ltd., Consulting Engineers, Hiroshima, Japan

**ABSTRACT:** Geosynthetic-reinforced soil walls have gained wide acceptance in the world as retaining walls of roads and so on. The functions of their facings and reinforcing materials laid in them vary, and different design methods have been proposed to date. The present paper describes the experimental results of an outdoor, full-scale, reinforced soil wall and the evaluation of the results, the experiment being a part of a series of experimental studies to elucidate the reinforcing mechanism of geosynthetic-reinforced soil walls with concrete facings and establish a design method which takes account of the effect of such wall facings.

The test wall of 8 m-high was constructed on a soft ground, and its facing was of concrete blocks. Its behavior has been observed during the construction and for two years thereafter. During the time period, it was exposed to heavy rains and not so large earthquakes. The focus of this paper is the evaluation of the stability of reinforced soil walls based on the experimental results.

**KEYWORDS:** Geosynthetic-reinforced wall, Field test, Design, Long-term observation, Stability analysis

## 1 INTRODUCTION

Various approaches have been taken to the design and construction of geosynthetic-reinforced soil walls. In particular, researchers have proposed a number of design methods, maintaining that wall facings contribute to the reinforcing effect of the walls (Tatsuoka 1992, Leshchinsky 1993, NCMA 1993, and Gotteland et al. 1992). Regarding roads of which less severe constraint of deformation is required, the Public Works Research Institute (PWRI) of the Ministry of Construction has been pursuing experimental studies on the reinforcing effect of various types of wall facings (Tajiri et al. 1996, Nakajima et al. 1996, and Ochiai & Fukuda 1996). As shown in Figure 1, a full-scale vertical reinforced soil wall of 8 m-high with concrete-block facings (under an overloaded embankment of 9.8 kN/m<sup>2</sup>) was constructed, and its behavior has been observed during the construction and for two years thereafter. The present paper compares and contrasts the observed behavior with the

behavior assumed and predicted by the current design method, and discusses subjects which require due consideration in the design of reinforced soil walls in future.

## 2 SPECIFICATIONS OF TEST WALL

To design the test wall shown in Figure 1, its design conditions were set based on the previous test results and so on. The banking material was sandy soil, and its internal friction angle  $\phi_s'$ , cohesion  $c'$ , and unit weight  $\gamma_s$  were 29°, 0 kN/m<sup>2</sup>, and 18.6 kN/m<sup>3</sup>, respectively. The dimensions of the concrete blocks to be used were 50 cm in height, 100 cm in width, and 35 cm in depth, and their hollows were to be filled with crushed stone. Their unit weight was 21.1 kN/m<sup>3</sup>. A zone of crushed stone about 30 cm thick was to be provided at the back of the concrete-block facing as a drainage, and its internal friction angle  $\phi_g'$  and unit weight  $\gamma_g$  were 45° and 19.6 kN/m<sup>3</sup>.

The internal friction angles between materials were set as follows:  $\delta_1=(2/3)\phi=19^\circ$  between banking soil and blocks,  $\delta_2=0$  between reinforced soil mass and banked soil behind,  $\delta_3=(2/3)\phi_g=30^\circ$  and  $\delta_3=(1/2)\phi_g=22^\circ$  (two cases) between blocks,  $\delta_{bf}=\delta_3$  between blocks and concrete foundation, and  $\delta_{sg}=\phi_s'=29^\circ$  between banking soil and reinforcements. Reinforcing geosynthetic to be used was geogrid (Tensar SR-55), of which the design tensile strength  $T_d$  was 29.4 kN/m.

To determine the arrangement of the reinforcements, comparative design was performed by using the following design methods: PWRI method (Onodera et al. 1992), Geogrid Research Board (GRB) method (Yamanouchi & Fukuda 1993), Leshchinsky method (1993), and monolithic wall method which assumes that short reinforcements and a facing unite with each other to exert the soil retaining effect. Figure 2 shows the stability analysis mode by the PWRI method. For the stability analysis under the seismic condition, the horizontal seismic coefficient  $k_h$  of 0.10 was assumed.

Figure 3 summarizes the specifications of reinforcements found by the comparative calculation. The focus of this study was put on the verification of the reinforcing mechanism by

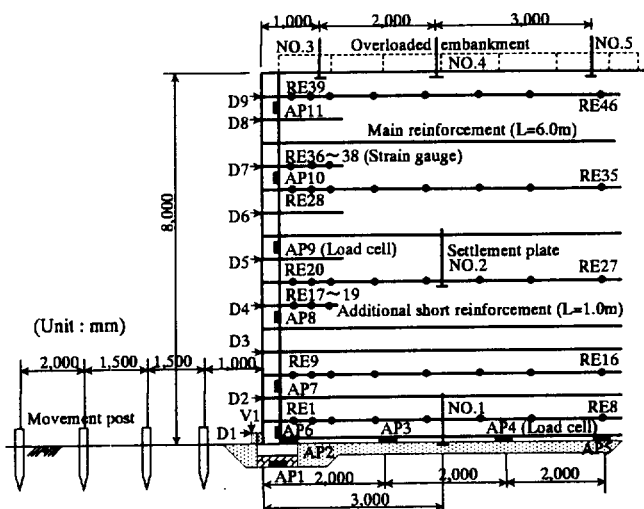


Figure 1. Cross-section and reinforcement pattern of test wall.

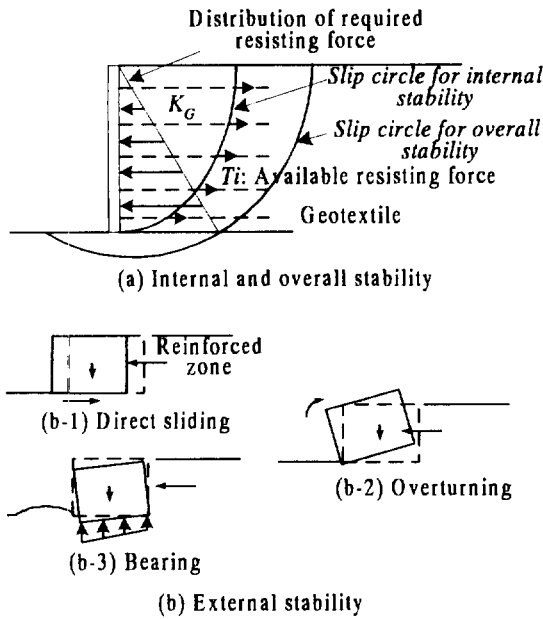


Figure 2. Failure mode of PWRI's design method.

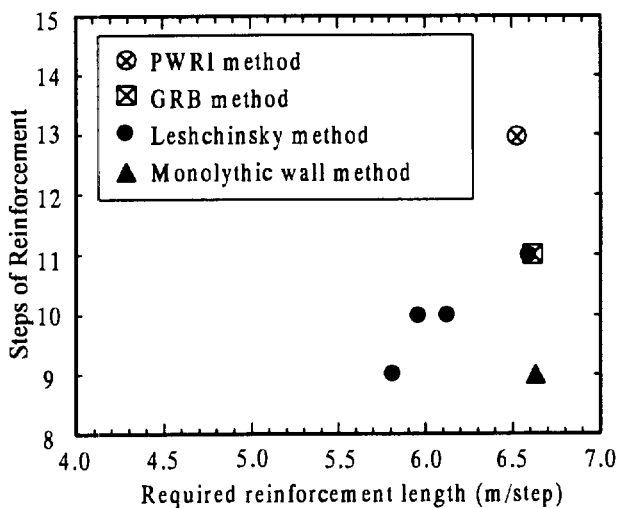


Figure 3. Required reinforcement length and steps.

constructing the test wall into a critical state, the calculation results taken into account. Namely, the test wall was based on the ordinary condition, the number of reinforcement layers was set at 11 on reference to the results by the Leshchinsky method, and the length of reinforcements  $L$  was set at 6.0 m (see Figure 1). To prevent the blocks not connected to main reinforcements from coming out of the wall surface, short reinforcements of 1.0 m-long were connected to them. The wall given these conditions and specifications, its stability was calculated by the PWRI's method as shown in Table 1. The overall stability  $F_s$  by the slip circular method was found to be 1.055, a state near the critical condition. Under the seismic condition of  $k_h=0.10$ , it ( $F_s$ ) was found to be 0.917, an unstable state.

Table 1. Stabilities of test wall calculated by PWRI method.

Analysis mode	Ordinary condition	Seismic condition ( $k_h=0.10$ )
Overall stability (Circular slip)	$F_s=1.055 < 1.2^*$ NO	$F_s=0.917 < 1.0^*$ NO
Direct sliding	$F_{sd}=2.142 > 1.5^*$ OK	$F_{sd}=1.844 > 1.2^*$ OK
Overturning (Eccentricity)	$ e =0.690 < L/6^*$ OK	$ e =0.566 < L/3^*$ OK
Bearing capacity	$q_{max}=252 < q_a^*$ NO	$q_{max}=264 < q_a^*$ NO

$L$ : length of main reinforcement, (=6.0m).

$q_a$ : allowable bearing capacity, (=49kN/m<sup>2</sup>) estimated from  $N$ -value (6) after Nakajima et al. 1996.

\*: design criteria.



Photo 1. Overview of test wall (June 1997).

### 3 FIELD MEASUREMENT OF TEST WALL

The long-term observation of the test wall has been conducted with the measuring instruments shown in Figure 1 for about 800 days including the construction period. The wall experienced the heavy rainfall of 81.5 mm/d ( $t=189$  d) and the of 191.5 mm/d ( $t=559$  d). The wall was also exposed to three small to medium earthquakes, but maintained its stability as Photo. 1.

#### 3.1 Horizontal Displacements of Test Wall

Figure 4 shows the displacements of the wall surface measured during the observation period. The maximum horizontal displacement was approximately 100 mm, and the wall surface took a bulgy shape, the center portion in height most prominent. The displacements immediately after the construction were small enough.

Since the overhanging of wall surfaces mars their scenes and offends our sense of security, it would be preferable to give the wall surfaces small backward leans in their construction. The deformation of the wall slowed down considerably and settled after some 800 days passed in the observation.

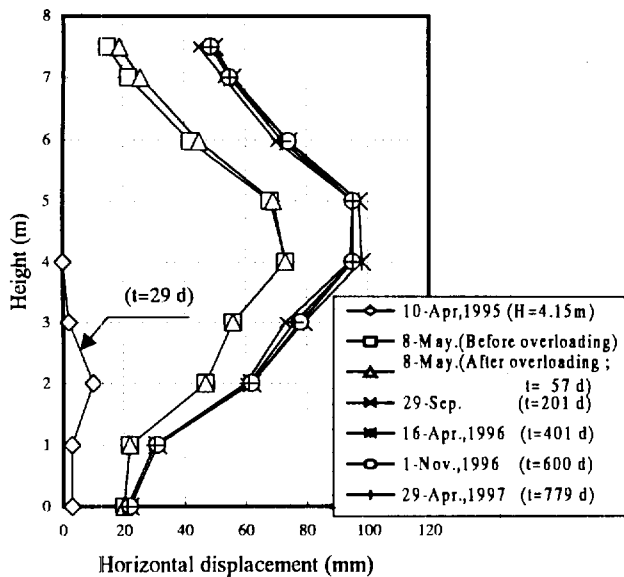


Figure 4. Horizontal displacement of test wall.

### 3.2 Earth Pressure on Wall Facing and Subgrade Reaction

Figure 5 shows the distribution of earth pressure on the back of the facing during and after the construction of the wall. The measured values were larger in the upper zone and smaller in the lower zone than the values calculated on the basis of Coulomb's earth-pressure theory.

As shown in Figure 6, the subgrade reactions were equal to or smaller than the overburden pressure in the area distant from the facing, and exceeded largely the pressure by the dead weight of the concrete blocks at the bottom of the facing. This does not

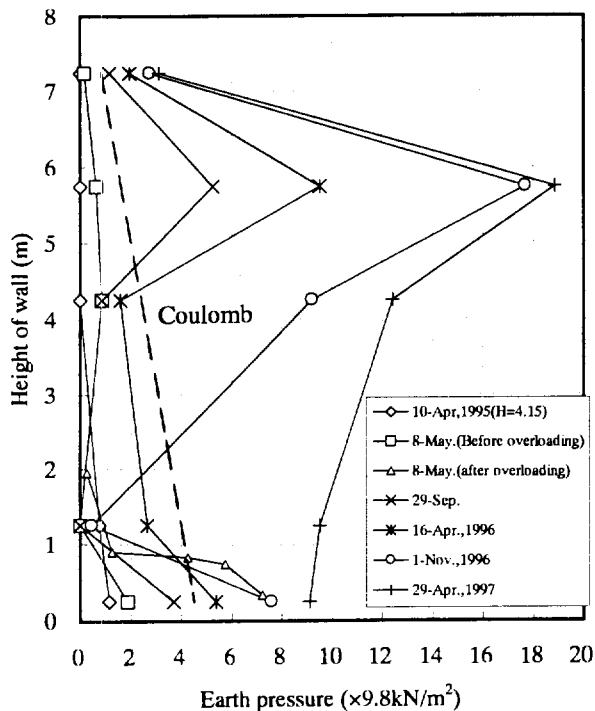


Figure 5. Earth pressure distribution on back of facing.

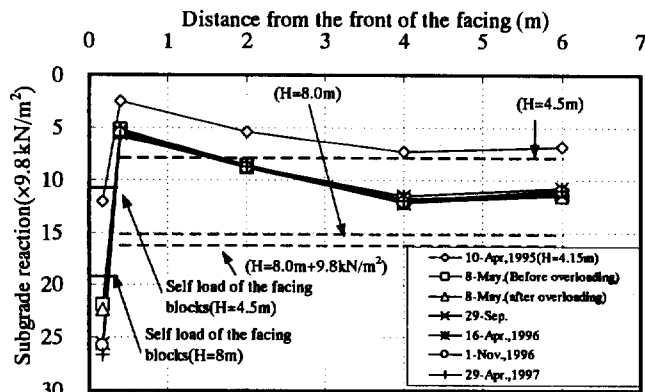


Figure 6. Distribution of subgrade reaction at bottom.

agree with the assumption, made in the design manual of the PWRI regarding the external stability analysis for the bearing capacity of foundation grounds, that the reinforced zone of an embankment behaves as a rigid body and the distribution of the subgrade reaction takes a trapezoidal shape, the reaction decreasing linearly from the facing toward the rear.

### 3.3 Strain of Reinforcements

Figure 7 shows the distribution of the strain of the reinforcements measured by foil strain gauges bonded on them. The maximum strain of each reinforcement was observed in the immediate vicinity of the facing. This distribution pattern is typical of walls with high-rigidity facings. At the completion of the test wall, the maximum strains were approximately 1%, 8.8 kN/m in terms of tensile force, which were smaller than the design strength of 29.4 kN/m. The maximum strains of the additional short reinforcements were at the same level as those of the main reinforcements.

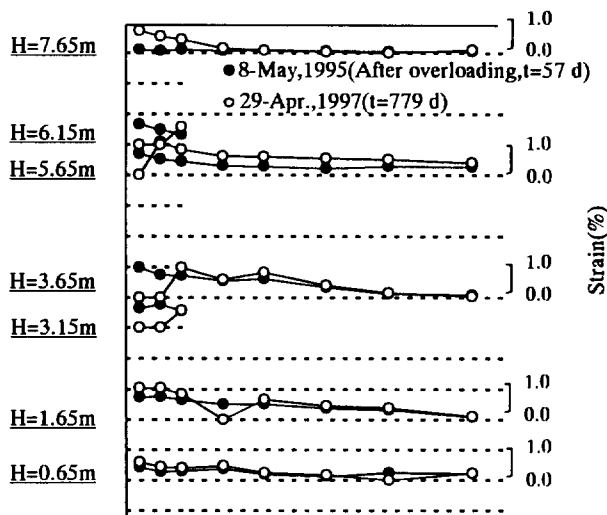


Figure 7. Distribution of strain of reinforcements.

## 4 DISCUSSION ON STABILITY OF TEST WALL

### 4.1 External Stability Analysis

In the PWRI design method, its external stability for the bearing capacity of the foundation ground is examined by checking whether the subgrade reaction is contained within the bearing capacity or not. The top layer of the foundation ground of the test wall was a filled Kanto-loam layer 2.15 m thick. As its  $N$ -value was about 6, its bearing capacity was estimated at 49 kN/m<sup>2</sup> or so. On the other hand, the maximum subgrade reaction was estimated at 252 kN/m<sup>2</sup> under the ordinary condition and 264 kN/m<sup>2</sup> under the seismic condition ( $k_s=0.10$ ), suggesting the instability of the test wall. Besides, the subgrade reactions observed were about 261 kN/m<sup>2</sup> under the facing and about 117 kN/m<sup>2</sup> under the embankment. Thus, it can not be explained why the test wall has maintained its stability.

On the other hand, since almost the whole test wall consisted of soil and it could basically be regarded as an embankment, another stability analysis was performed by using a circular slip surface which runs into the foundation ground. The soil-filling history of the ground taken into account, its strength parameters in the original state and in the state immediately before the construction of the test wall were estimated. With the safety factor  $F$ , of 1.027 thus found, the stability of the test wall could be explained (Nakajima et al., 1996).

Thus, it was suggested that the external stability analysis for the bearing capacity of foundation grounds can basically and advantageously be replaced by the circular slip stability analysis using slip surfaces which run into the foundation grounds.

#### 4.2 Stability Analysis under Seismic Conditions

The test wall underwent three small to medium earthquakes so far in 1996: the first was of  $M=4.7$  and estimated acceleration at Tsukuba 14 gals on August 16; the second,  $M=6.2$  and 26gals on September 11; and the third,  $M=5.4$  and 45 gals on December 21. The stability analyses of the wall under the third earthquakes (45 gals,  $k_s=0.05$ ) turned out as follows: the safety factors against slip circle  $F_s=0.989<1.0$ ; the safety factors against direct sliding  $F_{sd}=2.326>1.2$ ; and the stabilities against overturning  $e=0.373<L/3$ , indicating the instability against slip circle in particular. Nevertheless, the wall maintained its stability during the earthquakes. Accordingly, it would also be necessary to review the seismic-stability analysis method of the PWRI design method.

## 5 CONCLUSIONS

Based on the long-term observation results of the full-scale reinforced test wall 8-meter high, the behavior of the test wall was compared and contrasted with that assumed and predicted by the PWRI's design method, to identify future subjects toward the establishment of a more rational design method. Main findings are as follows:

1. The arrangement of the reinforcements of the test wall was determined to construct the wall into a critical state under the ordinary condition, critical when evaluated by the PWRI design method. During the some 800 days observation, the test wall was exposed to heavy rains and small to medium earthquakes. Although the test wall, given such specifications, was supposed to lose its stability, it maintained its stability. Accordingly, it is necessary to establish a more

rational design method in future.

2. The PWRI design method is built on the concept of limit equilibrium. However, the following inconsistencies were observed: (i) the measured earth pressures on the back of the test wall's facing in the lower zone were smaller than the active earth pressures estimated by the Coulomb's earth-pressure theory, (ii) the measured values of the tensile force on the reinforcements were smaller than the values estimated in designing the test wall, and (iii) the distribution of the subgrade reaction did not take the trapezoidal shape which is assumed of concrete retaining walls, and the design and measured values of the subgrade reaction exceeded the bearing capacity of the foundation ground.
3. The bearing capacity, one factor in analyzing the external stability of walls, need not be examined, if their external stability is examined by the circular slip stability analysis using slip surfaces which run into their foundation grounds.

## REFERENCES

- Gotteland, Ph., J. P. Gourc, H. Wilson Jones and J. Baraize (1992) Cellular walls associated with geosynthetics: A laboratory model study, *Proc. Int. Symp. on Earth Reinforcement Practice (IS Kyushu '92)*, Fukuoka, Japan, pp.337-343.
- Leshchinsky, D. (1993) Geosynthetic reinforced steep slopes and walls: Effects of facing blocks, *1st Tokushima Int. Seminar on Slope Stability Engineering*, Tokushima, Japan, pp.95-133.
- Nakajima, T., N. Toriumi, H. Shintani, H. Miyatake and K. Dobashi (1996) Field performance of a geotextile reinforced soil wall with concrete facing blocks, *Proc. Int. Symp. on Earth Reinforcement Practice (IS Kyushu '96)*, Fukuoka, Japan, pp.427-432.
- NCMA (1993) "Design manual for segmental retaining walls (Modular Concrete block retaining wall systems) 1st edition", National Concrete Masonry Association, Virginia, USA, 336p.
- Ochiai Y. and N. Fukuda (1996) Experimental study on geotextile-reinforced soil walls with different facings, *Proc. 1st European Geosynthetics Conf. (EUROGEO 1)*, Maastricht, Netherland, pp.113-120.
- Onodera, S., S. Naemura, A. Nakane and S. Maruo (1992) A design method for steep reinforced embankments with geotextiles, *Proc. Int. Symp. on Earth Reinforcement Practice (IS Kyushu '92)*, Fukuoka, Japan, pp.391-396.
- Tajiri, N., H. Sakaki, J. Nishimura, Y. Ochiai and K. Dobashi (1996) Full-scale failure experiments of geotextile-reinforced soil walls with different facings, *Proc. Int. Symp. on Earth Reinforcement Practice (IS Kyushu '96)*, Fukuoka, Japan, pp.525-530.
- Tatsuoka, F. (1992) Keynote lecture: Roles of facing rigidity in soil reinforcing, *Proc. Int. Symp. on Earth Reinforcement Practice (IS Kyushu '92)*, Fukuoka, Japan, Vol. 2, pp.831-870.
- Yamanouchi, T. and N. Fukuda (1993) Design and observation of steep reinforced embankment, *Proc. 3rd Int. Conf. on Case Histories in Geotechnical Engineering*, St. Louis, USA, Vol. 2, pp.1361-1378.



# Multi-Anchored Soil Retaining Walls with Geosynthetic Loop Anchors.

H. Brandl

Professor, Institute for Geotechnical Engineering, Technical University, Vienna Austria

**ABSTRACT:** The paper deals with reinforced modular block walls using loop anchors. The bearing behavior of such structures is the deadman principle, but there exists simultaneously a composite effect between modular units, straps, and soil. Accordingly, several hypotheses of calculation are presented, based on model tests and comprehensive in-situ measurements on construction sites since the year 1977. Recommendations for on-site installation, filling, and backfilling of the structure are also given.

**KEYWORDS:** Retaining walls, Slope stabilization, Geo „Others“, Design by Function

## 1 SCHEME OF LOOP ANCHORED WALL SYSTEMS

Figure 1. illustrates the scheme of a loop anchored wall system. Generally, the front side of the wall consists of L-shaped elements (modular prefabricated reinforced concrete units) arranged in displaced position to each other and connected by tension straps (loop anchors) to anchor elements (e.g. half tubes) on the back of the wall. Similarly, for embankments both facings can be constructed of L-shaped elements (e.g. Figure 3).

The core of the wall consists of soil being placed in layers and compacted. The prefabricated elements and the loop anchors prevent the soil from giving way. Thus the fill material increases the bearing capacity, and the whole structure acts as a composite body - similar to crib walls but more flexible. Accordingly, the effect of the loops is primarily not a soil reinforcement, and friction is merely of secondary importance.

In order to avoid long term corrosion problems and to provide a flexible behavior of the retaining wall, geosynthetics have been preferred since about 15 years as tie-elements: High modulus polyester has proved especially suitable. Aramid is relatively expensive but exhibits less strain and creep. Consequently, a combination of polyester and aramid yarns is especially useful in critical cases. Special loops consist of geocomposites comprising a polyester tie element with a strip drain, and this core being wrapped by a non-woven geotextile. These composite loops have proved suitable for low-permeable fill material of a high water content.

The retaining structure with anchor loops is not only used for retaining walls but also for

- Noise protection walls.
- Bridge abutments.
- Protective structures against avalanches, mud flows.
- Quay walls and bank protection.
- Increase of the height of embankment dams.

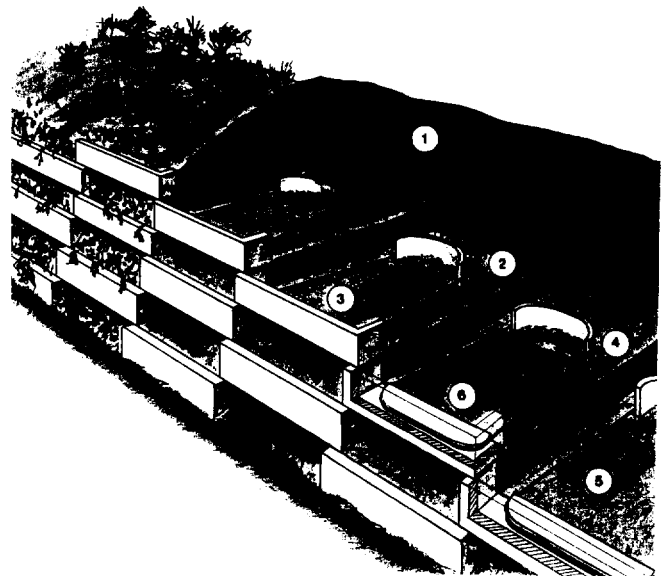


Figure 1. Loop anchored wall system - Schematical.

- |                               |                                  |
|-------------------------------|----------------------------------|
| 1 Natural soil or backfill    | 2 Fill material                  |
| 3 Modular wall facing element | 4 Anchor element                 |
| 5 Loop anchors                | 6 Section through facing element |

## 2 MODEL TESTS AND FIELD MEASUREMENTS

Small scale tests (1:20) in the laboratory were combined with 1:1 - field measurements on several construction sites. The maximum wall height was 21 m.

From Figure 2 it can be seen that overturning is the dominating mode of the global wall displacement. But in detail the structure does not tilt like an ideal monolith: There are differential movements among the layers, thus indicating internal shear deformations. The layers are pushed outside in steps, remaining rather horizontal. With

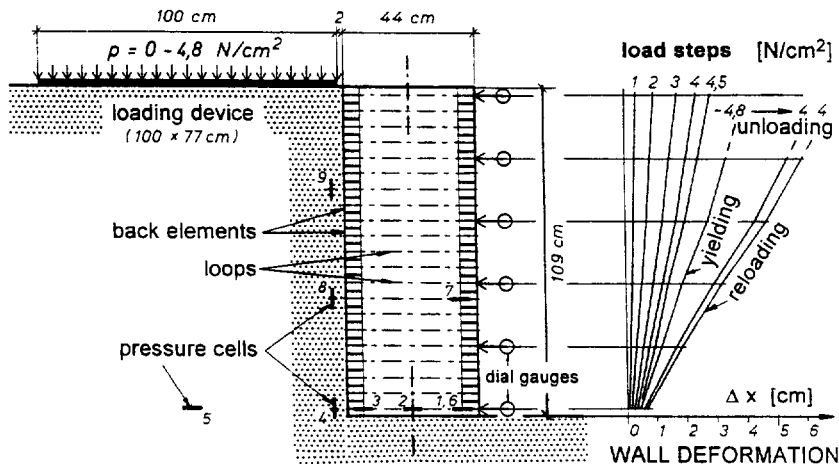


Figure 2. Laboratory test No.2. Scale 1:20, hence wall height  $H = 21,8\text{m}$  in nature.  $1\text{ N/cm}^2 = 10\text{ kPa}$

increasing surcharge load, structural failure begins on top of the wall where the composite behavior of the wall is not yet as strong as in greater depth. The bond effect among backfill, loops and modular elements increases with the overburden pressure. This could be proven especially clearly by cutting some of the loops. In this case a rearrangement of internal forces took place, thus avoiding failure to a high extent. Collapse of the wall is announced by large movements and does not occur suddenly.

This bearing deformation behavior is characteristic of multi-anchored soil retaining walls with geosynthetic loop anchors. It could be found not only in model tests but also

on numerous construction sites. Figure 3 shows a loop anchored retaining wall as a catch-system for avalanches and mud flows which threatened a highway and railroad on toe of a steeply inclined slope. Figure 4 illustrates the base pressure during the construction period and its long-term behavior. The stress distribution exhibits a maximum near the inner pressure cell which is caused by the embankment-like cross section of the retaining system. This differs widely from the behavior of gravity walls.

The tensile forces in the loops are plotted in Figure 5 showing a typical long-term decrease within the first years after wall completion. Four strain gauges were mounted on

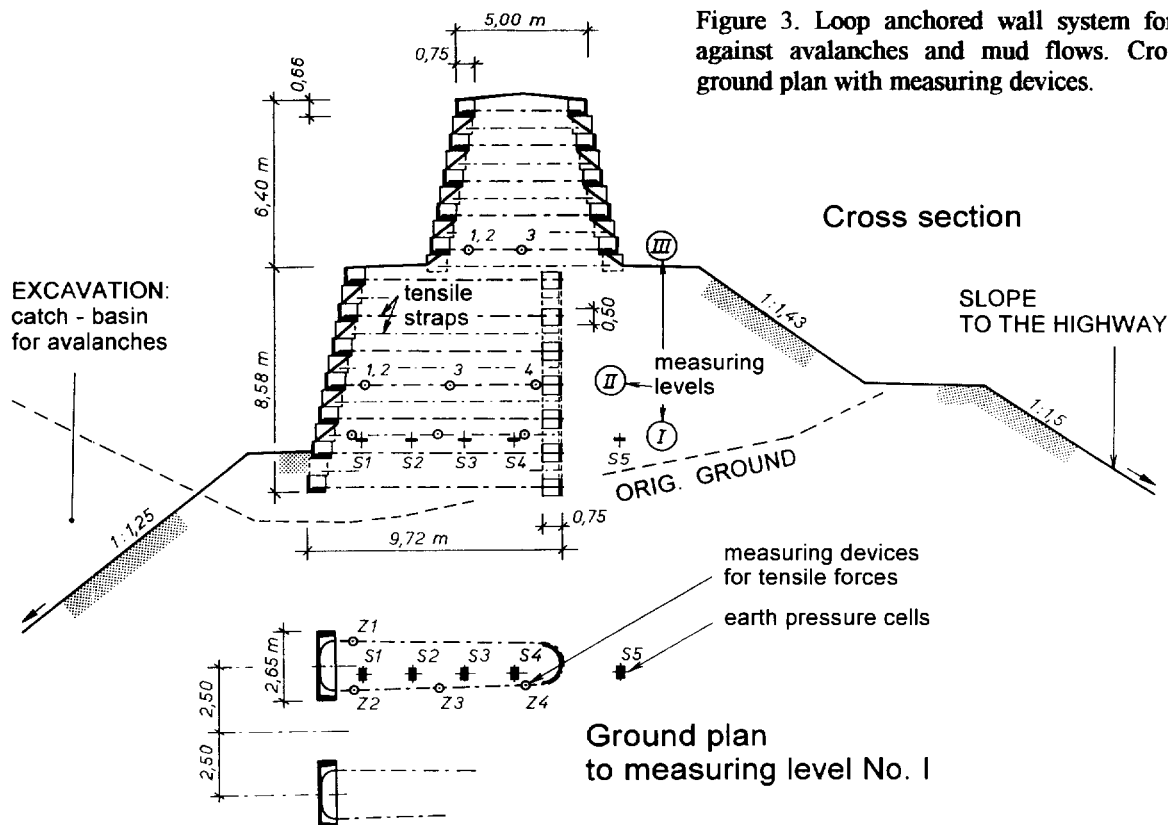


Figure 3. Loop anchored wall system for a catch-basin against avalanches and mud flows. Cross section and ground plan with measuring devices.

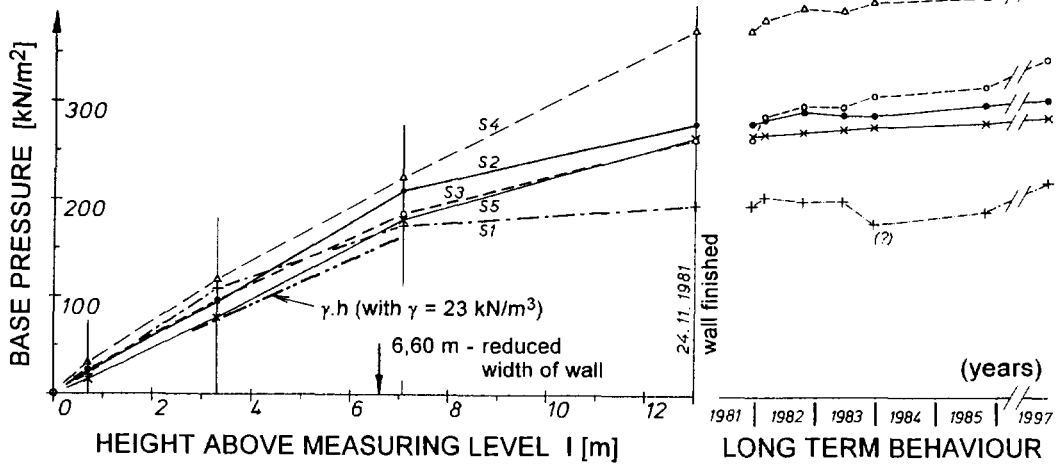
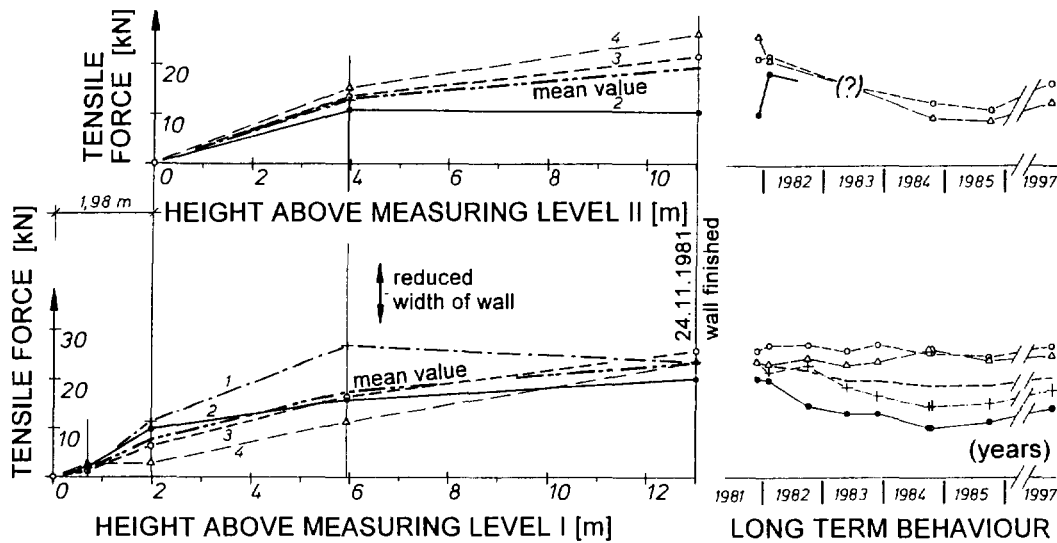


Figure 4. Measured base pressures versus wall height and long-term behavior (to Figure 3).

Figure 5. Measured tensile forces versus wall height and long-term behavior (to Figure 3).



each loop. The measured tensile forces are smaller than calculated, especially in the lower part of the retaining system. After reaching a certain overburden, additional wall heights cause less increase in tensile force than could be expected by the dead weight of  $\gamma \cdot z$  and  $\sigma_h = K \cdot \gamma \cdot z$ . This is caused by a variable coefficient of lateral earth pressure. Similar to reinforced soil,  $K$  varies with depth from  $K_0$  at the top, to  $K_a$  below several meters depth. Furthermore, low tensile forces can be explained by arching or silo pressure conditions in the fill and by an increasing modulus of the fill. A gradual increase of the bond effect between soil, loops, and anchor elements plays an additional role. Loops generally experience stress reduction, as the soil progressively takes over a higher portion of load. Creeping of the loops could be widely excluded, because some sections of the retaining system had loops of coated steel - and the results were fairly

similar. The difference between theoretical and actual tensile forces represents an additional safety factor compared to conventional calculation.

### 3 DESIGN AND CALCULATION

In order to develop a practicable design method, several hypotheses and theoretical assumptions were compared. Their accuracy and limits of application had to be verified on the basis of small scale tests, field experiments, in-situ measurements and site experience.

For design, external, internal, and local stability analyses have to be performed. The external stability comprises base sliding, overturning, and ground failure. It is calculated similarly to conventional retaining walls, the structure being considered a „quasi-monolith“, but with a statically

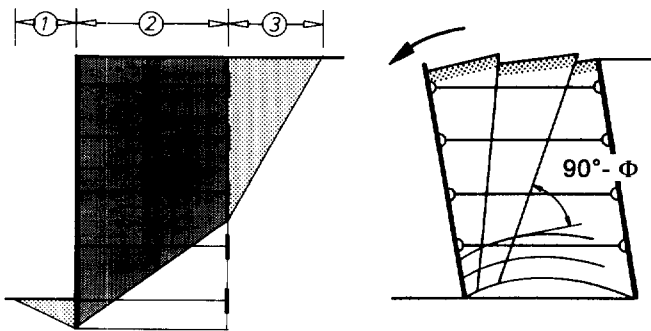


Figure 6. Internal failure mechanisms of loop anchored walls. Left: Block theory (assuming three slices). Right: Cofferdam scheme.

reduced, fictive width of the wall. According to the deformability of the wall, the active earth pressure can be assumed at the back of the wall and an angle of wall friction,  $\delta = \phi$ . The resultant of all acting forces should run generally within the core of the cross section. Commonly, block-like overturning is not a relevant failure mechanism.

The internal stability comprises three failure mechanisms: pull-out, tensile overstress, internal sliding (including possible slope failure). Furthermore, the local stability of the segmental wall units has to be proven: facing connection and bulging (shear transfer failure). The calculation can, above all, be performed similarly to that of cellular cofferdams, assuming a lateral earth pressure between the active limit value and the earth pressure at rest, depending on the stretchability of the loops.

For assessing the tensile forces,  $T$ , in the loops two boundary analyses have proved suitable:

$$T = K_{ah} \cdot \sigma_1 \cdot \Delta A \quad \text{.....for } \delta = \phi$$

$$T = K_a \cdot \gamma_f \cdot z \cdot \Delta A \quad \text{.....for } \delta = 0$$

whereby

$K_a$  = active earth pressure coefficient

$z$  = depth of the loop beneath top of wall

$\gamma_f$  = unit weight of the fill material

$\sigma_1$  = front edge pressure (fictious value of „quasi-monolith“)

$\Delta A$  = portion of the wall area referring to one loop

$\delta$  = angle of wall friction

$\phi$  = friction angle of fill material.

The maximum calculated  $T$  should be considered the design value.

The influence of surcharge loads on the back or directly on the crown of the wall can be assessed by conventional calculation methods. Traffic loads are idealized by static replacement loads. Contrary to reinforced soil, a friction loss along the tie elements caused by dynamic loads is not relevant.

Site observations have disclosed that the internal stability of loop anchored walls is actually higher than assessed by conventional calculation. This refers especially to internal

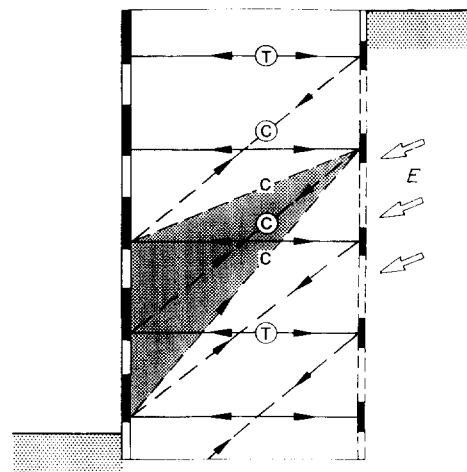


Figure 7. Idealization of soil (fill material) and structural members of a loop anchor wall system as a truss like retaining structure.

E = earth pressure

C = soil in compression

T = anchor loops acting in tension

sliding of slender structures. For a slenderness of  $B/H \geq 0.6$ , Janbu's block method has proved suitable. The methods of Kranz and others provide by far too small safety factors. Sliding analyses based on block theories (e.g. Figure 6/left) underestimate the actual safety factor of very slender structures. Numerous site observations have shown that in such cases values of only  $FS_{calc.} = 0.4$  to  $0.8$  are calculated, whereas the walls have been exhibiting a fully stable behavior since 10 years and more (checked by long term monitoring). Consequently, such slender structures should be designed similar to cofferdams with multiple anchorage (Figure 6/right).

Another calculation method idealizes the loop anchor wall system as a truss-like structure. According to Figure 7, the loops are the truss members acting in tension, and the soil between the loops and modular units represents the truss members in compression. This truss-like behavior increases with compaction degree of the fill material. A high compressive strength and dilatant properties of the soil enable it to interact with the loops and the anchor elements on the front and back side of the retaining structure. Vertical, possibly prestressed anchors through the prefabricated anchor elements at the back of the wall would provide further improvement.

Experience has shown that loop anchored walls hardly fail on a plane passing through the toe. Commonly, the critical failure plane runs through the face of the structure at a point  $1/4 H$  to  $1/3 H$  above the toe ( $H$  = wall height). In case of high surcharge loads, failure may occur at even higher points.

If inextensible (metallic) loops are used, the failure of the wall can occur rather rapidly according to potential overstress of adjacent loops - like a zip effect. Contrary to

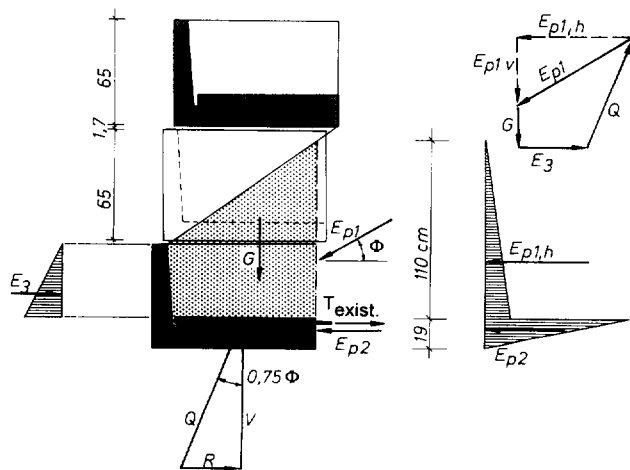


Figure 8. Forces on the facing element of a loop anchor wall system and force polygon for the soil fill on the concrete element.

$T_{\text{exist}}$  = existing tension force  
 $G, G_G$  = dead weights of soil and concrete element

that, overstressing of extensible loops (polymeric anchors) first of all leads to creep and only limited load shedding. The deformation increases, thus indicating in time the necessity of strengthening the structure.

The connection between the tie elements and the facing of a permanent soil reinforcement wall is a critical part of the design. Contrary to that, anchor loops allow a full strength solution without requiring special starter elements embedded in the modular facing. Figure 8 illustrates the load transfer in a typical modular structure. Vertical wall friction can be assumed  $\delta_v = \emptyset$ , and horizontal friction  $\delta_h = 0.75 \emptyset$ .

Loop anchored walls require smaller widths than conventional reinforced soil structures. This reduces the slope cut, which is especially important if the retaining structure has to be placed into unstable terrain. No special footing is necessary except on soft soil.

The structure allows adaptation to various site conditions, geometries, and varying loads, and it behaves fairly insensitive to differential settlement, to dynamic loads, and to earthquakes. Furthermore, full-face draining and intensive greenery planting are possible.

#### 4 LONG TERM BEHAVIOR

Regarding the long term behavior of loop anchored wall systems, two factors have to be considered before all: Creeping and effect of hydrolysis on polyester.

Monitoring of loop anchored wall systems has disclosed that creeping can be widely neglected. Figure 9 shows the tensile strength-extension characteristics of various loops. At a working stress level of about  $\leq 30\%$  for the initial ultimate tensile strength of geosynthetic straps, long term creep elongation could be expected less than 1% occurring

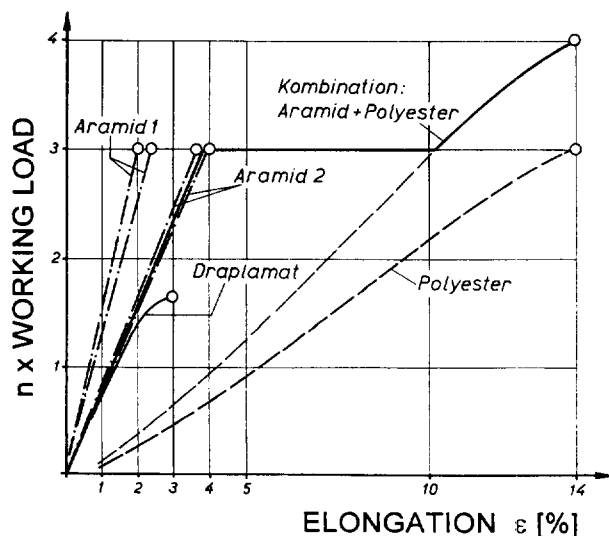


Figure 9. Tensile strength - elongation characteristics of various loops. Draplamat is a coated steel strap.

after construction. The (allowable design) extension is likely to be  $< 5\%$  in total for polyester and  $< 1\%$  for aramid and draplamat.

There is a significant difference between the load-deflection characteristics of a loop and a reinforcing strip. Contrary to laboratory tests on free tie elements, creeping gradually decreases on the site where the loops are embedded in soil. This effect increases with composite effect, hence with compaction degree and friction/adhesion. Changes in ambient operating temperature between 10 to 40 ° C practically do not alter the creep characteristics.

Draplamat consists of coated steel tendons and is cheaper than aramid. Polyaramid loops can exhibit even greater shear strength and lower extension than steel straps (Figure 9). Such tie elements are sometimes preferred for very high retaining structures and high loads. Mostly, the ultimate tensile strength of draplamat is similar to that of aramid, i.e.  $\sigma_T = 2600 \text{ N/mm}^2$ . The strain at failure is  $\epsilon_f = 3\%$  and 2 to 4% respectively. Commonly used polyester straps exhibit  $\sigma_T = 1050 \text{ to } 1250 \text{ N/mm}^2$  and  $\epsilon_f = 10 \text{ to } 14\%$ .

Composite loops consisting of aramid and polyester have proved suitable for structures in unstable slopes and seismic areas. Overstressing is indicated by a period of great deformation which is succeeded by strain hardening. This ductile behavior enables a timely strengthening of the structure before failure might occur. Consequently, such retaining systems are especially suitable for designing by the observational method.

When polyester fibres are directly exposed over longer periods of time at  $\text{pH} > 11$ , the presence of water (exactly OH ions) can have a detrimental and destructive effect, resulting in chain scission, reduced molecular weight and strength loss. Consequently, a coating of polyester loops is

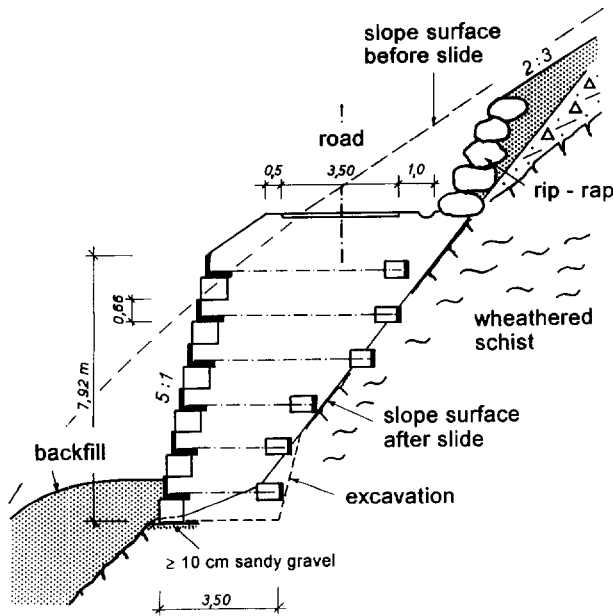


Figure 10. Loop anchored wall to reconstruct a road in a steep slope after landslide had occurred.

sometimes required. Generally, hydrolysis is not relevant if well engineered materials are used for loop anchored wall systems.

## 5 CONSTRUCTION PRINCIPLES

Commonly, indigenous and waste fill materials can be used for loop anchored wall systems. This provides significant savings in construction costs. The maximum grain size of the fill should not exceed 2/3 of the thickness of a layer. Cohesive or cohesive-frictional material provides more stable structures than purely frictional fill. On the other hand, sufficient drainage is essential if the retaining structure supports a slope. In such cases the grains finer than 0,06 mm should be limited to 15%. Furthermore, this value avoids frost damages within the composite structure. Sandwich filling, with alternating cohesive and non-cohesive layers has also proved suitable.

Usually, the fill material and the backfill of the structure should be compacted to  $D_{pr} = 97$  to 100% of standard Proctor density. The higher value is for widely grained fill material and a distance of more than 1 m behind the back of the wall. Near the front face, a lower compaction is preferred (about  $D_{pr} = 92\%$ ) to avoid local damage and to facilitate the planting of greenery. Compaction should begin about 1 m behind the face elements and proceed toward the backside of the wall. Thus, a slight prestressing of the loops is obtained, and the front blocks remain in their position. The back members of the deadman anchorage have to be well embedded in densely compacted soil. The front zone shall be compacted as last part.

During wall construction, the anchor loops must be protected from local overstress (e.g. passing of heavy vehicles or site equipment). This can be performed by a cover of sand, by a stable coating, or by excavating small trenches where the loops are placed. Polyester loops should be isolated from direct contact with concrete facing elements. Accordingly, a coating is recommended if polyester loops are installed. Commonly, robust loop coatings of polyethylene or PVC are used. Coating of the modular concrete elements has also proved suitable.

The concrete elements do not require a special interlock, e.g. by slotting dowels into preformed locating holes. Experience has shown that an accurate positioning of successive layers of blocks can be fully obtained simply by a precise installation of the elements. But bituminous soft-fibrous boards should be placed between the concrete elements to avoid local overstressing and edge cracking. Furthermore, such interlayers improve the flexible behavior of the structure, and they may compensate possible installation deficiencies. Flexible interlayers, covering the whole contact zone, have proved more suitable than small boards.

Commonly, loop anchored wall systems are stepped back at 5 to 15 cm per layer to provide an attractive face inclination and to improve planting conditions. Furthermore, facing elements can be colored to give specific aesthetic effects. Small unit sizes allow an adaption to various geometry, including stepped foundations and wall heights and varying length of anchor loops (e.g. Figure 10).

The main advantages of the loop anchor wall system are:

- Modular standards of the pre-fabricated elements.
- The assembling of the wall requires only a light crane; no special technical knowledge is required.
- Short construction period.
- The excavated soil can be used as fill material in most cases.
- No footings (except on soft subsoil).
- Well adaptable to locally differing conditions (geometry, soil, loads, etc.).
- Rather insensitive to differential settlements, to dynamic and cyclic loads, and to earthquakes.
- No sudden rupture in case of overloading, but gradually increasing failure indications, due to the great plastic reserves.
- Excellent drainage of the fill and backfill.
- Sufficient place for plant growth (hence also „green walls“).

## REFERENCES

- Brandl, H., Dalmatiner, J. (1986) „New earth retaining structure and other retaining structures of reinforced or multi-anchored earth“, Volume 280 of *Straßenforschung*, Federal Ministry of Economic Affairs, Vienna, Austria.

# Mechanically Stabilized Earth Wall Design: External Stability

M.S. Meyers, PhD, PE

Senior Geotechnical Engineering Specialist, U.S. Army Corps of Engineers, St. Paul District, St. Paul, Minnesota, USA

R.A. Wetzel, PhD, PE

E.S. McCullough, PhD, PE

Professors, Department of Civil and Environmental Engineering, University of Wisconsin-Platteville, Platteville, Wisconsin, USA

R.R. Berg, PE

Consultant, Ryan R. Berg & Associates, Inc., St. Paul, Minnesota, USA

**ABSTRACT:** Design of mechanically stabilized earth (MSE) walls includes internal and external stability analyses. External stability, which includes sliding, overturning, bearing capacity, global stability, and compound stability analyses, generally governs the required length of reinforcement and the wall embedment depth. This paper discusses the components of external stability design of MSE walls, the focus being on bearing capacity and the impact of non-generalized site conditions on reinforcement lengths and embedment depths required to satisfy bearing capacity and sliding design criteria. Results indicate that the minimum L/H ratios of 0.6 or 0.7 taken for granted by many designers are not satisfactory for non-generalized site conditions. This paper is directed towards members of the geosynthetics community who design and construct MSE walls.

**KEYWORDS:** Bearing capacity, Segmental retaining walls, Geosynthetic reinforcement, Foundations, Embedment depth.

## 1 INTRODUCTION

Design and construction of mechanically stabilized earth (MSE) walls has dramatically increased with the advent of segmental retaining wall (SRW), or modular block, units. Design of MSE walls is routinely completed by many engineers (e.g., civil, structural, geotechnical) with varying technical expertise. The need to fully understand the concepts of MSE wall design appears to have diminished with the widespread availability of computer software and design charts provided by manufacturers, suppliers of geosynthetic reinforcement and SRW units, and others.

Design of MSE walls includes internal and external stability analyses. Most designers find that completing the internal stability design, which tends to focus on the economic placement of the geosynthetic reinforcement, is straightforward. For very generalized site conditions, such as a wall with horizontal backslopes and front slopes, general design rules-of-thumb may be satisfactory for determining the reinforcement length. For non-generalized site conditions, however, such as a wall with a front slope and/or backslope, external stability is likely to govern the design of the wall, especially with respect to required reinforcement lengths and wall embedment depth.

External stability includes: sliding, overturning, bearing capacity, global stability, and compound stability. Many designers do not have all of the tools required to complete all of the components of the external stability analysis for non-generalized site conditions. Most current MSE wall design software products do not address all of the components of external stability design for non-generalized site conditions.

This paper discusses the components of external stability design of MSE walls. The focus of the paper is on bearing capacity and the impact of non-generalized site conditions on required reinforcement lengths and wall embedment depths.

The purpose of the paper is threefold: (i) to rekindle a classical geotechnical engineering oriented approach to the design of MSE walls with respect to external stability; (ii) to highlight the significance of non-generalized site conditions on bearing capacities for MSE wall system foundations; and (iii) to disseminate findings regarding the ultimate bearing capacity of MSE wall system foundations, for both generalized and non-generalized site conditions.

## 2 CURRENT DESIGN PRACTICE

### 2.1 Design Methodology

Several design guides for MSE wall systems are available. This discussion will focus on two of the generic design guides which are available: the National Concrete Masonry Association (NCMA) design manual (1996); and the Federal Highway Administration (FHWA) design guidelines (Elias and Christopher 1997). The general design approach for both methods consists of two interrelated but separate procedures: design for internal stability; and design for external stability. A generic MSE wall cross-section is presented in Figure 1.

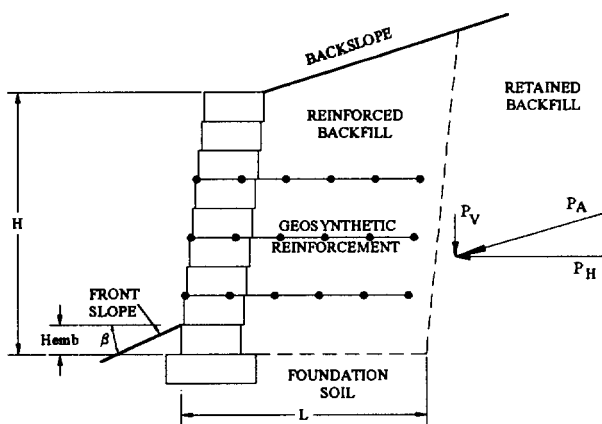


Figure 1. Typical geosynthetic-reinforced MSE wall cross-section (after NCMA, 1997).

### 2.1.1 Internal Stability

Internal stability refers to the interactions between the soil, facing units, and geosynthetic reinforcement in the reinforced soil zone. The spacing and tensile strength of the reinforcing layers are determined in this analysis, along with a check of the connection strength between the facing units and the reinforcement.

### 2.1.2 External Stability

The reinforced soil zone is considered to act as a composite gravity mass for the purposes of external stability analyses other than composite stability analyses. Forces acting on this mass include: the weights of the soil and facing units; the lateral earth pressure of the retained backfill; and any surcharge loads. Sliding, bearing capacity, overturning, settlement, compound stability, and global stability are possible failure modes that must be considered.

### 2.1.3 Empirical Design Criteria

The base width,  $L$ , of the reinforced soil zone is usually established from external stability analyses. In addition, certain minimum values for  $L$  have been established from experience. The NCMA guidelines recommend that  $L$  shall not be less than  $0.6H$  regardless of the results of stability calculations. FHWA guidelines recommend a minimum  $L$  of  $0.7H$ .

To insure a safe allowable bearing capacity is achieved, minimum wall embedment depths,  $H_{emb}$ , have been established for the bottom of the wall below finished grade. These values vary from  $H/20$  for walls with a horizontal slope in front of the wall to  $H/5$  for slopes of 3 horizontal to 2 vertical (3H:2V). A minimum wall embedment depth of 0.5 m, except for structures founded on rock, where no

embedment of the wall is required, is stated in the FHWA guidelines. NCMA guidelines require a minimum wall embedment of 0.15 m.

## 2.2 Lateral Earth Pressures

Lateral earth pressures are calculated differently in the two design procedures. With the NCMA guidelines, lateral earth pressures for both internal and external analyses are based on Coulomb earth pressure theory, which can account for the inclination of the wall facing units, the backslope angle, wall friction, and MSE mass-retained backfill friction. The vertical component of earth pressure is neglected in NCMA internal and external stability calculations.

Using the FHWA guidelines, lateral earth pressures are based on Coulomb theory for external stability and Rankine theory for internal stability. Face batters are ignored for batters less than or equal to 10 degrees from the vertical. The earth pressure direction is considered to be parallel to the backslope angle for external stability. A horizontal earth pressure direction is used for internal stability, with and without sloping backfills.

## 2.3 Bearing Capacity

As this paper is primarily concerned with bearing capacity determinations, the analysis methods for sliding, overturning, settlement, compound stability, and global stability are not discussed herein; a complete discussion of these analyses is contained in the literature (Elias and Christopher 1997; Holtz et al. 1997; Simac et al. 1993; and Berg et al. 1989).

Conventional bearing capacity analyses are carried out assuming that the reinforced soil mass acts as a continuous strip footing of width,  $L$ . The vertical stress on the base of the footing should be less than the allowable bearing capacity of the foundation soil. The vertical stress is assumed to act uniformly over a footing of effective width,  $B'$ , which is determined from

$$B' = L - 2e \quad (1)$$

where  $e$  is the eccentricity of the resultant vertical force on the base. The ultimate bearing capacity,  $q_{ult}$ , may be determined from the Terzaghi bearing capacity equation using the Vesic bearing capacity factors:

$$q_{ult} = c N_c + q N_q + 0.5 \gamma B' N_\gamma \quad (2)$$

Allowable bearing capacity,  $q_{all}$ , is determined by dividing the ultimate bearing capacity by an appropriate factor of safety, which is typically 2.0 for MSE wall systems (NCMA, 1997; U.S. Army Corps of Engineers, 1989 and 1990) to 2.5 (Elias and Christopher, 1997):

$$q_{all} = q_{ult} / FS \quad (3)$$



Design procedures in the FHWA guidelines require that the eccentricity,  $e$ , not exceed  $L/6$ , and if it does, the reinforcement length must be increased. A limitation on eccentricity is not required in the NCMA procedures.

Both the NCMA and FHWA design procedures consider only the vertical components of foundation loads in ultimate bearing capacity calculations. Thus, effects of the inclination of the resultant foundation load, which typically reduce the ultimate bearing capacity of a foundation, are neglected.

The NCMA and FHWA design procedures do not address the presence of a ground slope in front of the wall, except with respect to general guidance and recommendations of minimum embedment depths for typical ground slopes in front of the wall. The ultimate bearing capacity of a wall with a front slope is reduced by an amount proportional to the angle  $\beta$  of the front slope, assuming no bench in front of the wall. A ground slope bearing capacity factor is included in the bearing capacity equation (Bowles, 1996). Equation (2), with  $\beta$  measured counterclockwise in degrees from the horizontal, is modified to:

$$q_{ult} = c N_c g_c + q N_q g_q + 0.5 \gamma B' N_\gamma g_\gamma \quad (4)$$

where:

$$g_c = 1.0 - \beta/147 \quad (5)$$

and

$$g_q = g_\gamma = (1 - 0.5 \tan \beta)^5 \quad (6)$$

Assuming a cohesionless soil and all other conditions equal, a 3H:1V front slope reduces the ultimate bearing capacity by approximately 60 percent; a 2.5H:1V front slope reduces the ultimate bearing capacity by approximately 68 percent; and a 2H:1V front slope reduces the ultimate bearing capacity by approximately 76 percent. These are staggering reductions in ultimate bearing capacity values, which are typically not directly accounted for in most MSE wall design software.

Bowles (1996) also presents a procedure for determining the ultimate bearing capacity of foundations on slopes, with and without a bench in front of the foundation, independent of the application of a ground slope bearing capacity factor to the general bearing capacity equation.

A goal of this paper is to verify the NCMA and FHWA minimum embedment depth and reinforcement length guidelines and to enlighten the reader as to a more thorough understanding of the impacts of various front slope and backslope combinations on the ultimate bearing capacity of MSE wall systems.

### 3 GEOTECHNICAL SITE CONDITIONS

#### 3.1 Generalized Site Conditions

MSE wall systems are often designed for generalized sites conditions, such as: a horizontal front slope; a nominal surcharge loading; adequate foundation soil shear strengths; and a depth to groundwater which does impact the bearing capacity of the foundation soils. For these generalized site conditions, the guidance and recommendations regarding embedment depths and L/H ratios may well be applicable. In many instances however, especially of late, many MSE wall systems are being carried to extreme heights in locations where the generalized site conditions discussed above do not exist. Such conditions are referred to in this paper as non-generalized site conditions.

#### 3.2 Non-Generalized Site Conditions

Many MSE walls are being designed and constructed with backslopes and ground slopes in front of the wall which can vary from 3H:1V to 1.5H:1V. In addition, foundation soil shear strengths may be lower than is typically assumed for generalized site conditions (Meyers et al. 1997). These non-generalized site conditions obviously result in lower ultimate bearing capacities than would be determined for the generalized site conditions. In addition, compound stability may govern the design in some instances. As such, the general guidance and recommendations regarding embedment depths and L/H ratios may not provide sufficient safety factors against failure.

## 4 METHODOLOGY

### 4.1 General

A spreadsheet was developed to analyze the sliding stability and ultimate bearing capacity of MSE wall foundations for the generalized and non-generalized site condition combinations presented in Table 1. A cohesionless soil with an angle of internal friction equal to 30 degrees and having a unit weight of 19.6 kN/m<sup>3</sup> for the wall fill, retained backfill, and foundation soil were assumed for these analyses. Only the NCMA methodology was used for the analyses. The NCMA bearing capacity equations were modified to include a ground slope factor, assuming no bench in front of the wall. Analyses include determination of bearing capacity factors of safety and L/H ratios.

### 4.2 L/H Ratio Determinations

The minimum length of geosynthetic reinforcement required to just meet a factor of safety equal to 1.5 against sliding failure was determined for various wall height, surcharge,

**Table 1. Combinations Analyzed For Ultimate Bearing Capacity of MSE Walls.**

Case	Front Slope	Back Slope	Surcharge (kN/m <sup>2</sup> )	Embedment Ratio Denominator <sup>a</sup>
1	0	0	0	20, 10, 7, 5
2	0	3H:1V	0	20, 10, 7, 5
3	0	2H:1V	0	20, 10, 7, 5
4	0	0	12	20, 10, 7, 5
5	3H:1V	0	0	20, 10, 7, 5
6	3H:1V	3H:1V	0	20, 10, 7, 5
7	3H:1V	2H:1V	0	20, 10, 7, 5
8	3H:1V	0	12	20, 10, 7, 5
9	2H:1V	0	0	20, 10, 7, 5
10	2H:1V	3H:1V	0	20, 10, 7, 5
11	2H:1V	2H:1V	0	20, 10, 7, 5
12	2H:1V	0	12	20, 10, 7, 5

<sup>a</sup>Wall embedment depth equal to H/Embedment Ratio Denominator (e.g.  $H_{emb} = H/5$ ).

and backslope combinations. The critical sliding plane was taken as the reinforced fill-foundation soil interface (i.e., at depth equal to H). This required reinforcement length, or a minimum reinforcement length of 0.6H, whichever was greater, was then used in the bearing capacity computations to determine the factor of safety against bearing capacity failure for various wall heights, backslope, front slope, surcharge, and wall embedment depths. A minimum embedment depth of 0.15 m was used. A bench in front of the wall was not included in the analyses.

Minimum length of geosynthetic reinforcement required to just meet a factor of safety equal to 2.0 against bearing capacity failure were determined for various wall heights, backslope, front slope, surcharge, and wall embedment depths. The minimum L/H ratio for the various backslope, front slope, embedment depth, and surcharge combinations was, thus, defined as the longer of the lengths required to: (i) meet a factor of safety of 2.0 against bearing capacity failure; (ii) meet a factor of safety of 1.5 against sliding failure; and (iii) meet a minimum L/H ratio of 0.6.

## 5 RESULTS

### 5.1 Bearing Capacity Factors of Safety Determinations

Typical bearing capacity factor of safety results are presented in Figure 2, which plots the bearing capacity factor of safety against the foundation embedment depth (as a ratio of the wall height) for several different front slopes of a typical MSE wall condition assuming a horizontal backslope and a surcharge of 12 kN/m<sup>2</sup>. As is to be expected, for a horizontal front slope, the factors of safety are well above 2.0 and indicate that a minimum embedment ratio of H/20 or 0.15 m, which ever is greater, should be satisfactory with respect to the sliding and bearing capacity components of external stability, for walls varying in height from 1.5 to 12 m.

The bearing capacity factors of safety are reduced dramatically when the only variable modified is the front slope, which was increased from horizontal to 3H:1V. A minimum embedment ratio of H/20 or 0.15 m is still satisfactory for the wall height and embedment ratio combinations analyzed. However, with the factor of safety approaching 2.0 for the shorter embedment depths, the designer should have a higher degree of confidence in the definition of the design parameters used in the sliding and bearing capacity analyses.

For a 2H:1V front slope, a factor of safety of 2.0 is not attained for most wall height and embedment depth ratio combinations. Either a greater geosynthetic reinforcement length is required or an increased embedment depth ratio is required. Since an embedment depth ratio of H/7.5, which results in a bearing capacity factor of safety of just 2.0 for a wall height of 12 m, corresponds to an embedment depth of 1.8 m, it may be more economical to increase the effective width of the footing by increasing the length of geosynthetic reinforcement.

### 5.2 Minimum L/H Ratios

Typical minimum L/H ratio results are presented in Figure 3, which is a bar graph plot of the range of L/H ratios required to satisfy both sliding and bearing capacity design requirements against the various combinations of front slopes, backslopes, and surcharges for wall heights which vary from 1.5 m to 12 m, assuming an embedment depth ratio of H/20 and no bench in front of the wall. A thick horizontal line is drawn across the bar graphs at an L/H ratio equal to 0.6, the minimum L/H ratio recommended by the NCMA Manual.

An L/H ratio greater than 0.6 is required to satisfy the sliding and bearing capacity requirements for many of the design cases. The following conditions require a L/H ratio greater than 0.6:

1. A backslope of 2H:1V, regardless of the front slope.
2. A front slope of 2H:1V, regardless of the backslope.
3. A front slope of 3H:1V, if a backslope other than horizontal is used.

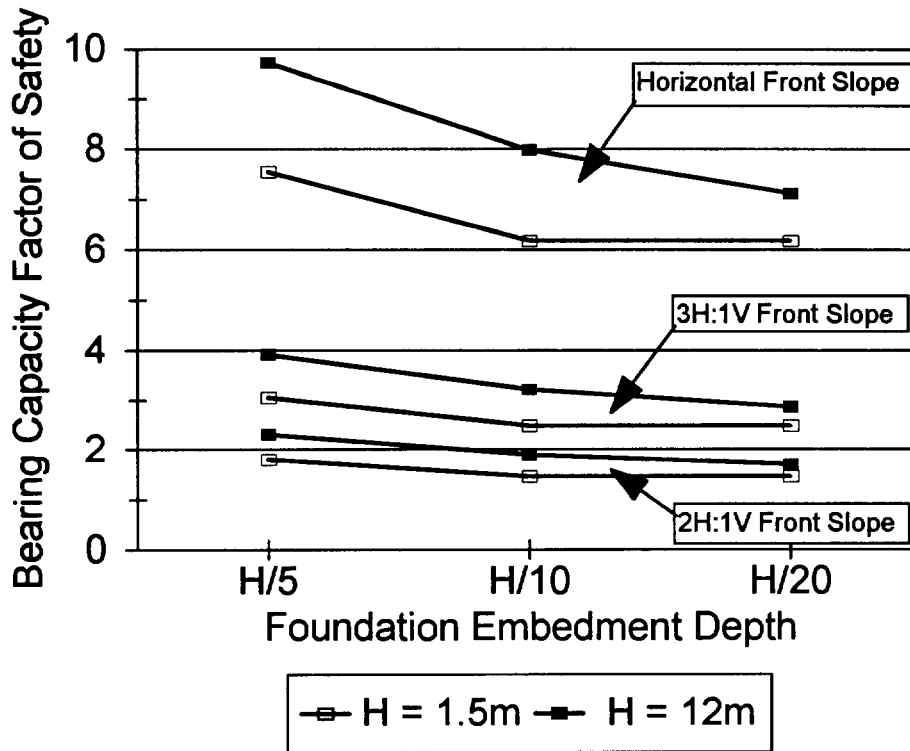


Figure 2. Typical bearing capacity factors of safety for various wall embedment ratios.

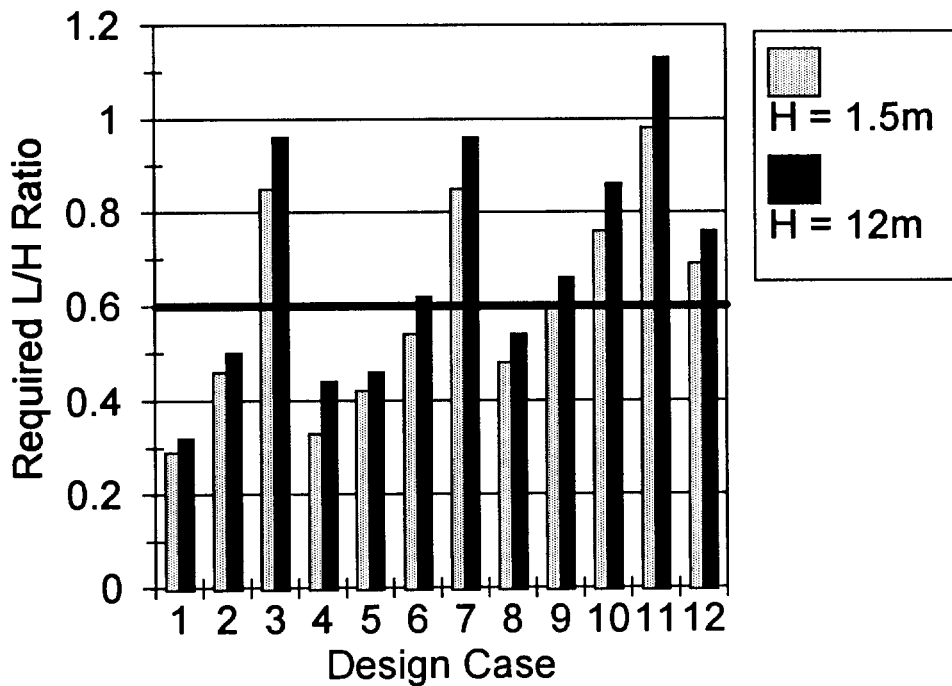


Figure 3. Minimum L/H Ratios for the combinations listed in Table 1.

Since the embedment ratio of  $H/20$  represents the shortest embedment depth investigated, the required  $L/H$  ratios for increased wall embedment depths are not quite as large. However, the same design cases (No. 1, 2, and 3 noted above) require  $L/H$  ratios greater than 0.6 for wall embedment depth ratios of  $H/10$ ,  $H/7$ , and  $H/5$ .

## 6 CONCLUSIONS

This paper has presented a basic review of the determination of the ultimate bearing capacity of MSE wall systems. The impact of various combinations of front slopes, back slopes, surcharges, embedment depths, and wall heights on ultimate bearing capacity is presented and discussed.

Conclusions, based on the assumptions previously listed, are:

1. The ground slope in front of a MSE wall system can significantly impact the ultimate bearing capacity beneath an MSE wall.
2. The magnitude of the angle of the ground slope in front of an MSE wall is proportional to the reduction in ultimate bearing capacity for the wall.
3. A backslope of 2H:1V requires an  $L/H$  ratio greater than 0.6, regardless of the front slope and wall embedment depth used.
4. A front slope of 2H:1V requires an  $L/H$  ratio greater than 0.6, regardless of the backslope and wall embedment depth used.
5. A front slope of 3H:1V requires an  $L/H$  ratio greater than 0.6, if a backslope other than horizontal is used, regardless of the wall embedment depth used.
6. A  $L/H$  ratio of 0.6, with a wall embedment depth ratio of  $H/20$ , is most likely satisfactory for generalized site conditions limited to horizontal front slopes and backslopes and a surcharge of  $12 \text{ kN/m}^2$  or less.

## 7 RECOMMENDATIONS

The intent of this paper was to investigate the impact of non-generalized site conditions on the bearing capacity of MSE wall systems. The authors note that performance of comprehensive sliding, bearing capacity, and compound stability analyses are particularly important for all projects with non-generalized site conditions, especially where a front slope or backslope of any magnitude is to be used. The site conditions will dictate the minimum reinforcement length,  $L$ , and wall embedment depth ratio for the MSE wall structure.

## 8 DISCLAIMER

The opinions and recommendations included in this paper are solely those of the authors and do not represent the views of the US Army Corps of Engineers or the University of Wisconsin-Platteville.

## 9 REFERENCES

- Berg, R.R., Chouery-Curtis, V.E., and Watson, C.H. (1989) "Critical Failure Planes in Analysis of Reinforced Slopes", *Geosynthetics '89*, IFAI, San Diego, CA, USA, pp. 269- 278.
- Berg, R.R. and Meyers, M.S. (1997) "Analysis of the Collapse of a 6.7 m High Geosynthetic-Reinforced Wall Structure", *Geosynthetics '97*, IFAI, Long Beach, CA, USA, Vol. 1, pp. 85-104.
- Bowles, J.E. (1996) *Foundation Analysis and Design, Fifth Edition*, McGraw-Hill Book Company, New York, USA.
- Elias, V. and Christopher, B.R. (1997) *Mechanically Stabilized Earth Walls and Reinforced Soil Slopes Design and Construction Guidelines, Participants Manual, FHWA Demonstration Project 82, Ground Improvement*, Federal Highway Administration, Washington, D.C., USA, 371 p.
- Holtz, R.D., Christopher, B.R., and Berg, R.R. (1997) *Geosynthetics Engineering*, Bitech Publishers, Vancouver, B.C, Canada, 452 p.
- Meyers, M.S. and Schwanz, N.T. (1993) "MSE Segmental Block Wall System in a Riverine Environment", *Geotechnical Fabrics Report*, IFAI, Volume 11, Number 4, pp. 22-27.
- Meyers, M.S., Schwanz, N.T., and Berg, R.R. (1997) "Specifying and Bidding Segmental Concrete Faced MSE Walls on U.S. Army Corps of Engineers, St. Paul District Projects", *Geosynthetics '97*, IFAI, Long Beach, CA, USA, Vol. 2, pp. 789-801.
- National Concrete Masonry Association, (1997) *Design Manual For Segmental Retaining Walls (Modular Block Retaining Wall Systems), Second Edition*, Herndon, Virginia, USA.
- U.S. Army Corps of Engineers (1989) *EM 1110-2-2502, Retaining and Flood Walls*, U.S. Army Corps of Engineers, Washington, D.C., USA.
- U.S. Army Corps of Engineers (1990) *ETL 1110-2-322, Retaining and Flood Walls*, U.S. Army Corps of Engineers, Washington, D.C., USA.

# Brick-Faced Retaining Walls Reinforced with Geosynthetics - A Numerical Analysis

M. Isabel M. Pinto

Assistant Professor, Department of Civil Engineering, University of Coimbra, Coimbra, Portugal

R. V. C. Pereira,

Research Assistant, Department of Civil Engineering, University of Coimbra, Coimbra, Portugal

M. L. Lopes

Assistant Professor, Department of Civil Engineering, University of Porto, Porto, Portugal

A. Mendonça

Research Assistant, Department of Civil Engineering, University of Porto, Porto, Portugal

**ABSTRACT:** The paper presents a study on the behaviour of brick-faced retaining walls reinforced with geosynthetics. This new method of construction for low height retaining walls combines the reinforced earth techniques with a conventional brick wall. While the walls are being built reinforcement sheets are anchored to the wall by the bed joints of the brickwork. After cure, backfilling is done in layers and a surcharge load is applied.

The influence of the reinforcement configuration's length and spacing is studied by using a numerical model based on the finite elements method. The reliability of the model is checked by comparing the numerical results with those obtained from laboratory studies on small scale models. A brief description of the bidimensional model used is presented and followed by the definition of the geometry of the analysed structure. The backfill, reinforcement and face materials of the retaining wall are characterized.

**KEY WORDS:** Geosynthetic reinforcement, Retaining walls, Finite element analysis, Nonwoven Fabrics.

## 1 INTRODUCTION

Nowadays retaining walls reinforced with geosynthetics are being constructed frequently throughout the world. Therefore the establishment of reliable criteria of behaviour for each type of these structures is of the utmost importance.

This paper presents a study carried out on brick faced retaining walls reinforced with geosynthetics, built on rigid foundations. The effect of varying the reinforcement configuration both its length and spacing was investigated by using a two dimensional numerical model based on the finite elements method. The validity of the model is checked by comparing the results with those obtained from laboratory studies on small model walls.

This study follows an experimental test program (Pinto 1992, Pinto and Cousens 1996) on this type of wall and the development of a numerical model for reinforced retaining walls (Lopes 1992, Lopes et al 1994).

## 2 EXPERIMENTAL STUDY

The method of construction is similar to that proposed by Dalton (1977) for low height retaining walls and combines the reinforced earth technique with a conventional brick wall.

The walls were built "in situ" in a test tank near its free end. The internal dimensions of the tank are 240 mm wide x 490 mm high x 630 mm long. It is made mainly of steel in order to ensure minimum deformations so that plane strain conditions could be considered. The walls were 300 mm high x 240 mm wide and half a brick thick (20.5 mm).

The reinforcement material was a non-woven fabric used as interfacing in dressmaking, with a deformability modulus of 6.9 kN/m and a thickness of about 0.3 mm.

The walls were built with scale model bricks sawn from full size bricks "class B engineering bricks" as recommended by BS 5628 (1978). While the walls were being built, reinforcement sheets were anchored to the wall by the bed joints of the brickwork. After cure backfilling was done in 30 mm layers (each layer being compacted by a small vibrating plate in order to achieve the required density) while the reinforcement were extended horizontally into the backfill. Finally a surcharge load was applied.

Different reinforcement lengths and spacings were tested. The walls were instrumented in order to measure the wall movement and the horizontal earth pressure acting on the rear face of the wall.

## 3 NUMERICAL MODEL

The numerical model was developed for reinforced retaining walls and simulates the construction process. It is based upon the finite elements method and assume the validity of the plane strain conditions. The soil and the face are simulated by bidimensional elements with 5 nodes (Doherty et al 1969), the soil-face and the soil-reinforcement interfaces by joint elements with 4 nodes (Goodman et al 1968) and the reinforcement by elements with 2 nodes.

The construction process was simulated according to Kulhawy (1977). When a finite element is activated its self weight is divided by the element nodes and applied to the system. The deformability modulus of these elements is very small in order to simulate a material with weight and

without stiffness, however, before the placement of the next layer of backfill (next stage) the deformability modulus returns to its real value. The vertical and the horizontal stresses correspond to the overburden pressure, and to the at rest state respectively. The movement of the nodes of the activated elements is considered to be the same as the top nodes of the previous elements.

## 4 NUMERICAL ANALYSIS

### 4.1 Problem Conditions

In order to carry out the study a total of 5 finite element meshes were created, one for an unreinforced wall, and four for reinforced walls. These include two lengths (8 and 12 cm) and two spacings (3 and 4 brick courses, i. e., 45 and 60 mm respectively) for the reinforcement.

Figure 1 shows a finite element mesh for the wall reinforced every 3 brick courses with 12 cm long reinforcement sheets.

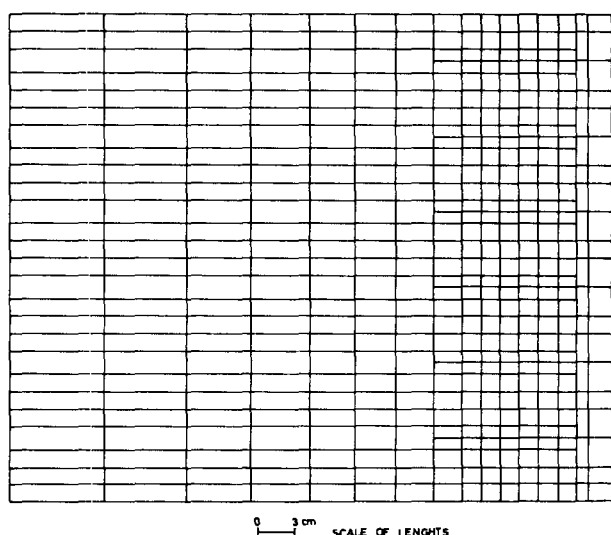


Figure 1. Finite element mesh.

Each mesh starts with only 20 elements, corresponding to the face of the wall. New elements are progressively activated in order to simulate the backfilling process: 300 for the backfilling, 126 for the interfaces and 48 for the reinforcement. Each reinforcement element is activated immediately after the placement of some soil on top of it. At the end of the backfilling stage the full mesh (which is activated in 10 steps) has a total of 494 elements and 495 nodes. The surcharge is then simulated by an equivalent load applied to the upper nodes of the top elements.

The boundary conditions were defined taking into account the geometry of the test tank (left lateral boundary) and the foundation condition (bottom boundary). In the former, the horizontal movement is prevented while in the latter, neither horizontal nor vertical movements are allowed in order to simulate a rigid foundation.

The soil of the backfill is a medium grain size containing about 15% of fine sand, with limiting densities of 14.4

$\text{kN/m}^3$  and  $16.8 \text{ kN/m}^3$ . Other characteristics of the soil are given in Table 1.

Table 1. Soil characteristics.

$\gamma$ ( $\text{kN/m}^3$ )	$K_0$	$\phi$ ( $^\circ$ )	$c$ (kPa)	$\nu$	$E$ (kPa)
16.3	0.36	40	0	0.35	7000

$\gamma$  denotes density,  $K_0$  at rest coefficient,  $\phi$  angle of friction,  $c$  cohesion,  $\nu$  Poisson's ratio and  $E$  deformability modulus.

Table 2 shows the characteristics of the interfaces. The deformability modulus of the wall was assumed to be 25000 kPa after comparative studies on unreinforced walls.

Table 2. Interface characteristics.

	Soil - Reinforcement	Soil - Face
$c_a$ (kPa)	0	0
$\text{tg } \delta$	0.73	0.75
$K_t$ (kPa/m)	2000	750

$c_a$  denotes adhesion,  $\delta$  angle of friction and  $K_t$  stiffness modulus.

### 4.2 Results

#### 4.2.1 Reliability of the numerical model

The reliability of the numerical model was checked by comparing the numerical results with those obtained from the laboratory tests. The comparisons were made both during the backfilling stage and under a surcharge load equivalent to a 270 mm high embankment on top of the backfill. In general a good degree of agreement was found when comparing the movement of the wall and the horizontal pressures acting on the rear face of the brickwall.

The influence of the increase of the backfill on the movement of the wall is shown in Figure 2 for a wall reinforced every 3 brick courses with 8 cm reinforcement length.

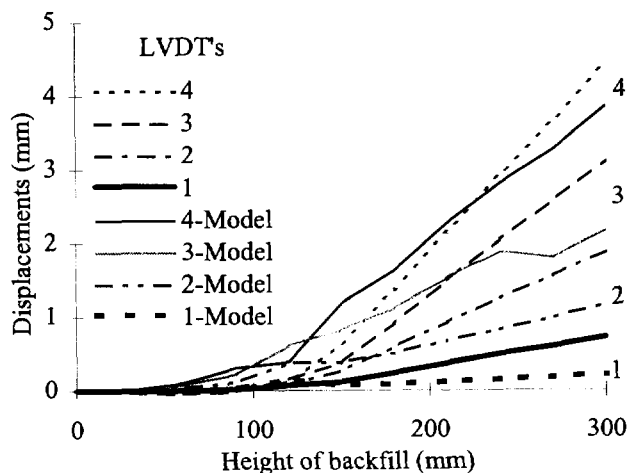


Figure 2. Displacements during backfill.

Figure 2 shows the variation of the displacement of the wall at different heights: 40, 115, 200 and 280 mm from the base of the wall, which corresponds to the position of the LVDT's 1, 2, 3 and 4 respectively. This figure shows in general, good agreement between the results obtained from the numerical model and those obtained from the laboratory tests. Small differences are however noticed as the values from the numerical model are lower than those from the laboratory. This is more evident near the end of backfilling stage and was also noticed during surcharging.

Figure 3 shows the displacements along the height of a wall reinforced every 4 brick courses with 8 cm reinforcement length during surcharging. The results from the numerical model and the laboratory test show a similar profile with values close to each other, but again, with the numerical model giving lower values when compared with the laboratory tests.

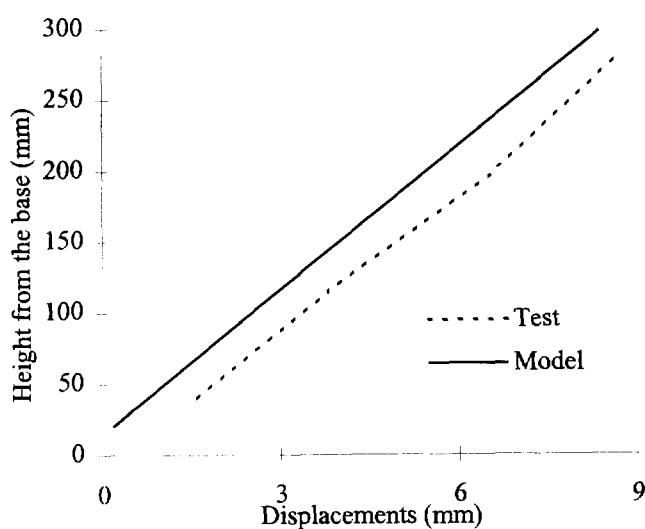


Figure 3. Displacements during surcharging.

The difference observed might be explained by a combination of two effects: the compaction which is not simulated by the numerical model and was found to be important during the laboratory test program (Cousens and Pinto 1996); and the restriction of displacement on the base of the wall imposed by the boundary conditions of the numerical model necessary to simulate the rigid foundation.

#### 4.2.2 Influence of the reinforcement configuration

A study of the influence of the reinforcement length and spacing configuration was carried out. The movement of the face of the wall (Figure 4) and the stresses developed on the reinforcement (Figure 5) were considered.

When comparing the curves plotted in Figure 4, corresponding to the same reinforcement length (i.e. 3b.c.-8 cm with 4b.c.-8 cm and 3b.c.-12 cm with 4b.c.-12 cm), it can be seen that displacements decrease with a decrease of spacing for both reinforcement lengths.

Comparisons between curves corresponding to the same spacing (i.e. 3b.c.-8 cm with 3b.c.-12 cm and 4b.c.-8 cm with 4b.c.-12 cm) reveal a decrease of displacements with

an increase of length for both reinforcement spacings.

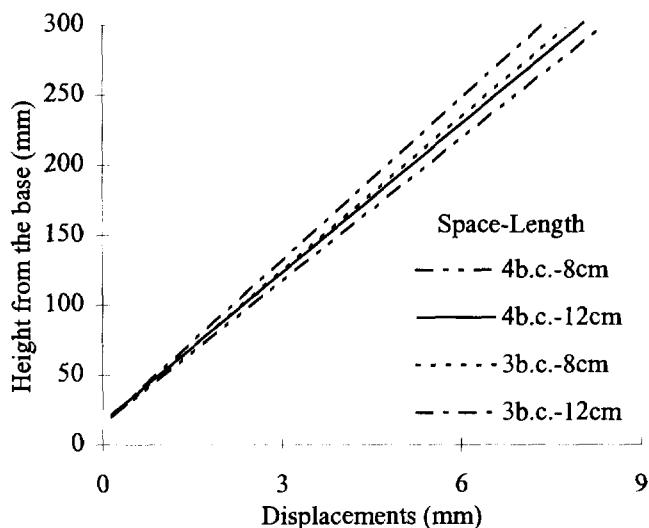


Figure 4. Displacements during surcharge for different reinforcement conditions.

The influence of the reinforcement configuration can also be studied comparing curves 3b.c.-8 cm and 4b.c.-12 cm of Figure 4. These curves correspond to walls with the same total amount of reinforcement ( $1152 \text{ m}^2$  for each wall) although differently distributed along the height of the wall. Figure 4 shows smaller displacements for the situation with lower spacing (3b.c.-8 cm) as opposed to that with long reinforcement (4b.c.-12 cm), suggested that the spacing is more important than the length of the reinforcement.

Figure 5 shows the variation of the stresses along the reinforcement length for walls with different reinforcement conditions. The curves plotted correspond to the most solicited layers of each wall which are those positioned at about mid-height. However, similar results were obtained for other layers. All curves show a non-linear behaviour, characteristic of highly deformable materials. The stresses are highest at the connection with the wall, and decrease towards the free end, which is characteristic of rigid walls (Shen et al 1979). Unlike walls with flexible faces, walls with rigid faces do not follow the vertical movement of the soil mass, consequently some bending takes place on the reinforcement, which generates tensile stresses.

The influence of the spacing can be studied comparing curves 3b.c.-8 cm with 4b.c.-8 cm and 3b.c.-12 cm with 4b.c.-12 cm in Figure 5. A decrease of the stresses can be related to a decrease in spacing, for both lengths. The influence seems to be more important on walls with the longest reinforcement.

When comparing curves corresponding to the same spacing (i.e. 3b.c.-8 cm with 3b.c.-12 cm and 4b.c.-8 cm with 4b.c.-12 cm) it can be seen that higher stresses are associated with shorter reinforcement, for both spacings, and specially for lower spacing.

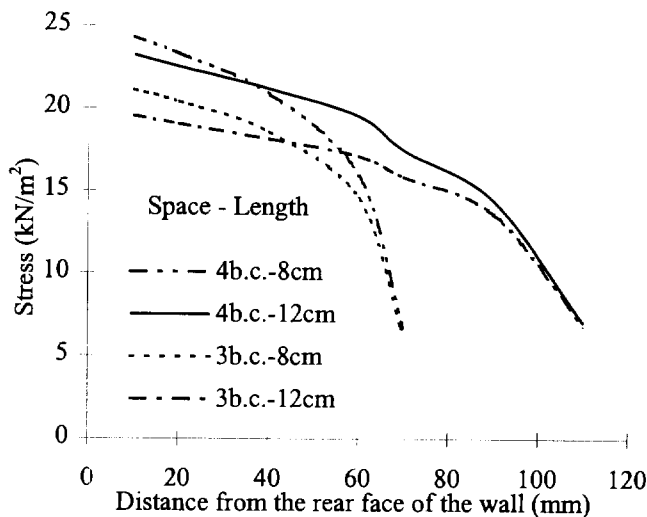


Figure 5. Stresses along the reinforcement length during surcharge for different reinforcement conditions.

Comparing stresses on walls with the same amount of reinforcement (i.e. 3b.c.-8 cm and 4b.c.-12 cm) it can be seen that lower stresses are associated with lower spacing. This is in agreement with the findings relating to the movement of the wall where the most important factor was found to be the spacing as opposed to the length. The difference of stresses between the two reinforcement situations increases towards the top of the wall.

## 5 CONCLUSIONS

A satisfactory degree of agreement was found when comparing the numerical results with those obtained from the laboratory tests.

From the study carried out it can be concluded that both the reinforcement length and spacing are important as far as the behaviour of the structure is concerned.

In fact, small movement and low stresses on the reinforcement are associated with longer reinforcement and lower spacing between reinforcing layers. This might be explained by the relative movement between the soil and the face of the wall which decreases both with the increase of the reinforcement length and with the decrease of the reinforcement spacing. Due to this movement some bending takes place on the reinforcement generating tensile stresses. The lower the movement the lower the generation of these stresses.

The spacing seems more important than the length of the reinforcement for both the movement of the wall and the development of tensile stresses on the reinforcement.

## ACKNOWLEDGMENTS

The authors would like to express their thanks to the financial support of JNICT through the Project

PBIC/C/CEG/2387/95, to PRAXIS XXI of the "Ministério da Ciência e Tecnologia" and FEDER through the Project 3/3.1/CEG/2598/95 and to the Scholarship PRAXIS XXI/BM/8009/96.

## REFERENCES

- BS 5628: Part1. (1978) "Structural Use of Masonry", British Standards Institution.
- Cousens, T.W. and Pinto, M. Isabel M. (1996) "The Effect of Compaction on Model Fabric Reinforced Brick-Faced Earth Retaining Walls", International Symposium on Earth Reinforcement, Fukuoka, Balkema, Rotterdam, ISBN 9054108339, Vol. 1, pp. 339 - 344.
- Dalton, D.C. (1977) "Fabric Reinforced Brick Retaining Wall", West Yorkshire Metropolitan County Council, Internal Report.
- Doherty, W.P., Wilson, E.L. and Taylor, R.L. (1969) "Stress Analysis of Axisymmetric Solids Utilizing Higher Order Quadrilateral Finite Elements", Report No. S.E.S.M. 69-3, Structures and Materials Research, Department of Civil Engineering, University of California, Berkeley.
- Goodman, R.E., Taylor, R.L. and Brekke, T.L. (1968) "A Model for the Mechanics of Jointed Rock", Journal of the Soil Mechanics and Foundation Division, Vol. 94, SM3, pp. 637-659.
- Kulhawy, F.H. (1977) "Embankments and Excavations", Chap. 16, "Numerical Methods in Geotechnical Engineering", C. Desai and J. Christian Eds. McGraw-Hill Book Company, New York.
- Lopes, M.L. (1992) "Muros Reforçados com Geossintéticos", PhD Thesis, University of Oporto, Porto, Portugal (in Portuguese).
- Lopes, M.L., Cardoso A.S. and Yeo, K.C. (1994) "Modelling Performance of a Sloped Reinforced Soil Wall using Creep Functions", International Journal of Geotextiles and Geomembranes, Vol. 13, No. 3, pp. 181-197.
- Pinto, M. Isabel M. (1992) "Model Studies of Fabric-Reinforced Brick-Faced Earth-Retaining Walls", PhD Thesis, University of Leeds, U.K.
- Pinto, M. Isabel M. and Cousens, T.W. (1996) "Geotextile Reinforced Brick Faced Retaining Walls", International Journal of Geotextiles and Geomembranes, Vol. 14, No. 9, pp. 449-464.
- Shen, C.K., Mitchell, J.F., DeNatale, J.S. and Romstad, K.M. (1979) "Laboratory Testing and Model Studies on Friction in Reinforced Earth", Proceedings of the International Conference on Soil Reinforcement, Paris, pp. 169-174.



# Large Deformations FEM Analysis of a Reinforced Earth Structure

R. Arab

Lirigm, Joseph Fourier University, Grenoble, France

P. Villard

Lirigm, Joseph Fourier University, Grenoble, France

J.P. Gourc

Lirigm, Joseph Fourier University, Grenoble, France

**ABSTRACT:** This paper describes the use of finite element (FE) method in large deformations to predict the behaviour of reinforced soil walls loaded on the top by a concrete slab load. The measured results are compared to the numerical ones for both the simulations done. A parametric study was also carried out to investigate the effect of some important parameters for design, such as the geotextile length, the facing stiffness and the position of top load application considering a geotextile-reinforced retaining wall with a continuous and vertical facing.

**KEYWORDS:** Finite element analysis, Retaining wall, Geotextile reinforcement, Top load.

## 1 INTRODUCTION

This paper outlines the use of the finite element (FE) method for the analysis of two full scale experimentations on segmental walls (4.35 m height by 5 m wide) loaded on the top and constructed with extensible reinforcement : one with non woven geotextile and another with woven geotextile. The reinforcement distribution in the two reinforced walls are not exactly the same as illustrated in Figures 1 and 2, this is justified by the difference in mechanical properties between the two geotextiles. The experimentation was performed and reported by Gourc et al., (1995). The analysis of the reinforced soil walls was performed using a finite element program GOLIATH developed at Lirigm which is appropriate to simulate the great deformations of this kind of structures and the membrane behaviour of the geotextiles in the slinding process.

The comparison between the predicted and the experimental results shows the difficulties to simulate correctly field prototype structures behaviour.

In this study, the effect of some parameters such as reinforcement length, facing stiffness and the position of load application is examined, considering a reinforced-retaining wall with a continuous and a vertical facing.

## 2 NUMERICAL MODELLING

### 2.1 Materials

A plane strain finite element analysis in large deformations was performed using the finite element (FE) program GOLIATH. The finite element mesh adopted for the analysis is shown in Figure 3. The fill is modelled by three

node isoparametric elements. The soil was assumed to be an elastic-perfectly plastic material with a Mohr-Coulomb failure criterion ( $E_s$ ,  $\nu_s$ ,  $c_s$ ,  $\Phi_s$ ) with a non associated flow rule with a dilatancy angle  $\psi_s$ . The unit weight of the soil is  $\gamma_s = 19 \text{ kN/m}^3$ . The foundation of the structure is supposed to have an elastic behaviour ( $E = 60 \text{ MPa}$ ,  $\nu = 0.33$ ).

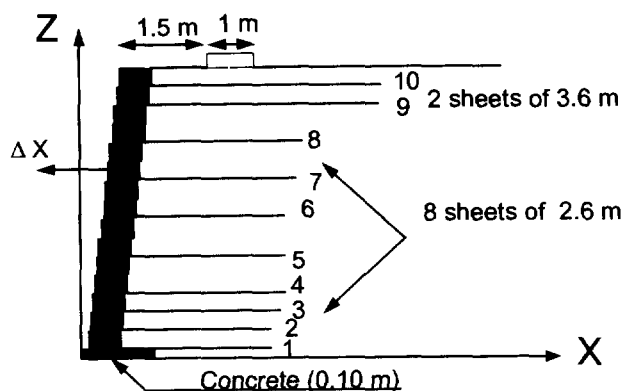


Figure 1. Non Woven wall (NW) profile and notations

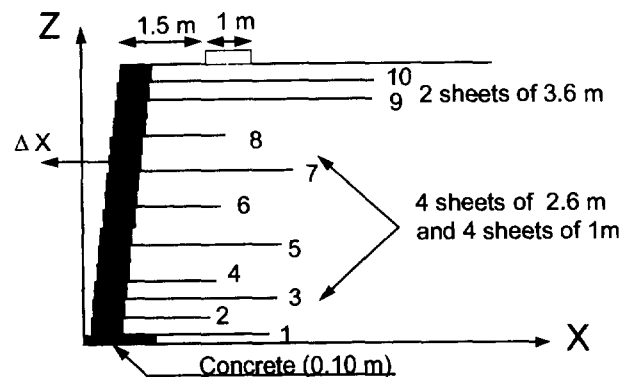


Figure 2. Woven wall (W) profile and notations.

The facing is modelled using four node isoparametric elements and was supposed to be elastic ( $E_f, \nu_f$ ) with a unit weight  $\gamma=22 \text{ kN/m}^3$ . Backfill, foundation, and facing element are modelled in large strain.

The facing is assumed to be continuous and the sheets are assumed to be fully bonded to the soil (no relative displacement).

The geotextile sheets were modelled using linear elastic bar elements in large displacement with negligible compressive strength and no bending stiffness (which allows the simulation of the membrane behaviour).

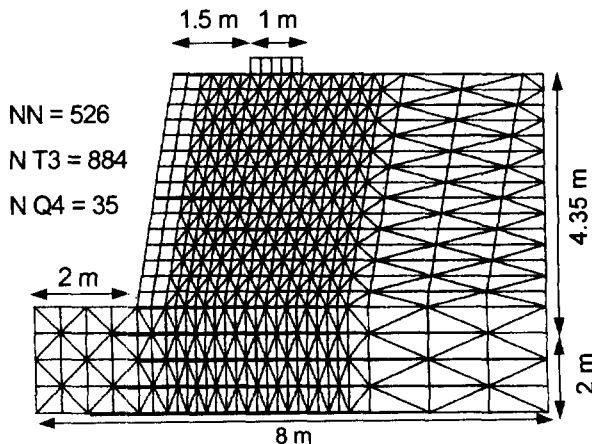


Figure 3. Finite element mesh adopted.

The geotextile stiffness are respectively  $J_{NW}=95 \text{ kN/m}$  and  $J_W=340 \text{ kN/m}$  for a non woven and woven fabrics.

## 2.2 Construction and loading

The compaction process is not simulated in this analysis. The full height of the wall is initially constructed applying body forces on the structure with ten load increments of 0.1g. Then the concentrated load is applied step by step through a linear elastic slab ( $E = 1500 \text{ MPa}, \nu = 0.2$ ) with 10 kPa increments until 100 kPa, followed by 2.5 kPa increments until failure.

The two reinforced walls have been analysed by Arab et al., 1996 using the set 1 of parameters as summarised in Table 1 which was modified after additional laboratory test (set 2) as indicated in table 1.

Table 1. soil and facing parameters for the modelisation

	$E_s$ (MPa)	$\nu_s$	$\phi_s$ (°)	$\psi_s$ (°)	$E_f$ (MPa)	$\nu_f$
Set 1	20	0.3	36	6	25	0.2
Set 2	35	0.3	36	16	20	0.2

## 3 RESULTS OF ANALYSIS

The predicted slab settlements versus surcharge  $Q$  obtained

with the two sets of parameters, are compared to the experimental one, respectively on Figures 4 and 5 for the two reinforced walls. The large settlement values considered shall be noticed.

For low value of the top load, the predicted settlement of the slab is very close to the measured one. It is worth noting that below the critical surcharge (breakpoint) the deformations and the displacement for the two structures are very small. Above this surcharge value the deformations increase significantly with the top load.

The measured slab settlement curves versus top load shown a breakpoint which corresponds to about 130 kN/m called the "critical surcharge". This is not predicted by the simulations. The breakpoint is very significant for designer because below it, only small deformations and displacements occur.

In the case of the Non Woven wall (NW) the predicted settlement obtained great with the two sets of parameters is lower than the measured one, particularly the solution calculated with the first set. However for the Woven structure (W) the measured settlement curve is enclosed by the numerical ones.

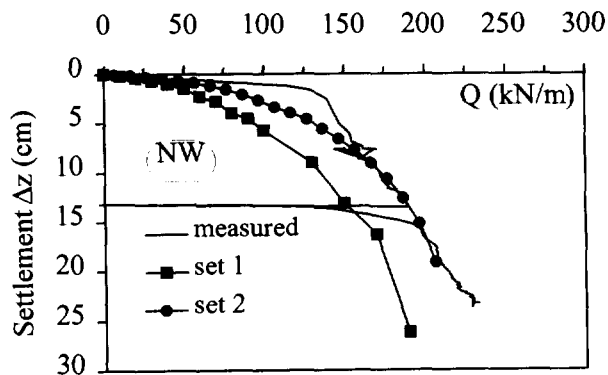


Figure 4. Slab load settlement versus top load (NW wall).

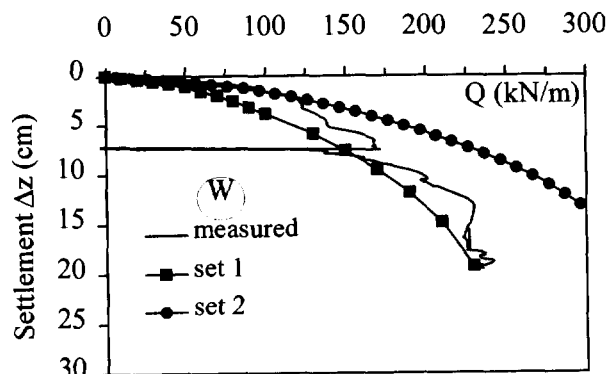


Figure 5. Slab load settlement versus top load (W wall).

The low settlement measured below the "critical surcharge" in the case of the Non Woven wall (NW) is probably due to the compaction effect. Under compaction, the extensibility and the texture of the geotextile combined

to the fine sand used to construct the Non Woven (NW) reinforced wall induce a better improvement of the mechanical characteristics than in the case of the Woven structure (W).

#### 4 PARAMETRIC STUDY

A parametric study was carried out to investigate the effect of mechanical and geometric parameters for gaining an insight into the effects of several of the important design factors, such as the geotextile length, the facing stiffness and the position of top load application considering a geotextile-reinforced retaining wall with a continuous and vertical facing. The structure geometry, the finite element mesh and the material properties of backfill, foundation, facing used are those corresponding to set 2 as summarised in Table 1 unless otherwise stated. The geotextile stiffness adopted corresponds to the non woven fabrics ( $J_{NW}=95$  kN/m).

##### 4.1 Effect of geotextile length (L)

The effect of reinforcement length  $L$  is examined by considering different lengths of reinforcement while the height  $H$  of the wall reinforced by eight sheets with a constant spacing  $\Delta H=0.58$  m is kept the same. The range of  $L/H$  considered varies from 0.36 to 0.8. As shown in Figure 6 the influence of increasing length of the geotextile is no more significative when  $L$  reaches  $0.5H$ . The short reinforcement sheets ( $L/H=0.36$ ) contribute to the increasing of the bearing capacity as demonstrated by comparison with the unreinforced retaining wall (No reinf). This demonstrates that not only the reinforcement tensile beyond the failure surface will be considered in the design methods.

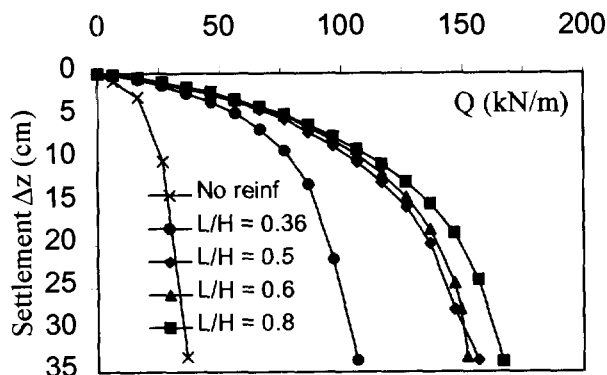


Figure 6. Effect of reinforcement length on the slab settlement under surcharge.

##### 4.2 Effect of wall facing stiffness

The rigidity of the wall facing depends of the construction mode. The effect of facing stiffness on the performance of

geosynthetic-reinforced soil retaining wall is not fully understood and is usually ignored in the design. An analysis is performed considering a retaining wall reinforced by  $N_p=8$  sheets of geotextile. The sheets are equally spaced,  $\Delta H=0.58$  m and are 2.6 m long ( $L/H=0.5$ ). Different facing stiffness were examined ( $E=5, 10$  and  $20$  MPa). A wrapped facing was also analysed ( $E=0$  MPa). The slab settlement versus surcharge and the lateral deflections of the facing induced by a top load of  $Q=60$  kN/m for all the cases considered are illustrated respectively on Figures 7 and 8.

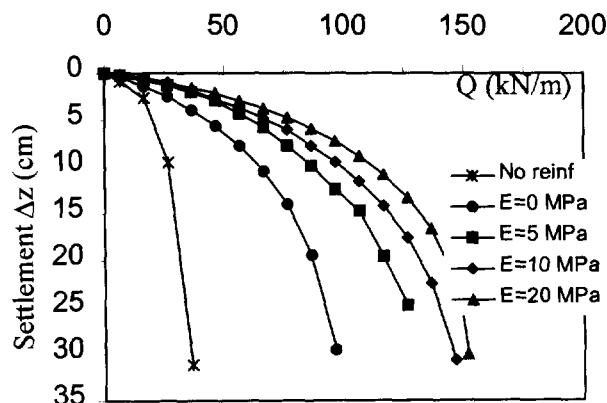


Figure 7. Effect of facing stiffness (E) on the slab load settlement.

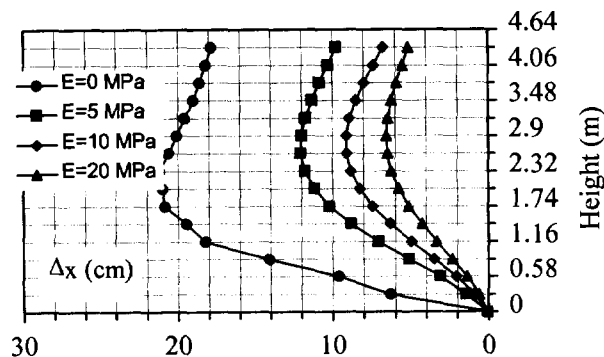


Figure 8. Effect of facing stiffness (E) on the wall facing horizontal deflection  $\Delta x$ .

In the absence of a facing or with a facing of low stiffness, the wall deformed greatly, particularly at high top load.

##### 4.3 Effect of the position of top load

To examine the effects of the position of the top load, different distance of slab position from wall face were considered ( $d=1, 1.5$  and  $2.5$  m). The height of the wall, the number of reinforcement layers and their length were the same as previously i.e. ( $H=4.35$  m,  $N_p=8$ ,  $L/H=0.5$ ). The slab settlement curves versus top load are illustrated in Figure 9 for the three cases. When the rear of the geotextile is not horizontally beyond the upstream

corner of the slab, the failure occurs roughly as in the case corresponding to  $d = 2.5$  m. The mean shear strain field ( $\epsilon_1 - \epsilon_3$ ) for the cases  $d = 1.5$  m and  $d = 2.5$  m are shown in Figures 10 and 11. We notice from these patterns that when the reinforcement length does not include horizontally the slab width a shear band develops from downstream side of the slab to the bottom of the facing.

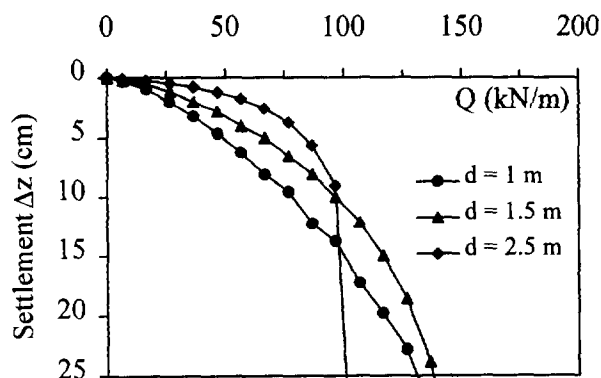


Figure 9. Effect of the point application of the top load on the slab settlement.

## 5 CONCLUSION

A finite element method has been used to model two experimental walls reinforced by extensible reinforcement. Despite the assumption done, the predicted results are quite satisfactory until large deformations. However some physical phenomenon observed are not predicted like the experimental "breakpoint" of the diagram surcharge-settlement. To simulate this phenomenon, it would be necessary to take into account the compaction effect and the construction stages. However lack of experimental data on the compaction mode and effect makes such approach very difficult.

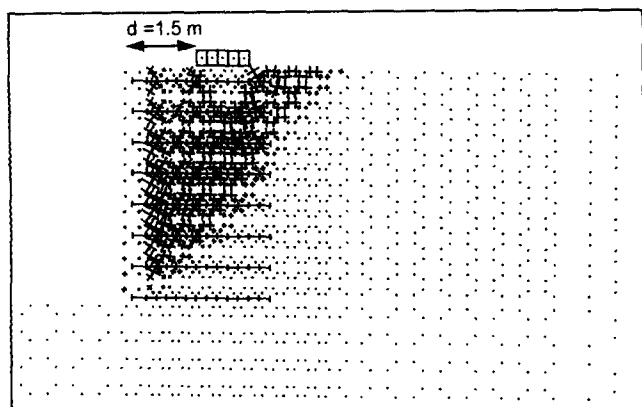


Figure 10. shear strain field ( $\epsilon_1 - \epsilon_3$ ) induced by a top load  $Q=90$  kN/m (scale : 1.5).

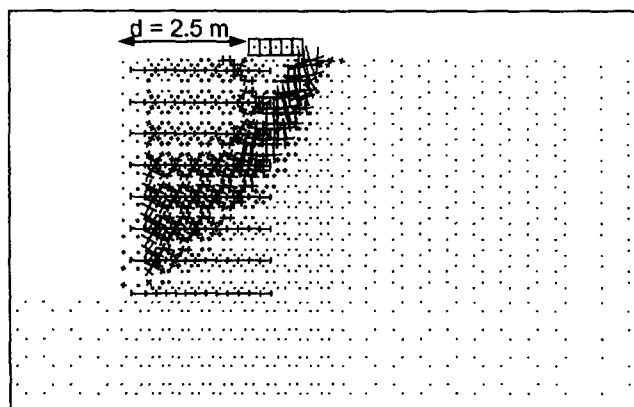


Figure 11. shear strain field ( $\epsilon_1 - \epsilon_3$ ) induced by a top load  $Q=90$  kN/m (scale : 1.5)

In addition, numerical simulations have been performed to investigate the effects of some parameters on the behaviour of reinforced soil wall loaded on the top. The parameters considered included the reinforcement length, the facing stiffness and the point of application of the top load. All of these parameters influence the behaviour of the structure. But the most important geometric parameter is the ratio of the reinforcement length to wall height. For a ratio equal or greater than 0.5 there is no significant increasing on the bearing capacity. It is also found that the reinforcement length has to be extended beyond the potential failure surface developing from the upstream side of the slab to cover the width of the slab load.

## REFERENCES

- Arab R., Villard P, Gourc J.P (1996). Mechanism of Reinforcement from two field trials. *International Symposium on Earth Reinforcement Practice, Kyushu, Japan*, pp. 303 - 308.
- Arab R. (1997). Modélisation des massifs renforcés sollicités localement en tête. Doctorat thesis, University Joseph Fourier of Grenoble.
- Gourc J.P., Gotteland P.H., Haza E., Perrier H., Baraize E. (1995) Geotextile reinforced structures as bridge abutments : full scale experimentation, *Geosynthetics 95, Nashville, USA*, pp. 79-93.
- Ling H.I., Tatsuoka F. (1995). Simulating Performance of GRS-RW by Finite Element Procedure. *Journal of Geotechnical Engineering*. vol.121, n°4, pp. 330-340.
- Helwany M.B., Tatsuoka F., Tateyama M., Kojima K. (1996). Effects of facing rigidity on the performance of geosynthetic-reinforced soil retaining walls. *Soils and Foundation. Japanese geotechnical Society*. vol. 36, n°1, pp. 27- 38.

# Evaluation of Foundation Support for Geosynthetic Reinforced Soil Wall on Sloping Ground

J. Otani

Associate Professor, Department of Civil & Environmental Engineering, Kumamoto University, Kumamoto, Japan

T. Hirai

Manager, Mitsui Petrochemical Industrial Products, Tokyo, Japan

H. Ochiai

Professor, Department of Civil Engineering, Kyushu University, Fukuoka, Japan

S. Shinowaki

Graduate Student, Department of Civil & Environmental Engineering, Kumamoto University, Kumamoto, Japan

**ABSTRACT:** The purpose of the paper is to evaluate the effects of deformation of geosynthetic reinforced soil wall backfill on the bearing resistance of the foundation ground using the results of finite element analysis. Here, the reinforced soil wall constructed on relatively soft sloping ground, which is a real construction site in Japan, is taken into consideration and a series of parametric study is conducted, in which the effects of the condition of foundation ground and a backcut angle behind the reinforced backfill are discussed, and also the effectiveness of soil improvement at the toe of the wall is also evaluated. The conclusions drawn from this study are: (1) the effect of the backcut angle behind the reinforced backfill on the bearing resistance of foundation ground is less, so that this effect does not have to be considered on the design calculation of bearing capacity; and (2) when the foundation ground is relatively soft, the deformation property of the reinforced backfill deeply affects to the reaction at the base of the reinforced backfill. The soil improvement technique at the base of the reinforced backfill is one of the effective methods.

**KEYWORDS:** Bearing Capacity, Finite Element Analysis, Reinforcement, Retaining Walls, Steep Slope

## 1 INTRODUCTION

Applications of geosynthetics to the embankment or retaining wall have been most popular technique among all the earth reinforcement practices around the world. This is because the behavior and failure mechanism of these reinforcing structures have been successfully evaluated under the contributions by many researchers. The results of these researches have been presented in recent international conferences and symposia (e.g. Proceedings edited by Yamanouchi et al., 1988, Ochiai et al., 1992, and Ochiai et al., 1996). But recently, such as in Japan, these applications have been applied to more severe conditions such as relatively soft sloping ground or various backcut angle behind the backfill. And those conditions have to be considered on the stability calculation in order to design these structures safely.

In the current design method, the stress distribution at the base of the retaining soil wall has been assumed by the moment equilibrium with assumption of Coulomb earth pressure theory. However, this distribution is affected by the deformation and strength properties of the reinforced backfill and it also depends on the property of foundation ground. These properties have not been considered in the current design method so far and besides, in-situ conditions at the construction site, e.g. the backcut angle, is variously changed.

The purpose of the paper is to evaluate the effects of deformation of geosynthetic reinforced soil wall backfill on the bearing resistance of the foundation ground using the results of finite element analysis. Here, the reinforced soil

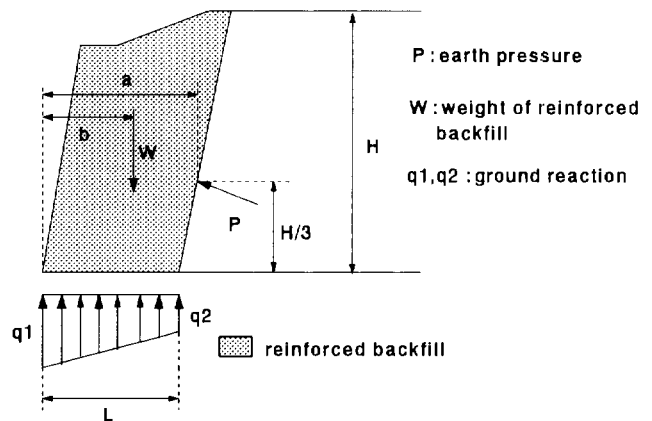


Figure 1. Forces on the reinforced backfill in the design.

wall constructed on relatively soft sloping ground, which is a real construction site in Japan, is taken into consideration and a series of parametric study is conducted, in which the effects of the condition of foundation ground and a backcut angle behind the reinforced backfill are discussed. And also the effectiveness of soil improvement at the toe of the wall is also evaluated.

## 2 CALCULATION OF BEARING RESISTANCE ON CURRENT DESIGN METHOD

Current design calculation of the stability concerning bearing capacity of foundation ground at the base of the reinforced backfill is summarized based on the design

manual by Public Works Research Center(PWRC) in Japan. This design calculation is based on the equilibrium of all the loads subjected to the reinforced backfill as shown in Fig.1. As shown in this figure, the ground reaction at the base of the reinforced backfill is always set to be trapezoidal shape and this is based on the assumption that the ground under the backfill is always rigid and the effect of ground settlement is not evaluated in the design method. As described above, the application of these structures is extended to the relatively soft foundation ground nowadays. When the foundation ground is relatively soft or the backcut angle behind the reinforced backfill is changed, this trapezoidal assumption may not be true and has to be examined. This is a key issue here in this paper and is discussed based on the results of finite element analysis.

### 3 FINITE ELEMENT ANALYSIS

#### 3.1 Problem to be solved

The finite element analysis is conducted for the real construction site in Japan and this is shown in Fig.2(a). The geosynthetic reinforced soil wall was constructed on the sloping foundation with its slope angle of  $25^{\circ}$ . The ground conditions are also shown in the figure and these are summarized as follows:

- For natural ground:
  - a) Ground I: clay with gravel (SPT N-value = 2 - 5);
  - b) Ground II: weathered dacite (SPT N-value = 12 - 50);
  - c) Ground III: dacite (SPT N-value is more than 50).
- For artificial ground:
  - d) Reinforced ground: compacted Ground I;
  - e) Improved ground: improved by cement.

It is noted that the Ground I is a sloping soft ground and the application of soil improvement technique at the toe of the wall was taken into consideration. The geogrid type of reinforcing material was used at the site. As shown in Fig.2(a), there are 11 layers of geogrid and three different types were used (Tensar SR55, SR80 and SR110), in which SR110 was used for the first four layers from the bottom, SR80 for fifth to seventh layers and SR55 for top four layers.

#### 3.2 Method of analysis

In order to evaluate not only 1) the effect of backcut angle behind the reinforced backfill but also 2) that of soil improvement in the ground, a series of finite element analysis is conducted. The method used here is elasto-plastic finite element method using Drucker-Prager failure criterion with non-associated flow rule(Otani et al.,1992). The geogrid type of geosynthetics is modeled by beam element in the analysis with perfectly elasto-plastic assumption. The material properties were determined from material tests in laboratory. The interaction between soil and geogrid is ignored. The soil testings for both in-situ and laboratory have been conducted for the soils at this

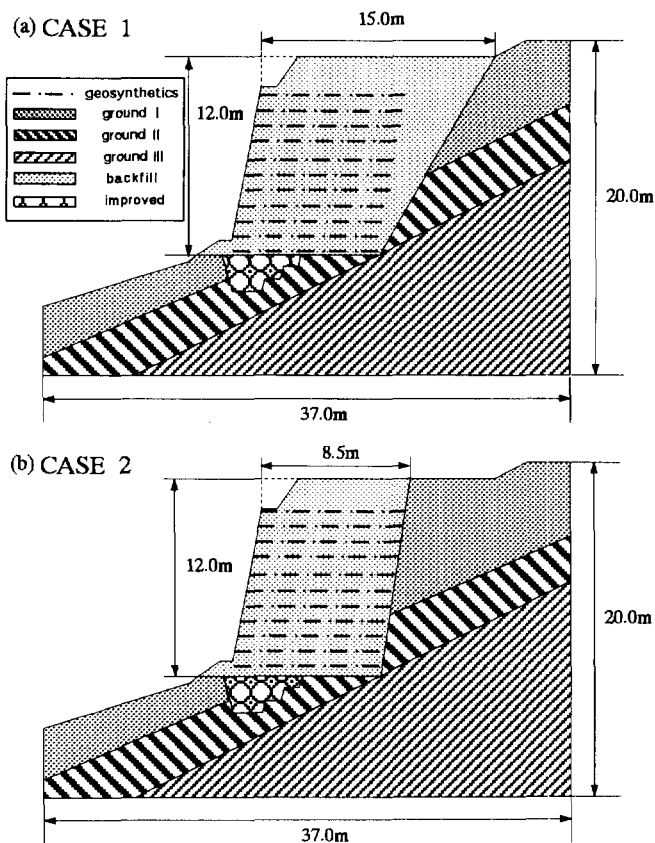


Figure 2. Problems to be analyzed.

construction site, so that the material property of the ground was determined from these testings and is shown in Table 1. In the analysis, the case shown in Fig.2(b) is also analyzed in order to evaluate the effect of backcut angle. The analysis is conducted with loading condition of step-by-step construction of the backfill. It is also noted that the joint element is used between natural slope and the backfill in order to express the discontinuity phenomenon, in which this interaction is modeled as a friction property with setting the shear stiffness of the soil itself in the joint element. The total cases of the analysis are listed as follows:

- CASE 1: ground condition of natural sloping ground as shown in Fig.2(a)
- CASE 1-1: for rigid foundation ground;
  - CASE 1-2: without improvement; and
  - CASE 1-3: with improvement,

- CASE 2: ground condition of natural sloping ground as shown in Fig.2(b)
- CASE 2-1: for rigid foundation ground;
  - CASE 2-2: without improvement; and
  - CASE 2-3: with improvement.

It is noted that the case of rigid foundation is also analyzed for the comparative study and this is conducted by assuming all the natural ground to be Ground III without improvement technique.

Table 1. List of material property of the ground.

	Young's modulus	poisson's ratio	cohesion	friction angle	unit weight
	$E(\text{kN/m}^2)$	$\nu$	$c(\text{kN/m}^2)$	$\phi(^{\circ})$	$\gamma(\text{kN/m}^3)$
ground I	$4.90 \cdot 10^3$	0.30	18.63	29	$1.67 \cdot 10^2$
ground II	$2.94 \cdot 10^4$	0.25	0.00	32	$1.77 \cdot 10^2$
ground III	$2.94 \cdot 10^5$	0.20	0.00	41	$2.62 \cdot 10^2$
backfill	$1.47 \cdot 10^4$	0.40	10.79	23	$1.63 \cdot 10^2$
improved	$5.88 \cdot 10^4$	0.35	95.12	31	$1.73 \cdot 10^2$

4 RESULTS AND DISCUSSION

Figure 3 shows the results of deformation for all the cases, in which CASE 1-1 is shown in Fig.3(a); Fig.3(b) for CASE 1-2; Fig.3(c) for CASE 1-3; Fig.3(d) for CASE 2-1; Fig.3(e) for CASE 2-2; and Fig.3(f) for CASE 2-3. Comparing the results between CASE 1-1 and CASE 1-2 or CASE 2-1 and CASE 2-2, the deformation around the base of the reinforced backfill for the case of rigid foundation is much less than that for the case of without improvement. The lateral deformation is also remarkable for the case of without improvement. But this is improved by the application of soil improvement technique as shown in Fig.3(c) and Fig.3(f). Figure 4 shows the results of both distributions of settlement and vertical pressure beneath the reinforced retaining backfill. Looking at the shape of stress distribution at the base of the

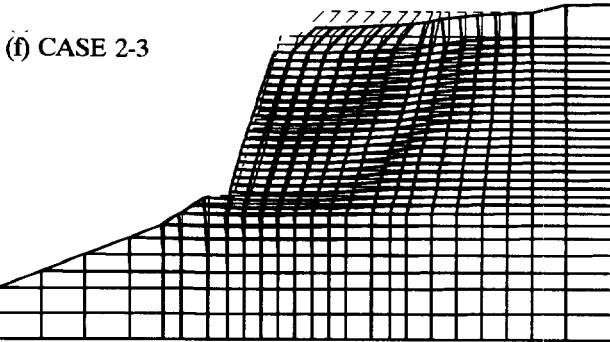
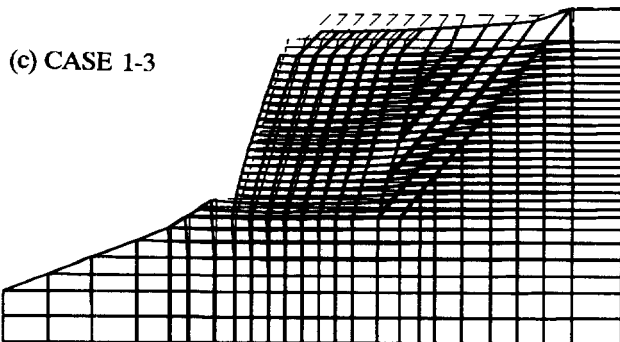
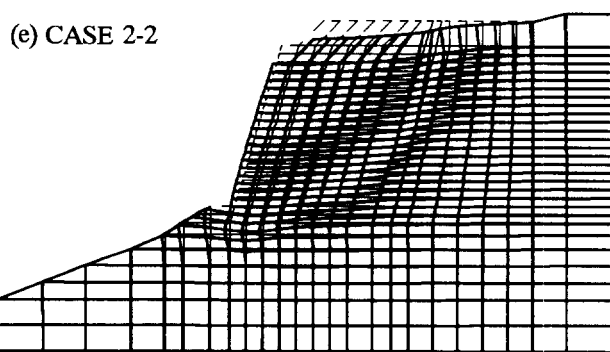
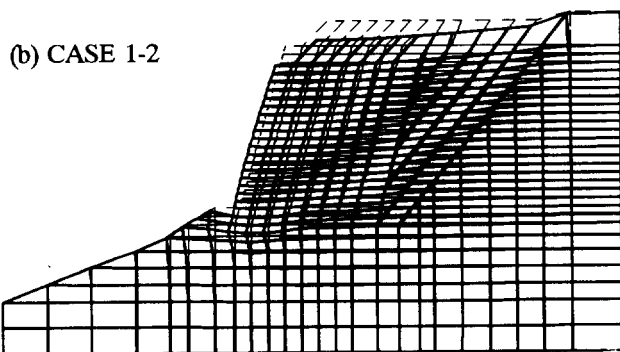
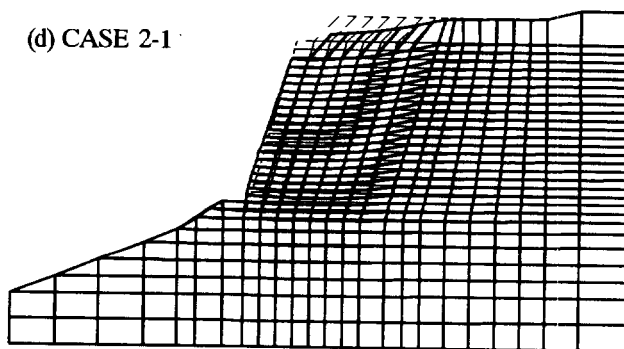
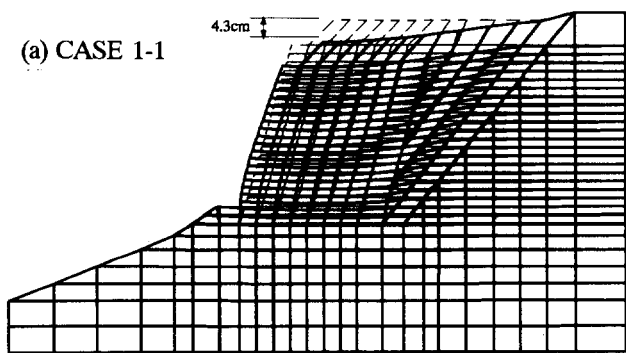
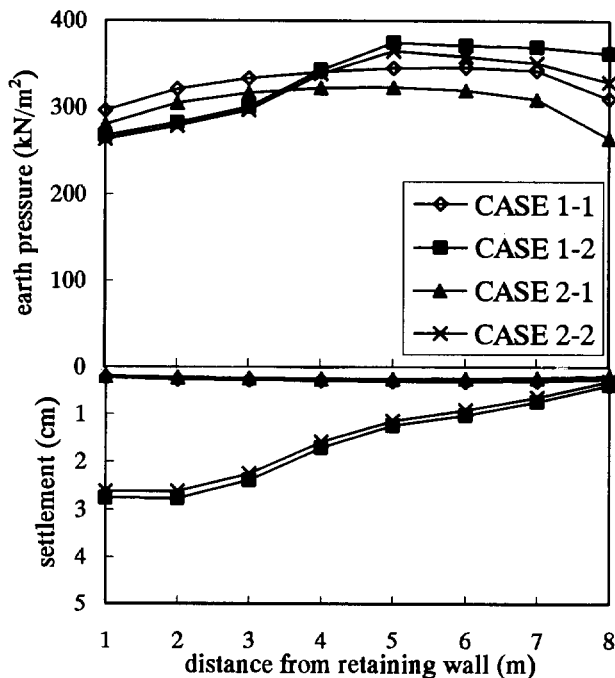


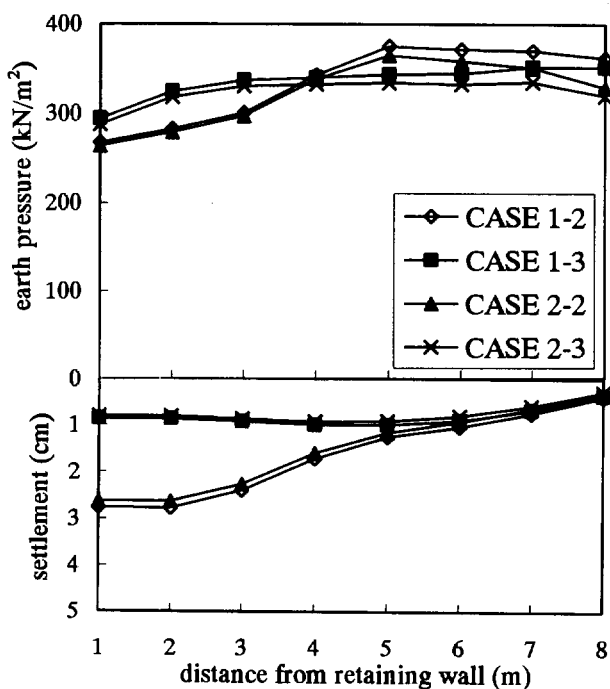
Figure 3. Deformation Property from analysis results.

backfill, it is not always the trapezoidal shape. So that it affects the calculation of overall stability for the reinforced soil wall and this depends on the deformation property of the reinforced backfill. It is also pointed out that not only

the force equilibrium on the reinforced backfill but also the local deformation around the toe of the wall have to be checked for its overall stability. For comparing the effect of slope angle of natural ground behind the reinforced backfill, it is obviously realized that it is not much difference between two cases (CASE 1 and CASE 2).



(a) Effect of rigidity of foundation ground



(b) Effect of soil improvement technique

Figure 4. Distributions of earth pressure and settlement at the base of reinforced backfill.

## 5 CONCLUSIONS

Recently, the earth reinforcement practice has been applied to the cases with more severe conditions such as on relatively soft sloping ground or various backcut angle behind the backfill. These conditions on the bearing capacity of foundation ground were evaluated.

The conclusions drawn from this study are listed as follows:

- (1) The effect of the angle of natural slope behind the reinforced backfill on the bearing resistance of foundation ground is less, so that this effect does not have to be considered on the design calculation of bearing capacity.
- (2) When the foundation ground is relatively soft, the deformation property of the reinforced backfill deeply affects to the reaction at the base of the reinforced backfill. Therefore, this should be considered in the design calculation.
- (3) For overall stability of the reinforced wall on relatively soft sloping ground, not only the force equilibrium on the reinforced backfill but also the local deformation around the toe of the wall should be checked.
- (4) The improvement technique around the toe of retaining wall makes the settlement less and earth pressure equivalent at the base of the reinforced backfill.

The field measurements such as earth pressure and deformation of the reinforced backfill at this site are still on the way at this moment. When the results of this paper is compared with this in-situ measurement, it is promised that the analysis results are quantitatively evaluated.

## REFERENCES

- Ochiai,H.,Hayashi,S. and Otani,J.(1992) "Earth Reinforcement Practice", Balkema, Rotterdam, Netherlands.
- Ochiai,H., Yasufuku,N. and Oomine, T.(1996) "Earth Reinforcement", Balkema, Rotterdam, Netherlands.
- Public Works Research Center (PWRC) (1994) "Design and construction manuals of geotextile-reinforced structures", (in Japanese).
- Otani,J., Ochai,H. and Hayashi,S.(1992) "Restraining effect of geogrid reinforced soil in finite element analysis", IS Kyushu '92, JGS, Fukuoka, Japan, Vol.1, pp.147-150.
- Yamanouchi,T., Miura,N. and Ochiai,H.(1988) "Theory and Practice of Earth Reinforcement", Balkema, Rotterdam, Netherlands.



# PARAMETRIC STUDY FOR GEOSYNTHETIC REINFORCED WALLS UNDER SUSTAINED EARTHQUAKES

**A. Carotti**

Professor, Dept. of Structural Eng., Politecnico di Milano, Milan (Italy)

**P. Rimoldi**

Director, Tenax SpA, Geosynthetics Division, Viganò (Italy)

## Abstract

The Authors propose a newtonian model for the dynamics of geogrid reinforced soil retaining walls, based on a scheme with lumped masses having elastic, viscous and coulombian interactions. The model allows to evaluate the local amplifications by integrating the elasticity and inherent damping with the contribution of the geogrid layers. The aim of the present paper is the drawing, for the different cases analyzed, of design charts which will allow engineers to evaluate the number and characteristics of the geosynthetic reinforcing layers required to satisfy given safety requirements, as a function of the characteristic parameters of the earthquake. A trial-and-error procedure for the seismic analysis of geogrid reinforced walls is outlined.

**Keywords:** Geogrids, Dynamic Mechanical Analysis, Retaining Walls, Seismic Design, Seismic Loads.

## 1. INTRODUCTION

A non-linear multidof newtonian model for the seismic dynamics of slopes and walls on horizontally accelerated bedrock (Carotti and Rimoldi, 1997), is taken as the basic mathematical and computational support for a pseudo-static design procedure for geosynthetic reinforced walls.

From the multidof model, a series of 2-D response spectra and design charts have been obtained; from such plots the following kinematic and mechanical information can be deduced:

- maximum values of the seismic response at the top of the wall;
- spectral values of the active coefficient of earth pressure  $K_{aE}$  under seismic condition.

Based on these charts, a trials-and-errors procedure for checking the seismic feasibility of statically designed reinforcements is presented for various peak accelerations at bedrock and various frequency contents of the accelerogram.

A first major group of parameters are discussed in the present paper; successive developments, which are under way, will take into consideration other characteristics, including the interlayer stiffness and viscous damping.

## 2. NON-LINEAR NEWTONIAN MODEL WITH GEOGRIDS

From laboratory tests (Montanelli and Moraci, 1997), we assume the following mechanical actions between the geogrids and the soil layers on top and bottom, as a consequence of the soil-geogrid interlocking:

1. an increase of the interlayer soil stiffness, proportional to the elastic stiffness of the geogrids. From monotonic tensile tests on geogrids (Fig. 1) the load-strain curve has been reduced to a tri-linear curve and the stiffness value in each linear segment have been identified. We have focused the attention on the 1<sup>st</sup> stage, with strain threshold  $\epsilon_1 = 0.03$ . If  $L_g$  is the geogrid length in the direction of the seismic acceleration,  $F$  is the tensile force applied to the geogrid and  $\Delta l$  its elongation, we postulate that, in condition of interlocking between the geogrids and the soil layers, the contributed inter-layer stiffness is:

$$K_{gi} = \frac{F}{\Delta l} = \frac{F}{\epsilon_1 \cdot L_g} \quad (1)$$

2. An increase of the interlayer viscous damping force, equal to the inherent viscous damping of the geogrid. From sinusoidal cyclic tests (Montanelli and Moraci, 1997) with frequency  $f = 1.0$  Hz (see Fig. 2) and from the examination of an average elliptical cycle, the average viscous force  $F_{vinc}$  (force in counterphase

to the velocity, when the displacement is nil) has been obtained, together with the value of the peak velocity (product of the peak displacement, obtained from the test plot, and of the circular frequency  $\omega = 2\pi f$  of the test). From the ratio force/velocity the damping coefficient is immediately obtained. In details :

$$C_{gi} = \frac{F_{visc}}{\Delta l \cdot \omega} = \frac{F_{visc}}{\epsilon \cdot L_g \cdot \omega} \quad (2)$$

where  $\Delta l$  is the differential interlayer displacement ( $x_i - x_{i-1}$ ), when perfect interlocking between soil and geogrid has been assumed.

3. An increase of the interlayer damping due to the friction between the geogrid and the soil layers, under the weight of the soil. The frictional damping due to the i-th geogrid (where N is the number of geogrid layers) is:

$$F_{Ci} = -tg \phi_{sg} \cdot g \cdot \sum_{k=i}^n M_k \cdot sign(\dot{x}_k) \quad (3)$$

where the signum function  $sign(\dot{x}_k)$  introduces the non linearity in the model. The direction of the frictional force is determined by the sign of  $\dot{x}_k$ . In Eq. (3)  $\phi_{sg}$  is the soil-geogrid interface friction angle; g is the gravity acceleration.

The Newtonian equations of motion for the N-DOF non-linear model with geogrids (N soil layers with N geogrid layers) can be obtained taking into account the elastic stiffness  $K_{gi}$ , the viscous damping  $C_{gi}$  and the Coulomb-type friction force  $F_{Ci}$  induced by the geogrids, defined in Eq.s (1)÷(3).

Indicating with  $\hat{M}$  the distributed load on top of the wall, the Newtonian equation of motion for the i-th layer is:

$$M_i \cdot \ddot{x}_i = -K_i(x_{i-1} - x_i) - C_i(\dot{x}_{i-1} - \dot{x}_i) + K_{i+1}(x_i - x_{i+1}) + C_{i+1}(\dot{x}_i - \dot{x}_{i+1}) - K_i(x_{i+1} - x_i) - C_i(\dot{x}_{i+1} - \dot{x}_i) + K_{i+1}(x_i - x_{i+1}) + C_{i+1}(\dot{x}_i - \dot{x}_{i+1}) + tg \phi_{sg} \cdot g \cdot \left( \sum_{k=i}^n M_k + \hat{M} \right) sign \dot{x}_i - tg \phi_{sg} \cdot g \cdot \left( \sum_{k=i+1}^n M_k + \hat{M} \right) \cdot sign \dot{x}_{i+1} = -M_i \cdot \ddot{x}_i \quad (4)$$

where  $g \cdot \left( \sum_{k=1}^n M_k + \hat{M} \right)$  represents the total gravity load acting on the i-th geogrid layer.

### 3. CONTROL OF DYNAMIC EQUILIBRIUM FOR GEOGRID REINFORCED WALLS

The steady dynamic equilibrium for a 1-DOF (one Degree Of Freedom) linear oscillator under sinusoidal resonant excitation is described in Fig. 3, where the inertia force is balanced - at maximum displacement

- by the elastic recalls.

In this non-linear model (see Carotti and Rimoldi, 1997), the contribution of the friction force to the equilibrium (at maximum displacement) of the i-th reinforced layer of the wall must be taken into consideration.

In the present research, a geogrid reinforced earth wall is assumed, with a cohesionless backfill and possible permanent surcharge loads on the top surface; the vertical spacing  $S_v$  of the geogrids and the overall length L are taken as constant.

Here the following hypotheses are introduced:

- the static earth pressure  $P_{st}$  is balanced even in seismic conditions by the friction  $F_{C_i}$  and by the tensile strength  $T_{g_i}$  of the geogrids;
- in seismic conditions, the forces  $F_{C_i}$  furtherly provide an increase of damping, the forces  $T_{g_i}$  provide an increase in terms of damping and stiffness;
- the dynamic earth pressure  $Pa_d$  can be obtained through the superposition of effects of the static earth pressure  $Pa_s$  and the seismic earth pressure  $Pa_{ge}$  (suffix "G" for geogrids and "E" for earthquake):

$$Pa_d = Pa_s + Pa_{GE} \quad (5)$$

- The earth pressures can be described with the Rankine type equations:

$$Pa_d = \frac{1}{2} Ka_d \gamma H^2 \quad (6)$$

$$Pa_s = \frac{1}{2} Ka_s \gamma H^2 \quad (7)$$

$$Pa_{GE} = \frac{1}{2} Ka_{GE} \gamma H^2 \quad (8)$$

Therefore :

$$Pa_d = \frac{1}{2} (Ka_s + Ka_{GE}) \gamma H^2 \quad (9)$$

and :

$$Kad = Ka_s + Ka_{GE} \quad (10)$$

- due to the previous hypothesis, the dynamic forces can be studied independently from the static ones; therefore now on only the equilibrium of the dynamic forces will be considered.

The conditions of dynamic equilibrium and the mechanical interaction between the two adjacent layer, (i-1)-th and i-th, are described in Fig. 3, which gives an imagine at maximum displacement (zero velocity) of the wall. Being in conditions of zero velocity, at this point of time the viscous damping force  $F_v$  is zero.

As said above, only the dynamic forces are

considered here, without the static earth pressure  $P_{a_i}$ .  
 Let  $F_{IN_i}$ ;  $F_{e_{(i-1)}}$ ;  $F_{e_i}$  represent, respectively, the overall inertia force and the elastic recalls above and under the  $i$ -th layer; and let  $F_{c_{(i-1)}}$ ;  $F_{c_i}$ ;  $P_{agE_i}$  represent the upper and lower Coulomb friction force, and the active earth pressure due to the  $i$ -th layer.

With the assumption that the 1<sup>st</sup> modal shape is dominating (Carotti and Rimoldi, 1997), then all the displacements of the single layers are in phase. Hence we can assume that there is a balance between the elastic recall forces of the soil itself: therefore  $F_{e_i}$  is almost equal to  $F_{e_{(i-1)}}$  and computationally they can be neglected.

Under these hypotheses, in condition of dynamic equilibrium we have (see Fig. 3):

$$P_{axE_i} = F_{IN_i} + T_{g_i} \quad (11)$$

$$F_{IN_i} = -M_i \cdot \ddot{x}_{v2}$$

where  $T_{g_i}$  is the tensile strength in the geogrid under the  $i$ -th soil layer (see Fig. 3):

$$T_{g_i} = F_{c_i} \quad (12)$$

When the expression of Eq. 8 is introduced, a pseudo-static expression for the coefficient of active earth pressure  $K_{agE}$  under seismic excitation can be obtained:

$$K_{agE} = \frac{2 \cdot P_{agE}}{\gamma \cdot H^2} \quad (13)$$

#### 4. PRELIMINARY PARAMETRIC DISCUSSION

The following design parameters has been taken into consideration for discussing the effects of geosynthetic reinforcement on the seismic response of the wall.

##### a) Soil:

$$\gamma = 18 \text{ kN/m}^3 ; \phi = 25^\circ - 40^\circ ; c = 0$$

$$\text{shear modulus } G = 10^4 \text{ kN/m}^2 ;$$

$$H = 3 \text{ m} - 6 \text{ m} - 9 \text{ m}.$$

The first three natural frequencies and damping ratios for the 3 m and 6 m high walls, without reinforcements, are given in Table 1.

Tab. 1 - Natural frequency  $f$  and damping ratio  $\xi$  for some of the walls considered in the parametric study.

	H = 3 m.		H = 6 m.	
	f (Hz)	$\xi$ (%)	f (Hz)	$\xi$ (%)
1st mode	5.63	4.9	2.95	1.3
2nd mode	14.43	14.3	8.8	3.8
3rd mode	25.89	22.6	14.45	6.3

##### b) Geogrids:

We have considered the geometrical and mechanical characteristics of the TENAX TT401 Samp mono-oriented geogrid, which have the following properties:

$$\text{Unit weight: } w = 0.77 \text{ Kg/m}^2$$

$$\text{Polymer density: } \rho = 0.950$$

$$\text{Tensile strength: } T = 80 \text{ kN/m}$$

$$\text{Elongation at peak: } \varepsilon_{peak} = 13\%$$

$$\text{Strength at 2\% strain: } T_{2\%} = 26 \text{ kN/m}$$

$$\text{" " 5\% " : } T_{5\%} = 48 \text{ kN/m}$$

Taking into consideration the cross sectional area of the longitudinal stretched rib of the geogrids:  $A_r = 1.6 \text{ mm} \times 6.5 \text{ mm} = 10.4 \text{ mm}^2$ , and a number of 50 ribs/m, the resistant section is:  $Ar = 5.2 \times 10^{-4} \text{ m}^2/\text{m}$ :

And therefore,

$$\sigma_{peak} = T/Ar = 154 \text{ MPa}$$

$$E_{peak} = \sigma_{peak} / \varepsilon_{peak} = 1185 \text{ MPa}$$

$$\sigma_{2\%} = T_{2\%} / Ar = 50 \text{ MPa}$$

$$E_{2\%} = \sigma_{2\%} / 0.02 = 2500 \text{ MPa}$$

Other data used in the model are:

- soil-geogrid interface friction angle:

$$\phi_{sg} = \arctan(\tan \phi / f_{ds})$$

where the direct shear factor  $f_{ds}$  has been assumed equal to 0.80;

- constant vertical spacing:  $S_v = 0.6 \text{ m}$ ;

- geogrid length:  $L = 0.5 H - 1.0 H$

where  $H$  is the wall height.

##### c) bedrock excitation:

the following classes of acceleration time histories have been implemented:

c1) a stationary gaussian zero-means white noise, low-pass filtered with fixed bandwidth (0,5 Hz) and variable peak acceleration, varying between 0.1 g to 1.1 g.

c2) as above but with parametrically fixed peak acceleration  $a_g = 5 \text{ ms}^{-2}$  and variable bandwidth: all the bandwidths considered have the same left cut-off frequency (zero Hz) and different right cut-

off frequencies, ranging from 1 Hz to 10. By this way the effects of many historic earthquakes can be modelled and simulated: from very low frequency “near-fault” earthquakes, to earthquakes with increasingly wider bandwidths as the San Salvador (1986), Mexico City (1985) and El Centro (1940) records.

Using these types of bedrock excitation it is possible to obtain the following spectra:

**1. spectra under excitation c1:** spectra of top relative displacement and top absolute acceleration of active earth pressure coefficient  $K_{agE}$  and the overall active earth pressure  $P_{agE}$  for two different geogrid lengths, are given in Figg. 4, 5, 6. Such spectra are obtained by plotting the maximum value of the response quantity (extracted from the time history) vs the peak acceleration of the bedrock.

The family of parabolic curves are monotonically increasing with the base peak acceleration. Both  $K_{agE}$  and  $P_{agE}$  decrease with increasing geogrid length  $L$ .

**2. spectra under excitation c2:** spectra as above vs variable bandwidth of the bedrock acceleration, are given as well in Fig. 4, 5, 6, respectively for the 3 m, 6m, 9m high walls. The amplification effect when the seismic bandwidth includes the natural frequencies of the wall (see Tab. 1) is evident: spectra show the possibility of controlling such amplifications by means of geogrid reinforcements of variable lengths.

Note 1: the 1<sup>st</sup> mode of vibration is dominating in reinforced soil structures. Hence resonance occurs around the frequency of the 1st mode (compare Figg. 4, 5 with Tab.1).

Note 2: For soil without geogrids, in order to stress the influence of geogrids, the model has taken into account only the viscous damping and not the Coulombian one (which has been accounted for in the model with geogrids). As a consequence the model for soil alone is not sensitive to the parameter  $\phi$  (in favour of safety); hence in the charts all the curves without geogrids are the same. This limitation will be eliminated in the future developments of the model.

## 5. DESIGN CHARTS FOR GEOGRID REINFORCED WALLS IN SEISMIC CONDITIONS

The analysis has been extended to the ranges of practical interest of the main soil and geogrid parameters. Design charts are given in Figures 4, 5 and 6. The following procedure can be used for the seismic analysis of geogrid reinforced walls:

**STEP 1:** design the reinforced block in static conditions. Adopting, as example, the “tie-back wedge” method, the following three parameters shall be determined :

- minimum length of geogrids  $L_{min}$ ,
- vertical spacing  $S_v$ ,
- overall number of geogrids:  $n_{grid}$ .

**STEP 2:** the seismic input is established. At first, a standard 0 - 5 Hz bandwidth and variable peak acceleration are assumed (characteristic statistical parameters of the time record, including RMS, crest-factor and variance, can be imposed),

**STEP 3:** the design charts in Figg. 4 - 6 are then entered and the seismic active pressure coefficient  $K_{agE}$  is obtained.

**STEP 4:** the dynamic earth pressure coefficient  $K_{ad}$  is determined with Eq. 10; then the stability analysis of Step 1 is re-calculated with reference to  $K_{ad}$  and allowing for a reduction of the safety factor FS according to each National Code (usually a 20% reduction of FS is envisaged in the seismic Codes for earthworks, e.g.: a reduction from 1.3 to 1.06 of the  $FS_{\text{overturning}}$ ; a  $FS_{\text{pullout}}$  reduction from 1.5 to 1.2 etc.)

**STEP 5:** if any of the before mentioned checks at Step 4 are not satisfied, then by a trials-and-errors procedure the following corrections may be introduced:

- increase the number of geogrids and/or the geogrids length  $L$ ,
- with these new values, the design procedure starting from Step 3 is repeated,
- as long as all the checkouts are satisfied.

**STEP 6:** the sequence from Step 2 to Step 5 can be repeated for a different choice of the seismic input.

If the effects of variable bandwidths and fixed peak-acceleration must be investigated, spectra at the bottom in Figures 4 -6 will be considered.

## REFERENCES

Carotti A., Rimoldi P., (1997) “Time and Frequency Domain Analysis for the Seismic Design of Geogrid-Reinforced Soil Slopes and Walls”, Proceedings of Geosynthetics '97 Conf., Long Beach, Ca (USA).

Montanelli F., Moraci N. (1997) “Behaviour of Geogrids under cyclic loads”, Proc. Geosynthetics '97 Conf., Long Beach, California, USA.

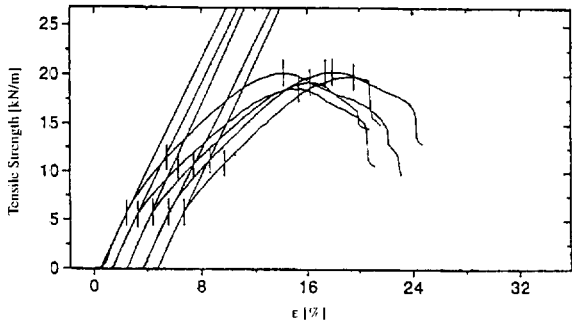


Figure 1: Scheme of the mechanical interaction between soil layers and geogrids in conditions of dynamic equilibrium at maximum displacement (from Carotti and Rimoldi, 1997).

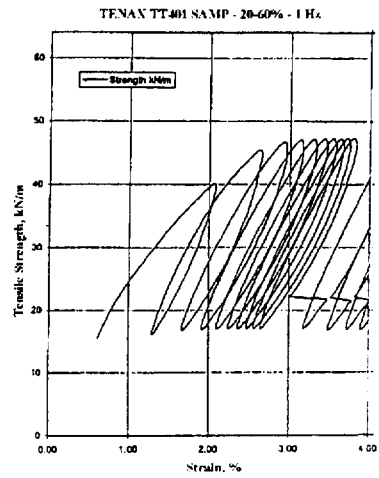
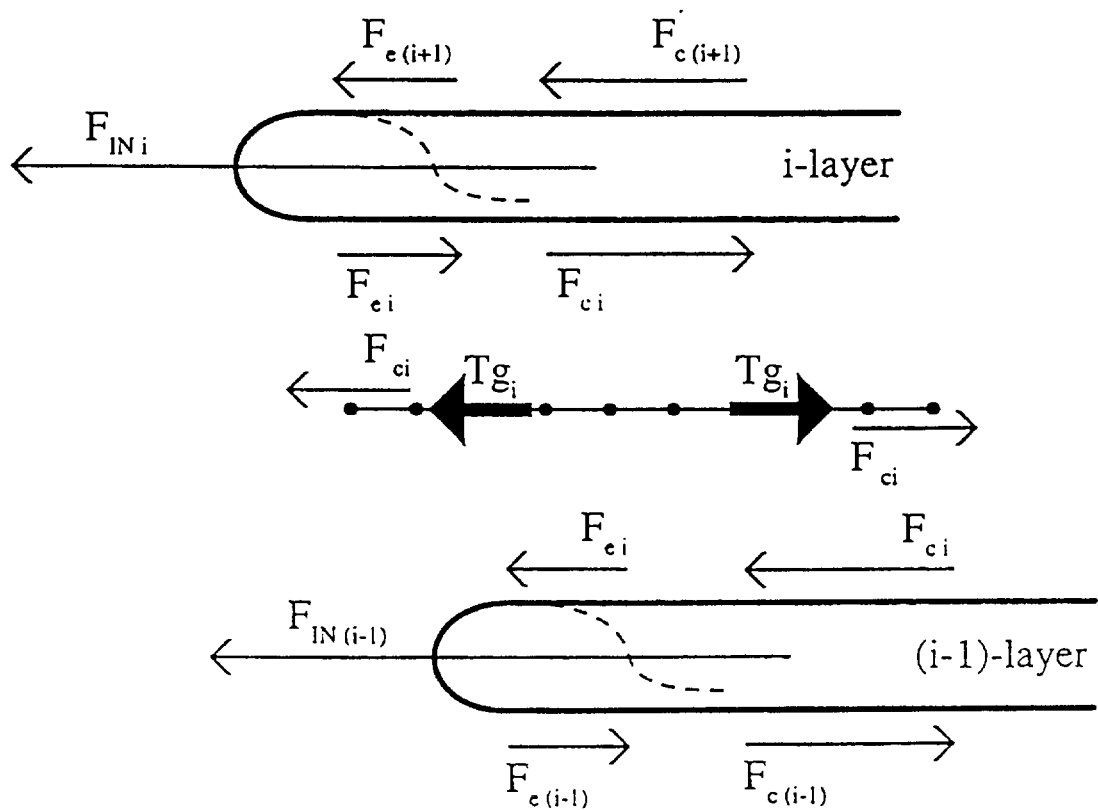


Figure 2: A cyclic tensile test for a typical HDPE geogrid (from Carotti and Rimoldi, 1997).



Force field at maximum displacement:  
 $F_e$  = Interlayer elastic recall force field  
 $F_c$  = Interlayer coulombian friction force field  
 $F_{IN}$  = Inertial force field

Figure 3: Scheme of the mechanical interaction between soil layers and geogrids in conditions of dynamic equilibrium at maximum displacement.

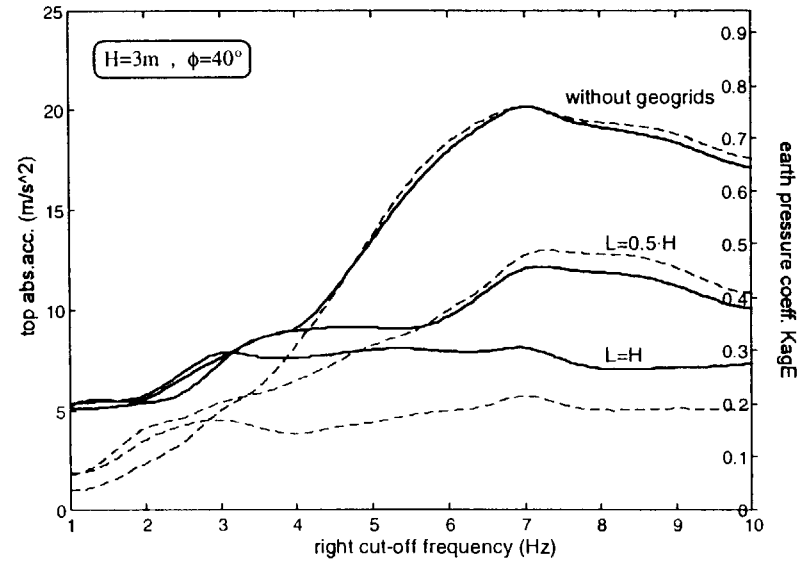
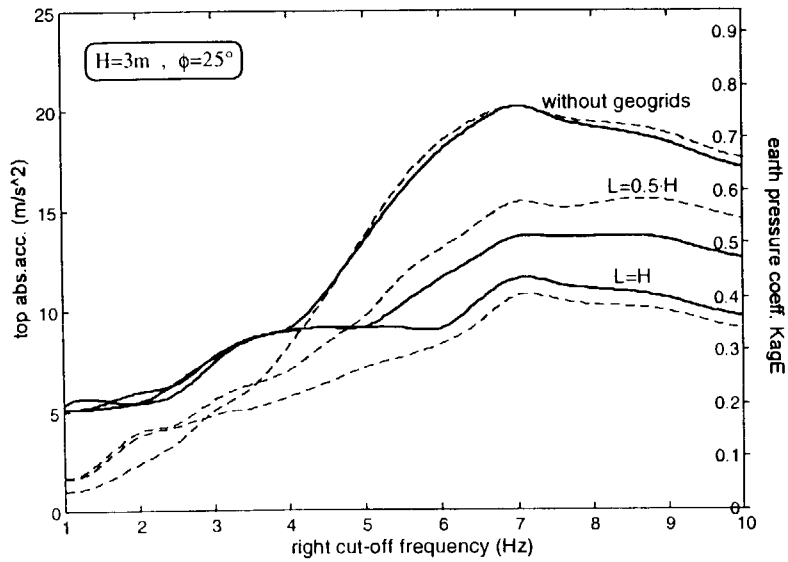
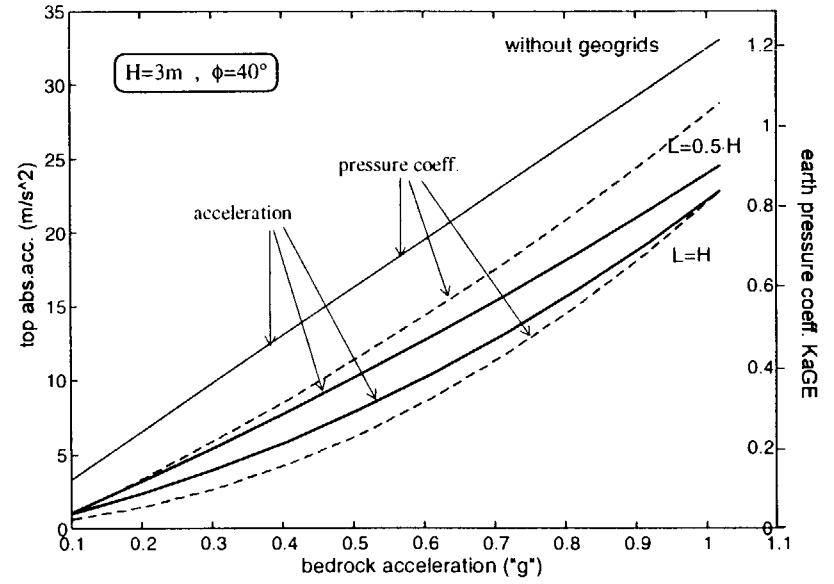
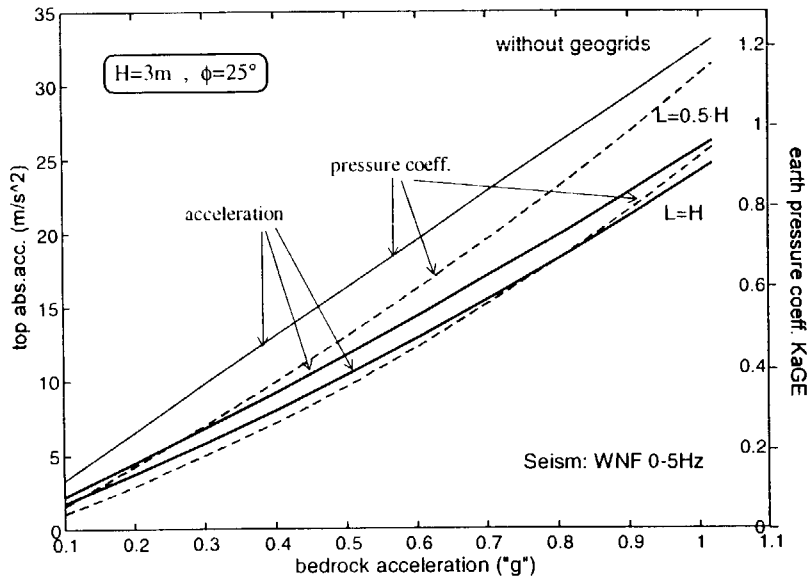


Figure 4 : Design charts for a 9.0 m high wall.

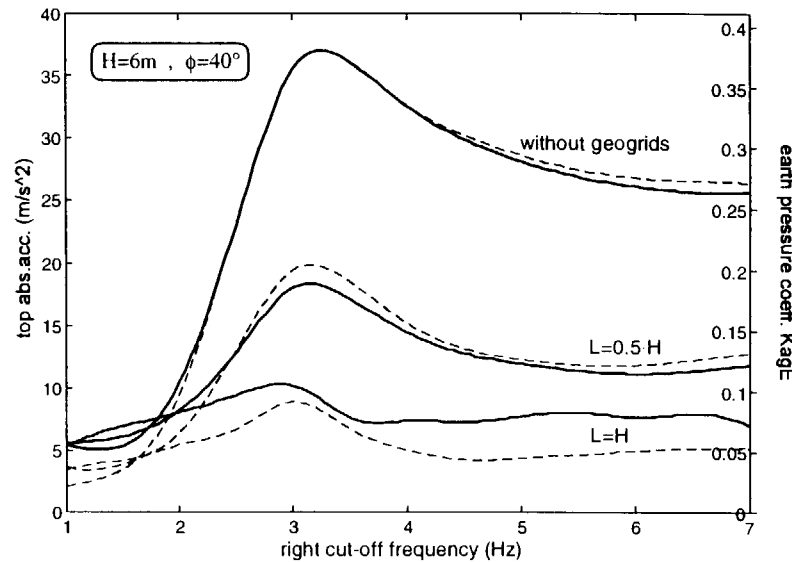
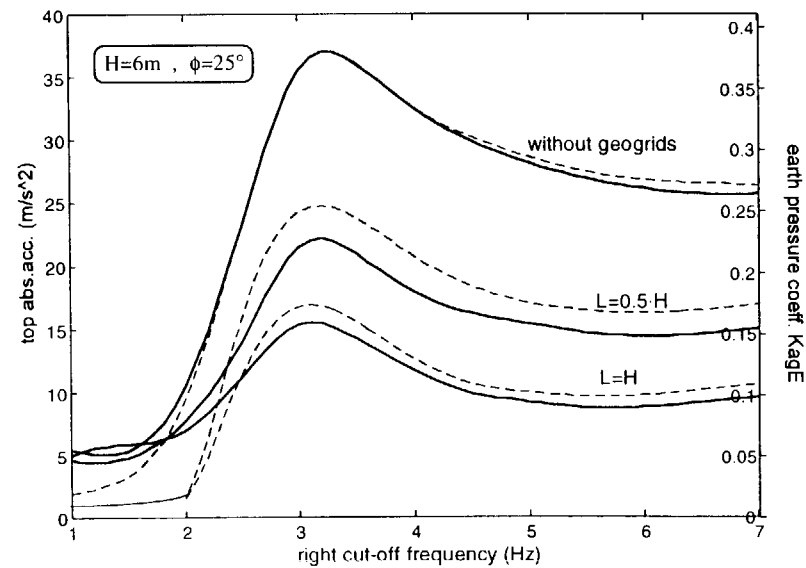
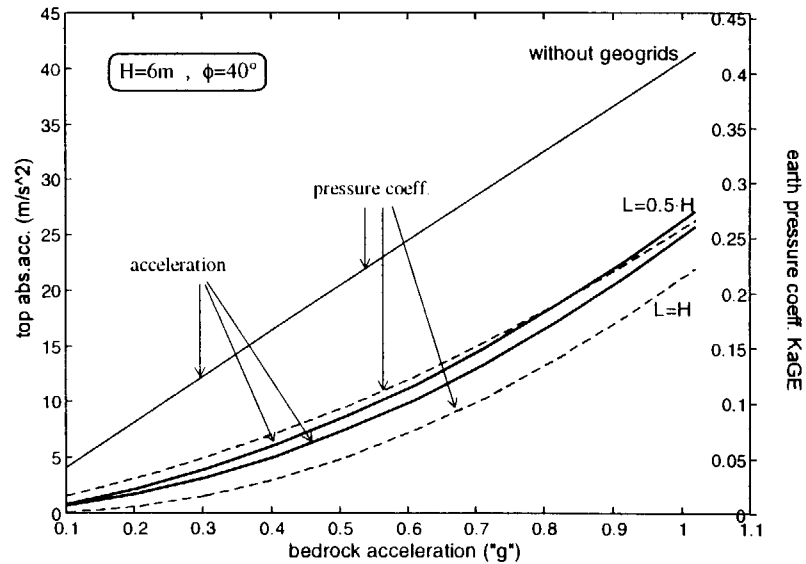
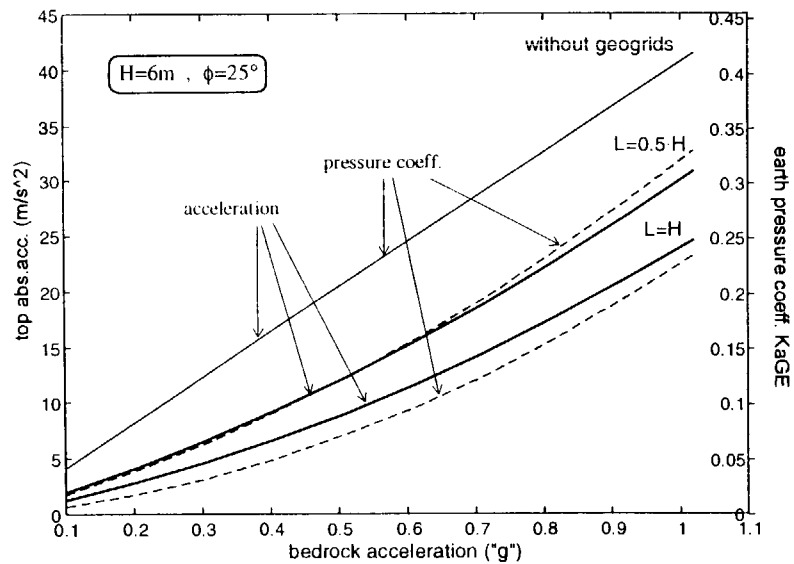


Figure 5 : Design charts for a 6.0 m high wall.

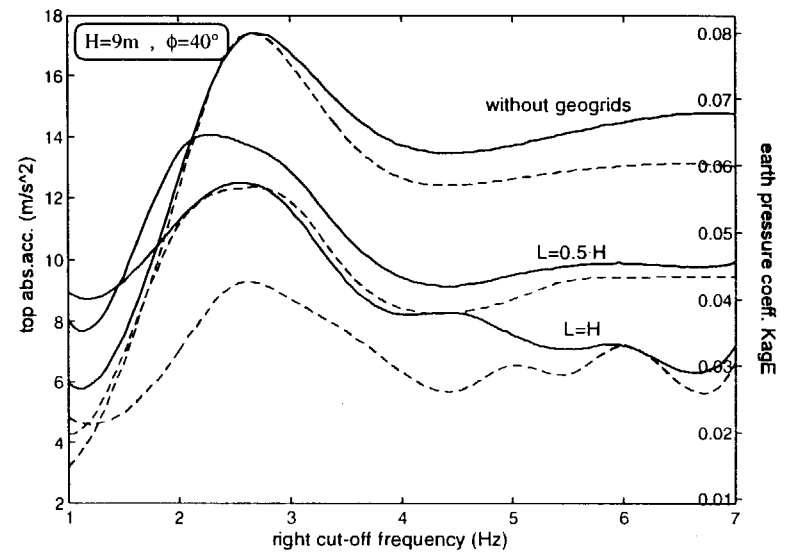
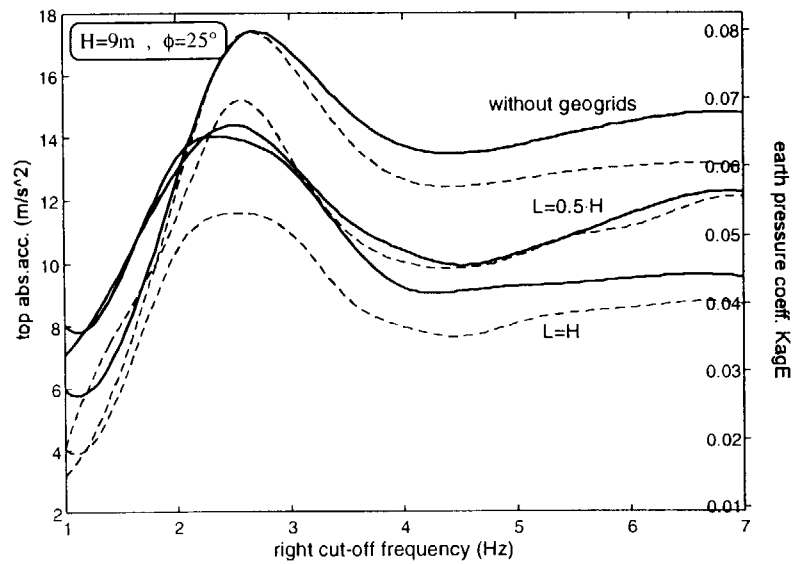
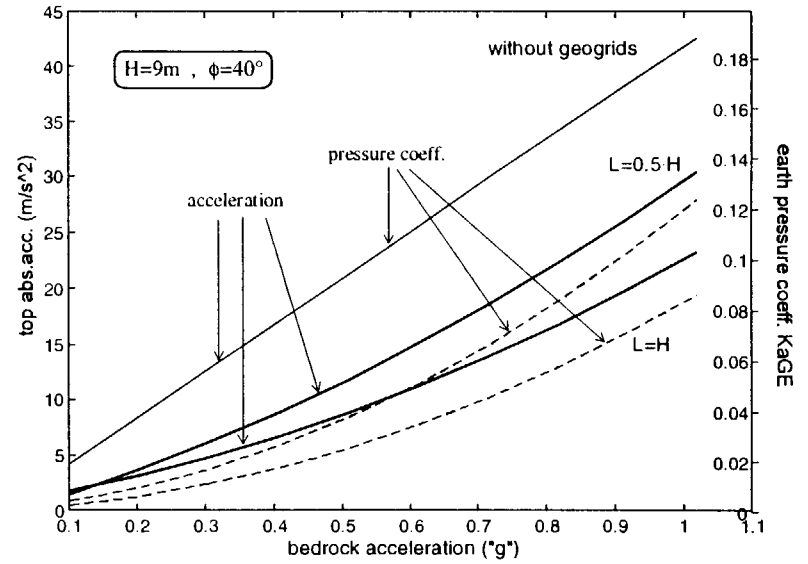
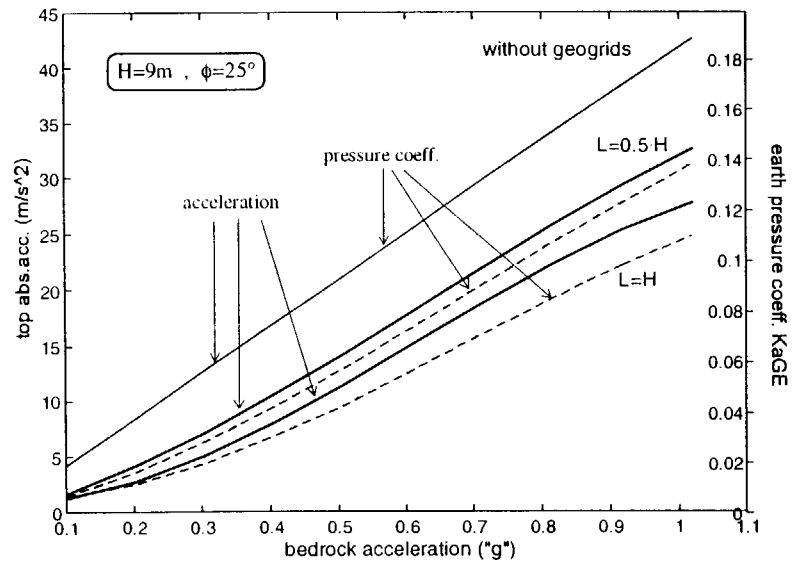


Figure 6 : Design charts for a 9.0 m high wall.



# Influence of Reinforcement Stiffness, Length and Base Condition on Seismic Response of Geosynthetic Reinforced Retaining Walls

R.J. Bathurst

Professor, Department of Civil Engineering, Royal Military College of Canada, Kingston, Ontario, Canada

K. Hatami

Research Associate, Department of Civil Engineering, Royal Military College of Canada, Kingston, Ontario, Canada

**ABSTRACT:** The paper reports selected results from a set of numerical experiments that were carried out to investigate the influence of reinforcement stiffness, length and base boundary condition on the seismic response of a geosynthetic reinforced full-height panel wall. The two-dimensional explicit finite difference program FLAC was used to carry out the numerical experiments. The paper illustrates how program FLAC may be a useful research tool to corroborate current empirical guidelines for the pseudo-static analysis and design of geosynthetic reinforced wall structures or to propose new guidelines. For example, the numerical results illustrate that the dynamic response of the simulated walls is very sensitive to base foundation condition.

**KEYWORDS:** Retaining walls, Geosynthetic reinforcement, Seismic analysis, Finite difference, Parametric study.

## 1 INTRODUCTION

In North America, geosynthetic reinforced soil walls are routinely designed using pseudo-static limit-equilibrium methods for sites with peak horizontal ground accelerations  $\leq 0.29g$ . A limitation of pseudo-static methods is that they cannot consider the effect of duration of seismic loading, acceleration amplification through the backfill soil, and foundation condition on the development of reinforcement loads and structure deformations (Bathurst and Alfaro 1996; Bathurst and Cai 1995). The results presented in this paper are part of an ongoing project directed at understanding the dynamic response of geosynthetic reinforced wall structures due to earthquake. The results presented in this paper show that the two-dimensional explicit finite difference program FLAC may be a useful tool to investigate the seismic performance of reinforced wall structures. Ultimately, numerical simulation results of the type demonstrated here may be used to verify or modify currently accepted pseudo-static design methods.

## 2 MODEL

The example walls were chosen to have the same height and number of uniformly spaced reinforcement layers as the base case example reported by Rowe and Ho (1992) (Figure 1). A preliminary set of static analyses were carried out using the same geometry, material properties and reinforcement layout as that reported by Rowe and Ho to confirm that FLAC (version 3.30) analyses for the end of construction loading case give similar results to their finite element analyses. However, boundary conditions were then modified for the current study to accommodate the need for a larger mesh and other details related to the two different foundation conditions investigated.

Each wall was modeled as a continuous panel with a height of 6.0 m and a width of 0.14 m. The bulk and shear moduli of the wall were  $K_w = 20,000$  MPa and  $G_w = 10,000$  MPa, respectively. The wall was hinged at its toe using beam elements. The soil was modeled as a purely frictional elastic-

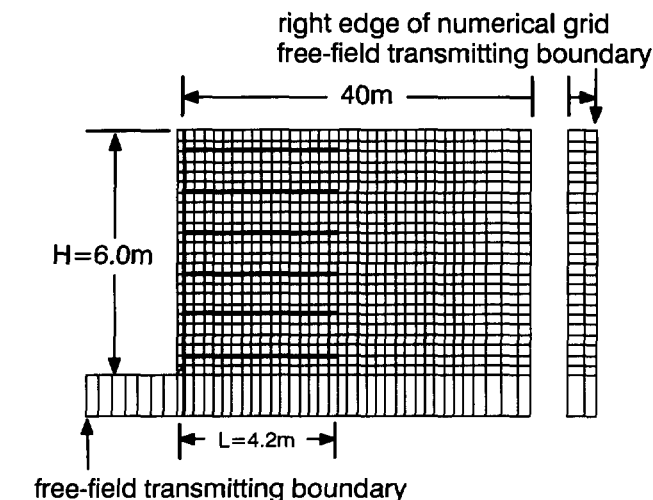


Figure 1. Numerical grid for example problem with fixed base condition.

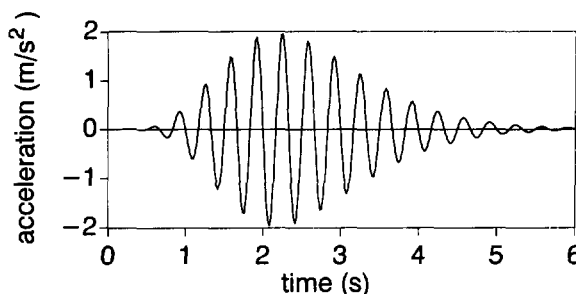


Figure 2. Base acceleration-time history.

plastic material with a Mohr-Coulomb failure criterion and non-associated flow rule. The friction angle of the soil was  $\phi = 35^\circ$ , dilatancy angle  $\psi = 6^\circ$  and unit weight  $\gamma = 20$  kN/m<sup>3</sup>. The bulk and shear moduli of the soil were  $K_s = 27.5$  MPa and  $G_s = 12.7$  MPa, respectively.

A uniformly spaced reinforcement was considered in the model. The reinforcement was modeled using linear elastic cable elements with negligible compressive strength and an equivalent cross-sectional area of  $0.002 \text{ m}^2$ . The stiffness of the reinforcement ( $J$ ) was a variable in this set of parametric analyses. The tensile yield strength of the reinforcement was  $T_{\text{yield}} = 200 \text{ kN/m}$  to ensure that reinforcement rupture was not a failure mechanism.

The interface between the reinforcement (cable elements) and the soil was modeled by a grout material of negligible thickness with interface friction angle  $\delta_g = 35^\circ$ . The bond stiffness and bond strength of the grout model were taken as  $k_{\text{bond}} = 2 \times 10^6 \text{ MN/m/m}$  and  $s_{\text{bond}} = 10^3 \text{ kN/m}$ , respectively. The interface and grout properties were selected to simulate a perfect bond between the soil and reinforcement layers. The soil-wall and soil-foundation interfaces (for the sliding wall cases) were modeled using a thin soil layer of  $0.05 \text{ m}$  thick. However, the friction angle of the interface layer between the reinforced soil and the panel wall was set to  $\phi_{\text{int}} = 20^\circ$  and the dilatancy angle to  $\psi_{\text{int}} = 0^\circ$ .

The numerical grid was selected to represent an infinitely wide region. To achieve this condition the soil region was extended to  $40 \text{ m}$  beyond the back of the wall and a *free field* boundary condition was applied at the truncated boundaries at the left and right edges of the grid to allow for the radiation of elastic waves to the far field.

The soil and reinforcement elements were constructed in layers while the panel wall was braced horizontally. The propped panel supports were then released in sequence from the top of the structure as reported by Rowe and Ho. After static equilibrium was achieved, the full width of the foundation was subjected to the acceleration history illustrated in Figure 2.

Table 1. Numerical simulation configurations.

Test	Base condition	L/H	J (kN/m)
1	fixed	0.7	500
2	fixed	0.7	1000
3	fixed	0.7	2000
4	sliding	0.7	500
5	sliding	0.7	1000
6	sliding	0.7	2000
7	fixed	1.0	500
8	fixed	1.0	1000
9	fixed	1.0	2000
10	sliding	1.0	500
11	sliding	1.0	1000
12	sliding	1.0	2000

### 3 PARAMETRIC ANALYSES

The test configurations considered in the current investigation are summarized in Table 1. The base foundation condi-

tion was either fixed (i.e. the toe of the wall was slaved to the foundation but was free to rotate) or free to slide horizontally along a thin  $0.05 \text{ m}$  thick layer of soil and rotate about the toe. The stiffness ( $J$ ) and length ( $L$ ) of the reinforcement were also varied as shown in the table. The synthetic horizontal acceleration record shown in Figure 2 was applied to nodes along the entire base of the numerical grid at equal time intervals of  $\Delta t = 0.05 \text{ s}$ . The accelerogram simulates a ground motion with both increasing and decaying peak acceleration portions. The peak amplitude of the input acceleration was  $0.2g$  with a dominant frequency of  $3 \text{ Hz}$  which is typical of medium to high-frequency content earthquakes. A mass proportional damping of  $\zeta = 0.05$  was assumed for the model. The total duration of the input excitation was limited to  $6 \text{ seconds}$  in order to minimize computational time.

## 4 RESULTS

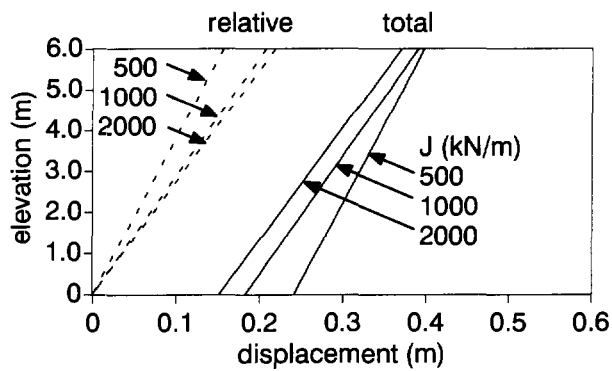
### 4.1 Wall Displacements

Wall displacements predicted at the end of the excitation period are shown in Figure 3. For the same base condition, the *total* wall deflections diminish with increasing reinforcement stiffness. Similarly, for the same base condition and reinforcement stiffness, there is less total wall displacement for  $L/H=1.0$  compared to configurations with  $L/H=0.7$ . However, the plots show that for the range of reinforcement stiffness values used, the base condition (fixed or sliding) has a greater influence on wall deflection than the magnitude of reinforcement stiffness. In addition, the *relative* wall deflections taken with respect to the wall toe are less for the sliding foundation case than for the fixed toe case.

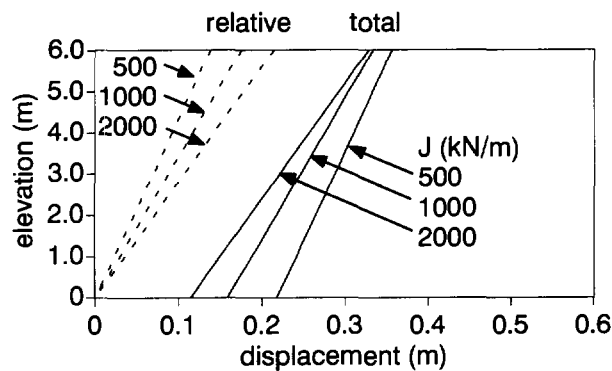
### 4.2 Reinforcement Forces

In general, reinforcement forces were observed to accumulate with duration of seismic shaking. Figure 4 shows the relative distribution of axial forces in the reinforcement layers at the end of the  $6 \text{ second}$  acceleration record. The reinforcement forces at the connections were almost always greater than the internal reinforcement forces at all stages of the numerical experiments including end of construction. This trend can be attributed to the relative downward movement of the reinforced soil zone relative to the continuous wall panel.

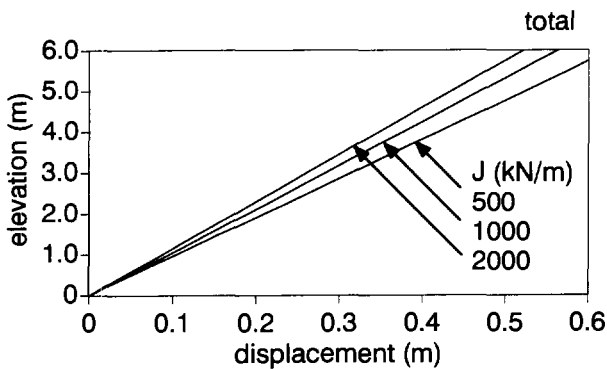
Figures 5a and 5b show the distribution of maximum *total* reinforcement force (typically at the end of the shaking duration when ground accelerations have returned to static conditions) and the distribution of forces at the end of construction for each experiment (initial). The largest reinforcement forces at the end of construction and after dynamic loading were predicted for the sliding foundation case. The distributions of maximum total reinforcement forces are very different for sliding and fixed foundation cases. The influence of toe fixity and the structural panel member on reinforcement forces is clear in the two figures. The maximum reinforcement force occurs at the bottom layer for the sliding cases while the peak reinforcement layer occurs at the second from bottom layer for the fixed toe condition. The maximum total



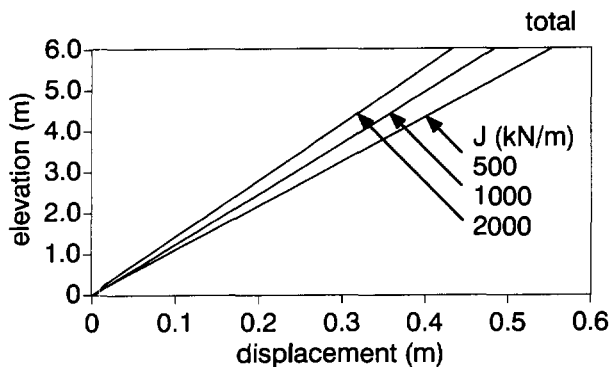
a) sliding base ( $L/H=0.7$ )



b) sliding base ( $L/H=1.0$ )



c) fixed base ( $L/H=0.7$ )



d) fixed base ( $L/H=1.0$ )

Figure 3. Wall displacements predicted at end of seismic record (time = 6 s).

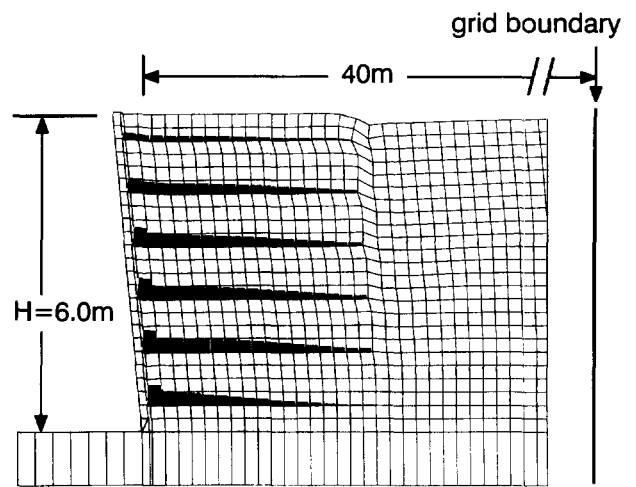


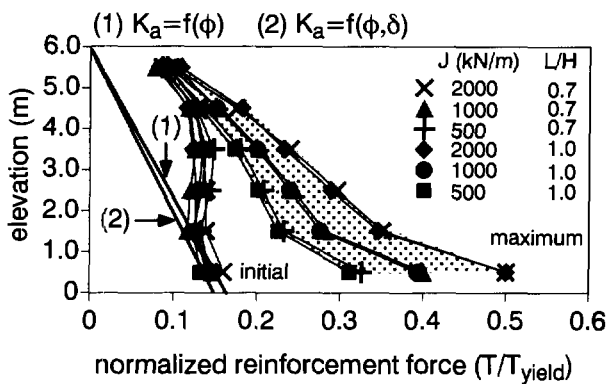
Figure 4. Reinforcement forces at  $t = 6$  s for fixed base condition with  $L/H=0.7$  and  $J=2000$  kN/m.

reinforcement force distributions are relatively insensitive to reinforcement ratio ( $L/H$ ) for the two values investigated but relatively sensitive to the reinforcement stiffness value under dynamic loading. Reinforcement loads increase with reinforcement stiffness. Superimposed on these two figures are predicted reinforcement forces using Rankine earth pressure theory and Coulomb earth pressure theory. These curves do not capture the trend in reinforcement loads at the end of construction for both foundation conditions and are generally very much lower in magnitude than the peak reinforcement forces generated as a result of shaking.

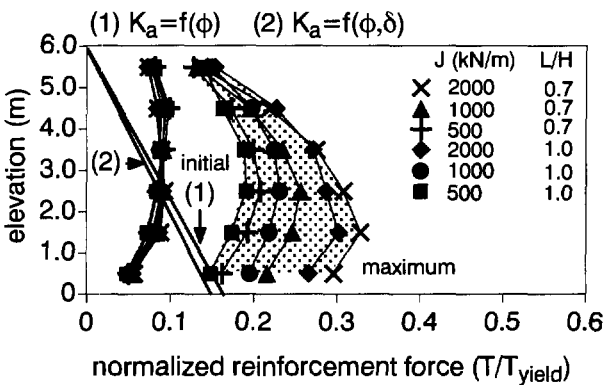
Figures 6a and 6b show the peak dynamic increment force recorded in all simulations. These values are calculated by subtracting the total dynamic load curves in Figure 5 from the corresponding initial static values. Superimposed on the figures are the predicted dynamic increment forces using the current AASHTO (1996) method with a peak ground acceleration of 0.2g. In general, the empirical AASHTO method underestimates the magnitude of additional reinforcement forces. In addition, the trend in additional reinforcement load cannot be captured by the empirical AASHTO curves for the fixed toe condition.

#### 4.3 Other

Figure 7 shows a plot of shear zones in the failed volume of soil within the reinforced zone and in the retained fill. This figure is typical of all numerical simulations reported in this paper. There was no evidence of a well-defined Rankine type failure surface contained within the reinforced soil zone. Rather, the reinforced soil zone acted as a parallel sided monolithic mass. Large shear strains were recorded at the wall-soil interface and at the reinforced soil-retained soil interface. The failure volume can be approximated by a bilinear wedge with the orientation of the linear segment in the retained soil approximately  $31^\circ$  from the horizontal. This failure surface orientation is consistent with Mononobe-Okabe earth pressure theory when ground acceleration amplification is considered (i.e. peak accelerations in the soil were as great as 2 to 3 times the 0.2g peak input value at the base of the structure).

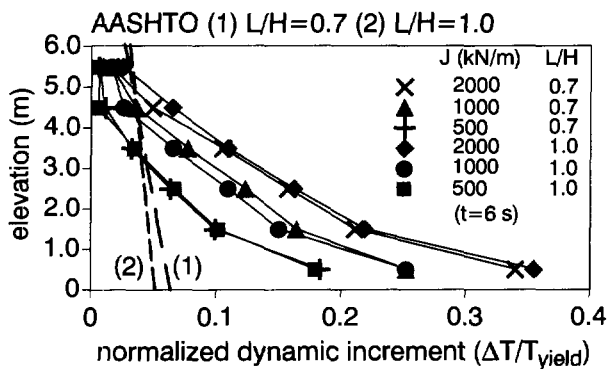


a) sliding base (total forces)

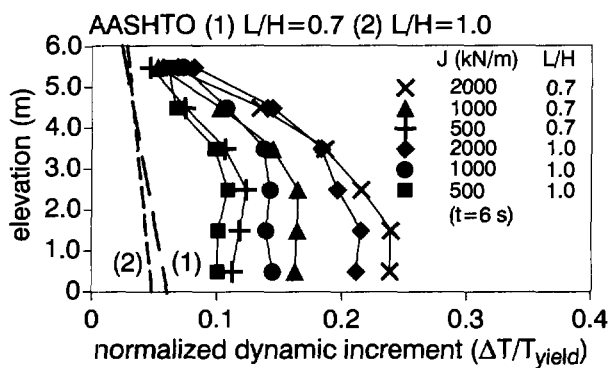


b) fixed base (total forces)

Figure 5. Total reinforcement forces.



a) sliding base (dynamic increment force)



b) fixed base (dynamic increment force)

Figure 6. Dynamic increment reinforcement forces.

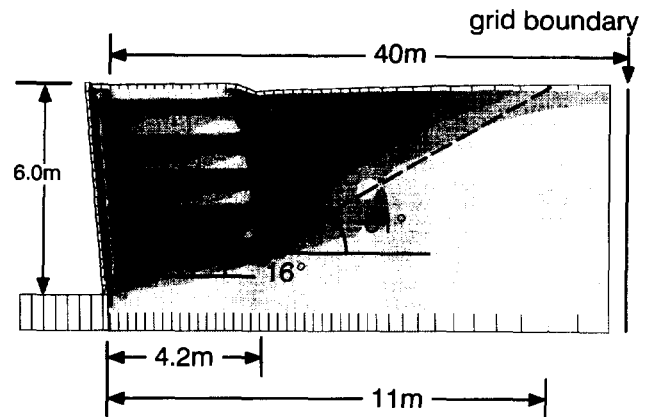


Figure 7. Shear zones at  $t = 6$  s for fixed base condition with  $L/H=0.7$  and  $J=2000$  kN/m.

## 5 CONCLUSIONS

Program FLAC holds promise as a numerical simulation tool to investigate the seismic response of geosynthetic reinforced soil walls. In particular, the numerical results may be used to corroborate current empirical guidelines for the pseudo-static analysis and design of geosynthetic reinforced wall structures or to propose new guidelines. More work remains to investigate a wider range of wall geometries and facing types before predictions based on program FLAC can be used as an aid to the development of simplified seismic design guidelines. However, it is important to note that the seismic response values reported in this paper have not been verified against laboratory models of any scale. The writers are currently carrying out reduced-scale shaking table tests of geosynthetic reinforced soil walls that will be used to calibrate numerical simulations and to verify simulation results.

## ACKNOWLEDGMENTS

The funding for the work reported in the paper was provided by the Department of National Defence (Canada).

## REFERENCES

- AASHTO (1996) *Standard Specifications for Highway Bridges*, 16th Edition, American Association of State Highway and Transportation Officials, Washington, D.C., USA, 677 p.
- Bathurst, R.J. and Alfaro, M.C. (1996) "Review of seismic design, analysis and performance of geosynthetic reinforced walls, slopes and embankments", *Proc. of the Int. Symp. on Earth Reinforcement Practice*, IS-Kyushu'96 Fukuoka, Kyushu, Japan, 12-14 November 1996, 30 p.
- Bathurst, R.J. and Cai, Z. (1995) "Pseudo-static seismic analysis of geosynthetic reinforced segmental retaining walls", *Geosynthetics International*, Vol. 2, No.5, pp. 789-832.
- FLAC (1995) (Version 3.30) Itasca Consulting Group, Inc. 708 South Third Street, Minneapolis, MN 55415, USA.
- Rowe, R.K. and Ho, S.K. (1992) "A review of the behavior of reinforced soil walls", *Proc. of the Int. Symp. on Earth Reinforcement Practice*, IS-Kyushu'92, Fukuoka, Japan, 11-13 November 1992, pp. 801-830.

# The Verrand High Reinforced-Soil Structure

G. Sembenelli

Geotechnical Consultant, SC Sembenelli Consulting, Milan, Italy

P. Sembenelli

Geotechnical Consultant and Managing Director, SC Sembenelli Consulting, Milan, Italy

**ABSTRACT:** The Verrand Embankment is a 27.5 m High Reinforced Soil Structure topped by a 10 m high unreinforced embankment, located at the bottom of a steep V-shaped valley, in the Italian Alps. Scope of the structure, which was completed by the end of 1996, was threefold: providing a stabilising weight to the natural slope, providing a disposal for material from tunnel excavation and providing access beyond the embankment. The reinforced portion mainly consists of three 9 m high blocks, with face angle about 60° from the horizontal. The reinforcements are non-woven geotextiles. The Paper describes the project geometry, fill and reinforcing materials as well as the construction sequence. Monitoring data, collected since the early construction phases, are also presented and discussed.

**KEYWORDS:** Reinforced slope, Geotextiles, Case study, Construction, Deformations

## 1 INTRODUCTION

A new highway connecting the Monte Bianco Tunnel with the city of Aosta, in the Italian Alps, requires the construction of a bridge, some 600 m long, parallel to a very steep slope, about 35 to 40° from the horizontal. The slope forms the left side of a V-shaped valley, created by the Dora Baltea River.

The geology of the site is quite complex. Originally, the valley was filled by a very large earth and rock slide. During the latest glaciation the slide materials were overconsolidated by the action of a thick layer of ice. Locally, concretions of carbonate-rich waters had also formed. By the end of Würmian glaciation the increased erosive potential of the river deeply cut the overconsolidated deposits. The slope material, which is observed today, can be described as a silty sand matrix containing gravel and large boulders, slightly cemented. The surficial part of the mass is often decompressed. The natural water table daylight in the bottom half of the slope.

Presently the slope is close to limit conditions and repeated slides of limited extent occur, whenever the river cuts into the toe of the slope. A particularly large slide took place, in the early years of the century, near the village of Verrand.

Pier #4 of the bridge is located within the perimeter of this slide. It was thus decided that the slope had to be stabilised with a high buttressing embankment.

The steepness of the valley sides imposed the use of reinforced soil technologies, so that the volume of fill and thus the stabilising weight could be maximised. As a side result of this solution, a large volume of muck from nearby tunnel jobsites could be disposed in an environmentally acceptable way.

## 2 PROJECT DESCRIPTION

The Verrand Embankment, shown in plan on Fig. 1, is a 27.5 m High Reinforced Soil Structure overlaid by 10 m of unreinforced, 1.5H to 1V embankment. The structure is some 150 m long for a total volume of about 120 000 m<sup>3</sup>, out of which 50 000 m<sup>3</sup> are reinforced fill.

The reinforced portion mainly consists of three 9 m high blocks, with face angle of 60° from the horizontal. The blocks are stepped to create 5 m wide sloping berms, almost parallel to the riverbed grade. A 5 m wide service ramp runs on the lower berm and cuts the second and third blocks. A ramp was necessary for construction and to provide access beyond the buttress.

The area where the lower block is founded was cleaned and excavated to reach a competent foundation. Also the natural slope was cleaned and stepped in order to get a better interlocking with the new fill. This operation was carried out as filling progressed.

The toe of the HRSS had to be protected from river action by a cyclopean wall, about 4 m high. Additional riverbed training and erosion preventive works are presently underway.

A deep drainage was located at the contact between fill and natural slope, in order to keep water away from the reinforced fill. The drainage system consisted of two sloping collectors along the sides and one collector at the toe. All collectors were created backfilling a trench with selected gravel, wrapped in a geotextile separator. The drainage system also included geonet bands placed on the slope at 10 m spacings, across the collectors. Drainage in form of bands instead of a continuous sheet was selected in order to avoid creating a low friction contact between the new fill and existing slope. In addition, a number of nearly horizontal drain holes heading in the main drainage collector were drilled to depress the piezometric level as far as possible inside the slope. The main collector discharges to the river, on both sides of the embankment.

A surface drainage system was also foreseen. Rain water is collected and carried to the river by a system of ditches and collectors, running along the berms and along the slopes. Collectors along the slopes are included in the facing system and consist of trapezoidal channels on galvanised steel.

## 3 THE REINFORCED SOIL

The first step in designing a reinforced soil structure is selecting the facing technology, on account that it strongly

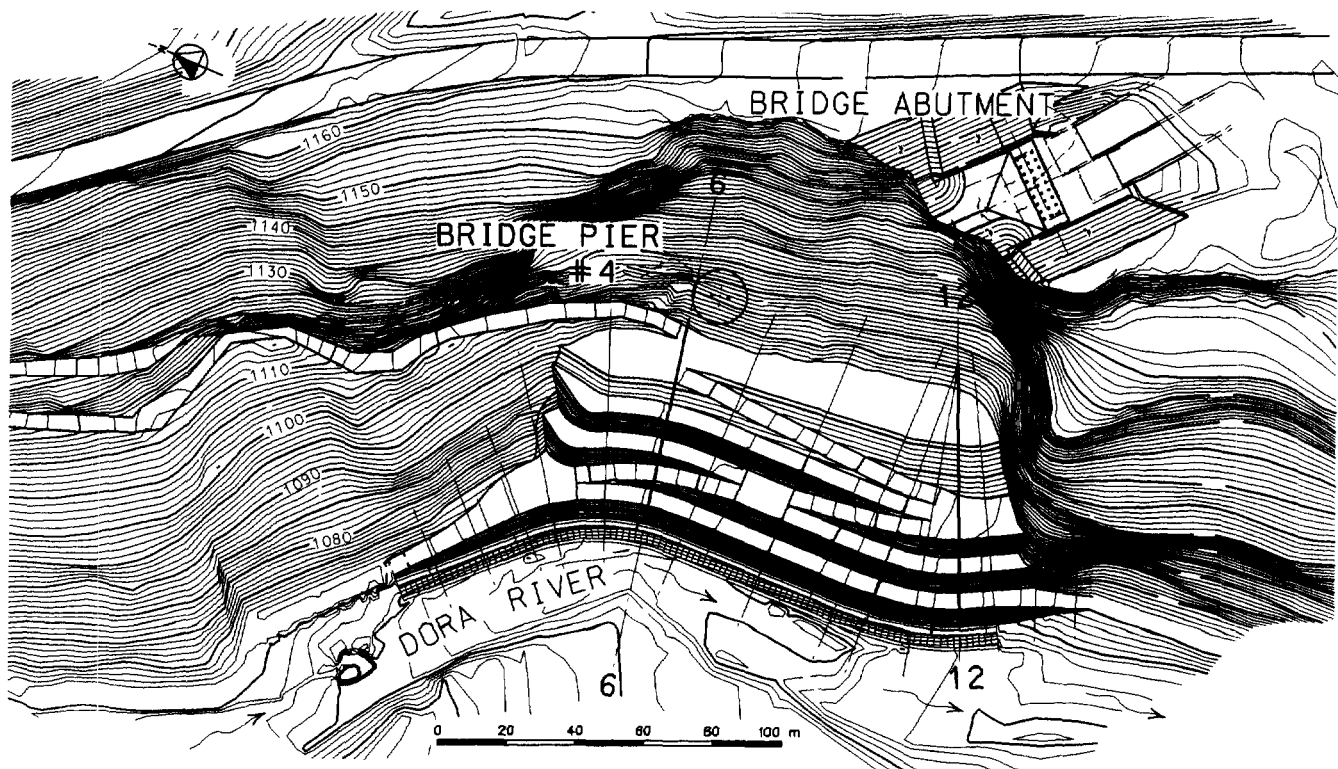


Figure 1. Plan of the Verrand High Reinforced Soil Structure

influences the construction process and the overall structural behaviour. Due to environmental constraints, it was chosen one patented facing systems, resulting in a completely grassed surface, once construction completed.

The basic element of the selected facing technology are 0.5 or 0.6 m high, L-shaped forms made by a welded wire steel mesh, left in place. Each form element is to be bent to an angle which is the one selected for the slope. Short steel tendons holding the two arms of the forms keep the section undeformed during lift compaction. A light woven geotextile is placed inside the form to retain the soil. The fill material is usually spread and compacted in half form high lifts, stopped 0.4 m short from the form. A band of topsoil is placed between the woven geotextile and the lift edge, in order to create a support for vegetation growth. The surface is finally hydroseeded so that it becomes completely and permanently grassed in a short time.

The appearance of the grassed surface at Verrand HRSS before and after hydroseeding is shown in Fig. 2.

An heavy vibrating roller is normally used to provide the necessary compaction effort. The roller actually used at Verrand was a DYNAPAC CA35 Class (7 static tons on drum), instead of the specified CA 25 class (5 static tons on drum). The roller moves parallel to the slope, covering the whole spread of both fill and topsoil placed over the geotextiles, up to the forms.

#### 4 MATERIALS FOR CONSTRUCTION

The fill material placed within the reinforced section was

well graded crushed rock with a relatively large sand and silt fractions, obtained by processing tunnel muck. This material mainly came from tunnelling in schists. The tunnel muck was first crushed in order to reduce its maximum grain size to 150-200 mm and then mixed with material obtained from open air excavations. The latter material was added considering that a relatively high content in sand and silt fines could reduce the potential for damaging the reinforcements.

The specifications for fill materials could not be excessively tight, on account of the fact that random tunnel muck from different excavations fronts were used to supply the needed volume.

The backfill was basically the same material with maximum size in the order of 500 mm. No processing was required for the backfill.

The reinforcements used at Verrand were anisotropic nonwoven geotextiles, continuous filament, needle-punched, Polyester (PET) fibre of three grades, manufactured by Fritz Landolt A.G., Switzerland. The nominal tensile strengths of the geotextiles were 40, 100 and 120 kN/m and their main characteristics are summarised in Table 1.

The reinforcements of grade 1000 and 1200 are quite thick and sometimes the unrolled sheets were undulated. This required special care during placement, in order to avoid wrinkles under the lifts, which might reduce the overall stiffness of the reinforcements. The above deformation were mainly considered to be a consequence of the production process.



Figure 2. View of the Verrand High Reinforced Soil Structure after completion. Vegetation is not yet fully developed in the upper part.

Table 1. Main characteristics of geotextiles FLN-TEXA used as reinforcement at Verrand HRSS

Type	Mass	Machine direction		Transverse direction	
		Strength	Elongation at failure	Strength	Elongation at failure
[-]	[g/m <sup>2</sup> ]	[kN/m]	[%]	[kN/m]	[%]
350	350	48.5	36.8	21.8	37.6
1000	900	115.5	38.3	47.8	36.2
1200	1050	132.7	40.1	55.4	39.6

Geotextiles survivability was checked by full scale tests, under the worst expected condition, i.e. with the coarsest fill compacted in 0.3 m thick lifts. After placing the geotextiles sheets on a compacted layer of fill, 3 additional fill lifts were spread and compacted with the same roller used in construction. The reinforcements were then carefully dug out. Exhuming operations are very difficult and

some additional damage is inevitably produced.

The most damaged zones of the unearthed sheets were thoroughly mapped. From those zones, specimens were taken, described and tested according to UNI-8639 (Italian) Standard. This testing procedure requires 100 mm wide and 200 mm long tubular (folded) specimens (Cazuffi et al., 1986).

Damages were not uniformly distributed over the geotextiles, but rather concentrated in patches. This is probably related to coarse particles segregation processes in the fill, as shown in Fig. 3. The tendency for damages to concentrate close to the outer slope was observed. Apparently segregation tends to increase along the edge of a given lift. Special attention should be devoted to avoid excessive segregation and hence excessive damages near the face, considering that here tensile stresses are the greatest. The extent of the damaged areas was about 50% of the reinforcements width.

Damage was classified under three main types: tears, through-going punctures and partial punctures. Tears were large damages probably related to the unearthing operations and were not considered in the analyses. Through-

going punctures are the most significant damages on account that they produce an appreciable loss of strength. They are small cuts, either rounded or linear, randomly oriented, 10 to 30 mm long. Partial punctures are small indentations, where the filaments are displaced and not necessarily cut.

Within the most damaged zones, the number of observed through-going punctures ranged from a minimum of 40 per square meter (30 per sq. yard) to a maximum of 100 to 120 per square meter (80 to 100 per sq. yard). The corresponding average strength loss was in the order of 50 to 60%. The above results could be observed on all the reinforcement examined and are in good agreement with previously published works (Sembenelli, 1995).

On account that the most damaged zones spread over about half the width of each reinforcement, it may be concluded that the actual strength retained by the whole reinforcement is 70 to 75% of that of the undamaged material. Correspondingly, the appropriate Factor of Safety to account for installation damage is  $F_d = 1.35$  to 1.45.

Our observations suggest that the maximum particle size has more influence on the width of the damaged areas than on the level of damage itself.



Figure 3. Compacted fill material surface under a reinforcement. Segregation of coarse particles in foreground is clearly visible

## 5 DESIGN OF THE REINFORCEMENT DISTRIBUTION AND LENGTH

The selection of the reinforcement requirements (force and length) was based on the limit equilibrium. In the Writers' opinion, when dealing with complex High Reinforced Soil Structures, this is still the most suitable design tool available.

The total horizontal force necessary for equilibrium was determined on a homogeneous unreinforced cross section. The required tensile force to be taken by the reinforcements was then computed as the force required for obtaining a minimum Factor of Safety  $F_s = 1.3$  against sliding. The computations were carried out with the Simplified Janbu Method, working directly on horizontal forces.

The assumed geotechnical characteristics of the fill material were: total unit weight  $TUW = 21 \text{ kN/m}^3$ , cohesion  $c = 0 \text{ kPa}$  and angle of friction  $\phi = 35^\circ$ . Tri-axial CD strength values, obtained from 100 mm diameter, compacted specimens, were larger than the assumed ones. However, a conservative value of the friction angle was selected to take into account the reduction of friction at high confining pressures and high strain levels. With this, the conditions of the lower block and situations of excess of silty fines were covered.

Several design sections were analysed, in order to cover all typical configurations. On each section a number of potential sliding surfaces were selected, so that part of a single block as well as one or more blocks were cut. The computed maximum horizontal force needed for equilibrium at each potential sliding surface was hence distributed over its height. Finally, the minimum required reinforcement was computed as the envelope of the above values.

The geotextiles tensile strength values were reduced to account for installation damage, long term durability and creep. The Design Strength was finally assumed to be 27% of the Wide-Width (500 mm) strength determined according with CNR-UNI (Italian) standards (Cazzuffi et al., 1986).

The length of the reinforcements was selected so that the computed minimum factor of safety for surfaces passing just beyond the reinforcements would be  $F_s = 1.3$ .

Detailed drawings of each reinforcement level were provided to the Contractor to ensure a proper distribution of the overall strength and to minimise wastage. This required a large number of construction drawings including plans, front views and cross sections. The curved contours of the reinforced embankment surface required detailed drawings to show the exact location in plan of both the reinforcement sheets and their overlaps.

The heaviest reinforcements were located within the lower blocks, not only to fulfil strength requirements but also to provide greater stiffness. Grade 350 reinforcements were used only locally in the very upper portion of the upper block. Additional reinforcements at the base of the top unreinforced fill were introduced to reduce the earth pressure on the reinforced blocks.

A typical reinforcement distribution is shown in Fig. 4. It is worth noting that the inner side profile of the reinforcements is stepped in order to meet the overall stability requirement.



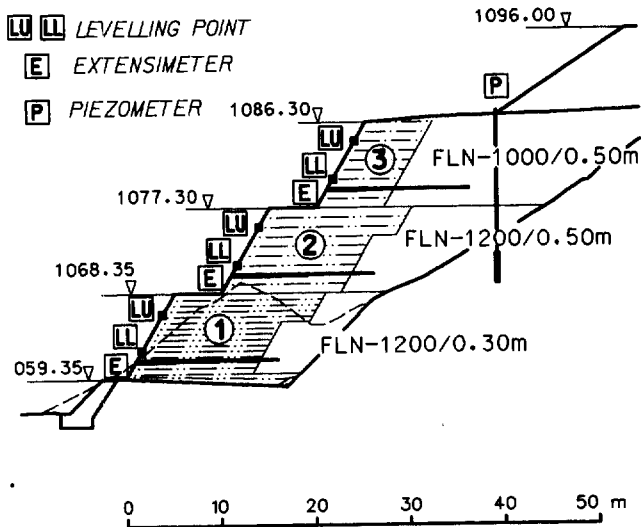


Figure 4. Design cross section 12 with blocks numbering, reinforcements and instrumentation

## 6 CONSTRUCTION

Construction started in summer 1994. The lower block and about 3 m of the mid block were completed by November 1994. From winter 1994 through April 1996, construction was stopped, due to non-technical reasons. Fill could not be placed between late November and early April anyway, on account of the cold climate.

After resuming construction, the reinforced portion was completed early in September 1996 and the unreinforced fill was hence added to final grade. Actual construction took about 9 months.

The flow of material from neighbourhood excavations was slow so that a standard production, say 300 to 500 m<sup>3</sup>/day for a crew of 3 men, could not be sustained.

Hydroseeding was carried out early in 1996 for the lower part, already completed at that time, and at the end of 1996, for the upper blocks. Some delay between completion of construction and seeding is usually tolerated, though not beneficial for the facing which remains unprotected.

A large flood, in the order of 600 m<sup>3</sup>/s, occurred in the summer of 1996. The estimated return period of such flood was 50 years. The water level rose to the top of the toe wall, but no effects were noted on the reinforced embankment, though a scour, up to 2 m deep, produced in the riverbed.

## 7 BEHAVIOUR

Since early construction, vertical and horizontal displacements were monitored, with topographic surveys of reference points at cross sections 6 and 12. On the same cross

sections, long-base extensometers were placed to measure horizontal average strains. Due to installation problems, however, no one of the bases gave reliable readings.

The selected reference points were special plates and the heads of the extensometers. Horizontal displacements were measured from stations located on the opposite bank of the river, so that the distance between station and measuring points was in the order of 100 m. The location of the reference points on cross section 12 are shown in Fig. 4. Plates and extensometers are similarly located in section 6. It should be noted that the extensometer 2E in section 6 is below the service road.

The main data recorded are summarised in the time histories of Fig. 5 and 6. The shape of all displacement

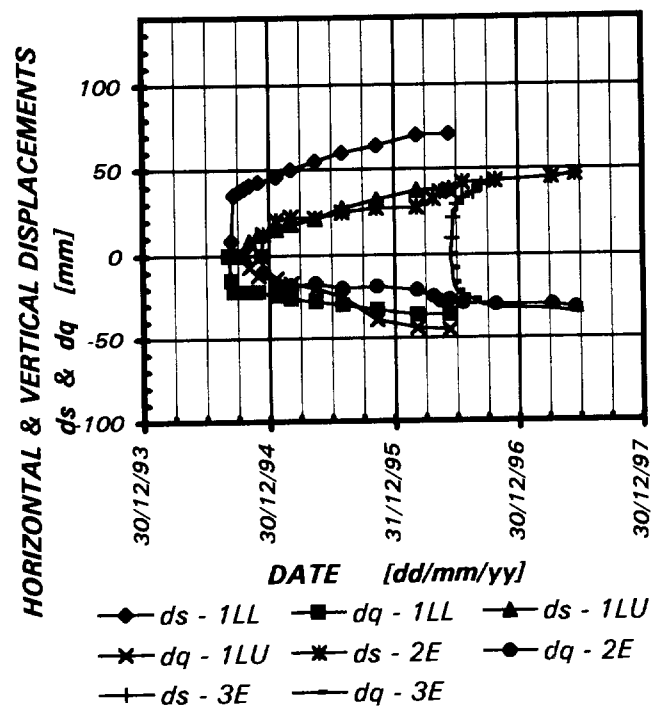


Figure 5. Horizontal and vertical displacements measured on section 6. See Figure 3 for key

curves is hyperbolic and a horizontal asymptote appears to be reached after 9 months, from completion.

At Section 6, the maximum horizontal displacements is in the order of 70 mm, on the lower plate of the lowest block. The upper blocks exhibited lesser horizontal displacements, in the order of 50 mm. Vertical displacements range between 30 and 45 mm.

At Section 12, the measured horizontal displacements of the lower block are somehow larger, with maximum in the order of 100 mm. The horizontal displacements of the upper blocks were approximately 50 mm. Vertical displacements are about 70 mm, in the lower block, and 40 mm, above.

The normalised Horizontal Displacements with respect to the relevant height vary over a wide range, between

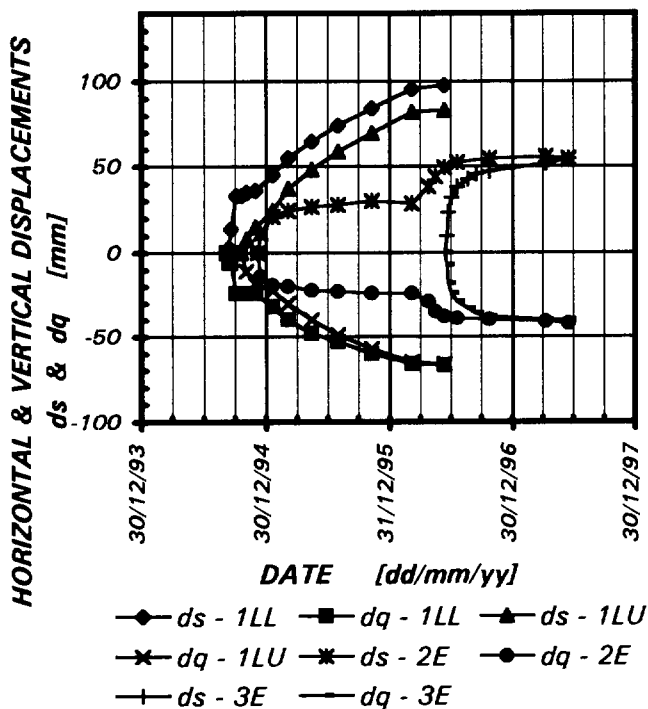


Figure 6. Horizontal and vertical displacements measured on section 12. See Figure 3 for key

$ds/H = 0.25\%$  to  $ds/H = 0.56\%$ . A good correlation between the normalised height and the average slope above the reference point, to which displacements are referred, seems to exist as shown in Fig. 7. Data from Champagne HRSS, a similar structure built according with the same facing technology, are also included for reference (Semenelli, 1995). The experimental points from Verrand HRSS fit to a logarithmic curve, with a satisfactory correlation. Only one point from Champagne HRSS lays close to the above fitting curve while the other ones lay on an almost parallel curve. This latter points actually refer to a different condition, which included an arched facing and geogrids reinforcements (Semenelli, 1994).

All points, which fall close to the fitting curve, are related to structures built with well graded (silty) sand and gravels, reinforced with non-woven geotextiles.

Casagrande Standpipe Piezometers will also be installed in order to monitor the water table in the long term.

#### ACKNOWLEDGMENTS

The Owner of the Monte Bianco-Aosta Highway is RAV - Raccordo Autostradale Valle d'Aosta spa, Roma, Italy. The permission for publishing the above is deeply acknowledged.

VIADOTTI COURMAYEUR a.t.i., a Joint Venture headed by ASTALDI spa, Roma, Italy, is the Contractor in charge of construction. Most of the measurements were carried out by the Contractor's personnel, whose support is also acknowledged.

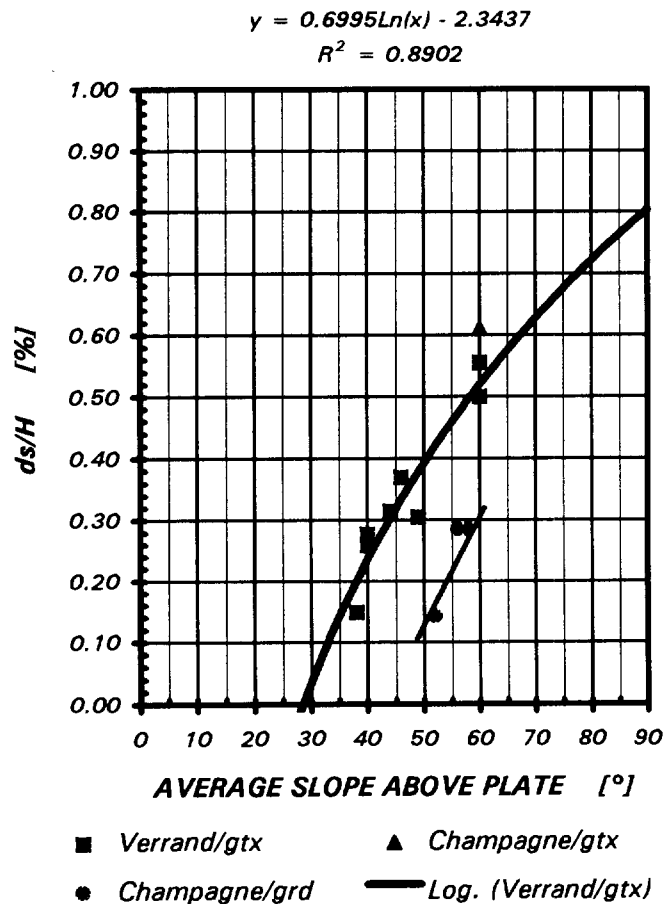


Figure 7. Normalised horizontal displacements vs. average slope

#### REFERENCES

- Cazzuffi, D., Venesia, E., Rinaldi, M., and Zocca, A. (1986) "The Mechanical Properties of Geotextiles: Italian Standard and Interlaboratory Test Comparison" *Third International Conference on Geotextiles, Geomembranes and Related Products*, Vienna, Austria, Vol. 3, pp. 695-700
- Christopher, B.R., Gill, S.A., Giroud, J.P., Juran, I., Mitchell, J.K. and Dunicliff, J. (1989) *Design and Construction Guidelines for Reinforced Soil Structures*, Report No. FHWA-RD-89-043, McLean, VA
- Jewell, R.A. (1990) "Strength and Deformations in Reinforced Soil Design" *Fourth International Conference on Geotextiles, Geomembranes and Related Products*, The Hague, Netherlands, Vol. 3, pp. 913-946
- Semenelli, G. and Semenelli, P. (1994) "Experiences with High Reinforced Soil Slopes" *Fifth International Conference on Geotextiles, Geomembranes and Related Products*, Singapore, Vol. 1, pp. 479-482
- Semenelli, G. and Semenelli, P. (1995) "An Approach to High Reinforced Soil Structures" in *The Practice of Soil Reinforcing in Europe*, Ed. by T.S. Ingold, Thomas Telford, London, UK, pp. 139-152

# GEOGRID REINFORCEMENT OF SLOPES FOR EARTHQUAKE RESISTANCE AT THE NEW U.S. EMBASSY IN CARACAS, VENEZUELA

J.R. Lambrechts

Vice President, Haley & Aldrich, Inc., Cambridge, Massachusetts

**ABSTRACT:** Construction of a new U.S. Embassy building in Caracas, Venezuela posed a number of site stabilization challenges that were overcome with extensive use of geosynthetics. The new site contained several deep, steep sided valleys that had been previously filled in an uncontrolled manner. These 15 to 30 m thick fills were stabilized by installing more than 200,000 sq.m. of geogrid to provide necessary seismic stability in what was the largest application of geogrids in South America, and ranks high in worldwide use at a single building site. Two large walls supported with geo-mechanical stabilization were incorporated into slope stabilization design. This paper reviews the site conditions, design requirements that prompted the use of geogrid stabilization, and the unique application for stabilizing long sloping valley fills placed on bedrock.

**KEYWORDS:** Geogrids, Slope stabilization, Reinforcement, Seismic design.

The construction of the new U.S. Embassy building in Caracas, Venezuela required extensive site stabilization with geogrid to make the long, steep slopes on the site resistant to the local severe earthquake design conditions. Stability considerations that were incorporated into slope reinforcement designs required special construction to provide resistance to interface sliding of reinforced fill along the surface of underlying sloping bedrock. Other applications of geosynthetics included support of retaining walls and surface slope stabilization using cellular confinement systems in landscape areas of steep final ground surface.

## 1 SITE CONDITIONS

### 1.1 Local Geology

The site of the new embassy is in the Alameda area of southeastern Caracas, near the top of a high ridge that rises more than 150 m above a major southern trending valley corridor in this city of 5 + million people. At the edge of the Caribbean tectonic plate, the region is seismically active, and mountains and hilly terrain are present throughout. The bedrock in the area of the embassy is a dark gray micaceous, calcareous schist, which is a member of the Las Mercedes Formation.

The local hilly topography results from erosion of the bedrock. The tropical environs has produced deep weathering of the bedrock. A mantle of residual soils that has developed over the weathered bedrock is typical for such environs, with gradual transition from weathered bedrock upward through decomposed bedrock, which becomes residual soils, and finally topsoil.

### 1.2 Original Site Preparation for Development

An area of several square miles south and east of the embassy site was developed in the early 1980's, with level

building lots being formed on previously steep sloping hillsides. The initial site development in the early 1980's involved considerable earthwork to make level building lots in the originally hilly terrain. This involved bulldozing off topographic high ridges to fill in the deep intervening, incised valleys.

Several building lots were combined to make a site large enough to accommodate the security needs of a U.S. Embassy. Most of the embassy site had been transformed from hilly terrain, to a series of relatively level plateaus by extensive cutting and filling. Figures 1.a and 1.b present the pre- and post-development site topographic conditions, with the major fill areas labeled. The principal building and land uses of the new embassy are also indicated.

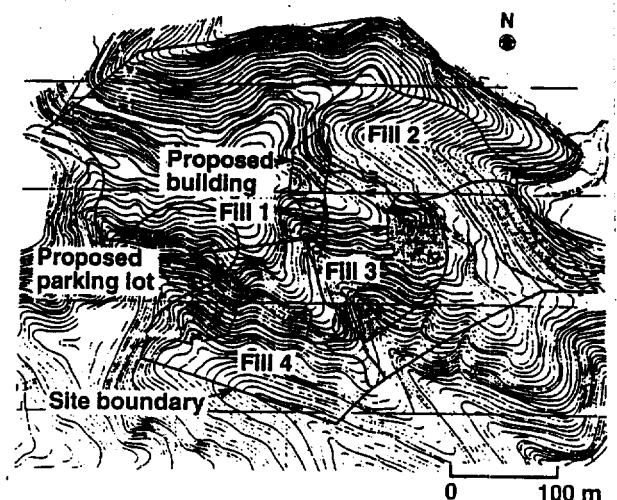


Figure 1.a Pre-Development Site Topography

## 2 DESIGN CONSIDERATIONS

Site use requirements for the proposed embassy necessitated adding fill on the slopes of Fills 2 and 3, and changes in grading on Fill 4. Also, in certain areas adjacent to the new building, filling was necessary for landscaping, with slopes as steep as 45 deg. However, the calculated stability of the Fill slopes existing before construction was marginal for even static conditions. Conditions for Fill 2 are shown on Figure 2, indicating new fill necessary for required final site grading and critical stability surfaces. Similar Factors of Safety were found for Fill 3. Factors of Safety were calculated using the program GEOSLOPE for the Janbu procedure to study irregular sliding models. The constraining effects of the buried valleys were considered, and applied by increasing the calculated Factors of Safety by 10 %, per findings of Baligh and Azzouz (1975).

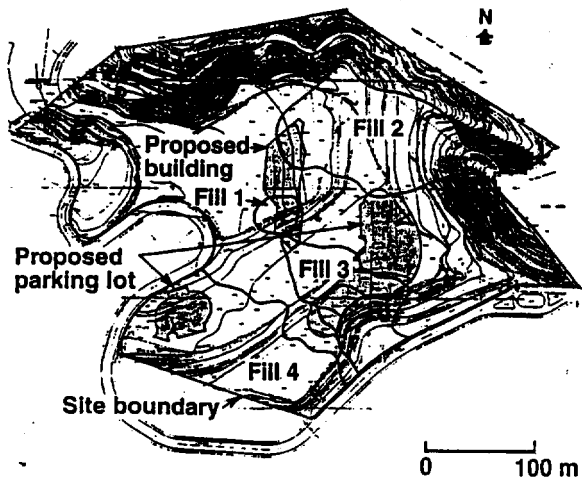


Figure 1.b Conditions After Development Grading

Ground surface across the majority of the developed site area varies El. 945 m to El. 990, but lower levels to El. 915 occur at the bottom (east end) of Fill 2. Bedrock was exposed at ground surface after site development in the flat areas and on slopes between the Fills. Only about half of the Fill 4 area, at the southwest side of the site, is within the site limit, with the remainder continuing across the road and onto the sites on the other side of the street. Similarly, Fill 3 continues downhill beyond the site limit and road, and beneath the lot across the street. The design of stabilization for each Fill area had to account for these conditions.

The Fills were found to be 20 m to 35 m thick, with density being generally loose to compact. The fill was a mixture of the topsoil, the residual soils, and the decomposed and weathered bedrock. Gradation of fill generally varied from silty coarse to fine sand, to medium to fine sandy silt, all with trace clay and rock fragments. Some organic matter was also randomly present. Since there had been little clearing and grubbing prior to valley filling, in many borings topsoil and residual soil were found below fill. Also, as a result of the bulldozing of ridges, vegetation was sometimes found buried in bottoms of fills. Based on results of test boring Standard Penetration Test N-values, the following strengths were assigned to the various strata:

Stratum	Friction Angle (deg)	Unit Weight (kN/m <sup>3</sup> )
Uncompacted Fill	30	19.6
Residual Soil (& Topsoil)	25	20.4 (18.8)
Decomposed Rock	35	21.2
Schist Bedrock	40	22.0
Compacted Backfill	33	20.4

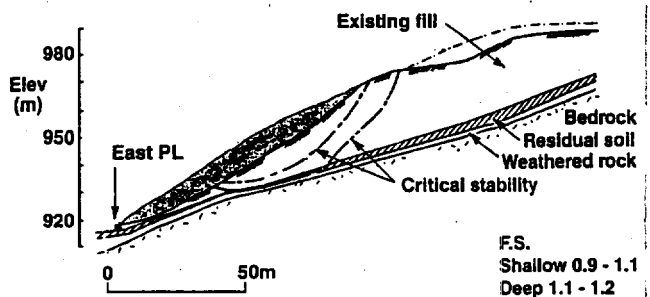


Figure 2. Stability Conditions of Original Fill 2

Primary geotechnical design considerations stem from the severe regional seismicity, which requires design for Richter magnitude 7.0. From earlier site specific seismicity study, the design earthquake was determined to produce bedrock horizontal acceleration of 0.30g. This was used in seismic slope stability analyses, which lowered calculated factors of safety to considerably below 1. Major reconstruction of the large site fills was therefore imperative.

Design for developed site required static Factor of Safety of 1.5, and for seismic conditions a FS of at least 1.0, plus the requirement that toe of slope not move beyond the property line as result of earthquake shaking. To satisfy these requirements, it was found necessary to remove and replace considerable amount of the existing fill in the three major Fills.

## 3 DESIGN OF SLOPES USING GEOGRID

In designing the stabilized fills for surface slopes as steep as 2 hor. to 1 vert., extensive use of geogrid reinforcement was essential to meet design criteria. Slope stability Factors of Safety were calculated using friction angle of reinforced fill judged to be at least 5 deg. more

than compacted backfill; i.e., 38 deg. Generalized profile through Fill 2 in Figure 3 shows the extent of reinforced fill necessary to meet design requirements for both the resist deep seated and shallow instability. As indicated, the dynamic conditions were the more severe, and thus necessitated more geogrid than would have only static considerations.

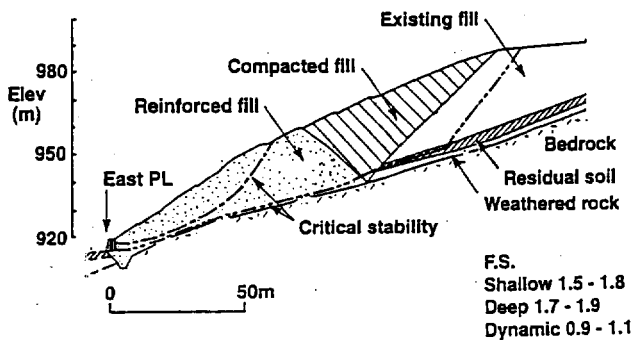


Figure 3 Calculated Stability for Reinforced Fill Buttress in Fill 2

However, design consideration was necessary to prevent a possible sliding surface from occurring on the interface between reinforced fill and bedrock, which would have been at the lower strength of the unreinforced fill. A means was devised to anchor the geogrid reinforced fill into the bedrock using "step cuts" into the weathered rock (below the decomposed rock). The need to "tie" the reinforced fill into the bedrock illustrated in Figure 4; the  $T_g$  force would have to be developed to bolster base friction is to prevent sliding along the bedrock surface.

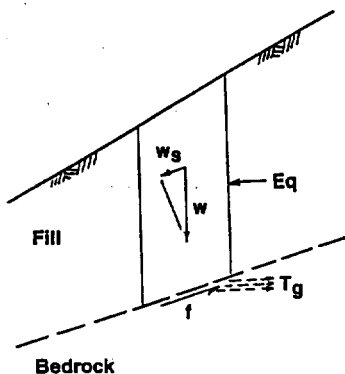


Figure 4 Sliding Block Model for Slope Stabilization

The necessary tension force from the geogrid was determined from the slope stability calculations as increments of load applied to bottoms of slope slices to hold the slice in place, thus supplementing base friction. The geogrid force,  $T_g$ , provides the increase in frictional

resistance to make up the 5 deg. difference in friction angle between the compacted unreinforced fill and the reinforced fill. This force was then converted into equivalent length of geogrid using reasonable grid spacings and applying the equation shown in Figure 5. The equation parameters were derived from FHWA (1989).

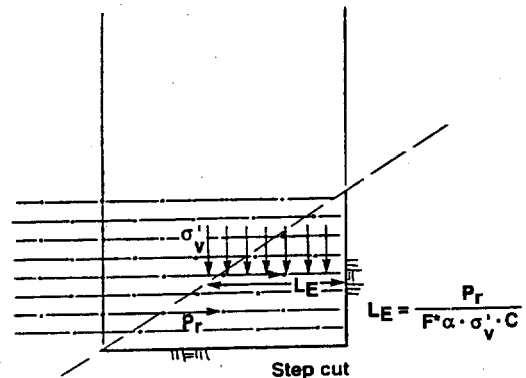


Figure 5 Model for Determining Embedment Length

The key feature to make the geogrid reinforcement effective was the use of "step cuts" into the top of bedrock, as shown in Figure 5. The width of the step cuts had to be long enough to engage the  $L_e$  of the geogrid. This was generally accomplished by limiting the height of cut to 2 m. since the slope of bedrock was relatively gentle, see Figure 3. The upper layers of geogrid in each step cut were less than fully effective, but this was taken into account in the overall stabilization design.

Further, the effectiveness of the engagement zone was enhanced by use of coarse to medium sand as a 1 m minimum thickness "slope drain" layer between the reinforced fill and bedrock. The slope drain contained less than 5% fines and is used to keep piezometric pressures from building up in the base of the reinforced fill. Although bedrock was not found to freely yield groundwater, infiltration over the life of the project from surface irrigation, rainfall, or the surface drainage system were considered possible sources which the slope drain would protect against. Leaks in drain pipe lines are considered possible given the seismic potential of the area.

The non-uniformity of the valley fills led to intricate zoning of the reinforced fills in design drawings. Typical sections of the fills are shown on Figures 6.a, 6.b and 6.c. In the Fill 3, the stability of the on-site fill was provided for with the arrangement shown in Figure 6.a. The Fill 3 section proceeded further downslope beyond the property limit, so the deeper overall stability of the valley fill could not be fully improved. However, the reinforcement provided makes the slope within the site secure against earthquake loadings.

At the sides of the Fill 3 valley, the soil fill was joined to the bedrock as shown in Figure 6.b, with a series of step cuts. Also of importance in the design of the geogrid

was the retained fill wall at the top of the slope which was designed as a geogrid supported precast concrete wall. Spacing of geogrid layers is shown on the cross-sections. At both locations above Fill 3, a retaining wall was constructed to achieve area needed for parking lots. The wall was designed to use pre-cast concrete panels supported by geogrids extended back sufficient distance for seismic loading conditions.

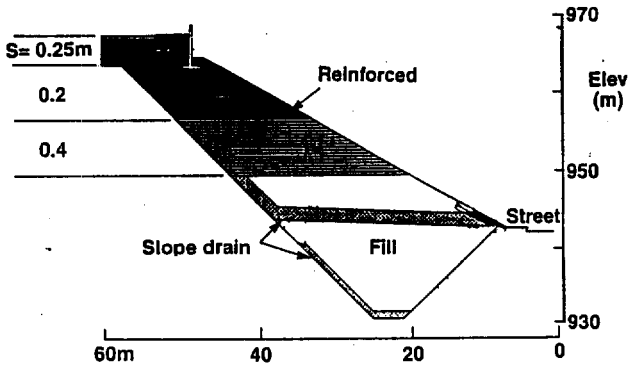


Figure 6.a Fill 3 Deep Buttress

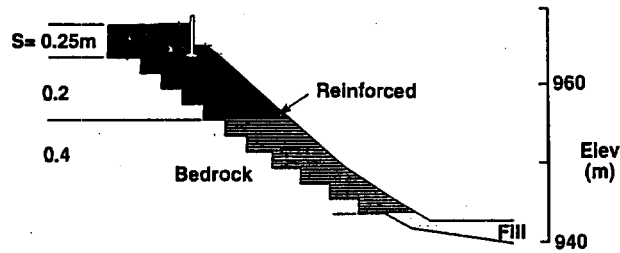


Figure 6.b Fill 3 Provisions for Fill over Rock Slope

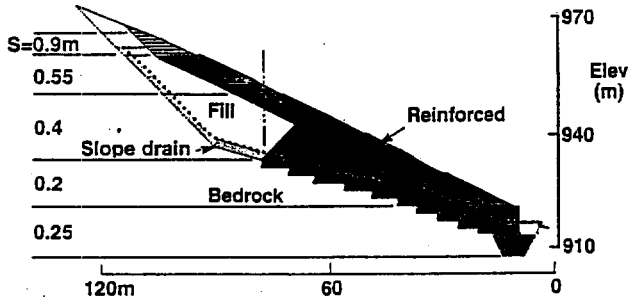


Figure 6.c Fill 2 Cross Section of Reinforcement

Fill 2 profile shown on Figure 6.c provides heavy reinforcement at the toe to create a buttress, with geogrids anchored in the step cuts. Further up the slope, reinforcement was provided only to provide stability of the

"surficial" slope, since the overall stability was sufficient with the large buttress formed in the bottom part of the slope. At the bottom of the Fill 2 slope, another retaining wall was provided for grade separation at the property line. It also will act as buttress in the event adjacent ground support is removed (by earthquake or excavation).

The contract documents set the following requirements for geogrid material:

Weight, per square m.	644 g/sq.m
Minimum Opening Size, in.	15.2 mm
Long-Term Allowable Design Load determined per GRI GG4 (1991)	14.6 kN/m

Material chosen by the Contractor was Mirafi 10 T. In limited areas around the building where small slopes were reinforced to provide 45 deg. inclinations, Mirafi 7 T was used, since the LTADL was less. To maintain landscape slopes adjacent to the building that were at 45 deg. inclinations stable against surface runoff, Geoweb cellular confinement system was installed and interconnected with the layers of geogrid.

Stabilization of the three large fills to provide site slopes, roads and parking areas that would be stable under the design earthquake conditions involved removal of deep fill, and reconstruction with geogrid reinforced backfill. At the time of installation in 1992-3, the more than 200,000 sq.m of geogrid used was the largest installation in South America. About 8,500 sq. m of cellular confinement was also installed.

#### ACKNOWLEDGMENTS

The Foreign Buildings Office of the U.S. Department of State supervised the design and construction of the Caracas embassy project, and their permission to publish this paper is gratefully appreciated. Project Architect was Gunnar Birkerts Associates of Birmingham, MI. Ammann and Whitney of New York City was the site civil engineer. General Contractor for the construction was Perini International, of Framingham, MA. Haley & Aldrich served as the geotechnical consultant for the project, including design of the geogrid system, and provided on-site geotechnical consultation during building foundation and geogrid installation during earthwork construction.

#### REFERENCES

Baligh, M. and Azzouz, A. (1975), "End Effects on Stability of Cohesive Slopes", Journal of the Geotechnical Engineering Division, ASCE, Vol. 101, No. GT11, Nov., pp. 1105-1117.

FHWA (1989), "Reinforced Soil Structures", Report No. 89-043, Vol. 1, Nov. 1989.

# The Construction of Steep Reinforced Slopes in Hilly Terrain

C.R. Lawson  
CEO, TC Nicolon Asia, Malaysia

T.W. Yee  
Manager, TC Nicolon Asia, Malaysia

**ABSTRACT:** The flexibility of reinforced soil makes it an ideal solution for the construction of steep reinforced slopes in hilly terrain. However, due to the nature of hilly terrain, four major construction constraints can arise. These are the lack of a firm foundation on which to construct the reinforced slope; excavation instability or the occurrence of bedrock that limits the width of the base of the reinforced zone; the presence of groundwater emanating into the excavation from behind the reinforced zone; and the overall instability of the hilly terrain that limits the geometry of the reinforced slope. A parametric study was performed to evaluate the effect of these constraints on reinforced slope stability. Guidelines for maximising reinforced slope geometry, the role of drainage, and the modular approach to design are given for reinforced slopes constructed in hilly terrain.

**KEYWORDS:** Reinforced slopes, Hilly terrain, Construction constraints, Slope geometry, Drainage, Instability

## 1 INTRODUCTION

The use of reinforced soil as a technique to construct steep, stable slopes is a common practice. Today, much is known of the performance of reinforced soil slopes designed and constructed to "standard" geometries. Standard geometries include the presence of a flat, firm foundation beneath the reinforced slope; no limitations on the width of the reinforced zone for stability purposes; and no unusual loading regimes above the reinforced zone.

Reinforced soil is also an ideal technique for the construction of steep slopes in hilly, or mountainous, terrain. The technique results in a retaining structure that is flexible (i.e. it can undergo deformation without exhibiting structural distress) and highly cost-effective. This is important because the topography of hilly terrain dictates the adoption of significant earthworks structures, in some cases founded on suspect and unstable foundation materials. In addition, groundwater is normally present in this type of topography. This is particularly so in tropical climates where heavy rainfall can result in severe groundwater conditions. In this environment the construction of stiff, brittle structures is to be avoided.

In South East Asia, development effort is spreading from the coastal areas into the hinterland of many countries. For the majority of these countries, large areas of the hinterland consist of hilly and mountainous terrain. The overall topographical and geomorphological geometry of this terrain coupled with the need to maximise stable earthworks platforms for infrastructure and other development purposes results in reinforced slopes of significant magnitude. Slope heights over 20 m and slope angles greater than 60 degrees are not uncommon.

An example of such a reinforced slope, whose final height will be over 40 m, is shown in Figure 1 (it is currently at a height of 30 m). It should be emphasised that slopes of this magnitude require good construction quality. Two examples of good construction quality shown in this

example is the use of grass-impregnated soil bags for the slope facing and the use of tiered catchment drains for the collection of surface and subsurface water run-off. The use of grass-impregnated soil bags enables a stable slope face to be developed while at the same time promotes quick vegetation growth. The use of tiered catchment drains enables the quick removal of surface water run-off as well as being the exit drains for the subsurface drainage galleries within the reinforced slope.

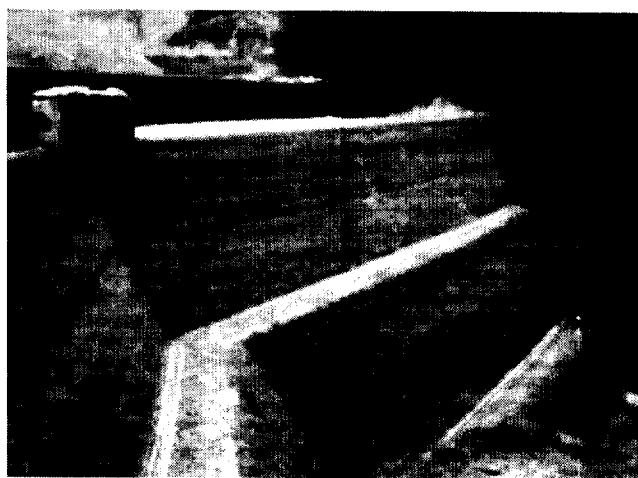


Figure 1. Example of a high, reinforced slope constructed in hilly terrain.

## 2 REINFORCED SLOPE CONSTRAINTS IN HILLY TERRAIN

The geomorphological and topographical nature of hilly, or mountainous, terrain poses considerable constraints on the design and construction of steep reinforced slopes. The general geomorphology is similar to that shown in Figure 2a where the terrain consists of a soil-filled slope overlying a dipping bedrock stratum. The soil-filled slope either has formed naturally or is the result of the dumping of earthfill

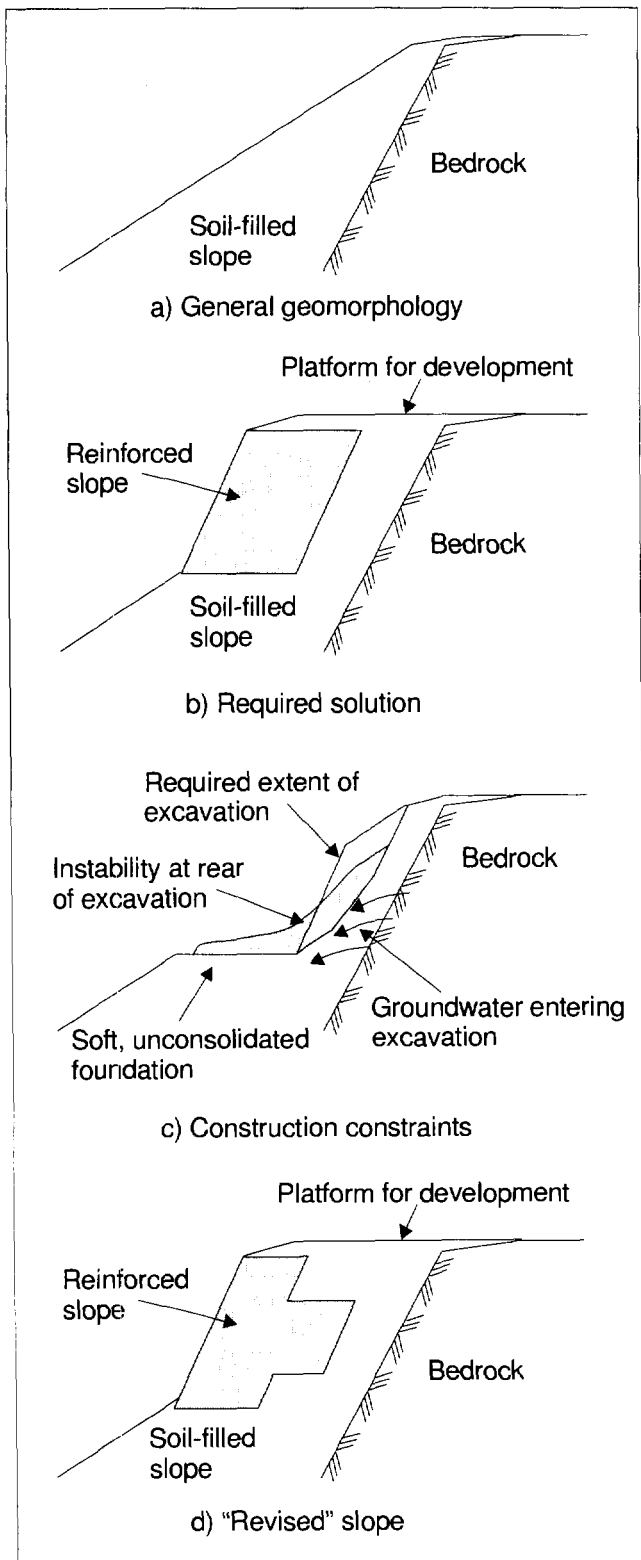


Figure 2. Constraints on construction of reinforced slopes in hilly terrain.

from nearby construction sites. In South East Asia these soils are normally saprolytic, residual or colluvial deposits. In many instances these soils are not compacted and

consequently exhibit relatively high hydraulic conductivities enabling easy penetration by groundwater.

When a reinforced slope of standard geometry is proposed for construction in this type of terrain (Figure 2b) a number of constraints may exist that considerably affects the final design geometry. These are (Figure 2c):

- The ability to excavate the soil-filled slope in order to provide an adequate base width for the reinforced slope. Slope instability at the rear of the excavation may limit the base width possible.
- The foundation at the base of the reinforced slope may be uncompacted and soft. This may constrain the geometry of the reinforced slope.
- The presence of groundwater during excavation of the soil-filled slope can promote slope instability at the rear of the excavation and can prevent the formation of a firm foundation beneath the proposed reinforced slope.

While each of the above constraints has a marked effect on the design geometry of the final reinforced slope it is impossible to foresee these events with any degree of certainty until construction is in progress. Consequently, in many instances it is necessary to carry out a revised reinforced slope design once the construction constraints are known. To accommodate these construction constraints the final design geometry of the reinforced slope may resemble that shown in Figure 2d.

The revised reinforced slope geometry shown in Figure 2d is not what one would consider a "standard" reinforced slope geometry inasmuch as:

- The foundation surface dips down from the toe of the reinforced slope and is not horizontal.
- The foundation may not be firm but may be soft and compressible.
- Instability at the back of the excavation limits the width of the reinforced zone at the base of the reinforced slope.
- The presence of the bedrock stratum may limit the extent of the reinforced zone and may concentrate shear stresses behind the reinforced zone.

Because of the above features, the use of design procedures based on "standard" geometries is only of limited use. When establishing an appropriate, safe geometry for the required reinforced slope all of the above features need to be considered. Because of some of the unusual topographical and geomorphological features involved in hilly terrain it is important to have an understanding of their effect on the resulting geometry of the reinforced slope. This is especially the case where required reinforced slope heights are to be maximised.



Table 1. Geotechnical parameters used in the parametric study.

	Reinforced soil	Foundation soil			Backfill soil	Bedrock
		Firm	Moderate	Soft		
Bulk density ( $\text{kN/m}^3$ )	18	18	16	15	18	22
Friction angle ( $^\circ$ )	35	35	32	30	35	45
Cohesion (kPa)	150	150	20	10	10	5,000
Bulk modulus (MPa)	115	115	65	15	85	20,000
Shear modulus (MPa)	70	70	40	10	50	15,000

### 3 PARAMETRIC STUDY

To evaluate the effect of various geometric and material parameters on the stability of reinforced slopes in hilly terrain a parametric study was performed. It was considered that the boundaries of external stability were important aspects that required assessment for reinforced slopes constructed in hilly terrain. In addition, stresses and deformations were also considered important parameters for investigation. Because of the specific nature of this type of terrain and the need to evaluate the effect of foundation compressibility as one of the aspects of reinforced slope stability, it was concluded that a sophisticated modelling procedure would be required. Consequently, the parametric study was performed using a continuum method approach (FLAC 1995).

#### 3.1 Slope Geometry Analysed

A slope geometry indicative of that encountered in hilly, or mountainous, terrain was used as a basis for the parametric study. This is shown in Figure 3. The reinforced zone has variables  $H$ ,  $L$  and  $\beta$ .

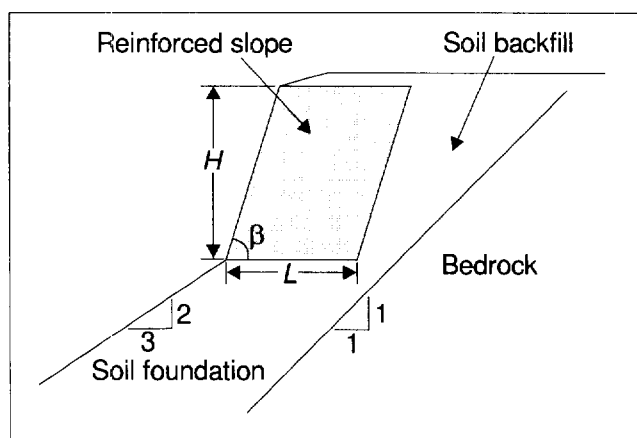


Figure 3. Reinforced slope geometry used in the parametric study.

A bedrock stratum, on a 1:1 dipping plane, is present near the heel of the reinforced zone. The presence of this bedrock stratum concentrates shear stresses within the backfill zone behind the reinforced zone, thus accelerating a potential global failure mode. The location of the bedrock stratum also restricts large vertical deformations at the heel

of the reinforced zone. This condition is considered common in hilly terrain.

The reinforced zone is seated on a soil foundation with a surface slope of 3:2 ( $34^\circ$  to the horizontal). This slope angle is close to the natural angle of repose for various soil types and is considered common in hilly terrain.

#### 3.2 Material Parameters Used

The various geotechnical parameters used in the study are listed in Table 1. The soil in the reinforced zone was assumed a compacted cohesive-frictional fill indicative of the saprolytic, residual and colluvial soils found in South East Asia. In the reinforced zone, the reinforcement was modelled by means of an additional apparent cohesion within the compacted soil. To ensure the maintenance of internal stability within the reinforced zone the layers of reinforcement would have to impart an apparent cohesion of 130 to 140 kPa according to the method proposed by Hausmann (1976). Consequently, a total cohesion of 150 kPa was assumed for the reinforced zone.

Three different foundation soil conditions were adopted for the parametric study – firm, moderate and soft (see Table 1). Standard design methods for reinforced slopes always assume a firm foundation beneath the reinforced slope. While never specifically stated, a firm foundation can be assumed to be one where it is impossible for a bearing failure to occur, or where another type of external instability occurs before the onset of bearing failure. For the parametric study, the firm foundation has been given the same properties as the reinforced zone. This was done to ensure that foundation failures beneath the reinforced zone could not occur, given the specific geometry of the problem. With a foundation having these properties the only external failure modes are global, sliding, compound or overturning instability.

The soft foundation soil parameters listed in Table 1 may be considered indicative of loosely placed soil or fill. While not implicit, groundwater may be also present within the loose fill.

The moderate foundation soil parameters are considered indicative of naturally deposited soil without any form of densification carried out. This is considered to be the most prevalent type of foundation condition encountered in hilly terrain in South East Asia.

It has been assumed that the soil backfill consists of compacted local soil taken from the excavation of the

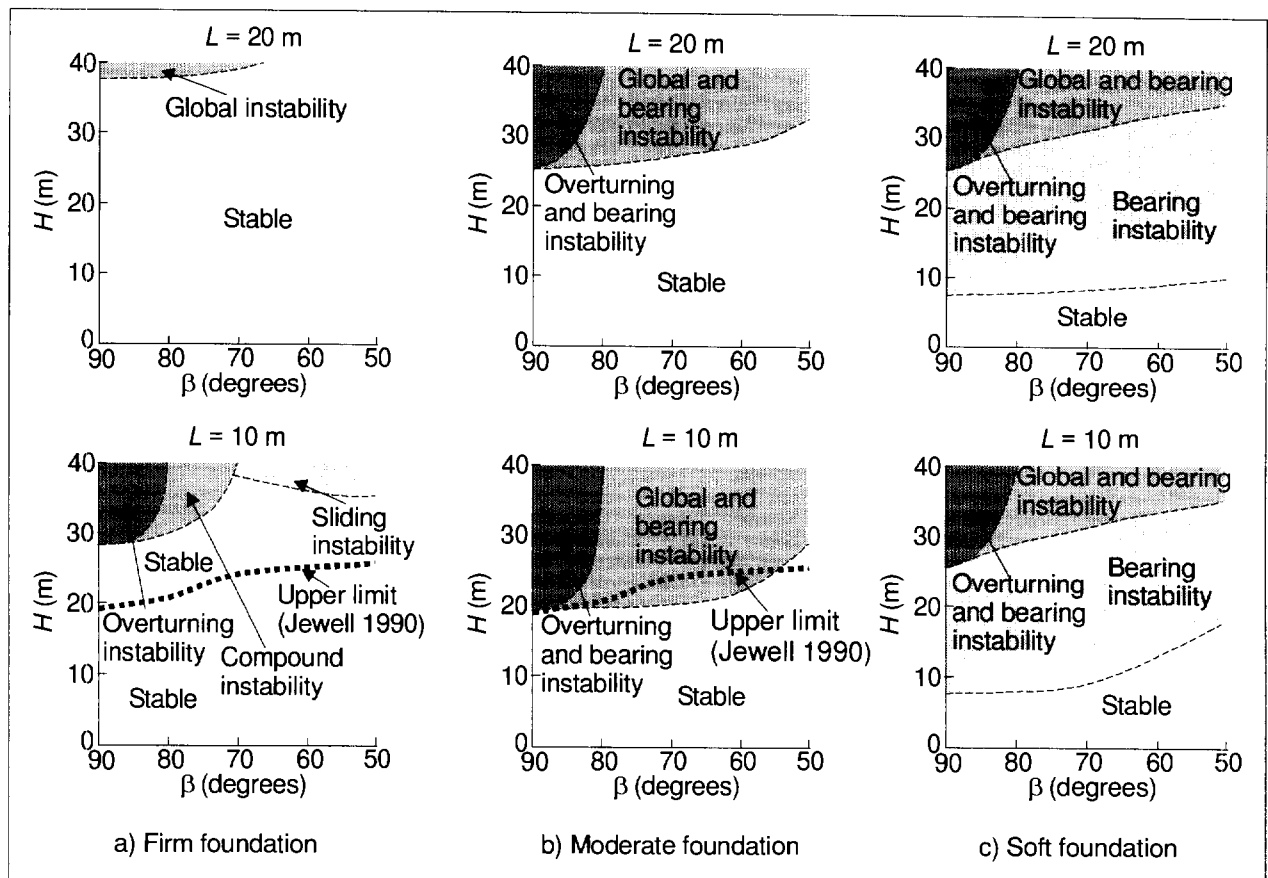


Figure 4. External stability boundaries for reinforced slopes constructed according to the geometry shown in Figure 3.

reinforced slope. The bedrock is an incompressible stratum that cannot fail internally.

For the parametric study, a reinforcement layer was included at the base of the reinforced slope. The inclusion of this layer was not to enhance the internal stability of the reinforced zone but to determine what additional tensile loads are exerted on the base reinforcement layer, given the different foundation conditions and potential failure modes occurring. In addition to the base reinforcement layer a horizontal interface was included between the reinforcement layer and the surface of the soil foundation. This interface layer was given a bond coefficient  $a' = 0.7$  which, while being lower than expected for modern geosynthetic reinforcements, would be considered to provide conservative (i.e. safe) stability solutions.

A second interface was included between the compacted backfill and the rear of the reinforced zone. For this interface a bond coefficient of  $a' = 1.0$  was used for all cases.

### 3.3 External Stability Boundaries for Reinforced Slopes

From the parametric study it was possible to determine the boundaries of acceptable external stability for reinforced slopes analysed according to the geometry shown in Figure 3. Figure 4 contains plots of regions depicting stable and unstable behaviour for the cases of reinforcement length  $L$

$= 10$  m and  $L = 20$  m and for firm, moderate and soft foundation conditions.

For the firm foundation case, Figure 4a, and for reinforcement length  $L = 20$  m global instability begins at around 40 m height for the reinforced slope. Global instability occurs along the boundary of the bedrock stratum (see Figure 3). "Standard" design methods such as the chart method proposed by Jewell (1990) would indicate that significantly higher slopes were possible for  $L = 20$  m, however, these methods cannot take into account the geomorphological features shown in Figure 3. For the reinforcement length  $L = 10$  m case shown in Figure 4a external instability can be induced by overturning, compound or sliding depending on the reinforced zone geometry. The calculated upper limit according to Jewell (1990) has also been plotted. The results show that an additional slope height of 8 to 10 m can be adopted compared to that calculated using "standard" design methods.

For the moderate foundation case, Figure 4b, and for reinforcement length  $L = 20$  m the onset of external instability occurs around 25 to 30 m in height depending on the slope angle. The onset of global and bearing instability occurs before other forms of instability, e.g. sliding, etc. Comparison with the firm foundation case shown in Figure 4a shows the effect of the change in foundation properties on the achievable reinforced slope geometry. For the

reinforcement length  $L = 10$  m case shown in Figure 4b external instability is also induced by global and bearing but (as expected) at a lower slope height than for  $L = 20$  m. The calculated upper limit according to the design charts of Jewell (1990) has also been plotted. The results show that there is fair agreement, however, this is considered to be by chance as “standard” design methods cannot account for bearing instability, which is the major mode of instability in this case.

For the soft foundation case, Figure 4c, and for reinforcement length  $L = 20$  m the onset of external instability occurs around 8 to 10 m in height depending on the slope angle. As to be expected the dominant mode of instability is bearing failure. For the reinforcement length  $L = 10$  m case shown in Figure 4c external instability is also induced by bearing failure at comparable slope heights to the  $L = 20$  m case.

### 3.4 Vertical Stress at Base of Reinforced Slope

The vertical stress acting across the base of the reinforced slope was also recorded from the parametric study. This stress was derived in the form of a vertical stress ratio (VSR), being:

$$VSR = \frac{\sigma'_{vb}}{\gamma H} \quad (1)$$

where:  $\sigma'_{vb}$  = vertical stress along the base of the reinforced slope;  $\gamma$  = bulk density of the soil in the reinforced slope; and  $H$  = height of the reinforced slope.

While the vertical stress at the base of the reinforced slope varies across the width of the reinforced zone, for simplicity, the vertical stress ratio at the toe of the slope ( $VSR_{toe}$ ) and at the heel of the slope ( $VSR_{heel}$ ) were the only two locations recorded.

Figure 5 shows the results obtained for the firm foundation case. At the toe of the reinforced slope (Figure 5a)  $VSR_{toe}$  ranges from 1.2 to 0.35 according to slope angle and  $H/L$  ratio. For slope angles greater than  $75^\circ$   $VSR_{toe} \geq 1.0$ . This is consistent with retaining wall theory. For slope angles less than  $75^\circ$   $VSR_{toe} < 1.0$ , the value reducing as the slope angle reduces. At  $\beta = 75^\circ$ ,  $VSR_{toe} = 1.0$ .

At the heel of the reinforced slope (Figure 5b) the magnitude of  $VSR_{heel}$  is greatly dependent on the  $H/L$  ratio of the slope. Relatively high values of  $VSR_{heel}$  are obtained for  $H/L = 0.5$ . The reason for this is the effect of the development of full friction between the reinforced zone and the soil backfill. This effect reduces as the slope angle reduces. For  $H/L = 1.0$  there is still some effect of backfill friction giving  $VSR_{heel} > 1.0$  for slope angles greater than  $55^\circ$ . For  $H/L \geq 1.5$  the effect of backfill friction is negligible and consequently,  $VSR_{heel} = 1.0$  for slope angles greater than  $65^\circ$ .

Figure 6 shows the results obtained for the moderate foundation case. In general, the results are similar to those

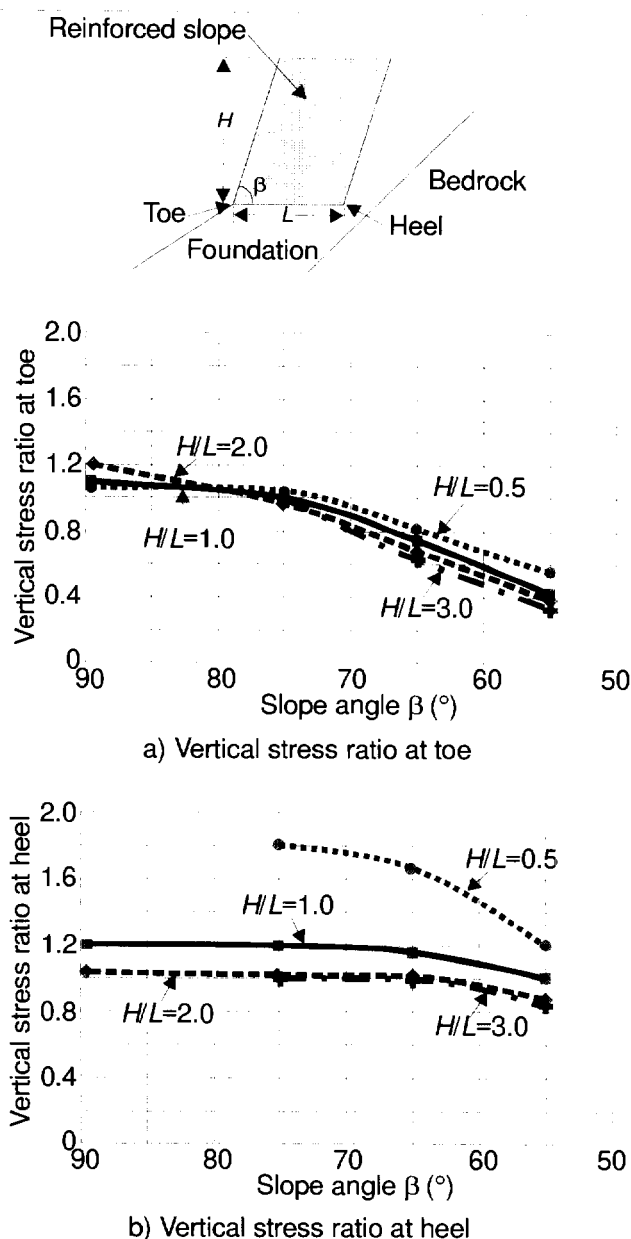


Figure 5. Vertical stress ratio at the base of the reinforced slope for the firm foundation case.

presented in Figure 5 for the firm foundation case. However, the moderate foundation, being more compressible than the firm foundation, enables a more uniform stress distribution to develop across the base of the reinforced zone than is the case with the firm foundation. Consequently, the curves plotted in Figure 6 show more agreement between the  $VSR_{toe}$  and  $VSR_{heel}$  values than is the case for the firm foundation.

### 3.5 Additional Load in Reinforcement at Base of Reinforced Slope

Standard design methods that assume the presence of a firm foundation calculate reinforcement loads according to

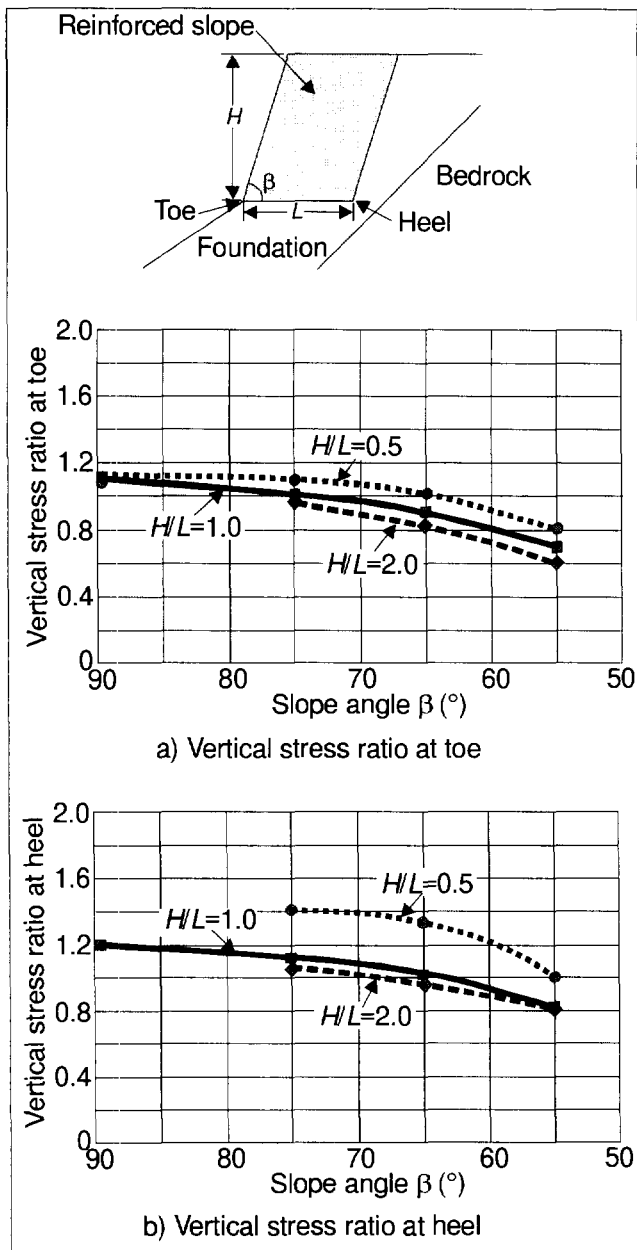


Figure 6. Vertical stress ratio at the base of the reinforced slope for the moderate foundation case.

internal stability requirements only. However, in situations where the foundation is compressible additional tensile loads may be imparted to the reinforcements as the reinforced slope deforms. These additional tensile loads would be a maximum at the base of the reinforced slope. The parametric study was also used to calculate the magnitude of these additional tensile loads imparted to the reinforcement layer at the base of the reinforced slope.

Table 2 contains a summary of the results obtained. It is noted that for stable conditions the additional loads imparted to the base reinforcement layer are relatively small and may be neglected for all cases except the soft foundation case. For the soft foundation case the additional loads are greatest, at around 10 kN/m. For most reinforced

slope applications the design loads carried by the reinforcements are between 30 and 60 kN/m. Thus, only for soft foundation conditions would the additional reinforcement load be significant.

Table 2. Additional reinforcement load at base of reinforced slope due to different foundation conditions.

Foundation	Additional reinforcement load	
	Stable conditions	Onset of instability
Firm	$\approx 1$ kN/m	$\geq 20$ kN/m
Moderate	$\approx 3$ kN/m	$\geq 30$ kN/m
Soft	$\approx 10$ kN/m	$\geq 40$ kN/m

However, at the onset of instability the additional load applied to the base layer reinforcement increases significantly, even for the firm foundation case. This increase in reinforcement load should provide added incentive to ensure that reinforced soil slopes do not approach external instability as the additional loads applied to the base layer reinforcements could lead to their premature rupture with subsequent collapse of the structure.

#### 4 THE ROLE OF DRAINAGE

The influence of good drainage on the performance of reinforced slopes constructed in hilly terrain should not be underestimated. This is especially the case in wet, tropical climates where significant flows of surface and subsurface water can occur. In these environments well- designed and constructed drainage systems are essential and should be considered an integral part of reinforced slope design and construction.

Water may penetrate the constructed slopes in two ways – as groundwater flow from the existing undisturbed deposits behind the slopes, and as surface water run-off due to rainfall. To accommodate these events a recommended drainage layout is shown in Figure 7.

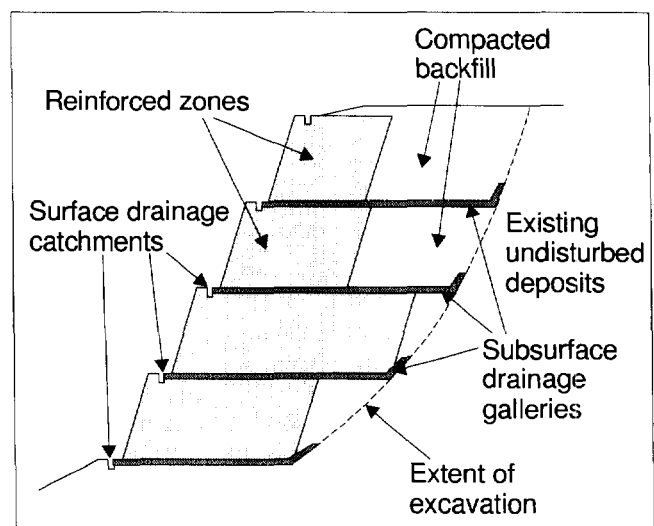


Figure 7. Recommended layout of drainage system within high, reinforced slopes.

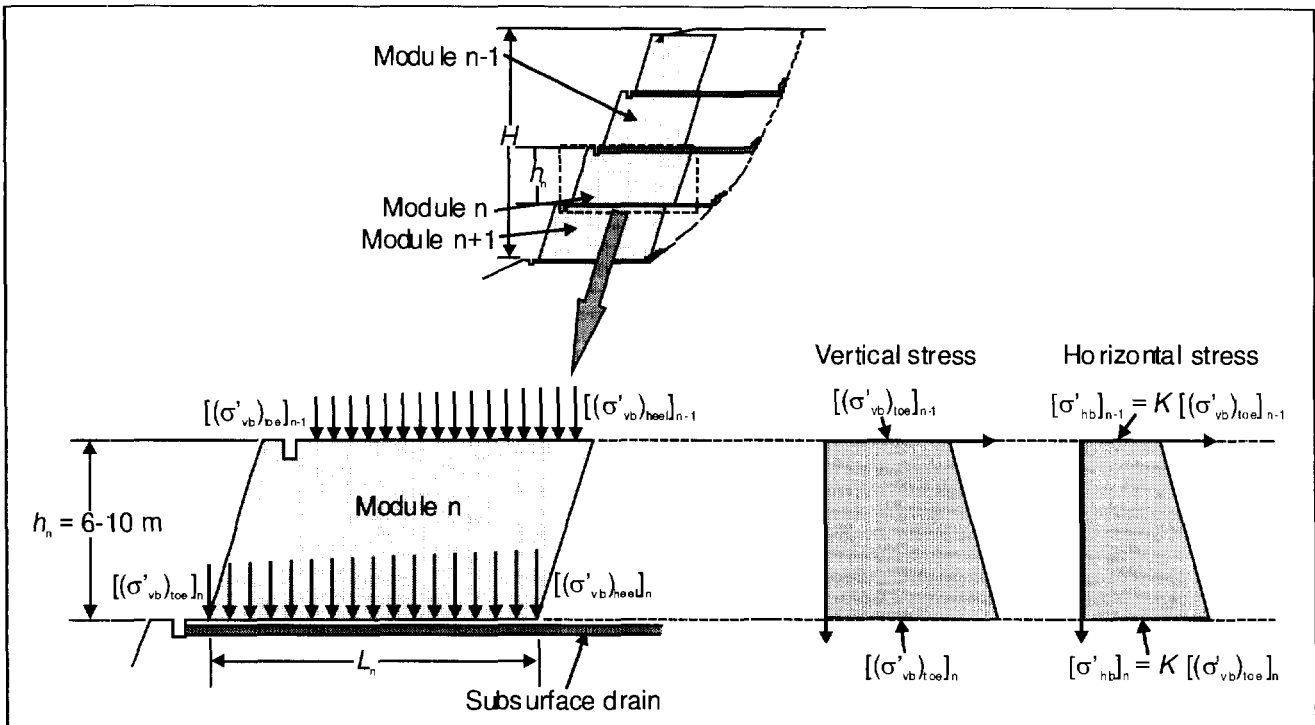


Figure 8. Modular approach to the design of steep reinforced slopes.

To ensure the effective removal of groundwater from behind the constructed slope subsurface drainage galleries should be constructed within the fill zone, preferably at every tier level in the reinforced slope. Since the compacted backfill material is normally the same material as that excavated at site, when replaced and compacted it exhibits significantly less hydraulic conductivity than the adjacent undisturbed deposits. Consequently, to remove the groundwater effectively it is essential that the subsurface drainage galleries be extended beyond the compacted backfill zone to interface with the existing undisturbed deposits. The subsurface drainage galleries can be of the form of drainage blankets or feeder drains. The materials used for the drains are normally small aggregates (for drainage) with geotextile filters. The outlets of the subsurface drainage galleries extend beneath the reinforced soil zones and exit within the surface catchment drains at the toes of the reinforced slope tiers.

If the excavated soil is suitable it is normally used with the geosynthetic reinforcement to construct the reinforced soil zones. This is common practice in South East Asia where the saprolitic, residual and colluvial soils exhibit good shear resistance when combined with geosynthetic reinforcement. The use of the locally available soil also provides the most economical solution. When these soils are compacted to form the reinforced zones it is difficult for surface water to penetrate these fills especially when one considers the nature of the surface geometry of steep slopes. Consequently, surface water damage is normally confined to surface erosion. To protect against surface erosion, open catchment drains should be constructed at the toe of each reinforced zone tier to prevent excess surface

run-off, Figure 7. To prevent surface soil loss it is normal practice either to use an erosion control mat on the surface of the slope or to use grass-filled soil bags. Grass-filled soil bags are normally used for the steeper reinforced soil slopes.

## 5 MODULAR APPROACH TO DESIGN

The design of steep reinforced slopes in hilly, or mountainous, terrain lends itself to a modular approach inasmuch as the reinforced slope can be divided into similar regions, or modules, within the height of the reinforced slope. Each module can be assessed for internal stability as well as sized appropriately to ensure external stability of the whole reinforced slope. A modular approach to design also enables added flexibility in the sizing of the individual modules, standardisation and simplification of the reinforced soil components within each module, and the ability to readily re-size specific modules if construction conditions are not the same as assumed during the design phase.

Figure 8 shows the general basis for the modular design approach. The reinforced slope is designed as a series of reinforced soil modules. Each module consists of its reinforced soil zone along with its associated integral drainage system. Each reinforced soil module can be 6 to 10 m in height, but is more commonly 6 to 8 m. During construction, it is common practice to step-back the face of each succeeding module between 1 to 1.5 m. This enables enough space for the construction of the surface catchment drain.

The length of each module,  $L_n$  in Figure 8, needs to be assessed with regard to the maintenance of internal and external stability. The results shown in Figure 4 may be used as a basis for the assessment of external stability.

The internal stability of each module is assessed by plotting the horizontal stress distribution through the module and ensuring that there is adequate reinforcement capacity to resist the horizontal stresses. The procedure used to determine the horizontal stress distribution through each module is shown in Figure 8. First, the vertical stress distribution at the top and the base of each module is determined, e.g. by using the results in Figures 5 and 6. Second, the vertical stress distribution through each module can then be determined using the vertical stress at the toe of each module as the basis. Third, the horizontal stress distribution can then be determined by adopting an appropriate value of  $K$ , the ratio of horizontal to vertical stress. Values of  $K$  as proposed by Jewell (1990) may be used. Checks for adequate reinforcement bond capacity can be performed by deriving a vertical stress distribution through each module based on the vertical stress at the toe and the heel of each module.

## 6 CONCLUSIONS

The paper has concentrated on a specific, but important, aspect of reinforced slopes – that of their construction in hilly, or mountainous, terrain.

While the use of “standard” design methods may be appropriate for assessing the internal stability of reinforced slopes constructed in this type of terrain, their use for assessing the overall dimensions of the reinforced zone for external stability purposes is not appropriate. Specific aspects such as local topography and geomorphology, as well as foundation conditions need to be considered, and these can result in significantly different solutions compared with those solutions provided using standard design methods and charts.

Good drainage should form an integral part of any reinforced slope design in hilly terrain, especially in tropical climates where high rainfall is prevalent. Attention to the controlled removal of both surface and subsurface water is crucial for good performance.

A modular approach to the design of steep reinforced slopes offers a number of advantages over the conventional approach of considering the reinforced zone as one single mass. Its major benefit lies in the flexibility of being able to consider the reinforced slope as separate regions (modules) that can be sized according to their location in the slope, and reinforced according to the magnitude of the vertical stresses acting at the top and the bottom of each module. The modular approach enables a number of the components of reinforced slope design to be standardised, and allows the slope geometry to be easily adjusted according to local construction conditions.

## REFERENCES

- FLAC (1995) *Fast Lagrangian Analysis of Continua*, Itasca Consulting Group, Version 3.3.
- Hausmann, M.R. (1976) “Strength of Reinforced Earth”, *Proceedings Eighth Australian Road Research Conference*, Vol.8, Section 13, pp. 1-8.
- Jewell, R.A. (1990) “Revised Design Charts for Steep Reinforced Slopes”, *Reinforced Embankments, Theory and Practice*, Thomas Telford Ltd, UK. pp. 1-30.

# Case Study. Bluewater Retail & Leisure Destination - Major reinforced soil slopes to form steep sided new lakes.

J.H. Dixon

Tensar International Ltd, New Wellington Street, Blackburn, UK

**ABSTRACT:** Bluewater is a new £360M (\$580M) retail and leisure destination located in a former chalk quarry in England. Enabling Works involved bulk filling and the formation of a number of lakes. Two of these lakes were formed with slopes at  $70^{\circ}$  to the horizontal, about 10m high, and which in places were surcharged with highway embankments. Lakes 1 and 2 were constructed with several hundred linear metres of reinforced soil slopes, incorporating high density polyethylene uni-axially oriented geogrids. Lake 1 was also lined with a geomembrane which, to avoid damage could not be placed on or near the slope face. The geomembrane was therefore located underneath and behind the rear face of the reinforced soil block. This detail posed unusual design considerations involving sliding stability and the analysis of a number of load cases for different combinations of water level. The design and construction of these lakes including three innovative facing details are discussed.

**KEYWORDS:** Geogrid, Steep slope, Reinforced embankment, Geomembrane lake liner.

## 1 INTRODUCTION

Bluewater, developed by Lend Lease is located approximately 30km east of London. On completion, in March 1999, it is intended to be the largest and most prestigious retail development in Europe, containing 140,000m<sup>2</sup> of retail space, 13,000 car parking spaces, nearly 12,000m<sup>2</sup> of leisure space and with a million trees and shrubs landscaping the area.

The site is located in a former deep chalk quarry. The construction of several lakes was included within an Enabling Works contract which principally involved bulk filling with approximately 3M m<sup>3</sup> of a local silty sand. Two of the lakes, Lakes 1 and 2, were formed with steep sides in order to maximise their water volume and depth for environmental reasons.

Lake sides sloping at  $70^{\circ}$  to the horizontal and approximately 10m high were selected. In places these slopes were to be surcharged by highway embankments and landscaping fill under a later contract. The Client's Consulting Engineer, Waterman Partnership, recognised at an early stage the economic and practical advantages of reinforced soil techniques.

As the ground water level was known to vary significantly it was decided to line Lake 1 with a geomembrane in order to retain a constant lake water level. There were concerns about the long-term durability of the geomembrane and in particular its vulnerability to potential damage from burrowing wildlife or boat impact if it were placed on, or close to, the slope surface. It was therefore decided to locate it underneath and up the rear face of the reinforced soil block.

## 2 REINFORCED SOIL DESIGN

### 2.1 Outline Design Brief

The Engineer invited Tensar International Ltd to assist with specialist design support in developing the reinforced soil design beyond the concept stage.

Lake 1, with the geomembrane lining located below the reinforced soil block, presented two unusual reinforced soil design challenges:

- The potential for sliding of the reinforced soil block over the geomembrane.
- The combination of the large number of possible water levels (within both the lake and the external ground) and various imposed loadings conditions, phased with the subsequent highway and landscaping contracts.

Furthermore, the design brief called for a low-cost durable face with a 120 year life and high security against wash out of the fill.

#### 2.1.2 Basic Design Parameters

The fill which was to be sourced from an adjacent quarry was a silty fine sand (Thanet Sand). Its design parameters were:

$$\phi'_{cv} = 31^{\circ}, c' = 0, \gamma_{opt} = 19.3\text{kN/m}^3 \text{ and } \gamma_{sat} = 20.2\text{kN/m}^3$$

A series of 30cm x 30cm laboratory shear box tests was commissioned to measure the frictional shearing resistance between the various specified geosynthetic materials and this fill.

The selected lining system was 1mm thick modified low density polyethylene (LDPE) geomembrane protected by a 700g/m<sup>2</sup> polypropylene needle punched geotextile. The critical interface shearing angle ( $\phi_{is}$ ) for this combination was measured at  $20^{\circ}$ .

Two strengths of high density polyethylene (HDPE) geogrid reinforcement were selected; Tensar 40RE (Type 1) and Tensar 80RE (Type 2). These are manufactured from extruded sheets and orientated (stretched) in the machine direction. Their Index QC strength in the longitudinal direction is 40kN/m and 80kN/m respectively and rib thicknesses ( $t_f$ ) 0.7mm and 1.3mm and ( $t_b$ ) 1.9mm and 3.6mm respectively (Figure 1). Shear tests on these two grid types with the chosen fill material indicated friction angles in excess of  $26^\circ$  (i.e. a coefficient of soil interaction  $\mu > 0.8$ ).

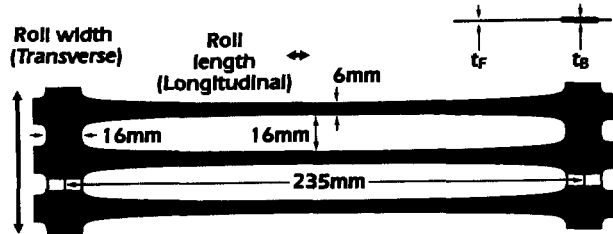


Figure 1 Geometry of the grid reinforcement

## 2.2 External Stability

The shear box testing confirmed that a critical potential failure mechanism for Lake 1 was sliding over the geomembrane lining system. It was therefore decided to incline the lining at an angle  $\alpha$  of approximately  $5^\circ$  below the reinforced soil block (This equated to a fall of 1.5m from toe to heel over the width of the block).

The basal reinforcement layer remained horizontal and was positioned a minimum distance of 100mm above the lining system at the face. This ensured that the critical interface frictional value would not be further reduced.

The factor of safety against sliding over the inclined geomembrane was calculated by resolving forces about the geomembrane (Figure 2).

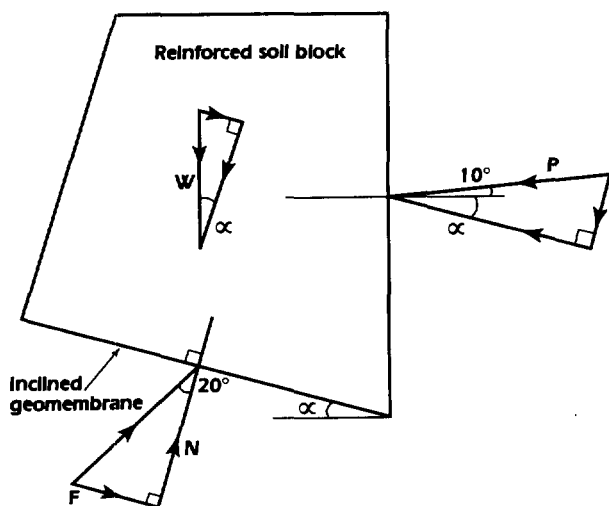


Figure 2 Force resolution on reinforced soil block.

Note: the net mobilising force ( $P$ ) is assumed to act on an angle to the rear of the reinforced soil wall =  $\frac{1}{2} \times \phi'_{ls}$ .  $W$  = weight of the reinforced soil block and  $F$  and  $N$  are the frictional and normal forces acting on the inclined geomembrane.

By resolving forces perpendicular to the geomembrane:

$$W \cos \alpha + P \sin (10^\circ + \alpha) = N \quad (1)$$

By resolving forces parallel with the geomembrane:

$$F = N \tan 20^\circ \quad (2)$$

$$FoS = \frac{F + W \sin \alpha}{P \cos (10^\circ + \alpha)} \quad (3)$$

$$FoS = \frac{[W \cos \alpha + P \sin (10^\circ + \alpha)] \tan 20^\circ + W \sin \alpha}{P \cos (10^\circ + \alpha)} \quad (4)$$

Where FoS = Factor of Safety against sliding over the lining system. (i.e. the resisting force divided by the sliding force).

FoS for design was specified as 1.5 for the temporary condition and 2.0 for the completed works. Figure 3 shows the cross section through the north side of Lake 1 and the particular loading condition which was found to be critical for sliding stability i.e. the condition prior to the placement of landscaping fill and with the lake water level lower than its final design level.

The width of the reinforced soil block is dimensioned to provide sufficient weight ( $W$ ) to satisfy FoS.

Lakes 1 and 2 were also checked for other external stability conditions, including sliding over the reinforcement.

## 2.3 Internal Stability

The specialist designer's experience of other reinforced soil structures with a similar geometry was that design principles based on the German Institut für Bautechnik (DIBt) would produce a stable and economical solution. Internal stability calculations take the form of a two-part wedge analysis through the reinforced soil block. A series of two-part wedges are examined with the lower part of the wedge originating at the structure face and passing through the block, and the upper part of the wedge passing up the back face of the reinforced soil block. The active pressure, above that point where the lower part of the wedge cuts the back face of the reinforced soil block, is added to the disturbing forces acting on the two-part wedge to give the total disturbing force. In the case of internal stability, the resultant active



force is taken to act on angle equal to the friction angle of the soil block rear face.

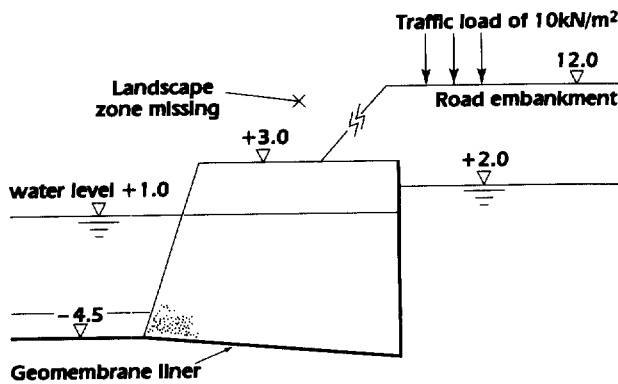


Figure 3

Reinforcement must be provided to resist the disturbing force on each two-part wedge by intercepting the wedge being considered. The two-part wedge stability calculation should be carried out from the toe of the structure, the bottom grid layer, at all levels where the grid spacing alters and at every level where the grid type alters.

The reinforcement design strength is obtained from the creep-limited strength appropriate to the design life and in-soil temperature. Specific partial factors are then applied to take account of such factors as installation damage. Finally, an overall FoS = 1.75 is applied to the strength.

The reinforcement layout was derived by analysis with lower part wedge angles ( $\theta$ ) set at  $3^\circ$  intervals (Figure 4) using the specialist designer's computer program - Winwall. (Tensar International, 1995)

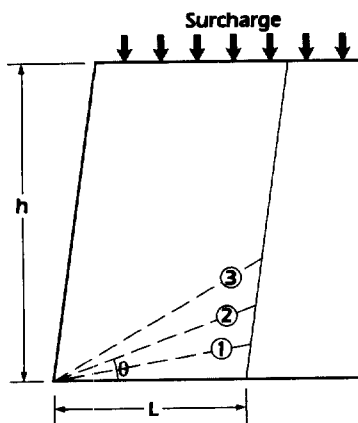


Figure 4 Two-part wedge analysis.

For Lake 1, the critical condition for internal stability was identified as the completed structure fully landscaped under the rapid 'draw-down' condition with the lake empty (perhaps during a future maintenance operation) and the backfill behind the reinforced soil block fully saturated. A typical reinforcement layout for the north side of Lake 1 is shown in Figure 5. The maximum vertical reinforcement spacing was set at 60cm.

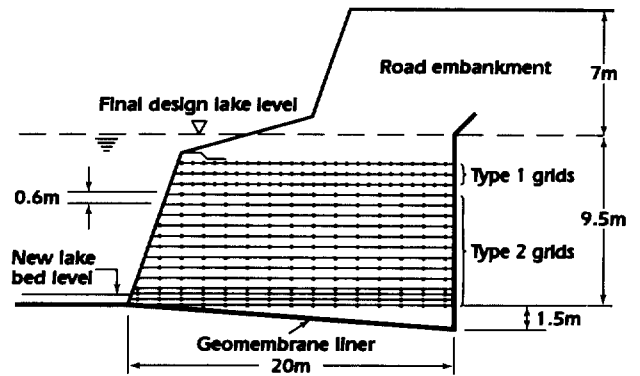


Figure 5 Typical reinforcement layout.

Note: The road embankment (part of a later contract) was constructed using reinforced soil.

#### 2.4 Face Detail

The face of the reinforced slopes had to be relatively inexpensive while possessing high durability and damage resistance. The Engineer ruled out a proprietary segmental concrete block face on the grounds of cost, and instead selected a geogrid wrap-around face. With this detail, the horizontal reinforcement layers are extended up the temporarily supported face of the fill and then returned back horizontally and connected with a full-strength joint to the next layer of reinforcement. There was sufficient information on the durability of the specified grids to satisfy long-term serviceability questions (Wrigley, 1987).

The face also had to remain permeable and retain the silty sand fill. Attention was therefore focused on the selection of a geotextile filter to line the wrap-around face. It was recognised that any damage or malfunction of this geotextile could lead to a steady wash out of fines and ultimately to collapse.

Netlon 1004R geotextile was specified. It has independent certification from the German Federal Waterways Authority (BAW) based on rigorous performance testing with a range of soils including silty sand. These tests assess:

- filter performance by filtering a real soil in turbulent conditions and also examining the resultant permeability after impregnation with soil particles.
- residual tensile strength following exposure to abrasion (16 x 5000 revolutions of a rotating drum containing gravel and water).
- puncture resistance in a test replicating rock armour units being dropped on a soil supported sample.

This non-woven geotextile is manufactured by needle punching two separate geotextiles, one containing staple (short) fibres of polypropylene and the other, a polyester, to create an integrated 800g/m<sup>2</sup> duplex material. This efficient double layer arrangement provides a coarse fibre pre-filter which, additionally, interacts with the soil to achieve a degree of mechanical stabilisation of soil particles which may otherwise be prone to migration.

Despite this certified evidence of the geotextile's robustness and field experience with similar products under extremely severe test conditions (Dixon et. al, 1990), the Engineer was concerned about its vulnerability to damage e.g. from accidental impact, burrowing animals, nesting birds and long term exposure to ultra violet (UV) radiation.

The Engineer, therefore, specified an outer grid wrap-around face retaining a 15cm wide layer of 5 - 10cm sized hard durable fill as cover protection to a geotextile wrap-around local to the face of the silty sand fill (Figure 6).

With the specified grids it is possible to create a full-strength connection between adjacent lengths using an HDPE bodkin (Figure 7). In a wrap-around detail this bodkin provides a more positive joint than simply relying on a frictional anchorage. Furthermore, when the higher grid length is tensioned during installation this helps pull the lower wrap-around face tight.

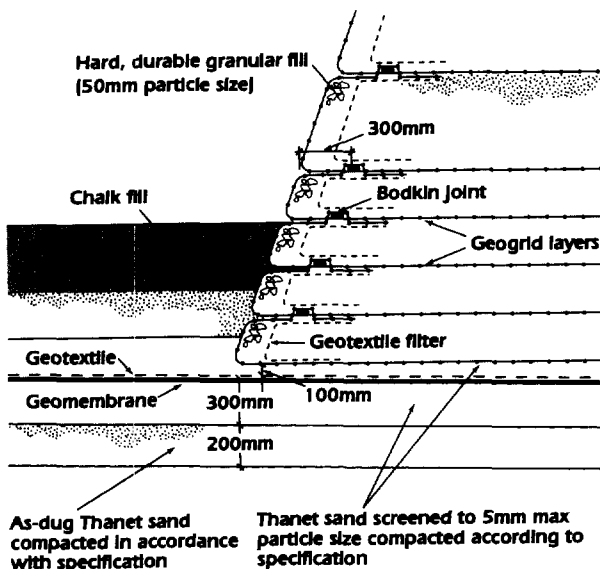


Figure 6 Cross-section showing face detail.

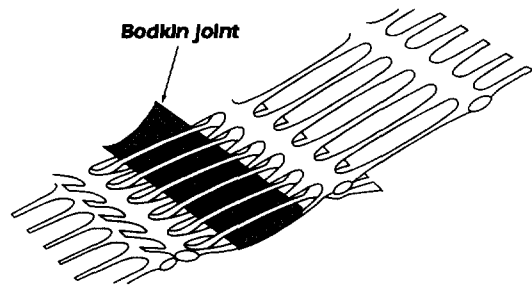


Figure 7

### 3 CONSTRUCTION

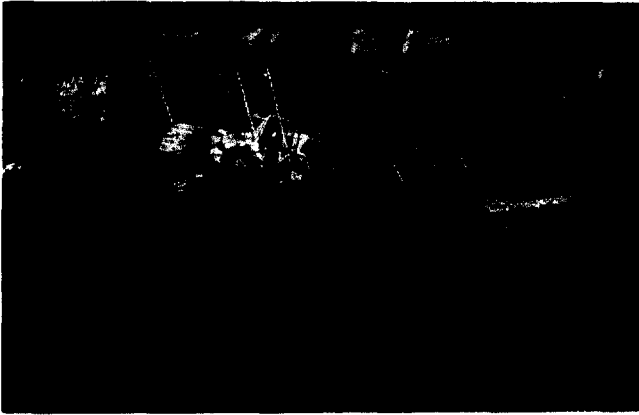
#### 3.1 Contract Award

The Enabling Works contract was let by Bluewater Construction Management Team (BCMT) to O'Rourke Civil Engineering Limited in early 1996 following a competitive tendering process. O'Rourke chose to use the specified geosynthetics. They appointed a specialist sub-contractor to supply and install the lining system for Lake 1 and opted to construct the reinforced soil slopes themselves.

#### 3.2 Lake 1

Lake 1 is oval in plan with a perimeter slope length of approximately 500m. Reinforced soil installation began in April 1996. The Contractor selected a 2.4m high timber formwork system, supported by scaffold tube and fittings, for temporary support to the grid wraparound face (Figures 8 & 9). A 60cm high inner plywood former with lifting holes, tapering in cross section from 20cm at the top to 15cm at the bottom, was used to form the inner geotextile wrap-around.

The grids were cut to design length on site. Bodkin joints were used to avoid wastage from end of roll off-cuts. These lengths were abutted against the inside face of the shutter and nominally joined by cable ties to avoid any gaps opening during installation. The internal former was then placed against the grid face and the geotextile was wrapped around the internal face of the former. A geotextile overlap of 50cm was specified. The silty sand fill was placed and compacted in lifts to a depth of 60cm. This fill was found to have sufficient short-term cohesion that the former could be carefully raised and the resulting void filled, by hand, with coarse material without any slumping of the geotextile face.



Figures 8 & 9

The grid wrap-around face was next returned over the coarse fill and connected to the next grid layer using a bodkin. The free end of the upper grid was then hand tensioned using a steel beam.

The face of Lake 1 was slightly reprofiled by local steepening to accommodate 20cm horizontal ledges at the top of each 2.4m lift on which the shutter could be seated. The overall slope remained at 70°. (The geomembrane which extended up the rear of the reinforced soil block also required its own temporary shuttering).

These details resulted in relatively slow outputs of around 40 - 50m<sup>2</sup> of completed face area per day using two gangs. In order to improve this, the Contractor developed a face detail which replaced the shutter and plywood former with an internal steel mesh former. This was produced by site cutting 5mm diameter steel mesh sheets and bending them into 'U' shaped units 60cm high x 28cm wide. These units were positioned to act as a permanent face former (Figure 10) and then filled with the coarse fill. Since the steel mesh aperture was 20cm x 20cm, the vertical face of the unit was lined with geogrid Type 1 before filling. The top of the unit was cross braced using steel tie wire.

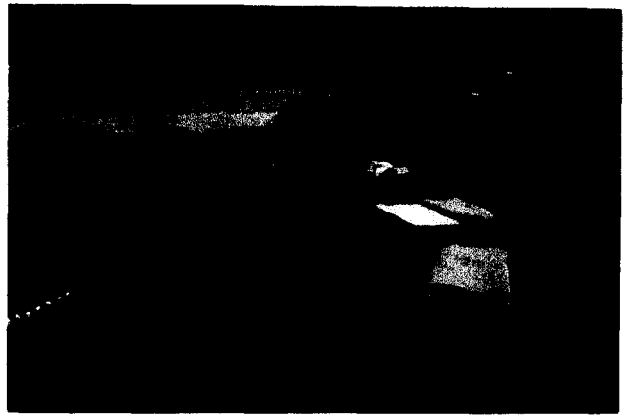


Figure 10

The geotextile was then wrapped up the rear face of the filled unit and the bulk fill placed behind. The main grid length was then wrapped up the front face of the unit and bodkined and tensioned as normal.

This alternative method proved a little quicker, particularly for the higher levels, although the alignment, while acceptable, was less consistent.

The reinforced soil slopes of the Lake are constructed with approximately 60,000m<sup>2</sup> and 80,000m<sup>2</sup> of geogrids Types 1 and 2 respectively supplied in 50m x 1.3m rolls. They were constructed in approximately 3 months.

### 3.3 Lake 2

The water level of Lake 2 was designed to fluctuate with that of the surrounding chalk aquifer and so no geomembrane lining was necessary. About half of the slope length of Lake 2 was formed from the existing chalk quarry face.

Reinforced soil construction took place in the Winter and Spring of 1997. In order to simplify and accelerate installation the Contractor, with assistance from the grid manufacturer, proposed a radically different face comprising site-cast, ordinary-Portland-cement concrete blocks (with 50MPa 28 day compressive strength). These blocks were 2.7m long, 0.6m high and 0.3m wide and contained either one or two layers of 'starter' lengths of cast in Type 2 geogrid (Figure 11). The deeply embedded thick transverse bar of the grid has been shown to provide an anchorage in excess of the design strength of the reinforcement.

HDPE grids have been shown to be unaffected by the highly alkaline environment associated with concrete embedment. (Wrigley, 1987)

This solution was attractive to the Contractor who had already established a batching plant on site and estimated

that he could produce blocks at about a third the cost of typical proprietary segmental units.

For simplicity, the blocks were produced with a stepped vertical face and so the slope profile was amended (Figure 12).

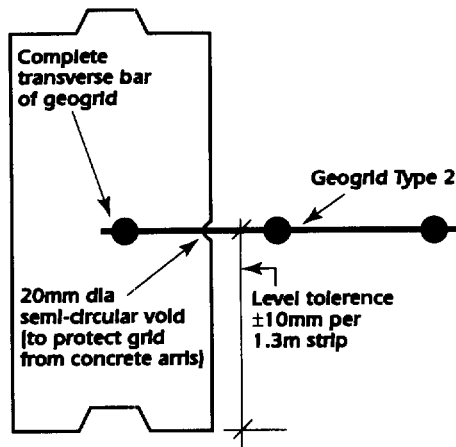


Figure 11 Cross-section of typical block.

These blocks overcame the need for both the shuttering and the coarse fill. The main grid lengths were connected to the starters using bodkins and the geotextile was used to prevent wash out of fines through any small gaps between blocks.

The blocks were cast at a rate of up to 36 per day. Over 1,000 blocks each weighing approximately 1 tonne were required. Installation was much less labour intensive when compared to Lake 1.

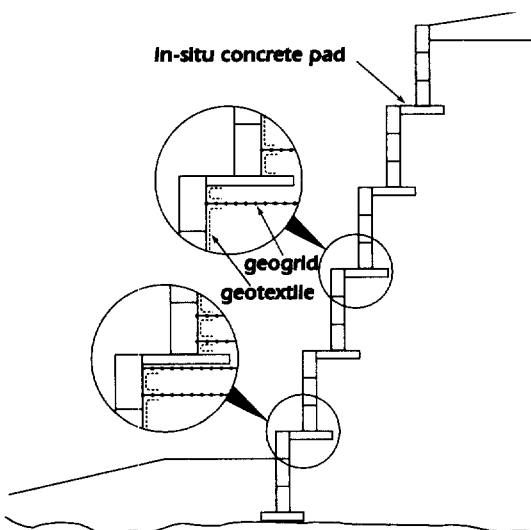


Figure 12

#### 4 CONCLUSIONS

This paper explains the design approach used to address the unusual situation of a reinforced soil lake slope overlying a geomembrane lining system.

The construction details of the three reinforced steep slope facings on this major UK project are also described.

Although the retail park is not scheduled to open until early 1999, Lake 1 (lined) had been substantially completed by the end of 1996 and Lake 2 by the Spring of 1997. There has been no sign of any movement or instability in the reinforced soil structures.

#### ACKNOWLEDGEMENTS

The writer is indebted to Lend Lease, BCMT, Waterman Partnership and O'Rourke Civil Engineering Limited for permission to produce this paper and to J Cannon who carried out much of the original reinforced soil design.

#### REFERENCES

- Tensor International (1995) In-house Publication "Winwall, Version 1.14, In-house reinforced wall and slopes design program to Institute für Bautechnik and UK DoT reinforced slope design method (HA68/94)".
- Dixon, J.H. and Osborn, S. (1990) "Field trials to evaluate geotextile puncture resistance", *Proc 4<sup>th</sup> Int Conf on Geotextiles, Geomembranes and Related Products*, Balkema, Rotterdam. P641 ISBN 90 61 911192.
- Wrigley, N.E. (1987) "Durability long-term performance of Tensor polymer grids for soil reinforcement," *Materials Science and Technology*, Vol 3.

# Soil Bioengineering\Biotechnical Stabilization Of A Slope Failure

Robbin B. Sotir

Principal, Robbin B. Sotir & Associates, Marietta, Georgia

John T. Difini

Engineer, Haley & Aldrich, Inc., Cambridge, Massachusetts

Andrew F. McKown

Vice President, Haley & Aldrich, Inc. Cambridge, Massachusetts

**ABSTRACT:** This paper describes the basic principles of steep slope stabilization using soil bioengineering to reconstruct and stabilize a section of slope along Massachusetts Turnpike at Mile 79.3 E.B. Discussions will focus on the principles of soil bioengineering and reinforced soil slope (RSS) designs, benefits of this interdisciplinary environmentally sound approach, and case study details: vegetation harvesting and storage, design, installation and project status as of October 1997. Design of a fill material, satisfying both agronomic needs of vegetative components and engineering requirements for slope stability, is described. Meeting environmental and aesthetic goals was paramount.

Use of tensile inclusions made from live branches and polymeric geogrids made it possible to construct a highly steepened 4V:1H vegetated earthen buttress slope.

RSS is useful in constructing steepened slopes, improving stability and reducing required fill volumes. Soil bioengineering uses woody vegetation installed perpendicular to the slope face on constructed fill terraces. The installed branches offer immediate reinforcement as supplemental tensile inclusions.

**KEYWORDS:** Soil Bioengineering, Biotechnical, Slope, Stabilization, Vegetation.

## 1 INTRODUCTION

Mechanically stabilized earth (MSE), or reinforced soil slope (RSS) embankment systems are commonly used for the widening and reconstruction of existing roads and highways. This paper focuses on the benefits achieved by combining the principles of soil bioengineering and reinforced soil slope design to reconstruct a failed slope on the Massachusetts Turnpike.

## 2 SYSTEM OVERVIEW

### 2.1 Soil Bioengineering and Biotechnical Slope Stabilization Techniques

Soil bioengineering techniques have been used around the world for centuries and were used in the United States by the Department of Agriculture's Soil Conservation Service in the 1930s. They have since been incorporated into the USDA's National Resources Conservation Service Engineering Field Handbook as Chapter 18, "Soil Bioengineering for Upland Slope and Erosion Control." Soil bioengineering uses mechanical, hydrological, biological, and ecological principles to develop living structures for the stabilization and revegetation of cut and fill slopes. Living woody plant material forms the main structural component. Soil bioengineering is typically used in conjunction with sound engineering data and design, a fact that is especially evident on this project.

In this case, live cuttings from woody plants were installed in the ground in specific configurations and served immedi-

ately as soil reinforcements, horizontal drains, barriers to earth movement and hydraulic pumps or wicks. Much the same as with geogrids, additional stabilization occurs when the roots develop along the length of the embedded stems. Woody vegetation, when properly designed and installed in these specific configurations, can create stable, composite earth masses. Its functional value has been well established. These cuttings can be used alone or in combination with geosynthetic materials.

When living vegetation is combined with inert components such as geogrids, the approach is referred to as biotechnical stabilization. Essentially the vegetated geogrid is a composite of soil bioengineering and an RSS system in which the slope will always be dependent upon the RSS structural measures for stability. This case study project represents an excellent example of how to combine technologies.

### 2.2 Engineering a Reinforced Soil Slope

The design approach to engineering an RSS is a generic process that is typical from slope to slope.

### 2.3 Anticipated Benefits

The combination of RSS and soil bioengineering systems typically provides the following benefits:

- Immediate slope stabilization and erosion control
- Elimination of the need to purchase additional rights-of-way since slopes can be reconstructed at very steep angles
- Reduction of maintenance costs, as there is no need to return to the site to add soil or gravel, or to hydroseed
- Modification of soil moisture regimes using backslope

drainage systems and/or the brushlayer branches which act as wick drains

- Enhancement of opportunities for wildlife habitat and ecological diversity
- Improved aesthetic quality and scenic beauty through revegetation and naturalization of the slope.

### 3 CASE STUDY

#### 3.1 Project Site

The project site is located immediately adjacent to the eastbound lane of the Massachusetts Turnpike at Mile 79.3 in Charlton, Massachusetts. The slope was approximately 144.87 meters (475 feet) in length, ranged from 3.05 meters (10 feet) to 15.25 meters (50 feet) in height and had a slope angle of approximately 1V:1.5H. Stabilization was needed to remediate ongoing surficial sloughing failures. These failures ultimately formed a large exposed, unvegetated area that was increasingly vulnerable to progressive surface erosion and further failure. Groundwater seepage, saturated surficial soils, and seasonal freeze-thaw cycles exacerbated the instability of this north-facing slope. On both sides of the failed area, the slope was well vegetated and appeared stable; however, it was apparent that the failure was expanding on both sides, as shown in Figure 1.

Subsurface conditions at the site include widely graded, slightly cohesive, dense to very dense glacial till overlain by shallow surficial topsoil and forest mat. Bedrock is typically located within 3.05 meters (10 feet) of the base elevation of the slope. However, during construction an outcrop of poor rock was discovered along a 7.62 meter-long (25 feet) section of slope. The rock sloped unfavorably toward the roadway and required controlled blasting to cut it to a stable surface on which the slope could be reconstructed.

#### 3.2 Project Background

Due to the nature and extent of the failure conditions, the Massachusetts Turnpike Authority (MTA) decided it was imperative to correct this situation by reconstructing the slope. See Figure 1. If not treated, these conditions would inevitably lead to further slope failures, additional maintenance costs and an expanding, unsightly, unvegetated slope along a scenic



Figure 1. Overall view of the project from the west-bound lane (Sept. 1994), prior to slope excavation and slope reconstruction

stretch of the Turnpike. A concrete barrier was installed along the base of the slope to contain the failed soil mass and prevent it from moving onto the roadway.

The aim of the project was to design and construct a 4V:1H earthen buttress immediately in front of the cut slope to provide internal, external, and compound stability. The soil bio-engineering approach was adopted to meet the requirement of an aesthetically pleasing and environmentally sound reconstruction, and to assist in controlling internal drainage. This combined approach uses vegetated geogrids to provide the much-needed surficial stability and to support long-term vegetative growth with almost no maintenance requirements. The geogrid is a hybrid design that incorporates brushlayers in the frontal, wrapped portion of the RSS. Over time the live branches take root and increase the internal stability of the reinforced slope.

#### 3.3 Remedial Design

The remedial design called for excavating the failed slope back approximately 6.1 meters (20 feet) to the same slope angle (4V:1H) as the proposed slope and constructing a steepened, biotechnically stabilized earthen buttress. The slope was stabilized with layers of primary and secondary geogrids, burlap, vegetated geogrids at the face, and live fascines over the top of the finished slope. Figure 2 shows a cross section depicting the existing slope (dashed line) and the remedial design.

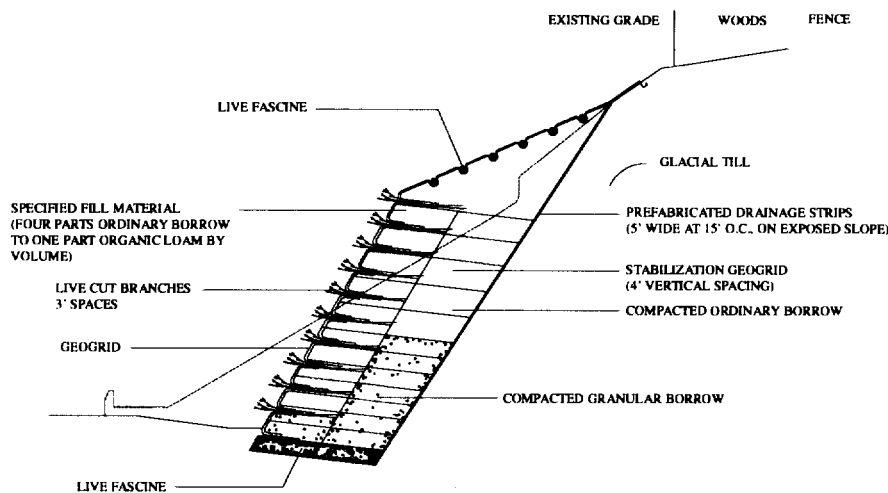


Figure 2. Cross section of remedial slope design

The primary geogrid was designed to provide global, internal, and compound stability to the slope. This grid extends approximately 6.1 meters (20 feet) from the face to the back of the slope. The vertical spacing of the primary geogrid is .61 meter (2 feet) over the lower half of the slope and 1.22 meters (4 feet) over the upper.

As shown in Figure 3, the secondary geogrid, burlap, and brushlayers (which together constitute the vegetated geogrid) were primarily designed to provide facial stability to the slope. As shown in Figure 2, the secondary geogrid and burlap "wrap" the face of each vertical lift between each row of brushlayer branches. The burlap temporarily prevents soil from sloughing out of the face through the grid openings until the plant materials produce leaves and roots. The face wrap extends .91 meters (3 feet) into the slope at the bottom of each vertical lift and five feet at the top. All lifts were constructed using a continuous batter board to control the slope of the face. A front view of the vertical and lateral limits of the vegetated geogrid lifts and brushlayers is provided in Figure 4.

Brushlayers consisting of 2.44 to 3.05 meter (8 to 10 feet) long willow (*salix* sp.) and dogwood (*cornus* sp.) branches were placed on the constructed earthen terraces between each .91 meter (3 feet) vertical lift. These brush-layers, which are installed in layers with the growing ends exposed, extend from the face approximately 3.05 meters (10 feet) back to the mid-point of the slope. During the growing season, these brushlayers will root and produce leaves, stabilizing the face of

the slope. They will also provide some measure of internal stability initially and over the long term. The alternating sequence of constructed earthen terraces and live branch brushlayers is shown in Figure 5.

Drainage panels (1.52 meters (5 feet) wide, spaced 4.57 meters (15 feet) on center) that extend vertically along the back side of the slope were designed to accommodate the migration of groundwater into the reinforced portion of the slope, preventing the buildup of hydrostatic pressures in that area. These panels connect

into a .305 meter (1-foot) thick crushed-stone drainage layer at the base of the slope, which extends the full length and width of the slope.

As shown on Figure 1, four types of backfill were used to reconstruct the slope in addition to the crushed-stone drainage layer at the base. These backfills are granular borrow, ordinary borrow, 50/50 mix, and specified fill. The first three constitute the structurally competent "core" while the specified fill at the face provides a media amenable to plant growth. The specified fill used in the front 3.05 meters (10 feet) of each lift is a blended material consisting of four parts ordinary borrow to one part organic loam by volume. It should be noted that the lifts were constructed to slope away from the face (~20°)



Figure 3. Close-up view of the vegetated geogrid along the front face.

For design of

the slope, stability analyses were conducted to determine: (1) the width of the reinforced zone required to provide a minimum safety factor of 1.5 for deep-seated failure surfaces, and (2) the vertical spacing and design strength of soil reinforcement elements required to provide a minimum factor of safety of 1.3 for both internal

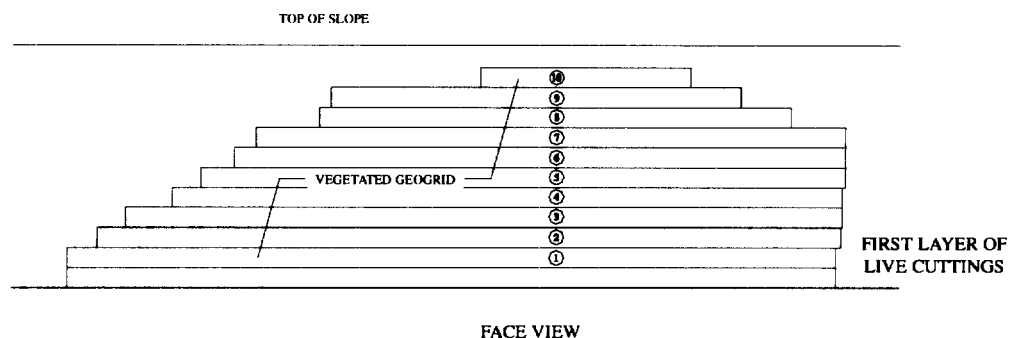


Figure 4. Front view of as-built slope illustrating limits of slope remediation activities.

and that fertilizers were added to each lift to further optimize the growing conditions for the installed brushlayers.

A 1V:3H cut was made above the steep slope and live fascine bundles were installed to prevent surface erosion and to rapidly revegetate the slope with woody plant materials. As illustrated in Figure 6, a live fascine is a collection of live cut branches grouped together in a bundle and secured with twine. The bundle was placed in trenches and anchored with dead stout stakes and live stakes. These structures provide immediate mechanical stabilization and erosion control and will eventually grow and reinforce the surface soil mantle. In this particular application, they also act as a drain, collecting water and transporting it laterally to both ends of the site.

### 3.4 Stability Analyses

A series of slope stability analyses were conducted to design the RSS and assess the stability of the slope under temporary construction conditions (i.e., the cut slope condition). These analyses were conducted using the University of

and compound failure surfaces. For temporary construction conditions, stability analyses were conducted to configure the cut so that a minimum factor of safety of 1.2 was maintained during the construction process. The computer output for the global stability analysis used to determine the lateral extent of the reinforced zone is provided in Figure 7. The failure surface yielding a minimum factor of safety of 1.5 generally defines the extent of the reinforced zone.

### 3.5 Agronomic and Geotechnical Considerations

The design and construction of this slope presented several



Figure 5. The alternating sequence of constructed earthen terraces and live branch layer



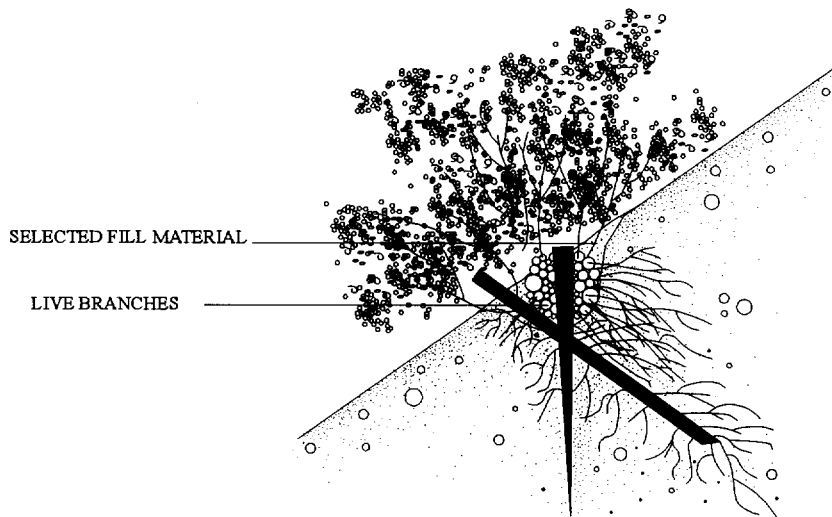


Figure 6. Establishing live fascine.

challenges involving the need to balance agronomic and geotechnical requirements. The factors to be balanced were these: (1) the need for water and nutrients in the slope to sustain and promote vegetative growth versus the desire to remove water so as to eliminate hydrostatic pressures; (2) the need to use organic matter in the slope to provide nourishment for plant growth and development versus the desire to construct the slope with free-draining, inorganic, granular soils; and (3) the need to construct the slope during the fall and winter months while the vegetative plant materials were in a dormant state versus the desire to construct the slope during warmer weather to prevent soil freezing problems and weather delays. A final agronomic consideration was that the plant materials needed to be properly stored following harvesting to protect them from shock. A brief discussion of each of these topics follows.

• **Drainage** - The original design called

for a continuous backslope drainage system to intercept groundwater before it enters the reinforced portion of the slope and divert it to the gravel subbase and drainage system beneath the slope. The backslope drainage system was originally designed to consist of free-draining crushed stone, with filter fabric against the naturally deposited gla-

cial soils. However, since it was desirable to allow some water to migrate to the willow and dogwood branches in the slope, the design was modified to utilize 1.52 meter (5 feet) wide prefabricated drainage strips spaced 4.57 meters (15 feet) on center in place of the continuous crushed-stone backslope layer. That allows some groundwater to migrate into the reinforced zone without permitting hydrostatic pressures to develop on the back side of this zone. The brushlayers also function as horizontal drains, reducing the possibility of hydrostatic pressures.

• **Organic material** - To provide favorable conditions for plant growth, it was desirable from an agronomic standpoint to incorporate organic material in the backfill. To accommodate this, the outer 3.05 meters (10 feet) of slope, starting approximately 1.52 meters (5 feet) up from the base of the slope, was backfilled with a blended material consisting of four parts of ordinary borrow to one part loam by volume. By carefully selecting the mixture and the location within the slope and checking the global stability and location of failure planes, it was possible to satisfy both the agronomic and geotechnical design requirements.

• **Construction time frame** - The freezing of subgrade soils that contain high organic material and water was a daily concern, since the construction was done mostly during the winter

since the construction was done mostly during the winter

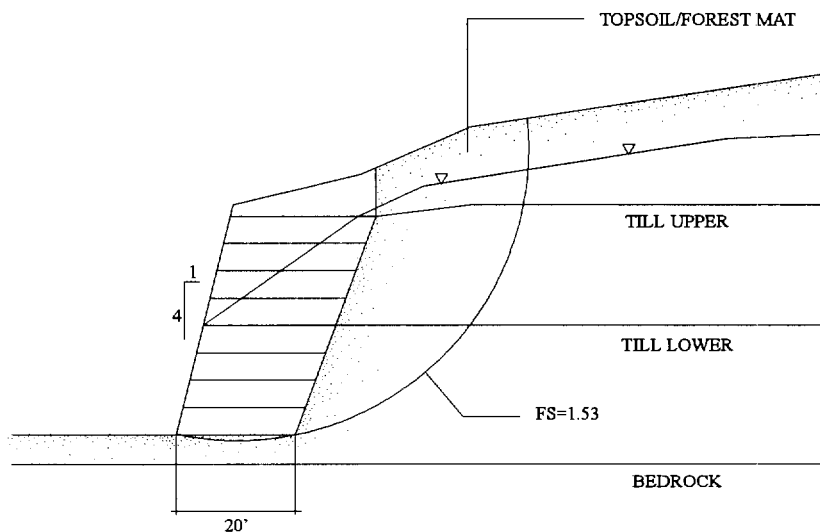


Figure 7. Factor of safety for deep-seated global failure surface.



Figure 8. The condition of the project site, July 1996.

months. To minimize the impact of freezing, the lifts were adequately compacted at the end of each workday, and were inspected the following day for the occurrence of heave or formation of ice lenses; in addition, unsuitable frozen subgrade soils were removed when needed. Furthermore, frequent snow-storms limited the number of workdays on the project's already tight schedule. Accumulating snow, which had to be plowed from the previously constructed lifts before work could continue, shrunk staging and storage areas significantly. It should be noted that a near record snowfall in excess of 254 centimeters (100 inches) occurred during the winter this slope was constructed, following an unseasonably warm fall.

• Harvesting, handling and storage of cuttings - The harvesting of suitable, biotechnically capable plant material and installation of the soil bioengineering systems needed were carefully planned, coordinated and maintained. Numerous potential harvest sites were located before the project started. Sites were then selected based on the quality of material, site accessibility, and proximity to the project site. These harvesting sites contained large stands of willow (*Salix* sp.), a species well-suited for soil bioengineering construction. Refrigerated trucks were used to transport and store the live cut branches, which allowed the cuttings to be stored for long periods of time, such as a month or more. Proper temperature and humidity controls were maintained to keep the branches in dormancy and prevent the cuttings from dying out. The use of refrigerated trailers allowed the contractor to transport larger quantities of material to the site, providing installation crews with immediate access to live cuttings when needed and improving overall operations and efficiency.

#### 4 CONCLUSIONS

The face of the major slope reconstruction, the vegetated geogrid, looks very good. As shown in Figure 8, the slope is stable and the vegetation is well developed. The cut slope above is also well vegetated and appears stable.

This biotechnical installation should continue to root and grow, thus providing for increased surface protection, soil reinforcement, and an aesthetically pleasing revegetated slope. Over time, natural invasion from the surrounding plant community is expected to occur, causing the system to blend into the naturally wooded scenic setting of the area. Thus the long-term mechanical and ecological goals of the project will be satisfied.

#### REFERENCES

- Gray, D.H. and Sotir, R. (1995). *Biotechnical and Soil Bioengineering Slope Stabilization. A Practical Guide for Erosion Control*, John Wiley & Sons, New York, NY, USA.
- Kraebel, C.J. (1936). *Erosion control on mountain roads*. USDA Circular No. 380, 43 pp.
- Coppin, N., Barker, D., and Richards, I. (1990). *Use of Vegetation in Civil Engineering*. Butterworth's: Sevenoaks, Kent, England.
- Gray, D.H. and Leiser, A.T. (1982). *Biotechnical Slope Protection and Erosion Control*, Van Nostrand Reinhold, New York, N.Y. USA.

# Finite Element Analysis of instrumented geogrid reinforced slope

A. Ghinelli

Professor, Department of Civil Engineering, Florence University, Italy

M. Sacchetti

Researcher, Department of Civil Engineering, Florence University, Italy

**ABSTRACT :** A 15 m high green faced reinforced slope was built in 1996 to consolidate a landslide situated on the Montone hill in the province of Perugia (Italy). The reinforced slope was built using as fill material locally available soils and as reinforcement HDPE mono-oriented extruded geogrids. A section of the slope has been fully instrumented in order to verify its long term behavior. To evaluate the field stress and deformation behavior of the Montone reinforced slope a finite element analysis has been carried out. The paper describe the model technique developed to evaluate the filed stress and deformation of steep reinforced slope using special interface elements. The results of finite element analysis are in good agreement with the field measured results.

**KEYWORDS:** Steep slope, Geogrids, Field test, Finite Element analysis

## 1 INTRODUCTION

The Montone hill located in the province of Perugia (Italy), was interested in the past by several instability and erosive phenomena along its slopes, which caused great damage at historical buildings and at road network.

During the last decades important landslides concerned the North-East slope of Montone hill, particularly along the Montone-Pietralunga main road. These phenomena that involved an area of about 15.0 m high and 200.0 m long, produced in proximity of the Fosso Fornaci a road interruption.

In one of the sub-project for the consolidation of the Montone hill, near the Fosso Fornaci, was foreseen to restore the interrupted main road and to stabilize the natural slope by rebuilding it with the local soils reinforced with HDPE geogrids. The reinforced slope presents a maximum height of 15.5 m and a length of about 53.0 m (see Figure 1). Due to the importance of the project, a section of the slope has been instrumented in order to verify its long-term behavior.

The paper deals with the stress and deformation analysis of the Montone reinforced slope by finite element analysis. A procedure to model the fill soil, the reinforcements and the soil-reinforcement interaction using discrete finite elements are described. The properties of the soil fill and of the reinforcement geogrids are also presented.

Field measurement taken over two months period after construction are reported and compared with numerical analysis results.

The paper shows a good agreement between compared results. This fact highlights the possibility to use element finite methods to predict filed behavior of reinforced slopes without rigid face and with a complex geometry.

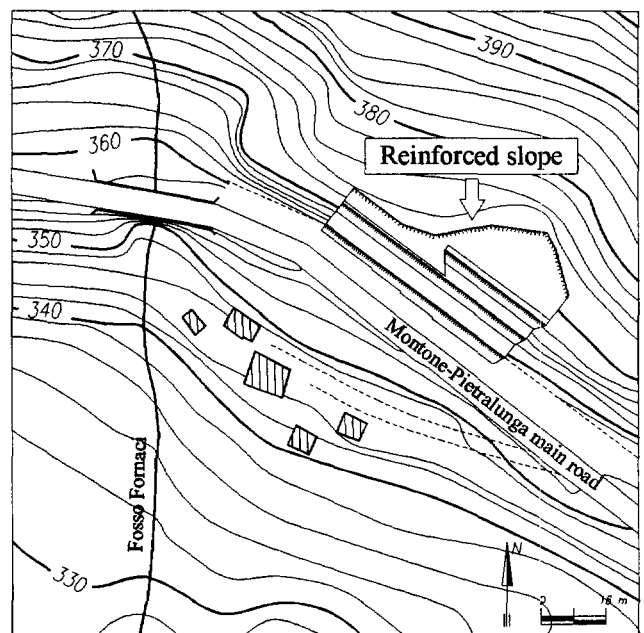


Figure 1. Reinforced slope location

## 2 REINFORCED SLOPE DESCRIPTION

In the last decades the North-East slope of Montone hill was interested by important landslides and erosive phenomena that produced in proximity of the Fosso Fornaci an interruption of the Montone-Pietralunga main road.

For better understanding the reasons of slope instability an intensive geophysical and geotechnical test campaign and a back-analysis study on the old landslide bodies were carried out (Coluzzi et al., 1997).

To restore the interrupted main road and to stabilize the natural slope a green faced reinforced slope was built. The

construction commenced in the summer of 1996 after the landslide body has completely been removed from the main road and after the existing ground surface has been remodeled.

The reinforced slope shows a running length of 53.0 m and a maximum height of 15.5 m, split up in three bodies respectively of 5.3, 5.6 and 4.6 m of height, with 1:1.73 side slope, separated by two horizontal berms of 4.1 m and 3.1 m length (see Figure 2).

As above mentioned the reinforced slope was built using as fill material locally available soils and as reinforcement HDPE mono-oriented extruded geogrids. In particular the entire slope was supplied of 23 reinforcement layers, 0.65 m vertically spaced, with length variable between 4.5 m and 3.15 m.

The green faced reinforced slope was built using the TENAX RIVEL system (Rimoldi et al., 1996), which consist in the use of sacrificial steel mesh form-works that help in the face construction and permit to obtain a very uniform geometry of the slope. A thick drainage system was placed beneath the reinforced bodies.

The Jewell method (Jewell, 1990) was used to design the reinforced slope, whereas global stability analysis was carried out using the STABGM, a code based on the Bishop's modified method (Coluzzi et al., 1997).

The main geotechnical properties of the fill soil and mechanical properties of the reinforcement geogrids

adopted to design are reported in Table 1.

Table 1. Geotechnical properties of the fill soil and mechanical properties of the reinforcement geogrids adopted to limit equilibrium design

	Unit	Design value
<b>FILL SOIL</b>		
Unit weight	[kN/m <sup>3</sup> ]	19.7
Friction angle	[°]	26
Effective cohesion		-
Interstitial pressure ratio	[-]	0
<b>REINFORCEMENT</b>		
Peak tensile strength	[kN/m]	60
Strength at 2% strain	[kN/m]	17
Long term design strength	[kN/m]	25

## 2 INSTRUMENTATION

Due to the importance of the project, a section of the was provided with extensive instrumentation.

The main purpose of the instruments installed is to

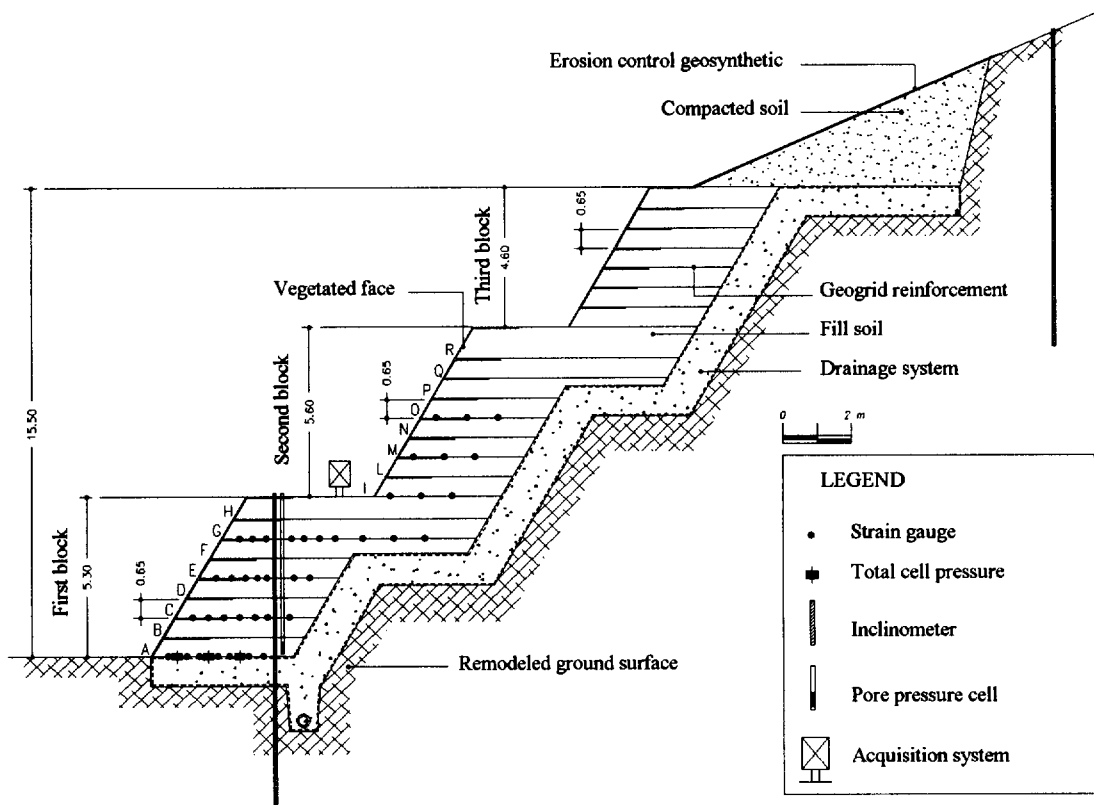


Figure 2. Cross section of the instrumented geogrid reinforced slope

check the overall deformation of the slope and to indicate the long-term behavior of the reinforcements under field stress conditions. Moreover, field measurements are very valuable input data for subsequent numerical analysis with finite element method.

The instrumented section was equipped with 40 strain gauges (electrical wire resistance type) positioned on geogrid ribs of the first and second reinforced block; 3 total vertical pressure cells positioned at the bottom of the first reinforced block; 2 vertical inclinometers installed on the first block and on the top of the third block; 1 pore pressure cell and 1 acquisition system installed on the first block (see Figure 2). Descriptions of instrumentation types and installation procedure are detailed in Coluzzi et al. (1997).

The strain gauges and total pressure cells has been activated after construction, whereas inclinometers and pore pressure cell are not yet active. After about one month measurements 9 strain gauges are "dead".

### 3 FINITE ELEMENT ANALYSIS

For reinforced slopes, deformation and stability are the two main concerns. Nevertheless an accurate assessment of deformations in field condition can only be achieved through a stress-deformation analysis, such as a finite element analysis.

To evaluate the field stress and deformation behavior of the Montone reinforced slope a finite element model of the entire structure has been developed. The numerical simulation has been performed using the CRISP90 computer code (Britto et al., 1990), developed at Cambridge University in the eighties, which uses many soil constitutive models, and capable to simulate drained and undrained geotechnical problems with static load conditions. In particular to simulate the field behavior of steep reinforced slope, without rigid facing, a modeling technique has specifically been developed. This technique foresees to use the following elements:

- "BAR" elements, with linear-elastic or linear elasto-plastic behavior, for reinforcements.
- "LSQ" (Linear Strain Quadrilateral) and "LST" (Linear Strain Triangle) elements, with linear elastic-plastic behavior, for fill soil.
- "SLIP" elements, with behavior based on the Goodman & Taylor (1968), for soil-reinforcement interface.
- "LSQ" and "LST" elements, with linear-elastic behavior, for foundation soil.

To obtain a true and correct forecast of the stress and deformation behavior of reinforced slope by numerical finite element analysis it is necessary to define and subsequently to simulate the very complex interaction mechanisms establishing between the fill soil and the

reinforcement geogrids. In this pattern the use of "SLIP" elements with frictional and adhesive behavior, which permits relative displacements, seems to be able to simulate the above mentioned interaction mechanics.

The finite element model created consist of 2107 nodes and 872 elements (161 reinforcement elements, 322 interface elements and 389 soil elements) (see Figure 3). Computational problems connected with the dimension of the overall stiffness matrix imposed heavy limitations on the elements number of soil foundations. Therefore we decided upon to model a little portion of natural slope with very simple linear-elastic elements having adequate resistance and stiffness to support the reinforced body.

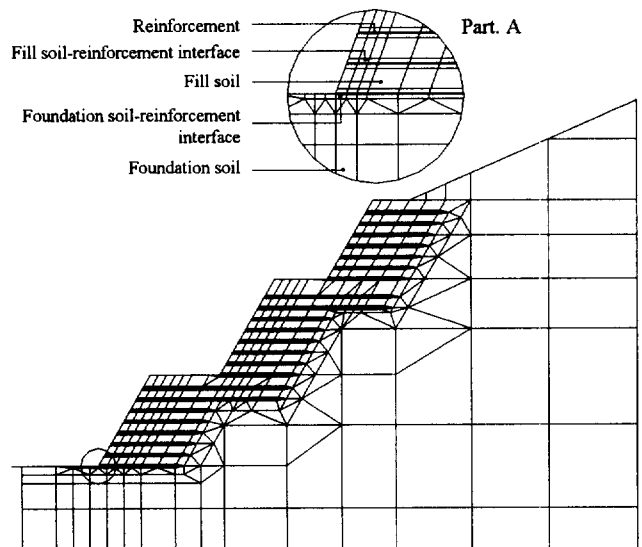


Figure 3. Finite element model

### 4 MATERIAL PROPERTIES

With the final purpose to obtain a more realistic numerical simulation a series of field tests on the reinforced slope and laboratory tests on materials taken from reinforced bodies were carried out. From these tests were assessed the most important mechanical parameters to introduce into numerical model. The tests undertaken are:

- Field density tests, carried out on all three reinforced bodies, that supplied the unit weight of the fill soil.
- Field pull-out tests, performed on geogrid layers, about 0.50 m wide with different anchorage length, purposely embedded into the bottom reinforced body, that given the pull-out factor of reinforcement.
- Rigid plate load tests, carried out on the first reinforced body using circular plates with 300 mm and 600 mm diameter, that supplied the principal deformation parameters of the fill soil.
- Classification tests, performed on several samples of

fill soil taken from reinforced slope, that supplied the limit indexes and the particle size distributions.

- Direct shear tests with standard box of 60x60 mm, performed on samples of fill taken from reinforced slope, that given the shear resistance of fill with particle size finer than ASTM10 sieve.
- Tensile creep tests, carried out on geogrids samples, using different tensile loads and temperatures (Cazzuffi et al., 1997), taken from the reinforced slope after end construction, that given the long-term tensile stiffness of reinforcement.

The most important test results achieved are summarized in Table 2.

Table 2. Geotechnical properties of fill soil and mechanical properties of reinforcement geogrids adopted to finite element analysis

	Unit	Design value
<b>FILL SOIL</b>		
Unit weight	[kN/m <sup>3</sup> ]	18.4
Friction angle	[°]	33
Effective cohesion	-	-
Initial elastic modulus	[MPa]	35.2
Poisson ratio	[-]	0.2
<b>REINFORCEMENT</b>		
Tensile stiffness	[kN/m]	500
<b>FOUNDATION SOIL</b>		
Unit weight	[kN/m <sup>3</sup> ]	20.0
Friction angle	[°]	23
Effective cohesion	[kPa]	100
Elastic modulus	[MPa]	10
Poisson ratio	[-]	0.4
<b>INTERFACE</b>		
Pull-out coefficient	[-]	1

## 5 FINITE ELEMENT ANALISYS RESULTS

The state of deformation at end construction of the Monotone reinforced slope, achieved with numerical analysis, is showed in Figure 4.

Figure 5 shows the comparison between the distribution of reinforcement strains achieved with numerical analysis (light dots and dashes) and achieved from field measurement (dark dots) after two months of the end construction, relating to the first reinforced body (layers A to H). Figure 6 shows the same comparison relating to the second reinforced body (layers I to R).

With reference to numerical analysis results, all layers presents the same shape strain distributions, excepting the

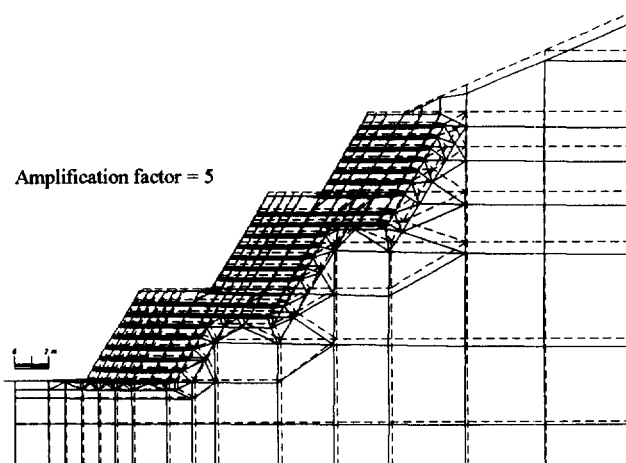


Figure 4. Deformation state of entire reinforced slope

layers G and H on the first body and Q and R on the second body. In particular the second layer of each body (respectively B and L) has the largest strain whereas the top layer (respectively F and P) has the smallest. The peak reinforcement strains occurred in the bottom layers closer to the slope surface than the top layers. The very particular strain profiles of layers G and H on the bottom body and Q and R on the second body are mainly related to their specific border conditions.

From Figures 5 and 6 it is also possible to highlight a close affinity between measured values and calculated values, excepting the at layers A and G. The reasons of this disagreement may be attributable to specific border conditions. In fact for layer A the distribution of strains along its length depends also from foundation soil-geogrid interface characteristics, while for layer G the distribution of strains is influenced by different confinement pressure conditions and different support soils along its length. The presence of a second peak in the strains profile in proximity of different contour condition confirm the above mentioned consideration.

At the last Figure 7 shows a very good agreement between numerical and measured distribution of total vertical pressure at the bottom of the first reinforced body. In the same figure the total vertical pressure has been compared also with "static" pressure due at the weight of reinforced slope. The different envelope is obviously due to thrust of backfill.

## 6 CONCLUSION

To evaluate the field stress and deformation behavior of the Montone green faced reinforced slope a finite element model of the entire structure has been carried out. A modeling technique has specifically been developed to simulate the field behavior of reinforced slope without

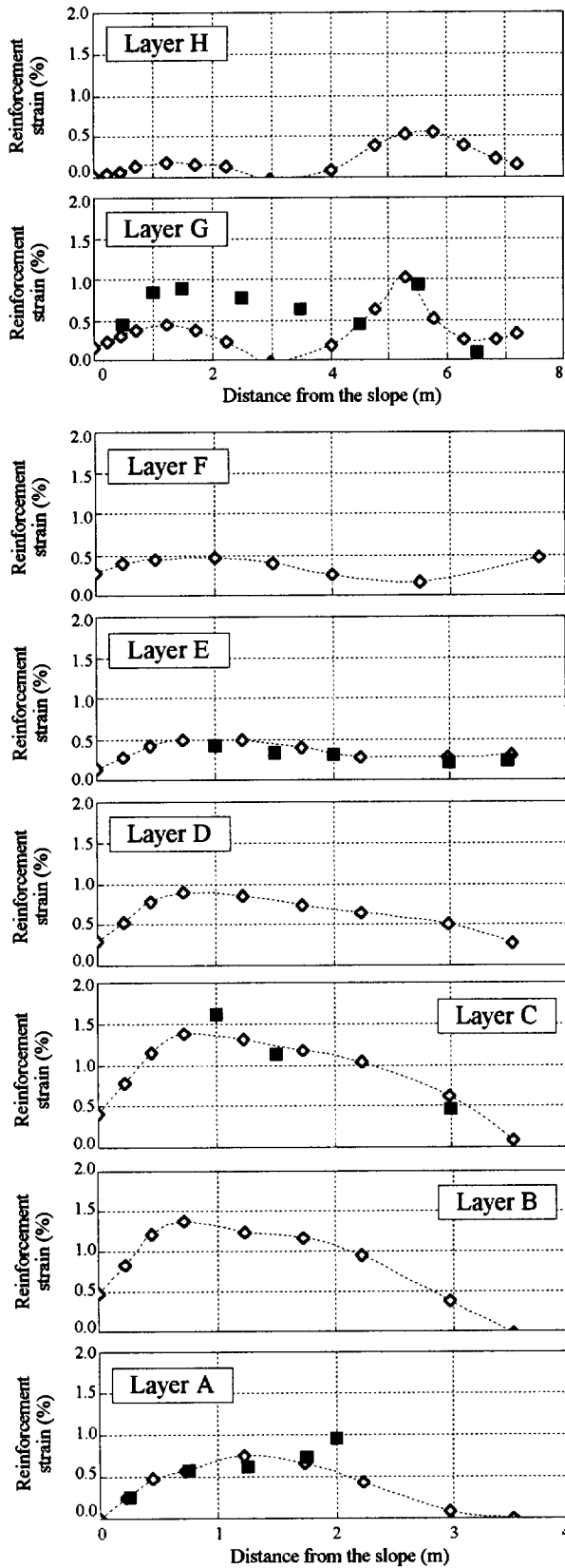


Figure 5. Strain distributions on the reinforcement geogrids of the first reinforced block

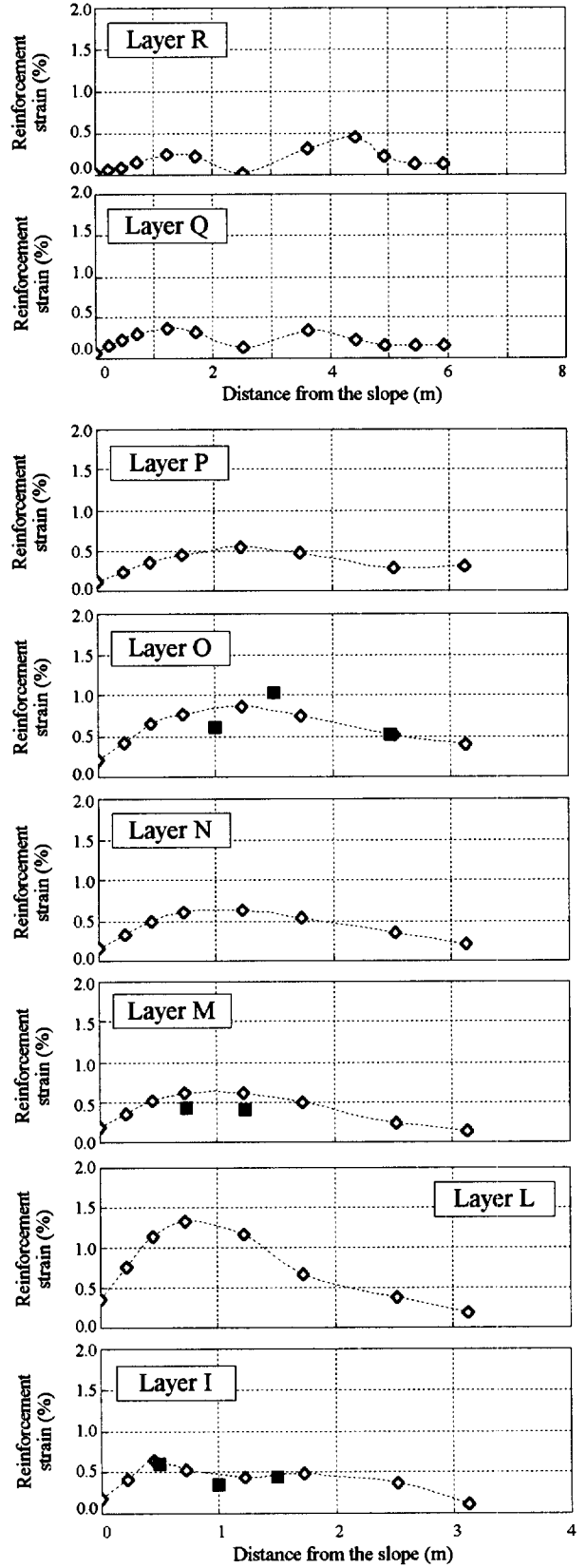


Figure 6. Strain distributions on reinforcement geogrids of the second reinforced block

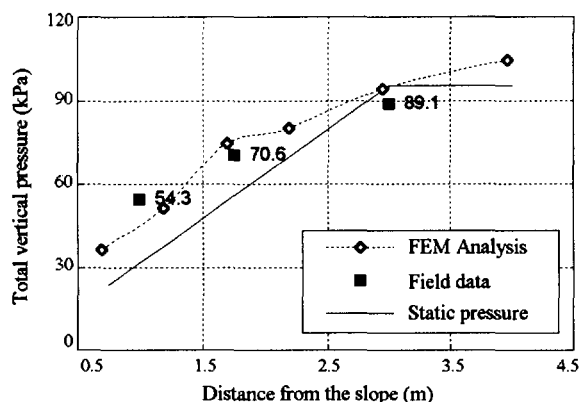


Figure 7. Total vertical pressure at the bottom of the first reinforced block

rigid facing which foresee the use of “SLIP” elements with frictional and adhesive behavior, which permits relative displacements, to simulate the complex interaction mechanisms establishing between the soil fill and the reinforcement geogrids.

A series of field and laboratory tests was carried out to assess the most important mechanical parameters to introduce into numerical model.

The performance of the Montone reinforced slope was monitored by a specific instrumentation installed in a section of the slope during its construction. Field measurement showed the mobilization of tensile resistance on the geogrids and the distribution of total vertical pressure at the base.

The strain distribution results of finite element analysis are in good agreement with field measurement results taken after two months of the end construction. Nevertheless the border conditions have a remarkable influence on the base reinforcement layer and on the layers disposed between each reinforced body. This influence is negligible in the others reinforcement layers.

The good agreement achieved confirm the validity of modeling technique developed and highlights the concrete possibility to use of element finite methods to obtain detailed information about stress and deformations under field condition.

## ACKNOWLEDGMENT

The field measurement is a co-operative project in association with the Department of Civil Engineering of Florence University, TENAX SpA, Viganò, Italy, and R.P.A., Perugia, Italy. The contribution of these organization is acknowledged.

A particular acknowledgment to the SEAS SpA, Perugia, Italy, for precious assistance given during the execution of all the field tests.

## REFERENCES

- Britto, A. and Gunn, M. (1990) *Critical State Soil Mechanics via Finite Elements*, Ellis Horwood Limited, Chichester, England.
- Cazzuffi, D., Ghinelli, A., Sacchetti, M. and Villa, C., (1997) “European Experimental Approach to the Tensile Creep Behaviour of High-Strength Geosynthetics”, *Geosynthetics'97*, Long Beach, CA, pp.253-266.
- Coluzzi, E., Montanelli, F., Rimoldi, P. and Zinesi, M. (1997) “Preliminary Results From an Instrumented Geogrid Reinforced Slope for The Stabilisation of The Montone Hill in Central Italy”, *International Symposium on Mechanically Stabilized Backfill (MSB)*, Colorado USA.
- Goodman, R.E., Taylor, R.L. and Brekke, T.L. (1968) “A Model for The Mechanics of Joined Rock”, *Journal Soil Mechanics Foundations Division*, ASCE, Vol. 99, pp.637-659.
- Jewell, R.A. (1990) “Strength and Deformation in Reinforced Soil Design”, *Proc. IV Int. Conf. on Geotextiles, Geomembranes and related Products*, The Hague, Netherlands, pp.913-946.
- Rimoldi, P. and Jaecklin, F. (1996) “Green Faced Reinforced Soil Walls and Steep Slopes: The State-of-The-Art”, *Geosynthetics: Applications, Design and Construction*, De Groot, Den Hoedt & Termaat Editors, Balkema, Rotterdam, pp.361-380.



# The Assurance Of Durability

John H Greenwood

ERA Technology Ltd, Cleeve Road, Leatherhead KT22 7SA, UK

**ABSTRACT:** The design engineer requires assurance that the geosynthetics he uses will function over a particular service lifetime. This paper introduces the CEN Guide to Durability which provides guidance to the user of geotextiles for non-reinforcing and, to a limited extent, reinforcing applications on the resistance to weathering, chemical and biological effects. "Normal service conditions" are defined for which testing is restricted to a minimum and there is exemption for materials where there is sufficient field experience. The designer of reinforced soil will require in addition information on potential reductions in strength, expressed as partial safety factors, and methods are described for deriving these factors expressed as in BS 8006.

**KEYWORDS:** Degradation, Polymeric ageing, Predictions, Reinforcement, Safety factors

## 1 INTRODUCTION

The design engineer requires assurance that the geosynthetics he uses will function over a particular service lifetime. In the absence of long-term experience, it is necessary to make predictions, which of necessity are based on changes in properties measured over shorter periods, or under more severe or accelerated conditions. For most applications an assurance of a minimum level durability is sufficient, and standards committees on both sides of the Atlantic have defined practical tests intended to assure a minimum durability.

Reinforced soil design requires additional calculation of the reduction in strength due to environmental or other factors and the calculation of a corresponding partial factor for use in design.

## 2 NON-REINFORCING APPLICATIONS

### 2.1 "Normal Service Conditions" and When to Test

The CEN Guide to Durability of Geotextiles and Geotextile-Related Products (CEN 1998) has been written by members of Working Group 5 (Durability) of CEN Technical Committee TC189, Geotextiles, to guide the user and to provide the background to the recommendations it makes. Starting with definitions of durability, "required" and "available" properties, design life and end of life, it then describes the polymer structure, polymer types and manufacturing processes relating to the principal types of geotextile. The environments above and below ground are noted, with particular reference to the temperature, humidity, organic and chemical content of soils and of their potential effects on the polymer. In addition mechanical

load will cause creep or rupture, particularly of soil reinforcements, while transverse load in coarse soils can lead to mechanical damage and to compressive creep of drainage composites. Under some circumstances mechanical load can accelerate chemical attack (or vice versa), although this is not seen as a major problem in the highly oriented polymers used in fibres and geogrids.

The final chapter of the Guide provides guidance on what testing is necessary and when, introducing the concept of a window of "normal service conditions" for which only very limited testing is necessary. Recognising that the geotextiles have been used for upwards of 25 years after which, with few exceptions, the only significant degradation found has been that caused by mechanical damage, the normal service conditions are defined as:

- functional design lifetime less than 25 years
- pH value between 4 and 9
- soil temperature not greater than 25°C
- natural soil, excluding landfills and contaminated land.

It is recognised that the soil may be dry, partially or fully saturated, aerobic or anaerobic, and may contain common transition metals in ionic form such as  $\text{Fe}^{2+}$  and  $\text{Fe}^{3+}$ .

For non-reinforcing applications in natural soil where the geotextile has a functional design life of less than five years, even when the soil structure itself has a longer lifetime, the only tests required are for mechanical damage and weathering. For all other applications with design lives of up to 25 years, screening tests for the hydrolysis of polyester and for the oxidation resistance of polypropylene and polyethylene will be required in addition. A soil burial

test for biological resistance is not required for these polymers, but should be performed on new materials, vegetable based products, geocomposites, coated materials and any others of doubtful quality (such as materials recycled after consumer use). Other polymers require separate assessment, including polyamides which can be subject to both hydrolysis and oxidation.

An important feature of the Guide is the inclusion of a clause allowing manufacturers to use a demonstration of satisfactory long-term service as an alternative to screening tests. The user will decide whether the site conditions experienced were sufficiently similar to the new design conditions for the field evidence of good durability to be accepted, and whether the new product is sufficiently similar to the old. So far, most studies on exhumed samples have shown little evidence of degradation other than mechanical damage due to compaction in coarse fills on installation. The assessment of field experience is mentioned further in Section 3.8.

## 2.2 Mechanical Damage

A simulated site test for mechanical damage has been described by Watts and Brady (1990) and a database of measurements has been compiled by Allen and Bathurst (1994). The results are generally expressed as a reduction in tensile strength (see below, Section 3.4), but for visual observation holes and tears may be more significant for applications in filtration and separation.

## 2.3 Weathering Tests

The screening test for weathering test, ENV 12224, will be a fluorescent tube test based on current practice in artificial weathering and is described further in Greenwood et al. (1996). Drawing on the results of intercomparison tests on a range of stabilised and specially prepared unstabilised geotextiles, the Guide recommends that, unless they are to be covered on the day of installation, all materials should be subjected to accelerated weathering for a UV radiant exposure (total ultraviolet light below 400 nm wavelength received per unit area) of 50 MJ/m<sup>2</sup>. This corresponds to approximately 250 hours in a weatherometer and to one summer month's exposure on site in southern Europe. As with mechanical damage, loss of strength is taken as the indicator of degradation for all applications, since it can be measured quantitatively and more accurately than, for example, hydraulic permeability.

For applications in soil reinforcement or otherwise dependent on long-term strength, geotextiles which retain over 80% of their strength in the weathering test should be covered within one to four months, while those which retain 60% to 80 % of their strength should be covered within 2 weeks. For non-reinforcing applications the acceptable bands of retained strength are over 60% and 20% to 60% respectively. The time to cover depends on the season and location in Europe, it being unreasonable to apply the same

rule on a hot summer's day by the Mediterranean as on a short winter's day in Scandinavia. If the material fails the test it has to be covered on the day of installation.

Correlation between the reduction in strength and the time to cover on site is believed to be a useful and practical concept. Extended artificial weathering tests using similar methods are required for materials which are to be exposed for longer durations.

## 2.4 Hydrolysis and oxidation

Apart from the soil burial test for biological resistance (ENV 12225), which was described by Greenwood et al (1996), the only tests required for non-reinforcing applications with service lives from 5 to 25 years are the screening of polyester geotextiles for resistance to internal hydrolysis and of polypropylene, polyethylene and polyamide for resistance to oxidation. It is well established that normal textile grade polyester degrades slowly under moist conditions, and high tenacity polyesters even more slowly. Based on current quality control practice in polyester manufacture, ENV 12447 proposes immersing the geosynthetic in water at 95°C for 8 weeks and determining the percentage reduction in strength. This is a simple and directly relevant screening test that avoids the problems of determining carboxyl end-group count and molecular weight. The screening test for oxidation of polyethylene and polypropylene is an oven ageing test at 110°C for polypropylene and at 100°C for polyethylene. The passmark is 50% of tensile strength and the durations are longer for reinforcing than for non-reinforcing applications.

## 2.5 Beyond Normal Service Conditions

Outside the "window" of normal service conditions the Guide recommends the designer to consider further tests. For example, for pH values below 4 and above 9, screening tests in concentrated alkali and in acid under aerobic conditions have been developed. For landfill sites, contaminated land, or for very long durations under hydrolysing or oxidising conditions, Arrhenius type accelerated testing should be considered.

# 3 REINFORCING APPLICATIONS

## 3.1 General

The design of reinforced soil is not covered in detail by the CEN Guide to Durability but is governed by codes such as BS 8006 which specify a safety factor  $f_m$  for the durability of the material which is applied to the design strength. Design lives are long, typically 50 to 120 years. Definition of  $f_m$  requires a numerical estimate of the reduction in strength that will occur by the end of the design life.  $f_m$  is the product of several partial safety factors (>1) as listed in Table 1 but for only some of them does the code specify the

means of calculation. Methods for deriving these factors from the properties of the reinforcement are not included in the Guide, but some have been drafted elsewhere (for example WSDOT 1997). The following Sections are intended to point out some of the items which should be addressed.

Table 1. Partial safety factors as defined by BS 8006: 1995.

$f_{m11}$	applied where the base tensile strength is not the characteristic strength	statistical*
$f_{m112}$	= 1.0 for polymers	
$f_{m21}$	statistical scatter of long-term data	statistical
$f_{m22}$	uncertainty of extrapolation	uncertainty
$f_{m211}$	mechanical damage	reduction
$f_{m212}$	long-term effect of mechanical damage	uncertainty
$f_{m22}$	chemical effect of the soil environment	reduction/ uncertainty

\*For the use of these definitions see Section 3.9

### 3.2 Specifications

The general service environment including the soil types, temperatures and gradations, the expected loads and the design life must first be defined. The information required includes:

- tensile properties including characteristic strength
- creep and rupture tests
- damage tests
- chemical description of the material
- chemical durability tests
- field experience (if any)
- quality assurance statement.

The range of loads, temperatures, times and soil gradations used, in particular those for the creep and rupture tests, must correspond to the service environment. Without a complete set of data it is necessary to resort to default and uncertainty factors which too often turn out to be controversial. The ultimate goal must be to define a procedure which is independent of the operator and excludes all uncertainty factors.

### 3.3 Separation of Long-Term Strength from Long-Term Strain

Until there is an integrated theory of creep and stress-rupture the calculation of partial safety factors for strength and strain should be kept separate. While strength is sensitive to mechanical damage and to environmental influences such as weathering and possible long-term

chemical degradation, creep strain at lower loads is affected by little except load and temperature.

### 3.4 Mechanical Damage

As mentioned in Section 2.2, the effect of mechanical damage is generally expressed as the ratio in strengths of a damaged material compared with the undamaged material and expressed as a percentage. The partial safety factor  $f_{m211}$  will then be the inverse of the ratio. Methods are being developed for performing damage tests in the laboratory using standard fills. The reduction in strength for the fills on the site being considered can be interpolated by plotting the reductions in strength against a soil parameter such as  $d_{50}$  (WSDOT 1997).

Very little information exists on the effect of mechanical damage on long-term strength, if any, and in this situation the method of Allen and Bathurst (1996) could be used to define  $f_{m212}$ .

### 3.5 Environmental effects

The principal potential degradation mechanisms for commonly available geotextiles are those which are the subject of screening tests (Section 2.1). Internal hydrolysis, the slow degradation of polyester fibres in water irrespective of pH, has been studied by a number of authors and the reduction in strength of high tenacity fibres has been predicted. From measurements of both retained strength and molecular weight after immersion in water (pH7) at elevated temperatures the rate of bond breakage can be derived as a function of temperature. The strength of the polyester at long times and lower temperatures can then be derived by extrapolation using Arrhenius' formula. The predictions in Table 2 use the calculations of Burgoyne and Merii (1993) for the two fibres they used, PET1 and PET2, while the results of Schmidt et al (1994) for tests at 50 to 70°C have been extrapolated assuming that the rate of loss of strength is linearly proportional to the rate constant. All refer to high tenacity fibres with number-average molecular weight  $M_n > 25000$ . A similar calculation has been made by Salman et al (1997) for a polyester with  $M_n = 18200$ .

Table 2. Percentage retained strength following internal hydrolysis.

	50 years		120 years	
	20°C	30°C	20°C	30°C
Burgoyne (PET1)	98	92	96	87
Burgoyne (PET2)	96	85	92	74
Schmidt et al.	95	89	85	64
Salman et al.	84	54	62	0

These predicted reductions in strength can be used to derive the reduction factor  $f_{m22}$ . It should be noted that the data

refer to saturated conditions and that internal hydrolysis will take place more slowly in unsaturated soils. Alkaline hydrolysis, which reduces the strength due to surface attack, should be considered in addition for soils with a pH of 9-10 or above.

There is no generally accepted method for predicting the reduction in strength of polyolefins due to oxidation, but that of Salman et al (1997) provides an example.

Extrapolations based on logarithmic scales as in Arrhenius' method can have wide confidence limits and an estimate should be made of the sensitivity of any prediction to changes in the input data. It may therefore be necessary to set an additional factor to account for the uncertainty of the extrapolation, but this factor should be handled separately as described in Section 3.9.

Weathering is discussed in Section 2.3. If a reduction in strength is anticipated due to weathering during installation, then this must be included in the calculation of  $f_{m22}$ .

### 3.6 Stress-Rupture

As with all extrapolations, stress-rupture results must be examined for any evidence of a change of behaviour, whether in the shape of the curve, the elongation at break or the appearance of the broken specimen. Any change in the mechanism of failure will invalidate the extrapolation.

Long-term design strength is currently predicted by fitting a curve to the stress-rupture data, conventionally plotted as in Fig. 1, and extrapolating it from shorter times at high loads to longer times at lower loads. The most commonly used fit is:

$$T = T_0 - b \log t \quad (1)$$

where  $T$  is applied tension (load) expressed as a percentage of the tensile strength of the same batch of material,  $t$  is time and  $T_0$  and  $b$  are constants. With  $x = \log t$ ,  $y = \sigma$ , and the subscript  $av$  indicating a mean,

$$S_{xx} = \sum (x_i - x_{av})^2 \quad (2)$$

$$S_{yy} = \sum (y_i - y_{av})^2 \quad (3)$$

$$S_{xy} = \sum (x_i - x_{av})(y_i - y_{av}) \quad (4)$$

$$b = S_{xy} / S_{yy} \quad (5)$$

and the straight line fit is:

$$T_0 = y_{av} - x_{av} / b \quad (6)$$

The regression line is then extrapolated to the design lifetime to give the unfactored design strength  $T_{CR}$ , again as a percentage of the batch tensile strength. The regression line is expected to cross the line  $T = 100\%$  at a time comparable with the duration of a tensile test.

Table 3: Example of stress-rupture results (fictitious).

load as % tensile strength		time to rupture (h)	
85		1.2	
85		7	
85		21	
80		19	
80		61	
80		225	
75		345	
75		716	
75		2,014	
70		3,970	
70		9,836	
70		>18340	
$x_{av}$	2.351	$b$	-0.214
$y_{av}$	77.5	$n$	12
$S_{xx}$	19.06	$K$	0.0442
$S_{yy}$	375	$t$	1.812
$S_{xy}$	-80.27	$s$	0.4340
predicted stress rupture load for 1000000 h			60.5%
lower confidence limit for 1000000 h			54.7%
$f_{m121}$ based on statistical procedure			1.11

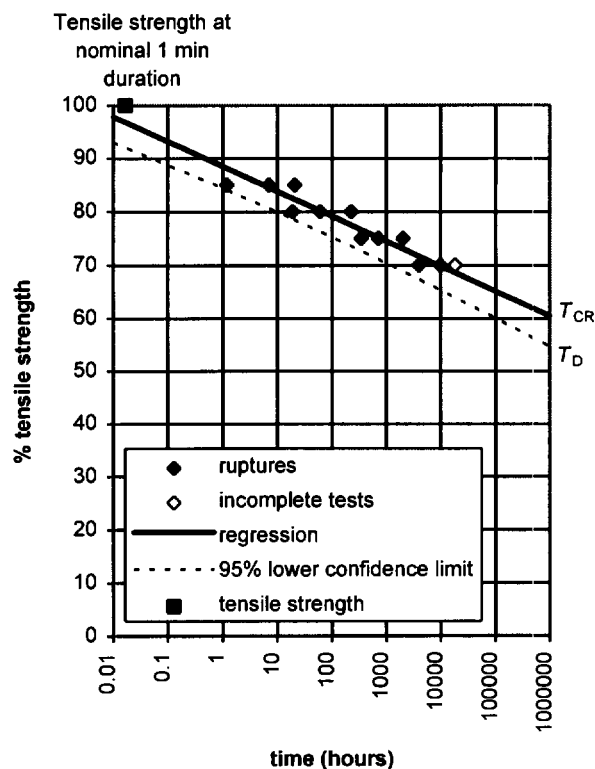


Fig. 1 Stress-rupture diagram

Statistically, the lower confidence limit is given by a formula which combines the variance of the data with the variance of the gradient of the line:

$$y = y_{av} + b(x - x_{av})/K - (ts/K)[K(1 + 1/n) + (x - x_{av})^2/S_{yy}]^{1/2} \quad (7)$$

where  $n$  is the number of measurements,  $t$  is the value of Student's  $t$  corresponding to  $(n - 2)$  and the appropriate (one-sided) probability level, and

$$s = [(S_{xx} - S_{xy}^2/S_{yy})/(n - 2)]^{1/2}; \quad K = b^2 - t^2 s^2/S_{yy} \quad (8)$$

This curve forms the lower branch of a hyperbola that draws away from the stress-rupture line on extrapolation and meets the design life at  $T_D$  such that  $T_{CR} / T_D = f_{m121}$  (see example with numerical data in Table 3 and stress-rupture diagram in Fig. 1). WSDOT (1997) defines the reduction factor as equalling  $100/T_{CR}$  and applying it to the MARV strength, which in the BS 8006 system is equivalent of applying  $f_{m111}$  and then setting  $f_{m121} = 1$ . In either case it is important not to double-count the variability due to scatter. The question of whether design should more correctly be based on residual strength has been raised elsewhere (Greenwood 1997).

Methods for defining  $f_{m122}$ , the uncertainty factor which reflects the considerable step of predicting 50 to 120 year performance from rupture data over much shorter periods, are based on the duration of the longest test result. The methods allow extrapolation up to ten times without further penalty and then increase  $f_{m122}$  progressively to reach values of 2 for extrapolation by a factor of 100 based on  $T_d$  (BS 8006), or 1.2 or 1.4, depending on the likelihood of a knee, based on the confidence limit as defined by WSDOT (1997). Following current practice in the calculation of stress-rupture characteristics, it is proposed that the duration of an incomplete rupture test should be acceptable for this procedure provided that it lies to the right of the curve as in Fig. 1.

Any such procedure should include measurements made at different temperatures, firstly to allow design strengths to be defined for different design temperatures and secondly to accommodate predictions made by time-temperature shifting. If this is done, the longest duration used to define  $f_{m122}$  may be redefined as the longest test after time-temperature shifting (WSDOT 1997). A maximum temperature shift of 20°C below the lowest test temperature is proposed.

Measurement of stress-rupture data is laborious, expensive and can give similar results on similar products. Small and Greenwood (1991) combined results from a range of polyethylene geogrids to produce a general stress-rupture curve for the range. Such measurements on products from the same range of products are generally acceptable but the rules for acceptance require definition (WSDOT 1997).

### 3.7 Combination of Partial Safety Factors

Following Greenwood and Yeo (1996) partial safety factors should correctly be classified and combined as follows:

reduction factors	multiply
statistical factors	combine statistically to give the correct final probability level
uncertainty factors	choose an appropriate overall factor not less than the largest partial factor

The resultant factors defined by the three classes should then be multiplied.

### 3.8 Creep Strain

In the absence of a satisfactory method for predicting the creep of the soil-reinforcement composite, current practice is to measure the unrestrained creep of geosynthetics for soil reinforcement in air. This yields maximum and thus conservative values for strain.

The comments made at the start of Section 3.6 concerning the extrapolation of stress-rupture apply equally well to creep. Again, there is no fundamental materials based equation for curve fitting. The equation

$$\varepsilon = \varepsilon_0 + \varepsilon_1 \log t \quad (9)$$

is normally sufficient for polyester and a power law

$$\varepsilon = \varepsilon_0 + \varepsilon_1 t^n \quad (10)$$

is a useful model for the primary creep of polyethylene with  $\varepsilon =$  strain.  $\varepsilon_0, \varepsilon_1$  and  $\varepsilon_2$  (below) are all functions of applied load, the shape of which is reflected in the isochronous curves. For polyethylene it is necessary to predict the onset of secondary (constant strain rate) creep. This can be done by adding a constant strain rate term  $\varepsilon_2 t$  and curve fitting to tests at higher values of load which exhibit secondary creep. If a relation is established between  $\varepsilon_2, T$  and applied load, for example by using Sherby-Dorn diagrams, then the onset of secondary creep can be predicted at lower values of  $T$ .

As for stress-rupture, creep strain curves can be time-temperature shifted, offering the possibility of abbreviated testing (see for example Thornton et al 1997). It should be noted, however, that since the elongation at break is itself a function of time and temperature the shift factor for creep strain may differ from that for stress-rupture of the same material.

The accuracy of the prediction of creep strain has been examined by Müller-Rochholz and Koslowski (1996) and found to lie within 0.7% strain for polyesters and polyethylene at 7% strain, predicted from 24 h to 24000 h. These levels of accuracy are comparable with the variability in short term creep modulus, suggesting that a partial safety factor for uncertainty of strain extrapolation is superfluous. As 10 year creep strain measurements on polyester based products are become available, the only partial safety factor

required for creep strain extrapolated to 100 years, given that temperature has already been taken into account, should be to reflect the variability in the initial strain or modulus of the material. This argument will not apply to creep rupture data until corresponding 10 year data are available.

### 3.9 Field Experience

The above predictions will increasingly be complemented, and eventually replaced, by experience from site. Statements that no degradation took place should always be accompanied by an estimate of what degradation might have been predicted given the site conditions. A conclusion that "no degradation occurred, and none was expected" serves only as a demonstration that no unexpected phenomena are present.

## 4 CONCLUSIONS

A document on the durability of geotextiles is in place for the guidance of civil engineers. Further details are necessary to cover the definition of partial safety factors used in the design of reinforced soil.

### ACKNOWLEDGEMENTS

I acknowledge the many contributions made by members of CEN TC189/WG5 toward the first part of this publication. The second part is based partly on work supported by the Geotechnical Engineering Office, Hong Kong, and is published with the permission of the Director of Civil Engineering of the Hong Kong Government. The views expressed are those of the author. The Directors of ERA Technology Ltd are thanked for permission to publish.

### REFERENCES

- BS 8006: (1995) *Code of Practice for Strengthened/Reinforced Soils and Other Fills*, British Standards Institution, London
- CEN (1998). *Geotextiles and Geotextile-related products: Guide to Durability*. CEN Report, Brussels, in press.
- ENV 12447 (1997). *Geotextiles and Geotextile-Related Products. Method for determining the resistance to hydrolysis*. CEN, Brussels
- ENV 12224 (1996). *Geotextiles and Geotextile-Related Products. Determination of the Resistance to Weathering*. CEN, Brussels.
- ENV 12225 (1996). *Geotextiles and Geotextile-Related Products. Method for determining the microbiological resistance by a soil burial test*. CEN, Brussels.
- Allen, T.M. and Bathurst, R.J. (1994) "Characterisation of Geosynthetic Load-Strain Behaviour after Installation Damage", *Geosynthetics International*, Vol. 1, No. 2, pp. 181-199.
- Allen, T.M. and Bathurst R.J. (1996) "Combined Allowable strength Reduction Factor for Geosynthetic Creep and Installation Damage", *Geosynthetics International*, Vol. 3, No. 3, pp. 407-439.
- Burgoyne, C.J. and Merri, A.L. (1993) "Hydrolysis tests on polyester yarns", Cambridge University Department of Engineering Technical Report CUEDID-Struct/TR138, Cambridge, U.K.
- Greenwood, J.H., Trubiroha, P., Schröder, H.F., Franke, P. and Hufenus R. (1996) "Durability Standards for Geosynthetics: the Tests for Weathering and Biological Resistance", *Geosynthetics: Applications, Design and Construction*, eds. de Groot, M., den Hoedt, G. and Termaat, R.J., Balkema, Rotterdam, Netherlands, pp. 637-642.
- Greenwood, J.H. and Yeo, K.C. (1996) "Assessment of Geogrids for Soil Reinforcement in Hong Kong", *Earth Reinforcement*, eds. Ochiai, H., Yasufuku, N. and Omine K., Balkema, Rotterdam, Netherlands, pp. 363-367.
- Greenwood, J.H. (1997) "Designing to Residual Strength of Geosynthetics Instead of Stress-Rupture", *Geosynthetics International*, Vol. 4, No. 1, pp. 1-10.
- Müller-Rochholz, J. and Koslowski, C. (1996) "Creep prediction", *Geosynthetics: Applications, Design and Construction*, eds. de Groot, M., den Hoedt, G. and Termaat, R.J., Balkema, Rotterdam, Netherlands, pp. 1027--1030.
- Salman, A., Elias, V., Juran, I., Lu, S. and Pierce, E. (1997) "Durability of Geosynthetics Based on Accelerated Laboratory Testing", *Geosynthetics '97*, Long Beach. IFAI, St. Paul MN, USA, pp. 217-234.
- Schmidt, H.M., te Pas, F.W.T., Risseeuw, P. and Voskamp, W. (1994) "The hydrolytic stability of PET Yarns under medium alkaline conditions", *Fifth International Conference on Geotextiles, Geomembranes and Related Products*, Singapore, Vol. 3, pp. 1153-1158.
- Small, G.D. and Greenwood, J.H. (1993) "A Review of the Phenomenon of Stress-Rupture in HDPE Geogrids", GEO Report No 19, Geotechnical Engineering Office, Hong Kong, 77p.
- Thornton, S.J., Allen, S.R. and Thomas, R.W. (1997) "Approaches for the Prediction of Long-Term Viscoelastic Properties of Geosynthetics from Short-Term Tests", *Geosynthetics '97*, Long Beach. IFAI, St. Paul MN, USA, pp. 277-291.
- Watts, G.R.A. and Brady, K.C. (1990) "Site damage trials on geotextiles", *Fourth International Conference on Geotextiles, Geomembranes and Related Products*, The Hague, Netherlands, pp 603-607
- WSDOT (1997) "Geosynthetic Reinforcement Product Submission and Approval Requirements". *Test Method 925*. Washington State Department of Transportation, USA.

# Long-Term Experience with Reinforced Embankments on Soft Subsoil: Mechanical Behavior and Durability

K.-H. Blume

Dipl.-Ing., Federal Highway Research Institute, Bergisch-Gladbach, Germany

D. Alexiew

Dr.-Ing., HUESKER Synthetic GmbH & Co., Gescher, Germany

**ABSTRACT:** Two projects of embankments on soft ground with high-strength basement reinforcement are shortly described. Started in 1981 and 1986, respectively they belong to the first one's using preloading plus reinforcement for autobahns and highways in Germany. Site conditions, construction stages, measurement data and evaluation are presented, including long-term reinforcement strain measurements. The geotextiles are still under tension. In 1995 high-tenacity polyester woven was exhumed from underneath the first embankment and analyzed for evaluation of durability. Important preliminary results are reported, showing negligible loss of strength in 14 years. In conclusion, findings and recommendations for focal points of design, long-term reinforcement behavior and durability are summarized.

**KEYWORDS:** Embankments, Reinforcement, Long-term-measurements, Soft soils, Durability

## 1 INTRODUCTION

In Germany, in the construction of highways on soft saturated subsoils, increased use is being made of the preloading method. The advantages compared to soil replacement are not only the high cost savings but also countryside, environmental and ground water protection. The development of the preloading method is closely connected with the development of geosynthetics. The reinforcement function is of particular importance as it can be required not only to ensure the short-term stability during construction, but also the final long-term stability.

Since around 1970, the Federal Highway Research Institute (Bundesanstalt für Straßenwesen -BASt) has been involved in such projects on federal highways and autobahns. Investigation and measuring programs have been performed on large-scale test embankments. The aim was to ascertain the behavior of the soft subsoil and the long-term behavior of high-strength geosynthetic reinforcement. Some of the experimental embankments were just loaded up to ground failure to verify the assumptions and results of the stability calculations.

For the Federal autobahn project BAB A 26, connecting the cities of Hamburg and Stade, a test embankment was built near the town of Rübke (designated as 'Rübke-embankment' here) by the BASt in 1981, simulating a real autobahn-section on saturated peat with high-strength basement reinforcement. The project, materials used and deformation behavior until now are reported below.

Based on this experience the entire highway B 211 at the town of Grossemeer was built in 1986 under similar conditions using a reinforcement of even higher strength (designated as 'Grossemeer-embankment' here). The measurements in this case were extended by direct strain measurements on the high-strength woven used, which are continued up to now. The project, materials and most important measurement results including the long-term strains are shortly described.

In autumn 1995, after a 14-years-service period, parts of the high-tenacity polyester woven from underneath the 'Rübke-embankment' were exhumed. Tests and analyses were carried out for evaluation of durability. The most important findings are also presented.

## 2 TEST EMBANKMENT AT RÜBKE

### 2.1 Description Of The Full-Scale Test

The dimensions of the embankment were in compliance with the standard cross section RQ 26 planned for the autobahn. Geometry and essential characteristic values of the peat subsoil are shown in Figure 1. The consolidation calculations resulted in a required preloading height of 3.6 m. A part of preloading had to be removed after consolidation. The stability calculations were performed according to DIN 4084 (Bishop's method) modified by reinforcement retaining force. Only low short- and long-term strains were allowed. The calculations resulted in a reinforcement mobilizing at least 90 kN/m at maximum 5% short-term strain, with an ultimate tensile strength (UTS) of at least 200 kN/m and ultimate strain  $\leq 10\%$ . Only 1% creep strain in two years was allowed under 90 kN/m tension force. A high-strength polyester woven geotextile (Stabilenka® 200) was selected. The test comprises preloading with a subsequent consolidation period of just under two years, removal of preload, a reloading and the long-term measurements of the deformation behavior.

The test embankment was constructed directly on the terrain without any soil replacement. First of all the woven was laid on the grass in July 1981.

Loads, heights and settlements to date are shown in Figure 2.

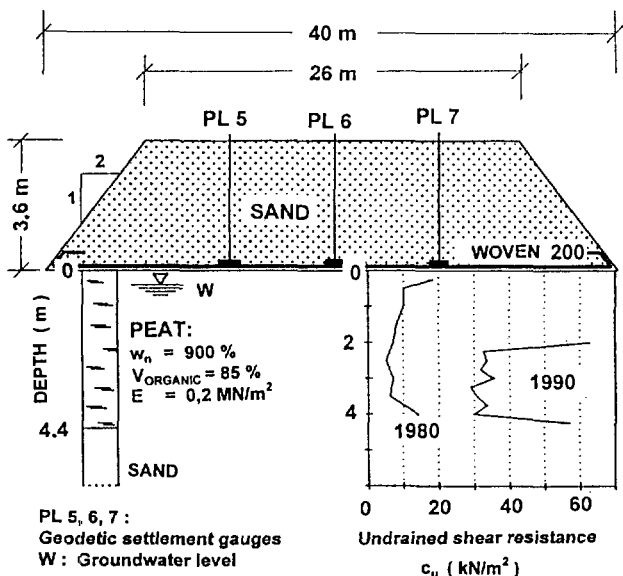


Figure 1. Full-scale test embankment at Rübke (not to scale).

## 2.2 Course Of The Test And Measurement Results

Measurements of settlement, pore water pressure, base pressure, inclination and groundwater level were performed.

In this test, it was not possible to perform strain measurements directly on the fabric. Because, at this time, a measuring system with robust, precise and water-proof strain gauges was not available. Four years later, long-term resistant strain gauges were developed and applied for the 'Grossenmeer-embankment' (see section 3).

The development of the settlement shows a significant drop in the settlement rate, which was below 1 cm/year in the first year after the reloading. Nowadays the settlement rate is less than 0.5 cm/year with a decreasing tendency. The BAST is continuing the measurements.

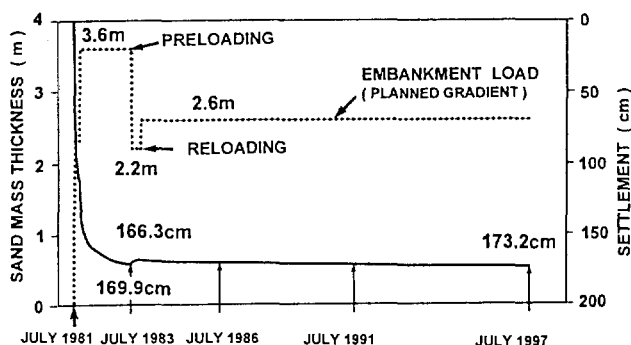


Figure 2. Load and settlement at Rübke from July 1981 until July 1997.

The high permeability of the peat in the unconsolidated state has made a rapid consolidation settlement easier.

For an embankment thickness of 2.3 m, the degree of consolidation was already 80% after two-months. Very high primary settlements of around 1.1 m were measured. The

transition primary / secondary settlements at a degree of consolidation of 90% occurred after 5.5 months. The total settlement of the peat mounted to around 1.6 m. The peat was compressed by around 40%.

The average strain of reinforcement derived from the settlement profiles (not shown) amounted up to 3%. Maxima and minima could not be registered due to absence of strain gauges (compare with section 3, 'Grossenmeer').

During filling and consolidation relatively low horizontal displacements occurred at the toe of embankment: maximum 18 cm in the peat and 12 cm on the ground surface. In a distance of 10 m from the toe of the embankment horizontal displacements of 1 cm to 3 cm were registered. The increase of undrained shear strength is shown in Figure 1.

## 2.3 Assessment Of The Measurement Results

The measurement results confirmed the feasibility of controlled construction of reinforced embankments on very weak subsoil (peat) by preloading, removing of preload and partial reloading to justify the final gradient. Due to the controlled preloading and the reinforcement, no failure-type deformations occurred, neither in the embankment nor in the foundation soil. The high-modulus geotextile (see section 2.1) allowed only small lateral spreading/squeezing deformations. Based on the average strain only the reinforcement looked understressed compared to design assumptions and calculations. But note, that strain (and tensile force) could had been higher e.g. in the usually critical zone (from the point of view of stability) under the slope and near the toe (see section 3.3). Summarizing: the simplified design calculations according to DIN 4084 agreed well enough for engineering purposes with the measured behavior. Nevertheless, continuous measurements are an important tool to control the construction progress.

The measurement results and the collected experience from July 1981 until March 1985 were adequate to recommend the preloading method with high-strength reinforcement for the entire new autobahn route BAB A 26.

## 3 HIGHWAY EMBANKMENT AT GROSSENMEER: TEST AND REFERENCE SECTIONS

### 3.1 Description Of The Project

Due to the positive results from the 'Rübke-embankment', the BAST recommended the preloading method with geotextile reinforcement for the construction of the new federal interstate highway B 211 at the town of Grossenmeer.

The BAST performed measurements on two sections. The first one with steeper slopes, called here 'test embankment', had to be integrated later after reshaping in the standard highway embankment. The second one, called here 'reference section', was already from the beginning a standard highway embankment. The test program was extended here by direct short- and long-term strain measurements of



the high-strength basement reinforcement.

The highway embankment at Grossenmeer has a length of around 2 km. The weak subsoil consists of layers of peat and organic silts in all 3 m to 5 m thick, underlayered by dense sand. According to pre-design calculations, typically an embankment thickness of 4.5 m height was selected for the stage of consolidation (preloading). The consolidation period was expected to be about two years. After that layers of different adequate thickness had to be removed to fit the planned final gradient.

The following design soil parameters were assumed for the stability calculations according to DIN 4084:

Soft subsoil: Undrained shear strength  $c_u = 8 \text{ kN/m}^2$   
Unit weight  $\gamma_n = 11 \text{ to } 13 \text{ kN/m}^3$   
Sand: Angle of internal friction  $\phi' = 32.5^\circ$   
Unit weight  $\gamma_n = 18 \text{ kN/m}^3$

The calculation resulted in an allowable embankment height of only 2.6 m without reinforcement. To achieve the aimed preloading height of 4.5 m and the required FOS = 1.2 (global stability, temporary stage) according to DIN 4084, a reinforcement tensile force of about 200 kN/m was required (Blume 1995, Blume 1996). For reasons of deformation compatibility the corresponding short-term strain was limited to 5%, and the total strain (short-term plus creep) was not allowed to exceed 6% for several years. Based on the stress-strain and creep curves a high-tenacity polyester woven with an UTS = 400 kN/m and 10% ultimate strain was selected (Stabilenka® 400).

The earthwork for the entire 2 km-stretch was carried out from June 1986 until June 1987, followed by a consolidation period of 15 months. After then in some sections the embankment thickness had to be increased additionally from 4.5 m up to 6.5 m (including the 'reference section', see below) to compensate the unexpected high settlements. After a new consolidation period of 17 months, parts of the preloading thickness were removed in March 1990 for fitting the final gradient. The highway was opened to traffic in October 1990.

Since October 1990, after the end of the measurements directly accompanying construction, measurements have been and are being performed on the long-term deformation behavior of the subsoil, of the completed highway and on the strain behavior of the basal reinforcement.

### 3.2 Description Of The Tests

The main aim of both the 'test embankment' and the 'reference section' was to provoke the highest possible stress in the woven, selecting sections of the highway having particularly unfavorable subsoil conditions. Knowledge was to be gained of the long-term behavior of the reinforcement.

Under the 'test embankment', which was planned as a 'crash test', extremely high reinforcement stress had to be generated by rapid construction (4.5 m in four days), and by a steep slope of 1 V : 2 H. Nevertheless, ground failure had to be avoided because of the later integration in the stan-

dard highway embankment, after reshaping. Around 40 m away, in the 'reference section' with a standard (flatter) slope of 1 V : 3 H, the loading process lasted around a year.

For the direct geotextile strain measurements, the BAST developed a suitable strain measuring system which does not influence the strain of the fabric. Robustness, precision and water-resistance were proved in advance in contact with soil and under water also.

Settlements, pore water pressure, inclination and groundwater level of the subsoil were measured. The strain measurements were performed on, in total three cross sections, two of them in the 'test embankment' and one in the 'reference section'. In each case 9 strain gauges were installed at 2 m space. Additionally, settlement gauges were placed near the strain gauges (Figure 3 a, d).

### 3.3 Measurement Results And Assessment

The most important results are depicted in Figure 3 a, b, c for the 'test embankment' and in Figure 3 d, e, f for the 'reference section'. Note, that embankment material, single layer thickness, height (4.5 m) and reinforcement are the same.

The construction periods and slope inclinations are quite different, as mentioned above.

In Figure 3 b, c the graphs show the development only within the first 4 days (height from zero to 4.5 m). After that the increase in strain became less and, after 2 months, came almost to a halt (not shown). In the subsequent 25 months the strains asymptotically came up to a maximum final strain of about 7% below the slope and 6% below the center of the embankment (not shown).

In Figure 3 e, f the graphs show the processes within around one year (height from zero to 4.5 m stepwise). The line with the number 1 corresponds to the 4<sup>th</sup> day (1.5 m sand), and with the numbers 2 to 5 to the 30<sup>th</sup> day after placing of the respective sand layer, at nearly constant time intervals.

Although the distance between the 'test embankment' and the 'reference section' is only around 40 m, the subsoil conditions seem to be considerably different, resulting in unexpected high settlements of the latter. In both cases a weak zone below the slopes was identified. Nevertheless, slope failure was not observed in the embankment body itself, neither for the 'test embankment', nor for the 'reference section'. On the contrary, the horizontal displacement of the subsoil near the toes became large, for the 'test embankment' up to 40 cm, destroying the inclinometer tubes. The ground tended to a 'squeezing-out', but a real failure did not occur. Note, that the typical subsoil-squeezing-mode cannot be checked by Bishop's method (DIN 4084) used for design calculations. Nowadays this mode should be checked e.g. according to Michalowski and Lei Shi (1993).

The reasons for the surprisingly high reinforcement-strains (and corresponding stresses) below the slopes in both cases are apparently both the weak zones and the squeezing-out tendency.

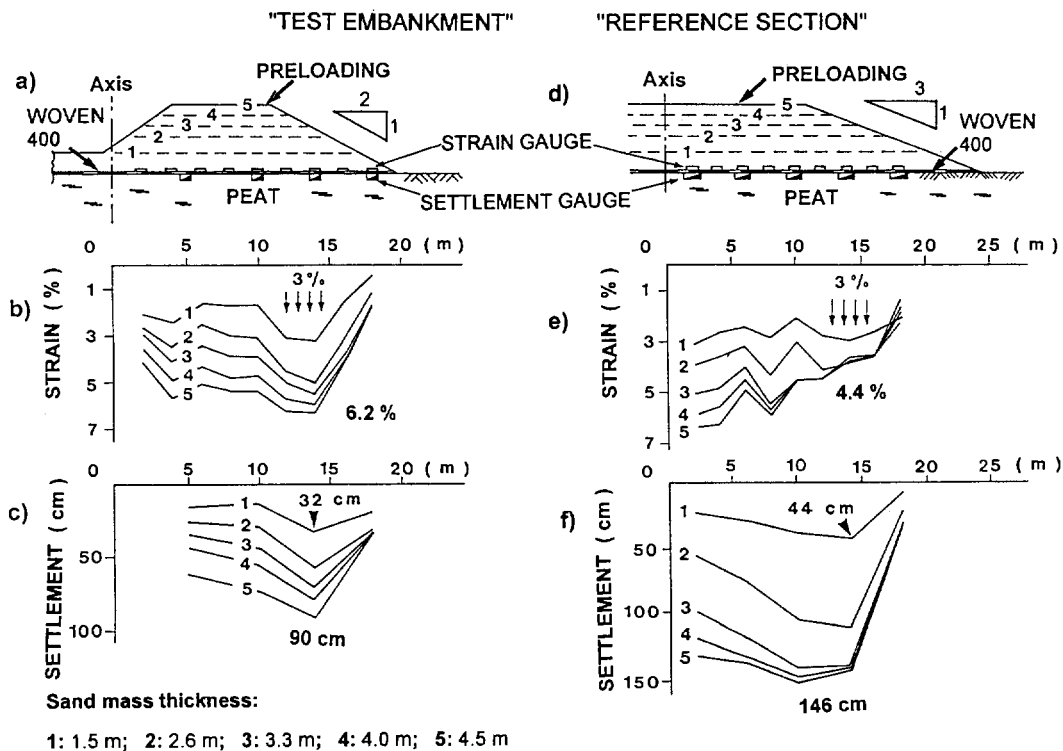


Figure 3. Grossemeer: construction stages, settlements and strains

The strain increase and the horizontal deformations came to a halt shortly after completion of the construction. Based on the observation, it can be concluded that the reinforcement prevented both slope failure of the embankment and ground failure due to squeezing of the soft layers.

The reinforcement strains exceeded at some locations the values of 5% (short-term) and 6% (long-term) assumed in design. The real mobilized tensile forces were higher than expected according to the stability calculations (DIN 4084, Bishop's method). The stress ratio (tensile force/UTS) exceeded 50% clearly.

In 1993, the strain measurements in the 'test embankment' were terminated due to adjacent building activities. Only the results of the continued long-term measurements from the 'reference section' are reported below.

Note, that in Figure 3 d, e, f only the period from June 1987 to June 1988 is depicted. After that in Autumn 1988 the height of the 'reference section' was increased to 6.5 m to compensate the high settlements, and was reduced again just in Spring 1990 (Figure 4).

So far, at the center of the embankment, maximum strains between 6.8% and 7.6% and maximum settlements of the soft subsoil of between 190 cm and 205 cm have been measured. The strains presented in Figure 4 from commencement of construction in July 1986 until July 1997 remained practically unchanged after removal of the preloading height and opening of the highway to traffic in October 1990.

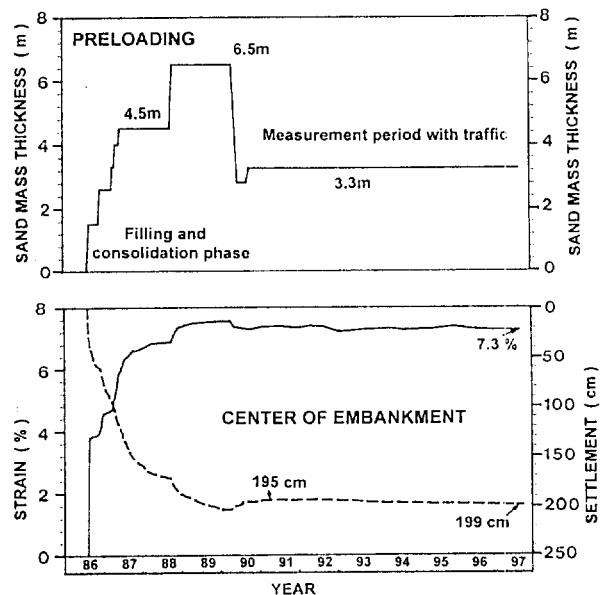


Figure 4. Variation of load, strain and settlement in the Grossemeer 'reference section' (1986 to 1997).

The constant strain level indicates that the reinforcement is still under tension after 10 years. It is difficult to evaluate the effective tensile forces from the registered strains with high precision now. In comparison with the short-term behavior a reduction in the effective tensile stress could be expected theoretically due to some factors. Relaxation could

play a (negligible) role; for the high-tenacity polyester used relaxation due to creep is very low. Furthermore, installation/compaction damage and environmental effects could have reduced the really available mobilized tensile force.

For the evaluation of relaxation the isochrones could be used, and the percentage of installation damage in sands is known in good confidence, being in the range of 5% to 10% for the reinforcement used. For evaluation of environmental effects the best way is to exhume and analyze an analogous reinforcement material, which has been embedded under similar conditions for a long time. For this purpose the Rübke-embankment offered a good possibility (see section 2).

#### 4. INVESTIGATION OF A HIGH-STRENGTH POLYESTER WOVEN AFTER 14 YEARS EMBEDDED IN SOIL

##### 4.1 Description Of Exhumation And Tests

In 1995, the BAST initiated the investigation of exhumed fabric samples. Since it is not possible to take samples from Grossemeer, the BAST proposed, samples to be taken at Rübke (see section 2).

In September 1995, around 120 m<sup>2</sup> of the high-strength woven were exhumed from the embankment base after 14 years in use. The entire geotextile was lying below the terrain in the peat and groundwater due to settlements. By an excavator, embankment parts were removed down to the woven, from the slope to the center of embankment. At the beginning, it was possible to remove the remaining sand by hand. Due to the rapid rising of water, it was unavoidable to pull out and up most of the woven directly by the excavator. Thus, abrasion and damage of the fabric could not be fully avoided.

It was observed during uncovering, that the woven was still under tension before cutting. A considerable effort was necessary to lift up the edge of the woven by a shovel (Figure 5). This observation corresponds to the strains under the Grossemeer 'reference section', which indicate considerable tensile forces until today also (Figure 4). Discoloration of the fabric due to contact with the rotted grass and the peat were clearly visible. In some places, grains of sand had penetrated its structure.

Samples for the testing institutes, participating in the investigations, were taken from four different geotextile areas after exhumation, corresponding to defined different positions in the base.

For each of the four areas the following tests were performed:

- (1) Yarn tensile tests according to DIN 53834, T 1 with 15 individual tests per each area
- (2) Analyses for determination of the carboxyl end groups (CEG) and of the molecular weights of the high-tenacity polyester
- (3) Scanning electron microscopy (SEM) of filaments
- (4) Chemical analysis of the groundwater (pH-values).

##### 4.2 Evaluation Of The Results Available To Date

The evaluation of the investigations regarding durability are almost completed. The most important results to date are presented here. The final evaluation and details will be reported separately.

The results of yarn tensile tests form a better criterion for evaluation of strength loss due to environmental effects than the wide-width strip tests. Damage caused by installation, compaction and (in this case) removal and exhumation, and sand-grain inclusions in the woven structure has a less pronounced influence on the cleaned single yarn (although it can not be eliminated). The graphs in Figure 6 show the stress-strain behavior of the exhumed yarns. Each curve represents the average of 15 tests per area.



Figure 5. Rübke: the woven being still under tension after 14 years.

The specific yarn strength of the 'virgin' (brand new) high-tenacity polyester used (Diolen<sup>®</sup>: CEG < 27 meq/kg; number average molecular weight  $M_n > 25000$ ; further exact data are known also) is shown in Figure 6, too. To perform a durability evaluation on the safer side, an increased possible average value of 'virgin' strength of 86 cN/tex (instead of 84.6 cN/tex) could be assumed. Thus, the residual strength is around 83% of the 'virgin' strength. The ultimate strain is practically unchanged. Note, that the yarn-strength-loss of around 17% includes (in chronological order) the effects of weaving of the yarns producing the fabric, of installation and compaction damage, of biological and chemical degradation (chemical attack plus hydrolysis) and of exhumation process.

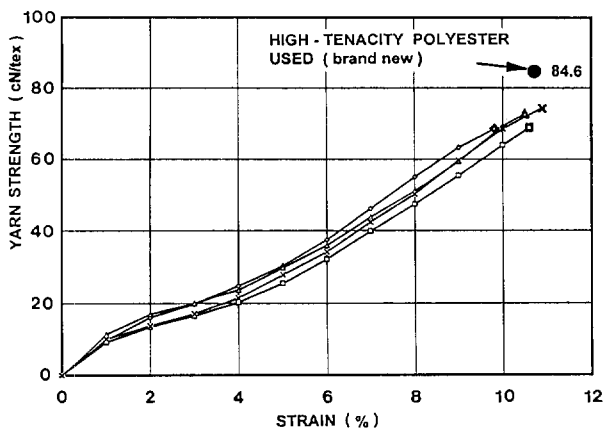


Figure 6. Specific yarn strength after 14 years in soil under groundwater level for the four different sampled areas according to DIN 53834, T 1.

The loss of yarn-strength due to the manufacturing process is 7% to 12%, on the average 9% (HUESKER Synthetic 1996). Further, for the woven mentioned loss of strength during compaction in sands of 5% to 10% has been observed. The loss of strength due to exhumation process is hardly to be identified exactly, but it can be set to 1% to 5% in this case. (Note, that a gentle exhumation was not possible, as mentioned above.)

The comparison of the percentage terms described above (weaving, compaction and exhumation) with the registered total loss of yarn-strength of about 17% results in 0% to 3% loss of strength due to environmental effects in this case.

Further, the SEM-photomicrographs performed indicate no chemical damage of the filament surface; it is completely smooth.

The comparison of molecular weights and number of CEG of 'virgin' and exhumed material leads so far to the conclusion, that 1% to 2% of strength-loss could be caused by changes in the polymer itself.

These latter evaluations of the microscopic and chemical investigations correspond well to the evaluation of loss in strength based on mechanical yarn-tests as mentioned earlier.

The pH-value of the groundwater is 6.6 on the average. This fact together with the SEM leads to the conclusion, that no chemical attack ('external' hydrolysis) has taken place.

The loss of strength of about 1.5% per 10 years, evaluated by different methods in this case, may be explained by 'internal' hydrolysis ('aging') in the groundwater and (unlikely) by biological effects (rotted grass, peat).

## 5 SUMMARY AND CONCLUSIONS

Two projects of embankments on soft subsoil with high-strength basement reinforcement have been started in Germany in 1981 ('Rübke') and 1986 ('Grossenmeer')

respectively.

The 'Rübke-embankment' is a pure test-embankment for the autobahn BAB A 26. The 'Grossenmeer-embankment' is an integral part of the federal highway B 211. In both cases high-modulus polyester woven is used with 200 kN/m and 400 kN/m UTS, respectively, and 10% ultimate strain. For stability calculations DIN 4084 (Bishop's method) has been used, modified by reinforcement force. Measurement programs are performed up to now, including direct strain measurements at 'Grossenmeer'.

Woven from 'Rübke' was exhumed after 14 years under tension below groundwater to evaluate durability.

1. Stability calculations according to DIN 4084 are correct enough to prevent failure of embankment and/or subsoil, at least when high tensile force at low strain is mobilized to restrain deformations.
2. High-moduli for a long period (low creep) are important, because the reinforcement works after consolidation also. In the projects described it is still under tension after 15 and 11 years, respectively.
3. The high-strength reinforcement used proved to resist overstressing successfully for a long period.
4. Local weaker subsoil zones can easily result in reinforcement overstressing and/or failure tendency; it should be kept in mind when selecting safety factors.
5. Subsoil squeezing-out is recommended to be checked additionally to DIN 4084-calculations by other methods.
6. The analyses of durability and operation conditions indicate in this case, that (internal) hydrolysis under stress in groundwater is the main reason for the registered negligible loss of strength.
7. The loss of strength due to 'aging' (environmental effects) is 1.5% to 2% in 14 years for the high-tenacity polyester woven used.

## REFERENCES

- Blume, K.-H. (1995) "Großversuch zum Tragverhalten textiler Bewehrung unter einer Dammaufstandsfläche", 4. Informations- und Vortragsveranstaltung über "Kunststoffe in der Geotechnik", Special Issue 1995, DGGT, Germany, pp. 78 - 88.
- Blume, K.-H. (1996) "Long-term measurement on a road embankment reinforced with a high-strength geotextile", EuroGeo 1 1996, Maastricht, The Netherlands, Conference proceedings, Balkema, Rotterdam, 1996, pp. 237 - 244.
- HUESKER Synthetic GmbH & Co. (1996), "Internal test reports summary", Gescher, Germany (unpublished).
- Michalowski, R.L., Lei Shi (1993), "Bearing capacity of nonhomogeneous clay layers under embankments", Journal of Geotechnical Engineering, Vol. 119, 1993, No. 10, ASCE, pp. 1657 - 1669.

# Durability of Polyester and Polypropylene Geotextiles Buried in a Tropical Environment for 14 Years

J.W. Cowland  
Geotechnical Engineering Office, Hong Kong

K.C. Yeo  
Geotechnical Engineering Office, Hong Kong

J.H. Greenwood  
ERA Technology, United Kingdom

**ABSTRACT:** The demolition of a 14 year old embankment on soft clay provided the opportunity to exhume samples of the geotextiles that had been used to reinforce the base. Specimens of these woven polyester and woven polypropylene geotextiles were then tested to assess their durability. From tensile and hydrolysis tests it was found that the polypropylene geotextile largely retained its strength, and the polyester geotextile lost about 15% of its strength. A portion of the polyester strength loss was attributed to hydrolysis.

**KEYWORDS:** Durability, Polyester, Polypropylene, Geotextiles, Tropical Environment.

## 1. INTRODUCTION

In 1982, a 3.5 km long coastal road embankment was constructed on soft clays in a tidal area of Hong Kong. The base of this embankment was reinforced with woven polyester and woven polypropylene geotextiles. Figure 1 shows a typical cross-section of the embankment.

In 1996, part of this embankment was demolished to make way for a river improvement scheme, which provided the opportunity to exhume some of these materials. Large pieces of both the polyester and the polypropylene geotextiles were carefully removed from the embankment by hand, and tests were carried out to determine their durability.

Tensile tests were carried out to determine the strengths of the recovered geotextiles, and they were also examined under a scanning electron microscope to determine the extent of site damage. Carboxyl end group counts, and molecular weight determinations, were performed on the polyester geotextile to evaluate the extent of hydrolysis. This paper presents the results of these durability tests.

## 2. GEOTEXTILES

A single layer of reinforcing geotextile was used beneath the embankment. Rolls 5 m wide were placed on the intertidal mud flats and stitched together. The project commenced with a polyester geotextile, which was substituted in places by a polypropylene geotextile. The exhumation encountered areas of both materials.

### 2.1 Polyester

The woven polyester geotextile was a multifilament material, with a weight of 450 g/m<sup>2</sup>. Quality control tests at the time of construction demonstrated a characteristic tensile strength of 200 kN/m in the warp. The maximum tensile strength was often 220 kN/m, at a strain of 8%, with a 10% strain at break. In the weft the characteristic tensile strength was 45 kN/m, with a 20% strain at break.

Ten strain gauges were attached to one roll of the polyester geotextile during laying, and a 9% extension was recorded after the placing of the fill material.

### 2.2 Polypropylene

The woven polypropylene geotextile was a fibrillated tape material, with a weight of 570 g/m<sup>2</sup>. Quality control tests demonstrated a characteristic tensile strength of 200 kN/m in the warp, with a strain of 12% at the maximum tensile strength, and 40 kN/m in the weft.

## 3. ENVIRONMENT

The coastal road embankment was constructed in the intertidal zone of a mangrove swamp. The geotextiles were placed by hand directly onto the very soft dark grey organic silty clay, which contained a large number of shells. The fill material, essentially a brown gravelly silty sand of granitic origin, was mechanically placed on top in 0.5 m layers.

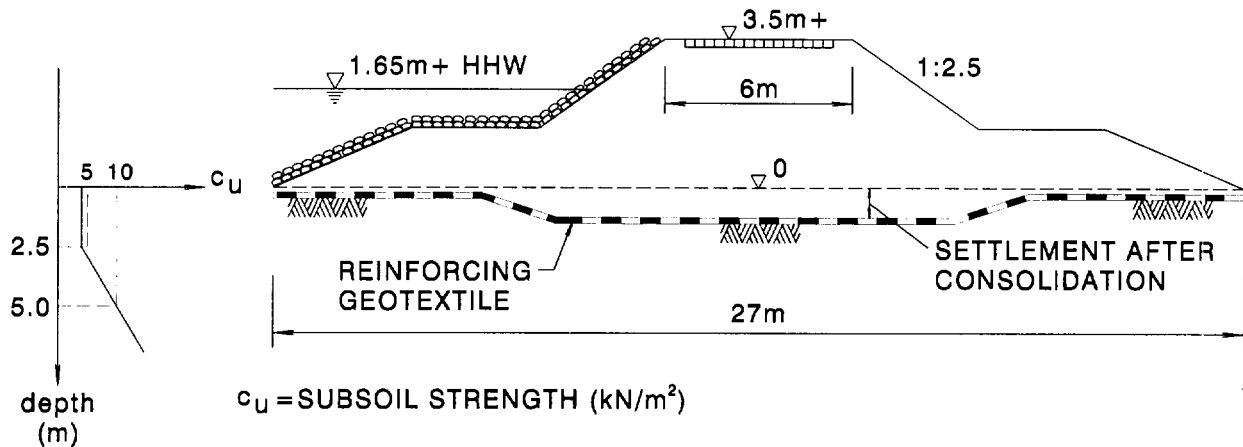


Figure 1. Cross-Section of the Embankment

During exhumation, pieces of pH indicator paper were placed in the water surrounding each geotextile, and they all indicated a pH of 7. It should be noted, though, that the portion of the exhumed embankment where the polyester geotextile was located was adjacent to the estuary of the Shan Pui River, which flows through the Yuen Long Industrial Estate, and is polluted.

The Hong Kong Observatory has been measuring soil temperature, for agricultural purposes, for over 25 years. At a depth of 3 m below ground level, the average soil temperature has consistently been found to be 26°C.

#### 4. EXHUMATION AND SAMPLE SELECTION

The polypropylene geotextile was encountered during the initial stage of demolition of the embankment. With the full cooperation of the site staff, careful hand excavations were then made to recover large pieces of both the polyester and the polypropylene geotextiles. These large pieces were then washed with a hose of water to remove some of the adhering soil, their appearance carefully observed and recorded, before being transported to the laboratory.

The appearance of the black polypropylene geotextile was relatively uniform, and appropriate samples were taken for tensile testing, and examination for site damage.

The white polyester geotextile had more marked differences in appearance, especially in colour. One area was greyish white, and showed some signs of installation damage, whilst another area was stained brown and grey. Samples for testing were selected from areas that were visually undamaged (to the human eye), although stained.

#### 5. DURABILITY TESTING

##### 5.1 Tensile Tests

Ten specimens of the polyester geotextile, and ten specimens of the polypropylene geotextile, were subjected to wide width tensile tests, in accordance with BS 6906: Part 1 (1987), except that individual specimens were tested at different rates of strain. Two specimens of each geotextile were tested in the warp direction at 100, 10, 1, 0.1 and 0.01 per cent/minute strain. The specimens were gripped with roller clamps, and their extensions measured using a non-contacting video extensometer.

The results are shown in Table 1. Examples of the load strain curves for both the polyester and the polypropylene geotextiles, at a constant strain rate of 10%/min, are shown in Figure 2. None of the polyester specimens showed any visible signs of damage before testing, although some staining was evident on all specimens. Specimen F of the polypropylene material showed visible fraying of some of the warp fibres, and this probably accounts for the low value of tensile strength.

The results are summarised in Figure 3.

##### 5.2 Scanning Electron Microscope Examination

Three specimens of the polypropylene geotextile were examined in a scanning electron microscope, one on both sides. Their appearance, as shown in Plate 1, was typical of a fibrillated tape geotextile. Most of the damage was confined to the surface. Both warp and weft were damaged equally. Soil residue had penetrated the textile.

Table 1. Tensile Test Results

Rate of strain (%/minute)	Polypropylene Geotextile			Polyester Geotextile		
	Sample	Maximum strength (kN/m)	Strain at maximum strength (%)	Sample	Maximum strength (kN/m)	Strain at maximum strength (%)
100	A	246.4	10.7	A	168.2	5.5
100	B	259.5	11.2	B	153.8	4.9
10	C	216.9	12.6	C	177.7	5.5
10	D	215.4	11.5	D	164.2	5.4
1	E	213.1	14.5	E	173.9	5.5
1	F	†144.8	11.1	F	142.2	5.1
0.1	G	210.9	15.3	G	159.1	5.3
0.1	H	167.2	13.7	H	163.8	5.2
0.01	I	160.6	15.6	I	108.8	3.7
0.01	J	188.6	20.8	J	140.5	5.2

† Damaged specimen

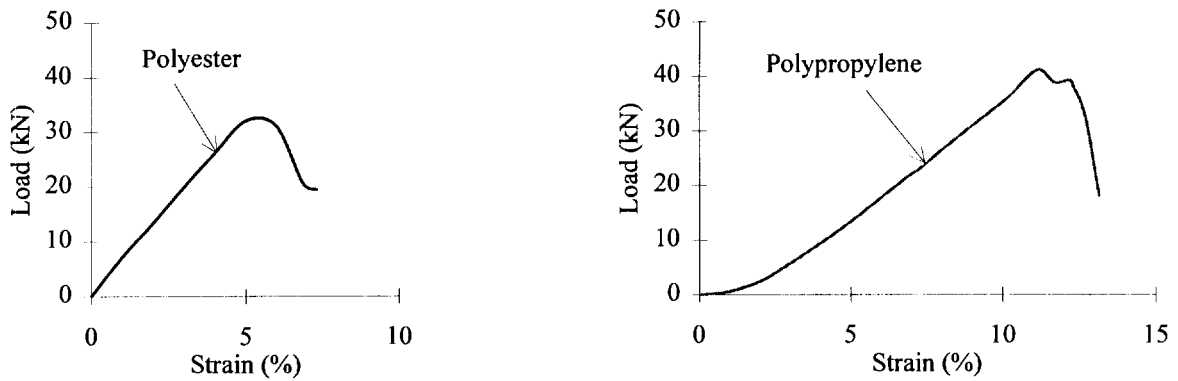


Figure 2. Examples of Load Strain Curves

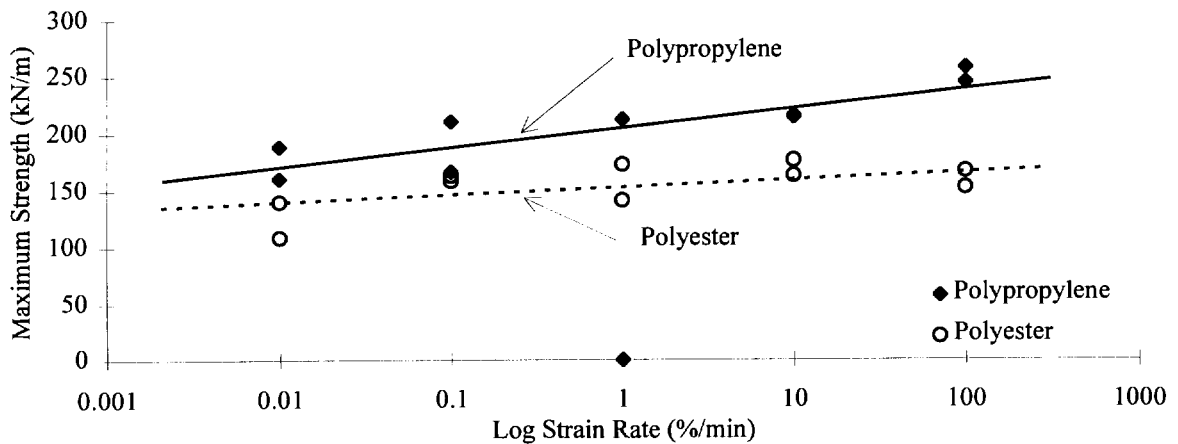


Figure 3. Change of Maximum Tensile Strength with Strain Rate

Plate 1. Scanning Electron Micrograph of Polypropylene Geotextile

Plate 2. Scanning Electron Micrograph of Polyester Geotextile

Plate 3. Scanning Electron Micrograph of Polyester Geotextile

Plate 4. Scanning Electron Micrograph of Polyester Geotextile



Table 2. Hydrolysis Test Results

Specimen	Staining	Intrinsic viscosity	Viscosity molecular weight	Carboxyl end group (CEG) (meq./ $\mu$ g)			Mean CEG (meq./ $\mu$ g)
1	Greyish white	1.08	38,200	28.9	25.9	29.8	28.2
2	Grey / brown	0.61	19,200	30.4	30.1	29.8	30.1
3	Grey / brown	0.64	20,300	29.6	30.2	29.4	29.7

Two specimens of the polyester geotextile, one from the area stained brown and grey, and the other from the area stained greyish white, were examined in the scanning electron microscope. There was no damage visible to the unaided eye in either specimen. Examples of the micrographs are shown in Plates 2, 3 & 4; in which the warp direction is horizontal.

Locally there was damage to the fibres in the form of splits, indentations or openings in the fibre surface parallel to the axis. In places the surface of the fibres appeared flaky. This was sometimes, but not always accompanied by local distortion, as shown in Plate 3. Individual soil particles and smeared areas were present, primarily attached to the warp fibres.

X-ray analysis of an area stained brown and grey showed that the smeared areas contained aluminium, silicon and some iron, and were therefore likely to be from an iron containing clay. Analysis of the discrete particles showed that some were clay, but others consisted mostly of sulphur. Analysis of an area stained greyish white found similar distributions of sulphur containing particles. The clay was found to contain silicon and aluminium as before, but no iron.

### 5.3 Hydrolysis Tests

Nine carboxyl end group tests were carried out on the polyester geotextile, using the non-aqueous titration method of Pohl (1954), but with bromocresol green as the indicator. Three tests were performed on a specimen of the material stained greyish white and six were performed on two specimens of the material stained brown and grey. The results are shown in Table 2.

Three intrinsic viscosity measurements were made, in accordance with ISO 1628-1 (1984), using o-chlorophenol as the solution medium; from which the viscosity molecular weight, which approximates to the weight average molecular weight, was then calculated. These results are also shown in Table 2.

## 6. DISCUSSION OF RESULTS

### 6.1 Polypropylene

The loss of strength of the polypropylene geotextile after burial for 14 years was relatively insignificant. Also, as shown by comparison of a test at 10%/minute strain (Figure 2) and the original properties, there was little change to the strain characteristics.

In addition, examination in the scanning electron microscope found only surficial surface damage to the material. Thus, it is concluded that this woven polypropylene geotextile has survived installation, and burial in the ground for 14 years at 26°C., with little change.

### 6.2 Polyester

The polyester geotextile lost about 15% of its strength after installation and burial for 14 years in a saturated ground at 26°C.

From Table 1 it can be seen the strain at maximum strength was less than that measured before installation. Figure 2 shows that the strain at break was also less. The relatively flat gradient of the polyester change of strength with strain rate plot, shown in Figure 3, indicates that it is not particularly strain rate sensitive.

The carboxyl end group test results ranged from 26 to 30 equivalent ends/microgram, which when compared with the range of 25 to 50 normally required for the production of high tenacity polyester fibres, indicates little hydrolytic degradation. The results for the material stained brown and grey were slightly higher than for the greyish white material.

The weight and number average molecular weights of the original geotextile are believed to have been at least 33,000 and 12,400 respectively. The intrinsic viscosity measurements and molecular weight determinations showed that material from the areas stained brown and grey was only two thirds of the original molecular weight.

Taking all these measurements into account, especially the loss of molecular weight, it is concluded that a portion of the 15% loss of strength of this woven polyester geotextile was due to hydrolysis. The rest may be due to installation damage (Brady et al, 1994).

The analysis of Burgoyne and Merii (1993) and the Arrhenius diagram of Schmidt et al (1994) both predict a loss of less than 5% due to hydrolysis after 14 years in saturated soil at 26°C. Salman et al (1997) predict a larger loss, and Schmidt et al indicate that a 30% loss of molecular weight would be associated with a 14% loss of strength.

The relationship between a change of carboxyl end group count and the change in the molecular weight depends on the distribution of molecular weights. Local hydrolysis may be associated with the presence of metal ions in the degraded areas.

This loss of strength does not preclude the use of similar polyester geotextiles for the basal reinforcement of embankments on soft clay, as the strength of the reinforcement is only required for a few months, until the clay has consolidated. It is suggested, though, that similar durability studies be carried out on polyester geotextiles and geogrids exhumed from permanent reinforced fill.

#### ACKNOWLEDGEMENTS

This paper is published with the permission of the Director of Civil Engineering of the Hong Kong Special Administrative Region Government. J.H. Greenwood thanks the Directors of ERA Technology for permission to publish.

The authors wish to thank G.W. Lovegrove and F. Teague for their records and recollections of the construction of the embankment, and Mrs. P.J. Howard for performing the scanning electron microscopy.

#### REFERENCES

- Brady K.C., Watts G.R.A., Nagarkatti A.S. & Greenwood J.H. (1994). "Installation Damage Trials on Geotextiles", Research Report 382, Transport Research Laboratory, Crowthorne, U.K.
- British Standards Institution (1987). BS 6906: Part 1. "Methods of Test for Geotextiles: Determination of the Tensile Properties using a Wide Width Strip", BSI, London.
- Burgoyne C.J. & Merii A.L. (1993). "Hydrolysis Tests on Polyester Yarns", Cambridge University Department of Engineering Technical report CUEDID-Struct/TR138, Cambridge, U.K.
- International Organisation for Standardisation (1984). ISO 1628-1: "Guidelines for the Standardisation of Methods for the Determination of Viscosity Number and Limiting Viscosity Number of Polymers in Dilute Solution", ISO, Switzerland.
- Pohl H.A. (1954). "Determination of Carboxyl End Groups in a Polyester, Polyethylene Terephthalate", Analytical Chemistry, Volume 26, pp. 1614-1616.
- Salman A., Elias V., Juran I., Lu S. & Pierce E. (1997). "Durability of Geosynthetics Based on Accelerated Laboratory Testing", Geosynthetics 97, Long Beach, U.S.A., pp. 217-234.
- Schmidt H.M., te Pas F.W.T., Riseeuw P. & Voskamp W. (1994). "The Hydrolytic Stability of PET Yarns Under Medium Alkaline Conditions", Proceedings of the 5th International Conference on Geotextiles, Geomembranes and Related Products, Singapore, Volume 3, pp. 1153-1158.

# Study on Creep-Rupture of Polyester Tendons : Full Scale Tests

P. Orsat  
Freyssisol, Freyssinet International and Cie, Velizy, France

M. Khay  
Centre d'Experimentation Routiere, Le Grand Quevilly, France

M. Mc Creath, Linear Composites Ltd, Keighley, United Kingdom

**ABSTRACT:** The behaviour under creep of polymeric materials used to reinforce soil structures is an essential criterion in the study of the durability of structures. The report presents the results of full-scale tests carried out to study the behaviour under creep of polyester tendons. Loading tests to rupture were performed on tendons for assumed life periods of 2, 10, 30, 100, 300 and 1000 days. Samples taken before rupture at different ages allow determination of the residual strength characteristics of the tendons. The results obtained confirm the law of the linear behaviour of creep rupture versus the logarithm of time. It also shows that the residual strength of tendons subjected to creep tests remains greater than that calculated from the stress rupture curve and very close to the initial test strength of polymeric materials.

**KEYWORDS:** Polyester, creep rupture, residual strength, creep.

## 1 INTRODUCTION

The results of creep rupture tests on polyester fibres are generally expressed in the form of creep rupture curves of the type: load in relation to log (time) as shown in Figure 1. The admissible tension load at time "t" is determined by extrapolation of the tensile strength data obtained from creep tests at time  $t_0$ . Safety coefficients are applied to the tensile strength to allow for uncertainty due to extrapolation. Knowing the true strength of the material under the effect of creep related to time is of major interest when defining these safety coefficients.

It is important, therefore, to establish the residual strength of tendons used i.e. what is their actual breaking load  $Tf_1$  at time " $t_1$ ", under a given load applied  $Tf_2$ , when off loading takes place some time before creep rupture, as per the creep rupture line at time " $t_2$ " (Figure 2).

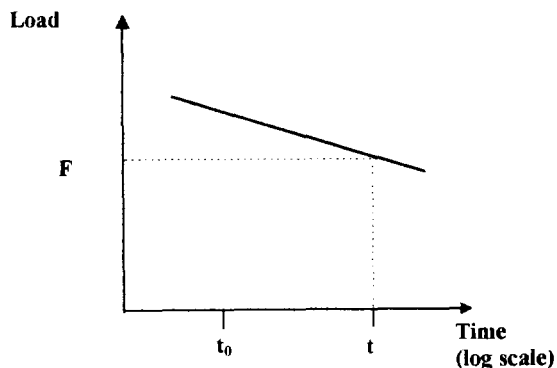


Figure 1. Creep rupture curve.

The report presents the results of a study carried out in order to establish the characteristics of creep rupture of polyester cables used as tendons in reinforced fill and to evaluate their residual strength before rupture (Linear Composites Ltd 1995).

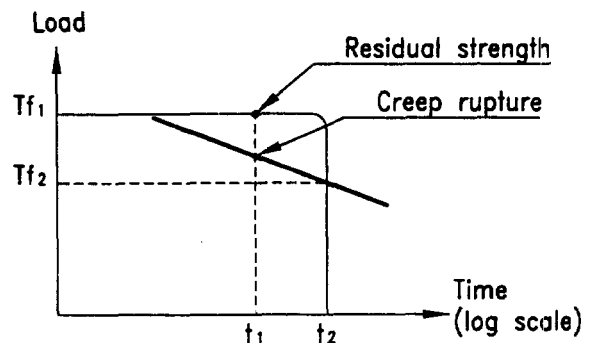


Figure 2. Residual strength.

## 2 TESTS

The loading test was performed to full scale in a covered test pit under ambient atmospheric conditions. A device allowed maintenance and monitoring of the temperature in the pit at about 18°C. Tendon test pieces were loaded to a constant value calculated for different rupture times. For each series, the tests were continued on the one hand up to creep rupture of the test pieces, and on the other hand by

taking samples at different times before rupture for determination of their residual strength in a laboratory tensile test.

## 2.1 Tested Material

For this study and for experimental purposes, the tests were performed on Parafil polyester tendons of the same nature as polyester reinforced strips used in the reinforced fill. These were composed of polyester fibres covered with a polyethylene sheath. The test pieces, prepared specially for these tests, were 550 mm long and comprised two termination devices at their extremities.

## 2.2 Loading Weights

These tendons are characterised by:

- their Nominal Breaking Load "N.B.L." defined as 10 kN,
- their actual breaking load i.e. the mean of 20 samples tested as initial reference. However, this value can vary between various series of samples tested due to termination dimension as pre-tensioning conditions during samples preparation.

The weights consist of concrete blocks which are adjusted by adding additional weights before loading the samples.

## 2.3 Table 1

This table gives the plan of the experiments carried out. The set of samples was prepared successively for the tests. In general, 16 samples were loaded for each creep rupture point and 6 samples for each strength retention point.

Table 1. Plan of experiments performed.

Phase	Reference	Loading for		Test performed		Type	
	Sample	Test pieces	Rupture at (days)	Test pieces	Time (day)	Test pieces	
0		2	5	2	5	Creep	
1	1	20	2	12	2	12	Creep
			10	16	10	16	Creep
			30	14	30	14	Creep
2	2	20	100	40	2.10	4x6=2	Resi. strength
					30.60	4	
					100	16	Creep
					30	6	Resid. strength
					300	34	100
3	3	5	1000	24	200	6	
					300	16	Creep
					30	6	
					100	6	Resid. strength
					200	6	Resid. strength
			300	6			

## 2.4 Determination of Creep Rupture Loads

The calculation of the creep rupture loads for each phase of the tests was determined from the experimental results obtained during a previous study and readjusted by a series of rupture tests under creep. This relationship subsequently recalculated after each test phase, was used for calculating the weights for the following phase. The weights were calculated with reference to the tensile strength of the test samples.

## 2.5 Determination of the Reference Tensile Strength

Characterisation of the 550 mm long tendons due to be tested was established using tensile tests at a strain rate of 100 mm/min. Table 2 gives the results for the tendons for the three series of samples tested.

Table 2. Reference tensile strength.

Series	1		2		3	
Samples	20		20		5	
	Loads kN	Extension at rupture (%)	Loads kN	Extension at rupture (%)	Load kN	Extension at rupture
Mean	15.85	10.09	14.72	9.7	15.57	10.3
S.D. <sup>1</sup>	20	0.31	56	0.5	71	0.7
V.C. <sup>2</sup> %	1.3	2.9	3.8	4.8	4.5	7.0

<sup>1</sup>Standard Deviation - <sup>2</sup>Variation Coefficient

All tendons tested came from the same batch of cable. However, slight changes were introduced in the termination conditions (dimension and pre-stressing rate during preparation stage). This can explain the slight changes observed for reference tensile strength measurement between phases.

## 3 TEST RESULTS

Table 3 gives the creep test results. The graph in Figure 2 shows an adjustment by linear regression of the relation load - f(log(time)) with very good correlation.

The creep rupture equation line obtained is:

$$Tf(\%) = 88.8 - 2.38 \log(t_{\min}) \quad (1)$$

where: Tf(%) = actual breaking load (in % of original breaking load) at time t ; and t = time in minutes.

This equation has been established using creep rupture results at 2, 10, 30 and 100 days. It will be confirmed by 300 days tests which are still on going.

**Table 3. Rupture time under creep.**

Phase	Weight values (kN)	Rupture time under calculated creep (day)	Rupture under observed creep (day)		
			Mean	S.D. <sup>1</sup>	V.C. <sup>2</sup> %
0	13.40	2	0.05	0.05	100
	12.62	2	1.21	0.91	74.9
1	12.41	10	10.34	7.47	72.2
	12.20	30	15.51	10.81	69.7
2	11.95	100	81.87	62.61	76.5
3	11.75	300	*	*	*

\* Test under way

<sup>1</sup> Standard Deviation - <sup>2</sup> Variation Coefficient

Table 4 gives the results of the determination of residual strength for tendons subjected to creep tests. These show that, for different loads and before termination of their foreseeable life span, the residual strength is not affected by the load (Cf. Figure 3).

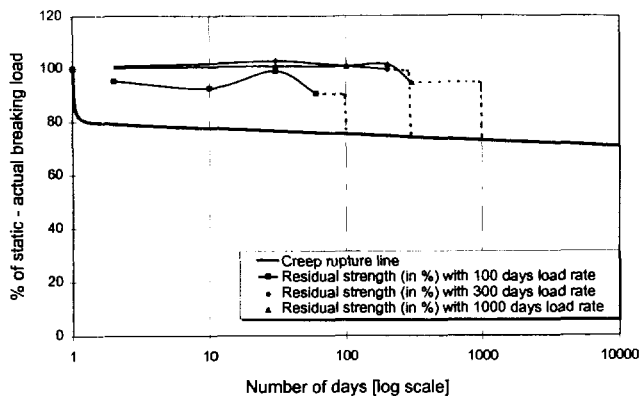


**Figure 3. Creep rupture curve and residual strength.**

**Table 4. Residual strength of tendons subjected to creep test.**

Phase	Refe. <sup>3</sup> (kN)	Time of rupture calculated creep <sup>4</sup> (day)	Age of the test (day)	Measure residual strength % of the reference tension		
				Mean	S.D. <sup>1</sup>	V.C. <sup>2</sup> %
2	14.72	100 (81,2%)	2	95.2	4.6	4.9
			10	92.5	3.5	3.7
			30	99.0	4.8	4.8
			60	90.4	1.7	1.9
			300	102.8	3.1	3.0
3	15.57 (75,5%)	100 (74,2%)	100	100.8	5.3	5.2
			200	99.5	1.9	1.9
			30	100.9	8.8	8.7
			1000	100.7	6.2	6.2
			200	101.4	2.3	2.3
		300	94.5	7.1	7.5	

<sup>1</sup> Standard Deviation - <sup>2</sup> Variation Coefficients - <sup>3</sup> Reference

<sup>4</sup> Rate of loading in relation to reference

For phase 2, the variations observed, as well as the fall in measured residual strength, may result from problems related to the termination devices on the tendons, which were improved for phase 3.

#### 4 DISCUSSION

The objective of this project was to firmly establish the long-term tensile behaviour of Paraweb soil reinforcing products. However, the creep and creep rupture behaviour of webbing is difficult to study because slip-free methods of holding the web are complex and expensive and preclude the multi-sample approach. Polyester cable was used in this work to simulate webbing because it performs in an identical manner to the equivalent web and is easier to hold in standard terminations. The breaking load of the cable was limited to about 15 kN so that the concrete weights could be restricted to a maximum of 14 kN.

The test results for creep rupture and strength retention are shown in Tables 3 and 4 and graphically in Figure 3. The anticipated creep rupture performance was confirmed and the regression equation established.

Evidence of retention of strength under load approaching 100% is clearly demonstrated for three different loads (it is clear that the phase 2 results were slightly lower than anticipated. This was due to minor termination difficulties which were resolved for phase 3).

Evidence is also presented confirming the retention of initial strength until close to the creep rupture point.

This strength retention phenomenon brings into question the current techniques (based on creep rupture) used to establish safety factors for design loads. The following example demonstrates the anomaly:

- taking the Characteristic Breaking Load (CBL mean - 1.64 SD) of series 2 as 13.8 kN,
- assume a typical factor of safety (which includes the effects of creep rupture) of 3 on CBL,
- the design load for the tendons becomes:

$$DL = \frac{CBL}{3} = \frac{13.8}{3} = 4.6 \text{ kN}$$

- using the creep rupture equation, if we calculated the time to rupture for a load of 4.6 kN from:

$$\log(t_{\min}) = \frac{88.8 - 31.25}{2.38}$$

this results in  $t = 2.3 \times 10^{18}$  years.

The evidence presented in this paper suggests that if this tendon was off-loaded after "only" 120 years its breaking load would still be close to 100%.

It is believed, therefore, that the phenomenon of strength retention should be a major consideration when calculating design loads. Clearly, providing the final design load is below the predicted creep rupture load for 120 years, safety factors should be applied to the retained load i.e. the initial strength of the geotextile. In addition any factors for transient load increases during the life of the structure should be based on the retained, i.e. initial strength.

## 5. CONCLUSION

1. This work has confirmed the linear nature of the creep rupture performance of polyester tendons on a load versus log time basis.
2. The residual strength of the tendons when subjected to the creep tests remains far above the creep rupture curve and is unaffected by time under load until close to the creep rupture life.
3. A new approach to design load safety factors should be considered which take into account residual strength (as opposed to the current BNSR 1991).

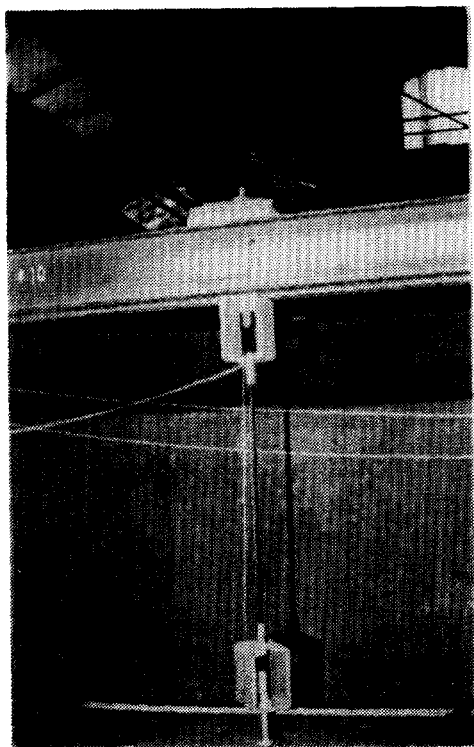


Figure 3. Close view of sample under testing

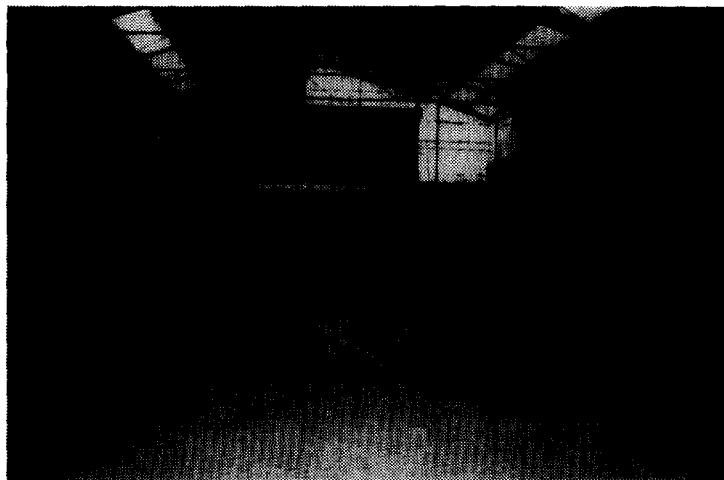


Figure 5. A pit view with all the samples under testing.

## ACKNOWLEDGMENTS

The authors wish to thank Messrs H. Perrier, G. Vincelas and D. Lozach for their participation in the tests. The study was financed by the Freyssiol Department of Freyssinet International and Cie and by Linear Composites Ltd.

## REFERENCES

- BNSR (1991) Commission Géotextile et Produits Apparentés "Safety coefficients for geotextiles and products" - Project GTX 71.
- Linear Composites (1995) "Note on creep and the application of creep / stress rupture curves to the choice of design values".

# Coated PET-geogrids, wovens and yarns - comparison of longtime performance under tension

J. Müller-Rochholz

Professor, Department of Civil Engineering, Fachhochschule Münster, Labor für Baustoffe, Münster, and Institute for textile Building and Environmental Techniques (tBU), Germany

D. Alexiew

Chief Engineer, HUESKER Synthetic, Gescher, Germany

C. Recker

Civil Engineer, Fachhochschule Münster and tBU, Germany

S.E. Lothspeich, P.E. (civil engineer), HUESKER Inc., Charlotte, NC, USA

**ABSTRACT:** The load/deformation behavior of geogrids is the dominant characteristic for the bearing behaviour of the composite soil-geogrid. As deformations of soil shall be small during implementation of geogrid and very small after construction high modulus at low deformations and low creep are the aims. As polyester normally has a orientation phase at low deformations the attempt was made to use other polyester yarns for geogrids. Short-time and creep tests show significantly better behavior in initial load bearing capacity and creep behavior.

**KEYWORDS:** Creep, Design deformation, Polyester, Geogrid

## 1 INTRODUCTION

The coaction of reinforcing geosynthetic and soil is the basis of design methods. Examples are given by OECD Expert Group I8 (1991). The following figures are taken from the OECD report.

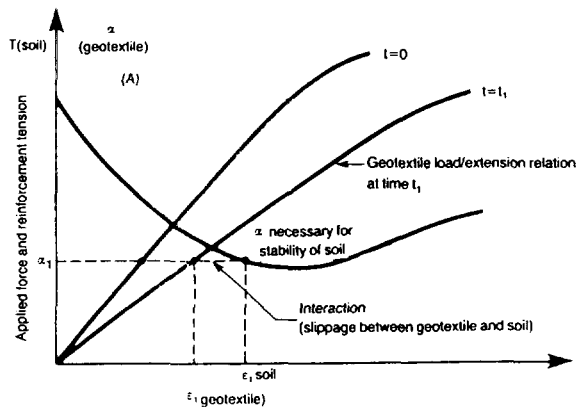
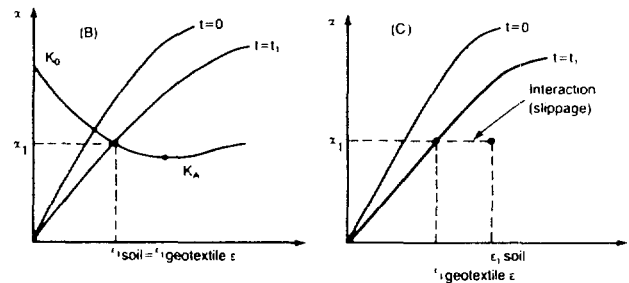


Figure 1 a. Calculation of slope stability and compatibility of soil and geotextile reinforcement



(A) General principles of calculation of the internal stability  
(B) Two part wedge method  
(C) Displacement method

Figure 1 b. Calculation of slope stability and compatibility of soil and geotextile reinforcement

The curves show load/extension curves for the geosynthetic („isochronous stress-strain curves) and the soil curve. Independent from the design approach, it is to be seen that a steeper curve for  $t = t_1$  (for example  $t_1 = 10^6$  h = 114 years) leads to structures with low movement. A big difference between  $t = 0$  and  $t = t_1$  leads to movement in a post construction phase i.e. service period. For the post construction deformation values are given between .5 % for rigid structures and 1 % for not sensitive structures by the OECD Expert Group I8 (1991).

So a reinforcing material should have a curve with low deformation in the design-relevant area

(deformations of  $\leq 3\%$ ) and the smallest difference possible between  $t = 0$  and  $t = t_1$ .

As some polymers have orientation phases of the macro molecules at relativ low deformation, this orientation should be eliminated by stretching during production or other thermo-mechanical pretreatment.

This investigation deals with two types of polyester (PES-) yarns and grids woven from these yarns.

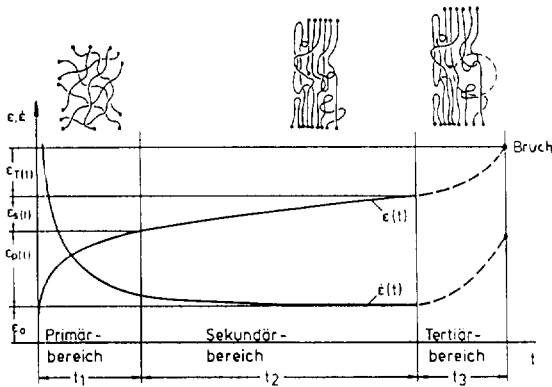
## 2 GENERAL DEFORMATION BEHAVIOR

Geosynthetics deformation behavior is influenced by

- deformation in the textile structure
- polymer type
- thermo-mechanical treatment of tapes, yarns, fibres etc.

The deformation in the textile structure of woven materials may be influenced by kind of weaving and warp tension. Knitwear may have straight load bearing elements, thus having no construction deformation. The same is valid for extruded and stretched grids.

Polyester materials are characterized by a orientation phase between 20 and 30 % of short-time strength. The phenomenon is visualized in Figure 2 (C. Koslowski, 1996) versus time, as this orientation occurs under sustained load at lower stresses.



- $\epsilon_T$  = tertiary creep deformation
- $\epsilon_s$  = secondary creep deformation
- $\epsilon_p$  = primary creep deformation
- $\epsilon_0$  = initial deformation

Figure 2. Creep deformation and creep rate

## 3 TARGET OF THE INVESTIGATION

The tests reported here should show, whether a different yarn [called New Technology (NT) in this report] gives better performance at low deformation values than a

standard PES-yarn. Short-time tensile, tensile creep and creep rupture tests were conducted, this report deals with short-time tensile and creep tests.

### 3.1 Short-time Tests

The short-time tests were carried out with two grids of identical nominal maximum force. All tests were performed on identical equipment by same staff according to ISO 10319 i. e. 1 % preload, 20 %/min strain rate, videoextensometer. Figure 3 shows the stress-strain curves, which (best to be seen for the product with 150 kN/m) miss the typical orientation phase, characterized by a degressive gradient from about 1 % strain up to 4 %. Also the ultimate deformation is about 9 % for the NT-materials compared with about 12 % for the standard material.

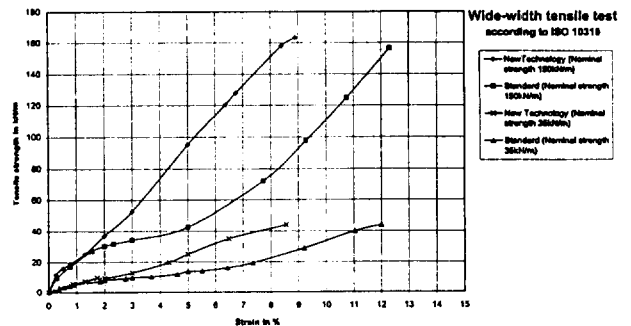


Figure 3. Stress-strain curves - woven polyester-geogrid

### 3.2 Creep Tests

For the creep comparison we took old values for the standard materials [published by J. Müller-Rochholz and R. Kirschner at the 4<sup>th</sup> International Conference on Geotextiles, Geomembranes and Related Products, The Hague, Netherlands (1990)], therefore sometimes stress/strength values and temperatures are close but not identical.

Creep curves for yarn and geogrids of different strength woven of this yarn are shown in Figures 4 a and b. The problem in testing is to be seen by the remark „clamp failure“. If stress level is very close to the bearable load, any lateral stress may cause rupture.



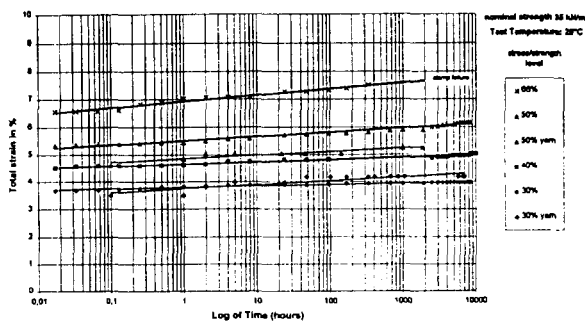


Figure 4 a. Creep curves - woven polyester-geogrid „new technology“ (35 kN/m)

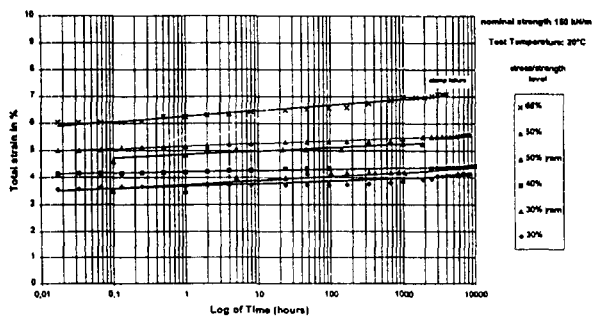


Figure 4 b. Creep curves - woven polyester-geogrid „new technology“ (150 kN/m)

Figure 5 shows 1 year NT-values at 30 % stress level and 3 years lines of standard PES of lower (= 25 %) stress level, showing ca. 1 % higher strains for the lower stress level of standard yarns.

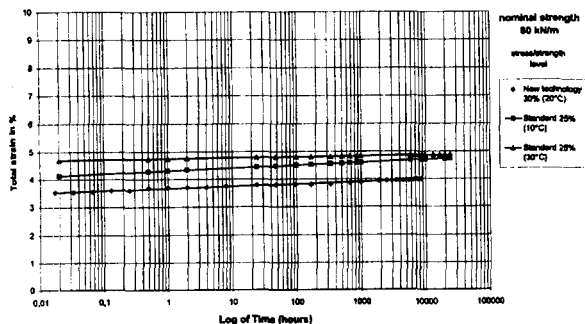


Figure 5. Creep curves - woven polyester-geogrid

In Figure 6 identical stress levels (50 %) of products are compared at differing temperatures showing the low influence of temperature for PES and ca. 2 % less strain for the NT-materials. In this figure results of yarn creep tests supplied by the producer are plotted additionally. There is a different stress level for the standard yarn. The coincidence of yarn and product strains shows low construction influence.

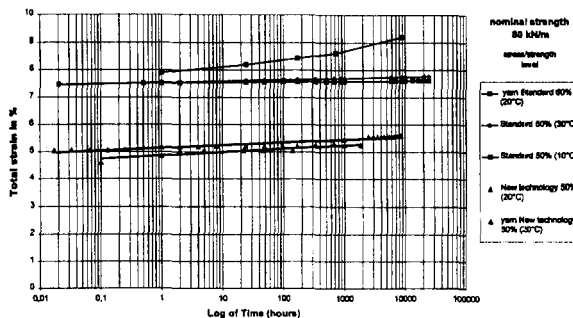


Figure 6. Creep curves – woven polyester-geogrid (80 kN/m)

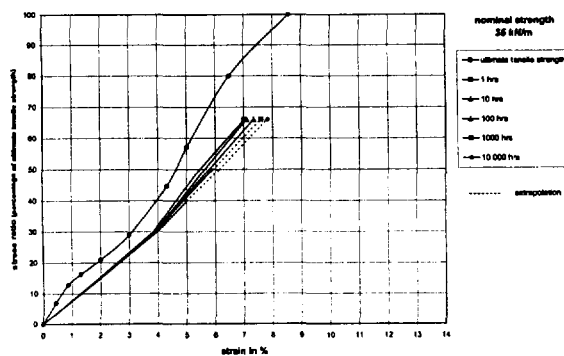


Figure 7. Isochronous curves – woven polyester-geogrid „new technology“

From these creep curves isochronous stress-strain curves were derived, showing in Figure 7 the close lines for 1 h up to 10000 hrs. Two lines of Figure 7 are transferred to Figure 8 to see the difference between the products with different yarns; which leads to strain differences f. e. at 20 % stress-level of > 3,5 % strain at 10000 hrs for standard to < 1,5 % for NT-products or at strain level of 2 % to stress levels from 5 % (standard) to 15 % (NT).

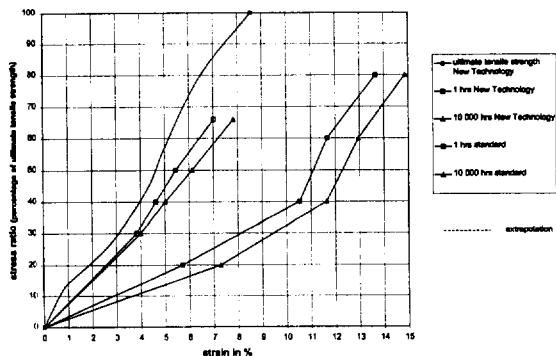


Figure 8. Isochronous curves – woven polyester-geogrid

#### 4 CONCLUSION

It can be shown that the thermo-mechanical treatment of yarns (here: Polyester) may lead to significant changes in the load deformation behavior especially in the application relevant area of admissible deformations/stresses. So the load bearing capacity at 2 % strain is tripled.

#### REFERENCES

- OECD Expert Group I8 (1991) *Ground Engineering Applications of Geotextiles in Road Construction and Maintenance*, Transport and Road Research Laboratory Crowthorne, UK.
- Koslowski, C. (1996) *Geokunststoffe, Extrapolation von Kurzzeitkriechversuchen ( $\leq 1000$  h) auf Langzeitwerte*, Final thesis work at Fachhochschule Münster
- Müller-Rochholz, J., Kirschner, R. (1990) "Creep of geotextiles at different temperatures", *4th International Conference on Geotextiles, Geomembranes and Related Products*, The Hague, Netherlands, Editor G. den Hoedt A.A. Balkema/Rotterdam/Brookfield

# The Effect of Oxygen Pressure, Temperature and Manufacturing Processes on Laboratory Degradation of Polypropylene Geosynthetics.

A. Salman  
Consultant, Westbury, NY

V. Elias  
Principal, V. Elias and Associates P.A., Bethesda, MD.

A. DiMillio.  
Geotechnical Research Project Manager, Federal Highway Administration, McLean, VA.

**ABSTRACT:** To qualify geosynthetics for in ground reinforcement use, it becomes mandatory to assess their durability within a short time with respect to environmental parameters to which they will likely be subjected for 75 to 100 years. This requires the development of accelerated tests permitting prediction of potential degradation under actual use conditions. It is known that polyolefin may oxidize resulting in polymeric molecular chain breaks directly resulting in strength loss of the material. The available studies of polyolefins oxidation indicate that rates of oxidation are very low at ambient temperatures, however in the context of the lifetime of civil engineering applications, may not be negligible. Comprehensive studies of polyolefin oxidation indicated that the rate of reaction among other factors, depends on the oxygen partial pressure in the system as well as on temperature. Complex antioxidant mixtures are commonly used to reduce the rate of oxidation for commercial polyolefin products during processing and in end use.

**KEY WORDS:** Geosynthetics, durability testing, oxidation, life prediction, antioxidant consumption

## 1. RESEARCH OBJECTIVES

This study was focused on considering the prime factors affecting the rate of degradation which are temperature, oxygen partial pressure, manufacturing process and effectiveness of antioxidants.

The scope of this reported research was limited to the laboratory investigation of thermooxidative degradation of a few typical commercial products selected to represent geosynthetic materials potentially used in highway applications. It is only a part of a larger FHWA study to develop durability testing protocols for geosynthetics.

The scope of the study is limited in that:

- a small number of commercial geosynthetic products are considered;
- only "severe" conditions of treatment, as compared to the in-service conditions, are used to accelerate degradation to achieve measurable chemical and mechanical changes during 2 to 3 years of laboratory incubation time.

## 2. LABORATORY ASSESSMENT PROCEDURES

The basic principles of thermooxidative degradation of polyolefin polymers indicate that environmental conditions such as oxygen partial pressure may have a significant impact on the rate of mechanical deterioration caused by oxidation. In order to assess the influence of oxygen partial pressure on the rate of mechanical degradation for

polyolefin geosynthetics, the following initial conditions have been selected for accelerated laboratory testing:

1. Oven aging in circulating air (21% O<sub>2</sub>) to represent surface and near surface conditions
2. Oven aging in stagnant atmosphere containing 8% O<sub>2</sub> balanced by N<sub>2</sub> to represent reduced oxygen found in reinforced fills (Yanful, 1993).

The overall effect of antioxidant additives is assessed by testing a specially manufactured polypropylene textile P-3a. This material is identical to the commercial products P-3 in terms of polymeric composition and manufacturing, except that it was manufactured with a minimum amount of additives required for production purposes.

## 3. GEOSYNTHETIC MATERIALS TESTED

Results from 2 commercial and 1 research grade geotextiles are reported in this study. The materials are differentiated by manufacturing process, composition and antioxidant additives. The main characteristics are shown in Table 1.

### 3.1 Testing procedures

The testing procedure consists of: (i) sample preparation; (ii) oven aging of prepared samples at different levels of oxygen concentration (iii) mechanical testing to determine tensile strength using a Wide Width Strip Test (ASTM D-4595); (iv) chemical testing to determine Oxygen Induction Time (OIT) by Differential Scanning Calorimetry

Table 1. Major characteristics of selected commercial polyolefin geosynthetic products.

Product code	Type	Unit weight (g/m <sup>2</sup> )	Tensile strength (kN/m)	Antioxidant type
P-3	PP Needlepunched-continuous filament non-woven geotextile	440	1.20±0.06	Hindered Amine (HALS), with trace carbon additive for color
P-3a	PP Needlepunched-continuous filament nonwoven textile	200	0.35±0.03	Research grade manufactured with a minimum amount of additives
P-4	PP Needlepunched staple nonwoven geotextile	370	1.50±0.05	Phenolic and phosphite

(DSC) at 175°C; and (v) analysis of surface morphology by SEM and/or optical microscopy. The major features of the testing procedure are outlined below.

To perform accelerated thermodegradation of polyolefin geosynthetics in air (21% O<sub>2</sub>), forced-draft ovens with a temperature uniformity of ±1% and substantial fresh air intake are used in a compliance with ASTM D-3045, "Heat aging of plastics without load". To conduct aging in a stagnant atmosphere containing 8% O<sub>2</sub>, a special chamber was designed and manufactured. This apparatus provides a temperature uniformity of ±1°C, and allows control of oxygen concentration in the chamber. The specimens are suspended in the oven or in the chamber without pretension and without touching each other.

The temperature of exposure varied from 50° to 90°C. At least 5 consecutive retrievals were made over the period of aging at each specific condition with each retrieval represented by a minimum of 5 specimens.

The study further indicated that Oxidative Induction Time (OIT) measurements for these geotextiles appeared to be ineffective in monitoring strength degradation for the products tested.

Measurements of remaining OIT for the geotextiles reported did not correlate with remaining strength or antioxidant consumption as measured by induction time.

#### 4. LABORATORY ACCELERATED DEGRADATION RESULTS

Each of the selected geosynthetic products tested exhibits a unique pattern of degradation under the tested environmental conditions. Surface morphology studies are discussed in the context of measurable deterioration of mechanical properties observed for the aged geosynthetics.

##### 4.1 Nonwoven continuous filament geotextiles, P-3 and P-3a

The monitoring of weight changes during exposure to elevated temperatures in different atmospheres, indicated

no statistically significant variation of weight for the P-3 and P-3a geotextiles.

SEM study of the fiber surface morphology indicated that there are no apparent changes on the fiber surface on a microlevel, for either geotextile, aged in different atmospheric environments and at temperatures varying from 50° to 90°C.

The progressive strength loss versus time for the P-3 and P-3a geotextiles, are shown on Figure 1, indicates a non linear strength loss and the presence of an induction period. The induction period is defined as the initial period of oven aging, when no statistically significant changes of a tensile strength is observed. The P-3a geotextile exhibits no induction period for the same range of test temperatures.

One of the properties which affects the rate of thermooxidation processes is the composition and concentration of antioxidant additives in commercial products. The effect of antioxidant additives on the rate of mechanical degradation of polyolefin geosynthetic products is clearly illustrated by the relative performance of two products, P-3 and P-3a. The P-3 product contains a HALS type of antioxidant additive, and P-3a is a specially manufactured textile with only a minimum amount of antioxidants required for production purposes. The beneficial effect of antioxidants is clearly demonstrated by the summarized comparisons between degradation rates for these two products which is shown in Figure 1. There is an indication that at the lowest temperature tested of 50°C, the effect of the antioxidants is more pronounced than at the highest temperature of exposure of 80°C which is closer to the upper limit of effectiveness of about 135°C, for HALS type antioxidants (Fay, King, 1994).

Samples of the P-3 commercial geotextile were exposed to elevated temperatures of 70°, 80° and 90°C in a stagnant atmosphere of 8% oxygen balanced by nitrogen. The summary of results is shown on Figure 2.

Results indicate that the rate of mechanical degradation in stagnant diluted air is much slower than the rate of degradation in circulating air ovens. It can be observed that in stagnant diluted air (8% O<sub>2</sub>) P-3 exhibits an initial

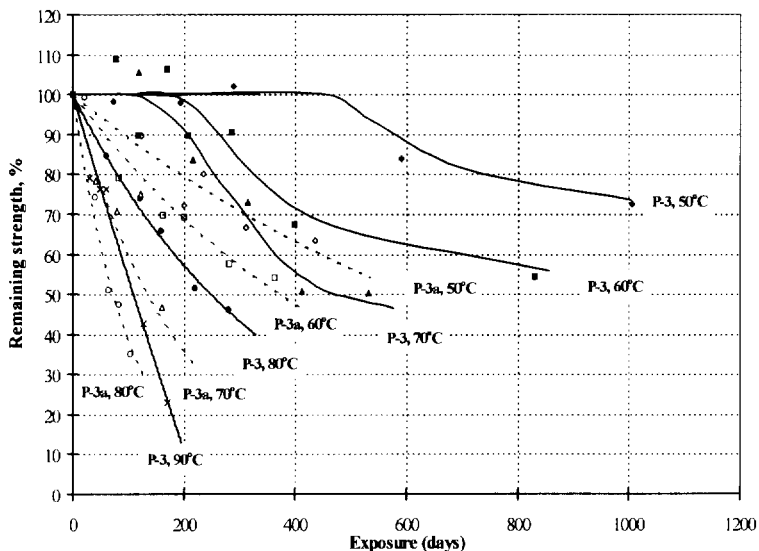


Figure 1. Effect of antioxidant additives on the rate of thermooxidation for the P-3 commercial product and P-3a research grade textile.

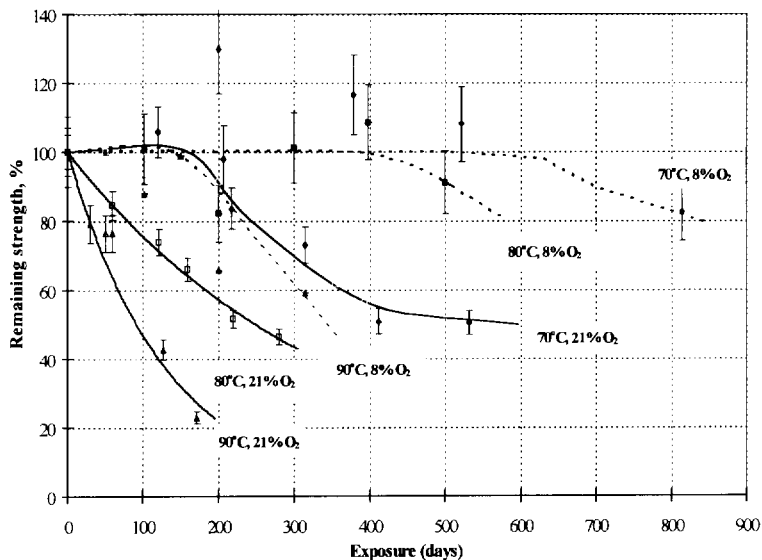


Figure 2. Tensile strength for continuous filament geotextile P-3 during oven aging in stagnant diluted air at 8% O<sub>2</sub> and in circulating air at 21% O<sub>2</sub>.

tensile strength increase when tested at 70°C. However, tensile strength decreases with exposure time.

#### 4.2 P-4, nonwoven staple geotextile

Commercial geosynthetic P-4 does not exhibit shrinkage or swelling over the period of aging in circulating air and stagnant diluted air ovens.

Analysis for microscopic changes on fiber surface morphology has been conducted by SEM of fibers "as received" and fibers taken from the specimens aged in circulating air oven at 50°C. The virgin fibers appear to

be smooth and clean, however, there are traces of initial cracks on the surface of virgin fibers transverse to the fiber length. The SEM study further indicates a progressive development of circumferential cracks on the fiber surface during exposure to elevated temperatures in circulating air.

The SEM study of fiber surface morphology for this geotextile aged in stagnant diluted air (8% O<sub>2</sub>) at 70 °C, indicated no development of circumferential cracks on the surface of fibers after the 473-day thermal treatment. No changes of the fiber diameters have been observed.

Weight changes for P-4 measured over the period of exposure to elevated temperatures in different atmospheric conditions are minimal. The weight changes measured vary within the range of 0 to 2 percent.

The observed development of fiber cracking explains the rapid loss of tensile strength during thermooxidation in intense circulating air. It appears that this material loses 50% or more of its initial strength during the first 50 days of exposure in temperatures varying from 50° to 80°C as shown on Figure 3.

The results of mechanical testing for P-4 aged in a stagnant atmosphere of diluted air (8% O<sub>2</sub>, 92% N<sub>2</sub>) are at first quite unexpected. The specimens aged at 70° and 80°C in stagnant diluted air exhibit a strength increase by factor of 1.8 after first 80 days of exposure followed by statistically insignificant changes of tensile strength. However, no tensile strength increase is observed at 90°C. The summarized experimental results for mechanical degradation in these conditions are also shown on Figure 3.

#### 4.3 Summary of laboratory data on the rate of mechanical deterioration caused by thermooxidation

Results of tensile strength monitoring for these two polypropylene geosynthetics, indicate that each of the products studied, exhibits a unique pattern of tensile strength changes during exposure to elevated temperatures under differing environment conditions (oxygen partial pressure). However, the common features are as follows:

1. Oven aging in stagnant diluted air at 8 percent oxygen results in the decrease of the rate of tensile

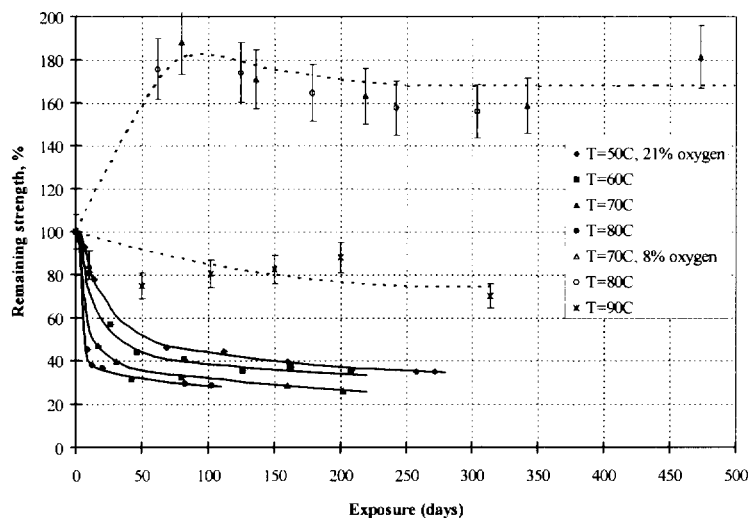


Figure 3. Tensile strength loss for geotextile P-4, aged in circulating air at 21% O<sub>2</sub> (solid line) and at 8% O<sub>2</sub> (dashed line).

- strength loss as compared to the rate observed in circulating air (21% O<sub>2</sub>) at the same temperature.
2. The two commercial products tested, exhibit a different morphology in their virgin state. SEM microphotographs at a magnification of 3000x reveal the presence of initial crazes/cracks on the surface of virgin fibers for nonwoven staple geotextile P-4. There is no indication of surface imperfections under the same magnification, for the virgin fibers of the nonwoven continuous filament product, P-3. This difference in fiber morphology is one of the causes for the differences in degradation patterns for P-3 and P-4 product.
  3. Staple product P-4 exhibits very low resistance to oxidation in circulating air (21% O<sub>2</sub>) at elevated temperatures which results from intensive surface cracks growth over the period of aging. By contrast, the continuous filament product P-3 exhibits no fiber surface crack development during oxidation under the same conditions, and a much lower rate of mechanical deterioration.
  4. Aging in stagnant diluted air (8% O<sub>2</sub>) results in the healing of the initial crazes on the fiber surface of the P-4 product. This may explain the tensile strength increases by a factor of about 1.5-1.6, observed in stagnant diluted air. Product P-3 exhibits the increase of tensile strength by a factor of 1.2-1.3, under the same conditions of aging.
  5. It appears that the effectiveness of antioxidant package can be measured by the developed induction time for products with no cracks or crazes in their as manufactured state.

Intensive surface crack growth in circulating air as well as crack healing in stagnant diluted air, indicate that there may be other or additional mechanisms to ther-

mooxidation, which contribute to mechanical degradation for staple product P-4 under accelerated temperature testing. The crack disappearance phenomena may occur due to an increase of molecular diffusion rate in the polymer leading to crack healing, analogous to the cold welding of metals. When the rate of diffusion and crack healing prevails over the rate of oxidation, a strength gain effect is observed. This adds to the complexity of the degradation process at high temperatures and brings to question the validity of oven aging as the appropriate accelerator for thermooxidative degradation studies especially for products which exhibit initial cracks/crazes in their as manufactured state.

The nonwoven continuous filament product, P-3, exhibits a more classic behavior and the temperature accelerated data lends itself to analysis within a framework of polymer chemistry.

## 5. A NUMERICAL MODEL FOR DEGRADATION RATE AND LIFE EXPECTANCY

The main objective of durability studies for commercial geosynthetic products is to estimate a degradation rate and corresponding life expectancy for in-service conditions.

The results of tensile strength losses for P-3 during oven aging in circulating air (21% O<sub>2</sub>) at elevated temperatures up to 70°C exhibit a substantial period of time with no changes of mechanical strength followed by a nonlinear decay of strength. Experimental data obtained in stagnant diluted air (8% O<sub>2</sub>), show a significant decrease in the rate of mechanical degradation as compared to the rate in circulating air (Figure 1). These patterns of degradation indicate that conventional "Arrhenius modeling" as suggested in the literature (Wisse and Berkenfield, 1982; Koerner, Lord and Hsuan, 1992) may be too simplistic to describe the degradation behavior of geosynthetic products. Therefore, the basic principles of kinetics of chemical reactions in general, and kinetics of thermooxidation in particular, such as the Basic Autoxidation Scheme (BAS) (Bolland, 1948; Kelen, 1982) must be considered in formulating an appropriate numerical model for materials which in their virgin state are completely intact and exhibit no cracks/crazes.

An interpretation procedure using BAS has been recently developed by the authors (Salman, Elias et al., 1997) and is used to interpret the laboratory results for P-3, which exhibits a more classic behavior.

## 5.1 Interpretation Procedure

In chemical kinetics (Adamson, 1973) the rate  $R$  of a reaction  $A+B+C+\dots \rightarrow \text{Products}$  at constant temperature is expressed as a function of composition of the system, according to mass action law as:

$$-\frac{d[P]}{dt} = R = k[A]^x[B]^y[C]^z \quad (1)$$

where  $[A]$ ,  $[B]$ , and  $[C]$  are the concentrations of reactants, and  $k$  is the rate constant being independent of the concentration of the reactants but dependent on temperature.

The order of the rate law is the sum of the exponents ( $x+y+\dots$ ). The important cases are zero, first and second-order reactions. The rate should be determined experimentally (Atkins, 1986).

The rates  $k$  of most reactions increase with temperature according to the Arrhenius law as:

$$k = Ae^{-E_a/RT} \quad (2)$$

with  $A$  - the pre-exponential factor, usually considered as a constant which is independent of temperature;  $E_a$  - the activation energy;  $R$  - the ideal gas constant; and  $T$  - the temperature in  $^{\circ}\text{K}$ .

The kinetics of autoxidation for the general case of antioxidant presence, consist of two phases. The first phase (induction period) describes the consumption of antioxidants, with the reaction constant for consumption defined by an Arrhenius-type dependency. During the second phase, the oxidation and corresponding mechanical degradation is described by the kinetics of the BAS.

The data usually obtained in the laboratory, does not provide sufficient information on the kinetics of antioxidant depletion during aging. Therefore, the order of reaction for antioxidant consumption cannot be determined directly from experimental data. Analysis of integrated rate laws for kinetics of chemical reactions (Adamson, 1973) yield a general expression for induction time versus temperature at any given level of antioxidant depletion  $[A]/[A_0]=c$ . Assuming that the reaction constant for antioxidant consumption obeys the Arrhenius law, the following relationship is indicated:

$$\ln \frac{1}{t_{ind}} = C_1 + C_2 \frac{E_a}{RT} \quad (3)$$

where  $C_1$  and  $C_2$  are the constants for a particular antioxidant and given level of depletion  $c$ .

This relationship (3) suggests a procedure for estimating induction time at a given temperature  $T_0$   $^{\circ}\text{K}$  as follows:

1. The induction period  $t_{ind}$  is determined at each temperature of exposure, defined as the period of no statistically

significant changes in mechanical strength. It is determined by extending a tangent line to the slope of the post induction degradation curve until it intersects the no strength loss line. With limited data it requires some judgment.

2. A linear regression analysis is conducted for the function  $\ln(1/t_{ind})$  versus the reciprocal temperature ( $1/T$   $^{\circ}\text{K}$ ). The obtained linear equation  $\ln(1/t_{ind}) = a(1/T)+b$  is used to find the value of the induction period at any given temperature,  $T_0$   $^{\circ}\text{K}$  as follows:

$$t_{ind} = 1/\{ \exp[a(1/T_0)+b] \} \quad (4)$$

The determination of induction period at elevated temperatures is shown in Figure 4 for P-3 commercial geosynthetic, aged in circulating air at 21 percent oxygen and reduced oxygen at 8 percent.

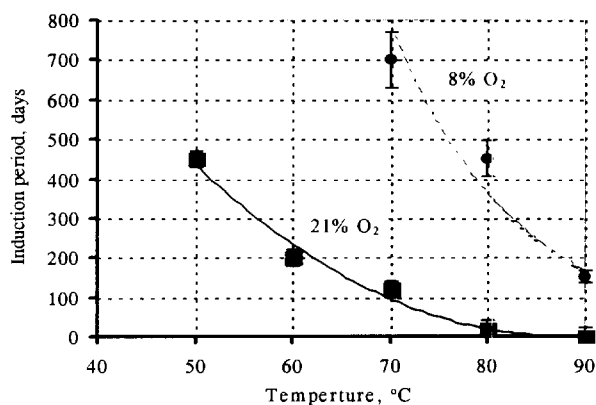


Figure 4. Induction period for P-3 aged in circulating air at 21% (solid line) and 8% (dashed line)  $\text{O}_2$ .

3. The solution of the equation for linear regression of  $\ln(1/t_{ind})$  versus reciprocal temperature at  $20^{\circ}\text{C}$  (Figure 5), yields a value for P-3 of anticipated induction period  $t_{ind} = 51$  years at 21%  $\text{O}_2$  and 240 years at 8%  $\text{O}_2$ . For P-3a which does not exhibit an induction period at the temperature tested, no prediction at ambient temperature can be made from the data.

Interpretation of data for mechanical degradation observed in the post induction period, requires the determination of the order of reaction for the product tested, with a subsequent estimate of anticipated rate of degradation (strength loss per 100 years) or time to 50 percent strength loss at any given temperature. In this study zero-, first- and second-order reactions are considered. The procedure of determining the order of reaction and degradation rate estimates are as follows:

1. Functions representing the kinetics of zero-, first- and second-order are used to fit the experimental data for the measured mechanical degradation, after the induction period for each temperature of aging.

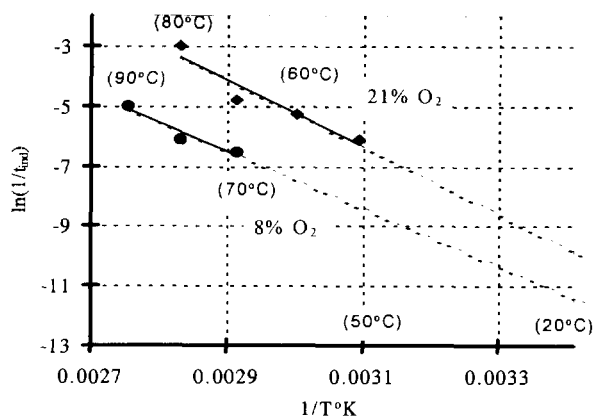


Figure 5. Linear regression analysis of  $\ln(1/t_{ind})$  versus  $1/T^\circ K$  for P-3.

2. The obtained values of the logarithm of reaction constant  $\ln(k)$  for the chosen type of kinetics, are plotted versus reciprocal temperature of aging (Arrhenius plot).
3. A linear regression analysis is used to find the equation for  $\ln(k)$  as a function of reciprocal temperature  $1/T$ ,  $\ln(k) = a(1/T) + b$ . This equation yields the value of  $k$  for the temperature of interest,  $T_0$ ;  $k(T_0) = \exp[a(1/T_0) + b]$ .
4. The obtained  $k(T_0)$  value of the rate constant is used to calculate a normalized retained strength at a given time  $x(t) = F(t)/F_0$  or to calculate time  $t_i$  to reach certain level of retained strength  $c = F/F_0$  at a given temperature  $T_0$  K for a specific reaction:

$$x(t) = 1 - k(T_0)t; t_i = \frac{1 - c}{k(T_0)} \text{ - for zero-order reactions; } \quad (5)$$

$$x(t) = \exp(-k(T_0)t); t_i = \ln(1/c)/k(T_0) \quad (6)$$

- for first-order reactions; and

$$x(t) = \frac{1}{1 + k_1(T_0)t}; t_i = \frac{1 - c}{k_1(T_0)c} \quad (7)$$

- for second order reactions law.

The results of exponential curve fitting corresponding to a first-order reaction which has the greatest likelihood ( $R^2$ ) for approximating the experimental data, are shown in Figure 6.

A first-order reaction is predicted by the BAS model for kinetics of mechanical degradation of polyolefins without antioxidants at a constant oxygen pressure. Therefore, the priority in the selection of the reaction order, is given to the exponential law (first-order).

Figure 6 summarizes the result of a linear regression analysis for the reaction constant  $k$  corresponding to a first-order reaction for mechanical degradation for P-3 in circulating air at 21 percent oxygen.

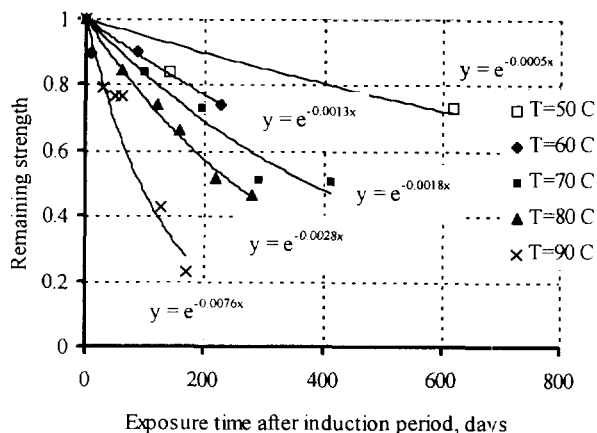


Figure 6. Exponential curve fitting corresponding to a first-order reaction, after an induction period, for P-3 at 21%  $O_2$ .

The solution of a linear regression line equation and sequential substitution of the obtained value of the reaction constant  $k$  into a first-order reaction, yields an estimate of 50 percent strength loss at 20°C of 38 years after the induction period of 51 years at 21%  $O_2$  and 240 years at 8%  $O_2$ . The obtained estimates of anticipated strength is valid only for the conditions of testing, e.g. circulating air at 21%  $O_2$  and in stagnant diluted air at 8%  $O_2$ .

It appears, that the estimate for the induction period of 51 to 240 years with no strength loss, suggests that antioxidant consumption rate and ambient regime primarily determine the practical durability of this commercial product.

For the research grade textile P-3a, the interpretation of data in circulating air at 21%  $O_2$ , yields an estimate of anticipated time to 50 percent strength loss at 20°C as of 29 years. This result is in a good agreement with the estimate of degradation rate after the depletion of antioxidants, for the P-3 geotextile. The interpretation of data in stagnant diluted air at 8%  $O_2$  yields an estimate of anticipated time to 50% strength loss at 20°C as of 47 years for the P-3a textile which is a decrease by a factor of 1.6 when compared to the degradation rate in air at 21%  $O_2$  (FHWA, 1997). This result is in general agreement with an estimate of the reduction of the degradation rate in diluted air at 8%  $O_2$  based on the integrated law of chemical kinetics (Equation 1).

Arrhenius equation for reaction rate constant could be rewritten as:  $\ln(k) = C - U/RT$ , where  $U$  is apparent activation energy, and  $R = 8.31$  J/mol. Solving this equation with respect to  $U$ , one obtains value of  $U = 61$  kJ/mol, which is in a reasonable agreement with the value of 65 kJ/mol, reported by Wisse and Birkenfeld (1982) for PP geosynthetic with extracted antioxidants tested at 21%  $O_2$ .

Tests for P-4 in stagnant diluted air indicate that some process other than oxidation, controls the behavior of this



material at elevated temperatures. Therefore, both elevated temperature aging results and the numerical model developed within the framework of BAS, cannot be directly applied to laboratory data obtained for the P-4 product or other products with initial cracks or circumferential cracks developed during aging at elevated temperatures. For these geosynthetics, alternate testing methods at ambient temperature and elevated oxygen pressure (50 to 100 atm) as indicated by the BAS, result in mechanical degradation rates in for shorter time and may be more applicable.

## 6. ALTERNATE TESTING PROTOCOL AT ELEVATED OXYGEN PRESSURE

In a simplified process of polyolefin oxidation, it is assumed that the rate of reaction at constant temperature depends on the concentration of original polymer [A] and the concentration of oxygen [B], in equation (1). Data reported in the literature (Kelen, 1982) indicate that the rate of oxidation may be proportional to the concentration of oxygen in the system, which corresponds to a first order reaction. Therefore, an increase in oxygen pressure should result in the proportional increase of the rate of mechanical degradation for polyolefins. For example, the exposure of polyolefin based geosynthetics to an atmosphere of pure oxygen may result in the acceleration of the degradation rate by a factor of 5 as compared to the rate anticipated in air (21% oxygen) at ambient temperature. The further increase of oxygen pressure to 50 atm should result in an acceleration of the reaction by a factor of 250, as compared to the rate of oxidation under ambient conditions.

### 6.1 Testing conditions and experimental results

An atmosphere of pure oxygen at a pressure of 50 and 100 atm has been selected for an initial feasibility assessment of high oxygen pressure accelerated degradation for polyolefin geosynthetics. It is anticipated that this condition may accelerate the degradation rate by a factor of 250 in 50 atm and by a factor of 500 in 100 atm as compared to the rate under ambient (1 atm, 21% O<sub>2</sub>, 20°C) conditions. Strip size specimens of three geosynthetics previously tested (P-3, P-3a and P-4), were placed in high pressure chamber filled with pure oxygen at 50 and 100 atm at 20°-22°C. The chamber was ventilated and refilled with oxygen once a day.

Tensile strength tests were conducted on strip-size specimens for materials as received and after the incubation. Relative changes of tensile strength are presented in Table 2.

### 6.2 Interpretation of test results

The simplified and preliminary kinetics for oxidation under oxygen pressure yields an acceleration factor of 250 for oxygen pressure of 50 atm and factor of 500 for oxygen pressure of 100 atm. Strength losses from oven aging in circulating air at 21% oxygen and under high pressure oxygen incubation at ambient temperature were calculated within the framework of the Basic Autoxidation Scheme and are shown on Table 3. The comparison is based on strength losses in equivalent periods of time.

Table 2. Tensile strength loss for geosynthetics aged in pure oxygen at 50 and 100 atm and 20°C.

Condition	Equivalent time at ambient condition*, years	Strength loss, %			
		Material			
Oxygen pressure, atm	Incubation time, days		P-3	P-3a	P-4
50	60	40	0	42	10
100	30	40	0	N/A	N/A
100	90	120	16	N/A	N/A

\* 21% O<sub>2</sub>, 20°-22°C

Table 3. Comparison between oven aging and high oxygen pressure strength loss estimates.

Equivalent time at ambient conditions, years	High pressure oxygen strength loss, % (oven aging strength loss estimate, %)		
Material ⇒	P-3	P-3a	P-4
40	0/(0)	42/(63)	10/(100)
80	N/A/(50)	N/A	N/A
120	16/(100)	N/A	N/A

N/A - not available

Results of this limited study indicate that oxygen pressure can be used as an accelerator and that a preliminary acceleration factor can be predicted by the simplified kinetics of oxidation for polyolefins. The estimates of strength loss over 40 years based on data developed under high oxygen pressure conditions are within the range of estimates obtained in oven aging in circulating air for some products or yield more reasonable results as indicated by actual performance. As expected, the P-3 product with an estimated 50 years induction period, exhibits no tensile strength loss over a period equivalent to 40 years. The research grade textile P-3a yields a strength loss of 42% tested under high oxygen pressure condition which is in reasonable agreement with the 63% strength loss over 40 years, obtained for oven aging in circulating air. The difference may be attributed to the

intrinsic variability of mechanical properties for the P-3a product, nonuniformity of the degradation process at different temperatures and in high oxygen pressure etc.

Furthermore and of significant importance is the preliminary finding that the estimated strength loss in 40 years measured for the P-4 nonwoven staple fiber geotextile is more consistent with the anticipated and reported performance for this geosynthetic. Interpretation of P-4 losses from oven aging protocols suggests a 50% strength loss in 6.5 years, which is unreasonable in light of the actual performance of this material over 10 years as measured from retrieved sites. Examination of P-4 samples incubated under high oxygen pressure indicates no changes in surface morphology.

## 7. SUMMARY

Interpretation of experimental data suggests the following:

1. Kinetic models developed within the framework of the Basic Autoxidation Scheme (BAS) appear to provide a satisfactory analysis of the experimental data and permit conservative estimates of time against strength loss at ambient temperature to be made for products which exhibit no cracking/crazes in their as produced state.
2. The rate of antioxidant depletion and the rate of mechanical degradation in stagnant diluted air appears to be lower than in circulating air and may provide better model of in-ground conditions.
3. Products with effective antioxidants may exhibit induction times well in excess of their useful life in civil engineering applications. Oven aging temperatures must be low enough to permit measurements of induction time, which is a method to quantify the effectiveness of the antioxidant package.
4. High oxygen pressure appears to be a viable accelerator for oxidative strength loss measurements and appears to be a viable testing protocol for products where high temperature changes the surface morphology. However more development is necessary to establish more exact relationships.
5. Estimates of strength loss versus time under ambient conditions based on high oxygen pressure degradation are in a satisfactory agreement with estimates obtained from oven aging in circulating air for the monofilament product tested.

## ACKNOWLEDGMENTS

This study was funded by Federal Highway Administration under DTFH 61-91-R-00054, "Durability of Geosynthetics for Highway Applications". Their permission to publish the developed data is appreciated. We wish to acknowledge the contributions of T.M. Allen for his con-

tinuous interest and suggestions and Dr. V.V. Krongauz for his helpful discussions.

## REFERENCES

- Adamson A.W., 1973, "A textbook of physical chemistry", Academic Press, New York, 1079 p.
- Atkins P.W., 1986, "Physical chemistry" Third edition, Oxford University Press, 857 p.
- ASTM D-3045, Heat aging of plastics without load", American Society for Testing and Materials, Philadelphia, PA, USA.
- ASTM D-4595, "Standard Test Method for Tensile Properties of Geotextiles by the Wide-Width Strip Method", American Society for Testing and Materials, Philadelphia, PA, USA.
- Bolland J.L., 1948, "Kinetic studies in the chemistry of rubber and related materials. VI. The benzoyl peroxide catalyzed oxidation of ethyl linoleate", *Trans. Faraday Soc.*, Vol. 44, pp. 669.
- Fay J.J., King R.E., 1994 "Antioxidants for geosynthetic resins and applications", *Proc. 8th Conference GRI, Dec. 94*, Philadelphia, pp. 74-91.
- FHWA, 1997, "Durability of geosynthetics for highway applications", Draft Final Report, DTFH 61091-R-00054.
- Kelen T., 1982, "Polymer degradation" Van Nostrand Reinhold Company, New York, p. 211.
- Koerner R.M., Lord A., Hsuan Y.H., 1992, "Arrhenius modeling to predict geosynthetic degradation" *Geotextiles and Geomembranes*, No 11, pp. 151-183.
- Salman A., Elias V., Juran I., Lu S., Pearce E., 1997, "Durability of geosynthetics based on accelerated laboratory testing", *Geosynthetics '97*, San Diego, CA, pp 217-234.
- Wisse J.D.M., 1988, "The role of thermo-oxidative aging in the long-term behavior of geotextiles". *Durability of geotextiles, RILEM*, Chapman and Hall, London, pp. 207-216.
- Wisse J.D.M., Birkenfeld S., 1982, "The long term thermo-oxidative stability of polypropylene geotextiles in the Oosterschelde Project", *Second International Conference on Geotextiles*, Las Vegas, USA, Vol 1, pp. 283-288.
- Yanful E.K., 1993, "Oxygen diffusion through soil covers on sulfuric mine tailings", *Journal of Geotechnical Engineering*, Vol. 119, No. 8, pp. 1207-1228.

# Conventional and Stepped Isothermal Methods for Characterizing Long Term Creep Strength of Polyester Geogrids

J. S. Thornton

President and Principal Scientist, Texas Research International, Inc., Austin, Texas, U.S.A.

J. N. Paulson

Vice President, Strata Systems, Inc., Atlanta, Georgia, U.S.A.

D. Sandri

Western Regional Engineer, T.C. Mirafi, Inc., Lake Forest, California, U.S.A.

**ABSTRACT:** Conventional methods of time-temperature superposition (TTS) are compared to a new procedure for time-temperature superposition called the stepped isothermal method (SIM). Creep and creep rupture properties of two polyester geogrid products are investigated. The conventional TTS approaches studied consumed a total of 18,000 hours of test time. In addition with both polyester products it was found difficult to separate temperature dependence of creep strain response from specimen to specimen variation in elastic strain response to loading events. Using the new SIM method, over 15 load specific master creep modulus curves were generated, some of which extended to over 100 year design lifetimes, each from a single specimen in a test that was completed in less than 18 hours. The results of the conventional and SIM procedures were found to be equivalent for the polyester products examined.

**KEYWORDS:** Time-temperature superposition, shift factors, unconfined creep tests, creep strain, creep modulus, creep rupture, polyester fibers, geogrid, accelerated testing.

## 1 INTRODUCTION

The Stepped Isothermal Method (SIM) for time-temperature superposition (TTS) has been formally introduced at this symposium in a companion paper [Thornton, et. al. (1998)] emphasizing the theoretical aspects of the procedure development and giving examples selected from tests on a polyester (PET) yarn. Thornton, et.al (1997) described SIM for a single temperature step on a wide width PET geogrid sample.

The present paper introduces the application of SIM to two PET fiber based geogrid products designated Product A and Product B from two different geosynthetic material manufacturers in the USA.

Utilization of TTS principles have been applied often to polypropylene and polyethylene products. However, extensive use of TTS for polyester products has been inhibited by three factors. First the creep rates for PET, which are generally linear (or nearly so) in semilog plots, are relatively low, in the range of 0.1 to 0.2% strain per time decade. Secondly, the specimen to specimen variation in the load vs. strain relationship is relatively high, given the small resultant creep strains. A 1% uncertainty in strain level for a given load is not atypical. The third factor is that the temperature dependence of creep curves under the same applied load is comparatively small. Differences in exposure temperatures of 20°C cause less than 1% difference in creep strain at the same exposure time. The above factors conspire to make the TTS process for PET so uncertain that many replicate samples are needed to establish the shift factors and the proper strain level locations for shifted creep curves.

SIM overcomes these difficulties because a master curve is

generated on a single sample which is maintained under load as it is exposed to a series of isothermal dwells separated by increasing temperature steps. Because recovery is prevented by this procedure, the master curve is made up of juxtaposed segments in contrast to the overlapped segments that comprise a conventional master curve. When specimens are taken to rupture, the shifted times to rupture obtained from the SIM procedure can be used to construct creep rupture curves. The experimental efficiencies that result from SIM lead to large cost and time savings.

## 2 OBJECTIVE

The objective of this paper is to introduce the application of the SIM to the characterization of long term creep and creep-rupture of two PET based geogrid products. The results of conventional time-temperature superposition are provided for comparison purposes.

## 3 MATERIALS AND METHODS

Products A and B are from two different manufacturers in the U.S.A. The methods of construction differ significantly, Product A is manufactured by the weft insertion weaving process and Product B is manufactured by a knitting process. Both products are coated to protect the fibers from abrasion. Comparative load vs. strain and secant modulus vs. strain curves for the two materials are given in Figure 1. Both products are made from high tenacity, high molecular weight (>25,000), alkali tolerant (max. 30 carboxyl end group) fibers. The double hump in both load vs. strain curves is

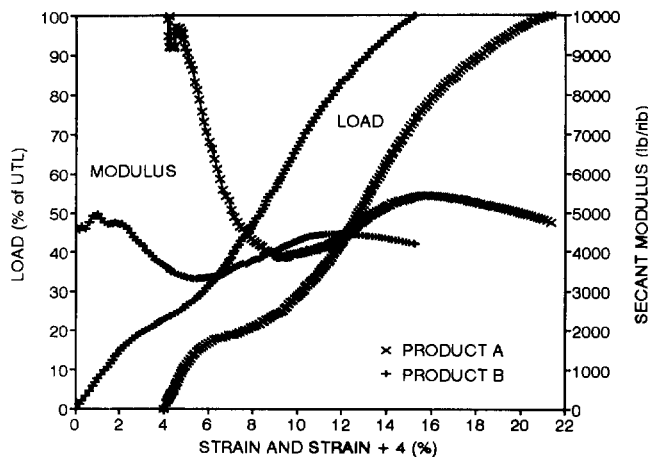


Figure 1. Load and secant modulus vs. strain curves for Products A and B.

characteristic of drawn PET fibers. The initial modulus of Product A is higher than that of Product B due to construction differences. Both products exhibit gradual peaks in secant modulus at strains corresponding to about 75% of the ultimate tensile strength (UTS).

The stepped isothermal creep and creep rupture tests were performed by TRI/Environmental, Inc. of the U.S.A. These tests were all performed in a Model 3111 Instron environmental chamber modified with a Watlow Series 982 temperature controller at a series of temperatures 14°C apart beginning at 26 ± 0.5°C. The 26°C starting temperature was sufficiently above laboratory ambient temperature that adequate temperature control could be achieved by heating only. The tests were performed in an Instron 4505 Load Frame under computer control. Strain was monitored using an extensometer (typically Instron 2620-T24) with a nominal gage length of 2 in. The load cell used was Instron with a rated load capacity of 2248 pounds.

The conventional creep tests on Product A and creep-rupture tests on Product B were performed by ERA Technology, Ltd. of the U.K. Test conditions were 20 ± 2°C/65 ± 2% RH, 40 ± 2°C and 60 ± 2°C for both test programs. Two ribs were utilized in the creep tests and a single rib in the creep rupture tests. The gage lengths were 60mm and 75mm. Roller grips and dead weight loading frames were used in both tests and the strain transducers used were LVDTs.

The Product A and B materials used in SIM tests by TRI and conventional tests by ERA were from different manufacturing lots.

## 4 RESULTS AND DISCUSSION

### 4.1 Creep of Product A

#### 4.1.1 Conventional Time-Temperature Superposition

Figure 2 shows the results of eleven long term creep tests of Product A. The tests were conducted at 21, 31 and 56% of

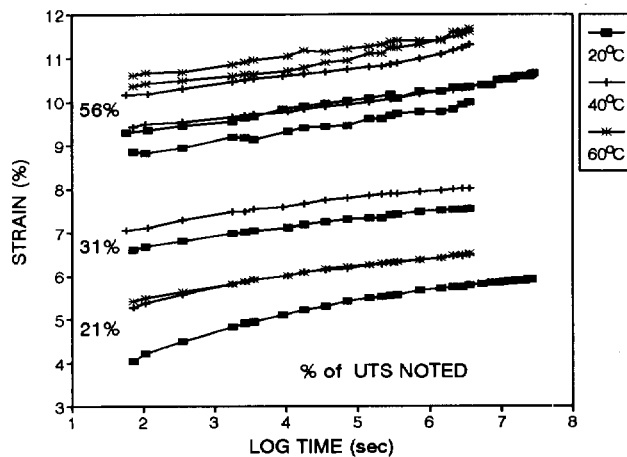


Figure 2. Creep strain vs. log time for Product A at 21%, 31% and 56% of UTS and 20°C, 30°C and 40°C.

the ultimate tensile load of the material and at 20, 40 and 60 degrees Celsius. Two of the tests at 20°C were of 8000 hour duration (one at 21% UTS and one at 56% UTS) and the balance of the tests were 1000 hour duration. Replicate tests were performed at 56% UTS at 20, 40 and 60°C.

These data illustrate one of the major problems with conventional time-temperature superposition of PET products: specimen-to-specimen variation tends to mask the effect of temperature on test results. In Figure 2 at 21% of UTS, the creep strain curve for 60°C lies on top of the creep strain curve for 40°C. At 56% of UTS, one creep strain curve at 20°C lies over another at 40°C. Also at 56% of UTS, the separation between the two 40°C curves is nearly as great as between the higher 20°C curve and the lower 60°C curve. Clearly, it can be concluded from Figure 2 that the specimen-to-specimen variation exhibited is of the same magnitude as a 20°C change in test temperature.

Figure 3 presents the averages of the two creep strain results at each temperature for 56% of UTS. The average curves display reasonable separation despite variability of the individual curves.

Figure 4 shows the creep data of Figure 3 in terms of creep modulus, which is the quotient of the creep stress by the creep strain. As discussed in the companion paper [Thornton, et.al (1998)] creep modulus, as a more fundamental quantity, is preferred over creep strain when comparing the properties of different materials or even different lots of the same material.

Conventional time-temperature superposition was applied to the creep modulus data of Figure 4 to obtain the master curve of Figure 5. The 40°C and 60°C curves were shifted horizontally to the right (representing an acceleration) until they overlapped the 20°C curve in a reasonable fashion. The horizontal shift of creep strain vs. log time data on a semi log plot is equivalent to multiplying the time for each data point of the curve by the same shift factor. The logarithm of the shift factor is the horizontal distance along the log time scale that the curve is moved. The logarithm of the shift factor used on the 40°C data was about 2.5 and that for the 60°C data was about 5. This means that the 40°C curve was shifted

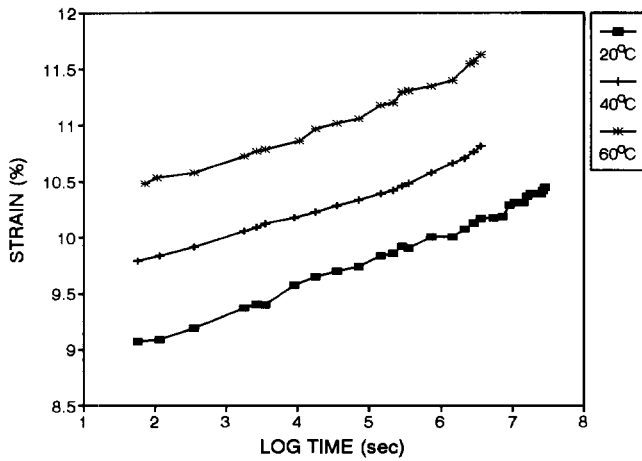


Figure 3. Creep strain vs. log time for Product A at 56% of UTS and 20°C, 30°C and 40°C. Results to 1000 hr. are the average of 2 specimens; results beyond 1000 hr. (20C) are from one specimen shifted vertically to continue the trend established up to 1000 hr.

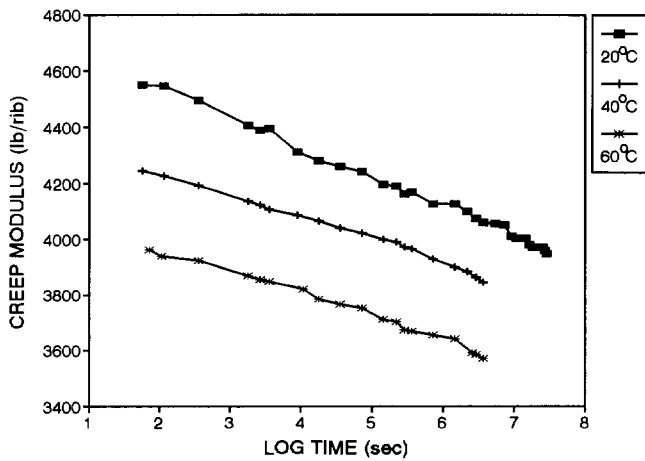


Figure 4. Creep modulus vs. log time for Product A at 56% of UTS and 20°C, 30°C and 40°C.

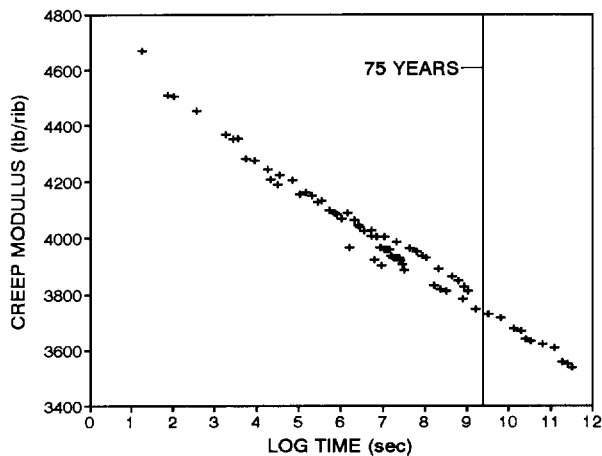


Figure 5. Master creep modulus vs. log time for Product A at 56% UTS for a reference temperature of 20°C.

To the right by two and one-half decades and the 60°C curve was shifted to the right by five decades to achieve the master curve. Since the 20°C curve was fixed in this procedure, 20°C became the reference temperature.

#### 4.1.2 Stepped Isothermal Method (Product A)

Four tests which represent replicate specimens tested at 40% and 56% of UTS were completed on Product A. Since the SIM procedure is described in some detail in the companion paper, only a brief description of the procedure as applied to one of the 40% UTS tests (1801) is given here. The stepped temperature profile for test 1801 is shown in Figure 6, where thermocouple readings representative of the temperatures of the specimen and the grips are displayed. Note that there is a brief exposure to 99°C, which is well above the glass transition temperature (often quoted as 82°C) of PET.

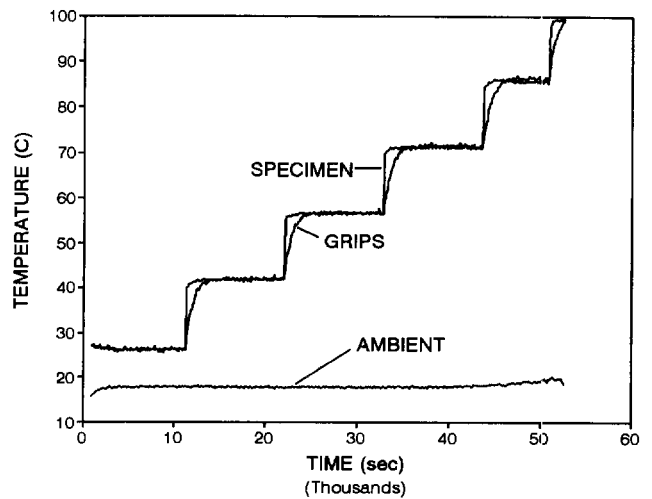


Figure 6. Stepped temperature profile for SIM test 1801 (40% UTS).

The first four isothermal steps are each about 10,800 sec. long, the fifth step about 7000 sec. long and the final step is about 1700 sec. in length. The creep response under the influence of the constant applied load and the temperature profile is presented in Figure 7. The first strain response at 26°C is a normal and complete creep curve, while the subsequent responses at 42°C, 57°C and so on, appear normal, only lacking the initial ramp up portions. Thus, each new temperature exposure sets off a fresh creep response under the constant applied load. Additional interesting features of this graph are the thermal contractions that accompany the increases in temperature. A negative coefficient of expansion is a characteristic of PET fibers. The one shown here is about 35 parts per million per degree Celsius. The load and strain data of this figure were converted to creep modulus and plotted in Figure 8.

Figure 9 contains the creep modulus information of Figure 8 plotted against log time. In addition, the creep modulus responses for the second through the sixth temperature steps

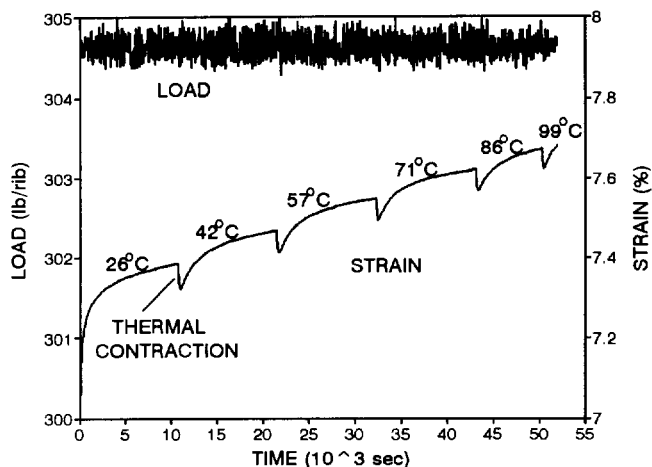


Figure 7. Creep strain response and applied load vs. time for SIM test 1801 (40% UTS).

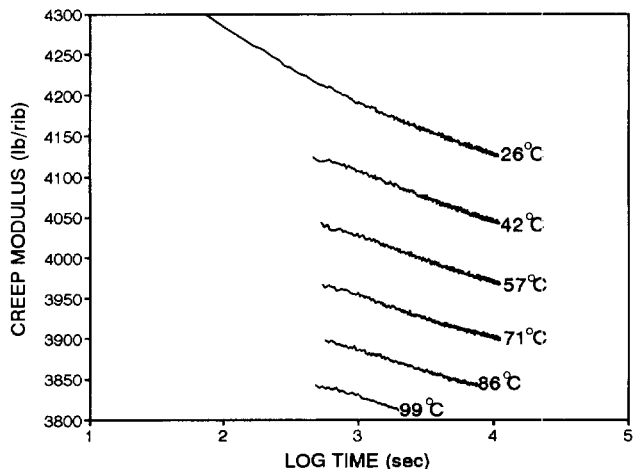


Figure 10. Creep modulus vs. log time for SIM test 1801 (40% of UTS) showing effect of vertical shifts to eliminate thermal contractions between steps.

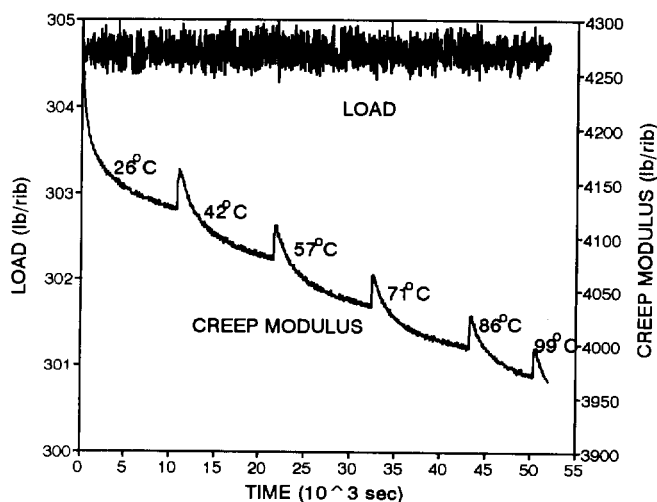


Figure 8. Creep modulus and applied load vs. time for SIM test 1801 (40% UTS).

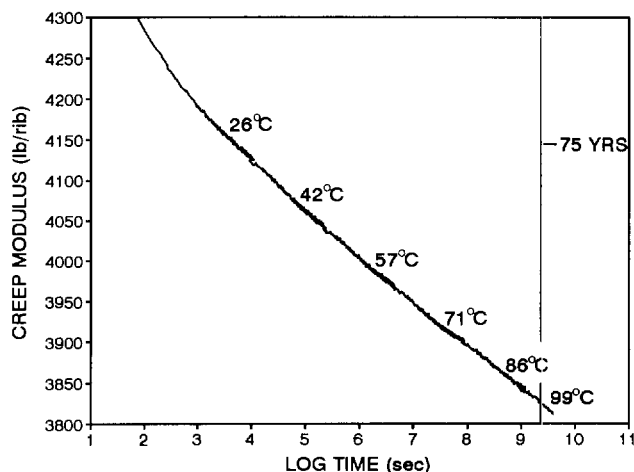


Figure 11. Master creep modulus vs. log time for SIM test 1801 (40% of UTS).

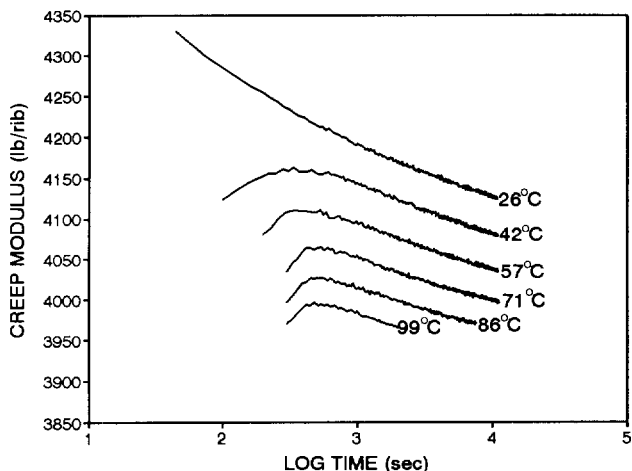


Figure 9. Creep modulus vs. log time for SIM test 1801 (40% UTS) with effect of rescaled start times.

are rescaled to new starting times between 100 and 300 seconds, increasing 2 to 2.5 on the log scale. The next figure, Figure 10 shows the intermediate result of vertical shifts to remove the thermal contractions from the creep data.

Finally, the master creep modulus curve is obtained by horizontal shifts of the segments stacked up in Figure 10 to achieve the result shown in Figure 11 for the reference temperature given by the first step, 26°C. The duration depicted by this master curve is 9.596665 log seconds which converts to over 100 years. Without the 99°C segment of 1700 sec. The shifted time would have been about 32 years.

Master creep modulus curves for the other three tests were created using the method just described.

#### 4.1.3 Comparison of Conventional and SIM Results

Master creep modulus curves for the tests described in the previous two sections are shown in Figure 12. The agreement

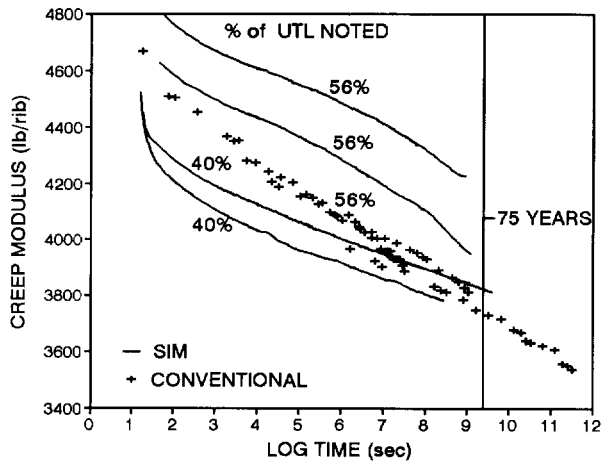


Figure 12. Master creep modulus vs. log time curves by conventional and SIM for Product A at 56% and 40% of UTS.

is quite good especially considering the data were generated several years apart on two different lots of material at separate laboratories.

The separation between the two 56% and the two 40% SIM curves are indicative of specimen to specimen variation. Since data from six specimens were combined to give the conventional (56%) curve, the individual effect of specimen-to-specimen variation is somewhat suppressed, but the overall scatter in the data for the conventional curve reflects uncertainty in both specimen-to-specimen variations and selections of the factors used for the time-temperature shifts. A set of creep strain curves, were computed from the master creep modulus curves and are presented in Figure 13.

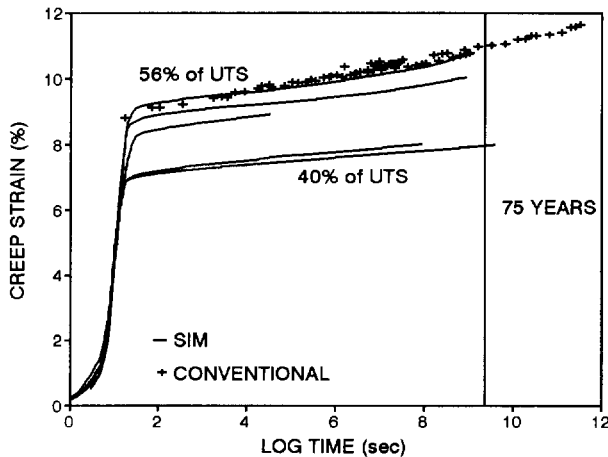


Figure 13. Strain response to long term loading at 40% and 56% of UTS for Product A.

Figure 14 consists of curves relating the cumulative shift factors used in the time-temperature superposition procedures to create the master curves. The single curve of the factors used to generate the conventional master curve is the one on the left of this figure. A family of four curves to the right define the shift factors for the four SIM master curves. The

SIM shift factor curves are essentially the same, appearing not to depend on load level. The slopes of the conventional and SIM curves differ somewhat as do the origins of the curves. The difference in the origins is arbitrary, depending only on the selection of reference temperature. The difference in slopes is not so arbitrary, but given the sample to sample variation problems inherent in the conventional master curves may not be significant. Note that the shift factor curve that extends to 99°C maintains linearity and constant slope beyond the reach of the other curves.

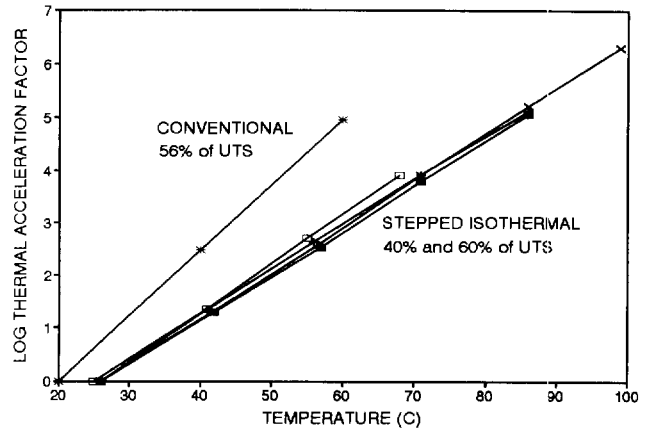


Figure 14. Shift factors used to construct the Product A master creep modulus curves.

## 4.2 Creep-Rupture of Product B

### 4.2.1 Conventional Time-Temperature Superposition

There are several ways to do conventional TTS for creep rupture data. The first starts with separate linear regression plots of the rupture strengths vs. log times to rupture for each test temperature. The regression lines for each plot are then shifted horizontally along the log time axis to achieve the optimum fit of a combined regression line through all the data. If, in addition to the rupture strength and time-to-rupture data there are creep strain measurements available, as in the present case, then it is possible to obtain additional estimates of the shift factors using the creep modulus curves at the different test temperatures, in a manner similar to that illustrated in Section 4.1.1. The two ways just described should give similar creep rupture regression lines. However, if at the same rupture stress the creep strains at rupture vary with temperature then the factors for shifting rupture regression lines will differ from those for shifting creep modulus curves.

Figure 15 presents the separate linear regression plots of rupture load as % of UTS vs. log time to rupture for tests performed at 20°C, 40°C and 60°C. The regression lines are not parallel, which makes the TTS uncertain. Horizontal shifts to make the regression lines colinear resulted in several visually acceptable curves, using shift factors between 1.91 and 2.3 for the 40°C to 20°C shift and 3.8 and 4.6 for the 60°C to 20°C shift.

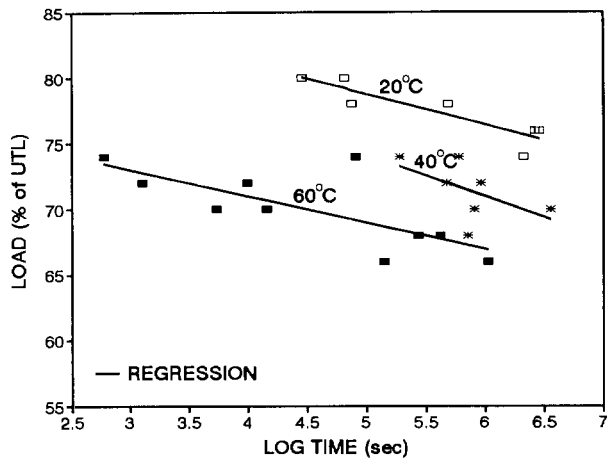


Figure 15. Conventional Load vs. time to rupture data with regression Lines for Product B at exposure temperature of 20°C, 40°C and 60°C.

Creep strain data taken during the creep rupture tests are presented in Figure 16, and the creep modulus curves derived therefrom are shown in Figure 17. Notice that the creep modulus data tend to be separated by test temperature, more so than the creep strain data. The natural groupings of the creep modulus data suggest they can be shifted en masse, despite the slightly different load levels applied at the three test temperatures. This is a consequence of the fact that as a quotient, modulus does not change as much as load with strain in the 65 to 80% load range (see Figure 1). More exact estimates of the log shift factors might be obtained by examining smaller groups of individual curves arranged by applied load. However, this would work only to the extent that sample to sample variation effects were controlled by testing numerous replicates. Figure 18 presents the modulus data of Figure 17 shifted by factors of 1.95 (40°C to 20°C) and 3.90 (60°C to 20°C). Using these factors, the data of Figure 15 are shifted to give the master curve of Figure 19.

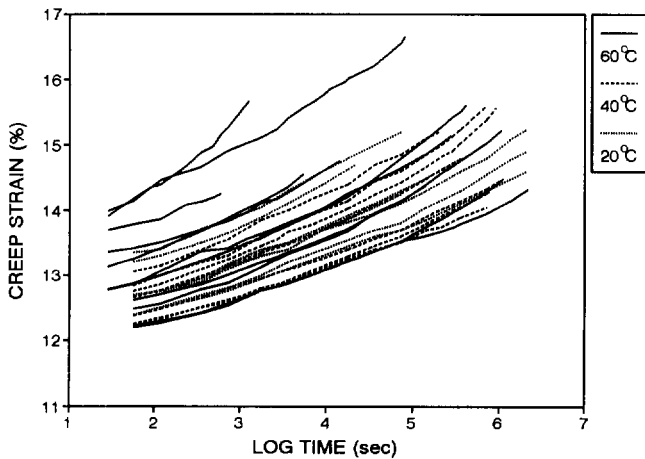


Figure 16. Creep strain vs. log time curves for the conventional Product B rupture tests.

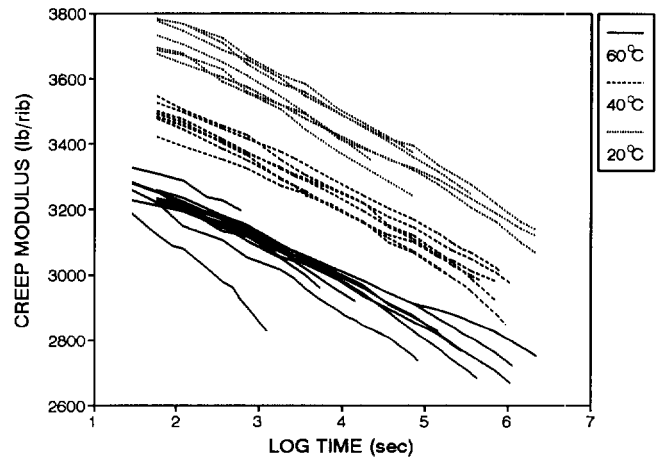


Figure 17. Creep modulus vs. log time curves for the conventional Product B rupture tests.

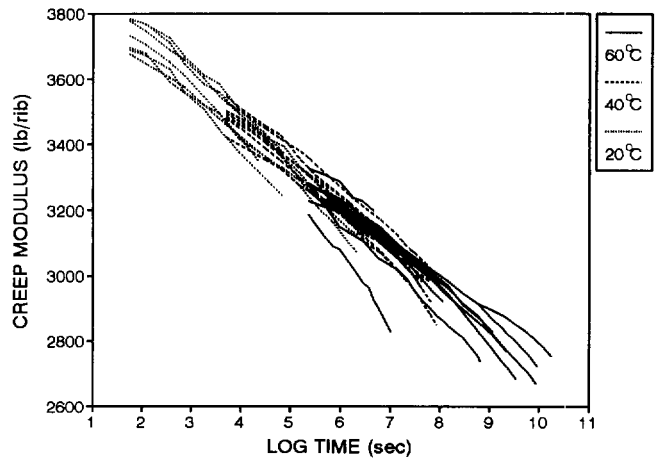


Figure 18. Shifted creep modulus curves for the conventional Product B rupture tests.

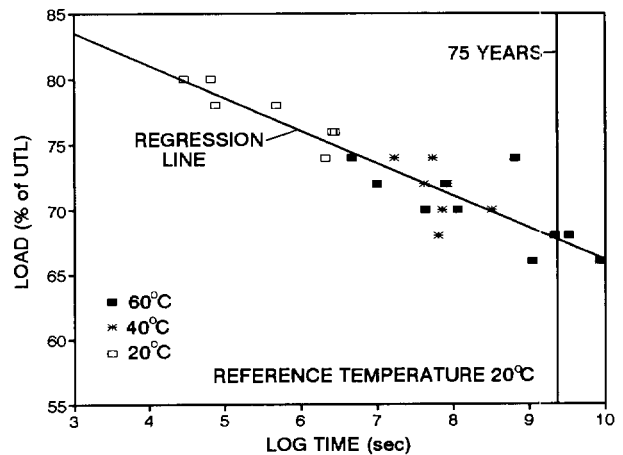


Figure 19. Conventional master load vs. log time to rupture data and regression line at a 20°C reference temperature.



#### 4.2.2 Stepped Isothermal Method (Product B)

Creep modulus master curves for each specimen were generated using the same procedure described in Section 4.1.2. These are displayed in Figure 20. Note that 5 of the curves terminated in rupture, and the balance did not. We use the term runout to describe the result of a test where rupture did not occur before the test was terminated. Runouts that are close to the loads resulting in rupture can be used in the statistical analysis to help locate the regression line.

Figure 21 presents the creep strain curves derived from the creep modulus master curves.

An expanded set of creep-rupture loads vs. log times to rupture for the SIM tests are shown in Figure 22. The runout loads and log times, included for information, were not included in the regression calculation. The 75 year rupture load at a reference temperature of 26°C is 65.6% of UTS. Less than one decade of extrapolation beyond the temperature shifted results was needed to return this result.

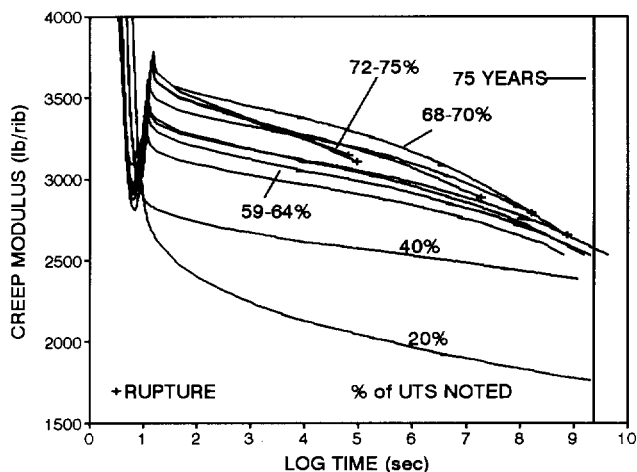


Figure 20. Master creep modulus vs. log time curves for SIM tests on Product B. Load levels and rupture events are noted.

Table 1 provides a guide to the shifted rupture times of Figures 20 - 22. The log shift factors used to construct this table are based on 0.093 decades per °C. Thus a 14°C temperature step creates a time shift of about 1.3 decades.

Table 1. Logarithm of the shifted times at the reference temperature (26°C) corresponding to the unshifted times at the exposure temperatures.

Range Shifted time Log $A_T(t-t')$	Maximum value	
	Exposure Temperature, °C	Unshifted cumulative time, sec
0.0-4.0	26	$1 \times 10^4$
4.0-5.3	40	$1 \times 10^4$
5.3-6.7	54	$1 \times 10^4$
6.7-8.0	68	$1 \times 10^4$
8.0-9.3	82	$1 \times 10^4$

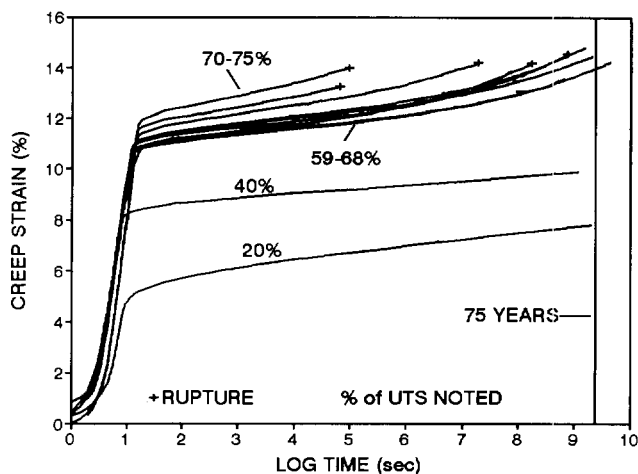


Figure 21. Creep strain curves computed from the data of Figure 20.

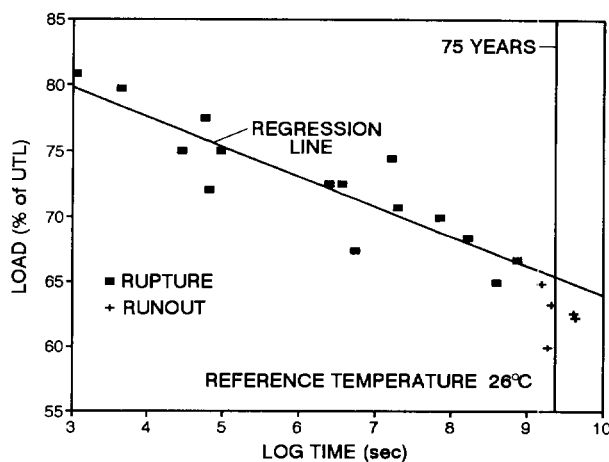


Figure 22. SIM master load vs. log time-to-rupture data and regression line for Product B.

#### 4.2.3 Comparisons

Regression lines for the conventional and SIM creep rupture results are compared in Figure 23, and shift factors used to accomplish TTS, in Figure 24. Rupture loads at 75 years for a reference temperature of 20°C are 67.7% for conventional and 66.5% for SIM TTS. Despite an apparent small difference in shift factors for the conventional and SIM approaches, results for the regression lines and the projected rupture loads at 75 years are very close. Figure 25 compares all shift factors for Products A and B.

### 5 CONCLUSIONS

- The use of SIM as a special application of TTS for polyester geogrids appears to be validated by the results presented herein. Differences, if any, in the shift factors obtained in SIM and conventional approaches are not large.

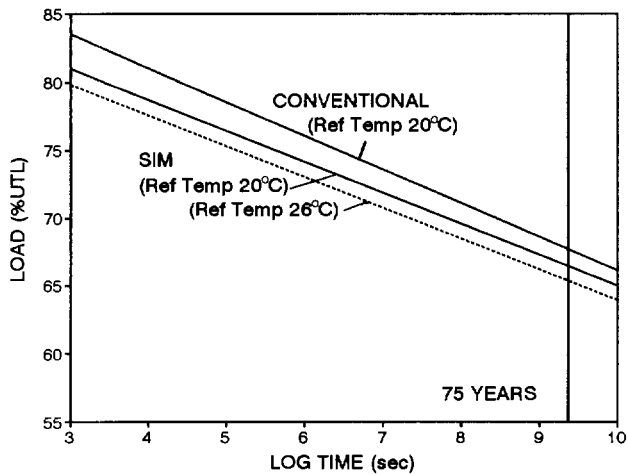


Figure 23. Comparison of conventional and SIM regression lines for Product B.

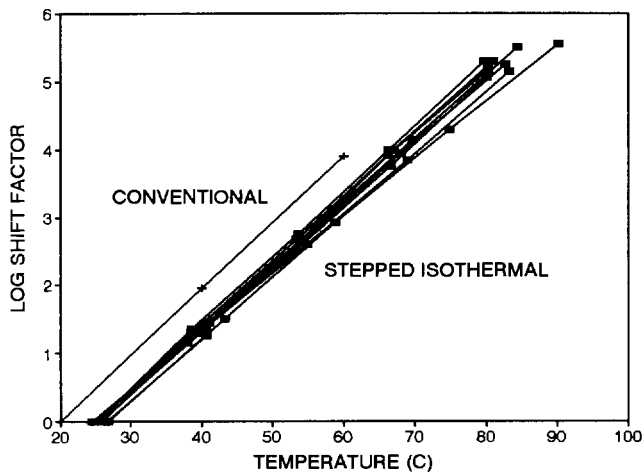


Figure 24. Comparison of log shift factors for Conventional and SIM rupture master curves.

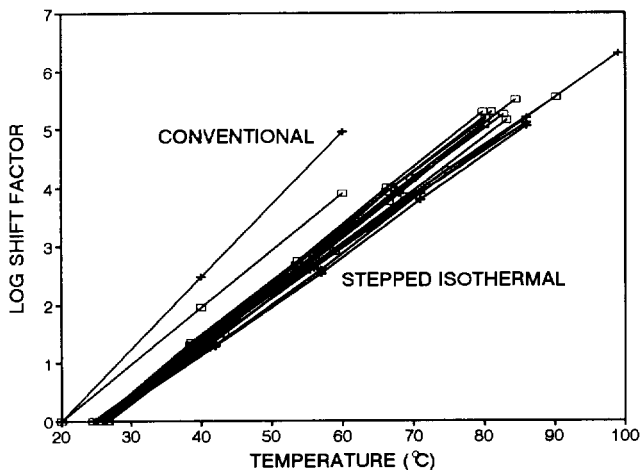


Figure 25. Comparison of all shift factors for creep and creep rupture for Products A and B.

- An advantage of SIM in this regard is that it reduces the uncertainty of shift factors used to construct master curves.
- Since a SIM master curve is generated from a single specimen, the precise location of the completed curve is uncertain, due to specimen-to-specimen variation. This is not a great disadvantage if several SIM tests are to be done, as in developing a creep rupture curve. Alternatively, if only a single SIM test is done and its location is important, the location can be determined from the results of a few very short term conventional creep experiments.
- The apparent insensitivity of SIM master curves to abrupt transition behavior for tests at 40% of ultimate and higher at and above the glass transition temperature is consistent with a creep mechanism associated with they crystalline regions of the polymer.
- The slopes of SIM generated creep strain curves increase significantly with increase in applied load, but the shift factors are not greatly sensitive to applied load for the range of loads studied here. Thus the increases in slopes are not caused by decreases in shift factors.
- The shift factors for Products A and B (Figure 25) are similar despite differences in construction and load vs. strain behavior confirming the notion that the shift functions are manifestations of basic material properties.
- Obtaining creep strain data in conjunction with performing creep rupture tests is recommended where TTS is to be done. If rupture times at elevated temperatures are shifted based on the basis of achieving superposition of creep strain or modulus curves then the shift factors for creep and those fro rupture will be the same. Rupture times from SIM tests can be obtained no other way.

#### ACKNOWLEDGMENTS

The authors are indebted to Dr. John H. Greenwood for helpful suggestions and experimental efforts at ERA Technology, Ltd., for both products A and B over several years, Shawn L. Arnett of TRI/Environmental, Inc. and J.M. Palmer of ERA are acknowledged for conducting the experimental program. Funding from Texas Research International, Inc., Strata Systems, Inc., and T.C. Mirafi, Inc. is greatly appreciated. T.C. Mirafi, Inc. is also acknowledged for providing seed funding for SIM development.

#### REFERENCES

- Ferry, J.D. (1980) *Viscoelastic Properties of Polymers*, 3rd Edition, John Wiley and Sons, New York, NY, USA.
- Thornton, J.S., Allen, S.R., Thomas, R.W. and Sandri, D. (1998), "The Stepped Isothermal Method for TTS and Its Application to Creep Data on Polyester Yarn," *Sixth Int'l Conference on Geosynthetics, Atlanta, USA*.
- Thornton, J.S., Allen, S.R., and Thomas R.W., (1997), "Approaches for the Prediction of Long Term Viscoelastic Properties of Geo Synthetics from Short Term Tests," *Geo '97, IFAI, Vol. 1, Long Beach, CA, USA, pp 277-291*.

# The Stepped Isothermal Method for Time-Temperature Superposition and Its Application to Creep Data on Polyester Yarn

J. S. Thornton

President and Principal Scientist, Texas Research International, Inc., Austin, Texas, U.S.A.

S. R. Allen

Vice President and Program Manager, TRI/Environmental, Inc., Austin, Texas, U.S.A.

R. W. Thomas

Vice President and Technical Director, TRI/Environmental, Inc., Austin, Texas, U.S.A.

D. Sandri

Western Regional Engineer, T. C. Mirafi, Inc., Lake Forest, California, U.S.A.

**ABSTRACT:** The stepped isothermal method (SIM) is a new procedure for assessing the long term viscoelastic behavior of polymeric materials. SIM is a special case of time-temperature superposition (TTS) that is convenient for characterizing viscoelastic materials. It utilizes a single specimen which is loaded continuously through a sequence of timed isothermal exposures at increasing temperature in stair step fashion. Generating master curves involves rescaling the times for the elevated temperature and utilizing horizontal shifts in such a way that smooth curves are achieved. Relationships between the rescaling times and the resulting horizontal shift factors as well as the relative magnitudes of the temperature and time steps are investigated to demonstrate that the SIM can tolerate reasonable variations in these parameters and provide master curves and shift factors comparable to those obtained by conventional time temperature superposition. Conventional and SIM results are obtained on a 3 ply, 1000 denier poly(ethylene terephthalate) yarn. PET is an ideal object for study because its creep properties are well behaved. Also, as the basic ingredient for a number of commercially viable geosynthetic fabrics and grids, the properties of PET yarn are of special interest on their own.

**KEYWORDS:** Stepped isothermal method, time-temperature superposition, shift factors, unconfined creep tests, creep strain, creep modulus, creep rupture, polyester yarn, accelerated testing.

## 1 INTRODUCTION

Polymer scientists have been using time-temperature superposition techniques for at least 4 decades to describe long term viscous or viscoelastic properties of polymers [see, for example, Ferry (1980)]. The fundamental notion is that elevating temperature accelerates the response to mechanical load. Deformations, such as creep strain, occur relatively rapidly when load is first applied, but the rate of increase decreases with time. Consequently, graphs produced with log time as the abscissa are indispensable for describing viscoelastic behavior.

The precise way that increasing temperature accelerates these physical processes, governs how creep response can be "shifted" along a log time scale. Ferry (1980) refers to TTS as the method of reduced variables for corresponding states. A temperature dependent time factor,  $a_T$ , relates the ratio of the time,  $t_T$ , for a viscoelastic process to proceed a given amount at an arbitrary temperature to the time,  $t_R$ , for the same process at a reference temperature.

$$a_T = \frac{(t_T)}{(t_R)}$$

At temperatures greater than the reference temperature  $a_T$  is less than 1. For this reason, some in the accelerated testing business refer to  $a_T$ , as an attenuation factor and  $A_T$ , defined as its reciprocal, as an acceleration factor. Both, collectively, are referred to as shift factors.

Early master creep (or relaxation) curves using TTS were specialized to small strain linear viscoelastic situations. Single specimens were used (to reduce specimen to specimen variation) and these were permitted to recover between creep exposures by removing the load (without removing the specimen from the apparatus to avoid problems of repeatable clamping stress transfers) for a time period that was long compared to the loading time between creep tests (10 times the loading time would generally effect 99+% recovery of the creep strain of the prior creep test).

Most engineering applications that engage time-dependent behavior of polymeric materials deal with non-linear viscoelastic behavior. For such situations, creep master curves are generated using several specimens to reduce the uncertainties of non-identical specimens, and each is only tested one time because recovery is generally too complex to consider doing. Hence, the corresponding states must come from averaging a range of states from the several specimens tested at each exposure temperature. Despite the preoccu-

pation of this paper with large strain nonlinear viscoelastic effects we believe it will be helpful preparation to review the Boltzman Superposition Principle, which is the first mathematical statement of linear viscoelasticity.

From this brief review we will see that tracking the creep response to a series of loading steps includes starting a new clock with each new step. Boltzman (1876) proposed that, a) the creep response of a material is a function of the entire loading history, and b) each loading step is treated as an independent event, and c) the total creep response is the sum of the individual responses to those independent events. In mathematical notation the time dependent strain  $e(t)$  is

$$e(t) = \int_{-\infty}^t D(t-t') \frac{d\sigma(t')}{dt'} dt'$$

The integral is over all time to the present hence the limits are from  $-\infty$  to  $t$ . The first factor  $D(t-t')$  is the compliance function where  $t'$  symbolizes the times at which increments of stress  $d\sigma$  are applied; so that  $t-t'$  starts a new clock that activates the compliance function at the application of each stress increment. The second factor  $d\sigma(t')/dt'$  represents the loading program which is summed by the integration process. The response of a linear viscoelastic material to a two-step loading program is illustrated in Figure 1. As illustrated in this figure, each loading event begins a new clock and evokes an independent creep response. The new creep response is on top of (added to) the background of continuing responses to the history of loading events. The idea of a series of loading events activating new responses and starting new clocks at  $t-t'$  will be utilized for explaining the SIM as we shall see shortly.

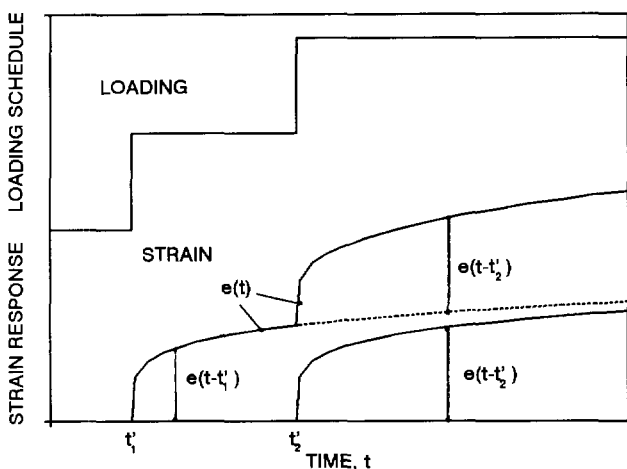


Figure 1. Boltzman Superposition Principle applied to the case of two loading steps

## 2 THE SIM PROCEDURE

The stepped isothermal method (SIM) procedure for creep consists of a series of timed isothermal creep tests performed

at a sequence of increasing temperatures. These are somewhat analogous to the loading steps of the previous section. As in an ordinary creep test, the load is held constant and the creep strain is measured for the duration of the test. The number, heights and the durations of the temperature steps are designed to produce a master curve of creep compliance (or preferably its reciprocal, the creep modulus) over a long term period defined by the test objective. For the geosynthetics community, long term generally means 75 years or sometimes 1,000,000 hours, which is 114 years. For our work on PET, we've found that 14°C temperature steps and 10,000 second isothermal step durations are convenient and workable for most tests on PET base products. Five 10,000 second isothermal exposures between 26°C and 82°C will usually achieve the desired long term objective. The time step of 10,000 seconds has been used frequently in the literature [see, for example, Murayama et.al (1968)]. Also, in previous work, Thornton, et.al (1997) showed that as the basis for long term extrapolations creep and relaxation modulus curves at 3 hours were as well developed as curves at 24 hours for that purpose. The typical starting temperature of 26°C comes from desiring a temperature above our maximum summer laboratory ambient temperature of 23°C that could be controlled by heating only. The typical ceiling temperature of 82°C came from the temperature usually assigned as the glass transition temperature for PET. Above 82°C one would ordinarily expect to encounter glass transition behavior with PET. However, as we'll see later, at high loads the creep mechanism engages crystalline regions of the polymer which do not participate in the glass transition. Our study of shorter and longer times and higher and lower temperature steps has confirmed that our standard SIM temperature steps of 14°C and time steps of 10,000 sec, while aggressive, are usually acceptable.

Preparation for the SIM test involves mounting the specimen in the grips, achieving temperature equilibrium, and applying a small (< 1%) preload on the specimen. Ramping the load to the predetermined stress level begins the test. This is done rapidly (typically 60%/minute strain rate) to minimize the creep deformation that occurs during the ramp-up process. We've gotten into the habit of "starting the clock" for the first leg of the creep test at the start rather than the end of the ramp. This preserves the ramp-up process for the record. With generally less than 20 seconds involved in the ramp-up and 75 or 114 years the long term objective, a starting time correction from the start to the peak of the ramp has no measurable impact on the final master curves.

The first creep exposure of the SIM procedure is a normal creep test in the sense that the specimen does not have a history of creep loading. The second and subsequent creep exposures are complicated slightly by having the thermal histories of the previous steps. This slight complication however, represents the essence of the SIM method. Since recovery is not permitted during the time that the temperature step takes place, and since the temperature step is accomplished rapidly, within 1 to 2 minutes, the mechanical

state of the sample is nearly the same after the temperature step as it was before the temperature step took place. Inherent in the SIM is the necessity that the corresponding states at both the lower and the higher temperature are stable ones that would be readily achievable under, say a conventional TTS approach. That condition would not be achieved if, for example, the temperature step was so large that the sample had to undergo a rapid change to achieve a steady state creep rate.

Just as each loading step is treated as an independent event for Boltzman's Principle, we assign a starting time,  $t'$  on the old clock to each temperature step. The time on the new clock starts at 0 which is obtained by setting  $t-t' = 0$ . The response history for the thermal steps is easier to account for than with the loading steps because the load has not changed. The assumption is that with the temperature step only the rate of creep has been changed, not the mechanism. Based on the notion that for a pair of corresponding states obtainable at two temperatures, the one at the higher temperature must have occurred at an earlier time than the one at the lower temperature, we begin the rescaling procedure by finding that earlier time,  $t'$ , that represents the virtual starting time of the higher temperature step. Exactly how we choose  $t'$  is illustrated in Figure 2.

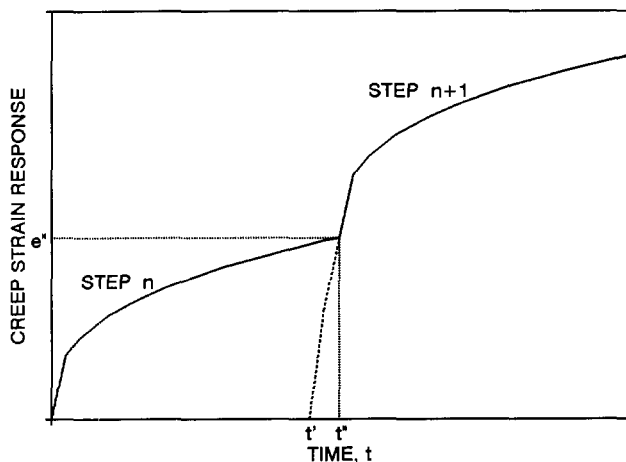


Figure 2. Strain response for two temperature steps

Here, we see the strain response for two temperature steps. In Figure 2 the precise time of the application of temperature step  $n + 1$  is  $t''$ . In the SIM at  $t''$ , the effect of history has been to bring the strain response to  $e^n$ . In a hypothetical independent creep test at the temperature of step  $n + 1$  the creep strain  $e^n$  would have been achieved at a time  $t_i$  after the start time. Overlaid on Figure 2, the starting point of that hypothetical creep curve would be at  $t'$ . Thus,  $t_i = t' - t''$ . We refer to the value of  $(t-t')$  at the beginning of the step (i.e. at  $t = t''$ ) as the initial value of  $t-t'$ . We know that we have the best value for  $t'$  if the slopes of the creep curves in semi logarithmic representations are the same before and after the temperature change.

In the SIM procedure it is necessary to remove the effects of thermal expansion to insure that the strain response is due to loading effects only. This is accomplished by a simple vertical shift for each temperature change.

The final SIM procedural step is the horizontal shifts to achieve juxtaposition of the creep modulus segments. If the rescaling step has achieved the slope matching boundary condition, then there will be little if any effort needed to determine the horizontal shifts needed. In practice, we generally do the rescaling and the horizontal shifting steps together in an iterative fashion to achieve a smooth creep modulus master curve.

The SIM procedure just described for processing creep modulus data is summarized in bullet form in Table 1.

Table 1. SIM procedure for processing creep modulus data

- Plot the creep strain and creep modulus data as function of linear time to identify the times for the temperature step changes.
- Using creep modulus as the parameter of interest, plot this parameter vs. log time.
- Rescale the times for the individual creep modulus segments by plotting them vs. the logarithm of the initial value of  $(t-t')$  where  $t'$  is adjusted to account for history. This will be achieved when the slope of the beginning of a new segment is exactly the same as the ending slope of the previous segment.\*
- Remove thermal expansion effects by vertical shifts.
- Shift horizontally to achieve exact juxtaposition of the rescaled and vertically shifted individual creep modulus segments.\*

\*the rescaling and shifting steps may require some iteration.

### 3 OBJECTIVE

The objective of this paper is to introduce the SIM and a standard protocol for its use. This will be accomplished by first comparing SIM results using the standard protocol to conventional TTS results and next by examining the effects of variations from the standard protocol. Finally, demonstrating the effectiveness of SIM by using it to characterize the long term creep and creep rupture properties of a polyester yarn, completes this introduction.

### 4 MATERIALS AND METHODS

Figure 3 represents stress vs. strain and secant modulus vs. strain curves for a 3 ply polyester yarn chosen for the current investigation on the basis of its well behaved creep properties and commercial importance. The rapid loading secant modulus is included in this illustration because the creep modulus is a secant modulus. When the loading path up a stress-strain curve is interrupted at a particular stress for a creep test, the beginning creep modulus for the creep test will

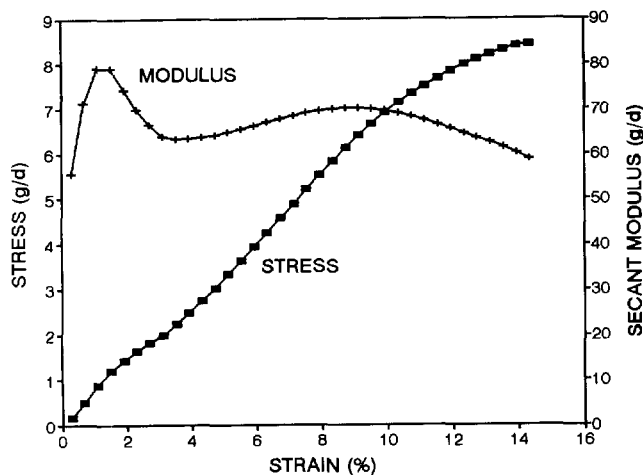


Figure 3. Stress and secant modulus vs. strain for the 3 ply, 1000d polyester yarn under rapid loading conditions.

be the same as the rapid loading secant modulus at that stress. Most of the tests reported in this paper were conducted in the vicinity of the second modulus peak at stresses between 5 and 7 g/d. Note that the secant modulus varies only within a range of about 3% around 70 g/d, in that stress range. The creep mechanism probably involves some straightening and breaking of tie molecules between crystalline regions in vicinity of the second modulus peak. Even for creep tests at stresses as low as 3 g/d the mechanism is probably similar to that of the higher stresses. At stresses below about 1.5 g/d the creep mechanism is associated more with the initial modulus peak and involves conformational changes involving the breakdown of the entanglement network as well as molecular uncoiling [Van den Heuvel et.al. (1993)]. This figure shows that initial creep modulus for tests at less than 1.5 g/d applied stress will be substantially higher than tests at above 3 g/d applied stress.

The creep tests were all performed in a Model 3111 Instron environmental chamber modified with a Watlow Series 982 temperature controller at a series of temperatures 14°C apart ± 0.5°C. The 26°C starting temperature was sufficiently above laboratory ambient temperature that adequate temperature control could be achieved by heating only. The tests were performed in an Instron 4505 Load Frame under computer control. Strain was computed from cross head travel and a 10 inch gage length. Instron Model 2111 "horn" grips were used along with an Instron load cell with a rated load capacity of 224 pounds. The specimen and the grips were completely enclosed in the environmental chamber.

## 5 RESULTS AND DISCUSSION

### 5.1 Conventional TTS

As a special case of TTS, SIM should provide master curves as good as and potentially better than the conventional procedure. Thus, the ability of SIM results to match exactly those of conventional TTS is not the goal; to show they give

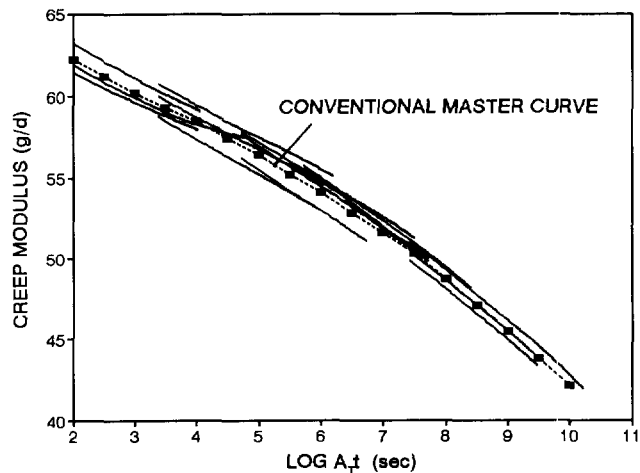


Figure 4. Conventional master creep modulus curve.

comparable results, builds confidence in both procedures.

A total of 15 polyester yarn specimens, consisting of 3 each at the temperatures of 26, 40, 54, 68, and 82°C were tested for creep at an average stress of 62% of UTL over time periods of 10,000 to 60,000 sec. The resulting creep modulus curves were shifted to obtain a good visual representation by a conventional master creep modulus curve. These results are shown in Figure 4. Note the range of the individual modulus values is 3 to 5% of the master curve values. The conventional master curve appears in some of the subsequent figures to provide a comparison with SIM master curves.

### 5.2 Standard SIM Steps

Figures 5 through 9 illustrate the SIM applied to a yarn specimen subjected to a constant stress of 5.21 g/d, which is about 62% of the ultimate tensile strength (UTS) of this material. Figure 5 shows the measured creep strain and the computed creep modulus as a function of linear time. Each time step is approximately 10,000 sec and each temperature

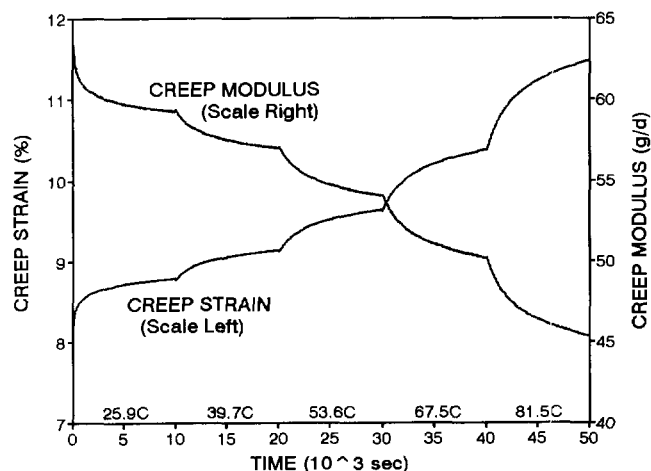


Figure 5. Creep strain and creep modulus vs. linear time for a specimen tested at 62% of UTS.

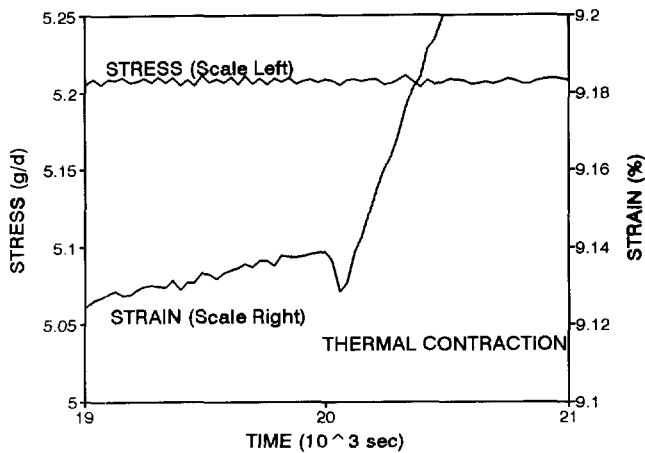


Figure 6. Enlargement of a portion of Figure 5 showing a thermal contraction after a 13.9°C temperature step.

step approximately 14°C beginning at 25.9°C and ending with 81.5°C as shown along the bottom of the figure. There are tiny cusps at the temperature step change points which are manifestations of a negative thermal expansion coefficient ( $\alpha_T$ ). One of them is shown in enlarged scale in Figure 6. The magnitude of  $\alpha_T$  for this example is about 7ppm/°C. Such negative thermal expansions are easy to identify because they produce length changes opposite to the creep strains. Positive thermal expansions may require separate experiments to quantify. Next, Figure 7 presents the creep modulus data as a function of log time. The effect of the time rescaling step is illustrated in Figure 8. Rescaling has a dramatic effect on the shapes of the curve segments. Part of this is due to the nature of logarithmic scales, but as indicated earlier, the initial slopes of the rescaled curves are influenced by the new starting times. Figure 9 gives the master creep modulus curve resulting from the horizontal shifts. The abscissa is now labeled LOG  $A_T [t-t']$  to indicate the data has been both rescaled and shifted.

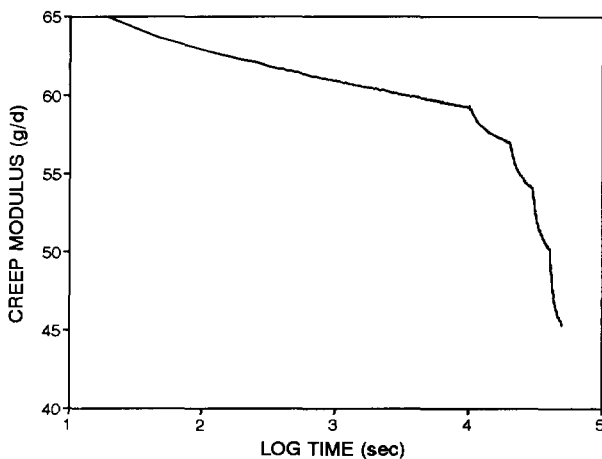


Figure 7. Creep modulus data from Figure 5 plotted vs. log time.

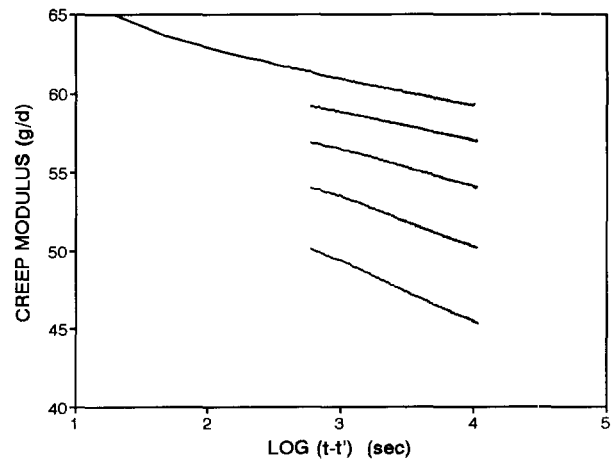


Figure 8. Creep modulus data from Figure 7 rescaled for new starting times vs. log  $[t-t']$

### 5.3 Effect of the Choice of $t-t'$ on $A_T$

The purpose of this section is to explore the effect on  $A_T$  of non optimum selections of rescaling times  $t-t'$ , when generating master curves.

Figure 10 displays the influence of three choices for rescaled times  $t-t'$  on the shapes of the resulting creep modulus master curves. The middle curve, labeled 600s, for the initial value of  $t-t'$ , is near optimum, and this is the same curve displayed in Figure 9. The other two do not show slope continuity at the points of juxtaposition. One of these shows concave features for  $t-t'$  considerably larger than optimum, in this case 1500s, the other convex features for  $t-t'$  considerably smaller than optimum, here 300s. The reach of the master curves is governed by the horizontal shift factors, and by inspection we observe that a smaller value for  $t-t'$  requires a larger log  $A_T$  to achieve juxtaposition, and visa versa. A quantitative relationship between the initial value of  $t-t'$  and the average log shift factor per degree of temperature

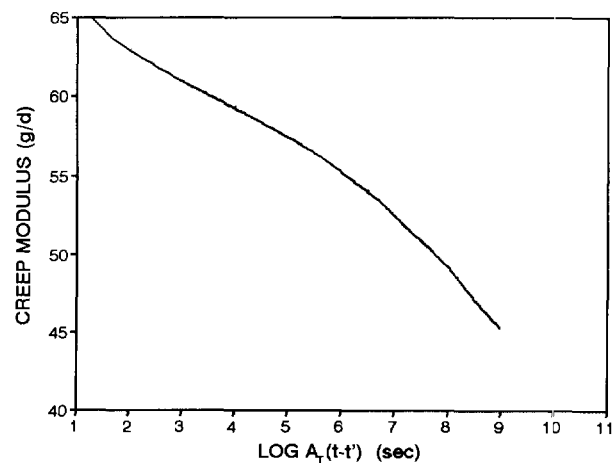


Figure 9. Creep modulus data from Figure 8 horizontally shifted to achieve the master curve shown.

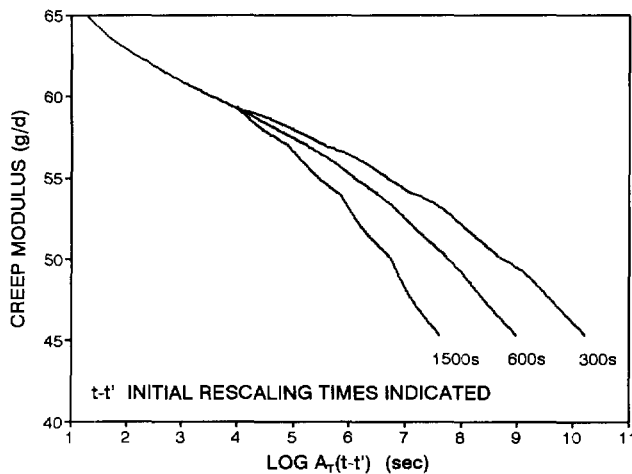


Figure 10. Effect of choice of rescaling times on the shape of the creep modulus master curve.

step, is given in Figure 11.

Figures 10 and 11 show that while it is possible to generate master curves that achieve juxtaposition with a wide combination of  $t-t'$  and  $A_T$  selections, there will be a much limited selection of combinations (perhaps only one optimum combination) where the slopes of the adjacent curve segments will match at the points where they meet. For clarity, we have exaggerated the effects on  $A_T$  and the resulting master curves by illustrating the effects of large deviations from optimum selections of  $t-t'$ . Near optimum selections of  $t-t'$  are easy to achieve, however, and uncertainties in the reach of resulting master curves are not expected to be above 0.1 log cycle.

#### 5.4 Effect of Time and Temperature Step Magnitudes

When designing a SIM test it is important to pick the times at each temperature increment and the size of the temperature changes imposed to achieve the desired results. One of the important requirements is that the temperature step bridges

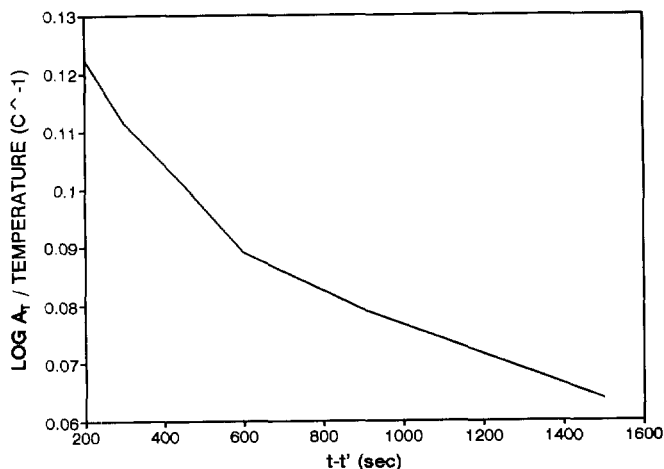


Figure 11. Effect of rescaling times on the horizontal shift factors used to construct master curves.

two corresponding states. The only way we know to effect this is to insure that both states be very nearly steady states, by which we mean that the creep rates are not changing (at least not rapidly) with time. Thus, the creep rate,  $de/d\log t$ , before a temperature step would be ideally, exactly the same as after the step. This situation we desire will be more achievable for small temperature steps and large time steps, but that is the direction of higher cost.

The matrix of SIM tests we conducted to explore the effect of time and temperature step magnitudes is given in Table 2. The conditions studied were A through G. The two not studied were cases Y and Z, the conditions for which were considered too extreme to be instructive. The A through G tests were conducted on yarn specimens loaded to 62% of UTS. The number of steps and the maximum temperature

Table 2. Matrix of SIM tests on variable time and temperature steps

Step times, sec	7°C steps	14°C Steps	28°C Steps
1000	A(9)[82]	B(5)[82]	Y
10,000	C(7)[68]	D(5)[82]	E(3)[82]
100,000	Z	F(4)[68]	G(3)[82]

achieved in the SIM tests are given in parentheses and brackets respectively. All tests were started at 26°C. The results of the SIM tests are presented in Figure 12. The SIM results have been normalized to a creep modulus of 62.4 g/d at log time 2 and are presented with a creep modulus curve developed by conventional TTS which was also normalized to 62.4 at log time 2. We note that three of the SIM results compare favorably with the conventional results, these are conditions C, D and F. Conditions A and B result in smooth

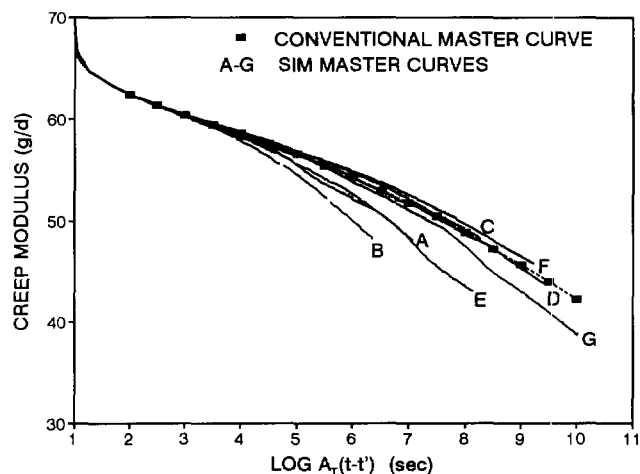


Figure 12. Resulting creep modulus master curves from the variable time and temperature steps of the Table 1 Matrix, compared to the conventional master curve of Figure 4. All curves have been normalized to a modulus of 62.4 g/d at log time 2 (sec).



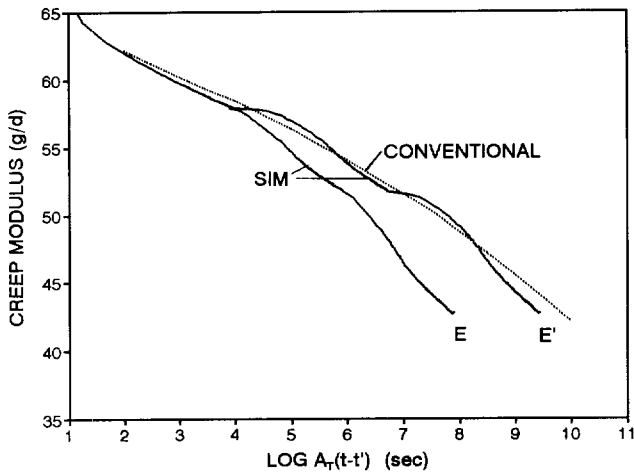


Figure 13. Characteristic curve shapes for an excessive temperature step (condition E of Table 2).

master curves, but the short reach of these curves indicate clearly that the time steps are inadequate for stable creep conditions to have been achieved. Conditions E and G do not result in smooth master curves despite achieving both the slope matching and juxtaposition boundary conditions. Condition E is examined in more detail in Figure 13.

Slopes are matched at the points of juxtaposition in curve E of Figure 13, yet a convex curvature followed by a concave curvature indicates that the creep rate accelerated immediately after the temperature step change. A larger shift factor would bring the steady state regions of the curves into a better alignment with the conventional TTS data as shown in curve E' but at the expense of slope matching at the points of juxtaposition.

SIM tests conducted with inadequate temperature or time steps will result in master curves of shorter reach than those with adequate steps. The exaggerated examples investigated here would be easy to identify and rectify by substituting tests utilizing smaller temperature and/or longer time steps. More

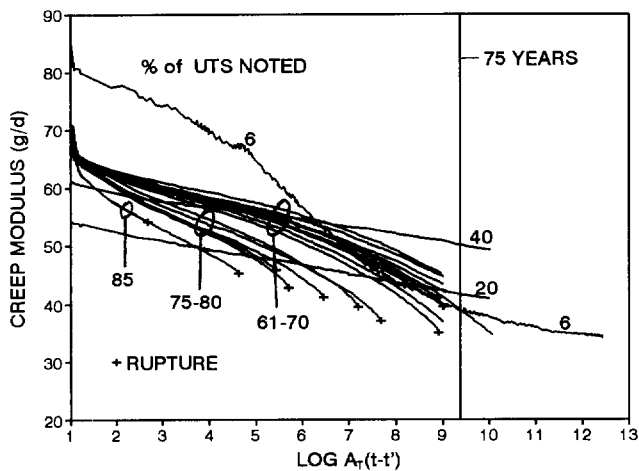


Figure 14. Creep modulus master curves as a function of stress level.

subtle inadequacies might go undetected, but would result in master curves that would err on the conservative side.

Conditions C, D, and F yield satisfactory SIM master curves. Condition D, as the most economical is recommended as a standard protocol for PET.

### 5.5 Effect of Stress Levels

To assess the effect of stress levels on the master creep modulus curves and the associated shift functions, over twenty-five creep tests were performed at stress levels between 6% and 85% of the 26°C UTS. Nine of the specimens were taken to rupture. These nine were among the ones tested at above 67% of UTS. Following the SIM procedure, the raw creep data was converted to master creep modulus curves, and the resulting family of curves is presented in Figure 14. Note that at the very lowest stress (6%) the beginning creep modulus values are higher than those at the higher stresses. Also, note that the modulus curve of 20% falls below the one at 40%. These are natural consequences of the trend in the secant modulus curve in Figure 3. The shift factors for those master curves are graphed against the step temperatures in Figure 15. The results presented in Figure 15 indicate that the shift factors for the low stress master curves are higher than those generated at higher stress levels. This may be understood in terms of the differences in the creep mechanisms operative at the different stress levels. Refined creep strain curves, computed from the master creep modulus curves of Figure 14 are presented in 16.

The several creep ruptures indicated in Figure 16 are associated with creep strain curves that display higher creep rates but otherwise appear as reasonable creep curves. The shift factors used to generate the curves leading to rupture are not distinguishable from those at lower stresses down to 61% of UTS, most of which do not lead to rupture (see Figure 15, Stress > 61%).

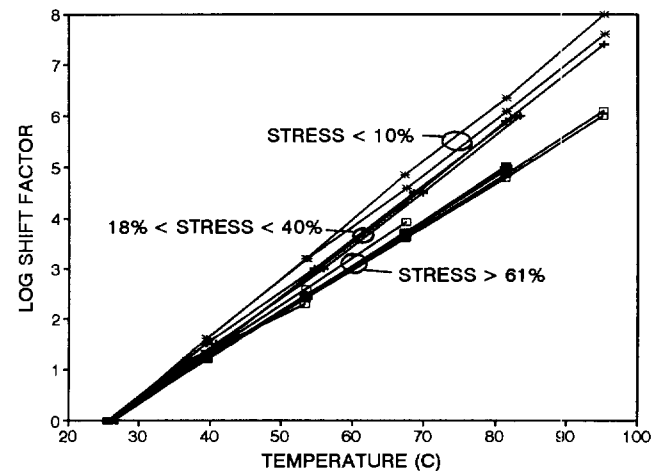


Figure 15. Shift factors vs. temperature for the master curves of Figure 14.

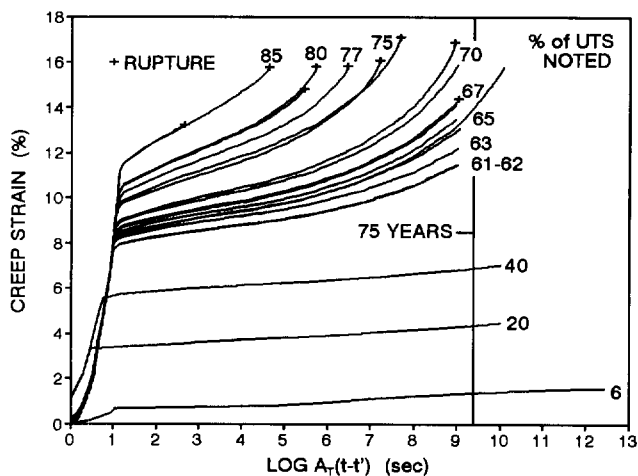


Figure 16. Creep strain vs log time curves computed from the master curves of Figure 14

The plot of creep rupture stress vs. log time to rupture is presented in Figure 17. Nine rupture points are indicated along with three run out points. Significantly, one data point goes well beyond the 75 year time line, so that the 75 year intercept is a conservative interpolation rather than an extrapolation. The 75 year intercept of the regression line is at 68% of the 26°C UTS. Table 3 provides a guide to the shifted rupture times of Figure 17.

Table 3. Logarithm of the shifted times at the reference temperature (26°C) vs the unshifted times at the exposure temperatures.

Shifted time Range $\log A_T(t-t')$	Maximum values (approximate)	
	Exposure Temperature, °C	Unshifted cumulative time, sec
0.0-4.0	26	$1 \times 10^4$
4.0-5.3	40	$2 \times 10^4$
5.3-6.7	54	$3 \times 10^4$
6.7-8.0	68	$4 \times 10^4$
8.0-9.3	82	$5 \times 10^4$

## 6 CONCLUSIONS

- Utilization of SIM for TTS reduces the uncertainty of the shift factors used to construct master curves.
- Both the conventional and the stepped isothermal methods of time-temperature superposition can produce master curves that extend well beyond 100 years.
- Utilization of SIM reduces greatly the test time needed for characterizing long term creep properties over conventional TTS or extrapolation methods.
- The time and temperature steps of 10,000 sec and 14°C appear to be acceptable for SIM creep testing of PET yarn under most conditions.
- Inadequate temperature and or time steps result in master

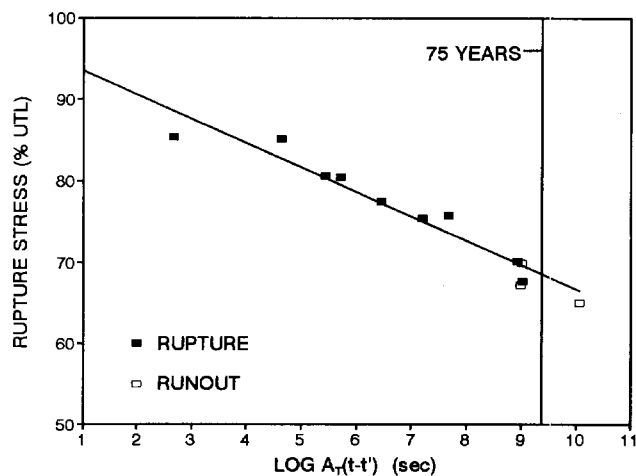


Figure 17. Creep rupture data and regression line for the polyester yarn.

curves with shorter reach than curves generated from tests with adequate steps, but such inadequacies will be conservative.

- The shift factors for creep display a linear direct dependence on temperature and an inverse dependence on stress, the latter may be caused by a difference in creep mechanism between low and high applied stress levels.
- Since creep rupture is merely an event that takes place at the end of a creep strain curve, the shift factors used to generate the creep strain vs. shifted time curves are the factors that determine the shifted time of the rupture event.

## ACKNOWLEDGMENTS

The authors are indebted to Shawn L. Arnett of TRI/Environmental for conducting the experimental program. Funding from T.C. Mirafi, Inc. and Texas Research International, Inc. for research leading to the discovery of the SIM as well as the characterization of the 3 ply PET yarn reported herein is gratefully acknowledged.

## REFERENCES

- Ferry, J.D. (1980) *Viscoelastic Properties of Polymers*, 3rd Edition, John Wiley and Sons, New York, NY, USA.
- Heuvel, C.J.M. v.d., Heuvel, H.M., Faassen, W.A., Veurink, J., and Lucas, L.J., (1993), "Molecular Changes of PET Yarns during Stretching Measured with Rheo-Optical Infrared Spectroscopy and Other Techniques," *J. Appl. Polymer Sci.*, Vol. 49, pp. 925-934.
- Murayama, T., Dumbleton, J.H., and Williams, M.L., (1968), "Viscoelasticity of Oriented Polyethylene Terephthalate," *J. Appl. Polymer Sci.*, Vol. 6, pp. 787-793.
- Thornton, J.S., Allen, S.R., and Thomas R.W., (1997), "Approaches for the Prediction of Long Term Viscoelastic Properties of Geo Synthetics from Short Term Tests," *Geosynthetics '97*, IFAI, Vol. 1, Long Beach, CA, USA, pp 277-291.

# Modeling and Extrapolation of Creep Behavior of Geosynthetics

Te-Yang Soong

Research Engineer, Geosynthetic Research Institute, Drexel University, Philadelphia, Pennsylvania, USA

Robert M. Koerner

Professor and Director, Geosynthetic Research Institute, Drexel University, Philadelphia, Pennsylvania, USA

**ABSTRACT:** The creep behavior of geosynthetic materials can be described by a rheologic model consisting of a finite number of Kelvin units connected in series, i.e., the so-called Kelvin-chain model. With properly selected spring moduli and dashpot viscosities, the combined effect of all Kelvin units in the model can be used to describe the results of experimental creep data. Once such a model is established, it can then be used to extrapolate the creep behavior of the tested material beyond the laboratory measured time frame. This paper presents a systematic procedure for obtaining the optimum model based on relatively short-term creep data. The long-term predicting capability of the model is then justified by supplemental experimental data.

**KEYWORDS:** Creep, Modeling, Geotextile, Geogrid, Geomembrane, Geosynthetic Clay liner, Geocomposite Edge Drain

## 1 INTRODUCTION

Whenever stresses are imposed on a viscoelastic material like geosynthetics (via tension, compression, shear, torsion, bending, etc.), they must somehow be internally sustained by the material's molecular structure. If the stresses remain constant over a sufficiently long period of time, the molecular structure will attempt to accommodate them via some type of deformation, e.g., the creep phenomenon. Examples of applications where creep is of concern are the following:

- Tensile creep of geotextiles in mechanically stabilized earth structures,
- Tensile creep of geogrids in mechanically stabilized earth structures,
- Compressive creep of geonets and drainage geocomposites in the liner systems of landfills,
- Out-of-plane deformation of geomembranes in landfill and waste pile covers due to differential settlement and up-lifting gases,
- Internal creep shear of geosynthetic clay liners on steep side slopes
- Compressive deformation (creep) of geopipes in various situations.

In actual designs, creep is generally included via reducing the allowable stress by a proper creep reduction factor, Koerner (1998). In an ideal situation, the creep reduction factors are determined experimentally, e.g., conducting 10,000-hour (or longer) creep test at several stress levels.

Unfortunately, creep tests are by their nature time-consuming and thus expensive. Furthermore, accurate creep tests are difficult to perform owing to the difficulty in maintaining the desired environment over a long period of time. In this study, a rheologic model which provides long-term prediction capability is presented. It is hoped that via careful interpretation and extrapolation of short-term creep data, accurate long-term creep behavior can be predicted.

## 2 THE KELVIN-CHAIN MODEL

It has been shown that the creep behavior of a wide range of materials can be described by a Kelvin-chain model which consists of a finite number of Kelvin units in series, Roscoe (1950). In addition, a spring can be added to the original Kelvin-chain model. This provides to the model the capability of simulating the initial instantaneous (elastic) strain which is typically seen in creep measurements. Figure 1 shows the modified Kelvin-chain model used in this study.

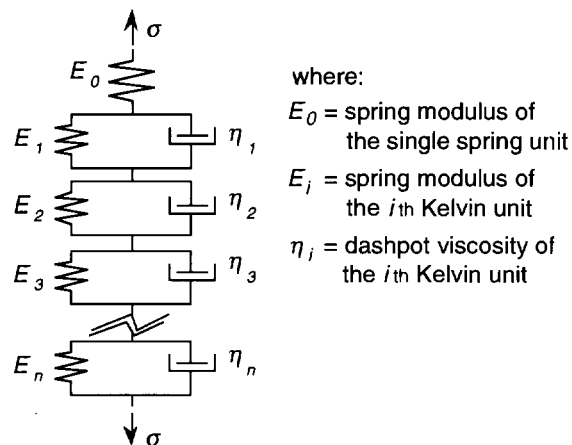


Figure 1. The Kelvin-chain model

A Kelvin unit consists of a spring and a dashpot in parallel. In the Kelvin-chain model, each Kelvin unit is identified by the letter "i" and characterized by a retardation time,  $\tau_i$ , where  $\tau_i = \eta_i / E_i$ . Experiences show that in an ideal Kelvin-chain model, the spring modulus in each Kelvin unit is generally inversely proportional to its corresponding dashpot viscosity. In other words, Kelvin units consisting of high-modulus springs possess dashpots with low viscosities. The relative degrees vary. When such

a model is subjected to an external stress,  $\sigma$ , as seen in Figure 1, an instantaneous deformation is created in the single spring. Note that this deformation stays constant regardless of the time scale as long as the applied stress remains. Subsequently, the Kelvin units with higher spring moduli and lower dashpot viscosities will be deformed. Note that such deformations will also be retarded more rapidly. Succeedingly, the units with lower spring moduli will respond to the external stress owing to the higher resistance from the dashpots. However, continuous deformations will be observed in these units over a longer period of time, until their corresponding retardation times are reached.

Figure 2 illustrates the above concept by plotting a set of creep data along with the calculated curve corresponding to a Kelvin-chain model consists of four Kelvin units and a single spring. It is seen that the calculated curve (a superposition of five individual curves) accurately modeled the experimental data. The individual behavior of each component in the model is also shown in the figure where the concept of "retardation time" is clearly demonstrated.

### 3 THE MODELING PROCEDURE

To utilize a Kelvin-chain model, the creep behavior is viewed as a so-called strain function:

$$\epsilon(t) = \epsilon_0 + \sum_{i=1}^n \frac{1}{E_i} (1 - e^{-t/\tau_i}) \quad (1)$$

where:  $\epsilon_0 = 1/E_0 =$  the elastic strain (i.e., strain induced immediately after the stress is applied) caused by a unit stress (i.e.,  $\sigma = 1$ ). Note that the end of the elastic deformation portion of the experimental data, i.e.,  $\epsilon_0$ , is defined herein as the point of which the second derivative first changes its sign, generally from negative to positive. In Equation 1, the retardation times,  $\tau_i$ 's, are values which can be arbitrarily chosen providing some restrictions are satisfied, Bazant (1988), Bazant and Prasanna (1989). However, any two adjacent Kelvin units having a relationship of  $\Delta(\log\tau_i) = 1$  generally gives sufficiently smooth creep curves; Bazant and Xi (1995). That is to say, if the smallest retardation time is chosen as  $10^{-3}$  hour, the subsequent retardation times will generally be selected as  $10^{-2}$  hr.,  $10^{-1}$  hr.,  $10^0$  hr.,  $10^1$  hr., etc.

Furthermore, an "N"-unit Kelvin-chain model can generally simulate creep data of "N" orders of magnitude on the time scale. Note, however, if extrapolation of the experimental data is desirable, more Kelvin units are necessary. For example, if a extrapolation out to  $10^4$  hours is desirable using a 1000-hour creep data (i.e., one-order extrapolation), one additional Kelvin unit with retardation time of  $10^4$  is necessary.

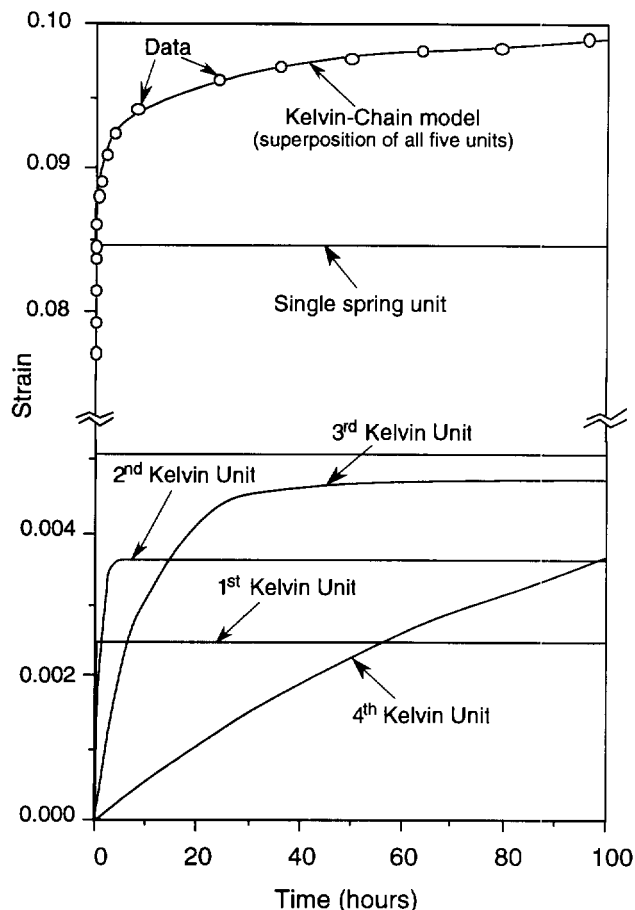


Figure 2. Creep data simulated by a Kelvin-chain model consisting of four Kelvin units and one single spring.

As to the selection of  $E_i$ 's, it is determined by optimum fitting of the creep data under the constraints of the pre-selected retardation times.

It is clear that a regression analysis (optimum fitting) for determining six or more unknowns (numbers of  $E_i$ 's, in this case) can be extremely time consuming. A procedure which reduces the numbers of the independent variables to only two, regardless the actual number of  $E_i$ 's, is recommended herein.

The following expression is proposed to serve the aforementioned purposes [see Bazant and Xi (1995) for detailed mathematical derivations]:

$$\frac{1}{E_i} = 1.151(a)(3\tau_i)^3 \left[ \frac{-2n^2(3\tau_i)^{2n-3}(n-1-(3\tau_i)^n)}{(1+(3\tau_i)^n)^3} + \frac{n(n-2)(3\tau_i)^{n-3}(n-1-(3\tau_i)^n) - n^2(3\tau_i)^{2n-3}}{(1+(3\tau_i)^n)^2} \right] \quad (2)$$

In Equation 2, “a” and “n” are the new targeted unknowns (instead of  $E_i$ 's) associated with the modeled creep data. Note that the new fitting involves only two variables and is obviously much simpler.

By varying the two independent variables “a” and “n” in Equation 2, different combinations of  $E_i$ 's with respect to the pre-selected retardation times,  $\tau_i$ 's, can be obtained. This allows a comparison of each calculated result of Equation 1 to the actual experimental data. The calculated result is then optimized using the least-squares approximation (weighting by “time” is recommended) and iteration of this process will eventually converge on the actual experimental data. The resulting optimum model can then be used to predict experimental creep behavior beyond the actual measured data.

#### 4 EXAMPLES

Six sets of very different geosynthetic materials creep data were used to verify both the simulating and the long-term predicting capabilities of the proposed Kelvin-chain model. They are the following geosynthetic materials:

- (a) 1500-hr tensile creep of a nonwoven needle-punched PP geotextile at 50% of its wide-width tensile strength at a temperature of 22°C [Allen et al (1982)],
- (b) 10,000-hr tensile creep of a PET geogrid at 70% of its short-term tensile strength at a temperature of 23°C (data courtesy of Strata Systems, Inc.),
- (c) 1000-hr confined tensile creep of a stiff, unitized HDPE geogrid at 60% of its ultimate tensile strength under a normal stress of 28 kPa at approximately 23°C [Wilson-Fahmy et al (1995)],
- (d) 20,000-hr biaxial tensile creep of a HDPE geomembrane under a constant stress ( $\approx 60\%$  of its ultimate strength) at approximately 23°C [Duvall (1993)],
- (e) 1,000-hr internal shear creep of a geosynthetic clay liner (GCL) at 40% of its short-term shear strength at approximately 23°C,
- (f) 1,000-hr compressive creep of a edge-drain geocomposite at 45% of its short-term compressive strength at approximately 23°C (data courtesy of Monsanto Company).

The results are shown in Figures 3 to 8 corresponding to each of the above tests, respectively. Note that the results shown in Figure 4 are plotted on a logarithmic scale to give a different perspective. Seen in each of the figures are (1) initial portion of the data (one order of magnitude shorter in time than the entire data), as solid circles, for establishing the Kelvin-chain model; (2) the optimum Kelvin-chain model calculated creep behavior, as solid curves; (3) one order of magnitude extrapolation using the established model, as dashed curves and (4) the rest of the creep data, as

open circles, for verifying the predicting capability of the model.

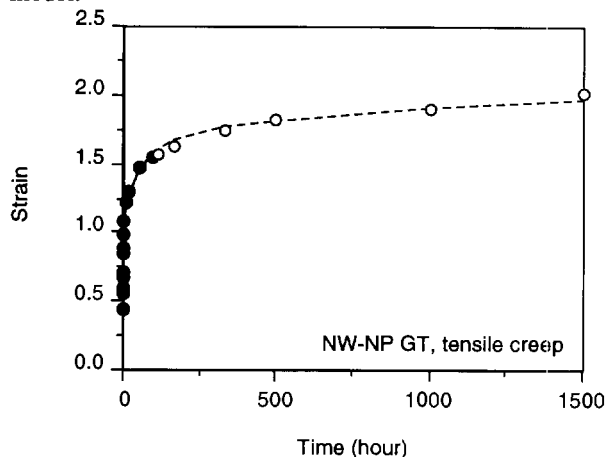


Figure 3. Experimental and modeled data of material (a)

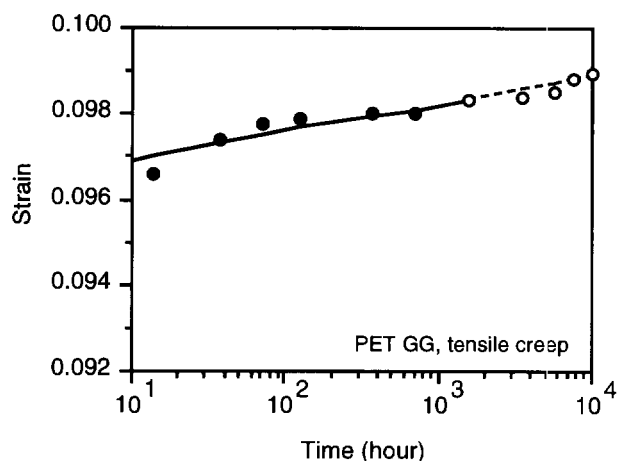


Figure 4. Experimental and modeled data of material (b)

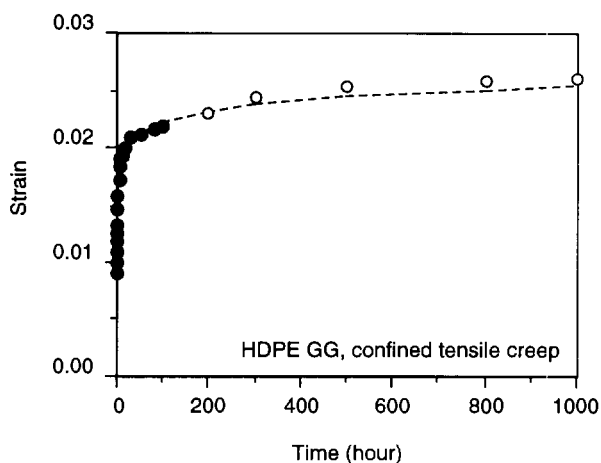


Figure 5. Experimental and modeled data of material (c)

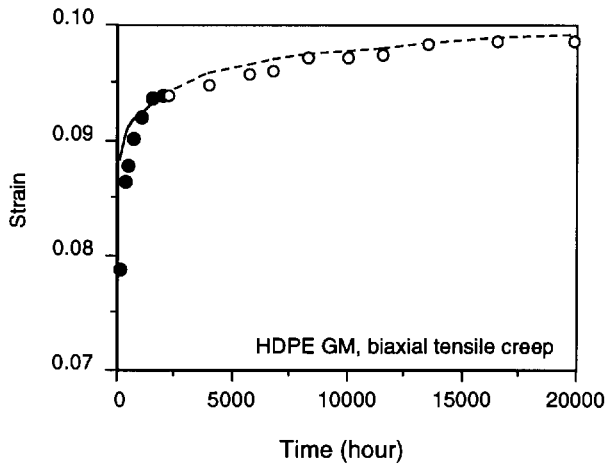


Figure 6. Experimental and modeled data of material (d)

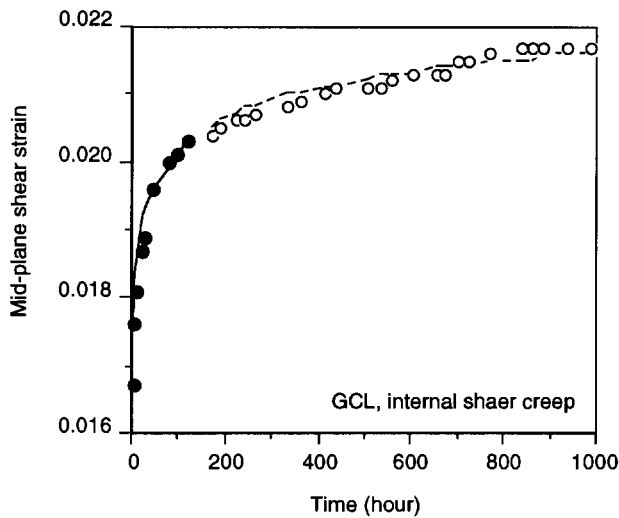


Figure 7. Experimental and modeled data of material (e)

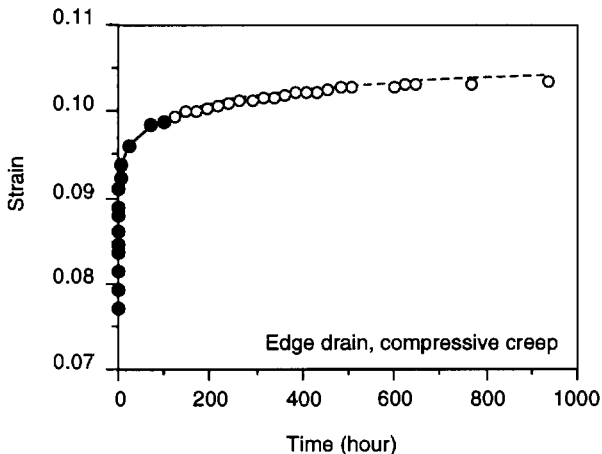


Figure 8. Experimental and modeled data of material (f)

## 5 SUMMARY AND CONCLUSIONS

Geosynthetics, being viscoelastic materials, must be evaluated for their creep sensitivity under a variety of constant stress situations. Laboratory tests can be performed for relatively long time periods, yet extrapolation to site specific lifetimes is usually necessary and the technique used is obviously critical. The Kelvin-chain model presented in this paper, and its application to a wide variety of geosynthetic materials, is shown to result in an accurate prediction of the data and is recommended for general use. This model is shown to be viable for at least one order of magnitude based on the results presented herein. Analytically it is possible to extrapolate beyond one order of magnitude, but substantiate data is sparse and further corroboration is required in this regard.

## 6 ACKNOWLEDGMENT

The funding for the preparation of this paper was provided by the Geosynthetic Institute's consortium of member organizations and the U.S. EPA. Financial support via David A. Carson under contract CR-821448 is sincerely appreciated.

## 7 REFERENCES

- Allen, T., Vinson, T.S. and Bell, J.R. (1982) "Tensile Strength and Creep Behavior of Geotextiles in Cold Regions Applications", *2nd Int. Conf. on Geotextiles*, Las Vegas, NV, USA, Vol. 3, pp. 775-780.
- Bazant, Z.P. ed. (1988) *Mathematical Modeling of Creep and Shrinkage of Concrete*, John Wiley & Sons, Inc., New York, NY, USA
- Bazant, Z.P. and Prasannan, S. (1989) "Solidification Theory of Concrete Creep II: Verification and Application", *J. Engrg. Mech.*, ASCE, Vol. 115, No. 5, pp. 1691-1703.
- Bazant, Z.P. and Xi, Y. (1995) "Continuous Retardation Spectrum for Solidification Theory of Concrete Creep", *J. Engrg. Mech.*, ASCE, Vol. 121, No. 2, pp. 281-288.
- Duvall, D.E. (1993) "Creep and Stress Rupture Testing of a Polyethylene Geomembrane Under Equal Biaxial Tensile Stress", *Geosynthetics '93*, IFAI, Vancouver, BC, Canada, Vol. 2, pp. 817-830.
- Koerner, R. M. (1998) *Designing with Geosynthetics*, 4th Ed., Prentice Hill Book Co., Englewood Cliffs, NJ, 792 pgs.
- Roscoe, R. (1950) "Mechanical Models for the Representation of Viscoelastic Properties", *British J. of Appl. Physics*, Vol. 1, pp. 171-173.
- Wilson-Fahmy, R.F., Koerner, R.M. and Harpur, W.A. (1995) "Long-Term Pullout Behavior of Polymeric Geogrids", *J. Geotech. Engrg.*, ASCE, Vol. 121, No. 10, pp. 723-728.

# Slow Strain Rate Modulus Assessment Via Stress Relaxation Experiments

Te-Yang Soong

Research Engineer, Geosynthetic Research Institute, Drexel University, Philadelphia, Pennsylvania, USA

Arthur E. Lord, Jr.

Professor, Department of Physics & Atmospheric Science, Drexel University, Philadelphia, Pennsylvania, USA

**ABSTRACT:** Geosynthetics are usually deformed very slowly in actual applications. Conversely, most mechanical properties (e.g., modulus) are determined in the laboratory under relatively fast strain rates. The use of such experimental values in engineering design is felt to give an inaccurate assessment of actual behavior. This paper presents a procedure to simulate laboratory generated stress relaxation test results by the Maxwell-Weichert rheologic model. Once such a model is established and calibrated, it can be used to determine the more realistic, “design-oriented”, modulus of the tested material. In this paper, the 0.3% secant modulus of a 1.5 mm HDPE geomembrane tested at various strain rates was successfully predicted using the Maxwell-Weichert model. It is felt that the same approach can be applied to other geosynthetic materials for determining realistic moduli values for use in engineering design.

**KEYWORDS:** Modeling, Geomembranes, Modulus, Stress relaxation

## 1 INTRODUCTION

Geosynthetics are usually deformed very slowly (i.e., on the order of weeks, months or years) in actual applications. Conversely, most mechanical properties (e.g., modulus) are experimentally determined in the laboratory under relatively fast strain rates (i.e., on the order of seconds, minutes or hours). Since it is well known that the mechanical properties of viscoelastic materials like geosynthetics are strongly strain-rate dependent, the use of such experimental values in actual engineering design is a concern in that changing in the polymer structure, e.g., stress relaxation, cannot occur as it likely does in the field.

In this paper, a Maxwell-Weichert rheologic model established using laboratory generated stress relaxation test results at fast strain rates, is presented. Once such a model is established and calibrated, it can be used to calculate values of modulus at slow strain rates. It is hoped that via the above procedure, more suitable initial moduli values for the use of engineering design can be determined.

## 2 BACKGROUND

The strong dependence of mechanical properties on how fast the material is deformed (time scale) is a result of the viscoelastic nature of geosynthetics. Two well-known examples of such dependence are the stress relaxation behavior and the strain-rate dependent modulus. Both phenomena are illustrated graphically in Figure 1. Conceptually, two replicate specimens are deformed to a specific strain level,  $\epsilon_0$ , under two different strain rates, i.e.,  $\dot{\epsilon}_1$  and  $\dot{\epsilon}_2$ . This strain level is then held constant for both cases and the stresses are monitored over time. Eventually, after considerable time, the curves come to the same equilibrium residual stress level. It is seen, in the left-hand

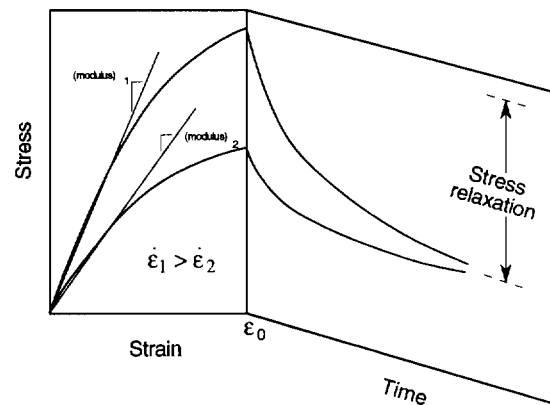


Figure 1. Viscoelastic nature of geosynthetics illustrated by the strain-rate dependent secant modulus and the stress relaxation behavior.

portion of the curves, that the modulus (in this case, a secant modulus) of the tested material is proportional to the strain rate. Regarding the right-hand portion of the curves, the trend of decreasing stresses with time demonstrates the concept of stress relaxation.

It is reasonable to assume that the above two phenomena are inter-related since both of them are results of the unique viscoelastic nature of the tested material. It is also reasonable to assume that using the result of one experiment (e.g., a stress relaxation test) one should be able to predict the result of a related test (e.g., the strain-rate dependent modulus). The objective of this study is to develop the above concepts.

## 3 THE MAXWELL-WEICHERT MODEL

Figure 2 shows the Maxwell-Weichert rheologic model used in this study, Aklonis et al (1972). A typical model consists of “N” Maxwell units, which are springs and dashpots in series, placed in a parallel combination with a single spring at the end. The springs represent the elastic properties ( $E$  is the elastic modulus) and the dashpots represent the viscous properties ( $\eta$  is the dashpot viscosity) of the modeled material. In this study, the units become less strong and more viscous as one moves to the right in the parallel combination. Each Maxwell unit is characterized by a spring modulus,  $E_i$ , and a corresponding retardation time,  $\tau_i$ , where  $\tau_i = \eta_i/E_i$ . The final spring, with an elastic modulus of  $E_R$ , represents the totally relaxed or residual modulus value.

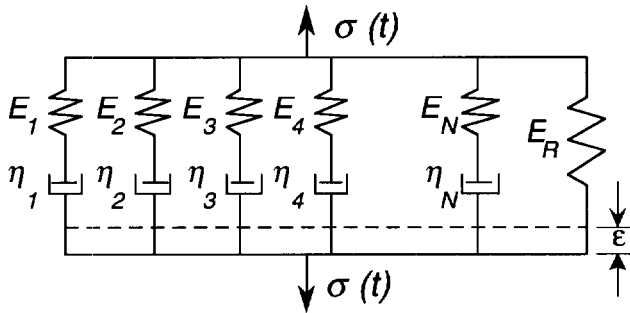


Figure 2. A Maxwell-Weichert model subjected to a constant strain.

In a typical stress relaxation test, it takes an initial stress to deform a Maxwell-Weichert model to reach the desired strain because of the resistance of all Maxwell units has to be overcome. In stress relaxation tests, this is the maximum stress. Once the desired strain is reached, the dashpots start to flow and therefore release the stresses in the springs. As a result, the stress required to maintain a constant strain decreases with time. Since the units in a Maxwell-Weichert model consist of dashpots with viscosities over a wide range, i.e., some dashpots can be easily stretched and others are more difficult, they can be used to simulate stress relaxation of geosynthetics at different stages. Ultimately, when the stresses in all Maxwell units are fully dissipated, the residual stress is modeled by the final spring.

When a Maxwell-Weichert model is subjected to a constant strain, as in a stress relaxation test, the following expression can be used to describe the stress/strain relationship in each of the Maxwell units:

$$\frac{d\varepsilon_i}{dt} = \frac{d\varepsilon}{dt} = \frac{1}{E_i} \frac{d\sigma_i}{dt} + \frac{\sigma_i}{\eta_i} = 0 \quad (1)$$

where  $\varepsilon_i$  = strain in unit “i”,  $\varepsilon$  = the constant strain applied and  $\sigma_i$  = stress in unit “i”.

The solution of Equation 1, which represents the stress in unit “i” at any time “t”, is as follows:

$$\sigma_i(t) = \sigma_{i0} e^{-\frac{t}{\tau_i}} \quad (2)$$

where  $\sigma_{i0}$  = the initial stress in unit “i”.

The total stress at any time “t” in the entire Maxwell-Weichert model, is the sum of the stresses in all of the elements, i.e.,

$$\sigma(t) = \sigma_{10} e^{-\frac{t}{\tau_1}} + \sigma_{20} e^{-\frac{t}{\tau_2}} + \dots + \sigma_{N0} e^{-\frac{t}{\tau_N}} + \sigma_R \quad (3)$$

where  $\sigma_R$  = the stress in the final single spring.

Alternatively, the stress relaxation process can be described by a time-dependent relaxation modulus,  $E(t)$ , where

$$E(t) = \frac{\sigma(t)}{\varepsilon} = \sum_{i=1}^N \left( \frac{\sigma_{i0}}{\varepsilon} e^{-\frac{t}{\tau_i}} \right) + \frac{\sigma_R}{\varepsilon} \quad (4)$$

or

$$E(t) = \sum_{i=1}^N (E_i e^{-\frac{t}{\tau_i}}) + E_R \quad (5)$$

Equation 5 can then be used to simulate the stress relaxation test results. Figure 3 illustrates the modeling concept by plotting a set of stress relaxation data along with the calculated curve corresponding to a Maxwell-Weichert model. This example consists of four Maxwell units and a single spring. It is seen that the calculated curve (a superposition of five underlying individual curves) accurately modeled the laboratory data. The individual behavior of each unit in the model is also shown in the figure.

In Equation 5, the retardation times,  $\tau_i$ 's, are values which can be arbitrarily chosen. If we choose adjacent Maxwell units to have a relationship of  $\Delta(\log \tau_i) = 1$ , it generally gives satisfactory simulation. That is to say, if the smallest retardation time is chosen as  $10^{-3}$  hour, the subsequent retardation times will generally be selected as  $10^{-2}$  hr.,  $10^{-1}$  hr., 1 hr.,  $10^1$  hr., etc. As to the selection of  $E_i$ 's, they are determined by optimum fitting of the stress relaxation data under the constraints of the pre-selected retardation times.

#### 4 MAXWELL-WEICHERT MODELING OF HDPE GEOMEMBRANES USED IN THIS STUDY

Large-scale stress relaxation test results on a commercially available 1.5 mm thick HDPE geomembrane were used to illustrate the use of Maxwell-Weichert model. See Soong, et al (1994) for a detailed description of the laboratory test setup and conditions. The tests were conducted at five



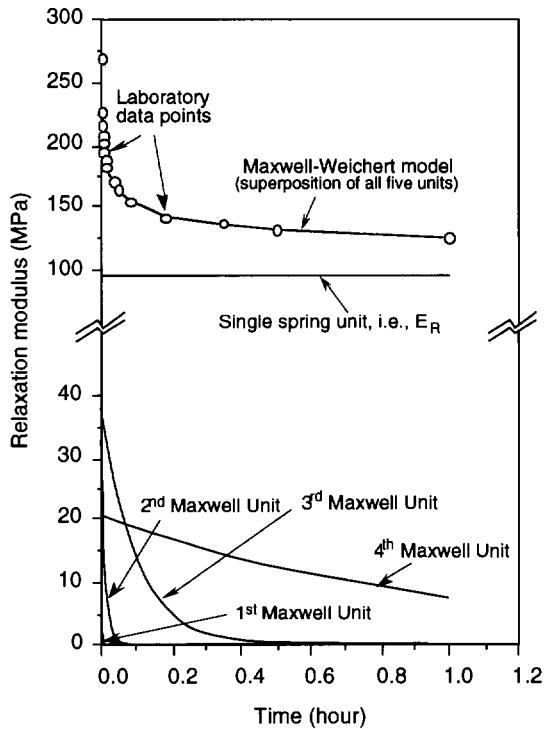


Figure 3. Stress relaxation data simulated by a Maxwell-Weichert model consisting of four Maxwell units and one single spring.

different temperatures under a constant tensile strain of 3%. Seven Maxwell units with retardation times varying from  $10^{-4}$  to  $10^2$  hours and one additional spring were used in each of the five models for five different temperatures. The values of  $E_i$ 's in all of the models were determined by applying a least-squares regression procedure, under the restraints of the pre-selected retardation times, until the calculated behavior converged to the laboratory results. The laboratory data along with the calculated relaxation behavior are shown in Figure 4 by plotting the relaxation modulus against time on a log-log scale. There is excellent agreement between the laboratory and the calculated results.

Once a Maxwell-Weichert model is established, it can be used to calculate the modulus of the modeled material at different values of strain rate. The following section presents the detailed procedure.

## 5 CALCULATING THE STRESS UNDER VARIOUS STRAIN RATES

When the modeled material, e.g., a geomembrane, is deformed under a constant strain rate "C", the following expression can be used to describe the stress/strain relationship in each of the Maxwell unit:

$$\frac{d\epsilon_i}{dt} = \frac{d\epsilon}{dt} = \frac{1}{E_i} \frac{d\sigma_i}{dt} + \frac{\sigma_i}{\eta_i} = C \quad (6)$$

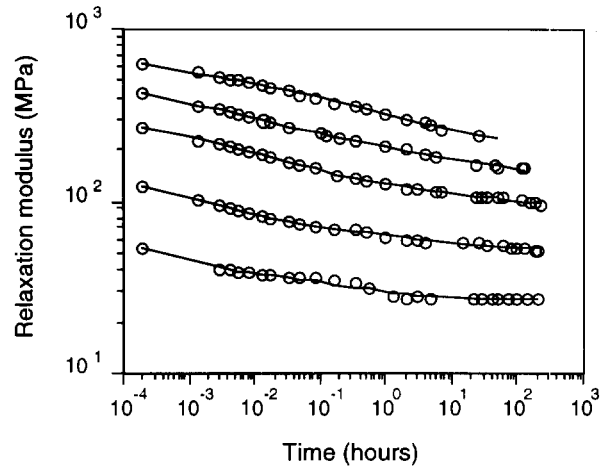


Figure 4. Laboratory generated (open circles) and calculated stress relaxation behavior (solid lines) of a 1.5 mm thick HDPE geomembrane at various temperatures.

Equation 6 can be solved as:

$$\sigma_i(t) = C\tau_i E_i (1 - e^{-\frac{t}{\tau_i}}) \quad (7)$$

Consequently, the expression for the entire model can be written as:

$$\sigma(t) = C \left[ \sum_{i=1}^N \tau_i E_i \left( 1 - e^{-\frac{t}{\tau_i}} \right) \right] + C(E_R)t \quad (8)$$

Since the experimental data was developed at 3% strain, we must modify Equation 8 if it is to work for general values of strain (e.g., 0.3% strain).

Popelar, et al (1990) presented an empirical relationship to incorporate the strain dependence in the establishing of viscoelastic models for HDPE pipes. The relationship was interpolated and extended for this study and the following expression, a modification of Equation 8, results:

$$\sigma(t) = C \left[ \sum_{i=1}^N \tau_i \left( \frac{E_i}{a + b(Ct)} \right) \left( 1 - e^{-\frac{t}{\tau_i}} \right) \right] + \left( \frac{E_R}{a + b(Ct)} \right) Ct \quad (9)$$

where  $Ct = \epsilon =$  strain at time "t".

Table 1 lists values of the constants "a" and "b" corresponding to various strain levels used for conducting the stress relaxation tests. Note that when the desired strain level is equal to that used in the stress relaxation test, no modification is necessary.

Table 1. Constants in Eq. 9 as a function of strain level

Strain level used in the stress relaxation test, $\epsilon_p$	Constants <sup>1</sup> in Equation 10	
	a	b
1.0%	0.70	30.5
2.0%	0.53	23.3
3.0%	0.43 <sup>2</sup>	18.9 <sup>2</sup>
5.0%	0.31	13.7
7.5%	0.23	10.2
10.0%	0.19	8.1

1. Values are for modulus in units of MPa.

2. Appropriate constants for this study.

## 6 JUSTIFICATION OF CALCULATED INITIAL MODULUS VALUES

The 0.3% secant modulus of the tested HDPE geomembrane can be determined as follows:

1. A strain rate, i.e., a value of "C", is assumed.
2. The relation " $0.3\% = Ct$ " gives the value of "t".
3. The time "t" is inserted into Equation 9 to obtain the corresponding stress,  $\sigma(t)$ , at 0.3% strain.
4. The relation " $\sigma(t)/0.003$ " gives the 0.3% secant modulus of the modeled material.

The above procedure was applied to five separate Maxwell-Weichert models corresponding to five different temperatures over a range of strain rates from 0.0001% to 100% per minute. The results are shown in Figure 5 by plotting the 0.3% secant modulus against strain rate on a log-log scale. The experimental values of some supplementary tensile tests conducted at 30°C under various strain rates are also shown, in open circles, to exam the validity of the aforementioned prediction procedure. As seen in the figure, the agreement between the experimental data and the calculated values is quite satisfactory.

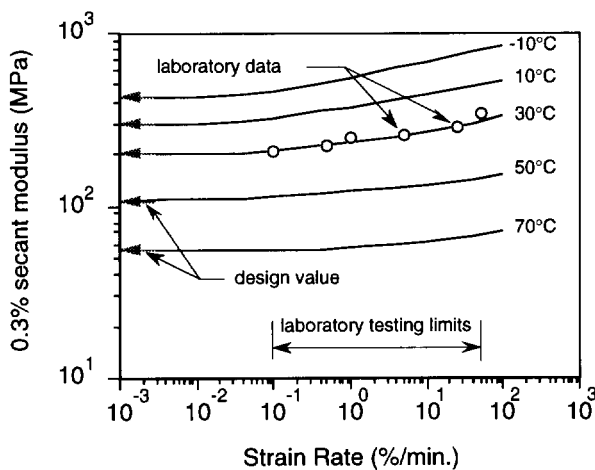


Figure 5. Strain-rate dependent 0.3% secant moduli of the 1.5 mm HDPE geomembrane used in this study.

Also seen in Figure 5 is that at a given temperature, the values of 0.3% secant modulus of the tested HDPE geomembrane remain practically unchanged when strain rates are slower than 0.01% per minute. Such values are considered more suitable in engineering design than those obtained routinely in the laboratory. Such recommended design moduli of the tested HDPE geomembrane are collected and re-plotted against temperature in Figure 6. It is felt that this type of data, shown here for modulus, is the type of data that should be used in design to simulate field conditions.

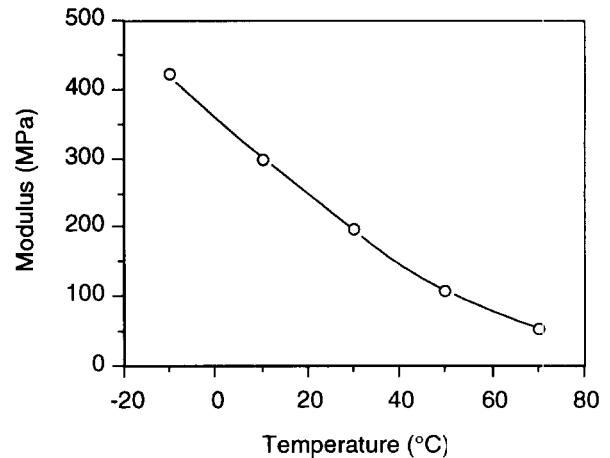


Figure 6. Design modulus of the HDPE geomembrane used in this study (corresponding to a very slow strain rate, i.e.,  $\leq 10^{-2}\%$ /min simulating a situation of stress relaxation).

## 8 CONCLUSIONS

This paper presents a recommended procedure to simulate stress relaxation test results by the Maxwell-Weichert rheologic model. Once such models are established and calibrated, they can be used to determine realistic, "design-oriented", moduli of the modeled material and thereby assess the stress relaxation phenomenon. To verify the procedure, the 0.3% secant moduli of a 1.5 mm HDPE geomembrane at various strain rates were successfully predicted.

## 9 ACKNOWLEDGMENT

The funding for the preparation of this paper was provided by the Geosynthetic Institute's consortium of member organizations and the U.S. EPA. Financial support via David A. Carson under contract CR-821448 is sincerely appreciated.

## 10 REFERENCES

- Aklonis, J.J., Macknight, W.J. and Shen, M. (1972) *Introduction of Polymer Viscoelasticity*, Wiley-Interscience, New York, NY, USA.
- Popelar, C.F., Popelar, C.H. and Kenner, V.H. (1990), "Viscoelastic Material Characterization and Modeling for Polyethylene", *Polymer Engineering and Science*, Vol. 30, No. 10, pp. 577-586.
- Soong, T.-Y., Lord, A.E., Jr. and Koerner, R.M. (1994) "Stress Relaxation Behavior of HDPE Geomembranes", *5th Intl. Conference on Geotextiles, Geomembranes and Related Products*, Singapore, Vol. 3, pp. 1121-1124.

# Long term behavior characterization of soft composite under biaxial loading

P. MAILLER

Geosynthetic tests manager, Institut Textile de France D.R. LYON, av, Guy de Collongue, BP 60, 69132 Ecully cedex

M. SOTTON

General manager, Institut Textile de France D.R. LYON, av, Guy de Collongue, BP 60, 69132 Ecully cedex

**ABSTRACTS:** Amongst the many composite materials, soft composites containing a thermo-plastic matrix with textile reinforcement are used in civil engineering and building construction in the form of tensile membranes.

To justify permanent use of these structures, it is necessary to know their stiffness and failure behavior, and to predict their long term behavior under combined loading. So we must develop experimental characterization techniques and rheological models taking into account the specific properties of these materials and their long term behavior.

The material studied is a polyvinylchloride reinforced with high tenacity polyester plain weave fabric and is used for tensile or inflatable structures.

**KEYWORDS:** Durability, Soft composite, Biaxial loading, Creep, Rheological behavior

## 1 INTRODUCTION

The aging of reinforced PVC fabrics is caused mainly by superficial cracks of the matrix. The exposed fibers are then attacked by U.V.. The main characteristics affected are the tensile strength and the tear strength. These characteristics can fall by up to 60%. So it is necessary to characterize, to predict and to model this aging to take it into account in the time of building conception.

This paper presents a theorico experimental method for the characterization of long term behavior of soft composites. The study is made on a coated fabric but the method can easily be apply to every kind of soft composites

As it is shown on figure 1 this characterization can be done by accelerated tests at the scale of the constituents (fiber, matrix) or at the scale of the textile architecture. The prediction must be validated by real time tests.

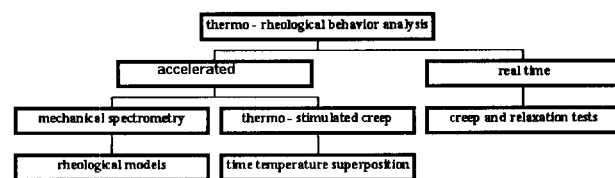


Figure 1 : Study organigram

## 2 MATERIAL STUDIED

The material studied is a high tenacity plain weave polyester (ref. ENKA 174 S) coated with PVC. The weight of the coated fabric is 800 g/m<sup>2</sup> for a thickness of 0.6 mm and a fiber content of 24%. The PVC has no mechanical properties, is only used to protect the polyester from U.V. attack. The material is orthotropic on the scale of the textile architecture and behaves as a membrane.

## 3 VISCOELASTIC MEASUREMENT

### 3.1 Elaboration of rheological model

Simple viscoelastic tests were performed at different frequencies with a DMTA (Dynamic Mechanical Thermal Analysis).. To choose a well suited model, we draw with the experimental results Cole-Cole diagrams (Cole et al. 1941) and we compare those diagrams with model ones. The results are shown on figure 2. The complex modulus  $E^*$  can be written

$$E^* = E' + iE'' \quad (1)$$

Cole-Cole diagrams are made by plotting  $E''$  modulus as a function of  $E'$  modulus.

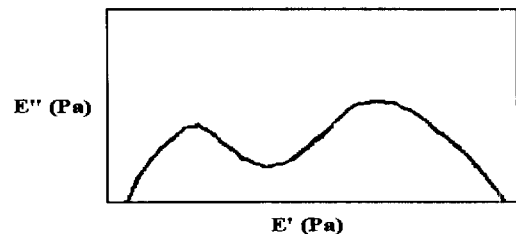


Figure 2 : Evolution of  $E'$  and tangent  $\delta$  with temperature

Our experimental results can be approached by a Zener bipolarabolic model (Huet et al. 1984). This model can be done either with an assembly in series or/and parallel of springs and dashpots or with an assembly in series or/and parallel of fractional elements. The basic fractional is a model of one mechanism (spring pot) which constitutive law satisfies : (Koller 1984)

$$K.D_t^\alpha . X(t) = F(t) \quad (2)$$

where  $\alpha$  is the order of the fractional derivation ( $0 \leq \alpha \leq 1$ ). After several mathematical operations we obtain the equation of the model. (equation 3 and figure 3)

$$E^*(i\omega) = E_0 + \frac{E_\infty - E_0}{1 + (i\omega\tau)^{-k} + \delta(i\omega\tau)^{-h}} \quad (3)$$

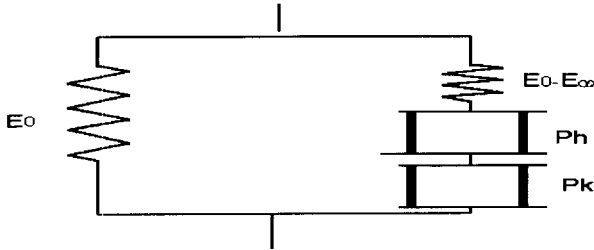


Figure 3 : Limited biparabolic Zener

The values of the parameters  $h, k, E_0$  are determined by enlarging the external parts of Cole-Cole diagrams. In order to determinate the value of  $E_\infty$ , we divide every part of Cole-Cole diagram in two zones. The first one corresponding to high frequencies is approximated to an arc of a circle whose center is under the real axis, the second corresponding to low frequencies is approximated to an arc of a circle whose center is under the real axis and cuts it in  $E_\infty$ .

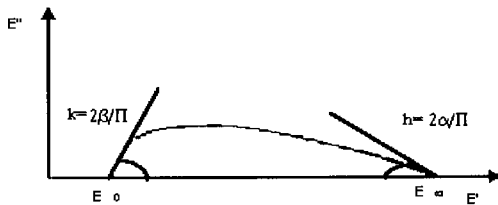


Figure 4 : Determination of the different parameters

To determinate the value of  $\delta$ , we give arbitrary values of the term  $\omega\tau$  and we adjust the value of  $\delta$  until the experimental and calculated values are matched. (figure 5)

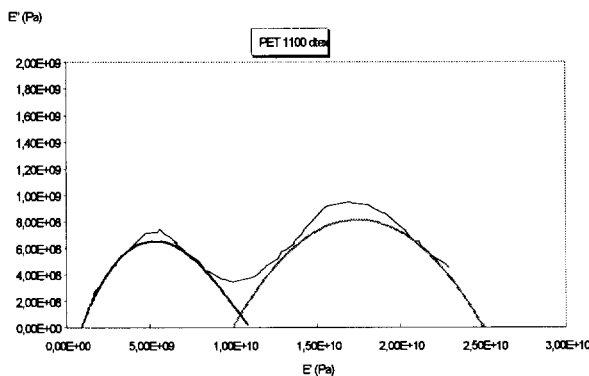


Figure 5 : Experimental/theoretical Cole-Cole

Table 1 gives the values of the parameters of the model for the polyester fibers.

zone 1					zone 2				
E0 GPa	E∞ GPa	h	k	δ	E0 GPa	E∞ GPa	h	k	δ
2.9	11	0.22	0.13	2.5	9.9	25	0.14	0.14	1

From equation (3) of Zener model it is possible to find temporal expressions (relaxation modulus  $E(t)$  and creep modulus  $J(t)$ ). Operational relaxation and creep modulus can be expressed with the help of Carlson Laplace transforms'. (Boufera et al. 1990), (Cost 1964) Equations 4 and 5 give us the temporal expression of the relaxation ( $E(t)$ ) and creep ( $J(t)$ ) functions.

$$E(t) = E_0 + \frac{E_\infty - E_0}{1 + \left(\frac{t}{\tau}\right)^k + \delta\left(\frac{t}{\tau}\right)^h} \quad (4)$$

$$J(t) = \frac{1 + \left(\frac{t}{\tau}\right)^k + \delta\left(\frac{t}{\tau}\right)^h}{E_0\left(1 + \left(\frac{t}{\tau}\right)^k + \delta\left(\frac{t}{\tau}\right)^h\right) + E_\infty - E_0} \quad (5)$$

### 3.2 Time temperature superposition

In the second part of this investigation, we determine the time variation of  $E(t)$  by application time temperature superposition. The tests are made on the DMTA between -150 °C and 200 °C at five frequencies (0.3 to 30 Hz). Superposition of the data curves permits us to obtain a master curve for a reference temperature of 25 °C.

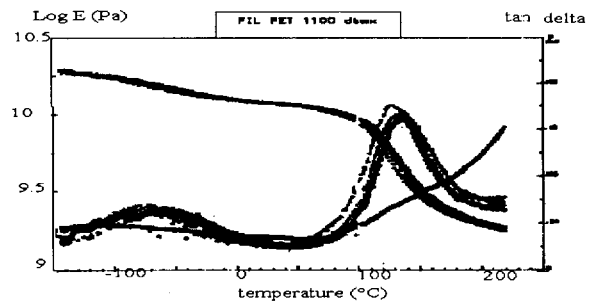


Figure 6 : Test at several frequencies on polyester fiber

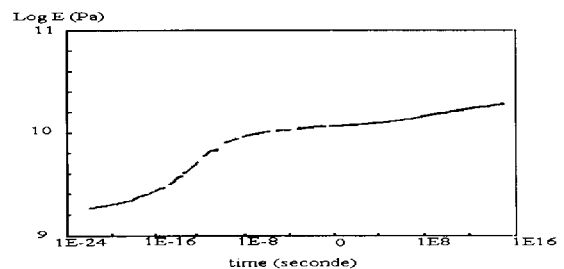


Figure 7 : Master curve at 25 °C for polyester fiber

This master curve can be fitted with an exponential function (Kabir 1984).

$$E = E_0 \cdot t^a \quad (6)$$

where  $\log E_0 = 10.09$  Pa and  $a = -0.013$  Pa/s.

In this part we have determined the creep curves of polyester fibers either by applying the time temperature superposition principle or by mechanical spectrometry and definition of a rheological model.

#### 4 THERMOSTIMULATED CREEP ON LARGE DIMENSION SPECIMENS

The Institut Textile de France in collaboration with the Laboratoire Mécanique et Matériaux Université Lyon 1 (with the support of the Région Rhône Alpes) have developed a biaxial testing apparatus to carry out tests on large dimension specimens on soft or stiff composites. (Mailler 1996)

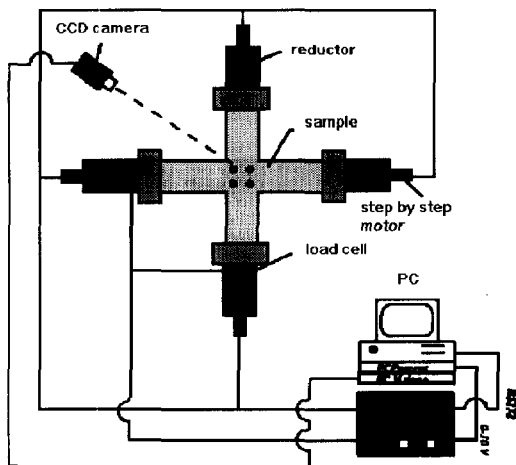


Figure 8 : Biaxial testing apparatus

The mains characteristics of this apparatus are given below.

- maximum load of 15 000 daN,
- sample of  $1 \times 1 \text{ m}^2$  with a maximal deformation of 50%,
- four step by step motors permit to drive the apparatus either in displacement or load with several load or displacement ratio between the two axes,
- a thermal enclosure permits us to realize test between  $-40 \text{ }^\circ\text{C}$  to  $200 \text{ }^\circ\text{C}$ .

We made a series of creep test in the following conditions:

- 1/1 320 daN/30 cm in warp and 320 daN/30 cm in weft,
- 2/1 320 daN/30 cm in warp and 160 daN/30 cm in weft,
- 1/2 160 daN/30 cm in warp and 320 daN/30 cm in weft.

The displacements are measured in the central part of the specimen with an optical method. Using a CCD camera, we follow the displacement of the barycentre of marks drawn on the surface of specimen.

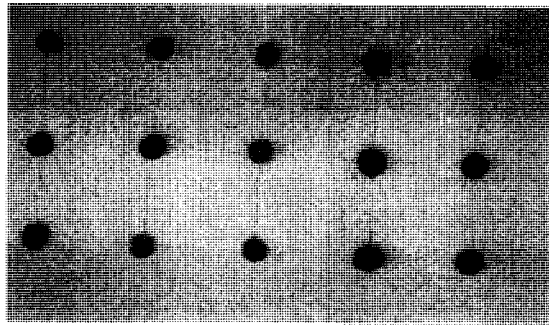


Figure 9 : Biaxial specimen (marks on surface)

The strains are then calculated using a pseudo finite element made with four points. These strains are calculated in the center of these elements and take into account the large deformations of this kind of material.

Figure 10 illustrates biaxial creep curves at  $25 \text{ }^\circ\text{C}$  for a load ratio of 1:1.

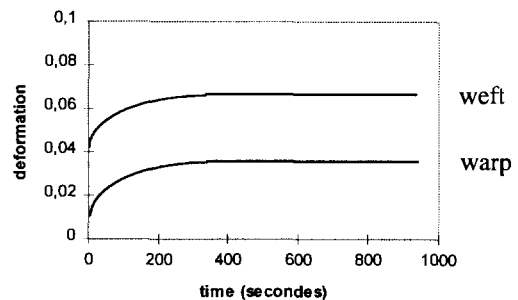


Figure 10 : Biaxial creep curve at  $25 \text{ }^\circ\text{C}$  (1/1)

With similar curves at several temperature we construct a master curve taking into account the stresses applied in the central part of the specimen and using an inverse method to calculate the E modulus. The basis of this method is given below.

At a given time we have,

$$\begin{bmatrix} \sigma_1 \\ \sigma_2 \end{bmatrix} = \begin{bmatrix} \varepsilon_1 & \varepsilon_2 & 0 \\ 0 & \varepsilon_1 & \varepsilon_2 \end{bmatrix} \times \begin{bmatrix} C_{11} \\ C_{12} \\ C_{22} \end{bmatrix} \quad (7)$$

where  $\sigma_i$  are the stress,  $C_{ij}$  are the coefficients of the rigidity matrix and  $\varepsilon_i$  the strain.

If we consider two different times on two different tests (for example two load ratios) we have,

$$\begin{bmatrix} \sigma_{11}^1 \\ \sigma_{21}^1 \\ \sigma_{11}^2 \\ \sigma_{21}^2 \end{bmatrix} = \begin{bmatrix} \varepsilon_1^1 & \varepsilon_2^1 & 0 \\ 0 & \varepsilon_1^1 & \varepsilon_2^1 \\ \varepsilon_1^2 & \varepsilon_2^2 & 0 \\ 0 & \varepsilon_1^2 & \varepsilon_2^2 \end{bmatrix} \times \begin{bmatrix} C_{11} \\ C_{12} \\ C_{22} \end{bmatrix} \quad (8)$$

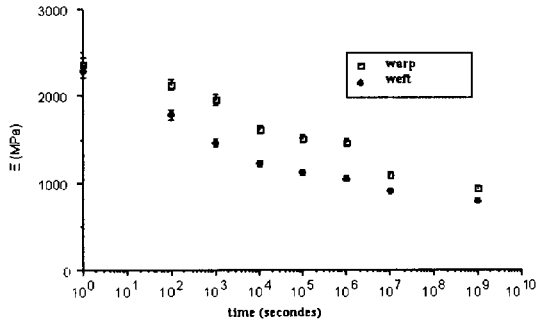


Figure 11 : Biaxial master curve at 25° C

These curves can be fitted by a logarithmic function:

$$E(t) = E_0 + a \log t \quad (9)$$

where a warp = -170 MPa/s , a weft = -165 MPa/s ,  $E_0$  warp = 2400 MPa,  $E_0$  weft = 2060 MPa

In an attempt to validate this predicted creep curves, we carried out real time tests on specimens exposed during 380 days in situ at Lyon. We measured the displacement under a constant load and we defined the creep curves (Figure 12). The knee indicates an augmentation of deformation du to higher temperatures in summer time.

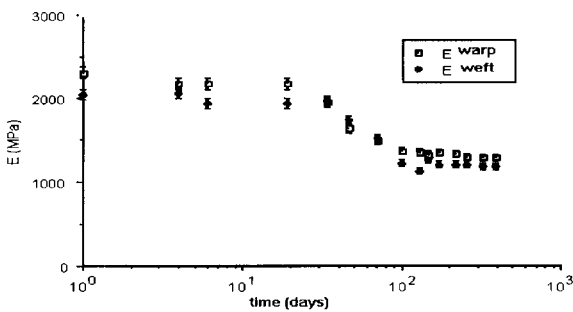


Figure 12 : Creep curves obtained by real time tests

## 5 CONCLUSION

All those results can be compared with real time tests (Figure 12). The three different approaches (at the scale of the constituents, at the scale of the textile architecture and the real time tests) give us similar results.

In a general point of view this results are similar to the literature (Toyada et al 1990,1992,1994) and give a residual tension stress of 50% in 3 years with a little evolution in 7 years. This is in accordance with our results which show us an asymptotic stabilization of creep.

This work permits the designers to take the durability into account during the design process.

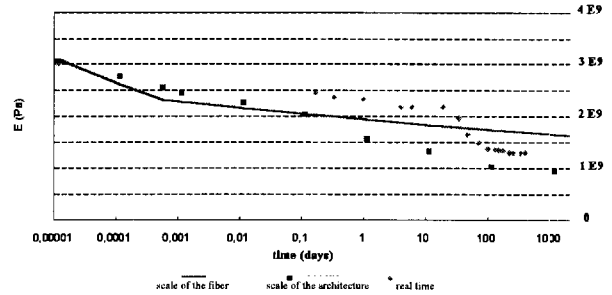


Figure 13 : Comparison of real time test and accelerated tests

## REFERENCES

- Cole K.S., Cole R.H. (1941) "Dispersion and absorption in dielectrics; Alternative current characteristics". T Chem Phys. vol 9 p341
- Huet C., Bourgoin D., Richemond S. (1984) "Rhéologie des matériaux anisotropes" Compte rendu du 19 ème colloque national annuel, Paris Cepadues ed p 591
- Koller R. C. (1984) "Application of fractional calculus to the theory of viscoelasticity" Journal of Applied Mechanics vol. 51 pp 299-307
- Boufera A., Doan C., Hamelin P. (1990) "Comportement viscoélastique des matrices polymères" Comportement des composites à renforts tissus - Comportement dynamique des composites. Ed Pluralis 1990 pp 47-68
- Cost T. (1964) "Approximate Laplace transform inversion in viscoelastic stress analysis" AIAA journal vol. 2 pp 2157-2166
- Kabir (1984) "In isolation and soil behavior of geotextile" Theses University of Glasgow
- Mailler Ph. (1996) "Rhéologie des membranes composites souples orthotropes sous chargement multi axial" Thèse de doctorat UCB LYON I 1996
- Toyada, Nireky, Juntunen, Ohnuma (1990) "Durability of PVC coated fabrics for membrane structures" I.A.S.S.S. Dresden and Cottbus
- Toyada, Wu, Tori (1992) "Deterioration with time of PVC coated fabric for tent warehouses, some experimental results" Textile Composite in Building Construction Part 1, Ed Pluralis
- Toyada, Sakabe, Tori, Itoh, Konishi (1994) "Weatherability of membrane structure materials as determined by their exposure conditions" ESN I Gakkaishi, vol. 50 N° 10

# A Model for the Ultimate Pull-out Resistance of Geogrids

R.H. CHEN

Professor, Institute of Civil Engineering, National Taiwan University, R.O.C.

Y.S. LEE

Ph.D. Candidate, Institute of Civil Engineering, National Taiwan University, R.O.C.

**ABSTRACT:** A three-parameter model is proposed to predict the ultimate pull-out resistance of geogrids. Twenty-seven pull-out tests were performed using three types of geogrids embedded in Ottawa Sand and kaolinite clay. The proposed model can take into account the nonlinear relation of the ultimate resistance with the normal stress. Using this model and analyzing the test results, the above mentioned phenomenon can be described and the ultimate resistance can be predicted very well.

**KEYWORDS:** Pull-out test, Ultimate pull-out resistance, Geogrid.

## 1 INTRODUCTION

In the design of reinforcements, laboratory pull-out tests are performed to understand the pull-out resistance of reinforcements in soils. The parameters needed in the limit equilibrium methods, such as apparent cohesion  $c$  and frictional angle  $\phi$  are obtained. It is a common practice to employ the Mohr-Coulomb criterion for the design. However, this criterion does not usually predict the ultimate pull-out resistance very well. Hence, a three-parameter model for predicting the ultimate pull-out resistance is presented in this study to take into account the deformation modulus of geogrids and applied normal stress. This model was verified by twenty-seven pull-out tests. According to the results verified, this model can describe the relation between the ultimate pull-out resistance and the applied stress, and predicts the ultimate pull-out resistance of other geogrids.

## 2 THE PROPOSED MODEL

In design practice, the assumptions on the pull-out resistance of geogrids in soils are: (a) the shear stress at the interface between geogrid and soil is constant, (b) the shear stress at the interface follows the Mohr-Coulomb criterion. Hence the pull-out resistance is presented as:

$$\tau = c + \sigma \tan \phi \quad (1)$$

$$P = 2 A \tau \quad (2)$$

where:

$\tau$ : the shear stress at the interface

$c$ : apparent cohesion intercept

$\sigma$ : applied normal stress

$\phi$ : frictional angle

$P$ : ultimate pull-out resistance

$A$ : embedded area of geogrids

On the other hand, the proposed three-parameter model is

as follows:

$$\tau = \sigma \left[ a_1 + a_2 \exp\left(-a_3 \frac{\sigma}{E}\right) \right] \quad \text{for sandy soils} \quad (3)$$

$$\tau = a_1 + \sigma a_2 \exp\left(-a_3 \frac{\sigma}{E}\right) \quad \text{for cohesive soil} \quad (4)$$

$$E = \frac{T}{\epsilon} \quad (5)$$

where:

$a_1, a_2, a_3$ : parameters to be determined.

$E$ : deformation modulus of geogrid, which can be determined by Eq.(5).

$T$ : the tensile force of geogrid in the tensile strength test.

$\epsilon$ : the strain of geogrid in the tensile strength test.

In this model, the  $a_1$ ,  $a_2$  and  $a_3$  parameters are obtained by pull-out tests. Eq.(3) is suitable to sandy soils, and Eq.(4) is suitable to cohesive soils. This proposed model compared with the Mohr-Coulomb criterion has the following characteristics:

1. The model uses the applied normal stress  $\sigma$  and the geogrid deformation modulus  $E$  to describe the ultimate pull-out resistance.
2. If the modulus of geogrid is infinite, the pattern of the simplified proposed model is similar to the ordinary shear strength model such as Mohr-Coulomb criterion.
3. The expansion of the exponential function in Eq.(3) or Eq.(4) has infinite terms. For this reason, the proposed model is convenient to describe test results smoothly, compared to the Mohr-Coulomb criterion that has only two parameters.

Table 1. Fundamental properties of geogrids.

Item (kN/m)	Grid A	Grid B	Grid C
Ultimate tensile strength	110	80	55
Deformation modulus at 5% strain	1320	960	660
Deformation modulus at 10% strain	880	640	440

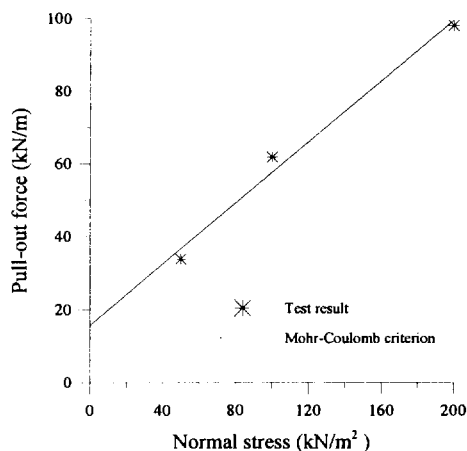


Figure 1. Normal stress versus ultimate pull-out resistance for grid A embedded in Ottawa Sand ( $D_r=85\%$ ).

### 3 TEST EQUIPMENT AND TEST MATERIAL

The dimension of the pull-out box is 60cm  $\times$  35cm  $\times$  20cm (length  $\times$  width  $\times$  height). The range of pulling rate is from 0.0006 to 107 mm/min. The capacity of pulling force is 12.5 tons applied by electric motor. The vertical load system consists of a rubber air bag and a jack. Load cells and LVDT are used to measure the pulling force and the displacement. A data acquisition device, an AD card, and a personal computer are used for test controlling and recording. Test materials include geogrid, sand, and clay. The material properties of three types of Tensar geogrid used in the tests are summarized in Table 1. The sand is Ottawa sand (No. C109) that has specific gravity 2.65, maximum void ratio 0.732, and minimum void ratio 0.387. The strength parameters are  $c = 0.7 \text{ kN/m}^2$ ,  $\phi = 36^\circ$ , for relative density  $D_r = 85\%$ ; and  $c = 5 \text{ kN/m}^2$ ,  $\phi = 32^\circ$ , for  $D_r = 50\%$ . The clay is kaolinite that has specific gravity 2.62, maximum dry density 12.8  $\text{kN/m}^3$ , the optimum water content 31.5%. The strength parameters from the consolidated undrained test are  $c = 18 \text{ kN/m}^2$ ,  $\phi = 15.6^\circ$ , for dry unit weight  $\gamma_d = 12.4 \text{ kN/m}^3$  and water content  $\omega = 29\%$ .

The dimension of geogrid specimen is 45 cm  $\times$  10 cm (length  $\times$  width), there are three apertures in the longitudinal direction and five apertures in the transverse direction. The distance between the first transverse rib and the front wall of

Table 2. The ultimate pull-out resistance.

#### (a) Ottawa Sand ( $D_r=85\%$ )

Normal stress ( $\text{kN/m}^2$ )	Grid A (kN/m)	Grid B (kN/m)	Grid C (kN/m)
50	33.8	30.9	28.2
100	61.8	57.2	47.9
150			56.2
200	98.1	74.7	

#### (b) Ottawa Sand ( $D_r=50\%$ )

Normal stress ( $\text{kN/m}^2$ )	Grid A (kN/m)	Grid B (kN/m)	Grid C (kN/m)
50	25.3	22.0	18.5
100	48.2	42.1	33.5
150		53.0	51.2
200	86.1		

#### (c) Clay

Normal stress ( $\text{kN/m}^2$ )	Grid A (kN/m)	Grid B (kN/m)	Grid C (kN/m)
50		18.2	15.1
100	26.5	24.5	17.5
200	35.9	30.7	23.5
300	43.0		

the pull-out box is 12 cm. The pulling rate is 1 mm/min.

### 4 TEST RESULTS AND ANALYSIS

The ultimate pull-out resistance of test results is summarized in Table 2. According to the test results, the ultimate resistance increases with the normal stress but the relation is not proportional. The example using the Mohr-Coulomb criterion together with the pull-out test result is shown in Figure 1. From the figure, the Mohr-Coulomb criterion does not appear to be very accurate in regression result, but also the cohesion intercept is greater than zero in sands. Considering the aforementioned phenomenon, a three-parameter model is therefore proposed. The procedure used to analyze the test result is described in the following:

#### 1. Determine the deformation modulus.

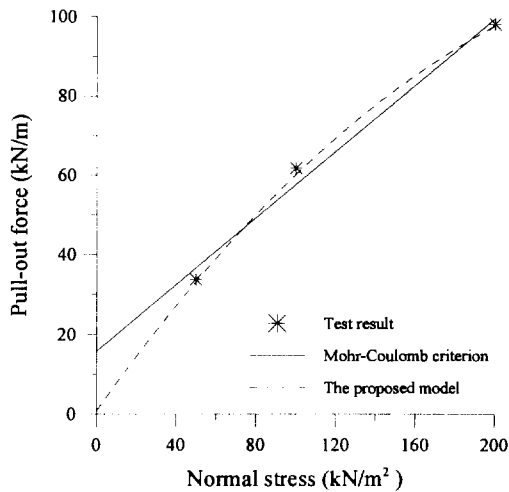
Geogrid is a flexible material, and its modulus varies with strain. Hence a predictive model must take this behavior into consideration. For simplicity, the proposed model adopts the deformation modulus as the secant modulus at 5% strain when the strain is less than 5%, and the secant modulus at 10% strain for strain more than 5%.

#### 2. Determine $a_1, a_2$ and $a_3$ parameters.

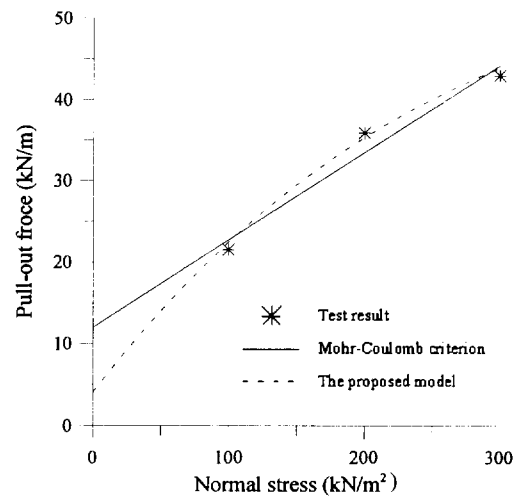
The three parameters are to be determined by using Eq.(3) for sands, and using Eq.(4) for clays.

#### 3. Compute the ultimate pull-out resistance.

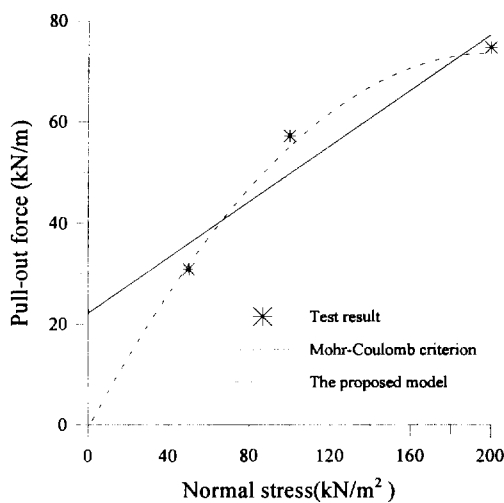




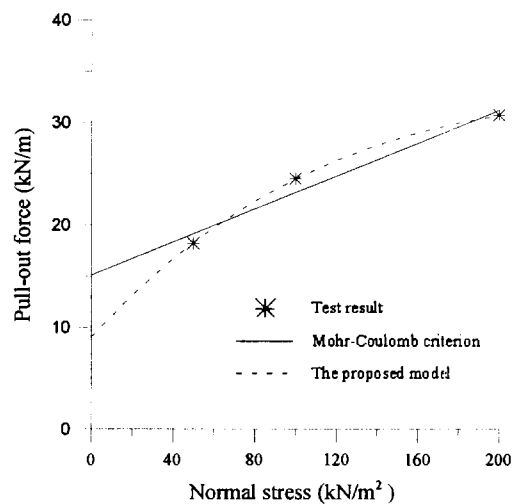
(a) Grid A



(a) Grid A



(b) Grid B



(b) Grid B

Figure 2. The comparison of the proposed model and Mohr-Coulomb criterion for pull-out tests in Ottawa Sand ( $D_r=85\%$ ).

Figure 3. The comparison of the proposed model and Mohr-Coulomb criterion for pull-out tests in clay.

The ultimate pull-out resistance is computed considering various modulus and normal stress using Eq.(3) for sands and Eq.(4) for clays.

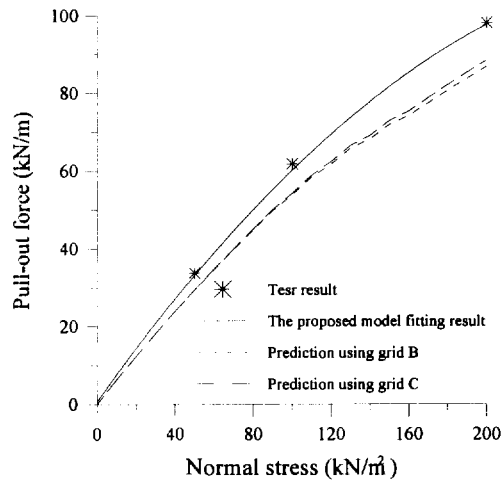
The parameters for computation are summarized in Table 3. The comparison of the proposed model and the Mohr-Coulomb criterion for the ultimate pull-out resistance of geogrids in sands are shown in Figure 2.

It is obvious that the proposed model is better than the Mohr-Coulomb criterion. For instance, the proposed model describes the relation of the ultimate pull-out resistance and the normal stress very well and the apparent cohesion intercept is zero. The model also describes non-proportional relation of the ultimate pull-out resistance with the normal stress. In the other case for kaolinite clay, the comparison is

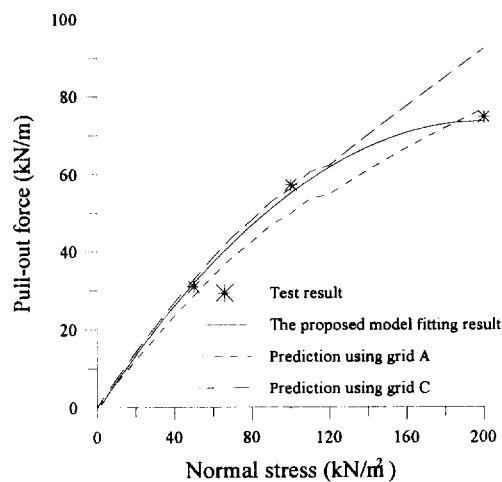
shown in Figure 3. Analyzing and comparing the result, the result from this model is similar to that of the Mohr-Coulomb criterion. Besides, this model predicts the ultimate pull-out resistance well.

From the above mentioned results, the proposed model is a good application to predict the ultimate resistance for alternating normal stress.

Furthermore, the proposed model seems also be able to predict the ultimate pull-out resistance of other geogrids. For instance, it predicts the ultimate resistance of geogrid B by using the parameters of geogrid A or C. The results of this prediction are shown in Figure 4. It is found that the predictions are within 10%~20% error. In engineering practice, it seems acceptable.



(a) Grid A/Ottawa Sand (Dr=85%)



(b) Grid B/Ottawa Sand (Dr=85%)

Figure 4. The result of the proposed model predicting the ultimate pull-out resistance.

## 5 CONCLUSIONS

Summarizing from the mentioned explanation and discussion, the advantages of the proposed model are as follows:

1. The dimensionless term  $\sigma/E$  is used to describe the ultimate pull-out resistance, and its application on studying test result shows good.
2. Although there are three parameters in this model, more than two parameters in the Mohr-Coulomb criterion, the convenience and power of this model is justified.
3. As the modulus  $E$  approaches infinity, the model can be simplified to become a special case of the Mohr-Coulomb criterion.
4. The model predicts the ultimate pull-out resistance of

Table 3. Parameters of the proposed model.

(a) Ottawa Sand (Dr=85%)

Item	$a_1$	$a_2$	$a_3$
Grid A	0.46	0.37	6.2
Grid B	0.23	0.47	3.0
Grid C	0.25	0.45	3.0

(b) Ottawa Sand (Dr=50%)

Item	$a_1$	$a_2$	$a_3$
Grid A	0.42	0.17	5.5
Grid B	0.14	0.55	5.0
Grid C	0.37	0.065	6.0

(c) Clay

Item	$a_1$	$a_2$	$a_3$
Grid A	4.0	0.22	2.2
Grid B	9.0	0.22	3.4
Grid C	11.7	0.07	0.7

geogrids more well than the Mohr-Coulomb criterion. It also can be used to predict the ultimate pull-out resistance of other geogrids within acceptable error.

5. Using this model, the non-proportional relation of the ultimate resistance with the normal stress can be described.

## REFERENCES

- F.H.W.A. (1991) *Reinforced Soil Structures, Design and Construction Guidelines*, Vol. 2, U.S. Department of Transportation, D.C., USA.
- Ingold, T.S. (1984) "A Laboratory Investigation of Soil-Geotextile Friction", *Journal of Ground Engineering*, Vol. 17, pp.21-28.
- Koerner, R.M. (1990) *Designing with Geosynthetics*, 2nd ed., Prentice-Hall, New Jersey, USA.
- Lee, Y.S., Chen, R.H., and Chen, T.C. (1996) "A Three-Parameter Model for the Ultimate Pull-out Force of Geogrids", *Proceedings of the International Symposium on Earth Reinforcement*, Fukuoka, Japan, pp.69-72.

# An Approach to Analyze the Pull-out Resistance of Woven Geotextiles

Ashoke K. Karmokar

Assistant Professor, Department of Material Systems Engineering, Tokyo University of Agriculture and Technology, Faculty of Technology, 2-24-16 Naka-cho, Koganei-shi, Tokyo 184-0012, Japan

Hisayoshi Kabeya

Professor, Department of Material Systems Engineering, Tokyo University of Agriculture and Technology, Faculty of Technology, 2-24-16 Naka-cho, Koganei-shi, Tokyo 184-0012, Japan

**ABSTRACT:** The pull-out resistance of geotextiles is generally the result of complex phenomena occurring at the soil-geotextile interface. In this study, an attempt is made to analyze the pull-out resistance by considering that soil shearing and soil-geotextile friction at the interface are liable to develop the resistance. The usefulness of this approach is pointed out in terms of the prediction of pull-out resistances of soil-geotextile system. For illustration, the pull-out resistances of two woven geotextiles with Toyoura sand are predicted, and compared with those of experimental values. The surface asperity of geotextile is identified as an important factor influencing shearing and friction components at the interface.

**KEYWORDS:** Friction, Geotextiles, Pull-out Resistance, Shear Strength, Woven Fabrics

## 1 INTRODUCTION

The operational circumstances of many soil structures reinforced with geotextiles reveal that the geotextile is at least partly subjected to a pull-out force. This is leading to the pull-out method which is used for the evaluation of soil-geotextile interfacial interaction. The results of a pull-out test are, however, difficult to interpret because of complex interactions at the interface. Nevertheless, a few attempts at a numerical approach have been made to analyze the behavior involved in the pull-out operation of a geogrid (Wilson-Fahmy and Koerner 1993; Yogarajah and Yeo 1994), but hardly any attempts have ever been made for a geotextile. This is probably because of the structural complexities that a geotextile presents compared with a geogrid. In this study, a semi-empirical approach is adopted to analyze the pull-out resistance developed by the woven geotextiles with sand. The structural parameters of the geotextiles and their interactions with the sand are well accounted for in this approach.

## 2 ANALYTICAL PROPOSITION

The pull-out resistance is assumed to be developed due to interactions comprising soil shearing and soil-geotextile friction. Therefore, pull-out resistance (P) could be written as

$$P = S + F \quad (1)$$

where, S = shearing force, F = frictional force. Let the total area at the interface be A, out of which the areas responsible for soil shearing and soil-geotextile friction are A1 and A2, respectively. Thus, Equation (1) becomes

$$P = \tau \cdot A1 + f \cdot A2 \quad (2)$$

where,  $\tau$  = soil shear stress, f = soil-geotextile frictional force per unit area. The relationship for the determination of frictional force is

$$f = \mu_f \cdot N \quad (3)$$

where,  $\mu_f$  = coefficient of friction between soil and raw material of geotextile (hereafter the raw material frictional behavior is termed as 'skin-friction'), N = normal stress.

To predict pull-out resistance, therefore, we need the values of  $\tau$ ,  $\mu_f$  and shearing/friction area at the interface.

## 3 MODEL ILLUSTRATION

For illustration, two plain woven geotextile samples were considered, and their interactions with Toyoura sand were taken into account. A few details of the geotextile samples and sand are given in Table 1 and Figure 1, respectively.

A prototype apparatus (Kabeya et al. 1993) was used for conducting the pull-out experiments. Four levels of normal pressure, e.g., 2.5, 5.0, 7.5, and 10.0 kPa, were maintained on the soil-geotextile-soil system during experiments (low pressures were to avoid fabric deformation inside soil).

Table 1 Specifications of woven geotextile samples.\*

Descriptions	Sample (S1)	Sample (S2)
Polymer type	Polypropylene	Polyester
Yarn type	Flat tape	Multi-filament
Yarn count (Tex)	130 × 120	530 × 530
Yarn crimp (%)	4.3 × 1.6	5.5 × 3.7
No. of yarns (/cm)	6.3 × 6.3	5.6 × 5.6
Thickness (mm)	0.60	1.00
Area density (g/m <sup>2</sup> )	170	600

\*Samples were obtained from Taisei Corporation, Japan

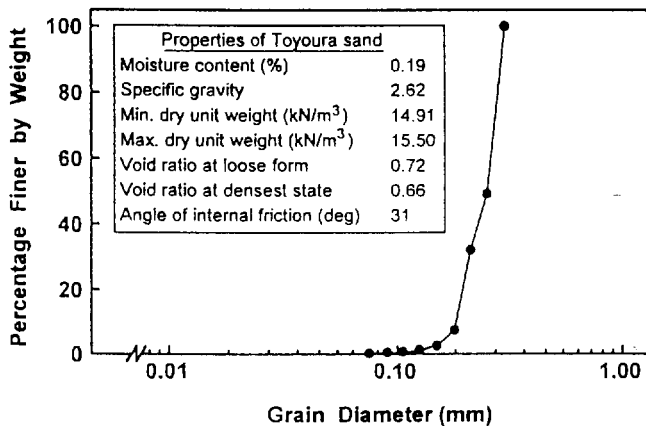


Figure 1 Grain size distribution of Toyoura sand.

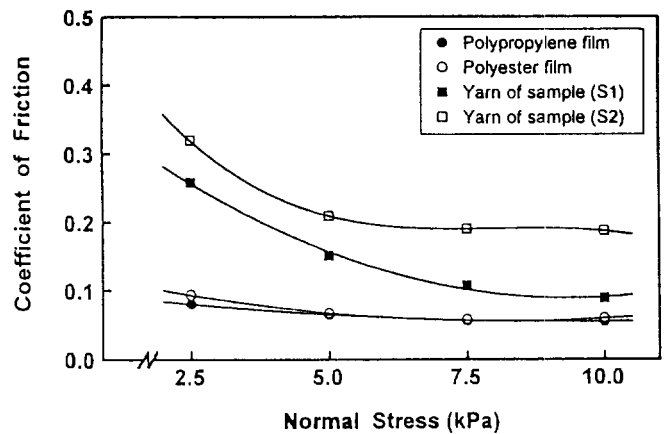


Figure 2 Skin-frictional coefficient with Toyoura sand.

### 3.1 Frictional Experiments

The polymer types of the two selected geotextiles were polypropylene (sample S1) and polyester (sample S2). Consequently, the pull-out tests on polypropylene (PP) and polyester (PET) films with sand were carried out for determining the sand-geotextile skin-friction coefficients. By this method, however, the frictional representation may not be truly possible, as finishes in the geotextile and the film are necessarily different. Thus, to find out the actual frictional coefficients, the following approach was used.

The individual yarn was unraveled from the geotextile sample and heat-set under decrimped-taut condition. The decrimped yarn was then used in the pull-out experiments with Toyoura sand. In pull-out experiments, therefore, the occurrence of soil shearing at the interface which may be initiated by the crimps was very unlikely, as the yarn was decrimped and merely tape or filament (with marginal twists) in kind. Consequently, the yarn-sand pull-out resistance development was thought to be solely due to friction. The sand-film (geotextile) skin-friction coefficient is obtained by using the following empirical relationship

$$\mu_f = F' / (A' \cdot N) \quad (4)$$

where,  $\mu_f$  = coefficient of skin-friction,  $F'$  = frictional force,  $A'$  = interfacing area,  $N$  = normal stress.

The results are shown in Figure 2 where it may be seen that the set of values obtained by the above approach are higher than those obtained with the respective films. These differences in values could be attributed to their different surface textures. However, the coefficients of skin-friction obtained here could reasonably be taken as actual values.

### 3.2 Shearing Experiments

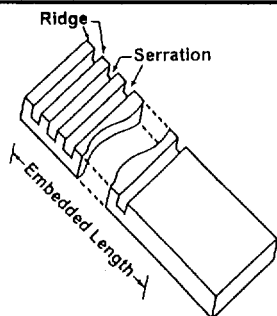
For characterizing the shear behavior of sand, generally, we conduct direct shear box tests in laboratory. However, possibly a different state occurs due to different shearing

situations at the soil-geotextile interface in the pull-out method, and at the interface of the two boxes in the direct shear box method. At the soil-geotextile interface, the soil shear behavior is believed to be influenced by the presence of the surface concavities of the geotextile. The concavity wall may put up passive bearing resistance to the soil shear stress. As concavities are numerous, so the contribution of passive bearing resistance to soil shear stress is also significant. In the direct shear box test, such resistance comes only from the back wall of the shear box for total interface area, and consequently, the shear stress occurring with this method is lower in value. Thus, it is important to conduct shear tests under simulated pull-out interfacing conditions, so that the passive bearing resistance of soil brought by cross elements could be taken into account.

For this, channel-like parallel serrations were engraved on acrylic plates (Table 2). Each plate was then used as the reinforcing element in the pull-out experiments. The conditions maintained in the experiments were similar to those during soil-geotextile pull-out testing. The engraved area on the plate (channel) is believed to be responsible for soil shearing, and the flat area to be responsible for friction in the pull-out operation. With defined areas for shearing and friction on the plate, it was possible to distinguish the soil shearing and soil-acrylic plate friction components, provided the sand-acrylic plate frictional coefficient was known. For the sand-acrylic plate frictional coefficient, the pull-out tests on smooth acrylic plates with Toyoura sand were conducted.

Figure 3 was drawn to show the trend of soil shear stress against serration width in the acrylic plate for different levels of normal pressure. The shear stress corresponding to the pitch of respective geotextile samples could now be obtained from this figure by extrapolating the respective trends. It is noteworthy to mention at this stage that as the shear area in the acrylic plate decreases, the variability in pull-out resistance (i.e., soil shear stress) increases. This is one of the reasons why we did not use acrylic plates with serration widths of less than 5 mm in this study.

Table 2 Specifications of serrated acrylic plates.



Designation of plates	P20	P15	P10	P5
Number of serration	2	3	4	5
Serration length (mm)	48	48	48	48
Serration width (mm)	20	15	10	5
Serration depth (mm)	5	5	5	5
Shearing area (cm <sup>2</sup> )	23.2	26.1	23.2	14.5
Ridge width (mm)	10	10	10	10
Friction area in 10 cm embedded length (cm <sup>2</sup> )	92.8	89.9	92.8	101.5

### 3.3 Interfacial Shearing and/or Friction Area

Evaluating the shearing/friction area at the soil-geotextile interface is a two stage process, namely, the measurement of the surface roughness of geotextile samples, and the correlation between surface roughness and soil properties involved in the interface interaction process. The brief description for each of the stages is given below.

#### 3.3.1 Evaluation of surface roughness

An empirical approach was followed for measuring the surface roughness of geotextile samples because the two other commonly used methods e.g., mechanical scanning and laser scanning methods, were tried, but they failed to give definite outcomes, due to procedural limitations. In this method, replicas of the two geotextile samples were reinforced with a contrasting color matrix to form a solid block. The block was then milled gradually (in cross-plane direction) at regular intervals. For milling, a precision end-milling machine was used in our laboratory. The milling was done for a cut-out thickness of 0.1 mm in each step. Therefore, it may be said that the technique used here characterizes the surface as a combination of undulating lines, as may be obtained in other scanning methods. The photograph of each milled surface (i.e., at steps of 0.1 mm milled thickness) was taken with a camera fixed to the milling machine. As a next process, each photographic negatives was enlarged by a projector and imaged over the sensitive screen of a digitizer. The digitizer was interfaced with a computer, by which undulating lines were digitized into corresponding numerical values of  $X_i$ , as the distance along the fabric plane, and  $Y_i$ , as the distance of surface contours from the top fabric plane (see inset of Figure 4).

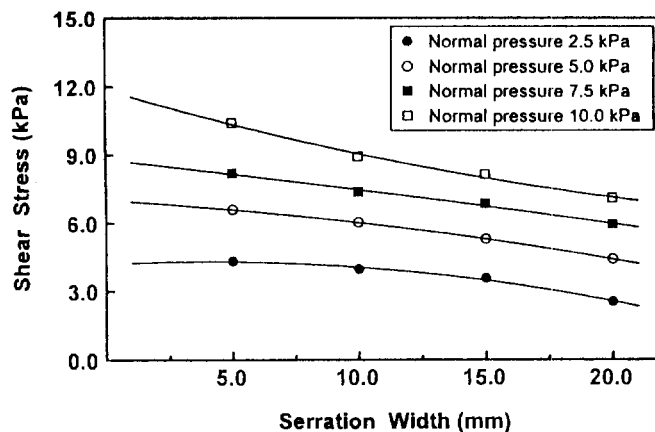


Figure 3 Effect of serration width on shear stress.

Consequently, two dimensional arrays ( $X_i$ ,  $Y_i$ ) for each undulating line were obtained. The reassembling of these undulating lines by a computer program gives a view of the surface of the geotextile sample, as shown in Figure 4.

#### 3.3.2 Correlation of surface roughness with soil properties

The two parameters, namely, the depth, and the slope of surface concavities were used for expressing the surface roughnesses of geotextile samples. These two parameters were then weighed, as stated below, against the two soil parameters, viz., the average soil particle diameter ( $D_{50}$ ), and the soil shear angle ( $\phi$ ) of Toyoura sand, respectively, for determining interfacial shearing/friction area.

The measurements of concavity depths at different points at distances 0.1 mm apart yield a frequency distribution for each of the geotextile samples. It is assumed that when the absolute concavity depth at any point (element) is more than the size of soil particle employed, then that element will be responsible for soil shearing at the interface. On the other hand, if the concavity depth is less than the size of the soil particle, the element will be responsible for friction at the interface. Thus, corresponding to the value of concavity depth equals to average soil particle diameter ( $D_{50}$ ) of Toyoura sand, the percentage of elements causing shearing and friction at the interface may be found out. By knowing the total embedded area maintained during experiments (both faces of the geotextile), we were able to calculate the interfacial shearing and friction area.

Similarly, the concavity slopes calculated between any two consecutive measuring points (0.1 mm apart) give a frequency distribution for each geotextile sample. It is our assumption that when the calculated slope is less than the angle of soil shearing ( $\phi$ ), that slope will be responsible for soil-geotextile friction, and when the slope is more than the angle of soil shearing, that slope will be responsible for soil shearing at the interface. Using the same line of action stated above, therefore, we were able to draw a partition in the population of concavity slope distribution.

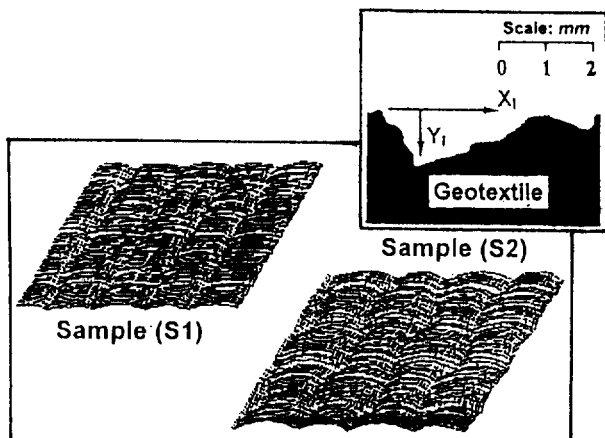


Figure 4 Surface view of geotextile samples.

However, it is a common perception that the interfacial interactions between soil and geotextile are quite complex phenomena, and the ways we tried to correlate concavity depth and concavity slope with soil properties individually may not be totally justified. This is because, even if there is sufficient concavity depth (greater than particle diameter), interfacial soil shearing may not occur when the slope at that point is less than the shear angle of the soil. Similarly, it may be argued that, even if the concavity slope is higher than the soil shear angle, the interfacial shearing may not occur when the concavity depth is less than the particle diameter. For this reason, therefore, an attempt was also made to introduce the interaction between concavity depth and concavity slope, for finding the correct shearing and/or friction area at the interface.

### 3.4 Calculated Pull-out Resistance

Using the three sets of shearing/friction areas, obtained from the concavity depth distribution, the concavity slope distribution, and the interaction of the two, the pull-out resistances were calculated. It were observed that the pull-out resistances calculated using the areas corresponding to depth distribution and slope distribution were in poor agreement with those obtained experimentally, although the general trends were found the same. In contrast, the pull-out resistances calculated using the interaction induced shearing/friction areas were in good agreement with the experimental pull-out resistances (Figure 5). As stated before, the reason for this may be the interactive effects due to both the depth and the slope of surface concavities of geotextiles, rather than individual actions.

## 4 SUMMARY

With the multiplicity of structural parameters of geotextiles and complexities in the design procedure for geotechnical applications, we very often encounter the

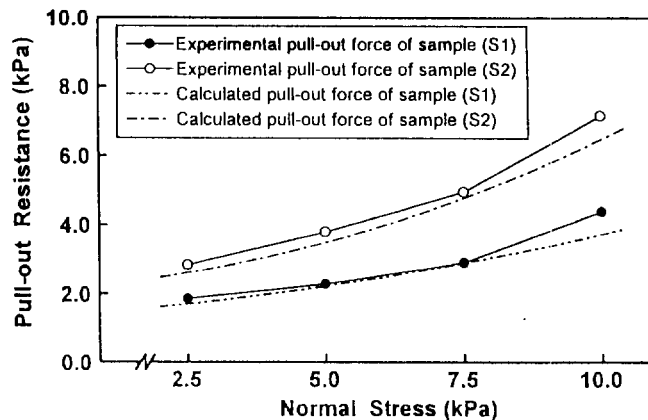


Figure 5 Experimental/calculated pull-out resistance.

need to know the pull-out force that a geotextile will exert with the soil type. Using the proposition described before, we may have the option of dealing with the problem of determining pull-out resistance. By knowing the soil-geotextile skin-friction behaviors, the soil shearing properties, and the interfacial shearing or friction areas for the soil-geotextile system, we could proceed to calculate the constituents shearing and friction at first, and then the pull-out resistance.

The illustration reported in this study indicates that depending on the surface asperities of the geotextile, and their interactions with the soil, the contributions of shearing and friction in the pull-out resistance will vary. It is identified that the effect of the surface asperity of the geotextile is merely to influence the shearing and friction area at the interface. Comparisons of experimental and calculated values of the pull-out resistance show that the correlation between surface asperities and soil properties for evaluating the interfacial shearing and/or friction area is an interactive process of factors such as depth and slope of surface concavity of geotextiles.

## REFERENCES

- Wilson-Fahmy, R.F. and Koerner, R.M. (1993) "Finite Element Modeling of Soil-Geogrid Interaction with Application to the Behavior of Geogrids in a Pull-out Loading Condition", *Geotextiles and Geomembranes*, Vol. 12, pp. 479-501.
- Yogarajah, I. and Yeo, K.C. (1994) "Finite Element Modeling of Pull-out Tests with Load and Strain Measurements", *Geotextiles and Geomembranes*, Vol. 13, pp. 43-54.
- Kabeya, H., Karmokar, A.K., Kamata, Y. and Tsunoda, S. (1993) "Influence of Surface Roughness of Woven Geotextiles on Interfacial Frictional Behavior — Evaluation Through Model Experiments", *Textile Research Journal*, Vol. 63, No. 10, pp. 604-610.

# A NEW APPROACH IN MODELING OF SOIL-GEOTEXTILE INTERFACE BEHAVIOR IN PULLOUT TESTS

S. B. Mallick,  
Civil Engineering Department, Auburn University

D. J. Elton  
Civil Engineering Department, Auburn University

and

S. Adanur  
Textile Engineering Department, Auburn University

**ABSTRACT:** A nonlinear elastic finite element model was developed using GAP elements to investigate the failure criteria and the separation behavior at the soil-geotextile interface during pullout tests. Pullout resistance calculated from this model was compared to that obtained from laboratory pullout tests reported earlier in the literature. The data showed the pullout resistance obtained from the finite element model was approximately equal to that obtained from the laboratory pullout tests. Results from the model also indicated the existence of material nonlinearity close to pullout load application point.

**KEY WORDS:** Finite element, Numerical modeling, Interface-element, Geotextile, Pullout

## 1. INTRODUCTION

When a geotextile is used as reinforcement material in a slope, one of the predominant causes of failure is the slippage or pullout of geotextile from the soil mass. Such a behavior can be modeled by the pullout tests in a laboratory. A simple experimental set-up was designed and pullout tests were carried out in the laboratory (Mallick et. al, 1997). In conjunction with experimental study a theoretical model is required to visualize the pullout mechanism. Such a model can be validated against the results obtained from the laboratory pullout tests.

Finite element analysis conducted by Katagiri et. al (1990) has shown a linear relationship between normal pressure and shear stiffness of the soil-geotextile interface. A joint element technique was used to connect the upper and lower surface of the geogrid with the soil particles. The results showed that the analyzed strain sufficiently agreed with the measured strain. Floss and Gold (1990) conducted a finite element analysis on the efficiency of a single geotextile reinforced two-layer system. Soil continuum was modeled by an eight node isoparametric element with quadratic shape functions. The geotextile was modeled with isoparametric bar elements. To model the soil-geotextile interaction, thin-layer elements were used at the interface. An elastoplastic nature of analysis with

Mohr-Coulomb yield criterion was adopted to limit the transfer of load from the soil to the geotextile.

Wu ( 1987) also developed a finite element model to predict the stress-deformation behavior of a soil-fabric system. The interface region was modeled by connecting the nodes with unilateral normal and tangential springs. The fabric was represented by a special element which could only withstand tension. No resistance to bending and compression was allowed in this element. To simulate the viscoelastic behavior of the polymeric geogrid, varying elastic moduli was used for different sections of the geogrid in a finite element analysis. The residual shear modulus at the interface was selected on the basis of the assumption that the partial slippage would occur once the shear strength was reached.

A review of literature shows that the behavior of the soil-geotextile interface depends on the successful modeling of load transfer mechanism from geotextile to soil. This mechanism is again dependent on the choice of a proper element to model the soil-geotextile interface. This study was carried out to investigate the applicability of a new type of interface element in modeling a pullout test with geotextiles.

## 2. MODELING OF INTERFACE WITH GAP ELEMENTS

In the numerical model developed in this study a new type of element was used to model the soil-geotextile interface.

Ten isotropic GAP elements were used to model the load transfer mechanism at the soil-geotextile interface. Slip-separation behavior of the interface is governed by the status of the GAP elements. The GAP or friction element (available in the element library of MSC/NASTRAN) has several advantages over the thin-layer or spring elements previously used to model the soil-geotextile interface. This is because GAP elements can simulate several situations which are observed in a pullout test. These situations are:

Open GAP: Simulates no contact at the interface

Closed GAP: Simulates the contact between soil and geotextile at the interface under vertical loading

GAP sticking with static friction: Simulates the building of pullout resistance at the interface.

Resistance increases until the pullout load overcomes the static friction at the interface. After the static friction is overcome, GAP elements start slipping with kinetic friction and pullout resistance drops as the reinforcement is pulled out of the soil layers. A horizontal shear stiffness for the gap element was used to simulate the frictional force at the interface. As the load was applied, the stick-slip behavior of the interface was examined with the behavior of GAP elements under the specified loading condition.

### 3. NUMERICAL MODELING OF PULLOUT MECHANISM

A two dimensional plane strain nonlinear model was developed to simulate the stress-strain behavior of a geotextile subjected to a pullout load (Figure 1). A large scale general purpose computer program, MSC/NASTRAN, was used to analyze the model. The above model was tested for initial pullout displacement of 40 mm. For this displacement, stress-strain relationship for soil and geotextile materials were considered to be linearly elastic. For the correct simulation of stick-slip behavior of the interface, geometric nonlinearity was incorporated in the model.

### 4. ELEMENTS AND PARAMETERS USED FOR THE MODEL

Soil: Cover material was modeled using a elastic, four node, isotropic, quadrilateral element. The following material properties were used for the quadrilateral elements:

Modulus: 100 Mpa  
Poisson's ratio: 0.3  
 $\phi$ : 32 degrees  
c: 0 (dry sand)

Interface Element: The following parameters were selected as the properties of the GAP elements.

axial stiffness: 80.E+7 N/m<sup>2</sup>  
transverse stiffness: 9.E+7 N/m<sup>2</sup>  
coefficient of static friction: 3.0  
coefficient of kinetic friction: 0.1

Reinforcement: Reinforcement was modeled with four one dimensional linear rod elements with no bending stiffness. The following parameters were selected as the properties of the rod elements.

thickness: 0.001m  
modulus: 5250 kN/m

Loading: The above model was tested for a 7 kPa normal pressure and 40 mm pullout displacement at the tension end of the geotextile. Ten iterations were used in the model to reach 40 mm forced displacement.

## 5. EXPERIMENTAL

Details of the experimental study can be found from Mallick et. al (1997). A simple pullout box was designed and pullout tests were conducted with different types of geotextiles and sands. Figure 2 shows the details of the experimental set-up. A pullout load was applied at the rate of 1 mm/min at the tension end of the geotextile. Pullout load and the corresponding front end displacement were measured during a pullout test.

## 6. RESULTS

Figure 3 shows the calculated (from finite element model) and measured load-displacement behavior at the front end of the geotextile. From the output it was observed that the calculated load response of the geotextile at different displacement levels are very close to the load measured during the experiment. Calculated loads are slightly higher than the measured loads at all displacement levels.

Figure 4 shows the calculated pullout resistance along the length of the geotextile. From the results it can be noted that the pullout resistance obtained from element number two is smaller than that obtained for element number one. This discrepancy in the output shows the need for a varying modulus input for the different sections of the geotextile. As the pullout resistance sharply increases from element 3 to element 4, nature of the load response graph shows a need for nonlinear modeling for the geotextile material close to the load application point.



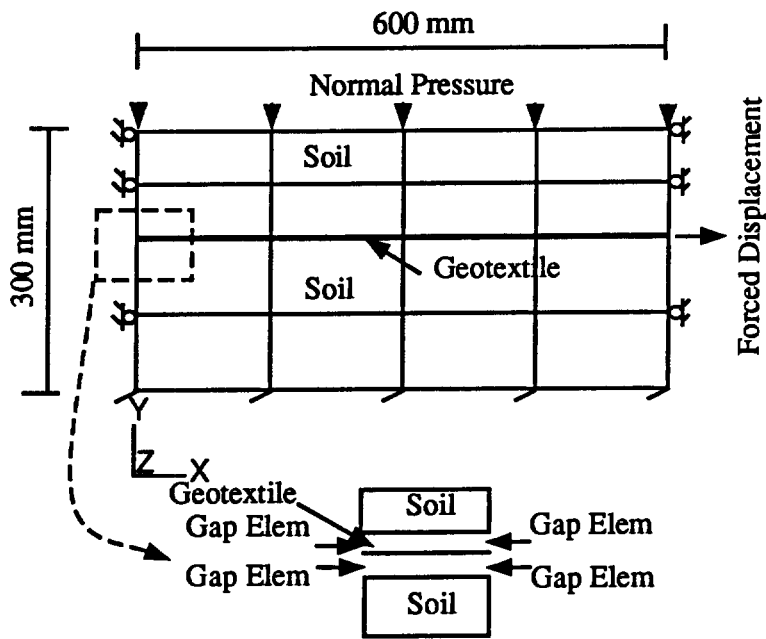


Figure 1. Finite Element Model

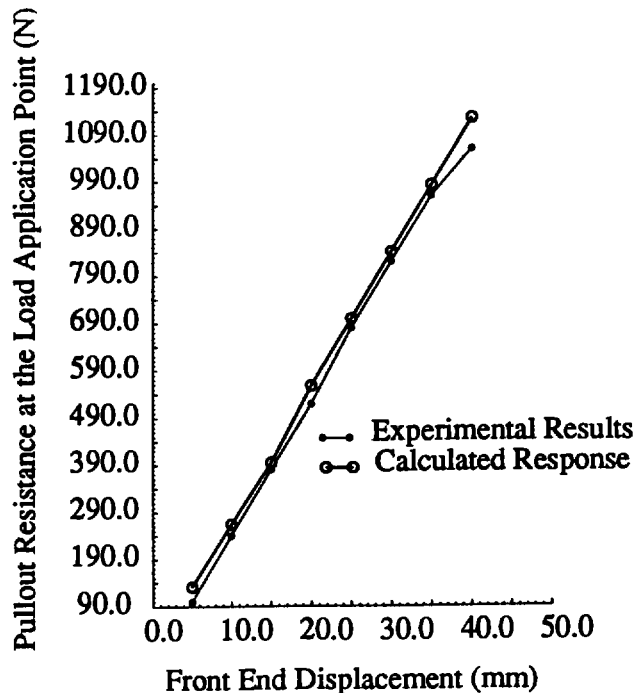
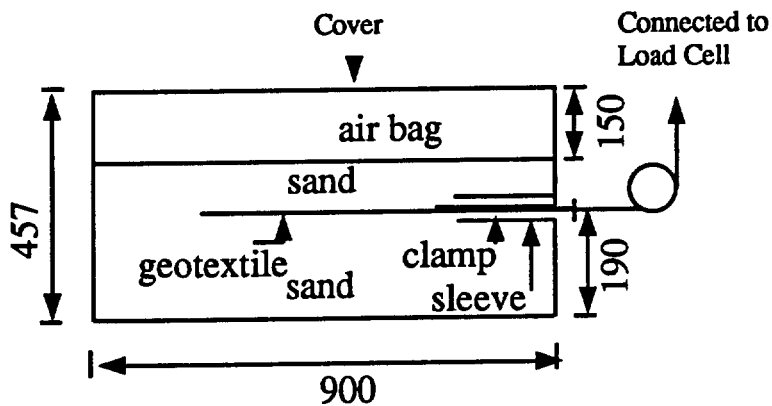


Figure 3. Calculated and Measured Load-Displacement Behavior at the Front End of Geotextile (Element No. 4)



Note: all dimensions are in mm

Figure 2. Experimental Setup

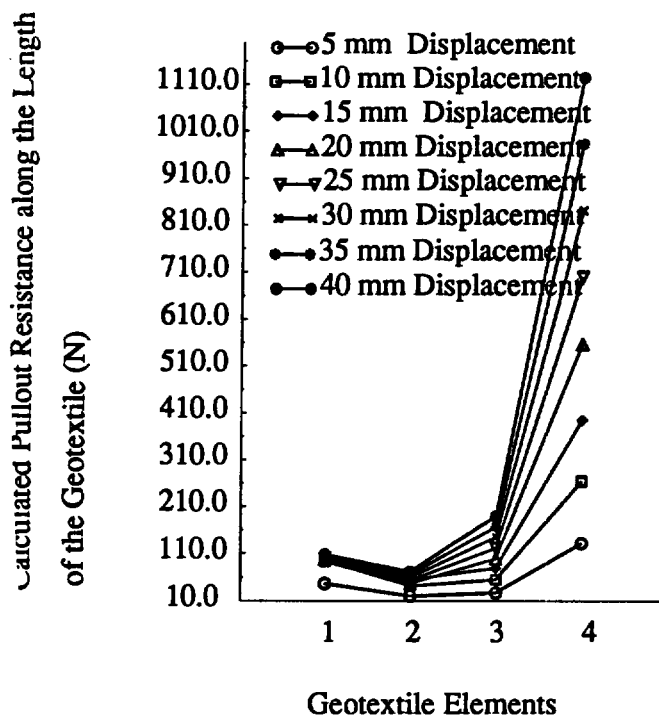


Figure 4. Calculated Pullout Resistance along the Length of Geotextile

From the force-displacement output of GAP elements it was observed that up to 15 mm displacement, all ten GAP elements were sticking to the rod elements and no slip was calculated at the interface. At 15 mm displacement, GAP elements 5 and 10 (both at the load application point) started slipping with kinetic friction. No sliding was observed from the analysis.

Analysis of Fabric Reinforced Sand", Ph.d. Dissertation, 1987, The University of Michigan, Ann Arbor.

Yogarajah, I., and Yeo, K. C., "Finite Element Modeling of Pullout Tests with Load and Strain Measurements", *Geotextiles and Geomembranes*, 13 (1994) pp 43-54

## 7. SUMMARY AND CONCLUSION

A finite element model was developed to simulate the behavior of a geotextile under pullout load. GAP or friction elements were used to simulate the contact problem at the soil-geotextile interface. Data showed that the model can accurately predict the pullout resistance developed at the front end of the geotextile. Analysis results show that the pullout resistance in the reinforcement increased sharply from element three to element four (at the load application point). This sharp increase in the load response indicate that a nonuniform stress distribution due to a nonlinear stress-strain behavior exists close to tension end of the geotextile. This particular stress-strain behavior can be modeled with localized nonlinear-elastic stress-strain relationship.

From the results of the analysis it can be concluded that, even for the small displacement of 40 mm at the front end of the geotextile, local material non-linearity should be incorporated into the model. GAP element properties should be selected with extreme caution because the performance of the model depends on the correct stick-slip behavior of the gap elements.

## 8. REFERENCES

Floss, R. and Gold, G., "Use of the FEM for the Single Reinforced Two-Layer System", *Geotextiles, Geomembranes and Related Products*, Den Hoedt (ed.), 1990, Balkema, Rotterdam, ISBN 90 61911192.

Katagiri, T., Haneda, H., Mamoru, M., Steep Reinforced Embankment Using Geogrid: Laboratory Pullout Test of Geogrid and Its Finite Element Analysis", *Geotextiles, Geomembranes and Related Products*, Den Hoedt (ed.), 1990 Balkema, Rotterdam, ISBN 90 6191 1192

Mallick, S. B., D. J. Elton., and S. Adanur. An Experimental Characterization of Soil-Woven Geotextile Interface in Large Box Pullout Tests. *Proceedings of Geosynthetics '97*, IFAI, Volume 2, page 927 -940. Wu, Cho-Sen, "Finite Element

# Influence of Grid Configuration on Interface Shear Strength Soil/Geogrid Systems

T. Zettler

Research Assistant, Department of Civil and Environmental Engineering, Syracuse University, Syracuse, New York

G. Kasturi

Research Assistant, Department of Civil and Environmental Engineering, Syracuse University, Syracuse, New York

S. K. Bhatia

Chair, Department of Civil and Environmental Engineering, Syracuse University, Syracuse, New York

A.H. Abdel-Rehman

Assistant Professor, National Research Center, English Research Institute, Pilot Laboratory, Dokki, Cairo, Egypt

R. Bakeer

Professor, Department of Civil and Environmental Engineering, Tulane University, New Orleans, Louisiana

**ABSTRACT:** Despite the increased use of geogrids in modern engineering practice, there is a lack of information on their in-situ performance. The performance of geogrids vary based on manufacturing and design conditions. Each type of geogrid has a different grid configuration or aperture sizes. To assure a sufficient design one should learn about the basic mechanism of soil/geogrid interaction and influence of their configuration on their performance. This paper presents the results of a study of the influence of grid configuration on the direct shear strength of geogrid-soil interfaces. The results demonstrate that there is an optimum configuration which offers the optimum interaction between soil/geogrid. The results of this study have been the basis of development of a new soil/geogrid interface finite element.

**KEYWORDS:** Friction, Finite Element Analysis, Geogrids, Reinforcement, Shear Strength

## 1 INTRODUCTION

Over the last two decades, inclusion of geosynthetics in soil reinforcement has greatly increased. Their material properties allow for an increased stability of foundation soils, retaining walls, and many other earth structures. Practical experience coupled with field performance has demonstrated the positive impact of geosynthetic inclusions in regard to economics and stability of the reinforced continuum.

Structures are increasingly built on difficult soils and larger and higher walls are being built; the need for reinforcement mechanisms such as geosynthetics becomes more apparent.

Inclusion of this media in design introduces a tensile strength factor to a soil mass which previously was largely only able to support compressive stresses.

Due to their ability to carry large tensile stresses, geogrids are being used more frequently especially in the design of retaining walls. However, their behavior in shear and pullout conditions is complex and still not clearly understood.

In addition to the adhesion and friction components acting on the interface surfaces of the geogrids with soil, other shear stress components can also affect the

interaction behavior of geogrids. Passive stresses due to the interlocking of soil particles along the cross ribs would definitely influence the measured resistance.

In general, the geogrids offer a three-fold advantage as a reinforcement:

1. offers tensile strength to soil;
2. offers shear resistance due to the friction between the transverse and longitudinal ribs of the grid;
3. offers additional pull-out resistance due to the bearing resistance of the soil interlocked within the grid holes.

When employing a geogrid into a design, there are two potential failure mechanisms:

1. "Bond Resistance Mechanism". The geogrid must be properly anchored into the soil. If there are no provisions made for this, the geogrid would have the potential to "slide out". Then, failure will occur above and below the soil reinforcement interface.
2. "Direct sliding". If the reinforcement interface does not have a large enough interface frictional strength, the soil either above or below the

reinforcement would have the potential to slide along the reinforcement. This occurs when the soil/reinforcement strength is less than that of the actual soil by itself.

Design of geogrids changes according to their function and manufacturing process. Each geogrid may differ in aperture size, configuration, and tensile strength. Geogrids available today have uniaxial or biaxial configurations.

Configuration of the geogrid openings plays an important role in their performance. The ratio of the open space area to the total surface area, dimensions of the openings, and orientation of the openings are some factors that would affect a geogrid performance.

In order to have optimum benefit of geogrids, the designer must have a general knowledge of the characteristics of both the "pullout" and "direct shear" capabilities of the specific geogrid. At the present time, there is little information to be found concerning these capabilities for a general type of geogrid. In addition, there is not enough information on in-situ behavior of geogrids.

To provide a step towards understanding basic understanding of soil-geogrid interaction, this research concentrated on the effects of varying the grid configuration and hole size in a series of direct shear tests while keeping the aperture ratio fairly constant. Thus, any variance seen in the shear strength capability would be a direct result of the configuration alone and is, therefore, indicative of the passive resistance during shearing. Due to time limitation, pullout resistance was not investigated.

As mentioned earlier, it would be impossible to test every possible configuration of geogrids. Currently, work is in progress to create a finite element model which would simulate the various types of soil/geosynthetic interface reactions (Abdel-Rehman 1997). The experimental data presented in this paper has been used to verify the finite element.

The results reported in this paper will be used to verify a numerical interface model and element with more applicable postulates to accurately describe the geogrid performance in a finite element analysis. Once the model has been proven, it can be used to simulate many configurations and situations.

## 2 LITERATURE REVIEW

Rowe and Fisher (1985) conducted tests concerning both the pullout and shear strength characteristics of geotextiles and geogrids. For testing purposes, a geogrid with openings representing approximately 55

percent of the gross area of the material was used. Thus, the ribs represented 45 percent of the gross area.

In shearing of geogrid/soil, Rowe and Fisher (1985) observed that "the soil adjacent to the geogrid moves relative to both the ribs of the geogrid and the soil in the openings of the ribs". In their research, "recognizing that the rib-soil interface represents approximately 45 percent of the gross area, the apparent friction angle can be determined from:

$$\tan^{-1} (0.45 \tan \phi_{\text{rib-soil}} + 0.55 \tan \phi_{\text{soil}}) \quad (1)$$

where:  $\phi$  = interface friction angle. They observed that in direct shear tests the interface friction angles were similar whether the grid was sheared in the longitudinal direction or the transverse direction ( $\phi_{\text{rib-soil}} = 31.5^\circ$ ). Also, the angle was similar to that of the soil itself ( $\phi_{\text{soil}} = 31-32^\circ$ ).

Reasoning presented for such behavior was that "in direct shear, the entire rib-soil interface and soil-soil interface between ribs is mobilized and hence the apparent friction angle is close to that of the soil". The work by Rowe and Fisher was one of the first to focus on geogrid/soil interaction. However, they did not focus on different configurations of the geogrid. Bergado et al. (1993) also conducted research on geogrid/soil interaction. With geogrids, "the direct shear interaction mode is controlled not only by the friction between the soil and the grid surface but also by the friction of the soil itself" (Bergado et al. 1993). The resistance due to direct shear has two components including the shear resistance between the soil and the reinforcement-plane surface area, and the soil-to-soil shear resistance at the grid opening (Jewell et al. 1984). Jewell et al (1984) and Bergado et al. (1993) also provided understanding on the interaction of soil/geogrids mechanics during shearing. The direct shear resistance can be quantified as:

$$P_s = \sigma_n A [\alpha_{ds} \tan(\delta + (1 - \alpha_{ds}) \tan \phi_{ds})] \quad (2)$$

where:  $\phi_{ds}$  = friction angle of soil in direct shear;  $\delta$  = skin-friction angle between soil and reinforcement shear surface;  $\alpha_{ds}$  = ratio between reinforcement shear area and total shear area;  $\sigma_n$  = normal stress at the shear plane; and A = total shear area.

From this research, Bergado et al. concluded that depending on the apertures of the grid, the shear resistance between the grid and soil can be equal to or larger than the shear resistance of the soil itself (1993).

This added resistance would come from the passive resistance created along the rib interface.

### 3 SCOPE OF RESEARCH

#### 3.1 Test Apparatus

The device used for direct shear testing was built specifically to test the interface properties of geosynthetics, including geogrids. The equipment consists of a computer, a control panel, and a split shear box. The machine is fully automated and computer controlled and built according to ASTM D5321 standards for direct shear testing.

The control panel is used to operate the split shear box. It displays the normal load being applied by a set of pneumatic pistons located below the shear box. It also displays the horizontal and vertical displacements occurring during the testing. LVDTs are placed in contact with the upper shear box for horizontal displacement measurement and in contact with the loading yoke for vertical displacement measurement. The control panel also controls the rate of shear displacement via a worm gear connected to the lower box.

The split shear box consists of top and bottom parts. The top part, which remains stationary at all times, has the dimensions of 30.5 by 30.5 by 5.1 cm. The bottom part, which is displaced, has dimensions of 40.6 by 30.5 by 5.1 cm. The bottom part is longer than the top part to allow for a larger displacement area. The top and bottom parts are slightly separated to eliminate added friction.

#### 3.2 Soil Properties

Soil used for the testing is a mostly fine grained sand. Properties are as follows:  $C_u = 0.45$ ;  $C_c = 1.23$ ;  $d_{10} = 0.52$  mm;  $d_{40} = 0.29$  mm;  $d_{60} = 0.15$  mm;  $\phi_{soil} = 32.3^\circ$ .

#### 3.3 Geogrid Configurations

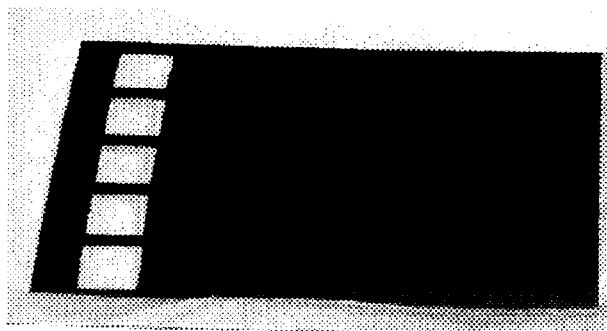
Simulated geogrid sheets were using in the tests. The geogrids are made from samples of high density polyethylene (HDPE) solid sheets (geomembrane). The HDPE is a 60 mil. HDPE sheets were cut to the dimensions of 33 by 47 cm. The different geogrid patterns are then designed and cut into the sheet

Nine patterns were tested. The patterns were determined such that constant opening areas are maintained as much as possible. In doing so, any differences in the results among the different configurations would be a result of additional passive stresses of the new configuration.

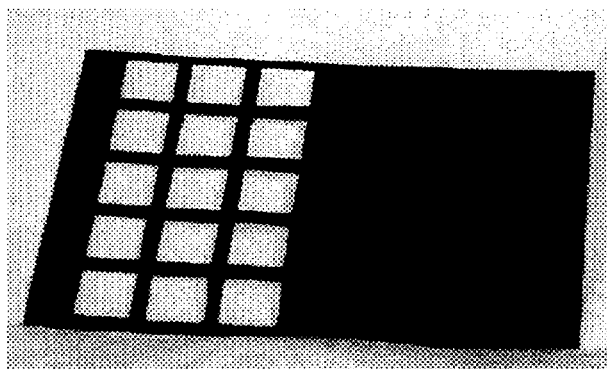
Each hole, independent of the pattern, was cut to be 25 cm<sup>2</sup>. Three different holes sizes are used: Series A (5 by 5 cm), Series B (2.5 by 10 cm), and Series C (4

by 6.4 cm). Each sample of a particular hole size has an increasing number of rows of holes.

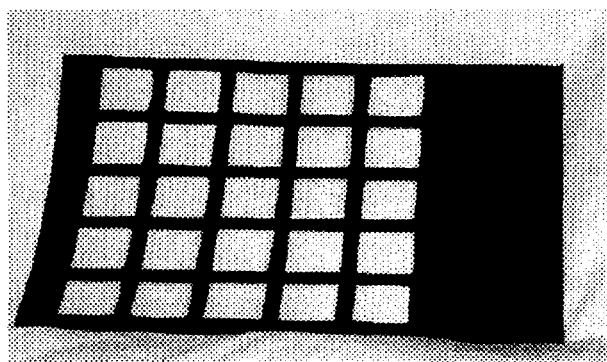
The nine samples were as follows: 5 by 5 cm holes with 1, 3, and 5 rows (Figure 1); 2.5 by 10 cm holes with 1, 2, and 3 rows oriented longitudinally; and 4 by 6.4 cm holes with 2, 4, and 6 rows oriented transversely.



Pattern 1



Pattern 2



Pattern 3

Figure 1. Typical configuration of geogrids (Series A).

### 4 TESTING PROGRAM

Several tests were performed to ensure the repeatability of the tests. For the geogrids/soil tests the bottom part of the direct shear machine was filled

with sand and tamped by hand for compaction. The geogrid was secured to the bottom part of the machine. Only the end of the geogrid being pulled (closest to the control panel) was securely clamped. This is done to limit stretching of the sample. The opposite end is left free. The top part is then placed on top and filled with sand. Again the sand is tamped by hand. The top part is slightly raised after the addition of the sand to eliminate added friction between the two metal surfaces of the top and bottom parts of the direct shear machine. The loading apparatus is then added to apply the normal load.

Tests were conducted in the dry state. Each test was run at a normal load of 69.64 kPa, representing an average normal stress.

During shearing, the bottom part of the machine is pulled at a displacement rate of one mm/min. Total testing time was approximately one hour with the data acquisition recording performance every minute.

Several experiments were conducted on a pure sheet of HDPE geomembrane (60 mil) to provide a reference for tests on the geogrids. The interface friction angle of the HDPE geomembrane with the same sand used in the rest of the testing was measured to be  $\delta_{\text{nb soil}} = 23.5^\circ$ .

Each geogrid is tested at least three times while attempting to keep all conditions the same. Figure 2 shows the full set of results of three tests under the same conditions. The subsequent figures represent average values of three identical tests.

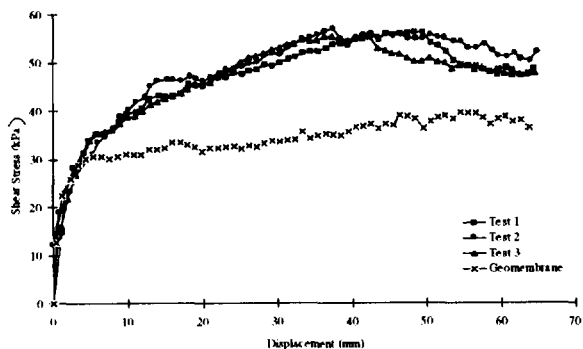


Figure 2. Shear stress vs. displacement (5 by 5 cm holes and 5 rows) (See Figure 1).

As can be seen in Figure 2, results of the three tests are fairly consistent. The slight variations can be attributed to minor differences in normal loading application or set up of the test. For example, the degree of compaction may vary since it is performed manually.

## 5 TEST RESULTS

The results are presented in Figures 3, 4, and 5, and in these figures each curve represents an average of three tests. Results for the geomembrane are also the average of three tests.

### 5.1 Geogrid Sample A: 5 by 5 cm Holes

As can be seen below, the holes in the geogrid provided an added component of resistance over the geomembrane (Figure 3). However, it is not until five rows of squares in the geogrid are used that a substantial increase is evident. There is a slight increase in resistance on the membrane for geogrids with one and three holes. The first two patterns did not show a peak in shear strength. This could be due to the thin width of the grid between holes which may have resulted in some stretching during the testing.

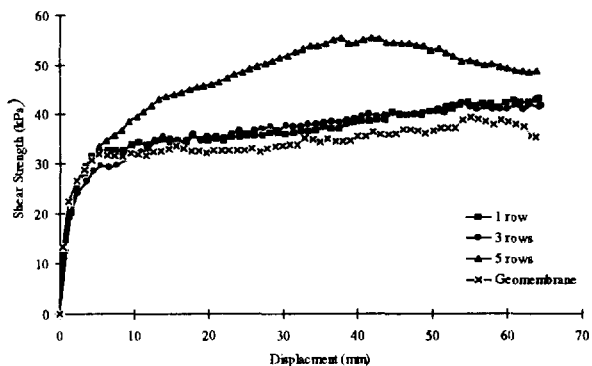


Figure 3. Results of sample A: shear stress vs. displacement (See Figure 1).

### 5.2 Geogrid Sample B: 2.5 by 10 cm Holes

For this sample, there was a steady increase in the added component of resistance over the geomembrane (Figure 4). However, in all geogrids with one row, there was no real added resistance. It should be noted that as the shearing continued the patterns showed a distinct peak and increase in resilience, however, the residual shear strength for both were very similar. The third pattern with five rows of holes reached and maintained a much larger shear resistance over the membrane.

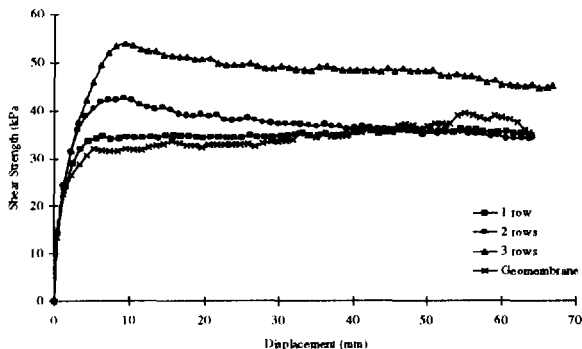


Figure 4. Results of sample B: shear stress vs. displacement.

### 5.3 Geogrid Sample C: 4 by 6.4 cm Holes

This test showed similar results as for Sample B. However, shear resistance was slightly larger than for Sample B.

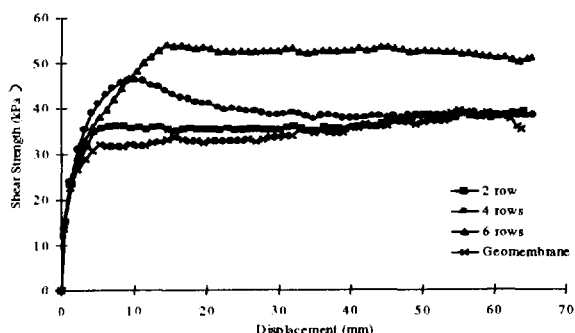


Figure 5. Results of sample C: shear stress vs. displacement.

## 6 DISCUSSION

All samples (A, B, and C) were prepared such that the aperture ratio stayed approximately similar for the different patterns (Table 1). The aperture ratio is the ratio of the area of the holes to the total area of the sample before cutting.

For the first test of each series (aperture ratio in the range of 8 to 13 percent), there is no noticeable amount of added resistance.

For Series B and C, there is some added resistance as the ratio increased to approximately 25 percent. However, in Series A there was not much of an advantage to increasing the aperture ratio to 25 percent.

Once the ratio increased to 40 percent, there is a significant resistance added by the grid.

The results given in Table 1 demonstrate that the configuration of the grid does have an effect on the shear resistance of the continuum.

Table 1. Calculated Data for the various grid configurations.

Series	Pattern	Aperture Ratio	$\delta_{\text{measured}}^*$	$\delta_{\text{measured}}^{**}$
"A" 5 by 5 cm holes	1 row	8%	24.3	31.7
	3 rows	24%	25.7	31.4
	5 rows	40%	27.2	38.6
"B" 2.5 by 10 cm holes	1 row	13%	24.7	27.3
	2 rows	26%	25.9	31.5
	3 rows	39%	27.1	37.5
"C" 4 by 6.4 cm holes	2 rows	13%	24.7	29.2
	4 rows	23%	25.7	33.6
	6 rows	34%	26.7	37.8

Notes: \*See equation (1). \*\*See equation (3).

Values for the "apparent" friction angle ( $\delta$ ) were determined using the equation provided by Rowe and Fisher (1985) and given in Table 1. To determine the "measured" friction angle from the test results, the maximum shear stress was obtained for each configuration, assuming cohesion equal to zero:

$$\delta_{\text{measured}} = \tan^{-1} (\tau_{\text{max}} / \sigma) \quad (3)$$

where:  $\sigma$  = normal stress.

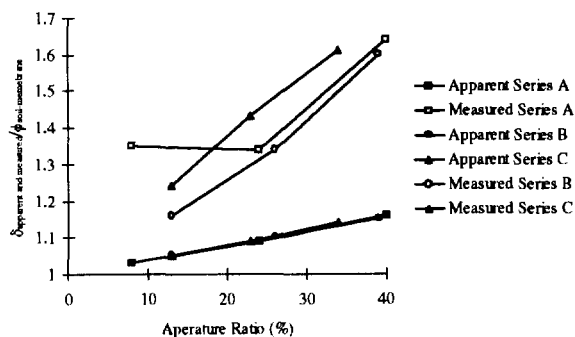


Figure 6. Apparent versus measured friction angles.

Figure 6 shows that the apparent friction angle was always less than the measured friction angle (calculated using equations 1 and 3 respectively). At times, these values may even exceed the interface friction angle of the soil alone. This can be attributed to many factors.

After conducting a test, it was often observed that the sand particles have moved up and long the surfaces of the ribs. This may cause the friction angle

to increase as it would if the membrane were textured in that area.

Also, it was noted that the sand had to move up and then along the ribs before the shearing could occur. This created an almost wave-like pattern on the membrane which offered an extra resistance surface. As the number of holes in a pattern increases, the resistance magnifies creating the large measured friction angle.

It was also observed that holes near the edge of the pattern did not contribute as much resistance as did the holes in the center. Thus, when patterns were tested with holes only in the center there is a large increase in measured resistance. To verify this, a pattern was cut in which one row of square holes (50 by 50 cm) was placed only in the center of the grid (see results in Figure 7).

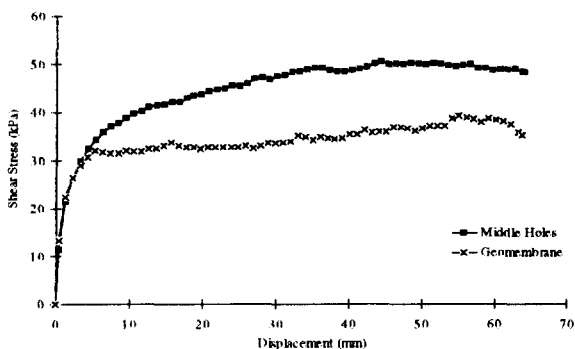


Figure 7. Testing with one row of squares in center of grid: shear stress versus displacement.

As can be seen when comparing results of Figures 3 and 7, the maximum resistance obtained was greater when the holes were in the center. This indicates that more resistance is generated by the center holes.

In the case of Series A (Figure 1), the ribs between the holes were relatively thin. Some stretching or twisting may have occurred during shearing. This may explain the lack of a defined peak shear strength in the first two patterns in the series (Figure 3). Because of the lack of a definite peak value, it is difficult to evaluate the measured friction angle accurately.

This being the case, it appears that Series C offered the most benefit, since the apparent friction angles versus measured are the most similar.

This research provides a basic study on the mechanisms of geogrids/soil. The results are being used by Tulane University to test and verify a finite element model being developed (Abdel-Rehman, 1997). In order to develop such a model, basic test results such as this one are necessary for verification. Ongoing research is being conducted in this field by

the two universities involved in this research. It is promising that the model will allow for even more definite results of a most suitable configuration of geogrid based on actual design criteria.

## 7 CONCLUSION

The results presented show that grid patterns, location, and aperture ratio significantly influence interface frictional resistance. The following general conclusions can be determined:

1. Grid configuration plays a vital role on the shear strength capability of a geogrid. Certain configurations provide larger amounts of passive resistance over other patterns.
2. The results of this study has been used as a basis of a finite element program being developed for modeling soil-structures reinforced with geosynthetics.

## ACKNOWLEDGMENTS

The writers would like to thank those individuals who helped with this research. Especially, we would like to thank Ms. Kristen Refkofsky for the many hours spent on testing geogrids.

## REFERENCES

- Abdel-Rehman, A. (1997) "Modeling of Soil/Geosynthetic Interaction in Reinforced Earth Works", *Ph.D. Dissertation*, Civil Engineering, Tulane University.
- Alfaro, M.C., Hayashi, S., Miura, N. and Watanabe, K. (1995) "Pullout Interaction Mechanism of Geogrid Strip Reinforcement", *Geosynthetics International*, Vol. 2, No. 4, pp. 679-698.
- Bergado, D.T., Chai, J.C., Abiera, H.O., Alfaro, M.C. and Balasubramaniam, A.S. (1993) "Interaction between Cohesive-Frictional Soil and Various Grid Reinforcements", *Geotextiles and Geomembranes*, Vol. 12, pp. 327-349.
- Jewell, R.A., Milligan, G.W.E., Sarsby, R.W. and Dubois, D. (1984) "Interaction between Soil and Geogrids", *Proceedings of Symposium on Polymer Grid Reinforcement*, Thomas Telford Ltd., London, pp. 18-19.
- Rowe, R.K., and Fisher, D.G. (1985) "Determination of Soil-Geotextile Interface Strength Properties", *2<sup>nd</sup> Canadian Symposium on Geotextiles and Geomembranes*.



# Soil Interaction Characteristics of Geotextiles and Geogrids

M. Koutsourais  
Regional Manager, TC Mirafi, USA

D. Sandri  
Senior Engineer, TC Mirafi, USA

R. Swan  
GeoSyntec Consultants, USA

**ABSTRACT:** Geosynthetic design in soil reinforcement applications require that the soil interaction characteristics of the reinforcement product be evaluated. The soil interaction characteristics are determined by performing direct shear and pullout tests under a specific soil condition and range of normal pressures. Polymeric reinforcement products used in soil reinforcement applications consist of geotextiles and geogrids which vary in texture, flexibility and open area. This paper presents soil interaction data of geotextiles and geogrids in both cohesionless and cohesive soil types. The data is used to compare soil interaction properties for various geosynthetic reinforcement products in both cohesionless and cohesive soils. Results indicate that geogrids and geotextiles offer similar soil interaction values. Interaction coefficients range from 0.9 to 1.0 in sands and from 0.6 to 0.9 in clays depending on geosynthetic surface texture, stiffness and applied normal stress.

**KEYWORDS:** Friction, Geogrids, Geotextiles, Pull-out resistance, Pull-out test, Reinforcement, Shear strength, Woven fabrics

## 1 INTRODUCTION

Geogrids and geotextiles are often used to construct reinforced retaining walls, steepened slopes, embankments on soft foundations, vertical landfill expansions, and soil veneer covers of landfills. However, a generally accepted but incorrect belief exists among Civil engineering professionals that geogrids interact or interlock with the soil being reinforced better than do geotextiles such as woven polyester fabrics. As a result, geogrids are often chosen over equally well-suited geotextiles. In order to curtail such mis-selection of materials and encourage accurate selection of design parameters, the interaction between the soil and the geosynthetic reinforcement must be evaluated.

Today, soil reinforced structures are designed with a variety of geosynthetics and soil types. The soil interaction characteristics between various geosynthetics and fine grained (clay) soils becomes increasingly important as more and more reinforced soil structures are designed with marginal (cohesive) fill materials and various types of geotextiles and geogrids. As a result, quantifying the soil interaction characteristics between these materials and developing design values for various soil and geosynthetic combinations is essential.

In keeping with current state-of-practice design references (AASHTO (1992), Christopher et. al. (1990), Simac (1993)), minimum anchorage lengths ( $L_a$ ) may vary from 0.3 to 1 meter (1 to 3 ft). The actual required embedment length is a function of the amount of effective overburden (i.e. depth of reinforcement), soil type above and below the

geosynthetic, and the interaction properties between the soil and geosynthetic.

Many researchers (Batt (1991), Cowell (1993) Geoservices (1990), Ingold (1983), Jewell (1980), Juran (1988), Koerner (1986), O'Dowda (1987), Palmeira (1990), Rowe (1985), Swan (1987)) have investigated the soil interaction characteristics between geosynthetics and sand. Cowell and Sprague (1993) presents a comparative study of pullout data and soil interaction values between woven polyester geogrids and high-strength, high-modulus polyester geotextiles in a uniform fine sand. The results presented by Cowell and Sprague (1993) and of previously published research show that geogrids and geotextiles provide similar soil interaction coefficients in sand between 0.90 and 1.0.

To supplement the research documented by Cowell and Sprague (1993) and others, direct shear testing of various high-strength polyester and polypropylene geotextiles in sand was conducted as well as both direct shear and pullout testing of polyester geogrids and high-strength polyester and polypropylene geotextiles in a lean clay. The data can be used to compare the results obtained by direct shear and pullout testing for determination of the coefficient of interaction. The data can also be used to compare the soil interaction properties of various geosynthetic reinforcement products and to develop recommended design soil interaction properties in different soil conditions.

## 2 TESTING CONCEPTS, AND TYPICAL RESULTS

### 2.1 Purpose

The direct shear and pullout tests measure the total resistance to sliding and pullout of a geosynthetic with a soil substratum and superstratum. Total sliding and pullout resistance may be a combination of sliding, rolling, interlocking of soil particles and geosynthetic surfaces, and shear strain within the geosynthetic specimen. The data developed can be used in the design of geosynthetic-reinforced retaining walls, steepened slopes, and embankments constructed on weak foundation soils. The data is also useful for applications in which the geosynthetic is subject to sliding such as applications which require the geosynthetic to be placed on a slope and for determination of geosynthetic overlap requirements.

The interaction developed between the soil and the geosynthetic is determined by performing direct shear and pullout tests under various soil types and a range of normal pressures. The data obtained is used to determine the coefficient of shear-stress-interaction,  $C_i$ , which measures a reinforcement product's efficiency in transferring stresses from adjacent soil particles to the geosynthetic reinforcement. The coefficients are simply the percentage of the internal shear strength of the soil that can be mobilized at the soil/geosynthetic interface as shown by equation (1).

$$C_i = \tau_i / \tau_s = (c_a + \sigma_n \tan \delta) / (c + \sigma_n \tan \phi) \quad (1)$$

where:

- $\tau_i$  = shear stress at interface
- $\tau_s$  = shear stress of soil
- $\delta$  = interface friction angle
- $\phi$  = internal friction angle of soil
- $c_a$  = interface adhesion
- $c$  = soil cohesion
- $\sigma_n$  = normal soil pressure

The coefficient of interaction is used in reinforced soil structure design to determine required reinforcement embedment lengths beyond the anticipated failure plane to prevent pullout of the reinforcement. A commonly accepted method of calculating this embedment length beyond the failure plane,  $l_a$ , is indicated by equation (2).

$$l_a = (P \times FS_{po}) / (2 C_i (c + \sigma_n \tan \phi)) \quad (2)$$

where:

- $P$  = Pullout force per unit length of reinforcement
- $FS_{po}$  = Design factor-of-safety with respect to pullout

The coefficient of soil and geosynthetic interaction can be expressed only in terms of the soil used in testing and is a function of the applied normal stress, soil gradation,

plasticity, in-place density, and moisture content, as well as the unique physical and mechanical characteristics of the geosynthetic. However, it is useful for design guidance to be able to characterize  $C_i$  values by geosynthetic and soil "type".

### 2.2 Direct Shear

The direct shear test used to determine the shear resistance of a soil/geosynthetic combination is ASTM D5321-92, "Standard Test Method for Determining the Coefficient of Soil and Geosynthetic or Geosynthetic and Geosynthetic Friction by the Direct Shear Method". The coefficient of friction between a geosynthetic and soil is determined by placing the geosynthetic and one or more contact surfaces, such as soil, within a direct shear box. A constant normal stress is applied and a tangential (shear) load is imposed on the apparatus such that one section of the box moves in relation to the other. Shear loading is applied via a 10 cm/min (0.04 in/min) constant rate device capable of measuring load.

The shear force is recorded as a function of the horizontal displacement of the moving section of the shear box. The test is performed for a minimum of three different normal stresses. The peak and/or residual shear stress is plotted against the applied normal stresses with the test data represented by a "best fit" straight line whose slope is the coefficient of friction between the two materials where the shearing occurred. The y-intercept of the straight line provides the 'adhesion' as measured by the test.

### 2.3 Pullout

The general test method used to determine the pullout resistance of a geosynthetic in soil is GRI GG-5/GT-6 - "Geogrid/Geotextile Pullout". The pullout test is performed by compacting soil in the lower half of the pullout box with subsequent placement of the geosynthetic specimen on top of the compacted soil and attached to a loading harness. The soil is then compacted in the upper half of the pullout box. The specific normal stress is applied to the upper layer of compacted soil through the use of a rigid loading platen and dead weight for the normal stress or through the use of an air bladder loading system. After application of the normal stress, the pullout specimen is immediately subjected to a 10 cm/min (0.04 inch/minute) constant rate of extension "pullout" force. Pullout displacement continues until a constant or decreasing load is recorded or the geosynthetic sample fails in rupture. Tests which fail in rupture would require re-doing at lower normal stresses in order to induce slippage and hence measurement of resistance to sliding.

The pullout force is recorded as a function of the horizontal displacement of the pullout specimen. The test is performed for a minimum of two different normal stresses. The peak pullout force is plotted against the applied normal stresses used for testing. The coefficient of interaction,  $C_i$ ,

is back-calculated using equation 3.

$$C_i = (P)/(2 I_a (c + \sigma_n \tan \phi)) \quad (3)$$

### 3 TEST PROGRAM

#### 3.1 Geosynthetic Types

The reinforcement products chosen for this research consist of a woven polypropylene geotextile (W, PP, GT), woven polyester geotextiles (W, PET, GT) and polyester geogrids (W, PET, GG). Table 1 summarizes the geosynthetic types investigated.

Table 1. Summary of Geosynthetic Materials Investigated

P r o d	Type <sup>1</sup>	Weight, g/m <sup>2</sup> (osy)	Ultimate strength, kN/m (lbs/ft)	Weave
A	W, PP, GT	420 (12)	70 (4800)	twill
B	W, PET, GT	440 (13)	105 (7200)	plain
C	W, PET, GT	680 (20)	200 (13800)	twill
D	W, PET, GT	950 (28)	300 (20580)	basket
E	W, PET, GG	186 (5.5)	39 (2700)	knitted
F	W, PET, GG	390 (12)	109 (7460)	knitted

<sup>1</sup>W = woven, PET = polyester, PP = polypropylene, GT = geotextile, GG = geogrid

The products were chosen based on their different structure, weave pattern and polymer type. This range of products also compliments the matrix of products tested and presented by Cowell and Sprague (1993). They ranged in ultimate tensile strength from 73 kN/m (5000 lbs/ft) to 364 kN/m (25000 lbs/ft).

The woven polypropylene geotextile evaluated in the program is characterized as being relatively stiff, having a rough surface texture and exhibiting a low percent open area (<30%). The woven polyester geotextiles evaluated are characterized as being flexible, having a smooth surface texture and exhibiting a low percent open area. The coated polyester geogrids evaluated are characterized as being flexible with a high percent open area (>30%). The samples tested cover a range of weights, tensile strengths and weave patterns as noted in Table 1 for detailed evaluation and comparison.

#### 3.2 Soil Types

The two soil types tested in conjunction with the geosynthetic products referenced above include a uniform fine sand (SP) and a lean clay with sand (CL). Figure 5 illustrates the gradations of the two soil types.

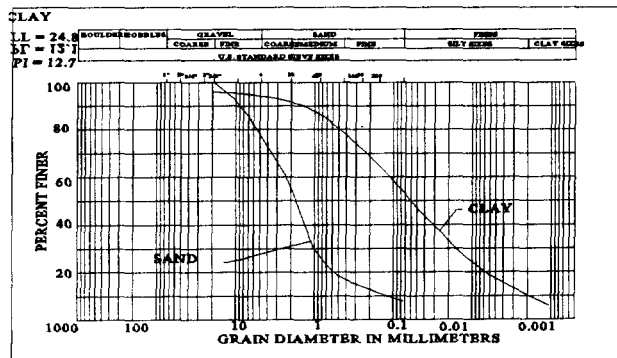


Figure 5. Soil Gradation Curves

#### 3.3 As-tested soil properties

A modified proctor was performed on the sand in accordance with ASTM D1557. The maximum dry density was determined to be approximately 18.4 N/m<sup>3</sup> (117 pcf) at an optimum moisture content of 8.8%. Post test evaluations indicated an average 94% of maximum dry density at an average moisture content of 17.4% had been achieved.

The clay soil used for direct shear and pullout testing had a liquid limit (LL) = 24.8; plastic limit (PL) = 12.1; plasticity index (PI) = 12.7; maximum dry unit weight of 18.6 N/m<sup>3</sup> (118.5 pcf); and optimum moisture content of 12.5%. The clay was moisture conditioned for compaction to 95% of the maximum dry unit weight and 1% dry of the optimum moisture content based on ASTM D698.

#### 3.4 Matrix of Test Conditions

Tables 2 and 3 summarize the program matrix and conditions for direct shear and pullout testing, respectively. All direct shear samples were 30.5 cm wide by 30.5 cm long.

Samples used in pullout testing are noted below. Pullout samples had dimensions of 45.7 (wide) by 91.5 (long) cm. An exception to the above was in test number 1 where the sample was 46.5 cm by 92.7 cm.

**Table 2. Summary of Direct Shear Test Conditions**

Test no.	Soil type	P r	Initial soil conditions <sup>1</sup>		Normal stress (Pa)
			$\gamma_d$ , kN/m <sup>3</sup>	$\omega$ , (%)	
1	Sand	A	17.2	17.4	34, 69, 103
2	Sand	B	17.2	17.4	34, 69, 103
3	Sand	C	17.2	17.4	34, 69, 103
4	Clay	A	17.5	11.5	14, 28, 55
5	Clay	B	17.5	11.5	14, 28, 55
6	Clay	D	17.5	11.5	14, 28, 55
7	Clay	E	17.5	11.5	14, 28, 55
8	Clay	F	17.5	11.5	14, 28, 55

<sup>1</sup>  $\gamma_d$  = Dry unit weight,  $\omega$  = water content

**Table 3. Summary of Pullout Test Conditions**

Test no.	Soil type	P r	Initial soil conditions <sup>1</sup>		Normal stress (Pa)
			$\gamma_d$ , kN/m <sup>3</sup>	$\omega$ (%)	
1	Clay	A	117.5	11.5	14, 28
2	Clay	B	117.5	11.5	14, 28, 55
3	Clay	C	117.5	11.5	28, 55
4	Clay	D	117.5	11.7	7, 14
5	Clay	E	117.5	11.4	28, 55

<sup>1</sup>  $\gamma_d$  = Dry unit weight,  $\omega$  = water content

## 4 RESULTS

A summary of the direct shear results in sand (TRI, 1995) is shown in Table 4. Soil interaction coefficients via direct shear testing range between 0.92 and 1.0.

A summary of the direct shear and pullout test results in clay (GeoSyntec, 1996) are shown in Tables 5 and 6, respectively.

The soil interaction coefficients for the flexible polyester geotextiles and geogrids range from 0.71 to 0.93 in direct shear and from 0.82 to 0.91 in pullout under the full range of normal stresses tested. The soil interaction coefficients for the woven polypropylene geotextile range from 0.58 to 0.64 in direct shear and 0.66 to 0.71 in pullout.

**Table 4. Summary of direct shear results in sand - peak sliding resistance (N/m<sup>2</sup>) vs normal stress**

Test No.	Soil	P r	Normal Stress, Pa			Friction angle, $\delta$	C <sub>i</sub>
			34	69	103		
	C/S <sup>1</sup>	-	26	44	65	32 °	-----
1	Sand	A	25	44	61	30 °	0.9
2	Sand	B	38	65	92	32 °	1.0
3	Sand	C	35	55	78	32 °	1.0

<sup>1</sup> C/S = Control Sand

### 4.1 Interpretation of results

The results demonstrate that direct shear and pullout testing in sand will yield similar soil interaction coefficients for all geosynthetic types tested. These values are typically in excess of 0.90 and provide good agreement with results of pullout testing presented by Cowell and Sprague (1993) on similar products.

Similar results which demonstrate high sand-geosynthetic action values are abundant in the literature. No significant correlation appears to exist between percent open area, reinforcement geosynthetic texture, its stiffness or other such properties. All reinforcement geosynthetics seem to do well in sand.

Results of direct shear testing in clay provide interaction values ranging from 0.71 to 0.93 for polyester products and somewhat lower values of 0.58 to 0.64 for polypropylene product A. The results demonstrate a lack of correlation between interaction behavior and percent open area or geosynthetic structure. However, the data suggests superior polyester performance when compared to polypropylene. In fact, the high-strength polyester geotextiles provide interface shear strengths as great as the internal shear strength of the soil itself. Further, the peak interface shear strengths were all mobilized at approximately the same displacement (5 cm) as was the peak strength of the soil itself. Good compatibility exists between each geosynthetic type and sand.

In general, the results of pullout testing in clay are in agreement with those noted above for direct shear testing in clay.

Compared to direct shear results, pullout testing provides approximately 13% to 17% higher soil interaction values at low normal stresses of less than 20 Pa (< 4 psi) and essentially the same soil interaction values at higher normal stresses (>28 Pa (4 psi)).

The flexible polyester geosynthetics provide approximately 25% higher soil interaction values when compared to the stiff woven polypropylene geotextile. The

woven polyester geotextiles provide similar soil interaction values when compared to the geogrids.

Observations from the test results indicate that the percent open area of the geosynthetic has negligible, if any, influence on the soil interaction coefficients in clay. However, the surface texture and stiffness or rigidity of the geosynthetic has a significant effect on the soil interaction within clay. The geotextile weave pattern has negligible, if any, effect on the soil interaction characteristics of the geotextile.

## 5 DESIGN RECOMMENDATIONS

Table 7 provides soil interaction coefficients for use in conservative design of reinforced soil structures. Values are subject to verification testing during construction.

The results provided herein and found in the literature suggest that relatively high interaction values can be confidently employed with all reinforcement geosynthetics irrespective of texture, percent open area or polymer type. An interaction coefficient in sand of 0.9 is recommended.

Greater variability is observed in interaction testing in clay. Test results incorporating polyester reinforcement geosynthetics range from 0.7 to 0.9+. Therefore, a

conservative guidance value of 0.7 appears to be reasonable.

A slightly lower design interaction value of 0.6 is recommended for polypropylene products used in clay.

Design values recommended above range from 0.6 to 0.9 with values used for critical structures being verified by actual soil-geosynthetic testing during construction. However, it is also recommended that validation testing during construction be required on a selective basis with great consideration for its true impact on design. A parametric study of most reinforcement applications will demonstrate that the greatest factor affecting required embedment length is normal stress (i.e. reinforcement depth), not  $C_i$ . In practice, its affect on structure design and performance is only significant in the upper portions of reinforced soil structures. In fact, once below a depth of about 1 m (3 ft), the embedment length of most commonly marketed reinforcement geosynthetics is governed by minimum embedment length criteria rather than  $C_i$  or pullout.

Recognizing the true impact of soil-geosynthetic interaction for each design scenario will guide the designer in evaluating whether to use the above recommended values or require testing during construction.

Table 5. Summary of Direct Shear Results in Clay - Peak Sliding Resistance ( $N/m^2$ ) vs. Normal Stress (psi)

Test No.	Soil	Product	Normal Stress, Pa			Adhesion, $c_a$ ( $N/m^2$ )	Friction Angle, $\delta$	$C_i$
			14	28	55			
	Control Clay	---	16.5	28.2	49.6	6211	38	-----
4	Clay	A	9.6	17.2	31.7	1911	28	0.58 - 0.64
5	Clay	B	11.7	22.0	44.1	477	38	0.71 - 0.89
6	Clay	D	13.1	24.1	46.2	1911	39	0.79 - 0.93
7	Clay	E	13.1	22.7	43.4	2388	37	0.79 - 0.88
8	Clay	F	13.8	23.4	44.6	3822	36	0.83 - 0.89

Table 6. Summary of Pullout Test Results - Ultimate Pullout Capacity ( $N/m$ ) vs. Normal Stress

Test No.	Soil Type	Product	Normal Stress, Pa				$C_i$
			7	14	28	55	
1	Clay	A		20,030	36,400		0.66 - 0.71
2	Clay	B		25,500	45,500		0.82 - 0.91
3	Clay	D			45,500	80,200	0.88 - 0.90
4	Clay	E	17,800	27,400			0.83 - 0.89
5	Clay	F			44,600	78,700	0.87

**Table 7. Recommended Design Soil Interaction Coefficients**

Product	Sand	Clay	
		PET	PP
Rough textured, stiff PP GT	0.9	--	0.6-0.7
Smooth textured, flexible PET GT and GG	0.9-1.0	0.7-0.9	--
Recommended value	0.9	0.7	0.6

**REFERENCES**

AASHTO Interim Specifications (1992), "Standard Specification for Highway Bridges", Fourteenth Edition, 1989 as amended by the Interim Specification.

ASTM (1996), "Standard Test Method for Determining the Coefficient of Soil and Geosynthetic or Geosynthetic and Geosynthetic Friction by the Direct Shear Method", Volume 04.09.

ASTM, Draft Standard Test Method D 35.01.87.02, "Measuring geosynthetic Pullout Resistance in Soil".

Batt, D. and Bowers, M. (1990), "Preliminary Report of Pullout Testing of Miragrid 5T in Sand in the University of Cincinnati Pullout Box", May.

Christopher, B.R., Safdar, A.G., Giroud, J.P., Juran, I., Mitchell, J.K., Schlosser, F., and Dunncliff, J., (1990), Reinforced Soil Structures, Volume I. Design and Construction Guidelines, FHWA-RD-89-043, November.

Cowell, M.J. and Sprague, C.J. (1993), "Comparison of Pull-Out Performance of Geogrids and Geotextiles", Geosynthetics, '93 Conference, Vancouver, BC, Canada, pp. 579-592.

GeoServices, Consulting Engineers, Inc. (1990), "Pullout and Interface Direct Shear Testing of Miragrid 7T Geogrid and Perini Project Number 126", May, Norcross, GA.

GeoServices Consulting Engineers, Inc. (1990), "Pullout Testing of Selected Mirafi Geogrids", GeoServices Project No. P1268, April, Norcross, GA.

GeoSyntec Consultants, Inc. (1996), "Nicolon/Mirafi Geogrid and Geotextile Direct Shear and Pullout Testing within Compacted Clay Soil", Draft Report No. GLI3839.

Geosynthetic Research Institute (1991), "Test Method for Geogrid Pullout", GG5.

Geosynthetic Research Institute (1992), "Test Method for Geotextile Pullout", GT6.

Ingold, T.S. (1983), "Laboratory of pull-out testing of geogrid reinforcements in sand", Geotechnical Testing J., ASTM, 6(3), pp. 101-111.

Jewell, R.A. (1980), "Some effects of reinforcement on the mechanical behavior of soil", Thesis presented to Cambridge University, Cambridge, UK, in partial fulfillment of the requirements for the Degree of Doctor of Philosophy.

Juran, I., and Chen, C.L., (1988) "Soil-Geotextile Pull-out Interaction Properties: Testing and Interpretation", Proceedings of the TRB 67th Annual Meeting, January 11-4, 1988, Paper No. 870159, pp. 38

Juran, I., Knochenmus, G., Acar, Y.B. & Arman, A. (1988), "Pull-out response of geotextiles and geogrids", Proc. Symp. on Geosynthetics for Soil Improvement, ASCE, Nashville, USA, Geotechnical special publication No. 18, pp. 92-111.

Koerner, B. (1986), "Direct shear/pull-out tests on geogrids", Report No. 1, Department of Civil Engineering, Drexel University, USA.

O'Dowda, C.S. and Barratt, D.A. (1987), "Field Pull-Out Tests on Geogrids", Ground Engineering Division Structures Dept., Transport and Road Research Laboratory, Crowthorne, Berkshire.

Palmeira, E.M., and Milligan, G.W.E., (1990) "Large Scale Pull-out Test on Geotextiles and Geogrids", 4th International Conference on Geotextiles Geomembranes and Related Products, Vol. 2, pp. 743-746.

Rowe, R.K., Ho, S.K. & Fisher, D.G. (1985), "Determination of soil-Geotextile Interface Strength Properties" Second Canadian Symp. on Geotextiles, pp. 25-34.

Simac, M.R., Bathurst, R.J., Berg, R.R., Lothspeich, S.E. (1993), Design Manual for Segmental Retaining Walls, National Concrete Masonry Association, First Edition, Herndon, VA.

Swan, R.H., (1987) "The Influence of Fabric Geometry on Soil/Geotextile Shear Strength", Geotextiles and Geomembranes, 6, pp. 81-87.

TRI Environmental, Inc. (1995), "Test Results for Interface Friction Tests", TRI Log No. E3001-70-09, Test Dates 6/24-29/1995, June.

# Performance of Geotextile-Reinforced Embankment on Soft Bangkok Clay

D.T. Bergado and P.V. Long

Professor and Research Associate, School of Civil Engineering, Asian Institute of Technology, Bangkok, Thailand.

P. Delmas and K.H. Loke

Polyfelt/Bidim Geosynthetics, Bezons, Cedex, France and Polyfelt Sdn. Bhd., Kuala Lumpur, Malaysia.

N. Miura

Professor and Director, Institute of Lowland Technology, Saga University, Saga 840, Japan.

**ABSTRACT:** Three full scale test embankments were constructed to failure on soft Bangkok clay. One of the embankments was unreinforced and served as control embankment. The second embankment was reinforced with multi-layer reinforcements consisting of four layers of low strength nonwoven geotextiles. The third embankment was reinforced with one layer of high strength (200 kN/m ultimate strength) nonwoven/woven geotextile at the base. The test embankments were constructed using silty sand and were fully instrumented. The geotextile reinforcements were also instrumented to measure their deformations. Back-analyses were made using the limit equilibrium method. The primary failure occurred at the same deformation as the unreinforced embankment during the bearing capacity failure in the foundation. Just prior to this stage, the limiting strain in the geotextile can be taken equal to the critical strain at 3% and the direction of the reinforcing force can be taken as horizontal. The secondary failure occurred at the embankment collapse coinciding with the rupture of the reinforcement and the limiting strain can be taken as the sum of the critical strain during primary failure and localized strain during secondary failure and the direction of the reinforcing force can be taken as bisectonal. The results confirmed the existence of soil/geotextile composite behavior that modified the soil shear strength at the intersection of the failure plane and geotextile reinforcement. Consequently, the respective collapse heights of the multi-layer and high-strength geotextile-reinforced embankments were 1.1 and 1.6 times the unreinforced embankment.

**KEYWORDS:** Geotextiles, Nonwoven fabrics, Reinforcements, Embankments, Soft soils

## 1 INTRODUCTION

In this paper, the performances of 3 full scale test embankments, constructed on soft Bangkok clay, have been described and analyzed. All three test embankments have been built to failure. The unreinforced embankment served as control embankment and was designated as CE embankment. The second embankment, designated as MGE embankment, was reinforced with 4 layers of low strength, nonwoven, needle-punched geotextile consisting of one layer of TS700 (280 g/m<sup>2</sup> and ultimate strength of 19 kN/m) and 3 layers of TS420 (130 g/m<sup>2</sup> and ultimate strength of 9 kN/m). The third embankment, the HGE embankment, was reinforced with one layer of high-strength, woven/ nonwoven (composite) geotextile (PEC 200) with nominal mass of 700 g/m<sup>2</sup> and ultimate strength of 200 kN/m. The geotextile instrumentations and preliminary theoretical analyses have been published previously (Bergado et al, 1994; Loke et al, 1994). The objectives of this paper are to present, evaluate, and analyze the performances of all 3 test embankments based on the measured and monitored data and subsequent theoretical back-analyses using the limit equilibrium method (LEM). Most of the data and results presented in this paper were derived from the work of Long (1997) under the supervision of the first author.

## 2 SITE CONDITION AND SOIL PROFILE

The layout of the test embankments is given in Figure 1. The embankment designations CE, MGE, and HGE have been defined previously. Two boreholes down to 12 m depth and 6 field vane tests down to 10.5 m depth were done. The locations of boreholes and vane tests are also shown in Figure 1. Continuous Shelby tube (inside diameter = 0.075 m) samples were obtained from the boreholes while undrained shear strength at 0.50 m intervals were obtained from the vane tests. The generalized soil profile and soil properties are presented in Figure 2. The uppermost 11 m in the soil profile can be divided into 3 sublayers. The weathered crust forms the topmost 2 m thick sublayer consisting of heavily overconsolidated reddish-brown clay. This sublayer is underlain by a soft, grayish clay sublayer down to about 8 m depth with natural water content varying from 60 to 80%. The medium stiff clay sublayer with silt seams and fine sand lenses can be found from 8 to 11 m depth. The liquid limit of the soft clay ranges from 70 to 102% and the plasticity index is about 60%. The groundwater level at the test site varied seasonally from 0.50 m depth in the rainy season to 1.50 m depth in the dry season. The undrained shear strength from field vane test are also given in Figure 2.

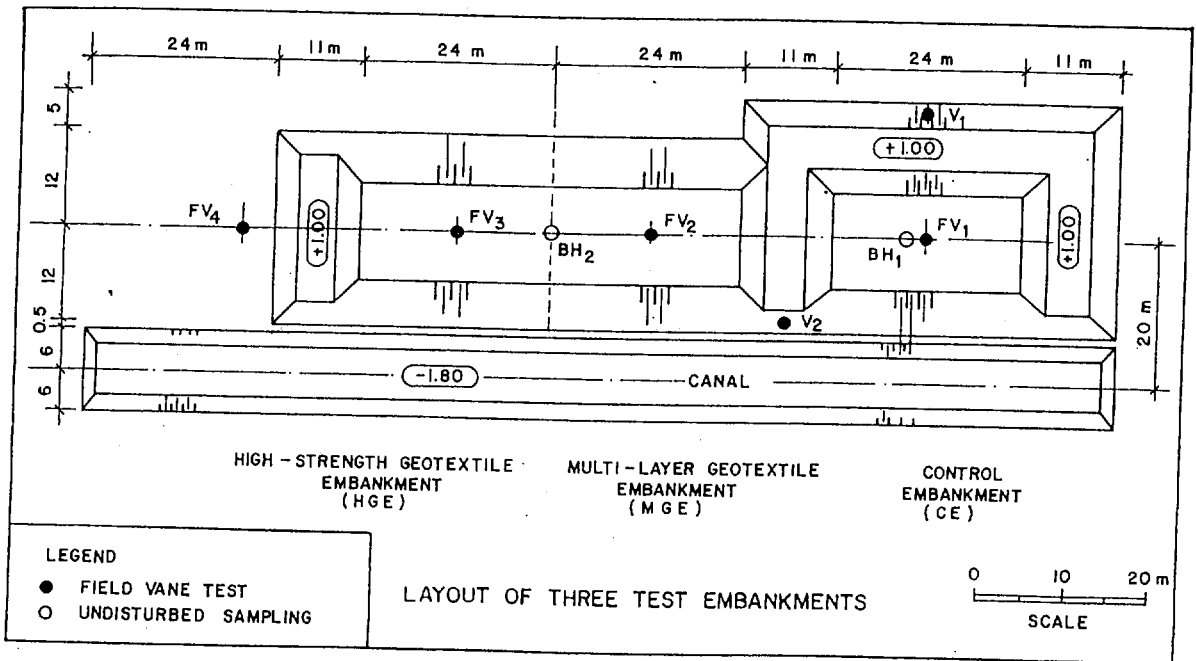


Figure 1. Layout of test embankments with locations of field investigations.

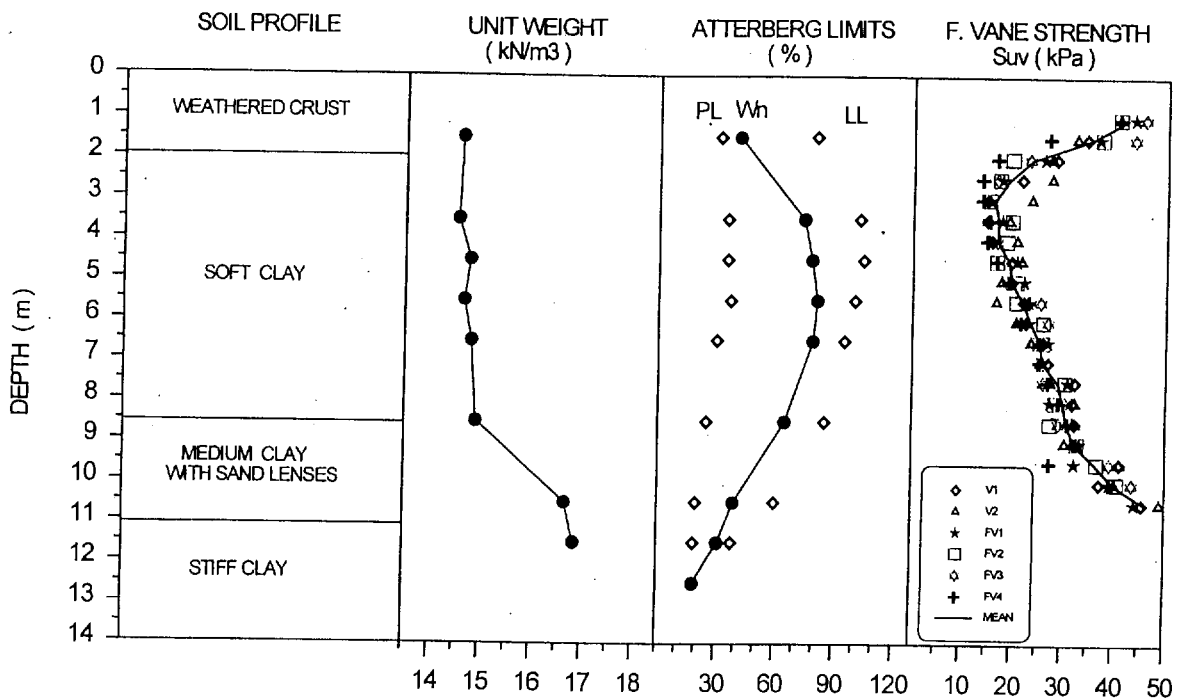


Figure 2. General soil profile and soil properties at the site.



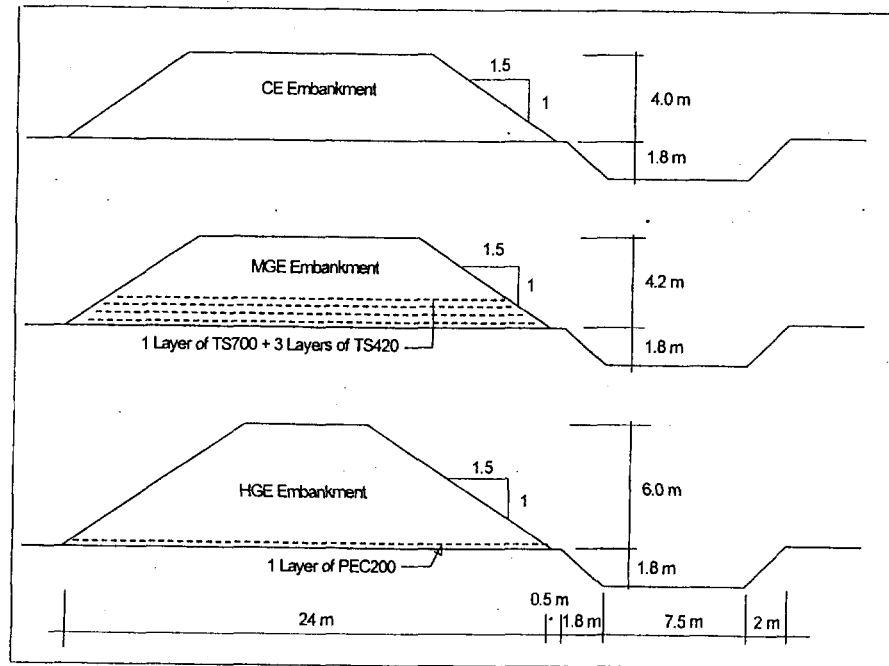


Figure 3. Cross-sections of three test embankments.

### 3 EMBANKMENT DESIGN AND INSTRUMENTATIONS

The cross-sections of the three test embankments are given in Figure 3. All embankments were designed with side slopes of 1V to 1.5 H. A canal was excavated to 2 m deep and 7.5 m wide along the toe of the test embankments to reduce the volume of fill required to reach failure and to ensure that the failure will occur in the canal side.

The silty sand, widely used locally for highway construction, was utilized as embankment material. Using standard Proctor compaction, the maximum dry density and optimum moisture content were obtained as 18 kN/m<sup>3</sup> and 10%, respectively. The failure envelopes from large (shearing area = 0.54 m<sup>2</sup>) and conventional (shearing area = 0.0032 m<sup>2</sup>) shear box tests for the embankment material compacted to 95% of standard Proctor compaction with water contents of 9.5% and 13.0% are plotted in Figure 4. The conventional and large shear box test results correspond to peak and critical state strength parameters, respectively.

The foundation instrumentation of MGE and HGE embankments is presented in Figure 5. The same instrumentation system was used for CE embankment except for surface settlement, S2, and standpipe piezometers SP4, SP5 and SP6. The instruments consisted of piezometers, surface and subsurface settlement plates, and inclinometers for measuring pore pressures, vertical settlements and lateral displacements, respectively. The displacements in the geotextiles reinforcements were measured by wire extensometers, Glotzl extensometers, and 100 mm long special strain gages (Figure 6).

### 4 EMBANKMENT CONSTRUCTION TO FAILURE

Before the embankment construction, the ground surface was cleared by excavating to 0.20 m depth and levelled. Then, the canal was excavated. Immediately, thereafter, the control embankment (CE) was constructed in layers with compaction lift thickness of 0.30 m. The sequences of embankment construction are shown in Figure 7. Very small deformations were observed at embankment height lower than 2.50 m. The magnitudes and rates of vertical settlements as well as the lateral movements increased significantly when the embankment height exceeded 3.5 m corresponding to 65 kPa embankment loading. The CE

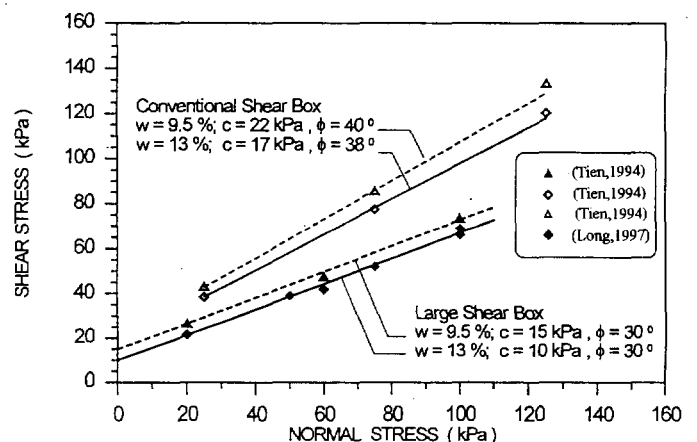


Figure 4. Failure envelopes of embankment fill from conventional and large scale direct shear tests.

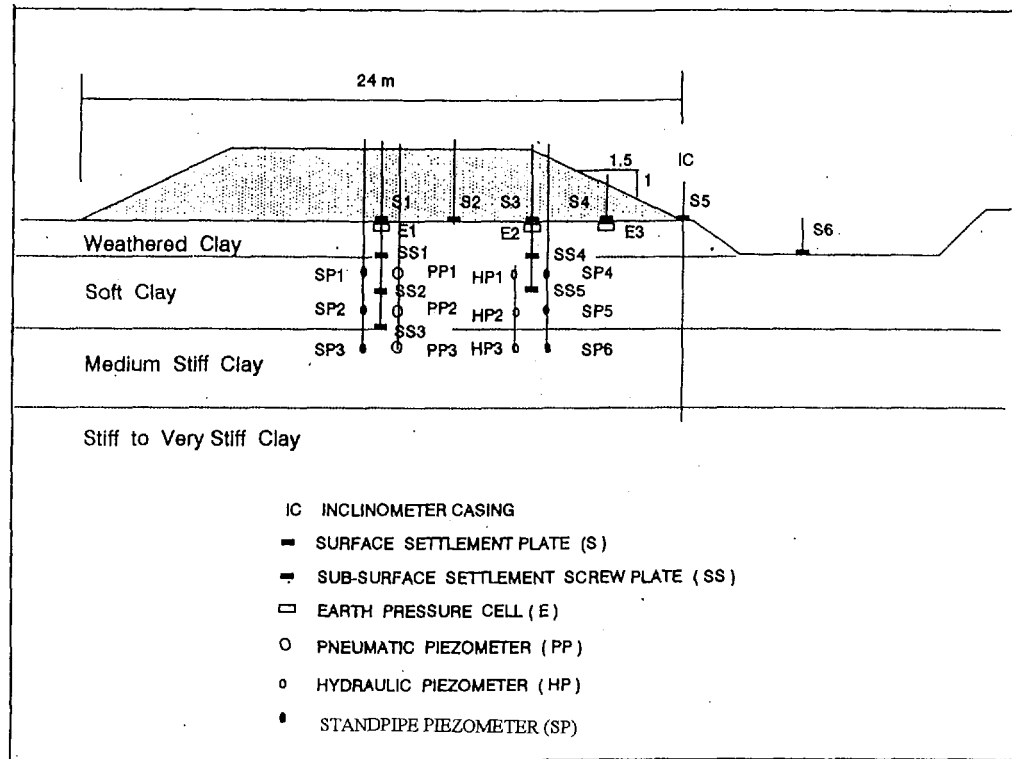


Figure 5. Foundation instrumentations of the embankments.

embankment reached a net height of 4 m (or 80 kPa embankment loading) at failure. The measured excess pore pressures from pneumatic piezometers are plotted in Figure 8 together with the rate of embankment loading. The cross-section measured after failure is plotted in Figure 10 including the failure locations indicated by bamboo stakes and by inclinometer.

Both MGE and HGE embankments were built at the same time with the same rate of filling, construction procedure and quality control as the CE embankment (see Figure 7). Up to the embankment height of 3.75 m or 75 kPa embankment load, the measured strains in the geotextiles were smaller than 1.0%. The rates of vertical and lateral displacements as well as geotextile strains increased significantly when the embankment height exceeded 3.75 m. At this stage, the maximum strains in the geotextile reinforcements were 3% and 2.3% in the MGE and HGE embankments, respectively. The failure of MGE embankment occurred at 4.2 m height (88 kPa embankment loading) that completely ruptured the low strength geotextile reinforcement. The MGE embankment failure induced deformations in the HGE embankment. The cross-section of MGE embankment at failure as compared with CE embankment is also shown in Figure 10. During the failure stage of MGE embankment, the measured maximum strain in the high strength reinforcement was 8.5% which indicated that the induced failure caused 6% additional strain in the high strength reinforcement. The HGE em-

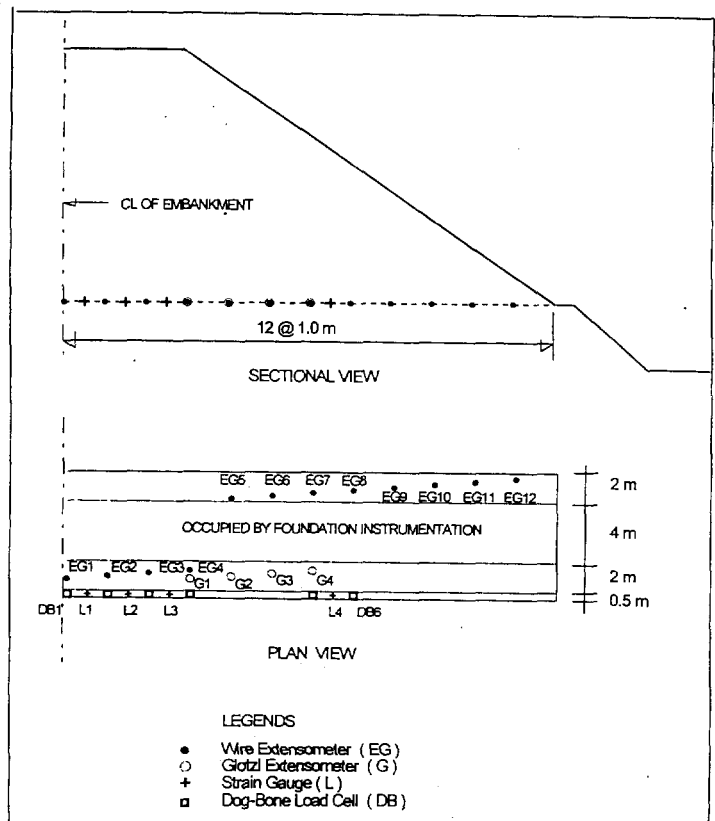


Figure 6. Geotextile instrumentations in HGE embankment.

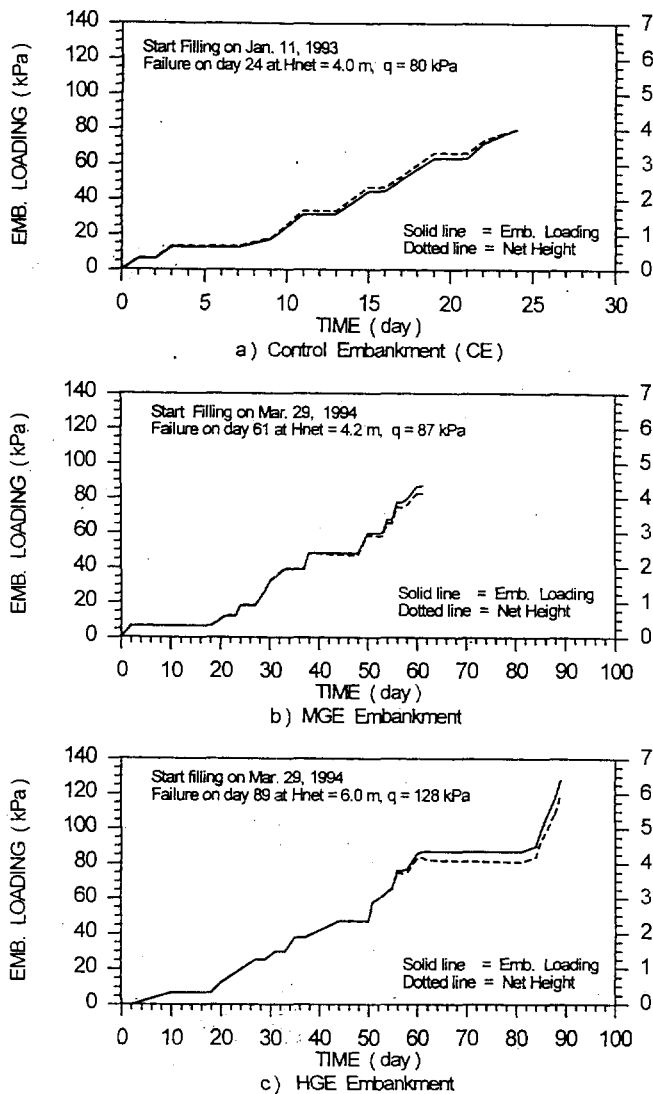


Figure 7. Construction sequences of three test embankments.

bankment height was further increased until a net height of 6 m (or 128 kPa embankment loading) was reached wherein the maximum recorded displacement was 670 mm corresponding to 12% strain and rupture of the high strength reinforcement. The excess pore pressures from pneumatic piezometers underneath the HGE embankment are given in Figure 9 together with the rate of embankment loading. The measured displacements in the high strength reinforcements at selected locations from wire extensometers are plotted in Figure 11 together with the base of embankment construction.

The collapse height corresponds to the maximum net embankment height that can be constructed. The net embankment height is defined as the difference between the current embankment crest elevation and the original elevation of the embankment base. The critical height, on the other hand, is the height at which the deformations in the foundations are equal to that of the unreinforced embankment prior to failure. Thus, the critical height and the collapse height can be considered as the embankment heights corresponding to the bearing capacity failure of the founda-

tion (primary failure) and the collapse of the reinforced embankment together with its foundation (secondary failure), respectively.

There were 35 rainy days during the construction of MGE and HGE embankments as compared to none for CE embankment. Thus, the actual collapse loads of MGE and HGE embankments were 88 kPa (4.6 m fill thickness) and 128 kPa (6.7 m fill thickness) which are, respectively, 1.1 and 1.6 times higher than the CE embankment.

## 5 CRITICAL STRAIN IN GEOTEXTILE REINFORCEMENT

The critical strain in geotextile reinforcement,  $\epsilon_c$ , is defined as the maximum strain mobilized in the reinforcement when the reinforced embankment reaches the critical height (prior to primary failure). The measured strains prior to primary failure of HGE and MGE embankments are 2.3% and 3.0%, respectively. The Almere test embankment (Rowe, 1992) reinforced by one layer of geotextile yielded the strain of 2.5% at critical height of 2.05 m. The Sackville embankment (Rowe et al, 1995) using one layer of polyester woven geotextile yielded 3% strain at 5.7 m fill thickness when primary failure occurred. The critical strain of 3% was also obtained at Guiche test embankment (Delmas et al, 1992) with one layer of woven/nonwoven geotextile. Thus, the critical strain lie in a small band of values ranging from 2.3 to 3.0% for a very large range of geotextile stiffness ranging from 350 kN/m to 5,000 kN/m in various soil profiles.

## 6 BACK-ANALYSES OF STABILITY USING LIMIT EQUILIBRIUM METHOD

The limit equilibrium method (LEM), assuming circular slip surface, was used for back-analyses of stability in both

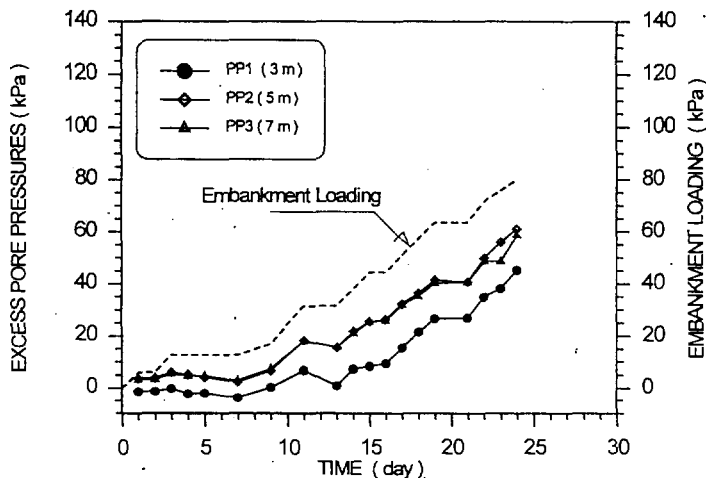


Figure 8. Excess pore pressures from pneumatic piezometers in CE embankment.

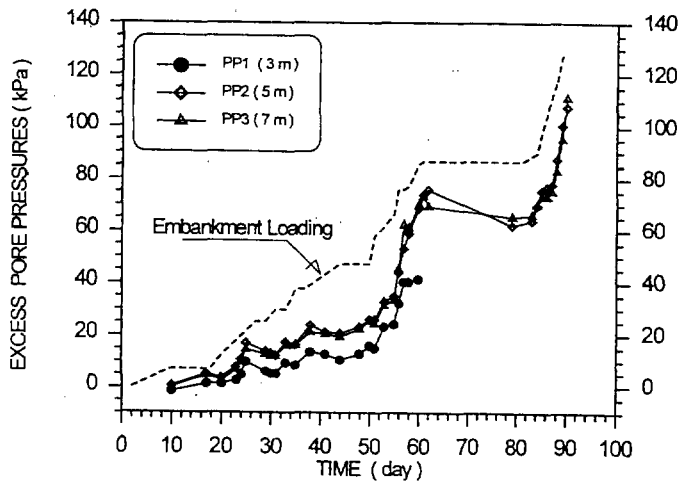


Figure 9. Excess pore pressures from pneumatic piezometers in HGE embankment.

unreinforced and reinforced embankments. The computer software PCSTABL6 (Purdue University) based on Bishop's simplified method (Bishop, 1955) with modification to include the effect of the reinforcement, was utilized.

For the CE embankment, the field compaction have total unit weight ( $\gamma$ ) of 18.5 kN/m<sup>3</sup> and moisture content ( $\omega$ ) of 9.5%. Corresponding to this condition, the peak strength consists of 40 degrees friction angle and 22 kPa apparent cohesion and the corresponding critical state values were 30 degrees friction angle and 15 kPa apparent cohesion (see Figure 4). The mean values of the field vane shear strength with correction factor of 0.80 were used as undrained strengths of the soft clay foundation. The calculated factor of safety for the actual slip surface of CE embankment at 4.0 m net height were 1.02 and 0.98 for the strength parameters of embankment fill at peak and post-peak, respectively.

For the stability of MGE and HGE embankments, the reinforcing force can be either assumed as a free-body force or a force modifying the soil strength. Following the approach of Bonaparte and Christopher (1987), the former assumption was applied in the HGE embankment and the latter assumption was used in the MGE embankment. For the case of the reinforcement modifying the soil shear strength, the resultant force in the direction tangent to the slip surface,  $T_R$ , can be calculated as follows:

$$T_R = T(\cos \alpha + \sin \alpha \cdot \tan \phi) \quad (1)$$

in which  $\alpha$  is the angle between the direction of the reinforcement and the tangential direction of the slip circle, and  $\phi$  is the friction angle of the embankment fill.

The direction of reinforcement force at the onset of failure can be represented by the inclination factor,  $I_f$ , defined as follows:

$$I_f = 1 - \alpha/\alpha_0 \quad (2)$$

where  $\alpha_0$  is the angle between the initial (horizontal) direction of the reinforcement and the tangential direction of the slip surface. The values of  $I_f$  of 0, 0.5, and 1.0 correspond to horizontal, bisectonal, and tangential directions, respectively. The reorientation of the reinforcement is caused mainly by the bending of reinforcement due to local deformation. Thus, the value of inclination factor,  $I_f$ , should be selected according to the magnitude of the localized strain in the geotextile,  $\epsilon_{lc}$ , at the vicinity of the slip surface. From the results of large direct shear tests and finite element modeling (FEM), Bergado et al (1996) suggested that the maximum value of  $I_f$  is 0.50 corresponding to the bisectonal direction. The bisectonal direction has also been successfully assumed by Rowe and Soderman (1984), Low and Duncan (1985) and Rowe (1992).

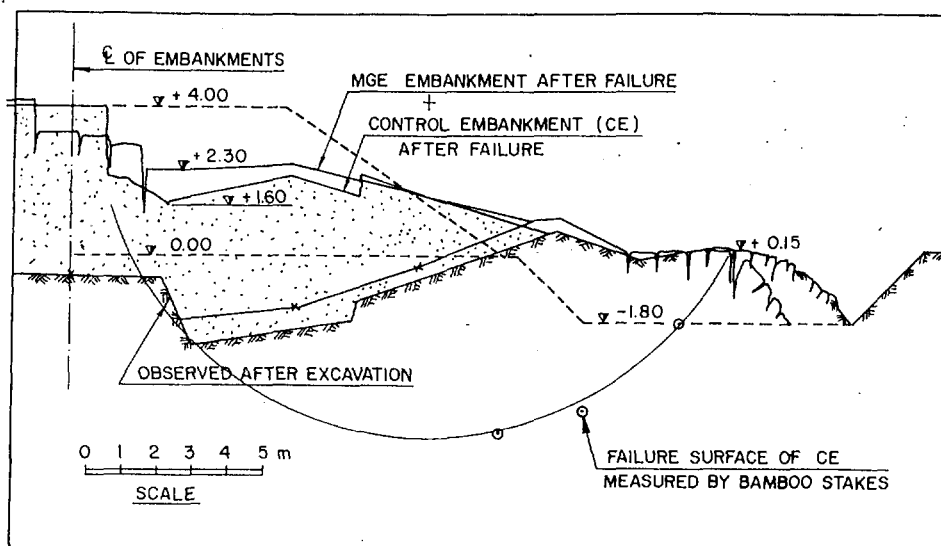


Figure 10. Cross-section of CE and MGE embankment after failure.

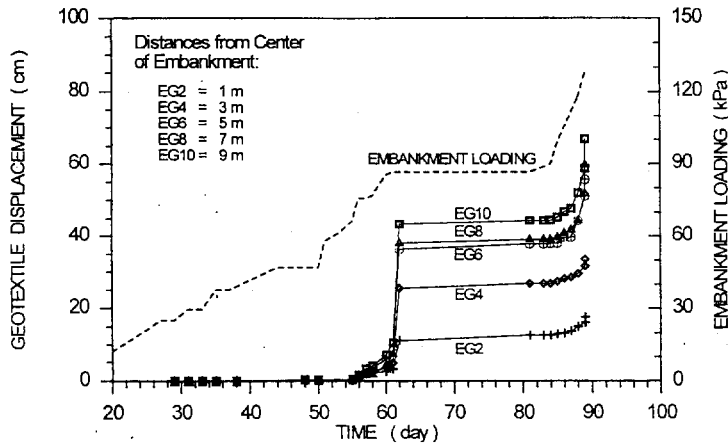


Figure 11. Displacements in geotextile measured by wire extensometer.

The ultimate reinforcement force,  $T_{ult}$ , was computed corresponding to the value of the limiting strain,  $\epsilon_{lm}$ , which includes the localized strain,  $\epsilon_{lc}$ , whenever  $I_r$  is greater than 0. The strength parameters of backfill soil correspond to the field compaction condition ( $\gamma_t = 19.2 \text{ kN/m}^3$  and  $w = 13\%$ ) influenced by rainy days. The corresponding friction angle ( $\phi$ ) and apparent cohesion ( $c$ ) were  $\phi = 38$  degrees and  $c = 17 \text{ kPa}$  at peak strength, respectively, and  $\phi = 30$  degrees and  $c = 10 \text{ kPa}$  at critical state, respectively. The undrained strengths in the soft clay foundation were similar as the CE embankment.

The failure of MGE embankment at 4.2 m net height was back-analyzed. At the critical height, assuming peak strength parameters of embankment fill, no localized geotextile deformation ( $\epsilon_{lc} = 0$ ) and horizontal direction of reinforcing force ( $I_r = 0$ ) with measured strain of reinforcement of 3%, the factor of safety (FS) was 0.98. At the onset of failure (FS = 1.0) with  $I_r = 0.5$  (bisectonal direction of reinforcing force and using critical state strength parameters of embankment fill, the back-analyzed geotextile strain was found to be 13%.

The stability of HGE embankment at net embankment heights of 4.2 m (critical height) and at 6.0 m (collapse height) were back-analyzed. Using the measured strain in the geotextile of 2.3% and assuming  $I_r = 0$  and peak strength parameters for embankment fill, the calculated FS was 1.0. This indicates that the HGE embankment reached critical height at 4.2 m and the bearing capacity failure (primary failure) was unavoidable, even without the interference of MGE embankment. After induced failure of adjacent MGE embankment, the measured strain in the high strength geotextile was 8.5% corresponding to tensile strength of 145 kN/m. At this stage, assuming  $I_r = 0.5$  and using critical strength parameters of embankment fill, the safety factor of 1.25 was obtained. Therefore, the embankment construction can be continued which was done. The HGE embankment collapse at net embankment height of 6 m with measured strain in the geotextile of 12 to 14% corresponding to rupture strength of 200 kN/m for high

strength geotextile. At 6 m net height, the FS value for HGE embankment was found to be 1.0 using either the actual failure surface or the most critical and deeper failure surface. Therefore, regardless of the influence of MGE embankment failure at net height of 4.2 m, the HGE embankment should fail at net embankment height of 6.0 m.

## 7 MAGNITUDE AND ORIENTATION OF REINFORCING FORCE

Two important variables are involved in the circular slip stability analyses, namely: the inclination factor,  $I_r$ , and the limiting strain,  $\epsilon_{lm}$ , at the onset of failure. Based on the measured strain, the results of back-analyses by LEM indicated that reinforcing force can be horizontal direction ( $I_r = 0$ ) at critical height just prior to bearing capacity failure (primary failure) as well as the reinforcing force can be bisectonal ( $I_r = 0.50$ ) at collapse height. Rather than assumed arbitrarily, an improved method is introduced to estimate the limiting strain,  $\epsilon_{lm}$ , as follows:

$$\epsilon_{lm} = \epsilon_c + \epsilon_{lc} \quad (3)$$

in which  $\epsilon_c$  is the critical strain corresponding to the critical height (just prior to bearing capacity failure or primary failure) and  $\epsilon_{lc}$  is the localized strain associated with the slip failure. The value of  $\epsilon_c$  was found to be 2.3% to 3% as mentioned previously. Based on large direct shear tests and subsequent FEM modeling, Bergado et al (1996) proposed a new method to calculate the localized strain,  $\epsilon_{lc}$ , as follows:

$$\epsilon_{lc} = 225 (I_r) (S^{-0.4}) \quad (4)$$

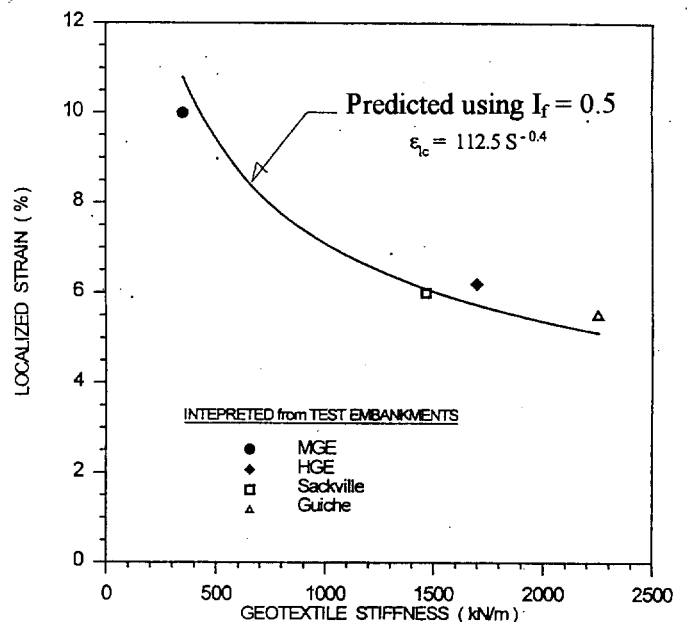


Figure 12. Localized strains in geotextile from field data and as predicted by Equation 4.

The value of  $S$  is the total stiffness of all reinforcement layers in the embankment and should be determined as secant stiffness at 5% strain. The value of  $I_r$  can be assumed as  $I_r = 0$  or  $I_r = 0.50$  corresponding to critical embankment height and collapse height, respectively. Equation 4 is plotted in Figure 12 for various values of stiffness,  $S$ . The data derived from Sackville (Rowe et al, 1995) and Guiche (Delmas et al, 1992) embankments are also included in Figure 12.

## 8 CONCLUSIONS

The full scale test embankment program including the site conditions, instrumentations, and embankment construction have been described. The test embankment program yielded valuable data which can be used to improve the design method of geotextile reinforced embankment on soft ground. Based on the results, the following conclusions can be made:

1. The geotextile reinforcements improved the collapse heights of MGE and HGE embankments by 1.1 and 1.6 times, respectively, higher than CE embankment.
2. The critical strain,  $\epsilon_c$ , in the geotextile reinforcement just prior to bearing capacity failure or primary failure of foundation soil can be taken as 2.3 to 3% irrespective of geotextile stiffness and condition of the foundation soil.
3. The limiting strain,  $\epsilon_{lm}$ , at slip failure can be taken as the sum of critical strain,  $\epsilon_c$ , and the localized strain,  $\epsilon_{lc}$ , associated with the slip failure.
4. The geotextile reinforced embankment on soft ground with limitation on foundation deformation not exceeding the unreinforced embankment just prior to the bearing capacity failure or primary failure (embankment height,  $H < \text{critical height, } H_c$ ), the mobilized tensile force in the reinforcement can be obtained assuming the limiting strain equal to critical strain which can be taken as 3% ( $\epsilon_{lm} = \epsilon_c = 3\%$ ). The direction of reinforcing force can be taken as horizontal ( $I_r=0$ ) and the peak strength parameters of embankment fill are suitable.
5. For embankments designed with allowable large deformations where the embankment height,  $H$ , can exceed the critical embankment height,  $H_c$ , the mobilized reinforcing force should correspond to the limiting strain,  $\epsilon_{lm}$ , which is the sum of critical strain,  $\epsilon_c$ , and localized strain at failure,  $\epsilon_{lc}$ . The value of  $\epsilon_{lc}$  can be obtained from the in-soil stiffness of the reinforcement using  $I_r = 0.50$  and using the shear strength parameters of embankment fill at critical state.
6. For single layer reinforcement placed directly on the ground at the base of embankment, the reinforcing force can be taken as free-body force. For multi-layer reinforcements with frictional embankment fill, the effects of reinforcing force in modifying the soil strength at the vicinity of failure surface should be considered.

## ACKNOWLEDGEMENTS

The authors are deeply indebted to the generous financial support of Polyfelt Geosynthetics, Austria and to their past and present staff such as G. Werner, K.H. Loke, J. Smith, P. Delmas, and B.R. Christopher for their technical advises and suggestions.

## REFERENCES

- Bergado, D.T., Long, P.V., Loke, K.H., Christopher, B.R. and Delmas, P. (1994), "Geotextile Reinforcement in Full Scale Test Embankment on Soft Ground", *Proc. Fifth Intl. Conf. on Geotextiles and Geomembranes and Related Products*, Singapore, pp. 21-24.
- Bergado, D.T., Long, P.V. and Werner, G. (1996) "Deformation Behavior of Geotextile Reinforcement at Vicinity of the Shear Surface", *First European Geosynthetics Conference (EuroGeo 1), Maastricht, The Netherlands*, pp. 177-182.
- Bishop, A.W. (1955) "The Use of Slip Circle in the Stability Analysis of Slopes", *Geotechnique*, Vol. 5, No. 1, pp. 7-17.
- Bonaparte, R. and Christopher, B.R. (1987) "Design and Construction of Reinforced Embankments over Weak Foundation", *Transp. Res. Record* 1153, pp. 26-39.
- Delmas, P., Queroy, D., Quaresma, M. and De Saint, A. (1992) "Failure of an Experimental Embankment: Guiche", *Geotextiles and Geomembranes and Related Products*, Den Hoedt (ed.), Balkema Printers Rotterdam, the Netherlands.
- Loke, K.H., Ganeshan, V., Werner, G. and Bergado, D.T. (1994) "Composite Behavior of Geotextile Reinforced Embankment Soft Clay", *Proc. Fifth Intl. Conf. on Geotextiles and Geomembranes and Related Products*, Singapore, pp. 25-28.
- Long, P.V. (1997) "Behavior of Geotextile-Reinforced Embankment on Soft Ground", *Doctoral Engineering Dissertation*, School of Civil Engineering, Asian Institute of Technology, Bangkok, Thailand.
- Low, B.K. and Duncan, J.M. (1985) "Analysis of the Behavior of Reinforced Embankment on Weak Foundation", *Report VPI/CE-CT-85-H*, Virginia Polytechnic Institute, Blacksburg, V.A., U.S.A.
- Rowe, R.K., Granendran, C.T., Landva, A.O. and Valsangkar, A.J. (1995) "Construction and Performance of a Full Scale Geotextile Reinforced Test Embankment, Sackville, New Brunswick", *Canadian Geotechnical Journal*, Vol. 23, pp. 512-534.
- Rowe, R.K. (1992) "Reinforced Embankments on Cohesive Deposits", *International Symposium on Application of Geosynthetics Technology*, Jakarta, Indonesia, pp. 1-19.
- Rowe, R.K. and Soderman, K.L. (1987) "Reinforcement of Embankment on Soils Whose Strength Increases with Depth", *Geosynthetics '87*, New Orleans, pp. 266-277.
- Tien, M.H. (1994) "An Investigation of Interaction of Geotextile and Low Quality Backfill Soil by Direct Shear Tests", *Master of Engineering Thesis*, Asian Institute of Technology, Bangkok, Thailand.

# Reinforced Piled Embankments in Sweden - Design Aspects

Y. Rogbeck  
M Sc, Swedish Geotechnical Institute, Linköping, Sweden

S. Gustavsson  
M Sc, Scandiaconsult, Malmö, Sweden

I. Södergren  
M Sc, Swedish National Road Administration, Borlänge, Sweden

D. Lindquist  
B Sc, Swedish Geotechnical Institute/University of Washington, Seattle, USA

**Abstract:** This paper describes a case study of a reinforced piled embankment and presents a proposed calculation model. The height of the embankment was 1.7 m, which is lower than that normally accepted for embankment piling according to Swedish regulations. The project includes a field study of displacement and strain in the reinforcement for the alternatives soil fill and cavities below the reinforcement. The cavities were simulated by using foam mattresses below the reinforcement. Displacements at the reinforcement level in the area with soil fill were about 20 mm, while displacements over the mattresses were about 200 mm, i.e. 10 times larger. Calculations were carried out using two analytical models, BS 8006 and Carlsson, and a finite difference method, FLAC. Comparisons are made between measured values and calculated values. In this case the FLAC calculations are judged to give a good picture of the actual behaviour in the construction. The analytical models are too conservative because they do not take the foundation support from the soil beneath the reinforcement into account. The various calculation models were compared to each other and a suggestion for design using an analytical model is made. The model is two-dimensional but an attempt was made to take the three-dimensional behaviour into account. This was done in this case by taking the three-dimensional load and distributing it over the two-dimensioned surface. Aspects of design are provided.

**Keywords:** Geogrids, Piles, Embankments, Reinforcement, Design, Case study.

## 1. MÖNSTERÅS CASE STUDY

Embankment piling has been used in Sweden for many years. During recent years some projects have been carried out with reinforcement over embankment piling or deep stabilisation. Monitoring has been carried out in an embankment at Mönsterås.

The case study was of a reinforced piled embankment constructed in 1996 on a section of Route 632 in Mönsterås, Sweden. The Swedish National Road Administration (SNRA) ordered the construction, Scandiaconsult managed it and the Nordic Construction Company was the contractor. The field studies were carried out by Scandiaconsult and the Swedish Geotechnical Institute (SGI). A number of different alternatives were studied in the process of selecting soil improvement on the stretch of road in question, explained below.

- Excavation/refill. Discarded because of the effects this would have on the surroundings. Both on the nearby quay construction and the environment. Furthermore, it would require considerable heavy truck traffic in central Mönsterås.
- Light fill. For sufficient load relief, the light fill would cause uplift at the maximum groundwater level.
- Concrete mat foundation on piles. Feasible but expensive, about twice as expensive as embankment piling.

### 1.1 Soil conditions

The soil consisted of an upper layer of 1 to 3 m of fill beneath which was 2 to 4 m of loose sediments of gyttja and clay which rest on sand and till. The depth to the bedrock was not carefully examined but is probably limited. The thickness of the soil layer in a cross-section of the embankment area varies.

The fill was deposited over a long period of time. The oldest part of the fill was placed with a grillage beneath it. The fill consisted mainly of non-cohesive soil but there was also some

wood and construction waste. The fill varied in stiffness. For design calculations, a dimensioning friction angle of  $32^\circ$  was used.

The gyttja, the thickness of which varies between 0.5 and 2.0 m, contained layers of silt and fine sand. The gyttja was loose with an uncorrected shear strength, according to field vane shear tests, between 10 and 50 kPa. The water content varied between 40 % and 200 % with one measurement of 430 %. For design calculations, a dimensioning, undrained shear strength of 8 kPa was used.

The clay, the thickness of which varied between 0.5 and 2.0 m, contained layers of fine silt. The uncorrected shear strength of the clay varied, according to vane shear tests, between 10 and 70 kPa. The water content varied between 20 % and 60 %. For design calculations, a dimensioning, undrained shear strength of 10 kPa was used.

Both the gyttja and the clay were assessed as being normally consolidated for the existing conditions.

The composition and thickness of the till were not closely examined, but generally it had a high relative stiffness. However, in some areas there were looser layers of sand in the upper surface of the till. For design calculations, a dimensioning friction angle of  $35^\circ$  was used.

Parts of the embankment area have been flooded at the maximum groundwater levels.

### 1.2 Design and construction

The construction consisted of precast concrete piles which were driven down to a firm bottom. The length of the piles was 3 to 6 m. Pile caps were placed above the piles covering 25 % of the embankments surface area. The reinforcement consisted of a biaxial polyester geogrid, with 84 kN/m tensile strength at break and a tensile strength of 16 kN/m at 3 % strain according to EN ISO 10319 (TexGrid TG 75-75). The geogrid was laid in one layer. The embankment fill consisted of crushed rock, 0 to 200 mm. A cross-section of the construction is shown in

Figure 1. The height of the embankment is 1.7 m which is lower than that normally accepted in Swedish regulations. In order to obtain permission to build the construction, the designer was forced to verify that the design would function as intended. Verification took place through calculations supplemented with field monitoring.

The embankment fill was compacted with a 2-ton roller. The first layer over the reinforcement was 0.5 m when compacted. Thereafter compaction took place in 0.3 m lifts. In the area with measurement equipment, a 600 kg vibratory plate compactor was used in order not to destroy the monitoring equipment. The fill was placed in two stages. In the first stage fill was placed to 0.7 m over the reinforcement and in the second stage to the total of 1.6 m above the reinforcement.

### 1.3 Design

For design of the soil reinforcement, calculations were carried out according to British Standard (BS 8006, Draft) 1995, Equation 1 and according to (Carlsson 1987), Equation 2. The most significant differences between the models are the forces in the reinforcement due to the vertical load. These differences arise from the way that the models analyse the arching effect. These forces are compared in Table 1. The results differed, in this case with the lowest forces in the reinforcement according to BS 8006. The procedure used in BS 8006 produces relatively large jumps in the calculation results at certain embankment heights. The jumps depended on whether or not an arching effect arose and how the load was distributed between piles and reinforcement. Care should be taken, especially with new standards and results should be checked which are near such limits. The geometry of the Mönsterås project was close to such a limit. The SNRA therefore decided to carry out such a check within the framework of the SGIs planned work on the regulations for the SNRA in Sweden.

The calculations according to BS 8006 are as follows:

For  $H > 0.7$  (c-a) the distribution over pile load/soil load is;

$$p'_c / \sigma'_v = (C_c \cdot a / H)^2$$

For  $H > 1.4$  (c-a) the distributed load on and the force in the soil reinforcement are;

$$W_T = \frac{1.4c f_{fs} \gamma (c-a)}{c^2 - a^2} [c^2 - a^2 (p'_c / \sigma'_v)]$$

$$T_{rp} = \frac{W_T (c-a)}{2a} \sqrt{1 + \frac{1}{6\epsilon}} \quad (1)$$

The calculations according to Carlsson are as follows:

$$d = (c-a) \sqrt{\frac{3\epsilon}{8}}$$

$$P_b = \frac{(c-a)^3}{16 \tan 15^\circ} \gamma \frac{1}{2d} \sqrt{1 + \frac{16d^2}{(c-a)^2}} \quad (2)$$

- Where  $H$  = embankment height (1.7 m)  
 $c$  = centre distance between pile caps (2.4 m)  
 $a$  = pile cap width (1.2 m)  
 $d$  = displacement (d)  
 $C_c$  = pile type factor, end-bearing piles ( $1.95 H/a - 0.18$ )  
 $\gamma$  = unit weight of embankment fill ( $20 \text{ kN/m}^3$ )  
 $f_{fs}$  = partial coefficient for soil load (1.0)  
 $\epsilon$  = strain  
 $W_T$  = the distributed vertical load acting on the reinforcement (kN/m)  
 $T_{rp} = P_b$  = force in the reinforcement (kN/m)

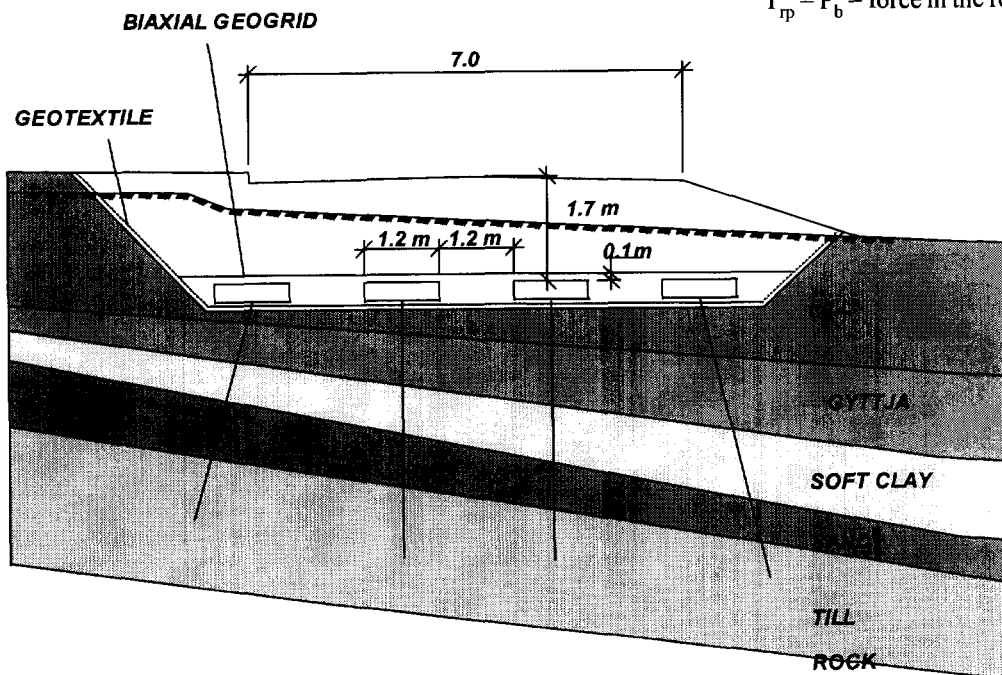


Figure 1. Cross-section of Route 632 in Mönsterås.



Calculations using the BS 8006-model (fictive three-dimensional) gave a force on the basis of the vertical load between the pile caps of 18 kN/m at a strain of 6 %. Calculation according to Carlsson (two-dimensional) gave a force of 26 kN/m and a displacement of 0.18 m at a corresponding strain. In order to verify these results, other calculations were carried out using the two-dimensional finite difference program, Fast Lagrangian Analysis of Continua (FLAC), Version 3.30 (Itasca 1995). The calculations showed that there was arch formation, even for the low embankment height studied here, and that the displacement at the road surface was negligible. Calculations were carried out for cases with both cavities and soil fill under the reinforcement. The elastic modulus times area, EA = 400 kN/m, was used for the FLAC calculations. In implementation, however, a somewhat more rigid reinforcement was used. Table 1 shows the results from the calculations.

Table 1. Design results of the analytical and finite difference models.

Method	Strain $\epsilon$ (%)	Displacement d (m)	Force $F_v$ (kN/m)
Carlsson	2	0.10	42
	6	0.18	26
BS 8006	2	0.10	28
	6	0.18	18
FLAC Foundation support cavity	0.08	0.01	1
	3.5	0.13	14

#### 1.4 Field monitoring of strain and displacement in the reinforcement

The quality control was supplemented with measurements in an attempt to clarify the effect of the reinforcement and compare measured values with the calculation models. The monitoring was carried out in two areas of the embankment, as shown in Figure 2. One area consisted of the normal construction with soil fill between the pile caps. The other area consisted of foam mattresses between two rows of pile caps in order to simulate a cavity under the reinforcement. The mattresses were 0.55 m high and had an area of 1.2 m by 6.0 m. The monitoring consisted of vertical displacement and strain measurements in the reinforcement and displacement measurements on the road surface.

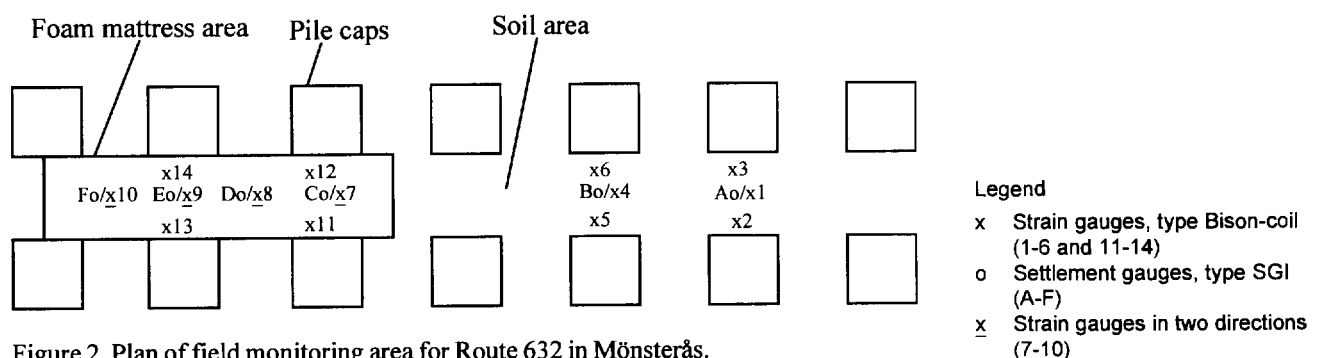


Figure 2. Plan of field monitoring area for Route 632 in Mönsterås.

The vertical displacements of the reinforcement were measured using settlement gauges, type SGI. The measurement results are shown in Figure 3. The displacement in the area with the soil fill was about 20 mm. Displacement measured over the mattresses between the pile caps was 173 and 206 mm while displacement on the diagonal was 212 and 213 mm. The larger displacement on the diagonal is probably due to three-dimensional effects. However, the full effect is not obtained since the mattresses are only lying between the pile caps in one direction and soil fill is between the pile caps in the cross direction.

The strains in the geogrids were measured with Bison coil strain gauges screwed into the geogrids. They are designed for synthetic geogrids and have a measurement accuracy of 2.5 micrometers. Theoretically, the largest strains are obtained at the cap edge. Where there is a cavity under the reinforcement, the strain is nearly uniform between the pile caps. To examine the differences between the cap edge and the middle of the cavity, measurements were carried out both between the pile caps and at the cap edge. The strain measurements between the caps also gave the opportunity to compare these with measured displacements. Field measurements of horizontal movements were made, which were then calculated into strains and forces.

The strains are shown in Figures 4 and 5. The strain gauge locations are shown in Figure 2. In spite of a high measurement accuracy in the strain gauges, the distribution of results at the pile cap edge is large. This may be due to edge

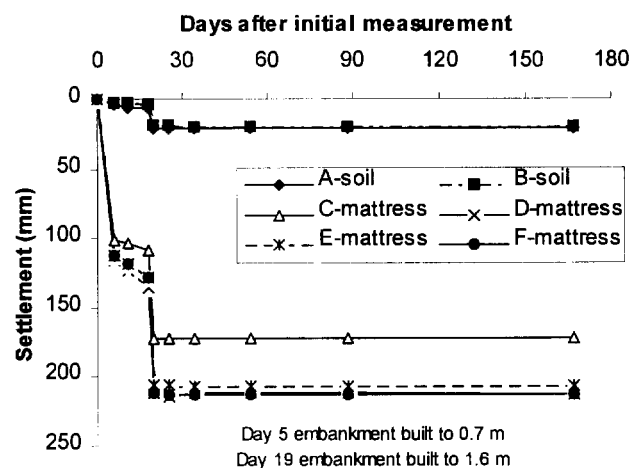
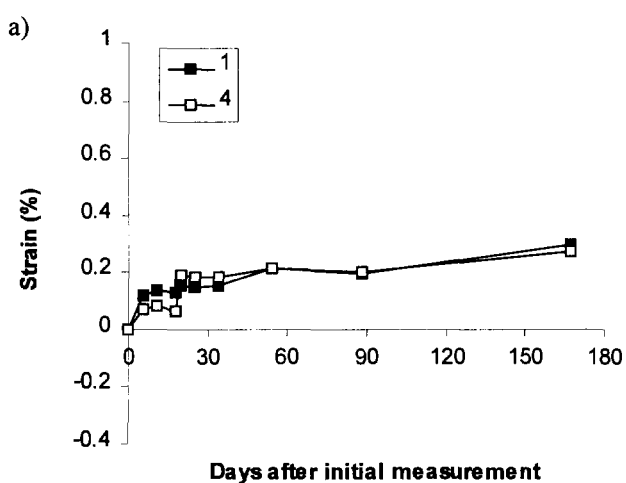


Figure 3. Measured vertical displacement in the area with soil fill and foam mattresses respectively.

effects. In the mattress area the strains close to the edge of the pile caps were 0.5, 1.6, 2.1 and 4.5 %. At the midpoint between and along the pile caps the strains were 0.4, 0.6, 0.7 and 1 %. At the midpoint between and across the pile caps they were 1.8, 2.9, 3.0 and 3.2 %. Corresponding tensile forces were 5 to 23, 4 to 9 and 12 to 17 kN/m.

### 1.5 Monitoring of displacements on the road surface

The displacements on the road surface were measured with settlement plates placed 0.7 m under the surface and surrounded by protective tubing. The embankment fill material was assessed as being non-susceptible to frost heave. Measurements of the displacements in the surface did not begin until all the embankment fill had been placed in November 1996. Displacements also occurred during the laying and compaction processes. Unfortunately these displacements could not be documented.



The measured displacements varied between 5 and 10 mm. Most of these were formed within one month after the embankment fill had been completed. No significant differences on the road surface were observed between the area with and without mattresses.

### 1.6 FLAC calculations to evaluate the field behaviour

To find the reasons for the differences between predicted and measured displacements and geogrid strains supplementary FLAC calculations were carried out. The primary aim was to study the case where a cavity arises under the reinforcement between the pile caps.

The embankment was symmetrical about its centre line so only one side of the embankment was modelled. If the mattress had also been used in side sections, rather than just the centre of the embankment, the modelled section could have been reduced to 1.2 m in width. Instead, the modelled section

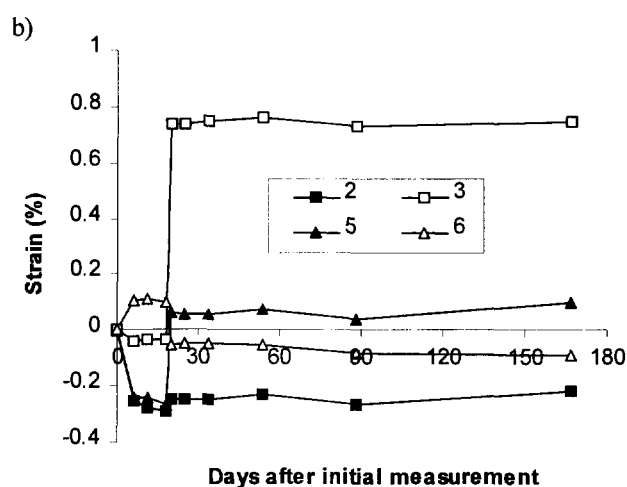


Figure 4. Measured strains in the reinforcement for case with soil.  
a) along and in the middle between the pile caps.  
b) across and at the pile caps.

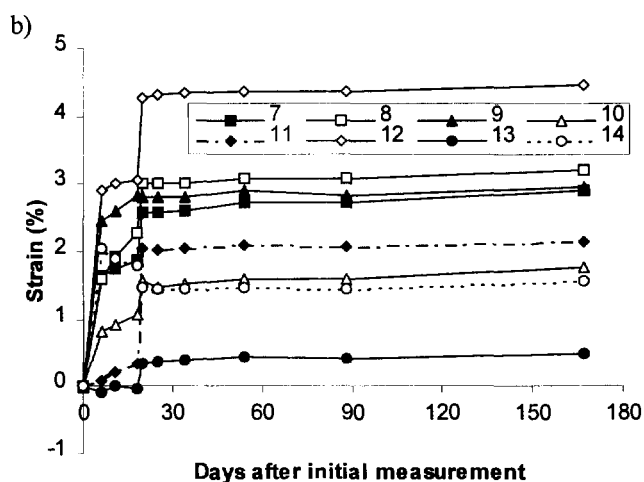
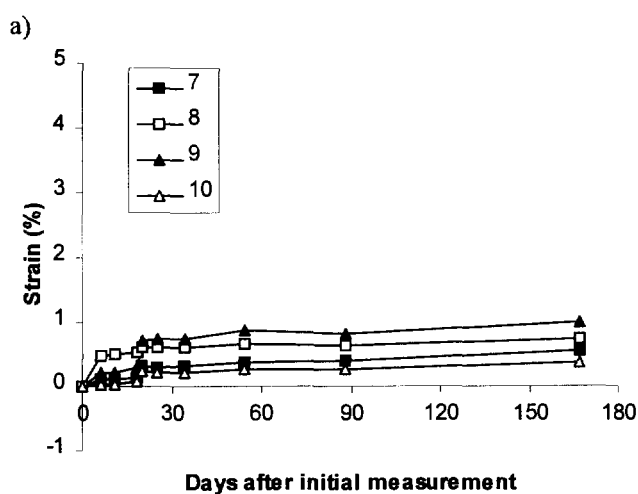


Figure 5. Measured strains in the reinforcement for case with soil fill and foam mattresses.  
a) along and at the midpoint between the pile caps.  
b) across the pile caps both at the midpoint between and at the pile caps.

was 3.6 m wide and 2.15 m high. It spanned horizontally from the centre of the mattress area across a footing and soil area to the centre of the second footing. Vertically it spanned from the bottom of the mattress to the top of the fill. The material locations were shown in Figure 1. A variety of grid meshes were tested. A 36 x 28 grid was selected to optimise the calculation time and precision of the results.

The geogrid was modelled using the cable element in FLAC. Values used in this analysis for the cable element are shown in Table 2. The cable element was chosen, rather than the beam element, because the cable element can model the soil/geogrid interaction. The Mohr-Coulomb plasticity model was used for the soil. The mattress was modelled elastically with its moduli based on laboratory unconfined compression tests. Finally, the footings were modelled as null elements with fixed boundary points.

Table 2. Cable element input values used to model a geogrid.

FLAC parameter	Magnitude and units
elastic modulus · area	600 kN/m
perimeter	2 m/m
yield	75 kN/m
kbond	17,000 kPa (maximum)
sbond	0 kPa
sfriiction (assumed = soil)	42°

Ideally the kbond and sbond should be obtained from laboratory and field pullout tests using the fill material. Because these tests were not available, Equation 3, based on the definitions in (Itasca 1995), was used to obtain values for the kbond.

$$kbond = (sbond + perimeter \cdot \sigma' \cdot \tan(sfriiction)) / \delta_{max} \quad (3)$$

The perimeter was chosen to be the maximum of 2 m for the geogrid, as opposed to its surface area, because there is frictional resistance on both the top and bottom of its surface and significant passive resistance where the holes in the grid meet the spanning grid elements.  $\sigma'$  is the overburden pressure at the level of the geogrid. It should be noted that the kbond increases with the overburden pressure as the embankment is constructed. Finally,  $\delta_{max}$  is the geogrid displacement when the maximum pullout resistance is reached. For the geogrid used in this project 3 mm was used.

The maximum displacement occurred at the mattress/geogrid interface at the midpoint between pile caps. The displacement and tensile force distribution in the geogrid are shown in Figure 6.

Compaction of the fill was modelled as a static pressure applied during the construction of the embankment. The compactive effort was modelled by adding an equivalent static load of 20 or 50 kPa and stepping to equilibrium. When equilibrium was reached the load was removed and FLAC stepped again to a new equilibrium. The equivalent static load used in FLAC for compaction was only an estimate. Therefore, two values were chosen in-between the compaction equipment's static load and its centrifugal vibratory force of 12 and 100 kPa, respectively. The incremental displacements and the effect of the static compaction loads for the base case are shown in Figure 7. The compaction was modelled at 0.5, 0.7, 1.0, 1.3 and 1.6 m embankment heights. The effect on displacement at the geogrid was only significant for the first two compactions.

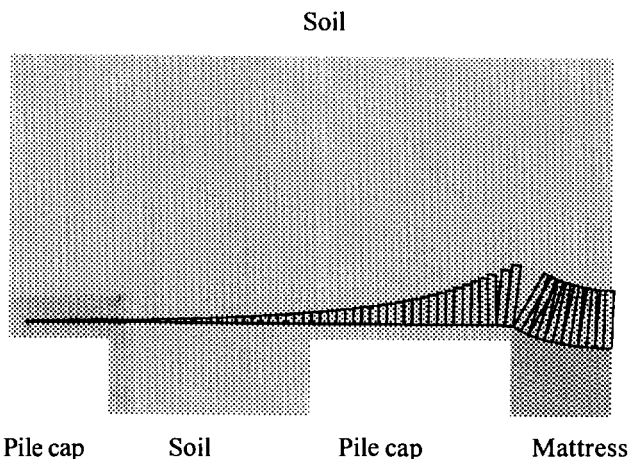


Figure 6. Base case displacement and tensile force distribution in the geogrid.

Figure 7. Base case maximum geogrid settlement versus embankment height.

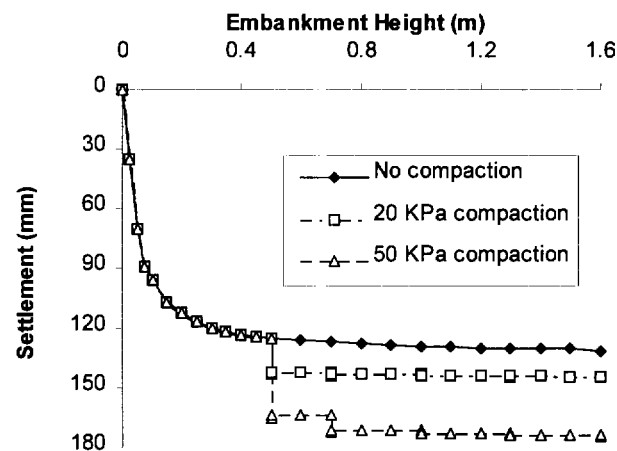


Figure 7. Base case maximum geogrid settlement versus embankment height.

The arching effect between pile caps reduced the incremental portion of load carried by the geogrid as the fill height increased. Thus the displacement did not increase at the same rate as the embankment was constructed. The arching effect between pile caps is shown in Figure 8. Figures 6 and 8 show that the surface displacement is relatively small.

Five models were analyzed in FLAC. The base case model had the geogrid, mattress, pile caps, and fill all modelled as they are in the field. A fictive 3D model attempted to account for the three dimensional effects of the lateral spacing between pile caps by increasing the weight of the fill by the equivalent increased area of 50 %. Next, air was modelled between all the pile caps to compare the design assumptions with the FLAC results. Because the air was modelled in all the areas around the pile caps the geogrid had relatively high tensile stresses from settlements on both sides of the pile cap. Also the geogrid was not able to move toward either side as it could in the mattress case. Compared to the mattress model, the air model had smaller displacements and higher geogrid tensile forces and strains. The final two models had soil modelled below the geogrid as it was in most of the embankment. Unlike the mattress and air, the soil was stiffer than the gytija below the footing. Therefore much of the displacement

## Soil

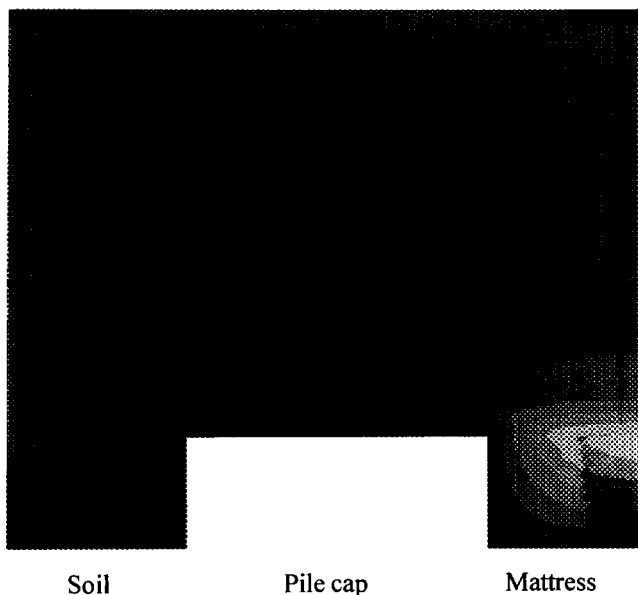


Figure 8. Arching effect as shown by y-displacement contours.

occurred in the gytja. Thus the soil models required that the lower fill and gytja be included in the calculations. The material properties of the gytja were not known with much certainty, so the soil model calculations are provided to show only approximate magnitudes.

The results from the FLAC calculations are summarized in Table 3.

In these models the most important input parameters affecting the magnitude of the settlement in the embankment were the following: moduli of the soil or mattress between pile caps, elastic modulus times area of the cable, amount of compaction, depth of fill when compacted, the soil/geogrid bond properties and the fill properties.

## 1.7 Comparison between calculations and field measurements

A comparison was made between the values obtained in design and the values measured for vertical displacements and forces in the reinforcement.

For the case with the mattress the calculated tensile force was 10 kN/m and the displacement about 0.14 m in FLAC. Modelling compaction of the fill increased the displacement between 10 and 50 mm and the tensile force between 3 and 9 kN/m. The forces measured in the area with mattresses were generally somewhat higher than calculated, as was the displacement. One of the causes may be three-dimensional behaviour. FLAC calculations in two dimensions were estimated to give a good understanding of the behaviour of the construction, but it was somewhat uncertain. One way of taking the three-dimensional behaviour into account was to increase the density by 50 %, which corresponds to a load distribution according to Figure 11. Such a calculation gave a displacement of 0.18 to 0.2 m when the compaction effect was taken into account. This was closer to the results in the field which were 0.17 to 0.21 m. The strain in the geogrid in the field between the caps was 3 %, which the FLAC calculation also showed for the compaction case. For the case with soil below the geogrid the displacement according to the FLAC calculation was 12 mm and the tensile force was 0.4 kN/m without compaction. If the fictive three-dimensional effects were taken into account as mentioned above then the calculated displacement was 23 mm. Modelling compaction of the fill increased the displacement between 10 and 45 mm and the tensile force between 1 and 9 kN.

In the soil case the displacements without compaction corresponded better to the field measurements. On the other hand the displacements are small and there are large uncertainties in the properties for the soil below the pile caps. Therefore the model of the case with mattresses is more reliable.

Because the resistance of the foundation soil is considerable the analytical calculation models in this case gave a misguided picture of the actual behaviour of the construction. The FLAC calculations on the other hand gave a good picture of the behaviour on the condition that the pertinent input data was used. If a cavity should arise under the reinforcement then the analytical models are thought to be appropriate, but the three-dimensional effects should be taken into account.

Table 3. Results from FLAC.

Model Description	Maximum Settlement* (mm)	Maximum Cable Tensile Force (kN)	Maximum Cable Strain (%)
Base case no compaction	141	10	1.7
Base case 20 kPa compaction	155	13	2.2
Base case 50 kPa compaction	188	19	3.1
Fictive 3-D no compaction	171	14	2.3
Fictive 3-D 20 kPa compaction	181	17	2.8
Fictive 3-D 50 kPa compaction	205	23	3.9
Design grid air no compaction	152	15	2.4
Design grid air 20 kPa compaction	167	18	3.0
Design grid air 50 kPa compaction	195	25	4.2
Soil case no compaction	12	0.4	0.07
Soil case 20 kPa compaction	22	1.5	0.25
Soil case 50 kPa compaction	56	7	1.2
Soil fictive 3-D no compaction	23	1.6	0.3
Soil fictive 3-D 20 kPa compaction	35	3.5	0.6
Soil fictive 3-D 50 kPa compaction	70	11	1.8

\* The results are shown to the nearest mm for comparison purposes only. Model predictions are not this precise.

## 2. PROPOSED ANALYTICAL CALCULATION MODEL

With an active reinforcement, the size of the caps can be reduced. It is also possible to choose a lower embankment height than the 2.5 metres which is today the lowest permitted in Swedish regulations.

In order to be able to propose a model which is suitable for design of reinforcement over embankment piling, the SGI carried out a pre-study by the assignment of the SNRA where a number of calculation models were compared. In that comparison, BS 8006 appeared to be a promising model. In the second stage of the project, BS 8006 was compared with FLAC calculations to get a closer idea of the actual behaviour. That comparison showed that at the degree of cap coverage which is normally used in Sweden between 20 to 30 % (to be compared with those on which the method is based, which are usually around 8 to 16 %) the calculations did not agree. Better agreement was reached when Carlsson's method was compared to the FLAC calculations. This method had been modified to take into account the three-dimensional effects and reduced embankment heights.

### 2.1 Prerequisites

The calculation assumes arch formation and that the reinforcement is deformed during loading. The reinforcement is assumed to be placed in one layer. The function of the reinforcement is greatest if it is placed closest to the pile caps, but it should for practical reasons be about 0.1 m above the pile caps.

In order to ensure that the displacements in the road surface are not too large, the embankment height should be at least as large as the distance between the pile caps, a minimum of 1.0 m high, and the degree of cap coverage should be at least 10 %.

It is recommended that calculations should be carried out for an initial strain of a maximum of 6 % and with a remaining creep strain after the construction period and during the lifetime of the construction of an additional 2 % at most. Figure 9 shows the symbols used in the proposed calculation model.

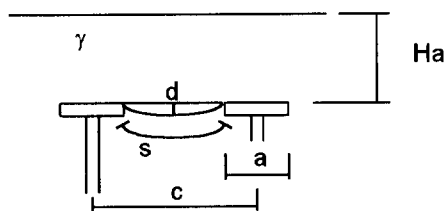


Figure 9. Symbols used in the proposed calculation model.

where  $c$  = distance between the pile centres (m)  
 $a$  = side length of the pile caps  
 $Ha$  = embankment's height above the reinforcement (m)  
 $\gamma$  = unit weight of embankment fill ( $\text{kN/m}^3$ )  
 $d$  = maximum displacement of the geosynthetic (m)  
 $s$  = arc length of the displaced geosynthetic (m)

### 2.2 Vertical load transfer

The method is based on the formation of an arch which spreads the soil load onto the pile caps. The cross-sectional area of the soil under the arch, which is the load carried by the rein-

forcement geogrid, is approximated using the soil wedge described in Figure 10. This applies even if the embankment height is lower than  $(c-a)/2 \cdot \tan 15^\circ$ , which is the height of the soil wedge.

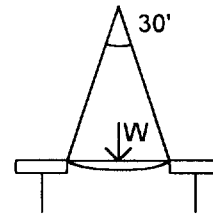


Figure 10. The soil wedge which is carried by the geosynthetic.

The weight of the soil wedge,  $W$ , according to Figure 10 is:

$$W = \frac{(c-a)^2}{4 \cdot \tan 15^\circ} \cdot \gamma \quad \text{kN per metre in depth.}$$

The arc length of the geogrid when it is displaced by the load of the soil wedge, can be calculated as follows:

$$s = (1 + \epsilon)(c-a) = c-a + \frac{8}{3} \cdot \frac{d^2}{c-a}$$

where the displacement,  $d$ , is dependent on the strain in the geosynthetic,  $\epsilon$ , according to:

$$d \approx (c-a) \sqrt{\frac{3}{8} \cdot \epsilon}$$

The force in the reinforcement,  $F$ , in two-dimensions is calculated using the catenary equation:

$$F_{2D} = W \cdot \frac{(c-a)}{8d} \sqrt{1 + \frac{16d^2}{(c-a)^2}}$$

The three-dimensional effects are estimated through load distribution according to Figure 11, where the load is distributed over the surface according to the figure and is taken up by the reinforcement along the edge of the pile cap. The force is calculated as follows:

$$F_{3D} = \frac{1 + c/a}{2} F_{2D}$$

where,

$F_{3D}$  = the dimensioned force in the reinforcement due to the vertical load in three dimensions

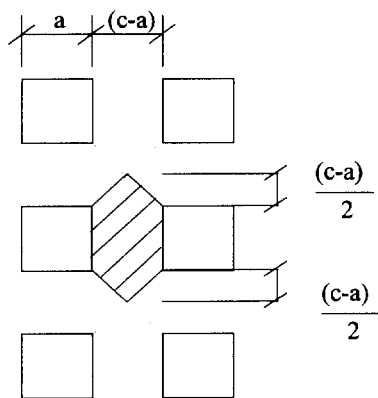


Figure 11. Load distribution to estimate the forces in the three-dimensional case.

### 2.3 Transverse sliding across the bank and pull-out of the reinforcement

For the necessary reinforcement length on account of transverse sliding across the bank, the bond length and the pull-out length of the reinforcement can be determined according to BS 8006.

## 3. CONCLUSIONS

In design with analytical models, the foundation support of the soil between the pile caps is not normally taken into account, but field measurements showed that the effect can be considerable. For the relatively low embankment height used here, it appeared that the displacement which arises in the reinforcement does not affect displacements in the road surface. In this case, the FLAC calculations are judged to give a good picture of the actual behaviour of the construction. Three-dimensional effects should however be simulated. Here they were fictively simulated by increasing the density of the fill.

Analytical calculation models are judged reasonable if there is a risk that a cavity will arise under the reinforcement. They are though often more conservative than if FLAC calculations are made for cavities. The proposed calculation model has proved to give better agreement with the FLAC calculations than other methods at the degrees of cap coverage which are normally used in Sweden, i.e. 20 to 30 %. Soil with poor properties can give support initially but settlement can arise even after the construction period. Thus in low embankments there is a risk that settlement which arises after the completion of the road could cause displacements in the road surface, and this must be taken into account in design. The force in the reinforcement is also greater if the soil settles than if there is resistance. Future changes to the load situation, e.g. a ground water lowering, can affect the foundation support of the soil and in such cases it should be assumed that a cavity has arisen.

Compaction of the fill above the reinforcement significantly affects the tensile force and moderately affects the displacement of the reinforcement. This is very important if the compaction is carried out at low fill heights above the reinforcement. The effect of compaction is not normally taken into account in calculations but should be considered if foundation support from the soil is assumed.

The results of the field study showed a large difference in the strain measurements close to the pile cap edge, possibly due to edge effects. This makes the cap edge strains difficult to compare with the calculation model. The strains measured in the center of the pile caps show a smaller difference and compare well with the FLAC model. Some effects of three-dimensional behaviour could be seen in the field measurements. A larger area with mattresses would have better simulated what actually happens if a cavity appears under the reinforcement. In this case the measurements were conducted on a road construction and the risk of having to rebuild large areas of the embankment, if the displacement of the road surface proved too great, was not acceptable.

For many cases the analytical calculation models that assume cavities below the geogrid are too conservative in estimating the forces in the geogrid. The finite difference model showed much better agreement with field measurements because it included the soil foundation support beneath the reinforcement. A study by (Jones et al, 1990) concluded that current simplified analytical procedures are conservative due to quantifying the arching mechanism and that they can not accurately take into account partial foundation support. There is a need for finite element or difference methods to model the complex interaction behaviour. Additional full-scale field testing and modelling is necessary to better understand the processes involved here.

The three-dimensional effects should be studied with field studies using larger areas with simulated cavities. Modelling should also be done with three-dimensional programmes to verify the differences between two- and three-dimensions. Until three-dimensional programmes become more common there is a need to model in two-dimensions, with relevant additions to take the three-dimensional behaviour into account.

## ACKNOWLEDGEMENTS

The authors would like to thank Mr. F. Burman, SGI, who carried out the measurements, Mr. M. Åberg, SNRA, assistant project leader, Mr. P-E Bengtsson, SGI, for his views on the choice of parameters and Mr. T. Eng, Engtex, for help with the properties of the reinforcement.

The project described in the article was funded by SNRA and SGI.

Douglas Lindquist's participation in the project was possible thanks to a grant from the Valle Scandinavian Exchange.

## REFERENCES

- British Standard, BS 8006 (1995) *Code of practice for strengthened/reinforced soils and other fills*. BSi.
- Carlsson B. (1987) *Reinforced soil, principles for calculation*, Terratema AB, Linköping. (In Swedish).
- Itasca Consulting Group, Inc. (1995). *Fast Lagrangian Analysis of Continua (FLAC) Version 3.3 User's Manual*.
- Jones, C.J.F.P., Lawson, C.R., Ayres, D.J. (1990) Geotextile reinforced piled embankments, *4th Int. Conf. on Geotextiles, Geomembranes and Related Products*, The Hague, 28 May-1 June 1990, page 155-159.

# Embankment Support Over Piles Using Geogrids

C G Jenner and R A Austin

Tensar Division, Netlon Limited, New Wellington Street, Blackburn, UK

D Buckland

Clwyd County Council Highways Department, Clwyd, UK

## ABSTRACT:

The construction of embankments over soft ground is a common engineering problem. In situations where the underlying soil is highly compressible or for approach embankments to bridges, minimising the total and differential settlement of a new road construction can govern the method of construction.

The paper describes the use of stiff biaxial polypropylene geogrids within granular fill to support embankment loads above piles and vibro concrete columns, VCCs. This technique has been used successfully on many road embankment projects in Europe due its cost effectiveness and ability to deliver an effective embankment support system within a short time frame.

The design and construction of geogrid reinforced load transfer platforms is discussed, including the platform used on the A525 Rhuddlan Bypass in North Wales, where due to underlying soil conditions, a piled solution employing VCCs was used, to carry the embankment loads through the soft layers into the firmer strata below.

To ensure that the load transfer platform (LTP) performed as expected, instrumentation was included in the platform construction to monitor platform settlement, geogrid strains and deflections. The installation and results of the instrumentation monitoring are described.

**KEYWORDS:** Embankments, Geogrids, Piles, Design, Monitoring

## 1 INTRODUCTION

The growing use of geosynthetic solutions for construction over soft and variable ground confirms their importance in overcoming complex geotechnical problems.

Increasingly utilised under embankments constructed on piles or vibro concrete columns (VCCs), is a geogrid reinforced granular load transfer platform. Used in several major UK projects, the technique is growing in popularity in Europe because it offers a rapid, cost effective solution within a predictable construction programme.

The platform functions by transferring loads imposed by the embankment to pile caps via a grid-reinforced basal layer. Biaxial geogrids, with high stiffness at low strain, are placed in several layers to interlock with, and reinforce the granular fill to create a flexurally stiff platform which distributes loads evenly and reliably to the piles. The supporting piles or VCCs pass through the soft soil layer and transmit load to the stable ground beneath, thus reducing settlement and removing the need to pre-consolidate the ground to remove permanent settlement and improve ground bearing properties.

## 2 LOAD TRANSFER PLATFORM CONCEPTS

The design of a load transfer platform can be carried out in different ways:

1. Tension membrane approach, using high strength tension membrane theory.
2. Improved arching approach, using low strength reinforcement.

The most common approach for embankment support over piles is to adopt the tension membrane approach. This requires the reinforcement to carry the full amount of any vertical load above the geosynthetic, less allowance for load shedding in the overlying fill.

The improved arching approach differs from the tension membrane theory only in respect to the calculation of the vertical load shedding and relies on the ability of the reinforcement used to interlock with the granular embankment fill and enhance the natural arching angle of the fill, thus reducing the vertical load to be supported by the reinforcement. Both design methods can be carried out in accordance with the limit state design principles defined in BS 8006.

When constructing load transfer platforms using the improved arching approach, the mechanism of load transfer is one of arching taking place in the granular platform. The purpose of the geogrids spanning across the pile/VCC heads is to enhance the transfer of vertical loading onto the piles/VCCs and subsequently through the piles/VCCs to the foundation soils.

In order to control differential settlement at the proposed ground surface, the geogrids need to adequately retain the soil between the arching angles of adjacent VCCs. A minimum height of fill above the load transfer platform of at least the platform thickness is normally employed to ensure that the arch is always loaded and that the VCC positions are not reflected up to the ground surface causing surface undulations.

Stiff integral biaxial geogrids, due to their unique element geometry and junction strength, interact with the fill and create a composite beam where the fill's shear strength properties are utilised effectively. The improved arching design approach is specific to a type of integral geogrid which has been proven to enhance the natural arching angle of granular fill when a multi-layer solution is employed, Guido 1987.

Research into the load transfer characteristics of the geogrid/fill composite has shown that the load spread through fill can be conservatively taken as  $45^\circ$  providing that the peak internal angle of friction of the fill is at least this value.

Whichever design approach is used, the design must ensure that the geosynthetic is sufficiently well anchored in the fill material, to permit the transfer of the design load into the reinforcement. This requirement can lead to long anchorage lengths where high strength reinforcement solutions are employed.

Geogrid load transfer platforms designed adopting the enhanced arching approach have been successfully used on a number of major projects in Europe, including the Gdansk Urban Highway, Topolnicki 1996 and the Second Severn Crossing Toll Plaza, Maddison et al. 1996.

### 3.0 CASE STUDY

#### 3.1 A525 Rhuddlan Bypass

Rhuddlan is a small town standing between the coastal town of Rhyl and the main A55 trunk road, in Denbighshire (formerly Clwyd), North Wales. During the summer months large traffic volumes leave the A55 and travel through the centre of Rhuddlan on their way to the coast causing severe congestion.

In May 1995 a two year £11 million contract was started for the construction of 2km of 7.3m wide two lane dual carriageway bypass to the town, which included upgrading an existing section of highway and the construction of a

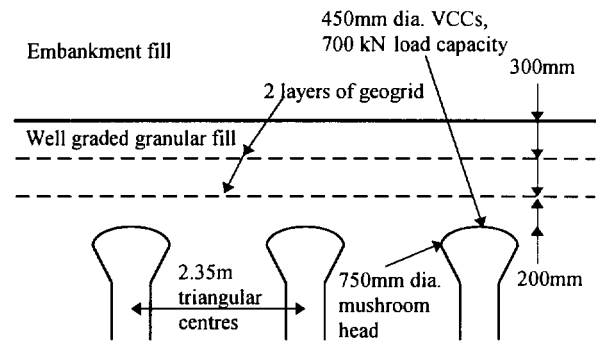


Figure 1 Typical cross-section through Rhuddlan bypass load transfer platform.

430m long 11-span twin deck viaduct, with a 46m centre span over the River Clwyd.

The approach embankment to one side of the viaduct crossed an area of 7-8m of peat and soft silty alluvial strata overlying sands and gravels. To support the embankment over this area the construction contract specified cast in situ driven piles under a 800mm thick un-reinforced rolled concrete supporting raft. Contractor Edmund Nuttall proposed a VCC and load transfer platform solution as an economic and rapidly constructed alternative to the specified design.

The accepted solution for the embankment support was to install VCCs at the appropriate centres to support the loads from the embankment which varied in height from 4m to 7m. The layout of the VCCs was a triangular pattern with centre to centre dimensions of 2.65m, 2.35m, 2.05m, and 1.75m, the closer centres supporting the higher sections of the embankment.

#### 3.2 Load transfer platform design

The geogrid reinforced load transfer platform varied in height, 650mm, 800mm and 950mm, depending on the particular VCC layout with the number of geogrid layers being 3No. in the 950mm thick sections and 2No. in the 800mm and 650mm sections. As the distance between the VCCs reduced the load transfer platform thickness required for the arching mechanism to develop also reduced.

The LTP was designed assuming a grid strain of 5% in 120 years. This level of strain was assumed to represent the ultimate limit state condition for the platform, which can only occur in conditions where the underlying soil would degrade or collapse, i.e. waste fills. Such conditions did not occur on this site. For the in-service condition some support to the fill beneath the developed arch will always be provided by the underlying soil, leading to a reduced level of strain in the geogrid. A typical cross section through the construction used is shown in Figure 1



Table 1 Properties of Geogrids used in the Rhuddlan Bypass Load Transfer Platform

Grid Property		Tensar SS1	Tensar SS2
		Grid Type 1	Grid Type 2
Quality Control Strength*	LD	12.5 kN/m	17.5 kN/m
	TD	20.5kN/m	31.5 kN/m
Approximate Peak Strain	LD	12.0%	12.0%
	TD	10.0%	10.0%
Load at 2% Strain*	LD	4.5 kN/m	7.0 kN/m
	TD	6.0 kN/m	12.0 kN/m
Load at 5% Strain*	LD	9.5 kN/m	14 kN/m
	TD	15.0 kN/m	23.0 kN/m
Typical Rib Thickness	LD	0.7mm	1.20mm
	TD	0.5mm	0.90mm

\* Determined as a lower 95% confidence limit in accordance with ISO 2602 1980 (BS 2846 Part 2 1981).

and properties of the reinforcement used are given in Table 1. Approximately 18 000m<sup>2</sup> of biaxial geogrid was installed to construct the 6000m<sup>2</sup> of load transfer platform over VCCs installed by Keller Foundations Ltd.

Due to the critical nature of the project the Client, Clwyd County Council requested the Contractors alternative design was subjected to Category II checks and certification. An independent verification of the design was therefore carried out by Clwyd County Council's Design and Construction Division Bridges Group - the designer of the structures.

### 3.3 Monitoring of geogrid strain

To ascertain the performance of the load transfer platform, the bridge designer specified that strain gauges and inclinometers were installed in the reinforced fill. At two locations, inclinometer and strain gauges were installed to monitor development of the arch and geogrid strain.

Prior to installation of the strain gauges, a calibration exercise was undertaken in a tensile testing machine to correlate the strain recorded by the gauges with the actual strain in the grid, Figure 2.

On site, vibrating wire strain gauges were clamped in pairs to both layers of grid, at the centre of the geogrid design span geogrid to measure strain over a 260mm gauge length, Figure 3. At locations A and B, an inclinometer and two pairs of strain gauges were installed on each layer of grid. Station A was under the viaduct bank seat with a vertical pressure of 121 kN/m<sup>2</sup> applied to the top of the reinforced fill. At Station B the platform was supporting a 4m high embankment.

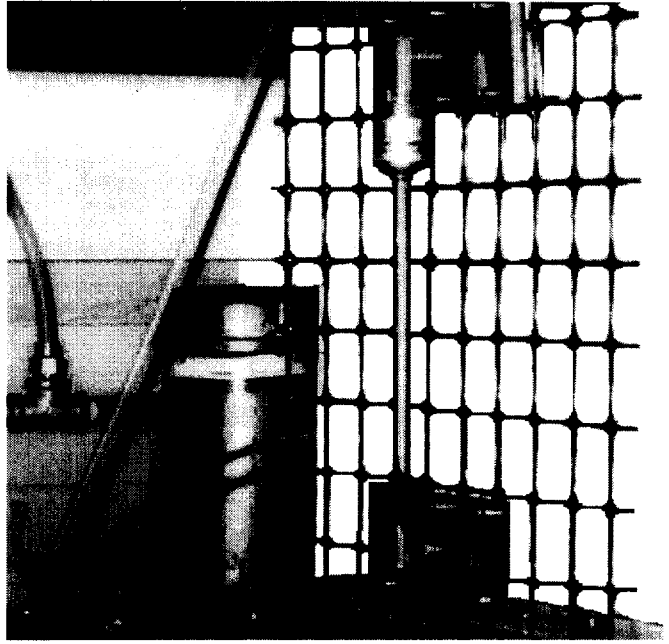


Figure 2 Laboratory calibration of strain gauges.

### 3.4 Results of strain monitoring

Readings taken over a period of one year show that strain developed in the grid during construction, after which the strain remained virtually unchanged, Figure 4 & 5. Once the initial strain had developed during construction the LTP rapidly achieved a state of equilibrium and the grid strains stabilised, with no evidence of creep being apparent. As used in the LTP design, partial support of the fill under the arch was shown to have occurred by a reduced level of strain in the geogrid from that assumed being recorded.

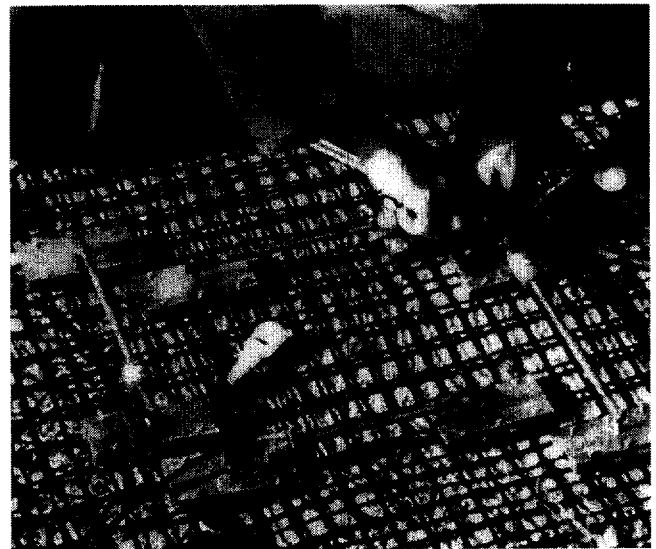


Figure 3 Installation of strain gauges on geogrid

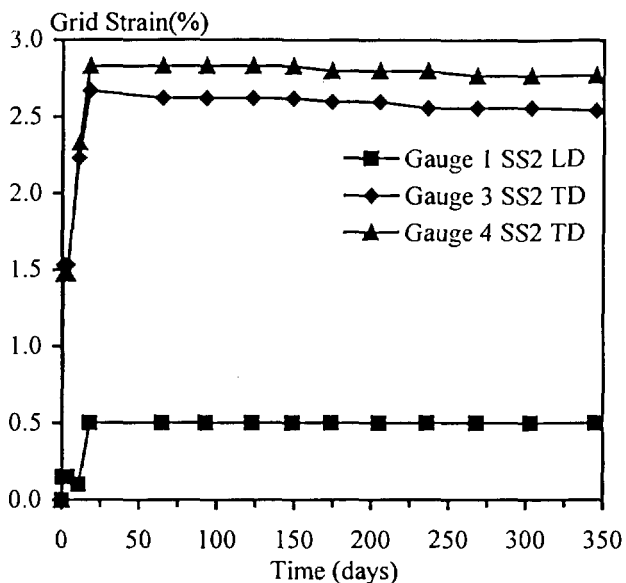


Figure 4 Geogrid strain readings at Station B Lower Grid - Grid Type 2

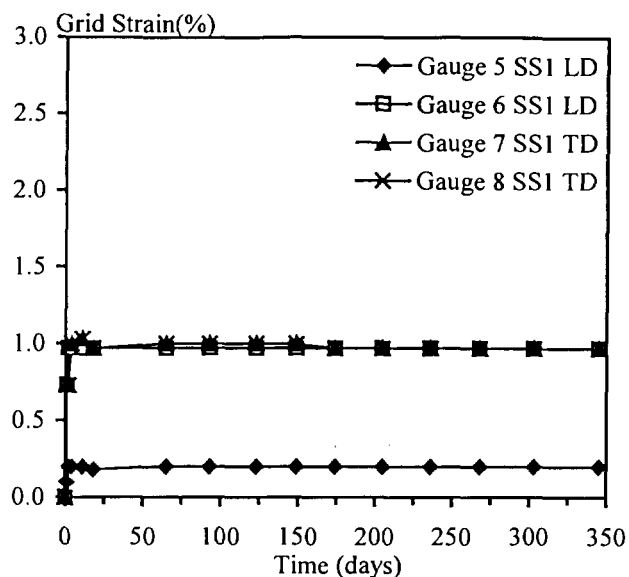


Figure 5 Geogrid strain readings at Station B Upper Grid - Grid Type 1

One of the simplified assumptions made during the design check was that half the weight of the fill under the arch would be supported by the foundation soil and half by the geogrid layers. It was further assumed that the strain in the upper grid would be less than that in the lower grid. The initial strain calculated by this approach was found to be of similar magnitude to that recorded by the strain gauges over the monitoring period.

#### 4.0 CONCLUSIONS

1. The geogrid reinforced load transfer platform used on the Rhuddlan Bypass project provided a cost effective solution to the problem of embankment construction over soft ground.
2. The monitoring undertaken revealed that the geogrid reinforcement was providing restraint to the fill to enable enhanced arching within the fill to occur.
3. Recorded geogrid strains were as allowed for in the design.
4. Due to the interlock of the geogrid with the fill and the development of a composite material, no evidence of creep of the geogrid was recorded.
5. Higher grid stains were recorded in the lower grid than the upper grid as anticipated in the design.
6. The use of low strength, stiff biaxial geogrids and the enhanced arching design approach is a viable alternative to the use of high strength reinforcement and tension membrane theory, for the construction of embankments over piles.

#### ACKNOWLEDGEMENTS

The Authors wish express their thanks to the Highways and Transportation Department of the former Clwyd County Council and subsequently the Technical Services Department of Denbighshire County Council for the provision of monitoring data for inclusion in this paper.

#### REFERENCES

- British Standards Institution. BS 8006:1995, "Code of practice for strengthened reinforced soils and other fills", BSI, London.
- Guido, V.A., Knueppel, J.D., Sweeny, M.A., 'Plate Loading Tests on Geogrid-Reinforced Earth Slabs', Proceedings: Geosynthetics '87, IFAI, New Orleans, USA. pp. 216-225.
- Maddison, J.D., Jones, D.B., Bell, A.L. and Jenner, C.G., (1996), "Design and performance of an embankment supported using low strength geogrids and vibro concrete columns", Geosynthetics: Applications, Design and Construction, Proceedings EuroGeo1, Balkema, Maastricht, Holland, pp. 325-332.
- Topolnicki, M, (1996), "Case History of a geogrid-reinforced embankment supported on vibro concrete columns", Geosynthetics: Applications, Design and Construction, Proceedings EuroGeo1, Balkema, Maastricht, Holland, pp. 333-340.

# Two- and Three-Dimensional Numerical Analysis of the Performance of Piled Embankments

G. Kempton  
Consultant, Terram Ltd, Pontypool, UK

D. Russell  
Geotechnical Engineer, Foundations & Geotechnics Division, Mott MacDonald, UK

N. D. Pierpoint  
Geotechnical Engineer, Foundations & Geotechnics Division, Mott MacDonald, UK

C. J. F. P. Jones  
Professor of Geotechnical Engineering, University of Newcastle-Upon-Tyne, UK

**ABSTRACT:** Empirical methods have been in use for some time to design geosynthetic materials to carry embankment loads over piles. Some methods have used simple two-dimensional models based on little more than load spreading procedures which generally ignore three-dimensional effects. Other methods have attempted to address the three-dimensional nature of the problem by basing the design method on behaviour observed in experimental work. The paper describes work which has been carried out using two- and three-dimensional finite difference techniques that better represents the problem's full complexity. A study has been carried out which compares the two- and three-dimensional analyses for various piled embankment geometries. A comparison is also made between the two and three-dimensional finite difference analyses and the current British design standard, BS 8006. The paper also gives recommendations for design.

**KEYWORDS:** Design, Embankments, Finite Element Analysis, Geosynthetic Reinforcement, Soft Soils.

## 1. INTRODUCTION

Construction of roads, railways and buildings is increasingly carried out on foundations that would previously have been considered unsuitable. In order to construct these structures with confidence and within the available time it is often necessary to adopt a piled solution. Piles are installed through the soft subsoil material. The piles are much stiffer than the subsoil and therefore differential settlements occur. These differential movements generate shear stresses within the embankment which increase the load on the piles and decrease the load on the subsoil. This mechanism is called arching.

In order to place the relatively expensive piles as far apart as possible, a relatively inexpensive geosynthetic material is included at the base of the fill. The geosynthetic picks up the vertical load not carried directly by the piles and goes into tension. The difficulty in design is to assess the amount of vertical load which is carried by the geosynthetic and the tension which this load generates in the geosynthetic.

A typical piled embankment layout is shown in Figure 1. For analysis and design a two-dimensional (2D) model, Figure 2, has often been used. However, in reality, the problem is three-dimensional (3D), Figure 3.

A research project has been undertaken to better understand the behaviour of the piled embankment system. The finite difference programs FLAC and FLAC<sup>3D</sup> (ITASCA, 1993) have been used to carry out a series of 2D and 3D numerical analyses. These are compared to assess the appropriateness of each approach.

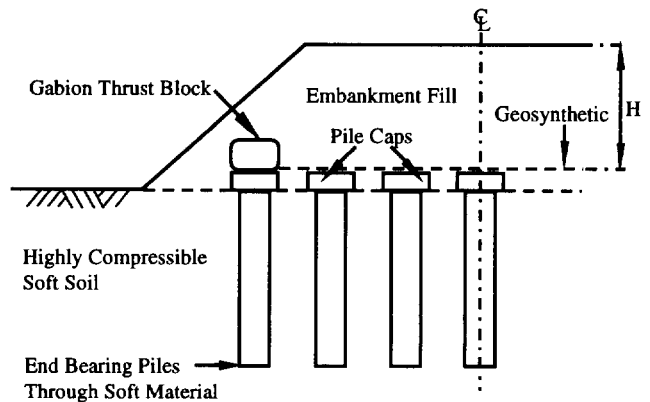


Figure 1. A cross-section through a typical piled embankment.

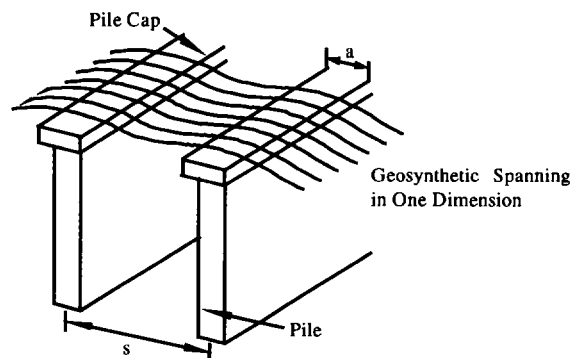


Figure 2. Two-dimensional representation of the piled embankment problem.

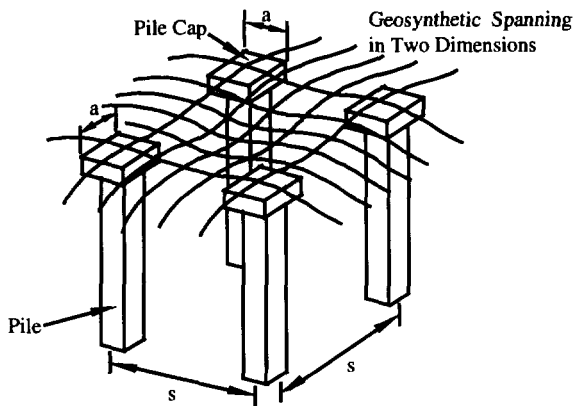


Figure 3. Three-dimensional representation of the piled embankment problem.

Due to the uncertainty of the subsoil behaviour it is generally assumed that the entire vertical load of the embankment is carried by the piles, either by soil arching or transferred by the geosynthetic.

In order to compare design methods a parameter, the Stress Reduction Ratio  $S$  has been defined (after Low, Tang and Choa, 1994). The Stress Reduction Ratio is defined as the ratio of the average vertical stress carried by the geosynthetic  $p_r$  to the average vertical stress  $\gamma H$  due to the embankment fill of height  $H$ :

$$S = \frac{p_r}{\gamma H} \quad (1)$$

The stress reduction ratio  $S$  is written  $S_{2D}$  or  $S_{3D}$  for two- and three-dimensional conditions respectively.

## 2. NUMERICAL ANALYSIS

An initial series of 2D numerical analyses was performed using the finite difference program FLAC. A cross section of the embankment was considered in plane strain for which the pile is represented as a strip foundation. A typical mesh geometry is shown in Figure 4(a).

However, the piled embankment problem is truly 3D (Figure 3); neither plane strain nor axisymmetric analyses accurately reproduce the behaviour. (In axisymmetric analysis, an umbrella shaped arch resting on a single central pile cap is produced). A second series of analyses was performed using the 3D finite difference program FLAC<sup>3D</sup>. A typical mesh geometry for these analyses is shown in Figure 4(b). In 3D the arching can be thought of as producing a dome resting on four pile caps. In both the 2D and 3D analyses, the fill material was modelled as linear elastic with a Mohr-Coulomb yield criterion ( $E' = 20 \text{ MPa}$ ,  $\nu' = 0.2$ ,  $\phi' = 30^\circ$ ,  $c' = 5 \text{ kPa}$  and  $\gamma = 20 \text{ kN/m}^3$ ). The geosynthetic, installed at the base of the fill, consisted of one-dimensional linear elastic elements capable of sustaining axial tension but no bending (a single line of elements in 2D and a grid of elements in 3D with a stiffness  $J = 9500 \text{ kN/m}$ ). In the analyses presented the subsoil was not included (which reproduced

the assumption made in all current design methods), although analyses have subsequently been carried out where the subsoil was included. The pile was assumed rigid with the base of the mesh fixed vertically to represent the pile cap.

For both the 2D and 3D analyses, the embankment fill material was modelled as being installed in a number of lifts. After each lift deformation occurs and the geosynthetic tension increases. The analysis therefore models an embankment constructed very slowly under drained conditions with full consolidation of the subsoil between lifts.

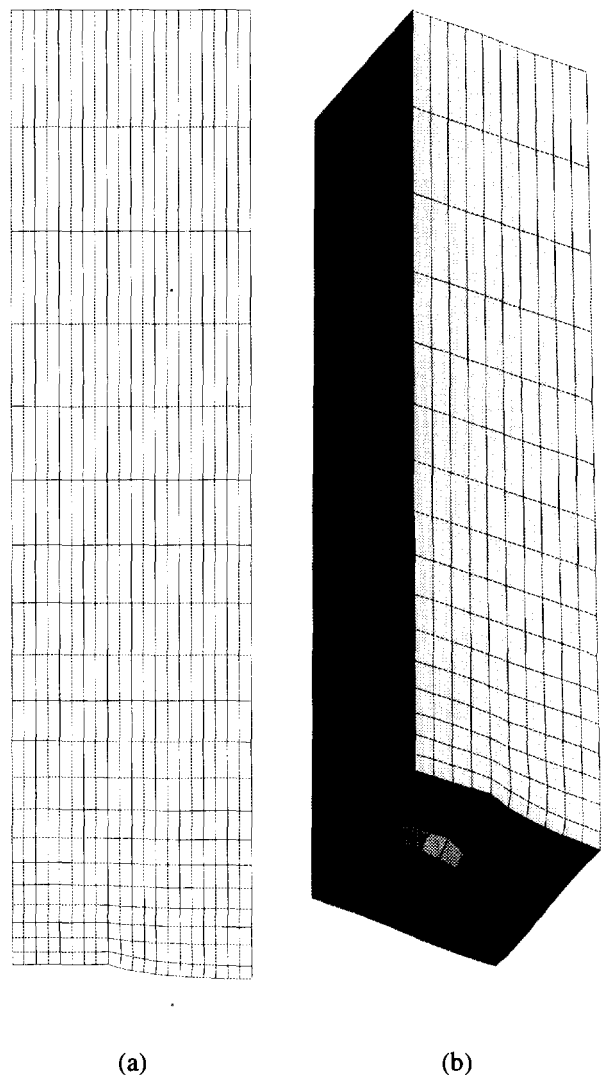


Figure 4. Mesh geometry for (a) 2D analyses, and (b) 3D analyses.

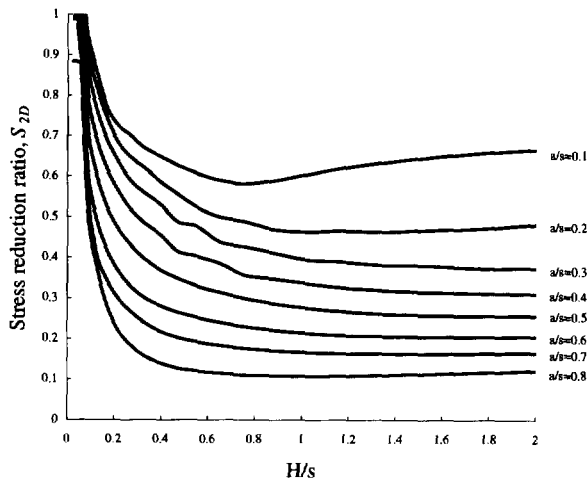


Figure 5. Stress reduction ratio in two-dimensional analyses.

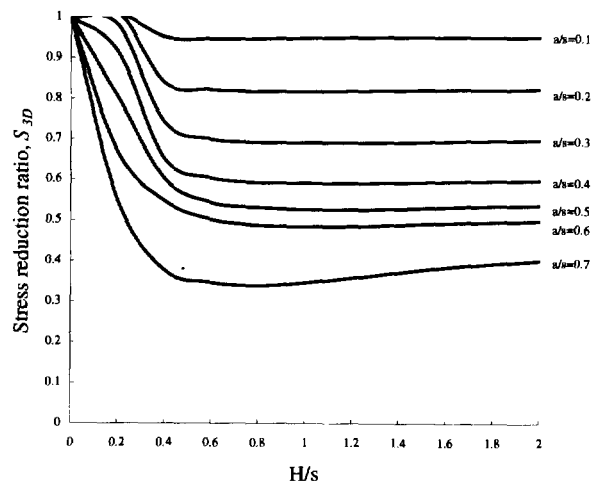


Figure 6. Stress reduction ratio in three-dimensional analyses.

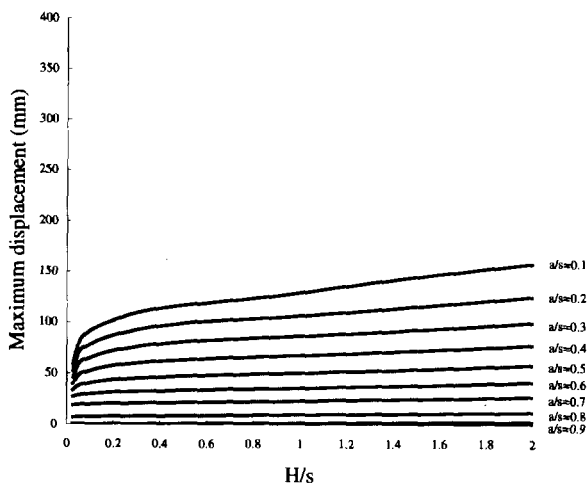


Figure 7. Maximum displacement in two-dimensional analyses.

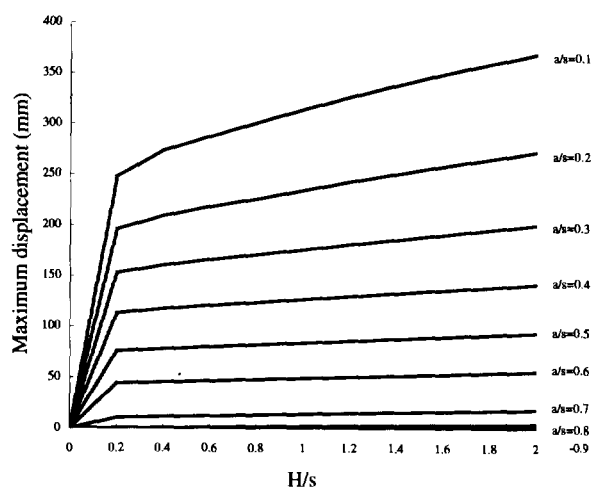


Figure 8. Maximum displacement in three-dimensional analyses.

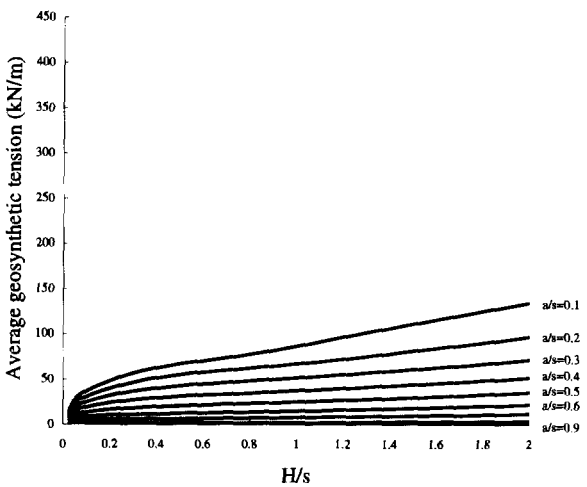


Figure 9. Average geosynthetic tension in two-dimensional analyses.

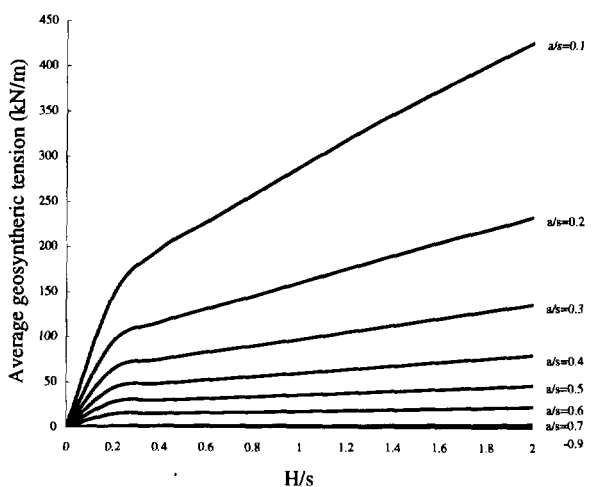


Figure 10. Average geosynthetic tension in three-dimensional analyses.

Analyses were performed in which the pile width  $a$  to pile spacing  $s$  ratio was varied with the fill and geosynthetic properties held constant. The behaviour of the system was assessed in terms of the stress reduction ratio (Figure 5, Figure 6), the average tension generated in the geosynthetic (Figure 7, Figure 8), and the maximum displacement at the base of the embankment (Figure 9, Figure 10), for 2D and 3D analyses respectively.

### 3. DISCUSSION OF ANALYSIS RESULTS

In both the 2D and 3D analyses, the stress reduction ratio decreases as  $a/s$  ratio increases. This is a result of the piles being closer together allowing arching to develop. Also, the stress reduction ratio decreases as the height increases until a critical height is reached after which the stress reduction ratio is virtually constant. This behaviour is explained by the ability of the arching mechanism to develop as the height increases. There is a point at which 'full arching' develops. When this occurs the load carried by the geosynthetic increases proportionally to the embankment height.

The stress reduction ratio determines the maximum displacement and the geosynthetic tension. The higher the stress reduction ratio the larger the maximum displacement and the larger the geosynthetic tension.

The numerical analyses presented demonstrate the need to analyse the piled embankment in 3D rather than 2D. Comparing Figures 6 and 7, it can be seen that the stress reduction ratio is significantly higher in the 3D analyses than in the 2D analyses for any given  $a/s$  ratio. Consequently, the maximum displacement at the base of the embankment and the tension generated in the geosynthetic are underestimated if the 3D nature of the problem is ignored. This behaviour is intuitively correct as the proportion of pile is less in the 3D case ( $a^2/s^2$ ) than in the two-dimensional case ( $a/s$ ).

### 4. BS 8006 DESIGN METHOD

The method used in the current BS 8006, Code of practice for strengthened/reinforced soils and other fills (1995) to design geosynthetics over piles was initially developed by Jones et al. (1990). An assessment of the degree of arching taking place in the embankment fill is made using Marston's formula for positive projecting subsurface conduits (Spangler and Handy, 1973; Young and O'Reilly, 1983). BS 8006 introduces a critical height concept, Figure 11, with the critical height assumed to be equal to  $1.4(s-a)$ , where  $s$  is the pile spacing and  $a$  is the width of the pile cap.

If the embankment height is below the critical height Figure 11(a), the load carried by the geosynthetic is the embankment load reduced due to the arching in the embankment fill plus any surcharge loading on the top of the embankment. For embankment heights greater than

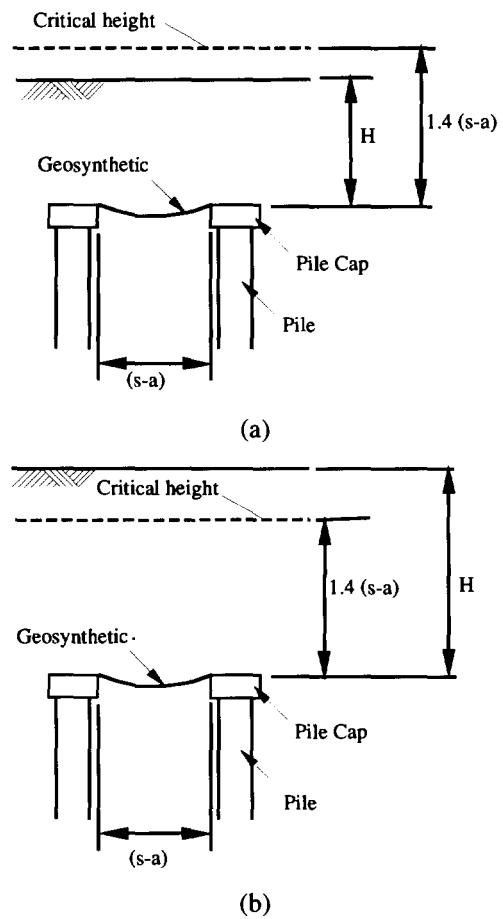


Figure 11. BS 8006 critical height concept.

the critical height, Figure 11(b), it is assumed all loads above the critical height are transferred directly to the piles as a result of arching in the embankment fill.

The load on the geosynthetic is assumed to be a distributed load between adjacent pile caps and the resultant deflected shape of the geosynthetic a parabola. The tension in the geosynthetic, ignoring partial factors of safety, is calculated using the following equation:

$$T = \frac{w_T(s-a)}{2a} \sqrt{1 + \frac{l}{6\varepsilon}} \quad (2)$$

where  $w_T$  is the distributed load on the geosynthetic and  $\varepsilon$  is the strain in the geosynthetic.  $w_T$  can be calculated using one of the following expressions, depending on the embankment height:

For  $H > 1.4(s-a)$

$$w_T = \frac{1.4s\gamma(s-a)}{s^2 - a^2} \left[ s^2 - a^2 \frac{p'_c}{\sigma'_v} \right] \quad (3)$$

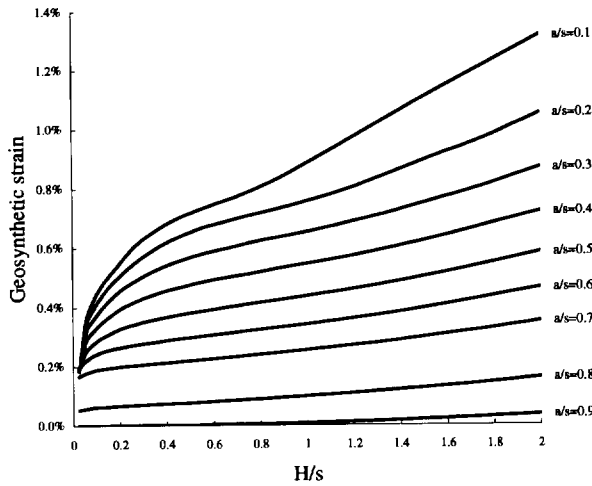


Figure 12. Geosynthetic strain from 2D FLAC analyses.

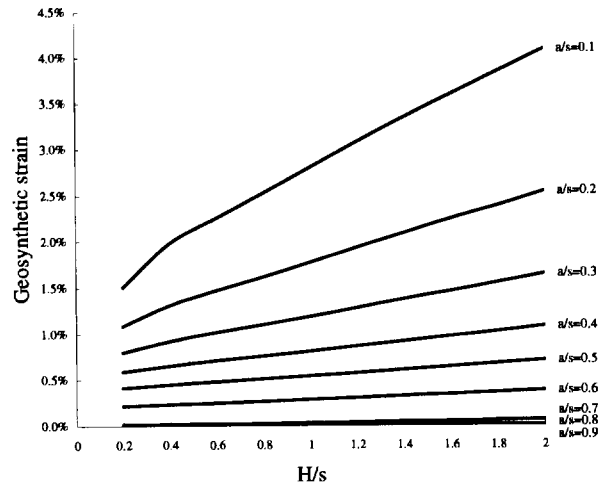


Figure 13. Geosynthetic strain from 3D FLAC analyses.

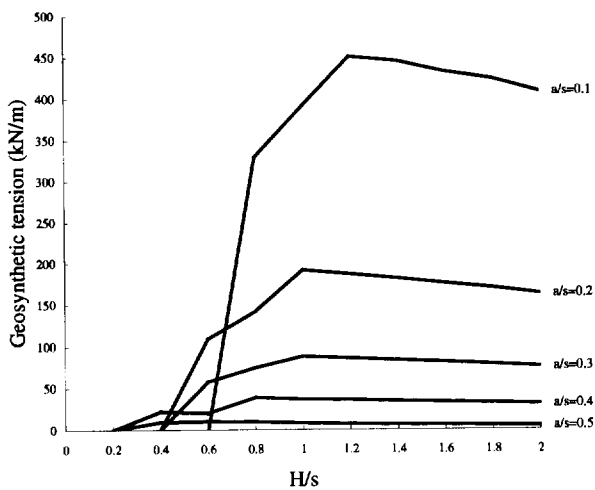


Figure 14. Geosynthetic tension in 2D based on BS 8006.

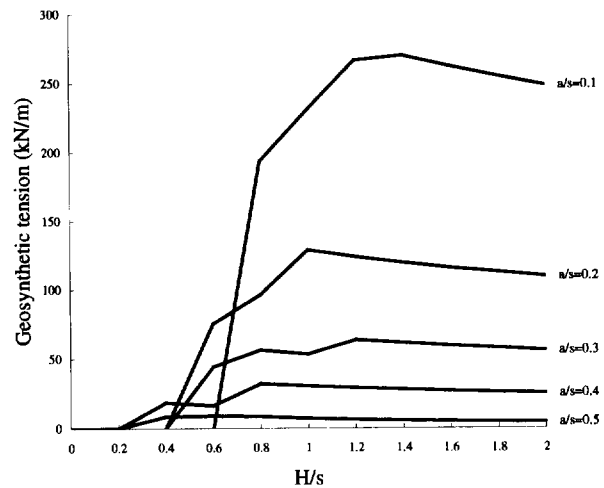


Figure 15. Geosynthetic tension in 3D based on BS 8006.

For  $0.7(s-a) \leq H \leq 1.4(s-a)$

$$w_T = \frac{s(\gamma H + w_s)}{s^2 - a^2} \left[ s^2 - a^2 \frac{p'_c}{\sigma'_v} \right] \quad (4)$$

Where  $\gamma$  is the soil unit weight,  $w_s$  is a uniformly distributed surcharge loading,  $p'_c$  is the vertical stress on the pile cap and  $\sigma'_v$  is the average vertical stress at the base of the embankment.  $p'_c/\sigma'_v$  can be calculated using the following expression:

$$\frac{p'_c}{\sigma'_v} = \left[ \frac{C_c a}{H} \right]^2 \quad (5)$$

Where for the end bearing pile used in this study  $C_c$  is defined as:

$$C_c = 1.95 \frac{H}{a} - 0.18 \quad (6)$$

Partial factors of safety have been omitted from the above equations. No account is taken of the subsoil in assessing the load to be carried by the geosynthetic. BS 8006 recommends that the initial design strain should be limited, for practical purposes, to less than 6%.

For comparison purposes the tension in the geosynthetic was calculated for  $H/s$  ratios from 0.2 to 2.0 and  $a/s$  ratios from 0.2 to 0.8. The design strain values used in Equation 2 were taken from both the 2D and 3D FLAC analyses in Figure 12 and Figure 13, respectively. The tensions determined from the BS 8006 design method are presented in Figure 14 for 2D and Figure 15 for 3D.

A marked difference was found between the geosynthetic tensions calculated using BS 8006 and those resulting from the FLAC analyses.

It was found that BS 8006 overestimated the geosynthetic tension for all geometries in 2D and underestimated the tension in 3D. For  $a/s$  between 0.2 and 0.6 and with  $H/s$  between 0.6 and 1.4 the BS 8006 geosynthetic tensions were approximately 30% lower than the 3D FLAC analysis. For the other

geometries the difference was larger. For values of  $a/s$  less than 0.6 BS 8006 gave a negative tension value. If the BS 8006 partial load factor for soil unit weight is applied, all calculated geosynthetic tensions are 30% higher.

## 5. RECOMMENDATIONS FOR DESIGN

The analyses presented have been compared with various design methods (Russell and Pierpoint, 1997). The comparison showed that there is a reasonable agreement with the Terzaghi (1943) and the Hewlett & Randolph (1988) design methods. The other design methods used in the UK, BS 8006 (1995) and Guido (1987), appear to give results that differ significantly from the numerical analyses for some geometries. The most appropriate design method is dependent on the geometry of the particular piled embankment.

The major uncertainty is the vertical load that the soft subsoil can carry in the long term without producing excessive settlement. This is a very difficult prediction to make as the stiffness of the fill, geosynthetic, piles and subsoil all contribute to the distribution of stresses and therefore, displacement. If the subsoil contribution is overestimated then large settlements of the surface of the embankment can result (Azam et al, 1990). Currently the authors recommend a conservative approach to design with the contribution from the subsoil calculated based on the allowable settlement at the surface of the embankment. This contribution may be negligible for high embankments but can be significant for low embankments or lightly loaded building floor slabs.

Research is underway to look at the role of the subsoil in more detail and to provide recommendations for design. In the mean time the use of numerical analysis methods is strongly recommended.

## 5. CONCLUSIONS

A series of 2D and 3D numerical analyses have been carried out to investigate the behaviour of piled embankments. The analyses show large differences between the 2D and 3D cases. A 3D model is required to accurately model the wide range of piled embankment geometries used in practice.

The 3D parametric study has shown that the minimum stress reduction ratio develops at an  $H/s$  ratio of approximately 0.5. A significantly lower stress reduction ratio is calculated in 2D analyses.

A comparison was made between the BS 8006 design method and the 2D and 3D FLAC analyses. BS 8006 overestimated the geosynthetic tension when compared with FLAC 2D and under estimated the tension when compared with FLAC 3D.

Recommendations for design have been made. The major uncertainty is the amount of vertical load that can be resisted by the subsoil. Due to the current lack of

information, the authors recommend a cautious approach. For high embankments, the resistance from the subsoil is likely to be a small proportion of the total load. For lower embankments, or building slabs, the subsoil resistance may be significant but must be assessed with care to ensure that the long term surface settlements meet construction specifications.

## REFERENCES

- Azam, T., Ramsn, K. and Ali, F. H. (1990), Geotechnical assessment of distressed piled embankments on soft ground, *Seminar on Geotechnical Aspects of the North South Expressway*, Kuala Lumpur, Malaysia.
- BS 8006 (1995), *Code of Practice for strengthened/reinforced soils and other fills*, British Standards Institute.
- Guido, V.A., Kneuppel and Sweeney, M.A. (1987), Plate loading tests on geogrid-reinforced earth slabs, *Geosynthetics '87*, New Orleans, pp. 216-225.
- Hewlett, W.J. and Randolph, M.F. (1988), Analysis of piled embankments, *Ground Engineering*, Vol. 21 No. 3.
- ITASCA Consulting Group Inc (1993), *FLAC/FLAC<sup>3D</sup> - Fast Lagrangian analysis of Continua*. ITASCA Consulting Group, Minneapolis, Minn, USA.
- Jones, C.J.F.P., Lawson, C.R., Ayres, D.J. (1990), *Geotextile reinforced piled embankments, Geotextiles, geomembranes and related products*, Den Hoedt (Ed), 1990, Balkema, Rotterdam, pp. 157-159.
- Low, B.K., Tang, S.K. and Choa, V. (1994), Arching in Piled Embankments, *Journal of Geotechnical Engineering*, ASCE, Vol. 120. No. 11, pp. 1917-1937.
- Russell, D. and Pierpoint, N. D. (1997). A numerical investigation of the behaviour of piled embankments. *Ground Engineering*, November, Thomas Telford.
- Spangler, M.G. and Hardy, R.L. (1973), *Soil Engineering*, Intext Education Publishers, New York.
- Terzaghi, K. (1943), *Theoretical Soil Mechanics*, John Wiley & Sons, New York.
- Young, O.C. and O'Reilly, M.P. (1983), *A guide to design loadings for buried rigid pipes*, Transport and Road Research Laboratory, UK.



# Geogrid and Geocell Reinforced Secondary Road Over Deep Peat Deposit

Juha Forsman

Research Engineer, Viatek Group Ltd, Espoo, Finland

Eero Slunga

Professor, Soil Mechanics and Foundation Engineering, Helsinki university of Technology, Espoo, Finland

Pentti Lahtinen

Development Manager, Viatek Group Ltd / SGT, Luopioinen, Finland

**ABSTRACT:** A reinforced secondary road on the top of a 10 meter thick peat deposit has been constructed at the peat bog of "Leteensuo" in the southern part of Finland. The secondary road contains three different reinforced test sections: two geogrid reinforced and one geocell reinforced sections. This paper presents the description of the construction, field instrumentation and observations of the test sections. The bearing capacity and the settlement of the reinforced roads have been analysed by manual calculation methods. After construction the calculations have been verified on the basis of field observations.

**KEYWORDS:** Unpaved Roads, Geogrids, Geocell, Instrumentation, Case study

## 1. INTRODUCTION

A secondary road (Y607) has been constructed on the top of a peat surface using synthetic georeinforcements. The road forms a part of the Finnish Georeinforcement Research and Development Project, which has been introduced by Friberg et al. (1994).

The secondary road on the top of peat contains three different reinforced test sections: two geogrid reinforced and one geocell reinforced sections. The situation of the test sections is beside the Highway between Helsinki and Tampere at Leteensuo peat bog about 15 km to north-west of the city of Hämeenlinna. The private secondary road is constructed beside the highway at summer 1996.

## 2. TEST SITE

### 2.1 Geology

In the middle of the peat deposit of Leteensuo the thickness of peat layer is 9...10 m and the degree of humification of it is medium (H4-6) or high (H7-10), Figure 1. On the edges of the deposit the degree of humification is high (H=von Post classification). Under the peat layers there is 5...6 m of clay on the top of glacial till. The level of ground water is near the ground level.

### 2.2 Index Properties of the Peat

The index properties of the peat samples [water content ( $w$ ), density ( $\gamma$ ), ash content ( $A_s$ ), acidity (pH), void ratio ( $e$ ) and the degree of humification ( $H$ )] are presented in Figure 2 at station number 244 (Figure 1).

The water content of the peat is about 500...1000 % at the

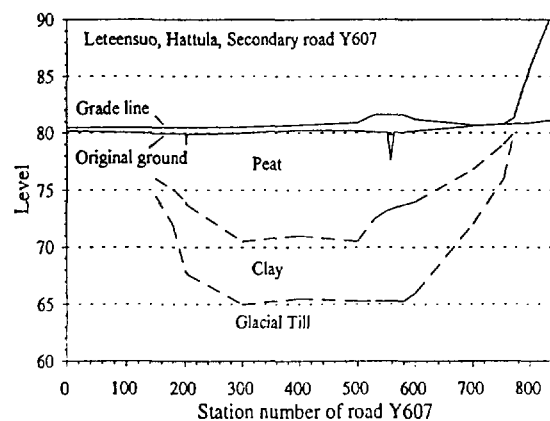


Figure 1. Profile of the secondary road at Leteensuo.

depth of 1...10 m and 300...500 % at the depth of 0...1 m.

### 2.3 Strength and Deformation Parameters of the Peat

The undrained shear strength of the peat has been determined by vane test ( $c_u$ ) and fall-cone test ( $c_{uk}$ ), Figure 2. Drained and undrained triaxial tests with undisturbed peat have been performed using standard triaxial apparatus. The triaxial tests have been performed at a strain rate of 0,6 %/h and with  $\sigma_3 = 10...20$  kPa. The strength and deformation parameters have been determined at strains  $\epsilon_1 = 1,6..15$  %. The drained Young's modulus varies between 380..150 kPa at strains 1,6..15 % at the depth of 0,8..1,0 m, between 360..100 kPa at the depth of 1,3..2,4 m and between 355..80 kPa at the depth of 3,1..5,3 m.

The undrained Young's modulus varies between 580..140 kPa at strains 1,6..15 %. Cohesion varies between 0.4 kPa and the angle of friction between 3..19°. The peat seems to behave like a yield hardening material, without any rupture.

The strength properties of the peat have been determined also by direct shear tests. One dimensional compression of the peat has been studied by means of incremental loading and constant rate of strain oedometer tests. The results of those laboratory tests have been presented more comprehensively by Lojander et al. (1996).

### 3. TEST STRUCTURES

The secondary road of Leteensuu contains two geogrid and one geocell reinforced test sections.

The reinforcements have been used to increase the bearing capacity and to reduce the settlement differences of the road. The road embankment has been constructed by the Finnish National Road Administration of Häme Region.

The geogrid or geocell reinforced structures are: 1xgeogrid+crushed gravel (Ch 90..200 and 680..750, Fig. 3a), Geocell+LECA (Ch 200..300, Fig. 3b) and 2xgeogrid+LECA (Ch 590..680, Fig. 3c).

The test structures are illustrated as designed. The fulfilled thicknesses of the aggregate layers were mainly higher than designed. The fulfilled layer thicknesses at the instrumented stations, 170, 240 and 650, are presented in the brackets in Figure 3. The fulfilled layer thickness varies quite much at the 1xgrid and 2xgrid -structures. The layer thickness of the geocell structure does not vary significantly. The layer

thickness has been measured by ground penetrating radar (GPR) survey after construction.

The LECA, Light Expanded Clay Aggregate, has been used as a light-weight fill because of the expected large settlements of the road.

## 4. MATERIALS OF THE TEST STRUCTURES

### 4.1 Aggregates

In the 1xgeogrid+crushed gravel -structure there was used crushed gravel with a grain size of 0-65 mm as a bearing layer. In the geocell structure the 500 mm high geocell was filled with blown LECA with a grain size of 4-20 mm. In the 2xgeogrid+LECA -structure there was used about 500 mm layer of LECA with a grain size of 0-65mm. Over the LECA there was a layer of crushed gravel as a bearing layer. Uppermost there was surface layer of gravel (0-16mm). The strength and deformation parameters of the aggregates are presented in Table 1.

### 4.2 Geosynthetics

Geogrid Tensor SS30 (grid A) has been used at the bottom of the test structures 1xgrid+crushed gravel and geocell+LECA. Geogrid Tensor SR55 (grid B) has been used as a vertical grid of the geocell structure. Geogrid Fortrac 35/20 (grid C) has been used in the test structure 2xgrid+LECA. The properties of the grids are presented in Table 2.

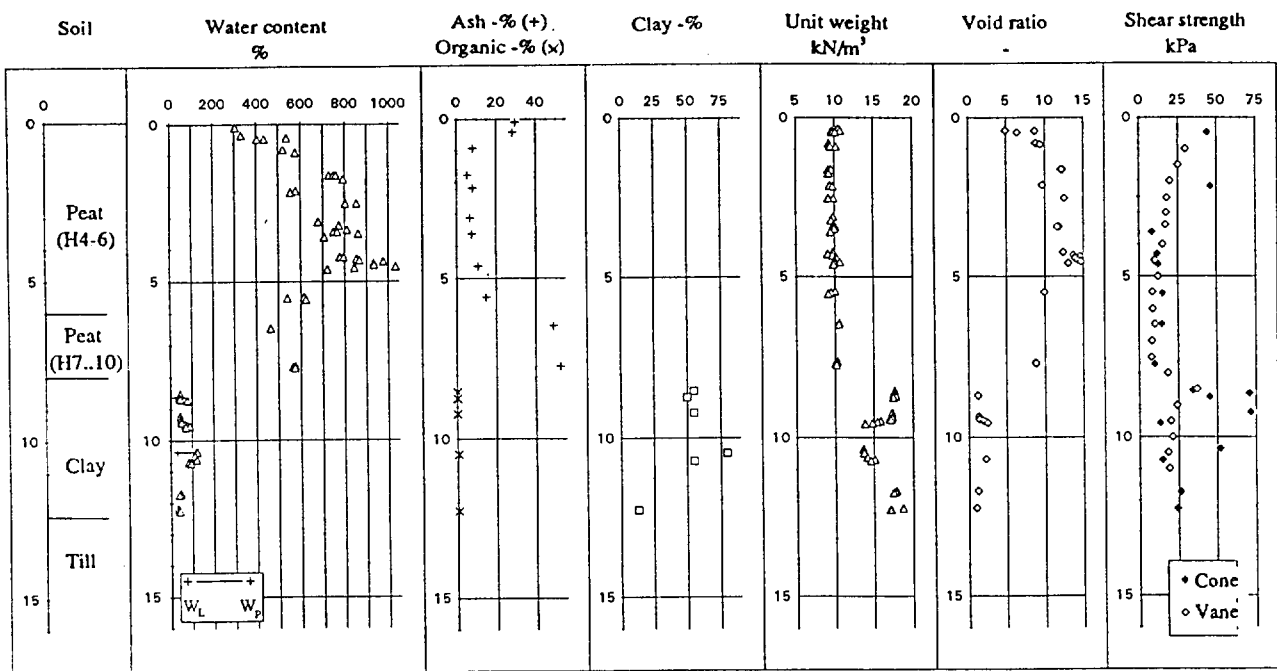


Figure 2. Index properties and undrained shear strength of peat and clay of Leteensuu at station 244.

Table 1. Index, strength and deformation properties of the aggregates.

	Crushed gravel 0-65 mm	LECA 4-20 mm	LECA 0-65 mm
$\gamma_0$ [kN/m <sup>3</sup> ]	19,45	2,99...3,07	4,49...4,81
<b>triaxial test</b>			
$\phi_p   c_p$ [°   kPa]	43,8   0	44,5   2	44,5   2
$\phi_c   c_c$ [°   kPa]	42,6   0	40,0   2	40,0   2
$E_{d50}$ [kPa]	9...26	11...13	14...16
$E_{dr}$ [kPa]	47...143	-	56

Polypropylene grid A is extruded biaxially drawn. Polyethylene (HDPE) grid B is extruded uniaxially drawn. Polyester grid C is woven and coated with PVC. The weight of grid A is 300 g/m<sup>2</sup>, grid B 500 g/m<sup>2</sup> and grid C 210 g/m<sup>2</sup>.

## 5. CONSTRUCTION

### 5.1 Installation of the Geogrids

All test structures have been built during May-July 1996 in three sections. Over the levelled subsoil there was first put a needlepunched nonwoven geotextile. Over the textile there

Table 2. Properties of the reinforcements.

Label	Index strength kN/m	$F_{max}^d$ = UTS kN/m	$\epsilon_{max}^d$ %	$J_{sec}^d$ $\epsilon = 2   6 \%$ kN/m
A <sup>a</sup>	30 / 30 <sup>a</sup>	32,6	9,4	780   535
B <sup>b</sup>	55 / - <sup>b</sup>	50,5	10,1	905   650
C <sup>c</sup>	35 / 20 <sup>c</sup>	36,6	11,4	305   230

a. Biaxially drawn    b. Uniaxially drawn    c. Woven  
a. and b. Netlon Limited (1984, 1995)  
c. DIN 5387, preload 5mN/tex or ASTM 1682/B52576  
d. ISO/DIS 10319.2, Tested at Helsinki Univ. of Tech.

was put the base grid A or C. In the 1xgeogrid structure and in the geocell structure the base grid was installed in the longitudinal direction of the road except the 4 pieces of grid in the 1xgeogrid structure. One of those pieces was instrumented with strain gauges. In the 2xgrid+LECA -structure all grids were installed in transverse direction of the road.

Grid B in the geocell structure was cut to a width of 0,5 m. The grid was installed vertically by wooden piles and nylon cord in the transverse direction of the road. Between the transverse grids there were installed other vertical grids. The grids are connected to each other with iron bars. Vertical grids are connected to base grid with cable ties, Fig. 3b.

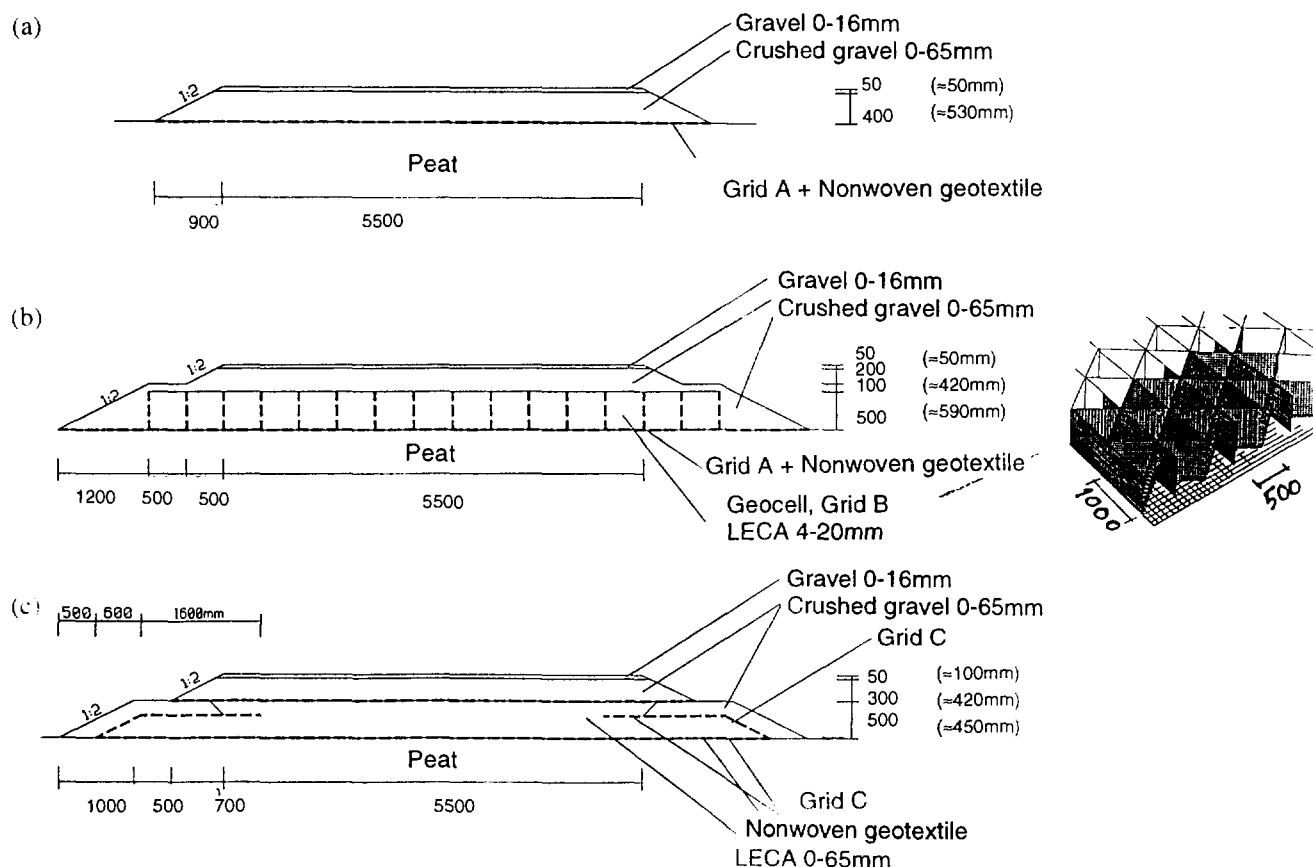


Figure 3. Geogrid and geocell reinforced test structures: (a) 1 x geogrid + crushed gravel, (b) geocell + LECA, (c) 2 x geogrid + LECA. The fulfilled layer thickness are presented in the brackets.

## 5.2 Installation of the Aggregates

The installation of crushed gravel and LECA of the test structures of 1xgrid and 2xgrid+LECA was performed by lorry and excavation machine. The installation of LECA to geocells was performed by blowing.

The precompaction of the aggregate layers was done by the excavation machine with caterpillar tread. All test structures have been compacted by a vibratory roller.

## 6. INSTRUMENTATION

### 6.1 Instruments

The test structures are extensively instrumented. The principles of the instrumentation are presented in Figure 4.

The instrumentation and control methods include: vertical magnetic probe extensometers, horizontal hydrostatic profile gauges, settlement plates, horizontal extensometers, strain gauges, plate load tests and falling weight deflectometer tests (FWD).

### 6.2 Installation of the Instruments

The vertical magnetic probe extensometers were installed at stations 241,5 and 651,5 to measure the settlements of the ground at different depths. An extensometer consists of ring magnets sliding on a central access pipe and fixed in the ground at preselected measuring levels. A special probe travels within the access tube and observes the positions of the magnets outside the tube.

To measure the settlements and the shape of the base of the road embankment there were installed flexible PEH-pipes for the horizontal hydrostatic profile gauges at the peat surface at six stations.

The horizontal extensometers were installed to stations 171 and 651 to measure the horizontal movements of the base of the road embankment about 0,1...0,15 m above the surface of the peat. The measuring units, precision potentiometers, were installed at the centre line of the road and the anchor plates were installed about 1,3 and 2,7 meters to the side from the centre line of the road. When the anchor plate moves the voltage of the potentiometer changes. The changes are converted to millimetres by a calibration factor determined in laboratory.

The strain gauges were glued to grids to measure the strains of the grids at stations 170, 240 and 650. The strain gauges were glued to the elements of the grids. The measured strains are converted to tensions of the reinforcements by a calibration factor determined in laboratory.

At the surface of peat there were installed 4 steel plates ( $\phi=0,45$  m) and at the surface of the LECA 2 steel plates ( $\phi=0,30$  m) for plate bearing tests.

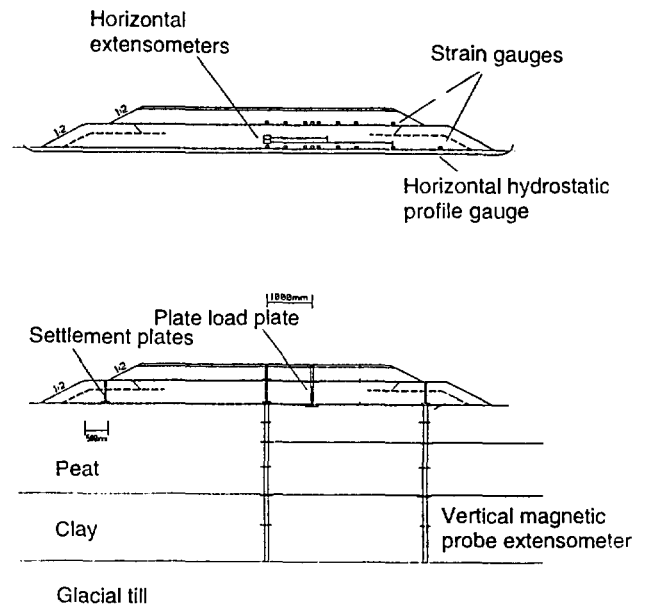


Figure 4. The principles of the instrumentation of the test structures.

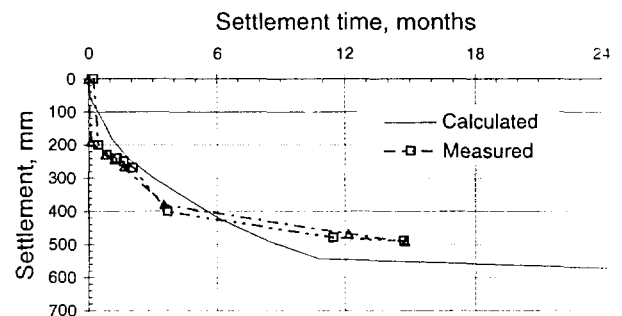


Figure 5. Calculated and measured settlement of the geocell structure at station 240.

## 7. RESULTS

### 7.1 Settlements

The settlements at the centre line of the test structures from summer -96 to 8/97 are: 0,41 m at station 174, 0,51 m at station 239..250 and 0,54 m at station 649. The settlements are directly dependent on the thickness of the peat layer (Figure 1). The measured settlements are quite near to the manually calculated settlements during one year, Figure 5. In this case it is really wise to use LECA as a light-weight fill to keep the road surface over the peat surface. The surface of the 1xgeogrid+crushed gravel -structure is now, 1.5 years after construction, about at the same level as the peat surface and in this situation the drainage of the road structure is very bad.

The settlements at different depths in the ground are not illustrated in this article, but they equal quite well to the precalculated deformation distribution.

## 7.2 $E_2$ -modulus

The  $E_2$ -modulus at the surface of the peat and LECA has been measured at stations 170, 240, 650 and 700 in 7-8/96, 9/96 and 8/97. The  $E_2$ -modulus was 2..5 MPa and 27..36 MPa. The  $E_2$ -modulus of the road has been measured at the surface by plate load and by FWD-tests, Table 4. The FWD-tests have been made at intervals of 10 or 5 m about 1 m to both sides from the centre line. By plate load and FWD-test measured  $E_2$ -modulus are very near each other. Plate load and FWD-tests in 7-8/96 were made before the installation of the surface gravel (0-16mm).

When looking at the results of the plate load and FWD-tests one has to keep in mind that the  $E_2$ -modulus changes very much at different stations along the road because of the varying thickness of the embankment and the strength of the peat layer. It can be seen from the Table 4 that the  $E_2$ -modulus of the structure 2xgeogrid+LECA is increasing by the time.

## 7.3 Strains and Tensions of the Georeinforcements

The measuring results of the strain gauges have been converted to tensions by a calibration factor ignoring the potential effects of the creep of the synthetic geogrids and the effects of the confining stress to the modulus of the grid.

The mobilised tension of the base grid of the 2xgeogrid+LECA -structure is illustrated in Figure 6. The tandem-axle with twin tyres is above the strain gauges. The axle-group load of the lorry is approximately over 16 ton. In Figure (a) there is a lorry laden with gravel on the middle of the embankment (Fig. c) and there is illustrated the total mobilised tension of the grid (=tension before the loading + tension caused by the lorry). In Figure (b) there are the changes of the tension of the grid caused by the lorry on the embankment. In Figures (a) and (b) the continuous line illustrates the case when both axles of the tandem-axle are loaded (Fig. d). The dashed line illustrates the case when the whole load is on one axle of the tandem-axle (Fig. e).

The loading with lorry was repeated with all test structures. The mobilised tension of the base grids was 4..5 kN/m in 1xgrid+crushed gravel, geocell+LECA and 2x geogrid+LECA -structures. The mobilised tension of the upper grid of the 2xgeogrid+LECA -structure was about 1..1,5 kN/m. The changes of the mobilised tension of the lower edge of the vertical grid of the geocell were about 3 kN/m.

The lorry loading of the test embankments has been made almost immediately after the construction of the embank-

ment. About 2..4 months later when repeated the loading the mobilised tension has been lower because of the installation of the surface of the road and the strengthening of the peat due to the consolidation.

## 7.4 Deterioration of the Surface of the Test Structures

The rutting and the deterioration in the form of potholes on the surface of the test structures have been observed ocularly. The shape of the surface has also been measured by the means of levelling. On the basis of the observations after 1 year of the construction there are mostly potholes on the surface of the 1xgrid+crushed gravel -structure. On the surface of the 2xgrid+LECA there are very few potholes but on the surface of the geocell -structure there are more potholes. The most rutted test structures are the 1xgrid and geocell -structures while the surface of the 2xgrid+LECA has behaved better.

## 8. ANALYSIS BY MANUAL CALCULATION

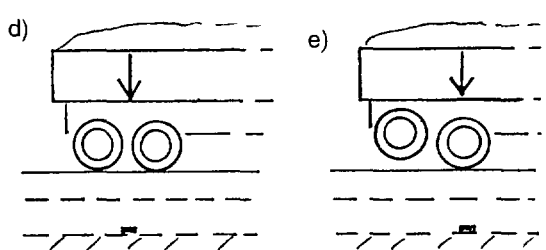
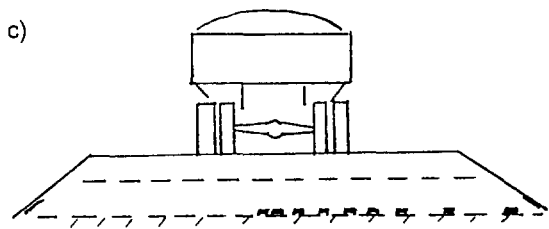
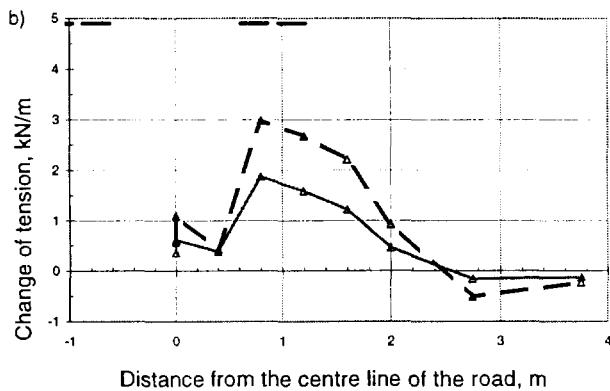
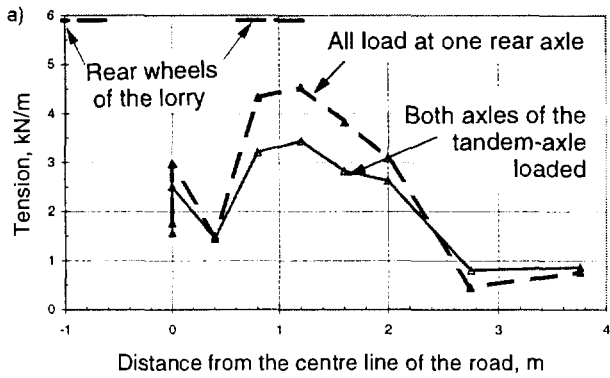
The tension of the grid of the 1xgrid structure has been calculated using the methods presented by Giroud & Noiray (1981) and Housby & Jewell (1990). Both methods are for a clay base but in the absence of a better method those are used also for a peat base. In the calculations the next assumptions have been adopted: axle load 100 kN, number of passes 10 000, rut depth 150 mm and the shear strength of the base 25 kPa.

When using the method of Giroud & Noiray the calculated thickness of the embankment is 0,73 m and tension of the base grid is 8 kN/m. When using the method of Housby & Jewell the calculated thickness of the embankment is 0,77 m and tension of the grid is 10 kN/m. The calculated thickness of the road structure is a little bit bigger than the fulfilled thickness ( $\approx 0,6$  m). The calculated tensions of the grid are about twice as big as the measured ones (4..5 kN/m) in the 1xgrid and 2xgrid -structures.

The method of Housby & Jewell is based on the combination of the bearing capacity of the clay subgrade and the effect of the horizontal stresses in the fill/clay interface. The method of Giroud & Noiray is concentrated to the tensioned membrane effect and the bearing capacity of the clay subgrade. According to the theory of Housby & Jewell the tension of the grid is concentrated near the loading point while in the theory of the tensioned membrane the tension is supposed to be distributed evenly to a very large area. When

Table 4.  $E_2$ -modulus measured by plate load and FWD-tests at 7-8/96, 9/96 and 5/97.

Station	FWD-tests, MPa				Plate load test, MPa, $E_{2\text{ average}}$		
	$E_2$ , 9/96	$E_{2\text{ average}}$ , 9/96	$E_2$ , 5/97	$E_{2\text{ average}}$ , 5/97	7-8/96	9/96	8/97
90...200	17...69	45	34...95	58	36	53	49
200...300	14...83	43	28...95	55	49	67	65
590...680	38...75	55	40...93	69	50	68	89



- - - - - Geogrid C  
 ■ Strain gauge  
 / / / / Peat

Figure 6. Mobilised tension of the base grid of the 2 x grid + LECA-structure caused by a lorry on the embankment. (a) Tension before loading + tension caused by the lorry. (b) The change of the tension of the grid caused by the lorry on the embankment.

studying Figure 6 one can see that the tension is not very largely distributed but the tension is concentrated quite near the loading point.

### 9. CONCLUSIONS

When constructing a road on a peat area there are two main problems: the low bearing capacity of the peat and the large settlements. The low bearing capacity can be increased and the differences in settlements can be reduced by geogrids. In the case of Leteensuu an adequate bearing capacity of the road has been achieved by a moderate low embankment with geogrids. One and a half years after the construction of the test structures there are no significant differential settlements at the road surface.

The measured tensions of the base grids are about half of the precalculated ones with the methods presented by Giroud & Noiray (1981) and Houlsby & Jewell (1990). The distribution of the tension agrees quite well with the distribution assumed by the theory of Houlsby & Jewell. On the basis of the test construction of Leteensuu it seems to be possible to use both of the dimensioning methods of Giroud & Noiray and Houlsby & Jewell on the peat base.

### ACKNOWLEDGEMENTS

The authors like to thank the "Georeinforcement" -project for the financing and promoting of the laboratory tests and the instrumentation of the test structures. Thanks are due also to the organisation of the Finnish National Road Administration of Häme Region for the construction of the test structures.

### REFERENCES

Friberg, P., Lahtinen, P., Slunga, E. & Suni, H. (1994). Finnish Georeinforcement Research and Development Project. *Fifth international conference on geotextiles, geomembranes and related products*, Singapore. 5-9.9.1994. Vol. 3, pp. 1169-1172.

Giroud, J.-P. & Noiray, L. (1981). Geotextile-Reinforced Unpaved Road Design. *Journal of the Geotechnical Engineering Division, (ASCE)*, Vol. 107, No. GT9, pp. 1233-1254.

Houlsby, G. T. & Jewell, R. A. (1990). Design of reinforced unpaved roads for small rut depths. *4th international conference on geotextiles, geomembranes and related products*, The Hague. 28.3.-1.4.1990. Vol. 1, pp. 171-176.

Lojander, M., Forsman, J. & Takala, J. (1996). Mechanical properties of Leteensuu peat. *XII Nordiska Geoteknikermötet*, Reykjavík. 26-28.6.1996. Vol. 1, pp. 123-128.

# CONSTRUCTION OF HIGHWAY EMBANKMENT ON SOFT MARINE SOIL USING JUTE GEOTEXTILES

P.Jagannatha Rao

Senior Consultant, Lea Associates South Asia Pvt Ltd., New Delhi

Bindumadhava

Project Manager, Consulting Engineering Services (P) Ltd., New Delhi

N. Venisri

Engineer, Consulting Engineering Services (P) Ltd., Hyderabad

**ABSTRACT** : The paper presents case study of design and construction of 1.5m high embankment resting on 4m deep soft marine clay subsoil layer. In order to ensure adequate initial factor of safety, it was found necessary to provide a reinforcing fabric at the base of the fill and jute geotextile was successfully used for this purpose. Jute being biodegradable the natural fibre fabric suffers loss of strength with time. In the present case, it was found that the post construction gain in the undrained shear strength of the soft clay subsoil is adequate to compensate the loss in the strength of reinforcing fabric after it is placed in the soil. Thus, the factor of safety always remains at the design level. Construction of the embankment was completed in April 1996 and post construction monitoring showed the embankment performance to be satisfactory.

**KEYWORDS** : Jute geotextile, Reinforcement, Embankments.

## 1.0 INTRODUCTION

A major deepwater port was developed at Kakinada in Andhra Pradesh, India and within the port area, a highway network was under construction for transporting cargo from ships to godowns. At the proposed location, subsoil is soft clay upto 4m depth and water table is at about 0.5m below the ground level. The area gets submerged during high tide. Highways constructed earlier faced many problems during and after construction such as subsidence of the fill during construction, excessive post construction settlements, lateral spreading of fill material, etc. It was observed that sometime as much as 30% of the fill sinks into the soft subsoil during spreading of the fill, thus necessitating use of larger quantities of costly granular fill material, pushing up the cost of construction.

In order to mitigate the above problems, various alternatives were examined among which jute geotextile has shown itself to be a promising one from performance as well as cost considerations. The use of geotextiles to improve the performance of embankments over soft subsoil is an effective and well tried form of reinforced soil construction. Geotextiles may be used to improve

- i) embankment stability against bearing capacity failure
- ii) stability against slope failure through the foundation

- iii) allow controlled construction over very soft or difficult foundation soils and make possible more uniform settlement of the embankment.
- iv) act as separator between the embankment material and soft subsoil
- v) function as drainage blanket for draining of pore water during consolidation.

Reinforcement on soft soil is most effective when placed at or close to the foundation surface.

Factor of safety of embankment is usually at its lowest during and immediately after construction and increases thereafter. The increase is a function of the gain in strength of the soft clay. Thus, reinforcement has to be effective only for a short term, the duration depending on the consolidation characteristics of the soft clay layer. In such cases, long term durability of the geotextile reinforcement is of secondary concern.

The reinforcement is needed essentially to improve the stability during construction phase and in the period of consolidation during which the soil attains the required strength. The concept, shown in fig (1) is given by Jewell (1996) and forms the basis of design in the present instance.

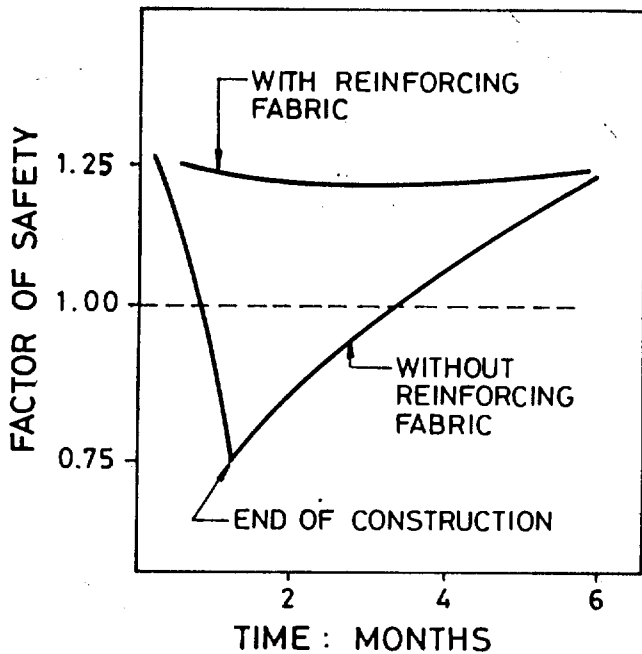


Figure 1 : Variation in factor of safety of fill on soft ground, with and without reinforcing fabric. Based on Jewel (1996)

The primary loading from an embankment is due to the self weight of the embankment fill, which causes horizontal stresses in the fill, which in turn produce lateral forces (i.e.) outward shear stresses. The resulting outward shear stresses which act on the foundation surface reduce the bearing capacity of the foundation subsoil. Hence, the primary role of the reinforcement is to resist the outward shear stresses and relieve the foundation of the effect of lateral forces, thereby increasing the allowable height of the embankment. A layer of reinforcement placed in the embankment would resist lateral displacement by exerting an inward shear stress on the foundation surface thus reduce the lateral spreading of the foundation soil. Since the geotextile is placed between the embankment fill and the subsoil, it also performs the function of separator thereby eliminating the possibility of the soft subsoil squeezing upward into the costly granular fill. This geotextile along with a sand cushion also acts as a drainage layer facilitating the escape of pore water during the consolidation phase.

### 1.1 Properties of Subsoil

The subsoil upto a depth of 4m from the ground level is mainly clay with occasional mixture of silty sand. The average liquid limit and plasticity index were 60 and 28 percent respectively. The soil in general was found to have a natural moisture content ranging from 70% to 80% with bulk density varying from 1.3 Mg/m<sup>3</sup> to 1.45 Mg/m<sup>3</sup>. Average undrained shear strength of the soil was found to

be 6.0 kN/m<sup>2</sup> from in-situ vane shear tests, compression index ( $C_c$ ) 0.225 and coefficient of consolidation ( $c_v$ )  $2.0 \times 10^{-7}$  m<sup>2</sup>/ sec.

### 1.2 Design Aspects

Design of geotextile used for reinforcement is based on the methodology given by Jewel (1996) and is as follows:

Height of fill ( $H$ ) = 1.5m

Unit weight ( $\gamma$ ) = 16.6 kN/m<sup>3</sup>,

Angle of internal friction  $\phi = 30^\circ$

Depth of foundation soil  $D = 4.0$  m

Undrained cohesion  $C_u = 6$  kN/m<sup>2</sup>

Thus vertical stress due to fill ( $\sigma_v$ ) =  $16.6 \times 1.5 = 24.9$  kN/m<sup>2</sup>.

Factor of safety (FS) against bearing failure for the unreinforced embankment.

$$= \frac{cN_c}{\gamma H} = \frac{6 \times 3.14}{24.9} = 0.75$$

$N_c = 3.14$  in the unreinforced state.

Thus, the bearing capacity is not adequate without reinforcement at the base level. By providing a geotextile reinforcement, the bearing capacity factor,  $N_c$  increases to  $\pi + 2 = 5.14$

and the factor of safety works out to

$$\frac{6 \times 5.14}{24.9} = 1.23$$

which is a satisfactory value.

The horizontal force to be resisted by tension in the fabric is estimated as

$$P_a = K_a \gamma H^2 / 2$$

$$= \frac{0.33 \times 16.6 \times 1.5 \times 1.5}{2} = 6.16 \text{ kN/m}$$

Hence, required design tension in the fabric = 6.16 kN/m

For a fabric having a tensile strength of 20 kN/m, the factor of safety available is 3.2 and is thus adequate. Once the embankment is in place, the soft clay consolidates and improves in shear strength.

With an average  $c_v = 2 \times 10^{-7}$  m<sup>2</sup>/sec, the time required for 90% consolidation works out to 205 days or about seven months.



Settlement was estimated to be the order of 175 to 200mm, by using standard calculations.

Strength gain at the end of consolidation is of the order of  $\Delta S_u = 0.18 \times \Delta \sigma'_v = 0.18 \times 24.9 = 4.48 \text{ kPa}$

Average undrained cohesion at the end of consolidation would thus be of the order of (6.0 + 4.48) say 10 kPa. Factor of safety of the embankment at the end of consolidation without any reinforcing fabric would thus be

$$FS = \frac{10 \times 3.14}{16.6 \times 1.5} = 1.26 \text{ which is satisfactory.}$$

Thus the use of an even a relatively low strength geotextile helps to maintain the factor of safety at an acceptable level of 1.26.

At the end of 7 months, when the strength gain due to consolidation has occurred, the increased shear strength of the subsoil ensures the minimum required factor of safety. The strength of fabric is no longer needed to provide reinforcing effect.

### 3.0 CHOICE OF FABRIC

In the preceding section, it was demonstrated that a fill can be built on the soft clay by placing a geotextile fabric and a low strength one is adequate. A variety of such geotextiles are manufactured from petroproducts. However, in certain areas of the world, natural fibres such as jute, coir, sisal, kenaf are being increasingly studied and evaluated for use in various geotechnical engineering applications. The objective of such efforts is to make use of desirable properties of above fibres, make a wider variety of fabric products available for geotechnical engineers where suitable use can be found and in some instances with cost advantage, provided performance criteria are met. The 5th International conference on geosynthetics held in September 1994 in Singapore devoted a special session to Natural Fibre Fabrics. This session has clearly impressed the engineers with the potential of natural fibre fabrics for use in geotechnical engineering applications. These fabrics compliment the range of applications of petrobased fabrics.

Since jute is available in India in abundance, a United Nations Development Programme (UNDP) sponsored project on the "Development and Promotion of Jute Geotextile" is in progress in India covering the period 1992-1997. The Indian Jute Mills Association (IJMA) is the coordinating agency for the project. Development of jute and jute based geotextiles, their evaluation and characterization and the use of such fabrics in full scale experimental constructions form objectives of the project. Efforts were concentrated on carrying out full scale field experiments to demonstrate and evaluate the capabilities of selected varieties of jute fabrics for use in surface erosion control of slopes, drainage, separation and to a limited extent, reinforcing function. The fact that jute fabric is

biodegradable, with a limited life and deteriorates in a short period of about two years was always kept in mind in the planning and operation of the project and choice of experimental installations. Full scale field experiments covering these applications have been implemented at different locations in India. Ramaswamy (1994) presents in detail the application of jute geotextiles in erosion control, drainage as well as reinforcement.

As explained in section 1 and shown in design in section 2, in the present instance, it is adequate if the reinforcing function of the fabric is available for period of seven months. The use of fabric has essentially helped in overcoming problems in the placement of the fill and initial low factor of safety. Thus, fabric with a limited life can be tried in this project and its performance evaluated by the field trial. Accordingly, jute geotextile fabric having the basic properties given in Table 1 was chosen for use in the project.

Table 1 : Properties of Jute Geotextile

S.No	Property	Test Value
1	Thickness	3 mm
2	Weight	750 gsm
3	Tensile Strength	20 kN/m
4	Elongation	30%
5	Puncture Resistance	350 N
6	Overlap length	30 cm

The woven jute geotextile fabric was treated with cuproammonium sulphate to increase resistance of the fabric to biodegradability. Talukdar et al (1994) have studied the influence of various chemicals such as copper naphthenate etc. with acrylic binder on the resistance to microbial attack when buried in soil. The results were very encouraging and showed that jute fabrics treated with selected chemicals have better resistance to microbial attack under conditions of burial in soil. Venkatappa Rao et al (1994) have shown on the basis of a careful study that the decrease in the narrow strip tensile strength of soil embedded in soil and remaining in submerged condition is only of the order of 35% after four months. Mohiuddin (1994) provides data to indicate that in jute fabrics treated with copper naphthenate and such other chemicals, the loss of strength is retarded. Thus, it was reasonable to consider that jute fabric used would serve the reinforcing function in adequate measure, in the design life of 7 months.

#### 4.0 INSTALLATION OF GEOTEXTILE

At present, jute geotextile being an experimental product is available in roll width of 0.75m only. Hence, fabrics were stitched at site, using a portable stitching machine to obtain the requisite width. The stitching operation was easy, reliable and fast. Before spreading the geotextile, the site was cleared of any extraneous materials and tree/plant roots. A layer of sand 150 mm thick was spread to serve as a levelling course. The geotextile was laid with its warp direction (strong direction) parallel to the width of the embankment. Top width of the embankment was 7.0m and side slope 1 v1 to 2h1. A trench of size 0.5 x 0.5m was dug in the soil at either toe line of the embankment and along its length. To provide anchorage, the geotextile was placed in the trench. The trench was back filled with sand placed in layers and compacted. The fabric was stretched manually after spreading on the ground so as to render it free of wrinkles and establish good contact with soil and fill. An overlap of 0.30m was provided between two rolls of geotextiles. After spreading the geotextile and anchoring it along the edges, a sand cushion of 30 cm thick was placed to protect the geotextile from damage due to moving vehicles. Placing of fill upto the requisite height was done by rear dumping and spreading. The fill was then compacted by a 6 ton roller. Nearly 300 m of embankment was built under the programme. Construction of the embankment was completed in April 1996. Settlements were observed subsequent to the construction. Simple standpipe type settlement gauge was installed for this purpose. It was found that the settlements conformed to the estimated value. The physical condition of the fill and its surface were monitored periodically and were found to be satisfactory.

The cost of jute geotextile used in the project is of the order of Rs. 18/- or US\$ 0.50 and thus proved to be highly economical compared to products based on petrochemicals, which are costlier in India.

#### 5.0 CONCLUSION

An embankment was built on soft clay subsoil, using geotextile as a reinforcing layer at the base. the geotextile was required to serve as reinforcing fabric for a period of 7 months only. Subsequently the strength gain in the soft clay was adequate to keep the embankment stable. The performance of the fill was found satisfactory. The project demonstrates that where site conditions enable the designer to rely on reinforcing properties of geotextiles for a limited time period, it is possible to use natural fibre geotextile in such applications. This has the effect of finding suitable range of conditions where natural fibre based geotextile can be used in geotechnical applications.

#### ACKNOWLEDGEMENT

The project was carried out as a part of the UNDP sponsored project "Development and Promotion of Jute Geotextiles". The overall coordinating agency was the Indian Jute Mills Association, Calcutta. The work reported herein was carried out by the authors, while they were at the Central Road Research Institute, New Delhi and the senior author was coordinating the project. The authors thank all concerned in the above organisations for their cooperation in successfully completing the project. The authors also wish to thank officials of Kakinada port and JNTU college of Engineering, Kakinada for help at site in various phases of the project.

#### REFERENCES

- Jewell, R.A (1996) Soil Reinforcement with Geotextiles, 1st Ed., Construction Industries Research and Information Association, London.
- Mohiuddin. G. (1994). Jute geotextiles. 2nd International Workshop on Geotextiles, Central Board of Irrigation and Power, 1994. pp.70-76. New Delhi
- Ramaswamy. S.D (1994). Potential of Jute Assembled Soil Stabilisers. 2nd International Workshop on Geotextiles, Central Board of Irrigation and Power, New Delhi, 1994. pp. 77-85.
- Talukdar, M.K. Mukherjee, D. and Ghosh S.K. (1994), Performance of Certain Antimicrobial Treated Nonwoven Jute Fabrics. Fifth International Conference on Geotextiles, Geomembranes and Related Products, Singapore 1994, Vol.2 pp. 849-852
- Venkatappa Rao, G. and Abid Alikhan, M. and Narayana Sarma, G.V. (1994). Durability of Geotextiles. Fifth International Conference on Geotextiles, Geomembranes and Related Products. Singapore 1994. Vol. 2. pp.857-860.

# PERFORMANCE OF GEOTEXTILE REINFORCED EMBANKMENTS ON VERTICALLY DRAINED SOFT MUDS

K.C. Yeo & J.W. Cowland  
Geotechnical Engineering Office, Hong Kong

**ABSTRACT:** Twenty kilometres of flood protection embankments have been constructed on soft muds in the north-west of Hong Kong, using woven polyester geotextiles as basal reinforcement. Prefabricated vertical drains were installed to accelerate consolidation of the muds. An extensive instrumentation programme was carried out to monitor the performance of the embankments. This paper outlines the design and construction of the embankments. Typical instrumentation results are given, and performance of the embankments are discussed.

**KEYWORDS:** Case Study, Embankments, Soft Soils, Geotextiles, Pre-fabricated Vertical Drains

## 1 INTRODUCTION

The northwestern part of Hong Kong contains a broad alluvial floodplain. Development of this low-lying area generally requires the construction of raised platforms. Provision of major flood drainage is essential for land use planning as flood discharges develop rapidly due to heavy rainfall in the wet season.

A series of drainage channel projects are being carried out in these areas to alleviate the flood problem and to

improve the drainage systems. The case study presented in this paper consisted of the construction of three drainage channels of width 125m to 480m, and of lengths 3.2km(Contract A), 4.4km(Contract B) & 2.3km(Contract C) respectively. Small embankments 4m high were constructed on each side of these drainage channels over an area which had been used extensively for fish farming, with small bunds forming the boundaries of the ponds. Figure 1 shows the location of the site.

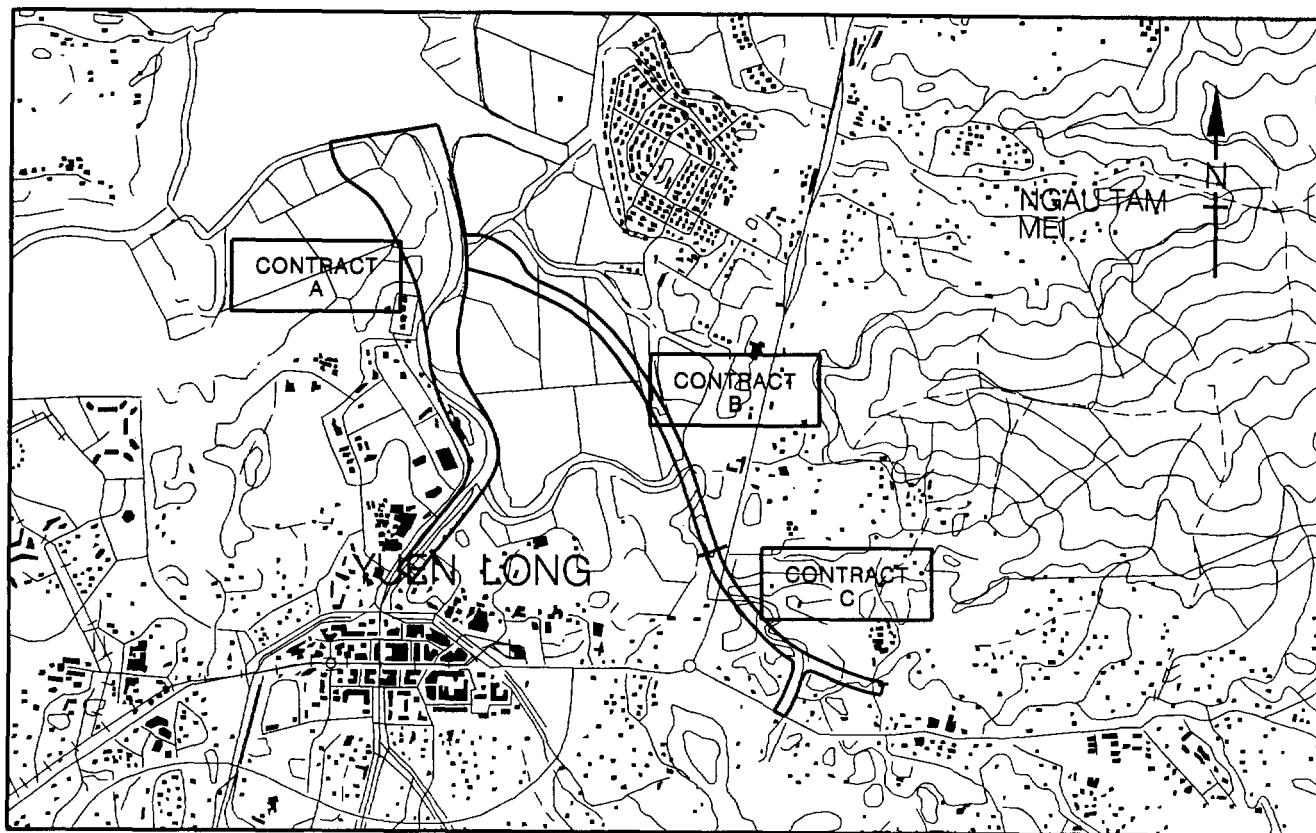


Figure 1. Location of the Site

## 2 GEOLOGY

The geology of the area comprises muds overlying older alluvial sediments which rest on residual weathered rocks of volcanic or meta-sedimentary origin. The stratigraphy of the site can be categorised as follows:

**Fill:** generally granular in nature and exists in the bunds of the fish pond area, with thickness varying from 1 to 3 metres.

**Pond deposits:** generally a very soft to soft dark brown to dark grey silty clay exists at the bottom of the fish ponds for a depth of 1 to 1.5 metres.

**Estuarine/Marine deposits:** generally a very soft dark grey to black silty to sandy clay with shell fragments, with thickness from 2 to 8 metres.

**Alluvial clay/silt:** generally a firm to stiff light grey to pinkish brown with reddish brown mottled sandy silty clay with varied depth.

**Alluvial sand/gravel:** generally a medium dense to dense grey to brownish yellow/light grey silty/ gravelly sand with varied depth.

The thickness of the alluvium was between 10 to 30 metres. It does not possess a uniform succession of strata, but varies from location to location. The insitu materials below the alluvial deposits are coarse tuff/granodiorite. Figure 2 shows the geology of the site.

## 3 DESIGN AND CONSTRUCTION

The embankments were formed by filling on the existing ground. For embankments constructed over soft muds, the stability of the embankments has been improved by a combination of measures, i.e. installation of prefabricated vertical drains (PVD), application of geotextile reinforcement, staged construction with wide berms and partial removal of pond deposits. As the preconsolidation

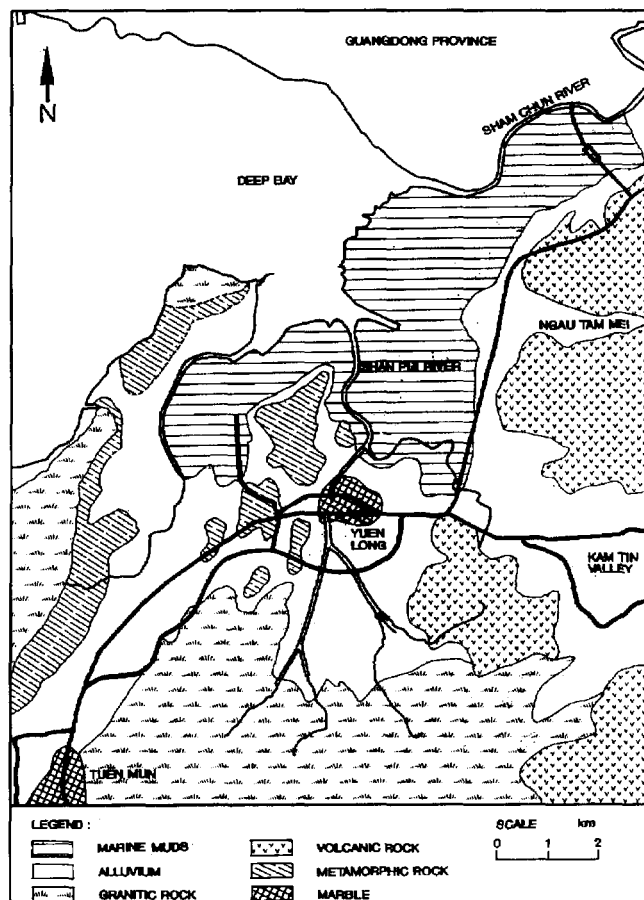


Figure 2. Geology of the Site

pressure of the alluvium was generally higher than the embankment load, most of the settlement occurred only in the marine sediment. The soil parameters adopted for the embankment design are summarised in Table 1. In general, they are on the conservative side.

Table 1. Geotechnical Design Parameters

Design Parameters				Type of Deposit				
				Marine Deposit	Alluvial Clay	Alluvial Silt	Alluvial Sand	Alluvial Gravel
Unit Weight (kN/m <sup>3</sup> )				16	19	20	19	19
Shear Strength Parameters	Short Term	Undrained Shear Strength	S <sub>u</sub> (kPa)	10	40	40	-	-
	Long Term	Effective Cohesion	c' (kPa)	3	4	0	0	0
		Effective Angle of Friction	φ' (Deg)	25	33	33	35	35
Parameters for Settlement	Preconsolidation Pressure		P <sub>o</sub> ' (kPa)	NC	150 - 300	150 - 300	-	-
	Compression Ratio		C <sub>c</sub> / (1+e <sub>o</sub> )	0.15 - 0.3	0.11 - 0.16	0.12 - 0.18	-	-
Analysis	Recompression Ratio		C <sub>r</sub> / (1+e <sub>o</sub> )	0.015 - 0.03	0.015 - 0.025	0.018 - 0.03	-	-

A typical cross section of the embankment, showing the layout of the geotextiles, prefabricated vertical drains and instrumentation, is shown in Figure 3. The construction adopted both "partial removal of pond deposits" and "no excavation" approaches. The primary basal reinforcements used were a layer of woven polyester geotextile (two different brands) of characteristic strength of 800kN/m or 600kN/m. A second layer of woven polyester geotextiles were used as a separator with characteristic strength of 400 kN/m or 200kN/m. Two different types of PVD (grooved and spun core) were installed to a depth of approximately 15 metres through the marine deposits, to accelerate the consolidation of the foundation soil.

They are simple to read and can be read from a station which is remote from the work area with little interference to the construction activity. However, they are not robust and some of the piezometers were damaged during construction. A number of the pneumatic piezometers were found to malfunction after installation, and yielded erratic results. Therefore it is important to consider the use of more than one type of piezometer for cross checking. For future projects it would be advisable to install some standpipe piezometers to supplement pneumatic piezometers at selective locations for reference.

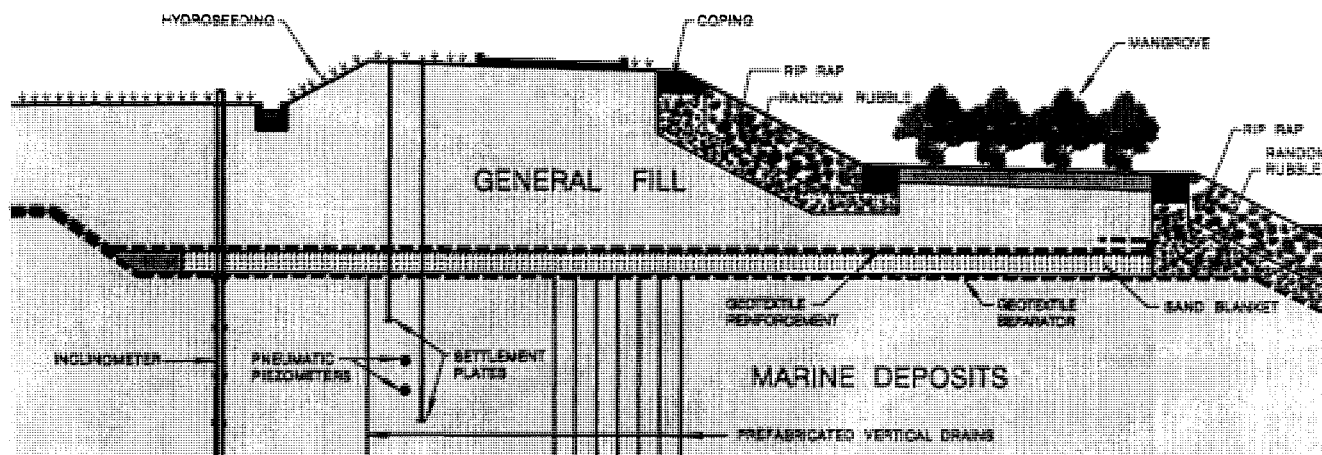


Figure 3. Typical Section of the Embankment

#### 4 INSTRUMENTATION

An extensive network of geotechnical instrumentation was installed, to monitor ground deformation and groundwater pressures during construction of the embankments. More than fifty cross-sections (at 100 metres interval) along the embankments were monitored using pneumatic piezometers, inclinometers (with and without extensometers) and settlement plates, during and after construction.

For embankments constructed over pond and estuarine/marine deposits, monitoring of the excess pore water pressure dissipation within the mud was critical for controlling the filling rate of the embankment. In addition, there were fish ponds along both sides of the channels, and lateral movement of the soft deposits may have damaged the bunds of the fish ponds. Thus it was important to monitor this movement. It was also important to measure the settlement of the mud over time, so that the timing of laying the black top of the service road on the crown of the embankment could be determined.

##### 4.1 Piezometers

Pneumatic piezometers were widely used in this project.

##### 4.2 Inclinometers and Extensometers

Inclinometers were installed to monitor the magnitude and the rate of lateral movement of the foundation soils below the embankment. Casing inclination data were provided in two mutually perpendicular near-vertical planes. Horizontal deformation of the transverse sections was of particular interest as the behaviour of the embankment would be assumed to be in plane strain.

Extensometers were used in conjunction with inclinometers to monitor the changing distance between two to four positions beneath the vertical axis of a particular section, i.e. vertical compression of the foundation soils. Two different types of extensometers were used, i.e. spring anchor extensometers attached outside the inclinometer casing, and flexible corrugated polyethylene pipe with induction coil rings where inclinometer casing was inserted inside the pipe. As the accuracy of extensometers is only 10 - 20 mm. Settlement plates are a useful alternative.

##### 4.3 Settlement Plates

Settlement plates were used to quantify the magnitude of settlement of the embankments with time. Two types of

settlement plates were used, i.e. shallow settlement plates and deep settlement plates. The shallow settlement plate was a 1m x 1m steel plate welded to a hollow tube which was extended with fill height, installed at the base of the embankment before filling. The deep settlement plate was a 110 mm diameter circular plate welded to an steel bar, which was also extended, and installed at the base of the soft deposits by drillhole. The settlement of the plates were monitored using surveying techniques throughout construction. The difference between the settlement measured by the shallow and the deep settlement plates represented the actual settlement of the layer of the soft deposits at any time.

The accuracy of the plate settlement measurement using conventional surveying equipment was found to be close to millimetres.

## 5 TYPICAL INSTRUMENTATION RESULTS

A typical set of instrumentation results is shown in Figures 4 to 9. Figure 4 summarises the locations of all the instrumentation. The fill level was increased to approximately 4m at the crown in October 1995, as indicated in Figure 5, and a typical set of piezometer measurements shows that the excess pore pressure has built up slowly, and then dissipated over the next three months, as shown in Figure 6. This indicates that the prefabricated vertical drains were working satisfactorily. The ground water re-established at a new level after that, and then fluctuated with seasonal changes. Figure 7 shows the increase in settlement, from the monitoring data of the settlement plates, in response to the increase in pore water pressure during the same period. The increase in settlement reduced when the pore water pressure stabilised, and the

rate of settlement became insignificant. Figures 7 & 8 show the settlement monitoring results at the crown (by extensometers) and at the berm (by settlement plates). The total settlement which occurred at the crown of the embankment was about 150mm, while the settlement which occurred at the berm was about 70mm.

Two plots were employed for the interpretation of inclinometer data. The 'cumulative' plot gave a more graphic representation of the actual deformation pattern and was most commonly used. The 'change' plot, which plots the gradient of the 'cumulative' plot, accentuates the location of the deformation zone, which is useful to identify the shear zone (squeezing) and its magnitude. In general, the shear deformation is expressed in degrees. Figure 9 shows typical cumulative and shear deformation plots in the transverse direction for the inclinometer at a typical section. The plane on which the maximum shear strain occurred was at about 2m below the existing ground level. From the drillhole records, this level coincided with the location of the interface between fill and marine deposits. The magnitude of the maximum shear strain was less than 1 degree.

## 6 PERFORMANCE OF EMBANKMENTS

The performance of the embankments has been assessed from the monitored behaviour of the instrumentation. The fill level has reached a full height of approximately 4 metres. The excess pore water pressures within the marine deposits have dissipated satisfactorily, with an undissipated pore water pressure of only about 5-10 kPa. In general, the settlement plates have provided reasonably good information on the compression of the marine deposits. The shallow and deep settlement plates indicated that the

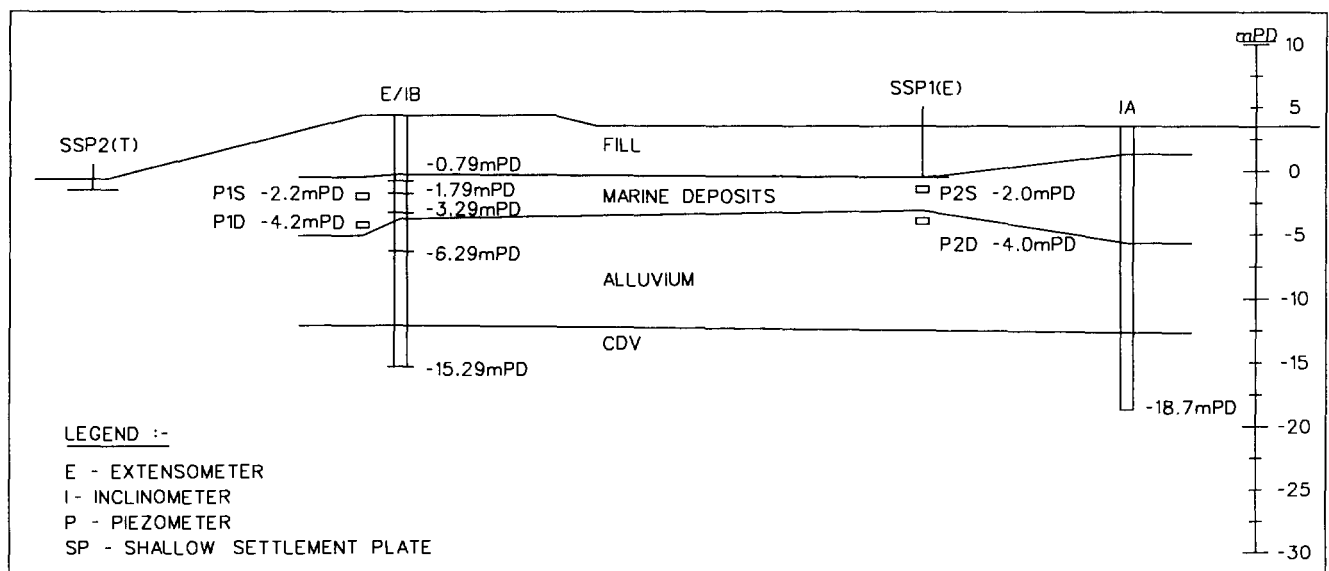


Figure 4. A Typical Instrumentation Section

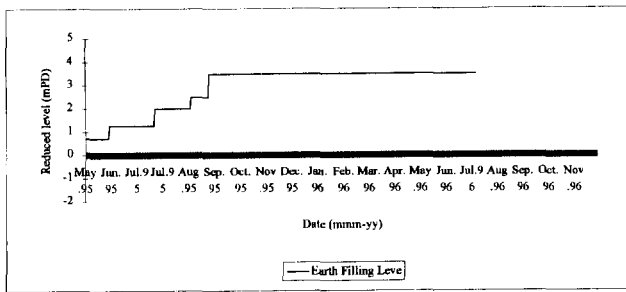


Figure 5. Fill Level Plot

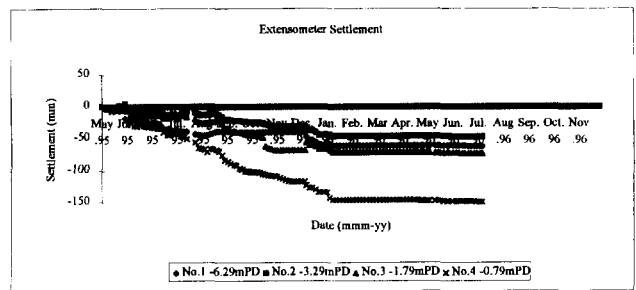


Figure 7. Settlement Plot

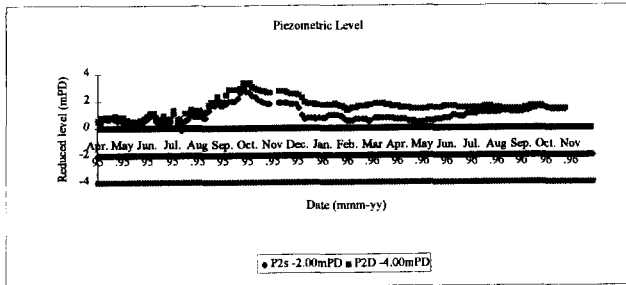


Figure 6. Piezometer Plot

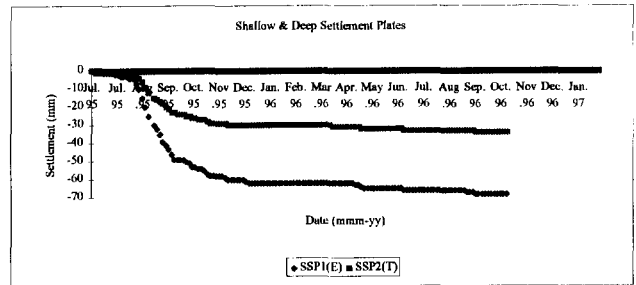


Figure 8. Settlement Plot

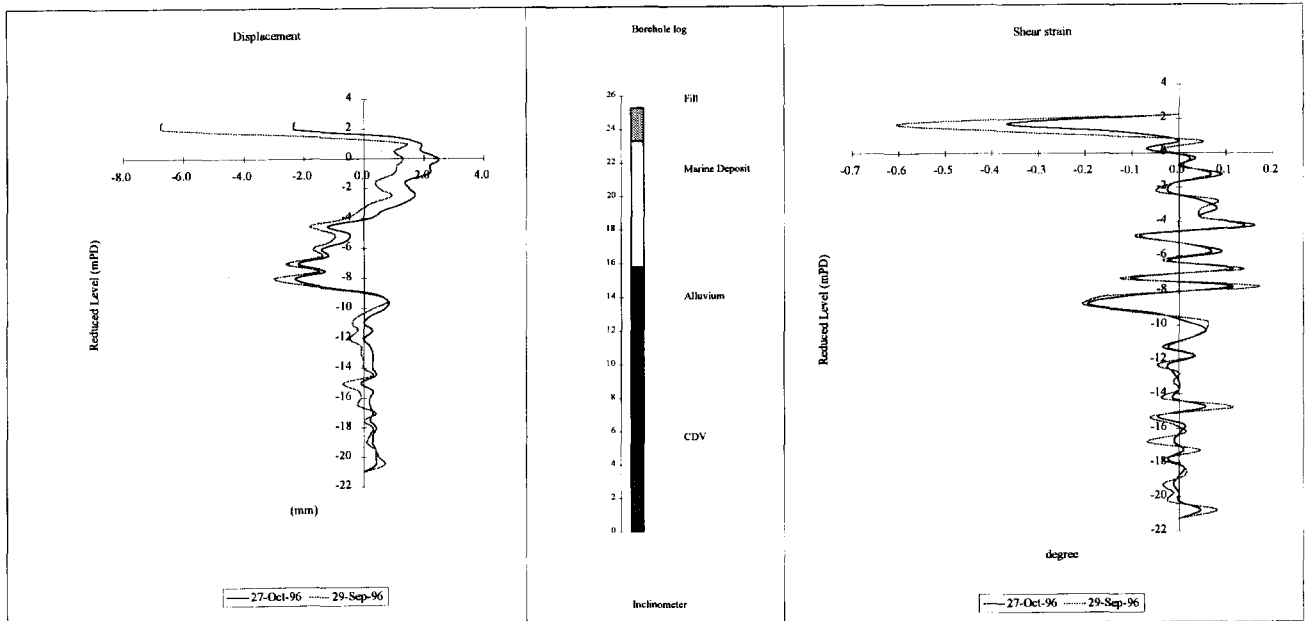


Figure 9. Inclinerometer Plots

settlement for the marine deposits at the embankment crown was between 250mm to 350mm, depending on the thickness of marine deposits, which ranged between 4m to 6m. At the berm of the embankment, the settlement measured by using extensometers was between 60mm to 150mm with thickness of the marine deposits ranged from 6m to 8m. In general, the rate of settlement was insignificant 4-6 months after the end of construction. The inclinometer with extensometer was used to monitor the horizontal and vertical deformation of the ground at

selected locations. At this site it was used to monitor the lateral movement of the earth bunds adjacent to fish ponds. It was found that squeezing of the marine deposits underneath the embankment occurred at the interface between the stiffer alluvium and the marine deposits. In general, the cumulative deformation ranged from 30mm to 100mm along the drainage channel. The maximum shear deformation, in general, occurred at the interface of the marine deposits and the alluvium, with a magnitude of between 0.5° to 2°.

## 7 COMPARISON OF PERFORMANCE

To assess the effectiveness of the performance of the embankments, four cases of trial embankments on soft soil foundations, which employed similar reinforcement materials or had similar site conditions as Hong Kong, were

It is suggested that a way forward to improve the economy, efficiency and effectiveness of the design of embankments on soft soil foundations in Hong Kong is to construct a trial embankment, to define the critical conditions, and to conduct back analyses, so that the design parameters can be more accurately determined.

Table 2. Comparison of Embankment Performance

Case	Reinforcement Material	Su(kN/m <sup>2</sup> )	Soft Clay Depth (m)	Berm	Fill Height (m)	Rft. Strain (%)	Rft. Load (%)	PVD
1986 France Test Embankment	Polyester Woven 225/60	30 Const.	24	Yes (4.5m)	7 8.75 (failed)	2.5	50	No
1989 Canadian Test Embankment	Polyester Woven 216	30 Const.	10	Yes (3.5m)	4 8.2 (failed)	2		No
1982 Hong Kong Deep Bay	Polyester Polypropylene Woven 200/200	5-10 Linearly Increase Ratio 0.25	12	Yes (0.8m)	3.5	9		No
1988 Malaysia Trial Embankment	HDPE Geogrid 80	5-10 Linearly Increase Ratio 0.3	14	No	6	5	40	Yes (Not Functioned)
	HDPE Geogrid 110 × 2			Yes (3m)	8.50	2	25 × 2	Yes (Not Functioned)
1995 Hong Kong DSD Contract A	Polyester Woven 800/100		10	Yes (2m)	4			Yes

reviewed (Delmas, Ph. et al (1992), Rowe, R.K. et al (1994), Cowland, J.W. et al (1997) & Malaysian Highway Authority (1989)).

A comparison of the performance of these trial embankments and the Hong Kong embankment are summarised in Table 2. Although the reinforcement load and strain in the Hong Kong embankments have not been measured, the comparison does indicate that the design of the geotextile reinforcement for these flood protection embankment was conservative.

## 8 CONCLUSIONS

The use of vertical drains in combination with basal reinforcement proved to be a cost-effective means to construct embankments over soft ground without removal of the muds.

Both types of polyester woven reinforcement geotextiles and the prefabricated vertical drains that were used performed satisfactorily. They enhanced the short-term stability of the embankments and accelerated the time of consolidation of the muds.

Instrumentation plays a important role during construction to ensure safety of the construction work, allow control of the construction pace, and to provide data for measurement of quantities.

The performance of the embankments was very much better than the calculated performance assumed in design, reflecting the conservatism in the choice of soil parameters.

## ACKNOWLEDGEMENTS

This Paper is published with the permission of the Director of Civil Engineering of the Government of the Hong Kong Special Administrative Region.

## REFERENCES

- Cowland, J W, Yeo K C & Greenwood, J H (1998) "Durability of polyester and polypropylene geotextiles buried in a tropical environment for 14 years", *Paper submitted to the Sixth International Conference on Geosynthetics*.
- Delmas, Ph., Queyroi, D., Quaresma, M., De Saint, Amand & Puech, A. (1992) "Failure of an experimental embankment on soft soil reinforced with geotextile: Guiche", *Geotextiles, Geomembranes and Related Products*, Den Hoedt (ed.) @ 1992 Balkma, Rotterdam.
- Dunnicliff, J (1988) "Geotechnical Instrumentation for Monitoring Field Performance", John Wiley & Sons, 577p.
- Malaysian Highway Authority (1989) "Factual report on performance of the 13 trial embankments", *Proceedings of Int. Sym. on Trial Embankments on Malaysian Marine Clays*, Kuala Lumpur, vol.I.
- Rowe, R.K. & Gnanendran, C.T. (1994) "Geotextile strain in a full scale reinforced test embankment". *Geotextiles and Geomembranes 13*, pp 781-806.



# Influence of Geometry and Construction Sequence on Reinforced Embankments on Soft Soils

J.L. Borges

Auxiliary Professor, Department of Civil Engineering, Faculty of Engineering, University of Porto, Portugal

A.S. Cardoso

Associate Professor, Department of Civil Engineering, Faculty of Engineering, University of Porto, Portugal

**ABSTRACT:** In order to study the influence of some parameters, namely the embankment geometry and construction sequence, on the geotechnical behaviour of reinforced embankments on soft soils, a numerical model based on the finite element method is used. The settlements, horizontal displacements, stresses in the reinforcement (geosynthetic) and global stability are analysed. Several conclusions are indicated.

**KEYWORDS:** Embankments, Finite Element Analysis, Reinforcement, Settlement Analysis, Soft Soils.

## 1 INTRODUCTION

In this paper, the influence of two parameters - embankment width and construction sequence (Fowler and Haliburton, 1980; Christopher and Holtz, 1985; Haliburton et al., 1982; Koerner and Welsh, 1980; Ingold and Miller, 1988; Holtz, 1990) - is studied.

A numerical model based on the finite element method (Borges, 1995) is used and, basically, its theoretical hypotheses are: a) validity of the plane strain conditions; b) coupled formulation of the flow and equilibrium equations considering the constitutive relations (elasto-plastic models) formulated in effective stresses (extension of Biot's consolidation theory); this formulation is applied at any phase of the problem, either during the embankment construction or in the post-construction period; c) utilisation of the critical states model  $[p,q,\theta]$  (Lewis and Schrefler, 1987; Borges, 1995) to simulate the constitutive behaviour of the foundation and embankment soils; d) utilisation of a hardening elasto-plastic model to simulate the «instantaneous» constitutive behaviour of the reinforcements; e) simulation of the viscous behaviour of the geosynthetics (time-dependent constitutive relations) using a rheological model based on the serial association of Kelvin's units; f) simulation of the constitutive behaviour of the soil-geosynthetic interfaces using a hardening elasto-plastic model.

These studies involve the numerical results of a reference embankment, reinforced and unreinforced (analyses 1A and 1B, respectively). Firstly, the results of these cases are compared to the results of other two cases (analyses 2A and 2B) which are similar to the first ones except to their width, that is smaller. Secondly, having the purpose to verify the influence of the way each embankment layer is constructed (in this case, starting, or not, from its extremities to its middle), the results of other analysis (3A) are introduced.

## 2 DESCRIPTION OF REFERENCE PROBLEM

The analyses 1A and 1B are similar except in the fact that the first one has a reinforcement in the embankment base and the second one does not. They model a 28 days continuous construction of an embankment of 2 m height, symmetric, with a final platform of 10.6 m width and slopes inclined  $V/H=2/3$ . The foundation is a 5 m depth saturated clay that lays on a rigid and permeable soil (lower boundary of the problem). Figure 1 shows the finite elements mesh. Only the 2D elements are represented; the geosynthetic and the soil-geosynthetic interfaces are modulated by one-dimensional elements put between the foundation and the embankment elements.

The embankment construction was simulated activating successively the elements that form the different embankment layers. Four layers of 0.5 m were considered. Total time of construction was 28 days (7 days by layer).

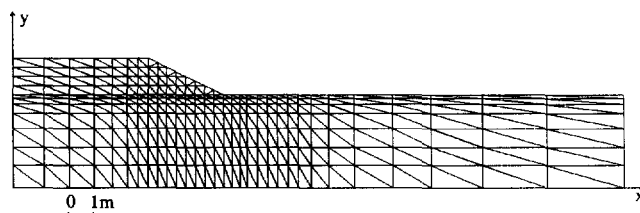


Figure 1. Finite element mesh

The constitutive relations of the embankment and of the foundation were simulated using the critical states model  $[p,q,\theta]$  with the parameters indicated in Table 1. Tables 2 and 3 show other geotechnical properties and the depth variation of the coefficient of earth pressure at rest,  $k_0$ , and of the over-consolidation ratio, OCR, in the foundation.

Figure 2 shows the mechanical behaviour of the geosynthetic and soil-geosynthetic interfaces (elastoplastic

models). The geosynthetic thickness is 2 mm and its elastic modulus is  $1.5 \times 10^6$  kPa. Normal and tangential stiffnesses of the soil-reinforcement interfaces are  $2.0 \times 10^7$  kPa and  $1.6 \times 10^4$  kPa, respectively.

Table 1. Parameters of the critical states model [p,q,θ] for the foundation and the embankment

	$\lambda$	$k$	$\Gamma$	$N$
Foundation	0.22	0.02	3.26	3.40
Embankment	0.03	0.005	1.80	1.817

Table 2. Geotechnical properties of the foundation and the embankment

	$\gamma$ (kN/m <sup>3</sup> )	$v'$	$\phi'$ (°)
Foundation	17	0.25	30
Embankment	20	0.30	35

Table 3. Coefficient of earth pressure at rest,  $k_0$ , and over-consolidation ratio, OCR, in the foundation

Depth (m)	$K_0$	OCR
0 - 1	0.7	2.43
1 - 1.8	0.7 - 0.5	2.43 - 1
1.8 - 5	0.5	1

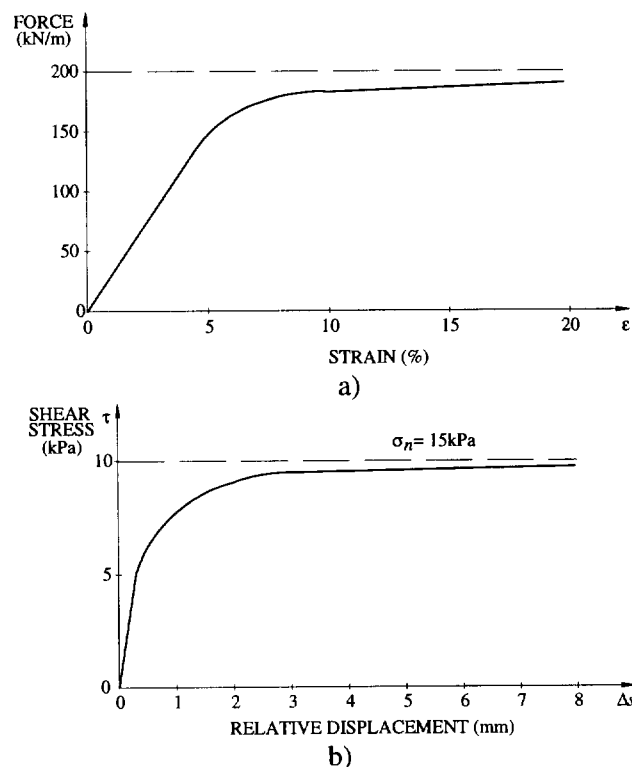


Figure 2. Constitutive curve of the: a) geosynthetic; b) soil-geosynthetic interface

### 3 INFLUENCE OF EMBANKMENT WIDTH

Because the 2D character of the problem, it is natural that the alteration of the embankment geometry - namely the embankment width - influences the behaviour, either in terms of displacements or in terms of global stability.

To study this question two analyses were done (2A and 2B), which are, as said, similar to the reference analyses (1A and 1B), except to their width, that is smaller (see Figure 3).

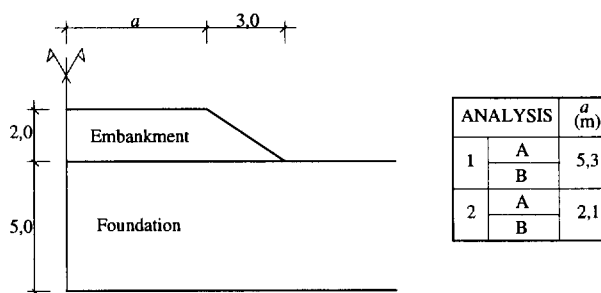


Figure 3. Embankment geometry

Relatively to the geosynthetic traction forces, Figure 4 shows that their maximum values are similar (either at the end of construction or at the end of consolidation) in the 1A and 2A analyses, which shows that the maximum value of the traction, as explained by Borges (1995), does not significantly depend on the embankment width. Increasing this parameter, only increases the area of the geosynthetic in which the traction force has approximately a uniform value (similar to the maximum one), in the middle zone of the embankment base.

Relatively to the embankment settlements (Figure 5), one can see that, in terms of decrease of maximum value of the settlements due to the geosynthetic, this decrease can be more effective in larger embankments. However, the influence on the differential settlements under the embankment platform can be observed in both cases. It is interesting verify that the maximum settlement value increases with the embankment width (different geometry of the problem determines different stresses in the foundation and, consequently, different maximum settlement value at the end of the consolidation).

In terms of global stability, it should be noted that the embankment geometry, namely the  $b/h$  relation (see Figure 6), influences the type of failure surface that can occur, i.e., the probability of occurring a failure surface as the one presented in Figure 6a (without cutting the embankment and the reinforcement) is greater when the  $b/h$  parameter has a small value. In this case the geosynthetic does not directly contribute with its strength to the global stability, so the embankment width can determine the role of the reinforcement on failure mechanism.

Using the numerical results and limit equilibrium assumptions, it can be obtained the failure surfaces

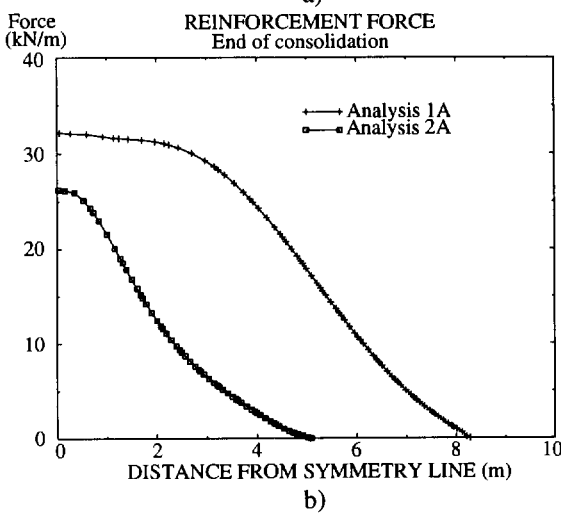
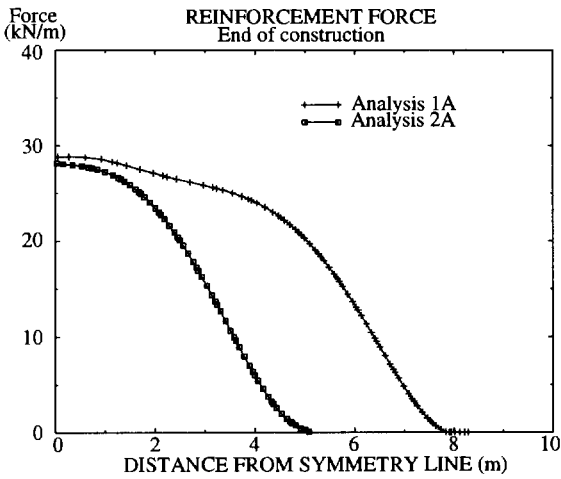


Figure 4. Influence of the embankment width on the reinforcement forces: a) at the end of construction; b) at the end of consolidation

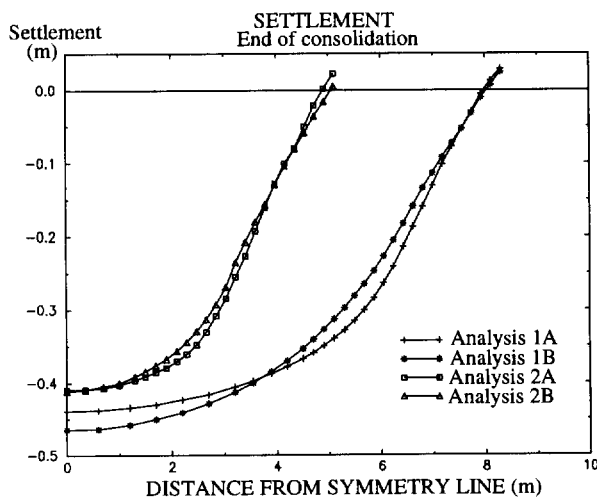


Figure 5. Influence of the embankment width on the embankment settlements at the end of consolidation

concerning the four analysed cases. Figure 7 shows those (cylindrical) surfaces and the respective global stability coefficients, at the end of construction. These calculations were done by a computer program that, in each analysed cylindrical surface, compares acting and failure tangential forces (obtained from the results of the numerical model and the strength characteristics of the materials).

The results show that the increase of the global stability due to the reinforcement (comparing 1A to 1B and 2A to 2B) is less effective for small values of  $b/h$  because failure surfaces could be similar to the one represented in Figure 6a. It was the case of 2A analysis.

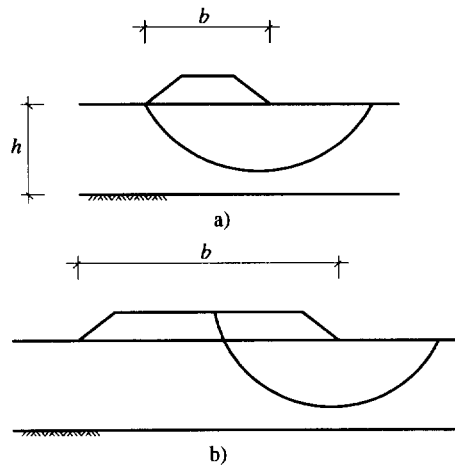


Figure 6. Influence of embankment width on the type of global failure

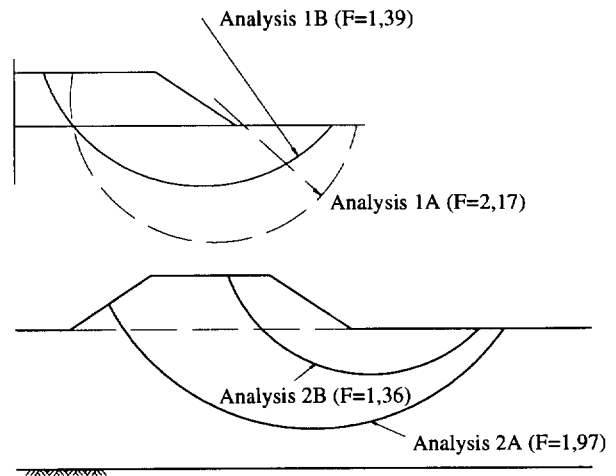


Figure 7. Failure surfaces and respective global stability coefficients (F) at the end of construction.

#### 4 INFLUENCE OF CONSTRUCTION SEQUENCE

To verify the influence of the way each embankment layer is constructed (temporal and spatial evolution), the results

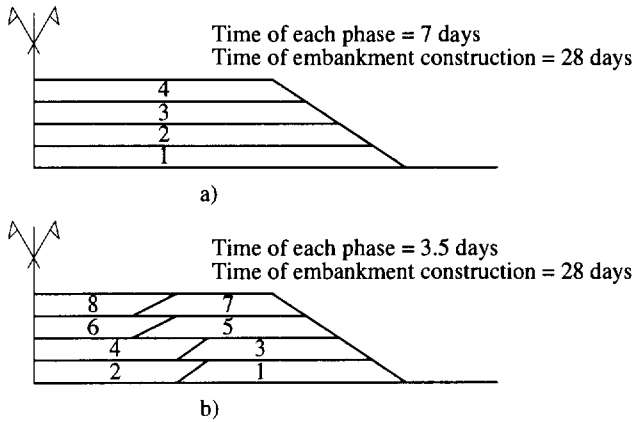


Figure 8. Embankment construction phases: a) analyses 1; b) analyses 3

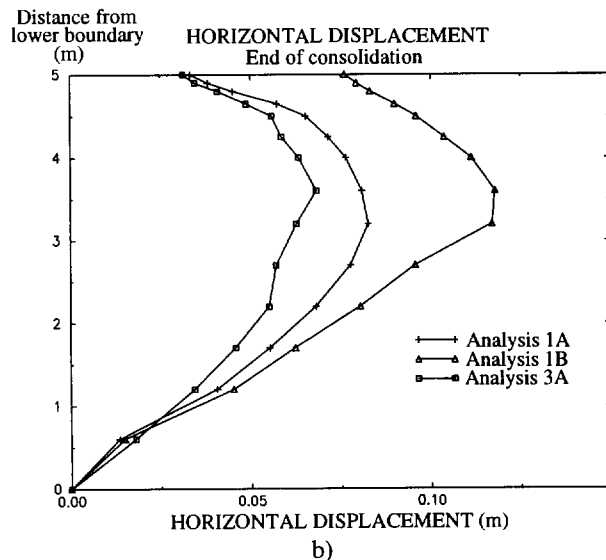
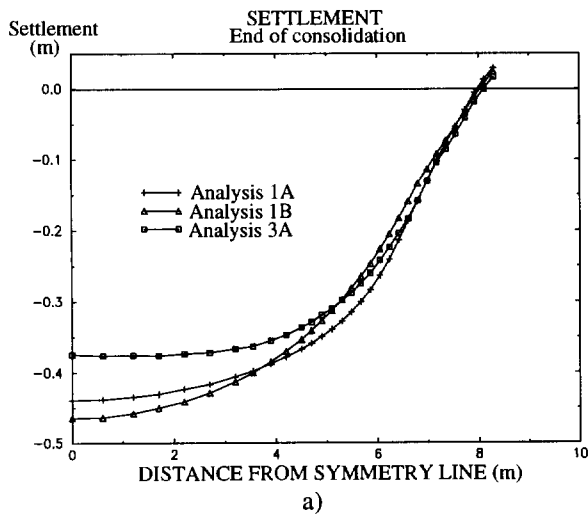


Figure 9. Influence of construction procedures on the: a) settlements; b) horizontal displacements at the vertical line 3.2 m distant from symmetrical line.

of other analysis (3A) are introduced. This analysis is similar to the reference one, 1A, except in what concerns the construction sequence of each layer (see Figure 8).

From the analysis of the numerical results, it can be concluded that the most important alterations concern the long time settlements (Figure 9a). These settlements are significantly reduce in terms of maximum and differential values.

The reason of that behaviour (Borges, 1995) is related to the fact that, at the end of construction, the distribution of excess pore pressures in the middle of the foundation loaded zone is more uniform. This fact implies a decrease of the shear strains in the foundation, which, consequently, leads to the reduction of settlements (as seen in Figure 9a) and of horizontal displacements, as it can be seen, for example, at the vertical line 3.2 meters distant from symmetry line (Figure 9b).

#### ACKNOWLEDGEMENTS

The writers acknowledge the funding for the work reported in this paper that was provided by the PRAXIS/2/2.1/CEG/42/94 project.

#### REFERENCES

- Borges, J. L. (1995) "Aterros sobre solos moles reforçados com geossintéticos - Análise e dimensionamento", *PhD Thesis in Civil Engineering*, Faculty of Engineering, University of Porto, Portugal.
- Christopher, B. R. and Holtz, R. D. (1985) *Geotextile Engineering Manual*, Federal Highway Administration, Washington, D.C., FHWA-TS-86/203, 1044 pp.
- Fowler, J. and Haliburton, T. A. (1980) "Design and Construction of Fabric Reinforced Embankments", *The Use of Geotextiles for Soil Improvement*, Preprint 80-177, ASCE Convention, pp. 89-118.
- Haliburton, T. A.; Lawmaster, J. D. and McGuffey, V. E. (1982) *Use of Engineering Fabrics in Transportation Related Applications*, Final Report Under Contract N° DTFH61-80-C-0094.
- Holtz, R. D. (1990) "Design and Construction of Geosynthetically Reinforced Embankments on Very Soft Soils", *International Reinforced Soil Conference*, Glasgow, pp. 391-402.
- Ingold, T. S. and Miller, K. S. (1988) *Geotextiles Handbook*, Thomas Telford, London.
- Koerner, R. M. and Welsh, J. P. (1980) *Construction and geotechnical engineering using synthetic fabrics*, John Wiley and Sons, Inc., New York.
- Lewis, R. W. and Schrefler, B. A. (1987) *The Finite Element Method in the Deformation and Consolidation of Porous Media*, John Wiley and Sons, Inc., New York.

# Design Guidance for Reinforced Soil Structures with Marginal Soil Backfills

Barry R. Christopher, Ph.D., P.E.  
Christopher Consultants, Roswell, Georgia, USA

Jorge G. Zornberg, Ph.D., P.E.  
GeoSyntec Consultants, Huntington Beach, California, U.S.A.

James K. Mitchell, Ph.D., P.E.  
Virginia Polytechnic Institute and State University, Blacksburg, Virginia, U.S.A.

**ABSTRACT:** Use of marginal, poorly draining backfill to construct reinforced soil structures offers significant advantages for numerous applications. This paper reviews the issues associated with using such soils with an emphasis on the use of permeable inclusions as a design alternative to provide internal drainage of the reinforced zone. Case histories demonstrating the successful use of permeable inclusions for addressing both internal and external seepage problems are presented. Adverse conditions of excessive moisture and pore water pressures within the poorly draining backfill are identified. Finally, preliminary guidance for reinforced soil structures using poorly draining backfills is provided to account for these adverse conditions in their design.

**KEYWORDS:** Reinforcement, Design, Seepage Control, Shear Strength, Drainage.

## 1 INTRODUCTION

Granular soils have been the preferred backfill material for reinforced soil construction due to their high strength and ability to prevent development of pore water pressures. Stringent specifications regarding selection of granular backfill are provided, for example, by the United States FHWA guidelines (Elias and Christopher, 1996). However, if granular fills were not readily available, or if substantial cost benefits resulted from relaxing fill specifications, poorly draining soils (e.g. silty or clayey soils) have been used in practice. In these cases, proper understanding of the conditions leading to wetting of the fill and to the development of pore water pressures is imperative for an adequate design.

Although marginal soils have been successfully reinforced using impermeable reinforcements (e.g. geogrids, woven geotextiles, metallic reinforcements), failures have also been reported. These failures generally occurred if the generation of pore pressures or seepage related conditions were not correctly addressed during design (Mitchell and Zornberg, 1995).

A promising approach for design of reinforced marginal soils is to promote lateral drainage in combination with soil reinforcement. This may be achieved by using geocomposites with in-plane drainage capabilities or thin layers of granular soil in combination with the geosynthetic reinforcements. This design approach may even lead to the elimination of external drainage requirements. The potential use of permeable inclusions to reinforce poorly draining soils is well documented (e.g. Tatsuoka et al.,

1990; Zornberg and Mitchell, 1994; Mitchell and Zornberg, 1995). The focus of this paper is on the implementation of this technology by providing design guidance based on experience gained in recent case histories. Emphasis is placed on the identification of the adverse conditions that may result in wetting and pore water pressure development within the reinforced marginal fill.

This paper initially identifies the problems related to the use of marginal soils and the potential use of permeable inclusions as a design alternative. Next, experiences from the technical literature and by the authors on recent case histories are presented. Finally, preliminary guidance is provided, considering the identified adverse conditions, regarding the design of reinforced soil structure using poorly draining backfills.

## 2 BACKGROUND

### 2.1 Reinforcing Poorly Draining Backfills: Identification of Adverse Conditions

Significant problems are associated with the use of marginal soils in reinforced soil construction. The use of comparatively wet soils leads, for example, to construction problems associated with compaction difficulties during placement. However, the most serious concerns are related to stability problems associated with the potential development of pore water pressures or loss of strength due to wetting within the reinforced fill mass. The following three adverse conditions of pore water pressure generation and/or loss of

strength due to wetting are of concern when reinforcing poorly draining backfills (Fig. 1):

*Condition (a): Generation of pore water pressures within the reinforced fill.* When fine grained, poorly draining soils are used in reinforced soil construction (particularly if placed wet of optimum moisture), excess pore water pressure can develop during compaction, subsequent loading, and surcharging. The designer must then account for these pore water pressures for the evaluations of stability and consolidation-induced settlements.

*Condition (b): Wetting front advancing into the reinforced fill.* This is the case for fills placed comparatively dry (i.e. no pore water pressure generation is expected during construction). However, loss of soil shear strength may occur due to wetting of the backfill soils as a consequence of post-construction infiltration. This loss of strength due to wetting could be expected, even if no positive pore water pressures are generated and no seepage flow configuration is established within the fill.

*Condition (c): Seepage configuration established within the reinforced fill.* Seepage flow may occur within the reinforced soil mass, for example, in the case of sliver fills constructed on existing embankment side slopes and cut slopes in which infiltration occurs from the adjacent ground. Significant seepage forces may occur either during rainy or spring thaw seasons. Water level fluctuations and rapid draw down conditions can also induce seepage forces in structures subjected to flooding or constructed adjacent to or within bodies of water. Seepage forces may also occur during ground wetting, inducing an additional destabilizing effect to the loss in shear strength described by Condition (b).

## 2.2 Reinforcing Poorly Draining Backfills: Permeable Inclusions as Potential Design Alternative

The potential benefits of using marginal soils to construct steepened slopes are significant and include:

- reduced cost of structures that would otherwise be constructed with expensive select backfill;
- improved performance of compacted clay structures that would otherwise be constructed without reinforcements; and
- use of materials, such as nearly saturated cohesive soils and mine wastes, that would otherwise require disposal.

However, the significant benefits of using poorly draining soils as backfill material can be realized only if a proper design accounts for the three adverse conditions listed in Section 2.1. The use of permeable reinforcements is a potential design alternative to properly handle these conditions, as follows:

*Condition (a):* Pore water pressures generated during construction within the reinforced poorly draining fill could be dissipated if the geosynthetic inclusions are used not only as reinforcements, but also as lateral drains. New applications in the use of geosynthetics for stabilization in land reclamation projects could be developed. For example, acceleration of drainage of hydraulically dredged materials could be achieved.

*Condition (b):* A problem frequently reported for embankments of (unreinforced) compacted cohesive soils is the development of surface tension cracks and the subsequent loss of soil strength due to soaking. The wetting front and development of surface tension cracks have been observed by the authors and other investigators (Tatsuoka et al., 1990) to extend only down to the region above the first geosynthetic layer. If the reinforcement is permeable, water that might normally accumulate in the crack can drain when the crack reaches the first layer of reinforcement.

*Condition (c):* Permeable reinforcements can prevent the development of flow configurations with destabilizing seepage forces within the embankment fill. Internal drainage is of particular concern in road widening projects, because of the potential water seepage from cut slopes into the reinforced fill. Although the adverse effect of seepage forces in engineered slopes could be prevented by designing special drainage systems, a more economical design alternative is to combine drainage and reinforcement capabilities by using permeable reinforcement elements.

In addition to addressing stability problems, the use of permeable inclusions may also be of benefit during construction. Wet soils typically must be dried to provide desired compaction levels and associated design strengths. However, it has been verified that permeable inclusions (e.g. nonwoven geotextiles) help in the compaction of the

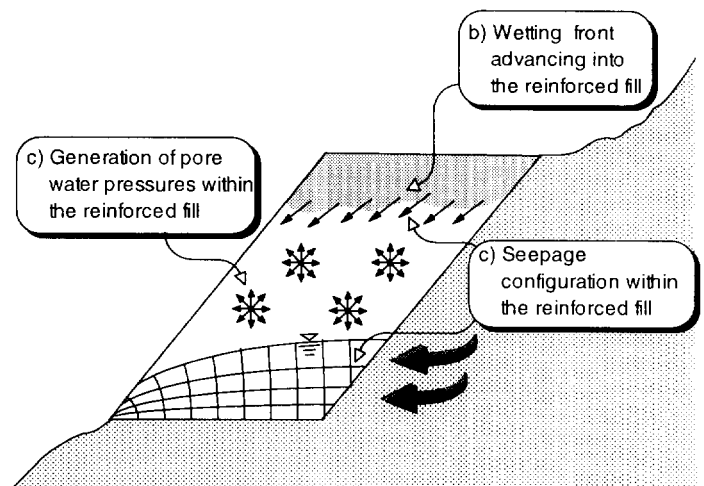


Fig. 1. Different conditions of concern in reinforced soil slopes using poorly draining backfills.

fill both by allowing better distribution of the compaction effort and by draining excess pore water pressure induced during compaction (Indraratna et al., 1991; Zornberg et al., 1995). On several projects, water has even been observed seeping out of the geotextile during compaction of such soils placed wet of optimum. The most significant improvement in compaction has been reported for low plasticity clayey and silty soils. Although some compaction improvement has been observed in plastic soils, the influence would not be nearly as significant. In either case, drying may still be required to facilitate placement and compaction, especially in very wet soils. Test pads are recommended to determine the actual placement requirements and compaction improvements. The increased rate of settlement would also expedite the construction of structures with a low tolerance for settlement (e.g. roads, bridges and buildings) that may be supported by the reinforced structure.

### 3. EXPERIENCE IN THE USE OF REINFORCED POORLY DRAINING FILLS

Although there are no generally accepted design guidelines for reinforced soil structures using marginal soils, good performance has been observed in cases where the generation of pore water pressures within the fill was mitigated. The observed performance of a 5.6 m high experimental structure built using silt backfill in Rouen, France is a good example (Perrier et al., 1986). Pore water pressures were monitored within the silt backfill. The structure consisted of sections reinforced with woven geotextiles and a section reinforced with a composite nonwoven/geogrid. Fig. 2 shows positive and negative pore water pressures as a function of time recorded at different locations within the fill. The pressure sensor behind the reinforcement region recorded placement excess pore water pressures of as much as 60 kPa at the end of construction. Along the woven geotextile, 3.5 m from the wall face, positive pore water pressures on the order of 20 kPa were registered at the end of construction and dissipated in 350 days. Along the composite geotextile, on the other hand, negative pore water pressures were registered over the entire length of the reinforcement, even at the end of construction. The negative pore water pressure recorded for the geocomposite most likely developed due to the ability of the geosynthetic to maintain partial saturation in the soil or to the unsaturated condition of the geosynthetic itself. Pore water pressures along the composite geotextile were systematically lower than those recorded along the woven textile.

Permeable reinforcements were also used to control pore water pressure during construction and to accelerate post-construction consolidation as part of the reconstruction of an embankment in Pennsylvania (Wayne et al., 1996). A sink hole developed in a section of state

route SR54 due to the collapse of an abandoned railroad tunnel. The traditional repair would have involved the removal and replacement of the 15 m high embankment. However, the native soil (a sandy clay of high moisture content) was deemed unsuitable backfill due to potential stability and settlement problems. Consequently, due to the high cost of granular fill as replacement material (estimated as \$19.60/m<sup>3</sup>), the Pennsylvania DOT decided to use geosynthetics to provide both drainage and reinforcement to the native soil used as fill. The estimated cost savings are \$200,000 (based on an as built cost of \$4/m<sup>3</sup> for the native

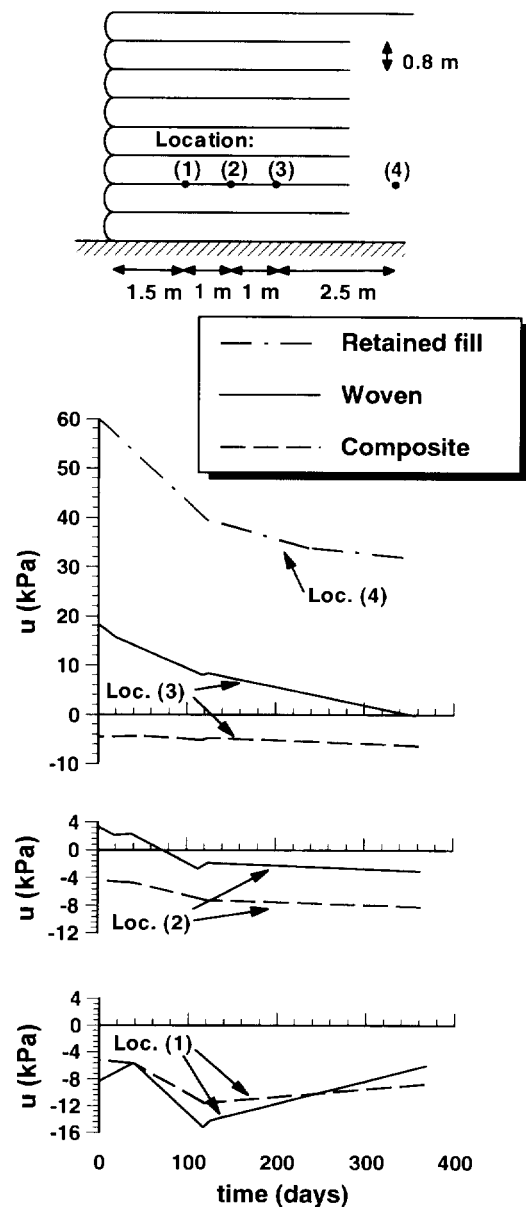


Fig. 2. Pore water pressures ( $u$ ) in the Rouen reinforced wall, along a woven and a nonwoven/geogrid composite, within a silty backfill (redrawn after Perrier et al., 1986).

soil plus the geotextile). Based on the results of field tests used to evaluate pore pressure response, a nonwoven geotextile was selected to allow pore pressure dissipation in the native soil. The geotextile, with an ultimate strength of 16 kN/m, also provided reinforcement to the 1.5H:1V side slopes. Placement of geotextiles at each compacted lift (0.3 m spacing, i.e. 0.15 m drainage path), led to full dissipation of pore water pressure within approximately 4 days. Only approximately 25% of the pore water pressures were dissipated during the same time period in zones that did not contain geosynthetics. Piezometers installed at the base and middle of the slope confirmed the test pad results. Fig. 3 shows the development and subsequent dissipation of pore pressure during and following construction of the embankment. Geotextile deformations in the side slope were monitored and found to be less than the precision of the gages ( $\pm 1\%$  strain).

There is also good evidence that permeable geosynthetic reinforcements can reduce the influence of external seepage behind the reinforced soil mass (e.g. in cut slope applications). Recent centrifuge model studies evaluated the performance of unreinforced and reinforced steep slopes constructed with clay (Mahmud, 1997). Seepage was induced into the reinforced clay by maintaining a constant water level at the back of the structure. Measurement of pore pressure across the base of the structure, indicated a lower phreatic surface if the slope was constructed using permeable geosynthetic reinforcements than if the slope was unreinforced (Fig. 4).

The use of permeable reinforcements to reduce external seepage problems was also demonstrated in a recent project which included one of the highest geotextile-reinforced slopes in the U. S. (Zornberg et al., 1995). As part of a highway widening project, the Federal Highway Administration constructed a permanent, 15.3 m high geotextile-reinforced slope. Several characteristics were unique to the design: the structure was higher than usual geotextile-reinforced slopes, it involved the use of both a high modulus composite and a nonwoven geotextile, and it was constructed using indigenous soils (decomposed granite) as backfill material. Internal drainage was a design concern because of the potential seepage from the fractured rock mass into the reinforced fill, and because of the potential crushing of decomposed granite particles that was anticipated to reduce the hydraulic conductivity of the fill. Widening of the original road was achieved by converting the existing 2H:1V unreinforced slope into a 1H:1V reinforced slope. The final design adopted a high strength composite geotextile in the lower half of the slope and a nonwoven geotextile in the upper half. Piezometer measurements indicated that a seepage flow configuration did not develop within the reinforced soil mass even during the spring thaw, when seepage water infiltrated from the backslope fractured rock into the reinforced fill.

Additional evidences that good structure performance is dependent on maintaining a low water pressure in poorly

draining backfills was provided by Tatsuoka et al. (1990) and Mitchell and Zornberg (1995). However, practice has led theory, and a consistent design methodology for design of reinforced soil structures using poorly draining backfills has not been developed yet.

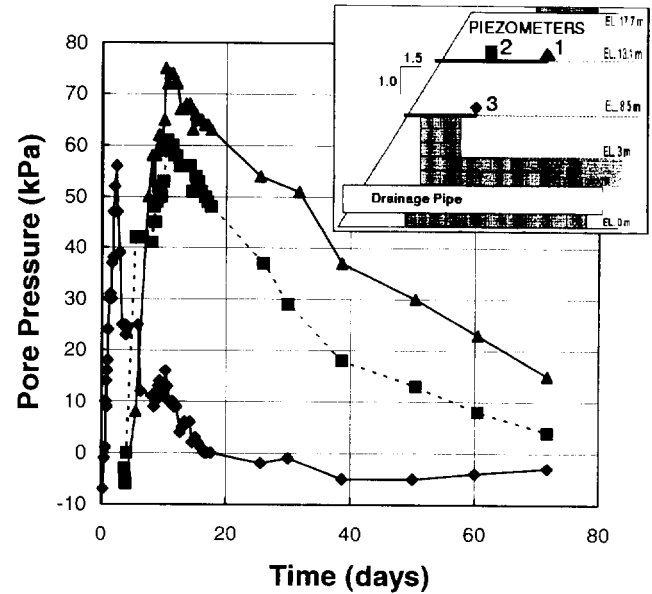


Fig. 3. Pore water pressure measurements in the SR54 reinforced slope (redrawn after Wayne et al., 1996).

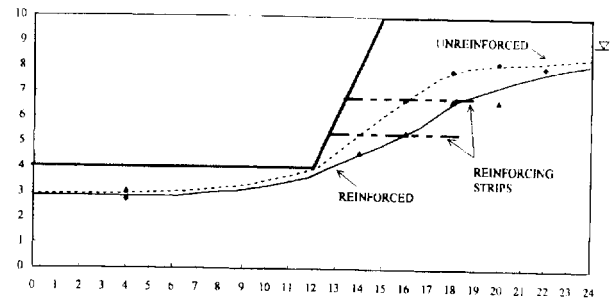


Fig. 4. Centrifuge model results showing the elevation of the phreatic surfaces for unreinforced and reinforced slopes (Mahmud, 1997).

## 4. DESIGN GUIDANCE

### 4.1 General Considerations

Good performance in reinforcing marginal soils depends on accounting for excess pore water pressure development within the fill material. Design criteria involved in the use of reinforcement-drainage geocomposites differ from those developed for conventional soil reinforcement applications. A total stress analysis, considering soil parameters representative of placement conditions, usually has been



adopted in the analysis of impermeable conventional reinforcements. The design generally leads to the use of reinforcements with a comparatively high tensile strength to account for a low soil shear strength and the presence of seepage forces. Reinforcement embedment length is comparatively large to account for reduced pullout resistance. External drainage of the reinforced soil structure has often been considered as part of the design to intercept ground water at the back of the structure.

The general design philosophy for permeable inclusions that is proposed in this paper is that transmissivity of the geosynthetic inclusion should be selected so that the geosynthetic inclusions can carry the full in-plane flow without developing positive pore water pressures along the soil-reinforcement interface. While it is also possible to design for positive pore water pressures at the interface, such a design requires evaluations that are beyond the scope of this paper. Consequently, the design procedure described below is only for reinforced soil structures in which the reinforcement transmissivity is conservatively selected so that flow is not impeded within the geosynthetic. The proposed design methodology assumes no build up of excess pore pressure within the permeable reinforcements.

The analysis should account for the three adverse conditions listed in Section 2.1 in order to determine the tensile strength and pullout requirements. The general design philosophy proposed herein is to consider a two-phase evaluation:

*Analysis (i)* in each adverse condition is performed ignoring the drainage contribution provided by the reinforcements.

This is a total stress analysis which considers that stability is mostly provided by the reinforcements with minimum contribution of the soil shear strength. Due to the conservative nature of this assumption, a relatively low design factor of safety is suggested.

*Analysis (ii)* in each adverse condition is performed accounting fully for the drainage contribution provided by the reinforcements (i.e. zero pore water pressure is considered within the reinforced fill for analysis purposes). Considering that no pore water pressures are assumed to develop, this is an effective stress analysis. Design factors of safety used in conventional engineering practice are considered in this case.

#### 4.2 Designing for Condition (a): Pore water Pressures Generated within the Reinforced Fill

There is good evidence that geosynthetics with adequate transmissivity and vertical spacing on the order of every compaction lift or every other compaction lift (e.g. 200 to 300 mm) can dissipate excess pore pressure along the interface of the permeable inclusions during construction (Bourdillon et al., 1977). However, excess pore water pressures may develop within the soil mass between

geosynthetic layers during construction, especially if highly plastic soils are used as backfill material. Considering the difficulty in accurately evaluating the distribution of pore water pressures generated during construction a two-phase analysis is proposed. These analyses, summarized in Table 1, are as follows:

- i) Total stress analysis ignoring reinforcement lateral drainage. This analysis neglects the dissipation of pore water pressures through the permeable inclusions to provide a conservative estimate of the stability of the structure at the end of construction. Considering the short-term condition and the conservative assumptions in this analysis, a factor of safety of 1.1 is recommended. This analysis determines minimum reinforcement requirements that will preclude collapse during construction of the structure. That is, it provides reinforcement requirements for a short-term situation in which stability is provided mostly by the tensile forces in the reinforcements with only a minor contribution by the undrained shear strength of the backfill. The undrained soil shear strength of the backfill for this analysis should be based on unconsolidated undrained (UU) triaxial tests. The specimens should be prepared at representative field densities and moisture placement conditions, and tested at these placement conditions under project-specific confining pressures. Although the authors consider testing under unsaturated conditions is an adequate approach, testing under fully saturated conditions represents an additional degree of conservatism that the designer may consider on a project-specific basis.
- ii) Effective stress analysis accounting for full lateral drainage by the reinforcement. Full drainage of the reinforced fill is assumed for the long-term conditions. This analysis provides a realistic evaluation of the long-term stability of the structure, because dissipation of pore water pressures generated during construction should have occurred through the permeable inclusions. This analysis determines the minimum reinforcement requirements that will provide adequate stability under long-term conditions following dissipation of pore water pressures generated during construction of the structure. It is emphasized that the transmissivity of the reinforcements should be selected so that generation of pore water pressures is prevented at the soil-reinforcement interface. Typically, the soil shear strength should be based on isotropically consolidated undrained (CIU) triaxial tests performed on saturated samples with pore pressure measurements or on consolidated drained (CD) triaxial tests. The long term design factor of safety typically required for reinforcement of granular fills (e.g. 1.3 to 1.5) should be used in this analysis.

Table 1. Summary of Analyses for Reinforced Soil Structures with Poorly Draining Backfills

<i>Condition</i>	<i>Characteristics</i>	<i>Analysis i: Ignoring lateral drainage</i>	<i>Analysis ii: Accounting for full drainage</i>
<i>a) Generation of pore water pressures within reinforced fill</i>	Type of analysis:	Total Stress	Effective Stress
	Case:	Generation of pore pressures due to short-term loads	Long-term drained condition due to lateral drainage
	Design Criteria:	FS = 1.1	FS = 1.3 to 1.5 (*)
	Reinforcement Transmissivity:	Ignored in analysis	Conveys fully the flow from consolidation process
	Soil shear strength:	$\phi$ and $c$ from UU tests. Specimen condition: as placed	$\phi'$ and $c'$ from CIU or CD tests. Specimen condition: saturated
<i>b) Wetting front advancing into reinforced fill</i>	Type of analysis:	Total Stress	Total Stress
	Case:	Loss of shear strength due to soaking	Unsaturated condition maintained due to permeable reinforcements
	Design Criteria:	FS = 1.1	FS = 1.3 to 1.5 (*)
	Reinforcement Transmissivity:	Ignored in analysis	Prevents advancement of wetting as defined by testing
	Soil shear strength:	$\phi$ and $c$ from CIU tests. Specimen condition: saturated	$\phi$ and $c$ from CIU or CD tests. Specimen condition: highest anticipated moisture
<i>c) Seepage flow configuration established within reinforced fill</i>	Type of analysis:	Total Stress	Effective Stress
	Case:	Development of seepage forces within fill	Saturation of fill, without development of seepage forces due to permeable reinforcements
	Design Criteria:	FS = 1.1	FS = 1.3 to 1.5 (*)
	Reinforcement Transmissivity:	Ignored in analysis	Conveys fully the seepage flowing into the backfill
	Soil shear strength:	$\phi$ and $c$ from CIU tests. Specimen condition: saturated	$\phi'$ and $c'$ from CIU or CD tests. Specimen condition: saturated

(\*) Design criteria for Analysis (ii) should be selected based on design guidelines for reinforced soil structures with granular backfill.

The reinforcement tensile strength eventually selected is the higher value obtained from analyses (i) and (ii). Moreover, the minimum reinforcement length selected for design should be the larger value defined from the two analyses. Note that the analyses described above address internal stability. However, the required length of the reinforcement must also consider external stability of the structure. External stability should consider the undrained soil shear strength for the fill retained behind the reinforced zone if it is to be constructed with similar marginal fill. For cut slopes appropriate pore water pressure assumptions should be made for field conditions.

It should be noted that an effective stress analysis could have been proposed to evaluate the short-term stability of the structure, instead of the total stress Analysis (i). An effective stress analysis would more accurately account for the in-plane drainage capacity of the geosynthetic and the corresponding increase in soil strength. Also, an effective stress analysis would facilitate evaluation of the backfill placement rate that would lead to

an acceptable stability factor of safety during construction. The difficulty in this approach is the accurate determination of the pore water pressures within the fill. They could be estimated from direct measurements in field trials (e.g. test pads) or sealed laboratory specimens (one lift thick with a geosynthetic on the bottom and top connected to drain lines) subjected to stress levels anticipated during construction. Alternatively, pore pressures could be theoretically estimated based on one-dimensional consolidation theory and the assumption of full saturation of the backfill material during construction. An evaluation of this approach is beyond the scope of this paper.

#### 4.3 Designing for Condition (b): Wetting Front Advancing into the Reinforced Fill

As loss of strength may occur because of a wetting front advancing into the reinforced fill. Geosynthetic transmissivity requirements should be established to avoid

advancement of wetting front for expected conditions. A two-phase analysis is also proposed in this case. These analyses, summarized in Table 1, are as follows:

- i) Total stress analysis ignoring the effect of lateral drainage in preventing advancement of a wetting front. This analysis is performed using shear strength properties of the reinforced soil mass defined using saturated specimens. The results of this analysis provide an estimate of the stability of the structure under an advancing wetting front. This analysis is conservative because the backfill is assumed fully saturated, which should not occur in actual practice because the wetting front is intercepted by the permeable reinforcements. Consequently, a factor of safety of 1.1 is recommended in this case. Water pressure that may develop as water fills surface cracks (induced by desiccation, freeze/thaw, or slope movements) should be accounted using boundary water pressures in the analysis.
- ii) Total stress analysis accounting for the effect of lateral drainage in preventing advancement of a wetting front. The total shear strength is defined from unsaturated specimens prepared at the highest moisture anticipated in the fill. Note that the total shear strength defined from unsaturated specimens should be higher than the effective shear strength of the fill. A total stress analysis is considered in this case, instead of an effective stress analysis, in order to account for the beneficial effect of the negative pore water pressures in the unsaturated reinforced fill. The shear strength of the reinforced fill above the top reinforced layer (which may become saturated) should be obtained from saturated specimens. This analysis provides a realistic evaluation of the stability of the structure because it accounts for the lateral drainage of the geosynthetic reinforcements.

#### 4.4 Designing for Condition (c): Seepage Configuration Established within the Reinforced Fill

Post-construction pore water pressures could be generated by a seepage configuration developing within the backfill material. Such a flow configuration may develop seasonally during rainy periods or during spring thaw. A seepage configuration may also develop due to water level fluctuations in structures subjected to flooding or constructed adjacent to or within bodies of water. Finally, seepage forces could be induced by surface water infiltration. The seepage configuration can be determined for an unreinforced embankment using flow nets for seepage analysis. Transmissivity requirements in the geosynthetic inclusions are such that each reinforcement should convey fully the flow quantity it intercepts (as estimated from a flow net defined in an unreinforced

slope). A two-phase analysis is also proposed in this case. These analyses, summarized in Table 1, are as follows:

- i) Total stress analysis ignoring reinforcement lateral drainage. This analysis considers seepage forces defined from a flow configuration that would develop in an unreinforced slope. The results of this analysis provide a conservative estimate of the stability of the structure during a seasonal rapid configuration of seepage flow within the fill. The conservatism of this analysis is because (1) the backfill is assumed as fully saturated, which may not occur in actual practice, and (2) the seepage configuration does not account for the lateral drainage provided by the reinforcements. Therefore, a relatively low factor of safety of 1.1 is recommended in this case (note that seepage forces are considered in the analysis).
- ii) Effective stress analysis accounting for full reinforcement lateral drainage. Full drainage of the reinforced fill is assumed for the typical condition of the structure. This analysis provides a realistic evaluation of the long-term stability of the structure because it accounts for the lateral drainage of the geosynthetic reinforcements. No seepage forces are considered to develop within the reinforced fill if the reinforcements provide adequate internal drainage.

As indicated, the transmissivity and number and location of layers should be selected so that the geosynthetics have in-plane drainage capacity to accommodate the full seepage flowing into the reinforced fill. Otherwise, external groundwater and surface water control systems (e.g. base and back drains and surface collectors) must be incorporated into the design. The soil shear strength in the two analyses (total and effective stresses) should be determined using saturated samples in order to account for the potential loss of shear strength under soaked conditions.

#### 4.5 Reinforcement Requirements

Mechanical and hydraulic properties that must be characterized for alternative reinforcement-drainage geocomposite systems include: tensile strength, pullout resistance, drainage, and filtration. These four characteristics should be carefully evaluated and quantified in order to assess the overall performance of the structures under consideration. The evaluations include at least the following considerations:

- Tensile strength requirements of the geosynthetic, determined as indicated in Table 1, will be typically higher for reinforcement of marginal fills than conventional free draining material. Consideration should be given to soil creep in the determination of long-term design strength.

- Pullout resistance, which require special consideration due to the potential development of pore water pressures at the soil/reinforcement interface and to the creep potential of cohesive soils. For the total stress analyses in Table 1, total stress shear strength properties should be used. For the effective stress analyses, effective shear strength properties should be considered.
- Transmissivity requirements should account for the different conditions indicated in Table 1 (i.e. the total flow induced by consolidation or seepage must be accommodated without inducing positive pore water pressures within the reinforcements). There is good evidence that transmissivity values equivalent to those of needlepunched nonwoven geotextiles are adequate to freely drain cohesive type soil and dissipate excess pore pressure along the interface, provided spacing is on the order of every lift or every other lift of compacted soil (e.g. Bourdillon et al., 1977). They should also be high enough to prevent advancement of a wetting front. Test pads could be used to evaluate the suitability of selected geosynthetics. Increased transmissivity may be required based on flow net analysis of externally induced seepage (Condition c).
- Filtration requirements needed to minimize clogging of the geocomposite should also be evaluated. Design guidance is provided in Holtz et al. (1997) and Koerner (1994).

## 5 CONCLUSIONS

Marginal poorly draining backfill can be used to safely construct reinforced steepened slopes provided internal and external seepage forces have been accounted for in the analysis. Adverse conditions include: (a) the generation of pore water pressures within the reinforced fill (either during construction or subsequent loading); (b) a wetting front advancing into the reinforced fill, which may cause loss of soil shear strength in a fill initially placed in a comparatively dry condition; and (c) a seepage flow configuration established within the reinforced fill due to seepage from the retained soil or fluctuations in the water level for structures constructed adjacent to or within bodies of water.

Reinforcements with in-plane drainage capabilities offer a design alternative for mitigating these adverse conditions. A two-phase analysis is proposed when using permeable reinforcements to account for both short and long-term conditions. Although the design approach is supported by theoretical soil mechanics, it relies heavily on field experience. Therefore, an element of conservatism is inherently included in the proposed methods. Further refinement of this guidance is being developed by the authors in order to provide quantitative transmissivity requirements for the case of pore water pressures developed during construction. Recommendations are

provided herein regarding the selection of soil shear strength properties and design criteria for the analyses.

## REFERENCES

- Bourdillon, M., Didier, G., and Gielly, J., 1977, "Utilisation des Produits Non-tissés pour le Drainage," *Proc. Intl. Conf. on the Use of Fabrics in Geotechnics*, Paris, Vol. 2, pp. 279-284.
- Elias, V., and Christopher, B.R., 1996, "Mechanically Stabilized Earth Walls and Reinforced Soil Slopes, Design and Construction Guidelines" Department of Transportation, FHWA, Washington D.C., 367 p.
- Holtz, R.D., Christopher, B.R. and Berg, R.B., *Geosynthetic Engineering*, 1997, BiTech Publishers Ltd., Richmond, British Columbia, Canada, 452 p.
- Indraratna, B., Satkunaseelan, K.S., and Rasul, M.G., 1991, "Laboratory Properties of a Soft Marine Clay Reinforced with Woven and Nonwoven Geotextiles", *Geotechnical Testing J.*, Vol. 14, No. 3, pp. 288-295.
- Koerner, R.M., 1994, *Designing With Geosynthetics*, 3rd Edition, Prentice-Hall Inc., Englewood Cliffs, 783 p.
- Mahmud, M.B., 1997, "Centrifuge Modeling of an Innovative Rapidly Installed and Economical MSES for Marginally Stable Slopes" Ph.D. Dissertation, Rensselaer Polyt. Inst., Troy, NY, 240 p.
- Mitchell, J.K., and Zornberg, J.G., 1995, "Reinforced Soil Structures with Poorly Draining Backfills. Part II: Case Histories and Applications," *Geosynthetics International*, Vol. 2, no. 1, pp. 265-307.
- Perrier, H., Blivet, J.C., and Khay, M., 1986, "Stabilization de Talus par Renforcement tout Textile: Ouvrages Experimental et Reel," *Proc. Third Intl. Conf. on Geotextiles*, Vol. 2, Vienna, pp. 313-318.
- Tatsuoka, F., Murata, O., Tateyama, M., Nakamura, K., Tamura, Y., Ling, H.I., Iwasaki, K., and Yamauchi, H., 1990, "Reinforcing Steep Clay Slopes with a Nonwoven Geotextile," *Performance of Reinforced Soil Structures*, Thomas Telford Ltd., pp. 141-146.
- Wayne, M.H., K.W. Petrasic, Wilcosky, E., and Rafter, T.J., 1996, "An Innovative Use of a Nonwoven Geotextile in the Restoration of Pennsylvania SR54," *Proc. Geofilters '96*, Montreal, pp. 513-521.
- Zornberg, J.G., and Mitchell, J.K., 1994, "Reinforced Soil Structures with Poorly Draining Backfills. Part I: Reinforcement Interactions and Functions," *Geosynthetics International*, Vol. 1, no. 2, pp. 103-148.
- Zornberg, J.G., Barrows, R.J., Christopher, B.R., and Wayne, M.H., 1995, "Construction and Instrumentation of a Highway Slope Reinforced with High Strength Geotextiles". *Proc. Geosynthetics '95*, Nashville, TN, Vol. 1, pp. 13-27.

# Reinforcement of a Saudi Sabkha Soil Using Geotextiles

S.A. Aiban, O.S.B. Al-Amoudi, I. Ahmed, H.I. Al-Abdul Wahhab

Assistant Professor, Assistant Professor, Research Assistant and Associate Professor, respectively, Department of Civil Engineering, King Fahd University of Petroleum and Minerals, Dhahran, Saudi Arabia

**ABSTRACT:** Sabkha soils are well distributed over many parts of the world. Paved roads constructed on sabkha terrains often suffer different classes of damage due to the low load-carrying capacity of sabkha deposits, especially when becoming wet. This calls for the improvement of sabkhas prior to any construction. An experimental program was conducted to assess the performance of a problematic sabkha soil from eastern Saudi Arabia and to improve its strength using different techniques. In this paper, the effects of chemical additive type, dry density, moisture content and exposure conditions on the strength and deformation characteristics of the sabkha are presented. The results indicated that the sabkha had an acute water sensitivity depicted by a complete loss of strength when the samples were compacted at moisture contents other than the optimum value or when the sabkha was inundated with water. The results also showed that cement and lime had a marginal effect on the strength of this sabkha while geotextile significantly enhanced its load-bearing capacity.

**KEYWORDS:** Sabkha, Geotextile, Subgrade, Chemical stabilization, Water sensitivity.

## 1 INTRODUCTION

Sabkha is originally an Arabic expression to describe indefinitely saline flats that are underlain by sand, silt and clay, and often encrusted with salt. It is an equilibrium surface whose level is largely controlled by the prevailing climatic and hydrological conditions (Johnson et al. 1978). These soils are defined as the subaerial evaporite flats that border partially landlocked seas (called coastal sabkhas), or cover a number of continental depressions (called inland or continental sabkhas), both types usually form under hot and arid climates; and are associated with shallow groundwater tables (Al-Amoudi 1995).

Sabkha is widely distributed in the Arabian Peninsula, especially in the well-populated cities along the Arabian Gulf and Red Sea coasts (Al-Amoudi et al. 1992). Along the western and southwestern shores of the Arabian Gulf, these soils are generally viewed as unconsolidated, heterogeneous, layered or unlayered sediments, that are bathed in highly concentrated brines. Their outer surfaces are generally composed of hygroscopic salts which, when dampened, can render the normally stable surface crusts impassable. These characteristics make the sabkha susceptible to collapse upon flooding.

Sabkha soils are not confined to the Arabian Peninsula, but are well distributed over the globe with various nomenclatures, and often highly bewildering (Ellis 1973). Sabkha extends over many parts of the Middle East, including Egypt, Sudan, Libya, Tunisia,

Algeria and Ethiopia. Sabkha also exists in India, Australia, Southern Africa, Mexico as well as in California, Utah and Texas in the USA (Al-Amoudi et al. 1997).

### 1.1 Characteristics of Sabkha Soils

During the last two decades, with the upsurge in oil prices, the Arabian Gulf countries have gone through a spectacular phase of both industrialization and urbanization. Inevitably, some of this construction was located on sabkha flats and, therefore, several problems developed in road construction, such as cracking, ravelling, formation of huge potholes and rutting (Farwana and Majidzadeh 1988), despite the fact that the necessary precaution had been taken. A major contributory factor is the very low bearing capacity of the sabkha soil, which often leads to the formation of depressions and excessive differential settlement (Al-Amoudi et al. 1995). The surficial layers of sabkha deposits are well known for their generally low strength, with SPT N-values of 0 to 8, rarely exceeding 10. In addition, there are three other concerns when dealing with sabkha soils (Al-Amoudi et al. 1995). Firstly, the concentrated nature of sabkha brines, which is often four to six times that of a seawater from the same vicinity, can be drawn into the permeable layers of a construction (such as a road) by capillary action and can recrystallize therein, causing expansion and blistering at the surface. Secondly, the severe climatic conditions, under which

sabkha deposits usually develop, can contribute to the instability of the sabkha soil by phase alteration. Lastly, the mineral grains in the sabkha matrix are bonded together by cements that are somewhat water-soluble, such as halite, gypsum, anhydrite and/or aragonite, thus making the sabkha susceptible to collapse upon wetting.

These characteristics mean that sabkha soils do not comply with routine design requirements, as neither their bearing capacity nor compressibility meet normal constructional practices (Al-Amoudi 1994). Such a situation calls for the improvement of sabkha soil prior to any construction to avoid future problems. A recent search of the literature (Al-Amoudi 1995) indicates that many deep soil densification techniques (i.e. vibroflotation, vibroreplacement, dynamic compaction, etc.) have been implemented for large-scale constructions, with varying degrees of success. Chemical stabilization, using cement, lime and emulsion, did not bring a guaranteed improvement for all types of sabkha (Aiban et al. 1996). Geotextiles have also been used to stabilize sabkha soils in both preliminary laboratory studies and the field. Despite the reported success achieved through the use of geotextiles as a means of reinforcing the sabkha soil and/or drainage control, practicality and durability remain the critical factors (Al-Amoudi 1994). Presently, there is relatively meager information on the usage of geotextile for aggregate bases/subbases constructed over weak soils, such as sabkha. Such applications are of great potential to the construction industry in the Arabian Gulf and elsewhere.

This research program was initiated when lime and cement failed to stabilize a problematic "clayey" sabkha soil. Therefore, geotextiles were proposed to improve the load-bearing capacity of this sabkha. Accordingly, an experimental program was initiated to assess the performance of sabkha soil with and without geotextile. Although there are currently many parameters under investigation, the paper reports the effect of density, moisture content and exposure conditions (i.e. as-molded vs. soaked) on the strength and deformation characteristics of sabkha soils.

## 2 EXPERIMENTAL PROGRAM AND RESULTS

The sabkha sample was retrieved from the gigantic Ar-Riyas sabkha in eastern Saudi Arabia. The characteristics of this sabkha have been described in detail by Al-Amoudi et al. (1997) and Johnson et al. (1978). The soil was collected to embody all the layers up to the water table excluding the salt crust. After being transported to the laboratory, the soil was spread on plastic sheets for air drying and the lumped pieces were broken down using plastic hammers until all the

material passed ASTM # 4 sieve. The soil was thereafter thoroughly mixed, allowed to air dry and stored in plastic drums until testing.

### 2.1 Geomorphology of the Sabkha

The sabkha surface was observed to be covered by non-crystallized, pure halite layer 3 to 4 cm thick. A layer of brownish clay with anhydrite impurities was the second layer in succession and had a thickness of 2 to 3 cm. A band of anhydrite of about 6 to 7 cm thick was encountered followed thereafter by dark brown clay that had an apparent plasticity and contained some cubical crystals of clear halite (sodium chloride). Thereafter, a layer of halite cubes was encountered at a depth of 20 to 22 cm. The water table is shallow and was encountered at the top of the halite layer which is only 20 cm below the ground surface. Some air bubbles were observed after excavation, indicating the presence of artesian flow. The sabkha layering is shown in Figure 1.



Figure 1. Layering characteristics of the sabkha.

### 2.2 Sabkha Classification and Compaction

The USCS and AASHTO systems were used to classify the sabkha soil. In addition to water, the characterization tests were conducted using sabkha brine from the same vicinity. The grain-size distribution curves are shown in Figure 2. The plastic limit values

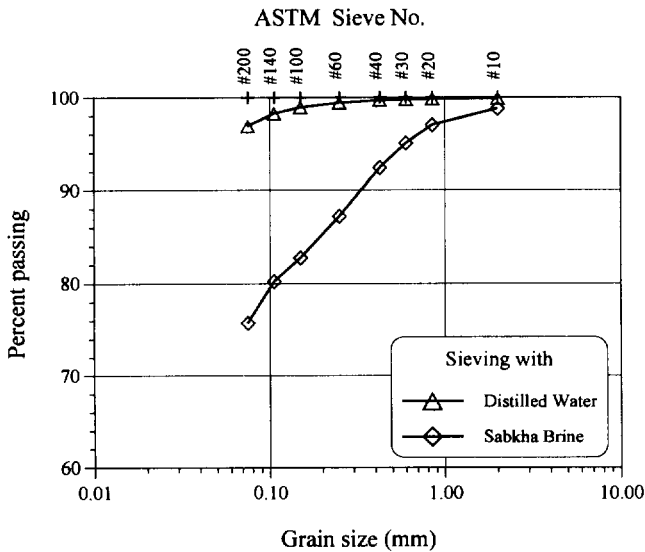


Figure 2. Grain-size distribution of the sabkha.

were 21% and 28% when distilled water and sabkha brine were used, respectively. The corresponding plasticity indices are 17.1% and 13.4%. Based on the sabkha brine results, the soil is classified as CL and A-6 according to the USCS and AASHTO systems, respectively.

The modified Proctor (i.e. compaction) test (ASTM D 1557) was used to determine the maximum dry density ( $\gamma_{d \max}$ ) and optimum moisture content ( $w_{opt}$ ). The California-bearing ratio (CBR) test (ASTM D 1833) was conducted for samples prepared at different moisture contents to assess the moisture sensitivity of the sabkha. The variation of the dry density and CBR values with the molding moisture content is shown in Figure 3. The CBR results clearly indicate the acute water sensitivity of the sabkha; the as-molded CBR value could reach 64 on the dry side of optimum while on the wet side of optimum, the CBR was as low as 3 only. In addition, the CBR at the  $w_{opt}$  was much lower than those at lower moisture contents. Furthermore, the soaked CBR did not exceed 2 regardless of the molding moisture content.

### 2.3 Chemical Stabilization

The CBR results in Figure 3 indicate a complete loss of strength when the samples were compacted on the wet side of optimum at a moisture content corresponding to 95% of the  $\gamma_{d \max}$ . The complete strength loss calls for stabilization of the sabkha prior to its usage. Different percentages of portland cement and lime were used to increase the strength of the sabkha and improve its water sensitivity, however, the improvements cannot be considered significant. The results in Figure 4 reveal

that only the addition of 10% cement can, at best, double the maximum unsoaked CBR value after 7 days of curing. These additions reduced the water sensitivity of the sabkha, but could not bring out significant improvements as compared with other sabkhas where an increase in the strength in excess of ten times has been reported (Aiban et al. 1996; Al-Amoudi et al. 1995). It was, therefore, decided to use geotextile to improve the bearing capacity of this sabkha.

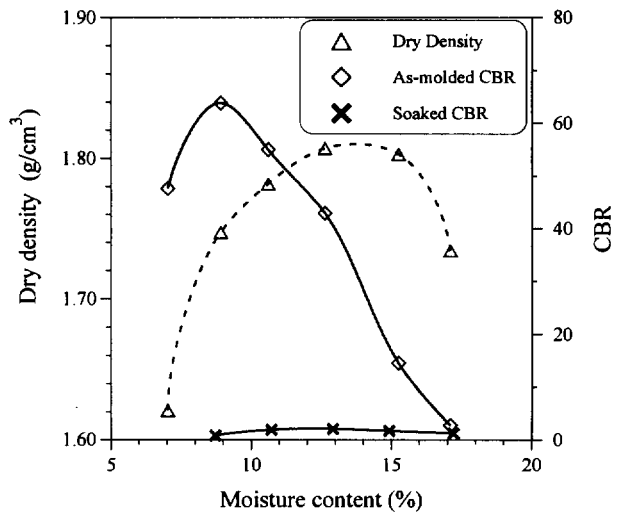


Figure 3. Variations of dry density and CBR values with molding moisture content for untreated sabkha.

### 2.4 Mold Fabrication

At present, relatively meager information has been developed concerning the use of geotextiles as reinforcement in aggregate bases or under foundations. This is particularly true when using weak and heterogeneous soils, such as sabkhas, as part of a pavement layer system. The only documented laboratory work on the use of geotextiles with sabkha soils is that of Abduljauwad et al. (1994). However, the mold used in their investigation was relatively small and had a diameter of only 320 mm. In this experimental program, a large-scale setup was fabricated at the University central workshop to conduct "representative" tests on sabkha soil reinforced with locally-produced geotextiles. The setup consists of a stainless steel mold having a diameter of 750 mm and a height of 350 mm with a wall thickness of 6.4 mm. The mold rests on a square stainless steel plate having the dimension of 1100 × 1100 mm and 16.5 mm in thickness. Stainless steel material was used in the setup because of the chemical aggressivity of the sabkha. To soak the samples, four

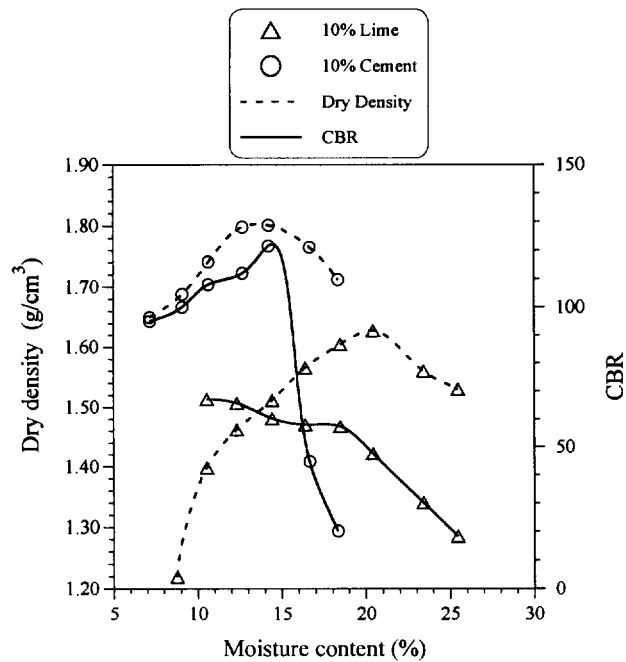


Figure 4. Variation of dry density and unsoaked CBR values with moisture content for sabkha samples treated with 10% cement or lime.

holes were made in the lower portion of the mold which were connected to the top reservoir containing the soaking fluid. The bottom reservoir was provided to maintain a constant water level when testing soaked samples. The setup is schematically shown in Figure 5.

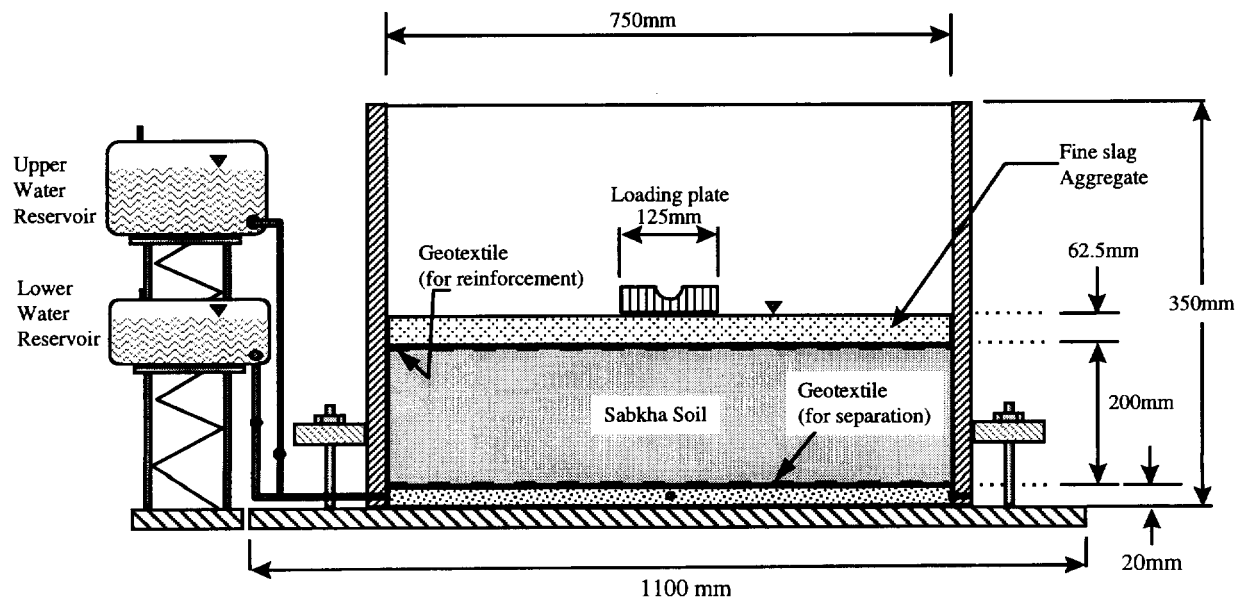


Figure 5. The experimental setup for the sabkha-geotextile system.

## 2.5 Sample Preparation and Testing

The sabkha samples were prepared in the large-scale mold as follows (Figure 5): First, a 20 mm layer of coarse sand filter was laid in the mold, thereafter, a layer of geotextile was spread over the sand, which acted as a separator between the sand filter and sabkha matrix while allowing water to flow in an upward direction when the sabkha samples were soaked. The sabkha soil was mixed with the specific amount of water in a large mixer, then a known weight of soil was placed in the mold and compacted to the required dry density using the static compaction method by means of a large jack which acted against a strong reaction beam. The soil was compacted in three lifts of 70, 60 and 70 mm thicknesses. The reinforcing layer of geotextile was thereafter placed on top of the compacted sabkha soil followed by a 62.5 mm thick layer of fine (0.15 to 4.76 mm in size) steel slag aggregate, which was pluviated to its maximum density. The technical specifications of the geotextile are summarized in Table 1. The geotextile is a locally produced non-woven needle punched fabric manufactured from polyester fibers.

So far, all testings of the geotextile-reinforced sabkha were performed under static loading. A displacement control loading was applied using an electrical motor and the deformation rate was set at 1 mm/min. The load was applied on a stiff circular plate having a diameter of 125 mm and a thickness of 10 mm. The load was measured using a load cell while the deformation was measured using four LVDT's mounted on top of the loading plate.



Table 1. Technical specifications of the geotextile used as reported by the manufacturer.

Property	Standard	Unit	ALYAF-400
Weight	ASTM D5261	gm/cm <sup>2</sup>	400
Thickness under 2 kN/m <sup>2</sup>	ASTM D5199	mm	4.5
Strip tensile strength (Longitudinal/transverse)	DIN 53857	N	925/1650
Grab tensile strength (Longitudinal/transverse)	ASTM D4632	N	1025/1525
Grab elongation (Longitudinal/transverse)	ASTM D4632	%	>80/>80
Cone penetration	BS 6906-6	mm	8.5
Permeability, k	BTTG, UK	cm/s	0.14

The loading plate was selected to be circular for many reasons including: (1) to simulate tire imprints which can be assumed circular for the majority of problems (Yoder and Witczak 1975), (2) to allow direct comparison with the California Bearing Ratio (CBR) results due to the relative similarities in the two systems since the CBR applies the load through a circular piston, and finally (3) to enable future theoretical simulations using both numerical procedures and analytical calculations due to the existence of similar solutions for axisymmetric problems.

The loading plate was chosen to have a diameter of 125 mm so that a clearance of 312 mm (five times the radius of the plate) from the sides of the mold can be maintained. This was intended to avoid any boundary interference from the sides of the mold. In addition, there will be enough distance from the end of the geotextile to provide anchorage of the geotextile and thus prevent failure due to pull out of the geotextile.

Figure 6 depicts the results for the specimens prepared at 90% and 95% of the maximum dry density ( $\gamma_{d \max}$ ) on the dry side of optimum and tested under "soaked" conditions, with and without the geotextile reinforcing layer. The data therein indicates that the strength of the system increased significantly when a geotextile layer was introduced. The ultimate strength of the sample without geotextile layer was 68 and 76 kgf at a deformation of 30 mm for the samples prepared at 90 and 95% of  $\gamma_{d \max}$ , respectively. When a geotextile layer was incorporated in the system, the ultimate strength increased to 248 and 265 kgf for the same deformation. This corresponds to an improvement in the ultimate strength of 365% and 350% compared to that of the corresponding samples without any geotextile layer. With an average improvement of about 357%, the soil-geotextile systems successfully improved the strength of

the present sabkha soil more than the improvement attained using cement or lime at a dosage of 10% by weight of the dry soil.

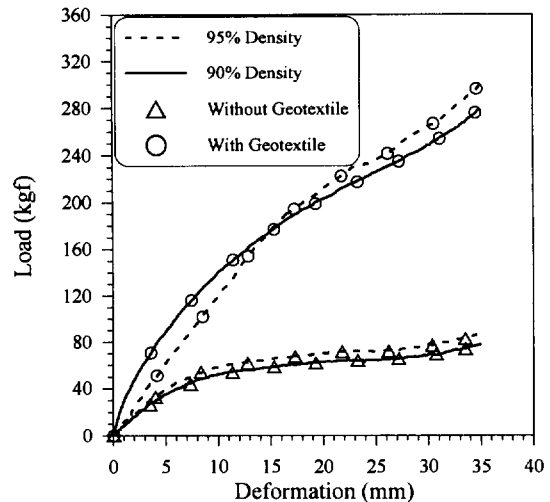


Figure 6. Load deformation curves for soaked sabkha soil with and without geotextile reinforcement.

It is worth mentioning that the two sets of load-deformation curves for the 90 and 95% relative compaction are almost identical regardless of the sabkha's initial density or moisture content. This is mainly ascribable to the fact that the strength of the sabkha is completely lost upon soaking and, thus, the soaked sabkha samples have the same strength. However, the reinforcing geotextile layer improves the load-carrying capacity of the sabkha significantly irrespective of its initial state. It is believed that the fine slag aggregate and some other factors have an effect on these results. It is the intention of the research team to vary the thickness of the fine slag aggregate and the geotextile (type and properties) and investigate their effects, in order to optimize the design of geotextile-sabkha systems.

### 3 CONCLUSIONS

This experimental program was conducted to compare the influence of chemical additives and geotextile on the load-carrying capacity of a clayey sabkha soil. The results clearly indicated the acute water sensitivity of the sabkha, as evidenced by the complete loss of strength when the samples were prepared at moisture contents other than the optimum value or when the sabkha was soaked. The results also demonstrated the fact that

chemical additives did not improve the strength significantly even when 10% cement or lime was added. However, the use of geotextile improved the load-carrying capacity of the sabkha up to four times that without geotextile. This was the case even for lower degrees of compaction such as 90% of  $\gamma_d$  max. The utilization of problematic sabkha sites seems to be possible with the use of geotextile; a possibility where other stabilization techniques failed.

In addition, the future program will include testing of cement-treated sabkha samples using the 750 mm mold. This will allow a direct comparison between the effectiveness of the chemical stabilization and geotextile. The boundary conditions of the two sets will be identical except for the treatment procedures. It should be clear that the data presented in this paper does not directly compare the chemical stabilization and the improvement using geotextile, nevertheless, the results vividly demonstrated the poor response of sabkha to chemical stabilization. On the other hand, the data clearly indicates the significant improvement of the load-carrying capacity of the sabkha-geotextile system. Both the CBR and loading in the large 750 mm mold simulate a punching problem albeit with some variation in the boundary conditions.

#### ACKNOWLEDGMENTS

The authors acknowledge the support provided by King Fahd University of Petroleum and Minerals (KFUPM), and King Abdulaziz City for Science & Technology (KACST). Thanks are extended to Mr. Hassan Zakariya Saleh for his assistance.

#### REFERENCES

- Abduljawwad, S.N., Bayomy, F.M., Al-Shaikh, A.M. and Al-Amoudi, O.S.B. (1994) "Influence of Geotextiles on the Performance of 'Saline' Sebkhah Soils", *Journal of Geotechnical Engineering*, ASCE, Vol. 120, No. 11, pp. 1939-1960.
- Aiban, S.A., Al-Abdul Wahhab, H.I. and Al-Amoudi, O.S.B. (1996) *Identification, Evaluation and Improvement of Eastern Saudi Soils for Constructional Purposes*, Progress Report No. 4, KACST AR-14-61, Riyadh, Saudi Arabia.
- Al-Amoudi, O.S.B. (1994) "Chemical Stabilization of Sabkha Soils at High Moisture Contents", *Engineering Geology*, Vol. 36, Nos. 3/4, pp. 279-291.
- Al-Amoudi, O.S.B. (1995) "A Review of the Geotechnical and Construction Problems in Sabkha Environments and Methods of Treatment", *Arabian Journal for Science & Engineering*, Vol. 20, No. 3, pp. 405-432.
- Al-Amoudi, O.S.B., Abduljawwad, S.N., El-Naggar, Z.R. and Rasheeduzzafar (1992) "Response of Sabkha to Laboratory Tests: A Case Study", *Engineering Geology*, Vol. 33, No. 2, pp. 111-125.
- Al-Amoudi, O.S.B., Aiban, S.A. and Al-Abdul Wahhab, H.I. (1997) "Variability and Characteristics of Eastern Saudi Sabkha Soils", *XIV International Conference on Soil Mechanics and Foundation Engineering*, Balkema, Rotterdam, Netherlands, Vol. 1, pp. 17-20.
- Al-Amoudi, O.S.B., Asi, I.M. and El-Naggar, Z.R. (1995) "Stabilization of an Arid, Saline Soil Using Additives", *Quarterly Journal of Engineering Geology*, Vol. 28, No. 4, pp. 369-379.
- Ellis, G.I. (1973) "Arabian Salt-bearing Soil (Sabkha) as an Engineering Material", *TRRL Report LR 523*, Crowthorne, Berkshire, England.
- Farwana, T.A. and Majidzadeh, K. (1988) "An Investigation into the Use of Emulsified Asphalt in the Stabilization of Sandy Sabkha", *Proceedings, 3rd IRF Middle East Regional Meeting*, Riyadh, Saudi Arabia, Vol. 3, pp. 3.203-3.213.
- Johnson, H., Kamal, M.R., Pierson, G.O. and Ramsay, J.B. (1978) "Sabkhahs of Eastern Saudi Arabia", In S.S. Al-Sayari and J.G. Zlot (eds.), *Quaternary Period in Saudi Arabia*, Springer-Verlag, Berlin, pp. 84-93.
- Yoder, E.J. and Witczak, M.W. (1975) *Principles of Pavement Design*, 2nd ed., John Wiley & Sons Inc., New York.

# Long-term Deformation of Reinforced Cohesive Soil Fills and Walls

M. Fukuoka

Dr., Public Works Research Center, Tokyo, Japan

**ABSTRACT:** This paper describes a method of estimating long-term deformation of geosynthetic reinforcing walls or embankments mainly due to percolation of rainwater. The triaxial compression test commonly used for obtaining coefficient of linear deformation and Poisson's ratio cannot be used for gravel-mixed soil or unsaturated soil which change soil constants by percolation of rainwater, under low level stresses and long-term loading tests. Moreover, uniform results are very difficult to obtain, because apparatuses differ from place to place and individual errors in tests are large. It is rather common to construct reinforced walls and embankments in front of original slope, a large unreinforced part is left. Deformation of the total structure is influenced by the deformation of the unreinforced part. Method of calculating deformation by use of coefficient of linear deformation is presented by utilizing an actual example. Finally, the behavior of the surface on the reinforced part, which gets high earth pressure by absorbing much rainwater, is analysed. Shear deformation in the reinforced part is presented.

**KEYWORDS:** Deformation, Testing, Walls, Soil deformation, Design.

## 1 INTRODUCTION

The author presented a paper titled "Well Documented Case Study of a Reinforced Soil Wall", at the 5th International Conference of the IGS In Singapore in 1994 with M. Itoh et al. (Itoh et al. 1992)

The backfill soil was a cohesive soil prevailing in the central region of Japan's mainland, and the reinforcement was a polyethylene geogrid widely used in Japan.

The purpose of this wall was to test applicability of cohesive soils for reinforcing soil structures. The wall was 7.5m high and has a front slope of 1 to 0.3. Geocomposite strips for drainage were inserted in the fill. After completion of the fill, the wet season followed for about 5 months. Total amount of rainfall was about 400mm, which is about 30 percent of the annual rainfall.

Vertical and horizontal deformations at the shoulder were 880mm and 374mm, respectively. Maximum pore water pressure in the fill was 20 kPa. It is clear that the cause of major deformation is due to the percolation of rainwater into the fill. Strain gages, extensometers, pore water pressure meters, earth pressure cells, settlement plates, horizontal displacement rods and deformation plates at the front wall were installed in the test wall. Material tests for both soil and geogrid were conducted in the laboratory. As no such well documented records like these were found, the author asked M. Itoh to translate the full report into English.

It was distributed to the members of the IGS, who came to the meeting room of the IS-Kyushu. The author hoped that this report be used for cooperative research work aiming for forecasting long-term behavior of reinforcing walls and embankments. The author has been studying this report from various angles of investigation. This paper describes in part the results of this studies as such.

## 2 BEHAVIOR OF FILL PART WITH NO REINFORCEMENT

Figure 1 is the reinforced part of the test wall with instrumentation layout. Table 1 is properties of geogrid. Figure 2 illustrates strain versus tension of the geogrid. Table 2 gives soil properties.

Figure 3 illustrates the section of the test wall including both reinforcing and non-reinforcing parts. The area ratio between reinforced and non-reinforced parts is  $46\text{m}^2 : 85\text{m}^2 = 1:1.5$  from Fig.3.

The area of non-reinforced part is very much larger compared with that of reinforced part. Table 3 gives horizontal displacement of the wall face and the boundary plane between reinforced and non-reinforced parts. Horizontal elongation of the non-reinforced part is much larger than that of the reinforced part at the upper portion of the test wall. As stated above, the non-reinforced part of the fill is very important upon discussing displacement of reinforcing walls. But there were no monitoring systems here, because we were not aware of the importance. The author could not help but use case records which he gathered himself for the purpose of analyzing the behavior of this part. The non-reinforced part can be assumed as a backfill supported by a kind of retaining wall. Regarding the reinforced part of the wall as a common retaining wall, the unreinforced part is backfill. As the reinforced part is massive and heavy, it has enough power of retaining backfill. The face between the reinforced and unreinforced parts can be regarded as a front face of the backfill. The inclination of the face is 1:0.3. The author has about 50 well documented case records of earth pressure measurement, some of which are described in the references at the end of this paper. As the results of earth pressure measurements, wall height and inclination of the back side of the retaining wall are more important than other conditions like soil properties and method of compaction. Therefore, the author determines the earth pressure coefficient based on the case records. Some of the selected case records are described here. Finally, the earth pressure coefficient is decided as 0.3. The earth pressure measurement in the soil mass is terribly difficult. The author has several case records now, and is hoping that a chance will come in the near future. Figure 4 is a gravity concrete retaining wall. Three panel type earth pressure gages, 2m in width, were installed to the back of the wall. Figure 5 shows the earth pressure for 3 large concrete block retaining walls. Coefficients of earth pressure  $K$  are described for comparison. Distribution of earth pressure is not triangular. The panel type earth pressure gages are installed not only on the back face of the retaining wall but also on the slope behind the backfill as shown in Fig.6. Precision of the measurement can be checked by using those gages surrounding the backfill. Coefficient of earth pressure is as low as 0.15, which is due to the thickness of the backfill and low energy of compaction. A small-scale laboratory model test was conducted in order to study the effect of backfill width. Sketch of the backfill and test results are given in Fig. 7. The horizontal axis is the coefficient of

earth pressure and vertical axis is the ratio between thickness and height of the backfill (B/H). Inclination of the back face of the retaining wall is 1:0.5. The coefficient of earth pressure decreases remarkably in accordance with the decrease of the B/H, and becomes nearly equal to the final value of the coefficient of earth pressure with the increase of the B/H larger than 0.5. Figure 8 illustrates the external forces acting on the boundaries of the non-reinforced part. The weight of the non-reinforced part is 1.463 MN/m. The earth pressure on the boundary between reinforced and non-reinforced parts is 179 kN/m, assuming the coefficient of earth pressure is 0.3. Reaction from the original ground surface is calculated by the force polygon in the figure. Normal and tangential components of the reaction and mobilized angle of friction are obtained as shown in the figure. Using

cohesion  $c=48$  kPa and friction angle  $\phi=25^\circ$  from the triaxial compression test, safety factor against sliding is computed. The factor of safety is 6.2. As a matter of fact, such soil constants are too large. Even when considering these conditions, such high factor of safety sufficiently verifies that no sliding, deformation shall be caused. Factor of safety against sliding increases with coefficients of earth pressure higher than 0.3. The factor of safety against sliding decreases with lower coefficient of earth pressure, but this part is absolutely safe. Because the inclination of the original ground surface is gentle. If the inclination is  $45^\circ$ , the situation changes entirely. The non-reinforced part moves out horizontally toward the surface of the wall as the fill settles. There is a case example showing such a phenomenon. Distribution of normal and shear stresses along the original ground

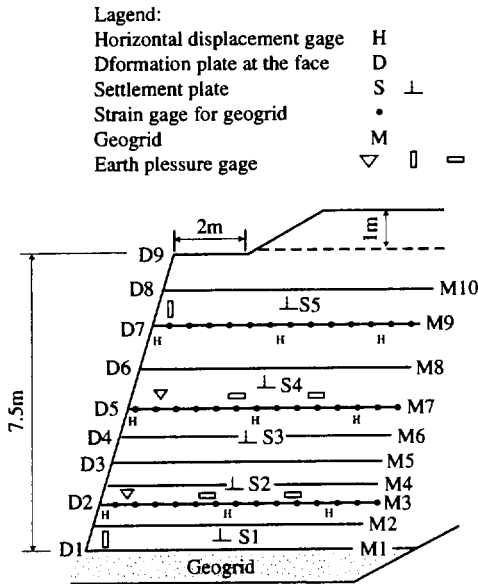


Figure 1 Instrumentation layout.

Table 1 Geogrid properties

Opening dimensions:	110x22mm
Tension at failure:	78kN/m
Elongation at maximum strength:	17%
Material:	Polyethylene

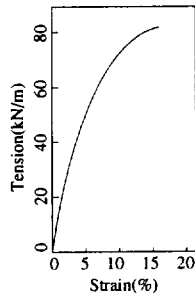


Figure 2 Strain versus tension for geogrid

Table 2 Soil properties

Grain size:	sand 23.3%, silt 53.3%, clay 23.4%
Natural water content:	$w_n = 25.0\%$
Liquid limit:	$w_l = 54.6\%$
Plastic limit:	$w_p = 26.8\%$
Maximum dry density:	$\rho_{dmax} = 1.48 \text{ Mg/m}^3$
Optimum water content:	$w_{opt} = 26.4\%$
Angle of internal friction:	$\phi = 20.6^\circ$
Cohesion:	$c = 42.2 \text{ kPa}$

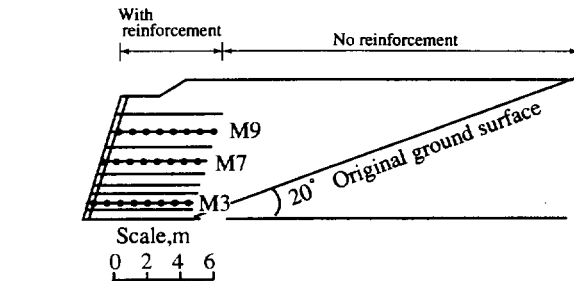


Figure 3 Cross section of the test wall.

Table 3. Horizontal displacement of the wall face, boundary between reinforced and unreinforced parts, and elongation of reinforced part.

Position	May 8			October 7		
	M9	M7	M3	M9	M7	M2
Wall face	23	33	20	242	160	62
Boundary, reinforced & non-reinforced	15	16	4	154	73	17
Elongation of reinforced part parts	8	17	16	88	87	45

Notes: May 8 is date of end of construction.

October 7 is date of end of measurement.

M9, M7, M2 are reinforcing mats in Fig. 3.

Unit: mm

How to read: The wall face at M3 level moved 23mm during construction. It was moving through the rainy season, and finally the amount of movement reached 242mm. Movement of the boundary of reinforced and non-reinforced parts are 15mm (May 8) and 154mm (October 7). Accordingly, elongation of the reinforced part is 23-15=8mm (May 8) and 62-17=45mm (October 7).

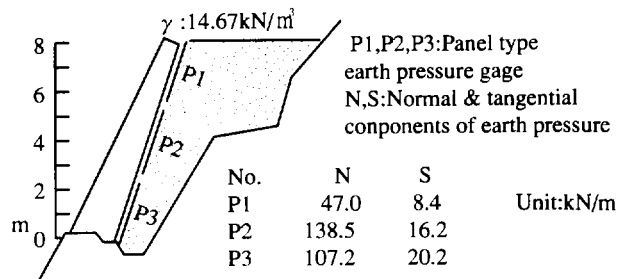


Figure 4 Concrete gravity wall.

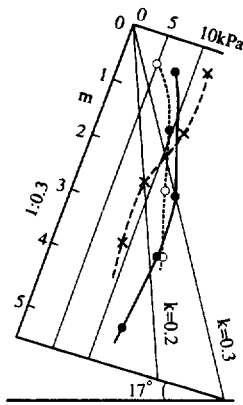


Figure 5 Normal component of earth pressure against large concrete block walls.

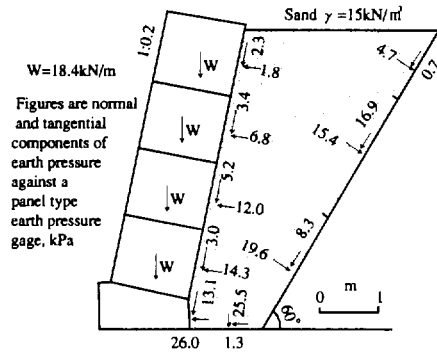


Figure 6 Large concrete block retaining wall.

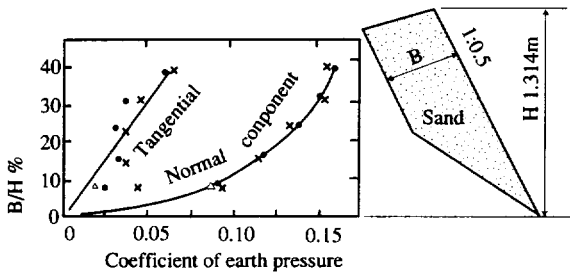


Figure 7 Relationship between thickness of backfill and earth pressure.

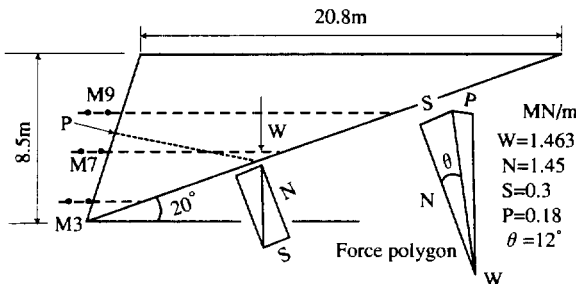


Figure 8 Unreinforced part of the test wall. Method of analyzing earth pressure on the front wall and the back slope of the backfill.

surface is not uniform or triangular as shown in Fig. 6. Maximum shear stress is about 2 times larger than the average value for this case. Therefore, it is necessary to maintain a higher factor of safety to prevent sliding movement. Figure 8 illustrates positions of mats M3, M7 and M9. Records of horizontal displacement gages are indicated in Table 3. Displacement of the surface between the reinforcing and non-reinforcing can be inferred by this table. The lengths of the dotted lines in the figure are widths of the non-reinforced part. They are 2.4, 8.2, 12.9 m respectively. Assuming the strains are uniform along those lines, those strains are calculated as shown in Table 4. Comparing these values with strains at the tail ends of the mats measured by strain gages, quite a neat coincidence was recognized. Vertical settlements were measured by the settlement plates. The variation of those thicknesses between two settlement plates are obtained. These variations are calculated in the form of strain and described in Table 4.

Table 4. Variation of vertical and horizontal deformation in the form of strain.

Position	Horizontal strain			Vertical strain		
	~5/8	~10/7	5/8~10/7	~5/8	~10/8	5/8~10/7
M9	0.108	1.19	1.09	S4~S5	0.75	8.80
M7	0.182	0.89	0.71	S3~S4	0.87	5.92
M3	0.167	0.71	0.54	S2~S3	0.46	16.36
				S1~S2	0.42	12.48
(Position)				(Layer)		

As the forces on the boundary and weight of the backfill are obtained, stress distribution is obtained by trial and error method. This rough method of calculation may be sufficient at this stage.

According to the author's case records, earth pressure does not change so much, if the retaining wall moves forward after the completion of it.

Therefore, only horizontal strain in taking into account and the changes of m and E are back-calculated using equations (1) and (2).

$$\epsilon_h = \frac{\sigma_h}{E} - \frac{1}{mE} \left\{ (\sigma_h + \sigma_v) \frac{1}{m} + \sigma_v \right\} \dots \dots \dots (1)$$

$$\epsilon_v = \frac{\sigma_v}{E} - \frac{1}{mE} \left\{ (\sigma_h + \sigma_v) \frac{1}{m} + \sigma_h \right\} \dots \dots \dots (2)$$

The results are described in Table 5. m-values are ranging between 3.08~3.98, E-values between 0.45~7.30 MPa. E-values before May 8 which had ranged between 2.46~7.30 MPa, decreased to 0.49~1.30 MPa at the end of the test on October 7. The reduction caused a drop by 1/10 of original values.

We can realize how the increase of moisture content has a large effect on soil constants. The wide variety of m and E values are mainly due to the non-uniformity of soil kinds and distribution of moisture content.

Table 5. Coefficient of linear deformation E and Poisson's ratio 1/m in the non-reinforcing part.

Period	~5/8			~10/7			5/8~10/7		
	M9	M7	M3	M9	M7	M3	M9	M7	M3
E:MPa	5.25	7.30	2.46	0.45	1.10	0.83	0.49	1.30	1.25
m	3.35	3.08	3.98	3.39	3.32	3.85	3.39	3.37	3.79

There are a lot of monitoring systems set up in the reinforced part of the wall. Twelve conventional earth pressure gages were installed. No. 1 and 12 measure horizontal earth pressure or stress. No. 2, 3, 4 and No. 7, 8, 9 measure two-dimensional earth pressure, namely, horizontal, vertical and shear stresses. No. 5, 6, 10 and 11 measure only vertical stress. These were located behind the wall face. The other 8 gages were located 1.5m behind the wall face. Table 6 describes earth pressure and horizontal strain 1.5m behind the wall face.

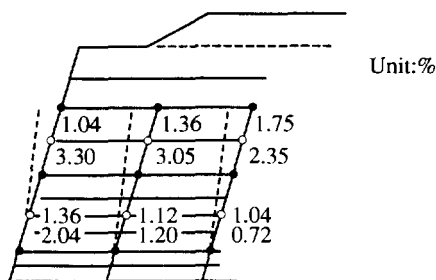
Table 6. Earth pressure near the front face of the wall.

NO.		5/8	5/16	6/20	7/1	10/20
12	$\sigma_h$	2.2	1.4	4.4	5.2	5.1
7,8,9	$\sigma_v$	45.6	67.0	77.5	37.7	40.5
	$\sigma_h$	11.1	9.9	5.5	37.7	34.3
	$\tau$	+5.2	+5.35	-2.30	-22.7	+2.30
	$\epsilon_h$	0.465	0.800	0.891	0.710	1.302
2,3,4	$\sigma_v$	79.1	112.7	116.0	37.7	74.4
	$\sigma_h$	21.8	30.6	14.6	2.2	1.7
	$\tau$	-5.45	-5.35	-16.1	-7.85	-6.7
	$\epsilon_h$	0.477	1.043	1.017	1.106	1.507

Note:  $\sigma_v, \sigma_h, \tau$  : kPa ;  $\epsilon_h$  : %  
 12→Earth pressure cell which is between D7 and D8,  
 7,8,9→earth pressure cells which are between D5 and D6, and  
 2,3,4→earth pressure cells which are between D2 and D3 in Fig.1.  
 + and - signs of shear stress and counter clockwise and clockwise directions, respectively.  
 Rainy season : 5/16~7/1

Looking at the table, earth pressure changes in wide range with the lapse of time. The strain along the reinforcements are elongated in accordance with the horizontal deformation of the soil. As this soil is not elastic, this elongation is never recovered. Vertical stress  $\sigma_v$  and  $\epsilon_h$  rapidly increase with the start of rainy season. Horizontal stress  $\sigma_h$  of No. 7, 8 and 9 increases gradually with time. Horizontal stress of No. 2, 3 and 4 is large in rainy season. Shear stress is low, and sometimes changes their sign from plus to minus. Shear stress for No. 2, 3 and 4 is high in rainy season.

This paper deals with shear deformation of the fill by use of data from horizontal displacement gages. Figure 9 illustrates distribution of shear strain. Upper figures indicate the shear strains between May 8 and June 20, which is the first part of rainy season, and the lower figures are that between June 20 to October 7, which is the main part of rainy season with much rain. Shear strain in the main part of rainy season is larger than that of the first part.



Legend: ○ : Points measured  
 Upper figure : shear strain before rainy season, | between two points  
 Lower figure : shear strain during rainy season, | marked with ●

Figure 9 Distribution of shear strain, at points marked with ○

1. A large deformation occurred by percolation of rain water, when a geogrid reinforced test wall with cohesive soil backfill was exposed to the wet season. Deformation of the wall is caused by reduction of soil constants with increase of moisture content. The deformation of soil is irreversible, and the elongated reinforcement caused by the soil deformation is left intact. Therefore, a method of soil test for measuring soil constants is needed. It is important to use a simple laboratory test with no individual errors.

2. There are many cases where the triangular unreinforced part comes behind the reinforced part. Effect of deformation on this part is large to estimate total deformation of the wall. Method of estimating such deformation by use of coefficient of linear deformation and Poisson's ratio is described.

3. Front face of a reinforced soil wall was exposed to percolation of rainwater causing marked change in earth pressure.

This then caused major deformation, whereupon colossal permanent deformation is caused in reinforcing material. Decrease of soil constants may also induce this phenomenon and increase strain in the reinforcement.

4. Shear strain in the reinforced part of the test wall increased with amount of percolated rain.

ACKNOWLEDGMENTS

The author would like to thank M. Itoh of Maeda Corporation for providing us with the report of Toyoshina test wall.

REFERENCES

Fukuoka, M., Akatsu, T., Katagiri, S., Iseda, T., Shimazu, A., Nakagaki, M. (1981) Earth Pressure Measurements on Retaining Walls, Case History Volume, 9th International Conference on Soil Mechanics and Foundation Engineering, Tokyo, pp. 237-296.  
 Fukuoka, M. (1984) Earth Pressure on Retaining Walls and Buried Pipes, International Conference on Case Histories in Geotechnical Engineering, St. Louis, Vol. 1, pp. 351-362.  
 Fukuoka, M., Tani, S., Ihara, S., Ishizaki, H., Takano, G. (1990) Stability of Retaining Wall Reinforced by Continuous Fiber During Earthquakes, Proc., 4th International Conference on Geotextiles, Geomembranes and Related Products, the Hague, Vol. 1, pp. 27-32.  
 Fukuoka, M., Okedoi, K., Ozaki, K., Nakayama, K., Ihara, S. (1992) Stability of Fiber Reinforced Sand Retaining Walls, Proc., 2nd International Conference on Recent Advances in Geotechnical and Soil Dynamics, St. Louis, Vol. 1, pp. 643-648.  
 Fukuoka, M. (1994) Friction at Upper and Lower Faces and Tension in Reinforcing Sheets, Proc. on Geotextiles, Geomembranes and Related Products, Singapore, pp. 243-246.  
 Itoh, M., Shirasawa, M., Itoh, A., Kumagai, K., Fukuoka, M. (1994) Well Documented Case Study of a Reinforced Soil Wall, Proc. on Geotextiles, Geomembranes and Related Products, Singapore, pp. 255-258.

# Development Of Woven Geotextiles For Reinforcing Cohesive Soil Filled Slopes - A New Approach

S. Anbahan Ariadurai

Research Student, Department of Textiles, UMIST, Manchester, United Kingdom

Ian L. Whyte

Senior Lecturer, Department of Civil and Structural Engineering, UMIST, Manchester, United Kingdom

Prasad Potluri

Lecturer, Department of Textiles, UMIST, Manchester, United Kingdom

**ABSTRACT:** Reinforced ground structures using cohesive soils are difficult to design due to problems relating to consolidation and poor internal drainage. Due to these inherent drawbacks cohesive soils are seldom used as fill materials in reinforced embankments. However, when a geotextile with good filtration and drainage properties is used as a reinforcement, cohesive soils could be successfully used as back-fills in steep embankments. There are few instances of needle-punched nonwoven fabrics, possessing superior hydraulic conductivity, have been used as reinforcements in embankments with back fills of cohesive soil. Non-woven textiles, however, are inferior in tensile properties when compared with the woven textiles. In reinforcement applications, the primary quality required of the fabric is superior tensile properties. Woven geotextiles, which have the required tensile properties, have not been tried as reinforcement for cohesive soils because of their poor transmissivity. Owing to this draw back in woven geotextiles the amount of research done on the transmissivity of woven geotextiles is minimal. By designing novel and innovative woven fabric structures it is possible to increase the transmissivity of the woven geotextiles without sacrificing the tensile properties. This paper presents a new approach that enables woven geotextiles to be designed with superior tensile properties and adequate transmissivity for use as reinforcement in cohesive soil filled earth structures. A theoretical model, derived from the first principles, which predicts the transmissivity values of woven geotextiles is discussed. Laboratory results from tests conducted on some woven geotextiles substantiate the theoretical models and the data is presented.

**Keywords -** Geotextiles, Woven Fabrics, Reinforcement, Transmissivity, Tensile Strength

## 1 INTRODUCTION

In recent years, use of geosynthetics has become accepted as a technically sound and cost-effective solution in solving many geotechnical and environmental problems. In the construction of reinforced earth filled embankments, when the in-situ soil is not suitable as a fill - cohesive soils such as clay, it is usual to fill the structure with a suitable imported granular material. With ever increasing cost in material handling, use of readily available materials from the site is one of the best cost-effective options available. However, use of cohesive soils as back-fill in steep embankments has gained little acceptance due to their inherent low permeability and excess pore water pressures. Therefore, if geotextiles of adequate draining capacity and tensile characteristics are developed and used with the in-site cohesive materials considerable savings can be achieved.

A few case histories of test embankments with cohesive soil back fills employing needle-punched nonwoven fabrics are reported (Tatsuoka et al. 1986, Ling et al., 1993). Further, when the motorway M25, between Junctions 15 and 16 on the west side of London in the UK, was widened, the embankment was reinforced with a combination of a geogrid and a nonwoven geotextile (Leiper, 1995). The soil

in this case was recompacted London Clay. Fabian (1990) too has successfully used needle-punched nonwoven geotextiles to reinforce test embankments built with cohesive fills. However, there are no reports of woven geotextiles being attempted as reinforcement for cohesive soils. The main limitation of the currently available woven geotextiles is their poor drainage capabilities. According to the United Kingdom's Department of Transport requirements, the design life for steep slopes is not less than 60 years if the slope is regarded as an earthwork or 120 years if the slope is regarded as a structure (Ingold 1994). Strength and creep are vital properties to provide such a long life; woven fabrics are capable of providing these properties better than nonwovens or any other fabric type. Thus, if the draining capacity of woven geotextiles is considerably improved, they would become the most suitable geotextile material to reinforce a cohesive soil-filled structure.

In order to design woven geotextiles which have the capacity to drain the estimated quantity of water a suitable theoretical model is required. This paper presents a geometrical model which can estimate the transmissivity of woven fabrics. The model, which is validated by laboratory results, is then used to engineer novel woven fabric structures which give improved transmissivity.

## 2 ESTIMATES OF REQUIRED DRAINAGE

A clay reinforced slope can act as a frictional fill in terms of the effective critical state angle of shearing resistance, provided any excess pore water pressures are rapidly dissipated. The required drainage is a function of the soil consolidation properties, geometry of the reinforcement layers and excess pore water pressures generated by construction. An estimate of the drainage is made using the following assumptions: the clay is fully saturated, with permeability  $k = 10^{-8}$  m/s, and compressibility  $M_v = 0.25$  m<sup>2</sup>/MN, subjected to a total normal stress increase  $\Delta\sigma = 200$  kN/m<sup>2</sup> (equivalent to a basal layer in a 10 m high fill) with geotextile reinforcement drains at a relatively wide spacing of 0.5 m and of length 7.5 m. The clay layer between the reinforcement is assumed to be in one dimensional consolidation, with the excess pore water pressure isochrones modelled as a parabolic function. The rate of discharge from the clay is given by the hydraulic gradient (slope of the isochrone) at the clay surface.

At any time 't' the total volume of water expelled from the clay is equal to the settlement volume at that time:

$$V = 2 d L_{GT} b_{GT} R M_v \Delta\sigma \quad (1)$$

at time:

$$t = \frac{T_v d^2}{c_v} \quad (2)$$

where, d = maximum drainage distance,  $L_{GT}$  = length of the geotextile,  $b_{GT}$  = width of the geotextile, R = average degree of consolidation,  $M_v$  = coefficient of volume compressibility,  $\Delta\sigma$  = total stress increment,  $T_v$  = time factor and  $c_v$  = coefficient of consolidation.

For the assumed values, the total volume of water discharged per metre width by consolidation is 0.1875 m<sup>3</sup>. Hence, 90% consolidation (0.169 m<sup>3</sup> water) takes 3.7 hours.

The rate of discharge per square metre from the clay fill (above and below the geotextile layer) is given by

$$Q = \frac{4 k \Delta\sigma}{\gamma_w \sqrt{12 c_v t}} \text{ for } T_v < \frac{1}{12} \quad (3)$$

where, Q = rate of discharge and  $\gamma_w$  = unit weight of water. From equation (3), the rate of discharge of water from the soil when the isochrone reaches the centre of the clay layer can be calculated to be less than 10<sup>-7</sup> m<sup>3</sup>/s/m<sup>2</sup>, this occurs approximately one hour after the assumed instant load application. Clays typically have permeability of 10<sup>-7</sup> m/s or less, often about 10<sup>-9</sup> m/s, and if permeable layers with permeability of 10<sup>-4</sup> m/s, or greater, are incorporated, then these will act as effective drains.

The computations involved for calculating the required transmissivity for the geotextiles are lengthy and complex (Giroud, 1981). However, one dimensional consolidation theory provides an indication as to the efficiency of these drains. Accordingly, geotextiles placed at small vertical spacing (0.5 m or less), can rapidly consolidate the clay and dissipate excess pore water pressures. The total volume of water is relatively small and the discharge rate diminishes rapidly with time.

## 3 THEORIES OF FLUID FLOW

Predicting the fluid flow through textile materials has largely been studied with the help of the general theories of fluid flow through porous media. In all of these theories, the fluid flow is given as a function of the total pore space available in the fabric mass and the specific area. However, as the structure of woven fabrics are very different from other porous media, with two distinct drainage paths - within the yarns and between the yarns - a need for a specific theoretical model for woven fabrics was realised.

As a result, a theoretical model which predicts the in-plane fluid flow in woven geotextiles is developed from first principles. This model is found to predict the flow of water in woven fabrics more accurately than the available general models for flow through porous media.

The Poiseuille equation for the average laminar flow velocity through straight parallel capillary tubes of constant circular cross-section is,

$$V = \frac{R_h^2 \Delta p}{8\mu L} \quad (4)$$

and hence

$$Q = \frac{R_h^2 \Delta p}{8\mu L} A \quad (5)$$

where, V is the velocity of the fluid,  $\Delta p$  the pressure difference,  $\mu$  the viscosity of the fluid, L the length of the drainage medium, A the area of cross-section and  $R_h$  the hydraulic radius.

When the Poiseuille's equation is extended to non-circular channels it becomes,

$$Q = \frac{R_h^2 \Delta p}{k \mu L} A' \quad (6)$$

where, A' area of the pore space in the channels and k shape constant which depends on the shape of the channel. However, the cross-sectional area of the pores in the channels is  $A\epsilon$ , where,  $\epsilon$  is the porosity. Therefore, equation (6) can be written as,



$$Q = \frac{R_h^2 \Delta p}{k \mu L} A \epsilon \quad (7)$$

Thus, if the hydraulic radius  $R_h$  of the woven fabric is estimated, from equation (7), the rate of discharge can be calculated.

The hydraulic radius is defined as,

$$R_h = \frac{\text{cross sectional area of the pore}}{\text{wetted perimeter}} \quad (8)$$

When the flow of fluid through a woven fabric is considered, it is clear that there exist pores between the yarns and within the yarns. As the structural parameters of the two porous media are different, it is prudent to treat the two separately. The overall coefficient of in-plane permeability is then obtained by combining the two.

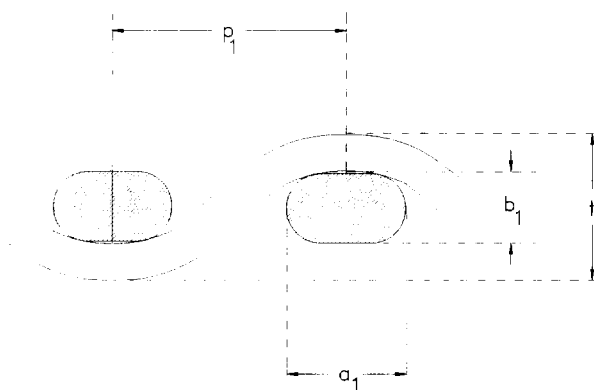


Figure 1. Cross-section of two consecutive yarns in an intersection unit

Figure 1 shows a cross-section of two consecutive yarns of a woven fabric in a plane containing the axis of an intersecting weft yarn. The yarns are considered to have the Kemp's race track sectional geometry (Kemp, 1958). If the major diameter of the warp and weft yarns are ' $a_1$ ' and ' $a_2$ ' respectively, and the minor diameter of the warp and weft yarns are ' $b_1$ ' and ' $b_2$ ' respectively and the distance between the centre of two adjacent warp yarns is ' $p_1$ ', we have,

$$\text{total cross-sectional area between two consecutive yarns} = t \times p_1$$

where,  $t$  is the thickness of the fabric.

However, the area of solid in the cross-section =  
area of the warp yarn + area of the weft yarn.

$$\text{Area of the warp yarn} = \frac{\pi b_1^2}{4} + b_1(a_1 - b_1) \quad (9)$$

$$\text{Area of the weft yarn} = l_2 b_2 \quad (10)$$

where,  $l_2$  is the length of weft yarn between the planes

containing the axes of consecutive warp yarns.

$$\text{However,} \quad l_2 = p_1(1 + c_2) \quad (11)$$

where,  $c_2$  is the crimp in the weft yarn. Therefore,

$$\text{Area of the weft yarn} = b_2 p_1(1 + c_2) \quad (12)$$

Hence, Total area of solid

$$= \left\{ \left[ \frac{\pi b_1^2}{4} + b_1(a_1 - b_1) \right] + [b_2 \cdot p_1(1 + c_2)] \right\} \quad (13)$$

Therefore, Area of void between the yarns

$$= t p_1 - \left\{ \left[ \frac{\pi b_1^2}{4} + b_1(a_1 - b_1) \right] + [b_2 p_1(1 + c_2)] \right\} \quad (14)$$

$$\text{Wetted perimeter of the pore} = 2p_1 + \pi b_1 + 2 l_2' \quad (15)$$

where,  $l_2'$  is the length of yarn in the partial geometry of the Kemp's race track section. Further,

$$l_2' = l_2 - (a_1 - b_1) \quad (16)$$

Therefore, wetted perimeter of the pore

$$= 2p_1 + \pi b_1 + 2[p_1(1 + c_2) - (a_1 - b_1)] \quad (17)$$

Substituting (14) and (17) in (8) we get,

$$R_h = \frac{t p_1 - \left\{ \left[ \frac{\pi b_1^2}{4} + b_1(a_1 - b_1) \right] + [b_2 p_1(1 + c_2)] \right\}}{2p_1 + \pi b_1 + 2[p_1(1 + c_2) - (a_1 - b_1)]} \quad (18)$$

A similar treatment is done to find the rate of discharge within the yarns. Considering circular cross-sectional filaments, if the diameter of a single filament in a multi-filament yarn of race track geometrical shape is  $d_f$ , the hydraulic radius for the flow within the yarn is derived.

The porosity of the yarn,

$$\epsilon_y = 1 - \frac{\text{Volume of filament yarns}}{\text{Total volume of yarn}}$$

Considering racetrack geometry and unit length,

$$\text{Total volume of warp yarn} = \left[ \frac{\pi b_1^2}{4} + b_1(a_1 - b_1) \right]$$

Considering circular filaments,

$$\text{Volume of filaments in warp yarn} = \frac{\pi d_f^2}{4} n_f$$

where  $n_f$  is the number of filaments in the yarn.

Therefore, porosity in yarn

$$\varepsilon_y = \left\{ 1 - \frac{\left[ \frac{\pi b_1^2}{4} + b_1 (a_1 - b_1) \right]}{\left( \frac{\pi d_f^2}{4} n_f \right)} \right\} \quad (19)$$

The total cross sectional area of the yarn, considering the race track sectional geometry,

$$= \left[ \frac{\pi b_1^2}{4} + b_1 (a_1 - b_1) \right] \quad (20)$$

Then the cross-sectional area of the pore

$$= \left[ \frac{\pi b_1^2}{4} + b_1 (a_1 - b_1) \right] \varepsilon_y \quad (21)$$

$$\text{total wetted perimeter} = \pi d_f n_f \quad (22)$$

where,  $n_f$  is the number of filaments in the yarn.

Therefore,

$$R_h = \frac{\left[ \frac{\pi b_1^2}{4} + b_1 (a_1 - b_1) \right] \varepsilon_y}{\pi d_f n_f} \quad (23)$$

If the geometrical parameters of the fabric and the yarn are known, the hydraulic radius of the inter-yarn and the intra-yarn porous media can be calculated using equations (18) and (23) respectively. Thus, the rate of discharge between the yarns and within the yarns can be calculated using equation (7) if the appropriate shape constants and the porosity values are known. It is assumed that the shape of the pore within the yarns is of an equilateral triangle and in-between the yarns a rectangular triangle. Therefore, the respective shape constants are 1.67 and 1.63 (Munson et al, 1990). Once the rate of discharge is known the coefficient of in-plane permeability and subsequently the transmissivity of the fabric can be estimated using the equations (24) and (25).

$$\theta = \frac{Q L}{W H} \quad (24)$$

where,  $\theta$  = hydraulic transmissivity,  $W$  = width of the specimen,  $H$  = difference in total head across the specimen and  $L$  = length of the specimen.

$$k_p = \frac{\theta}{t} \quad (25)$$

where,  $k_p$  = coefficient of in-plane permeability and  $t$  = thickness of the geotextile.

In Figures 2 and 3, results obtained by the developed theoretical model, indicated by the name UMIST, and other general models are compared with the laboratory results obtained at various normal stress levels. The hydraulic transmissivity testing was performed in accordance with ASTM D 4716 - 87 (ASTM, 1987). The distinctive advantage of this model is its capability to predict the flow in any composite structure which has a number of drainage paths. Fabric C1 is commercially available and M2 is a fabric made in the laboratories of the Department of Textiles of UMIST. Two other fabrics, M1 and M3, made in the laboratory and a second commercial fabric C2 were also tested for their transmissivity. In Table 2 is given the specifications of all the five fabrics tested.

Table 2. Specifications of the fabrics tested.

Fabr	Weave	Fabric sett		Yarn count		Area density (g/m <sup>2</sup> )	Thickness ** (mm)
		ends/cm	picks/cm	warp (tex)	weft (tex)		
M1	Plain	4.6	3.33	2200	220	1202	1.70
M2	Matt	4.25	4.27	2200	220	1160	1.66
M3	* Double	4.72	2.36	2200	220	2139	3.60
C1	Twill	4.00	5.14	337	330	297	0.93
C2	Plain	5.91	9.84	228	108	224	0.83

\* The count, and the sett correspond to both face and back fabrics individually. \*\* Thickness at 2 kN/m<sup>2</sup> stress level.

#### 4 A NOVEL WOVEN FABRIC

A novel woven fabric which incorporates porous tubes in its structure is designed to enhance the drainage property of the woven geotextile without sacrificing its tensile properties. In this fabric two sets of fabrics are woven on top of one another with a tubular structure, into which the porous tubes are inter woven. The whole composite fabric is woven on a shuttle loom. The laboratory transmissivity results obtained are presented in Figure 4 along with the results obtained for fabrics M1, M2 and M3 developed at the laboratory of UMIST.

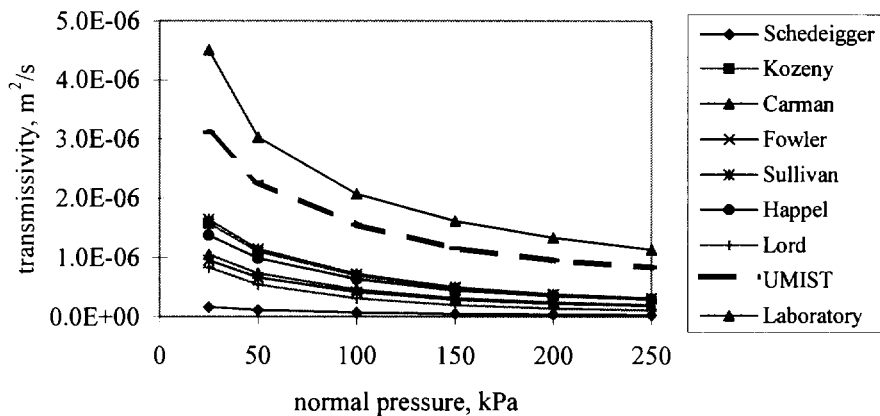


Figure 2. Transmissivity - normal pressure relationship for various theories - Fabric C1

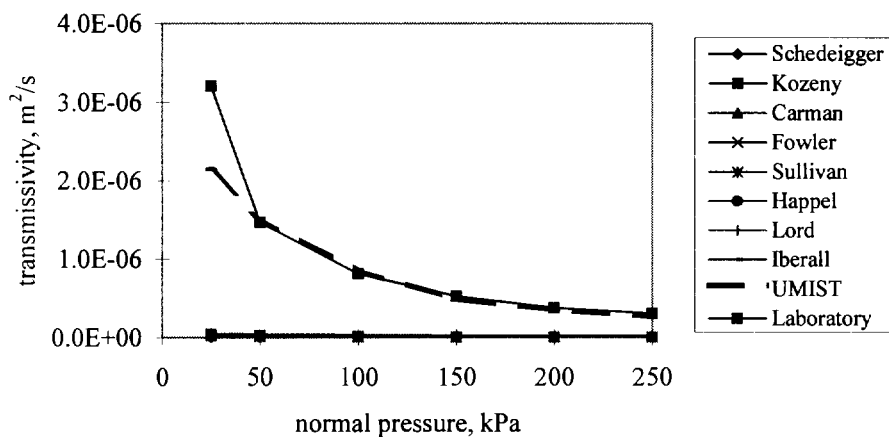


Figure 3. Transmissivity - normal pressure relationship for various theories - Fabric M2

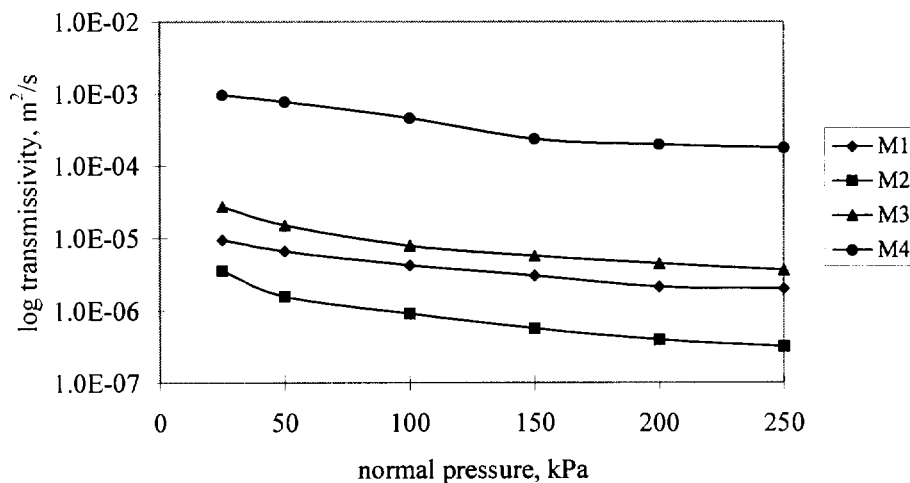


Figure 4. Log transmissivity - normal pressure relationship - Fabrics M1, M2, M3 and M4

## 5 TENSILE PROPERTIES

Tensile behaviour of the fabrics are of great importance when the geotextile is to be used for reinforcement applications. One of the most critical property is the tensile stiffness, which must be as high as possible to avoid any undesirable deformations and movements in the soil structure. Therefore, during the design and manufacturing of the geotextile fabric careful consideration was given to keep the warp crimp to a feasible minimum level. For typical slopes a maximum allowable reinforcement elongation of 5% will result in outward face deflections of no greater than 100 to 150 mm (Jewel, 1996). From the estimated initial load - strain curve shown in Figure 5, it is clear that the maximum strain levels in all the designed fabrics are within the permissible levels.

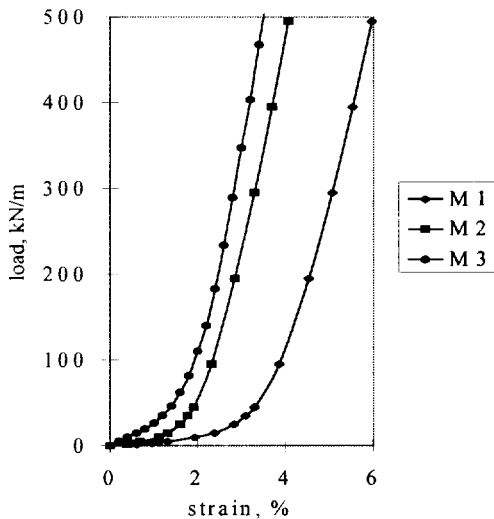


Figure 5. Estimated initial load - strain relationship of fabrics M1, M2 and M3

## 6 DISCUSSION AND CONCLUSIONS

From Figure 2 and 3 it is apparent that the proposed theoretical model for the flow of water in the plane of the woven fabrics is fairly accurate in predicting the actual flow levels compared to the other general theories of flow in porous media. Although the prediction at lower stress levels is comparatively farther from the actual values, at higher stress levels, which are the stress levels encountered in the field, the predictions are reasonably accurate. Tests done on other three fabrics also follow a similar trend. However, for fabric M3, the predictions at lower levels are comparatively away from the measured values. Nevertheless, at 150 kPa and beyond, the predictions are similar to the other fabrics. Giroud considered a geotextile basal drain to an embankment and calculated that a transmissivity of  $3.1 \times 10^{-7} \text{ m}^2/\text{s}$  allowed the geotextile to effectively work as a

drain for compressive stresses of less than about 1 MPa (equivalent to a 50 m high embankment). From Figure 4, where the transmissivity of the geotextiles at various stress levels are indicated, it is clear that the innovative geotextile M4 possesses a transmissivity value that is 100 - 1000 times higher than the transmissivity value predicted by Giroud. Further, from the results given in Figure 4 it can be deduced that with suitable geotechnical designs even geotextiles M1 and M3 can successfully be used as reinforcement geotextiles functioning as drains in clayey soils. Although the cost of these fabrics are higher than the fabrics available in the market, preliminary cost calculations suggest that the savings obtained by the use of in-site soils over imported material will override the fabric cost.

The theoretical model presented in this paper does not take into consideration the fact that soil particles can partially fill the pores in the fabric structure. It is envisaged to study this effect in future research. However, the transmissivity of the novel fabric M4 is sufficiently high to take into account any partial blockage that may occur.

## REFERENCES

- ASTM D 4716-87 (1987) Standard test method for constant head hydraulic transmissivity (in-plane flow) of geotextiles and geotextile related products. Annual Book of ASTM Standards, Vol. 04.09. pp 53 - 56
- Fabian, K. (1990) "Time dependent behaviour of geotextiles reinforced clay walls", *Fourth International Conference on Geotextiles, Geomembranes and Related products*, A. A. Balkema, The Hague, Netherlands, Vol. 1, pp. 33 - 38.
- Giroud, J. P., (1981) "Designing with Geotextiles", *Materiaux et Constructions*, Vol. 14, pp 257 - 272.
- Ingold, T.S. (1994) *The Geotextiles and Geomembranes Manual*, Elsevier Advanced Technology, Oxford, UK.
- Jewell, R.A.(1996) *Soil Reinforcement with Geotextile*, CIRIA Special Publication - 123, London, UK.
- Kemp, A. (1958) "An Extension of Pierce's Cloth Geometry to the Treatment of Non-circular Threads", *Journal of the Textile Institute - Transactions*, Vol. 49, pp T44 - T48.
- Leiper, Q. (1995) "A Reinforced Soil Solution for the M25", *Geotechnical Engineering in Highway Design and Construction*, UMIST, Manchester.
- Ling, Hoe I., Tatsuoka Fumio, Wu Jonathan T.H. and Nishimura Jun. (1993) "Hydraulic Conductivity of Geotextiles under Typical Operations Conditions", *Geotextiles and Geomembranes*, Vol. 12, pp 509 - 542.
- Munson, Bruce R., Young, Donald F. and Okiishi, Theodore H. (1990) *Fundamentals of Fluid Mechanics*, John Wiley & Sons, New York.
- Tatsuoka, F., Ando, H., Iwasaki, K. and Nakamura, K. (1986) "Performances of Clay Test Embankments Reinforced with Non-woven Geotextile", *Third International Conference on Geotextiles, Geomembranes and Related Products*, Vienna, Austria, pp 355 - 360.

# Large Scale Pullout Tests of Geotextile in Poorly Draining Soils

S. H. Chew, S. A. Tan

Lecturer and Senior Lecturer, Department of Civil Engineering, National University of Singapore, Singapore

K. H. Loke

Regional Technical Manager, Polyfelt Asia Sdn. Bhd., Malaysia

P. H. Delmas

Vice-president, Development Application Europe, Polyfelt

C. T. Ho

Formerly Research Scholar, Department of Civil Engineering, National University of Singapore, Singapore;  
Civil Engineer, Civil Engineering Department, Housing and Development Board, Singapore

**ABSTRACT:** The use of geosynthetics in soil reinforcement applications has been increasingly popular in recent years. Geosynthetic reinforced soil walls are commonly backfilled with clean sand. In regions where clean sand is not cheaply and easily available, a cost-effective design of the wall is to use locally available soil, that may not be free draining. As a result, the designs of reinforced slopes and walls have to take into consideration of the probable build-up of excess pore water pressures, especially during rainy seasons. In recent years, effort is focused on the development of geosynthetic material that can perform not only reinforcement functions but act as a drainage medium as well. Such soil-reinforcement material can rapidly drain off excess pore water to maintain the stability of the system. This paper reports a series of large scale pullout tests in locally available residual soil which is poorly draining.

**KEYWORDS:** Geotextile, Reinforcement, Pullout tests, Drainage, Deformation.

## 1 INTRODUCTION

The growth of the petrochemical industries in the recent years has led to the development of numerous synthetic products for various geotechnical engineering purposes. One of the many applications is the use of such materials for reinforcement purposes. This includes using geosynthetic products for slope stabilisation, erosion control, reinforcement of steep slopes as well as construction of vertical earth walls. The use of geosynthetics for soil reinforcement applications, especially, depends on the characteristics of the soil-geosynthetic interface which, in turn, is dependent on the effective stress at the interface. When granular material is used as the backfill material, the effective stress at the interface is more stable due to the unlikelihood of build-up of excess pore water pressure.

Granular backfill, however, may not be easily and cheaply available in many areas, especially in Southeast Asian regions. Under such circumstances, the more cost effective way of constructing reinforced earth walls would be to use the locally available residual soil which is lateritic in nature. Lateritic soils are cohesive-frictional soils but they are not free draining in nature. The soil strength is also dependent on its in-situ water content and soaking may lead to a drastic reduction in the expected strength of such material (Bergado et al. 1993). There is an impending threat of build-up of excess pore water pressure

at the soil-geosynthetic interface during heavy raining seasons, leading to the possibility of instability of the soil mass. Hence, in order to effectively use such material as backfill for reinforced soil system, the geosynthetic used must have the dual function of reinforcing the soil mass and, at the same time, drain away pore water in the soil mass. The essential design criteria for such system were outlined in Chew and Loke (1996).

## 2 PULLOUT TESTS

### 2.1 Test Apparatus

The Department of Civil Engineering at National University of Singapore (NUS) has developed a large scale pullout apparatus capable of performing large scale pullout tests on geosynthetic material of various configurations. Recommendations from Farrag et al. (1993) were studied extensively and used as guidelines in the development of the pullout apparatus at NUS. The apparatus measured 1.5 m in length, 1.5 m in width and provides for 30 cm of soil sample to be placed below and on top of the geosynthetic specimen to be tested. Horizontal sleeve plates are provided at the front wall of the pullout apparatus to eliminate boundary effects due to the front wall. The apparatus performs the pullout process at constant strain rate, driven

by a hydraulic machine. Detail description of this large scale pullout apparatus can be found in Chew et al. (1997).

In the first few series of pullout tests performed, the main objectives were to test the ability of the apparatus to function as desired. The series of pullout tests performed by Ng (1995) showed that the pullout apparatus is able to perform pullout at slow constant rates and that boundary effects were minimal. Subsequently, the apparatus were further modified by Ho (1996) to increase its testing capabilities by incorporating drainage systems into the apparatus. The aims of the improvements and modifications were to enable the apparatus to perform pullout tests in various soils, from granular to lateritic.

## 2.2 Geotextile Material

The geosynthetic material used in the two pullout tests is the PEC-75/25, a high-strength geotextile produced by Polyfelt. Theoretically, this material is a geocomposite as it comprised of a woven geotextile mechanically bonded to a nonwoven geotextile. This geotextile has multi-filament woven polyester yarns in grid-like pattern bonded to thermally bonded nonwoven polypropylene sheet. The maximum tensile strength of the geotextile is 75 kN/m along the longitudinal direction and 25 kN/m along the transverse direction. It derives its strength from the woven polyester yarns while the polypropylene sheet provides a drainage medium.

## 2.3 Soil Sample

The soil sample used is the locally available residual soil from the western part of Singapore. The soil is lateritic in nature and its optimal compaction is at water content of about 20%. However, it turns soggy and loses strength rapidly when soaked in water for long periods of time. The soil is reddish brown in the colour and consists of well-graded silty sand. Dry sieving tests on the soil revealed that the soil contains about 10-14% of silts, with a  $D_{50}$  of 0.24 mm and  $C_u$  of 6.2.

## 2.4 Test Program

A number of series of pullout tests were conducted in the last few years using the NUS Large Scale Pullout apparatus. Various type of geosynthetics has been tested with both sand and with residual soils as backfill material. Tests results were found to be consistent, and with good repeatability. In this paper, the test results of two pullout tests with residual soils will be reported. The first pullout test aimed to study the pullout resistance of the geotextile when embedded in residual soil at its in-situ moisture content. The soil sample in test 1 was prepared and compacted to an average density of 1905 kg/m<sup>3</sup> and an average moisture content of 23.5%. In the second test, the objective was to study the reduction in the pullout resistance

of the geotextile in residual soil when the soil is soaked with water to simulate ponding conditions. In this test, the soil was first compacted to an average density of 1887 kg/m<sup>3</sup> and an average water content of 23.3%. The soil sample in the test 2 was then subjected to 20 cm of water ponding for 4 days continuously in order to soak the soil sample in the pullout apparatus. In both tests, the rate of pulling at the front of apparatus was 0.80 mm per minute and the tests were carried out until total pullout had occurred. There was also no additional surcharge applied to the surface of the soil backfill, i.e. the pullout tests were conducted under low stress conditions.

## 2.5 Instrumentation

Aluminium strips with strain gauges were used to measure the pullout resistance mobilized by the geotextile in the course of the pullout process. The aluminium strips were pre-calibrated and a total of 8 were used for measuring the pullout resistance. These were mounted at the front of the geotextile and connected to the clamping plate in front of the pullout apparatus which was pulled forward at a constant and very slow rate by the hydraulic machine.

Displacements at various locations of the geotextile were measured using thin tell-tale wires, with the help of potentiometers with travel range of 100 mm. A total of 7 tell-tales were used in each of the two tests. In addition, potentiometers were used to measure the displacements at the front end of the geotextile. Each of the potentiometers was connected to the data acquisition system together with the strain gauges for the aluminium strips. Readings were recorded at 30 second intervals.

In test 2 where soaking of the soil sample occurred, there was anticipation of possible build-up of excess pore water pressure during the compaction and pullout test. In this test, miniature pore water pressure transducers were used to measure the pore water pressure at various parts of the soil sample. Two of such transducers were placed near the soil-geotextile interface: one just in front of the sleeve plates and the other, about 60 cm from the front wall.

# 3 PULLOUT RESPONSE OF GEOTEXTILES

## 3.1 Peak pullout resistance

The pullout responses of the geotextile in residual soil under different soil conditions are shown in figures 1. In test 1, where the soil is compacted at its in-situ moisture content, it can be seen that the pullout resistance of the geotextile increased steadily with front displacement until an apparent peak. The peak pullout resistance registered in the first pullout test was 23.2 kN while in the soaked pullout test, the peak pullout strength was measured at 19.4 kN. This indicates a drop of 16.4% in the peak pullout

resistance when the soil is pond with water. What was worthy to note was the change in the strength of the residual soil before and after the soaking process. Cone penetrometer tests on the soil sample showed an average CBR value of 3% in test 1. For test 2, where the soil was thoroughly soaked for 4 days, the CBR value dropped to an average of only about 1.5%, with the soil at the interface having only 0.75% in CBR value. This showed that the pullout resistance of the geotextile fell by only 16.4% when the strength of the soil at the interface dropped by almost 75%.

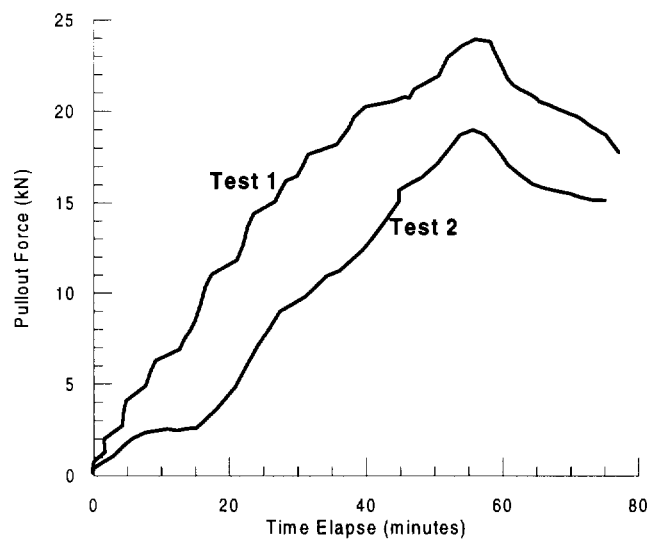


Figure 1 : Pullout response of geotextile in residual soil in tests 1 and 2.

### 3.2 Displacements during pullout

Figures 2 and 3 show the total displacements measured at various locations of the geotextile for test 1 and test 2 respectively. By total displacements, it meant that the magnitude of displacements recorded consisted of both displacement due to sliding of the geotextile against the soil at the soil-geotextile interface, as well as displacement due to material stretching of the geotextile.

It can be seen that the differential displacement between the front end of the geotextile and a point 30 cm from the front wall was lower for test 2 as compared to test 1. This is expected as the peak pullout resistance that can be mobilised in the second test was lower than the first test, substantiating the fact that the residual soil backfill at the interface was indeed weakened by the soaking process. Note that the first 30 cm of the geotextile was not embedded in soil. Thus this section of the geotextile was undergoing a process similar to the wide-strip tensile test.

Another important observation made in the two pullout tests was that in test 1, the differential displacement between two

consecutive locations along the embedded length of the geotextile was less uniform. Differential displacements were larger at locations nearer to the front wall than locations further from the front wall. This meant that the geotextile developed higher levels of strain nearer to the front wall than at locations further from the front wall. In test 2, however, it was observed that the differential displacement seemed to be quite uniform along the length of the geotextile, showing that the strain development was rather uniform along the length of the geotextile.

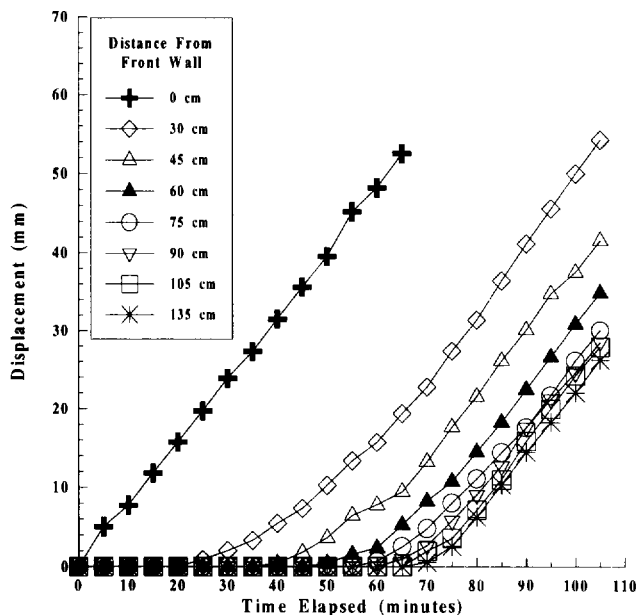


Figure 2 : Displacements at various locations of the geotextile during pullout test 1.

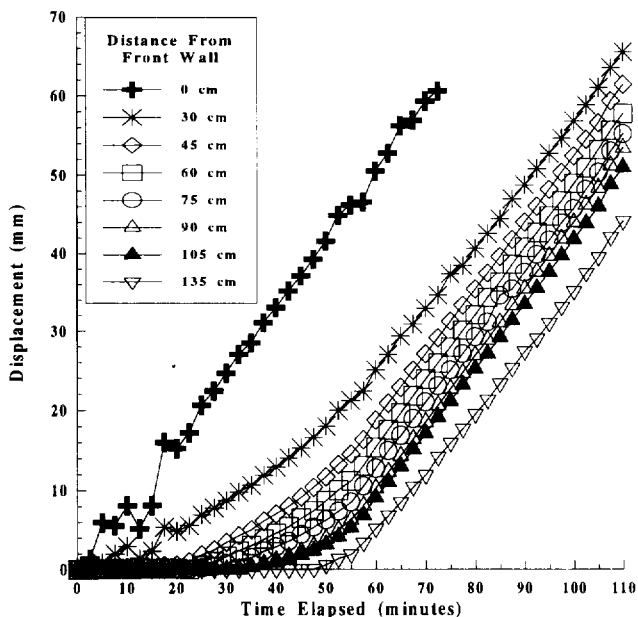


Figure 3 : Displacement at various locations of the geotextile during pullout test 2.

### 3.3 Pore water pressure measurements

During test 2, pore water pressure transducers were installed in various locations to measure the pore water pressure during the compaction and the pullout stages. While the hydrostatic pore water pressure is about 1.0 kPa at the location 10 cm below the surface of the soil, as indicated as PPT4. The pore water pressure transducer at this point (PPT4) measured a pore pressure of about 3.5 kPa through the test, indicating that there is a built-up of excess pore water pressure of about 2.5 kPa. However, at the location of the soil-geotextile interface, where the hydrostatic pressure is about 2.5 kPa, the pore pressure transducer PPT2 gave pore water pressure reading of practically zero through out the pulling process. This indicates that the geotextile is capability of draining away the water effectively and functioned not only as reinforcement but also as a drainage medium.

Interesting results were obtained from the pore pressure transducer near the sleeve plate (PPT3). At the location of soil-geotextile interface, the transducer just in front of the sleeve plates (PPT3) registered some development of excess pore water pressure during the pullout process, reaching the peak total pore water pressure of about 6.5 kPa at the elapse time of about 60 minutes, which corresponds to the time when peak pullout force occurred. Subsequently, the pore water pressure dissipated rapidly when the geotextile was undergoing pullout.

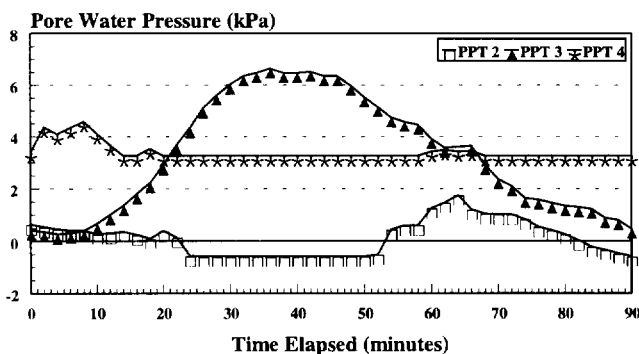
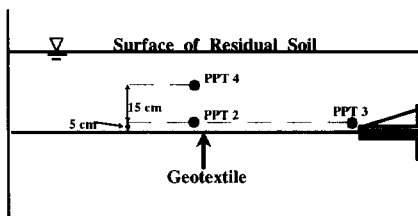


Figure 4 : Pore water pressure measurements during test 2.

## 4 CONCLUSIONS

The use of residual soil as backfill material for the construction of geosynthetics steep slopes and earth walls

is feasible only if proper drainage mediums are also provided to rapidly drain off the pore water to prevent potential build-up of excess pore water pressure. Hence, the geosynthetics material not only have to functioned as a reinforcement material but also as a drainage medium. One such material is the composite geotextile which consists of high-strength polyester yarns for reinforcement purposes, and a porous nonwoven polypropylene sheet for drainage function. The two large scale pullout tests reported here indicate that high-strength geotextile, coupled with drainage capability, can provide a rational choice as the reinforcement material. The test results indicates that the pore pressure at the soil-geotextile interface is practically zero, except at location near the sleeve plate, while the soil mass above the geotextile were having some excess pore water pressure. This seems to suggest that the geotextile is capable of dissipating excess pore water pressure rapidly during the pullout test. With the provision of this drainage function, peak pullout force dropped by only 16.4% when the residual soil is subjected to ponding. With the use of such material for reinforcement purposes, the reinforced soil concept can be further extended to regions where granular material is not readily available as backfill material.

## REFERENCES

- Bergado, D.T., Macatol, K.C., Amin, N.U., Chai, J.C., Alfaro, M.C. and Anderson, L.R. (1993) "Interaction of Lateritic Soil and Steel Grid Reinforcement", *Canadian Geotechnical Journal*, Vol. 30 No. 2, pp. 376-384.
- Chew, S.H. and Loke, K.H. (1996) "Design Criteria for Reinforced Soil Structures using Poorly Draining Backfills", *Proceeding, 12<sup>th</sup> Southeast Asia Geotechnical Conference*, Kuala Lumpur, Malaysia, pp. 137-145.
- Chew, S.H., Tan, S.A., Ho, C.T. and Loke, K.H. (1997) "Case studies and Large scale Tests on Geosynthetic Soil Reinforcement with Regional Soils", *International Conference on Ground Improvement Techniques*, Macau, pp. 121-129.
- Farrag, K., Acar, Y.B. and Juran, I. (1993) "Pullout Resistance of Geogrid Reinforcements", *Geotextiles and Geomembranes*, Vol. 12, No. 2, pp. 133-159.
- Ho, C.T. (1996) *Pullout Response of Geotextile in Dry and Wet Soils*, B(Eng) Thesis, Department of Civil Engineering, National University of Singapore, Singapore.
- Ng, L.F. (1995) *Pullout Resistance of Geosynthetics Using Large Scale Pullout Apparatus*, B(Eng) Thesis, Department of Civil Engineering, National University of Singapore, Singapore.



# Soft Clay Embankment Reinforced by Geosynthetic Horizontal Drains

M. Kamon

Professor, Disaster Prevention Research Institute, Kyoto University, Uji, Kyoto, Japan

T. Akai

Chief Engineer, Technology Research Institute of Osaka Prefecture, Izumi, Osaka, Japan

M. Fukuda

Manager, Osaka Soil Test Laboratory, Osaka, Japan

Y. Nanbu

Chief Engineer, Obayashi Corporation, Osaka, Japan

**ABSTRACT:** A full-scale test embankment reinforced with geosynthetic horizontal drains (GHDs) was carried out. The GHDs consisted of geocomposite materials and had the functions of reinforcement and drainage. Two kinds of GHDs and slope facing materials were selected, and a soft clay generated from an excavation was used for the filling material. The soft clay embankment, reinforced by GHDs, was designed to be 10 meters high with a steep slope angle. Limit values for the safety of the embankment were selected.

During and after the embankment execution, the settlement and the deformation of the embankment, the induced elongation of the GHDs, the strengths of the filling material, etc. were carefully monitored. The results obtained reveal that the soft clay embankment is stable and that the GHDs provide sufficient reinforcement.

**KEYWORDS:** Embankment, Geocomposites, Reinforcements, Soft Soils, Steep Slope

## 1 INTRODUCTION

Recently, embankments reinforced with geosynthetic materials have been used as one of the general construction methods for stabilizing embankments. The good mechanical properties of geogrid, a typical reinforcing material, are widely recognized for their applicability to reinforced embankments filled with sandy soils. Due to the lack of drainage, inferior quality soil such as surplus soil from construction sites can not be used for filling material in reinforced embankments. When soft clay of a low strength is used as a filling material for embankments, the filling is expected to increase in strength owing to consolidation by the effects of dewatering. Therefore, we have developed GHDs which are not only superior strength but also high permeability (Kamon et al. 1994).

This paper describes the results of a case study involving newly developed GHDs applied to a reinforced embankment filled with a soft clay soil.

## 2 OUTLINE OF THE TEST EMBANKMENT AND BASIC PROPERTIES OF GHDS

Two GHDs were applied to a reinforced embankment 10 meters in height. Plastic cores covered by nonwoven fabric (improved mechanical characteristics) and the reinforced nonwoven fabric (reinforced with high tensile strength yarn) were used. The width of each GHD was 0.3 meters. The basic material properties of the GHDs are summarized in Table 1.

The construction site is in the southern part of Osaka Prefecture, and surplus clay soil from an excavation in

Table 1. Basic properties of geosynthetic horizontal drains

Materials	Zone A	Zone B
	(Plastic core covered by nonwoven fabric)	(Reinforced nonwoven fabric)
Thickness (mm)	3.6	8.7
Unit density (g/m <sup>2</sup> )	1636	1581
Pull-out strength (kN)		
at 5% elongation	6.1	8.3
at failure	6.5	12.2
Tensile strength (kN/m)		
at 5% elongation	43.5	43.8
at failure	82.8	72.9
Elongation at failure (%)	32.1	11.4
In-plate permeability (cm/s)		
Normal stress at 98.0kPa	1.6x10 <sup>-1</sup>	3.2x10 <sup>-1</sup>
Normal stress as 294.0kPa	1.6x10 <sup>-1</sup>	1.0x10 <sup>-1</sup>

this area was used. The ground conditions in this area include Pleistocene deposits, and the excavated clay soil was in a slightly overconsolidated state.

Table 2. Physical properties of filling material used

Density of solid particle (Mg/m <sup>3</sup> )	2.686
Water content (%)	44.2
Clay fraction (<5 μm) (%)	63.3
Liquid limit (%)	57.4
Plasticity (%)	35.3
Cohesion, c <sub>u</sub> (kPa)	88.2
Internal friction angle, φ (°)	23.7
Preconsolidation stress, p <sub>c</sub> (kPa)	426.3
Coefficient of consolidation, c <sub>v</sub> (cm <sup>2</sup> /day)	0.589

### 3 DESIGN OF THE SOFT CLAY EMBANKMENT REINFORCED BY GHDS

The physical properties of the clay soil are indicated in Table 2. The liquidity index was approximately 63% and the clay soil became very soft after remolding.

Based on the in situ failure test results (Kamon et al. 1996), a highly soft clay embankment reinforced by GHDS was constructed. A section of the embankment is illustrated in Figure 1. GHDS were placed over 50% of the embankment with the staggered arrangement shown in this figure. The design factors of the slope stability are summarized in Table 3, which was modified from the Japanese design manual (1992).

The stability of the embankment was calculated according to the following rotational slip method.

$$F_s = \frac{R \cdot \Sigma (c_i \cdot l_i + (W_i \cdot \cos \theta_i + T_i \cdot \sin \theta_i) \cdot \tan \phi_i + T_i \cdot \cos \theta_i)}{R \cdot \Sigma (W_i \cdot \sin \theta_i)} \quad (1)$$

where  $c_i$  = cohesion of the soil (kPa),  $w_i$  = clod weight,  $\phi_i$  = angle of internal friction (degree), and  $T_i$  = tensile strength of material (kN/m).

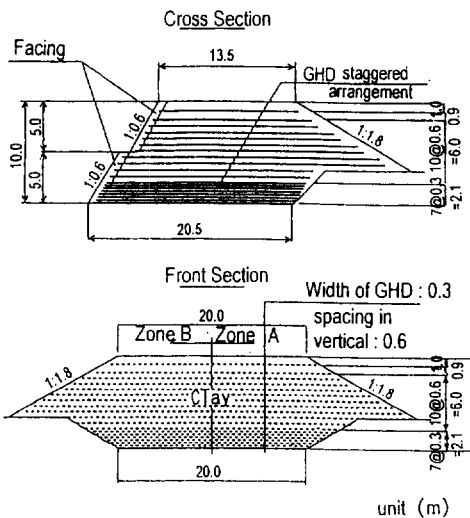


Figure 1. Section of the test embankment

As  $T_i$  value, we selected the smaller value between the ultimate tensile strength  $T_a$  and the pull out resistance  $T_{pi}$  of GHDS.  $T_{pi}$  was calculated by Equation (2), namely,

$$T_{pi} = 2 \cdot (0.5c_i + 1.0 \cdot \sigma_v \cdot \tan \phi_i) \cdot L_{ei} \quad (2)$$

where  $\sigma_v$ : vertical earth pressure which works upon the anchorage part of the material at each layer,  $L_{ei}$ : anchorage length of the material at each layer,  $F_s$ : safety factor,  $R$ : radius of the rotational slip surface,  $l_i$ : arch length of the slip surface which was divided into sections, and  $\theta_i$ : sliding angle at the center point of the slip surface which was divided into sections.

The embankment had two different zones reinforced by two different GHDS, each 10 meters high and with a

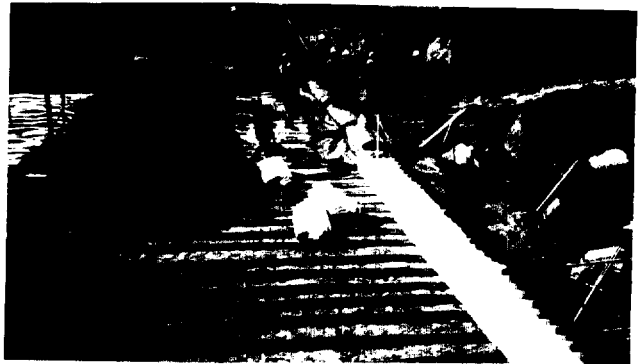


Figure 2. Filling work with GHD and facing material



Figure 3. Completed filling work of 10 m-embankment

Table 3. Design factors and the calculation result of the slope stability

Calculation method of slope stability	Sliding circle method
Seismic design factor	$k_h = 0.2$
Arrangement of GHDS	Staggered; 50%
Design strength of soil (remolded)	$c = 29.4 \text{ kPa}$ , $\phi = 0$
Safety factors	Sliding circle (static): 1.3 (dynamics): 1.0 Pull-out safety (static): 2.0 (dynamics): 1.2
Design strength of GHDS	Static (by the creep test result) Dynamics (at 5% elongation by tensile test result)
Calculation result of slope stability	Static: without reinforced = 0.976 with reinforced = 1.405 Dynamics: without reinforced = 0.730 with reinforced = 1.015

1:0.6 slope angle. Figures 2 and 3 show the embankment reinforced by the GHDs during and after the filling work. Two types of facing materials were newly developed and applied to zones A and B, the details of which are omitted in this paper.

## 4 MONITORING RESULT

### 4.1 Monitoring System of the Embankment

The filling works were carried out smoothly in both zones. To monitor the slope stability, inclinometers, tensiometers, multi-layer settlement gauges, earth pressure gauges, relative displacement meters, and groundwater monitoring wells were installed in the embankment in order to certify the deformation of the embankment and the status of the GHDs. These monitoring instruments with automatic measuring systems (Figure 4) were mainly installed on the slope and around the predicted sliding circle. The measuring points for each parameter are indicated in Figure 5.

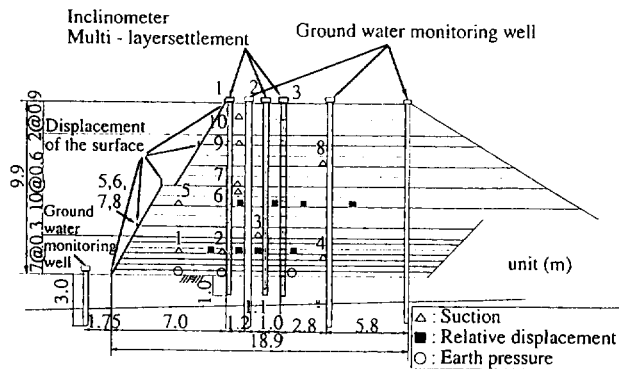


Figure 4 Monitoring system of the embankment

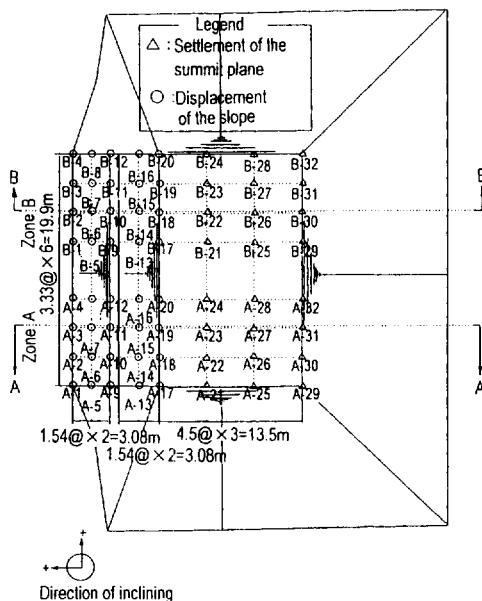


Figure 5. Monitoring points of the embankment

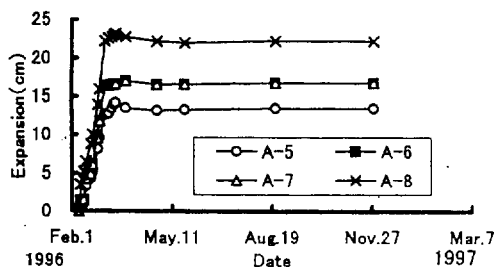


Figure 6. Behavior of the deformation of slope surface

### 4.2 Deformation of the Embankment

Figure 6 indicates horizontal displacements at the 3-meter high slope of the embankment measured by surveying the total stations. A large horizontal outward deformation at the early stage of the filling work includes a lateral movement by the overburden load as well as the self-weight effect of the filling machine. After the completion of the filling work on March 22, 1996, the horizontal deformation was very small and the embankment became stable by the consolidation of the clay soil.

### 4.3 Elongation of the GHDs

The results of measuring the strain of the GHDs are illustrated in Figure 7. Strain gauges were set on the fourth and the tenth GHDs where they would be close to the predicted sliding circle. The extensions of the GHDs as well as the compressions were obtained during the filling work. The maximum strains were relatively small values (0.8 to 1.0 %). After the completion of the embankment, no additional strain was observed in the GHDs. This means that the embankment was quite stable.

The difference in the embankment's deformation behavior between zones A and B depends on the elongation and the friction of the GHDs used, but the difference was very small in this case study.

### 4.4 Physical Properties of the Filled Soft Clay

The shear strength of the filled soil during the filling work was measured by a cone penetration test. Figure 8 shows the results of the distribution of cohesion in the embankment. The results are in zone A and the controlled value was 30 kPa. As the shear strength was less than 30 kPa with a height of 3 - 5 meters, additional filling was carefully performed with the confirmation of the stability analysis. Since the safety of the soft clay embankment is at its lowest in the early stage of the execution, the safety factor of the embankment increased in the drainage function of the GHDs after the completion of the embankment.

The variation in suction for the embankment (zone A) during a rainy season is illustrated in Figure 9. Tensiometers at points A3, 7, and 9 are directly set on the GHDs

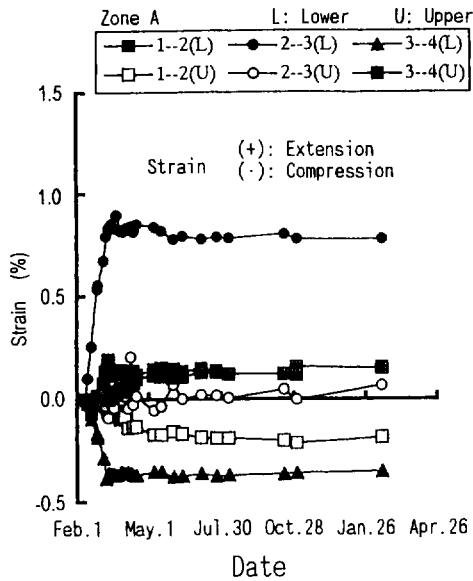


Figure 7(a). Behavior of elongation of GHD (Zone A)

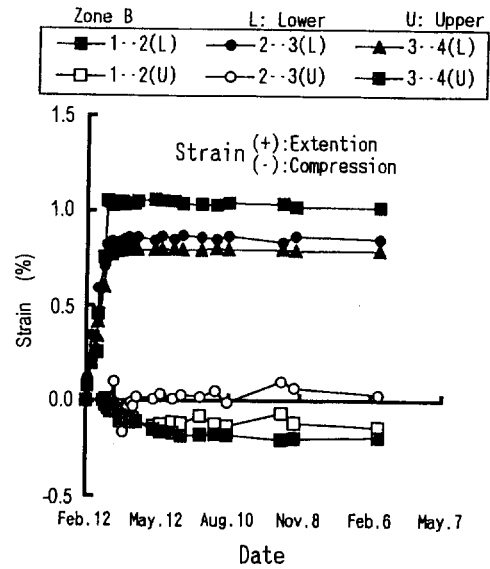


Figure 7(b). Behavior of elongation of GHD (Zone B)

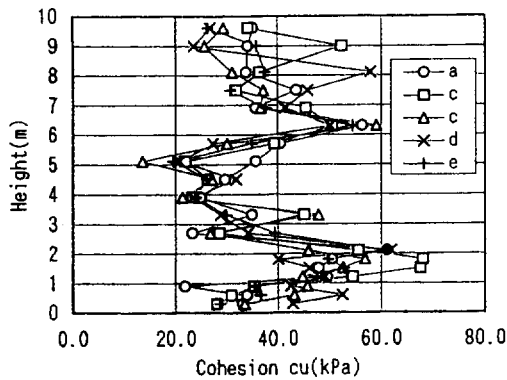


Figure 8. Cohesion distribution of the embankment

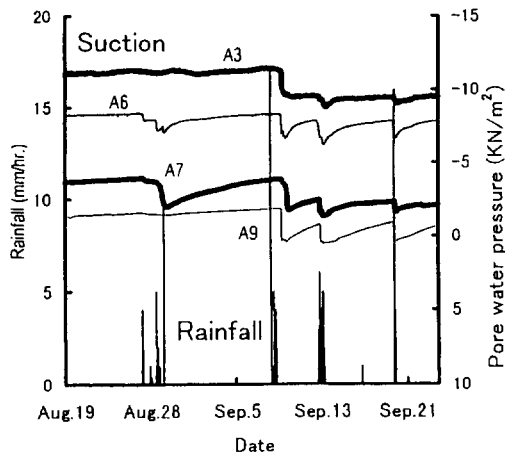


Figure 9. Behavior of tensiometers with rainfall

and A6 was set in the center of the soft clay. The data show negative porewater pressure because of the Pleistocene clay that was filled. This suction (negative porewater pressure) decreases with rainfall, at the surface of the embankment in particular, and increases with dissipation due to the high permeability of the GHDs. It is seen that the GHDs had a high drainage effect and that the safety of the embankment was maintained even with a heavy rainfall.

## 5 CONCLUSION

The GHDs showed a sufficient tensile reinforcing function and the soft clay embankment with a steep slope was safely constructed using them. The reinforcing and drainage effects of the GHDs can be estimated because of the monitoring results, in particular from the deformation behavior of slope surface and elongation data of the GHDs. Consequently, the GHDs can be used practically in designing reinforced embankments filled with soft clays which are usually disposed of as construction waste.

## REFERENCES

Kamon, M., Akai, T., Fukuda, M. and Nanbu, Y. (1996) "In Situ Failure Test of High Water Content Soft Clay Embankment Reinforced by GHDs", *IS-Kyushu '96*, JGS, Fukuoka, Japan, Vol. 1, pp. 215-220.

Kamon, M., Akai, T., Fukuda, M. and Yaida, O. (1994) "Reinforced Embankment Using Geosynthetic Horizontal Drains", *Proc. 5th ICG*, Singapore, Vol. 2, pp. 791-794.

Public Works Research Institute (1992) *Design Manual for Reinforced Earth by Geotextile*, Civil Engineering Research Center, Tokyo, Japan.

# Centrifuge Modeling of an Innovative MSES for Marginally Stable Slopes

M. B. Mahmud

Lecturer, Faculty of Civil Engineering, Universiti Teknologi Malaysia, Johor Bahru, Johor, Malaysia

T. F. Zimmie

Professor, Department of Civil Engineering, Rensselaer Polytechnic Institute, Troy, New York, USA

**ABSTRACT:** Centrifuge model tests were performed to study the feasibility of a new installation method for the construction of mechanically stabilized earth structures (MSES) using geotextile reinforcement. The proposed method allows wide strips of geotextile to be driven horizontally and directly into existing and marginally stable slopes, similar to the installation of vertical wick drains. It does not require excavation of the soil behind the slope face, thus offering a rapid and economical solution for slope stabilization. Model geotextile strips simulated high strength non-woven geotextiles, which serve both as horizontal drain and reinforcement. The contribution of each function to the stability of marginally stable slopes in soft soil is presented in this paper. Typical results from centrifuge model studies show good agreement with other numerical analyses.

**KEYWORDS:** centrifuge modeling, geotextile reinforced slopes, soil reinforcing, low cost slope stabilization

## 1 INTRODUCTION

Centrifuge model tests were performed to study the feasibility of a new installation method for the construction of mechanically stabilized earth structures (MSES) using geotextile reinforcement. Conventional geotextile reinforced slopes utilize geosynthetics such as geogrids and geotextiles in the form of continuous sheets. These materials are installed in place after excavation of the slope and successive placement of selected soil as backfill. The proposed method allows wide geotextile strips to be driven horizontally and directly into existing and marginally stable slopes, similar to the installation of vertical wick drains. The geotextile strips perform dual functions, both as horizontal drains and reinforcement. Since excavation of the soil behind the slope face is not required, the method offers a rapid and economical solution to slope stabilization. The advantages of the proposed method over conventional MSES are summarized in Table 1.

Table 1. Conventional MSES versus the proposed method

Conventional MSES	Proposed Method
<ul style="list-style-type: none"><li>• require excavation/removal of "bad" soil</li><li>• use selected/imported backfill</li><li>• time consuming (constructed in layers)</li><li>• require formwork/temporary supports</li><li>• some need specially designed facing</li><li>• high cost</li></ul>	<ul style="list-style-type: none"><li>• insitu installation on existing slope (minimal or no excavation)</li><li>• utilize existing soil</li><li>• rapid installation</li><li>• no formwork/temporary support</li><li>• minimal facing (surface erosion control)</li><li>• economical</li></ul>

## 2 SOFT SOIL SLOPES

Various full scale studies have been performed dealing with geotextiles performing multiple functions in the stability of reinforced slopes in soft saturated soil. Tatsuoka and Yamauchi (1986) reported on full scale studies performed on two clay test embankments reinforced with planar sheets of non-woven geotextile. The multiple functions of the geotextile, i.e. drainage, tensile reinforcement and compaction control, were the major considerations in the study. Two embankments were constructed using locally available volcanic ash clay, and were fully instrumented to monitor the performance of the embankments over a period of 1.5 and 3 years. The non-woven geotextiles used served well as pore pressure dissipators and the immediate dissipation of pore water pressure was observed after a period of heavy rainfall. The non-woven geotextile was about 3-4 mm thick with an in-plane permeability of  $2 \times 10^{-1}$  to  $3 \times 10^{-2}$  cm/sec and provided the required drainage and hence stabilized the slopes.

Kamon and Akai (1996) constructed full scale reinforced embankments to study the effect of geosynthetic horizontal drains (GHD) on the stability of the embankments. Various types of newly designed GHDs were used in the study. The GHDs were similar to vertical wick drains. The inner cores were wrapped with woven or non-woven geotextiles. These materials were about 12 mm thick, had maximum tensile strengths of about 74.5 kN/m, and exhibited very high in-plane permeabilities. GHD strips, 30 cm wide, were installed during the construction of the clay embankments. The use of GHDs improved the stability of the slopes, increasing the factors of safety (FOS) to about 1.43 and 1.55, compared to a FOS of 1.163 using only conventional geotextiles. Kamon et al. concluded that GHDs can serve the dual functions of reinforcement and drainage for stabilizing soft clay embankments.

It should be noted that the GHDs were installed in a similar manner to conventional MSES systems, i.e. the slopes were excavated in order to install the GHDs or reinforcement.

Loke et al. (1994) also studies the multi-functioning behavior of geotextile-reinforced embankments on soft clay. The full scale embankments, reinforced and unreinforced, were constructed to failure. High strength and multi-layers

non-woven needle punched geotextiles were used in the study. The use of the high strength non-woven geotextiles provided the required drainage and reinforcement for the embankment. Theoretical analyses, using finite difference methods, were performed to determine the critical height of the embankment. The results from the analyses confirmed the behavior of the full scale slope.

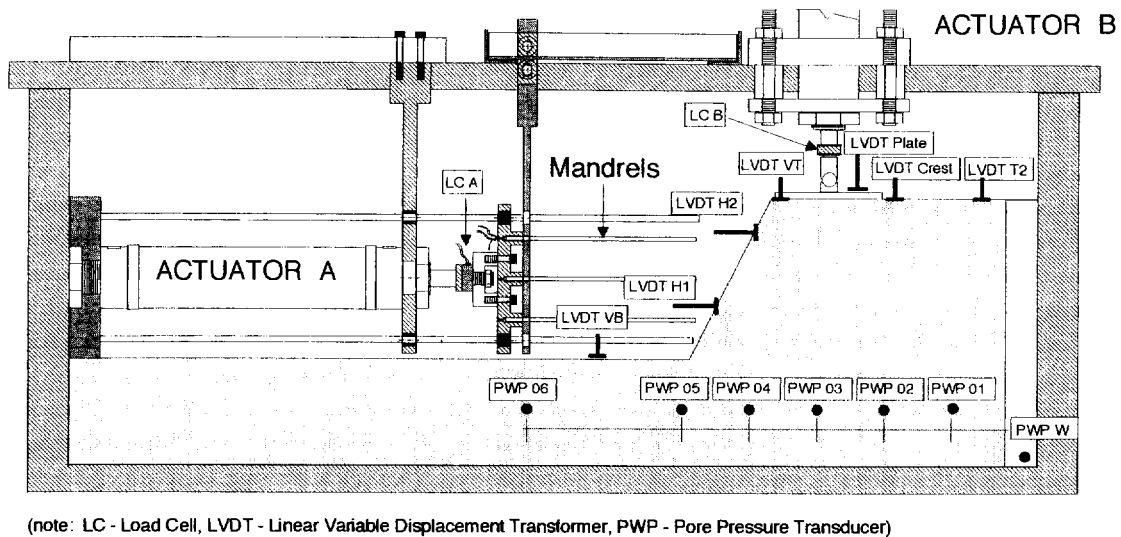


Figure 1 The experimental setup showing various instrumentation used in the study

### 3 CENTRIFUGE TESTING

#### 3.1 Experimental Setup

The geotechnical centrifuge at Rensselaer was used to perform all model tests presented herein. The capability and performance of the centrifuge, and a summary of various research projects that have been performed using the centrifuge is presented by Van Laak et al. 1997. Model slopes with a slope angle of 63° (1H:2V) were constructed in a large centrifuge strong box (60.96 cm wide x 91.44 cm long). Two actuators, Actuator A and Actuator B shown in Figure 1, were used to drive the mandrel and apply surcharge loading, respectively.

Soft clay material was used in the model slopes which were accelerated to marginal g-levels (factor of safety close to one) to simulate near failure conditions of the slopes. Geotextile strips were then inserted into the slopes, using the remotely controlled mandrel driver, at that particular high g-level (while the centrifuge was rotating). The slopes were then loaded to failure.

Various instrumentation used in the models are shown in Figure 1. Details dealing with the instrumentation and calibrations are presented elsewhere (Zimmie and Mahmud, 1996a).

#### 3.2 Testing scheme

Four model tests are presented in this paper. The models are Unre301, Rein301, Unre403 and Rein401 which represent an unreinforced slope with surcharge loading, reinforced slope with surcharge loading, unreinforced slope with seepage and reinforced slope with seepage, respectively.

Models Unre301 and Rein301 were spun up to 8 g in the centrifuge and maintained at this g-level for a few minutes, then the g-level was increased to 16 g and again maintained at that g-level for a few minutes before finally being increased to 25 g. The surcharge loading was introduced at the 25 g-level, and the load was monitored by the load cell attached to the loading plate. For model Rein301, six geotextile strips were inserted at 25g, prior to the application of crest loading. Both Actuator A and Actuator B (Figure 1), were utilized in the model. Actuator A moves horizontally, inserting geotextile strips housed inside the mandrels into the soil. This operation occurs while the centrifuge is in motion and the model is at the specified high acceleration level in order to simulate prototype soil stresses in the slope. Actuator B is used to apply a surcharge loading on the slope after the strip installation process is complete. Load cells are used to continuously monitor the driving force and surcharge loading.

Models Unre403 and Rein401 were spun up to 25 g in increments of 5 g. The models were maintained at that g level for several minutes before introducing the water. Water was fed into a reservoir behind the slope, from a water tank mounted on the shaft of the centrifuge. An automatic shut-off valve with a remote switch located in the centrifuge control room was used to control the flow of water in flight. Two perforated plates were placed at the headwater and tailwater sides to allow flow within the model. For model Rein401, six reinforcing and drainage strips were inserted at 25 g before introducing the water at the back of the slope.

Centrifuge modeling requirements were carefully observed to achieve similitude. Additional details concerning centrifuge modeling laws pertinent to this study are presented in Zimmie and Mahmud (1996b).

#### 4 RESULTS AND DISCUSSIONS

The crest settlements of models Unre301 and Rein301 plus corresponding loads that caused failure are shown in Figures 2 and 3 respectively. The unreinforced slope model resisted an applied crest load of about 27.2 kg (60 lbs) and the reinforced slope a load of 45.4 kg (100 lbs). Both tests showed approximately the same amount of settlement to failure but the reinforced slope resisted a higher load, as expected. Using limit equilibrium analyses, the factor of safety (FOS) for the unreinforced and reinforced slopes were 1.24 and 1.62 respectively, prior to the application of surcharge loading. The FOS at failure was about 0.45 for both models, computed using the maximum applied loads, indicating that failure probably occurred at load values slightly less than the maximum. Details results and the failure mode of these slopes are presented in Mahmud and Zimmie (1997).

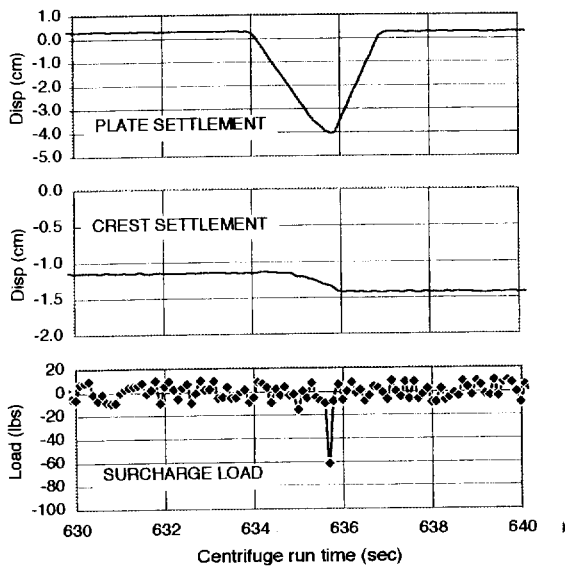


Figure 2 Unreinforced slope with surcharge loading

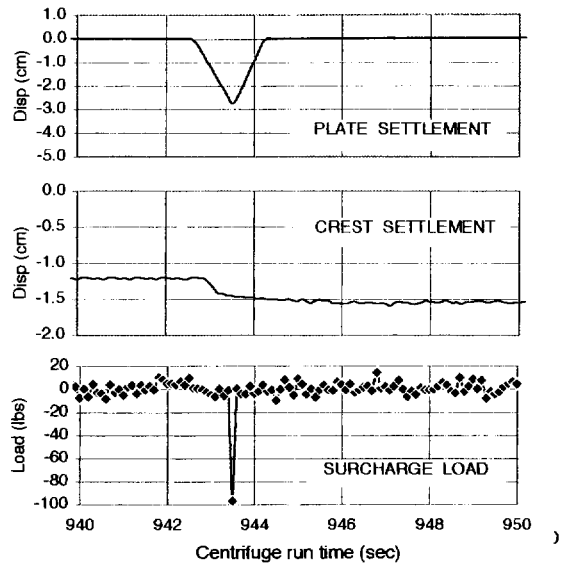


Figure 3. Reinforced slope with surcharge loading

Model Unre403 and Rein401 were performed to emphasize the drainage function of the geotextile strips. The difference in water table between the unreinforced and reinforced slopes plotted from pore pressure transducer data is shown in Figure 4. As shown, the installation of six strips into the slope significantly lowered the phreatic surface and increased the stability of the slope. The FOS of the unreinforced and reinforced slopes computed by limit equilibrium analysis were 0.8 and 1.1 respectively.

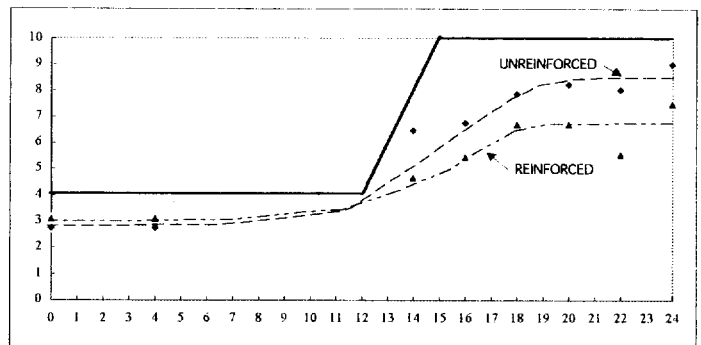


Figure 4. Phreatic surfaces for unreinforced and reinforced slopes (dimension in model units- inches)

#### 5 CONCLUSIONS

The use of geosynthetics as reinforcing elements in reinforced walls can result in savings of about 20-50% as

compared to the use of metallic strips [Christopher and Holtz (1985), and Mitchell and Villet (1987)]. The new installation technique proposed herein will even further reduce the overall construction cost of mechanically stabilized earth structures (MSES). Detailed analysis of the cost of the proposed method is presented by Mahmud (1997). A comparison of unit costs between the proposed method and other reinforced soil structures is shown in Figure 5. Unit costs of the other structures were provided by Holtz et al. (1995). The proposed method is very economical compared to other MSES, largely due to the fact that no excavation of the slopes is required.

This method can rapidly stabilize marginally stable slopes or slopes near failure. The practicality, and time and cost saving aspects of this new method will be beneficial in various slope stabilization schemes including marginally stable embankments, existing slopes and cut slopes.

The centrifuge modeling techniques used in this study are quite economical and less time consuming than the alternative of full scale prototype testing. In fact, it would have been economically impractical to conduct full scale testing during this stage of the study. Proper scaling conditions were carefully observed, and the results of the centrifuge model tests should agree well with the results of full scale tests.

Obviously the feasibility and cost effectiveness of the proposed methodology can only be truly verified after full scale slope installations are completed.

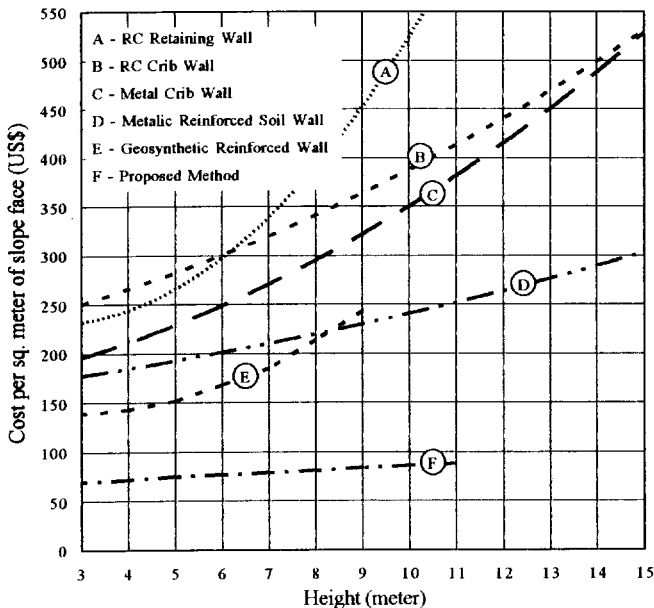


Figure 5. The cost comparison between the proposed method and other methods for reinforcing slopes.

## REFERENCES

- Christopher, B. R. and Holtz, R. D. (1985), "Geotextile Engineering Manual", National Highway Institute, FHWA, DTFH 61-80-C-00094.
- Holtz, R. D., Christopher, B. R. and Berg, R. R. (1995), "Geosynthetic Design and Construction Guidelines", FHWA HI-95-038 (May 1995), NHI, Fed. Highway Administration, US-DOT, Washington D. C.
- Kamon, M. & Akai, T., (1996), "In Situ Failure Test of High Water Content Soft Clay Embankments Reinforced by GHDs", In H. Ochiai, N. Yasufuku and K. Omine (eds.), *Earth Reinforcement - Proc. of the International Symposium*, Vol. 1, Fukuoka, Japan: Balkema, Rotterdam, pp. 215-220.
- Loke, K. H., Ganeshan, V., Werner, G. and Bergado, D. T. (1994), "Composite Behaviour of Geotextile Reinforced Embankment on Soft Clay", *Proceedings of the Fifth International Conference on Geotextiles, Geomembranes and Related Products*, G. P. Karunaratne, S. H. Chew and K. S. Wong (eds), International Geotextile Society, Singapore, pp. 25-28.
- Mahmud, M. B. (1997), "Centrifuge Modeling of an Innovative, Rapidly Installed and Economical MSES for Marginally Stable Slopes", Ph. D. Thesis (July 1997), Rensselaer Polytechnic Institute, Troy, New York.
- Mahmud, M. B. & T. F. Zimmie (1997), "The Influence of Surcharge Loading on the Stability of Directly Installed MSES", *Proc. of the International Symposium on Mechanically Stabilized Backfill (MSB)*, Denver, Colorado.
- Mitchell, J. K. and Villet, W. C. B. (1987), "Reinforcement of Earth Slopes and Embankments", NCHRP Report no. 290, TRB, National Research Council, Washington D.C.
- Tatsuoka F. and Yamauchi, H., (1986), "A Reinforcing Method for Steep Clay Slopes using a Non-woven Geotextile", *Geotextile and Geomembranes*, vol. 4, pp. 241-268.
- Van Laak, P., Elgamal, A-W., Zimmie, T. F., and Adalier, K. (1997), "Experimental Facilities: The RPI Geotechnical Centrifuge Facility", *NCEER Bulletin*, vol 11, no. 2, State University of NY at Buffalo, April 1997, pp. 12-17.
- Zimmie, T. F. and Mahmud, M. B. (1996a), "Instrumentation for Centrifuge Modeling of Geotextile Reinforced Slopes", In H. Ochiai, N. Yasufuku and K. Omine (eds.), *Earth Reinforcement - Proc. of the International Symposium*, Vol. 1, Fukuoka, Japan: Balkema, Rotterdam, pp. 847-852.
- Zimmie, T. F. and Mahmud M. B. (1996b), "Centrifuge Modeling of a Rapidly Installed MSES", In H. Y. Fang and H. Inyang (eds), *Environmental : Proc. of the 3rd International Symposium*, Vol. 1 Technomic, Lancaster, PA, pp. 795-804.



# Hydraulic Effects of Using Dual-Function Geosynthetics in the Design of Multi-layer Structures

PH. GOTTELAND,  
Assistant Lecture, L.I.R.I.G.M.laboratory, Grenoble University, France.

**ABSTRACT:** This article presents some works to try to model the behavior of multi-layer structures combining a soil having what would be considered as poor mechanical properties for construction purposes, and Dual-Function (draining-reinforcing) Geosynthetics (DFG). We focus on this paper on the hydraulic modeling of a composite soil geosynthetics. We consider for the DFG geosynthetic only the transmissive capacity of the geosynthetic drain for accelerating the dissipation of uplift pressures. Effect of the geosynthetic transmissivity is shown for two types of soil. Modeling of the effect of a local damage of the drain is presented.

**KEYWORDS:** Drainage, Geocomposites, Modeling, Transmissivity, Installation damage

## 1 INTRODUCTION

One advantage of using flexible geosynthetics for ground reinforcement would seem to be the possibility of using soils of poor quality, with a high percentage of fines, often with high initial water content and highly sensitive to water. The concept involves associating a drainage function and a reinforcing function for the inclusion (Dual-Function Geosynthetics: DFG). Thanks to the high transmissive capacity of the geosynthetic with high permeability draining function, interstitial uplift pressures induced by placing the soil can be quickly dissipated. At the same time, the tensile strength of the reinforcing geosynthetic improves the mechanical stability of the structure provided by the consolidation of the material (Figure 1).

A modeling system was already presented (Gotteland et al. 1996) with some results of the combined draining-reinforcing effect of a dual-function inclusion for the construction of multi-layer structures alternating a layer of soil with a geosynthetic sheet. We focus on this paper on the hydraulic modeling and on numerical results obtained to assess the effect of some parameters.

## 2 EMBANKMENTS CONSIDERED

The types of structure concerned are linear structures with vertical or sloping facing with the length being much greater than the other dimensions: height  $H$  and width  $B$ . Calculations can thus be made in the plane of the structure. The structures could be multi-layer, alternating a layer of soil with a Dual-Function Geosynthetic DFG, of length  $B$ , placed horizontally with a spacing of  $D_h$ .

The soil supplied is the same and homogeneous over the entire height of the embankment.

The embankment facing is considered as a perfect drain; the upstream boundary between the structure and the in situ soil is considered to be either perfectly draining, or perfectly impermeable depending on the type of construction.

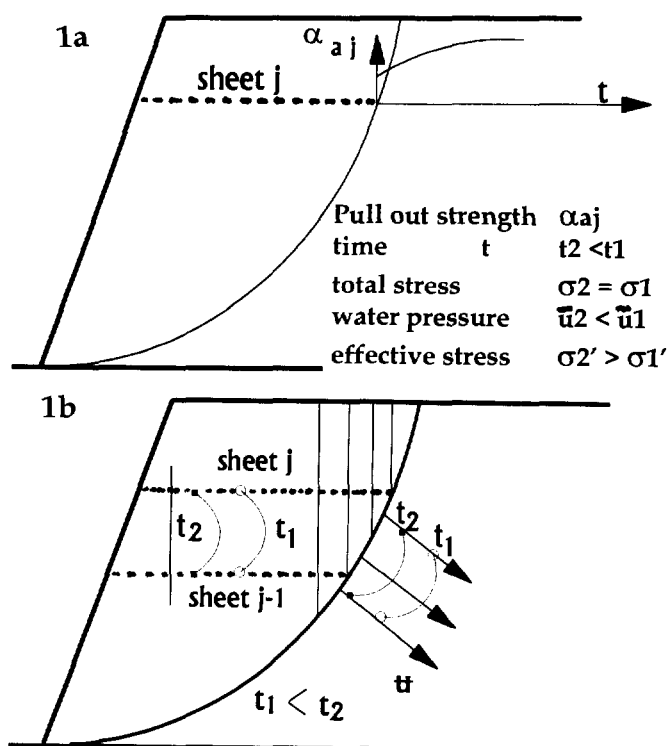


Figure 1: increase of the pull-out strength of the DFG (1a), increase of the shear strength of the soil (1b), by lowering of the pore water pressure in the structure

### 2.1 The soils

The soils considered in this study are homogeneous fine soils (clays, silts), with high initial water content and permeability,  $k_s$ , between  $10^{-8}$  and  $10^{-10}$  m/s. A saturated state may be achieved on completion of placing operations. Compacting may give rise to permeability anisotropy (vertical and horizontal permeability may be different).

## 2.2 Dual-Function Geosynthetics (DFG)

The DFG inclusions considered are made up of an association of a draining geosynthetic and a reinforcing geosynthetic, for example by the combination of a non-woven and a woven fabric.

As far as only drainage is concerned (hydraulic function), the functional characteristic is the transmissivity  $\theta g$  [ $m^2/s$ ] with  $\theta g = kg \cdot e$  ( $kg[m/s]$  permeability,  $e[m]$  thickness).

## 2.3 Draining properties of DFG in the presence of soil

Contact with the soil and applied stresses, over time, lead to a reduction in draining properties of geosynthetics as well as a reduction in soil permeability in the surrounding filtration area. This is known as the clogging phenomenon. The laws governing the variation in these properties are still being studied but simplified approaches can be considered.

The more simple modeling is to consider the transmissivities could be reduced all a long the drain compared to the same values on virgin geosynthetics in order to take these phenomena into account ( $\theta g$  initial =  $\theta g$  reduced  $\sim 2 \times 10^{-8} m^2/s$ ).

We present one other possibility : local reducing of the drain transmissivity for example to modelise a localized clogging or problems of water penetration in the drain.

## 3 INTERSTITIAL UPLIFT PRESSURES IN A SOIL-GEOSYNTHETIC DRAINING COMPOSITE.

For the hydraulic study, the multi-layer structures studied are broken down into identical elementary element, either by considering two half draining geosynthetic enveloping a soil layer of thickness  $Dh$ , or two soil half-layers enveloping a geosynthetic (Figures 2).

For modeling purposes, the construction of a element  $j$  is assumed to be instantaneous and completed after time  $T_j$ . The time  $T$  [days] is the time in days since the start of embankment construction (layer  $j=1$ ),  $t=T-T_j$  [days] is the relative time since construction of module  $j$ . The construction time between completion of two successive elements is  $Dt$  [days].

The stress  $\sigma$ , generated by the weight of the soil layers, is applied uniformly to each element and is imposed instantaneously when constructing the next overlayer.

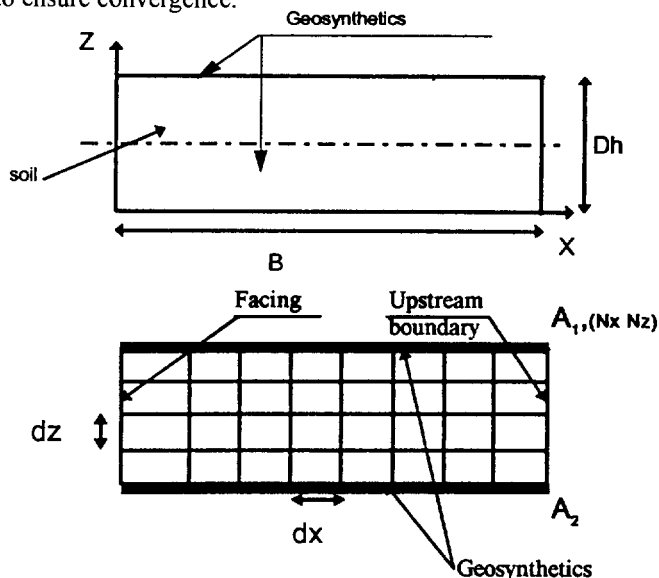
The deadweight of the element  $j$  studied is not taken into account.

The soil has an isotropic, linear elastic behavior; after placing, it is assumed to be saturated in water, a fluid considered to be incompressible. The stress  $s$  created by an instantaneous increase in interstitial uplift pressure  $\bar{u}$ ,  $\bar{u}(x, z, t=T-T_j=0) = \sigma$ .

The transmissivity  $\theta g$  of the geosynthetic is constant with time. Flow in the geosynthetic drain obeys Darcy's law.

The evaluation method for  $\bar{u}(t)$  is based on the theory of consolidation. Two approaches are possible: flow in the soil may be considered to be unidirectional (Auriault et al. 77) or two-directional (Bourdillon 76, Gotteland 91).

We consider here the hypothesis of two directional flow in the soil. The consolidation problem is resolved by a finite-difference numerical method. The system is broken down into discrete elements in space (rectangular mesh) and time (explicit scheme). The degree of error in the evaluation of uplift pressures will depend on the size of the mesh  $dx/dz$  (a smaller mesh giving a more accurate result) and on the time step, which must be less than the critical time step in order to ensure convergence.



Figures 2: elementary element, discrete mesh

## 4 MODELING OF CONSTRUCTION

Each element of the multi-layer structure can be studied separately. For each, the effect of the construction stack of successive element on the change in interstitial uplift pressures must be assessed.

A detailed modeling procedure was proposed (Gotteland 91, Gotteland et al 96) in order to assess the effect of the following main parameters on the dissipation times of interstitial uplift pressures in the elements:

- Construction phasing  $Dt$  [days]
- Initial uplift pressure  $\bar{u}(t=0) = \bar{u}_{comp}$  [kPa] (initial remnant pressure after compacting effect)
- Thickness of modules  $Dh$  [m]
- Transmissivity of the geosynthetic  $\theta g$  [ $m^2/s$ ]
- Horizontal and vertical permeability of the soil  $k_x, k_z$  [m/s]
- etc.

We retain for this paper, the following simplified modeling procedure : Hypothesis of instantaneous construction of the complete structure ( $Dt=0$ ), with combined influence of compacting and total overload generated by the weight of overlying modules on the consolidation ( $\bar{u}(t=0) = \bar{u}_{comp} + (n-1) \cdot \bar{u}_{stat}$ ,  $\bar{u}_{comp}$  is the initial remnant pressure after compacting effect,  $\bar{u}_{stat}$  increasing by the weight of the soil from an additional element, simplified model 2, Figure 3).

This model provide a greater safety margin because it does not make allowance for consolidation during construction.

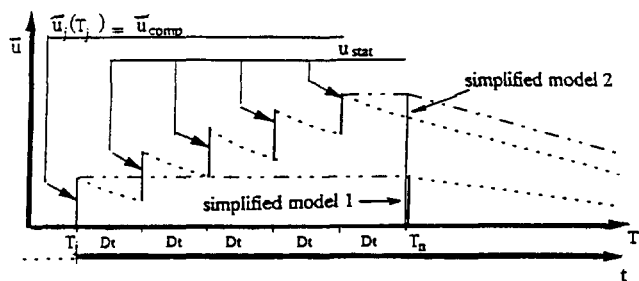


Figure 3: Theoretical modeling of the variation of the uplift pressure during and after construction.

## 5 STUDY

Some characteristic results of a parametric study are presented in order assess the influence of the variation in transmissivity  $\theta_g$  of the DFG. Three soils are considered :

	Soil 1 (clay)	Soil 2 (Silty clay)	Soil 3 (Clayey silt)
$k_s$ [m/s]	$1,7 \cdot 10^{-10}$	$1,6 \cdot 10^{-9}$	$2,6 \cdot 10^{-9}$
$\gamma_s$ [kN/m <sup>3</sup> ]	17,5	17.5	17.5
$Cvs$ [m <sup>2</sup> /s]	$1.47 \cdot 10^{-7}$	$5.4 \cdot 10^{-7}$	$2.8 \cdot 10^{-7}$

$k_s$  [m/s]: permeability,  $\gamma_s$ : soil density [kN/m<sup>3</sup>],  
 $Cvs = k_s \cdot E_{oed} / \gamma_w$  with  $E_{oed}$ : oedometric modules of the soil [kPa],  $\gamma_w$ : water density [kN/m<sup>3</sup>]

Only the uplift pressure distribution in the element at the base is calculated ( height of the structure  $H = 7$  m, length  $B =$  variable , geosynthetic spacing  $D_h = 1$  m) with impermeable upstream boundary.

The instantaneous construction hypothesis is considered:  
 $\bar{u}(t=0) = 105$  [kPa] (simplified model 2, Figure 3)

### 5.1 Influence of the transmissivity $\theta_g$ of the DFG

Figure 4 shows the variation in dissipation time required to obtain 10% maximum residual uplift pressure in the module in the vicinity of the impermeable upstream boundary (time  $t$  such that  $\bar{u}(t)_{max} / \bar{u}(t=0) = 10\%$ ). as a function of DFG transmissivity  $\theta_g$ .

An interesting phenomenon is seen to occur as a result of the modeling calculation: for low transmissivity values, maximum uplift pressures are dissipated faster in soil 1 (clay) than in soil 3 (silt), and even compared to soil 2 for extremely low values, although soil 1 has lower permeability.

For a more important length  $B$  of the drain, the observed phenomena exist for greater value of  $\theta_g$ . In the same way, if the thickness  $D_h$  is smaller ( $D_h = 0.5$  m) the same phenomenon is amplified. Notice, that these values of  $\theta_g$

are similar of real values of  $\theta_g$  for non-woven geotextiles used for D.F.G.

For high transmissivity values ( $\theta_g = 10^{-5}$  m<sup>2</sup>/s), the uplift pressure decreases rapidly in the drains for both soils: drainage occurs mainly through the geosynthetic drains. The soil with the high  $Cvs$  value dissipates the interstitial uplift pressures more quickly.

For a lower transmissivity value ( $\theta_g = 10^{-7}$  m<sup>2</sup>/s), the uplift pressure in the drains takes much longer to decrease. The explanation seems to be that, for soil 1, the ratio  $\theta_g / k_s$  is such that most drainage of the soil takes place through the geosynthetic drains. For soil 3, given the low  $\theta_g$  value, flow is mainly horizontal through the soil; as a result, the drain is subjected to high uplift pressure. Consequently, the draining time being longer, the residual uplift pressure (maximum at the impermeable upstream boundary), is higher for the more permeable soil. Figure 5 shows the uplift pressure distribution for two times  $t = 10$  and  $20$  days for soils 1 and 3 and for  $\theta_g = 10^{-7}$  m<sup>2</sup>/s of the DFG.

The using of a geosynthetic drain seems to be really efficient for low permeability of soil (clay) compared to higher permeability of soil (clayey silt).

The ratio of geosynthetic transmissivity to soil permeability ( $\theta_g / k_s$ ) therefore plays a major role. What can we expect in real life of draining system?

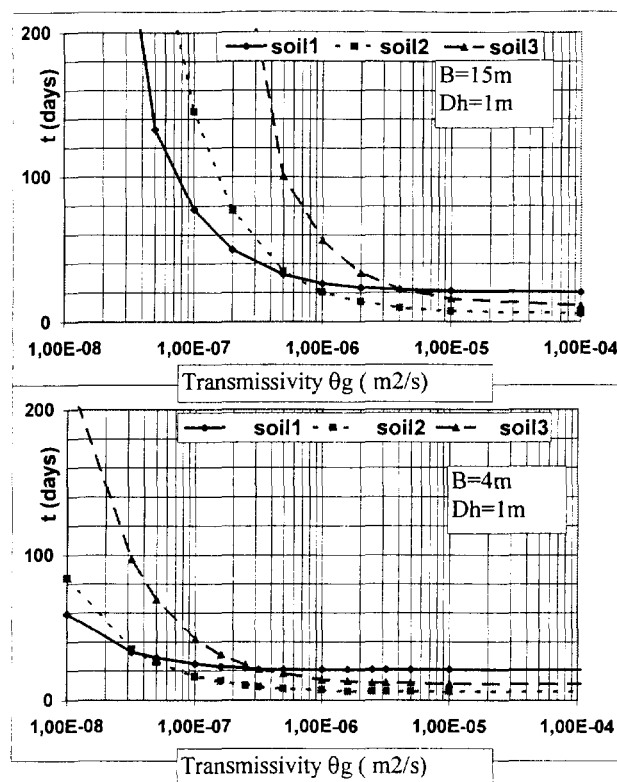


Figure 4: variation in dissipation time ( $\bar{u}(t)_{max} / \bar{u}(t=0) = 10\%$ ) as a function of transmissivity  $\theta_g$  ( $B = 4m, B = 15m$ ).

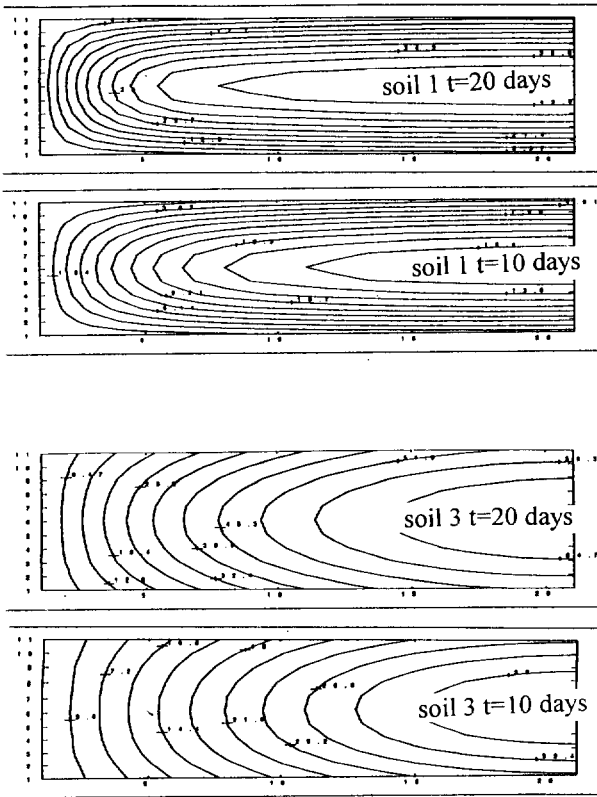


Figure 5: uplift pressure distribution in soil 1 and soil 3 ( $\theta_g = 10^{-7} \text{ m}^2/\text{s}$ ,  $B=4\text{m}$ ,  $d_h=1\text{m}$ , two times 10 and 20 days)

### 5.2 Influence of a localized decrease of $\theta_g$

We show the influence that could have a localized reduce of the DFG transmissivity. This decreasing could be produced: by a local damage of the drain, a decreasing of the thickness of the drain induced by a construction blemish, a water moisture penetration difficulty of the drain. This last phenomena was already observed for non-woven geosynthetics.

We had solved this problem with a numerical method;  $\theta_g$  is locally reduced: ( $\theta_g$  locally reduced =  $\theta_g/100$ ) in the application treated. In function of the place of the damage, we had an uplift pressure discontinuity in the damage DFG: the uplift pressure is increased at the back and is decreased in front of the damage, in comparison with undamaged DFG (Figure 6). This induce an over distribution of the water flow in the soil-DFG composite: the uplift pressure increase in the undamaged DFG and it is more efficient.

## 6 CONCLUSIONS

The use of draining-reinforcing dual-function geosynthetics (DFG) means that it is possible to consider employing poor quality soils to build reinforced-earth structures.

From this first original approach, the effect of the main parameters involved can be judged, although it should be

stressed that this is only the preliminary stage of research on this subject. An instrumented structure will have to be built and monitored to refine the hypotheses considered and modeling procedures in order to establish a necessary validation base.

## REFERENCES

- Auriault J.L., Cordary D., Giroud J.P., Gourc J.P. (1977) *Etude théorique du rôle des drains textiles dans la consolidation des remblais*. 1st International Conference on Soils and textiles, Paris, pp.273-278.
- Bourdillon M., (1976) *Utilisation des textiles non tissés pour le drainage, application aux remblais de sols fins en cours de consolidation*, Doctoral thesis, Lyon France
- Khay M. (1978) *consolidation de remblai au moyen d'un non tissé; Remblais expérimentaux*, rapport cete, Rouen France
- Gotteland Ph. (1991) *Renforcement des sols par géosynthétiques: dimensionnement et validation*, doctoral thesis Grenoble, France
- Gotteland Ph., Gourc J.P., Aboura A. (1996) *Benefits of using Dual-Function Geosynthetics in the design of multi-layer Structures* Proceedings Geofilters'96, Montreal, pp 553-562

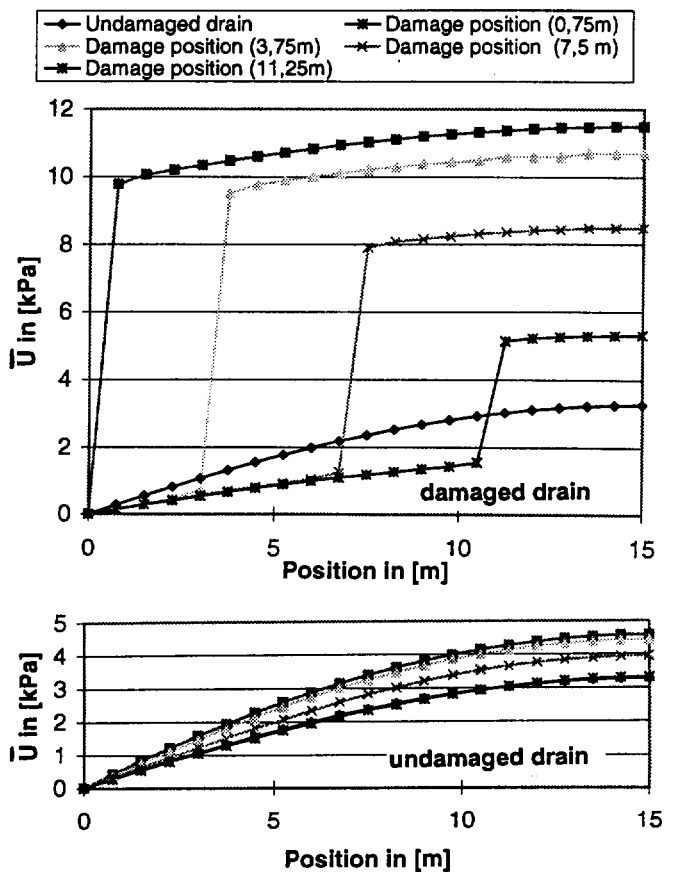


Figure 6: uplift pressure in the damaged and undamaged DFG ( $\theta_g$  locally reduced =  $\theta_g/100$ ,  $\theta_g=10^{-7} \text{ m}^2/\text{s}$ ,  $B=15\text{m}$ )

# The Mobilized Strength of Prefabricated Vertical Drains

W. Voskamp  
Akzo Nobel Geosynthetics bv

G. Troost  
Akzo Nobel Geosynthetics bv

G. R. Koerner  
Geosynthetic Research Institute, Drexel University, Philadelphia, PA USA

**ABSTRACT:** This paper focuses on the mobilized strength of prefabricated vertical drains, or PVDs, and is based on the results of theoretical, laboratory and field testing on prototype PVDs. Used herein are PVD simulated units known as load-elongation measuring strips, or LEMS. Results of the paper show that the typical strength of commercially available PVDs are well in excess of the required strength when installed by properly functioning construction equipment.

**KEYWORDS:** Drainage, Wick Drains, Tensile Strength and Survivability

## 1 INTRODUCTION

PVDs have replaced conventional sand drains over the past 20 years, by providing an economical solution to rapidly consolidate fine grained saturated soils. When building on such compressible soils, large settlements are anticipated. As the soil cannot compress at a greater rate than release of the excess pore water pressure, such settlement can continue for a long period of time. PVDs are used to expedite this release of pore water hence they decrease the time for settlement and greatly facilitate the stabilization of such sites.

PVDs are approximately 100 mm wide by 2 to 5 mm thick. They are delivered on site in large rolls. Most PVDs consist of a synthetic drainage core surrounded by a nonwoven heat bonded or mechanically bonded geotextile filter. They are installed vertically in the ground by a pile driving type of construction equipment known as a "wick sticker". Spacings are typically at 1 to 5 m throughout the soil to be stabilized. The length of the drains are site specific but usually extend to the bottom of the soft soil involved.

Once the PVDs are installed over a large area, a surcharge load is placed on the ground surface to mobilize excess pore water pressure in the foundation soil. The expulsion of the water is coincident with consolidation of the soil resulting in settlement at the ground surface. Additional surcharge load is placed in incremental lifts in accordance with the design requirements. The duration of the load depends on the soil characteristics, PVD spacing and type of PVD utilized.

There is a wealth of information available on the technique and a tremendous number of PVDs have been successfully installed around the world. The design method for determining the consolidation time versus PVD spacing as well as the required flow rate has been fully described in the literature. For example, Hansbo [1979]

has developed the relationship usually used to determine the PVD spacing as a function of the desired consolidation time. Holtz, et al. [1991] has given guidance on the flow rate capacity of PVDs in the unkinked and kinked conditions.

Conversely, the mechanical strength requirements of PVDs has seen little quantitative analysis and discussion. The only reference, Kremer, et al. [1983], reports the need for a PVD tensile strength of 500 N at a corresponding minimum strain of 2%. They also suggest a maximum strain of 10%. This upper strain limit is imposed in order to avoid unwanted deformations that might compromise the drain's dimensions and thus flow capacity. The technical background for these tensile strength and strain values is not known. Thus, the pursuit of a more rigorous numerical and experimental treatment of the tensile strength requirements during installation of PVDs is the purpose of this paper.

The tensile strength of PVDs is a consideration both during installation and during consolidation. Installation challenges the drain's strength as it threads through rollers of the wick sticker. The strength of the PVD is also challenged during the mandrel withdrawal process. Both of these situations are exacerbated by high installation speeds. In addition, the tensile strength may also be an issue when the drains are collectively used to resist a circular arc failure of the weak, sensitive soil. A large number of PVDs "sewn into the ground" and working as a unit will intercept and resist such a circular arc failure. This, however, is a design issue and is not addressed in this paper.

The paper will describe theoretical, laboratory and field research aimed at determining the mobilized strength of PVDs. The paper will conclude with generic recommendations on the required strength of PVDs based on the results of this investigation.

## 2 INSTALLATION

Typical equipment used to install PVDs is shown in Figure 1. Lighter trackhoe mounted units are sometimes used when the PVDs are relatively short, e.g., less than 15 m deep. Collectively, we will refer to all PVD installation equipment as "wick stickers". Wick stickers contain a mandrel which encases and carries the PVD while it is being driven. Mandrel designs are product specific. Rhombic mandrels with tapered ends are often used for high speed driving in soft soils. T-shaped mandrels reinforced with a longitudinal steel fin and fitted with harden steel driving tips are used when hard surface layers need to be penetrated. Mandrels are designed to minimize disturbance of the ground and to reduce smear and remolding of the soil adjacent to the PVD.

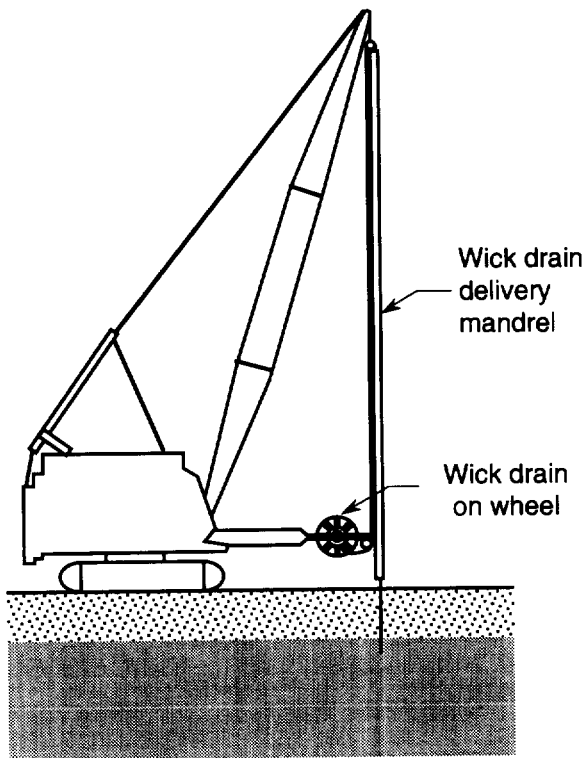


Figure 1. PVD installation rig, a wick sticker.

At the bottom of the mandrel the PVD is fixed to an end assembly that remains in the ground as the mandrel is withdrawn. The purpose of the end assembly is to keep the PVD fixed at the bottom of the soil layer while at the same time keeping soft soil from entering the mandrel as it is driven.

## 3 THEORETICAL CONSIDERATIONS

PVDs strengths are challenged during installation partly from the drain's self weight and partly from friction between the drain and various parts of the installation equipment. Worst case scenarios are envisioned as maximum forces are developed in the PVD when the mandrel accelerates from a full stop to full speed. Four limiting conditions are identified. These conditions are when the drain is pulled from the roll, as the drain passes through the conveyance system and under the lower roller, as the drain passes over the fixed cylindrical guide roller at the top of the rig, and when the mandrel is retrieved from the penetrated soil leaving the PVD in place.

The first condition investigated is when the drain is initially pulled off the roll. This is a process where the drain is drawn into the mandrel of the installation equipment. This incremental rather than continuous process requires the use of peak rather than average speed for the calculations. By using an angular acceleration of the roll with peak velocity of the wick sticker, a required force of only 14 N is mobilized in the PVD. This occurs at the beginning of each drive when there is a full roll of drain on the reel. The situation is analytically suggested to be as follows:

Velocity of Roll

$$V_{ave} = \frac{L}{D} = \frac{18\text{m}}{18\text{sec}}$$

$$V_{ave} = 1\text{ m / sec}$$

$$2\left(\frac{1}{2}(1)V_{peak}\right) + 16\text{ 1 / peak} = 18$$

$$V_{peak} = 1.06\text{ m / sec}$$

Acceleration of PVD Roll

$$a = \frac{V_{peak}}{t} = \frac{1.06\text{ m / sec}}{1\text{ sec}} = 1.06\text{ m / sec}^2$$

$$\alpha = \frac{a}{r} = \frac{1.06}{0.6} = 1.77\frac{\text{rad}}{\text{sec}^2}$$

Center of Gravity of PVD Roll

$$k^2 = \gamma^2 + r^2$$

$$k = \sqrt{(.1)^2 + .6^2}$$

$$k = 0.61\text{ m}$$

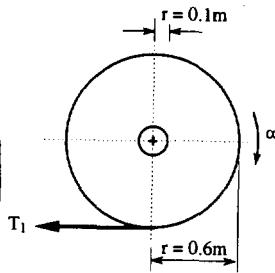
$$\text{mass}_{\text{max}} = m = 25\text{ kg}$$

$$\Sigma M_o = I\alpha$$

$$T_1(0.6) = \frac{1}{2}mk^2\alpha$$

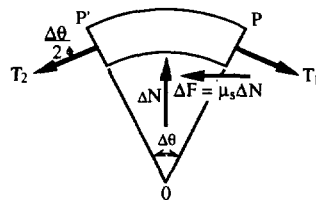
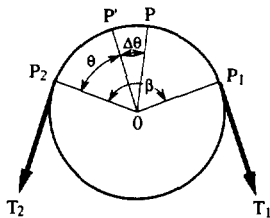
$$T_1 = \frac{1}{0.6} \left[ \frac{1}{2}(25)(0.61)^2(1.77) \right]$$

$$T_1 = 13.6 \text{ N}$$



Note, this is the maximum force due to the fact that  $m$  and  $\alpha$  decrease as the drain is utilized off of the roll.

In the second condition, the drain passes through the conveyance system and under the lower roller. There exists a relationship between the tension in the drain before it enters and after it leaves the roller. This relationship is based on the assumption that the drain is just about to slide into motion. By taking a free body diagram of a small element of the drain the forces acting on the drain are the two forces of tension, the normal component of the reaction of the roller and the friction force. A relationship is obtained knowing that motion is imminent by letting the angular change of the drain approach zero. As seen in the following calculations, only 25 N of strength is required of the PVD in such a condition.



$$\Sigma F_x = 0: (T + \Delta T) \cos \frac{\Delta\theta}{2} - T \cos \frac{\Delta\theta}{2} - \mu_s \Delta N = 0 \quad (1)$$

$$\Sigma F_y = 0: \Delta N - (T + \Delta T) \sin \frac{\Delta\theta}{2} - T \sin \frac{\Delta\theta}{2} = 0 \quad (2)$$

Solving Eq. 2 for  $\Delta N$  and substituting Eq. 1

$$\Delta T \cos \frac{\Delta\theta}{2} - \mu_s (2T + \Delta T) \sin \frac{\Delta\theta}{2} = 0$$

Divide by  $\Delta\theta$

$$\frac{\Delta T}{\Delta\theta} \cos \frac{\Delta\theta}{2} - \mu_s \left( T + \frac{\Delta T}{2} \right) \frac{\sin(\Delta\theta / 2)}{\Delta\theta / 2} = 0$$

Let  $\Delta\theta$  approach zero

$$\frac{dT}{d\theta} = \mu_s T = 0 \quad \frac{dT}{T} = \mu_s d\theta$$

By integration

$$\ln \frac{T_2}{T} = \mu_s \beta \quad \text{or} \quad \frac{T_2}{T} = e^{\mu_s \beta}$$

Given

$$\beta = \pi \text{ rad, and}$$

$$\mu_s = 0.2$$

Since:

$$F = T_1 = 13.6 \text{ N}$$

Therefore the PVD experiences the following after it exits the lower roller

$$T_2 = e^{\mu_s \beta} T_1$$

$$T_2 = e^{(.2)(3.14)} (13.6)$$

$$T_2 = 25 \text{ N}$$

In the third condition, the PVD is considered to be sliding over the roller at the top of the rig. The tensile force in the PVD is calculated by assuming geometric and frictional characteristics of an upper roller for typical construction equipment. The calculations are similar to that of the lower roller. Liberties were taken in estimating the frictional characteristic of the roller. Conservative values were chosen assuming that the roller would seize-up and become partially fixed. Regardless of these conservative assumptions, a relatively low force of 47 N was mobilized in the PVD for this condition.

Upper Roller

$$T_3 = e^{\mu_s \beta} T_2$$

$$T_3 = e^{(.2)(3.14)} (25)$$

$$T_3 = 47 \text{ N}$$

The fourth condition is when the mandrel is withdrawn and pulled out of the soil leaving behind the drain and its end assembly. As stated previously, the end assembly anchors the PVD and keeps soft soil out of the mandrel. It is possible, however, that some soil can enter the bottom of the mandrel. This in turn will impede release of the drain and subject it to a tensile force by snagging the PVD at the tip of the mandrel. Assuming such a condition exists, the end assembly constitutes the resisting force, where the

friction caused by the soil in the end of the mandrel constitutes the driving force. The calculation and assumptions associated with this condition follows. This worst case scenario results in a mobilized strength of approximately 103 N in the PVD.

### 3.1 Friction in the Mandrel

Using Mohr-Coulomb criteria

$$\tau = \sigma_n \tan \phi + c$$

$$\tau = c \text{ assuming } \phi = 0$$

$$\tau = c = 10,000 \text{ Pa for typical soft clay}$$

$$\Sigma F_y = T_4 - 2\tau e A = 0$$

$$T_4 = 2\tau e A$$

$$T_4 = 2(10,000)(30\%)(.1)$$

$$T_4 = 600 \text{ N}$$

However can such a force be mobilized in the drain?

### 3.2 Bearing Capacity of End Rod

$$Q_o = Q_p + Q_s$$

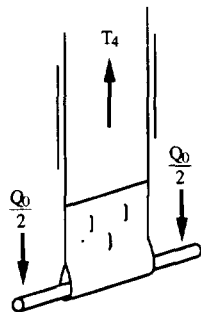
$$Q_o = A_p p_o + 0$$

$$Q_o = A_p (cN_c + 9N_a)$$

$$Q_o = .002(10,000)(5.14)$$

$$Q_o = 103 \text{ N}$$

Since  $Q_o \ll T_4$ ,  $T_4$  will never be mobilized and therefore  $Q_o$  governs



## 4 LABORATORY INVESTIGATION

The purpose of the laboratory investigation was twofold; to verify, or refute, the theoretical values just calculated (wherein many assumptions were required) and to develop a means of determining the mobilized strength of PVDs in the field. To aid us in these pursuits, we constructed a laboratory wick sticker simulator. A schematic diagram of the laboratory wick sticker simulator is shown in Figure 2. The simulator was constructed in the high bay region of GRI's soils laboratory. The high bay allowed for an upper fixed roller height of 10 m above the floor level.

By positioning a load cell at different locations along the PVD path, one could check the mobilized strength of the drain along the path. Results from this exercise showed that the first, second and third conditions resulted in average load cell responses of 10 N, 18 N and 150N

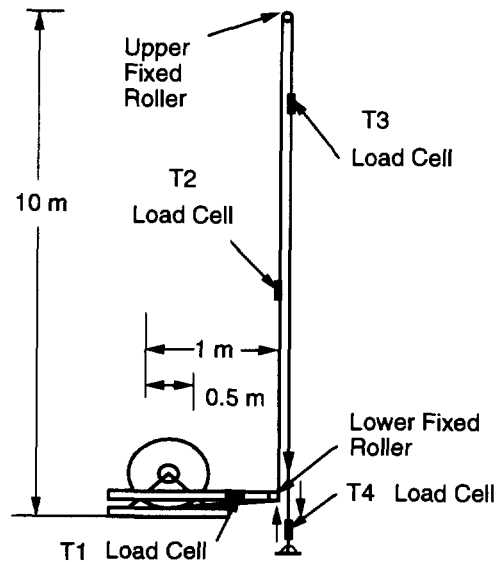


Figure 2 Schematic of laboratory wick sticker simulator.

respectively. To simulate the fourth condition we had to make up a model in the soils lab of an end assembly attached to a PVD being pulled from a freshly remolded column of soft soil. The PVD experienced widely different loads in this simulation depending on the amount of friction imparted in the mock mandrel. Loads in the PVD varied from 25 to 250 N.

These laboratory simulations were interesting, however, it was clear that we could not use the load cell out in the field. It was too cumbersome and fragile to withstand the rigors of field work. Hence we set out on developing a means of determining the mobilized strength of PVDs remotely. Six different techniques were attempted to measure the load elongation response of the PVD. They included:

- Foil strain gages similar to those used by Risseeuw [1986] and Guglielmetti, et al. [1996]
- Load sensitive film which changes color upon being stressed to different levels
- Spray applied coatings which crack to varying degrees after being stressed
- Hole punching to reduce PVD strength
- Side cutting PVD to incrementally reduce its strength
- Development of a simulated PVD unit called "Load-Elongation Measuring Strip" (LEMS)

Of all the techniques attempted, the LEMS showed the most promise. This specially prepared PVD consisting of a polyamide (3 x 3) grid fabric as a core, heat bonded between two 160 g/sq. m. nonwoven PET geotextiles. At 2 m intervals along the LEMS, the geotextile was cut away and specific number of polyamide yarns were cut. This left known numbers of yarns intact which allowed the LEMS to



model progressively weaker PVDs. This procedure was used to develop the curves shown in Figure 3. From this data an average breaking strength of 78 N per yarn was obtained. For comparison purposes, Figure 4 shows the tensile strength behavior of commercially available PVDs. For all tests of Figure 3 and 4 the gage separation was maintained at 100 mm and the strain rate was 10 mm/min.

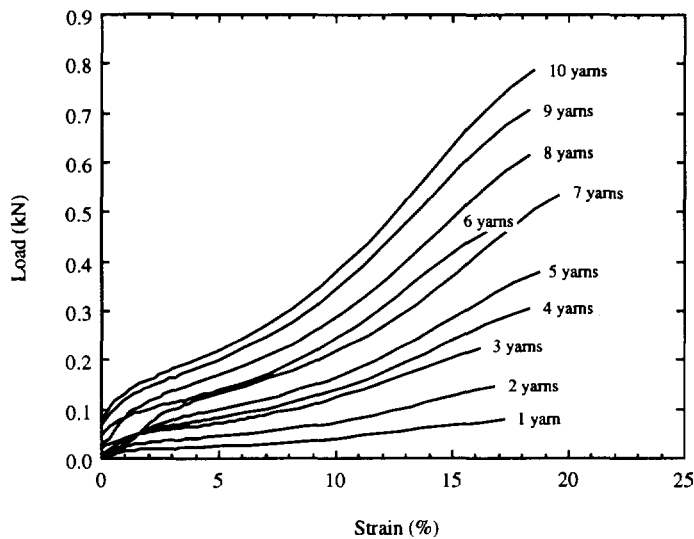


Figure 3 Load elongation behavior of LEMS.

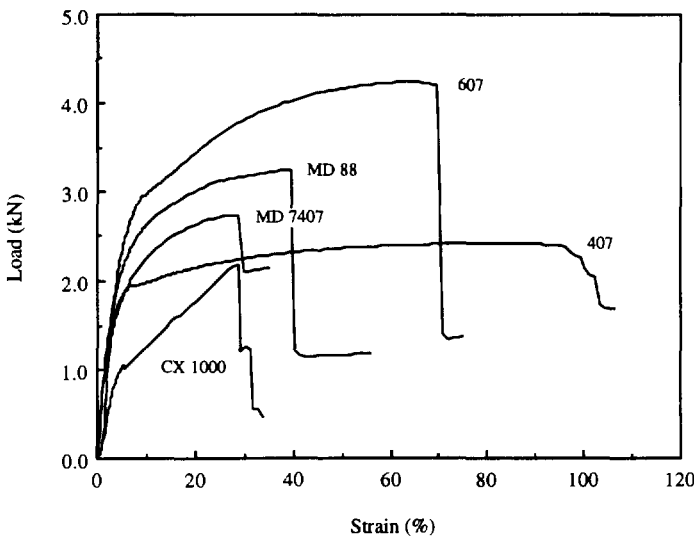


Figure 4 Commercially available PVD load elongation responses.

With the LEMS now calibrated insofar as its strength per yarn is considered, laboratory trials on the wick sticker simulator were undertaken. In conducting these trials friction in the rolls was increased using a brake and weight assembly to sequentially cause failure of the LEMS. The results of approximately 27 trial runs (with different numbers of uncut yarns) provided the results of Figure 5. The trend is linear resulting in a slope of 75 N per yarn. This roughly agrees with the tension testing in the constant rate of extension machine as noted previously. Equipped with this confirmation, we took the LEMS to the field to try and verify our theoretical and laboratory findings.

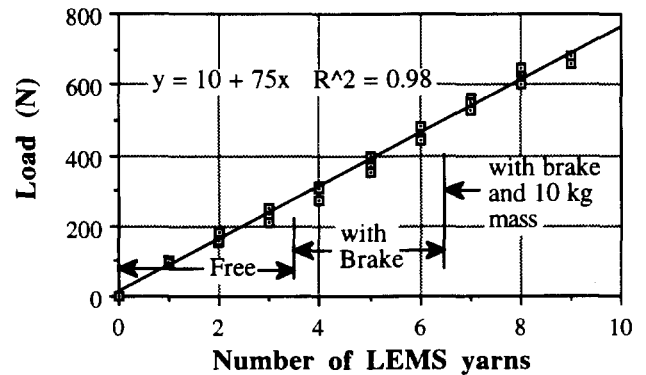


Figure 5 Results of LEMS calibration on simulator.

## 5 FIELD INVESTIGATION

Field trials with the LEMS material were conducted at a major soft soil stabilization project at the Philadelphia International Airport. Through the cooperation of Day & Zimmerman Infrastructure, Inc. and Geotechnics America, Inc. (the PVD contractor) a field trial of the LEMS was conducted in October of 1997.

As reported by Koerner [1997], the results of the field work are summarized in Table 1.

Table 1 - Field Behavior of LEMS at the Philadelphia International Airport.

No. of Yarns in LEMS	Resulting Strength of LEMS (N)	No. of Repeat Trials	Result of Each Trial
20	1540 N	2	pass/pass
14	1080 N	2	pass/pass
10	770 N	3	pass/pass/pass
5	390 N	3	pass/pass/pass
3	230 N	2	fail/fail

The results of Table 1 indicate that the mobilized PVD strength for this particular construction equipment and site condition is between 390 and 230 N. It must be clearly stated that it is believed that site conditions and

construction equipment will influence results. However, these limited results are insightful none-the-less.

## 6 SUMMARY AND CONCLUSION

It appears from theoretical calculation, laboratory testing and a limited field investigation that the strength of most commercially available PVDs are greater than required for installation. In addition, it appears that the current trend of increasing the strength requirements of PVDs is unfounded. At present, there does not appear to be any tangible reason for increasing PVD strengths over and above those that are currently being manufactured. For example, Figure 4 indicates that available PVD tensile strengths are from 2000 to 4000 N. Most commercially available PVDs meet or exceed equipment imposed installation stresses as demonstrated in this paper.

In light of the low values of mobilized PVD strengths developed in this study, e.g.,

- theoretically: 14 to 103 N
- experimentally: 10 to 250 N
- field: 230 to 390 N

we are confident in stating that there is an inherent factor of safety for most commercially available PVDs. Of all installation conditions described, it appears that withdrawal of the mandrel is the governing strength condition. Loads during withdrawal of the mandrel are site specific. They depend on the type of anchor plate and will only take place at the tip of the PVD where it connects with the end assembly.

The requirement for discharge of water at this location is limited since it is at the end of the drain. The load in the rest of the drain is probably less than 230 - 390 N. It is interesting to note that this corresponds with an elongation of approximately 2-4% for most PVD.

It is concluded that all commercially available drains have strengths and elongation's at break which are much higher than necessary. Hence, the available factors of safety for mobilized strength is in the range of 4 to 11. We question if the higher factors of safety are warranted in the event that ones construction equipment is functioning properly and geometrically equipped to drive the specific PVD delivered to the specific job site.

## ACKNOWLEDGMENTS

The research project was carried out under the general support of the GSI consortium of member organizations. Appreciation is extended in this regard. The authors would like to specifically thank Mr. Timothy Kruppenbacker, construction manager of Day and Zimmermann, Inc. and Mr. John Case, controller of

Geotechnics America, Inc. for their assistance with our field effort.

## REFERENCES

- Guglielmetti, J. L., Koerner, G. R. and Battino, F. S. (1996), "Geotextile Reinforcement of Soft Landfill Process Sludge to Facilitate Final Closure: An Instrumented Case Study," Proceedings of GRI-9 Conference on Geosynthetics in Infrastructure, Enhancement and Remediation," R. M. Koerner and G. R. Koerner, Eds., GII Publ., Philadelphia, Pennsylvania, USA.
- Hansbo, S. (1979), "Consolidation of Clay by Band Shaped Prefabricated Drains," *Ground Engineering*, Vol. 12, No. 5, pp. 21-25.
- Holtz, R. D., Jamiolkowski, B., Lancellotta, R. and Pedroni, R. (1991), "Prefabricated Vertical Drains: Design and Performance," Butterworth Heinemann, London.
- Koerner, G. R. (1997), "Field Installation of Prefabricated Vertical Drains," Proceedings of GRI-11 Conference on Installation of Geosynthetics, R. M. Koerner Ed., GII Publication, Philadelphia, Pennsylvania, USA.
- Kremer, R. J., Oostveen, J. P., Van Weele, A. F., DeJager, W. J. and Meyvogel, I. J. (1983), "The Quality of Vertical Drainage," Proceedings of the Eight European Conference on Soil Mechanics and Foundation Engineering, Helsinki, Vol. 2, pp. 721-726.
- Risseuw, P., "Manual for the Attachment of Strain Gauges for Measuring Deformations of Stablenka Reinforcing Fabrics," Enka Industrial Systems, Holland, 1986, p. 23.

# Investigation on Some Factors Affecting Discharge Capacity of Prefabricated Vertical Drain

Norihiko MIURA

Professor, Department of Civil Engineering, Saga University, Saga 840, Japan

Jinchun CHAI

Associate Professor, Department of Civil Engineering, Saga University, Saga 840, Japan

Kiyomitu TOYOTA

Graduate Student, Department of Civil Engineering, Saga University, Saga 840, Japan

**ABSTRACT:** A series of laboratory tests have been conducted to investigate the effects of (a) trapped air bubbles in drainage path, (b) folding (no kinking) of drain, (c) confining drain by clay, and (d) elapsed time (long term), on discharge capacity of prefabricated vertical drain (PVD). The test results indicate that confining the drain by rubber membrane yielded a much higher discharge capacity than that in clay. It suggests that the discharge capacity test of PVD should be conducted by confining the drain in clay. Also, the discharge capacity reduces significantly with elapsed time, and the long term behavior of PVD should be considered in design. For most commercially available PVDs, a long term discharge capacity of less than 100 m<sup>3</sup>/year is tentatively suggested for design. The possible air bubbles trapped in the drainage path of PVD has some effect on discharge capacity, and the test data from this study showed about 20% reduction due to this factor. The folding of the drain does not have obvious influence on discharge capacity because it does not change both length and cross sectional area of drainage path much.

**KEYWORDS:** Prefabricated vertical drain, Laboratory test, Hydraulic conductivity, Drainage.

## 1 INTRODUCTION

Installing the vertical drain into ground can shorten the drainage length of the deposit significantly, and with some surcharge loading, the engineering properties, in terms of the compressibility and undrained shear strength, of the deposit can be substantially improved. The development of prefabricated vertical drain (PVD) has made this method more attractive due to the portability of the material and lower installation cost. During past few decades, vertical drain improvement has been widely used in soft soil engineering.

For a given soil condition, the behavior of vertical drain improved subsoil is controlled by: (a) drain spacing and equivalent drain diameter, (b) smear effect, and (c) discharge capacity of drain (well resistance). The drain spacing is a known factor and the equivalent drain diameter of PVD can be reliably calculated based on the geometry of the PVD. However, smear effect and discharge capacity have to be determined experimentally. At present, the method for determining the discharge capacity of PVD has not been standardized, and the values reported in the literature are not consistent. Most test methods confine the drain by rubber membrane, such as ASTM D4716-87, and determined values are usually high. However, some low values were reported for confining the drain in clay (e.g. Hansbo 1983). An ideal discharge capacity test should simulate the drain installation, confinement of clay on the filter sleeve of drain, and the deformation of drain during consolidation. It is obvious that a full scale test could be expensive if it is possible. For a small scale laboratory test to be valid, it must consider the important influence factors. In order to improve the laboratory test method and advance the prediction ability on the behavior of vertical drain improved

subsoil, there is a need to investigate the main influencing factors on discharge capacity of PVD.

In this paper, the effect of (a) possible air bubbles trapped in the drainage path, (b) folding (no kinking) of drain which most likely will occur in the field due to consolidation of soil, (c) confining the drain by clay, and (d) elapsed time (long term) on discharge capacity of PVD are systematically investigated. First, the unit cell (a drain surrounded by a soil cylinder) consolidation theory is briefly reviewed to indicate the effect of discharge capacity on the rate of consolidation. Then the laboratory test methods as well as results are presented. The suggestions are made on improving the test method on discharge capacity of PVD.

## 2 A BRIEF REVIEW ON UNIT CELL THEORY

The basic theory of vertical drain consolidation is unit cell theory which was first proposed by Barron (1948). Further studies on unit cell behavior were made by Yoshikuni and Nakanodo (1974) and Hansbo (1981). Since Hansbo's theory is relatively simple, it has been widely used. The derivation of the theory is based on equal vertical strain assumption. The resulting equation for average degree of radial consolidation ( $\bar{u}_h$ ) of a unit cell is as follows:

$$\bar{u}_h = 1 - \exp(-8T_h / \mu) \quad (1)$$

$$T_h = \frac{C_h t}{D^2} \quad (2)$$

$$\mu = \ln \frac{n}{s} + \frac{k_h}{k_s} \ln s - \frac{3}{4} + \pi \frac{2l^2 k_h}{3q_w} \quad (3)$$

Where  $C_h$  is the horizontal coefficient of consolidation,  $t$  is time,  $D$  is the diameter of unit cell,  $k_h$  is the horizontal permeability of soil,  $k_s$  is permeability in smear zone,  $l$  is drainage length,  $q_w$  is discharge capacity,  $n=D/d_w$ , and  $s=d_s/d_w$  ( $d_w$  is the diameter of drain, and  $d_s$  is the diameter of smear zone). The last term in Equation 3 represents the well resistance. It can be seen that the larger the discharge capacity,  $q_w$ , the smaller the well resistance, and the higher the rate of consolidation. For example, assuming  $l=15$  m and  $k_h=10^{-8}$  m/sec, if  $q_w$  is less than  $100$  m<sup>3</sup>/year, it will have a considerable influence on consolidation rate of vertical drain improved subsoil.

### 3 APPARATUS AND TEST METHODS

#### 3.1 Apparatus and Test Procedure

The apparatus used is a modified triaxial device as shown in Figure 1. The main cell has a diameter of 200 mm and height of 600 mm. The drain sample is set inside the cell similar to that of setting the triaxial test sample. The lower pedestal is fixed at the bottom of the cell and connected to the inlet water flow system. The upper pedestal is movable (for adjusting the length of drain sample) and connected to the outlet water flow system. The drain length can be

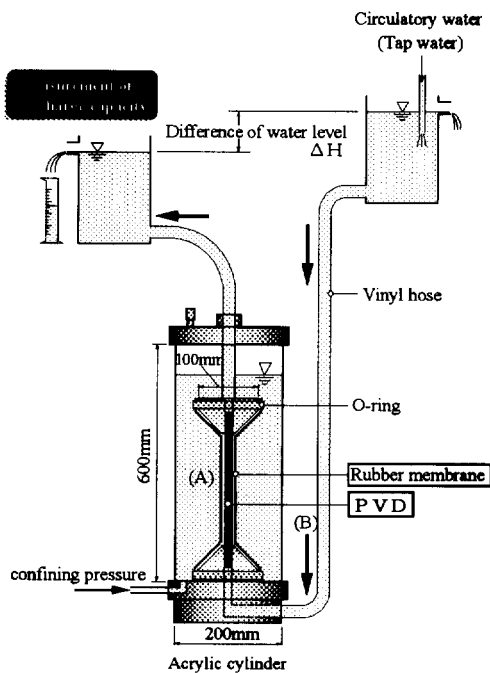


Figure 1. Set-up of discharge capacity test apparatus

tested is 200 mm to 400 mm. The shape of pedestal is made as: one end is cylindrical for fixing the membrane, and rectangular at another end to connect the drain. In this way, when confining the drain by rubber membrane, there will be no gap between membrane and drain. The length of drain inserted into the slot of upper and lower pedestal is about 30 mm each. The diameter of the pedestal is 100 mm. Except the main cell, there are inlet and outlet water containers. The inlet water container is linked with water supply system, and outlet water container is connected to discharge capacity measuring device. After the drain is installed, the cell is filled with water up to about 80% full, and confining pressure is applied by air pressure through an air pressure regulator. For investigating the effect of folding, the drain is folded at one and two point for 10% and 20% vertical strain, respectively. The methods for investigating the possible trapped air bubble effect and confining the drain by clay are described as follows.

#### 3.2 Method for Investigating the Effect of Trapped Air Bubbles

It is considered that installing a drain into ground, the water from soil gradually enters the drain along the whole length of the drain, and there might be some air bubbles trapped into drainage channels. In order to study the possible trapped air bubble effect, a simple air bubble generation device is newly developed. A thin plastic tube is connected to an air tank through an air pressure regulator. Then the tube is placed at the bottom of the drain sample through an inlet hose as shown in Figure 2. The amount of air bubbles generated can be controlled by adjusting the air pressure regulator. The generated air bubbles enter the drain following the water flow. The main test steps are:

- (1) Set-up the drain sample and apply the desired confining pressure as well as hydraulic gradient.

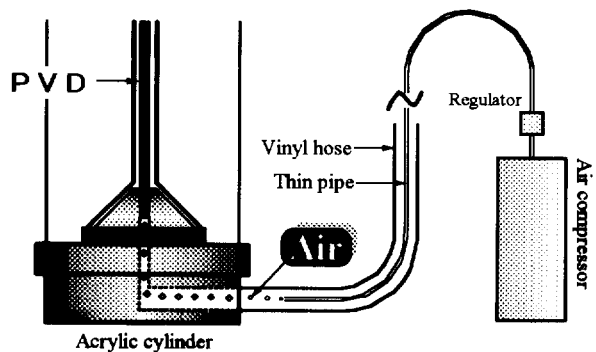


Figure 2. Method for generating air bubbles

- (2) Generate the air bubbles with a diameter of about 1 mm, and a speed of about 100 bubble/min. This process is continued for about 4-6 hours.

- (3) Close the air bubble generation system, and let the water flow continue for more than 2 hours to steady the flow. Then measure the discharge capacity.

### 3.3 Test Procedure for Confining the Drain by Clay

Hansbo (1983) recognized the importance of confining the drain by clay on determining the discharge capacity. However, due to convenience, most discharge capacity tests conducted by manufacturers are confining the drain by rubber membrane. One of the purposes of this investigation is to compare the discharge capacities determined by clay confinement and membrane confinement. The test method proposed in this study for testing the drain in clay is simple and can test the full size of drain. The following main steps are followed during test:

- (1) Connect the drain sample to lower pedestal, fix the membrane to lower pedestal also, and set the mould for preparing the clay sample in position.
- (2) Make clay sample. The remoulded clay with a water content close to the liquid limit is put into the mould layer by layer keeping the drain in the middle. The diameter of the clay sample is 100 mm. After the required height of clay sample is reached, the upper pedestal is installed and the drain is connected to outlet flow system. Care needs to be paid to prevent the contamination of the top of drain by clay.
- (3) Consolidate the clay sample. For removing the mould, a suction of about 10 kPa is applied to the clay sample. After confining pressure is applied, the suction is gradually released and the sample is left for consolidation under lateral pressure.
- (4) Measure discharge capacity. After the consolidation of clay sample is finished, the discharge capacity is measured under desired hydraulic gradient.

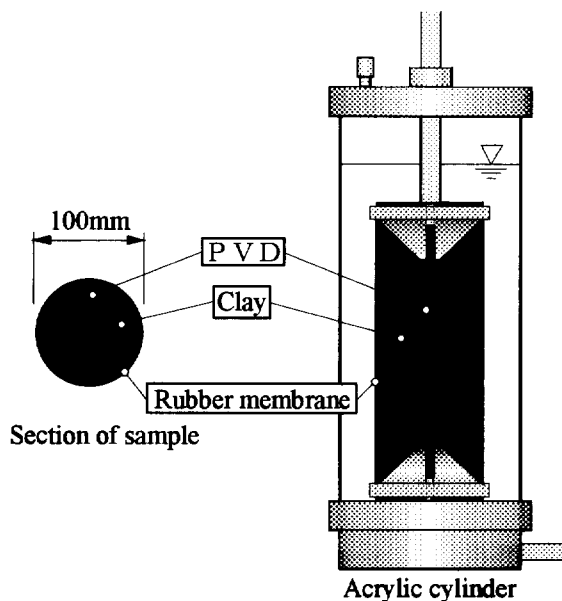


Figure 3. Set-up of confining the drain by clay

The set-up of the drain confined by clay is illustrated in Figure 3. With this method, a test with one consolidation pressure and several hydraulic gradients requires 10 days to complete.

### 3.4 Considering the Head Lose in Hose System


Another factor which has been noticed during the investigation is head loss in the hose of the test equipment. Since the discharge capacity of drain confined in membrane is normally high, ignoring the head loss in the hose does not introduce much error. For testing the drain in clay, which is close to field condition, the head loss in the testing system needs to be considered. The calibration of the head loss in the hose system can be made by conducting the test without installing a drain sample.

## 4 TEST RESULTS AND DISCUSSIONS

### 4.1 Materials Used

The PVD adopted in this study is a commercial products and its properties are summarized in Table 1. The soil used is remoulded Ariake clay. Its index properties are: specific gravity,  $\rho_s$ , of 2.60, plastic limit,  $w_p$ , of 42.8%, and liquid limit,  $w_l$ , of 105.0%. The soil consists of 57.0% clay, 41.7% silt, and 1.3% sand particles. The rubber membrane used has a thickness of 1.0 mm.

Table 1. Physical properties of PVD

Size (mm)	Thickness	2.6
	Width	94
Drainage channel	Depth(mm)	1.5
	Width(mm)	1.8
	No. of channel/drain	40
Unit weight (g/m)		90
Material	Filter	Spun bonded polyester
	Core	Polyolefin
Connection condition between filter and core		Fixed
Structure		

### 4.2 Short Term Test Results

For ease in quantifying each influencing factor, the test results of confining a straight drain in a rubber membrane are considered as basic ones and other test results are compared with them. The confining pressures for the basic test were 49 and 392 kPa, and hydraulic gradients were

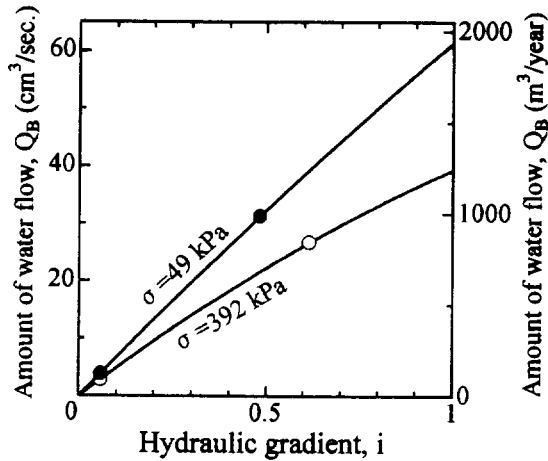


Figure 4. Results of basic test

about 0.08 and 0.8. The results are plotted in Figure 4. It can be seen that as a general tendency the discharge capacity is reduced with increased confining pressure. It is the same as the results reported in the literature (e.g. Hansbo 1987). If extrapolating the results to unit hydraulic gradient ( $i=1.0$ ), a discharge capacity of 1981  $m^3/year$  and 1307  $m^3/year$  can be obtained for confining pressures of 49 kPa and 392 kPa, respectively. The short term test results are summarized in Figure 5. A discharge capacity ratio is used in the figure, which is defined as the amount of water flow,  $Q$ , divided by the corresponding value of basic test,  $Q_b$  ( $Q/Q_b$ ). Following discussions can be made for short term test results.

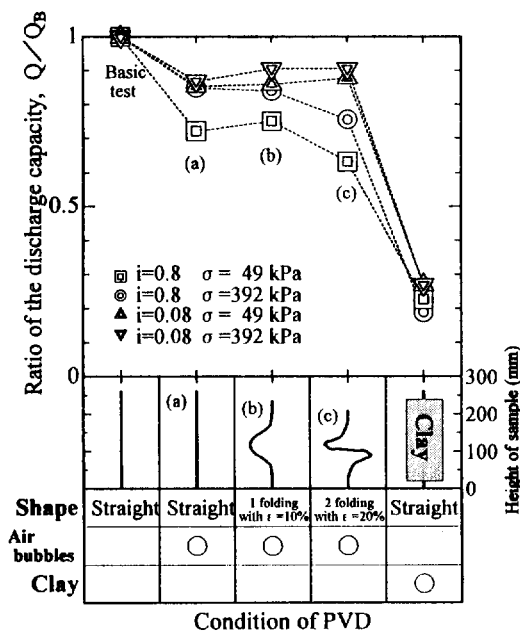


Figure 5. Summary of short term test results

(1) Confining the drain by a rubber membrane can not simulate the actual field condition and the discharge capacity test for determining the design value should confine the drain with clay. When confined by a rubber membrane, it results in a much higher discharge capacity than that in clay. For the case investigated, the clay value is only about 20% of membrane value. Three possible reasons for reduction on discharge capacity of PVD in clay can be considered.

(a) Reducing the cross sectional area of drainage channel due to deformation of filter under pressure. This has been considered as the main reason. After the test, it was observed that the filter was considerably deformed and the cross sectional area of drainage channel was reduced to 70-50% of original value as shown in Figure 6. The left side of Figure 6 was made by stamping the actually used soil sample on paper. Since the amount of reduction on cross-sectional area is a function of stiffness of filter, as a supplementary information, the tension force versus tension strain relationship of the filter was determined by the laboratory wide strip test, with a strain rate of about 1%/min as shown in Figure 7. For the case of confined in rubber membrane, due to the tension stiffness of membrane, filter can not deform as freely as that in clay.

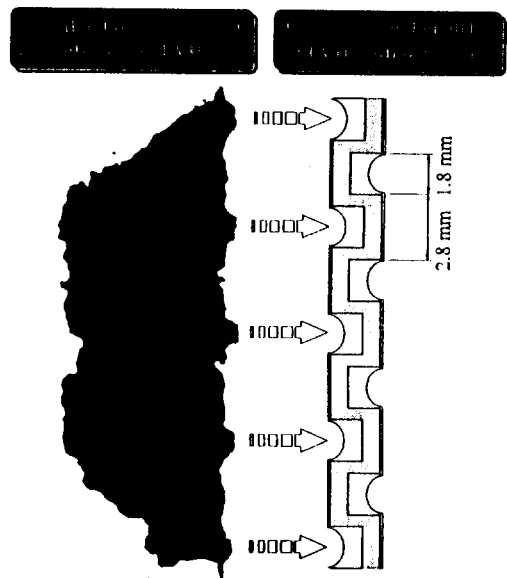


Figure 6. Deformed shape of clay sample adjacent to drain

(b) Reducing the conductivity of filter in longitudinal direction due to soil particles penetrating into the opening of filter. When confining the drain in rubber membrane, the filter may act as a part of vertical water flow path. In the case of confined by clay, the clay particles will enter the opening of the filter and reduce the conductivity of filter. Since the thickness

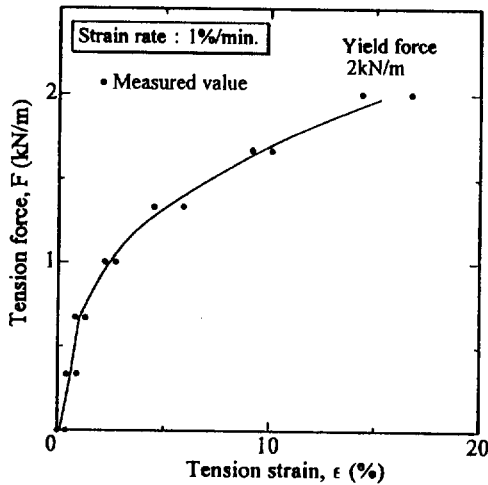


Figure 7. Tensile force versus tensile strain curve for filter

of the filter is only about 0.2 mm, this effect is a minor one.

(c) Clay particles enter the drainage channel. Although the most of filters commercially used satisfy the filtration criteria, the experimental evidence indicates that some amount of very fine particles entered the drainage path and forming loose flocculated sediments on the wall of drainage path. It is considered that the formation of the flocculated sediments is a function of chemical contents of clay.

(2) It seems that not much air bubbles can remain in the drainage path. The data from this study show that the trapped air bubbles reduced the discharge capacity about 20%.

(3) Considering a vertical strain up to 20%, the folding of the drain has minimal effect on discharge capacity, which supports the conclusion drawn by Hansbo (1983). This factor can be explained as the folding of the drain does not change both the length and cross-sectional area of drainage path much. The kinking was not considered in this study because it rarely occurs in the field.

#### 4.3 Long Term Test Results

Only one test of confining the drain in clay was tested for about 5 months. The conditions were: confining pressure of 49 kPa and hydraulic gradient of 0.08. This confining pressure approximately represents the lateral earth pressure in subsoil under a 5 m high embankment or at 10 to 15 m depth of natural subsoil. A lower hydraulic gradient is adopted because, in the field, the average value during consolidation process may not be high. The long term test results are shown in Figure 8, which indicate that the discharge capacity was continuously reduced with elapsed time except the last measurement point. It has been understood that in the interval between the last two measurements, the inlet hose (about 30 mm in diameter and flexible) had been stepped on several times unexpectedly.

Stepping on the water flow hose is just like applying pressure pulses to water flow system. It was observed that some flocculated fine particles were pressured (due to stepping) out of the drainage channel of drain and deposited on the wall of the outlet hose. Based on these results, it is considered that the reasons for the reduction of discharge capacity with elapsed time are (1) creep behavior of filter which reduces the cross-sectional area of drainage path, and (2) clogging caused by flocculated fine particles. As shown in Figure 8, for the case investigated, the creep effect is evaluated as the difference between last measurement point and the reading at about 1 week of elapsed time, which reduced the discharge capacity about 30%. The most reduction can be attributed to the clogging effect which is a function of soil type and filter type. The chemical analysis about the flocculated fine particles as well as the clay mineral is going on and the results will be reported in the future. The discharge capacity reduction with elapsed time was also reported by Koda et al. (1986) for confining the Geodrain in organic soils. For a drain, it is normally expected to work at least half a year. Therefore, in design, long term behavior of drain should be taken into account.

#### 4.4 Discussions

From this investigation, it shows that the most important factors affecting the discharge capacity of PVD are: (a) confining condition, and (b) the duration of test. Therefore, for determining the design value of discharge capacity, the test should be conducted by confining the drain by clay and tested for a longer period (may be few month). If comparing the results from this study with those reported in the literatures, the following comments can be made.

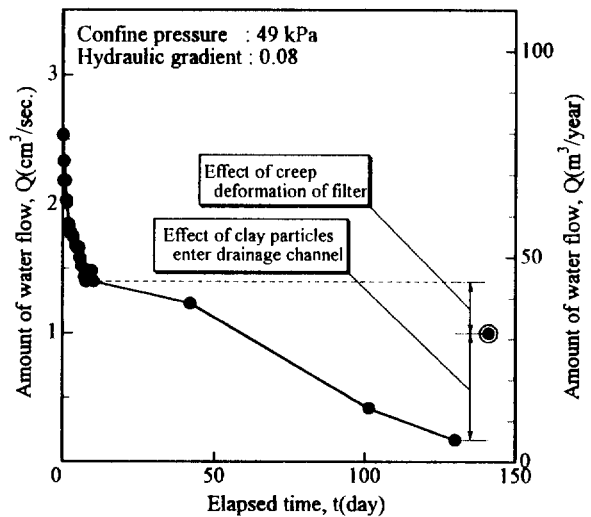


Figure 8. Long term discharge capacity test results

(1) The values of confining the drain by rubber membrane are comparable with the data reported by manufacturers. Due to the apparent high discharge capacity, it may be considered that the well resistance of PVD can be

ignored in design. However, the results of this study suggest that the high value for confining the drain by rubber membrane may not represent the field condition, and well resistance may be an important design factor, especially for long drains. The discharge capacity of confining the drain by rubber membrane may only be used as a quality control test.

(2) In clay short term (about 1 week) value of discharge capacity is in the lower range of the data summarized by Hansbo (1987). Comparing with the specifications about required discharge capacity as summarized by Bergado et al. (1996), it can be seen that with a discharge capacity of few hundreds  $m^3/year$ , the most specifications can be satisfied. However, the most specifications have no clear requirement about long term behavior.

(3) The long term in clay value (about 5 months) from this study is higher than the data reported by Hansbo (1983) by using the revised CTH (Chalmers University of Technology) method for the similar drain. The revised CTH method also confined the drain in clay with a test duration of less than 1 month. Whether the CTH method considered the head loss in the hose system is not clear, and if not, it might be the reason for the lower value of discharge capacity. The relative lower value of discharge capacity of PVD was also reported by Jamiolkowski et al. (1983). The field discharge capacity may vary with the type of drain, type of clay, and designed consolidation period, but as a rough reference, it is recommended that for most commercial PVD, a design discharge capacity of less than  $100 m^3/year$  can be used.

## 5 CONCLUSIONS

Four influence factors on discharge capacity of PVD are experimentally investigated. These factors are: (a) possible trapped air bubbles in drainage path, (b) folding of drain, (c) confining the drain by clay, and (4) long term behavior. From the test results, following conclusions can be drawn:

1. The discharge capacity of PVD confined in clay is significantly lower than that confined by rubber membrane. It is strongly recommended that for determining the design value, the discharge capacity test should be conducted by confining the drain in clay. The test of confining the drain by rubber membrane not represents the field condition and it might be used for quality control purpose only.
2. The discharge capacity of PVD reduces significantly with elapsed time. For the case investigated, the

long term minimum value is only about 10% of the value at 1 week. This indicates that for design vertical drain improvement, long term behavior of PVD should be considered. For most commercial PVD, a design long term discharge capacity of less than  $100 m^3/year$  is tentatively suggested.

3. The possible air bubbles trapped in drainage channel has an effect on discharge capacity. For the case investigated, it shows that the discharge capacity was reduced by about 20% due to the effect of trapped air bubbles.
4. The folding of drain does not influence discharge capacity significantly because it does not change both the length and cross sectional area of drainage path much.

## REFERENCES

- Barron, R. A. (1948) "Consolidation of fine-grained soils by drain wells", *Trans. ASCE*, Vol. 113, pp. 718-742.
- Bergado, D.T., Manivannan, R., and Balasubramaniam, A.S. (1996) "Proposed criteria for discharge capacity of prefabricated vertical drain", *Geotextiles and Geomembranes*, Vol. 14, pp. 481-505.
- Hansbo, S. (1981) "Consolidation of fine-grained soils by prefabricated drains", *Proc. 10th Int. Conf. Soil Mech. and Found. Eng.*, Stockholm, Vol. 3, pp. 677-682.
- Hansbo, S. (1983) "How to evaluate the properties of prefabricated drains", *Proc. of 8th ECSMFEE*, Helsinki, Vol. 2 pp. 621-626.
- Hansbo, S. (1987) "Design aspects of vertical drains and lime column installations", *Proc. of the 9th southeast Asian Geotechnical Conference*, Bangkok, Vol. 2, pp. 8-1 to 8-12.
- Jamiolkowski, M., Lancellotta, R., and Wolski, W. (1983) "Pre-compression and speeding up consolidation, General Report", *Special Session 6, Proc. Eighth Europe Conf. Soil Mech. and Found. Engrg.*, Rotterdam, A.A. Balkema, pp. 1201-1226.
- Koda, E., Szymanski, A., and Wolski, W. (1986) "Laboratory tests on Geodrains durability in organic soils", Seminar on Laboratory Testing of Prefabricated Band-Shaped Drains, Milan, Italy.
- Yoshikuni, H. and Nakanodo, H. (1974) "Consolidation of soils by vertical drain wells with finite permeability", *Soils and Foundations*, Vol. 14, No. 2, pp. 35-46.



# Design of a New Geocomposite Vertical Wick Drains for Ground Improvement

J. N. Mandal

Department of Civil engineering, Indian Institute of Technology, Powai, Mumbai-400076, India.

V. S. Kanagi

Department of Civil engineering, Indian Institute of Technology, Powai, Mumbai-400076, India.

**ABSTRACT:** During the past few decades, an increasing need has arisen for various types of civil engineering projects on construction sites underlain by thick deposit of soft cohesive soils. Parallel to the development of the sand drains, different types of prefabricated vertical strip drains were developed and were used exclusively in various projects. In this paper, a new cylindrical prefabricated geocomposite drain (environmental friendly coir and jute) has developed and can be used to accelerate the consolidation of soil thereby making the site available for the use in short time. The relatively low cost of manufacture and installation makes this drain quite attractive. A design methodology has been developed and the results are presented in the form of design charts for the handy use.

**KEYWORDS:** Prefabricated vertical drains, Soft soils, Drainage, Filtration, Geocomposite.

## 1 INTRODUCTION

In the recent years many civil engineering projects have been under-taken on the sites which are underlain by thick deposits of soft cohesive soils. In such situations a ground improvement technique is essentially needed to provide adequate soil properties viz., bearing capacity and tolerable post construction total and differential settlements. Preloading and precompression are frequently used in combination with vertical drains, (Hausman, 1990. Holtz, 1987 and Johnston, 1970) especially in areas of very thick deposits of soft soils with high percentage of moisture content. The main purpose of vertical drains is to accelerate the consolidation time by shortening the drainage path. Usually sand drains are used for these purposes (Bergado, et al., 1992). The prefabricated drains were first introduced into the field of geotechnical engineering by Kjellman (1948). Improvement of the Kjellman wick drain included using a grooved plastic core in place of cardboard.

The various types of prefabricated vertical drains, their common installation methods and pertinent characteristics have been documented. (Jamiolkowski et al., 1983 and Koerner, 1994). Most of the prefabricated drains made of natural materials viz., jute and coir has also been studied. (Lee et al., 1989; Ramaswamy, 1994; Dastidar, 1969; Dinesh Mohan, 1977; Sengupta, 1980 and Mandal and Shiv, 1992). As two components of natural geocomposite drains (i.e. jute and coir) are readily available in the Indian subcontinent at low cost, an attempt has been made in the present paper to develop a new design methodology to install geocomposite drains in soft cohesive soils. The design charts are also presented for handy use.

## 2 GEOCOMPOSITE DRAINS

Generally geocomposite drains are made of synthetic materials, yet some geocomposite drains are made of natural fibre extracted from jute and coir. Different configurations of natural geocomposite drains are shown in Figure-1. The schematic diagram of a natural geocomposite drain for which the nomogram is developed is shown in Figure-2.

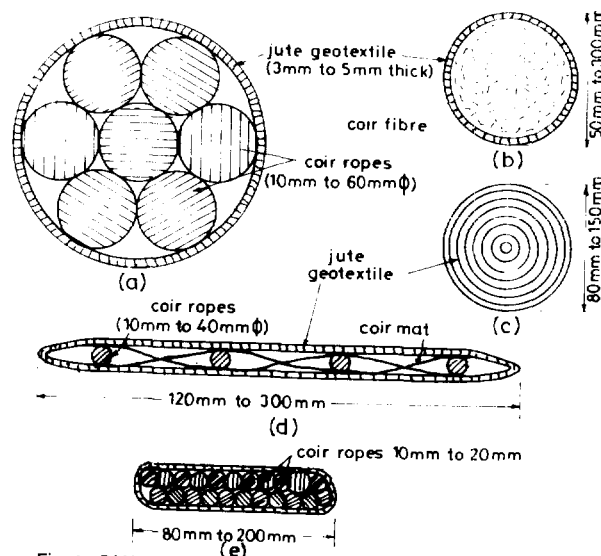


Fig. 1. Different types of geocomposite drains

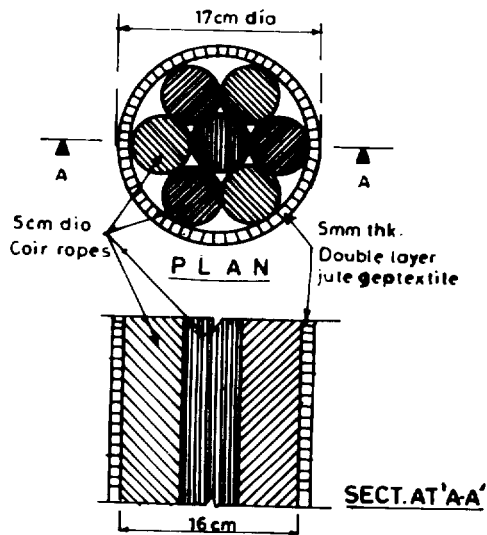


Fig. 2 Geocomposites vertical wick drain

Seven coir ropes of diameter 10mm to 60mm are grouped to form one geocomposite drain. These ropes are tied with jute rope at a spacing of 60cm. This group of coir rope is then wrapped with double layer of jute geotextile. The geocomposite drain diameter varies from 50mm to 200mm. The coir ropes provide longitudinal channels to allow percolation where as the filtering quality of the drain is furnished by the two jute burlap layers.

This geocomposite drain can be designed and manufactured to suit the needs of the specific requirements of different soil improvement projects. It is flexible, rugged, resistant to clogging adequately strong in tension and sufficiently durable. The properties of this geocomposite drain and a typical natural soil are given in Table 1. Jute and coir are by nature strong and not easily decomposable under adverse environmental conditions. The geocomposite drain is relatively resistant to chemical action and loses its strength usually after two years of installation in soft marine clay. (Ramaswamy, 1994)

Table 1 Properties of geocomposite drain and soil

a) Material

1) Jute fibre

Thread diameter : 1.5 to 2.0 mm  
weight: 450 g/m<sup>2</sup>  
Tensile strength = 13 KN./m

2) Coir rope

Rope diameter: 10mm to 60mm.  
weight: 350 g/m<sup>2</sup>  
Tensile strength = 11 KN./m

b) Geocomposite drain

- i) Components : seven number of coir ropes of diameter 10mm to 60mm wrapped by double layer jute geotextile.
- ii) Diameter: 100mm to 200mm.
- iii) Filter cover permeability  $> 10^{-3}$  cm/sec.
- iv) Axial permeability :  $> 10$  cm/sec for confining pressure up to 330 KN /sq.m

c) Marine clay

specific gravity = 2.65  
liquid limit = 78%  
plastic limit = 38%  
plasticity index = 40%

2.1 Function of Natural Geocomposite Drain

The function of geocomposite drains are:

1. The jute fiber has the capacity to accept water through the filter jacket and work as water absorbent material.

2. The coir has the capacity to discharge the water quickly out of the consolidation soil strata.

The natural geocomposite drain has a unique structure that enhances the function as a filter fabric has high permeability and restricts the erosion of soil particles. At the same time it allows very fine particles from the soil to flow in and out of the drain without clogging. Removal of very fine sand particles is beneficial as this allow larger particles to form a highly permeable soil network against the fabric.

3 DESIGN CONSIDERATION

The procedure for the design of vertical drains are based on Terzaghi's one dimensional consolidation theory as suggested by (Barron, 1948, Richart, 1959, Kjellman, 1948 and Hansbo, 1979)

3.1 Design Parameters:

The spacing of the vertical drain is governed by

- soil properties
- boundary and drainage conditions
- desired degree of consolidation
- time available for consolidation
- drain installation pattern and
- height of surcharge or fill load.

The degree of consolidation, surcharge intensity, settlement, pore water pressure and drain parameters are interrelated. The degree of improvement of soil properties depends on percentage settlement, dissipation of pore water pressure, increase in effective stress or

increase of shear strength and the drain spacing can be obtained from (Barron, 1948). A more rigorous approach to drain design has been used in Europe and utilizes a combination of Kjellman's, (1948) original work and Hansbo (1979), the relevant design equation follow:

$$t = \frac{D^2}{8Ch} \left[ \frac{l_n \left( \frac{D}{d} \right)}{1 - \left( \frac{d}{D} \right)^2} - \frac{3 - \left( \frac{d}{D} \right)^2}{4} \right] l_n \frac{1}{1-U}$$

which can be simplified, since  $d/D$  is small, to

$$t = \frac{D^2}{8Ch} \left[ l_n \left( \frac{D}{d} \right) - 0.75 \right] l_n \frac{1}{1-U} \quad (1)$$

where :  $t$  = consolidation time

$Ch$  = coefficient of consolidation for horizontal flow

$d$  = equivalent diameter of the wick drain ( $\approx$  circumference /  $\pi$ )

$D$  = sphere of influence of the wick drain (for a triangular pattern use 1.05 times the spacing, for a square pattern use 1.13 times the spacing)

$U$  = average degree of consolidation.

From equation 1 a nomogram has been developed which relate degree of consolidation, coefficient of consolidation  $Ch$ , and the required drain spacing. The results are plotted in a graphical form as shown in Figure-3.

#### 4 CONSTRUCTION PROCEDURE

Geocomposite drains can be lowered into the drill holes made by readily available piling equipment. Koerner (1994) has given varieties of base plates to attach geocomposite drains at bottom of lanes. Similar types of drain plates can be used for lowering the natural geocomposite drain. A coir fabric at the ground surface is proposed for quick drainage of dissipated water beneath the embankment, instead of costly sand blanket. Since geocomposite drain allows faster consolidation the embankment layer thickness may also be increased to complete work at the earliest.

#### 5 CONCLUSIONS

The natural geocomposite vertical drain has been developed to speed up the consolidation process for various types of construction on sites underlain by thick deposits of soft clays. It is flexible, resistant to clogging, resistance to ultraviolet rays, relatively more permeable, strong in tension and sufficiently durable, low cost and environmental superiority over geosynthetics. As with synthetic geocomposite drains the natural geocomposite drain can be designed and manufactured to suit the specific requirements of different soil improvement projects.

#### ACKNOWLEDGMENTS

The authors are grateful to Prof. S. P. Sukhatme, Director IIT, Powai, Bombay, for his encouragement and the use of facilities.

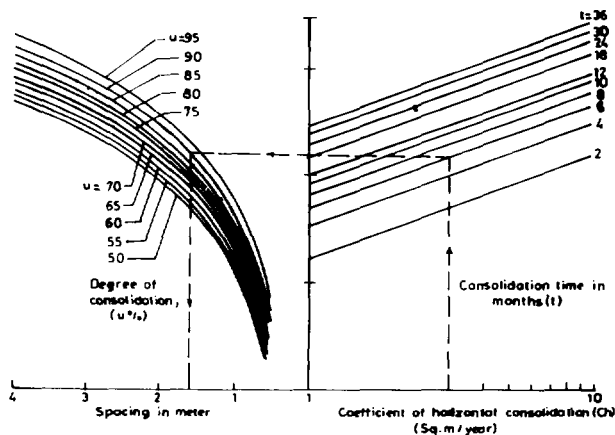


Fig. 3 Nomogram for geocomposite drain (15 cm diameter)

## REFERENCES

- Barron, R. A. (1948), "Consolidation of Fine Grained Soils by Drain Wells", ASCE, Transaction, Paper No. 2346, Vol. 113, PP. 718-754.
- Bergado, D. T., Alfaro, M. C. and Balsubramaniam, A. S. (1992), "Improvement of Soft Bangkok Clay using Vertical Drains" *Geotechnical Engineering Bulletin*, Vol. 1, No. 2, PP. 3-30.
- Dastidar, A. G. , Gupta, S. and Ghosh, T. K. (1969), "Application of Sand Wick in Housing Project, Int. Conf. on Soil Mechanics and Foundation Engineering, Mexico, PP. 59-64.
- Dinesh Mohan (1977), "Consolidation of Ground by Vertical Rope Drains" *Indian Geotech Journal*, Vol 7, No. 2, PP. 106-115.
- Hansbo, S. (1979), "Consolidation of Clay by Band-Shaped Prefabricated Drains", *Ground Engineering*, Vol. 12, No. 5, pp. 16-25.
- Hausman, M. R. (1990), "Engineering Principle of Ground Modification", McGraw Hill International Edition, P.632.
- Holtz, R. D. (1987), "Preloading with Prefabricated Vertical Strip Drains" *Geotextile and Geomembrane*, Vol. 6, PP. 109-131.
- Jamiolkowski, M., Lancellotta, R. and Wolski, W. (1983), "Precompression and speeding up consolidation", General report, specially session 6, Proc.8th ECSMFE, Helsinki, Vol.3, PP. 1201-1226.
- Johnston, S. J.(1970), "Foundation Precompression with Vertical Sand Drains" *Journal of Soil Mech. and Foundation Division*, ASCE, Vol. 96, No. 1, PP. 145-175.
- Kejellman, W. (1948), "Accelerating Consolidation of Fine Grained Soils by Means of Cardboard Wicks", *Proceeding Second Int. Conf. On Soil Mech. and Foundation Engineering*, Rotterdam, Vol. 2, PP. 302-305.
- Koerner, R. M. (1994), "Designing with Geosynthetics", Prentice Hall Englewood Cliffs, New Jersey, Second Edition, USA.
- Lee, S. L., Karunaratne, G. P., Yong, K. Y., and Ramaswamy, S. D. (1989), "Performance of Fiber Drain in Consolidation of Soft Soils", *Proc. 12th Int. Conf. SMFE. Rio De Janeiro, Brazil*, PP. 1667-1670.
- Mandal, J. N. and Shiv, A. (1992), "CAD on Geocomposite Vertical Strip Drains" *Construction and Building Material*, Vol. 6, No. 4, PP. 219-225.
- McGown, A., Marsland, A., Radwan, A. M. and Gabar, A. W. (1980), " Recording and Interpreting Soil Macrofabric Data", *Geotechnique*, Vol. 30, PP. 417-447.
- Ramaswamy, S. D. (1994), "Potential of Jute Assembled Soil Stabilizers", *Proc. 2nd. Int. Workshop on Geotextiles*, 11-12 Jan. New Delhi, PP 77-85.
- Sengupta. D. P. (1980), " Sub-strata Treatment for a Building using Rope Drains", *Indian Geotech. Journal*, Vol. 10, No. 4, PP 322-332.
- Richart, F. E. (1959), "Review of the Theories Sand Drains", *ASCE Trans. Vol. 124*, Paper No. 2999, PP. 709-739.
- Wissa, E. A., Davis, E. H., Christian, J. T. and Heibergs, S., "Consolidation at Constant Strain", *ASCE Journal. of Geotechnical Engg.* Vol. 97, pp. 1393-1413.

# Critical Evaluation of Laboratory Drain Tests Simulating Field Conditions

G.P. Karunaratne

Formerly Associate Professor, Department of Civil Engineering, National University of Singapore

S.A. Tan

Senior Lecturer, Department of Civil Engineering, National University of Singapore

S.H. Chew

Lecturer, Department of Civil Engineering, National University of Singapore

S.L. Loh

Research Scholar, Department of Civil Engineering, National University of Singapore

**ABSTRACT:** The discharge capacity of vertical drains is found to be significantly affected by the testing conditions. This paper presents the drainage performance of prefabricated vertical drains (PVD) under simulated field conditions, using a new drain testing apparatus. This apparatus can simulate realistic field conditions for vertical drains in soft clay deposits. Due to large ground settlement in soft clay, vertical drains may subject to excessive strains and formation of kinks. In general, such drains will have a lower discharge capacity than straight drains. Therefore, in addition to the realistic field properties of soil, critical evaluation of the laboratory determined discharge capacity is needed to understand the field performance of PVD. The testing conditions that can be simulated in this apparatus include varying confinement pressure, kinking of drains and packing in clayey soils. It is seen that different types of prefabricated vertical drains have significantly different discharge capacities under similar testing conditions. A comparative study of the discharge capacity of four drains under various test conditions is also presented in this paper.

**KEYWORDS:** Prefabricated vertical drains, Confining air pressure, Discharge capacity, Kinking, Testing

## 1 INTRODUCTION

Prefabricated vertical drains (PVD) are often used to accelerate consolidation of soft clay soils in ground improvement projects. Many types of prefabricated vertical drains are available in the market. To determine the suitability of a drain for a given project an evaluation of discharge capacity is needed. A new drain testing apparatus for PVD was developed at the National University of Singapore (NUS), to closely simulate the field conditions in such tests. The simulated testing conditions include varying confining pressure, kinking of drains and packing of clay around them. Four types of PVDs were tested under these conditions.

Hansbo (1983) recommended that testing of vertical drains should be carried out by placing it in an impervious soil. Lawrence and Koerner (1988) examined the influence of the kinks on the discharge capacity of drains. Based on these two conditions the discharge capacity of kinked drains that have packed clay around them is an important condition to be specified. The results of such tests with the new apparatus are discussed in this paper.

## 2 NUS DRAIN TESTING APPARATUS

A vertical drain testing apparatus was designed and fabricated to determine the discharge capacity and the transmissivity of prefabricated vertical drains (Loh, 1996). The design of the apparatus adheres closely to the ASTM Standard D4716-87 specifications and the conditions stated in the Hansbo (1983) 'ideal test'. The apparatus consists of three main detachable components: a constant head inlet reservoir, an outlet reservoir and a transparent, cylindrical compressed air chamber as shown in Figure 1.

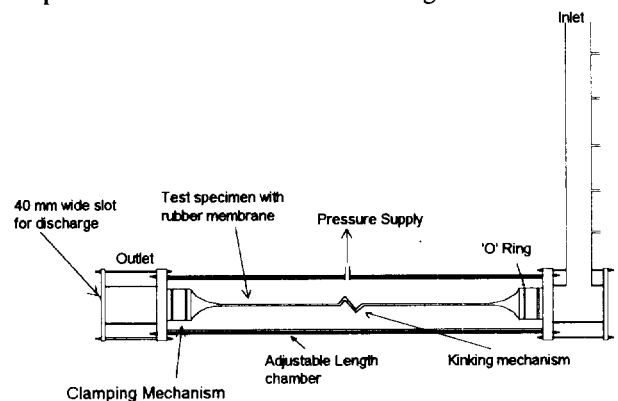





Figure 1: Schematic diagram of the NUS drain testing apparatus (Loh, 1996)

Table 1: Physical properties of the PVD tested

	VD1	VD	VD3	VD4
Mass/unit area (g/mm <sup>2</sup> ) x10 <sup>-4</sup>	11.81	2.92	4.06	3.4
Core type	Coir	Polypropylene	Polypropylene	Polyester
Core structure		 Continuous channel	 button extrusion	XXXXXXXXXX nylon web
Sleeve filter	Double layer of woven Jute	Polypropylene non-woven	Polypropylene non-woven	Polyester non-woven
Dimensions (W mm x t mm)	100 x 8	100 x 6	100 x 6	100 x 6

The compressed air chamber is designed to be large enough to accommodate a kinking mechanism, which consists of two angle plates. The angle plates can be placed against the drain to form a kink at any desired angle. Hence the discharge capacity of kinked drains can be determined. Remoulded clay can be packed around the drain, which is then encased in a rubber membrane, in order to ensure that the effective lateral pressure of the soil against the drain sleeve is acting as in the field. The liquidity index of the remoulded clay was 0.6 to 0.7. With this layer of clay coming into contact with the drains, there will be a better simulation of the field conditions.

### 3 TYPES OF DRAINS

Four types of prefabricated vertical drains were investigated in this apparatus. VD1 is made of natural fibres of jute and coir. Two layers of jute burlap (Lee et al 1996) envelop four coir strands of 5-6mm in diameter made of coconut fibre. VD2, VD3 and VD4 are geosynthetic drains with different core types and core structures. VD2 has continuous rectangular channels whereas VD3 has button extrusions formed on the polypropylene core. VD4 has a polyester nylon web type of core (Hausmann, 1990). Salient physical properties of the four prefabricated vertical drains are shown in Table 1.

### 4 TEST RESULTS

#### 4.1 Confining Pressure

The four PVDs were tested under a range of confining pressures from 20kPa - 300kPa, which is equivalent to a lateral pressure in 30m-40m thick submerged soft clay. High confining pressure is needed to determine the discharge capacity of such PVD installed at great depths. Figure 2 shows the results for the four drains tested. For all drains, it is noted that with an increase in confining pressure, there is a reduction in discharge capacity. This is to be expected as reported by Hansbo (1993), Kamon et al (1992) and Broms et al (1994). The filter sleeve squeezes

into the core with increased confining pressure and hence the effective cross-sectional area of the core is reduced, leading to a reduction in the discharge capacity.

VD1 has the lowest discharge capacity among the drains tested. VD2 and VD3 have polypropylene non-woven filter sleeves, which were partially squeezed into the channels in the core at large confining pressures. This reduction in core space causes a drastic reduction in the discharge capacity. It is observed that the discharge capacity of VD4 is lower than that of VD2 at low confining pressures, but is the highest among the four at 300 kPa pressure. The relatively high discharge capacity is due to the relative stiffness of the nylon web type of core structure and the filter sleeve. The relatively high stiffness is more effective in preventing the filter sleeve from being squeezed into the core at high confining pressures.

#### 4.2 Type of Confinement

It is very important to have a close simulation of the field conditions of the drains in a study of this type. Besides changing the hydraulic gradient and confining pressure, tests were conducted using different confinement methods for each PVD. These included packing of clay around the PVD, with or without a stiff plate, as prescribed in the ASTM in applying pressure on the PVD.

Hansbo (1983) commented that the determination of the discharge capacity of a drain wrapped in a film of polyethylene and placed between two steel plates is inaccurate in this regard. He recommended that, in order to determine the discharge capacity of a drain, clay should be packed around the drains to ensure that the effective lateral pressure of the soil acting on the drain sleeve is similar to that in the field. The ASTM specification and the testing conditions used by many other workers, for instance Chang et al (1994), are similar without any clay directly around the drain. Hence from the above discussion, it was decided to determine the discharge capacity of PVDs with the placement of a rigid plate, as per ASTM, and to compare the results with those conducted with clay packed PVDs, as

proposed by Hansbo (1983). Two rigid perspex plates placed on either side of the PVD served the purpose.

In Figure 3, the drains lined with rigid (perspex) plates have nearly always a larger discharge capacity than those without rigid plates. The drains with the packed clay around fall in between the discharge capacities measured with and without perspex plates. Hence, clay packing is a closer simulation of the field conditions.

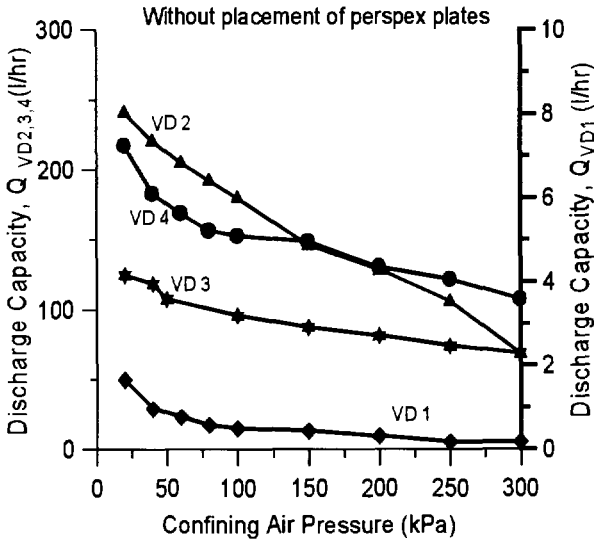


Figure 2: Discharge capacity of different types of PVD

#### 4.3 Kinking of Drains

Another field condition likely to be encountered is the kinking of drains (Lawrence and Koerner, 1988). Two series of kinking tests were conducted. In the first series, an artificial kink with 135° angle was introduced. The second series was a “natural” kink carried out by imposing a 25% axial strain on the drain, similar to the drain deformation in the field. Lawrence and Koerner (1988) observed that with kinks in the PVDs, there is a reduction in discharge capacity.

Figure 4 shows the discharge capacity of straight and kinked drains and Figure 5 shows the percentage reduction of the discharge capacity of kinked drains compared to the straight drains. It is clear that the discharge capacity of straight drains is always higher than that of kinked drains. Although straight VD2 showed much higher discharge capacity than VD3, kinked VD2 showed a greater percentage reduction in discharge capacity than kinked VD3 at 135°. It is apparent that VD3 has a more rigid core structure than VD2. At a confining pressure of 350 kPa, the percentage reduction of discharge capacity for VD4 is the lowest, whereas VD2 has the highest reduction. Tests were also performed with artificial and natural kinks.

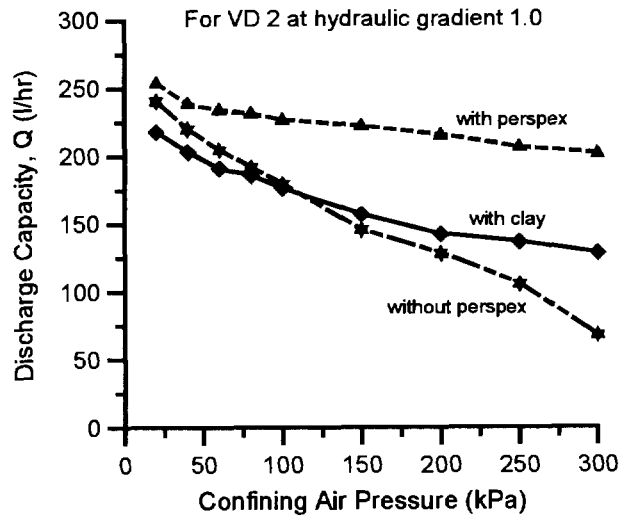


Figure 3: Discharge capacity of VD2 under confinement with/without stiff perspex/clay around

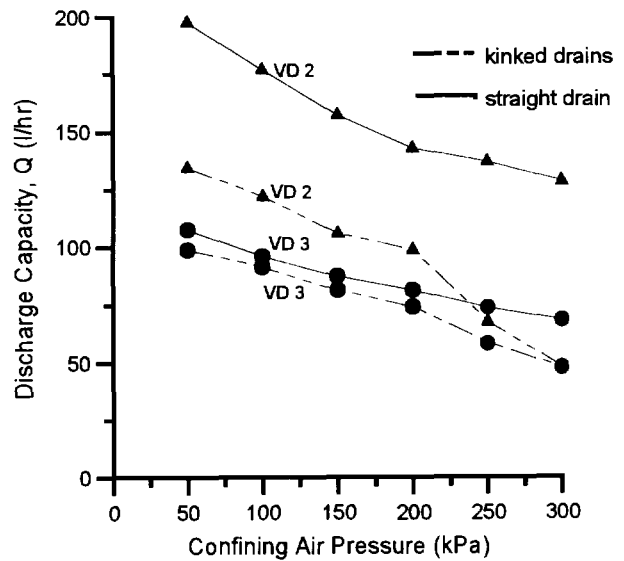


Figure 4: Discharge capacity of kinked and straight drains

Figure 6 gives a comparison of results for the two series of tests with artificial and natural kinks. Drains with natural kinks tend to have a higher discharge capacity than drains with artificial kinks. Discharge capacity of kinked drains obtained from natural kink is more realistic as kinks are formed naturally in the field. Figure 7 shows the discharge capacity of drains with natural kinks and clay packing around the drain. The discharge capacity of VD4 is the highest in the kinked condition. This type of drain has a nylon web type of core which is robust and does not collapse much when kinked. Also its filter sleeve is relatively stiff compared to those of VD2 and VD3 and hence it is not squeezed into the core at high confining pressure. In the case of VD1 the discharge remains very low both in the straight and kinked conditions.

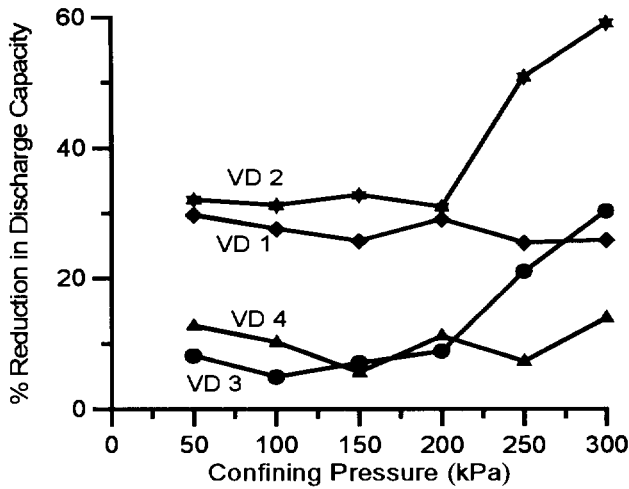


Figure 5: Percentage reduction in discharge capacity of kinked drains

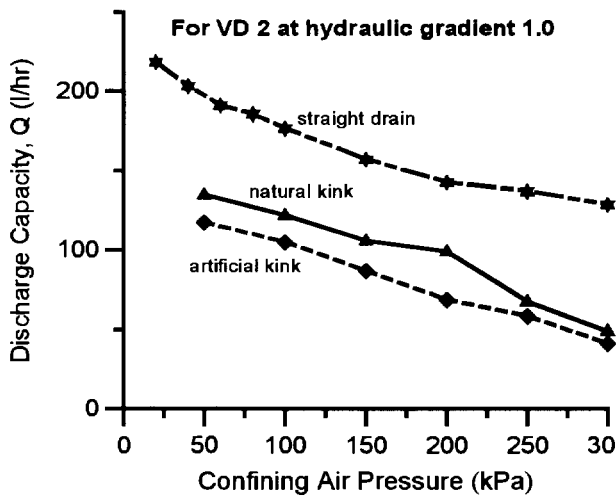


Figure 6: Discharge capacity of VD2 with different types of kinks

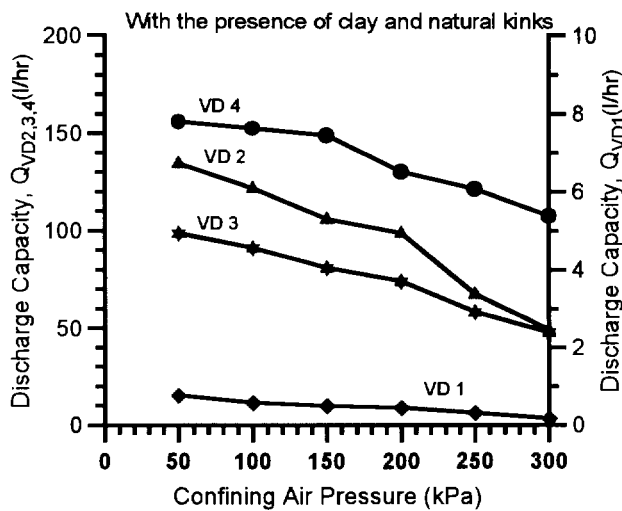


Figure 7: Discharge capacity of PVD with 25% axial compression

## 5 CONCLUSION

Four types of PVDs were tested in a new apparatus. It is observed that the core structure of the drain plays an important role in the estimation of the discharge capacity. In testing PVDs, the method of confinement of PVDs has a great influence on the discharge capacity. Different confinement modes can yield considerably different results. Other conditions such as kinking of drains are also important when choosing a PVD for a given project. To be more realistic in the measurement of discharge capacity, the confinement pressure on PVD should be applied through a packed layer of clay, where the PVD is to be used, and a natural kink should also be incorporated during the test.

## 6 REFERENCES

- ASTM D4716-87 (1987), "Standard Test Method for Constant Head Hydraulic Transmissivity (In-plane flow) of Geotextiles and Geotextile related products".
- Broms B.B., Chu J. and Choa V. (1994), "Measuring the Discharge Capacity of Band Drains by a New Drain Tester", *Proceedings of Fifth International Conference on Geotextile, Geomembranes and Related Products*, Singapore, vol. 2, pp 803-806.
- Chang D.T.T., Liao J.C. and Lai S.P. (1994), "Laboratory Study of Vertical drains for a Ground Improvement Project in Taipei", *Proceedings of Fifth International Conference on Geotextile, Geomembranes and Related Products*, Singapore, vol. 2, pp 807-812.
- Hansbo, S. (1983), "How to Evaluate the Properties of Prefabricated Drains", *Proceedings VIIIth ECSMFE*, Helsinki, vol. 2, pp 621-626.
- Hansbo, S. (1993), *Ground Improvement*, Chapman and Hall, CRC Press, Florida, USA
- Kamon M., Pradhan T.B.S and Suwa S. (1992), *Soil Improvement - Current Japanese Materials Research vol. 9*, ELSEVIER Science Publisher Ltd and The Society of Materials Science, Japan
- Hausmann, M. R. (1990), *Engineering Principles of Ground Modification*, McGraw-Hill International Editions.
- Lawrence C.A. and Koerner R.M. (1988), Flow Behaviour of Kinked Strip Drains, *Proceeding Geosynthetic for Soil Improvement - Geotechnical Special Publication No. 18*, pp 22-39.
- Lee S.L. Karunaratne G.P., Aziz M.A. and Yong K.Y. (1996), "Fibredrain and its application in land reclamation and ground improvement", *Proceedings of Joint NUS-Fukken seminar on Land Reclamation and Ground Improvement*, Singapore, pp 1-28.
- Loh S.L. (1996), *Vertical Drains Capacity Test*, B.Eng. Thesis, National University of Singapore.



# Geotextiles for the ElDorado International Airport in Colombia

A. Malagón

Civil Engineer, Manager of Ingeniería & Geosintéticos Ltda, Santafé de Bogotá, Colombia, South America

**ABSTRACT:** This document presents the case history of the utilization, between 1996 and 1997, of 1,220,000 m<sup>2</sup> of woven geotextiles, reinforcing the foundation of embankments constructed on soft soils, and 25,000 m<sup>2</sup> of nonwoven geotextiles for filtration, on the second runway of the ElDorado International Airport. In Colombia, geosynthetics have been used since the 1980s; however this is the first job that has been reinforced by high tensile strength geotextiles. The foundation soil at the project site consists of a deep deposit of lacustrine origin, poorly consolidated. The original design was based on improving the characteristics of the soil's resistance through preconsolidation by overload, with the use of wick drains. The building contractor, based on a further investigation of the subsoil, presented and obtained the approval of an alternative, that does not contemplate the preconsolidation nor the wick drains, but rather includes the reinforcement of the foundations of the embankments by woven geotextiles.

**KEY WORDS:** Airport Construction, Soft Soils, Wick Drains, Geotextiles, and Reinforcement

## 1. INTRODUCTION

The use of geosynthetics in Colombia was initiated during the 1980s with the utilization of geotextiles for soil separation and filtration, with the specific purpose of avoiding contamination of structures below pavements and porous mediums in drainage systems. Later, geotextiles were used to reinforce foundations and to construct mechanically stabilized soil retaining walls. In the beginning of the nineties decade, the use of geomembranes started mainly to avoid or diminish leaks in such works as (a) water storage, (b) wastewater treatment and (c) disposition of solid contaminants. Other geosynthetics such as geogrids, geonets, and so on, have been used occasionally in limited quantities.

The development of the geosynthetics market in Colombia, without being very great, has been faster than the diffusion and acquisition of the necessary technical know-how for its correct use and specification. In Colombia, there are no technical norms that regulate the specification, the design and the construction with geosynthetics nor is there an impartial entity that can duly assess the engineer. The industry, along with some universities and engineering firms, has made great efforts to spread the technology but the results are limited and in some case arguable.

On the other hand, Colombia suffers from a lack of runways and transportation infrastructure, which has led some investigators to calculate that Colombia is behind its own necessities by about thirty years. To overcome this problem, the Colombian government has decided recently to grant licenses for the most important construction projects and for the rehabilitation of roads, city streets, airports and seaports. Both national and international firms have been invited. This is the case of the ElDorado International Airport, which handles some of the heaviest air traffic in the world with only one runway. The construction of the second runway has been contracted, by granting a license for a term of seventeen years. The

contractor is a consortium of the Spanish firm Dragados and the Colombian firm Conconcreto.

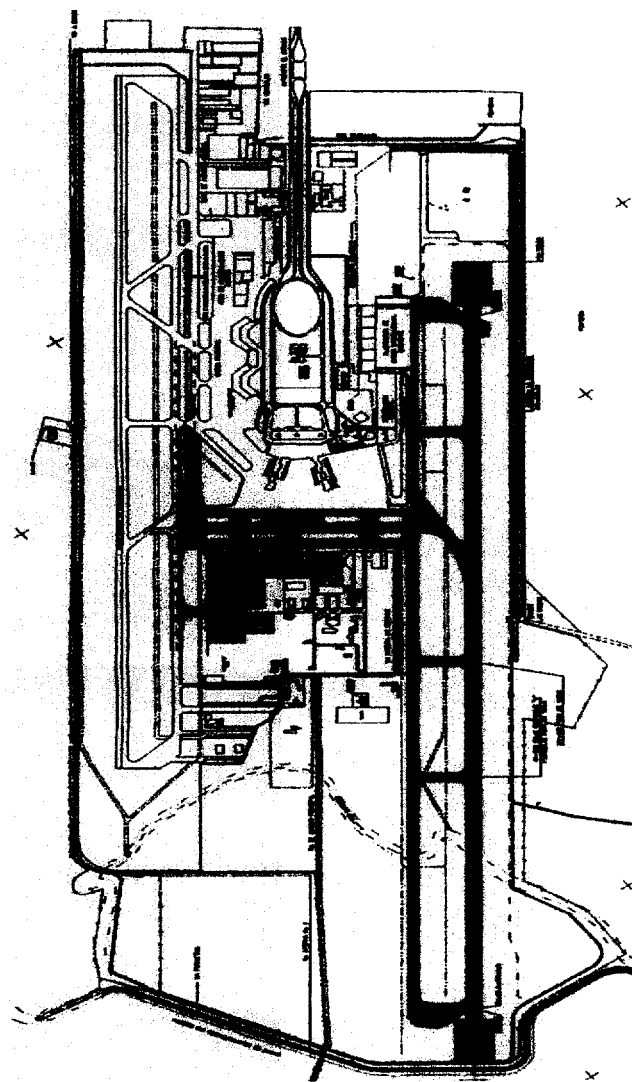


Figure 1. General plan view of the project

The soil on which the runway is being constructed, is a deposit of some 300 meters deep (for this project about 60 meters have been recognized as soft), consisting of lacustrine origin soils mainly clayey with presence of volcanic ash and also some sand lens. The runway goes in an east-west direction which is 3,800 meters long and crosses the Bogotá river bed which was rectified by means of a canal of some 600 meters long, which made the construction possible (see Figure 1). Figure 2 shows the side view of the runway. As can be observed, the initial 2,600 m of the runway - Sector 1 - rest directly on the top layer of native clays, while the final 1,200 m of the runway - Sector 2 - rest on a embankment with maximum height of 4.0 m.

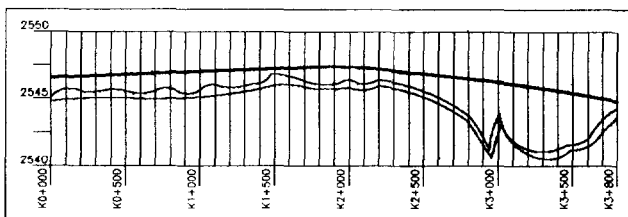


Figure 2. Side view of the runway

The investigation of the subsoil demonstrated its incapacity to support the loads of the embankments and that the runway would suffer great differential settlements, unless adequate measures were taken to avoid this. The designer specified a process of preconsolidation: induced by an overload caused by an embankment 5 meters high, accelerated by the installation of wick drains placed 1.80 meters apart and 10 meters deep (see Figure 3).

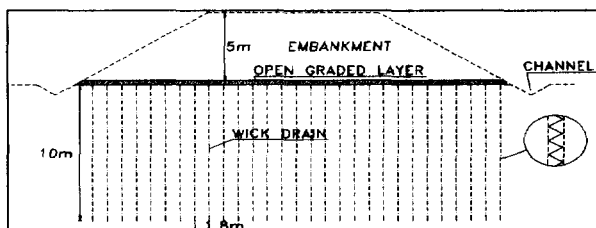


Figure 3. Preconsolidation typical transverse section of the full scale test embankment.

The contractor furthered the investigation of the subsoil through traditional mechanical drilling and through the Cone Penetration Test (CPT), with a continuous measurement of interstitial pressure. In Santafé de Bogotá at that time, there had been no one with the experience required for the project in the use of CPT equipment. When the original design was done, the designer did not have the information that the constructor obtained through his own additional investigation. The results of this investigation made it possible to characterize better the subsoil and led to the conclusion that the treatment of preconsolidation could be avoided. Consequently, the contractor recommended embankment foundation reinforcement in lieu of the acceleration of settlements.

In order to confirm the performance of the original design, a full-scale test embankment has been constructed and monitored.

## 2. ORIGINAL DESIGN : IMPROVEMENT THROUGH PRECONSOLIDATION

### 2.1 Foundation Soil

The soils at the work site are predominantly arguieulous of high plasticity (CH), very soft, and belong to the lacustrine deposit named *Sabana* formation, whose depth beneath the runway is 60 m as a minimum. The water table is 1 or 2 m below the terrain surface. According with the bidding documents, there are two geotechnical zones along the runway: Zone 1, on the Bogotá river valley that presents a layer of fine sands located between 4.0 and 11.0 m below the surface, resting on the typical soils of the *Sabana* formation. Zone 2, located out of the Bogotá river valley where the typical geotechnical profile of the *Sabana* formation is present. The designer specified the use of wick drains in order to improve the resistance of the foundation but mainly to make it uniform. This preconsolidation treatment was designed also to reduce the expected differential long-term settlements between zone 1 and 2, due not only to the geotechnical differences but also taking into account the variable height of the embankment (from 0 to 4.0 m).

The wick drains were specified to have a depth of 10 m; 1.80 m spaced and interconnected on the surface through a granular material layer of high permeability. This layer was designed to capture and evacuate the expelled water from the soil, thanks to the application of the overload of an embankment 5.00 meters in height (Figure 3). The estimated time necessary for the completion of the preconsolidation process was 15 months.

### 2.2 Pavement Structure

In the solicitations, two alternative pavement designs were specified: (a) flexible pavement composed by 13 cm of asphalt carpet, over 38 cm of standard asphalt base and 90 cm of granular material, meeting specifications of subbase course. And (b) rigid pavement composed by 38 cm of concrete slab, over 20 cm of standard asphalt base and 90 cm of granular subbase material.

### 2.3 Embankment Material

Table 1. Embankment material specifications.

CHARACTERISTIC	SPECIFIED	REAL
Maximum Grain Size	75mm	75 mm
% passing No. 200 sieve	<15%	13.5%
Liquid Limit ( $I_L$ )	25%	23%
Plasticity Index ( $I_p$ )	6%	6.7%
CBR	-	38

These specifications correspond to a local material, called "Recebo", with a soil friction angle ( $\phi$ ) that varies between 25° and 30° when compacted, and is composed by a mix of fine and granular soils.

### 3. DEFINITIVE DESIGN : REINFORCEMENT OF THE FOUNDATION WITH GEOTEXTILES

Three typical transversal sections were analyzed: (a) transversal section of the runway, (b) transversal section of the platforms and (c) transversal section of the perimeter roadways for vehicle transit.

This document refers mainly to the runway and platforms reinforcement, though it includes the technical characteristics of low strength geotextiles used to reinforce the perimeter roadways.

Based on the new exploration of the subsoil, the contractor was able to establish more precisely the characteristics of the foundation soil and to analyze, for the embankment material used (see Table 1), the two transversal typical sections of the runway (see Figure 4).

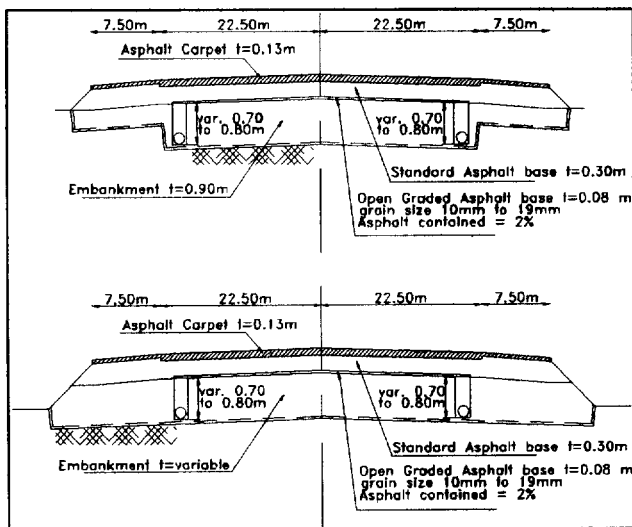


Figure 4. Reinforced Typical Transverse Sections.

Following the design method proposed by Koerner (1990) to determine the required functions of a geotextile in the foundation of embankments on soft soils, the contractor determined the primary and secondary functions of the geotextile. According with the contractor criteria, separation is the primary function for low height embankments, while for high height embankments, depending on the governing mode of failure, reinforcing could be of primary importance (see Figure 5). When Toe or Spreading are the governing failure modes, reinforcement and separation are the geotextile primary functions. When Base failure is governing, separation is the primary geotextile function. For Sector 1, the geotextile was designed for separation. For Sector 2 by means of comparing the embankment height (H), the soft soil depth (D) and the embankment width (B), a toe failure was

determined to be the governing mode and the geotextile was designed for separation and reinforcement.

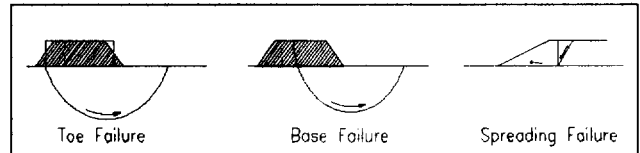


Figure 5 Mode of Failure

#### 3.1 Geotextile Design for Separation Function

The contractor, considering puncture as the most probable separation geotextile-breaking mode, used the following equation to determine the required geotextile puncture resistance:

$$F_{p_{req}} = (\pi d_i d_a) p' S' \quad (1)$$

Where,

$F_{p_{req}}$  = Required geotextile puncture resistance (kN)

$d_i$  = Geotextile opening size (m)

$d_a$  = Average diameter of the puncturing aggregate (m)

$p'$  = Pressure exerted on the geotextile (kPa)

$S'$  = Shape factor of the aggregate particles

$$S' = (1-S)$$

$S$  = sphericity

$S = 0.4$  for crushed stone

Taking into account that the foundation soils have a passing 200 ASTM sieves > 50%, the contractor decided to specify O95 < 0.3 mm. In consequence for  $d_i = 0.3$  mm,  $p' = 490$  kPa (imposed by the construction trucks) and  $d_a = 70$  mm, we have:

$$F_{p_{req}} = (\pi)(0.3 \times 10^{-3})(70 \times 10^{-3}) 490 (1-0.4)$$

$$F_{p_{req}} = 0.01940 \text{ kN} = 19.40 \text{ N}$$

Using a factor of safety against puncture of 2.0,

$$F_{p_{reqd}} = 38.8 \text{ N}$$

#### 3.2 Geotextile Design for Reinforcement

Using a computer program for geosynthetics design, the contractor determined the required tension at 20% of elongation ( $T_{20}$ ), based on the following parameters:

Table 2. Geotextile for reinforcement design parameters

Design parameter	Symbol	Unity	Value
Embankment Height	H	M	3.50
Elongation at failure	$\epsilon_f$	%	$\leq 20$
Fill material Shear stress	$\tau_f$	kPa	19
Foundation soil Shear stress	$\tau_s$	kPa	17.8
Soft soil depth	D	M	14
Angle of slopes to horizontal	$\beta$	°	26
Fill material Unit weight	$\gamma_f$	kN/m <sup>3</sup>	17.8

Geotextile resin		PP
Uniform surcharge load	$q_a$	kPa 10
Damage during construction partial factor	$f_{m1}$	1.1
Loss of resistance for 20 year partial factor	$f_{m2}$	1.24
Global Factor of Safety	FS	1.5

The computer program calculates the required  $T_{20}$  and minimum anchor length  $L_a$  using the Bishop stability method of analysis. For the runway, the results was:

$$T_{20} = 70 \text{ kN/m}$$

$$L_a = 47 \text{ m}$$

#### 4. PRELIMINARY RESULTS OF THE MONITORING ON THE TEST EMBANKMENT AND ON THE FINAL EMBANKMENT

##### 4.1 Test Embankment

The test embankment, 160 m length by 80 m wide and 5 m high, with slopes 2H:1V (see Figure 6), was constructed near the runway where one can expect the largest velocities of settlement, due to the presence of a sand layer in the stratum. As Figure 6 shows, the test embankment was divided in three zones:

Zone A: on top of foundation soil treated with wick drains installed as defined in the original design (1 wick drain / 2.80 m<sup>2</sup>),

Zone B: on top of foundation soil treated with wick drains installed more closely (1 wick drain / 2.0 m<sup>2</sup>),

Zone C: embankment on top of foundation soil without wick drains.

To monitoring the test embankment performance, the following set of instruments was installed:

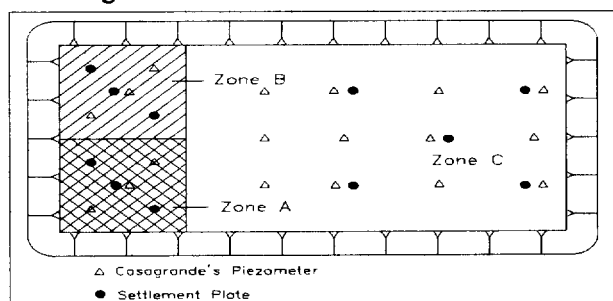


Figure 6 Plant View of the Test Embankment

Table 3. Set of instruments installed in the test embankment

Instrument	Quantity
Casagrande's piezometer	11
Settlement plate	18
Extensometer	3 (60 m length)
Continue Settlement line	4

These instruments allow for the measurement of settlements at the foundation level and to evaluate continuously their space variation.

Table 4. Results of settlement plates

Zone	Settlement (mm)	Instrument
A	80	Settlement plate N° 3
B	115	Settlement plate N° 6
C	158	Settlement plate N° 14

Table 5. Maximum excess of pore water pressure (kPa)

Zone	Depth (m)	$\Delta u$ (kPa)	Piezometer
A	10	4.9	N°3
	20	21.6	N°1
	30	15.7	N°2
B	10	9.8	N°6
	20	38.3	N°4
	30	30.4	N°5
C	10	1.9	N°11
	20	29.4	N°10
	30	32.4	N°9

Due to space limitations it is not possible to include in this document more detailed information about these provisional test embankment results, but the initial contractor's conclusions are:

- Measured settlements are smaller than those expected and occur at a velocity near to the expected one,
- The greater part of settlements during the construction occurs in the top 20 m of the stratum,
- Apparently there is not important influence of the wick drains on settlements,
- According with the settlement distribution in the test embankment, differential settlements would occur in the runway (in the order of 5 cm). This magnitude of differential settlements have registered in airports with similar foundation conditions than EIDorado Airport (San Francisco Airport, Mexico City Airport)

##### 4.1 Final Embankment

The final embankment foundation was reinforced by a high strength woven geotextile. During construction, no monitoring instruments were installed. At the moment of this writing the contractor is starting a plan of topography measurements. As the contractor has been able to establish through geotechnical studies and embankment tests, settlements will occur on the runway. However thanks to geotextile reinforcement, abrupt differential settlements will not appear. According to the measurements the magnitude of the general settlement because of consolidation is small and will be compensated by repaving maintenance works, which are normal for this type of construction.

## 5. REQUIRED AND SUPPLIED SPECIFICATIONS FOR THE GEOTEXTILES

### 5.1 Geotextile for the Runway and Platforms

The contractor specified the following necessary characteristics of the woven geotextile to reinforce the runway and platforms:

Property	Un	Value
Ultimate tensile strength	KN/m	70 x 56
Elongation at break	%	< 13
O <sub>95</sub>	µm	< 300

### 5.2 Geotextile for the Perimeter Roadways

The contractor specified the following necessary characteristics of the separation woven geotextile for perimeter roadways:

Property	Un	Value
Ultimate tensile strength	KN/m	25 x 25
Elongation at break	%	50 to 70
O <sub>95</sub>	µm	< 150
Flow Capacity Normal to the plane	L/m <sup>2</sup> .s	0.0319
Thickness	Mm	>3.00
Puncture Strength	N	4000

### 5.3 Geotextiles for Filtration in Drainage System

The pavement drainage system leads infiltrated and ground water, by the open graded asphalt base, to the lateral drainage lines, which are trench drains filled with open graded material including a 100 mm size pipe, wrapped up by nonwoven needle punched geotextile.

Table 6. Characteristics of the geotextiles used.

#### a) Woven geotextile Geotex 4x4 for runway

Property	UN	MARV	Typical
Polymer Type		PP	
Wide Width	KN/m	70x70	81.4x80.5
Tensile Strength			
Wide Width	%	14x12	19x19
Elongation			
Mullen Burst	kPa	8270	8960
Trapezoidal Tear	N	820x845	1335x1310
AOS	Mm	0.600	0.600-0.425
Permittivity	s <sup>-1</sup>	0.60	
Permeability	L/m <sup>2</sup> /s		54
Water Flow Rate	l/m/m <sup>2</sup>	1830	
UV Resistance	%	80	80

#### b) Woven geotextile Geotex 200 ST for the perimeter roadways

Property	UN	MARV	Typical
Polymer Type		PP	
Wide Width	KN/m	21x21	22.7x27.1

Tensile Strength			
Wide Width	%	15	11x19
Elongation			
Mullen Burst	kPa	3100	3440
Trapezoidal Tear	N	330	420x420
AOS	Mm	0.425	0.300
Permittivity	Sec <sup>-1</sup>	0.07	
Permeability	l/m <sup>2</sup> /s		11
Water Flow Rate	L/m/m <sup>2</sup>	240	
UV Resistance	%	90	90

#### c) Nonwoven geotextile NT1600 for filtration in drainage system

Property	UN	Typical
Polymer Type		PP
Grab Tensile Strength	N	420
Elongation at Break	%	80
Mullen Burst	kPa	1205
Trapezoidal Tear	N	160
AOS	Mm	0.150
Permittivity	Sec <sup>-1</sup>	2.2
Permeability	Cm/s	4.8 x 10 <sup>-2</sup>

## 6. METHOD OF CONSTRUCTION

### 6.1 Preparation of the Foundation Soil

Geosynthetics installation guidelines for reinforcement of embankments foundation on soft soils recommend: (a) to install the reinforcement over the terrain, without removing the vegetation and (b) to induce - within adequate limits - the development of the resistance in the reinforcement. However, in this case, the organic soil was removed.

### 6.2 Placement and Joint Systems of the Geotextile

The geotextile was extended in the normal direction along the centerline of the runway, in such a way that the greatest stress was applied in the roll direction.

At first, an instruction was given to sew the geotextile through the interlocking method, recommended by the British Standard Guides 8006 (see Figure 7), in order to guarantee the maximum possible stress transmission. In Colombia neither high strength yarn nor sewing machines to make double chain stitch were available. In consequence, in some spots it was observed that seams could not support the stress due to the extension and compactness of the fill material. To fix that, a new instruction was given to use overlaps whose dimension was adjusted according to the CBR value of the foundation soil in the different zones of the project.

### 6.3 Extension and Compacting of the Fill Material.

This operation was initiated in the zones where the foundation soil was found to have the greatest bearing

capacity. The material was discharged over the geotextile, on firm areas and was distributed in such a way that, when it was spread out a layer of 0.35 m of thickness, before compacting, was obtained. Bulldozers were used on this job of the type CAT D-7 equipped with caterpillars of standard width. Although this kind of equipment exerts high pressure on the soil, the geotextile was able to support those high construction loads. But the seams (see reasons in 6.2) gave way in some places, something which was made evident by observing local failures.

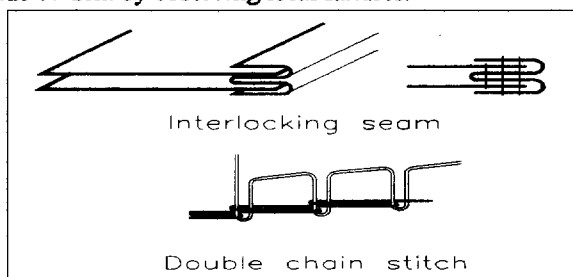


Figure 7. Types of seams.

An initial compacting was applied with the bulldozers and then the final compacting was applied with a vibrator roller until the specified density was achieved.

Some points that showed rutting during construction, due to faults in the subgrade soil, were repaired by adding material, until the geotextile was deformed sufficiently so as to supply the required strength in order to stabilize the filling.

When the adequate bearing capacity was obtained in the first layer, two more layers were added and compacted, until the final projected level was obtained.

On the embankment crest level a hot asphalt spray was applied, on top of which the structure of the pavement was constructed. It was made up of a layer 8 cm of open graded asphalt base, a 30-cm thick standard asphalt base and a carpet layer of 13 cm. The open graded layer was specified for the purpose of improving the drainage conditions of the structure which has a lateral slope of 1.5% and is interconnected with a system of lateral drainage lines, that discharge every 50 m (see Figure 4).

## 7. CONCLUSIONS

The final design of the embankment foundation reinforced with geotextiles has sped up the construction and it is functioning in accordance with what was established by the contractor. This is without the necessity of overload and drainage and has also resulted in being more economical.

This job demonstrates that geosynthetics offer economic alternatives in construction, that are reliable and of great use for modern engineering projects in both developed countries and in those countries found to be in the process of development. In this case, the geotextiles have made it possible:

- (a) to obtain and make uniform the stability conditions of the embankment, which are required by the project, without the necessity of improving the characteristics of the subgrade soil;
- (b) to carry out the work in a shorter period of time and
- (c) To utilize embankment filling material that is available near the construction site, which translates into considerable savings on transport costs.

The construction job represents an important contribution to the development of the specification, design and construction of works carried out with geosynthetics in Colombia, a country where a tremendous academic effort is required in order to ensure that these products are used according to rational criteria.

The relative extensive use of geosynthetics in Colombia is based generally on the intuition of engineers who have seen proof of beneficial effects of these products in their different applications. Only in some cases, such as the second runway at EIDorado International Airport, do the required specifications of the reinforcement correspond to a technically calculated design.

The lack or absence of adequate design has led to partially or totally faulty projects, which have been carried out with geosynthetics in Colombia and this also has meant a lower pace of growth in this market.

The reduced diffusion of rational analytic methods for design with geosynthetics means that only a handful of engineers have the necessary technical information for designing with these products.

As a result, we continue resolving a lot of geotechnical problems by means of traditional technologies that are more costly, not only in terms of money but also in terms of time and the environment.

We hope that the importance and good results of this project will encourage engineers in Colombia, as well as other countries to construct with geosynthetics. To do this we need to utilize sound geotechnical principles to analyze, design and specify geosynthetics and to construct according with the designer and manufacturer recommendations.

## ACKNOWLEDGMENTS

The writer would like to thank Engineers Fernando Bolinaga and Fernando Roman of Dragados and Intecsa, for their help to get the necessary data for this document. The writer also acknowledges the cooperation of the Project Directors, Engineers José Antonio López, Fernando Abadía and José Ignacio Quirós; of the Project Field Director Eng. José Luis Pasión and the Project Technical Director Eng. Pablo Quirós, and of the contractor consortium field engineers, not only because of their cooperation, but especially because of their interest to get the best results in this geosynthetics reinforced job. Finally I would like to thank Engineers Henry Angulo and Rodrigo Arévalo who have made the graphics and Mr. Albert Klein for the translation necessary for this paper.

# Testing and Analysis of Soft Foundation Treatment for Donggang Diking Project

Q. Y. Luo

Senior Engineer, Zhejiang Institute of Water Conservancy and Hydraulic Power, Huajiachi, Hangzhou, China

**ABSTRACT:** A seawall for Donggang diking project is 3635m long and 5.3m to 7.5m high, with a diked area of 2.45km<sup>2</sup>. The foundation consists of silty clay with high water content, high compressibility and low strength. A seawall section having a height of 5.3m to 6.0m was treated with geotextile reinforced foundation mattress; meanwhile, a seawall section having a height of 6.0m to 7.5m was improved using plastic drainage plates. To meet the needs of two treatment schemes the observation instruments had been installed in the seawall, covering observation duration of 830 days and 710 days, respectively. The test results obtained are mainly presented and analysed in this paper. Findings show that the two treatment schemes adopted for this project have achieved excellent effect and the construction of the seawall was smoothly accomplished with faster speed and shorter time. Also, it shows that there is difference in consolidation effect between the two schemes and the popularization and application should be carried out in line with local conditions.

**KEYWORDS:** Seawall, Soft foundation, Plastic drainage plate, Geotextile, Observation result analysis

## 1 INTRODUCTION

Donggang diking project is located in Shenjiamen of Zhoushan City, Zhejiang Province, which is the largest fishing harbour in China, and is close to Putu Island of Zhoushan Archipelago which ranks among the most celebrated Buddhist Meccas in China. The diked area during the first construction period covers 2.45km<sup>2</sup> and has been already completed, in which the development and construction of harbour, industry, commerce and tourism are being conducted.

The seawall for Donggang project involves a total length of 3635m. The beach ground elevation of the seawall line ranges from -1.3m to -3.5m (Huanghai Elevation, the same below). The top elevation of the seawall is 4.0m and the seawall height varies from 5.3m to 7.5m. The design high and low tide levels are 2.84m and -2.8m, respectively. It is a sea area with strong wind, high wave and larger tidal range. The seawall foundation consists of silty soft clay which has high water content and compressibility as well as low strength. The foundation stabilization treatment consists mainly of;

- Geotextile reinforced foundation mattress. The applied area of geotextile included the seawall of less than 6m high. The seawall sections were connected with the land areas at both ends and were 1505m long in total, in which the geotextiles laid were more than 100000m<sup>2</sup>.

- Plastic drainage plate. It was used for the 6m to 7.5m high seawall which was extended into the sea area so as to make the foundation be precompressed, drained and consolidated. The seawall length was 2130m and the plastic drainage plates of 850000m were

driven into the foundation.

In order to verify the stabilization effect of the soft clay foundation, control the construction rate and realize information construction, in accordance with the two treatment schemes a representative seawall with a length of 100m was selected as a test section, respectively. Instruments were embedded to carry out long-term observation. The series of readings which have been obtained started on November 29th, 1992 and ended on March 13th, 1995 and an observation duration lasted eight hundred and thirty days. Now, the test results derived in the course of construction are described as follows.

## 2 FINDINGS FOR GEOTEXTILE SCHEME

The top elevation of the seawall is 4.0m and the seawall is 6.0m high. The cross-section of the seawall is shown in Figure 1. The seawall cross-section was chosen through stability calculation and analysis for several schemes. The cross-section of the seawall treated by geotextile reinforced foundation mattress is more economical than a conventional scheme (natural foundation), in which a counter weight fill of 15m was shortened. The mattress with a thickness of 1.0m, consisted of two layer polypropylene woven fabrics and a crushed stone layer, is an important component part of the seawall. The geotextile utilized was a 60kN/m product and the characteristic indexes are shown in Table 1. The foundation can be divided into four soil strata and the buried elevation and soil characteristic indexes for each layer are listed in Table 2. The observation instruments were installed in November, 1992 and the location is shown in Figure 1. The instruments which were buried in the seawall include five ground

settlement plates(s), four settlement pipes (Fs) in layers, two clinometers(F), fifteen pore water pressure meters(u), six earth pressure cells (P) and two water level pipes (c). Also, the strength measurement was carried out with vanes(Cu). The seawall was filled in five stages starting on November 29th, 1992 and the crest elevation of the dyke reached 4.0m up to September, 1994. Earth material used for closure was placed in four stages. The top elevation of the seawall reached 2.6m up to November, 1994.

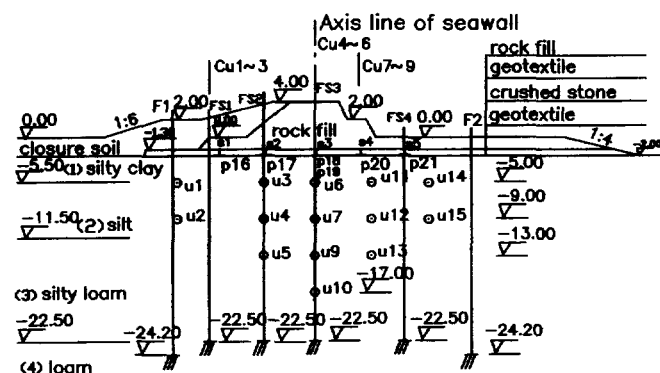


Figure 1. Seawall cross-section and observation instrument layout

Table 1. Main characteristic indexes of geotextile

Mass per unit area	Trapezoidal tearing strength		Ball rupture strength	Strip tensile 10 × 5			
	Longitudinal	Lateral		Tensile strength	Tensile strength rate	Tensile strength	Tensile strength rate
(g/m <sup>2</sup> )	(kN)	(kN)	(kN)	Radial (kN)	Radial (%)	Lateral (kN)	Lateral (%)
285	1.26	0.59	2.13	3.34	31	1.53	22

Table 2. Main characteristics of the foundation soil

Soil type	Water content (%)	Void ratio	Coef. of consolidation (cm/s <sup>2</sup> )	Quick shear	
				Cohesion (kPa)	Angle of inter. friction (°)
Silty clay	44.3	1.24	$2.9 \times 10^{-3}$	11.8	8.5
Silt	54.3	1.47	$1.29 \times 10^{-3}$	8.7	3.5
Silty loam	35.6	0.96	$2.69 \times 10^{-3}$	13.9	13.5
Loam	26.4	0.71	$2.75 \times 10^{-3}$	1.92	12.2

### 2.1 Ground Settlement

The graph of the settlement quantity of  $S_1 \sim S_3$  and time is shown in Figure 2. The settlement curve under the action of each stage loading is presented in Figure 3. Up to the end of March, 1995, the accumulated settlement quantities of  $S_2$  and  $S_3$  at the top of the seawall

were 116.7cm and 115.7cm, respectively. The steady settlement quantity was 152cm based on the calculation of their measured settlement curves.

### 2.2 Stratified Settlement

Taking  $FS_3$  as an example, as can be seen in Figure 4, the settlement quantity of ninety percent occurred in the first and second earth layers having a thickness of 9.5m below the ground surface. The accumulated settlement quantities of  $FS_2$  and  $FS_3$  at the top of the seawall were 114.2cm and 103.2cm, separately, basically identical with that of the corresponding ground settlement plates.

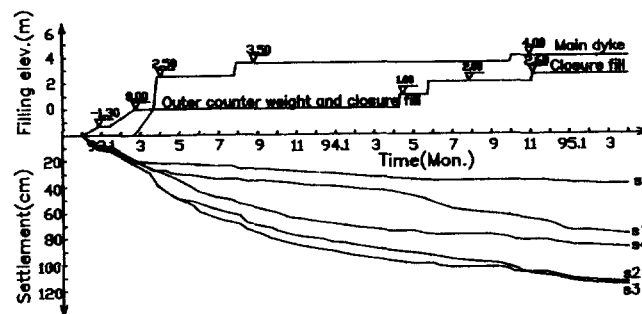


Figure 2. Graph of filling elevation and ground settlement

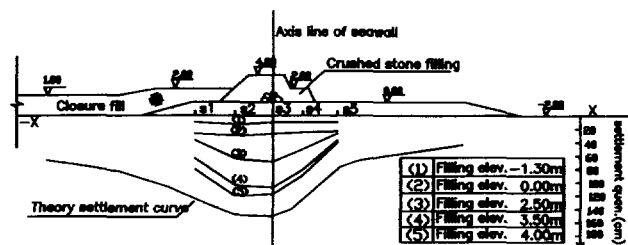


Figure 3. Settlement curve of each stage loading

### 2.3 Pore Water Pressure

Presenting some measuring points nearby the centre line of the seawall as examples, the graph of the foundation pore water pressure and time in the course of filling the seawall is plotted in Figure 5. It can be seen from Figure 5 that the pore water pressure of  $U_6$  in a shallow layer was more easily dissipated than that of  $U_9$  and  $U_{10}$ . Loading in a thin layer was advantageous to the dissipation of pore water pressure. The pore pressure increment of  $U_6$  was dissipated by twenty percent after one month for the third-stage loading and by thirty-nine percent after four months. It was dissipated by sixty-one percent after one month for the fourth-stage loading and fully dissipated after four months.



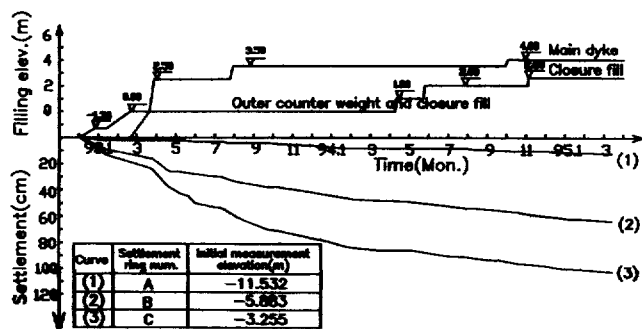


Figure 4. Graph of filling elevation and stratified settlement

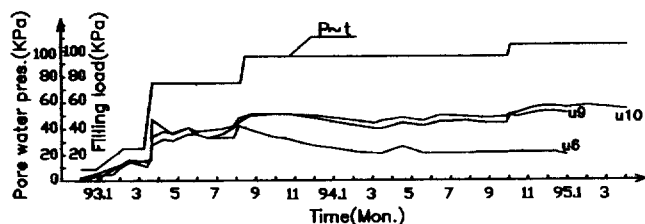


Figure 5. Graph of filling load and pore water pressure

Figure 6 that, if the elevation of  $-8\text{m}$  was looked upon as a demarcation line, the foundation strength above it would be increased in varying degrees, in which the foundation strength increased greatly near the ground surface; taking the foundation of elevation of  $-5\text{m}$  as an example, the strength had risen to 1 to 1.8 times; it did not almost increase below the elevation of  $-8\text{m}$ .

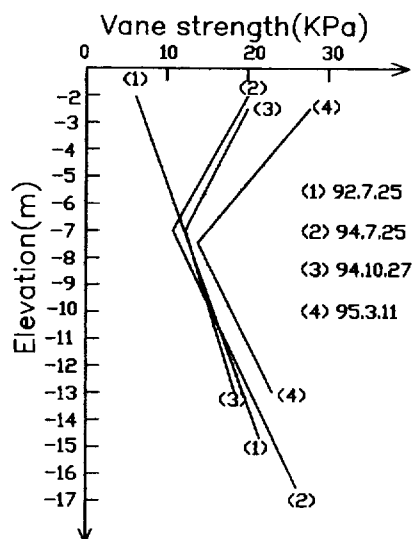


Figure 6. Test results of vane strength

## 2.4 Horizontal Displacement

The accumulated displacement quantity of  $F_1$  started from December, 1992 and ended in January, 1994 was 110mm. The horizontal displacement quantity was increased and developed to a deeper layer as the height of the seawall was raised and the maximum displacement occurred in the foundation surface layer.

## 2.5 Earth Pressure

Six earth pressure cells were embedded into the foundation below a geotextile reinforced foundation mattress and five of them are functioning normally. The average value of the ratio of the measured earth pressure was raised along with the increase of load, i. e. it was 0.26 for the second - stage loading, 0.43 for the third - stage loading, 0.66 for the fourth - stage loading and 0.73 for the fifth - stage loading.

## 2.6 Foundation Strength

The experimental results of vanes in the natural foundation and during three different construction periods are summarised in Figure 6. It can be known from

## 3 FINDINGS FOR PLASTIC DRAINAGE PLATE SCHEME

The crest elevation of the seawall is 4.0m and the seawall is 7.5m high. The cross - section of the seawall is given in Figure 7. The seawall cross-section was chosen after stability of conventional (natural foundation) and plastic drainage plate schemes had been calculated and analysed according to different water levels and loading. The stability and safety coefficient of the cross-section adopted was only about 0.8 if a conventional (natural foundation) scheme was used. It shows that the effect of plastic drainage plate scheme is excellent. Plastic drainage plates were driven at a range of 36m, with a spacing of 1.4m and a driven depth of 15m. The drainage blanket consisted of crushed stone of less than 10cm in grain diameter was 2.2m in thickness. The plastic drainage plate used is made of polythene cross core bonded with nonwoven fabrics and its performance indexes are listed in Table 3. The beach ground elevation of the seawall was  $-3.5\text{m}$ , in which the foundation is divided into five soil layers. The buried elevation and property indexes for each soil layer are listed in Table 4 and the location of instruments is given in Figure 7.

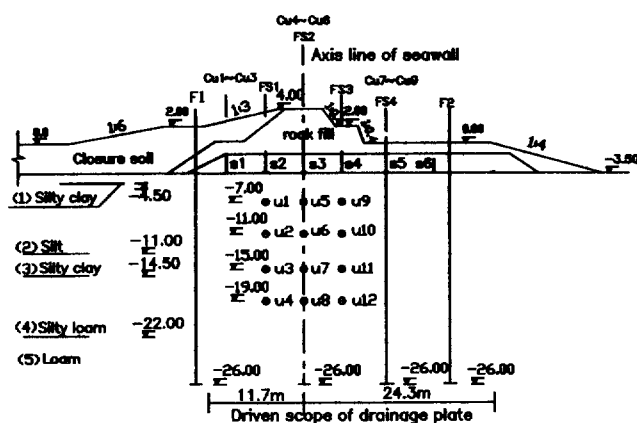


Figure 7. Seawall cross-section and observation instrument layout

Table 3. Main characteristic indexes of plastic drainage plate

Item	Unit	Indexes	Conditions	
Thickness	mm	4		
Wideness	mm	100		
Longitudinal passing water	cm <sup>3</sup> /s	25	Lateral pressure 350kPa	
Filter film permeability coefficient	cm/s	$5 \times 10^{-4}$	Specimen submerged in water for 24h	
Filter film equivalent aperture	mm	0.075	Equal to $O_{80}$	
Composite tensile strength	kN/10cm	1.3	At elongation rate of 10%	
Filter film tensile strength	Longitudinal	N/cm	25	At elongation rate of 10%
	Lateral	N/cm	20	At elongation rate of 10%

Table 4. Main characteristics of the foundation soil

Soil type	Water content (%)	Void ratio	Coef. of consolidation (cm <sup>2</sup> /s <sup>2</sup> )	Quick shear	
				Cohesion (kPa)	Angle of inter. friction (°)
Silty clay	49.3	1.38	$2.53 \times 10^{-3}$	11.7	7
Silt	59.2	1.63	$5.88 \times 10^{-4}$	13.0	2
Silty clay	49.6	1.35	$8.67 \times 10^{-4}$	21.0	2
Silty loam	36.9	1.00	$2.88 \times 10^{-3}$	15.0	17
Loam	32.0	0.88	$1.60 \times 10^{-3}$		

The observation items covered six ground settlement plates (s), four stratified settlement pipes (Fs), two clinometers (F) and twelve pore water pressure meters (u); meanwhile, the strength measurement was conducted with vanes (Cu). The installation of obser-

vation instruments was finished from June 14th to June 25th, 1993. All observation work ended till March 27th, 1995 and it took us seven hundred and ten days.

The construction of the seawall, which was divided into six stages, was accomplished between April 9th, 1993 and October 27th, 1994. The work lasted five hundred and sixty days, including an intermittent period. The construction of earth material for closure was performed in four times and lasted five hundred and four days from October 1st, 1993 to February 28th 1995. The filling graph of the seawall is given in Figure 8.

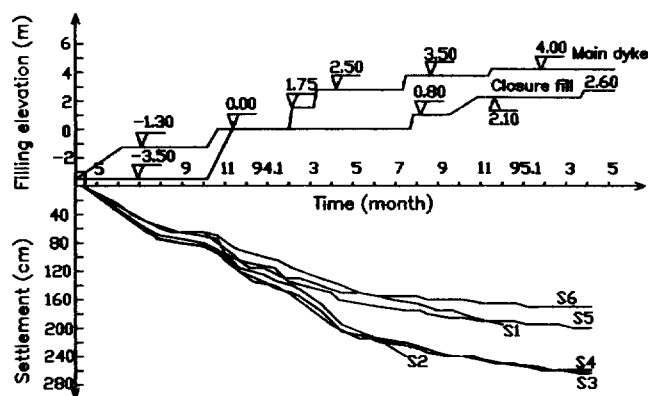


Figure 8. Graph of filling elevation and ground settlement

### 3.1 Ground Settlement

The graph of the settlement quantity and time is plotted in Figure 8 and the settlement curve of the seawall foundation is shown in Figure 9. As for the first and second stage loading the settlement increment of filling height per metre was larger, about 41cm, respectively; for the third to sixth stage loading the increment was very near, about 28.5cm, respectively. This was because the settlement increment for the first and second stage loading included an instantaneous settlement and an additional settlement induced by disturbed foundation in the course of driving plastic drainage plates. The settlement rate during load stage was all larger, in which the maximum settlement rate amounted to 4.6cm per day. At the end of observation the accumulated settlement quantity of S<sub>3</sub> near the seawall axis line was 260.2cm and the consolidation degree was about ninety percent.

### 3.2 Stratified Settlement

There are numerous data about stratified settlement. Citing FS<sub>2</sub> near the seawall axis line as an example the settlement graph at different measuring points is shown in Figure 10. The total settlement quantity of each soil

layer amounted to 254.8cm, close to 260.2cm for the accumulated settlement quantity of  $S_3$ . The settlement quantity in silty layer (Elevation-3.5m to -11.0m) made up fifty-nine percent of the total, the settlement quantity in silty clay layer (Elevation -11.0m to -14.5m) twenty percent and the settlement quantity in silty loam (Elevation -14.5m to -22.0m) twenty-one percent.

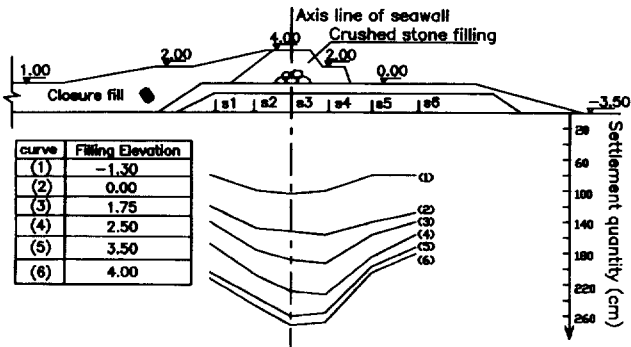


Figure 9. Settlement curve of seawall foundation

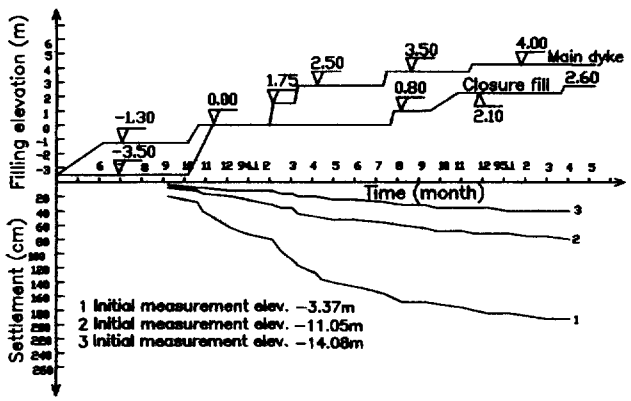


Figure 10. Graph of FS2 stratified settlement

### 3.3 Horizontal Displacement

Taking  $F_2$  embedded near the sea side as an example, the distribution curve of the horizontal displacement quantity along the direction of depth in different construction period is presented in Figure 11. The horizontal displacement quantity increased as the addition of load. The maximum horizontal displacement quantity was equal to 203.6mm, which occurred near the elevation of -8.0m and affected the silty loam layer at the elevation of -22m.

### 3.4 Foundation Strength

The vane strength at the elevation of 2.5m increased more obviously than that of the natural foundation

under the action of the fourth-stage loading in May, 1994. At the elevation of -7.25m (half of the seawall height) it was 2.11 times higher than the natural strength. It was 1.78 times at the elevation of -11.0m and it was 1.57 times at the elevation of -14.75m. It was obvious that the foundation strength would further rise with the increase of loading and pre-compression time. The vane tests had not been done afterwards because of the reasons of construction and management.

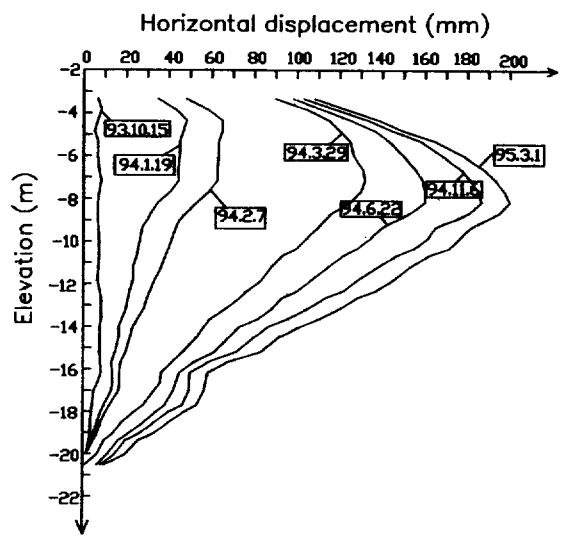


Figure 11. Curve of horizontal displacement along depth

### 3.5 Pore Water Pressure

According to the statistics of the data obtained from twelve pore pressure cells the pore water pressure rose with filling of the seawall, but it was quickly dissipated. Presenting  $U_1$ ,  $U_3$  and  $U_9$  as examples, the coefficients of pore pressure under the action of second-stage loading were greatest. Its average value equalled 0.79 and surpassed the normal standard limit. However, the coefficients of the pore pressure under the action of other different stage loading were smaller, i.e. 0.49 for the third-stage loading, 0.38 for the fourth-stage loading, 0.34 for the fifth-stage loading and 0.25 for the sixth-stage loading. Practice shows that plastic drainage plates have achieved the excellent effects of drainage and stabilization.

## 4 CONCLUSIONS

Based on the results analysed above, the main conclusions can be concluded as follows:

4.1 The seawall foundation of Donggang diking project is a silty clay with high water content, high

compressibility and low shear strength. For a treatment of this kind of foundation, geotextiles were used as a reinforced foundation mattress and plastic drainage plates as precompression, drainage and stabilization according to the seawall height. The information construction was performed based on the in-situ test results. The seawall was successfully accomplished with faster speed and shorter time and the desired results have been achieved. The methods also have a reference role for a design and construction of similar projects on a soft clay foundation.

4.2 The seawall of 6.0m high which was treated with geotextile reinforced foundation mattress was actually accomplished within twenty-two months. It reveals from the analysis of the test data that the intermittent time of the fourth-stage loading can be reduced from fourteen months to four months. Therefore, if it was not due to untechnical reasons, the seawall would be finished during twelve months. The seawall of 7.5m high, treated with plastic drainage plates, was practically finished during eighteen months. According to the analysis of measured data, the intermittent time for each loading could be shortened except the third-stage loading and it was entirely possible to construct the seawall within twelve months.

4.3 The settlement rate, horizontal displacement rate and pore water pressure coefficient are three main indexes of monitoring the stability of a project and controlling construction rate. As for the seawall treated with two approaches the maximum settlement rate reached 3.2cm to 5.2cm per day, the maximum horizontal displacement rate 4.8mm per day and the pore

water pressure coefficient 0.76 during loading. These three indexes greatly exceed the conventional standard limit and in fact the seawall is always in a stable state.

4.4 The approaches to treating seawall by geotextiles and plastic drainage plates attain the purpose of stabilization foundation. The former exerts a less influence on the stabilization foundation depth, amounting to 6m to 9m, i. e. equivalent to 1 to 1.5 times of the seawall height. The latter's influence scope surpasses the driven depth of plastic drainage plates with a length of 15m; it comes up to the whole silty clay layer, i. e. equivalent to 2.5 times of the seawall height.

## ACKNOWLEDGMENTS

The author wishes to thank Senior Engineers Liao Shude and Hu Henan, as well as Engineers Zhang Mingqiang, Chen Xiuliang, Wu Wenhua and Wu Yunbiao for finishing the study work cooperatively.

## REFERENCES

- Sun Pengzhou et al (1991) "Geological Report on Donggang Reclamation Development Project in Putu", Zhoushan Water Survey Office, Zhoushan, Zhejiang, China.
- Min Longyou et al (1993) "Preliminary Design on Polder for Donggang Polder Development No. 1 Project in Zhoushan", Zhejiang Design Institute of Water Conservancy & Hydroelectric Power, Hangzhou, China.

# Electrokinetic Geosynthetics and their Applications

I. M. Nettleton \* +, C.J.F.P. Jones \*, B.G. Clarke \* & R. Hamir #

\* Geotechnical Group, Department of Civil Engineering, Newcastle University, UK

+ Transport Research Laboratory, Riccarton, Edinburgh, Scotland, UK.

# Department of Civil Engineering, University Sains Malaysia, Malaysia

**ABSTRACT:** Increasing demands for construction materials, land and the redevelopment of derelict land are leading to the development of new technologies, and the integration of existing ones. It is with the above challenges in mind that the development of electrically conductive geosynthetics (Electrokinetic Geosynthetics EKGs) has come about. EKGs may provide filtration, drainage and reinforcement, which can be enhanced by electrokinetic processes, such as electro-osmosis and ion migration. In addition to the electrokinetic processes, it is possible to incorporate enhanced transmissivity, sorption, wicking, and hydrophilic characteristics into the new geosynthetics. The availability of new materials and production techniques, together with the need for new engineering solutions, to complex environmental and ground engineering situations, have rendered feasible and desirable the inclusion of these properties into a new range of geosynthetics. This paper describes the concepts behind the development of a new generation of geosynthetics, and the laboratory testing of prototype materials and experimental applications.

A series of laboratory experiments have been undertaken which investigated the feasibility of employing EKGs and electro-osmotic consolidation for the improvement of fine grained low permeability fills. These tests showed accelerated dissipation of pore pressures; reduction of moisture contents; and increases in soil strength and adhesion to reinforcement, over and above that from conventional consolidation. Investigations into environmental applications for EKGs have demonstrated that they can be used for integrated electrode and wellpoint installations for electrokinetic remediation of contaminated ground. Investigations have demonstrated the sorption properties of EKGs, in respect of heavy metals.

**KEYWORDS:** Geosynthetics, Reinforcement, Electrokinetic, Drainage, Environmental Engineering.

## 1. INTRODUCTION

The increasing demands for construction materials, land and the redevelopment of derelict land are leading to the development of new technologies, and the integration of existing technologies. The development of *electrically conductive geosynthetics* (EKGs) is an example of this. The concept is to develop a range of geosynthetics which in addition to providing filtration, drainage and reinforcement can be enhanced by electrokinetic techniques for the transport of water and chemical species within fine grained low permeability soils, which are otherwise difficult or impossible to deal with.

The ability of electrokinetic phenomena to move water, charged particles and free ions through fine grained low permeability soil is well established. Electrokinetic phenomena will occur in any soil; however, in medium to coarse grained soils electrokinetic phenomena provide a less effective transport mechanism than hydraulic flows, due to high permeability of the soil.

The first application of electrokinetic phenomena for civil engineering processes was undertaken by Casagrande in 1939 for the dewatering and stabilisation of railway cuttings at Salzgitter, Germany, Casagrande (1952). Since then there have been many other applications of electroosmosis for dewatering and stabilisation of soils, including: (i) The use of electroosmosis for dewatering and strengthening Norwegian quick clays, Bjerrum *et al* (1967); (ii) Electroosmotic stabilisation of West Branch Dam, Fetzer (1967); (iii) Electroosmotic treatment to improve pile friction, Milligan (1994).

## 2. ELECTROKINETIC TRANSPORT PHENOMENA

There are five principle electrokinetic phenomena within soil: Streaming Potential, Migration Potential, Electroosmosis, Ion Migration and Electrophoresis. The first two of these phenomena are concerned with the generation of electrical potential due to the movement of charges and charged particles respectively. The remaining three are concerned with the transport mechanisms developed upon application of an electrical field across a soil mass.

### 2.1 Electroosmosis

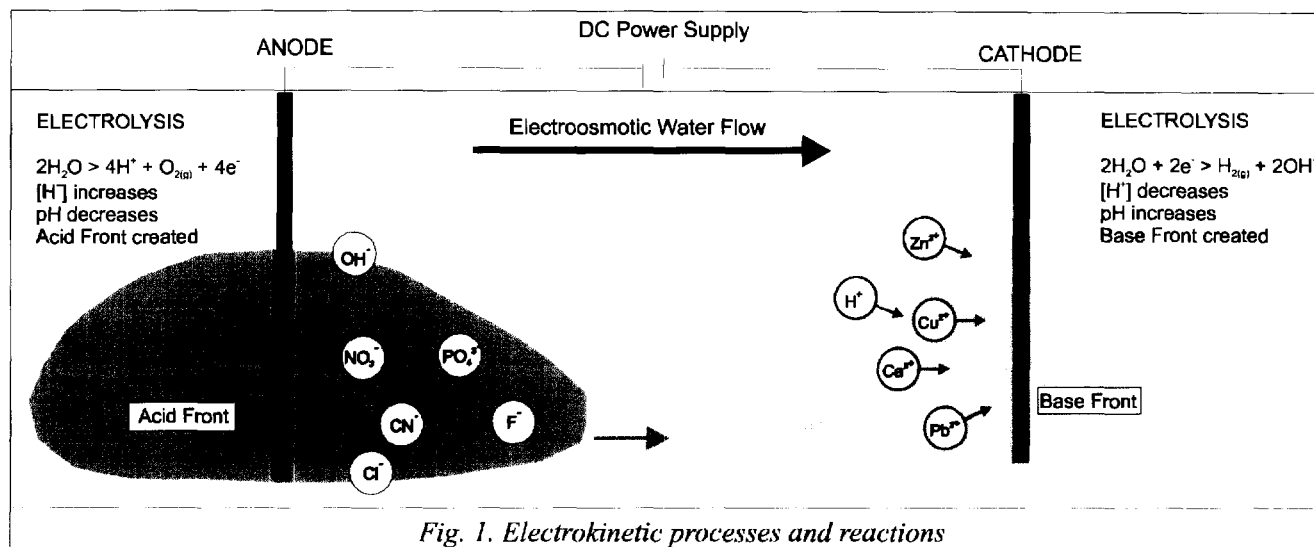
When an electrical field is applied across a fine grained soil mass cations are attracted to the cathode and anions to the anode, Fig. 1. As the ions migrate they carry their hydration water with them, and exert a frictional force on the water around them. Hence, there is a flow of water to both the anode and the cathode. In order to maintain charge neutrality, however, there are more cations than anions in the pore fluid of a soil containing negatively charged clay particles. Therefore, there is a net flow of water to the cathode, Gray & Mitchell (1967).

The electroosmotic flow of water through a soil can be expressed in the form of Darcy's equation for water flow:

$$q_A = k_e i_e A \quad (1)$$

where  $q_A$  is the flow rate,  $i_e$  is the potential gradient  $\Delta V/\Delta L$ ,  $A$  is the cross-sectional area and  $k_e$  is the coefficient of electroosmotic permeability.

The electroosmotic permeability ( $k_e$ ) for most soils lies in the range  $1 \times 10^{-9}$  to  $1 \times 10^{-8}$  m<sup>2</sup>/Vs, Lageman *et al* (1989),



and is independent of pore size, Casagrande (1949).

If both the anode and cathode are open (to water flow) then electroosmosis will “pump” water through a soil. However, if the anode is closed and the cathode open, then electroosmosis will generate negative pore pressures. The magnitude of these is given by:

$$u = \frac{k_e}{k_h} \gamma_w V \quad (2)$$

where  $k_e$  is the electroosmotic permeability,  $k_h$  is the hydraulic permeability,  $\gamma_w$  is the unit weight of water and  $V$  is the applied voltage. If the total stress does not change during electroosmosis then the magnitude of the effective stress is proportional to the negative pore pressure generated at the anode.

### 2.2 Electromigration or Ion Migration

The application of an electrical field across a soil mass causes migration of the free ions and ion complexes, which are present within the pore fluid, to the appropriate electrode, Lageman *et al* (1989) and Hellowell (1994).

Lageman *et al* (1989) report the average mobility of ions in soils as  $5 \times 10^{-8} \text{ m}^2/\text{Vs}$ , which is an order of magnitude greater than the electroosmotic permeability. Hence, anions can usually overcome the electroosmotic flow and migrate towards the anode.

### 2.3 Electrophoresis

When a DC electrical field is applied across a particulate suspension positively charged particles are attracted to the cathode and negatively charged particles are attracted to the anode. Most clay colloids are negatively charged and are therefore, attracted to the anode.

Electrophoretic mobilities reported by Lageman *et al* (1989) and by van Olphen (1977) are in the ranges  $1 \times 10^{-10}$  to  $3 \times 10^{-10} \text{ m}^2/\text{Vs}$  and  $1 \times 10^{-8}$  to  $3 \times 10^{-8} \text{ m}^2/\text{Vs}$  respectively. Hellowell (1994) attributes the discrepancy to differences in the moisture content of the medium. Electrophoresis has found applications in the densification of sludges and mine tailings, Lo *et al* (1991a). Esrig (1968) reports that the process is inconsequential for most naturally occurring soils.

## 3. GROUND IMPROVEMENT AND REINFORCEMENT USING EKGS

Electroosmotic treatment of soils generates negative pore pressures and thereby increases the effective stress, leading to consolidation of the soil. The end result is similar to that gained by the application of a surcharge; however, unlike vertically surcharging a soil mass, there are no stability problems, as the pore pressures generated are negative rather than positive. Electroosmosis may also be used to accelerate the dissipation of positive pore pressures resulting from vertical surcharging. Indeed, once the positive pore pressures have been dissipated electroosmosis can be continued for further consolidation, due to the generation of negative pore pressures. The maximum negative pore pressure due to electroosmotic consolidation will be generated at the anode, Esrig (1968). These processes increase the *strength* of the soil and the *bond* characteristics of the soil and the reinforcement.

Electroosmosis often leads to increases in strength of cohesive soils, due to chemical cementing of the soil fabric, Mitchell (1991).

### 3.1 Laboratory Tests - Consolidation

A number of laboratory tests have been conducted to evaluate the use of conductive geotextiles as electrodes in electroosmotic consolidation. The tests using an electroosmotic cell simulated the reinforcement, electrodes and the drainage configuration expected in reinforced soil applications.

A number of geosynthetic electrodes were considered and compared with a perforated copper disk. The initial type 1 geosynthetic electrode was formed from a non-woven, needle punched geotextile. A copper wire of 300 mm length and 1 mm diameter was inserted at the centre of the geotextile. Copper wire was chosen to inhibit the generation of oxygen at the anode. Any oxygen generated at the anode combined with the copper to form copper oxide, which is a good conductor of electricity.

The samples were prepared from Grade E Kaolinite (SILT) slurry at water contents of 1.5 times the liquid limit to ensure they would be fully saturated. The electroosmotic permeability was  $k_e = 3.4 \times 10^{-9} \text{ cm/sec per volt/cm}$  and hydraulic permeability  $k_h = 6 \times 10^{-7} \text{ cm/sec}$ .

Initially the soil was consolidated with an effective stress of 25 kPa. Electroosmotic tests were conducted with vertical pressures of 50 and 100 kPa to simulate the imposed load of fill material. During the tests, pore pressures, current and voltage variations across the soil sample were recorded. After treatment, tests were carried out to determine the water content and strength of the soil.

**Negative Pore Pressure**

Figure 2 shows the change in pore pressure at the anode during electroosmotic consolidation using type 1 geosynthetic electrodes with different applied voltages.

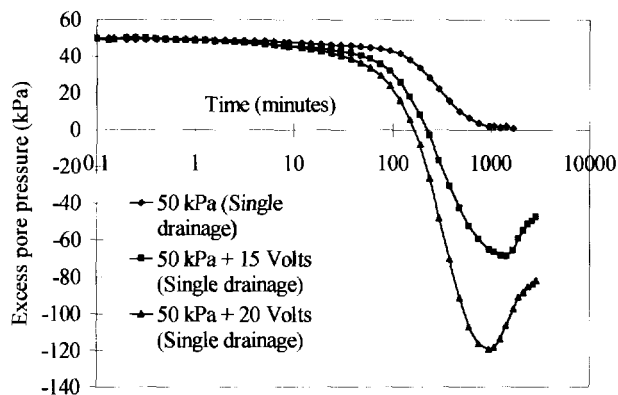


Fig. 2. Excess pore pressure versus time for normal consolidation and for electroosmotic consolidation.

Initially the back pressure was lowered by 50 kPa to simulate an applied vertical pressure. After the current was switched on the pore pressure at the anode decreased until it equalised the back pressure, signifying full dissipation of the positive pore pressure. As the test continued, the pore pressure at the anode decreased to a value lower than the back pressure, signifying the generation of the negative pore pressure. Upon reaching a maximum negative value, the pore pressure increased before stabilising at a lower negative value. Figure 2 shows that the positive pore pressure generated by the vertical loading was reduced to zero in a shorter time by the application of electroosmosis. The results concur with the theoretical solution by Wan *et al* (1976).

**Vertical Strain**

The vertical strain-time curves are as shown in Figure 3. The electroosmotically induced vertical strain curve was similar to the consolidation due to vertical load. The vertical strain increased from 9.7% for consolidation with a normal load to 13% with the incorporation of electroosmotic consolidation.

**Water Content**

The moisture content profile is as shown in Figure 4. It indicates that moisture content for soil consolidated by a combination of vertical load and electroosmotic consolidation is lower than soil consolidated only with a vertical load.

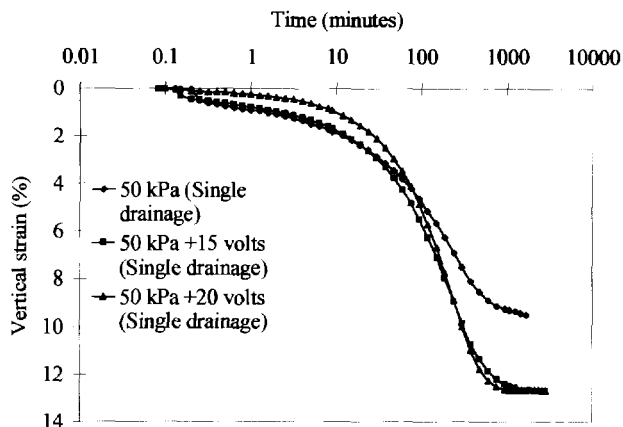


Fig. 3. Vertical strain versus time for normal consolidation and for electroosmotic consolidation.

The shape of the water content distribution indicates that the lowest water content was at the centre of the specimen. However, the water content at the anode was still significantly reduced. The water content profile agrees with the finding of Lo *et al* (1991b).

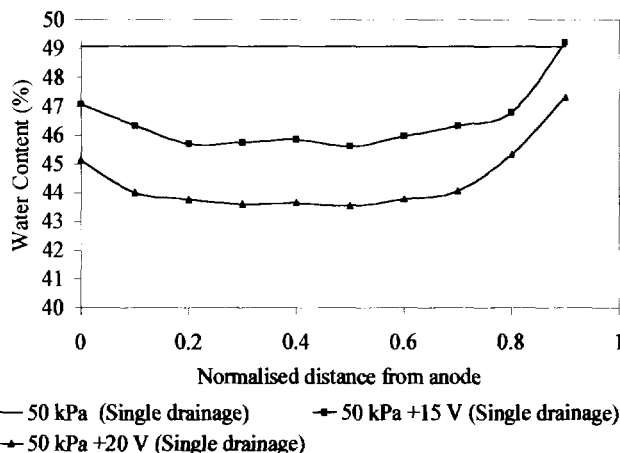


Fig. 4. Water content variation across soil specimens consolidated by vertical loading and by electroosmosis, with a closed anode.

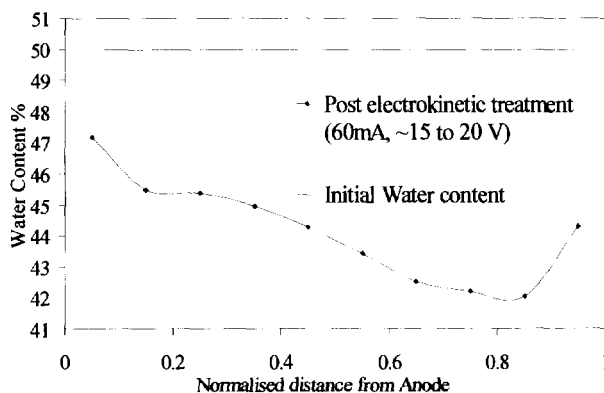


Fig. 5. Moisture content profile across electrokinetically treated soil, open anode and cathode conditions.

As a comparison Figure 5 shows the water content profile across a soil sample subjected to electrokinetic treatment, but with an an "open" anode and cathode. This allows water into and out of the soil. The largest degree of dewatering occurs at the cathode, due to a high resistance zone which develops close to the cathode. This high resistance zone causes a localised increase in the voltage gradient and, hence, an increase in electroosmotic flow in this region.

#### Shear Strength

The undrained shear strength of the soil was determined at a depth of 30 mm from the surface. The test showed an increase in the shear strength up to 128% for an applied voltage of 20 volts, Table 1.

Table 1. Increase in shear strength when using electrokinetic geosynthetic reinforcement.

Soil	Shear Strength kPa	% Increase
50 kPa vertical pressure	11	-
50 kPa vertical pressure + 15V	19	72
50 kPa vertical pressure + 20V	26	128

#### 3.2 Laboratory Tests - Soil-Reinforcement Bond

The use of electrically conductive geosynthetic reinforcement can be shown to increase soil-reinforcement bond. A series of pullout tests have been undertaken at Newcastle University to illustrate this concept. The objective of the tests was to study the effect of an electroconductive reinforcement on bond performance under undrained conditions. This represented the most severe case in the use of cohesive fill in a reinforced soil structure.

The tests were performed in a specially designed pullout cell and were conducted on soil strengthened by vertical overburden and also by a combination of overburden and electroosmotic consolidation.

Commercially available grade E kaolin was used for the tests. The soil was mixed at a water content of about 52% which was about 3% below the liquid limit.

A drainage layer which also served as the cathode was first placed at the bottom of the cell. The soil was then placed in the cell and compacted manually. The anode was inserted at mid height of the sample. Another layer of conductive geosynthetic was placed at the top of the soil sample forming a second cathode. Hence a two way drainage configuration was used to accelerate the consolidation process.

The soil was consolidated by the application of vertical pressure or by a combination of vertical pressure and electroosmotic consolidation. The vertical pressure was applied by a hydraulic jack capable of providing a constant vertical pressure. A potential difference of 30 volts was

applied by means of a direct current power supply unit with a maximum output current of 1 ampere.

After the completion of the consolidation process, the cell was turned sideways and bolted to the platen of the frame of the triaxial testing machine. A slit cover was then removed, exposing the geosynthetic reinforcement. The pullout resistance and the vertical displacement were automatically recorded by a load cell and LVDT respectively. After the pullout tests, laboratory vane shear tests were carried out on the soil sample close to the anode. A small portion of the soil sample was also taken for the determination of the water content.

#### Bond Strength

The increase in reinforcement-soil bond due to the use of electrically conductive reinforcement is shown in Table 2. The results show that the increase ranged from 54% to 209% at different overburden pressures.

Table 2. Increase in Shear and Soil Reinforcement Bond strengths using an electrokinetic geosynthetic.

Consolidation Pressure kPa	% Increase in Shear Strength	% Increase in Bond Strength
110	150	209
140	203	113
356	72	54

#### 4. ENVIRONMENTAL APPLICATIONS OF ELECTROKINETIC GEOSYNTHETICS

The electrokinetic processes described in Section 2 can be applied to the remediation and containment of contaminants within the ground. Indeed, electrokinetic remediation is the only technique for the in situ remediation of contaminated fine-grained soils and the groundwater within them (NATO/CCMS 1993). The following are the electrokinetic processes which can be utilised for contaminant remediation and containment:

- Ion migration may be utilised to transport metals and polar contaminants to the relevant electrode, where they may be removed (Lageman *et al* 1989).
- Ion migration may be utilised to transport nutrients to enhance bioremediation (Figure 6).
- Electroosmosis may be utilised to flush contaminants from the soil (Lageman *et al* 1989).
- Electrosorption of contaminants.

In addition because the soil mass acts as a resistor the ground heats up (Lageman *et al* 1989 reports temperature rises of between 20 and 40 °C) and this phenomena may be used to volatilise organic contaminants (Lageman 1995), and to stimulate bioremedial action.

Electrokinetic transport of nutrients has been investigated in a tank containing grade E Kaolinite (Section 3.1). The tank was 400mm long with three wellpoints inserted at 100mm spacings along the length. Nitrate solution (500mg/l) was placed in the electrode reservoirs, an electrical current of 60mA was set across the tank, and porewater samples were taken from the three wells twice a



day. Figure 6 shows the Nitrate breakthrough curves obtained. Well/01 was located 100mm from the anode, well/02 was located at the centre of the tank, and well/03 was located 100mm from the cathode.

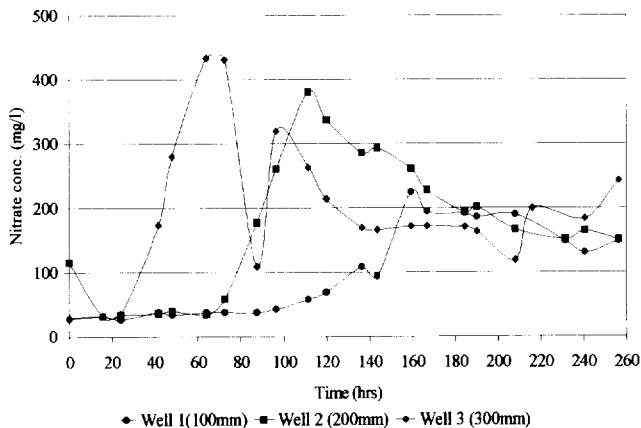


Fig. 6. Graph showing transport of Nitrate by ion migration.

## 5. ELECTROKINETIC GEOSYNTHETICS

The new EKGs can take the form of single materials, which are electrically conductive, or composite materials, in which at least one element is electrically conductive. They can be of the same basic form as present day filter, drainage, separator and reinforcement materials, but offer sufficient electrical conduction to allow the application of electrokinetic techniques for ground improvement and remediation.

There are a number of materials which can be used to produce electrically conductive geosynthetics. The principle conductive materials which have been considered and evaluated at Newcastle include:

- Carbon Fibre Materials.
- Conductively Filled Polymers.
- Metallic Fibres (Metal fibres, metallised fibres or metal coated fibres).
- Composites formed from conductive/non conductive elements.

The metallic fibres have been discounted due to corrosion durability problems. Both the carbon fibre and conductively filled polymer materials show great promise as base materials for the new EKGs, and are discussed below.

### 5.1 Conductively Filled Polymers

Organic polymers with all carbon backbones are insulators (eg polyethylene PE, polyvinylchloride PVC, ethylvinylacetate EVA) and can be used for electrical insulation. However, if carbon black, carbon fibres or finely divided metals are used as fillers in such organic polymers, then conductive ( $10^{-5}$  to 1 s/cm) composites may be created, Cowie (1991). In these composites it is the filler which conducts and not the polymer.

If carbon black is used as the conductive filler then a loading of between 20 and 30 wt % will be required to

produce a suitable conductivity. The structure and mixing of the carbon black filler plays an important role in determining the properties of the conductive polymer. There are two main types of carbon structure of interest, the Low structure, which is a jumbled array of carbon spheres, and the High structure, which is a chain of spheres, giving a higher conductivity.

An activated carbon black or carbon fibre filler may also be introduced to increase the sorption characteristics of polymeric materials. Sorption is another potential function of EKGs.

### 5.2 Carbon Fibre Materials

Carbon fibres are representative of graphite materials; they are electrically conductive ( $> 10^2$  s/cm) and chemically stable. High modulus carbon fibres are expensive and their use is limited to specialist applications where high stresses, high temperatures and radiation exposure are expected. The lower modulus carbon fibres are cheaper, their production simpler and the raw materials more abundant, Ermolenko *et al* (1990).

Activated carbon fibres (ACFs) have an open microporous structure which provides sorption sites. They provide similar or higher sorption than activated carbon particles and their shape allows more rapid and greater sorption than is found with carbon particles, Ermolenko *et al* (1990). The low modulus materials have many of the features required for the production of electrically conductive geosynthetics.

### 5.3 EKG functions and design

During electrokinetic treatment utilising EKGs water will flow from the soil and into the EKG at the cathode, and oxygen and hydrogen will be formed and flow into the anode and cathode respectively. The gas and water have to be dissipated to prevent the build up of pore pressures. Hence, the EKG must act as a filter and a drainage material:

- Filtration - to allow the free passage of water from the soil to the drainage system.
- Transmissivity - to transport water and gas out of the system without hindrance.

The EKG must also distribute the electrical current to the pore fluid within the fine grained soil being treated. Any interface resistance to the transfer of current from the electrodes to the soil is a potentially large source of electrical inefficiency for electrokinetic treatment. The higher the interface resistance, the lower will be the effective voltage gradient or current flow for electrokinetic treatment. Factors affecting the pore fluid/electrode interface resistance include:

- Form of the electrodes
- Gas generation during the process
- Current densities - high values lead to electrode polarisation.

Electrode configuration plays an important role in determining the magnitude of interface resistance. An important consideration is the presence of ground water in the porous structure of the geosynthetic. This makes its

whole surface act as an electrode. A major advantage of the use of a geosynthetic electrode is that the surface area can be much larger than traditional electrodes, and the structure is open to the flow of water and gas.

From a study of the electrode requirements for electrokinetic treatment it is clear that a band drain type electrode seems to be the most promising design (Nettleton, 1996). A band drain can be made to act as a local distributor of electrical current by incorporating carbon black fillers into the base polymer for either the geotextile filter or the drainage component of the band drain. Due to the electrical current requirements for electrokinetic treatment a stringer will be required to conduct and distribute the bulk of the current throughout the band drain. The stringer could take the form of a metallic wire coated with a conductive polymer to prevent corrosion due to electrolysis at the electrodes (Nettleton, 1996).

## 6. CONCLUSIONS

The development of electrically conductive geosynthetic materials offers significant new application areas for geosynthetic products, ranging from accelerated consolidation of soft soils to soil decontamination and pollution control. The use of electrically conductive reinforcement in reinforced soil structures is beneficial as the concept is fully compatible with, and has a positive influence on, the parameters controlling the reinforcement mechanisms.

## ACKNOWLEDGEMENTS

The authors would like to express their thanks to the Engineering and Physical Sciences Research Council and the British Council in Japan for their support during this research. In addition the authors would like to thank Mitsui Petrochemical Industrial Products Ltd. and Netlon Ltd. for supplying materials and production facilities.

## REFERENCES

- Bjerrum, L., Mowm, J. and Eide, O. (1967). "Application of electro-osmosis to a foundation problem in a Norwegian quick clay", *Geotechnique*, Vol. 17, pp. 214-235.
- Casagrande, I. L. (1949). "Electro-osmosis in soils", *Geotechnique*, Vol.1(3), pp. 159-177.
- Casagrande, L. (1952). "Electrical stabilisation in earthwork and foundation engineering", *Proc. Conf. on Soil Stabilisation*, Massachusetts, USA.
- Casagrande, L. (1952). "Electro-osmotic stabilisation of soils", *Journal of the Boston Society of Civil Engineers*, Vol. 39, pp. 51-83.
- Cowie, J. M. G. (1991). *Polymers: Chemistry & Physics of Modern Materials* (2nd ed.), Blackie, Glasgow, UK. 436 p.
- Ermolenko, I. N., Lyublinter, I. P. and Gulko, N. V. (1990). *Chemically modified carbon fibers and their applications*, Verlagsgesellschaft mbH, Weinheim, Germany. 304 p.
- Esrig, M. I. (1968). "Pore pressures, consolidation and electrokinetics", *Journal of Soil Mechanics and Foundation Division*, ASCE, Vol. 94 (SM4), pp. 899-921.
- Fetzer, C. A. (1967). "Electro-osmotic stabilisation of West Branch Dam", *Journal of Soil Mechanics and Foundations Division*, ASCE, Vol. 93 (SM4), pp. 85-106.
- Gray, D. H. and Mitchell, J. K. (1967). "Fundamental aspects of electro-osmosis in soils", *Journal of the Soil Mechanics and Foundations Division*, ASCE, Vol.93 (SM6), pp. 209-236.
- Hellawell, E. (1994). *Modelling transport processes in soil due to hydraulic density and electrical gradients*, PhD Thesis, Cambridge University, UK.
- Lageman, R. (1995). Personal Communication.
- Lageman, R., Pool, W. and Seffinga, G. A. (1989). "Electro-reclamation: state-of-the-art", *In NATO/CCMS 3rd Int. Conf. on Demonstration of Remedial Action Technologies for Contaminated Land and Groundwater*, Nov. 6-9 1989, Montreal, Canada, pp. 115-136.
- Lo, K. Y., Ho, K. S., & Incullet, I. I. (1991a). "A novel technique of electrical strengthening of soft sensitive clays by dielectrophoresis". *Canadian Geotechnical Journal*, Vol. 29, pp. 599-608.
- Lo, K. Y., Ho, K. S. and Incullet, I. I. (1991b). "Field tests of electroosmotic strengthening of soft sensitive clay", *Canadian Geotechnical Journal*, Vol. 28, pp. 74-83.
- Milligan, V. (1994). "First applications of electro-osmosis to improve friction pile capacity - three decades later", *In Proc. 13th Int. Conf. on Soil Mechanics and Foundation Engineering*, Jan. 5-10 1994, , New Delhi, India. Balkema: Rotterdam, The Netherlands, Vol. 5, pp. 1-5.
- Mitchell, J. K. (1991). "Conduction phenomena: from theory to geotechnical practice", *Geotechnique*, Vol. 41 (3), pp. 299-340.
- NATO/CCMS (1993). "Demonstration of Remedial Action Technologies for Contaminated Land and Groundwater". (Final Report No. EPA/600/R-93/012a) North Atlantic Treaty Organisation, Committee on the Challenges of Modern Society.
- Nettleton, I. M. (1996). *Electro-Bioremediation*. 1<sup>st</sup> year interim report for EPSRC Contract No. GR/K20590. Geotechnical Group, University of Newcastle upon Tyne, UK.
- van Olphen, H. (1977). *An introduction to clay colloidal chemistry*, (2nd Ed.), Wiley Interscience: New York, USA. 318 p.
- Wan, T. W. and Mitchell, J. K. (1976). "Electro-osmotic consolidations of soils", *Journal of Soil Mechanics and Foundation Division*, ASCE, Vol. 102, (GT5), pp. 503-507.

# A Study of the Behavior of Geogrid Reinforced Stone Column

J.S. Sharma

NTU-PWD Geotechnical Research Centre, Nanyang Technological University, Singapore

**ABSTRACT:** The bearing capacity of a stone column is mainly governed by the bulging failure near its top end. The performance of a stone column can be improved by providing layers of reinforcement in the top region. In this paper, the behavior of geogrid reinforced stone column is explored using the finite element method. Results are presented from a parametric study using a unit cell finite element mesh in which the number, spacing and the stiffness of the geogrid were varied. It was found that increasing the number of geogrid layers results in an increase in the bearing capacity and a reduction in the bulging of the stone column. Decreasing the spacing of geogrid layers also increases the bearing capacity of the stone column. However, decreasing the spacing to less than 0.5 times the diameter of the stone column does not result in appreciable increase in bearing capacity. An inexpensive, low stiffness reinforcement installed at correct spacing is good enough to provide significant increase in the bearing capacity of the stone column.

**KEYWORDS:** Bearing Capacity, Finite Element Analysis, Geogrids, Soft Soils, Stone Columns

## 1 INTRODUCTION

It has become a common practice to install stone columns for improving the bearing capacity of soft clay deposits. When a soft clay layer installed with stone columns is loaded, a redistribution of vertical stress takes place. Most of the vertical stress is carried by the stone column because it is significantly stiffer than the soft clay. As a result, the stone column deforms laterally into the surrounding soil. For stone columns with lengths greater than a certain critical length, it is widely accepted that their load carrying capacity is governed by the bulging failure near their top end irrespective of whether they are end bearing or penetrate partially into a medium stiff soil layer (Madhav and Miura, 1994). The reason for this is the shear strength of the surrounding soft soil near the top end of the stone column is fairly low and therefore, the soil is unable to provide sufficient lateral resistance to the bulging. Experiments on stone columns have indicated that maximum bulging occurs at a depth approximately equal to 1 to 1.5 times the diameter of the stone column (Hughes et al., 1975; Madhav, 1982). The occurrence of bulging failure limits the ultimate load carrying capacity of a stone column regardless of the stiffness of the stone column material.

The magnitude of lateral stresses imposed by the stone column on the surrounding soil can be reduced by reinforcing the stone column near its top end using layers of geogrid. As a result, the bulging of stone column is reduced and its load carrying capacity is increased. The effectiveness of this technique has been demonstrated experimentally by Madhav (1982). Madhav et al. (1994) have proposed a limit equilibrium based method for the design of such stone columns. Their method is simple to use but it does not take into account the effect of slip at the stone column-soil interface and the stiffness of the reinforcement. In this paper, the behavior of geogrid reinforced stone columns is explored using the finite element method. A parametric study was conducted using a

“unit cell” finite element mesh in which the number, the spacing and the stiffness of the geogrid were varied. The finite element code was validated against the results of a field trial on a single stone column (Hughes et al., 1975) prior to its deployment in the parametric study.

## 2 FINITE ELEMENT ANALYSIS

### 2.1 The Mesh

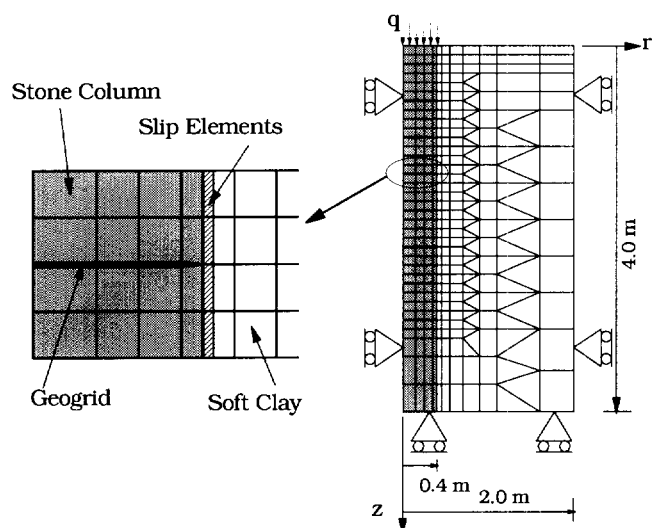


Figure 1. The finite element mesh

Figure 1 shows the details of the finite element mesh used in the present study. It is an axisymmetric unit cell mesh with the central axis of the stone column as the axis of symmetry. The diameter of the stone column is 0.8 m whereas the diameter of the unit cell soil cylinder is 4 m, giving the replacement ratio, i.e. the ratio of the volume of stone column to the volume of the unit cell soil cylinder, equal to 0.04 or 4%. Only top 4 m of the stone column has been

modelled. The justification for this the fact that at depths greater than 2 to 3 diameters, the deformation of the stone column is negligible (Hughes and Withers, 1974).

The stone column has been modelled using 8-noded quadrilateral elements with displacements unknown. The surrounding soil has been modelled using 6-noded triangular and 8-noded quadrilateral elements with displacements and pore pressures unknown. The geogrid has been modelled using very thin (0.01 m thickness) 8-noded quadrilateral elements. The interface between the stone column and the surrounding soil has been modelled using 6-noded slip elements. No slip elements are provided at the geogrid-stone column interface.

## 2.2 Constitutive Modelling of Materials

The stone column has been modelled as Elastic-Perfectly Plastic material with Mohr-Coulomb failure criterion. The surrounding soft clay is considered as normally consolidated and is modelled as an Elastic-Perfectly Plastic material but with Tresca failure criterion. The undrained shear strength of the soft clay increases linearly with depth. The geogrid has been modelled as Linear Elastic material. The slip elements at stone column-soft clay interface have also been modelled as Elastic-Perfectly Plastic material with Mohr-Coulomb failure criterion. Following the experience of Balaam and Poulos (1982), the stone column-soft clay interface is assumed as purely cohesive, i.e. zero angle of friction but a finite value of cohesion. The cohesion at the stone-column-soft clay interface at any level is taken as 80% of the undrained shear strength of soft clay at that level. Table 1 lists all the parameters chosen for the above four types of materials.

Table 1. Parameters for the stone column, soft clay, geogrid and the stone-column-soft clay interface

Parameter	Stone Column	Soft Clay	Geogrid	Inter-face
$c_o$ (kPa)	1.0	1.2	—	1.0
$m_c$ (kPa/m)	0.0	1.94	—	1.55
$\phi$ (Degrees)	40.0	0.0	—	0.0
$E_o$ (kPa)	40,000	720	2,500,000	600
$m_E$ (kPa/m)	9200	1150	0.0	900
$\nu$	0.3	0.49	0.3	—
$\gamma_{bulk}$ (kN/m <sup>3</sup> )	18.0	18.0	18.0	—
$t$ (m)	—	—	0.01	0.04

Notes:  $c_o$  — cohesion at ground level,  $m_c$  — rate of increase of cohesion with depth,  $\phi$  — angle of internal friction,  $E_o$  — Young's modulus at ground level,  $m_E$  — rate of increase of Young's modulus with depth,  $\nu$  — Poisson's ratio,  $\gamma_{bulk}$  — bulk unit weight,  $t$  — thickness.

## 2.3 Stages in a Typical Analysis

A typical finite element analysis in the present study has following stages:

1. In-situ stage: This is the start of the analysis. At this stage of the analysis, the whole mesh contains only the soil elements.
2. Installation of stone column and geogrid layers: In this stage, the soil elements that are occupying stone column space are removed from the mesh and the elements representing stone column and geogrid are added to the mesh.
3. Loading of stone column: In this stage, the stone column is loaded at its top end using displacement control. The displacement is applied in very small increments (0.0002 m per increment) to prevent any divergence from the stress-strain curve.

## 2.4 Validation of the Finite Element Code

Before a finite element mesh is used for a parametric study, it is imperative to validate it against good quality experimental data. The main purposes of the validation are to ensure that the mesh is sufficiently refined and to check that the constitutive models used are satisfactory. For the validation, it was decided to make use of the results of a field trial on a single stone column reported by Hughes et al. (1975). This field trial is supplemented with extensive site investigation data which includes undrained shear strength profile of the soil, in-situ lateral stresses, and the soil modulus obtained from in-situ pressuremeter tests. Almost all the input parameters were taken directly from the site investigation data with the exception of the permeability of the soil which was taken to be  $2 \times 10^{-9}$  m/s in horizontal direction and  $1 \times 10^{-9}$  m/s in the vertical direction. Since the full loading of the stone column was very quick (total time = 0.5 hour), the soil can be assumed to be undrained. Therefore, the finite element simulation can be considered to be insensitive to small differences in permeability of the soil.

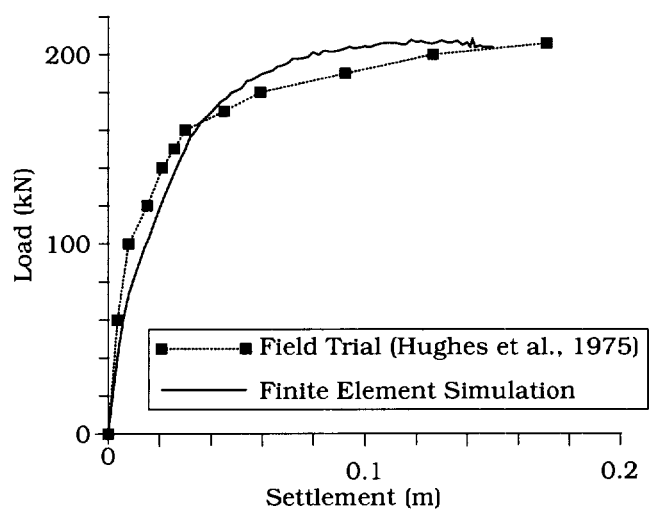


Figure 2. Measured and simulated load-settlement curves (after Hughes et al., 1975)

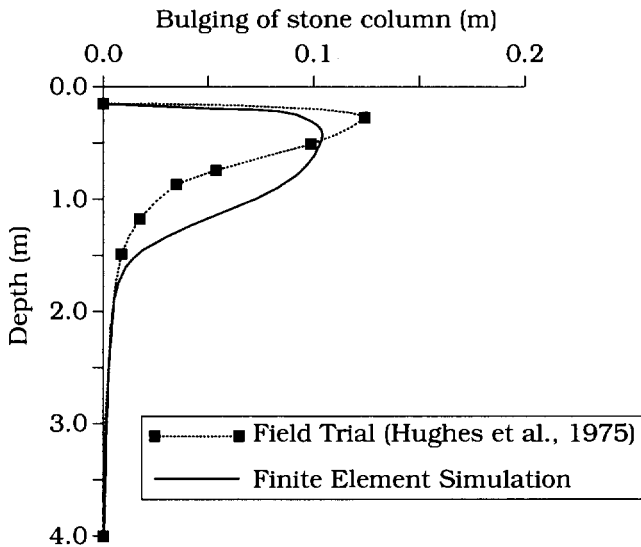


Figure 3. Measured and simulated bulging of stone column (after Hughes et al., 1975).

Detailed account of the finite element simulation can be found in Sharma (1997). Due to lack of space, only two main comparisons are described here. Figure 2 shows the comparison between the measured and the simulated load settlement curves. As seen from Figure 2, there is good agreement between the two curves. The measured and simulated deformation of the stone column at the end of loading are shown in Figure 3. Once again, the agreement between the two curves is satisfactory.

### 3 PARAMETRIC STUDY

As mentioned previously, the main parameters in the present study are: the number, spacing and the stiffness of the geogrid. Table 2 lists these parameters and their range.

Table 2. Range of parameters for the geogrid

Parameter	Range
Number of geogrid layers	0 to 5, in steps of 1
Spacing of geogrid layers	0.5 to 3 times the diameter of stone column
Elastic Modulus of geogrid (kPa)	100,000 to 2,500,000

#### 3.1 Effect of Number of Reinforcement Layers

In this series of finite element runs, the number of geogrid layers was increased from 0 to 5 in steps of 1. The spacing of these layers was kept constant at 0.5 times the diameter of the stone column ( $d_{sc}$ ) and the elastic modulus ( $E_r$ ) of the geogrid was taken equal to  $2.5 \times 10^9$  N/m<sup>2</sup>. Figure 4 shows the load-settlement curves for the stone column.

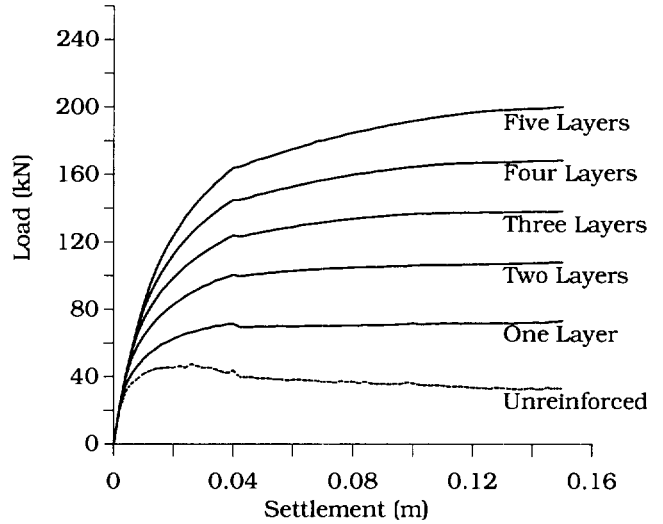


Figure 4. Effect of number of layers on the load-settlement response of stone column

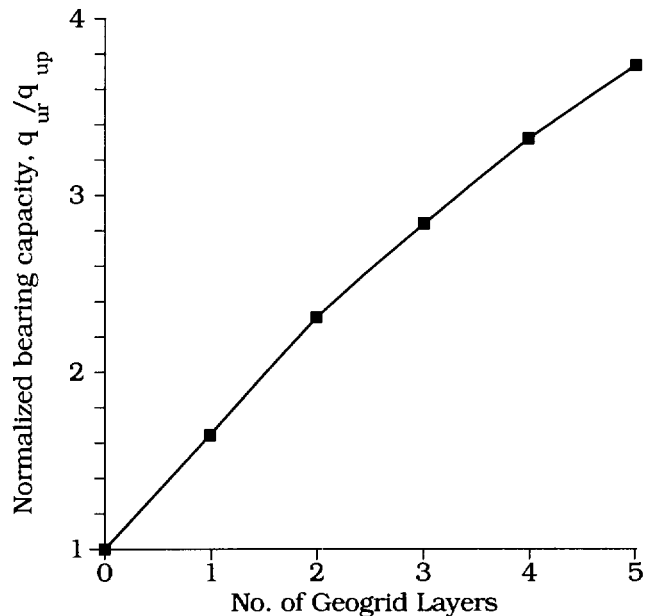


Figure 5. Variation of normalized bearing capacity of stone column with number of geogrid layers

Figure 5 shows the normalized bearing capacity of the stone column ( $\theta = q_{ur}/q_{up}$ ) plotted against number of geogrid layers. In figure 5 and in subsequent figures,  $q_{ur}$  is the ultimate bearing capacity of a reinforced stone column and  $q_{up}$  is the ultimate bearing capacity of an unreinforced stone column. It is clear from figures 4 and 5 that inclusion of geogrid layers in the stone column results in significant improvement in the load bearing capacity of the stone column. For example, the load bearing capacity of a stone column reinforced with three layers of geogrid is more than

twice that of an unreinforced stone column. The variation between  $\theta$  and the number of geogrid layers is almost linear. However, it does tend to flatten slightly as the number of layers are increased beyond 3 which implies that it may not be economical to put more than 3 layers of reinforcement.

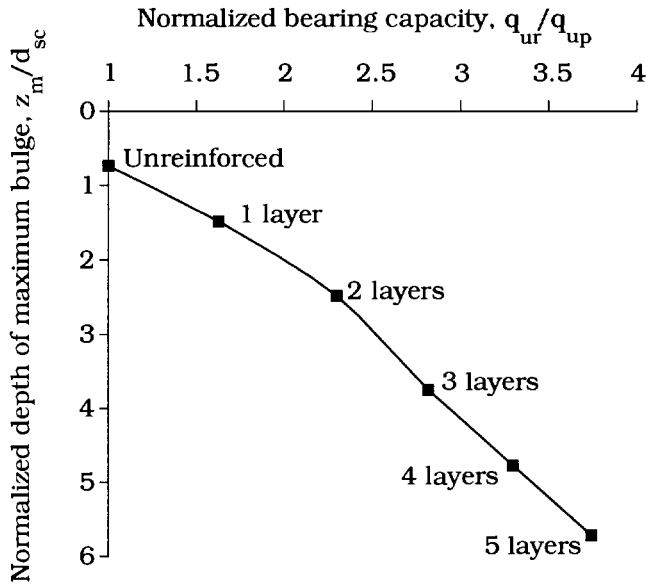


Figure 6. Variation of normalized depth of maximum bulging with normalized bearing capacity of stone column.

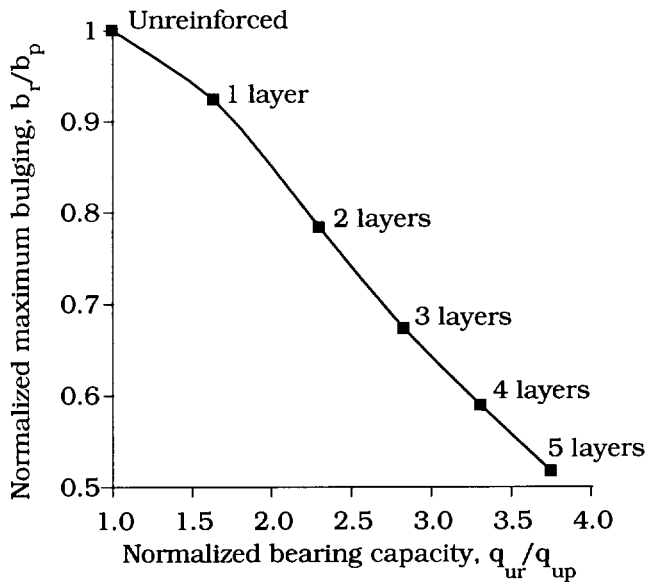


Figure 7. Variation of normalized maximum bulging with normalized bearing capacity of stone column

Figure 6 shows normalized depth of maximum bulging ( $\zeta = z_m/d_{sc}$ ) of stone column plotted against  $\theta$ . In this figure,  $z_m$  is the depth at which maximum bulging takes place. It can be seen from figure 6 that the increase in bearing capacity is

achieved by pushing the point of maximum bulging deeper, i.e. the failure mechanism is now benefiting from higher lateral resistance from the surrounding soil.

Increasing number of geogrid layers not only pushes the point of maximum bulging deeper but also reduces the amount of maximum bulging as seen from Figure 7 which shows normalized maximum bulging ( $\beta = b_r/b_p$  where  $b_r$  is maximum bulging for reinforced stone column and  $b_p$  is the maximum bulging for unreinforced stone column) plotted against  $\theta$ . For example, the amount of maximum bulging for a stone column reinforced with 3 geogrid layers is less than 70% of that for an unreinforced stone column. The reduction in amount of maximum bulging is achieved by redistribution of the lateral deformation of stone column over a longer section as shown in Figure 8.

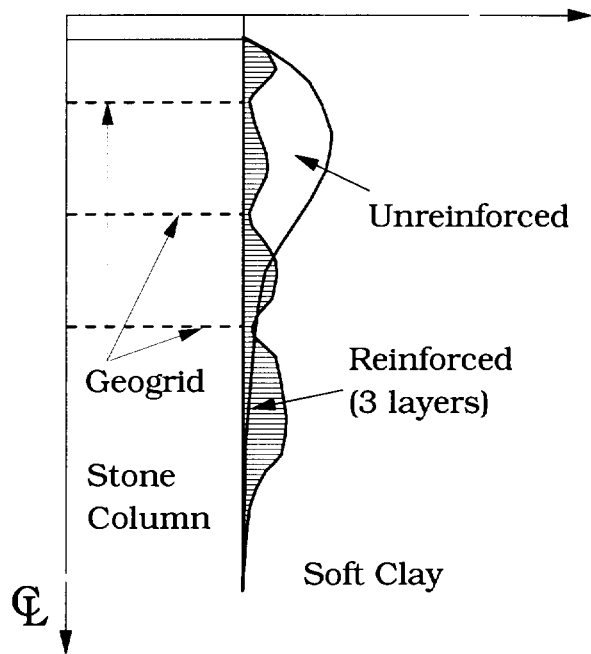


Figure 8. Redistribution of lateral deformation of stone column due to the presence of geogrid layers.

### 3.2 Effect of Spacing of Reinforcement Layers

For this series of finite element runs, the stone column was reinforced with three geogrid layers.  $E_r$  for geogrid was taken equal to  $2.5 \times 10^9 \text{ N/m}^2$ . Figure 9 shows normalized spacing of the geogrid layers ( $\lambda = s_r/d_{sc}$  where  $s_r$  is the spacing of geogrid layers) plotted against  $\theta$ . It can be seen from figure 9 that the maximum benefits of reinforcing the stone column are achieved when the spacing of reinforcement is between 0.5 to 1.5 times the diameter of the stone column. A spacing closer than 0.5 times the diameter would not result in any significant increase in the bearing capacity. Also, the combined action of multiple

layers of reinforcement, i.e. redistribution of lateral deformation of stone column, is not achieved effectively if the spacing of the reinforcement is greater than twice the diameter of the stone column. As a result, the increase in bearing capacity of the stone column is not significant.

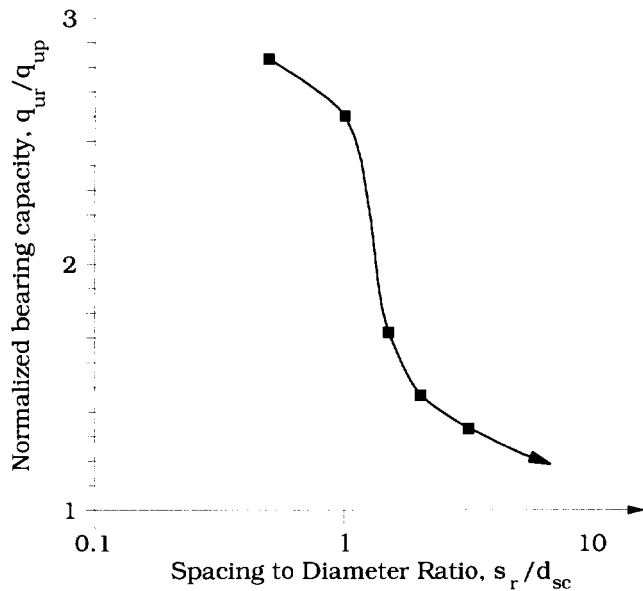


Figure 9. Effect of spacing of geogrid on the bearing capacity of the stone column

### 3.3 Effect of Stiffness of Reinforcement

In this series of finite element runs, the stone column was reinforced with three layers of geogrid spaced at 0.5 times the diameter of the stone column. Figure 10 shows elastic modulus of the geogrid ( $E_r$ ) plotted against  $\theta$ . The bearing capacity of a reinforced stone column increases as the stiffness of the reinforcement is increased. The increase is very dramatic when the stiffness is increased from  $E_r = 0$  (unreinforced case) to  $E_r = 1 \times 10^8 \text{ N/m}^2$ . However, beyond a certain stiffness ( $E_r > 10 \times 10^8 \text{ N/m}^2$ ), the increase is not significant. This implies that one need not use an expensive high stiffness reinforcement in order to improve the bearing capacity of stone column. Even a cheap, low stiffness reinforcement installed at correct spacing would provide significant increase in the bearing capacity of the stone column.

Figure 11 shows maximum tension in the geogrid plotted against  $E_r$ . It can be seen from figure 11 that a stiffer reinforcement attracts more tension but does not contribute significantly towards improving the bearing capacity of the stone column. Provision of a low stiffness reinforcement would result in a relatively flexible stone column with low levels of tension in the reinforcement. Such a flexible stone column would deform more uniformly than the one installed with very stiff reinforcement. This would result in the

bulging being distributed over a greater length, thus preventing localised bulging failure and resulting in improved bearing capacity.

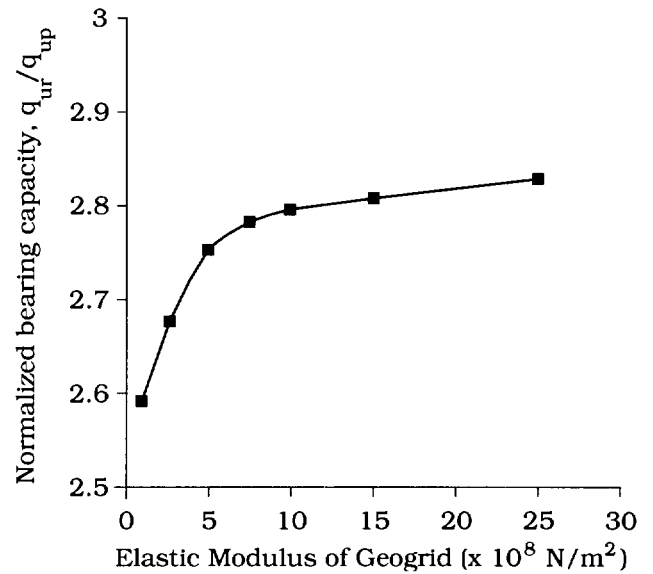


Figure 10. Effect of stiffness of geogrid on the bearing capacity of stone column

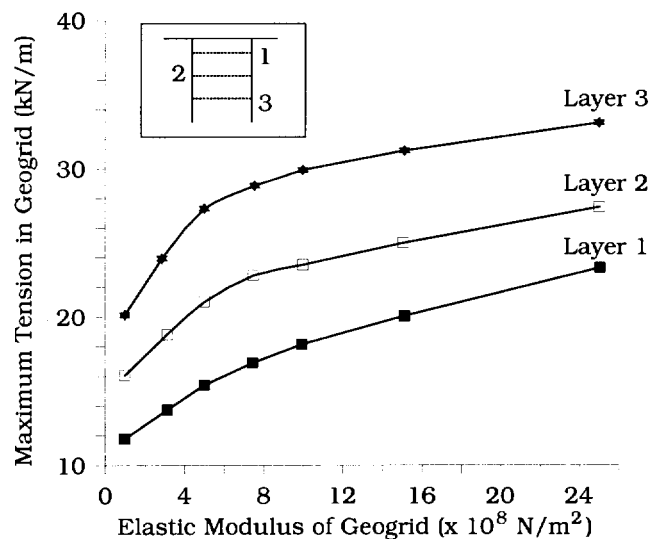


Figure 11. Effect of the stiffness of the geogrid on the magnitude of maximum tension induced in the geogrid

## 4 CONCLUSIONS

A parametric study of the behavior of geogrid reinforced stone column has been conducted using a finite element unit cell mesh which has been validated against the results of a field trial. The number, the spacing and the stiffness of

geogrid were the main parameters. It was found that increasing number of layers of geogrid increases the bearing capacity of the stone column. It also reduces the bulging of stone column and pushes the point of maximum bulging deeper. The inclusion of geogrid layers results in redistribution of lateral deformation of stone column and therefore, facilitates much more effective transfer of lateral stresses from stone column to the soft clay.

Installing geogrid layers at closer spacing also increases the bearing capacity of the stone column. The optimum spacing of geogrid layers was found to be between 0.5 to 1.5 times the diameter of the stone column. Installation of geogrid layers at spacing closer than 0.5 times the diameter of stone column does not result in appreciable increase in the bearing capacity of the stone column.

The increase in bearing capacity of stone column due to increase in stiffness of geogrid is quite dramatic when the elastic modulus of geogrid is increased from zero (unreinforced) to  $1 \times 10^8$  N/m<sup>2</sup>. However, increasing the elastic modulus beyond  $10 \times 10^8$  N/m<sup>2</sup> does not result in appreciable increase in the bearing capacity. A stiffer reinforcement also tends to attract more tension. Based on these two observations, it can be concluded that it is better to reinforce the stone column using a less stiff reinforcement installed at a spacing between 0.5 and 1.5 times the diameter of the stone column. Such a system would be more flexible and would be able to deform more uniformly than the one installed with stiff reinforcement. This would in turn result in bulging being distributed over a greater length, thus preventing localised bulging failure and improving the bearing capacity of the stone column.

#### ACKNOWLEDGEMENT

The author has benefited greatly from numerous stimulating discussions with Prof. M.R. Madhav of Indian Institute of Technology, Kanpur and would like to take this opportunity to thank him for all his help and encouragement.

#### REFERENCES

- Balaam, N.P. and Poulos, H.G. (1982). The Behaviour of Foundations Supported by Clay Stabilised by Stone Columns. *Research report No. R424*, School of Civil and Mining Engineering, University of Sydney.
- Hughes, J.M.O. and Withers, N.J. (1974). Reinforcing of soft cohesive soils with stone columns. *Ground Engineering*, Vol. 7, pp 42-49.
- Hughes, J.M.O., Withers, N.J. and Greenwood, D.A. (1975). A Field Trial of the Reinforcing Effect of a Stone Column in Soil. *Geotechnique*, Vol. 25, No. 1, pp 31-44.
- Madhav, M.R. (1982). Recent Development in the Use and Analysis of Granular Piles. *Symposium on Recent Development in Ground Improvement Techniques*, Bangkok, pp 117-129.

Madhav, M.R., Alamgir, M. and Miura, N. (1994). Improving Granular Column Capacity by Geogrid Reinforcement. *Fifth International Conference on Geotextiles, Geomembranes and Related Products*, Singapore, Vol. 1, pp 351-356.

Madhav, M.R. and Miura, N. (1994). Soil Improvement, Panel Report on Stone Columns, *Thirteenth ICSMFE*, New Delhi, India, Vol. 5, pp 163-164.

Sharma, J.S. (1997). A Parametric Study of the Behaviour of Reinforced Stone Columns. *Technical Report No. NTU/GRC/97-2*, NTU-PWD Geotechnical Research Centre, Nanyang Technological University, Singapore.



# Geosynthetic Reinforced Unpaved Roads on Very Soft Soils: Construction and Maintenance Effects

E.M. Palmeira

Associate Professor, Department of Civil Engineering, University of Brasilia, Brasilia, Brazil

**ABSTRACT:** Geosynthetics can be used in unpaved roads on soft subgrades to increase bearing capacity and reduce fill consumption. When unpaved roads are built on very soft soils and with poor construction techniques excessive deformations of the geosynthetic layer can occur during the construction of the road caused by the traffic of bulldozers and trucks on thin layers of fill. This paper examines the effects of the road construction on the strains in extensible geosynthetic reinforcements. A methodology to estimate geosynthetic strains caused by construction is presented and its results suggest that significant geosynthetic strains can be developed during road construction. The influence of surface maintenance on the bearing capacity of reinforced and unreinforced unpaved roads is also investigated. A methodology to estimate the bearing capacity of this type of road after surface repair is presented. The predictions by this methodology compared well with model tests results available in the literature.

**KEYWORDS:** geosynthetic, reinforcement, unpaved roads, geotextile strains, surface maintenance.

## 1 INTRODUCTION

The construction of embankments on soft soils is generally a problem in routine geotechnical engineering works. In the case of unpaved roads the main load on the embankment is usually due to the weight of the trucks rather than the weight of the fill material itself. High vertical stresses can reach the soft foundation causing excessive deformation or local failures that may lead to interruptions of the traffic and to transportation cost increases. The use of geosynthetics for the reinforcement of unpaved roads on soft subgrades has been a common solution for the increase of road bearing capacity, besides minimizing fill consumption, foundation deformation and road surface rutting.

Several methodologies have been presented so far dealing with the design of reinforced unpaved roads or with the estimate of bearing capacity of this type of structure (Ferreira Jr, 1995). A common feature of these methodologies is to assume the geometrical characteristics of the problem as shown in Figure 1. This assumption does not take into account geosynthetic or subgrade deformations caused by the construction of the road. However, in the case of very soft subgrades (undrained strength at the surface below 15 kPa) large deformations of the subgrade can be caused by construction vehicles such as bulldozers and loaded trucks that bring the fill material for the road construction. In such cases the first deformations on the geosynthetic layer will be caused by these vehicles while spreading and compacting the fill or trafficking on thin layers of fill. In many cases the compaction of the fill material is simply provided by the bulldozer weight and the traffic of the trucks used in the construction of the road.

This paper deals with geosynthetic deformations caused during construction of the road and how they can be

estimated. The behaviour of this type of road after surface maintenance is also approached, particularly for the case of narrow unpaved roads.

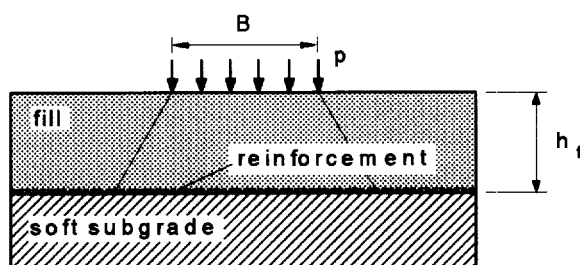


Figure 1. Typical approach for reinforced unpaved roads.

## 2 GEOSYNTHETIC DEFORMATIONS CAUSED BY ROAD CONSTRUCTION

The construction of unpaved roads on soft soils usually involves the following steps: cleaning of the ground surface, laying of the geosynthetic layer (if present), spreading of the fill material and fill compaction by appropriate equipments. Because of site conditions or project characteristics some of these steps may not be executed in many cases, such as cleaning of the ground surface and fill compaction by usual compaction equipments. Frequently the compaction of the fill is provided by the bulldozer and the traffic of trucks and at this initial stage the road is continuously repaired until a final height of compacted fill is reached for which further loads can be sustained for a certain period of time until maintenance is required. During spreading of fill on the geosynthetic layer the bulldozer operator can cause severe rutting and geosynthetic deformations due the combination

of the bulldozer weight and thin fill layers. A simple analysis of the mechanics of the problem is shown in Figure 2, where the vertical stress caused by the bulldozer weight is assumed as a uniformly distributed stress (strip load). If the fill strength is neglected, equilibrium along the vertical direction leads to an expression for a conservative estimate of the minimum compacted fill layer below the bulldozer track in order to avoid failure of the fill and excessive rutting:

$$h_0 = \frac{b}{\tan\theta} \left( \frac{p}{N'_c c_0} - 1 \right) \quad [1]$$

where:  $h_0$  is the minimum fill height (when the factor of safety equals to unity),  $p$  is the vertical stress on the surface,  $b$  is half of the track width,  $\theta$  is the load spreading angle,  $N'_c$  is the bearing capacity factor for the foundation and  $c_0$  is the soft soil undrained strength at the surface.

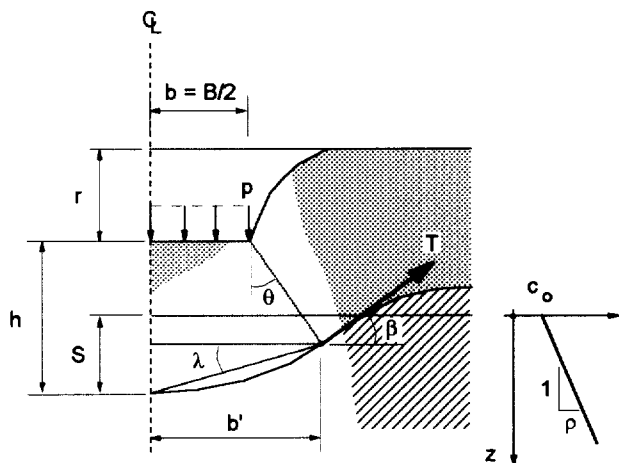


Figure 2. Failure mechanism during spreading of the fill.

A mean value for the subgrade undrained strength can replace the value of  $c_0$  if a less conservative estimate is desired. However, the value of  $c_0$  is chosen at this stage because not all the efforts acting on the system are being considered in expression 1, such as inertia forces and vibrations. For the case of reinforced roads the value of  $N'_c$  to be used is equal to  $\pi + 2$  and for unreinforced roads the value given by the expression below (Houlsby et al, 1989) is suggested:

$$N'_c = 1 + \frac{\pi}{2} + \cos^{-1}\alpha + \sqrt{1 - \alpha^2} \quad [2]$$

where  $\alpha$  is the ratio between the mobilized outward shear stress and the undrained strength at the subgrade surface.

If the bulldozer moves on a fill layer with thickness equal or smaller than the value given by equation 1 a significant vertical displacement at the foundation soil surface will occur. This settlement will reach to a depth where equilibrium is maintained depending on the subgrade undrained strength and on the force mobilized in the reinforcement. This depth can be also estimated considering the vertical equilibrium in Figure 2, which for the reinforced case yields to:

$$S = \frac{pb - T \sin\beta}{\rho N_c (b + h \tan\theta)} - \left( \frac{c_0}{\rho} + 2b \right) \quad [3]$$

where  $S$  is the maximum settlement at the subgrade surface,  $T$  is the geosynthetic tensile force,  $\beta$  is the inclination of  $T$  to the horizontal direction,  $N_c$  is the bearing capacity factor for a foundation with inclined base ( $\lambda$ , in Fig. 2) and  $\theta$  is the load spreading angle in the reinforced case. Due to the assumed trapezoidal shape of the deformed fill below the load (Fig. 2) and assuming no shear stress at the geotextile-subgrade interface the bearing capacity factor in this case ( $N_c$ ) can be obtained by (Houlsby and Wroth, 1983, and Palmeira and Cunha, 1993):

$$N_c = \pi + 2 - 2\lambda \quad [4]$$

where  $\lambda$  is the angle between the fill wedge base and the horizontal (Fig. 2).

Palmeira and Cunha (1993) performed model tests with unpaved roads reinforced with extensible geotextiles subjected to severe rutting caused by successive stages of footing loading and surface repair. Empirical expressions were obtained to estimate  $\beta$ ,  $\lambda$  and the average geosynthetic tensile strain ( $\epsilon$ ) as a function of the maximum vertical displacement at the fill-subgrade interface normalized by the footing width. These expressions were developed for roads with ratios  $h_f/B \leq 0.7$  (Fig. 1) and are presented below:

$$\frac{\beta}{\pi} = 0.237 + 0.191 \log_{10} \frac{S}{B} \quad (\beta \text{ in radians}) \quad [5]$$

$$\frac{\lambda}{\pi} = 0.156 + 0.133 \log_{10} \frac{S}{B} \quad (\lambda \text{ in radians}) \quad [6]$$

$$\epsilon = 0.5 \sqrt{1 + 3.5 \tan^2 \lambda} + \frac{0.27}{\tan \lambda} \ln(1.87 \tan \lambda + \sqrt{1 - 3.5 \tan^2 \lambda}) - 1 \quad [7]$$

Figure 3 presents some comparisons between values of geotextile strain ( $\epsilon$ ) versus  $S/B$  predicted by equation 7 and observed by different researchers (for  $h_f/B \leq 0.7$ ). The results from model tests were inferred from deformed

shapes of the reinforcement layer or obtained by strain measurements in the reinforcement. A good agreement between predicted and observed values can be noted.

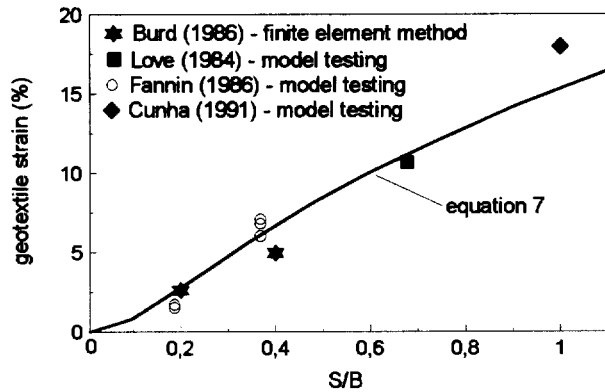


Figure 3. Predicted and observed values of geotextile strains.

Laboratory tests on model unpaved roads have also consistently shown that the load spreading angle in the reinforced fill can be significantly greater than in the unreinforced fill (Love, 1984, Palmeira and Cunha, 1993 and Palmeira and Ferreira, 1994). Palmeira and Ferreira (1994) observed load spreading angles between 21 to 34° for reinforced roads and between 6 to 17° for the unreinforced ones.

The value of  $S$  depends on the fill thickness ( $h$  in Fig. 2) below the bulldozer track. This thickness depends on the bulldozer operator experience and is likely to be highly variable in different parts of the road depending on the subgrade undrained strength and stiffness at its surface. If  $h$  is significantly smaller than  $h_0$  (equation 1) and depending on the subgrade strength the rut depth required for equilibrium can be even greater than  $h$  and soft soil may reach the fill surface through fill cracks. This is certainly more critical for the unreinforced case, but depending on the value of  $h$  high geotextile strains can be developed because of this excessive deformation of the system. These strains are not taken into account if the available design methods are applied for unpaved roads on very soft soils or when poor construction techniques are employed.

Assuming a linear relationship between tensile force and tensile strain for the geotextile, expressions 1 and 3 can be combined to obtain the following expression relating maximum vertical displacement at the fill-subgrade interface ( $S$ ) to geotextile strain ( $\epsilon$ ) in dimensionless terms:

$$\frac{S}{B} = \frac{\frac{p}{c_0} - 2 \sin \beta \frac{J}{c_0 B} \epsilon}{N_c \frac{\rho B}{c_0} \{1 + k [\frac{1}{(\pi + 2) c_0} p - 1]\}} - (\frac{c_0}{\rho B} + 1) \quad [8]$$

where  $k$  is the ratio between  $h$  and  $h_0$ .

Figures 4 to 6 show charts obtained from the iterative solution of equations 4 to 8 to estimate the geotextile deformation for  $k = 0.5$  and for different values of the dimensionless terms. The geotextile strain due to road construction may then be taken into account in conjunction with the strains caused by the traffic of vehicles on the road to estimate the total geotextile strain. The associated settlement  $S$  can be estimated by equation 8 and can then be compared with the value of  $h$  ( $h = k h_0$ , with  $h_0$  given by equation 1).

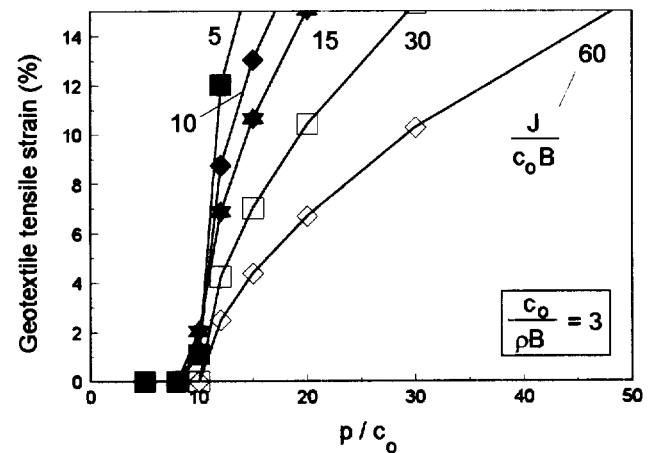


Figure 4. Geotextile strain versus  $p/c_0$  for  $c_0/(\rho B) = 3$ .

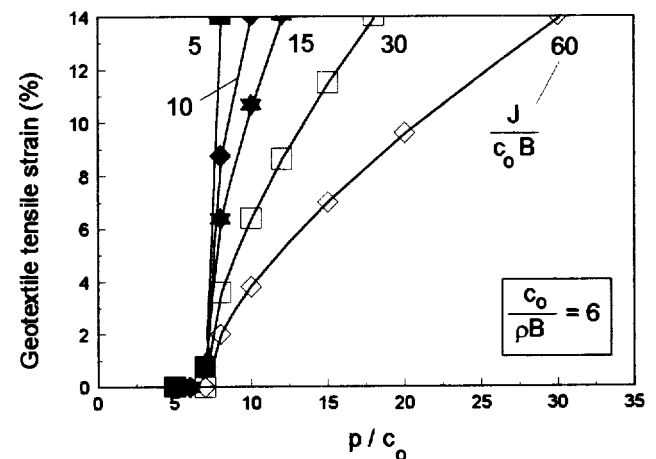


Figure 5. Geotextile strain versus  $p/c_0$  for  $c_0/(\rho B) = 6$ .

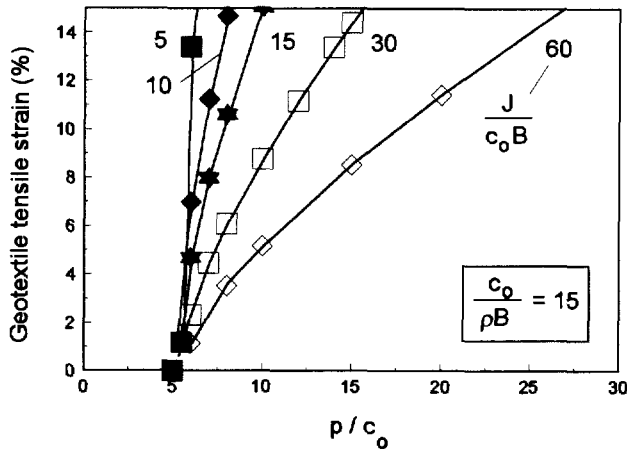


Figure 6. Geotextile strain versus  $p/c_0$  for  $c_0/(\rho B) = 15$ .

### 3 BEARING CAPACITY OF UNPAVED ROADS AFTER SURFACE MAINTENANCE

#### 3.1 Theoretical Development

Figure 7 shows the failure mechanism assumed after a repair of the road surface after excessive rutting has occurred under plane strain conditions. This is the case of narrow roads and poor maintenance conditions, where the surface repair is made just by filling the rut and compacting the new material. The region ABCD is inside the compacted material while the block CDEF is composed of the original failed road. It is assumed that failure in the repaired region will develop along vertical planes (plane BC in Fig. 7) due to the punching mechanism of the block underneath. This is consistent with the observation of failure mechanisms in model roads which suffered successive stages of surface repair and loading (Palmeira and Cunha, 1993). For stiff fill materials the block ABCFED is assumed to behave as a rigid mass being pushed into the soft subgrade. A vertical stress distribution throughout the repaired region ABCD similar to the one employed by Terzaghi (1943) for the study of tunnels in soil is adopted (Fig. 8). The yielding base DC controls the failure mechanism of the repaired region and the horizontal stresses along plane BC drops during loading, being assumed that active conditions are reached. This assumption is corroborated by predictions of horizontal stresses in a elastic layer with a yielding base (Poulos and Davis, 1974). Based on these hypotheses the vertical stress at the base of the rut can be derived:

$$\sigma_b = p \cdot e^{-2k_{ap} \tan \phi' \frac{r}{B}} - \frac{2c' - \gamma B}{2k_{ap} \tan \phi'} (1 - e^{-2k_{ap} \tan \phi' \frac{r}{B}}) \quad [9]$$

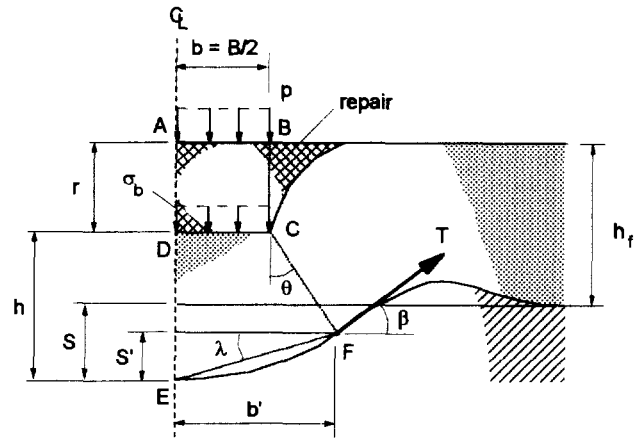


Figure 7. Failure mechanism after surface repair.

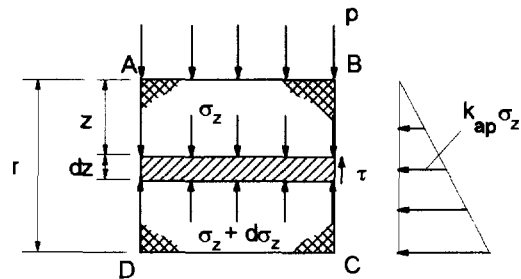


Figure 8. Vertical stress distribution in block ABCD

where  $\gamma$  is the specific weight of the fill,  $k_{ap}$  is the active earth pressure coefficient and  $c'$  and  $\phi'$  are the shear strength parameters of the soil used for the repair (peak values).

According to Figure 9 the study of the equilibrium of block CDEF and the bearing capacity of the subgrade yields to:

$$\sigma_b = \frac{b'}{b} \sigma + \frac{b'}{b} \tan \lambda \tau - \frac{W}{b} + \frac{T \sin \beta}{b} \quad [10]$$

where  $\sigma$  is the foundation bearing capacity,  $\tau$  is the shear stress at the reinforcement-subgrade interface (assumed equal to the undrained strength of the subgrade),  $W$  is the weight of block DCEF and  $T$  is the tensile force in the reinforcement (if present).

The bearing capacity of the foundation soil is given by (Palmeira and Cunha, 1993, Figs. 7 and 9):

$$\sigma = N_c C_u + \gamma h_f + \gamma_s (S - S') \quad [11]$$

where  $\gamma_s$  is the specific weight of the subgrade material and  $h_f$ ,  $S$  and  $S'$  are the dimensions given in Figure 7. The value of  $N_c$  is given by Equation 4, where  $\lambda$  is given by

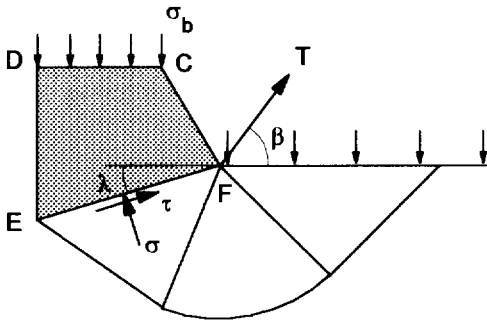


Figure 9. Failure mechanism of the soft subgrade.

equation 6 for reinforced roads and by the following expression (Palmeira and Cunha, 1993) for the unreinforced case ( $\lambda_{unr}$  in radians):

$$\frac{\lambda_{unr}}{\pi} = 0.247 + 0.236 \log_{10} \frac{S}{B} \quad [12]$$

Rewriting equation 9 yields to:

$$p = \sigma_b \cdot e^{\frac{2k_{ap} \tan \phi' r}{B}} + \frac{2c' - \gamma B}{2k_{ap} \tan \phi'} (e^{\frac{2k_{ap} \tan \phi' r}{B}} - 1) \quad [13]$$

The values of  $\sigma_b$  and  $\sigma$  are calculated by equations 10 and 11, respectively, using appropriate values of  $\lambda$  and  $\theta$  for the reinforced and unreinforced cases.

The case in which a series of repairs are made is schematically presented in Figure 10. The same approach presented above can be used and in this case the load capacity after the second repair can be obtained by:

$$p = \sigma_a \cdot e^{\frac{2k_{ap} \tan \phi' r}{B}} + \frac{2c' - \gamma B}{2k_{ap} \tan \phi'} (e^{\frac{2k_{ap} \tan \phi' r}{B}} - 1) \quad [14]$$

with:

$$\sigma_a = \sigma_b \cdot e^{\frac{2k_{acv} \tan \phi'_{cv} r_0}{B}} + \frac{2c'_{cv} - \gamma B}{2k_{acv} \tan \phi'_{cv}} (e^{\frac{2k_{acv} \tan \phi'_{cv} r_0}{B}} - 1) \quad [15]$$

where  $r_0$  is the depth of the first rut repaired (corresponding to block A'B'CD, in Fig. 10),  $r$  is the depth of the second rut repaired (block ABB'A', in Fig. 10) and  $k_{acv}$ ,  $c'_{cv}$  and  $\phi'_{cv}$  are the fill active earth pressure coefficient and strength parameters under constant volume, which are the relevant ones for the shear strength along the

vertical planes of the first rut (already failed). Similar expressions can be developed for a number of repairs greater than 2 if the subgrade continues to control the failure mechanism. As the fill becomes thicker failure may take place inside the fill material itself (Palmeira and Ferreira Jr., 1994).

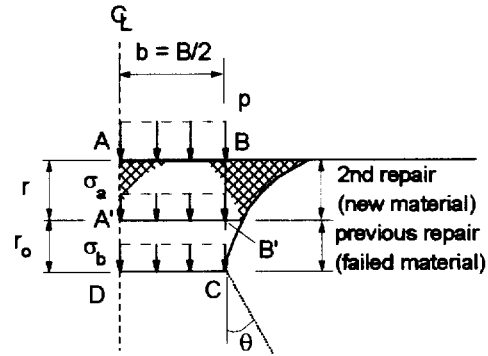


Figure 10. Two successive repairs of the road surface.

### 3.2 Comparisons Between Predicted and Observed Values of Road Bearing Capacity After Maintenances

Predictions by the methodology developed above were compared with model test results presented in the literature (Cunha 1991; Palmeira and Cunha 1993; Palmeira and Ferreira Jr. 1994; Ferreira Jr. 1995). These model tests are schematically shown in Figure 11. Different types of soils were used as fill materials ( $\gamma = 16$  to  $18 \text{ kN/m}^3$ , mean particle diameter ( $D_{50}$ ) =  $0.13$  to  $1.20 \text{ mm}$ , coefficient of non uniformity =  $1.6$  to  $36$ ,  $c' = 0$  to  $2.9 \text{ kPa}$ ,  $c'_{cv} = 0$ ,  $\phi' = 35$  to  $50^\circ$  and  $\phi'_{cv} = 31$  to  $38^\circ$ ). Up to three surface repairs were made on the road surface in some cases, as shown in Figure 10. The soft subgrade consisted of a saturated layer of kaolin. A rigid metal footing (plane strain conditions) provided the load on the road surface which was applied at a undrained constant rate of displacement. A model needle-punched nonwoven geotextile ( $75 \text{ g/m}^2$ , thickness =  $0.5 \text{ mm}$ , wide strip tensile strength =  $3.3 \text{ kN/m}$ , tensile strain at failure =  $70\%$  and tensile stiffness =  $4.9 \text{ kN/m}$ ), made of polyester, was used in the reinforced tests. This reinforcement would simulate an extensible geotextile presenting a tensile stiffness of the order of  $60 \text{ kN/m}$  in prototype conditions. Additional information on the materials used and testing methodology can be found in Palmeira and Cunha (1993) and in Palmeira and Ferreira Jr. (1994).

Figure 12 shows comparisons between predicted and observed values of  $p/C_u$  at failure for each loading stage. The value of the undrained strength at a depth equal to  $B$  was used to normalize the values of footing pressure in Figure 12. A reasonably good agreement can be observed

between predicted and observed values of  $p/C_u$  and the scatter can be partially explained by the scatter of the values of undrained strength besides some limitations of the approach.

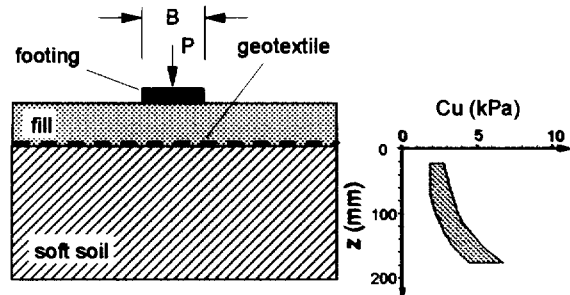


Figure 11. Schematic view of the model tests performed.

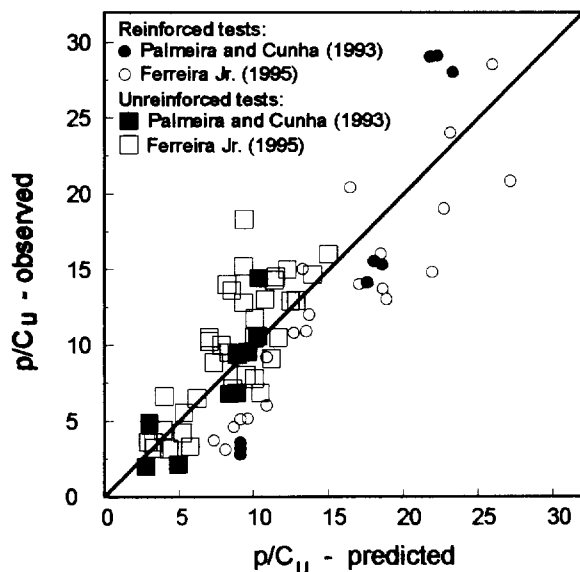


Figure 12. Comparisons between predicted and observed values of  $p/C_u$ .

#### 4 CONCLUSIONS

This paper presents some aspects regarding geotextile deformation during unpaved road construction and bearing capacity of this type of road after surface maintenance. It is observed that significant strains can be mobilized in extensible geotextiles during road construction on very soft subgrades. A methodology is presented for the estimate of these strains. In spite of the limited amount of data available, results from model tests and finite element analyses compared well with predicted values of the variation of geotextile strain ( $\epsilon$ ) with the normalized settlement at the soft soil surface ( $S/B$ ).

The presence of the geosynthetic has a marked effect on the bearing capacity of the unpaved road after maintenances. A proposed methodology has also been presented which improves a similar methodology previously presented in Palmeira and Cunha (1993). Good comparison was observed between predictions by this methodology and model tests results.

#### ACKNOWLEDGEMENTS

The Authors would like to thank the University of Brasilia, CNPq, CAPES/Brazilian Ministry of Education and Rhodia-Ster for supporting the present work.

#### REFERENCES

- Burd, H. J. (1986) "A Large Displacement Finite Element Analysis of a Reinforced Unpaved Road", *D.Phil. Thesis*, University of Oxford, UK, 222 p.
- Cunha, M.G. (1991) "Model Studies of Geotextile Reinforced Unpaved Roads", *MSc Thesis*, University of Brasilia, Brazil (in Portuguese), 130 p.
- Fannin, R.J. (1986) "Geogrid Reinforcement of Granular Layers on Soft Clay - A Study at Model and Full Scale", *D.Phil. Thesis*, University of Oxford, UK, 221 p.
- Ferreira Jr., L.G.F. (1995) "Model Studies on the Influence of Geotextile Reinforcement on the Failure and Deformation Mechanisms of Unpaved Roads", *MSc. Thesis*, University of Brasilia, Brazil (in Portuguese), 181 p.
- Houlsby, G.T. and Wroth, C.P. (1983) "Calculation of Stresses on Shallow Penetrometers and Footings", *OUEL Report No.1503/83*, Univ. of Oxford, UK, 18p.
- Houlsby, G.T., Milligan, G.W.E., Jewell, R.A. and Burd, H.J. (1989) "A New Approach to the Design of Unpaved Roads - Part I", *Ground Engineering*, April, pp. 25-29.
- Love, J.P. (1984) "Model Testing of Geogrids in Unpaved Roads", *D.Phil. Thesis*, University of Oxford, 216 p.
- Palmeira, E.M. and Cunha, M.G. (1993) "A Study of the Mechanics of Unpaved Roads with Reference to the Effects of Surface Maintenance", *Geotextiles and Geomembranes*, Vol. 12, No. 2, pp. 109-131.
- Palmeira, E.M. and Ferreira Jr., L.G.F. (1994) "The Behaviour of Unpaved Roads Under Large Rutting Conditions", *Fifth International Conference on Geotextiles, Geomembranes and Related Products*, Singapore, Vol. 1, pp. 135-138.
- Poulos, H.G and Davis, E.H. (1974) "Elastic Solutions for Soil and Rock Mechanics", John Wiley and Sons, New York, USA, 411 p.
- Terzaghi, K. (1943) *Theoretical Soil Mechanics*, John Wiley and Sons, New York, USA.

# Numerical Analysis of a Pavement Base Reinforced with Geogrid

Mauricio Abramento

IPT- Instituto de Pesquisas Tecnológicas do Estado de São Paulo, Brasil

**ABSTRACT:** This paper presents results of a detailed numerical analysis, using the finite differences software FLAC, comparing the behavior of an unreinforced and geogrid reinforced pavement base. The study was developed for designing a flexible pavement (pavers over crushed stone and sand) to be built in an intermodal yard located in Brazil. Preliminary studies showed that the crushed stone layer collapses under the high imposed loads (transtainers with design wheel load of 35tf), suggesting its reinforcement with geogrids. The results of numerical analysis showed that the pavement performance improved substantially with three layers of geogrid (long-term strength of 50kN/m) evenly spaced in the crushed stone, inhibiting plastification of the materials and reducing the magnitude of plastic displacements at surface.

**KEYWORDS:** Geogrid, Base reinforcement, Pavement, Numerical analysis.

## 1 INTRODUCTION

One of the many applications of geosynthetics is reinforcement of coarse material for sustaining heavy loads. For example, Walls and Galbreath (1987) present a case of ballast reinforcement with geogrid, while Raymond et al. (1993) show the use of a layer of geogrid for reinforcing a sand for gantry cranes tracks. This paper presents results of a detailed numerical analysis, using the finite differences software FLAC, comparing the behavior of an unreinforced and geogrid reinforced pavement base. The study was developed for designing a flexible pavement to be built in an intermodal yard located in Brazil. Very heavy vehicles (transtainers) for handling containers from large ships will circulate in the area. The vehicles have a very high design wheel load of 35tf, corresponding to an unusual applied pressure on the pavement of about 12kgf/cm<sup>2</sup>.

## 2 PAVEMENT LAYERS

Figure 1 shows the pavement system and main soil layers involved in the problem, from top to bottom: a) 15cm thick high strength articulated concrete blocks (pavers); b) crushed stone compacted with high energy (pavement base), with thickness to be determined, ranging from 0.6m (geogrid-reinforced) to 1.2m (unreinforced); c) 3.0m thick dense sand; and d) 8.0m thick compressible clay layer. Geotechnical and pluviometric peculiarities resulted in this system, in particular large differential settlements expected due to consolidation of the soft clay layer. The pavement

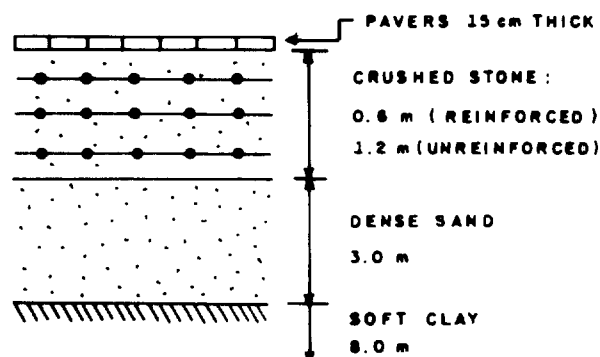


Figure 1. Pavement system (not to scale)

system should act as a reservoir, holding large volumes of water from heavy rainfalls. A numerical analysis was carried out to assess the stability and possible reinforcement of the crushed stone layer, considering heavy wheel loads.

## 3 SOIL PARAMETERS

In order to analyze the pavement behavior, it is necessary to estimate the strength (friction angle) and deformability parameters for the sand and the crushed stone layers. The friction angle is the most important parameter, since it indicates the possibility of failure of pavement as well as magnitude of plastic displacements due to the wheel load.

The following equation, proposed Barton and Kjaernsli (1981) was used for determining the crushed stone peak friction angle  $\phi_p$ :

$$\phi_p = R \log (S/\sigma'_n) + \phi_b \quad (1)$$

In this equation, R is a particle shape factor (which depends on the crushed stone porosity after compaction), S is a factor depending on the unconfined compressive strength of the original rock (gneiss),  $\sigma'_n$  is the mean confining stress, and  $\phi_b$  the residual friction angle of crushed stone. Depending on the position of the wheel, two conditions for confining stresses were considered. Far from the wheel, stresses due to compaction prevail in the crushed stone (estimated as 0.1MPa) and immediately under the wheel the static load from the transtainer is dominant (1.0MPa). Stiffness of the crushed stone was estimated from the literature. For the sand, the strength and deformability parameters were determined from triaxial compression tests. Table 1 summarizes the parameters used in the analysis:

Table 1. Parameters used in the numerical analysis.

Condition	Crushed Stone		Sand	
	E (MPa)	$\phi_p$	E (MPa)	$\phi_p$
minimum $\sigma'_n$ (far from wheel)	300	55°	170	37°
maximum $\sigma'_n$ (under wheel)	100	46°	140	33°

In all FLAC analyses, the Mohr-Coulomb constitutive model was used for simulating the behavior of dense sand and crushed stone layers, while elastic model was considered for the reinforcement layers. The effect of dilatancy for the dense sand and crushed stone layers was explicitly included in all analyses. The Poisson's ratio was assumed as 0.33 for both materials.

#### 4 UNREINFORCED CRUSHED STONE BASE

The bearing capacity of the unreinforced crushed stone was initially verified through the classical Terzaghi (1943) formulation, considering a cohesionless soil and rectangular load at the surface. The  $N_y$  factors were determined as proposed by Kumbhojkar (1993) for the range of friction angles assumed in the analysis. The safety factor with respect to general failure for the crushed stone decreases from as high as 7.7 considering small confining pressures (far from the wheel load in Table 1), to as low as 0.96 for high confining pressures, immediately under the wheel. The results suggested that the crushed stone could

be reinforced in order to avoid its plastification due to the heavy loads prevailing in the pavement.

The thickness of the crushed stone layer determines the magnitude of loads on the dense sand layer underneath. This problem was analyzed supposing the stress distribution proposed by Giroud and Noray (1981). The results indicated that the crushed stone layer should be over 80cm thick in order to yield a factor of safety  $FS > 2.0$  with respect to bearing capacity for the sand layer, and over 100cm for  $FS > 3.0$ . If the sand is required to work within elastic conditions, it is generally recommended a high value of factor of safety with respect to bearing capacity. These results motivated the use of reinforcement layers in the crushed stone.

#### 5 GEOGRID REINFORCED CRUSHED STONE BASE

In order to minimize plastic deformations and rutting, and maximize safety factor against failure for the crushed stone and dense sand layer, reinforcement the crushed stone layer is proposed. The use of three layers of geogrid within the crushed stone layer was preferred in order to achieve better stress distribution (Huang and Tatsuoka, 1990). A single layer of reinforcement could also be used in the crushed stone, but the stress redistribution in the layer would not be as much efficient, and the loads carried by the geogrid would be much higher.

Loads in the reinforcement layers were initially quantified using the analytical model proposed by Binquet and Lee (1975). In this model, the loads along the reinforcements are expressed as a function of the depth, number and spacing of reinforcements, width of applied load and bearing capacity of the soil. The crushed stone layer was taken as 60cm, in order to verify the efficiency of the reinforcement on the bearing capacity of the sand layer. Considering three layers of reinforcements evenly spaced in the crushed stone at 20cm, loads in the reinforcements were estimated as varying from 47kN/m for the top layer to 56kN/m for the bottom layer.

Both the unreinforced and reinforced 60cm crushed stone behavior were further analyzed using the finite differences program FLAC (Fast Lagrangian Analysis of Continua). This program, developed by Itasca Consulting Group (USA), allows flexibility in modeling the behavior of the many materials involved (crushed stone, sand, reinforcement layers). Figure 2 shows the grid used in the numerical simulation. Conditions presented in Table 1 were analyzed, each one with and without reinforcement, resulting a total of four cases. The following properties were considered for the reinforcement layers, corresponding to those of commercially available geogrids: Elastic modulus 500MPa, thickness 2.5mm and ultimate tensile strength 100kN/m. These values do not account for installation damage.



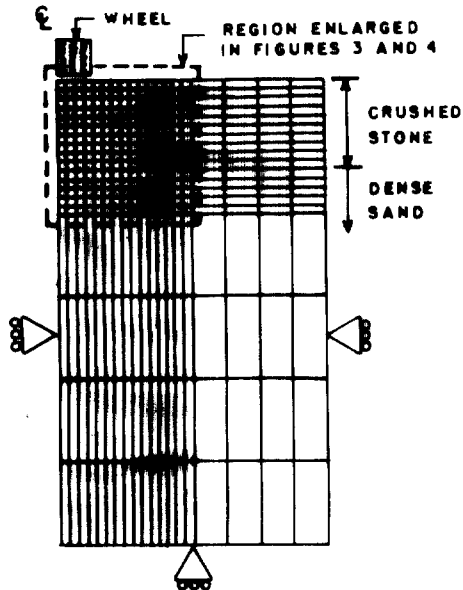


Figure 2. Grid for FLAC analysis.

The following additional hypotheses were considered for the problem: plane strain conditions, Mohr-Coulomb plastification criteria for both the sand and crushed stone and elastic behavior for the reinforcements. Only half of the geometry was considered in the grid due to symmetry of the problem (Figure 2).

Results are presented in Figures 3 and 4 for the critical case of minimum strength parameters presented in Table 1 (immediately under the wheel), without and with reinforcement, respectively. Basically, the failure mechanism for the unreinforced crushed stone observed in the analytical model is confirmed in the numerical analysis, as shown in Figure 3. In this case, there are large upward displacements at the surface and downward displacements immediately under the wheel. There is a general plastification in both crushed stone and dense sand layers. The results show that introducing three reinforcements in the crushed stone layer is very efficient, inhibiting almost completely plastification in both crushed stone and dense sand layers, as shown in Figure 4. Displacements at the surface and within the layer are also drastically reduced. The loads in the reinforcement layers vary from 47kN/m for the bottom layer to 24kN/m for the superficial layers. The maximum value for the axial load in the bottom layer compares relatively well with the one determined with the analytical model of Binquet and Lee (1975), while their model overestimates the loads for the more superficial reinforcement layer. Table 2 summarizes the results obtained in the numerical analysis. In general, the results show that reinforcement is generally more efficient in the critical case of minimum peak friction angle, when loads along geogrids and benefits in the system are maximized.

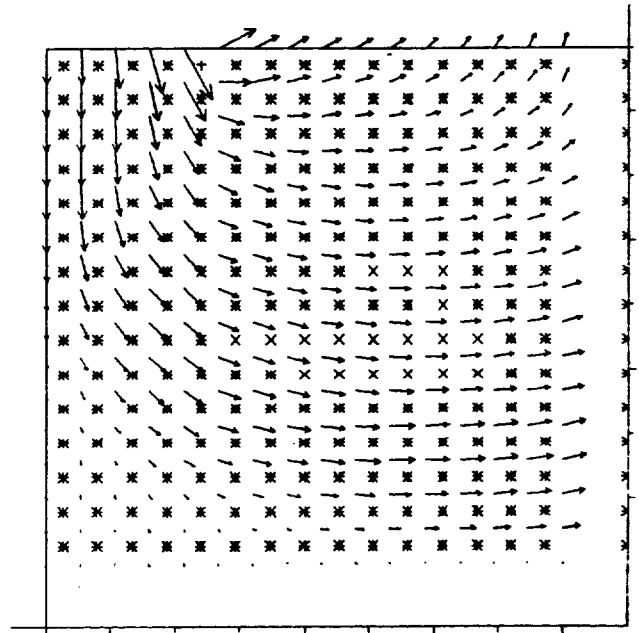


Figure 3. FLAC results, unreinforced crushed stone case. Legend: Max. displacement vector=30cm. Plastification: \* At yield; X Elastic.

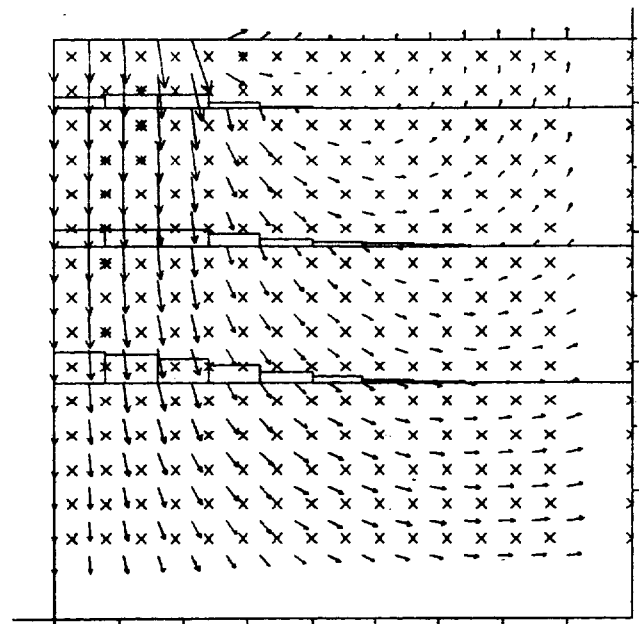


Figure 4. FLAC results, reinforced crushed stone case. Legend: Max. displacement vector=4.5cm. Plastification: \* At yield; X Elastic. Reinforcements load distribution also shown.

Table 2: Summary of numerical analyses and results.

Case	Maximum displacements (cm)	Plastification	Geogrid loads (kN/m)
1: $\phi$ p max unreinf.	1.9	localized	-
2: $\phi$ p max reinf.	1.8	no	5.5 to 9.5
3: $\phi$ p min unreinf.	>30	generalized (failure)	-
4: $\phi$ p min reinf.	4.5	no	24 to 47

## 6 GEOGRID CHARACTERISTICS AND INSTALLATION

In order to choose the correct reinforcement, it is necessary to multiply the maximum loads determined in the numerical analyses by a general factor of safety. One of the most important aspects to be accounted for is the installation damage of reinforcement, since very high energy will be employed for compacting the crushed stone layer. The amount of damage should be assessed by means of large scale laboratory tests. For example, Watts and Brady (1994) carried out a series of high energy compaction tests using crushed stones over geogrids, suggesting factor of safety against damage varying from 1.3 to 1.7. Koerner (1993) also suggests FS values in this range. Creep, chemical and biological damage should also be taken into account for determining the suitable reinforcement. In order to minimize the effects of installation damage, the reinforcement could be placed within two thin layers of grit, avoiding direct contact of the coarse material with the geogrid layers for improved protection.

## 7 CONCLUSIONS

This paper presents results of a numerical analysis with FLAC on the behavior of unreinforced and geogrid reinforced pavement base to be constructed in a intermodal yard. The results show that the unreinforced crushed stone base collapses under the high imposed loads, suggesting its reinforcement with geogrids. The number and position of geogrid layers were initially estimated using simplified closed-form solutions originally developed for reinforcement of shallow foundations, which resulted in a reinforcement configuration consisting of three layers of geogrids with long-term strength of 50kN/m evenly spaced within the crushed stone base. Results of numerical finite difference analyses on this reinforcement configuration showed that the pavement performance improved in the

following ways: a) inhibiting the plastification of the crushed stone base and the dense sand layer; b) reducing the magnitude of plastic and elastic displacements at the pavement surface and within the layers; and c) reducing the thickness of the crushed stone base from 1.2m to 0.6m, without causing collapse of the dense sand layer underneath. The introduction of reinforcement could also drastically reduce maintenance frequency, one of the major aspects related to container terminal management (Meletiou and Knapton, 1987).

## ACKNOWLEDGEMENTS

The author is grateful to IPT and CNPq for support in the research work.

## REFERENCES

- Barton, N. and Kyaernsli, B. (1981) "Shear Strength of Rockfill", *ASCE Journal of Geotechnical Engineering*, Vol. 107, No. GT7, July, p. 873-891.
- Binquet, J. and Lee, K.L. (1975) "Bearing Capacity Analysis of Reinforced Earth Slabs", *J. Geot. Eng. Div. Proc. ASCE*, Vol. 101, GT12, p. 1257-1276.
- Giroud, J.P. and Noiray, L. (1981) "Design of Geotextile Reinforced Unpaved Roads", *J. Geot. Eng. Div. ASCE*, Vol. 107, n. GT9, pl. 1233-1254.
- Huang, C.C. and Tatsuoka, F. (1990) "Bearing Capacity of Reinforced Horizontal Sandy Ground", *Geotextiles and Geomembranes*, v. 9, p. 51-82.
- Koerner, R. (1993) "Designing with Geosynthetics", Prentice Hall.
- Kumbhojkar, A.S. (1993) "Numerical Evaluation of Terzaghi's  $N\gamma$ ", *ASCE Journal of Geotechnical Engineering*, Vol. 119, n.3, pp. 598-607.
- Meletiou, M. and Knapton, J. (1987) "Container Terminal Pavement Management", *UNCTAD Monographs on Port Management*, Monograph n.5., 51 p.
- Raymond, G.P. Abdel-Baki, M. Karpurapu, R.G. and Bathurst, R.J. (1993) "Reinforced Granular Soil for Track Support", *ASCE Special Conference on Grouting, Soil Improvement and Geosynthetics*, p.1104-1115.
- Terzaghi, K. (1943) "Theoretical Soil Mechanics", John Wiley and Sons, NY.
- Walls, J.C. and Galbreath, L.L. (1987) "Railroad Ballast Reinforcement Using Geogrids", *Geosynthetics '87*, New Orleans, p. 38-45.
- Watts, G.R.A. and Brady, K.C. "Geosynthetics: Installation Damage and the Measurement of Tensile Strength", *5th International Conference on Geosynthetics*, Singapore, p. 1159-1164.

# Improvement of Bearing Capacity of Soft Clay Using Geogrids

Y. Tanabashi

Civil Engineering Dept., Nagasaki University, Bunkyo-machi 1-14, Nagasaki 852, Japan

K. Yasuhara

Dept. of Urban and Civil Engineering, Ibaraki University, Hitachi, Ibaraki 316, Japan

K. Hirao

Dept. of Civil Engineering, Nishinippon Institute of Technology, Kanda 1633, Fukuoka-ken, 80003, Japan

N. Kiyokawa

Mitsui Petrochemical Industrial Products Co., Ltd., Yushima, Tokyo, 101, Japan

H. Itoh

CTI Engineering Co., Ltd., Nihonbashi Honmachi, Tokyo, 103, Japan

**ABSTRACT:** A number of 1g laboratory model footing tests have been carried out to find out which geosynthetics and methods of placement are optimal for giving sufficient bearing capacity for both the trafficability of construction machines and the construction of earth structures on soft soils. To study the effect of sand mat placement, in particular, a numerical simulation was performed using a procedure in which the Sekiguchi-Ohta constitutive model for soft clay was combined with a truss element for the geogrid and Goodman's joint element for interaction between the sand and geogrid. Based on Biot's theory of three-dimensional consolidation, a finite element model was formulated to analyse the deformation and failure mode of the soft clay in the laboratory model tests both with and without the geogrid and sand mat. Typical results from the calculations give a good prediction of the effectiveness of sand mat placement for decreasing settlement, and, therefore, improving the bearing capacity of soft clay. It is concluded that this must be due to an increase in bending stiffness caused by combining the sand mat with the geogrid.

**KEYWORDS:** Bearing capacity, Geosynthetics clay liners (GCL), Model tests, Finite element analysis, Friction

## 1 INTRODUCTION

In previous papers (Hirao et al., 1992; Yasuhara et al., 1994), the authors have emphasized that composite geosynthetics which are non-woven geosynthetics reinforced with woven geosynthetics in-between are best for improving the bearing capacity of soft clay. This composite geosynthetic has a higher tensile strength than the non-woven geosynthetic hitherto used, and in addition has the advantage of giving high friction in soft clay (Hirao et al., 1992). There is no significant improvement in bearing capacity when a geogrid is placed directly over the surface of a soft clay, because the frictional force developed between the geogrid and soft clay is very small (Hirao et al., 1992) and it cannot follow the large deformations of the soft clay.

In order to establish a suitable procedure for the use of geogrids to improve the bearing capacity of soft clay, 1g laboratory model tests were conducted. In particular, a focus was placed on which effect of (i) restraintment, (ii) combination with woven or non-woven geosynthetics and (iii) combination with sand mat contributes most to increasing bearing capacity.

## 2 EXPERIMENTAL PROGRAMME

### 2.1 Outline of Model Tests

A soil tank with 2 m width, 0.5 m length and 1.0 m depth, as illustrated in Fig. 1, was used for the model tests. The properties of the clay were:  $G_s = 2.62$ ,  $w_L = 107\%$ ,  $I_p = 66$ . Details are given in previous papers (Hirao et al., 1992, 1996). Soft clay mixed with water to a moisture content  $w_i$  of 130% was poured into the soil tank to form a 40cm or 80cm thickness clay layer. The average vane shear strength of the model clay layer after

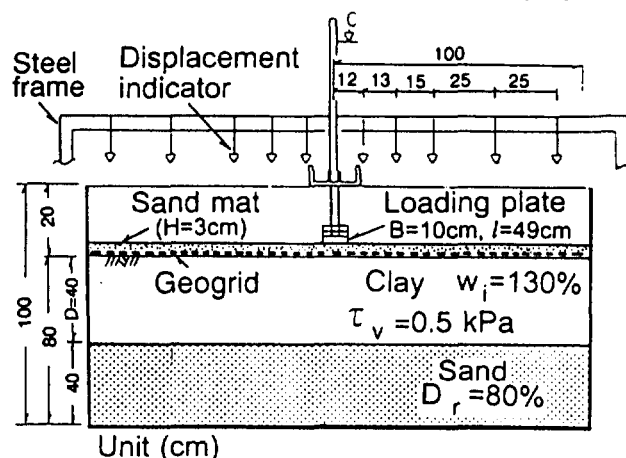


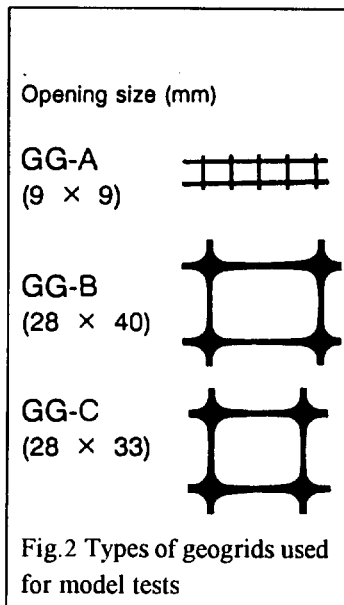
Fig. 1 Testing apparatus for model tests

pouring was 0.5 kPa and was almost constant with depth.

A layer of geogrid was firstly placed directly over whole the surface of the clay layer with a 2m width and 0.5m length. Then a sand mat of 3cm thickness was laid onto the geogrid. To obtain the load versus settlement curves, several kinds of model footing tests were carried out in which step loads were applied to the soft clay reinforced with a geogrid. For comparing the effects of different reinforcements, plate loading tests were also conducted on soft clay without a sand mat and geogrid as well as tests with the combined use of geogrids with non-woven geofabrics.

A vertical load of 1.0 kPa was applied in each step to a plate 10cm wide, 49cm long and 48 Pa in weight until the clay layer failed. The loading duration of each step was 15 min.

A lateral restraint was provided by a tension force developed by a counter weight on the edge of geogrids as is shown in Fig. 1.



## 2.2 Properties of Geogrids Used

Table 1 summarizes the mechanical properties of the three kinds of geogrids used. The differences between the three geogrids illustrated in Fig. 2 were in the size of the opening, tensile strength, frictional force and bending stiffness of which the later two were determined using methods proposed by Hirao et al. (1992, 1996).

Table 1 Mechanical properties of geotextiles used

Material	Symbol	Thickness or Opening (mm)	Bending Stiffness $B_G$ ( $N \cdot cm^2$ )	Stiffness $l$ (cm)	Description
Woven Fabric	WF	0.5	9.3	11.3	-----
Composite Fabric	CF-B	4.0	11.3	16.0	-----
Geogrid	GG-A	9×9	23.1	33.9	-----
	GG-B	28×40	129.4	75.3	-----
	GG-C	28×33	185.2	85.3	-----

As will be mentioned later, the size of the opening is an important factor in the improvement of the bearing capacity of soft clay because of its relation to the magnitude of mobilized friction and the interlocking effect.

## 3 RESULTS FROM EXPERIMENTS

The bearing capacity for reinforced models is defined by the applied load at the yielding point,  $p_{y,n}$  for non-reinforced and  $p_{y,r}$  for reinforced cases in the settlement,  $S$ , versus load,  $p$ , curves. The results relating to the improvement of the bearing capacity of soft clays reinforced with geogrids were taken from the model

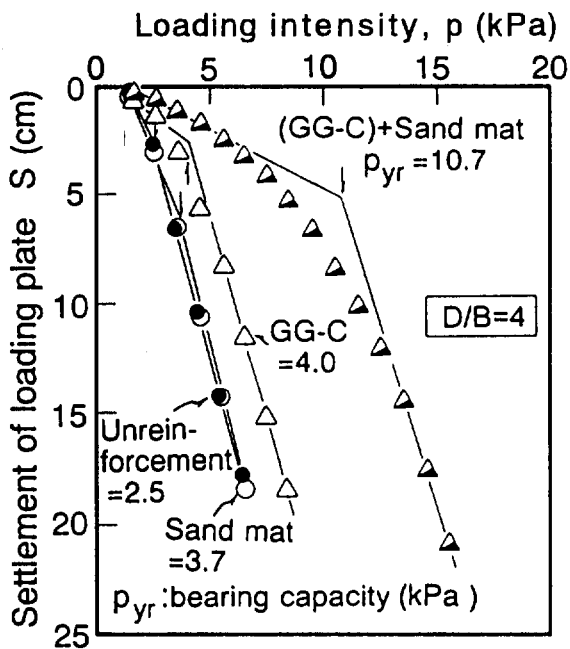


Fig. 3 Representative  $p$  vs.  $S$  curves obtained by model tests

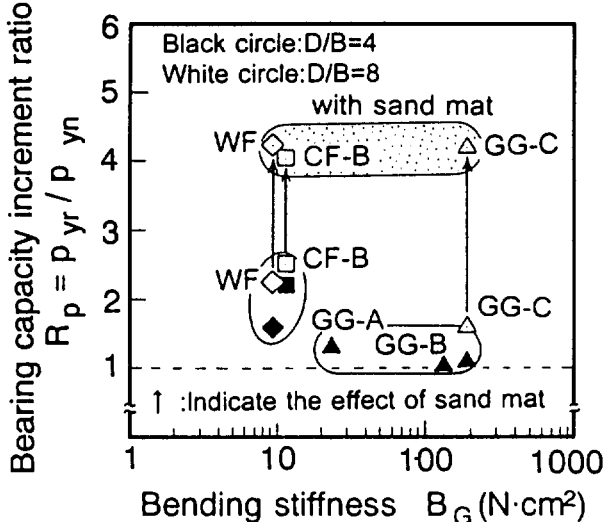


Fig. 4 Effect of bending stiffness on increase in bearing capacity of soft clay

tests described in the previous section. Figs. 3 to 6 illustrate the effects of the above-mentioned factors on the settlement,  $S$ , vs. vertical stress,  $p$ , curves.

As can be seen in Fig. 3, the bearing capacity with no reinforcement is very small because the model ground consists of extremely soft clay. A small increase in bearing capacity can be observed in Fig. 3 due to the size of the geogrid's mesh.

The ratio of the bearing capacity,  $p_{yr}$ , of soft clay improved by reinforcement with geogrids to that,  $p_{ym}$ , for no geogrids, is denoted by  $R_p$ . Fig. 4 and Fig. 5 show the effects of both the bending stiffness of geogrids and the stiffness of woven and composite geofabrics, respectively. It can be seen from these results in Figs. 4 and 5 that the placement of a geogrid with a large bending stiffness does not necessarily increase the bearing capacity of soft clay, although the bending stiffness of the geogrid is larger than the composite geofabric. This tendency is irrespective of the thickness of the clay (Hirao et al., 1996). On the other hand, it is also seen from these figures that a combination of sand mat with each geosynthetic markedly increases the bearing capacity, independent of the kind of geosynthetic. The reason for these differences will be discussed later.

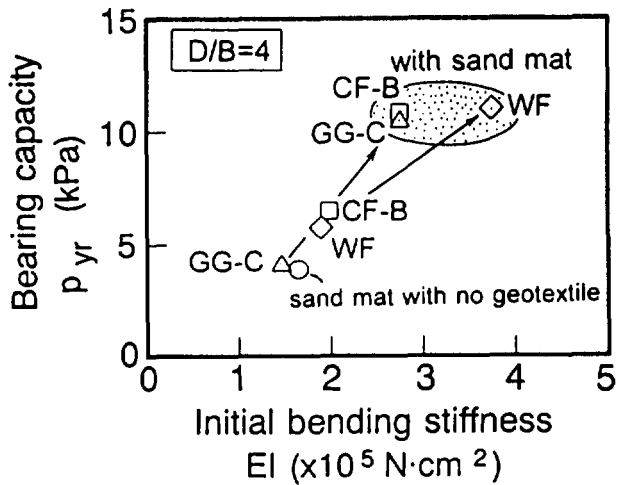


Fig. 5 Relation between initial bending stiffness and bearing capacity with and without sand mat

#### 4 EVALUATION OF SAND MAT EFFECT USING FEM ANALYSIS

##### 4.1 Analysis of Laboratory Model Tests

A FEM analysis of the behaviour of an embankment on soft clay with and without geogrids and sand mats was conducted using a model incorporating the effect of the interaction of the geogrid

and soft clay, as summarized in Table 1. The analytical procedure used the elasto-visco-plasticity model developed by Sekiguchi and Ohta (1977) for clay, by using a beam element for modeling the geogrid and a joint element for the interaction between geogrid and soil, respectively. The model also incorporated Biot's theory of three-dimensional consolidation for a coupled analysis. In a previous paper (Tanabashi et al., 1992), the model was successfully applied to the results from model footing tests on soft clay with and without geogrid and sand mat.

The geometry of the model analyzed is shown in Fig. 6 and corresponds to the laboratory model test where the width of the loading plate  $B$  was 10 cm, the depth of the clay layer  $D$  was 40 cm and the thickness of the sand layer was 3 cm. The analysis focused on the effect of the sand mat on the improvement of bearing capacity of a soft clay with and without a geogrid. The embankment on clay was modeled with and without sand mat

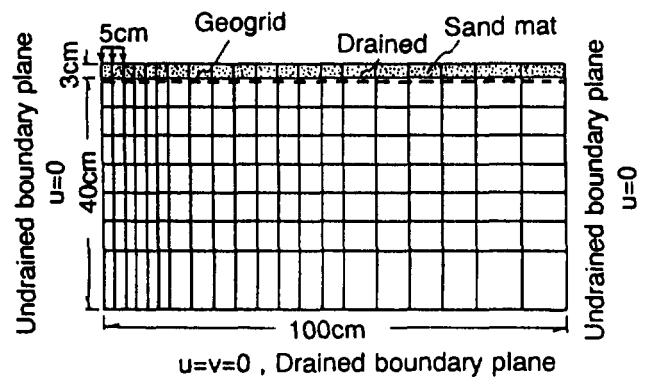


Fig. 6 Finite element mesh and boundary condition used for model tests

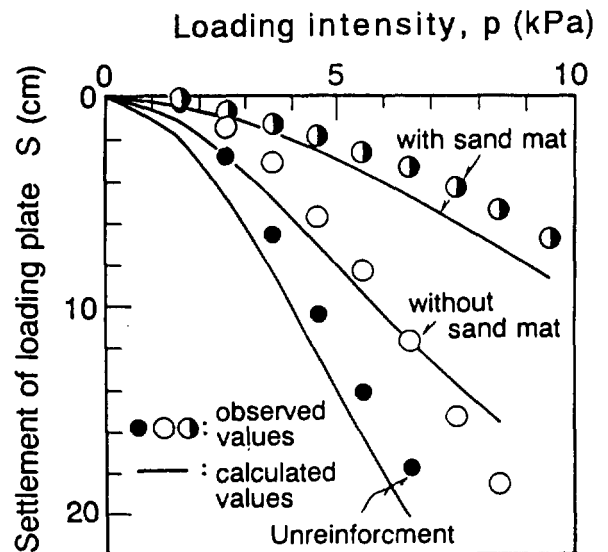


Fig. 7 Comparison of  $p$  vs.  $S$  curves for model tests with and without sand mat

and geogrid and was divided into 210 nodes and 200 elements for the FEM analysis as is also shown in Fig. 6. The boundary conditions for displacement were complete restraint on the bottom and horizontal restraint on lateral surfaces. In addition, the hydraulic boundary conditions were assumed to be drained at the bottom and surface and undrained on the sides. The parameters necessary for the present analysis were determined indirectly from plasticity indices, as proposed by Iizuka and Ohta (1987). The settlement versus load curves calculated using the FE analysis based on the Sekiguchi and Ohta model (Sekiguchi and Ohta, 1977) were compared in Fig. 7 with those observed in laboratory model tests which includes the results without geogrid and sand mat. Fig. 7 suggests that the method proposed for analyzing the reinforcement effect gives a reasonable prediction of the settlement versus load relations with and without geogrid and sand mat.

The model was also capable of simulating the deformation of the soft clay model both with and without reinforcement. Fig. 8 illustrates a family of results from model tests with and without a sand mat under an applied load,  $q = 8.4$  kPa. It can be seen

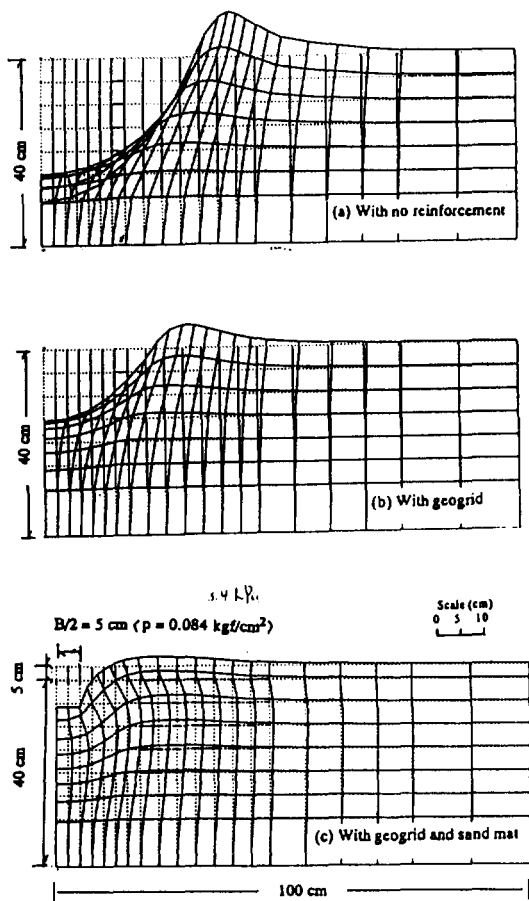


Fig. 8 Typical deformation diagrams obtained from numerical simulations

from Fig. 8 that in the case of soft clay alone or with a geogrid the ground deforms as if it is failing, while for soft clay with a geogrid and sand mat the settlements and lateral displacements are clearly restrained. This is due to the composite effect in which the sand mat restricts the movement of the geogrid and thus produces an increase in bearing capacity.

#### 4.2 Numerical Verification for Field Conditions

Numerical experiments using the proposed model were carried out to demonstrate the effect of a sand mat on the improvement of the bearing capacity of soft clay with a geogrid, under in-situ conditions with a typical profile just like as under model footing test condition as illustrated in Fig. 7. For this calculation, the following conditions were assumed: (i) depth of clay layer,  $D$ , 4, 6, 8, 10, 12 m; (ii) depth of clay layer to loaded area ratio,  $D/B$ , 1.33, 2.00, 2.67, 3.33, 4.00, and; (iii) the thickness of sand mat was kept constant equal to 30 cm. The boundary and drainage

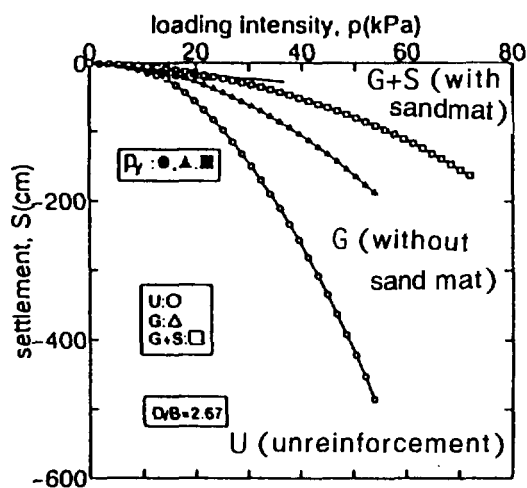


Fig. 9 Typical  $p$  vs.  $S$  curves obtained from numerical simulations

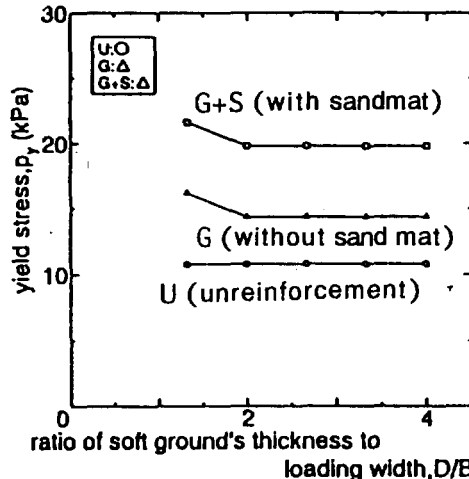


Fig. 10 Calculated relationship between  $p_y$  and  $D/B$

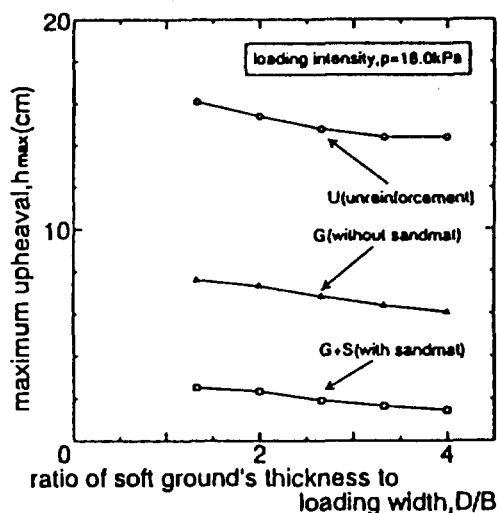


Fig. 11 Calculated relationship between maximum upheaval,  $h_{max}$  and  $D/B$

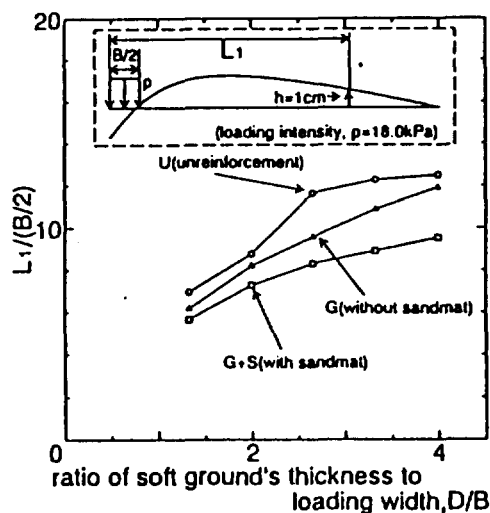


Fig. 12 Relation between normalized critical distance,  $L_1/(B/2)$  and  $D/B$

conditions were the same as those adopted in the analysis of the laboratory model tests. Typical settlement versus load relations for  $D/B = 2.67$  are shown in Fig. 9. The effect of geogrid and geogrid with sand mat on settlement control in soft clay is illustrated in the  $p$  versus  $S$  curves in Fig. 9 by the fact that the settlement increases linearly beyond the yield point with increasing applied loads, but increases abruptly in the case of no reinforcement. However, it is interesting to note that this yielding load becomes larger for reinforced compared with unreinforced models but is independent of the  $D/B$  as shown in Fig. 10. It is also notable that the bearing capacity improvement

due to a sand mat combined with a geogrid is considerable. The applied yielding load, increases by up to 1.8 times compared with no reinforcement. The advantage of a sand mat with geogrids is also observed in the deformation of soft clay under applied load. The amounts of maximum settlement, maximum heave and lateral distance of heave in soft clay are shown in Fig. 11 and Fig. 12 for cases with and without sand mat and geogrid. It is concluded from these comparisons that both settlement and lateral displacement of soft clay reinforced with geogrid and sand mat are not influenced by  $D/B$ .

The results calculated using the proposed model are presented in Fig. 13 in the form of the relation between  $S/D$  and  $d/S$  which is conventionally used for the stability control of soft clay under embankments (Matsuo and Kawamura, 1977). In this representation, it is assumed that soft clay fails when a  $S/D$  versus  $d/S$  path reaches the line for  $1/F = 1$  where  $F$  is a safety factor for stability. When we read off from data in Fig. 13, obtained by calculating for cases with and without a sand mat and  $D/B = 2.67$ , it is clear that the applied load  $p_{pr}$  for  $F = 1$  with sand mat and geogrid is larger than that for no reinforcement.

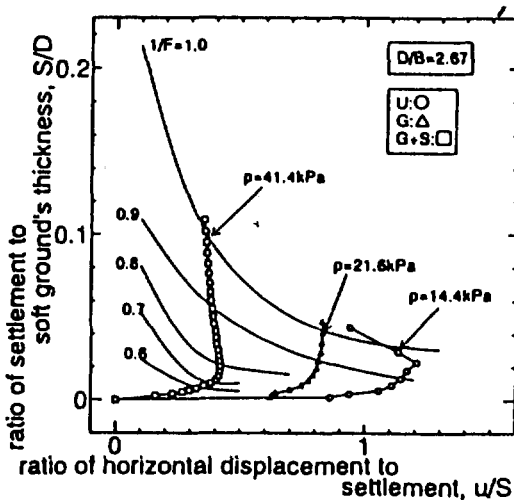


Fig. 13 Calculated relationship between  $S/D$  and  $d/S$

## 5 CONCLUSIONS

- 1) The direct placement of geogrids on the surface of a soft clay does not improve its bearing capacity.
- 2) There is little increase in the bearing capacity of a soft clay if a tensile force is applied by weighting the edge of a geogrid. The reason for no improvement is due to either the frictional

force or the interlocking effect being not exerted between the geogrid and clay.

3) Combined non-woven geosynthetics with geogrid gives an advantage by increasing bearing capacity.

4) The bearing capacity is markedly improved by an underlying sand mat combined with a geogrid. This effect is caused by an increase in bending stiffness of the composite of geogrid and sand mat as well as the higher frictional force developed between sands and geogrids compared with a geogrid only.

5) The effect of a sand mat on bearing capacity improvement and displacement control in soft clay has been successfully analyzed using a modified model which incorporates the effect of the interaction of the geogrid and sand mat.

#### ACKNOWLEDGEMENT

The authors would like to express their gratitude to Ikegami, M. (the executive director of Mitsui Petrochemical Industrial Products Co., Ltd.) who offered some kinds of geosynthetics and the 1g model footing testing apparatus used in this study.

#### REFERENCES

- Hirao, K., Yasuhara, K., Takaoka, K., Nishimura, J. and Tanabashi, Y. (1992) : Laboratory model tests on the application of composite fabrics to soft clay ground, Proc. IS-KYUSHU92, Vol. 1, pp. 601 - 606.
- Hirao, K., Yasuhara, K. and Tanabashi, Y. (1996) : Effect of bending stiffness of geotextiles on bearing capacity improvement of soft clay, Proc. IS-KYUSHU96, Vol. 1, pp. 591 - 596.
- Iizuka, A. and Ohta, H. (1987) : A determination procedure of input parameters in elasto-viscoplastic finite element analysis, Soils and Foundations, Vol. 27, No. 3, pp. 71 - 87.
- Matsuo, M. and Kawamura, K. (1977) : Diagram for construction control of embankment on soft ground, Soils and Foundations, Vol. 17, No. 3, pp. 37 - 52.
- Sekiguchi, H. and Ohta, H. (1977) : Induced anisotropy and time dependency in normally consolidated clay, Proc. 9<sup>th</sup> Intn'l Conf. SMFE, Specialty Session, No. 9, pp. 163 - 175.
- Tanabashi, Y., Hirao, K. and Yasuhara, K. (1992) : Numerical analysis for bearing capacity improvement of soft clay ground reinforced with geotextiles, Proc. IS-KYUSHU92, Vol. 1, pp. 701 - 706.
- Tanabashi, Y., Itoh, H., Hirao, K. and Yasuhara, K. (1996) : In-situ investigation and numerical estimation for bearing capacity improvement of very soft ground reinforced with geotextiles, Proc. IS-KYUSHU96, Vol. 1, pp. 685 - 690.
- Yasuhara, K., Hirao, K. and Tanabashi, Y. (1994) : Geofabrics

application to reinforcement of soft ground, Proc. Intn'l. Symp. Fiber Science and Technology, Vol. 1, pp. 511 - 512.



# The Bearing Capacity of a Reinforced Sand Layer Overlying a Soft Clay Subgrade

M.J. Kenny

Lecturer, Department of Civil Engineering, University of Strathclyde, Glasgow, UK

**ABSTRACT:** Recent interest has developed in the use of geosynthetics for forming a fill layer over soils which have very low bearing capacity. However, the reinforcement mechanism is not clearly understood. A programme of laboratory scale plane-strain bearing capacity tests under monotonic loading has been carried out which considers the reinforcing mechanism of the geosynthetic. Analysis of the test results show that the interpretation of the reinforcing mechanism is highly dependent upon the values assumed for the various model parameters. The results further suggest that in order to function effectively as a reinforcement over very soft clays, the geosynthetic should possess a significant component of in-plane bending stiffness.

**KEYWORDS:** Bearing capacity, Reinforcement, Shallow foundations, Soft soils, Unpaved roads.

## 1 INTRODUCTION

Recent interest has developed in the use of geosynthetics for forming a fill layer over soils which have very low bearing capacity, so that a construction platform can be formed. Although the technique has been successful in practice, there has been considerable disagreement concerning the reinforcement mechanism. After carrying out dimensional analysis of model loading tests, Fakher et al. (1996) concluded that the in-plane bending stiffness is the dominant factor when constructing over very soft soils. However, the current design methods for unpaved roads consider only tensile stiffness in the analysis of the mechanisms of reinforcement.

Many of the design methods have been developed from laboratory scale plane-strain bearing capacity tests under monotonic loading. This paper reports the results of a programme of such model tests carried out at the University of Strathclyde. Although the reinforcement used possessed insignificant bending stiffness, analysis of the reinforcing mechanism has allowed consideration of the relative importance of both tensile and bending stiffness in the bearing capacity of a reinforced sand layer over a soft clay subgrade.

## 2 BACKGROUND

In recent years, two different approaches have been adopted for the design of unpaved roads. The first approach is typified by the design method of Giroud and Noiray (1981). It attributes the improvement in the road performance to the reinforcement acting as a tensioned membrane as rutting develops and an increased subgrade bearing capacity due to subgrade confinement. Burd (1995) further developed membrane theory to produce a model in which the deformed reinforcement shape is obtained from a set of membrane equations. In contrast, the second

approach proposed by Milligan et al. (1989) neglects membrane action but considers that the reinforcement reduces the shear stresses developed at the surface of the subgrade, thus increasing the subgrade bearing capacity. It is thus more appropriate for small deformations. Despite these differences, the two approaches have the following common features :

1. They are derived from a stress distribution model common in the bearing capacity analysis of layered soils (Kenny and Andrawes, 1997). Giroud and Noiray (1981) assume a value of  $\tan^{-1}0.6$  for the stress distribution angle  $\alpha$  (see Figure 5) for both the unreinforced and reinforced road, while Milligan et al. (1989) state that the stress distribution angle should be derived from observation and experience.
2. The allowable subgrade bearing capacity is greater in the reinforced than in the unreinforced case. Both Giroud and Noiray (1981) and Milligan et al. (1989) have proposed modified subgrade bearing capacity factors.
3. The recommended stress distribution angles are the same in both the unreinforced and reinforced cases, although the presence of the reinforcement has been shown to improve the stress distribution.

## 3 EXPERIMENTAL SET UP

A strip footing 0.12 m wide was used in all tests. The test tank has inner dimensions of 2.0 m length, 1.4 m height, and 0.3 m width and parallel glass sides, as shown in Figure 1, and contained a soft clay subgrade overlain by Leighton Buzzard sand. The displacement fields were recorded at intervals of 10 mm footing penetration and analysed using the stereo-photogrammetric technique.

The soft clay subgrade was simulated by an artificial clay known as Glyben (Kenny and Andrawes, 1997), which is manufactured by mixing a sodium-bentonite clay

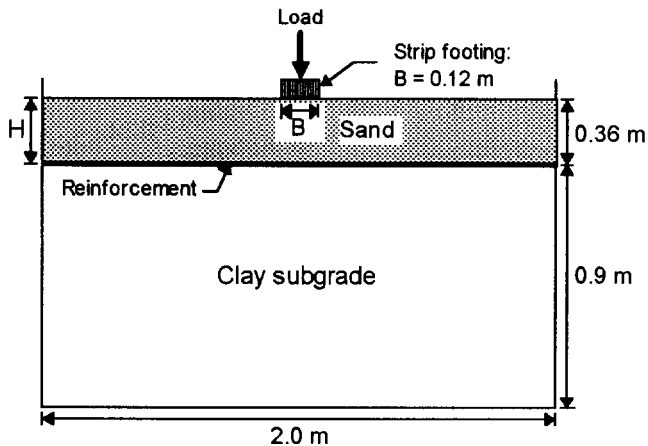


Figure 1. The experimental set up.

(Fulbent 570) and glycerine, the resulting shear strength depending on the mix proportions. A large number of undrained triaxial tests and vane shear tests were carried out over the period of the study, which demonstrated that Glyben behaved generally as a  $\phi_u = 0$  material under quick undrained loading, with an average  $c_u$  of  $10.6 \text{ kN/m}^2$ . Since Glyben samples are formed by compaction, the material unavoidably contains a small proportion of trapped air (approx. air voids content = 8%). However, the material was completely insensitive to handling and gave excellent repeatability during testing.

The fill material used was a uniformly graded coarse Leighton Buzzard sand placed using an air activated spreader in a dense state, with a mean porosity of 34.5% (porosity limits ; 34.0% - 44.5%). The operational angle of friction  $\phi'$  for the sand placed at this density was found to be  $48.5^\circ$ .

The reinforcement of the upper sand layer was provided by a single layer of geogrid type reinforcement placed at the sand-clay interface. Although no attempt was made to correctly scale all aspects of the problem, the reinforcement used can be considered to be a reduced scale model geogrid. It consists of welded polypropylene filaments of 0.5 mm diameter with grid openings of  $6.1 \text{ mm} \times 7.1 \text{ mm}$  on average. The load-extension properties of the geogrid were investigated using a range of strain rates of relevance to the current investigation.

In the experimental programme, bearing capacity tests were carried out for clay subgrade alone ( $H/B = 0$ ), and with and without the reinforcement layer for  $H/B$  ratios of 0.25, 0.75, 1.0, 1.5 and 2.0.

#### 4 EXPERIMENTAL RESULTS

The stress-settlement relationships for unreinforced and reinforced sand overlying clay shown in Figure 2 are representative of the test programme as a whole. Since

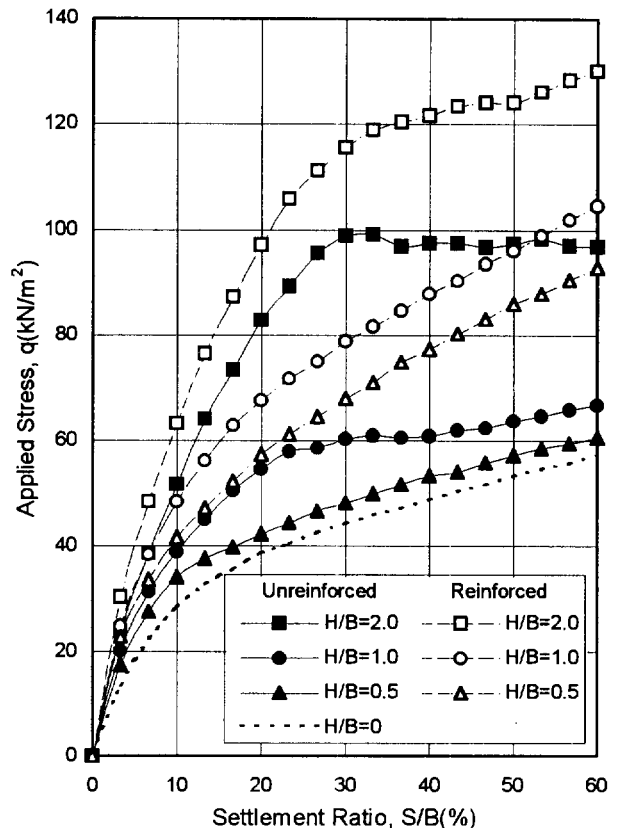


Figure 2. Stress-settlement relationships for unreinforced and reinforced sand over clay.

there is no observable post-peak, strain softening for the clay alone, this stress-settlement behaviour is consistent with a local shear failure of the subgrade due to the compressibility of the material. For unreinforced sand over clay, the ultimate stress can be more readily identified from the peak in the stress-settlement curve, particularly for large  $H/B$  ratios. As for clay alone, there is no clearly defined failure point in the reinforced case. In unpaved road design, a maximum rut depth (i.e. footing settlement) is a more appropriate criteria.

The displacement fields recorded during the later stages of footing penetration are given in Figures 3 and 4 for  $H/B$  ratios of 0.5 and 2.0 respectively. In general it was observed that for small sand depths the deformation of the sand/clay interface was more uniform when reinforcement was present. This indicates improved stress-distribution in the reinforced case. There was also a tendency for the sand beneath the footing to be displaced outwards when no reinforcement was present, particularly for large sand depths and at low footing settlements. This lateral displacement reduced when reinforcement was used. This is consistent with observations of Milligan et al. (1989), but the effect was less pronounced.

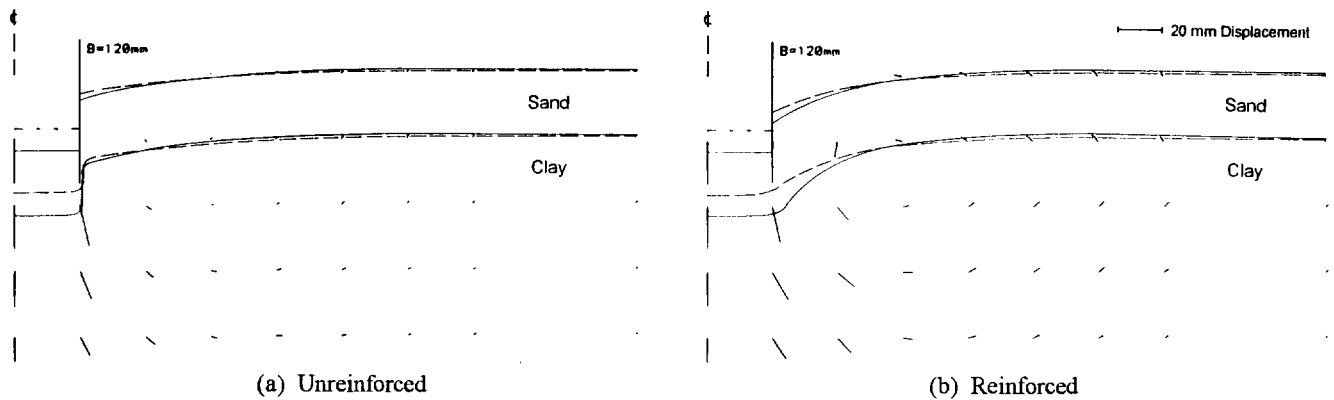


Figure 3. Displacement vectors for  $H/B = 0.5$  (Footing settlement,  $S/B = 42-58\%$ ).

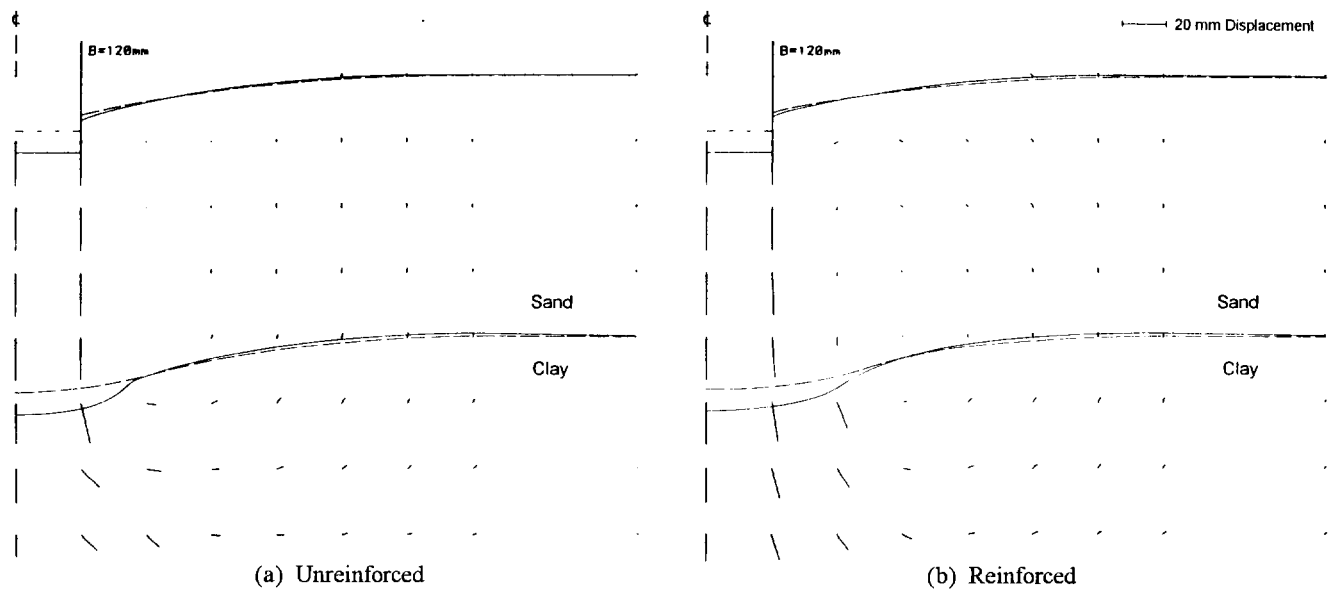


Figure 4. Displacement vectors for  $H/B = 2.0$  (Footing settlement,  $S/B = 42-58\%$ ).

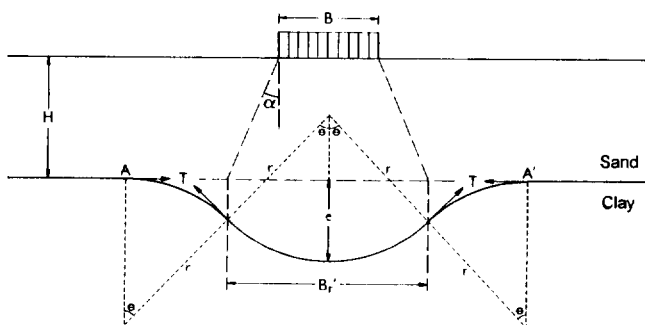


Figure 5. Analysis of membrane forces (after Gourc, 1983).

## 5 THE REINFORCEMENT MECHANISM

If we consider a typical stress distribution model with membrane action, as shown in Figure 5, the contribution of the reinforcement tension to the bearing capacity can be

calculated. Since very little subgrade heave was observed during footing penetration, the membrane analysis proposed by Gourc (1983) assuming four circular segments was adopted. This method is sufficient for illustrative purposes, although Burd (1995) gives a more rigorous treatment of reinforcement equilibrium.

From Figure 5 it can be seen that the contribution to the bearing capacity from stress distribution through the upper sand layer,  $q_d$ , is:

$$q_d = q_c \frac{B'}{B} \quad (1)$$

The subgrade reaction  $q_c$  was taken from the clay alone curve in Figure 2 at the same footing settlement. The membrane force which opposes the applied stress is equivalent to the vertical projection of the reinforcement tension at the stationary points. The maximum reinforcement tension is limited by the anchorage capacity.

Denoting the contribution to the bearing capacity due to membrane action by  $q_m$ , it follows that:

$$q_m = 2T \sin \theta / B \quad (2)$$

The angle  $\theta$  and the reinforcement strain depends on the footing settlement,  $S$ . Having determined the strain in the reinforcement and estimating the strain rate from the rate of penetration of the footing, the tension  $T$  was obtained from the load-strain properties of the reinforcement. The bearing capacity of the footing,  $q$ , can be determined by summing the contributions from stress distribution,  $q_d$ , and membrane action,  $q_m$ . The bearing capacities were calculated using a commonly assumed stress distribution angle of  $\alpha = 30^\circ$  and using the actual values measured during the test programme. These are compared with the experimental values,  $q_{exp}$ , in Table 1.

Table 1. Comparison of experimental and predicted bearing capacities for reinforced sand over clay.

Test details			Bearing capacity (kN/m <sup>2</sup> )			
H/B	S/B	B' <sub>r</sub> /B	q <sub>d</sub>	q <sub>m</sub>	q	q <sub>exp</sub>
0.5	0.33	1.58*	78.7	3.7	82.4	71.0
		1.2**	59.9	7.0	66.9	71.0
0.5	0.58	1.58*	78.7	12.2	90.9	92.0
		1.2**	72.7	21.8	94.5	92.0
1.0	0.33	2.16*	107.8	1.8	109.6	81.8
		1.58**	78.6	3.8	82.4	81.8
1.0	0.58	2.16*	130.9	6.0	136.9	103.6
		1.6**	97.0	12.3	109.3	103.6

Note : \* denotes values calculated using  $\alpha = 30^\circ$ ; \*\* denotes values calculated using measured values of  $B'_r$  (distance between points of inflection of sand/clay interface).

It can be seen that by using a stress distribution angle  $\alpha$  of  $30^\circ$ , the calculated membrane forces are approximately 50% of those calculated using the observed values of  $\alpha$ . In addition, the bearing capacity tends to be overpredicted using  $\alpha = 30^\circ$ . A similar analysis of the unreinforced tests gave a larger overprediction, particularly at small displacements when the sand thickness is large, which can be attributed to the lack of lateral restraint of the sand.

## 6 CONCLUSIONS

Based on the experimental results and analysis presented above, the following conclusions can be drawn:

1. In the present investigation, the commonly assumed values of the stress distribution angle were larger than those observed experimentally and resulted in overprediction of the bearing capacity. This seems to oppose the observation of Burd (1995) that the stress distribution angle tends to be greater for soft than firm

clays. This discrepancy could be due to the compressibility of the subgrade.

2. It has often been concluded that the improvements in the load carrying capacity of unpaved roads due to membrane action are insignificant and may therefore be neglected. However, these conclusions appear to be based on the method by which they are calculated rather than on observed behaviour. In the present investigation, the use of a more realistic stress distribution angle rather than the commonly assumed values greatly increased the calculated membrane forces, suggesting that membrane action does make a significant contribution, particularly for small subbase thicknesses. Unpaved road field trials carried out by Sigurdsson and Fannin (1997) confirmed the importance of membrane action for small subbase thicknesses.
3. In reinforcing very soft ground, the contribution to the bearing capacity from the subgrade reaction after load spreading through the fill would be insignificant so that a tensile reinforcement would rely upon membrane action to support the traffic loading. Even assuming that adequate anchorage and subbase-geogrid interlock is maintained, deformation is likely to be excessive under traffic loading. Therefore a geosynthetic with significant in-plane bending stiffness would be beneficial to the performance of the structure.

## REFERENCES

- Burd, H.J. (1995) "Analysis of membrane action in reinforced unpaved roads", *Canadian Geotechnical Journal*, Vol. 32, pp. 946-956.
- Fakher, A., Jones, C.J.F.P., & Zakaria, N.A.B. (1996) "The influence of dimensional analysis on the interpretation of model loading tests on reinforced ground", *Proc. Int. Symposium on Earth Reinforcement*, Kyushu, Japan, pp. 585-589.
- Giroud, J.P. & Noiray, L. (1981) "Geotextile-reinforced unpaved road design", *Jour. Geotech. Eng. Div.*, ASCE, Vol. 107, No. GT9, pp. 1233-1254.
- Gourc, J.P. (1983) "Quelques aspects du comportement des geotextiles en mecanique des sols", *PhD thesis*, University of Grenoble, France.
- Kenny, M.J., & Andrawes, K.Z. (1997) "The bearing capacity of footings on a sand layer overlying soft clay", *Geotechnique*, Vol. 47, No. 2, pp. 339-345.
- Milligan, G.W.E., Jewell, R.A., Houslyby, G.T. & Burd, H.J. (1989) "A new approach to the design of unpaved roads - part II", *Ground Engineering*, Vol. 22, No. 8, pp. 37-42.
- Sigurdsson, O., & Fannin, R.J. (1997) "Construction and performance of a geosynthetic reinforced unpaved road", *Proc. Ground Improvement Geosystems*, Thomas Telford, London, pp. 322-328.

# Supporting Capability of Geogrid Reinforced Soil Foundations

N. Yasufuku

Associate Professor, Department of Civil Engineering, Kyushu University, Fukuoka, Japan

H. Ochiai

Professor, Department of Civil Engineering, Kyushu University, Fukuoka, Japan

K. Kawamata

Engineer, Electric Power Development Co. Ltd.

**ABSTRACT:** Geogrid reinforced sandy soil foundations are often used to improve the supporting capability of soft soil foundations. The vertical load applied on a geogrid reinforced foundation is transmitted to the supporting soil over a wider area, thus, improving the soil's ability to support the foundation load. In order to examine the effect of the vertical load propagation due to geogrid reinforced sandy soils foundation, a series of model loading tests was carried out with different reinforced soil foundation thicknesses and number of geogrids horizontally placed in sandy soils. In addition, a method estimating the effective thickness for geogrid reinforced foundation design is presented based on experimental and theoretical considerations.

**KEYWORDS:** reinforcement, geogrid, soil foundation, vertical load propagation, bearing capacity

## 1 INTRODUCTION

The working platform usually consists of geogrid reinforcement laid within a uniform layer of cohesionless fill on the surface of soft soils. Although a number of methods have been used to construct a fill layer over the soft soil, there seems to be no general agreement with respect to the reinforcement mechanism and load spreading effects.

Reinforced sandy soil foundations with geogrid horizontally placed on soft soil ground are often used to improve the supporting capability of soft soil ground in an economical way. The vertical load applied on the reinforced soil foundations is transmitted to the supporting foundation within a wider area, subsequently, providing the supporting foundation with greater bearing capacity. It is considered that the spreading effects depend on the factors shown in Table 1. It is therefore essential to investigate the properties of vertical load propagation in the reinforced soil foundation with geogrids with reference to the influence factors in

Table 1. Typical factors related to load spreading effects in reinforced sandy soil foundations with geogrid

Term	Influence factors
Reinforced soil ground with geogrid	1. Thickness, 2. Number and position of reinforcement layers, 3. Reinforcement length
Soil property	1. Unit weights of soils, 2. Strength parameters
Geogrid property	1. Tensile strength, 2. Friction property

Table 1. This will develop a rational way of determining the reinforced geogrid soil foundation thickness in practical design. In this paper, the effects of the foundation thickness and the number of reinforcement layers on the spreading effects in reinforced sandy soil foundations with geogrid are investigated using the results of model loading tests and a few theoretical considerations.

## 2 EXPERIMENTAL PROCEDURE

Figure 1 shows the layout of the experiment. On the floor of a 1.08 m wide, 0.4 m deep, 0.8 m high container, twenty-one aluminium blocks (0.05 m wide, 0.4 m long) were lined up.

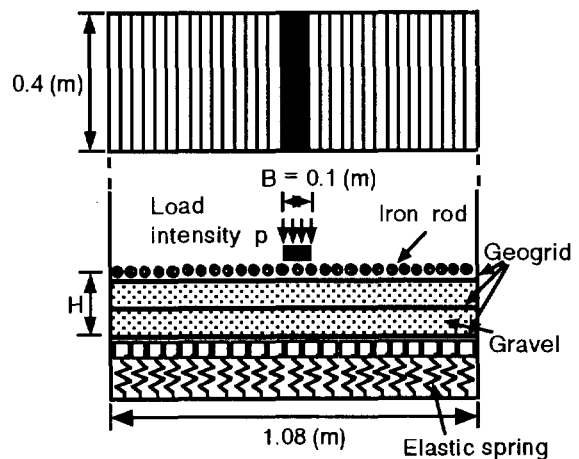


Figure 1 Experimental setup

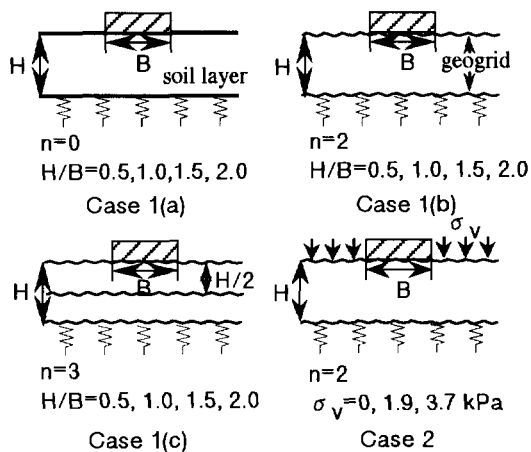


Figure 2 Groups of tests

Two elastic springs were fixed under each aluminium block and the vertical deformation of each spring was measured by a dial gauge attached alongside. The elastic springs with an elastic stiffness of  $k=3.14$  (kgf/mm) were used to represent the supporting soil, possessing an elastic modulus of subgrade reaction  $k_g=3077$  kPa/m. The model reinforced soil foundation with geogrid were made of fine gravel. The average dry density was  $16.4$  kN/m<sup>3</sup> and the internal friction angle was 41 degrees (Ochiai et.al.,1994). The tests performed are schematically shown in Figure 2. They consists of the following two cases:

Case 1 aims to study the effects of number of reinforcement layers on the vertical load propagation properties. The spreading effect is also investigated in relation to the thickness of reinforcement layer. Case 2 aims to discuss the spreading effect of vertical load through reinforced gravel foundations with geogrid under different overburden pressures. The tensile strength of geogrid used is 14.7 (kN/m). The size of each model is 1.08 m wide, 0.40 m long and 0.05, 0.1, 0.15 or 0.20 m thick. The loading plate of 0.1 m wide and 0.4 m long is placed on the model reinforced gravel foundation, which is then vertically loaded while controlling displacement. The rate of displacement was 1 mm/min.

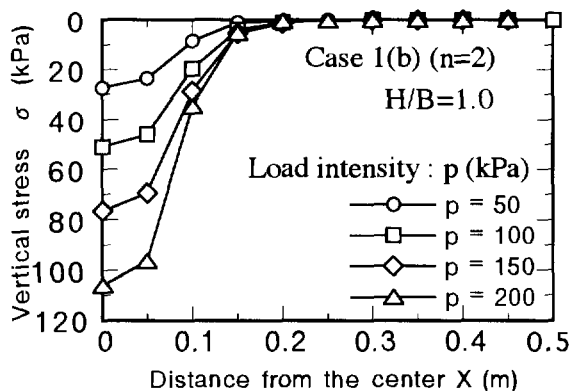


Figure 3. Typical vertical stress distribution

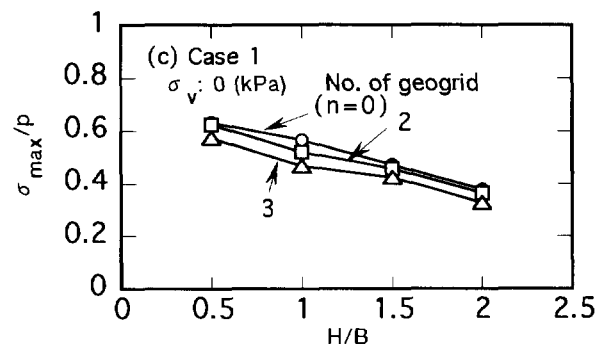
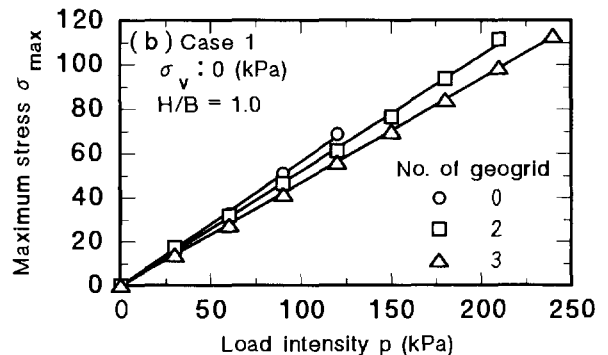
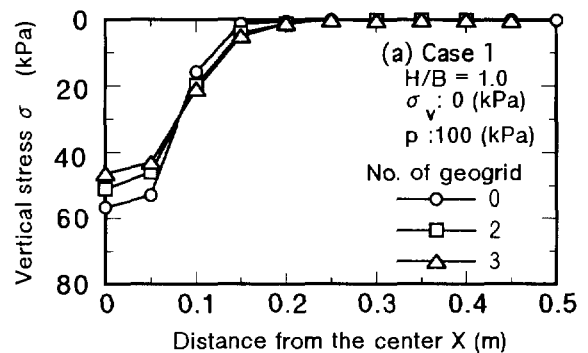


Figure 4 Characteristics of load spreading effect related to number of reinforcement layer

### 3 EXPERIMENTAL RESULTS

#### 3.1 Vertical Stress Propagation

Figure 3 shows the vertical stress distribution at the supporting foundation under the reinforced gravel layer with two geogrids (Case 1(b) at  $H/B=1.0$ ) generated by several load intensities  $p$ . It can be seen from this figure that the vertical stress distribution was convex with a maximum vertical stress  $\sigma_{max}$  at the center. It is also obvious that the magnitude of  $\sigma_{max}$  increases with the increasing load intensity  $p$ , and that the magnitude is always smaller than the values of  $p$ .

#### 3.2 Maximum Vertical Stress

Figures 4 and 5 show the effects of number of reinforcement

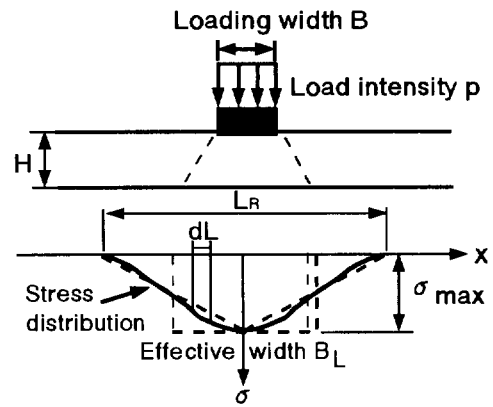
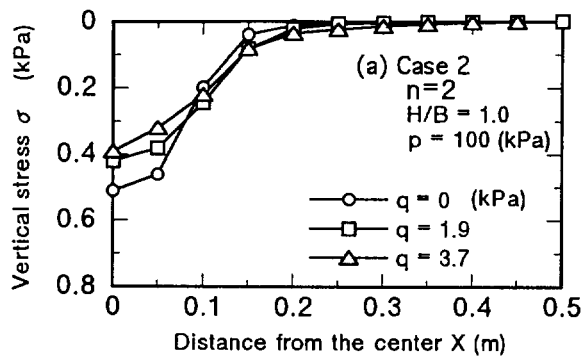


Figure 6 Definition of effective width BL

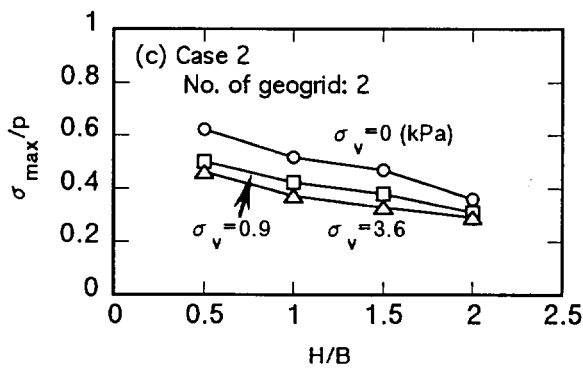
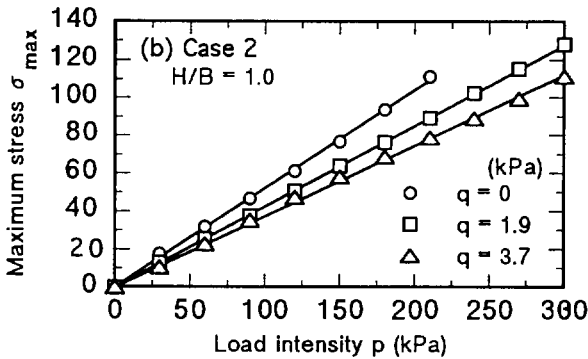


Figure 5 Characteristics of load spreading effect related to overburden pressure

## 4 THEORETICAL CONSIDERATIONS

### 4.1 Definition of Effective Width

When loading is applied to a reinforced gravel layer with geogrid, the resulting stress distribution becomes convex with a maximum vertical stress  $\sigma_{max}$  at the center of the base as is schematically shown in Figure 6. Here, in order to reasonably estimate the spreading effects of the reinforced gravel foundation, effective width  $B_L$  is introduced which is defined as an apparent stress distribution width. When considering that  $\sigma_{max}$  is uniformly transmitted to a given supporting subgrade due to a load intensity  $p$ , and then the  $\sigma_{max} B_L$  balances with  $pB$ , the following equation can be given (see Figure 6):

$$pB = \int \sigma dL = \sigma_{max} B_L \quad (1)$$

Eq.(1) can also be rewritten as;

$$\frac{B_L}{B} = \frac{1}{\frac{\sigma_{max}}{p}} \quad (2)$$

As shown in Figures 4 and 5,  $\sigma_{max}/p$  is constant irrespective of load intensity, and it is therefore obvious from Eq.(2) that  $B_L/B$  also becomes constant. In addition, it is important to point out that as the  $\sigma_{max}/p$  becomes smaller and  $B_L/B$  becomes larger, the spreading effect of reinforced gravel layer increases.

When a triangular stress distribution with width  $L_R$  is assumed as shown in Figure 6 which is approximately true (see Figures 4 and 5), the relationship between  $L_R$  and  $B_L$  is represented by

$$L_R = 2B_L \quad (3)$$

layer and overburden pressure on the magnitude of maximum vertical stress  $\sigma_{max}$ . It is found from these figures that 1)  $\sigma_{max}$  decreases with the increasing number of reinforcement layer and overburden pressure (see Figures 4(a) and 5(a)), and that 2) the  $\sigma_{max}$  develops in proportion to the applied vertical stress over a wide load intensity region, irrespective of the two factors mentioned above (see Figures 4(b) and 5(b)), and also that 3) not only the values of  $\sigma_{max}/p$  decrease with the increasing  $H/B$  but also the influence of the two factors on  $\sigma_{max}/p$  gradually decreases with the increasing  $H/B$  (see Figures 4(c) and 5(c)). Similar properties have already been shown in the results of geogrid-mattress loading tests (Ochiai, et. al.,(1994); Yasufuku, et. al.,(1996)).

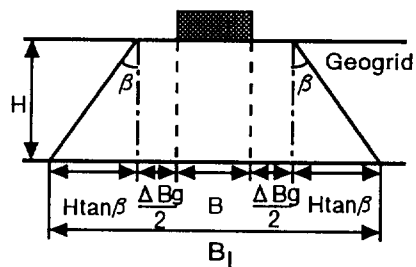


Figure 7 Schematic view of load spreading effect

#### 4.2 Geogrid Spreading Effects $\Delta B_g$

When a loading plate of width  $B$  is placed on a reinforced gravel layer with geogrid, the applied vertical load is transmitted to the supporting subgrade through the gravel layer. An idea of load spreading is schematically shown in Figure 7. Based on this idea, the total spreading effect  $B_L$  can be divided into two parts: one is geogrid spreading effect  $\Delta B_g$ , which is due to soil-geogrid interaction and the other is  $2H \tan \beta$ , which is due to thickness of gravel layer. Thus, the net spreading effect normalized by  $B$  is given by

$$\frac{B_L - B}{B} = \frac{\Delta B_g}{B} + 2 \frac{H}{B} \tan \beta \quad (4)$$

where,  $\beta$  is defined as spreading angle through a reinforced gravel layer.

The computed relationship between  $(B_L - B)/B$  and  $2H/B$  are shown in Figure 8, together with the experimental data, in which Figure 8(a) indicates the effects of number of reinforcement layers on the net spreading effect, and also Figure 8(b) clarifies the dependence of the effect on the overburden pressure. Here the experimental plots were obtained from Eq.(1) with measured values of  $\sigma_{max}/p$ , and the solid lines are based on Eq.(4), in which spreading angle  $\beta$  was estimated to be 27 degrees, that is  $\tan \beta = 0.5$ , irrespective of number of reinforced layers and overburden pressure. It can be found from these figures that the normalized spreading effect of geogrid  $\Delta B_g/B$ , which is evaluated as the value of  $B_L/B$  at  $H/B = 0$ , increases with the increase in the number of reinforcement layers and overburden pressure, at least in the case of normalized thickness  $H/B$  less than 2. In addition, it can be seen that Eq.(5) can reasonably represent the mechanism of spreading effects in the reinforced gravel layer with geogrid.

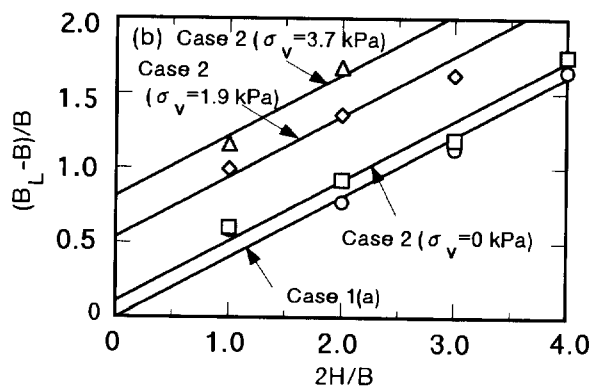
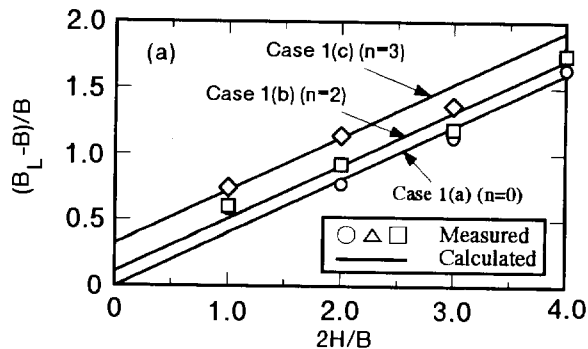


Figure 8 Relationship between  $(B_L - B)/B$  and  $2H/B$

#### 4.3 Estimation of Geogrid Reinforced Thickness

In a practical design, it is necessary to properly estimate the thickness of reinforcement layer  $H$  against an allowable bearing capacity  $q_a$  in the supporting soft layer. When  $q_a$  is considered to be  $\sigma_{max}$ , and substituting Eq.(4) into Eq.(1), the following equation is obtained;

$$pB = q_a (B + 2H \tan \beta) + q_a \Delta B_g \quad (5)$$

where  $q_a \Delta B_g$  represents an internal force taken by the reinforcement spreading effect  $\Delta B_g$ . As was discussed by Ochiai et. al., (1986), taking the spreading effect as  $G_e$  and comparing with Eq.(5),  $G_e$  is given by ;

$$\begin{aligned} G_e &= q_a \Delta B_g \\ &= pB - q_a (B + 2H \tan \beta) \end{aligned} \quad (6)$$

Further, considering that  $\tan \beta = 0.5$  ( $\beta = 27^\circ$ ), Eq.(6) is easily rewritten as:

$$\frac{H}{B} = \frac{p}{q_a} \left( 1 - \frac{G_e}{pB} \right) - 1 \quad (7)$$



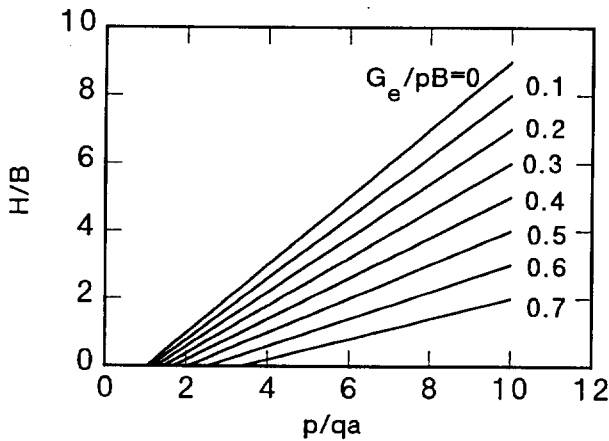


Figure 9 Chart of determining reinforcement thickness  $H$  against geogrid spreading effect  $G_e$

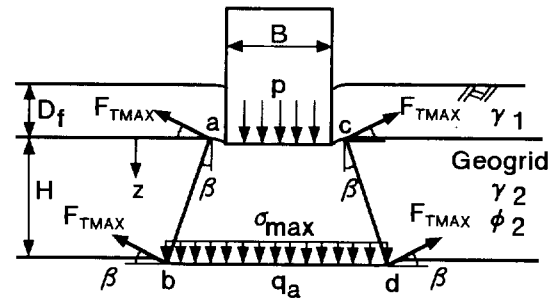


Figure 10 Idea of load spreading effect

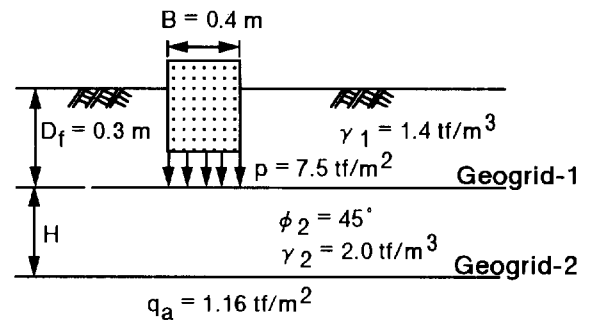


Figure 11 Example of design condition

Figure 9 shows the  $H/B$ - $p/q_a$  relationship calculated from Eq.(7) with various values of  $G_e/pB$ . It is important to note that the estimation of  $G_e$  is needed in order to obtain the thickness of reinforcement layer using Eq.(7). To estimate  $G_e$  in a concrete way, the following assumption can be made; 1) the spreading effects can be produced due to the maximum tensile force  $F_{Tmax}$  in geogrids and the direction is perpendicular to line  $ab$  ( $cd$ ) as shown in Figure 10, that is, the angle between the direction of the force and that of the horizontal plane becomes the load spreading angle  $\beta$  ( $\tan\beta=0.5$ ). 2)  $F_{Tmax}$  can be mobilized by maximum tensile shear stress  $\tau_{max}$  in the range of the load spreading width  $2H\tan\beta$  and 3) the shear stress  $\tau_{max}$  is due to the internal friction between soil and geogrid. A similar idea has been reported by Yang et. al.,(1994).

Base on these assumptions, the tensile force  $F_{Tmax}$  is represented by

$$F_{Tmax} = \tau_{max}(2H \tan \beta) = \sigma_v \tan \delta (2H \tan \beta) = \sigma_v H \tan \delta \quad (8)$$

where,  $\delta$  and  $\sigma_v$  are the friction angle in the soil-geogrid interaction and vertical stress acting on the geogrid respectively. Here, for simplicity  $\sigma_v$  is assumed to be equal to the overburden pressure. Therefore, the spreading effect  $G_e$  in geogrid is estimated by ;

$$G_e = \sum_{i=1}^n F_{Tmax,i} \sin \beta = \sum_{i=1}^n \sigma_{v,i} H \tan \delta \sin \beta \quad (9)$$

where,  $n$  is defined as numbers of reinforcement layer and,

$\sin\beta$  is almost equal to 0.45 from the definition of  $\beta$ . It is easy to understand that when substituting Eq.(9) into Eq.(7), the proper thickness,  $H$ , can be obtained under a certain design condition.

Now, as an application of this model, the following example is considered. The design condition is shown in Figure 11. In this case, the vertical stresses  $\sigma_{v1}$  on geogrid-1 and  $\sigma_{v2}$  on geogrid-2 are evaluated as :

$$\sigma_{v1} = \gamma_1 d_f \quad ; \quad \sigma_{v2} = \gamma_2 (d_f + H) \quad (10)$$

and substituting Eqs.(8), (9) and (10) into Eq.(7), and after some calculation, the thickness  $H$  is computed as follows:

$$H = \frac{-A_2 + \sqrt{A_2^2 - 4A_1A_3}}{2A_1} \quad (11)$$

where,  $A_1 = \gamma_2 \tan \delta \sin \beta$ ,  $A_2 = 2\gamma_1 d_f \tan \delta \sin \beta + q_a$  and  $A_3 = -(p - q_a)B$ . It is important to note that in this case, using this equation, the thickness,  $H$ , is computed as 1.20 m which is about a half compared with the thickness in the case without geogrid ( $G_e=0$ ) which is about 2.18 m calculated using Eq.(7).

## 5 CONCLUSIONS

The vertical load spreading effect of reinforced soil foundation with geogrids is investigated both experimentally and theoretically. The main conclusions obtained are as follows :

1. The vertical load propagation on the surface of subgrade has a convex shape with the maximum vertical stress  $\sigma_{max}$  at the center of applied vertical stress  $p$ .
2. The maximum vertical stress  $\sigma_{max}$  developed is proportional to the applied vertical stress  $p$ . The ratio,  $\sigma_{max}/p$ , is influenced by the thickness of reinforced soil foundations, numbers of geogrids and the overburden pressure.
3. Effective width  $B_e$  is proposed to express the load spreading effect in reinforced soil foundation with geogrid which has two parts: one is geogrid spreading effect and the other is the effect due to the thickness of soil layer.
4. An estimating method is proposed to calculate the thickness of reinforced foundations in design practice using the proposed effective width  $B_e$  and the considered soil-geogrid interaction mechanism.

## ACKNOWLEDGMENTS

The authors would like to thank Prof. J.W. Ju of Suncheon National University, Korea and Mr. M. Nakashima of Kyushu University, Japan for their support during the experiments.

## REFERENCES

- Ochiai, H., Matsushita, H. and Hayashi, S. (1986) "Foundations for Buildings on Grounds Contained Sulphuric Ion", *Tsuchi-to-Kiso*, Vol.34, No.6, pp.45-50 (in Japanese).
- Ochiai, H., Tsukamoto, Y., Hayashi, S., Otani, J. and Ju, J.W. (1994) "Supporting Capability of Geogrid-Mattress Foundation", 5th International Conference on Geotextiles, Geomembranes and Related Products, Singapore, pp.321-326.
- Yang, J, Ochiai, H. and Hayashi, S. (1994) "Evaluation of Bearing Capacity of Geogrid Reinforced Foundation", *Jour. of Geotechnical Engineering, JSCE*, No.505/III-29, pp.123-132, (in Japanese).
- Yasufuku, N, H.Ochiai, K.Omine, S.Ohno, K.Kawamata and Y.Tsukamoto (1996) "Evaluation of the Bearing Capacity Improvement of Geogrid Mattress", *Proc. of Int. Symp. on Earth Reinforcement (IS Kyushu '96)*, Vol.1, pp.703-708.

# Theoretical Solutions for Stress and Strain Fields of a Geosynthetic-Reinforced Foundation Vertically Loaded by a Concentrated Force

Jie Han

Design Engineer, Ph.D., Tensar Earth Technologies, Inc., Atlanta, GA 30328, USA

**ABSTRACT:** Geosynthetics can be used as reinforcements in soils to provide improved bearing capacity and reduced settlement for structural footings or pavement systems. Existence of geosynthetics in a foundation tends to alter the stress and strain fields due to the difference in elastic moduli and strengths between geosynthetics and soils. Geosynthetic-reinforced soil system can be treated as inhomogeneity and inclusion problems as studied in micromechanics of composites. The concept is to represent the inhomogeneities of geosynthetics in soil as the inclusions of eigenstrains in a homogeneous medium. Derivation of the solutions to determine stress and strain fields of the geosynthetic-reinforced foundation vertically loaded by a concentrated load is presented in this paper, in which the Eshelby eigenstrain tensor is introduced.

**KEY WORDS:** Geosynthetic, reinforcement, foundations, inclusion, stress-strain relations.

## 1 INTRODUCTION

Early studies conducted by Binquet and Lee (1975a, b) on geosynthetic-reinforced foundations demonstrated the effectiveness of geosynthetics in increasing bearing capacity of soils. The use of this kind of foundation has attracted more attention in the past few years. A number of model tests have been performed by several researchers (Huang and Tatsuoka 1990; Omar et al. 1994; Yetimoglu et al. 1994). Those tests mainly focused on finding out the optimized configuration of the geosynthetic layers in soil such as the location of the top layer, the spacing between adjacent layers, the width of reinforcement, and the number of layers. However, very few theories have been developed so far to study the mechanisms behind the experimental results. Binquet and Lee (1975b) assumed that the normal and shear stresses along the upper surface of the geosynthetic reinforcement follow Boussinesq's solution. Shukla and Chandra (1994) established a model to analyze the settlement response by treating a geosynthetic layer as an elastic membrane and solving the equilibrium equations under vertical and horizontal loads on the membrane. In those papers, the existence of the geosynthetics was not taken into account in the calculation of applied stresses on the geosynthetics due to the external loads on the upper surface. In reality, the existence of geosynthetics in the foundation disturbs the whole stress and strain fields as indicated by Kurian et al. (1997) using a finite element method.

## 2 THEORIES OF INHOMOGENEITY AND INCLUSION PROBLEMS

A material  $\Omega$  with different elastic moduli from those of a matrix  $D-\Omega$  as shown in Figure 1 is called an inhomogeneity in micromechanics. The existence of the material  $D$  will disturb the applied stresses in the domain  $D-\Omega$  (Mura 1983).

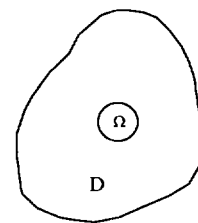


Figure 1 Inhomogeneity and inclusion (Mura 1982)

The disturbed stress field can be simulated by an eigenstress field resulting from a fictitious eigenstrain  $\epsilon_{ij}^*$  in the domain  $\Omega$  in a homogeneous material. The so-called eigenstrain was defined by Mura (1982) as a nonelastic strain such as thermal expansion, phase transformation, initial strains, plastic, and misfit strains, etc. Eigenstress is a self-equilibrated internal stress induced by one or several eigenstrains in a body without any other external force and surface constraint. The domain  $\Omega$  with the eigenstrain  $\epsilon_{ij}^*$  and the same elastic moduli as those in the matrix  $D-\Omega$  is called an inclusion.

Due to applied external forces, the stress-strain relation for the inhomogeneity problem can be expressed as (Mura 1982)

$$\sigma_{ij}^0 + \sigma_{ij} = C_{ijkl}^* (\epsilon_{kl} + \epsilon_{kl}^0) \quad \text{in } \Omega \quad (1)$$

$$\sigma_{ij}^0 + \sigma_{ij} = C_{ijkl} (\epsilon_{kl} + \epsilon_{kl}^0) \quad \text{in } D-\Omega \quad (2)$$

where  $\sigma_{ij}^0$  and  $\epsilon_{kl}^0$  are the stress and the strain induced by external forces without any inhomogeneity, and  $\sigma_{ij}$  and  $\epsilon_{kl}$  are the stress and the strain due to the presence of the inhomogeneity. As pointed out by Eshelby (1957), the

inhomogeneity problem can be treated as an equivalent inclusion problem by including the eigenstrains as follows:

$$\sigma_{ij}^0 + \sigma_{ij} = C_{ijkl}(\varepsilon_{kl} + \varepsilon_{kl}^0 - \varepsilon_{kl}^*) \quad \text{in } \Omega \quad (3)$$

Equalizing Equation (1) and Equation (3) yields

$$C_{ijkl}^*(\varepsilon_{kl} + \varepsilon_{kl}^0) = C_{ijkl}(\varepsilon_{kl} + \varepsilon_{kl}^0 - \varepsilon_{kl}^*) \quad \text{in } \Omega \quad (4)$$

### 3 MODELING OF A GEOSYNTHETIC-REINFORCED FOUNDATION

Figure 2a is a case occurring in geotechnical practice. The geosynthetic layer has two major functions in resisting the applied load  $P$  on the surface: soil confinement and membrane effect. This problem can be modeled as an ellipsoidal inhomogeneity or inclusion in a half space as shown in Figure 2b. This model can be further decomposed into two problems as shown in Figure 3. The problem in Figure 3a is a Boussinesqi problem while the problem in Figure 3b is an inclusion problem. The solutions to the stresses  $\sigma_{ij}^0$  and strains  $\varepsilon_{kl}^0$  for Boussinesqi's problem can be found in many textbooks. Therefore, the aim of this paper is to investigate the inclusion problem.

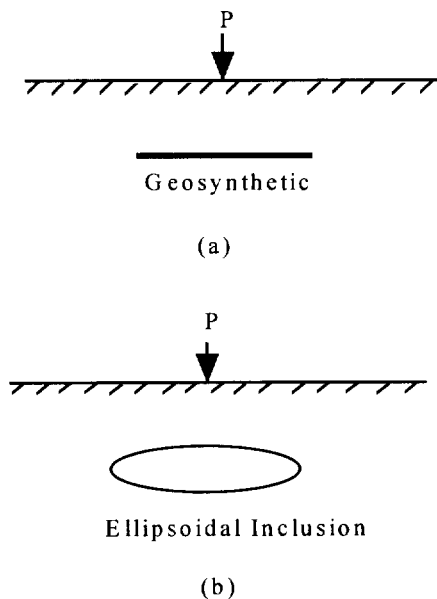


Figure 2 Modeling of a Geosynthetic-Reinforced Foundation

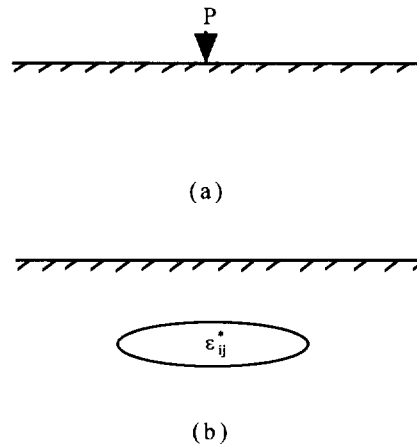


Figure 3 Decomposition of the Problem

### 4 SOLUTION FOR STRESS AND STRAIN FIELDS

The displacement  $u_i(\bar{x})$  induced by the eigenstrain  $\varepsilon_{ij}^*$  in the semi-infinite domain can be expressed by (Seo and Mura 1979)

$$u_i(\bar{x}) = \int_{\Omega} C_{jkmn} \varepsilon_{mn}^*(\bar{x}') \frac{\partial}{\partial x'_k} G_{ij}(\bar{x}, \bar{x}') d\bar{x}' \quad (5)$$

where  $G_{ij}(\bar{x}, \bar{x}')$  are Green's functions and  $C_{jkmn}$  are elastic constants. Green's functions  $G_{ij}(\bar{x}, \bar{x}')$  for the semi-infinite isotropic medium have been obtained by Mindlin (1936) and rewritten by Seo and Mura (1979) in their paper as follows:

$$G_{ij}(\bar{x}, \bar{x}') = \frac{1}{16\pi\mu(1-\nu)} \left\{ \frac{3-4\nu}{R_1} \delta_{ij} + \frac{1}{R_2} \delta_{ij} + \frac{(x_i - x'_i)(x_j - x'_j)}{R_1^3} \right. \\ \left. + \frac{(3-4\nu)(x_i - x'_i)(x_j - x'_j)}{R_2^3} + \frac{2x_3 x'_3}{R_2^3} \left[ \delta_{ij} - \frac{3(x_i - x'_i)(x_j - x'_j)}{R_2^2} \right] \right. \\ \left. + \frac{4(1-\nu)(1-2\nu)}{R_2 + x_3 + x'_3} \left[ \delta_{ij} - \frac{(x_i - x'_i)(x_j - x'_j)}{R_2(R_2 + x_3 + x'_3)} \right] \right\} \\ G_{3j}(\bar{x}, \bar{x}') = \frac{(x_j - x'_j)}{16\pi\mu(1-\nu)} \left[ \frac{(x_3 - x'_3)}{R_1^3} + \frac{(3-4\nu)(x_3 - x'_3)}{R_2^3} \right. \\ \left. - \frac{6x_3 x'_3 (x_3 + x'_3)}{R_2^5} + \frac{4(1-\nu)(1-2\nu)}{R_2(R_2 + x_3 + x'_3)} \right] \\ G_{i3}(\bar{x}, \bar{x}') = \frac{(x_i - x'_i)}{16\pi\mu(1-\nu)} \left[ \frac{(x_3 - x'_3)}{R_1^3} + \frac{(3-4\nu)(x_3 - x'_3)}{R_2^3} \right. \\ \left. + \frac{6x_3 x'_3 (x_3 + x'_3)}{R_2^5} - \frac{4(1-\nu)(1-2\nu)}{R_2(R_2 + x_3 + x'_3)} \right]$$

$$G_{33}(x, x') = \frac{1}{16\pi\mu(1-\nu)} \left[ \frac{3-4\nu}{R_1} + \frac{8(1-\nu)^2 - (3-4\nu)}{R_2} + \frac{(x_3 - x'_3)^2}{R_1^3} + \frac{(3-4\nu)(x_3 + x'_3)^2 - 2x_3x'_3}{R_2^3} + \frac{6x_3x'_3(x_3 + x'_3)^2}{R_2^5} \right] \quad (6)$$

where  $R_1^2 = (x_1 - x'_1)^2 + (x_2 - x'_2)^2 + (x_3 - x'_3)^2$ ;  
 $R_2^2 = (x_1 - x'_1)^2 + (x_2 - x'_2)^2 + (x_3 + x'_3)^2$ ;  
 $\mu =$  shear modulus;  
 $\nu =$  Poisson's ratio.

The effect of the free surface has been included in the above equations by containing the term  $R_2$ .

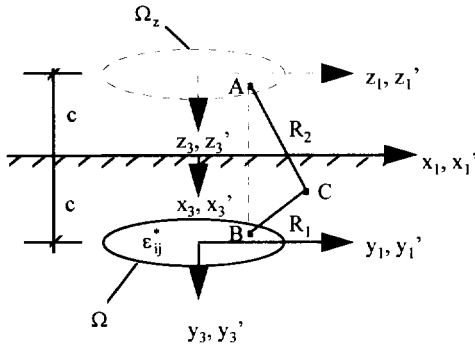


Figure 4 An Ellipsoidal Inclusion in a Half Space (After Seo and Mura 1979)

Assume a circular geosynthetic sheet with a radius  $R$  horizontally buried in a half space has a constant thickness  $t$  in  $x'_3$  direction, which is much less than the dimensions in  $x'_1$  and  $x'_2$  directions. The vertically applied load  $P$  passes through the center of the geosynthetic sheet. The variation of eigenstrains in the thickness direction is negligible. Due to the geometric symmetry and the location of the applied load, the eigenstrains are symmetric to  $x'_1$  and  $x'_2$  axes.

From Equation (5), the relationship between the strain disturbance and the eigenstrain can be expressed by

$$\epsilon_{kl} = \frac{1}{2} (u_{k,l} + u_{l,k}) = \int_{\Omega} C_{opmn} \epsilon_{mn}^* (\bar{x}') g_{klop}(\bar{x}, \bar{x}') d\bar{x}' \quad (7)$$

$$\text{where } g_{klop}(\bar{x}, \bar{x}') = \frac{1}{2} \left[ \frac{\partial^2 G_{ko}(\bar{x}, \bar{x}')}{\partial x_1 \partial x_p} + \frac{\partial^2 G_{lo}(\bar{x}, \bar{x}')}{\partial x_k \partial x_p} \right].$$

Substituting Equation (7) into Equation (4) yields

$$\epsilon_{kl}^* (\bar{x}) = K \int_{\Omega} C_{opmn} \epsilon_{mn}^* (\bar{x}') g_{klop}(\bar{x}, \bar{x}') d\bar{x}' + F_{kl}(\bar{x}) \text{ in } \Omega \quad (8)$$

where  $K = I - C_{ijkl}^{-1} C_{klij}^*$  and  $F_{kl}(\bar{x}) = K \epsilon_{kl}^0$ .

A variety of numerical methods can be adopted to solve Equation (8). A numerical integration technique is introduced herein. Equation (8) can be expressed as (Wang et al 1977):

$$\epsilon_{kl}^* (\bar{x}_1) = F_{kl}(\bar{x}_1) + KC_{opmn} A_{\Omega} \sum_{j=1}^n w_j \epsilon_{mn}^* (\bar{x}_j) g_{klop}(\bar{x}_1, \bar{x}_j) \quad (9)$$

where  $\bar{x}_1$  and  $\bar{x}_j$  are integral points,  $\bar{x}_1 = (x_1, x_2)$ ,  $\bar{x}_j = (x'_1, x'_2)$ , and  $x_1^2 + x_2^2 \leq R^2$  and  $(x'_1)^2 + (x'_2)^2 \leq R^2$ ;  $w_j =$  weight factor;  $n =$  number of integral point;  $A_{\Omega} =$  integral area, equal to the area of geosynthetic sheet.

Equation (9) can be rewritten in matrix forms as

$$\mathbf{E} = \mathbf{F} + \lambda \mathbf{G} \mathbf{W} \mathbf{E} \quad (10)$$

$$\text{or } \mathbf{H} \mathbf{E} = \mathbf{F} \quad (11)$$

where  $\mathbf{H} = \mathbf{I} - \lambda \mathbf{G} \mathbf{W}$ ;  $\mathbf{I} = n \times n$  unit matrix;  
 $\lambda = K C A_{\Omega} t$ ;  $\mathbf{G} = (G_{ij})$ ;  $\mathbf{E} = (\epsilon_{kl}^* (\bar{x}_1), \epsilon_{kl}^* (\bar{x}_1), \dots, \epsilon_{kl}^* (\bar{x}_n))^T$ ;  
 $\mathbf{F} = (F(\bar{x}_1), F(\bar{x}_1), \dots, F(\bar{x}_n))^T$ ;  $\mathbf{W} = (w_1, w_2, \dots, w_n)$ .

After solving the eigenstrains  $\epsilon_{kl}^*$  at integral points from Equation (11), the strain disturbance  $\epsilon_{kl}$  can be computed by using the numerical integration technique and substituting  $\epsilon_{kl}^*$  into Equation (7). Then, the stress and strain fields can be obtained from Equation (1) and Equation (2).

## 5 FUTURE STUDIES

This paper only focuses on the development of theoretical solutions for stress and strain fields of a geosynthetic-reinforced foundation vertically loaded by a concentrated force. Parametric studies need to be done in the future to investigate influential factors and develop design charts for this problem, which will be very beneficial to researchers and engineers.

## 6 SUMMARY

By mean of the concepts and methodologies in micromechanics, the geosynthetic-reinforced foundation is modeled as an inclusion problem. The stress and strain disturbance due to the presence of a geosynthetic sheet in a half space is simulated by applying an eigenstrain in the region of the geosynthetic sheet. Using the solutions obtained by Mindlin (1936) for a force at a point in the interior of a semi-infinite solid and the stress-strain

relationship proposed by Eshelby (1957) for a general inclusion problem, the eigenstrain for the inclusion is computed. The stress and strain fields for a geosynthetic-reinforced foundation vertically loaded by a concentrated force is formulated.

## ACKNOWLEDGMENTS

The author would like to thank Mr. Philip Egan, the President of Tensar Earth Technologies, Inc., for his review and comments.

## REFERENCES

- Binquet, J. and Lee, K.L. (1975a). "Bearing Capacity Tests on Reinforced Earth Slabs", *Journal of Geotechnical Engineering*, ASCE, Vol. 101, No. 12, pp. 1241-1255.
- Binquet, J. and Lee, K.L. (1975b). "Bearing Capacity Analysis of Reinforced Earth Slabs", *Journal of Geotechnical Engineering*, ASCE, Vol. 101, No. 12, pp. 1257-1276.
- Eshelby, J.D. (1957). "The Determination of the Elastic Field of an Ellipsoidal Inclusion and Related Problems", *Proceedings of the Royal Society, Series A*, Vol. 241, pp. 376-396.
- Huang, C.C. and Tatsuoka, F. (1990). "Bearing Capacity of Reinforced Horizontal Sandy Ground", *Geotextiles and Geomembranes*, Vol. 9, pp. 51-82.
- Kurian, N.P., Beena, K.S., and Kumar, R.K. (1997). "Settlement of Reinforced Sand in Foundations." *Journal of Geotechnical and Geoenvironmental Engineering*, Vol. 123, No.9, pp. 818 - 827.
- Mindlin, R.D. (1936). "Force at a Point in the Interior of a Semi-Infinite Solid", *Physics*, Vol. 7, May, pp. 195-202.
- Mura, T. (1982). *Micromechanics of Defects in Solids*, Martinus Nijhoff Publishers, The Hague, 587p.
- Omar, M.T. (1994). "Bearing Capacity of Foundation on Geogrid-Reinforced Sand", *XIII CIMSTF*, New Delhi, India, pp. 1279-1282.
- Seo, K. and Mura, T. (1979). "The Elastic Field in a Half Space due to Ellipsoidal Inclusions with Uniform Dilatational Eigenstrains", *Journal of Applied Mechanics*, Vol. 46, September, pp. 568-572.
- Shukla, S. and Chandra, S. (1994). "A Generalized Mechanical Model for Geosynthetic-Reinforced Foundation Soil", *Geotextiles and Geomembranes*, Vol. 13, pp. 813-825.
- Wang, L.X., et al. (1977). *Mathematical Handbook* (in Chinese), Higher Education Publisher, Beijing, 1398p.
- Yetimoglu, T., Wu, J.T.H., and Saglamer, A. (1994). "Bearing Capacity of Rectangular Footings on Geogrid-Reinforced Sand", *Journal of Geotechnical Engineering*, Vol. 120, No. 12, pp. 2083-2099.

# Bearing Capacity of Strip Footing on Geogrid-Reinforced Slope

C. S. Yoo

Assistant Professor, Department of Civil Engineering, Sung Kyun Kwan University, Seoul, Korea

D. Y. Lee

Researcher, Geotechnical Engineering Division, Korea Institute of Construction Technology, Seoul, Korea

**ABSTRACT:** This paper presents the results of laboratory model footing tests on the bearing capacity behavior of strip footing on geogrid reinforced slopes. For the model tests, the reinforced slopes were artificially created using the raining technique with sand. A wide range of conditions were analyzed by varying geogrid reinforcing patterns. Furthermore, model tests were simulated using finite element analysis with the aim of investigating the mechanics behavior of the reinforced slope such as failure mechanism and force distribution in geogrid. Based on the results of model tests, both qualitative and quantitative relationships were established between the bearing capacity and the geogrid design parameters such as depth, length, and number of geogrid layers.

**KEYWORDS:** Geogrid, Bearing capacity, Slope, Model test, Strip footing, Finite element analysis.

## 1. INTRODUCTION

Geogrids are often used as slope reinforcement for construction of slopes to angles steeper than those constructed with the fill material being used. When a strip footing is constructed adjacent to such a reinforced slope, the bearing capacity behavior of the footing would be significantly different than that of unreinforced slope. To design such a strip footing on a reinforced slope requires a bearing capacity determination method. Most of the previous studies mentioned above, however, have been focused on horizontally leveled ground, and therefore, no rational method of bearing capacity determination for a shallow foundation on reinforced slope is available up to date. Therefore, much still needs to be investigated in order to develop a generally acceptable design method for shallow foundations on reinforced slope.

This study was undertaken with the aim of investigating the mechanistic behavior of geogrid-reinforced slope under strip load as well as the bearing capacity behavior of strip footings on reinforced ground using experimental and numerical studies.

## 2. LABORATORY MODEL TESTS AND FINITE ELEMENT ANALYSIS

### 2.1 Laboratory Model Tests

The laboratory model tests were conducted in a test box made of 60 mm-thick wood, having an internal dimension of 1.2m (length) x 0.8m (depth) x 0.3m (width). One side of the test box was cleared using a plexiglass for ease of observing failure mechanism during the test. The

inside walls of the test box were greased to minimize the friction with ground and the edges of the foundations as much as possible. Although no slip sheets were attached onto the inside walls, no appreciable friction was observed during the test. Furthermore, a rough base condition of a 80mm-wide model footing made of steel was achieved by attaching a sand paper at the bottom.

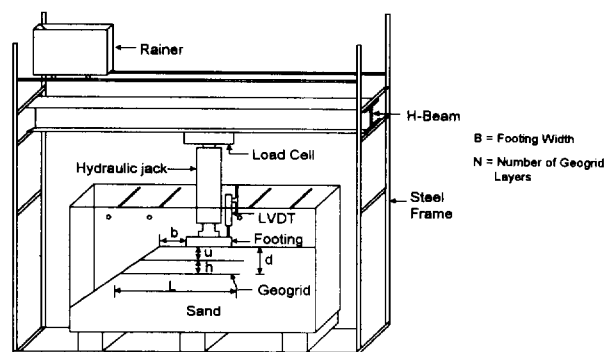


Figure 1. A schematic view of model test box with symbols used in this study.

The artificial ground was constructed with fine sands by the raining technique. The effective size( $D_{10}$ ), uniformity coefficient( $C_u$ ), and coefficient of gradation( $C_c$ ) for sand were 0.36 mm, 1.61, and 1.1, respectively. The tests were conducted on a ground with a slope of 1(H):0.67(V) at a relative density of approximately 70%. The slope of the ground was artificially formed by removing the sand with a vacuum after forming horizontally leveled ground. In order to

evaluate the consistency of the placement density during raining, small cans were placed at different locations in the test box. In the test, the Fortrac geogrids by Huesker Synthetic GmbH Co, which has relatively smaller size of apertures, were used in order to reduce a possible size effect. The mechanical properties of the ground and the geogrid are summarized in Table 1. Note that the Young's modulus of the geogrid was back calculated after performing several computer runs.

During the tests, the model footing was loaded using a hydraulic jack at a rate of 1.0 mm/min. The applied footing load and the settlement were measured using a load cell and two LVDTs, respectively. A schematic view of model test box with the symbols used in this study is seen in Fig.1.

Table 1. Mechanical property of the ground and geogrid.

	Ground	Model Footing	Geogrid
Young's modulus E (kN/m <sup>2</sup> )	2500	2.1E08	1700000
Poisson's ratio $\nu$	0.35	0.17	-
Friction angle $\varphi$ (degree)	42	-	-
Cohesion (kN/m <sup>2</sup> )	0	-	-
Unit weight(kN/m <sup>3</sup> )	16	-	-
Tensile strength (kN/m)	-	-	55

## 2.2 Finite Element Analysis

A series of finite element analysis using a commercial code DIANA(1996) were conducted on selected conditions in order to investigate the mechanistic behavior of reinforced slope under strip load. In the finite element modeling, the foundation ground was discretized using isoparametric 8-node elements, while the geogrid using embedded reinforcement element. The embedded reinforcement element is a special type of element provided by DIANA, which can model the grid pattern of reinforcement. The vertical and horizontal boundaries were modeled by placing the y and x direction rollers, respectively, and were placed in accordance with the test configuration.

In the analysis, the footing and geogrid were characterized as a linear elastic material, while the foundation soil being an elasto-plastic material obeying Mohr-Coulomb failure criterion. The mechanical properties tabulated in Table 1 were used as input parameter for analysis. Fig. 2 shows a typical finite element mesh used in the analysis.

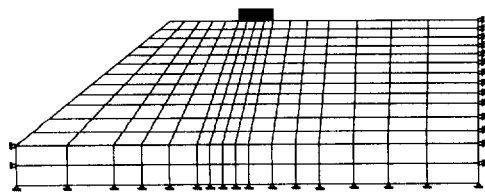


Figure 2. Finite element mesh used in the analysis.

## 3. MECHANICAL BEHAVIOR OF REINFORCED SLOPE UNDER STRIP LOAD

### 3.1 Failure Mechanism

The failure mechanism was investigated using the results of model tests and finite element analysis. To observe the failure mechanism during the model tests, horizontal layers of colored sand were placed and photos were taken at various stages of loading to trace the failure surface. The failure patterns for the finite element analysis, on the other hand, were traced using the maximum shear strain ( $\epsilon_1 - \epsilon_3$ ) contours. Figs 3 and 4 show the failure patterns for unreinforced and reinforced slopes, respectively. Note that the results were obtained at the footing settlement level of  $S_v/B=0.15$  ( $S_v$ =footing settlement;  $B$ =footing width), which is beyond its ultimate level for both cases, and that the failure patterns both from the model tests and finite element analysis shown in Figs 3 and 4 are qualitative drawings.

As can be seen in Fig 3 for unreinforced slope, a typical slope failure pattern is observed, which initiates from the footing edge opposite to the slope and progresses toward the slope. The failure pattern for a reinforced slope with three layers of geogrid presented in Fig. 4 demonstrated that due to the reinforcement, the failure surface is not well developed in the reinforced zone, indicating the improved load bearing capacity of the slope. Inspection of the failure pattern reveals that it is desirable to place the geogrids across the potential failure line for unreinforced case so that the geogrid can tie back the potential sliding wedge against outward movement.

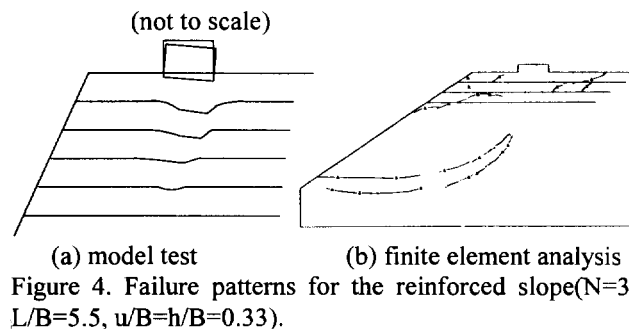
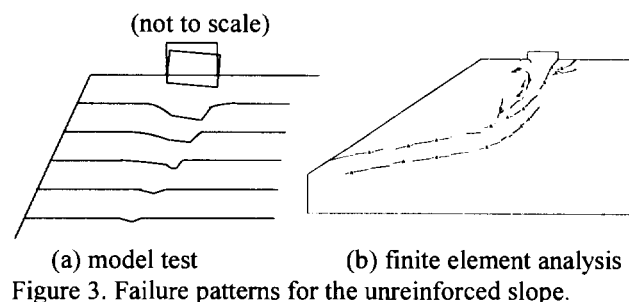


Figure 4. Failure patterns for the reinforced slope ( $N=3$ ,  $L/B=5.5$ ,  $u/B=0.33$ ).



### 3.2 Traction Force Distribution in Geogrid

Fig. 5 shows typical examples of the traction force distributions in geogrids obtained from the finite element analysis at different footing settlement levels ( $S_v/B=0.05$  and  $0.1$ ). It is seen that the peak values of tensile force in each layer of geogrid occurs at the points where the slip surface and the geogrid intersect, as one can expect. Furthermore, it is also observed that as the footing load level increases, the traction force in the lower level of geogrid considerably increases while no significant increase is seen in the upper level.

Another finding in this figure is that the traction force distributions are approximately symmetrical from the potential failure surface, and reach nearly zero values at about  $2.0B$  from the peak point. This trend indicates that the geogrid needs to be extended beyond the potential failure surface with at least a length of  $2.0B$  for anchoring effect. Therefore, it seems reasonable to assume in the relevant design calculation a symmetrical triangular reinforcement force distribution at its apex at the intersection point with a potential failure surface for unreinforced case.

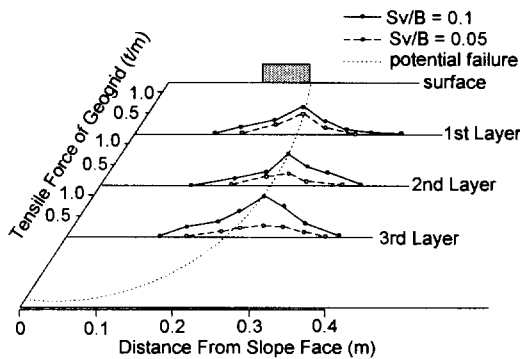


Figure 5. Traction force distributions in geogrids

## 4. BEARING CAPACITY BEHAVIOR

Based on the results obtained from the model tests, the bearing capacity behavior of strip footing on reinforced slope was analyzed. In the analysis, the normalized bearing capacity ratio ( $BCR=q_r/q_{ur}$ ) was used, where  $q_r$  and  $q_{ur}$  being bearing capacity values for reinforced and unreinforced slope, respectively.

### 4.1 Effect of length of geogrid

Das et al.(1994) has reported that there exists a critical length of geogrid beyond which the geogrid has no further reinforcing effect. In order to investigate the variation of bearing capacity with the length of geogrid( $L/B$ ), several conditions were tested by varying  $L/B$  for  $N=3.0$  and  $u/B=h/B=0.33$ . Fig. 6 shows the relationship between BCR and  $L/B$  for  $b=1.5B$ , indicating that BCR increases

with increasing  $L/B$  until  $L/B$  reaches its critical value of approximately 5.5 from the slope and becomes almost constant thereafter, indicating  $(L/B)_{cr}=5.5$  in this case.

A similar trend can be observed for  $b=3.0B$  as seen in Fig. 6, showing the critical length of approximately  $7.0B$ . The extended length beyond the failure surface corresponds to approximately  $3.0B$  for both cases( $b=1.5B$  and  $3.0B$ ), implying that the geogrid must be extended approximately  $3.0B$  beyond the potential failure surface to have maximum reinforcing effect. This trend supports the traction force distribution pattern.

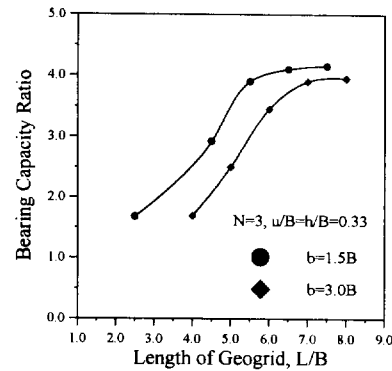


Figure 6. Variation of BCR with  $L/B$

### 4.2 Effect of depth of reinforced zone

The variation of bearing capacity with the depth of reinforced zone( $d/B$ ) was investigated by increasing the number of layers( $N$ ) while maintaining  $L/B=(L/B)_{cr}$  and  $u/B=h/B=0.33$ . The relationship between BCR and  $d/B$  for  $b=1.5B$  and  $0B$  is summarized in Fig. 7. As can be seen in this figure, BCR increases almost linearly with  $d/B$  until  $d/B=2.5$  and becomes nearly constant thereafter, indicating  $(d/B)_{cr}=2.5$ . Note that Das et al.(1994) reported  $(d/B)_{cr}$  of 2.0 for horizontally leveled ground for both sand and clay. This discrepancy may be attributed to the fact that the influencing zone is deeper for a sloped ground than a leveled ground.

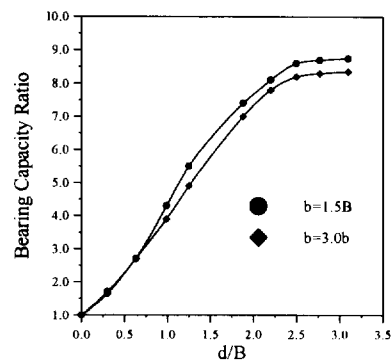


Figure 7. Variation of BCR with  $d/B$

### 4.3 Effect of $u/B$ and $h/B$

The effects of  $u/B$  and  $h/B$  on the bearing capacity were investigated while keeping  $L/B$  at a constant value of  $(L/B)_{cr} = 5.5$ . Fig. 8 shows the variation of BCR with  $u/B$  for  $N=1, 2$ , and  $3$  cases with  $h/B=0.75$ . As can be seen in this figure, for  $N=1$ , the BCR increases with  $u/B$  up to approximately a maximum value of  $1.0B$  and decreases thereafter, indicating  $(u/B)_{cr}=1.0$ . Note that Das et al.(1994) reported  $(u/B)_{cr}$  of approximately  $0.4$  for horizontally leveled ground. For  $N=2$  and  $3$ , although a similar trend is observed,  $(u/B)_{cr}$  appears to decrease with increasing the number of geogrid layers( $N$ ); i.e.,  $(u/B)_{cr} = 0.8$  for  $N=2$  and  $(u/B)_{cr} = 0.6$  for  $N=3$ . This trend may be explained in terms of deep footing effect suggested by Huang et al.(1994). The deep footing effect is a mechanism that a part of reinforced zone behaves as a part of the footing and transfers a major part of the footing load into a deeper zone. Therefore, as the reinforced zone becomes thicker, the reinforced zone acting as a part of the footing should be located closer to the footing in order to maximize its reinforcing effect.

The variation of BCR with  $h/B$  can be observed in Fig. 9 for  $N=2.0$  and  $3.0$ . The results obtained for the conditions at a fixed value of  $u/B=0.33$ . As noticed, the trend is similar to that for the variation of BCR with  $u/B$ . However, the critical value of  $h/B$  appears to be nearly constant approximately  $(h/B)_{cr}=0.8$  regardless of  $d/B$ .

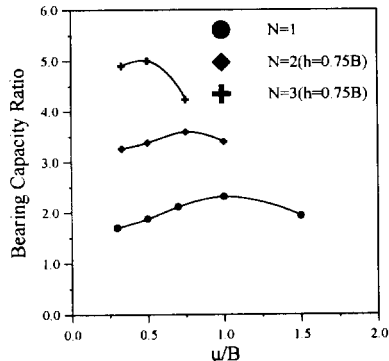


Figure 8. Variation of BCR with  $u/B$

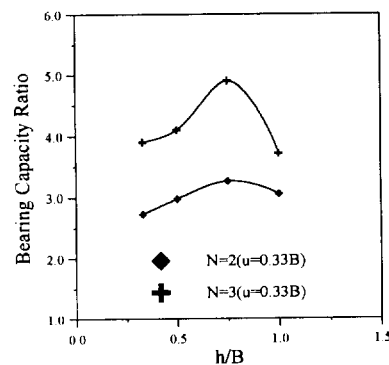


Figure 9. Variation of BCR with  $h/B$

### 5. CONCLUSIONS

The mechanistic behavior of geogrid-reinforced slope and the bearing capacity behavior of a strip footing on the slope were investigated using both experimental and numerical approaches. A wide range of boundary conditions were tested by varying the reinforcing pattern. The results of model tests and finite element analysis were used to identify the failure mechanism and the traction force distribution in geogrids, and also to establish both qualitative and quantitative relationships between the bearing capacity of a strip footing on reinforced slope and the reinforcing pattern. Based on the results of this study, the following conclusions can be drawn:

1. A symmetrical force distribution with its apex at the intersection point with a potential failure plane can be assumed for traction force distribution in geogrid.
2. The geogrid must be extended at least  $3.0B$  beyond a potential failure surface in order to maximize the reinforcing effect.
3. The reinforced zone must be extended to approximately  $2.5B$  below footing base for maximum reinforcing effect.
4. The critical value of  $u/B$  varies between  $0.6 \sim 1.0$  depending on the number of geogrid layers( $N$ ), while  $(h/B)_{cr}$  being nearly constant value of  $0.8$  regardless of  $N$

### REFERENCES

- Akinmusuru, J. O. and Akinbolade, J. A.(1981) "Stability of Loaded Footings on Reinforced Soil", *Journal of the Geotechnical Engineering*, ASCE, Vol. 107, pp. 819-827.
- Das, B. M., Khing, K. H., Shin, E. C., Puri, V. K., and Yen, S. C.(1994) "Comparison of bearing capacity of strip foundation on geogrid-reinforced sand and clay", *Proc. 8<sup>th</sup> Inter. Conf. on Computer Methods and Advances in Geomechanics*, Morgantown, WA, USA, pp 1331-1336.
- DIANA(1996), User's Manual, Release 6.1, TNO Building Construction Research
- Fragaszy, R. J. and Lawton, E.(1984) "Bearing Capacity of Reinforced Sand Subgrades", *Journal of the Geotechnical Engineering*, ASCE, Vol. 110, pp.1501-1507.
- Giroud, J. P. and Noiray, L.(1981) "Geotextile-Reinforced Unpaved Road Design", *Journal of The Geotechnical Engineering*, ASCE, pp. 1233-1252.
- Huang, C., Tatsuoka, F., and Sato, Y.(1994) "Failure Mechanisms of Reinforced Sand Slopes Loaded with a Footing", *Soils and Foundations*, Vol. 24, No. 2, pp. 27-40

# A Study on the Coir Reinforcement for Strengthening Soft Soil Subgrades

Dr. K. Rajagopal  
Associate Professor  
Department of Civil Engineering  
Indian Institute of Technology Madras  
Chennai, India 600 036

Mr. S. Ramakrishna  
Assistant Engineer  
National Highways Department  
Secretariat of Public Works, MS Building  
Bangalore, India 560001

**ABSTRACT:** Coir is a naturally occurring fibre available at relatively low cost in many tropical countries. A number of products can be manufactured from coir fibre for geotechnical applications. The strength and other properties of these products compare favourably with those made of synthetic materials. Through laboratory plate load model tests, this paper examines the suitability of coir geotextiles for construction of unpaved roads over soft soil subgrades. The soft subgrades of 1 m depth (CBR < 0.5) were prepared in a test tank of plan dimensions 1.5 m × 1.5 m. Base course layers of varying thickness values (with and without coir reinforcement) were constructed on top of this subgrade. The results from these tests have clearly illustrated the benefit of using coir reinforcement in such cases.

**Key Words:** geotextiles, coir reinforcement, subgrades, plate load tests, unpaved roads

## 1 INTRODUCTION

The coir is a naturally occurring fibre derived from the husk of coconut fruit. It is abundantly available at very low cost in many tropical countries. A number of products can be manufactured from coir fibre for geotechnical applications, such as geogrids, geotextiles, geomats etc. These products were found to last for as long as four to six years within the soil environment depending on the physical and chemical properties of the soil, Ramakrishna (1996). In many instances, the strength of subgrade soil increases in course of time as the soil undergoes consolidation induced by the traffic loads. For such applications the natural reinforcement products are ideally suitable, Rao and Balan (1994). The current paper describes the results from investigations carried out on coir geotextile reinforced soft soil subgrades.

## 2 MATERIALS USED IN TESTS

### 2.1 Clay Soil

The clay soil used in this investigation had plastic and liquid limits of 15% and 42% respectively. This soil can be classified as CI according to the Indian Standard Classification System, IS 1498-1978. The cohesive strength and friction angle of the clay soil are 21.2 kPa and 1.3° respectively.

### 2.2 Gravel Soil (murum)

The gravel soil (murum) contains 48% gravel size particles, 48% sand size particles and 4% silt and clay size particles. The specific gravity of this soil was found to be

2.75. This soil is classified as A-2-4 (0) as per AASHTO classification system and is rated as a good sub-base material. The cohesive strength and friction angle of this soil are 10 kPa and 44.9° respectively.

### 2.3 Coir Geotextile

The coir geotextiles used in this investigation are commercially available floor mats which are woven from coir fibres. The coir fibres are twisted into a rope form and these ropes are woven in weft and warp directions to form the mat. These mats have approximately the same strength in both the principal directions. The thickness of these mats is dependent on the diameter of the twisted ropes used in forming the mat. The geotextile (coir mat) used in this investigation had a thickness of 7.2 mm at a standard normal pressure of 2 kPa. The mass per unit area of this mat was 1,396 g/m<sup>2</sup> at a room temperature of 30°C.

The ultimate tensile capacity of this mat was found to be 37 kN/m at a strain of 43% from wide-width tensile tests performed according to ASTM D4595 standards. The secant modulus of this material at 10% strain is 110 kN/m. The seam strength, determined according to the suggested ASTM procedures, was found to be 24 kN/m. The seams were stitched using strong nylon thread with 25 mm overlap on both sides of the seam.

The cohesive strength and friction angle of clay-coir geotextile interface were found to be 22.6 kPa and 8.2° respectively. The same properties for gravel-coir interface are 40 kPa and 32.3° respectively. A comparison of these strength properties with those of individual materials shows that coir geotextile has excellent interface strength properties. This may be because of the rough nature of the coir and its natural affinity towards the water and clay because of surface charges.

### 3 LABORATORY PLATE LOAD TESTS

#### 3.1 Test Facility

The plate load tests were performed within a test tank of plan dimensions 1.5 m × 1.5 m and 1.2 m deep. The loading was applied through a 100 kN capacity proving ring using a hydraulic jack. The test tank was centrally located below a reaction frame for applying plate loads. The plate was of 300 mm diameter (D) to simulate the Equivalent Single Wheel Load (ESWL).

#### 3.2 Preparation of Test Bed

The soft clay soil bed was prepared by sedimentation technique under vacuum pressure to simulate the soft natural subgrade. The soil was initially mixed manually using crowbars at 160% water content. This slurry was kept under a low vacuum pressure of 19.6 kPa for three days to drain out the water and remove the entrapped air. Then it was subjected to a consolidation pressure of 98 kPa until the rate of deformation has decreased to less than 0.01 mm per minute. The method of test bed preparation was adapted from the work reported by Kuntiwattanakul et al. (1995). The entire consolidation process took approximately 8 to 10 days for each preparation. This procedure had created soft subgrades with a CBR value of approximately 0.4. The thickness of soft clay layer was maintained at around 900 mm for all the tests.

The gravel sub-base course was prepared directly on top of this clay layer. The gravel layer was compacted at optimum moisture content using a 10 kg drop hammer falling through a height of 500 mm.

The gravel layer was compacted to 80% maximum density in all the tests. The compacted sub-base course was allowed to mature for one day by covering it with a polythene sheet. The coir geotextile reinforcement was introduced during the compaction stage itself.

The above procedure of preparing the clay and gravel layers was repeated for all the tests performed in this present investigation so that the test conditions remain uniform for the entire range of tests.

#### 3.3 Test Programme

The following series of plate load tests were carried out in this investigation with the following four configurations.

- Series 1: soft clay subgrade alone
- Series 2: gravel sub-base course over soft clay subgrade.
- Series 3: gravel sub-base course over soft clay subgrade and one layer of coir geotextile at clay-gravel interface.

- Series 4: gravel sub-base course over soft clay subgrade and two layers of coir geotextile, one at clay-gravel interface and the other at mid-depth of gravel layer.

In Series 2-4, six sub-base layer thickness (h) values of 100, 150, 200, 250, 300 and 350 mm were considered. In subsequent sections, the results from these tests are referred to by these series numbers.

#### 3.4 Test Procedure

The general test procedure for plate load tests as described in *Indian standard IS 1888:1982 (Reaffirmed 1988)* was adopted for all the tests. The loading was applied through a 300 mm diameter plate. The applied load was measured using a pre-calibrated 100 kN capacity proving ring. The settlement of plate and the soil surface were measured using a total of six dial gauges. In the case of tests with reinforcement layers, the coir geotextile was placed at the required levels after wetting.

Each load increment was applied as either 10% of the estimated ultimate load or the load required to produce 1 mm settlement, whichever is lesser. Each load increment was kept constant until the rate of settlement reduces to less than 0.025 mm per minute. The load and the corresponding deformations were recorded after the settlements have stabilised under each load increment, which was typically 6 to 12 hours. The loading was continued until a total plate settlement of 150 mm has occurred which took approximately 6 days.

After each test, the gravel layer was carefully removed. After that, the top 400 mm thick clay soil in the tank bed was replaced with puddled clay having 40% water content. This test bed was once again pre-consolidated under 98 kPa surcharge pressure which took 2 to 3 days to stabilise. This re-formed clay bed had the same properties as the originally prepared clay bed as confirmed by results from in situ vane shear tests. On this, fresh gravel layer of required thickness was laid in the same manner as discussed earlier.

### 4 RESULTS AND DISCUSSIONS

The plate load test carried out on clay bed showed that it is an extremely soft subgrade with an ultimate bearing capacity of 20 kPa. Hence, it can be expected that the provision of gravel sub-base with or without coir reinforcement will significantly improve its load bearing capacity. Typical improvement in the performance obtained with the provision of gravel layer with and without reinforcement layers is illustrated in Figure 1.

Handwritten text at the bottom of the page, possibly a signature or initials.

In general, the performance has improved with the increase in the thickness of gravel layer. The provision of a geotextile layer at the clay-gravel interface has further increased the load bearing capacity of subgrade. When an additional layer of geotextile was placed at the mid-height of the gravel layer, the ultimate capacity and stiffness has tremendously increased.

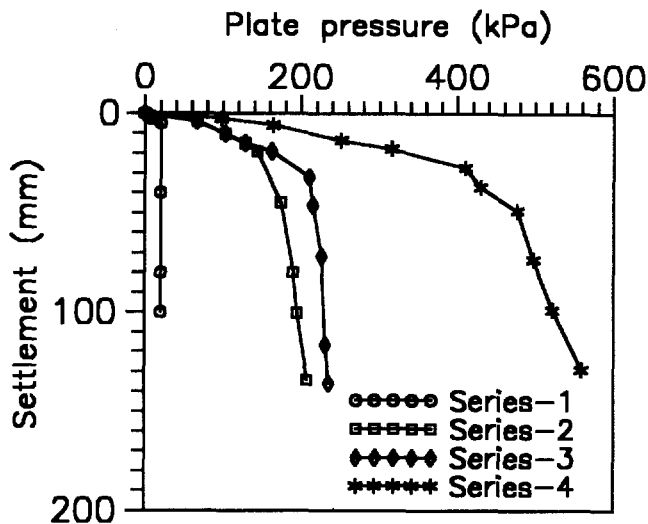


Figure 1. Performance with 150 mm thick gravel layer

The ultimate pressures developed from various tests are compared in Table 1 which clearly show the improvement in the performance with the provision of coir geotextile reinforcement.

From the results shown in Figure 1 and Table 1, it can be seen that the provision of a single layer reinforcement at the clay-gravel interface does not improve the load bearing capacity very much. The effect of single layer of geotextile is significant when gravel layer is thicker than 200 mm. When a thin layer of gravel is provided, there may not have been an adequate bond with the coir geotextile for the load transfer to take place. In the case of two layers of coir geotextile, the reinforcement layer at the mid-depth of gravel prevents its lateral spread and hence higher loads are mobilised in coir reinforcement which contributes to the increase in ultimate pressures. This can also be explained by the good bond between the coir and the gravel as shown from the interface shear strength properties (Section 2.3).

In the case of unreinforced and single layer reinforcement cases, the ultimate pressures have developed within a settlement of 15 to 40 mm whereas the two layer system had developed ultimate pressures at much higher settlements in the range of 100 mm (Figure 1). This result once again confirms the advantage of placing the additional reinforcement layer within the gravel layer.

In addition to the reinforcement action, the geotextile layer at clay-gravel interface functions as a separator and filtration and drainage medium as it has good compressibility characteristics. On the other hand, the layer within the subbase contributes mainly to the strength and stiffness of subgrade. It is evident from this experimental results that stiffness of the coherent mass is also an important parameter as reported by Douglas and Valsangkar (1992).

Table 1 Ultimate pressures (kPa) from plate load tests

Thickness of gravel layer (h)	unreinforced subbase layer	one layer of reinforcement	two layers of reinforcement
100 mm	100	120	400
150	200	220	550
200	240	250	750
250	300	360	900
300	370	440	1000
350	400	500	1150

From the plate load test data, the pressures developed for different thicknesses of gravel layers at various rut depths (settlement levels) were developed. This data is plotted in a non-dimensional form in Figure 2 for a rut depth of 75 mm. Similar charts were developed for other rut depths also. In these figures the thickness of gravel layer (h) is normalised with respect to the diameter of plate (D) and the plate pressure at any settlement is normalised with respect to the ultimate bearing capacity of soft clay layer (20 kPa) denoted as the Bearing Capacity Ratio (BCR). This term BCR indicates the relative improvement in the bearing capacity of subgrade with the provision of gravel layers with or without reinforcement. These charts can be used for designing the thickness of subbase layer over soft subgrades for a given BCR and the diameter of wheel base.

The above data is presented in a different form in Figure 3 for Indian Road Congress (IRC) standard wheel load of 22.25 kN. Similar curves have also been developed for other standard wheel loads. It is evident from this chart that the thickness of subbase can be substantially reduced with the use of coir geotextile reinforcement. At rut depths less than approximately 10 mm, the gravel layer can not mobilise enough shear strength which results in the requirement of very thick subbases, as is evident from the initial steep slope of curves.

## 5 ILLUSTRATIVE EXAMPLE

Design a subbase course to increase the load bearing capacity to 500 kPa of soft clay subgrade whose ultimate bearing pressure is 25 kPa. Consider the Equivalent

Single Wheel Loads (ESWL) of 28 kN and 48 kN having a tire pressure of 580 kPa. Design the subbase course for allowable rut depths of 25, 50 and 75 mm.

Design: The following step-by-step procedure illustrates the design process using the design charts developed in this investigation.

Step 1: Calculate the Bearing Capacity Ratio (BCR) at the ultimate bearing pressures.

$$BCR = \frac{\text{required ultimate bearing pressure on subbase course}}{\text{ultimate bearing capacity of subgrade}}$$

In the present example,  $BCR = \frac{500}{25} = 20$

Step 2: Calculate the contact area of the wheel as the ratio of ESWL and the tire pressure. From these, the equivalent diameters of contact area are calculated for the two wheel loads as 250 mm and 325 mm respectively.

Step 3: Obtain the required h/D ratios for rut formations of 25, 50 and 75 mm from the design charts. The results are given in Table 2.

Table 2 Design of subbase thickness over soft subgrades

Design Case	Design base course thickness (mm)			Savings in thickness (mm)	
	gravel alone (A)	gravel + one layer reinf. (B)	gravel + two layer reinf. (C)	Savings for B over A	Savings for C over A
i) r = 25 mm P = 28 kN P = 48 kN	300 360	268 321	153 183	32 39	147 177
ii) r = 50 mm P = 28 kN P = 48 kN	288 345	255 310	108 129	33 35	180 216
iii) r = 75 mm P = 28 kN P = 48 kN	275 330	250 300	83 100	25 30	192 230

in which r is the rut depth and P is the wheel load. As can be seen, the single layer reinforcement does not result in much savings in subbase thickness. On the other hand, when an additional layer is provided within the subbase, significant savings are achieved.

## 6 CONCLUSIONS

The use of coir geotextiles for construction of subbase layer over soft subgrades is studied in this paper. Various engineering properties of coir geotextiles have been reported in this paper. These properties are comparable to those of intermediate to high density polypropylene based geotextiles. The plate load tests have clearly indicated the capability of coir geotextiles in improving the stiffness and load bearing capacity of soft subgrades. Hence, the coir geotextiles are suitable for cost-effective field applications.

## REFERENCES

- Douglas, R. A. and Valsangakar, A.J. (1992) "Unpaved Geosynthetic-Built Resource Access Roads: Stiffness Rather than Rut Depth as the Key Design Criterion", *Journal of Geotextiles and Geomembranes*, 11, pp. 45-59.
- Kuntiwattanukul, P., Towhata, I, Oshishi, K. and Seko, I. (1995) "Temperature Effects on Undrained Shear Characteristics of Clay", *J. Soils and Foundations*, 35, pp. 147-162.
- Ramakrishna, S. (1996) *Investigation on Applications of Coir Reinforcement in Geotechnical Engineering*, Thesis submitted for award of Master of Science degree, Indian Institute of Technology Madras, Chennai.
- Rao, G.V. and Balan. K. (1994) "Coir Geotextiles-A Perspective", *Proc. of 2nd Int. Workshop on Geotextiles*, CBIP, New Delhi, India, pp. 119-126.

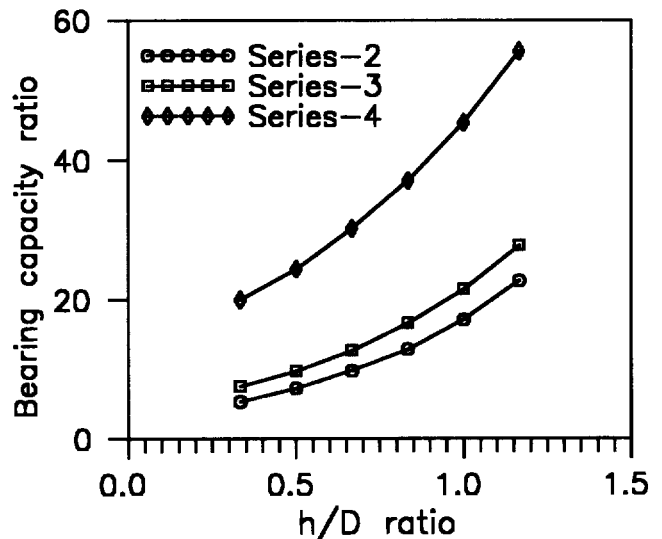


Figure 2 BCR for a rut depth of 75 mm

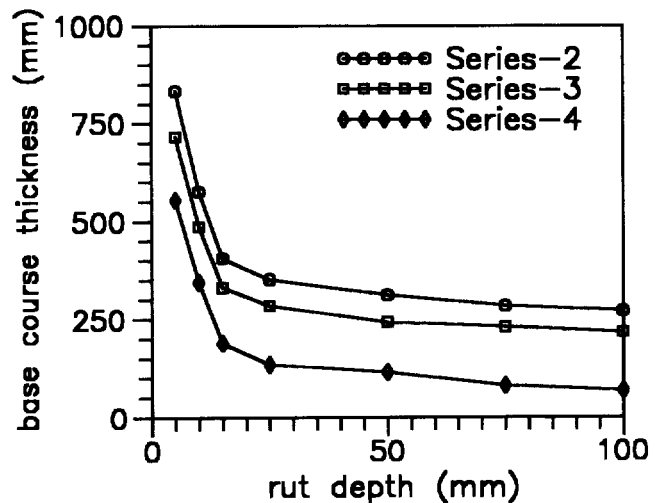


Figure 3. Design chart for wheel load of 22.25 kN

# Treatment of container stockyard using Stress distribution ability of geonet

Hong Zhu

General Manager, YiChang Netlon Geosynthetics Ltd, Hubei Province, China

Dao hong Ruan

Engineer, YiChang Netlon Geosynthetics Ltd, Hubei Province, China

**ABSTRACT:** This paper presents the technical characteristics of geonet, the effect of stress distribution of geonet was initially observed in eastern China in the winter by a lively trial which can be defined as "NET - ICE TRIAL", The interacting mechanism between geonet and soft soil was analyzed based on lots of laboratory tests, three in - situ plate load tests were carried out on the site which is close to Yangtze River with extensive dredged sand areas of soft soil depth up to 8m. The results showed that bearing capacity of soft soil can be increased about one times undisturbed soil bearing capacity after a layer of geonet was paved horizontally, two layers of geonets lead to four times the bearing capacity of soft soil. The total amount of settlement was reduced by 22% , differential settlement was reduced by 35% . compared with the method of dynamic consolidation, the new technique has advantage of quick speed construction and low cost.

**KEYWORDS:** Container stockyard, Geonet, Stress distribution

## 1 INTRODUCTION OF APPLICATIONS

The use of geonets in China dates back to the early 1980's when the materials were first manufactured in China. The early projects were mainly in soil reinforcement, drainage and filtration. In the late 1980's the applications increased to projects involving embankment foundation consolidation, bridge approach details, reflection cracking of asphalt pavements, slope protection, leachate collection, leakage detection in landfills and coastal erosion protection. The application areas range from highways and railways to hydraulic engineering.

As the applications of geonets increased the construction departments required more information with regard to calculations and theory and this generated large interest in the academic world. A large number of Universities and Research Institutions became involved in studying the principles of geonets in different applications.

The Ministry of Communications considered the setting up of a project to research the mechanism of geonets and then the National Eight - Five Plan research project entitled "Application Research of Geonets in Bridge Abutment and Soft Soil Treatment of High Grade Road" was appraised by them on October 1995. The research into the mechanisms of geonets was promoted very deeply at this stage and this research became a history of the development of geonets in China.

A typical application of geonets is described as "Reinforce-

ment of Soft Soil Container Stockyard Project"

## 2 SELECTION OF GEONET MESH

Geonets have a great number of application areas which can be described as follows:

- 1) Soft soil reinforcement
- 2) Slope protection
- 3) Drainage

Laboratory tests have shown that the mesh shape is very important for stress distribution and that a hexagonal shaped aperture is the best as it is both stable and has low elongation. The order of stability of geonets according to tensile tests is: Hexagonal mesh > diamond mesh > square mesh. Although the tensile strengths are different in the longitudinal and transverse directions this is not important as long as the difference is not too large. If the difference is too large then the reinforcement of soft soil can not be achieved.

The selection of the appropriate mesh is also dependent on the grading of the fill material. In the project described later in this paper, the container stockyard, granular materials (dredged sand) were used and therefore a larger mesh size was selected.

The actual tensile strength of the geonet used, weight 660g/m<sup>2</sup>, tested in the laboratory is greater than the specified value of 5.8 KN/m but it is still not high. Is it possible for this material; to reinforce the soft soil? The answer will be found af-

ter the field tests and laboratory trial are completed.

### 3 THE PHENOMENON OF NET - ICE STRESS DISTRIBUTION

On a container stockyard project where the soft soil foundation was overlain by a geonet reinforced pavement the mesh had been placed on a compacted surface when suddenly the weather became worse. It snowed and the mesh became frozen in ice.

The same load was then imposed on two different ice surfaces, one with the mesh and one without, and the stress distribution of the geonet was observed directly in the two ice surfaces.

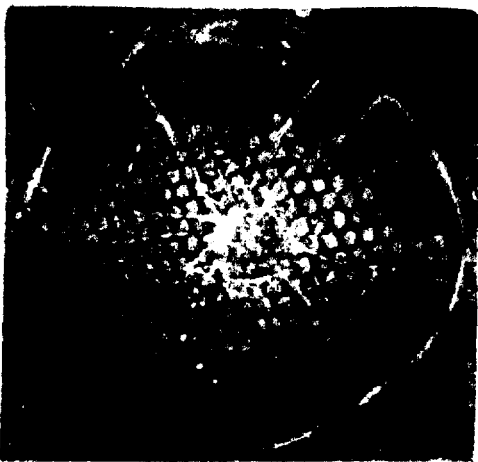


photo 1



photo 2

IN photo 1, with the geonet, the thin ice surface cracked but didn't break with white stress circles radiating from the central load. This showed how the load was distributed over a large area with the same geometry as the loaded area. In photo 2 the ice was broken and no distribution occurred.

This was the first time that the phenomenon of "live" stress distribution had been seen on a working site and this was defined as the NET - ICE TRIAL.

now given

R: radius of stress distribution

r: radius of central load

$S_R$ : area of stress distribution

$S_r$ : area of central load

An equation was obtained by measure on the construction site

$$\text{so } R = 5r$$

$$\frac{S_R}{S_r} = \frac{\pi R^2}{\pi r^2} = \frac{(5r)^2}{r^2} = 25 \quad (1)$$

This equation means that the area of stress is increased by 25 times as compared with the loaded area and shows how the bearing capacity of soft soil can be increased. The NETICE TRIAL shows the distribution mechanism in transmitting the load evenly onto a much larger bearing area.

25 times as compared with the loaded area and shows how the bearing capacity of soft soil can be increased. The NETICE TRIAL shows the distribution mechanism in transmitting the load evenly onto a much larger bearing area.

### 4 LABORATORY TEST

In order to illustrate quantitatively the geonet mechanism in improving bearing capacity of soft soil lot of tests have been completed in the past five years.

The trial chooses the mid liquid limit silty clay to do three trial cylinder shape samples.

Sample c is pure clay.

Sample d one layer of geonet is used

sample E three layers of geonets are used c (see fig 1)

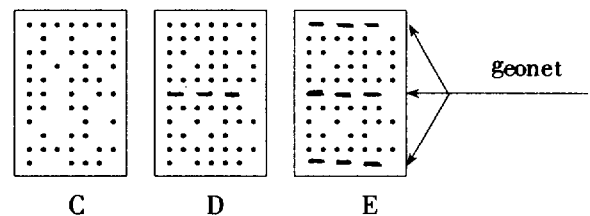


Figure 1.

The trial is unconfined compression strength test, test results are as follows (table 1)

Table 1:

Sample mode	C			D			E		
Sample no.	1	2	3	1	2	3	1	2	3
load(kg)	720	722	722	1520	1522	1523	5239	5240	5241
compression strength(kpa)	408.1	409	409	860.6	861.7	862.3	2966.2	2966.7	2967.3
(mean) strength	408.4			861.1			2966.8		

The bearing capacity is increased significantly by geonet, the value of sample D is 2.1 times the value of sample C and sample E is 7.3 times sample C, results show:

- 1) the bearing capacity of soil is improved with the increase of quantity of geonet.
- 2) the bearing capacity is increased by one time when a layer of geonet is paved.

NET - ICE TRIAL and laboratory test of using geonet to increase the bearing capacity of soil provide enough evidences for construction projects, but all the research data in theory need to be confirmed by actual applications.



## 5 CONTAINER STOCKYARD TREATMENT

### 5.1 soil properties

The container stockyard is situated in Jiang Shu province. The harbour area is about two hundred thousand square metres, forty thousand of which will be used as a container stockyard.

The soil profile can be divided into three layers which are described, from top to bottom, as follows:

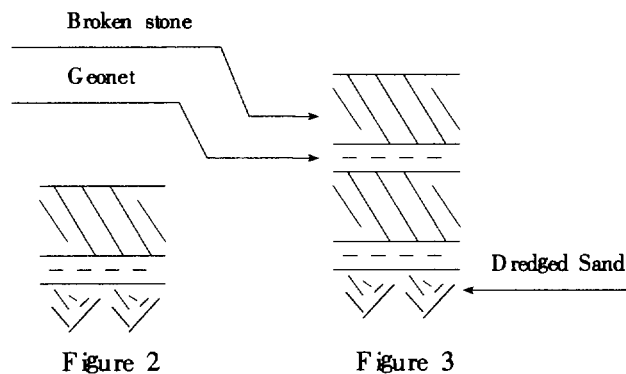
Layer 1: 4 – 5m of pump – dredged yellow fine sand mixed with cohesive soils, saturated and highly compressible. This soil is very susceptible to liquefaction. Particle sizes range from 0.074mm to 0.25mm.

Layer 2: 2 – 3m of mucky clay, brownish yellow and grey in colour, saturated and highly compressible.

Layer 3: Fine sand and intermittent silty clay layers. Moderate to low compressibility with a higher bearing capacity.

The dredged sand was placed two years ago and consolidation of the mucky clay had already occurred due to the overburden load. The groundwater level is not influenced significantly by the water levels of the Yangtze River because of the cofferdam. The only water ingress is due to natural rain water.

The conventional method of treating container stockyard is dynamic consolidation but this method has high cost and slow construction speed, moreover, easily effected by weather. The cross section of new method is shown as follows. (see fig 2):



### 5.2 construction procedure

- 1). Dredged sand is compacted by bulldozer twice times.
- 2). Geonet is unrolled and laid directly over the dredged sand, with an overlap of 150mm between individual sheets, and pinned with "U" shape steel pins at 1.0m spaces.
- 3). Backfill broken stone with 60% clay and 40% granular material.
- 4). Compact backfill, using vibratory roller operating without vi-

bration twice at the beginning and with the vibration for another twice times at one hour interval. The maximum vibrating force is 30 tons.

- 5). Pave the second layer geonet repeat the same procedure.

During the compacting operation in one area in Fig 2 liquefaction occurred. This was assumed to be because the placing and compacting operation had taken place too quickly. It was then suggested that there should be a 1 hour interval between compaction passes and that the fill thickness should be no more than 0.8m – 1m.

### 5.3 bearing capacity test

Three in situ plate load tests were carried out, two of them were finished on the structure of Fig 2 and Fig 3 respectively, another one is for ground which had been treated by dynamic consolidation with 10 tonnes hammer at 10 meters high. The size of plate is 1m by 1m. The results see table 2.

Table 2

load(kn)	measured settlement (mm)		dynamic consolidation
	one layer of geonet	two layers of geonets	
50	7.86	4.42	8.30
100	9.53	5.84	12.23
150	14.38	6.06	16.35
200		6.64	
250	32.58	9.04	
300	39.83		
designed bearing capacity(Mpa)	80	150	150
tested value	125	250	155

Notes: The bearing capacity of undisturbed soil is 60 kpa

Table 2 shows the bearing capacity of two layers of geonets structure is twice times the one layer geonet structure. Interlock between geonet and granular material forms a high density and shear resistant layer which distribute vertical loads also indicate the horizontal elasticity of geonet and granular material is very good, thus the total settlement can be reduced. This concept is confirmed by modulus of resilience test.

Table 3.

Structure mode	one layer of geonet	two layers of geonets
modulus of resilience (Mpa)	711.25	991.89
mean value	706.21	1061.48

Note: The modulus of resilience of undisturbed soil can't be measured.

#### 5.4 Unit weight test (table 4)

Table 4.

Item	Natural soil	one layer of geonet	two layers of geonets	dynamic consolidations
water content %	17.71	13.13	12.56	
unit weight kn/m <sup>3</sup>	16.2	18.3	18.6	18.3

The unit weight of geonet structure changes little. It is increased by 10% to 13%, compared with nature soil the compactness can reach 93.8% to 95.9%.

#### 6 ANALYSIS

It can be seen from Table 2 that the bearing capacity of soft soil has increased significantly. when granular material is compacted over geonet, it partially is penetrates and projects through the apertures creating an interlocking action between granular material and geonet mesh. This interlock enables the mesh to resist horizontal shear from the fill and thereby mobilise the maximum bearing capacity of the soft soil. Mechanical interlock creates a flexurally stiff platform which distributes load evenly and minimizes different settlement, geonet prevents lateral movement of particles at the base of the fill layer, helps the fill to retain its full design strength by preventing contamination by soft soil thus controlling the amount of the more expensive fill.

#### 7 CONCLUSIONS

The following conclusions are drawn:

1. Geonet can increase the bearing capacity of soft soil of dredged sand significantly, reduce the total amount of settlement and control the different settlement.
2. Geonet can distribute vertical load evenly, mechanical interlock between geonet and granular fill plays an important role in reinforcement of soft soil.
3. Tensile strength of geonet is not the main factor in improving soft soil.
4. The further rules of stress distribution of geonet need to be researched.

#### ACKNOWLEDGEMENTS.

The authors would like to thank Chang Sha University of Communications for its support. The authors also acknowledge Netlon Ltd Uk for its technical help.

#### REFERENCES

- Ali Fakher and Colin Jones (1996) "Land Reclamation Using Super Softclay Proceedings of the Second International Conference on Soft Soil Engineering, Nanjing, China" pp. 775 - 780
- D. H Ruan and Y. J. Pang (1996) "NETE Geonet Applications In Civil Engineering Foundation Treatment" pp. 37 - 40
- Y. Chen, R. H. Ying and Q. S. Zhang (1993) "Laboratory Research Using Netlon Geonets Consolidate Embankment"

# A GEOTEXTILE-WRAPPED AGGREGATE HIGHWAY DRAIN EVALUATION

Gerald P. Raymond

Professor Emeritus, Queen's University, Kingston, Ontario, Canada, K7L 3N6.

Richard J. Bathurst

Professor, Department of Civil Engineering, Royal Military Collage of Canada, Kingston, Ontario, Canada.

Jerry Hajek

Senior Pavement Management Engineer, Ministry of Transportation of Ontario, Downsview, Ontario, Canada.

**ABSTRACT:** Presented are results from excavations at two edge drain locations adjacent to a freeway pavement (i.e., a limited access divided highway with at least two lanes in each direction). The pavement was built on a high fill of recompacted clayey gravel (GC). Typical Atterberg limits of the fines were  $LL \approx 25$ ;  $PL \approx 16$ ;  $PI \approx 9$ . Directly on the clayey gravel subgrade was a 152 mm cement treated base followed by 229 mm of structural portland cement concrete pavement. Adjacent to the pavement edge was a 3 metre-wide paved shoulder ending in a continuous curb and gutter fitted with catch basins about every 100 m. In 1982 a geotextile-wrapped aggregate pavement edge drainage system was retrofitted through the paved shoulder. The objective of the investigation was to evaluate the performance of the drainage system. From the observations and tests made on the recovered soil samples conclusions and recommendations are stated.

**KEYWORDS:** Drainage, Edge drain, Geotextile, Pavement, Performance evaluation.

## INTRODUCTION

As part of an evaluation of Ontario's highway pavement drainage practice, excavations were made at two edge drain locations adjacent to a freeway pavement on June 4/1992. The pavement was built in 1970 on a high fill of recompacted clayey gravel (GC,  $LL \approx 25$ ;  $PL \approx 16$ ;  $PI \approx 9$ ) and the drains were added in 1982. Figure 1 is a schematic of the pavement edge and edge drain cross section obtained from the construction drawings. Built directly on the clayey gravel subgrade was a 152 mm thick cement treated base followed by 229 mm thick portland cement concrete slab. Adjacent to the pavement edge was a 3 metre wide paved shoulder ending with a continuous curb and gutter and catch basins about every 100 m. The edge drainage system was retrofitted through the paved shoulder as a geotextile-wrapped coarse open graded aggregate (OGA) containing a 100 mm corrugated perforated polyethylene pipe placed 50 mm above the trench base (and base portion of the geotextile). The pipe centre line was to be located 762 mm from the edge of the concrete pavement. The wrapped stone was to be 325 mm thick and its top level with the cement treated base.

## OBJECTIVE

The objective of the investigation was to evaluate the effectiveness of the pavement drainage system some ten years after installation. Also of interest was the condition of the geosynthetics (geotextile and plastic pipe) used in the

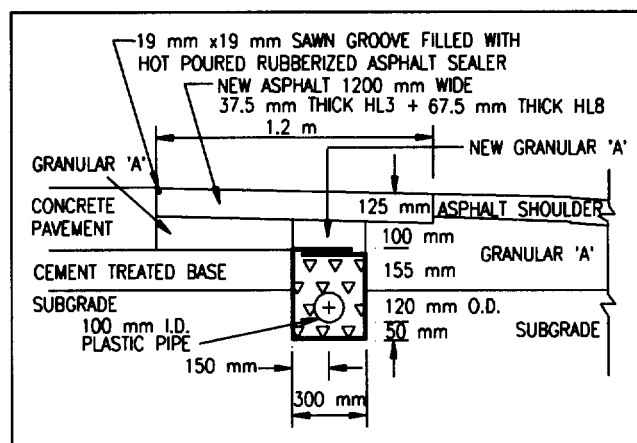


**Figure 1. Cross section from construction drawings.**

drainage system.

## GEOSYNTHETICS

The geotextile was a needlepunched staple fibre product with the following properties: filtration opening size = 100  $\mu\text{m}$ ; mass/unit area = 230  $\text{g}/\text{m}^2$ ; grab strength = 550 N at an elongation of 75% at failure. The pipe was a corrugated perforated polyethylene product with a nominal inside diameter of 100 mm, and a nominal outside diameter of 125 mm.

## WEATHER AND STORM DRAINAGE CONDITIONS

The weather the day and night before the excavations had been intermittent rainfall. On the day of the excavations the weather was overcast with intermittent sunshine. The temperature at 7:00 am, which was the start of the excavating, was 14°C. The highway surface drainage was discharged via curb and gutters to catch basins. The catch basins were connected to a deep storm sewer.

## POSITION OF EXCAVATIONS AND OUTLETS

Both excavations were made on the shoulder side of the shoulder/pavement edge area of six contiguous same direction traffic lanes near catch basins which were located at the curb. The longitudinal grade of the Highway was about 2%. The cross-sectional slope of the pavement was about 2.5% and the shoulder about 6%.

## EXCAVATION TP1 (STATION 16+568)

The first excavation (TP1) was made adjacent to a transverse pavement joint at chainage 16+568. The shoulder/pavement surface showed considerable settlement of the shoulder. Figure 2 shows the surface profile measurements taken at both excavations. Figure 3 shows the typical cross section observed at the first excavation TP1. The cross section measurements were taken at both ends of this excavation some 300 mm apart. Little difference was noted between the measurements of the same items. The drainage pipe was not connected to the catch basin at this location. The structural concrete portion of the pavement is about 240 mm thick. The cement treated base was of poor quality either due to deterioration or initial mix. Its thickness was estimated to be 150 mm in accordance with the construction drawing. The geotextile-wrapped aggregate drain was installed adjacent to the edge of the cement treated base. Its centre line was located 780 mm from the edge of the pavement and its width was 420 mm. It extended from the surface elevation of the cement treated base layer into the clayey gravel subgrade for a total thickness of 300 mm. Thus the portion of geotextile forming the base of the drainage system was 540 mm below the pavement surface elevation. Above the upper (top) portion of the geotextile was a thickness of 140 mm of Granular 'A' covered by a thickness of 100 mm of asphalt concrete which formed the shoulder surface.

Figure 4 shows the pipe and the clean condition of the aggregate beside and above the pipe inside the geotextile. Figure 5 shows the fouled cemented condition of the aggregate on the bottom inside of the geotextile wrap. Migration of subgrade fines through the geotextile into the clear stone was visible. Seepage water has washed some of the fines through the clear stone and deposited them on the geotextile. The base portion was wet and once the geotextile was removed a very thin depth of ponded water was evident.

Overall, the top of the drainage pipe was approximately at the same level as the bottom of the cement treated base.

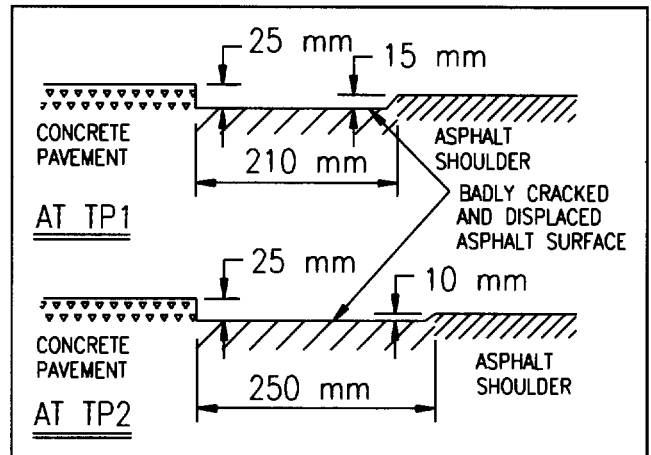


Figure 2. Surface profiles at pavement edge/shoulder.

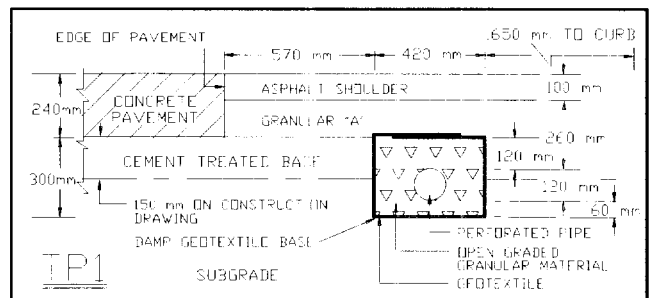


Figure 3. Cross section at Excavation TP1.



Figure 4. Open graded aggregate and pipe within geotextile.

Once the geotextile had been sampled the excavation was extended back to the pavement edge where a transverse joint existed. It was noted that pumping had eroded a portion of the pavement at this joint. Deposited in the eroded portion was black granular type material. This black material was probably fines from the asphalt pavement shoulder. Sampling

the black soil proved difficult and no representative sample was obtained.

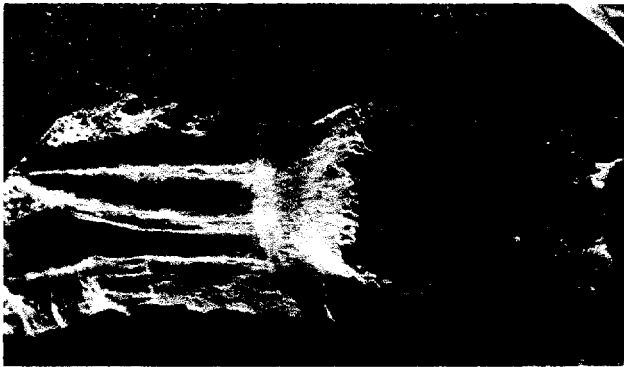


Figure 5. Geotextile condition: side and base.

### EXCAVATION TP2 (CHAINAGE 16+532)

The second excavation (TP2) was made near a catch basin and resulted (prior to enlargement) in much the same findings as the first excavation (TP1). Figure 2 shows the settlement between the pavement edge and the geotextile drain. Figure 6 shows the cross section measurements observed.

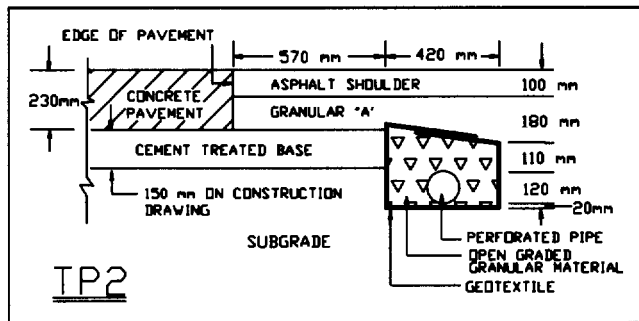


Figure 6. Cross section at Excavation TP2.

The curb catch basin was offset about 1.5 metres from the aggregate drain. The excavation was then enlarged to determine if the edge drain was connected, via an outlet pipe, to the catch basin. Indeed it was, and at the outlet chainage, the drainage pipe was turned down slightly. Figure 7 is a plan of the T-junction connecting a non-perforated outlet pipe, running at a right angle to the pavement, to the catch basin. The T-junction was wrapped in geotextile that was bedded on about 150 mm of Granular 'A'. Figure 8 shows a profile view along the perforated pipe highlighting the turned down condition at the T-junction. The slight turndown at the junction of the two pipes (perforated and non-perforated) picked up any water draining along the 50 mm of aggregate located below the perforated pipe in the geotextile-wrapped aggregate drain. Figure 9 shows a profile view along the

outlet non-perforated pipe connection. The connection pipe was cemented into the catch basin wall. Water collecting in the Granular 'A' below the T-junction and below the outlet pipe was trapped by the surrounding clayey gravel since there was no allowance for drainage at the catch basin connection.

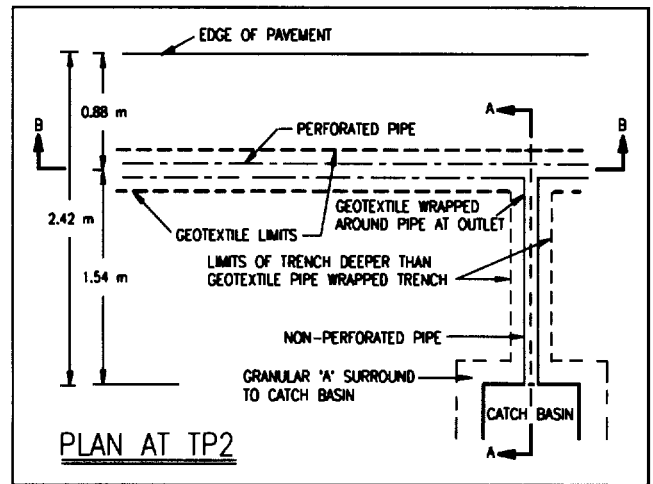


Figure 7. Plan view of outlet connection.

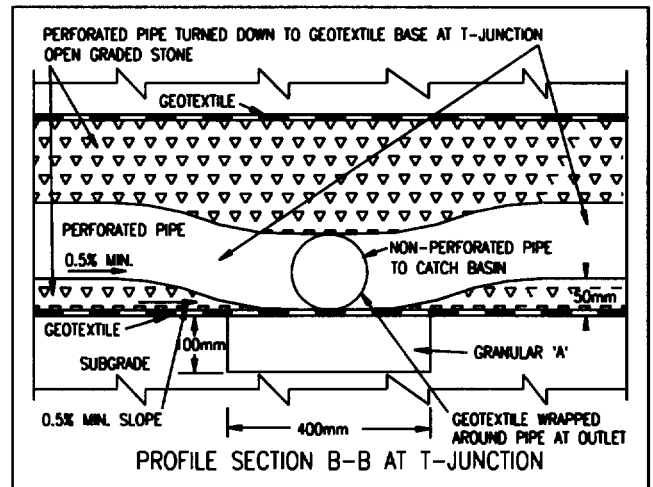


Figure 8. Section B-B: Profile of pipe at T-junction.

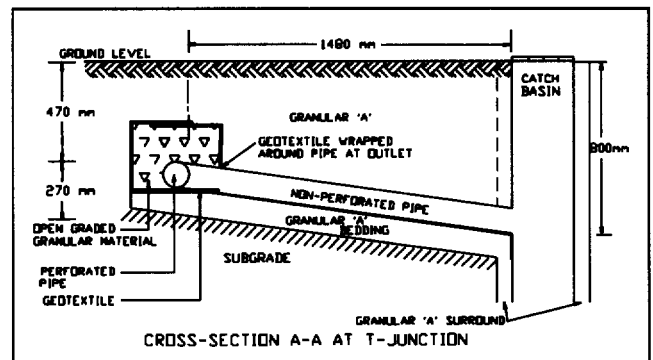


Figure 9. Section A-A: Connection to catch basin.

## LABORATORY RESULTS

All soil samples recovered from the excavations were subject to grain size analysis. Figure 10 shows the grain size analysis curves from Excavation TP2. The samples from within the geotextile were open graded aggregate with only small amounts of material passing the 75  $\mu\text{m}$  sieve. The material trapped in the geotextile graded from 1 mm down to 50% passing the 75  $\mu\text{m}$  sieve. The Granular 'A' materials graded in accordance with the MTO specification except at the 75  $\mu\text{m}$  limit which was slightly greater than permissible (i.e. 10% to 12 % compared with MTO limits of 2%-8% for Granular 'A'). This quantity of fine sized material within a broad grading granular material indicated the probability of a relatively low permeability of Granular 'A'. Confirmation was obtained by permeability tests on the recovered Granular 'A' samples. The average coefficient of permeability of the as-recovered samples was  $2.8 \times 10^{-5}$  cm/s and after washing on a 75  $\mu\text{m}$  sieve  $2.6 \times 10^{-2}$  cm/s; an increase of nearly 1000 times.

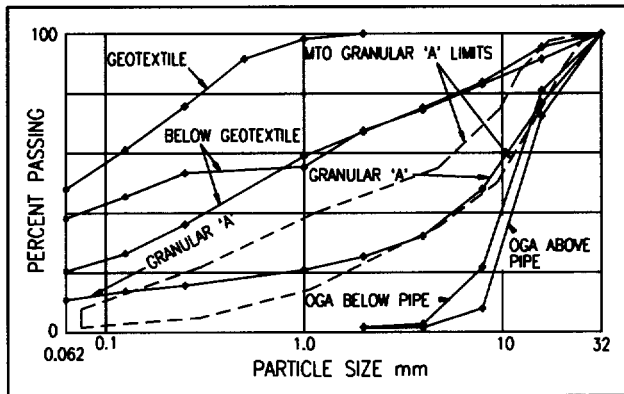


Figure 10. Grading of Excavation TP2 soil samples.

The geotextiles examined in the field and on return to the laboratory showed no sign of obvious damage. There were no holes or severely worn areas that might cause concern that the properties were less than those originally specified in 1982. A good indication of the remaining overall strength was the considerable force needed to remove a small area of the geotextile in the field. This considerable force inflicted no observable damage.

## DISCUSSION

The results of the investigation show that placing a geotextile-wrapped trench drain some distance away from, and separated from, the pavement edge by relatively impermeable Granular 'A' prevented or significantly reduced internal drainage of the area below the structural concrete. The results of this poor drainage were clearly seen at the transverse joint uncovered at the first excavation. At this

joint there was evidence of (a) pumping, (b) erosion of the concrete at the joint base, (c) heave/settlement on the shoulder at the pavement edge (Figure 2) and (d) deterioration of the quality of the cement treated base. Retrofit geotextile-wrapped trench drains should be located adjacent to the pavement edge with the geotextiles against the supporting pavement layers. To prevent subgrade pumping, a filter capping granular material continuously graded down to the 75  $\mu\text{m}$  sieve should be used with any cement treated base.

There was no evidence that the geotextile or the pipe had sustained any damage that would cause concern regarding its ability to continue to function as it has over its ten years in-situ. The sides and top of the geotextile were relatively clean. The main fouling was at and above the base, which is the whole purpose of the clear stone bedding below the pipe. Provision should be made to allow drainage of any granular bedding material placed below any outlet pipes connected to catch basins.

## CONCLUSIONS AND RECOMMENDATIONS

Excavations were made at two granular edge drain locations on the shoulder of a major Ontario freeway. From the observations and tests made on the recovered soil samples, the following conclusions and recommendations are made.

Retrofit geotextile-wrapped trench drains should be located next to the pavement edge.

Geotextiles, if used, should be placed tight against the supporting layers of the concrete pavement.

The need for a 50 mm bedding of open graded aggregate at the base of trench drains was clearly demonstrated at both excavations. The bedding material trapped sediment that otherwise would have accumulated in the drainage pipe reducing the pipe's ability to function effectively.

Evidence of migration of subgrade fines into the open graded aggregate above the cement treated base was observed. Drainage alone does not stop subgrade pumping.

No evidence was noted of loss of ability to function of either the geotextile or pipe.

Evidence of accumulation of fines in the trench drain demonstrated that a geotextile is required.

The T-junction detail illustrated in Figure 8 is recommended.

## ACKNOWLEDGEMENT

Gratefully acknowledged is the considerable cooperation and help provided by Ministry of Transportation of Ontario (MTO) personnel who provided the excavation equipment and manpower. Particular thanks are extended to Ms. P. Marks and Mr. S. Senior of the MTO for their significant contributions to this paper. The views expressed in this paper are those of the authors and not necessarily the MTO.

# Deformations and Damage of Non-Woven Geotextiles in Road Construction

A. Watn

Senior Scientist, SINTEF Civil and Environmental Engineering, Norway

G. Eiksund

Research Scientist, SINTEF Civil and Environmental Engineering, Norway

Å. Knutson

Head of Division, Norwegian Public Road Administration, Road Research Laboratory, Norway

**ABSTRACT:** SINTEF Civil and Environmental Engineering have performed a research project in two phases on non-woven geotextiles in road constructions. The first phase was a large-scale laboratory test aimed to study the effect of non-woven geotextiles on road deformations at cyclic loading. The second phase was a field test aimed to study the resistance against damage of the geotextiles during construction. The project focused on the correspondence between properties from index tests and the observed behaviour. A clear correspondence was found between the initial tension stiffness of a geotextile and the deformation after cyclic loading. Low correlation was found between observed damage during construction and the evaluation criteria used for classification of geotextiles in Norway. To take into account these findings it is recommended a revision of the evaluation criteria. It is also proposed a survivability criterion based on a combination of deformation energy and stress-strain properties to cover the construction and lifetime requirements.

**KEYWORDS:** Geotechnical Engineering, soil, geotextile, damage.

## 1 INTRODUCTION

The criteria for evaluating strength and deformation properties for non-woven geotextiles used in separation and filtration in roads have been discussed for more than twenty years. The first systems for evaluation and classification of geotextiles for separation and filtration in roads were introduced by the Norwegian Road Research Laboratory (NRRL), (Alfheim and Sørli, 1977). Later several systems have been introduced but generally the classification requirements are mainly empirically based, and to some extent dependent on local conditions and experiences (Forschungsgesellschaft für straßen- und Verkehrswesen, 1994, Rathmayer, 1993, AASHTO, 1990). The evaluation criteria and the index test methods which are used, differ between the systems and a possible co-ordination between the systems have been discussed since their introduction.

### 1.1 The Norwegian classification system

Geotextiles for separation and filtration in roads are in Norway divided into four classes dependent on the type of material (maximum grain size) to be used against the geotextile:

Class 1: Generally not used

Class 2: Sand and gravel with max. diameter 50 mm

Class 3: Crushed stone with max. diameter 100 mm

Class 4: Blasted rock with max. diameter 2/3 of the layer thickness

The classification is based on an evaluation of results from the static puncture tests and the cone drop tests. The tested product will achieve points from the results in the tests referring to each criterion and the classification is then dependent on the total sum of points. For the static puncture test (CBR- test, ISO 12236:1996) the measured force and deformation are used to calculate a corresponding tension (force/mm) and strain (%). The classification criterion is based on the derived tension and strain, the maximum tension, the elongation strain at failure and the tension increase from 20 % to 70% strain (or until strain at failure if less than 70%). The average hole diameter is used as evaluation criterion for the cone drop test (Schalin 1995).

### 1.2 Relevant properties and test methods

There is a clear need for establishing a more fundamental understanding of the required characteristics of the geotextile to fulfil its functions (separation and filtration) in the road. The required properties must reflect the environmental loads imposed on the geotextile during the installation, construction and service lifetime. A theoretical sound correlation between the required properties and the corresponding required parameters found from index tests should be established. A combination of index tests, large scale performance tests, full scale field tests and collection of experiences from the field is believed to be the best way to establish such a correlation.

2 RESEARCH PROJECT

SINTEF Civil and Environmental Engineering have performed a research project on non-woven geotextiles in road constructions. The NRRL and has participated with observers and supervisors in the project. The project focused on the correspondence between geotextile properties found in index tests and the observed behaviour in laboratory and the field. The first project phase (SINTEF 1996) included index tests and large scale laboratory load test. This part aimed to study the effect of stress-strain properties on non-woven geotextiles on road deformations at cyclic loading. The second phase was a field test (SINTEF 1997) aiming to study the resistance against damage of the geotextiles during the construction. Non woven geotextiles with different production technology and area weight were used in the research projects.

2.1 Laboratory tests

2.1.1 Index tests

The index tests included cone drop tests, static puncture tests and wide width tensile tests. The tests were performed on virgin samples and on samples extracted after the load test. In addition the effect of thermal cycling and stress strain behaviour under frozen conditions were tested. Six different non-woven geotextiles were tested, three corresponding to class 2 and three corresponding to class 3. The geotextiles used in the laboratory tests corresponding to class 3 are listed in Table 1.

Table 1. Class 3 geotextiles used in the laboratory test.

Reference	Type of product	Nominal area weight (g/m <sup>2</sup> )
SNP 3A	Staple fibre, needle punched, polypropylene	190
CNP 3B	Continuous filament, needle punched, polypropylene	160
CTP 3C	Continuous filament, thermally bonded, polypropylene	190

A summary of the results from the static puncture tests and the falling cone test on virgin samples for class 3 products is presented in Table 2.

Typical load displacement curves from the static puncture test are shown in Figure 2. Observe the differences in initial stiffness between the different geotextiles.

The thermal cycling had no significant effect on the results from the index test measurements.

Table 2 Results from initial index testing of the geotextiles.

Ref	Weight g/mm <sup>2</sup>	Static Puncture test		Falling cone
		Max force, N	Displ.at max. force, mm	Average hole diameter, mm
SNP 3A	197.8	2380	57	14
CNP 3B	171.5	2252	44	24.2
CTP 3C	190.8	1970	50.8	19.1

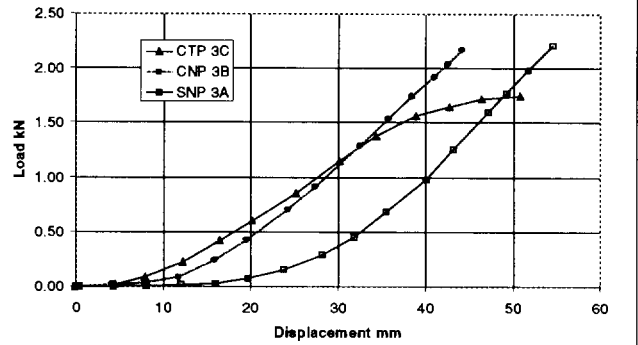


Figure 1. Typical load displacement curves for the class 3 geotextiles.

2.1.2 Large scale load test

The large scale laboratory testing was performed in a 12.5 m long and 1.8 m wide test bin filled with a 650 mm thick layer of soft clay with 2-3 kPa undrained shear strength. The geotextiles was placed on the clay and covered with 150 mm of crushed stone as shown in Figure 2. The geotextile test samples were 2 x 1.8 m. Cyclic and static load was then applied on a circular plate with diameter 250 mm on the bearing layer. The geotextiles used in the large scale laboratory test are listed in Table 1.

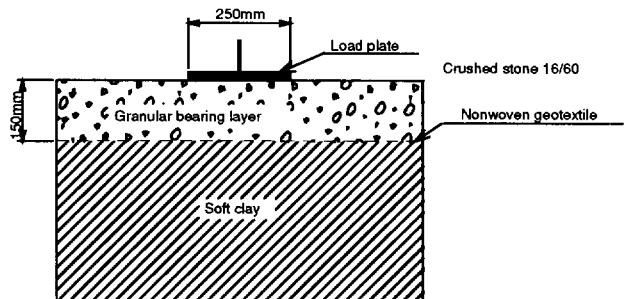


Figure 2. Bearing layer construction.

A cyclic load with frequency 1 Hz and amplitude 0-4 kN was applied on the load plate. A load of 4 kN corresponds to an average applied stress under the load plate of 81.5 kN/m<sup>2</sup>. The gradually developing displacement on the geotextile beneath the load plate was measured during the



test, the resulting deformation profiles after 1000 cycles are presented in Figure 3.

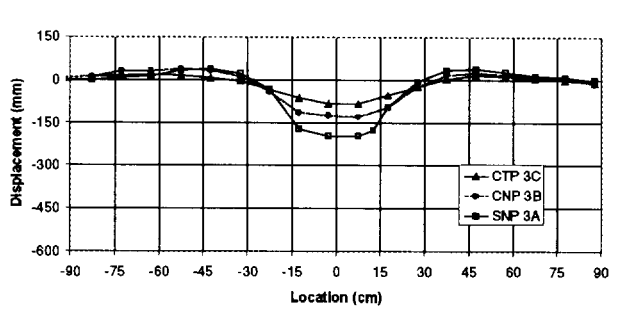


Figure 3. Measured vertical displacement profile of the geotextiles after completed load test.

### 2.1.3 Evaluation of results

There are considerable differences in the measured deformations and strains in the geotextile in the load test. The observed deformations correspond well with the load displacement relations, Figure 2, measured in the static puncture test. The average strain of the geotextiles was measured to be 10.3%, 4.6% and 1.4% for SNP 3A, CNP 3B and CTP 3C, respectively. Converted to displacement in the static puncture test these strains correspond 19 mm, 12 mm, and 7 mm displacement. Figure 4 shows that the load corresponding to the strain levels is approximately 0.08 kN for all the three geotextiles. In the same figure, the area under the load displacement curve, named as the deformation energy, is shaded. Note that the deformation energy based on these results is about the same for all the tested geotextiles, even with large differences in the strain level.

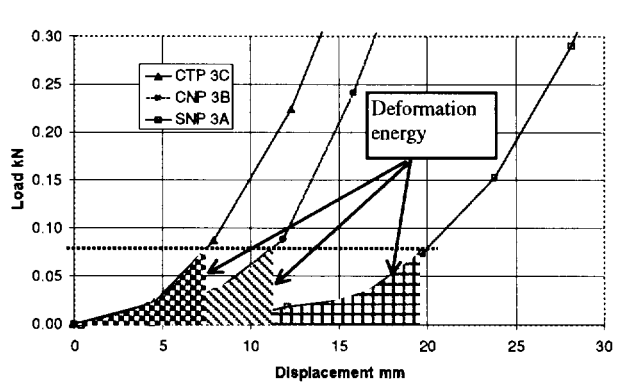


Figure 4. Force-strain relationship related to measured strain for the geotextiles in the load test

This test shows that the strain developing at a typical cyclic loading is strongly dependent of the initial stiffness. A criterion that is aimed to cover the need for remaining

strength after construction should include the effect of initial stiffness.

## 2.2 Full scale field tests

### 2.2.1 Test set up

The test was performed outdoor on frozen uneven ground. The material in the ground consists of fill masses with silt, sand, clay and occasional stones. Due to rainfall just before and under the installation the upper 50-100 mm of the underground was saturated and muddy during the installation. As the temperature was decreasing during the test, this upper layer was frozen at the time of the extraction. Geotextiles used in the field test are listed in table 3.

Table 3. Geotextiles involved in the testing.

Reference	Type of product	Nominal area weight (g/m <sup>2</sup> )
CNP 4A	Continuous filament, needle punched, polypropylene	320
SNP 4B	Staple fibre, needle punched, polypropylene	330
SNP 4C	Staple fibre, needle punched, polypropylene	320
CTP 4D *)	Continuous filament, thermally bonded, polypropylene	350
SNP 4E	Staple fibre, needle punched, calendered on one side, polypropylene	300
CTP 4F **)	Continuous filament, thermally bonded, polypropylene and polyethylene	350

\*) Not previously classified in class 4 in Norway

\*\*\*) Tested in a separate field test

The geotextile CTP 4F was tested in a separate test together with CTP 4D that was also tested together with the other products. The results for CTP 4D are used as reference basis for comparing the results. The field test also included five geotextiles from class 2 not reported in this paper. The results from the index tests on virgin material are presented in Table 4. The load deformation relation curves from the static puncture test are shown in Figure 5.

Table 4. Results from index tests on the class 4 geotextiles.

Ref	Measured area weight $g/m^2$	Strength increase 20 - 70% strain N/mm	Push through tension N/mm	Push through strain %	Hole diameter mm	Number of points acc. to the Norw. classif.	Corresp applic class
CNP 4A	310.7	18.94	34.32	60.86	15.90	35	3
SNP 4B	359.0	23.20	38.28	70.78	12.10	44	4
SNP 4C	314.4	17.17	26.17	87.08	10.10	44	4
CTP 4D	353.1	10.60	33.87	70.12	13.90	41	4
SNP 4E	302.3	19.13	28.44	85.46	13.10	44	4
CTP 4F	345.9	14.3	38.9	51.4	20.9	35	3

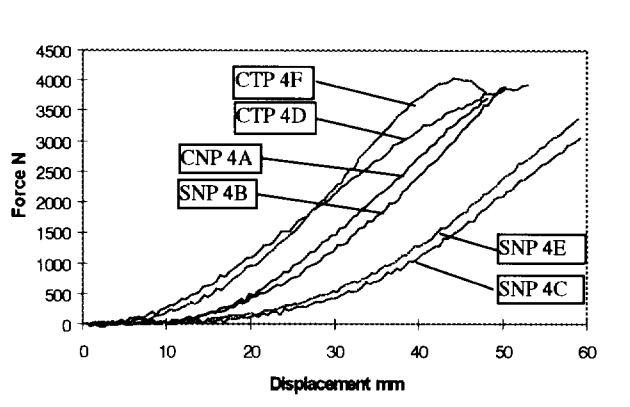


Figure 5. Measured force and displacement from the static puncture test.

The principle for the test fill is shown on Figure 6. The geotextiles were placed directly on the ground and then covered with fill material by the use of a pay loader. The covering was done sideways to ensure that each of the geotextiles was treated equally. For the class 4 material, blasted rock with a maximum diameter of 800 mm was used for the fill. The largest rock fragments were flaky shaped thus a fill height 500 mm was possible.

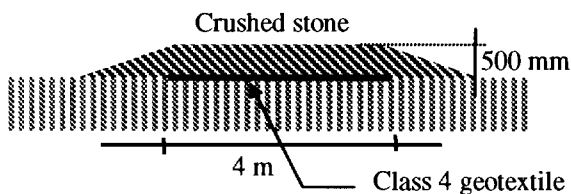


Figure 6. Principle for the test fill.

The fill material was compacted with a heavy vibrating roller with three overpasses along the centre line and on the shoulders on top of each fill. One week after the installation the fill material was removed. The top of the fill material was removed carefully with an excavator. The

geotextile was then tied to the excavator and carefully lifted out.

### 2.2.2 Test results

The amount of damage and deformation of the geotextiles were observed during the extraction. By the visual inspection during extraction some damage in terms of holes could be seen on all the geotextiles. The degree of damage varied. The geotextiles SNP 4B and CTP 4D was less damaged than average, SNP 4C and CNP 4A average damaged while SNP 4E and CTP 4F most damaged. During the extraction it could be observed that the underground was more even under the products having a high initial stiffness compared to the others.

After extraction the samples were brought to the laboratory where the damages (number and size of holes) were counted and measured. The distribution of holes within different diameter ranges is shown in Figure 7.

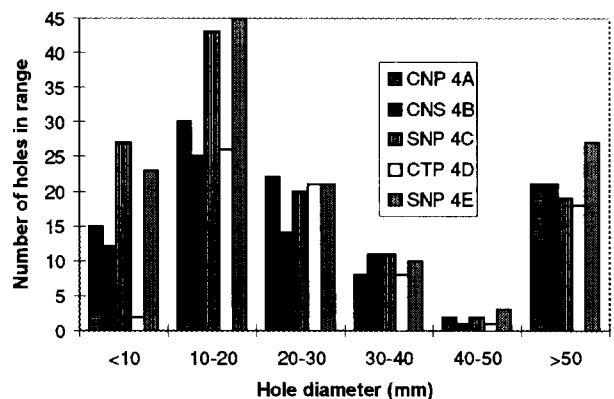


Figure 7. Distribution of holes.

### 2.2.3 Evaluation of results

In order to correlate the observed damage with index test results the degree of *Damage* on a geotextile is defined as the sum of the measured hole diameters. The *Resistance*

against damage for one product can then be defined as the average damage divided by the damage on each geotextile as shown in Table 5, that is, the higher number the less damage. In the table the measured damage is normalised with respect to the average value for the five geotextiles, that is, a factor of 1.15 means 15 % less damage than the average.

Table 5. Resistance against damage.

Ref	Damage (Sum Of hole diameter)	Resistance against damage (Average damage)/ (damage)
CNP 4A	2793	1.07
SNP 4B	2613	1.15
SNP 4C	3157	0.95
CTP 4D	2655	1.13
SNP 4E	3759	0.80
CTP 4F	-	0.40*)

\*) Based on a scaling of the results

As CTP 4F was tested in a separate test the results can not be compared directly with the others. The additional field test with the geotextiles CTP 4D and CTP 4F used a less heavy compaction equipment resulting in considerably less damage on CTP 4D compared with the first part of the test.

However, by using the results for CTP 4D as a reference basis a possible comparison of the degree of damage can be done. This way of scaling the degree of damage is quite uncertain since it is based on the damages on one geotextile only, but still it illustrates the much higher degree of damage found for CTP 4F compared to the other products tested.

The resistance against damage and the results from the index tests are used to evaluate the requirements in the classification system. The relevancy of an index test parameter for survivability of the geotextile is studied by correlating the parameter with the *resistance against damage* as defined above. The area weights are also included in the correlation. The results of the correlation are shown in Table 7. The test results from geotextile CTP 4F was not included in the correlation.

Table 6. Correlation between index test results and resistance against damage.

Parameter	Correlation
Weight/m <sup>2</sup>	0.81
Strength incr. 20-70%	-0.11
Failure strength	0.84
Strain to failure	-0.77
1/(Cone drop hole diam)	-0.26
Number of points	-0.36

The parameters showing best correlation with the resistance against damage is the *push through strength* and the *area weight*. The criteria for *strength increase*, and the *number of points* shows poor correlation. The *strain to failure* and the *cone drop hole diameter* shows a fair negative correlation. The poor correlation for the number of points is remarkable. The low correlation is mainly caused by the fact that the two geotextiles with the most damage have full score based on the criteria in the index test.

The results from the index test do not point out an obvious candidate among the parameters that may explain why CTP 4F should be so severely damaged. In the primary tests the best correlation with the resistance against damage was found for the unit weight and the failure strength. This was not the case for CTP 4F that gives a high score on both unit weight and failure strength. Geotextile CTP 4F has, however, a relatively low value both for *strain to failure* and the *inverse of the cone drop hole diameter*. These low values may partly explain some of the higher degree of damage for the CTP 4F geotextile.

Both CTP 4D and CTP 4F are thermally bonded geotextiles, having a high initial stiffness. As shown in Figure 5, the force-displacement relations from the static puncture test are relatively similar for these to geotextiles compared to the other geotextiles tested. The large difference in degree of damage between CTP 4D and 4F is not reflected by similar differences in the index test results, with a possible exception for the deformation at failure. The damage on CTP 4F is therefore probably caused by material properties not measured in the index tests. A possible explanation may be the properties on the brittleness in the failure or the tear propagation for the geotextile.

### 3 CONCLUSIONS AND RECOMMENDATIONS

The project has provided useful information for evaluating relevant properties and requirements for geotextiles to be used for separation and filtration in roads. There are considerable differences in stress strain properties of the geotextiles that is also reflected in the behaviour in the field. Noticeable differences are found in the susceptibility for damage during installation. The criteria used in the existing systems for classification and specification do not seem to reflect properly the behaviour in the field. A revision of the criteria is therefore clearly needed.

The deformation of the geotextiles when subjected to loading, that is, in terms of rutting during installation and construction, is clearly linked to the initial stiffness of the geotextile. A criterion for geotextile survivability is clearly relevant, but has to reflect the behaviour during installation, construction and service lifetime. A criterion for geotextile survivability is suggested based on a combi-

nation of requirements for deformation energy and remaining stress and strain till failure. The principle is presented in Figure 8.

The deformation energy related to the installation and construction should be chosen with respect to the type of fill material, construction equipment and type of underground.

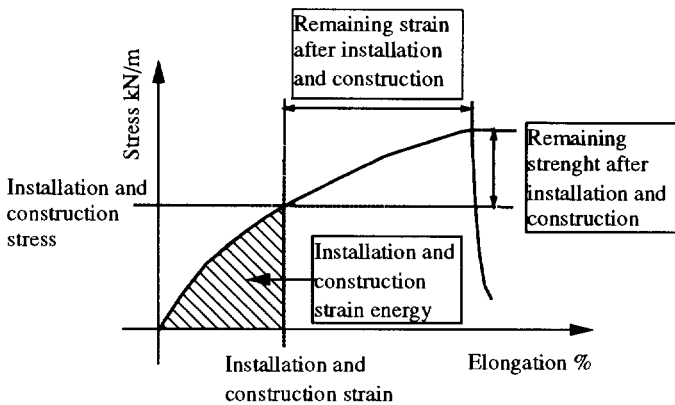


Figure 8. Survivability criterion principle.

The requirements for remaining strength and strain to failure should reflect the expected loads and deformations (settlement) for the service lifetime.

The final criteria should be based on a collection of data from laboratory and field tests correlated with long-term experiences from the field. The field experience should include different type of geotextiles, fill materials, subsoil conditions and construction equipment. This should preferably be done as joint project involving several countries, producers, public authorities and research organisations.

#### ACKNOWLEDGEMENT

The authors would like to thank Du Pont de Nemours (Luxembourg) S.A. for funding the work and the purchasers of non-woven geotextiles in Norway for providing free samples for testing. We would also like to thank Ingrid Sødergren from Vägverket, Sweden for participating as observer in the field test and for useful contribution to the discussion.

#### REFERENCES

AASHTO (1990): "Standard Specifications for Geotextiles". *American Association of State Highway and Transportation Officials*, M288-90, Washington DC.  
 Alfheim S.L., Sørli A. (1977): "Testing and classification of fabrics for application in road constructions. *Intern.*

*Conf. on the use of fabric in geotechnics Paris 1977. Vol 2, pp 33-338.*

CEN TC 189: "General and specific requirements for geotextiles and geotextile related products used in the construction of roads and other trafficated areas" Preliminary draft.

Forschungsgesellschaft für Straßen- und Verkehrswesen (1994): "Merkblatt für die Anwendung von Geotextilien und Geogittern im Erdbau des Straßbaus".

Rathmayer, H (1993): "Nonwoven Geotextiles in Road constructions. Quality Requirements- The VTT-GEO Geotextile Specification". *Finnish National Road Administration*, FinnRA Reports 71/1993.

Rathmayer H. (1980) : "Long-term behaviour of geotextiles installed in road constructions in Finland since 1973. *Väg-och vattenbyggaren* 1980:7/8, pp 33 -36.

Schaln, L (1995): "A comparison among the Swedish, the Finnish and the Norwegian requirements for separation layers of geotextiles". *Norwegian Road Research Laboratory*, internal report nr 1786 (in Swedish).

SINTEF (1996): "Non-Woven Geotextiles in Road Constructions." Report.

SINTEF (1997): "Non-woven geotextiles - Field test on damage during installation." Report.

# Rut Prediction for Roadways with Geosynthetic Separators

Wen-Sen Tsai, Moh and Associates, Inc., Taipei, Taiwan, Republic Of China

Robert D. Holtz

Professor, Department of Civil Engineering, University of Washington, Seattle, Washington, USA

**ABSTRACT:** Laboratory model tests that simulated field loading conditions were conducted to evaluate the performance of geotextiles separators. In the tests, rut depth was determined for various geotextiles, thickness of aggregate, subgrade soils, and the number of loading cycles. A rut prediction formulation for unpaved of roadways was developed, based on the Giroud and Noiray (1981) design procedure for unpaved roads. The prediction formula is verified by the rut measurement in a full scale field test.

**KEY WORDS:** geotextiles, separation, unpaved roads, model tests, rut prediction, design

## 1 INTRODUCTION

That geotextiles can markedly improve the performance of unpaved roadways constructed on soft foundation soils is well established. Although the primary geotextile function is separation, performance of unpaved roads is also significantly enhanced by the filtration, drainage, and reinforcement functions provided by the geotextile.

Ruts in the roadway surface are probably the most important indicator of roadway performance. Excessive or premature rutting is a good indication of either subgrade or aggregate failure, or both. Hence, the influence of geotextiles on the development of ruts can be used to evaluate their performance in unpaved roadway systems. Consequently, in this research, ruts were measured in laboratory scale model tests on subgrade-geotextile-aggregate systems. Cyclic plate load tests were conducted on three different thicknesses of base course aggregate, various types and weights of separator geotextiles, and two soft subgrade soils. The geotextiles investigated included heatbonded nonwovens, needlepunched nonwovens, and a woven silt-film. The results were used to develop a prediction equation for rut depths in unpaved roads. This rut prediction formula considers the base course thickness, subgrade strength, and number of loading cycles. The formula also predicted reasonably well the results of a full scale road test.

## 2 TEST SETUP, SOILS, GEOTEXTILES, AND PROCEDURES

Since the performance of geotextiles has been found to be strongly affected by the loading conditions, e.g. loading level and loading frequency, loading parameters used in this study modeled loading conditions experienced by separation geotextiles in the field. This was done by having stress levels applied to the geotextile due to a

dynamic load in the test the same as in the field.

Furthermore, the boundary of the test apparatus did not interfere with the failure zone in the subgrade, when and if the subgrade experienced a shear failure under a dynamic load.

An 80 kN single axle load, termed the equivalent single axle load (ESAL), is used in the AASHTO pavement design method and a tire pressure of 620 kPa is common for loaded dump trucks. The contact area between the tire and pavement for this loading, expressed as a ratio of wheel load and tire pressure, was 0.0645 m<sup>2</sup>.

A 0.416 m<sup>3</sup> steel drum, (Figure 1) contained layers of soils and was used to simulate a common roadway. The top layer was aggregate, which was underlain by a layer of soft soil 300 mm thick. More details about the setup can be found in Tsai (1995) and Tsai and Holtz (1997).

### 2.1 Subgrade Soils and Aggregate

Two different soils, a silty (ML) soil and a clayey (CL) soil, were used as the subgrades in the study. The silty soil was a tailing material from washed crushed rock. The clayey soil was obtained by mixing the silty soil with 5% bentonite by weight. The crushed stone aggregate (GP) was similar to the base material used by The Washington State Department of Transportation (WSDOT) for pavements. Table 1 shows the basic properties of these three materials.

### 2.2 Geotextiles

Six different separator geotextiles, all polypropylene, were tested. Types and relevant properties and given in Table 2.

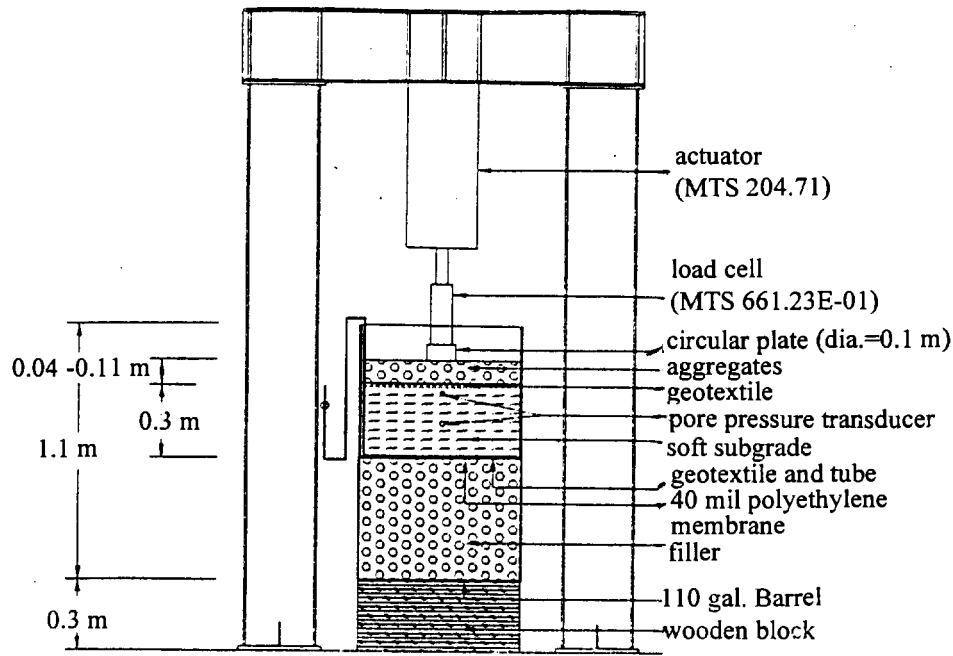


Figure 1. Experimental Setup

Table 1. Basic properties of the silty soil, the clayey soil and the aggregate.

Property	Silty Soil	Clayey Soil	Crushed Stone
% passing US No. 200 sieve	81	82	0
Coefficient of Uniformity	25	NA	3.6
Coefficient of Curvature	1	NA	1.3
Plastic Limit, %	27	24	NA
Liquid Limit, %	38	46	NA
Unified Soil Classification System	ML	CL	GP
Permeability, cm/sec	$1.2 \times 10^{-7}$	$2.9 \times 10^{-8}$	NA
Maximum Dry Density, kg/m <sup>3</sup>	1580	1622	1922
Optimum Moisture Content, %	20.5	20.3	NA

### 2.3 Test Procedure

Testing procedure reported by Tsai and Holtz (1994), Tsai (1995) and Tsai and Holtz (1997) was followed in all tests reported in this paper.

Table 2. Nominal physical and mechanical properties of geotextiles used in the study.

Geo-textile	Structure	Thickness	Mass per Unit Area	Grab Strength
		ASTM D 1777 mm	ASTM D 3776 g/m <sup>2</sup>	ASTM D 4632 kN(%)
NP4	Nonwoven	1.3	142	0.511 (50)
NP6	Nonwoven	1.8	204	0.711 (50)
NP8	Nonwoven	2.3	268	0.933 (50)
HB4	Nonwoven	0.4	132	0.578 (100)
HB6	Nonwoven	0.5	197	1.000 (90)
SF4	Woven	NA	136	0.801 (15)

### 3 RUT MEASUREMENTS

In the model tests, the rut depths were determined based on the readings of a built-in LVDT in the MTS actuator that applied load to the circular plate.

A total of 19 tests were conducted in this study. Among the tests, three different aggregate base thicknesses, six different separators, two different subgrade soils, and four different subgrade strengths were used (Tsai, 1995; Tsai and Holtz, 1997).

Figure 2 shows a typical development of rut depth on the aggregate surface in a test where the geotextile was found to have survived. From this figure, we can see that

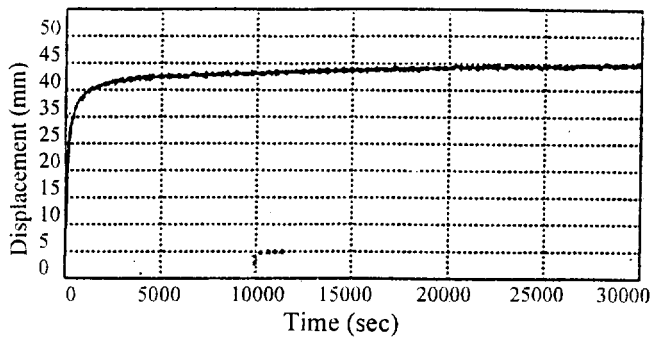


Figure 2. Typical development of rut depth on aggregate surface.

the rate of rut depth development was high initially, and then decreased with the number of cycles.

A summary of the measured ruts obtained in the tests are shown in Table 3. In this table, the notation of form A-B-C-D-E to identify each test. A is the thickness of the base course in mm; and B represents the type of separator used in the test. If it was a geotextile, then its mass per unit area (in oz/yd<sup>2</sup>) is also given. NP represents a needlepunched nonwoven geotextile; HB is a heatbonded nonwoven, , and SF represents a slit-film woven geotextile. GF represents a graded granular filter separator, while MEM represents an impervious plastic membrane. Null means that no geotextile was used.

The subgrade soil type was represented by C, while D represents the subgrade strength in CBR. E represents the sequence of a test, if the test was repeated.

In some tests, local shear failure of the subgrades was experienced, especially the softer ones (40-NP4-Silt-0.5, 40-NP4-Silt-1, etc.). These tests generally had large ruts, some as deep as 147 mm. The ruts for these tests that failed were not used for rut prediction.

Note that the rut depth of Test 40-MEM-Silt-2 was greater than rut depths in tests with separators of lower moduli, e.g. 40-HB6-Silt-2, 40-NP4-Silt-2, 40-NP8-Silt-2. Similarly, the test with the clayey subgrade (Test 40-NP4-Clay-2) had a deeper rut (63 mm) than test 40-NP4-Silt-2 (45 mm) which had the same experimental parameters except subgrade soil type. This can be explained by the long-persisting high pore pressures in the clay, as discussed by Tsai and Holtz (1997). This high pore pressure reduced the modulus of the subgrade, and thus higher plastic subgrade deformation occurred.

The ruts discussed in this section are not equivalent to the ruts that would occur in the field, since the results are determined from scale model tests. Since a fixed wheel path is simulated in these test, the ruts obtained in laboratory tests are probably greater than in the field.

#### 4 RUT PREDICTION BASED ON LABORATORY TEST RESULTS

Table 3. Ruts and depressions on subgrade surfaces after dynamic loading

Notation	Rut on Aggregate Surface (mm)	Depression Depth on Subgrade Surface (mm)	Depression Diameter on Subgrade Surface (mm)	Ratio of Depression Depth to Rut Depth (%)
110-HB4-Silt-2	18	14	229	78
110-NP4-Silt-2	20	9	152	45
110-SF4-Silt-2	18	6	165	33
110-Null-Silt-7	20	4	NA <sup>a</sup>	20
110-Null-Silt-2	49	30	203	61
110-Null-Silt-1	154	110	191	71
55-HB4-Silt-2 <sup>b</sup>	130	203	140	156
40-GF-Silt-2	118	123	152	104
40-MEM-Silt-2	50	51	203	102
40-HB4-Silt-2	94	122	229	130
40-HB4-Clay-2	70	140	203	200
40-HB6-Silt-2	42	44	216	105
40-NP4-Silt-2a	45	44	191	98
40-NP4-Silt-2b	46	51	216	111
40-NP4-Clay-2	63	74	254	117
40-NP4-Silt-1	97	279	107	288
40-Np4-Silt-0.5	147	152	330	103
40-NP8-Silt-2	41	41	NA	100
40-SF4-Silt-2	46	64	191	139

a. Depression was very small and it was difficult to determine the depression zone.

b. The shaded rows indicate the tests where geotextiles were found to have failed.

The results from the laboratory model tests reported here can be used to predict the rut depths in the field with various subgrade strengths, base course thicknesses and geotextile separators. Then it may be possible to determine rut depths for given base course thicknesses using projected traffic loads during the road's service life. In 1981 Giroud and Noiray, proposed a design method for unpaved roads, both with and without geotextiles. In their procedure, the geotextile was used to increase the bearing capacity of the subgrade from elastic "bearing capacity", actually the maximum shear stress, or  $N_c = \pi$  to ultimate bearing capacity  $N_c = (\pi + 2)$ , due to the subgrade confinement and stress reduction on the subgrade surface provided by the geotextile. They also considered the effect of traffic load using empirical data presented by Hammit (1970) and Webster and Alford (1978). The design formula proposed by Giroud and Noiray is shown below.

$$h'_o = \frac{119.24 \log N + 470.98 \log P - 279.01r - 2283.34}{c_u^{0.63}} \quad (1)$$

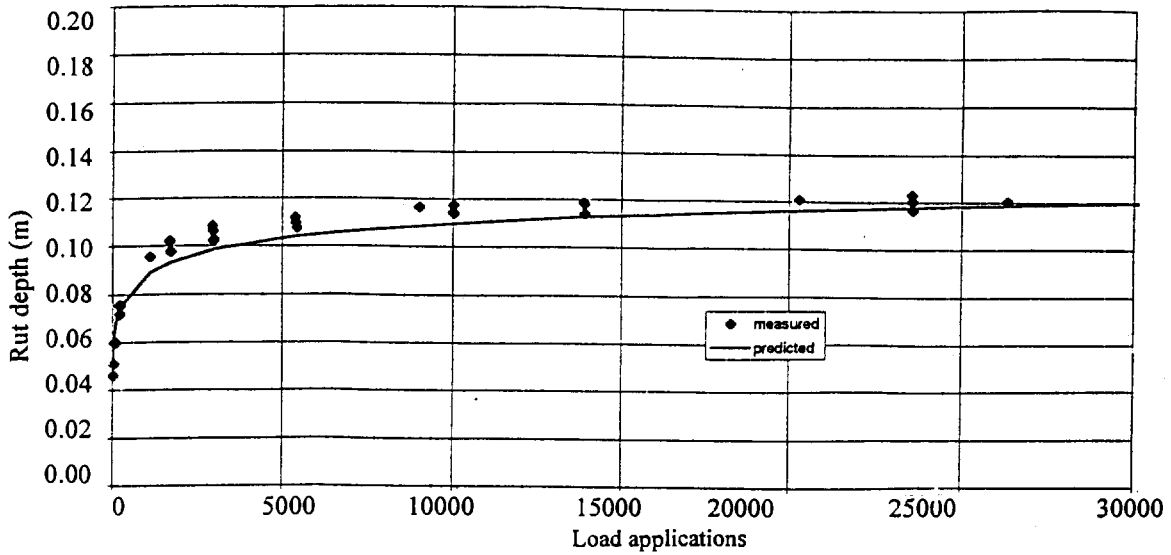


Figure 3. Measured and predicted ruts for Test 40-NP4-Silt-2

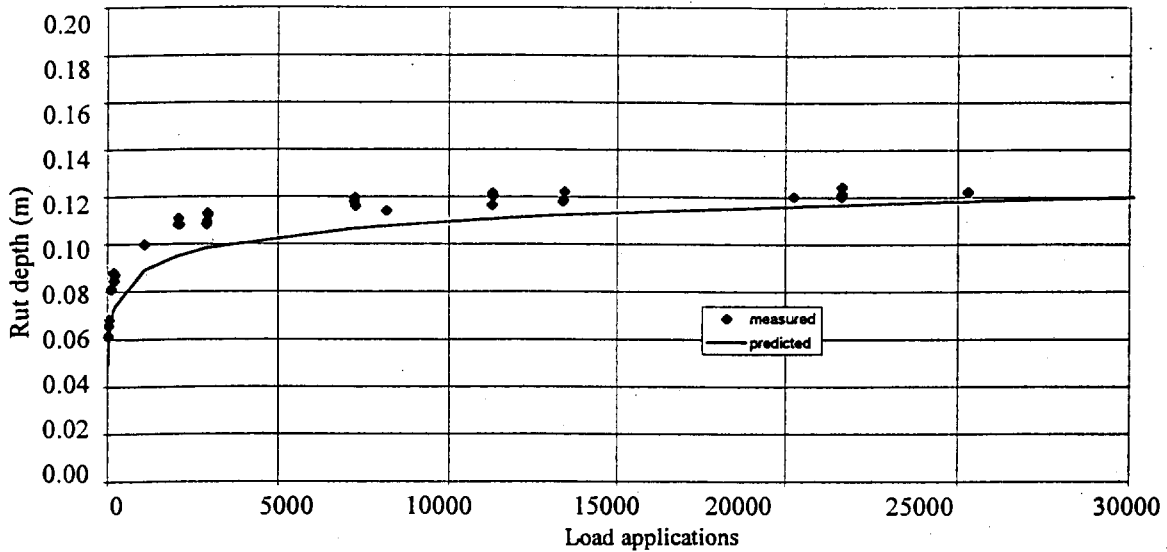


Figure 4. Measured and predicted ruts for Test 40-SF4-Silt-2

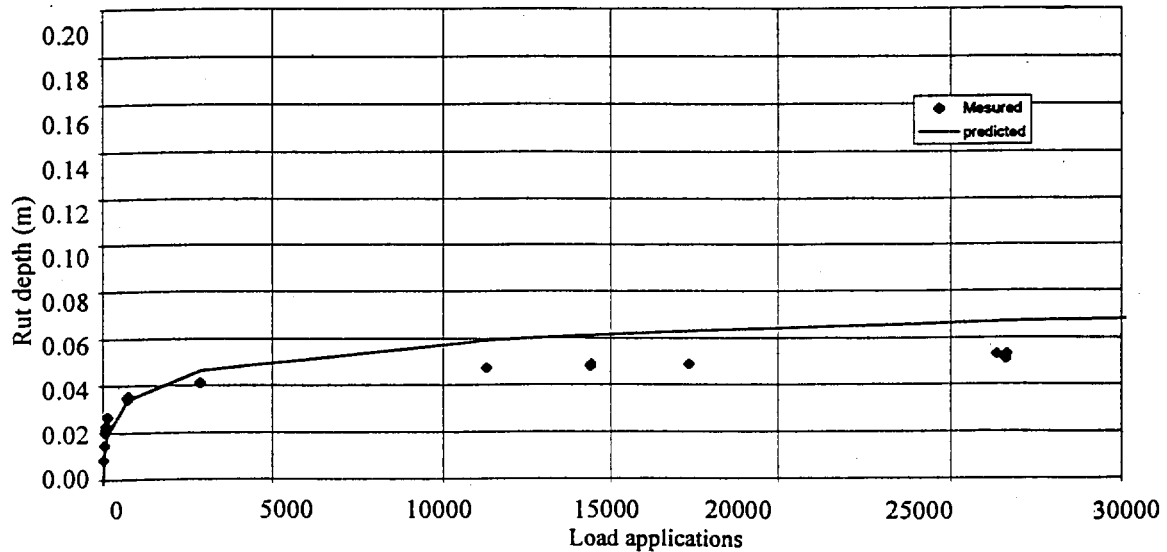


Figure 5. Measured and predicted ruts for Test 110-Null-silt-2



where

$h'_0$  = aggregate thickness (case without geotextile, when traffic is taken into account), in m

$c_u$  = undrained cohesion of subgrade soil, in Pa

$N$  = number of applications of load  $P$

$P$  = axle load, in N

$r$  = rut depth, in m

Equation 1 can be rearranged to obtain:

$$r = -8.18 + 0.186 \log N - 0.00358 c_u^{0.63} h'_0 + 0.733 \log P \quad (2)$$

This equation is of the form:

$$r = A + B \log N + C c_u^D H + E \left( \frac{k}{H} \right) \quad (3)$$

where  $A$ ,  $B$ ,  $C$ ,  $D$  and  $E$  are parameters, and where  $H$  is aggregate thickness, in meters, for the case with or without geotextile.

The laboratory results (Tsai, 1995) showed that the presence of geotextiles can reduce ruts if the geotextile can survive during its service life. However, the tests also showed that geotextile type did not affect rut depth, probably because of the strength of the subgrade and the types of geotextiles tested. Thus Equation 3 does not include geotextile modulus but instead a term  $E(k/H)$ , where  $k = 1$  if a geotextile is present, and  $k = 0$  if no geotextile is present. Using the laboratory results obtained previously, a regression analysis was conducted. The model tests have a scale of 1:2.75. Therefore, the measured ruts in the laboratory tests were multiplied by 2.75 to reflect field rut depths.

A statistics program, *NLREG*, was used to perform a non-linear regression analysis on the results of the laboratory model tests which did not have a subgrade failure or a failed geotextile. In the regression analysis, the sample size was 330, and from these results, Equation 3 can be expressed as:

$$r = 0.260 + 0.009176 \log N - 0.3935 c_u^{0.1465} H - 0.01689 \left( \frac{k}{H} \right) \quad (4)$$

The proportion of variance explained ( $R^2$ ) and the standard error of estimate were 0.88 and 0.0128, respectively.

Equation 4 is used only with an equivalent single axle load (EASL or 80 kN), and  $N$  is the corresponding number of passages of ESAL. On the other hand, Equation 2 can be used for the design of unpaved roads without geotextiles and also applies for any axle loads besides ESAL. This is why the coefficients of Equation 4

are different from those of Equation 2. Figures 3, 4 and 5 illustrate the development of both measured ruts from some typical laboratory model tests and their predicted values based on Equation 4. These tests represent various loading conditions with respect to base course thickness, subgrade strength, and geotextile separators. From these figures, we can see that Equation 4 provides a reasonable prediction for these three tests. Other results in Tsai (1995) provide similar agreement.

## 5 USE OF THE RUT PREDICTION FORMULA FOR FULL SCALE ROAD TEST RESULTS

The results of the full scale road test described in Tsai et al. (1993) were used to verify the new rut prediction formula. In the full scale road test, ten wheel passes were applied using a loaded dump truck weighing 214 kN. The rear axle of the truck was a tandem axle and supported about two-thirds of the gross weight of the loaded dump truck, i.e. 143 kN. Based on Giroud and Noiray (1981), either single axle of the tandem axle carries an axle load equivalent to:

$$0.6 \times 143 \text{ kN} = 86 \text{ kN} \quad (5)$$

The equivalent number of the passages of the single axle load is:

$$2 \times N = 2 \times 10 = 20 \quad (6)$$

The number of the passages of the tandem axle thus can be expressed in equivalent single axle load (ESAL) and is shown below.

$$N = 20 \times \left( \frac{86 \text{ kN}}{80 \text{ kN}} \right)^{3.95} = 27 \quad (7)$$

Equation 4 was used to calculate the ruts in the full scale road test. Figure 6 shows the values versus the measured values of the rut depths for the sections with 150 and 300 mm thick base courses in the full scale road tests (Tsai et al., 1993). Unfortunately, the subgrade strengths immediately below each location where the ruts were measured were not known. Hence, the mean values of subgrade strengths (shown in Tsai et al., 1993) in each section are used to predict the ruts. Figure 6 shows that many of the predicted values of the ruts are in the range of the measured values, so Equation 4 can be used to reasonably well predict the ruts with 150 and 300 mm base courses. Predictions are not made for the sections with 450 mm thick base course in the full scale road test, because the largest equivalent base course thickness in the laboratory

model tests was only 300 mm. Therefore, some tests with thicker base course are needed to improve this equation for such cases.

## 6 CONCLUSIONS

By modifying Giroud and Noiray's (1981) design equations, a new rut prediction formula based on the results of laboratory tests on scale model subgrade-geotextile-aggregate systems was developed. The formula takes into account base course thickness, subgrade strength, type and weight of geotextile separators, and number of loading cycles. The ruts measured in typical laboratory model test, compared well with their predicted values. The results of full scale road tests were also used to verify the rut prediction formula, up to an equivalent base course thickness of 300 mm. The predicted values tended to be greater than the measured values.

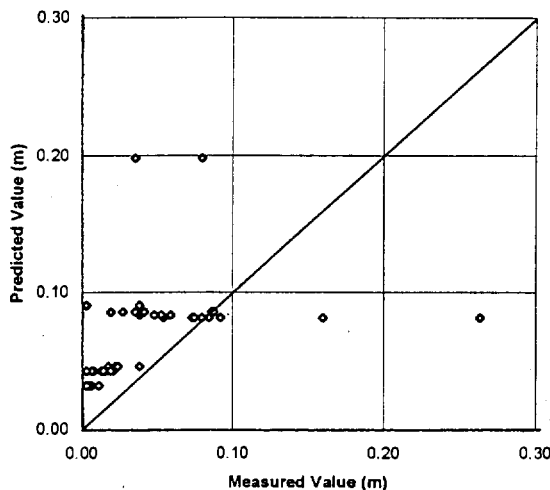


Figure 6. Predicted versus measured values of rut depths for the full scale road test

## REFERENCES

- Giroud, J.-P., and Noiray, L. (1981) "Geotextile-Reinforced Unpaved Road Design," *Journal of the Geotechnical Engineering Division, ASCE*, Vol. 107, No. GT9, pp. 1233--1254.
- Hammit, G. (1970) "Thickness Requirements for Unsurfaced Roads and Airfield Bared Base Support," *Technical Report S-70-5*, United States Army Engineer Waterways Experiment Station, Vicksburg, Miss., July.
- Tsai, W.-S. (1995) "Evaluation of Geotextiles as Separators in Roadways," *Ph.D. Thesis*, University of Washington, Seattle, Washington, pp. 173
- Tsai, W.-S. and Holtz, R. D. (1994) "Performance of Geotextile Separators in Laboratory Model Tests",

*Proceedings of the Fifth International Conference of Geotextiles, Geomembranes, and Related Products*, Singapore, Vol. 2, pp. 663-666.

Tsai, W.-S. and Holtz, R. D. (1997) "Laboratory Model Tests to Evaluate Geotextile Separators in Service", *Proceedings Geosynthetics '97 Conference*, Long Beach, Vol. 2, pp. 633-646.

Tsai, W.-S., Savage, M. B., Holtz, R. D., Christopher, B. R., and Allen, T. (1993) "Evaluation of Geotextiles as Separators in a Full Scale Road Test," *Proceedings Geosynthetics '93 Conference*, Vancouver, Canada, Vol. 1, pp. 35--48.

Webster, S. L., and Alford, S. J., (1978) "Investigation of Construction Concepts for Pavements Across Soft Ground," *Technical Report S-78-6*, United States Army Engineer Waterways Experiment Station, Vicksburg, Miss., July.

# Quantifying the Separation Characteristic of Geosynthetics in Flexible Pavements

Imad L. Al-Qadi

Associate Professor, The Via Department of Civil Engineering, Virginia Tech, Blacksburg, VA

Brian J. Coree

Visiting Assistant Professor, The Via Department of Civil Engineering, Virginia Tech, Blacksburg, VA

Thomas L. Brandon

Associate Professor, The Via Department of Civil Engineering, Virginia Tech, Blacksburg, VA

Salman A. Bhutta,

Doctoral Candidate, The Via Department of Civil Engineering, Virginia Tech, Blacksburg, VA

Alexander K. Appea,

Graduate Student, The Via Department of Civil Engineering, Virginia Tech, Blacksburg, VA

**ABSTRACT:** A field experiment was conducted in which geosynthetics were used at the base/subgrade interface in instrumented sections of a flexible pavement on a rural highway in Bedford County, Virginia. The sections were monitored for two-and-one-half years under local traffic. In this paper, development of a transition layer (intermixing at the base course-subgrade interface) is hypothesized when geosynthetic is absent. An analysis of Falling Weight Deflectometer (FWD) data confirmed the hypothesis in the thinner base (100 mm) sections. The results so far obtained from thicker base sections (150 mm and 200 mm) are inconclusive.

**KEYWORDS:** Geotextiles, Geogrids, Pavements, Separation, Falling Weight Deflectometer.

## 1 INTRODUCTION

To examine the geosynthetic benefits in pavement system and validate an earlier laboratory investigation at Virginia Tech (Al-Qadi et al., 1996, Smith et al., 1995), a section of rural highway in Bedford County, Virginia, was selected in 1994 for an experimental project involving the use and evaluation of geosynthetic functions between a fine-grained subgrade and a granular base course. The experimental section comprised part of a route realignment project undertaken by the Virginia Department of Transportation (VDOT). It was hypothesized that under the action of traffic and environment the subgrade would, in the absence of a separation material, be pumped into the granular base and/or the base course material would penetrate into the subgrade thereby compromising the structural capacity of the pavement.

### 1.1 Site Description

Nine experimental sections, each of approximately 15 m in length, were constructed as part of the realignment of Route 616 in Bedford County, Virginia. The pavement construction comprised a nominal 90 mm hot-mix asphalt (HMA) wearing course surfacing over a granular base. The thickness of the base varied throughout the nine

sections: 100 mm thick in sections 1 through 3, 150 mm in sections 4 through 6, and 200 mm in sections 7 through 9. The subgrade was a weak, reddish brown CH (AASHTO A-7-6) soil, except under sections 5 and 6 where it was identified as ML (AASHTO A-5). These materials were found to have soaked CBR values in the range 6 to 10% at in-situ moisture-density values.

Samples of all construction materials were taken from in-situ and tested in the Materials Laboratory at Virginia Tech. Conventional tests were performed on all recovered materials (HMA: Marshall parameters at 50-blows, asphalt extraction and aggregate gradation; base course: gradation, moisture content, moisture-density and CBR; subgrade: gradation, moisture content, moisture-density and CBR). Extra testing was undertaken on these materials to provide more fundamental material properties (HMA: resilient modulus and creep compliance; base and subgrade: resilient modulus).

The HMA had an asphalt content of about 6.2% by weight of mixture, an average air-void content of 4.6% and an average VMA of 17.9%. The average Marshall Stability and Flow values were 12.3 kN and 10 flow-units. The resilient modulus,  $M_R$ , of field specimens ranged from 3160 MPa at 5°C to 2620 MPa at 40°C. Creep compliance curves were obtained from all field and bulk samples.

The granular base material complied with VDOT specification for a type 21-B base. It classifies as a GW

soil and has an optimum moisture of 6.1% at a density of 22.3 kN/m<sup>3</sup>. Remolded samples were tested for resilient modulus,  $M_R$ , and can be expressed in terms of the bulk stress,  $\theta$ , with an average result of:

$$M_R \text{ (MPa)} = 650\theta^{0.62} \quad (1)$$

Two types of geosynthetic materials were placed at the base/subgrade interface: a woven geotextile and a geogrid. Sections 1, 4, and 7 served as control sections with no geosynthetic at the base/subgrade interface, while the geotextile was placed in sections 2, 5, and 8. The geogrid was likewise installed in sections 3, 6, and 9. The experimental matrix is shown in Table 1. The pre-installation properties of the geosynthetics used are listed in Table 2. The geosynthetics were also tested after three years of field service to determine the installation, construction practice, environmental, and vehicular loading effects on these properties. A 0.6 m x 3.6 m (lane width) piece of each geosynthetic was obtained after excavating the pavement in October 1997. Both geosynthetics were found in excellent condition, and their properties are shown in Table 3. Analysis of changes in the geosynthetic properties and gradation of base and subgrade material after three years of service will be presented in a future publication.

Table 1. Experimental Matrix.

Section Type	Base Thickness		
	100 (mm)	150 (mm)	200 (mm)
Control	1*	4	7
Geosynthetic	2	5	8
Geogrid	3	6	9

\*Denotes section number

Table 2. Characteristics and Properties of Geosynthetics Used (before testing).

Material	Direction	Ultimate	
		Strength (kN/m)	Elong. (%)
Geotextile	Warp	27	23.6
	Fill	25	9.9
Geogrid	Machine	19	8.9
	X-Mach	33	9.3

Construction started in April 1994 and was effectively completed by September 1994. This period included a significant amount of time and effort devoted to installing and checking the various instruments embedded in the pavement. The pavement was opened to traffic in September 1994 (Al-Qadi et al. 1996).

Table 3. Characteristics and Properties of Geosynthetics Used (after testing).

Material	Direction	Ultimate	
		Strength (kN/m)	Elong. (%)
Geotextile	Warp	18	14.8
	Fill	25	12.5
Geogrid	Machine	19	12.4
	X-Mach	32	14.1

## 1.2 Traffic

Traffic volume rates were recorded automatically by the installed instrumentation and varied from 300 vehicles per day in winter to more than 700 vehicles per day in summer.

Three calibration tests were run; a flat-bed truck was used at different axle loads, tire pressures and speeds. This was designed to provide a basis for calibration and validation of the installed instrumentation, and to yield a complete response matrix against which a mechanistic pavement design method, under development, could be validated.

## 1.3 Section Monitoring

Monitoring of the experimental sections was undertaken using two approaches. The first consisted of a series of embedded instrumentation designed to monitor and record traffic, temperature, moisture, pressure, and strains at various points within the pavement sections and on the geosynthetics. A data acquisition system was set up to collect all the appropriate readings from the instrumentation when triggered by the passage of a vehicle. Accumulated data was periodically transmitted electronically to the Materials Laboratory at Virginia Tech for storage and analysis. The second approach relied upon periodic, seasonal visits to the site to measure and record visible distress indicators, although only permanent deformation (rutting) was found to have occurred, to subject the test sections to Falling Weight Deflectometer (FWD) testing for structural evaluation, and, on occasion, to scan the sections using ground penetrating radar (GPR). This paper discusses the rutting and FWD test results

## 2 FIELD MONITORING

The test sections were periodically monitored to provide information relative to surface distresses (rutting) and to perform noninvasive, nondestructive structural evaluations of the different sections.

## 2.1 Rutting

Rutting was measured using a straight-edge method. Two readings were taken on each section during each visit. The magnitude of rutting was defined as the greatest gap between the straight-edge laid upon the pavement transverse to the direction of traffic and the pavement surface. This method would not distinguish between settlement or compaction rutting and plastic flow/heave rutting, however, it is noted that there was no indication of plastic flow/heave distortion of the pavement surfaces. Figures 1 and 2 summarize the development of rut depths during the monitoring period for sections 1 through 3 and 4 through 9, respectively.

From Figures 1 and 2, it is immediately apparent that the rutting histories of sections 1, 2, and 3 stand apart from those in sections 4 through 9, which are statistically identical. In these sections, the magnitude of rutting not only exceeds that in the others, but the rate at which it accumulated is seen to be increasing. Indeed, it has been observed that since about August 1996, the rutting measured in section 1 has exceeded the maximum criterion of acceptability (25 mm), and the rate at which it is accumulating is accelerating.

The rutting that occurred during the first few months of traffic is mainly due to "normal" initial rutting from compaction under traffic. As can be noted, the rutting observed in the first four months is almost the same for all sections. The sharp increase in rutting (in all sections) just before October 1996 is due to the application of two weeks of heavy truck loading to accelerate rutting. The relatively low rutting in sections 4 through 6 was due to the greater wander in the area of the intersection.

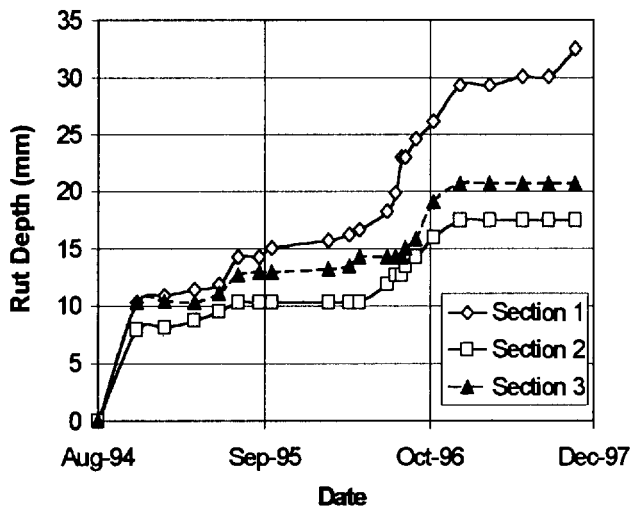


Figure 1. Rut Depth for Sections 1 through 3.

## 2.2 Falling Weight Deflectometer (FWD)

The Virginia Department of Transportation (VDOT) FWD was chosen to perform seasonal structural evaluations of the test sections. This device, which drops a calibrated mass onto a circular plate (radius 150 mm) in contact with the pavement surface, records the magnitude of the applied load, and the vertical deformation response of the pavement surface at the center of the loaded plate and a six locations offset from the loaded axis.

Two types of analysis may be performed on FWD data. The simplest and most direct analysis relies on computing a Surface Modulus,  $E_0$ , defined as the applied load divided by the measured axial deformation. This value is analogous to a spring constant (kN/mm), and provides a gross measure of the overall structural value of the pavement system, including the subgrade. A more sophisticated analysis is possible using various techniques of "back-calculation" which seek to match the observed pavement response to that returned by a mathematical model of a layered linear elastic half-space. This technique generally relies upon varying the linear elastic moduli of the component material layers until a satisfactory match to the observed surface deflection is achieved.

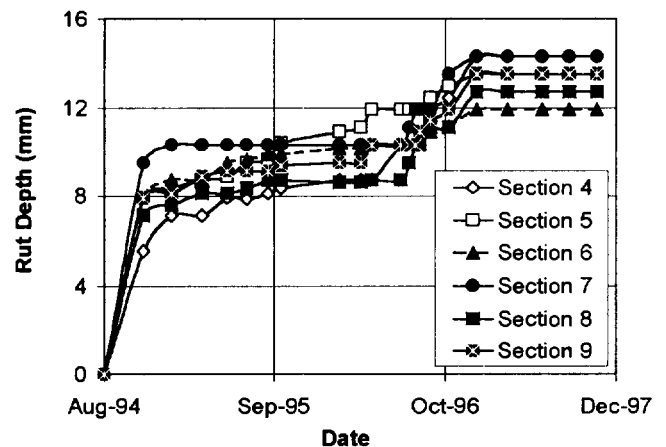


Figure 2. Rut Depth for Sections 4 through 9.

### 2.2.1 Surface Modulus ( $E_0$ )

The surface modulus of each section was computed for each of the seasonal site visits. This technique is simple because it requires that no assumptions be made relative to the thickness or elastic response of component layer materials. However, it is subject to modification in HMA surfaced pavement due to the effects of temperature upon the viscoelasticity of the asphalt bound materials, and can be further influenced by the presence of an effective rigid

layer underlying the pavement at some depth. The results of these analyses are shown in Figure 3.

It can be seen from Figure 3 that the overall pavement responses of sections 1, 2, 3, and 9 stand out as being distinct from those in sections 4, 5, 6, 7, and 8 which are remarkably consistent. This apparent difference is ascribed to the details of the design of this road section, which was relocated to transform an intersection into a curve. Consequently, in spite of a significant excavation (mainly in sections 4 through 8), the sections at each end of the new construction are somewhat influenced at some depth by the presence of previously undisturbed and compacted subgrade materials. This will also explain the increased surface moduli observed in these sections; the authors believe that this is due not to stronger pavement sections, but to residual pre-compacted subgrade.

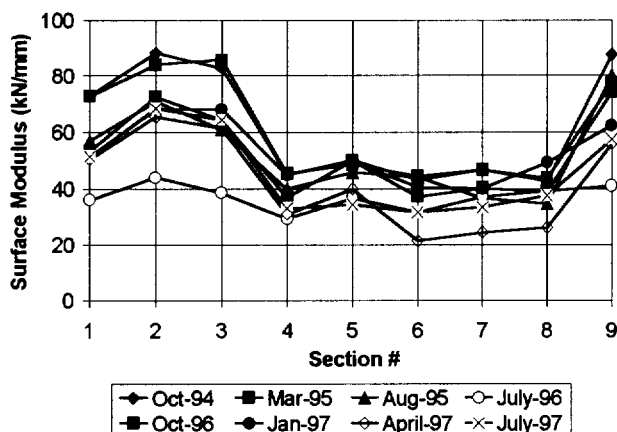


Figure 3. FWD-derived Surface Moduli (MPa).

Nonetheless, if the surface moduli for sections 1, 2 and 3 are closely examined, it will be seen that for all FWD tests, the surface modulus of section 2 (geotextile) exceeds that of section 3 (geogrid), which in turn exceeds that of section 1 (control). This pattern is also observed in sections 4, 5, and 6 (150 mm base) and in sections 7 and 8 (200 mm base), and would tend to indicate that the geotextile may contribute more to the structure than other sections (Al-Qadi et al. 1997).

### 2.2.2 Detailed FWD Analysis

FWD measured deflection profiles were plotted for different periods. The purpose of this exercise was to define any inconsistency, which might occur in the measurements taken by the geophones. Figures 4 and 5 are typical measured deflection basins for different load levels in July 1997 for sections 1 and 2.

The collected FWD field data was further analyzed using proprietary software, MODULUS version 5.0,

developed by the Texas Department of Transportation (TxDOT) and the Texas Transportation Institute (TTI).

This package takes as input pavement responses recorded in the field and the thicknesses of each physical material layer. The elastic parameters ( $E$ ,  $\nu$ ) of any layer except the subgrade may be either fixed or bounded within a range supplied by the user. The program then performs a search algorithm, varying the “slack” variables until an optimal match between the measured and computed deflection basins is found. The output from this program is the “optimal” set of layer moduli consistent with the measured values and the set layer property constraints.

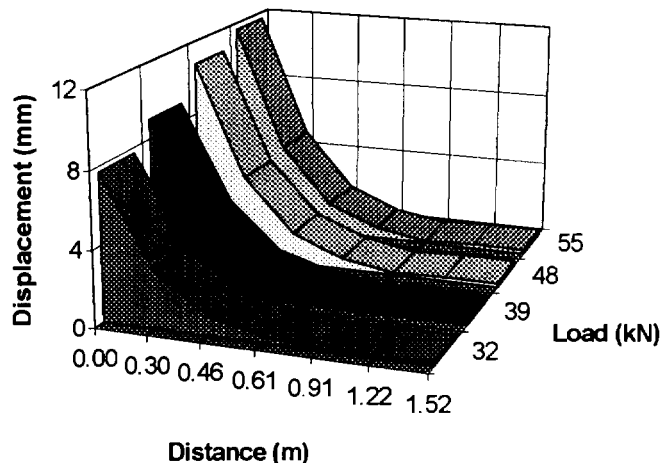


Figure 4. Deflection Basin Profile (July 1997), Section 1.

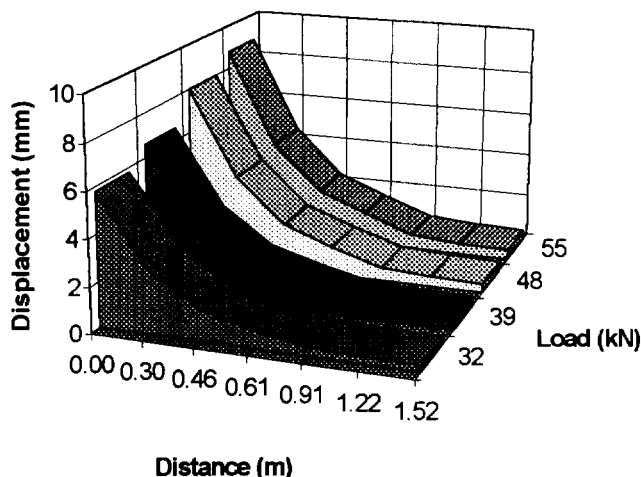


Figure 5. Deflection Basin Profile (July 1997), Section 2.

MODULUS uses an internal routine to detect the presence and depth of effective rigid layers deep within the pavement. This is important, and has been found to significantly influence the returned moduli. In this project, MODULUS did indeed detect an effective rigid bottom

layer at a varying depth of 0.5-7.5 m (mostly above 2.0 m) below the pavement surface. Further data analysis indicates that the variation in depth to rigid bottom layer did not have any significant effect on the result pattern.

Due to the relatively thin HMA surfacing layer, the elastic properties of this layer were input and fixed by the authors based upon appropriate measured pavement temperatures and the laboratory resilient modulus characterization of specimens obtained from the field. The nominal elastic parameters of the granular base layer were also provided and fixed by the authors based upon laboratory measurements (Al-Qadi et al. 1996). The only parameter returned by MODULUS, therefore, was the subgrade modulus (Figure 6). This analysis confirms the differential response between the different treatments.

For most of the FWD results, the subgrade “apparent” resilient moduli of the sections with geotextile are greater than their corresponding control sections or geogrid stabilized/ reinforced sections. This may be attributed to a weaker base course layer in the latter sections as compared to the corresponding geotextile stabilized sections, which is consistent with the “pumping of subgrade fines into the base course layer and/or intermixing at the base-subgrade interface” hypothesis.

### 2.2.3 Base-Subgrade Interface Intermixing Model

One of the important functions of geosynthetics in pavements is stabilization, which is its ability to isolate and provide a barrier against the base course-subgrade intermixing (Koerner and Koerner 1994, Al-Qadi, et al., 1994, Jorenby and Hicks, 1986; Lair and Brau, 1986). The extent of contamination and the material properties of the intermixing layer are of critical importance in determining the performance of pavements. Although the concept of base course contamination has been realized for sometime (Yoder and Witczak, 1975), an estimate of its contribution to the reduction in pavement service life is still needed to be quantified. The following section details the approach adopted to determine the extent of contamination in this project.

The hypothesis put forth in the study was the development of a transition layer between the subgrade and base layer in the absence of a geotextile. To determine the transition layer thickness developed in control and (may be) geogrid stabilized reinforced sections, an independent layer of resilient modulus value between the base and subgrade was added and the “geotextile subgrade resilient modulus” was considered in the calculations as reference. After adding the transition layer with known properties to the control pavement system, a back-calculation procedure was adopted to determine the subgrade resilient modulus. This is an iterative process where the thickness of the transition layer is changed gradually to yield a subgrade resilient

modulus approximately equal to that of the geotextile stabilized section.

For example, the subgrade resilient modulus, from the data collected in August 1995, for section 1 (100 mm control section) was 105 MPa, where the geotextile stabilized section had a subgrade resilient modulus of 110 MPa. A transition layer thickness of 13 mm at a resilient modulus of 138 MPa was needed to increase the subgrade resilient modulus to 110 MPa. Over the next 8 months the transition layer increased to 64 mm. The thickness further increased to 69 mm by October 1996 indicating asymptotic stabilization of intermixing layer versus time (see Figure 7). Further tests show insensitivity to greater contamination/ intermixing.

For the thicker base course sections (150 mm and 200 mm), the MODULUS program becomes insensitive to changes in transition layer thickness. This implied that the FWD back-calculation procedure could not estimate the contamination layer thickness accurately in the thicker base course sections (150 mm and 200 mm) at this time.

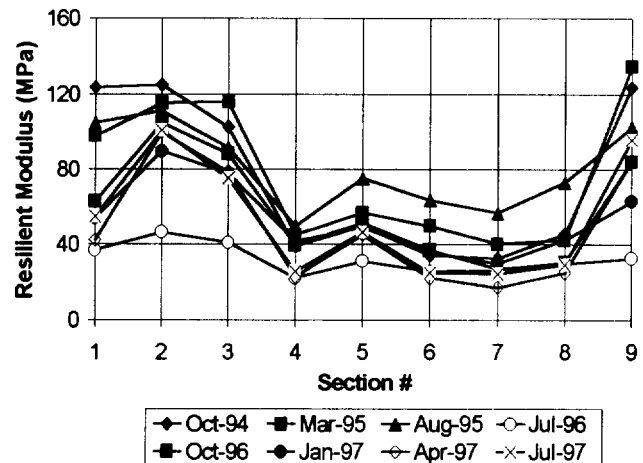


Figure 6. Apparent Subgrade Resilient Modulus Variation over Time.

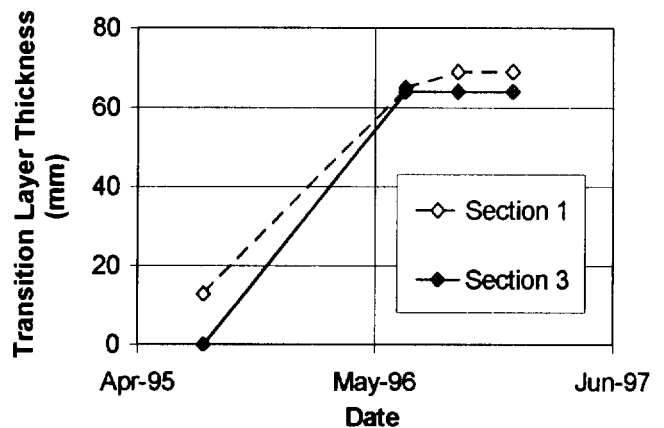


Figure 8. Development of Transition Layer.

### 3 CONCLUSIONS

The results of this field experiment and analysis of the data derived from non-destructive monitoring (rutting and FWD) suggest a clear difference in performance when geosynthetic is included in the pavement system; specially in the thinner base sections (1 through 3), while the short duration of the project prevent any clear distinctions being made in the thicker base sections (4 through 9) at his time. Within sections 1 through 3, the benefit of the geotextile is noted by comparison with the performance (rutting) of the control to the other sections; equally, a simple analysis of FWD data suggests that the degree of intermixing at the base-subgrade interface is a function of the geosynthetic used - no intermixing in the geotextile section, and delayed or reduced intermixing in the geogrid stabilized/reinforced section. MODOLUS program was used to obtain the extent of intermixing at the base course-subgrade interface in the 100 mm test sections over a period of 17 months (August 1995 to January 1997). It was found that the degree of intermixing can be quantified. However, for the thicker base course sections (150 mm and 200 mm) the back-calculation (so far) turns insensitive and the difference in performance between sections is within the numerical accuracy of the computer model.

### 4 ACKNOWLEDGEMENTS

The authors acknowledge the financial support by the Virginia Center for Innovative Technologies and the Amoco Fabrics and Fibers Company. The authors also acknowledge the VDOT support in providing the FWD testing for this study. The invaluable help by Barney Barnhart and Jeff Kesler of VDOT is greatly appreciated.

### 5 REFERENCES

- Al-Qadi, I. L., Brandon, T. L., Smith, T. A., and Lacina, B. A. (1994) "How Do Geosynthetics Improve Pavement's Performance," *Proceedings of Material Engineering Conference*, San Diego, CA, USA, pp. 606-616.
- Al-Qadi, I. L., Brandon, T. L., Bhutta, S. A., Appea, A. K., and Lacina, B. A. (1996) *Field Testing of Geosynthetically Stabilized Pavement Sections*, The Charles E. Via, Jr. Department of Civil Engineering, Virginia Tech, Blacksburg, VA, USA.
- Al-Qadi, I. L., Brandon, T. L., and Bhutta, S. A. (1997) "Geosynthetically Stabilized Flexible Pavements," *Geosynthetics '97*, IFAI, Long Beach, CA, USA, pp. 647-662.
- Brandon, T. L., Al-Qadi, I. L., Lacina B. A., and Bhutta S.A. (1996) "Construction and Instrumentation of Geosynthetically Stabilized Secondary Road Test Sections," *Transportation Research Record*, No. 1534, Washington, D.C., USA, pp. 55-57.
- Jorenby, B. N. and Hick, R. G. (1986) "Base Course Contamination Limits," *Transportation Research Record*, No. 1095, Washington, D.C., USA, pp. 86-102.
- Koerner, R. M. (1994) *Designing With Geosynthetics*, 3<sup>rd</sup> Edition, Prentice-Hall Inc., Englewood Cliffs, NJ, USA.
- Koerner, R. M. and Koerner, G. R., (1994) *Separation: Perhaps The Most Underestimated Geotextile Function*, Geotechnical Fabrics Report, Industrial Fabrics Association International, St. Paul, MN, USA, pp. 4-10.
- Laier, H. and Brau, G. (1986) "The Use of Geotextile in Road Construction under Intensive Dynamic Loading," *Third International Conference on Geotextiles*, Vienna, Austria, pp. 995-1000.
- Smith, T. E., Brandon, T. L., Al-Qadi, I.L., Lacina, B. A., Bhutta, S.A., and Hoffman, S. (1995) *Laboratory Behavior of Geogrid and Geotextile Reinforced Flexible Pavements*, The Charles E. Via, Jr. Department of Civil Engineering, Virginia Tech, Blacksburg, VA, USA.
- Yoder, E. J. and Witczak, M. K (1975) *Principles of Pavement Design*, 2<sup>nd</sup> Edition, John Wiley and Sons, Inc., New York, NY, USA.



# Geosynthetic-Reinforced Pavements: Overview and Preliminary Results

S.W. Perkins

Assistant Professor, Department of Civil Engineering, Montana State University, Bozeman, Montana, 59717, U.S.A.

M. Ismeik

Postdoctoral Research Associate, Department of Civil Engineering, Montana State University, Bozeman, Montana, U.S.A.

M.L. Fogelsong, Y. Wang, E.V. Cuelho

Graduate Research Assistants, Department of Civil Engineering, Montana State University, Bozeman, Montana, U.S.A.

**ABSTRACT:** Montana State University (MSU), with support from the Montana Department of Transportation (MDT), has initiated a laboratory and analytical based research program to study and quantify the benefits derived by the addition of geosynthetics to the base course layer of flexible pavements, where the function of the geosynthetic is one of reinforcement. The objectives of the study are to verify previous work showing the positive benefit of using geosynthetics for base course reinforcement, to quantify the stress-strain response of laboratory-scale reinforced pavement test sections such that mechanisms of reinforcement can be more clearly understood and described, and to develop a comprehensive methodology for the design of such pavements. The purpose of this paper is to describe on-going research work at MSU, plans for laboratory testing and analytical modeling, and to present preliminary results from several completed test sections. Details of the test facility and instrumentation used to quantify behavior are presented.

**KEYWORDS:** Pavements, Base Course, Reinforcement, Laboratory Tests, Geogrids, Geotextiles

## 1 INTRODUCTION

Geogrids and geotextiles have been examined and used in practice for reinforcement of the base course layer of flexible pavements for over the past sixteen years, with both successes and failures having been reported. Early attempts using geotextiles (Brown et al., 1982; Ruddock et al., 1982; Halliday and Potter, 1984) indicated very little improvement in rut development characteristics that could be attributed to geotextile reinforcement. For studies involving both geogrids and geotextiles, Anderson and Killeavy (1989), Barksdale et al. (1989) and Cancelli et al. (1996) have demonstrated that geogrids are superior to geotextiles when used as a reinforcement member, while Al-Qadi et al. (1994) showed that superior performance was seen when a geotextile was used.

These studies involving both materials have provided insight into the importance of the roles of separation and filtration and the ensuing effect on reinforcement potential. The only study available where appreciable mixing of the base course and subgrade soils in control sections was noted (Al-Qadi et al., 1994) also corresponds to the one showing superior performance by the geotextile. Other studies exhibiting more moderate amounts of mixing, and indicative of conditions for which separation and filtration functions were not as critical (Anderson and Killeavy, 1989; Barksdale et al., 1989) indicate that improvement due to geogrid reinforcement can still be observed, but perhaps not to the extent had separation and filtration functions been incorporated into the section designs. On the other extreme, studies exhibiting no problems with mixing (Cancelli et al., 1996; Collin et al., 1996; Haas et al., 1988; Mirua et al., 1990; Moghaddas-Nejad and Small, 1996; Webster, 1993) have

demonstrated significant improvement with geogrid reinforcement for properly designed sections.

Improvement in pavement performance has been observed in laboratory-scale experiments involving stationary circular plates to which a cyclic load has been applied (Cancelli et al., 1996; Haas et al., 1988; Miura et al., 1990), test tracks incorporating moving wheel loads (Barksdale et al., 1989; Collin et al., 1996; Moghaddas-Nejad and Small, 1996; Webster, 1993) and full-scale roads constructed with normal construction equipment (Anderson and Killeavy, 1989; Mirua et al., 1990). Improvement has been defined in terms of an extension of the life of the pavement, or the amount by which the base course layer could be reduced such that equivalent performance is seen. Reinforced pavements have been shown to have a life typically 3 to 10 times that of a similar unreinforced section, while a reduction of base thickness ranging from 22 to 50 % has been observed. Performance has typically been measured in terms of accumulated rut depth with increasing load cycle application.

Improvement has been seen for all levels of rut depth below that corresponding to an inoperable condition (25 mm). Measurement of strain on geogrid layers has shown that strain is developed immediately upon the first load application and well before any appreciable rut is developed in the pavement, provided the reinforcement was properly placed in the base layer. Strain measurements have indicated that these materials are engaged in a tensile capacity and that the level to which strain develops is closely related to the amount of improvement observed. These results indicate that this application is well suited for flexible pavements which cannot tolerate significant surface deformations and remain operational. Perkins and Ismeik (1997) have provided a more comprehensive review of studies addressing this application.

Despite the positive successes reported from field and laboratory based studies, this application has not been widely applied in practice and its use has been discouraged by a number of state departments of transportation. The overriding obstacle preventing the use of this application lies in the absence of an accepted design technique which accounts for the variables believed to control pavement performance. MSU, with support from the MDT and Federal Highway Administration, has initiated a laboratory and analytical based research program to study and quantify the benefits derived by the addition of geosynthetics to the base course layer of flexible pavements, where the function of the geosynthetic is one of reinforcement. The objectives of the study are to verify previous work showing the positive benefit of using geosynthetics for base course reinforcement, to quantify the stress-strain response of laboratory-scale reinforced pavement test sections such that mechanisms of reinforcement can be more clearly understood, and to develop a comprehensive methodology for the design of such pavements. The step from the observation of behavior in laboratory experiments to the development of a design solution will be accomplished through the development of a finite element model of a reinforced pavement. Once the model is shown to reasonably match the behavior observed in the laboratory experiments, the model will be used in a parametric study to evaluate the influence of variables thought to impact reinforced pavement performance. The purpose of this paper is to describe the ongoing research work at MSU, the plans for laboratory testing and analytical modeling, and to present preliminary results from several completed laboratory test sections.

## 2 OVERVIEW OF RESEARCH PROGRAM

The MDT faces conditions in the eastern portion of the state where quality gravel sources for road construction are scarce and associated haul costs of such material are high. Subgrade conditions in this region consist of A-6 to A-7 soils, resulting in relatively low subgrade support values and relatively thick base course sections. Faced with these conditions, MDT has been interested in investigating the possible use of geosynthetics as reinforcement in the base course layer. MSU developed an early plan to construct a series of full-scale test sections along an existing or new roadway with these sections containing electronic instrumentation to measure pavement response. To investigate the suitability of proposed instrumentation and installation techniques, a pilot test section was constructed in the Summer of 1995 with results reported by Perkins and Lapeyre (1996, 1997).

The results of this instrumentation study indicated that excessive uncertainty existed in the installation and operation of instrumentation in an outdoor, field-scale test site and that successful completion of the originally planned approach was questionable. An alternate approach was then proposed where similar instrumentation used in the pilot test section would be used along with new devices to monitor the behavior of test

sections constructed in a laboratory setting. This facility is described in this paper and essentially consists of a large reinforced concrete box in which pavement test sections are individually constructed and loaded with a 40 kN load cyclically applied to a 305 mm diameter circular plate resting on the pavement surface. The pavement test sections contain an extensive array of instruments to measure stress, strain, moisture content and temperature. Stress and strain response is measured in the pavement layers both during a dynamic load cycle and between load cycles to monitor the accumulated response with increasing load cycle.

It is anticipated that between 10-15 sections will be constructed and loaded over the course of the study. Geosynthetic type (geogrid versus geotextile), geosynthetic position within the base layer, subgrade type and strength and stiffness characteristics, and base and asphalt concrete (AC) thickness are anticipated as variables to be included in the study. The variables included in these sections are not intended to cover all possible pavement configurations but rather are intended to provide a description of response for a representative cross section of variables. The modeling portion of the study is intended to be used to supplement the experimental data by providing analytical predictions of behavior for those conditions not physically tested.

In conjunction with the experimental portion of the study, a finite element model of the laboratory-scale pavement sections is being developed. The model is being developed to match the stress, strain and deflection response observed in the 10-15 experimental test sections. Once confidence in the model is developed by this step, the model can be used to predict response of a wide range of pavement configurations for which experimental data is not available. Results from this parametric study will then be combined to form a design methodology suitable for use by flexible pavement designers. The form of this design methodology has not been defined at this point, but will most likely consist of simple equations and design charts which account for the variables found to be most influential on reinforced pavement response.

The modeling portion of the study is being accomplished through the use of a commercial finite element program and user defined material constitutive laws. Haas et al. (1988) and Miura et al. (1990) showed that in a similar test arrangement, tensile strains as great as 1.8 % were observed in geogrid reinforcement for surface rut depths less than 25 mm. Cyclic tension tests performed by Bathurst and Cai (1994) and preliminary tests performed by the authors indicate that for strains of this magnitude, simple isotropic linear elastic material models are inadequate. In anticipation of the need to predict strains of this magnitude, a series of monotonic, cyclic and sustained load tests are being performed on the geogrid and geotextile being used in this study. The monotonic load tests are being used to define the orthotropic elastic-plastic properties of the materials, where the in-plane shear modulus is thought to be particularly important in defining pavement response. Sustained load tests will provide intrinsic creep properties of the geosynthetics. Cyclic tension tests will be

used to calibrate a non-linear, combined isotropic/kinematic hardening model which will model the ratchetting effect observed in repeated load tests. Ratchetting refers to the accumulation of plastic strain with increasing load cycle number for cyclic tests performed under constant load amplitude.

Ratchetting effects are also observed under compressive deviatoric loads in soil materials and will be modeled through the use of a bounding surface plasticity model. An interface model will be used between the base soil and the geosynthetics and will consist of a simple elastic-plastic Coulomb type friction law. It is anticipated that the elastic stiffness response will need to be normal stress dependent. The interface model will be calibrated from pull-out tests where the pull-out arrangement will be modeled as a boundary-value problem using the finite element model being developed. A standard viscoelastic model will be used for the asphalt concrete.

The research approach of collecting data from experimental test sections, using a model to match the observed behavior, using the model in a parametric study to examine the influence of a wide range of variables and using these results to establish a design solution to the problem is being applied to laboratory-scale experiments under stationary load conditions. Part of the reason for first exercising this approach in the laboratory is to establish its feasibility. Recognizing that different behavior is to be expected under conditions of a moving wheel load, if this approach is found to be successful, the authors intend to pursue an additional phase to the project where experiments are conducted in a test-track facility where more realistic loads can be applied to the pavement. The same research approach can then be applied, with the resulting design solution reflecting the moving wheel load case.

The remainder of this paper describes the laboratory test facility developed to evaluate reinforced flexible pavements under idealized load conditions. Preliminary results from a geogrid reinforced section and an unreinforced section are presented. These results are preliminary in that the primary function of the sections was to examine the performance of the proposed instrumentation and installation techniques. For this reason, the full array of instruments planned for subsequent sections was not included. While care was taken to make the two sections as comparable as possible, minor differences as noted existed.

### 3 LABORATORY TEST FACILITY

#### 3.1 Test Box and Loading Arrangement

Laboratory-scale pavement test sections are being constructed in a reinforced concrete box having inside dimensions of 2 m by 2 m in plan and 1.5 m in height. The box consists of four sides having an open bottom and with the concrete laboratory floor serving as the bottom face. The front face of the box is removable to facilitate excavation of the test section.

Two I-beams were set into the wall forms prior to the placement of wet concrete. The I-beams were placed parallel to each other along opposite walls perpendicular to the front wall. The upper flanges of each I-beam act as rails for the load frame to move along.

The load frame consists of an additional two I-beams which span between the two I-beams embedded in the concrete wall. The ends of the load frame I-beams are attached to a carriage assembly allowing the load frame to roll from the front to the back of the box. Attached to the two load frame I-beams is a second carriage assembly upon which the load actuator is mounted. This second carriage assembly allows the load actuator to roll along the load frame I-beams, hence allowing the load actuator to move from side to side in the box. The two carriage assemblies allow the load actuator to be positioned at any point along the plan dimensions of the box. Figure 1 shows a photograph of the box and load frame.

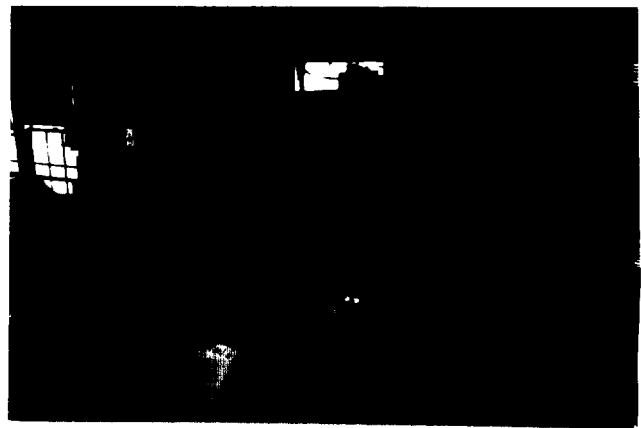


Figure 1. Test box and load frame.

The load actuator consists of a 305 mm diameter bore pneumatic cylinder with a 75 mm stroke. The threaded end of the actuator's piston is attached to a load cell having a range of 90 kN. A 55 mm diameter steel rod is attached to the other side of the load cell and extends down to and rests on a 305 mm diameter steel plate having a thickness of 25 mm. The end of the rod resting on the steel plate is rounded and sits inside a similar shaped recess in the plate, thus allowing the plate to rotate during loading. A waffled rubber pad 4 mm in thickness is placed between the steel plate and the AC surface to aid in providing a uniform pressure distribution on the AC surface.

A pneumatic binary regulator is used to control the time-history of air pressure supplied to the load cylinder. The pneumatic regulator is in turn controlled by a computer which sends a series of binary signals to the regulator's four solenoid valves allowing the division of the single inlet pressure into any one of fifteen equally spaced outlet pressures. Control of the binary signals is provided by the same software used for data acquisition.

Inlet pressure to the binary regulator is controlled and monitored by a standard gage and regulator. The binary regulator allows for any shaped load pulse to be specified and approximated by fifteen points for each of the ascending and descending portions of the pulse. Due to the limited number of points available for approximating load pulse curves, a simple triangular pulse with a linear rise time, a hold time at peak load, a linear fall time and a pause time between pulses has been specified. Two pulse durations of 0.5 and 1 Hz have been used, with times for the periods described above being 0.6, 0.3, 0.6 and 0.5 s for the 0.5 Hz pulse and 0.3, 0.2, 0.3 and 0.2 s for the 1 Hz pulse. Inlet pressure to the binary regulator has been set to give a peak load of 40 kN, corresponding to a load plate pressure of 550 kPa.

Two types of loads were applied to the pavement. The first type consisted of the application of a single load pulse at 25 different locations within the box. Application of these loads allowed for the careful examination of response from the different sensors. The second type of load consisted of a series of repeated loads when the load plate was placed at the center of the box. The 1 Hz load pulse was used for the repeated cycle tests for both sections 1 and 2 and the single pulse tests for section 2. The 0.5 Hz pulse was used for the single pulse tests for section 1.

### 3.2 Pavement Layer Materials and Thickness

The preliminary test sections reported in this paper used a slow curing cold mix asphalt concrete. This material was used due to the unavailability of hot mix asphalt during the time period in which the preliminary test sections were constructed. Hot mix asphalt is being used for subsequent test sections. The cold mix was heated in a mobile trailer-mounted oven prior to placement and compaction. Compaction was accomplished by a hand-operated vibratory plate compactor. Compacted thickness of the AC layer for sections 1 and 2 were 70 and 75 mm, with bulk density values of 21 and 22 kN/m<sup>3</sup>, respectively. Results of laboratory tests on the cold mix asphalt are given in Table 1. A grain size distribution of the aggregate used in the mix is given in Figure 2.

A crushed stone base course meeting the MDT specifications for crushed top surfacing, type A, grade 3 is being used for all test sections. The grain size distribution for the material is shown in Figure 2, where it is seen that 100 % of the material passes the 19 mm sieve.

Sections 1 and 2 contained a compacted base section thickness of 200 mm. The material was compacted at a water content ranging between 5 to 6.5 %, resulting in dry density values of 21 kN/m<sup>3</sup>. Measurement of dry density and water content during excavation of the sections indicated that the water content dropped to 4.5 to 5 % with the dry density remaining essentially unchanged.

A fine silty sand consisting of the fines trapped in the baghouse of a hot mix plant were used for the subgrade. The material has 40 % fines with a liquid limit of 18 % and a plastic limit of nearly the same value, classifying the material

Table 1. Cold mix asphalt concrete properties.

Property	Section	
	1	2
Marshall stability, lb (T-245)	9620	9620
Marshall flow (T-245)	15	15
Density, g/cm <sup>3</sup> (T-245)	2.31	2.31
Asphalt content, % (T-164)	5.0	5.0
Rice specific gravity (T-209)	2.48	2.48
Air voids, %	17.9	13.8
Penetration (T-49)	51	51
Kinematic viscosity (T-201)	554	554
Specific gravity of aggregate	2.61	2.61

Note: T designations refer to AASHTO test specifications

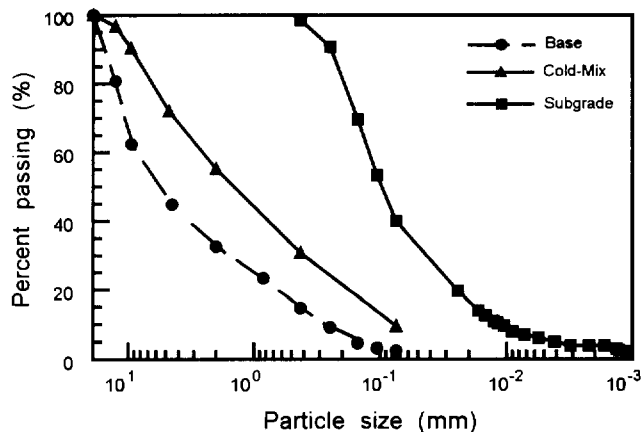


Figure 2. Grain size distributions of AC aggregate, base and subgrade.

as a SM or A-4. A grain size distribution of the material is given in Figure 2. Modified Proctor compaction tests indicate that the material has a maximum dry density of 18.2 kN/m<sup>3</sup> occurring at a water content of 11.5 %. The material was compacted in the box at a water content of 14.5 % and at an average dry density of 17.5 kN/m<sup>3</sup>. Laboratory CBR tests on this material at this water content and dry density and in-situ Dynamic Cone Penetration (DCP) tests indicate a CBR of approximately 15. This material was not replaced between sections 1 and 2. Only the asphalt concrete, base and geogrid were removed between sections 1 and 2.

Section 1 contained an extruded, polypropylene, biaxial geogrid placed in the base course at a level of 40 mm above the base course - subgrade interface. The geogrid has a mass per unit area of 215 g/m<sup>2</sup>, an aperture size of 25 by 33 mm in the machine and cross-machine directions, respectively, and

a wide-width ultimate tensile strength of 13 and 20 kN/m in the machine and cross-machine directions, respectively. Section 2 was unreinforced.

The remaining test program will use hot mix asphalt for all sections. A second subgrade consisting of a highly plastic clay will be used for approximately one-half of the program with the silty sand being used for the other half. The clay will be prepared at a water content to produce a weak subgrade having a CBR of approximately 3-4. A woven geotextile will also be incorporated into the test program. Other variables to be included are base course and asphalt concrete thickness, and geosynthetic position.

### 3.3 Instrumentation

The two preliminary test sections described in this paper contained a limited number of instruments compared to sections which are currently being constructed with hot mix asphalt. The primary purpose of these preliminary test sections was to examine the performance and installation procedures of instruments to be used in later sections. The two sections discussed in this paper contained one asphalt concrete strain gage, 12 soil pressure cells, 8 soil strain gages and four foil strain gages mounted to the geogrid specimen in section 1. In addition, 8 LVDT's were used to monitor surface deformation of the asphalt concrete layer and the load cell was used to monitor applied load.

The single AC strain gage was used only in section 2. The strain gage was a H-type gage marketed by Dynatest. The gage was placed at the bottom of the AC layer. The stress cells placed in the base course and subgrade were also marketed by Dynatest and have a diameter of 68 mm and a thickness of 13 mm. Cells having two different ranges of 200 and 825 kPa were used. Four stress cells were placed in the base course layer, two being oriented to measure vertical stress and two to measure stress in the horizontal direction. The centerline of the stress cells was 120 mm below the top of the base course layer and were placed at a radius of 400 mm from the center of the box. The two cells measuring horizontal stress were oriented to measure stress in the radial direction when the load was placed in the middle of the box. Four stress cells were also placed in the upper portion of the subgrade at a distance of 130 mm below the top of the subgrade (level 1) and in a similar configuration as those contained in the base. Two additional cells were placed at levels of 430 mm (level 2) and 705 mm (level 3) below the top of the subgrade. At each level, one cell was placed at a radius of 400 mm to measure vertical stress while the other was placed to measure radial stress at this same radius.

Strain in the base and subgrade soils was measured using a LVDT mounted between rectangular end plates measuring 15 by 50 mm and 5 mm thick. The gage length between the end plates was nominally 80 mm. Four LVDT's were placed in the base course and four in the top layer of the subgrade in a similar configuration to the stress cells placed at these two levels.

On the geogrid used in section 1, four bonded resistance (foil) strain gages were placed on ribs located at a radius of 400 mm from the center of the box. Two gages were placed to measure radial strain in the machine direction of the geogrid while the other two were placed to measure radial strain in the cross-machine direction when the load was placed in the center of the box. The geogrid was placed 40 mm above the bottom of the base.

Data acquisition and control has been established to control the time-history of the load application and to trigger the collection of data. Two types of tests were performed on each section. After the construction of a section, the load frame was moved to 25 different points within the box to apply a single pulse of load. The full time history of each sensor was collected for each of the 25 locations. Once these tests were completed, the load plate was moved to the center of the box where a repeated load was applied. During the application of this repeated load, the peak and baseline reading of each instrument was measured and collected for the majority of the applied load cycles. The baseline reading corresponds to a time when no load was applied to the pavement and represents a permanent response corresponding to that particular load cycle, while the peak reading corresponds to a time when the peak load was applied. In addition to this data, the full time history of each sensor was measured for specified load cycle numbers.

## 4 EXPERIMENTAL RESULTS

### 4.1 Transient Response To A Single Load Pulse

At each of the 25 load locations, three separate single pulse load tests were conducted. Figure 3 illustrates three load traces from one of the 25 load locations for sections 1 and 2, where the shape of the load pulse curve is identical for each of the three applications. The spike on the descending branch of the curve is due to some small feedback in the binary control valve. Figure 4 illustrates the time-history response of stress cells located in the base and subgrade for sections 1 and 2 when the load was applied directly above the sensor. The data shows that in the base the vertical stress was slightly higher in the reinforced section, while in the subgrade the stress was slightly less. Figure 5 shows the time-history of radial stress in the base and subgrade when the load was applied at a radius of 310 mm from the sensor.

The peak response of stress cells located in the base layer and oriented to measure vertical, radial and tangential stress were recorded from various time-history records as the load was applied at different locations. Figure 6 illustrates the variation in these peak measurements with respect to the lateral distance from the load plate to the sensor, where positive stresses correspond to compression. For each stress parameter and at each lateral location, three data points are given corresponding to the three tests performed at that location. Figure 6 illustrates the reproducibility of the results.

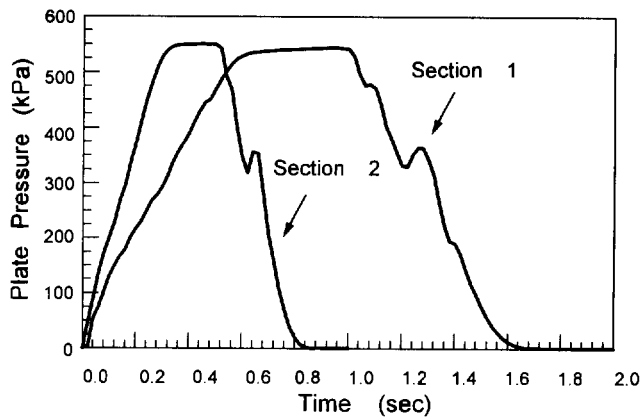


Figure 3. Load pulse time-history.

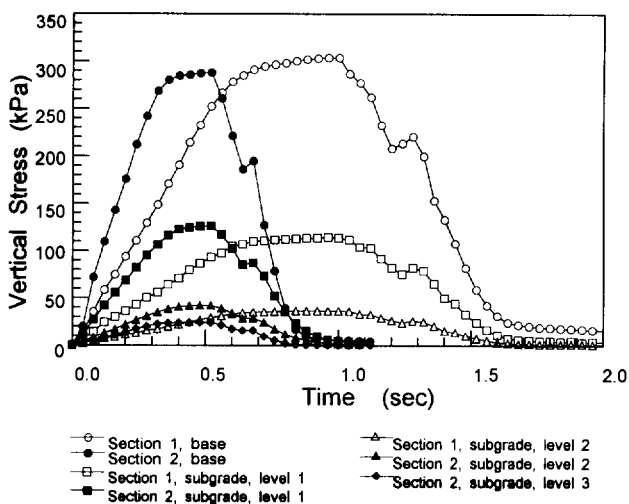


Figure 4. Vertical stress time-history in base and subgrade.

The curves shown in Figure 6 correspond to general trends sketched to match the available data points and were not developed from rigorous analyses. This is also true for the curves shown in Figures 7 and 8.

Figure 7 shows results of vertical, radial and tangential strain in the base in a similar fashion as Figure 6, where positive strain corresponds to contraction. Figure 7 shows more scatter than Figure 6 and is due mainly to the influence of compaction induced during the first and second load applications on the subsequent load applications at that same location.

Figure 8 illustrates radial and tangential strain induced in the geogrid in section 1 due to single load pulses applied at various locations, where positive strains correspond to tension. The results indicate that as much as 0.17 % tensile strain is induced in the geogrid immediately below the centerline the load. Radial tensile strains quickly vanish to zero at a radius of approximately 200 mm, which is 50 mm greater than the radius of the load plate. Beyond this

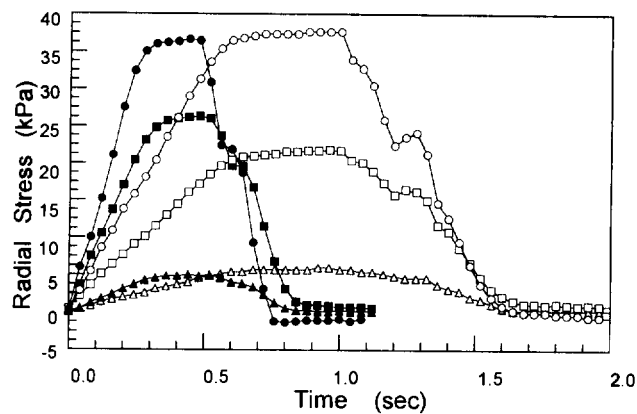


Figure 5. Radial stress time-history in base and subgrade.

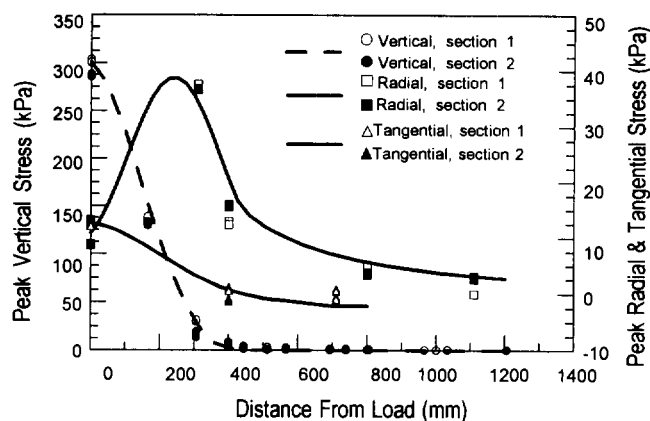


Figure 6. Peak vertical, radial and tangential stress in base.

region strains become compressive, reaching a peak compressive strain at a radius of approximately 300 mm, whereafter they approach zero. In the tangential direction, the strains are seen to be in tension for all points away from the load and approach zero at a radius of 800 mm.

The results shown in Figure 8 have the same trend as the results for radial and tangential strain in the base shown in Figure 7, indicating that in regions where the base experiences extensional strains, the base interacts with the geogrid to transfer tension to the reinforcement. These results indicate that the primary function of the geogrid is in preventing lateral spread of the base course and that anchorage of the geogrid is not needed in such an application.

#### 4.2 Transient and Permanent Response to Multiple Load Cycles

Upon completion of the single pulse tests, the load plate and frame were moved to the center of the box where a repeated load was applied. The mean and standard deviation of the

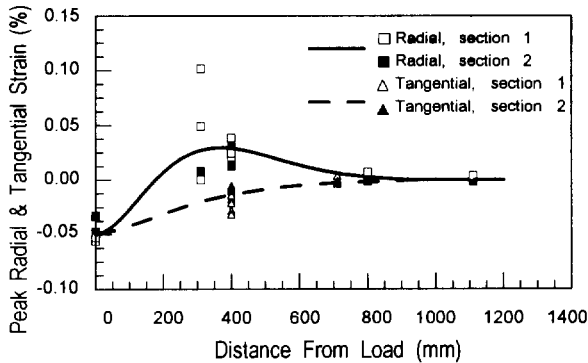
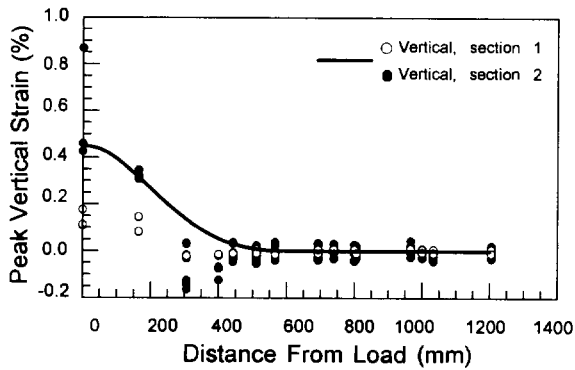


Figure 7. Peak vertical, radial and tangential strain in base.

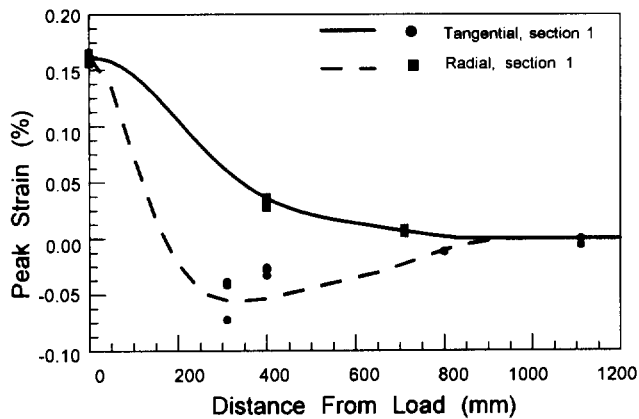


Figure 8. Peak radial and tangential strain in geogrid.

applied pressure was 548 and 4.0, and 550 and 4.3 for sections 1 and 2, respectively. Figure 9 shows the plate pressure versus average plate deformation observed during the first load application for sections 1 and 2. Figure 10 shows the development of surface deformation with load cycle number, where for each section three curves provided. The “peak” curve corresponds to the average plate deformation measured at the point in time where the applied load reached a maximum for that cycle. The “permanent” curve corresponds to the deformation immediately prior to when the load was applied. The “transient” curve corresponds to the

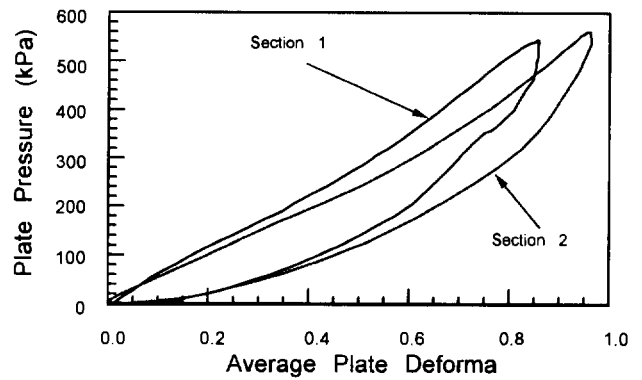


Figure 9. Load versus deformation for first cycle.

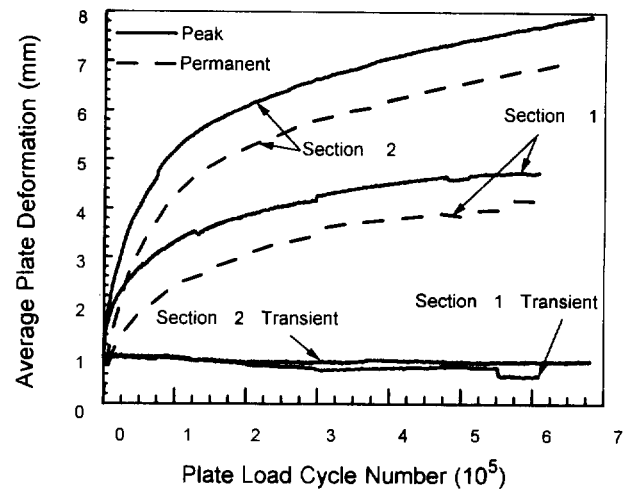


Figure 10. Deformation versus cycle number.

difference between the “peak” and “permanent” curves and represents the dynamic or transient deformation for each load cycle. Figure 9 indicates that the dynamic stiffness of section 1 is slightly greater than section 2 for the first load cycle. The transient response Figure 10 shows that both sections become slightly more stiff with increasing load cycle, with section 1 experiencing a slightly greater increase in stiffness for load cycle numbers greater than 250,000 as compared to section 2. Section 2 shows a more rapid rate of rut depth than section 1, while section 1 appears to have reached a plateau when the rut depth in section 2 continues to increase linearly with cycle number.

Visual inspection of the asphalt from sections 1 and 2 indicated that the asphalt in section 1 was more stiff and less susceptible to flow than that in section 2 even though the laboratory results, including the Marshall and penetration tests, indicate that the materials were identical and the density and thickness in section 2 were greater than section 1. Temperature of the asphalt prior to compaction was not measured, but it is believed that this is the main difference

between the materials causing the behavior observed. Thus it is not clear if the geogrid in section 1 is responsible for the improvement in behavior observed or if the improvement is due to the difference in asphalt. The additional sections being constructed as part of this project will clarify this point.

## 5 CONCLUSION

Preliminary results from a study designed to examine the reinforcement function of geosynthetics in flexible pavements have indicated the compatibility between extensible strains in the base and the development of tensile strain in the geogrid, indicating the reinforcement function of the material. The comparison of stress and strain measures in the soil layers indicated only slight differences between a reinforced and unreinforced section for the application of a single load pulse. This is to be contrasted against the significant difference observed in rut development for repeated cycle tests, indicating that examination and modeling of repeated load behavior is necessary to understand the mechanisms of reinforcement. Additional work being performed by the authors will help illustrate these mechanisms for pavement variables believed to influence performance.

## ACKNOWLEDGMENTS

The authors gratefully acknowledge the financial support of the Federal Highway Administration and the Montana Department of Transportation through contract number 8106 and the Tensar Corporation for the donation of geogrid material.

## REFERENCES

- Al-Qadi, I.L., Brandon, T.L., Valentine, R.J., Lacina, B.A. and Smith, T.E. (1994) "Laboratory Evaluation of Geosynthetic Reinforced Pavement Sections" *Transportation Research Record* 1439, Washington DC., USA, pp. 25-31.
- Anderson, P. and Killeavy, M. (1989) "Geotextiles and Geogrids: Cost Effective Alternate Materials for Pavement Design and Construction", *Proceedings of the Conference Geosynthetics '89*, San Diego, CA, USA, pp. 353-360.
- Barksdale, R. D., Brown, S. F. and Chan, F. (1989) "Potential Benefits of Geosynthetics in Flexible Pavement Systems", *National Cooperative Highway Research Program Report No. 315*, Transportation Research Board, National Research Council, Washington DC, USA.
- Bathurst, R.J. and Cai, Z. (1994) "In-Isolation Cyclic Load-Extension Behavior of Two Geogrids", *Geosynthetics International*, Vol. 1, No. 1, pp. 1-19.
- Brown, S.F., Jones, C.P.D. and Brodrick, B.V. (1982) "Use of Non-Woven Fabrics in Permanent Road Pavements", *Proceedings of the Institution of Civil Engineers*, London, UK, Part 2, Vol. 73, pp. 541-563.
- Cancelli, A., Montanelli, F., Rimoldi, P. and Zhao, A. (1996) "Full Scale Laboratory Testing on Geosynthetics Reinforced Paved Roads", *Proceedings of the International Symposium on Earth Reinforcement*, Fukuoka/Kyushu, Japan, November, Balkema, pp.573-578.
- Collin, J. G., Kinney, T. C. and Fu, X. (1996) "Full Scale Highway Load Test of Flexible Pavement Systems With Geogrid Reinforced Base Courses", *Geosynthetics International*, Vol. 3, No. 4, pp. 537-549.
- Haas R., Wall, J., and Carroll, R.G. (1988) "Geogrid Reinforcement of Granular Bases in Flexible Pavements," *Transportation Research Record* 1188, Washington DC, USA, pp. 19 - 27.
- Halliday, A.R. and Potter, J.F. (1984) "The Performance of a Flexible Pavement Constructed on a Strong Fabric", *Transport and Road Research Laboratory, Report 1123*, Crowthorne, Berkshire, UK, 15 p.
- Miura, N., Sakai, A., Taesiri, Y., Yamanouchi, T. and Yasuhara, K. (1990) "Polymer Grid Reinforced Pavement on Soft Clay Grounds", *Geotextiles and Geomembranes*, Vol. 9, pp. 99-123.
- Moghaddas-Nejad, F. and Small, J. C. (1996) "Effect of Geogrid Reinforcement in Model Track Tests on Pavements", *Journal of Transportation Engineering*, Vol. 122, No.6, pp. 468-474.
- Perkins, S.W. and Lapeyre, J.A. (1996) "*In-Field Performance of Geosynthetics Used To Reinforce Base Layers; Phase I: Instrumentation Selection and Verification*", Report No. FHWA/MT-96/8126-1, U.S. Department of Transportation, Federal Highway Administration, Washington, DC, USA, 160p.
- Perkins, S.W. and Ismeik, M. (1997) "A Synthesis and Evaluation of Geosynthetic Reinforced Base Layers in Flexible Pavements: Experimental Work", *Geosynthetics International*, Vol.4, No.6.
- Perkins, S.W. and Lapeyre, J.A. (1997) "Instrumentation of a Geosynthetic - Reinforced Flexible Pavement System", *Transportation Research Record* 1596, Washington, DC, USA.
- Ruddock, E.C., Potter, J.F. and McAvoy, A.R. (1982) "A Full-Scale Experiment on Granular and Bituminous Road Pavements Laid on Fabrics", *Proceedings of the Second International Conference on Geotextiles*, Las Vegas, Nevada, USA, Vol. 2, pp. 365-370.
- Webster, S. L. (1993) "Geogrid Reinforced Base Courses For Flexible Pavements For Light Aircraft, Test Section Construction, Behavior Under Traffic, Laboratory Tests, and Design Criteria", *Technical Report GL-93-6*, USAE Waterways Experiment Sta., Vicksburg, MS, USA, 86 p.



# Cost Versus Reinforcing Effectiveness of Geotextiles in Pavement Works in Greece

A.G. Kokkalis

Assistant Professor, Democretus University of Thrace, Civil Engineering Department, 67100 Xanthi, Greece

**ABSTRACT:** Geotextile reinforced pavements might be both economically and technically advantageous over their conventional counterparts, especially under poor subgrade conditions. In this paper a systematic method of estimating possible cost implications of including a geotextile in the subgrade-subbase interface are discussed. The cost evaluations are obtained on the basis of the thickness of the aggregate layer which can be replaced by the geotextile been laid in the pavement-subgrade interface, so that the two structure have identical load-deformation behavior. The load-deformation behavior is evaluated by regression formulas, which have been derived from pavement finite element analysis and verified through field experiments. Reinforced pavements might provide numerous others indirect savings and conveniences, such as a more solid roadbed, a shorter construction time, ease in construction methods, savings in maintenance costs, higher factors of safety, acceptability of marginal materials etc. These factors were not included in this economic evaluation and all promote the reinforced alternative. The results obtained have been verified in several case studies.

**KEYWORDS:** Geotextiles, Reinforcement, Pavements, Unpaved roads, Road construction

## 1 INTRODUCTION

Geotextiles have already a 25-years history of successful applications in many fields of geotechnical engineering. A field of particular interest is that of highway and pavement works. In Greece the first relevant application of geotextiles took place in a highway in Peloponnese in 1977. Since then geotextiles established a widespread use in pavement engineering works. Nowadays, they are systematically used in most major highway schemes, like the Patra-Athens-Thessaloniki-Border and the Egnatia motorways. This constantly increasing application rate urged for a systematic analysis of the effectiveness of geotextile inclusion in a pavement system and the cost implications this involves.

A research activity concerning the reinforcing and other beneficial actions of geotextiles been laid in the pavement-subgrade interface was run at the Aristotle University of Thessaloniki since 1985 and at the Democretus University of Thrace lately.

## 2 REINFORCING ACTION OF GEOTEXTILES

A geotextile been laid at the subgrade-subbase interface fulfills any one of the actions of reinforcement, separation, filtration and in few cases drainage. It should be mentioned that in most cases more than one of the above functions act simultaneously. Of interest for this paper is the reinforcement function. This function is expressed, as a rule, in a dual manner, i.e. lateral restraint and membrane action. Membrane action is the most obvious one: as the pavement is deformed by the loads, the geotextile been laid on the top of the subgrade is also deformed. Assuming that no slip occurs the geotextile is strained. The vertical constituent of the stresses developed balance part of the applied load. At the cost of substantial displacement and

ignoring the parameter of creep relaxation, the ultimate loading of the system can markedly increase (Sellmeijer 1993; Espinoza 1994). However, it has become obvious that the membrane effect mechanism fails to accurately predict the benefits that can be obtained from the inclusion of geotextiles at low deformations (Little 1992; Milligan et al. 1989). Non-woven products with relatively low stiffness is unlikely to produce any benefit at all if included in any membrane effect analysis. Nevertheless, experience has shown that there is a clear improvement to the performance of the pavement with the inclusion of low stiffness geotextiles. This improvement is mainly attributed to lateral restraint i.e. the stretched geotextile inhibits the lateral displacements of the aggregates. Another positive effect is that the subgrade just outside the traffic loading area is also loaded more or less vertically, through the stressed geotextile, which ensures maximum bearing capacity of the system. Furthermore, the aggregate layer acts like a beam spreading the load over a larger area. (Sellmeijer 1990, 1993). Finally, the separation and filtration functions, which the geotextile simultaneously performs, ensure the integrity, purity and stiffens of the aggregate layer which mobilize a plastic stress-strain state with higher factors of safety (Little 1992). The exact value of all these mechanisms is hard to evaluate analytically.

There are a profusion of methods for estimating the reinforcing effectiveness of geotextiles in pavements, ranging from the purely empirical to the use of finite elements models. It is the author's opinion that the latter methods, through calibration by full-scale experiments, permit any type of reinforcing action to be evaluated and included.

A finite element program was used herein to calculate the stress-strain fields in a great variety of weak pavements (which can also be considered as subbases of typical pavements) either reinforced or not with geotextiles. The

program analyses the pavement-subgrade system as a three-dimensional axially symmetric multi-layered problem (Snaith et al. 1980). The wheel load is specified as a uniformly distributed pressure over a circular contact area. The boundary conditions of the system are: horizontal restraint at the lateral boundaries and both horizontal and vertical restraint at the base boundary. Material properties are specified for each layer of the system. The resilient modulus of each layer may be either linear or dependent on any number of stress regimes. The elastic analysis employs a successive over-relaxation technique to obtain the stress in each element of the finite element grid. When the elastic analysis is completed a non-iterative procedure makes use of the computed stress values and suitable creep equations to calculate the vertical permanent strain for each element. The strains are then converted to deformations and summed for each column of the grid to yield the overall surface permanent deformation profile.

The fabric has been modeled using a layer of its approximate thickness (for typical non-woven heat-bonded geotextiles their typical thickness has been taken as 1 mm). Since in practice local reinforcement of the soil structure occurs in the vicinity of the fabric, two transitional layers have been introduced, one above and one below the fabric layer having similar thickness as the geotextile itself. Thus, the abrupt change in resilient modulus between the fabric and its adjacent layers has been reduced, since these transition layers have intermediate characteristics between the fabric and the adjacent layers themselves.

A large number of the independent variables i.e. resilient modulus of geotextile, resilient modulus of subgrade and thickness of aggregate layer are then combined. Not taking into account the various numbers of load repetitions, 567 combinations as a total have been solved.

Characteristic permanent deformation profiles obtained from these pavement models are compared with those measured in the field from full scale experiments made in similar pavements. Although the deformation predicted were consistent with those measured, weighting factors were, as a rule, necessary, so that the computed values coincide with those observed in the field experiments. These calibration factors were specified for each layer.

The purpose of the field experiments involved was the determination of the load-deformation characteristics of subbases, either reinforced or not with geotextiles. Cycled plate bearing tests were carried out on the various model pavements. Model pavements were 4 by 4 meters in plan and founded on generally weak subgrades. Loads were applied through a rigid 0.3 meters diameter plate to approximate wheel load contact area. Loads also have magnitudes approximating standard wheel load and were applied on variable thickness granular pavements either reinforced or not with geotextiles. The geotextile anchorage was sufficient to ensure that no lateral slip would occur.

The results were subsequently statistically analyzed so that prediction formulas were developed through which the

thickness of the granular layer could be obtained. This procedure, although it introduces inevitable inaccuracies, is preferable, since applying a prediction formula is considerably simpler than formulating and solving the finite element program for any new set of data. Additionally, it helps the study of the economic consequences of pavement geotextile reinforcement. However, it should be constantly kept in mind, (Palmeira and Cunha 1993; Douglas and Valsangar 1991) that it is difficult to predict geotextile reinforced pavement deformation by simple relationships. More detailed information for the whole procedure is given in Kokkalis, (1990).

The regression formulas obtained are, for pavements without geotextile reinforcement:

$$e_{pl} = 13.0 \frac{1}{E_{SG}^{0.70}} + 18.5 \frac{1}{H_{ag}^{0.63}} + 1.1(\log N)^{0.88} + 2.2 \frac{(\log N)^{1.21}}{E_{ag}^{0.88}} - 3.4, (R = 0.991) \quad (1)$$

$$\text{where: } E_{ag} = 0.19H_{ag}^{0.45}E_{SG} \quad (2)$$

and in the case of geotextile reinforced pavements:

$$e_{pl} = 13.0 \frac{1}{E_{SG}^{0.70}} + 18.5 \frac{1}{H_{ag}^{0.63}} + 1.1(\log N)^{0.88} + 5.1 \frac{1}{E_g^{0.21}} + 2.2 \frac{(\log N)^{1.21}}{E_{ag}^{0.88}} - 6.2, (R = 0.978) \quad (3)$$

$$\text{where: } E_{ag} = 0.12(\log E_g)H_{ag}^{0.45}E_{SG} \quad (4)$$

where:  $e_{pl}$  is the permanent deformation of the whole structure measured in mm,  $E_{SG}$  and  $E_{ag}$  are the resilient modulus of the subgrade and the aggregate layer respectively measured in MPa and  $E_g$  is the resilient modulus of the geotextile measured in KPa,  $H_{ag}$  is the thickness of the aggregate layer expressed in cm for equations (1) and (3) and in mm for equations (2) and (4) and  $N$  is the number of standard load repetitions applied to the pavement.

Care has been taken so that equations (1) and (3) yield consistent results.

The limitations of the formulas obtained are:  $E_{SG} < 50$  MPa and  $H_{ag} < 60$  cm.

A sensitivity analysis conducted on the derived formulas showed, as expected, that the single most important parameter affecting the required pavement thickness is the deformation behavior of the subgrade. Of most interest for this research is the sensitivity of the design equation to the thickness of the granular layer of the pavement and to the resilient modulus of the geotextile: permanent deformation is four times more sensitive to the parameter "thickness of aggregate layer" than to the parameter "modulus of the geotextile".

Apart from the field experiments, the whole procedure involved laboratory experiments for the determination of the interactional characteristics between the geotextile and the surrounding material, the determination of the stress-strain relationship of geotextiles when acting in isolation and when they are confined in the soil-aggregate environment of the project. It is this confined resilient modulus ( $E_g$ ) that has been used in the analysis. To obtain  $E_g$  a large shear box (30 X 30 cm) has been properly modified so that it could include and stress a geotextile specimen. The specimen was kept in contact with representative soil been laid underneath and graded aggregate been laid on top of the specimen. The geotextile specimen in this soil-geotextile-aggregate system was subsequently stressed whilst been compressed by loads equivalent to the traffic and dead loads which really apply to the system. Apart from few difficulties which arose and easily confronted this procedure of determining the confined stress-strain behavior of geotextiles could be regarded as successful (Kokkalis and Papacharisis 1989). From the derived stress-strain diagram, the values of  $E_g$  used were those corresponding to the actual strain the geotextile develops in situ.

### 3 COST IMPLICATIONS OF GEOTEXTILE INCLUSION

Geotextile reinforced pavements, apart from offering certain technical advantages, may consist an economically competent alternative as well. Numerous factors are affecting the relevant economic analysis, so that a generalized solution is unattainable. Each case study has its own prevailing economic parameters. It should be mentioned herein that, from a literature review it can be concluded, that in cases of soft subgrades, geotextile reinforced pavements usually present economic advantages.

The economic analysis of the reinforcing action of geotextile is based on the obvious fact that the stronger the geotextile, the greater the thickness of the subbase layer which could be replaced so that the two structures have identical load-permanent deformation behavior.

Apart from the substitution of part of the aggregate layer, geotextiles been laid on soft subgrades might also indirectly affect certain cost items by:

1. speeding up the construction,
2. creating a more solid working surface,
3. facilitating construction practice,
4. extending working periods,
5. reducing maintenance cost,
6. reducing vehicle operating cost,
7. making marginally rejected soil materials acceptable,
8. attaining higher factors of safety and
9. making the removal of soft surface layers not necessary.

It worth's mentioning for item 5., that maintenance cost for Greek secondary roads amounts up to 60% of the

original construction cost over the whole design life of the road (Nikou 1988).

As it has been previously reported, all the above potential indirect savings are very difficult to be included in an economic analysis. In the analysis presented herein three cost items are taken into account, i.e. purchase cost of geotextiles and aggregate, transport cost and application cost. It should be commented that the application of geotextiles does not demand any specific machinery which should otherwise be included as a cost item. These three cost items have been applied to a number of pavement construction projects in Greece, where there were a geotextile inclusion. It is obvious that the range of unit costs is broad, whilst they are simultaneously critical for the results of the evaluation. Typical unit costs used are (1 ecu = 1.15 U.S. dollars):

1. purchase and transport cost of geotextiles: 1.0 ecu/m<sup>2</sup>,
2. application cost of geotextiles: 0.1 ecu/m<sup>2</sup>,
3. supply cost of aggregates: 0.08 ecu/m<sup>2</sup>/cm of layer thickness,
4. transport cost of aggregates: 0.001 ecu/km/cm of layer thickness,
5. construction cost of aggregate layer: 0.02 ecu/m<sup>2</sup>/cm of layer thickness,

From the above figures and through the equations (1) and (3) it can be derived that, assuming the mean transportation distance of aggregates as being 10 km, the reinforced pavement would be cost-effective if the geotextile could replace more than 10 cm of the thickness of the aggregate layer. This is the case when  $E_{SG} < 40$  Mpa. If  $E_{SG} < 25$  Mpa then the reinforced pavement becomes less expensive even if there is an adjacent source of aggregates. It is obvious that as the subgrade becomes softer, (in which case geotextile inclusion becomes more effective) and as acceptable aggregates can be only obtained from sources being farther away, geotextile reinforcement becomes economically advantageous. The economic influence of the resilient modulus of geotextile can hardly assessed, since it means both higher purchase cost and higher replacement potential. The quotation of the cases where geotextile reinforced pavements are cost effective can not be farther described, since the result depends on each specific data set.

Woven geotextiles possess much higher resilient modulus and are simultaneously more expensive. It would have been interesting to evaluate the cost efficiency of their application on the base that they, obviously, could replace a thicker layer of aggregates. However, the amount of bond that a geotextile can develop with the surrounding soil sets limits to the exploitation of very high modulus. In relevant full scale trials slip surfaces evidently developed for large deformations. It is accepted (Palmeira and Cunha 1993) that, in the long term, the use of a highly frictional medium modulus (like non-woven geotextiles) reinforcements may be capable of producing greater overall cost savings than the use of high modulus geotextiles.

#### 4 CONCLUSIONS

The main conclusion drawn is that the cost implications of geotextile inclusion in pavements depend on the specific conditions of each project. In general, the thickness of the unbound subbase, which the geotextile could replace, costs as much as the supply and application of the geotextile itself, provided that a non-woven product is selected. Woven geotextiles present certain problems which, combined with their higher supply cost, make their application rather expensive.

The most important parameter affecting the economic analysis is the load-deformation behavior of the subgrade. As the subgrade becomes softer the geotextile inclusion solution becomes cost-effective. Availability of acceptable aggregate material is the next important parameter. The economic influence of the resilient modulus of geotextile can be hardly assessed, since it means both higher purchase cost and higher replacement potential.

It should be mentioned that the analysis is limited in the direct construction cost elements of the pavement. If other indirect savings and conveniences, such as providing a more solid roadbed, a shorter construction time, facilitation in construction methods, savings in maintenance and vehicle operating costs, increased factors of safety, acceptability of marginal materials, were included in the analysis, the economic supremacy of geotextile reinforced pavements over weak subgrades is expected to become evident.

#### ACKNOWLEDGEMENTS

The author is indebted to KEDE (Central Laboratory of the Ministry of Public Works) which supported the experimental procedure providing the necessary equipment and personnel. The author also wants to express its gratitude to the Civil Engineering Laboratories of the Aristotle University of Thessaloniki in which a series of experiments have also been performed.

#### REFERENCES

- Douglas, R.A. and Valsangar, A.J. (1991) "Unpaved Geosynthetic Built Resource Access Roads: *Stiffness* Rather than *Rut Depth* as a Key Design Criterion", *Geotextiles and Geomembranes*, No. 10, Elsevier Science Limited, pp. 45-59.
- Espinoza, R.D. (1994) "Soil-Geotextile Interaction: Evaluation of Membrane Support", *Geotextiles and Geomembranes*, No. 13, Elsevier Science Limited, pp. 281-293.
- Kokkalis, A.G. and Papacharisis, N. (1989) "A Simple Laboratory Method to Determine In-Soil Behavior of

- Geotextiles", *Geotextiles and Geomembranes*, No. 8, Elsevier Science Limited, pp. 281-293.
- Kokkalis, A.G. (1990) "A Theoretical and Experimental Approach to the Reinforcement of Secondary Roads", Ph.D. Thesis, *Aristotle University of Thessaloniki, Civil Engineering Department*, Thessaloniki, Greece, 560 p.
- Little, P.H. (1992) "A Review of Two European Design Methods for Geotextile Reinforced Unpaved Roads", *Highways and Transportation*, Vol. 39, No. 8, Institution of Highways and Transportation, England, pp. 19-22.
- Milligan, G.W.E., Jewel, R.A., Houlby, G.T. and Burd, H.T. (1989) "A New Approach to the Design of Unpaved Roads", *Ground Engineering*, April, pp. 25-29.
- Nikou, N. (1988) "A Proposal for Forest Roads Design Standards", Ph.D. Thesis, *Aristotle University of Thessaloniki, Civil Engineering Department*, Thessaloniki, Greece, 560 p.
- Palmeira, E.M. and Cunha, M.G. (1993) "A Study of the Mechanics of Unpaved Roads with Reference to the Effects of Surface Maintenance", *Geotextiles and Geomembranes*, No. 12, Elsevier Science Limited, pp. 109-131.
- Sellmeijer, J.B. (1990) "Design of Geotextile Reinforced Paved Roads and Parking Areas", *Forth International Conference on Geotextiles, Geomembranes and Related Products*, The Hague, Volume 1, pp. 177-182.
- Sellmeijer, J.B. (1993) "MGEO: A Low-Volume Road Designer", *Geotextiles and Geomembranes*, No. 12, Elsevier Science Limited, pp. 471-477.
- Snath, M.S., McMullen, D., Freer-Hewish, R.J. and Shein, A. (1980) "Flexible Pavement Analysis", Final Technical Report, *European Research Office*, Grant No DAERO-78-G-125, 203p.

# A Study on Preventing And Repairing Road Frost Boiling by Applying Geotextile in Daqing Area

Jingan Cao

General Engineer, Daqing Oil Field Construction Design And Research Institute, Daqing, Heilongjiang Province, China

Zizhong Huang

Civil Engineer, Daqing Oil Field Construction Design And Research Institute, Daqing, Heilongjiang Province, China

Diangou Zhao

Engineer, Road Engineering Corporation of Daqing Oil Administration Bureau, Daqing, Heilongjiang Province, China

Jing Dai

Engineer, Road Engineering Corporation of Daqing Oil Administration Bureau, Daqing, Heilongjiang Province, China

**ABSTRACT:** This paper reports on the achievements in test research of applying needle-punched geotextile to prevent and repair road frost boiling and its application and dissemination in Daqing. The indoor simulated tests and outdoor road repairing tests have been begun since 1990. By these tests and analysis of gained data, the key technical question for preventing and repairing the road frost boiling have been solved and a complete set of design and construction methods also have been summed up. Theory and facts have proved that it is the ideal method by applying geotextile to prevent and repair road frost boiling in the seasonal freezing zone. This method is convenient for construction, excellent effect and notable economic and social benefits.

**KEYWORDS:** Freeze/thaw Behavior, Geotextiles, Geomembranes, Road Construction, Separation

## 1 INTRODUCTION

Daqing Oil Field is situated in the middle of Songnen plain in China, which is a seasonal freezing zone. During spring thawing period, under harmful factors, frost boiling becomes so severe that about 20 km road needs to be repaired in Daqing annually.

Many methods were tried to prevent and repair road frost boiling for many years, but its effects are all unsatisfactory. In 1990, a new way was found for preventing and repairing road frost boiling, which is to employ geotextile. Facts have proved that it is of excellent effect and notable economic benefit to apply geotextile to prevent and repair road frost boiling.

## 2 REASONS AND PREVENTIVE METHOD OF ROAD FROST BOILING

Road frost boiling is a peculiar phenomenon in the seasonal freezing zone. Frost effect increases the water content in subgrade in winter, and the extra water can not be drained off during spring thawing period, which makes subgrade be over-moistured, and reduces its load-bearing capacity. Under the load of running trucks, there appears springing, chapping, bulging and mud pouring, then the whole road is destroyed.

Frost boiling results from the comprehensive effect of 5 factors such as water, soil, temperature, pavement, and the load of running trucks. According to several years experience on repairing road frost boiling, it is believed that water is the major factor of 5 factors. In Daqing the water in the subgrade mainly comes from underground water, so the key of preventing road frost boiling is to cut off the ascent of

capillary underground water. In order to solve this problem, the test research of applying geosynthetics to prevent and repair road frost boiling was carried out.

## 3 INDOOR TESTS

Two kinds of material, geotextile and geomembrane, were used in the indoor tests.

### 3.1 Separating Water and Isolated Heat Tests

The selected soil sample was a clay with medium liquid limit, a typical soil in Daqing. Its water content was 18.5% and its dry density before test was  $1.68 \text{ g/cm}^3$ . The soil sample was put into five round freezing containers (shown in Figure 1). Then the freezing containers were sent into

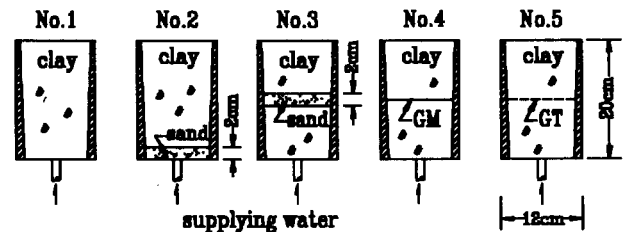


Figure 1. Sample model type.

freeze room. The samples were froze from the top of freezing containers while supplying enough water to the bottom of samples. Freezing continued 310 hours simulating the soil sample's natural state. At last, the test ended when the

whole samples were frozen. All the measured data is listed in Table 1.

Table 1. The measured data of sample.

Content	Sample for comparison			Geo-memb	Geo-textile
	No.1	No.2	No.3	No.4	No.5
Measured value					
Frost heaving amount (mm)					
Upper 10cm	9.0	11.7	11.6	3.4	1.7
Under 10cm	17.1	12.8	8.1	14.9	12.0
Water content after freezing (%)					
Upper 10cm	26.6	26.6	20.5	13.9	16.7
Under 10cm	29.9	31.6	27.8	34.8	30.8
Temperature in the middle of samples (°C)					
At the beginning	12.7	12.8	13.0	A.M.132 B.M.137	A.T.12.5 B.T.13.6
Temperature at top is -1	1.4	1.4	1.1	A.M.-1.1 B.M.-1.5	A.T.1.1 B.T.2.0
Air temperature is -9	-3.5	-3.2	-2.7	A.M.-2.1 B.M.-0.9	A.T.-2.6 B.T.-1.0
At the end of test	-1.0	-1.7	-1.1	A.M.-1.1 B.M.-0.8	A.T.-1.1 B.T.-0.8

Note: A.M. is the abbreviation for above the membrane; B.M. is the abbreviation for below the membrane; A.T. is the abbreviation for above the textile; B.T. is the abbreviation for below the membrane.

From Table 1 it can be seen that, after freezing under the condition of saturation water, the water content of the upper layer soil sample in container No. 4 and 5 is evidently less than that of the samples for comparison, and the frost heaving amount decreases more than 60%, while the temperature under the geomembrane and the geotextile is clearly higher than that of samples for comparison. Therefore, geomembrane and geotextile are rather effective to separate water, and geotextile can particularly isolate heat to a certain degree.

### 3.2 Freeze-thaw Resistance and Corrosion Resistance Tests

A freeze -thaw test was carried out under the temperature from -20 °C to 10 °C. After dipped into water, polyester geotextile was made to undergo 300 freeze-thaw cycles. Its tensile strength only decreased 21% as much as the original tensile strength, which mean polyester is good at freeze-thaw resistance.

In the corrosion resistance test(resisting acid and alkali), the polyester geotextile was soaked into the water solution of different pH values, and measured its strength which is listed in Table 2. The polyester textile was also dug out, which was buried in soil (pH = 9) for two years, and its

measured strength only decreased 1.9%. The above tests proved that the polyester textile has a certain corrosion resistance .

Table 2. Measured strength of polyester textile in corrosion resistance test.

Soaking time (days)	pH value				
	1.54	4.24	7.00	9.26	11.81
Tensile strength (N/5 cm)					
90	775	877	805	786	723
180	738	795	787	786	649
Strength decrease after 180 days (%)					
	7.8	0.7	1.7	1.9	19.0

Notes: The original tensile strength of geotextile (500 g/m<sup>2</sup>) is 801 N/5 cm.

## 4 TEST ROAD

The test road section is on an Oil Field main line which is 10 m wide in subgrade and 7 m wide on bituminous concrete pavement. Most of the road sections are wet or overwet because of the high underground water level and the water beside the road all the year. Moreover, a busy traffic of heavy trucks can be found on the road. There was always frost boiling since the road was built up in 1984. Up to 1989, the severe frost boiling stopped traffic. It was determined to repair this road thoroughly and to build a test road in the road section where frost boiling was most severe. The test road was began to build in June 1990, and was completed in July. To meet test conditions, there was no drain beside the road, and the height of subgrade embankment was less than the standard so that the road was over-wet.

### 4.1 Test Plans

In view of the reason of road frost boiling, three tests by sealing, separating and replacement were carried out.

#### 4.1.1 Sealing in this plan

Ice gathering zone in subgrade was wrapped with impermeable geomembrane in order to form a water-tight zone for water in the vertical direction, to protect this zone from water on the ground, to cut off the ascent of capillary underground water, to cut down the height of ice gathering zone, to lighten the freeze and subsidence of subgrade, to improve the whole strength of subgrade and prevent frost boiling.

#### 4.1.2 Separation in this plan

Separation, drain filtration and reinforcement characteristics of the geotextile were introduced to prevent road from frost boiling.

During spring thawing period, the water content of the subgrade is high and the strength is low. Under the repeat-

edly load of running trucks, base course material is easily pressed into the subgrade soil, while the mud is easily squeezed upwards. With these two acting together, then there appears frost boiling. After geotextile has being laid, there is no frost boiling. Having dug the road, it can be seen that base course material does not mix with the subgrade soil. It is the geotextile that plays the role of separation.

The test road was dug to be observed the water content of subgrade soil during spring thawing period. The result is there was less ice grains in the soil above geotextile than below it, and the water content in the latter was 1.1 times that of the former. Both indoor test and field observation prove that geotextile can cut off the ascent of capillary underground water from positive temperature zones to negative temperature zones.

Geotextile can drain water away in both vertical and horizontal directions. The measured coefficient of permeability of the soil and the geotextile in the test road were respectively  $1.98 \times 10^{-4}$  cm/s and  $5.5 \times 10^{-1}$  cm/s, the latter being more than 2700 times of the former. Thus water can be drained away along the cross slope through geotextile when the water content of the soil below the geotextile is high. In addition, geotextile laid between structural layers and it can bear load together with road surface and subgrade, and spread stress. Therefore, geotextile reinforces the road.

#### 4.1.3 Replacement method

Replacement method, an usual method, is to replace the frozen subgrade soil with non-freeze or weak freeze material in order to reduce the water content of the subgrade, prevent subgrade from freezing and subsiding, keep the stability of subgrade and protect road from frost boiling.

#### 4.2 Sections of Test Road and Pavement Structure

Based on the severity and contrast condition, the 550 m long test road was equally divided into 11 sections in which 4 sections were for sealing test, 4 sections for separating test and the other for replacement test.

The pavement structure was designed along with the 3<sup>rd</sup> class road standard. The structural composition and thickness were determined referring to the requirement of strength and freeze-thaw resistance, see Table 3.

#### 4.3 The Selection of Geosynthetics

##### 4.3.1 Geomembrane

The geomembrane is made of polyvinyl chloride(PVC), whose density is 200 g/m<sup>2</sup>.

##### 4.3.2 Geotextile

The selection of the geotextile is the key of the separating plan. Geotextile should play roles of separation, drainage, filtration and reinforcement, so its effective opening size(EOS) and strength are very important.

Table 3. Test road pavement structure.

Thickness of the base course	Structural type						
	Sealing		Separation		Replacing embankment		
	I-1 (cm)	I-2 (cm)	II-1 (cm)	II-2 (cm)	III-1 (cm)	III-2 (cm)	III-3 (cm)
Slag lime soil	15	15	20	15	20	20	20
Gravel lime soil	-	-	-	-	15	15	-
Lime soil	15	15	30	15	20	40	30
Soil wrapped by geo-membrane	20	40	-	-	-	-	-
Soil	-	-	-	30	-	-	-
Geotextile	-	-	One layer		-	-	-
Sand and gravel	-	-	-	-	20	-	-

Note: The road surface course is 9 cm thick bituminous concrete; the allowable rebound deflection of pavement is 0.57 mm (The standard axial loading is 60 kN).

The mechanism of separation is similar to filtration mechanism in irrigation works, requiring the effective opening size of geotextile matches the grain diameter of subgrade soil in order to protect soil from capillary rising and drain water off without blocking. Then the following formulation should be satisfied:

$$d_{15} < O_{90} < d_{85} \quad (1)$$

where:  $O_{90}$ , the effective opening size of geotextile;  $d_{15}$  and  $d_{85}$  are respectively diameter of protected soil grain with 85% and 15% passing on standard screen.

Strength according to reference, the tensile strength should satisfy following formulation:

$$0.75 < \frac{\text{transverse tensile strength}}{\text{longitudinal tensile strength}} < 1.25 \quad (2)$$

The selected geotextile should meet strength requirements, and should be durable enough to resist aging and erosion by acid and alkali. Considering the widespread saline soil in Daqing, on the basis of indoor tests, field observation and relevant references on polyester geotextile, the polyester geotextile was selected as working geosynthetics.

#### 4.4 The Determination of Location of Geosynthetics

Another key in both sealing and separating plans is to determine the location of the geomembrane and geotextile in the road cross section. We believe geosynthetics should be laid in the place with the most water content in the subgrade. Referring to the geological reference, the location is 0.6~0.8 m below the road surface, which was also proved by field test. The detailed direction in construction is shown in Figure 2.

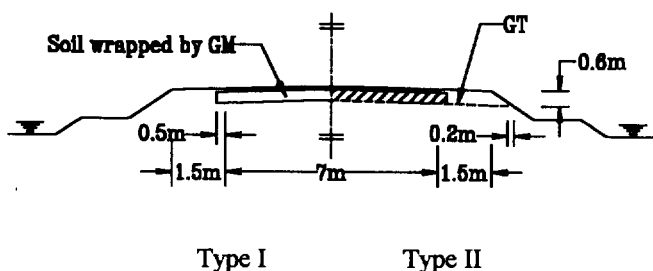


Figure 2. Road cross-sectional profile.

## 5 TEST EFFECT AND ECONOMIC BENEFIT

### 5.1 Test Effect

From the completion of the test road up to the end of 1996, most of the sections worked well except some damaged parts of the road surface on a few sections of sealing plan, though the real traffic volume was 45% more than the designed traffic volume. Since this road was built, two year systematic observation and three year detailed observation on road surface strength, evenness, crack, freeze-thaw, subgrade water content and freeze depth at 527 observing places have been carried out, and more than 20,000 data have been obtained. The measured rebound deflection during spring thawing period which is one of the major effect factors on the road, is listed in Table 4.

Table 4. The measured rebound deflection of road surface.

Type	III-1	II-1	I-2
Mileage	250m~300m	300m~350m	350m~400m
	(mm)	(mm)	(mm)
1990 Oct.	0.094	0.129	0.160
1991 Apr.	0.395	0.352	0.481
1992 Apr.	0.391	0.418	0.556
1993 May	0.350	0.378	0.556
1994 Apr.	0.365	0.509	0.793
1995 May	0.409	0.545	0.973
1996 May	0.388	0.494	0.845

The sealing plan resulted in a low road surface strength and a large rebound deflection, which were far from the design requirement. Especially the rebound deflection of type I-1 road section during spring thawing period in 1994 reached 1.1 mm, and a 5 m<sup>2</sup> local part on road surface was damaged. In addition, there were many underground pipelines across road in the Oil Field. The geomembrane will be destroyed when these underground pipelines are dug out. So, the sealing plan is unsuitable for using in Daqing Oil Field.

The replacement method resulted in a thick pavement structure layer and a greater reduction of strength. The rebound deflection during spring thawing period in 1995 was 12.1% more than that in 1994. Moreover, it had a too great amount of work and too much cost (\$18 per square meter)

to be adopted.

The separating plan met the designed strength requirement with a little reduction of strength. For example, the rebound deflection during spring thawing period in 1995 was only 7% more than that in 1994. Besides, it had a thin structural layer, little amount of work, low cost (\$17 per square meter) and an excellent effect. Especially, structure of type II-1 is a structure with advanced technology and better economic benefit for preventing and improving road frost boiling in freeze area.

### 5.2 Economic Result

Referring to the settlement of test road, the separating plan saved \$1 per square meter than the replacement method. Because the test road worked effectively during the first spring thawing period after its completion, this technique was disseminated in the same year, and the construction method was improved, so \$1.3 per square meter was saved.

In the past seven years, more than 640,000 m<sup>2</sup> geotextile have been applied to 45 roads (total length 50 km), and saved \$928,000 (direct expense). Besides, because preventing road from frost boiling and avoiding detours during the construction period, the transport efficiency was improved 54%, and \$600,000 transport expense was saved annually. Therefore, both economic benefit and social benefit are notable.

## 6 CONCLUSION

Facts have proved that this is a new technique with convenient construction, excellent effect and notable economic benefit and social benefit, to apply geotextile to prevent and repair road frost boiling in severe cold area. We believe that the selection of textile and laying elevation are two keys of this technique. In Daqing, the suitable geotextile is polyester geotextile with 500 g/m<sup>2</sup>, effective opening size being 0.08~0.1mm and laying elevation usually being about 0.7 m below the road surface.

## REFERENCES

- Hong, Y.W. (1992) *Geosynthetic in Engineering Practice*, 1<sup>st</sup> Edition, Heilongjiang Provincial Hydraulic Bureau, Harbin, Heilongjiang province, China.



# Laboratory Study of the Dynamic Test System on Geogrid Reinforced Subgrade Soil

Dave Ta-Teh Chang

Associate Professor, Dept. of Civil Engineering, Chung Yuan University, Chung Li, Taiwan, R.O.C.

Wei-Jen Wang

Graduate Research Assistant, Dept. of Civil Engineering, Chung Yuan University, Chung Li, Taiwan, R.O.C.

Yao-Hung Wang

Research Assistant, Dept. of Civil Engineering, Chung Yuan University, Chung Li, Taiwan, R.O.C.

**ABSTRACT** : While geosynthetics were considered for pavement reinforcement, the R and CBR properties are no longer sufficient to govern the pavement thickness design. Resilient modulus testing has replaced static penetration testing as it more accurately simulates the in situ conditions on the pavement. Using geogrids of different types, this research studied their reinforcement effects on the subgrade, and the variation in reinforcement effects when geogrids were placed in varied depth during the application of repeated loadings. Repeated load test results show that geogrid reinforcement is highly effective as reflected in factors related to foundation stiffness and the amount of deformation associated with repeated addition of heavy loads. And it was found that improvement of the foundation stiffness is significantly related to the stiffness and initial modulus of the geogrid.

**KEYWORDS**: Bearing Capacity, Geogrids, Pavement, Reinforcement.

## 1 BACKGROUND

The function of geosynthetics in pavement reinforcement is to reduce the amount of deformation when a pavement is subject to loadings. Among various geosynthetics, geogrid is preferable for pavement reinforcement under high loadings. This is principally due to the interlocking between the geogrid and the soil. The fundamental properties of geogrid, such as light weight, resiliency, ease of installation, high modulus to strain resistance, acid resistance, and longer life span, make it an ideal geosynthetic for such applications.

Previously, the capacity of a reinforced pavement structure was determined by static penetration tests. However, the actual loadings by vehicles are dynamic, and such static tests may no longer meet today's requirements. In this study, the effects of geogrids in pavement reinforcement are examined under dynamic loadings. Dynamic tests of this type are not yet in common practice.

## 2 COEFFICIENT OF SUBGRADE REACTION

The coefficient of subgrade reaction was originally defined by Terzaghi (1955) :

$$k_s = \frac{q}{y} \quad (1)$$

in which  $k_s$  = coefficient of subgrade reaction, [KN/m<sup>3</sup>];  $q$  = uniform loadings, Kpa ;  $y$  = deformation under static pressure [m].

Coefficient of subgrade reaction is frequently applied in foundation engineering for the computation of stiffness of subgrade. Upon actual application, this coefficient needs to be calibrated as provided by Terzaghi (1955).

For cohesive soil, then

$$k_s = k_p \times \frac{A_p}{A} \quad (2)$$

For cohesionless soil, then

$$k_s = k_p \left( \frac{A+1}{2A} \right)^2 \quad (3)$$

in which  $k_p$  = coefficient of subgrade reaction derived from the test ;  $A$  = area of foundation. ;  $A_p$  = area of plate ;

When the loading plate is of rectangular shape, then

$$k_s = k_p \left( \frac{m+0.5}{1.5} \right)^2 \quad (4)$$

in which  $m$  = size of the rectangular plate =  $L/B$ .( $B$ : width of foundation)

Many indirect ways and/or empirical formula are available for calculating the coefficient of subgrade reaction. For example, from consolidation tests

$$k_s = \frac{1}{m_v \times H} \quad (5)$$

in which  $m_v$  = coefficient of volumetric compressibility ;  $H$  =  $0.5B \sim 1.0B$ .( $B$ : width of foundation), or by CBR and the like. From the above, it can be seen that size, shape and rigidity of plate, soil properties, and other variables can affect the coefficient of subgrade reaction.

### 3 BEARING CAPACITY RATIO ( BCR )

For more suitable application in pavement reinforcement design , Bearing Capacity Ratio (BCR) is then suggested by Mandal and Sah (1992) as follows :

$$BCR = \frac{q_r}{q_{ur}} \quad (6)$$

in which  $q_r$  = ultimate bearing capacity after reinforcement ;  $q_{ur}$  = ultimate bearing capacity before reinforcement.

Using this ratio, the effect of reinforcement by geosynthetics under static pressure can be determined.

### 4 MATERIALS

In this study, weathered mudstone is used to provide the soft subgrade layer for the testing. General properties of weathered mudstone are shown in Table 1.

Table 1 General properties of weathered mudstone

Properties	Values
Liquid limit, (%)	34.3
Plastic limit, (%)	21.6
Plastic Index	12.7
Maximum dry density, ( g/cm <sup>3</sup> )	1.68
Optimal Moisture Content	
O.M.C. (%)	17.5
Cohesion, (kg/cm <sup>2</sup> )	0.5
Specific Gravity	2.7
Internal friction angle	17°

The specimen was prepared using 95% compaction and a moisture content of O.M.C.+2%, to the in situ condition.

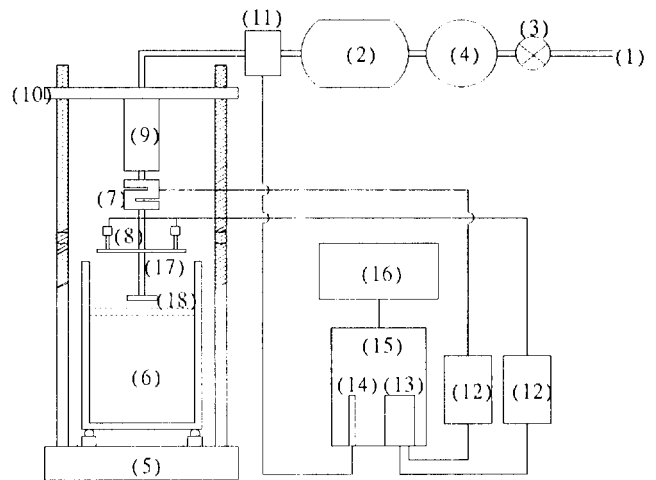
As for geosynthetics, flexible geogrids of two different strength levels are used and are identified as the H-geogrid and the L-geogrid. Their general properties are shown in Table 2 below.

Table 2 General Properties of Geogrids

	H-Geogrid	L-Geogrid
Characteristic	flexible	flexible
Material	polyester	polyester
Size of opening	2cm × 2cm	2cm × 2cm
Elongation at breaking, %	14	17
Ultimate rib strength [kN/m]	232.0	107.9
Tensile modulus [kn/m]	1657.1	634.7

Notes : Rib tensile strength test was based on the method of GRI-GG1.

### 5 TESTING SYSTEM SETUP AND PROCEDURES



(1)Pneumatic system (2)Air tank (3)Valve (4)Pressure gauge (5)Platform (6)Test box (7)Load cell (8)LVD (9)Pressure cylinder (10)Beam (11)Electromagnetic valve (12)Amplifier (13)AD/DA converter (14)Time control card (15)Computer (16)Laser printer (17) Rod (18)Loading Plate

Figure 1. Layout of test system

The testing system used in this study is arranged according to the resilient modulus testing device provided by Chang et al.(1991), and the layout is given in Figure 1. A metal box with a dimension of 0.457 m(length) × 0.457 m(width) × 0.762 m(height) is used for molding soil specimen. Newmark Charts (Newmark, N.M., 1942) were used to compute the transfer of stress below the circular plate. To enable the stress to decrease to the lowest level of 6% underneath the center of circular plate, the thickness of the soft specimen should be at least three times the width of plate. For a plate of 0.1016 m in diameter, the depth of mudstone computed in this test was 0.3 m.

To cope with the pneumatic system used in this test, plates of two different diameters 0.0508 m and 0.1016 m were used. The test was initially performed for each geogrid in four runs at 4 different embedded depths, which are 0.2, 0.4, 0.6 and 1.0 in terms of D/R (embedded depth/radius of plate).The determined best ratio was used for the rest of the tests.

AASHTO T274-82 (1983) method was followed to perform the dynamic loading with levels of 19.6(0.2), 39.2(0.4), 58.8(0.6), 78.4(0.8), 98.0(1.0), 117.6(1.2), 137.2(1.4), and 156.8(1.6) Kpa(kg/cm<sup>2</sup>). As this test is related to the study of pavement reinforcement, the typical M<sub>R</sub> Test details were followed in the selection of frequency of loading, contact interval, and loading waveform. In this case, the frequency is 0.33 Hz, the contact interval is 0.1 sec., and the loading is of triangular waveform.

## 6 RESULTS AND DISCUSSIONS

### 6.1 Effects of Stress Levels, Loading Numbers and Embedded Depth

Typical results are illustrated in Figure 2. A higher dynamic coefficient of subgrade reaction was observed under smaller stress, because smaller deformation resulted under the smaller stress. Under stress at the range between 19.6(0.2) to 117.6(1.2) Kpa(kg/cm<sup>2</sup>), the dynamic coefficient decreased abruptly. When the stress is greater than 117.6(1.2) Kpa(kg/cm<sup>2</sup>), the dynamic coefficient becomes constant. To demonstrate the trend of this curve, more tests have been performed using loading stresses of 29.4(0.3), 58.8(0.6), 88.2(0.9), 117.6(1.2), and 147.0(1.5) Kpa(kg/cm<sup>2</sup>).

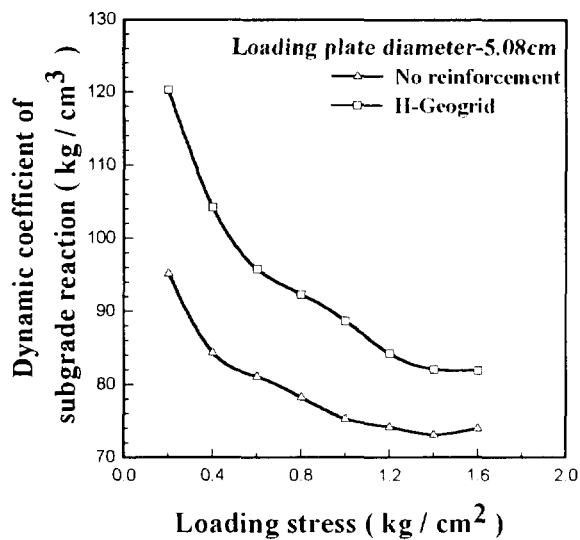


Figure 2. Responded dynamic coefficient of subgrade reaction with and without reinforcement

According to Chang et al (1991) study, in the first cycle (the first 200 loadings) of the test, the  $M_R$  values could vary in an irregular way. Several groups of tests have been conducted to verify this phenomenon, and the results are shown in Figure 3. Only H-geogrid, and 5.08cm-plate were used in these tests for determining number of loading for the rest of the program. It can be seen that during the first 200 loadings, the dynamic coefficient of subgrade reaction increases gradually, and after the first 200 loadings, the dynamic coefficient of subgrade reaction becomes stable although slight deviations are still observed. To neutralize these deviations, an averaged value was taken from loading no. 201 to loading no. 500 as the dynamic coefficient of subgrade reaction.

Regardless of whether the loadings are applied by the big plate or the small plate, during the first 200 loadings, the readings of the dynamic coefficient of subgrade reaction

increase gradually. Reasons for this phenomenon could be that: ① the plate was not in complete contact with the mudstone surface, resulting in a larger deformation at the beginning; ② repeated loadings will compact the mudstone, and when the mudstone is compacted to a certain extent, the dynamic loading stress will transfer to a lower elevation in the mudstone. After 150~200 loadings, a certain degree of compaction will result, and the coefficient of subgrade reaction becomes stable accordingly. After 200 loadings, although the coefficient curve still shows some uncertainties, generally speaking, the value is close to a constant. The occurrence of uncertainties is relatively rare in the case of a large plate. This is because the effect of uneven compaction on a large plate is insignificant in comparison to that on a small plate.

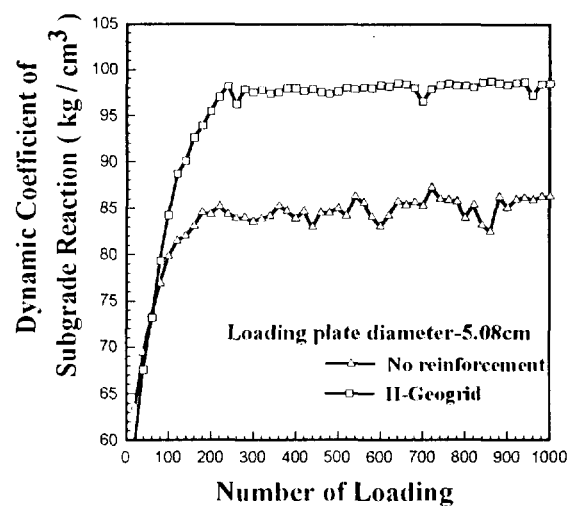


Figure 3. Significance of loading numbers for the performance

### 6.2 Effects of Geogrid Strength

Figure 4. indicates that the best reinforcement occurs when  $D/R = 0.2$ . The effects diminish for deeper embedded depth. For  $D/R \geq 0.6$ , the effect of reinforcement becomes negligible. These findings are equivalent to the studies by Mandel and Sah (1992).

A series of tests were carried out at the best embedded depth (i.e.,  $D/R = 0.2$ ), to compare the effect of reinforcement by geogrids of different mesh sizes and plates of different dimensions. Findings indicate that the strength of H-geogrids is two times that of L-geogrids; whereas the dynamic coefficient of subgrade reaction after reinforcement by H-geogrids is more or less the same as that by L-geogrids (Fig.5 and Fig.6). It could be concluded that the effect of reinforcement is not directly related to the strength of geogrids but the tensile modulus (or stiffness) of the geogrid materials.

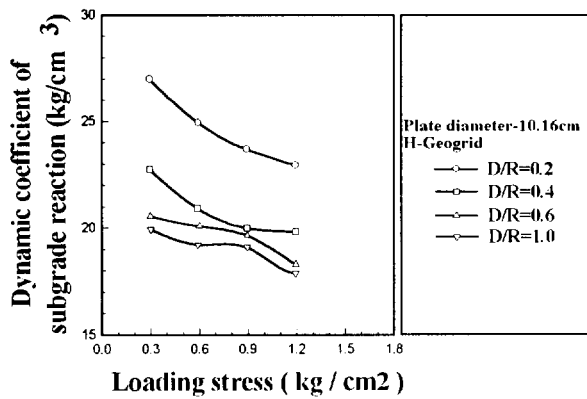


Figure 4. Effect of different embedded depth for 10.16cm diameter plate

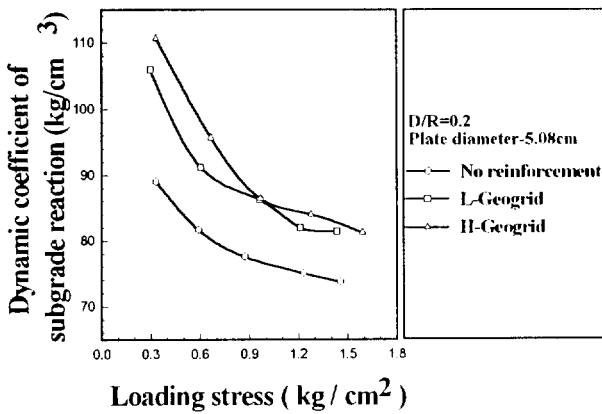


Figure 5. Dynamic coefficient of subgrade reaction with varied loading levels. (5.08cm-plate at D/R=0.2)

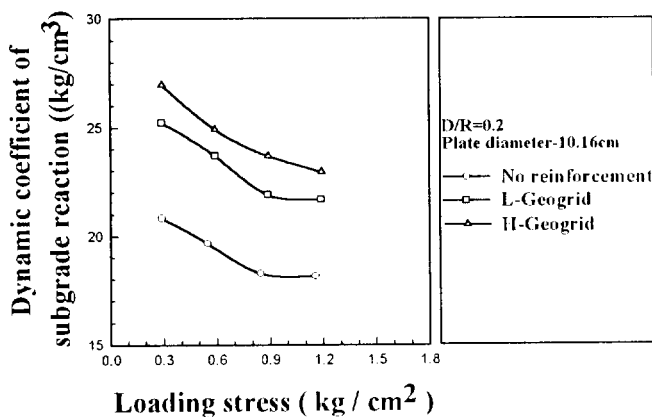


Figure 6. Dynamic coefficient of subgrade reaction with varied loading levels. (10.16cm-plate at D/R=0.2)

## 7 CONCLUSIONS

- (1) The effect of geogrids in pavement reinforcement is confirmed.
- (2) The best reinforcement occurs when  $D/R = 0.2$ . The effects diminish for deeper embedded depths. For  $D/R \geq 0.6$ , the effect of reinforcement becomes negligible.
- (3) Both the dynamic coefficient of subgrade reaction and the amount of permanent deformation can be used for the determination of the effect of reinforcement. The effect of reinforcement is not directly related to the strength of geogrids but to the stiffness of the geogrid materials.
- (4) The level of the dynamic coefficient of subgrade reaction is related to the size of the plate, deformation of geogrids, and the interface properties between geogrid and mudstone (such as interlocking, friction).

## REFERENCES

- AASHTO, "Standard Method of Test for Resilient Modulus of Subgrade Soils.", 1983, AASHTO Designation, No.T274-82.
- Chang, Dave Ta-Teh, Chen-En Chiang, and Chun-Young Chang, "Modified Testing Device to Evaluate MR Properties on Fly Ash Treated Subgrade Soil", pp 88~95, ASTM Geotechnical Testing Journal, March, 1991.
- Mandal, J. N. and Sah, H. S. , November, 1992, "Bearing Capacity Tests on Geogrid-Reinforced Clay", Geotextiles and Geomembranes.
- Newmark, N.M, 1942. "Influence Charts for Computation of Stresses in Elastic Soil". University of Illinois Engineering Experiment Station, Bulletin No.338.
- Terzaghi, "Evaluation of Coefficients of Subgrade Reaction", Geotechnique, Vol.5, pp.297~326, 1955

# Performance prediction model for asphalt overlays with geotextile interlayers on cracked pavements

R. M. Rodrigues

Associate Professor, Geotechnical Department, Instituto Tecnológico de Aeronáutica, São José dos Campos, Brazil

**ABSTRACT:** The paper presents the development of a mechanistic-empirical model for the prediction of reflective cracking on asphalt overlays with the use of a geotextile as interlayer, considering only the effect of traffic loads. The model is based on an interpretation of laboratory experimental data obtained by Majidzadeh et al (1984). The finite element method and concepts of fracture mechanics are used in this process. It is shown that different mechanisms for the reflective cracking process must be considered in function of the temperature and a proposition is made of a general model.

**KEYWORDS:** Reflective crack prevention, Pavements, Geotextiles, Finite element analysis, Asphalt overlay

## 1 INTRODUCTION

Reflective cracking in asphalt concrete overlays placed over cracked or jointed pavements is a major concern for design. The interface between the overlay and the cracked pavement is the best place to apply remedial measures, since it is at this location that the controlling stresses for the reflective cracking process occur. Geotextile-asphalt interlayers are an effective solution but a comprehensive design method is still lacking for cost-benefit evaluations. A model is suggested for practical application and it is the result of a mechanistic interpretation of laboratory test data obtained by Majidzadeh et al (1984).

## 2 EXPERIMENTAL DATA

Majidzadeh et al (1984) conducted repeated load tests on beams supported by elastic foundation (Figure 1) with the purpose of evaluating reflective cracking life of asphalt concrete overlays applied over cracked pavements. They performed tests with and without the presence of an asphalt impregnated geotextile membrane interlayer placed between the overlay and the cracked asphalt concrete (AC) or Portland cement concrete (PCC) layer. Tests were performed at two temperatures (4.4°C and 22.2°C). The asphalt concrete mix was a FAA P-401 with 5.9% in weight of AC-20 asphalt and 3.4% air voids. The existing crack was sawed to a width of 3.2 mm. Several combinations of layer thickness ( $h_1$ ,  $h_2$ ) and applied surface vertical pressure ( $q$ ) were considered for each test configuration. Three geotextiles were considered and designated as being of low, medium and high tensile moduli. The performance of these geotextiles on the increase of reflective cracking life was nearly the same, with a slightly greater beneficial effect with the ones of higher moduli. For this reason, the analysis here performed employed the average of the test results for all geotextiles considered. According to Majidzadeh et al (1984), this result would be a consequence of the asphalt impregnation with different rates (from 0.3 to 0.9 l/m<sup>2</sup>) of the three geotextiles, which tended to saturate them, leading to a more uniform behavior.

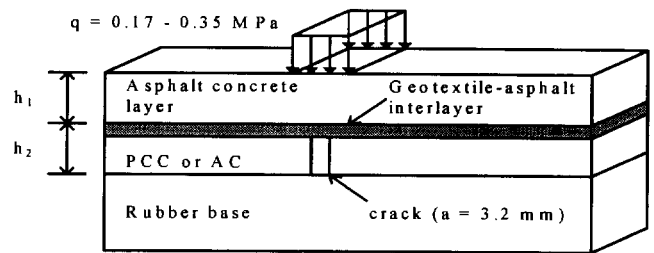


Figure 1. The experiment of Majidzadeh et al (1984).

## 3 ANALYSIS OF TEST RESULTS

Two dimensional finite element modeling (plane stress) was employed in the simulation of the test configuration of Figure 1. Only standard constant strain triangle elements were utilized for all materials, with a special mesh refinement at the crack tip. Each analysis had the objective of evaluating the stress state at the critical point in the asphalt concrete overlay. This point is situated immediately above the existing crack, on the underside of the overlay. The parameter chosen for this evaluation was the distortion energy density ( $U_d$ ), which includes only the strain energy due to shear, leaving out the volumetric strains, since these latter strains are not related to fatigue cracking. Besides, this parameter is known to be less susceptible to suffer inaccuracies in the finite element method, when compared to stresses or strains. For these analyses, the asphalt-geotextile membrane interlayer was not included on the finite element mesh. So, even in the tests where the geotextile was present, the calculated values of  $U_d$  referred to a situation where the overlay was placed without the geotextile. The observed number of load cycles to a complete reflection of the crack ( $N_f$ ) was correlated with the calculated values of  $U_d$  by:

$$N_f = A \left( \frac{1}{U_d} \right)^B \quad (1)$$

where A and B are material constants.

It was also analyzed the possible effect of the inclusion on this regression of the overlay thickness ( $h_1$ ), in the form:

$$N_f = A \left( \frac{1}{U_d} \right)^B h_1^C \quad (2)$$

Regression results are shown on Tables 1 and 2, together with the coefficient of determination ( $r^2$ ) and the standard error of estimate (s). It can be seen that parameter  $U_d$  is strongly correlated with reflective cracking, independently of support conditions, applied load and overlay thickness. Besides, for  $T=22.2^\circ\text{C}$  the inclusion of  $h_1$  on the regression was significantly beneficial, while for  $T=4.4^\circ\text{C}$  that is not the case. At  $4.4^\circ\text{C}$  the correlation between  $N_f$  and  $U_d$  is stronger than at  $22.2^\circ\text{C}$  and, for this latter temperature, it is highly desirable to include  $h_1$  on the model. So, while  $U_d$  alone is sufficient to explain reflective cracking at  $4.4^\circ\text{C}$ , there is an effect at  $22.2^\circ\text{C}$  that is controlled by  $h_1$ . A possible interpretation for these results is that there is a stable crack progression through the overlay thickness with load repetitions after the occurrence of fracture at the bottom of layer, for the temperature of  $22.2^\circ\text{C}$ . At  $4.4^\circ\text{C}$  the asphalt concrete mixture would be a fragile material, making the crack progression to be of little importance in relation to the period necessary for fracture beginning at the critical point.

The inclusion of a geotextile-asphalt interlayer significantly increases reflective cracking life, specially for the lower temperature, as indicated by parameter A. At  $4.4^\circ\text{C}$  the influence of  $U_d$  on  $N_f$  is strongly affected by the inclusion of the geotextile interlayer, since the inclination of the  $\log U_d \times \log N_f$  line changes from 1.883 to 0.8589. It is impossible, therefore, to consider geotextile action as of a Stress Absorbing Membrane Interlayer (SAMI) type, since there would not be a well defined reduction factor that could be applied to the calculated values of  $U_d$  for the case of overlay without geotextile in order to predict the greater reflective cracking life with the inclusion of the membrane. A definition of such reduction factor would require, instead, the use of a reduction function (a reduction factor varying with  $U_d$ ), implying in a non linear SAMI action. This hypothesis must, however, be discarded, in light of the excellent correlation observed between  $N_f$  and the  $U_d$  values calculated without the inclusion of the geotextile interlayer on the finite element analyses.

Table 1. Overlay without geotextile interlayer (9 points).

	T = 4.4°C		T = 22.2°C	
	Eq. (1)	Eq. (2)	Eq. (1)	Eq. (2)
A	4.3616	9.2624	8.765	0.1514
B	1.883	2.119	2.051	1.8048
C	-----	-0.9074	-----	2.732
$r^2$	0.851	0.874	0.784	0.957
s	0.4606	0.4906	0.6413	0.3095

Table 2. Overlay with geotextile interlayer (6 points).

	T = 4.4°C		T = 22.2°C	
	Eq. (1)	Eq. (2)	Eq. (1)	Eq. (2)
A	$1.178 \times 10^4$	$1.307 \times 10^4$	15.87	0.2356
B	0.8589	0.8796	2.4193	1.6227
C	-----	-0.0967	-----	3.6547
$r^2$	0.964	0.965	0.728	0.874
s	0.1291	0.1476	0.871	0.641

#### 4 OVERLAY WITHOUT GEOTEXTILE

Several studies have shown the validity of Paris' law for fatigue cracking prediction on asphalt concrete (Luther et al 1976). According to this law, crack progression can be predicted by a model of the form:

$$\frac{dc}{dN} = aK_1^b \quad (3)$$

where  $c$  is the crack length,  $N$  is the number of cycles of the stress intensity factor  $K_1$ , and  $a$  and  $b$  are material properties. The stress intensity factor is a parameter that describes the stress field in the vicinity of a crack tip.

The irregular path followed by a crack that goes around aggregate particles puts doubts, however, as to the relevance of stress intensity factors calculations on this so heterogeneous material. The crack progression could be viewed, maybe, as a sequence of discrete ruptures of aggregate particles bonds along this irregular path. Besides, the results on Tables 1 and 2 indicate that reflective cracking life is controlled, to a high degree, by the distortion energy applied at the critical point on the underside of the overlay. Combining these two arguments, one could describe the process of consisting of two stages. During the first one, there would be happening the fracture under repeated loads of the aggregate bonds at the critical location. Conventional fatigue laws under controlled stress would be sufficient to predict duration of this stage. Tensile strength of the asphalt concrete is the major controlling factor in this case. The fracture occurrence would imply in the rupture of bonds of aggregate particles on the critical location and an initial length for this original crack would be on the order of magnitude of the maximum particle diameter ( $\phi_{max}$ ). After this, there begins a new mechanism where the crack thus formed serves as a means to redirection the dissipated energy to the formation of new free surfaces, resulting on the extension of the crack. A low speed for crack progression depends on the ability of the material to dissipate strain energy through plastic distortion rather than through formation of new free surfaces at the crack tip. Therefore, a fragile material will have a faster crack progression than a more ductile one.

These considerations can be expressed by the following model:

$$N_f = N_0 (1 + F_{PT})^\beta \quad (4)$$

$$F_{PT} = \alpha (h_1 - \phi_{max}) \quad (5)$$

$$N_0 = M \left( \frac{1}{U_d} \right)^{n/2} \quad (6)$$

where:  $N_0$  = number of load cycles for the fracture on the critical location of the overlay, where the distortion energy density is equal to  $U_d$ ;  $F_{PT}$  = crack progression factor ( $\geq 0$ );  $\alpha$  = mixture parameter related to crack progression under repeated loads;  $M$  and  $n$  = fatigue parameters of the asphalt concrete mixture.

This model implies in the fact that crack reflection life ( $N_f$ ) is controlled by the fatigue life of the critical region on the underside of the asphalt concrete layer ( $N_0$ ), and that the formed crack must propagate through the entire overlay thickness ( $h_1$ ) from the initial fracture, whose length is of the order of magnitude of  $\phi_{max}$ . Crack speed progression is controlled by parameter  $\alpha$ , which is equal to zero when the material has a fragile behavior and increases from zero as the material becomes of a visco-elasto-plastic nature. If  $\alpha=0$  (crack propagation is unstable) the value of  $\beta$  has not any influence on  $N_f$ , but if  $\alpha > 0$  the value of  $\beta$  will influence crack reflection life. Therefore,  $\beta$  is related to the stable crack progression process and has the meaning of a fracture material parameter, in the same sense as with the fracture parameters of Paris' Law.

Parameters  $M$  and  $n$  of equation (6) must be determined from stress controlled bending fatigue tests, which are well known to represent fracture formation at the critical zone and do not incorporate significant crack propagation effects. From analysis of several tests of this kind, the following relations can be stated:

$$N_0 = K \left( \frac{1}{\varepsilon} \right)^n \quad (7)$$

$$n = 1.813 - 0.1046 \log_e K \quad (8)$$

where  $\varepsilon$  is the maximum tensile strain applied. Parameter  $n$  must be measured in repeated load or creep tests and parameter  $K$  can be calculated by equation (8). In the state of pure bending the following relation is valid:

$$\varepsilon = \left[ \frac{3U_d}{E_R (1 + \nu)} \right]^{1/2} \quad (9)$$

where  $E_R$  is the resilient modulus and  $\nu$  is the Poisson's ratio. For the asphalt concrete employed, values of  $E_R$  are 10545 MPa at 4.4 °C and 3515 MPa at 22.2°C. Poisson's ratio was not measured and a typical value of 0.33 was adopted, as is usual in pavement analysis.

Therefore, the following correspondence can be established between equations (6) and (7):

$$M = K \left[ \frac{E_R (1 + \nu)}{3} \right]^{n/2} \quad (10)$$

Applying this relation to the values of  $M$  determined by regression of data from tests at 4.4°C without geotextile (Table 1, equation 1), results:  $K = 6.8273 \times 10^{-9}$  and  $n=3.77$ . Substituting this value of  $K$  on equation (8) the predicted value for  $n$  is 3.78, which is nearly the same value determined from regression. This implies that  $\alpha = 0$  for  $T=4.4^\circ\text{C}$ . At this temperature the asphalt concrete mixture is, as expected, a fragile material.

Considering now the experimental data for  $T=22.2^\circ\text{C}$  and overlay without geotextile, the fitting of the model was done varying  $\alpha$  as the basic parameter and determining  $M$ ,  $n$  and  $\beta$  by linear regression analysis. For any fixed value of  $\alpha$  the model adjustment to the experimental data is the same ( $r^2=0.957$  and  $s = 0.3095$ ). The absolute error of estimate is the same as for the direct regression of equation (2). Results are shown on Table 3 where it can be seen that exponent  $n$  of the fatigue law is the same for all values of  $\alpha$  and equal to 3.61. Only for  $\alpha = 0.143$  there is agreement between the value of  $M$  predicted by equations (8) and (10) and the value of  $M$  determined by regression to the experimental data, as can be seen at the rightmost column of Table 3. The resulting value of  $\beta$  is equal to 5.246.

Table 3 - Model fitting for  $T = 22.2^\circ\text{C}$ .

$\alpha$	$M$	$n$	$\beta$	$K (\times 10^{-8})$	$K(\text{eq. 8})/K$
0.100	1.544	3.61	6.561	4.0731	1.178
0.120	1.428	3.61	5.833	3.7673	1.089
0.143	1.313	3.61	5.246	3.4587	1.000
0.150	1.278	3.61	5.103	3.3725	0.975
0.200	1.078	3.61	4.373	2.8446	0.822
0.500	0.494	3.61	3.054	1.3036	0.377

## 5 GEOTEXTILE EFFECT

The model for overlay without geotextile can be applied to help in the interpretation of the data for the tests with geotextile. The increase in reflective cracking life due to the geotextile inclusion is given by:

$$\Delta N = N_f - N_{OV} \quad (11)$$

where  $N_f$  is the reflective cracking life with geotextile and  $N_{OV}$  is the predicted reflective cracking life for the overlay without geotextile, as given by equation (4). Figure 2 shows the calculated values of  $\Delta N$  for the tests conducted by Majidzadeh et al (1984), where it can be seen a clear dependence of  $\Delta N$  with  $U_d$ , the distortion energy density at the crack tip on the overlay calculated without the inclusion of the geotextile.

There is a trend for convergence for low values of  $U_d$  of the relations between  $\Delta N$  and  $U_d$  for the two temperatures considered, allowing the proposition of the following model:

$$\Delta N = 5.0 \times 10^5 \left( \frac{U_d}{1 \text{ kPa}} \right)^\xi \quad (12)$$

where:  $\xi = -0.677$  for  $T = 4.4^\circ\text{C}$  (with mean error of 16 %) and  $\xi = -2.10$  for  $T = 22.2^\circ\text{C}$  (with mean error of 27 %).

There are several experimental evidences showing that extension of reflective cracking life with the inclusion of geotextiles is a consequence of a crack arrest process, in which dissipated energy is deviated from the formation of new free surfaces at the critical zone on the overlay to propagation of a horizontal crack at the geotextile-pavement interface (Montestruque 1996). In this way, the possibility of writing equation (12) as an expression of experimental data would be a result from a stable horizontal crack progression, which could be described by a law analogous to Paris' Law:

$$\frac{dl}{dN} = AU_d^B \quad (13)$$

where  $l$  is the horizontal crack length, and  $A$  and  $B$  are fracture parameters for the geotextile-pavement bond. This hypothesis will be valid only if  $B > 0$ , since horizontal crack progression speed must increase with the distortion energy supply on the crack tip region. Integrating equation (13) and considering that  $U_d$  varies only slightly with horizontal crack extension (since this horizontal crack is of small length), one could write:

$$\Delta N = \frac{1}{A} \int_0^{l_{crit}} U_d^{-B} dl = \frac{l_{crit}}{A} U_d^{-B} \quad (14)$$

where  $l_{crit}$  is the critical length reached by horizontal crack, after which dissipated energy goes to the generation of new free surfaces at the crack tip on the overlay.

Comparing equations (12) and (14) one concludes that  $\xi = -B$ . Since  $\xi < 0$  the condition  $B > 0$  is satisfied, giving support to the hypothesis that increase in reflective cracking life can be interpreted as the result of a deviation of dissipated energy from the critical zone of the overlay to the

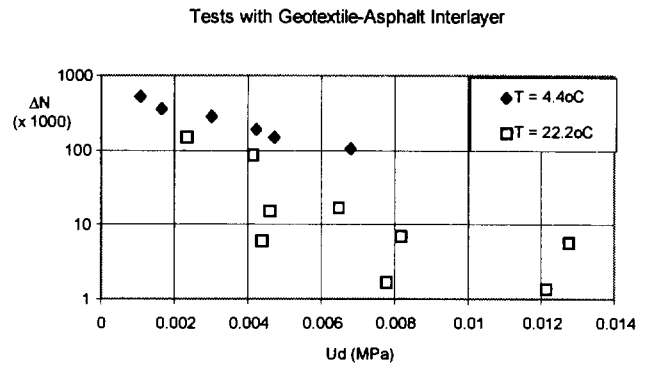


Figure 2. Increase in reflective cracking life with geotextile.

generation of a small localized rupture between geotextile and overlaid pavement. Parameter  $B$  influences the horizontal cracking process and is temperature dependent. Since the bond and the other materials involved are of asphaltic nature, this dependence is conceivable.

## 6 CONCLUSION

Reflective cracking life of asphalt overlays with the presence of an asphalt-geotextile membrane interlayer can be predicted by first estimating reflective cracking life without the interlayer (equation 4). This number of load cycles is then added to the delay predicted by equation (12). The model should be applied to field data in order to better evaluate its consistency. Material parameters relevant for the model are:  $\alpha$  (degree of fragile behavior in function of temperature),  $n$ ,  $\phi_{max}$  and  $E_R$  for the asphalt concrete, and  $\xi$  for the geotextile-pavement bond, at design temperature.

## REFERENCES

- Majidzadeh, K., Ilves, G., Sklyut, H. & Kumar, V.R. (1984) *Mechanistic Methodology for Airport Pavement Design with Engineering Fabrics. Volume I: Theoretical and Experimental Base*, Report No. DOT/FAA/PM-84/9,1, Federal Aviation Administration, Washington, D.C., USA, 161 p.
- Montestruque, G.E.V. (1996) "Estudo de Sistemas Anti-Reflexão de Trincas na Restauração de Pavimentos Asfálticos", MSc Thesis, Instituto Tecnológico de Aeronáutica, ITA, São José dos Campos, SP, Brasil, 141p.
- Luther, M.S., Majidzadeh, K. & Chang, C.W. (1976) Mechanistic Investigation of Reflection Cracking of Asphalt Overlays. *Transportation Research Record 572*, p. 111-122, TRB, Washington, D.C.



# EFFECTIVENESS OF SYNTHETIC INTERLAYERS IN BITUMINOUS PAVEMENTS

G. DONDI  
D.I.S.T.A.R.T. DEPARTMENT  
UNIVERSITY OF BOLOGNA, ITALY

## ABSTRACT

The insertion of interlayers in bituminous pavements is quite widespread, although designers tend to use a wide range of synthetic interlayers, from nonwoven low-modulus to high strength polyester geotextiles, not always on the basis of their technical properties. This paper describes the results obtained in an experimental study carried out by our Department, based upon a series of dynamic tests. In order to simulate the road pavement, full-scale square samples were employed: in a steel box, partly filled with rubber, two bituminous concrete layers with different interlayers were placed. In some specimens, deep artificial grooves were made in order to examine a damaged existing pavement. The specimens were dynamically loaded up to failure, with the aim of achieving a simulation of fatigue failure, allowing to better understand sample behaviour. Static tests were carried out at intermediate stages during the dynamic loading. The results of the reinforced specimens, in terms of displacements and rut depths, demonstrated the advantages of interlayers insertion: geosynthetics appear to be able to delay the surface cracking due to reflection of fissures from the underlying layers. Failure cracking patterns can now be reported due to the completion of laboratory experimentation. Such patterns, which may be very different in the case of overlays standing on pre-fissured bases, show the benefits of interposing geosynthetics in pavements.

**KEYWORDS:** Pavements, Fatigue, Reinforcements, Reflection, Cracking, Prevention

## 1. INTRODUCTION

One of the main problems related to the durability of road pavements is represented by surface cracking, induced by fatigue, thermic effects and underlying cracking, i.e. for rehabilitation of cobbled roads (Fig. 1).

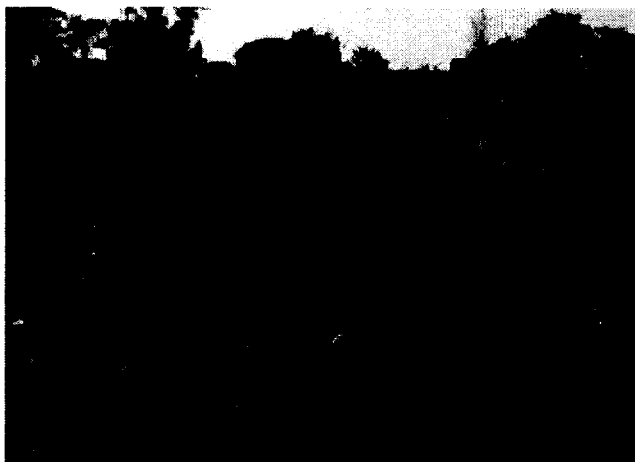


Figure 1. Cobbled surface of Via Appia, 2000 years old Roman road.

The interposition of geosynthetics as interlayers in asphalt pavements (often referred to as “reinforcement”), to prevent the mentioned phenomena, is quite widespread and has generally proved to be successful. Nevertheless, an overall accepted design method still does not exist. There are a lot of questions still pending regarding the best and worst type of interlayer (nonwoven geotextiles, geogrids, etc.), the appropriate position of installation and the opportunity of the insertion of interlayers also in new projects.

A reply has not yet been given to all these questions; however, with the laboratory experimentation described in this paper and the information obtained in situ with another experiment underway, an attempt has been made to contribute to the assessment of the behaviour of bituminous pavements containing synthetic interlayers. Only macro-reinforcement we will be considered in this article (Fig. 3); i.e., the interlayers that are well defined in the bituminous mix. This subject has already been studied in the past, from a theoretical point of view by our Department (Dondi and Righi, 1990), (Dondi, 1994) and, more recently, a large number of experiments were carried out. In an initial stage, for a preliminary static evaluation, some “three point bending” tests on asphalt beams: without interlayers (UR), with nonwoven geotextiles (GX) and with polyester (PET) geogrids (GG). Then created 24 specimens (1.4x1.4m) were created, having many different types of interlayers and degrees of disturbance (Fig. 2).

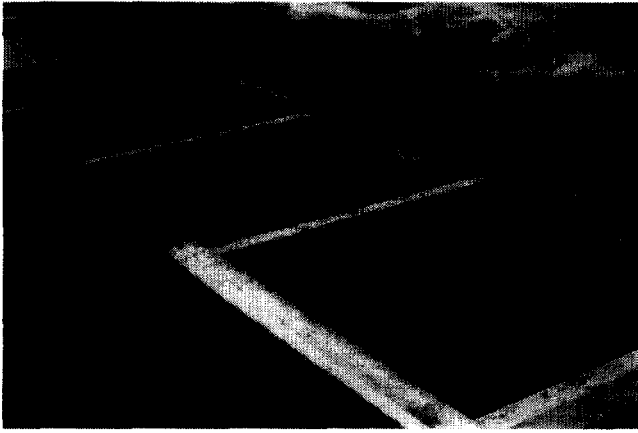


Figure 2. Sample preparation: in some, the longitudinal artificial cuttings can be seen.

It's well known that the reinforcement of asphalt requires high temperature resistant polymers: indeed, with modified binders, during compaction, the mix reaches high temperatures (140-150 °C and higher). For this reason, it was considered that the use of at least PP or PET geosynthetics would be necessary.

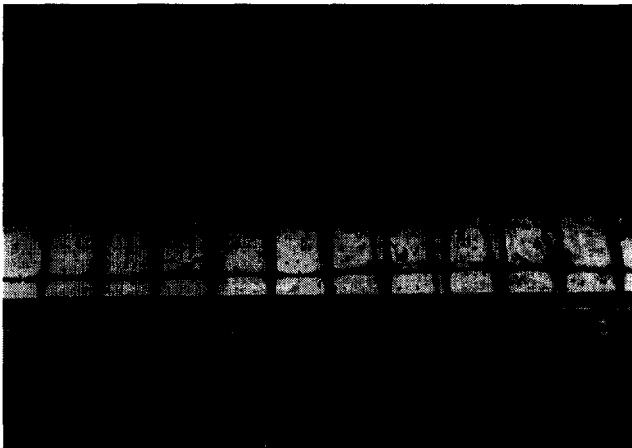


Figure 3. Detail of a polypropylene geogrid insertion in a specimen.

The insertion of nonwoven geotextiles in a flexible pavement generally causes a strength decrease, despite a better overall behaviour. For this reason, some stiffer geogrids or composites may be preferred. Furthermore, the latter theoretically appears to provide a better solution since it improves the linking with the upper bituminous layer also without any tack coat upon the interlayer surface.

## 2. PRELIMINARY PHASE

In the preliminary stage of the research, it was verified that, according to Judycki (1990), the best loading methodology

was, for many reasons, the three point bending test since stresses and strains are more realistic. The samples were 100 mm wide, 85 or 100 mm high, and 600 mm long. The interlayer, when present, was placed 35 mm over the bottom of the sample. The rate of loading was approximately 50 mm/min', as also suggested by Kunst e Kirschner (1993) and all the tests were carried out using a bituminous mix, with a 5% of 80/100 penetration grade bituminous binder.

The grain size distribution curve of the aggregate is represented in Fig. 4, with the binder fuse of the Italian National Roads Administration.

As interlayers, we employed two geosynthetics currently used for road pavements: a nonwoven polypropylene geotextile (Grab Test, ASTM D-4632: 18 kN/m,  $\epsilon_f=55\%$ ); and a polyester woven geogrid (Tensile strength: 60 kN/m). The tack coat was obtained with a cationic emulsion containing 70% of 80/100 bitumen, modified with 5 % Styrene-Butadiene-Styrene (SBS-R) modifier with radial structural arrangement.

Results showed that the most important improvement with interlayers was the increased capability of bearing high loads even after failure, i.e. a higher ductility.

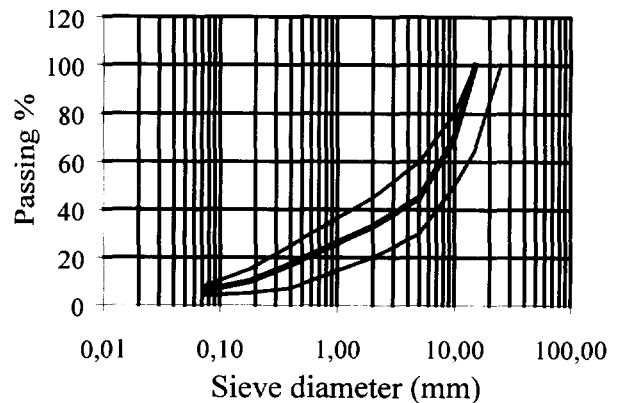


Figure 4. Grain size curve of the bituminous mix.

## 3. LABORATORY DYNAMIC TESTS

In a second stage described in this paper, we carried out more specific dynamic tests in order to better simulate traffic loads and boundary conditions (Dondi 1996). The first step of this research project consisted in a comparison of the results obtained with numerical models such as BISAR (De Jong 1973) and F.E.M. non linear models (Fig. 5), such as FENLAP (De Almeida 1993).

FENLAP is a computer program written in FORTRAN 77 language by J.R.de Almeida. This program performs a finite element calculation of an axi-symmetric solid and is designed for the structural analysis of pavements. It can run both on mainframe and on personal computers. FENLAP uses rectangular elements, distributed over a rectangular

grid. A mesh with up to 23 columns and 23 rows, corresponding to a maximum of 484 elements (22 in each direction) may be analysed. The maximum number of layer which can be considered is 5. Due to the axi-symmetry, all nodes on the left side of the mesh are assumed to be on rollers, allowing vertical displacements but preventing radial ones. For the vertical boundary on the right side and for the lower boundary, several boundary conditions may be adopted as options. Nine different material models are given as an option for the stress-strain relationships of each layer; the main models and the corresponding elastic constants follow:

- 1) Linear elastic isotropic (all type of materials): 5 parameters, vertical Young's modulus  $E$  and Poisson's ratio  $\nu$ ;
- 2) Brown's (fine grained soils): 4 parameters, initial Young's modulus  $E_1$ ,  $\nu$ ,  $A$  and  $B$ .

As non-linear models can be used in FENLAP, the program follows an iterative procedure in which the elastic properties are successively adjusted, for they depend on the values of stress computed. At each iterations, an error check is performed by comparing the new elastic moduli with the elastic ones determined in the previous iteration. If failure criteria are considered, the stresses are also compared with the values obtained in the previous iteration. When both errors fall below an admissible tolerance specified by the user, converge is said to be achieved and the iteration procedure is stopped.

In particular, we tried to establish the different behaviour of semi infinite and confined multilayered system with trial moduli. It was discovered that, in order to avoid significative boundary effects, the minimum dimension of square specimens was approximately 1.5x1.5 m.

Consequently, we created a bituminous concrete strip, approximately 36 m long, in two stages (two layers): after completion of the first one, artificial cuttings were also realised in some areas to represent the rehabilitation of a fractured pavement.

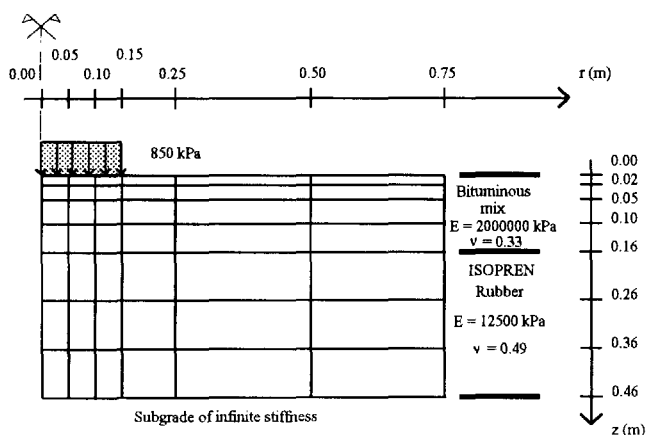


Figure 5. Numerical mesh (of the samples) for numerical analysis.

Various kinds of interlayers were then inserted; these specimens have the characteristics described in Table 1.

A steel box was then built to contain the asphalt specimens and the underlying layers (Fig. 6). The load was applied by means of a circular steel plate, with a diameter of 0.3 m standing on a rubber layer with the function of minimizing stress concentration related to plate stiffness.

To enhance only the behaviour of asphalt, and with the aim of reducing the uncertainties as much as possible, we decided to build the foundation bed with rubber.

This allows to minimise uncertainties related to resilient behaviour of granular materials and increases the reproducibility of the tests (Fig. 6).

Besides the traditional mechanical tests, other experiments were carried out in order to assess the complex modulus ( $E_c$ ) and the phase shift angle ( $\phi$ ) of the asphalt specimens.

From the laboratory results of a simple static creep test, we obtained at a temperature of 25°C:  $E_c = 800$  MPa and  $\phi = 40^\circ$ .

Table 1. Characteristics of specimens tested

a) Non Lesioned bituminous concrete (NL)
a.1) Unreinforced Specimen (UR);
a.2) Specimen with nonwoven geotextile interlayer (GX);
a.3) Specimen with bi-directional woven polyester (PET) geogrid (GG) interlayer;
a.4) Specimen with bi-directional polypropylene (PP) geogrid (RA) interlayer ;
a.5) Specimen with polypropylene (PP) geocomposite (GT=GX+GG) interlayer.
b) Lesioned bituminous concrete(LE)
b.1) Unreinforced Specimen (UR);
b.2) Specimen with nonwoven geotextile interlayer (GX);
b.3) Specimen with bi-directional woven polyester (PET) geogrid (GG) interlayer;
b.4) Specimen with bi-directional polypropylene (PP) geogrid (RA) interlayer;
b.5) Specimen with polypropylene (PP) geocomposite (GT=GX+GG) interlayer.
GX: tensile strength $S_t = 18$ kN/m (long.), 8 kN/m (trans.); yield strain $\epsilon_y = 55\%$ (long.), 40% (trans.).
GG: tensile strength $S_t = 60$ kN/m (long.), 54 kN/m (trans.); yield strain $\epsilon_y = 14\%$ (long.).
RA: tensile strength $S_t = 20$ kN/m (long.), 20 kN/m (trans.); yield strain $\epsilon_y = 13\%$ (long.), 10% (trans.).
GT: tensile strength $S_t = 20$ kN/m (long.), 20 kN/m (trans.); yield strain $\epsilon_y = 13\%$ (long.), 10% (trans.).

All the asphalt specimens, made outside in a single 36 meters long strip as described previously (see also Fig.2), were then cut away, brought in the laboratory, and placed directly on the rubber (settled down)in the steel box. Hence, as far as stiffness is concerned, the rubber represents both the foundation and the subgrade layers. The

asphalt specimens have a total thickness of 160 mm, arranged as follows (Fig. 6):

1. a 60 mm-thick asphalt layer bottom, in some cases fissured (indicated in the text as “LE”, whereas the other non-fissured samples are referred to as “NL”), by cutting it with a steel tool to a depth of 50 mm;
2. the interlayer, when present, fixed with a cationic bituminous emulsion (1000 gr/m<sup>2</sup> approximately ) tack coat;
3. a 100 mm-thick asphalt layer top.

In order to evaluate the minimum thickness of overlays, since some practical applications suggest that such a limit exists, we also realised some “REVERSE” samples (RE) in which the bottom asphalt layer was 100 mm thick (instead of 60 mm) and the overlay 60 mm thick (instead of 100 mm).

The load was applied with a hydraulic jack, controlled by the data acquisition system, at a frequency of 5 Hz. The shape of the loading wave is approximately sinusoidal and has an initial amplitude ( $\Delta V_0$ ) of 60 kN, in the range 5-65 kN. During the tests and in some cases with very high displacements, it was necessary to reduce this amplitude in order to maintain the original frequency.

Two reference grid patterns, 100x100 mm and 50x50 mm in the central portion, were sketched on the surface of the samples previously covered with white paint, to allow reporting the failure pattern vs. number of cycles.

Surface displacements, at different distances from the loading plate, were monitored with inductive transducers connected to an Instron data acquisition system (Fig. 6 )

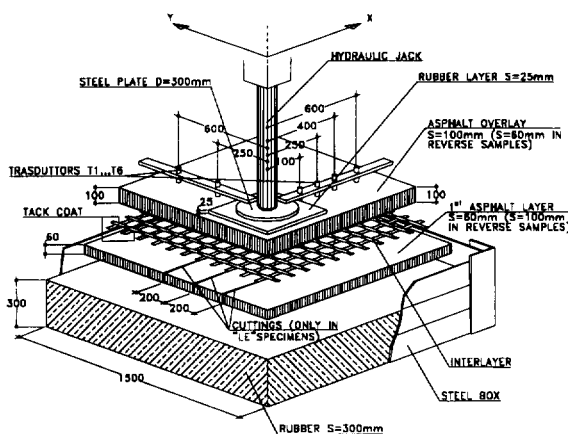


Figure 6. Sample composition.

In some tests, the acquisition of the temperature gradient to which the specimen is exposed during and after the test, by means of a temperature survey in several points

and at various depths of the specimen, achieved by the installation of thermic probes with automatic data acquisition.

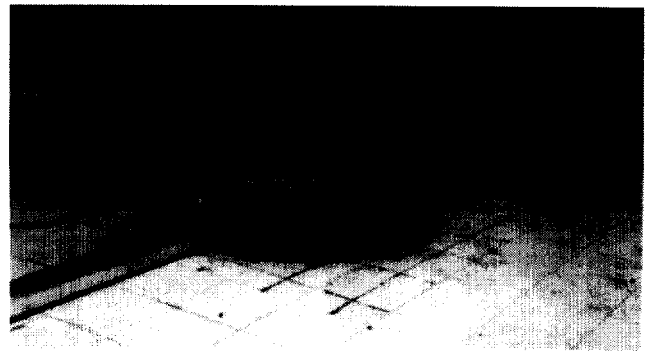


Figure 7. A specimen after  $5 \times 10^5$  loading cycles

## 4. INTERPRETATION OF RESULTS

At the end of the tests (each one is approximately three days long), all the samples showed highly significant permanent displacements (Fig. 7), although the degree of damage was very different. Furthermore, cracks appeared later in specimens and their extension was much smaller than in samples without geosynthetics.

### 4.1 Cracking Pattern

As previously described, it is to be pointed out that the failure behaviour of the various types of samples differs substantially.

In non-lesioned samples (NL), cracking starts in radial directions on the free surface: this behaviour was previously observed by other authors (Kief et al., 1994, and therefore we could assume that this is normal for pavements whose unique factor of degradation is repetitive loading. In lesioned samples (LE), the cracking pattern, as shown in Fig. 9 for  $5 \times 10^5$  cycles, follows the alignment of artificial cuttings.

The estimation of the benefit brought by the interlayers can be made by analysing the tables reported in this paragraph.

#### 4.1.1 Normal Samples

The tables (Tab. 2 and Tab. 3) refer respectively to the specimens NL and LE.

These tables summarize the percentages of damaged surface ( $A_{les}$ ) in comparison to the total area ( $A_t$ ), and the decrease of cracking ( $\Delta A_{les}$ ) in the different situations (UR, GX, GG, GT and RA) in respect to the unreinforced the specimen (UR) at the end of every single test, after  $5 \times 10^5$  loading cycles.

The surface under the loading plate was not included in the calculation of the total area.

Table 2. Percentages of the damaged surface in comparison to the total surface of the specimen (NL specimens).

Sample	NL-UR (%)	NL-GX (%)	NL-GG (%)	NL-GT (%)	NL-RA (%)
$A_{les}/A_t$	43	24	17	23	21
$\Delta A_{les}/A_t$	-	-44	-60	-47	-51

Table 3. Percentages of the damaged surface in comparison to the total surface of the specimen (LE specimens).

Sample	LE-UR (%)	LE-GX (%)	LE-GG (%)	LE-GT (%)	LE-RA (%)
$A_{les}/A_t$	38	13	10	9	17
$\Delta A_{les}/A_t$	-	-66	-74	-76	-55

The benefit had by the interlayer seems extremely high for all the type of interlayers and it is not excessively influenced by its modulus. In particular if we consider the NL specimens, we may observe a maximum improvement of 60 % (GG-PET and GT) while, for the remaining synthetic interlayer, the benefit proves to be quite steady at a range from 45% to 50%.

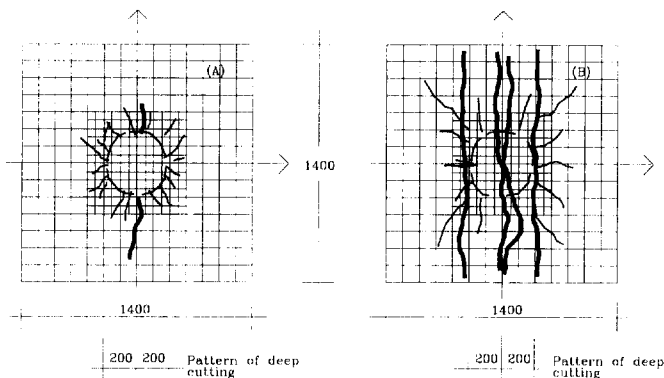


Figure 8. Cracking after  $5 \times 10^5$  cycles in two samples: one, on the left, has an interlayer (NL -GX) and the other does not (NL -UR).

Instead, with regard to the LE series we obtain an maximum improvement of 74-76% (GT-PP and GG-PET) while, for the remaining materials, the improvement is sufficiently homogeneous with values between the 55% and the 66%.

Therefore, the improvement is more evident for the LE specimens although, also in this case, it is not strictly proportional to the strength of the interlayers.

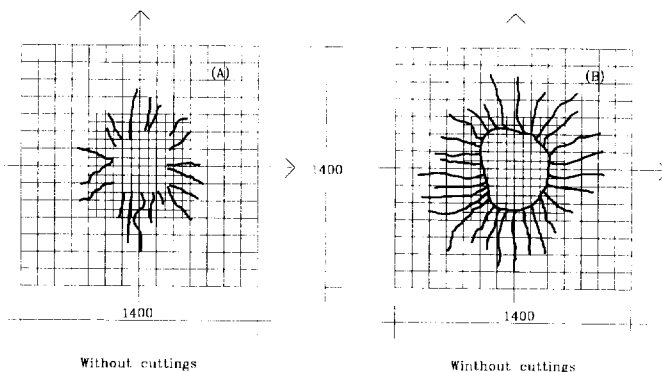


Figure 9. Cracking after  $5 \times 10^5$  cycles in two samples: one, on the left, has an interlayer (LE -GX) and the other does not (LE -UR).

#### 4.1.2 Reverse Samples

Also in these samples, characterised as previously specified by a thin overlay, the insertion of an interlayer reduces the cracking set, although the benefit is much more moderate than in the previous case.

Table 4. Results of "REVERSE" (RE-NL) specimens.

Sample	RE NL-UR (%)	RE NL-GX (%)	RE NL GG (%)	RE NL GT (%)	RE NL RA (%)
$A_{les}/A_t$	43	n.d.	31	28	34
$\Delta A_{les}/A_t$	-	n.d.	-28	-35	-21

The benefit achieved by the interlayer comes to a maximum improvement of 35 % (GT) while, for the remaining materials, the benefit proves to be quite steady at a range from 21% to 28%. Furthermore, with regard to the "reverse" series and unlike specimens with normal section, a very prominent, circular crack appears, at the edge of load mark, from which the previously mentioned radial cracks depart.

This confirms that the insertion of interlayers near the surface, as was foreseeable, must be taken into account with extreme caution.

#### 4.2 Settlements

When analysing deformations settlement of non-fissured samples (NL), it is necessary to point out the difference between permanent deformations (visco-plastic deformation) and reversible ones (visco-elastic deformation).

##### 4.2.1 Visco-plastic settlements

Permanent deformations, in the case there are no artificial cuttings, depend on the presence of interlayers, as is

pointed out by Fig. 10. In this case, it appears evident that their extent is related to the modulus of the interlayer.

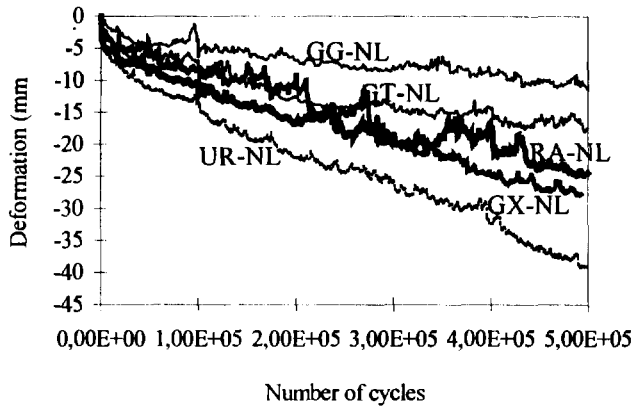


Figure 10. Permanent deformations under loading surface vs. N°. of cycles.

#### 4.2.2 Visco-elastic settlements

Instantaneous deformations, with analogy to the previous case and in the same non lesioned condition, are also influenced by the presence of interlayers.

Hence, it's possible to assert that, when there are synthetic interlayers, NL specimens stiffness (not the resistance) increases in strict proportion to the modulus of interlayers. The improvement is made much more evident by increasing the number of loading cycles. This can be explained, order than by the fatigue behaviour, also by taking the specimens temperature into account. In fact, this conspicuously increases while the test is being carried out (Tab.5): this is due to the dissipation of the deformation energy, which is transmitted by the hydraulic jack.

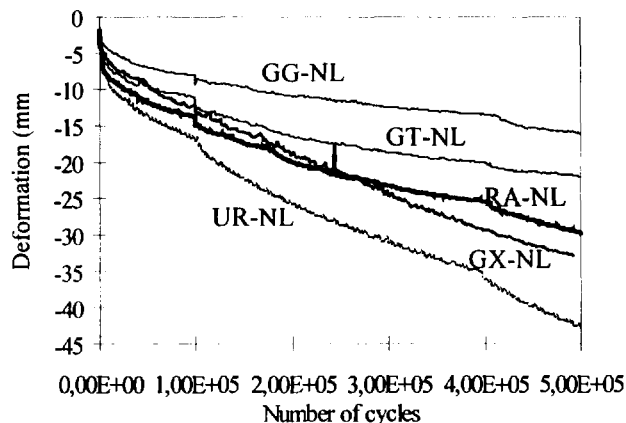


Figure 11 Instantaneous deformations under loading surface vs. N° of cycles.

It's also particular interesting to compare the details of the results obtained on two LE specimens, for which the behaviour appears significantly different in comparison with NL ones.

Table 5. Continuous logging of temperature in the specimen.

Load Cycle x10 <sup>3</sup>	Air Temp. C°	Probe 1 C°	Probe 2 C°	Probe 3 C°	Probe 4 C°
0	22.2	21.7	21.7	21.6	21.3
50	22.4	22.6	22.0	21.7	21.3
100	22.7	23.3	22.4	21.8	21.3
150	22.3	23.9	22.7	21.8	21.2
200	21.9	24.5	23.1	21.9	21.0
250	21.7	25.4	23.6	22.2	21.2
300	21.4	25.8	23.9	22.3	21.1
350	21.1	26.2	24.2	22.4	21.1
400	21.6	26.6	24.5	22.6	21.2
450	22.0	27.0	24.8	22.8	21.3
500	22.5	27.2	25.0	22.9	21.4

We now consider:

1. Lesioned specimen, without interlayers (LE-UR).
2. Lesioned specimen, with a nonwoven geotextile as interlayer (LE-GX).

In this case, maximum deformations (under loading) are surprisingly similar for specimens with (GX) and without interlayers (UR), while pseudo-elastic deformations follow a different behaviour: after  $4 \times 10^5$  cycles, instantaneous settlements significantly increase in LE-UR specimens while they tend to be constant in the LE-GX specimen (see Fig. 12)

When analysing the total settlement of fissured specimens (see Fig. 12), the two curves for UR and GX samples are so close that no differences can be noticed.

So, contrarily to the NL case, we don't record any stiffness increase consequent to the introduction of a nonwoven geotextile in this case.

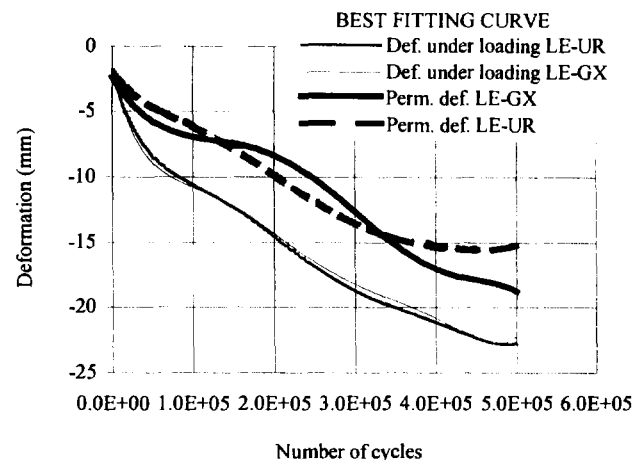


Figure 12. Settlement under loading surface vs. N° of cycles.

When taking into consideration the elastic fraction of the displacement, we can see that, prior to a certain number

of cycles (i.e. approximately  $4 \times 10^5$ , Fig. 12) the curves are quite similar. After this limit, there is a rapid increase of settlements in UR samples.

We can conclude that with LE specimens there is no reduction of permanent deformation but that the overall behaviour of LE-GX sample is better, considering the increase of pseudo-elastic stiffness.

## 5. IN SITU TESTS

In order to validate laboratory tests, we have created an experimental field by reproducing, in a lane of the Centro Padane Motorway S.p.A., A21 Piacenza-Cremona-Brescia (Fig.13), some sections very similar to those tested in the laboratory.



Figure 13. Experimental field in a motorway lane.

During rehabilitation works of the upper bituminous layer, deep cuttings were made (50-70 mm) in the binder layer (Fig. 14) between the edges of the road, in a 10 m wide and 120 m long area.

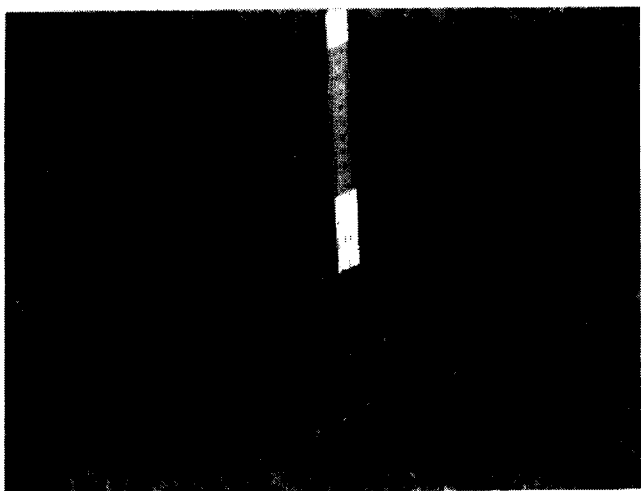


Figure 14. Detail of the groove.

These cuttings were regularly spaced at 500 mm to represent existing cracks (Fig. 15).

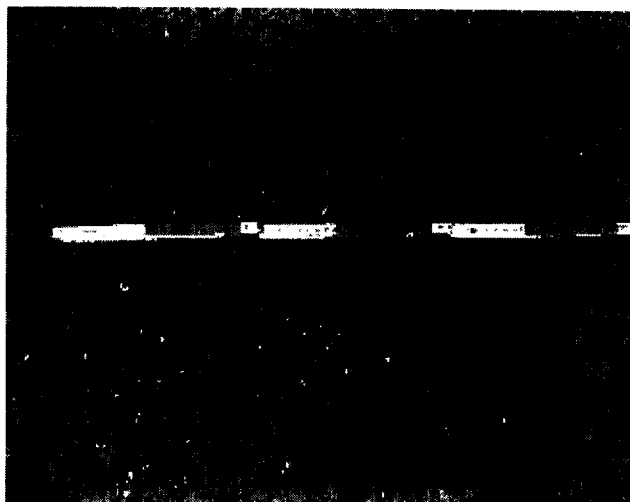


Figure 15. Detail of the distance between the grooves.

Then interlayers of different types, similar to those previously employed in laboratory tests, were laid down only on some parts of the lesioned field, on a bituminous tack coat (Fig. 16).

Finally, the lane was repaved with a layer of 90-100 mm thick asphalt. In order to evaluate the real traffic volume and composition, we also arranged in the vicinity a digital axles counter and an inductive load-measurement device.

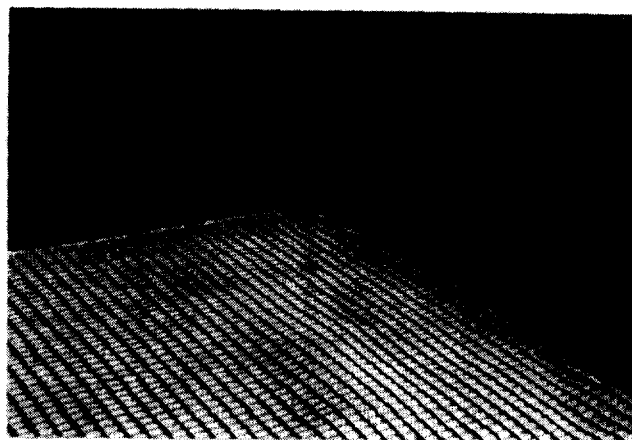


Figure 16. Detail of the reinforcement laying.

The experimental field, after nine months, performs well and there is no evidence of cracking reflection, neither in sections with deep cuttings and without interlayers, but the test is still continuing and we expect the results in next months.

## 6. CONCLUSIONS

The insertion of "high modulus" geosynthetics in upper bituminous layers requires a correct sequence of the following operations:

- thorough cleaning, through blowing and brushing, of the laying plane, or better through hydraulic jetting;
- sealing of the possible cracks through bituminous coat casting;
- laying of a first bituminous emulsion tack coat, possibly with elastomer;
- laying of the interlayer by means of a roller, equipped with clutch, able to provide low pretensioning stress;
- settlement of the surface by means of a clipper shearing machine for removing protrusions, resulting from a not perfectly homogeneous laying;
- laying of a second bituminous emulsion tack coat, possibly elastomer (it is not necessary if geogrids are used);
- laying and compaction of the subsequent asphalt layer.

When summarizing the achievable benefits, we may state that:

- advantages are particularly outstanding with geogrids and composites in critical conditions, such as heavy loads and for overlays of intensely fractured pavements;
- there is a significant improvement of the ductility of bituminous layers;
- with polyester geogrids, there is also a slight increase in ultimate strengths, without interlayer failure;
- in any case, also with nonwovens insertion with a good tack coat, the presence of an interlayer delays the cracking reflection and guarantees the durability for the overlays;
- the pseudo-elastic stiffness of the pavement is slightly increased and the degree of cracking is, in any case, much lower;
- with regard to the reduction of cracking ratio, the benefit brought by the interlayer seems extremely high for all types of interlayers and is not strongly influenced by the strengths and the moduli of this ratio. For the LE specimens and therefore with regard to the reflection of pre-existent cracking, the improvement is much more evident than for the NL specimens;
- it is absolutely unwary to place the interlayers too near the surface: the minimum coverage is 70 – 80 mm thick;
- recycling is allowed.

When designing a reinforcement, the following criteria should be followed.

When the geosynthetic is placed into the bituminous layers, it is necessary to observe some simple, but basic instructions during the laying of the interlayers: the laying

stage is, in fact, fundamental, principally in order to guarantee a monolithic pavement. It's well-tested, in fact that an inadequate link between the layers, especially when geosynthetics with high bitumen absorption capacity are used, i.e. nonwovens and composites, can cause a quick failure of the pavement.

## ACKNOWLEDGEMENTS

The Author wishes to thank Mr. Rimoldi, TENAX S.p.A., for laboratory facilities and Mr. Salvadori (Centro Padane Motorway S.p.A., A21 Piacenza-Cremona-Brescia, Italy) for his help for the realisation of in situ experimental field.

## REFERENCES

- De Almeida Rocha, J. C. G., (1993) "Analytical Techniques for the Structural Evaluation of Pavements", Thesis submitted to the University of Nottingham, Department of Civil Engineering, for the degree of Doctor of Philosophy.
- De Jong, D.L., Peutz, M.G.F., and Korswagen, A.R. (1973) "Computer Program Bisar, Layered systems under normal and tangential surface loads".
- Dondi, G., and Righi, P.V. (1990) "Rinforzo delle sovrastrutture stradali", Quaderno AIPCR: "L' Impiego dei geotessili e prodotti affini nelle opere stradali", XXI Convegno Nazionale Stradale, 11-15 giugno, Trieste, pagg. 9-18.
- Dondi, G., (1994) "Three dimensional finite element analysis of a reinforced paved road", Proceedings of the 5th International Conference on Geotextiles, Geomembranes and Related Products, Sept., Singapore.
- Dondi, G., (1995) "Le pavimentazioni flessibili rinforzate mediante geosintetici", Estratto dagli Atti del Convegno Naz.: "La ricerca nel settore delle infrastrutture interportuali e aeroportuali", 28-29 giugno, Trieste.
- Dondi G., (1996). "Laboratory test on bituminous mixes reinforced by geosynthetics", 3<sup>rd</sup> International RILEM Conference on Reflective cracking in pavements, October 2-4, Maastricht, NL.
- Dondi G., (1997) "Full scale dynamical testing on reinforced bituminous pavements", Geosynthetics '97 International Conference, 11-13 March, Long Beach, Cal., U.S.A.
- Judycki, J., (1990) "Bending test of asphaltic mixture under static loading", Proceedings of the fourth Intern. RILEM Symposium, October, Budapest.
- Kunst, P.A.J.C., and Kirschner, R. (1993) "Comparative laboratory investigations on polymer asphalt inlays", Geosynthetics '93 Conference Proceedings, March, Vancouver, British Columbia.
- Kief, O., Livneh, M., Ishai, I. and Altus, E. (1994) "Experimental and analytical approaches for studying reflective crack retardation", Proceedings of the 5th International Conference on Geotextiles, Geomembranes and Related Products, Sept., Singapore.



# Geotextile Within Asphalt Overlay on a Brazilian Road: A 13-Year Case Study

P.R. Aguiar  
MULTIGEO Eng. Associados, São Paulo, Brazil

C.E.L. Paiva  
Professor, Geotechnical and Transport Engineering Dept., Faculdade de Engenharia Civil, UNICAMP, São Paulo, Brazil

**ABSTRACT:** This paper examines the use of geotextile within an asphalt overlay on a rural road with medium traffic 13 years after application. Testing was carried out using four 300m long experimental sections of the road. Each one was further divided in two areas: a field test area with geotextile use and a control covered with ordinary asphalt. Different thicknesses of asphalt overlays were used. Data concerning the current pavement surface and structural stages are presented and compared with the original ones. Finally, some conclusions about the four sections are drawn and the concept of the technique employed is evaluated.

**KEYWORDS:** Asphalt overlay, geotextiles, pavements, rehabilitation, reflective crack prevention.

## 1 INTRODUCTION

The SP-52 in São Paulo, Brazil, carries medium traffic from the city of Cruzeiro to the boundary between the states of São Paulo and Minas Gerais. Local temperatures range from 10°C to 38°C.

In 1984 asphalt overlays were laid on the road in order to overcome severe pavement deformations. Four experimental sections with similar pavement structures were chosen for this study and each section was further divided in two areas: one of them received a geotextile reinforced overlay, while the second one was covered with conventional pavement for comparison.

The present work examines the current road surface conditions and compares deflection measurements carried out in 1984, in 1985 and in 1997, 13 years later.

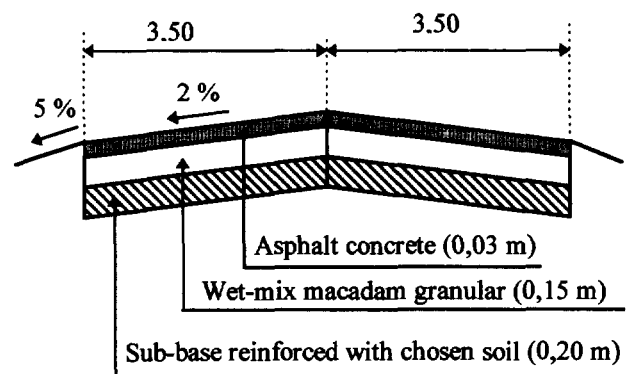
## 2 PREVIOUS PAVEMENT CONDITIONS

The transversal section of the SP-52, built in 1967, consisted of a 0.03m thick asphalt concrete layer over a 0.15m thick wet-mix macadam granular base and a 0.20m thick sub-base reinforced with chosen soil, as shown in figure 1.

In 1981 the Average Daily Traffic (ADT) was 1121 vehicles, 29% of which were commercial (trucks and buses). In 1983 the pavement presented many surface deformations such as longitudinal cracking, alligator cracking, sinking, potholes, holes and localized

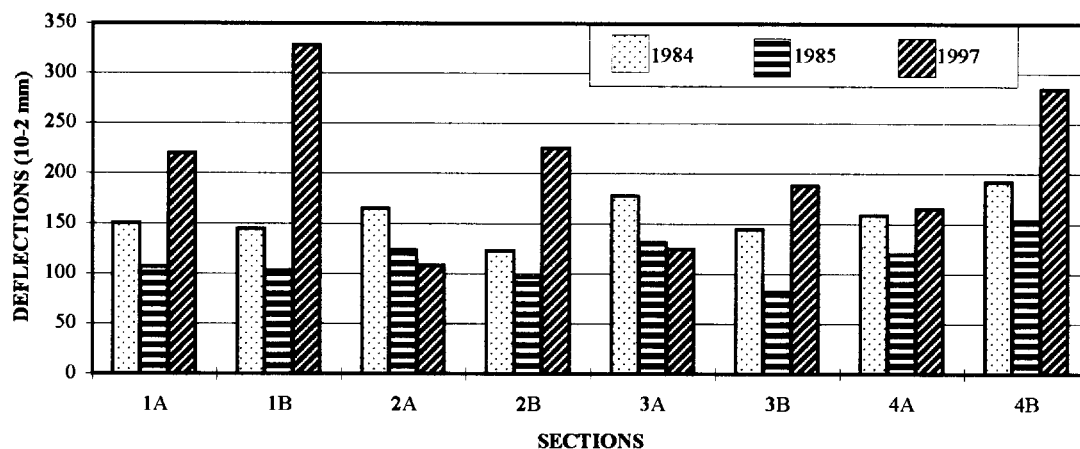
patches. To solve these problems the pavement needed improvements in the base course and drainage system as well as repairs to the cracked surface course.

Figure 1: Previous pavement transversal section

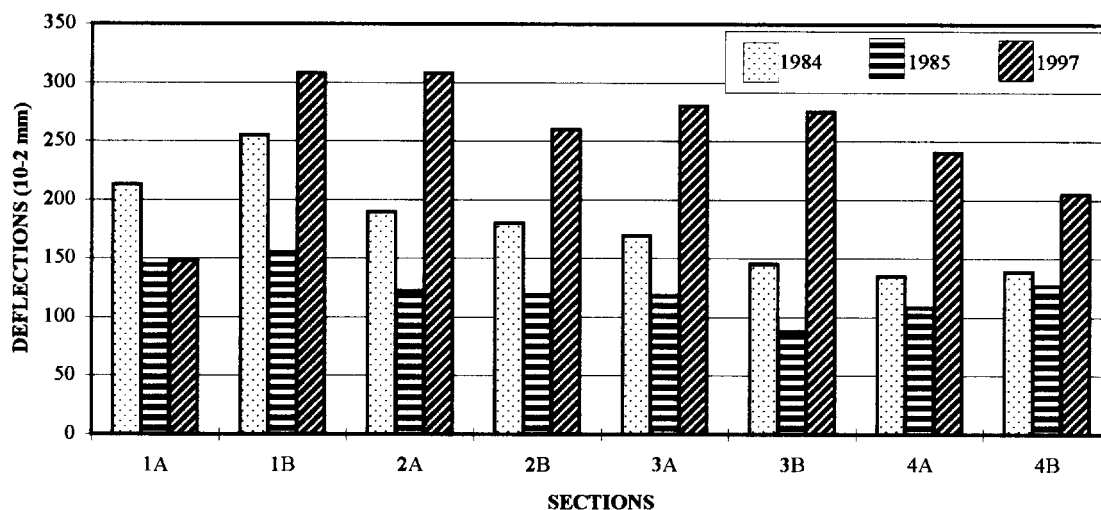


Four 300m long sections were chosen for the experimental design. Pavement structural conditions were done by means of Benkelman beam deflection measurements, taken in 1984 (before the overlay), in 1985 (4 months later) and in 1997 (13 years later). Figures 2 and 3 show the internal and external lane deflections, respectively.

**Figure 2: Internal Lanes-Deflections**



**Figure 3: External Lanes-Deflections**



### 3 THE OVERLAY INSTALLATION

Since there were no project criteria considering geotextile reinforcement conditions in Brazil in 1984, the sections were designed according to the usual method based on USACE and thus ignoring the geotextile reinforcement properties.

Each 300m long section was divided in two areas with similar characteristics. The compositions of the pavement sections laid on each of them between May and June, 1984, are shown in figure 4.

A 100 % polyester non-woven continuous filament geotextile called BIDIM OP-20 (RHODIA-STER S/A) was employed (200 g/m<sup>2</sup>, 15 kN/m wide width tensile NF G-38014, 30-35% elongation). In the beginning and at the end of each section the geotextile was attached to the previous pavement with metallic staples in order to avoid sliding.

Table 1 summarises the main occurrences during installation (left and right sides of the road were named considering the São Paulo (Cruzeiro) - Minas Gerais direction), whereas figures 2 and 3 show deflection measurements done in 1985.

Figure 4: Overlays transversal sections

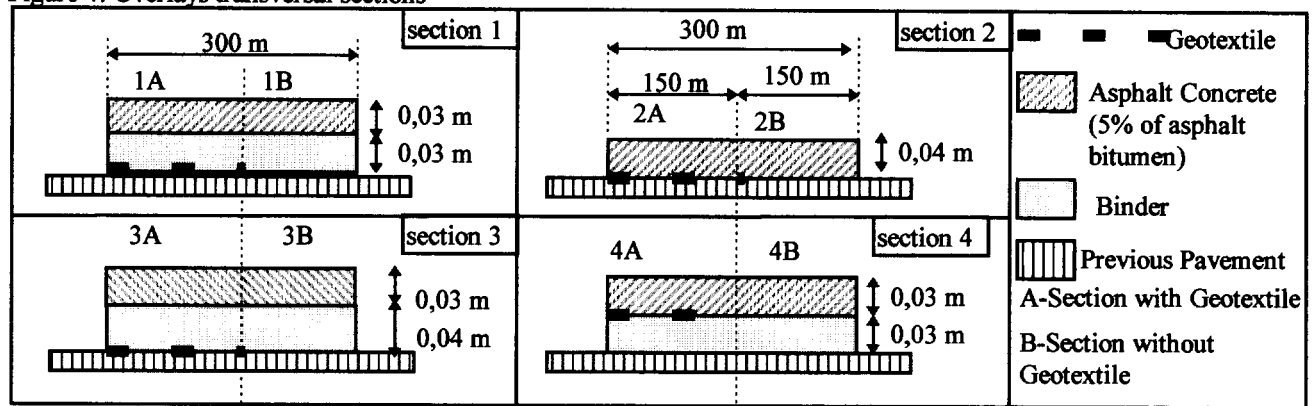


Table 1: Main Occurrences during overlay installation.

Sections	Lane (*)	1 <sup>ST</sup> Tack Coat (L/m <sup>2</sup> ) (**)	2 <sup>ND</sup> Tack Coat (L/m <sup>2</sup> ) (**)	Observations
1.A	Right	0,90	0,50	Great number of wrinkles, some of them removed.
	Left	0,87	0,94	
2.A	Right	0,80	0,90	Right side without wrinkles; left side with few wrinkles, eliminated by brushing; deteriorated base without any treatment.
	Left	0,70	0,62	
3.A	Right	0,70	1,00	Section in curve, with occurrence of wrinkles in its internal side. The geotextile was cut and juxtaposed with prior pavement.
	Left	0,60	0,90	
4.A	Right	0,50	1,40	Wrinkles removed by means of cutting and juxtaposing it with prior pavement.
	Left	0,70	0,90	

(\*) São Paulo-Minas Direction

(\*\*) Cationic Asphalt Emulsion

#### 4 13 YEARS LATER

In 1995 an analysis made by the Department of Roads of São Paulo State (DER,1995) considered the pavement area to be good, with 14% of cracking, 0.05% of potholes and 0.30% of sinking. The ADT was then 1936 vehicles, 27% of which were commercial.

However, a more recent evaluation carried out in 1997 showed that there was an accelerated pavement damage in the last two years (figures 2 and 3). The current surface conditions were considered regular, with 32% of cracking severity, 5% of potholes and 30% of patches.

Table 2 summarises the observations during the 1997 evaluation.

#### 5 CONCLUSIONS

The last deflection measurements presented in figures 2 and 3 as well as the surface deformations observed (table 2) lead to the conclusion that most of the analysed sections are at the end of their expected lifetime. These

results differ somewhat from the ones obtained in 1995, when the pavement condition was considered good.

Comparing areas 1B to 1A and 2B to 2A one can conclude that the geotextile inlay acted as a reflective cracking barrier, albeit there were no significant differences either between areas 3A and 3B or between 4A and 4B.

Although sections 1 and 4 had the same asphalt concrete thickness, the former is very damaged while the latter is in good conditions. The reason for this disparity may lie on their positions on the road. Section 1 is located on a hill and immediately after a road police station, whereas section 4 presents no obstruction for free flow of commercial vehicles.

An intensive surface damage with alligator cracking was observed in a small segment of area 1A. Some small asphalt concrete pieces could be removed and it turned out that in the damaged area the course thickness was only 0.02m instead of the specified 0.03m. Therefore the asphalt concrete has come apart from the pavement after 10 years in operation.

Table 2: Conditions of the Sections in April 1997

Section	Lane	(MG-Cruzeiro)	(Cruzeiro-MG)	Observations	Concept
1A	Int	OK	TT BI	Block cracking	Regular
	Ext	TB AI	TL+TT MI		
1B	Int.	TB AI	TB AI	Block cracking, alligator cracking	Regular
	Ext	J MI	J AI		
2A	Int	OK	TB MI	Several segments in good state and others in regular state with alligator cracking	Regular
	Ext	TL+T BI	J AI		
2B	Int	TL+T MI	TL+TT BI	Transversal and longitudinal cracking; few segments with alligator cracking	Regular
	Ext	T AI	TL+TT MI		
3A	Int	TT BI	OK	Segments in good state and others with alligator cracking	Regular
	Ext	OK	J AI		
3B	Int	TT+T BI	OK OK	Segments in good state and others with alligator cracking	Regular
	Ext	L BI	TL+J AI		
4A	Int	OK	OK	Good state	Good
	Ext	OK	TL BI		
4B	Int	OK	OK	Good state	Good
	Ext	OK	OK		

TB: block cracking TL: longitudinal cracking AI: high intensity BI: low intensity Ext: External lane  
 J: alligator cracking TT: transversal cracking MI: medium intensity Int: Internal lane OK: Good  
 Regular: 25 to 50 % of surface defects; Surface cracking length lower than 3,5 m. PSI between 2,0 and 3,0.  
 Good: 5 to 25 % surface defects. PSI between 3,0 and 3,8.

Residual asphalt for geotextile impregnation was used in much smaller amounts than in the USA, in order to keep the geotextile drainage capacity and avoid the usual exudation that occurs in tropical countries.

There are still few overlays with geotextile in Brazil. A rise in such applications is expected, since some highways are now private and their owners take only high cost-benefit solutions. From our results it is thus possible to advise a 20% increase in the asphalt emulsion for the forthcoming geotextile applications.

#### ACKNOWLEDGMENTS

The authors would like to thank to the DER-Department of Roads of São Paulo, head and local offices, for the equipments and data of pavement system management of SP-52 road, and RHODIA-STER S/A by the data presented.

#### REFERENCES

- Aguiar, P.R. (1984) "Relatório sobre a aplicação do geotêxtil BIDIM no recapeamento da rodovia SP-52", *RHODIA Report*, São Paulo, SP, Brazil.
- Aguiar, P. R.(1985) "Avaliação e Planejamento da Aplicação BIDIM em Recapeamento Asfáltico" *RHODIA Report*, São Paulo, SP, Brazil.
- DER-Departamento de Estradas de Rodagem do Estado de São Paulo (1995) "Levantamento de condições de pavimento - Rodovia SP-52", São Paulo, SP, Brazil.
- Paiva, C.E.L, Aguiar, P.R. (1996) "Análise comparativa de algumas obras de recapeamento asfáltico com aplicação de geotexteis" *30ª Reunião Anual de Pavimentação*, ABPv, Salvador, BA, Brazil, pp 1458-1466.
- UNICAMP- Universidade Estadual de Campinas (1997) "Levantamento de condições existentes do pavimento da rodovia SP-52", Campinas, SP, Brazil

# Fracture Behaviour of Geosynthetics in Asphalt Layers

R. Lugmayr  
Technical Consultant, Polyfelt Geosynthetics., Linz, Austria

**ABSTRACT:** The fracture behaviour of different overlay systems was determined due to a research from Tschegg et al (1998). Using a new wedge splitting procedure with deep notched drilling cores the fracture properties of the interfaces geosynthetic reinforcement - asphalt layers and the resistance to crack growth of reflection cracks in three different overly systems was determined in this paper. The test was carried out with a polypropylene needle-punched nonwoven geotextile, a flexible geocomposite interlayer consisting of polypropylene needle-punched nonwoven reinforced with high strength glass filaments and a stiff polypropylene geogrid with a nonwoven fixed on the junctions. The result of the research of Tschegg et al (1998) was evaluated and discussed in this paper from the practical engineers point of view.

**KEYWORDS:** Adhesion, Asphalt Overlay, Fractures, Geocomposites, Geogrids

## 1 INTRODUCTION

Formation and propagation of reflection cracks in bituminous pavements are unsolved problems in theory and practical application until today. It is necessary to characterize the fracture behaviour of the basic components in order to be able to calculate, model and simulate cracks. The fracture behaviour and bond strength of bonds between the asphalt layers, has to be determined.

The fracture behaviour of bituminous overlays and the bond strength was basically investigated due to the research at the Technical University in Vienna, Austria (Tschegg et al 1995a,b, 1997). In order to characterize the fracture behaviour of different overlay systems using typical geosynthetic products further research (Tschegg et al. 1998) was also done. The propagation of reflective cracks of the whole system and crack propagation of the interface was investigated. The determined results are of great scientific and practical interest. The results are evaluated and discussed in this paper from the practical engineers point of view. Preliminary a short description of the research procedure (Wedge splitting test and experimental details) Tschegg and Co-worker (1998) is shown.

## 2 PRINCIPLE OF THE TESTING METHOD

In Figure 1 a core specimen of asphalt pavements with mounted loading device and displacement gauge is depicted. Specimens are placed on a narrow linear support in a compression testing machine.

The specimen has a rectangular groove with a starter notch at the bottom of the groove. For interface tests (fracture test of the adhesive bond) , the specimens are oriented in a way, that the interface is aligned in the plane defined by starter notch and linear support. In order to characterize the fracture mechanical properties of the crack propagation the

Geosynthetic Interlayer is placed normal to the plane starter notch and linear support. A deep notch simulates the reflective crack up to the geosynthetic of the wearing course. A crack is forward to (through) the interface into the overlayer of the specimen during the fracture test due to the splitting force (loading condition: bending).

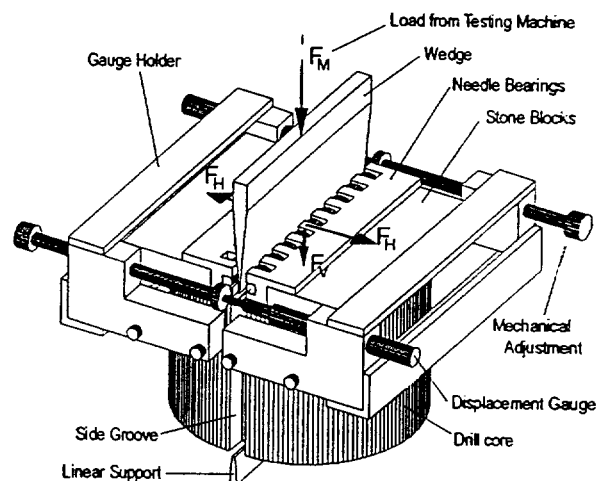


Figure 1: Test arrangement for drill core-specimen (according to Tschegg 1986)

Two load transmission pieces are placed in the groove and a wedge is inserted between them. The wedge transmits a force  $F_M$  from the testing machine to the specimen. The slender wedge exerts a large horizontal force component  $F_H$  and a small vertical force component  $F_V$  on the specimen. The force  $F_M$  is determined with a load cell in the testing machine. More details of the testing method is described in Tschegg et al 1995a and Tschegg 1997.

### 3 EXPERIMENTAL DETAILS

#### 3.1 Material, specimen shape and size

From a bituminous base layer sample, of Austrian standard type BT I 16 (crushed aggregates, maximum grain size 16 mm, binder content 4.8-4.9 % of 100 pen-bitumen), plates of 70 - 80 mm thickness were produced. Compaction was performed with a vibration roller. Thus the asphalt aggregate mixture and production of the layer was similar to that, which is used in road construction. The plate surfaces were treated with a water jet until all binders and fine aggregates were removed from the surface. In this way a road with traffic was simulated.

Further drilling cores with a diameter of 200mm and a height of 120mm with and without interlayer were produced. In order to simulate a reflective crack the wearing course was then cut down of 10mm above the interlayer. Additionally two 50mm deep side notches were cut to eliminate border influences of the specimen. The ligament area has a dimension of 100x55mm and is large enough that the size effect has no influence on the test results. Two stone plates were glued onto the front face of the drilling core parallel to the starter notch. They act as a groove for taking up the loading device. In the case of the stiff geogrid interlayer it was distinguished between specimen with one and two bars (Fig. 2) in order to evaluate the influence of different bar number in the ligament area on the fracture behaviour.

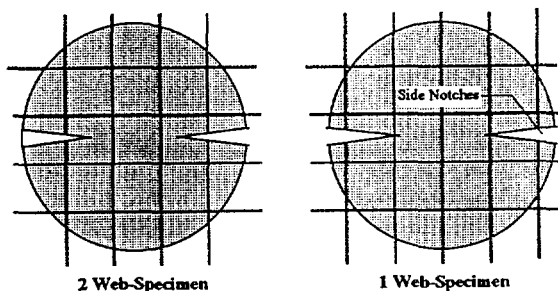


Figure 2 : One and two bar specimen

#### 3.2 Testing conditions and evaluation

The vertical load of the testing machine is transferred into the sample via a wedge ( $\alpha/2=15^\circ$ ) and two load transferring pieces. The load is applied over a roller bearing in order to eliminate any friction forces which would influence the results.

Testing was performed with a mechanical compression testing machine with a load capacity of 5 kN. Unstable crack growth was not observed in any of the tests. The cross-head velocity was 2 mm/min in all tests. Before testing, the specimens were stored in a cooling chamber with a control

accuracy of  $\pm 0,5^\circ\text{C}$  for approximately 24 hours. Testing temperatures were  $-10^\circ\text{C}$ ,  $0^\circ$ , and  $+10^\circ\text{C}$ .

Investigated interlayers were installed according to the producer recommendations. Used interlayer systems were:

- A) Geotextile, flexible polypropylene needle-punched nonwoven ;
- B) Geocomposite, polypropylene needle-punched nonwoven reinforced with flexible high strength glass fibers;
- C) Geogrid, stiff pre-stressed deformation resistant polypropylene grid with nonwoven fixed on the junctions;
- D) Control specimen without interlayer.

The complied load-displacement curves (in the following LDC) are characterizing the fracture behaviour fully, so this curves were used as a basis for the following test evaluation.

The fracture energy (energy which is necessary to split the specimen completely) describe the resistance against crack propagation. The area under the LDC is proportional to the fracture energy. The fracture energy can be obtained simply from the LDC. After dividing the established fracture energy with the area of fracture (projection) the specific fracture energy was obtained. This result is a parameter which is independent of shape and dimension of the specimen.

#### 3.3 Interface fracture behaviour

The different fracture behaviour of the four interface types is best described by the shape of the post-peak section of the LDC in Fig.3. Without interlayer the curve drops very quickly after the maximum values has been reached, compared to geotextile interlayer. This means that with increasing crack mouth opening, without interlayer no more forces are transmitted, whereas with the fibers of the nonwoven geotextile probably bridge the crack and allow a transmission of forces (bridging effect). The surface structure of the geotextil interlayer and the geocomposite interlayer do not differ considerably. Therefore the geotextile shows a more shallow shape of the curve than geocomposite only in the very late post-peak section of the LDC. Due to the included glass fibers of the geocomposite the stiffness increased slightly and reduces insignificantly the bridging effect in the interface crack.

The nonwoven component fixed on the geogrid is extremely stiffened by the geogrid. The fibers are coarser, and the fiber structure is more dense, which results in a smoother and less felted surface of the nonwoven. With the geogrid, the binder cannot guarantee the bonding of the fibers to the base course. The bridging effect is thus small, as the nonwoven can be easily delaminated from the base course. This results in a much lower resistance against crack propagation compared to the other interlayer systems.

The area under the LDC represents the resistance against crack propagation. Figure 3 describe qualitative the high resistance against interface crack elongation of the "Geotextile and the flexible Geocomposite". The low resistance of the "Control and stiff Geogrid" specimen can be also obtained from Fig. 3.

### 3.4 Reflective Cracking Behaviour

The LDC of reflective cracking tests give the best overview of high resistance against crack propagation of interlayer systems. The fracture energy for the crack opening obtained from the LDC are determined till the crack meet the overlay surface.

The obtained specific fracture energies  $G_f$  is direct proportional to resistance against crack propagation. They are drawn up as  $G_f/G_{f0}$ , ( $G_{f0}$ =spec. fracture energy of specimen "Control") in figure 4. The figure point out very clear the excellent performance of geosynthetics to resistance of crack propagation at temperatures  $-10^\circ\text{C}$  to  $+10^\circ\text{C}$ . The "flexible Geocomposite" perform best of all investigated geocomposites.  $G_f$ -values of the "stiff geogrid" are not determined in the investigation Tscheegg et al (1998) due to the low adhesion bonding of the interlayer. At temperatures  $0^\circ\text{C}$  and  $10^\circ\text{C}$  the adhesive bond strength is reduced due to the stiff geogrid. In fact, the specimen were detached during testing and the determination of LDC was not possible (Tscheegg et al 1998).

For the long term behaviour of an asphalt wearing course the energy which is consumed at the beginning of the crack formation is decisive, where the cracked pavement can still fulfill its function. Therefore the specific fracture energies consumed up to a crack opening width of 4 mm at the testing temperature of  $-10^\circ\text{C}$  have been plotted in figure 5. This figure point out very clear the highest values of the consumed energy and the best resistance against crack opening of the flexible Geocomposites. This could be observed from small to large openings of cracks. Under equal conditions of loading the expected lifetime of the system with flexible Geocomposites versus the other tested systems is much longer.

More detailed information of increasing the resistance against crack propagation in asphalt overlayers can be found in the publication Tscheegg et al (1998).

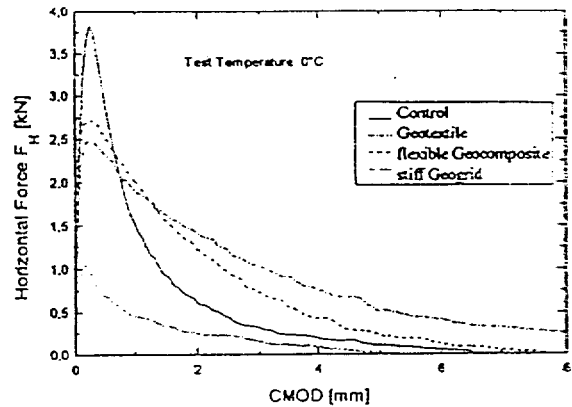


Figure 3 : Load-displacement-curve

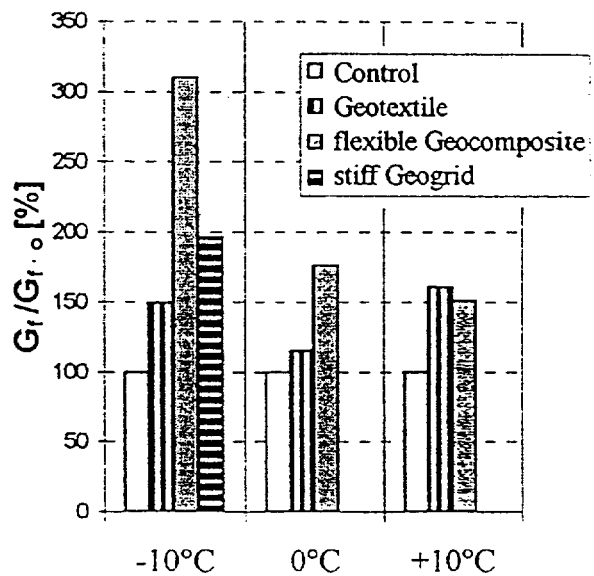


Figure 4: Specific fracture energy  $G_f/G_{f0}$

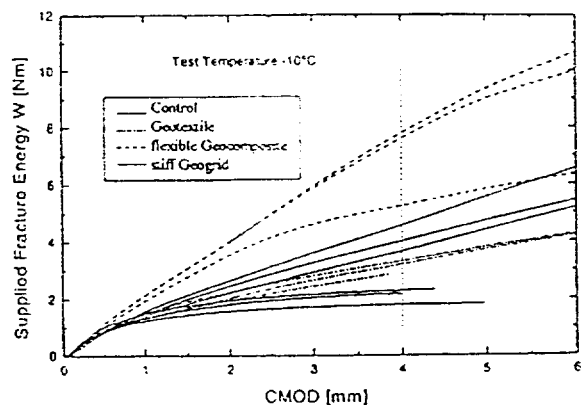


Figure 5: Supplied fracture energy acc. to Crack-opening-displacement

#### 4 DISCUSSION AND CONCLUSION

The fracture mechanical parameters differ considerably for different interlayer systems. A high resistance against crack propagation is achieved by interlayers with flexible (low stiffness) and a good bonding to the asphalt layer by the polymermodified bituminous binder.

Maximum force values ( $F_{max}$ ) from the LDC of the four investigated overlay systems (taken from Figure 3) considerable differences were found at 0°C. The  $F_{max}$  value is comparable with the values of the pull-of-test. Specimen without interlayer ("Control") show the highest values. However the highest resistance against crack propagation in the interface are achieved with Geotextile and flexible Geocomposite. The conclusion is that the adhesion bonding (calculated of max. strength) gives no statement of the fracture behaviour. Only the parameter  $G_f$  and a sound evaluation of the fracture behaviour results in a respectable statement of adhesive bond strength.

The normalized specific fracture energy  $G_f/G_{f0}$  (resistance against reflective crack propagation versus bonding without geosynthetics) shows the different fracture behaviour of overlay systems much more precisely than the strength values (calculated from  $F_{max}$ ) taken from the LDC.

A high resistance against crack propagation was achieved with the flexible geocomposite interlayer with high strength glass fibers at temperatures of -10°C and 0°C. At higher temperatures, the differences were smaller.

The Load-displacement-curves show the consumption of energy during crack propagation as a function of Crack-mouth-opening-displacement and allow the judgement of the crack retarding effect of interlayers. The optimum performance is achieved by interlayers which consume most of the energy in the early post-peak section. If this effect starts at high Crack-mouth-opening-displacement values (i.e. in the late post-peak section) the overlay is already cracked and the interlayer has no significant beneficial effect.

It could be proven by the experiments (Tschegg et al 1998) that interlayers with good bonding to the asphalt show the highest resistance against reflective crack propagation.

#### 5 SUMMARY

On different overlay systems, the fracture behaviour of the interface between interlayer and asphalt layer have been investigated with regard to reflection crack propagation using the wedge splitting method according to Tschegg.

The described wedge splitting method is suitable for the description of interface cracking and reflection cracking in overlay systems. Drill cores can be used as specimens, which are easy to be gained and handled, and need only slight modification. The testing procedure is simple and can be performed in a straight forward an inexpensive way.

For the practical engineer, this fracture test method can help to control and judge the construction quality of pavements with regard to crack formation.

With reference to the maximum splitting force  $F_{max}$  best performance is shown by the conventional homogeneous system without interlayer.

Due to the most inhomogeneous system the largest decrease is given with the stiff geogrid interlayer.

The best resistance against reflective crack propagation is illustrated by the flexible geocomposite interlayer and the geotextile interlayer.

#### REFERENCES

- Tschegg, E.K. (1986), Equipment and appropriate specimen shapes for tests to measure fracture values (in German), patent AT- 390328.
- Tschegg E.K., G. Kroyer, D.M. Tan, S.E. Stanzl-Tschegg and J. Litzka (1995b), Investigation of bonding between asphalt layers on road construction. ASCE J. of Transp. Eng., Vol. 121, No.4, pp 309-316
- Tschegg E.K., (1997), An efficient Fracture Test Method for Bituminous Materials and Layer Bonds, in Proc. „Mechanical Test for Bituminous Materials“, ed. By H.D. Benedetto and L. Francken, Of the fifth intern. RILEM symposium MTBM Lyon 97, France, pp 405-41.
- Tschegg E.K., (1998) Fracture Behaviour of Geosynthetic Interlayers in Road Pavements, ASCE J. of Transp. Eng. in press 1998
- Dondi G. (1996), Laboratory test on bituminous mixes reinforced by geosynthetics. Proc of RILEM Conf. "Reflective Cracking in Pavements", Maastricht, pp 231-240
- Jaecklin F.P. and J. Scherer (1996), Asphalt reinforcing using glass fibre grid "Glasphalt". Proc of RILEM Conf. "Reflective Cracking in Pavements", Maastricht, pp 268-277
- Molenaar A.A.A.(1993). Evaluation of pavement structure with emphasis on reflecting cracking. State of the Art and Design Recommendations, Liege, March 1993
- Polyfelt (1986) Design and Practice Manual for Geotextiles



# Response Investigation and Design Guidelines for Asphalt Pavements with an EPS Geofoam Sub-base

M. Duškov

Consultant Pavement Engineering, Oranjewoud BV, Rotterdam, The Netherlands

L.J.M. Houben

Head of Road and Railroad Research Laboratory, Delft University of Technology, Delft, The Netherlands

A. Scarpas

Research Associate, Delft University of Technology, Delft, The Netherlands

**ABSTRACT:** The use of Expanded PolyStyrene (EPS) Geofoam instead of traditional "heavy" sand for pavement sub-base can reduce or even eliminate the additional load on the subsoil, thus decrease or eliminate the settlement of pavement structures on a compressible subsoil. The experiences with EPS geofoam are very promising but a uniform design procedure does not yet exist for this type of structure. Optimisation of the existing EPS pavement design guidelines and their improvement has demanded materials research on EPS, the use of three dimensional finite element pavement models and in situ full-scale measurement. Extensive materials research provided data for the stress-strain response of EPS under representative loading and environmental conditions. 3-D modelling enabled critical evaluation of existing design methodologies by analyzing pavements with different roadbases, different EPS types and different asphalt thicknesses. In situ measurements by means of built-in strain transducers in asphalt provided data for verification of the 3-D modelling.

**KEYWORDS:** Geofoam, Road Construction, Soft Soil, Finite element analysis, Material Tests

## 1 INTRODUCTION

This paper deals with the use of Expanded Polystyrene (EPS) Geofoam as a light-weight sub-base material in pavement structures. In comparison with other sub-base materials EPS has, besides an extremely low density and a low modulus of elasticity, a low water absorption and a low thermal conductivity. Through a substantial reduction of the pavement's weight, EPS as a sub-base material offers a major new solution for reduction of the settlements of new road structures and roads to be widened in areas with soils of poor load-bearing capacity. Such areas are present in the western and northern parts of the Netherlands. The application of EPS however affects the performance of the overlying structure. To investigate, on one hand, to which extent the EPS characteristics influence the overall pavement behaviour and, on the other, the long term durability of EPS in relation to varying environmental conditions, materials research on EPS, in-situ measurements and numerical analyses of the structural behaviour of pavements with an EPS sub-base have been carried out. Based on the research findings the current Dutch design guidelines have been revised and optimized.

## 2 MATERIALS RESEARCH

The extensive testing of the EPS material involved the characterization of the elastic and permanent deformation behavior under both repetitive and static loadings, the water ab-

sorption of EPS, as well as the mechanical properties of EPS15 and EPS20 after water absorption and freeze-thaw cycles (Duškov 1997). Summarizing the experimental results it can be stated that:

- ❑ EPS absorbs water very slowly and to a limited extent. The maximum percentage of water, that EPS20 will absorb, is 2% v/v. The maximum percentage will rapidly increase, however, if EPS is overloaded and its cell structure is damaged.
- ❑ The dynamic E modulus of EPS20 under the loading conditions corresponding to the maximum expected values for pavement sub-base conditions, has the values which are somewhat larger than the value of 5 MPa which is normally used in pavement design procedures.
- ❑ The Poisson's ratio value of EPS20 of 0.10 seems to be appropriate for design purposes.
- ❑ Low temperatures, water absorption level and exposure to freeze-thaw cycles, separately or combined, have no negative influence on the mechanical behaviour of EPS.
- ❑ Under a static stress of about 20 kPa corresponding to the dead weight of the pavement top layers, the creep of EPS20 amounts a few tenths of a percent. The practical consequence is a small additional permanent vertical deformation of the pavement structure caused by creep of the EPS sub-base layer. The main part of this creep however occurs during construction of the overlying layers.
- ❑ The ultrasonic test method has potential to be used on site to determine the elastic modulus at various positions of EPS blocks for quality control purposes. Additional work has to be done, however, to validate the test procedure.

### 3 IN SITU MEASUREMENTS

In order to get an insight into the structural behaviour of flexible pavement structures with an EPS sub-base, asphalt strains and surface deflections have been measured on the Matlingeweg in Rotterdam. The considered pavement structure was of interest for investigation because of its sub-base, which consists of a 1.0 m thick EPS layer, combined with a heavy traffic loading. The measurements were carried out by means of the Falling Weight Deflectometer (FWD) and four strain transducers built-in at the bottom of the asphalt layer. Overlaying of the pavement structure has taken place much earlier than it was originally planned because severe cracking occurred at the pavement's surface within a few weeks after reconstruction.

The temperature dependent behaviour of the asphalt layer disables a direct comparison between the measured strain values. It implicates that those values have to be translated to a reference temperature before comparison. The back-calculated E-values in the pavement structure layers were used to transform the measured asphalt strain values to a reference temperature and to present the trend of the transformed strain values as a function of the pavement structure age.

The following conclusions and recommendations regarding the pavement condition in general (after 3 years in service) and the elasticity moduli of the pavement layers in particular are drawn:

- The back-calculated very low E-values for the sand capping layer (from 40 to 65 MPa) and the crushed masonry/concrete base (from 80 to 85 MPa) before overlaying highlight the inability of the EPS to provide a proper support to the roadbase in the considered pavement structure with a 130 mm thick asphalt layer. Correspondingly insufficient support of the roadbase to the asphalt layer resulted in a critically high asphalt strain of about  $192 \mu\text{m/m}$  ( $T=20^\circ\text{C}$ ). Use of overestimated E-values for the roadbase materials was probably the main reason for the inappropriate pavement design.
- Open joints between the EPS blocks in a sub-base can have very serious consequences for the design life of pavement structures, and thus have to be avoided by all means. The joints between the blocks in various layers should not coincide with each other. Open joints are especially risky in the case of an EPS sub-base which consists of only one EPS layer. The longitudinal joints between the EPS blocks should not be close to a wheel track. An adequate (lateral) support of the blocks is necessary to prevent any movement of the blocks.
- The back-calculated E-value of the EPS sub-base ranges from 10.4 to 19.7 MPa, which is somewhat higher than the elasticity moduli found in literature for the EPS types under consideration (EPS25 and EPS30).
- The back-calculated E-value of the asphaltic concrete layer varied between 5,000 and 25,000 MPa, due to the

temperature range of  $0.2^\circ\text{C}$  to  $31.0^\circ\text{C}$ , during the various FWD measurements. The E-modulus was about 10,500 MPa for the reference temperature  $T=20^\circ\text{C}$ .

- The E-value of the crushed masonry/crushed concrete base ranged from 140 to 600 MPa after overlaying. The modulus found for the sand varied between 70 and 150 MPa. In some measurements the values found for the crushed masonry/concrete base were lower than could be expected for this unbound material. In order to design an appropriate pavement thickness on an EPS sub-base the E-values obtained in this study for the unbound base and sand layer are suggested to be used as input data in calculations of the design life.
- The asphalt strain remained more or less constant in the 3-year period after overlaying. The constant value of the strain is a sign of a good condition of the pavement structure. The maximum horizontal tensile asphalt strain amounts to about  $85 \mu\text{m/m}$  at the reference asphalt temperature of  $20^\circ\text{C}$ .

### 4 3-D FINITE ELEMENT ANALYSIS

#### 4.1 Modelled Pavement Structures

The three-dimensional (3-D) finite element analysis of pavement structures with an EPS sub-base layer is necessary since it allows modelling of the block structure in the EPS sub-base, in contrast with two-dimensional or axial symmetric pavement models. Three separate 3-D analyses were carried out. Firstly, a 3-D pavement structure model was developed with a single vertical interface layer next to the wheel load. Secondly, a polder road was analyzed; in this case a much more complex model was developed to analyze the effects of: *a)* different block patterns, *b)* various EPS types in the sub-base and *c)* a concrete capping layer, on the stress and strain values in the pavement layers. Finally, using experiences from the previous analyses, a model for a motorway pavement structure was designed with a simplified EPS block structure to investigate the consequences of implementation of EPS (instead of sand) on the behaviour of (Dutch) motorway pavement structures.

The analysis of single-joint pavement structure model was performed to investigate whether the existence of an open joint in the sub-base does affect the pavement behaviour. In this particular analysis one interface layer was used to model the vertical joint. The wheel load was placed just adjacent to the joint to enforce maximum shear forces in the layer above the EPS sub-base. Also the effects of using a concrete (capping) layer above the EPS sub-base and a somewhat different EPS type were determined.

The polder road analysis was carried out because in the western part of the Netherlands a great number of polder roads are located in areas with a low bearing capacity subsoil. These polder roads, constructed in the traditional

way on soft, saturated subsoil, are subjected to (uneven) settlements. The use of EPS, particularly in the sub-base of these roads, is likely to offer a solution for the settlement problems by reducing the weight of the pavement structure. Once designed, the 3-D polder road model enabled the analysis of the effects of different block patterns in the sub-base on the pavement structure behaviour. The complexity of the model was defined by the need of modelling different block patterns by means of a single mesh.

The last finite element analysis was performed on a model for a motorway pavement structure with layer thicknesses corresponding to the usual values for Dutch motorways (see Figure 1). 3-D modelling of the heaviest loaded road type was done to determine to which extent building-in of EPS blocks in the sub-base influences its structural behaviour. The reference was an identical structure with a sand sub-base layer. Additionally, the effects of a concrete capping layer above the EPS blocks were investigated. Based upon the results of the previous analyses the motorway model was simplified compared to the polder road model. A single vertical joint was designed in the EPS layer and the axle load was placed next to that joint.

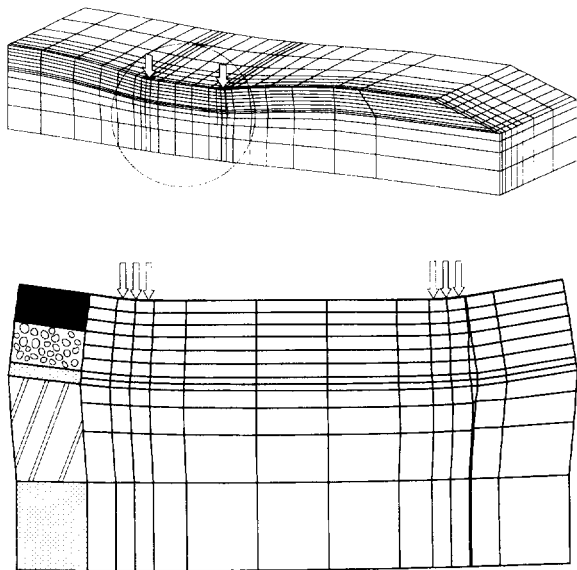


Figure 1. Resulting deformations due to a 100 kN axle load in a motorway pavement structure with an implemented EPS sub-base

All described models and analyses were realized by the means of the three-dimensional version of the finite element program CAPA (Computer Aided Pavement Analysis) (Scarpas 1995). The implemented interface elements allowed a flexible simulation of mechanisms in joint faces making this program one of the best of its kind.

#### 4.2 Concluding Remarks on 3-D Finite Element Analyses

- ❑ Open joints between the EPS blocks in the sub-base significantly affect the behaviour of pavement structures with an unbound roadbase. The wide joints make it impossible to support properly the above-laid unbound base. This results in insufficient support of the roadbase to the asphalt layer. Consequently, higher stress and strain values occur in the asphalt layer under the wheel load with as final result a shorter life of the pavement structure.
- ❑ Implementation of a concrete capping layer above the EPS sub-base neutralizes the (negative) influence of the joints between the EPS blocks on the pavement behaviour. Such a capping layer ensures enough support to the unbound roadbase layers above this layer, also in the case of existing open joints between the EPS blocks.
- ❑ The maximum vertical stress values occurring in the EPS sub-base layers under the 100 kN standard axle load do not exceed the linear-elastic region experimentally determined for this material.
- ❑ Application of a denser (and more costly) EPS type with a somewhat higher elasticity modulus in the sub-base has only a very limited influence on the horizontal strain values at the bottom of the asphalt layer and, therefore, on the overall behaviour of pavement structures with an EPS sub-base.
- ❑ In the case of the polder roads the existence of open vertical joints in the EPS sub-base results into approximately 10% higher horizontal asphalt strains under the 100 kN standard axle load when a wheel load is located above such a joint. Accordingly, if longitudinal open joints coincide with a wheel track it could lead to a reduction of the pavement life with about 40%.
- ❑ EPS sub-bases where the blocks are laid in various patterns deform somewhat different under traffic load. Different sub-base behaviour occurs along the joints between the EPS blocks. However, the absolute deformation differences are so small that the effects on the structural pavement behaviour are of no practical importance.
- ❑ The (negative) influence of the division of the sub-base into two sublayers seems to be very limited. Still, building-in the EPS blocks in at least two sublayers in the sub-base is recommendable to avoid continuous vertical joints. Avoiding open joints between the EPS blocks demands accurate laying and in order to do this it is easier to use less thick blocks because block dimensions always deviate somewhat.
- ❑ In case of the polder road, pavement strengthening by increasing the asphalt layer thickness with 30% (extra 50 mm) or by building-in a 150 mm thick cement treated capping layer above the EPS sub-base appeared to be similarly beneficial with respect to the horizontal asphalt strain. The realized asphalt strain reduction amounts to approximately 30% resulting in a 6 times longer pavement life.

- The horizontal strain values at the bottom of the asphalt layer of the motorway pavement structure with the sand sub-base are approximately 40% lower than the corresponding values above an open joint in the EPS sub-base. As a result of this the reduction of the pavement life would amount to about 12 times if the EPS sub-base has been built-in with a wide joint exactly along the wheel track.
- The implementation of a concrete capping layer above the EPS sub-base enables the design and construction of light-weight pavement structures with an EPS sub-base, suitable for heavily loaded motorways. Its design life is even longer than that of the corresponding traditional structures with a sand sub-base.

## 5 DESIGN GUIDELINES

### 5.1 Current Dutch Design Guidelines

Generally speaking, the current Dutch design procedure for pavement structures with an EPS sub-base includes three steps. In the first step the list of requirements is being established by defining both the boundary conditions and the design starting points. In the next step it is checked whether the implemented light-weight sub-base assures sufficient reduction, if not elimination, of settlements without danger of upward movements due to buoyancy. Repeated calculations for different sub-base thickness values in the assumed pavement structure lead iteratively to the optimum EPS layer thickness. Finally the durability of the considered pavement structure and built-in materials is checked for the expected traffic loading during the design life. Based on these calculations the thickness of the upper pavement layers above the EPS sub-base has to be determined.

The boundary conditions are: in-situ subsoil conditions, groundwater level and traffic intensity. Important subsoil conditions are the geotechnical profile, the density and thickness of the layers, the sensitivity to settlements, the soil mechanical history (settlements in the past) etc. The starting points, i.e. arbitrarily defined preconditions, are: the pavement design life expressed as the number of 100 kN standard axle load repetitions, the street level, and pavement material characteristics of the previously selected type of pavement structure.

This design procedure differs to a certain extent from the Dutch design procedure that is followed in the case of application of a traditional sand sub-base. The differences regard the weight-balance and the buoyancy calculations. Both calculations serve the purpose of determining the proper thickness of the EPS sub-base. With "proper EPS sub-base thickness" is meant such a thickness that subsoil settlements are eliminated or reduced to an acceptable amount; water absorption in the EPS sub-base is taken into account in the subsoil stress calculation by assuming an EPS

density of 100 kg/m<sup>3</sup>. The excavation depth for the EPS material may be restricted by considering the buoyancy forces for the case of highest possible ground water level. Even if areas are flooded the upper pavement layers must be heavy enough to keep the EPS sub-base in position. In the buoyancy calculation the dry density of the EPS sub-base material is used. The minimum safety factor recommended for buoyancy calculations amounts to 1.1 (De Wijs and Hengeveld 1988).

Once the proper EPS layer thickness has been determined the design procedure continues with calculation of the pavement design life based on the Shell Pavement Design Manual (1978). This mechanistic procedure is the main pavement design method used in the Netherlands. The Shell Pavement Design Manual considers the horizontal tensile strain at the bottom of the asphalt layer and the vertical compressive strain at the top of the subgrade to be of critical importance for the design. The asphalt strain value has to be limited in order to prevent asphalt fatigue cracking while the limitation of the vertical strain serves to prevent excessive permanent deformation in the subgrade. In the Manual strain values are given as a function of the allowable number of load applications. So, by knowing the strain values, one is able to determine the pavement design life expressed as 'allowable number of 100 kN axle load repetitions'.

### 5.2 Shortcomings of Current Design Guidelines

The missing part in the discussed current design procedure for pavement structures with an EPS sub-base is a design criterion regarding the EPS material. There is no established maximum value for either strain or stress occurring in the EPS layer due to the traffic load, the limit value which should not be exceeded because of negative effects on the material behaviour.

The strain occurring in the EPS layer is a result of the dead weight of the upper pavement layers, on one hand, and the traffic loading, on the other. Generally speaking, the higher the (static) strain component due to the dead weight, the lower the (dynamic) component due to the traffic loading. The static strain due to the dead weight of a thin pavement structure (where a relatively high dynamic strain can be expected) amounts to about 0.2% (Duškov 1997).

Cyclic loading test results point out that EPS15 does not accumulate permanent deformations under combined static and cyclic stress of 15 kPa and 20 kPa respectively. The related total strain amounted to 0.6%. EPS20 resisted a cyclic stress component of 30 kPa, i.e. undergoing cyclically a total strain of about 0.7%, without permanent deformation.

Based on the results reviewed above it may be stated that as long as the elastic deformation in the EPS sub-base due to repeated (traffic) loads is limited to 0.4%, then permanent deformation of the EPS blocks is negligible and will have no influence on the pavement behaviour. Therefore, the

design criterion for the EPS layer should be a maximum strain value of 0.4%.

In completed pavement structures the strains in the EPS sub-base due to the traffic loads are unlikely to be critical. More problems can be expected in the construction phase before all layers are built-in. If the EPS layer is overstressed by the construction traffic driving on (unbound) base layers, the effective EPS elasticity modulus is reduced and the water absorption increases.

Pavement analyses by means of both multi-layer (Duškov 1991) and finite element models (Duškov 1996) pointed out a negligible influence of the EPS thickness on the structural pavement behaviour. Due to the low elasticity modulus the EPS block layer simply does not contribute to the load distribution and functions only as a fill material.

Since the stress and strain values in the pavement layers are independent of the thickness of the EPS sub-base it is possible to determine the pavement design life before carrying out settlement and buoyancy calculations. As input value an unit EPS thickness, e.g. 0.5 m, could be applied. The advantage of such an approach is that the upper pavement layers can be designed first and their total weight thus is known before carrying out the weight-balance calculation and determining the thickness of the EPS layer.

### 5.3 Revised Design Guidelines

Based on the considerations given in the previous chapters the following guidelines for the design of pavements with an EPS sub-base are given.

- ⇒ In designing the pavement it must be realized that EPS20 blocks in contact with water will absorb about 2% v/v of water. EPS15 blocks will absorb more water, probably about 3% v/v. Although these volume percentages are low it means a considerable increase in weight which has to be taken into account when designing roads with EPS sub-bases. The usually assumed maximum density of saturated EPS of 100 kg/m<sup>3</sup> contains a high safety factor, a density of 50 kg/m<sup>3</sup> seems to be a more realistic value.

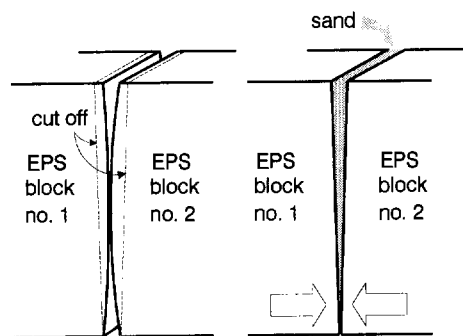


Figure 2. Filling up of joints between deviated blocks

- ⇒ During construction much attention should be paid to proper placement of the EPS blocks. All joints should be closed and load transfer across the joints should be promoted. As in the case with concrete block pavements, filling of the joints with jointing sand is strongly recommended. In order to be able to fill the joints a V type joint is recommended (Figure 2). Blocks with such joints can be easily made.
- ⇒ The EPS thickness has a negligible influence on the structural behaviour of the pavement. Therefore, first the upper pavement layers should be designed by using an unit EPS thickness, e.g. 0.5 m, and then, when the exact dead weight of the upper pavement layers is known, the weight-balance calculations should be performed and the proper EPS thickness determined. The revised design procedure, including the  $\epsilon_{EPS}$  criterion, is shown in Figure 3.

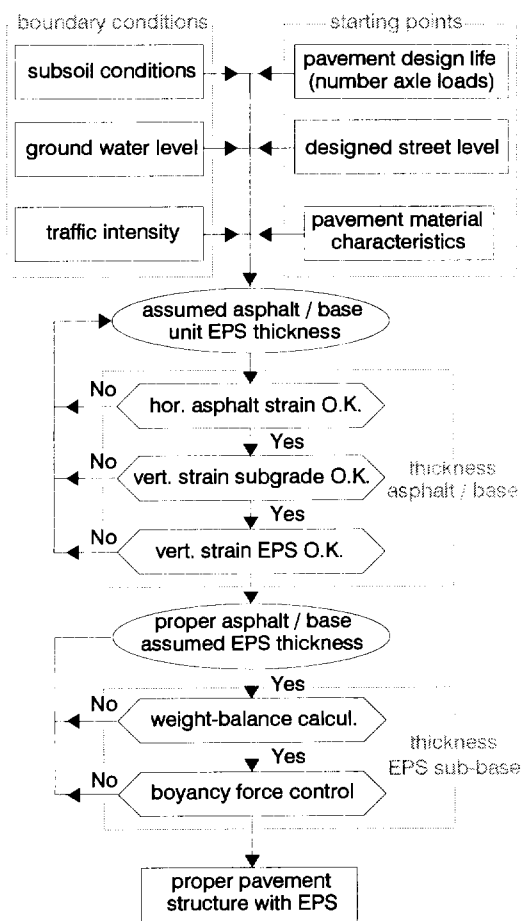


Figure 3. Flowchart of the revised Dutch design procedure (incl. EPS strain criterion) for flexible pavement structures with an EPS sub-base

- ⇨ Longitudinal joints between EPS blocks must not coincide with a wheel track because it will result into a significant reduction of the pavement life. The EPS block pattern should be designed such that longitudinal joints are located between the wheel tracks.
- ⇨ As long as the elastic deformation due to repeated (traffic) loads is limited to 0.4%, then permanent deformation of both EPS15 and EPS20 blocks is negligible and will have no influence on the pavement behaviour. Therefore, the vertical strain value of 0.4% should be used as the design criterion for the EPS layer.
- ⇨ During the construction phase, which is the most critical phase, special measures (such as steel planking) should or could be taken to ensure that the maximum allowable EPS strain value of 0.4% is not exceeded. Overloading EPS results in a lower modulus of elasticity and a higher water absorption.
- ⇨ The presence of an EPS sub-base in a pavement structure has a significant influence on the stress and strain development in the pavement. *If granular materials are placed immediately on top of the EPS layer* then the stiffness of such a layer is low and in fact much lower than is normally expected. Consequently, unbound material modulus values reduced up to 50% should be used as input data for design purposes.  
Unbound base materials that have the potential to develop a high stiffness do not pay off. Also relatively expensive self-cementing materials (e.g. blast furnace slags) seem to be not adequate above an EPS sub-base as cementing does not develop because of a significant amount of movement in the structure caused by the heavy traffic loads.
- ⇨ For design purposes a minimum elastic modulus of 5 MPa can be adopted for EPS20. In the case of EPS15 a minimum modulus of 4 MPa should be used.
- ⇨ Neither the modulus of EPS nor its other characteristics will deteriorate due to environmental influences like repeated wetting and freeze-thaw cycles.
- ⇨ The application of denser (and more expensive) EPS types with a somewhat higher elasticity modulus has no significant effects on the overall pavement behaviour. The use of EPS15, the lightest EPS type, instead of EPS20 can reduce the material costs considerably. However, one has to realize that the vertical strains in EPS15 will be about 1.25 times greater than those in EPS20, while the criterion  $\epsilon_{\text{EPS}} \leq 0.4\%$  is still valid.
- ⇨ Application of a cement treated capping layer on top of the EPS sub-base has a tremendously beneficial effect on the performance of the pavements. Such a capping layer neutralizes the effects of open joints between the EPS blocks, guarantees sufficient support to overlaying unbound base material even under high traffic intensity and eliminates any restriction for use of cheaper low-density EPS types. A cement treated capping layer is therefore strongly recommended.

- ⇨ Although additional work needs to be done to validate the test procedure modulus testing by means of the ultrasonic method is very promising for quality control of the blocks on site.

## 6 ACKNOWLEDGEMENT

Shell Nederland Chemie BV, Road and Hydraulic Engineering Division of the Ministry of Traffic, Public Works and Water Management (DWW-RWS), and Stybenex BV are gratefully acknowledged for sponsoring this research into EPS geofam.

## 7 REFERENCES

- Duškov, M. (1997) *EPS as a Light-Weight Sub-base Material in Pavement Structures*, PhD Thesis, Delft University of Technology, Delft, The Netherlands, p 251.
- Duškov, M. (1996) *3-D Finite Element Analyses of Pavement Structures with an EPS Geofam Sub-base*, Proc. Int. Symp. on EPS Construction Method, EPS TOKYO '96, Tokyo, Japan, pp. 48-57.
- Duškov, M. (1991) *Use of Expanded Polystyrene Foam (EPS) in Flexible Pavements on Poor Subgrades*, Proc. Volume 1, Int. Conf. on Geotechnical Engineering for Coastal Development, Yokohama, Japan, pp. 783-788.
- Scarpas, A. (1995). *CAPA Finite Elements System*, FEMA User's Manual, Faculty of Civil Engineering, Delft University of Technology, Delft, The Netherlands, p 55.
- Shell Pavement Design Manual* (1978), Shell International Petroleum Company Limited, London, UK.
- Wijs de, W., Hengeveld, H. (1989) *Roads on Expanded Polystyrene Foam* (in Dutch), Foundation for Building Research, Rotterdam, The Netherlands, p. 101.

# Particles Washout Associated With The Retention Of Broadly Graded Soils By Geotextiles

Jean Lafleur

Professor, Département de Génie Civil, Géologique et des Mines, Ecole Polytechnique de Montréal, Montréal, QC, Canada

**ABSTRACT:** Engineering sense suggests that the filtration opening size  $O_f$  of a filter does not need to be smaller than the smaller particles of a retained base to fulfill its function. Research on the filtration of broadly graded soils has shown however, that some finer particles are washed out in the process of soil filter bridge formation near the interface zone. The model proposed by Lafleur et al. (1989) relates the mass of washout and the associated settlement to the retention ratio of the combination  $R_R (= O_f/d_f)$  and to the broadness coefficient of the retained soil  $C_b (= O_f/d_o)$ . Compatibility tests between square mesh sieves and three different broadly graded bases were made. The results have confirmed the validity of the existing model.

**KEYWORDS:** Filtration, piping, Gradient Ratio test, woven geotextiles, seepage control.

## 1 INTRODUCTION

The main function of a filter is to retain soil particles without altering the flow of water. Current selection criteria are based on geometric and hydraulic considerations supplemented by experimental evidence from which success or failure has been assessed. Success involves implicitly that there is no washout of soil particles. Giroud (1996) admits however, *that soil retention does not require that the migration of all soil particles be prevented. Soil retention simply requires that the soil behind the filter remains stable.* The amount of washout has been recognized as an important factor in the interpretation of compatibility tests (Austin et al., 1997, Fannin et al., 1994, Honjo et al., 1996, Lafleur et al., 1996, Bhatia et al., 1996). The overall performance of a drainage structure is related to the washout that produces two detrimental effects:

- ▶ formation of voids and caverns near the filter interface, that transmit uneven subsidence at the surface;
- ▶ filling and clogging of downstream water conveyance systems.

The severity of the loading is not the same for every application. For example, a dynamic environment such as beneath roads or erosion control applications is more aggressive on the particles than a static, continuous flow. The consequences of washout may also vary. In dams, concentrated washout and piping lead to the formation of sinkholes at the crest. Austin et al. (1997) have demonstrated that a 150 mm diameter and 100 m. long drainage pipe with a 3% slope can be completely filled at the lowest point in the profile when washout is in the order of 0.25 kg/m<sup>2</sup>.

## 2 PREDICTION OF WASHOUT

Before a filter/base combination attains equilibrium, appreciable washout can occur, especially in broadly graded soils. Lafleur et al. (1996) have shown that for nonwoven geotextiles, the

particles migration is less than 2.5 kg/m<sup>2</sup> provided that for internally stable soils,

$$R_R < 1$$

where:

$R_R$  = retention ratio =  $O_f/d_f$

$O_f$  = filtration opening size obtained from hydrodynamic sieving

$d_f$  = base indicative size

=  $d_{35}$  for uniform soils ( $C_u \leq 6$ )

=  $d_{30}$  for broadly ( $C_u > 6$ ) linearly graded soils

=  $d_{30}$  for broadly concave upward graded soils

=  $d_G$  for broadly gap graded soils ( $d_G$  is the lowest size of the gap)

For internally unstable or suffusive soils, the filtration process is different. Suffusive soils are broadly graded with gradation curves that are markedly concave upward or that show a gap below 30% passing. It has been shown by Kenney and Lau (1985) that for such soils, finer particles can move within the coarser grains skeleton. These movable particles can form a cake near the base/filter interface if  $O_f$  is too small. This phenomenon is called blinding or external clogging. To avoid this risk, the filter must have a minimum opening size. At the other extreme, to avoid piping,  $O_f$  must be less than a given value,  $d_f = d_{30}$  and

$$1 < R_R < 5$$

Lafleur et al. (1989) have studied the self-filtration or bridging that develops near the interface zone separating broadly graded soils from filters. They presented a model to evaluate the amount of base washout  $M_p$  induced in the

process and the associated settlement  $\Delta H$ . Some assumptions had to be made:

- ▶ the combination is compatible i.e. the retention ratio is smaller than 5;

- ▶ the soil near the interface is divided into  $m$  layers, with

$$m = \left\lceil \frac{\log C_B}{\log R'_R} \right\rceil \quad \text{and } C_B = \text{breadth coefficient} = O_p/d_o$$

- ▶ all the fines smaller than the opening size of each upstream layer are washed out. The constriction size of the remaining particles is equal to their minimum grain size divided by the ratio  $R'_R$  taken equal to 9 (Sherard et al., 1984).

The induced settlement is given by

$$\Delta H = d_{100} \sum_{j=1}^m \left( \frac{P_j}{100} \right)$$

$P_j$  = percent in mass finer than  $(O_p/R'_R)^j$  originally present in the  $j$ th layer and  $i = j - 1$

The mass of washout is equal to

$$M_p = \rho_D \cdot \Delta H \quad \text{where } \rho_D = \text{dry density of the base}$$

An extensive testing program was designed to bring some experimental support to the above model and to verify the accuracy of the assumptions.

### 3 TESTING PROGRAM

The program involved broadly graded soils with different gradations filtered by square mesh sieves. The filtrimeter shown on Fig. 1 was used. Its diameter is 197 mm such as to minimize wall effects for samples containing coarse particles. Four lateral piezometers at distances of 55, 90, 130, 180 mm respectively from the filter, allowed the evaluation of the local permeabilities. Water was circulated downward at an overall gradient of 5 through the soils. The downstream part of the filtrimeter was submerged to maintain positive pressure head throughout the samples. The sieve openings were 19.1, 9.52, 4.76 and 2.00 mm and the filters designated 19, 10, 5 and 2 respectively.

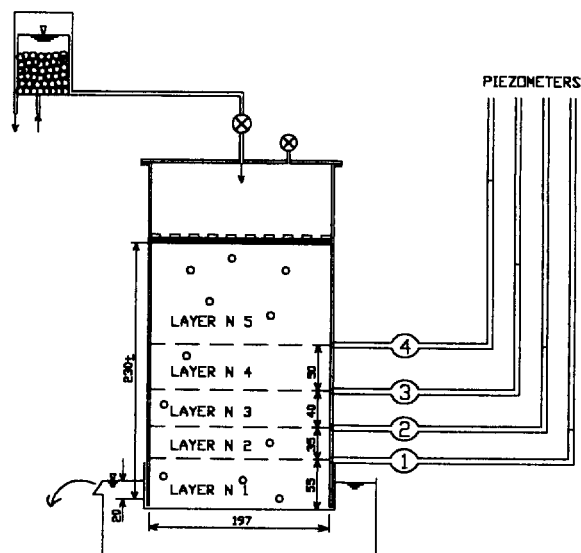


Fig. 1 Filtrimeter for screen tests

The soils were reconstituted either from natural subrounded particles (G) or spherical glass beads (B) comprised between 0.1 and 19 mm in size. Their gradations are described on Fig. 2 and Table 1: rectilinear (R), gap-graded (D) and concave upward (C). They are internally stable and broadly graded. Although their coefficients of uniformity varies between 7 and 21, their coefficients of curvature do not lie between 1 and 3, so they cannot be classified as "well-graded". Their indicative size  $d_i$  (arrows on Fig. 2) varies between 0.7 and 3.0 mm.

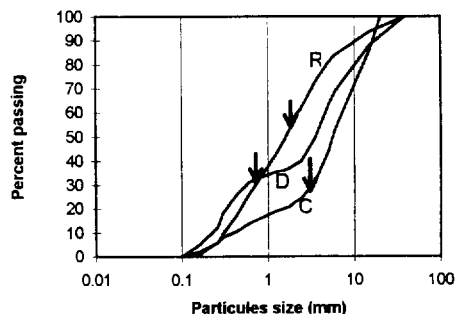


Fig. 2 Gradation curves of tested bases



Table 1 Base soil gradation properties

base	$d_{10}$ mm	$d_{85}$ mm	$d_f$ mm	$C_u$	$C_c$
R	0.29	6.6	1.8	6.9	0.77
D	0.22	11.8	0.7	20.0	0.31
C	0.37	13.6	3.0	18.9	3.59

The tests lasted 150 minutes and vibrations were applied by tapping with a rubber hammer on the sides of the permeameter. Equilibrium was interpreted on the basis of the shape of the local permeability curves. At the end of the tests, the mass of passing particles was recorded and the samples were cut for gradation analyses into 5 slices, limited at the top and at the bottom of the sample and at the level of the piezometers.

#### 4 RESULTS

The Table 2 gives an overview of the test results. The retention ratio  $R_R$  of the combinations varies between 0.7 and 27 and those for which the model applies ( $R_R < 5$ ), have been highlighted. One can appreciate the convergency between the model and the measurements, from the computed relative errors  $\Delta$ . It appears that, although the measurements are in the same order of magnitude as the calculations, the model underestimates the amount of washout. The shape of the particles may have played a role since for a given opening size, the washout is nearly the double with the spherical grains (tests B). These are more mobile than the subrounded particles G and thereby, more susceptible to washout.

The Fig. 3 is a logarithmic plot of the mass of washout versus the retention ratio for all the tests of this program:  $M_p$  increases regularly with  $R_R$ . At the critical  $R_R$ -value of one, the plot indicates that  $M_p$  varies between 8 and 50 kg/m<sup>2</sup>, which is more than the previously mentioned limit of 2.5 kg/m<sup>2</sup>. This discrepancy can be related to the structure of the filter. The metallic mesh sieves used in the tests are similar to a woven geotextile and they have a large Percent Open Area (POA), varying between 62 and 75%. This is much more than the current woven geotextiles for which POA ranges between 1 and 20% (Mlynarek and Lombard, 1997). For purpose of comparison, the results of compatibility tests made by these authors (designated ML) have been reported on Fig. 3. They have been classified as low POA ( $\leq 10\%$ ) and high ( $40\% > POA > 10\%$ ). The influence is obvious: for a  $R_R$ -value of one,  $M_p$  is equal to 0.24 kg/m<sup>2</sup> for POA <10 and to 0.92 kg/m<sup>2</sup> for POA > 10.

Physically, when the ratio between the solid retention structure (filaments) and the opening voids is higher, there is relatively more surface to retain particle so that bridging and retention are easily promoted. Giroud (1996) arrived at similar conclusions when he demonstrated that for nonwoven geotextiles with given thickness and fibres diameter, the opening size is smaller with lower porosity.

Table 2 Tests results and comparison

	$R_R$	$\Delta H$ (mm)			$M_p$ (kg/m <sup>2</sup> )		
		meas	calc	$\Delta\%$	meas	calc	$\Delta\%$
GR19	10.6	137.0			201.0		
GR10	5.6	52.9			88.4		
GR5	2.8	15.5	13.4	-14	27.1	18.6	-31
GR2	1.1	5.1	11.3	+122	7.5	15.7	+109
BR19	10.6	-			394.8		
BR10	5.6	-			366.0		
BR5	2.8	23.9	9.4	-61	41.0	14.5	-65
BR2	1.1	6.8	7.3	+7	12.0	11.1	-8
GD19	27.1	76.0			128.8		
GD5	7.1	9.7			17.4		
GD2	2.8	6.8	6.7	-1	11.8	9.5	-19
BD19	27.1	-			393.7		
BD10	14.3	105.8			187.0		
BD5	7.1	18.5			34.0		
BD2	2.8	10.2	5.2	-49	19.4	8.4	-57
GC19	6.3	51.9			87.1		
GC10	3.3	13.3	5.1	-62	24.4	8.0	-67
GC5	1.7	4.8	4.4	-8	9.0	6.1	-32
GC2	0.7	2.2	3.8	+73	5.4	5.4	0
BC19	6.3	-			394.0		
BC10	3.3	126.6	4.9	-96	220.0	7.3	-97
BC2	0.7	6.7	2.6	-61	17.0	4.1	-76

Fannin et al. (1994) have performed modified Gradient Ratio tests on nonwoven geotextiles and different soils. Their results (FVS) have also been plotted on Fig. 3 separating uniform (U) and well-graded (WG) base soils. The shape of the  $M_p$ - $R_R$  curve is different: for well graded soils it is gradual, for uniform soils, it shows a sharp quasi vertical break around  $R_R = 1$ .

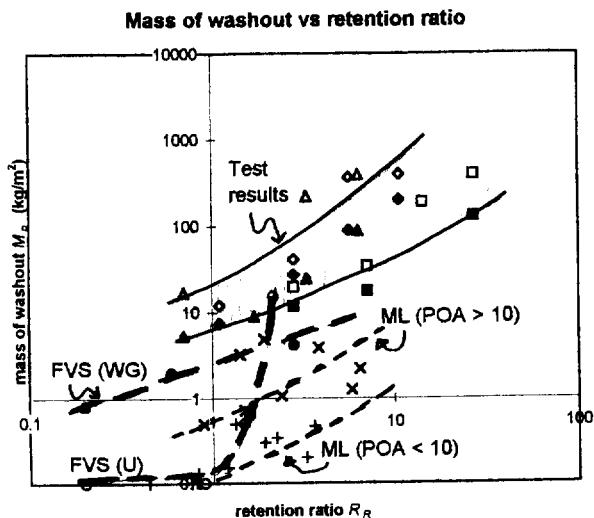


Fig. 3 Mass of washout versus retention ratio

## 5 DISCUSSION AND CONCLUSION

The amount of washout associated with the filtration of broadly graded soils was evaluated from screen tests using square conventional sieve mesh with different opening sizes.

The results have confirmed the validity of the approach suggested by Lafleur et al. (1989). The retention ratio  $R_R$  between the opening size of a filter and the indicative size of the base, is the most important factor intervening in the amount of washout. The experimental relationship between  $M_p$  and  $R_R$  is gradual for broadly graded soils while for uniform soils, it shows a marked bend around  $R_R = 1$ . The success or failure of a filter for broadly graded soils is therefore quite subjective because it depends on the amount of tolerable washout. Finally, the results have disclosed that the Percent Open Area and by extension, the porosity, play a role in the rearrangement of the particles near the interface. The lower the value, the lower the washout.

## ACKNOWLEDGMENT

The author wishes to acknowledge the diligent work of Khaireddine Sakrani, who performed the tests as partial fulfilment for his M.Sc.A. degree and of Sebastien Lopez, who helped in the preparation of this paper.

## REFERENCES

- Austin, D.N., Mlynarek, J. & Blond, E. (1997). Expanded anti-clogging criteria for woven filtration geotextile. *Geosynthetics '97*, IFAI, Long Beach, CA, USA, Vol. 2, pp. 1123-1144.
- Bhatia, S.K., Moraille, J., Keith, K. & Smith J.L. (1996). Comparative performance of granular vs. geotextile filters in the laboratory. *GEOFILTERS '96* edited by Lafleur & Rollin, Montréal, QC, Canada, pp. 449-460.
- Fannin, R.J., Vaid, Y.P. & Shi, Y.C. (1994) Filtration behaviour of nonwoven geotextiles. *Canadian Geotechnical Journal*. Vol. 31, No. 4, pp. 555-563.
- Giroud, J.P. (1996). Granular filters and geotextile filters. *GEOFILTERS '96* edited by Lafleur & Rollin, Montréal, QC, Canada, pp. 565-680.
- Honjo, Y., Haque, M.A. & Tsai, K.A. (1996). Self-filtration behaviour of broadly and gap-graded cohesionless soils. *GEOFILTERS '96* edited by Lafleur & Rollin, Montréal, QC, Canada, pp. 227-236.
- Kenney, T.C. & Lau, D. (1985). Internal stability of granular filters. *Canadian Geotechnical Journal*, Vol. 22, No. 2, pp. 215-225.
- Lafleur, J., Eichenauer, T. & Werner, G. (1996). Geotextile filter retention criteria for well graded cohesionless soils. *GEOFILTERS '96* edited by Lafleur & Rollin, Montréal, QC, Canada, pp. 429-438.
- Lafleur J., Mlynarek J. & Rollin A.L. (1989). Filtration of Broadly Graded Cohesionless Soils. *Journal of Geotechnical Engineering*, ASCE, Vol.115, No.12, pp.1747-1768
- Mlynarek, J., & Lombard, G. (1997). Significance of percent open area (POA) in the design of woven geotextile filters. *Geosynthetics '97*, IFAI, Long Beach, CA, Vol. 2, pp. 1093-1107.
- Sherard J.L., Dunnigan, L.P. & Talbot, J.R. (1984). Basic properties of sand and gravel filters. *Journal of Geotechnical Engineering*, ASCE, Vol. 110, No. 6. pp. 684-700.

# Geotextile Characteristic Opening Size: The Influence of Some Test Parameters

Barroso, Madalena C. P.

Research Assistant, National Civil Engineering Laboratory (LNEC), Lisbon, Portugal

Lopes, Maria da Graça D. A.

Senior Research Officer, National Civil Engineering Laboratory (LNEC), Lisbon, Portugal

**ABSTRACT:** Designing a geotextile for filtration applications requires information on the characteristic opening size of the geotextile. Several techniques are available for measuring the characteristic opening size, but there is no one universally accepted. Three test methods are usually used: dry sieving, hydrodynamic sieving and wet sieving. The wet sieving test method was used to study the influence of some test parameters (soil granulometry, water flow rate and vertical amplitude) on the results of opening size measurement. For this purpose six nonwoven geotextiles were used. The results showed that the test conditions can indeed influence results of the measurement of characteristic opening size.

**KEYWORDS:** Geotextile, Wet sieving test method, Characteristic Opening Size

## 1 INTRODUCTION

Where geotextiles are used as filters they must perform two functions simultaneously. One is to retain fine soil particles and the other is to allow the seepage of water from the retained soil. The ability of the geotextile to filter is a function of the size and distribution of the pores and the porosity. However, the distribution of the pores within the geotextile is difficult to determine. As a result, several indirect test methods have been developed. Three techniques are used: dry sieving, standardised in the United States, United Kingdom, Belgium and the Netherlands; hydrodynamic sieving, standardised in Canada, France and Italy; and wet sieving, standardised in Germany, Austria and Switzerland. For a given geotextile the results obtained are dependent on the test method used (Bhatia & Smith, 1995).

In order to obtain a unified standard in Europe, the different existing national standards are being harmonised under the auspices of the European Committee for Standardisation (CEN). An index test has been developed based on the wet sieving technique. A specific parameter, the Characteristic Opening Size (COS also called  $O_{90}$ ), indicates the size of the largest grain size particle that can pass through the geotextile.

A final draft European Standard was authored by Technical Committee 189 and was recently submitted for formal vote to the European countries (prEN ISO 12956). Before becoming a standard the test method was validated. It was necessary to clarify the influence of some specific parameters, in order to determine the best test conditions. During the work on standard harmonisation, intercomparison tests were performed in several countries. The results obtained have shown that  $O_{90}$  can be affected by test conditions, as reported by Faure (1996).

In this context, a test programme has been carried out in Portugal's National Civil Engineering Laboratory (LNEC), to study the influence of some test parameters, namely the soil granulometry, the vertical amplitude and the water flow rate.

## 2 DESCRIPTION OF THE TEST PROCEDURE

The tests were performed based on final draft of the European Standard prEN ISO 12956 (Geotextiles and geotextile related products—Determination of the characteristic opening size).

The principle of the test is to sieve a well graded granular material (usually soil) through a geotextile specimen. The specimens are soaked in water at laboratory temperature and leave it to saturate for at least twelve hours. Then they are placed in the clamping device on the sieving apparatus (figure 1). For each specimen, a soil mass of 7,0 kg per square meter of exposed sieving area is spread on the geotextile and watered by means of a spray nozzle. The water supply is open and it is adjusted by the operator in order to spray uniformly over whole specimen ensuring that all soil particles are wetted, but do not allow the water level to rise above the granular material. The amplitude of sieving is adjusted to a sufficient level to agitate the soil particles. During 10 minutes of sieving all water and soil passing through the specimen are collected. The passed soil is dried and weighed. The particle size distribution is plotted on a semi-logarithmic graph with sieve size on the horizontal axis and the cumulative percentage of the combined passed granular material on the vertical axis. The Characteristic Opening Size corresponds to the  $d_{90}$  of the particle size distribution curve ( $O_{90}=d_{90}$ ).

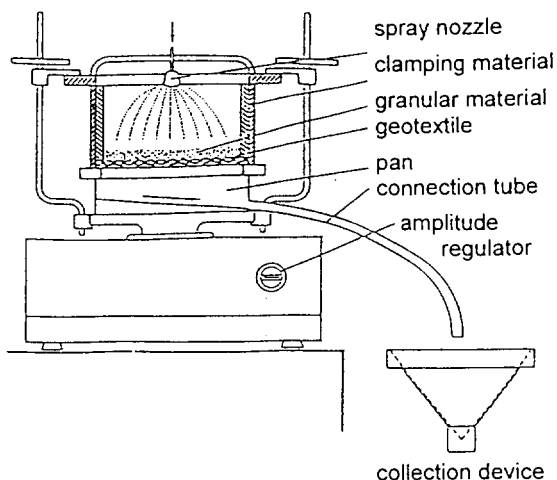


Figure 1. Example of apparatus.

### 3 MATERIALS TESTED

Six nonwoven geotextiles were used in this work. Table 1 presents the fabrics tested.

Table 1. Geotextiles tested.

Geot.	Manufacturing process	Polymer type	Mass per unit area (g/m <sup>2</sup> )
A	Needlepunched nonwoven	Polyester	133
B	Needlepunched nonwoven	Polypropylene	242
C	Needlepunched nonwoven	Polypropylene	476
D	Heatbonded nonwoven	Polypropylene	139
E	Needlepunched nonwoven	Polyester	134
F	Needlepunched nonwoven	Polyester	293

### 4 TEST PROGRAMME

Before the experimental programme started, the repeatability of the test method was studied. Geotextile B was selected to evaluate the  $O_{90}$  of over forty-eight specimens. The tests were performed with a vertical amplitude of 0,75 mm and with an average water flow rate of 1,4 l/min (at a pressure of 200 kPa). The soil used was the Soil 2 (see figure 2). The  $O_{90}$  obtained was:

- average = 84  $\mu$ m

- standard deviation (s) = 4,5  $\mu$ m
- coefficient of variation = 5,2 %

Based on these values the repeatability of the test method was judged to be good.

During the tests several problems occurred:

- the soil tended to agglomerate on the surface of some specimens, preventing the soil from passing through the geotextile. When this happened, the water flow rate was increased until the agglomerate was broken up;
- water accumulated above some specimens. In these cases, the water flow rate was reduced to avoid soil particle loss.

Following the repeatability tests, the  $O_{90}$  test conditions were studied. Firstly three geotextiles were tested with several soils. Then another three geotextiles were tested with different amplitudes and two water flow rates. Table 2 shows the parameters analysed and the geotextiles used.

Table 2. Parameters analysed.

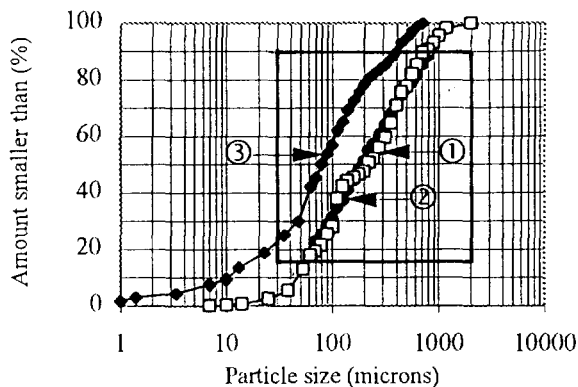
Geotextile	Repeat-ability	Soil granul.	Amplitude	Water flow rate
A			•	•
B	•		•	•
C			•	•
D		•		
E		•		
F		•		

### 5 TEST RESULTS AND DISCUSSION

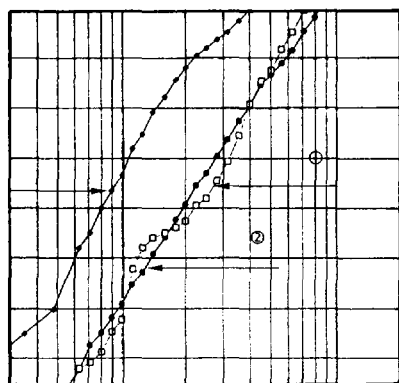
#### 5.1 Influence of Soil Granulometry on $O_{90}$

Three soils were used (figure 2 a). According to the CEN draft test method, the soil used must fulfil the following requirements: it must be cohesionless; the uniformity coefficient ( $C_u$ ) must be greater than 3 and smaller than 20; the soil must not be gap-graded; and the assumed  $O_{90}$  must be between  $d_{20}$  and  $d_{80}$ . Table 3 presents the features of the soils used.

Soil 1 was initially analysed using the ASTM series of sieves, which has fewer sieves than the ISO series. As result, the soil granulometry was not well defined for the particle sizes used to estimate  $O_{90}$ . Therefore, a new soil (Soil 2) was made up. The difference in particle size distribution obtained for Soils 1 and 2 (see figure 2 b) show how important it is to use a higher number of sieves, to define properly the soil granulometry.



(a)



(b)

Figure 2: (a) Particle size distribution of the soils used; (b) detail on difference of Soil 1 and Soil 2.

Table 3. Characteristics of the soils.

Soil 1	Soil 2	Soil 3
$C_u = 6,8$	$C_u = 5,9$	$C_u = 10,3$
$d_{20} = 75 \mu\text{m}$	$d_{20} = 67 \mu\text{m}$	$d_{20} = 25 \mu\text{m}$
$d_{80} = 532 \mu\text{m}$	$d_{80} = 583 \mu\text{m}$	$d_{80} = 218 \mu\text{m}$

The tests were performed with an average water flow rate of 1,8 l/min (at a pressure of 200 kPa). The amplitude selected was 0,75 mm. The results obtained are presented on table 4.

It seems that the  $O_{90}$  values are dependent on the soil used, especially for geotextiles with smaller mass per unit of area, since the one with higher mass per unit area only showed a slight difference in  $O_{90}$ .

Several problems occurred during the tests:

- water accumulated above some specimens of geotextile F when tested with Soil 1, and above some specimens of

geotextiles D, E and F, when tested with Soil 3. The wet sieve pan outlet did not drain the water quickly enough. The solution adopted was to decrease inflow and the amplitude until the water drained;

- it was difficult to keep the amplitude constant for some specimens of geotextiles A, B and C tested with Soils 1 and 2. Changes occurred without any apparent cause. When this occurred, the operator had to adjust the amplitude manually.

Table 4. Variation of  $O_{90}$  with the soil granulometry.

Geotextile	Soil 1	Soil 2	Soil 3
	$O_{90} (\mu\text{m})$	$O_{90} (\mu\text{m})$	$O_{90} (\mu\text{m})$
D	119	125	113
E	118	122	111
F	118	116	110

### 5.2 Influence of Amplitude on $O_{90}$

The tests started with geotextile B carried out with three vertical amplitudes of 0,75 mm, 1 mm, and 1,25 mm, keeping the water flow rate constant (2,4 l/min, at a pressure of approximately 200 kPa). Since the time available to perform the tests was very limited and because the results obtained with geotextile B showed a very small difference in  $O_{90}$  for amplitudes higher than 1 mm, the geotextiles A and C were tested only with amplitudes of 1 mm and 1,25 mm. Nevertheless, it is believed that the results for geotextiles A and C would also follow the same trend, thus producing similar results to those given by geotextile B for amplitudes below 1 mm.

Soil 2 was used in the tests. The overall results are presented in figure 3.

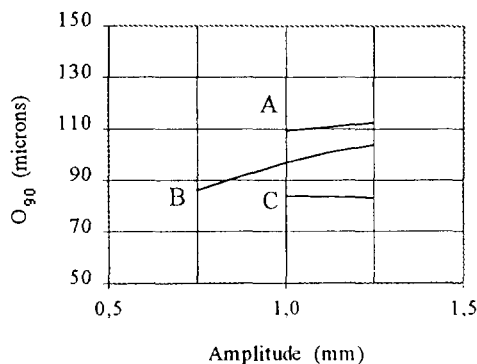


Figure 3. Variation of  $O_{90}$  with the amplitude.

The results showed only a slight variation in  $O_{90}$  with the increasing amplitude for amplitudes above 1 mm.

Several observations were made during the tests:

- the same problem with soil agglomeration on the surface of the geotextiles previously reported also occurred with some specimens of geotextiles A and C, when tested with the amplitude of 1 mm, and with some specimens of geotextile A at an amplitude of 1,25 mm. In these cases, the solution adopted was to increase the water flow rate until the agglomerate was broken up;
- the difficulty with accumulation of water, also occurred with some specimens of geotextile C, when tested with both amplitudes, and with some specimens of geotextile B during the tests performed with an amplitude of 1,25 mm; once more the water flow rate was reduced;
- it was difficult to keep the amplitude constant when some specimens of geotextile A were tested. It decreased without any explanation. When this occurred, the operator had to adjust the amplitude manually.

### 5.3 Influence of Water Flow Rate on $O_{90}$

The tests were performed with two water flow rates: 2,4 l/min (at a pressure of approximately 200 kPa) and 3,0 l/min (at a pressure of approximately 300 kPa), keeping the vertical amplitude constant (1 mm). Soil 2 was used in the tests. The results obtained are presented in figure 4.

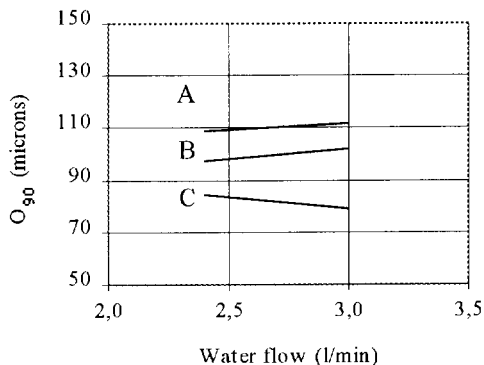


Figure 4. Variation of  $O_{90}$  with the water flow rate.

The results showed that there are no significant differences in  $O_{90}$  values obtained when water flow rate is varied, for the soil used.

During the tests several problems occurred:

- the soil tended to agglomerate on the surface of some specimens of the geotextiles A and C, preventing the soil from passing through the geotextiles. When this occurred the water flow was reduced once more. As tests

progressed, soil agglomerates moved freely over the geotextile specimens;

- water accumulated above some specimens of the geotextile C, due to air that was trapped inside the top chamber. When this happened, the test was stopped and the water was allowed to flow through the inlet pipe, before the test was continued.

## 6 CONCLUSIONS

Based on the test results the following was concluded:

- (1) for nonwoven geotextiles, soil granulometry seems only to influence  $O_{90}$  values for geotextiles with small mass per unit area. However, only a few geotextiles were tested, therefore, it is difficult to know if this influence may be attributed to the variability of the nonwoven geotextiles themselves;
- (2) for nonwoven geotextiles, the  $O_{90}$  appeared not to be influenced by amplitude, when the amplitude was higher than 1 mm;
- (3) for nonwoven geotextiles, the  $O_{90}$  seemed not to be affected by the water flow rate.

These conclusions must be seen in the light of the small number of tests that were performed, and the experimental difficulties encountered. The authors suggest that more tests should be carried out using different types of geotextiles.

## ACKNOWLEDGEMENTS

The authors wish to thank to Programme Praxis XXI of Ministry for Science and Technology and to FEDER, for financial support under its Project 3/3.1/CEG/2598/95.

## REFERENCES

- Bhatia, S. K. & Smith, J. L. (1995) "Sieving techniques for measuring pore openings—an open question", *Proceedings of the Geosynthetics '95 Conference*, Nashville, Tennessee, USA, Vol. 1, pp. 281-295.
- Faure, Y. H. (1996) "Characteristic opening size of geotextiles: European intercomparison tests for standardisation", *Proceedings of the 1st European Geosynthetics Conference*, Eurogeo, Maastricht, Netherlands, pp. 1047-1054.
- prEN ISO 12956 (1996) Geotextiles and geotextiles related products - Determination of the characteristic opening size.

# Permeability Requirements For Geotextile Filter Design

R.J. Fannin,  
Assoc. Professor, Department of Civil Engineering, University of British Columbia, Vancouver, B.C., Canada

Y.C. Shi  
Sembawang Engineering and Construction Pte Ltd., Singapore

Y.P. Vaid  
Professor, Department of Civil Engineering, University of British Columbia, Vancouver, B.C., Canada

**ABSTRACT:** Inconsistencies in design of geotextile filters are reported, with reference to current regulatory guidance. Results of laboratory Gradient Ratio tests are then described, and used to illustrate the role of a unified approach to interpretation of soil-geotextile compatibility that accounts for hydraulic gradient, permeability, and excess water head (or porewater pressure) across the filter.

**KEYWORDS:** Filtration; Geotextiles; Gradient Ratio Tests; Permeability; Seepage Control

## 1. INTRODUCTION

Design requirements for a geotextile in filtration applications include soil retention, permeability and strength. The permeability requirements are intended to promote an unimpeded flow of water through the filtration zone. Approaches used in design are derived from empirical relationships comparing the permeability of the geotextile filter ( $k_F$ ) to that of the soil ( $k_S$ ). The USFHWA (Christopher and Holtz, 1985) and Canadian Foundation Engineering Manual (CGS, 1993) require that for filtration of fines in critical or severe applications:

$$k_F > 10 k_S \quad (1)$$

and for filtration of clean medium to coarse sands:

$$k_F > k_S \quad (2)$$

More recently Giroud (1996) has proposed separate design criteria for the pore water pressure, to limiting value of 10% of the compressive stress, and for an excessive reduction in flow rate, to a limit of 10% of that in the soil without a filter. The limit values of 10% in the criteria, which are arbitrary and based on judgement, yield the following relationships:

$$k_F > 10 k_S i_S \quad (\text{excessive pore water pressure}) \quad (3)$$

$$k_F > k_S \quad (\text{excessive flow rate reduction}) \quad (4)$$

In laboratory testing, the relative permeability of the soil and the permeability of the geotextile are evaluated to ensure compatibility. One example is the Gradient Ratio test (ASTM D5101) which allows the permeability of the soil-geotextile composite zone ( $k_{sg}$ ) to be compared with that of the soil ( $k_S$ ). Piping of material adjacent to the geotextile yields a value of  $GR_{ASTM} < 1$ , while in contrast clogging yields a value of  $GR_{ASTM} > 1$ , where ports 3, 5 and 7 define  $GR_{ASTM} = i_{57}/i_{35}$  (see Fig. 1). The basis for a unified interpretation of the GR test was presented (Fannin et al., 1994a), in which the historic limiting criterion of  $GR_{ASTM} < 3$  for compatibility of geotextile and soil was shown, from continuity of flow, to yield an implicit permeability ratio given by:

$$k_{57} > 0.33 k_{35} \quad (5)$$

This criterion for clogging, proposed by Haliburton and Wood (1982) and later adopted by regulatory agencies, differs markedly from the companion empirical criteria for permeability reported above, most notably that of Giroud (1996) for excessive pore water pressure. In this paper, results are presented to illustrate the development of this composite zone with time. The objective is to assess the implications of apparent contradictions in the permeability and clogging criteria advocated for filter design.

## 2. GRADIENT RATIO (GR) TEST RESULTS

A program of tests was performed on selected combinations of 10 soils (4 uniformly graded and 6

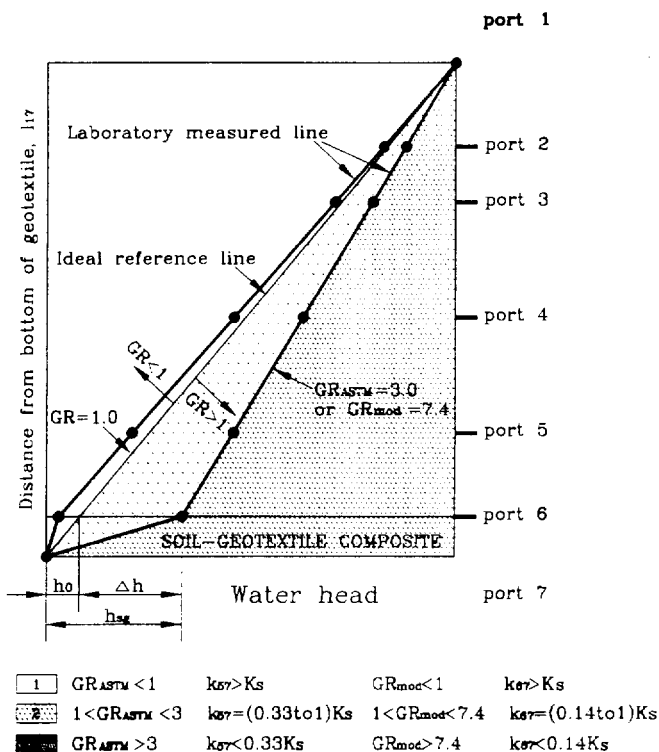


Fig. 1. Schematic unified interpretation of the gradient ratio test.

broadly graded) and 4 needle-punched nonwoven geotextiles (Shi, 1993; Fannin et al., 1994a). The GR permeameter was modified to include 3 ports in addition to those specified in the ASTM test method, as follows: port 6 is located only 8 mm above the top surface of the geotextile specimen, port 4 is located midway between ports 3 and 5, and port 2 is located 13 mm above port 3.

Measurements were taken of the water head at each port, and the resulting flow rate, at four values of imposed system hydraulic gradient in the range  $i_{17} = 1$  to 10.

Values of permeability in the soil ( $k_{35}$ ) and in the very thin soil-geotextile composite zone ( $k_{67}$ ) were then deduced, together with a  $GR_{mod}$  given by  $k_{35}/k_{67} (= i_{67}/i_{35})$ . A similar approach has been reported by Austin et al. (1997).

Results are reported for two of the broadly graded soils (BML74 and BML90) with one nonwoven needle punched geotextile, for which material properties are reported in Tables 1 and 2. The variation of permeability with time, see Fig. 2, shows a permeability in the composite zone which is greater than of the soil for BML90 (a silt with trace of sand) but less than that of the soil for BML74 (a sandy silt). The behaviour appears independent of system gradient. The stable response over time is attributed in part to the technique used in sample

Table 1 Properties of the soils

Description	Code	$D_{85}$ ( $\mu\text{m}$ )	$D_{50}$ ( $\mu\text{m}$ )	$D_{15}$ ( $\mu\text{m}$ )	$C_u^a$	$K_{35}^b$ (m/s)
Silt with sand	BML74	246	43	12	5.5	$1 \times 10^{-6}$
Silt	BML90	57	22	9	4.1	$1 \times 10^{-6}$

<sup>a</sup>Coefficient of uniformity ( $D_{60}/D_{10}$ )

<sup>b</sup>Typical value

Table 2 Properties of the nonwoven geotextile

FOS ( $\mu\text{m}$ )	Thick- ness (mm)	Mass/unit area ( $\text{g}/\text{m}^2$ )	Grab strength (N) MD/CMD <sup>a</sup>	Elongation (%) MD/CMD
150	1.6	199	677/720	53/102

<sup>a</sup>MD = Machine direction; CMD = Cross-machine direction

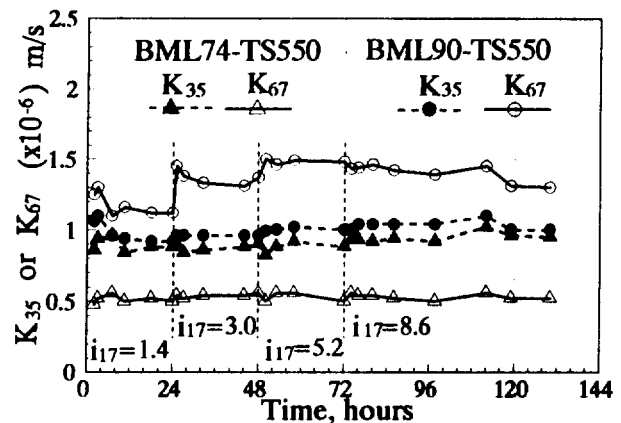


Fig. 2. Permeability of soil and soil-geotextile composite.

preparation, which ensures full saturation of the soil and geotextile (Fannin et al., 1994b).

### 3. EXCESS WATER HEAD LOSS

A relationship for excess water head loss  $\Delta h$  was presented by Shi et al (1996), where with reference to Fig. 1:

$$\Delta h = h_{sg} - h_0 \quad (6)$$

from which it can be shown that:



$$\Delta h = \frac{10i_{17} (GR_{mod} - 1)(\ell_{17} - 10)}{10 (GR_{mod} - 1) + \ell_{17}} \quad (7)$$

and all dimensions are in millimeters.

It is almost independent of the thickness of the upstream soil ( $\ell_{17}$ ) when  $\ell_{17}$  exceeds 1000 mm, see Fig. 3(a), however, it is proportional to  $GR_{mod}$  and  $i_{17}$ , see Figs. 3(b and c).

Typical values of the hydraulic gradient equivalent to  $i_{17}$  are reported after Giroud (1996) and Luettich et al (1992) in Table 3. Assuming that  $\ell_{17} = 1000$  mm, the water head loss is calculated for  $GR_{mod} = 7.4$ ; the losses do not exceed 120 mm for hydraulic gradients less than 2.0. An excess water head loss of 596 mm is predicted for an hydraulic gradient of 10.

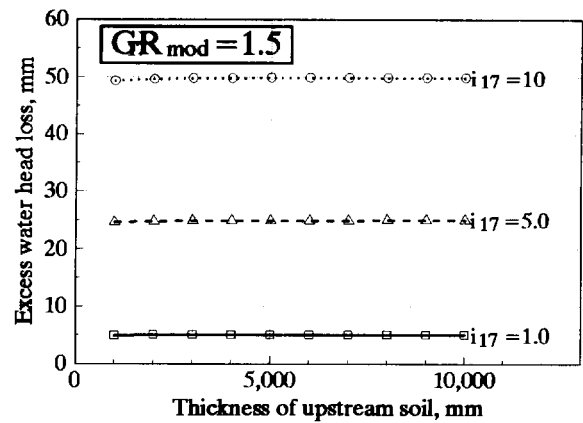
Table 3 Typical hydraulic gradients and corresponding excess water head loss ( $\ell_{17} = 1000$  mm,  $GR_{mod} = k_{35}/k_{67} = 7.4$ ).

Application	Typical hydraulic gradient	Excess water head loss $\Delta h$ (mm)
Standard dewatering trench	1.0	60
Inland channel protection	1.0	60
Pavement edge drain	1.0	60
Vertical wall drain	1.5	89
Landfill leachate collection / detection removal system	1.5	89
Landfill leachate collection removal system	1.5	89
Dam toe drains	2	119
Dam clay cores	3 to >10	178 to 596
Shoreline protection	10	596
Liquid impoundment with clay liners	>10	>596

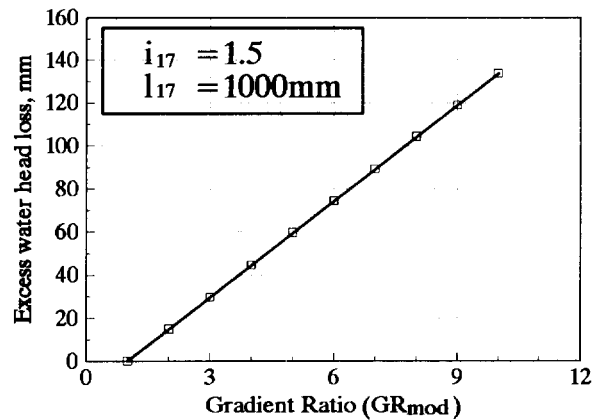
Notes: Typical hydraulic gradients developed after Giroud (1988) and Luettich et al (1992), critical applications may require designing for higher gradients than those given.

Values of  $\Delta h$  determined for the two Gradient Ratio tests described above are reported in Table 4. Given the average gradient ratio ( $GR_{mod}$ ) of 1.7 developed in testing soil BML74 with the geotextile,  $\Delta h$  is found to be in the range 8 to 10 mm, for a system hydraulic gradient ( $i_{17}$ ) of 1.4 and  $\ell_{17}$  varying from 100 to 10,000 mm. The range is 50 to 60 mm when  $i_{17} = 8.6$ . The losses are associated with a partial clogging of the geotextile filter zone.

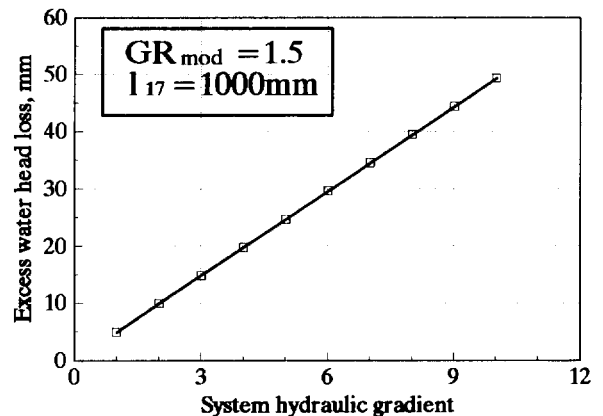
In contrast, an average gradient ratio ( $GR_{mod}$ ) of 0.8 developed for soil BML90 with the geotextile. A gradient



(a)



(b)



(c)

Fig. 3. Variation of excess water head (from eqn. 7).

ratio less than unity indicates the soil-geotextile composite is more permeable than soil being retained, yielding negative values of  $\Delta h$ .

Table 4 Excess water head loss for soils BML74 and BML90 with TS550 (mm)

$l_{17}$ (mm)	BML74	-TS550	BML90	-TS550
	$i_{17} = 1.4$	$i_{17} = 8.6$	$i_{17} = 1.4$	$i_{17} = 8.6$
100	8.2	50.6	-2.6	-15.8
1000	9.6	59.2	-2.8	-17.1
10,000	9.8	60.1	-2.8	-17.2

#### 4. CONCLUDING REMARKS

1. The gradient ratio test provides a means of evaluating the compatibility of a soil and geotextile with reference to permeability of the soil being retained.
2. The excess head loss ( $\Delta h$ ) in the soil-geotextile composite zone is shown from theoretical analysis to be almost independent of thickness of the upstream soil, but proportional to the system hydraulic gradient ( $i_{17}$ ) and gradient ratio (GR).
3. A series of trial calculations indicates the value of excess water head loss ( $\Delta h$ ) induced by a  $GR > 1$  is relatively small for applications governed by a system hydraulic gradient between 1 and 2, and gradient ratio  $GR_{mod} < 7.4$  and therefore  $GR_{ASTM} < 3$ .
4. There is a need to better link design criteria for  $k_F$  and  $k_S$ , with laboratory performance data from Gradient Ratio tests yielding values of  $k_{sg}$ . It is proposed that excess water head loss ( $\Delta h$ ), which can be used in design assessments of performance and related stability analyses, is the most appropriate parameter.

#### ACKNOWLEDGEMENTS

The research was funded by the Natural Sciences and Engineering Research Council of Canada (NSERC). The Ontario Ministry of Transportation supplied the geotextile materials.

#### REFERENCES

- ASTM D5101-96 Standard Test Method for measuring the soil-geotextile system clogging potential by the gradient ratio, Annual Book of ASTM Standards, ASTM Philadelphia.
- Austin, D.N., Mlynarek, J. and Blond, E. (1997). Expanded anticlogging criteria for woven filtration geotextiles. Geosynthetics '97, pp. 1123-1144, IFAI, St. Paul, MN.
- Canadian Geotechnical Society, Canadian Foundation Engineering Manual, 3rd edition, Vancouver, B.C.
- Christopher, B.R. and Holtz, R.D. (1985), Geotextiles Engineering Manual, U.S. Federal Highway Administration, Report FHWA-TS-86/203, pp. 1044.
- Fannin, R.J., Vaid, Y.P. and Shi, Y.C. (1994a), Filtration behaviour of nonwoven geotextiles, Canadian Geotechnical Journal, Vol. 31, No. 4, pp. 555-563
- Fannin, R.J., Vaid, Y.P. and Shi, Y.C. (1994b), A critical evaluation of the gradient ratio test, ASTM Geotech. Testing Journal, 17: 35-42.
- Giroud, J.P. (1996), Granular and geotextile filters, Proceedings of Geofilters'96, Montreal, Quebec, 29-31 May, pp. 565-680.
- Haliburton, T.A. and Wood, P.D. (1982), Evaluation of U.S. Army Corps of Engineers gradient ratio test for geotextiles performance, Proceedings of the second international conference on geotextiles, Las Vegas.
- Luetlich, S.M., Giroud, J.P. and Bachus, R.C. (1992), "Geotextile filter design guide", Geotextiles and Geomembranes, Special Issue on Geosynthetics in Filtration, Drainage and Erosion, Vol. 11, Nos. 4-6, pp. 433-441.
- Shi, Y.C., Fannin, R.J. and Vaid, Y.P. (1996), Evaluation of geotextile filter behaviour using the Gradient Ratio test, Proceedings of Geofilters'96, Montreal, Quebec, 29-31 May, 469-480.
- Shi, Y.C. (1993), Filtration behaviour of nonwoven geotextiles in the gradient ratio test, M.A.Sc. thesis, Univ. of British Columbia, Vancouver, Canada.

# Geotextiles Filter Design by Probabilistic Analysis

Urashima, Denise C.

Student, Department of Geotechnique, Aeronautical Institute of Technology, São José dos Campos, São Paulo, Brazil

Vidal, Delma

Professor, Department of Geotechnique, , Aeronautical Institute of Technology, São José dos Campos, São Paulo, Brazil

**ABSTRACT:** A methodology to obtain the parameters to design needle-punched nonwoven geotextiles filters based upon probabilistic analysis and in-suspension filtration tests is proposed. The superposition of theoretical pore size distribution curve and that obtained by in-suspension filtration tests allows one to estimate the distance between confronts, essential to use the probabilistic theory. This paper presents tests results and analysis for thin geotextiles (mass per unit area less than 200 g/m<sup>2</sup>) and a design procedure that shows the versatility of this method.

**KEYWORDS:** Design, Filtration, Geotextiles, Nonwoven Fabrics, Probability

## 1 INTRODUCTION

The good performance of geotextiles in filtration functions has been reported in practical engineering thus becoming one of the most popular geosynthetics applications in the world. In recent years, research has been conducted at several laboratories in order to obtain a better knowledge of mechanisms and parameters associated with filtration problems.

Filter design is usually based on Terzaghi's proposition, empirically or semi-empirically adapted by different authors. However, these design procedures don't allow a complete understanding of the filtration phenomena. It is impossible to estimate the filter thickness needed to retain the soil particles.

Silveira(1965) proposed a probabilistic analysis to study the carrying of soil particles in a filter. This analysis gives us the filter thickness needed to retain the soil particles, if the filter pore size distribution curve and the average distance between confrontation particle/filter voids are known.

This paper presents a procedure to obtain the necessary parameters to design thin needle-punched nonwoven geotextiles filter (mass per unit area less than 200 g/m<sup>2</sup>), combining Gourc's(1982) and Silveira's(1965,1993) propositions, to estimate the distance between confronts. Some results are presented and examples discussed to show the relevance of the adopted procedure.

## 2 THEORETICAL ANALYSIS

From a probabilistic analysis of carrying spherical particles through a protective filter, Silveira(1965) proposes to establish the necessary filter thickness to retain a determined diameter soil particle.

This proposition analyses the particle path through the filter. Taking the confidence level as P', the probability, P,

of a defined diameter particle, d, to be retained by a pore size smaller than it, before a number N of voids confronts, assuming that each confrontation is a independent event, necessary to satisfy the condition:

$$P' \equiv 1 - P^N \quad (1)$$

In other words, it is possible to determine the number of pore confronts necessary to warrant the particle retention when it tries to cross the filter thickness by:

$$N \equiv \log(1 - P') / \log P \quad (2)$$

Considering the average distance between confronts as s, the total filter thickness,  $t_{GT}$ , necessary to retain a defined particle diameter is given by:

$$t_{GT} = s N \quad (3)$$

Therefore, to carry out this analysis it is necessary to know the average distance between confronts and the probability of the particle finding a pore size smaller than itself, represented by the pore size distribution curve. Both these parameters are difficult to obtain.

The filter pore size distribution curve has been evaluated by several experimental methods. Several of them are discussed by Bathia et al.(1994) and Fisher et al.(1993). Some are very complex, others are not compatible with geotextiles.

Silveira(1993) proposed to realise in-suspension filtration tests with different filters thickness and to evaluate the pore size distribution curve by retro-analysis using his probabilistic theory. In this case, it is necessary to estimate the average distance between confronts.

For the granular filters, the average distance between confronts can be evaluated in function of granular filter particle diameters. In the case of geotextiles, this supposition can not be used because the geotextiles fibres

are not necessarily in contact, and the Silveira(1993) proposition can not be directly applied.

To solve this problem, the Silveira's proposition was combined with a theoretical analysis to obtain the filter pore size distribution curve for needle-punched nonwoven geotextiles, proposed by Gourc(1982) in which case the accumulated probability, Q, of finding a pore size smaller than a defined diameter, d, is obtained by the expression:

$$Q = 1 - \exp [ - ( \eta \pi d^2 / 4 + \lambda d / 2 ) / n_{GT} ] \quad (4)$$

where  $n_{GT}$  is the geotextile porosity and the parameters  $\eta$  and  $\lambda$  can be calculated from the fibre diameter,  $d_f$ , by:

$$\eta = 8 ( 1 - n_{GT} ) / ( \pi^2 d_f^2 ) \quad (5)$$

$$\lambda = ( 2 + 4 / \pi ) ( 1 - n_{GT} ) / d_f \quad (6)$$

### 3 TESTS AND MATERIALS

To carry out this work the authors analysed several fabrics available in Brazil. This paper presents results obtained with thin fabrics, usually employed in filtration functions, and separated into three groups, each one having the same production characteristics, as shown in Table 1.

Table 1. Needle-punched nonwoven geotextiles group characteristics

product	filament	polymer	$d_f$ (mm)
A	continuous	PET	0.022
B	staple	PP	0.030
C	staple	PP	0.026

All fabrics were analysed for their physical characteristics: thickness, mass per unit area, and fibre diameter. Specimens with 150 mm diameter and having physical characteristics close to the average value were selected and submitted to a special in-suspension filtration tests described in Urashima and Vidal(1997).

These tests, illustrated on Figure 1, were conducted to evaluate the bigger particle passing across the filter on the first one seepage front, under severe flow conditions (the particles are been transported by flow). These results can be compared to the hydrodynamic opening size tests results, where the particles are submitted to several seepage front (2000 cycles).

The soil particle used in these tests were obtained from a granite powder, selected after analysis in repeated sieving tests, compounded from uniform single fractions (105/88, 88/75, 75/66, 66/53, 53/44, 44/37, <37  $\mu$ m).

### 4 RESULTS

Physical characteristics of the geotextiles are presented in

Table 2. The theoretical pore size distribution curves obtained from Gourc(1982) are presented in Figure 2.

Some results of the in-suspension filtration tests are presented on Figure 3.

Table 3 presents an abstract of experimental and analytical values.  $O_{95, sf}$  is the 95 % opening size measured in suspension filtration tests. The distances between confronts presented were obtained considering a confidence level,  $P' = 98 \%$ , and theoretical pore size distribution curves in Figure 1.

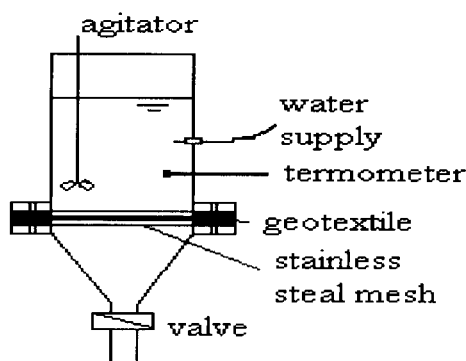


Figure 1. The test apparatus scheme.

Table 2. Geotextiles physical characteristics

geotextile	$M_A$ ( $g/m^2$ )	C.V. (%)	$t_{GT}$ (mm)	C.V. (%)	$n_{GT}$ (%)
AA	158	7.7	1.33	7.4	91.4
AB	181	6.3	1.55	5.3	91.5
BA	167	3.9	1.67	5.4	88.9
BB	198	5.9	1.86	3.7	88.2
CA	129	8.9	0.93	8.3	85.6
CB	135	8.0	1.00	5.8	85.0

Table 3. Experimental and analytical results

geotextile	thickness (mm)	$O_{95, sf}$ (mm)	distance between confronts (mm)
AA	1.33	0.070	0.459
AB	1.55	0.059	0.448
BA	1.67	0.044	0.234
BB	1.86	0.041	0.219
CA	0.93	0.062	0.345
CB	1.00	0.054	0.347

These results show that the adopted methodology provides a very close evaluation of distances between confronts, for fabrics with same production characteristics.

Fabrics with mass per unit area greater than 200  $g/m^2$

present distances between confronts increasing with thickness. For example, to the BC geotextile ( $t_{GT} = 2.28\text{mm}$ ) and CC ( $t_{GT} = 1.74\text{mm}$ ) this distance was 0.367 and 0.518, respectively. Their analysis has been improved to confirm and comprehend this tendency.

## 5 CALCULATIONS

The procedure to specify geotextiles satisfying retention criteria, can take several paths:

- Defining a soil particle diameter to retain (for example,  $d_{85}$  in well graded soil or  $d_{50}$  or an other value in function of soil characteristics), and choosing a geotextile (pore size distribution curve, distance between confronts and thickness known) to obtain the retention confidence level of this diameter;
- Defining a soil particle diameter to retain, to determine the necessary thickness to retain this diameter with a given confidence level, for each geotextile group (for example, A, B or C);
- For a chosen geotextile with pore distribution curve, distance between confronts and thickness known, to verify the soil particle to be retained with a specified confidence level;

With the retention or clogging criteria verified, it is necessary to analyse the permeability and survival criteria to complete the geotextile specification.

A well graded soil with  $d_{85}$  equivalent to 0.11 mm can be used to demonstrate a case of needle-punched nonwoven geotextile filter design, satisfying the retention criteria.

In this case, if it is possible to consider that this soil

particle diameter can retain the soil particles smaller than itself, two attitudes can be adopted:

- to determine the thickness necessary to retain  $d_{85}$  particle diameter for the geotextiles groups analysed,
- to determine the retention confidence level of this particle diameter for a specified geotextile.

From equations 2, 3 and 4:

$$t_{GT} = s \log(1 - P') / \log(1 - Q) \quad (7)$$

for a confidence level  $P'$  equal to 99.9 %,  $Q$  obtained from Figure 1 or equation 4 and  $s$  obtained from Table 3, we have for:

- geotextiles group A:  $t_{GT} > 1.38 \text{ mm}$
- geotextiles group B:  $t_{GT} > 0.84 \text{ mm}$
- geotextiles group C:  $t_{GT} > 0.75 \text{ mm}$

and the geotextiles AB, BA and CA can be adopted.

If the geotextile AA ( $t_{GV} = 1.35 \text{ mm}$ ) is available, the retention confidence level to retain the  $d_{85}$  soil particle, determined from equations 2, 3 and 4 is 99.88%.

Comparing these results with a traditional retention criteria like the one proposed by the French Geotextiles and Geomembranes Committee (CFGG), considering the best soil condition, the geotextile hydrodynamic opening size needs to be lower than 0.138mm. In this case, the geotextiles of the group A can not be adopted (AA -  $O_{95,H} = 0.21 \text{ mm}$ , AB -  $O_{95,H} = 0.17 \text{ mm}$ ).

It is necessary to remember that Silveira's proposition takes into consideration the most critical situation, i.e. the particles are been transported by flow.

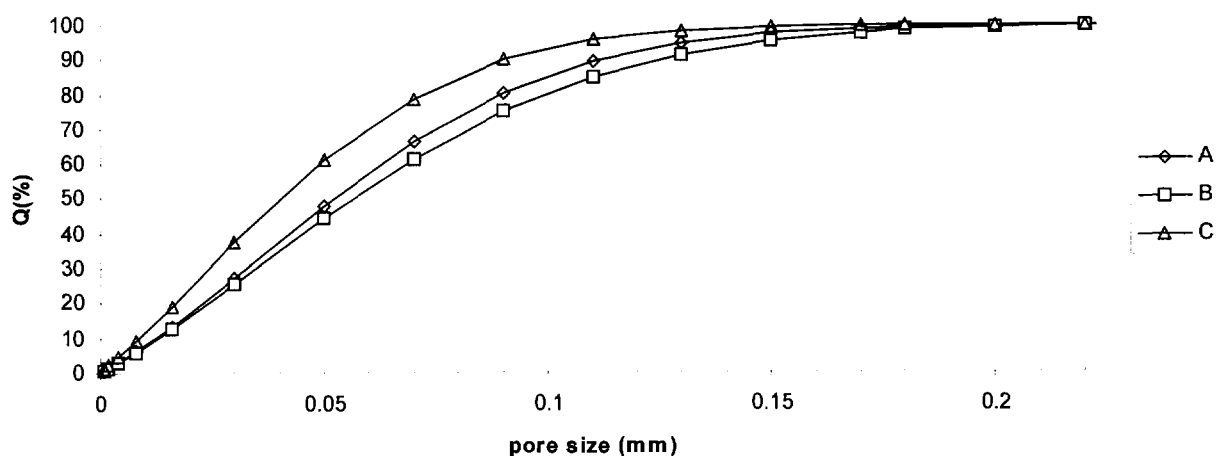


Figure 2. Theoretical pore size distribution for the analysed geotextiles groups.

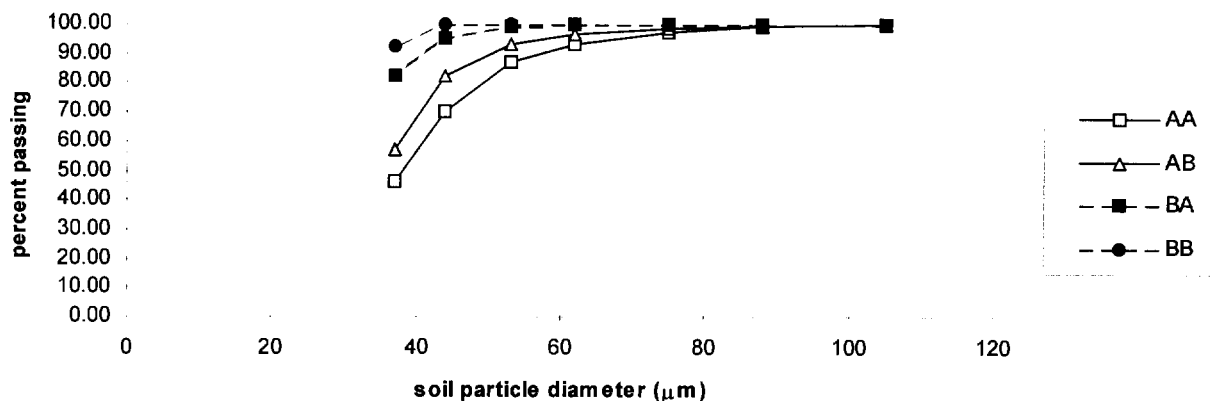


Figure 3. Grain size distribution curves of the soil passant mass observed in some in-suspension filtration tests.

## 6 COMMENTS

Although Silveira's (1993) procedure can not allow us to determine directly the pore size distribution curve of geotextiles because the average distance between confronts are not known and we do not have several fabric thicknesses with the same production characteristics (each fabric thickness represents one point of the curve), his proposition is interesting to evaluate the average distance between confrontations, if the pore size distribution curve can be obtained by an other method.

From the results of in-suspension filtration tests, conducted according to the probabilistic theory suppositions, and the theoretical pore size distribution curve proposed by Gourc (1982), it is possible to evaluate the average distance between confronts.

Each geotextile or group of fabrics that presents the same production characteristics can be analysed and have their filtration parameters evaluated.

To define a production line (group of geotextiles presenting the same fabric filtration characteristics) it is necessary to have a good technological control of the production procedure that warrants the same characteristics. The nonwoven geotextiles are very sensitive to a variation of the needle intensity. Anyway, the analysis of in-suspension filtration tests results can detect the fabric variations.

Fabrics with mass per unit area greater than 200 g/m<sup>2</sup> need to be better studied to verify if the observed variation on the average distance between confronts with apparently the same production characteristics is a function of the in-suspension filtration tests methodology adopted, or intrinsic fabric variation. Tests with larger specimens are been carried out to improve our knowledge.

The superposition of the theoretical pore size distribution curve and in-suspension filtration tests results looks to be an applicable proposition for thin geotextiles.

## ACKNOWLEDGEMENTS

This research was partially supported by FAPESP (São Paulo Research Support Foundation).

## REFERENCES

- Bhatia, S.K., Smith, J.L., Christopher, B.R. (1994). Interrelationship between pore openings of geotextiles and methods of evaluation. *Fifth International Conference on Geotextiles, Geomembranes and Related Products*, Singapore, pp. 705-710.
- Fischer, G.D., Holtz, R.D., Chistopher, B.R. (1993) A critical review of geotextile pore size measurement methods. *Geofilters'93 - International Conference on Filters and Filtration Phenomena in Geotechnical Engineering*, Karlsruhe, Germany, pp 83-90.
- Gourc, J.P. (1982) Quelques aspects du comportement des géotextiles en mécanique des sols, *Université Scientifique et Médicale de Grenoble, Institut Polytechnique de Grenoble*, Grenoble, France.
- Silveira, A (1965) An analysis of the problem of washing through in protective filters. *VI International Conference on Soil Mechanics and Foundation Engineering*. Montreal, Canada, pp 551-555.
- Silveira, A (1993) A method for determining the void size distribution curve for filter materials, *International Conference on Filters and Filtration Phenomena in Geotechnical Engineering*. Karlsruhe, Germany, pp.71-73.
- Urashima, D.C., Vidal, D. (1997) Filtration opening size by in suspension tests. *Symp. on Recent Developments in Soil and Pavement Mechanics*, Rio de Janeiro, Brazil, 25-27 jun.

# Filter behaviour of hydraulically and mechanically damaged geotextiles

YH Faure, Y. Kehila

LIRIGM, University Joseph Fourier, Grenoble, France

**ABSTRACT :** In this paper, a geotextile filter is considered hydraulically « damaged » when it is clogged by soft soil and mechanically damaged when it is punched or torn by gravels during installation. Specific tests were performed to damage hydraulically non-woven filters by filtration of fine soil in suspension (critical conditions for clogging). Physical properties and filtration characteristics of filters like filtration opening size are analysed to show their influence on velocity of clogging. Clogging occurs when the filtration opening size is smaller than the  $d_{max}$  of the fine soil and the velocity of clogging is very sensitive to the geotextile density (or porosity). Three levels of damage action were applied to damage filters mechanically. A lot a perforations are necessary to produce variation of filtration opening size when it is determined by sieving method (wet sieving or hydrodynamic sieving). A very deformable geotextile is less damaged than a rigid one.

**KEYWORDS :** Filtration, Degradation, Clogging Tests, Non-woven fabrics

## 1 INTRODUCTION

A lot of studies have been carried out in the past in order to analyse geotextile filter behaviour and, in general, clean undamaged specimens are tested. However, during on-site installation, geotextiles are laid mostly on a soft, saturated fine soil and, as a result, filter pollution (or clogging) occurs when operatives walk on the geotextile. Moreover, when the gravel layers are subsequently placed on the filter, mechanical damage may occur, such as punctures or tears. In both cases, the geotextile filter is considered to be hydraulically or mechanically damaged.

This paper presents the experiments carried out and the results obtained, indicating the filter behaviour of different textile structures.

## 2 HYDRAULIC DAMAGE: FILTRATION OF WATER LOADED WITH SOIL IN SUSPENSION

In order to study the effect of hydraulic damage, a filtration test was performed on a sample of water loaded with soil in suspension. This test, presented in a previous paper by Faure et al. (1993), reproduces the critical conditions encountered when installing the geotextile on site: the soil in the trench is often very muddy and the geotextile must filter the soil carried in suspension in the water without clogging. Then, when the soil has consolidated and is in close contact with the filter, the water is no longer charged with particles in suspension, or contains only very little (on condition that the internal stability of the soil to be filtered is established). It is necessary to check that the clogging level during the initial stage is not too high, and it would be beneficial if the circulating clear water could help unclog the geotextile, thereby ensuring better subsequent operation of the system.

### 2.1 Description of the filtration test

The test assembly consists of the following components - two upstream reservoirs, one for supplying water loaded with soil particles in suspension, and one constant-level reservoir to ensure the circulation of clear water (a three-way valve is used to switch instantaneously from one reservoir to the other),  
- a constant discharge pump to provide a constant solid and liquid flow when clogging is not too high,  
- a sample holder (effective diameter: 50 mm),  
- a constant-level downstream reservoir.

A pressure sensor is connected to the circuit 0.15 m upstream of the geotextile. This sensor monitors the time-dependent increase in pressure due to filter clogging.

### 2.2 Soil used

The retention criteria for geotextiles filters are based on the characteristic “geotextile filtration opening” size,  $O_f$ . If the value of  $O_f$  has been correctly chosen, the granular skeleton of the soil is retained (Giroud, 1996) and the risk of

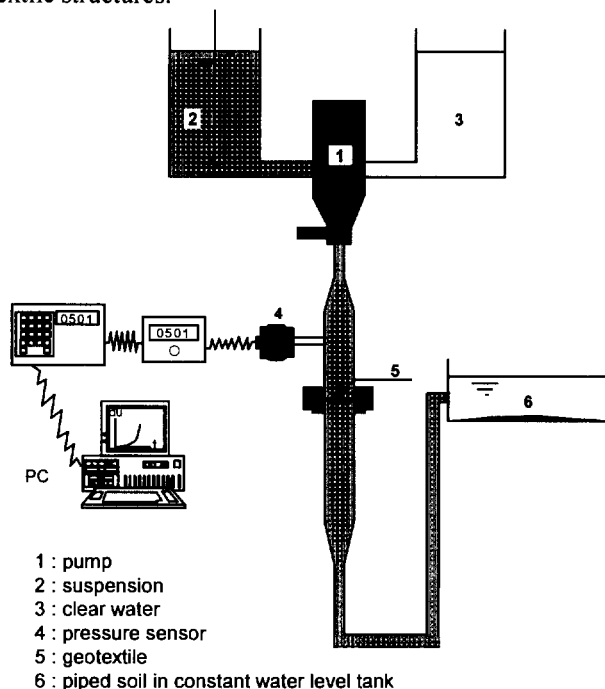


Figure 1: Diagram of the test assembly used for filtering soils in suspension

clogging during the initial operating period of the filter is due only to the fine elements in the soil. This is the reason why the retention criterion of the CFG (French Geosynthetics Committee) requires a filtration opening  $O_f$  greater than  $80 \mu\text{m}$ , in the case of coherent soils, to allow particles smaller than  $80 \mu\text{m}$  to pass through the geotextile.

For the filtration tests on loaded water, a clayey soil was used with upper particle size limited to  $80 \mu\text{m}$ . The particle size range of this pottery-type clay (Figure 2) was measured without deflocculant because, during the test, it is used without deflocculant.

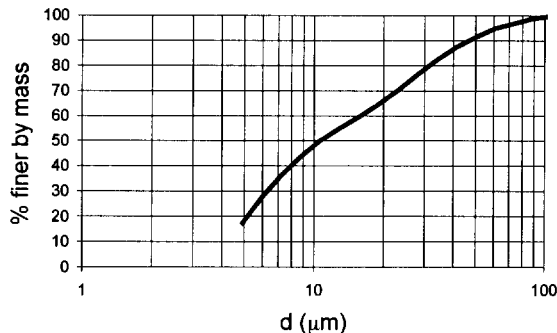


Figure 2: Particle size range of the soil for filtration tests of soil in suspension

### 2.3 Characteristics of geotextiles tested

All the geotextiles are made of non-woven polypropylene. The distinguishing parameters (cf. Table 1) are mass per unit area  $\mu_g$ , thickness  $T_g$  and fibre diameter  $d_f$ . Porosity can be then calculated by mean of :

$$n = 1 - \frac{\mu_g}{\rho_f T_g} \text{ where } \rho_f \text{ is the density of the fibres.}$$

Table 1: Characteristics of geotextiles tested (mean values)

Géotextile Lirigm name	Structure	$\mu_g$ g/m <sup>2</sup>	$T_g$ mm	$d_f$ mm	n %	O90 (Hyd. S) $\mu\text{m}$
CF130a	nw-needlepunched.	126	1.1	26	87.5	85
CF130b	nw-needlepunched.	127	1.3	37	89.4	155
HB130	heatbonded	137	0.5	42	70.2	140
SF130	nw-needlepunched.	134	2.5	31	94.2	175
CF300a	nw-needlepunched.	292	2.6	26	87.8	65
CF300b	nw-needlepunched.	286	2.8	37	88.9	105
HB300	heatbonded	294	0.8	42	60.1	65
SF300	nw-needlepunched.	269	3.9	31	92.5	100
CF400a	nw-needlepunched.	400	3.45	26	87.4	61
CF600a	nw-needlepunched.	633	4.5	26	84.7	59
CF600b	nw-needlepunched.	617	4.4	37	84.8	50
CF800a	nw-needlepunched.	816	5.9	26	85.0	60
SF1100	nw-needlepunched.	1119	7.8	49	84.7	101

The density of the geotextile is :  $\rho_g = \frac{\mu_g}{T_g}$

SF geotextiles are made with short fibres while CF materials are made with continuous filaments. The HB geotextiles are heat-bonded.

### 2.4 Test procedure

After installing the test sample and saturating the system, soil particles are tipped into the reservoir filled with water (capacity 25 l). The concentration  $C_o$  of the suspension is 0.5, 1 or 2 g/l. A mechanical stirrer ensures that the suspension remains homogeneous at all times. The flow rate is imposed by the pump with a speed of 40 mm/s. When the particles come into contact with the filter, recording of the pressure « u » starts. This pressure gradually increases. Then, when the clogging level is too high, the pressure suddenly increases at a much faster rate until the safety valve is tripped. (Figure 3). Overpressure is defined by the difference :  $u - u_o$  ( $u_o$  is the measured value of  $u$  at the beginning of the test with clear water).

### 2.5 Influence of geotextile structure

Figure 3 shows that the mass per unit area is not the main parameter governing the clogging rate: when  $O_f$  is greater than  $d_{max}$  of the soil (cf. CF300b and SF300), no clogging occurs: the pressure has hardly increased after all the water has flowed through. On the other hand, with a filtration opening size  $O_f < d_{max}$ , clogging occurs all the faster as the porosity is lower (HB300 and CF300a).

The density  $\rho_g$  ( $= \mu_g / T_g$ ) was calculated for each geotextile sample. This parameter gives an indication of the compactness of the fibrous medium (like the porosity).



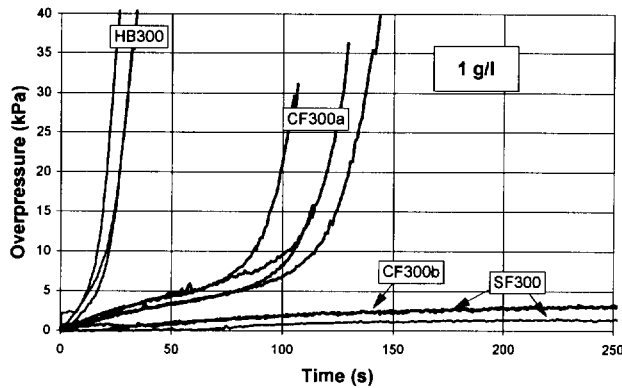


Figure 3: Influence of geotextile structure 2.6 Influence of geotextile density (or porosity)

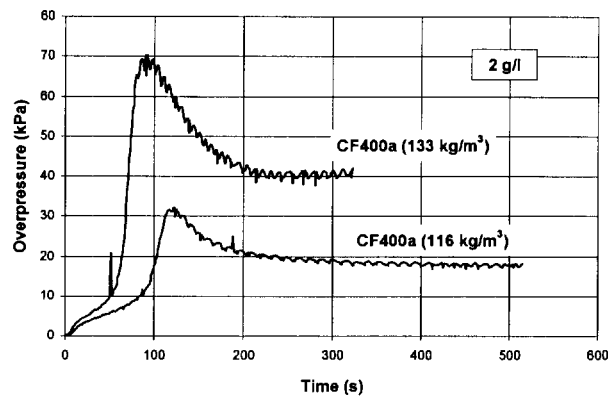


Figure 4: Clogging - Unclogging curves

To study the clogging phenomenon, the clogging rate was defined by the slope of the straight line tangent to the clogging pressure curve before the “elbow” ( $V_c = \Delta u / \Delta t$ )

Figure 5 shows the variation in  $V_c / C_o$  (to compare tests conducted with different concentrations  $C_o$ ) as a function of  $\rho_g$  for CFa geotextiles of the same fibre diameter and same needle-punched structure. Despite the dispersion, the compactness (or the porosity) would indeed seem to be the parameter most influencing the filter clogging rate, regardless of the weight per unit area. Clogging therefore occurs mainly on the surface or in the first layers of fibres.

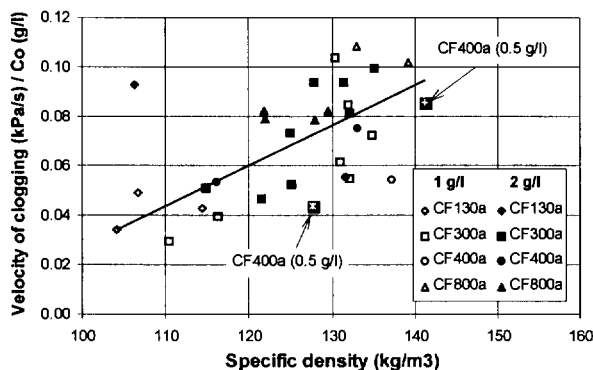


Figure 5: Determining role of geotextile density

## 2.7 Unclogging

The ease with which a geotextile is likely to become clogged is controlled by the injection of clear water, always with a flow speed of 40 mm/s, as soon as the pressure reaches 10 kPa. The graphs in Figure 4 illustrate this phenomenon and clearly show the role of compactness (for CF400a filters). A high density filter remains less permeable than a low density filter although its clogging level was the same as the low density filter.

## 3 MECHANICAL DAMAGE:

If a geotextile incurs mechanical damage, during the installation procedure (punctures, tears), its filtration characteristics, permeability and filtration opening size are modified: the permeability increases and the filtration opening size as well. The question is to know whether these variations will disturb the filtering behaviour of the geotextile and, if so, in what proportions, and is it still operational after this damaging action?

- The permeability increases: this is a positive effect with regard to the permeability condition required by the filter criteria. However, a permeability test after a damaging action enables the level of filter damage to be estimated.

- The filtration opening size increases: the geotextile is now not so efficient at retaining the soil. To estimate the damage incurred on a geotextile, is the transmission observation method objective?

Damaging action tests were conducted with three stress levels and the filtration opening size of the damaged samples was then measured by wet sieving and by hydrodynamic sieving

### 3.1 Levels of damaging actions

Level 1: Tests were carried out according to the draft European Standard Procedure for simulating site damage. A geotextile specimen is laid between two gravel layers (corundum SD 5-10 mm) and subjected to cyclic loading of 900 kPa with a frequency of 1 Hz for 200 s (Figure 6).

Level 2: The test device used is the same as before. The damage is produced by a 230 mm square plate with 57 ASTM punches (ASTM D 5494 standard), Figure 7. The point of each punch has a pyramidal shape and the base is circular (25 mm diameter). Together, they form a triangular arrangement with a side length of 25 mm. The geotextile is laid on an 80 mm thick layer of sand (0-2 mm). The cross-section of the cell containing the sample is small (250 x 250 mm), slightly larger than the punch plate. The punches are in direct contact with the geotextile. A load of 380 kPa is applied (i.e. 0.35 kN per punch), for 200 cycles at 1 Hz.

Level 3: The punches consist of 23 mm high cones with an apex angle of 40° (Figure 8). 19 cones are fixed on a support plate in a triangular arrangement with a 60 mm side length. A load of 0.60 kN per cone, or an equivalent pressure of 150 kPa, is applied at 1 Hz for 200 cycles.

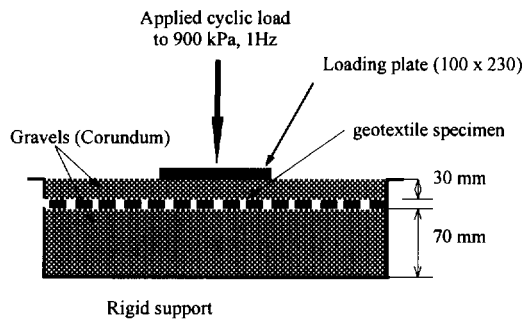


Figure 6: Test device for the level 1 damage test

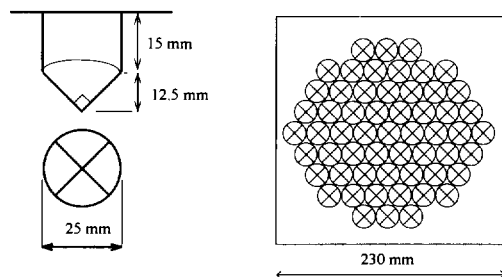


Figure 7: ASTM punches for the level 2 damage test

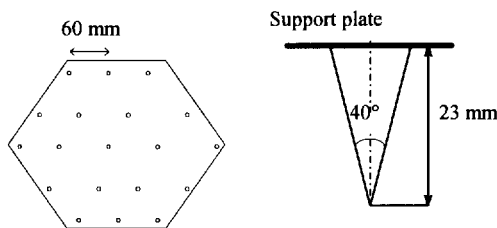


Figure 8: Cones for the level 3 damage test

### 3.2 Results (Figure 9)

Not all the geotextiles were systematically subjected to the same stress levels. Depending on the results obtained, a higher or lower level was not necessarily applied. For example, when the HB130 geotextile suffered considerable damage at level 2, it was not considered necessary to apply level 3.

**Level 1 :** With level No 1 damaging action, only the HB130 geotextile would appear to have suffered any damage: many of the filaments are broken and perforation marks are visible. However, measurement of the O90 opening by the wet sieving test shows only a slight increase in O90: from 117 to 142 $\mu$ m.

For the other geotextiles no damage was observed or measured.

**Level 2 :** With level 2, of the 130 g/m<sup>2</sup> geotextiles, only the SF130 kept the same O90 value, although it suffered considerable strain. The heavier geotextiles (300 g/m<sup>2</sup>), despite showing the marks of the punches after the test, have suffered only minor damage and their O90 value has hardly increased, even for HB300.

**Level 3 :** With the stress applied at level 3, all the geotextiles are perforated: cone holes are clearly visible by

shining a light through the sample, although the size of the holes varies depending on the geotextile.

For the highly deformable SF300 and SF1100, the cone hole diameters are much smaller than those of the CF300a, in which the holes are more like cuts. However, it is worth noting that although the holes are several millimetres in size, the values of O90 remain well under 1 mm. There are two reasons for this:

- after the damage test, with the samples at rest, the perforations and cuts in the needle-punched material tend to close with time, a feature that is not found in heat-bonded geotextiles,
- the number of perforations (only 7) inside the sample (200 mm diameter) tested by wet sieving or hydrodynamic sieving is not sufficient. During sieving, a small quantity of soil passes through the holes and the proportion of large particles is insufficient.

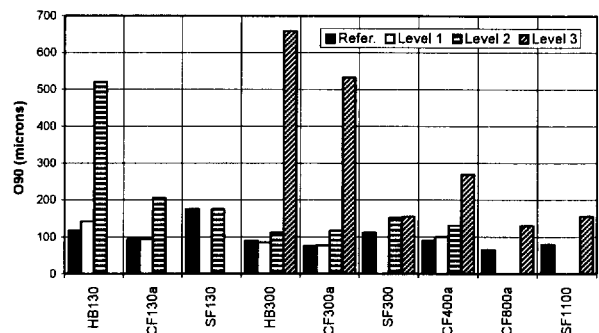


Figure 9: O90 histogram after the damaging action

## 4 CONCLUSION

This study of the hydraulic behaviour of geotextile filters after incurring hydraulic or mechanical damage has highlighted the role played by characteristic parameters.

**Hydraulic damage** (water loaded with soil particles in suspension): filter clogging is delayed when the filtration opening size is greater than the  $d_{max}$  value of the soil in suspension. With an Of value equal to or slightly lower than the value of  $d_{max}$  of the tested soil in suspension (here  $d_{max} = 80 \mu$ m), the risk of clogging increases when the filter porosity is smaller.

**Mechanical damage:** the filtration opening size of geotextile filters is not modified at level 1. In order for the filtration opening size test to be sensitive to the filter damage, the number of perforations must be sufficiently great like with the level 2 damage test.

## REFERENCES

- Faure, YH., Elamir, A., Farkouh, B., Gendrin, P., Reisinger, P. (1993) « Geotextile filter behaviour with critical filtration conditions » *Proc. 1st Int. Conf. Geo-Filters*, Karlsruhe, pp 209-116.
- Giroud, JP. (1996) « Granular filters and geotextile filters » *Proc. 2nd Int. Conf. Geo-Filters*, Montreal, pp 565-680.

# Large-scale Performance Tests to Evaluate Filtration Processes

Th. Kossendey

LGA-Geotechnical Institute, Nuremberg, Germany

G. Karam

Du Pont de Nemours, Luxembourg, Luxembourg

**ABSTRACT:** The long-term filter performance of 5 geotextiles differing in permittivity, thickness, mass per unit area and type of polymer was studied experimentally in large permeameters supplied with three different soils. In three test series, the geotextile samples of 500 mm diameter were submitted to steady state seepage under different hydraulic gradients for 6 to 24 months. In the first two performance tests, the water flow was in the direction of gravity. The third test series simulated the case of upward water flow. Although the geotextiles differed in their parameters, their filter performance exhibited very similar characteristics and satisfied the requirements for stable filter performance. A detailed microscopic investigation into the soil structure directly above the geotextiles confirmed that the geotextiles formed an internal soil filter with a bridging network.

**KEYWORDS:** Long-Term Filtration, Clogging tests, Performance Evaluation, Microstructure

## 1 INTRODUCTION

Geotextile filters function adequately when they retain a majority of the soil particles at the interface between a finer and a coarser soil and permit the flow of water through the pores of the soils and the geotextile filter without any water pressure build up upstream of the filter. Many investigations were carried out to obtain reliable criteria for the design of geotextile filters, but it is difficult to predict the long-term filter behaviour. The long-term performance of geotextile filters depends primarily on the following factors:

- the properties of the filter,
- the properties of the soils,
- the type of water flow.

Since these major factors are variable, it is not possible at the present time to predict the long-term filter performance of different geotextiles quantitatively on a theoretical basis. The long-term filter performance can only be evaluated correctly on the basis of either field experience or large scale performance tests under well defined boundary conditions which can be related to the in-situ situation.

## 2 TESTING PROGRAMME

### 2.1 Soils used for the performance tests

According to the geotextile filter criteria currently applied in Germany (FGSV 1994), a soil is called a "problem soil" regarding the geotextile filtration, if any one of the following criteria applies:

- $C_u = d_{60}/d_{10} < 15$  and the soil contains some fines  $< 0.06$  mm
- $> 50$  % content of the grain size fraction  $0.02$  mm  $< d < 0.1$  mm
- $I_p < 15$  % (if not available: content of clay / content of silt  $< 0.5$ )

The fine-grained silt used for long-term filtration test

was a loess from a road construction site in the Central Hesse area, about 30 km north of Frankfurt/Main.

The soils A and B were blended from different quartz fractions. Thus, it was possible to design cohesionless soils with gradation curves which met the above-mentioned criteria for a "problem soil" with respect to geotextile filtration.

The soils used in the permeation tests fully satisfied all criteria for a "problem soil". The grain size distributions are shown on Figure 1. Details of the soil parameters used in the tests are given by Kossendey et al. (1996b).

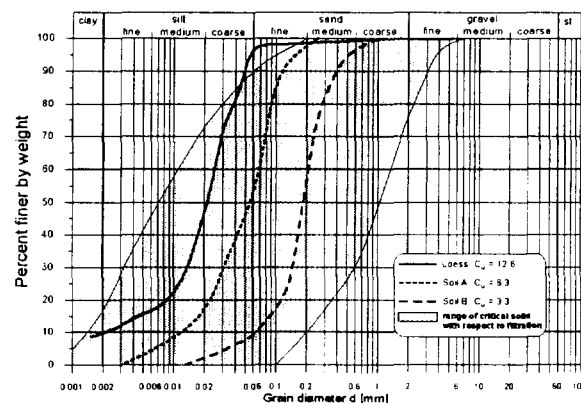


Figure 1. Grain size distributions of the soils used in the long-term permeation tests

### 2.2 Geotextiles

5 different nonwovens (3 heat-bonded, PP and 2 needle-punched, PET) geotextiles were selected for the long-term performance tests. They comprised geotextiles of various polymers and different manufacturing technologies in a wide range of their properties. Details of the selected geotextiles are given in table 1. Their properties were determined by index tests at the laboratory of the LGA-Geotechnical Institute. The results of these tests served as reference data for the evaluation of changes in the geotextile properties after the long-term permeation.

### 2.3 Permeameter circuit

The test equipment used in these test series consists of 3 supply containers and 4 permeameters per circuit arranged radially around the supply container. They have a diameter of 50 cm and a height of 167.5 cm. A detailed description of the permeameters was given previously by Gartung et al. (1994) and Kossendey et al. (1996b).

### 2.4 Test conditions

In total, three long-term filtration test series differing in their boundary conditions were carried out. For the first two test series, a mesh was placed upon the conical bottom plate with a discharge opening at the centre in each of the permeameters. The geotextile sample was installed above the mesh and attached to the permeameter by a fixing ring. The soil layer was placed on the geotextile. The first long-term test series was carried out under a hydraulic gradient of  $i=3$  regarding the soil layer above the geotextiles. This hydraulic gradient falls into the range of typical hydraulic gradients for drainage applications under steady-state flow conditions, as noted by Davindenkoff (1976) and Luettich et al. (1992). During the second test series the hydraulic gradient was selected as  $i = 12$  to observe the permeation behaviour under higher hydraulic gradients. The permeation of the tests was in direction of gravity. In order to examine the filtration behaviour of a system geotextile/soil under conditions of upward permeation against the direction of gravity, a third test series was implemented with a hydraulic gradient  $i = 2,5$  (figure 2). The soil layers of each test implementation were only slightly compacted to test the filtration behaviour for the worst case.

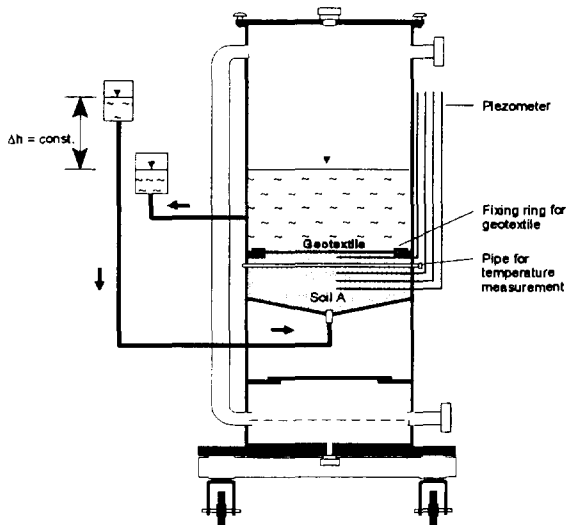


Figure 2. Schematic sketch of the test with upward permeation

The test liquid (tap water) permeated uniformly through the system geotextile/soil. The determined values of dissolved oxygen in the different circuits were between 4.2 ppm and 5.5 ppm. Following the definition of de-aired water (maximum at 6 ppm), the criterion for the oxygen

content of de-aired water was met in the filtration tests.

### 2.5 Analysis of the microstructure

In order to analyse the microstructure at the interface geotextile/soil influenced by the interaction between geotextile and soil, microscopic sections were prepared. The undisturbed soil samples taken after the end of the tests were saturated by a resin in the same way as by water in the filtration tests to prevent the soil samples from any disturbance. The viscosity of the resin was similar to the water that permeated the system geotextile/ soil.

## 3 TEST RESULTS

### 3.1 Performance tests with a hydraulic gradient $i = 3$

During an initial period of approximately four weeks, an increase in the system permeability of the permeameters with the loess soil was observed. In spite of the increase in permeability, no soil particles were detected by the collecting glass. After about four weeks, the permeability of all permeameters began to decrease. With increasing test duration, the permeameters showed only small differences in the system permeabilities. They followed the same trend towards constant values. The system permeabilities of the permeameters are given in Figure 3. The coefficient of permeability of the loess soil tested by small scale index test was  $1.2 \cdot 10^{-8}$  m/s. The observed permeabilities of the large scale system geotextile/soil never fell below this value, so the permeabilities of the system soil / geotextile were higher than that of the small soil sample at all times. The reason for the discrepancy may be local variations in the density of the large permeameter sample, and associated inhomogeneities in the distributions of the coefficient of hydraulic conductivity.

The behaviour of the system permeabilities in the permeameters with soil A and soil B are similar to the results of the tests described by Kossendey et al. (1996a, 1996b). In permeameter with geotextile NP1 an additional load of 20 kPa was applied. The system permeabilities began to increase in all permeameters. In contrast to the test with the loess soil, the initial period of increasing permeabilities lasted only a few days.

Except for a slight cloudiness of the test liquid which could not be quantified, no particle migration was observed in the test circuit with soil A at the beginning of the tests. Although the geotextile HB1 was not dimensioned with respect to the criteria of FGSV, it satisfied the requirements for a sufficient filter performance. The greatest amount of migrated soil particles of NP1 was detected during the first 2 hours. With increasing test duration, the geotextile showed a stabilization like in the other permeameters. The reason for the higher amount might be details in the filling procedure of the permeameter. The cumulative amount of the migrated soil particles is given in table 1.

Table 1. Cumulative amount of migrated soil

Geotextile	Amount of migrated soil [g/m <sup>2</sup> ]	Soil
HB 1	19.02	A
HB 2	14.80	A
HB 3	5.97	A
NP 1*	78.38	A
HB 1	24.27	B
HB 2	9.15	B

\* with 20 kPa load

After that initial period, the flow rates became consistent and the various permeameters showed only very small differences. As a result of higher compaction of the soil layer, the measured permeabilities in the permeameters with geotextiles NP1 and HB2 (soil A) were lower. The system permeabilities of the permeameters with soils A and B stabilized to equilibrium conditions after 100 days, and then they varied only in a very small range for the remainder of the test period. Like in the test with the loess soil, there were no discernible differences in the performance between the types of geotextile. The system permeabilities are given also on figure 3.

The permeameters which were filled with soil B and the permeameter with the geotextile HB 1 and soil A showed a slight decrease in their permeabilities after 300 days, while all of the other permeameters were constant in their permeabilities. After the monthly addition of a disinfectant against microbiological growth, an immediate increase in the permeabilities of the treated permeameters was observed. Although a biofilm of algae was not observed at the surface of the soil layer, probably a microbial growth within the pores of the soil had to lead to a reduction of the system permeabilities. The measured permeabilities of the dismantled geotextiles were smaller than those of the virgin geotextiles by a factor of 10 at maximum, but they never fell below the permeability of the test soils.

### 3.2 Performance test with a hydraulic gradient $i = 12$

Two heat-bonded and two needle-punched nonwovens were selected for a second test series to evaluate the filter

performance under a hydraulic gradient of  $i = 12$ . In a first step, a layer of soil A with 5 cm thickness installed without compaction in the permeameters was permeated.

The development of the permeabilities of both tests under the hydraulic gradient  $i = 12$  was similar to the results of the first test series. After an initial period of increase, the permeabilities began to decrease slightly. The measured amount of migrated soil was higher than in the test with a hydraulic gradient  $i = 3$ , but after 2 hours permeation no measurable amounts of soil were detected. After a test duration of 85 days, the soil layer in the permeameters was brought into suspension to simulate the extreme case of the destruction of the internal soil filter. Like in the first test, there were no discernible differences in the performance between the geotextile types. The measured amounts of migrated soil were higher than the results before the disturbance, but piping of the soil stopped within 3 hours. A distinct trend of a better performance of thicker products regarding the retention of particles was not observed. The system permeabilities and the cumulative amount of migrated soil particles are given on Figures 4 and 5.

### 3.3 Performance tests with upward permeation

Four nonwovens (two heat-bonded and two needle-punched) were selected for a third test series to evaluate the filter performance with upward permeation under a hydraulic gradient  $i = 2.5$ . The behaviour of the permeabilities was similar to the results of the two test series mentioned above. During an initial period of about 10 days, the permeabilities showed a nonuniform permeation behaviour. After that initial period, the permeabilities in all permeameters adjusted to constant flow rates. In order to simulate the frequent case of interrupted water flow in a subsurface drainage system, the upward permeation of the test system was stopped after 40 days. After the renewed start of the permeation, following an initial period of instability, the system permeabilities remained again relatively constant with time. The system permeabilities are given on Figure 6.

Table 2. Geosynthetics used in the long-term permeation tests

	Geotextile	Polymer	Mass per unit area [g/m <sup>2</sup> ]	Thickness (2 kPa) [mm]	$O_{90,w}$ [mm] <sup>1</sup>	$k_v$ (20 kPa) [m/s] <sup>2</sup>	Permittivity (20 kPa) [s <sup>-1</sup> ] <sup>2</sup>
heat-bonded	HB 1	PP	113	0.44	0.18	$4.0 \cdot 10^{-4}$	1.34
	HB 2	PP	195	0.56	0.13	$2.4 \cdot 10^{-4}$	0.55
	HB 3	PP	300	0.82	0.09	$3.2 \cdot 10^{-4}$	0.42
needle-punched	NP 1	PET	250	2.97	0.10	$2.2 \cdot 10^{-3}$	0.83
	NP 2	PET	365	4.02	0.09	$2.3 \cdot 10^{-3}$	0.55

<sup>1</sup> measured by wet sieving (draftDIN 60500-6)

<sup>2</sup> related to 10° Celsius and 1 geotextile layer, surcharge loads are given in brackets

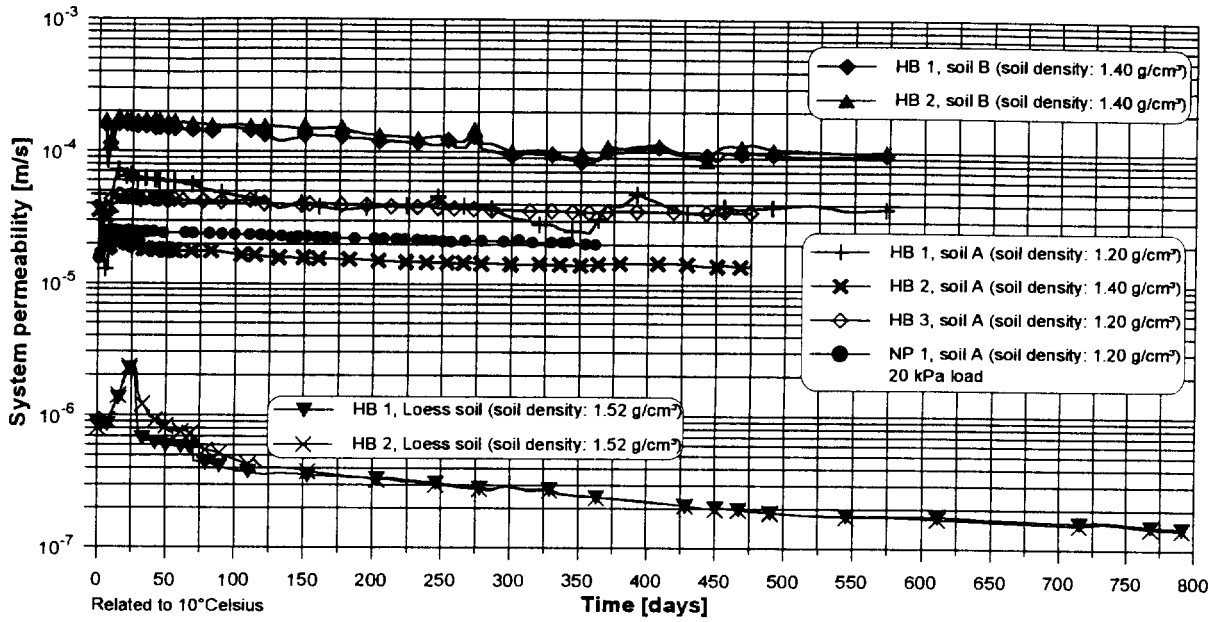


Figure 3. Permeabilities of the different systems of geotextile/soil (downward permeation, hydraulic gradient  $i=3$ )

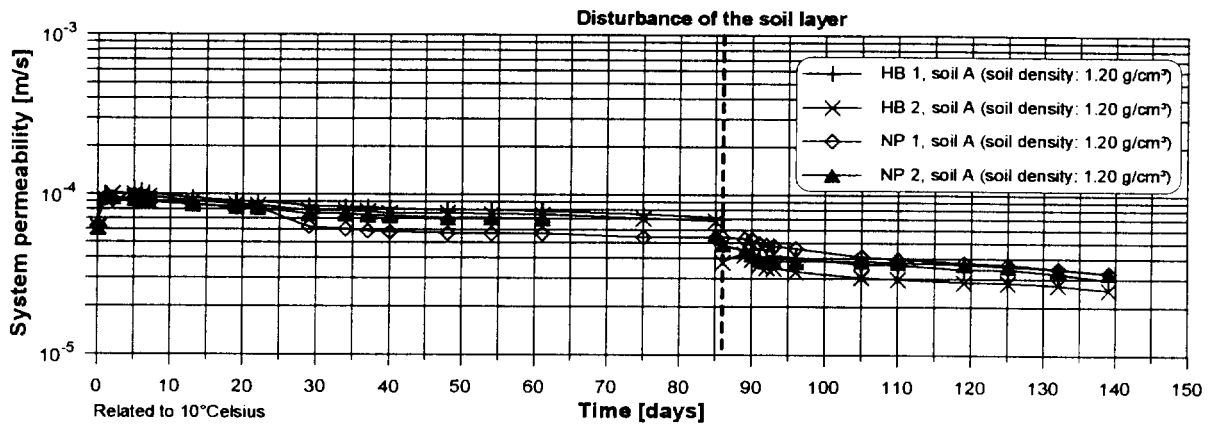


Figure 4. Permeabilities of the system of geotextile/soil A (downward permeation, hydraulic gradient  $i=12$ )

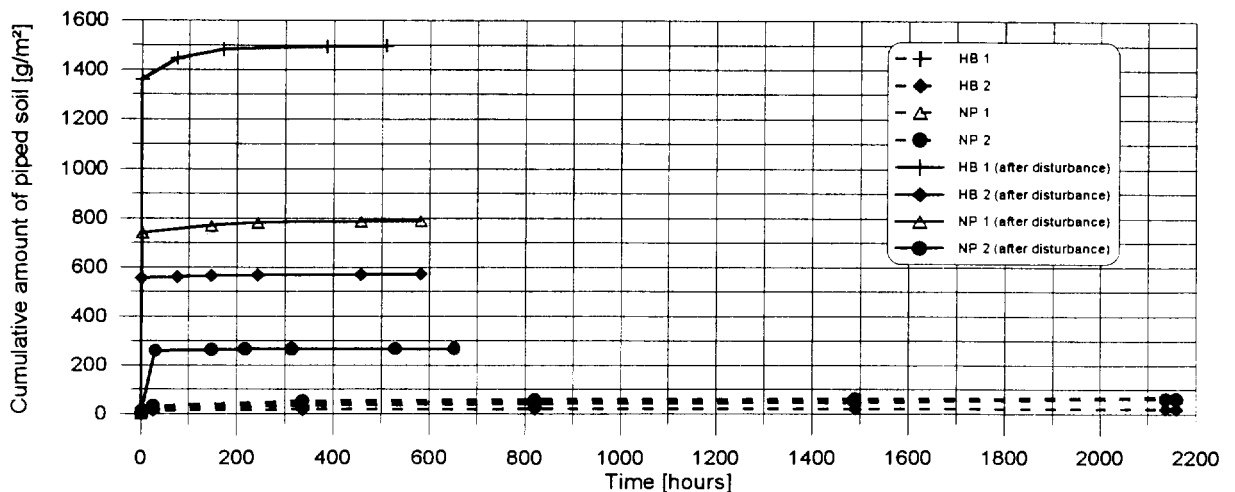


Figure 5. Cumulative amounts of piped soil (hydraulic gradient  $i=12$ )

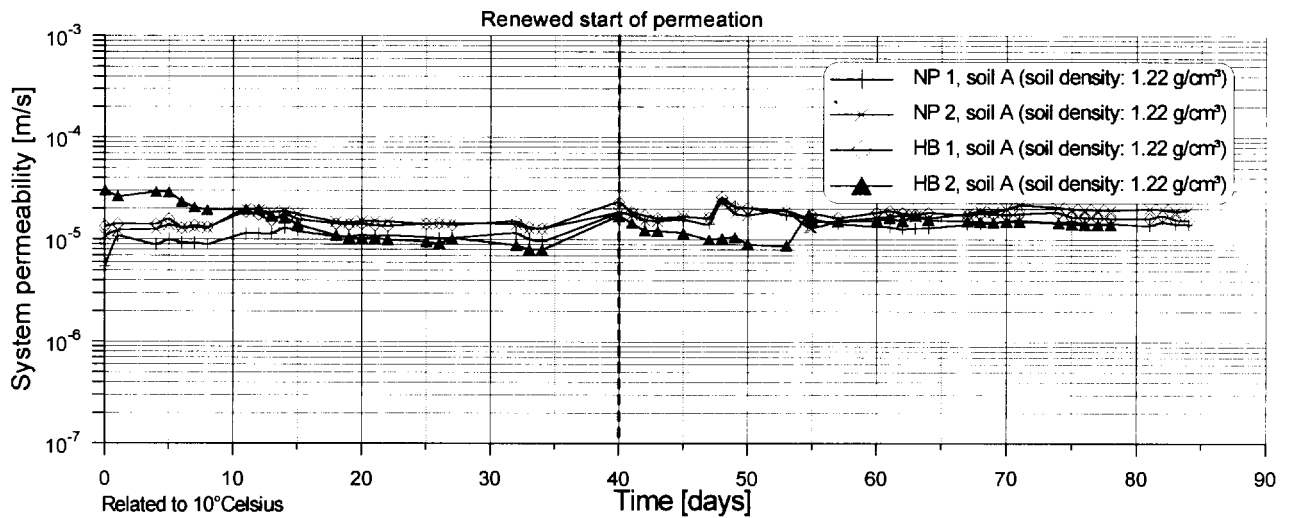


Figure 6. Permeabilities of the system of geotextile/soil A (upward permeation, hydraulic gradient  $i=2.5$ )



Figure 7. Microstructure at the interface Geotextile HB2/ Soil A (2<sup>nd</sup> Test series; hydraulic gradient  $i=12$ )

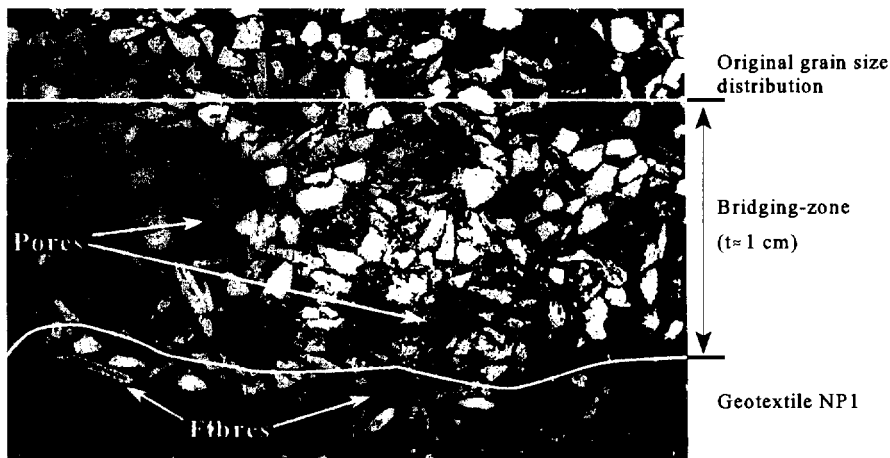


Figure 8. Microstructure at the interface Geotextile NP1/ Soil A (2<sup>nd</sup> Test series; hydraulic gradient  $i=12$ )

#### 4 MICROSTRUCTURAL ANALYSES

During the dismantling of permeameters of the test series permeated downward, undisturbed geotextile/soil samples were prepared for microscopic analyses. In all analysed microscopic sections, it was observed that soil particles

formed an internal soil filter in the form of a bridging network above the geotextiles. The geotextile filter layers acted as a catalyst for the formation of this internal filter system of the soil. The thickness of the bridging-zone was dependent on the hydraulic gradient. The thickness of the bridging-zone observed in the tests under the hydraulic

gradient  $i = 3$  was 5 mm at maximum and about 1 cm in the tests under a hydraulic gradient  $i = 12$ . A trapping of finer soil particles by the filter layer was noticed only in tests with the needle-punched geotextiles. However, the penetration was about 0.5 mm, so that the phenomena of deep filtration discussed by Heerten (1993) was not observed. The microstructures of soil A and the geotextiles HB2 and NP1 are given on figures 7 and 8.

## 5 CONCLUSION

Although the tested geotextiles differed in their material parameters, their filter performance exhibited essentially the same characteristics. They satisfied the requirements of stable permeation conditions. A review of the test results published by Kisskalt (1992), by Gartung et al. (1994) and by Kossendey et al. (1996a, 1996b), revealed that this observation applies to the geotextiles and test soils studied by Kisskalt and by Kossendey et al. as well. The test duration of up to 800 days and the large scale of the test equipment admit the application of these findings to conditions which are encountered in engineering practice (steady-state-flow conditions and lower hydraulic gradients). The opening size  $O_{90,w}$  (measured by the wet sieving method) of most of the recently obtainable nonwovens falls into the region from 0.07 to 0.13 mm. Following the obtained test results, it has to be assumed that geotextiles which meet the retention criterion based on  $O_{90,w}$  will perform successfully under these boundary conditions.

Along with the results of previous research investigations (Kisskalt 1992 and Kossendey et al., 1996a, 1996b), the findings of these long-term studies in filtration with 25 different geotextiles and 6 critical soils regarding filtration are a wide basis for the assessment of the long-term filter performance. All results confirmed that the thickness of a geotextile layer is not a relevant criterion for filtration under steady-state-flow conditions and the retention criterion based on  $O_{90,w}$ , has proved to be a reliable basis for the dimensioning of geotextile filter layers. Field examinations of geotextiles installed up to 15 years ago (Rollin et al., 1994 and Mlynarek et al., 1994) confirm the results with respect to the long-term performance.

The test results of the long-term test series reported in the present paper and compared to results of previous test series carried out at the LGA-Geotechnical Institute can be summarized as follows:

- all permeameters showed the same flow behaviour with increasing test duration
- stable flow conditions were obtained in all permeameters
- the system permeability was independent of the type of geotextile
- the thickness of a geotextile filter layer had definitely not any influence on the filtration behaviour under test conditions described above
- the microscopic analyses indicated that the

geotextile filter acts as a catalyst for the formation of an internal soil filter based on a bridging network

- the phenomenon of deep filtration was not observed
- no measurable migration of soil particles occurred after 48 h, stable hydraulic conditions were obtained in all permeameters
- even relatively openly designed geotextiles performed successfully
- no failure of the geotextile filter by clogging was found during the performance tests

## 6 REFERENCES

- Davidenkoff, R. (1976) "Anwendung von Filtern im Wasserbau", W. Ernst & Sohn, Berlin, Germany.
- draftDIN 60500-4 (1997) "Prüfung von Geotextilien.- Bestimmen des Wasserdurchlässigkeitsbeiwertes  $k_{v,konst}$  senkrecht zur Geotextilebene unter Auflast bei konstantem hydraulischen Höhenunterschied"
- draftDIN 60500-6 (1994) "Bestimmung der Öffnungsweite  $D_w (O_{90})$ "
- FGSV Forschungsgesellschaft für Straßen- und Verkehrswesen (1994) "Merkblatt für die Anwendung von Geotextilien und Geogittern im Erdbau des Straßenbaus", FGSV, Cologne, Germany, 72 p.
- Gartung, E., Kossendey, Th. & Murray, H. R. (1994) "Long-term filter function of nonwovens: large scale performance tests", *5. Int. Conf. on Geotextiles*, Singapore, Vol 2, pp. 729-732
- Heerten, G. (1993) "A contribution to the improvement of dimensioning analogies for grain filters and geotextile filters", *Geofilters '92*, Balkema, Karlsruhe, Germany, pp. 121-128.
- Kisskalt, J. (1992) "Kunststoffe in der Geotechnik - Deponiebau mit Geokunststoffen-", *Veröffentlichungen des Grundbauinstitutes der Landesgewerbeanstalt Bayern*, Vol. 68, LGA, Nuremberg, Germany, 405 p.
- Kossendey, Th., Gartung, E. & Lawson, C.R. (1996a) "Long-term performance tests for verification of current geotextile filter criteria", *Geofilters '96*, Bitech Publishers Ltd., Montreal, Canada, pp. 275-284
- Kossendey, Th. & Karam, G. (1996b) "A Critical Review of the Current Filter Criteria on the Basis of Long-Term Performance Tests", *EuroGeo 1*, Balkema. Maastricht, The Netherlands, pp. 961 - 968
- Luettich, S. M., Giroud, J. P. & Bacchus, R. C. (1992) "Geotextile filter design guide", *Geotextiles and Geomembranes*, Vol. 11, Special issue 1992: 355-370. Barking: Elsevier Science Publisher
- Mlynarek, J., Bonnell, R. B., Broughton, R. S. & Rollin, A. L. (1994) "Long-term effectiveness of subsurface agricultural drainage systems", *5. Int. Conf. on Geotextiles*, Singapore, Vol 2, pp. 725-728
- Rollin, A. L., Mlynarek, J., Hoekstra, S. E. & Berkhout, H. C. (1994) "Geotextile thickness: A relevant filter design criterion", *5. Int. Conf. on Geotextiles*, Singapore, Vol 2, pp. 795-698



# The Performance of a Geotextile Filter in Tropical Soil

M.G. Gardoni

Civil Engineer, University of Brasilia, Brasilia, Brazil

E.M. Palmeira

Associate Professor, University of Brasilia, Brasilia, Brazil

**ABSTRACT:** Problems with granular filters in residual soils from quartzite is well known by the Federal District Highway Department, Brasilia, Brazil. These soils are structurally formed by clusters of fine particles. However, geotextile filters have been used successfully under these conditions. This paper investigates a geotextile drain in residual soil from quartzite that have been performing well for the last 10 years. Soil and geotextile samples were collected from the drain and tested in the laboratory. Chemical and microscopic analyses were performed on the residual soil and on samples of the geotextile. Current filter criteria were also used and the results obtained suggest that the accuracy of a criterion prediction may be a function of the procedure used to obtain grain size distribution of the soil and on cluster resistance to high gradients. In general the drain is in good operational conditions.

**KEYWORDS:** nonwoven geotextile, filter, residual soil, geotextile permeability, filter criteria.

## 1. INTRODUCTION

Geotextile draining systems have consistently performed well in highways around Brasilia, Federal District, Brazil. In several similar situations granular filters have clogged when in contact with residuals soils from quartzite, which is very common in the region. Besides, local government environmental agencies have been very strict on the exploitation and use of natural materials such as sand and gravels. This causes these materials having to be transported from distant places for drain construction, which increases significantly the cost of granular drains in comparison to synthetic drains. Because of these reasons geotextile drains have become increasingly competitive in comparison to natural drains and the Federal District Highway Department has increased the acceptance of geotextile drainage systems in the region.

This paper presents a study of a 10 years old geotextile drain built in the BR-020 highway, close to Brasilia, in a region of residual soils from quartzite. The study involved the inspection of the geotextile in situ, collection of geotextile, soil and water samples for laboratory tests.

## 2. CHARACTERISTICS OF THE DRAIN, MATERIALS AND EQUIPMENTS USED

### 2.1 Drain characteristics

The drain in the BR-020 highway was constructed in a region of residual soil and weathered rock from quartzite, with the presence of meta-siltstone and meta-claystone. The drain is 400 m long at each side of the road and was constructed in a 0.6 m wide and 1.5 m deep trench. Figure 1 shows schematically the drain geometrical characteristics.

### 2.2 Soil, water and geotextile characteristics

A trench was excavated alongside the drain to collect soil and geotextile samples for testing. Undisturbed soil samples as well as geotextile samples on the side and on the top of the drain were collected. Visual inspection showed that the geotextile layer was in good state not being observed any damage that might have been inflicted to the geotextile during construction. The drain, as a whole, was in very good operational conditions. At this stage it was also very clear the greater contamination of gravel material not protected by the geotextile. Water samples were also collected for analyses.

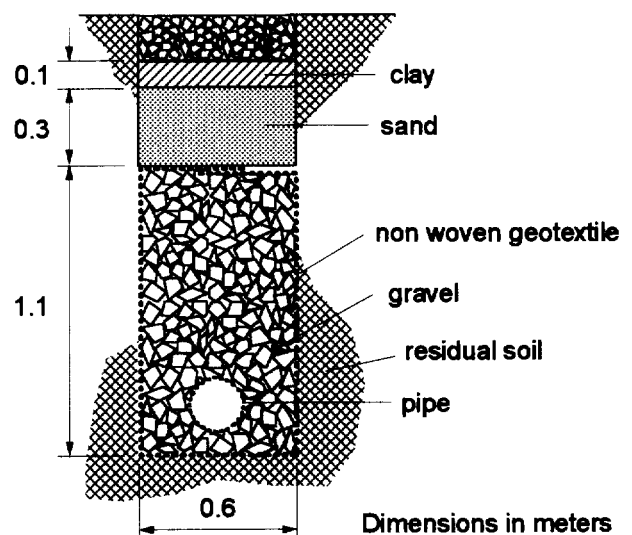


Figure 1. Drain characteristics.

Standard laboratory tests were performed on the residual soil samples for the determination of grain size distribution, void ratio, moisture content, etc. Table 1 summarizes the main characteristics of the soil. The soil is

a fine sand (83% of sand particles) and its grain size distribution is shown in Figure 2. Two curves for the grain size distribution of the residual soil are presented in this figure. One is the curve obtained with the sedimentation test using deflocculant (standard procedure) and the other is the result with the sedimentation test without the use of deflocculant. The reason for the latter type of sedimentation test is due to the fact that soils in this region are commonly structurally composed of clusters of soil particles, forming strong larger grains, which may be loosened by the action of the deflocculating agent used in the tests but not necessarily by water flow in a drain or in filtration tests. Therefore, for the use of filtration criteria, the grain size curve obtained without the use of deflocculant may be the appropriate one under these circumstances. Figure 2 shows a marked difference between results of sedimentation tests with and without the use of deflocculant.

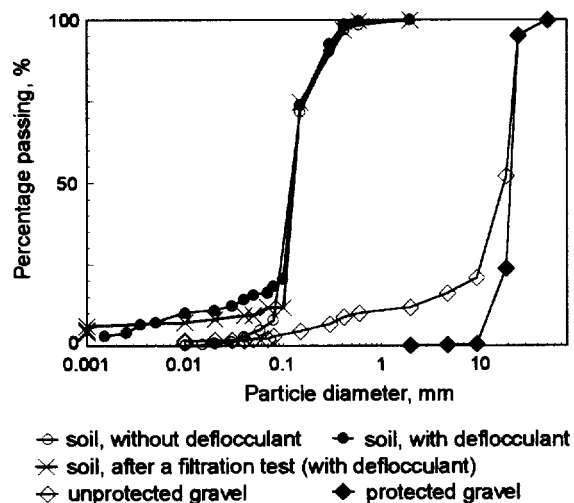


Figure 2. Grain size distributions of the soils.

Table 1. Soil properties.

Natural moisture content, %	11.4
Specific gravity (in situ), kN/m <sup>3</sup>	22.6
Void ratio	0.33
Density of the soil particles	2.71
Permeability coefficient, cm/s	$80 \times 10^{-4}$

It is important to note that depending on the grain size distribution chosen for filter design the values of grain diameters obtained can be significantly different. The same applies to the value of the coefficient of non-uniformity of the soil (CU) which may be 1.4 or 19, depending on the curve used. The latter value suggests that if the pack of grains is destroyed by the action of the water the soil can be highly sensitive to suffusion.

Chemical and mineralogical tests were also performed in the residual soil such as methylene blue and X-rays diffractometry. These tests yielded to results of coefficient of activity for the fine fraction of the soil equal to 6.88 g/g, specific surface of 7.35 m<sup>2</sup>/g and cations exchange capacity of 0.8 meq/100. Results of the chemical analysis are presented in Table 2. The soil can be then classified as a low activity lateritic soil. This was confirmed by the presence of kaolinite as the predominant clay mineral in the soil fine fraction in X-rays diffractometry tests.

Table 2. Chemical composition of the soil.

Substance	Percentage (%)
SiO <sub>2</sub>	89.10
Fe <sub>2</sub> O <sub>3</sub>	1.12
Al <sub>2</sub> O <sub>3</sub>	2.53
CaO	0.13
MgO	0.06

Tests with samples of the underground water in the region revealed a pH equal to 7.95 and low values of turbidity (0.7 NTU) and iron content (0.23 mg/l). These values are close to the values observed for distilled water.

A nonwoven needle punched geotextile, made of polyester, commercially available under the name Bidim OP20, was used to envelope the gravel material (Fig. 1). Table 3 presents the main characteristics of the geotextile used.

Table 3. Geotextile characteristics.

FOS, mm	0.130
AOS, mm	0.12-0.21
t <sub>GT</sub> , mm	2.2
k <sub>n</sub> , cm/s	0.55

Notes: FOS - filtration opening size (AFNOR G 38017); AOS - apparent opening size (ASTM D4751-87); t<sub>GT</sub> - geotextile thickness; k<sub>n</sub> - geotextile permeability coefficient normal to its plane (ASTM D4491-89).

### 2.3 Experimentals

Filtration tests with undisturbed soil samples and the same type of geotextile used in the drain were performed in the laboratory as well as geotextile permeability tests with geotextile samples exhumed from the drain. A permeameter similar to the one presented by Calhoun (1972) was employed for the filtration tests, which is composed of a pvc cell that can accommodate 100 mm diameter soil samples. A total system gradient of 2 was adopted for the filtration tests. The equipment also allows the execution of gradient ratio tests. However, for the present case the definition of gradient ratio may be irrelevant due to the fact that undisturbed samples, rather

than reconstituted samples, were tested. So, heterogeneities in the undisturbed soil mass can affect the value of the gradient ratio obtained. Nevertheless, the general procedure recommended by ASTM (1991) for gradient ratio tests (ASTM D 5101-90) was followed in the present case.

For the conformance of the cylindrical external face of the soil sample to the cylindrical internal surface of the permeameter cell the soil sample side was covered by a layer of paraffin which was then trimmed appropriately to achieve a satisfactory match between soil and cell diameters. The internal wall of the permeameter cell was greased to avoid any preferential flow along the soil-cell interface. Filtration tests with durations as long as 2500 hours ( $\cong$  3.5 months) were performed.

Distilled water was used in the laboratory tests and its composition after having crossed the soil sample was monitored during the test to assess variations in pH, turbidity, total iron and electrical conductivity.

To assess the loss of permeability of the geotextile in the drain after 10 years of operation the carefully exhumed geotextile samples were subjected to permeability tests in the laboratory. The equipment in this case is similar to the one presented in ASTM (1991) for the determination of the permeability of geotextiles normal to its plane (ASTM D 4491-89).

Investigations of the state of the exhumed samples of geotextile were also carried out using electronic microscopy. For this analysis samples of exhumed geotextile were firstly totally impregnated by polyesterene resin under vacuum. Slices of these samples could then be cut for the analysis by an electronic microscope.

Additional information on materials, equipments and methodologies can be found in Gardoni (1995).

### 3. RESULTS OBTAINED

#### 3.1 Filtration test

Figure 3 shows the result of a filtration test with an undisturbed residual soil sample and the same geotextile used in the drain. Approximately 2000 hours were necessary for the stabilization of water flow conditions.

At the end of the long term filtration test the soil mass close to the geotextile (one third of the original sample height) was tested for void ratio determination. It was observed that the void ratio increased from 0.33 to 0.53 in that region. This suggests that some level of suffusion occurred during the long term filtration test. This can be also inferred from the grain size distribution of the soil sample close to the geotextile after the filtration test, which is also presented in Figure 2 (grain size analysis with the use of deflocculant). This indicates that the mobility or dispersion of soil clusters may be dependent of the gradient used in the test.

Figure 2 also shows the grain size distributions of the gravel materials enveloped by the geotextile and on top of the drain (Fig. 1). It can be observed that the unprotected gravel was significantly contaminated by the fines from the residual soil while the gravel inside the drain was clean.

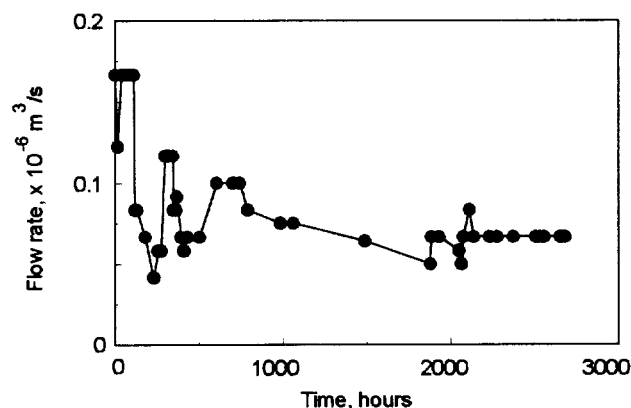


Figure 3. Flow rate versus time in a filtration test.

The analysis of the water that passed through the soil sample in comparison to the standard distilled water showed high values of turbidity and increases on iron content and pH, as shown in Table 4. These results suggest that there was iron precipitation under laboratory conditions.

Table 4. Water composition at the entrance and at the exit of the soil sample (end of the test).

Stage	ph	(1)	(2)	(3)	(4)
Entrance	6.8	0.028	0.38	3.10	1.8
Exit	7.1	2.22	82	10.6	7.4

Notes:

(1) - total iron (mg/l); (2) - turbidity (NTU); (3) electrical conductivity ( $\mu$ S/cm) and (4) - total dissolved solids (mg/l).

#### 3.2 Geotextile permeability

The geotextile samples taken from the drain side and top as well as the sample used in the filtration test discussed above were tested to assess their loss of permeability under field and laboratory conditions. Firstly, for this comparison, a series of geotextile permeability tests were performed on virgin samples of the same geotextile in order to determine its average permeability coefficient and the scatter of test results. As the mass per unit area of thin geotextiles can vary markedly along the geotextile layer, several samples of varying mass per unit area were tested. The results of normal geotextile permeability of virgin samples versus geotextile mass per unit area are presented in Figure 4 where a rather constant average normal

permeability with mass per unit area can be observed as well as a significant scatter of test results.

The results of permeability tests with geotextile samples from the drain and from the filtration test are also presented in Figure 4 and in Table 5. A reduction of geotextile permeability of 50 to 60% with respect to the average permeability of the virgin samples can be observed for the exhumed geotextile samples. The geotextile sample used in the filtration test retained only about 5% of its original normal permeability. These results suggest that much more severe conditions occurred in the laboratory filtration test than in the field (larger gradient, for instance). Nevertheless, the values of permeability coefficient or geotextile permittivity are still significantly high for practical purposes, as shown in Table 5.

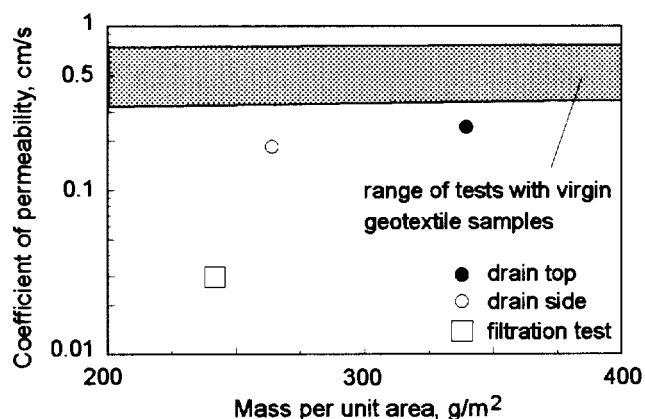


Figure 4. Geotextile permeability test results.

Table 5. Geotextile permeability tests results.

Geotextile specimen	$t_{GT}$ (mm)	$M_A$ ( $g/m^2$ )	$k_n$ (cm/s)	$\psi$ ( $s^{-1}$ )
Drain top	1.6	340	0.24	1.50
Drain side	1.6	264	0.19	1.19
Filtration test	2.0	242	0.03	0.15

Notes:  $t_{GT}$  = geotextile thickness,  $M_A$  = geotextile mass per unit area,  $k_n$  = geotextile coefficient of permeability and  $\psi$  = geotextile permittivity.

### 3.3 Evaluation of filter criteria

As mentioned earlier in this work, for a proper application of filter criteria the grain size characteristics of the soil in contact with the geotextile have to be well determined. In the case of the residual soil investigated in the present work the value of relevant grain diameters depend on the use or not of deflocculant in the sedimentation test. Because the soil mass is mainly composed of coarse "grains" composed of clusters of particles that may or may not be dispersed by water flow or migrate through the soil

mass, the designer has to decide which grain size distribution curve should be used for design purposes. The aim of this section is to evaluate the results obtained by some design criteria available in the literature for the drain under investigation. The following filter criteria were employed: French Committee on Geotextiles and Geomembranes (CFGG, 1986), Canadian Geotechnical Society (CGS, 1992), Carroll (1983), Christopher and Holtz (1985), Giroud (1982), IRIGM (Grenoble)/Ecole Polytechnique de Montreal (Faure et al, 1986), Mlynarek et al (1990), Ontario Ministry of Transportation (OMT, 1992), University of British Columbia - UBC (Fannin et al, 1994), United States Federal Highway Administration (USFHWA, Christopher and Holtz, 1985) and United States Army Corp of Engineers (USACE, 1977). Table 6 summarises the results of filter criteria evaluation. It can be observed that most of the criteria would lead to the acceptance of the use of geotextile while only two would reject its use as filter for the residual soil. It is interesting to note that the criterion presented by Giroud (1982) would not be entirely applicable for the grain size distribution curve obtained in the sedimentation test with deflocculant because to some extent the soil could be considered as a gap graded soil by that criterion. Nevertheless, if the criterion was also applied in this case the geotextile would have failed to meet filter requirements. The geotextile may fail or not by the criterion presented in Mlynarek et al (1990) depending on the value of the apparent opening size used for the geotextile (maximum or minimum value in Table 3).

Table 6. Evaluation of filter criteria

Criterion	Grain Size Analysis	
	Without deflocculant	With deflocculant
CFGG (1986)	F	F
CGS	P	P
Carroll (1983)	P	P
Christopher & Holtz (1985)	P	P
Giroud (1982)	P	NA/F
Mlynarek et al (1990)	F/P	P
IRIGM/EPM	F	F
OMT (1992)	P	P
UBC	P	NA
USFHWA	P	P
USACE	P	P

Notes: F - geotextile failed; P - geotextile passed; NA - criterion is not applicable, F/P - failed or passed (see text for comments) and NA/F - Not applicable or failed (see text for comments).

From the results presented in Tables 1 and 5 it can be observed that the permeability coefficient of the exhumed geotextile samples is of the order of 25 times the soil permeability coefficient, which satisfies current

permeability criteria such as the ones presented by Carroll (1983), Giroud (1982) and Christopher and Holtz (1985)

### 3.4 Microscopic investigations of exhumed geotextile samples

The exhumed geotextile samples were observed under optical and electronic microscopes and photographs of some of the specimens are presented in Figures 5 to 8. In general it could be observed that the geotextile was in good conditions with the sample taken from the side wall of the drain with a greater degree of clogging but still maintaining a large amount of its openings free from soil particles, as shown in Figure 5. This is reasonable since water flow is more (or only) significant along the sides of the drain. Figure 6 shows that the grains retained in the geotextile were formed by clusters of soil particles, as commented earlier in this work. Figure 7 shows a detail of one of these clusters. These results emphasises the difficulty related to the choice of appropriate soil particle diameters to use in filter criteria for residual soils. Figure 8 shows that clay particles or clusters were also found bonded to individual geotextile fibers. Some level of damage of the geotextile fibers could be identified and may have been caused during drain construction or by the action of microorganisms. Figures 5 to 8 show that after 10 years of existence the geotextile layer is in good operational condition.



Figure 5. General view of the geotextile openings.

## 4. CONCLUSIONS

This work investigated the condition of a 10 years old geotextile drain in a residual sandy soil from quartzite. Clogging of granular drains in contact with this soil is common and nonwoven geotextiles have been successfully used as alternatives for granular drains. The main conclusions of the present work are summarised below:

. The geotextile was able to retain the fines from the residual soil and the enveloped gravel material in the drain was very clean in contrast to the contaminated gravel material in regions where geotextile layers were not used.

. Geotextile permeability tests suggest a 70% loss of the original permeability under field conditions for the drain investigated. The permeability loss observed in a laboratory filtration test was significantly greater than in the field which was probably due to the soil-geotextile system in the laboratory having been subjected to more severe conditions than the ones found in the field. The destruction of soil clusters and the consequent intensity of suffusion is also likely to be dependent of the gradient of flow.

. The investigation of the condition of the geotextile pores after 10 years of operation showed that a large amount of free pores is still available.

. Geotextile filter design for soils formed by clusters of particles is a complex task. The results presented in this work shows that the acceptance or not of a geotextile filter by current criteria or the applicability of some criteria can be even dependent of the procedure adopted in the grain size analysis of the soil. Soil chemical and mineralogical analyses are useful tools for the understanding of long term behaviour of geotextile drains in tropical soils. In spite of the encouraging results obtained in the present work, further research is required for a better understanding on the behaviour of geotextile filters in tropical soils.

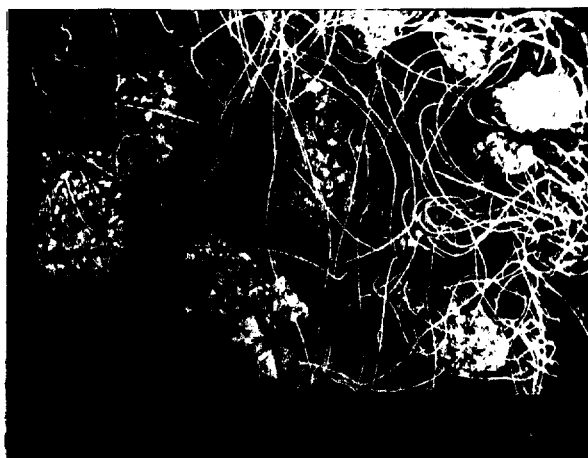


Figure 6. Clusters of particles retained in the geotextile.

## ACKNOWLEDGEMENTS

The authors are indebted to the following institutions that helped to make this work possible: Federal District Highway Department, University of Brasília, CAPES - Brazilian Ministry of Education and Rhodia-Ster. Dr. Cristina Brandão and Prof. Elliot W. Kitajima, from the

University of Brasilia, gave important contributions to the chemical and microscopical analyses performed, respectively.



Figure 7. Detail of a cluster of particles.



Figure 8. Fine particles bonded to a geotextile fiber.

## REFERENCES

- ASTM (1991) "ASTM Standards on Geosynthetics", 2nd Edition, Philadelphia, PA, USA, 104 p.
- Calhoun, C.C. (1972) "Development of Design Criteria and Acceptance Specifications for Plastic Filter Cloths", *Technical Report S-72-7*, US Army Corps of Engineers, Waterways Experimental Station, Vicksburg, USA.
- Carroll, R.G. (1983) "Geotextile Filter Criteria", *Transportation Research Record 916*, USA, pp. 46-53.
- CFGG (1986) "Geotextiles Manual", Comité Français sur les Géotextiles et Geomembranes, Association Française de Normalisation, France, 64 p.
- CGS (1992) "Canadian Foundation Engineering Manual", Canadian Geotechnical Society, 3rd Edition, Vancouver, BC, Canada.
- Christopher, B.R. and Holtz, R.D. (1985) "Geotextile Engineering Manual", U.S. Federal Highway Administration, Report FHWA-TS-86/203, 1044p.
- Faure, Y. Gourc, J.P., Brochier, P. and Rollin, A. (1986) "Soil-Geotextile Interaction in Filter Systems", *3rd International Conference on Geotextiles*, Vienna, Austria, Vol. 2, pp. 671-676.
- Gardoni, M.G. (1995) "Evaluation of the Applicability of Laboratory Tests and Filter Criteria for the Use of Geotextile Drains in the Federal District", *MSc Thesis*, University of Brasília, Brazil (in Portuguese), 177 p.
- Giroud, J.P. (1982) "Filter Criteria for Geotextiles", *2nd International Conference on Geotextiles*, Las Vegas, USA, Vol. 1, pp. 103-108.
- Fannin, R.J., Vaid, Y.P. and Shi, Y.C. (1994) "Filtration Behaviour of Nonwoven Geotextiles", *Canadian Geotechnical Journal*, 31, pp. 555-563.
- Mlynarek, J., Lafleur, J. and Lewnadowski, J.B. (1990). "Field Study on Long Term Geotextile Filter Performance", *4th International Conference on Geotextiles, Geomembranes and Related Products*, The Hague, The Netherlands, Vol.1, pp. 259-262.
- OMT (1992) "Material Specification for Geotextiles", *Ontario Provincial Standard Specification 1860*, Ontario Ministry of Transportation, Canada.
- USACE (1977) "Civil Works Construction Specification for Plastic Filter Fabric", United States Army Corps of Engineers, *Construction Guide Specification No. CW-00215*, Washington, DC, USA.

# Effect of Cavities Between Soil and Geotextile Filter on Permeability

Prof. Dr. Erol Güler

Professor, Department of Civil Engineering, Boğazici University, Turkey

Emir Baran

Former M.Sc. Student, Turkey

**ABSTRACT:** During the placement of the geotextile filter, some free space can be left between the in-situ soil and the filter fabric. There is the possibility that the soil particles that separate from the soil matrix will accumulate on the surface of the filter geotextile and create an impermeable layer, which is called blinding. The aim of this study was to observe whether such blinding process really occurs. This was investigated by preparing samples with cavities of cylindrical shape. The diameters and the heights of the cavities varied. Two types of geotextiles, one of them needle-punched and the other spun-bonded, that are most commonly used as filters were used in the tests. Permeability tests conducted on the samples revealed that the presence of cavities did not cause any reduction in the permeability for the given clay and two geotextiles that have been used, compared to the permeability of the samples without cavities.

**KEYWORDS:** Blinding, Geotextile, Filtration, Permeability

## 1 INTRODUCTION

Geotextiles used for filtration and related applications should have similar functional criteria to those of aggregate filters. The fabric to soil system should permit free liquid flow across the plane of the fabric without clogging while preventing the escape of soil particles. There are several modes of failure that need to be considered in the design of a geotextile filter. The design for filtration, retention and long term clogging properties of geotextile filters has been studied by many researchers. (Giroud, 1982, Luettich et. al., 1994) Another possibility of failure is blinding. During the placement of the geotextile filter, some free space can be left between the in-situ soil and the filter fabric. There is the possibility that the soil particles that separate from the soil matrix will accumulate on the surface of the filter geotextile and create an impermeable layer. The aim of this study (Baran, 1996) was to observe whether such blinding process really occurs. This was investigated by preparing samples with cavities of cylindrical shape. The diameters and the heights of the cavities varied. Two types of geotextiles that are most commonly used as filters were used in the tests. One of the geotextiles was a needle-punched and the other a spun-bonded geotextile. Hydraulic conductivity tests were conducted on samples prepared with cavities.

## 2 METHODOLOGY

A mixture of kaolinite and bentonite clay was used in the tests. The percentages of kaolinite and bentonite were 75% and 25% respectively. Geotechnical properties of the clay mixture used in this study are given in Table 1.

In each sample, the geotextile filter was placed over gravel, and the soil sample with a cavity was placed over the

geotextile. The gravel used was a uniform sized gravel passing No. 4 sieve.

Table 1. Geotechnical properties of clay

Properties	Values
Dry unit weight( $\text{kN/m}^3$ )	15.2
Optimum water content(%)	23
Specific gravity	2.69
Activity	0.29
Smaller than 2 $\mu\text{m}$	47.1
Liquid limit(%)	85
Plastic limit(%)	25
Plasticity index(%)	60

Two types of geotextiles were used in all tests. The first one was nonwoven, needle-punched and the other one was nonwoven, spun bonded. The basic characteristics of the geotextiles used are listed in Table 2 and 3.

Table 2. Properties of spun-bonded geotextile

Properties	Test Method	Unit	Values
Unit weight	ASTM D3776	$\text{g/m}^2$	68
Thickness under 2 kPa pressure	ASTM D 1777	mm	0.36
Tensile strip test	BS/6906/1	kN/m	3.3
Permeability	EMPA/ITF	m/s	25E-04

The clay samples were prepared in an air-dried condition as a powder and mixed with each other properly before adding water to it. Then water was gradually added to the samples until the desired water content was reached. The samples prepared were allowed to sit for 24 hours to allow for the moisture to distribute evenly. All the samples were compacted at two percent dry of optimum. The compaction was conducted according to Standard Proctor compaction method as outlined in ASTM Standard D 698-78, Method A.

Properties	Test Method	Unit	Values
Unit weight	ASTM D3776	g/m <sup>2</sup>	95
Thickness under 2 kPa pressure	ASTM D 1777	mm	1.0
Tensile strip test	ASTM D 4595	kN/m	5.9
Permeability vertical under pressure 2 kN/m <sup>2</sup>	Franzius Inst.	cm/s	0.5
Permeability vertical under pressure 200 kN/m <sup>2</sup>	Franzius Inst.	cm/s	0.06

In preparation of samples which had cavities, special mold-bases as shown in Figure 1a, were laid down at the base of the compaction mold. Different mold bases with varying heights and diameters were used.

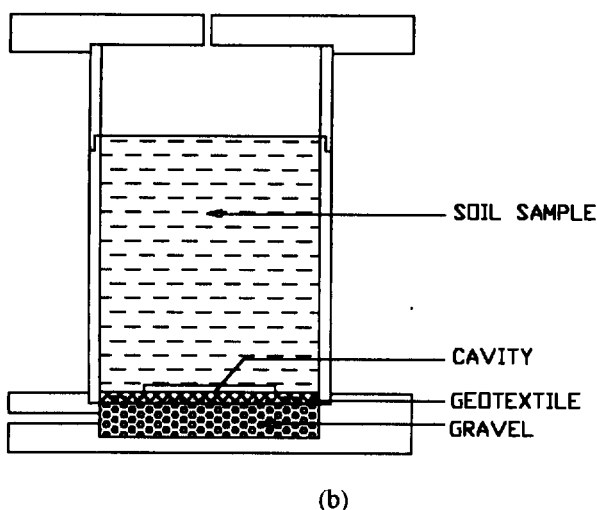
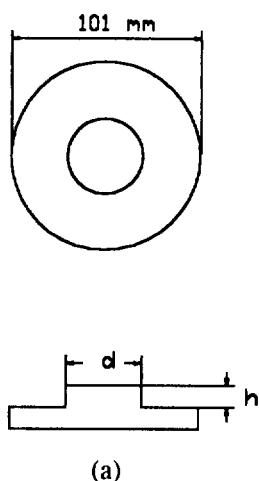


Figure 1. a) Special mold bases used to form cavities, b) Cross-section of a typical test sample

The chosen heights and diameters of the cavities were as follows: mold bases with height (h) of four mm and with height of six mm; For each height of cavity, there were three different diameters (d), twenty, forty and sixty mm.

After compaction, the mold bases under the samples were removed carefully leaving the cavities in the sample. The samples were placed over geotextile which was laid over a gravel layer because in a subsurface drainage installation, the downstream side of the geotextile is usually supported by gravel or rock. Cross section of a typical test sample is shown in Figure 1b.

Falling head permeability tests were conducted on the specimens in the molds in which they were compacted. Hydraulic head was on the average 135 cm. Measurements of the permeability tests were continued until permeability values reached an equilibrium condition.

### 3 TEST RESULTS

Permeability tests which were conducted on the samples which did not have a cavity, are given in Table 3.

Table 3. Result of permeability tests on samples without cavities

Sample type	Permeability (cm/s)
Soil only	$5.14 \times 10^{-8}$
Soil with spun-bonded geotextile	$5.58 \times 10^{-8}$
Soil with needle-punched geotextile	$7.83 \times 10^{-8}$

The results of the tests with varying cavity geometry and type of geotextile used are given in Table 4 and Table 5.

Table 4. Result of permeability tests on samples with spun-bonded geotextile, Permeability(cm/s)

Diameter (mm)	20	40	60
Height (mm)			
4	$6.80 \times 10^{-8}$	$9.03 \times 10^{-8}$	$8.55 \times 10^{-8}$
6	$8.48 \times 10^{-8}$	$1.07 \times 10^{-7}$	$9.77 \times 10^{-8}$
			$1.06 \times 10^{-7}$

Table 5. Result of permeability tests on samples with needle punched geotextile, Permeability(cm/s)

Diameter (mm)	20	40	60
Height (mm)			
4	$8.35 \times 10^{-8}$	$9.74 \times 10^{-8}$	$9.55 \times 10^{-8}$
6	$9.8.3 \times 10^{-8}$	$1.10 \times 10^{-7}$	$1.31 \times 10^{-8}$
			$1.38 \times 10^{-7}$

Permeability test results versus surface area of the cavities can be seen in Figure 2 for spun-bonded geotextiles and in Figure 3 for needle punched geotextiles. Surface area is described as the surface through which the



water leaves the soil and enters the cavity. Therefore, the surface area is calculated as the sum of the circular section plus the peripheral area of the cylindrical cavity. For spun-bonded geotextiles, increasing the diameter, increased the permeability value slightly. Further increase in diameter of the cavity did not result in further increases, instead a slight decrease was observed. Increasing the height of the cavity resulted in higher permeabilities for all diameters. When needle punched geotextiles were used, increasing the diameter revealed similar results with those of spun-bonded geotextiles when cavity height was 0.4 cm. However, increasing the cavity diameter further caused an increase in permeability for the cavity height of 0.6 cm.

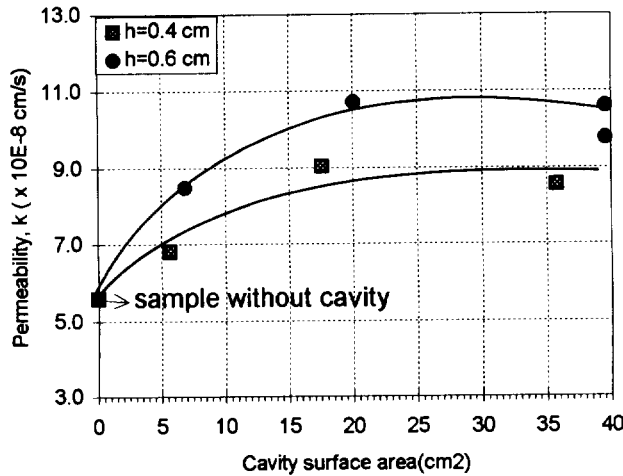


Figure 2. Permeability versus cavity surface area for spun bonded geotextiles

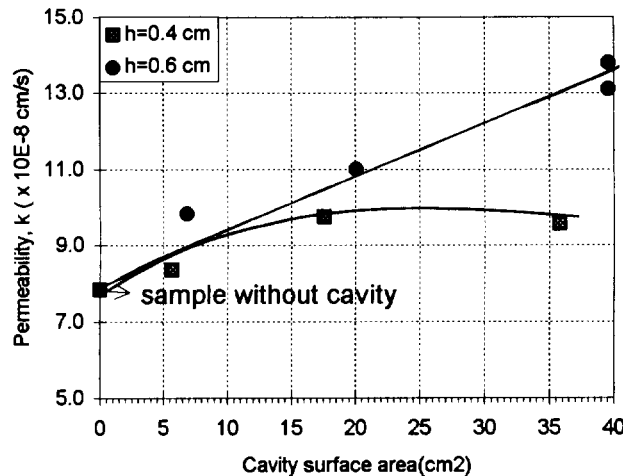


Figure 3. Permeability versus cavity surface area for needle punched geotextiles

Permeability results for both types of geotextiles were also plotted against the volume of the cavity. The permeability results versus volume of the cavities are

shown in Figures 4 and 5 for spun-bonded and needle-punched geotextiles respectively. Similar conclusions can be drawn from these figures.

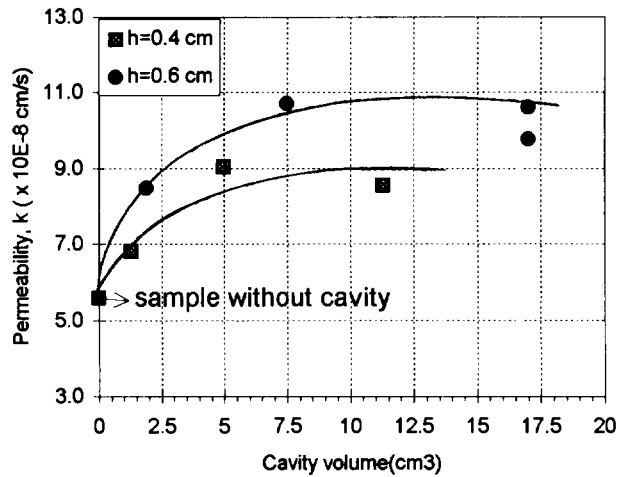


Figure 4. Permeability versus cavity volume for spun bonded geotextiles

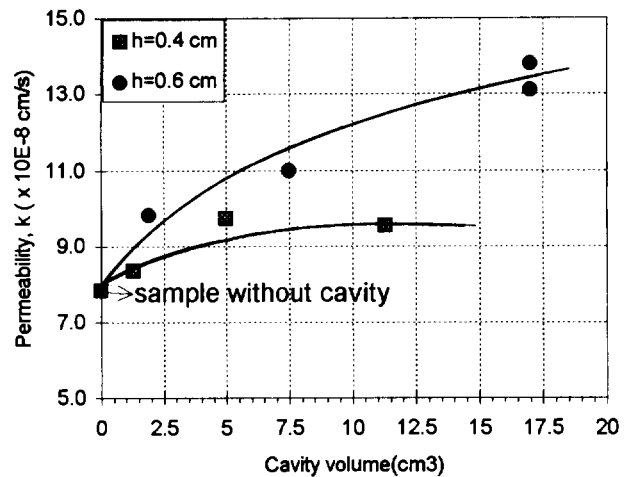


Figure 5. Permeability versus cavity volume for needle punched geotextiles

#### 4 CONCLUSIONS

Permeability tests conducted on the samples revealed that the presence of cavities did not cause any reduction in the permeability for the given clay and the two types of geotextile that have been used compared to the permeability of the samples without cavities. A slight increase of the permeability was observed for smaller sized cavities. It was determined that the increase in the height of the cavity causes consistently an increase in the

permeability. An initial increase in the permeability was measured with an increase in the diameter. For spun bonded geotextiles, increasing the size of the cavity causes an increase in the permeability for up to a maximum permeability level. Increasing the size of cavity beyond this point slightly decreases the maximum permeability value. For needle punched geotextiles, the trend is similar for the cavity height of 0.4 cm. However, for a cavity height of 0.6 cm this reversal in behaviour is not observed and a further increase in permeability is measured with increasing cavity size. This indicates that the danger of blinding is even less for needle punched geotextiles, for the given cavity sizes.

## REFERENCES

- ASTM (1989) *American Society for Testing Materials*, Annual Book for ASTM, Easton, March, 1989.
- Baran, E.B. (1996) Effect of Cavities Between Soil and Geotextile on Permeability, *Master Thesis*, Bođaziçi University.
- Giroud, J. P. (1982) "Separation Criteria for Geotextiles," *Proceeding of Second International Conference on Geotextiles*, Las Vegas, Vol.1, pp. 103-108
- Luetlich, S. M., J. P. Giroud, and R. C. Bachus (1994) *Geotextile Filter Design Guide*, Georgia,

# Theoretical Basis for the Development of a Two-Layer Geotextile Filter

J.P. Giroud

Senior Principal, GeoSyntec Consultants, 621 N.W. 53rd Street, Suite 650, Boca Raton, Florida, USA

P. Delmas

Technical Director Polyfelt Group, Bidim Geosynthetics, 9 rue Marcel Paul, Bezons, France

O. Artières

Project Leader, Bidim Geosynthetics, 9 rue Marcel Paul, Bezons, France

**ABSTRACT:** This paper presents a description of the structure of nonwoven geotextiles, including the constriction size distribution curve and the opening size distribution curve, and a theoretical model that leads to a minimal required number of constrictions to ensure homogeneous opening size of the geotextile. Then, an analysis of the mechanism of filtration is presented, which quantifies the probability for a particle to be retained by (on or in) a nonwoven geotextile filter or to pass through the filter. This analysis shows that a needle-punched nonwoven geotextile filter having the minimal required number of constrictions is preferable to a thicker nonwoven geotextile filter. This leads to the concept of a two-layer geotextile filter where filtration is provided by a layer of needle-punched nonwoven material constructed with fine fibers and mechanical properties are provided by a layer of needle-punched nonwoven material constructed with coarse fibers.

**KEYWORDS:** Geotextiles, Nonwoven, Filtration, Opening size, Theory.

## 1 INTRODUCTION

Ever since geotextiles have been used as filters, filter thickness has been a subject of discussion. This paper sheds some light on the subject while providing a theoretical basis for the development of a two-layer geotextile filter. In Section 2, an analysis of the structure of nonwoven geotextiles shows that the opening size of nonwoven geotextile filters decreases with increasing thicknesses of geotextiles made from the same nonwoven material. In Section 3, an analysis of the mechanism of filtration shows that the probability for a particle to be retained by a geotextile filter depends on the thickness of the geotextile. It is concluded in Section 4 that a relatively thin needle-punched geotextile filter is desirable in many practical cases. However, a thin geotextile filter may not have the required mechanical properties to withstand mechanical damage and to resist deformations that could alter its opening size. To that end, a two-layer filter has been developed. This filter associates two layers of needle-punched nonwoven material: a layer constructed with fine fibers and having a thickness selected to provide optimal filtration characteristics; and a layer constructed with coarse fibers providing the required mechanical properties.

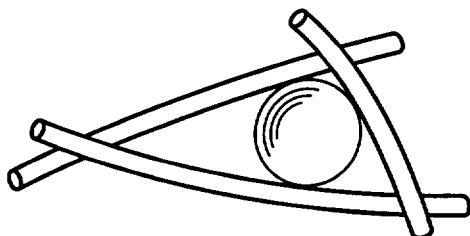


Figure 1. Constriction size.

## 2 STRUCTURE OF NONWOVEN FILTERS

### 2.1 Basic Definitions

#### 2.1.1 Constrictions

To pass through a nonwoven geotextile filter, a particle must pass between fibers. A constriction is a passage delimited by three or more fibers which are nearly, but not necessarily exactly, in the same plane. The size of a constriction can be defined as the diameter of the sphere which can just pass through the constriction (Figure 1). A constriction is different from a pore. Whereas a constriction is strictly defined, a pore is a loosely defined portion of the pore volume, i.e. the volume located between the fibers.

#### 2.1.2 Constriction Size Distribution Curve

If a block of nonwoven material is considered (i.e. a three-dimensional sample, not a quasi two-dimensional sample such as a geotextile), and if this block is large enough to be representative, it contains a representative set of the constrictions which exist in the considered nonwoven material. This set of constrictions is represented by a constriction size distribution curve (Figure 2, Curve C).

The constriction size distribution curve is an intrinsic characteristic of the nonwoven material. Therefore, it is related to parameters that characterize the nonwoven material (e.g. the porosity,  $n$ , and the fiber diameter,  $d_f$ ), but it is not related to parameters that depends on the geotextile, such as the geotextile thickness. Constriction sizes range from  $C_0$ , the size of the smallest constriction in the considered nonwoven material, to  $C_{100}$ , the size of the

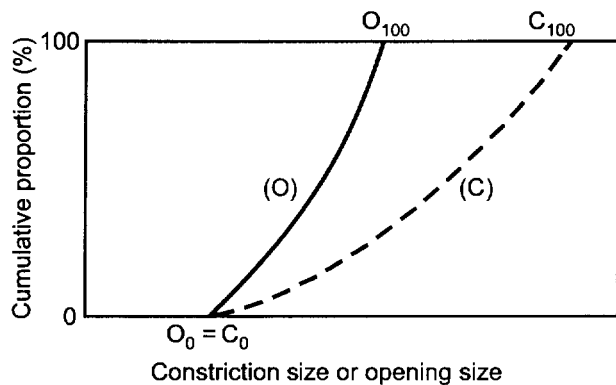


Figure 2. Constriction size distribution curve (C) and opening size distribution curve (O) for a nonwoven geotextile.

largest constriction in the considered nonwoven material;  $C_{100}$  is such that 100% of the constrictions in the considered nonwoven material are smaller than or equal to  $C_{100}$ .

One could argue that the size of the smallest constriction is  $C_0 = 0$  because there is always the possibility that three fibers will meet at the same point, thus delimitating a passage with a zero size. However, from the viewpoint of filtration, constrictions with a size that is zero or very small should not be considered because a particle that meets such a constriction will not be stopped; instead, it will be diverted laterally. (The particles do not have to follow a straight path, and they naturally select the path of least resistance.)

### 2.1.3 Filtration Path

A soil particle that travels in a nonwoven geotextile filter follows a certain filtration path (Figure 3). A filtration path is tortuous, but its general direction is approximately perpendicular to the plane of the geotextile. As it travels along a filtration path, a particle passes through constrictions until it meets a constriction which is smaller

than it is. Unless it diverts the particle, this constriction stops the particle. The level at which a particle is stopped depends on the filtration path (Figure 3): this is an important consideration in the analysis of the filtration mechanism. Of course, if the considered particle is not stopped by a constriction, it passes through the geotextile.

### 2.1.4 Opening Size

In each filtration path, there is a constriction that is smaller than the others. This constriction plays an essential role: it determines the size of the largest particle that can pass through the geotextile following the considered filtration path. This constriction is called the *controlling constriction* of the considered path, a terminology proposed by Kenney et al. (1985) for sand filters. In a given filtration path, the size of the controlling constriction is the *opening size* of the filtration path; therefore, the opening size of a filtration path is the size of the largest particle which can travel through the geotextile filter following this filtration path.

### 2.1.5 Opening Size Distribution Curve

In a nonwoven geotextile filter, there are many filtration paths, and these paths are all different. A given particle can be stopped in a certain filtration path, but it may pass through the filter if it follows another path. Each filtration path is characterized by its opening size. Therefore, a geotextile filter is characterized by an opening size distribution curve (Figure 2, Curve O). The size of the openings of a nonwoven geotextile (i.e. the sizes of the openings of the various filtration paths of the geotextile) range from  $O_0$ , the size of the smallest opening in the considered nonwoven geotextile, to  $O_{100}$ , the size of the largest opening in the considered nonwoven geotextile. It will be shown in Section 2.2.4 that  $O_0$  is equal to  $C_0$ ;  $O_{100}$  is such that 100% of the filtration paths in the considered geotextile have openings that are smaller than or equal to  $O_{100}$ . In other words, 100% of the openings of a geotextile are smaller than or equal to  $O_{100}$ . The opening size distribution curve is a characteristic of the geotextile and, in particular, the largest opening,  $O_{100}$ , is a characteristic of the geotextile, called the *opening size of the geotextile*. The opening size of a geotextile is the size of the largest particle that can pass through the geotextile provided it migrates individually through the geotextile and it is not attracted electrostatically or otherwise to the geotextile fibers.

## 2.2 Relationship Between Constrictions and Openings

### 2.2.1 Influence of the Thickness of a Nonwoven Filter

The constriction size distribution curve is an intrinsic characteristic of the material that constitutes a geotextile whereas the opening size distribution curve is a

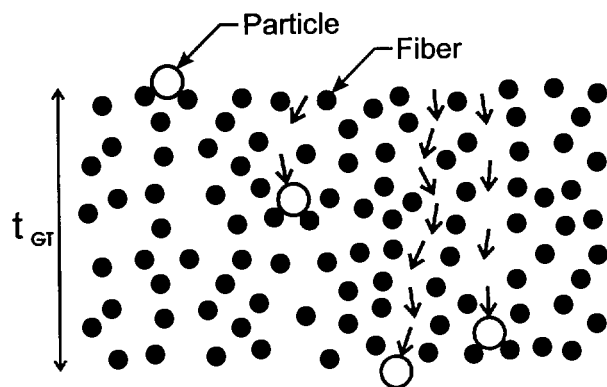


Figure 3. Filtration paths ( $t_{GT}$  = geotextile thickness).

characteristic of the geotextile. The relationship between the constriction size distribution curve of the material that constitutes a geotextile and the opening size distribution curve of this geotextile depends on the thickness of the geotextile. To establish the relationship between these two types of curves, three nonwoven geotextiles with different thicknesses are considered. These three geotextiles are assumed to be made with the same nonwoven material (i.e. a material characterized by a given fiber diameter, a given porosity, and a given type of fiber arrangement).

Two extreme cases will be considered first, the case of a nonwoven geotextile with a zero thickness (Section 2.2.2) and the case of a nonwoven geotextile with an infinite thickness (Section 2.2.3); then the case of a nonwoven geotextile with a finite thickness will be considered (Section 2.2.4).

### 2.2.2 Infinitely Thin Nonwoven Geotextile

In a hypothetical infinitely thin nonwoven geotextile, each filtration path has only one constriction. Therefore, the opening size of each filtration path is equal to the size of the unique constriction of this filtration path. As a result, in the case of a hypothetical infinitely thin nonwoven geotextile, the opening size distribution curve is identical to the constriction size distribution curve (Figure 4, Curve 4).

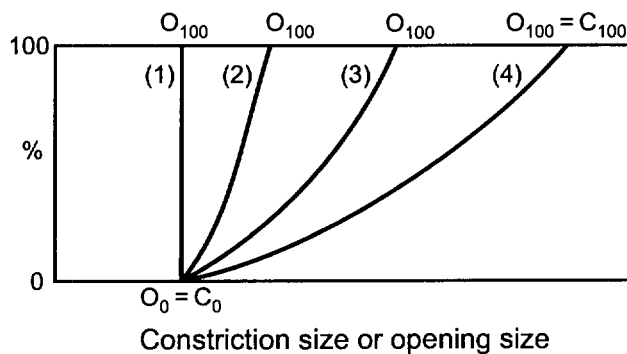


Figure 4. Opening size distribution curves for four geotextiles made from the same nonwoven material, but having different thicknesses: (1) infinitely thick, (2) thick, (3) thin, and (4) infinitely thin. (Curve 4 is also the constriction size distribution curve for the four geotextiles.)

### 2.2.3 Infinitely Thick Nonwoven Geotextile

In a hypothetical infinitely thick nonwoven geotextile, each filtration path contains an infinite number of constrictions. Therefore, in this case, there is a 100% probability that all constriction sizes are present in each filtration path. Thus, each filtration path contains the smallest constriction,  $C_0$ . When a filtration path contains the smallest constriction, this constriction is the controlling constriction. Therefore,

in a hypothetical infinitely thick nonwoven geotextile, all filtration paths have the same controlling constriction, hence the same opening size ( $O_0 = O_n = O_{100} = C_0$ , where  $0 < n < 100$ ). As a result, the opening size distribution curve of this geotextile is a vertical line (Figure 4, Curve 1). In other words, in a hypothetical infinitely thick nonwoven geotextile, all filtration paths have the same opening size, which is the opening size of the geotextile and which is equal to the smallest constriction size.

### 2.2.4 Nonwoven Geotextile Having a Finite Thickness

The case of a nonwoven geotextile having a finite thickness is considered. Elementary calculations show that, in typical nonwoven geotextiles, the number of filtration paths is greater than  $1000/\text{cm}^2$ . Therefore, if the considered specimen is large enough to be representative, it contains a very large (quasi infinite) number of filtration paths. The probability that at least one filtration path contains the smallest constriction is virtually 100%. When a filtration path contains the smallest constriction,  $C_0$ , this constriction is the controlling constriction, i.e. the opening size of the filtration path. A filtration path which has an opening size equal to the size of the smallest constriction is, of course, a filtration path that has the smallest opening size. Therefore,  $O_0 = C_0$  (Figure 2).

In a given filtration path, the number of constrictions, in the case of a typical nonwoven geotextile, is not very large (for example, between 10 and 50, as indicated in Section 2.3.3). Therefore, the probability that the smallest constriction is present in all filtration paths is smaller than 100%. As a result, a certain number of filtration paths have a controlling constriction (i.e. an opening size) greater than  $C_0$ . Therefore,  $O_n > C_0$ .

The largest constriction size is  $C_{100}$ ; therefore, the largest possible opening size is  $C_{100}$ . However, for a filtration path to have such an opening size, would require that all the constrictions of this filtration path be equal to  $C_{100}$ . But, in a given filtration path, the probability that all the constrictions are identical is virtually zero. Therefore, the maximal opening size that a filtration path may have (i.e. the opening size of the geotextile) is smaller than the maximal constriction size. Therefore,  $O_{100} < C_{100}$ .

The relationship, demonstrated above, between the constriction size distribution curve and the opening size distribution curve of a nonwoven geotextile having a finite thickness is illustrated in Figure 2. The opening size distribution curves of two nonwoven geotextiles with a finite thickness are shown in Figure 4: Curve 2 for a relatively thick geotextile and Curve 3 for a relatively thin geotextile. In Figure 4, it is important to note that Curve 4, which is the opening size distribution curve for the hypothetical infinitely thin nonwoven geotextile, is also the constriction size distribution curve for all four nonwoven geotextiles made with the same nonwoven material.

## 2.3 Theoretical Model of Nonwoven Geotextile Filters

### 2.3.1 Description of Chart

A theoretical model of the structure of nonwoven geotextiles (Giroud 1996) made it possible to develop a chart (Figure 5) that provides relationships between the following parameters: the geotextile opening size,  $O_{100}$ , the thickness of the geotextile,  $t_{GT}$ , the diameter of the fibers,  $d_f$ , and the porosity of the geotextile,  $n$  (solid curves for a given value of the porosity, and dashed curves for a given value of  $\mu_{GT}/(\rho_f d_f)$  where  $\mu_{GT}$  = geotextile mass per unit area,  $\rho_f$  = fiber density, and  $d_f$  = fiber diameter). This chart is in good agreement with the results of numerous tests performed on needle-punched (and some heat-bonded) nonwoven geotextile filters (Giroud 1996). The chart also gives an approximate value of the average number of constrictions,  $m$ , that a particle traveling through a nonwoven geotextile filter can be expected to pass through (dotted curves in Figure 5).

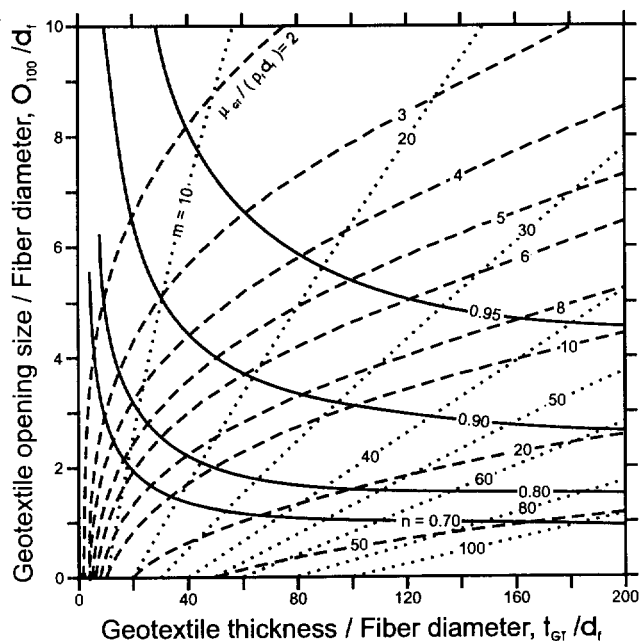


Figure 5. Chart giving three relationships between the geotextile opening size/fiber diameter ratio and the geotextile thickness/fiber diameter ratio for nonwoven geotextile filters.

### 2.3.2 Size of Constrictions

The chart in Figure 5 shows that, for a given nonwoven material characterized by its porosity,  $n$ , the opening sizes of geotextiles having different thicknesses made with this nonwoven material decrease for increasing thicknesses (solid curves) and tend to reach an asymptote as the

geotextile thickness (and the geotextile mass per unit area) tend toward infinity. The horizontal asymptotes of the solid curves in Figure 5 correspond to the case of the hypothetical infinitely thick nonwoven geotextile used in the demonstrations presented in Section 2.2.3. Therefore, the geotextile opening size that corresponds to the horizontal asymptotes in Figure 5 is a theoretical value of the smallest opening size,  $O_0$ , and the smallest constriction size,  $C_0$  ( $O_0 = C_0$ , as demonstrated in Section 2.2.4). On the other hand, the chart does not provide information on the size of the largest constrictions ( $C_{100}$ ) because the theoretical model used to establish the chart presented in Figure 5 is not valid for extremely small values of the geotextile thickness/fiber diameter ratio (e.g.  $t_{GT} / d_f < 10$ ); in other words, the chart presented in Figure 5 cannot represent the case of the hypothetical infinitely thin nonwoven geotextile discussed in Section 2.2.2.

### 2.3.3 Influence of the Number of Constrictions

In Section 2.2, the parameter used to compare geotextiles was the geotextile thickness. This was appropriate because the geotextiles considered had the same porosity and fiber diameter. In Sections 2.3.3 and 2.3.5, it will be seen that the appropriate parameter to compare nonwoven geotextiles having different porosities and/or fiber diameters is the number of constrictions.

The difference  $O_{100} - O_0$  between the geotextile opening size,  $O_{100}$  (i.e. the size of the largest opening of the geotextile), and the value of the asymptote of the solid curves in Figure 5,  $O_0$  (i.e. the size of the smallest opening of the geotextile), characterizes the homogeneity of the geotextile filter with respect to opening size: a small value of  $O_{100} - O_0$  indicates an homogeneous geotextile, whereas a large value indicates an heterogeneous geotextile. The chart in Figure 5 shows that, for less than approximately 15 constrictions ( $m < 15$ ),  $O_{100} - O_0$  is large, whereas, when the number of constrictions is greater than approximately 25 to 30,  $O_{100} - O_0$  is small and does not significantly decrease with increasing geotextile thicknesses. Therefore, it may be *qualitatively* said that: (i) to avoid using an heterogeneous geotextile filter, the number of constrictions should be greater than 15; and (ii) in cases where a very homogenous geotextile filter is required, the number of constrictions should be greater than approximately 25-30.

A very homogenous filter is required in cases, such as bank protection systems, where a large amount of particles must pass through the filter to ensure filtration while minimizing the risk of clogging. Indeed, in these cases, if the range of opening sizes of the filter is large, there is a high probability that the filter will stop some particles smaller than the geotextile opening size,  $O_{100}$ .

An attempt to *quantitatively* determine the required value of the number of constrictions consisted of performing the four following calculations (not shown

here, but to be published elsewhere): (i) the derivative of  $(O_{100} - O_0) / d_f$  with respect to  $t_{gr} / d_f$ ; (ii) the derivative of  $(O_{100} - O_0) / d_f$  with respect to  $\mu_{gr} / (\rho_f d_f)$ ; (iii) the ratio  $(O_{100} - O_0) / d_f$ ; and (iv) the ratio  $(O_{100} - O_0) / O_0$ . These four calculations gave four relationships between the geotextile porosity and the minimal values required for the number of constrictions,  $m$ , to ensure that  $O_{100} - O_0$  does not vary significantly as a function of the considered parameter, i.e.  $t_{gr} / d_f$ ,  $\mu_{gr} / (\rho_f d_f)$ ,  $d_f$ , or  $O_0$ . A parametric study, based on these four relationships, showed that the required minimal number of constrictions is of the order of 15 to 40 depending on the geotextile porosity and the considered parameter, with numbers of constrictions equal to or greater than approximately 25-30 being required to obtain a very homogeneous filter.

### 2.3.4 Influence of Geotextile Porosity

The chart presented in Figure 5 shows that the porosity of the nonwoven *material* has a large influence on the geotextile opening size. Nonwoven *materials* that have the same porosity and fiber arrangement are said to have the same structure. They are represented by a curve  $n = \text{constant}$  in Figure 5. Nonwoven *materials* that have the same structure differ only by the diameter of the fibers; and their constriction sizes are proportional to the fiber diameter. Thus, for nonwoven *geotextiles* made with nonwoven *materials* that have the same structure, the constriction size distribution curves: (i) are proportional to the fiber diameter; and (ii) consequently, in the traditional semi-logarithmic axes, are derived from one another by translations. Nonwoven *geotextiles* that have the same structure differ in general by their thickness; these geotextiles have the same constriction size distribution curve but different opening size distribution curves.

A parametric study, based on the theoretical model described in Section 2.3, showed that the geotextile porosity has a significant influence on the opening size values that can be achieved. The usually required opening sizes (e.g. 70 to 200  $\mu\text{m}$ ) can be provided economically (i.e. using relatively fine fibers and relatively small masses per unit area) by a nonwoven geotextile that has the minimal number of constrictions mentioned in Section 2.3.3 (i.e. 25-30) if the geotextile porosity is in the 0.85 to 0.95 range, which is typical for needle-punched nonwoven geotextiles, whereas nonwoven geotextiles with porosities smaller than 0.7 would require very coarse fibers and/or very large masses per unit area to have the usually required opening sizes while meeting the above minimal number of constrictions. The parametric study also showed that, with the typical porosities of needle-punched nonwoven geotextiles, it is possible to obtain geotextile opening sizes of the order of 80  $\mu\text{m}$  by using fibers having a diameter of 25  $\mu\text{m}$ , and of the order of 150  $\mu\text{m}$  or more by using fibers having a greater diameter (e.g. 30 to 50  $\mu\text{m}$ ).

### 2.3.5 Importance of Constrictions

A parametric study, based on the theoretical model described in Section 2.3, showed that nonwoven geotextiles having the same number of constrictions and the same opening size ( $O_{100}$ ) have approximately the same opening size distribution curve regardless of the values of the geotextile porosity and fiber diameter (provided, of course, that the appropriate relationship exists between porosity and fiber diameter to achieve the given  $O_{100}$ ). This important finding shows that the number of constrictions is the most significant parameter for comparing geotextile filters. Also, when two nonwoven geotextiles have approximately the same opening size distribution curve, they have approximately the same constriction size distribution curve because approximately identical cumulative probability curves (i.e. the opening size distribution curves) must be based on approximately identical statistical sets (i.e. the constrictions).

## 3 ANALYSIS OF THE FILTRATION MECHANISM

### 3.1 Filtration Probabilities

Consider the two curves defined in Section 2.1, the constriction size distribution curve (which characterizes the material of which the geotextile is made) and the opening size distribution curve (which characterizes the geotextile). Both curves are cumulative probability curves. Thus, the constriction size distribution curve gives the probability,  $P_c$ , that a particle of size  $d$  will be retained at the surface of the geotextile and, correlatively, the probability,  $1 - P_c$ , that the particle will not be retained at the surface of the geotextile (Figure 6). The particles which are not retained at the surface of the geotextile either are retained in the geotextile or pass through the geotextile, and the opening size distribution curve gives the probabilities related to these two possibilities: the opening size distribution curve gives the probability,  $P_o$ , that a particle will be retained by (on or in) the geotextile and, correlatively, the probability  $1 - P_o$  that a particle will not be retained, i.e. will pass through the geotextile (Figure 6). Thus, the following probabilities can be defined: probability that a particle will pass through the geotextile,  $P_{\text{PASS}} = 1 - P_o$ ; probability that a particle will be retained in the geotextile,  $P_{\text{IN}} = P_o - P_c$ ; probability that a particle will be retained on the geotextile,  $P_{\text{ON}} = P_c$ ; and probability that a particle will be retained by (on or in) the geotextile,  $P_{\text{RETAIN}} = P_o = P_{\text{ON}} + P_{\text{IN}}$ .

Four situations can be considered depending on the size,  $d$ , of a particle relative to the extremities of the two curves ( $O_0$ ,  $O_{100}$ ,  $C_0$  and  $C_{100}$ ): (i) if  $d > C_{100}$ , the particle is retained at the surface of the geotextile because, in this case, there is no constriction larger than  $d$  ( $P_{\text{RETAIN}} = P_{\text{ON}} = 1 = 100\%$ ,  $P_{\text{PASS}} = 0$ ); (ii) if  $O_{100} < d < C_{100}$ , the particle cannot pass

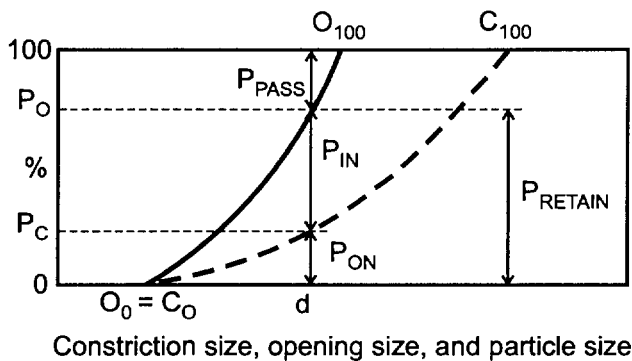


Figure 6. Probability that a particle will pass through a geotextile or will be retained in or on the geotextile.

through the geotextile because there is no filtration path with an opening size greater than  $d$ , and the particle either moves into the geotextile until it meets a constriction that stops or it remains at the surface of the geotextile if it happens that the constriction that stops it is at the geotextile surface ( $P_{\text{RETAIN}} = P_{\text{ON}} + P_{\text{IN}} = 1 = 100\%$ ,  $P_{\text{PASS}} = 0$ ); (iii) if  $O_0 < d < O_{100}$ , the particle has all of three possibilities, it can be retained in or on the geotextile or it can pass through the geotextile ( $P_{\text{ON}} + P_{\text{IN}} + P_{\text{PASS}} = 1 = 100\%$ ); and (iv) if  $d < O_0$ , the particle passes through the geotextile ( $P_{\text{RETAIN}} = 0$ ,  $P_{\text{PASS}} = 1 = 100\%$ ).

### 3.2 Influence of Number of Constrictions on Filtration

In Section 2.3.3, it was shown that a minimal number of constrictions of 25-30 was required to ensure that the geotextile filter is very homogenous. The filtration analysis that follows shows that a greater number of constrictions may be more detrimental than beneficial.

The probabilities indicated in Section 3.1 and illustrated in Figure 6 can be used to compare the mode of particle retention by different geotextiles. Retention is a complex mechanism that includes the *retention* of skeleton particles and the *non-retention* of fine particles (Giroud 1996). Therefore, two particles will be considered: a skeleton particle of size  $d_s$ , which should be retained (Section 3.2), and a fine particle of size  $d_p$ , which should not be retained (Section 3.3). As indicated by Giroud (1996), skeleton particles are retained by a filter if the filter opening size is equal to or less than  $\lambda d_s$ , where  $\lambda$  is a factor greater than one that accounts for particle bridging (hence a "factored size",  $\lambda d_s$ , for the skeleton particles).

Two nonwoven geotextiles with the same opening size,  $O_{100}$ , are compared in Figure 7. This is a typical situation faced by a designer who has to make a choice between two apparently equivalent geotextile filters. These two geotextiles are assumed to have different opening size distribution curves and, consequently, they have different values of  $O_0$  and  $O_{100} - O_0$ . Therefore, they have different

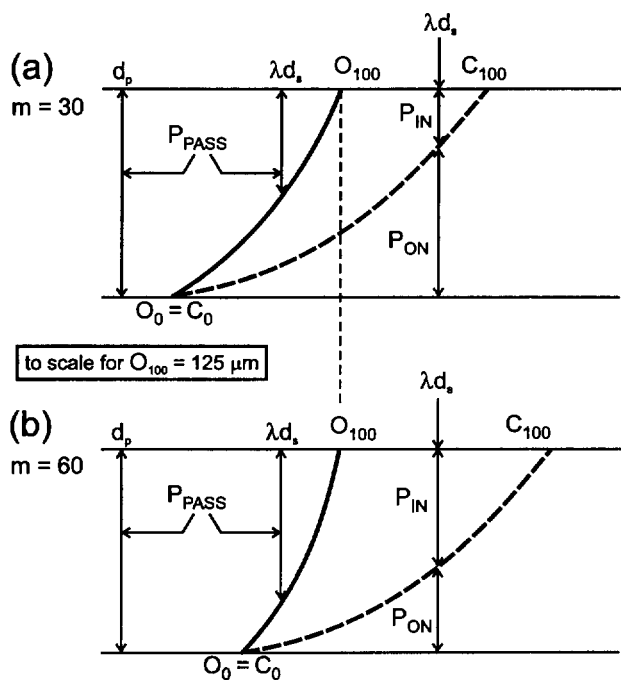


Figure 7. Probabilities of retention of two particles, one being a skeleton particle of size,  $d_s$ , the other being a fine particle of size,  $d_p$ , by two nonwoven geotextile filters having the same opening size,  $O_{100}$ , and having: (a) 30 constrictions ; (b) 60 constrictions.

numbers of constrictions, according to Section 2.3.3. The geotextile represented in Figure 7a has 30 constrictions, i.e. a number of constrictions sufficient to ensure that the geotextile filter is very homogenous (see Section 2.3.3), whereas the geotextile represented in Figure 7b has 60 constrictions. These two geotextiles, having a different  $O_0$ , have different constriction size distribution curves. Combining the demonstrations presented in Sections 2.3.4 and 2.3.5 shows that the two constriction size distribution curves must be derived from one another by translation in the traditional semi-logarithmic axes. It is seen in Figure 7 that a particle of size  $d_s$  such that its factored size is greater than the geotextile opening size ( $\lambda d_s > O_{100}$ ), as should be the case if the filter is properly designed, is: (i) more likely to be retained *on* the geotextile in the case of a nonwoven geotextile filter having 30 constrictions than in the case of a nonwoven geotextile filter having a greater number of constrictions; and (ii) correlatively more likely to be retained *in* the geotextile in the case of a nonwoven geotextile filter having 60 constrictions than in the case of a nonwoven geotextile filter having 30 constrictions. Skeleton particles move less and, therefore, the skeleton structure is less disturbed if more particles are retained *on* than *in* the geotextile filter (see Section 2.1.3 on the level at which a particle is stopped). Also, if, as a result of a design error or an unexpected variation of the soil characteristics, the skeleton particle factored size is smaller than the filter



opening size ( $\lambda d_s < O_{100}$ ), Figure 7 shows that less skeleton particles pass through the geotextile filter in the case of the filter having 30 constrictions than in the case of the filter having more constrictions.

From the above analysis, it appears that a nonwoven geotextile filter having 30 constrictions is preferable to a nonwoven geotextile filter having more constrictions because: (i) in the normal case where the soil skeleton particle factored sizes are greater than the geotextile opening size, the nonwoven geotextile filter having 30 constrictions retains soil skeleton particles with less disturbance of the skeleton structure than a nonwoven geotextile filter having more constrictions; and (ii) in the case where (as a result of a design error or an unexpected variation of the soil characteristics) the soil skeleton particle factored sizes are smaller than the geotextile opening size, the nonwoven geotextile filter having 30 constrictions is more likely to retain skeleton particles than a nonwoven geotextile filter having more constrictions.

### 3.3 Influence of Porosity and Fiber Diameter

As pointed out at the beginning of Section 3.2, it is important not only to retain the skeleton particles, but also *not to retain* the fine particles that must pass through the filter to prevent clogging. To that end, the smallest geotextile opening size,  $O_0$ , must be larger than a minimal value which can be determined as follows.

According to Mitchell (1970), grout particles flow easily through a soil being grouted if they are smaller than 1/25 times the  $d_{15}$  of the soil, i.e. smaller than 1/5 times the size of openings between the soil particles, since openings in granular materials are approximately equal to  $d_{15}/5$  according to Kenney et al. (1985). This may be adapted to geotextile filters as follows. The soil particles most likely to cause filter clogging are the particles that may exhibit cohesion and may, therefore, adhere to fibers or to other particles. Particles that may exhibit cohesion are the particles smaller than approximately 5  $\mu\text{m}$ . Therefore,  $O_0$  should be greater than approximately 25  $\mu\text{m}$ .

A parametric study based on the model presented in Section 2.3 showed that  $O_0$  significantly depends on the geotextile porosity and fiber diameter and that, for usual values of needle-punched nonwoven geotextile porosity and fiber diameter,  $O_0$  is always significantly greater than 25  $\mu\text{m}$ . Therefore, the typical particles likely to cause clogging should pass easily through usual needle-punched nonwoven geotextile filters. Thus, it appears that the *non-retention* of fine particles is a criterion that is easily met by usual needle-punched nonwoven geotextile filters.

In conclusion, the comparison between two needle-punched nonwoven geotextile filters should be made essentially on the basis of the *retention* of the skeleton particles and not on the basis of the *non-retention* of fine particles. This approach is used in Section 3.4.

### 3.4 Retention of a Non-Uniform Soil

The method illustrated in Figure 7 can be extended to the case where the size of the skeleton particles ranges within two known limits (non-uniform soil). This case is illustrated in Figure 8, which shows that the various retention probabilities are proportional to areas delimited by the constriction size distribution curve and the opening size distribution curve. Figure 8 leads to the same conclusions as Figure 7: (i) in the case where all of the skeleton particles are greater than the opening size of the filter ( $d_s > O_{100}$ ), the skeleton particles are more likely to be retained *on* a nonwoven geotextile having 30 constrictions than *on* a nonwoven geotextile having more constrictions; and (ii) in the case where the range of skeleton particles includes sizes that are smaller than the opening size of the filter ( $d_s < O_{100}$ ), the amount of skeleton particles likely to pass through a nonwoven geotextile filter having 30 constrictions is smaller than through a nonwoven geotextile filter having more constrictions. Essentially, Figure 8 shows that a nonwoven geotextile filter having 30 constrictions is more reliable than a nonwoven geotextile filter having more constrictions because it is less sensitive to variations of the soil particle size distribution curve.

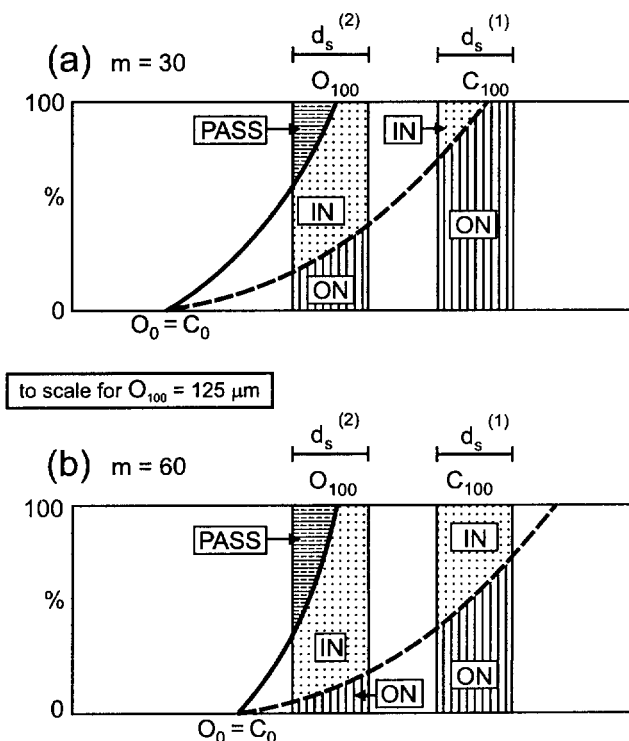


Figure 8. Probabilities of retention of skeleton particles by two nonwoven geotextiles having the same opening size,  $O_{100}$ , but having different numbers of constrictions : (a)  $m = 30$ ; (b)  $m = 60$ . Two soils are considered: (1) all of the skeleton particles are larger than  $O_{100}$ ; (2) some of the skeleton particles are smaller than  $O_{100}$ .

#### 4.1 Concept of Two-Layer Filter

Based on the analyses and discussions presented in Sections 2 and 3, a needle-punched nonwoven geotextile filter having approximately 25 to 30 constrictions is recommended for applications where a very homogenous filter is required. However, while such a geotextile can provide adequate filtration performance, it may not have the required mechanical properties to withstand mechanical damage and to resist deformations that could alter its opening size. Based on these considerations, a series of two-layer filters has been developed. These filters associate two layers of needle-punched nonwoven material: a functional layer constructed with fine fibers and having the required thickness to provide approximately 25 to 30 constrictions for optimal filtration characteristics; and a protective layer constructed with coarse fibers providing the required mechanical properties to protect the layer of fine fibers. For example, in one of the filters of the series, the fiber diameter is 25  $\mu\text{m}$  for the fine fibers and 50  $\mu\text{m}$  for the coarse fibers, each of the two layers having a mass per unit area of 200  $\text{g}/\text{m}^2$ , hence a total mass per unit area of 400  $\text{g}/\text{m}^2$  for the two-layer nonwoven geotextile filter.

#### 4.2 Opening Size of a Two-Layer Geotextile Filter

To minimize the risk of clogging, particles that pass through the layer of fine fibers should pass easily through the layer of coarse fibers. To that end, the opening size of the layer of coarse fibers must be significantly larger than the opening size of the layer of fine fibers. If this condition is met, only the layer of fine fibers must be considered when filter criteria are used, i.e. there is no need for special filter criteria for two-layer geotextile filters if there is a large difference of opening sizes between the two layers; the relationship between the opening sizes of the two layers depends on several parameters (such as porosity, thickness, and fiber diameter) and it is necessary to check on a case-by-case basis that the opening size of the layer of coarse fibers is much larger than the opening size of the layer of fine fibers. This can be done using the chart presented in Figure 5. For example, in the case of the two-layer geotextile filter described in Section 4.1, the following values are obtained: (i) for a fine fiber layer having a mass per unit area of 200  $\text{g}/\text{m}^2$ , a fiber diameter of 25  $\mu\text{m}$  and a porosity of 0.87: number of constrictions, 25; thickness, 1.7 mm; and opening size, 70  $\mu\text{m}$ ; and (ii) for a coarse fiber layer having a mass per unit area of 200  $\text{g}/\text{m}^2$ , a fiber diameter of 50  $\mu\text{m}$  and a porosity of 0.87: thickness, 1.7 mm; and opening size, 190  $\mu\text{m}$  (the number of constrictions is irrelevant for the coarse fiber layer). It appears that, for the considered two-layer geotextile, there is a large difference between the opening sizes of the two layers.

This paper shows that the performance of nonwoven geotextile filters is significantly influenced by the porosity of the nonwoven material and the thickness of the geotextile. Both parameters govern the number of constrictions, i.e. the number of passages between fibers that a particle has to go through. An analysis of the structure of nonwoven geotextiles (Section 2) shows that a number of constrictions equal to or greater than approximately 25 to 30 should ensure homogeneity of the filtration characteristics. An analysis of the filtration mechanism (Section 3) shows that the probabilities for soil particles to be retained by, or to pass through, a geotextile filter can be derived from a comparison of the constriction size distribution curve of the geotextile material and the opening size distribution curve of the geotextile. The analysis shows that, in the practical situations reviewed, a better performance may be expected from a nonwoven geotextile filter with approximately 25-30 constrictions than from a nonwoven geotextile filter with more constrictions. These considerations led to the development of two-layer nonwoven geotextile filters. However, in addition to providing the theoretical basis for the development of two-layer filters, this paper shows that considerable information is now available regarding the structure of nonwoven geotextiles and the understanding of filtration mechanisms in geotextiles. In particular, this paper shows that, to analyse filtration mechanisms, it is necessary to use the entire opening size distribution curve, and not only the geotextile opening size, and that it is also necessary to use the constriction size distribution curve. This should open up the way to new filter design methods.

#### ACKNOWLEDGMENTS

The authors express their gratitude to K.L. Soderman for his comments, and to K. Holcomb and S.L. Berdy for their assistance in the preparation of this paper.

#### REFERENCES

- Giroud, J.P., 1996, "Granular Filters and Geotextile Filters", *Proceedings of GeoFilters '96*, Lafleur, J. and Rollin, A.L., Editors, Montréal, Canada, May 1996, pp. 565-680.
- Kenney, T.C., Chahal, R., Chiu, E., Ofoegbu, G.I., Omange, G.N. and Ume, C.A., 1985, "Controlling Constriction Sizes of Granular Filters", *Canadian Geotechnical Journal*, Vol. 22, No. 1, pp. 32-43.
- Mitchell, J.K., 1970, "In-Place Treatment of Foundation Soils", *Journal of the Soil Mechanics and Foundation Division*, ASCE, Vol. 96, No. SM1, January 1970, pp. 73-110.

# Aquatextiles: Use of Nonwoven Geotextiles for Filtration in a Municipal Water Treatment Plant

E. A. Richards

Professor, Department of Human Ecology, University of Alberta, Edmonton, Alberta, Canada T6G 2N1

J. D. Scott and D. W. Smith.

Professors, Department of Civil and Environmental Engineering, University of Alberta, Edmonton, Alberta, Canada T6G 2G7

**ABSTRACT:** Particle removal in municipal water treatment involves adsorption, sedimentation and filtration. The particles vary from materials in true solution to coarse suspensions and range in size from colloidal materials to coarse particles. This research explores the use of nonwoven geotextiles to enhance a pretreatment, screening procedure prior to rapid sand filtration. Laboratory and field tests were conducted to determine long term filtration efficiencies for a polypropylene, needlefelt fabric at a municipal water treatment plant.

Removal efficiency of particles was determined by particle counting. Scanning electron microscopy was used to elucidate the filtration process. A variety of capture phenomena are involved for suspended particles less than 20  $\mu\text{m}$ : entrapment, surface attraction and aggregation. This research shows that a nonwoven fabric with openings of 300  $\mu\text{m}$  can successfully remove particles less than 10  $\mu\text{m}$ . This innovative work represents new technology and is an opportunity for new markets for traditional needlefelt and new geotextiles. In this application these textiles would be better named aquatextiles.

**KEYWORDS:** Water Treatment, Filtration, Geotextiles, Aquatextiles, Nonwoven Fabrics, Environmental Engineering.

## 1 INTRODUCTION

Since their inception in the early 1970's geotextiles have become widely used in geotechnical applications. New markets for geosynthetics have concentrated on third generation: textiles designed for specific installations. Use of woven and nonwoven geotextiles has increased in what have now become traditional applications. This research project was designed to study new uses for conventional geotextiles in water treatment engineering rather than in geotechnical engineering. Innovative applications could open new markets for standard and new geotextile fabrics.

The objective of this research was to explore the possibility of using geotextile materials in filtration operations in municipal water treatment. Geotextiles have been used successfully in subsurface drainage applications since 1970 and it appeared possible to transfer that technology to the area of water treatment. Geotextiles appear to be promising filter media due to the variety of fibers and fabric constructions available commercially.

Liquid-particle separation in potable water treatment involves a wide range of techniques broadly divided into filtration and sedimentation. The main purposes of separation are to decrease waterborne disease through reduction in the number of harmful microorganisms and to increase aesthetics through reduction of suspended solids. Filtration in water treatment differs markedly from subsurface filtration/drainage applications in that the concentration of suspended particles is low and the volume of water flowing through a filter is very high.

The research project involved four components: development of a laboratory protocol for using textiles as a water filtration medium, testing a variety of geotextiles as possible media choices, development of a long term, field testing protocol and field testing at a municipal water treatment plant. The objective of this paper is to report the results of field testing where geotextiles were used for particulate removal at a municipal water treatment plant.

## 2 MATERIALS AND METHODS

### 2.1 Screening Studies

In the initial laboratory evaluation of potential fabrics a filtration device was designed which consisted of a simple filter apparatus with a constant pressure drop (Richards *et al.*, 1997). The particulate suspension used was the test dust for the American National Standard/NSF International Standard for Drinking Water Treatment Units at a concentration of 10 mg/L. Eleven polypropylene geotextiles were tested in the laboratory and six fabrics were selected for additional laboratory testing at a water treatment plant. One fabric was chosen for further testing and the filtration device was modified to meet the demands of long term, field testing (Figure 1). The apparatus consisted of a peristaltic pump set to give a constant flow, the filtering device, a surge tank and a constant pressure drop tank. Change in pressure was measured with a float device in the surge tank, which was connected to a

Lakewood datalogger. The filtration device consisted of an enclosed glass funnel with exit ports for air bubbles. The fabric sample was placed at the center of the funnel, resting on a wire mesh.

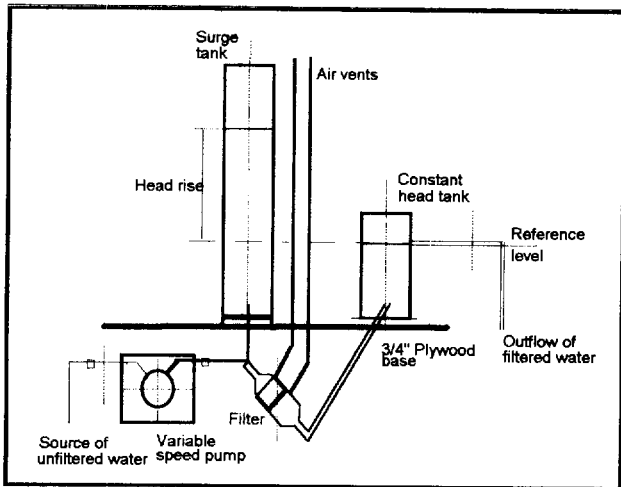


Figure 1. Profile view of experimental equipment for field testing in a municipal water treatment plant.

## 2.2 Fabric

The fabric selected for long term testing was a needlepunched, nonwoven, polypropylene fabric. The fabric mass and thickness as measured in the laboratory were 457 g/m<sup>2</sup> and 4.14 mm under a load of 2 kPa. The manufacturer's specification states a permittivity of 0.7 sec<sup>-1</sup> at a flow rate of 34 L/(m<sup>2</sup>s) and an apparent opening size of 300 μm. This is a relatively thick, standard goetextile which is commonly used for underground drainage applications.

## 2.3 Experimental Procedure

The treatment steps at the Rossdale Water Treatment Plant located on the Saskatchewan River follow a standard procedure for municipal water purification (Figure 2). A coarse screening to remove large debris is followed by alum/polymer flocculation and coagulation to remove

suspended particles. The water is softened with lime and the calcium carbonate precipitate over 20 μm in size settles through tube settlers in a still basin. There are additions of carbon dioxide to adjust the pH after softening, of chlorine for disinfection and of fluorine prior to final settling in the contactor basin. Filtration through a sand filter is the final treatment step prior to distribution to the city.

For this experimental program the influent was taken from the beginning of the contactor basin, after the addition of carbon dioxide, chlorine and fluorine. Of interest in this research were the particles in the water after softening, predominantly calcium carbonate, with sizes 20 μm or less, not including submicron sized particles. The influent was pumped from the still basin to the equipment, in excess of that needed for the testing, to keep the velocity of the influent constant at 10 m<sup>3</sup>/(m<sup>2</sup>hr). Testing was conducted from October to December in 1996 at the Aqualta Rossdale Water Treatment Plant in Edmonton, Alberta, Canada.

## 2.4 Influent Characteristics

The influent remained relatively constant with respect to the distribution of particle sizes, from 1 μm up to and including 20 μm, but varied with respect to the number of particles from day to day and within a given experiment. During the testing period the total number of particles/mL varied from 2,090 to 20,370. The distribution of particles showed a peak at the five μm size, with the number of 15 and 20 μm particles remaining relatively constant. During each run of 6 to 11 hours there would be a change in influent over time with one or two peak periods. There was no consistency for the time during the day for the peaks and they did not relate to plant operations. Figure 3 illustrates the change in influent over time for Run 30.

## 2.5 Removal

Filter performance is measured by effluent water quality. Removal efficiency, expressed by percent removal for the number of particles of a given size, was determined by particle counting with an HIAC/ROYCO Model 8000A particle counter. Particles less than 20 μm were

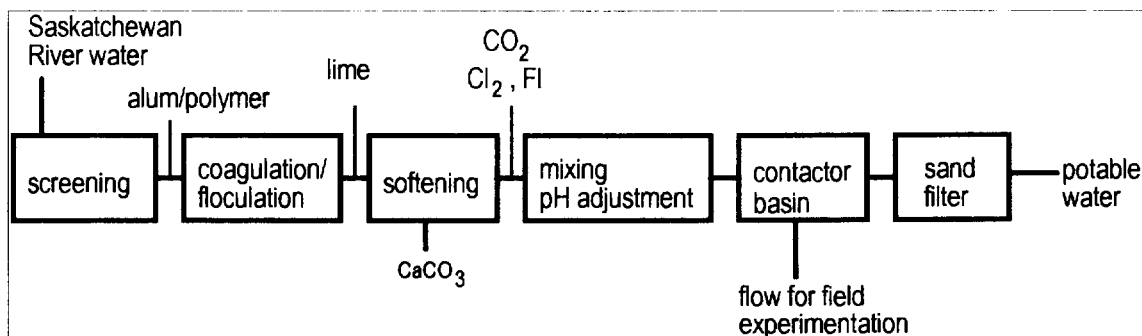


Figure 2. Steps in the municipal water treatment process at the Aqualta Rossdale Water Treatment Plant, Edmonton, Alberta,

counted. Four and five  $\mu\text{m}$  particle removals were of particular interest as the *Cryptosporidium parvum* cyst which causes Cryptosporidiosis (diarrhea) is about 4  $\mu\text{m}$  in diameter.

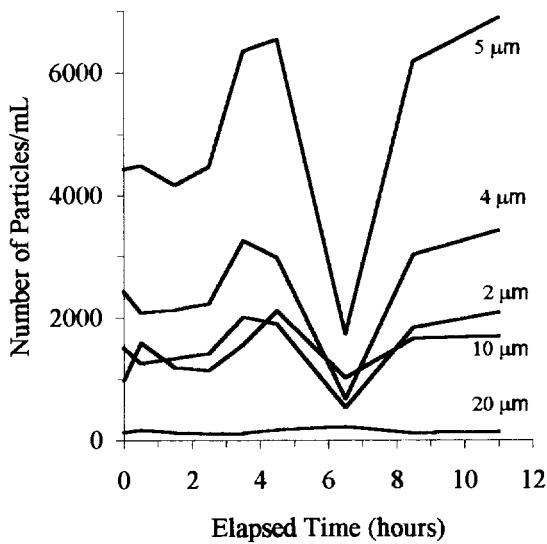


Figure 3. Change in influent particle size over time, Run 30, December 12, 1996.

### 3 FIELD TEST RESULTS

#### 3.1 Removal

Removal of particles varied with time. For each experimental run there was an initial period of adjustment, followed by an increase in removal to a peak of removal efficiency, and then declining removal. The time of peak removal for different runs varied between 0.5 to 3.5 hours (Figure 4).

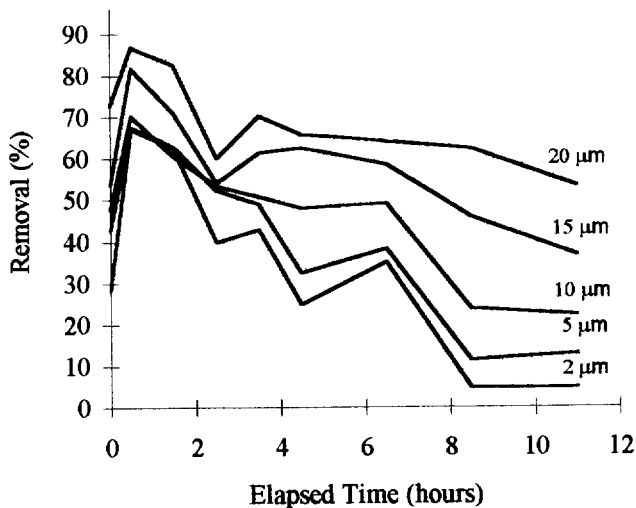


Figure 4. Removal efficiency over time showing the periods of initial adjustment, peak removal and declining removal for one layer of fabric, Run 30.

Examination of removal curves for all runs shows a similar pattern. The removal pattern is not smooth but shows a zigzag shape, especially after 4.5 hours. It appears that when the particulate loading on the filter reaches a critical level, particles detach from the fibers. The fabric is then able to capture particles more efficiently with a subsequent increase in removal efficiency. When the fabric is again unable to hold more particles the particles are detached. However, gradually the removal efficiency of the filter decreases with time. Varying the thickness of the filter layer by using additional layers of fabric increased the removal efficiency slightly.

#### 3.2 Headloss

There was an increase in headloss with time as shown in Figure 5. As the number of layers of fabric increased, the headloss increased. An examination of the patterns of increased head required to maintain a constant flow velocity showed variations between runs as well as with the number of layers of fabric. An examination of headloss increase with the cumulative number of particles captured showed a consistent pattern. The cumulative number of 2 to 5  $\mu\text{m}$  sized particles increased and then levelled off. The cumulative number of particles over 10  $\mu\text{m}$  continued to increase with time. When this data is compared to the patterns of headloss it is the larger particles, the 10 to 20  $\mu\text{m}$  particles, which determine headloss.

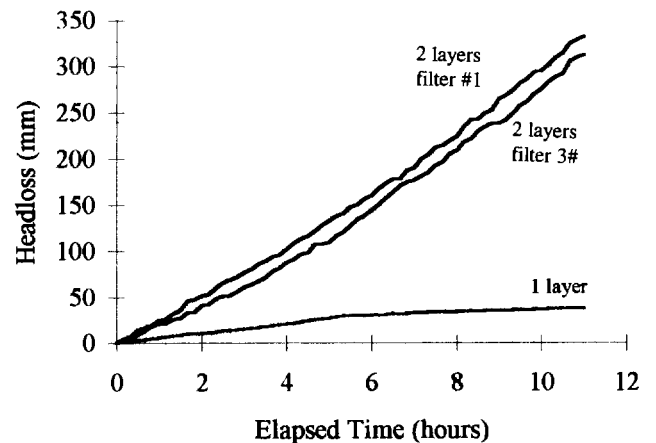


Figure 5: Pattern of headloss with one and two layers of fabric for concurrent tests, Run 30.

#### 3.3 Scanning Electron Microscope

An Hitachi 2-2500 scanning electron microscope was used to examine fabric specimens after filtration. Examination of the photomicrographs showed an increasing number of particles captured with time (Figure 6). At the end of a filtration run the fabrics were loaded with calcium carbonate particles which were attached to

the surface of the fibers. Cracks or roughness on the surface of the fibers also served as anchoring points for the calcium carbonate. As time increased an aggregation of small particles was observed.

#### 4 DISCUSSION

While particle counting is a useful technique for measuring filtration efficiency it is the SEM analysis which elucidates the capture phenomena. SEM analysis shows a variety of removal phenomena of the suspended particles. It is postulated that the transport mechanisms of interception, inertia and sedimentation occur. The attachment mechanisms involve surface attraction between the calcium carbonate and the polypropylene fibers. In addition there appears to be entrapment of the calcium carbonate between adjacent fibers and aggregation of the particles on the fibers and between adjacent fibers. Detachment mechanisms were thought to be the result of particle shearing and scour due to an increase in interstitial fluid velocity.

The retention of particles less than 10  $\mu\text{m}$  by nonwoven fabrics suggests that these fabrics could be used to enhance traditional water treatment practices when the influent contains suspended particles. While ideally a filter medium would remove all 4 and 5  $\mu\text{m}$  sized particles to ensure removal of the *Cryptosporidium parvum* cysts, removal of 40% of this sized particles puts a decreased load on the sand filter. By placing a needlefelt fabric upstream of a sand filter the filtration run of the sand filter can be extended, thus increasing run length and efficiency.

#### 5 CONCLUSIONS

1. Nonwoven geotextiles show sufficient removal



Figure 6. Scanning electron photomicrographs. Various times of capture of calcium carbonate particles a) 1.0 hour (Run 29), b) 10.75 hours (end, Run 29). c) Capture phenomena of surface attachment  $\rightarrow$ , entrapment  $\blacktriangleright$ , and aggregation  $\Rightarrow$ .

performance, for limited time periods, to be of interest as a potential medium for removal of 2 to 10 micron particles in water treatment applications. It is suggested that these textiles be termed aquatextiles, rather than geotextiles.

2. The removal over time of 2 to 10 micron particles is a function of the particle size. There appears to be a limit to the amount of particles that a nonwoven fabric can hold that is specific to each particle size. Near this limit the retention of particles becomes somewhat unstable.

3. A polypropylene fabric with an apparent opening size of 300 microns effectively captured 2 to 20 micron particles. The influence of fabric structure and fiber composition on removal will be a promising area of filtration research.

4. Increasing the thickness of the fabric layer through using two layers of fabric increased particulate removal.

5. The use of nonwoven textiles in water treatment filtration applications will offer new markets for traditional geotextile fabrics as well as an opportunity to develop new fabrics with better capture properties.

#### ACKNOWLEDGEMENTS

The authors wish to thank: Mr. Riyaz Shariff and the operators at the Aqualta Rosedale Water Treatment Plant, Edmonton, Alberta; Dr. Ming Chen, University of Alberta, for his supervision of the electron microscope work; and Mr. J. Dobroseilski of AMOCO Fabrics and Fibers Company for supplying the experimental fabrics.

#### REFERENCES

Richards, E. A., Smith, D. W. and Scott, J. D. (1997) Use of textile materials to enhance water treatment operations. 1997 CSCE/ASCE Environmental Engineering Conference, Edmonton, Alberta, 1695-1706.

# Turbulence and dynamics in the falling head test

Adam Bezuijen

Sen. Consultant, Delft Geotechnics, Delft, the Netherlands.

**ABSTRACT:** The falling head test is elaborated theoretically. A closed form solution is presented for the course of the head loss in time during such a test, neglecting the contribution of inertia. Furthermore the influence of the mass of the oscillating water column is investigated. The governing equations are presented. Simulations with these equations show good agreement with the results of measurements. The results of calculations show that dynamics can have a distinct influence on the result of the test. Not only if oscillations are observed in the head loss over the geotextile, but also if only a monotone descending head loss is found in the test.

**KEYWORDS:** Laboratory tests, Permeability, Falling head test, Forchheimer, Inertia effects.

## 1 INTRODUCTION

A falling head test can be performed quicker than a constant head test. Electronic data acquisition equipment is necessary for the falling head test, but the price for this equipment decreases every year. Inter laboratory tests have shown that comparable results can be obtained with both tests. Both tests are incorporated in the CEN-Norm "Water flow capacity perpendicular to the plane, without load" prEN 12040 of the TC189 "Geotextiles" (CEN, 1955). It therefore can be expected that the falling head test will be used more and more in the future.

The principle of the falling head test is shown in Figure 1. A geotextile is placed in a U-shaped tube with a valve. The valve is closed before the test and there is a difference in water level in both sides of the tube. At the beginning of the test the valve is opened and the water starts to flow. Continuous monitoring of the pressure, with the pressure gauge shown, allows to monitor the water level in the tubes as a function of time, from which the head loss over the geotextile can be calculated. The water flow capacity of the geotextile tested on is determined by the head loss over the geotextile and the flow through the geotextile.

Evaluation of the results of a falling head test is nowadays automated by means of a computer program, in which the permittivity at a certain head loss is calculated from the measured head loss and its rate of decrease. In this paper a different approach is followed. The differential equation that governs the flow in a falling head test is solved analytically, assuming the Forchheimer flow equation. Using this formula the parameters in the flow equation are determined by non-linear regression.

## 2 THEORY

### 2.1 Turbulence

Using the Forchheimer relation and neglecting dynamic terms, the relation between head loss and specific discharge can be written as:

$$h = a_h q + b_h q^2 \quad (1)$$

Where  $h$  is the head loss,  $q$  the specific discharge and  $a_h$  and  $b_h$  are coefficients determining the permittivity of the geotextile with dimensions of  $s$  and  $s^2/m$  respectively.

In a falling head test there is a relation between the change in head loss and the specific discharge:

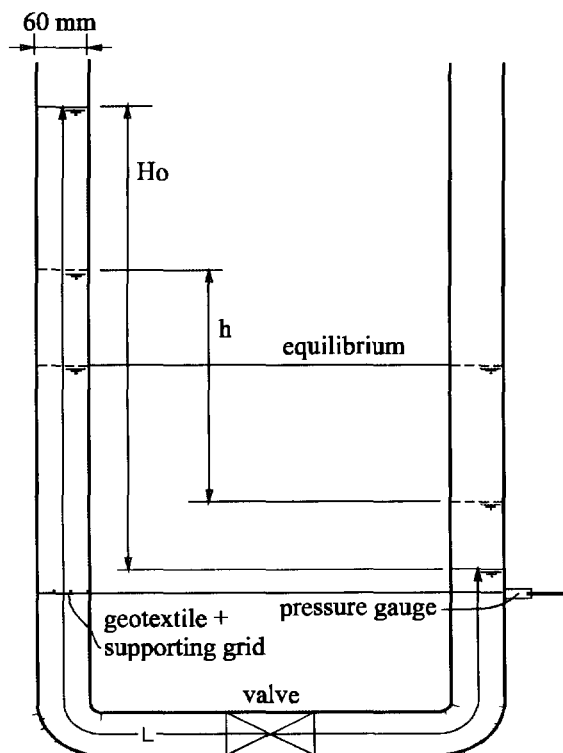


Figure 1: Sketch of a falling head apparatus.

$$q = -\alpha \frac{dh}{dt} \quad (2)$$

$\alpha$  depends on the geometry of the falling head apparatus. For the normal apparatus with two equal tubes, as shown in Figure 1,  $\alpha=0.5$ . If there is a constant head at the down flow side (this is the case if there would be no tube right from the valve in Figure 1),  $\alpha = 1$ . Inserting equation (2) in (1) and rearranging leads to the following differential equation:

$$\alpha^2 b_h \left(\frac{dh}{dt}\right)^2 - \alpha a_h \left(\frac{dh}{dt}\right) - h = 0 \quad (3)$$

Since  $\frac{dh}{dt} < 0$  (it is a falling head test), this can also be written as:

$$\frac{dh}{dt} = \frac{1 - \sqrt{1 + 4b_h h / a_h^2}}{2\alpha b_h / a_h} \quad (4)$$

Substituting

$$z = 1 - \sqrt{1 + 4b_h h / a_h^2} \quad (5)$$

the differential equation reads:

$$dz - \frac{1}{z} dz = \frac{dt}{\alpha a_h} \quad (6)$$

Taking at  $t = 0$ ,  $z = z_0$ , and calculating  $z_0$  from (5), assuming that  $h=H_0$  at  $t=0$ , (6) leads to:

$$\frac{t}{\alpha a_h} = z - z_0 - \ln \frac{z}{z_0} \quad (7)$$

Substituting back equation (4) leads to the final relation between  $t$  and  $h$ :

$$t = \alpha a_h \left[ \sqrt{1 + 4 \frac{b_h H_0}{a_h^2}} - \sqrt{1 + 4 \frac{b_h h}{a_h^2}} - \ln \left( \frac{\sqrt{1 + 4 \frac{b_h h}{a_h^2}} - 1}{\sqrt{1 + 4 \frac{b_h H_0}{a_h^2}} - 1} \right) \right] \quad (8)$$

Figure 2 shows the result of a comparison between measurements on a relatively impermeable geotextile (the influence of dynamics in the test was expected to be small) and a calculation using Equation (8), in which  $a_h$  and  $b_h$  were obtained by non-linear regression on the measurement data, showing almost perfect agreement.

## 2.2 Dynamic effects

If the geotextile is very permeable, the inertia of the water column cannot be neglected. The head loss not only contributes to overcome the flow resistance in the geotextile, but also contributes to accelerate or decelerate the water column. An extreme example is the falling head test on a circular plate as was performed in the CEN round robin test (Dierickx, 1995), but it was also found in some permeable geotextiles, see Figure 3. To describe the results of

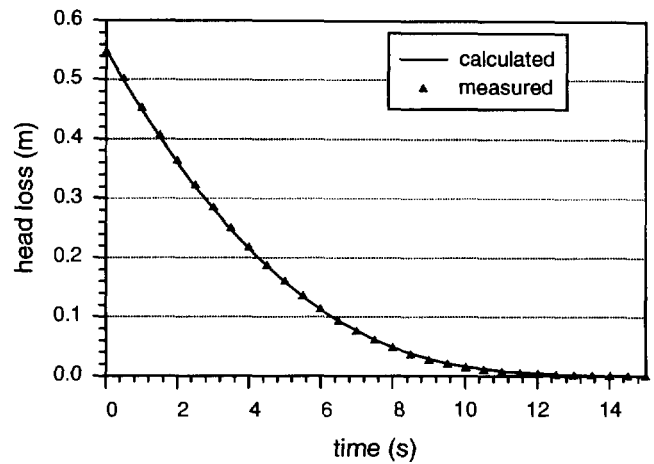


Figure 2: Falling head test on a less permeable geotextile (G2, see Section 2.2) and fit using Equation (8),  $a_h=2.44$  s,  $b_h=148$  s<sup>2</sup>/m.

such tests equation (1) was extended with a term that includes inertia of the water column in the falling head apparatus. Taking this into account equation (1) reads:

$$h = a_h q + b_h |q|q + \frac{L}{g} \frac{dq}{dt} \quad (9)$$

The absolute sign is now necessary because the possibility of flow reversal. Using (2), (9) can be written as:

$$\alpha^2 b_h^* \left(\frac{dh}{dt}\right)^2 - \alpha a_h \left(\frac{dh}{dt}\right) - \alpha \frac{L}{g} \frac{d^2 h}{dt^2} = h \quad (10)$$

Where  $b_h^* = b_h$  if  $q > 0$  and  $b_h^* = -b_h$  if  $q < 0$ . In this way the absolute sign in equation (9) is incorporated.

This equation was solved using an explicit finite difference scheme, using the following approximations:

$$\frac{dh}{dt} \approx \frac{h_{i+1} - h_i}{\Delta t} \quad \text{and} \quad \frac{d^2 h}{dt^2} \approx \frac{h_{i+1} - 2h_i + h_{i-1}}{\Delta t^2} \quad (11)$$

Where  $h_i$  is the head loss at time step  $i$  and  $\Delta t$  is the time increment between 2 time steps. Inserting (11) in (10),  $h_{i+1}$  can be written as:

$$h_{i+1} = \frac{-B + \sqrt{B^2 - 4AC}}{2A} \quad (12)$$

with:

$$A = \alpha^2 \frac{b_h^*}{\Delta t^2}$$

$$B = -\alpha \left[ 2\alpha \left(\frac{b_h^*}{\Delta t}\right)^2 h_i + \frac{a_h}{\Delta t} + \frac{L}{g\Delta t^2} \right] \quad (13)$$

$$C = \left( \alpha \frac{a_h}{\Delta t} + \alpha^2 \frac{b_h^*}{\Delta t^2} h_i - 1 \right) h_i + \alpha \frac{L}{g\Delta t^2} (2h_i - h_{i-1})$$



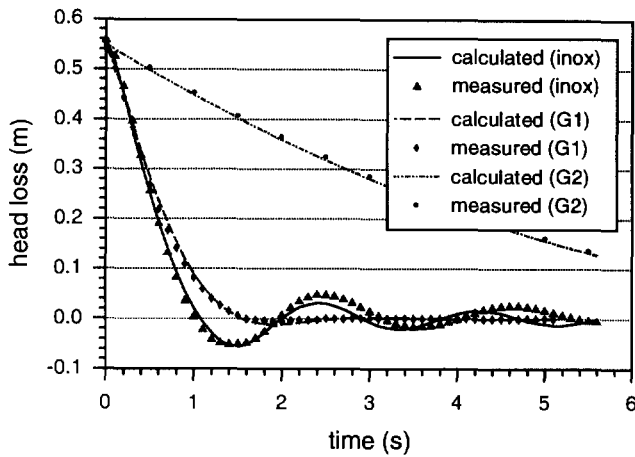


Figure 3: Measured and calculated piezometric head for a perforated plate (inox) and two different geotextiles.

Using these equations it is also possible to simulate the measured head loss in a falling head test as a function of time also for very permeable material quite accurately, see Figure 3. This figure shows measurements and calculations for 3 different geotextiles: The perforated plate used in the CEN tests and two geotextiles with different permeability. UCO (Terrasafe) 4000, which will be referred to as G1, a needle punched slightly head bonded nonwoven with a thickness of approximately 3.8 mm and Lotrak 16/15, referred to as G2, a woven geotextile (tape/tape) with a thickness of approximately 0.5 mm. The permeability of G2 is clearly less than that of G1. The whole curve of G2 is shown in Figure 2.

### 3 INFLUENCE DYNAMICS ON PARAMETERS

In the CEN norm “Water flow capacity normal to the plane, without load”, prEN 12040, dynamics is not taken into account. Time  $t=0$  is the time the valve is completely opened and the first time  $dh/dt=0$  is taken as the end of the test. The permeability of the geotextile is determined in this part of the curve, assuming that the difference in the head loss is zero when  $dh/dt=0$ , see Figure 4, which is a modified version from the figure in the norm. Figure 3 shows that the head loss can be less than zero due to dynamics. If this is the case, the curve is shifted along the Y-axis before the evaluation, to obtain a head loss of zero at  $dh/dt=0$ .

Taking one value for the parameters  $a_h$  and  $b_h$  in equations (12) and (13), it is possible to calculate the influence of dynamics by changing the length  $L$  of the water in the tube. The larger this length the larger the influence of dynamics. The CEN procedure described above and the non-linear regression technique can be used to obtain values for  $a'_h$  and  $b'_h$ . (the accents indicate that the parameters are determined in a different way) using the solution without dynamics, Equation (8). If the CEN procedure is cor-

rect, then  $a'_h$  and  $b'_h$  should be equal to the input values for  $a_h$  and  $b_h$ .

This procedure was performed for the 3 different values of  $a_h$  and  $b_h$ , describing the permeability of the materials mentioned before. Table 1 shows the results of this procedure.

Table 1: Calculated values of the Forchheimer coefficients  $a_h$  (s) and  $b_h$  ( $s^2/m$ ) and the velocity (VI) (m/s) and head loss (HI) (m) index. See also text.

	Perf. Plate				G1			G2		
L (m)	1.6	0	1.6	3	1.6	0	1.6	1.6	0	1.6
	D				D		D			
$a_h, a'_h$	0.01	0.0	0.0	0.0	0.65	0.63	0.16	2.4	2.3	2.2
$b_h, b'_h$	3.5	3.4	3.6	3.6	2.8	2.8	4.6	148	148	151
VI ( $\cdot 10^{-3}$ )	120	120	120	120	61	62	88	12	12	12
HI ( $\cdot 10^{-3}$ )	1.6	1.4	1.5	1.5	14	14	5.0	108	106	105

The column with D presents the parameters  $a_h$  and  $b_h$  used in the calculation including dynamics (equations (12) and (13)), resulting in the fits of Figure 3. When values for  $a_h$  and  $b_h$  were found, calculations were run with the same  $a_h$  and  $b_h$  for various lengths of the water column  $L$  (0, 1.6 and for the perforated plate also 3 m). The results of those calculations were used as an input for determination of  $a'_h$  and  $b'_h$  (presented in the columns with  $L = 0, 1.6$  and 3 m without D). The method described in prEN 12040 has been used to obtain the part of the curve appropriate for calculations and Equation (8) and non-linear regression to obtain the parameters  $a'_h$  and  $b'_h$ . For the theoretical case  $L=0$  (in reality the length of the column must always have a certain length, but this value is used to exclude the last term in equation (9)) there is no influence of dynamics. In that case the parameters  $a'_h$  and  $b'_h$  should be the same as  $a_h$  and  $b_h$  used in the dynamic calculation (D). In this case the procedure is just a check of the accuracy of both solutions. If  $L$  has a realistic length, there can be deviations. The calculation with  $L=1.6$  m shows the influence of dynamics on the result of the test for the equipment used. The values for  $a'_h$  and  $b'_h$  mentioned for  $L=1.6$  m are the values that will be found using the procedure of prEN 12040, thus

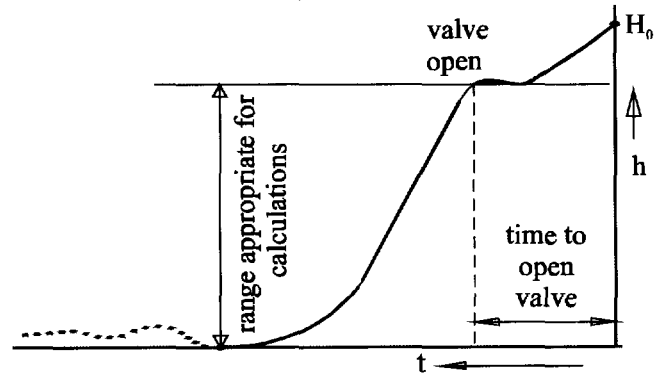


Figure 4: Sketch from prEN 12040 (modified) to calculate the water flow capacity.

neglecting dynamics.

The procedure of prEN12040 was slightly changed. The time the valve is completely opened is never known exactly and therefore the part of the curve with the steepest gradient is taken as the beginning of the test. In case the results are influenced by dynamics, this is a bit later than the moment the valve is open. A difference of approximately 0.3 s was found in the tests.

#### 4 DISCUSSION ON THE RESULTS

Table 1 shows that the parameters used in the numerical calculations are in close agreement with  $a'_h$  and  $b'_h$  when the numerical results for  $L=0$  are fitted with equation (8). This means that without dynamic effects both solutions correspond to each other, as could be expected. Small deviations occur due to the finite differences used in the numerical method. The small value of  $a_h$ , used to simulate the behaviour of the perforated plate, could not be found when the result of the numerical calculation with  $L=0$  was used to obtain  $a'_h$ . The influence of such a small value of  $a_h$  can be found in the damping of the oscillations (for  $\text{time} > 2$  s in Figure 3), but is negligible in the first part of the curve, where turbulent flow is dominant.

The results of the non-linear regression on the numerical simulations with a finite length  $L$  (and therefore influenced by dynamics), result in different values of  $a'_h$  and  $b'_h$  compared with the results for  $L=0$ . Remarkably the difference is only small in case the parameters for the perforated plate are used, but significant for geotextile G1 and still perceptible for the much less permeable geotextile G2. The parameters  $a'_h$  and  $b'_h$  differ considerably from  $a_h$  and  $b_h$  for G1. It is known that slight changes in the results of falling head tests can lead to relatively large changes in the parameters  $a_h$  and  $b_h$  (Bezuijen et al. 1994). However, also the velocity index and head index differ significantly. For G1 the This means that the procedure as suggested in prEN 12040 will not lead to the right values of  $a_h$  and  $b_h$  when there is an influence of dynamics. If dynamics has an influence, the flow capacity of the material is overestimated. Neglecting dynamics for geotextile G1 leads to a velocity index VI that is 30 % too high and to a head loss index that is 180 % too low.

For geotextile G2 the influence is only small. However, simulations has shown that for geotextiles with a velocity index of 34 mm/s, dynamics has still a considerable influence for an apparatus with a length of 1.6 m water column. For such a geotextile there will be hardly any overshoot in the head loss below zero, as is still present in geotextile G1 (see Figure 3). Neglecting dynamics for a geotextile with a velocity index of 34 mm/s leads to a VI that is 14% too high and a HI that is 47 % too high.

From this it can be concluded that is not sufficient to look at overshoot in the head loss to determine whether or

not dynamic effects have an influence. The influence depends on the apparatus, but is significant (errors of more than 14 % and up to 180%) for the apparatus shown in Figure 1, with a water column of 1.6 m length, when the head loss reaches values close to zero between 1.5 and 4 seconds.

#### 5 CONCLUSIONS

This study has led to the following conclusions:

1. The results of a falling head test on geotextiles can be described with Equations (12) and (13). In case dynamic effects can be neglected Equation (8) can be used.
2. The procedure as presented in prEN 12040 to deal with dynamic effects that occur in a falling head test on permeable geotextiles can lead to inaccurate results, even if no overshoot is visible in the head loss versus time plot. Considerable errors (from 14 % up to 180 %) were found when the head loss reaches values close to zero between 1.5 and 4 seconds.
3. The error found when using the procedure of prEN 12040 was largest in the head loss index.
4. It is advised to include the influence of dynamics in the interpretation of a falling head test when relatively permeable geotextiles are tested, or to use a constant head test.
5. More tests are needed to determine the entire range where dynamics has an influence.

#### ACKNOWLEDGEMENT

I would like to thank Dr. W. Dierickx of the Belgian Research Station for Agricultural Engineering for providing the measurement data and for stimulating discussion.

#### REFERENCES

- Bezuijen A., Köhler H.-J. and Abromeit H.-U. (1994) "Geotextile permeability as a function of temperature", 5<sup>th</sup> Int. Conf. on Geotextiles, Geomembranes and Related products, Singapore, 5 - 9 September, pp 655-658.
- Dierickx W. (1995) "Research and Intercomparison Tests Necessary for the Harmonisation of Standards on Geotextiles, Task 4: Water Permeability Intercomparison". EC Measurement and Testing Project 0169, Document 0169/4/6, November.
- CEN (1995) *Geotextiles and geotextile-related products - Determination of the water permeability characteristics normal to the plane, without load*. PrEN 12040:1995, July.

# Factors Affecting Hydraulic Transmissivity of Geocomposite Drain Systems

Nader S. Rad

Laboratory Director, GeoSyntec Consultants, Geomechanics and Environmental Laboratory, Alpharetta, Georgia, USA

Cuneyt Gokmen

Program Manager, GeoSyntec Consultants, Geomechanics and Environmental Laboratory, Alpharetta, Georgia, USA

James M. Stalcup

Operation Manager, GeoSyntec Consultants, Geomechanics and Environmental Laboratory, Alpharetta, Georgia, USA

**ABSTRACT:** Effects of various testing parameters on the hydraulic transmissivity of geocomposite drain systems commonly used in leak detection and leachate collection systems of modern landfills are investigated. A laboratory testing program was performed utilizing different geonet, geotextile, geomembrane and geosynthetic clay liner (GCL) products. The test results indicate that, the configuration of the geocomposite system, the intensity and the duration of the sustained vertical stress, and the hydraulic gradient can strongly influence the hydraulic transmissivity of a geocomposite drain.

**KEYWORDS:** drainage, geonets, geocomposite, transmissivity, laboratory testing

## 1 INTRODUCTION

Modern landfill liner-system design commonly includes leak detection and leachate collection systems, which often consist of a geonet sandwiched between two geotextile layers, or between a geotextile and a geomembrane layer (both configuration herein are referred to as geocomposite drains). Hydraulic transmissivity of a geocomposite drain is known to be affected by various factors including: (i) physical characteristics of the geonet, geotextile, and when applicable, geomembrane components, (ii) the intensity and duration of the applied vertical stress, (iii) the hydraulic gradient, and (iv) presence of an overlying geosynthetic clay liner (GCL). The effects of these parameters on the hydraulic transmissivity of geocomposite drains were studied with a laboratory testing program utilizing different geonet, geotextile, geomembrane and GCL products in various geocomposite drain configurations.

## 2 TEST EQUIPMENT AND SETUP

The constant head hydraulic transmissivity test method described by the American Society for Testing and Materials (ASTM) test standard D 4716 was utilized in the testing program. A simplified schematic diagram of the test equipment and setup is presented in Figure 1. Referring to the figure, hydraulic transmissivity is calculated utilizing the following equation:

$$\theta = \frac{Q}{B \times (h/L)} \quad (1)$$

where,  $\theta$  is the hydraulic transmissivity ( $m^2/s$ ),  $Q$  is the volume of discharged fluid per unit time ( $m^3/s$ ),  $L$  is the length of the specimen ( $m$ ),  $B$  is the width of the specimen ( $m$ ), and  $h$  is the difference in the total head across the specimen ( $m$ ). The hydraulic gradient is equal to the ratio of  $h$  to  $L$ .

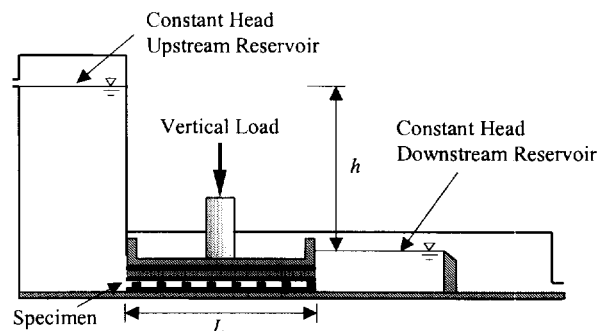


Figure 1. Schematic diagram of the test equipment and setup.

## 3 TEST MATERIALS

One geomembrane, two different geonets, three different geotextiles and one GCL product were used in the testing program. Table 1 provides general information on each product.

## 4 TEST SPECIMEN CONFIGURATION

Referring to Figure 2, the following test specimen configurations were used:

Table 1. Test material general information.

Test Material			
Designation	Type	Trade Name	Remarks
GM	Geomembrane	Gundline HD	High density polyethylene, smooth, $t=1.5$ mm
GN1	Geonet	Tensar NS140551	Polyethylene, $t=5.0$ mm, $\theta=1E-3$ m <sup>2</sup> /s @ $\sigma=720$ kPa and $i=1.0$
GN2	Geonet	NSC PN 3000	Polyethylene, $t=5.0$ mm, $\theta=1E-3$ m <sup>2</sup> /s @ $\sigma=720$ kPa and $i=1.0$
GT1	Geotextile	LINQ Typar 3601	Polypropylene, nonwoven, $M_A=203$ g/m <sup>2</sup> , AOS=0.1 mm, and $\psi=0.1$ s <sup>-1</sup>
GT2	Geotextile	Amoco 4557	Polypropylene, nonwoven, $M_A=407$ g/m <sup>2</sup> , AOS=0.15 mm, and $\psi=1.1$ s <sup>-1</sup>
GT3	Geotextile	Polyfelt TS750-Reg	Polypropylene, nonwoven, $M_A=349$ g/m <sup>2</sup> , AOS=0.15 mm, and $\psi=1.3$ s <sup>-1</sup>
GCL	GCL	Claymax	Primary backing: Amoco 4034, polypropylene, woven, $M_A=98$ g/m <sup>2</sup> Secondary backing: Chicopee (a very thin woven geotextile)

$t$ : thickness (mm),  $M_A$ : mass per unit area (g/m<sup>2</sup>), AOS: apparent opening size (mm),  $\psi$ : permittivity (s<sup>-1</sup>),  $\sigma$ : vertical stress (kPa), and  $i$ : hydraulic gradient (-)

Configuration I - a geonet sandwiched between two geomembranes to evaluate the baseline hydraulic transmissivity of the geonet.

Configuration II - a composite of a geotextile and a geonet sandwiched between two geomembranes to evaluate the effects of a single geotextile layer over the geonet on its transmissivity.

Configuration III - a GCL placed over the geotextile component of a geocomposite drain (secondary backing against the geotextile) to evaluate the effects of an overlying GCL on the transmissivity of a geocomposite drain.

Configuration IV - a GCL directly placed over a geonet (primary backing directly against the geonet) to evaluate the effects of an overlying GCL on the transmissivity of a geonet.

duration (i.e., the period of applied vertical stress) varied from several days in the case of Tests 1 through 7 to approximately 120 days in the case of Tests 8 and 9.

Table 2. Summary of laboratory testing program.

Test No.	Config. No.	Test configuration (from top to bottom)							
		GM	GCL	GT1	GT2	GT3	GN1	GN2	GM
1	I	x						x	x
2	II	x		x				x	x
3	II	x		x			x		x
4	II	x			x		x		x
5	II	x				x	x		x
6	III	x	x	x			x		x
7	III	x	x			x	x		x
8	III	x	x	x				x	x
9	IV	x	x					x	x

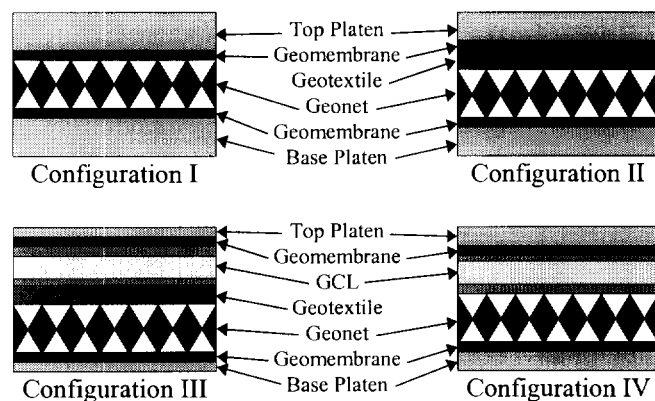


Figure 2. Schematic diagram of four different test configurations.

## 5 TESTING PROGRAM

Nine transmissivity tests were performed, as presented in Table 2. The tests were performed utilizing vertical stresses ranging from 24 to 766 kPa and hydraulic gradients ranging from 0.1 to 0.5. These boundaries were selected to encompass commonly encountered field conditions. Test

## 6 TEST RESULTS

The test results are graphically presented in Figures 3 to 7. The results and the observations made during the tests are summarized in the following paragraphs.

Hydraulic gradient - Referring to Figures 3, 5 and 6, it appears that higher hydraulic gradients result in lower measured transmissivity values. This suggests that as the hydraulic gradient increases the flow regime becomes turbulent and Darcy's law may not be fully applicable (Williams, et al., 1984 and Cancelli, et al., 1987).

Geotextile - Referring to Figure 3 (a), it appears that presence of a geotextile over a geonet reduces its transmissivity. This is likely due to penetration of the overlying geotextile into the geonet channels (Williams, et al., 1984 and Koerner, 1990).

As illustrated in Figure 3 (b), the type of the overlying geotextile may have a significant impact on the hydraulic transmissivity of a geocomposite drain. For the geonets and geotextiles used in this investigation, the test results indicate that the hydraulic transmissivity may decrease by approximately half an order of magnitude when the heaviest/thickest geotextile is used.

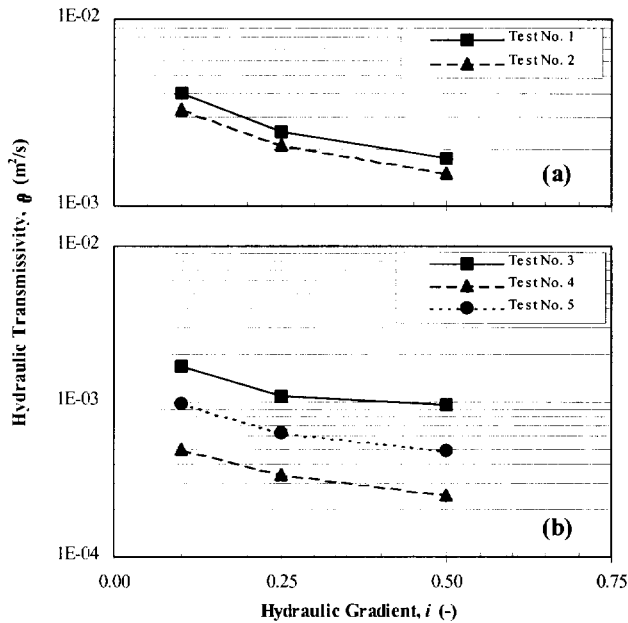


Figure 3. Effect of geotextile on transmissivity of geocomposite drains ( $\sigma=766$  kPa).

**Vertical Stress** - The effect of the vertical stress on the transmissivity of geocomposite drains is depicted in Figure 4. Referring to the figure, hydraulic transmissivity decreases as the vertical stress increases. The decrease in the hydraulic transmissivity is likely due to: (i) compression of the geonet ribs, and (ii) increasing penetration of the overlying geotextile into the net (Williams, et al., 1984 and Fannin and Choy, 1995). As presented in the figure, for the geotextiles and geonets used in this investigation the

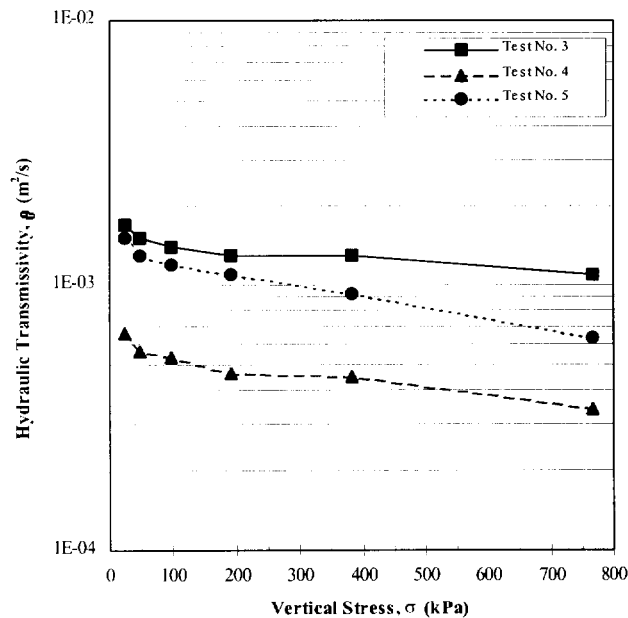


Figure 4. Effect of vertical stress and geotextile on the transmissivity of the geocomposite drains ( $i=0.25$ ).

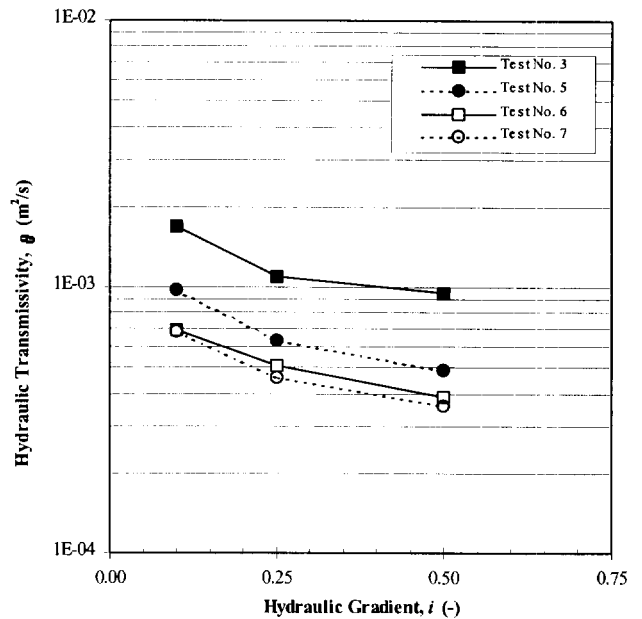


Figure 5. Effect of GCL on transmissivity of geocomposite drains with various geotextiles ( $\sigma=766$  kPa).

transmissivity may decrease by 30 to 60% as the vertical stress increases from 24 to 766 kPa. In general, the heavier/thicker the geotextile the stronger the decrease in the overall transmissivity of the geocomposite drains.

**GCL** - As illustrated in Figures 5 and 6, presence of an overlying GCL may reduce the transmissivity of a geocomposite drain by 30 to 70 %. Referring to Figure 5, the effect of GCL on the transmissivity is generally dependent on the type of geotextile used to separate the GCL from the geonet. For the materials used in this investigation, the reduction in the transmissivity was less when a heavier/thicker geotextile was used. It should be noted, however, that this observation contradicts the results presented in Figure 3 (b). Thus, more research in this area is needed before a final conclusion can be drawn.

As presented in Figure 6, direct placement of a GCL on a geonet results in approximately an order of magnitude reduction in its transmissivity. Notwithstanding the transmissivity reduction, direct placement of GCL on a geonet may be an economical approach for some landfill designs. It should be noted, however, that the geotextile backing of the GCL placed against the geonet should have appropriate mechanical and physical properties to: (i) withstand potential damage under the applied vertical stress and construction activities, and (ii) limit migration of bentonite from the GCL into the geonet.

**Duration of vertical stress** - The effects of the duration of sustained vertical stress on transmissivity of geocomposite drains are presented in Figure 7. Referring to the figure, the transmissivity of a geocomposite drain decreases as the duration of the applied vertical stress increases. For the geocomposite drains and test duration used in this

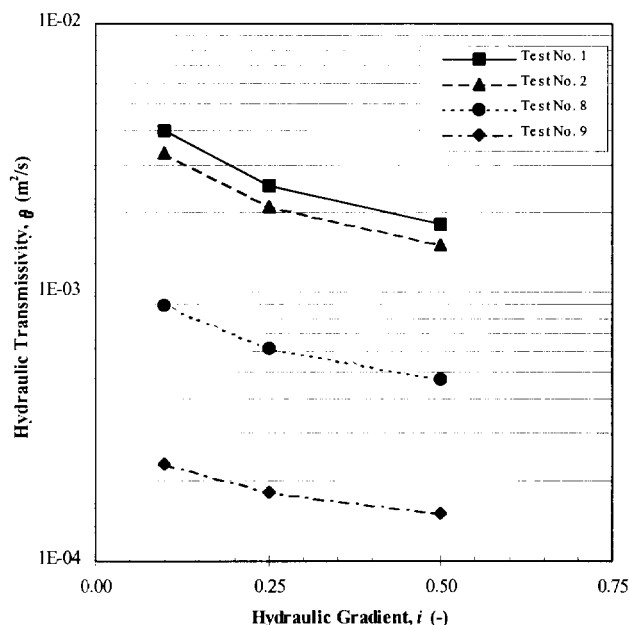


Figure 6. Effect of GCL on transmissivity of geocomposite drains with or without geotextile ( $\sigma=766$  kPa).

investigation most of the reduction occurred in the first 50 to 60 days. The maximum transmissivity reduction was approximately 30 to 40%. The observed decrease in the transmissivity is likely due to: (i) creeping of the geonet ribs (Smith and Kraemer, 1987), and (ii) creeping of the overlying geotextile into the geonet channels.

## 7 CONCLUSION

The purpose of this investigation was to evaluate the effect(s) of various parameters on the hydraulic transmissivity of geonets and geocomposite drains. Based on the results obtained in this study the following conclusions can be drawn:

(i) the higher the hydraulic gradient the lower the hydraulic transmissivity value;

(ii) the higher the vertical load the lower the hydraulic transmissivity value;

(iii) an overlying geotextile may reduce the hydraulic transmissivity of a geonet due to possible penetration of the geotextile into the geonet channels;

(iv) the physical and mechanical properties of the material(s) used in a geocomposite drain affect its overall transmissivity;

(v) direct placement of a GCL on a geonet may strongly reduce its overall hydraulic transmissivity due to penetration of GCL and possible migration of its bentonite component into the geonet channels;

(vi) presence of a layer of geotextile between the GCL and the geonet reduces the GCL effect on the transmissivity of the geonet; and

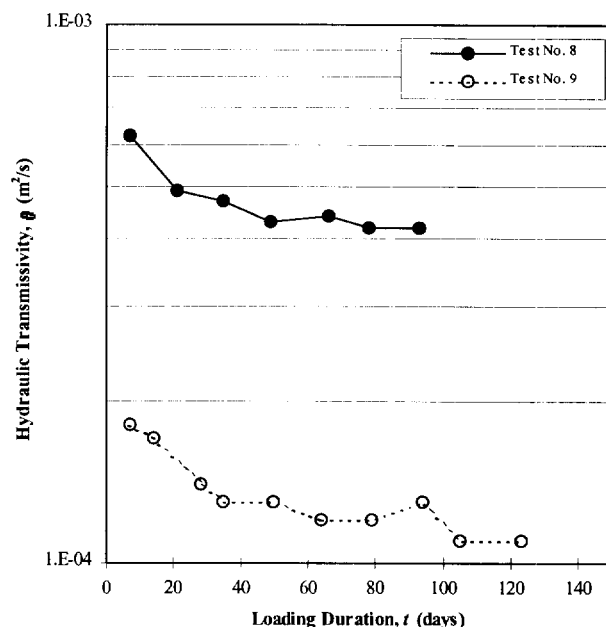


Figure 7. Long-term effect of applied vertical stress on the transmissivity ( $\sigma=766$  kPa,  $i=0.25$ ).

(vii) long-term application of vertical stress may reduce hydraulic transmissivity of a geocomposite drain.

The authors recommend that the actual design configurations be simulated, as closely as possible, in the laboratory to determine representative field hydraulic transmissivity values.

## REFERENCES

- ASTM (1993) *Annual Book of ASTM Standards, Volume 04.08*, Philadelphia, PA, 1470 p.
- Cancelli, A., Cazzuffi, D. and Rimoldi, P. (1987) "Geocomposite Drainage Systems: Mechanical Properties and Discharge Capacity Evaluation", *Geosynthetics '87*, IFAI, Vol. 2, New Orleans, LA, pp. 393-404.
- Fannin, R. J. and Choy H.W. (1995) "Factors Influencing the Long-Term Flow Capacity of Geonets", *Geosynthetics '95*, IFAI, Nashville, TN, pp. 267-280.
- Koerner, R.M. (1990) *Designing with Geosynthetics*, Second Edition, Prentice Hall, Englewood Cliffs, N.J., 652 p.
- Smith, A.D. and Kraemer, S.R. (1987) "Creep of Geocomposite Drains", *Geosynthetics '87*, IFAI, Vol. 2, New Orleans, LA, pp. 422-433.
- Williams, N., Giroud, J.P., and Bonaparte, R. (1984) "Properties of Plastic Nets for Liquid and Gas Drainage Associated with Geomembranes", *Proceedings of the International Conference on Geomembranes, Vol. II*, Denver, CO, pp. 399-404.

# Comparison of transmissivity tests DIN-ASTM-CEN

J. Müller-Rochholz

Professor, Department of Civil Engineering, Fachhochschule Münster, Labor für Baustoffe, Münster, Germany

Z. Bronstein

Institut für textile Bau-und Umwelttechnik, Greven, Germany

**ABSTRACT:** Working on harmonising tests, there were 3 different test available. They differ in specimen size, lateral pressure material, water input to specimen. These standards were tested in comparison on a set of identical materials with different hydraulic gradients. The results are given in plots flow us hydraulic.

**KEYWORDS:** Hydraulic transmissivity, In-plane flow, Drainage capacity, Drainage, Transmissivity

## 1 INTRODUCTION

World wide trade needs generally accepted technical values for the products traded. The work on international standards in the International Standard Organisation ISO is accelerated in the geosynthetic area by the Vienna-contract, which states a common speed and a mutual acceptance of standards between ISO and the Comité Européenne de Normalisation CEN. For drainage applications of geosynthetics the drainage capacity is the design parameter. This property may be tested by prEN ISO 12958 November 1995 or ASTM D 4716-87 or an old German Proposed made by Franzius Institute (DIN 60500 T7). This comparison included 10 Materials and the 3 standardised methods.

## 2 DEFINITIONS

**In-plane water flow capacity:** The volumetric in plane rate of water per unit width of the GTX or GRP, at defined gradients and loads, in a direction parallel to the plane of the product.

**Transmissivity  $\theta$ :** The in-plane water flow capacity of the GTX or GRP under laminar conditions at a hydraulic gradient of unity.

**Hydraulic gradient  $\Delta h$ :** Ratio of the head loss in the GTX or GRP to the distance between two mesasuring points.

## 3 TEST METHODS

The 3 methods described in

- prEN ISO 12958 November 1995
- ASTM D 4716-87
- Franzius Institute method
- 

are synoptic shown in fig. 1, 2 and 3.

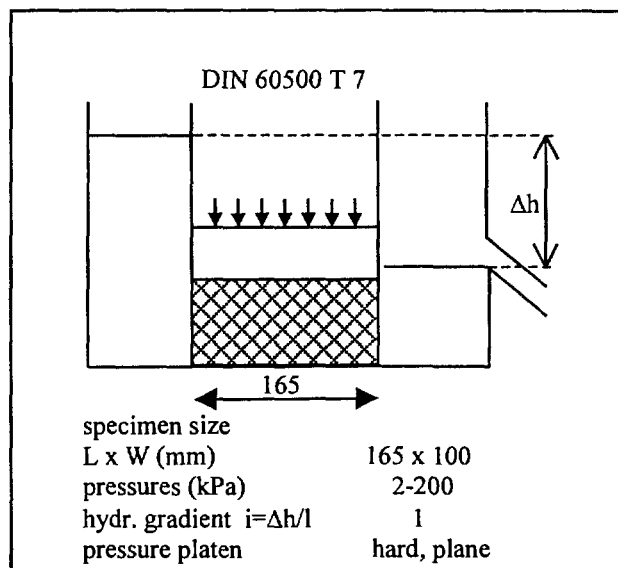


Figure 1: Schematic sketch of test condition DIN 60500 T7

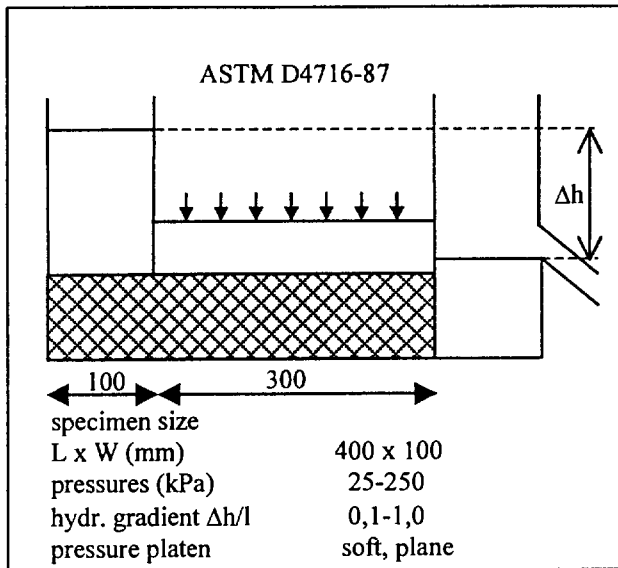


Figure 2: Schematic sketch of test condition ASTM D4716-87

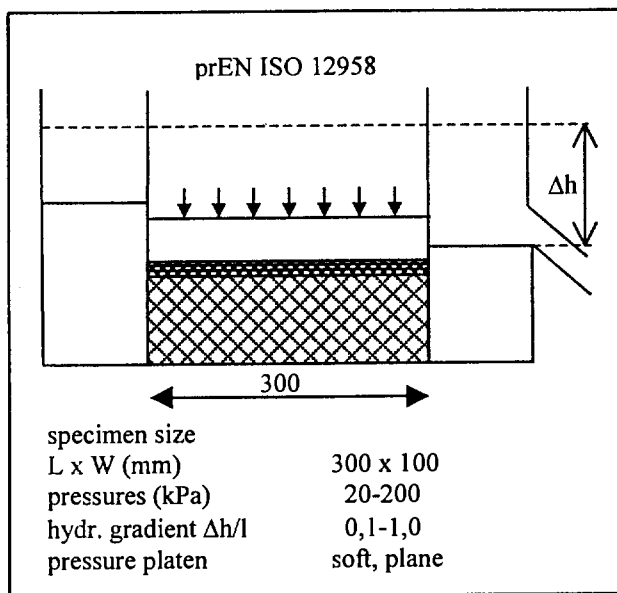


Figure 3: Schematic sketch of test condition prEN ISO 12958

The differences are specimen size, water input direction to specimen, kind of confining plate material.

### 3 MATERIALS TESTED

A wide set of materials covering typical products for drainage application were tested, the generic description is given hereunder.

#### Number of Materials

-Random wire mats	-	4
-Oriented wire mats	-	1
-extruded geonet	-	2
-Cuspated sheet	-	1
-nowoven composite	-	1
-PE foam-particle	-	1

### 4 RESULTS

The results of comparison tests are given in figures 4 to 8.

#### Influence of pressure on drainage materials

The generic products show different behaviour, the lines of flow vs stress drop rapidly for random wire products, show less decrease for oriented wires and again less for geonet and cuspated film type products. Be aware that the flow axis is scaled differently, the flow at 2 kPa for wire products is very high.

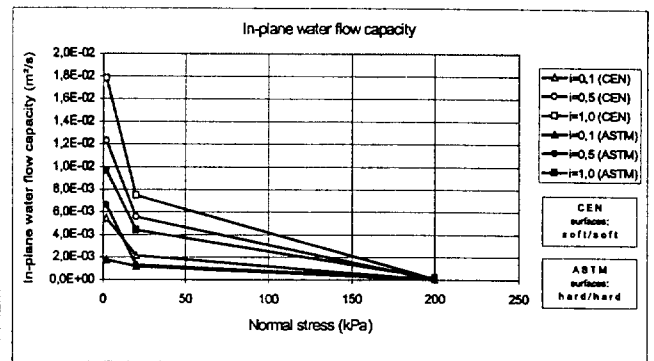


Figure 4: Oriented PA wire between nonwovens (Sterz, Breuer 1995, Ehler, Rohde 1995)

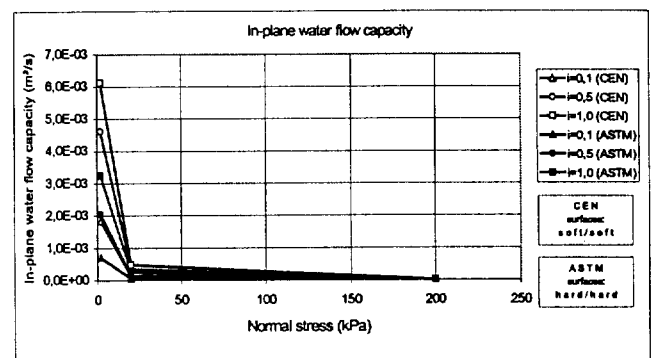


Figure 5: Random PP wire between nonwovens (Sterz, Breuer 1995, Ehler, Rohde 1995)



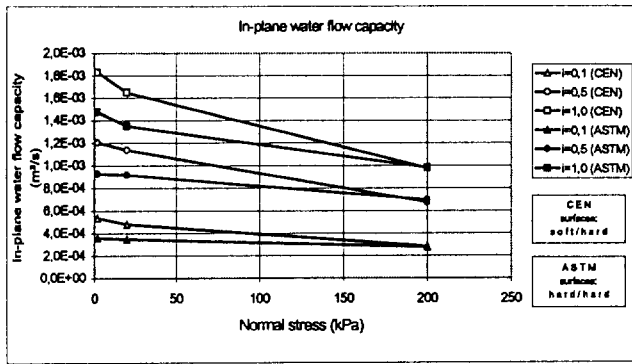


Figure 6: Extruded geonet with nonwoven (Sterz, Breuer 1995, Ehler, Rohde 1995)

Influence of hard/soft platen

The soft (cellular rubber) platen of CEN simulating soft soil pressure on the geotextile filter leads to a strong decrease of the curves ( see fig 7) by confining the flow section.

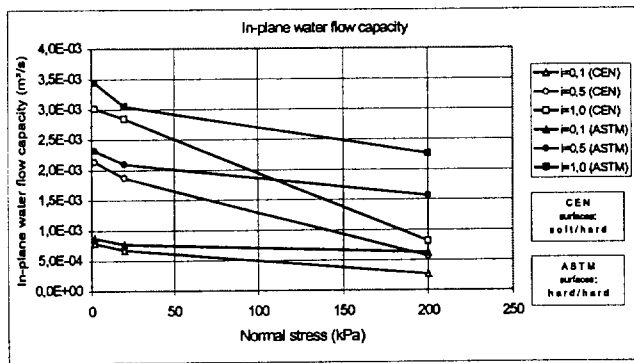


Figure 7: Cuspated sheet with nonwoven (Sterz, Breuer 1995, Ehler, Rohde 1995)

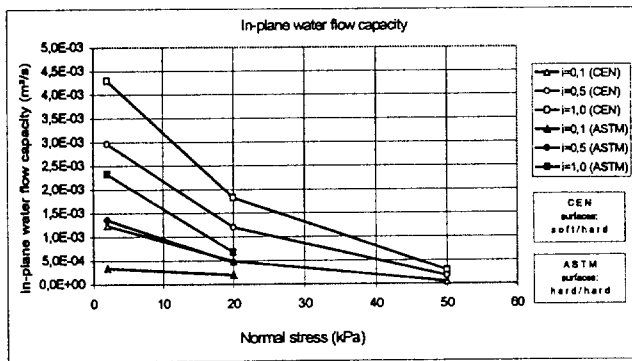


Figure 8: PE foam-particles with nonwoven cover (Sterz, Breuer 1995, Ehler, Rohde 1995)

Influence of gradient

The dependence from gradient is not always linear (see fig 9), so if a value measured at a gradient not equal to 1 is than calculated for Transmissivity at gradient 1, the mistake is significant.

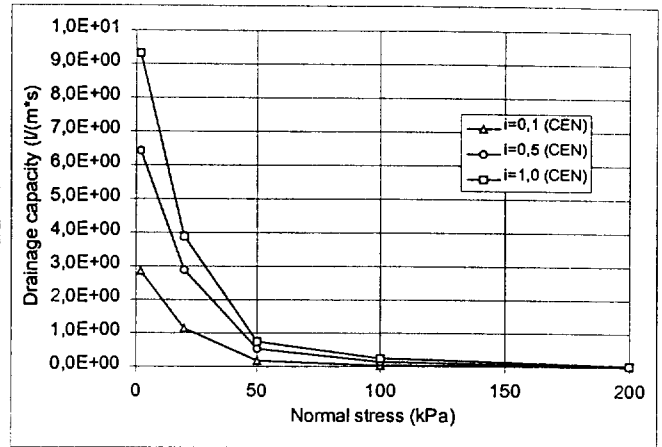


Figure 9: PE foam-particles with nonwoven

Influence of test method

From the curves given in fig 4 .. 8 tables were derived, giving the comparative values for the 3 standard methods for 3 materials (see table 1, 2, 3). Roughly evaluated the test according to ISO and CEN leads to product specific correlation values, a factor, valid for all materials is not extractable.

$\sigma$ kPa	$\theta$ (CEN) m <sup>2</sup> /s	$\theta$ (ASTM) m <sup>2</sup> /s	$\theta$ (Franzius) m <sup>2</sup> /s
2	0,0208	-	0,1100
20	0,0013	0,0006	0,0120
200	0,0002	0,0001	0,0047

Table 1. Random wire mat (Sterz, Breuer 1995)

$\sigma$ kPa	$\theta$ (CEN) m <sup>2</sup> /s	$\theta$ (ASTM) m <sup>2</sup> /s	$\theta$ (Franzius) m <sup>2</sup> /s
2	0,0050	-	0,0216
20	0,0003	0,0004	0,0024
200	< 0,0001	< 0,0001	< 0,0001

Table 2. Random wire mat between nonwoven (Sterz, Breuer 1995)

$\sigma$ kPa	$\theta$ (CEN) m <sup>2</sup> /s	$\theta$ (ASTM) m <sup>2</sup> /s	$\theta$ (Franzius) m <sup>2</sup> /s
2	0,0009	-	0,0063
20	0,0007	0,0014	0,0049
200	< 0,0001	0,0001	0,0009

Table 3. Extruded geonet with nonwoven (Sterz, Breuer 1995)

## REFERENCES

Draft prEN ISO 12958 (CEN)

*Geotextile and, geotextile-related Products-  
Determination of WaterFlow Capacity in their Plane*  
European Committee for Standardization.

ASTM D 4716-87

*Standard test Method for Constant Head Hydraulic  
Transmissivity (In-Plane Flow) of Geotextile and  
geotextile-related Products*  
ASTM Committee D-35.

D. Sterz, W. Breuer

*Transmissivity of difference drainage materials by  
CEN-test*

Fachhochschule Münster, Münster, Germany 1995

E. Ehler, I. Rohde

*Transmissivity of difference drainage materials by  
ASTM D4716-87*

Fachhochschule Münster, Münster, Germany 1995

# The Optimization Analysis Between Processing Parameters and Physical Properties of Geocomposites Composed of Multi-layered Nonwovens

H.Y. Jeon

Associate Professor, Department of Textile Engineering, Chonnam National University, Kwangju, Korea

J.Y. Kim

Research Associate, Department of Textile and Apparel Technology and Management, North Carolina State University, Raleigh, NC, USA

**ABSTRACT:** The geocomposites of needle punched(NB) and spunbonded(SB) nonwovens having reinforcement and drainage functions were manufactured by thermal bonding method. The physical properties (e.g. tensile, tear and bursting strength, permittivity) of these multi-layered nonwovens were varied by processing parameters - temperatures, pressures, bonding periods etc. - in manufacturing by thermal bonding method. Therefore, it is very meaningful to optimize the processing parameters and physical properties of the geocomposites by thermal bonding method. An algorithm has been developed to optimize the process of the geocomposites using an artificial neural network (ANN). The geocomposites were employed to examine the effects of manufacturing methods on the analysis results and the neural network simulations have been applied to predict the changes of the nonwovens performances by varying the processing parameters.

**KEYWORD:** Multi-layered nonwovens, Thermal bonding method, Processing parameters, Optimization analysis.

## 1 INTRODUCTION

The function of nonwoven geotextiles are reinforcement, separation, filtration, drainage and liquid barrier (Ingold 1994; Koerner 1994). Multi-layered nonwovens as a kind of geocomposites are manufactured by needle punching or thermal bonding to develop the above one or two functions of geotextile (Lünenschloss and Albrecht 1981; Gourc, Faure, Rollin and LeFlear 1982). Especially, in the case of application to thermal bonding to manufacture geocomposites (multi-layered nonwovens), the processing parameters e.g. temperature, pressure, time etc, were affected by the physical properties of geocomposites. From this view, it is very reasonable that the optimization analysis is applied to examine the deviations and correlations between these parameters.

Process optimization is one of the most important topics in modern non-woven research because it directly influences many physical properties of the thermal bonded nonwoven geocomposite. It has been known that there exist very complicated interaction between processing parameters and material properties. The popular regression approaches always neglects some significant interactions between processing parameters in order to simplify the model and often have some difficulty in finding a reliable multivariable nonlinear model which must be considered as a model.

Very recently, the feed-forward multi-layered neural network approach has been widely used in many areas of engineering and science (Hornik 1989). Commonly, the neural networks can be employed in order to analyze some of the most complex non-linear system. The recent theoretical work has proven that neural networks can be

successfully applied to express most classes of continuous functions with bounded inputs and outputs with any specified precision (Sharpe 1994).

In this paper, a neural network algorithm for optimizing the correlations between physical properties and processing parameters of multi-layered nonwovens to be manufactured at the different processing conditions was used and the optimum condition of these was derived from analytical results.

## 2 EXPERIMENTAL

### 2.1 Manufacturing of Geocomposites

Spunbonded(SB) nonwoven(18g/m<sup>2</sup>) of polypropylene filament(7d) and needle punched(NB) nonwoven (163g/m<sup>2</sup>) of polypropylene staple fiber (12d) were used as raw materials for geocomposites composed of multi-layered nonwovens. A special designed thermal bonding apparatus was used to bind geocomposites and the plate which are available to heat and press was adapted to thermal bonding apparatus.

#### 2.1.1 The processing conditions

Processing conditions of thermal bonding for manufacturing geocomposites composed of multi-layered nonwovens are as follows:

- (1) Temperatures: 180 ~ 190 °C (at 2 °C intervals)
- (2) Pressures: 4, 5, 6 kgf/m<sup>2</sup>
- (3) Times: 2, 3, 4 seconds

## 2.1.2 Types of geocomposites

The following types of geocomposites were manufactured at the above conditions:

- (1) NP-thermal bonded
- (2) NP/SB
- (3) NP/NP
- (4) SB/NP/SB

## 2.2 Physical Properties

Physical properties of multi-layered nonwovens were estimated in accordance with the following ASTM methods:

- (1) Tensile strength for MD (machine direction) and CD (cross direction)- ASTM D 4632-91
- (1) Tear strength - ASTM D 4533-91
- (2) Bursting strength - ASTM D 3786
- (3) Permittivity - ASTM D 4491-92

## 3 NEURAL NETWORK

In this paper, the feedforward back propagation algorithm is applied to model manufacturing process of non-woven materials. A basic multi-layer neural network structure is shown in Figure 1 depicting the hidden layer, and output layer.

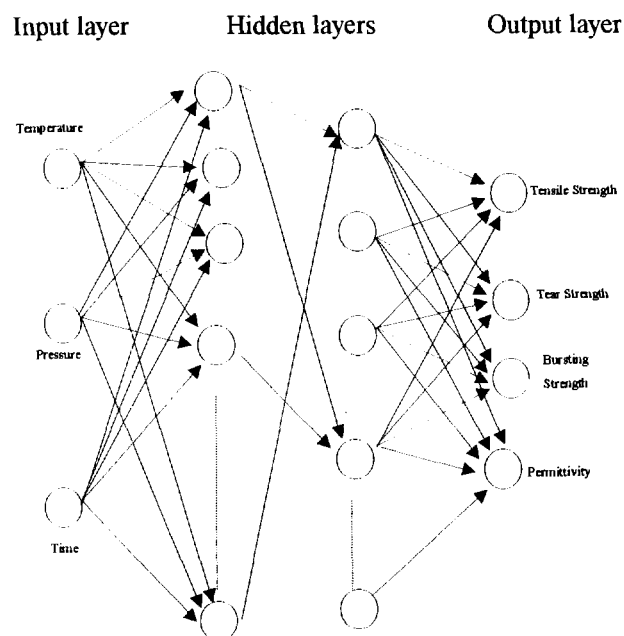


Figure 1. Architecture of a neural network having two layers.

This neural network has one input layer, one output layer, and any number of hidden layers. Each network consists of nodes (neurons). The input layer of the neural network takes information from the outside world and sends it to the nodes in the hidden layers. Similarly, the output layer of the neural network transmits the processed information to the external world.

To apply an  $m$ -variate signal input to a one-layer neural network consisting of  $n$  neurons each having  $m$  weights, we multiply an  $m$ -variate vector  $X$  ( $x_1, x_2, \dots, x_{m-1}, 1$ ) with the  $(n \times m)$ -variate weight matrix  $W$ . The result is an  $n$ -variate net input vector  $s$  ( $s_1, s_2, \dots, s_n$ ). Then, we can show how each component  $s_j$  is calculated for layer 1:

$$s_j = \sum_{i=1}^n w_{ji} v_i + b_j = w_j T \cdot v + b_j, j=1,2,\dots,k \quad (1)$$

The index  $j$  spans the  $n$  neurons, while  $i$  spans the  $m$  weights in the  $j$ th neuron. The number of weights in the neuron is one of more than the number of input variables,  $x_i$ ; the remaining one input variable is the bias, which is always equal to 1.

The quantity  $s_j$  is processed by an activation function to give the output  $o_j$  of the  $j$ th neuron:

$$o_j = f(s_j) \quad (2)$$

The input consists of process variables such as pressure, temperature and processing time. The network output are predicted values of physical properties at possible process conditions. The network training is performed using the nonlinear least square methods. The error at the output neuron can be defined as

$$E = \frac{1}{2} (t_k - o_k)^2 \quad (3)$$

where  $t_k$  is the target value of the output neuron. The backpropagation algorithms make use of the gradient descent methods for minimizing  $E$ . The error signal defined by

$$\delta_j = -\frac{\partial E}{\partial o_j} \quad (4)$$

leads to the result of general delta rule

$$\Delta w_{ji} = \eta \delta_j o_i \quad (5)$$

where  $\eta$  is an adaptation gain and  $\delta_j$  is computed based on whether or not neuron  $j$  is in the output layer. If neuron  $j$  is one of the output neurons, then

$$\delta_j = (t - o_j) o_j (1 - o_j) \quad (6)$$

On the other hand, if neuron is not in the output layer,

$$\delta_j = o_j (1 - o_j) \sum_i \delta_i w_{ji} \quad (7)$$

For a fast convergence, the momentum with gain  $\alpha$  will be introduced by following equation:

$$\Delta w_{ji}(k+1) = \eta \delta_j o_i + \alpha \Delta w_{ji}(k), \quad (8)$$

(, where k is the iteration step. )

#### 4 RESULTS AND DISCUSSION

The feedforward back propagation algorithm based on the generalized delta rule and the minimum mean squared error (MSE) principle were used for the data sets. In a feedforward network, the processing units can be divided into several layers: input layer, hidden layers and output layer. The input components consist of process variables such as pressure, temperature and processing time which are considered to be the important parameters. Outputs of the network are the predicted physical properties at the given process condition. The number of units in the hidden layers were set to be 16 following a series of optimization experiments. The networks have been used for training hundreds of experimental data sets, namely, pairs of process conditions and physical properties of different multi-layered nonwovens produced by varying the process conditions.

The prediction results are shown in Figures 2-5. As shown in the figures, several physical properties were predicted quite well with small errors. Figure 2 shows predicted permittivity at different process conditions. From this, it is known that a high permittivity value can be obtained when geocomposites are made at 180°C. Same tendency like this is observed for short processing time and lower temperature ranges. But in very high pressure and long processing time, the property is deteriorated significantly below unacceptable region. Figure 3 shows effect of process condition on tear strength of nonwovens. It was clearly seen that process time affects significantly the tear strength in such a way that longer process time enhances the tear strength over whole temperature regions investigated. But pressure effect is really negative, that is, high pressure caused the decrease of tear strength of nonwovens. Tensile strength difference and burst strength of geocomposites represented in Figure 4 and Figure 5, show the same tendency of the case of tear strength. In Figure 4, tensile strength difference between MD and CD doesn't depend on processing conditions except for 190°C. Using a simulation model, we tried to find some optimal process conditions which optimize several physical

properties in such a way that permittivity, tensile, tear strengths are maximized and tensile strength difference is minimized. From this, it is known that the optimum condition is found to be 182°C, 3sec and 4.9 kgf/cm<sup>2</sup>, respectively.

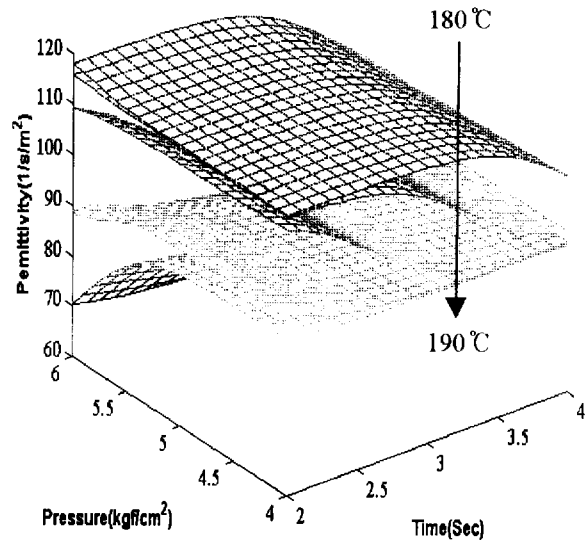


Figure 2. Prediction of permittivity using neural network.

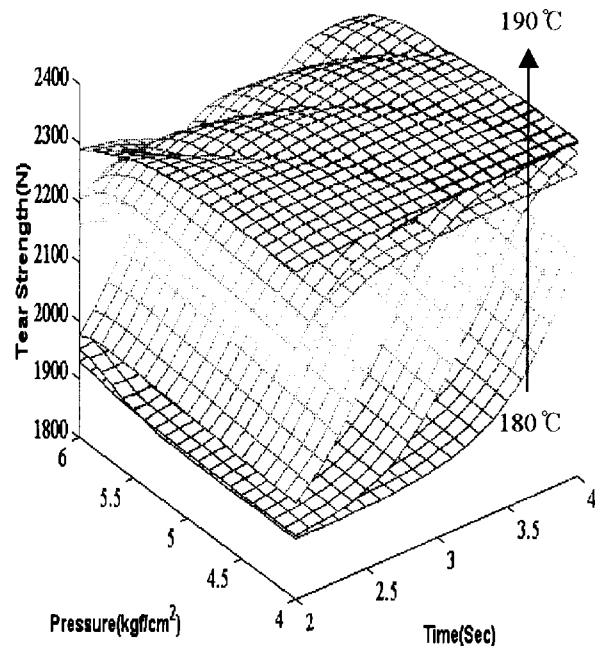


Figure 3. Prediction of tear strength using neural network.

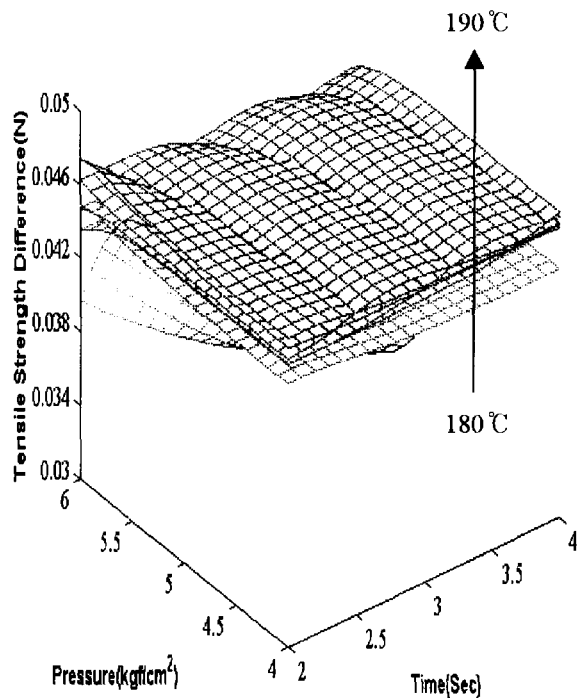


Figure 4. Prediction of tensile strength difference.

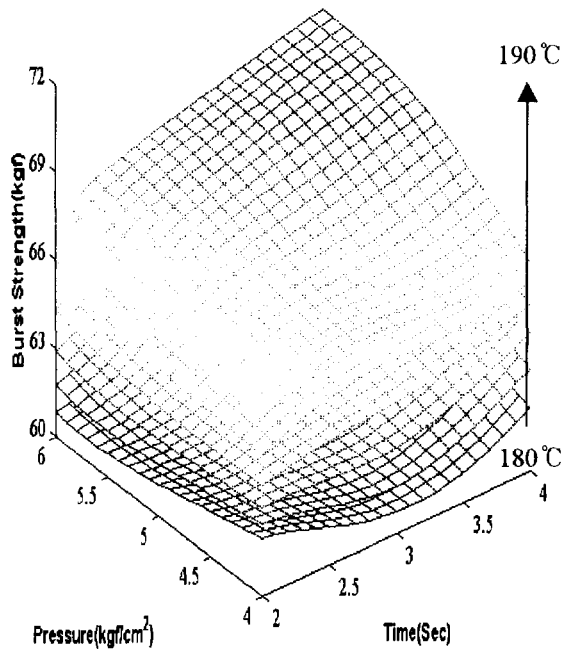


Figure 5. Prediction of burst strength using neural network.

The optimization analysis by neural network were used to examine the relations between processing parameters and physical properties of multi-layered nonwovens. Using this tool, we developed an algorithm for optimization of the geocomposite performances without a significant loss of physical properties. The simulated response surfaces were found to be highly effective in predicting the qualities of resulting geocomposites without actually producing them.

## REFERENCES

- Lünenschloss, J. and Albrecht, W. (1981) *Nonwoven Bonded Fabrics*, John & Sons, New York, pp. 178-313.
- Gourc, J.P., Faure, Y., Rollin, A., and LeFleaur, J. (1982) "Standard Tests of Permittivity and Application of Darcy's Formula", *Proc. 2nd Int. Conf. Geotextiles*, Las Vegas, NV, IFAI, Vol. 1, pp. 149-154.
- Masounave, J., Rollin, A., and Denis, R. (1981) "Prediction of Permeability of Nonwoven Geotextiles from Morphometry Analysis", *J. Microscopy*, 121 (1), pp. 99-110.
- Ingold, T.S. (1994) *The Geotextiles and Geomembranes Manual*, Elsevier Advanced Technology, Oxford, pp. 154-246.
- Koerner, R.M. (1994) *Designing with Geosynthetics*, Prentice Hall, Englewood Cliffs, pp. 67-327.
- ASTM Committee D-35 (1995) *ASTM Standards on Geosynthetics*, 4<sup>th</sup> ed.
- Booth, J.E. (1968) *Principle of Textile Testing*, London: Newnes-Butterworths Publ.
- Morton, W.E. and Heart, J.W. (1975) *Physical Properties of Textile Fibers*, New York: John Wiley & Sons.
- McGown, A., Andrawes, K.Z. and Kabir, M.H. (1982) "Load-Extension Testing of Geotextiles Confined in Soil." *Proc. 2nd Intl. Conf. Geotextiles*, Las Vegas, NV, IFAI, pp. 793-796.
- Bhat, N. and McAvoy, T.J. (1989) "Use of Neural Nets for Dynamic Modeling and Control of Chemical Process Systems", in *Proc. 1989 American Control Conf.* pp. 1342-1347.
- Hornik, K. (1989) "Multilayer Feedforward Networks are Universal Approximators", *Neural Networks*, vol.2, no. 5, pp. 359-366.
- Sharpe, R.N., Mo-yeun Chow, Brigg S. and Windingland L. (1994) "A Methodology Using Fuzzy Logic to Optimize Feedforward Artificial Neural Network Configurations", *IEEE Transactions on Systems, Man and Cybernetics*, Vol.24, No.5.
- Rustom, R., and Weggel, J. R. (1993) "A Study of Erosion Control System: Experimental Result", *Proc. Intl. Erosion Control Assoc.*, Indianapolis
- Theisen, M. S. (1992) "The Role of Geosynthetics in Erosion and Sediment Control: An Overview," *Journal of Geotextiles and Geomembranes*, Vol. 11

# Static and Cyclic Behaviour of Sand Reinforced by Mesh Elements

J.C. Morel

Research Scientist, Ecole Nationale des Travaux Publics de l'Etat, Lyons, France

J.P. Gourc,

Professor, Lirigm, University Joseph Fourier, Grenoble, France

**ABSTRACT:** The technique involving micro-reinforcement of sand by mesh elements is used for surface soil layers that are likely to be subjected to cyclic loading conditions. Based on the triaxial test, a comparative study of reinforced and non-reinforced sand is carried out. The behaviour of the sand is enhanced by the presence of the micro-reinforcement elements: under low cyclic loading, the reinforced soil has a higher elasticity; under high cyclic loading, the mesh elements take up the load and the compressive strength is improved.

**KEYWORDS:** Micro-reinforcement, Triaxial test, Cyclic loading.

## 1. INTRODUCTION

This research paper concerns the change in behaviour of a sand when it is reinforced with small polypropylene mesh elements with external dimensions of 100 mm x 50 mm. Each individual mesh is a 10 mm x 10 mm square. This type of reinforcement was designed by Mercer (Mercer et al., 1984) and optimised by Hytiris (Hytiris, 1986). The basic concept is the same as that of short-fibre reinforcement. However, the structure of the grid changes the implementation procedure and behaviour.

This type of reinforced sand has been the subject of a number of studies at the Lirigm, using the large shear box (Morel et al., 1997), and the biaxial compression test (Gourc et al., 1994, Morel et al., 1996) in plane strain conditions. The additional study presented here relates mainly to the behaviour of this material under cyclic compression using a triaxial testing apparatus.

Reinforced soils are reputed to have improved resistance to dynamic loading and fatigue compared to the same non-reinforced soils. Moreover, one of the main applications of this type of reinforcement concerns the surface layers subjected to repeated loading, for example as a result of traffic (this type of reinforcement can be used for unpaved roads). A comparative study of a sand with and without mesh elements would therefore seem to be of interest, especially as Lirigm was able to provide a high-performance triaxial test apparatus for cyclic loading.

Note that, in the case of the surface layer application, the reinforcing inclusions are required not only to improve the bearing capacity of the layer, but also to preserve its permeability, especially as this layer often serves as a draining layer. The compressibility under cyclic loading must therefore be reduced by the presence of the mesh elements.

## 2. EXPERIMENTAL CONDITIONS

The cyclic triaxial test apparatus at the Lirigm (Billet et al., 1990) can be used to test cylindrical samples of 70 mm diameter circular cross-section. The slenderness ratio (ratio of height to diameter) chosen here is equal to 1.9. The apparatus enables both the axial stress  $\sigma_1$  and the lateral stress  $\sigma_3$  to be cyclically slaved. During the tests described here, only  $\sigma_1$  will vary cyclically. The cyclic loading is sinusoidal with time (frequency of 0.5 Hz in this case). This apparatus has already been successfully used to study the liquefaction of geotextile-reinforced sand (Billet et al., 1994; Richa, 1992; Vercueil et al., 1997). The lateral confining stress is kept constant at 100 kPa in all the tests presented.

The sand used for these tests has already been studied on numerous occasions at the University of Grenoble. It is known as Hostun RF sand, a siliceous sand of mean diameter  $D_{50} = 0.35$  mm and uniformity coefficient  $C_u = 1.7$ . The grain density is  $\rho = 2.7$  Mg/m<sup>3</sup>.

Triaxial "static" compression tests were conducted for a unit weight value of 15 kN/m<sup>3</sup>, corresponding respectively to void ratios of  $e = 0.73$  and 0.66. All the "cyclic" compression tests were performed for  $e = 0.73$ , corresponding to a relative density  $D_r = 56\%$ .

The proportion of mesh elements added to the sand is characterised by the "reinforcement density,  $d_m$ " which, in %, is equal to the ratio of weight of mesh element with respect to the weight of the sand. It has been shown elsewhere (Gourc et al., 1994), that  $d_m = 0.4\%$  was the reinforcement density providing the best compromise between:

- the favourable effect of the increase in number of mesh elements, implying a greater quantity of mesh elements

subjected to tensile stress and thus improved overall strength of the reinforced soil.

- the unfavourable effect of the increase in number of mesh elements, involving disarrangement of the sand grains and thus a reduction in sand strength.

All the tests presented are for a value of  $d_m = 0.4\%$ . The sand - mesh elements mixture is made after having moistened the sand (sand water content  $w = 10\%$ ) in order to obtain isotropic distribution of the inclusions. To make allowance for the scale of the test sample, the meshes are cut into 50 mm x 25 mm elements, without any asperities to avoid piercing the test sample membrane.

### 3. BIAXIAL TRIAXIAL COMPARISON (STATIC)

The Lirigm biaxial compression prototype testing apparatus can be used to perform tests in plane strain state (Gourc et al., 1994) but, with its present set-up, it cannot be used for cyclic compression tests. As a previous publication by the same authors described a study of mesh-element reinforcement based essentially on the biaxial apparatus, it seemed of interest to compare triaxial test results with biaxial test results, under the same "static" compression conditions. The test sample for the biaxial test was 340 mm long in the main vertical compression direction, 150 mm wide and 60 mm thick. Another experimental difference is that the biaxial test samples have lubrication on the ends whereas the triaxial samples do not.

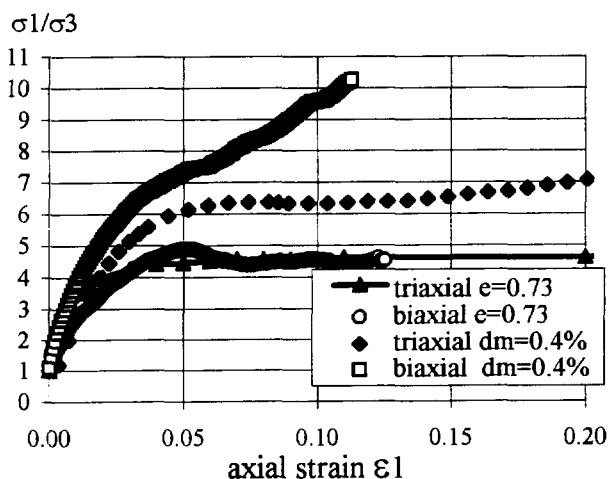


Figure 1 : Comparison of « static » tests, triaxial and biaxial tests

Lee (1970) and subsequently other authors showed on a non-reinforced sand that the angle of friction in the biaxial test is greater than the angle of friction in the triaxial test. This fact is confirmed by the tests described here.

Figure 1 compares the results obtained at Lirigm for a non-reinforced or reinforced ( $d_m = 0.4\%$ ) sand, presenting conventionally  $\sigma_1/\sigma_3$  as a function of axial strain  $\epsilon_1$ . The test is performed for an axial compression rate of 2 mm/min. In actual fact, this presentation can be justified

only in the small strain range. For large strains, localised failure occurs and the mechanism involved is a block-on-block sliding mechanism (Desrues et al., 1985), as shown on photo 1 for a reinforced sand sample at the end of the test. In such cases it is more proper to present  $\sigma_1/\sigma_3$  as a function of axial displacement: the curves obtained in biaxial and triaxial tests have much closer slopes in the large strain domain.

Generally speaking, the ductility of reinforced sand is clearly apparent. For the large strains reached, very few of the mesh elements had failed.

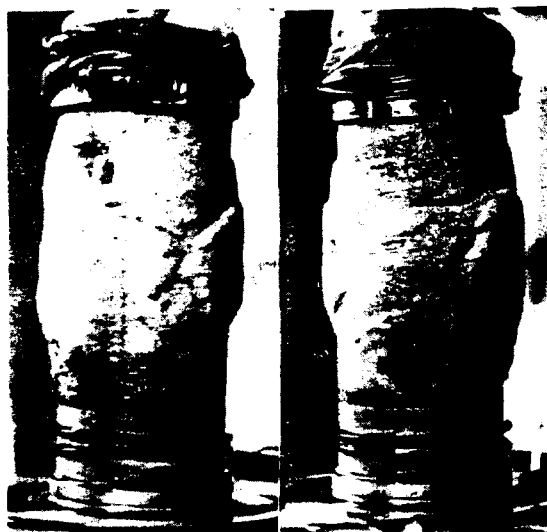


Photo 1 : Reinforced sand sample after failure at a « static » triaxial test.

### 4. BEHAVIOUR UNDER CYCLIC LOADING

The test procedure is similar in all cases:

- the confining pressure is kept constant (100 kPa),
- the first stage of the test ("static") corresponds to an increase in the deviatoric stress ( $\sigma_1 - \sigma_3$ ) of 200 kPa/min.
- the second stage of the test corresponds to 500 cycles of 0.5 Hz frequency and 100 kPa amplitude from the initial value of the pre-defined deviatoric stress,
- the third stage of the test ("static") corresponds to the continued crushing of the test sample at a vertical displacement rate of 9.6 mm/min.

Figure 2 shows the change in axial settlement of the test sample during the cyclic loading stage, for three initial values of the deviatoric stress : 100 kPa, 200 kPa and 500 kPa. The behaviour of non-reinforced and reinforced sand is compared, except for the 500 kPa initial deviatoric stress because the non-reinforced sand failed for a deviatoric stress of 350 kPa under "static" conditions.

- ♦ Settlement on initial loading ( $N = 1$ ) systematically reaches a greater value for the non-reinforced sand.
- ♦ The increase in vertical displacement with the number of cycles is also systematically higher for the non-reinforced sand.



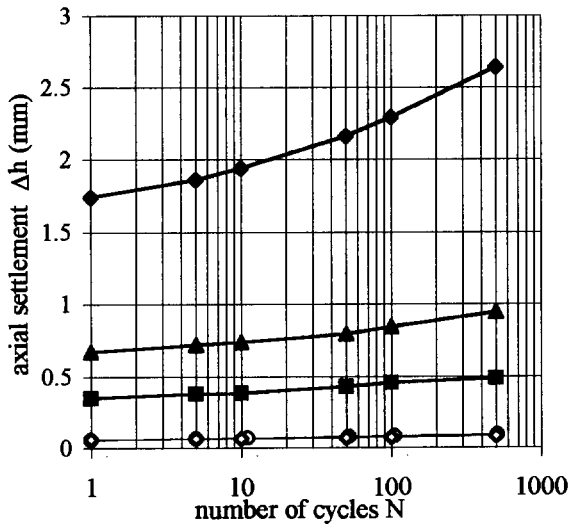
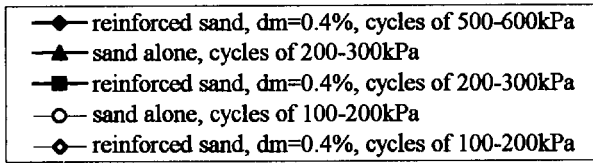


Figure 2: Cyclic loading stage: variation in vertical displacements as a function of number of cycles.

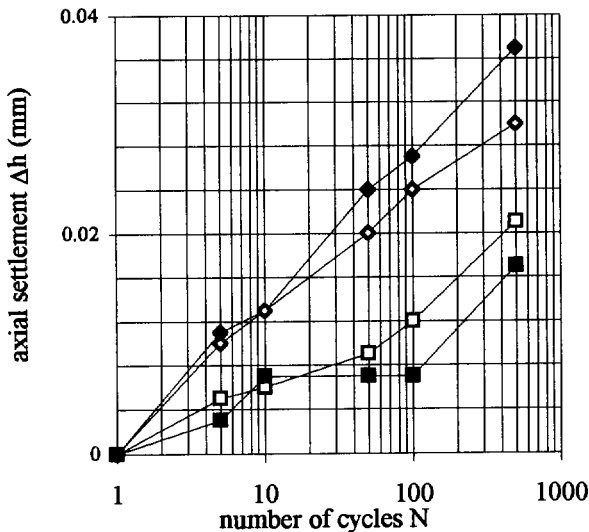
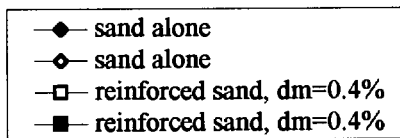


Figure 3: Cyclic loading stage (0-100kPa): variation in vertical displacements as a function of number of cycles, as from an initial loading of 100kPa

- ◆ A soil is generally considered to show acceptable behaviour under cyclic loading if the relationship between vertical displacement and log N is linear. In this case, it was found that this law is not obeyed for the non-reinforced sand (200-300 kPa) nor for the

reinforced sand (500-600 kPa). The samples show a clear deviation from elastic behaviour.

The cyclic loading domain (0-100 kPa) is interesting because it corresponds to a possible range of use (surface layer) of this type of reinforcement. Both the reinforced sand and the non-reinforced sand are a long way from their failure state. Figure 3 adopts the same presentation as figure 2, except that the displacement under initial loading (N = 1) is not taken into account. The displacement scale is obviously different from that in figure 2. Two tests performed under the identical conditions are presented on the same graph, thereby showing the good repeatability of this relatively difficult type of test.

Vertical displacement for the reinforced sand is halved but, more surprisingly, the variation is no longer linear for values of N greater than 100 cycles.

### 5. INFLUENCE OF CYCLIC LOADING ON STATIC BEHAVIOUR

Figure 4 compares the behaviour of non-reinforced and reinforced test samples under triaxial compression with and without transient cyclic loading of 500 cycles between 200 and 300 kPa: for the reinforced sand, it is found that the test curves with or without transient cyclic loading coincide after the cyclic loading stage as if the material had somehow "forgotten" its loading history.

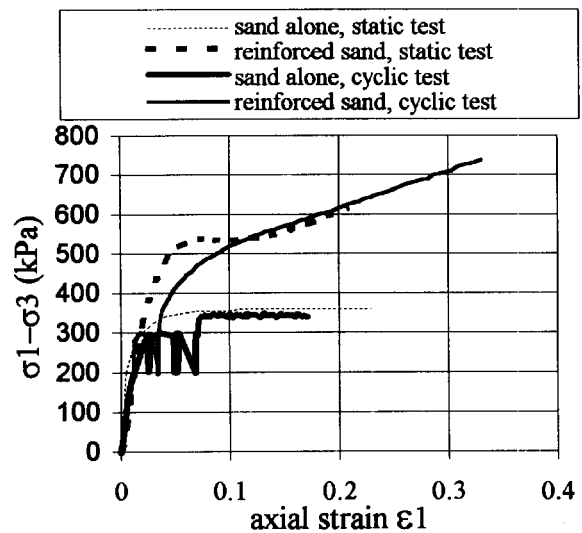


Figure 4: Comparative overall behaviour with and without transient cyclic loading (500 cycles) for reinforced or non-reinforced sand.

Figure 5 concerns only the reinforced sand and it is found that, contrary to the previous case, the cycles (500-600 kPa) well beyond the strength limit of the non-reinforced sand, have an effect on the post-cycle strength: the strength of the sand is increased through cyclic loading which has no doubt contributed to the mesh elements taking up the tensile stress. In a real-life situation, this could doubtless be obtained by controlled compacting.

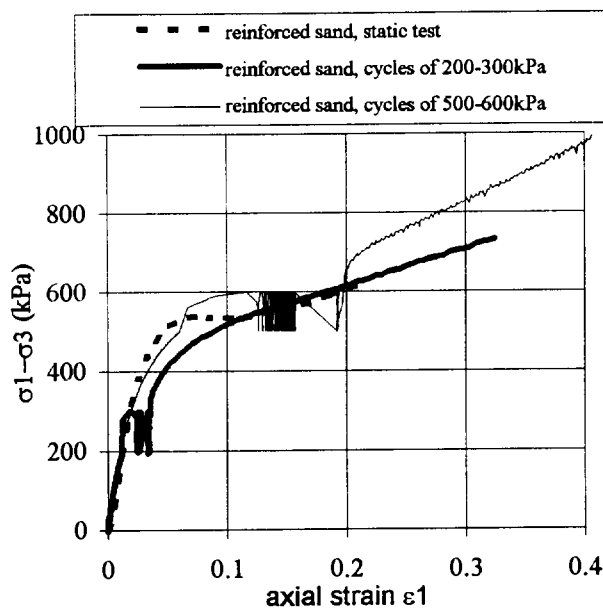


Figure 5: Comparative overall behaviour with and without transient cyclic loading (500 cycles) for reinforced sand.

## 6. INFLUENCE OF MESH-ELEMENT ORIENTATION

In the triaxial compression test, the direction of maximum strain is horizontal. The preferential orientation of the reinforcing inclusions should increase their efficiency. To verify this, a series of tests was conducted (fig. 6) in which the mesh elements are no longer placed randomly but in regularly spaced horizontal layers. In this case as well, the behaviour was compared for cases with and without cyclic loading. The reinforcement density ( $d_m = 0.4\%$ ) is the same for the mesh elements oriented horizontally or randomly.

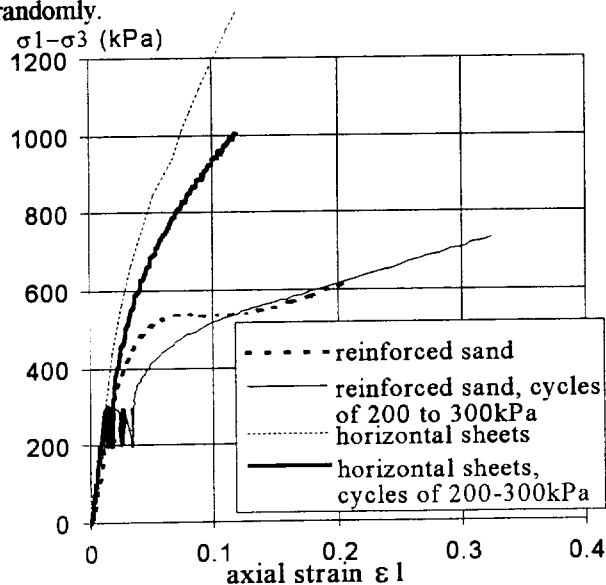


Figure 6: Comparative overall behaviour with and without transient cyclic loading (500 cycles) for horizontally or randomly reinforced sand.

For a given axial strain  $\epsilon_1$ , the deviatoric stress is notably higher for the sample with mesh elements arranged horizontally. The strain values obtained under cyclic loading conditions are also much lower for horizontal mesh elements. However, the tests were not continued long enough to obtain sufficient strain values to achieve a possible coincidence of the curves corresponding to the tests with or without cyclic loading.

## 7. CONCLUSIONS

Triaxial compression tests under cyclic loading conditions were undertaken and show that reinforcement using mesh elements is a high-performance method, not only under "static" loading but also under "cyclic" loading conditions. These observations should be used to improve their implementation procedures (pretensioning on compaction) and to find new applications.

## 8. REFERENCES

- Billet, P., Cordary, D., Gourc, J.P. (1990) "Compression biaxiale d'un composite sol-géotextile", *Symposium Textile Composites in Building Construction*, Lyon, pp. 215-227
- Billet, P., Cordary, D., Richa, B. (1994) "Laboratory study of sand liquefaction by the insertion of geosynthetics", *5th Int. Conference on Geosynthetics*, Singapore, pp. 537-540
- Desrues, J., Lanier, J., Stutz, P. (1985) "Localization of the deformation in tests on sand sample", *Engineering Fracture Mechanics*, Vol. 21, pp. 909-921
- Gourc, J.P., Morel, J.C. (1994) "Biaxial compression test on soil micro-reinforced by mesh-elements", *5th Int. Conference on Geosynthetics*, Singapore, pp. 365-368
- Hytiris, N. (1986) "A new method of soil stabilization", *P.h.d.*, University of strathclyde, Scotland
- Lee, K.L. (1970) "Comparison of plane strain and triaxial test on sand", *Journal of Soil Mechanics, ASCE*, May, pp. 901-921
- Mercer, F.B., Andrawes, K.Z., Mc Gown, A., Hytiris, N. (1984) "A new method of soil stabilization", *Symposium on Polymer grid reinforcement in civil engineering*, London, paper 8-1
- Morel, J.C., Gourc, J.P. (1996) "Reinforced soil failure : Analysis at the biaxial compression test", *Int. Symposium on Earth Reinforcement*, Balkema, Fukuoka, pp. 111-116
- Morel, J.C., Gourc, J.P. (1997) "Mechanical behaviour of sand reinforced by mesh elements", *Geosynthetics International*, Vol. 4, N° 5
- Richa, B. (1992) "Étude au triaxial dynamique de la liquefaction des sols renforcés par géotextiles", *Thesis Dr University J.F. Grenoble*
- Vercueil, D., Billet, P., Cordary, D. (1997) "Study of the liquefaction resistance of a saturated sand reinforced with geosynthetics", *Soil dynamics and earthquake engineering Journal*, (in press)

# Stabilization of Earth Slopes with Fiber Reinforcement

Garry H. Gregory

Vice President - Senior Geotechnical Consultant, Fugro South, Inc., Fort Worth, Texas, USA

David S. Chill

Business Manager – Geofibers Business Unit, Synthetic Industries, Inc., Chattanooga, Tennessee, USA

**ABSTRACT:** The use of fiber reinforcement (geofibers) for stabilization of earth slopes was investigated by laboratory testing of non-reinforced and fiber-reinforced clay soils in the direct shear and triaxial shear apparatus. Fiber contents included 0.2 and 0.25 percent by dry weight for this study. The test results show increases in maximum shear stress ( $\tau'$ ) at failure in the range of 20 to 50 percent for the fiber-reinforced specimens. Slope stability analyses were performed for a highway interchange embankment in Beaumont, Texas, USA, which had experienced repeated slope failures. The stability analyses produced an increase in calculated factor of safety from essentially one (imminent failure) for the non-reinforced case, to above 1.5 for the fiber-reinforced case. The slope was repaired with fiber-reinforced soil at a dosage rate of 0.25 percent, and has performed well to date.

**KEYWORDS:** Geofibers, Micro-reinforcement, Slope Stabilization, Earth slopes, Factor of Safety

## 1 INTRODUCTION

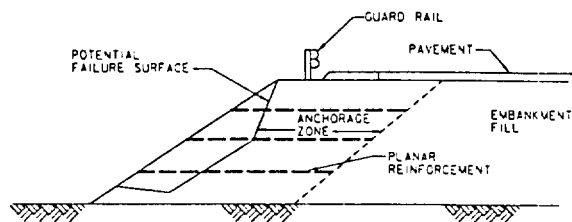
The use of geofibers for earth slope reinforcement has attracted significant interest in the past five years. Geofibers consist of relatively small fiber inclusions, distributed as an additive throughout the soil mass in the reinforced zone. Accordingly, the geofibers may be categorized as micro-reinforcement. Planar or continuous-sheet reinforcement elements, such as geotextiles and geogrids, are placed at discrete locations (usually horizontally) within the soil mass, with non-reinforced soil intervals between. Planar materials may be categorized as macro-reinforcement. Geosynthetic macro-reinforcement materials provide an effective solution to a wide variety of slope reinforcement problems, but have limitations in applications where the required anchorage zone is not available due to obstructions, as illustrated in Figures 1(a) and 1(b). Micro-reinforcement materials do not have these limitations since they reinforce the entire soil mass as a soil additive. The large anchorage zone is not required, and it is only necessary to extend the fiber-reinforced zone approximately 0.3 to 0.6 meters beyond the critical failure surface as illustrated in Figure 1(c). Therefore, micro-reinforcement geofibers can provide ideal solutions to slope stability conditions which previously were not practical with geosynthetics. The geofibers used in this study consisted of fibrillated polypropylene (FIBERGRIDS<sup>®</sup>, Synthetic Industries, Chattanooga, Tennessee, USA) in nominal 25 mm and 50 mm lengths.

## 2 BEAUMONT SLOPE

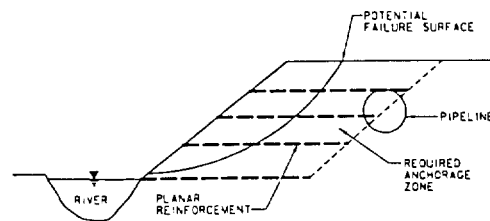
### 2.1 Project Description

The highway interchange embankment (Beaumont slope) is located at the intersection of U.S. Highway 69 and F.M. 347 in Beaumont, Texas, USA. The embankment is approximately 6 m in height at the tallest section, and has a slope ratio of 2.5 horizontal to 1 vertical (2.5H:1V) at the steepest section.

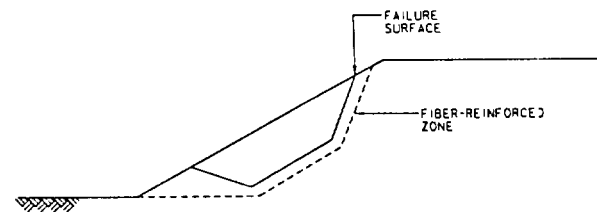
The fill soil in the slopes consists of a brown clay with some sand, gravel, and shells. The embankment soil has a liquid limit of 50, and a plastic limit of 17, with 68 percent passing the US No. 200 sieve. The material classifies as fat clay (CH), in accordance with ASTM D 2487. The



(a) anchorage-zone limitations from highway obstructions



(b) anchorage-zone limitations from pipeline obstructions



(c) large anchorage zone not required for geofibers

Figure 1. Anchorage-zone limitations of planar reinforcement compared to reinforced zone for geofibers.

embankment slopes on the northeast and northwest quadrants of this intersection had experienced repeated slope failures over the years. The failure-surface geometry typically consisted of a near-vertical scarp near the slope crest, a central failure surface about 1.5 to 2 m deep parallel to the slope, with an exit point about 1 to 1.5 m above the toe. These failures were typically repaired by excavating the failed areas and recompacting the same soil back into the

slope without the use of soil additives or reinforcement. In the fall of 1995 both the northeast and northwest slopes had failed again. The northeast slope was repaired as previously described, without reinforcement or additives. The northwest slope was repaired with geofibers reinforcement. The laboratory testing program, slope stability analyses, and slope repair details are presented in subsequent sections.

## 2.2 Conceptual Model

A conceptual model was developed of the slope failure mechanism for use in planning the laboratory testing program and slope stability analyses. Embankment slopes of clay soils, with height ranges of 6 to 10 m and slope ratios in the range of 2.5H:1V to 3H:1V, often experience shallow failures within a few years after construction. The compacted soils initially have relatively high shear strength values throughout, and may have a significant level of preconsolidation stress induced by the compaction process.

Slope stability analyses using the "as compacted" shear strength properties do not predict the shallow failures. From these analyses, it is apparent that the initial as-compacted shear strengths deteriorate with time in the shallow zone. The strength loss is caused by a number of factors such as desiccation, shrink-swell, water infiltration, and down-hill creep. The principal author has investigated a large number of shallow slope failures in clay soils. The loss of shear strength is not uniform throughout the shallow zone. Three distinct soil zones are usually present, consisting of a weak zone along the failure surface, a weathered zone above the failure surface, and the relatively undisturbed zone below the failure surface. The actual failure surface may be less than 10 mm thick in many cases. The material in the thin failure zone is usually of a soft, paste-like consistency, with a high moisture content. This zone has obviously lost the preconsolidation stress induced during the compaction process, and has degraded to a normally-consolidated condition at the shallow overburden pressure. Consequently, under effective-stress conditions, the soil in the failure zone will have  $c' = 0$ . The principal author has found similar thin, paste-like weak zones paralleling the surface at depths of about 1.5 to 2 m in adjacent embankments which had not experienced slope failures, but which later failed. Accordingly, it is believed that the weak normally-consolidated zone is created prior to actual failure by the weathering processes previously discussed, and by stress concentrations at the base of the weathered zone due to down-hill creep. The weathered soil in the zone above the failure surface generally contains many desiccation cracks and secondary weathering features, and the soil mass in this zone has a substantially lower shear strength than when initially compacted. However, this zone may still retain some long-term cohesion, and will exhibit a higher mass shear strength than the failure zone. The embankment soil below the failure surface in the deeper zone may remain relatively undisturbed and retain most or all of its initial shear strength. The laboratory testing program and slope stability analyses were performed in a manner consistent with the three distinct soil zones.

## 3 LABORATORY TESTING PROGRAM

### 3.1 Sample Preparation and Testing

The laboratory testing program included non-reinforced (control) and fiber-reinforced soil specimens. The direct shear tests were performed as consolidated-drained (CD)

tests, and included nominal 100-mm and 300-mm square specimens, and the ICU triaxial tests were performed on nominal 70 mm-diameter by 150 mm-length specimens. The direct shear tests included specimens prepared by standard compaction methods (95 percent ASTM D 698), and slurry-processed normally-consolidated (SPNC) specimens. All triaxial tests for this study were performed on specimens prepared by standard compaction methods. A consolidation test was also performed on a compacted specimen of the Beaumont clay, to determine the preconsolidation stress induced by the compaction process. The preconsolidation value was used in interpreting the direct shear test results.

The SPNC specimens were prepared by blending the soil in a mixer with sufficient water to form a thick slurry. The slurry was then partially consolidated in a 150-mm diameter CBR apparatus under approximately 70 percent of the normal stress to be used in the direct shear device. Following a consolidation period of about 24 hours, the sample reached a thick paste-like consistency, at which time it was removed from the CBR apparatus and trimmed into a 100-mm square shear box for testing. The remainder of the consolidation stage was completed in the direct shear machine, with the final consolidation stress equal to the normal stress to be used during the shear test. The normal stress range was selected to represent conditions along the actual failure surface in the slope. This procedure assured that the specimen would be normally consolidated during the test, to model the condition along the actual failure surface. Standard-compaction specimens were prepared using a controlled weight-volume relationship and static compaction techniques. The reinforced specimens were prepared by mixing the fibers and soil in a heavy-duty 19-liter mixer. Detailed descriptions of the sample preparation methods are available in a design guide for fiber-reinforced slopes (Gregory 1996).

### 3.2 Test Results

A total of 86 direct shear specimens and 32 triaxial shear specimens of clay soils were tested for this study. Twenty-one of the direct shear specimens were tested in the 300 mm square shear device, and the remainder were tested in the 100 mm square shear device. Twenty of the direct shear specimens and 12 of the triaxial shear specimens were performed for the Beaumont slope project. The remainder of the tests were performed for other slope projects or for research purposes.

Direct shear test results performed on 12 specimens of the Beaumont clay are presented on shear stress-normal stress plots in Figure 2. These tests were performed in a 100 mm square by 30 mm deep shear box. The geofibers were 25 mm in length for the reinforced specimens. The strain rate was 0.0076 mm/minute for all direct shear tests.

Figure 2 contains results for 8 specimens prepared with standard compaction methods. Figure 2 (a) was plotted using a bilinear fit. The first three points on each envelope have normal stress values below the preconsolidation stress induced by compaction ( $P_{cc}$ ), and the fourth point is above the  $P_{cc}$  value. Clay soils during shearing, with normal stresses below the preconsolidation stress, may exhibit significant effective cohesion ( $c'$ ), while those with normal stress values above the preconsolidation value exhibit  $c' = 0$  (Gregory and Doane, 1996). Accordingly, the strength envelopes in Figure 2(a) were fit with a bilinear line to obtain shear strength parameters in both the preconsolidated and normally consolidated (NC) ranges of normal stress. The test results show an increase of approximately 35 percent in  $c'$  for the reinforced specimens compared to the non-reinforced.

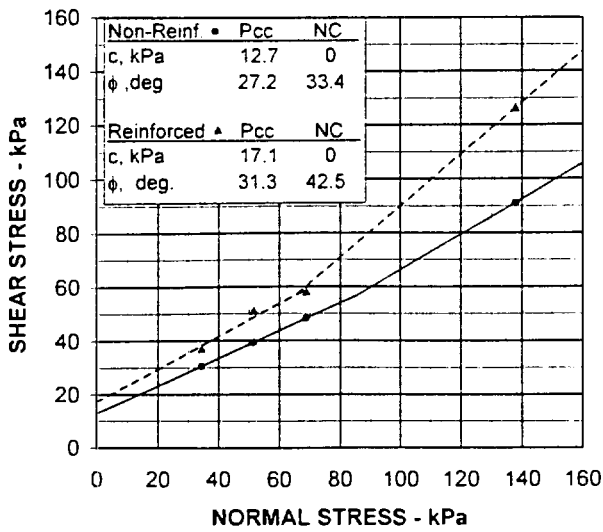
Increases in  $\phi'$  were 15 and 27 percent, respectively, for the preconsolidated and NC ranges of normal stress.

Figure 2(b) contains results performed on 6 specimens prepared by SPNC methods. The results in this figure were plotted with a linear fit since all specimens were normally consolidated during the tests. These results show an increase in  $\phi'$  of 33 percent for the reinforced specimens compared to the non-reinforced. Triaxial shear test results performed on 6 specimens of the Beaumont clay are presented in Figure 3. These specimens were prepared using standard compaction methods, and were performed as ICU tests, with pore-pressure measurements. A strain rate of 0.015 mm/minute was used for these tests.

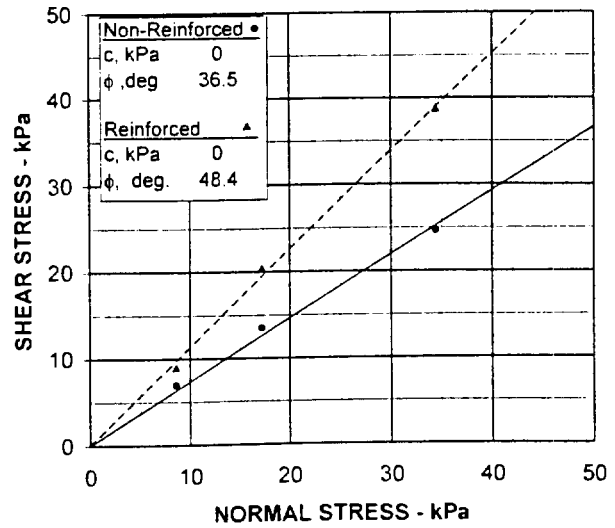
Figure 3(a) contains the results of three non-reinforced specimens plotted on a mohr-coulomb shear stress-normal stress diagram. Figure 3(b) contains the results of three specimens reinforced with 0.25 percent, 25 mm-long fibers. The test results on the specimens reinforced with 25 mm-long fibers in Figure 3(b) show an increase in  $\phi'$  of 16.5 percent, and an increase in  $c'$  of 8.5 percent, when compared to the control test results.

Four mechanisms are believed to be involved in the increased shear strength of fiber-reinforced soil. These mechanisms are : (1) friction between individual fibers and the surrounding soil, (2) adhesion between individual fibers and the surrounding soil, in soils exhibiting significant cohesion properties, (3) micro-bearing capacity of the soil mobilized during pull-out resistance of looped fibers crossing the shear plane, and (4) increased localized normal stress in the soil across the shear surface resulting from the pull-out resistance of the fibers during shearing of the soil. The individual interaction and contribution of these mechanisms to the apparent increase in shear strength is complex and difficult to determine accurately. However, the combined effects, including any synergistic effects, is relatively easy to determine by conducting shear strength tests on both non-reinforced and reinforced specimens, as was performed for this study.

A summary of average direct shear and triaxial shear test results from all specimens tested during this study is presented in Table 1.

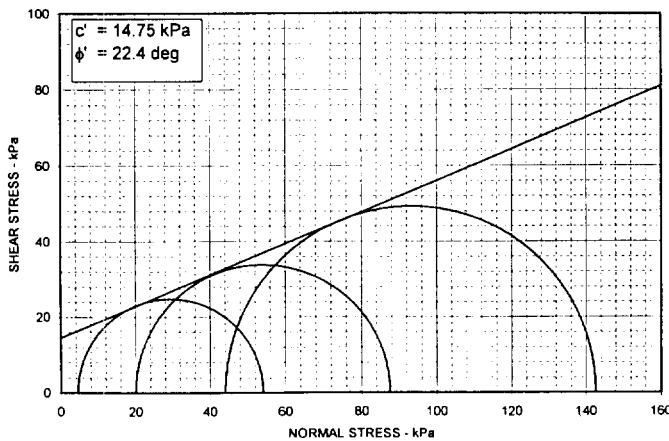


(a) Standard Compaction

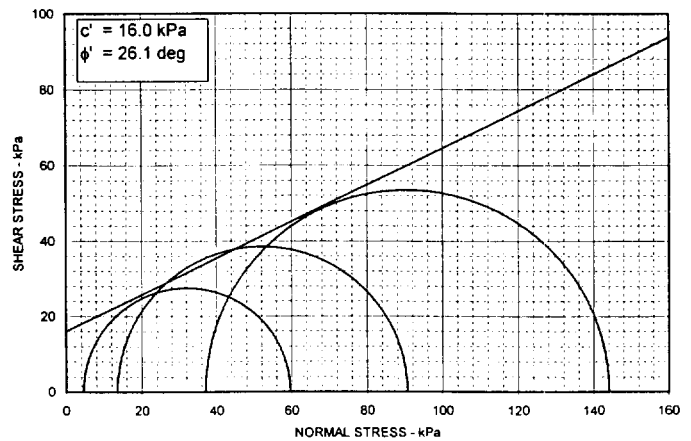


(b) SPNC Preparation

Figure 2. Direct shear test results on 100 mm Specimens.



(a) Non-reinforced Specimens



(b) Reinforced Specimens

Figure 3. Triaxial test results on 70mm diameter specimens.

Table 1. Summary of Direct Shear and Triaxial Shear Test Results (Average values, including 0.2 and 0.25 % fibers)

Test Description	Number of Specimens	$\phi'$ (Deg.)	$c'$ (kPa)
Direct Shear – 100mm Non-Reinforced	25	32.6	6.6
Direct Shear – 100mm Reinforced – 25mm Fibers	40	38.0	10.0
Direct Shear – 300mm Non-Reinforced	6	27.7	3.1
Direct Shear – 300mm Reinforced – 25mm Fibers	9	27.3	6.7
Direct Shear – 300mm Reinforced – 50mm Fibers	6	22.8	9.5
Triaxial Shear Non-Reinforced	9	22.0	14.8
Triaxial Shear Reinforced – 25mm Fibers	16	24.4	15.9
Triaxial Shear Reinforced – 50mm Fibers	7	30.8	15.4

It should be understood that the results in Table 1 are average values, based upon a range of fat clay (CH) and lean clay (CL) soils tested for this study. The averages for the direct shear tests in the 100mm device show increases of approximately 17 percent and 52 percent in  $\phi'$  and  $c'$ , respectively, for the reinforced specimens. The averages for the direct shear tests in the 300mm device show essentially the same  $\phi'$  values, and an increase in  $c'$  values of 116 percent for the specimens reinforced with 25mm fibers. The average results from the 300mm direct shear device also show a decrease of 21 percent in  $\phi'$  values and an increase of 206 percent in  $c'$  values for the specimens reinforced with 50mm fibers. The triaxial shear test average results show an increase in  $\phi'$  values of 11 percent and an increase in  $c'$  values of 7 percent for the specimens reinforced with 25mm fibers. The average triaxial results with the 50mm fibers show an increase of 40 percent in  $\phi'$  values, and an increase of 4 percent in  $c'$  values. In all cases where one shear strength parameter increased only a small amount or decreased slightly, the other parameter increased by a relatively large amount. Averaging the results in Table 1 for all clay types tested resulted in considerably more scatter than was observed for each individual soil type tested.

## 4 SLOPE STABILITY ANALYSES

### 4.1 Slope Geometry

The geometry of the existing slope, slide geometry, and subsurface stratigraphy were obtained from observations and measurements in the field, and from existing data and a new soil boring provided by the Texas Department of Transportation (TxDOT).

### 4.2 Soil Parameters

The soil parameters were obtained from the laboratory test results, adjusted in accordance with local practice. The unit weight values for the in situ soils were obtained from thin-wall tube samples taken from the boring. The unit weight values of the compacted soils were taken as 95 percent of maximum density as determined by ASTM D 698. Soil shear-strength parameters selected for the analyses are presented in Table 2. The labels and soil type numbers match those on the graphical output sheets from the

computer analyses, presented in subsequent sections. The unit weight values are not included in Table 2, in order to conserve space. Unit weight values of 18.9 and 20.9 KN/m<sup>3</sup> were used for moist and saturated unit weights, respectively.

### 4.3 Analysis Methodology

Slope stability analyses of the Beaumont slope were performed using the computer program GSTABL7, an enhanced version of PCSTABL6 (Humphrey and Holtz, 1986), modified by the principal author. The limit equilibrium method, using a sliding-block search routine and the Modified Janbu method (Janbu 1954, 1973), was used in the analyses.

Table 2. Soil Parameters Selected for the Stability Analyses  
Analysis of Initial Failure (Non-Reinforced)

Label	Soil type No.	$c'$ (kPa)	$\phi'$ (Degrees)
Surface-CH clay	1	9.3	24
Shoulder-CH clay	2	9.3	24
Weak-CH clay (failure surface)	3	0.0	32
Fill-CH clay	4	11.1	24
Base-CH clay	5	11.1	24
Deep-CH clay	6	11.1	24
<u>Analysis of Repaired Slope (Fiber-Reinforced)</u>			
Surface-CH clay	1	10.2	24
Shoulder-CH clay	2	10.2	24
Weak-CH clay (failure surface)	3	0.0	42
Fill-CH clay	4	11.1	24
Base-CH clay	5	11.1	24
Deep-CH clay	6	11.1	24

The shear strength of the failure surface zone (Weak-CH clay) was obtained from the direct shear test results on the SPNC specimens. The shear strength of the undisturbed embankment fill (Fill-CH clay) below the failure surface and in the protected shoulder of the roadway was obtained from the direct shear test results on the specimens prepared with standard compaction methods. In accordance with local practice and experience with similar soils, the  $\phi'$  and  $c'$  values obtained in the tests were reduced by approximately 12 percent for use in the analyses, to account for uncertainties in stratigraphic distribution and construction quality control.

The shear strength of the surficial soil in the weathered zone (Surface-CH clay) above the failure surface cannot be obtained readily with laboratory tests. Samples taken from this zone will not be representative of the desiccation cracks and secondary weathering features throughout the soil mass. However, the apparent shear strength of the weathered zone may be obtained by computer analyses, using the known data.

The shear strength values of the failure-surface and undisturbed-fill zones are known from laboratory test results. The geometry of the failure surface is known from observations and measurements in the field, following failure. It is also known that the stability factor of safety (resisting forces and moments divided by the driving forces and moments) for the slope at the time of failure was one or slightly below one. Therefore, stability analyses of the failed slope can be performed with the known shear strengths of the failure-surface and undisturbed fill zones, and an initial estimate of the mass shear strength parameters in the weathered zone. An iterative analysis can then be performed by changing the estimated shear strength

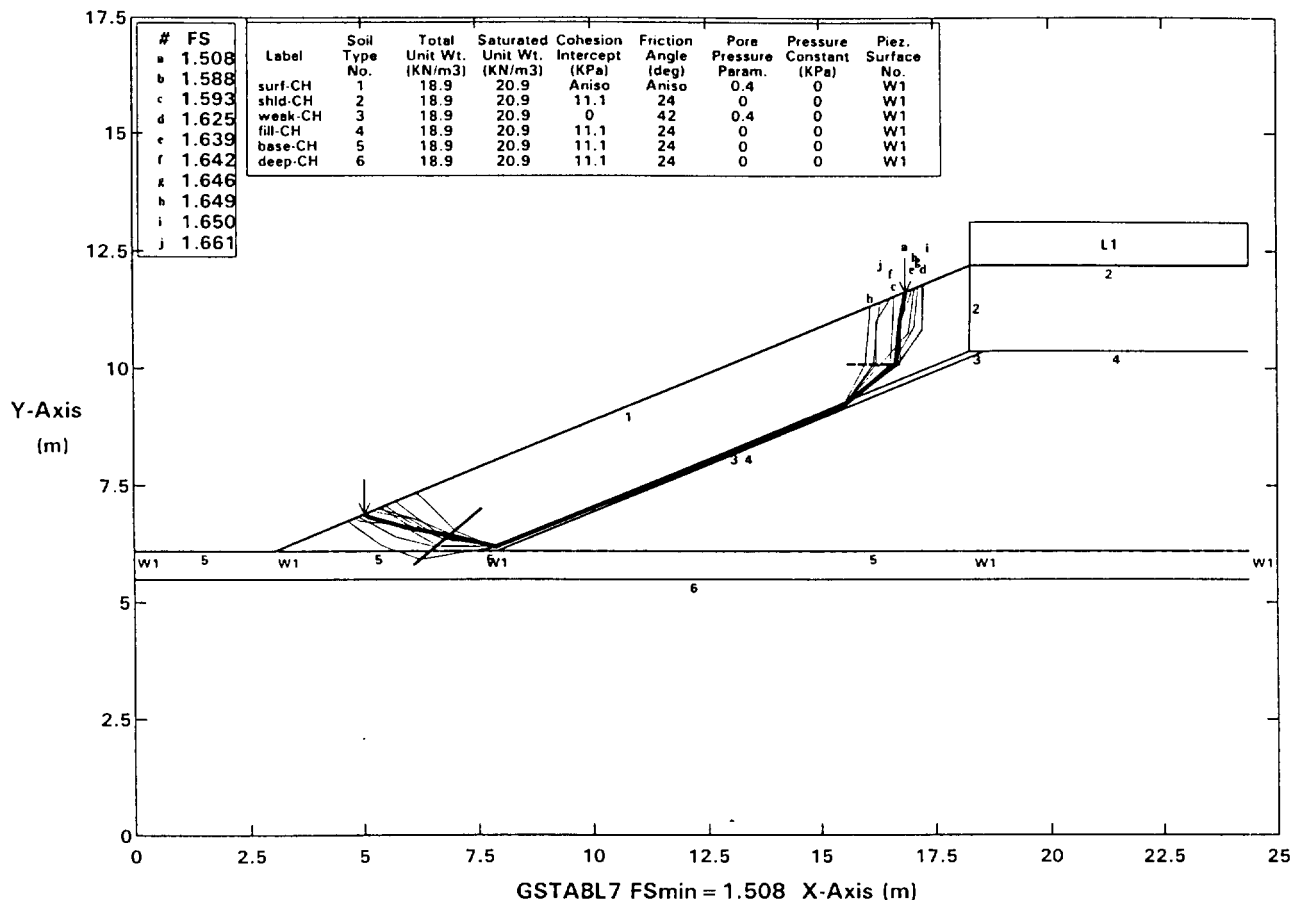


Figure 4. Graphical Computer output for the fiber-reinforced slope analysis.

parameters in each successive run until the calculated factor of safety converges to one or slightly below one. The changes in strength parameters can generally be applied uniformly to both  $\phi'$  and  $c'$ . It has been found from experience that a good initial estimate of the shear strength parameters for the weathered zone is approximately 50 percent of those of the undisturbed fill zone.

The mass shear strength of the fiber-reinforced weathered zone may be determined as follows. Assume that the ratio of the shear strength of the reinforced weathered zone to the shear strength of the fiber-reinforced laboratory specimens, is the same as the ratio of the shear strength of the non-reinforced weathered zone to the shear strength of the non-reinforced laboratory specimens. The shear strength of the non-reinforced weathered zone to be used in the ratio comparisons is the value determined in the iterative analyses discussed previously. This approach provides rational values of shear strength parameters in all soil zones, for both the initial failure condition and fiber-reinforced slope condition.

The stability analyses were performed using the sliding-block search routine by forcing the trial failure surfaces to pass through the failure zone parallel to the slope, while allowing the trial surfaces to exit near the upper and lower ends of the slope in a more random manner. The weathered zone was assigned anisotropic properties in the analyses,

with zero shear strength within zones plus or minus 10 degrees from vertical, to model tension cracks. The failure-surface zone was modeled as 150 mm thick for convenience in the analyses, although it is much thinner in the actual slope. For each analysis run, 110 trial failure surfaces were evaluated. The results of the slope stability analysis for the fiber-reinforced slope are presented in Figure 4 for illustration purposes. The initial failure analysis is not shown to conserve space. The 10 most critical (with respect to calculated factor of safety) trial failure surfaces are plotted in the figure. The most critical trial failure surface is shown with the heavy line. The failure surfaces are labeled with lower case letters, in ascending order of calculated factor of safety. The soil types are numbered below each boundary. The highway traffic loading at the top of the slope was included as a uniformly distributed load with an intensity of 9.6 kPa, and is shown on the figure by the designation L1. The ground-water surface detected in the boring is shown near the toe elevation with the designation w1. The ground-water surface and soil zones below the failure-surface zone were not used in the shallow failure analyses, but were used in a deep-seated global analysis performed for this slope, but not included in this study.

The slope stability analyses show an increase in calculated factor of safety from 1.007 (imminent failure) for the initial failure to 1.508 for the repaired, fiber-reinforced slope. This

is an increase in calculated factor of safety of approximately 50 percent due to the geofiber inclusion.

## 5 CONSTRUCTION AND PERFORMANCE

### 5.1 Construction

The slope was repaired in late November of 1995 in general accordance with the assumptions made in the analyses. The area was prepared by excavating the failed area approximately 0.6 m below the primary failure surface. The excavated soil was spread in approximately 200 mm-thick loose lifts prior to compaction. Geofibers were spread at the calculated dosage rate of 0.25 percent by dry weight of soil, and each lift was processed and the 25 mm-length fibers mixed into the soil with a minimum of three passes of a roto-till pulverizing mixer of the type commonly used in lime-subgrade stabilization. Each lift was compacted to approximately 95 percent of maximum dry density at a moisture in the general range of optimum to 5 percentage points wet of optimum in accordance with ASTM D 698. The fill was placed in essentially horizontal lifts.

### 5.2 Performance

The fiber-reinforced northwest slope has performed well to date. No additional signs of movement have been observed. The northeast slope at the same interchange was repaired without fiber reinforcement approximately six weeks prior to the northwest slope. The non-reinforced slope has again failed.

## 6 ADDITIONAL PROJECTS

The authors have been involved in more than 10 slope projects on which geofibers were utilized for slope repair and stabilization. These projects have included roadway embankments, pipeline embankments adjacent to rivers or creeks, and an earth-fill dam. One of the pipeline projects involved the use of geofibers for deep-seated stability, as well as shallow stability. The oldest installation of geofibers on these projects was completed approximately six years ago. Most of the other projects were completed within the past three years. These installations have performed well. A detailed discussion of these projects is not possible due to space limitations.

## 7 CONCLUSIONS

The use of geofibers for earth slope reinforcement was investigated by laboratory testing of non-reinforced and fiber-reinforced specimens of compacted clay soils. A highway embankment slope in Beaumont, Texas, USA, was used as the primary case study. Extensive slope stability analyses were performed for the initial failure and fiber-reinforced slope conditions. The factor of safety was increased from essentially one at the initial failure condition, to approximately 1.5 for the repaired slope using the same soil reinforced with geofibers.

Increases in effective shear strength ( $\tau'$ ) in the range of 20 to 50 percent due to geofibers inclusion were observed for this study, based upon  $\phi'$  and  $c'$  increases from laboratory tests and the slope geometries considered. Similar increases

in shear-strength parameters using fiber reinforcement have been reported by other researchers (Maher and Ho 1994, Alwahaab and Al-Ourna 1995, Nataraj and McManis 1997). Additional research and development of analysis methods for the reinforcement mechanisms and influence of fiber properties are needed. Ranjan, et al (1996) performed a study of these influences and proposed a model for analysis of fiber-reinforced cohesionless soils.

Based upon the results of this study, observation of actual installations of fiber-reinforced slopes, and research performed by others, the geofibers are a viable and cost effective method for slope repair using micro-reinforcement where macro-reinforcement elements may not be practical due to space limitations for the anchorage zone. The geofibers can provide solutions to an entire class of slope problems which were not previously practical with geosynthetics.

Additional research is desirable using a broader range of fiber lengths and soil types. Standardization of laboratory testing and analysis methods is needed. Additional case histories are needed, and are expected to occur at an accelerated rate due to the increased use of geofibers.

## REFERENCES

Alwahaab, R.M., and Al-Ourna, H.H., 1995. "Fiber Reinforced Cohesive Soils for Application in Compacted Earth Structures," *Geosynthetics '95 Conference Proceedings*, Nashville, Tennessee, USA.

Gregory, G.H., Fugro-McClelland, (Southwest), Inc., and Synthetic Industries, *Design Guide for Fiber-Reinforced Soil Slopes*, Version 1.0, October 1, 1996.

Gregory, G.H., and M.L. Doane, 1996. "Shear Strength of Fill With Direct Shear Device," *Proceedings of the Texas Section Fall Meeting*, Geotechnical Session, ASCE, San Antonio, TX, pp. 101-110.

Humphrey, D.N., and Holtz, R.D., Purdue University, Users Manual for STABL6, with *Reinforcing Layer Option*, JHRP86/18, October 1986.

Janbu, N., 1954. "Application of Composite Slip Surface for Stability Analysis," *European Conference on Stability of Earth Slopes*, Stockholm, Sweden.

Janbu, N., 1973. "Slope Stability Computation," *Embankment-Dam Engineering, Casagrande Volume*, Edited by R.C. Hirschfeld and S.J. Poulos, John Wiley & Sons, New York, pp. 47-86.

Maher, M.H., and Ho, Y.C., "Mechanical Properties of Kaolinite/Fiber Soil Composite," *American Society of Civil Engineers, Journal of the Geotechnical Engineering Division*, Volume 120, No. 8, August, 1994.

Nataraj, M.S., and McManis, K.L., 1997. "Strength and Deformation Properties of Soils Reinforced with Fibrillated Fibers," *Geosynthetics International*, Vol. 4, No. 1, pp. 65-79.

Ranjan, Gopal, Vasan, R.M., and Charan, H.D., "Probabilistic Analysis of Randomly Distributed Fiber-Reinforced Soil," *American Society of Civil Engineers, Journal of Geotechnical Engineering Division*, Vol. 122, No. 6, June 1996.



# Effect of Geotextile Reinforcement on the Stress-Strain and Volumetric Behavior of Sand

A.K. Ashmawy

Assistant Professor, Department of Civil and Environmental Engineering, University of South Florida, Tampa, Florida, USA.

P.L. Bourdeau

Associate Professor, School of Civil Engineering, Purdue University, West Lafayette, Indiana, USA.

**ABSTRACT:** Geosynthetic-reinforced soils exhibit a significant increase in strength compared with unreinforced soils. In this study, triaxial test results for a sand reinforced with horizontal geotextile inclusions and subjected to both monotonic and cyclic loading are presented. The influence of the inclusions on the stress-strain and volumetric behavior is investigated. It is shown that a large increase in deviator strength is attained when reinforcement is used. An increase in ductility is also observed, and is essentially due to the blocking of development and propagation of the shear band within the specimen. When subjected to cyclic loading, the reinforced sand accumulates less axial deformation than the unreinforced sand. Even though the unreinforced soil is contractive, a reduction in potential for volume change is introduced by the geotextile reinforcement. It is demonstrated that this reduction in volume change potential is mainly due to the increase in confinement.

**KEYWORDS:** Geotextiles, Reinforcement, Cyclic, Shear strength, Deformation.

## 1. INTRODUCTION

Over the past few decades, a large number of geosynthetic-reinforced earth structures, such as retaining walls, have been constructed worldwide. In order to better understand the reinforcement mechanisms acting in large-scale reinforced soil structures, it is necessary to first evaluate such mechanisms at the small-scale in a controlled laboratory environment. So far, three reinforcement mechanisms have been identified in the literature, namely passive or pullout anchorage, membrane action, and confinement enhancement (Ashmawy and Bourdeau 1995). Confinement enhancement has been attributed to the mobilization of shear stresses along the soil-geosynthetic interface, thereby reducing the lateral spread of the soil, as illustrated in Figure 1.

Most of the earlier experimental studies have focused on assessing the confinement enhancement mechanism under monotonic loading conditions. For example, Ingold and Miller (1983) investigated the confinement enhancement mechanism with the aid of radiographic analysis on clay specimens reinforced with plastic porous discs. The influence of the permeability of the reinforcement was examined in a study by Fabian and Fourie (1986) who tested high and low permeability inclusions. Ling and Tatsuoka (1994) conducted plane strain tests on a silty clay reinforced with three types of geosynthetics, to simulate the response of retaining walls.

Analytical models were proposed by Ingold and Miller (1983) and Chandrasekaran et al. (1989) to estimate the increase in monotonic strength of axisymmetric soil specimens reinforced with horizontal discs. In the latter model, the increase in strength is essentially expressed as a function of reinforcement spacing and specimen diameter. In both models, assumptions need to be made concerning the amount of shear stress mobilization along the reinforcement-soil interface.

One of the few studies dealing with the influence of confinement enhancement on the cyclic response of sand was conducted by Madani et al. (1979). The reinforcement material consisted of horizontal discs of aluminum foil, equally spaced along the triaxial specimen. It was concluded that the cyclic response of the reinforced sand essentially depends on the reinforcement spacing. In the present study, drained monotonic and cyclic triaxial tests are performed on sand reinforced with horizontal discs of woven and nonwoven geotextiles. The main purpose of the study is to

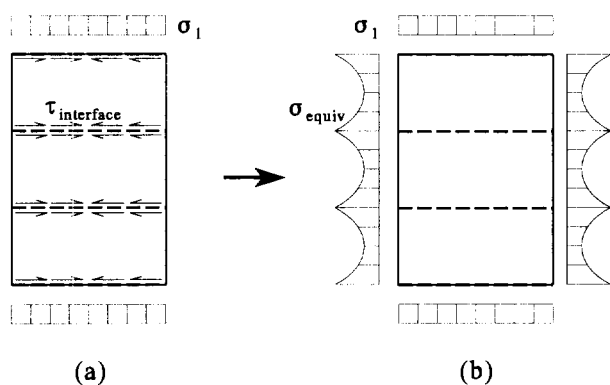


**Figure 1.** Confinement enhancement mechanism (a) interface shear stresses ; (b) equivalent confining pressure.

compare the performance of the specimens under monotonic and cyclic loading conditions, and to evaluate, experimentally, the contribution of confinement enhancement to the monotonic strength and to the deformability of the reinforced sand under cyclic loading.

## 2. TESTING PROGRAM

The tests were performed on a commercially available "Concrete Sand" reinforced with horizontal discs of woven and nonwoven geotextiles. The properties of the sand and the geotextiles are listed in Table 1 and 2, respectively.

Table 1. Properties of Concrete Sand.

Maximum unit weight	18.8 kN/m <sup>3</sup>
Minimum unit weight	15.5 kN/m <sup>3</sup>
Coefficient of uniformity	3.6
Coefficient of curvature	1.5
Specific gravity	2.65

Table 2. Properties of geotextiles.

Classification	Woven	Nonwoven
Product name	Stabilenka 200	Typar 3801
Mass/unit area <sup>a</sup>	450 g/m <sup>2</sup>	261 g/m <sup>2</sup>
Tensile strength <sup>b</sup>	220 kN/m	20 kN/m
Stiffness at 10% strain <sup>b</sup>	2000 kN/m	120 kN/m

<sup>a</sup> ASTM D3776

<sup>b</sup> ASTM D 4595

The 71 mm diameter sand specimens were moist-tamped at six layers, each 28.3 mm high. A target dry unit weight of 16.5 kN/m<sup>3</sup> was selected, corresponding to a relative density of 35%. In general, sands do not exhibit contractive behavior in axial compression except at very loose states or at high confining pressures. Consequently, dilation was observed for the unreinforced sand specimens tested under both undrained and drained conditions. Based on drained and undrained monotonic tests on the unreinforced sand, the effective angle of internal friction,  $\phi'$  was found to be 37°, within the effective confining stress range of 0 to 400 kPa.

The reinforcement was placed between the moist-tamped layers. In total, five horizontal discs of geotextile were equally spaced at 28.3 mm along each specimen. In addition, geotextile discs were placed at both specimen ends. The specimens were then saturated by flowing de-aired water and back-pressuring.

The testing program is outlined in Table 3. All tests were performed at a confining pressure of 50 kPa. It is believed that such low stress levels are typical in reinforced soil

applications, such as small retaining walls and embankments. For the cyclic tests, a deviator cyclic stress amplitude corresponding to 80% of the monotonic strength of the unreinforced soil was selected. Axial load and volume change were measured during the displacement-controlled monotonic tests, while axial deformation was recorded as a function of number of cycles during the load-controlled cyclic tests.

Table 3. Outline of the testing program.

Test	Loading mode	Geotextile
U-UR	Monotonic undrained	None (unreinforced)
M-UR	Monotonic drained	None (unreinforced)
M-NW	Monotonic drained	Nonwoven
C-UR	Cyclic drained	None (unreinforced)
C-NW	Cyclic drained	Nonwoven
C-WV	Cyclic drained	Woven

## 3. EXPERIMENTAL RESULTS

The monotonic test results indicate, as expected, a significant increase in terms of strength when the geotextile reinforcement is used. As shown in Figure 2a, the failure strength of the reinforced sand under drained conditions is approximately four times greater than that of the unreinforced. Although the initial stiffness is almost the same for both cases, the reinforced specimen exhibited less brittle behavior and reached its maximum strength at a much higher strain level. From the volume change versus axial strain plot in Figure 2b, it is concluded that the presence of geotextile reinforcement also reduces the potential of volume change.

Unreinforced undrained and drained, and reinforced drained stress paths are plotted in Figure 3, where  $p = \frac{1}{2}(\sigma_1 + \sigma_3)$ ,  $p' = \frac{1}{2}(\sigma'_1 + \sigma'_3)$ , and  $q = \frac{1}{2}(\sigma_1 - \sigma_3)$ . In the unreinforced undrained case, the stress path is distinctly traveling along the failure envelope beyond a mean effective stress of approximately 100 kPa. The strength increase introduced due to the presence of the reinforcement can be interpreted as an increase in the effective angle of internal friction ( $\phi'$ ). The apparent effective friction angle of the reinforced soil is 62°. An apparent increase in  $\phi'$  of 25° was therefore introduced by the nonwoven geotextile reinforcement.

Plots of cumulative axial and volumetric strain versus number of cycles are presented in figure 4. It is interesting to note the cyclic volume change response. Although the sand was dilative during monotonic loading, its cyclic behavior is purely contractive. This is attributed to the fact that, unlike monotonic loading, cyclic loading allows for a gradual rearrangement of particle packing, thereby causing continuous changes in soil structure as a function of loading

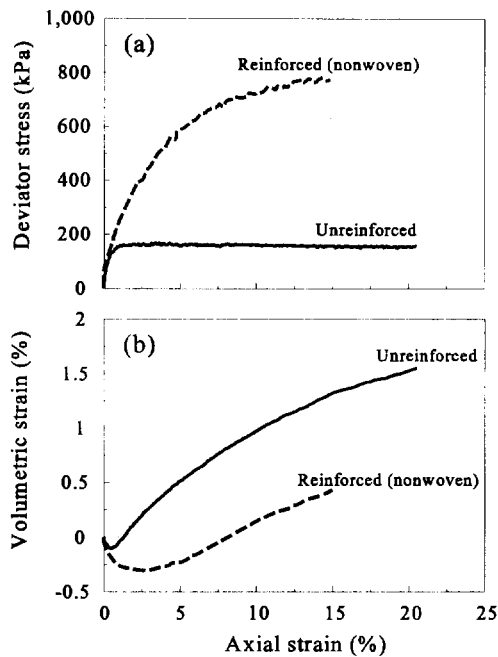


Figure 2. (a) Stress-strain and (b) volumetric response of unreinforced and reinforced concrete sand.

cycles. From a conceptual standpoint, if the amplitude of cyclic loading is not large enough to cause dilation during a given loading cycle, the volume will either remain unchanged, or more likely will slightly increase.

As shown in Figure 4, the use of geotextile reinforcement caused the rate and magnitude of cumulative axial strains to decrease. Also the tendency of the material to change its volume is smaller. This decrease in volume change tendency or potential is attributed to the enhanced lateral confinement provided by the geotextile reinforcement. The woven

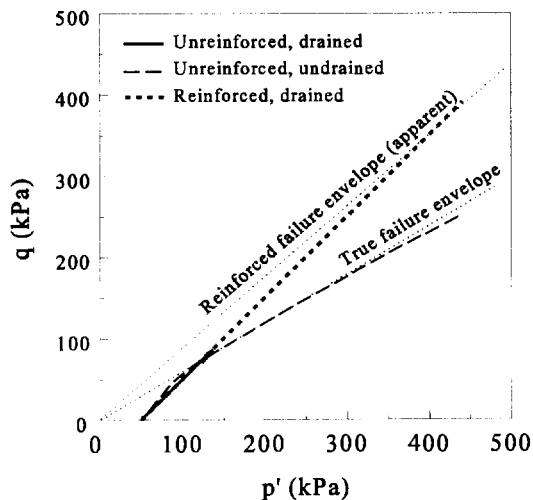


Figure 3. Stress paths and failure envelopes for unreinforced and reinforced specimens.

geotextile provided better reinforcement than the nonwoven. Although no tests were performed to characterize the sand-geotextile interface properties, it is believed that, because of its geometry, the woven geotextile pore size matches better the soil particle size.

#### 4. DISCUSSION

As mentioned earlier, the presence of the reinforcement during monotonic loading causes the sand to have a lower tendency for volume change under both drained and undrained conditions. In Figure 1, the mobilized frictional stresses along the interface act toward reducing the lateral or radial spreading of the material.

In the cyclic case, however, the sand is contractive rather than dilative, which may lead one to believe that the use of the reinforcement would be ineffective. It is difficult to understand the role of the reinforcement in this case without looking at the change in average area rather than volume, versus number of cycles. The plot shown in Figure 5 demonstrates that although the volume of all the specimens decreases with increasing number of cycles, the area does not. For the unreinforced case, the area of the specimen continuously increases, albeit at a decreasing rate, even at a high number of cycles. This outward radial spreading of the material, accompanied by the reduction in volume due to cyclic loading, causes a rapid increase in cumulative axial strains.

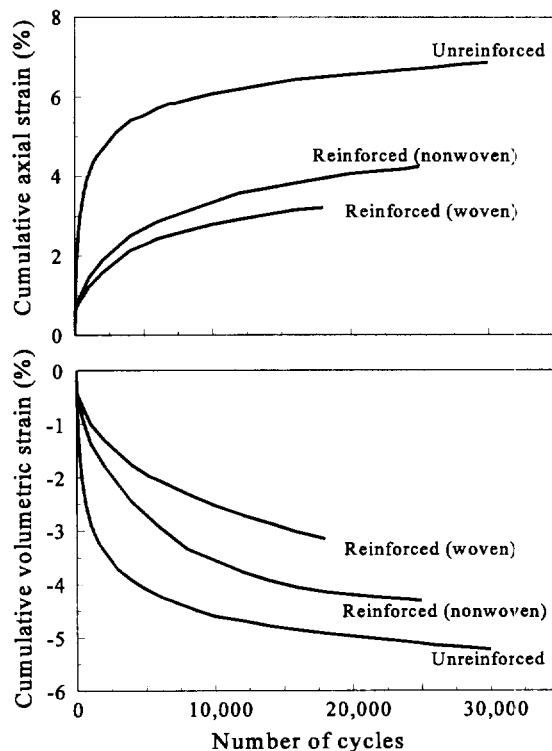
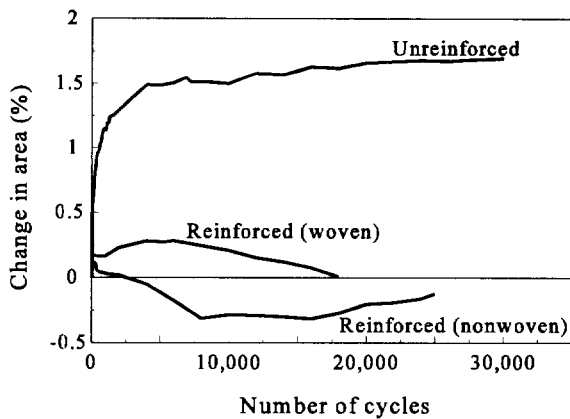


Figure 4. Variation in axial and volumetric strain as a function of number of cycles.



**Figure 5.** Change in specimen area as a function of number of cycles for the unreinforced and reinforced cases.

When geotextile reinforcement is used, the confinement enhancement causes a reduction in this radial spreading. After a very small initial increase in area during the first few cycles, the area of the specimen barely changes. Although a slight decrease of approximately  $10 \text{ mm}^3$  was measured beyond a certain point for the nonwoven-reinforced specimens, this does not seem to be logically possible and is essentially due to the low resolution of the volume change measurement system. A significant difference in change in area is, however, evident when the response of the reinforced specimens is compared with that of the unreinforced specimen. The additional enhanced confinement, physically reflected in the smaller change in area, causes an increase in the average effective confining stress within the soil, therefore reducing its tendency for volume change.

## 5. CONCLUSIONS

Monotonic and cyclic drained triaxial tests were performed on unreinforced and reinforced sand specimens. The reinforcement consisted of geotextile discs, both woven and nonwoven, placed horizontally at equal spacing along the specimens. The experimental results indicate that the presence of the reinforcement resulted in a significant increase in monotonic shear strength of the soil and a reduction in its cyclic deformability. The volume change potential decreased in both the monotonic and cyclic cases when reinforcement was used, regardless of the tendency for contraction or dilation of the unreinforced soil. Under both monotonic and cyclic loading, the reduction in volume change was attributed to the equivalent confinement enhancement introduced by the geotextile reinforcement. The confinement enhancement mechanism was verified experimentally by monitoring the change in average specimen area during loading.

## ACKNOWLEDGMENTS

Financial support was provided by the Swiss Federal Department of Transportation, Communication, and Energy, Grant No. OFR 2/92. The geotextile specimens were supplied by Reemay, Inc., and by the Nicolon Corporation. Additional support was supplied by the School of Civil Engineering at Purdue University.

## REFERENCES

- Ashmawy, A.K. (1995) "Analysis and Modeling of the Response of Geotextile-Reinforced Soil to Monotonic and Cyclic Loading", Ph.D. Thesis, Purdue University, West Lafayette, Indiana, USA, 268 pp.
- Ashmawy, A.K., and Bourdeau, P.L. (1995) "Geosynthetic-Reinforced Soils Under Repeated Loading: A Review and Comparative Design Study", *Geosynthetic International*, Vol. 2, No. 4, pp. 643-678.
- Chandrasekaran, B., Broms, B., and Wong, K.S. (1989) "Strength of Fabric Reinforced Sand under Axisymmetric Loading", *Geotextiles and Geomembranes*, Vol. 8, pp. 293-310.
- Fabian, K., and Fourie, A. (1986) "Performance of Geotextile-Reinforced Clay Samples in Undrained Triaxial Tests", *Geotextiles and Geomembranes*, Vol. 4, pp. 53-63.
- Ingold, T.S., and Miller, K.S. (1983) "Drained Axisymmetric Loading of Reinforced Clay", *Journal of Geotechnical Engineering*, ASCE, Vol. 109, No. 7, pp. 883-898.
- Ling, H.I., and Tatsuoka, F. (1994) "Performance of Anisotropic Geosynthetic-Reinforced Cohesive Soil Mass", *Journal of Geotechnical Engineering*, ASCE, Vol. 120, No. 7, pp. 1166-1184.
- Madani, C., Long, N.T., and Legeay, G. (1979) "Comportement Dynamique de la Terre Armée à l'Appareil Triaxial", *Compte Rendu, Colloque International sur le Renforcement des Sols*, Paris, France, Vol. 1, pp. 83-88. (in French)

# Numerical Simulation of Dynamic Behavior of Soil with Reinforcement

R.H. CHEN

Professor, Institute of Civil Engineering, National Taiwan University, R.O.C.

T.C. CHEN

Ph.D. Candidate, Institute of Civil Engineering, National Taiwan University, R.O.C.

**ABSTRACT:** Dynamic tests on soils with reinforcement are generally time consuming and expensive. Numerical simulation is another approach to improve the understanding of the dynamic behavior of reinforced soils. The numerical simulation of dynamic triaxial tests presented in this paper considers the reinforced soil a homogenous material with transversely isotropic property. The reinforcement is polyethylene sheets, representing the stiff reinforcement. For the purpose of comparison, laboratory tests are performed as well. As the results show, there is agreement between the simulation and the testing results.

**KEYWORDS:** Reinforced soil, Numerical simulation, Dynamic triaxial test.

## 1 INTRODUCTION

The property tests of reinforced soils are generally difficult to perform, because of difficulty preparing reinforced specimen and estimating representative specimen size. Moreover, due to lack of instruments and devices and the high operational skill needed, performing dynamic triaxial tests is not common. However, numerical simulation is another approach that may be used to improve our understanding of the dynamic behavior of reinforced soils. In this paper the numerical simulation is studied. Firstly, the reinforced soil is considered as a homogenous composite with nonlinear (or piece-wise linear) anisotropic elasticity constitutive properties. The cyclic loading and boundary conditions are similar to those of real tests. Numerical methods are used to evaluate the performance of this equivalent composite. For comparison, a series of dynamic triaxial tests are performed as well.

## 2 LITERATURE REVIEW

In numerically simulation of reinforced soils, two methods generally used, i.e., the separated method and the equivalent homogenous method. The former represents each component of reinforced soil, soil and reinforcement, are represented by different mathematical elements. The latter considers, from a macroscopic view, reinforced soil as a homogenous medium. The advantage of the separated method is that the interaction between soil and reinforcements as well as the internal forces of reinforcements can be found. However, it requires more complex parameters in numerical simulation, such as the material properties of both soil and reinforcements. Additionally, the interaction model between soil and reinforcements is needed and plays a very important role, yet an acceptable model has not been developed.

The homogenized approach employs the composite concept with anisotropic mechanical theory to characterize

the complex behavior of reinforced soils. Lesniewska (1996) pointed out that, to use this method the structure should be at least in accordance with mechanically homogeneity.

In homogenous methods, the reinforced soil can be simulated as an anisotropic homogenous medium by distributing the strength or the stiffness of reinforcements upon that of the soil element from a weighted viewpoint (Romstad et al. 1976; Sawicki 1983; De Buhan et al. 1989; Wu 1989; White and Holtz 1992). Among the anisotropic models, orthotropic and transversely isotropic models are most commonly used. In an equivalent homogenous method, Harrison and Gerrad (1972) considered the soil reinforced by non-extensible strips as an equivalent homogenous material in elastic condition. The stress-strain relation of reinforced soil is assumed cross-anisotropic elastic, and elastic constants were derived. However, the nonlinear property of reinforced soils was not considered.

## 3 NUMERICAL MODELING

### 3.1 Constitutive Relation

There are several considerations important in simulation. The composite concept is used to homogenize the reinforced soils into an equivalent homogenous medium with the transversely isotropic model to characterize reinforced soil. Since the stress-strain relation of soil is nonlinear, the soil behavior is simulated by a hyperbolic model. A plane strain condition is considered as well, because of considering real structures situation.

The scheme of soil and the reinforcement as well as the equivalent homogenous element are shown in Figure 1. Both the soil and the reinforcement are assumed isotropic.

In short, the constitutive model is derived and formulated as follows, according to the force equilibrium, strain compatibility, and anisotropy elasticity.

$$E_h = \frac{(A+B)^2 - (v_r A + v_s B)^2}{A+B}$$

$$\frac{1}{E_v} = \frac{1}{E_r}(\eta_r - 2v_r C) + \frac{1}{E_s}(\eta_s - 2v_s D) + \frac{2(C+D)}{\frac{E_r C}{v_r} + \frac{E_s D}{v_s}}$$

$$v_{hh} = \frac{v_r A + v_s B}{A+B}$$

$$v_{hv} = \frac{(1-v_r)A + (1-v_s)B}{A+B} [C+D]$$

$$\frac{1}{G_{vh}} = \eta_r \frac{2(1+v_r)}{E_r} + \eta_s \frac{2(1+v_s)}{E_s}$$

$$A = \frac{\eta_r E_r}{1-v_r^2}; \quad B = \frac{\eta_s E_s}{1-v_s^2}; \quad C = \frac{\eta_r v_r}{1-v_r}; \quad D = \frac{\eta_s v_s}{1-v_s}$$

$$E_s = E_{si} \left(1 - \frac{E_{si} \varepsilon}{(\sigma_1 - \sigma_3)_{ult} + E_{si} \varepsilon}\right)^{ns}; \quad E_{si} = K_s Pa \left(\frac{\sigma_m}{Pa}\right)^{ns}$$

where

$E_h$ : tangent modulus of the composite in horizontal direction

$E_v$ : tangent modulus of the composite in vertical direction

$v_{hh}$ : Poisson's ratio of the composite that characterizes the transverse strain in horizontal direction due to the horizontal stress.

$v_{hv}$ : Poisson's ratio of the composite that characterizes the transverse strain in horizontal direction due to the vertical stress.

$G_{vh}$ : shear modulus of the composite in vertical direction

$E_r$ : tangent modulus of the reinforcement

$v_r$ : Poisson's ratio of the reinforcement

$\eta_r$ : volumetric ratio of the reinforcement

$E_s$ : tangent modulus of the soil

$v_s$ : Poisson's ratio of the soil

$\eta_s$ : volumetric ratio of the soil

$E_{si}$ : initial tangent modulus of the soil

$K_s$ : soil constant

$ns$ : soil constant

$\sigma_m$ : mean stress

$\varepsilon$ : strain

$Pa$ : atmospheric pressure

### 3.2 Analysis Procedure

The FLAC computer program (1993) was used in the numerical analysis. The analytical procedure is shown in Figure 2. The constitutive law of the above formulae is introduced into numerical model by the FISH function of FLAC. Basically, FLAC code solves the fundamental governing equations of a continuum by an explicit finite difference method, thus the stress-deformation relation of a continuum is found. The step starts from the input of soil and reinforcement properties. The input of material

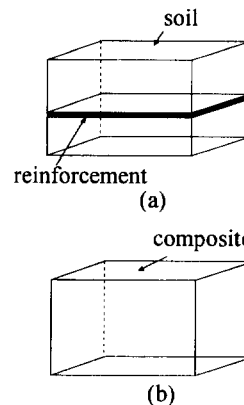


Figure 1. Schematic of (a) reinforced soil element, (b) equivalent composite.

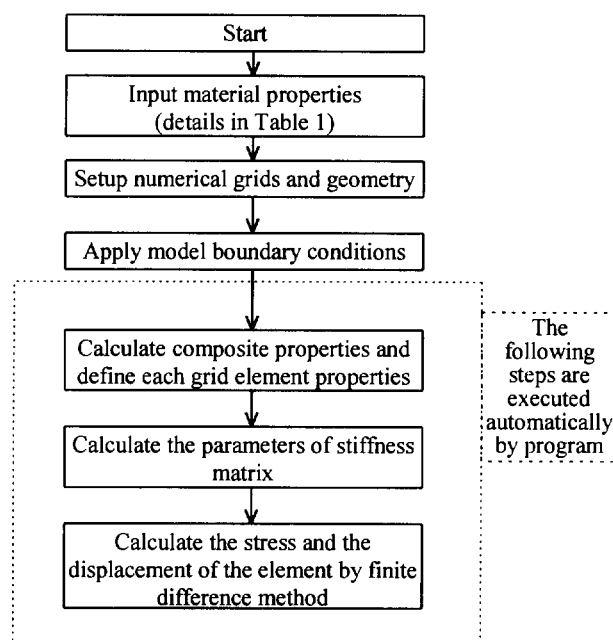


Figure 2. Numerical simulation procedure.

properties and parameters shown in Table 1 are adopted from soil and reinforcement testing, according to ATSM standard, individually. In addition, Table 2 lists the initial tangent moduli of the soil tested for hyperbolic model (Duncan and Chang 1970). The reinforcement is polyethylene sheet and is considered to be linear elastic in small strain conditions. The next step is generating the numerical grid and the boundary conditions. After completing this step, the remaining operations will be executed by the program until the result is found.

### 3.3 Dynamic Triaxial Test and Numerical Simulation Model

For qualitative comparison and simplicity, a series of

Table 1. Input parameters.

Property (unit)	Reinforcement	Soil
Poisson's ratio $\nu_r$	0.32	
Volumetric ratio $\eta_r$	0.03	
Young's modulus (MPa)	2171	
Poisson's ratio $\nu_s$		0.3
Volumetric ratio $\eta_s$		0.97
Material constant $K_s$		858.62
Material constant $n_s$		1.95
Yield stress (kPa)*		$(\sigma_1 - \sigma_3)_f$

\*Yield stress is calculated from the Mohr-Coulomb model.

Table 2. The initial tangent modulus of soil.

Confining pressure (kPa)	Initial tangent modulus (MPa)
50	189.69
75	260.02
100	303.66

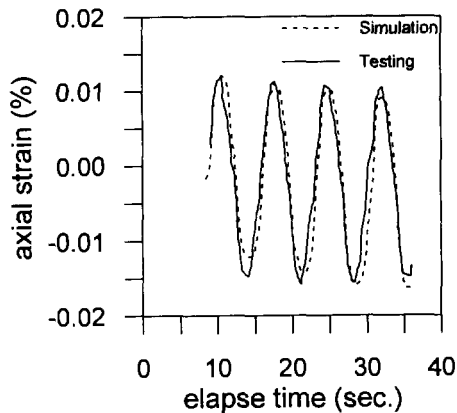


Figure 4. Axial strain versus elapsed time under 50 kPa confining pressure.

commonly used dynamic triaxial tests on reinforced soils are performed. This is because plane strain tests are rarely available in practice. The dynamic triaxial testing equipment is designed by Chan and Mulilis (U.C. Berkeley), and a cyclic loading and stress controlling device was used. The test methods are briefly mentioned below.

The soil is C109 Ottawa Sand, which consists primarily of rounded quartz particles. It is prepared with a relative density of 73%. The specimen is 71.2 mm in diameter, 171 mm in height. Three, equally spaced, horizontal layers of polyethylene sheet reinforcement were placed in the specimen. The polyethylene sheet is 68 mm in diameter and 0.2 mm thick. The Young's modulus and the tensile strength are 2171 MPa and 7.78 kN/m respectively, according to ASTM D4595-86 testing specification. Two different confining pressures 50 kPa and 75 kPa are applied.

In accordance with the test situation, the numerical model

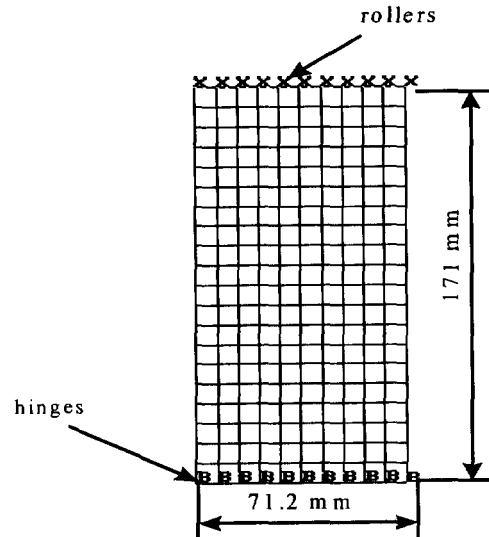


Figure 3. Numerical grid and boundary conditions of the specimen.

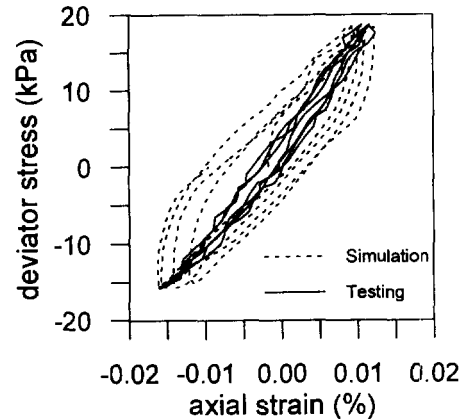


Figure 5. Deviator stress versus axial strain under 50 kPa confining pressure.

of the specimen is arranged as shown in Figure 3. Hinges are set at the bottom and rollers are set at the top of the core, respectively. The loading process used in the numerical analysis is similar to the testing procedure.

#### 4 RESULTS AND DISCUSSION

The comparison between testing and simulation results are shown in Figures 4 to 7. Figures 4 and 5 are for confining pressure equal to 50 kPa, and Figures 6 to 7 are for confining pressure equal to 75 kPa. In the figures, the dashed lines and solid lines stand for the simulation and test results, respectively.

Figure 4 shows that both the results appear a slightly viscous characteristic. The axial strain of numeric

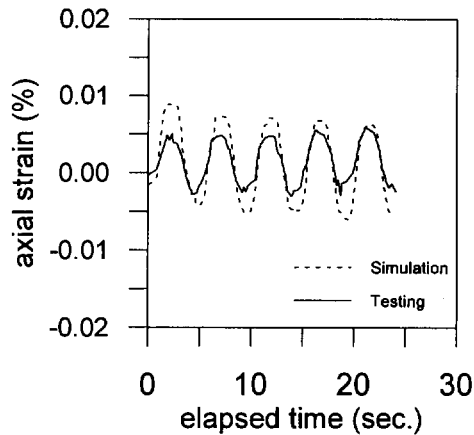


Figure 6. Axial strain versus elapsed time under 75 kPa confining pressure.

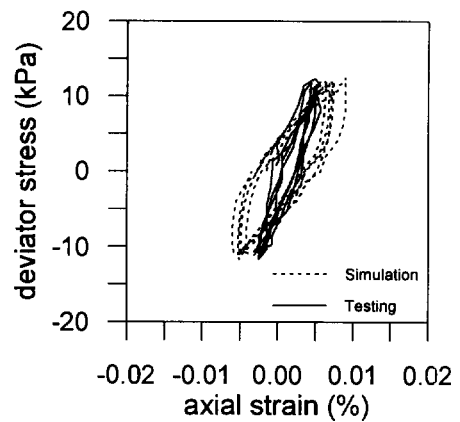


Figure 7. Deviator stress versus axial strain under 75kPa confining pressure.

simulation decayed with time, with each cycle of loading, and the hysteresis loops enlarged, shown in Figure 5. In contrast, the result from the testing maintained the same loop size than the simulation result. This is because the numerical model has introduced nonlinear properties of soil, and the viscous characteristic of reinforced soil is considered in this study. Thus, the simulation result shows the hysteresis behavior. It is noticed that the testing curve seems to be a little twist, this is because the curve is plotted from the raw testing data without regression. Except for the viscous influence, the amplitude and trajectory of axial strain in Figure 4 and the slopes of stress and strain in Figure 5 show good agreement.

In Figures 6 and 7, because the confining pressure increases, both average slopes of solid and dashed lines are larger than those in Figures 4 and 5. The hysteresis loops in Figure 7 are also more condensed than those in Figure 5. This means that the energy dissipation under higher confining pressure is less than under lower confining pressure for each cycle of applied load. The other evidence of this, finding in Figure 6, is the trajectory of the solid lines does not decay. The paths of both lines coincide but slightly differ in the maximum amplitude. This difference is due to testing device, non-uniformity in the cross sectional area of the specimen, imperfect homogeneity of a specimen, and not exactly plane strain condition of testing. However, the result of the simulation is reasonable. From the figures shown above, there is agreement between the simulation and the testing results.

## 5 CONCLUSION

This study attempts to characterize reinforced soils under cyclic loading by an equivalent homogenous approach. The reinforced soil is considered as a composite by employing

the transversely isotropic properties and nonlinear stress-strain relations. Comparison of results from dynamic triaxial tests and numerical simulation show that there is agreement between the two.

## REFERENCES

- De Buhan, P., Mangiavacchi, R., Nova, R., Pellegrini, G., and Salencon, J. (1989) "Yield Design of Reinforced Earth Walls by a Homogenization Method", *Geotechnique*, Vol. 39, No. 2, pp. 189-201.
- Duncan, J.M. and Chang, C.Y. (1970) "Nonlinear Analysis of Stress and Strain in Soils", *Journal of Soil Mechanics and Foundations*, ASCE, Vol. 96, pp. 1629-1653.
- FLAC program (1993) Itasca Consulting Group, Inc.
- Lesniewska, D. (1996) "Classification of Reinforced soil Structures Based on Their Possible Failure Mode", *Proceedings of the International Symposium on Earth Reinforcement*, Fukuoka, Japan, pp. 401-406.
- Harrison, W.J. and Gerrard, C.M. (1972) "Elastic Theory Applied to Reinforced Earth", *Journal of Soil Mechanics and Foundations*, ASCE, Vol. 98, pp. 1325-1345.
- Romstad, K.M., Herrmann, L.R., and Shen, C.K. (1976) "Integrated Study of Reinforced Earth - I: Theoretical Formulation", *Journal of Geotechnical Engineering*, ASCE, Vol. 102, pp. 457-471.
- Sawicki, A. (1983) "Plastic Limit Behavior of Reinforced Earth", *Journal of Geotechnical Engineering*, ASCE, Vol. 109, pp. 1000-1005.
- Wu, T.H. (1989) "Behavior of Soil - Geotextile Composites and Its Application to Finite Element Analysis", *Geosynthetics '89*, San Diego, USA, pp. 365-372.
- White, D.M. and Holtz, R.D. (1992) "Seismic Analysis of Reinforced Slope - A Review", *Proceedings of the International Symposium on Earth Reinforcement Practice*, Fukuoka, Japan, pp. 311-316.



# Rail Transport Support Upgradation - Potential Evaluation of Innovative Geosynthetics

V.K. Jain

Executive Director, Geotechnical Engg., Research, Designs & Standards Organisation, Ministry of Railways, Manak Nagar, Lucknow-226011, India.

A. Azeem

Geotechnical Research Engineer, Research, Designs & Standards Organisation, Ministry of Railways, Manak Nagar, Lucknow-226011, India.

**ABSTRACT:** Indian Railways have recorded manifold increase in traffic levels, speeds and axle loads in recent decades. Since the track formation was initially constructed to cater for a very low level of traffic, speed and axle load, the increase in structural demand on old formations have lead to severe failures. The paper examines the factors governing stability of subgrades, reviews the practice/methodologies of its design and strengthening. It also gives details and findings of field trials using low strength, low modulus geotextiles and geomeshes. Based on model studies, the potential of high strength, high modulus bi-oriented geogrids is established which is under evaluation through field trials.

**KEYWORDS:** Geogrids, Geotextiles, Model tests, Rail Road Applications, Reinforcement.

## 1 INTRODUCTION

On Indian Railways, manifold increase in traffic level, speed and axle loads have been recorded in the recent decades.

Parameter	Year		Projected (2000)
	1950	1996	
Traffic level (Gross Million Tonne)	100	400	500
Speed (Kmph)	75	140	160
Axle Load (tonne)	14	20.32	25

Most of this increase is on core routes known as golden quadrilateral of approx. length 11500 Kms. With liberalisation, Indian economy is growing at a targeted rate of 6 to 7% per year and railway traffic is expected to increase by 8 to 9%. As majority of track subgrades were initially constructed to cater for a very low level of traffic, axle loads and speeds, the manifold increase in traffic levels have placed a much greater level of structural demand on the existing track support. This has resulted in several subgrade failures. As on March 97, 750 Km of track is under permanent speed restriction due to weak subgrade. In addition, temporary speed restrictions are imposed during monsoons for about 500 Km. This results in slow down of trains, loss of carrying capacity and greater maintenance inputs.

Conventional method of subgrade improvement is replacement of poor subgrade with granular material. In most of the locations, the depth of replacement is worked

out to be 70cm and above. This is difficult to implement in field due to high volume of traffic and lack of track possession. This depth can be reduced by 30 to 40% if granular material is reinforced with one layer of high strength high modulus bi-oriented geogrids. With reduced depth, the work can be executed under running traffic conditions without needing track possession.

## 2 METHODOLOGY OF TRACK SUB-STRUCTURE DESIGN

Till recently, track subgrade designs were largely based on empirical approaches. Collaborated studies were carried out to assess the state of stresses inside the subgrade and to evolve a rational methodology for its design. Its main features are :

- i) The graphs have been developed for induced stresses for different modular ratios (ratio of elastic modulus of subgrade to elastic modulus of soil), depth of construction and axle load. A graph for 25t axle load is placed as Fig.1. (Yudhbir et- al,1993)
- ii) Undisturbed soil samples are collected from the site and are tested on Dynamic Triaxial Apparatus simulating field loading in laboratory to assess its threshold strength.
- iii) The depth of subgrade construction is designed on the principle that induced stresses on the soil should be less than its threshold strength.

## 3 SUBGRADE STABILIZATION TRIALS USING INNOVATIVE GEOTEXTILES.

Based on extensive literature studies, tentative specifications for geotextiles to be used for stabilization of

subgrade were formulated (Table-1). Trial laying of geotextiles conforming to the above specifications were undertaken on a problematic fine grained subgrade needing excessive maintenance inputs on a double line track. Geotextile was placed under a ballast cushion of 250mm, sandwiched between two nominal sand layers of thickness 50mm each. The post-treatment observations revealed that the upward migration of fines was checked by geotextile, however, the fabric continued to deform and eventually ruptured under outer rail seat (Fig.2). The study revealed that light weight, low modulus non-woven geotextiles are only effective in controlling upward migration of fines but could not contribute in arresting the shear failures.

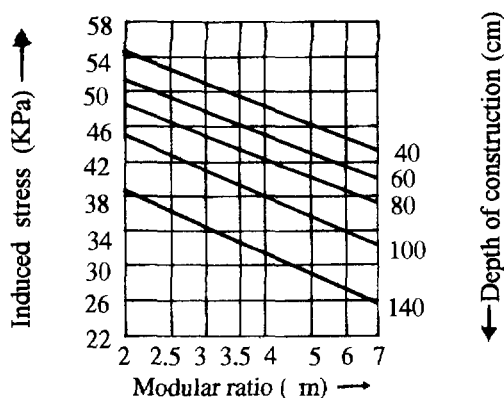


Figure 1. Induced Stresses at Subgrade( Yudhbir et- al,1993)

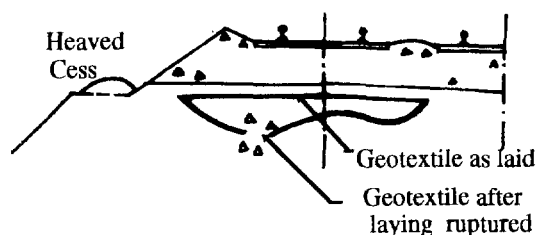


Figure 2. Subgrade Stabilization Trial using Geotextiles.

It was then decided to use available varieties of low strength, low modulus unoriented unstretched geomeshes (Netlon - India Grade CE 121, CE 131) in the similar fashion on problematic subgrades failing in shear on a single line track. Similar to geotextiles, this geomesh also continued to deform under passage of traffic and eventually ruptured near the rail seats (Fig.3).

Field trials using low modulus geotextiles as well as geomeshes amply demonstrated their limitations in preventing subgrade shear failures. The potential of high strength high modulus bi-oriented geogrids was thereafter evaluated.

Table 1. Specifications of Geotextile for Track Stabilizations

Parameters	Specifications
1. Composition	Polypropylene/Polyester. (Polyester to be used only in non-alkaline environment. Coloured fabric be preferred being more resistant to ultra Violet).
2. Mode of Manufacture	Non-woven, Needle punched
3. Denier	4 to 10.
4. Thickness (Under Surcharge pressure of 2 KPa)	3.00 mm and above.
5. Weight	400 gm/m <sup>2</sup>
6. Tensile strength (By cut strip test 200 x 50mm)	Min. 60 Kg.
7. Elongation at break (By cut strip test 200 x 50mm)	40% to 100%
8. Pore size	Max. 120 micron.
9. Equivalent\ Opening Size (EOS) 0 <sub>90</sub>	40 to 75 micron.

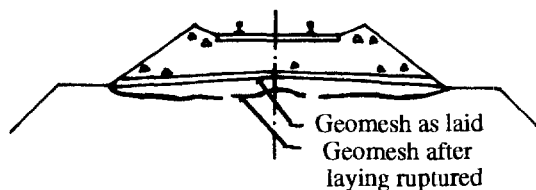


Figure 3. Subgrade Stabilisation trial using Geomesh.

#### 4 MODEL STUDIES

Model studies were carried out in the laboratory using a large size metal box 300 mm x 300 mm x 200 mm. The mould was filled with non-cohesive sub-ballast material conforming to Indian Railways specifications and compacted to desired density (90% of MDD). The test conditions included the following :

- i) Sub-ballast material only (unreinforced),
- ii) Sub-ballast with one layer of biaxially oriented geogrid (Tenax LBO 301) placed at the mid-height.

iii) Sub-ballast with two layers of biaxially oriented geogrid (Tenax LBO 301) placed at heights 1/3rd and 2/3rd respectively.

The relevant properties of biaxially oriented geogrid Tenax LBO 301 are as follows :

	MD	TD
• Peak Tensile Strength (KN/m)	19.5	31.6
• Yield Point Elongation (%)	16.0	11.0
• Aperture Size (mm)	30	40
• Unit Weight (gm/m <sup>2</sup> )	350	

The vertical load was applied through a square steel plate 125 mm x 125 mm size.

The ratio of mould dimension to footing dimension was 5.76 and its influence on test results are considered as marginal only.

The observations included recording of incremental vertical load and corresponding vertical deformations at the four corners of the box. The load deformation characteristics for the three test conditions are shown in Fig.4 which reveal the following :

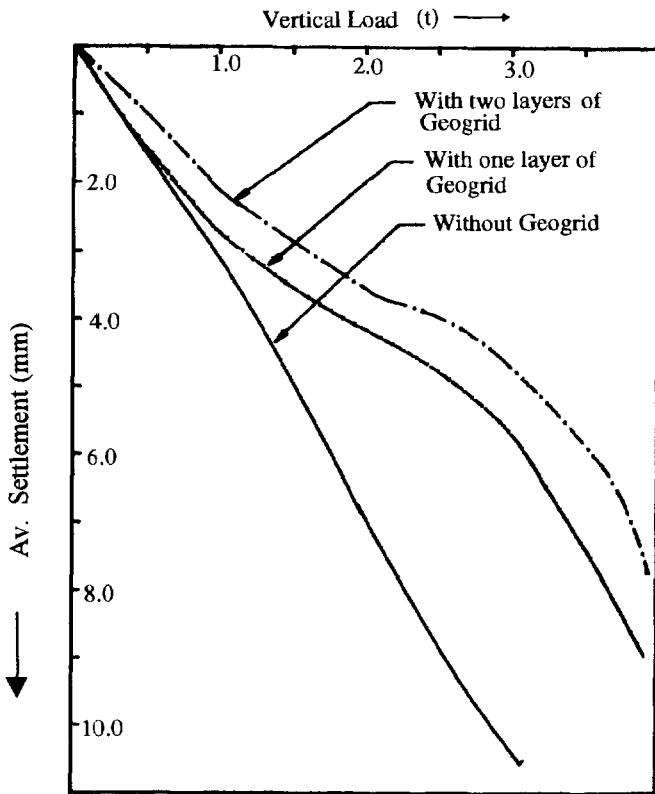


Figure 4. Model Studies – Load Deformation Curves with & without reinforcements

\* In all cases, settlement increased with increasing load. Settlement was maximum for unreinforced conditions.

\* Runaway deformations were noted at a vertical load of 3 tonnes in case of unreinforced sub-ballast and at 4 tonnes in case of reinforced sub-ballast.

\* When compared with unreinforced conditions at a vertical load of 3t. the percentage decrease in deformation was 46% in case of single layer reinforcement and 54% in case of double layer reinforcement.

\* Under these test conditions, the modulus of elasticity is worked out to be 63 MPa for unreinforced condition and 111 MPa for single layer reinforced condition. This data have been used for design of subgrade thickness for a case study on Cuttack-Bhadrak Section.

## 5 CASE STUDY

Cuttack-Bhadrak Section is a vital main line railway track between Howrah-Madras and connects Paradeep Port with Talcher-Shalimar. Maximum permissible speed of the section is 105 Kmph. A speed restriction of 30 and 50 Kmph is imposed on the stretch from Km 389/1 to 392/15 Dn line during rainy and dry seasons respectively due to weak subgrade. To strengthen the weak formation, detailed field investigations including testing of undisturbed and disturbed soil samples from site were undertaken by RDSO. The undisturbed soil samples have been tested in a Dynamic Triaxial Apparatus for confining pressure of 20 KPa (equivalent to a depth of 90 cm) and 35 KPa (equivalent to a depth of 180cm). With these values, a graph has been plotted between depth of construction and threshold strength of the soil. (Fig.5)

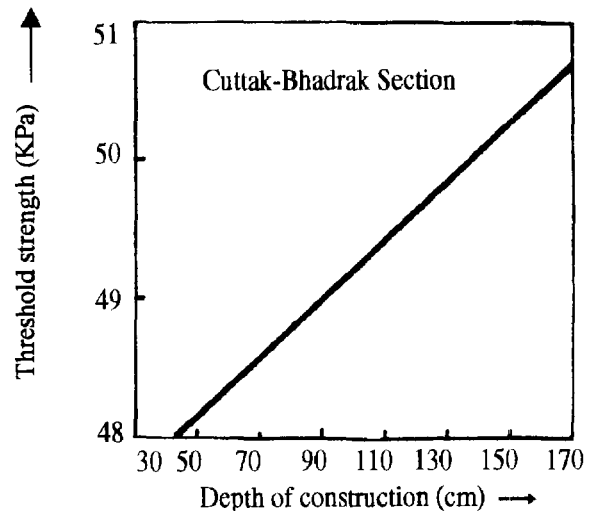


Figure 5. Threshold strength Vs Depth of Construction.

The depth of construction is worked out to be 75 cm (25 cm ballast + 50 cm sub-ballast). This depth is reduced to 55cm (25cm ballast and 30cm sub-ballast) by reinforcing sub-ballast with one layer of bi-oriented geogrid. Sample calculation is presented in Appendix-I.

With the use of geogrid reinforcement, the depth of sub-ballast is reduced from 50cm to 30cm, resulting in a saving of 40%. The most important feature of this design is that while interposing a sub-ballast of 50cm thickness requires track possession, no track possession is required for interposing 30cm thick sub-ballast layer. Since this is a core route, track possession is difficult. Therefore, provision of reinforcement will help in executing the work under running traffic.

## 6 CONCLUSION

Maintenance of railway subgrade is important due to manyfold increase in traffic levels, speeds and axle loads. Induced stresses in the subgrade should be less than threshold strength of the soil.

Strengthening of weak formation is required to be done under running traffic without track possession due to heavy traffic.

Soil is poor in tension. Provision of reinforcement will enhance the soil modulus.

Low strength low modulus geotextiles and geomeshes are not suitable for subgrade stabilisation.

High strength high modulus bi-oriented geogrid is more suitable for formation rehabilitation. One layer of geogrid reinforcement will reduce the sub-ballast thickness by about 40%.

Further studies would be needed to work out optimum modulus and strength characteristics of geogrid and sub-ballast characteristics for achieving higher economies, especially where depth of sub-ballast worked out is higher than 70cm.

## REFERENCES

- RDSO (1989) "State of the Art - Use of Geotextiles in Rail Track Foundation" *Civil Engineering Report No.C-261*, Manak Nagar, Lucknow.
- Singh, P.P. (1995) "Use of Geosynthetics in Railway formations to improve bearing capacity of subgrade soils". *Dissertation submitted for MS Degree*, BITS, Pilani, India.
- Yudhbir et-al (1993) "A Rational Approach to the Development of Design Methodology for Railway Formations" *Final Report*, IIT/Kanpur.

## Computations for depth of sub-structure

Eb	=	Young's Modulus of ballast
Esb	=	Young's Modulus of subballast
Es	=	Young's Modulus of soil
db	=	Depth of ballast
dsb	=	Depth of subballast
dt	=	Total depth of construction

Case-I - Without geogrid reinforcement:

db	=	25cm
dsb	=	50cm
dt	=	db + dsb = 75cm

Eb	=	130 MPa,
Esb	=	63 MPa (from model test)
Es	=	40 MPa

$$E_{eq} = \frac{E_b \times db + E_{sb} \times dsb}{db + dsb} = 85.33$$

$$\text{Modular ratio, } m = \frac{E_{eq}}{E_s} = \frac{85.33}{40} = 2.13$$

For dt = 75cm, Induced stress = 48.2 KPa (from Fig.1)

Threshold strength of soil = 48.7 KPa (from Fig.5)

Hence safe.

Case-II – Using one layer of geogrid reinforcement LBO-301:

db	=	25cm
dsb	=	30cm
dt	=	db+dsb = 55 cm

Eb	=	130 MPa
Esb	=	111 MPa (from model test)
Es	=	40 MPa
Eeq	=	119.63 & m = 2.99 (computed as in Case I above)

For dt = 55cm, Induced stress = 48 KPa (from Fig.1)

Threshold strength of soil = 48.3 KPa (from Fig.5)

Hence safe.

# The Use of Geotextiles for the Construction of the European High Speed Train Network

Frans De Meerleer  
Director - TEXION. Commercial Consultants to LYS-FABRICS, Belgium.

Frank Donckers  
General Manager Business Unit Raw Materials - IDEAL GROUP, LYS-FABRICS, Belgium.

**ABSTRACT:** The construction of a network of high speed trains in Europe involves the use of geotextiles for many applications. The Authors describe the general uses of geosynthetics in railway sub-ballast and construction applications, but point out those aspects where geotextiles play a particular part in assisting in the extreme environment of high speed train earthworks. The paper goes on to describe some actual applications where the main network has used geotextiles and outlines some of the difficulties involved in their specification, particularly bearing in mind the European decision to not standardise on geotextile classifications between Member Countries.

## 1 THE USE OF GEOTEXTILES TO ASSIST WITH SUBGRADE PROBLEMS

It has long been recognised that subgrade pumping beneath railways is a problem that can be ameliorated by the use of a geotextile at the ballast/subgrade interface. (Refs.1 & 2) The design difficulty has always been how to know which type of geotextile is the most suitable. With time, experienced railtrack engineers came to the opinion that low permeability and fine pore size were the preferable criteria for railways. The function of a geotextile beneath a railway is fundamentally different from that beneath a temporary access road or a permanent highway. The essential differences are a) that the ballast used to provide sleeper support is very coarse, uniform and angular, b) the regular repetition of the vibration from the axles can set up sympathetic resonant harmonic oscillations in the soil and c) the rail track system feeds a unique long distance wave of both negative and positive pressure into the ground ahead of the train itself.

The geotextile improves the structural integrity of the track and reduces the need for maintenance. It is generally considered (as shown in Fig.1), that the shedding of precipitation, caused by the fine pore size of the textile, is of particular benefit to the structural integrity of the track, whereas the filtration objective of the textile in preventing the upward migration of fines is of prime relevance to the maintenance requirements.

The new high speed train lines are multi-track systems (as opposed to low speed single track lines often encountered in developing countries), so maintenance is not such a critical problem as structural integrity. Therefore, in considering the geotextile requirements for this purpose, prevention of degradation of the subgrade is the main consideration. This logic has led to the conclusion that fine pore size and puncture resistance of the textile are the most important requirements. However, these properties can be found in a variety of different textiles including both woven and nonwoven types. Naturally, lightweight nonwovens are not suitable for this purpose since they can be

damaged too easily. However, the heavy grades of needlepunched and woven tape textiles have been selected for sub-ballast separation.

The European Union has made substantial progress with regard to the standardisation of design approach for all civil and structural engineering matters including geosynthetics. However, there has been the positive decision not to standardise the classification of geosynthetics for particular purposes. This appears to have been a pragmatic decision which holds the situation as at present, based upon different national, commercial and experience considerations for the utilisation of these products. No doubt this will have to be addressed in due course, but at the moment it leads to apparent anomalies in pan-European projects such as the high speed train system. Where the lines cross a national border, it has proved necessary to employ a different material because of different national preferences, experiences and classification systems, even though the ground conditions on each side of the border may be identical. The Authors feel that this should not be viewed as a failure of the concept of the European Union, but an indication of how difficult and time consuming it is to join together and blend a large number of sophisticated developed countries.

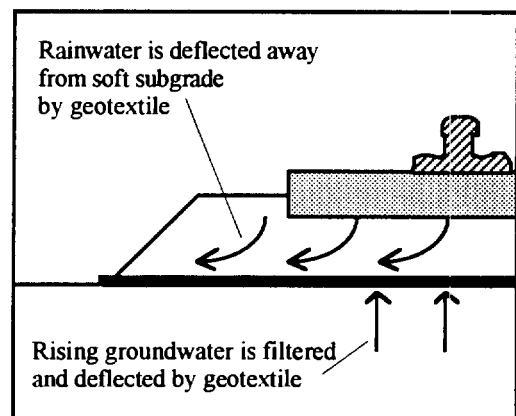


Fig.1. Rainfall shedding and pumping prevention by highly impermeable geotextile.

For, example, the Belgian Railways (N.M.B.S.) prefers to use nonwovens for this purpose, whilst the German Railways (D.B.) prefers woven tape products.

These filtration and drainage applications at sub-ballast level are particularly important in areas of cuttings, where water tables are high.

In addition to the prevention of contamination and saturation that a sub-ballast textile can provide, in high speed track conditions consideration must be given to the fundamental role of stress absorption. As can be seen in Fig.2 (Ref.3), although vertical stress is absorbed by the ballast layer, there is still a considerable amount of vertical stress remaining at the base of the ballast, to be passed down into the relatively soft subgrade. In embankment situations, where the subgrade is a pre-specified and pre-compacted material, and where drainage may be good, this stress may be absorbed adequately. However, a strong geotextile at this horizon can absorb stress and reduce the impinged load onto the subgrade. By reducing lateral shear stresses in the subgrade, the textile will help to increase its overall bearing capacity. Cohesive soils under shear exhibit a lower bearing capacity than those that are not. Under these circumstances - which include soft subgrades, wet subgrades and high speed train environments, it could be considered advantageous to choose stiffer woven products rather than nonwovens.

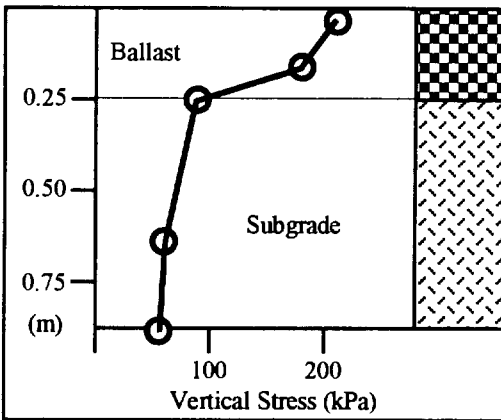


Fig.2. Typical variation of stress vertically beneath a rail line without the benefit of a geotextile (Ref.3).

The critically important contribution of a geotextile is shown in Fig.3 (Ref.4) which shows the typical results of a series of cyclical triaxial test in which the shear stress on the soil sample is continuously varied to simulate the passage of a high speed train.

Note that in this case, when the shear stress imposed on the soil exceeded  $65\text{kN/m}^2$ , the soil rapidly deteriorated with increasing induced strain until failure was reached at only 10,000 cycles. Below a shear of  $65\text{kN/m}^2$ , the soil stabilised up to and beyond one million cycles. The impact of

reducing shear on performance and maintenance cannot therefore be overstated. A high strength geotextile can contribute significantly to this providing that it has adequate durability (abrasion resistance and polymer longevity). There are doubts expressed about the potential longevity of woven slit film textiles, for example.

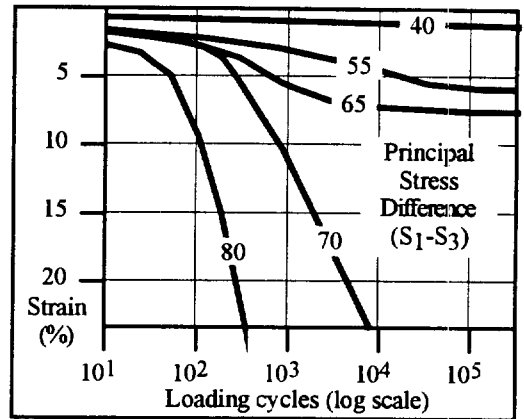


Fig.3. Effect of shear stress on cyclically induced cumulative strain in a soil without the benefit of geotextile (Ref.4).

## 2 GEOTEXTILES AS DRAINAGE COMPONENTS BENEATH NEW EMBANKMENTS

It is common to use geotextiles as separators at the base of new embankments. As mentioned previously, since in the case of high speed trains, structural stability is of paramount importance, the European system has commonly included the use of geotextiles as elementary separators at the base of embankments not only to act as construction aids, ensuring the highest level of integrity for the structure, but also as components in drainage elements, thus ensuring the reduction of water levels in the basal zones of the embankments. Especially where embankments are relatively more permeable than the underlying formation material, the use of low permeability geosynthetic textiles can lead to a reduction in received precipitation water in much the same way as is achieved beneath the ballast layer itself.

Once more, in this application, there have proved to be national differences, with the French Railways (S.N.F.C.) using woven geotextiles and immediately across the border, the Belgian Railways using nonwovens.

## 3 GEOTEXTILES AS REINFORCING COMPONENTS BENEATH NEW EMBANKMENTS

Even more so than highway embankments, high speed rail embankments are subject to potential lateral slope failures. The front of a high speed train

is preceded by a force wave within the rail and sleeper system which actively pushes down on the soil before the train arrives, followed by a continuously high surcharge load during the train passage. To counteract this effect, geotextiles are used in the sloping sides of banks as reinforcement layers and in particular, they are used as horizontal reinforcing layers at the basal horizon of embankments, to protect against slip circle failure. Not only are the dynamic forces greater with high speed trains, but as can be seen in Table 1, (Ref.5.) rail and sleeper weights also increase directly as the train speed increases. Although relatively small, this must also be taken into account in the slope design.

Axle wt. Tonnes	Speed Km/hr	Rail Wt. Kg/m
35	50	57
35	140	65
35	200	70

Table 1. Typical rail weights

It is interesting to note that although overall slope load is increased, the use of heavier weight rails reduces the direct shear loading of the ballast and sub-soil system. For example, increasing the rail weight from 48 to 68 kg/m diminishes soil shear stress by 20%.

The need for structural integrity is generated principally by the need for consistent and even track alignment both vertically and horizontally. Deformation levels that might be tolerated for ordinary railway trains are not permissible on high speed tracks.

South of Brussels, the Belgian Railways have employed the traditional high strength polyester woven geotextiles as the basal reinforcement layer for their sector of the European Network leading to Paris. This was not the usual standard reinforcing detail, but at the location of the River Zenne, the existing track structure had to be widened as well as refurbished to take the high speed traffic. The Zenne was running parallel to the old railway track and the widening involved displacing the river laterally to construct the new extension.

The cross section of this location is shown in Fig.4., where it can be seen that geotextiles were used to contain the entire fill body that infilled the old river bed and channel. The river was accommodated in a newly constructed canal built away from the new high speed track. Naturally, geotextiles were used in the banks of the canal as well, for erosion protection.

One of the interesting principles of the European High Speed Train Network is that the stations were to be located in the centre of cities to provide true

accessibility for the public. In practice, this meant that existing main line stations were to be upgraded for the new high speed trains.

This led to a problem experienced by the Japanese in the construction of their high speed inter-city trains - lack of space. In order to widen the track zone in city areas, it has become necessary to utilise reinforced soil technology as the most modern, cost-effective method of construction. Not only is reinforced soil construction cost-effective, but it is also environmentally friendly, permitting the adoption of a number of green grass and vegetated face finishes.

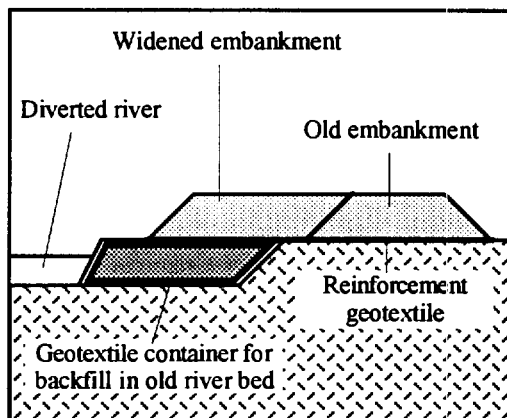


Fig.4. Widening of the Belgium - Paris sector parallel to the River Zenne.

The Japanese experience with earthquakes has highlighted the benefits of reinforced soil structures in areas of vibration. During recent major earthquakes, reinforced soil structures were invariable, the only ones left standing. In the light of these results, it is not surprising that reinforced soil should be adopted to support high speed train lines which are a major source of vibration.

#### 4 GEOTEXTILES IN THE CONSTRUCTION OF HIGH SPEED BRIDGES AND RAIL FLY-OVERS

The impermeability of bridge decks and fly-overs was a major concern for the Network designers. As a result of considerable technical input and research, a number of special composite geotextiles were developed impregnated with bitumen.

The geotextiles themselves were composite heavy nonwoven needlepunched (1500 g/m<sup>2</sup>) and strong woven (100 kN/m) which offered a cost-effective and reliable solution. Although well proven in laboratory testing, it is interesting to await the outcome of several years of real use to evaluate the results. Their use is shown in Fig.5.

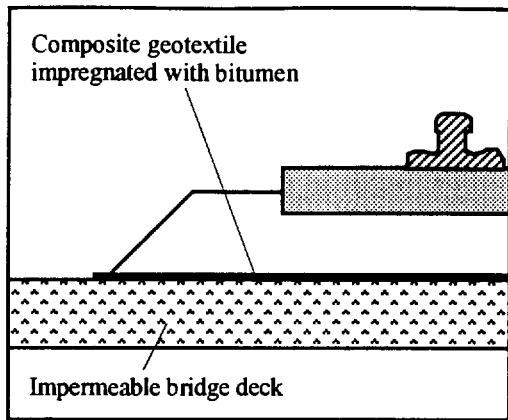


Fig.5. Location of bitumen impregnated composite between ballast and bridge decking.

### 5 LIFE EXPECTANCY OF GEOTEXTILES IN HIGH SPEED RAILWAY SYSTEMS

It is interesting to note that the life expectancy requirements of geotextiles in high speed designs varies depending upon where the textile is situated in the design. For example, the basal reinforcing geotextiles used to prevent slip circle failure should be designed to last in excess of 100 years, whereas, the sub-ballast textiles could be designed for less. The reasons for the less stringent requirements for the sub-ballast textile are that in addition to the ballast layer experiencing unavoidable deformations and in addition to potential frequent replacement of textiles during ballast maintenance, the predicted life of the concrete sleepers will, in any event, only be some 40 to 50 years, thus necessitating a major upper level refurbishment at that interval period. A longer planned life expectancy for the textile at this level would therefore not be cost effective.

Note: The Authors wish to acknowledge that the opinions expressed herein are their personal opinions and do not represent the views of their respective organisations.

#### References.

1. Membranes in Ground Engineering by P.R.Rankilor., Published by Wiley. 1981.
2. Designing with Geosynthetics by R.M.Koerner. Published by Wiley. 1986, (p159).
3. Track Geotechnology and Substructure Management. E.T.Selig and J.M.Waters. Published by Thomas Telford Services Ltd. U.K., 1994.
4. Design of Conventional Railtrack Foundations by D.L.Heath et al. Proceedings Inst.Civ.Eng. Vol. 51. Feb.1972.
5. Civil Engineer's Reference Book (4th Edition) edited by L.S.Blake. Published by Butterworths. U.K. 1989.



# Geosynthetic System for the Facing of Bovilla Dam

P. Sembenelli

Geotechnical Consultant and Managing Director, SC Sembenelli Consulting, Milan, Italy

G. Sembenelli

Geotechnical Consultant, SC Sembenelli Consulting, Milan, Italy

A. M. Scuro

Technical Director, Carpi Group, Arona, Italy

**ABSTRACT:** Bovilla Dam is currently the highest embankment dam incorporating a polymer (PVC) geomembrane installed within a system of geosynthetics, to provide the necessary waterproofing to the top 58 m of an 81 m high structure. Bovilla dam is the last of several such dams, of increasing height, designed and built in the last decade, along the lines set forth since the pioneering projects of 1959 - 1960. The position of the waterproofing system is on the upstream face of the dam, the waterproofing element is a 3 mm thick, plasticized and stabilised PVC geomembrane and the geosynthetic system is protected with a facing of cast-in-place, concrete slabs.

**KEYWORDS:** Dam, Geocomposites, Geomembranes, Protective cushioning, Seepage control

## 1 INTRODUCTION

Bovilla Dam, across Terkuze river in Albania, was originally designed as a concrete faced, gravel fill. It was not possible to reconstruct the basis for selecting a 1V/1.6H slope typical for rockfill but definitely steep for a sand-and-gravel fill. The design of the facing was developed around 1994 along the earliest schemes for such facings: a grid of concrete beams run under both the vertical and the horizontal joints of the facing slabs. The thickness of the slabs was about 0.5 m. The reinforcing of beams and slabs was quite complex and even more so was the system of the copper and PVC waterstops.

During the construction of the embankment, mostly built with alluvial gravel-and-sand, gulying of the upstream face by rainfalls developed. Attempts to reconstitute the face and recompact the fill gave unsatisfactory results. A growing concern for the end quality of the concrete facing and a compelling need to reduce both construction cost and time, suggested to look for alternate facing solutions.

A geosynthetic system essentially based on PVC geomembrane and geotextiles, finally proved to be a solution compatible with the fill materials, applicable notwithstanding of the slope of the face, requiring a much shorter placement time and nearly halving the cost of the design solution.

Late in 1994 the change in design was decided and design of the new facing system started. Placement of the bedding and drainage layer started in mid 1995 and was completed by the end of the year. Placement of the geosynthetic system started in May 1996 and was carried out in 3 parts: centre, left and right. The left and right parts were placed only after grouting of the foundation rock along the side beam was completed. For this reason placement of the 3 parts was not continuous. Placement of the geosynthetic system was completed in September and the waterproofing protection completed in November 1996. Figure 1 shows the upstream slope of Bovilla dam when placement of the waterproofing and protection were in progress. The net time required for the placement of the



Figure 1. Upstream slope of Bovilla dam in 1996. Protection has been completed in the centre part of the face.

geosynthetic system was 30 days with an average placement rate of 300 m<sup>2</sup>/day. The net time required to place the concrete protection was 100 days with an average placement rate of 90 m<sup>2</sup>/day.

The cost of the waterproofing system, including bedding, geosynthetics system, peripheral seal and concrete facing was on the order of 160 US\$/m<sup>2</sup>, in 1996 costs. All geosynthetics were imported from Italy and placement was directed by expatriate personnel.

## 2 THE FORERUNNERS OF TODAY'S DAMS

The first synthetic material tested as a waterproofing element was Butyl Rubber RI (Sabetta dam 1959) soon followed by Polyvinyl chloride PVC (Dobsina Dam 1960 and Terzaghi dam 1962). Low density polyethylene LDPE was used for the first time in 1964 (Toktogul cofferdam).

In later years the preferred choice became PVC in Europe and high density Polyethylene HDPE in the USA. According to a list of 83 earth and rock dams, major reservoirs and cofferdams waterproofed with geomembranes, prepared by the Senior Author, 54 structures have been built in Europe, 10 in Australasia, 5 in Africa and 14 in the Americas. PVC has been used on 33 known cases of the total. In Europe PVC has been used on 24 cases and in the Americas on 3 cases only. Waterproofings for high dams were mostly based on PVC. The Authors believe that part of PVC's success is due to the easily installed and well-performing welds possible with this polymer.

During the pioneering period, design practice developed along 2 lines: -i) thin geomembranes ( $< 0.5$  mm) and -ii) thick geomembranes ( $> 1.0$  mm). Thin geomembranes were selected mainly based on seepage loss considerations overlooking the possibility of damage during placement. Practical difficulties in welding very thin geomembranes, suggested using glued joints and often such geomembranes have been installed using folded connections. Negative experiences were the result of this type of design (Sembenelli 1995). Thick geomembranes and welded connections were adopted as a result of considering proper placement and welding as relevant requirements.

The selection of PVC and HDPE allowed production of continuous, high quality welds. Hot-air welding with hand-held blowers, soon evolved into machine welding by hot air and hot points. As a result of attention to the quality of the seams, the senior Author developed, in the early 70s the double track seam which made possible testing of the entire seams' length.

Bovilla is the latest example of more than 70 cofferdams, large reservoirs and dams designed along the concepts developed in Italy since Sabetta. The Italian practice always adopted thick geomembranes to provide extra strength against handling and placement damages and to allow high quality, controlled welds. Soon after the pioneering examples based on Butyl rubber RI and Chlorosulphonated polyethylene CSPE, Italian practice adopted PVC as the polymer. Quite early geocomposites consisting of a PVC geomembrane + a Polyethylene terephthalate PETP nonwoven geotextile were substituted for plain PVC sheets. Multi-layer geocomposites, incorporating a diffused reinforcement were developed and applied along this line of thinking.

The design of Bovilla dam was based on the experience gained with large scale testing, in designing and in supervising construction of several dams in Italy and abroad. Possibly the most significant experience related to the type of geocomposite adopted is Alpe Gera Dam (174 m high). The protection with cast in place concrete slabs was successfully adopted at Jibiya Dam (Sembenelli

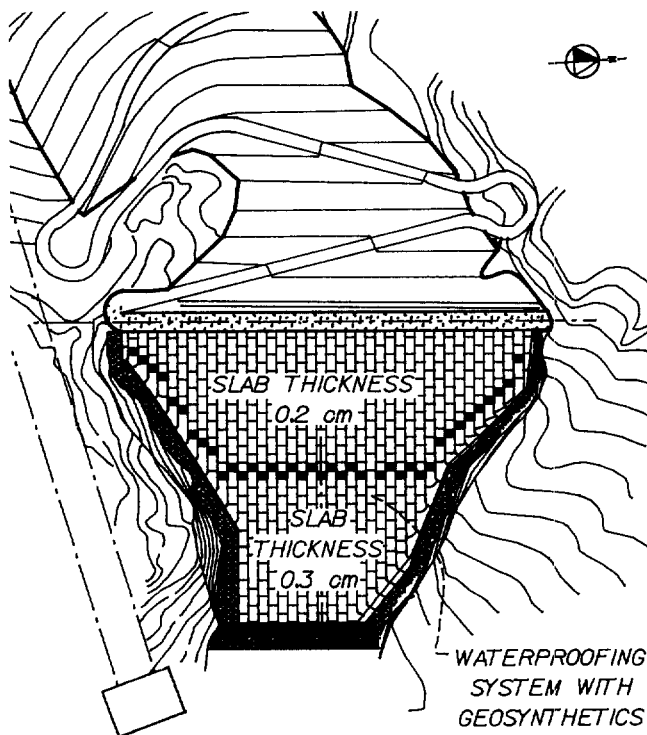


Figure 2. The plan of Bovilla dam with waterproofing based on a geosynthetic system and a cast-in-place concrete slab as a protection.

1990). The peripheral connection was perfected in the application of geomembrane waterproofings on several concrete dams like Pracana Dam.

## 3 THE EMBANKMENT OF BOVILLA

The dam, as shown in Figure 2, is placed in a narrow, winding gorge cut through a ridge of limestone rock just downstream from a tectonic contact with a schist formation. The relatively soft schists have been eroded and the limestone forms a long and high wall at the South-West end of the reservoir. A diversion tunnel has been cut through the limestone of the left bank. The limestone is heavily karstified and a large spring exists under the right abutment of the dam. Except for the excavation required to set the side beam, no excavation was carried out on the abutments. A deep, karstic niche was backfilled with concrete prior to filling against it.

At the upstream toe of the dam, river bottom rock was reached some 10 m below riverbed and the channel was filled with a concrete plug. The plug was raised some 15 m above riverbed elevation thus creating a gravity toe block nearly 25 m high. Figure 3 shows the cross section of Bovilla.

In order to condition the riverbed materials under the future fill, the rock on the sides of the gorge was demolished to a distance sufficient to permit the transit of construction equipment. Rock fragments covered by clean,

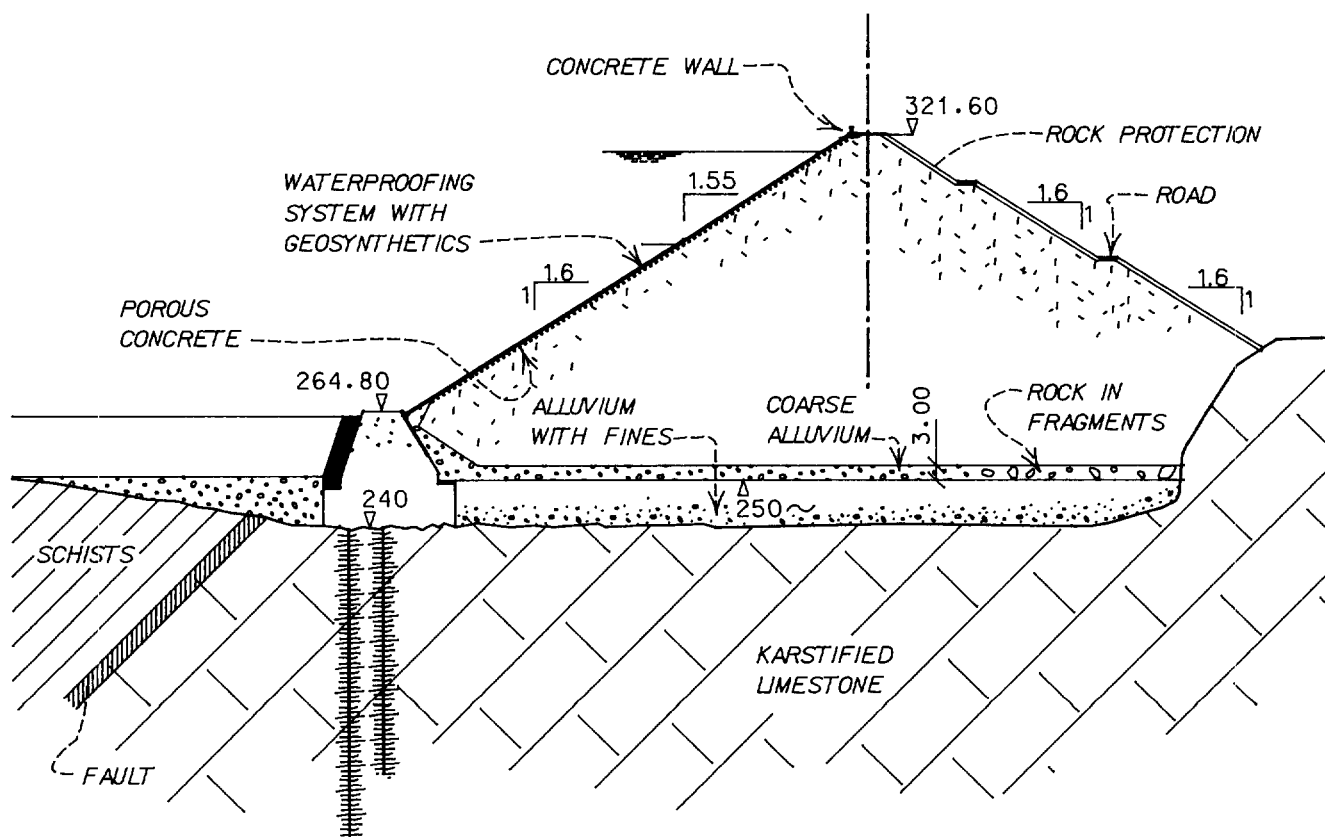


Figure 3. Main cross section of Bovilla dam on the Terkuze river. The maximum height of the dam is 81 m and the geosynthetic system has been applied over the top 57 m. The crest length of the dam is about 140 m.

coarse gravel were leveled and compacted in the riverbed channel thus creating an efficient bottom drain.

A substantial deposit of alluvial materials existed in the expanse of the reservoir and the embankment was filled with borrow-run sand-and-gravel. The alluvium is well graded and contains a certain amount of fines so that the permeability of the compacted embankment is quite low and certainly not uniform. The high percentage of fines was hindering proper compaction near the slope and favoured gullying along the compacted face. Difficulties experienced at properly filling and forming the face, suggested placing the centre and downstream parts of the fill only, while a proper solution was worked out. Hence the lower 40 m of the embankment were built in 2 separate stages which increased the potential for non uniform settlement of the face, under hydrostatic loads.

The rock line for the side beam was designed so as to obtain a profile in the plane of the face as regular as feasible. Fairly extensive excavations were necessary at given locations to smooth corners and to eliminate overhangs. The rock bench where the side beam had to be set, was designed with a gentle inward slope.

To eliminate gullying by rainwaters and to provide a free-draining, strong and uniform support to the waterproofing system, a sand-free, low-cement concrete was adopted which could be placed to produce a smooth surface. The specified aggregate size was 15 - 25 mm with  $C_u < 2$  and the cement just enough to hold the grains

together. Laboratory tests carried out on the cemented granular bedding proved that its coefficient of permeability was  $k > 1 \text{ cm/s}$ . The cemented granular bedding was placed from the top of the fill, as the fill was raised, in 2 m high bands, smoothed and compacted with a vibratory plate mounted on the arm of an excavator.

The thickness of the free-draining bedding layer was increased all along the periphery to widen the length of the contact between the drain and the abutment rock, with the aim of improving the collection of any seepage underpassing the side beam.

The toe block and side beam, part of the original design, had been cast as an unreinforced concrete block sitting over the abutment rock. As part of the design of the geosynthetic facing, the abutment surface, immediately below the side beam, was modified so as to avoid too steep as well as too flat profiles at the contact with the embankment. This was obtained by trimming the rock in excess or by concrete castings, where the abutment's rock was dipping too steeply.

A second stage reinforced concrete slab was placed over the surface of the side beam to reduce the danger of concentrated seepage in the concrete, which could eventually bypass the peripheral connection. Low pressure concrete grouting was applied systematically to the concrete-to-concrete and concrete-to-rock joints trough holes drilled from the face of the side beam.

As an additional measure against short circuit seepage,

the surface of the side beam's concrete, immediately above the geomembrane-to-concrete connection line, was treated with epoxy resins to fill honeycombs and hair cracks.

#### 4 THE WATERPROOFING SYSTEM

The waterproofing system of Bovilla dam was based on the previous designs of similar dams (Semenelli and Amigò 1996) and on experiences and studies regarding seepage flow through holed geomembranes. The choice of a geocomposite was dictated by the benefits provided by a geotextile backing, particularly if intimately connected to the geomembrane, in reducing the level of losses and in avoiding channelized flow under the liner (Fukuoka 1986).

The basis for selecting a geocomposite developed by the special Contractor CARPI was the proven performance of the liner under water heads far greater than that expected at Bovilla although, most of the precedents available were concrete or masonry dams (Scuero 1997). Other geosynthetics, like HDPE, would require finding adequate solutions to accept a more than tenfold larger coefficient of thermal expansion. A thermally stable geosynthetic makes much easier welding and protection with light weight slabs.

The waterproofing system, shown in Figure 4, consists of a 3 mm geomembrane coupled to a 700 g/m<sup>2</sup> geotextile. The geomembrane is a monolayer PVC (polyvinyl chloride) extruded from a straight-head extruder. The geotextile is a nonwoven, needle punched, continuous filament, PP (polypropylene) fibre. The coupling is obtained by calendaring the geotextile on the hot PVC sheet as it leaves the extruder. A selvedge of 50 mm is left on one side, for proper longitudinal welding of adjacent rolls. The geocomposite is produced in 2.05 m wide rolls of indefinite length.

Large scale loading tests were conducted on a high capacity cell. The support was the granular bedding, on 1 to 1 scale, and the maximum test pressure was 900 kPa i.e. 50 % in excess of the maximum expected water pressure on the face. Each test consisted of 3 loading-unloading cycles, with a first loading bench at 500 kPa, 24 hours of sustained load at 900 kPa and 6 hours recovery time in unloaded conditions in between cycles. The profile of the geocomposite under maximum load was obtained.

Another set of tests were carried out as shown in Figure 5 to simulate a collapse of the granular bedding surface. A sharp edge, vertical sided hole 0.3 m in diameter and 0.2 m deep was created under the geomembrane and a water pressure equal to 150 % of the full reservoir load was applied. The geocomposite stretched into the hole beyond the failure strain of the geotextile backing (about 34 % as determined with large scale burst tests) but the PVC geomembrane did not burst. The geotextile tore at an early stage of the test but, being on the underside of the geomembrane, its failure could not be observed in detail.

The geocomposite was factory cut to the exact lengths assigned by the design to each roll so that placement could be faster and more accurate, all horizontal seams could be eliminated, and wastage kept below 1 %.

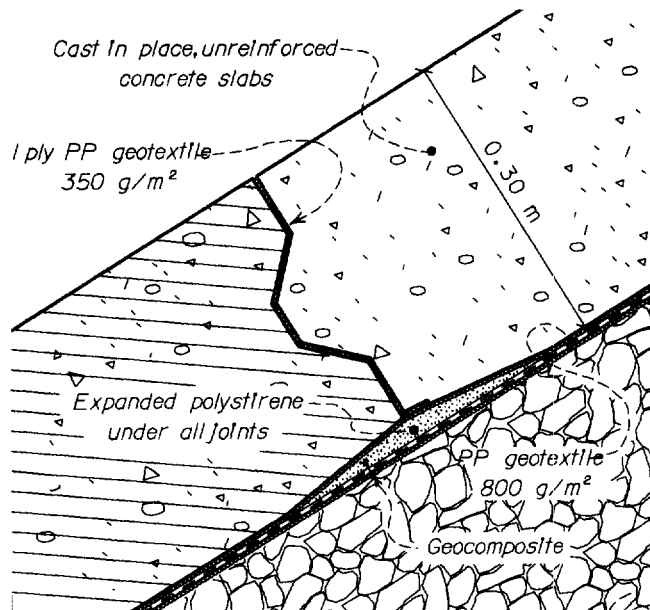


Figure 4. Cross section of the waterproofing system used at Bovilla dam.

Each roll of geocomposite was carried to the crest, unloaded and fastened to the concrete beam running along the upstream edge, with a tie down system (bolts and nuts). The roll was hence winched downslope and manually guided to its final position. The friction angle between geotextile and granular bedding was measured in the laboratory and proven to be 38°, about 20% larger than the slope angle. Hence a substantial grip developed between geotextile and granular bedding, enough to support the full dead weight of the geocomposite.

The geocomposite was ballasted against wind actions with strings of sand bags supported with ropes. The distance between ballast strings was about 6 m.

In spite of the ballast, however, a light but sustained wind circulating through the voids of the bedding layer, cut the frictional resistance to nearly zero and the full roll length ended hanging from the top beam. The geocomposite stretched about 0.5 % and some readjusting cuts had to be made at the toe of the slope.

The geocomposite was welded with butt welds 30 mm wide. Welds were all made with hot air equipment and about 50 % of the welding was manual. All welds were inspected and tested with a blade.

The design of the periphery of the geocomposite was such as to allow sharp, differential settlements of the fill with respect to the tie-down line. A reserve length of geocomposite was provided, sandwiched between anti-grip sheets of HDPE and nonwoven geotextile.

A geomembrane strip (without geotextile backing) was used to form the peripheral connection along the block toe and side beam. The connection was of the tie down type (bolts and nuts) with a prior application of a flattening polymer paste and soft rubber gasket. The tie down was obtained with embedded 10 mm bolts spaced 0.2 m and an 8 mm stainless steel flat profile and nuts. Each nut was

closed with a dynamometric wrench.

A detailed inspection of the geomembrane surface and a detailed approval procedure was specified prior to covering the geocomposite with the geotextile. This operation was deliberately done just before starting the casting operations so as to minimise the possibility that undetected damages could happen to the geomembrane while covered.

One of the key checks of the inspection was aimed at assessing the conditions of the supporting layer. Loose stones or other small objects accidentally entrapped under the geocomposite were located. A rule was set to decide when the characteristics of the geomembrane would not permit draping the foreign object, given its dimensions or shape. In such cases the geocomposite was slit open and the object removed. The cut was hence repaired by superimposing a piece of geomembrane.

## 5 THE PROTECTION OF THE GEOMEMBRANE

In many dams exposed geomembranes have been adopted with success and have proved their adequacy to a lasting service (Amigò 1994). Protection of the geomembrane is often avoided to allow inspection and easy maintenance while the presence of a protective layer may forbid checks and hinder repairs.

Protection also adds to the cost of the dam and may sometimes require an investment comparable to that of the waterproofing system itself. Timewise, protection requires, in general, construction times which are longer than those needed to place, weld and test the waterproofing system itself. The decision to protect the geosynthetic system needs therefore to be justified and, in general, light solutions are preferable to heavy ones.

The rationale for deciding to protect the facing of Bovilla was based on several reasons: the steepness of the gorge and the consequent danger of falling rocks, which would damage the waterproofing system, the steepness of the face reducing to nearly zero the possibility of supporting the geosynthetic system by friction and, finally, the remoteness of the site and the fear that the geosynthetics could be vandalised.

Cast in place, unreinforced concrete slabs were selected as protection. The thickness of the slabs was 0.3 m in the lower parts of the facing where the length of the free standing slab exceeds 100 m and was reduced to 0.2 m over the upper 50 m of the face. A nonwoven, needle punched, continuous fibre, PP (polypropylene) filament geotextile 800 g/m<sup>2</sup> was placed over the geocomposite to work as a decoupling layer, as well as a protection to the geomembrane against mechanical damage during concreting operations. The PP geotextile proved to work efficiently also as a light reinforcement to the slab (Sembenelli 1996).

Shear tests carried out on a large sample of the geocomposite resting on the granular bedding and covered with the specified geotextile, enabled the measurement of the actual friction at the geomembrane-to-geotextile interface. Tests proved that a friction angle of 22° was the maximum that could be relied upon. This angle is 70% of the slope angle. Therefore a substantial portion of the

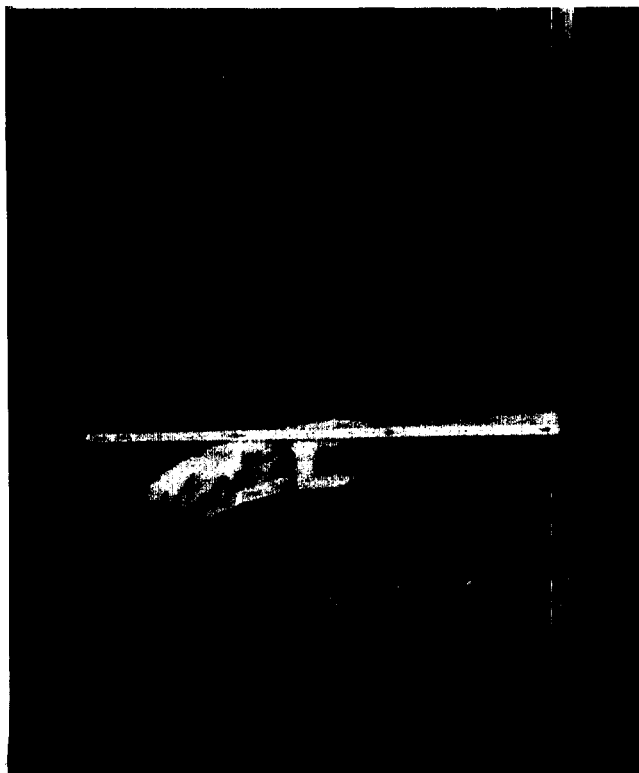


Figure 5. Large scale survivability test of the geomembrane simulating a collapsed hole in the bedding layer. The test was carried out in a high pressure vessel under 1.5 the maximum reservoir pressure. The granular support used in the testing chamber is the actual bedding placed on the dam.

protective slabs dead weight will have to be taken by the toe block. A reduction coefficient must be applied to the geotextile-to-support friction angle to account for the effects of construction and with related vibrations.

The joint pattern was based on continuous vertical and staggered horizontal joints. Shear keys were created along the sides of all slabs so as to block them, both ways. At horizontal joints, where appreciable angular deformations were considered likely to occur, through-going dowels were provided. Horizontal joints have the only purpose of allowing angular deformations to copy the deformed profile of the embankment facing, under full hydrostatic load. Horizontal joints are therefore obtained with the interposition of 1 ply of 350 g/m<sup>2</sup> geotextile. Vertical joints are assigned the key function of relieving any uplift pressure existing under the slabs upon draw down. A 3 ply packing of geotextile is therefore provided along them all. While along all horizontal joints the geotextile undergoes a substantial compression, negligible forces compress the geotextile interface along vertical joints. The in-plane permeability of the geotextile remains hence close to that of the material under a nominal normal stress. Slabs were cast in successive horizontal rows which allows halving the required length of forms as shown in Figure 6. The surface finish required for the slabs was obtained by straight-edge and trowel.

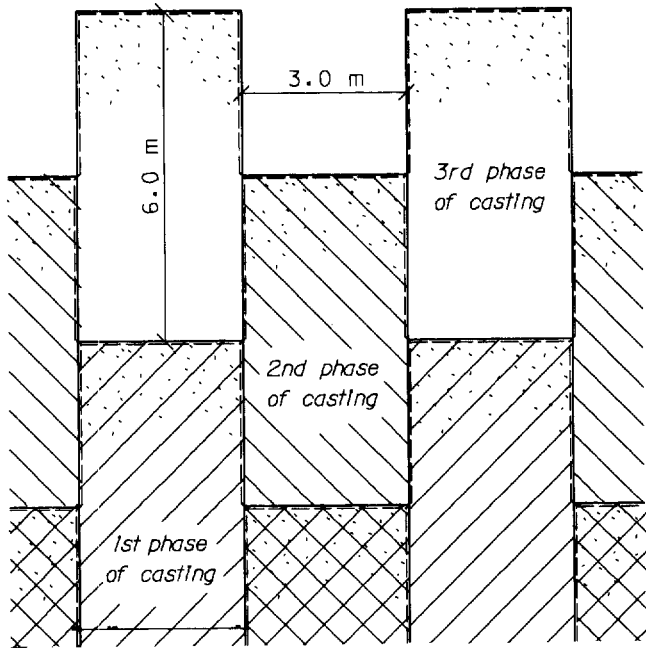


Figure 6. Joint pattern of the slabs forming the protection at Bovilla dam and casting sequence.

Each vertical slab rests, with most of its weight, against the toe block or against the side beam. Proper thickening

and reinforcement of the concrete section was hence introduced so as to keep the compressive stresses at the contact, within acceptable limits (the maximum compressive stress is on the order of 800 kPa). The design was developed so as to make each slab self-supporting. Several sections exist, along the side beam, where the contact line between the slab and the beam dips steeper than the concrete-to-concrete friction angle (assumed as 35°). Along such sections, the profile of the side beam was shaped in a jig-saw manner so as to prevent side way slippage of the slab foot.

An offset in the toe block profile locates the contact line between block and protection so that it stays off the vertical of the peripheral connection to ensure that the inevitable settlement of the edge of the facing slabs, with respect to the toe of the block, would not damage the connection. A styrofoam cap placed over the profile and the nuts, in its turn enclosed in a pocket of uniform sand, was added for the same purpose as shown in Figure 7.

Protection was placed from the bottom upward in 3 sections. The centre portion first was placed and, later, the 2 sides. The reasons for such unusual placement (which resulted in an increased length of side forms and in some complication in welding a geocomposite placed long before, to a newly laid one) were a need for drilling and grouting works along the side beam which could not be completed on time. Figure 8 shows the protection slabs during casting.

No personnel traffic was allowed on the geocomposite and/or on the geotextile. The Contractor thus selected to

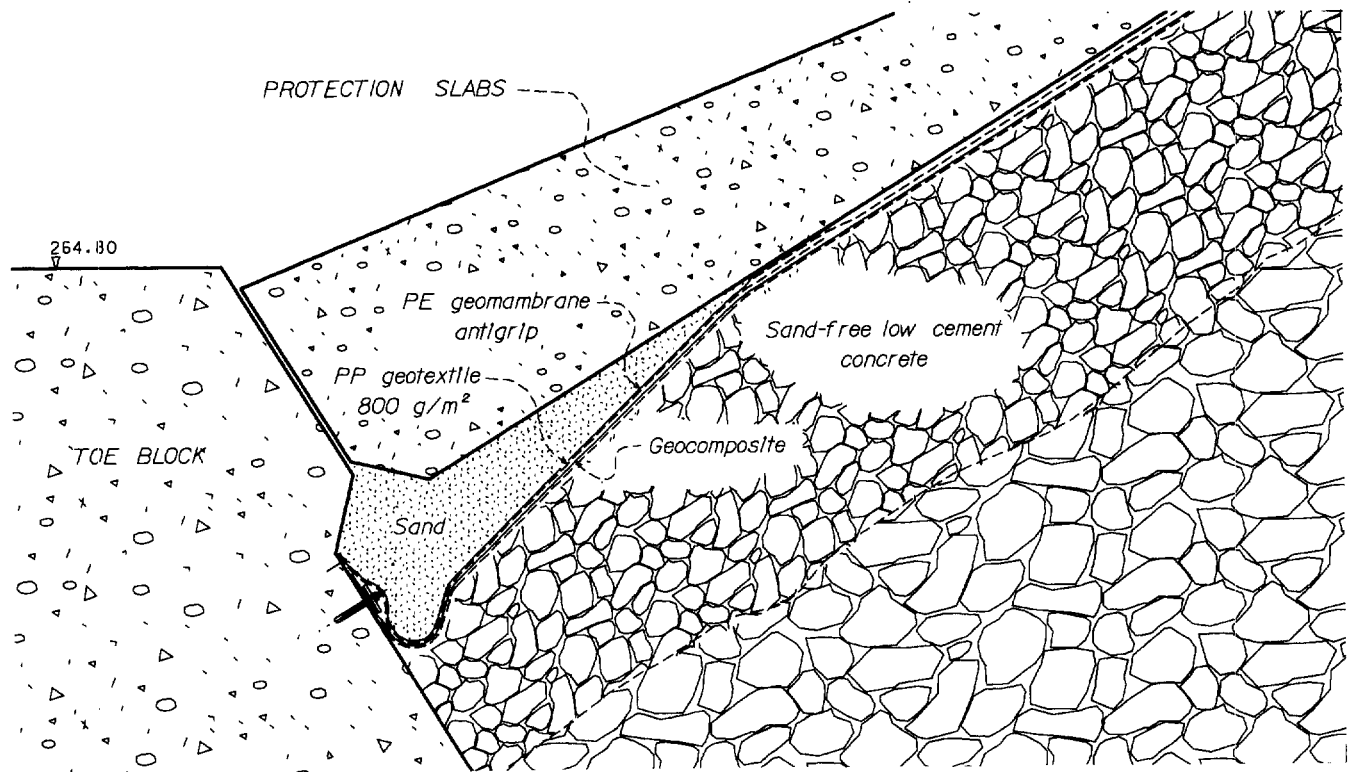


Figure 7. Connection between the waterproofing system and the toe block. A similar connection is used along the side beam.

serve the casting front from the toe of the dam. All walkways were arranged over the completed slabs and concrete was pumped to the placement zone.

A precast wave wall was part of the design of the crest of the dam. The precast elements were conceived so as to provide an early protection of the geocomposite from possible damage produced by falling objects.

## 6 THE MONITORING OF THE FACE

Monitoring localised water losses through the geomembrane is the main goal for a dam such as Bovilla. A diffused monitoring is possible today but still waiting further testing and certainly a costly measure. An overall monitoring system was hence selected which consisted of 3 open piezometers installed on the surface of the free draining bedding, immediately under the waterproofing system. The piezometer tips were limited to the lowest 2 m of the facing and piezometers pipes were of such diameter as to allow inserting a remote control electric pore pressure transducer at any later time in the future for continuous readings.

The size and distribution of the settlements of the face are of paramount importance for a waterproofing system based on geosynthetics. To survey settlements induced by the hydrostatic load, a lattice of reference points has been set into the concrete of the protecting slabs. Such points can be surveyed again when the reservoir is lowered and will make it possible to know the permanent deflection of the facing. Measuring the maximum inward deflection of a 110 m long face, while the reservoir pressure is on, is more complex and was not considered practicable at Bovilla. No post-loading readings are available so far.

## 7 CONCLUSIONS

Several successful dams in operation since 30 or more years prove that waterproofing earth and rock dams with geosynthetics is a viable and durable solution.

There has been a remarkable evolution as far as the type of the polymers most used in dams. Recent cases point to plasticized and stabilised PVC as the most widely used polymer nowadays.

Dams up to 60 m have been commissioned and all indications point to the adequacy of geosynthetics to build dams up to 100 m in height or even more. To the increasing height of dams (and acting water heads) Designers have answered with progressively more sophisticated "waterproofing systems" incorporating several layers of different geosynthetics. A similar evolution has taken place in welds, details of periphery, protections and QC procedures.

Specific testing and design procedures have been developed and are now available for a responsible design and a performing construction.

Monitoring equipments for the waterproofing system are becoming more and more sophisticated and tailored to suit modern solutions and needs.

It is not difficult to foresee that an array of geosynthe-



Figure 8. Close up of the cast-in-place, unreinforced concrete slab protection adopted at Bovilla dam.

tics will be more and more present in the dams of the future.

## REFERENCES

- Amigò, R. and Aguiar E. (1994) *Manual para el Diseño, Construcción y Explotación de Embalses Impermeabilizados con Geomembranas*, Consejería de Agricultura y Alimentación - Gobierno de Canarias
- Fanelli, G., Squero, A., Vaschetti, L. G. (1995) "PVC Membrane Protects Italy's Highest Dam", *Water Power & Dam Construction*, November 1995, pp. 20-23
- Fukuoka, M. (1986) "Large Scale Permeability Test for Geomembrane-Subgrade System", *Third International Conference on Geotextiles*, Vienna, Austria, Vol.III, pp.917-922
- Scuero, A. M. and Vaschetti, G. L. (1996) "Geomem-1998 Sixth International Conference on Geosynthetics - 1105

- branes for Masonry and Concrete Dams: State of the Art Report", *Geosynthetics: Applications, Design and Construction - First European Geosynthetics Conference*, BALKEMA, Maastricht, Netherlands, pp.889-896
- Sembenelli, P. (1990) "Engineering Geosynthetics in Design and Construction of Jibiya Dam", *Fourth International Conference on Geotextiles, Geomembranes and Related Products*, BALKEMA, The Hague, Netherlands, Vol. 2, pp. 419-424
- Sembenelli, P. (1994) "Geosynthetics in Embankment Dams", *Geotechnical Engineering Emerging Trends in Design and Practice*, OXFORD & IBH, New Delhi, India, pp. 279-304
- Sembenelli, P. (1995) "Lessons Learned from the Failure of Artik Dam", *Geosynthetics: Lessons Learned from Failures - Short Course Handout*, IFAI, Nashville, Tennessee, USA, (in print)
- Sembenelli, P. and Amigò, R. (1996) "Geomembranes for Earth and Rock Dams: State of the Art Report", *Geosynthetics: Applications, Design and Construction - First European Geosynthetics Conference*, BALKEMA, Maastricht, Netherlands, pp. 877-888
- SC - SEMBENELLI CONSULTING (1997) "Earth and Rock Dams with Synthetic Geomembranes as Waterproofing Elements - List and main data" - *Unpublished*



# Long Term Performance of Exposed Geomembranes on Dams in Italian Alps

Daniele Cazzuffi

ENEL Ricerca - Polo Idraulico e Strutturale, Milano, Italy

**ABSTRACT:** The paper presents the more recent results of an experimental program related to the behaviour vs. time of PVC geomembranes and PVC-PET geocomposites applied for rehabilitation of different types of dams owned by ENEL on the Alps. In particular, the behaviour vs. time of geosynthetics has been studied for the masonry dams of Lago Miller and Camposecco and for the concrete dams of Lago Nero, Piano Barbellino, Cignana and Pantano d'Avio. The considered geosynthetics are without any external protection and the related dams are in the West and Central regions of Alps at an elevation of more than 1,800 m above the sea level. The laboratory tests, carried out at the Special Materials and Geosynthetics Laboratories of ENEL Ricerca in Milano, allowed to determine the following characteristics: plasticizer content, hardness Shore A, tensile and water vapour transmission properties. According to the first observation programs and laboratory tests, the considered geosynthetics exhibit generally a satisfactory behaviour vs. time.

**KEYWORDS:** Dams, Geomembranes, Geocomposites, Laboratory Tests, Performance Evaluation.

## 1 INTRODUCTION

The first complete application of a PVC geomembrane at an old dam on the Alps was carried out in Italy in 1976 at the 11 m-high Lago Miller masonry dam, built between 1925 and 1926. Significant leakage led to the installation of a 2.0 mm-thick PVC geomembrane.

The geomembrane is also unprotected, so that it is exposed to the action of ice and ultra violet rays, particularly important as Lago Miller dam is located at an elevation of 2,170 m (Cazzuffi, 1987).

Another Italian installation of a PVC geomembrane for dam maintenance purposes was in 1980/1981 at the Lago Nero concrete dam. This 40 m-high structure was built from 1924 to 1929. A 2.0 mm-thick PVC geomembrane was placed without any external protection.

The 2.5 m-wide PVC geomembrane sheets were applied using a unique system, now patented by the firm Carpi, which allowed for continuous fastening along the vertical lines and also horizontal prestressing of the geomembrane itself.

A polyester needle-punched staple filament nonwoven geotextile (with a mass per unit area of 350 g/m<sup>2</sup>) was thermobonded in factory to the geomembrane, thus forming a geocomposite before application on site (Monari, 1984).

Other applications of PVC geomembranes to vertical upstream facings of old Italian concrete or masonry dams were performed more recently with very similar techniques. In the applications to Cignana and Piano Barbellino concrete dams, the stainless steel ribs are embedded in an extra layer of concrete placed on the upstream facing.

The maintenance of the Piano Barbellino dam was finished in 1987 (Photo 1): the geocomposite was constituted with a PVC geomembrane of 2 mm thickness and a PET geotextile of 1.5 mm thickness (Scuero, 1989). Differently, the maintenance of the Cignana dam was

achieved in 1988 and the geocomposite was constituted with a PVC geomembrane of 2.5 mm thickness and a PET geotextile of a 1.5 mm thickness.

Similar geosynthetic was applied in 1991-1992 on the cellular gravity concrete dam of Pantano d'Avio (Photo 2), 63 m height and built in the Fifties at the very remarkable elevation of 2,378 m (Cazzuffi, 1996).

Moreover, a PVC-PET geocomposite (with a geomembrane 2.5 mm thick) was applied in 1993 to the vertical upstream facing of Camposecco masonry dam (Photo 3), 27 m height and built in the Twenties at the considerable elevation of 2,337 m (Scuero and Vaschetti, 1996).

Table 1 summarises the characteristics of the 6 dams discussed in this communication (Lago Miller, Lago Nero, Piano Barbellino, Cignana, Pantano d'Avio and Camposecco), while Fig. 1 shows their location.

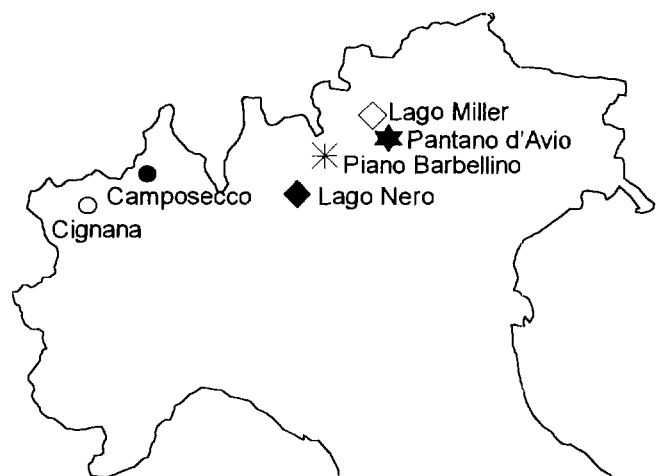


Figure 1. Location map of Italian dams on the Alps considered in the present paper.

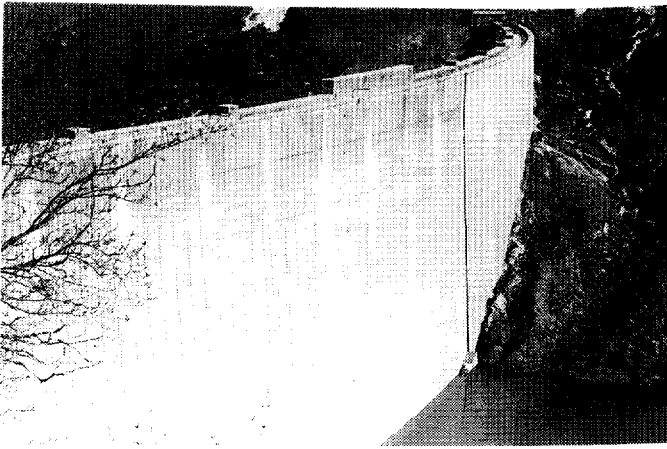


Photo 1. Piano Barbellino dam.

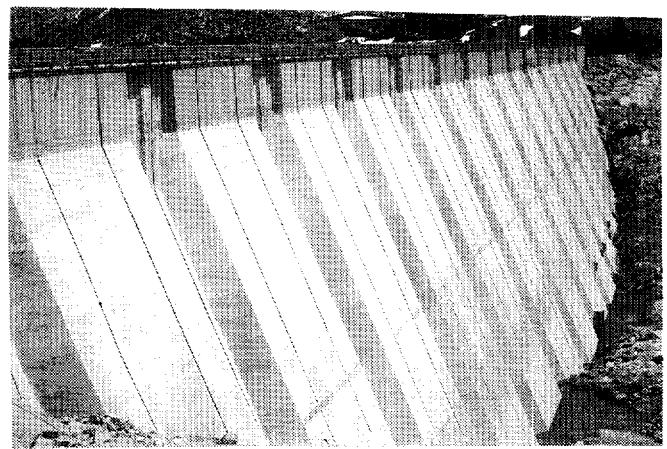


Photo 2. Pantano d'Avio dam.

## 2 OBSERVATION PROGRAM AND LABORATORY TESTS

During the recent observations (since 1995), different samples of geosynthetics were taken on the different dams, mainly on the upper part, exposed to weathering.

Only for the Pantano d'Avio dam (Photo 2) and for the third year sampling (Photo 4), samples were taken at the water level area submitted to the tidal range (dry and wetting zone).

The laboratory tests were carried out at the Special Materials and Geosynthetics Laboratories of ENEL Ricerca in Milano.

Among the different laboratory tests performed on the different geomembrane samples, the more relevant were as following:

- plasticizer content (according to ISO 6424);
- hardness Shore A (according to ISO R 868);
- tensile properties (according to ISO 527);
- water vapour transmission test (according to ASTM E 96).

For the geocomposite samples, the tests were performed only on the PVC geomembrane: the PET geotextile layer was taken away in laboratory, with the same methodology described also by Cazzuffi (1995).

Tests results on reference samples were only available for the Pantano d'Avio and Camposecco dams. Considering that the PVC geomembranes were produced by the same manufacturer, it was decided to use the same scale to show the results on all the samples taken on the different dams; the evolution of the properties vs. time since application is presented in Figure 2.

Table 1. List of dams considered in the paper (in chronological order according to geosynthetic application).

Dam	Lago Miller	Lago Nero	Piano Barbellino	Cignana	Pantano d'Avio	Camposecco
Type	M	C	C	C	CC	M
Height (m)	11.00	45.50	69.00	58.00	63.00	27.00
End of construction	1926	1929	1931	1928	1956	1930
Elevation (m)	2,170	2,024	1,868	2,158	2,378	2,337
Orientation	E	NW	E	W	S	NW
Slope (H/V)	Vertical	Vertical	Vertical	Vertical	0.5/1.0	Vertical
GM thickness (mm)	2.0	2.0	2.0	2.5	2.0	2.5
GM area (m <sup>2</sup> )	1,500	4,000	6,000	8,250	17,000	4,800
GM application	1976	1980/1	1987	1988	1991/2	1993
Legend	M: Masonry dam C: Concrete dam CC: Cellular gravity concrete dam GM: Geomembrane			E: East W: West S: South NW: North West		

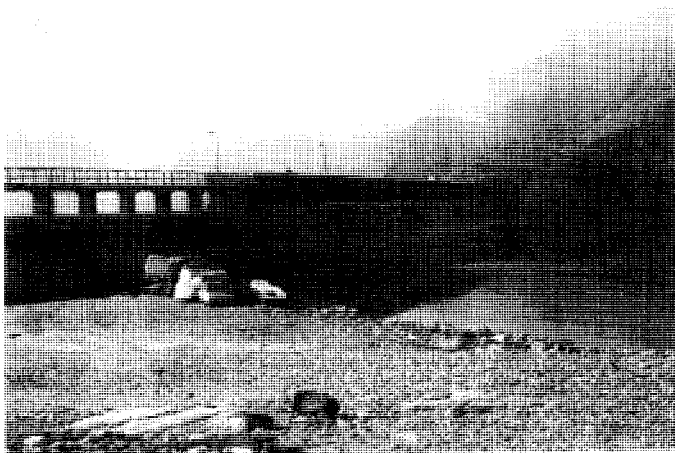


Photo 3. Camposecco dam.

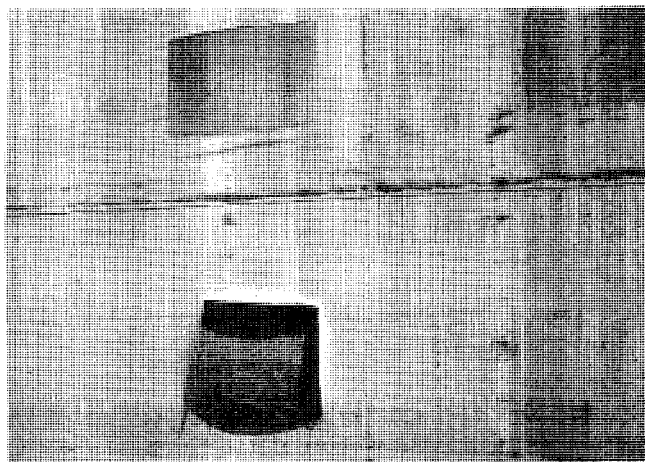


Photo 4. Location of the geomembrane sample exhumed in 1995 at Pantano d'Avio dam after 3 years since application.

### 3 CONCLUSIONS

The main results achieved by this extensive experimental program are as following:

- the PVC geomembranes exhibit generally a satisfactory behaviour vs. time;
- the plasticizer content exhibits a small decrease vs. time, even if it remains very high, for example about 28% after 19 years since application in Lago Miller dam;
- correspondingly, the hardness Shore A exhibits a certain tendency to limited increase, i.e. the geomembranes seem to be subjected to become a little bit more rigid;
- the results of the tensile properties confirm the above mentioned trend, i.e. the tensile strengths (both in longitudinal and transversal directions) generally tend to increase, while the corresponding strains tend to be subjected to limited decrease, thus forming a more rigid product;
- the water vapour transmission test results have been reported to permeability coefficient values according to the equations proposed by Giroud (1984) even if recently these equations have been questioned in literature (see, for example, Eloy-Giorni et al., 1996); in any case, being in this experimental study more interested to the comparative results than to the absolute values, it's important to remark that the permeability coefficient is quite constant vs. time, ranging from  $2 \times 10^{-13}$  m/s to  $1 \times 10^{-13}$  m/s.

Based on these results, similar rehabilitation systems of dams may be generalised, considering that a particular attention has to be taken into account during all phases of design and geosynthetic installation.

Finally, considering the lack of protection, survey and regular control during time of the geomembrane characteristics seem to be necessary.

Particular attention should be paid when geomembranes are exposed to South orientation, thus receiving the most of UV radiations.

### REFERENCES

- Cazzuffi, D. (1987) "The Use of Geomembranes in Italian Dams", *Water Power and Dam Construction*, Vol. 39 (3), pp. 17-21.
- Cazzuffi, D. (1995) "Experimental Study on the Behaviour vs. Time of Different Geosynthetics Used in Canals Owned by Enel", *Proceedings Rencontres 95*, Beaune, France, Vol. 2, pp. 9-15.
- Cazzuffi, D. (1996) "Réhabilitation de Barrages en Maçonnerie ou en Béton à l'Aide de Géomembranes: l'Expérience Italienne", *Comptes Rendus du Colloque Technique "Les géotextiles et les géomembranes dans les barrages"*, Paris, France, pp. 14.1-14.12.
- Eloy-Giorni, C., Pelte, T., Pierson, P., and Margrita, R. (1996) "Water Diffusion Through Geomembranes Under Hydraulic Pressure", *Geosynthetics International*, Vol. 3, No. 6, pp. 741-769.
- Giroud, J.P. (1984) "Impermeability: The Myth and a Rational Approach", *Proceedings International Conference on Geomembranes*, Denver, CO, USA, Vol. 1, pp. 157-162.
- Monari, F. (1984) "Waterproof Covering for the Upstream of the Lago Nero Dam", *Proceedings International Conference on Geomembranes*, Denver, CO, USA, Vol. 1, pp. 105-110.
- Scuero, A.M. (1989) "Waterproofing of the Upstream Face of Existing Concrete Dams with a PVC Geomembrane", *Proceedings Int. Conference on Upgrading and Refurbishing Hydro Power Plants (II)*, Zurich, Switzerland, pp. 291-303.
- Scuero, A.M., and Vaschetti, G.L. (1996) "Geomembranes for Masonry and Concrete Dams: State of the Art Report", *Proceedings of the First European Geosynthetics Conference EuroGeo 1*, Balkema, Maastricht, Netherlands, pp. 889-896.

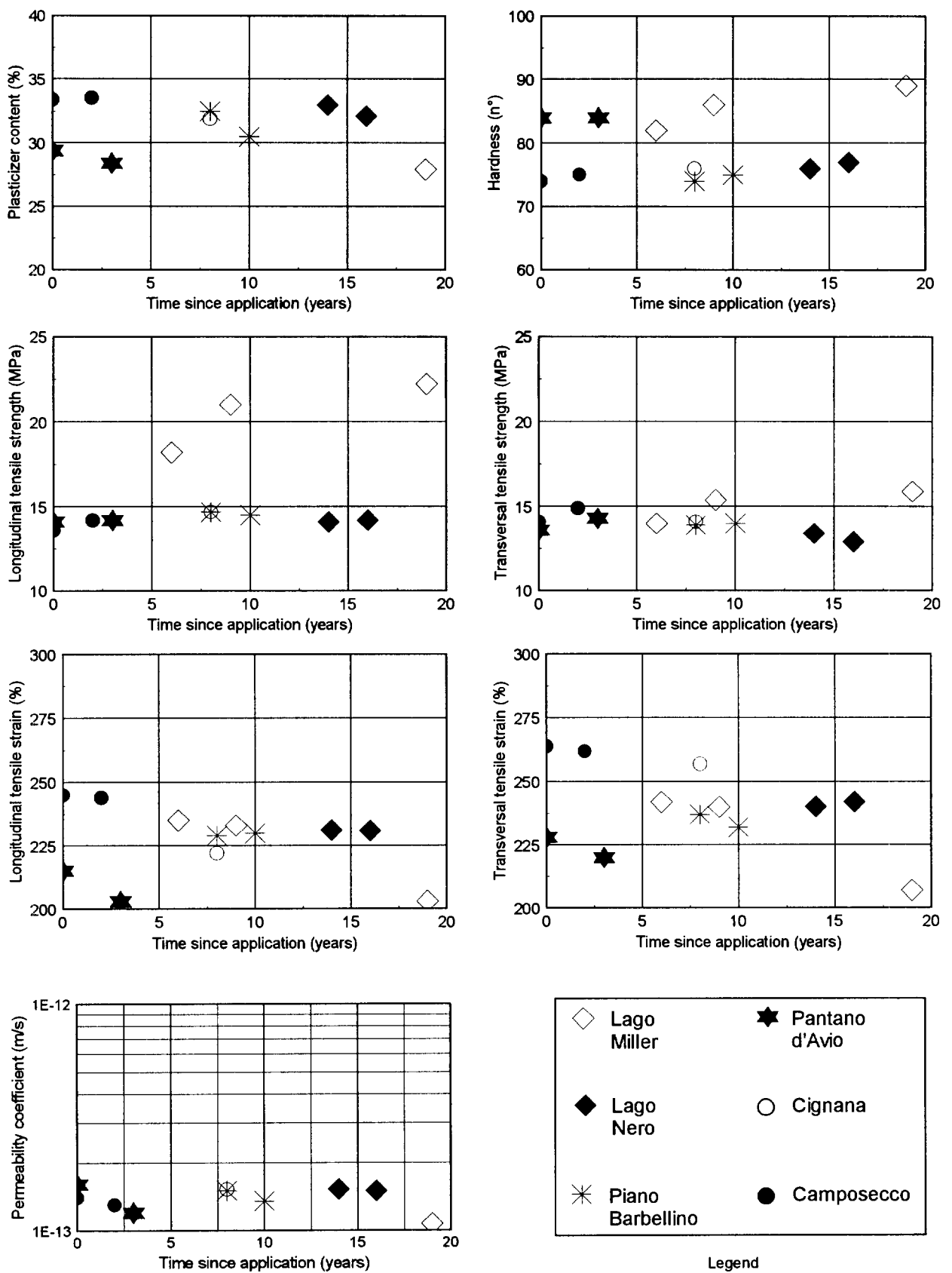


Figure 2 - Evolution of the main properties of PVC geomembranes vs time, after different years of application in the six considered dams (Lago Miller, Lago Nero, Piano Barbellino, Pantano d'Avio, Cignana and Camposecco).

# A Sail-Shaped Dam Made of High-strength Composite Geomembrane

Jiang Kun'e and Yuan Lixin

Research Institute of Water Resources and Hydropower, Liaoning Province, P. R. China

**ABSTRACT:** This paper recommends the design and construction of a membrane dam, also known as sail-shaped dam, made of high-strength composite geomembrane. The bottom edge of the dam is anchored onto the concrete base plate, and the top edge is hung on a cable across the river. The dam height may be regulated by changing the length of cable, even to flatten it to the base plate when discharging the flow. This new type of hydraulic flexible dam has an artistic profile and a distinctive style. The cost of this dam is also less than any other types of gate or dam with the same height. To date, two sail-shaped dams have been built on non-gated spillways of reservoir in our province and have made the most of the water projects.

**KEYWORDS:** Dams, Geomembranes, Composite materials

## 1 INTRODUCTION

The membrane dam, also known as sail-shaped dam, is a low-head water retaining structure made of high-strength composite geomembrane. The bottom and two side edges are anchored on a concrete base plate and side wall respectively, and the top edge is hung on cable across the river, the two ends of which are twined around winches located on both banks. The dam height may be regulated by changing the length of cable, raising the water level for irrigation or power generation, or flattening the dam on the river bed for discharging flood or navigation. When it is installed on a non-gated spillway of a reservoir, it can increase the common storage to make the most of the water project.

Building hydraulic flexible structures with geosynthetics is an initiative work. It is necessary to meet the requirements of strength, impermeability, and durability, as well as the frost-resistance if the structure is located in a cold region. Through a series of laboratory and field tests, we have selected polypropylene woven geotextile coated with ethylene vinyl acetate copolymers (EVA) to serve as the dam material to build sail-shaped dams on the spillways of Heiyushan reservoir (Fushun city) and Lanshan reservoir (Changtu county) in Liaoning province in 1996 and early 1997 respectively. The Lanshan sail-shaped dam has three continuous spans of 15m each, the two existing bridge piers are taken as the supports of cable transferring the cables to the winches by pulleys, so as to move the three spans synchronously. This type of structure is easy to construct, simple and convenient to operate, making it unnecessary to install pipelines and inflat/deflat equipment. therefore the cost of this system is the lowest as compared with other types of closed hydraulic flexible structures with the same height.

## 2 WORKING CONDITIONS AND DESIGN CALCULATION

### 2.1 Calculation of Configuration of Membrane

During the process of water-retaining, the membrane is subjected to tensile stress only when the water pressure is applied on it, no compressive stress and bending moment occur. and no stress in the direction of the dam axis, as it is long enough in compared with the height of dam. Therefore it is considered as two-dimensional problem.

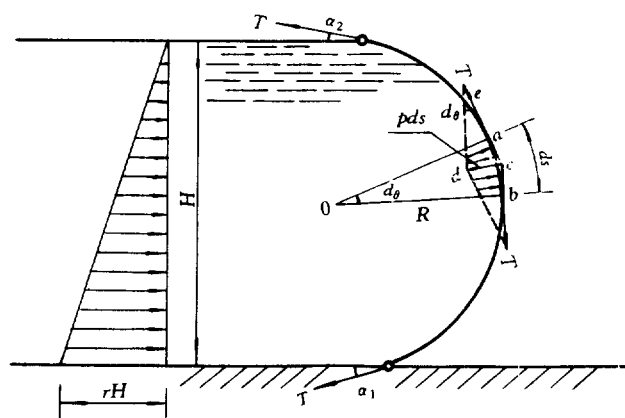


Fig. 1 Calculating sketch of membrane dam

When the water depth on the upstream side of membrane dam is  $H$ , and no water on the downstream side. The total upstream water pressure is  $P = \frac{1}{2} \gamma H^2$ , where  $\gamma =$  unit weight of water  $= 1 \text{ t/m}^3$ . From the equilibrium of all horizontal forces, we have:

$$T = \frac{\gamma H^2}{2(\cos\alpha_1 + \cos\alpha_2)} \quad (1)$$

in which: T = tangential tension of the membrane. In Fig.1, considering ds is very small,  $\widehat{ds} = ab$ .  $\Delta abo \sim \Delta ecd$ , then

$$\frac{R}{ab} = \frac{T}{cd} \quad \text{or} \quad \frac{R}{ds} = \frac{T}{pds}$$

where p = unit water pressure at that point, and R = radius of curvature. Therefore

$$R = \frac{T}{p} \quad (2)$$

Using above relationship, we can compute the geometric configuration of the membrane simply by diagrammatic method, the error of which will not exceed 5%, so it can meet the practical requirement. In the diagrammatic method, the upstream water depth is divided into a number of equal divisions, and the average unit water pressure of each division is computed, and the radius of curvature is calculated by Eq.2. Join circular arcs of each division together, to form finally the whole configuration of the membrane dam.

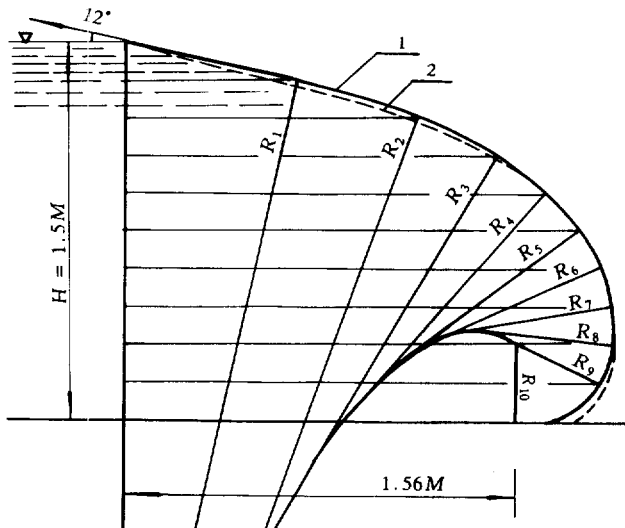


Fig. 2 Determine configuration of membrane dam by diagrammatic method: 1-computed curve, 2-Tested curve by hydraulic model study.

Now, we take the membrane dam of the spillway at Heiyushan reservoir as an example:  $H = 1.50\text{m}$ ,  $\alpha_1 = 0^\circ$ ,  $\alpha_2 = 12^\circ$ , We have

$$T = \frac{\gamma H^2}{2(\cos\alpha_1 + \cos\alpha_2)} = \frac{1 \times 1.50^2}{2(1 + 0.978)} = 0.569 \text{ tf/m or}$$

5.69 KN/m

Ten equal divisions are made for H, the radius of curvature of the first division is

$$R_1 = \frac{T}{p_1} = \frac{5.69}{\frac{1}{2}(0 + 1.5)} = 7.58\text{m}$$

Similarly, for the second division

$$R_2 = \frac{5.69}{\frac{1}{2}(1.5 + 3.0)} = 2.53\text{m}$$

The rest may be done in the same way. The configuration is drawn as in Fig. 2. From which, the total length of membrane is 3.05m, and the horizontal distance between anchor and crest is 1.56m.

## 2.2 Calculation of Cables

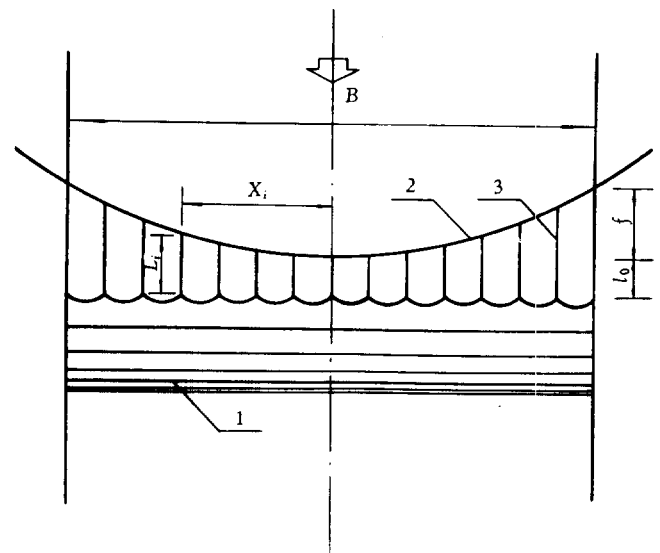


Fig. 3 Layout plan of membrane dam: 1-dam, 2-main cable, 3-secondary cables

The layout plan of the membrane dam is shown in Fig. 3. The main cable is a river crossing cable, and the secondary cables are used to tie the membrane dam onto the main cable. The spacing of which depends on the strength of membrane and the junction points. If the spacing is 1m, the tensile stress of each secondary cable is  $T = 5.69 \text{ KN}$ . The maximum tensile stress of the main cable may be computed by the following formula:

$$S_{\max} = \frac{TB^2}{8f} \sqrt{1 + 16 \frac{f^2}{B^2}} \quad (3)$$

Table 1. Test results of high strength composite geomembrane for sail-shaped dam.

Item	Unit	Amount	Remark
Weight	g/m <sup>2</sup>	975	
Total thickness	mm	1.2	
Thickness of EVA coater	mm	2 × 0.3	
Tensile strength(warp)	KN/m	42.6	Refer to ASTM D - 1682
(weft)	KN/m	38.7	
Elongation (warp)	%	7.05	Refer to ASTM D - 1682
(weft)	%	8.43	
Tearing strength	KN	1.04	Refer to ASTM D - 1117 - 80
puncture strength	MPa	1.7	Refer to ASTM D - 3780
Fatigue test	Times	100000	strength kept unchanged
Grab test	KN	11.0	Width of clamp = 30cm The tensile strength of the joint between membrane and cable.
Freez-thaw test	—	—	After 428 freezing-thawing cycles, tensile strength reduced by 24.5%.

In this example, we have

$$S_{max} = \frac{5.69 \times 15^2}{8 \times 5} \sqrt{1 + 16 \frac{5^2}{15^2}} = 53.34 \text{ KN}$$

If the curvilinear equation of main cable is

$$y = \frac{fx^2}{(\frac{B}{2})^2} = \frac{5x^2}{(\frac{15}{2})^2} = 0.0889x^2$$

$$(\frac{dy}{dx})^2 = 0.0316x^2$$

The length of the main cable

$$L = 2 \int_0^{B/2} \sqrt{1 + (\frac{dy}{dx})^2} dx = 2 \int_0^{7.5} \sqrt{1 + 0.0316x^2} dx$$

$$= 2 \left[ \frac{x}{2} \sqrt{1 + 0.0316x^2} + \frac{1}{2 \sqrt{0.0316}} \cdot \ln (x \sqrt{0.0316} + \sqrt{1 + 0.0316x^2}) \right]_0^{7.5}$$

$$= 2 \times 9.34 = 18.68m$$

The length of the secondary cable may be computed by following formula:

$$L_i = \frac{fx_i^2}{(\frac{B}{2})^2} + L_0 \tag{4}$$

In which:  $L_i$  = Length of the cable at point i,  
 $L_0$  = Length of the cable at center of span,  
 $x_i$  = Distance from center of span to point i.

If  $L_0 = 1.0m$ , Therefore:

$$L_1 = \frac{5 \times 1^2}{(\frac{15}{2})^2} + 1 = 1.089 \text{ m}$$

$$L_2 = \frac{5 \times 2^2}{(\frac{15}{2})^2} + 1 = 1.356 \text{ m}$$

The rest may be done in the same way.

In order to check the reliability of the results computed by approximate methods, we have conducted hydraulic model study (1: 5). It is indicated that the results are basically coincidence.

### 3 SELECTION OF MATERIAL

The sail-shaped dam is a hydraulic flexible structure exposed to the air and sunlight, or soaked in water over a long period of time, so that the flexible material must have sufficient tensile strength, watertightness, durability, tearing strength, flexibility, fatigue strength, and frost-resistance, etc. For this reason, after qualitative tests on several polymeric materials, we have decided to use polypropylene woven geotextile as the skeleton of composite geomembrane, and coated with ethylene vinyl acetate copolymers (EVA) adding an age-inhibiting agent. It is also required that the geotextile must be treated, so as to provide high cohesiveness with EVA. According to the concrete working condition of sail-shaped dam, we have conducted various tests of physical and mechanical

properties of processed material. The results are listed in Table 1.

An appropriate factor of safety should be considered in design of a sail-shaped dam, because of error in calculation, nonuniformity of skeleton material, loss of strength during operation, as well as the safety demand according to importance of the project, which is usually in the range of 3 to 5. The factor of safety of the two dams described in this paper are 6.8 and 11.1.

#### 4 JOINT OF THE MEMBRANES

Due to the limitation of the width of the geomembrane, it is necessary to piece together by lap joint. We have sewn up with polyamide fibre thread (density of stitches 2~3mm). The holes of needle are sealed by thermo-bonding EVA pieces of the same thickness to prevent from leakage. The test results of lap length and number of stitching rows effect on shearing strength are shown in Table 2.

Table 2. Test results of shearing stress of lap joint

Lap length (mm)	Number of stitching row	shearing strength (KN/m)
80	2	28.3
80	3	37.5
80	4	38.9

80mm lap length and 3-row stitches are adopted

#### 5 ANCHORAGE

The anchorage of a membrane dam on the concrete base plate or side wall is composed of built-in bolts (spacing 20cm), steel plate, pipe and channel. To punch bolt holes in the membrane is unnecessary. The pull-out resistance test was conducted before installation. The detail of anchorage is shown in Fig.4

#### 6 CONCLUSION

It is an attempt to use high-strength composite geomembrane to build low-head water-retaining structures, in order to open up the application of geosynthetics. Through careful design and experimental study, it is indicated that the properties of this special material can meet the requirement of working conditions of the dam. So far, two sail-shaped membrane dams, 1.17m and 1.5m high, 15m and 3×15m span, have been built on spillways of reservoirs in our province. This

simple type of structure with low engineering cost is a large benefit to the projects. Practice has proven that they are successful. However, the field observation is still taking place. At present, the height of the dam is limited by the strength of material. In order to acquire still greater results, it is necessary to take up effective measures to develop geosynthetics with higher strengths, to improve the lap joints, and to reduce wrinkles on the dam, so as to make the structure more perfect and safe.

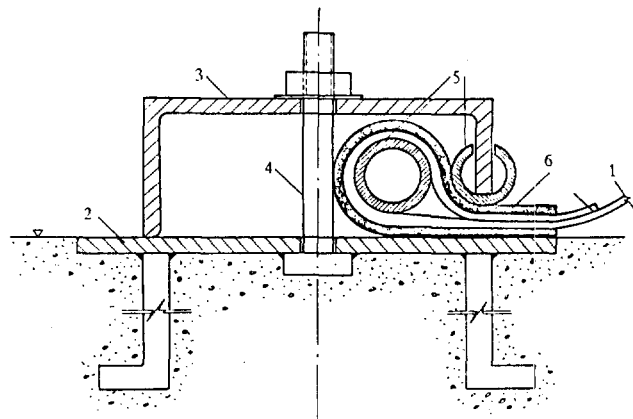


Fig. 4 Anchorage: 1-membrane, 2-steel plate, 3-channel, 4-built-in stainless steel bolt, 5-steel pipe, 6-rubber plate

#### REFERENCES

- B. E. Sergeev, et al, (1984) "Hydraulic Flexible structures", COLOS, Moscow, USSR. (in Russian). pp.9-38.
- Design Institute of Lanzhou Munciple Engineering (1979), "Design of Rubber Membrane Dams", *Proceedings of National Conference on Standardization of Dam Bag and Technical Exchange of Rubber Dams*, Benxi City, Liaoning Province, PRC. PP.300 - 319



# Use of a Synthetic Rubber Sheet for Surface Lining of Upper Pond at Seawater Pumped-Storage Power Plant

H. Shimizu

Director, Okinawa Seawater Pumped-Storage Project Construction Office, Electric Power Development Co., Ltd., Okinawa, Japan

Y. Ikeguchi

Deputy Manager, Okinawa Seawater Pumped-Storage Project Construction Office, Electric Power Development Co., Ltd., Okinawa, Japan

**ABSTRACT:** This paper presents a new technology for dam surfacing based on the use of rubber sheet which will be used in the construction of the world's first seawater pumped-storage power plant. The plant, presently under construction on Okinawa Main Island, is planned and financed by the Ministry of International Trade and Industry (MITI), Japan, with the Electric Power Development Co., Ltd. (EPDC), under a consignment contract with MITI, being in charge of surveys, research, designs and supervision of the construction. In designing this pilot plant, the sheet foundation design, the sheet anchoring method, selection of the sheet material, structural designs, and leakage water detection and dewatering system have been newly developed in consideration of the requirements imposed on a seawater pumped-storage power plant. This paper presents the design concept, construction work, the method and outcome of the quality management and observed behavior of sheets during typhoon conditions.

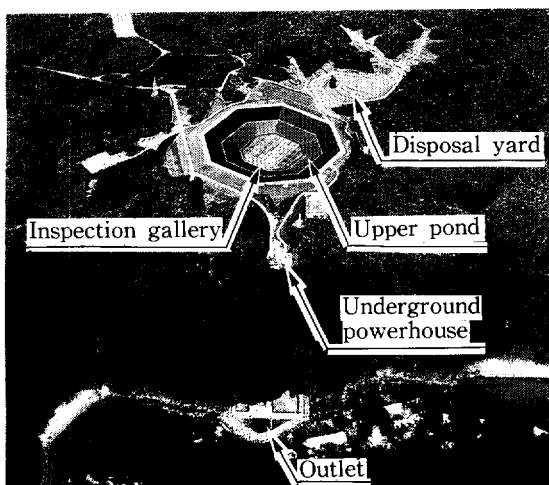
**KEYWORDS:** Construction, Dams, Design, Geomembranes, Pond Liners

## 1 INTRODUCTION

The objective of this plant is to develop seawater pumped-storage power generation technology for commercial use. The technology will be validated through a 5-year test operation and its application technology established accordingly.

The plant's upper pond is located on a plateau at approximately 150m elevation on the Pacific coast of Okinawa Main Island. The ocean is directly utilized as the lower pond. Power is generated at a maximum 30MW output at a powerhouse installed approximately 150m underground. As seawater is employed, a synthetic rubber sheet is used for the surface lining of the upper pond. Various new materials and new construction methods are also employed, including fiberglass reinforced plastic for the penstock. The seawater resistance and durability of each structure will be verified accordingly.

As a complicated configuration would provide difficulties in surface lining installation, the upper pond is designed with a layout of maximum possible simplicity. To improve workability, the dam body is an octagonal mortise earth fill dam. The slope is 1:2.5 (v:h) considering the stability of the embankment. Excluding the transition layer, the overall embankment volume is approximately 420,000m<sup>3</sup>. As shown in Figure 1, the surface lining is formed with a sheet anchor (filling concrete included), a transition layer (sheet foundation with crushed rock), and a lining sheet (main sheet, cushion fabric, cover sheet, etc.). The surface area of the sheet lining is approximately 53,000m<sup>2</sup>. Started in November, 1994, the surface lining work was completed in February, 1996.



Photograph 1. Panoramic view of the plant.

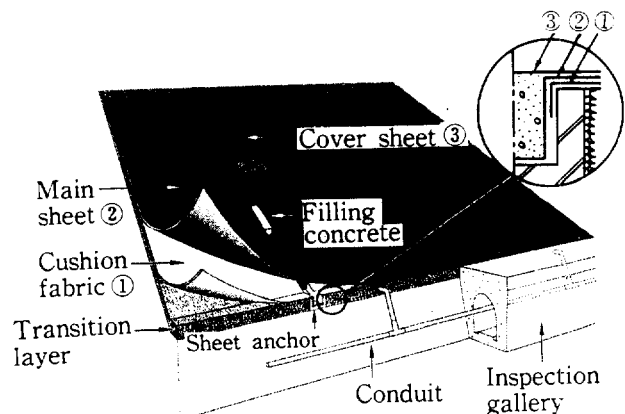


Figure 1. Structure of sheet lining.

## 2. SELECTION OF UPPER POND SURFACE LINING

### 2.1 Surface Lining Structure

The following conditions are required for the plant's

surface lining.

1. The lining materials are required to have virtually zero-permeability to provide a barrier preventing seawater leakage into the natural ground.
2. The surface lining is required to maintain impervious sealing performance against repetitive water level fluctuation.

Although it was possible to consider a concrete, asphalt or sheet lining as the surface lining, the sheet lining was finally selected for the following reasons. It is made of materials which provide a much lower permeability than concrete or asphaltic linings. Concrete lining has joints which present weak points in terms of the watertight integrity of the lining structure overall. Sheet lining construction costs are also lower than those for concrete or asphaltic linings.

In sheet lining structures, the sheet surface can either be exposed or protected by earth materials or concrete. Here, an exposed structure was selected as it permits easy repair in the event of sheet damage while assuring high reliability subject to appropriate maintenance inspection.

## 2.2 Sheet Materials

The following conditions are required for the plant's sheet materials.

1. As an exposed sheet lining structure was selected for the pumped-storage pond, the water level of which may be frequently changed, and with the plant located in sub-tropical Okinawa, sheet materials which provided less temperature sensitivity are suitable for the plant's sheet lining. (Temperature sensitivity shows extents of physical properties changes such as an ultimate elongation and a tensile strength caused by temperature change.)
2. Since the surface lining must be resistant to repetitive cyclic load and its structure must ensure impervious sealing performance in the location in which the intake and inspection gallery adjoin the structure, the sheet materials are more suitable due to their superior elongation and flexibility.

Table 1. Characteristics of the sheet materials.

Materials	EPDM	PVC	HDPVC	HDPE
Ultimate elongation(%)	450	300	400	700
Tensile strength(N/cm <sup>2</sup> )	750	1632	1423	2957
Temperature sensitivity				
at high temperature	L.S.	S.	S.	S.
at low temperature	L.S.	S.	L.S.	S.

Notes: Values in table are minimum values of the standard sheets. L.S. and S. denote less sensitive and sensitive.

Synthetic rubber (EPDM), soft polyvinyl chloride (PVC), high density soft polyvinyl chloride (HDPVC: specially developed PVC for improvement of the physical properties and feeling (like rubber) with increase of PVC molecular weight and the addition of plasticizer), or high density polyethylene (HDPE) are generally employed for the surface lining of sheet linings. The characteristics of the sheet materials are compared in Table 1. EPDM was

selected after studies and comparisons of the material performance and workability of these materials. Since HDPE provides a low elongation at yield (although its ultimate elongation is high.), HDPE was judged less suitable for the plant's sheet materials.

An outdoor exposure test near the site, bacteria proof test, seawater resistance test, and marine organism deposit test were carried out on the EPDM sheet used in this plant to determine its characteristics under near-real conditions. The long term durability of the EPDM sheet was confirmed.

## 3. DESIGN OF SUBGRADE FOR SURFACE LINING

The requirements for the subgrade of a rubber sheet lining for a seawater pumped-storage upper pond, are listed below:

1. It must provide a surface sufficiently hard to support the sheet, and ensure sufficient slope stability.
2. It drains the spring water from the natural ground, thereby dispersing the pore water pressure on the back of the sheet.
3. In the event of sheet failure, it diverts leakage water downward, finally leading to the inspection gallery built around the pond bottom, thereby preventing infiltration of seawater into the natural ground. (A dam body with a permeability coefficient in the order of  $10^{-4} \sim 10^{-6}$  cm/s has very low permeability.)
4. The residual air behind the sheet should be exhausted, because such air may inflate the sheet like a balloon when water is filled, or the negative pressure created by strong wind may pull the sheet up.

A crusher run with a maximum particle size of 20mm was selected from a number of materials meeting the above requirements in terms of water permeability and air porosity, with due consideration given to economy and seismic stability. The layer thickness was designed at 50cm. In this project, this crusher run foundation is termed the 'transition layer' as it is an intermediate transition layer between the dam body and the sheet lining.

## 4. DESIGN OF SHEET ANCHOR

### 4.1 Study of Sheet Anchoring Method

An exposed surface lining is used in this plant. In this structure, on-site adherence works may present structural weakness. For this reason, the concrete block anchoring method was adopted in order to alleviate on-site adhering works. In this method, the on-site sheet adhesions are embedded into specially designed U-shaped concrete blocks with filling concrete. No sheet-edge bonding work is performed on-site except for the cover sheets that provide an impervious lining over the anchoring works. As this anchor method is sufficiently heavy and wraps the sheet completely, it prevents wind damage experienced by anchoring by flat bar or by wrapping into buried pipe. Also, with the sheet surrounded by the sheet anchor, a sheet failure would not extend beyond the surrounding area.

## 4.2 Sheet Anchor Block Design

The following functions are required for the sheet anchor.

1. It must anchor the lining sheet firmly.
2. The main sheet surface must not adhere on site.
3. Its configurations and weight must be durable against sheet deformation resulting from an earthquake or a strong wind such as a typhoon.
4. It must provide an effective exhaust capability.

The U-shaped precast concrete blocks provide the functions given in 1, 2 and 3. To include the function described in 4, therefore, a precast unit with built-in PVC tubes was designed, as shown in Figure 2. One of the main reasons for designing a concrete block with built-in PVC tubes was that it requires less filtration installation area than the method which uses a buried perforated tube to prevent clogging of fine particles during stone crushing, thereby significantly reducing the risk of fine particle loss due to filter failure. Another reason was that it prevents the risk of sheet break due to subsidence of the transition layer caused by a tube break resulting from uneven settling of the transition layer. The exhaust tube also promotes drainage of leaked water in the event of sheet failure. A patent application for this type of sheet anchor structure has been filed.

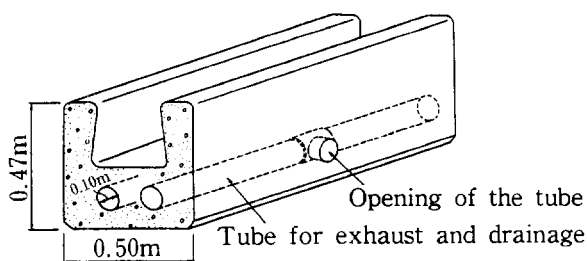


Figure 2. Anchor block.

## 4.3 Study of the Sheet Anchor Interval

According to this principle which is to eliminate on-site adhesion work on the exposed side of the sheet, the interval in the horizontal direction of sheet anchors was selected so that this would be as large as possible in reference to the maximum width of a sheet capable of being manufactured and transported to the construction site. This synthetic sheet is usually manufactured in 1.2 m wide belts which are joined at the manufacturer's plant into a single wide sheet. Considering the restrictions in the sheet transportation and the handling / fabricating limitations at the manufacturer's plant, the lateral interval of the anchor works was taken as 8.5m for slopes and 17m at the pond bottom.

For the interval in the slope direction, the sheet conditions during a strong wind such as a typhoon were considered. Strong wind induces negative pressure on the sheet surface. If air enters under the sheet, the sheet swells to maintain the balance of the inside and outside pressure. In this case, the sheet anchor intervals in the slope direction were determined considering the relationship between the sheet deformation (swell height) and the

anchor intervals in the slope direction. Regarding sheet deformation, a rectangular rubber sheet sample was anchored at its four sides and caused to swell with compressed air supplied from behind. In addition to this model experiment, numerical analysis was conducted with a finite element method (code name; ABAQUS) that permits the handling of super-elasticity materials such as rubber sheet. Where the aspect ratio (ratio of short side to long side at the sheet anchored area) was 1:2 and 1:5, the model test showed no significant difference in deformation under the same pressure. This analysis also indicated no significant difference in sheet deformation where the aspect ratio was larger than 1:2. The test indicated that deformation does not exceed a maximum 28% increase. It is, therefore, unnecessary to install a sheet anchor in the horizontal direction on the slope when the anchor intervals in the sheet horizontal direction are controlled. Consequently, the sheet anchor in the horizontal direction on the slope is located at the crest of the pond, berm, and at the toe of the slope.

## 4.4 Sheet Anchor Stability Against Sheet Swell

Sheet swelling due to strong wind induces tensile stress in the sheet and causes the sheet anchor to lift. In this case, sheet anchor stability was studied using the sheet deformation calculation model shown in Figure 3. The results of the study were compared with those of the previously described model test and it was confirmed that the values derived from the model test and the two-dimensional calculation model matched.

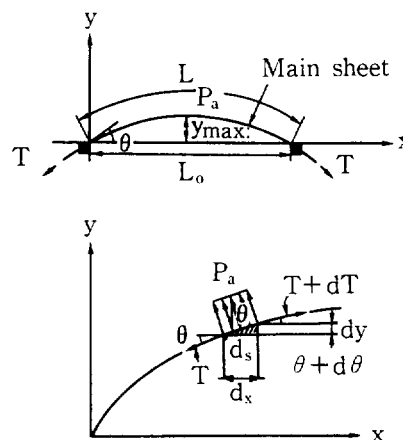


Figure 3. Sheet deformation calculation model.

The calculation method is outlined below. The negative pressure on the sheet,  $P_a$ , can be determined from equation (1).

$$P_a = \frac{\gamma_a}{2g} C v^2 \quad (1)$$

where:  $\gamma_a$  = weight of air unit volume;  $C$  = coefficient of wind force;  $v$  = wind velocity; and  $g$  = gravitational acceleration. The mechanical equilibrium of forces is expressed in equations (2) and (3).

$$T \sin \theta = P_a ds \cos \theta + (T + dT) \sin(\theta + d\theta) \quad (2)$$

$$T \cos \theta + P_a ds \sin \theta = (T + dT) \cos(\theta + d\theta) \quad (3)$$

where:  $T$  = tensile force induced in sheet; and  $\theta$  = swell angle. Relation of  $T = f(v, \theta, L_0)$  and  $L = f(v, \theta, L_0)$  is led from the equations (1) through (3). Also, the length of the sheet after swelling,  $L$ , can be determined from equation (4).

$$L = \frac{\sigma_t}{E} L_0 + L_0 \quad (4)$$

where:  $\sigma_t$  = tensile stress ( $T/A$ ) induced in sheet;  $A$  = cross area of sheet; and  $E$  = elasticity coefficient of EPDM sheet. Substituting the relative equation between  $E$  and  $\sigma_t$  obtained from the model experiment for Equation (4), leads to another equation, i.e.,  $L = f(v, \theta, L_0)$  due to the relation  $T = f(v, \theta, L_0)$ . Therefore, iteration the calculations for the unknown  $v$  and  $\theta$  until  $L$  obtained from the two equations match, the sheet deformation (deflection angle, swell height, and distortion) and the induced stress in response to the optional wind velocity can be calculated.

Assuming a sheet anchor interval of 8.5m and a deformation reaching the limit of  $\theta = 90^\circ$  (semicircle), the mean wind velocity, distortion, and tensile stress were calculated from the above equations. Consequently, the sheet distortion becomes 57.1% and the tensile stress  $118\text{N/cm}^2$  at approximately 43m/s wind velocity. These are sufficiently below the standard values of the main sheet (EPDM) shown in Table 2. The force toward the upper sheet anchor is determined from the tensile stress induced in the sheet is 4,710N/m, which is less than the sheet anchor weight of 5,370N/m. Assuming a sheet swell, the sheet anchor would therefore not be lifted.

## 5. DESIGN OF LINING SHEET

### 5.1 Member Structure and Lining Sheet Material

As described, the major lining sheet members for this plant are the main sheet, cushion fabric, and cover sheet. The functions and materials of each member are described hereafter.

#### 5.1.1 Main sheet

The main sheet is a trunk member of the lining sheet and inhibits seawater leakage. As the lining sheet of this plant is exposed, to improve its ozone resistance the proportion of EPDM in the rubber content is higher at a minimum of 70%.

The basic specifications are shown in Table 2. The thickness is established by considering the strength, resistance to irregularities, and workability. No special conversion of the plant production line was necessary for the 2.0mm thick EPDM sheet. The ultimate elongation is determined by considering the partial deformation. Since the sheet used in the plant was improved to reduce the tension set, its tensile strength exceeds that of the standard sheet ( $750\text{N/cm}^2$ ).

Table 2. Basic specifications of the main sheet.

Thickness (mm)	2.0~2.3
Ultimate elongation in tensile shear test (%)	450 or more
Tensile strength in tensile shear test ( $\text{N/cm}^2$ )	981 or more

Sheets joined and widened at the manufacturer's plant are used for the main sheet. To minimize irregularities in the adhering surface of the cover sheet by reducing the number of joints wrapped in the sheet anchor, the main sheet is joined in the slope direction. The tensile strength of the joints is greater than that of the original sheet. A test was performed to check its impervious sealing performance. The results confirmed there would be no air suction due to negative pressure. According to records regarding agricultural ponds, it is clear that with no water leakage through the joints, therefore, it provides the necessary high reliability.

#### 5.1.2 Cushion fabric

The cushion fabric prevents small irregularities and protrusion onto the surface of the transition layer and concrete from affecting the sheet. It protects the sheet from the edges of the crushed stone and concrete. It also prevents sheet failure due to local deformation as it makes the sheets installed surface smooth, thereby completely distributing sheet distortion to prevent local deformation of the base. (Elongation ratio in proportion to the same deformation is reduced.)

Long-fiber non-woven spun bonded fabric is generally used as the lining sheet cushion material. Compared with polyester and polypropylene, polyester was selected for the raw materials of the cushion materials, because of its excellent heat resistance and for water-proof performance. A repetitive hydraulic resistance test was carried out for the on-site sheet adhesions of which the base was a 20mm diameter simple grain material, assuming a loss of fine particles from the transition layer. Consequently, a minimum of  $800\text{g/m}^2$  is taken as the standard value of weight (mass per unit area).

#### 5.1.3 Cover sheet

The cover sheet provides an impervious sealing performance of the sheet anchor concrete surface which can become a weak point due to crack formation, etc. (The sheet anchor fixes the sheet mechanically. Its structure is dynamically stable. It does not, however, provide a water impervious seal.) Its material and specifications are the same as those of the main sheet.

### 5.2 Cover Sheet Adhesion Method

The adhering areas of the main and cover sheets are exposed. As this is the most important area for the water impervious seal of the surface lining, an adhesive tape (self-curing adhesive isobutylene-isoprene rubber tape) was used. The adhesive tape prevents condensation due to the adhesive when the sheet is cooled. Condensation can occur due to the heat of vaporization associated with the

adhesive's organic solvent. The isobutylene-isoprene rubber adhesive is initially combined with a curing agent. As this tape cures slowly, it eliminates any extra work required such as brushing, and results in a homogeneous adhesion surface.

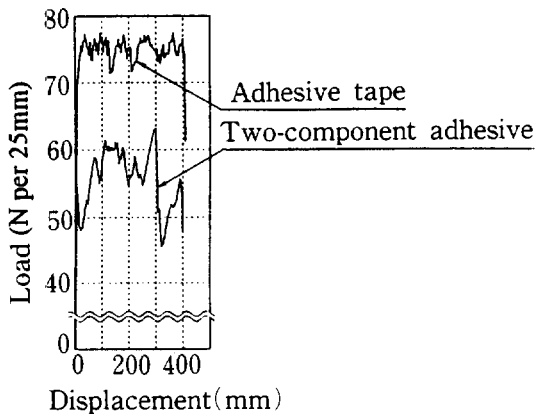


Figure 4. 180° peel test results

A 180° peel test was conducted on the adhering rubber sheet both after using a two-component adhesive and the adhesive tape. (Accelerated curing was used for test pieces at high temperature so that they provide the final adhesive strength.) The test results are shown in Figure 4. The peel strength of the adhesive tape is greater than that of the two-component adhesive. Here, the most important factor is that the adhesive tape shows smaller fluctuations in adhesive strength on peeling. Consequently, the adhesive tape ensures a higher water impervious seal. Adhesion with this tape prevents the formation of water leak routes.

## 6. QUALITY CONTROL IN SURFACE LINING INSTALLATION

### 6.1 Transition Layer Works

Stable quality is expected in the transition layer works since all materials are purchased from an existing crushing plant for concrete and road-base materials. In compaction, the finished density and surface conditions may, however, vary and quality control is, therefore, most important. The control standards were developed for precise quality control including a compaction method specifying the compaction equipment, spread depth, and tamping frequencies / times.

The control standards were developed based on the following basic conditions.

1. The material grain size shall be appropriate. The material shall be dynamically stable. Its structure shall also be stable in terms of the soil hydrology.
2. Compaction shall be sufficient.
3. The surface shall be smooth and dense.

The focal control points for the materials, compaction and surface finishing are grain distribution, dry density and flatness respectively. The controlled value of the field density was set at 1.92 t/m<sup>3</sup>, 70% of the relative density, in reference to the compaction test data for the material

containing natural water. This value was shown to provide sufficient strength for the embankment slope stability under the natural water content or saturation (postulating sheet failure) according to the triaxial compression test (CD test), and was selected with due consideration to its workability. Regarding the site density test method, the RI (radioisotope) method was used mainly as it allows measurement on the slope and is a simple method. The water replacement method was used in addition in the flat area and in the bottom of the crest and berm.

The quality control test showed that the values satisfied the control standards in all works (Table 3). The on-site permeability test also showed sufficient permeability for the transition layer. The site test conducted after compaction by the tamping method used in the actual installation showed that in the case of a minimum 10<sup>-2</sup> cm/s permeability coefficient, the transition layer performance of the residual air exhaust under the sheet was assured, with an air permeability coefficient in the order of 10<sup>0</sup> cm/s.

Table 3. Quality control test results of transition layer.

Items	Spec.	Ave.	Max.	Min.
Dry density (t/m <sup>3</sup> )	≥ 1.92	2.03	2.37	1.92
Permeability Coefficient (cm/s)	—	0.27	1.50	0.014

### 6.2 Lining Sheet Installation

For the lining sheet installation, control standards were developed to specify the installation conditions based on the temperature, humidity, wind velocity, etc., control method for the adhering area of the cover sheet, adhesion width of each member, and the adhesion location in detail.

Regarding the material quality, an inspection was conducted on all points of the basic specifications every 1,000m<sup>2</sup>. The rubber sheet quality may vary depending on the quality control in the raw material mixture process, pressure in the curing process, and the temperature control accuracy.

The cover sheet is the only member providing an impervious seal to the on-site sheet adhesions and thus requires a highly reliable adhesion. Quality control includes visual inspection and confirmation by touch to check for adhesion defects. Inspection with an inspection spatula confirmed no partial gaps remained not to adhere at the edges of the adhering areas. A negative pressure test was conducted throughout the adhering area. (Apply soapy water to the adhering area, depressurize at a minimum 0.51MPa over 10 seconds and check for foaming.)

Table 4. Quality control test results of adhesion work.

Items	180° peel strength	Tensile shear strength	
	(N per 25mm)	(N per 25mm)	
Curing period	7 days	7 days	3 months
Spec.	24.5 or more	196 or more	392 or more
Max.	80.4	503	631
Min.	29.1	314	405
Ave.	55.0	434	509

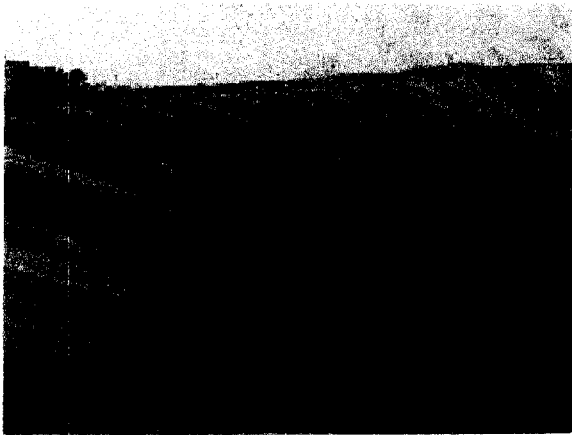
Test pieces produced under the same conditions were cured for 7 days, and the 180° peel strength and tensile shear strength were measured. The tests confirmed a stable adhering surface had been formed. The tensile shear strength was re-evaluated after a 3-month curing period and it was confirmed that the adhering area provided a strength equivalent to that of the main sheet. The test results are shown in Table 4.

## 7. OUTLINE OF WATER LEAK DETECTION AND DEWATERING SYSTEM

The system leads water leaking from the sheet to the inspection gallery (height=2.0m, width=2.0m) through the transition layer or PVC tube built into the sheet anchor. Since the groundwater from the drain hole on the ground is also led to the inspection gallery, it would be possible for the seawater and the fresh water to mix. To prevent such mixture, a pipe is installed from each conduit to each drain pit directly to collect the water. The leakage from the sheet only is pumped back to the upper pond. The groundwater is discharged to a nearby stream through a drainage tunnel. The seawater is, therefore, not discharged to the outside but returned to the upper pond and discharged back into the ocean after power generation. As the fresh water is discharged to the stream, the system is ecologically friendly.

Leakage from the sheet is detected by a salt analyzer (electronic conductivity measuring unit) and the fluctuation in the volume of leakage are measured by flow meter. Both instruments are installed on the conduit. To divide the slope into 55 and the bottom into 9 sections, a transparent conduit (acrylic) was installed to facilitate visual verification of the leakage locations in each section.

## 8. LINING SHEET BEHAVIOR UNDER STRONG WIND



Photograph 2. Sheet swell behavior in strong wind

In 1996, five typhoons approached Okinawa Main Island and provided opportunities to observe sheet swell behavior. When typhoon No.12 (Maximum instantaneous velocity; 49m/s, 10min. mean velocity; maximum 28m/s) approached in August, the water detection / dewatering

system piping, etc., had not been completed. Air was able to enter the sheet without restriction through the built-in sheet anchor tube. Consequently, a maximum sheet swelling of approximately 1.5m height took place (10min. mean velocity; maximum 18m/s, Photograph 2). The lining condition after the typhoon approach, was checked by visual inspection when it was confirmed that there were no problems such as sheet failure, and almost no residual sheet distortion or transition layer interruption.

Although typhoon No.21 approached in September, with an equal wind velocity, sheet swelling was controlled to approximately 1/3 by cutting off the air supply from the built-in sheet anchor tube. Since the crest road was paved, it was reasonable to assume that air inflow from the crest into the transition layer would be effectively prevented, thereby further controlling sheet swelling.

## 9. CONCLUSIONS

Following the completion of the lining in February, 1996, fresh water (rainfall and groundwater pumped up from the underground powerhouse) has been stored in the upper pond since June, 1996, to protect the lining sheet and to eliminate residual air from behind the sheet prior to the actual operation of the plant. No water leakage has occurred. This sheet lining has complete technically and has become the main development toward the realization of the world's first seawater pumped-storage power plant. Also, it raised the sealing confidence in the sheet lining used in agricultural ponds etc.

The paper presents the following suggestions for future projects with the rubber sheet lining for better technology.

1. Further improvement in the adhesion performance for on-site sheet adhesions is needed to enable application in ponds with larger water depths.
2. Transition layer material has been developed for low cost performance and better workability to meet the necessary functional performance.
3. Minimizing the 'human factor' in lining sheet installation would improve work stability and efficiency.
4. Where this lining is applied to store fresh water, the lining performance can be dropped to some degree compared with seawater storage. Cost reduction resulting from a more streamlined design will be the subject of a future project.

## ACKNOWLEDGMENTS

The writers wish to express their sincere gratitude to the members of MITI and all those concerned for their excellent cooperation and kind guidance.

## REFERENCE

- Takimoto, J. and Onoi, Y. (1997) "A Rubber Surface Pond on Strongly Weathered Rock Foundations for the Seawater Pumped-storage Power Plant", ICOLD Congress, 1997 Q.73, R.32, pp479-498.

# A Scheme of Using Geosynthetics to Treat Cracks on A Reservoir Blanket

Z.Y. Liu

Director, Technical Inquiry Committee of Water Conservancy Bureau of Hebei Province, China

**ABSTRACT:** A reservoir in the Hebei province of China has been in operation since 1961. A natural cohesive soil layer was used as the horizontal impervious blanket for the auxiliary dam. Cracks often occurred on the blanket and in the foundation of the dam during the operation. A scheme of using geosynthetics to treat the cracks was proposed. The scheme is composed of three reaches, namely, the anti-seepage reach, the drainage reach and the dam slope reach. Geomembrane, geomembrane-geotextile composite, and geopipes were used. A series of tests were made. The methods of testing and design will be presented in this paper.

**KEYWORDS:** Blanket, Cracks, Geocomposite, Design scheme.

## 1 INTRODUCTION

Huangbizhuang Reservoir in the Hebei Province of China was constructed from 1958 to 1961 with a catchment area of 23400 km<sup>2</sup> and a capacity of 1.21 billion cu. m. It has an auxiliary dam with a length of 7000 m and a maximum height of 19.2 m. The overburden layer of the foundation is composed of cohesive soil, sand, gravel and cobbles. The cohesive soil layer with thickness of 3~10 m was used as natural horizontal impervious blanket. A lot of cracks occurred on several parts of the blanket after storage of water for more than 35 years due to the unequal settlement of the soil layer under the water and dam load. The cracks were traditionally treated by digging ditches and backfilled with cohesive soil or by grouting with mud or cement. All of these measures had very little effect. In recent years some cracks were found under the dam and might extend in the foundation as far as the downstream side of the dam. It was found after exploration and excavation that most cracks on the blanket had silted up and those under the dam were mostly kept empty. It was generally considered that the cracks on the blanket would do little harm to the reservoir but those under the dam might cause seepage failure in the foundation. In order to refrain the water in the reservoir from flowing directly into the cracks under the dam and on the blanket near the dam, a scheme of using geosynthetics to treat the cracks was proposed. The whole work consists of a series of laboratory tests and a conceptual design. Geomembranes, geotextiles and geopipes were used in the scheme.

## 2 TESTS OF HYDRAULIC TRANSMISSIVITY OF THE SPACE BETWEEN THE GEOMEMBRANE AND THE SOIL

### 2.1 Test Equipment and Samples

#### 2.1.1 Test box

A box with size of 2.5 m × 0.5 m × 1.0 m is made of steel and divided into two stories. The height of each story is 0.5 m. Flange plates and rubber water-tight seal were used to prevent the leakage of water between stories. Inlet and outlet pressure gauges were installed as shown in Figure 1.

#### 2.1.2 Properties of geosynthetics and soil sample.

Two types of geosynthetics were used in the tests. One is PVC geomembrane with a thickness of 0.6 mm, and the other is geomembrane-geotextile composite composed of 0.45 mm PVC geomembrane and 210 g/m<sup>2</sup> needle-punched non-woven geotextile. Their properties are presented in Table 1.

Three kinds of soil samples were excavated from the blanket of the reservoir. Their properties are presented in Table 2.

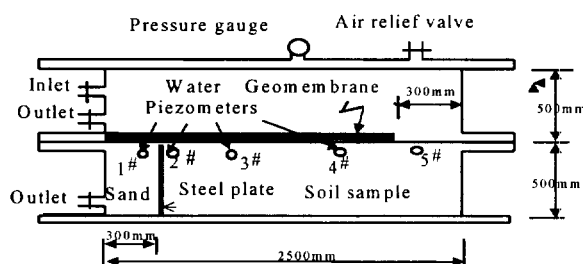


Figure 1. Test box.

Table 1. Properties of geosynthetics.

Types of geosynthetics	Thickness of geomembrane (mm)	Weight of geotextile (g/m <sup>2</sup> )	Stripe tensile strength (KN/m)	Elongation at break (%)
PVC geomembrane	0.6	—	9.49	282
PVC geomembrane-geotextile composite	0.45	210	12.44	83

Table 2. Properties of soil samples.

Soil samples	$\gamma_d$ (KN/m <sup>3</sup> )	Distribution of grain size (%)				Coefficient of permeability (cm/s)
		0.25-0.1 mm	0.1-0.05 mm	0.05-0.005 mm	<0.005 mm	
No.1	15.2	10.5	39.5	44.9	5.1	$7.09 \times 10^{-5}$
No.2	15.0		6.5	63.0	30.5	$2.63 \times 10^{-5}$
No.3	14.4	1.0	34.0	61.9	3.1	$9.23 \times 10^{-5}$

A mixture of three kinds of soil samples was used in the tests with a thickness of 0.5 m and dry density  $\gamma_d = 15 \text{ KN/m}^3$ . A sand drain with a width of 30 cm was placed at the outlet end of the box. A steel plate was welded on the front and back sides of the box to separate the sand drain from the soil sample. Geomembrane was put on the soil surface with a 30 cm gap to allow the water flowing into the geomembrane-soil interface. Glue was used to prevent leakage along the inner faces of the box. Four piezometers were put under the geomembrane with 1# on the sand and 2#, 3#, 4# on the soil. Another piezometer, 5# was put outside the geomembrane. Some pore pressure cells were buried in the soil sample. The detailed layout is shown in Fig. 1. The soil sample was pre-saturated. Water was supplied with varied heads of 1m, 3m, 6m and 9m. Each head was kept for 4 to 14 days until the discharge of the interface flow through the space between the geomembrane and the soil becoming stable. From the records of the pore pressure cells buried in the soil sample, the seepage water through the soil body was quite small and could be neglected.

Table 3. Results of Test No.1.

Water head H (m)	Duration (days)	Discharge ( $10^4 \text{ m}^3/\text{s}$ )	Reading of piezometers					Calculated results of each segment									
			5#	4#	3#	2#	1#	5#-4#, l=0.38m		4#-3#, l=1.0m		3#-2#, l=0.50m		2#-1#, l=0.05m		5#-1#, l=1.93m	
								$\Delta H$ (m)	$\theta$ ( $10^4 \text{ m}^3/\text{s}$ )	$\Delta H$ (m)	$\theta$ ( $10^4 \text{ m}^3/\text{s}$ )	$\Delta H$ (m)	$\theta$ ( $10^4 \text{ m}^3/\text{s}$ )	$\Delta H$ (m)	$\theta$ ( $10^4 \text{ m}^3/\text{s}$ )	$\Delta H$ (m)	$\theta$ ( $10^4 \text{ m}^3/\text{s}$ )
1.0	5	0.013	0.90	0.51	—	0.11	0.02	0.39	0.032					0.09	0.018	0.88	0.071
3.0	4	0.042	2.80	2.14	0.89	0.75	0.04	0.66	0.060	1.25	0.084	0.14	0.30	0.71	0.007	2.76	0.073
6.0	4	0.11	6.10	4.90	2.35	1.75	0.05	1.20	0.087	2.55	0.108	0.60	0.23	1.70	0.008	6.05	0.088
9.0	14	0.197	9.00	7.95	4.75	3.30	0.04	1.05	0.178	3.20	0.154	1.45	0.17	3.26	0.007	8.96	0.106

The above table shows that the values of transmissivity  $\theta$  vary significantly for different water heads at different positions along the interface. The factors affecting the values of  $\theta$  are : ①, the difference of water pressures above and below the geomembrane, ②, the water pressure acting on the soil surface, and ③, the head loss at the inlet and outlet of the interface. We can see that the values of  $\theta$  in the case of lower water heads ( $H=3 \text{ m}$  and  $H=6 \text{ m}$ ) at the inlet segment (between 5# and 4# piezometers) are smaller than those at the middle segments (between 4# and 3# piezometers, and 3# and 2# piezometers), which might be caused by the head loss at the inlet. But in the case of higher water head ( $H=9 \text{ m}$ ),  $\theta$  at the inlet segment becomes larger, which might be caused by the larger settlement of the soil body under higher water pressure and a larger space between the geomembrane and the soil being formed.

On the other hand, all the values of  $\theta$  at the outlet segment (between 2# and 1# piezometers) are smaller than those at other segments because the geomembrane at the outlet segment was subjected to a large pressure difference which made a large deformation of the geomembrane while the soil sample was subjected to a very small water pressure which made very little settlement of the soil body. Hence the interface space between the geomembrane and the soil is very small in this segment. At other segments the values of  $\theta$  vary with the water heads which made different deformations of the geomembrane and the soil sample and affected the transmissivity of the interface space between the geomembrane and the soil.

Eight tests were carried out from 1994 to 1995. The discharge of the interface flow, and the readings of the piezometers were recorded. The hydraulic gradients  $I$  between the piezometers were calculated and the hydraulic transmissivity  $\theta$  of each segment between every two piezometers can be calculated by the following equation:

$$\theta = \frac{Q}{BI}$$

where:  $\theta$  = hydraulic transmissivity of the space between geomembrane and soil ( $\text{m}^2/\text{s}$ );  $Q$  = discharge of interface flow ( $\text{m}^3/\text{s}$ );  $B$  = width of the box (m);  $I$  = hydraulic gradient between two piezometers,  $I = \Delta H/L$ ;  $L$  = distance between two piezometers(m);  $\Delta H$  = water heads difference between two piezometers(m).

The results of one of the tests, Test No.1, for example, in which 0.6 mm PVC geomembrane was used, are given in Table 3.

### 3 PERMEABILITY OF GEOMEMBRANES

The permeability of geomembranes can be determined by the WVT (Water Vapor Transmission) test method suggested by ASTM E96.

Haxo (1984) carried out a series of tests for different kinds of Polymeric membranes. The values of WVT can be converted into coefficients of permeability  $k$  by the following equation(after Lord and Koerner):

$$k = \frac{WVT}{S(R_1 - R_2) \times 1.175 \times 10^{10}} \Delta l$$

where:  $k$  = coefficient of geomembrane( $\text{cm}/\text{s}$ );  $WVT$  = Water Vapor Transmission( $\text{g}/\text{m}^2, \text{ day}$ );  $S$  = the saturation vapor pressure at test temperature( $\text{mm}$  of mercury),  $S = 32 \text{ mm}$  at  $20^\circ\text{C}$ ;  $R_1$  = the relative humidity within the test cup,  $R_1 = 1.0$  in Haxo's test;  $R_2$  = the relative humidity outside the test cup,  $R_2 = 0.2$  in Haxo's test;  $\Delta l$  = thickness of the membrane (mm).

The WVT test results and the corresponding values of  $k$  of PVC membrane are presented in Table 4



Table 4. Values of WVT and k of PVC membrane.

Thickness of PVC membrane(mm)	WVT(g/m <sup>2</sup> , day)	k(cm/s)
0.28	4.42	4 × 10 <sup>-12</sup>
0.51	2.97	5 × 10 <sup>-12</sup>
0.76	1.94	5 × 10 <sup>-12</sup>
0.79	1.85	5 × 10 <sup>-12</sup>

Hence the value k of PVC membrane ranges from 4 to 5 × 10<sup>-12</sup> cm/s.

#### 4 DESIGN SCHEME

##### 4.1 General Description

The width of the geocomposite on the blanket is 100 m, where cracks generally occurred and that on the dam slope is 70 m determined by the high water level. The Scheme is composed of three reaches on the cross-section, namely, the anti-seepage reach, the drainage reach, and the dam-slope reach. A single layer of 0.5 mm geomembrane with a length of 50m is put on the blanket of the anti-seepage reach, a composite made of 0.5mm geomembrane and 250g/m<sup>2</sup> needle-punched geotextile with a length of 50m on the drainage reach and a composite of geotextile-geomembrane-geotextile with a length of about 70m on the dam slope. A drainage system is provided to keep low water pressure under the geomembrane and geocomposite on the blanket. It consists of nine longitudinal drainage pipes at intervals of 10m, one transversal drainage pipe, a collecting well and a sump pump to collect and pump out seepage water. The layout is shown in Figure 2.

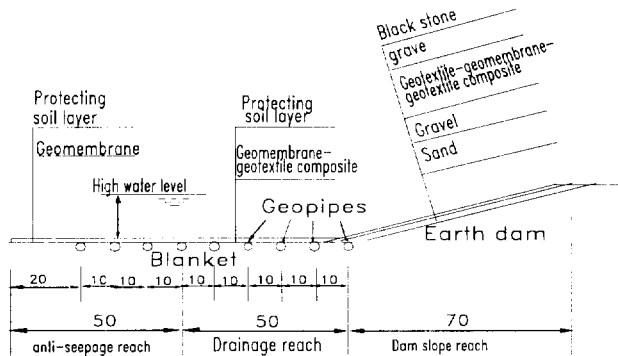


Figure 2. Cross-section of design scheme.

##### 4.2 Pressure Heads under the Geomembrane between Pipes.

###### 4.2.1 The water head equation under the geomembrane between two pipes (Figure 3)

Let the distance between any two pipes be 2L, set the origin at the mid-point of the interval between two pipes. Let y be the pressure head under the geomembrane at a distance x from the origin. The depth of water is 18m. The quantity of water permeating through the geomembrane will be

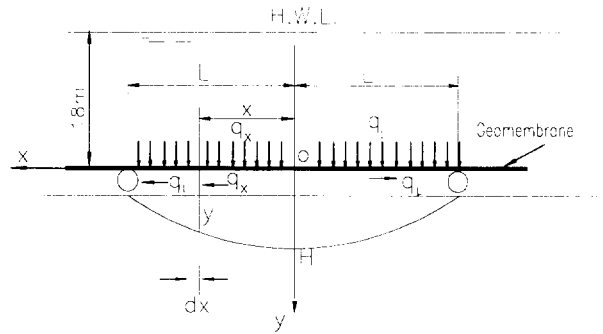


Figure 3. The curve of water head between two pipes

$$q = kIA = kIl \text{ per unit width} \quad (1)$$

where: q = quantity of water permeating through the geomembrane; l = length of permeating area, here l = dx, q = dq (m<sup>3</sup>/s per unit width); k = permeability of geomembrane, k = 5 × 10<sup>-12</sup> m/s; I = hydraulic gradient, I = ΔH/l, ΔH = difference of pressure head above and below the geomembrane, ΔH = 18-y; t = thickness of geomembrane, t = 5 × 10<sup>-4</sup> m

Substituting into eq.(1), we get: dq = 10<sup>-10</sup> (18-y)dx

The quantity of water permeating through the geomembrane from the origin O to a distance x will be q<sub>x</sub> = ∫<sub>0</sub><sup>x</sup> dq, or

$$q_x = 10^{-10} \int_0^x (18-y)dx \quad (2)$$

The interface discharge through the space between the geomembrane and the soil will be

$$q = I\theta \quad (3)$$

where: q = interface discharge (m<sup>3</sup>/s per unit width), at a distance x from the origin, q = q<sub>x</sub>; I = hydraulic gradient, here I = dy/dx; θ = transmissivity of the space. Hence

$$q_x = \frac{dy}{dx} \theta \quad (4)$$

Suppose the water pressure head y varies curvilinearly with x and the equation of the curve is

$$y = ax^2 + bx + c \quad (5)$$

The boundary conditions are: ① x = 0, y = H where H is the max. head at the origin; ② x = L, y = 0 because there is a drainage pipe at a distance L from the origin; ③ x = 0, dy/dx = 0, because at the origin no water would seep in opposite directions, and q = dy/dx θ = 0, therefore dy/dx = 0, substituting them into eq.(5) we get the pressure head equation

$$y = -\frac{H}{L^2} x^2 + H \quad (6)$$

4.2.2 The maximum head under the geomembrane between two pipes.

Substituting eq.(6) into (2)

$$q_x = \int_0^x 10^{-10} \left\{ 18 - \left( \frac{H}{L^2} x^2 + H \right) \right\} dx = 10^{-10} \left( 18x + \frac{1}{3} \frac{H}{L^2} x^3 - Hx \right) \quad (7)$$

which must be equal to the quantity of interface discharge represented by eq.(4), into which substituting eq.(6) we get

$$q_x = \frac{dy}{dx} \theta = \frac{d}{dx} \left( -\frac{H}{L^2} x^2 + H \right) \theta = -\frac{2Hx}{L^2} \theta \quad (8)$$

Balancing eq.(7) and (8)

$$10^{-10} \left( 18x + \frac{1}{3} \frac{H}{L^2} x^3 - Hx \right) = -\frac{2Hx}{L^2} \theta$$

we get the max. head at the origin

$$H = \frac{18x}{x - \frac{1}{3} \frac{x^3}{L^2} - \frac{2x}{L^2} \theta \times 10^{10}} \quad (9)$$

In the anti-seepage reach,  $L = 102 = 5\text{ m}$ ,  $\theta = 0.155 \times 10^{-6} \text{ m}^2/\text{s}$ , substituting into eq.(9) we get the max. head  $H = -0.146 \text{ m}$ .

In the drainage reach,  $L = 5\text{ m}$ ,  $\theta = 0.35 \times 10^{-6} \text{ m}^2/\text{s}$ , substituting into eq. (9) we get the max. head  $H = -0.064 \text{ m}$

4.2.3 Quantity of water flowing into pipes due to seepage and permeation.

By using equations (1) and (3) the quantity of water flowing into different longitudinal pipes at different positions could be estimated as shown in table 5.

Table 5. Quantity of water flowing into pipes.

Position of pipe	Quantity of water ( $10^{-8} \text{ m}^3/\text{s}$ per unit width)
The upstream pipe	16.7
Pipe in anti-seepage and drainage reach	1.8
Pipe at dam foot	7.2

4.2.4 Quantity of water flowing through the defects of the geomembrane.

In the design of a drainage system a defect of one hole with size of  $1 \text{ cm}^2$  per  $4000 \text{ m}^2$  of the geomembrane would be considered (Giroud, 1989). Accordingly the quantity of water flowing through the defect would be estimated by  $q = \mu A \sqrt{2gh}$ , where:  $\mu$  = discharge coefficient = 0.65;  $A$  = area of hole =  $1 \text{ cm}^2$ ;  $h = 18 \text{ m}$ . After substitution we get  $q = 1.22 \times 10^3 \text{ m}^3/\text{s}$  per  $4000 \text{ m}^2$ . The total length of three reaches of the geomembrane is about  $170 \text{ m}$ , hence  $4000 \text{ m}^2$  corresponds to a width of  $4000/170 = 23.5 \text{ m}$ . The quantity of water flowing through the defects per unit width will be  $q_6 = 1.22 \times 10^3 / 23.5 = 5.2 \times 10^5 \text{ m}^3/\text{s}$  (per unit width)

CONCLUSIONS

1. Cracks often occur in the foundation and on the blanket of an earth dam if it is built on a soil foundation and lined with a horizontal soil blanket. From economic and safety points of view the use of geosynthetics to treat the cracks might be more effective and appropriate than other measures. A scheme composed of three reaches, the anti-seepage reach, the drainage reach and the dam-slope reach, is recommended.

2. A drainage system must be provided to keep a low water pressure under the geomembrane. High water pressure under the geomembrane must be avoided because it might cause splitting action on the cracks, seepage failure of the soil foundation and rupture of the geomembrane during storage of water or rapid falling of water level. In this scheme there might be a high water pressure under the upstream part of the geomembrane (from the end to the first pipe), but it is quite far from the dam and would have little effect on the safety of the dam.

3. The functions of the geotextile affiliated with the geocomposite used in the drainage reach are to keep a further low water pressure under the geomembrane near the dam and to protect the geomembrane from being destroyed.

4. The quantity of water through the defects of the geomembrane is much greater than that due to seepage or permeation, anyway, it must be considered in the design of drainage pipes, and a certain factor of safety should be taken into account.

REFERENCE

Giroud, J.P. and Bonaparte R. (1989) "Leakage through Liners Constructed with Geomembranes -Part 1. Geomembrane Liners", *Geotextiles and Geomembranes*, Vol.1, No.1, Elsevier Science Publishers Ltd., U.K. p.64  
 Haxo, H.E. et.al. (1984) "Permeability of Polymeric Membrane Lining Materials" *Proceeding of International Conference on Geomembranes*. Denver, USA. pp.151 - 156.  
 Koerner, R.M. (1994) *Designing with Geosynthetics* (Third Edition) Prentice-Hall inc. New Jersey, USA. pp.432 - 433.

# Installation Damage Field Tests on a Geomembrane and Waterproofing of the SELVET Dam

**H. Girard**

Cemagref, Groupement de Bordeaux, 50 - avenue de Verdun, 33612 - Cestas Cedex, France

**D. Poulain**

Cemagref, Groupement de Bordeaux, 50 - avenue de Verdun, 33612 - Cestas Cedex, France

**C. Mine**

PRODIGE, 20 - Avenue des Chevaliers Tireurs, 73000 - Chambéry, France

**G. Potié**

SIPLAST, 12 - rue Cabanis, 75680 - Paris Cedex 14, France

**ABSTRACT :** The SELVET dam, located in the center of France, at an altitude of 1050 meters, was completed during the summer of 1996. It is 18 meters high and, with a crest length of 250 meters, can store 600 000 m<sup>3</sup> for drinking water purposes. Its backfill in stony gravel is waterproofed by a bituminous geomembrane placed on the upstream face. The choice of this geomembrane was the result of tenders from the relevant companies ; the design of the support and protection layers of the geomembrane and the implementation conditions are presented. In particular, field tests were performed to simulate installation damage during construction : 6 different structures were tested to define the Geomembrane Lining System (GLS), the purpose being to use local materials with sharp stones. Results of laboratory puncture tests are also given.

**KEYWORDS :** Geomembrane, Dam, Installation damage field test, Bi-axial tensile test, Puncture test, Slope stability

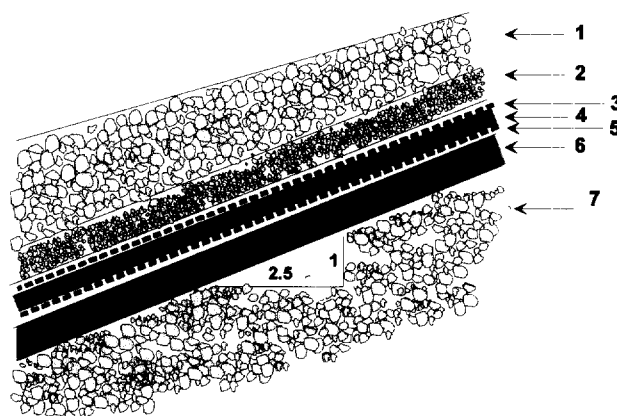
## 1 PRESENTATION

The substratum is a permeable basalt. The initial solution consisted of an embankment dam, constructed with a 0/150 mm basaltic random rockfill together with a watertight seal provided by a central diaphragm wall inserted in a silty gravel transition core (0/50 mm). A grout curtain was necessary to waterproof the foundation.

In this case an alternative solution was adopted using an elastomeric bitumen geomembrane placed on the upstream face. This was more economical and allowed the work to be completed in a shorter time. Because the fill was entirely random rockfill (0/150 mm) and not affected by rainwater, dam construction could take place in the winter.

The choice of the geomembrane was the result of tenders from the relevant companies and was justified by its competitive price and its references in France for this type of dam. The support and protection layers of the geomembrane had to satisfy the usual economic objectives for dams of this nature and the specific technical constraints at this site (in particular, resistance to puncturing from any sharp stones found in the fill and to the thick ice during winter). The final specification depended on installation damage tests realised under actual site conditions (on-site vehicles running over the protective layer). The six different Geomembrane Lining System (GLS) tested ranged from a minimum GLS, where the geomembrane was laid directly on the basaltic random rockfill (with any especially large stones removed) to the most complex one which was carried out with a bitumen stabilised support layer and anti-

puncturing geocomposites. The article describes these field tests and the results obtained from visual inspection and burst testing. These tests helped to determine the final choice for the GLS (figure 1). Its installation, together with the precautions taken and the stability calculations carried out are described in detail.



- 1 : 0 / 300 mm random rockfill ( 0.60 m to 1.40 m thick)
- 2 : 0 / 31.5 mm gravel (300 mm thick)
- 3 : Geocomposite (800 g/m<sup>2</sup>)
- 4 : Bituminous geomembrane (4 mm thick)
- 5 : Geocomposite (500 g/m<sup>2</sup>)
- 6 : Gravel - bitumen emulsion mix (150 mm thick)
- 7 : 0 / 100 mm random rockfill

Figure 1. Cross section of the Geomembrane Lining System

Complementary laboratory testing (puncture tests) was also performed for research purposes ; comparisons of the results of these tests were made with the results of the installation damage tests in the field.

## 2 ADVANTAGES OF A GEOMEMBRANE LINING SYSTEM (GLS)

### 2.1 Basic solution

A first study carried out in 1991 had evidenced that various types of dams could be considered for this site, namely in concrete (gravity dam), rock or earth. The geological and geotechnical surveys, continued in 1994 and 1995, evidenced that a flexible, backfill type dam was more suited to the context of the site than a concrete dam.

The materials available on the site consisted of :

- coarse 0/150 mm gravel, obtained by the blowing up of a basalt deposit situated on the right bank, providing large quantities of material ;
- 0/50 mm silty gravel in the bottom of the valley, but with an availability of only 30,000 m<sup>3</sup>.

Given these conditions, the typical profile adopted as a basic solution for the backfill included the following zones :

- a pseudo central core, 5 metres wide, in silty gravel sealed by a diaphragm wall in extension of a grouting curtain previously made in the foundation ;
- upstream and downstream fill in coarse gravel.

### 2.2 Type of dam retained

After consulting relevant firms, this basic solution was finally abandoned in favour of a homogenous backfill, with upstream sealing by a geomembrane. This choice was based on the following :

- it proved to be more economical (cost lower by approximately 10%) ;
- it provided the opportunity for an easier, later intervention on the grouting curtain then situated at the upstream toe of the dam ;
- it proved to be time-saving, as the grouting curtain and the backfill could be carried out simultaneously ;
- the construction of the backfill, solely in 0/150 mm coarse gravel, is less sensitive to the vagaries of climate and could therefore be considered in winter ;
- maintenance of silty gravel at the bottom of the valley is propitious for the sealing of the basin ;
- there is currently a considerable corpus of experience in the use of geomembranes for sealing dams, including large dams (ICOLD, 1991).

## 3 DESIGN OF THE GLS

### 3.1 Constraints specific to the site

The Geomembrane Lining System (GLS) had to meet the economic objectives specific to this type of small dam and the technical constraints specific to the site, in particular the mechanical aggressivity of the local materials proposed for support and protection, and the risk of thick ice in winter.

This latter factor resulted in the recommendation of protecting the entire surface of the geomembrane. The coarse 0/100 mm gravel of the upstream part of the backfill on which the GLS was to be installed was obtained by blasting on one of the slopes of the pond. It consisted of sharp stones without any cohesion, given the close grading of 50/100 mm and the absence of fines. Moreover, for economic reasons, use of rockfill, also obtained by blasting of the on-site basalt to obtain a grading larger than that of the backfill, had to be used for the protection of the geomembrane.

The geomembrane adopted was that proposed by the company awarded the contract, namely an elastomeric bitumen geomembrane with appropriate characteristics and references for the dam to be built.

### 3.2 Field damage tests

In such a context, damage tests of the geomembrane had to be made under installation conditions (figure 2) to determine the transition layers to be implemented on each side of the geomembrane. In view of the nature of the support and protection layers, the implementation of the protective structure by machines driving over the surface probably represented the highest risks of damage for the geomembrane.



Figure 2. View of the installation of the geomembrane on a test area.

Six on site tests were thus prepared. The geosynthetic materials used for the tests and the retained GLS were as follows :

- TERANAP 431 TP Elastomeric Bitumen Geomembrane, called GMB in the rest of the text, 4 mm thick and with a mass per unit area of 4.8 kg/m<sup>2</sup> ;

Table 1 : Geomembrane Lining Systems tested

Test N°	Support layer (over backfill)	Support geosynthetic	Sealing	Protective geosynthetic	Transition layer (under rip-rap)
1	Silty gravel from the site	None	GMB	GTX1	0/80 mm basalt (20 cm thick)
2	0/80 mm basalt	GTX2	GMB	GTX1	0/80 mm basalt (20 cm thick)
3	0/80 mm basalt	GCP2	GMB	GTX2	0/80 mm basalt (20 cm thick)
4	0/80 mm basalt	GCP2	GMB	GCP2	0/80 mm basalt (20 cm thick)
5	0/80 mm basalt covered with 6/10 mm fine gravel	GCP2	GMB	GTX2	Crushed quarry gravel 0/31.5 mm (20 cm thick)
6	0/80 mm basalt covered with 6/10 mm fine gravel	GCP2	GMB	GCP2	0/80 mm basalt (20 cm thick)

- heat-bonded, non-woven TERRAM geotextiles, type T6 or T7, called GTX1 and GTX2, 1.6 mm thick (NF 38-012, under 2 kN/m<sup>2</sup>) and with a respective mass per unit area of 280 and 330 g/m<sup>2</sup> (NF G 38-013) ;
- PRODRAIN 1-FT3 and 1-FT4 geocomposites, called anti-puncture geocomposites GCP1 and GCP2, with a mass per unit area of 500 and 800 g/m<sup>2</sup> respectively. They are composed of T3 (135 g/m<sup>2</sup> ; 0.9 mm) and T4 (190 g/m<sup>2</sup> ; 1.2 mm) geotextiles (same producer as T6 and T7, but thinner), with short textile fibers needle-punched on to them.

The lining systems tested were laid on the 0/150 mm coarse gravel backfill and topped with a 80 cm thick layer of 100/500 mm rip-rap, as described in Table 1.

The support layer was compacted in all the on site tests with a smooth, heavy vibrating roller, and the protection layers were positioned as work progressed by a loader driving over the rip-rap. The gravel placed above the geomembrane was compacted with a small tandem roller.

The tests were performed on a backfill installed for that purpose in the area of borrowed material, 15 m wide, with a 30 % slope, and 10 m long. Each test area was 2 m wide.

Two samples of 1 m<sup>2</sup> each of the geosynthetic materials installed were taken at random from each of the 6 tests. Analysis of the damage to the geomembrane included a detailed visual examination of the 12 samples and bi-axial tensile tests on the parts of each sample which appeared to have suffered the most damage.

Above all, the visual examination evidenced the following elements :

- severe damage on test No. 1, with punch marks over the entire surface, 8 of which came close to piercing ; more localized damage with nonetheless the presence of several impacts, close to piercing, in each of the tests Nos. 2, 3 and 4 (with one identified hole on test No. 2) ;

- the samples from tests Nos. 5 and 6 revealed only a few local, shallow punch marks.

### 3.3 Bi-axial tensile tests (Burst tests)

The bi-axial tensile tests were adopted to characterize, in the laboratory, the extent of the damage to the geomembrane. On the one hand, these tests integrated several parameters (tensile strength, deformability, leak detection, etc.) of particular interest in this case, and, on the other hand, were compatible with the short time-frame required by the site. Two samples were therefore cut from each of the 1 x 1 m panels taken from the site. These samples were taken from the areas which had visibly suffered the greatest damage (while avoiding the visually identified hole for which test would have been pointless).

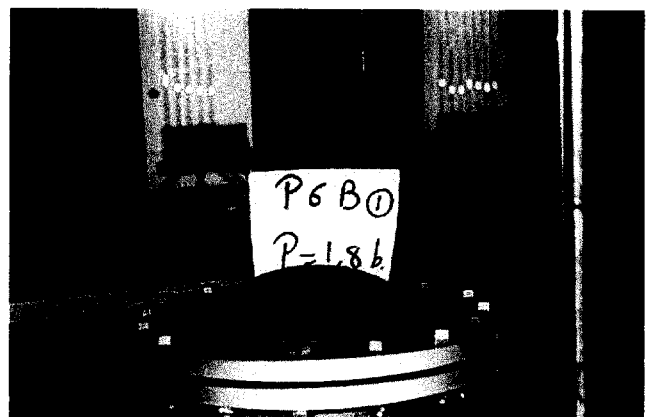


Figure 3. Bi-axial tensile test

The bi-axial tensile tests were performed on specimens with a diameter of 350 mm compressed by pressurised air with 200 mm diameter openings. The pressure was applied progressively in steps of 20 kPa, with a hold of 2 minutes between each step. Displacement was measured at the top of the geomembrane at the end of each step, and the burst pressure was recorded.

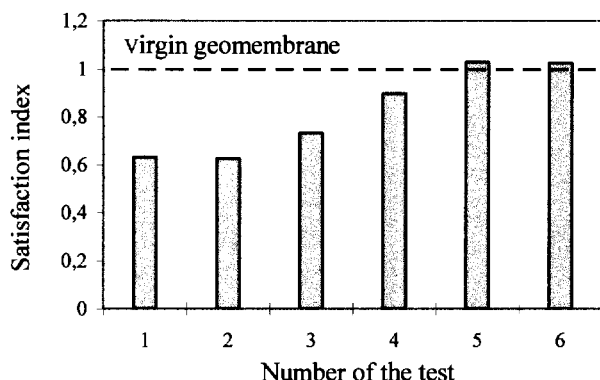


Figure 4. Summary of the bi-axial tensile tests for the 6 areas

The results of the tests were summarized in the form of a satisfaction index corresponding to the ratio between the mean of the displacements upon breakage recorded on the 4 samples from the same test area, and the mean of the displacements of 4 virgin samples. These values are shown in Figure 4.

Only the tests Nos. 5 and 6 gave a satisfaction index equal to 1, which confirmed the detailed visual examination of the geomembranes. Similar results were given by an equivalent index corresponding to the values of the bursting pressures.

### 3.4 Puncturing tests

These tests were performed after completion of the site, for research purposes, according to the French standard NF P 84-507, to determine the static puncturing resistance under the following conditions :

- . opening diameter = 45 mm,
- . punch diameter = 8 mm,
- . puncturing speed = 50 mm/min,
- . measurements : recording of the force applied and of the depth of the puncture.

For each GLS, 3 specimens were subjected to the test, whereas only one was taken for each geosynthetic tested.

The test was performed, of course, only on the geosynthetics. In that respect, it will be seen (Table 1) that test area No. 5 is the equivalent of test area No. 3 and test area No. 6 the equivalent of test area No. 4. The synthetic results shown in figure 5 correspond to the GLS of test areas 1 to 4. The GLS called « test area 7 » corresponds to the system implemented at the dam. For the static

puncturing test, the geosynthetics were arranged as in the field :

- . the smooth face of the geocomposite faced upwards (towards the punch) ;
- . for the GCP1 and GCP2 geomembranes, the « short fibre » face was in contact with the geomembrane.

Examination of the results in figure 5 evidence a better behaviour for test areas 4 and 6, which correlates with the results of the in-situ test areas (observations and results of the bi-axial tensile tests). The result for test area 7 is close to that of test area 6 (GLS of similar constitution). On the other hand, test area 5, the behaviour of which in-situ was considered satisfactory, behaves less well under static puncturing, whereas the GTX2 (used in test area 5) has a resistance equal to or greater than the GCP1 and GCP2 (test areas 4, 6 and 7). This evidences that the short fibres play a significant part in improving puncturing resistance.

In summary, the puncturing test is a simple test which provides valuable information for the comparison of the different geosynthetics tested for the protection of the geomembrane. It is, however, an index test which fails to take account of the granular layers of the support and protection structures, and cannot therefore be used alone for the sizing of a GLS. In our case, the in situ tests evidenced that the better quality of the support implemented for test area 5 compensates for the use of a less effective protective geocomposite.

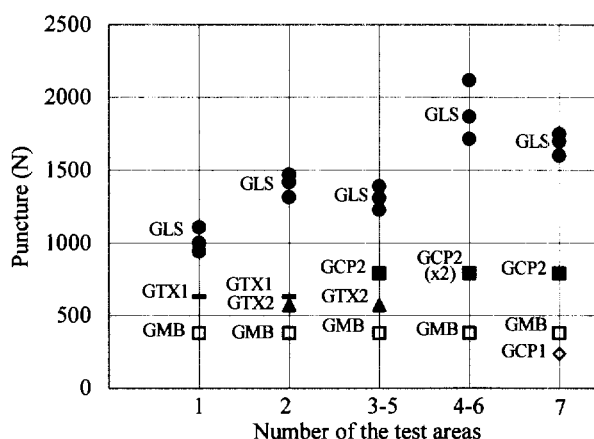


Figure 5. Summary results of the puncture tests

### 3.5 Description of the GLS adopted

Given the previously described on-site tests, it proved impossible to ensure a support layer solely with the on-site materials. At the very least, this layer had to be covered with fine gravel (tests Nos. 5 and 6). This solution, however, presented difficulties in implementation over a wide area (7,500 m<sup>2</sup>), due to the lack of cohesion of the gravel, which meant that the stones were likely to roll down the facing under the geomembrane upon its installation. To

avoid this installation difficulty, the support layer was finally made of gravel mixed with a bitumen emulsion. Under such conditions, with an improved quality of the support, it was decided to replace the GCP2 geosynthetic support under the geomembrane by a lighter-weight geocomposite (GCP1). Furthermore, to protect the geomembrane, the safest components of tests were adopted : the anti-puncturing geocomposite (test No. 6) and the crushed quarry gravel (test No.5). The GLS thus obtained is shown in figure1.

### 3.6 Stability of the GLS

To avoid eventual tensioning of the geomembrane, this one was installed with the smooth face uppermost. In these conditions, the weakest interface of the GLS as far as slippage stability is concerned consists of the contact between the geomembrane and the upper geotextile. The friction angle ( $\delta$ ) was measured between these two elements of the GLS with an inclined plane test (Gourc et al.1996 ; Girard et al. 1994). This test consisted of installing the geosynthetics to be studied on a flat frame, hinged on one side. The geosynthetics are then subjected to a low vertical stress by means of a layer of soil placed on the upper geotextile, held in place by a mobile, freely sliding frame (not fixed to the flat frame). The flat frame is then raised until slippage occurs along the interface being studied. The slippage angle is then measured. In the case in hand, the geomembrane was fixed to the flat frame ; the upper geotextile was then loaded with 30 cm of 0/31.5 mm gravel as used on the site. Slippage of the geotextile was obtained at values of 22 and 24 degrees (2 tests). A conservative value of 22° was taken in the calculations for the friction angle between the smooth face of the geomembrane and the upper geotextile.

The first stability calculation was performed taking account of a constant protection thickness equal to 1 metre, made up of a 30 cm layer of 0/31.5 mm gravel topped by 70 cm of random rockfill taken from the site. The mechanical characteristics adopted for these materials are  $c=0$  (zero cohesion) and  $\phi = 45^\circ$ . Furthermore, given the high permeability of these materials, it can be considered that when the dam is empty the protection layer is never saturated.

The calculations were performed according to the hypotheses defined above taking the highest profile of the upstream face. In this section, the total height of the slope is 17 m, with a slope of 1 / 2.5. The stability analysis is performed with the dam empty, by the blocks method (Soong and Koerner, 1996).

The safety coefficient thus obtained is equal to 1.22. This was considered too low, and to improve slippage safety the protection layer was therefore increased to 1.40 m at the foot of the slope and reduced to 0.60 m at the top. The calculations made with this variable thickness produced a slightly higher safety coefficient of 1.32. A calculation

performed using the ETAGE software (Soyez et al. 1990) developed by the Central Civil Engineering Laboratory (LCPC) produced the same result. We subsequently verified that slippage safety was also ensured during the filling of the dam ; in this case, the minimum coefficient obtained was equal to 1.20 at the beginning of the filling.

This profile with a variable thickness, as described above, was thus adopted for protection. The increase in the toe trench made it possible to increase considerably the slippage safety, which is thus ensured without taking account of tensile stress that can be absorbed by the upper geotextile (GCP2) anchored at the top of the slope.

## 4 IMPLEMENTATION OF THE GLS ADOPTED

A transition area (0/100 mm) was installed between the body of the backfill (0/150 mm) and the emulsified gravel, over a width of 3 metres, following completion of the grouting curtain at the toe of the upstream face. Its surface, parallel to the slope, was reworked with an excavator, and carefully finished by hand, to eliminate all of the larger pieces. The gravel-bitumen emulsion mix (0/14 mm) layer, 15 cm thick, was laid on the slope with a crawler-mounted loader and spread with a rake. Compacting was performed along the slope with a tandem roller anchored to the top of the slope, and the final surface then brushed.

The anti-puncturing geocomposite was then unrolled over the slope working downwards from the crest. The 2 m wide sections were sewn together. The geomembrane, delivered to the site in 4 m rolls, was unrolled downwards from the crest, the roll being hung from a hoisting tackle mounted on a shovel loader. The smooth face of the geomembrane was laid uppermost to avoid tensile stresses from settlement of the protection layer. A detailed pattern lay-out enabled the sections to be adapted to the length of the slope to avoid transverse joints.

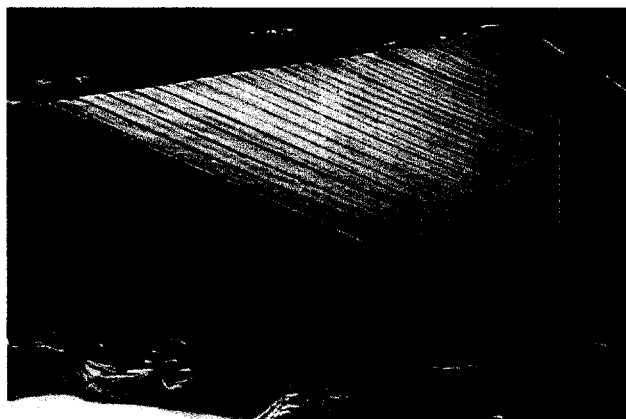


Figure 6. Installation of the geomembrane

Geomembrane sections were joined with a blow-torch,

with a 20 cm overlap. The project manager performed a visual inspection of all the seams.

The connection of the geomembrane to the grouting curtain at the foot of the slope was an important factor for sealing of the dam. The solution adopted consisted of lowering the geomembrane into a trench filled with concrete with the addition of bentonite (150 kg cement, 400 l with 10% of bentonite, 950 kg of 0/3 mm sand and 500 kg of 8/14 mm gravel). This trench was cut in the basalt with a trencher to a depth of 1 m along the centre line of the grouting curtain, then filled in 2 phases. The concrete was poured into the dam side part of the trench (using shuttering) to obtain a smooth vertical face. The geomembrane was then installed, and the upstream part of the trench filled. To improve the sealing of this sensitive transition area, an overlap strip of the same geomembrane (1 m wide) was then installed and seamed with the main geomembrane on one side and with the concrete (upstream part of the trench) on the other side. The geomembrane was anchored to the crest by a classic trench filled with gravel.



Figure 7. Installation of the protective layer of the GLS

The protection layer was installed as work progressed from the foot of the slope using a loader and a crawler-mounted shovel loader, after the installation of the top pierce-proof geocomposite. The two machines moved over the full thickness of the protection layer (gravel layer plus random rockfill) to restrict stresses on the geomembrane and to take advantage of the stability of the random rockfill resting at the foot of the slope up against a support fill.

## 5 CONCLUSION

The dam was built between October 1995 and August 1996, the backfill being completed during the winter. The installation of the GLS was performed without any particular difficulty between April and July 1996. The dam was filled in early 1997.

The damage on site installation tests made it possible to define a GLS adapted to the specific conditions of the dam with, in particular, the use of rip-rap taken from the site to form the protection layer.

The comparison between the results of the installation field tests (observations and bi-axial tensile tests) and laboratory puncture tests gave interesting information about the use of the latter.

## ACKNOWLEDGMENTS

We should like to thank the Viadène SIAEP, owner of the Selvet dam, the DDAF of Aveyron department and MERLIN consulting engineers, project managers who enabled us to complete this study and participated in the design and the construction of the GLS.

## REFERENCES

- Comité Français des Géotextiles et Géomembranes (CFGG), 1991 - *Recommandations générales pour la réalisation d'étanchéités par géomembranes*, 47 pp.
- Girard, H., Berroir, G., Gourc, J.P. and Mathieu, G. (1994) "Frictional behaviour of geosynthetics and slope stability of lining systems", *Fifth International Conference on Geotextiles, Geomembranes and Related Products*, Singapore, volume 1, pp. 339-342.
- Girard, H., Lefranc, M. and Tisserand, C. (1996) "Waterproofing and rehabilitation of dams by geomembranes in France", *First European Geosynthetics Conference, Geosynthetics: applications, design and construction, EUROGEO 1*, Maastricht, Netherlands, pp. 945-952.
- Giroud, J.P., (1992) "Geosynthetics in dams: two decades of experience", *Geotechnical Fabrics Report*, 10 (5), 6-9 and 10 (6), 22-28.
- Gourc, J.P., Lalarakotoson, S., Müller-Rochholz, H. and Bronstein, Z. (1996) "Friction measurement by direct shearing or tilting process - Development of a European standard", *First European Geosynthetics Conference, Geosynthetics: applications, design and construction, EUROGEO 1*, Maastricht, Netherlands, pp. 945-952.
- International Commission on Large Dams (ICOLD), 1991, *Watertight geomembranes for dams: state of the art*, Bull. 78, 140 pp.
- Soong, T.E. and Koerner, R.M. (1996) "Seepage induced slope instability", *Geotextiles and Geomembranes*, Vol. 14, pp. 425-445.
- Soyez, B., Delmas, Ph., Herr, Ch. and Berche, J.C. (1990) "Computer evaluation of the stability of composite liners", *Fourth International Conference on Geotextiles, Geomembranes and Related Products*, The Hague, Netherlands, Volume 1, pp. 517-522.



# BITUMEN GEOMEMBRANES IN IRRIGATION - CASE HISTORIES FROM A RANGE OF CLIMATES

B. Breul

Colas S.A., Direction Recherche et Développement, 92653 Boulogne Billancourt, France

R. Herment

Société des Pétroles Shell, Direction Bitumes, 92563 Rueil Malmaison, France

**ABSTRACT:** Bitumen was in use 5000 years ago for irrigation works that are still in good condition. Today, bituminous geomembranes are providing efficient, durable waterproof linings to irrigation canals, ponds and reservoirs throughout the world. They are either fluid-applied or delivered in rolls 4 metres wide. A survey of twenty irrigation dams around 10m high built between 1973 and 1983 in France with unprotected geomembrane facings found them performing well after 10-20 years service. Linings to a reservoir at Goudel in Niger and canals cut in laterite near Niamey have demonstrated their suitability in tropical climates. In North Africa, the Gulf States, Singapore, India and New Zealand, 5m-wide bituminous geomembranes have been in use on irrigation canals for some ten years and are still performing satisfactorily. In the USA, leaky areas on a large concrete-lined canal were stopped with an SBS bitumen-based geomembrane available in 4m widths in France.

**KEYWORDS:** Aging, Canal Liners, Case Study, Dams, Embankment, Geomembranes, Bitumen

## 1 INTRODUCTION

Five thousand years ago, crude petroleum was only accessible where it emerged from deep fissures in the ground. The heavy residue contained a high percentage of bitumen, which the ancients, especially in the Middle East, used for its waterproofing properties. Since those early times, it has been used to build and repair wells, reservoirs, canals and baths and consolidate irrigation canal embankments. Many of these constructions are still in good condition.

Bitumen emerged as a standard 20th century waterproofing material in civil and water engineering in the form of bituminous concrete, asphalt and bituminous geomembranes. The last-mentioned are lightweight materials that are easy to lay and repair, with waterproofing properties that make them ideal for irrigation works. They may take one of three forms:

- ◆ Bitumen can be sprayed onto a geotextile in situ (ISBGs)
- ◆ They may be prepared (prefabricated) in the factory and delivered to site in rolls (PBGs)
- ◆ An impervious asphalt may be laid on the canal or reservoir floor with the membrane confined to the sloping sides.

## 2 BITUMINOUS GEOMEMBRANE FOR IRRIGATION WORKS

The material underlying the lining must be free from grass or other organic matter, and well drained if it is not naturally impervious. Gas collection wells are also needed

if there is a risk of fermentation. It must be stable, smooth, with no sharp stones, and compacted to at least 90% Proctor optimum.

Although not always necessary, a protective covering should be added if the geomembrane is exposed to uplift pressures, wind suction, severe sunlight, impact, ice, debris, animals or wilful damage. It usually consists of unprocessed natural material although stabilisation with cement or bitumen reduces the thickness required.

Bituminous geomembranes, 3.3mm to 5.6mm thick with a density of 1.15, are three times heavier than polymer geomembranes, and therefore less affected by wind action.

## 3 EXAMPLES OF IN SITU BITUMINOUS GEOMEMBRANES

### 3.1. France

In situ bituminous geomembranes (ISBGs) were used in France in the early sixties under railway track and for renovating old roads; the ballast and top foundation courses respectively were removed to a depth of up to 800mm and the bituminous membrane was sprayed in two 3-5mm coats with a glass fleece or non-woven polyester geotextile in between, before covering with new material. The membrane isolates the overlying material from contaminated groundwater and shields the foundation from percolating surface runoff.

This approach was used again on the Huningue (1962) and Nord (1966) ship canals. It usefully reduces leakage through the canal floor. It must be protected on the banks against erosion and wave action.

When water reservoirs began to be lined in the seventies, it was found necessary to design special reinforcing arrangements to control root damage.

The choice of bitumen grade is governed by air temperatures at the site, altitude and exposure to sunlight. The bitumen is sprayed from a tanker through a spraybar at the rear or extending out to one side, horizontally or at an angle when spraying slopes. The geotextile is normally unrolled after the first coat has been sprayed.

The first application of an ISBG to a mountain reservoir 1800m asl in the French Alps was followed by several coastal reservoirs near Toulon with capacities ranging from 3000 m<sup>3</sup> to 40,000 m<sup>3</sup>, where the membrane was laid on pervious material and protected with 8cm of lean concrete.

Surface protection is not always necessary. Two small rockfill dams, 4-13m high, were built in 1973 and 1975 in southern France, each faced with an ISBG exposed to direct sunlight. The agricultural ministry's research institute CEMAGREF monitored the performance of the facings and reported the appearance of only one tear at the crest after eight years, which remained unchanged over the following seven years. A strip of geotextile that had not been impregnated with bitumen and had aged was easily repaired. The other dam showed no flaws after more than 20 years.

Use of ISBGs was slowed in France because the country's dense road network accessible to heavy trucks favoured prefabricated bituminous geomembranes, but they are an excellent answer for narrow inaccessible sites and for covering large flat areas.

### 3.2 USA

There has been a special ISBG working group within ASTM committee D35-10 since 1996.

#### 3.2.1. Irrigation Canals

The United States has a very extensive irrigation canal system and the US Bureau of Reclamation has issued tables correlating canal size and capacity, slopes, fill material and thickness.

#### 3.2.2. Reservoirs

American engineers use ISBGs to line large reservoirs with capacities in excess of 1 Mm<sup>3</sup>.

At Oakland, the ISBG is covered with 100mm of concrete and lies on a foundation of 10cm of dense and porous asphalt.

Engineers and scientists at the Department of Energy's Hanford site in Washington have developed a maintenance-free waste-site surface barrier made from natural materials that will last for 1000 years. They monitor a 5-acre prototype constructed in 1993 over a decommissioned wastewater disposal facility. There is a multi-layer barrier of various natural materials (sand, gravel, clay, etc.) 4.50 metres thick. In addition, an ISBG was laid on 150mm of asphalt.

## 4 PREFABRICATED BITUMINOUS GEO-MEMBRANE RESERVOIR LININGS

A few interesting examples are described in the following.

### 4.1. France: Embankments Less than 18m High

Seventeen water reservoirs impounded by rockfill embankments have been monitored by CEMAGREF over the last twenty years. Only four linings had protective coverings and all the underlying rockfill was free-draining. Reported damage was minor, consisting of a single case of a PBG being punctured by sharp stones underneath, one tear by vandals, and one section of seam that separated. The three spots were quickly repaired in a durable manner.

The only reported damage on the other embankments was minor damage to seams from plant roots, which was easily repaired. Mud curling was observed on the PBG without surface protection although it had no effect on watertightness and the process always stopped at the geotextile.

There are many other geomembrane linings ranging from 1500 m<sup>2</sup> to 10,000 m<sup>2</sup> in area all over France that have been giving complete satisfaction for the last twenty years.

### 4.2 France: Large Irrigation Works

Ospedal dam, 26m high, with a 5000 m<sup>2</sup> PBG facing laid on porous asphalt and a geotextile and protected with interlocking pavings, was built in Corsica in 1978 and remains in excellent condition, as evidenced by 19 years of periodic inspection.

In 1976, an irrigation reservoir was built at Gap in southern France with a 25,000 m<sup>2</sup> PBG facing, and Ortole rockfill dam in Corsica was completed with a similar 6800 m<sup>2</sup> facing. Problems were experienced with the poorly compacted soil when first filling the Gap reservoir. A tear in the geomembrane where it joined a concrete pipe allowed leakage to wash away material from the embankment, but it was easily repaired.

The Ortollo facing was laid on a elaborate base (25-30mm ballast impregnated with 3 kg/m<sup>2</sup> bitumen emulsion and 100mm cold laid asphalt) plus a geotextile. The protective covering was geotextile plus 140mm in situ fibre reinforced concrete (polypropylene fibre, length 30mm, weight 1kg/m<sup>3</sup>). All seams were 100% tested with an automatic ultrasound tester. The quality of construction enabled the structure to withstand exceptional floods successfully.

#### 4.3. Reservoirs in Hot Climates

From 1981 to 1983, large jobs ranging in size from 50,000 m<sup>2</sup> to 80,000 m<sup>2</sup> were completed in Saudi Arabia at Hail, Riyadh, Taif and Dorman at the Royal Palace. They included many ornamental ponds.

At Goudel near Niamey, a river water storage reservoir was lined with 4500 m<sup>2</sup> of PBG in 1981 and remains in good condition apart from some tears at junctions with concrete structures.

In 1989 at Palma, Majorca, 22,500 m<sup>2</sup> of PBG was used to line an aeration lagoon.

In 1991, reservoirs in the gulf of Marrakech had 90,000 m<sup>2</sup> of elastomeric bitumen PBG laid directly on the sand, without any protective covering.

In the same period, large reservoirs were lined with 30,000 m<sup>2</sup> PBG in Abu Dhabi.

In 1996, 110,000 m<sup>2</sup> of PBG was used at a settling pond in Nigeria.

All these prefabricated bituminous geomembranes performed well with respect to sunlight and temperatures in these hot climates.

## 5. CANALS

### 5.1. France

PBGs are used extensively for lining irrigation ditches and canals. Tests performed after fifteen years service near Le Mans revealed that PBGs covered with soil and grassed, were ageing well. They performed valuable service in controlling leakage from critical canal sections in the Freyssinet system. The largest job was the 260,000 m<sup>2</sup> of elastomeric bitumen PBG lining to the Nieffer canal near Mulhouse.

### 5.2. Very Hot Climates in Africa and Asia

Prefabricated bituminous geomembranes were effective in the construction of Ishagi canal, Iraq, in 1981 and the Mines d'Or canal at Poula in Burkina Faso. They also

successfully repaired the 64,000 m<sup>2</sup> of leaking concrete lining to the Tanorga irrigation canal in 1985, and controlled leakage over 22,000 m<sup>2</sup> of Tungabhadra canal in India in 1987. A geotextile underlay and slate gravel protective covering were provided for the Mines d'Or canal PBG.

### 5.3. North America

Two of three leaking sections of the Caspa District canal in Wyoming, USA, were repaired with 9000 m<sup>2</sup> and 60,000 m<sup>2</sup> elastomeric bitumen PBG in 1992 and 1994 respectively. The third, slightly larger (80,000 m<sup>2</sup>) section was repaired in 1995 by the canal operator's own employees.

When the West canal in Oklahoma was leaking in 152 places, PBG repairs to an 800m section restored irrigation supplies to 120 ha of farmland.

California has the densest canal system in the USA, and PBG has been used extensively to repair earth and concrete-lined canals.

Two water treatment ponds covering 75,000 m<sup>2</sup> and 6.50m deep, lined with elastomeric bitumen PBG, lost only 1 litre per square metre per day as against the design criterion of not more than 20 litres.

### 5.4. Special Problems in Livestock Farming Areas in Developing countries

Near Niamey in Niger, canals cut into the laterite were lined with 20,000 m<sup>2</sup> of PBG in 1991, and six years later, it was observed that:

- ◆ Canals in vegetable-growing areas were in good condition.
- ◆ Canals in livestock farming areas had been damaged at cattle crossings.
- ◆ Local residents had purposely torn the geomembrane in places to take water. It is also said that bituminous geomembrane material is popular for re-soling shoes.

This means that special measures are needed to combat damage of animal and human origin, such as fencing, thorn hedges, concrete cattle crossings and more water offtakes.

In Niger as in many other places, special care is needed when joining geomembrane to concrete, and should include firm cold jointing, double membrane thickness and clamp bars.

## 6. CONCLUSION

Laying bituminous geomembranes, with or without surface protection, is such a simple job that it can be successfully performed in many countries with standard tools and trained local labour, to build and repair irrigation canals and reservoirs. The examples described also illustrate that bituminous geomembranes are easy to repair, retain their waterproofing properties over time and age well.

The choice between in situ and prefabricated alternatives or combining bituminous geomembranes with asphalt is governed by local cost factors, since all three approaches have proved their worth.

## 7. ACKNOWLEDGEMENTS

Thanks are due to Messrs Siplast and Hypofors for permission to quote details of their jobs.

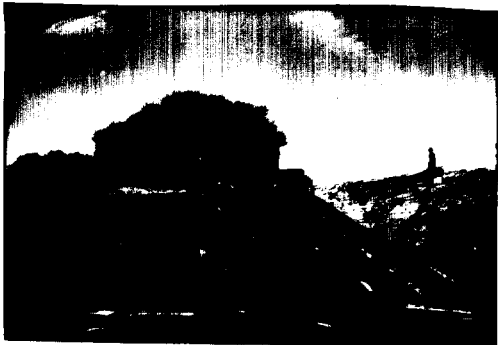
## REFERENCES

- Van Asbeck, W.F. (1962). *Bitumen in Hydraulic Engineering*, Vol 1, pp1-3
- Shell France brochure. La membrane bitume enterré, Nov 1974
- Dunglas, J., Lelu, V. and Chaigne, P. Revêtement de canaux d'irrigation par béton bitumineux étanche ou membrane bitume enterré. *Revue Eau et aménagement de la région provençale*. No.14, July 1977
- Alonso, Degoutte and Girard (1990). Result of Seventeen Years of Using Geomembranes in Dams and Basins. *Proc. 4th Int. Conf. On Geotextiles, Geomembranes and Related Products*. The Hague
- Wing, N.R. and Gee, G.W. (1994). Quest for the Perfect Cap. *Civil Engineering*. Nov. 1994
- Tisserand, C (1983). Un grand bassin à membrane non protégée. *Colloque Étanchéité superficielle*. Paris (CEMAGREF issue)
- ICOLD. Bulletin No. 38 Use of Thin Membranes on Fill Dams
- Bianchi, C., Rocca Serra, C. and Girollet, J (1979). Utilisation d'un revêtement mince pour l'étanchéité d'un barrage de plus de 20 mètres de hauteur. Communication C11. *Proc. 13th ICOLD Congress*. New Delhi 1979
- Breul, B. and Herment, R (1997). Bituminous Geomembrane Waterproof Lining to Manes Storage Reservoir. *Proc. Rencontres 97 Congress*, Reims 1997
- Shell Bitumes newsletter *Le Liant* No. 14, May 1996. Le barrage d'Ortolo

Shell Bitumes newsletter *Le Liant* No. 14, May 1996. Les géomembranes bitumineuses conquièrent l'Amérique



Colétanche bituminous geomembrane  
being laid at Ortolo dam



Reservoir lined with Colétanche  
at Goudel, Niger



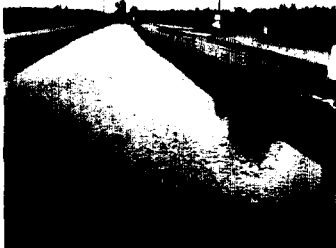
Canal lined with Colétanche  
near Niamey, Niger



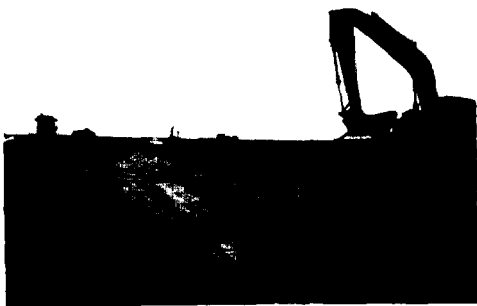
**Caspa Alcova, Wyoming (USA)**



**Caspa Alcova, Wyoming (USA)**



**Irrigation Canal, California (USA)**



**Altus, Oklahoma (USA)**

# Construction Technology of Geotextile Mattresses for Bank Protection of Liaohe River, Liaoning Province, P. R. China

Wang Dianwu,

Research Institute of Water Resources and Hydropower, Liaoning Province

Wang Xiaobai

Management Office of Agricultural Development Projects Using World Bank Loan, Liaoning Province

**ABSTRACT:** Since early 1980's, the experimental study of application of geotextiles to the bank protection of Liaohe river in our province has been carried on. We have innovated in construction technology, featuring the cold region in our country, such as sinking geotextile mattresses on/under the ice cover, and on a boat / floating bridge, etc. This paper briefs these construction methods, the properties of geotextiles in use for mattresses and the design principles are also provided.

**KEYWORDS:** Geotextiles, Embankments, Erosion control, Construction

## 1 INTRODUCTION

To handle dangerous section of a dike has always been the crux to river training works. Since last decade or so, geotextile mattresses have been used in such sections along the trunk of Liaohe river. According to the statistics, a total of 2 million sqm or more geotextiles were used in some 150 bank protection works. It has saved a great deal of investment and about 150 thousand tons of twig as compared with traditional fascine bundles and riprap works, which is corresponding to protecting thousands hectares of rapid growth forest, that is beneficial not only to ecological environment, but also to saving expense of transportation, as the total weight of 2 million sqm of geotextiles is only 300-500 tons, which is far less than that of twig. When the GT mattresses are used, the most appropriate construction method may be chosen, and the work efficiency could be increased by 50% or more, the quality of project and operating results may be guaranteed as well.

## 2 MANUFACTURE AND WEIGHT OF GEOTEXTILE MATTRESSES

### 2.1 Material of Geotextile Mattress

Five kinds of polypropylene woven geotextiles were used mainly in bank protection of Liaohe river. The main properties of GT are shown in table 1.

As seen by Table 1, the mechanical properties of the five kinds of GT can all meet the engineering requirement, but in consideration of that the larger the opening size, the lower the cost, so that, under the permissible filter condition, we choose the GT with opening size as large as possible.

According to laboratory filter test, field erosion

test and analysis on engineering practice for these five kinds of geotextile, the design criterion of filter is taken as:

$$O_{90} \leq A d_{90} \quad (1)$$

In which, the coefficient A is 10 for clay and loam; 2~5 for sandy loam and sand.

### 2.2 Determination of the Size of GT Mattress

Transversal (normal to the stream) length of the GT mattress is composed of two parts, i. e. the above-water part and under-water part. The transversal length of the above-water part is determined similar to the normal bank protection, and that of the under-water part will be calculated in reference to the thalweg if the main flow of the river is near the bank; or in reference to maximum eroding depth if the thalweg is far from the bank.

The transversal length of under-water GT mattress calculated with thalweg is:

$$L = L_1 + L_2 + L_3 \quad (2)$$

Where: L = total length of under-water GT mattress (m);  $L_1$  = length of mattress required for connecting to that of above-water part and for anchoring (m);  $L_2 = S_1 S_2 \sqrt{X^2 + H^2}$ , in which:  $S_1$  and  $S_2$  are coefficients of wrinkle and contraction under-water respectively. The actual measurement values for Liaohe river are  $S_1 = 1.4$  and  $S_2 = 1.05$ ; X = horizontal distance between thalweg and water surface on the bank during low water level (m); H = depth of water at thalweg during low water level (m);  $L_3 =$  overlength beyond the thalweg, or  $L_3 = K_0 h \sqrt{1 + m_0^2}$ ; in which:  $K_0$  = safety factor;  $m_0 =$

Table 1. Properties of GT used in the Bank Protection of Liaohe River

Polypropylene woven GT	Weight (g/sqm)	Thickness (mm)	Tensile strength (N/5cm)		Elongation per unit length(%)		Equivalent opening size $O_{90}$ (mm)	Permeability (cm/s)
			warp	weft	warp	weft		
A	100	2.0	496	408	26.0	20.0	0.70	$6.84 \times 10^{-4}$
B	110	2.5	511	666	28.6	25.0	0.72	$3.57 \times 10^{-3}$
C	103	2.1	584	526	13.0	17.5	0.15	
D			540	480	15.3	13.8	0.66	
E			392	357	19.5	17.5	0.33	

stable slope rate under-water;  $h$  = maximum eroding depth(m).

If transversal length of under-water GT mattress is calculated with maximum eroding depth, the total length of it will be:

$$L = L_1 + L_2 \quad (3)$$

where:  $L_1$  is the same as in Eq. (2);  $L_2 = K_0 h \sqrt{1 + m_0^2} (H_m + H_{max})$ . in which:  $H_m$  = mean depth during low water level(m);  $H_{max} = H_m(2B/R_m + 1)$ . in which:  $B$  = width of river corresponding to the bed forming discharge (m); and  $R_m$  = radius of curvature at river bend(m); and  $H_m$  = mean depth before erosion at the section in question.

The longitudinal length (in the direction of stream) of GT mattress was adopted 20 ~ 50m for on/under ice cover construction, and 10 ~ 20m for on boat/raft construction in Liaoning Province.

The dimension of GT mattress for base protection of spur /longitudinal dike may be computed by following formula:

$$L = l + m_1 h + l_0 + a \quad (4)$$

$$B = b + 2m_2 h + 2l_0 + a \quad (5)$$

In which:  $L$  and  $B$  = length of mattress parallel and perpendicular to the axis of dike, respectively, (m),  $m_1$  and  $m_2$  = end slope and side slope of dike, respectively,  $l$  = length of dike(m),  $b$  = top width of dike (m),  $l_0 = K_0 \sqrt{1 + m_0^2} h_s$ , where:  $h_s$  = depth of local erosion around the dike (m), which may be calculated by formula or determined by experiment, the actual measurement value for Liaohe river is  $h_s = 1.1 \sim 2.8m$ ,  $K_0$  and  $m_0$  are the same as in Eq. (2).  $a$  = additional length including wrinkle and contraction under-water(m).

### 2.3 Manufacture of Geotextile Mattress

The four edges around the GT mattress and every 0.50 ~ 0.60m in the transversal direction should fold up and sew into a sleeve-like pipe for penetrating nylon rope to act as reinforcements.

Now the factories can produce the GT mattress according to designed size and disposition of reinforcements.

### 2.4 Geotextile Mattress Weight

The types of weight for GT mattress are as follows:

1. precast concrete blocks put on sides of the mattress, and arranged in checkers inside the mattress, dump additional stone within the checkers make the mean weight up to  $1.2kN/m^2$ , and  $1.6kN/m^2$  for side one.
2. Put willow or oak twig bundles on two-layer GT mattress to form  $1.0 \times 1.0m$  checkers with riprap within it. The weight of which may be  $3.7 \sim 5.6 kN/m^2$ .
3. Earth pillow weight, this is a bag made of coated woven geotextile, filled with earth in situ, then sewn up. The length of which used in Liaohe river is 5 ~ 10m, 0.30 ~ 0.40m in diameter and single weight 10 ~ 20kN.
4. Put gabions, 0.30 ~ 0.60m in diameter, on edges of GT mattress; and arranged in checkers on it. Then dump riprap within checkers for 0.30 ~ 0.50m thick.
5. Combined weight of gabion, riprap, and earth pillow. The gabions are used for side weight and an additional weight of gabions at 10 ~ 20m spacing. The riprap or earth pillows are placed between the gabions. The weight is about  $1.0 \sim 2.0kN/m^2$

## 3 CONSTRUCTION TECHNOLOGY

### 3.1 Sinking Mattresses on Ice Cover

The construction period in our province is usually from the last ten days of December to the first ten days of March the following year.



Table 2. Field experimental results of ultimate bearing capacity of ice cover in Liaohe river area

Thickness of ice cover (cm)	Freezing period				Thawing period			
	10	20	30	40	10	20	30	40
Bearing capacity (kN/m <sup>2</sup> )	5.60	9.20	14.66	20.00	2.40	4.00	4.95	5.80



Figure 1. Sinking mattresses on ice cover

Dig an ice pit according to the size of GT mattress, construction period, designed weight and bearing capacity of ice cover.

The field experimental results of ultimate bearing capacity of ice cover for various thicknesses during freezing and thawing periods in Liaohe river area are listed in Table 2.

Place the GT mattress into the ice pit, the adjacent mattresses should be lapped or sewn on.

The weight should be put firstly on the downstream side of mattress, then extended progressively from upstream to downstream. When the weight reaches designed amount, the mattress body will sink itself uniformly within a short time.

With regard to the construction of GT mattress for base protection of spur /longitudinal dike, it should be done during thawing period when the bearing capacity of ice cover is greater, or determined in accordance with the law of thawing ice cover in local area, weight of dike, and loading of construction. To ensure safety for construction and shorten the time of construction as far as possible. The procedures are as follows: positioning on ice surface, spreading GT mattresses, putting weight on it, and building dike according to designed shape preliminarily. The dike deformed as soon as the thaw of river, to build again the dike to design section after thawing is basically stable.

### 3.2 Sinking GT Mattress Under Ice Cover

To dig through two longitudinal ice trenches, one near the bank and the other on the midstream side

of the mattress, and two transversal ice trenches at upstream and downstream ends. The trenches should not meet each other, they are used to pull mattress under ice cover. and to dump weight through them.



Figure 2. Sinking GT mattress under ice cover

Fold up the first GT mattress longitudinally and keep downstream end of it on the surface. Put the folded mattress on the upstream side of the first transversal ice trench.

Tie the upstream end of mattress to the piles driven through ice to the river bed, and hold down it on the ice cover with earth pillow.

Tie polyethylene (PE) ropes on each corner of downstream end of mattress(which is on the top of folded mattress), then throw the ropes into water through transversal ice trench and draw out from longitudinal ice trench (on the midstream side) by means of a stalk-hook. Then the mattress will follow the ropes passing through the water under ice cover, and be drawn out and put on the ice cover. The next mattress should then be sewn to the former. The rest may be done by the same way.

Throw the ropes into water through that longitudinal ice trench and draw out from another longitudinal ice trench (on the bank side). Pull the ropes to place the GT mattress (which floats on the water under ice cover), then fix it to bank and midstream ice surface. Finally, to give weight through transversal and longitudinal trenches on it. The mattress will sink onto the river bed.

### 3.3 Sinking GT Mattress on Boat/Raft

During bank protection construction period in

Liaoning province (the low water level period), the depth of water in the river is usually not more than 1.0m, and the velocity is about 0.5 ~ 1.5m/s. In practice, a realistic measure of sinking GT mattress by sliding it off while drawing the ropes in on the boat has been used. The main procedures of construction are as follows:

Positioning the two sides of GT mattress by transit or surveying rods, drive a pile on river bank and drop an anchor in river to fix steel rope used for guiding the boat to pull the GT mattress.

Place the GT mattress on the regulated slope of the bank, put and fix the precast concrete blocks on it. A steel pipe is installed on the front edge of the mattress. The PE ropes (16mm in diameter) spaced 2 ~ 3m centers are tied on the steel pipe and the boat.

The boat moves along the steel rope and pull the mattress with the PE ropes, the mattress will be developed gradually under the water until it reaches desired position.

Then, dump additional weight on the mattress from the boat.

### 3.4 Sinking GT Mattress on a Floating Bridge

The floating bridge is made up of raft or boat located near the river bank. The length of which should be longer than the transversal length (normal to the stream) of GT mattress. The loading capacity must be more than the total weight of earth pillows, gabions, and workers. The position of the floating bridge is held by steel or PE ropes to an anchor.

The procedure of sinking mattress is as follows:

Carry the processed GT mattress onto the floating bridge, which is rolled in transversal direction.

Make a sinking pillow (earth pillow or gabion) which is as long as the transversal length of mattress and wrapped up by the upstream end of the mattress, then sewn up with nylon thread.

Throw the GT mattress into the water as soon as the sinking pillow is completed. The rolled mattress will be opened up gradually and spread over the water surface under the floating bridge depending on dynamic force of flow.

Fasten the longitudinal reinforcement of mattress to the wooden piles on the bank to prevent the mattress from sliding to river bed while it is sinking. The drift is that the mattress travels downstream with the current during it sinks to the river bed. It is necessary to determine the drift by field experiment in advance, as the position of floating bridge used for sinking next GT mattress is related to this value and length of lapping joint of the two mattresses.

Put transversal side weight (earth pillow or gabion) onto the end of the mattress from the boat, and then dump bulk weight on it.

### 3.5 Placing GT Mattress Under Water

The discharge before flood season is very small on the upstream reaches of Liaohe river, even zero in some reaches. These cases would occur in medium and small sized rivers. During such period of time, the construction of GT mattress may be done simply by manpower. In this method, the mattresses should be constructed the same way as in sinking it on boat described above, then pull into place by standing in shallow water or opposite bank, or placing GT mattresses directly onto the river bed when the water depth is less than 1.0m, and then put the weight on it.

## 4 CONCLUSION

Through experimental study and engineering practice, some construction methods for placing GT mattresses in seasonal rivers in cold region have been developed. The method should be chosen in accordance with local conditions. However, practice has indicated that sinking GT mattress on ice cover is an optimal method for bank protection of frost-prone rivers in cold regions, because the construction on ice cover has following advantages:

1. Making mattresses, positioning, sinking mattresses, and placing weight will be more accurate, and easier to control the quality of construction.
2. The boat/raft and anchors are unnecessary for construction on ice cover. In addition, it is convenient to transport.
3. High efficiency, so as to shorten construction period and to save the cost of project.
4. Farmers are often employed in construction of bank protection work in China. The period from ice thawing till flood is the busy season in farming, while the winter is slack season, so that the labour force will be optimized.

## REFERENCES

- Wang Dianwu (1994) "Construction Technology of Geotextile Mattresses for Bank Protection" *Proceedings of Symposium on Rock and Soil Mechanics and its Application* Held by Chinese Young Scholars, Science Publisher, Wuhan, Hubei Province, P. R. China. pp. 502~506.
- Wang Dianwu (1994) "Filter Criteria of woven Geotextiles for Protective Works" *Proceedings of Fifth International Conference on Geotextiles, Geomembranes and Related products*, Singapore, 5-9 September 1994 Vol. 2 pp. 763~766.

# A New Structure for Protecting the Banks of Waterways

J. Yan

Research Engineer, Hydraulic Engineering Department , Nanjing Hydraulic Research Institute , Nanjing 210029, P. R. China.

**ABSTRACT:** This paper describes a new type of reinforcement for steep-faced embankment by roughened woven geotextile for protecting the bank of waterways. First , the authors have developed a new type of roughened woven geotextile , and have studied the engineering properties of roughened woven geotextile for reinforcing the soil body ( fractional coefficient between geotextile and clay about 0.4 ) . In this paper, the coupling calculation and analysis of stress-seepage for the soil body of embankment have been performed by finite element method for determining the design factors of this structure and laying disposition of the geotextile, at the same time the action of reinforcement materials on the stability of soil embankment have been considered . Finally, the paper describes a case of bank protection in a fourth-grade waterway. In comparison to the common type of bank protection engineering, the structure proposed in this paper have advantages of rapid construction, low cost, and high safety.

**KEYWORDS:** Waterway, Revetment , Friction, Woven Fabrics, Design.

## 1 INTRODUCTION

The purposes of bank revetment of waterways are primarily protect direct erosion and attack of shipping wave. Geotextile was usually put to use as geotextile soft caisson etc. in waterways in the past . But wrap-around reinforcement steep-faced embankment was applied to roads and railways etc. . We probes into applying wrap-around reinforcement steep-faced revetment in waterways in this paper, and proves its feasibility from selecting reinforcement materials and designing reinforcement embankment and analyzing states of stress-strain of embankment, calculating stability of embankment. Finally , the paper describes a case of bank revetment in a fourth-grade waterway, and it have success preliminarily .

## 2 ROUGHENED WOVEN GEOTEXTILE

We have researched and developed a new type of roughened woven geotextile (PP) for fitting the need of engineering, and have carried out the permeability characteristics testing, and engineering properties testing of woven geotextile in the laboratory, its properties are shown in table 1.

Table 1. Properties of woven geotextile (PP)

Test project	Unit	Measured value	Test method
Weight per unit	g/m <sup>2</sup>	290	GB/T 13762-92
Strip tensile	T	55.2	ASTM D4595
	W	52.2	
Trapezoidal tear	T	1.78	GB/T 13762-92
	W	1.60	
Permeability	cm/s	1.49×10 <sup>-3</sup>	NHRI-89
Frictional angle	$\mu_1$	21.9	Sample Size 200×200mm <sup>2</sup>
	$\mu_2$	30.0	

Notes:  $\mu_1$  = frictional angle between geotextile and loam ( ° ) ;  $\mu_2$  = frictional angle both geotextiles ( ° ) , GB/T = National Trial Standard of China , NHRI = Nanjing Hydraulic Research Institute .

## 3 DESIGN OF WRAP-AROUND REINFORCEMENT EMBANKMENT

When designing wrap-around reinforcement steep-faced embankment, we primarily take into account several aspects, such as high of embankment, length of embankment, gradient of embankment, loads of embankment, geological conditions of ground, and

characteristics of reinforcement materials and soil-filled . And define the rational position of reinforcement material in the soil-filled, the required reinforcement length, the vertical spacing , and the fold-over length.

We adopt to traditional way “ Limit equilibrium concepts” and design wrap-around reinforcement steep-faced embankment. Design ways in detail reference “Geotextiles” ( N.W.M.John,1987 ) , but we take into account simultaneously water pressure in course of designing in waterways .

#### 4 SEEPAGE-STRESS COUPLING CALCULATION

In fact, the stress within the body of the embankment will change the porosity of the fill, thus changing the permeability of the fill through the embankment body and affecting the distribution of seepage forces. In turn, seepage flow affects seepage forces and thereby influences the distribution of stress in the revetment. This indicates the need to simultaneously consider the interaction between stress fields and seepage fields. Seepage-Stress Coupling Calculation can give states of stress and strain during construction and using in reinforcement and the different positions of embankment body. the reinforcement will be rational used .

##### 4.1 Mathematical Modeling

###### 4.1.1 Seepage-Stress Coupling

The equations which represent the coupled seepage and strain in an embankment body are based on the Biot consolidation theory , stress equilibrium , a hyperbolic constitutive model for soil ( Duncan and Zhang, 1970 ; Duncan etc. ,1980 ) , and stress equilibrium and continuity of pore fluid ( Zhu and Shen , 1990 ) . These equations can be expressed in the following matrix form:

$$\left. \begin{aligned} [k][\Delta u] + \rho g [Q][h]^{n+1} &= [\Delta F_1] - [Q][h]^n \\ [Q][\Delta u] + ([s] + [R]\Delta t)[h]^{n+1} &= [\Delta F_2]\Delta t - [s][h]^n \end{aligned} \right\} \quad (1)$$

Where:  $[k]$  = stiffness matrix ;  $[\Delta F_1]$  = load increment matrix per unit volume ;  $[\Delta F_2]$  = constant matrix solved

using know value of hydraulic head ;  $[Q]$  = coupled seepage-stress matrix ;  $[s]$  = compression coefficient matrix of fluid ;  $[h]$  = hydraulic head matrix ;  $[R]$  = permeability matrix ; and  $[\Delta u]$  = displacement increment matrix .

##### 4.1.2 Modeling Reinforcement Geotextile

Tensile loads can be expected to develop in the geotextile as a result of deformations in the embankment body , One approach to model the relationship between load and strain is to assume a simple linear elastic model described by the following stiffness matrix :

$$k = \frac{AE}{l_e} \begin{bmatrix} \alpha^2 & \alpha\beta & -\alpha^2 & -\alpha\beta \\ \alpha\beta & \beta^2 & -\alpha\beta & -\beta^2 \\ -\alpha^2 & -\alpha\beta & \alpha^2 & \alpha\beta \\ -\alpha\beta & -\beta^2 & \alpha\beta & \beta^2 \end{bmatrix} \quad (2)$$

Where:  $l_e$  = length of linear element ; A = cross-sectional area of the linear element ;  $\alpha = \cos\theta$  ;  $\beta = \sin\theta$  ;  $\theta$  = orientation of the composite liner ; and  $E$  = elastic modulus of the reinforcement geotextile composite .

#### 5 The INTERNAL STABILITY OF REINFORCEMENT EMBANKMENT

There are a number of methods the model the internal stability of a slip surface in a steep-faced embankment. We adopt to the circular slip analysis methods of Bishop in which the tensile forces induced in the geotextile are assumed to generated an additional tensile power ( Ingold.I.S,1992 ) .

When calculating the geotextile vertical spacing , it should be assured that the tensile force acting on each geotextile layer does not exceeding the design tensile strength of the geotextile for that layer ( N.W.M. John,1987 ) .

#### 6 ANALYTICAL EXAMPLE

##### 6.1 Background

An example illustrating the application of these theories is taken from Zha-Jia-Su shipping line, it is a fourth-grade waterway, its typical cross-section and design results are shown in Fig 1.

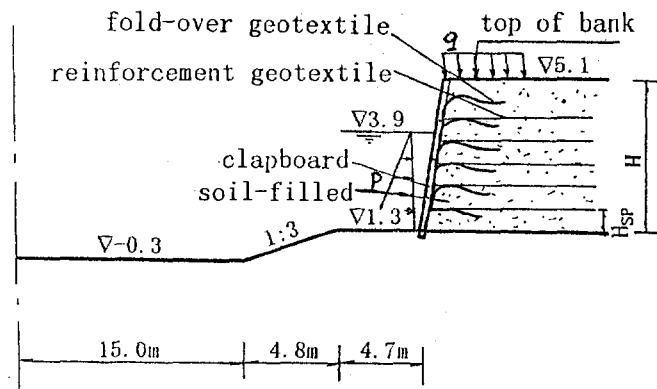


Fig 1. Zha-Jia-Su shipping line typical section and design results

### 6.2 Design of the Wrap-around Reinforcement Embankment Section

We Adopt to “ Limit Equilibrium Concepts ” and design the wrap-around reinforcement embankment in the Zha-Jia-Su shipping line. The design parameters in this example are summarized in table 2., and design results are shown in table 3.

Table 2. Design parameters for this example

H	H <sub>w</sub>	γ	μ <sub>1</sub>	μ <sub>2</sub>	φ'	Ta
3.8	4.2	19.3	21.9	30.0	24.0	52.2

Notes: H = height of embankment ( m ) ; H<sub>w</sub> = height of water level in waterway ( m ) ; γ = unit weight of soil-filled ( kN/m<sup>3</sup> ) ; φ' = internal frictional angle ( ° ) ; Ta = allowance tensile in the reinforcement geotextile (kN/m) .

Table 3. Design results for this example

H	β <sub>l</sub>	L	H <sub>sp</sub>	L <sub>f</sub>
3.8	80.0	4.0	0.6	1.5

Notes: β<sub>l</sub> = slope of embankment to the horizontal ( ° ) ; L = reinforcement length ( m ) ; H<sub>sp</sub> = vertical spacing of the reinforcement geotextile ( m ) ; L<sub>f</sub> = the fold-over length ( m ) .

### 6.3 Seepage-Stress Coupling Calculation

#### 6.3.1 Calculation Parameters and Conditions

In the case of seepage-stress coupling calculation of Zha-Jia-Su shipping line, the material parameters in this example are shown in table 4 and 5. The construction of embankment is divided six grades, each grade height of construction is 0.6 m, time of construction is six days, in addition to add two grades to fill water in waterway, so there are eight grades in calculation. In this example the calculations were based on 812 four-nod isoparametric elements with 884 nodes.

Table 4. Seepage parameters for example calculations

H <sub>up</sub>	H <sub>down</sub>	k <sub>s</sub>	k <sub>g</sub>
3.90	2.20	7.0×10 <sup>-6</sup>	1.49×10 <sup>-3</sup>

Notes: H<sub>up</sub> = The design water level ( m ) ; H<sub>down</sub> = the low water level ( m ) ; k<sub>s</sub> = permeability of soil-filled ( cm/s ) ; k<sub>g</sub> = permeability of geotextile ( cm/s ) .

Table 5. Soil-filled parameters for coupled calculations

R <sub>f</sub>	K	m	r	k <sub>b</sub>	k <sub>ur</sub>	c	φ
0.80	125	0.45	0.4	200	400	0.25	21.0

#### 6.3.2 Calculation Results

The soil-filled is homogeneous clays, and the geotextile permeability coefficient is much more than that of soil-filled, the isotonic lines is well-distributed in seepage zone, so the figures of contour lines of water head are omitted.

Since the geotextile liner is flexible and its deforms with the embankment, when tensile stress are developed in the embankment, they will be partially transmitted to the geotextile that in turn will mobilize tensile force. These tensile forces can then be expected to modify the distribution of stress and strain in the body of embankment. The calculation results using period of embankment are shown in Fig 2.

Fig 2 (a) and (b) show the distribution of major and minor principal stress of seepage-stress coupling calculation, the maximum values of them is respectively 7.85

kPa and 5.36 kPa , major and minor principal stress in

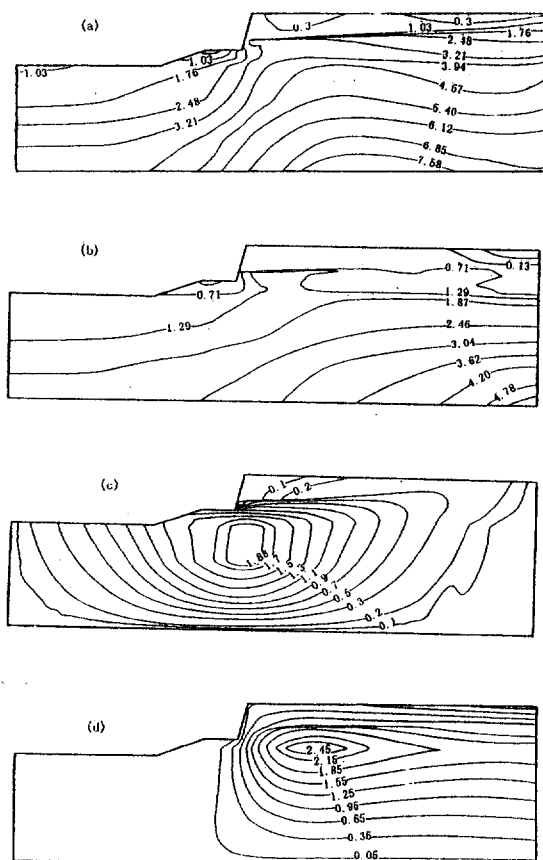


Fig. 2. The calculation results . ( a ) Contour lines of equal major principal stress ( kPa ) ; ( b ) Contour lines of equal minor principal stress ( kPa ) ; ( c ) Contour lines of horizontal displacement ( cm ) ; ( d ) Contour lines of vertical displacement ( cm ) .

reinforcement is respectively 3.24kPa and 1.66kPa, both of them are much less than  $T_a$  ( allowance tensile in the reinforcement geotextile ), but both of major and minor principal stress have a phenomenon of stress centralization in one-third height of reinforcement embankment , it indicted that it should lay the reinforcement in this position. Fig 2 ( c ) and ( d ) summarize horizontal and vertical displacement for seepage-stress coupling calculation , both of them are small , the maximum value of them is respectively 2.10cm and 2.74cm , the tensile stress which the deformation generated would not break off the reinforcement geotextile .

## 6.4 Stability Analysis

We Adopt to above theories to calculate the stability safety factor of embankment, including two kinds of reinforcement and non-reinforcement , the safety factor of each kind is respective 2.12 and 1.82 . Obviously ,the safety factor of reinforcement is larger than that of non-reinforcement , and the safety factor of reinforcement is satisfied with the civil engineering specification of China .

## 7 CONCLUSIONS

We prove the feasibility of using roughened woven geotextile to wrap-around reinforce embankments in a fourth-grade waterway . The seepage-stress coupled calculations and analyses show that woven geotextile can ensures that the reinforcement was laid the rational position and the less horizontal and vertical displacement of the embankment , stability calculations show that the reinforcement can increase the stability of embankment . some studies in this aspect are being performed to improve design methods and assess level and show advantages of this way.

## REFERENCES

- Zhu . B , and Shen .Z , 1990 , “ Calculations in soil mechanics ”, Shanghai scientific and technological press , Shanghai ,China ,( in Chinese )
- T. Tao , D .F. Li and J. Yan ,1995 , “ Calculation of coupled stress and seepage for dams with a geotextile /geomembrane composite liner ” ,Geosynthetics International. P707~721 .
- The initial design of transform engineering of Zha-Jia-Su shipping line , Chapter 1 , introduction of design , ZheJiang province ,China ,1993. ( in Chinese ) .

# Alternative Design and Construction of an Under Seawater Road Tunnel Using Geosynthetics in Greece

A. Kollios

Dr. Civil Engineer, Edafomichaniki Ltd, Athens, Greece

**ABSTRACT:** The construction of a 2,7 km length road tunnel and its approaches for the junction of two caps was designed with a net off-shore length of 700 m below sea-bed level. An extensive geological and geotechnical campaign was performed for the complexed foundation design. At this context an alternative water-proofing design concerning the immersed part of the tunnel sections was performed involving a special geomembrane type with hangers, that obviously offered a cost-effective solution and was approved for construction by the project Owner.

**KEYWORDS:** Case - Study, Design - by - Function, Geomembranes, Tunnel Construction.

## 1 INTRODUCTION

On the written instruction of a European contracting Joint-Venture, a detailed geological and geotechnical campaign was carried out as the basis for the detailed foundation design of an immersed tube tunnel crossing the Preveza - Aktion sea strait at the area of Western Greece. The investigations included geological mapping of the approaches to the tunnel and geotechnical drilling boreholes, both on-shore and off-shore, aiming at the determination of a detailed longitudinal geological soil section along the tunnel axis. The contractual design referred to separate tunnel sections as a girder box of 12,0 m width and 7,5 m effective height, incorporating base and roof slabs and side walls of 1,0 m thickness each. The immersed tunnel sections were to be placed immediately below sea-bed level and the maximum seawater height was approximately 26,0 m. Each tunnel section referring to the immersed part had a length of 135,0 m and was to be preconstructed on a dry dock, then by floating to reach the specific placement location.

The stratigraphy along the immersed tunnel axis presented the following geotechnical formations:

- I. The upper geological unit referred to rather loose, contemporary sea deposits involving grey silty sands and silts, with lenses and pockets of soft brown clays, extending to an average depth of 15 - 22 m below sea-bed level, being significantly deeper at the center part of the strait (reaching 40 m depth).
- II. The lower formation consisted of plioptiocene hard marls with intercalations of dense sandy and gravelly layers.

The tunnel immersed sections were designed to be founded by means of stone columns used for sub-soil improvement, in order to minimize the expected large settlements of the initially very loose alluvial deposits. The girder box section was originally designed to bear a 6-mm thick metal plate placed within the bottom slab, acting as a water-proofing element of the sensible tunnel section. An alternative design involving the use of geomembranes was then proposed to the contracting group, replacing successfully the metal plate and offering an interesting solution to the emerged problems. The geomembrane proposal was adopted and is actually under application of the project, to be finished by the end of the year 1998.

## 2 GEOMEMBRANE DESIGN

Water proofing of underground road tunnels under important hydrostatic pressures by geosynthetics involves the determination of the most involved property for geomembranes, the thickness of the liner. This property is directly related to the resistance to tear, to the puncture resistance and to the impact damage resistance. In fact a linear and sometimes exponential increase in resistance to the above mentioned actions is related to the geomembrane thickness increase.

In order to determine the minimum necessary operational geomembrane thickness, a rough estimate of the stress-strain conditions applied on the contractual girder box structure was performed using simple static analysis by a finite element method. The results of this analysis

allowed the determination of the most critical vertical stress applied on the geomembrane (Figure 1).

For the calculation, it was assumed that each preconstructed section of the tunnel was separately isolated by the proposed system, since the in-between joints were to be sealed by the contractually foreseen system of water stops.

The initial design of the minimum necessary function thickness of the geomembrane to be applied at the bottom of the tunnel sections referred to the determination of a cost-effective safety factor  $F$  considered as the ratio of the minimum necessary thickness to the allowable design thickness. This factor of safety  $F$  ranged from  $F=1,5$  to  $5,0$  depending on the polymere type, the special

construction conditions of the project, the method and the effectiveness of the quality control of the water - proofing system. The design of the allowable thickness of the liner was based upon the deformations to occur to the geomembrane during the construction and the life - time of the project. These deformations would mainly be construction deformations that would directly influence the relative displacements of the geomembrane during placement, since the presence of stone piles assured for a practically non - deformable foundation interface.

The allowable thickness design was performed according to R.M. Koerner, 1990 theoretical principles and the results were plotted at the following Figure 2.

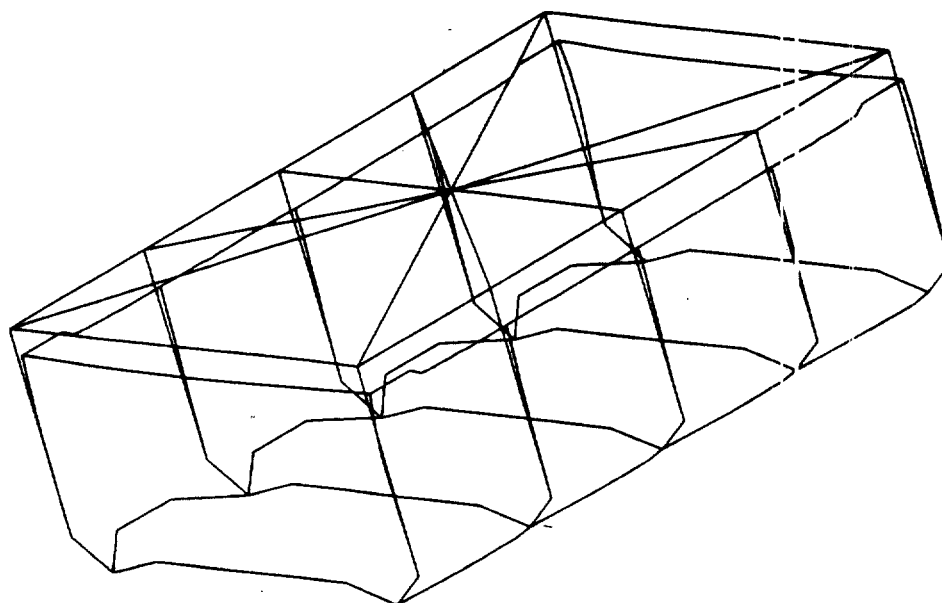


Figure 1. Indicative results of initial and deformed mesh of a typical tunnel section.

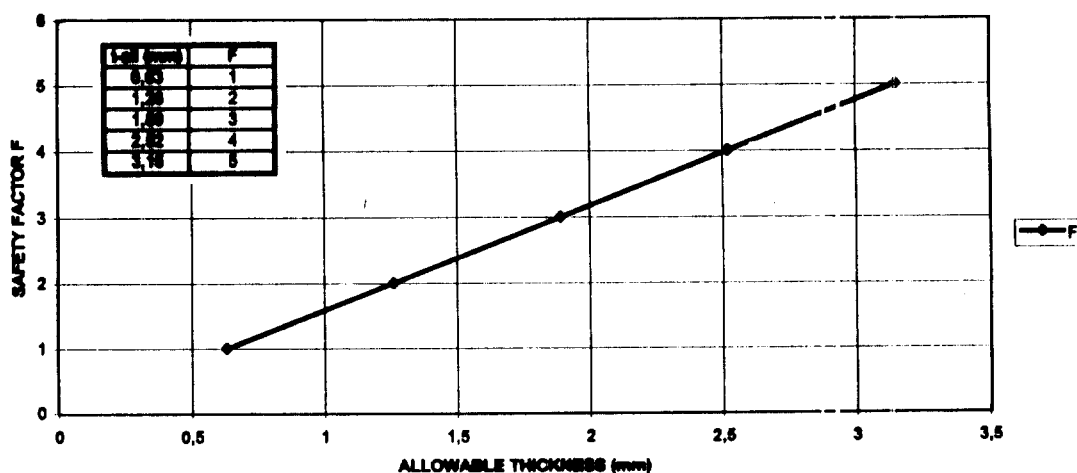


Figure 2. Correlation of the allowable thickness of the liner to the design safety factor



Based upon the final results, the alternative design for geomembrane selection proposed:

- a. A high density polyethylene geomembrane with a minimum thickness of 2,5 mm, corresponding to a safety factor of  $F_1 = 4$ , or
- b. A low density polyethylene geomembrane with a minimum thickness of 1,5 mm, corresponding to a safety factor of  $F_2 = 2$ .

All calculations were performed according to Eurocode 7, taking into consideration a seismic factor of  $a=0,30$ . g. As deduced by the analysis, the maximal vertical stress applied on the bottom geomembrane was calculated at the level of 300 KPa approximately.

### 3 CONSTRUCTION PROPOSALS

#### 3.1 General Considerations

The main factor of concrete desintegration in saline water is the influence of remaining chlorides within the concrete mass that create reinforcement corrosion. To avoid any such risks at the bottom of each tunnel section, the proposed use of a geomembrane, according to the design presented above, placed at the lower part of the concrete slab, exactly replacing the metal plate of 6 mm thickness initially planned, offers an interesting and rather cost-effective solution. In addition to that, water-proofing of also the walls and the roof of each section might also be adopted by the contractor, in conjunction with a high quality concrete mix, adequate for sea-water tunnelling purposes. The technical advantages of the proposal were evident in terms of quality control during construction, provided that the main geosynthetic placement rules would be completely respected.

#### 3.2 Construction Details

The geomembrane to replace the metal plate of 6 mm should be placed exactly at the same location, as contractually foreseen, i.e. at the lower limit of the concrete slab. For doing so, special conditions and care involved the following points:

- a. In order to assure a perfect adhesion of the geomembrane to the concrete slab (so that no detachment during construction and navigation of the sections occurred), the geomembrane should present the special section indicated at Figure 3.  
For this section, values of  $D$ ,  $d$  and  $H$  were such to assure for a perfect adhesion and that no lateral displacement of the geomembrane to the lower part of the slab might occur. The design called for  $D = H = 10 - 20$  mm and  $d = 5 - 10$  mm.
- b. The lower interface of the geomembrane would be in contact with the specially constructed bases placed on

the stone - piles levelled surface. Those specially constructed bases should be covered by plastic materials (such as teflon, thin plastic sheets) that did not need to present any life - time performance, but they should be applied only for the moment of placement. In this way, during placement, any wrong movement of the tunnel section would not transduce any secondary harmful friction of the membrane to the foundation bases (because of the protection provided).

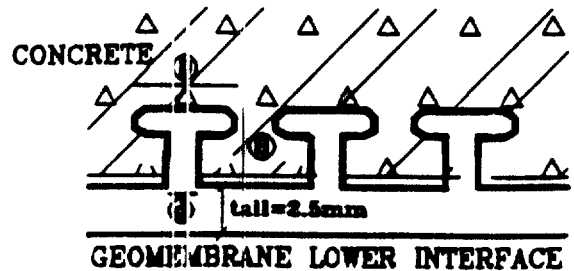


Figure 3. Special section of geomembrane to assure adhesion to the concrete slab.

- c. The remaining space between the foundation bases and the lower interface of the geomembrane should be filled with cement grout under pressure, according to the contractual specifications. Therefore, a life - time protection of the geomembrane was assured.
- d. Concreting of the slab over the geomembrane should be carefully executed, especially where the reinforcement is placed, so as not to create any short of damage due to scratches on the geomembrane.

In order to combine a complete waterproofing of all the design section of the tunnel according to the specifications used for geomembranes in underground constructions, the geomembrane protection of the bottom slab might also be placed over a 20 cm thick concrete base that would extend all around the section of the bottom, the walls and the roof of the section (outer girder box). This alternative proposal was not finally accepted and the contractually imposed water - proofing system was applied on site (sprayed polyurethane).

### 4 CONCLUSIONS

The use of a special type of geomembrane allowed a most interesting alternative solution for water proofing

the bottom slab of an under sea-water road tunnel, actually under construction, replacing the contractually foreseen metal plate and offering an important cost benefit (estimated at the level of 10% approximately over the total foundation cost). The existing geomembranes installation experience (mostly acquired during construction of multiple store - garages below ground level and the underground tube train and stations at the broader Athens area) combined with the strictly applied supervision, create the assurance for obtaining the most efficient water-proofing method for the final stage of function of the project, which is set to be fully realised by the end of 1998.

## ACKNOWLEDGMENTS

The author would like to thank Mr. S. Papaspyrou of Edafomichaniki Ltd for his review of the original manuscript as well as the site engineers Mr. S. Zafiratos and G. Kilimis from the contracting group for their help concerning the follow-up of the project. Special thanks are also due to Mr. G. Dernikos, project manager at the time of issue of the present alternative proposal for his directive ideas.

## REFERENCES

- EDAFOMICCHANIKI LTD (1994-1995) Geological and Geotechnical Investigations for Aktion - Preveza Junction, Athens, Greece.
- GEOFELT m.b.H (1994) Tunnelliner Information Data Sheets - Agruflex.
- Koerner, R.M. (1990) *Designing with Geosynthetics*, Second Edition, USA, pages 410-413.
- Kollios, A. (1995) *Waterproofing by Geosynthetics Alternative Proposal* - Aktion Preveza Junction - Preliminary Design and Specifications, Athens, Greece.
- POLYFELT Ges.m.b.H (1994) High Density Geomembranes - Polyline data sheet and specifications.

# Application and Testing of Geotextiles in Deep-draft Quays

Fengwu Liang

Senior Engineer, China Nanshan Development (Group) Incorporation, Shenzhen, China

**ABSTRACT:** Eight berths capable of taking ships up to 25000 DWT and 50000 DWT respectively were completed in Shenzhen port, in 1985 and 1995 separately. The berths are deep-draft quays of 11, 12.5 and 13.1 meters, behind which woven geotextiles were successfully placed as filters for trial. The durability of the geotextile requires further investigations since it was the first time that geotextiles were used in a large quantity in quay construction, instead of the conventional Crushed-stone filter courses. A blind shaft was built at one end of the quays. Field investigations and observation, a research institute has been commissioned to carry out the observation and investigation for ten successive years. In the shaft, synthetic bags, filled with the same quarry-run fills were placed at three different locations as the filter layers, i.e. underwater, intertidal zone and above water level.

**KEYWORDS:** Case Study, Geotextiles, Design, Walls, Filtration

## 1 THE CHANGES OF THE FILTER COURSES IN GRAVITY TYPE BLOCK QUAY

In a conventional gravity type block quay, the bulkhead wall is often a kind of retaining concrete block wall in a concrete stair type or gravity type. The block size is designed based on the lifting capacity of the crane held by the contractor. A large crushed stone riprap prism as filter courses is often used to keep the fills from leaking through the joints between the blocks to the front of the quay (Fig. 1). The quantity of works for construction of the quay is divided roughly into following parts:

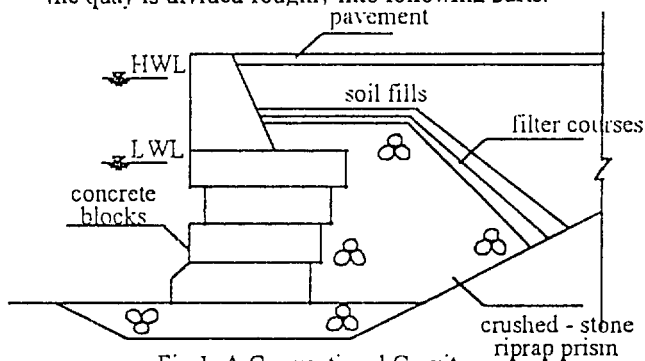


Fig 1. A Conventional Gravity Type Block

The two main factors affecting the cost and the construction period are item 2 and item 3. Usually, 20 percent of total cost and 50 percent of whole construction period will be spent on item 3. As new type construction materials are springing up in the wake of development in science and technology, scientist, after several decades hard work, eventually found out a new effective structure of gravity type quay to replace the conventional one. Eight berths each with capability of taking ships varying from 10,000 DWT to 50,000 DWT, had been successively built in Shenzhen China during the 10 years from 1985 to 1995. The structure of the quays was reformed not only on its blocks size but also on its filter courses by replacing crushed-stone riprap with woven synthetic fabrics. As a result of the reformation, the construction works were simplified enormously.

## 2 DESIGN OF THE FILTER COURSE IN BLOCK QUAYS

A gravity type solid-filled block quay, of good durability and flexibility to working loads as its advantages, is made up of many blocks which form many joints cross and down over the back of the blocks. In order to keep fills from leaking through the joints into the port, a reliable crushed-stone riprap filters should be built. If we want to adopt woven fabrics instead of crushed-stone riprap as filters, we need to reduce the number of joints, and to make the distribution of joints regular. According to our many years experience, a reinforced concrete hollow block in large size, which simplifies the distribution of joints, has been used in a deep-draft quay for 25,000 DWT in Chiwan harbour. The woven fabrics as filter courses were first time adopt in deep-draft quay with overall height 15m and draft 11m. As local soil and rock materials are easily accessible, it is convenient to unguarded quarry run rocks from Chiwan area as fills behind the hollow block quays. Closed H type reinforced concrete hollow blocks, weighing 200 t each, were designed for the quays. On top of the blocks are hollow relieving platforms with wave absorbing chambers. The longitudinal length of the hollow block along the quay is 3.5 m, and the width of the relieving platform which sits directly on top of the block is the same as that of the block, with no alternate joint between the two, thus leaving a vertical through joint every 3.5 m behind the quay. To facilitate placing synthetic fabrics and cut down their consumption, an independent strip of synthetic fabric was placed at every joint and the strip had a 1.00 m overlap on each side of the joint over the back of the block. Since the overall height of the block was about 10.00 m, the levelled foundation bed for the blocks would surely develop some irregularity, thus the joints between installed blocks would be far larger than the stipulated 5 cm in the construction code. Therefore, the largest allowable joint width was stipulated to be 10 cm -15 cm in the design. However, to prevent differential settlement of blocks causing excessive tension in the synthetic fabric strips, the designed width of the synthetic fabric strips was 25 cm.

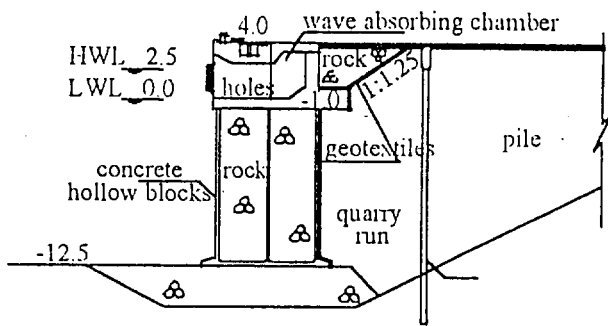


Fig 2. A Sectional View of A Gravity Type Hollow Block Quay with Wave Absorbing Chambers (Unit: m)

Synthetic fabric strip locking latch seat were embedded in the back walls of the blocks beside the joint. In order to lock the fabric to the back of the blocks, prepared holes were placed on the synthetic fabric strips in line with the position of the locking latch seat. To minimise difficulties of underwater operations, the connection of the locking latch seat and bolts with the synthetic fabric strips should be as simple as possible. The structure of a locking device is shown in Fig. 2.

Three types of woven synthetic fabric strips were designed and used at the cross section of the quays.

Type A: woven synthetic fabric strips of 2.25m x 12.00 m were used behind the hollow blocks.

Type B: woven synthetic fabric strips of 2.25 m x 4.50 m were placed on the cantilever extension of the relieving platforms.

Type C: woven synthetic fabric strips of 4.50 m wide were used beneath the stone prism placed behind the wave absorbing chambers to eliminate residual wave energy. The geotextiles were placed continuously with an overlap of 1.00 m.

As shown in Fig. 2c, loops were arranged both at the top end of type A and at the lower end of Type B to prevent soil grains from being washed out locally. The total consumption of geotextiles used for the 264m long berth accommodating ships up to 25000 DWT is 12000 m<sup>2</sup>.

In 1988 and 1995, 6 light weight gravity type quays each capable of taking ships up to 50,000 DWT were successively constructed in Chiwan Harbour and Mawan Harbour. This further developed and extended the application of Woven fabrics in deep-draft quays and make their section more economical and reasonable.

The light weight gravity type quay is a new type structure, specially designed for uneven distribution of geology, with bent structure upper and hollow blocks underwater. The combination of the upper bent with the railway can make over-water fills as a slope. This greatly releases the fills pressure upon the vertical bulkhead wall, and make filter courses set only behind the blocks for underwater all year long while the protection of filter courses for the over-water fills is unnecessary.

As is well known, the perfect way to extend the woven fabrics service life is to shelter it from ultraviolet

radiation. The light weight gravity type block quay in Chiwan, with its double ribbed upper bent, is an ideal method resolving this problem, with each hollow block weight under the relieving platforms within the crane lifting capacity 500 Ton. Joints are set every 7 metres covered with woven fabrics. The permeable bent and slope type bank protection are constructed above the relieving platforms. Thus, it not only provide a stable berthing condition, but also, due to the riprap being replaced and with no worry about the penetration through the stone and damage to filter course, simplifies the construction of stake foundation under the crane railway. And also, with the fills pressure and weight reduced, the pressure on the ground is released enormously. The woven fabrics make the construction easier and faster and cut down the cost by replacing the complicated crushed-stone filter courses. The quay, built with lower cost and higher quality using new materials and new technology, and with the tangled ground treatment problem resolved, was awarded a national silver medal on its perfect designing.

### 3 SELECTION AND PROTECTION OF WOVEN GEOTEXTILES

The woven geotextiles used as filters behind the quays should have the following properties:

1. Good in soil retention property and that in separating water and soil;
2. High water permeability to protect woven synthetic fabrics from being blocked up to form a detrimental water head;
3. Sufficient strength: tensile strength, impact strength, tear and puncture resistance;
4. Sufficient durability: good ultraviolet resistance, chemical corrosion resistance and sea water resistance.

The durability of geotextiles should not be affected by moulds eating rats and termites and by atmospheric temperature.

A new woven synthetic bag factory in Chiwan, manufacturing woven synthetic bags for chemical fertiliser, was completed and put into production at the time when the designs were completed. A research institute was then commissioned to carry out various tests for the physic-mechanical and chemical properties of the synthetic textile produced in the factory. It was finally decided to use the synthetics produced in this factory instead of the originally selected T7W7 woven geotextiles.

The main features of the woven geotextiles manufactured in this factory are as follows:

Longitudinal strength 2.5t/m

Latitudinal strength 2.5t/m

Impact resisting strength: Crushed when placed on concrete floor and stone of 30 kg dropped from a height of 2.00 m.

Chemical composition polypropylene

Unit weight 190g/m<sup>2</sup>

Permeability: No evident water head was observed during flume tests under sea flood and ebb condition simulated.

Laboratory tests showed that, no change in the tensile strength of the synthetic fabric was observed when the synthetic fabric was exposed to corrosive media of acid, alkali, salt and sea water. The resistance of the fabric against moulds was stable and their properties were also stable when they were subjected to oxygen blasting in normal atmospheric temperature: and no loss of weight was observed. From the outer appearance of the fabric, the colour, lustre and softness remained the same as that before the test. It was smooth surfaced, transparent and no abnormality had been observed in the texture of the fabric.

As the strength of the synthetic fabrics couldn't meet the designed requirements, it was decided to use two layers of the synthetic textile at each joint. Since anti-ageing agent was added to the polypropylene fabric, the synthetic fabric had a poor ultraviolet resistance. Practice proved that the textile would soon become brittle when they were exposed to sunshine. To prevent the textile from being exposed to sunshine, it is requested that the processed synthetic fabric strips should first be stored in dark rooms and then placed at night time or in cloudy days whenever it is possible, in order to prevent geotextile from being damaged by the dumping of rocks, a  $\Phi = 2\text{mm}$  wire netting with grids of  $3 \times 3\text{cm}$  was placed against the textile behind the quays as protection. A layer of rubble stone was ripped over the geotextile on the slope and then larger stones were placed.

#### 4 IMPORTANT REMARKS

Woven synthetic fabrics used as filters should first possess a porosity matching the permeability of the backfills so as to ensure an unimpeded drainage and the geotextile should not be liable to blocking. As a matter of fact, the permeability of commonly used woven synthetic fabric is usually higher than that of the adjacent soils. However, special attention should be paid to the gradual blockage of pores of geotextiles during their service.

A filter course is not formed by geotextiles themselves but formed when fine particles in the fills behind the fabric are washed off through the pores of the fabric and the remaining coarse grains form arch type structures around the pores while the soil beyond forms another granular filter course with different graded grains. The further away the soils is from the geotextile, the lower the permeability of soils becomes. A new natural filter course is thus formed, behind which are natural soils, and after such a natural filter is formed, soil grains will not be washed off any more as the soils behind it becomes stable (Fig. 3). Therefore, geotextiles don't work directly as a filter but help backfills forming a

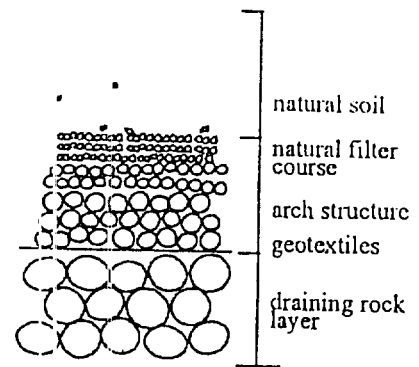


Fig. 3. Forming Process of A Filter Course

stable natural filter course. Proper selection of woven or non-woven synthetic fabrics according to the permeability requirement of a structure and the grain sizes of the fills is of great importance to a stable and effective filter course. The backfills for marine ports usually consist of rather coarse grains. Though the backfills are influenced by the complex alternating currents and waves during flood and ebb and the arch type structures behind the geotextiles are sometimes liable to failure. The squeezing action of the fills behind the geotextiles can generally keep the natural filter course stable and the pores and draining passages are not liable to salutation and blockage.

Geotextiles suitable should meet the requirements as follows:

- (1) For natural soils when the weight of soil particles passing sieves with a screen size of  $0.074\text{mm}$  (U.S. standard sieve #200) Accounts for less than 50% of the total weight;  $D_{85}(\text{soil})/E_{OS}(\text{geotextile}) \geq 1$  ( $E_{OS}$ : The effective pore size)
- (2) For soils other than above mentioned soil:  $E_{OS}(\text{geotextile}) < 0.211\text{mm}$  (U.S. standard sieve #70) But, when  $D_{85} < 0.074\text{mm}$ , it is not advisable to use geotextiles.
- (3) Geotextiles with  $E_{OS}$  smaller than  $0.149\text{mm}$  (U.S. standard sieve #100) should not be used as they are liable to blocking.
- (4) Within the limits stipulated in the criterion, geotextiles with larger pores should be used.

The above requirements only apply to specified soils and steady flow, and the influence of soil density has not been taken into account. However, those requirements can be considered properly in the case of soft and loose soils.

When geotextiles are used in quay structures, the following requirements have also to be followed.

- (1) The permeability ( $K$ ) of geotextiles should be greater than  $10K$  of soils, where  $K$  is the permeability parameter.
- (2) the slope ratio should be less than 3 so as to prevent the geotextile from blocking and corresponding tests should be carried out.
- (3) Unstable geotextiles or geotextiles with poor ultraviolet resistance should not be exposed to direct sunshine for more than 5 d.

## 5 LABORATORY TEST AND SITE OBSERVATION

In the national harbour engineering code, the service life of a gravity type quay should be more than 50 years. The polypropylene woven fabrics, instead of crushed-stone riprap, are applied in a quay structure for the first time. Its durability requires further investigation and observation. Some scientific research institutions have been commissioned to study the loss of its tensile strength and weight, and the changes of its outer appearance by submerging the fabrics into an acid liquid made up of artificial sea water and lactate for 6 month. In the middle of the quay, an observation well in which 2 series of samples, one series of soil and the other plate, were laid on both the place beneath low water and well ground to observe behavior of the fabrics in a long term of 10 years.

The results from both laboratory and observation are shown in Fig. 4:

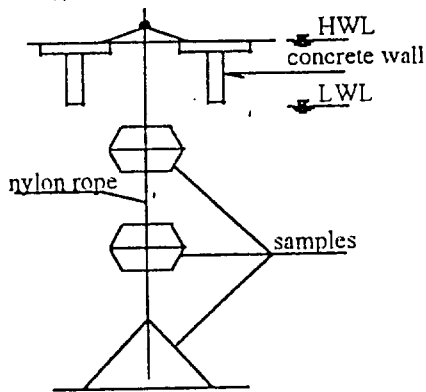


Fig 4. Samples Installation  
View on Testing Ground

The results from both laboratory and observation are shown in Fig 5.

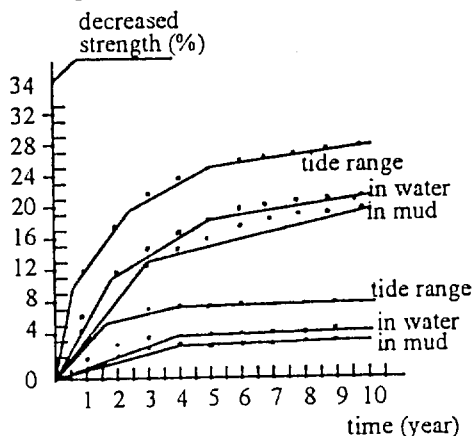


Fig 5. Relative Curve of Strength Loss  
and Exposing Period

From the above results, we can see:

1. In the laboratory test the polypropylene woven fabrics are not sensitive to sea water, acid, alkali, and bacterial corrosion at all.
2. The 10 years' observation demonstrates that the polypropylene woven fabrics corrosion and erosion by

nature sea water and mud is not serious.

3. In the water level changing area, due to the contact of fabrics with flls, the fabrics tensile strength decreased by 33.5 percent of which, by 26.5 percent in the first 3 years, and by 7 percent in the later 7 years in a slow decreasing rate. Under the low water level area, the tensile strength of the polypropylene woven fabrics decreased by 23.5 percent of which, 18 percent in the first 3 years and 5.5 percent in the later 7 years. The tensile strength-time diagram shows that the curve rate is more and more even at the time of 10 years later. By extension of the curve, we can calculate that the tensile strength of over water woven fabrics will have decreased by 50 percent while that of under water by 40 percent by the time in 50 years.

4. The above results also show that woven fabrics filter course and the concrete block with 50 years service life in gravity quays can match very well. When a type of anti-ageing woven fabrics with a longer durability are applied, the service life of a gravity quay is usually more than 70 years if it locates in a no accidents environment, especially in a no ice environment.

5. Woven fabrics filter course in a gravity quay should be set under water as fully as possible to shelter it from damage of the atmosphere and sunshine to extend its service life.

## 6 ECONOMIC BENEFITS

The economic benefits of woven synthetic fabrics used as filters for the quay for 25000 DWT ships in Chiwan Port are given in Table 1 as compared with that of filter drains and riprap prism filter course.

From the table, it can be seen that the filter course comprising synthetic fabrics produce a remarkable economic benefit which saved investment by 74% compared with the crushed-stone filter drains and by 76.1% compared with the riprap prism with crushed stone filter course and construction period is cut down by 1 to 4 times when geotextiles are used as a filter. Thanks to the using of geotextiles which are very easy to handle, the two hollow block deep-water quays were completed in just 9 months in spite of the complicated joints handled at the two ends of the quays, the time consuming bag-and concreting on the riprapped rock foundation bed and the special requirement for wave absorbing chambers on the upper part of the quay. Both quays have therefore been evaluated as excellent projects by the relevant authorities.

## REFERENCE:

1. Benhai Wei, and Len Jan (1997), "Total Report on Polypropylene Woven Fabric Performance Test in Chivvan Harbor" p5-9, Nanjing Hydraulic Research Institute, P.R.China
2. Benhai Wei (1989), "Report on Polypropylene Woven Fabric Performance Test in Chivvan Harbor" p4-7, Nanjing Hydraulic Research Institute, P.R.China

# Jute Geotextiles

U. Datta & P.K. Chatterjee

Indian Jute Industries' Research Association (IJIRA), 17 Taratola Road, Calcutta 700088, India.

B. Chottopadhyay & A. Ghosh

Civil Engineering Department, B.E. College (Deemed University), Howrah 711103 India.

**ABSTRACT:** A heavy duty open mesh woven jute fabric is perhaps the first geotextile, which has been in use for protection of slopes from erosion by rain and wind in Europe and America since early fifties. Lighter fabrics have been developed and their performance has been evaluated under various soil and climatic conditions. The results reveal that the fabrics reduce soil loss by about 90% and comparable with the performance of the existing product.

Woven jute fabrics for separation and filtration have been developed and found to be cost effective in river bank protection work replacing conventional granular filter. In this application the fabrics need chemical treatment for enhancement of durability. After successful trials under different soil and river conditions, the treated fabrics are being commercially used. Similarly treated fabrics have also been tried for construction of roads on soft soil as separator and found to be cost effective with encouraging results.

Jute non-wovens have been found suitable for filtration and drainage.

**KEYWORDS:** Erosion Control, Filtration, Separation, Embankments, Geotextiles

## 1 INTRODUCTION

Jute as a geotextile material is well known in Europe and America for protection of slopes from erosion by rain and wind. A heavy duty open mesh woven fabric in the name of Soil Saver/Geojute/Anti-Wash has been in use since fifties and the jute producing countries have been exporting the item since then. The demand of the product went up to as high as 100 M m<sup>2</sup>. In mid-sixties, when concept and application of geotextiles started, other natural and synthetic materials entered in this field of application. At present global demand of natural geotextiles is about 86.6 M m<sup>2</sup> - a recent survey reveals. Among the products, straw based products claim about 60% of the market, while jute and coir together claim about 37% and the rest 3% by others like wood-wool, synthetic etc. (Rickson et al. 1996). It has been reported that the decline in the demand of jute is due to nonavailability of the product in the market because of the fact that a few mills produce the product, which requires special type of processing equipment. For involvement of more number of mills in supply of the product, two products have been developed in consultation with the experts in this field. The products are of different open areas and their performance has been studied extensively. The results of the studies have been discussed in this paper.

The synthetic geotextiles are very expensive in the third world countries and so its application is limited. The civil engineers of the countries are looking for low cost alternatives for geotechnical constructions. Jute being one of the cheap fibres having good strength, structural stability, abrasion resistance etc. its properties for civil engineering applications have been evaluated by many

workers (Thomson 1985, Kabir 1988, Aziz 1991) and found to be useful for specific applications. A prefabricated fibre drain using jute fabric and coir rope was developed for consolidation of silty subsoil and used commercially in Singapore (Ramaswamy et al. 1984). Treated Jute Geotextiles for separation and filtration developed by IJIRA was used for protection of bank of the river Hooghly at Nayachar, opposite to Haldia Port (Datta et al 1990, Sanyal et al. 1993). The product is being used by the engineers of Irrigation & Waterways Directorate, Govt. of West Bengal for river bank protection work after extensive trials under various conditions of soil and river under their control. Results of the trials have been discussed here.

Similar fabrics were tried for construction of roads on soft soil as separator and encouraging results were reported. Jute nonwovens were also tried for construction of unpaved roads as well as for filtration and drainage of roads. The results are satisfactory (Rao et al. 1996).

## 2 FABRICS FOR CONTROL OF SURFACE SOIL EROSION

A heavy duty open mesh jute fabric is perhaps the first natural geotextile used in this field of application scientifically in early fifties in Europe and America. The fabric is made of thick yarns of 5 mm diameter, which requires special type of machinery for processing. Ludlow Jute Mills, an American firm in India set up a separate plant in their mills for manufacture of the product and developed special machinery in collaboration with a jute machine manufacturer. Other

mills also entered into the business to cater to the demand of the product. But from mid-sixties with the advent of other geotextiles of natural and synthetic origin in this field with the concept and application of geotextiles, its demand gradually declined to the present level. A recent market survey of the product revealed that nonavailability of the product in the market was one of the reasons for decline of demand. The experts suggested products, which could be produced by any mill having conventional jute processing machinery. For the purpose, IJIRA developed two varieties of Jute Mesh (JM) type I&II and tested the properties and performance in India and abroad. The specifications of the products including Soil Saver have been furnished in Table 1 below.

Table 1 Specification of Jute Geotextiles for Control of Surface Soil Erosion.

Jute Geotex tiles	Weight (g/m <sup>2</sup> )	Yarn diameter (mm)		No. of threads/dm		Width (Cm)
		Warp	Weft	Warp	Weft	
Soil Saver	500	5	5	6.5	4.5	122
Jute Mesh						
Type I	400	2	3	34	15	122
Type II	300	3	3	12	11	122

### 2.1 Properties

The physical properties of the materials tested by Soil Management Division, Silsoe College, U.K. and IJIRA are given in Table 2 along with the properties of the products available in the market for similar application.

Table 2 Physical properties of Jute and other geotextiles for Control of Surface Soil Erosion.

Properties	W O V E N				N O N W O V E N	
	Soil Saver	Jute Type I	Mesh Type II	Coir	Straw based	Synthetic
Weight (g/m <sup>2</sup> )	500	400	300	700	250	450
Thickness (mm)	5	3	3	4	8.5	18
Coverage (%)	55	60	40	60	100	85
Tensile Strength (KN/m)						
Warp	20	16	12	25	-	3.2
Weft	9.5	6	11	12	-	-
Water holding capacity(%)						
	600	500	400	280	700	90

### 2.2 Functions

When installed they act in two ways - 1. Arrest movement of soil particles, seeds and nutrients on the surface of the soil and 2. Help fast growth of vegetation, which covers the surface with a canopy of living mass as well as reinforces the soil with roots, protecting the surface from erosion by rain and wind permanently.

### 2.3 Trials and Results

The functional performance of Soil Saver is well known to the users for more than four decades; however, that of the new products has been studied by Silsoe College in UK and Tea Research Association as well as the Directorate of Forests, Govt. of West Bengal, in India in collaboration with IJIRA. Silsoe College studied the performance and compared it with the others while Tea Research Association studied soil loss of the hillocks of Cachar district in Assam, after plantation of tea using Jute Mesh Type I & II and compared it with that of bare plots. Forest Directorate used Soil Saver for protection of hill slopes in the district of Darjeeling in West Bengal through vegetation. The results of Silsoe College are shown graphically in Figure 1 & 2, while those carried out by Tea Research Association in Figure 3. The comparison of vegetation densities on treated and untreated areas of Darjeeling is given in Table 3. Vegetation density was measured six months after installation.

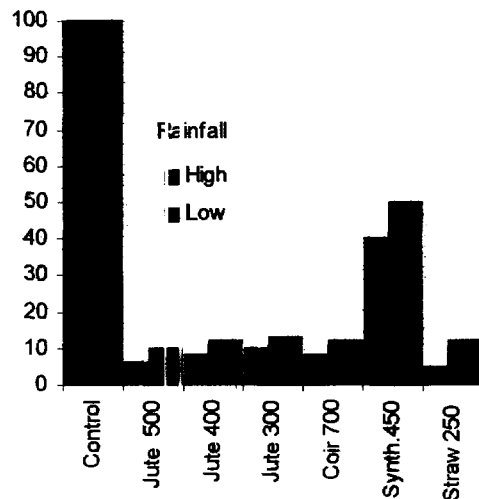


Figure 1 Soil loss (%) for different geotextiles treatment under different rain fall (Soil - Sandy loam)



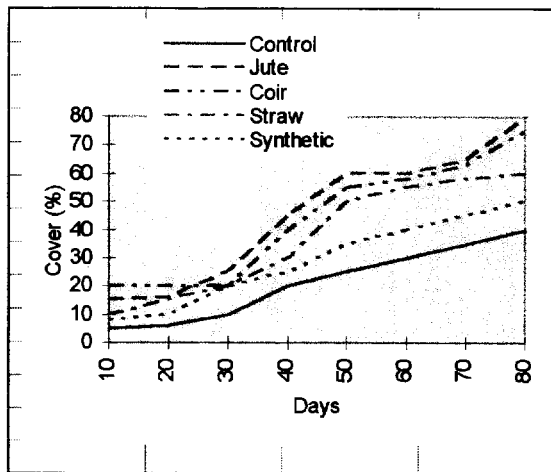


Figure 2 Vegetation cover (%) under different geotextiles with time (Soil-Sandy loam).

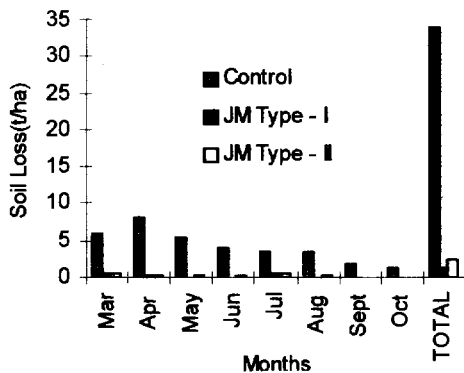


Figure 3 Soil loss under treatment of Jute Mesh Type I & II in different months of rainy season (Total rainfall - 2304 mm, Soil composition - Sand : 73%, Silt : 18% and Clay : 9%)

Table 3 Vegetation densities of treated and untreated areas

Plant species	Slope (60-65) <sup>o</sup>		Slope (30-45) <sup>o</sup>	
	Treated	untreated	Treated	untreated
Chipley	43	48	27	11
Kash*	45	21	58	30
Vimsing				
Patay	5	1	2	-
Guelo	1	1	17	1
Unio	9	12	12	2
Banmara	4	6	12	7
Amlisho	5	6	-	2
Kalimontey 10	-	-	-	6
Bansho	43	-	-	-
Raikhaney	-	2	6	1
Bhakatey	-	-	5	-
Total	165	97	139	60

\* Planted; Plant species (local names)

Soil composition - Sandy loam mixed with small stones;

Rain fall - above 3000 mm.

## 2.4 Selection of Fabrics

Selection of suitable fabric depends on the site conditions like gradient of the slope, intensity of rain fall, wind velocity and soil composition.

## 2.5 Installation

It is very easy to install. Any unskilled person can lay after training at site. After cleaning the surface and making it as smooth as possible the fabrics are laid after anchoring at the top of a slope and rolling down to the bottom, where it is anchored again and cut. The layers are to be overlapped by 10 cm side by side. The overlaps are fixed with the surface with the help of iron pegs of suitable size or living pegs made of tree branches, which may grow with time at intervals of one metre. End to end overlapping should be 15 cm and fixed with the ground keeping the finishing end on the top and starting end under. After installation, seeds of suitable plant/bush/legume may be spread over the treated area. Sapling/tree cutting may also be planted through the open areas if necessary. The treated area should be restricted from stamping and grazing till vegetation takes firm roots. Damage caused by chance should be repaired immediately placing fresh fabric on it and fixing it with the ground.

## 2.6 Discussion

It is evident from the above results that Soil Saver as well as the fabrics of type I & II are capable of reducing soil loss by around 90%, in spite of its less coverage compared to nonwovens as well as cover the surface with vegetation within three months. It is due to the fact that it is highly flexible, which increases by about 25% when wet. So, after first shower, it can establish intimate contact with soil surface reducing soil loss significantly. Moreover, it can absorb water to the extent of four to six times of its weight and helps reduce run off velocity considerably. The water is released in dry spell creating a moist atmosphere, which helps vegetation to grow fast. Apart from these properties jute has good insulation property, which again helps control the extremes of temperature for healthy growth of vegetation. After a period of one and a half years to two years it loses its strength while the biomass, which remains on the surface is not toxic, but increases water permeability of the soil.

### 3 FABRICS FOR SEPARATION AND FILTRATION

Development of such fabrics was initiated by Calcutta Port Trust in late eighties, when the trust was searching for low cost fabrics for protection of bank of the river Hooghly opposite to Haldia, a riverine port in Eastern India. Erosion of the bank was creating navigation problem for big ships. As synthetic geotextile for river bank protection is expensive in India, the Calcutta Port Trust approached IJIRA to develop fabrics for the purpose with specific properties like pore size, water permeability and durability for a reasonable period till siltation starts. For the purpose a twill woven fabric was designed and developed and treated with rot resistant chemicals and bitumen to enhance durability. Bitumen treatment was developed so that it maintains the pores of the fabric for filtration and water permeability across the plane of the fabric. The enhancement of durability of the fabric was measured in laboratory using standard methods IS:1623-1992 (BIS Hand Book 1996). The test results are given in Table 4.

Table 4 Results of Soil Burial Test

Incubation period (Week)	Loss in strength (%)		
	Control	Treated	
		Rot resistant chemicals	Rot resistant + Bitumen
3	90	5	2
6	100	50	20
9	-	90	50
12	-	100	80

A pilot trial on the bank observed strength loss around 30% after a year, when siltation was to the extent of 30 cm on the lower part of the bank. The engineers accepted the fabric for the bank protection work, and applied it commercially for protection of the bank to a stretch of 1.5 Km in 1992. The specification of the fabric is shown in Table 5.

Table 5 Specification of Jute Geotextile for Separation and Filtration

Physical properties		
Weight (g/m <sup>2</sup> )	-	760
No. of threads/dm Warp	-	102
No. of threads/dm Weft	-	47
Thickness (mm)	-	3
Weight after bitumen treatment (g/m <sup>2</sup> )	-	1200
Width (cm)	-	76
Pore size (O <sub>90</sub> ) micron	-	150

Mechanical Properties		
Strength (KN/m)	Warp	- 20 (Min.)
	Weft	- 20 (Min.)
Elongation(%)	Warp	- 5
	Weft	- 10
Puncture Resistance (Kg/cm <sup>2</sup> )		40
Hydraulic Properties		
Water permeability (L/m <sup>2</sup> /Sec.)		20
at water column of 10 cm.		

#### 3.1 Further Trials:

Directorate of Irrigation and Waterways, Govt. of West Bengal wanted to replace the conventional filter material for river bank protection work by geotextile due to the fact that quality filter material is not always available particularly in remote areas. They tried jute geotextile (filter) for protection of the banks of the Padma at Hasanpur, embankment of the river Phulahar at Ramayanpur as well as the banks of the river Hooghly at Barrackpore. Sunderban Development Board, Govt. of West Bengal has also used the material for protection of the approach road connecting a jetty constructed in a river subject to high tidal action in Patharpratima. The object of the trials was to compare its performance with that of conventional granular filter material. The above projects were completed in June'95, July'96, February '97 and August '96 respectively following the approved designs of the respective divisions. In these designs only the filter materials were replaced by Jute Geotextile (filter). The Civil Engineering Department of B.E. College tested soil of the sites and made necessary adjustment in the design for proper anchorage of the fabrics with overlapping. B.E. College is also monitoring the sites at regular intervals of time to assess the condition of the structures.

#### 3.2 River Characteristics and Soil Composition of the Sites

##### 3.2.1 Hasanpur

The Padma is a unidirectional river carrying about 30,000 cumec. of water during peak period July to October. From November water recedes and becomes stagnant during March to June. Right bank of the river at Hasanpur was subject to erosion. The bank was regraded to a slope of 2:1. The fabrics were anchored in a trench of 0.5m x 0.5m at the top and at the bottom it was anchored under a sausage of size 1 m x 3 m made of boulders of size 0.45m. A rip rap layer was placed on the fabric with two layers of boulders. The soil composition of the site is cited below.

Whitish grey sandy SILT (Sand - 30%, Silt-59% and Clay - 11%).

### 3.2.2 Ramayanpur

The river Phulahar becomes active from June to October, when it erodes its banks and sometimes causes flood. The embankment at Ramayanpur protects the villages and agricultural land nearby from the flood water. For protection of the embankment the project work was carried out to a stretch of 400 m, which is on a bend of the river and subject to erosion. The fabrics were anchored at the top in a trench of 0.5m x 0.5 m and at the bottom it was anchored under an apron of size 8m x 1m made of boulders of size 0.45 m. Two layers of boulder were placed on the fabrics as rip-rap. Soil composition of the site is given below.

Sandy grey SILT with little clay (Sand - 29%, Silt - 63% and Clay - 8%). Standard Proctor Test, OMC(%) - 12.4,  $\gamma_d$  Max ( $Mg/m^3$ ) - 1.7

### 3.2.3 Barrackpore

The Hooghly is a tidal river. In August-September the tidal waves rise upto 3 m when the river is full of water. The site is a bathing place, which was damaged with the time. Bank length of 20 m was repaired using Jute Filter on the slope after repairing. Jute Filter was laid on the slope with proper anchorage at the top and bottom and cement mortar blocks of size 0.5m x 0.5m x 0.10m were placed on the filter fabric. The soil composition of the site is given below.

Grey clayey SILT (Sand - 4.5%, Silt - 82% and Clay - 13.5%). LL-30.5, PL-19.5; Bulk density ( $Mg/m^3$ ) - 1.94, Water content (%) - 31, UC Strength ( $KN/m^2$ ) - 0.66.

### 3.2.4 Patharpratima

A jetty was constructed in the river Matla in Sunderban for water transport for benefit of the people of the area. The river is a tidal one and the tidal actions are severe in the spring (August-September). For protection of the approach road to the jetty, on the slopes of the road Jute Filter was applied with proper anchoring and brick blocks of size 0.5 m x 0.5m x 0.25m were placed on the fabrics. The soil composition of the site is highlighted below.

Grey clayey SILT with little sand (Sand - 0.4%, Silt - 78.6% and Clay - 21%) LL - 33.8, PL - 17.6, Standard Proctor Test, OMC(%) - 20.5,  $\gamma_d$  Max ( $Mg/m^3$ ) - 1.7.

### 3.3 Inspection Results

Hasanpur - No subsidence on the rip-rap on Jute Filter, while subsidence upto 15 cm was observed at places of that on the conventional filter materials after the flood of '95

Ramayanpur - No damage was observed after the severe flood in October'96

Barrackpore - It has been completed recently and it is too early to comment on it.

Patharpratima - No sign of displacement of the blocks is visible after seven months of tidal actions on the slopes.

### 3.4 Discussion

In bank protection work normally 150 mm thick layer of ballast of size 10 mm to 15 mm is used as filter, which does not function properly on all types of soil particularly on silty soft soil, as observed in Hasanpur bank protection work, which developed subsidence of the rip-rap structure at places. One of the disadvantages of granular filter is - it is difficult to maintain uniform thickness of the ballast over the length and breadth of the area under treatment, particularly when it is spread manually. Moreover, it is difficult to procure quality filter material in remote areas like Sunderban, where the Jetties constructed using available filter are damaged frequently under the tidal action of the rivers of the region.

The filter fabric is cheaper than the conventional filter material. Moreover, procurement and installation are very easy. Only care is to be taken during installation so that it is not ruptured. If it is damaged by chance, it may be repaired placing a piece of material on the damaged portion. It is a renewable resource and available in plenty. It is very cheap in comparison to synthetic geotextiles particularly in the third world countries.

After the above trials and realising the advantages, the Directorate has decided to apply the material commercially for bank protection work under their control and requisitioned materials for protection of both banks of a canal under Tista Barrage Project in Jalpaiguri to a stretch of 1.2 Km. The work will be completed by June, 1997. Further material for protection of bank of the river Mahananda is under negotiation.

Engineers sometimes expressed doubt about durability of the structures using Jute Geotextiles. In this context, it may be mentioned that the bank length of the Hooghly at Haldia treated in 1992 with Jute Geotextile is still in a good shape. It implies that though the strength of the fabric is not there the biomass which remains is acting as a filter or a natural filter has developed in the soil adjacent to the fabric and is working.

The fabric for separation and filtration has also been applied for construction of roads on soft soil by Kakinada Municipality in Andhra Pradesh in India. The site was a reclaimed area in the port of Kakinada, which is an

important port in South India. The road was made for moving trucks carrying cargo materials to port godowns. In this application width was increased by stitching the fabrics side by side. Construction of the road was designed by Central Road Research Institute, Delhi.

After one year the condition of the road satisfied the authorities, who has decided to increase the road length using similar fabric.

#### 4 CONCLUSION

Jute geotextiles are very cheap in comparison to synthetic geotextiles particularly in the third world countries and may find a big outlet. The jute producing countries may utilise their spare capacities of sacking product lines for the purpose with some modifications in machinery and structure of the fabrics to suit the requirements of geotextiles. Durability may be enhanced by chemical treatments in specific applications like bank protection work, road construction etc. While for protection of surface soil through establishment of vegetation, short durability is an advantage since the fabric becomes superfluous after growth of vegetation.

In India application of geotextiles is in an experimental stage and it is the right time to explore the ideas of application of Jute geotextiles to the practicing engineers in their respective fields. For the purpose, the Ministry of Textiles, Govt. of India and United Nations Development Programme (UNDP) have come forward to assist a project on development of Jute geotextiles for specific end uses under the leadership of the Indian Jute Mills Association. A number of Research and Development organizations and educational institutions are working in the project in their respective fields of expertise.

Object of geotextiles is to reduce cost of construction with good serviceability. In this context, Jute geotextiles have been found to be effective for protection of slopes, river bank protection, consolidation of silty sub-soil as well as roads on soft soil.

#### ACKNOWLEDGEMENTS

The authors are grateful to the Ministry of Textiles, Govt. of India and UNDP for funding the project activities. They are also grateful to the Indian Jute Mills Association, Calcutta for monitoring the project activities efficiently.

The authors acknowledge with thanks the co-operation extended by the engineers of Irrigation & Waterways Directorate, Forests Directorate, Sundarban Development

Board, Govt. of West Bengal for application of Jute Geotextiles.

Thanks are also due to the managements of the jute mills, who supplied materials as per specification and helped during development of the products as well as chemical treatments.

Thanks are due to the colleagues of the authors, who helped the project work directly and indirectly and also to the Directors of the institutions for their permission to present the paper.

#### REFERENCES

- Aziz, M.A. and Ramaswamy, S.D. (1991), "Properties of Jute Geotextiles for Civil Engineering Applications", *Text. Trends* Vol. 33 No. 12, PP. 29-40.
- Barooah, A.K. and Borbarah, B.C.(1997), *Use of Biodegradable Jute Geotextiles for Integrated Soil & Crop management in Tea (Part I)- Soil Conservation progress Report for 1995 & 96*, Tea Research Association, Tecklai Experimental Station, Jorhat, Assam, India.
- BIS (1996), *Bureau of Indian Standards Hand Book, Testing Jute Fabrics for resistance to attack by micro-organism (2nd revision)*, Bureau of Indian Standards, New Delhi, India
- Datta, U, Ghosh, S.N., Chatterjee, P.K., Krishnan, R.S. (1990), "Jute Geotextiles", Proc. *National Seminar on Jute R&D*, Delhi, April, PP 144-150.
- Kabir, M.H., Abedin, M.Z., Zakaria, M. and Saha, P. G. (1988), "Use of Jute Fabric as Soil Filter", Proc. *1st. Indian Geotextiles Conf.*, Bombay, Vol. 1, PP.G 15-23.
- Rao, P.J., Bindumadnav, Babu, G.L.S., Pathak, D.N. and Shah, A. J. (1996), "Use of Jute Geotextiles as Separator in Pavements - A case study", Proc. *National Seminar on Jute based Geotextiles*, New Delhi, PP.14-24
- Ramaswamy, S.D. and Aziz, M.A.(1984), "Jute fabric upon Coir grid matting for Stabilisation", Proc. *Int. Conf. on Road Development*, Paris, PP 775-779.
- Rickson, R.J. and Loveday, A. D.(1996), "Technical Specification and Market Study of Potentially important Jute Geotextile Products", Presented in *IJO Jute-Geotextile Conf.*, Dhaka, Bangladesh, Sept.'96.
- Sanyal, T. and Chakraborty, K.(1993), "Application of a Bitumenised Jute Textile in Bank Protection work in the Hooghly Estuary", *Geotextile & Geomembranes* Vol 13, PP 127-132.
- Thomson, J. (1985), "Jute Holds ground", *Textile Horizons*, Sept., PP. 23-29.

# ABRASION PROPERTIES OF GEOTEXTILES SUBJECT TO DYNAMIC LOADING

W.S.Alexander  
Business Development Manager, Amoco Australia

**ABSTRACT:** In many civil engineering applications geotextiles are subjected to dynamic loadings. These applications include use as a filter fabric beneath rock beaching, (rip-rap), and particularly in marine or tidal applications, which are subject to storm events. Also, to a lesser extent, dynamic loadings occur in railway and logging haul road applications.

This paper reviews the performance of commonly used geotextiles in these applications by exhuming geotextiles from a range of projects after a number of years. A testing program was undertaken to compare properties of geotextiles. Simple testing of geotextiles was carried out in mechanical agitators as well as in actual marine environment. The properties of a range of geotextiles, spun-bond, heat-bonded, continuous filament and staple-fibre non-wovens were compared before and after testing to establish the relative abrasion resistance of different geotextiles subjected to dynamic loading.

**KEY WORDS:** abrasion, geotextiles, case study, dynamic mechanical analysis testing

## 1 INTRODUCTION

Abrasion resistance is not widely considered an important characteristic of geotextiles. The proof of this statement is borne out by the lack of any abrasion performance parameters in commonly used geotextile specifications around the world. In civil engineering applications for geotextiles such as sub-soil drainage, roadway separation and liner protection abrasion is a secondary consideration. There are, however, applications where abrasion resistance is important to the long-term performance of the geotextile. These applications include the use of geotextiles as filters behind rock revetments as well as, to a lesser extent, in dynamic loading situations such as in railway track applications (ref.1) and unsealed haul roads.

## 2 EXISTING ABRASION TESTS

The ASTM currently has one standardised abrasion test for geotextiles, D4886, "Standard Test Method for Abrasion Resistance of Geotextiles (Sand Paper/ Sliding Block Method)". This test is, however, not widely used for the reasons already stated that abrasion is not widely accepted as being important as well as the general view that these tests are very severe and not a fair reflection of the actual abrasion mechanism in a given engineering application. It is difficult to specify what level of abrasion resistance is appropriate, according to D4886, for a given situation. Australian geotextile standards do not address the issue of abrasion although Austroads (ref.2) describe abrasion as "significant where there is repeated loading such as below rip-rap in shore protection or during placement of the first lift on an embankment/pavement when construction equipment must operate on a thin layer"

In Germany the BAW rotating drum test has been used for some years to carry out abrasion testing of

geotextiles. The author is not aware of further details of this test.

Two other standard textile abrasion tests, the Stolle and the Taber Abrasion test are, likewise, considered severe and inappropriate for testing geotextiles. Other abrasion tests have been put forward by Gray (ref.3) and Dine (ref.4), however these are not known to be widely used.

## 3 REVETMENT APPLICATIONS

Failures of geotextiles in revetment applications have been observed at La Canau, France 1985 and at Somers, Australia 1990. Storm events cause severe turbulent wave action, which has been shown to unravel and damage geotextiles. At Somers a non-woven, needle-punched, continuous-filament polyester geotextile failed after being subjected to wave action over only a few days. A replacement non-woven needle-punched, staple-fibre polyester geotextile was found to perform adequately when used in the same environment. Existing abrasion tests only consider the mechanical abrasion of geotextiles, caused by rock particles abrading the geotextile. Geotextiles should, ideally, be well secured by secondary armour rock however, in practice, when subjected to wave action there is some small movement of the geotextile. In some cases the geotextile will only be secured by large discrete rock units and relatively large movements of the geotextile between these rocks will occur. The structure of the geotextile must be adequate to prevent unravelling of the geotextile from this hydraulic loading as well as be resistant to mechanical abrasion caused by rubbing of the geotextile on rock.

#### 4 HYDRAULIC TESTING

Because of the difficulties of field testing geotextiles subject to wave action in a foreshore environment a simple test was devised to replicate the effects of dynamic wave action on geotextiles.

Geotextiles tested were 3 different commercially available Australian geotextiles, which are commonly used in revetment works. Each geotextile was a non-woven (NW), needle-punched (NP) type. Fibre type was either staple-fibre (SF) or continuous-filament (CF) and polymer was either polypropylene (PP) or polyester (PET). Samples of geotextile were placed in a domestic washing machine and agitated for given periods of time. (See Fig 1) Each agitation cycle was 12 minutes long and samples were tested for 4 and 8 cycles. The samples were visually inspected and Mass, Grab Tensile Strength and Mullens Burst Pressure were measured before and after testing. The results are detailed in Tables 1 and 2, and Fig 2 below:



Fig 1. Photo of Washing Machine Agitator

Table 1. Sample description

A	NW, NP, SF, PP
B	NW, NP, SF, PET
C	NW, NP, CF, PET

Table 2. Test Results

	Mass (gsm)			Grab (N)			Mullens (kPa)		
	B*	4	8	B*	4	8	B*	4	8
A	275	275	275	872	829	829	3500	3400	3400
B	298	298	298	550	550	550	2425	2425	2425
C	265	255	255	1100	1100	890	3300	3300	3300

\* Before

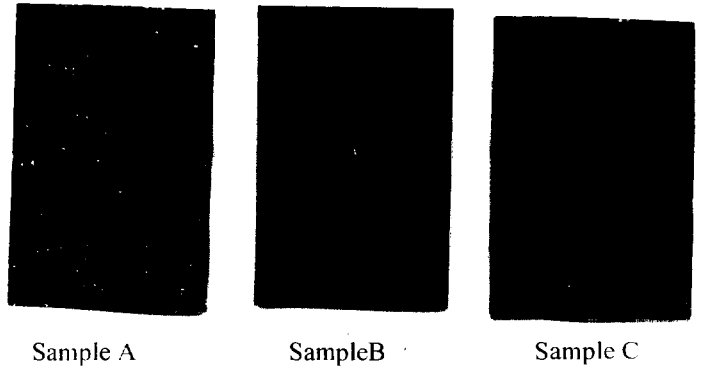


Fig. 2 Visual appearance of samples after testing (8 cycles)

#### 5 DISCUSSION OF RESULTS

From the above results it is clear that all geotextiles are subject to damage due to wave action, to varying degrees according to the type of structure of the geotextile. Visual inspection showed severe "fluffing" of samples B and C after 8 cycles (96 minutes in agitator). The structure of the geotextiles had begun to unravel. After 8 cycles sample C had virtually disintegrated. This appears to be due to sample C's lightly needled nature compared to the other more heavily needled staple-fibre fabrics. However, sample A showed little change in its visual appearance, even after 8 cycles, which may be explained by its tightly needled staple-fibre structure. The mechanical properties of each sample were affected to varying degrees. The mullens burst for each was largely unaffected. The grab tensile results for sample A showed a 5% reduction and for sample C showed a 20% reduction, which is a significant reduction and may indicate general strength reduction. Further mechanical strength testing of the sample is needed, such as wide strip tensile strength, trapezoidal tear strength and drop cone test, to determine if the mechanical properties are more broadly affected.

##### 5.1 Limitations of Results

This test should be seen as a useful index test to compare performance of different types of geotextiles. It is also useful to give broad guidance as to a geotextile's suitability for use in this type of application. The severe damage to sample C in this test closely replicates the damage sustained to this fabric at the Somers site and so gives a fair reflection of the damage that may occur in revetment applications. Because of the difficulty of replicating actual field conditions, ie coastal marine environment subject to tidal action, in the laboratory, it is

difficult to more accurately co-relate these results to field conditions and to standardise the test to set minimum acceptable performance limits. It is recognised that this testing regime is very severe and may not be appropriate to test abrasion of geotextiles in other applications such as roading or rail track. This test method only replicates turbulent wave action and does not take into account the mechanical abrasion of rock and soil particles rubbing against the geotextile. One improvement to the method would be to include rock particles in the agitator to help model field conditions more accurately. To this end testing has been conducted by others in Australia using a modified form of the LA Abrasion test, although the results have not been published. In this test, samples of fabric are fixed to the internal walls of a drum, which is filled with water and rocks. The drum is then rotated and the fabric samples are tested for the effects of water borne abrasion. The German BAW rotating drum test may also address this issue.

## 5.2 Recommendations

From this testing it would not be recommended to use geotextile C in revetment applications in marine applications due to the disintegration of the fabric's structure after 8 cycles in the test. The reduction in grab tensile may indicate a broad reduction in the strength properties of the geotextile.

## 5.3 Further Testing

Because of the limited nature of this project it is required to conduct further extensive testing to determine the reproduceability of the test method. Variables such as length of time of testing and addition of, and type of, rock samples need to be investigated.

## 6 CONCLUSIONS

The following conclusions were made based on this testing:

- abrasion is an important consideration in some engineering applications of geotextiles, such as revetment and rail track situations.
- abrasion is inadequately treated by current standard tests
- dynamic wave action causes stresses, other than mechanical abrasion, to occur in the geotextile
- a simple agitation test, using a domestic washing machine, was found to be a useful index test to compare performance of different geotextiles as well as to give broad assessment of suitability of geotextile for application

- field experience, together with agitator testing, show that some lightly needled continuous-filament non-wovens are not suitable for use in revetment applications in tidal environments
- The results of this testing together with field experience, indicate that staple-fibre non-woven geotextiles are most suitable for use in this application.

## ACKNOWLEDGEMENTS

The writer would like to thank Mr. G. Byrne of Vantree Pty Ltd for his assistance.

## REFERENCES

- Raymond, G. (1982) "Geotextiles for Railroad Bed Rehabilitation" *Second International Conference on Geotextiles*, Las Vegas, USA. pp.479-484
- AUSTROADS, (1990) *Guide to Geotextiles* pp.53
- Gray, C.G. (1982) "Abrasion Resistance of Geotextile Fabrics" *Second International Conference on Geotextiles*, Las Vegas, USA. pp.317-821
- Van Dine, D., Raymond, G. and Williams, S.E. (1982) "An Evaluation of Abrasion Tests for Geotextiles" *Second International Conference on Geotextiles*, Las Vegas, USA. pp. 811-816





# STABILITY CRITERIA FOR GEOSYSTEMS - AN OVERVIEW -

Krystian W. Pilarczyk

Manager R&D, Rijkswaterstaat, Hydraulic Engineering Division, Delft, The Netherlands, Fax +31-15-2611361

Mark Klein Breteler

Project Manager, Delft Hydraulics, The Netherlands

Theo Stoutjesdijk

Project Manager, Delft Geotechnics, The Netherlands

**ABSTRACT:** Geotextile systems such as bags, mattresses, tubes and containers filled with sand or mortar can be a good and often cheaper alternative for more traditional materials/systems as rock, concrete units or asphalt. These new systems were applied successfully in a number of countries and they deserve to be applied on a larger scale. Because of low price and easy construction these systems can be a good alternative for coastal protection and coastal structures in developing countries. The main obstacle in their application is however the lack of proper design criteria. An overview is presented on stability criteria of the existing geosystems and their limitations.

**KEYWORDS:** Geomattresses, Geobags, Geotubes, Design

## 1 INTRODUCTION

Various structures/systems can be of use in hydraulic and coastal engineering, from traditional rubble or concrete systems to more novel methods as geosystems and others. Within the scope of the research on the stability of rock and block revetments, much knowledge has been developed about the possible failure mechanisms and methodology on development of stability criteria under current and wave load (CUR/RWS, 1995a,b). Until recently, no or unsatisfactory design tools were available for a number of other (open) types of revetment and geosystems. This is why the design methodology for block revetments has recently been extended in applicability by means of a desk-study for a number of geosystems, such as sandbags and sand- and mortar-filled mattresses and tubes/containers. Also other stability aspects, such as soil-mechanical stability and residual strength were taken under consideration.

Geotextile systems utilize a high strength synthetic fabric as a form for casting large units by filling them by sand or mortar, or as curtains collecting sand. At this moment there is a relative large number of products of this type on the market provided by some specialistic companies all over the world. Mattresses are mainly applied as slope and bed protection. Bags are also suitable for slope protection and retaining walls or toe protection but the main application is construction of groins, perched beaches and offshore breakwaters. The tubes and containers are mainly applicable for construction of groins, perched beaches and offshore breakwaters. They can form an individual structure conforming functional

requirements for the project or as a component of the main structure. In general, the sand-filled structure can be used as: temporary structures to learn the natural interactions/responses, permanent structures at locations with relatively low wave attack ( $H < 1.5\text{m}$ ), or submerged structures where direct wave forces are reduced. The mortar-filled systems can resist much higher wave and current loading and, if necessary, can be interconnected by bars or by creating a special interlocking shape.

The main advantages of these systems in comparison with more traditional methods are: a reduction in work volume, a reduction in execution time, a reduction in cost, a use of local materials, a low-skilled labour requirement and possibility of using of locally available equipment.

This paper aims at giving a summary of the increased knowledge, especially that concerning the stability criteria for sand- and mortar-filled mattresses, bags and geotubes that have been made available.

## 2 STABILITY CRITERIA

### 2.1 Wave-load stability

There are two practical design methods available: the black-box model and the analytical model. In both cases, the final form of the design method can be presented as a critical relation of the load compared to strength, depending on the type of wave attack. For revetments, the basic form of this relation is:

$$\left(\frac{H_s}{\Delta D}\right)_{cr} = \frac{A}{\xi_{op}^{2/3}} \text{ with maximum } \left(\frac{H_s}{\Delta D}\right)_{cr} = 8.0 \quad (1)$$

In which: A = revetment (stability) factor (-),  $H_s$  = significant wave height (m),  $\Delta = \rho_s/\rho_w - 1$  = relative density (-),  $\rho_s$  = density of the protection material,  $\rho_w$  = density of water (kg/m<sup>3</sup>), D = thickness of the top layer (m), and  $\xi_{op}$  = breaker parameter (-). For porous top layers, such as sand mattresses and gabions, the relative density of the top layer must be determined, including the water-filled pores:

$$\Delta_m = (1 - n) \cdot \Delta \quad (2)$$

In which:  $\Delta_m$  = relative density including pores (-) and n = porosity of the top layer material (-).

The breaker parameter is defined as follows:

$$\xi_{op} = \frac{\tan \alpha}{\sqrt{H_s/L_{op}}} \quad (3)$$

In which:  $\alpha$  = slope angle (°),  $L_{op} = 1.56 T_p^2$  = deep-water wavelength at the peak period (m), and  $T_p$  = wave period at the peak of the spectrum (s).

The advantage of this black-box design formula is its simplicity. The disadvantage, however, is that the value of A is known only very roughly for many types of structures.

The analytical model is based on the theory for placed stone revetments on a granular filter. In this calculation model, a large number of physical aspects are taken into account. In short, in the analytical model nearly all physical parameters that are relevant to the stability have been incorporated in the "leakage length" factor. The final result of the analytical model may, for that matter, again be presented as a relation such as Eq. 1 where  $A = f(\Lambda)$ . For systems on a filter layer, the leakage length is given as:

$$\Lambda = \sqrt{\frac{b_f D k_f}{k'}} \quad (4)$$

with:  $\Lambda$  = leakage length (m),  $b_f$  = thickness of the filter layer (m),  $k_f$  = permeability of the filter or subsoil (m/s), and  $k'$  = permeability of the top layer (m/s).

With a system without a filter layer (a system placed directly on sand or clay) the permeability of the subsoil (eventually with gullies/surface channels) is filled in. For the thickness of the filter layer it is examined to which depth changes at the surface affect the subsoil. One can

fill in 0.3 m for sand and 0.03 m for clay. The values for D and  $\Delta$  depend on the type of revetment. When schematically representing a block on a geotextile on a gully on sand, the block should be regarded as the top layer and the combination of the geotextile and the small gully as the filter layer. The leakage length can be calculated using:

$$\Lambda = \sqrt{\frac{(k_f d_g + k_g T_g) D}{k'}} \quad (5)$$

with:  $k_f$  = permeability of the filter layer (gully) (m/s),  $d_g$  = gully depth (m),  $k_g$  = permeability of the geotextile (m/s),  $T_g$  = thickness of the geotextile (m), D = thickness of the top layer (m), and  $k'$  = permeability of the top layer (m/s).

To be able to apply the design method for placed stone revetments under wave load to other systems, the following items may be adapted:

- the revetment parameter A;
- the (representative) strength parameters  $\Delta$  and D;
- the design wave height  $H_s$ ;
- the (representative) leakage length  $\Lambda$ ;
- the increase factor  $\Gamma$  on the strength.

Only suchlike adaptations are presented in this summarizing paper. The basic formulas of the analytical model are given in (CUR/RWS, 1995a).

## 2.2 Flow-load stability

Severe flow attack may in practice occur on revetments, such as with flow over a steep slope and flow attack near many kinds of structures (downstream of sills, gates, discharge structures and the like). At these structures, the flow is often specifically determined by the geometry and the boundary conditions. With flow over a steep slope, such as on the downstream slope of a over-flow dam or dike, the situation is less ambiguous.

When the flow velocity is known well, or can be calculated reasonably accurately, Pilarczyk's relation (1990) is applicable:

$$\Delta D = 0.055 \frac{\Phi}{\Psi} \frac{K_T K_h}{K_s} \frac{u_{cr}^2}{2g} \quad (6)$$

in which:  $\Delta$  = relative density (-), D = characteristic dimension (m), g = acceleration of gravity ( $g=9.81 \text{ m/s}^2$ ),  $u_{cr}$  = critical vertically-averaged flow velocity (m/s),

$\Phi$  = stability parameter (-),  $\Psi$  = critical Shields parameter (-),  $K_T$  = turbulence factor (-),  $K_h$  = depth parameter (-), and  $K_s$  = slope parameter (-).

\* The stability parameter  $\Phi$  depends on the application. Some guide values are given below.

	Continuous toplayer	Edges and transitions
Riprap and placed blocks	1.0	1.5
Mattresses, gabions, and washed-in blocks	0.5	0.75

\* With the critical Shields parameter  $\Psi$  the type of material can be taken into account. Some guide values are given below.

Revetment type:	$\Psi$ (-)
riprap	0.035
loose, placed blocks	0.05
blockmats	0.07
gabions	0.07
sand and concrete mattresses	0.07

\* The degree of turbulence can be taken into account with the turbulence factor  $K_T$ . Some guide values for  $K_T$  are given below.

Situation:	$K_T$ (-)
Normal turbulence:	1.0
Increased turbulence (i.e. river bends)	1.5
Heavy turbulence (i.e. hydraulic jump)	2.0
Load due to water (screw) jet:	3.0 to 4.0

\* With the depth parameter  $K_h$ , the water depth is taken into account, which is necessary to translate the depth-averaged flow velocity into the flow velocity just above the revetment. The depth parameter also depends on the measure of development of the flow profile and the roughness of the revetment. The recommended formulas can be found in (Pilarczyk, 1990, Klein Breteler, 1996). The following indicative values for the water depth  $h > 2$  m are given below:

developed profile	:	$K_h = 0.2$
nondeveloped profile	:	$K_h = 0.4$

For shallow water and rough flow ( $h/k_s < 5$ ):  $K_h = 1.0$  ;  
 $h$  = water depth (m) and  $k_s$  = equivalent roughness according to Nikuradse (m);  $k_s \approx 0.05$  m for mattresses.

\* Slope parameter  $K_s$ . The stability of revetment elements also depends on the gradient under which the revetment is applied, in relation to the angle of internal friction of the revetment. This effect on the stability is taken into account with the slope parameter  $K_s$ , which is defined as follows:

$$K_s = \sqrt{1 - \left(\frac{\sin \alpha}{\sin \theta}\right)^2} \quad (7)$$

with:  $\theta$  = angle of internal friction of the revetment material ( $^\circ$ ) (about  $90^\circ$  for concrete mattresses and  $30$  to  $40^\circ$  for sand-filled systems) and  $\alpha$  = transversal slope of the bank ( $^\circ$ ).

With a downward flow along a steep slope it is difficult to determine or predict the flow velocity exactly, because the flow is very irregular (high turbulence, inclusion of air as a result of which the water level cannot be determined very well, etcetera). One is confronted with this when dimensioning the revetment of (the crest and) the inner slope of a dike in the case of flooding. In that case a design formula based on the discharge is preferable (Klein Breteler, 1996).

### 2.3 Soil-Mechanical Stability

The water movement on a revetment structures can also affect the subsoil, especially when this consists of sand. This effect is treated within the framework of the soil-mechanical aspects and can be of importance to the stability of the structure.

There are three aspects that will be discussed within the framework of soil-mechanical aspects:

- elastic storage;
- softening (liquefaction);
- drop in the water level.

These aspects and the accompanying damage mechanisms en design methods are discussed in detail below. Background information can be found CUR/RWS (1995a).

Elastic storage in the subsoil is connected with the permeability and stiffness of the grain skeleton and the compressibility of the pore water (the mixture of water and air in the pores of the grain skeleton). Because of these characteristics, wave pressures on the top layer are passed on delayed and damped to the subsoil of the revetment construction and to deeper layers (as seen perpendicular to the slope) of the subsoil.

This phenomenon takes place over a larger distance or depth as the grain skeleton and the pore water are stiffer. If the subsoil is soft or the pore water more compressible (because of the presence of small air bubbles) the compressibility of the system increases and large damping of the water pressures over a short distance may occur. Because of this, alternately water undertension and overtension may develop in the subsoil and corresponding to this an increasing and decreasing grain pressure.

Elastic storage can lead to the following damage mechanisms:

- lifting of the top layer;
- sliding of the top layer;
- sliding of the subsoil.

For the stability of the top layer, elastic storage could particularly be of importance if the top layer is placed directly on the subsoil without there being small gullies under the top layer and, if the permeability of the top layer is (locally) less than that of the subsoil. These conditions imply that the leakage-length approach according to the analytical model for the stability under wave load cannot be applied.

The stability of the subsoil may be jeopardized if, because of elastic storage, the grain tension decreases so strongly that insufficient shear stress can be absorbed in the subsoil to prevent sliding. The design method with regard to the different damage mechanisms connected with elastic storage are presented in the form of design diagrams. In these diagrams the permissible wave height is plotted against the thickness of the top layer and the slope gradient. If the revetment construction consists of a top layer on a filter layer, the thickness of the filter layer may in these diagrams be partially or completely (depending on the type of revetment) added to the thickness of the top layer.

Also through cyclic generation of water tension, water overtensions may occur in the subsoil, but with impermeable top layers also directly under the top layer. In sand, these watertensions can be calculated using the MCYCLE program developed by Delft Geotechnics. As the top layer becomes more impermeable, the water tension manifests itself closer to the surface of the slope. In the case of a very permeable top layer this is exactly the opposite. Softening (liquefaction) can be defined as follows:

A cyclic variable load causes compaction to occur in a

layer of sand. This leads to a decrease in the pore space. The water in the pores is subjected to pressure and will want to run off. At first, water overtension occurs. This causes a decrease in the contact pressure between the grains and with this the resistance to sliding. Finally, the water overtension might become so large that the contact pressure between the grains falls away completely. This is called softening or liquefaction.

The difference between liquefaction and elastic storage is that with liquefaction, water overtension is connected with a plastic deformation of a grain skeleton instead of an elastic deformation. Water overtension through softening occurs when the grain skeleton deforms plastically to a denser packing. From which follows that the dangers connected with liquefaction are smaller as the subsoil is compacted better during construction.

With regard to liquefaction, the following design rules are suggested for constructions with a reasonably compacted subsoil:

- With a top layer on sand there is no danger of liquefaction, if:
  - the slope gradient is gentler than or equal to 1:3,
  - the slope gradient is gentler than 1:2 and the wave height  $H_s$  is smaller than 2 m, or
  - the slope gradient is gentler than 1:2 and the subsoil is well-compacted.
- With a top layer on clay there is no danger of liquefaction.
- With a top layer on a granular filter there is generally no danger of liquefaction.

In these design rules hardly any distinction is made between types of revetment.

Through a drop in the water level a difference in the rise over the top layer may occur. A drop in the water level may occur as a result of tide or a ship passing through a waterway or canal. As with packed stone revetments, this is only a problem if any possible filter layer and the top layer are sanded up and because of this obtain a low permeability.

No calculations need to be made on this phenomenon if applies:

$$\frac{\Delta \sin \alpha}{2} \leq \Delta D \cos \alpha \quad (8)$$

in which:  $\Lambda$  = leakage length (m),  $\alpha$  = slope angle ( $^\circ$ ),  $\Delta$  = (representative) relative density of the top layer (-),  $D$  = (representative) thickness of the top layer (m).

### 3 TYPES OF STRUCTURES

#### 3.1 Concrete Mattresses

Characteristic of concrete mattresses are the two geotextiles with concrete or cement between them. The geotextiles can be connected to each other in many patterns, which results in each mattress system having its own appearance and properties. An example is given in Figure 1.

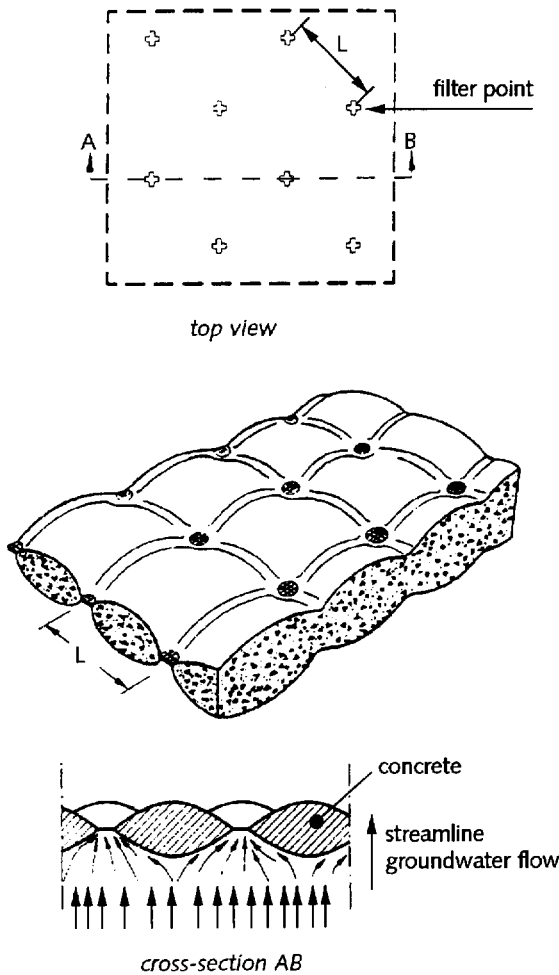


Figure 1 Example of concrete mattress

The permeability of the mattress is one of the factors that determine the stability. It is found that the permeability given by the suppliers is often the permeability of the geotextile, or of the so-called Filter Points. In both cases, the permeability of the whole mattress is much smaller. A high permeability of the mattress ensures that any possible pressure build-up under the mattress can flow away, as a result of which the differential pressures across the mattress remain smaller. The stability is there-

fore the largest with a large mattress permeability. In the long term, however, pollution of the Filter Points or the clogging of the geotextile can cause a decrease in the permeability.

##### 3.1.1 Design rules with regard to wave load

In the design rules for concrete mattresses with regard to wave load the calculation of the leakage length is adapted. This consideration, which is closely related to a consideration in accordance with the analytical model, results in a design formula in the form of the black-box formula.

During wave attack, the mattress will be exposed to a differential pressure which is directed upwards, as also is the case with packed stone revetments. This takes place the moment the wave has drawn back, just before the wave impact. Just as with packed stone revetments, the leakage length for this differential pressure is the most important construction-descriptive parameter. The leakage length ( $\Lambda$ ) can be calculated using Eqs. 4 or 5. The values of the leakage length may vary from about 0.5 to 10 m depending on the type (permeability) of the mattress, the permeability and thickness of the filter, and the presence of cavities under the mattress.

The failure mechanism of the concrete mattress is probably as follows:

- First, cavities under the mattress will form as a result of uneven subsidence of the subsoil. The mattress is rigid and spans the cavities.
- With large spans, wave impacts may cause the concrete to crack and the spans to collapse. This results in a mattress consisting of concrete slabs which are coupled by means of the geotextile.
- With sufficiently high waves, an upward pressure difference over the mattress will occur during wave run-down, which lifts the mattress.
- The pumping action of these movements will cause the subsoil to migrate, as a result of which an S-profile will form and the revetment will collapse completely.

The value of stability factor  $A$  in the design formula of the black-box model (Eq. 1) depends on the leakage length and the subsoil:  $A = 2$  to  $4$ . A permeable mattress on sand has a medium-sized or small leakage length and then the value of  $A$  is  $3$  to  $4$ . A low-permeable mattress on a filter has a large leakage length and therefore an  $A$ -

value of 2 to 3 (Figure 2). For the determination of the leakage length, one is referred to the analytical model.

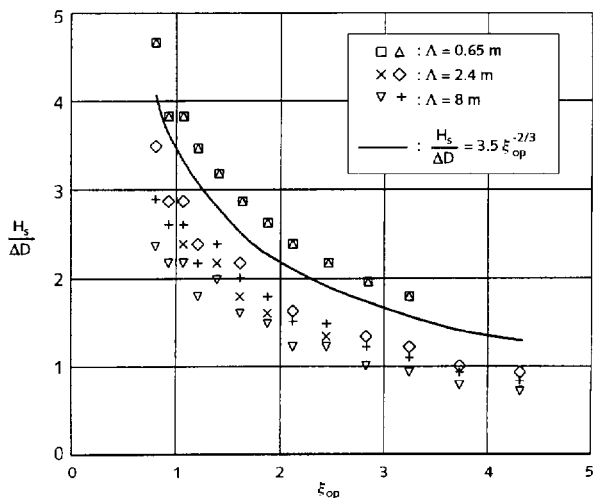


Figure 2 Calculation results for concrete mattresses

The representative relative density  $\Delta$  follows from the standard definition. For the representative thickness  $D$ , the average thickness should be filled in.

It can be concluded that, compared to the available data in literature, the derived stability relations give a safe estimation of the stability. Because the relations have not been verified sufficiently yet, it is not recommended to decrease the existing safety.

In the long run, the permeability of the top layer may diminish as a result of accretion and silting-up. This will have a negative effect on the stability, especially with systems with a leakage length smaller than approximately 2 m. If the leakage length is larger than 2 m, the effect of the permeability of the top layer on the stability is rather small.

### 3.1.2 Design rules with regard to flow load

A number of characteristic values for the critical flow velocity for concrete mattresses is given below.

Thickness	on slope	on bottom
50 mm	2.7 m/s	3.3 m/s
100 mm	3.9 m/s	4.7 m/s
200 mm	5.5 m/s	6.4 m/s

For the application of the design formula (Eq. 6), guide values for the constants are given in Section 2.2. For the representative thickness  $D$ , one should fill in the average thickness of the top layer.

### 3.1.3 Design rules with regard to soil-mechanical stability

The flow through a concrete mattress is concentrated in the Filter Points. The permeability of the systems filled with concrete lies approximately between  $1 \cdot 10^{-4}$  and  $5 \cdot 10^{-3}$  m/s. A concrete mattress is less flexible than a sand mattress and does not connect to the subsoil as well as a sand mattress. In contrast with sand mattresses, it is assumed that only the sliding of the whole mattress can occur and not just part of it.

#### \* Elastic storage

With regard to elastic storage, the following design example for a wave height  $H = 1$  m and a slope 1 on 3 is given. The required thickness of the mattress on sand for various failure mechanisms and wave steepness ( $S_{op}$ ) is equal to:

Failure type	$S_{op} = 0.03$	$S_{op} = 0.05$
Lifting of toplayer	0.35 m	0.25 m
Partial sliding toplayer	0.80 m	0.60 m
Sliding of toplayer	0.30 m	0.25 m
Sliding of subsoil	0.55 m	0.40 m

Concrete mattresses are mostly stiff and anchored at the top. Therefore, not the sliding and/or uplifting of the toplayer but the sliding of the subsoil is the most dangerous (for  $H=1$ m, the required thickness is 0.55m).

If the systems are placed on a filter, one can take into account an increase in the stability with regard to elastic storage. For the total thickness of a concrete mattress on a filter,  $D + b/\Delta$ , can be filled in, where  $b$  is the thickness of the filter.

#### \* Liquefaction

The design rules with regard to liquefaction do not differ from those presented in Section 2.3.

## 3.2 Sand Mattresses

A sand mattress consists of two geotextiles attached onto each other, between which sand is interposed. This way, a mattress is formed of sausages lying next to each other which run from the top to the bottom of the slope and which are interconnected. The lower geotextile is usually flat and the upper geotextile lies on top of it, in arches.

#### \* Construction/design/repair

The edges and connections of sand mattresses are vulne-

nable and must therefore be finished carefully. Mattresses lying next to each other can be sown together and the ends can be secured with for example ground anchors.

In actual practice, mattresses are not only threatened by the hydraulic load. The possibility of vandalism occurring, limits sand mattresses to being applied in places where unauthorized persons do not have access to. The system is also vulnerable to collision, (drifting) ice, floating bulky refuse, sunlight and chemical degradation.

**\* Stability**

Sand mattresses cannot be used when the significant wave height  $H_s$  is larger than 1.0 m (max. 1.5 m in case of properly compacted subsoil). Unfortunately, not much research has been conducted into the stability of sand mattresses. Besides Pilarczyk's design formula (1990), a small-scale model investigation, a desk study and a prototype experiment have been found. Based on these, the following value for A in the design formula (Eq. 1) is recommended according to the black-box model:  $A = 4$  to 5. In this formula the relative density including pores  $\Delta_m$  should be filled in for the representative relative density. For the representative thickness D of the mattress, the average thickness should be filled in:

$$100\% \text{ filled} : \frac{D}{D_d} = 0.7 \text{ to } 0.8$$

$$90\% \text{ filled} : \frac{D}{D_d} = 0.6 \text{ to } 0.7$$

with: D = average thickness of the mattress (m) and  $D_d$  = maximum diameter of the sausages (m).

Above a flow velocity of 1.5 m/s (max. 2 m/s), the sand in the mattresses is no longer internally stable. The design formula on stability against currents is given in section 2.2.

A sand mattress is relatively flexible and connects closely to the subsoil. The geotechnical design criteria are similar to those for the concrete mattresses.

**3.3 Geobags and geotubes**

Geobags or tubes can be filled with sand, gravel or concrete. The bags may have different shapes and sizes, varying from the well-known sandbags for emergency dikes to large flat shapes or elongated "sausages" (see Figure 3). The most common use for sandbags in hydraulic engineering is for temporary structures. The reasons why sandbags are not or hardly used for permanent structures are as follows:

- the resistance against flow load and wave load is relatively small;
- because the geosystems are prone to vandalism and the effect of sunlight, for example, the durability is relatively small;
- good design formulas are lacking;
- a construction made of sandbags looks ugly.

Major advantages of sandbags as construction material are the low costs and the simple processing. Uses for sand- or cement-filled bags are, among other things:

- revetments of relatively gentle slopes;
- temporary toe constructions in places where in due course vegetation should develop;
- (temporary) training walls/groins;
- temporary or permanent offshore breakwaters;
- temporary dikes surrounding dredged material containment areas.

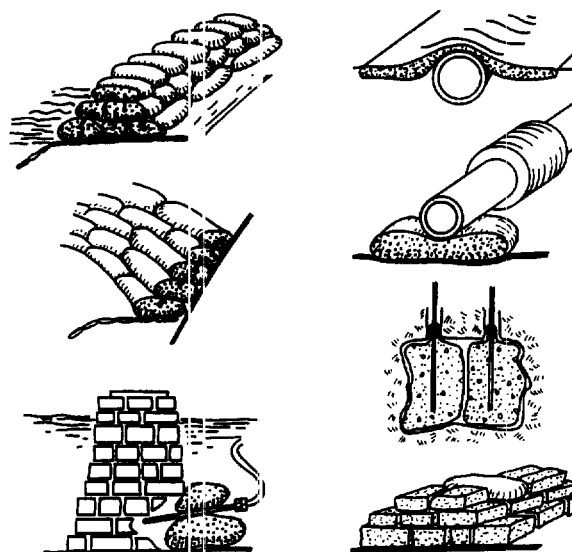


Figure 3 Application of geobags and containers

Because sand is easy to use and cheap, it is extremely suitable for temporary structures. Above a flow velocity of 1.5 to 2 m/s, the sandbags cannot be used for permanent applications because the sand is no longer internally stable.

Sandbags can be placed as follows:

1. *As a blanket:* One or two layers of bags placed directly on the slope. An "interlocking" problem arises if the bags are filled completely. The bags are then too round. A solution is not to fill the bags completely, so that the sides flatten out somewhat, as a result of which the contact area becomes larger.
2. *As a stack:* Bags stacked up in the shape of a pyramid. The bags lie half overlapping with the long side parallel to the shoreline.

When installing geosystems, one should see to it that this

does not take place on a rough foundation. Sharp elements may easily damage the casing of the element. Geosystems must not be filled completely. With a fill ratio of approximately 75% an optimum stability of the elements is reached. A sound soil protection is necessary if gravel (sand) sausages are used in circumstances where they are under attack of flow or waves.

Background information on geobags can be found in Pilarczyk (1995) and Wouters (1995).

New developments concern the large hydraulically filled geotubes and hydraulically or mechanically filled geocontainers (in combination with a split barge). Information on these systems can be found in Leshchinsky (1995), Pilarczyk (1996, 1997) and Den Adel et al (1996).

### 3.3.1 Design rules with regard to wave load

The stability relation of sand, gravel or cement bags which are used as protection elements on a slope appears to deviate somewhat from the formula according to the black-box model. For regular waves the recommended formula is as follows:

$$\left(\frac{H}{\Delta D}\right)_{cr} = \frac{3.5}{\sqrt{\xi_o}} \quad (9)$$

In which  $\Delta$  is the relative density if the pores are completely filled with water ( $\Delta_m$ ). The representative thickness  $D$  is the average thickness of the top layer, measured perpendicularly to the slope.

If this stability relation is combined with the relation found between  $H_s$  and  $H$ , (significant wave height with irregular waves and the wave height with regular waves) this results in the following stability relation:

$$\left(\frac{H_s}{\Delta D}\right)_{cr} = \frac{2.5}{\sqrt{\xi_{op}}} \quad (10)$$

For concrete sausages (tubes) used as a protection element on the crest of a low or underwater breakwater, it is found that the following stability relation for regular waves can be used:

$$\left(\frac{H}{\Delta b}\right)_{cr} = 3.2 \left(\frac{H}{L_0}\right)^{1/3} \quad (11)$$

In which  $b$  is the width of the sausage. Should two sausages be connected, the widths of both sausages together can be filled in for  $b$ .

If the sausage is placed with its longitudinal direction perpendicularly to the axis of the breakwater, the following stability relation applies:

$$\left(\frac{H}{\Delta l}\right)_{cr} = 1.0 \quad (12)$$

In which  $l$  is the length of the sausage.

### 3.3.2 Other design rules

Stability against current should be treated according to the rules given in Section 2.2.

The soil-mechanical stability should be treated according to the criteria mentioned in Section 2.3.

## 4 CONCLUSIONS

The geotextile systems can be a good and mostly cheaper alternative for more traditional materials/systems. These new systems deserve to be applied on a larger scale. Information presented on the stability criteria will be of help in preparing the preliminary alternative designs with geosystems. However, there are still many uncertainties in the existing design methods. Therefore, further improvement of design methods and more practical experience at various loading conditions is still needed.

## REFERENCES:

- CUR/RWS, 1995a. Design Manual for Pitched Slope Protection. CUR report 155. A.A. Balkema.
- CUR/RWS, 1995b. Manual on the use of rock in hydraulic engineering. CUR report 169. A.A. Balkema.
- Den Adel, H., Hendrikse C.H., and Pilarczyk, K.W., 1996, Design and application of geotubes and geocontainers, Proceedings of the 1st European Geosynthetics Conference (EuroGeo), Maastricht.
- Klein Breteler, M., 1996, Alternative open slope revetments, (in Dutch), Delft Hydraulics, H1930.
- Leshchinsky, Dov, and Leshchinsky, Ora, 1995, Geosynthetic Confined Pressurized Slurry (GeoCops): Supplement Notes for Version 1.0, May 1995 (Copyright Nicolon US and US Army Corps of Engineers).
- Pilarczyk, K.W. (ed.), 1990. Design of seawalls and dikes - including overview of revetments, in: Coastal Protection, A.A. Balkema (Publisher).
- Pilarczyk, K.W., 1995, Novel systems in coastal engineering; geotextile systems and other methods, Rijkswaterstaat, Delft.
- Pilarczyk, K.W., 1996, Geosystems in hydraulic and coastal engineering - An overview, Proceedings of the 1st European Geosynthetics Conference (EuroGeo), Maastricht, A.A. Balkema (Publisher).
- Pilarczyk, K.W., 1997, Application and design aspects of geocontainers, *Geosynthetics '97*, Long Beach, CA.
- Pilarczyk, K.W. and Zaidler, R.B., 1996, Offshore breakwaters and shore evolution control, A.A. Balkema Publisher, Rotterdam.
- Stoutjesdijk, T., 1996, Geotechnical aspects of alternative systems (in Dutch), Delft Geotechnics, H1930.
- Wouters, J., 1995, Stabiliteit van geosystemen (Stability of geosystems, in Dutch), Delft Hydraulics, H1930.



# Evaluation of Geosynthetic Fabric Containers to Contain Contaminated Dredged Sediment

Horace Moo-Young

Department of Civil and Environmental Engineering, Lehigh University, Bethlehem, PA, USA

Tommy Meyers

Environmental Engineering Division, Waterways Experiments Station, Vicksburg, MS, USA

Dan Townsend

Department of Civil Engineering, Louisiana State University, Baton Rouge, LA, USA

**ABSTRACT:** Recent changes in environmental regulations to protect the water column have prohibited the open water disposal of dredged sediment from the New York Harbor. As a result, the New York Harbor will lose about a foot of depth each year if the contaminated sediments are not dredged. Because of the restrictions and perceived political problems with dredging and open water disposal of the contaminated materials, the New York Port Authority investigated the use of geosynthetic fabric containers (GFC) to reduce the movement of contaminated sediments outside of the boundary of the disposal site and to decrease the impact of the sediment on the water column. This laboratory study investigates the migration of fines and contaminants through GFCs. Contaminated sediment was characterized for the physical and chemical properties. Laboratory filtration tests were conducted on the contaminated sediment and GFC configurations to determine the amount of total suspended solids that would be released to the water column.

**KEYWORDS:** Geotextiles, Filtration, Hazardous Containment, Apparent Opening Size

## 1 INTRODUCTION

The New York Harbor is a major industrial port on the East Coast of the U.S. where 4,500 ships carry \$60 billion per year worth of goods. River borne silts are sifting into the harbor's shipping channels and reduce the depth of the harbor. New York and New Jersey Port Authority continuously dredges to maintain channel depths for cargo ships and tankers. From 1990 to 1994, the average amount of dredged material was approximately 4.3 million cubic yards (5.6 million m<sup>3</sup>). Dredged material was disposed in the Atlantic Ocean, a few miles east of the Jersey Shore at the New York Bight Dredged Material Disposal Site. Recent changes in environmental regulations have restricted open water disposal of the sediment due to contamination. These restrictions on dredging have decreased the average amount of sediment dredged by 70% to 1.3 million cubic yards (1.7 million m<sup>3</sup>) in 1996. As a result, the New York Harbor will lose about a foot of depth each year if contaminated sediments are not dredged. Decreases in the harbor depth will have a severe impact, as larger cargo ships will dock at deeper ports.

Containing the contaminated sediment in a geosynthetic fabric container (GFC) for placement from split hull barges is one alternative that can reduce the movement of contaminated sediments outside the boundary of the disposal site and decrease the impact on the water column. After placement of the sediment, the

opening of the GFC is closed, transported to an aquatic disposal site where it is then released from the barge. When properly constructed, GFCs have performed well as hydraulic and geotechnical structures. Numerous projects have shown the beneficial uses of GFCs for dikes in shallow and deep-water energy (Fowler and Sprague, 1994; Risco, 1995).

This paper reports the findings on a laboratory study of the GFC performance with respect to the migration of fines and contaminants. In this study, laboratory filtration tests were conducted to provide information on the release of fines through GFCs.

## 2 MATERIALS

### 2.1 Dredged Sediment

Sediment (Category III by U.S. Army Corps of Engineers, New York District (CENAN) classification) from New York Harbor was used in this study. The sediment was mixed in a 250-gallon (1 m<sup>3</sup>) tank for three hours. Samples of the mixed sediment were collected for geotechnical and chemical analysis.

Three samples of the contaminated dredged sediment were analyzed for polycyclic aromatic hydrocarbons (PAHs), NH<sub>4</sub>, Total Organic Carbon, Arsenic, Cadmium, Chromium, Copper, Iron, Manganese, Lead, Mercury

and Zinc. Table 1 summarizes the standard procedures, detection limits, and chemical analysis on the sediment.

According to American Society for Testing and Materials (ASTM) designation D-2487, the sediment classifies as a sandy clay (CH). The initial water content (ASTM procedure D-2974) of the sediment was 207%, and the specific gravity (ASTM procedure D-854) of the sediment was 2.57. Consolidation tests were performed on sediment according to ASTM procedure D-2435 method A, and test results showed that the sediment was highly compressible with a compression index of 1.2.

## 2.2 Geosynthetics

A geosynthetic fabric container (GFC) is constructed by sewing one or more layers of geotextiles together to form a container that will support and contain a measured amount of saturated material. A woven polyester geotextile (fabric A) was used as the strength layer in the GFC. Four polypropylene nonwoven needle punched geotextiles were tested as potential filter layers for the GFC: fabric B (4 ounce/yd<sup>2</sup>), fabric C (8 ounce/yd<sup>2</sup>), fabric D (12 ounce/yd<sup>2</sup>) and fabric E (16 ounce/yd<sup>2</sup>). Physical and hydraulic properties of the geotextiles were determined using ASTM procedures and are shown in Table 2. Geotextiles in this study meet the recommended soil retention criteria which requires the apparent opening size (AOS) to be less than two to three times the soil particle size for which 85% of the total soil is finer (AOS < 2 or 3 d<sub>85</sub> where d<sub>85</sub> = 0.185 mm).

Table 1 Chemical analysis of sediment

Chemical	Procedure	sediment	
		Detection Limits	Average
		mg/kg	mg/kg
NH <sub>4</sub>	EPA-600-350.1	N/A	198
	EPA-CRL #324		
TOC	SM-5310	1	53,000
	EPA-CE-81-1		
Chromium	SW-846-7191	0.1	182
Copper	SW-846-7211	0.1	641
Iron	SW-846-6010	1.5	35400
Manganese	SW-846-6010	0.5	330
Mercury	SW-846-7471	0.2	2.05
Lead	SW-846-7421	0.1	429
Arsenic	SW-846-7060	0.5	20.3
Cadmium	SW-846-7131	0.01	12.4
Zinc	SW-846-6010	0.7	931
PAH	N/A	N/A	90.84

## 3 METHODS

### 3.1 Pressure Filtration Test

Bench top filtration tests were conducted to obtain information on the release of fines from geosynthetic fabrics of varying AOS. The filtration procedure described in this method simulates the migration of fines through a GFC. A vacuum pressure is applied to a filter media to separate liquids from solids. During a dredging operation, cake formation occurs after the GFC is filled with the sediment and is caused by self-weight consolidation. Cake formation also occurs after placement of the GFC in the disposal facility and is caused by consolidation under a hydrostatic pressure.

### 3.2 Apparatus

A Millipore Hazardous Waste Filtration System was used to conduct the pressure filtration tests, and this pressure filtration device is also used for the Toxicity Characteristic Leaching Procedure (TCLP) in hazardous waste testing (U.S. Environmental Protection Agency (EPA), 1982). The geosynthetic fabric was placed on a filter holder that was able to withstand pressures up to 100 psi (690 kPa). Five GFC configurations were tested: A, A + B, A + C, A + D, and A + E.

Three filtration tests were conducted on each fabric configuration at applied pressures of 5 psi (34.5 kPa) and 10 psi (69 kPa). Pressure was applied to the inlet of the filtration device using a compressed nitrogen cylinder. A relief valve on top of the chamber was used to adjust the pressure. A 250 ml graduated cylinder was used to measure the volume of filtrate.

Table 2. Geotextile properties

Fabric Properties	Units	Fabric				
		A	B	C	D	E
Thickness	mm	NP	1.8	2.7	3.7	4.7
	(mils)		70	105	145	185
Mass per unit area	g/m <sup>2</sup>	339	136	271	406	542
Permittivity	sec-1	NP	2.0	1.26	0.75	0.571
Apparent Opening Size	mm	0.25	0.21	0.21	0.15	0.15
	(US Sieve)	60	70	70	100	100

Note: NP-Not provided by manufacturer

### 3.3 Procedure

The geosynthetic fabric and filter chamber were initially weighed. The filter was then washed with deionized water, allowed to drip dry, and placed on the filter holder. The lower portion of the filtration apparatus was assembled, and to reduce the potential for migration of fines at the edges, the filter fabric slightly overlapped the filter holder. Approximately 500 grams of the sediment was weighed and placed into the filtration device, whereby the slurry was allowed to settle before running the test. The top plate was placed on top of the chamber and sealed. Silicone grease was used to reduce the loss of pressure between the chamber and the upper and lower plates. Pressure from the nitrogen cylinder was gradually applied on top of the sample, until the desired pressure was achieved. The volume of the filtrate was measured using a 250-ml beaker and recorded with respect to time. Tests were conducted until the pressure began to decrease, and no more filtrate passed through the filter. When consolidation of the sediment at the applied pressure was completed, the filter cake ruptured which caused a decrease in the applied pressure.

Total suspended solids (TSS) tests were conducted on the filtrate in the graduate cylinder using the Standard Method for Water and Wastewater procedure at 209F. The filtration apparatus was disassembled, and the filtered cake was weighed. The final water content of the filtered cake was obtained using ASTM procedure D-2216. Thirty filtration tests were conducted on the contaminated sediment from the New York Harbor; three replications were conducted for the five fabric configurations at filtration pressures of 5 (34.5 kPa) and 10 psi (69 kPa).

## 4 RESULTS

Initial and final TSS data indicate that there is low migration of the fines through the various filter configurations. Table 3 shows the filtration test results for tests conducted at 5 psi (34.5 kPa). The filtering efficiency was determined by comparing the final TSS of the filtrate to the initial TSS of the contaminated sediment as shown in equation 1 (Henry and Hunnewell, 1995; Christopher and Holtz, 1985).

$$FE = \frac{TSS_{initial} - TSS_{final}}{TSS_{initial}} \times 100 \quad (1)$$

where FE = Filtering Efficiency, %  
 $TSS_{initial}$  = initial TSS, mg/l  
 $TSS_{final}$  = final TSS, mg/l

For the filtration tests conducted on the various fabric configurations, the initial water content ranged from 180-

200%. The fabric configurations reduced the TSS migrating to the water column by an average factor of 1000. In all tests, the water flow through the fabric and sediment slowed with time. Initial and final TSS data indicate that there is low migration of the fines through the various filter configurations.

Figure 1 plots the TSS and fabric weight relationships for the filtration tests conducted at 5 psi (34.5 psi) with a minimum TSS concentration occurring at fabric D. Fabric E showed a sharp increase in TSS compared to fabric D. The TSS and fabric weight relationship at 10 psi (69 kPa) has a minimum TSS occurring at fabric D. These data indicate that fabric D has the lowest TSS concentration passing through the material.

Figure 2 plots the apparent opening size and total suspended solids relationship for tests conducted at 5 psi (34.5 kPa) and 10 psi (69 kPa). As the apparent opening size decreases, the total suspended solids concentration decreases.

## 5 SUMMARY AND CONCLUSION

The feasibility of using GFCs to contain contaminated sediment from the New York Harbor was studied. Laboratory filtration tests were conducted to determine the flow rate of suspended solids through a GFC system. Filtration testing provided an index test to determine the migration of fines through the fabrics. From these tests, it was shown that GFCs provide adequate filtration for dredge sediment. Utilizing the GFCs to contain contaminated dredged sediment will reduce the migration of fines in an open water disposal facility.

Table 3 Filtration test data at 5 psi (34.5 kPa)

Fabric Tested	Final	Initial TSS (g/l)	Final TSS (mg/l)	Average Flow (ml/min)	TSS Filtering Efficiency (%)
	Water Content (%)				
A	121	433.3	64.3	0.78	99.98
A + B	132.6	425.8	44.3	0.73	99.99
A + C	126	438.9	33.9	0.69	99.99
A + D	121	442.9	28.5	.68	99.99
A + E	112.7	44.8	68.4	0.87	99.98

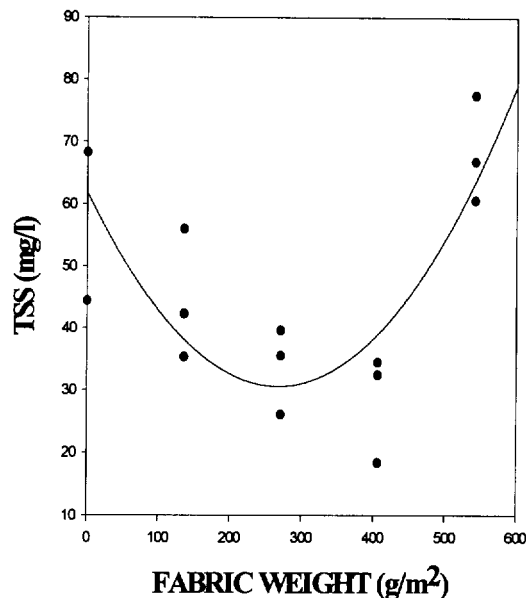


Figure 1. TSS and fabric weight relationship for filtration test at 5 psi (34.5 kPa).

#### ACKNOWLEDGEMENT

The Nicolon Corporation in Norcross, Georgia provided the geosynthetic fabrics for fine migration analysis. The authors would also like to thank the New York and New Jersey Port Authority for their support on the project.

#### REFERENCES

Christopher, B.R. and Holtz, R.D. (1985). "Geotextile Engineering Manual", FHWA-TS-86-203. Washington, D.C., Federal Highway Administration.  
 Fowler, J., Sprague, C.J., and Toups, D. (1994). "Dredged material-Filled Geotextile Containers,

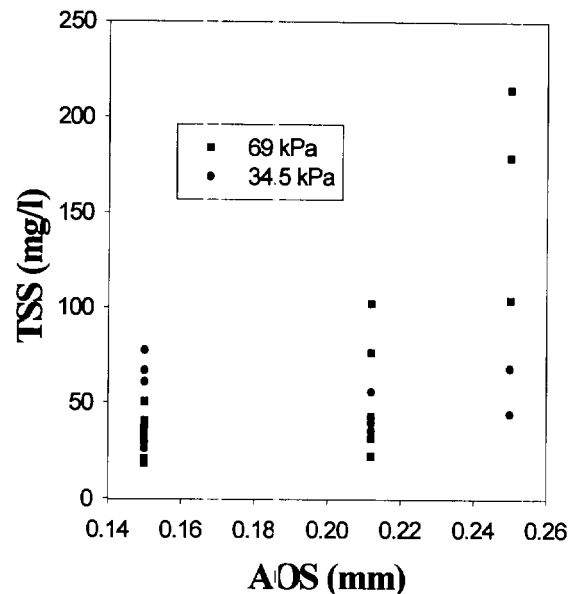


Figure 2. Relationship between TSS and AOS for filtration tests at 5 (34.5 kPa) and 10 (69 kPa) psi.

*Environmental Effects of Dredging Technical Notes*, U.S. Army Waterways Experiments Station, Vicksburg, MS.

Henry, K.S. and Hummel, S.T. (1995). "Silt Fence Testing for Eagle River Flats Dredging", *Cold Regions Research and Engineering Laboratory, Report 95-27*. Hanover, NH.  
 Risko, A.J. (1995). "Memorandum for the Record, FY 95 Marina Del Ray Detailed Project Summary," *U.S. Army Engineer District*, Los Angeles, Los Angeles, CA.  
 U.S. Environmental Protection Agency. (1982). "Test Methods for Evaluating Solid Waste," SW-846, 2nd ed., Office of Solid Waste and Emergency Response, Washington, D.C.

# Infrared Thermography of Damage in Geosynthetics

M.P. Luong

Professor, CNRS-LMS, Ecole Polytechnique, F-91128 Palaiseau, France

M. Khay

Civil Engineer, CETE Centre d'Expérimentation Routière, F-76121 Grand Quevilly, France

**ABSTRACT:** This paper aims to illustrate the use of quantitative infrared thermography as a nondestructive, noncontact, and real-time technique to detect the intrinsic dissipation that depicts the physical processes of damage and the mechanisms of geosynthetics failure. The parameter investigated in this experimental work is heat generation due to the energy dissipated by geosynthetics subject to tensile loading, up to failure. This experimental technique subsequently proposes a durability threshold, a loading limit beyond which geosynthetics fail.

**KEYWORDS:** Failure, Laboratory Tests, Materials Tests, Mechanical Properties, Tensile Strength.

## 1 INTRODUCTION

The use of geosynthetics in geotechnical engineering has been steadily increasing these last decades. It was initiated primarily by the manufacturers who sensed the need, developed, and marketed the products. The range of applications of geotextiles (Giroud 1980) is enormous: (i) filtration, drainage, earth dams, canals, coastal works, bank and shore protection, and in erosion prevention and control systems; (ii) stabilization of landslides, parking lots, paved and unpaved roads, roadways, and railroads on soft subgrades; and (iii) reinforcement of retaining structures, earth and waste slopes, and embankments. Geosynthetics (geotextiles, geogrids and geomembranes) can also be used together in a geocomposite system to provide multiple functions. Common applications of geocomposites are in hazardous waste containment systems and as prefabricated drainage layers. With the rapid recent growth in the use of these materials, civil engineers often have difficulty obtaining reliable mechanical characteristics for design, specifications, and construction with geosynthetics.

This paper emphasizes the application of infrared thermography to detect the occurrence of damage and to examine the mechanism and process of geosynthetics failure. Subsequently it proposes a limit of dissipative stability, defined as a drastic change in the rate of intrinsic dissipation.

## 2 THERMOGRAPHY BACKGROUND

Damage theories rely on assumed discontinuous phenomena at the microscopic scale. At the macroscopic scale, damage

parameters, considered as internal variables, are introduced according to the following main approaches: i) effective stress introducing a scalar continuous variable; ii) plasticity formalism suggesting phenomenological constitutive models that are widely used in engineering applications; and iii) micromechanics using micro- and macroscale relationships

Understanding damage requires making a clear distinction between the physical damage, the process of damage, and the manifestation of damage. This experimental work is based on the assumption that intrinsic dissipation and damage present the same evolution under loading up to failure as they occur in traditional strength tests.

The development of the thermo-visco-elastic-plasticity equations requires three types of basic assumptions (Dillon 1963, Kratochvil & Dillon 1969), leading to the following coupled thermomechanical equation:

$$\rho C_v \dot{T} = K \nabla^2 T - (\beta : \overset{4}{D} : \dot{E}^e) T + S : \dot{E}^I + r_0$$

where  $\overset{4}{D}$  denotes the fourth-order elasticity tensor,  $C_v$  ( $J.kg^{-1}.K^{-1}$ : Joule per kilogram per degree Kelvin) the specific heat at constant deformation and  $K$  ( $W.m^{-1}.K^{-1}$ : Watt per metre per degree Kelvin) the thermal conductivity.

This equation shows the potential applications of the infrared scanning technique in diverse engineering domains (detection of fluid leakages, nondestructive testing using thermal conduction phenomena, elastic stress measurements, and localization of dissipative phenomena). The detected temperature change, resulting from four quite different phenomena, must be correctly discriminated by particular test conditions and/or specific data reduction. This is the

main difficulty when interpreting the thermal images obtained from experiments under the usual conditions.

Infrared thermography is a convenient technique for producing heat pictures from the invisible radiant energy emitted from stationary or moving objects at any distance and without surface contact or any perturbation of the actual surface temperature of the objects viewed. The temperature rise ahead of a fatigue crack has been measured and thus proved using an infrared thermographic camera by Attermo & Östberg (1971). Attempts to measure and characterize the heat generated during the cyclic straining of composite materials have also been made. The scanning infrared camera was used to visualize the surface-temperature field on steel and fiberglass-epoxy composite samples (Charles *et al.* 1975) during fatigue tests.

A scanning camera, analogous to a television camera, utilizes an infrared detector in a sophisticated electronics system. It detects radiated energy and converts it into a detailed real-time thermal picture in a video system either in color or monochromatically. Response times are shorter than one microsecond. Temperature differences in the heat patterns are discernible instantly and are represented by several hues. The quantity of energy  $W$  ( $W.m^{-2}.\mu m^{-1}$ ), emitted as infrared radiation, is a function of the temperature and emissivity of the specimen. The higher the temperature, the more important the emitted energy. Differences of radiated energy correspond to differences of temperature. The infrared scanner unit in use comprises:

i.- a set of infrared lenses which focuses the electromagnetic energy, radiating from the object being scanned, into the vertical prism,

ii.- an electro-optical mechanism which discriminates the field of view in  $10^4$  pixels by means of two rotating vertical (180 rpm) and horizontal (18,000 rpm) prisms with a scanning rate of 25 fields per second,

iii.- a set of relay optics containing a selectable aperture unit and a filter cassette unit which focuses the output from the horizontal prism onto a single-element point detector, located in the wall of a Dewar chamber,

iv.- a photovoltaic SW short-wave infrared detector composed of Indium Antimonide InSb which produces an electronic signal output varying in proportion to the radiation from the object within the spectral response  $3.5 \mu m$  to  $5.6 \mu m$ ,

v.- a liquid nitrogen Dewar which maintains the InSb detector at a temperature of  $-196^\circ C$  allowing a very short response time of about one microsecond, and

vi.- an electronic control with preamplifier that produces a video signal on the display screen.

The received radiation has a nonlinear relation with the object temperature, can be affected by atmosphere damping, and includes reflected radiation from the object's surrounding. In consequence, calibration and correction procedures have to be applied. Knowing the temperature of the reference, the view-field temperature can then be calculated with a sensitivity of  $0.1^\circ C$  at  $20^\circ C$ . This infrared device is used to scan the following tests on geosynthetics.

### 3 TENSILE TESTING ON GEOSYNTHETICS

When reinforcing materials are deposited in embankments or slope, not only the deformation conditions of soil, but also the direction of reinforcing materials in soil influences the functions and effects of reinforcing materials. A geotextile may be subjected to various tensile loadings all over its life. The most common cases are caused by local irregularities of soil layer upon which it is placed. Rocks, stones, cracks or settlements in soil mass are frequent, even with a meticulous control of the earthwork. A great number of different tensile tests exist nowadays (Figure 1). Nevertheless there still exists the need for a good understanding of the failure mechanisms in order to specify a test procedure on geotextiles (Fayoux & Loulière 1984, Rollin *et al.* 1984).

A tensile force is gradually applied by a tension hydraulic actuator to a geotextile specimen while its length  $L$  is measured. Generally the nominal stress is expressed by the force  $F$  divided by the width  $b_0$  of the specimen and the strain  $\epsilon$  is obtained by dividing the increment  $\Delta L$  by the initial length  $L_0$ . Different types of tightening system have been devised for specimen gripping (Luong & Habib 1989).

Presently, most of the tensile characteristics (yield and failure, strain at yield and at failure) provided by laboratory tests - and so considered as references in civil engineering - are based on uniaxial standardized tensile tests such as AFNOR NFT 54102, DIN 53455 or ASTM D638. However the great influence of geosynthetic specimen geometry and



Figure 1 - 1D-tension tests on standardized specimens of various geosynthetics.

of the applied strain rate has been shown in literature (Gourc *et al.* 1986, Hoekstra 1988, Steffen 1984, Van Leeuwen 1977). The scattering of results caused by the influence of the specimen geometry and the sliding of the jaws can be reduced by measuring the strain in the central part of the specimen where failure occurs. It complicates the test procedure and needs more expensive equipment. Furthermore, the narrowing in the central part of the specimen may be very prejudicial to the validity of the measured elongation: very large strains occur at failure in contrast to limited lateral strains in reality.

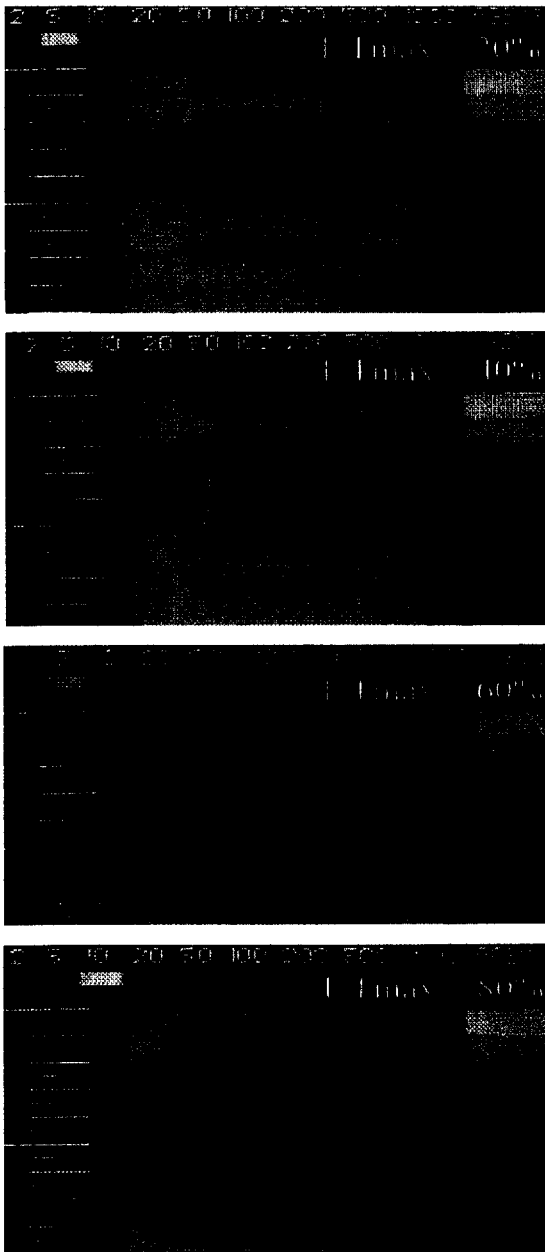


Figure 2 - Thermal images showing the failure process on a specimen of non-woven geotextile subject to 1D-tension test (0.5 °C for each color hue).

The principle of 2D-tension test is similar to the uniaxial tension test. The specimen is simultaneously loaded in two perpendicular directions with a 2D-tension frame. The lateral strain can be controlled, but in certain cases it would be closer to field conditions to maintain the deformation at the same value in the two dimensions. The stress-strain curves obtained in such test conditions would be particularly interesting for the designer. Unfortunately, in consideration to the ease of use and the cost of the required equipment, the generalization of the 2D-tension test seems to be not yet very realistic. The bursting test can be used as a more convenient alternative (Lucng & Bernhard 1990).

The proposed parameter, investigated in strength tests on geosynthetics, is heat generation due to the energy dissipated by the material that has been loaded up to failure (Figure 2). The contribution of the plasticity term is revealed by the rapid evolution of the heat dissipation once the stable reversible domain has been exceeded.

Geotextiles are dense fiber assemblies, usually defined as those in which the mechanics is dominated by fiber deformation predicted from assembly deformation. Thanks to the heat dissipation of the textile at large stresses, infrared thermography provides a ready mean to evidence what happens when the fabric yields: a) the effect of slippage from fiber ends, or false ends where fiber paths curve back on themselves, b) the cause of yielding and failure of bonds, either bond breakage or slippage of fibers through bonds, and c) the relevance of the geometry of fiber paths and binder distribution.

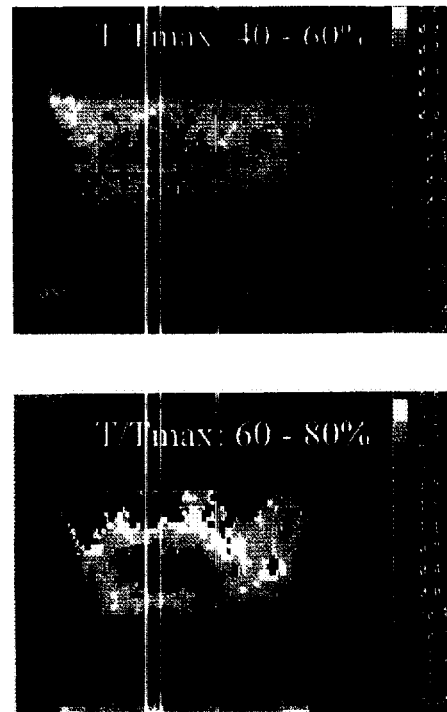


Figure 3 - Intrinsic dissipation evidencing the failure process on a specimen of non-woven geotextile subject to 1D-tension test (Temperature scale is given in °C).

The infrared scanner device displays a ten-color calibrated surface-temperature picture of the specimen. Each color hue corresponds to 0.2 °C. A computer-aided thermography software allowed the data reduction of the thermal images that shows heat generation between two loading levels (Figure 3). These thermal images provided quantitative values of the intrinsic dissipation of geosynthetics specimens subject to loading up to failure. The same procedure has been applied for each load step. The manifestation of the damage mechanism is revealed by a break of the intrinsic dissipation regime of the loaded specimen. Experimental results have been summarized in Figure 4 where it can be seen how a threshold of dissipative stability is determined using a graphical procedure. This provides a simple way to define a durability threshold for the tested material.

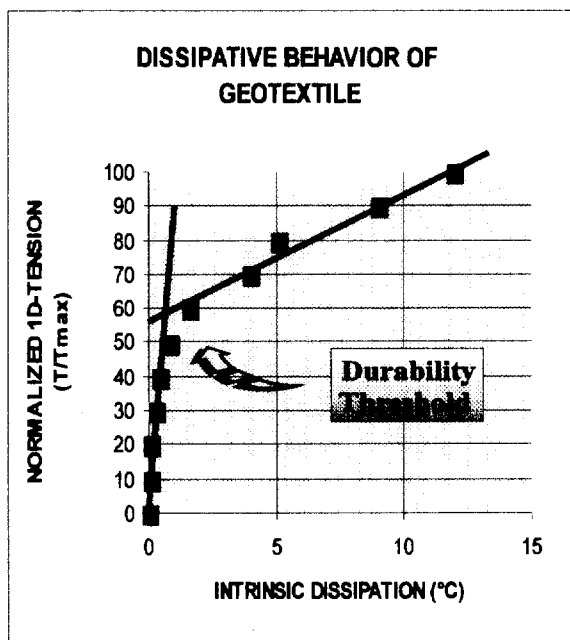


Figure 4 - Graphical determination of the durability threshold of a geotextile under tension.

#### 4 CONCLUDING REMARKS

This work has demonstrated that the intrinsic dissipativity of geosynthetics subject to tensile loading is the most sensitive and accurate manifestation of damage occurrence. Owing to the thermomechanical coupling, this useful technique provides a nondestructive real-time test with no contact to observe the physical processes of geosynthetics degradation, to detect the occurrence of intrinsic dissipation, and to estimate the evolution of dissipative behavior. It thus provides a measure of the material damage and permits evaluation of the sharp limit of a low accumulation of damage beyond which the material leads quickly to failure.

Infrared thermography can be used for the validation of new testing methods on geosynthetics, the development of

the mechanics of woven and non-woven geotextiles, particularly the relationships between the mechanical behavior of filaments and the fabric, and between the tensile strength as measured in various tests.

In addition the infrared thermographic analysis of geosynthetics under tension evidences the failure mechanisms of geosynthetics. Consequently it can be applied for the quality assessment and control of geosynthetics products.

#### REFERENCES

- Attermo, R. & Östberg, C. (1971), "Measurements of the temperature rise ahead of a fatigue crack", *Int. J. Fract. Mech.*, 7, II, 122-124.
- Charles, J.A., Appl, F.J. & Francis, J.E. (1975) "Using the scanning infrared camera in experimental fatigue studies", *Exp. Mech.*, 14(4), 133- 38.
- Dillon, O.W.Jr (1963) "Coupled thermoplasticity", *J. Mech. Phys. Solids*, 11, 21-23.
- Fayoux, D. & Loudière, D. (1984) "The behaviour of geomembranes to the soil", *Int.Conf. Geomembranes*, Denver, 175-180.
- Giroud, J.P. (1980) "Behaviour of geotextiles", *Mechanics of flexible fibre assemblies*, NATO ASI, E: Applied Sciences, 38, Sijthoff & Noordhoff.
- Gourc, J.P., Leclercq, B., Benneton, J.P., Druon, M., Puig, J. & Delorme, F. (1986) "Traction sur géomembrane: contribution à la définition d'un essai standardisé unique", *3rd Int. Conf. Geotextiles*, Vienna, 945-950.
- Hoekstra, S.E. (1988) "Review of bursting experiments on geomembranes", *RILEM TC103 MHG Meeting*, Montréal, 18 pages.
- Kratochvil, J. & Dillon, O.W. (1969) "Thermodynamics of elastic-plastic materials as a theory with internal state variables", *J. Appl. Phys.*, 40, 3207-3218.
- Luong, M.P. & Habib, P. (1989) "Thermographie infrarouge d'un géotextile non tissé soumis à la traction", *Materials and Structures / Matériaux et Constructions*, 22, 53-59.
- Luong, M.P. & Bernhard, C. (1990) "Bursting test: validation by 2D-tension test and infrared thermography", *4th Int. Conf. Geotextiles and Geomembranes*, May 28 - June 01, The Hague, The Netherlands, Balkema G.Den Hoedt, 573-578.
- Rollin A., Lafleur J., Marotte M., Dascal O. & Akber Z. (1984) "Selection criteria for the use of geomembranes to the soil", *Int. Conf. Geomembranes*, Denver, 493-499.
- Steffen H. (1984) "Report on 2D stress-strain behaviour of geomembrane with and without friction", *Int. Conf. Geomembranes*, Denver 181-185.
- Van Leeuwen J.H. (1977) "New methods of determining the stress-strain behaviour of woven and non woven fabrics in the laboratory and in practice", *Int. Conf. Use of Fabrics in Geotechnics*, Paris, II 299-304.



# Influence of Reinforcement Damage on the Pull-out Resistance of Geogrids

M.L. Lopes

Assistant Professor, Department of Civil Engineering, University of Porto, Porto, Portugal

T. Ayele

Ph.D. Student, Department of Geological Engineering, University of Bratislava, Bratislava, Slovakia

**ABSTRACT:** This paper studies the influence of reinforcement damage on the soil-reinforcement interaction mechanism by analyzing the results of pull-out tests carried out with pre-damaged reinforcements and a granular soil. The reinforcement tested was HDPE uniaxial geogrid and the soil was a well graded very gravelly sand. Testing equipment is described and soil and reinforcement materials are characterized physically and mechanically. To study the influence of reinforcement damage on its interaction mechanism with the soil, five different configurations of reinforcement damage and two different values of confinement stress were used. The role of damage configuration and of confinement stress on the pull-out behaviour of damaged geogrids is discussed. Finally, some general conclusions are put forward.

**KEYWORDS:** Geogrids, Damage, Interaction, Pull-out test, Pull-out resistance.

## 1 INTRODUCTION

Geosynthetics can be damaged during handling, placement, and construction operations, if enough care is not taken. The degree of reinforcement damage (extension, severity, and type) that can occur during those operations depends also on the types of machinery, soil, and reinforcement used.

Published field and laboratory test results generally consider reinforcement damage in terms of reduction in tensile and burst strength, grab, puncture and tear resistance, and number of holes per square meter (Razaqpur et al. 1993). Lately, some studies have been carried out accounting for reinforcement damage in terms of long term behaviour of geosynthetics (using creep tests for the assessment of damage) (Esteves, 1996).

However, when geogrids are used as soil reinforcement, particularly in walls and slopes, in addition to the short and long term tensile resistance requirements, the pull-out resistance must be sufficient to inhibit the failure by lack of pull-out resistance. To study the influence of a certain amount of damage on the pull-out behaviour of a high density polyethylene (HDPE) uniaxial geogrid, five different types of damage were simulated in the laboratory and the damaged specimens were tested in a pull-out apparatus. The influence of confinement stress on the pull-out behaviour of the damaged specimens was studied by carrying out tests under two different levels of confinement stress.

## 2 EQUIPMENT AND MATERIALS

The pull-out box used to study soil-geogrid interaction has internal dimensions of 1.53 m length, 1.00 m width, and 0.80 m height (Figures 1 and 2). The reduction of the influence of the top boundary on the pull-out resistance of the reinforcement and the uniform distribution of the

applied vertical stresses are achieved by placing over the top of the soil a smooth neoprene slab having a thickness of 0.025 m. To reduce the influence of the front wall on that resistance, a steel sleeve is used which extended 0.20 m inside the box. The pull-out force, obtained by a hydraulic system, is transmitted to the specimen by a clamp (Figure 3). The confinement stress is applied by placing ten small hydraulic cylindrical masses on the top of the box (Figure 2 and 4). The pull-out force and the confinement stress are measured by load cells (Figures 3 and 4). The frontal displacement and the displacements along the length of the reinforcement are measured by six linear potentiometers (Figure 2).

The soil used in the tests is granular as illustrated by the particle size distribution curve shown in Figure 5. The sand had a maximum and minimum dry unit weights of  $18.9 \text{ kN/m}^3$  and  $16.1 \text{ kN/m}^3$ , respectively. The dry unit weight of the sand used in the tests was  $17.5 \text{ kN/m}^3$ . The friction angles, defined by direct shear tests, for this unit weight and the two confinement stresses (24.1 kPa and 48.4 kPa) used in the pull-out tests were  $37^\circ$  and  $35.2^\circ$ , respectively, being zero the cohesion of the soil. The geogrid tested was a HDPE uniaxial geogrid with a tensile strength of 55 kN/m. Each specimen had 0.33 m width and 0.96 m confined length at the beginning of the test and was positioned at the middle of 0.60 m height of sand. The constant displacement rate applied in the tests was 1.8 mm/min. Figure 6 shows the dimensions and the position of the points of measurement of the displacements along the reinforcement for the undamaged specimen. Either, the dimensions and the position of the points of measurement, were the same for all specimens tested during the study.

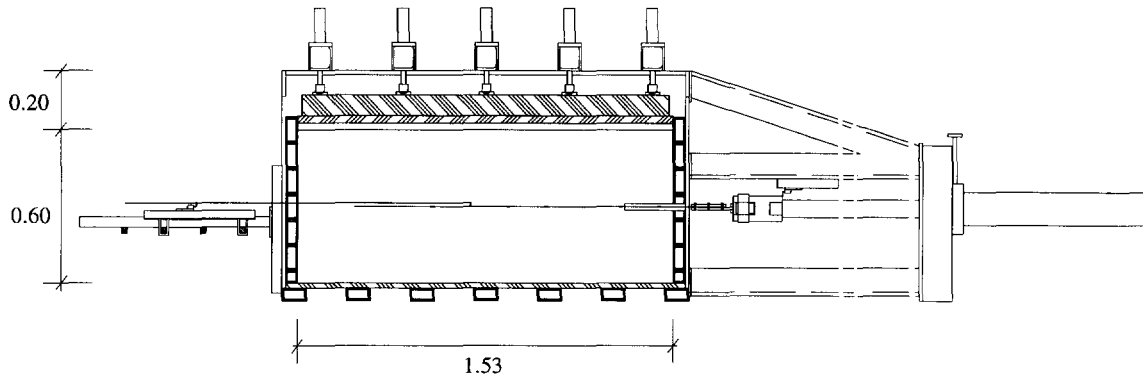


Figure 1. Pull-out box: schematic representation.

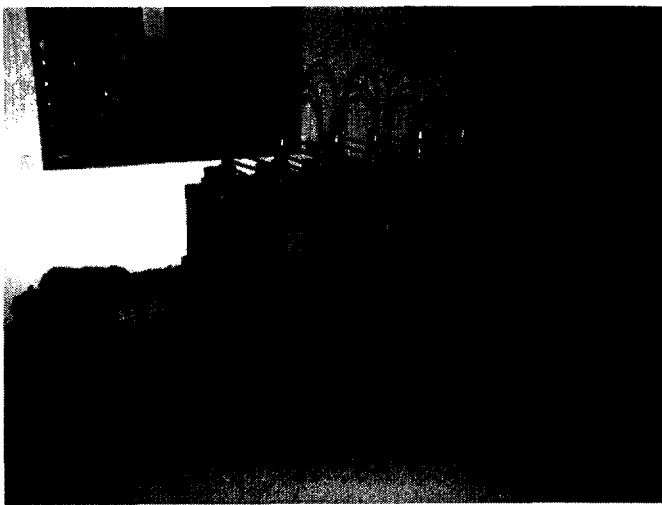


Figure 2. Pull-out apparatus - lateral view.

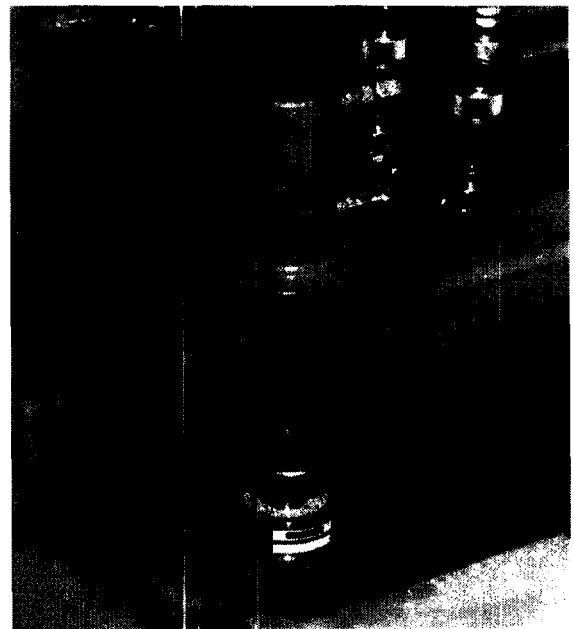


Figure 4. Confinement stress measurement system.

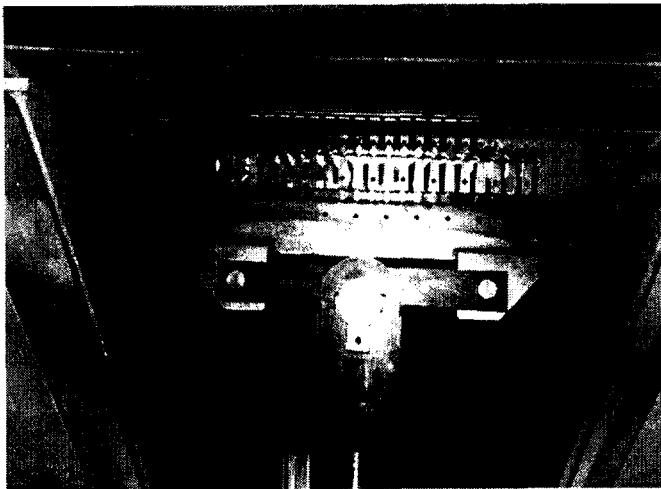


Figure 3. Clamp and load cell for measurement of pull-out force.

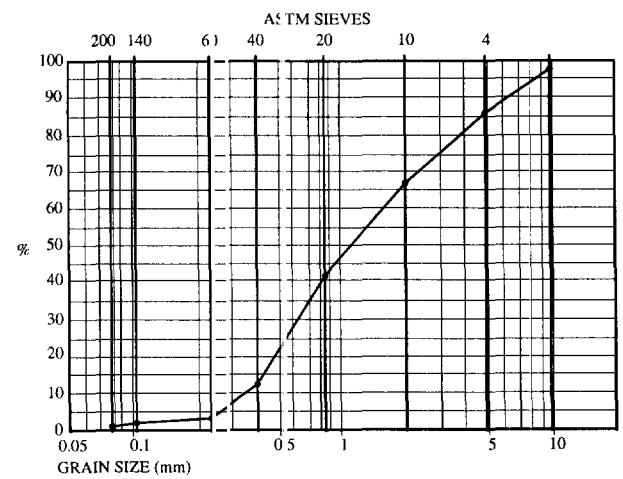


Figure 5. Granulometric curve of the soil.

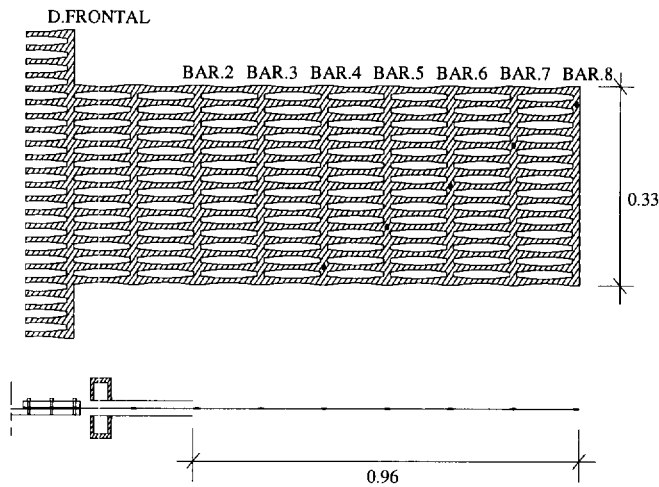


Figure 6. Undamaged specimen. Dimensions and position of the points of measurement of the displacements along the reinforcement.

### 3 ANALYSIS OF RESULTS

To study the influence of reinforcement damage on the pull-out behaviour of the geogrid, six pull-out tests were carried out for each confinement stress. One of the tests performed was with the undamaged geogrid (SPU) (Figure 6) and the others five with the damaged specimens. The various configuration of the damaged specimens (SP1, SP2, SP3, SP4, SP5) and the points of measurement of the displacements along the geogrid are presented in Figure 7. This figure represents only the confined geogrid at the beginning of the test.

The variation of the pull-out force with the front displacement of the reinforcement is presented in Figure 8 for specimens SPU, SP1 and SP5 under a confinement stress of 48.4 kPa. Specimens SP1 and SP5 had the same damage configuration (four ribs were cut adjacent to the mid-width of specimen), but its position along the length of the geogrid was different (SP1 at the middle and SP5 at the front). It can be seen that the pull-out behaviour of specimen SP5 is very similar to that of the undamaged specimen until failure occurs by lack of tensile strength (tensile failure) at a front displacement of 0.096 m. Specimen SP1 fails by lack of pull-out resistance (shear failure) at a front displacement of 0.142 m for a maximum pull-out force of 33.10 kN/m. The maximum pull-out force for the undamaged specimen (SPU) was 36.44 kN/m, at a front displacement of 0.087 m.

The displacements by strain along the geogrid measured in the tests with specimens SPU, SP1 and SP5 under a confinement stress of 48.4 kPa are present in Figure 9. It can be seen that the contribution of the posterior part of specimen SP5 for the pull-out resistance of its interface with the soil is zero. In fact, bars 6, 7 and 8 do not move during the test. The higher strain in the anterior part of the geogrid can be justified by the localization of the damage (just in the entrance of the sleeve). In fact, as the pull

out of the geogrid starts the damaged zone goes inside the unconfined area of the sleeve, deforms more than the undamaged specimen and fails by lack of tensile strength before starting the mobilization of shear stresses in its interface with the soil in the posterior part of the geogrid. As the front part of specimen SP1 was not damaged, during pull-out all the geogrid length contributes for the pull-out resistance of its interface with the soil, failing when this maximum resistance is reached. Specimen SP1 shows lower displacements by strain in bar 6 than in bar 8. The reason is the position of the linear potentiometer in bar 6 (just in the back limit of the damaged area), showing a localized reduction in movements due to damage, suggesting the easier penetration of the soil grains in the larger apertures of the geogrid in the damaged area, with consequent local increase of the interlock mechanism.

Figures 10 and 11 present the results of the pull-out tests in terms of variation of the pull-out force with the front displacement of the reinforcement for confinement stresses of 48.4 kPa and 24.1 kPa, respectively, for an undamaged specimen (SPU) and four damaged specimens (SP1, SP2, SP3 and SP4) (see Figure 7). Table 1 shows, for the two confinement stresses considered, the maximum pull-out force measured for each specimen tested, and the ratio between this force and that measured for the undamaged specimen. Analogous presentation can be seen in Table 2 for the front displacement for the maximum pull-out force.

The influence of the confinement stress in the pull-out resistance of the geogrid is presented in Figure 12. This figure shows the displacements by strain along the undamaged specimen for the two values of the confinement stress used in the tests (48.4 kPa and 24.1 kPa). It can be concluded that the increase in the confinement stress leads to a significant increase in the pull-out resistance of the reinforcement, increasing the maximum pull-out force about 71 % when the confinement stress changes from 24.1 kPa to 48.4 kPa. This behaviour suggests the importance of the skin friction mechanism in the pull-out resistance of the geogrid tested.

Figures 10 and 11 and Table 1 suggest that the behaviour of damage type SP1 and SP2 is distinct from that of SP3 and SP4. In fact, for the less damaged specimens (SP1 and SP2) the failure occurs by lack of pull-out resistance, as in the undamaged specimen (SPU), and for the heavily damaged specimens (SP3 and SP4) the failure mode is lack of tensile strength. In damage type SP1 and SP2, although the extensibility of the reinforcement increases (see Table 2) its stiffness is enough to mobilize shear stresses all along its length. The maximum pull-out force is similar or even greater than that of the undamaged geogrid. The greater values obtained are, probably, due to the local increase in the dimensions of the geogrid with consequent easier penetration of the soil grains in it, leading to a local increase of passive thrust mobilization on the bearing members of the grid (see Figure 9, bar 6). Damage type SP3 and SP4 due to the strong reduction of reinforcement stiffness in the damaged zone inhibits the mobilization of shear stresses in the length of the geogrid located behind that zone.

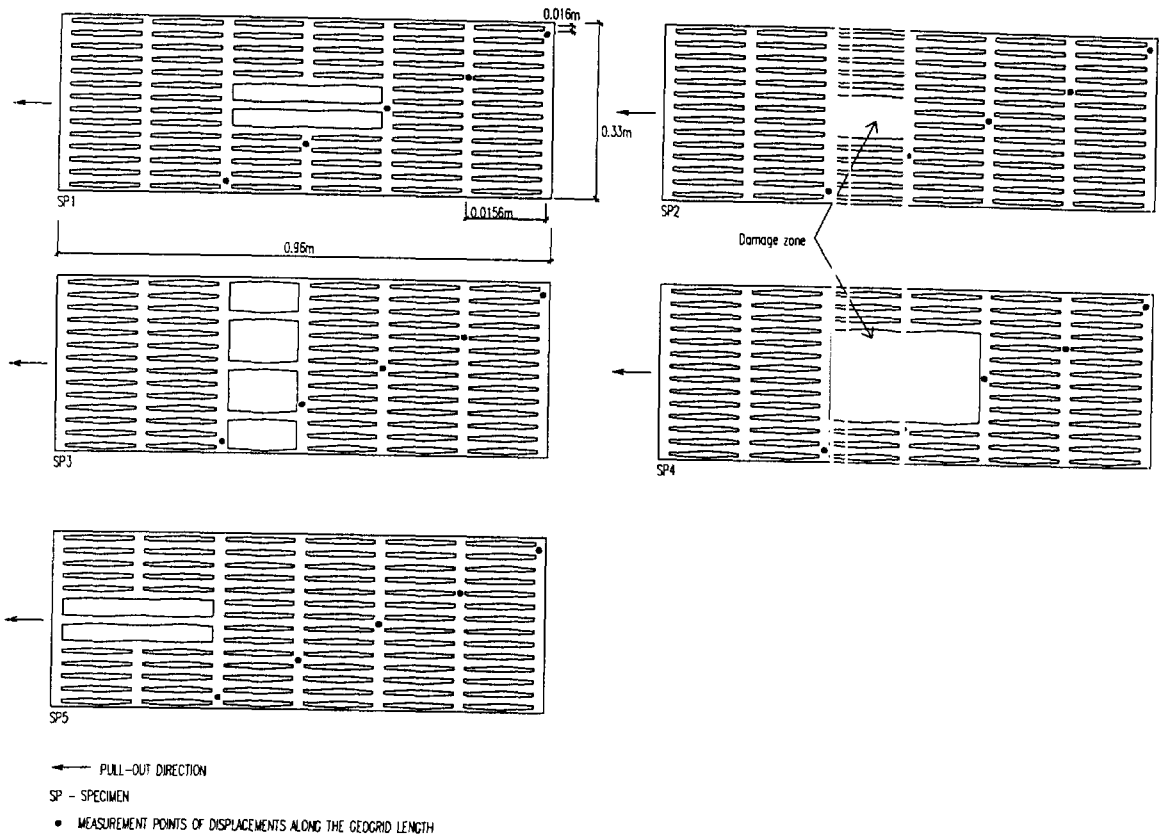


Figure 7. Geogrid damaged specimens.

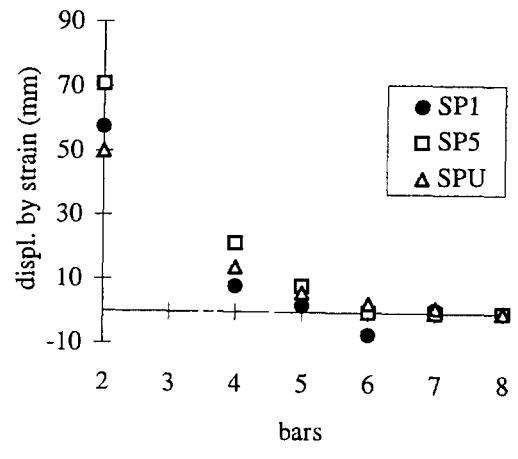
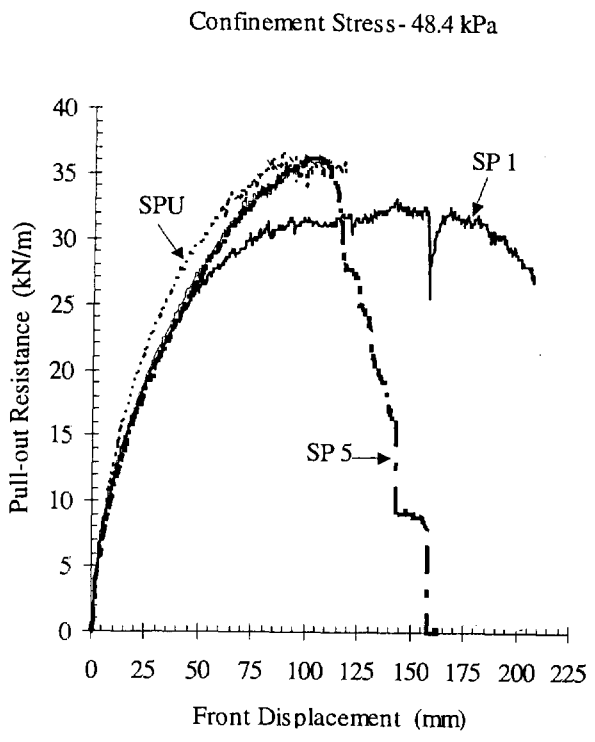


Figure 9. Displacements by strain along the geogrid (specimens SPU, SP1 and SP5,  $\sigma_{conf.}=48.4$  kPa).

In these cases only the remaining length contributes for the pull-out resistance of the reinforcement and failure occurs by lack of tensile resistance in the unconfined area of the sleeve.

The front displacement for the maximum pull-out force when the geogrid fails by lack of pull-out resistance (specimens SPU, SP1 and SP2) increases with damage (see Table 2). This is, the geogrid becomes more extensible with damage. This behaviour is more clear under a confinement stress of 48.4 kPa. In fact, for relatively similar values of maximum pull-out forces, the front displacement is about 45% to 63% higher when the specimen is damaged. The increase of confinement stress leads to an increase in maximum pull-out force and in front displacement for the maximum pull-out force. However, for damage configuration SP3 the influence of confinement stress is almost negligible.

The influence of damage is more important for higher confinement stresses. In fact, the extensibility of the damaged reinforcements increases more significantly, decreasing the ratio between the maximum pull-out forces of damaged and undamaged specimens when the confinement stress increases (see Tables 1 and 2).

Table 1. Ratio between maximum pull-out forces.

Specimens	24.1 kPa		48.4 kPa	
	Maximum pull-out force, T (kN/m)	$T_{(d. \text{ damaged})} / T_{(u. \text{ undamaged})}$	Maximum pull-out force, T (kN/m)	$T_{(d. \text{ damaged})} / T_{(u. \text{ undamaged})}$
SPU	21.26	1.00	36.44	1.00
SP1	26.14	1.23	33.10	0.91
SP2	25.51	1.20	37.35	1.02
SP3	21.26 *	1.00	21.86 *	0.60
SP4	17.61 *	0.83	28.24 *	0.77
SP5	-----	-----	36,10 *	0.99

Note: \* Tensile failure.

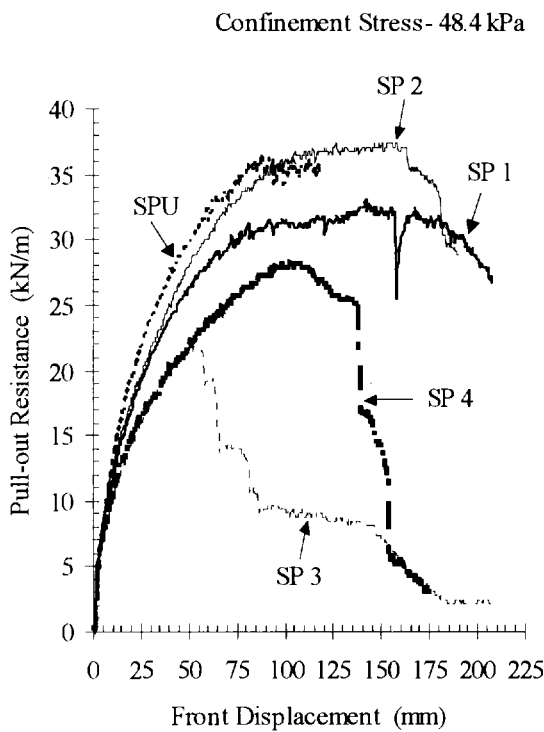


Figure 10. Influence of reinforcement damage on the pull-out behaviour of the geogrid for a confinement stress of 48.4 kPa.

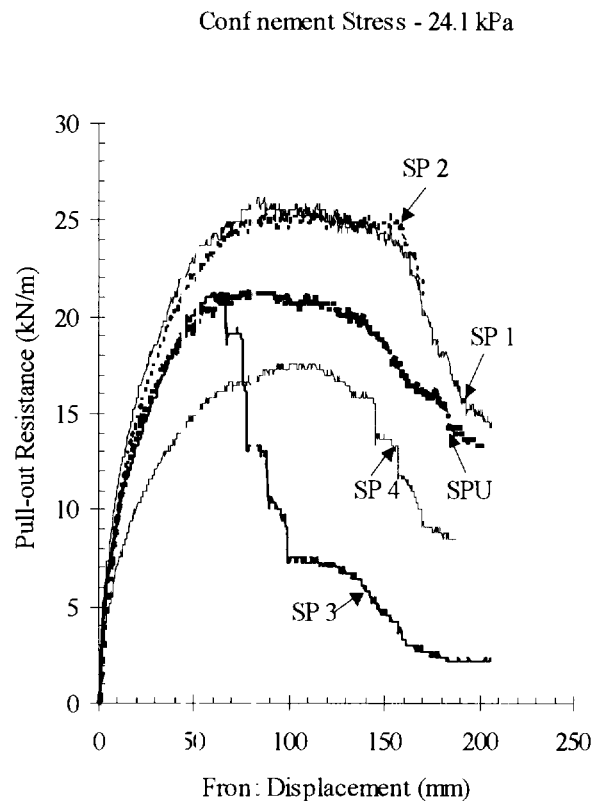


Figure 11. Influence of reinforcement damage on the pull-out behaviour of the geogrid for a confinement stress of 24.1 kPa.

Table 2. Front displacements for the maximum pull-out forces.

Specimens	24.1 kPa		48.4 kPa	
	Front displacement for the maximum pull-out force (m)	(ratio)	Front displacement for the maximum pull-out force (m)	(ratio)
SPU	0.072	(1.00)	0.087	(1.00)
SP1	0.082	(1.14)	0.142	(1.63)
SP2	0.097	(1.35)	0.126	(1.45)
SP3	0.060 *	(0.83)	0.053 *	(0.61)
SP4	0.094 *	(1.31)	0.098 *	(1.13)
SP5	-----	-----	0.096 *	(1.10)

Notes: Values in parentheses () are the ratio between front displacements for the maximum pull-out force of damaged and undamaged specimens; and \* means specimen tensile failure.

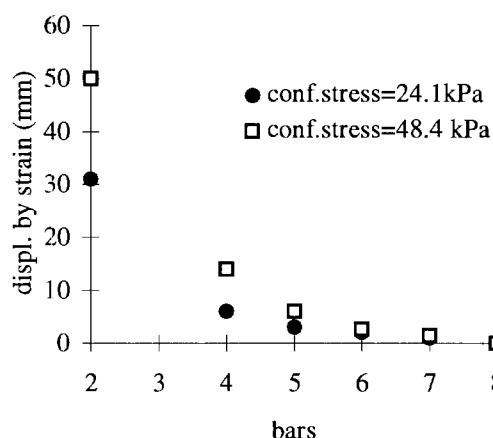


Figure 12. Influence of confinement stress on the displacements by strain along the geogrid (undamaged specimens).

#### 4 CONCLUSIONS

The study of the influence of reinforcement damage on the pull-out behaviour of a HDPE uniaxial geogrid embedded in a well graded very gravelly sand leads to the following major conclusions:

1. The localization of the same configuration of damage along the length of the geogrid can affect its pull-out behaviour, leading to tensile failure of the reinforcement when its location is near the front.

2. The configuration of damage can lead to a distinct behaviour of the geogrid: small damage leads to pull-out failure; large damage leads to tensile failure.
3. In general, damage increases the displacement at failure, the geogrid becoming more extensible.
4. In general, the increase of confinement stress leads to the increase of the maximum pull-out force and of the front displacement at the maximum pull-out force.
5. The influence of the geogrid damage on its pull-out behaviour increases significantly as the confinement stress increases, increasing the geogrid extensibility and decreasing the ratio between maximum pull-out forces of damaged and undamaged specimens.

#### ACKNOWLEDGMENTS

The authors would like to express their thanks to the financial support of Program PRAXIS XXI and of FEDER, Research Project 3/3 1/CEG/2598/95.

#### REFERENCES

- Esteves, S.A.C. (1996) "The Strength of Geosynthetics and Construction Damage Effects", *M.Phil. Thesis*, University of Strathclyde, Glasgow, UK, 288p.
- Razaqpur, A.G., Bauer, G.E., Halim, A.O.A. and Zhao, Y. (1993) "Pullout Resistance and Load-Slip Response of Mechanically Damaged Geogrids", *Geosynthetic Soil Reinforcement Testing Procedures*, ASTM STP 1190, Philadelphia, USA pp.195-206.

# Full-Scale Dynamic Tests on Geocomposites as Waterproof Layer and Reinforcement of the Surface of Embankment

J. ZHANG

Ph. D. Candidate, Department of Civil Engineering, University of Canterbury, Christchurch, New Zealand

D. Y. ZOU

Lecturer, Department of Civil Engineering, Southwest Jiaotong University, Sichuan, P. R. of China

**ABSTRACT:** The paper introduces the four groups of the full-scale dynamic tests which have been done to investigate the effects of the geosynthetic complex layers to behaviors of embankment. The results of system modulus, stresses, and settlements in the embankment for the tests are compared, some conclusions are obtained: the thickness of optimal complex layer is 100mm; special attention should be given to geosynthetics that is directly paid between subgrade surface and ballast. Because geosynthetics is used, mud stone can be used as fill in the embankment.

**KEYWORD:** Composite Material, Embankments, Railroad Applications, Separation

## 1 INTRODUCTION

Mud stone is a kind of poor quality soil that can not be used as filling in the embankment. The reason is that when the mud stone is saturated, its strength will be very low. However, railroad has to pass extensive mud stone areas. Hence, the soil will be improved to suit the design code. Comparing with soil improvement, geosynthetics is an economic method. When ground water, i. e., spring, is not present, geocomposites (geotextiles + geomembrances + geotextiles) not only prevent water above it into mud stone (Selig and Waters 1994), but also improve the stress state of the subgrade. Thus the disadvantage of mud stone can be overcome. When the geocomposites and subballast are used together, their functions will be used completely. However, in the geocomposites, geomembrance is very important to the design. Hence, It is necessary that the second subballast layer is inserted between subballast and subgrade. In this case, The thickness of geocomposites and the second subballast layer (the thickness is called complex thickness) ( Fig. 1) is a key to an economic and safe design.

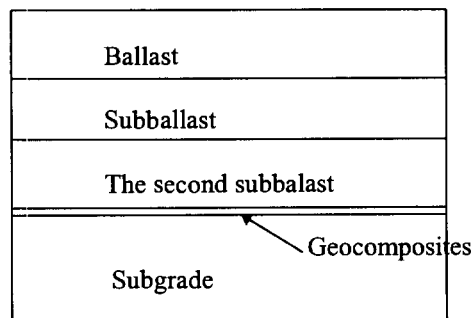


Figure 1. Confirmation of the embankment

For obtaining the optimal complex thickness, four complex thicknesses were tested. Comparisons of the stresses,

settlements and system moduli illustrate that the optimal complex thickness should be 100mm. The thickness assures the functions of subballast and avoids the abrasion and attrition between geocomposites and big particles..

## 2 MODEL TEST

### 2.1 Model and Material

The tests take 1:1 model to simulate the subgrade, ballast, subballast, sleeper. The size of the model box is 2.5m by 0.9m by 2.3m and it is made by steel frame and thick hard woods. In the analysis, because subgrade, subballast, ballast and superstructures are symmetry, only one-half of its section is taken.

According to measuring pressures on sites which illustrate that a axial weight will be taken by the successive 5 sleepers (Cui et al. 1994), maximum static pressure on the sleeper under the train wheel is 42 KN. However, because of the effects of track, train characteristics, and operating condition, measuring pressures on sites were in the range 45 KN - 60 KN. In terms of the above analysis, the static loading 45 KN and the dynamic maximum loading amplitude 15 KN were taken.

Subgrade clay was got from the site. special gravity  $G_s=2.67$ ; liquid limit  $W_L=36$ ; plastic limit  $W_p=23.1$ ; plasticity index  $I_p=13.5$ ; maximum dry density  $\rho_{dmax}=1.645g/cm^3$ ; optimal water content  $W_{opt}=20.5$ . In the filling, density was controlled by 95% maximum dry density.

The ballast was 250 mm thick. The subballast was 200 mm thick(Cui et al. 1994). The second subballast layer consists of sand and its thickness would be changed from 0 - 300mm.

The geocomposites consist of the two layers of non-woven geotextiles(Polyester) and a layer of geomembrance (PVC-Polyvinyl Chloride). Its weight is  $600g/m^2$  and thickness is about 2mm. Main parameters were measured in

the factory. tensile strength, puncture strength, and permeability strength were 600 N/5CM, 1.5MPa, 0.5 MPa, respectively. Before the tests, the ones were measured again which were 657 N/5CM, 1.92 KN, 0.825MPa, respectively(average value). A number of tests confirmed the parameters had change slightly.

## 2.2 Test Procedure

### 2.2.1 Test Equipment

All tests were done by the servo-hydraulic system. In the system, there are a displacement gauge and a load cell on the loading head. They measure total settlement and pressure. In the subgrade, displacement gauges, earth pressure cells, and acceleration gauges are setup along various height and away the loading center figure 2.

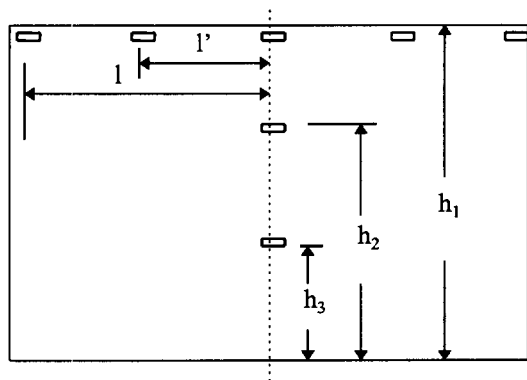


Figure 2. Location of instrument

### 2.2.2 Test Procedure

The test procedure should reflect situations on the site. Therefore, the thickness of the second subballast layer is a key factor, because it should spread stress from wheel load and prevent geomembranes from being punctured by big particles. At the same time, efficiency spreading stress by the second subballast layer was expected to be investigated. The four thicknesses of the second subballast layers which were 0mm, 100mm, 200mm, 300mm, respectively, were selected to the tests. According to different thickness, the location of some instruments were changed as followed: In model 1, the location of instruments were  $l=500\text{mm}$ ,  $h_1=850\text{mm}$ ,  $h_2=500\text{mm}$ ,  $h_3=200\text{mm}$ . In model 2, the location of instruments were  $l'=200\text{mm}$ ,  $h_1=750\text{mm}$ ,  $h_2=550\text{mm}$ ,  $h_3=350\text{mm}$ . In model 3, the locations of instruments were  $l'=200\text{mm}$ ,  $h_1=750\text{mm}$ ,  $h_2=550\text{mm}$ ,  $h_3=350\text{mm}$ . In model 4, the locations of instruments were  $l'=300\text{mm}$ ,  $h_1=75\text{mm}$ ,  $h_2=550\text{mm}$ ,  $h_3=350\text{mm}$  ( $l$  denotes distance from loading center;  $h$  denotes height from the bottom of box)

In the tests, the thickness and density of ballast and subgrade were the same. However, loading times would be

changed according to the cases. The loading times of the model 1 and 2 were one million times, respectively. The loading times of the model 3 and 4 were 500 thousand times, respectively. The different loading times among the models were decided by the total settlement.

## 3 RESULTS

### 3.1 Comparisons of deformation loading modulus

Deformation loading modulus  $E_v$  denotes the ratio of the stress and strain in the static loading. It will reflect the stiffness of system of the embankment (including ballast, subballast, geocomposites, and subgrade). For the new constructed embankment, initial deformation is very important. Therefore,  $E_v$  is important factor. The larger  $E_v$ , the smaller the settlement and the higher the density.

To investigate the change of the deformation loading modulus after the dynamic tests, the  $E_v$  was measured before and after the tests based on load plate test. The result of the model 1 is shown in figure 3.

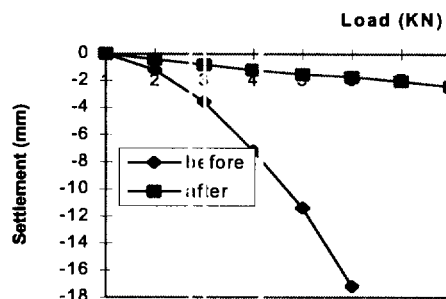


Figure 3. Relation between load and settlement before and after test in model 1

It denotes that the settlement of the embankment is clearly reduced after dynamic test, hence  $E_v$  increases greatly. The relation between the load and settlement is non-linear before test, but the relation becomes linear after test. Figure 4 reflects the relation between  $E_v$  and the thickness of the second subballast layer. The deformation loading modulus  $E_v$  of the four models are nearly the same before tests. However the  $E_v$  increases when the thickness of the second subballast layer increases from 0 to 200mm, but when the thickness of the one is equal to 300mm, its  $E_v$  has nearly no change. The results show that the thickness of the complex layer made by the second subballast layer and geocomposites will directly affect the stiffness and stability of the embankment and if the complex layer is too thick, its function will be reduced. The stress at the interface between geocomposites and the subgrade will directly affect the settlement of the embankment. Five earth pressure cells were setup on the interface. Figure 5 gives results of model 1 and 2.



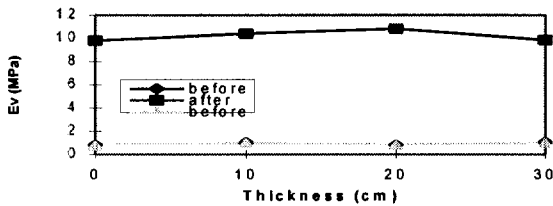


Figure 4. Relation between  $E_v$  and the thickness of complex layer

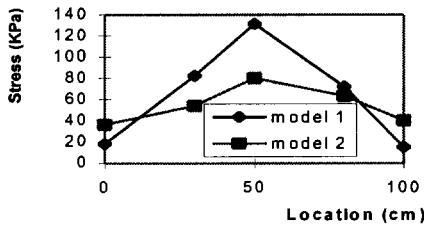


Figure 5. Stress of interface

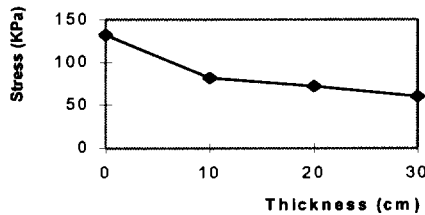


Figure 6. Relation between maximum stresses and thickness of complex layer

### 3.2 Stress at Interface Between Geocomposites and the Subgrade

These results show that the complex layer reduces the stress peak at the interface between the geocomposites and the subgrade. Figure 6 compares the maximum stress of the four tests which illustrate the complex layer has the function reducing stress, but the efficiency will gradually reduce as the thickness of the complex layer increases. Therefore, the optimum thickness of complex layer is very important in the embankment design.

### 3.3 Distributed Stresses Along the Depth

The distributed stresses along the depth of the embankment causes the settlement of the embankment. The complex layer reduces the stress at the interface between the complex layer and subgrade (figure 5), the layer also affects the distributed stresses. Figure 7 shows the results of the model 1 and 2. In the top of subgrade, the stresses in the model 1 are greater than the ones in the model 2. However, in the low part of subgrade, the stresses in the model 1 are smaller than the ones in the model 2. This result denotes

that although the complex layer reduces the stresses at the interface, the stress attenuation along the depth of the embankment in the model 2 is slower than that in the model 1. Special attention should be given to a high speed train. Geocomposites which affects stresses in the embankment is very interesting. Figure 8 is the result in which stresses were measured above and below geocomposites. It efficiently reduce stresses below geocomposites and change the value of the stresses of distribution along the depth of embankment. At the 100mm range above and below geocomposites, the stresses are reduced by about 30%.

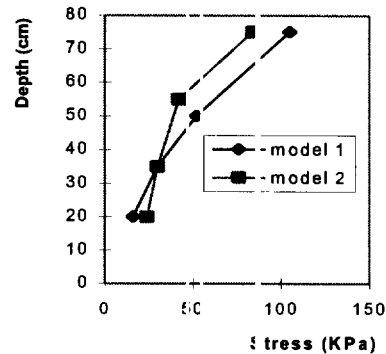


Figure 7. Distributed stresses in model 1 and 2

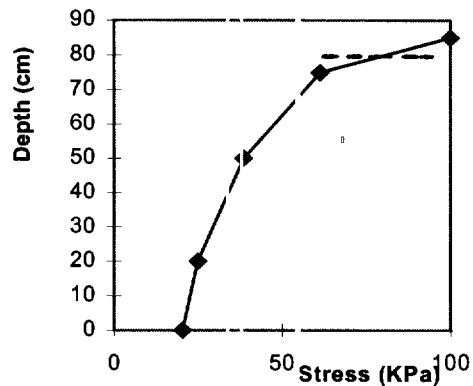


Figure 8. Effect of geocomposites on stress

### 3.4 Settlement of the Subgrade

The settlement of the surface of the subgrade will affect stability of the embankment and will increase cost of maintenance in the future and if settlement is greater, geocomposites will be in the dynamic extension state. Therefore, reducing settlement will be a key to the research. Figure 9 shows the results of settlement in the four models. These results illustrate that initial settlement is most part of total settlement. For example, initial settlement is 93% and 55% of the total settlement in the model 1 and 2, respectively. The result is conformable to stress analysis. Because the complex layer is on the surface of the subgrade, the settlement of subgrade is reduced greatly. If

the settlement in various models compares with the settlement of the model 1, the percent at model 2, 3, 4 is

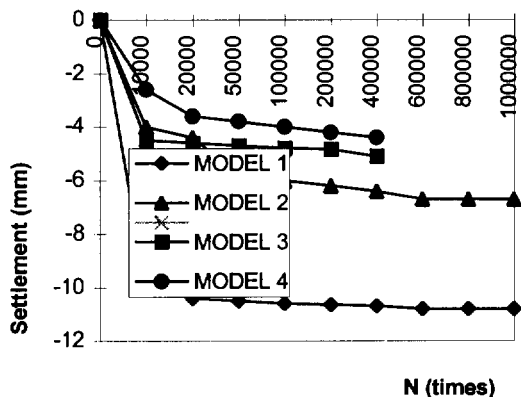


Figure 9. Surface settlement of embankment

37%, 52%, and 59%. The efficiency of the complex layer is very clear. Figure 10 shows settlement along the depth of

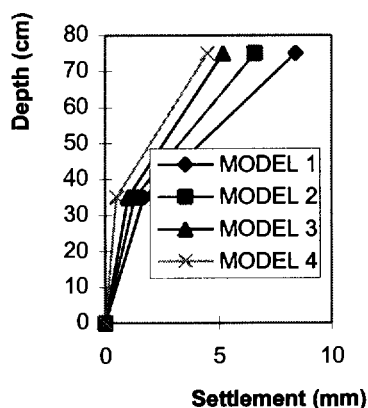


Figure 10. Distributed settlement along embankment

the embankment. The result shows that the settlement will reduce as the thickness of the complex layer increases. This is also conformable to the distributed stresses.

### 3.5 Situation of the Geosynthetics

After the four model tests, the geocomposites were checked by eyes and tests. In the model 1, the surface of the geocomposites is very rough. The reason is that big particles in the first subballast layer and ballast contact the surface of the geocomposites under dynamic loading. However, in the model 2, 3, 4, the surfaces of the geocomposites were still

new after tests. The reason is that the second subballast layer separates big particles and geocomposites and avoids their contacts.

Comparing geocomposite properties before and after the tests, tensile strength, puncture strength, and tear strength were nearly the same. It illustrates that the geocomposite qualities are well and meet the need of the project.

## 4 CONCLUSIONS

According to the above analysis, some conclusions can be obtained:

1. The static system modulus will increase with the thickness of complex layer. However the efficiency of complex layer will gradually reduce as its thickness increases. Because complex layers are inserted between subgrade and ballast, the amplitude of dynamic stresses is reduced. It illustrates that complex layers have efficiency spreading stress.
2. With respect to the maximum stress in the model 1, the maximum stress in the model 2, 3, and 4 reduce 36%, 38%, and 39%, respectively. With respect to the settlement of subgrade surface in the model 1, the settlement of subgrade surface in the model 2, 3, and 4 reduce 37%, 52%, and 59%. Compared to these results, in practice, the complex layer 100mm in model 2 is optimal thickness.
3. Compared to state of geocomposites after tests, if there is no the second subballast layer (in model 1), the surface of geocomposites become very rough, the reason is that big particles contact the surface of geocomposites under dynamic loading. If the case is taken, the geomembrance in the geocomposites may be punctured out in the future. Therefore, attention must be given that geocomposites are directly laid between subgrade surface and the first subballast layer.

## REFERENCES

- Cui, Y., Zhang, J., and Cho, X. W. (1994) *An Investigation of Subgrade Stresses in Field tests*, Project Report for Department of China Railroad, Report, Department of Civil Engineering, Southwest Jiaotong University, China
- Cui, Y., Zhang, J., and Cho, X. W. (1994) *Full-scale Dynamic Test on effect of loading frequency and subballast*, Project Report for Department of China Railroad, Report, Department of Civil Engineering, Southwest Jiaotong University, China
- Selig, E. T. and Waters, J. M. (1994) *Track Geotechnology and Substructure Management*, Thomas Telford Publications, London, England

# Performance Test to simulate Geotextile Puncture under dynamic cyclic Loading

G. Mannsbart

Technical Manager, Polyfelt Ges. m. b. H., Linz, Austria

H. Breymann

Head of Geotechnical Department, Testing and Research Institute for Civil Engineering, Salzburg, Austria

M. Moser

Head of Geotechnical Laboratory, Testing and Research Institute for Civil Engineering, Salzburg, Austria

**ABSTRACT:** Puncturing is one of the decisive stresses geotextiles are exposed to. For geotextiles used as separators under unpaved roads, the stress elongation behavior under dynamic puncture loading is of crucial importance. Dynamic and cyclic stresses caused by sharp edged aggregate have only been taken into account to a small amount in geotextile testing so far. On the basis of existing test methods (CBR-puncture according to EN 12236, Pyramid puncture according to ASTM 5494 and NFG 38019) a special test has been developed. The main modification is a cyclic up-and-down movement of the pyramid piston, which is pushed slowly into the geotextile.

The deformation and the puncture force are continuously measured, and the envelope of the obtained curves is the main characteristic of the geotextile behavior. Numerous test results have been obtained in the laboratory and will be cross-checked with the results from on-site trials. It is shown that needle punched non wovens perform very well. This is attributed to the rupture resistance and to the resistance to tearability of the product. To be able to withstand the harsh installation stresses, geotextiles have to show a clearly defined force elongation behavior in the dynamic cyclic loading test.

**KEYWORDS:** Dynamic mechanical analysis, Geotextiles, Installation Damage, Puncture Resistance, Separation

## 1 INTRODUCTION

Still the most common use of geotextiles is in road and pavement construction. Geotextiles increase stability and improve the performance of the subgrade by reducing deformations and by increasing the bearing capacity of the soil. (Polyfelt; 1986)

The primary function is separation, but also filtration, drainage, and strengthening of the soil may be regarded as secondary functions in road and pavement construction. The geotextile must prevent the movement of fines from the subgrades into the sub-base course. To be able to fulfill this requirement, it is necessary that the geotextile withstands all stresses during the installation phase.

Stresses occurring during installation are critical in most of the cases and therefore are regarded as decisive for design. Installation stress is understood here as the sum of puncturing, burst, and abrasive forces which occur during placement of the sub-base material as well as during compaction and loading by construction traffic. To simulate the forces exerted on a geotextile by a single sharp edged grain of the fill, a dynamic cyclic loading test has been developed.

## 2 TEST DESCRIPTION OF THE CYCLIC PYRAMID PUNCTURE TEST

### 2.1 Test Setup

When considering international specification tendencies, that aim to guarantee the separation function of geotextiles, one finds the CBR puncture resistance, Mullen Burst strength, and tear strength as essential specification criteria. In only a few standard specifications unit weight is also listed as a requirement. Dynamic and cyclic stresses caused by sharp edged aggregate have only been taken into account to a small amount in geotextile testing so far. (Bräu; 1996).

To be able to simulate the puncturing forces on a geotextile separator, a specific test method has been developed on the basis of existing test methods (CBR-puncture according to EN 12236, Pyramid puncture according to ASTM 5494 and NFG 38019; Werner; 1986). The main modification is a cyclic up-and-down movement of a pyramid-shaped piston, which is pushed slowly into the geotextile. By the use of this test the static and dynamic behavior of geotextiles under a pyramid load can be studied.

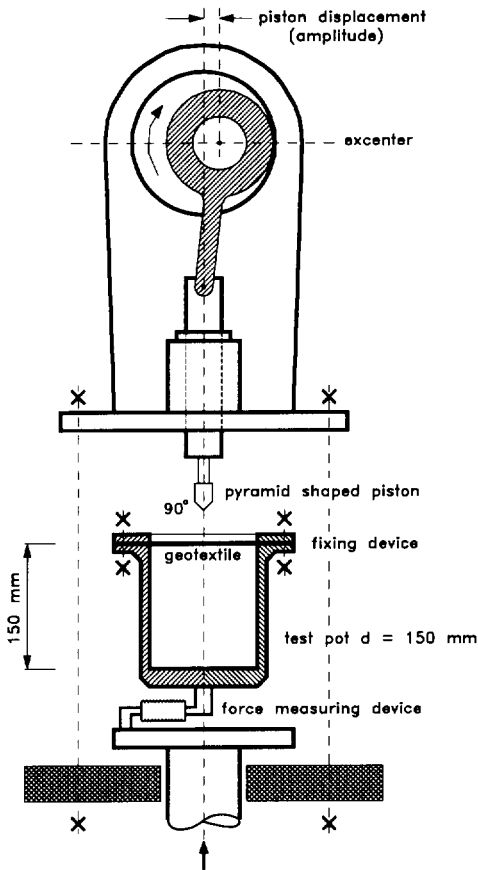


Figure 1: Scheme of the test device

The geotextile is positioned and fixed on a test pot. A pyramid shaped piston is used to simulate a sharp edged grain which exerts the stress during installation. The test pot has an inner diameter of 150 mm and a height of 150 mm. The fixing device was made in accordance with EN ISO 12 236.

Dynamic and static forces acting on the test pot due to the movement of the pyramid were measured.

For the dynamic puncture, the maximum value of the loading cycle is registered.

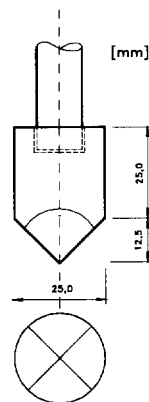


Figure 2: lay-out of the pyramid piston

## 2.2. Test Procedure

The test device offers the possibility to simulate both dynamic as well as static loading. Therefore, the test description is made in two parts.

### 2.2.1 Static Pyramid puncture test

In the static test, the piston is moved downward continuously until rupture occurs. The test is performed in analogy to EN ISO 12236. Instead of the cylindrical piston with 50 mm diameter the pyramid according to ASTM D 5494 is used (see Fig. 2). The velocity of the (upward) movement of the pot is  $10 \pm 1$  mm/min.

### 2.2.2 Dynamic Pyramid puncture test

In the dynamic test, the pyramid is exposed to cyclic up-and-down movement. The same 50-mm diameter cylindrical piston and the pyramid peak according to ASTM D 5494 are used.

The pyramid is moved up and down vertically by the use of an eccentric (see Fig. 3). At the same time, the test pot with the fixed geotextile is moved upwards against the oscillating pyramid. The force-elongation behavior is recorded.

The oscillating movement is achieved by an eccentric, which has an amplitude of  $\pm 5$  mm. The frequency of the vertical movement of the pyramid is 15 Hz.

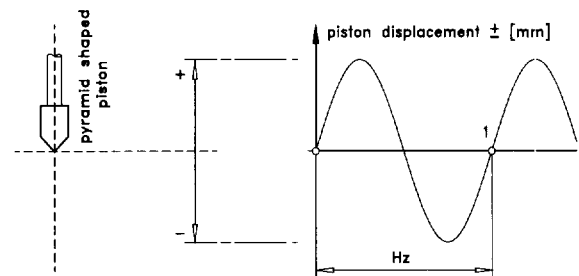


Figure 3: Principle of dynamic (cyclic) loading.

The stress for the dynamic test is characterized by the following parameters:

- vertical (upward) velocity of the pot (= velocity of the fixed geotextile) [mm/min]. The pot is moved upwards continuously by a special device with a velocity of 10 mm/min. The allowable tolerance is  $\pm 1$  mm/min.
- maximum vertical displacement of the pyramid during it's oscillating movement [mm]
- Frequency (strokes per second) for the movement of the pyramid [Hz]

For every type of geotextile at least five single tests (static, dynamic) at  $23 \pm 2^\circ\text{C}$  should be performed. The mean values  $F_{\text{stat}}$ ,  $F_{\text{dyn}}$  and the standard-deviation are calculated.

### 2.2.3. Test results

The static puncture force  $F_{stat}$  is the maximum value of the forces (in Newtons) measured during puncturing of the fixed geotextile specimen.

The dynamic puncture Force  $F_{dyn}$  is the maximum value of the dynamic forces (in Newtons) measured during puncturing of the fixed geotextile specimen. Here puncturing will be achieved by the superposition of the oscillating movement of the pyramid with the continuous upward movement of the pot.

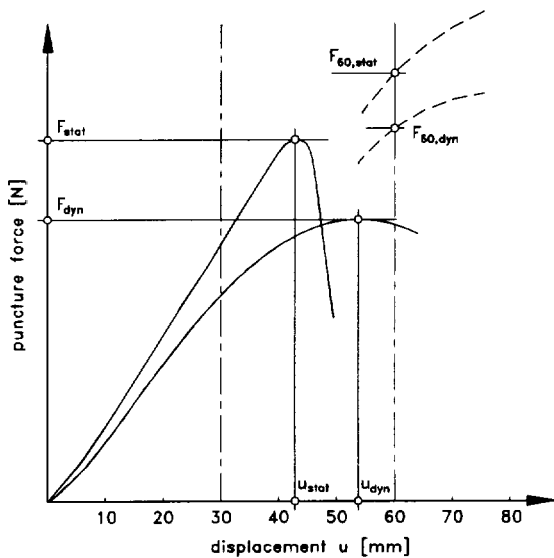


Figure 4: Graphical evaluation of the test results.

### 2.2.4 Boundary conditions

The test should be performed for at least 5 single specimens at  $23^\circ \pm 2^\circ$ . The curve of the force -elongation behavior is recorded.

The specimen has been prepared with a marking and cutting template and installed without any tension between the clamping rings.

The pot is fixed centered under the pyramid and the start-amplitude is fixed. For the start-amplitude of every test, the peak of the pyramid is lying without any tension on the surface of the fixed geotextile, and the pyramid has been set to the lowest point of the excenter.

The test is finished, if a decisive reduction of the puncture force is observed.

The evaluation is done according to the curves in Figure 4. The envelope curve of the arithmetic mean values is plotted.

The deformation has been determined by an electronic device in millimeters with an accuracy of  $\pm 0.1$  mm. The dynamic and the static puncture forces are given in

Newtons. The maximum of the obtained values is considered the puncture force.

### 2.2.5 Test report

In the test report the values obtained (static and dynamic puncture force) as well as the standard-deviation and the coefficient of variation are stated. A graphic evaluation (force-displacement curve) similar to the one given in figure 4 is enclosed.

## 3 TEST RESULTS

Large series of tests have been performed on various types of products. Thermobonded as well as needlepunched staple fibers and continuous filament nonwovens have been examined.

Among the results which have been obtained, results from a typical range of products are presented in this paper. Results for different grades of a specific polypropylene continuous filament nonwoven geotextile are given. The specimens have been tested with respect to both their static and dynamic puncture resistances. The properties of these products are given in Table 1.

Table 1 Properties of tested products

	Type A	Type B	Type C
CBR test [N]	2300	3500	4200
Tens. Str. [kN/m]	13.5	21.5	26.5
Elongat. MD/CD	80% / 45%	80% / 45%	80% / 45%
Weight [g/m <sup>2</sup> ]	200	315	400

At least 10 single tests have been performed for each of these grades. In Table 2 the mean values for the static puncture force ( $F_{stat}$ ) and the displacements at maximum load (Displ.-stat.) are given. Standard deviations and coefficients of variation obtained from these tests, are also shown in Table 2.

Table 2 Values obtained in the static puncture test

	Type A	Type B	Type C
F-stat. [N]	609.49	941.34	1285.20
Sdev	152.36	234.46	165.51
CVar	25	24.91	12.88
Displ.-stat.[mm]	42.8	42.90	47.60
Sdev	2.0	2.92	1.51
Cvar.	4.90	6.81	3.16

The graphical results for geotextile C are shown in Figure 5.

#### 4 ON SITE TESTS

To be able to show a correlation between laboratory and field tests, it is intended to perform onsite tests with sharp edged granular material on soft and weak subgrades.

For these tests sharp edged diabas granulate will be used and the performance of different geotextiles will be studied.

#### 5 CONCLUSION AND OUTLOOK

By a newly developed test method it is possible to evaluate the performance of a geotextile under dynamic loading. The properties of a product can be described by its behavior under static and dynamic puncturing and the force-deformation behavior can be quantified. By the use of the described test, a clearer more performance-orientated specification can be made possible.

An analysis of the first series of tests has shown the following significant results:

- The values for dynamic puncturing are far below the ones for the static tests.
- The shape of the curve is similar for both the static and the dynamic tests. Differences can mainly be seen in the behavior after rupture; the static tests show a sudden decrease, whereas the dynamic tests show a slow decrease.
- Static as well as dynamic tests show a relation between performance and the weight per unit area for each product type. However, the manufacturing process is of decisive importance for the performance of the geotextile. Therefore weight alone is not an adequate parameter for specification and should (if necessary) only be used as identification parameter.

It seems necessary to continue testing both in the laboratory as well as on full scale trials on site.

#### 6 REFERENCES

- Werner, G. (1986) Design criteria for the separation function of Geotextiles, 3rd intl. conference on Geotextiles, Vienna, Austria; Vol 1 pp 71 - 75;
- Bräu; (1996) Damage of Geotextiles during installation - Experience from real sites and research works, 1st European conference on geosynthetics, Maastricht, Netherlands, pp 145 - 150.
- Polyfelt (1986) Design and practice, Technical manual for Polyfelt TS.

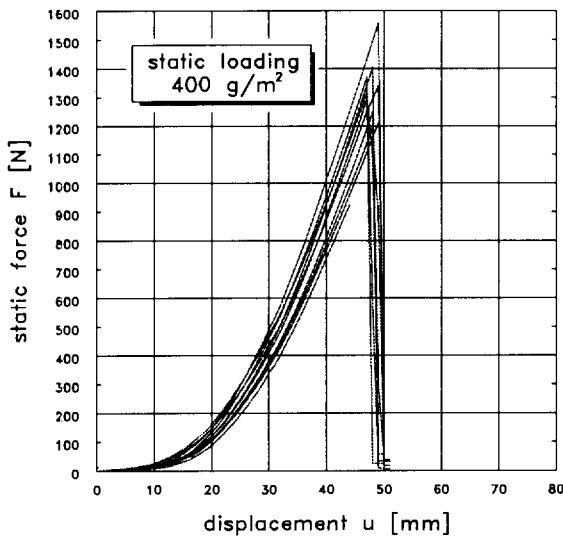


Figure 5: graphic results - static pyramid puncture test

In Table 3, the mean values for the dynamic puncture force (F-dyn.) and displacement at maximum load (Displ.-dyn.) are given along with their standard deviations and coefficients of variation.

Table 3 Values obtained by the dynamic puncture test.

	Type A	Type B	Type C
F-stat. [N]	511.95	780.40	955.27
Sdev	98.20	127.19	161.45
CVar	19.18	16.30	16.90
Displ.-stat.[mm]	45.20	41.10	50.50
Sdev	3.26	2.42	3.44
Cvar.	7.21	5.90	6.81

The graphical results for Geotextile C are shown in Figure 6.

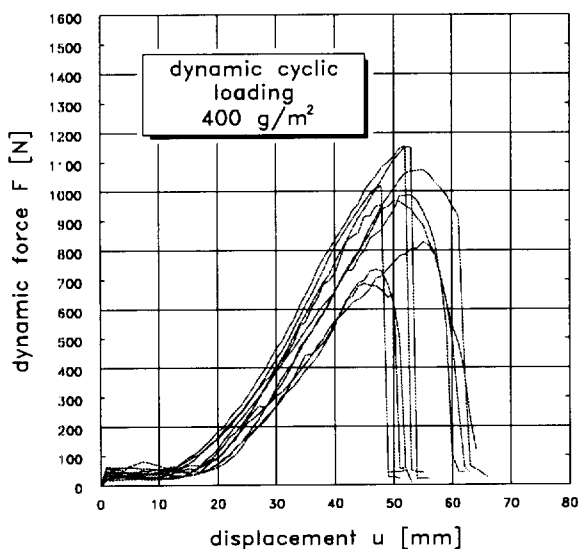


Figure 6: graphic results - dynamic pyramid puncture

# Author Index

Abdel-Rehman, A.H. ....	733	Breteler, M.K. ....	1165
Abramento, M. ....	891	Breul, B. ....	345, 1133
Adanur, S. ....	729	Breymann, H. ....	1193
Aguiar, P.R. ....	985	Bronstein, Z. ....	1059
Ahmed, I. ....	805	Buckland, D. ....	763
Aiban, S.A. ....	805	Cao, J. ....	963
Akai, T. ....	825	Cardoso A.S. ....	789
Al-Abdul Wahhab, H.I. ....	805	Cargill, K.W. ....	269, 481
Al-Amoundi, O.S.B. ....	805	Carlson, D.S. ....	279
Al-Quadi, I. ....	945	Carotti, A. ....	605
Alexander, W.S. ....	1161	Carroget, J. ....	345
Alexiew, D. ....	475, 663, 679	Carson, D.A. ....	427
Allen, S.R. ....	699	Cazzuffi, D. ....	1107
Allen, T.M. ....	491	Chai, J. ....	845
Andrawes, K.Z. ....	143	Chang, D.T. ....	967
Appea, A. K. ....	945	Chatterjee, P.K. ....	1155
Arab, R. ....	597	Chen, R.H. ....	721, 1083
Ariadurai, S. ....	815	Chen, T.C. ....	1083
Artières, O. ....	393, 1037	Chew, S.H. ....	257, 821, 855
Ashmawy, A.K. ....	1079	Chill, D.S. ....	1073
August, H. ....	239	Chottopadhyay, B. ....	1155
Austin, R.A. ....	501, 763	Christopher, B.R. ....	797
Averesch, U.B. ....	307	Clarke, B.G. ....	871
Ayele, T. ....	1183	Comer, A. I. ....	359
Azeem, A. ....	1089	Coree, B. J. ....	945
Bachus, R.C. ....	185, 523	Cowland, J.W. ....	411, 669, 783
Badu-Tweneboah, K. ....	261, 279	Cuelho, E.V. ....	951
Bakeer, R. ....	733	Dai, J. ....	963
Baran, E. ....	1033	Dao, H.R. ....	923
Barroso, M.C.P. ....	1005	Daniel, D.E. ....	427
Bathurst, R. J. ....	613, 929	Darilek, G.T. ....	273
Beech, J.F. ....	269	Datta, U. ....	1155
Bell, J.R. ....	491	De Meerleer, F. ....	1093
Bemben, S.M. ....	453	De, A. ....	443
Berg, R.R. ....	491, 587	Delmas, P. ....	747, 821, 1037
Bergado, D.T. ....	747	Difini, J.T. ....	643
Bezuijen, A. ....	1051	DiMillio, A. ....	683
Bhatia S.K. ....	733	Dixon, J.H. ....	637
Bhutta, S.A. ....	945	Donckers, F. ....	1093
Bindhumadhav ....	779	Dondi, G. ....	977
Bloquet, C. ....	393	Duquenois, C. ....	249, 355
Blume, K.H. ....	663	Durin, L. ....	249
Blümel, W. ....	447	Duskov, M. ....	993
Bonaparte, R. ....	427	Eberle, M.A. ....	205
Borges, J.L. ....	789	Eiksund, G. ....	933
Bouazza, A. ....	459	Elias, V. ....	523, 683
Bourdeau P.L. ....	1079	Elton D.J. ....	729
Boyle, S.R. ....	517	Fannin, R.J. ....	1009
Brachman R.V.I. ....	191	Faure, Y.H. ....	1017
Brandl, H. ....	581	Fillibeck, J. ....	417
Brandon, T.L. ....	945	Floss, R. ....	417

# Author Index

Fogelson, M.L. ....	951	Jain, V.K. ....	1089
Forsman, J. ....	773	Jakob, I. ....	239
Fredianelli, K.H. ....	465	James, G.M. ....	559
Frobel, R.K. ....	411	Jenner, C.G. ....	763
Frost, J.D. ....	433	Jeon, H.Y. ....	1063
Fukuda, M. ....	825	Jiang, K. ....	1111
Fukuoka, M. ....	811	Jones, C.J.F.P. ....	767, 871
Gardoni, M.G. ....	1027	Kabeya, H. ....	725
Gartung, E. ....	197, 285	Kadakil, H.U. ....	227
Gassner, F.W. ....	559	Kamon, M. ....	825
Gaumet, S. ....	393	Kanagi, V.S. ....	851
Ghinelli, A. ....	649	Karam, G. ....	1021
Ghosh, A. ....	1155	Karmokar, A.K. ....	725
Girard, H. ....	1125	Karunaratne G.P. ....	257, 855
Giroud, J.P. ....	185, 211, 261, 279, 1037	Kasturi, G. ....	733
Gleason, M.H. ....	211	Kavazanjian E., Jr. ....	219, 439, 465, 469
Gokmen, C. ....	1055	Kawamata, K. ....	905
Gotteland, P. ....	507, 511, 833	Kawamura, T. ....	545
Gourc, J.P. ....	487, 511, 597, 1069	Kehila, Y. ....	1017
Greenwood, J.H. ....	657, 669	Kelkar, A.D. ....	529
Gregory, G.H. ....	1073	Kempton, G. ....	767
Greguras, F.R. ....	405	Kenny, M.J. ....	901
Guan, Z. ....	375	Khan, A.J. ....	143
Güler, E. ....	1033	Khay, M. ....	675, 1179
Gustavsson, S. ....	755	Khire, M.V. ....	261
Hajek, J. ....	929	Kim, J.Y. ....	1063
Hamir, R. ....	871	Kiyokawa, N. ....	895
Han, J. ....	911	Knutson, A. ....	933
Hatami, H. ....	613	Koerner, G.R. ....	399, 839
Haza, E. ....	511	Koerner, R.M. ....	1, 301, 427, 707
Hendricker, A.T. ....	465	Koga, T. ....	565
Herment, R. ....	345, 1133	Kokkalis, A.G. ....	959
Hirai, T. ....	545, 601	Kollios, A. ....	1147
Hirao, K. ....	895	Konrath, L. ....	359
Hirata, M. ....	551	Koseki, J. ....	103
Ho, C.T. ....	821	Kossendey, T. ....	1021
Holtz, R.D. ....	517, 939	Koutsourais, M. ....	739
Hong, Z. ....	923	Kuhlman, C.J. ....	365
Horii, K. ....	103	Lafleur, J.P. ....	1001
Houben, L.J.M. ....	993	Lafleur, P. ....	331
Houlihan, M.F. ....	185, 211	Lahtinen, P. ....	773
Hsuan, Y.G. ....	233, 359, 371, 375	Lake, C.B. ....	233
Huang, Z. ....	963	Lalarakotoson, S. ....	487
Huff, W.J. ....	269	Lambrechts, J.R. ....	625
Hullings, D.E. ....	405	Lawson, C.R. ....	629
Iizuka, A. ....	551	Lee, D.Y. ....	915
Ikeguchi, Y. ....	1115	Lee, S.W. ....	433
Imaizumi, S. ....	201, 295	Lee, Y.S. ....	721
Ingold, T.S. ....	497	Lemonnier, P. ....	507
Ismeik, M. ....	951	Liang, F. ....	1151
Itoh, H. ....	895	Lindquist, D. ....	755



# Author Index

Liu, Z.Y. ....	1121	Ohmori, K. ....	551
Loh, S.L. ....	855	Olen, K.L. ....	481
Loke, K.H. ....	747, 821	Orsat, P. ....	675
Long, P.V. ....	747	Otani, J. ....	601
Lopes, M.D.G. ....	1005	Paiva, C.E.L. ....	985
Lopes, M.L. ....	593, 1183	Palmeira, E.M. ....	885, 1027
Lord, A.E., Jr. ....	711	Paulson, J.N. ....	691
Lothspeich, S.E. ....	679	Peggs, I.D. ....	365, 381
Lüders, G. ....	337	Penman, J. ....	501
Lugmayr, R. ....	989	Pereira, R.V.C. ....	593
Luo Q.Y. ....	865	Perkins, S.W. ....	951
Luong, M.P. ....	1179	Pierpoint, N.D. ....	767
Mailler, P. ....	715	Pierson, P. ....	355
Maisonneuve, C. ....	355	Pilarczyk, K.W. ....	1165
Mahmud, M.B. ....	829	Pinto, M.I.M. ....	593
Malagón, A. ....	859	Plankel, A. ....	475
Mallick, S.B. ....	729	Popelar, C.H. ....	365
Mandal, J.N. ....	851	Potié, G. ....	1125
Mannsbart, G. ....	1193	Potluri, P. ....	815
Mansour, R. ....	439	Poulain, D. ....	1125
Maranda, L. ....	331	Pradhan, S. ....	143
Marcotte, M. ....	323	Qureshi, S. ....	185
McCreath, M. ....	675	Rad, N. ....	1055
McGown, A. ....	143	Rajagopal, K. ....	919
McKelvey, J.A., III. ....	465	Ramakrishna, S. ....	919
McKown, A.F. ....	643	Rao, P.J. ....	779
Mendonca, A. ....	593	Raymond, G.P. ....	929
Meyers, M.S. ....	587	Recker, C. ....	679
Meyers, T. ....	1173	Reddy, K.R. ....	289
Miller, L.V. ....	273	Reid, R.A. ....	573
Mine, C. ....	1125	Richards, E.A. ....	1045
Mitchell, J.K. ....	797	Righter, G.K. ....	433
Miura, N. ....	747, 845	Rimoldi, P. ....	605
Miyaji, H. ....	201	Rodrigues, R.M. ....	973
Miyatake, H. ....	577	Rogbeck, Y. ....	755
Mlynarek, J. ....	323	Rollin, A.L. ....	331
Montgrain, F. ....	331	Rowe, R.K. ....	27, 191, 233
Moo-Young, H. ....	1173	Russel, D. ....	767
Moore, I.D. ....	191	Sabatini, P.J. ....	423
Morel, J.C. ....	1069	Sacchetti, M. ....	649
Morin, A. ....	355	Sadlier, M.A. ....	411
Moser, M. ....	1193	Saichek, R.E. ....	289
Mueller, W. ....	239	Salman, A. ....	683
Müller-Rochholz, J. ....	679, 1059	Sandri, D. ....	691, 699, 739
Munaf, Y. ....	103	Sangam, P. ....	233
Nanbu, Y. ....	825	Sarazin, P. ....	323
Nettleton, I.M. ....	871	Scarpas, A. ....	993
Nomoto, T. ....	295	Schaefer, V.R. ....	573
Ochiai, H. ....	545, 601, 905	Schicketanz, R.T. ....	307
Ochiai, Y. ....	577	Schmertmann, G.R. ....	279, 423
Ohta, H. ....	551	Schulze, D.A. ....	453

# Author Index

Scott, J.D. ....	1045	Villard, P. ....	487, 597
Scuero, A.M. ....	1099	von Maubeuge, K.P. ....	205
Sembenelli, G. ....	619, 1099	Voskamp, W. ....	839
Sembenelli, P. ....	619, 1099	Wang, D. ....	1139
Sharma, J.S. ....	877	Wang, W.J. ....	967
Sharma, H.D. ....	405	Wang, X. ....	1139
Shi, Y.C. ....	1009	Wang, Y. ....	951, 967
Shimizu, H. ....	1115	Watn, A. ....	933
Shinowaki, S. ....	601	Wetzel, R.A. ....	587
Skochdopole, T.R. ....	529	Whyte, I.L. ....	815
Slunga, E. ....	773	Wu, Y.N. ....	389
Smith, D.W. ....	1045	Yamaji, T. ....	545
Snow, M. ....	439	Yamakami, T. ....	551
Södergren, I. ....	755	Yan, J. ....	1143
Soderman K.L. ....	261	Yasufuku, N. ....	545, 905
Soong, T.Y. ....	1, 301, 707, 711	Yasuhara, K. ....	895
Sotir, R.B. ....	643	Yee, T.W. ....	629
Sotton, M. ....	715	Yegjian, M.K. ....	227
Soubra, A.H. ....	507	Yeo, K.C. ....	669, 783
Soupir, S.P. ....	573	Yokoyama, Y. ....	295
Sprague, C.J. ....	539	Yoo, C.S. ....	915
Stalcup, J.M. ....	1055	Yu, L. ....	389
Stark, T.D. ....	315	Yuan L. ....	1111
Stevenson, P.E. ....	529	Yuan, Z. ....	523
Stoewahse, C. ....	447	Zanzinger, H. ....	197, 285
Stoutjesdijk, T. ....	1165	Zettler, T. ....	733
Swan, R.H., Jr. ....	423, 439, 523, 739	Zhang, J. ....	1189
Tajiri, N. ....	577	Zhao, D. ....	963
Tan S.A. ....	257, 821, 855	Zimmie, T.F. ....	443, 829
Tanabashi, Y. ....	895	Zornberg, J.G. ....	469, 797
Tao, T.K. ....	389	Zou D.Y. ....	1189
Tateyama, M. ....	103, 565		
Tatsuoka, F. ....	103, 565		
Tatzky-Gerth, R. ....	239		
Thiel, R. ....	381		
Thomas, R.W. ....	349, 699		
Thornton, J.S. ....	691, 699		
Tognon, A.R.M. ....	191		
Touze, N. ....	249		
Townsend, D. ....	1173		
Toyota, K. ....	845		
Troost, G. ....	839		
Tsai, W.S. ....	939		
Tsuboi, M. ....	201, 295		
Tsukada, Y. ....	577		
Uchimura, T. ....	565		
Urashima, D.C. ....	1013		
Usher, S. ....	233		
Vaid, Y.P. ....	1009		
Venisri, N. ....	779		
Vidal, D. ....	1013		

# Subject Index

The pages listed indicate the first page of the paper in which the reference is found.

Abrasion .....	1161	Cyclic Loading .....	1069
Accelerated Testing .....	691, 699	Cyclic Triaxial Test .....	565
Adhesion .....	989	Dam .....	1099, 1107, 1111, 1115, 1125, 1133
Aging .....	27, 233, 375, 393, 1133	Damage .....	933, 1017, 1183
Airport Construction .....	859	Deformations .....	619, 811, 821, 1079
Analysis .....	1, 27, 511	Degradation .....	27, 657
Antioxidant Consumption .....	27, 683	Desiccation .....	27, 205
Apparent Opening Size .....	27, 1173	Design Deformation .....	679
Aquatextiles .....	1045	Design ....	1, 27, 143, 219, 227, 289, 491, 497, 501, 507, 755, 767, .....797, 811, 939, 1013, 1115, 1143, 1151, 1165
Asphalt Overlay .....	973, 977, 985, 989	Design By Function .....	381, 581, 1147
Base Course .....	951	Differential Settlement .....	295, 465
Base Reinforcement .....	891	Diffusion .....	27, 233, 239, 249
Bearing Capacity .....	587, 601, 877, 895, 901, 905, 967	Dilatancy Of Compacted Soils .....	551
Biaxial Tensile Test .....	1125	Direct Shear Tests .....	423, 443, 447, 453
Bias .....	399	Discharge Capacity .....	855
Biaxial Loading .....	715	Double-liner Systems .....	27, 269
Biotechnical .....	643	Drainage .....	629, 797, 821, 833, 839, 845, 871, 929, 1055, 1059
Bitumen .....	1133	Durability .....	27, 663, 683, 715
Blanket .....	1121	Dynamic Mechanical Analysis .....	605, 1161, 1193
Blinding .....	1033	Dynamic Triaxial Test .....	1083
Bridge Pier .....	565	Earth Slopes .....	1073
BS 8006 .....	501	Earthquake .....	219
Canal Liners .....	1133	Edge Drain .....	929
Caps and Closures .....	481	Elastoplastic Model .....	551
Case Histories .....	27, 103, 747	Electrokinetic .....	871
Case Study .....	269, 481, 619, 755, 773, 783, 1133, 1147, .....1151, 1161	Embankments .....	143, 501, 663, 755, 763, 767, 779, 783, .....789, 825, 1133, 1139, 1155, 1189
Centrifuge Modeling .....	829	Embedment Depth .....	587
Channel Tunnel .....	1093	End Restraint .....	545
Characteristic Opening Size .....	1005	Environmental Engineering .....	27, 871, 1045
Chemical Stabilization .....	805	Erosion Control .....	1139, 1155
Chemical Compatibility .....	27, 465	Exposed Geomembrane .....	211
Clogging .....	27, 185, 1017	Extrusion .....	323
Coir Reinforcement .....	919	Factor of Safety .....	(see Safety Factors)
Compacted Clay Liner .....	1, 27, 233, 417	Failures .....	337, 365, 559, 1179
Composite Material .....	715, 1111, 1189	Falling Weight Deflectometer .....	945
Composite Liner Systems .....	27, 233, 239, 307, 411, 417	Falling Head Test .....	1051
Compressive Creep .....	1059	Fatigue .....	977
Concentrated Top Load .....	511	Field Test .....	747
Confined Extension Test .....	523	Filter .....	27, 185
Construction .....	439, 559, 619, 1115, 1139	Filtration .....	1001, 1009, 1017, 1013, 1021, 1033, 1037, .....1045, 1155, 1173
Construction Constraints .....	629	Finite Difference Method .....	487, 613
Construction Quality Assurance .....	273	Finite Element Analysis .....	469, 487, 551, 593, 597, 601, .....649, 729, 733, 767, 789, 877, 895, 915, 973, 993
Container Stockyard .....	923	Flexible Polypropylene .....	359
Containment .....	27, 257	Foundations .....	587, 911
Cover System .....	1, 211, 219	Fractures .....	365, 989
Cracking .....	27, 977, 1121	Friction .....	227, 417, 443, 447, 453, 725, 739, 895, 1143
Creep .....	675, 679, 707, 715	Full-scale Loading Test .....	565
Creep Modulus .....	691, 699		
Creep Rupture .....	675, 691, 699		
Creep Strain .....	691, 699		

# Subject Index

Peel Separation .....	337	Seawall .....	865
Performance Evaluation .....	239, 257, 273, 285, 929, 1107	Seepage Control .....	1, 797, 1001, 1009, 1099
Permeability .....	27, 239, 249, 315, 1009, 1017, 1033, 1051	Segmental Retaining Walls .....	559, 587
Piles .....	755, 763	Seismic Analysis .....	613
Piping .....	1001	Seismic Design .....	103, 219, 227, 605, 625
Plastic Pipe .....	27, 191, 197	Seismic Loads .....	103, 219, 469, 605
Plate Load Tests .....	919	Seismic Stability .....	103, 219
Polyester .....	675, 679, 691, 699	Separation .....	939, 945, 1155, 1189, 1193
Polyethylene .....	371, 375, (see also HDPE)	Service Life .....	27
Polymeric Aging .....	27, 233, 355, 657	Settlement Analysis .....	469, 789
Polypropylene .....	359, 669, 683	Shallow Foundations .....	901
Pond Liners .....	1115	Shear Strength .....	315, 417, 423, 427, 453, 725, 739, 797, 1079
Precision .....	399	Slope Stability .....	27, 411, 475, 507, 581, 625, 643, 1073, 1125
Predictions .....	511, 657	Slow Crack Growth .....	371
Prefabricated Vertical Drains .....	(see Wick Drains)	Soft Soils .....	663, 767, 783, 789, 825, 859, 877, 901, 993
Preloading .....	565	Soft Foundation .....	865, 905, (see also Soft Soils)
Prestressing .....	565	Soil Confinement .....	523
Prevention .....	977	Soil Deformation .....	811
Probability .....	1013	Solid Waste Containment .....	27, 427
Proficiency Testing .....	399	Specifications .....	497, 529, 539
Protection .....	27, 279, 285, 289, 411	Stability .....	27, 405, 439
Protective Cushioning .....	27, 285, 289, 1099	Stabilization .....	643
Pull-out Resistance .....	725, 729, 739, 1183	Statistical .....	439
Pull-out Test .....	721, 739, 821, 1183	Steep Slope .....	1, 143, 481, 601, 637, 825
Puncture Test .....	285, 1125, 1193	Stepped Isothermal Method .....	699
Quality Assurance .....	337	Stone Columns .....	877
Quality Control .....	345	Strain Measurements .....	517
Railroad Applications .....	1089, 1093, 1189	Strain Gauges .....	517
Reflective Crack Prevention .....	973, 977, 985	Strain .....	523
Rehabilitation .....	985	Strength .....	439
Reinforced Embankments 637, 501, 663, 747, 783, 789, 825, 829		Stress Relaxation .....	711
Reinforced Soil .....	497, 565, 797, 805, 811, 815, 829, 905, 1083	Stress Distribution .....	923
Reinforced Slopes .....	581, 619, 625, 629, 649	Stress Cracking .....	27, 349, 355, 365
Reinforced Walls .....	103, 143, 491, 497, 501, 559, 573, 581, 587, 593, 601, 605, 613, 811	Stress Crack Resistance .....	27, 371
Reinforcement .....	143, 465, 469, 481, 491, 517, 539, 545, 559, 601, 625, 657, 663, 739, 755, 779, 789, 797, 815, 821, 859, 871, 885, 901, 905, 911, 967, 977, 1079, 1089, 1183	Stress Strain Relations .....	523, 911
Reinforcement Specifications & Guidelines .....	491	Subgrade .....	805, 919
Reservoir Liners .....	257, 637	Surface Maintenance .....	885
Residual Strength .....	675	Surface Roughness .....	433
Retaining Walls .....	103, 143, 491, 497, 511, 559, 573, 581, 597, 605, 613	Survivability .....	289, 839
Revetment .....	1143	Temperature Effects .....	27, 201, 249, 365, 573
Rheological Behavior .....	715	Tensile Strength .....	529, 815, 1179
Road Construction .....	993	Tensile Behavior .....	201
Rut Prediction .....	939	Tensile Strain .....	295, 839
Safety Factors .....	491, 497, 657	Testing .....	27, 345, 417, 453, 511, 517, 523, 529, 811, 855, 993, 1059, 1179
Sand .....	453	Theory of Elasticity .....	295
Seams .....	345, 349	Thermal Bonding Method .....	1063
Seams Quality .....	331	Thermal Stress .....	201
		Thermal Treatment .....	323
		Thermal Diffusivity .....	389
		Time Domain Reflectometry (TDR) .....	205

# Subject Index

- Geo "Others" .....581
- Geobags .....1165
- Geocells .....465, 767, 773
- Geocomposite Edge Drain .....707
- Geocomposites .....285, 825, 833, 989, 1055, 1099, 1107, 1121
- Geofibers .....1073
- Geofoam .....993
- Geogrid .....465, 469, 475, 481, 523, 539, 545, 565, 605, 625, 637, 649, 679, 691, 707, 721, 733, 739, 755, 763, 773, 877, 891, 905, 915, 945, 951, 967, 989, 1089, 1183
- Geomattresses .....1165
- Geomembrane .....27, 201, 227, 233, 239, 249, 261, 269, 273, 279, 289, 295, 307, 323, 331, 337, 345, 349, 355, 359, 365, 371, 375, 381, 399, 411, 417, 423, 433, 453, 459, 637, 707, 711, 1077, 1099, 1107, 1111, 1115, 1121, 1125, 1133
- Geomembrane Composite .....389
- Geomembrane Installation .....27, 307
- Geomembrane Waves (Wrinkling) .....27, 301, 307, 315
- Geonets .....443, 923, 1055
- Geopipes .....191, 197
- Geosynthetics .....27, 143, 185, 219, 523, 683, 865, 887, 911
- Geosynthetic Clay Liner (GCL) .....27, 205, 233, 315, 411, 427, 707, 895
- Geosynthetic Reinforcement .....103, 143, 487, 507, 551, 587, 593, 613, 767
- Geotechnical Engineering .....933
- Geotextiles .....27, 185, 227, 289, 295, 393, 433, 447, 459, 517, 523, 539, 573, 619, 707, 725, 729, 739, 783, 805, 815, 821, 859, 865, 919, 929, 933, 939, 945, 951, 973, 985, 1005, 1009, 1013, 1017, 1033, 1037, 1045, 1079, 1089, 1093, 1139, 1151, 1155, 1161, 1173, 1193
- Geotextile Reinforcement .....597, 747
- Geotextile Strains .....885
- Geotubes .....1165
- Gradient Ratio Tests .....1001, 1009
- HDPE .....27, 191, 233, 239, 249, 279, 301, 307, 323, 331, 337, 349, 365, 371, 375
- HDPE Waves .....(see Geomembrane Waves)
- Heat .....389
- Hilly Terrain .....629
- History .....491
- Hydraulic Conductivity .....27, 845
- In-situ Monitoring .....205
- Inclined Plane .....487
- Inclusion .....911
- Inertia Effects .....1051
- Instability .....629
- Installation .....27, 307
- Installation Damage .....289, 833, 1193
- Installation Damage Field Tests .....1125
- Instrumentation .....773
- Integral Abutment .....573
- Interaction .....1183
- Interface .....1, 405, 439
- Interface Element .....729, 733
- Interface and Internal Shear .....411
- Interface Shear Strength .....1, 405, 411, 423, 427, 433, 439, 443, 447, 459, 733
- Interface Testing .....1, 423, 447
- Intimate Contact .....27, 307
- Jute Geotextile .....779
- Kinking .....855
- Knit Fabrics .....529
- Laboratory Tests .....191, 249, 285, 295, 349, 389, 399, 423, 447, 453, 845, 951, 1051, 1055, 1107, 1179, (see also Testing)
- Laboratory Modeling .....301
- Landfill .....27, 185, 191, 197, 211, 219, 227, 233, 261, 269, 273, 279, 285, 289, 315, 393, 405, 447, 459, 469, 475, 481
- Landfill Cover .....1, 427, 443
- Landfill Liner .....27, 279, 315, 443
- Large Scale Performance Test .....1021
- Leachate .....27, 185, 233, 261
- Leachate Collection System .....27, 185, 191, 197
- Leak Detection .....27, 273
- Leakage .....27, 261, 269
- Life Prediction .....27, 683
- Limit State .....143, 501
- Limit Equilibrium .....1, 501, 507
- Liners .....27, 233, 261, 279, 289, 381, 405, 459, 487, 637
- Liquid Containment .....233
- Load Transfer .....763
- Long-term Measurements .....663
- Material Tests .....993, (see Testing and Laboratory Tests)
- Mechanical Properties .....529, 1179
- Mechanical Damage .....279, 355
- Micro-reinforcement .....1069, 1073
- Microscopic Investigation .....1021
- Mode of Failure .....279
- Model Tests .....103, 197, 895, 939, 1089
- Modeling .....27, 257, 707, 711, 833
- Modulus .....529, 711
- Moisture Content Measurement .....205
- Monitoring .....763
- Multi-axial Tension Test .....279
- Multilayered Nonwovens .....1063
- Nonwoven Geotextiles .....27, 593, 933, 1013, 1037, 1045, 1063
- Numerical Analysis .....729, 891, 1083
- Opening Size .....27, 1037
- Oxidative Induction Time .....27, 233, 375
- Oxidation .....27, 233, 375, 683
- Partial Factors .....143, 497
- Pavement .....573, 891, 945, 951, 967, 973, 977, 985

# Subject Index

Time Temperature Superposition .....	691, 699
Transmissivity .....	815, 833, 1055
Transmissivity Tests .....	1059
Triaxial Tests .....	1069, 1083
Tunnel Construction .....	1147
Ultimate Pull-out Resistance .....	721
Ultrasound .....	345
Ultraviolet Resistance .....	359
Ultraviolet Effects .....	393
Unconfined Creep Tests .....	691, 699
Unpaved Roads .....	773, 885, 901, 919, 939
Vegetation .....	643
Vertical Drains.....	(see Wick Drains)
Veneer Stability .....	1
Water Sensitivity .....	805
Water Treatment .....	1045
Waterway .....	1143
Waves .....	(see Geomembrane Waves)
Weathering Resistance .....	393
Weld Seams .....	337
Welding Parameters .....	331
Wet Sieving Test Method .....	1005
Wick Drains .....	783, 839, 845, 851, 855, 859
Wind Uplift .....	211
Woven Geotextiles .....	27, 529, 559, 725, 739, 815, 1143
Wrinkles .....	(see Geomembrane Waves)
Young's Modulus .....	201